

SEVENTH EDITION



Textbook of

RADIOLOGY AND IMAGING

VOLUME 2



David Sutton



نشر الکترونیکی
موسسه انتشاراتی
نوردانش



CHURCHILL
LIVINGSTONE

SEVENTH EDITION

***TEXTBOOK OF
RADIOLOGY
AND IMAGING***

VOLUME 11

EDITED BY

DAVID SUTTON MD, FRCP, FRCR, DMRD, [FCanAR](#) (Hon)

Consulting Radiologist
St Mary's Hospital and Medical School, London
Director, Radiological Department (1963-1984)
Consulting Radiologist, The National Hospital for Neurology
and Neurosurgery, London, UK.

ASSOCIATE EDITORS

Nuclear Medicine

PHILIP J.A. ROBINSON FRCP, FRCR

MRI

JEREMY P.R. JENKINS FRCP DMRD, FRCR

CT

RICHARD W. WHITEHOUSE BSc, MB ChB, MD, FRCR

Ultrasound

PAUL L. ALLAN MSc, MBBS, DMRD, FRCR, FRCP(Ed)

Cardiac Radiology

PETER WILDE BSc, MRCP, FRCR

Neuroradiology

JOHN M. STEVENS MBBS, DRACR, FRCR



CHURCHILL
LIVINGSTONE

CHURCHILL LIVINGSTONE
An imprint of Elsevier Science Limited

2003, Elsevier Science Ltd. All rights reserved.

The right of David Sutton to be identified as editor of this work has been asserted by him in accordance with the Copyright, Designs and Patent Act 1988.

No part of this publication may be reproduced, stored in a retrieval system, or transmitted in any form or by any means, electronic, mechanical, photocopying, recording or otherwise, without either the prior permission of the publishers (Elsevier Science Limited, Robert Stevenson House, 1-3 Baxter's Place, Leith Walk, Edinburgh EH 13AF) or a licence permitting restricted copying in the United Kingdom issued by the Copyright Licensing Agency Ltd, 90 Tottenham Court Road, London W 1 T 4LP.

First Edition 1969
Second Edition 1975
Third Edition 1980
Fourth Edition 1987
Fifth Edition 1993
Sixth Edition 1998

ISBN 0 443 071098
International Student Edition ISBN 0 443 07108X

British Library Cataloguing in Publication Data

A catalogue record for this book is available from the British Library

Library of Congress Cataloging in Publication Data

A catalog record from this book is available from the Library of Congress

Note

Medical knowledge is constantly changing. As new information becomes available, changes in treatment, procedures, equipment and the use of drugs become necessary. The editors, contributors and the publishers have, as far as it is possible, taken care to ensure that the information given in this text is accurate and up to date. However, readers are strongly advised to confirm that the information, especially with regard to drug usage, complies with the latest legislation and standards of practice.

The Publishers have made every effort to trace the copyright holders for borrowed material. If they have inadvertently overlooked any, they will be pleased to make the necessary arrangements at the first opportunity.

**ELSEVIER
SCIENCE** your source for books,
journals and multimedia
in the health sciences
www.elsevierhealth.com

Commissioning Editor: Michael J. Houston
Project Development Manager: Martin Mellor
Project Manager: Nora Naughton (Aoibhe O'Shea)
Designer: Sarah Russell

The
publisher's
policy is to use
paper manufactured
from sustainable forests

Printed in China by RDC Group Limited

CONTENTS

Cover illustrations: Vol 1: *Front*: Figs. 2.09; 1.60; 1.61A,B; 15.1 39B *Back*: Figs. 25.144; 2.8; 15.144; 26.43C
Vol 2: *Front*: Fias. 59.26A; 59.39; 58.94A-D; 59.37 *Back*: Figs. 33.7113; 55.43C; 58.43C

VOLUME 2

SECTION 1

Respiratory system

- 1 The normal chest: methods of investigation and differential diagnosis 1
Janet Murfitt, Philip J. A. Robinson, Richard W. Whitehouse, Andrew R. Wright, Jeremy P. R. Jenkins
- 2 The mediastinum 57
Roger H. S. Gregson, Richard W. Whitehouse, Andrew R. Wright, Jeremy P. R. Jenkins
- 3 The pleura 87
Michael B. Rubens, Simon P. G. Padley
- 4 Tumours of the lung 107
Michael B. Rubens, Simon P. G. Padley, Jeremy P. R. Jenkins
- 5 Pulmonary infections 131
Simon P. G. Padley, Michael B. Rubens
- 6 Diseases of the airways: collapse and consolidation 161
Michael B. Rubens, Simon P. G. Padley
- 7 Diffuse lung disease 187
Simon P. G. Padley, Michael B. Rubens
- 8 Miscellaneous chest conditions 217
Simon P. G. Padley, Michael B. Rubens
- 9 The paediatric chest 247
Catherine M. Owens, Karen E. Thomas

SECTION 2

Cardiovascular system

- 10 The normal heart: anatomy and techniques of examination 265
Peter Wilde, Mark Callaway
- 11 Acquired heart disease I: the chest radiograph 283
Mark Callaway, Peter Wilde
- 12 Acquired heart disease II: non-invasive imaging 317
Mark Callaway, Peter Wilde
- 13 Invasive imaging and interventional techniques 347
Peter Wilde, Mark Callaway
- 14 Congenital heart disease 363
Peter Wilde, Anne Boothroyd
- 15 Arteriography and interventional angiography 411
David Sutton, Roger H. S. Gregson, Paul L. Allan, Jeremy P. R. Jenkins
- 16 Phlebography 483
David Sutton, Roger H. S. Gregson, Paul L. Allan, Jeremy P. R. Jenkins
- 17 The lymphatic system 509
Graham R. Cherryman, Bruno Morgan

SECTION 3

Abdomen and gastrointestinal tract

- 18** The salivary glands, pharynx and oesophagus 533
A. H. A. Chapman, John A. Spencer, J. Ashley Guthrie, Philip J. A. Robinson
- 19** The stomach and the duodenum 575
A. H. A. Chapman, J. Ashley Guthrie, Philip J. A. Robinson
- 20** The small bowel and peritoneal cavity 615
Steve Halligan
- 21** The large bowel 635
Steve Halligan, Philip J. A. Robinson
- 22** The acute abdomen 663
Stuart Field, Iain Morrison
- 23** The abdomen and major trauma 691
Otto Chan, Ioannis Vlahos
- 24** The biliary tract 711
John Karani
- 25** The liver and spleen 737
Robert Dick, Anthony Watkinson, Julie F. C. Olliff, Philip J. A. Robinson, Richard W. Whitehouse
- 26** The pancreas 787
Janet Murfitt, Richard W. Whitehouse, Philip J. A. Robinson, Richard Mason, Paul A. Dubbins, Andrew R. Wright
- 27** The adrenal glands 825
David Sutton, Philip J. A. Robinson
- 28** The paediatric abdomen 849
Karen E. Thomas, Catherine M. Owens

VOLUME 2

SECTION 4

Genito-urinary tract

- 29** The urogenital tract: anatomy and investigations 885
Julian Kabala, Tim Whittlestone, David Grier, Philip J. A. Robinson
- 30** The kidneys and ureters 929
Julian Kabala, Carl Roobottom
- 31** The bladder and prostate 989
Julian Kabala, Gary N. Sibley, Jeremy P R. Jenkins, Paul Hulse

- 32** The urethra and male genital tract 1017
Julian Kabala, Philip J. A. Robinson, Raj Persad, Robert Jones
- 33** Obstetric ultrasound 1039
Roger Chisholm, Jeremy P R. Jenkins
- 34** Gynaecological imaging 1069
Mary Crofton, Jeremy P R. Jenkins

SECTION 5

Skeletal system: soft tissue

- 35** Congenital skeletal anomalies: skeletal dysplasias, chromosomal disorders 1107
Peter Renton, Ruth Green
- 36** Periosteal reaction; bone and joint infections; sarcoid 1153
Peter Renton
- 37** Avascular necrosis; osteochondritis; miscellaneous bone lesions 1179
Peter Renton, Ruth Green
- 38** Disease of joints 1201
Peter Renton, Ruth Green
- 39** Tumours and tumour-like conditions of bone (1) 1247
Mark Cobby, Iain Watt
- 40** Tumours and tumour-like conditions of bone (2) 1287
Mark Cobby, Iain Watt
- 41** Disorders of the lymphoreticular system and other haemopoietic disorders 1321
Mark Cobby, Iain Watt
- 42** Metabolic and endocrine disorders affecting bone 1351
Jeremy W. R. Young, Leonie Gordon
- 43** Skeletal trauma: general considerations 1371
Jeremy W R. Young
- 44** Skeletal trauma: regional 1389
Jeremy W R. Young
- 45** The soft tissues 1417
Jeremy P R. Jenkins, Janet Murfitt, Fritz Starer, Richard W Whitehouse, W Gedroyc
- 46** The breast 1451
Michael J. Michell, Chris Lawinksi, Will Teh, Sarah Vinnicombe

SECTION 6**Head and neck; CNS;
recent technical advances**

- 47** The pharynx and larynx: the neck 1489
*Peter D. Phelps, Philip J. A. Robinson, Richard W Whitehouse,
Andrew R. Wright, Julie F. C. Olliff*
- 48** The sinuses 1519
Swarupsinh V Chavda, Julie F. C. Olliff
- 49** Teeth and jaws 1531
Peter Renton
- 50** Ultrasound of the eye and orbit 1551
John A. Fielding
- 51** The orbit 1573
Michael I. Rothman, Gregg H. Zoarski
- 52** The petrous temporal bone 1597
Peter D. Phelps
- 53** The skull 1617
David Sutton
- 54** Neuroradiology of the spine 1643
John M. Stevens, Brian E. Kendall

- 55** Angiography in neuroradiology 1673
David Sutton, John M. Stevens, Katherine Mizkiel

- 56** Interventional neuroradiology 1707
Rolf Jager, Stefan Brew

- 57** Intracranial lesions (1) 1723
David Sutton, John M. Stevens, Katherine Mizkiel

- 58** Intracranial lesions (2) 1767
*David Sutton, John M. Stevens, Katherine Mizkiel,
Philip J. A. Robinson, Keith Dewbury*

- 59** Recent technical advances 1819
*Richard W Whitehouse, Philip I. A. Robinson,
Jeremy P. R. Jenkins, Paul L. Allan, Nicola H. Strickland,
Philip Gishen, Andrew R. Wright, Andrew P Jones*

Useful appendices 1847

- A. Centres of ossification 1847
- B. Glossary of CT terms 1850
- C. Glossary of MR terms 1852
- D. Radiopharmaceuticals for imaging 1855

Index to volumes 1 and 2

نشر الکترونیکی
موسسه انتشاراتی
نوردانش

CONTRIBUTORS

Paul L. Allan MSc, MBBS, DMRD, FRCR, FRCP (Ed)

Honorary Consultant Radiologist
Royal Infirmary
Edinburgh, UK

Stefan Brew MB, ChB, MHB (Hons), MSc, FRANZCR, FRCR

Consultant Radiologist
National Hospital for Neurology and Neurosurgery
London, UK

Anne Boothroyd MBChB, FRCR

Consultant Radiologist
Royal Liverpool Children's Hospital
Liverpool, UK

Mark Callaway BM, MRCP, FRCR

Consultant Radiologist
Bristol Royal Infirmary
Bristol, UK

Otto Chan FRCS, FRCR

Consultant Radiologist
The Royal London Hospital
London, UK

Anthony H. A. Chapman FRCP, FRCR

Head of Clinical Radiology
Leeds NHS Trust
Consultant Radiologist
St James's University Hospital
Leeds, UK

Swarupsinh V. Chavda MBChB, DMRD, FRCR

Consultant Radiologist
St James's University Hospital
Leeds, UK

Graham R. Cherryman M[3013, FRCR

Professor of Radiology

Honorary Consultant Radiologist

UHL NHS Trust
Leicester, UK

Roger Chisholm MA, MBBChir, MRCP, FRCR

Consultant Radiologist
Hope Hospital
Salford, UK

Mary Crofton FRCR, FRCP

Consultant Radiologist
Department of Radiology
St Mary's Hospital
London, UK

Mark Cobby MBChB, MRCP, FRCR

Consultant Radiologist
Frenchay Hospital
Bristol, UK

Keith Dewbury BSc, DMRD, FRCR

Consultant Radiologist
Southampton General Hospital
Southampton, UK

Robert Dick MB, BS(Syd), FRCAR, FRCR

Department of Radiology
Royal Free Hospital
London, UK

Paul Dubbins BSc, FRCR

Consultant Radiologist
Imaging Directorate
Derriford Hospital
Plymouth, UK

Stuart Field MA, MBBChir, DMRD, FRCR

Consultant Radiologist
Kent and Canterbury Hospital
Canterbury, UK

John A. Fielding MD, FRCP(Edin), FRCR

Consultant Radiologist
Royal Shrewsbury Hospital
Shrewsbury, UK

W. Gedroyc MRCP, FRCR

Consultant Radiologist
St Mary's Hospital
London, UK

Philip Gishen MB, BCh, DMRD, FRCR

Consultant Radiologist and Director of Imaging
Hammersmith Hospital
UK

Roger H. S. Gregson MSc, MB, FRCR, DMRD

Consultant Radiologist and Head of Training
University of Nottingham
Nottingham, UK

Ruth Green FRCR

Consultant Radiologist
Royal National Orthopaedic Hospital
Middlesex, UK

David Grier MBChB, MRCP, FRCR

Consultant Radiologist
Bristol Royal Hospital for Children
Bristol, UK

Leonie Gordon MD

Professor of Radiology and Nuclear Medicine
Medical University of South Carolina
Charleston,
South Carolina, USA

J. Ashley Guthrie BA, MRCP, FRCR

Consultant Radiologist
St James's University Hospital
Leeds, UK

Steve Halligan MBBS, MD, MRCP, FRCR

Consultant Radiologist
St Mark's Hospital
London, UK

Paul Hulse MRCP FRCR

Consultant Radiologist
Christie Hospital
Manchester, UK

H. Rolf Jager MD, FRCR

Consultant Radiologist
National Hospital for Neurology and Neurosurgery
London, UK

Jeremy P. R. Jenkins FRCP, DMRD, FRCR

Consultant Radiologist
Honorary Senior Clinical Lecturer
Manchester Royal Infirmary and University of Manchester
Manchester, UK

Andrew P. Jones MSc

Consultant Clinical Scientist
Head of MR Physics Group
Christie Hospital
Manchester, U K

Robert Jones BmedSci, BMBS, FRCS(Ed)

Urology Research Fellow
Bristol Royal Infirmary
Bristol, UK

John Karani MSc, MBBS, FRCR

Consultant Radiologist
King's College Hospital
London, U K

Julian Kabala MRCP, FRCR

Consultant Radiologist
Bristol Royal Infirmary
Bristol, UK

Brian E. Kendall FRCR, FRCP, FRCS

Consulting Radiologist
The National Hospital for Neurology and Neurosurgery
and the Middlesex Hospital
London, UK

Chris Lawinski BSc, MSc, MPhil

Consultant Physicist
King's College Hospital
London, UK

Richard Mason FRCS, MRCP, FRCR

Consulting Radiologist
Middlesex Hospital
University College of London Hospitals
London, UK

Michael J. Michell FRCR

Consultant Radiologist
King's College Hospital
London, UK

Katherine Mizkiel BM(Hons), MRCP, FRCR

Consultant Neuroradiologist
National Hospital for Neurology and Neurosurgery
London, UK

Bruno Morgan MA, MRCP, FRCR

Senior Lecturer and Honorary Consultant Radiologist
University Hospitals Leicester
Leicester, UK

Iain Morrison MB BS, MRCP, FRCR

Consultant Radiologist
Kent and Canterbury Hospital
Canterbury, UK

Janet Murfitt MB BS, MRCP, FRCR

Consultant Radiologist and Director of Diagnostic Imaging
St Bart's and The London NHS Trust
London, UK

Julie F.C. Olliff B Med Sci, BM BS, MRCP, FRCR

Consultant Radiologist
Honorary Senior Clinical Lecturer
University of Birmingham
Birmingham, UK

Catherine M. Owens BSc, MRCP, PFCR

Clinical Director Consultant Paediatric Radiologist
Department of Radiology
Great Ormond Street Hospital for Children
London, UK

Simon PG. Padley MRCP, FRCR

Consultant Radiologist
Chelsea and Westminster Hospital
London, UK

Raj Persad ChM, FRCS, FRCS(Urol), FEBU

Consultant Urologist
Bristol Royal Infirmary
Bristol, UK

Peter D. Phelps MD, FRCS, FRCR

Former Consultant Radiologist
Royal National Orthopaedic Hospital and University
College Hospital
Honorary Senior Lecturer
Institute of Orthopaedics
London, UK

Peter Renton FRCR, DMRD

Consultant Radiologist
Honorary Senior Lecturer
Royal National Orthopaedic Hospital
and University College London Hospitals
London, UK

Philip J.A. Robinson FRCP, FRCR

Professor of Clinical Radiology
University of Leeds
Consultant Radiologist
Leeds Teaching Hospitals
Leeds, UK

M. I. Rothman MD

Assistant Professor of Radiology, Neurosurgery and
Otolaryngology /Head and Neck Surgery,
Medical Director. Anna Gudelsky Magnetic Resonance Center
Baltimore,
Maryland, USA

Carl Roobottom MSc, MBChB(Hon), MRCP, FRCR

Consultant Radiologist
Derriford Hospital
Plymouth, UK

Michael B. Rubens MB, DMRD, FRCR

Consultant Radiologist and Director of Imaging
Royal Brompton Hospital
London, UK

Gary N. Sibley FRCS

Consultant Urologist
Department of Urology
Bristol Royal Infirmary
Bristol, UK

John A. Spencer MA, MD, MRCP, FRCR

Consultant Radiologist
St James's University Hospital
Leeds, UK

John M. Stevens MBBS, DRACR, FRCR

Consultant Radiologist
Department of Radiology
National Hospital for Neurology and Neurosurgery
London, UK

Nicola H. Strickland BM, BCh, MA(Hons)(Oxon), FRCP, FRCR

Consultant Radiologist
Hammersmith Hospital NHS Trust
London, UK

David Sutton MD, FRCP, FRCR, DMRD, [FCan.AR](#) (Hon)

Consulting Radiologist
St Mary's Hospital and Medical School, London
Director, Radiological Department (1963-1984)
Consulting Radiologist, The National Hospital for Neurology
and Neurosurgery
London, UK

Will Teh MBChB, MRCP, FRCR

Consultant Radiologist
Northwick Park Hospital
Middlesex, UK

Karen E. Thomas MA, BM BCh, MRCP, FRCR

Consultant Paediatric Radiologist
Hospital for Sick Children
Toronto
Ontario, Canada

Sarah Vinnicombe BSc, MRCP, FRCR

Consultant Radiologist
Department of Diagnostic Imaging
St Bartholomew's Hospital
London, UK

Ioannis Viahos MSc, MBBS, MRCP, FRCR

Research Fellow
Department of Diagnostic Imaging
St Bartholomew's Hospital
London, UK

Iain Watt FRCP, FRCR

Consultant Clinical Radiologist
Bristol Royal Infirmary
Bristol, UK

Anthony Watkinson Bmet, MSc, MBBS, FRCS, FRCR

Consultant and Senior Lecturer in Radiology
Royal Free Hospital
London, UK

Peter Wilde BSc, MRCP, FRCR

Consultant Cardiac Radiologist
Directorate of Clinical Radiology
Bristol Royal Infirmary
Bristol, UK

Richard W. Whitehouse BSc, MB ChB, MD, FRCR

Consultant Radiologist
Manchester Royal Infirmary
Manchester, UK

Tim Whittlestone MA, FRCS (Ebg), MD, FRCS(Urol)

Hunterian Professor of Surgery
Specialist Registrar in Urology
Bristol Royal Infirmary
Bristol, UK

Andrew R. Wright MA, MBBS, MRCP, FRCR

Consultant Radiologist
Honorary Senior Lecturer
St Mary's Hospital
Imperial College
London, UK

Jeremy W. R. Young MA, BM, BCh, FRCR

Professor and Chairman of Radiology, Medical University
of South Carolina
Charleston
South Carolina, USA

Gregg Zoarski MD

Department of Diagnostic Radiology
University of Maryland Medical Center
Baltimore
Maryland, USA

PREFACE

The First Edition of this Textbook was conceived in the 1960s and published in 1969. I, like many of my contemporaries began my studies in Radiology at the end of the Second World War. My first post as an ex military service registrar was in the Radiology Department of the National Hospitals for Nervous Disease at Queen Square. It was pure serendipity that I should thus become associated with James Bull, the only British radiologist trained in Scandinavian neuroradiological techniques, including percutaneous angiography. and at that time representing the most advanced aspects of radiology.

My training in percutaneous cerebral angiography laid the foundation for other percutaneous techniques which I was able to apply when appointed to St. Mary's hospital in 1952. Here again pioneer work had already begun exploiting the potential for new methods in vascular surgery.

As a result of this background we were able to publish in 1962 the first personal monograph based on an experience of more than ten thousand cases. (See Ch. 15).

X-Rays were discovered by Roentgen in 1895, and though the importance of the discovery was immediately realised and widely discussed the impact on medical practice was surprisingly slow. The diagnosis and treatment of fractures and lesions of bones and joints was the first area to be thoroughly studied and surveyed. At the same time, the dangers and potential hazards of the new rays were becoming apparent for the first time, as was the therapeutic use of X-Rays.

In the Post war period, pain and experience of a specialist radiologist was still a matter of considerable debate and concern. Broadly speaking, there were those who favoured a technical approach and pain, usually pure scientists or physicists, and others who preferred a largely clinical approach with a minimum of technical training. Thus advanced pain in medicine or trends in surgery was regarded by many as essential for high quality radiology. The British Faculty of Radiologists was expanding rapidly and soon became the Royal College of Radiologists. The FRCR thus became the essential higher radiological qualification on a par with the MRCP or FRCS, and the DMRD was of non-downgraded to a qualifying diploma.

At the time of this controversy, I took the opportunity to broaden my experience and expertise with the MD thesis, Membership of the Royal College of Physicians, London and Fellowship of the Faculty of Radiologists. This was undoubtedly the clinical, rather than technical approach to radiological expertise.

In 1955 I was appointed Editor to the Faculty Journal, and took the opportunity to persuade the Editorial Board to change its name to Clinical Radiology. Apart from showing where my own interest lay in the continual medico-political controversy between pure scientists (mainly physicists) and clinicians which many felt could adversely affect the future pain and examination

syllabus for Specialist Radiologists, the change was highly successful from a purely practical point of view. Sales rose by 300% (from 1000 to 4000 copies per annum).

The first edition of this popular text-book was published in 1969 and this seventh edition is still growing strongly at the mature age of thirty three years. Review of the last five editions cover a period of exponential growth in radiological facilities and imaging. New fields were just beginning to open at the time of the first edition and these included ultrasound and nuclear medicine. Computer tomography began in the 1970s to be overtaken in the 1980s by magnetic resonance. It was generally felt that CT would soon be out-moded, but the last few years have seen a remarkable comeback from CT in the form of multi-slice spiral CT. As a result the versatility, speed and scope of CT examinations has been transformed.

In general, we hope this book reflects British Teaching Hospital Practice in the field of Imaging. The ISE edition remains very popular with non British readers and the 6th Edition has also been translated into two further languages, Greek and Portuguese. We believe that much of its success is due to the decision to concentrate on Clinical rather than Technical aspects of our rapidly expanding and evolving speciality.

Whilst each new edition has emphasised clinical rather than technical progress, the student must also be aware of, and absorb, the technical advances. The new edition therefore includes a chapter devoted to explaining this area. Other features of this new edition are the complete rewriting by mainly new authors of major sections of the text. These include the Cardiac, GU, Paediatric, Small and Large bowel, Major Abdominal Trauma and Interventional Neuroradiology chapters. Other chapters have been revised by deleting obsolete material or including new material. Recent clinical advances are also reflected in the revision. Thus imaging and Staging of malignant tumors has been revised and updated in many areas, and the opportunity has been taken to integrate the latest version of the World Health Organisation (WHO) reclassification on a histopathological basis of primary cerebral tumours. The expansion of invasive and minimally invasive angiography is monitored, and discussed. However, this is to some extent balanced by the increasing use of interventional techniques.

Radiology is a graphic subject, and images and illustrations are its vital tool. This edition contains no less than 5600 illustrations, some 2000 of which are new.

As in previous editions, we would remind the student that large textbooks, like large animals, have a longer period of gestation. It is therefore important to keep up with the current literature and attend up to date seminars.

David Sutton

1002

29

THE UROGENITAL TRACT: ANATOMY AND INVESTIGATIONS

Julian E. Kabala

with contributions from Philip J. A. Robinson, Tim Whittlestone and from David Grier

ANATOMY

The kidneys and retroperitoneum, ureters, bladder and male genitalia are discussed.

The kidneys and retroperitoneum

The kidneys develop from three structures which succeed each other: the pronephros and the mesonephric and metanephric ducts. The pronephros develops during the 3rd week of gestation and regresses during the 4th to the 8th week, leaving no adult correlate. It is replaced by the mesonephric (wolffian) duct, which develops in males into the efferent ductules of the testes, the epididymis and the vas deferens and in females into the epoophoron and paroophoron. In the 5th week the kidney begins to develop from two separate cell lines arising from the metanephric duct: the ureteric bud and the metanephric blastema. The ureteric bud develops into the ureter, renal pelvis and (by multiple divisions of the upper end) the calyces and collecting ducts. The metanephric blastema develops into the Bowman's capsules, proximal and distal convoluted tubules, Henle's loops and the remainder of the renal parenchyma. The division of the ureteric bud into calyces gives rise to the underlying lobar structure of the kidney, each lobe consisting of a calyx and its associated collecting ducts and renal cortex. During development about 14 lobes develop which fuse initially to form an obviously lobulated kidney. Renal cortical cellular multiplication continues in early childhood, gradually smoothing out the lobar outline by around 5 years of age. In approximately 5% of individuals the lobar outline persists into adulthood.

The kidneys develop in the upper half of the pelvis and migrate cranially during the 4th to the 8th week of gestation. At the same time the kidneys rotate 90° medially so the renal pelvis lie on the anteromedial aspect of the kidney. Initially the kidneys are supplied by lateral sacral branches of the aorta but during ascent they acquire successively higher lateral branches of the aorta up to the definitive renal arteries at the level of first lumbar disc (L1-L2). Failure of

regression of the inferior arteries is common and gives rise to accessory renal arteries.

The kidneys come to lie in the retroperitoneal space high on the posterior abdominal wall. They are bean-shaped with their concave aspect pointing medially. The right kidney lies a variable distance lower than the left in most subjects, owing to the presence of the liver. In quiet respiration they move up and down approximately 2-3 cm but this may more than double with deep inspiration.

The hilum of the kidney is a vertical opening on the medial aspect which contains the renal pelvis. The renal vein and one or two branches of the renal artery pass through the hilum to enter the kidney anterior to the renal pelvis, a further branch of the renal artery passing through the hilum posterior to the renal pelvis. The hilum also contains fat, sympathetic nerve fibres and lymphatic channels that drain to the lateral aortic lymph nodes around the origins of the renal arteries from the aorta.

Renal tissue is divided into a peripherally placed cortex and the central medulla. The medulla consists of 8-16 pyramids, which contain the descending and ascending tubules and the collecting ducts. The apex of each pyramid projects into a calyx as a renal papilla. The cortex contains the glomeruli and the proximal and distal convoluted tubules. The superior end of the ureter expands to form the renal pelvis which divides into 2-4 major calyces, each of which divide into 2-1 minor calyces. Each calyx is indented by a papilla, which is the apex of a medullary pyramid. The calyces therefore have a characteristic shape with a well-defined extension around the convexity of the papilla (the fornices). The minor calyces drain into a major calyx via a neck (infundibulum). Often at the renal poles (especially the upper pole) several papillae drain into one large calyx. These are referred to as compound calyces and are particularly vulnerable to damage from reflux nephropathy (Fig. 29.1).

The ureter runs retroperitoneally down the anterior aspect of the psoas muscle, separated from it by the transversalis fascia. As it enters the pelvis it crosses over the anterior aspect of the common iliac artery bifurcation immediately in front of the sacroiliac joint. It descends along the lateral pelvic wall, just medial to the obturator

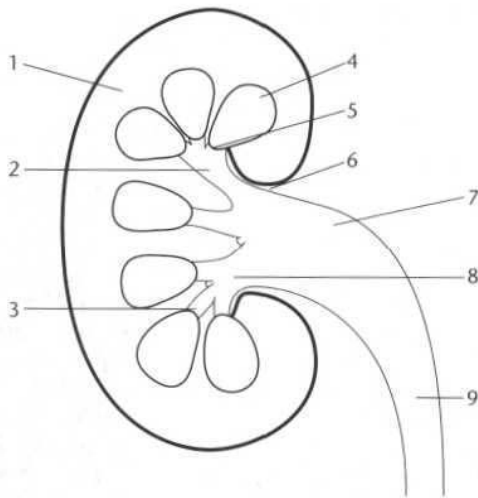


Fig. 29.1 Structure of the kidney. 1, Cortex; 2, compound calyx; 3, minor calyx; 4, medullary pyramid; 5, papilla; 6, renal sinus; 7, renal pelvis; 8, infundibulum of major calyx; 9, ureter.

internis, to the level of the ischial spine, from where it runs anteromedially until it enters the superolateral angle of the bladder base. The vas deferens crosses over the ureter, separating it from the bladder just before the ureters enter the bladder wall. The ureters run obliquely through the bladder wall for around 2 cm.

A fibrous capsule is closely applied to the renal cortex over the entire kidney apart from the hilum. The kidney is surrounded by perinephric fat and lies within a space partly enclosed by layers of fascia, traditionally referred to as the perinephric space (perirenal

space). The perinephric space is one of a number of spaces within the abdomen and pelvis that are important determinants of the direction of disease spread.

The transversalis fascia lines the inside of the abdominopelvic cavity, including the inferior aspect of the diaphragm, the posterior and medial surfaces of the anterior and lateral abdominal wall muscles respectively, the anterior aspect of the spinal column, psoas and paraspinal muscles and the superior aspect of the pelvic diaphragm. The major organs and their associated fascia develop within the space defined by the transversalis fascia. During embryological development, as the kidneys ascend from the pelvis the surrounding (perinephric) fascia forms a cone, with its apex superiorly. The perinephric fascia anterior to the kidney is often referred to as Gerota's fascia, the posterior fascia as Zuckerkindl's fascia and the enclosed space as the perinephric space (Fig. 29.2). It contains the kidney, the adrenal gland (anteromedial to the kidney on the left, superomedial to the kidney on the right), the upper ureter and the

nephric fascia and the adjacent transversalis fascia which contains only fat (the posterior pararenal space). This space is of interest to the interventional radiologist as a potential area in which to kink a guide-wire and mistakenly position a drain intended for the renal collecting system. There is a more substantial space anterior to the perinephric spaces between the anterior perinephric fascia and the posterior layer of the peritoneum, the anterior pararenal space. This contains the pancreas and duodenum centrally, with the ascending colon on the right and the descending on the left. These organs are therefore in direct contact with the anterior perinephric fascia.

Laterally the anterior and posterior perirenal fasciae fuse with the lateroconal fascia at the fascia trifurcation. The lateroconal fascia continues laterally and anteriorly to fuse with the parietal peri-

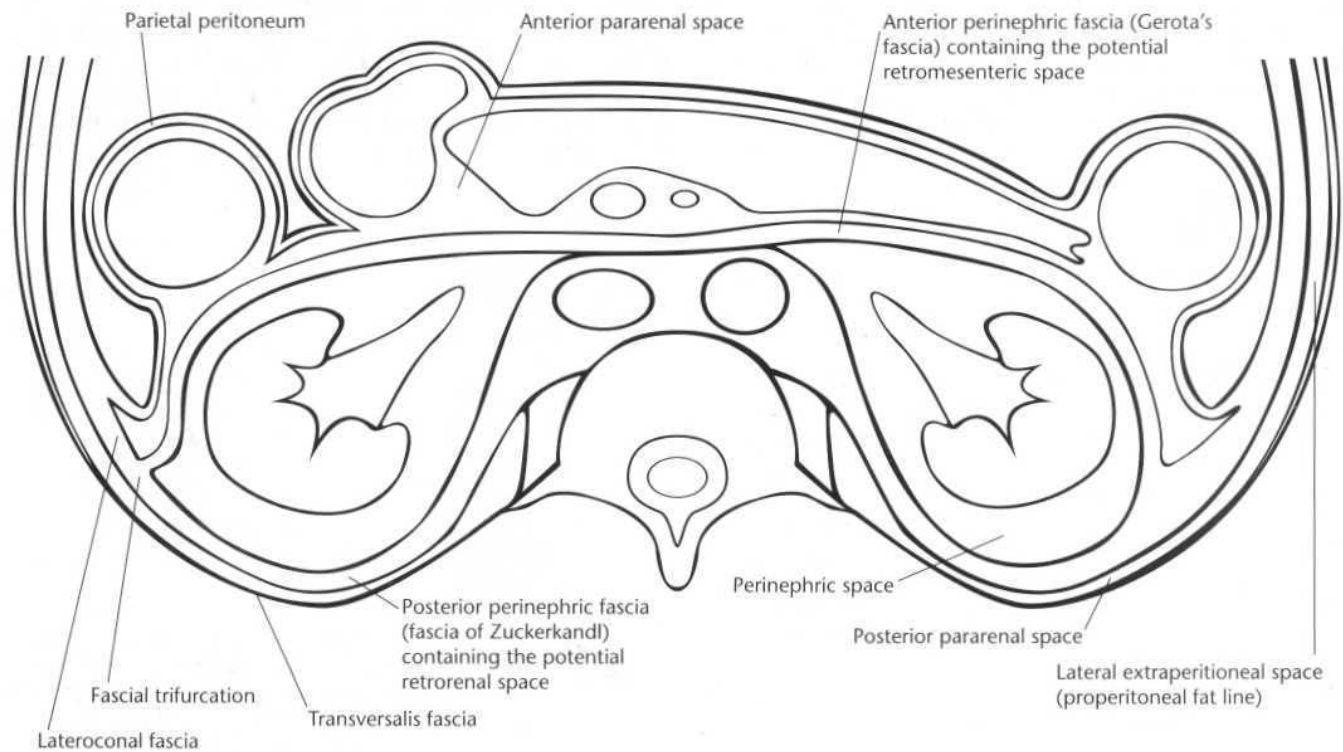


Fig. 29.2 Retroperitoneal fascial spaces.

toneum. Consequently the posterior pararenal spaces are continuous laterally with the fat-containing lateral extraperitoneal spaces (the properitoneal fat line) which lie between the parietal peritoneum and the transversalis fascia. Medially the posterior perinephric fascia fuses with the transversalis fascia over the paraspinal muscles, closing the posterior pararenal spaces medially. The line of fusion between the posterior perinephric and transversalis fasciae varies from cranial to caudal, being over the psoas muscle at the level of the superior renal pole and, more laterally, over the quadratus lumborum at the level of the inferior poles. Parts of both the perinephric and posterior perirenal spaces therefore lie directly over the psoas muscles, separated from them only by the transversalis fascia. This is an important route of spread of renal disease, particularly inflammatory processes, into the psoas muscle compartment and hence inferiorly into the pelvis and the iliacus muscle.

The anterior perinephric fascia and the combined posterior perinephric and transversalis fasciae run medially across the midline to meet with the corresponding fasciae on the contralateral side. This would imply the perinephric spaces can communicate with each other across the midline. Observation of the extension of disease within the perinephric space, however, shows that this does not occur as readily as would be expected if there was free communication. This problem is overcome by considering the layers of fasciae as laminated structures that arise embryologically from more than one layer and in certain areas contain potential spaces and communications. The anterior and posterior perirenal fasciae thicken medially and to some extent fuse, acting as a relative barrier to medial extension of disease. There is a potential space within the laminated anterior perinephric fascia (the anterior interfascial or retromesenteric space) that can eventually transmit disease processes across the midline. The posterior perinephric fascia is also laminated and contains a potential space (the posterior interfascial or retrorenal space). Fluid in either of these potential spaces may track to the other and also via the fascial trifurcation into the lateroconal fascia. Fibrous septae are found within the perinephric space running from the renal capsule to the perinephric fascia and act as potential conduits between the perinephric and interfascial potential spaces.

Superiorly (the apex of the cone of the perinephric fascia) the perinephric space is closed. Since the perinephric fascia originally develops as a cone around the kidneys, as they ascend it would be expected that the perinephric spaces remain open inferiorly. This, however, remains a matter of controversy and it has been suggested that the anterior and posterior layers of perinephric fascia fuse inferiorly in the iliac fossae, closing the perinephric spaces and forming a combined laminated fascia that continues inferiorly along the anterolateral aspect of the psoas muscles. In routine radiological practice the distinction does not appear to be important, as both descriptions offer mechanisms for disease to spread from the region of the kidneys inferiorly into the pelvic extraperitoneal spaces.

The relationships of the kidneys are as follows. Posteriorly the kidneys lie over the psoas and paraspinal muscles and the 12th (and on the left the 11th) ribs. Anterosuperiorly the kidneys are in contact with the adrenal glands and anteroinferiorly with the jejunum. Anterolaterally the kidneys abut the liver, and below it the hepatic flexure on the right (Fig. 29.3A); the spleen and below it the splenic flexure on the left (Fig. 29.3B). The other important anterior relationship is with the duodenum anteromedially on the right and with the pancreas and stomach anteromedially on the left.

The arterial supply and venous drainage of the kidneys are both extremely variable. The renal arterial supply is most commonly provided by a single lateral branch of the aorta, the renal artery, originating at the level of the first lumbar disc. The right renal artery has the longer course and runs posterior to the inferior vena cava. The renal arteries run posterior to their respective renal veins. The renal artery gives off the inferior adrenal and the renal capsular arteries and then classically divides into three branches as it enters the renal sinus, two running anterior to the renal pelvis, one posterior. The main renal branches subsequently divide into the interlobar arteries, which run centrifugally within the cortical tissue between the medullary pyramids. At the level of the base of the pyramids the interlobar arteries give off the arcuate arteries, which run along the line of the corticomedullary junction.

The venous drainage mirrors the arterial tree except that the kidneys are drained by five or six major venous branches, which most commonly combine to form a solitary renal vein that drains

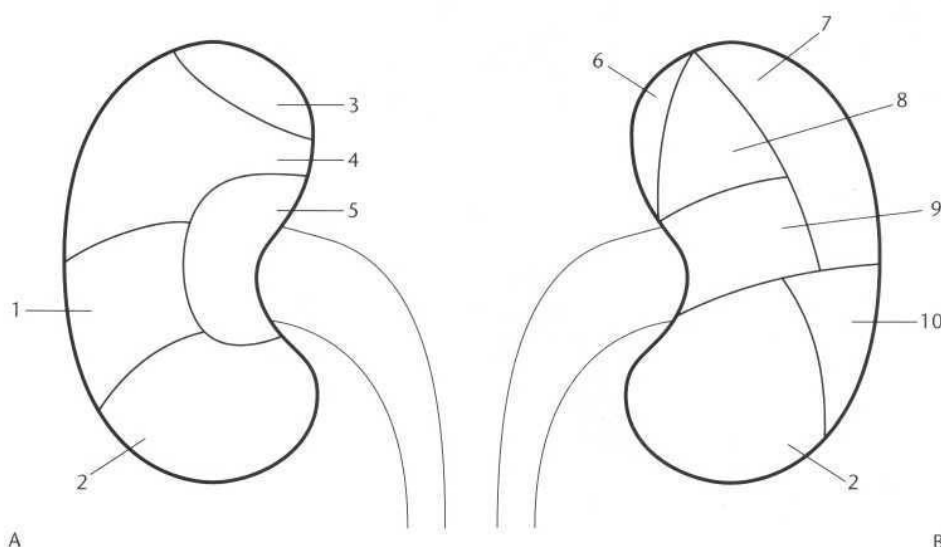


Fig. 29.3 Anterior relations of (A) the right kidney, and (B) the left kidney. 1, Hepatic flexure; 2, small intestine; 3, right adrenal gland; 4, liver; 5, duodenum; 6, left adrenal gland; 7, spleen; 8, stomach; 9, pancreas; 10, splenic flexure.

into the inferior vena cava, also around the level of the first lumbar disc.

The lymphatic drainage of the kidneys is to the lateral aortic lymph nodes around the origin of the renal arteries.

The bladder

The transversalis fascia continues inferiorly into the pelvis, where it is often referred to as the pelvic fascia. It lines the walls of the pelvis and overlying muscles, notably including the obturator internus laterally and the pelvic diaphragm inferiorly. The parietal peritoneum of the abdomen also continues inferiorly and is reflected over the pelvic viscera and fat-containing spaces of the pelvis, leaving most of the pelvic organs outside the peritoneal cavity. The umbilicovesical fascia is a large triangular fascia with its apex at the umbilicus. It extends inferiorly, dividing the prevesical space anteriorly from the perivesical space posteriorly and centrally. The cave of Retzius is the part of the prevesical space immediately posterior to the pubis. The prevesical space continues posterolaterally into the paravesical spaces (Fig. 29.4). These spaces are continuous superiorly with the properitoneal fat stripes (lateral extraperitoneal spaces of the abdomen) and the posterior pararenal spaces. The perivesical space contains the bladder, the urachus and the seminal vesicles. It is limited posteriorly by the reovesical septum (reetovaginal in the female).

The pelvic organs are supported by the pelvic floor, which is formed by the pelvic diaphragm. This separates the pelvic cavity superiorly from the perineum inferiorly. The pelvic diaphragm consists of the large levator ani and the small coccygeus muscles and their covering fascia. The puborectalis sling is a prominent part of the levator ani which runs around the lateral and posterior aspects of the anorectal junction and sweeps forward along the lateral margins of the prostate and inserts into the posterior aspect of the body of the pubis (Fig. 29.5).

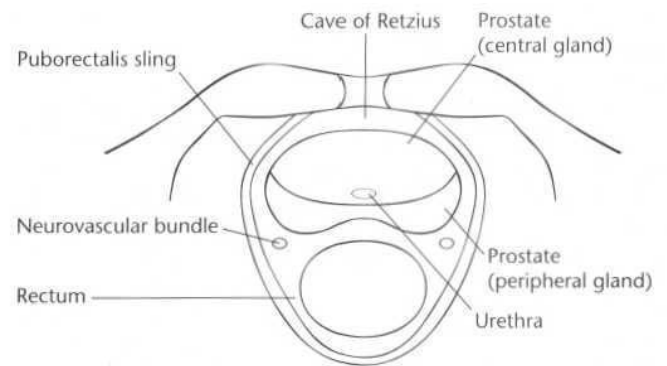


Fig. 29.5 The relationships of the prostate.

The urinary bladder lies immediately posterior to the pubic bones. When full it is roughly spherical but when empty it approximates to a pyramidal shape, having an apex and four roughly triangular surfaces: posterior (base), superior and two inferolateral. The apex lies immediately behind the upper margin of the symphysis pubis and gives rise to the urachus, which is the fibrous remnant of the allantois. The urachus runs superiorly in the extraperitoneal fat to the umbilicus as the median umbilical ligament. The superior surface of the bladder is covered in peritoneum and loops of ileum and/or sigmoid colon. The inferolateral surfaces relate anteriorly to the retropubic fat and pubic bones and posteriorly to the obturator internus (superiorly) and the levator ani (inferiorly).

The base of the bladder receives the ureters at its superolateral angles and gives rise to the urethra at its inferomedial angle. This rests on the prostate inferiorly, and the muscle fibres of the bladder wall run continuously into the prostate. The muscle fibres are thickened around the origin of the urethra as the (internal) sphincter vesicae. This area of the bladder is referred to as the bladder neck. The bladder mucosa is thrown into folds when the bladder empties.

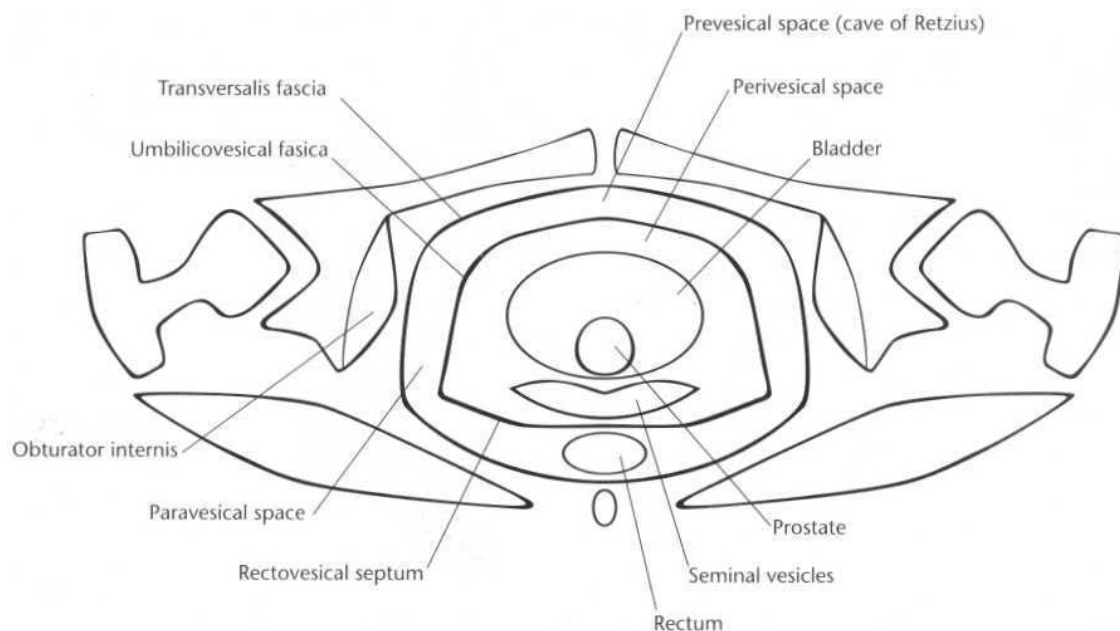


Fig. 29.4 The extraperitoneal spaces of the pelvis.

except over the base where it is firmly adherent to the underlying muscle layers. This region is referred to as the trigone. The superior border of the trigone is defined by a muscular ridge running between the ureteric orifices (the interureteric ridge). The upper part of the base is covered by peritoneum and lies anterior to the rectovesical pouch (utero-vesical pouch in the female), the lower part is subperitoneal and separated from the rectum by the vasa deferentia and seminal vesicles (vagina in the female).

The arterial supply is from the superior and inferior vesical arteries which arise from the anterior division of the internal iliac arteries, as described below. The common iliac arteries terminate at the pelvic inlet anterior to the sacroiliac joints by dividing into the external and internal iliac arteries. The external iliac artery runs along the medial border of the psoas muscle, following the pelvic brim to exit the pelvis under the inguinal ligament to become the common femoral artery as it enters the leg. The internal iliac artery enters the pelvis anterior to the sacroiliac joint with the ureter running inferiorly and crossing it anteriorly. At the level of the upper border of the sciatic notch the artery bifurcates into anterior and posterior divisions. Further branches are variable but classically include the umbilical artery (giving rise to the artery to the vas deferens and the superior vesical artery), the inferior and middle vesicle arteries, the internal pudendal, inferior gluteal and uterine arteries. Branches of the posterior division of the internal iliac artery are essentially musculoskeletal, being the iliolumbar, lateral sacral and superior gluteal arteries.

The venous drainage of the bladder is to the vesical venous plexus, which communicates inferiorly with the prostatic venous plexus and drains superiorly into the internal iliac veins.

Lymphatic drainage is into the internal and external iliac lymph nodes lying along the course of the respective arteries. These in turn drain into the common iliac nodes. The medial chains of the external iliac lymph nodes (obturator nodes) lie next to the lateral pelvic walls at the level of the acetabulum. They are frequently involved early in metastatic spread of bladder or prostatic cancers and are therefore often referred to as sentinel nodes. Small pelvic lymph nodes may be seen on CT and MRI and are regarded as normal when less than 10 mm in diameter.

The male genitalia and urethra

The prostate has roughly the shape of an inverted rounded cone/pyramid. It is a glandular organ enclosed by a fibrous capsule. It contains a substantial fibromuscular component which surrounds the prostatic urethra. It has a base, apex, anterior, posterior and two lateral surfaces. Superiorly its base relates to the bladder. Inferiorly its apex lies on the upper surface of the urogenital diaphragm. Anteriorly it relates to extraperitoneal fat in the retropubic space (cave of Retzius). Posteriorly the prostate is separated from the rectum by the rectovesical septum (fascia of Denonvillier), which is the fused walls of the inferior end of the rectovesical pouch. Laterally the prostate relates to the puborectalis, which is an important radiological landmark seen running backwards close to the lateral margin of the prostate and encircling the anorectal junction. The neurovascular bundle of the prostate lies in the angle between these two structures (Fig. 29.5).

The classical lobar anatomy of the prostate is unhelpful. The zonal anatomy is more useful clinically and pathologically. Three zones are described histologically: central, transitional and peripheral. The transition zone has a C shape lying against the anterior

and lateral aspects of the proximal urethra. The central zone lies against the posterior aspect of the proximal urethra and encases the transition zone posteriorly and superiorly. The peripheral zone surrounds the central zone and the distal urethra. Radiologically the central and transitional zones are indistinguishable and are commonly referred to collectively as the central gland. In young males the largest component of the prostate is the peripheral zone (70%), the transitional and central zones constituting 5% and 25% of the gland, respectively. The zonal architecture in young males cannot be clearly seen radiologically but it becomes more evident with advancing years. The transitional zone is the site of development of benign prostatic hyperplasia and with age increases in size and eventually dominates the gland.

The prostate is supplied by the inferior vesical and middle rectal arteries. Venous drainage is into the periprostatic venous plexus which communicates inferiorly with the dorsal vein of the penis and superiorly with the perivesical venous plexus, which in turn drains into the internal iliac veins. Lymphatic drainage is into the internal iliac nodes.

The seminal vesicles are paired lobulated sacs, approximately 5 cm long in the young adult male (becoming atrophic with age), lying on the posterior surface of the bladder. They run inferomedially into a narrow duct which joins with the duct of the vas deferens to form the ejaculatory duct. The ejaculatory duct pierces the prostate to enter the prostatic urethra on the verumontanum.

The male urethra is approximately 20 cm long and runs from the bladder neck to the external meatus, where it dilates to form the fossa terminalis (navicular fossa). It can be considered in three sections: prostatic, membranous and penile. The prostatic urethra is 3 cm long and runs from the bladder neck through the prostate. It is normally the widest part of the urethra. Its most notable feature is a longitudinal mound (verumontanum) along the posterior wall. At the centre of the verumontanum is a small diverticulum (prostatic utricle) which receives the ejaculatory ducts at its lateral margins. The urethra exits from the prostate just above the apex to become the membranous urethra. The membranous urethra is the shortest (1-1.5 cm) and least distensible section of the urethra. It is enclosed by the sphincter urethrae (external sphincter), which, along with the deep transverse perineal muscles and their covering fasciae, form the urogenital diaphragm. The urogenital diaphragm closes the arch formed by the pubic bones and separates the cavity of the pelvis from the perineum below.

The penile urethra can be subdivided into bulbar (proximal) and pendulous (distal) sections which relate to the root and body of the penis, respectively. The root is made up of three masses of erectile tissue, the centrally placed bulb and paired laterally placed crura. The bulb is attached to the underside of the urogenital diaphragm: it encases the proximal penile urethra and is surrounded by the bulbospongiosus muscle. The crura run along the posteromedial aspects of the pubic arch and are covered by the ischiocavernosus muscles. The bulb and the crura continue anteriorly into the body of the penis as the corpus spongiosum and the dorsolaterally placed paired corpora cavernosa, respectively. The urethra continues into the body of the penis encased by the corpus spongiosum and its distal expansion (the glans).

The scrotum is a pouch of skin that contains the testes, epididymis and spermatic cord. It has three layers from superficial to deep: skin, dartos muscle and Colles' fascia (continuous anterosuperiorly with the anterior wall membranous fascia-Scarpa's fascia). It is divided into two compartments by a midline fibrous

septum (median raphe). Each compartment contains a testicle, epididymis and proximal spermatic cord.

The testicles originate on the posterior abdominal wall around the level of the first lumbar vertebra. They descend retroperitoneally through the abdomen and with their associated neurovascular structures, lymphatics and ducts exit the pelvis via the inguinal canal around the 7th to 8th month of uterine life. They are preceded by a peritoneal diverticulum (processes vaginalis), remnants of which may persist into adult life. As they leave the pelvis they acquire a covering from each layer of the anterior abdominal wall which surrounds the spermatic cord and the testes. The transversalis fascia gives rise to the internal spermatic fascia, the internal oblique muscles to the cremasteric muscle and fascia and the external oblique aponeurosis to the external spermatic fascia. Deep to these three layers is the tunica vaginalis. This is a serous membrane (derived from peritoneum) with two layers: parietal, against the internal spermatic fascia, and visceral, which closely invests the testis and the epididymis. The tunica vaginalis envelops the testicle and applies it to the posterior scrotal wall. There is a potential space between these two layers which extends a little way along the spermatic cord and normally may contain up to 1-2 ml of serous fluid. In disease states a more substantial collection may be seen (hydrocele).

The outermost layer of the testicle is the tunica albuginea, a dense fibrous capsule. Posteriorly there is a vertical linear extension of the tunica albuginea into the testicular parenchyma (mediastinum of the testis). The testicle is divided into 200-400 lobules by numerous trabeculae that extend from the mediastinum. The lobules consist of interstitial tissue (which includes the androgen-producing Leydig cells) and 2-4 seminiferous tubules (which include the supporting Sertoli cells) that drain via a common tubule. These converge into a network of tubules at the mediastinum (the rete testis) that drain via 10-15 efferent tubules out of the testicle into the epididymis.

The epididymis consists of a convoluted common tubule with supporting tissue. Its upper, mid and lower portions may be referred to as the head, body and tail. Drainage is from the tail into the vas deferens. An embryological remnant a couple of millimetres long (so-called appendix or hydatid) may be identified related to the upper pole of the epididymis (derived from the mesonephric duct) or the testis (derived from the millerian duct).

The testicle is supplied by an end artery, the testicular artery, which originates from the aorta just below the renal artery. This runs inferiorly along the posterior abdominal wall on the surface of the psoas muscle and enters the scrotum via the inguinal canal within the spermatic cord. At the mediastinum of the testis the dominant testicular artery (sometimes referred to as the inferior testicular artery) divides into several capsular arteries which run around the testicular parenchyma just deep to the tunica albuginea. This layer has been referred to as the tunica vascularis. Branch arteries run from this layer towards the mediastinum, close to which further branching occurs, running back in the opposite direction. There may be an additional branch (transtesticular artery) which enters the mediastinum directly from the testicular artery and is often accompanied by a large vein. Before reaching the mediastinum the testicular artery also gives rise to the epididymal artery and a minor testicular branch (internal testicular artery), which enters the upper pole of the testicle and contributes to the capsular branches.

Venous blood drains from the posterior border of the testicle into an extensive venous plexus (the pampiniform plexus). The pampiniform plexus ascends within the spermatic cord with the testicular artery and the vas deferens. Classically the branches of the pampiniform plexus unite to form a single testicular vein (the internal spermatic vein) as it enters the abdomen via the inguinal canal. The testicular vein runs superiorly along the posterior abdominal wall in the retroperitoneum and terminates in the renal vein on the left and in the inferior vena cava just below the renal vein on the right. This, however, is extremely variable and often there are multiple collaterals to the renal or retroperitoneal veins, multiple terminal ostia and multiple testicular veins.

The spermatic cord runs from the testicle to the abdominal cavity via the inguinal canal. It contains the vital supply and drainage structures of the testicle surrounded by continuations of the three deep fascial layers of the scrotum (the internal spermatic, cremasteric and external spermatic fasciae). The contents include the testicular artery, pampiniform plexus, lymphatic vessels and the vas deferens. The veins are routinely visualised and are normally no more than 1-2 mm maximum diameter.

The lymphatic vessels follow the testicular artery and vein retroperitoneally to terminate in the first-echelon nodes (sometimes referred to as the sentinel lymph nodes) in the upper abdomen. On the left these are immediately lateral to the para-aortic lymph nodes and medial to the renal lymph nodes around the level of the first to the second lumbar vertebrae, while on the right they are in the paracaval region just below the renal vessels around the level of the first to the third lumbar vertebrae.

Drainage from these nodes is into the nodes between the renal vessels and the aortic bifurcation (paracaval from the right, para-aortic from the left and both potentially into the aortocaval centrally). Drainage from these nodes is superiorly to the para-aortic and paracaval nodes above the renal hila and extending retrocrurally into the mediastinum. In a minority the lymphatics drain directly into nodes at the level of the aortic bifurcation and occasionally directly into the common iliac nodes. Testicular lymph node drainage is usually to the ipsilateral nodes but bilateral drainage may occur, more often from the right than the left. These considerations are important when staging testicular malignancy.

The vas deferens is a muscular duct responsible for the transport of the sperm from the testicle to the urethra. It originates from the tail of the epididymis and leaves the scrotum in the spermatic cord. After passing through the inguinal canal it enters the pelvis at the deep inguinal ring, hooks round the lateral aspect of the inferior epigastric artery and runs posteroinferiorly on the lateral wall of the pelvis (on the obturator internus) to the level of the ischial spine, where it turns inferomedially to run along the posterior aspect of the bladder immediately anterosuperior to the distal ureters. The distal vas dilates to form the ampulla. This curves inferiorly where it joins the duct of the seminal vesicle to form the ejaculatory duct, which joins the urethra at the verumontanum.

INVESTIGATIONS

Plain films

The standard plain radiographic imaging of the urinary tract is the KUB (kidneys, ureters and bladder), which consists of a full length abdominal film and an upper abdominal (cross-kidney) film (Fig. 29.6). The films are taken with the patient supine using a low

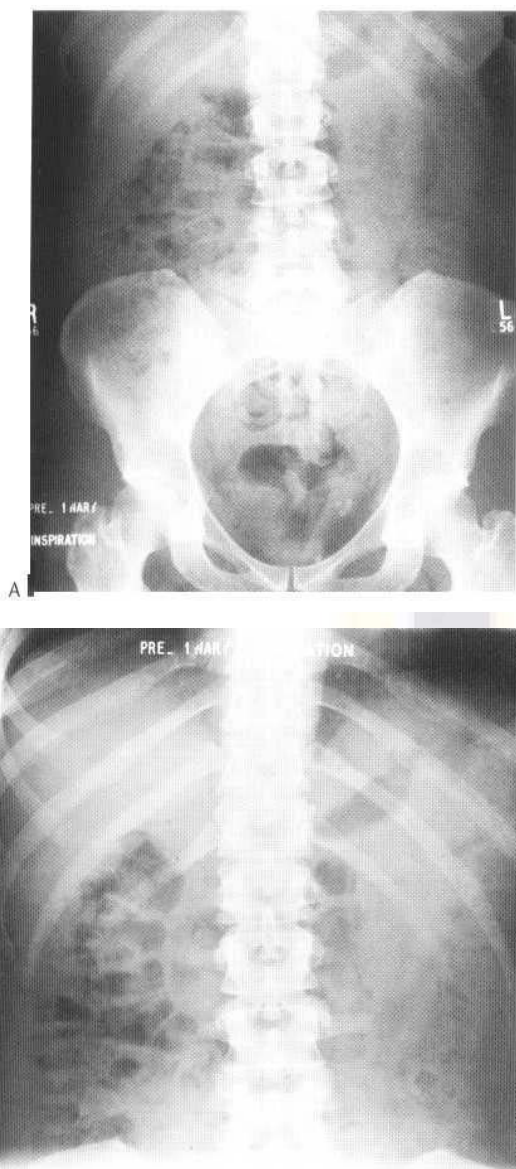


Fig. 29.6 The KUB. (A) Full length and (B) cross kidney films from a KUB examination. Several phleboliths are seen in the pelvis. They are characteristically smooth small rounded calcific areas with a tiny central radiolucency.

voltage technique (60-65 kV) to maximise soft-tissue contrast. The full length film is taken in inspiration using a 35 x 43 cm cassette positioned with the lower border at the symphysis pubis to ensure the urethra (particularly the prostatic urethra) is included on the film. The cross-kidney film is taken in expiration using a 24 x 30 cm cassette with the lower border 2.5 cm below the iliac crests.

The outline of several anatomical structures can be seen on the KUB, including renal, psoas and bladder outlines, much of the axial skeleton, the bowel gas pattern and the lung bases, all of which should be routinely inspected. A range of pathology may be observed in these and other structures but the KUB is a relatively unreliable diagnostic tool and, despite the occasional incidental finding in other systems, its principal use is in the assessment of urinary tract calculi. It is, however, extremely unreliable in the diagnosis of ureteric calculi, with an accuracy of only around 50%.

Box 29.1 Calcification on the KUB

Urinary tract

Renal: calculi, renal cell carcinoma, tuberculosis, arterial (atheroma or aneurysm)

Ureter: calculi, tuberculosis, schistosomiasis

Bladder: calculi, schistosomiasis, transitional cell carcinoma

Outside the urinary tract

Musculoskeletal: costal cartilage calcification

Hepatobiliary: gallstones, hepatic granuloma

Pancreas: chronic pancreatitis

Adrenal: tuberculosis, Addison's disease

Spleen: granuloma

Aorta: atheroma, aneurysm

Venous: phlebolith

Uterine: fibroid

Lymphatic: calcified lymph nodes (presumed postinfective)

There are numerous causes of calcification visible on the plain radiograph, with considerable overlap in their appearances, and a specific diagnosis is often not possible. The more common causes are listed in Box 29.1. The KUB is most usefully employed as part of an intravenous urogram (IVU) or to follow up a previously proven calculus.

Intravenous urography

The intravenous urogram (IVU) is the classic routine investigation of urology. With the advent of ultrasound its role is now much diminished and its future is the subject of considerable debate as other modalities, particularly spiral computed tomography (CT), become more widely available. At this date, however, it is still widely used and requires consideration. Currently the main indications are the investigation of persistent or frank haematuria, renal and ureteric calculi (particularly prior to endourological procedures), ureteric fistulas and strictures and complex urinary tract infection (including tuberculosis).

The IVU consists of a series of plain films taken after administration of an intravenous injection of a water-soluble iodine-containing contrast medium. There is considerable variation in the exact details of how an IVU is performed in different departments, although there should be general agreement on the underlying principles. Traditionally the patient was prepared with a period of 4 h starvation and fluid deprivation and the bowel purged with a strong laxative. Bowel preparation is now generally regarded as unhelpful and it was unpleasant for the patient: it has now largely been dispensed with. Occasionally the patient will feel nauseated after the IVU injection and rarely there will be a severe reaction with the need for cardiovascular and occasionally cardiopulmonary support. With this in mind, it seems reasonable to persist with avoidance of food for 2-4 h prior to the procedure. There has been a considerable body of work on the potential adverse effects of intravenous contrast on renal function and its relationship to the patient's fluid status. Traditionally fluid was restricted prior to the IVU in order to improve opacification of the collecting system. However, it has long been accepted that dehydration is associated with an increased risk of nephrotoxicity, which may be permanent in patients with diabetes mellitus, myeloma, hyperuricaemia, sickle-cell disease and pre-existing renal disease. The risk of irreversible damage to renal function in a previously healthy kidney due to the contrast injection is very low. This appears to be further reduced with avoidance of

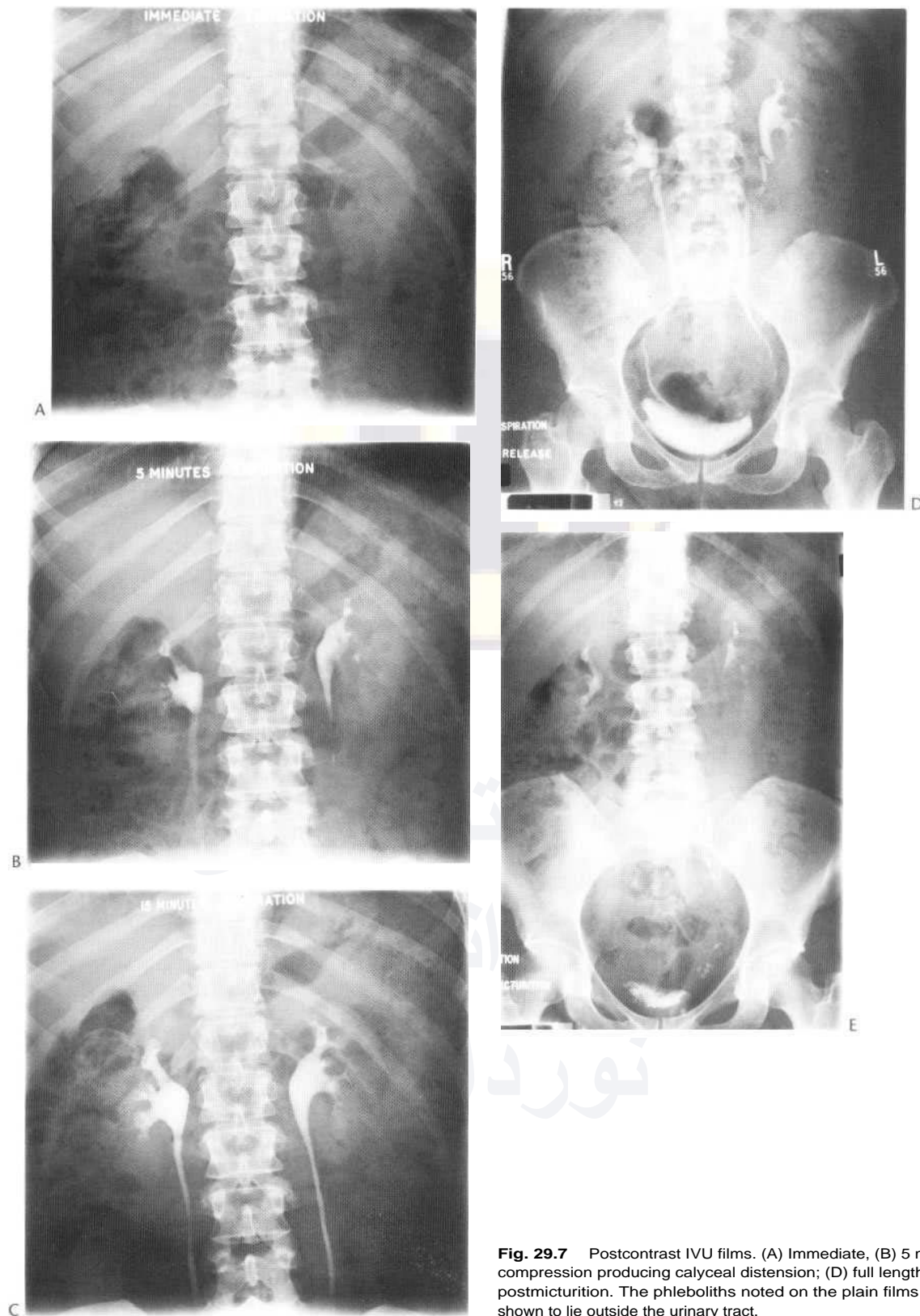


Fig. 29.7 Postcontrast IVU films. (A) Immediate, (B) 5 min, (C) 15 min film with compression producing calyceal distension; (D) full length release; (E) full length postmicturition. The phleboliths noted on the plain films (Fig. 29.6A) are nicely shown to lie outside the urinary tract.

dehydration. Modern non-ionic contrast agents do not provoke an osmotic diuresis and the degree of opacification is unlikely to be significantly altered by dehydration. Fluid restriction should therefore be avoided and if there is a risk that the patient is dehydrated before the IVU this should be corrected first.

The classical series of plain films (immediate, 5 and 15 min, full length release and postmicturition) is described, with mention of some of many potential modifications. A preliminary postmicturition plain film (KUB) is performed. This should be examined to check exposure factors, centring and obvious pathology, particularly urinary tract calcification. Intravenous contrast is given relatively rapidly by hand. The standard dose is 50 ml of 350-370 strength water-soluble contrast. Some understanding of the underlying structure of water-soluble contrast agents is desirable and a knowledge of potential adverse reactions and their treatment is imperative. These issues are discussed under water-soluble contrast (p. 926). At this point it is worth emphasising some safety features. Although modern contrast medium is exceptionally safe, there is a small risk of serious reactions. The most dangerous of these are the anaphylactoid-type hypersensitivity reactions. To minimise the risks

of these a routine inquiry about previous contrast exposure and allergy is recommended before administering the contrast medium. The injection should be through some form of indwelling cannula or needle that can be taped into place for the duration of the investigation. This allows emergency treatment to be administered if required, or a further injection of contrast if opacification is seen to be inadequate. There should also be a doctor (usually the radiologist) available in the X-ray department throughout the investigation. Most adverse events are likely to take place within the first few minutes after the injection. Emergency drugs, oxygen and resuscitation equipment should also be readily available. Treatment of contrast reactions is discussed on page 928, as is the specific problem of metformin interaction.

A cross-kidney film is taken immediately after contrast injection and at 5 min after the injection (Fig. 29.7). Abdominal compression is applied as soon as the 5 min film has been taken (a variety of devices are available for this) to inhibit ureteric drainage and promote distension of the pelvicalyceal systems, optimising their visualisation. A further cross-kidney film is taken at 12-15 min to demonstrate this.

Table 29.1 IVU modifications

Radiography	Modification	Purpose
Plain films	Additional obliques or tomograms	To assist the location of potentially intrarenal opacities. Rarely required; ultrasound and other imaging manoeuvres usually preferable
Nephrogram	Thick slice tomogram	To improve definition of the renal outlines
	Omit along with the 5 min film and take a solitary 3 min film	To reduce radiation dose
5 min film	Second injection of contrast	<ul style="list-style-type: none"> improve opacification of the pelvicalyceal systems if inadequate
15 min compression film	Series of 1 cm thick tomograms	<ul style="list-style-type: none"> differentiate between overlying shadows and filling defects within the collecting systems delineate the renal outlines when inadequately seen (better done with ultrasound)
15 min release film	Additional bladder views	<p>When the bladder is poorly filled on the release film (as is often the case) delayed films of the fuller bladder may be performed.</p> <p>When equivocal filling defects are seen in the bladder area oblique films may be performed</p> <p>The above additional bladder views are rarely indicated as they increase the radiation burden to the patient and the relevant clinical problems are better answered by ultrasound or cystoscopy. However, occasionally a small suspected calculus in the distal ureter may be confirmed with the appropriate oblique</p>
Full length post-micturition film	Bladder area only	if the upper tracts have already been adequately imaged then imaging the bladder area alone will reduce the patient's radiation burden
	Omit	The preceding films may have already provided all the information required from the investigation
Prone full length film	Additional view	Where the renal pelvis is dilated, contrast may be slow to pass into the ureter; this can be accelerated by positioning the patient prone when the heavier contrast will run anteroinferiorly into the ureter, often to the level of the obstruction. Simply asking the patient to sit or stand for a few minutes first may improve the result
Erect images	Additional radiograph or fluoroscopy	if it is difficult to determine whether or not there is a small ureteric calculus, an erect oblique radiograph of the ureter or screening the ureter in this position may be useful on rare occasions
Frusemide IVU	Administration of 20mg of frusemide intravenously after the 15 minute film with a further film 15 minutes later	if suspected pelviureteric junction obstruction is being investigated and there is no evidence of this on the standard IVU, this manoeuvre can be performed. It may provoke hydronephrosis and pain. It is rarely necessary if the patient is to be investigated with radionuclide renography, as is often the case in this situation

Compression is routinely omitted in children and should be avoided in a number of situations. It is contraindicated if there is an aortic aneurysm. If the patient's abdomen is tender it should also be avoided. This contraindication includes recent abdominal surgery and the acute painful abdomen, the latter including renal colic. In the case of renal colic, even if the patient can tolerate compression it is best avoided because it is unlikely to contribute to the investigation and potentially may exacerbate the tendency of the acute obstruction to provoke extravasation of urine at the fornices. If this does occur, however, it is not a cause for undue alarm as it is not uncommonly encountered spontaneously in renal colic and does not appear to be associated with adverse sequelae.

If the 15 min film is satisfactory the compression is removed and a full length film is taken immediately to offer the best opportunity of demonstrating the ureters. The patient is then asked to empty the bladder and a further full length film is taken to demonstrate drainage of the upper tract and the postmicturition bladder volume.

This classical series can be modified to deal with particular circumstances, to attempt to increase the sensitivity of the procedure or to reduce the radiation dose to the patient. Some of the most frequently employed modifications are detailed in Table 29.1. Three circumstances in particular are worthy of further comment.

When there is significant acute obstruction, usually due to calculi, there is delay in opacification of the collecting system. The delay may be considerable, up to 24 h or more. It is then necessary to perform the minimum number of additional films. The time interval between films traditionally is approximately doubled, with films taken at 0.5, 1, 2, 4, 16 and 24 h, as necessary; however, in order to minimise the radiation exposure, if there is no opacification of an acutely obstructed kidney at 30 min it is usually unhelpful to perform the next film before around 4 h after contrast injection. A further manoeuvre to minimise radiation dose in patients with a strong clinical suspicion of ureteric colic is to omit all films after contrast until a full length 15 min film is performed.

Patients with proven or suspected ureteric calculus may require one or more follow-up IVUs. These should have the minimum number of films required to answer the specific question, for example a full length plain and 15 min postcontrast film may be sufficient. It is very rarely necessary to perform an IVU on a pregnant patient. If it is required, the radiation exposure should be minimised. The collecting systems in pregnancy are capacious and the ureters exhibit poor peristalsis. Consequently a single full length preliminary film and a delayed solitary full length film around 30-45 min may well be enough.

The stereotypical appearances of the normal IVU are as follows. It takes approximately 12-20 s for contrast to reach the renal arteries following its intravenous injection. At this stage its concentration is maximal in the vascular compartment; however, this falls rapidly as the contrast medium begins to escape into the extracellular compartment and also undergoes rapid glomerular filtration and enters the renal tubules. In the first minute of the IVU healthy kidneys (assuming a normal cardiovascular system) show diffuse enhancement. This is referred to as the nephrogram. During the nephrogram phase the renal size (normally at least three vertebrae in length but no more than four) and outlines are best seen. In roughly the first half minute, contrast in the vascular compartment dominates and therefore the cortex is more enhanced than the medulla: this differentiation is sometimes visible on the immediate film of the IVU series (but regularly visible on CT performed at this stage). In the second half minute, contrast in the tubules

increases and enhancement of the kidneys is more diffuse. Contrast begins to appear in the calyces from around 1 min. From this time, in good quality films, contrast may also be visible in the collecting ducts as fine linear opacities running along the medullary pyramids towards the calyces. This may be referred to as pyelotubular stasis or, when less defined, as the medullary or pyramidal blush, and is a normal phenomenon.

Contrast in the normal calyces will begin to drain immediately into the pelvis and ureter and this phase may be referred to as the pyelogram. The successful application of compression impedes ureteric drainage and distends the pelvicalyceal system, producing optimal visualisation of the pelvicalyceal system around 12-15 min. After compression is released there is a transient increase in flow down the ureters and the release film offers the best chance of demonstrating the ureters. The normal ureters exhibit continual peristalsis and on a single film it is uncommon to demonstrate the entire length of both (or even either) ureters. They will often demonstrate smoothly narrowed areas (especially at the pelviureteric junctions and as they cross the iliac vessels in the pelvis) and more relaxed capacious areas. This is normal and how vigorously further efforts are made to demonstrate the entire length of the ureter depends on the clinical situation. In most situations partial visualisation of a non-obstructed but otherwise normal ureter is acceptable. If there is persistent haematuria or abnormal cytology further efforts to demonstrate the ureter are required and may include prone films, repeat IVU after a short interval and/or retrograde pyelography.

Ultrasound

Ultrasound of the urinary tract can be considered under three headings: ultrasound of kidneys and bladder, ultrasound of the male genitalia and ultrasound of the prostate.

Kidneys and bladder Routine ultrasound of the urinary tract consists of examination of the kidneys and the full urinary bladder and is probably now the most frequently performed radiological investigation of the urinary tract. The commonest indications are urinary tract infection and prostatism. Other indications include haematuria, obstruction, masses, calculi, congenital abnormalities, renal failure and assessment of transplants. It is frequently used to guide diagnostic or therapeutic procedures. Assessment of the postmicturition bladder volume is often also performed as part of the same examination, especially for prostatism. Most modern probes emit a broad band of ultrasound that can be biased towards high (for thin patients) or low frequency, usually within the 2-6 MHz range for abdominal and pelvic work. The position of the normal kidneys is extremely variable and the optimal window for visualisation has to be determined for each patient. Conventionally each kidney is examined subcostally from the loin with the patient in the lateral position, the side of interest uppermost. Often, however, complementary views can be obtained with the patient supine with a more lateral or intercostal approach.

On ultrasound the normal renal cortex appears slightly hypoechoic compared to the liver and spleen. It lies as a peripheral rim with normal invaginations (columns of Bertin) projecting inwards between the medullary pyramids (Fig. 29.8). The pyramids are markedly hypoechoic compared to the cortex in the first 6 months of life, becoming less hypoechoic with ageing and in some disease states. Corticomedullary differentiation is therefore most obvious in young adults and children, and the hypoechoic pyramids are



Fig. 29.8 Normal renal ultrasound; note the relatively hypoechoic pyramids and markedly hyperechoic fat containing sinus (centrally) compared to the cortex.

occasionally mistaken for the dilated calyces of a hydronephrosis. Arcuate arteries can be identified in 25% of the adult population as focal hyperechoic areas at the corticomedullary junction. The centrally placed renal sinus contains the calyces, infundihula, part or all of the renal pelvis, blood vessels, lymphatics, fibrous tissue and fat. It is the most hyperechoic part of the kidney, owing to the presence of fat. The normal renal pelvis may be seen within the sinus fat as an echo-free structure, especially with a full bladder in the female. Often it will decrease in size when the patient empties her bladder. This, and the absence of dilated calyces separating the sinus fat, allows differentiation from hydronephrosis. Most normal adult kidneys have a maximum length of 10-12.5 cm, although substantial numbers of normal kidneys may be seen within the 9-13.5 cm range. Kidneys are roughly related to the patient's size and show some decrease in length with age (especially above 80 years). A difference of 2.0 cm or more between the two kidneys raises the possibility of unilateral disease. Measurements of renal length on ultrasound are of the order of 0.5 cm less than on IVU, which suffers from radiographic magnification. Although areas of scarring and diffuse cortical loss are appreciated subjectively, it is difficult to measure cortical thickness objectively with any degree of accuracy. In young healthy adults cortical thickness is of the order of 2.5-3 cm at the poles and 1.5-2.0 cm elsewhere. This may

decrease substantially with age and be associated with an increase in the central sinus fat, a phenomenon also visible on IVU.

Doppler assessment of the renal artery flow in order to identify significant renal artery stenosis may be requested as part of the investigation of hypertension (discussed further under renal arterial disease) and early in the assessment of renal transplant viability.

The pelviureteric and vesicoureteric junctions may be seen on ultrasound, especially when diseased, but otherwise the normal ureter is not routinely demonstrated.

Routine examination of the bladder requires it to be moderately full. The normal bladder has a triangular shape in the sagittal plane, and that of a square with the corners rounded off in the transverse plane. The normal wall thickness is 2-3 mm when the bladder is moderately full (Fig. 29.9). In the investigation of bladder outflow obstruction an assessment of postmicturition residue is often requested. This is fraught with inaccuracies, related as it is to the bladder volume initially (both over- and underdistension may preclude normal emptying) and variability in the shape of the bladder. It is, however, a broadly useful tool and simple to employ. The bladder is assumed to be roughly elliptical and the maximum transverse, sagittal and craniocaudal dimensions are measured. There is usually a volume function on the ultrasound machine that will generate a volume from these figures, or they can be multiplied together and by the constant for an ellipse, which is 0.533 (or roughly a half). The prostate is routinely identified at the bladder base, especially when enlarged. The seminal vesicles are also often seen posterior to the bladder.

Male genitalia This investigation is most commonly requested for assessment of the scrotum, occasionally of the penis. The major indication for scrotal ultrasound is the investigation of mass lesions, including a hydrocele, when there may be concern about an underlying tumour. Ultrasound of the scrotum and groins may also be performed to localise and assess an ectopic testicle. A high-frequency probe, sometimes disparagingly referred to as a small-parts probe, is used. Again, modern probes will emit a broad range of frequencies within approximately the 7-12 MHz range. The normal testicle is ovoid, approximately 3.5 cm in length and 3 cm in diameter. It has a speckled intermediate echogenicity (Fig. 29.10). The mediastinum (the invagination of the tunica albuginea) along the posterior aspect is seen as an echogenic line parallel to the epididymis. The lobular structure of

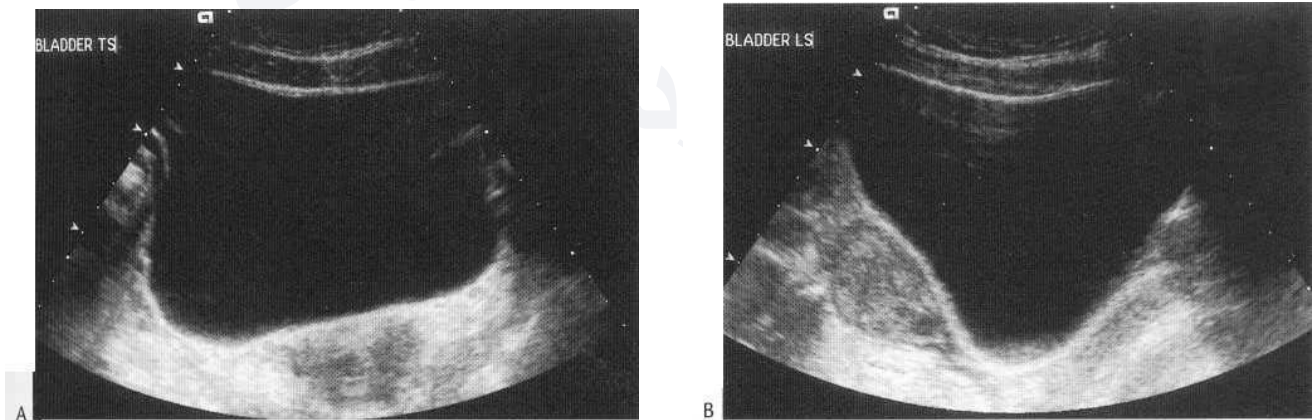


Fig. 29.9 Normal bladder ultrasound; note the thin smooth wall and the shape approximating to a rounded-off square in the transverse view (A) and a rounded-off triangle in the sagittal view (B).

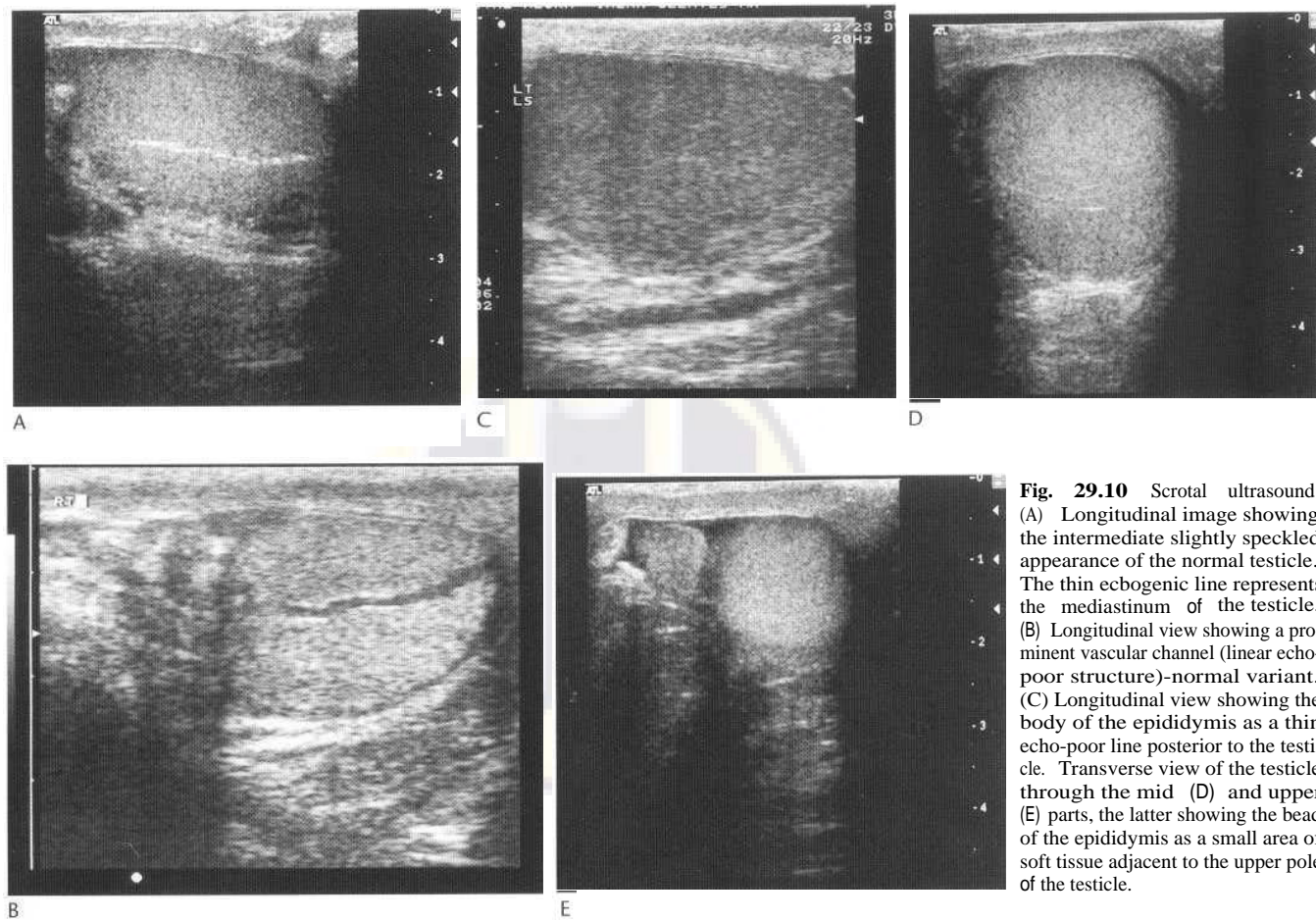


Fig. 29.10 Scrotal ultrasound. (A) Longitudinal image showing the intermediate slightly speckled appearance of the normal testicle. The thin echogenic line represents the mediastinum of the testicle. (B) Longitudinal view showing a prominent vascular channel (linear echo-poor structure)-normal variant. (C) Longitudinal view showing the body of the epididymis as a thin echo-poor line posterior to the testicle. Transverse view of the testicle through the mid (D) and upper (E) parts, the latter showing the bead of the epididymis as a small area of soft tissue adjacent to the upper pole of the testicle.

the testicle is very occasionally identifiable, with the interlobular septations visible as thin echogenic lines. The head (upper pole) of the epididymis lies lateral to the superior pole of the testicle, appears slightly more echogenic than the remainder of the epididymis and has a maximum diameter of 5-15 mm diameter. The epididymis tapers down through the body to the tail, which has a maximum diameter of 1-3 mm. Occasionally, small protuberances are seen at the head of the epididymis or the superior pole of the testicle and are the appendices of these structures. The scrotal skin and subcutaneous tissue is seen as a hyperechoic structure 5-7 mm thick.

Ultrasound of the penis is occasionally performed to assess mass lesions of the shaft, most commonly Peyronie's disease, although the clinical usefulness is debatable. Doppler ultrasound of the penis is most commonly performed in the assessment of impotence and is discussed under the relevant section.

Prostate The prostate can be seen at the bladder base on routine transabdominal scanning of the bladder. Apart from a rough idea of its size, little useful information is obtained using this route. Prostate ultrasound is performed using a dedicated medium- to high-frequency cavity probe (predominant frequencies around 4-7 MHz) positioned within the rectum. It is used in the investigation of suspected prostatic cancer, usually with multiple ultrasound-guided biopsies. It can also be used to assess the prostate

and seminal vesicles in infertility and (although its value is questionable) in prostatitis. The normal prostate is roughly bean-shaped, the concavity of the bean facing posteriorly. The transitional and central zones have the same intermediate echogenicity and are inseparable on ultrasound (Fig. 29.11). They can be referred to as the central gland, and increase in volume and heterogeneity with age as benign prostatic hyperplasia develops in the transitional zone. The peripheral zone is seen as an echogenic layer lying posteriorly. It is the site of most prostatic tumours, which usually appear as relatively echo-poor areas. Normal prostatic dimensions in the adult male are approximately 4 cm in the craniocaudal and transverse planes and 3 cm in the anteroposterior plane, with a maximum volume of 20-25 ml.

The seminal vesicles appear as paired lobulated echo-poor structures which often contain multiple small echo-free areas. The vasa deferentia appear medial to the seminal vesicles and superior to the prostate. They dilate normally near their termination (the ampullae). The periprostatic venous plexus is seen anterior to the prostate and is of variable prominence.

Direct contrast investigations

In this group of investigations water-soluble contrast is injected via some form of catheter directly into part of the urinary tract. The

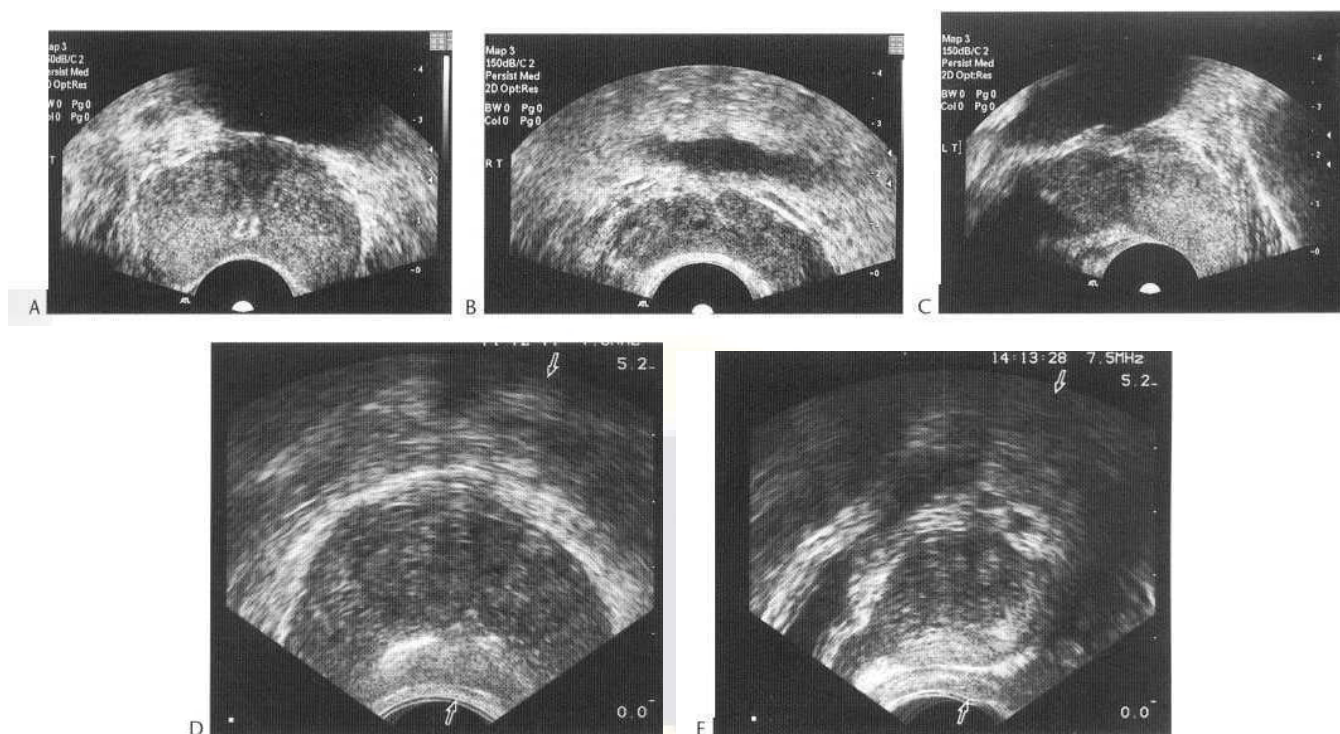


Fig. 29.11 Transrectal ultrasound of the prostate. (A-C) Young adult prostate. (A) Transverse section. There is a little calcification appearing as speckled echogenicity in the periurethral area, presumed to be related to previous prostatitis and urethritis. The prostate at this age shows poor zonal anatomy. (B) Transverse view of the normal paired echo-poor seminal vesicles. (C) Longitudinal view showing the subjacent puborectalis sling as a laminated, relatively echo-poor structure. (D, E) Transverse and longitudinal views of the prostate around middle to old age. The zonal anatomy is clearly seen with a relatively hyperechoic peripheral gland compared to the hypoechoic central gland.

following are considered under this heading: retrograde pyelography, cystography, loopography, stentography and urethrography. A further group of procedures, including antegrade pyelography, also involve direct injection of contrast into the collecting system but because they involve a percutaneous approach they are considered under the heading of non-vascular interventional procedures.

All of these procedures may potentially introduce infection into the urinary tract and care should be taken to use a sterile technique, and broad-spectrum antibiotics should be administered prior to the procedure.

Retrograde pyelography This investigation aims to optimally opacify the pelvicalyceal system and ureter. It usually follows an IVU and is indicated when there is persistent uncertainty about the diagnosis, particularly if there is haematuria and/or suspicious cytology. It is indicated to confirm or refute the presence of one or more filling defects within the collecting system, or to improve demonstration of the collecting system, either when there has been inadequate demonstration of part or all of the system or when the IVU is normal but the abnormal laboratory findings persist. It is occasionally used to demonstrate the lower end of an obstructed ureter.

The urologist positions catheters within one or both ureters cystoscopically and the patient is transferred to the X-ray department. Under screening control 5-20 ml of a 150 strength water-soluble iodine-containing contrast agent is injected via each catheter in turn. It is important to avoid injecting air bubbles, which can be mistaken for filling defects. The pelvicalyceal system and ureter should be adequately opacified but not overdistended.

Spot films should be taken prior to injection of contrast and then of the opacified pelvicalyceal system and ureter (Fig. 29.12). The ureteric catheter can be withdrawn to allow contrast injection at a site of concern after adequate images have been obtained higher up.



Fig. 29.12 Retrograde pyelogram demonstrating the pelvicalyceal system and ureter down to the vesicoureteric junction.

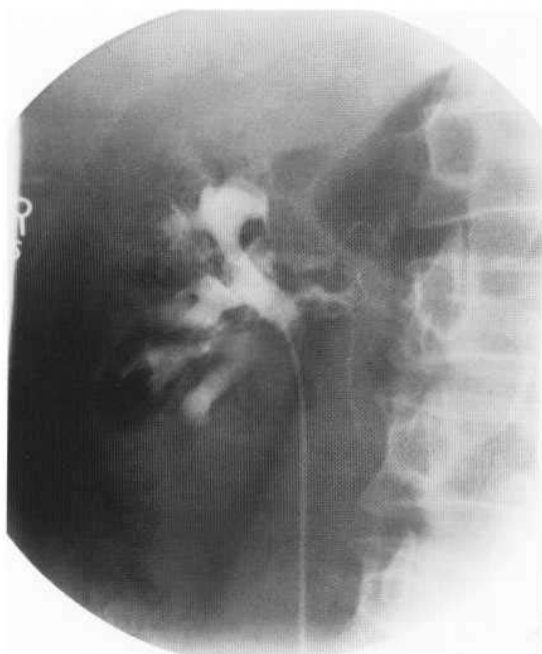


Fig. 29.13 Retrograde pyelogram with pyelosinus extravasation due to overdistension of the collecting system.

Overvigorous injection of contrast may lead to reflux of contrast into the collecting ducts (pyelotubular reflux) and forniceal rupture with contrast extravasation into the renal sinus (pyelosinus extravasation) or more extensively into the regional lymphatics or veins (pyelolymphatic and pyelovenous extravasation) (Fig. 29.13).

Loopography The classical urological diversion procedure is the fashioning of an ileal conduit, i.e. the use of a loop of ileum to

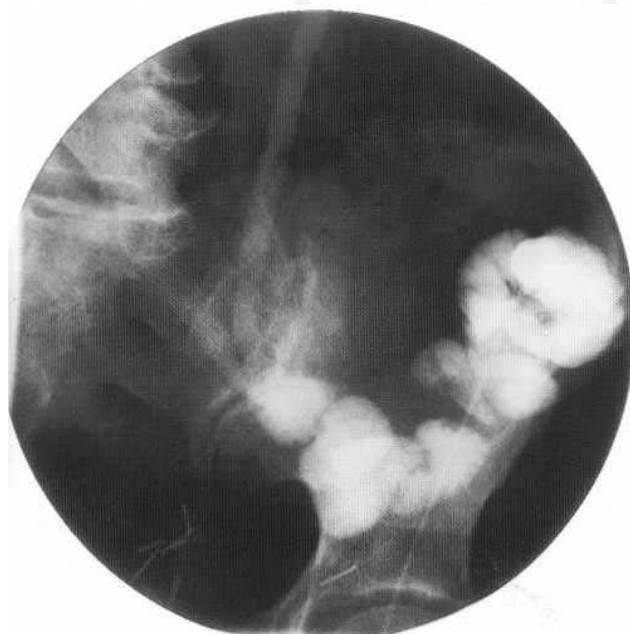


Fig. 29.14 Normal loopogram (conduitogram). Contrast outlines the ileal loop (which still demonstrates the typical small-bowel mucosal pattern) and freely refluxes into both ureters.

drain urine from the ureters to a cutaneous stoma. The standard investigation for ileal conduits is the loopogram. It can be performed in the immediate postoperative period to demonstrate the integrity of the surgical anastomoses, or later (after months or years) to differentiate between reflux (common) or obstruction (usually at the ureteroconduit junction, usually benign rather than recurrent tumour) when dilatation of the upper tracts has developed. A Foley catheter (12-16 gauge) is positioned so that its balloon lies a couple of centimetres into the conduit and is then cautiously inflated so as to produce a reasonable seal without overdistending the conduit. Between 20 and 40 ml of 150 strength contrast is injected under direct screening to outline the conduit, which is normally of the order of 12-15 cm long. Usually there is free reflux into the ureters and pelvicalyceal systems. A series of spot films are taken to record this. Obliques may be useful and the most important areas to study are the ureteroconduit anastomoses (Fig. 29.14). A rare complication of this procedure in patients with spinal injuries is the development of severe hypertension (autonomic dysreflexia) due to overdistension of the ileal loop.

Stentography Urologists routinely leave narrow gauge hollow stents running from the ureters into reconstructed bladders or ileal conduits in the immediate postoperative period. The stents run to the exterior either via the urethra or a cutaneous stoma. Stentography is frequently requested to demonstrate the integrity of the distal ureteric anastomoses within a few days of surgery. Between 10 and 20 ml 150 strength contrast is injected under direct screening via each stent in turn, which opacifies the upper tracts first, followed by drainage around the stents down into the bladder or diversion. Spot films are taken, again paying particular attention to the distal ureteric anastomoses (Fig. 29.15).

Cystography Cystography can be classified into three groups: micturiting cystourethrography (MCUG), dynamic cystography and simple cystography. The MCUG is primarily performed for the assessment of vesicoureteric reflux and is therefore essentially



Fig. 29.15 Normal stentogram demonstrating intact anastomoses between the ureters and the afferent loop of small bowel leading to the reconstructed neobladder.

an investigation of childhood. It is discussed in the paediatric investigations section below. Dynamic cystography is part of the urodynamics investigation of the lower urinary tract, and again is discussed below in the appropriate section.

Simple cystography is a relatively frequently performed and straightforward investigation in the adult. It is used to assess the integrity of the bladder following trauma or surgery or to investigate suspected fistulas involving the bladder (usually into the gastrointestinal tract, occasionally elsewhere such as the vagina). In the context of trauma the patient should be referred with a catheter already in place (either suprapubic or urethral if the referring surgeon can safely position one). A spot film should be obtained before contrast is administered. Approximately 250 ml of 150 strength contrast is infused into the bladder via a giving set. This should be done under frequent intermittent screening control so that extravasation can be identified as soon as it occurs. When the bladder has been filled or when extravasation is identified a spot film is obtained in the supine position. Ideally 45° oblique and lateral spot films should be obtained but the patient will often have significant pelvic trauma and this may not be possible. If a C-arm is available this may be useful but external splinting of the pelvis may degrade the images. In modern trauma management many patients will undergo CT scanning of the abdomen and pelvis after intravenous contrast. Under these circumstances repeating the images of the bladder 20 min after contrast is administered is at least as accurate as direct contrast cystography and obviates the need to transfer the patient to a different table for a further investigation.

When a patient has undergone radical prostatectomy or cystectomy, with preservation of the sphincter and reconstruction of the bladder using small bowel, a cystogram is often performed around 10 days postoperatively to demonstrate the integrity of the surgical anastomoses prior to removal of the urethral catheter. Only 100-150 ml of contrast is required and the patient will often complain of fullness at a significantly smaller volume, at which stage the infusion should stop. The patient is likely to be ambulant and adopt easily the positions required for the full series of images (Fig. 29.16). When a patient has a suspected vesical fistula, 250 ml of contrast can be used to maximise the chance of demonstrating the fistula. Again the patient usually has no trouble adopting the required positions.

Urethrography This can be performed via an ascending or descending approach. With advances in urethroscopy these procedures are required much less than formerly. Descending urethrography is usually part of the micturating cystogram and is rarely indicated in adults. When it is performed in adults the bladder should be adequately filled (with at least 200 ml of 150 strength contrast). The screening table should be positioned erect. Imaging is performed directly anteroposterior in females (Fig. 29.17) and in a 45° oblique projection in males (Fig. 29.18). Males are generally used to micturating while standing, often in unusual situations, and can manage with a bottle while screening is performed and spot films taken of the urethra and bladder base. Females are provided with a special drainage receptacle that is held between the thighs.

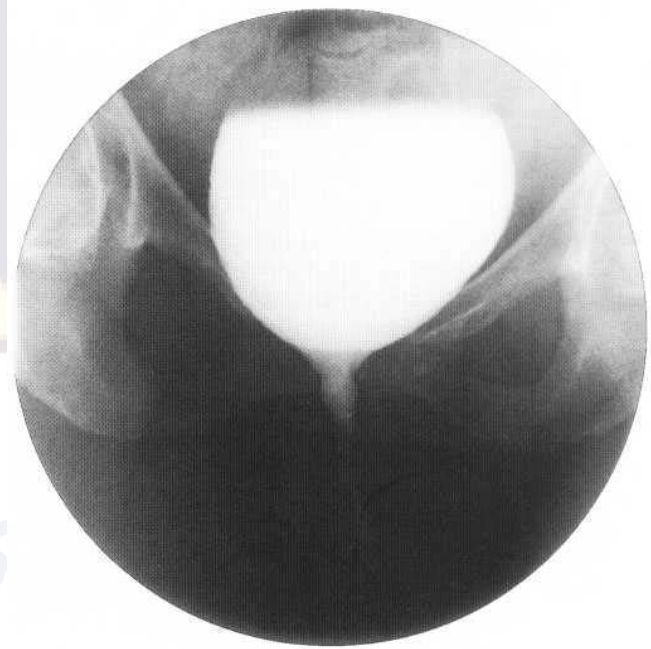


Fig. 29.17 Normal female micturating cystourethrogram showing the typical short open-necked female urethra.

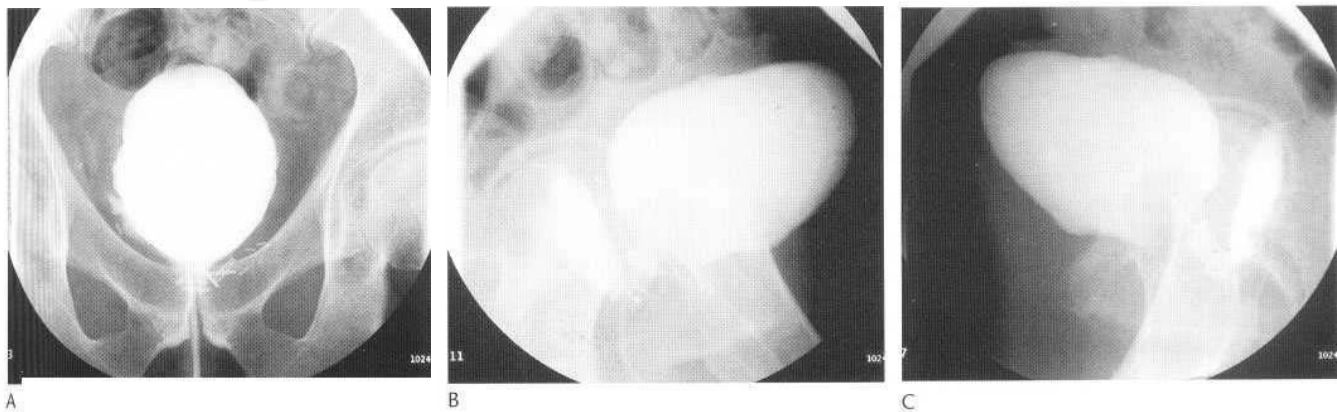


Fig. 29.16 Postprostatectomy cystogram. Supine (A), oblique (B) and lateral (C) views demonstrate a substantial extravasation arising from the right posterolateral aspect of the vesicourethral anastomosis.



Fig. 29.18 Descending urethrogram in a male. The entire length of the urethra is demonstrated as the bladder empties. A post-operative urethrorectal fistula is present with contrast tracking posteriorly from the prostatic beds.

Ascending urethrography is essentially confined to the male. It is used in the investigation of trauma, stricture and fistulas. The patient is positioned in a 45° oblique position with the dependent hip partly flexed to provide stability and ensure the urethra is not projected over bone. A 12-16 gauge Foley catheter is positioned with its balloon a couple of centimetres into the distal urethra. The balloon is gently partially inflated to provide a seal without undue trauma. Between 5 and 10 ml 150 strength contrast is injected gently into the urethra under direct screening and spot films are taken (Fig. 29.19). The urethra is usually easily opacified back to the urogenital diaphragm. In a minority of patients contrast will reflux into the posterior urethra and bladder. Usually, however, with ascending urethrography the prostatic urethra is not demonstrated. Overenthusiastic instillation of contrast into the urethra can be painful and produce extravasation of contrast into the corpora cavernosa (Fig. 29.20).

Female urethrography is rarely required, virtually all urethral pathology being better demonstrated on urethroscopy or transvaginal sonography.

Percutaneous interventional procedures

The common feature of all these procedures is the positioning of a cannula or drain percutaneously into the upper urinary tract under some form of image guidance. Included in this category are antegrade pyelography, percutaneous nephrostomy and nephrostograms, antegrade stent positioning and ureteric dilatation and percutaneous nephrolithotomy. The commonest complication of these procedures is infection, which is occasionally life-threatening. Where there is no evidence of infection at the start of the procedure a single intravenous injection of a broad-spectrum antibiotic (say cefuroxime 750 mg i.v.) 1-6 h prior to the procedure should be sufficient. If the urinary tract is known to be infected in advance there is a real risk of the procedure provoking Gram-negative septicaemia and hypotensive collapse. It is imperative the patient is then on an adequate course of broad-spectrum antibiotics and ideally, if circum-



A



B

Fig. 29.19 The normal male ascending urethrogram usually shows contrast flowing retrogradely as far as the junction of the bulbar and membranous urethra (A). Sometimes contrast will flow into the bladder and demonstrate the prostatic urethra (B). Note the smooth filling defect of the verumontanum within the prostatic urethra.

stances permit, should have been on antibiotics for at least 24 h prior to the procedure. Care should be taken to avoid overdistending the collecting system or any unnecessary manipulations, either of which may provoke bacteraemia. Less common complications include haemorrhage and bowel perforation. If the patient has known hepatic disease or other predisposition to coagulation defects, the platelet count and prothrombin time should be assessed prior to the procedure and abnormalities corrected. The risk of all complications increases with the complexity of the procedure and the size of the cannulas and drains ultimately employed.

Percutaneous nephrolithotomy is performed under general anaesthesia but otherwise these procedures are performed using local anaesthetic and are potentially painful. Adequate intravenous analgesia and sedation with appropriate pulse oximetry according to local protocols are therefore required. Following the procedure the patient requires an adequate period of observation, which usually involves at least overnight hospital admission, although simple



Fig. 29.20 Ascending urethrogram. A vigorous infusion of 150 strength contrast has been performed. The external sphincter has not relaxed (as is usually the case) and the anterior urethra is therefore overdistended with contrast extravasating and entering the corpora cavernosa.

diagnostic antegrade pyelography and some selected nephrostomies may be performed on an outpatient basis.

The initial percutaneous cannulation of the collecting system is usually performed under ultrasound guidance, fluoroscopy or a combination of both. Complex manoeuvres such as stent placement require fluoroscopy.

The other general point worth making is the value of an adequate incision in the skin. This is unnecessary if using only a line needle (21-22 gauge) but for most of these procedures a substantial catheter will be introduced and a skin incision of at least 5-10 mm is required; it should be at least 10-15 mm deep, traversing the superficial fascia. For percutaneous nephrolithotomy the length of the incision should be doubled.

Antegrade pyelography This is a relatively simple procedure. It is used to evaluate the cause and level of ureteric obstruction in the minority of patients in whom non-invasive imaging has not provided the information. It may also be the first step in performing a nephrostomy or the Whitaker procedure (discussed in the section on urodynamics). The patient is positioned approximately 45° semiprone and the pelvicalyceal system cannulated with a fine (22 gauge) needle. The general rule in gaining access to the pelvicalyceal system in all these procedures is that a puncture directly into the renal pelvis risks lacerating it. Ideally the puncture should be directed through the renal parenchyma into a suitable calyx and then into the pelvis. Confirmation of cannulation of the collecting system is obtained by aspirating urine. If this appears infected, the system should be drained and infection treated before proceeding with an antegrade pyelogram: 150 strength contrast is infused into the system to opacity it (Fig. 29.21). If the procedure is being performed for diagnostic purposes, a series of spot films of the ureter down to the level of the obstruction is taken. The flow of contrast down the ureter can be assisted by elevating the head of the screening table.

Percutaneous nephrostomy In this procedure a pigtail drain (usually 6-8F) with multiple holes is positioned in the pelvicalyceal system. It is indicated to drain urine from an obstructed system. Occasionally it is used to drain unobstructed systems to divert the urine flow and allow ureteric or vesical fistulas to heal. There are various methods and devices available to position a drain within the pelvicalyceal system of the kidney and the interventional radiologist is likely to be acquainted with a number of them but have a preferred method for routine use. A single-stab technique with a nephrostomy tube mounted on a cannula is available and, when successful, is the quickest method. This is most commonly performed under ultrasound guidance, although CT or even MRI have been used on occasion. Alternatively a sheathed needle (18 gauge) may be positioned (under ultrasound guidance or fluoroscopy after initial antegrade pyelogram) within the col-

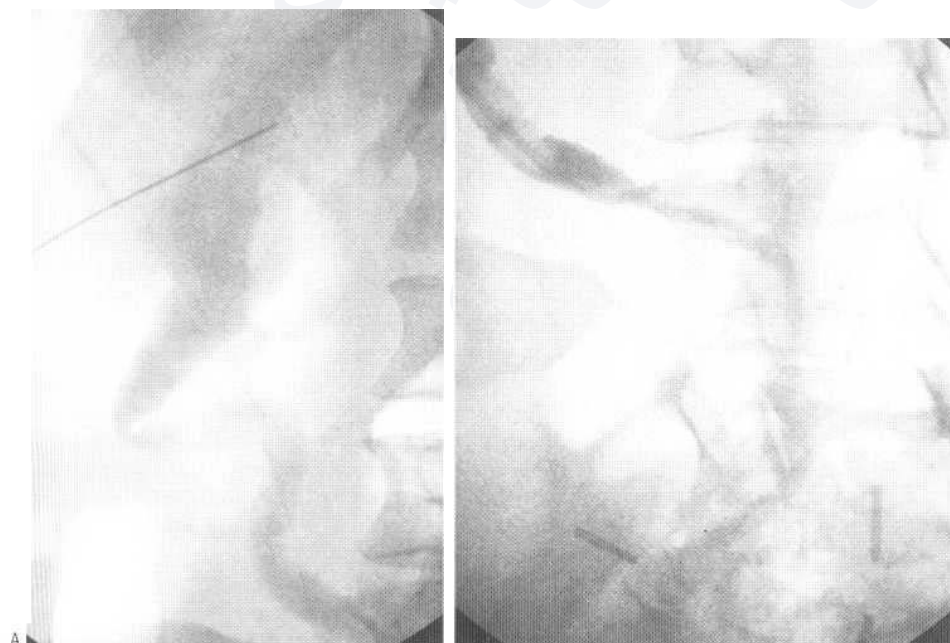


Fig. 29.21 Antegrade pyelography. The dilated pelvicalyceal system has been cannulated with a 22 gauge needle and opacified with 150 strength contrast (A). The ureter is dilated, shows marked medial displacement distally and tapers to a complete occlusion (B).

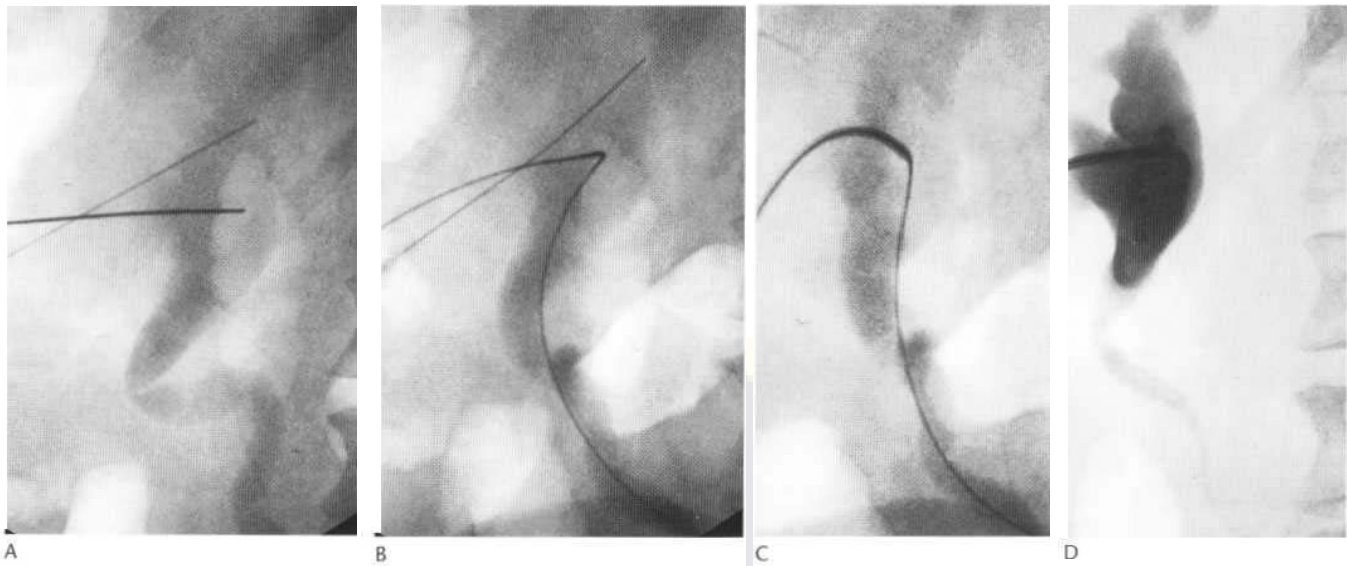


Fig. 29.22 Nephrostomy procedure using fluoroscopy and dual puncture technique. Having opacified the system through a fine-gauge needle a second puncture is made with a sheathed needle (A). A guide-wire is advanced through this into the pelvicalyceal system (and ideally for stability into the ureter) (B). The fine needle is removed and the sheathed needle exchanged for a dilator over the wire (C). The calibre of the dilator depends on the nephrostomy drain to be positioned and often comes as part of a nephrostomy set. For an 8F drain a dilator of 8 or 9F is usually employed. The dilator is exchanged for the drain, which is positioned, coiled up, in the renal pelvis (D).

lecting system and a conventional 35 gauge wire introduced through the sheath into the calyces and renal pelvis. This is used to guide one or more dilators and then the nephrostomy tube (a pigtail drain with multiple drainage holes) into position (Fig. 29.22). A further alternative is to position a fine wire through an initial fine needle puncture and dilate until a cannula sufficient to take a 35 gauge wire can be positioned.

Drainage of a perinephric or renal abscess is essentially a variation of this procedure. If the abscess is small, simple aspiration of pus via a sheathed needle may be sufficient. A multiple-hole pigtail drain can be positioned in a larger abscess using any of the above techniques, most commonly as a single-stab technique under ultrasound or CT guidance.

Nephrostogram A nephrostomy tube is positioned for therapeutic purposes but while it remains in position a nephrostogram can be performed. It is indicated to assess the obstructing lesion, either to evaluate its status (continued presence of a calculus, response of a malignancy to treatment) or obtain further diagnostic information if the cause of the obstruction has not yet been determined. It is also used to monitor the progress of fistulas. It is a very similar procedure to the antegrade pyelogram: 150 strength contrast is infused into the collecting system and spot films taken of the ureter down to the level of the obstruction. Where infection is present the procedure should be deferred until this has been adequately treated.

Antegrade stenting If the cause of the obstruction is unlikely to resolve within a few days of the percutaneous nephrostomy a ureteric stent can be positioned antegradely to relieve the patient of an external drain. This is most often performed for malignant obstruction. It can also be performed for non-obstructive problems such as a postoperative ureteric fistula or anastomotic breakdown. Under fluoroscopic guidance a 35 gauge wire is manipulated through the nephrostomy tube into the collecting system. It is convenient to replace the nephrostomy tube with an

angled catheter, such as a cobra, and use this and a suitable angled guide-wire to advance into the ureter and then across the obstructed area into the bladder. It is usual to dilate the constricted area, most simply with a rigid plastic dilator, and then position a double J stent from the pelvicalyceal system to the bladder (Fig. 29.23).

Percutaneous nephrolithotomy Percutaneous nephrolithotomy (PCNL) was developed as a minimally invasive alternative to open surgery for the treatment of renal calculi. Its role has been much reduced by the development of the even less invasive procedure of lithotripsy but it maintains an important role in patients with calculi resistant to lithotripsy (such as pure calcium phosphate or cystine calculi), where the size of the calculus would preclude successful lithotripsy (above 2.5 cm) and/or where there is likely to be a drainage problem (for example ureteric stricture). PCNL is performed under general anaesthesia; usually the patient is placed supine on the operating table and the urologist performs an initial cystoscopy with a view to positioning a thin catheter (5F) retrogradely through the ureter and into the pelvis of the kidney containing the target calculus. The patient is then repositioned semiprone with the side of the kidney of interest rotated approximately 45° upwards. Ideally the operating table will be articulated to allow some degree of flexion of the patient to separate maximally the ipsilateral subcostal margin and iliac crest. Contrast (150 strength) is infused via the ureteric catheter to opacify and distend the collecting system. A small amount of methylene blue is traditionally added to assist differentiation of blood-stained urine from a vascular puncture. Fluoroscopic screening of the kidney should identify the optimal site for access. This relates to the site of the stone. Calculi within the renal pelvis and/or mid or lower pole calyces can be accessed via a mid or lower pole calyx, which usually permits a subcostal approach. The desired calyx can usually be brought below the costal margin

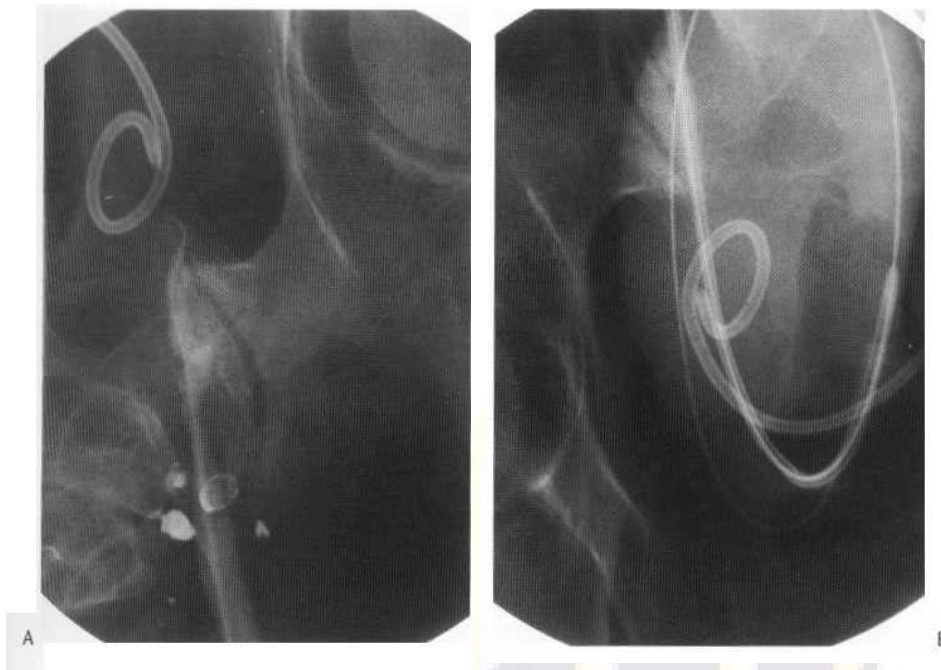


Fig. 29.23 Antegrade stent positioning. A guide-wire has been manipulated down the right ureter to the level of the obstruction (A). Note the distal end of a previously positioned left-sided stent is visible within the bladder. The guide-wire is advanced across the obstruction into the bladder. Following a dilatation step with a long 9F dilator the stent has been advanced along the wire so its distal end lies within the bladder (B). Once the wire is removed the distal end of the stent will adopt a pigtail configuration within the bladder. The upper end will behave similarly within the renal pelvis, provided care has been taken to ensure the upper end has been advanced sufficiently and does not lie within renal parenchyma.

by the anaesthetist holding the patient in an adequate inspiration while the initial percutaneous puncture is performed. This is made with a standard 18 gauge sheathed needle. A guide-wire (usually a 3 mm angled wire) is positioned through the needle into the target calyx and manipulated into the renal pelvis and ideally into the ureter. Initial dilatation to 9F is performed using plastic dilators, and then more significant dilatation is performed up to 28-30F. At this stage a hard plastic (Amplatz) sheath of this calibre is positioned over the dilatation system into the collecting system. The dilatation system is removed, allowing the urologist to gain access to the collecting system with a nephroscope. If an upper pole calyceal approach is required, the puncture is likely to be above the 12th rib. This is generally safe since the pleural reflection is usually around the 11th rib but punctures above this level should be avoided because of the risk of pleural trauma.

Different dilatation systems are available. One of the quickest and safest systems is a high-pressure balloon catheter that is inflated to 10 mm diameter with a screw-type syringe (Fig. 29.24). Occasionally there is difficulty in completely dilating the mid part of the balloon (usually at the level of the renal capsule) and an ancillary method must be employed. Graded plastic dilators are useful for this. On their own, however, multiple plastic dilators may prove troublesome and traumatic. Multiple metal dilators that lit sequentially over each other (telescopic dilators) are an effective and rapid method but should be used with care as they can cause considerable trauma if they drift forwards during the procedure.

Once adequate access to the system has been obtained, the urologist will inspect the inside of the collecting system, identify the calculus and remove it. Often the calculus must be broken up in situ, which is performed using some form of direct contact lithotripsy with an instrument introduced through a channel within the nephroscope and placed in direct contact with the calculus. After the calculus has been removed a percutaneous drain is positioned within the renal pelvis and the sheath is removed.

Major complications include infection (broad-spectrum antibiotics should be administered before the procedure), haemorrhage

and collateral organ damage. Haemorrhage is frequent but not normally severe. It usually originates from renal parenchymal trauma or rupture of vessels around the calyceal necks and stops relatively readily, either spontaneously or in response to a brief period of tamponade if the pelvicalyceal system fills with thrombus. More dramatic haemorrhage may result from damage to the vessels at the renal hilum if the dilatation system is allowed to drift too deep into the patient; this may be life-threatening and on rare occasions require emergency nephrectomy. Traumatic arteriovenous fistulas have also been reported and may produce florid haematuria and require selective arterial embolisation. Any of the surrounding organs may sustain damage and sequelae may include bowel perforation and pneumothorax. Although rare, these conditions should be considered during the postoperative period. A nephrostogram is usually performed 3-4 days after the procedure to demonstrate normal drainage (no obstructing stone fragments or ureteric damage) and good clearance of calculus.

Other percutaneous procedures

There are several other percutaneous urological procedures that involve techniques similar to those described above.

Having established a large percutaneous track, other forms of endoscopic intervention can be performed. *Inspection, biopsy and ablation of renal masses* may be performed but is rarely indicated and is associated with the risk of seeding tumour along the access track. More commonly *endoscopic pyelotomy* (endopyelotomy) is performed for the treatment of pelviureteric junction (PUJ) obstruction. A vertical incision is made through the full thickness of the wall of the PUJ. The danger of this procedure is the potential association of the condition with aberrant renal arteries that cross the PUJ and are at risk when the incision is made. They usually run anteriorly and therefore the incision should be made posterolaterally. A preoperative search for aberrant renal arteries should be performed, usually with contrast CT (CT angiography). Attempts have also been made to treat PUJ

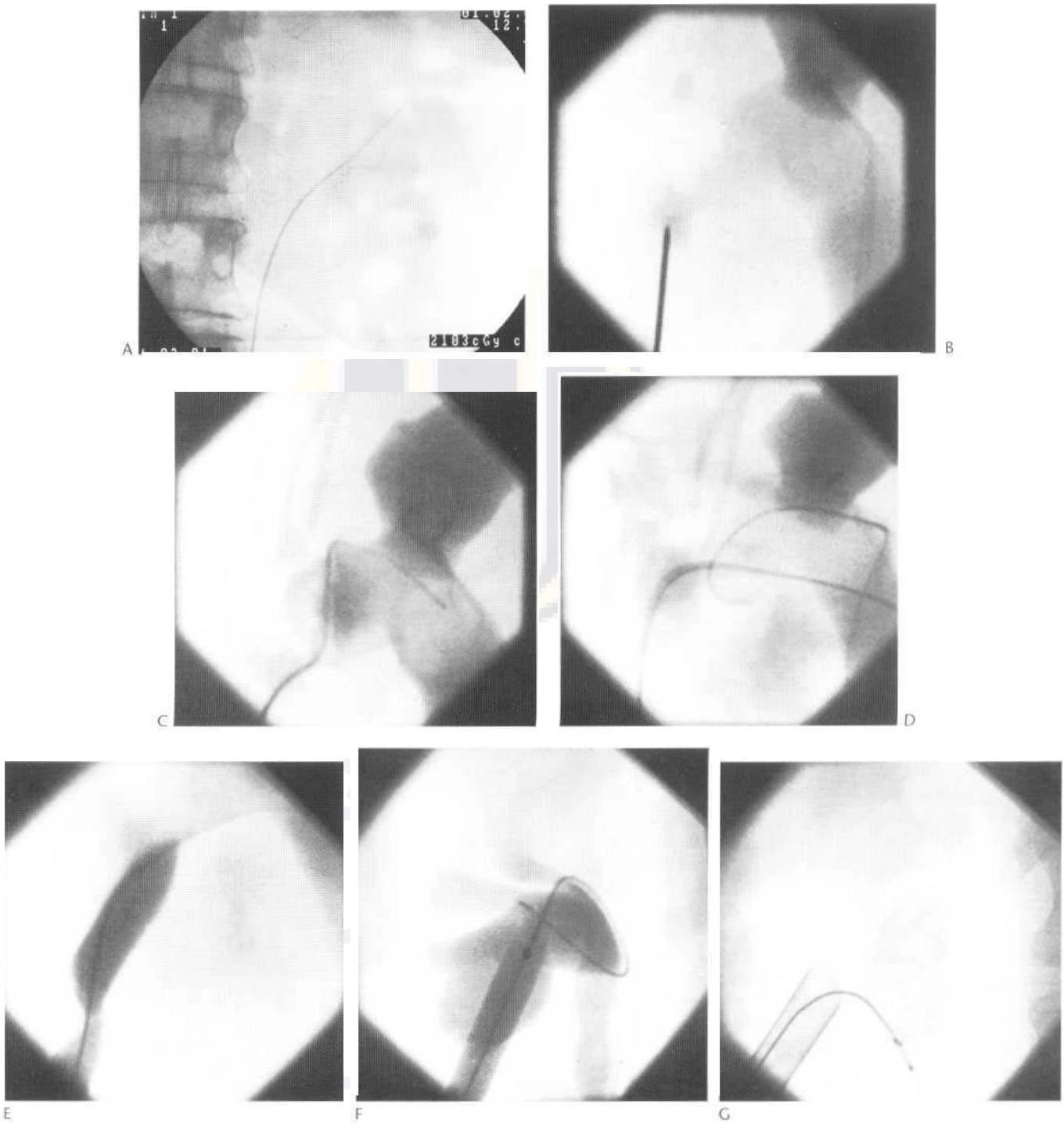


Fig. 29.24 Percutaneous nephrolithotomy. A faintly opacified staghorn calculus is present (A). A retrograde catheter is in position. After the system is opacified and dilated via the retrograde catheter a sheathed needle is used to cannulate one of the calyces (B). A guide-wire is advanced through the sheath into the calyx and manipulated into the renal pelvis adjacent to the calculus (C). An initial dilatation step is performed with an 8F dilator over the wire (D). A high-pressure balloon is positioned with its distal end in the collecting system. As it is inflated a waist at the level of the renal capsule is often the last part to dilate (E). Following inflation an Amplatz sheath is positioned over the balloon (F-example from a second patient). The balloon is deflated and removed, allowing the urologist access to the calculus. After the procedure fluoroscopy demonstrates adequate clearance of the stone (G).

obstination with *balloon dilatation*, either via antegrade (through a percutaneous track) or retrograde approaches, but the success rate is controversial.

Percutaneous renal cyst aspiration for diagnostic purposes. Once common, is now relatively rare, as Faith modern cross-sectional imaging the vast majority can be confidently categorised as benign.

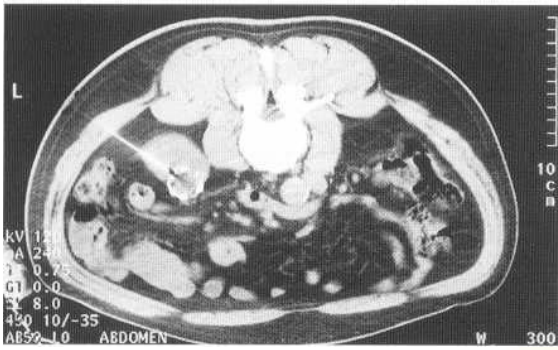


Fig. 29.25 Percutaneous cyst aspiration. A 22 gauge needle has been positioned within a heavily calcified cyst under CT guidance for diagnostic aspiration.

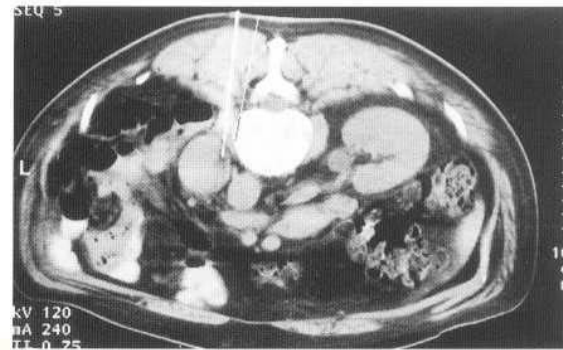


Fig. 29.26 CT-guided biopsy. An 18 gauge cutting needle has been positioned in a solid mass in the right renal bed under CT guidance. The core of tissue obtained confirmed recurrent renal cell carcinoma.

Fluid can be aspirated under ultrasound, CT or MRI guidance from complex cysts where there is a concern about potential malignancy. This is a simple procedure performed on an outpatient basis using a thin (21-22 gauge) needle and followed by a brief period of post-intervention observation (Fig. 29.25). Simple cysts are virtually always asymptomatic but on rare occasions the patient and the referring urologist put forward a reasonably convincing argument that a particular cyst, often large, is causing distressing loin pain. It is straightforward to position a needle within the cyst, usually under ultrasound guidance, and aspirate to dryness. This can be very time-consuming with a narrow-gauge needle and a plastic sheathed 18 gauge needle is recommended. When the cyst has been aspirated to dryness, a sclerosant can be infused into it to prevent recurrence. Absolute alcohol has been used but it is recommended that the needle is replaced by a small pigtail catheter to secure the position and drain the sclerosant after it is used. Contrast should also be injected into the cyst first to demonstrate the absence of extravasation (into the retroperitoneum, collecting system or vascular compartment). Arguably, a safer alternative is tetracycline (100 mg).

Percutaneous renal biopsy is easily performed under ultrasound, CT or MRI guidance. A core of tissue is obtained using a cutting needle. It is indicated in the assessment of diffuse renal disease. It is not routinely indicated for renal masses, which are usually characterised by cross-sectional imaging, but is useful in selected cases, for example when there is metastatic malignancy with a solid renal mass. These situations may warrant treatment with interferon for renal cell carcinoma but alternative chemotherapy for other malignancies and histological characterisation is required. Similarly, renal bed masses following nephrectomy or malignancies of unknown histology invading the kidney may require guided biopsy using similar techniques (Fig. 29.26).

Percutaneous procedures targeted to the bladder are less common because urologists have good access to the bladder lumen cystoscopically and are also confident at inserting suprapubic catheters clinically. Occasionally radiologists are involved in ultrasound-guided catheter placement and should be aware that the bladder wall is remarkably tough. For this reason, puncture of the full bladder with a sheathed needle, positioning of a stiff guide-wire into the bladder and multiple dilatation steps may be preferred to a single-stab technique. A simpler and quicker procedure that radiologists are required to perform from time to time is deflation of the balloon of an indwelling catheter. The problem arises from occlu-

sion of the channel to the balloon, which may occur in long-term catheters. An initial attempt to clear the channel with the stiff end of a guide-wire should be made, as this may solve the problem. If this fails, a line needle can be introduced under ultrasound guidance through the anterior pelvic wall into the bladder and into the catheter balloon, puncturing it (often quite dramatically) and deflating it, allowing the catheter to be removed.

Lithotripsy

Extracorporeal shock wave lithotripsy (ESWL) is the technique of shattering urinary tract calculi into fragments of 3 mm diameter or less with high-power ultrasound (shock waves). The resultant fragments are then passed in the urine. Early ESWL machines caused considerable discomfort to the patient and were relatively inefficient, requiring multiple sessions to obtain an adequate response. Conventional machines are much better tolerated (although this varies between patients) and achieve satisfactory results more rapidly. Renal calculi above 25 mm diameter respond to ESWL poorly because of the numerous fragments that are produced. These may remain predominately in the upper tract and provoke subsequent stone reformation or overwhelm ureteric drainage and lead to obstruction. They are often better treated with nephrolithotomy.

Shock waves are directed at the calculus under fluoroscopic or ultrasound guidance. Although ureteric and renal calculi can be treated with ESWL, a distal ureteric calculus may become difficult to image and inaccessible to the shock waves if it comes to rest anterior to the sacrum.

Prior to ESWL, patients undergo IVU examination, partly to assess the stone burden but more importantly to demonstrate adequate urinary drainage. If this is impaired (say due to ureteric strictures or bladder wall hypertrophy), the passage of the calculus fragments will be difficult and painful obstruction is likely to follow treatment. Under these circumstances passage of a double J stent retrogradely prior to ESWL may be necessary, or treatment of the calculus with nephrolithotomy may be preferred.

Usually the stone fragments pass without trouble but in up to 10% of cases there may be some degree of ureteric obstruction, as multiple stone fragments build up in the distal ureter (referred to as *steinstrasse* or *stone street*). This situation usually resolves with analgesia and an adequate fluid intake but in approximately a quarter of cases retrograde stenting or nephrostomy insertion is required.

The only other common complications are failure of treatment (inadequate fragmentation or poor clearance of fragments and subsequent reaggregation) or rapid recurrence of calculus, presumably related to residual fragments acting as a nidus. Less common complications include renal contusion, perinephric haemorrhage, fracture due to misdirected shock waves (usually of a transverse process) and possibly an increased incidence of long-term hypertension.

Vascular procedures

Renal angiography This procedure originally developed a role in the assessment of renal masses (particularly suspected renal cell car-

lesions, such as arteriovenous malformations and fistulas and aberrant or accessory renal arteries in patients undergoing live kidney donation. The vast majority of this diagnostic role (particularly the tumour work) is now better performed by cross-sectional imaging. Renal angiography is still useful in selected cases, usually combined with subsequent intervention, notably transluminal angioplasty for renal arterial stenosis or selective embolisation. The latter is performed for arteriovenous abnormalities and some cases of traumatic renal damage with continued bleeding. It may also be used in some inoperable renal tumours as a palliative treatment for haematuria. Standard angiographic technique is employed and there is a choice of embolisation materials, including feathered coils (Fig. 29.27), particulate material and absolute alcohol.

Angiography of the bladder and prostate is also largely performed as a prelude to intervention for troublesome or life-threatening haematuria, either due to inoperable tumour or postsurgical (usually transurethral prostatectomy) bleeding (Fig. 29.28).

Inferior vena cavography This procedure is obsolete for the assessment of vascular spread of renal cell carcinoma. Occasionally renal phlebography is performed to obtain blood for hormone (Usually renin) assay. Testicular phlebography is performed as a prelude to testicular vein embolisation for the treatment of varicoceles (Fig. 29.29). Although either the femoral or jugular vein can be used to gain access to the inferior vena cava, it is pleasanter for the patient to work from the groin; with modern low-friction catheters and wires, gaining access to the renal vein and then the testicular vein from the direction of the femoral vein is rarely a problem. It has to be emphasised, however, that the testicular vein is very prone to spasm if excess catheter and wire manipulation is performed, and this may preclude a successful outcome. The success rate of embolisation of the testicular vein (usually with metal coils) is of the order of 80%, which is comparable with surgery, the radiological procedure having a substantially lower morbidity.

Abnormalities of penile vascular supply are an important cause of erectile dysfunction and have been assessed with pudenda) angiography, cavernosography and duplex ultrasound. These are discussed in Chapter 32.

Vasography In this procedure the vas deferens is exposed surgically in the scrotum and cannulated. Two to three millilitres of water-soluble contrast is injected into the vas and spot films are taken to demonstrate areas of narrowing and occlusion. Its use in the investigation of male infertility is described in the appropriate section in Chapter 32.

Computed tomography

CT has a wide variety of indications, including the characterisation of renal masses, staging of urinary tract tumours and the assessment of inflammatory and traumatic processes, calculi and the causes of obstruction. It is also used to direct biopsies and the positioning of percutaneous drains. It may also be used to assess renal artery stenosis. Protocols vary between institutions but should conform to the same principles. They are tailored towards the clinical problem and common protocols are described below.

The gastrointestinal tract should be opacified before imaging for renal masses: 40 ml of 150 strength (or 20 ml of 300 strength) water-soluble iodine-base contrast diluted to 1 litre with fruit squash taken orally half an hour prior to the scan is a suitable protocol. An initial plain scan from the dome of the diaphragm to the iliac crests is performed, a suitable protocol being collimation of 8 mm, pitch of 1.5 and slice thickness of 7-8 mm. This is repeated after an intravenous injection of contrast. The timing is important, aiming towards imaging the kidneys while contrast is in the renal veins and inferior vena cava. This is usually optimal around 20-30 s from the start of the injection. With fast modern scanners 50 ml of 300 strength contrast is usually adequate. For lower tract tumours both the plain and postcontrast scans should be from the dome of the diaphragm to the symphysis pubis. A further 1 litre of dilute oral contrast taken 4 h before the scan is useful to image the large bowel and rectum. Alternatively, the same strength contrast can be administered immediately before the scan as an enema. All patients being investigated for malignancies should have a chest radiograph and some departments will also perform routine CT of the chest.

CT is commonly performed as a relative emergency for suspected acute urinary tract problems. When CT is performed for urinary tract calculi, both intravenous and oral contrast are avoided. Relatively narrow collimation (5-7 mm) with a pitch of 1.5-2.0 is recommended, bearing in mind that excessively narrow collimation increases the radiation dose to the patient. Using the wider collimation and higher pitch does not appear to significantly reduce the accuracy of the scan. The mAs should also be kept to a minimum. In the context of trauma, a protocol similar to the post-nephrogram phase described above for the investigation of renal masses is suitable. Repeat scanning after 6-8 min may demonstrate urinary extravasation, especially if there is suspected ureteropelvic disruption. In the assessment of renal or perinephric abscess, 8 mm slices are obtained prior to intravenous contrast and then again during the nephrogram phase. Opacification of the gastrointestinal tract with dilute oral contrast is useful in these cases. Spiral CT with a contrast infusion and relatively narrow collimation and image reconstruction (for example 3 mm and 1.5 mm respectively; pitch of 1-1.6) is suitable for demonstration of the renal arteries and major branches in the assessment of renal artery stenosis or in the preoperative work-up of patients for partial nephrectomy.

The normal renal parenchyma is of intermediate density, measuring between 30 and 60 HU (Fig. 29.30). The renal sinus and perinephric fat are low density, around -10 to -50. Following intravenous contrast the cortex enhances more rapidly than the medulla, appearing more dense from around 20 s to 60 s when there is maximum corticomedullary differentiation. Around 60-180 s the renal parenchyma becomes homogeneously high density, around 80-120 HU. After this, contrast appears in the collecting system. The ureter can be identified as it runs retroperitoneally along the

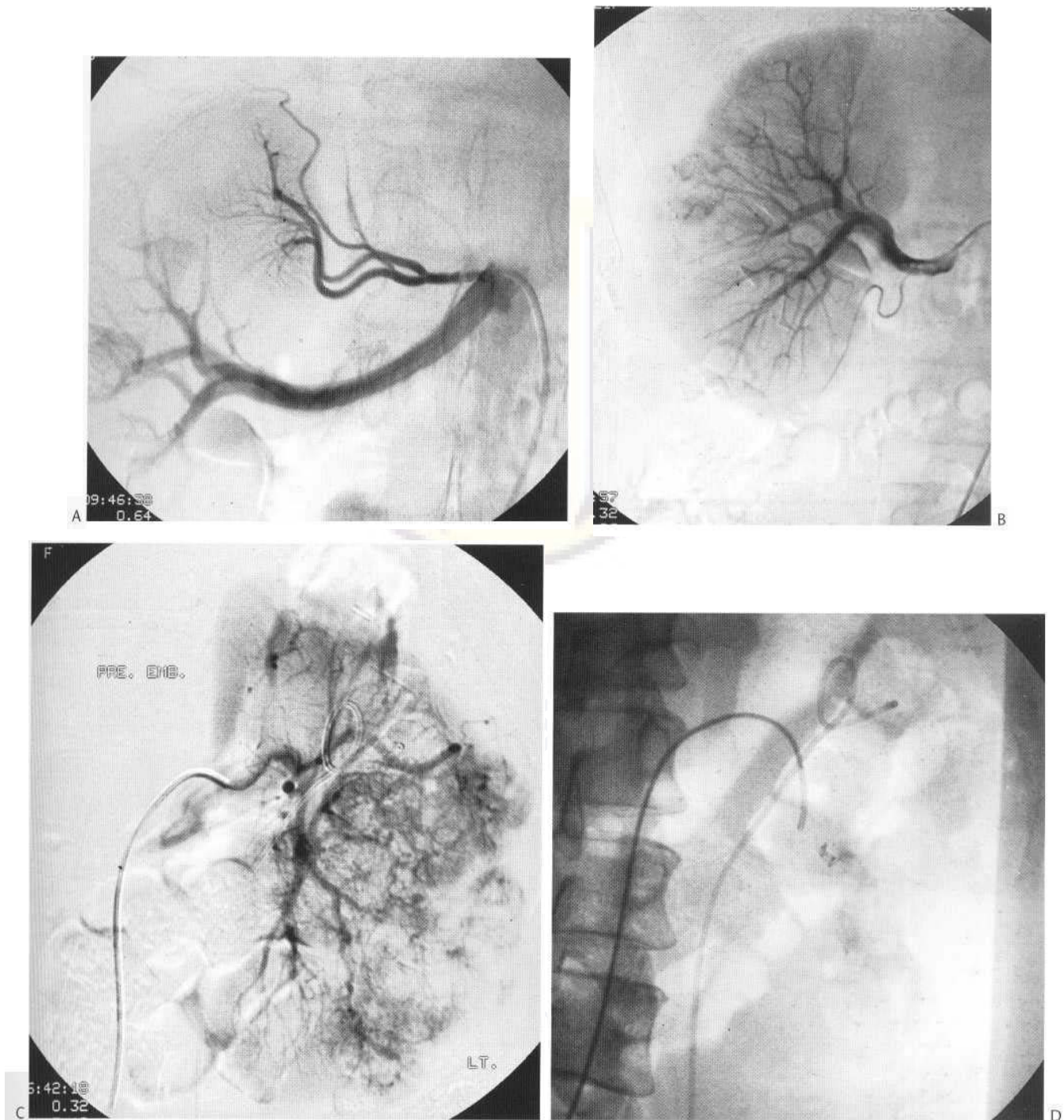


Fig. 29.27 Right renal angiogram showing a small upper pole accessory artery (A). Selective cannulation of the dominant renal artery demonstrates a small peripherally placed renal cell carcinoma (B). A larger renal cell carcinoma is shown on this left renal angiogram (C) with a characteristic malignant circulation (irregular disorganised vessels). Selective embolisation of part of the renal cell carcinoma has been performed (D).

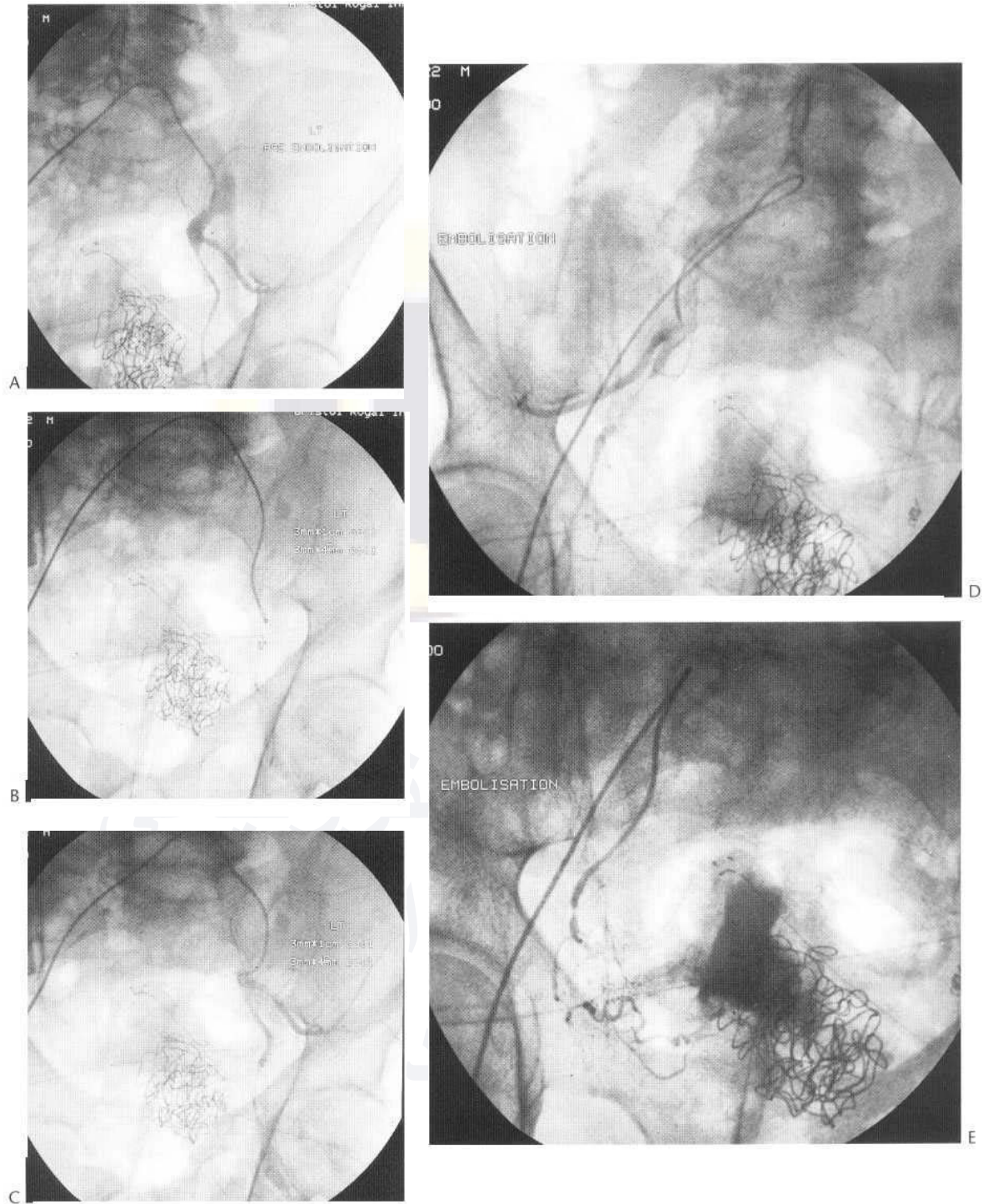


Fig 29.28 Pelvic angiography and tumour embolisation. The left internal iliac artery has been cannulated, by manipulating a catheter from the right femoral artery across the bifurcation, and its two major divisions (anterior and posterior) demonstrated (A). The patient is suffering severe immediate post-prostatectomy haemorrhage. A coil has been positioned in the anterior division (B) and the subsequent angiogram demonstrates successful obstruction of flow in this vessel (C). It is rare actually to demonstrate the bleeding point and, given the life threatening situation, it is often worth embolising both sides. Consequently in this case the right internal iliac artery has also been cannulated from the same femoral artery (D) and the anterior division of the internal iliac selectively cannulated (E). This injection shows the inferior vesical artery from which most of the bleeding is probably occurring and therefore this has also been occluded with a coil (F) (see over)

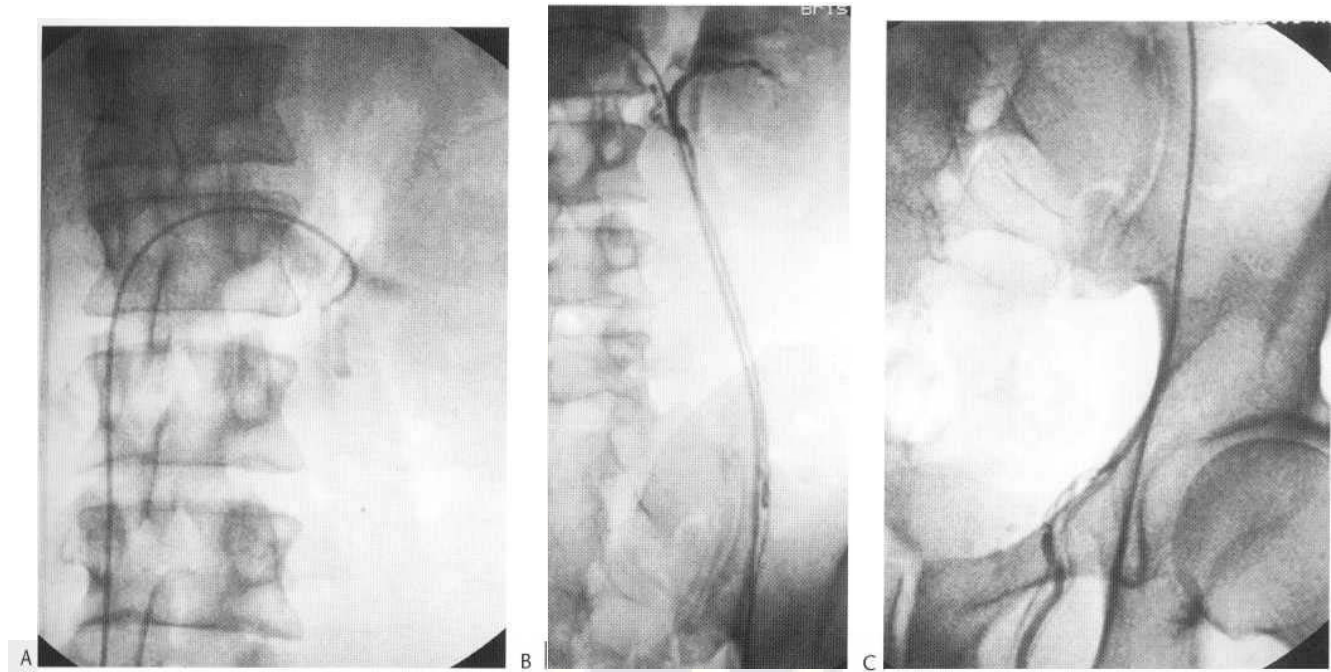


Fig. 29.29 Testicular vein embolisation. The left renal vein has been cannulated via the inferior vena cava (A). A testicular phlebogram performed once the catheter has been advanced down the testicular vein reveals a double testicular vein with multiple origins unprotected by valves, one of a number of variants associated with varicocele formation (B). The upper end of the varicocele is just visible once the catheter has been advanced to the inguinal ring (the varicocele itself should not be screened, to avoid irradiating the testicles) (C). The main testicular vein is occluded with multiple (2-4) coils along its length. Two are illustrated here (D). The most important is the distal one that also occludes the entry of the accessory testicular vein.

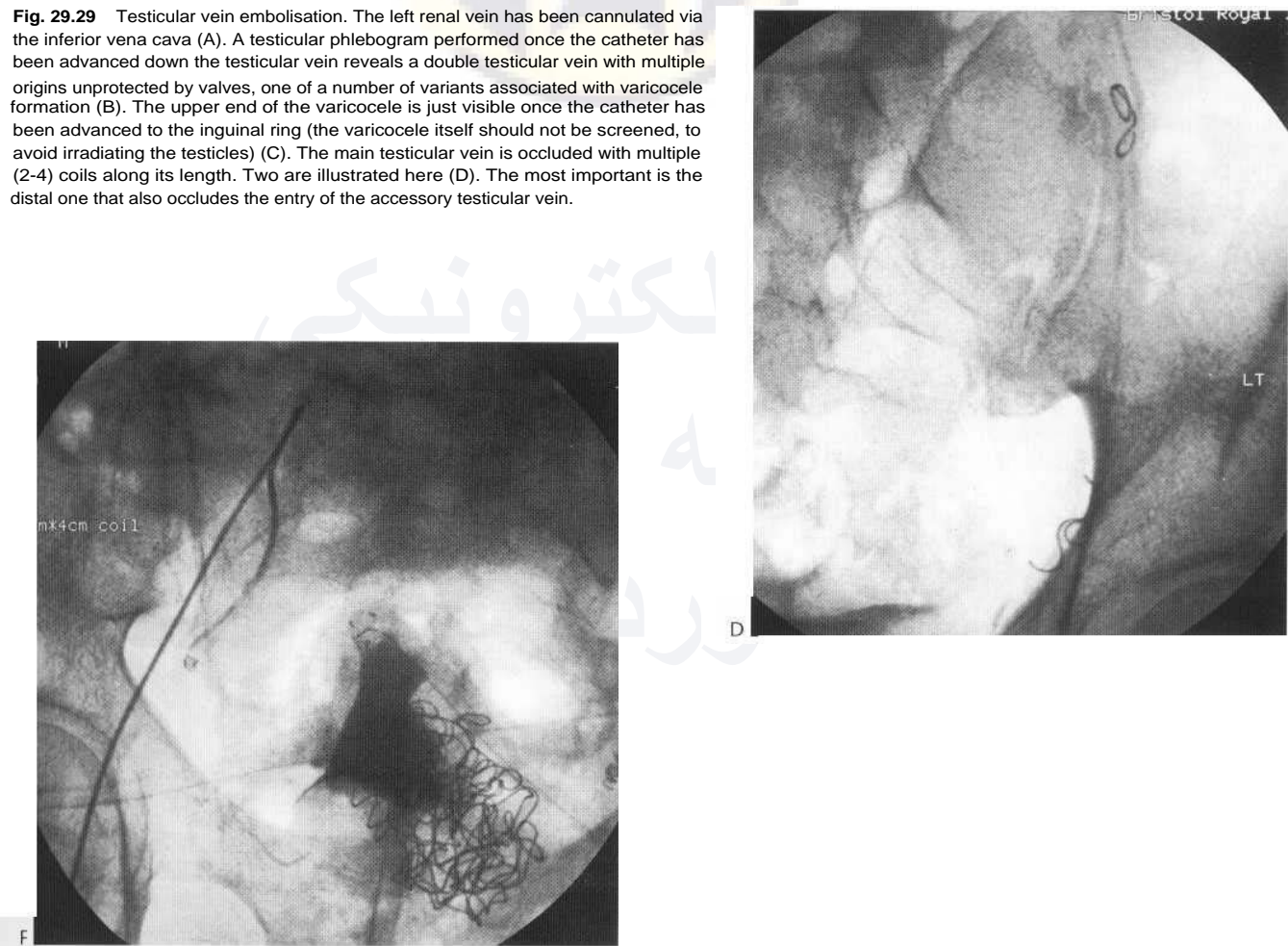


Fig. 29.28 (F) with satisfactory clinical response.

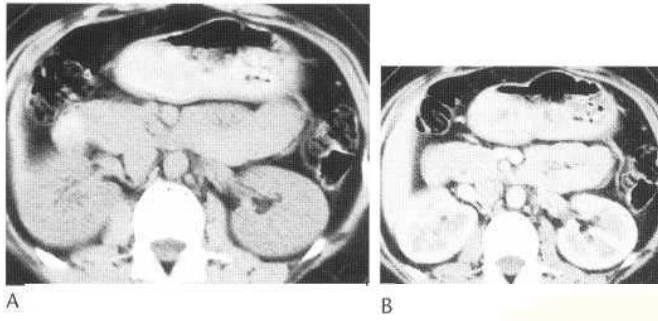


Fig. 29.30 Transverse CT through the midpart of the kidneys. Prior to contrast the kidneys are of intermediate density (A), similar to liver, spleen and blood vessels. During the nephrogram phase the cortex is seen to enhance earlier than the medullary pyramids (B).

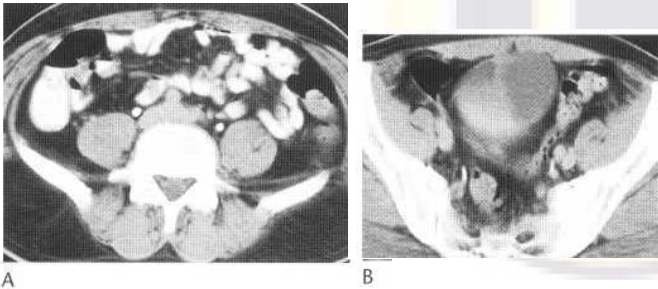


Fig. 29.31 Contrast-filled ureters entering the pelvis at the level of the iliac crest, running along the anterior aspect of the psoas muscles (A) and then around midsacral level crossing the iliac vessels and beginning to turn anteriorly (B).

medial aspect of the psoas muscle, especially when dilated or contrast-filled (Fig. 29.31).

After entering the pelvis the ureter runs posterolaterally to the level of the ischial spine, where it turns anteromedially and can be identified running in front of the seminal vesicles or vaginal fornices to reach the bladder base. The bladder is seen as a thin-walled structure between the urine and the fat. The seminal vesicles appear as tubular structures related to the superior aspect of the prostate, posterior to the lower bladder and anterior to the rectum. There is a fat plane between the seminal vesicle and the bladder (Fig. 29.32). The prostate is usually of homogeneous soft-tissue density but often shows multiple foci of calcification, increasingly from early adulthood onwards (Fig. 29.33).

On CT, normal lymph nodes are seen as soft-tissue density similar to unenhanced renal parenchyma, homogeneous apart from the possibility of a small area of fat at the hilum. Normal nodes are up to 10 mm in maximum transverse diameter in the para-aortic and iliac chains and 6 mm in the retrocrural region.

Magnetic resonance imaging

On T₁-weighted images the renal cortex is of similar signal intensity to liver. The medulla (containing more water) is slightly lower signal, similar to the spleen. On T₂-weighted and STIR sequences the kidneys are diffusely high signal, similar to spleen, although

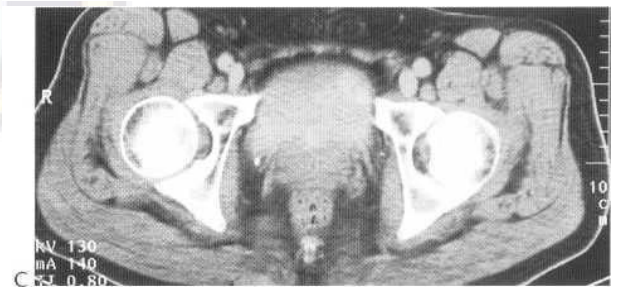
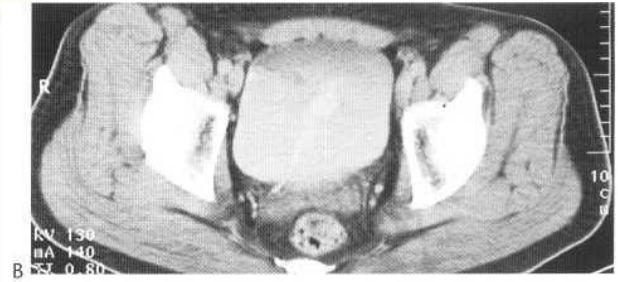
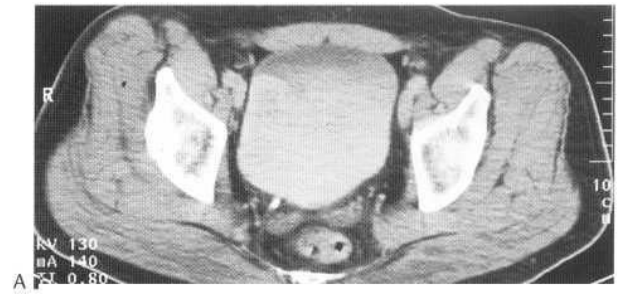


Fig. 29.32 CT of the pelvis showing the distal ureters just above the vesicoureteric junctions lying anterior to the seminal vesicles (A). The right ureter happens to contain a bolus of contrast at the time of the scan. (B) shows the ureters at the vesicoureteric junctions with a jet of opacified urine projecting from the right ureter into the bladder. Further inferiorly the prostate is seen just projecting into the bladder base (C).

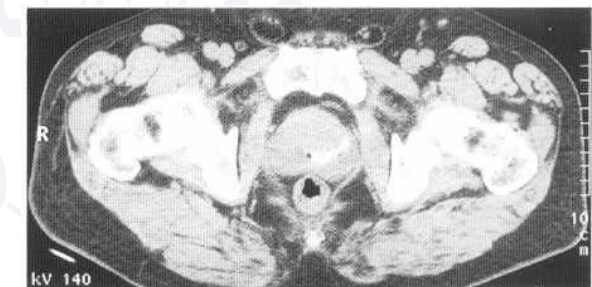


Fig. 29.33 Transverse CT of the prostate with focal calcification. The puborectalis sling is well demonstrated as a thin intermediate-density line encircling the anorectal junction and the prostate.

sometimes the medulla is seen to be of higher signal than cortex (Fig. 29.34). Gadolinium produces intense enhancement, the cortex first and then the medulla. This emphasises the corticomedullary differentiation, which is maximum around 20-60 s following contrast injection (Fig. 29.35). At around 60-180 s both the cortex and



Fig. 29.34 MRI scan of the normal kidneys. On the T₁-weighted sequence (A) the renal cortex is seen to be of higher signal than the medulla. The reverse is seen on the T₂-weighted (B) and STIR (C) sequences, with the medulla being of higher signal than the cortex (although both are relatively high signal).

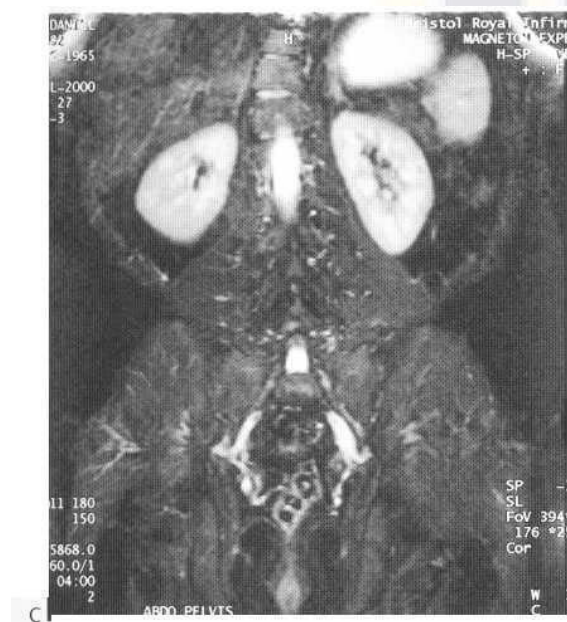


Fig. 29.35 MRI scan of the kidneys 30 s (A) and 90 s (B) following intravenous gadolinium showing the intense enhancement of the cortex and then both the cortex and the medulla.

medulla are intensely enhanced and there is little corticomedullary differentiation. Towards the end of this time contrast appears in the calyces, initially enhancing the urine but as the concentration in

urine rises the signal intensity may fall dramatically due to the hyperparamagnetic effect of concentrated gadolinium. This may also be observed in the region of the apices of the medullary pyramids (renal papillae), where the same phenomenon can be seen due to the high concentration of gadolinium in the collecting ducts.

The bladder wall is seen as a thin low-signal intensity line on

inside the bladder (Fig. 29.36). It is seen as an intermediate signal line on T₁-weighted images, similar to urine. The bladder wall enhances intensely with intravenous gadolinium. Differential enhancement of urine is seen in horizontal layers as contrast is excreted, again highly concentrated gadolinium causing a paradoxical fall in signal intensity.

Lymph nodes within the abdomen and pelvis appear as well-defined ovoid structures of intermediate signal on the T₁-

sequences. A small amount of fat is occasionally demonstrable at the lymph node hilum. Normal figures for size are the same as on CT.

The prostate zonal anatomy is seen from about the age of 5 years, before which there is insufficient central gland for contrast. The peripheral gland shows high signal on the T₁-weighted sequence, compared to the intermediate signal of the central gland (similar to skeletal muscle). The capsule is seen as a thin high-signal line, best seen with an endorectal coil. On the T₁-weighted sequence the prostate appears as an intermediate signal mass without visible zonal anatomy. Benign prostate hyperplasia produces nodularity and heterogeneity on all sequences, especially the T₁-weighted sequence. The seminal vesicles appear multicystic and high signal on the T₁-weighted sequence and intermediate signal on the T₂-weighted sequence.

The testes are homogeneous high signal on the T₂-weighted sequences, with low signal at the mediastinum and somewhat heterogeneous high signal within the epididymis. On T₁-weighted sequences the testes and epididymis are homogeneous and intermediate, similar to muscle.

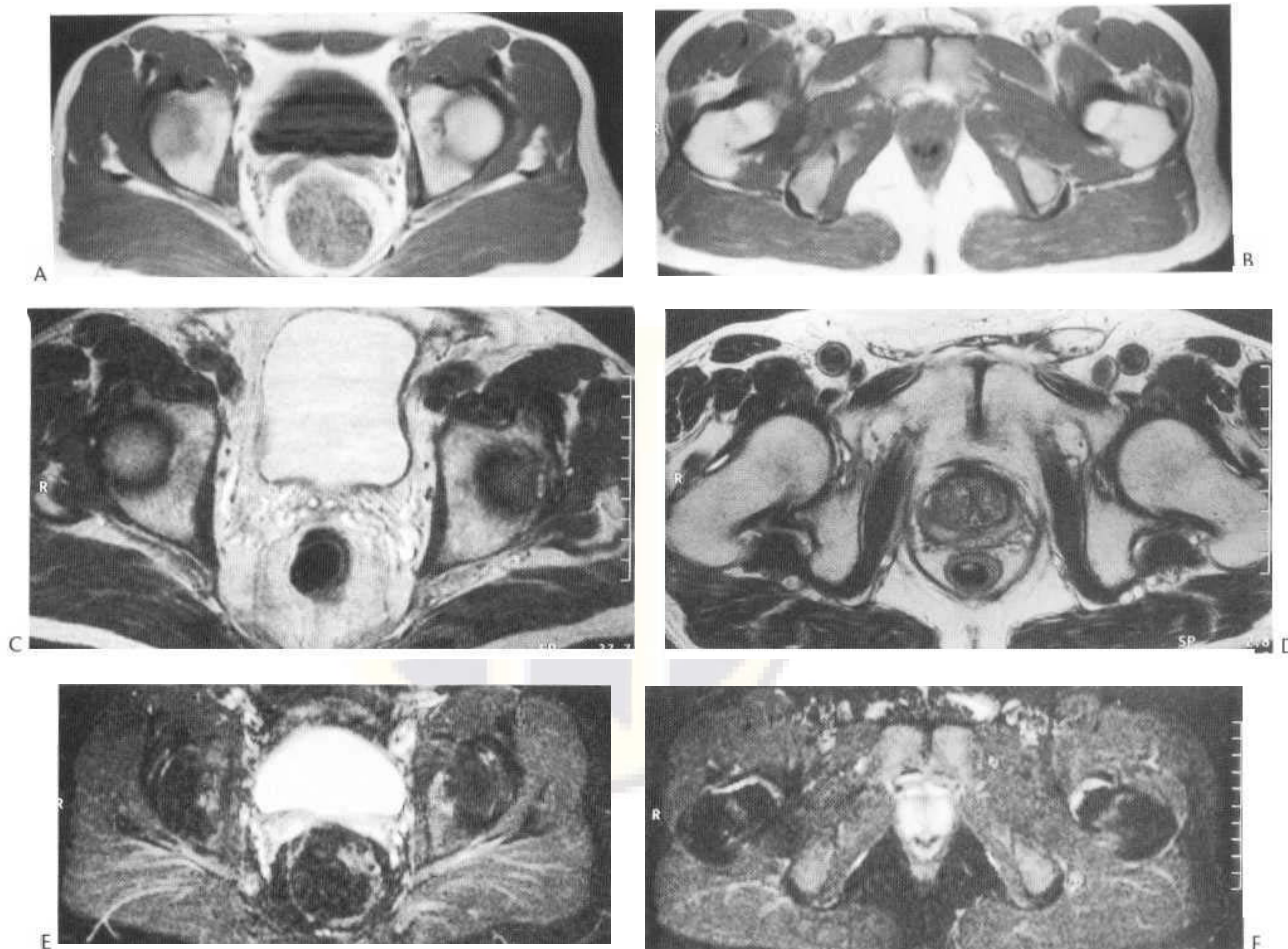


Fig. 29.36 MRI of the pelvis on the T₁-weighted sequence at the level of the bladder (A) and the prostate (B). The same levels (on a different patient) are seen on the T₂-weighted sequence (C,D) demonstrating the increased conspicuity of the bladder wall and the zonal anatomy of the prostate. Both sequences show the puborectalis sling well. The same levels are also shown on the STIR sequences (E, F).

RADIONUCLIDE IMAGING

Philip J.A. Robinson

The investigation of renal function is a key element in the management of most disorders of the urinary tract. Radioactive tracers that are excreted by the kidney are used to assess renal perfusion and excretory functions, while tracers that are retained in the kidney are used to demonstrate renal anatomy.

The 'intact nephron' concept In most renal disorders nephrons behave as independent functioning units, so that when any part of the nephron is diseased, the function of the whole nephron is affected. Whatever the primary site of pathology, whether at arterial, arteriolar, glomerular, tubular or ureteric level, the functional deficit can be assessed by the same techniques. Exceptions to this general rule occur in acute tubular necrosis and in some enzyme deficiencies when filtration and excretory functions may be dissociated.

Renal tracers Currently the most satisfactory tracer for imaging renal anatomy is dimercaptosuccinic acid (DMSA) labelled with technetium-99m. For investigating renal perfusion and excretion,

^{99m}Tc-labelled mercaptoacetylglycylglycylglycine (MAG3) is now usually preferred to earlier tracers excreted solely by glomerular filtration (e.g. diethylenetriaminepenta-acetic acid, DTPA) or by tubular secretion (orthoiodohippurate labelled with iodine-131 or iodine-123).

Stressing the system As with physiological investigation of other body systems, early disease is detected with greater sensitivity and accuracy by stressing the functions which are being investigated. Pharmacological stress may be conveniently regarded as the nuclear medicine equivalent of contrast enhancement in radiographic imaging. Diuretics are used to increase urine flow rates so as to reveal minor degrees of obstruction, and angiotensin-converting enzyme (ACE) inhibitors are used to expose and magnify the physiological disturbances associated with renal arterial disease.

Measurement of glomerular filtration rate (GFR)

GFR is used as a measure of global renal function in patients with known or suspected renal disease. It is also used to help plan treat-

ment in patients receiving nephrotoxic drugs, e.g. some chemotherapeutic agents for cancer. GFR is the volume of blood from which a solute which is wholly excreted by glomerular filtration is cleared in unit time, conventionally expressed as millilitres per minute. Tracers that are excreted almost entirely by glomerular filtration include the chelating agents EDTA and DTPA. EDTA can be labelled with chromium-51, DTPA with technetium-99m, and either of these radiopharmaceuticals can be used to estimate GFR. In order to avoid the inconvenience and potential inaccuracy of urine collection, GFR can be estimated from serial blood samples obtained at carefully timed intervals after injection of the tracer. The method assumes that uniform distribution of the injected tracer within the blood and extracellular fluid compartments occurs within 2 h after injection, and the subsequent rate of fall of activity in the blood, corrected for radioactive decay, is proportional to the rate of renal excretion. Assuming that the blood curve becomes linear after the initial phase of redistribution and equilibration, extrapolation of the linear part of the curve back to zero time will indicate the effective volume of distribution. GFR can then be calculated as the product of the distribution volume and the slope of the linear part of the curve.

DMSA scintigraphy

Radiopharmaceutical $^{99m}\text{Tc-DMSA}$ is extracted by and bound within the parenchymal cells of the proximal convoluted tubule. The extraction efficiency is rather low, so in the normal subject it takes about 3 h for approximately 50% of the injected tracer to become localised in the kidneys. Most of the other 50% is excreted unchanged in the urine. With renal failure, more of the injected activity accumulates in the liver and there is then appreciable biliary excretion. The state of hydration of the patient has little influence over the kinetics of DMSA, so no patient preparation is needed. The typical adult activity of 80 MBq should be scaled down for children according to body surface area. Adverse reactions are very rare.

Acquisition Because the concentration of DMSA in the renal parenchyma continues to increase while the levels in blood and in the extracellular fluid compartment gradually decline, the optimum time for imaging, with maximum kidney : background ratio, occurs 2-4 h after intravenous injection of the tracer. Images should be obtained at 2-3 h in children and 3-4 h in adults. For demonstration of renal anatomy, posterior and posterior oblique views are obtained. With marked renal asymmetry, and particularly with ectopic or transplant kidneys, an anterior view should also be obtained.

Interpretation The resolution of the images should be sufficient to demonstrate the demarcation of renal cortex and medulla (Fig. 29.37). The size, shape and location of both kidneys should be shown. Mass lesions of all types appear as non-functioning areas. Defects, deformities or scarring of the cortex should be recognised.

Divided renal function Because of the relatively high kidney: background ratio, and the stability of the tracer kinetics during the few minutes needed to acquire the images, $^{99m}\text{Tc-DMSA}$ studies offer the most accurate non-invasive method for the estimation of the distribution of function between the two kidneys. The contribution of each kidney is measured as its individual count rate

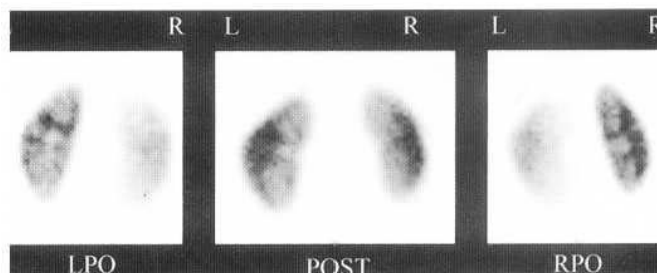


Fig. 29.37 Normal $^{99m}\text{Tc-DMSA}$ study. LPO = left posterior oblique; POST = posterior; RPO = right posterior oblique.

expressed as a percentage of the total counts from both kidneys, after background has been subtracted. With symmetrical kidneys, this estimate can be made satisfactorily from a single posterior view, but with asymmetric or ectopic kidneys it is important to obtain an anterior view and express split function as the geometric mean of percentage counts in the anterior and posterior views. Geometric mean is the square root of the product of the background-subtracted individual kidney counts in the two views.

Applications of DMSA scintigraphy

DMSA scintigraphy is used to locate the functioning renal tissue, differentiate renal cortex from soft-tissue masses in or adjacent to the kidney, to find scars or non-functioning areas of renal parenchyma and to establish the functional contribution of an abnormal kidney.

Renal ectopia and anomalies With horseshoe kidney (Fig. 29.38) the lower poles of both kidneys are joined by a bridge of renal tissue which lies anterior to the aorta and vena cava. This causes the ureters to take a more anterior course than usual, and there may be a degree of obstruction where the ureters cross the bridging renal tissue. DMSA is used to assess individual renal function, as well as to demonstrate the anatomical abnormality. The most common location for an ectopic kidney is in the midline of the pelvis (Fig. 29.39). Pelvic kidneys often show parenchymal distortion or [dysplasia](#), so again the estimation of divided renal function offers a useful supplement to the demonstration of the abnormal location and anatomy of the kidney. When multicystic

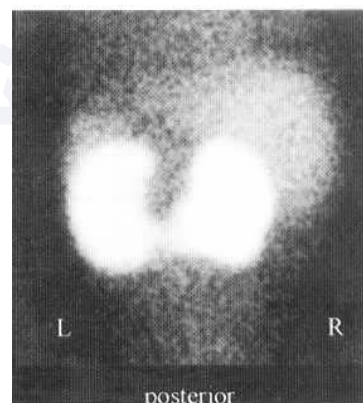


Fig. 29.38 Horseshoe kidney. $^{99m}\text{Tc-DMSA}$ showing bridging renal tissue between the lower poles of both kidneys.

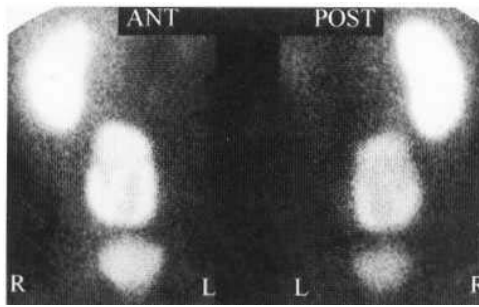


Fig. 29.39 Ectopic kidney. ^{99m}Tc -DMSA study showing right kidney in normal position; left kidney lying in the midline of the pelvis superior to the bladder.

dysplastic kidney is suspected, DMSA scintigraphy is used to confirm the total absence of function that is typical of this condition, and to differentiate it from other forms of unilateral cystic disease in infancy that are associated with preservation of some degree of renal function.

Renal masses and pseudomasses In a minor developmental anomaly, a portion of cortex may be infolded so as to lie adjacent to the renal pelvis, producing an apparent mass or 'pseudomass' on ultrasonography. Also known as 'prominent columns of,

by their concentration of DMSA at scintigraphy. Tumours, cysts or abscesses show no uptake of DMSA so they appear as photon-deficient areas in the renal images. The majority of true renal masses will be investigated satisfactorily by anatomical imaging but occasionally, particularly with bilateral disease, functional imaging with DMSA will be needed to establish the distribution of functional renal tissue. This may indicate which of two kidneys with bilateral tumours should be operated on first (Fig. 29.40), or whether the residual function on one side is sufficient to justify a conservative surgical procedure (e.g. partial nephrectomy) rather than the simpler but more drastic procedure of full nephrectomy.

Infection and scarring Infection in the renal parenchyma (acute pyelonephritis or acute nephronia) produces diminished function in the affected areas, often a small subsegmental wedge of the renal cortex. Under favourable conditions the infection may heal by resolution, and in such cases the anatomical integrity of the affected area is maintained and normal function is restored. In

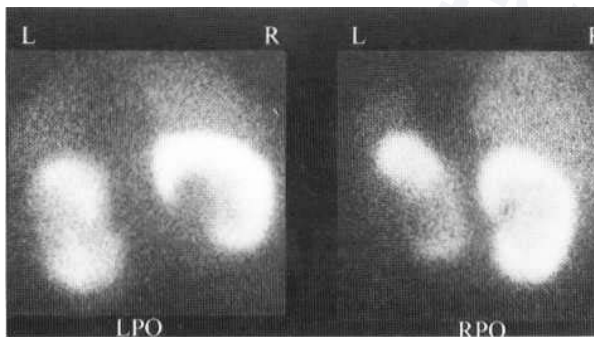


Fig. 29.40 Bilateral Wilms' tumours. ^{99m}Tc -DMSA study showing extensive replacement of the left kidney; smaller tumour at the hilum of the right kidney.

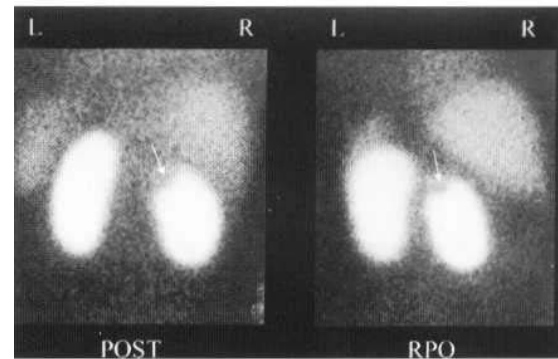


Fig. 29.41 Post infective scarring. ^{99m}Tc -DMSA study showing normal left kidney; scarred right upper pole (arrows).

more severe cases, focal scarring may ensue and the local functional deficit becomes permanent. Scarring is recognised as an area of indentation or discontinuity in the cortical image (Fig. 29.41). The severity of scarring may be expressed in terms of the extent of the lesion, the presence of multiple scars and by the distribution of renal function between affected and unaffected kidneys. Acute infection may produce total non-function in the affected area, indistinguishable from scarring, but in less severe cases may appear as an area of reduced function, with preservation of these areas can be confirmed as normal renal parenchyma within the normal renal outline. In kidneys with a duplex collecting system and two ureters, the upper pole cortex is often damaged by obstruction, or the lower moiety may be injured by reflux and infection. In such cases DMSA imaging can be used to establish the functional contribution of the upper and lower moieties in order to assist decisions on surgery to the kidney.

When to investigate? Although focal areas of diminished or absent function are well shown by DMSA scintigraphy, it must be remembered that acute infection and permanent scarring cannot be distinguished by this method. If the presence or extent of an acute lobar nephronia is under question, it is appropriate to carry out DMSA imaging at the time of the infection, or shortly afterwards. However, if the aim of DMSA imaging is to detect and monitor renal scarring, it is important to delay the examination for long enough to allow functional recovery to reach a maximum. The time interval required for this is variable, but it is recommended that DMSA for scarring should be delayed for at least 3 months (and probably 6 months) after the infective episode.

Dynamic renal studies

Radiopharmaceuticals Because nephrons under most circumstances act as individual functional units, it is not necessary to investigate perfusion, filtration, reabsorption and transit functions independently. In most circumstances, tracers which are handled differently by the kidney will produce similar results in the estimation of individual renal uptake and clearance. ^{125}I (excreted almost entirely by glomerular filtration) and ^{131}I

superseded by ^{99m}Tc -MAG3.

^{99m}Tc -MAG3 is loosely protein-bound in the circulation. A small proportion is filtered but a much higher proportion is secreted by the tubules, and although the extraction efficiency is not as good as

that of hippuran, the rate of excretion is much faster than with DTPA. Labelling with technetium-99m gives a lower radiation dose to the patient, with higher count rates giving better imaging and measurement statistics. The typical amount of activity administered for an adult is 100 MBq for excretion studies, or up to 200 MBq if perfusion imaging is also being performed.

DTPA is less costly and also quicker and easier to prepare than ^{99m}Tc -MAG3, and so it may be used in emergent situations where a rapid result is needed, particularly in respect of perfusion, e.g. with acute oliguria in the renal transplant recipient. Excretion is slower than with MAG3, count statistics are inferior, and a larger amount of activity needs to be administered (300 MBq for excretion studies and up to 800 MBq for perfusion imaging).

Diphosphonate agents used for bone scintigraphy (e.g. ^{99m}Tc -medronate) are also excreted almost entirely by glomerular filtration. In patients having scintigraphic surveys for bone metastasis, where there is no indication for imaging in the early vascular and soft-tissue phases, a satisfactory renal study may be obtained in the first 30-40 min after injection. Conventional bone imaging can be carried out 2-3 h later as normal, allowing both investigations to be completed at single visit.

Patient preparation Minor degrees of ureteric or outflow obstruction will not be detected if the rate of urine flow is slow. Also, giving a diuretic may be hazardous if the patient is already dehydrated. For these reasons it is essential that the patient is well hydrated at the start of the procedure. Preparatory instructions should encourage the patient to take plenty of fluid before attending for the procedure, and a further 300-500 ml of clear fluid should be given 30 min before injection.

Acquisition With the patient in a reclining (dentist's chair) or supine position, posterior view images are obtained with the gamma camera positioned so as to include both kidneys and the bladder. If deconvolution analysis is to be performed (see below), the heart should also be included in the field of view. Transplanted kidneys are normally located in the left or right iliac fossa so an anterior view is appropriate in these cases. If the patient is catheterised, the bag should also be within the field of view.

The radiopharmaceutical is given as a bolus injection into a peripheral vein. If an assessment of perfusion is required, it is important to deliver the bolus as tightly as possible. The volume of the injection is typically small (about 1 ml or less) and several techniques have been described for ensuring a speedy transit of the bolus to the central circulation.

Rapid image acquisition is required to demonstrate the perfusion phase, for example one frame per second for the first 30-40 s after injection. For the excretion phase, sequential images are acquired over periods of 10-30 s each for 20-30 min.

The supine position is preferred to sitting because it is more easily reproducible and there is less likelihood of the patient moving during the procedure. The disadvantage of the supine position is that a dilated but unobstructed (baggy) renal pelvis may not drain freely, so it is important to obtain a further spot view of the urinary tract with the patient sitting, after the dynamic acquisition has been completed. Additionally, a final spot view obtained after micturition is helpful to demonstrate the completeness of bladder emptying and to confirm prolonged hold-up in the obstructed upper tract.

Use of diuretics The sensitivity of dynamic renal imaging for detecting urinary tract obstruction is maximised by increasing the

urine flow rate in order to stress the system. Furosemide (frusemide) (normal adult dose 20-40 mg, scaled down by body surface area for children) produces a maximal diuretic response in the normal kidney within 5-10 min after injection. Currently there is no consensus on the optimum timing of diuretic injection. The most widely used technique requires intravenous furosemide to be given 15-20 min after starting the study (F+20 study). Image data are then collected for a further 15-20 min to determine the response of the kidneys to an increased flow rate. Alternatively, furosemide may be given 15 minutes before the injection of the radiotracer, in order to ensure that the patient is already undergoing a maximum diuresis at the start of data acquisition (F-15 study). Finally, some users prefer to give the furosemide and radiotracer simultaneously, so that a diuresis develops rapidly during the early part of this study. Each of these methods can produce satisfactory results, but each requires appropriately specific criteria for interpreting the results. The F+20 method has the advantage that it demonstrates a diuretic response, i.e. the change from resting to high urine flow rates, while the F-15 approach is thought to be more decisive in detecting minor degrees of obstruction.

Data analysis The image data is analysed by deriving time-activity curves from regions of interest placed over each kidney, from a background area around each kidney, from the bladder and from the heart (if included). After correcting the renal curves for background activity, the early part of the curves may be used to calculate split renal function. The kidney contains a mixture of short and long nephrons but it is known that the shortest parenchymal transit time within the kidney, i.e. the time taken for filtrate in Bowman's capsule and the proximal tubule to reach the renal pelvis, is 2.5-3 min, so it is safe to assume that none of the tracer entering the kidney during this period after injection will have reached the outflow tract. The relative renal function can then be expressed as the ratio of the area under the renogram curves of the two kidneys obtained during the period 40 s - 2 min 40 s after bolus injection of the tracer. The first 40 s are usually excluded in order to avoid errors that may be introduced by vascular structures overlapping the renal and background areas during the first pass of the tracer. If furosemide has been given during the procedure (F+20 technique), a numerical estimate of the diuretic response is calculated, e.g. by measuring the residual counts in the kidney 20 min after diuretic injection as a proportion of the maximum renal counts.

It may be helpful to confirm that an adequate diuresis has been achieved by measuring the average urine flow rate during the examination. This is achieved by having the patient empty the bladder immediately before starting the study, and also at the end of the study, and measuring the volume of urine generated during that time. Residual urine volume after micturition can also be assessed by comparing the counts in the bladder before and after micturition, and measuring the volume of urine passed.

Deconvolution analysis is a mathematical method of calculating what the output curve of an organ (in the case of the kidney, the renogram) would have looked like if the injection had been made as a bolus in the renal artery rather than into a peripheral vein. This is done by considering the observed renogram as a complex sum of a series of individual renograms that would have been obtained by sequentially injecting different amounts of tracer into the renal artery. The instantaneous concentrations entering the renal artery

are derived from the time-activity curve of the heart, so, knowing input of the tracer at each moment during the study, it is possible to differentiate the observed output function (the actual renogram) to derive a theoretical curve which represents the range of transit times between the renal artery and the renal pelvis. Although the calculation of mean parenchymal transit times offers a novel aspect of function in renal disease, the successful use of deconvolution methods requires meticulous attention to technique, and the added diagnostic value of their use in routine clinical practice remains uncertain.

Interpretation With MAG3, the images obtained during the first pass of the tracer illustrate vascular anomalies in the abdomen as well as the perfusion of the kidneys (Fig. 29.42). Images obtained 3-5 min after injection illustrate the size, shape and location of the kidneys. Serial images obtained during the excretion phase give a visual impression of relative renal function, rate of transit of activity through the renal pelvis, drainage from the pelvis in the sitting position, and the residual bladder volume after micturition.

The renogram gives several different indications of renal function. The initial, steeply rising part of the curve represents the delivery of circulating tracer to the kidney, and so the slope of this part of the curve is proportional to renal perfusion-the steeper the slope, the better the perfusion. As mentioned above, the area under the curve between 40 s and 2 min 40 s may be taken as a measure of the contribution of each kidney to overall renal function. The normal kidney produces a curve which peaks within a few minutes after injection and then falls (Fig. 29.42). The height of this peak repre-

sents the maximum amount of tracer which accumulates in the kidney. If the anatomical region from which the renogram is derived includes the renal pelvis, then the height of the peak is influenced by the volume of the pelvis-the reservoir effect of a baggy renal pelvis will produce a much higher peak on the renogram curve than a kidney of equal function with a small volume pelvis. However, the height of the peak is also affected by the uptake function of the kidney-with diminished function the magnitude of the peak activity is less. The time interval between the injection and the peak of the renogram (T_{max}) is prolonged in renovascular disease because the filtration pressure is reduced and the intrarenal transit times are slowed. However, a delayed T_{max} can also result from obstruction or from the reservoir effect of a dilated renal pelvis.

Response to diuresis The distinction between obstruction and the reservoir effect of an unobstructed but dilated renal pelvis can usually be made from the response to diuresis. With the normal kidney, administration of furosemide 20 min after MAG3 produces a rapid increase in urine flow so that activity retained within a baggy renal pelvis is displaced by urine containing much lower concentration of activity, so the observed count rate from the kidney falls. Various indices have been described to express the rate of elimination of tracer from the renal pelvis in response to diuretic stimulus, but there is no single index which is universally accepted. One simple approach is to say that if renal activity falls by more than 50% within 20 min of diuretic injection then obstruction is very unlikely. If the activity remains constant or increases, then obstruction is extremely likely. Activity falling by

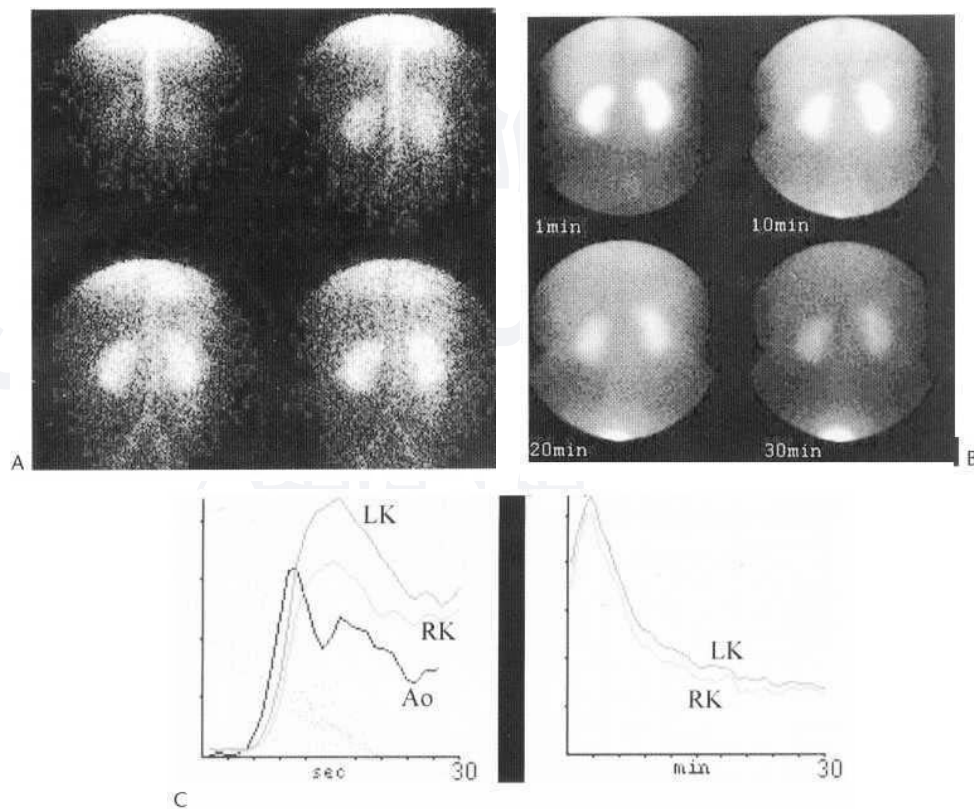


Fig. 29.42 Normal ^{99m}Tc-MAG3 dynamic renal study: (A) Part of the first-pass acquisition showing perfusion of aorta and both kidneys; (B) selected images from the excretion series with symmetrical uptake and clearance from both kidneys; (C) renogram curves from the perfusion sequence in the first 30 s (left) and the excretion curves up to 30 min (right). LK = left kidney; RK = right kidney; Ao = aorta.

less than 50% in 20 min may suggest low-grade obstruction but it is important also to consider the level of function within the affected kidney. Usually the first aspect of renal function to be affected in disease is the ability of the kidney to concentrate the urine, so the failing kidney is typically unresponsive to the doses of diuretic agents that would be effective in the normal kidney. Distinguishing between a kidney which is sufficiently damaged to prevent a normal diuretic response, and one with low-grade obstruction, remains difficult (see below). Low-grade obstruction is also suggested by a renogram which shows an incomplete fall-off in response to a diuretic stimulus, and then starts rising again—the delayed double-peak sign described by Homsy.

Captopril scintigraphy

With renal arterial disease, the perfusion pressure of the afferent glomerular arterioles is reduced, and filtration pressure is sustained by efferent arteriolar vasoconstriction mediated by the renin-angiotensin system. Administration of angiotensin-converting enzyme (ACE) inhibitors such as captopril blocks the efferent vasoconstriction, causing a fall in filtration pressure, which leads to a reduction in the GFR of the affected nephrons. Because of the reduced volume of glomerular filtrate, the mean transit time is prolonged and this in turn allows a greater reabsorption of water. These mechanisms produce in the captopril renogram the typical changes of diminished uptake, flattened peak and delayed T_{max}. In severe cases the clearance may be so slow that the curve continues rising throughout the period of observation.

Preparation For a captopril test, the patient should be off captopril and diuretics for 2 days, and off other ACE inhibitors for 7 days. Obtaining a baseline study without captopril intervention improves the specificity of the test. Pre- and post-captopril studies can be obtained on consecutive days, or even on the same day if the patient has good renal function. The patient should be normally hydrated. The effect of captopril on renal function is not mediated through a fall in systemic blood pressure, and such a fall is undesirable because it may cause changes in the renogram of the unaffected kidney. A small dose (25 mg) of captopril is given orally 1 h before injection of the radiopharmaceutical. The patient should be kept supine throughout and blood pressure should be monitored before, during and after the procedure. Because some patients are very sensitive to even small doses of captopril, a recommended precaution is to maintain an intravenous saline infusion with a period of the study to allow rapid treatment of any sudden hypotension.

Acquisition A 30 min dynamic study using ^{99m}Tc-MAG3 is carried out. Images are obtained at 1, 2, 5, 10, 20 and 30 min, with renogram curves for the whole study obtained in the usual way. ^{99m}Tc-DTPA may be used as an alternative in patients who have good renal function.

Interpretation As with unenhanced renal studies, interpretation of the captopril study is based on inspection of the images and analysis of the curves. The critical features indicative of renal vascular disease are reduced function and delayed transit. Affected kidneys are often small, although this is not a specific feature. The following grading system was used in a European multicentre study:

Grade I Mild delay in T_{max} (6–11 min using ^{99m}Tc-DTPA) with a falling excretion phase

Grade 2a More prolonged delay in T_{ax} (greater than 11 min) but still with an excretion phase

Grade 2b Continually rising or flat curve

Grade 3 As grade 2b, with marked reduction in function of the affected kidney.

With MAG3, T_{max} occurs earlier than the DTPA time quoted above.

Renal transplantation

The clinical setting of the transplant kidney provides differing and specific problems which require modifications in the technique for renal dynamic studies. Typically, the kidney is placed in the right iliac fossa, or sometimes on the left. An anterior view of the pelvis will encompass the kidney, ureter and bladder. Since there is only a single kidney, the question of split function estimation does not arise. Dynamic studies are obtained as normal, with perfusion and excretion imaging. In the context of post-transplant oliguria, calculation of a perfusion index is often helpful. This is derived by obtaining a time-activity curve from the parenchyma of the kidney and also a curve from the adjacent iliac or femoral artery. A fast bolus injection of the tracer results in a steeply rising arterial curve with a sharp peak (T_{ax}). After background subtraction, the areas under the arterial and renal curves are measured up to T_{III,II}. The ratio of these two areas, after normalisation for differences in the size of the regions of interest from which the curves were derived, defines the perfusion of the renal parenchyma relative to the blood flow through the adjacent large artery.

Transplant perfusion index = (flow in renal parenchyma/flow in iliac artery) x 100%.

Using this method of calculation, a perfusion index greater than 50% will usually be associated with good renal function.

Radionuclide cystography

This is the radionuclide analogue of X-ray micturating cystography with iodinated contrast media. In outline, the bladder is filled with fluid containing a non-absorbable radiotracer, and dynamic imaging of the urinary tract is carried out during micturition in order to detect vesicoureteric reflux. This may be achieved with direct instillation of the tracer into the bladder, but this approach does not capitalise on the major advantage of the radionuclide technique, which is the possibility of avoiding bladder catheterisation. Much more clinically useful is the technique of indirect cystography, which is basically similar but which uses as a starting point the full bladder at the end of a conventional dynamic renal study. Using ^{99m}Tc-MAG3, renal activity normally falls off to a considerable extent by the time the bladder is full, so the presence of baseline counts in the background and in the kidneys at the start of micturition is not a significant disadvantage.

Preparation and technique This is basically as for diuretic renography, described earlier. After completing the initial part of the study, including the response to diuresis, the patient is placed in a sitting or standing position and the camera repositioned to include both kidneys and the bladder within the field of view. Image frames of 5–10 s duration are collected during micturition. Time-activity curves are derived from the region of the bladder, each kidney individually, and also from regions along the line of each ureter.

Interpretation Vesicoureteric reflux is confirmed if there is an increase in kidney counts during micturition. Lesser degrees of reflux may appear as increased counts in the ureters, which may be transitory.

Applications of dynamic radionuclide studies

Urinary tract obstruction Obstruction implies increased resistance to flow, and resistance can only be assessed accurately by simultaneous measurements of pressure and flow. Such measurements require invasive techniques and so are unsuitable for routine clinical use. Anatomical imaging methods rely on demonstrating the structural abnormalities which cause obstruction and those which result from its effects, while radionuclide techniques demonstrate the alteration in flow caused by obstruction, as well as the consequent functional deficit that may follow.

With acute ureteric obstruction (e.g. by a stone), renal perfusion and glomerular filtration is maintained at first, and increased tubular reabsorption of water compensates, at least in part, for the cessation of urine flow, so that radiotracers continue to accumulate in the kidney. This mechanism gives rise to the characteristic obstructive renogram which shows a continuing rise (Fig. 29.43). A rather similar rising curve may also be produced by an unobstructed kidney if the extrarenal pelvis is large, causing a reservoir effect. However, in such cases an effective diuresis will wash out the contents of the renal pelvis, causing a rapid fall in the renogram (Fig. 29.44).

It may be argued that there is no such thing as partial obstruction-resistance to flow is either normal or increased. However, obstructions may be low-grade or high-grade, with minor or major changes in intrarenal pressure. High-grade obstruction is usually clearly shown on the renogram and its associated images. Recognising lesser degrees of obstruction is more difficult. The renal response to a diuretic is not an 'all or nothing' phenomenon, and

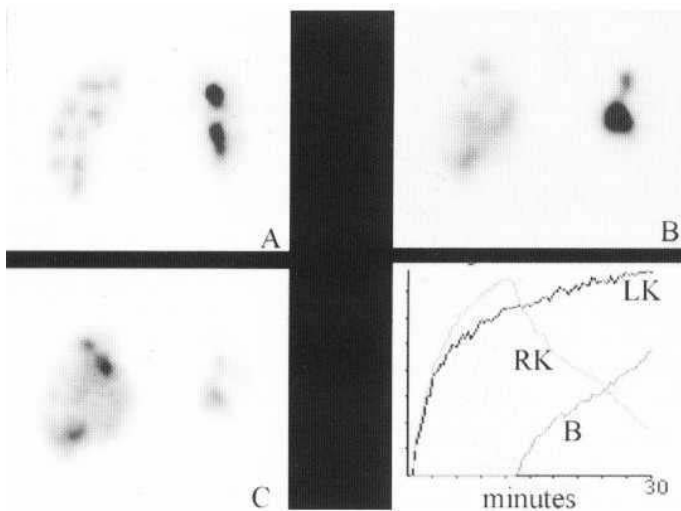


Fig. 29.43 Unilateral PUJ obstruction. ^{99m}Tc-MAG3 images at 1 min (A), 5 min (B) and 15 min (C), showing typical left hydronephrosis with normal clearance from the right kidney. Renogram curves (bottom right) show normal clearance on the right and an obstructed left side. LK = left kidney; RK = right kidney; B = bladder.

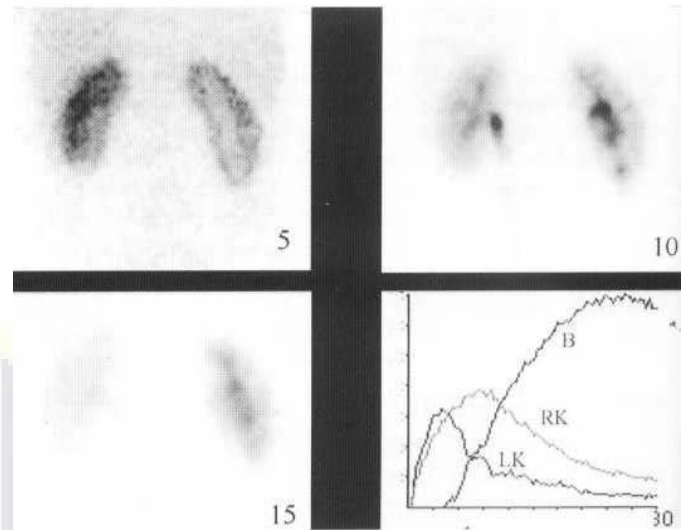


Fig. 29.44 Dilated but unobstructed renal pelvis. ^{99m}Tc images at 5, 10 and 15 min show rapid uptake and clearance from the left kidney; slower clearance from the right kidney. Renogram curves (bottom right) show normal left side and delayed peak on the right with rapid washout following furosemide (frusemide) injection. LK = left kidney; RK = right kidney; B = bladder.

with low-grade obstruction the kidney may show a transient and incomplete diuretic response. In some cases this results in the renogram beginning to rise again after a diuretic-induced fall (Homsy's double peak sign; Fig. 29.45), while in other cases the rate of fall of the curve may be less than expected. A similar problem arises in patients with diminished renal function—the

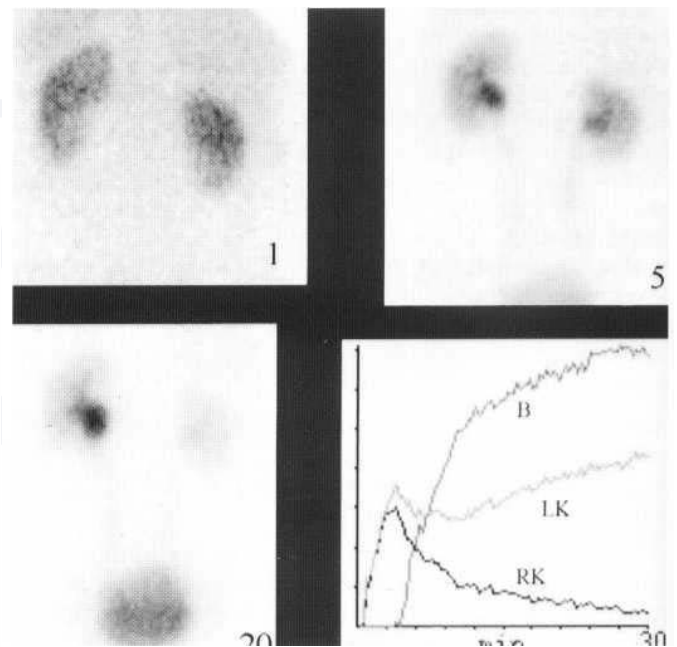


Fig. 29.45 Low-grade obstruction. ^{99m}Tc-MAG3 diuretic study images at 1, 5 and 20 min show normal uptake and clearance on the right; normal uptake on the left but incomplete clearance. Renogram curves (bottom right) show normal right side and normal uptake on the left but after an initial fall the excretion curve rises again (Homsy's sign). LK = left kidney; RK = right kidney; B = bladder.

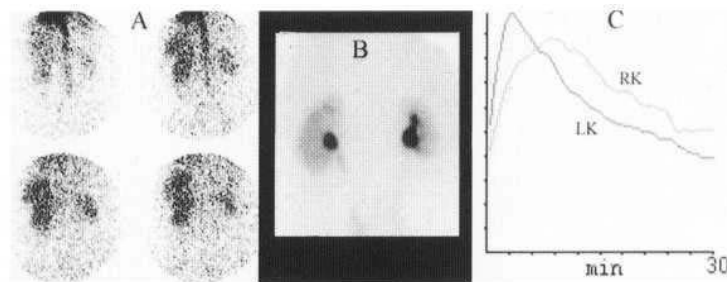


Fig. 29.46 Right renal artery stenosis. ^{99m}Tc -MAG3 dynamic study shows reduced blood flow to the smaller right kidney on the perfusion series (A), delayed excretion on the 15 min image (B), and the renogram curve (C) shows reduced uptake, delayed T_{max} and slower clearance from the right kidney. LK = left kidney; RK = right kidney.

affected kidneys may be unresponsive to diuretics, so the usual rapid fall in the renogram does not occur. When trying to distinguish between impaired but unobstructed kidneys that are unable to respond normally to diuretics and those with chronic obstruction and functional impairment, the concept of 'output efficiency' is helpful. This requires the diuretic response to be considered in relation to the uptake function of the kidney. If the input to the kidney is diminished, a 'normal' diuretic response cannot be expected. The rate of fall of the renogram during the diuretic phase should be compared with the rate of rise during the uptake phase—if the relationship between the two is the same as in a normal kidney, then obstruction is very unlikely.

Renovascular hypertension The main reason for investigating the renal tract in patients with hypertension is to detect the minority of patients with renal vascular disease that is treatable by anatomical means—angioplasty or surgery. However, it must be emphasised that renovascular hypertension may also result from small-vessel disease, which shows no specific features at angiography. Radionuclide studies will select out those hypertensive patients who have renovascular disorders, but cannot distinguish between large-vessel and small-vessel disease, as, whatever the level of arterial obstruction, the functional disturbance is similar.

Characteristic changes in the dynamic renal study are those of prolonged transit due to increased water reabsorption in the distal tubules, and diminished renal function associated with decreased blood flow caused by arterial narrowing. These changes are manifest by reduced gradient in the uptake part of the renogram, reduced and delayed T_{max} and prolonged transit times (Fig. 29.46). The affected kidney may be small or normal in size. Enhancement of the dynamic study with captopril magnifies these functional changes and unmasks some additional cases in which the baseline study is not diagnostic.

Captopril-enhanced renography has good results as a screening test for renovascular hypertension (sensitivity and specificity 80-90%) when the selection of patients for investigation is appropriate—a renal cause is more likely in patients who are young and those with severe or resistant hypertension. Discrepancies between scintigraphy and angiography occur because some patients with renovascular hypertension have only small-vessel disease, while angiographic renal artery stenosis occurs incidentally in a substantial proportion of elderly patients, and so may be associated with essential hypertension in occasional cases.

Acute renal failure The aim of scintigraphy is to discriminate between the potentially reversible condition of acute tubular necrosis (ATN) and those conditions that are progressive or irre-

versible (including acute or chronic renal failure). The rare but important occurrence of acute renal failure as a consequence of urinary tract obstruction must also be recognised. A ^{99m}Tc -MAG3 or DTPA study in ATN typically shows that renal perfusion is well maintained, even in the presence of anuria or severe oliguria. The GFR is relatively well preserved, but the filtered or secreted solutes either remain in the kidney or are reabsorbed (abnormally) from damaged tubules. Dynamic images show fairly good perfusion, with subsequent fading of the renal images and little or no excretion (Fig. 29.47). The renogram shows an initial vascular peak, which usually then falls in parallel with blood clearance curve.

With acute renal failure caused by intrinsic parenchymal disease or major vessel obstruction, perfusion is severely impaired or absent. With acute or chronic renal failure, a low level of excretion may persist, giving renograms with markedly impaired uptake phases and a flat excretion phase. In acute renal failure caused by obstruction, renal perfusion is well maintained.

Renal transplantation Although ultrasonography is the first-line technique for monitoring renal transplants, there are several indications for scintigraphy as a supplementary test when ultrasound is technically difficult or when its results are inconclusive or unexpected.

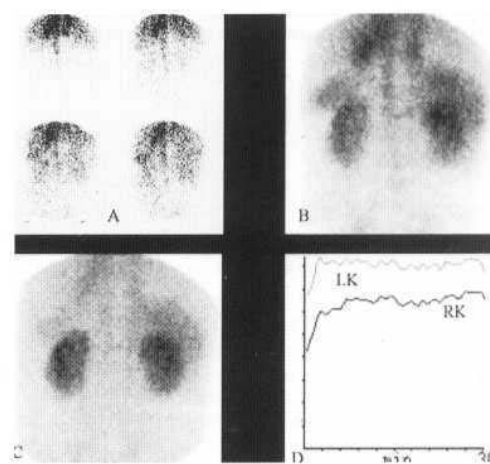


Fig. 29.47 Acute tubular necrosis. ^{99m}Tc -MAG3 study shows perfusion of both kidneys is reduced (A) and excretion images at 1 min (B) and 20 min (C) show persistent retention of the tracer in the kidney with no excretion. Renogram curves (D) show immediate uptake but no clearance. LK = left kidney; RK = right kidney.

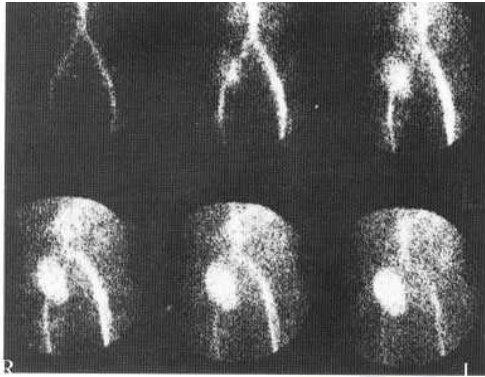


Fig. 29.48 Acute oliguria after renal transplantation. Anterior perfusion phase images from ^{99m}Tc-DTPA study show that blood flow to the transplanted kidney in the right iliac fossa is well maintained. Diagnosis: acute tubular necrosis.

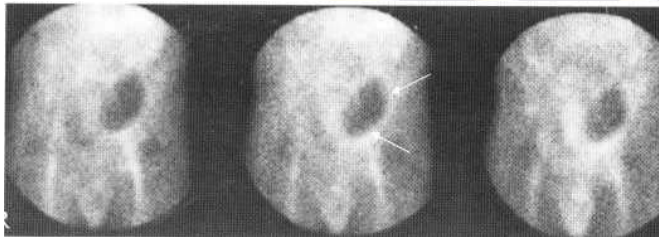


Fig. 29.49 Acute oliguria after renal transplantation. Anterior view dynamic images 2, 5 and 10 minutes after injection of ^{99m}Tc-DTPA show a photon deficient area which represents the totally ischaemic graft in the left iliac fossa; diagnosis: renal vein thrombosis.

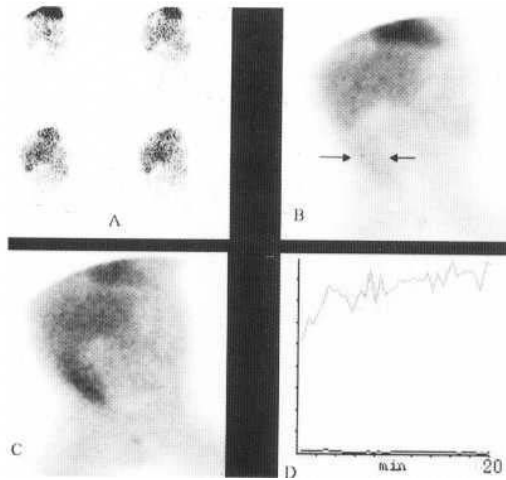


Fig. 29.50 Acute oliguria after renal transplantation. Anterior view perfusion images (A) and excretion images at 1 min (B) and 20 min (C) show severely impaired perfusion of the transplant kidney in the right iliac fossa with slowly increasing uptake but hardly any excretion to the bladder. Renogram curve (D) shows the typical flat curve of a badly-functioning kidney but without the initial vascular spike usually seen with acute tubular necrosis. Diagnosis: severe rejection.

In acute oliguria, particularly in the postoperative period, a perfusion study using ^{99m}Tc-MAG3 or DTPA gives an image of the distribution of blood flow within the kidney, and an estimation of its perfusion. With ATN, which is very common in the postoperative

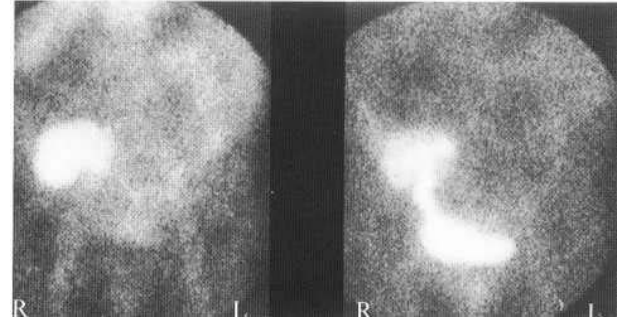


Fig. 29.51 Suspected obstruction in renal transplant. ^{99m}Tc-DTPA study shows good uptake at 2 min (left) with activity reaching the bladder via a distended ureter and collecting system at 20 min (right). Diagnosis: obstruction confirmed.

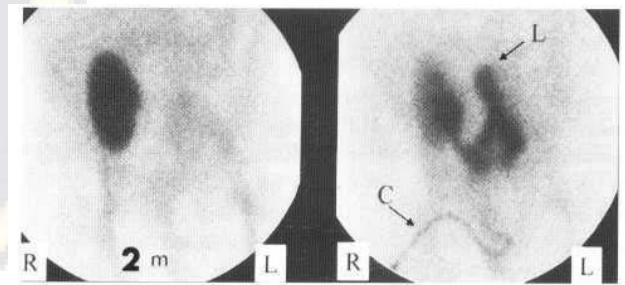


Fig. 29.52 Sudden deterioration in renal transplant function! study shows normal uptake at 2 min (left); at 20 min (right) some activity is draining via a bladder catheter (C) but much of the activity is leaking into the peritoneal cavity (L). Diagnosis: ureteric leak.

period after cadaveric transplantation, perfusion is relatively well maintained (Fig. 29.48). If oliguria results from thrombosis of the transplant renal artery or vein, the kidney becomes avascular and appears on scintigraphy as a photon-deficient area (Fig. 29.49). Acute rejection is associated with vascular obstruction at arteriolar level, and scintigraphy shows severely impaired perfusion, but enough to demonstrate the kidney is viable (Fig. 29.50). Although renography is not the method of choice for detecting outflow problems, the demonstration of delayed clearance of tracer from the renal pelvis supports the diagnosis of obstruction at the vesico-ureteric anastomosis (Fig. 29.51). Another cause of sudden deterioration in function, particularly in the postoperative period, is leakage of urine from the bladder or ureter, and again scintigraphy may be occasionally helpful in this situation (Fig. 29.52). Transplant renal artery disease is best demonstrated by magnetic resonance angiography.

Reflux and infection The major advantage of indirect radionuclide cystography is that it avoids the need for bladder catheterisation. The disadvantage is its lack of anatomical detail. For infants and children with suspected reflux disease, an appropriate strategy is to carry out X-ray micturating cystography at the initial assessment in order to detect anatomical abnormalities of the outflow tract as well as looking for reflux. Indirect radionuclide cystography can then be used as the follow-up examination to monitor response of reflux to treatment (Fig. 29.53). The indirect radionuclide method also allows monitoring of individual renal function. Using ^{99m}Tc-MAG3 as the tracer, renal images about 2 min after injection should be of sufficient quality

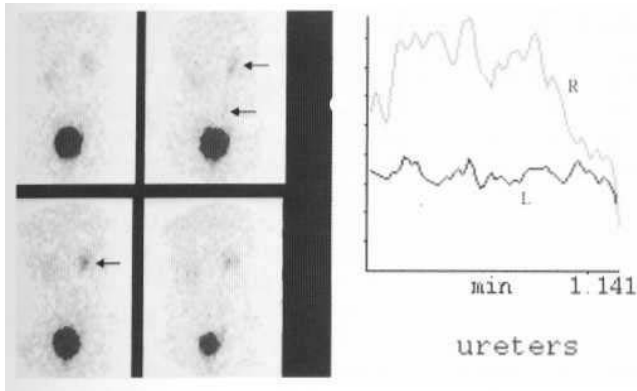


Fig. 29.53 Radionuclide cystography showing reflux. Selected images from the dynamic sequence obtained during micturition (left) show tracer appearing in the right kidney and ureter as the bladder empties (arrows). Time-activity curves over left and right ureters (right) show no reflux on the left and mild but prolonged episodic reflux on the right.

to show major scars, but DMSA scintigraphy produces better anatomical detail and a more accurate estimate of individual renal function.

URODYNAMICS

Tim Whittlestone

Urodynamic studies provide accurate and objective information on the pathophysiology of the lower urinary tract in patients with symptoms suggesting dysfunction of the bladder and/or urethra. The basis of urodynamics is the recording of pressure within the bladder (the cystometrogram) or urethra (the urethral profile) and the flow of urine (during voiding (the flow rate). The relationship between pressure and flow has been studied for 50 years but refinements in techniques and advances in technology, such as the addition of ultrasound and real-time imaging, have made urodynamics an accurate science.

In 1973 the multidisciplinary International Continence Society (ICS) realised the need for uniform standards and terms in urodynamic studies. The ICS has since published a series of recommendations that should be used when dealing with lower urinary tract function.

Lower urinary tract physiology

There are two distinct phases in lower urinary tract function: storage and micturition. During storage, the normal detrusor function is characterised by an increase in bladder volume as it fills with urine but no significant rise in bladder pressure or involuntary contractions. During this phase the urethral closure mechanism maintains a positive pressure and continence is achieved. When the bladder is full to its maximum functional capacity, sensory mechanisms signal to the cortex and the subsequent conscious desire to void may be inhibited or acted upon. During micturition, normal detrusor contraction effectively empties the bladder as the urethral sphincter mechanism relaxes. The pressure within the bladder during micturition (P_{det}) is the sum of the pressure generated by the

detrusor smooth muscle (P_{det}) and any contribution from abdominal wall straining (P_{abd}). Hence,

$$P_{det} = P_{ves} - P_{abd}$$

Common urodynamic disorders Lower urinary tract dysfunction may be caused by:

1. A disturbance of nervous control
2. Disorders of muscle function
3. Structural abnormalities.

Disturbances of nervous control The clinical picture is dependent upon the extent of denervation of the lower urinary tract. Complete lesions of the lower spinal cord decentralise the bladder and urethra; the bladder becomes acontractile and the urethral sphincter inactive. Bladder emptying then relies on abdominal straining. Lesions above the fifth lumbar segment preserve spinal reflexes but the coordination between the bladder and urethra is lost (detrusor sphincter dyssynergia). Cerebral damage may result in one of many Urodynamic disorders. Damage to the frontal lobes results in incontinence. Damage to the basal ganglia leads to involuntary bladder contractions (detrusor overactivity).

Disorders of muscle function Overactivity of the detrusor smooth muscle in the absence of any discernable cause (idiopathic detrusor instability) is a common Urodynamic finding and leads to urgency, frequency and urge incontinence. Many disease processes that reduce bladder compliance, radiotherapy being one common example, may compromise muscle function and reduce bladder capacity. Bladder outflow obstruction caused by prostatic enlargement may lead to either under- or overactivity of the bladder muscle.

Structural abnormalities Pelvic floor dysfunction, bladder neck descent and urethral sphincter incompetence are common urodynamic findings in postpartum women with stress incontinence. Bladder diverticula, often the result of chronically raised bladder pressure, are clearly seen with videourodynamics and may affect both the pressure and flow characteristics. Finally, there is a trend for urologists to reconstruct the lower urinary tract using bowel segments after total cystectomy. Both storage and voiding abnormalities may arise following reconstruction and synchronous cystometry and cystography can be invaluable in addressing these problems.

Urodynamic techniques

Urodynamics encompasses a number of complementary techniques of varying degrees of complexity, the application of which needs to be tailored to meet the clinical requirements of each patient. Those with particular relevance to the radiologist are:

- Ultrasound cystodynamogram
- Intravenous urodynamicogram
- Videocystometry.

Ultrasound cystodynamogram (USCD) The simplest investigation in the assessment of voiding dysfunction is the measurement of urinary flow rate using a volumetric flow meter. The device measures the volume of urine passed per unit time and the flow rate is expressed in millilitres per second. When the flow rate is combined with ultrasound the resulting USCD reveals more detailed information.

The subject usually attends for the investigation with a full bladder. The bladder is scanned with any ultrasound probe that allows adequate visualisation and the volume of urine is calculated; this is the functional bladder capacity. After the subject has voided into a suitably prepared flow meter, in private, the bladder is scanned once again to provide an assessment of the residual volume. This simple technique provides a non-invasive measurement of bladder emptying and urinary flow. It is particularly useful in the diagnosis of bladder outflow obstruction, the monitoring of patients with acontractile bladders and following surgical procedures on the lower urinary tract.

Intravenous urodynamicogram (IVUD) The IVUD is a combination of the conventional intravenous urogram and the assessment of urinary flow rates. It has largely been replaced by USCI).

In addition to the upper tract films of an intravenous urogram the patient performs a flow rate when the bladder feels full. The subsequent postmicturition film after voiding allows an assessment of the residual volume.

Videocystometry (VCMG) Generally, the majority of urodynamic units have neither fluoroscopic screening nor video recording facilities. However, the combination of synchronous cystography and cystometry with video recording (VCMG) is recommended in the assessment of complex cases, younger patients, neuropathic patients, those for whom corrective surgery has failed and patients with reconstructed bladders. Radiological screening provides real-time anatomical information during bladder filling and during micturition. It also allows the assessment of ureteric reflex, bladder neck support, the level of outflow obstruction and the competence of the urethral sphincter mechanism.

With the patient supine on the X-ray screening table the external urethral meatus is cleaned with antiseptic solution and 1% or 2% lignocaine gel is instilled into the urethra. A JOF filling catheter is inserted into the bladder and any residual urine drained. Fine-bore pressure catheters are inserted into the bladder and rectum (or vagina) and connected to fluid-filled pressure transducers

(Fig. 29.54). Subtraction of the rectal pressure from the bladder pressure allows the true detrusor pressure to be constantly displayed. The pressure transducers are zeroed to atmospheric pressure and raised or lowered to the level of the symphysis pubis. Care is taken to exclude air bubbles from the pressure lines and transducers. Contrast medium at room temperature is instilled into the bladder by a peristaltic pump at a constant rate (typically 50ml/min). When the patient senses that the bladder is full (first desire to void) the X-ray table is tilted to the standing position. Filling may continue until the maximum bladder capacity is reached (strong desire to void). The filling catheter is removed prior to voiding and the table turned to the oblique position. The patient voids into a standard flow meter. X-ray screening may be continuous throughout the investigation or at intervals, depending on the information sought by the investigator. The residual volume can be calculated at the end of voiding. It is common to ask the patient to inhibit micturition during the test—the 'stop test'. In men, contrast medium will be milked back from the distal sphincter proximally through the bladder neck and into the bladder. If there is bladder neck obstruction, contrast will be trapped within the prostatic urethra.

Videourodynamic equipment is becoming increasingly sophisticated but all systems allow the pressure and flow data to be displayed alongside the real-time cystogram. Video recording allows analysis later and demonstration of the results to other specialists.

Upper urinary tract urodynamics

Radiologists are often called upon to confirm upper urinary tract obstruction. Modern imaging techniques have largely dispensed with the need for upper tract urodynamics (the Whitaker test); however, in the absence of any definite obstructing lesion or calculus, where there is pelvic/lyceal dilatation and persisting symptoms upper tract studies may be of use. Under normal circumstances urine accumulates in the renal pelvis at a resting pressure of less than 5 cmH₂O. The pelvic pressure rises to 10 cmH₂O once dis-

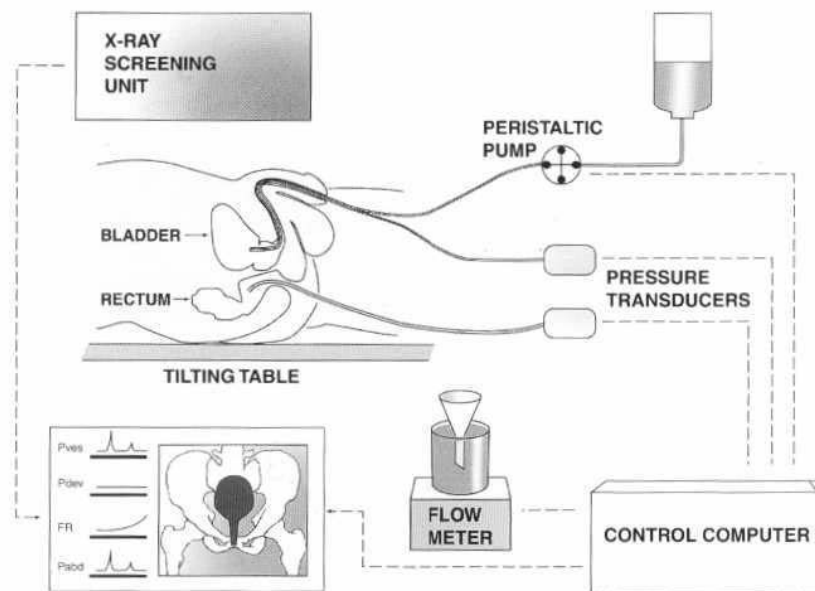


Fig. 29.54 Set-up for lower urinary tract urodynamics.

tended and urine enters the ureter to be transported to the bladder by ureteric peristalsis. In obstruction, peristalsis becomes disordered and the pressure in the renal pelvis will rise above physiological levels.

The Whitaker test is performed following insertion of a nephrostomy tube and can be supplemented by fluoroscopy to define the anatomy of the upper tracts simultaneously. Bladder pressure is constantly measured by an indwelling urethral pressure catheter. Dilute contrast is infused into the nephrostomy tube via one arm of a Y connector at 40 ml/min. The other arm of the Y is connected to a pressure transducer. The bladder pressure is continuously subtracted from the pelvic pressure. A pressure difference between the renal pelvis and bladder of less than 45 cmH₂O excludes obstruction. If the renal pelvic pressure exceeds bladder pressure by more than 22 cmH₂O obstruction is confirmed. Between 15 and 22 cmH₂O the result is equivocal. If both the bladder and renal pelvic pressure rise equally together, vesicoureteric reflex has occurred.

RADIOLOGICAL PROCEDURES IN CHILDHOOD

David Grier

This section will review the common imaging investigations of the urinary tract in children, together with relevant anatomy. Many of these techniques are similar to those used in adults but need some modification when applied to children, and a few are peculiar to children. Examinations in children may take longer to perform than equivalent studies in adults, but it is important to gain the trust and confidence of children and their parents if the examinations are to be successful. An awareness of radiation protection is important. Children are relatively more vulnerable to the deleterious effects of ionising radiation as they are still growing and have a longer life expectancy than adults. Examinations involving ionising radiation need to be justified and optimised if they are to be performed. Every attempt should be made to answer the clinical question using techniques that do not employ ionising radiation, especially ultrasound.

Ultrasound

The two most frequent indications for renal sonography are the evaluation of an antenatal abnormality (hydronephrosis or cystic change) and the investigation of a child who has had a urinary tract infection (UTI). Less common reasons include children with conditions associated with renal anomalies.

Renal anatomy The kidneys of neonates and young children differ from those of older children and adults in many respects, not just in size. There is a gradual transition in the sonographic appearance with age. The kidneys of a term neonate measure approximately 4–5 cm in length. Because there is no significant fat in the renal sinus around the hilar vessels and pelvis they lack the typical increased central hilar echogenicity seen in older children and adults. The renal contour may be quite lobular, reflecting persistent fetal lobulation. The medullary pyramids are usually very prominent and are of much lower echogenicity than the overlying cortex (Fig. 29.55). This may be so marked as to simulate dilated calyces unless this variation is appreciated. Some neonates in the first few days of life may demonstrate paradoxically echogenic

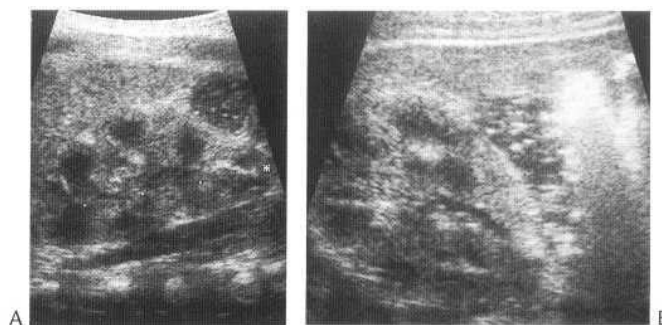


Fig. 29.55 Renal ultrasound. Corona (A) and transverse (B) images of a neonatal kidney demonstrating prominent hypoechoic medullary pyramids and no renal sinus fat.

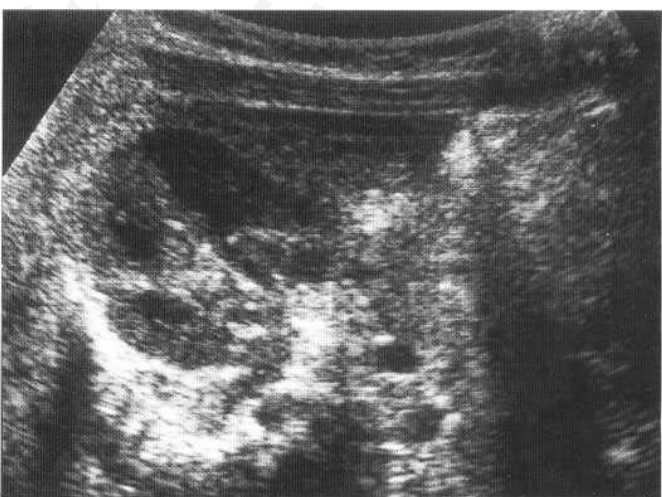


Fig. 29.56 Renal ultrasound. Corona (A) and transverse (B) images of the kidney of a 10-year-old child. The medullary pyramids are less conspicuous than in the neonatal period and there is now some echogenicity around the renal hilum.

medullary pyramids, which resolve once normal urine flow is established. This is due to deposition of proteinaceous deposits in the renal tubules (Tamm-Horsfall proteinuria), which are cleared as urine flow increases. The above appearances may be quite

striking in neonates, but become less obvious with increasing age as the kidney takes on a more typical adult configuration. Renal length also increases throughout childhood to the average adult length of 11 cm. In neonates the renal pelvis is often visible, although it should be less than 5 mm in transverse (AP) diameter. There is often a considerable extra-renal component to the pelvis.

In older children perisinus fat is laid down, producing the central hilar echogenicity within which is the renal pelvis. The medulla and cortex become more similar in echogenicity and are usually of slightly lower echogenicity than the adjacent liver and spleen. The contour of the kidney becomes smoother as fetal lobulation resolves (Fig. 29.56).

Technique The ultrasound examination should attempt to evaluate the whole urinary tract (bladder, ureters and kidneys). In all children, and especially those who are not toilet-trained, the examination should begin with the bladder in case it spontaneously empties before it has been imaged. It should be thin-walled (<3 mm) and contain clear urine. Stasis, infection or haemorrhage may cause urinary sediment or debris. Abnormalities such as wall thickening, diverticula, ureterocele and calculi should be sought. Ideally the bladder should be examined after voiding to give an estimate of residual volume, although this is not always possible in children who are not toilet-trained. Dilated ureters are identified posterior to the bladder as anechoic tubular structures which may alter their configuration due to peristalsis. Non-dilated ureters are not visible.

Good views of the kidneys can be obtained by scanning with the child prone—in most children the relatively superficial location of the kidneys facilitates good views. However, this is not always practicable in young babies, in whom excellent coronal views can be obtained instead. Images are obtained in longitudinal and transverse planes. Renal length should be assessed and related to age (or weight). Contour defects may suggest scarring if they are superficial to medullary pyramids (and hence calyces), or fetal lobulation if they are between pyramids. The kidneys should also be examined with the child supine. Dilatation of the renal pelvis and calyces is noted. The transverse diameter of the renal pelvis at its widest point is recorded. Duplex renal collecting systems may be identified in older children, even in the absence of dilatation, by a double renal sinus pattern (one for the upper and another for the lower moiety pelvis).

Fluoroscopy

Micturating cystourethrography This is the commonest fluoroscopic examination in infants and young children. The most frequent indications are the investigation of antenatal hydronephrosis and following a urinary tract infection. Less commonly it is used to evaluate siblings of children with vesicoureteric reflex and children with suspected structural abnormalities of the lower urinary tract.

It is a traumatic examination for child and the parents (and occasionally the operator) and exposes the child's gonads to a high radiation dose. This may be minimised by adequate justification, attention to collimation, minimal screening times and selection of the antiscatter grid. Dose-saving facilities on digital units are also important.

The urinary bladder is catheterised aseptically with a small catheter (6-S F) depending on the age of the child. This is taped loosely to the perineum to facilitate rapid removal. The bladder is

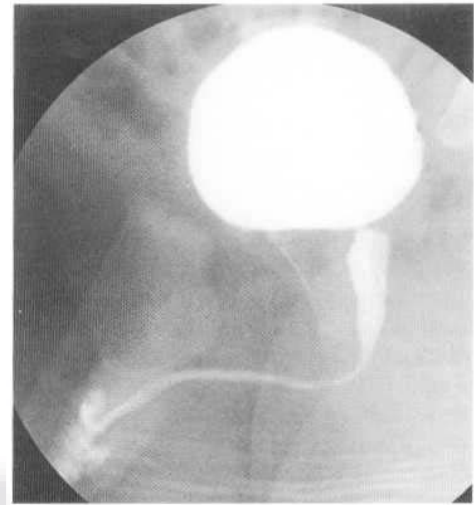


Fig. 29.57 Micturating cystourethrogram-male. An oblique voiding image demonstrates the whole urethra with no foreshortening. The filling defect in the posterior urethra represents the verumontanum.



Fig. 29.58 Micturating cystourethrogram-female. A supine voiding image in a female child. The urethra is shorter than the male and is straight.

then emptied through the catheter and a sample sent for culture. With the child supine on the screening couch, and gently restrained if necessary, dilute water-soluble contrast medium is dripped into the bladder from a bottle. The iodine content of the contrast medium should be about 150 mg/ml. An early filling image of the bladder is obtained in the supine (AP) position and then oblique views of the bladder base are taken when the bladder is nearly full (to look for reflux into the distal ureters). A voiding image of the urethra is required, especially in boys (Fig. 29.57). In girls the bladder should continue to be filled with the child supine until voiding begins around the catheter (Fig. 29.55). At this point the catheter is removed and spot films of the urethra are obtained during micturition. Images are then taken of each renal area to document the presence or absence of reflux to the level of the kidney.

With boys, the child needs to be positioned obliquely to open out the urethra (which would otherwise be foreshortened in the AP projection) and to equalise soft-tissue densities between bladder base and distal urethra. These views must include the bladder base and the tip of the penis. Cyclical filling of the bladder may increase the sensitivity for detection of vesicoureteric reflex at the expense of increased radiation dose. Antibiotics should be considered in those who have had a recent urinary tract infection and those with structural abnormalities, as detected by ultrasound.

Genitography This is required in the presence of structural abnormalities of the urogenital tract and in the presence of ambiguous genitalia. It is usually combined with micturating cystourethrography. Water-soluble contrast medium is injected gently into the perineal orifice and spot images obtained in the frontal (All) and lateral projections to delineate anatomy.

Loopography This is required to evaluate the anatomy and patency of distal small or large bowel after a defunctioning surgical procedure, prior to reconnection. This is commonly performed in infants with anorectal anomalies who may have an associated fistula to the urogenital tract (posterior urethra in boys and vagina in girls). The study is performed by introducing a small catheter into the distal stoma and injecting water-soluble contrast media by hand under high pressure. The distal bowel is distended and any fistula present has the best chance of being identified. The lateral projection is the most useful. Antibiotic cover is required because of the risk of bacteraemia and sepsis. This examination is usually performed in conjunction with a micturating cystogram.

Radionuclide radiology

General principles The commonest radionuclide investigations of the urinary tract in children are dynamic renography and static renal imaging. The former is helpful in the evaluation of the dilated urinary tract and the latter for the detection of structural abnormalities of the kidney, especially renal scarring after infection and positional abnormalities such as ectopia and aplasia. The activity of injected radiopharmaceutical is scaled down from adult doses and depends upon body weight, although there is an irreducible minimum activity consistent with satisfactory count rates and image quality. Sedation is required in less than 10% of patients in most centres with experienced staff used to working with children. A quiet environment, sufficient distraction, swaddling and immobilisation devices are helpful. The use of a topical anaesthetic cream and distraction techniques during injection are important.

Intravenous urography

This is not commonly performed in children as most clinical problems can be resolved with a combination of ultrasound and radionuclide techniques. The main indications for intravenous urography (IVU) are the clarification of structural renal and ureteric abnormalities, especially those of the collecting system, typically prior to surgical intervention. There is now no routine indication for the IVU in the evaluation of urinary tract infection and the detection of renal scarring in children. A non-ionic water-soluble contrast medium with an iodine content of 300 mg/ml is injected in a dose that depends on body weight (approximately 2 ml/kg to a maximum of 50 ml). Children are fasted for 3-4 hours prior to injection but bowel preparation is not required. Abdominal compression is not practicable in infants and young children and is not routinely used in older children. Tomography is unnecessary as line detail of

calyceal anatomy and renal contours is not sought, and because of the increased radiation dose.

It is prudent to obtain a plain film of the kidneys, ureter and bladder before contrast medium injection so as not to overlook calculi. The remaining radiographs should be tailored to answer the clinical question. An immediate film is not usually required and may be difficult to obtain if the injection is prolonged because of a small canula. A film at about 10-15 min after injection is sufficient to demonstrate normal pelvicalyceal anatomy, although delayed images will be required if there is collecting system dilatation. A further radiograph at about 20-30 minutes (after bladder emptying) is helpful in determining drainage from the collecting system. In the presence of upper tract dilatation, further delayed films will be required to completely display anatomy. A prone radiograph is useful in older children to demonstrate the ureters, and a lateral film is helpful in younger children and infants.

If bowel gas and contents obscure detail of the pelvicalyceal systems (particularly on the left), distending the stomach with gas may help. This may be achieved by getting the child to ingest a drink just prior to exposure, or in infants, by insufflation of air through an oesophageal tube passed for the purpose. The urinary bladder is not assessed as completely as in adults and is better evaluated with ultrasound. The functional significance of a distended renal pelvis may be assessed by the response to an intravenous injection of furosemide or an oral water load, especially in children with a history suggestive of intermittent pelviureteric junction obstruction. Indeed it may be useful to perform the IVU during an attack of pain.

Interventional procedures

These are performed less commonly in children than adults, although the principles of access and technique are similar. They generally require an anaesthesia, and may be performed in the radiology department, in the operating theatre or occasionally elsewhere (e.g. intensive care unit). All of these techniques require some form of imaging guidance. In children, ultrasound is the most useful modality for this because of its portability, lack of ionising radiation and ability to be used in 'real time'. (Caution should be exercised in the presence of clotting abnormalities, which should be corrected before the procedure.) The use of antibiotics should be considered, especially where the procedure is for suspected sepsis. It should be remembered that the presence of a dilated collecting system does not necessarily equate to obstruction and so drainage of such a system may not always be helpful.

Computed tomography (Fig 29.59)

CT of the kidneys is only rarely required in children. The commonest indications are blunt abdominal trauma and the evaluation of renal tumours (nephroblastoma, neuroblastoma and renal cell carcinoma and lymphoma). It is a high radiation dose procedure and so needs adequate justification. There is little role for CT scans of the kidney to be performed without intravenous contrast medium, unless one is looking specifically for calculi. The presence or absence of calcification within a renal mass is rarely helpful in the differential diagnosis. There is much less retroperitoneal fat in infants and young children compared with adults, so inherent contrast is less without the use of intravenous contrast medium. In trauma the use of intravenous contrast medium is mandatory to enable detection of focal or global areas of reduced or absent vascularity. It is sometimes helpful to obtain a plain radiograph of the abdomen directly after CT to demonstrate the renal collecting system and identify subtle leaks (especially after trauma).

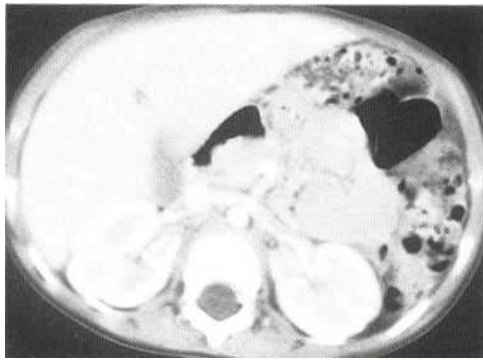


Fig. 29.59 Computed tomography. Axial image through renal hilum shows clearly the left renal vein and right renal artery. There is prominent fetal lobulation and corticomedullary differentiation.

Sedation or general anaesthesia will be required if the child is too young or ill to cooperate. In older children it is helpful to have an intravenous cannula in place prior to arrival at the CT scanner so that trust and cooperation are not jeopardised during the scan. Water-soluble contrast medium should be injected at a dose of 2 ml/kg (up to a maximum volume of 50 ml) just prior to scanning. Use of a pitch of 1.5 on spiral scanners is adequate. Slice thickness will depend on the size of the child and varies between 5 mm and 10 mm reconstructions.

Magnetic resonance imaging

MRI is in many ways an ideal modality for imaging children, as it does not use ionising radiation and has good soft-tissue contrast resolution and a multiplanar capability. Its disadvantages include relatively longer scan times, noise and the enclosed position of the patient in the scanner. Because of the frequent need for sedation or anaesthesia, the full potential of MR has not yet been exploited in young children. Its main role in children is in the staging of renal tumours, and in answering specific questions not resolved by ultrasound.

Gadolinium contrast medium may increase the conspicuity of intrinsic renal abnormalities. It can also be used in the form of a dynamic study, analogous to radionuclide renography, with regions of interest being drawn over both kidneys, and a plot made of renal transit of contrast medium through the kidney.

Sedation and anaesthesia

Most diagnostic imaging may be performed in infants and children without sedation and anaesthesia. A careful explanation of the procedure to the child and parents, calm and confident staff and a quiet environment will facilitate this. Examinations need to be tailored to answer the clinical question that has been posed. To obtain high-quality examinations of young and ill children, sedation or anaesthesia are frequently required. This particularly applies to MRI, CT and interventional procedures. Both CT and MRI have advantages and disadvantages, and local experience, circumstances and resources will determine which is most appropriate.

APPENDIX: WATER-SOLUBLE CONTRAST

Water-soluble contrast media are a group of compounds that absorb X-rays and therefore increase the radiodensity of the structure that

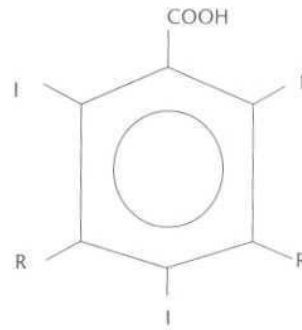


Fig. 29.60 Molecular structure of the building block for water-soluble contrast media.

contains them. In urological (and angiographic) practice they all depend on iodine atoms for their radiodensity. Original work with sodium iodide in the first third of the last century showed the usefulness of iodine-containing compounds as a contrast medium but this preparation was too toxic for clinical use. In the 1950s, relatively safe contrast media were developed based on a tri-iodinated benzene ring in which iodine atoms were attached to the benzene ring at the carbon atoms conventionally labelled 2, 4 and 6 (Fig. 29.60). The solubility of this compound depends on a carboxyl radical attached to the benzene ring at position 1. By varying the radicals attached to the remaining carbon atoms of the benzene ring (3 and 5), a family of contrast media were produced (diatrizoate, iohalamate, iothalamate and ioxithalamate). They were used extensively in intravenous urography, angiography and other conventional investigations such as retrograde pyelography, cystography and urethrography. Conventionally, contrast medium strength is described as milligrams of iodine per millilitre; commercial preparations having been available from 150 to 420, depending on the clinical application.

Although these compounds are extremely safe compared with many medical compounds they have a number of disadvantages. They all contain a carboxyl radical in order to be adequately water-soluble. This, however, is a proton donor and therefore they are all ionic salts, the cation being sodium or meglumine (or a mixture). Consequently, at therapeutic doses they have a high osmotic potential. Injected intravenously this is responsible for minor (but side-effects such as nausea and vomiting. Intravenously, there is an intense local sensation of heat and pain, worse in ischaemic limbs. The high osmotic potential also constitutes a substantial cardiovascular challenge, prohibits use in the sub-arachnoid space and is dangerous if aspirated into the lungs. In addition to these problems there is a rare but well-recognised risk of anaphylactoid sensitivity reactions that may lead to wheeziness, laryngeal oedema, cardiovascular collapse and fatalities. Although there is still considerable uncertainty about the exact mechanism involved in the latter group of idiosyncratic sequelae, it appears related at least in part to the high osmotic potential of these compounds. The osmolality of blood is approximately 290 mmol/kg water. 150 strength ionic contrast is approximately 701 mmol/kg, while 350-421 strength ionic contrast (the range used for intravenous urography) is approximately 2000 mmol/kg.

In the 1960s, therefore, a group of compounds, collectively referred to as non-ionic contrast media (compared to the pre-existing ionic contrast), were developed to overcome these problems. The non-iodine radicals at positions 3 and 5 (including the

ionic carboxyl radical) were replaced by long aminohydrocarbons which provide adequate solubility without ionising. This family of non-ionic contrast media maintain the radio-opacity of the previously available agents but with dramatically reduced osmotic potential. Examples of this type of compound are iopromide, iohexol, iopamidol, ioversol, iopentol, iobitridol and iomeprol. Further reduction in osmotic potential has been achieved by combining molecules into pairs producing non-ionic dimers such as iotrolan and iodixanol. At all concentrations the non-ionic contrast agents have an osmotic potential of the order of 40-50% (or less) compared with that of ionic compounds; 350-370 strength non-ionic (monomeric) contrast being approximately 800 mmol/kg, the non-ionic dimers being less than half this for equivalent iodine concentrations.

It is worth considering at this stage how these contrast media are used. Essentially contrast medium use can be considered in four categories:

- *Luminal filling* for example, pyelography (retrograde and antegrade), cystography and urethrography. Because contrast is injected directly into the lumen of the structure to be examined, only a relatively low concentration is required, 150 strength usually being sufficient. Very little contrast is absorbed during these procedures and therefore contrast-related side-effects are rare.
- *Angiography* for example, renal arteriography and testicular venography. The degree of contrast required for adequate imaging relates to the regional blood flow and the quality of the fluoroscopic equipment; 240-300 strength is usually employed.
- *Renal excretion*—essentially the IVU. This depends on adequate renal function and it is pointless attempting an IVU once the creatinine is above 500 $\mu\text{mol/litre}$. Even with good renal function a relatively high concentration of contrast is required, as it is administered intravenously and has to be filtered by the kidney; 350-370 strength contrast is generally used. Around 99% of intravenous (or intra-arterial) contrast is excreted by the kidneys, with a half-life of 1-2 h with normal renal function.
- *Parenchymal staining (enhancement)* essentially the postcontrast CT scan. With good quality equipment and correct timing, 300-350 strength contrast produces adequate contrast.

As indicated above all of the contrast media considered here are extremely safe. In lumen-filling urological procedures the risk of contrast-related side-effects is extremely remote. It is therefore safe to continue with the routine use of 150 ionic contrast medium for antegrade and retrograde pyelography, cystography, urethrography, conduitograms and related procedures unless the patient has a history of major contrast sensitivity reactions. In these circumstances the tiny amount of contrast that might be absorbed during the procedure could potentially provoke a significant reaction. It would therefore be best to avoid a contrast investigation, or if necessary use a gadolinium preparation, which has good radiodensity and because of its renal excretion can also be used for intravenous urography.

Intra-arterial use of ionic agents has long been discontinued because of its unpleasant local side-effects. Intravenous use of ionic agents is associated with a high rate of minor side-effects (approximately 5%, mainly nausea and vomiting), rarely with severe cardio-

vascular and hypersensitivity reactions, with occasional fatalities (11/214 033). Intravenous non-ionic agents have a much lower incidence of both major and minor side-effects, the largest study available suggesting an incidence of severe or very severe reactions being reduced from a rate of 0.04% with ionic agents (169 284 cases) to 0.004% with non-ionic agents (169 363 cases). Postcontrast nephrotoxicity also appears to be less frequent with low-osmolality contrast agents compared to high-osmolality contrast agents.

Initially because of cost considerations, non-ionic contrast agents were introduced only for patients most at risk of adverse reactions with ionic agents. This included children, the elderly, patients with a history of asthma, allergy or hypersensitivity, severe cardiopulmonary disease, renal impairment, diabetes mellitus or myeloma. In practice they are now universally indicated for intravenous use.

As well as reducing the rate of adverse reactions, the lower osmolality of the non-ionic contrast agents provokes less osmotic diuresis. This results in improved imaging, as the concentration of contrast in the collecting system, and hence its opacification, appears to be increased, although this potentially comes at the cost of reduced distension of the collecting system.

The following advice is taken from that of the Royal College of Radiologists on the management of reactions to intravenous contrast media. In the event of an adverse reaction of any severity, intravenous access should be maintained and the patient observed. For mild adverse reactions (nausea, vomiting, modest urticaria), this is likely to be sufficient, along with reassurance and where necessary an oral antihistamine. For more serious reactions, 100% oxygen at 10-15 l/min should be administered. Wheeze should be treated with nebulised salbutamol (5 mg in 2 ml). If hypotension develops, intravenous fluids are infused rapidly (Gelofusine 10-15 ml/kg). Bradycardia can be treated with atropine 0.6 mg, repeated every 5 min to a maximum of 3 mg. As soon as a cardiovascular disturbance develops, an anaesthetist/cardiac arrest team should be summoned urgently. If bronchospasm, urticaria or laryngeal oedema are developing, 500 mg of intravenous hydrocortisone can be administered intravenously. This may not, however, produce a response for some time and 10 mg of chlorphenamine (chlorpheniramine) given slowly over 1-2 min intravenously may be required. In the event of life-threatening hypotension/cardiovascular collapse, adrenaline (epinephrine) 500 μg (0.5 ml of 1/1000) should be given intramuscularly. Standard cardiopulmonary resuscitation procedures should be instituted as soon as cardiovascular collapse occurs.

A final point about intravenous contrast agents worth considering is the potential interaction with other drugs. The two in common use to be aware of are beta blockers and metformin. Beta blockers increase the risk of anaphylactoid reactions to contrast medium by up to three times. Stopping beta blockers before the examination is, however, also potentially dangerous and therefore it is extremely important to ensure the examination is fully justified and to remain aware of the potentially increased risk.

Lactic acidosis, a life-threatening metabolic disturbance, may develop in rare instances in diabetic patients given intravenous contrast while on metformin. This is related to renal excretion of metformin failing if there is renal insufficiency after contrast medium administration. However, metformin has a short half-life. The current advice therefore is for patients to stop taking it for 48 h from the time of the investigation and then have their renal function checked and shown to be normal before restarting it.

REFERENCES AND SUGGESTIONS FOR FURTHER READING

- Amis, F. S. (1999) Epitaph for the urogram. *Radiology*, **213**, 639-640.
- Barrett, B. J., Carlisle, E. J. (1993) Meta-analysis of the relative nephrotoxicity of high and low osmolality iodinated contrast media. *Radiology*, **188**, 171-178.
- Coakley, F. V., Hricak, H. (2000) Radiological anatomy of the prostate gland: a clinical approach. *Radiologic Clinics of North America*, **38(1)**, 15-30.
- Coll, D. M., Herts, B. R., Davros, W. J., Uzzo, R. G., Novick, A. C. (2000) Preoperative use of 3D volume rendering to demonstrate renal tumours and renal anatomy. *Radiographics*, **20**, 431-438.
- Dalla Palma, L. (2001) What is left of i.v. urography? *European Radiology*, **11**, 931-939.
- Emamian, S. A., Nielsen, M. B., Pederson, J. F., Yttc, L. (1993) Kidney dimensions at sonography: correlation with age, sex and habitus in 665 adult volunteers. *American Journal of Roentgenology*, **160**, 83-86.
- Ewan, P. W. (1997) Treatment of anaphylactic reactions. *Prescribers Journal*, **37(3)**, 125-132.
- Field, R., Middleton, W. D. (1992) Recent advances in sonography of the testis and scrotum. *Radiologic Clinics of North America*, **30(5)**, 1033-1053.
- Gore, R. M., Balfé, D. M., Aizenstein, R. I., Silverman, P. M. (2000) The Great Escape: interfascial decompression planes of the retroperitoneum. *American Journal of Roentgenology*, **175**, 363-370.
- Grossleld, G. D., Coakley, F. C. (2000) Benign prostatic hyperplasia: clinical overview and value of diagnostic imaging. *Radiologic Clinics of North America*, **38(1)**, 31-8.
- I leiken, J. P., Forman, H. P., Brown, J., J. (1994) Neoplasms of the bladder, prostate and testis. *Radiologic Clinics of North America*, **32(1)**, 81-98.
- Hogan, M. J., Coley, B. D., Jayanthi, V. R., Sides, W. E., Koff, S. A. (2001) Percutaneous nephrostomy in children and adolescents: outpatient management. *Radiology*, **218**, 207-210.
- Kabala, J. (1991) Attempting to increase the sensitivity of the plain film for ureteric; use of the full bladder. *British Journal of Radiology*, **64**, 1151-1153.
- Kahala, J. E., Kcoghane, S. R. (2001) Varicocele embolisation. *imaging* **13(1)**, 11-17.
- Kahala, J. E., Gillett, D. A., Persad, R. A., Penry, J. B., Gingell, J. C., Chadwick, D. (1991) Magnetic resonance imaging in the staging of renal cell carcinoma. *British Journal of Radiology*, **64**, 683-689.
- Katayama, H., Yamaguchi, K., Kozuka, T., Takashima, T., Seez, P., Matsuura, K. (1990) Adverse reactions to ionic and nonionic contrast media: a report from the Japanese Committee on the safety of contrast media. *Radiology*, **175**, 621-628.
- Katzberg, R. W. (1997) Urography into the 21st century: new contrast media, renal handling, imaging characteristics and nephrotoxicity. *Radiology*, **204**, 297-312.
- Kcoghane, S. R., Jones, L., Wright, M. P. J., Kabala, J. E. (2002) Percutaneous retrograde varicocele embolisation using tungsten embolisation coils: a five year audit. *International Journal of Urology and Nephrology* (in press).
- Kurhanewicz, J., Vigncron, D. B., Males, R. G., Swanson, M. G., Yu, K. K., Hricak, H. (2000) The prostate: MR imaging and spectroscopy. *Radiologic Clinics of North America*, **38(1)**, 115-138.
- Liu, W., Esler, S. J., Kenny, J. J., Goh, R. H., Rainbow, A. J., Stevenson, G. W. (2000) Low-dose nonenhanced helical CT or renal colic: assessment of ureteric stone detection and measurement of effective dose equivalent. *Radiology*, **215**, 51-54.
- Mastromatteo, J. F., Mindell, H. J., Mastromatteo, M. F., Magnant, M. B., Sturtevant, N. V., Shaman, W. P. (1997) Communications of the pelvic extraperitoneal spaces and their relation to the abdominal extraperitoneal spaces: helical CT cadaver study with pelvic extraperitoneal injections. *Radiology*, **202**, 523-530.
- Morcos, S. K., Thomsen, H. S., Webb, J. A. W., and members of the Contrast Media Safety Committee of the European Society of Urogenital Radiology (ESUR) (1999) Contrast media-induced nephrotoxicity: a consensus report. *European Radiology*, **9**, 1602-1613.
- Muttarak, M., Wilfred, C. G., Peh, C. G. (2000) CT of unusual iliopsoas compartment lesions. *Radiographics*, **20**, S53-S66.
- Nolte-Ernsting, C. C. A., Buckner, A., Adam, G. B., et al (1998) Gadolinium-enhanced excretory MR urography after low-dose diuretic injection: comparison with conventional excretory urography. *Radiology*, **209**, 147-157.
- Onishi, T., Oishi, Y., Suzuki, Y., Asano, K. (2001) Prognostic evaluation of transcatheter arterial embolization for unresectable renal cell carcinoma with distant metastases. *British Journal of Urology International*, **87**, 312-315.
- Persad, R., Kabala, J. E., Gillett, D., Penry, B., Gingell, J. C., Smith, P. J. B. (1993) Magnetic resonance imaging in the staging of bladder cancer. *British Journal of Urology*, **71**, 566-573.
- Royal College of Radiologists (1996) *Advice on the management of reactions to intravenous contrast media*. London: Royal College of Radiologists.
- Stacul, F. (2001) Current iodinated contrast media. *European Radiology*, **11**, 690-697.
- Thompson, N. W., Thompson, T. J., Love, M. H. S., Young, M. R. A. (2000) Drugs and intravenous contrast media. *British Journal of Urology International*, **85**, 219-221.
- Vasile, M., Bellin, M. F., Helenon, O., Mourcy, I., Cluzel, F. (2000) Imaging evaluation of renal trauma. *Abdominal Imaging*, **25**, 424-430.
- Whitfield, h. N. (1999) The management of ureteric stones. Part I: therapy. *British Journal of Urology International*, **84**, 916-921.
- Urodynamics**
- Abrams, P. H., Blaivas, J. G., Stanton, S. L., Andersen, J. T. (1988) The standardisation of terminology of lower tract function. *Scandinavian Journal of Urology and Nephrology*, **114**, 5-19.
- Chapple, C. R., Christmas, T. J. (eds) (1990) *Urodynamics Made Easy*. Edinburgh: Churchill Livingstone.
- Mundy, A. R., Stephenson, T. P., Wein, A. I. (eds) (1994) *Urodynamics: Principles, Practice and Application*. 2nd edn. Edinburgh: Churchill Livingstone.
- Whitaker, R. H. (1978) Methods of assessing obstruction in dilated ureters. *British Journal of Urology*, **45**, 15.
- Whittlestone, T. H., Persad, R. (2000) Radical cystectomy and bladder substitution. *Hospital Medicine*, **61**, 336-340.
- Nuclear medicine**
- Britton, K. E., Maisey, M. N. (1998) Renal disease. In: Maisey, M. N., Britton, K. F., Collier, B. D. (eds), *Clinical Nuclear Medicine*, pp. 389-424. London: Chapman and Hall.
- O'Reilly, P., Aurell, M., Britton, K. F., (eds), et al (1996) Consensus in diuresis renography. *Journal of Nuclear Medicine*, **37**, 1872-1876.
- Piepsz, A., Blafox, M. D., Gordon, I., et al (1999) Consensus on renal cortical scintigraphy in children with urinary tract infection. *Seminars in Nuclear Medicine*, **29**, 160-174.
- Taylor, A. (1999) Radionuclide renography: a personal approach. *Seminars in Nuclear Medicine*, **29**, 102-127.

30

THE KIDNEYS AND URETERS

Julian E. Kabala

with a contribution from Carl Roobottom

CONGENITAL LESIONS AND VARIANTS

Fetal lobulation Definitive renal tissue develops in utero from its embryological precursor (the metanephros) in response to local stimulation by the formation of adjacent calyces, as a consequence of the budding of the renal pelvis, which in turn develops from the upper end of the ureter. Renal tissue therefore develops as a series of 8-16 lobules and the lobulated structure remains apparent at birth. This feature gradually disappears over the first 5 years of life as the kidney grows. In up to 5% of the population, however, lobulation persists. This is of no clinical significance but it is important not to confuse it with the scars of reflux nephropathy. Characteristically in persistent fetal lobulation the parenchyma is of normal thickness (14 mm or more) with smooth indentations between the calyces. Where scarring results from vesicoureteric reflux the scars occur over the calyces, which are abnormally clubbed. The characteristic outline of fetal lobulation and its relationship to the calyces (or pyramids) can be seen on IVU, ultrasound, CT and MRI (Fig. 30.1).

Renal pseudotumours Prominent areas of normal renal tissue may develop and appear as mass lesions, particularly on IVU. They are of no clinical significance but may be misdiagnosed as neoplastic masses. A column of Bertin is commonly encountered. This variant is due to a prominent column of normal renal parenchyma, usually at the junction of the upper and middle thirds of the kidney. It is often bilateral. Careful study of it on ultrasound or contrast CT should demonstrate normal renal tissue (Fig. 30.2). A dromedary or splenic hump is a prominence of the superolateral border of the left kidney. Again it can be confirmed

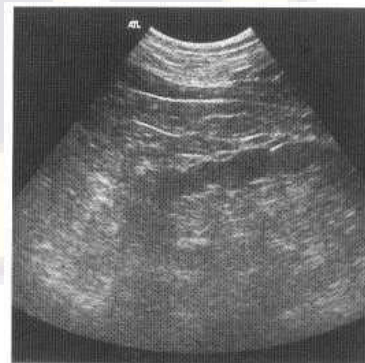


Fig. 30.1 Renal ultrasound demonstrating the characteristic pattern of persistent fetal lobulation.

to represent normal renal tissue on ultrasound (Fig. 30.3) or CT. DMSA scans have been performed to confirm normal renal tissue but this should rarely be necessary with modern imaging.

Renal agenesis Failure of the ureteric bud to reach the metanephros results in renal agenesis. Predictably the ipsilateral ureter and hemitrigone also fail to develop, although occasionally a blind-ending ureteric stump is present. Ipsilateral adrenal agenesis is seen in 10%. Associated ipsilateral urogenital abnormalities are common and include absence of the vas deferens, unicornuate uterus and absence or cyst of the seminal vesicle. Multiple anomalies in other systems may be present, particularly cardiovascular, gastrointestinal and musculoskeletal. The classical association is seen in the VATER syndrome where developmental lesions may include vertebral and ventricular septal anomalies, anorectal atresia, tracheal and oesophageal lesions (fistula and atresia) and radial bone abnormalities.

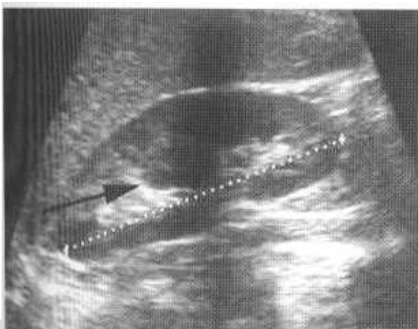


Fig. 30.2 (A) Longitudinal renal ultrasound scan showing a prominent column of Bertin (arrow). (B) Transverse scan showing the same feature (arrow).

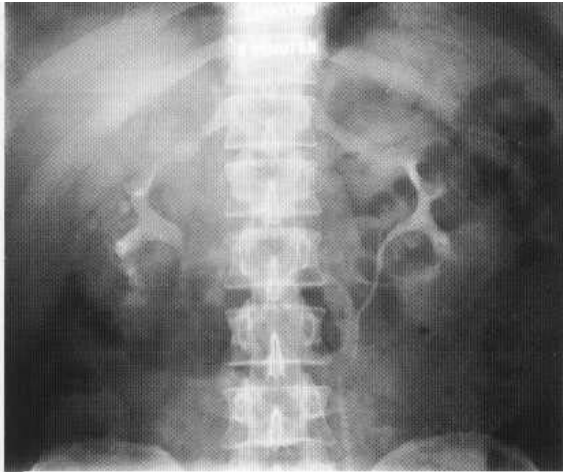


Fig. 30.3 Dromedary hump related to the lateral border of the left kidney on IVU (A) and ultrasound (B).

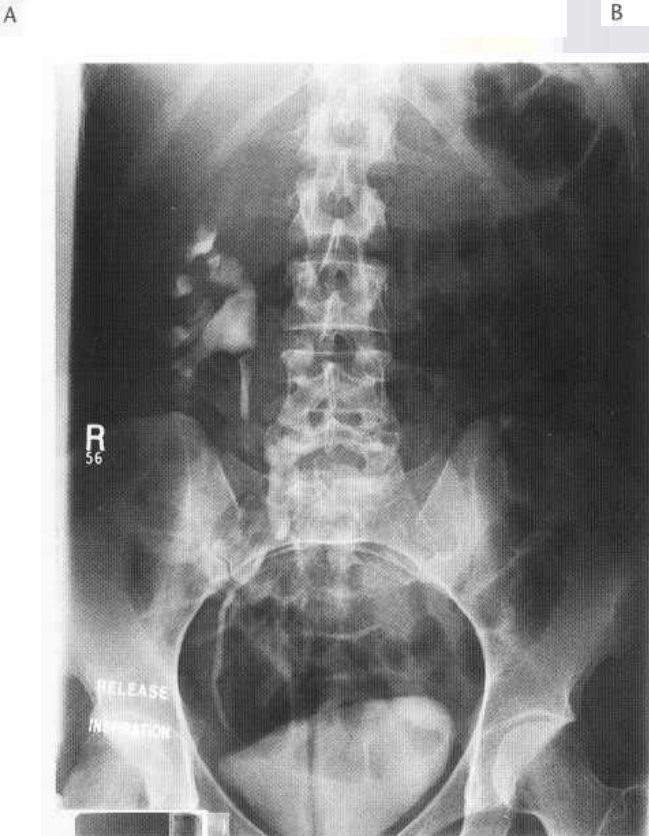


Fig. 30.4 IVU showing left renal agenesis with bowel gas within the left renal bed. The large right kidney shows a bifid renal pelvis, the mildest form of renal duplication.

Unilateral agenesis is not uncommon, occurring in up to 0.1 % of live births with a ratio of three males to one female. As an isolated lesion it is asymptomatic but there is an increased incidence of contralateral renal abnormalities, including ectopia and malrotation. Occasionally unilateral renal agenesis can be diagnosed on plain films by the absence of a renal outline and medial displacement of the splenic (on the left) or hepatic (on the right) flexure into the renal bed. The contralateral kidney, when normal, commonly shows compensatory hypertrophy and this may be visible on the plain film. These features are easier to see on ultrasound and IVU (Fig. 30.4). CT or radionuclide investigation demonstrating unilateral absence of renal tissue can be regarded as definitive. Failure to identify a kidney in the normal site may be due to agenesis, ectopia or nephrectomy. Occasionally a kidney becomes severely

atrophic following a major pathological insult (particularly vesicoureteric reflux or infarct) and may be overlooked, particularly on ultrasound.

Bilateral renal agenesis is rare (1/3000 live births). Oligohydramnios develops as a result of the in utero failure of urine production resulting in Potter's syndrome, with characteristic facies and early death from pulmonary hypoplasia.

Renal dysplasia This failure of development of normal renal tissue is usually unilateral and affects the whole kidney. Occasionally it is bilateral and leads to renal failure in infancy. Rarely it affects the upper pole of one kidney only. On ultrasound the kidney is small, with either a smooth outline or marked fetal lobulation. There is loss of corticomedullary differentiation and tiny cortical cysts may be visible. On IVU the kidneys excrete contrast, which demonstrates a lack of papillary development, the calyces appearing clubbed. There is an association with vesicoureteric reflux and numerous congenital syndromes including Beckwith-Wiedemann and Laurence-Moon-Biedl (Fig. 30.5).

Renal hypoplasia This condition is thought to arise as a result of an intrauterine insult, probably vascular, that impairs adequate development. The kidney is normal in shape and smooth in outline but is small, typically containing five or less calyces, which are also otherwise normal. Similarly the renal parenchyma is normally functioning but the global renal function is reduced in proportion to its size.

Supernumerary kidneys These are extremely rare, usually left-sided, hypoplastic and caudally positioned. Ureteric drainage may be separately into the bladder or into the normal kidney's ureter.

Rotational abnormalities Failure of normal developmental rotation (malrotation) leaves the pelviureteric junction pointing anteriorly. This relatively common, harmless anomaly produces a characteristic appearance on ultrasound, IVU (Fig. 30.6) and CT. Rarely overrotation occurs, leaving the pelviureteric junction pointing posteriorly.

Renal ectopia Failure of complete ascent of the kidney to the level of the second lumbar vertebra is relatively common, the kidney coming to lie anywhere from the pelvis upwards. Overascent is rare. There is usually an anomalous blood supply with multiple renal arteries from the aorta or iliac vessels at the level of the kidney. A pelvic kidney is encountered in 1/1000 live

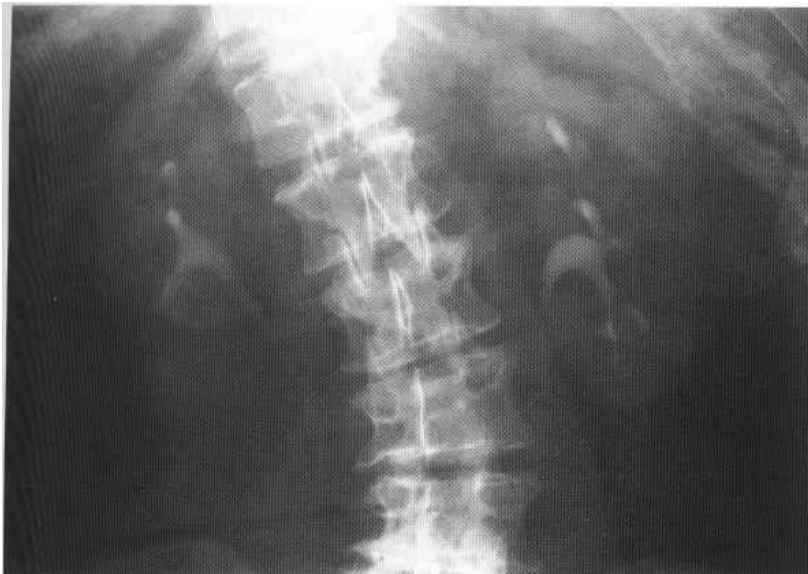


Fig. 30.5 Renal dysplasia in Laurence-Moon-Biedl syndrome showing poorly developed papillae and small communicating calyceal diverticula on IVU.



Fig. 30.6 Malrotation of the left kidney on IVU showing the anteriorly pointing renal pelvis projected over the calyces.

births, with a male predominance of around 1.5 to 1 (Fig. 30.7). The kidney is often small and the pelvic position is associated with an increased risk of trauma, vesicoureteric reflux and calculus formation (due to urinary stasis). There is also an increased



A



Fig. 30.7 Pelvic kidney seen on IVU (A) and (different patient) CT (B).

rate of contralateral renal anomalies, including agenesis and ectopia. When both kidneys remain in the pelvis they may fuse, producing the small pancake kidney, which is very frequently associated with other congenital anomalies.

Overascent is almost always limited by the diaphragm but there may be some superior herniation through a localised eventration, and very rarely a true intrathoracic kidney (Fig. 30.8).

Horseshoe kidney This is a common renal anomaly affecting 1/400 live births, with a 2 to 1 male predilection. In utero contact between the metanephric tissue of the developing kidneys results in a midline connection (isthmus) between the lower poles. The isthmus may be anything from a fibrous band to (more commonly) a block of renal tissue. The ascent of the combined kidneys is arrested in the low abdomen as the isthmus impinges on the inferior mesenteric artery. There is generally associated malrotation and accessory renal arteries. It is often associated with pelviureteric junction obstruction. There is an increased incidence of renal calculi, assumed to be due to relatively poor drainage of the pelvicalyceal systems with the ureters running anteriorly over the isthmus. Its low position directly over the spine also increases the risk of injury. Other associations include anomalies of the gastrointestinal tract and cardiovascular system, an increased risk of Wilms' tumour, medullary sponge kidney, Turner's syndrome and Ellis-van Creveld syndrome.

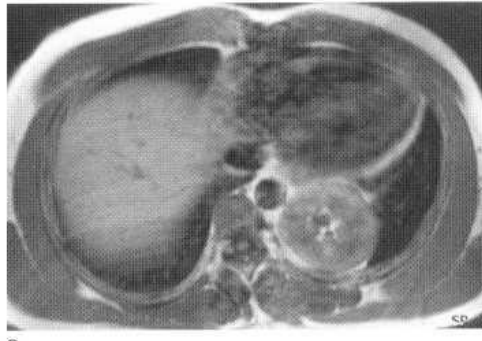
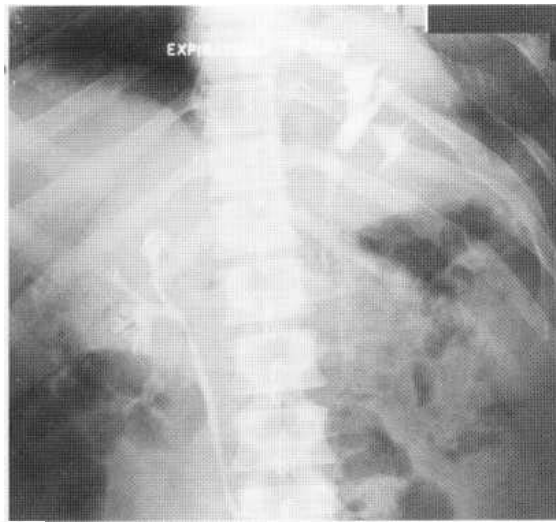


Fig. 30.8 Intrathoracic kidney seen on IVU (A) and a transverse T₁-weighted MR scan (B).

The characteristic configuration of a horseshoe kidney is often visible on the plain film but is better seen on the nephrogram phase of an IVU. The isthmus may be poorly seen due to its position overlying the lower lumbar spine, especially if it contains little renal parenchyma. The kidneys themselves are low lying, with their upper poles pointing superolaterally, lower poles inferomedially. The upper poles are usually at the same height. The pelvicalyceal systems point anteriorly and show fullness or some degree of stasis (Fig. 30.9). On ultrasound the kidneys are seen to lie low but the isthmus may be difficult to see and the diagnosis overlooked. CT or MR1 will reliably show the characteristic shape and position of a horseshoe kidney.

Crossed fused ectopia This can be regarded as a horseshoe kidney that has slipped superolaterally so that both kidneys come to lie on one side. The ureter draining the upper moiety inserts orthotopically on the ipsilateral side of the bladder. The lower moiety ureter also inserts orthotopically but into the contralateral

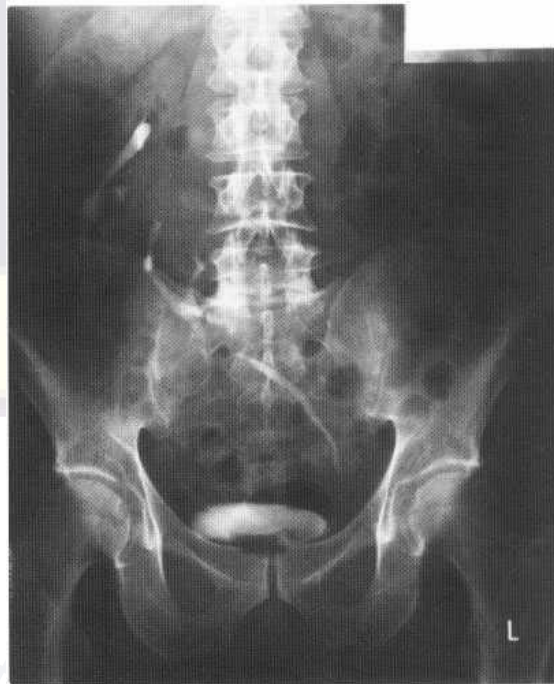


Fig. 30.10 Crossed fused ectopia demonstrated on IVU.

side of the bladder. Again there is a male predilection and it is more common on the right (Fig. 30.10).

Renal vascular abnormalities As the kidneys ascend they sequentially acquire and then lose arteries along the iliac arteries and then the aorta. Failure of involution of one or more of these is a common developmental variant and is seen in up to 25% of live

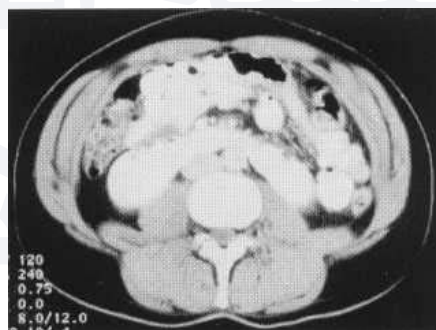
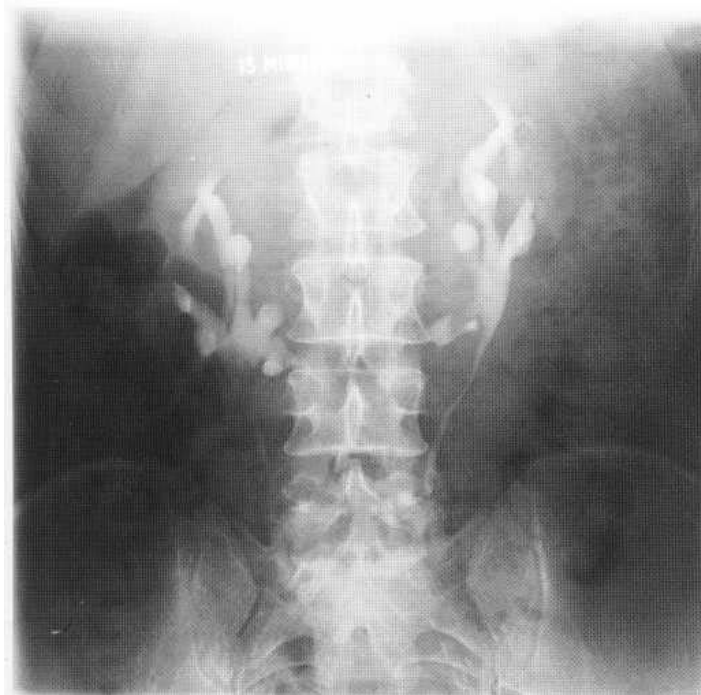


Fig. 30.9 IVU (A) demonstrating a horseshoe kidney. The isthmus of fused renal tissue across the midline is well seen on CT (B).

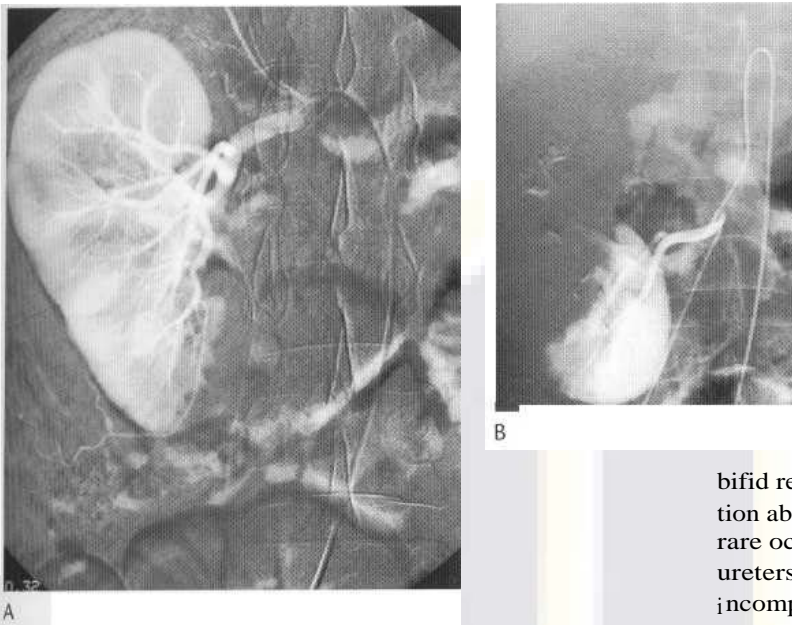


Fig. 30.11 (A) Main stem renal artery supplying the upper two-thirds of the kidney with (B) an accessory lower pole renal artery demonstrated on angiography.

births, most commonly a small lower pole artery (Fig. 30.11). The presence of an accessory renal artery is of significance and should be identified if certain surgical procedures are being considered (partial nephrectomy, endoscopic pyeloplasty and live renal transplantation). They are common in horseshoe and crossed fused kidneys. Accessory renal veins occur in up to 1/8 live births and are often retroaortic on the left.

Duplication abnormalities These are common, being found in 10% of the population. The most minor form of this condition is a

bifid renal pelvis, which is a normal variant. Otherwise duplication abnormalities (duplex kidneys) are characterised by two (on rare occasions more than two, up to six having been reported) ureters and renal pelvises. The duplication of the ureter may be incomplete (the ureters fusing at some point in their course and having a common distal ureter and orifice) or complete (both ureters having separate distal orifices). Incomplete duplication is almost always of no clinical significance, although in a small proportion of cases it may be associated with yo-yo reflux in which urine from one ureter refluxes back up the other ureter. This may lead to loin pain on micturition and urinary tract infection.

Completely duplicated ureters are associated with a number of potential problems. They may be associated with pelviureteric junction obstruction. The lower renal moiety drains via the ureter with the orthotopic insertion (i.e. inserts on the trigone in the anatomi-

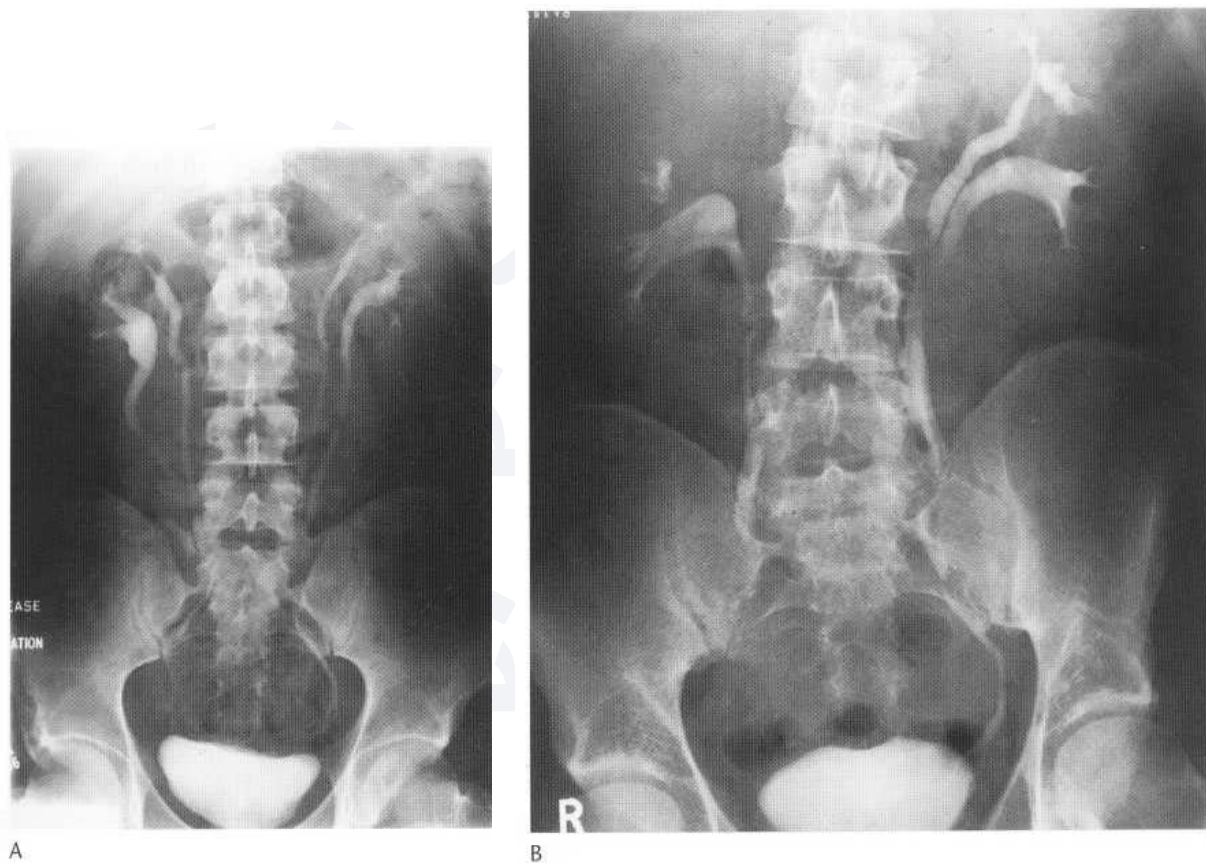


Fig. 30.12 Duplex ureters on IVU: complete bilateral (A) and partial left-sided (B).

cally correct site) but is often associated with vesicoureteric reflux. The ureter draining the upper moiety is inserted ectopically and its termination is always distal to the lower moiety insertion. This is usually within the bladder on the trigone inferior and medial to the orthotopic ureter but it may insert in a number of other sites. This is mainly within the bladder on the neck. In the male, the insertion is never inferior to the external sphincter and is therefore very rarely associated with incontinence. In the female, ureteric insertion into the urethra or vagina may occur and lead to continuous incontinence and vulnerability to ascending infection. There is often stenosis of the ureteric orifice with a variable degree of obstruction. The upper moiety ureter has a strong association with ureterocele formation, which is present in up to one-third of cases. Vesicoureteric reflux much less commonly affects the upper moiety.

An uncomplicated duplex kidney appears enlarged on all imaging modalities. The two collecting systems are visualised on IVU (Fig. 30.12), while the sinus fat surrounding the collecting



Fig. 30.13 Ultrasound of duplex kidney.

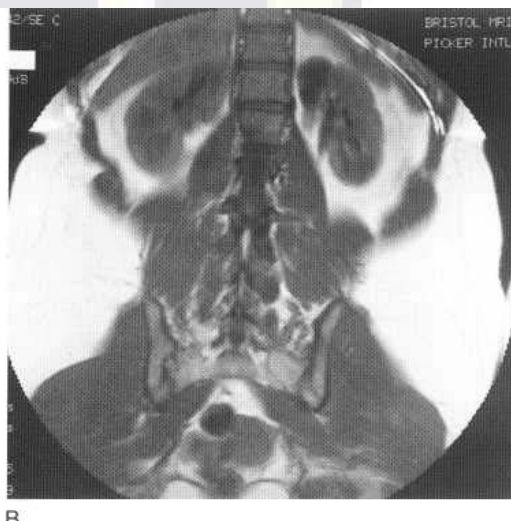
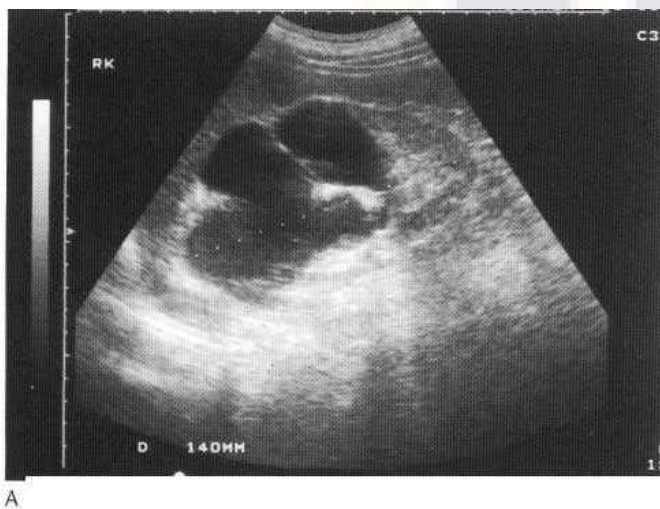


Fig. 30.14 (A) Ultrasound of duplex kidney with upper pole moiety hydronephrosis; there has been virtually complete loss of cortex from the upper pole moiety. Similar features seen on MRI in a different patient with a small, chronically hydronephrotic upper pole moiety (B).

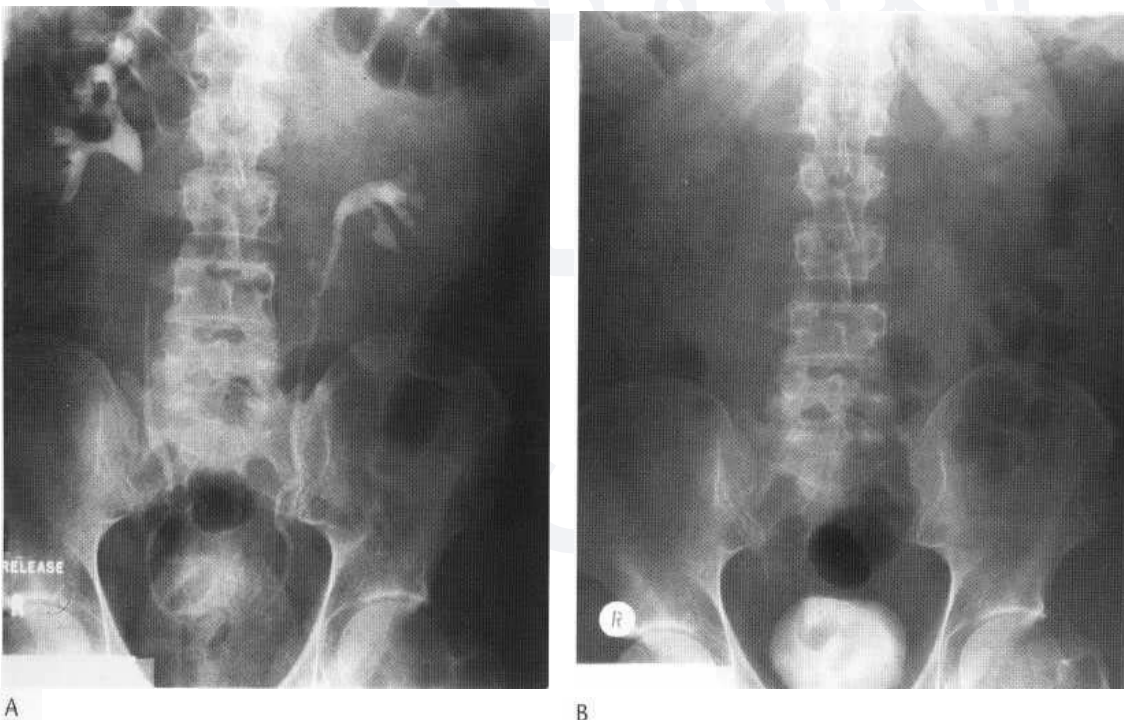


Fig. 30.15 The classical drooping lily sign on IVU (A). The lower pole moiety has been displaced inferolaterally by an upper pole hydro-nephrosis. This usually occurs due to obstruction of the upper pole moiety ureter at its orifice associated with ectopic insertion or a ureterocele. In this case it is due to a calculus in the upper pole moiety ureter (B).

systems of the two moieties and the renal parenchyma separating them are easily seen on ultrasound (Fig. 30.13). Analogous appearances are seen on CT and MRI (particularly good-quality T1-weighted images). The features of reflux nephropathy (cortical

scarring and clubbing of the calyces) may be present, most often affecting the lower moiety. If the upper moiety ureter is severely obstructed, the upper moiety becomes hydronephrotic and shows diffuse cortical loss, demonstrable on ultrasound, CT or MRI (Fig. 30.14). The upper moiety may opacify late or not at all and the hydronephrotic pelvis may displace the lower pole moiety inferiorly, giving rise to the so-called drooping lily sign (Fig. 30.15). On rare occasions three or more separate ureters have been seen on one side (Fig. 30.16).

ureterocele These are submucosal dilatations of the intramural distal ureter. They often project into the bladder lumen. They may become large and on occasion obstruct the other ipsilateral ureter of a duplex system and even the urethral orifice, provoking bilateral hydronephrosis. Most of them are associated with the upper moiety ureter of a duplex system and are therefore ectopic. These have a strong tendency to obstruction, sometimes severe, with marked hydroureter and hydronephrosis. There is a female preponderance of approximately 4 to 1.

A minority of ureteroceles are not associated with ureteric duplication and, although congenital, usually present in adults, often as incidental findings. They tend to be relatively small but may be associated with calculi and urinary tract infection. They are not usually associated with significant obstruction until complicated by calculi.

On IVU the ureterocele can be seen as a contrast-filled structure with a thin smooth radiolucent wall surrounded by contrast-containing urine in the bladder. This has been described as a cobra's head appearance. If the ureterocele is obstructed and the associated kidney non-functioning, it appears as a well-defined radiolucent mass within the opacified bladder (Fig. 30.17). On ultrasound it appears as a thin-walled purely cystic structure projecting into the bladder lumen at the site of ureteric insertion. Associated ureteric calculus and dilatation and hydronephrosis can also be seen.



Fig. 30.16 Triplex ureters demonstrated on IVU.

Ureteric diverticulum This is presumed to be an abortive form of ureteric duplication. It consists of a saccular or fusiform ureteric stump connected to the normal ureter. It predisposes to urinary tract infection and calculi.

Multicystic kidney This is a relatively common condition, which, if not detected antenatally, usually presents as a childhood abdominal mass. It is thought to be due to in utero failure of the ureteric bud to connect with the nephrons in the metanephric blastema. The ureter in turn fails to develop and is atretic, while the kidney becomes non-functioning. On ultrasound or CT the kidney is composed of non-communicating cysts of varying size. A variant of this condition (hydronephrotic multicystic kidney) has been described in which only the upper end of the ureter is atretic and the cysts within the kidney are arranged around a large central cyst, with which they may communicate. It has been suggested that this may represent an extremely severe form of intrauterine pelviureteric junction obstruction. Multicystic kidney is associated with an increased risk of contralateral pelviureteric junction obstruction.

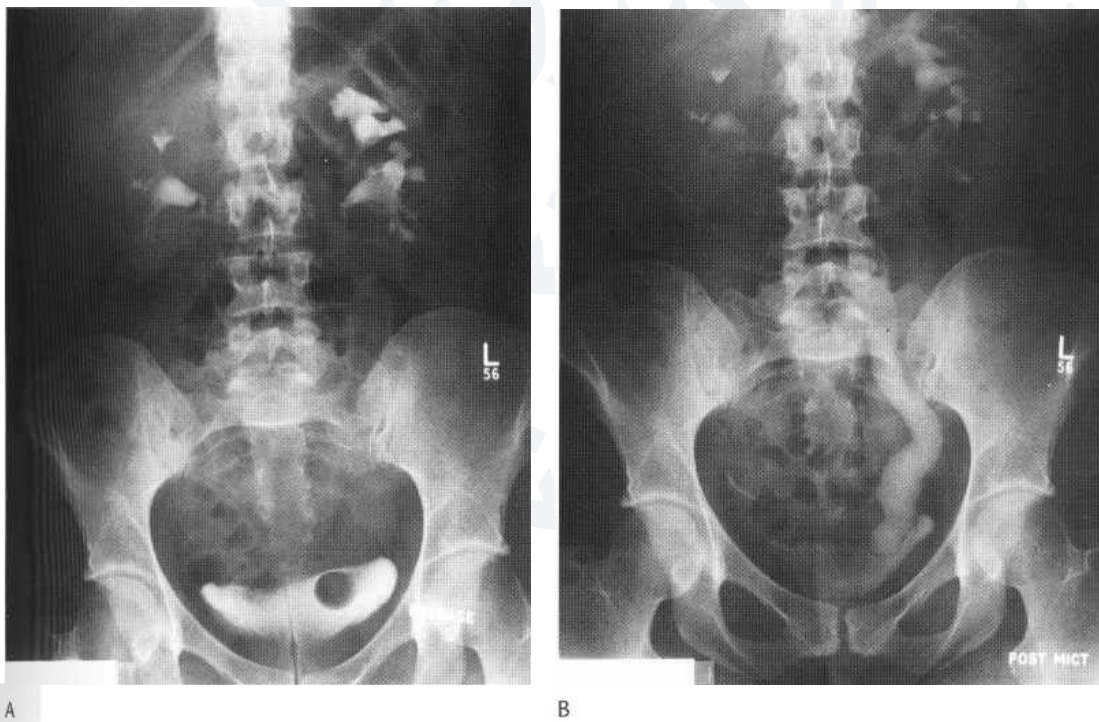


Fig. 30.17 Full length film from an IVU series showing a non-opacified partly obstructing ureterocele surrounded by opacified urine in the bladder (A). A later full length film shows opacification of the distended upper moiety ureter running down to the opacified ureterocele (B).

Polycystic kidneys Multiple cysts are seen in numerous congenital (mostly rare) syndromes, including Laurence-Moon-Biedl, Noonan's, Turner's and the trisomy syndromes. The most frequently encountered clinically important conditions in adults are polycystic disease of kidneys, tuberous sclerosis and von Hippel-Lindau syndrome. There are two principal types of polycystic kidneys: autosomal recessive and autosomal dominant.

In autosomal recessive polycystic disease of the kidneys (ARPK) the renal parenchyma is replaced by numerous tiny (1-8 mm) cysts. It has been referred to as infantile PCK but there are four subtypes (perinatal, neonatal, infantile and juvenile), so ARPK is the preferred term. Most present in the neonatal period with oligohydramnios and Potter's syndrome, with early death from respiratory failure. In the older subtypes renal function is better preserved. However, there is an association with periportal fibrosis and subsequent liver failure, which increases in frequency with age of presentation until the juvenile subtype, when the liver disease predominates. On ultrasound the kidneys are diffusely echogenic rather than cystic in appearance. On IVU there is a striated nephrogram thought to be due to contrast lying in the minority of preserved functioning tubules next to dilated non-opacified diseased tubules.

In autosomal dominant polycystic disease of the kidneys (ADPK) numerous cysts of varying size, often becoming extremely large, develop within the kidneys, gradually replacing normal renal parenchyma and ultimately producing renal failure. It usually presents between 20 and 39 years of age, although milder forms may not present until over 60 years and lack of renal failure has been observed in some patients up to 80 years of age. Presentation is usually with hypertension, renal insufficiency, complications of the multiple cysts (haematuria, pain and infection) or as an abdominal mass discovered on incidental clinical or imaging examination. There may be associated cysts in the liver (50% of cases), pancreas, spleen and lung; 15% have associated berry aneurysms and there is an increased incidence of coarctation and valvular heart disease. On IVU the plain films may show some cyst calcification. On the contrast films the kidneys are seen to be enlarged and the cysts may be visible as multiple well-defined non-perfused areas surrounded by normal areas of renal parenchyma. The calyces have a classical stretched appearance due to the presence of multiple cysts (Fig. 30.18). Ultrasound demonstrates multi-

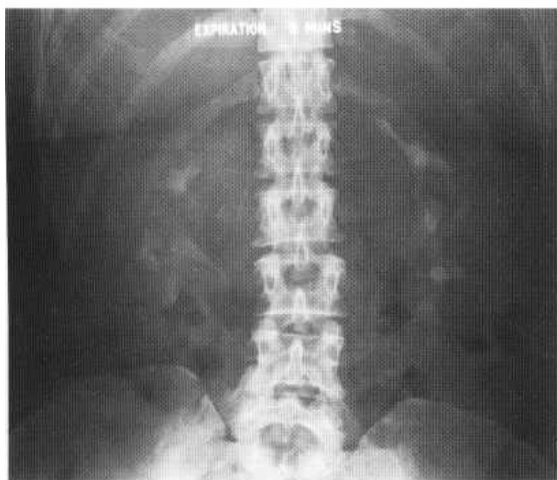


Fig. 30.18 IVU demonstrating the characteristic stretching of calyces by cysts in polycystic kidneys.

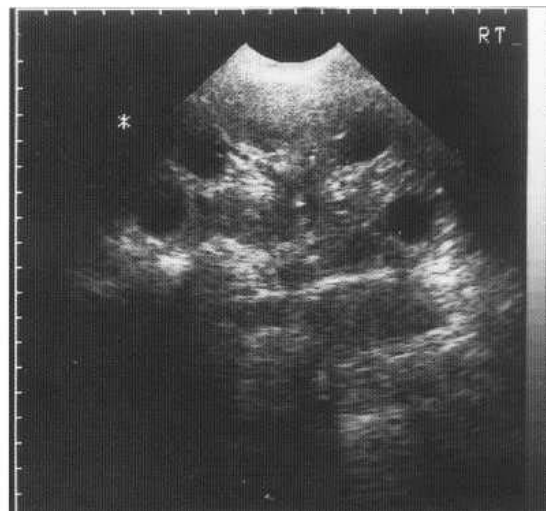


Fig. 30.19 Ultrasound showing relatively early polycystic disease with multiple simple cysts demonstrable.

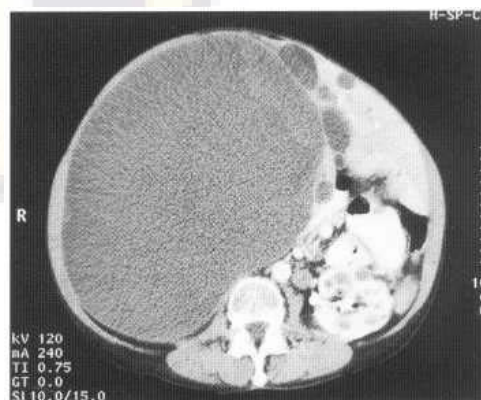


Fig. 30.20 CT scan showing multiple cysts in the left kidney. The disease in this patient is dominated by multiple hepatic cysts, the right lobe containing a particularly large one.

pie bilateral (but often asymmetrical) renal cysts of varying size and is more sensitive than IVU at the detection of small cysts in earlier disease (Fig. 30.19). In 10% of cases the disease is extremely asymmetrical but in virtually all cases it is bilateral and progressive. Initially the cysts are simple and separated by normal renal parenchyma. Over time they increase in number to produce marked bilateral renal enlargement, and the normal parenchyma disappears. The cysts are prone to haemorrhage and infection with episodes of pain, pyrexia and haematuria. As a result of this, some of the cysts may become thick-walled, septated, calcified and contain echogenic debris. CT and MRI will also show multiple cysts of varying size and contents (Fig. 30.20) with wall calcification more reliably demonstrated on CT. In patients with haematuria a small coexistent malignancy is extremely difficult to diagnose or exclude and occasionally serial imaging is required. There is a link at chromosomal level with tuberous sclerosis and some kidneys show features of both conditions in varying proportion (Fig. 30.21).

Tuberous sclerosis This is an autosomal dominant neurocutaneous disorder of low penetrance and extremely variable expressivity with a spectrum of central nervous system and cutaneous manifestations, including cerebral hamartomas, convulsions and adenoma sebaceum. Renal manifestations include multiple bilateral angiomyolipomas (Fig. 30.22) and cysts. There



Fig. 30.21 Ultrasound in a patient with tuberous sclerosis showing cysts and small echogenic angiomyolipomas in the kidney.

is a chromosomal link with autosomal recessive polycystic kidneys, which is likely to explain why sometimes in tuberous sclerosis the only renal abnormalities are multiple cysts.

Von Hippel-Lindau disease This is an autosomal dominant neurocutaneous disorder of incomplete penetrance and variable expressivity. Patients with this condition have a high incidence of multiple cysts in a variety of organs, including the kidneys (75%), liver and spleen; 50% develop pancreatic cysts, which may be associated with pancreatic insufficiency and diabetes. These patients are also prone to tumours in different organ systems, especially renal cell carcinoma (25-40% of patients, 75% multifocal), cerebellar haemangioblastoma, retinal angiomas and pancreatic adenocarcinomas and adenoma. There is also an asso-

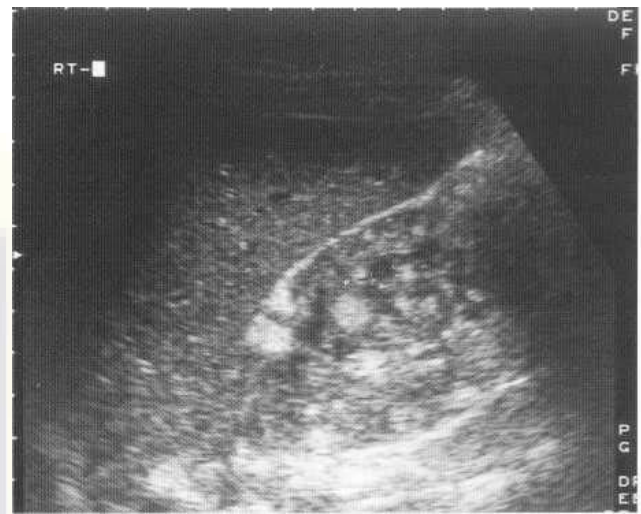


Fig. 30.22 Ultrasound of a patient with tuberous sclerosis showing multiple small, highly echogenic angiomyolipomas.

elation with endocrine tumours, which may be multiple, including phaeochromocytomas and islet cell tumours.

Medullary cystic disease This condition is characterised by medullary cysts. Along with the related juvenile nephronophthisis there is progressive tubular atrophy with resultant salt-wasting nephropathy and renal failure.

Medullary sponge kidney This is a common condition due to ectasia (fusiform or cystic) of the collecting ducts within the renal pyramids, seen in up to 1 in 200 IVUs. It is generally bilateral but may be unilateral or segmental, affecting as little as a single papilla. It is usually a benign incidental finding but there is a weak association with some tumours (Wilms' disease and phaeochromocytomas), other developmental lesions, such as horseshoe kidney, and distal renal tubular acidosis and some syndromes (hemihypertrophy, Caroli's and Ehlers-Danlos). On IVU

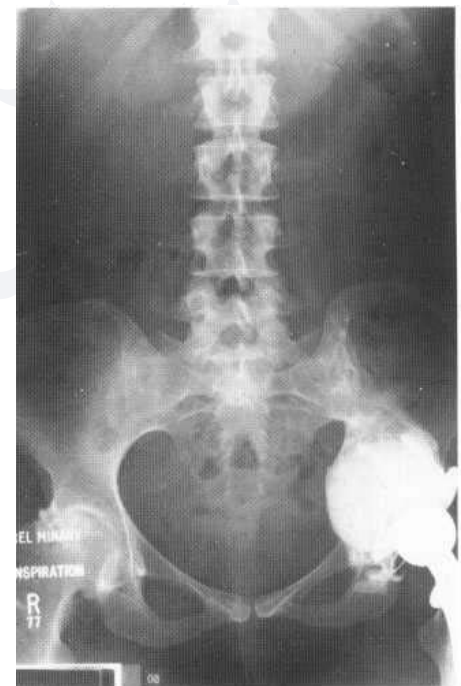
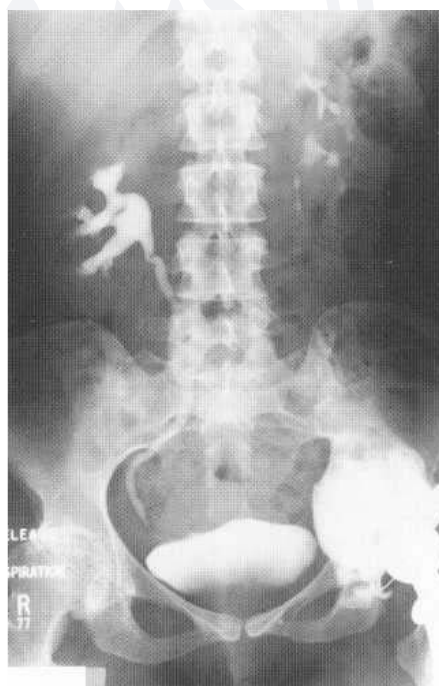
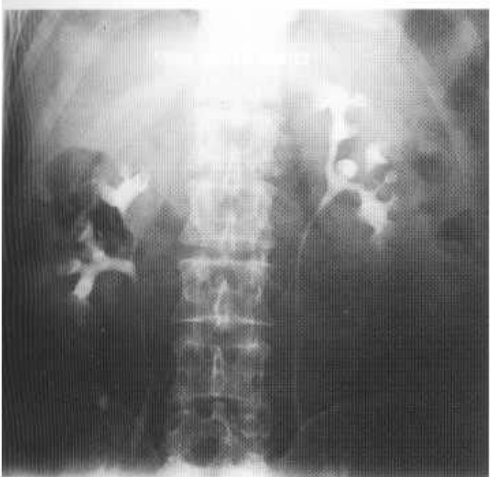


Fig. 30.23 Medullary sponge kidney on IVU showing linear (A) and saccular (B) ectasia of the collecting ducts. This is often associated with the formation of small calculi (C).

it is seen as multiple linear, sometimes saccular contrast collections within the medulla (Fig. 30.23). It should be borne in mind that a good-quality IVU will often show a papillary blush with some fine contrast streaking, which should not be overdiagnosed as medullary sponge kidney. The condition itself is asymptomatic and has no ultrasound features. However there is a tendency for small calculi to form within the ectatic tubules. These are often subtle but may become florid, producing the features of nephrocalcinosis. Calculi may pass into the calyces and beyond, producing ureteric colic.

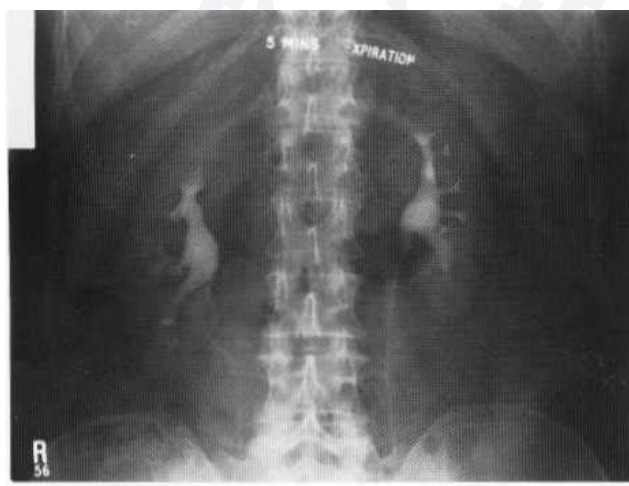
Calyceal diverticulum This is a common variant found in 1 in 250 IVUs and is an intraparenchymal cavity lined with transitional epithelium. The diverticula are usually a few millimetres in diameter (occasionally much larger) and communicate with a minor calyx, either centrally or at a fornix. Occasionally they arise from the infundibulum to a major calyx, rarely directly from the renal pelvis. They do not receive drainage from nephrons and therefore opacify during IVU after the rest of the calyces (Fig. 30.24). They may be identified on ultrasound, often being mistaken for a small cyst or hydrocalyx. Stasis within them leads to an increased risk of urinary tract infection and calculi.

Pelviureteric junction obstruction This condition has a spectrum of severity from severe antenatal hydronephrosis with global cortical loss to radiologically demonstrable hydronephrosis in the adult without apparent symptoms or loss of renal function. The cause of this condition is still not entirely clear and has provoked much controversy. Possibilities include an intrauterine ischaemic insult, excess collagen within the wall of the pelviureteric junction (PUJ) or the presence of aberrant blood vessels. Up to 20% are associated with an accessory renal artery running across the PUJ, which may be visible on the IVU as a smooth indentation. In some cases, however, the crossing blood vessels appear to be secondary to the development of the hydronephrosis and not the cause. The defining lesion is hydronephrosis that develops with a narrowed PUJ, which fails to relax and transmit the peristaltic wave to the ureter. Initially this is intermittent. In adult practice the typical presentation is of episodes of severe loin pain in a young adult, which may be related to the consumption of large quantities of fluid provoking a diuresis.

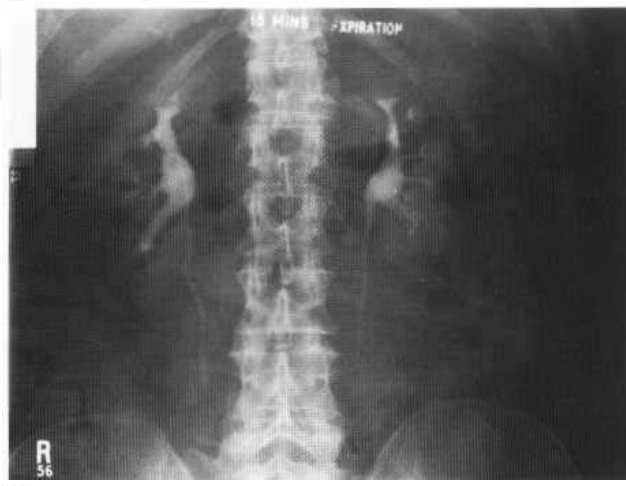


Fig. 30.25 Gross right hydronephrosis with failure of contrast excretion. Thin septae of renal tissue can just be seen separating the dilated non-opacified calyces. The left kidney is also affected, albeit to a lesser degree showing a tight pelviureteric junction and dilatation and clubbing of the calyces and renal pelvis.

During the acute episode there are features on IVU of severe acute obstruction, which include a delayed, increasingly dense nephrogram and delayed appearance (sometimes up to 24 h or more) of contrast within the collecting system. When opacification occurs it demonstrates clubbed calyces and a dilated pelvis. Prior to opacification of the pelvicalyceal system there may be a negative pyelogram, i.e. dilated calyces appearing as radiolucent areas surrounded by the denser areas of the nephrogram (Fig. 30.25). Contrast may be seen with a curvilinear configuration just peripheral to the calyces. This appearance has been termed 'crescents' and is thought to represent contrast stasis in collecting ducts displaced around distended calyces (Fig. 30.26). The PUJ is tightly closed and the ureter is often not opacified. Ultrasound will demonstrate a hydronephrosis without a dilated ureter. Where the ureter is not demonstrated at all, a retrograde pyelogram may be performed to confirm the nature of the diagnosis and ensure a neoplastic or other cause for the obstruction is not being overlooked. The urologist may have difficulty positioning the ureteric catheter all the way into the pelvis because there is often something of a U-bend at the upper end of the ureter in association with the hydronephrosis and poten-



A



B

Fig. 30.24 Calyceal diverticulum initially not seen on the 5 min IVU film (A) but fills retrogradely with contrast on the 15 min film (B).

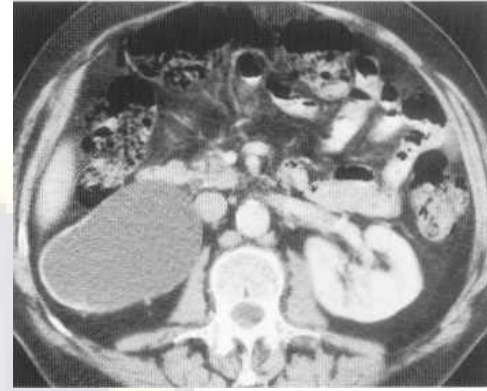


Fig. 30.27 Chronic right pelviureteric junction obstruction with almost complete cortical loss seen on CT.

tially related to an aberrant renal vessel. The investigation will demonstrate a normal-calibre ureter and usually contrast flows into the renal pelvis. It is important not to overfill the pelvis, partly to avoid extravasation and partly to avoid chemical pyelitis if a high concentration of contrast medium (particularly ionic) sits in contact with the urothelium of the obstructed system.

The episode of obstruction may be sufficiently painful and protracted as to require percutaneous drainage. More often it resolves spontaneously as the PUJ relaxes. It is in the nature of the condition, however, to progress to chronic significant obstruction with gradually progressive cortical loss, although the rate at which this occurs and the proportion of patients in which it occurs remains uncertain. This may happen silently and the hydronephrosis and cortical loss can become gross (Fig. 30.27). Ultimately this may present at any age as a result of calculus formation in the large pool of urine in the pelvicalyceal system and/or infection, which may be severe and progress to pyonephrosis. This often occurs acutely but is an occasional cause of non-specific malaise, weight loss and low-grade pyrexia, particularly in the elderly.

Milder cases are more difficult to diagnose. Typically the patient is a young adult with episodes of loin pain but an IVU or ultrasound is



Fig. 30.26 Bilateral pelviureteric junction obstruction (A). The left kidney is more severely affected, with contrast still visible in the collecting ducts as crescents. Classical right pelviureteric junction obstruction with kinking of the upper ureter (B). The same case after surgery (C) showing the straight medial edge of a pyeloplasty.

either equivocal or apparently normal, except perhaps for the presence of a sizeable extrarenal pelvis, which in itself is regarded as a normal variant. Ideally these patients should undergo IVU at the time of an acute episode of pain. Alternatively an IVU or renogram with a frusemide induced diuresis may provoke the characteristic obstructive appearances (and the pain).

Maximally severe cases are identified antenatally on routine ultrasound or within the first year of life during investigation for urinary tract infection or other abdominal condition. The condition is bilateral in 20% and associated with other urinary tract abnormalities such as multicystic disease of kidney, renal agenesis, renal duplication and vesicoureteric reflux.

If the kidney has reached the stage of marked global cortical loss then nephrectomy is the best treatment. Preoperative assessment may include a DMSA scan where there is doubt as to whether or not there is enough useful renal tissue to justify a more conservative approach. If the kidney is not so badly damaged as to be worth conserving, preoperative assessment may include a MAG3 renogram to confirm the degree of obstruction quantitatively and act as a baseline for postoperative assessment. The standard operation is pyeloplasty with opening and refashioning the PUJ. This gives a characteristic straight vertical medial edge to the renal pelvis, with the ureter arising from the inferomedial angle of the pelvis. The dilatation of the collecting system usually persists on postoperative imaging but there should be improvement of the drainage. Endoscopic pyeloplasty is sometimes performed. This involves cutting through the PUJ from the inside. It is important to exclude an accessory renal artery against the junction prior to the procedure; this can be done with angiography or more often now with CT or MR angiography. Retrograde balloon dilatation of the PUJ has also been tried but its success rate remains debatable (Fig. 30.28).

Congenital ureteric strictures The cause of these uncommon lesions is unproven but again theories include intrauterine

ischaemia. They are most frequently seen at the PUJ and the vesicoureteric junction. They result in hydronephrosis and loss of renal parenchyma, depending on their severity.

Retrocaval ureter The right ureter occasionally takes an aberrant course, running sharply medially posterior to the inferior vena cava and then dropping inferiorly towards the pelvis along a course medial to the pedicles. This may be apparent on IVU and may be confirmed with CT. It is rarely associated with hydronephrosis.

Primary megaureter This is felt to be due to congenitally abnormal musculature of the distal ureter, leading to focal failure of peristalsis. The ureter above the abnormal segment becomes dilated, sometimes massively. In severe cases dilatation involves the entire ureter and renal pelvis. Although the calyceal fornices usually remain sharp, they may also be involved if the condition is particularly severe (Fig. 30.29). It is bilateral in 25%. There is a male preponderance. It is associated with an increased risk of urinary tract infection and calculi (Fig. 30.30).

Megacalycosis and polycalycosis Occasionally the number of calyces is increased (polycalycosis) and/or have an abnormal shape, becoming rounded, with blunting or loss of the normal sharp fornices (megacalycosis) (Fig. 30.31). It is occasionally associated with megaureter.

Prune-belly syndrome It is thought that this condition arises following bladder outflow obstruction in utero due to urethral valves, with the development of hydroureters and hydronephrosis. The obstruction is overcome (otherwise renal failure and Potter's syndrome would develop) but the obstructive phase produces defective development of the anterior abdominal wall musculature and the ureteric musculature, with subsequent poor peristalsis and persistent non-obstructive dilatation of the collecting systems (Fig. 30.32). It is associated with cryptorchidism, defective prostatic

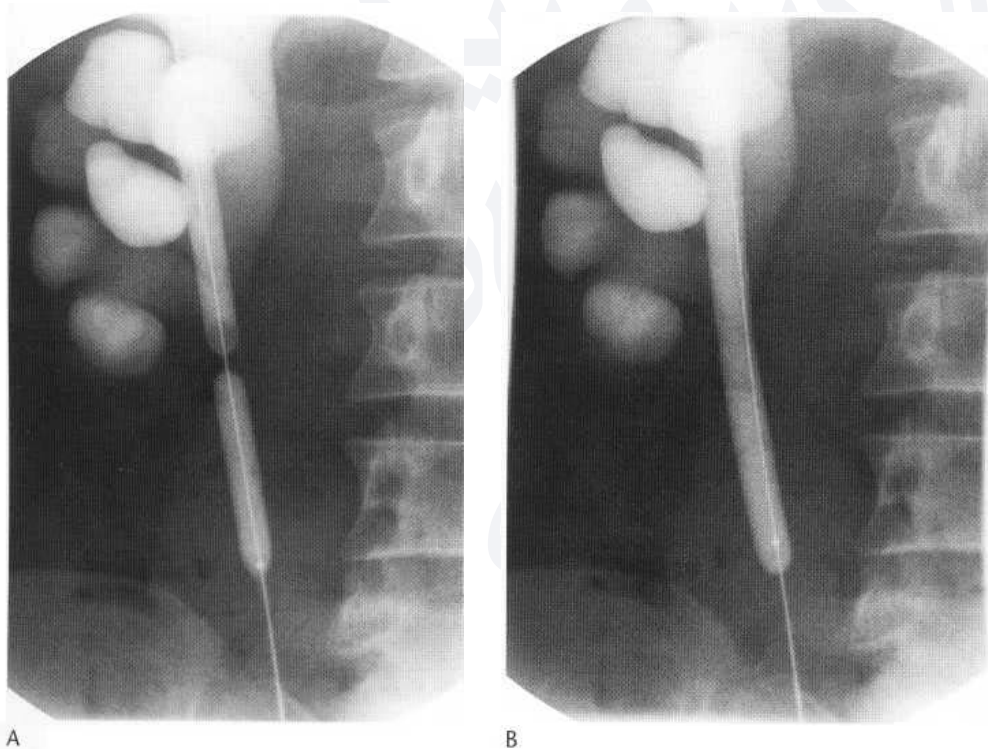


Fig. 30.28 Retrograde balloon dilatation of a pelviureteric junction obstruction: the balloon partly (A) and fully (B) dilated.

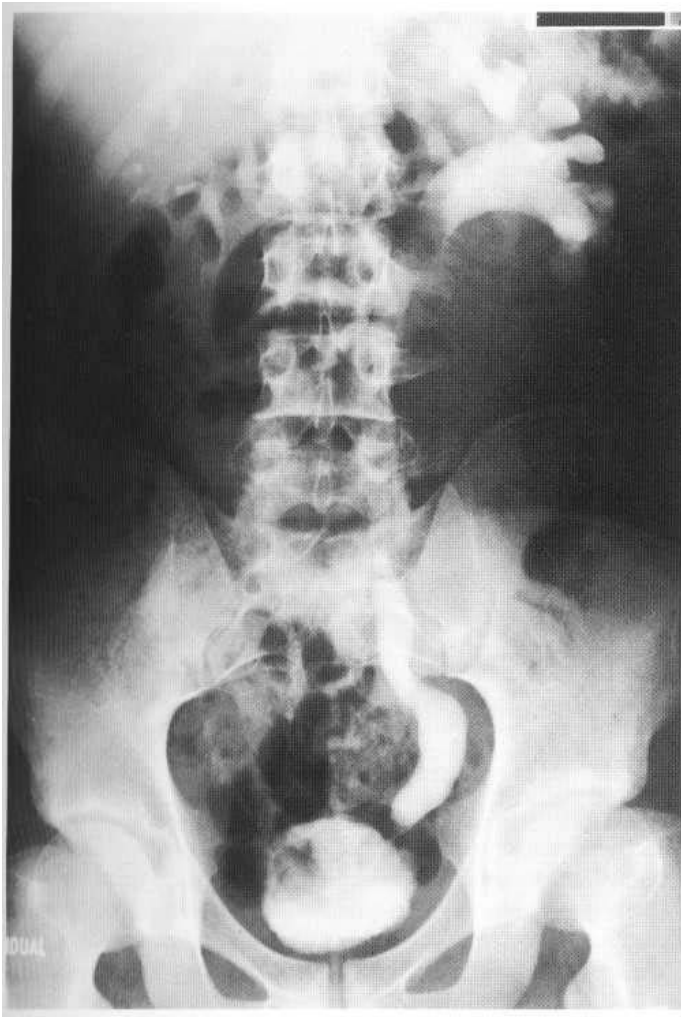


Fig. 30.29 Left megaureter on IVU showing dilatation of the entire length of the ureter with secondary pelvicalyceal dilatation.

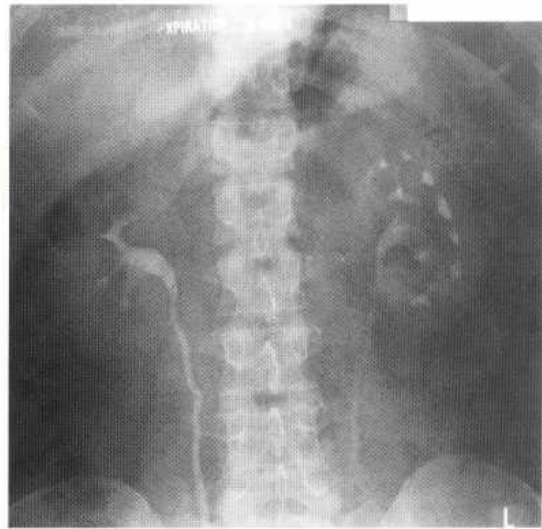


Fig. 30.31 Left megacalycosis with numerous calyces showing poorly developed flattened papillae.

development and urethral abnormalities, notably valves. Virtually all patients are male.

INFLAMMATORY DISEASE

Acute pyelonephritis This is an acute bacterial infection of the upper urinary tract. It is largely due to ascending infection with Gram-negative bacilli (most commonly *Escherichia coli*) and is associated with cystitis. It commonly affects females throughout adult life (when the urinary tract is otherwise usually normal) but is relatively uncommon in young adult males unless there is a structural or functional lesion of the urinary tract, such as inadequate bladder emptying. In older males it becomes more frequent in

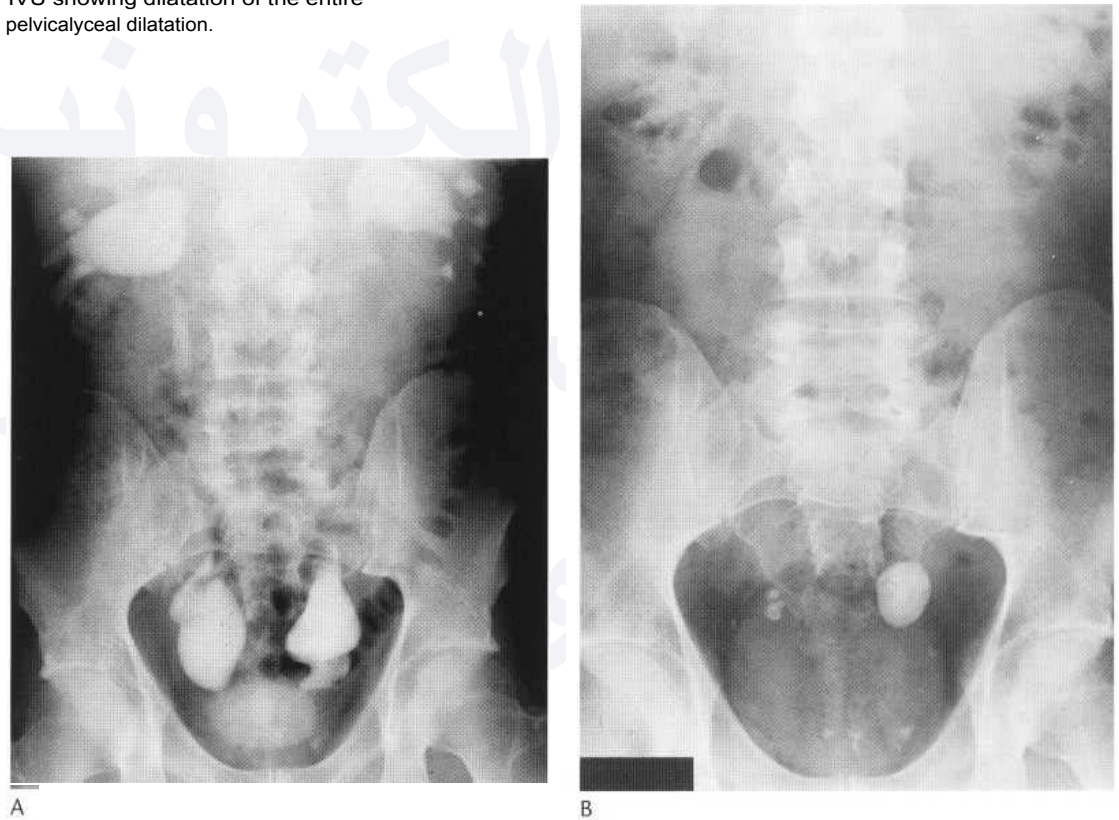


Fig. 30.30 Gross bilateral megaureters (A) with calculus formation within the dilated distal ureters (B).

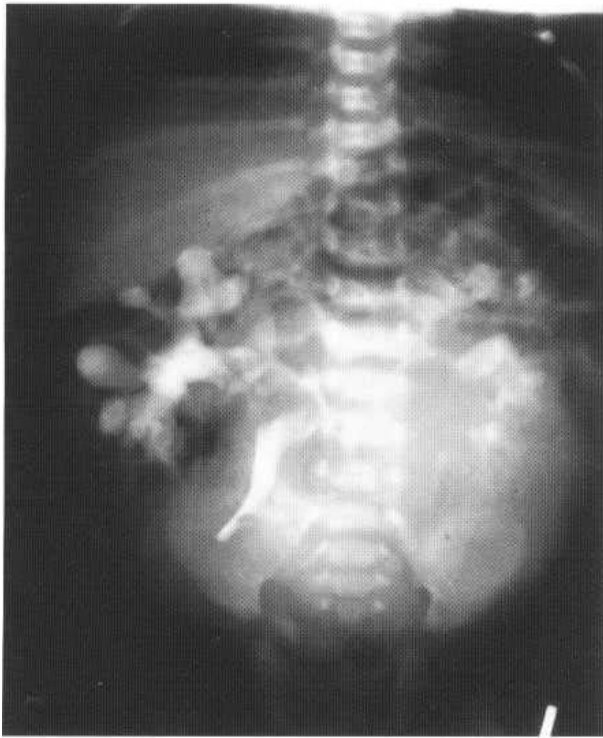


Fig. 30.32 IVU on an infant with prune-belly syndrome. There is gross overdilation of the bladder, bilateral hydronephrosis and hydroureters.

association with benign prostatic disease and consequent bladder outflow obstruction. It presents with pyrexia, loin pain and tenderness and often symptoms of cystitis.

Acute pyelonephritis requires no immediate investigations and is usually resolving within 72 h on appropriate antibiotic treatment. If the clinical picture is not improving by this stage, further imaging is required to investigate the possibility of an abscess (ultrasound or CT) or obstruction (ultrasound and/or IVU). Usually the IVU is normal. In one-third of cases, however, where the inflammatory process and oedema are more severe, IVU may show some of the

following features. The kidney may be smoothly enlarged and the calyces compressed by the adjacent swollen parenchyma. The affected kidney may show reduction in perfusion and function and a striated nephrogram. Rarely the infecting bacteria release an endotoxin that relaxes the smooth muscle of the ureter, which stops peri-

as if obstruction is suspected in the context of infection, relatively prompt drainage of the collecting system is required, usually by nephrostomy. Differentiation of obstructive from non-obstructive

infection there is usually significant delay in excretion of contrast on the IVU, or even on excretion from the affected kidney over several hours. On the other hand, if contrast appears within the collecting system within 5 or 10 min it is highly unlikely to be significantly obstructed. Similarly, ultrasound and MRI will often be normal but with more severe cases will show smooth renal enlargement. Ultrasound may show some diffuse reduction in echogenicity. Contrast-enhanced CT may demonstrate a striated nephrogram, global reduction in perfusion and function or wedge-shaped areas of abnormality and is more sensitive than IVU in showing these changes. CT may also demonstrate perinephric oedematous or inflammatory change. In a significant number of cases the pyelonephritic process is focal rather than diffuse and

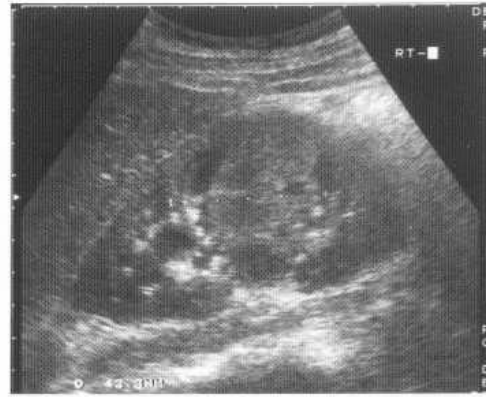


Fig. 30.33 Focal severe pyelonephritis appearing as a slightly heterogeneous mass.

leads to an area of localised swelling and reduced function within the parenchyma, which may appear as a mass of medium to low echogenicity on ultrasound (Fig. 30.33) and medium to low density on CT. When severe, this may appear as a mass on IVU, compressing the adjacent calyces. The older term for this lesion is acute lobar nephronia but it is more logical to refer to it as focal pyelonephritis. These features return to normal after the acute episode. An area of severe localised pyelonephritis, however, may progress to abscess formation. Following an acute episode of pyelonephritis the patient should be investigated to look for an underlying cause, particularly calculi, PUJ obstruction, inadequate bladder emptying and diabetes.

Emphysematous pyelonephritis This uncommon condition is a severe pyelonephritis with a gas-producing organism (generally Gram negative bacilli, especially *E. coli*), usually in elderly diabetic patients and frequently associated with ureteric obstruction. Gas develops within the renal parenchyma and may also spread to the perinephric space. There is often enough gas present to enable the diagnosis to be made on the plain film. CT, however, is more sensitive and will more accurately demonstrate the distribution of the gas. If it is diffusely throughout the kidney then emergency nephrectomy is indicated. Renal function will already have been destroyed and without surgery mortality may be in excess of 50%. If gas is localised to one part of the renal parenchyma a conservative approach with intravenous antibiotics and consideration of CT-guided and the ureter dilates. This may cause considerable concern, guided drainage may be appropriate. Gas in the pelvicalyceal system and ureter without gas in the renal parenchyma represents emphysematous pyelitis and can also be managed conservatively (Fig. 30.34). It is worth mentioning for completeness that gas bubbles can be difficult but if there is genuine obstruction with bubbles may be encountered in the collecting system in the absence of infection if they have gained access at the time of surgical instrumentation of the urinary tract (catheterisation, retrograde pyelography, etc.), or in the presence of a fistula to the skin or a gas containing viscus (Fig. 30.35).

Renal abscess Focal renal parenchymal inflammation may progress to liquefaction and abscess formation. This may be the sequel to untreated or resistant acute pyelonephritis or haematogenous spread of infection. The former is usually due to Gram-negative or anaerobic bacilli, the latter to *Staphylococcus aureus* and associated with a septic site elsewhere (skin or nasal cavity focus, intravenous drug abuse, infected central line) or impaired immunity, including diabetes. Haematogenous spread may lead to multiple and/or bilateral renal abscesses as well as abscesses else-



Fig. 30.34 Emphysematous pyelitis. (A) Plain film showing the characteristic configuration of gas in the collecting system. (B) CT demonstrating gas within the collecting system.

where in the body (particularly consider vertebral, pulmonary and cerebral metastatic spread). There may be marked loin pain and tenderness and severe pyrexia. IVU usually shows only a non-specific mass. The condition is better imaged with ultrasound or CT, which will show a heterogeneous mass (with irregular marginal enhancement on CT) containing single or multiple central

areas of cystic necrosis (Fig. 30.36). There is often considerable echogenic debris within the cystic areas on ultrasound. In severe cases gas may appear, best seen on CT. Perinephric inflammatory disease may also be identified.

Where there is a substantial liquefied area, ultrasound- or CT-guided positioning of a percutaneous drain may be useful. However, these patients often come to imaging at a relatively early stage of development of the abscess with only a tiny area of liquefaction demonstrable (2 cm or less). It is likely that these patients are better served by intravenous antibiotics and subsequent scanning to monitor resolution rather than premature intervention.

Perinephric abscess Renal infection of any severity may be associated with extension of disease into the perinephric space with the formation of a perinephric abscess. On IVU there is only indirect evidence such as loss of the psoas shadow, poorly seen renal outline and reduced or absent renal function manifested by failure to excrete or concentrate contrast. Ultrasound and CT will demonstrate a fluid or semifluid collection, often containing debris and septations and sometimes gas in the presence of the appropriate organisms (Fig. 30.37). Further extension of infection is largely determined by the anatomy of the retroperitoneal fascia) planes. Although disease may extend in any direction (including medially across the midline into the contralateral perinephric space), the course most often taken is directly posteriorly through the posterior perinephric fascia into the posterior perirenal space. From this site, further extension is often laterally into the lateral extraperitoneal space and lateral abdominal wall, posteriorly through the transversalis fascia into the psoas and quadratus lumb-



Fig. 30.35 Gas bubbles shown on IVU within the collecting system due to a fistula between the ureter and the small bowel in Crohn's disease.



Fig. 30.36 Renal abscess on postcontrast CT showing a liquid non-enhancing centre and an irregular enhancing wall.

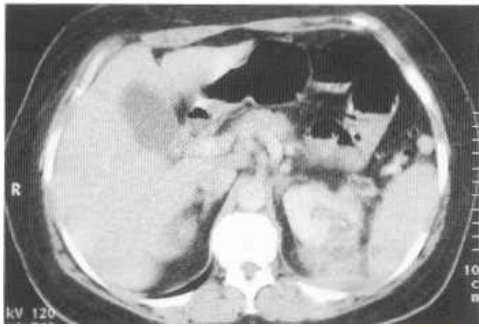


Fig. 30.37 Perinephric abscess on CT. There is an adjacent area of severe renal parenchymal inflammation with a tiny associated calculus. A small reactive pleural effusion is also present.

borum muscles and inferiorly along the psoas and then iliacus muscles into the pelvis.

Pyonephrosis Infection of an obstructed kidney may lead to pus developing within the renal pelvis and calyces (pyonephrosis). It may occur in association with any cause of obstruction but most frequently in the presence of calculi or the condition of undiagnosed PUJ obstruction. The imaging features are those of an obstructed system with particularly early or severe loss of renal function. Cross-sectional imaging may show evidence of thick pus and/or inflammatory debris within the dilated pelvicalyceal system (for example, echogenic areas on ultrasound or increased density on CT with possible layering). The infecting organisms are most commonly Gram-negative bacilli from ascending infection. Untreated, there is a danger of septicaemia, destruction of normal renal tissue and extension into surrounding areas. Treatment is by percutaneous drainage. This should only be performed with adequate antibiotic cover and a minimum of manipulation, as Gram-negative septicaemia and endotoxic shock are recognised and life-threatening complications of the procedure. Sometimes the situation develops insidiously over a considerable period of time, particularly in the elderly, and may then be associated with cortical loss and perinephric disease (Fig. 30.38).

Xanthogranulomatous pyelonephritis This is a chronic inflammatory process in which lipid-laden histiocytes invade and replace normal renal parenchyma. It is seen in the context of chronic urinary infection, usually with calculi, which are thought to provoke mild impairment of drainage, which initiates and propagates the disease. The infecting organism is usually *E. coli* or



Fig. 30.39 Xanthogranulomatous pyelonephritis on CT. There is a renal calculus but no hydronephrosis. Gas is seen in the collecting system in this case. The kidney has also begun to shrink and there is extension of the inflammatory process into the perinephric space and abdominal wall.

Proteus mirabilis. There is a marked female preponderance and 10% of patients are diabetic.

On IVU there is a non-functioning kidney, with calculi present in around 80%. Characteristically this is laminated or branched and fragmented. Initially the kidney may be enlarged and this may have a focal pattern simulating tumour (tumefactive xanthogranulomatous pyelonephritis) but ultimately there is renal atrophy, which may be marked. Ultrasound and CT show loss of normal corticomedullary differentiation and heterogeneity, which includes debris-containing cystic areas and calculi. The disease usually extends into the perinephric space with obliteration of tissue planes on all modalities (Fig. 30.39). With further extension through the layers of perinephric fascia the disease may extend into psoas muscle and the abdominal wall with the formation of a cutaneous fistula. Internal extension potentially leads to enteric fistulas. Enhancing areas of parenchyma may survive around the cystic areas, mimicking hydronephrosis. Where there is doubt a retrograde examination will show a contracted pelvicalyceal system and the absence of high-grade obstruction.

Tuberculosis Renal involvement is a feature of postprimary tuberculosis. Reactivation occurs at the corticomedullary junction. There is local infiltration into the parenchyma with subsequent papillary necrosis. Bacilli enter the collecting system and pyuria develops. Further progress of the disease is characterised by multifocal stricturing with impairment of drainage, formation of caseous pus and subsequent calcification. The classical features are seen on IVU. Strictures affect the calyceal necks, with the formation of hydrocalyces. Further strictures may be seen at the PUJ

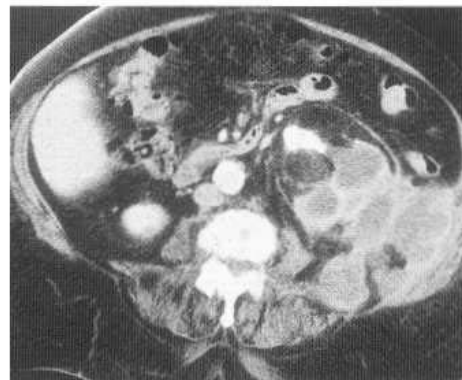


Fig. 30.38 Chronic pyonephrosis on ultrasound (A) and CT (B). There is marked cortical loss and modest dilatation of the collecting system. The CT also demonstrates the pelvic calculus responsible for the development of the condition, and a multiloculated perinephric abscess, which has extended laterally into the abdominal wall and posteriorly into the psoas muscle.

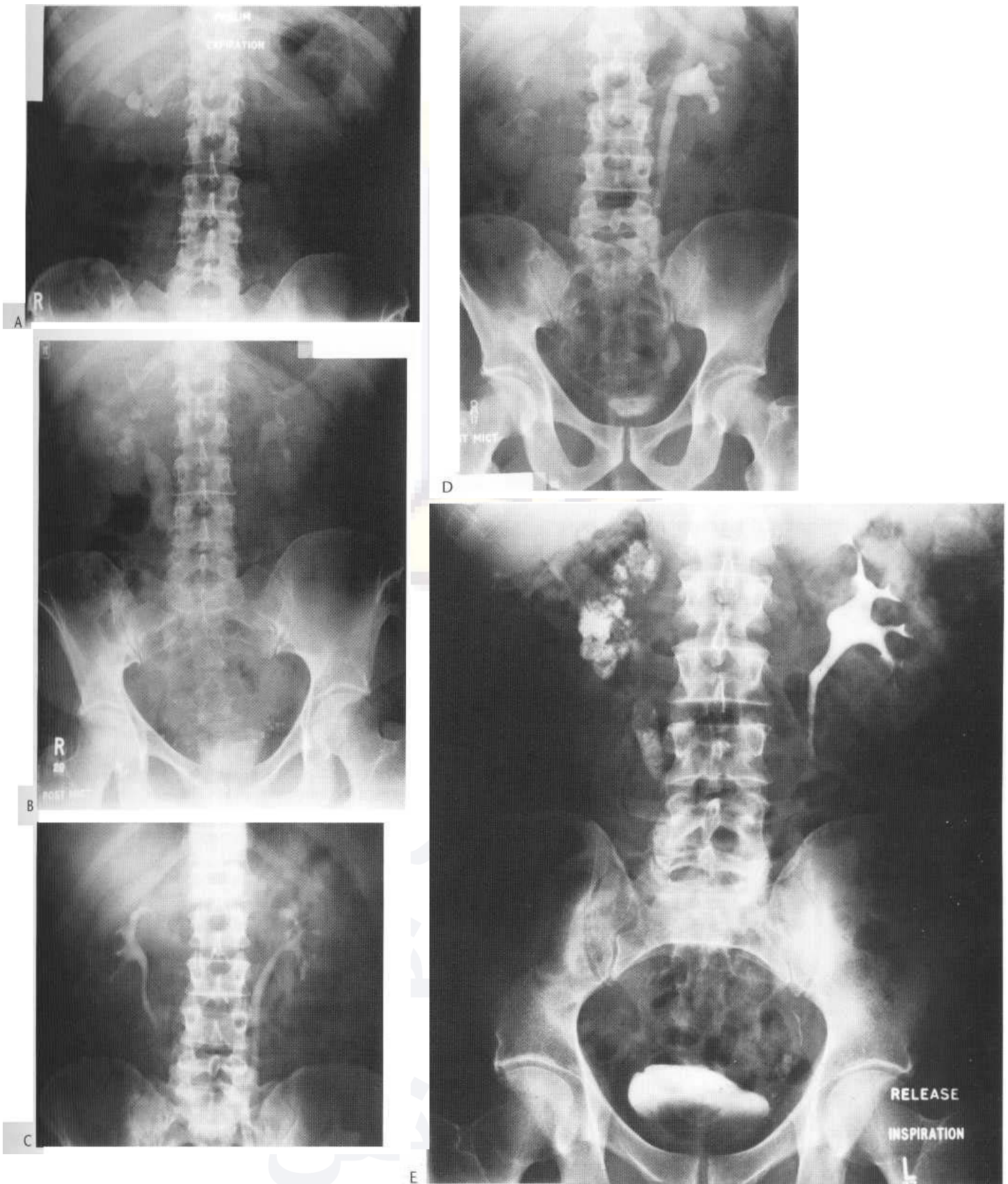


Fig. 30.40 Urinary tract tuberculosis. The plain film (A) demonstrates calcification within distended upper pole calyces. The IVU (B) shows strictures at the calyceal necks with hydrocalyces and fibrous stricturing of the renal pelvis and the ureter. The tomogram from an IVU on another patient (C) shows a stricture at the neck of the upper pole calyx. This progresses on treatment and the full length film from the IVU performed 6 months later shows the upper pole calyx has been completely amputated (D). Distal ureteric strictures are also present. Classical end-stage upper tract tuberculosis is the auto-nephrectomy (E) in which the chronically obstructed pelvicalyceal system is filled with calcifying caseous pus associated with complete renal parenchymal destruction. In this case there is also similar calcifying pus in an obstructed dilated upper ureter.

and at multiple levels in the ureter. The pelvis itself may become contracted. Significantly obstructed calyces accumulate pus and there is loss of parenchyma due to a combination of obstruction and destruction by the inflammatory process. Damaged areas and the Gaseous pus subsequently calcify. Badly affected areas become non-functioning (Fig. 30.40). When the pelvis is affected the entire hydronephrotic kidney may become non-functioning (tuberculous autonephrectomy). Ultrasound and CT will demonstrate hydrocalyces and/or a hydronephrosis, which may contain a considerable amount of debris, areas of calcification and parenchymal loss. Bacilli pass into the bladder, which also becomes inflamed and subsequently contracted. Presentation is usually with frequency and urgency. Although tuberculous lesions with subsequent calcification may develop at any site in the urinary tract, as a general rule the radiological changes are more pronounced in the upper urinary (kidneys and ureters), as against those seen with schistosomiasis, which predominates in the lower urinary tract.

Schistosomiasis Urinary tract schistosomiasis is caused by a parasitic blood fluke. It predominately affects the bladder but in up to 30% of cases also involves the ureter, particularly distally. Ureters are usually involved bilaterally but often asymmetrically. Parasitic ova deposited in the ureteric wall provoke an inflammatory reaction. In the early stage this may appear as multiple small inflammatory polyps. In the established disease the appearances are of strictures, often multiple, and linear calcification (Fig. 30.41).

Hydatid disease This arises from parasitic infection with the dog tapeworm *Echinococcus granulosus*. The usual intermediate hosts are pastoral animals, especially sheep. Tapeworm eggs from dog faeces are inadvertently consumed and develop into larvae in the intestine of the intermediate host. They pass through the intestinal wall and are disseminated throughout the body. They particularly

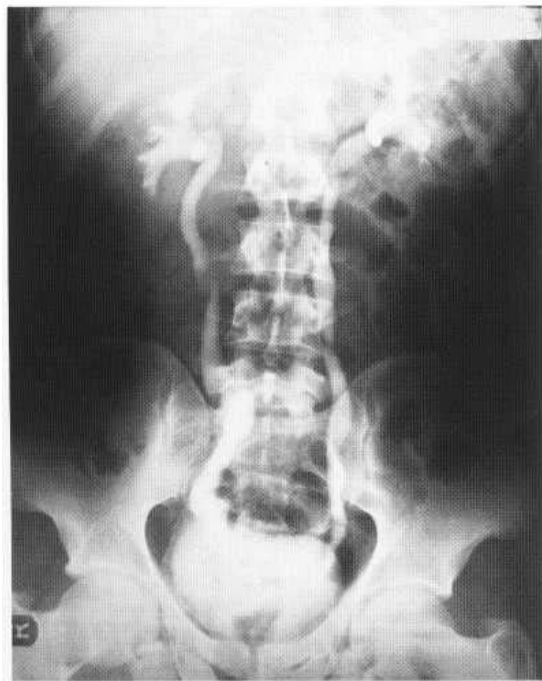


Fig. 30.41 Full length film from an IVU showing changes of schistosomiasis including bladder wall calcification with secondary ureteric and pelvic calyceal dilatation. (Courtesy of Dr Shadley Fataar, Royal Hospital, Muscat, Oman.)

infect the liver, rarely the kidney. The larvae develop into cysts. The wall of the cyst may calcify. On imaging, the classical appearance is of a multiloculated cystic mass, often with a dominant central cyst and multiple daughter cysts. Occasionally communication with the collecting system is visible on contrast studies.

Reflux nephropathy In this condition renal cortical scarring develops in association with dilated calyces. It is due to severe vesicoureteric reflux (VUR) and urinary tract infection in childhood. Because of its intimate relationship to VUR, it is worth considering this first.

Normally the ureter enters the superolateral angles of the trigone, penetrating the bladder wall at an oblique angle, giving rise to an oval ureteric orifice. This acts as a valve, preventing urine refluxing from the bladder into the ureter during micturition, the rise in intravesical pressure tending to close the orifice. In a small proportion of children the ureter takes a more direct course through the bladder wall, leading to a short intramural section and a round ureteric orifice which predisposes to reflux. Usually this is an isolated defect (although some cases are familial) but it is also encountered in association with a duplex system (usually the orthotopically inserted ureter of the lower moiety, sometimes the ectopic upper pole moiety ureter) and some other structural developmental lesions (prune-belly, paraureteric diverticulum). Although there remains some controversy, it seems most likely that VUR leads to reflux nephropathy only when it is severe enough to be associated with intrarenal reflux and infection. The insult to the kidney provokes scarring over the worst-affected calyces.

A grading system for VUR has been developed based on the appearances at micturating cystourethrography (MCUG). It is given below for reference:

- I-Reflux into the ureter alone; subdivided into reflux into part of the ureter only (Ia), all of the ureter without dilatation (Ib) and with dilatation (Ic)
- II-Reflux into the ureter and pelvis; subdivided into incomplete ureteric opacification without (IIa) and with (IIb) focal dilatation and complete ureteric opacification (IIc)
- III-Reflux into ureter and pelvis with mild dilatation; subdivided into fornices preserved (IIIa) and mildly blunted (IIIb)
- IV-Reflux into ureter and pelvis with moderate dilatation and preservation of the papillae; subdivided into partial (IVa) or complete (IVb) forniceal obliteration
- V-Reflux into ureter and pelvis with obliteration of the papillae; subdivided into subtotal papillary obliteration (Va) and total papillary obliteration with severe (Vb) or extreme (Vc) pelviureteric dilatation.

The more severe grades of reflux are demonstrable with radionuclide or ultrasound cystography. Usually the child presents with urinary tract infection (or septicaemia if severe) and management is generally conservative, aiming to control urinary tract infection and avoid its recurrence. Consequently intrusive investigation with MCUG (and the detailed grading described above) is uncommonly required and surgery rarely indicated. VUR has a tendency to improve with age and new scars are not thought to develop after 5 years of age.

Reflux nephropathy is usually asymmetrical or unilateral. The classical IVU appearances are of cortical scarring over clubbed calyces. This is most frequently seen at the renal poles, especially the upper pole because these are the sites of occurrence of com-

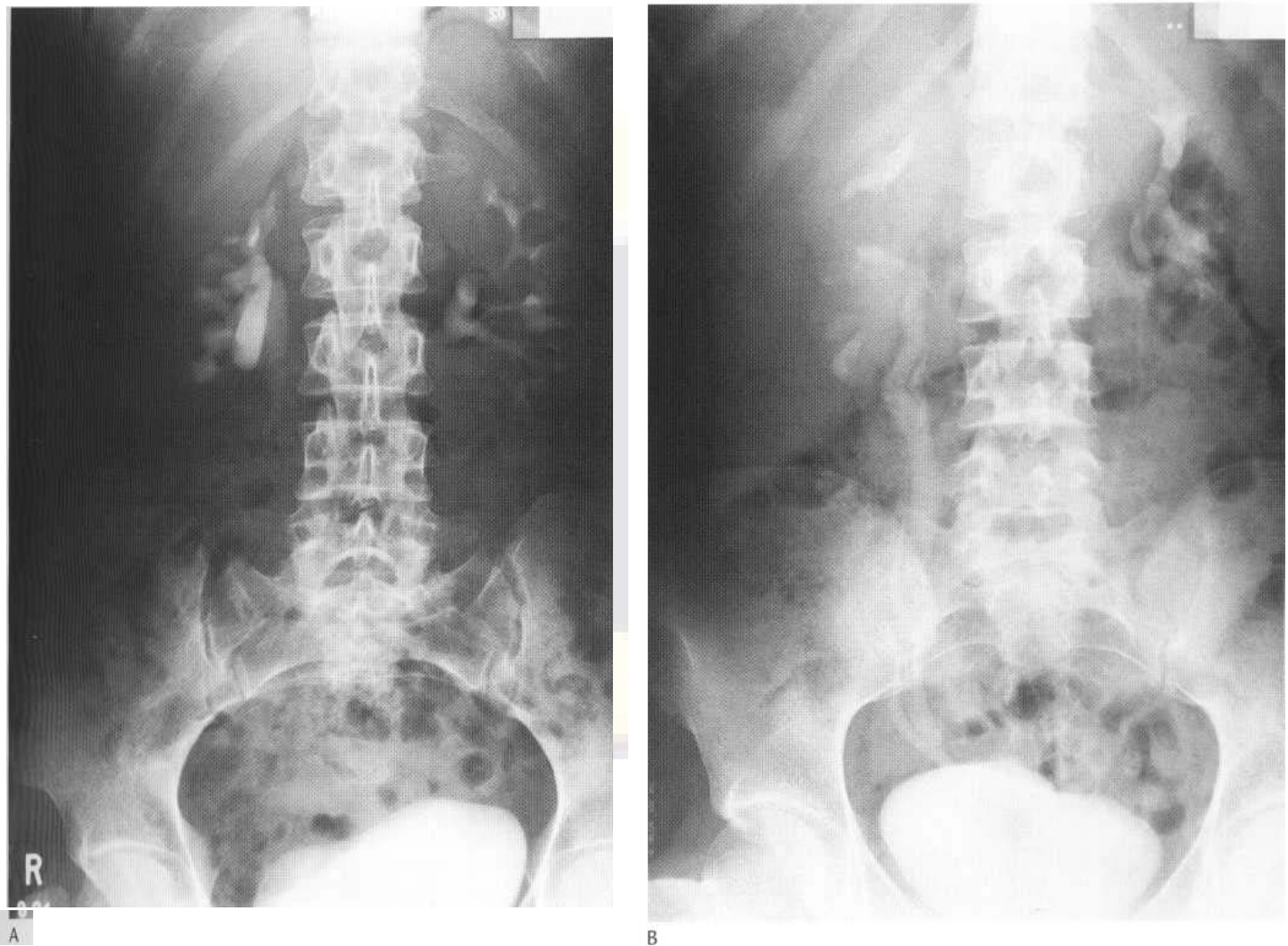


Fig. 30.42 IVU films showing the features of reflux nephropathy. (A) Severe right-sided disease with a small kidney, widespread cortical loss (maximal at the upper pole) and clubbing of the calyces. (B) Right-sided duplex system with diseased lower pole moiety showing clubbing of the calyces and cortical loss. The lower moiety ureter also shows persistent dilatation due to previous severe reflux.

pond calyces which are most susceptible to damage from reflux. The relationship of the scarring to underlying abnormal calyces differentiates the condition from vascular scarring and fetal lobulation (when the calyces are normal and, in the case of lobulation, the indentations are between calyces rather than directly over them). Badly affected kidneys grow poorly and are small, with diffuse cortical loss (Fig. 30.42). Severe continuing reflux in childhood may show capacious ureters and pelvicalyceal systems and there may be evidence of ureteric striations due to redundant mucosa. In adulthood, continued significant reflux is rare. Presentation of reflux nephropathy in adults is usually with recurrent urinary tract infection (which may be associated with pyelonephritis). If the nephropathy is severe, patients may present with hypertension and/or renal insufficiency. Focal areas of compensatory parenchymal hypertrophy may occur between the scars and, if prominent, may give rise to concern about the presence of a tumour, although on ultrasound or CT their appearance is of normal parenchyma. Ultrasound, CT and radionuclide imaging (DMSA) will all demonstrate the areas of scarring.

Although reflux nephropathy does not develop in the adult kidney in the way it does in childhood, a related condition is seen in patients with some lower urinary tract surgical procedures that

permit long-term significant reflux of potentially infected urine. The ureters and pelvicalyceal systems dilate and there is progressive diffuse loss of renal cortex and function. The condition is usually bilateral, although it may show considerable asymmetry. It is most commonly seen with an ileal conduit (Fig. 30.43) but is also encountered in other procedures, especially those involving ureteric reimplantation, for example ureterosigmoidostomy.

Rare inflammatory conditions

Pyeloureteritis cystica is an uncommon condition associated with chronic obstruction and/or infection. Multiple subepithelial cysts develop in the renal pelvis and/or ureter (usually the upper third) generally 1–4 mm in diameter (occasionally up to 20 mm) (Fig. 30.44). They appear as well-defined filling defects on IVU and retrograde pyelography. They are completely benign and asymptomatic, the patient presenting with symptoms from the associated condition. They may persist for months or years, even after removal of the cause.

Leucoplakia and **malacoplakia** are rare conditions seen in association with chronic urinary tract infection. They can affect any part of the urothelium but are more commonly seen in the bladder.

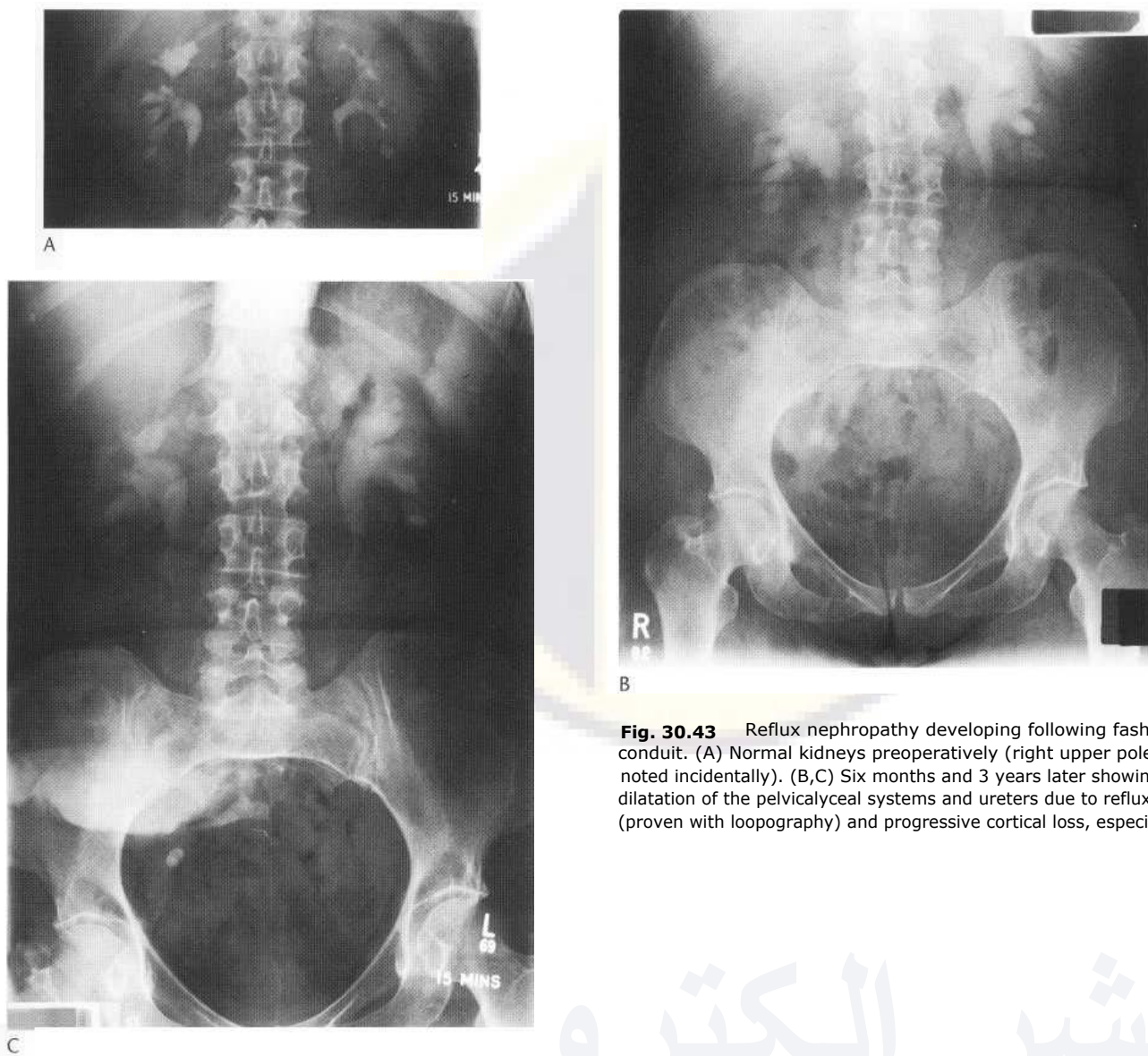


Fig. 30.43 Reflux nephropathy developing following fashioning of an ileal conduit. (A) Normal kidneys preoperatively (right upper pole compound calyx noted incidentally). (B,C) Six months and 3 years later showing non-obstructive dilatation of the pelvicalyceal systems and ureters due to reflux from the conduit (proven with loopography) and progressive cortical loss, especially on the left.

Leucoplakia appears as multiple small plaques of chronic inflammatory tissue arising from the urothelium with a predilection to progress to premalignant squamous metaplasia.

Malacoplakia is thought to be a mild form of chronic granulomatous disease (a defect of cell-mediated immunity). It characteristically appears as multiple filling defects (often bilateral), which may coalesce. The kidneys may appear diffusely enlarged and show decreased function. The filling defects may reach several centimetres in size and distort the calyces. Ultrasound appearances are of ill-defined heterogeneous masses. Occasionally only a solitary mass develops, which is indistinguishable from a renal neoplasm on the imaging features alone.

Chronic irritation of the transitional urothelium of any part of the urinary tract by infection and/or calculus predisposes to the development of squamous metaplasia, which in turn may lead to the formation and desquamation of masses of keratin (cholesteatoma). These appear on all modalities as non-specific filling defects. Classical associations are with stricturing chronic infections (tuberculosis, schistosomiasis) and other causes of chronic urinary tract obstruction.

Fungal renal infection (fungal pyelonephritis) is rare. It may occur due to haematogenous spread in patients with reduced immune competence (AIDS, chemotherapy and steroid treatment, transplantation and diabetes), especially in the presence of chronic indwelling central lines, and consequently is seen with involvement of other organs, especially the brain and lungs. Multiple medullary and cortical abscesses may develop with similar imaging features to *pyogenic abscesses*. Destruction of renal parenchyma occurs, particularly of the renal papillae, which allows fungal hyphae to escape into the renal pelvis with the formation of fungus balls, which in turn may pass into the ureters. Imaging modalities of all types demonstrate fungus balls as filling defects (usually multiple), 1-4 cm in diameter, hyperechoic on ultrasound and hypoechoic on CT. They may contain air, best seen on CT. Associated papillary necrosis, obstruction, renal abscesses and reduced renal function may also be demonstrated. Fungal infection (pyelonephritis and fungus balls) may arise via an ascending route, also associated with reduced immune competence. It is predisposed to by the presence of a long-term urinary catheter and may be secondary to pyogenic urinary tract infection. A variety of fungal species may be encountered- but the commonest is *Candida albicans*.

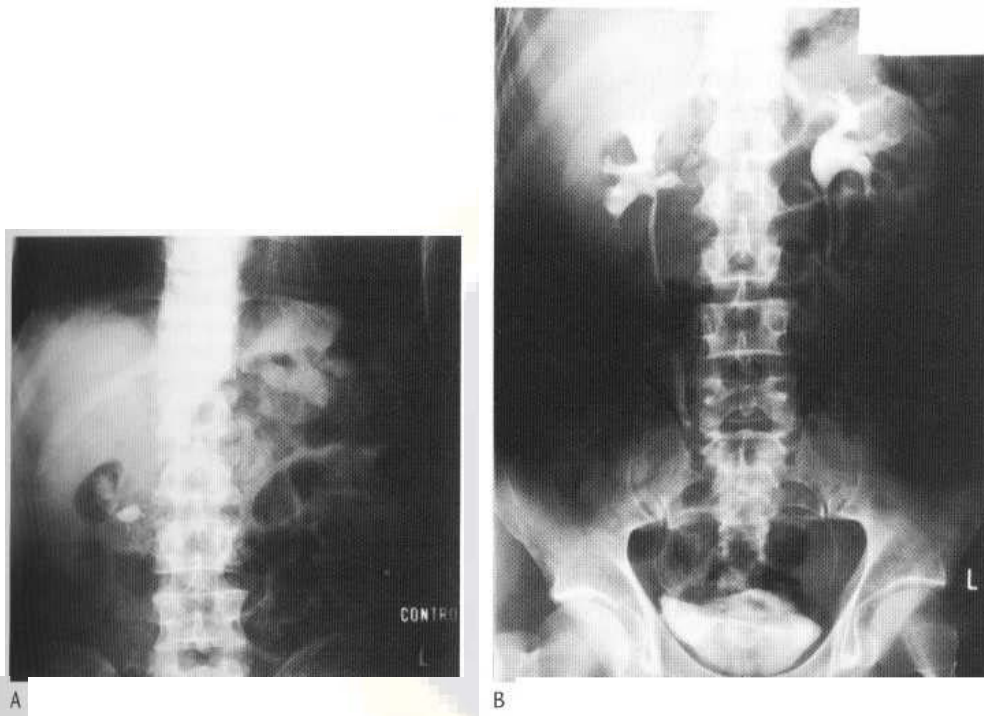


Fig. 30.44 Pyeloureteritis cystica. (A) Plain films showing a renal pelvic calculus (and incidental pancreatic calcification). (B) IVU demonstrating mild hydronephrosis due to the calculus, and multiple filling defects from the pelviureteric junction downwards due to the cyst of pyeloureteritis cystica.

RENAL MASSES

Renal masses may be single or multiple, affecting one kidney or both. The causes of a solitary mass include simple cyst, pseudotumour, tumour and abscess. Multiple masses have a similar differential but clearly causes may coexist; for example, simple cysts are extremely common and are often coincidentally present when a renal tumour is encountered. However, multiple and/or bilateral solid renal tumours are encountered from time to time. It is therefore extremely important to assess the contralateral kidney in the investigation of a tumour, both to ensure there is sufficient functioning renal tissue to allow nephrectomy to be performed and to identify whether or not a second tumour is present. Multiple renal cysts are usually simply idiopathic but there are a number of specific associations, described below. Multiple solid tumours are uncommon. They include metastases, lymphoma, multiple renal cell carcinoma and angiomyolipomas. The latter two have strong syndromic associations, notably Von Hippel-Lindau Syndrome with renal cell carcinoma and tuberous sclerosis with angiomyolipomas.

Benign renal masses

The commonest benign renal masses by far are *simple cysts*. Other benign masses include inflammatory lesions (*abscesses* and *severe focal pyelonephritis*) and *tumours*. The commonest benign tumour is the *angiomyolipoma* (hamartoma). All other benign tumours are rare. They include reninomas, vascular malformations and a variety of mesenchymal tumours.

Reninomas are tumours of the juxtaglomerular cells. They are typically seen in young patients (half are less than 20 years old) and are much more frequent in females. They produce renin and present with severe hypertension, secondary hyperaldosteronism and hypokalaemia. Because of their hormonal activity they are usually small (2-3 cm) at presentation. They appear as well-defined peripherally placed masses on all modalities, hyperechoic on ultra-

sound and poorly enhancing on CT. They may contain areas of haemorrhage and central necrosis and occasionally present with loin pain and rarely anaemia.

Arteriovenous malformations (AVMs) are rare. They are usually acquired following penetrating trauma (most often biopsy). Congenital AVMs are more common in females and are often not diagnosed until adulthood, when they present with haematuria. They are of variable size and may be quite small at presentation. On ultrasound they may be echo-poor or echogenic, depending on the size of the vascular spaces. Hypervascularity may be demonstrated with contrast CT or MRI or Doppler ultrasound, all of which may also demonstrate feeding artery and draining vein. Areas of curvilinear calcification may be present and best demonstrated on CT. Angiography should be diagnostic, with the demonstration of abnormal arterioles communicating with large venules and showing focal early venous filling.

Mesenchymal tumours may arise from any of the tissue elements within the kidney or renal sinus (neural, vascular, fibrous, muscular, fatty, etc.) or from multiple tissues (renal sinus teratoma). Appearances are usually non-specific and vary to a certain extent, depending on the dominant component. The most characteristic is a



Fig. 30.45 Renal sinus lipomatosis. CT demonstrates bilateral renal atrophy with increase in the volume of sinus fat.

pure lipoma with features on CT and MRI identical to fat. Much more commonly the amount of fat within the renal sinus increases significantly simply as a response to age-related renal atrophy. This is referred to as renal sinus lipomatosis. On IVU this produces narrowing and stretching of the calyces. On ultrasound, CT and MRI there is increase in the amount of sinus fat (Fig. 30.45). This process may also be seen in patients with marked renal atrophy from other causes (severe infection or ischaemia) or in the absence of renal atrophy in some patients with Cushing's disease or steroid treatment.

Historically, small solid renal tumours (less than 3 cm diameter) have been described as adenomas. Histologically, they may appear less aggressive than renal adenocarcinomas and tend not to metastasise. There is, however, no scientific basis for this distinction. Histologically, they are not distinct from small adenocarcinomas and even at this size they do occasionally metastasise. It is more logical therefore to consider them as early renal cell carcinomas with a generally favourable prognosis and abandon the term adenoma.

Cysts Cysts and cystic lesions of the kidneys are considered in the following categories: simple cysts, parapelvic and peripelvic cysts, complex renal cysts and acquired cystic disease of (Fig. 30.47). Both of these modalities show a well-defined mass with smooth walls having a thickness of no more than 2 mm.

Simple renal cysts are extremely common, being encountered in adulthood, increasing in frequency with age, and are present in 25-50% of subjects over the age of 50. The vast majority of simple renal cysts are asymptomatic. They are occasionally large enough to be palpable on routine clinical examination or by the individual themselves. Rarely they are thought to cause chronic pain, become infected or undergo haemorrhage (spontaneously or in the context of trauma). They have a thin fibrous wall lined with cuboidal epithelium and contain clear serous fluid. They are thought to arise from blocked tubules and originate mostly from the cortex.

Most cysts are not visible on plain radiographs but occasionally if they are large enough they can be identified as well-defined soft-



Fig. 30.46 Right renal cyst on IVU appearing as a well-defined avascular mass displacing the adjacent calyces.

tissue makes. They are frequently seen on IVU as well-defined non-enhancing masses that distort the adjacent renal outline and pelvicalyceal system. In the parapelvic position they may be associated with fullness of the pelvicalyceal system (Fig. 30.46) but they are not associated with significant obstruction. These features, although suggestive of simple cysts, overlap with cystic or poorly vascular neoplasms and require confirmation with ultrasound or CT. On ultrasound cysts are seen as echo-free masses with distal acoustic enhancement. One or two fine septations may be seen. Multiple cysts, especially in the parapelvic region, may mimic hydronephrosis. They can be differentiated by the demonstrable absence of communication between the cysts and the different pattern of echo-poor areas within the central echogenic fat. On CT cysts are usually low density, similar to water (0-20 HU) but occasionally they may be higher density (40-100 HU), assumed to be due to the presence of protein or blood products following previous infection or haemorrhage. The important feature on CT is the absence of enhancement with intravenous contrast. Analogous features are seen on MRI.

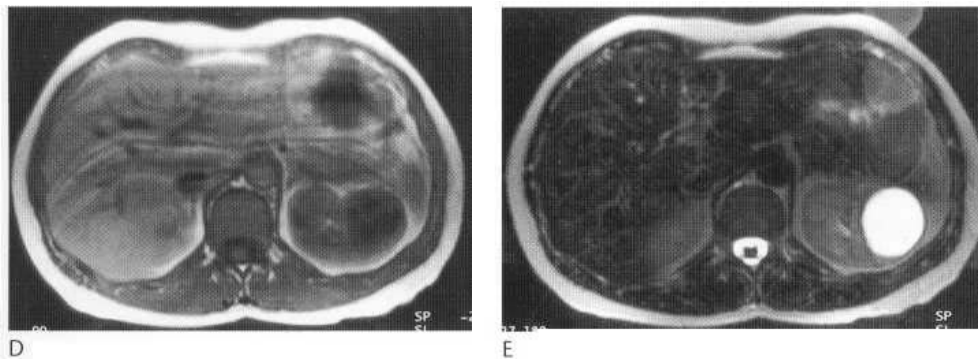
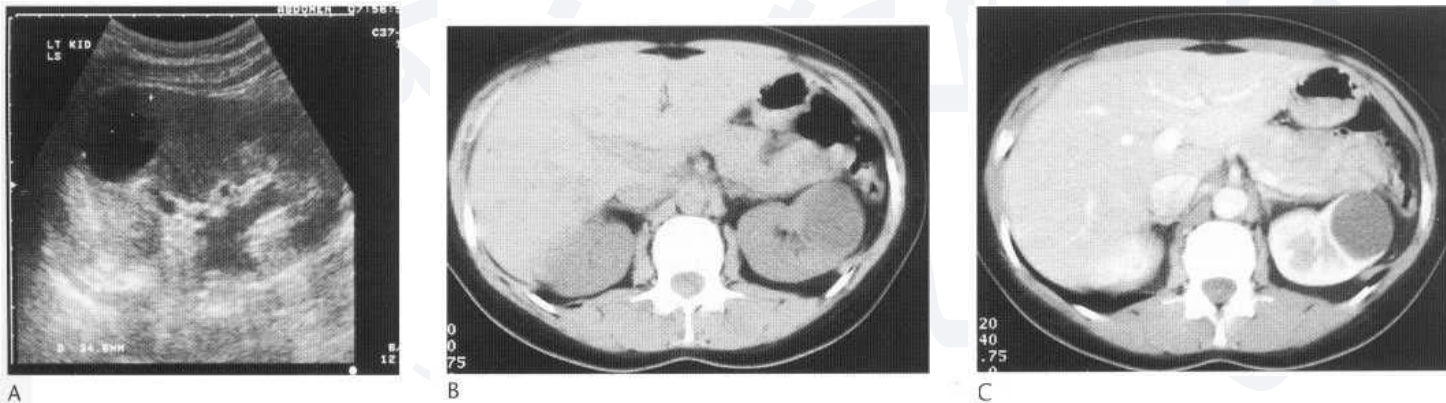


Fig. 30.47 Renal cyst on ultrasound (A) appearing as a well-defined echo-free mass without significant wall thickness and distal acoustic enhancement. On CT the cyst is of water density (B) and shows no enhancement with intravenous contrast (C). On MRI the cyst has the same signal intensity as water, being low signal on the T₁-weighted sequence (D) and high signal on the T₂-weighted sequence (E).

Simple renal cysts that originate from renal parenchyma medially may project into the renal sinus and are described as *parapelvic cysts*. There may be a solitary cyst or a few of varying size. Another common purely cystic lesion is the *peripelvic cyst*. Characteristically these are small and multiple and lie between the calyceal infundibula. They are thought to be lymphatic in origin and may be congenital. On rare occasions they produce focal hydronephrosis but otherwise are of no clinical significance. Both parapelvic and peripelvic cysts may demonstrate stretching and compression of the calyces on IVU, similar to the appearances with marked renal sinus lipomatosis. On ultrasound they have the typical appearance of centrally placed cysts but may be mistaken for a hydronephrosis. However, they do not communicate with each other or separate the central sinus echoes in the way that hydronephrosis does. In practice the clinical picture and imaging appearances of parapelvic and peripelvic cysts overlap to such a degree that the distinction between the two is not relevant in routine practice and both groups

of cysts are often referred to as parapelvic cysts, which seems perfectly justifiable.

Simple cysts are benign lesions with no malignant potential and, once a confident diagnosis is made on any of the above cross-sectional modalities, they can be confidently ignored. However, if a lesion does not rigidly fulfil the above criteria then a more significant diagnosis must be considered. Cystic lesions have been classified into four categories to allow some statement about their malignant potential to be made. The original description was of the CT features but in practice analogous features can be identified on ultrasound and MRI. Category I corresponds to a simple cyst, as described above, having a well-defined thin wall and homogenous water-density non-enhancing contents. Category II cysts may show a few thin (1 mm) septa and fine peripheral calcification. Density on CT may be increased, presumed to be due to previous infection or haemorrhage. Ultrasound of these lesions may show an echo-free lesion or increased echogenicity. These cysts are highly likely to be

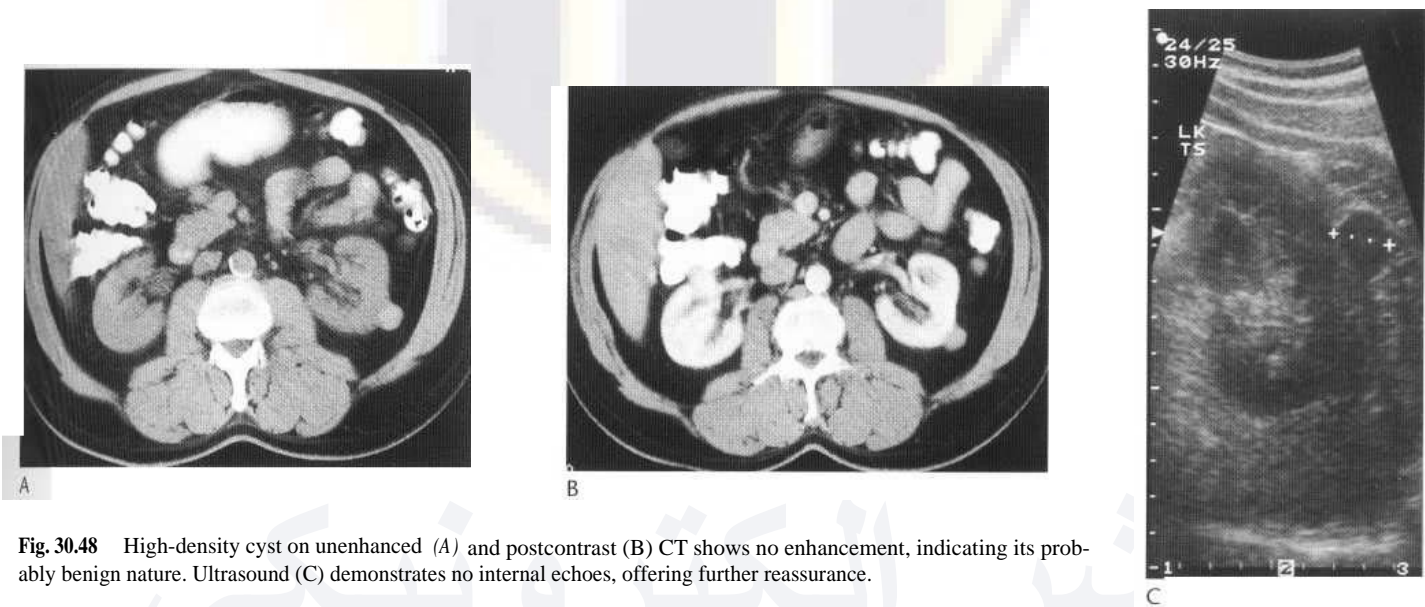


Fig. 30.48 High-density cyst on unenhanced (A) and postcontrast (B) CT shows no enhancement, indicating its probably benign nature. Ultrasound (C) demonstrates no internal echoes, offering further reassurance.

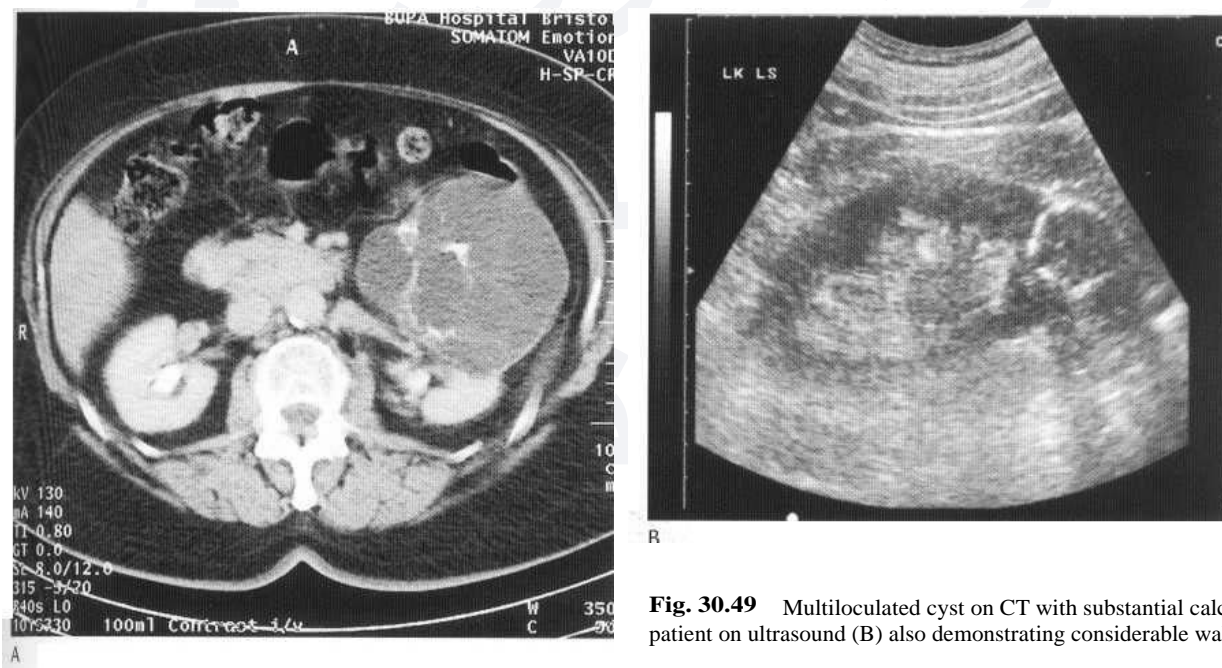


Fig. 30.49 Multiloculated cyst on CT with substantial calcific area (A). Different patient on ultrasound (B) also demonstrating considerable wall calcification.

benign but it may be useful to repeat the ultrasound after 6 months to confirm lack of progression (Fig. 30.48). Features of category III cysts include dense and/or thick areas of calcification and multiple, irregular or thickened (above 1 mm) septae (Fig. 30.49). Category IV cysts show solid areas of enhancement and irregular thickened walls and septae that may also enhance (Fig. 30.50). The usefulness of this classification is that the higher the category the more likely the lesion is to represent a renal malignancy. Approximately 90% of category IV lesions and 60% of category III lesions are malignant. Both these categories are therefore best treated with surgical excision. Approximately 25-30% of category I lesions are malignant. Image-guided aspiration of cyst fluid for cytology and interval scanning if no malignant cells are found is likely to be safe for these lesions.

Acquired cystic disease of dialysis After 3 years of dialysis over 50% of patients develop multiple cysts within the native kidneys. They are usually numerous and small (occasionally some become very large). The epithelium of the cyst walls is thought to be dysplastic and in up to 7% of long-term dialysis patients develops into renal cell carcinoma, albeit of relatively benign behaviour with a low metastatic potential.

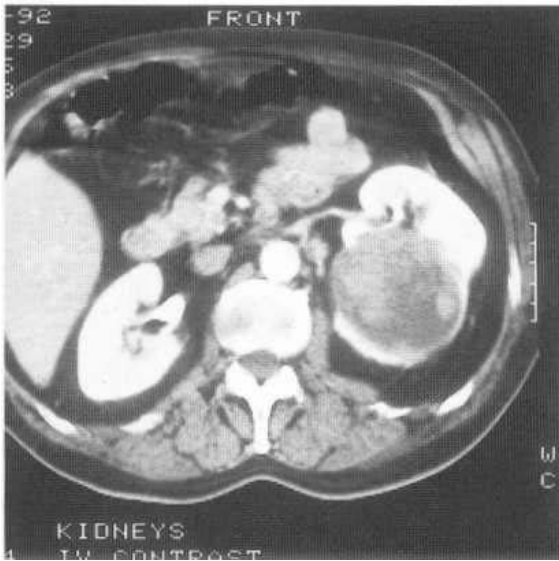


Fig. 30.50 Well-defined cystic lesion with substantial irregular enhancing areas signifying probable malignancy.

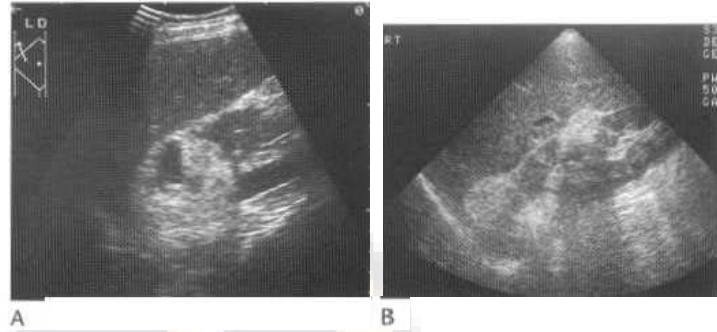


Fig. 30.51 Ultrasound appearances of angiomyolipomas. (A) Large lower pole predominantly echogenic mass (solitary angiomyolipoma). (B) Multiple well-defined purely echogenic masses (multiple angiomyolipomas in tuberous sclerosis).

Angiomyolipoma These are benign hamartomas consisting of varying proportions of angiod, myoid and lipoid tissue. They may be extremely vascular and contain small aneurysms with a predilection to bleed as the mass enlarges. Classically they have been described as large at presentation but increasingly small angiomyolipomas are being identified incidentally on ultrasound or CT: 80% are seen in adults between 30 and 50 years of age, with a marked female predominance. Under these circumstances they are small, solitary and asymptomatic; 20% are seen in patients in association with tuberous sclerosis (of whom 80% have angiomyolipomas). They are then usually multiple and bilateral. They tend to enlarge with age and become prone to haemorrhage. Predictably, therefore, the earlier they are encountered the more likely for this progression to happen. Presentation is usually as an asymptomatic mass, incidental finding on abdominal imaging or with symptoms due to haemorrhage into the lesion (pain and/or haematuria). Haemorrhage into the lesion may be marked and on occasion catastrophic. IVU generally is normal when the lesions are small, showing one or more non-specific masses when larger. If there is a substantial area of fat within the tumour this may be identifiable on the plain film as an area of reduced density, but this is rare.

Ultrasound demonstrates a well-defined predominantly echogenic mass (Fig. 30.51). They are homogenous when small but increasingly become heterogeneous as they enlarge. CT and MRI will demonstrate some fat in over 90% of cases (Fig. 30.52); CT showing areas of low density (20 HU or less), MRI showing high signal on T₁- and T₂-weighted images and a virtual signal void on

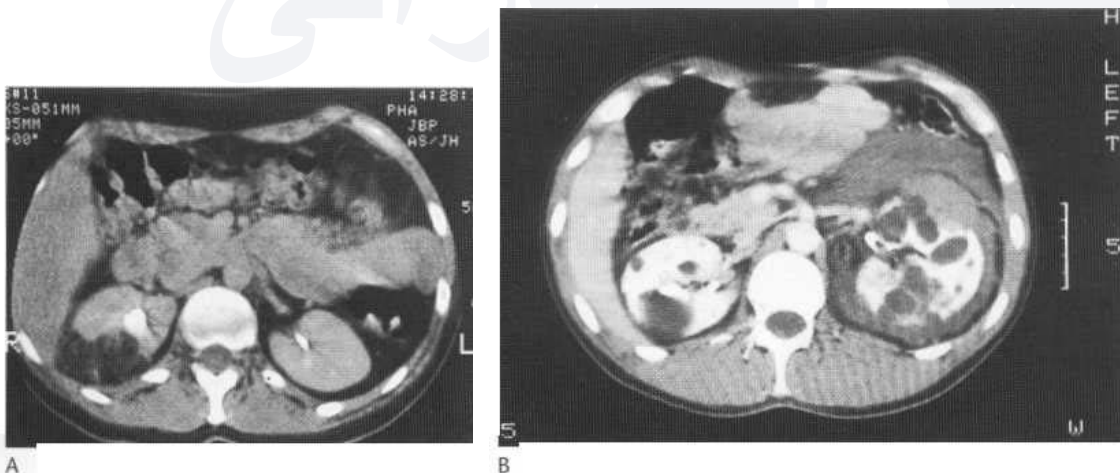


Fig. 30.52 CT showing predominantly fat-density solitary angiomyolipoma (A) and multiple purely fat-density bilateral angiomyolipomas (B) in tuberous sclerosis. The latter case has presented with a left-sided perinephric haemorrhage seen as a soft-tissue rim around the kidney but delineated externally by the perinephric fascia.

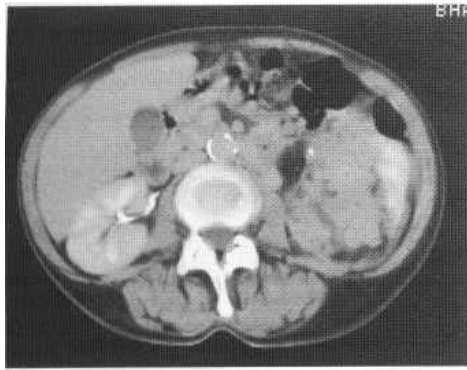


Fig. 30.53 Large left-sided angiomyolipoma with small fat-density areas but predominantly appearing as an enhancing soft-tissue mass.

the STIR sequence. Although there are rare reports of Wilms' tumours and renal cell carcinomas containing a little visible fat, in practice the presence of fat on CT or MRI is virtually diagnostic of angiomyolipoma. The amount of fat, however, is extremely variable. The non-fatty areas of the lesions are intensely vascular and show marked enhancement with intravenous contrast (Fig. 30.53). Acute haemorrhage may be seen on CT as areas of high density within the lesion and in the perinephric space (Fig. 30.54). Blood and blood breakdown products may be seen on MRI, with complex signal appearances. In the subacute phase there is usually high signal on T₁- and T₂-weighted sequences. As the thrombus matures there is gradual reduction in signal, ultimately with areas of signal void due to haemosiderin. Angiography is not required to make the diagnosis but on occasion may be considered with selective embolisation in mind to control bleeding, especially if there is only a solitary kidney. The angiogram will show intense vascularity, small aneurysms and early venous filling.

The only hazard with angiomyolipomas is *haemorrhage*, which is most likely to happen with masses over 4 cm in diameter and those that are growing rapidly. Therefore if the tumour is less than 4 cm diameter it can simply be monitored with ultrasound every 6-12 months. Around one-quarter will increase in size within 4 years. Over 4 cm, half will grow within 4 years. The rate of growth is faster in tuberous sclerosis. Prophylactic surgery can be considered if the lesion is enlarging rapidly.

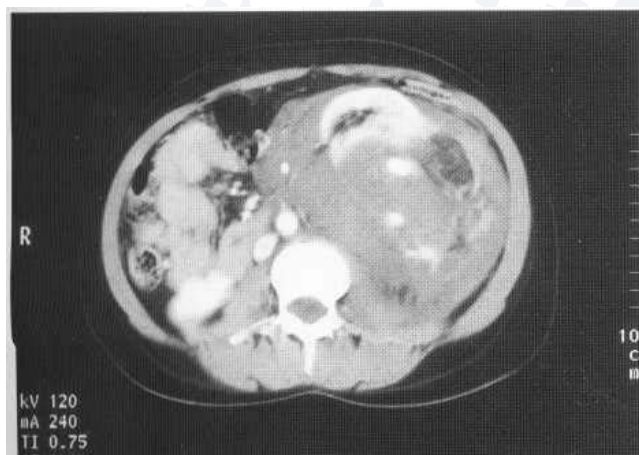


Fig. 30.54 Left-sided angiomyolipoma with brisk haemorrhage, some of which is sufficiently acute to appear as ill-defined high-density areas on CT.

Malignant renal masses

The single most common renal malignancy in adults is *renal cell carcinoma*. Renal malignancy is less frequent in childhood and is most often *Wilms' tumour*. Other malignancies include those arising from primitive renal tissue (such as *multiloculated cystic nephroma*), *oncocytoma*, *renal medullary carcinoma*, *sarcoma*, *lymphoma* and *metastases*. Invasion of renal parenchyma from the collecting system is seen sometimes with advanced transitional cell carcinoma and occasionally squamous cell carcinoma.

Renal cell carcinoma Renal cell carcinoma accounts for approximately 85% of adult renal malignancies, with a male to female predominance of approximately 2.5:1. It represents 3% of new cancer diagnoses and has an incidence of 11/100 000, which appears to be rising. Median age of onset is 55 years but occasional cases may be encountered in young adults and children. Renal cell carcinoma usually originates from the proximal convoluted tubule within the cortex, although less common histological variants, such as the papillary cystadenocarcinoma, originate from further distally within the nephron. There is an increased incidence of renal cell carcinoma in Von Hippel-Lindau disease and long-term renal dialysis.

Advanced renal cell carcinoma has a wide variety of symptoms, usually related to metastases and/or tumour bulk (loin mass, malaise, anorexia, pyrexia of unknown origin). More commonly they present as haematuria or as an incidental mass on CT or ultrasound of the abdomen for some other condition. Renal cell carcinoma may metastasise to bone, brain, lung, liver and soft tissues. It is not rare to see an apparently solitary metastasis from a renal cell carcinoma, especially to bone or soft tissue, and they are characteristically expansile, vascular and (in the case of bone) osteolytic. Sometimes the metastatic disease is the presenting symptom. There have been improvements in chemotherapy of disseminated renal cell carcinoma, particularly with the use of interferon, and a simple examination to assess the kidneys (usually ultrasound) is justified in patients with metastatic disease of unknown origin. Occasionally tumours produce an erythropoietin-like substance and present as polycythaemia or one of its complications. On rare occasions they present as spontaneous perinephric haemorrhage.

The IVU is the traditional modality used to investigate haematuria. Large tumours may be visible as a soft-tissue mass on the preliminary plain films. Up to 10% of renal cell carcinoma show some calcification on plain films. Similarly, if calcification is seen in association with a renal mass then it is most likely to represent a renal cell carcinoma, especially if the calcification is dense, central and amorphous. Following contrast injection renal cell carcinoma is usually detected as a mass which displaces the adjacent calyces and distorts the renal outline (Fig. 30.55). Occasionally the appearances are of a mass with loss of renal function if the tumour has occluded the renal vein. Renal cell carcinoma usually shows similar enhancement to normal renal tissue on the nephrogram but a minority of tumours are poorly vascular and therefore have an appearance similar to simple cysts and require further investigation, usually with ultrasound to confirm their nature. One-third of tumours less than 3 cm diameter are not seen in IVU and therefore, even if this investigation is normal, further investigation with ultrasound should be considered, especially if haematuria persists.

Ultrasound, CT and MRI will each reliably diagnose the vast majority of renal cell carcinomas. On ultrasound renal cell carci-

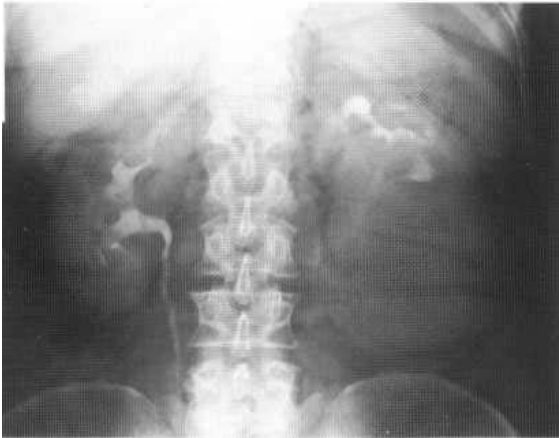


Fig. 30.55 Renal cell carcinoma on IVU. The tumour appears as a large left lower pole mass distorting the adjacent pelvicalyceal system.

Renal cell carcinoma usually appears as a solitary mass bulging from the renal outline. It is usually iso- or hypoechogenic compared to normal kidney but around 10% may be hyperechoic, especially if small. Most show some heterogeneity, although small lesions may not. Areas of hyperechogenicity with acoustic shadowing may be seen if macroscopic calcific foci are present (Fig. 30.56). On CT and MRI the features are of a soft-tissue mass that is at least partly solid, often lobulated and associated with loss of the normal renal architecture in the area affected. Generally, smaller tumours appear more homogeneous and well defined, becoming more heterogeneous, containing more substantial areas of necrosis and becoming less well defined as they enlarge. On CT they are usually isodense or hypodense compared to normal renal tissue, occasionally hyperdense. They enhance variably with intravenous contrast but almost always less than normal renal tissue (Fig. 30.57). Around a third have detectable areas of calcification. On MRI they appear of intermediate signal on the T₁-weighted sequence, high signal on STIR and variable but often intermediate to high on T₂-weighted sequences. In 10-15% of cases the tumour is predominantly cystic but evidence of malignant tissue is still usually apparent in the form of enhancing soft-tissue areas within the walls of the lesion. Occasionally renal cell carcinoma is predominantly infiltrating,



Fig. 30.57 Renal cell carcinoma on CT appearing as a heterogeneously enhancing mass associated with destruction of the normal renal architecture.

showing obliteration of normal renal architecture on ultrasound, MRI and CT with little mass effect. The important differential diagnosis in these cases is infiltrative transitional cell carcinoma invading renal parenchyma, which is treated with nephroureterectomy. Radiological clues to this condition are obliteration of renal sinus fat and tumour within the pelvicalyceal system.

Once the diagnosis has been made the tumour should be staged. Two formal systems are available. The Robson classification (Box 30.1) and the TNM classification of the International Union

Box 30.1 Staging of renal cell carcinoma-Robson classification

- Stage I Limited by the renal capsule
- Stage II Tumour has breached the renal capsule (perirenal involvement) but is limited by Gerota's fascia
- Stage IIIa Tumour invasion into renal vein or inferior vena cava
- IIIb Tumour involvement of regional lymph nodes
- IIIc Venous and lymph node invasion
- Stage IV Invasion of adjacent viscera or distant metastases



A



B

Fig. 30.56 Renal cell carcinoma on ultrasound. Two examples, one appearing as a solid mass of intermediate echogenicity replacing the normal renal architecture (A) and the other similar apart from substantial central necrosis (B).

Box 30.2 TNM staging of renal cell carcinoma*Primary tumour (T)*

TX	Primary tumour cannot be assessed
T0	No evidence of primary tumour
T1	Tumour limited to the kidney; 7.0 cm or less in maximum diameter
T2	Tumour limited to the kidney; above 7.0 cm in maximum diameter
T3a	Tumour extends into perinephric tissue (including the adrenal gland) but remains confined by Gerota's fascia
Tab	Tumour extends into the renal vein or inferior vena cava below the diaphragm
T3c	Tumour extends into the inferior vena cava above the diaphragm
T4	Tumour invades beyond Gerota's fascia

Nodal status (N)

NX	Regional lymph nodes cannot be assessed
N0	No regional lymph node metastasis
N1	Metastasis in a single regional lymph node
N2	Metastasis in more than one regional lymph node

Distant metastasis (M)

MX	Distant metastases cannot be assessed
M0	No distant metastases
m1	Distant metastases

Against Cancer (Box 30.2). The TNM classification is more detailed and incorporates the general principles of tumour staging found throughout the TNM system. The Robson classification is the one most commonly used routinely. Its advantages are its simplicity and good correlation with prognosis as well as indicating specific problems the surgeon may encounter.

Ultrasound is very often performed as part of the diagnostic process for renal cell carcinoma, and initial staging is undertaken. However, the accuracy of ultrasound staging is inferior to that of CT and MRI, which are usually indicated for definitive preoperative staging. Both CT and MRI are over 90% accurate for most aspects of staging except the differentiation between stage I and stage II. The error rate for this is of the order of 50%. Tumours that are confined by the renal capsule (stage I) should show a normal perinephric space (Fig. 30.58). Tumour extension through the renal capsule (stage II) may show bulk tumour in the perinephric space (Fig. 30.59). This differentiation may be difficult. Tumours may breach the capsule without showing bulk tumour outside it. Secondary signs to be sought under these circumstances include



Fig. 30.58 Stage I renal cell carcinoma on postcontrast CT. The tumour is small and confined to the kidney.

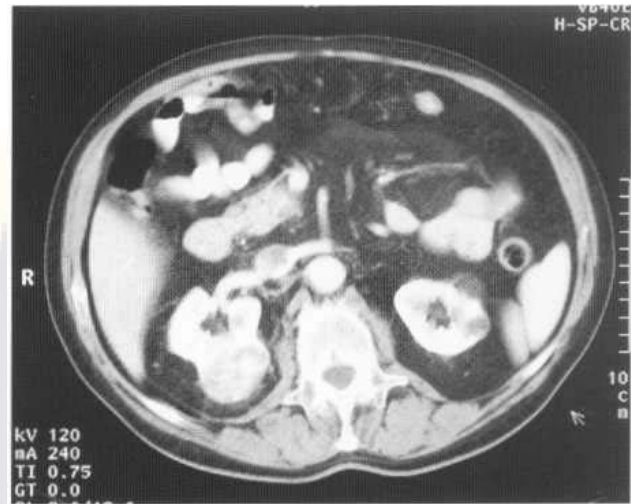


Fig. 30.59 Stage II renal cell carcinoma on postcontrast CT. The tumour extends to the margin of the kidney and shows some local nodular extension through the renal capsule.

tumour extending to the margin of the kidney and having an ill-defined peripheral outline, thickening of the perinephric fascia and soft-tissue strands within the perinephric space. These features, however, may also occur in some stage I tumours due to adjacent reactive inflammatory or oedematous change. Renal cell carcinoma also acquires a collateral or parasitic blood supply which is often visible in the perinephric space and may be mistaken for tumour extension through the capsule. Conventionally stages I and II are treated with radical nephrectomy and show little prognostic difference. Currently, however, nephron-sparing surgery (partial nephrectomy) is increasingly being offered under certain circumstances. These include situations where there is only one functioning kidney and/or where the tumour is small (less than 4 cm diameter) and localised, especially if there is a possibility of a more benign pathology such as an oncocytoma. In these patients it becomes much more important to attempt accurate differentiation between stage I and II. It is also important to perform a careful study of the healthy renal tissue on the affected side and in the contralateral kidney, as tumours may be multifocal within the same kidney or bilateral in up to 2%. Partial nephrectomy also depends on being able to preserve a separate blood supply to the remaining healthy renal tissue and therefore generally requires preoperative assessment of the renal vasculature, usually performed with MR or CT angiography.

Stage III tumours are treated with radical nephrectomy and thrombectomy and/or lymphadenectomy. MR and CT are both highly accurate in the demonstration of venous invasion. Renal cell carcinoma has a predilection to invade the renal vein at the hilum and extend along it into the inferior vena cava (Fig. 30.60). Further extension is usually superiorly with the flow of blood, occasionally as far as the right atrium. Sometimes tumour extends into the contralateral renal vein. Interestingly it is almost always intraluminal tumour, the inferior vena cava wall itself being rarely invaded. The disturbance of blood flow in the inferior vena cava may lead to thrombus formation and pulmonary emboli. On CT, if there is adequate opacification of the venous system the demonstration of a filling defect within the renal vein and/or inferior vena cava is highly reliable, good-quality spiral CT having an accuracy of the order of 96%. Care must be taken to evaluate all sections to avoid

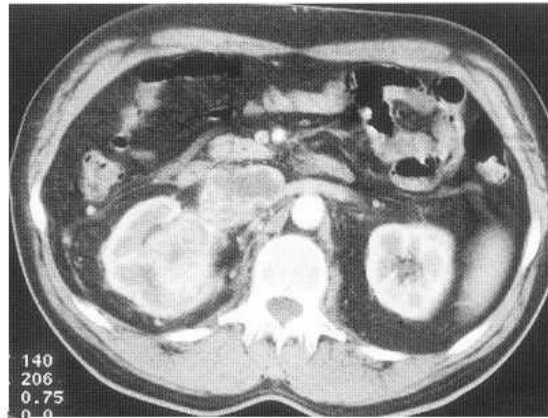
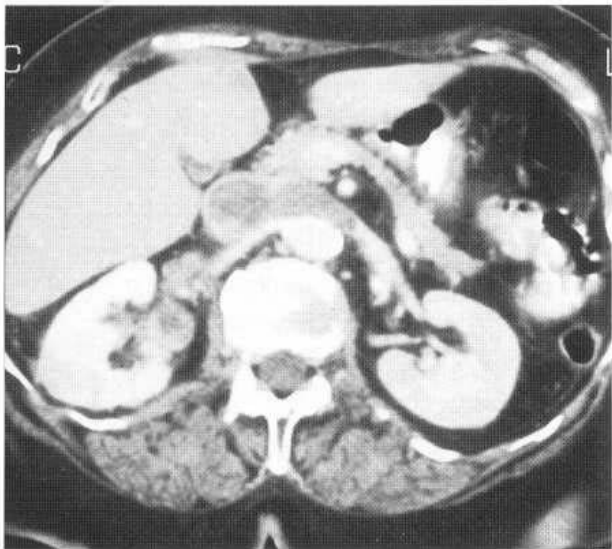


Fig. 30.60 Renal cell carcinoma with vascular involvement. (A) Ultrasound shows tumour as a soft-tissue nodule of intermediate echogenicity within the inferior vena cava. Postcontrast CT (B, different case) shows a right renal cell carcinoma extending along the renal vein into the inferior vena cava and (C) into the contralateral renal vein.

A

B



C

because tumour in the inferior vena cava may cause upstream blood in the vena cava below the renal veins to slow down sufficiently to appear as a high-signal column that may be mistaken for retrograde extension of tumour. It is important to assess extension into the contralateral renal vein and the superior limit of inferior vena cava involvement. Extension to the level of the hepatic veins or right atrium requires the involvement of a hepatic or cardiac surgeon. Usually the lymphatic drainage from the kidney follows the renal veins to the lateral aortic nodes close to the origins of the renal arteries. These are usually the first nodes to be involved with metastatic carcinoma. Drainage from this site is via the lumbar trunks to the cisterna chyli. Occasionally lymphatic channels bypass the first-order nodes and drain directly to the mediastinum. The overall accuracy for staging lymph node involvement with CT is around 83-89% and depends on the detection of lymph node enlargement above 1 cm diameter (Fig. 30.62). Unfortunately this leads to a substantial number of false positives due to reactive inflammatory hyperplasia (up to 43% in some studies). Enlargement above 2 cm diameter is almost always due to metastases. Microscopic metastasis without enlargement is uncommon. MRI staging depends on the same criteria and therefore has a similar accuracy.

misdiagnosing a central stream of unopacified blood returning from the lower limbs as tumour. On MRI, tumour within the blood vessels is well demonstrated on good-quality conventional sequences as a soft-tissue mass compared to the signal void of flowing blood (Fig. 30.61). The appearances can be complex

Stage IV tumours (Fig. 30.63) show invasion into adjacent organs. The organs involved are predictable from the relationships of the kidneys and include posterior extension into the psoas muscle and quadratus lumborum, superiorly into the adrenal glands, later-

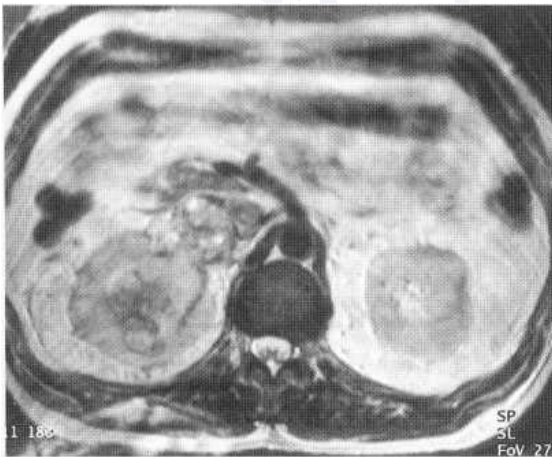


Fig. 30.61 Heterogeneous mass of renal carcinoma in the right kidney on MRI (T_2 -weighted sequence) extending along the right renal vein into the inferior vena cava.

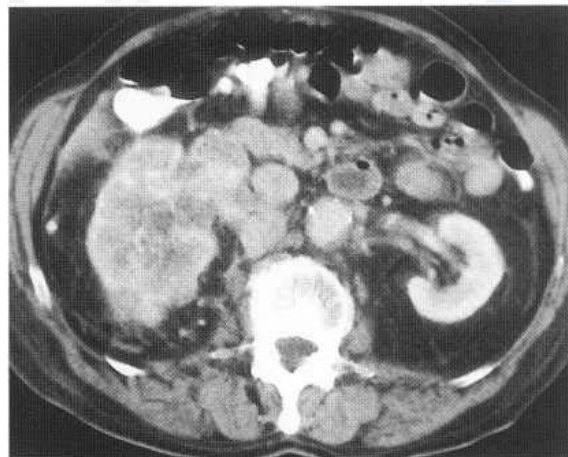


Fig. 30.62 Large right renal cell carcinoma with lymph node metastases including a large node that is displacing the inferior vena cava anteriorly.

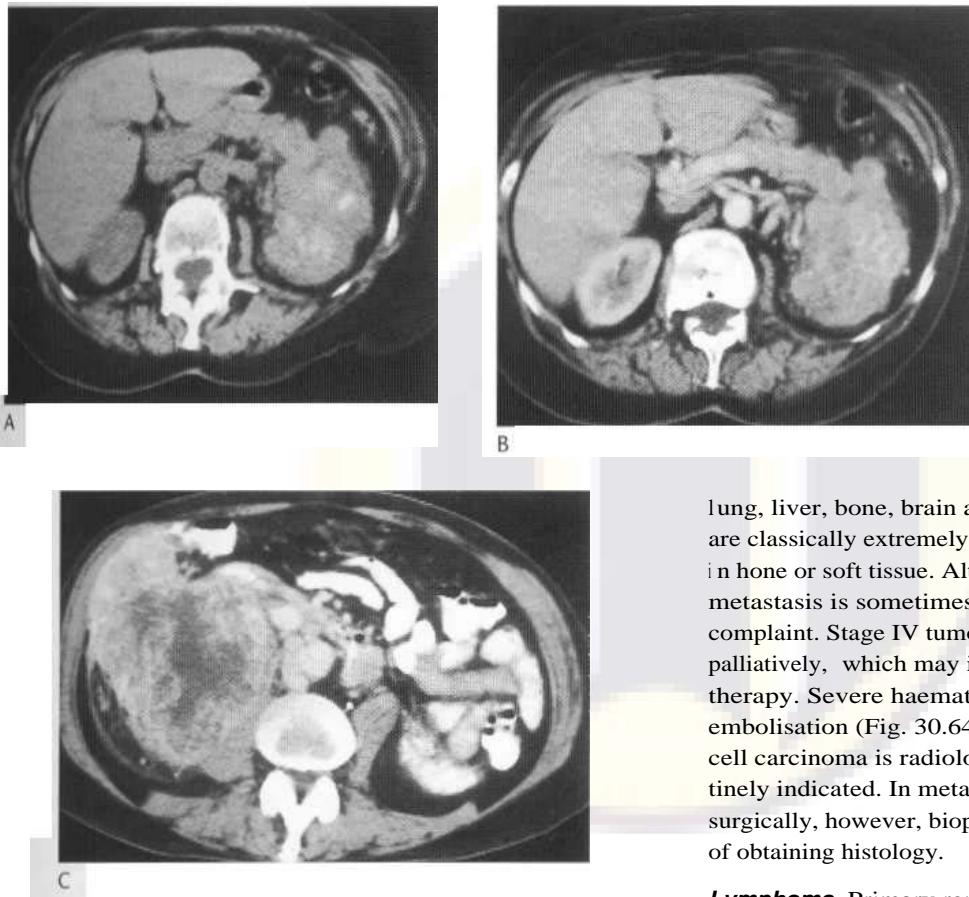


Fig. 30.63 Stage IV tumours. Left renal cell carcinoma with areas of calcification seen on the unenhanced CT (A). The tumour has invaded into the tail of the pancreas (B). Right renal cell carcinoma invading the psoas muscle, anterior abdominal wall and adjacent bowel (C).

ally into the abdominal wall, posterosuperiorly into the diaphragm, and anteriorly into colon, liver and duodenum (on the right) and pancreas, jejunum, stomach and spleen (on the left). Loss of the fat line between the tumour and adjacent structures on CT or MR1 is common and in itself does not necessarily indicate invasion, the diagnosis requiring the demonstration of density/signal change and/or enlargement. Common sites for distant metastases include

lung, liver, bone, brain and soft tissue throughout the body. They are classically extremely vascular and may be expansile, especially in bone or soft tissue. Although they are usually multiple, a solitary metastasis is sometimes encountered and may be the presenting complaint. Stage IV tumours have a poor prognosis and are treated palliatively, which may include surgery, chemotherapy and radiotherapy. Severe haematuria may be palliated with renal arterial embolisation (Fig. 30.64) or radiotherapy. The diagnosis of renal cell carcinoma is radiological and preoperative biopsy is not routinely indicated. In metastatic disease that is being managed non-surgically, however, biopsy is often required as it is the only means of obtaining histology.

Lymphoma Primary renal lymphoma is rare. Involvement of the kidney is usually secondary to extensive disease elsewhere in the abdomen. Renal involvement may take a variety of forms. Most commonly extensive retroperitoneal lymphoma extends along the lymphatics into the renal sinus and perinephric space and may penetrate into the parenchyma to produce multiple (occasionally solitary) intrarenal masses. Renal involvement is usually bilateral. The commonest manifestation on IVU is ureteric displacement by

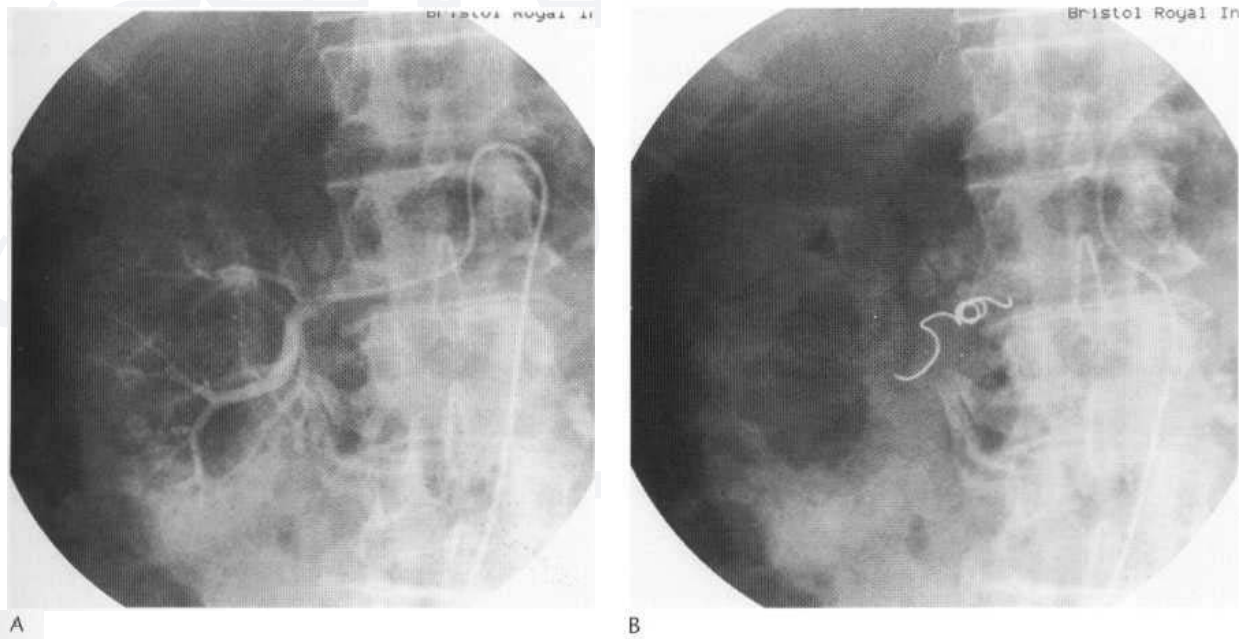


Fig. 30.64 Right renal angiogram (A) demonstrating the malignant circulation of a renal cell carcinoma. Embolisation with an intra-arterial coil (B) has been performed.

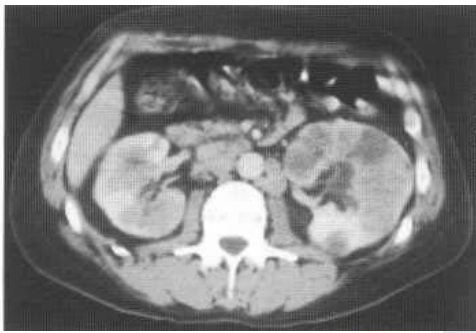


Fig. 30.65 Renal lymphoma on postcontrast CT. There are bilateral relatively well-defined intermediate to low-density deposits of lymphoma.

para-aortic and/or iliac lymphadenopathy with variable hydronephrosis. Direct renal involvement may be seen as one or more non-specific masses with corresponding distortion of the renal outline and pelvicalyceal system. On ultrasound renal deposits are generally echo-poor, often markedly so, even being echo-free, but, unlike cysts, not showing distal acoustic enhancement. Diffuse renal infiltration occasionally occurs, usually bilaterally, producing global renal enlargement demonstrable on all modalities. This is rare and more commonly seen with leukaemia. On CT there is usually widespread marked abdominal lymphadenopathy. Deposits of lymphoma are seen within the renal sinus and parenchyma and are usually well defined, homogeneous and of similar or slightly reduced density compared to normal renal parenchyma (Fig. 30.65). They enhance with intravenous contrast but to a lesser degree than normal renal tissue, and they are usually most visible during the nephrogram phase. Disease may also be identified in the perinephric space. Haemorrhage, calcification and cystic areas are rare. These features are mirrored on MRI. The deposits are usually well-defined and homogeneous with intermediate signal on the T₂-weighted sequence, intermediate to low on T₁-weighted sequence and high signal on the STIR sequence. Enhancement is poor.

Leukaemia Leukaemic involvement of the kidneys is more often a feature of lymphocytic than granulocytic leukaemia. It results in bilateral symmetrical renal enlargement, which may be gross.

Ultrasound, CT and MRI may show diffuse infiltration with loss of the normal renal architecture. Hypoechoic/low-density areas may develop in relationship to areas of haemorrhage. A focal mass of leukaemic cells may be demonstrated (chloroma). Renal insufficiency is common and may relate to orate nephropathy. Orate calculi and blood clot are common filling defects within the collecting system.

Renal metastasis Metastases to the kidneys are common at post-mortem (usually small and multiple) but rarely clinically significant or evident during life. Haematogenous spread of tumours to the kidney occurs most commonly from primary malignancy of the breast, bronchus, gastrointestinal tract, malignant melanoma and lymphoma. Occasionally a solitary deposit is seen, more usually there are multiple bilateral masses easily demonstrated on ultrasound, CT or MRI. Features on these three modalities are similar to those of renal cell carcinoma (Fig. 30.66). Rarely there is diffuse infiltration with obliteration of the normal architecture, especially with squamous cell carcinoma metastases from the bronchus. The imaging features are then similar to infiltrating transitional cell carcinoma.

The kidneys may also be involved by direct extension of tumour from neighbouring organs, particularly pancreas, adrenal and occasionally gastrointestinal tract.

Oncocytoma These are benign renal tumours with no malignant potential. Although suggestive of the diagnosis, imaging and even biopsy features overlap with those of renal cell carcinoma so a definitive preoperative diagnosis is not possible. However, consideration of the diagnosis may allow the surgeon to opt for a partial rather than a radical nephrectomy. On IVU the oncocytoma appears as a mass, indistinguishable from a renal cell carcinoma, and often large. On ultrasound classically the mass is isoechoic with normal renal tissue and as it enlarges above 5 cm or so shows a central stellate echo-poor scar (necrotic area). There may be an apparent pseudocapsule formed by compression of adjacent normal renal tissue. CT and MRI features are similar to a well-defined renal cell carcinoma which is relatively homogeneous apart from the frequent occurrence of a poorly enhancing irregular central scar (Fig. 30.67). The remainder of the tumour shows

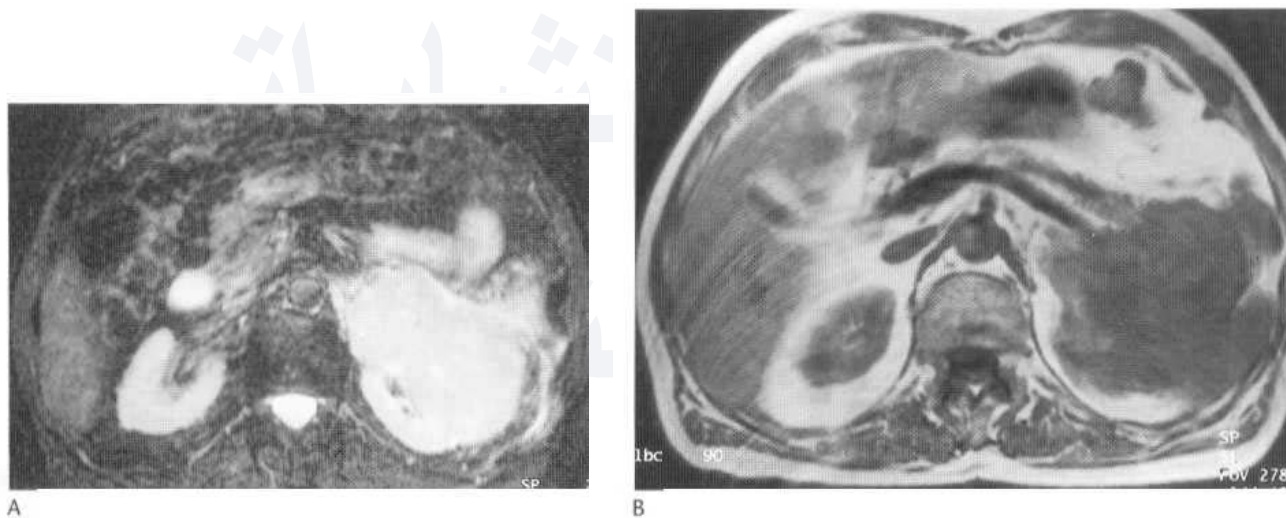


Fig. 30.66 Renal metastasis on STIR sequence (A) and T-weighted MRI (B). Features of the mass are essentially identical to a primary renal cell carcinoma.

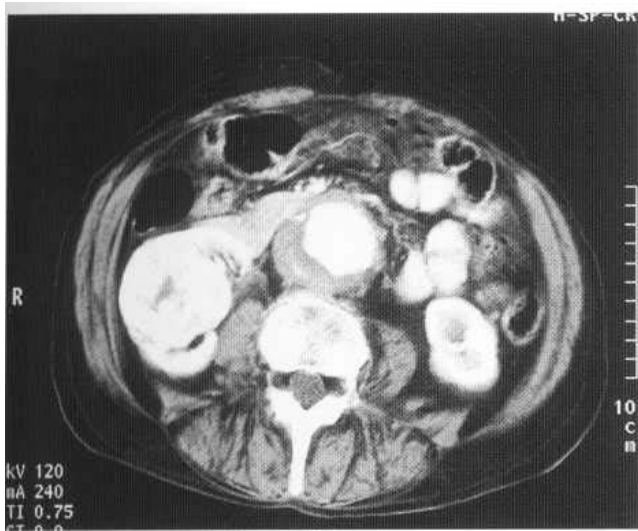


Fig. 30.67 Renal oncocytoma on CT appearing as a well-defined intensely enhancing mass with central non-enhancing scar.

good enhancement (often not as intense as normal renal tissue). Angiography classically shows regular radially orientated arteries (spoked-wheel appearance) but again, although this is suggestive of the diagnosis, it is not specific.

Transitional cell carcinoma This malignancy originates from the transitional epithelium of the renal pelvis, ureter or bladder and usually presents with haematuria. It is most common in the bladder (by far) and least common in the ureter (roughly 25:2.5:1). It constitutes approximately 5-10% of renal malignancies. It is rare in childhood but may present at any age in adulthood, most commonly in the seventh decade with a male predominance. There is an increased risk of its development in the presence of a variety of urothelial irritants (smoking, exposure to aniline dyes and other organic chemicals, analgesic abuse and chronic urinary tract infection, vesicoureteric reflux, obstruc-

tion and/or calculi). The development of a transitional cell carcinoma (TCC) at any site in the urinary tract appears to be a manifestation of instability of the urothelium and there is a significant risk of metachronous and synchronous tumours within the bladder, ureters and either pelvicalyceal system. A wide range of figures is quoted: up to one-quarter of renal TCC is associated with a synchronous tumour (usually within the bladder or the ureter) and up to one-third are associated with a metachronous tumour (two-thirds of these being in the bladder), usually within 4 years of initial tumour presentation. Contralateral renal TCC may be seen in up to 6%. Early tumours are confined to the collecting system but, as they advance, classical extension is into renal parenchyma (up to 25% of renal pelvic tumours) and the retroperitoneum. Haematogenous metastases are rare but lymph node spread is common. Although a routine staging system is not employed, tumours can be staged using a TNM classification. Tumours of stage T2 or less are confined to the renal pelvis or ureter, having invaded no further than the muscularis. T3 tumours extend into renal parenchyma or peripelvic (or periureteric) tissue; T4 tumours into adjacent organs or through the kidney into perinephric fat.

On IVU TCC is seen as an irregular mass projecting into the pelvicalyceal system. It may be sessile or polypoidal and may be associated with obliteration of one or more of the calyces (Fig. 30.68). In the upper urinary tract it virtually never shows calcification on plain films. Depending on size and site there may be associated hydronephrosis or hydrocalyx. The kidney may become non-functioning on IVU in the presence of extensive parenchymal invasion. The differential diagnosis of a filling defect on IVU includes other malignant tumours (metastases, renal parenchymal malignancy invading the collecting system), thrombus, non-opaque calculus and a variety of rare causes (sloughed papilla, fungus balls, pyeloureteritis cystica and gas bubbles). The two most important are thrombus and non-opaque calculi, which are reliably differentiated with CT. Thrombus has a characteristic serpiginous appearance on IVU and a tendency to resolve rapidly (Fig. 30.69). It is encountered with any cause of haematuria, including TCC.

Retrograde pyelography will also demonstrate TCC as a filling defect of variable irregularity; it may be performed to confirm the

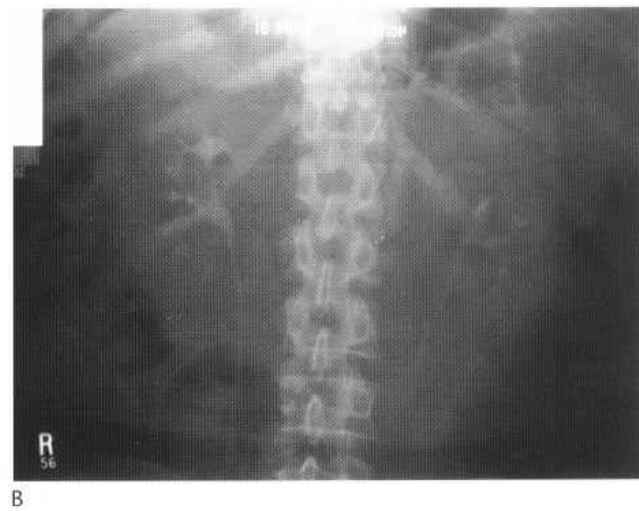


Fig. 30.68 (A) Large transitional cell carcinoma seen as a substantial filling defect in the left renal pelvis. (B) More subtle transitional cell carcinoma almost completely obliterating the left upper pole major calyx and showing marked irregularity of the remaining urothelium in that area.



Fig. 30.69 Well-defined serpiginous filling defect in the right renal pelvis extending a little way into the upper ureter. This represents thrombus in a patient overcoagulated with warfarin and presenting with haematuria. The filling defect and haematuria resolved completely once normal coagulation was restored.

IVU features and offers the urologist the opportunity of obtaining urine from the affected pelvicalyceal system for cytology and inspecting the bladder cystoscopically for synchronous lesions.

of TCC, especially when small. The most common appearance is a relatively echo-poor mass within the central hyperechoic area. It may be associated with a dilated calyx or hydronephrosis. Renal parenchymal invasion may be detected as an ill-defined hypoechoic area of (often subtle) expansion of renal tissue (Fig. 30.70). Appearances may be complex: areas of keratin production in squamous metaplasia or occasional encrustation of the tumour with calcium may produce echogenic areas similar to calculi or fat (Fig. 30.71). Chronic focal or global renal obstruction is both a predisposing cause of the condition and a potential sequel and the tumour may therefore coexist with inflammatory debris and [calculi](#).

CT is indicated to confirm the diagnosis of tumour (rather than, for example, poorly opaque calculus) and stage the lesion. TCC is reliably demonstrated from 1 cm diameter upwards. Calcification is rare (less than 2% of cases). The tumour appears as an ill-defined mass slightly denser than urine but hypodense (or sometimes iso-intense) compared to normal renal tissue with a density value of between 8 and 30 HU. TCC is less vascular than renal cell carcinoma and usually enhances poorly with intravenous contrast.



Fig. 30.70 Relatively echo-poor deposits of transitional cell carcinoma obliterating the normal renal architecture in the upper pole.



Fig. 30.71 Substantial transitional cell carcinoma showing a mixed echo-poor and echogenic pattern and a mild associated hydronephrosis.

However, is not particularly specific or sensitive in the detection, when there is infiltration into renal parenchyma these

tumours may have very similar density and enhancement to renal cell carcinoma. These features contrast with the other major differential diagnosis, thrombus, which is slightly denser (20-55 HU) and does not enhance at all. When large, the tumours characteristically obliterate the sinus fat, a feature not seen with renal cell carcinoma (Fig. 30.72). There may be associated hydronephrosis or hydrocalyx. Analogous features are seen on MRI (signal intensities being similar to normal renal tissue; sometimes slightly less on the T₁-weighted sequence and slightly more on T₂) but this modality is currently regarded as no more sensitive than CT and potentially less [so](#) in the demonstration of small tumours.

Squamous cell carcinoma This is an uncommon tumour constituting less than 10% of urothelial tumours. It is generally associated with metaplasia of the urothelium secondary to chronic irritation, usually due to chronic urinary tract infection with calculi present in at least 50%. It is often therefore associated with a structurally or functionally abnormal urinary tract. It has similar radiological features to TCC but is often more aggressive and faster growing (Fig. 30.73).

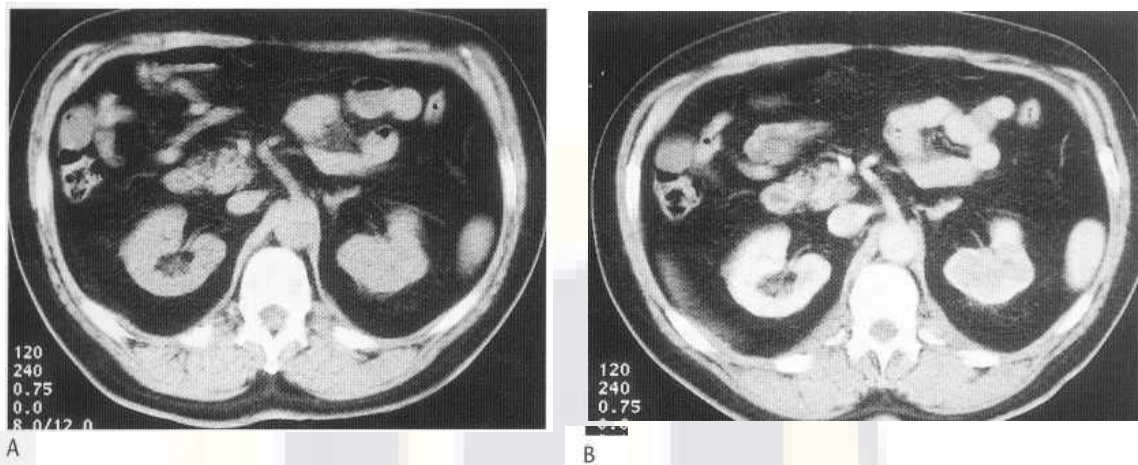


Fig. 30.72 Infiltrating left upper pole transitional cell carcinoma with similar density to normal renal tissue obliterating the sinus fat (A) and enhancing slightly less than normal renal tissue (B).

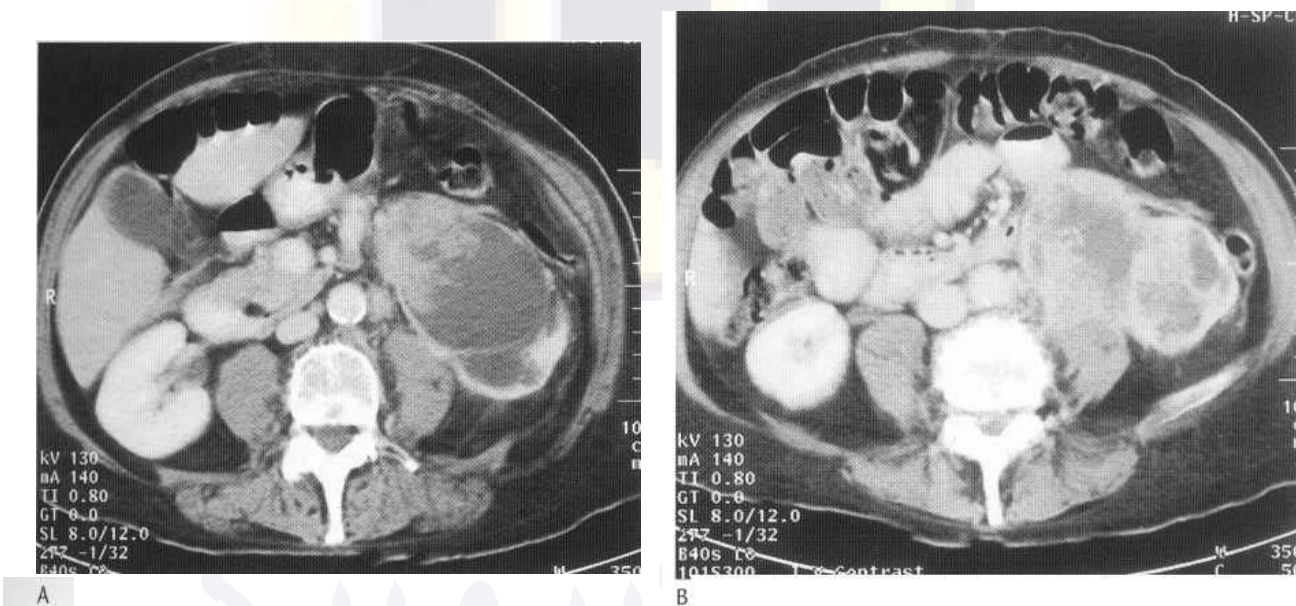


Fig. 30.73 Squamous cell carcinoma developing within a chronic hydronephrosis (A). The tumour has extended out of the collecting system and is invading the psoas muscle (B).

Wilms' tumour Wilms' tumour is a malignant tumour that arises from embryological precursors of renal parenchyma (metanephros). The tumour usually develops within the kidney, occasionally in the retroperitoneum. It occurs rarely in young adults but constitutes around 90% of renal tumours in childhood. There is a peak incidence at the age of 3-4 years; it is uncommon above the age of 5 and rare in the neonate. Tumours may be bilateral in up to 13% of cases. There may be an association with a number of developmental conditions, including hemihypertrophy, aniridia and genitourinary abnormalities (cryptorchidism, hypospadias, stale pseudohermaphroditism, progressive glomerulonephritis). Around 1% have been described as familial.

Presentation is usually with a palpable mass, often detected on examination for another condition, particularly trauma. It rarely presents with haematuria or pain. Hypertension is present in 25% due to excess renin production.

Ultrasound demonstrates a solid renal mass, usually large and predominantly of intermediate to low echogenicity. The tumour is generally heterogeneous due to areas of necrosis and sometimes



Fig. 30.74 Ultrasound of a Wilms' tumour showing the characteristic irregular multicystic appearance.

haemorrhage, calcium and even fat (Fig. 30.74). CT similarly shows a low-density heterogeneous poorly enhancing mass containing substantial cystic/necrotic areas, sometimes with foci of calcification and fat (Fig. 30.75). On MRI the tumour is low signal on the T₁-weighted sequence and high on T₂-weighted images. Although malignant, the tumour tends to displace rather than invade adjacent structures. However, there may be invasion into the renal vein and extension into and along the inferior vena cava, usually superiorly, occasionally into the right atrium. Metastasis is most frequently to the lungs and regional lymph nodes, sometimes to the liver.

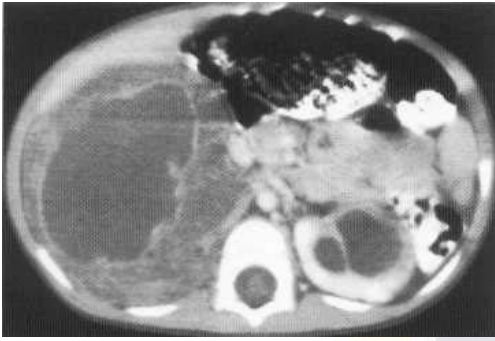


Fig. 30.75 CT scan of bilateral Wilms' tumours showing an irregular multicystic appearance.

Other tumours of primitive renal tissue

Nephroblastomatosis is not in itself a tumour but is closely related to Wilms' tumour. It consists of multifocal or diffuse areas of metanephric blastema within the kidneys persisting beyond 36 weeks gestation. These tumours are most frequently encountered in the peripheral cortex or columns of Bertin. They are found incidentally in up to 1/3 of infants but have the potential to transform into Wilms' tumours and are thought to be responsible for up to 40% of unilateral and 99% of bilateral Wilms' tumours. On CT the

commonest appearance is of multiple poorly enhancing low-density subcapsular nodules. On MRI they appear relatively low signal on both T₁-weighted and T₂-weighted sequences and on ultrasound (although less easily demonstrated) as echogenic nodules. Diffuse nephroblastomatosis leads to renomegaly, which may appear diffusely echo-poor. On contrast studies these cases may also show striated enhancement.

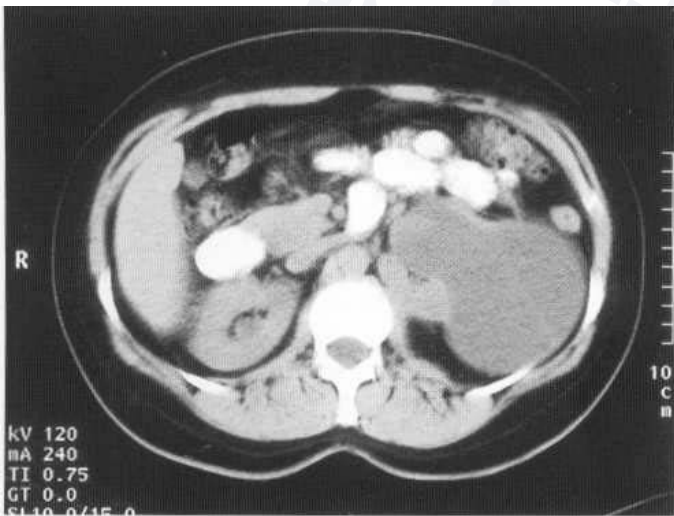
The commonest (albeit rare) tumour of primitive renal tissue encountered in adults is the **multilocular cystic nephroma**. It is thought to originate from primitive metanephric blastema. It has an intriguing bimodal age distribution, with 50% appearing at under 3 years of age (predominantly in males) and the remainder in adults (predominantly in females above the age of 40). Pathologically the lesion appears as a cyst with septae that contain renal tissue of variable maturity. It has been referred to as an adult Wilms' tumour but it does not contain expansile masses of nephroblastomatous tissue. On IVU it usually appears as a non-specific mass but its multicystic nature is occasionally visible as multiple non-enhancing areas. It may characteristically bulge into the renal pelvis. Ultrasound, CT and MRI will show a well-defined multiloculated mass, often with an apparent capsule. There is little or no enhancement with intravenous contrast (Fig. 30.76). Calcification is not a feature. It is an indolent tumour but may extend through the renal capsule. Partial nephrectomy is usually curative, although incomplete excision may lead to local recurrence. It does not metastasise.

Mesohlastic nephroma (fetal renal hamartoma) is the commonest renal tumour in the neonate, most cases presenting by the age of 3 months, rarely above 12 months. It is solid but may contain cystic, haemorrhagic and necrotic areas. It is locally infiltrative and may recur if incompletely resected, and on rare occasions metastasise to lungs, brain and bone.

Renal medullary carcinoma This is a rare malignancy originating from the medulla at its interface with the renal pelvis. The mean age of presentation is 20 years (range 10-39) and it is virtually confined to patients with sickle-cell trait or haemoglobin SC disease. It is extremely aggressive with a poor prognosis,



A



B

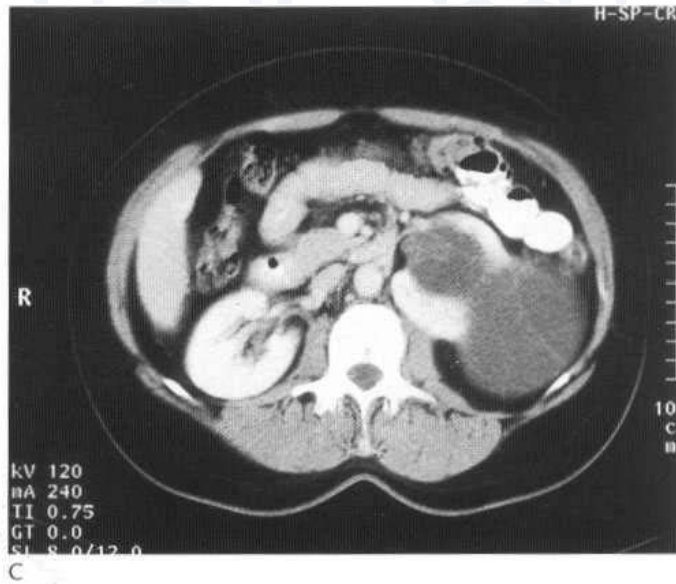
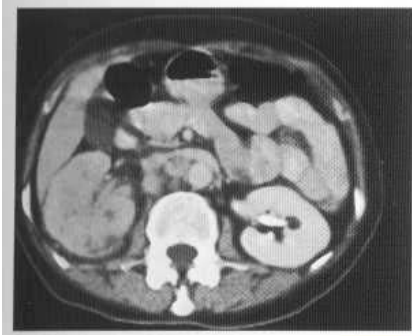


Fig. 30.76 Multilocular cystic nephroma on ultrasound (A) and CT before (B) and after (C) contrast. Note the lesion typically bulging into the renal pelvis.



CT of renal sarcoma shows generally expanded kidney with areas of tumour enhancing less well than normal renal tissue.

invading into the renal pelvis and showing early involvement of the lymphatic and vascular structures. Radiologically it behaves like an invasive transitional cell carcinoma, showing an ill-defined heterogeneous central mass involving the renal sinus and associated with dilated calyces. There may be satellite nodules within renal parenchyma and early distant metastases.

Sarcomas Renal sarcomas are rare, representing 3% or less of all renal malignancies in adults. They include a variety of histologies, depending on the tissue of origin. The majority are leiomyosarcomas, the remainder include rhabdomyosarcoma, chondrosarcoma and fibrosarcoma. Clinically and radiologically they are similar to renal cell carcinoma and appear as large soft-tissue masses, although areas of fat may be seen with a liposarcoma and bone with an osteosarcoma. Sarcomas arise most often from the renal capsule or sinus and this location may suggest the diagnosis (Fig. 30.77). They tend to metastasise haematobeneously Lymphadenopathy is therefore usually notably absent. They have variable aggressiveness but they are difficult to eradicate and the prognosis is poor.

The indeterminate mass

Most masses encountered in the kidneys are *simple* cysts and provided they fulfil the criteria described above can be safely assumed to be benign. The majority of solid masses are *renal cell carcinoma* and are treated with radical nephrectomy. The remaining renal masses are to some extent indeterminate: being neither an obvious benign cyst nor an obvious renal cell carcinoma. They may be considered in three categories: cystic lesions, solid lesions not typical of renal cell carcinoma and small lesions.

Multilocular cystic renal lesions have a wide differential, many inflammatory processes (renal abscess, focal xanthogranulomatous pyelonephritis, hydatid disease), segmental multicystic kidney and tumours (cystic renal cell carcinoma, Wilms' tumour and cystic nephroma). There may be clinical indicators to some of these conditions. The Bosniak classification of cystic lesions, as described above, is probably the best currently available approach to the remainder, with the options of guided biopsy/fine-needle aspiration and repeat interval imaging in appropriate cases.

It is generally safest to assume that a solid renal mass is a renal cell carcinoma and should be treated with radical or partial nephrectomy. However, imaging features may modify that approach. A **centrally placed lesion** that is more infiltrative than expansile raises the possibility of *transitional cell carcinoma* requiring nephroureterectomy. If the lesion is particularly well defined the possibility of a relatively benign lesion (oncocytoma, arteriovenous malformation) needs to be considered. Multiple

and/or **bilateral renal lesions** should prompt a search for features of metastases or lymphoma and may require biopsy. The **presence of fat** is highly suggestive of *angiomyolipoma*, even when only a very small amount of fat is present. These benign lesions are best left alone or, if large and/or expanding and the risk of haemorrhage is a concern, they are best dealt with by nephron-sparing surgery. Occasionally non-neoplastic lesions such as focal pyelonephritis or infarct may produce a localised mass. The clinical and imaging features (if necessary with sequential imaging) should confirm the benign diagnosis.

As the quality of scanning equipment improves and the general population undergoes increasingly frequent scanning for a variety of indications, small asymptomatic renal masses are often incidentally identified. Lesions that are 1.5-3.0 cm in diameter can usually be adequately categorised as simple cysts, probably renal cell carcinomas or indeterminate lesions to be considered as above. Very **small lesions** (below 1.5 cm) may be difficult to categorise, especially, for example, if there is an equivocal lesion on CT and the patient's build does not permit adequate visualisation with ultrasound. In these circumstances it would seem reasonable to repeat the imaging after 6 months and then subsequently yearly. If the lesion grows to more than 2 cm diameter, removal, probably with a partial nephrectomy, would be appropriate.

RENAL VASCULAR DISEASE

Renal arterial infarct The renal artery is an end artery and if it is occluded the kidney will infarct. Causes include thrombosis (usually due to atheroma), trauma, renal artery dissection, arteritis and embolus. Acutely the patient presents with pain, haematuria and proteinuria and may have fever and leucocytosis. On IVU the affected kidney is non-functioning (no nephrogram or contrast excretion into the calyces). On ultrasound the kidney is acutely swollen and may appear echo poor. There is no Doppler trace obtainable from the intraparenchymal or mainstem renal arteries. CT and MRI will demonstrate a swollen kidney with no enhancement with intravenous contrast (although there may be a rim of peripherally perfused parenchyma if the capsular artery is preserved) (Fig. 30.78). Over a period of weeks or months the kidney will atrophy dramatically, becoming small and fibrous. Chronically infarcted kidneys may be difficult to identify on ultrasound due to their small size and loss of most of the parenchyma

only part of the kidney, the size of which is determined by the size

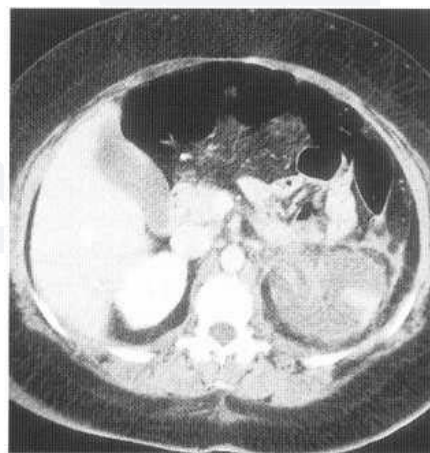


Fig. 30.78 Contrast CT scan of a renal infarct in a patient with arteritis. The left kidney is almost entirely non-perfused apart from a partial peripheral rim.

of the artery affected. IVU may show a wedge-shaped defect on the nephrogram, apex pointing towards the hilum, but this is better seen on contrast CT as a wedge of reduced perfusion. The capsular artery is an early branch of the renal artery and is often preserved. Consequently in around 50% of cases a sliver of perfused cortex is seen over the peripheral aspect of the infarct, against the capsule. Ultrasound may show a subtle wedge of reduced echogenicity and absent Doppler arterial signal. Again the infarcted renal tissue atrophies and later IVU, ultrasound, CT and MRI will demonstrate a focal scar.

Renal artery stenosis Significant renal artery stenosis (reduction of the internal diameter by at least 60%) is a potentially treatable cause of hypertension which is often severe and resistant to treatment. The vast majority of cases are due to atheroma but in younger adults fibromuscular dysplasia is seen in up to one-third. Other causes are rare and include arteritis (polyarteritis nodosa, Takayasu's disease, etc.) and compression of the renal artery by retroperitoneal masses. Renal artery stenosis (RAS) is the cause of hypertension in less than 1% of cases and it is therefore important to avoid overinvestigating vast numbers of individuals who do not have the condition. Unfortunately no single investigation is ideal and there remains considerable controversy over the best approach to this problem.

The IVU is no longer indicated to investigate this condition, usually being normal unless RAS is very severe. On rare occasions characteristic features may appear on an IVU performed for a different indication. The affected kidney may be small and smooth (RAS is probably the commonest cause of this). The reduced perfusion on the affected side produces a late nephrogram but because the contrast-containing urine within the tubules progresses slowly it becomes more concentrated than the unaffected side, ultimately giving rise to a hyperdense nephrogram. Similarly there is late appearance of contrast into the pelvicalyceal system and again this becomes hyperdense. Notching of the ureter due to compensatory hypertrophy of the ureteric artery (derived from the lumbar arteries) is extremely rare.

Initial ultrasound investigation is a logical first step in the investigation of RAS. It is a simple non-invasive way to determine the presence of two kidneys and exclude an obvious structural abnormality or coexistent condition that may relate to the hypertension (renal scarring, hydronephrosis, calculus disease and rarely renal or adrenal tumours). Ultrasound will also demonstrate if there is an obvious size disparity (more than 2 cm) between the kidneys and whether or not one kidney is abnormally small, both features that suggest unilateral RAS.

A variety of options for further investigation are available and the choice will tend to reflect local skills and enthusiasm. Doppler assessment of the mainstem renal artery may be performed. Colour imaging may demonstrate visually a change at the site of a stenosis and offer guidance for spectral sampling. The diagnosis of a significant stenosis is based on the functional information obtained by spectral sampling. A stenosis increases the peak systolic velocity and it has been suggested that a renal:aortic velocity ratio of more than 3.5 or an absolute velocity above 180-200 cm/s indicates a stenosis of more than 60%. There is still fierce debate about the usefulness of this technique, the published figures for accuracy varying enormously (0-98% for sensitivity, 37-99% for specificity). It is also difficult to perform the examination routinely, the technical failure rate being up to 90%. An alternative is to

perform spectral analysis on intrarenal arteries. RAS of less than 75% is not detected with this technique. More severe stenoses are characterized by reduction in the ascending slope of the systolic peak, which can be measured as reduced acceleration (below 3 m/s/s), lengthened time to systolic peak (above 0.07 s) and increased resistive index (above 5%) and pulsatility index (above 0.012) of the affected kidney compared with the other side. Unfortunately the correlation of RAS diagnosed from these criteria compared with more direct investigations is poor. The introduction of ultrasound contrast agents and continued developments in scanners is likely to improve this technique, which currently offers the best hope for a safe routine test for RAS.

Patients who are strongly suspected of RAS on clinical and/or ultrasonographic grounds may progress to further investigation with CT, MRI or functional radionuclide studies (described in Chapter 29).

CT angiography is an extremely useful investigation but exposes the patient to a considerable amount of radiation and should not therefore be used as a first-line investigation. The scan should be performed during the vascular phase, 15-25 s after the start of an intravenous infusion of 90-150 ml of 300 strength contrast at 3-5 ml/s. Recommended parameters are: collimation of 3 mm, pitch of 1.5-2.0 and reconstruction interval of 1-2 mm. Images can be reconstructed in multiple planes (Fig. 30.79) and maximum intensity projection performed for a 3D display. There is considerable variability in the suggested accuracy of the technique but it does appear to be of the order of 92% sensitivity and 83% specificity for RAS of 70% or greater.

MR angiography has the advantage that it avoids ionising radiation. Its disadvantage has been image degradation by patient movement (especially respiration), inability to see distal renal arteries and poor resolution compared with CT. As stronger and faster gradients are developed the situation is improving. Initially time of flight and phase contrast techniques were employed but these are being replaced by T₂-weighted contrast-enhanced acquisitions, with significant improvement in the images. There is a tendency for MR angiography to overestimate the severity of the stenoses and, once again, the published accuracy varies considerably but at best is of

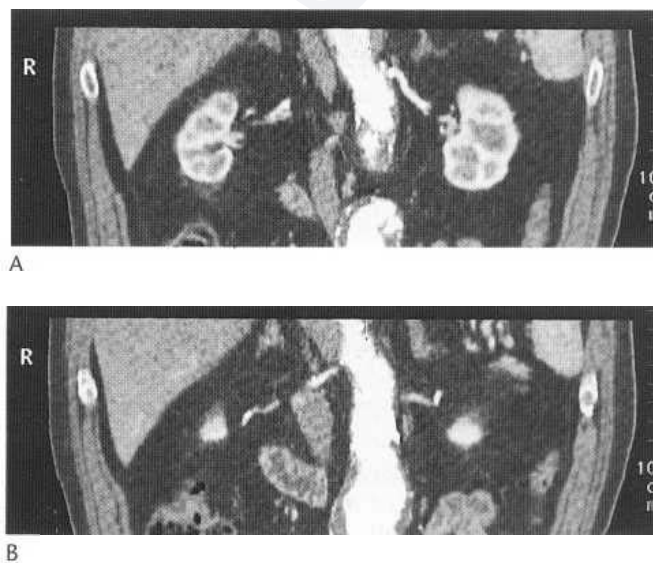


Fig. 30.79 CT angiogram (coronal reconstruction). A tight stenosis of the origin of the right renal artery is demonstrated.



Fig. 30.80 Angiogram demonstrating multiple short smooth stenoses of the right renal artery in fibromuscular dysplasia.

the order of 95% sensitivity and 90% specificity for RAS of 50% or worse.

The conventional gold standard investigation for the diagnosis of RAS has been percutaneous arteriography. Its place as a diagnostic test is much reduced in view of the non-invasive investigations considered above. However, if a significant RAS has been diagnosed, treatment with percutaneous renal arterial angioplasty may be indicated. Intra-arterial angiography will then be performed as the first step in the therapeutic procedure (Fig. 30.80).

Renal artery aneurysm This is usually due to atheroma and may act as a source of thrombotic emboli with subsequent infarction of part or all of the renal arterial supply.

Renal vein thrombosis This uncommon condition classically presents as loin pain and haematuria. It may be idiopathic but far more often there is an identifiable association such as abnormal coagulation (especially disseminated intravascular coagulation), connective tissue disease, amyloid, sepsis, trauma, pressure by lymph nodes or tumour and some haemoglobinopathies. An important cause is nephritic syndrome, which is usually due to minimal change glomerulonephropathy in children and membranoproliferative glomerulonephritis in adults, the latter having an association with malignancy, especially carcinoma of the bronchus. The development of renal vein thrombosis under these circumstances is associated with marked worsening of the proteinuria. If thrombosis is complete and occurs abruptly the imaging features are similar to those of an arterial infarct (non-functioning swollen kidney) except for Doppler ultrasound, which demonstrates loss of the venous rather than the arterial signal. If there is subacute or partial thrombosis then in the early stage all modalities will demonstrate smooth renal enlargement. The IVU will show a delayed but subsequently hyperdense nephrogram and pyelogram, with either normal calyces or some evidence of compression due to parenchymal swelling.

Notching of the ureter by dilated venous collaterals is occasionally seen. Ultrasound appearances include loss of the normal corticomedullary differentiation and diffuse reduction in echogenicity. The kidney may appear generally hypodense on CT. Thrombosis can be demonstrated within the renal vein with ultrasound. CT or MRI. Chronically the kidney becomes small and atrophic. Although renal cell carcinoma often invades the renal vein and inferior vena cava, it is remarkably rare for it to manifest with the clinical or radiological features of a renal vein thrombosis, presumably because the onset is insidious and the kidney manages to establish a satisfactory collateral drainage.

Shock nephrogram This is the delayed onset of a dense nephrogram with the disappearance of contrast from the pelvicalyceal systems. This indicates profound hypotension during an IVU, usually secondary to an adverse reaction.

CALCULI AND OBSTRUCTION

Renal and ureteric calculi

The formation of upper tract calculi is a common problem. It appears to be due to minerals crystallising out of urine in a normal urinary tract. There is a predictable increased risk of stone formation in conditions where the urine contains a high concentration of minerals, particularly calcium. Spending time in a hot climate or in a heat wave or becoming recurrently dehydrated in sporting or occupational activities are the commonest associations. Soave patients exhibit a familial tendency. A small but significant minority of patients have a specific biochemical cause. Hypercalciuria is the most common and may be due to excess loss by the kidneys in normocalcaemic states or in association with hypercalcaemia, which has a number of causes (discussed under nephrocalcinosis) but is most commonly due to hyperparathyroidism. Structural abnormalities predispose to stone formation, particularly those involving urinary stasis, for example pelviureteric junction obstruction. The presence of infection is also an important cause. Once one factor is present others may develop; for example, a calculus may impede drainage from a calyx or the renal pelvis, increasing the risk of infection, further calculus development and worsening drainage.

Over 90% of calculi are radiopaque on plain films (Fig. 30.81) and virtually all on CT. Most of these are calcium salts, usually a mixture of oxalate and phosphate, sometimes pure phosphate or oxalate. They are highly radiopaque, particularly calcium phosphate calculi. Small-bowel disease or resection predisposes particularly to the formation of oxalate calculi, which may have a speckled or punctate appearance (Fig. 30.82). The higher the oxalate content compared to the phosphate content, the greater the ease of treatment with lithotripsy. A minority of stones (up to 10% in some series) are largely composed of struvite (magnesium ammonium phosphate). These are poorly radiopaque when pure but they often contain some calcium phosphate (triple phosphate calculi), which increases radiodensity. They are associated with infection with urea-splitting bacteria (notably *Proteus mirabilis*). They may become large and branching (staghorn, i.e. extending into adjacent calyces) and are often laminated (Fig. 30.83). Although they shatter relatively easily with lithotripsy, their large size means that they are often better treated with percutaneous nephrolithotomy. The formation of calculi is often thought to be initiated by mineral deposition on a nidus of mucoprotein matrix. Occasionally calculi consist of

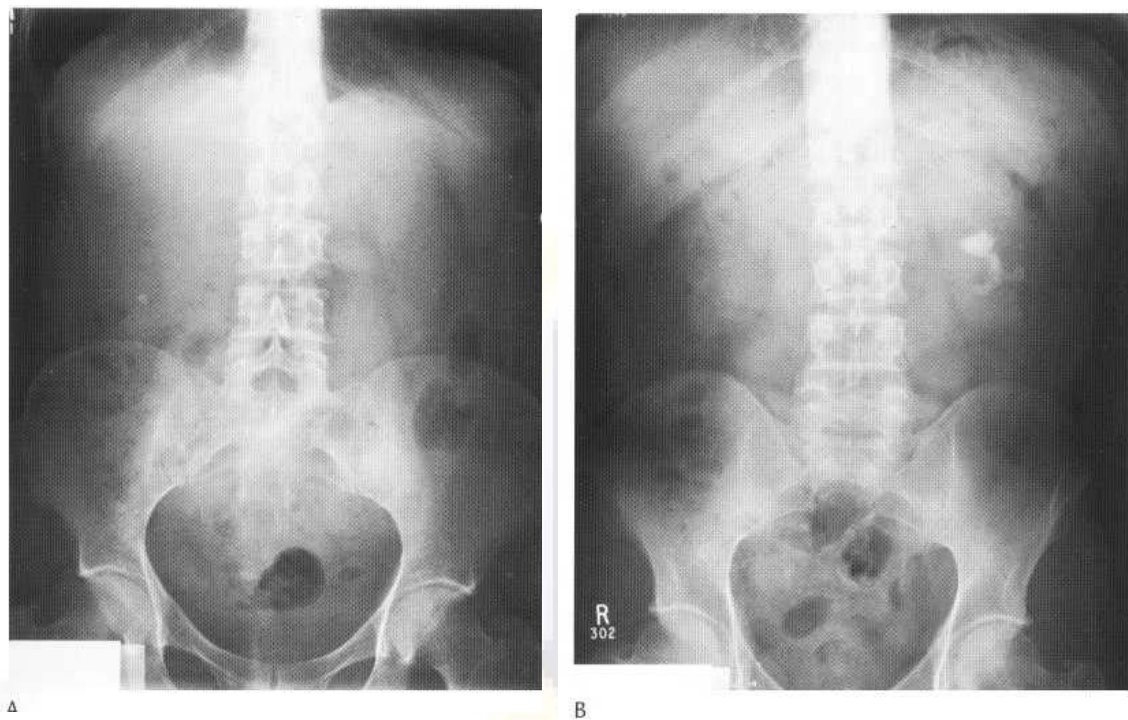


Fig. 30.81 (A) Small right renal calculus visible on plain film and larger calculus (B) in the left lower pole major calyx.

relatively pure matrix. They are radiolucent and only form in alkaline urine, usually in association with *Proteus* infection.

In less than 10% a variety of other calculi are encountered, often associated with abnormal metabolic states. Urate calculi occur with increased uric acid excretion in the urine, usually associated with gout, occasionally with other causes of hyperuricuria, such as hypercatabolic states with increased turnover of nucleoproteins (for example, patients with leukaemia or lymphoma and/or undergoing chemotherapy). They are radiolucent on plain films but easily seen on CT (Fig. 30.84). Cystine calculi are seen in patients with cystinuria, an inherited renal tubular disorder with loss of the amino acids cystine, ornithine, arginine and lysine in the urine. They are only modestly radiopaque due to their sulphur content and have an amor-

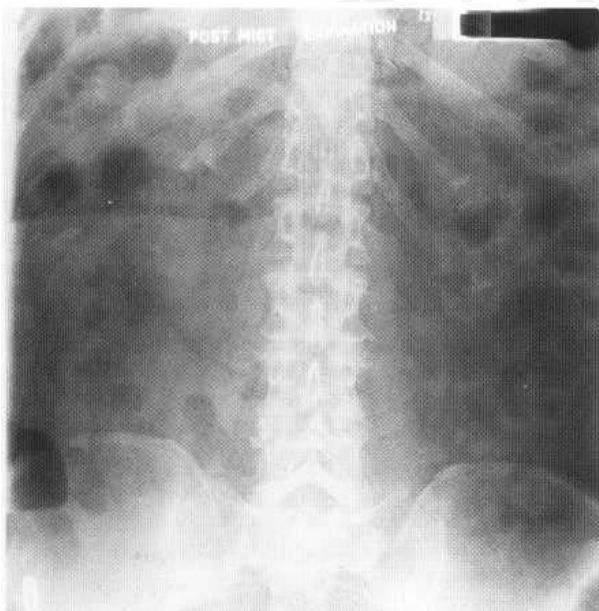


Fig. 30.82 Multiple punctate calculi in hyperoxaluria secondary to small bowel resection.

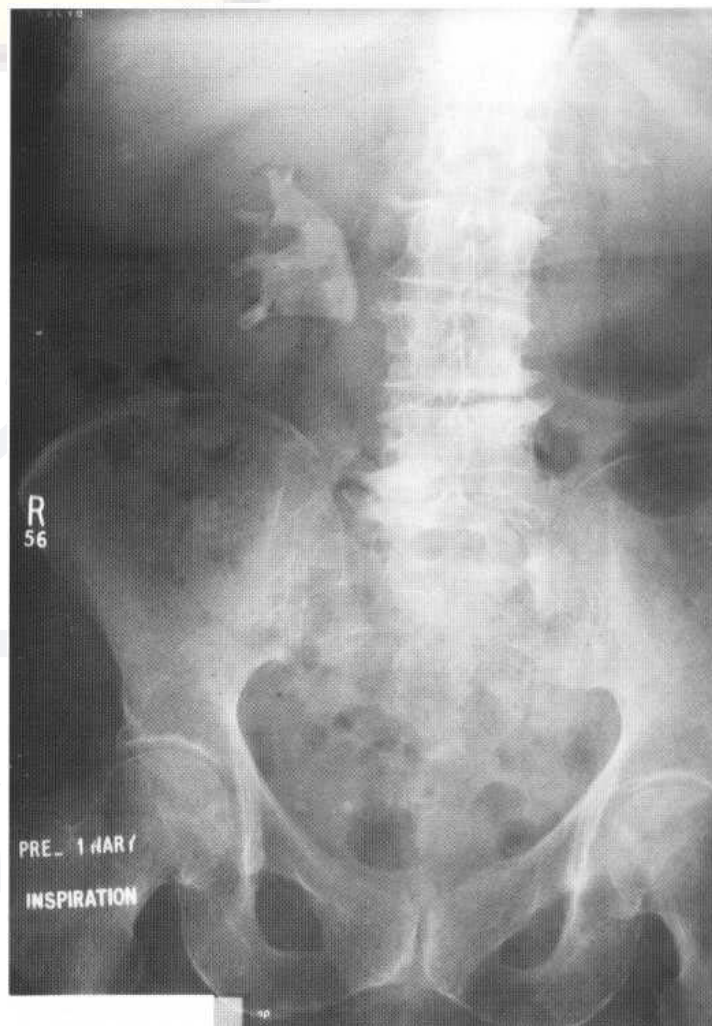


Fig. 30.83 Plain film showing large right staghorn calculus.

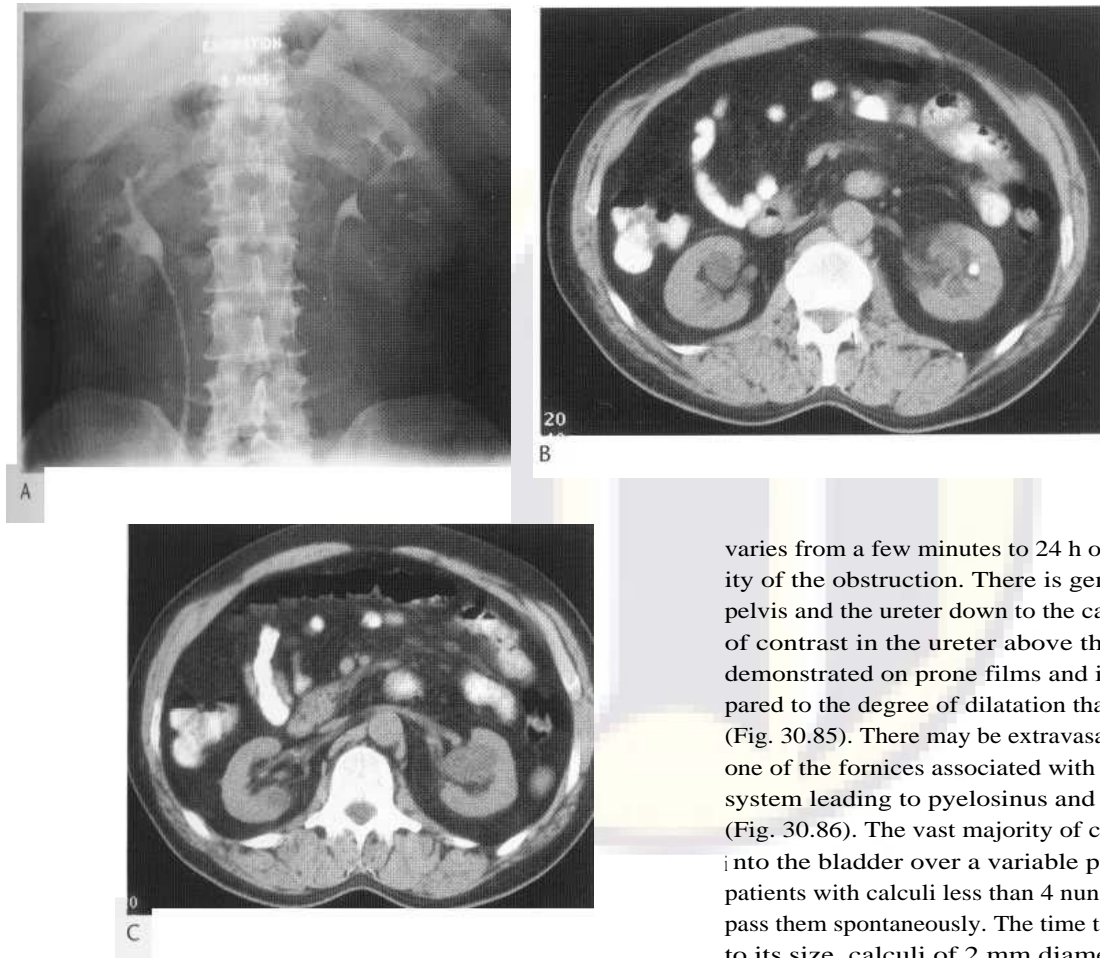


Fig. 30.84 Radiolucent urate calculus, not visible on plain film, appearing as a well-defined filling defect in the collecting system of the left kidney (A). A larger mass is also visible distorting the left pelvicalyceal system. CT confirms that the small filling defect is a urate calculus (B) and the larger one a parapelvic cyst (C).

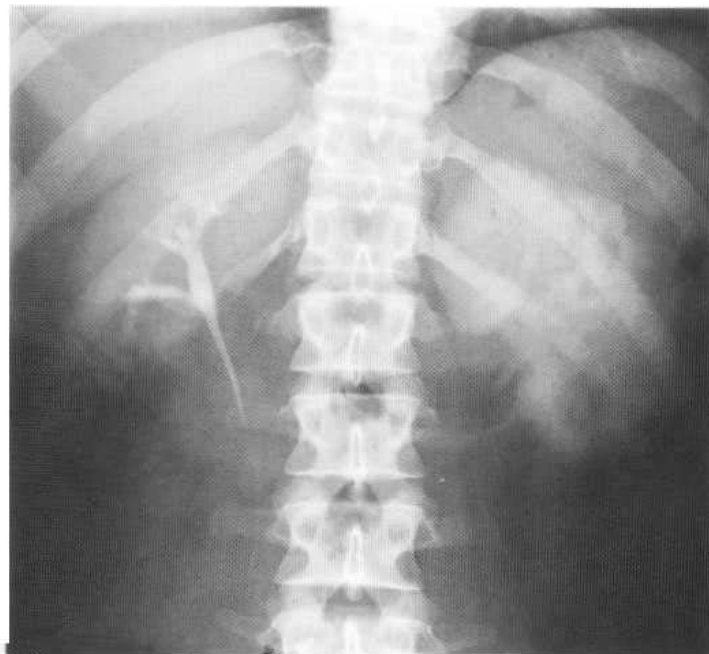
phous ground-glass appearance. Xanthine calculi are extremely rare: they are radiolucent and associated with defective oxidation of purines. Treatment of AIDS patients with protease inhibitor agents such as indinavir may lead to crystalluria and tiny radiolucent calculi.

Small calculi that remain in the calyces are generally asymptomatic but may be associated with microscopic haematuria. As they enlarge it is debatable whether or not they are associated with pain until they provoke some degree of calyceal or pelvic obstruction. Migration of small calculi into the ureter is common and presents with colic. This provokes severe prolonged pain radiating from the loin into the ipsilateral pelvis. The pain moves distally as the calculus progresses, often being maximum as the calculus struggles to enter the bladder. Once in the bladder it usually exits via the urethra with remarkable ease. There is usually haematuria, generally microscopic, occasionally frank. Plain films are not very useful in ureteric colic. They demonstrate other renal calculi with reasonable reliability but are extremely inaccurate in confirming ureteric calculus, small ones often being overlooked while innocuous areas of calcification such as phleboliths are often misdiagnosed as calculi. The traditional modality for investigating ureteric calculi has been the IVU. This demonstrates the relationship of a suspected calculus on the plain film to the urinary tract, confirming its location within the collecting system. In most patients with ureteric colic there is some degree of obstruction, manifested by delay in the appearance of the nephrogram and contrast excretion into the pelvicalyceal system. The affected kidney is often modestly enlarged. The delay

varies from a few minutes to 24 h or more depending on the severity of the obstruction. There is generally some distension of the pelvis and the ureter down to the calculus, with a standing column of contrast in the ureter above the calculus. This is often best demonstrated on prone films and is usually relatively mild compared to the degree of dilatation that occurs in chronic obstruction (Fig. 30.85). There may be extravasation of contrast from rupture of one of the fornices associated with high pressure in the obstructed system leading to pyelosinus and pyelolymphatic extravasation (Fig. 30.86). The vast majority of calculi progress down the ureter into the bladder over a variable period of time; at least 95% of patients with calculi less than 4 mm diameter would be expected to pass them spontaneously. The time taken to pass the calculus relates to its size, calculi of 2 mm diameter taking a mean of 8 days, calculi over 4 mm a mean of 22.1 days. Calculi most commonly arrest (usually temporarily) over the sacrum, as the ureter crosses the iliac artery, or at the vesicoureteric junction in the intramural ureter, both sites of relative narrowing. They can be extremely difficult to demonstrate on IVU when they come to lie over the sacrum. They may be associated with considerable mucosal oedema when they impact at the vesicoureteric junction (Fig. 30.87). Calculi are seen as filling defects on the postcontrast film, and sometimes in the presence of heavy haematuria there may also be visible thrombus within the collecting system (Fig. 30.88).

Ultrasound usually demonstrates mild hydronephrosis on the symptomatic side (Fig. 30.89). As indicated above, in acute obstruction the degree of distension is usually mild and the ultrasound appearances often overlap with normal. If minimal changes are taken to represent ureteric colic, ultrasound achieves a reasonable degree of sensitivity (95%) but at the cost of a low specificity of around 67%. Calculi within the calyces and renal pelvis can be seen as highly echogenic foci with dense distal acoustic shadowing (Fig. 30.90). It is rare to demonstrate calculi within the ureter but they may be seen at the vesicoureteric junction (Fig. 30.91) associated with some local ureteric distension. Despite its shortcomings, ultrasound has the advantage of not subjecting the patient to ionising radiation and has been recommended as the initial choice in the investigation of calculi in childhood.

Spiral CT is now increasingly replacing the IVU in the investigation of ureteric colic and can be regarded as the investigation of choice where it is available. A suitable protocol is collimation of 5-7 mm, pitch of 1.5-2 and slice reconstruction of 3 mm. The advantages of CT include the avoidance of an injection of contrast



A



B



C

Fig. 30.85 Dense nephrogram with delay in appearance of contrast in the left collecting system characteristic of high-grade obstruction (A). Eventually contrast outlines a mildly distended ureter down to a calculus at the left vesicoureteric junction (B) with the calculus just visible on the plain film (C).

medium and a rapid result without having to wait for several hours if there is high-grade obstruction. Spiral CT is thought to be highly accurate, with a sensitivity of 94%, and specificity of 97%, compared with 52% and 94% for IVU (and much worse for ultrasound) and 19% and 97% for ultrasound. CT has the potential advantage of making alternative relevant diagnoses (diverticulitis, appendicitis, cholecystitis, etc.) in patients with acute abdominal pain. However, it exposes the patient to a significant radiation burden. Estimates of the magnitude of this vary and it may represent three times the radiation of a three-film emergency IVU. However, if additional IVU films are required the relative disadvantage is reduced. Efforts should also be made to perform the CT with the minimum mAs. This may reduce image quality but should not affect its diagnostic usefulness for ureteric colic, and a radiation exposure not significantly different from IVU may be achievable. Essentially all ureteric calculi are radiopaque on CT (the only exception being protease inhibitor crystals). Demonstration of the calculus within

the ureter confirms the primary diagnosis. This is usually straightforward as there is often some prominence (albeit mild) of the

must be taken to avoid misdiagnosing iliac artery calcification or phleboliths as calculi. Calculi usually demonstrate a rim of soft tissue, which helps distinguish them. Secondary signs of urinary tract obstruction provide confirmation of the diagnosis and offer a measure of the degree of obstruction. Prominence of the renal pelvis may merely be due to an extrarenal pelvis. Dilatation of the intrarenal collecting system and hydroureter are more significant. The obstructed kidney may also be enlarged. There is often stranding within the perinephric fat, due to fluid within the bridging septa secondary to high lymphatic pressure (Fig. 30.93). If the changes are particularly gross but focal, this is likely to be due to fornical rupture. The pyramids may normally appear remarkably dense on unenhanced CT (white pyramid sign) and this may be absent on the obstructed side or in the presence of infection. Differentiation between calculi that have passed into the bladder and are lying against the vesicoureteric junction from those still impacted at the junction can be achieved with prone scanning.

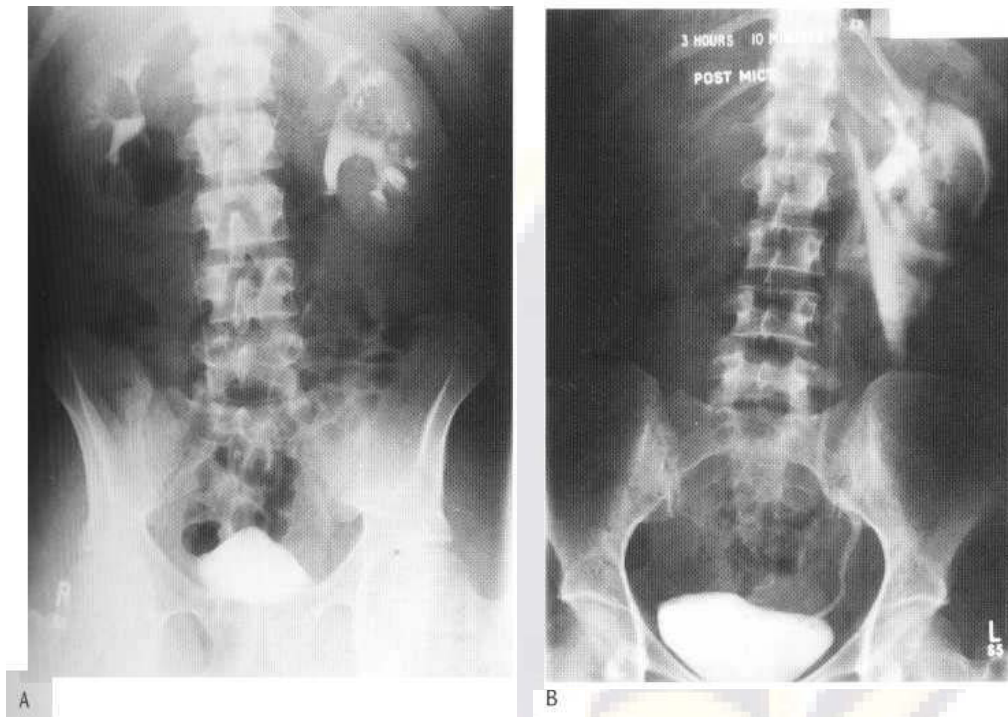


Fig. 30.86 Pyelosinus extravasation (A) in high-grade obstruction with leakage of contrast around the upper pole calyces, which have become ill-defined. Contrast is entering the lymphatic vessels (arrow), pyelolymphatic extravasation. More profuse extravasation is occasionally seen with forniceal rupture (B).

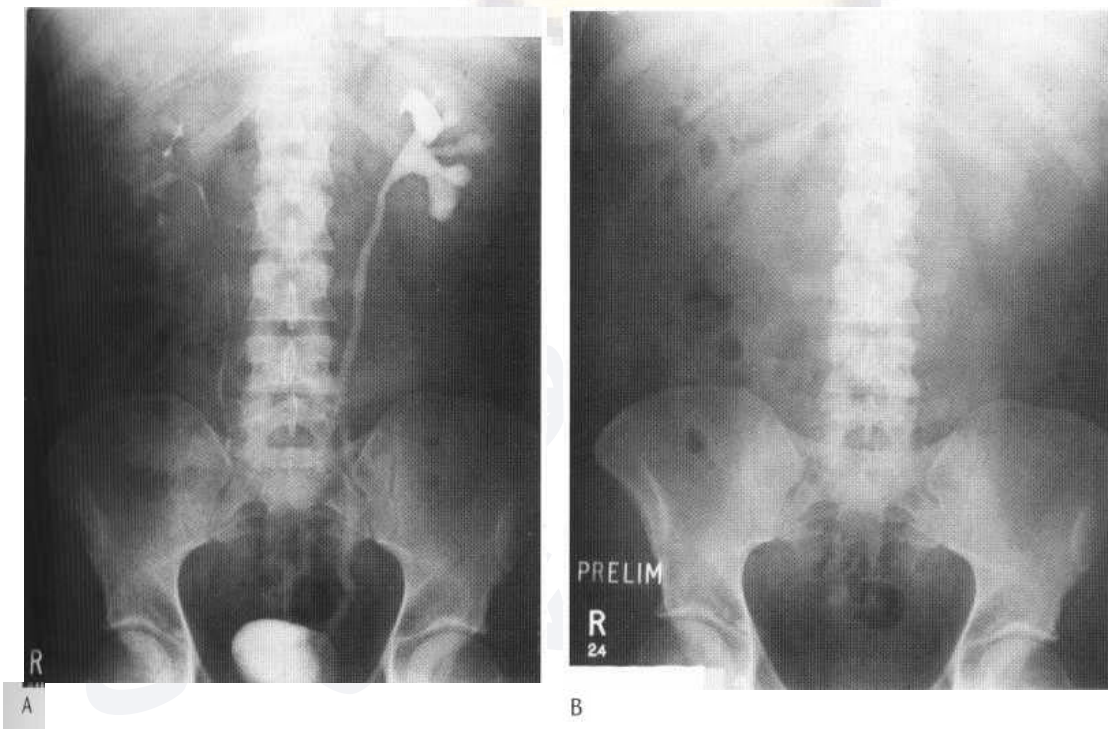


Fig. 30.87 Full length film from an IVU series (A) showing stasis and mild fullness in the left ureter and considerable oedema around the vesicoureteric junction due to a small calculus visible on the plain film (B).

As indicated above, ureteric calculi usually pass spontaneously. If adequate pain relief cannot be achieved and the calculus is not progressing, especially if there appears to be high-grade obstruction or infection, a percutaneous nephrostomy can be positioned to relieve symptoms and drain the system. This may provoke ureteric relaxation and subsequent calculus passage. It also offers the possibility of subsequent diagnostic nephrostograms or therapeutic antegrade stent positioning. It also stabilises the situation while urgent lithotripsy is organised. Calculi that are in the distal ureter may, however, be better managed with retrograde stenting and/or ureteroscopic removal.

The pattern of growth of calculi within the renal calyces is variable. Small ones may remain unchanged over years or migrate into the renal pelvis or ureter and provoke recurrent episodes of colic. Alternatively they may remain in the calyces and enlarge at a variable rate, sometimes developing into a staghorn calculus. Treatment options include open nephrolithotomy (rarely indicated and only for very large calculi), percutaneous nephrolithotomy (for large calculi), extracorporeal shock wave lithotripsy (ESWL) and observation. Percutaneous nephrolithotomy and ESWL are discussed in Chapter 29.



Fig. 30.88 Small ureteric calculus (small arrow) associated with haematuria and thrombus (large arrow).



Fig. 30.89 Ultrasound showing a relatively marked hydronephrosis.

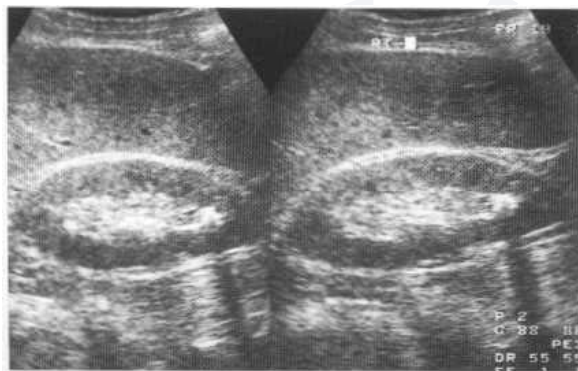


Fig. 30.90 Small solitary renal calculus on ultrasound seen as an echogenic focus with marked distal acoustic shadowing.

Hydronephrosis and hydroureter

A large renal pelvis alone is not hydronephrosis, it may simply represent a prominent extrarenal pelvis, which is a normal variant. Hydronephrosis is dilatation of the renal pelvis and calyces. At its most mild it is seen on IVU as blunting of the fornices but with preservation of the papillae. With increasing severity the papillae become flattened and ultimately appear concave as the calyces balloon out. With chronic obstruction the signs are more pronounced and diffuse cortical loss develops. Renal function begins to



Fig. 30.91 Small calculus in the distal dilated ureter seen as an echogenic focus on ultrasound.

be lost with poor or absent excretion of contrast on IVU. After prolonged obstruction (months or years) there may be almost complete cortical loss. Ultrasound is excellent for the diagnosis of chronic obstruction and is also the first-line investigation in searching for a cause (Fig. 30.94). As indicated above, ultrasound is often more equivocal in acute obstruction, although improvement in accuracy with Doppler techniques has been reported. Spectral analysis of interlobar or arcuate arteries may demonstrate increase in the resistive index in the obstructed kidney. This reflects reduction in the blood flow and is seen in a number of other conditions, including acute renal parenchymal disease. A resistive index above 0.70, or more than 0.08 more than the contralateral kidney, is suggestive of obstruction in the appropriate clinical situation.

Pelviureteric junction obstruction is associated with isolated hydronephrosis but obstruction below the level of the pelviureteric junction is associated with some degree of ureteric distension (hydroureter). Again this is most marked with chronic obstruction, where there is often also considerable tortuosity of the ureter. The major causes of obstructive hydronephrosis (most associated with hydroureter) are as follows:

- Calculi-renal pelvic (hydronephrosis alone), ureteric
- Pelviureteric junction obstruction
- Tumours
 - extrinsic compression of the ureter in the retroperitoneum (usually lymph node metastases) or pelvis (gynaecological malignancy, bladder, prostate or rectosigmoid carcinoma)
 - urothelial tumour of the ureter or pelviureteric junction
- Inflammatory mass lesions (Crohn's disease, appendix or diverticular abscess)
- Other ureteric stricture (see below)
- Other ureteric filling defect (see below)
- Retroperitoneal fibrosis
- Pregnancy hydronephrosis and hydroureter.

Hydronephrosis may also be seen in some non-obstructive states. The commonest are postobstructive hydronephrosis (often accompanied by atrophy), when a previous obstruction has been relieved, severe vesicoureteric reflex and primary megaureters. Continued passage of an excessive volume of urine may also produce these appearances, for example in diabetes insipidus. Non-obstructive hydronephrosis and hydroureter are also occasionally seen in severe

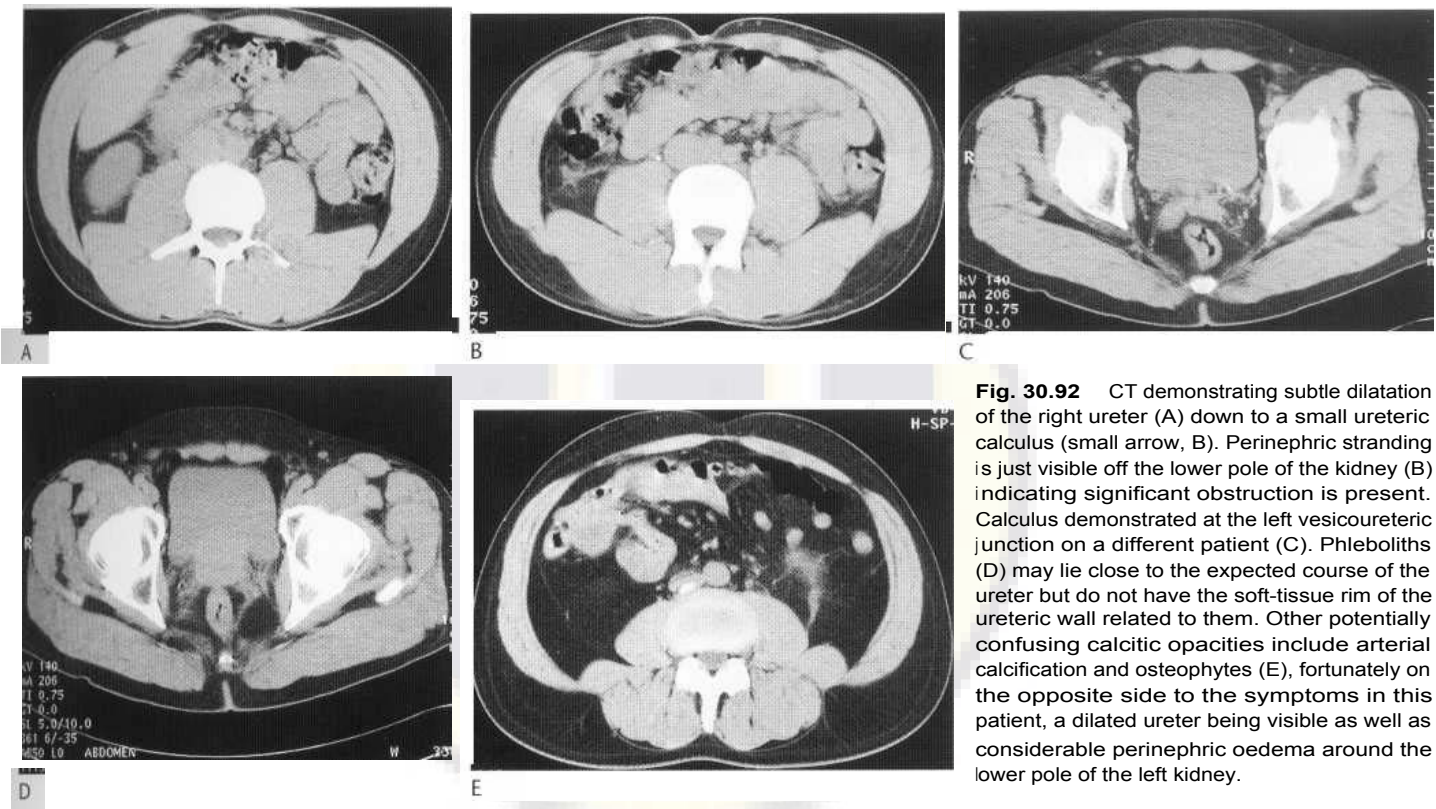


Fig. 30.92 CT demonstrating subtle dilatation of the right ureter (A) down to a small ureteric calculus (small arrow, B). Perinephric stranding is just visible off the lower pole of the kidney (B) indicating significant obstruction is present. Calculus demonstrated at the left vesicoureteric junction on a different patient (C). Phleboliths (D) may lie close to the expected course of the ureter but do not have the soft-tissue rim of the ureteric wall related to them. Other potentially confusing calcific opacities include arterial calcification and osteophytes (E), fortunately on the opposite side to the symptoms in this patient, a dilated ureter being visible as well as considerable perinephric oedema around the lower pole of the left kidney.

pyelonephritis due to the release of an endotoxin that inhibits ureteric peristalsis.

Pregnancy hydronephrosis and hydroureter

Non-obstructive dilatation of the upper two-thirds of the ureters and pelvicalyceal systems often occurs during pregnancy, due to smooth muscle relaxation under the stimulus of the hormones of pregnancy (particularly progesterone). It is usually more pronounced (or exclusively) on the right, presumably related to compression of the ureter by the uterus (the left side being protected by the sigmoid colon). It usually returns to normal 3-6 months postnatally. A proportion, however, remain dilated. The reason for this is uncertain and theories include coexistent urinary tract infection during pregnancy or particularly severe dilatation in pregnancy. The IVU demonstrates dilatation of the upper two-thirds of the ureter, which tapers smoothly to normal caliber as it crosses the iliac vessels (Fig. 30.95).

Occasionally during pregnancy the patient complains of loin pain, which may be extremely severe. It is usually right-sided and may be associated with hydronephrosis which is significantly greater than expected for simple hydronephrosis of pregnancy. The cause is unclear. The condition may present a considerable dilemma because it is difficult to exclude other causes of hydronephrosis, particularly ureteric colic, as it is desirable to avoid irradiating the fetus. Elevation of the resistive index on Doppler ultrasound may help diagnose significant obstruction, and MR gadolinium excretion urography may gain a role. Most cases can be managed with serial ultrasound scanning, observation and pain relief but some patients are sufficiently symptomatic to require a nephrostomy positioned under ultrasound (or MR) guidance.

UPPER URINARY TRACT TRAUMA

Renal trauma Up to 90% of renal injury is due to blunt rather than penetrating injury. It is seen in up to 10% of patients with significant abdominal trauma, and when severe is associated with injury to other organs in up to 80%. Conversely, when the kidney is the only organ damaged the injury is minor in around 98% of cases. A wide range of pre-existing renal abnormalities predispose to renal injury, sometimes in the context of relatively minor trauma. This may relate to a vulnerable position (as with transplant kidneys, horseshoe kidneys and crossed fused ectopia where there is a more anterior location and proximity to the rigid spine or iliac crest) or less robust areas of tissue, often combined with increased bulk (tumours, especially angiomyolipomas and renal cell carcinomas, cysts and hydronephrosis from any cause) (Fig. 30.96). The paediatric kidney is also more vulnerable, arguably due to the relatively large size of the kidney.

The most widely accepted indications for imaging the kidneys after blunt abdominal trauma are gross haematuria or microscopic haematuria plus another sign of renal damage, in particular shock (systolic pressure 90 mmHg or below), or significant other associated injuries. Microscopic haematuria alone is rarely associated with significant renal injury. However, severe injuries of the vascular pedicle or pelviureteric junction may occur with microscopic haematuria. Imaging of patients with microscopic haematuria is therefore indicated if the patient has sustained substantial trauma to the renal area that may be associated with these sorts of injury (contusions/haematoma over the flank, fractures of the lower ribs, transverse processes or thoracolumbar spine). There is also an increased risk of significant renal damage in children with blunt trauma and patients of any age with penetrating trauma. These patients should also be investigated even if only microscopic haematuria is present.

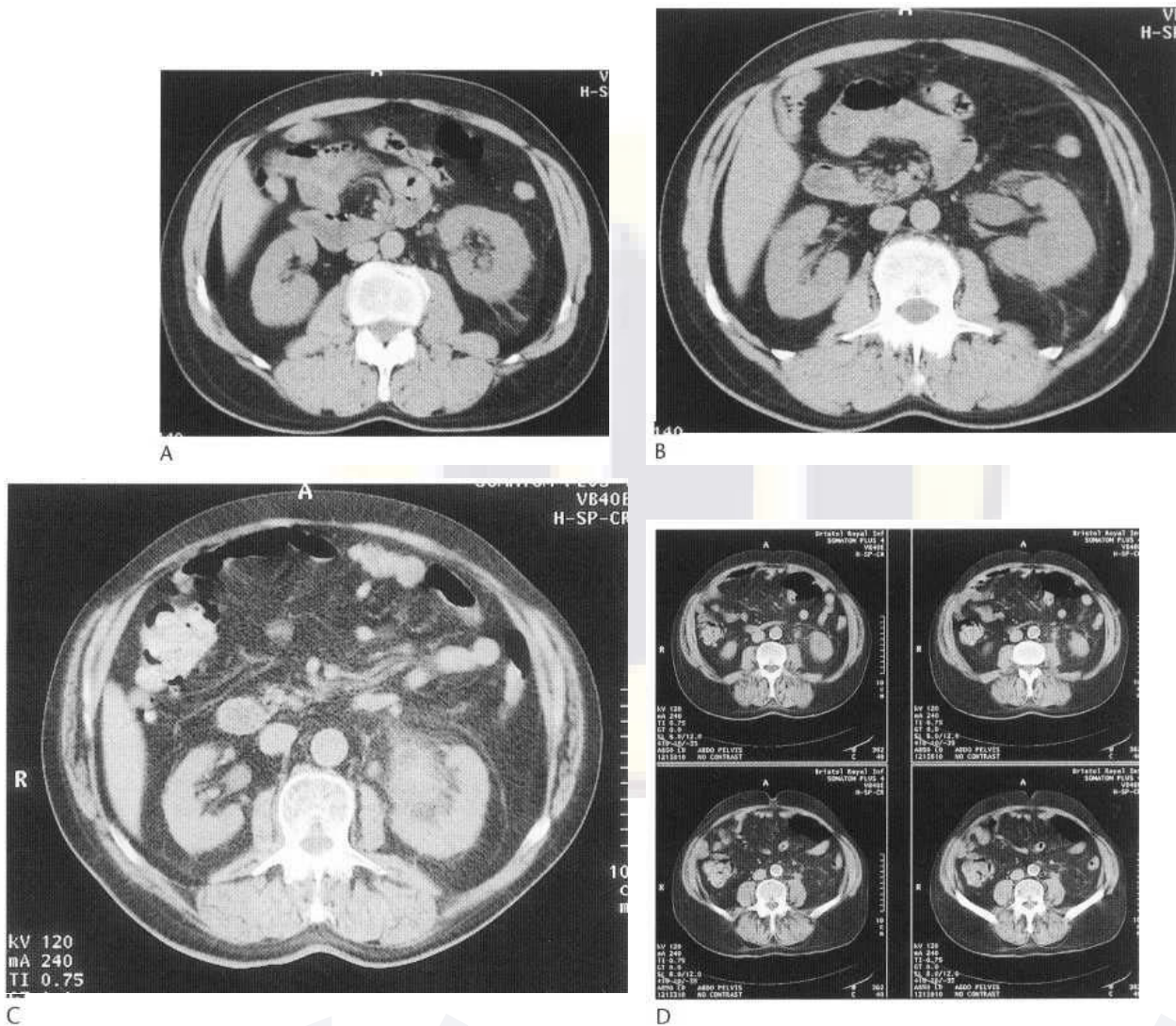


Fig. 30.93 CT showing modest perinephric stranding characteristic of significant obstruction from a ureteric calculus (A). In addition to these changes this second case shows a small fluid collection adjacent to the anterior lip of the renal hilum indicating a fornix rupture (B). The acute hydronephrosis is generally mild, as demonstrated in this third example (C), but the asymmetry between the sides is useful (although this patient demonstrates a slightly full extrarenal pelvis on the asymptomatic side). There is mild perinephric stranding on the symptomatic (left) side but considerable ill-definition around the renal pelvis, suggesting some extravasation into the renal sinus. This can be seen to track down along the dilated ureter, giving it a shaggy appearance (D).



Fig. 30.94 Ultrasound of chronic diffuse cortical loss, demonstrating

Historically the IVU was the favoured modality for the assessment of renal trauma. It has now largely been replaced by cross-sectional imaging. In the haemodynamically unstable patient destined for emergency laparotomy a single shot IVU (full length film 15 min after contrast injection) may be considered. It may offer

confirmation of the presence of a functioning contralateral kidney and some gross information about the injured kidney. The absence of unilateral excretion suggests a major vascular injury (usually renal artery avulsion). Large retroperitoneal, perinephric and subcapsular haematomas may be identified as soft-tissue swelling, often (in the case of retroperitoneal bleeding) with loss of the psoas shadow. Disruption of the pelvicalyceal system may be seen as extravasation of opacified urine. The quality of the IVU done under such circumstances is likely to be poor and if the patient has significant hypotension there may be little or no secretion bilaterally. With the increased availability of modern last CT scanners it is becoming increasingly unlikely that even the abbreviated IVU will be deployed in the trauma situation.

Ultrasound has been extensively used in trauma. Parenchyma], subcapsular and perinephric haematoma can be seen acutely as echo-poor areas, becoming more heterogeneous and echogenic with time. Disruption of renal parenchyma with capsular tears and urinomas may be identified. Colour flow and spectral Doppler may allow

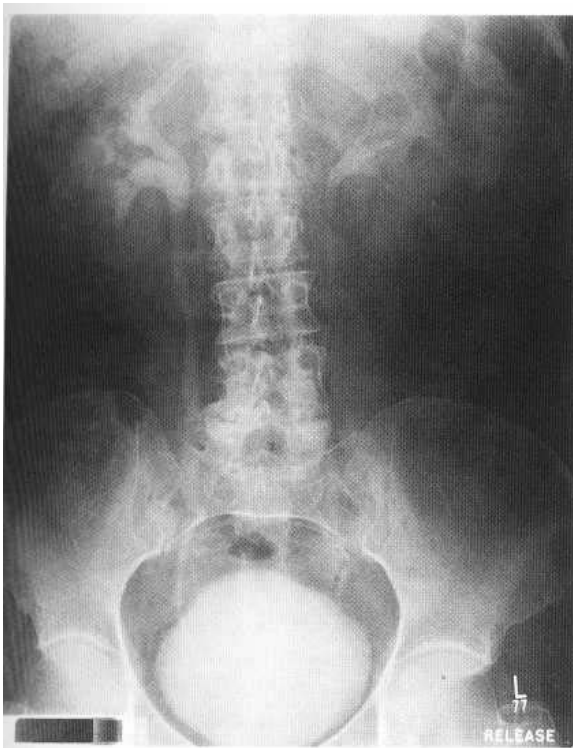


Fig. 30.95 Persistent dilatation of the upper two-thirds of the right ureter due to previous pregnancy.

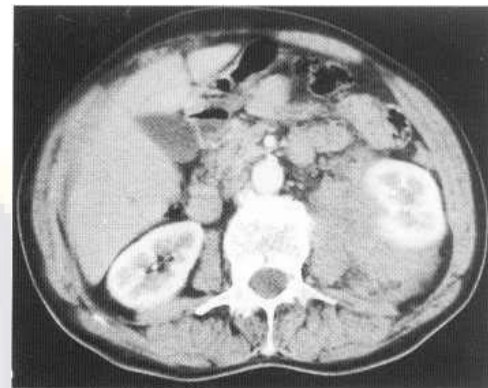


Fig. 30.97 Contrast CT showing large predominantly posterior perinephric haemorrhage.

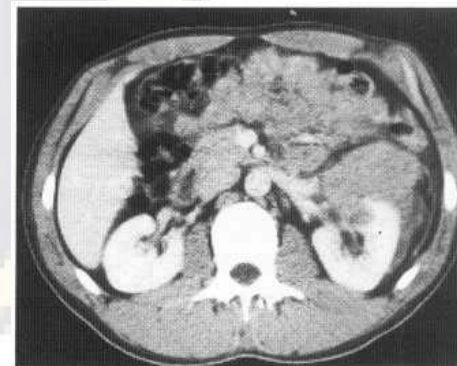


Fig. 30.98 Contrast CT showing a laceration of the kidney in the vicinity of the anterior lip of the renal sinus with a large associated haemorrhage.



Fig. 30.96 CT demonstrating traumatic rupture of a pre-existing pelvi-ureteric junction obstruction following relatively minor trauma. There is copious extravasation of urine and contrast medium.

diagnosis of pedicle injuries. Ultrasound, however, may be suboptimal in the trauma patient, with areas of tenderness precluding adequate imaging. Significant renal injuries may be missed, with up to 80% of parenchymal lesions being overlooked.

CT is currently the imaging modality of choice, allowing assessment of the entire abdomen, including the liver and spleen, for coexistent injuries. It is the most accurate technique for assessing renal injury. The abdomen and pelvis should be scanned from the diaphragmatic dome to the pubic symphysis with contrast. A suitable protocol is to commence scanning 30 s after the start of an injection of 50-100 ml of 300 strength at 2-3 ml/s, collimation 7 mm, pitch 1.3, reconstruction interval of 7 mm. Hyperacute areas of haemorrhage appear as ill-defined hyperdense areas. The bulk of the haematoma on most scans will be more established and appear of intermediate density. The haematoma may be described as

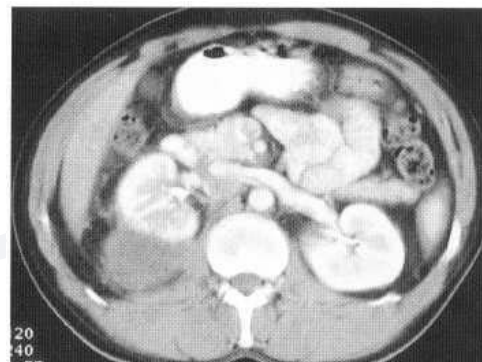
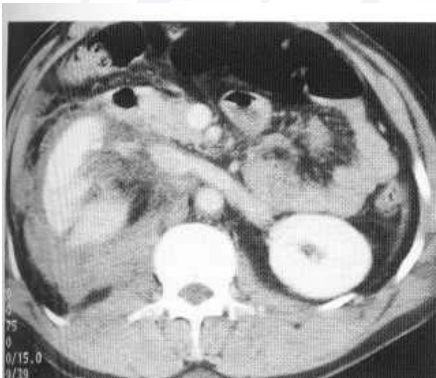


Fig. 30.99 Contrast CT showing a fracture through the centre of the kidney with considerable circumferential perinephric haemorrhage (A). Two months after conservative management there has been impressive healing of the kidney and resorption of most of the haemorrhage (B).

A

B

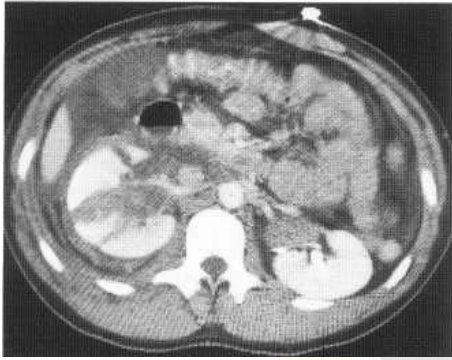


Fig. 30.100 Contrast CT showing a shattered kidney (multiple fractures).

parenchymal, subcapsular, perinephric or any combination of these. Subcapsular blood is seen as a crescentic low-density area following the convexity of the outer aspect of the renal cortex. Perinephric haematoma surrounds the kidney as it enlarges. They are usually mostly posterior, displacing the kidney forwards (Fig. 30.97). If the collection is predominantly medial, pelviureteric disruption should be considered. Renal lacerations/tears appear as irregular low-density linear areas crossing the parenchyma (Fig. 30.98). Fractures are lacerations that extend from the hilum to the external surface of the kidney (Fig. 30.99). Multiple renal fragments are referred to as a shattered kidney (Fig. 30.100).

The commonest vascular injury to the kidney is renal artery disruption/avulsion, which appears as non-perfusion of the kidney (Fig. 30.101). There may be some peripheral perfusion preserved due to the early take-off of the capsular artery. Traumatic renal artery dissection may be identified on CT and be associated with focal infarcts. Traumatic renal vein thrombosis is also seen and leads to a persistent nephrogram, sometimes with thrombus being

the pelviureteric junction is associated with injuries at this site. If there is total disruption, the ureter fails to opacify; if the laceration is incomplete, contrast appears in the ureter.

MRI is thought to have a similar accuracy to CT in the assessment of renal trauma. It may have some role where there is contrast allergy but otherwise the logistical problems of the modality generally exclude its routine use in acute trauma.

The most widely used imaging classification of renal injuries is that described by Federle. It is an easy intuitive system to follow,

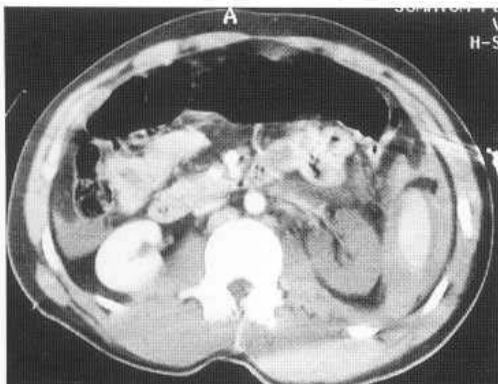


Fig. 30.101 Contrast CT of traumatic renal arterial avulsion. The left kidney is completely non-enhancing (non-perfused). There is a small amount of blood along the line of the renal vessels and a modest haemorrhage related to the spleen.

Box 30.3 Classification of renal trauma

Federle imaging classification		AAST classification	
Category	Injury	Grade	Injury
I	MINOR	1	Contusion and/or non-expanding subcapsular haematoma
	Contusion		
	Cortical laceration not extending into a calyx		
II	Cortical laceration more than 1 cm not extending into a calyx	2	Cortical laceration less than 1 cm not extending into a calyx
		3	Cortical laceration more than 1 cm not extending into a calyx
III	MAJOR	4	Cortical laceration extending to the corticomedullary junction or into the collecting system
	Cortical laceration extending into the collecting system (renal fracture)		
IV	CATASTROPHIC	5	Renal artery or vein injury with contained haemorrhage Renal pedicle avulsion Shattered kidney
	Renal pedicle injuries		
	Shattered kidney		
	Pelviureteric junction injuries		

categorising injuries into four groups (minor, major, catastrophic and injuries to the pelviureteric junction). The American Association of Surgery (AAST) have described a surgical classification which has also been used in the literature. Since the vast majority of imaged but only a minority will undergo surgery, the Federle classification is much more useful for the radiologist. Fortunately the two classifications show considerable overlap and their main features are listed together in Box 30.3 to illustrate this.

Penetrating injuries are uncommon and usually relate to gunshot or stab wounds. A significant number follow medical intervention, particularly renal biopsy. High-velocity gunshot wounds may be associated with catastrophic renal injuries; stabbing is more likely to be associated with lacerations of varying severity (Fig. 30.102). All (especially medical intervention) may lead to vascular injuries, including traumatic arteriovenous fistulas.

Around 95% of renal trauma is represented by minor lacerations and parenchymal contusions and does not require surgery. A small minority are haemodynamically unstable, often with multiple injuries, and require emergency laparotomy with either no imaging or possibly portable ultrasound while the patient is being prepared for surgery. The remaining group of patients are those with major or catastrophic injuries but with haemodynamic stability. Current opinion favours conservative management where possible with these patients. Most major lacerations will heal without intervention, even with a shattered kidney. Where a patient is stable but has evidence of continued bleeding (for example, demonstrable expanding haematoma with a continued need for transfusions), angiography with selective embolisation may have a role. Renal pedicle injuries with loss of perfusion to the kidney require arterial repair within a few hours if the kidney is to be preserved. However, results are poor and the surgery is hazardous and difficult.

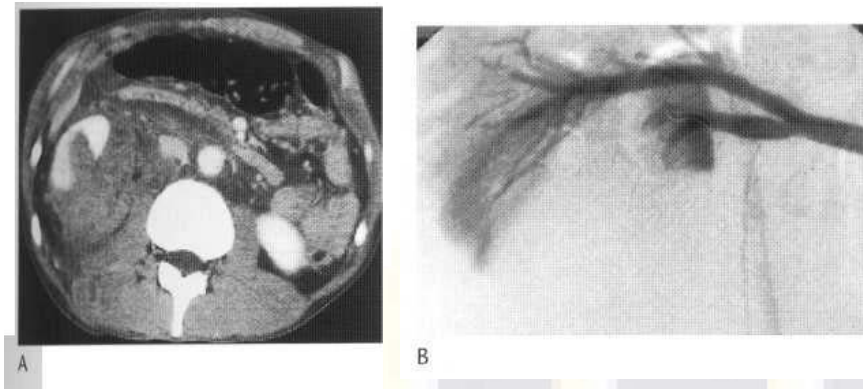


Fig. 30.102 Stab wound resulting in laceration of the lower pole of the right kidney with considerable associated haematoma shown on contrast CT (A). This was successfully treated with selective coil embolisation (B).

Complete pelviureteric disruption also requires surgery but partial disruption usually heals spontaneously. Persistent urinary extravasation can be treated with retrograde or antegrade stenting. Perinephric collections of urine or blood will tend to resorb over time. Large and/or infected collections may be treated with percutaneous drainage.

There is an increased risk of subsequent hypertension following renal trauma and this is particularly seen where there has been a substantial subcapsular haemorrhage. The increased intracapsular pressure impairs the renal arterial supply, impairment that may be exacerbated with healing and the development of perinephric fibrosis and renal atrophy (the Page kidney).

Ureteric trauma Ureteric trauma constitutes less than 1% of urinary tract trauma. Unlike renal and bladder trauma it is usually penetrating. It is occasionally due to severe deceleration with avulsion, usually at the pelviureteric junction, less often the upper third of the ureter and very rarely elsewhere in community-acquired injuries. It is more frequent in children, presumably because they are sufficiently flexible to permit the hyperflexion required to produce the injury. An important subgroup of injuries is those acquired through medical intervention, particularly gynaecological surgery for malignancy.

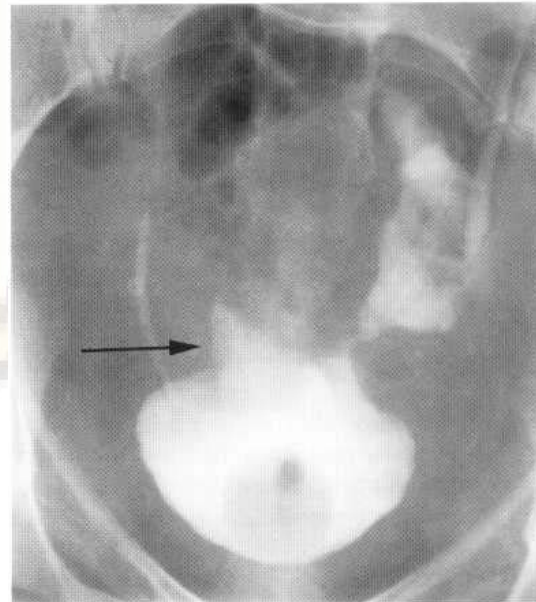


Fig. 30.104 Damage to the left ureter during pelvic surgery with severe distal ureteric stricturing, extravasation and fistulation into the vagina (arrow indicates contrast in the vagina).



Fig. 30.103 Bilateral extravasation from the distal ureters following radical pelvic surgery. The ureters also show smooth tapered stricturing in the pelvis with bilateral hydronephrosis and dilatation of the proximal ureters, worse on the right.

Other serious injuries are often present and may lead to the ureteric trauma being overlooked. Although there is usually haematuria, it may be absent in up to one-third of cases. Features include contrast extravasation, formation of a urinoma and occasionally ureteric discontinuity. On IVU there may be mild to moderate fullness of the pelvicalyceal system and extravasation at the site of the tear (Fig. 30.103). If it is complete, the ureter will fail to opacity below it. Fistulation into other structures may occur (Fig. 30.104). These features can also be demonstrated on a retrograde pyelogram, although this is not usually necessary. If the tear is partial then it will heal with a stent, albeit with the risk of late stricture formation. Complete avulsion requires surgical repair.

DIFFUSE AND MULTIFOCAL RENAL PARENCHYMAL ABNORMALITIES

A number of pathological processes (some of which have already been discussed above) produce global or multifocal changes in the imaging appearances of one or both kidneys. These appearances include changes in the size and outline of the kidneys and the presence of multiple calcified areas.

Small scarred kidneys The commonest causes are reflux nephropathy (characterised by abnormally clubbed calyces opposite the scars) and renal infarcts (the scars occurring between normal calyces). Other conditions include papillary necrosis and previous surgery (usually unilateral).

Small smooth kidneys Bilateral small smooth kidneys are most commonly seen as a late stage of numerous pathological processes. The commonest is probably renal arterial insufficiency (hypertensive nephrosclerosis, bilateral renal artery stenoses and/or small vessel disease), although these may be associated with scarring. Chronic glomerulonephritis and the end-stage of other nephropathies (hereditary, analgesic, etc.) also lead to small smooth kidneys. All of these processes lead to loss of the normal renal architectural pattern on ultrasound, with a general increase in echogenicity. Medullary cystic disease is responsible for small kidneys with cysts.

A unilaterally small kidney with clubbed calyces is likely to be due to postobstructive atrophy, although the appearances overlap with reflux nephropathy (when the cortex is thin and the kidney particularly small, scars may not be evident). Generally at least 1 week of high-grade sterile obstruction is required to produce irreversible obstruction. There is associated renal pelvic and ureteric ectasia. The commonest cause of a small smooth kidney with normal calyces is longstanding renal artery stenosis. Other causes include developmental hypoplasia, previous renal vein thrombosis, radiotherapy and trauma with subcapsular haematoma.

Smooth renal enlargement The commonest cause of bilateral smoothly enlarged kidneys is diabetes, often before it has become clinically apparent. Acute global renal insults of all sorts lead to bilateral renal swelling and include acute glomerulonephritis, acute nephropathy (AIDS, mate, etc.), interstitial nephritis and renal involvement in connective tissue diseases (systemic lupus erythematosus, Wegener's, etc.). Diffuse infiltration with tumour (leukaemia, occasionally lymphoma or myeloma) also produces this appearance. Rare causes include amyloidosis, acromegaly, autosomal recessive polycystic kidneys and hereditary depositional diseases.

The commonest cause of unilateral smooth renal enlargement is acute obstruction, when the diagnosis is usually obvious clinically and from other imaging features. Other acute renal insults may produce unilateral smooth enlargement and include acute pyelonephritis and acute vascular disturbances (main arterial or

venous occlusion, acute arteritis including recent radiotherapy). Any of these conditions may be associated with a heterogeneous or striated nephrogram and global reduction or loss of renal function. Infiltration with tumour (leukaemia, lymphoma, transitional cell carcinoma, renal cell carcinoma and metastases—especially squamous cell carcinoma) or an inflammatory process (tumefactive xanthogranulomatous pyelonephritis) may occasionally present as unilateral renal enlargement.

Compensatory hypertrophy of a kidney following loss or long-standing disease of the other kidney is worth mentioning for completeness. The kidney is normal apart from increase in size and cortical thickness. It is rarely pronounced above the age of 60 and is occasionally lumpy. Hypertrophy of one kidney is also seen in the syndrome of hemihypertrophy.

Renal insufficiency and failure

Less than 10% of patients presenting with unpaired renal function have an obstructive cause. Nevertheless, this is the single most important condition to diagnose or exclude because it is also the most treatable. Ultrasound is the standard method for this and in the subacute or chronic situation ultrasound is usually highly accurate, as discussed above. After obstruction has been excluded, other causes may be considered. This is essentially the realm of medical renal disease, which includes numerous conditions, many of which will give rise to similar imaging features. Ultrasound is again the most useful modality. The IVU is likely to be of poor quality as renal function worsens (and there may be no visible excretion at all) and may potentially exacerbate the renal deterioration.

Ultrasound will determine the presence of two kidneys and their sizes. This is of interest because normal-sized kidneys in the presence of renal failure suggests an acute cause with potentially an ongoing condition amenable to treatment. Small kidneys indicate chronicity. Ultrasound may also demonstrate areas of scarring (arterial or due to reflux nephropathy), calcification and cystic disease. Global changes in echogenicity may be present and, with Doppler, major vascular events may be detected (arterial or venous infarction).

In acute nephropathies there may be swelling of the cortex. This may retain normal echogenicity. In some cases of acute glomerulonephritis, acute tubular necrosis and acute interstitial nephritis the cortex may increase in echogenicity, emphasising corticomedullary differentiation.

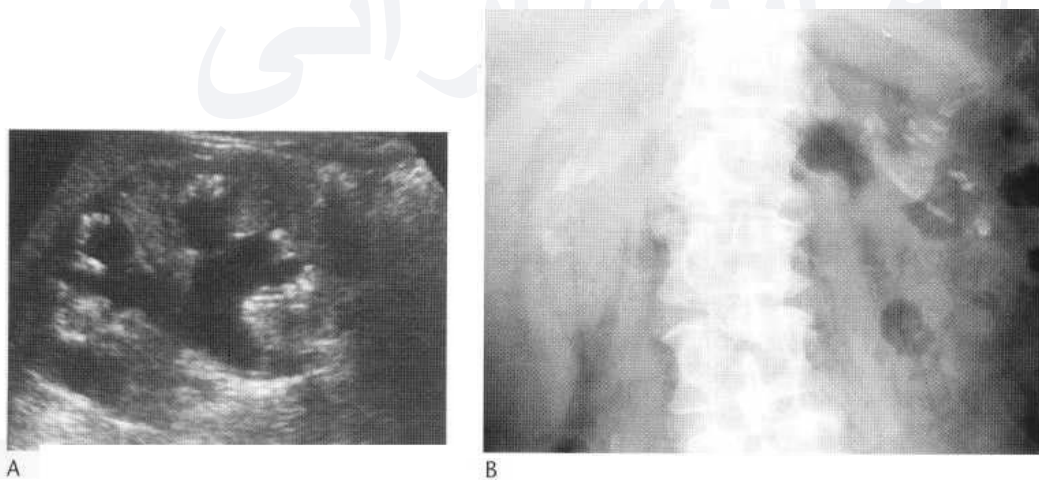


Fig. 30.105 Ultrasound of a patient with medullary sponge kidney showing multiple small echogenic areas in the papillae due to tiny calculi in the collecting duct (A). There is also hydronephrosis and proximal hydroureter due to a ureteric calculus. Plain film nephrocalcinosis (B) in a different patient.

Most chronic conditions associated with renal insufficiency lead to small kidneys with increase in the central echogenic fat, global cortical loss and disappearance of the corticomedullary differentiation. The kidneys may also become generally more echogenic.

Nephrocakinosis This refers to the presence of multiple foci of calcification within the renal parenchyma, conventionally excluding focal dystrophic calcification as found in renal tuberculosis and renal cell carcinoma. It may be cortical or medullary.

Cortical nephrocalcinosis is uncommon and usually associated with chronic renal failure and small kidneys. It is confined to the peripheral 2 cm of the renal tissue and is often thin, being referred to as tramline or eggshell calcification. The most common causes are acute cortical necrosis and chronic glomerulonephritis. Acute cortical necrosis occurs in response to a severe, usually hypotensive, renal insult, such as perinatal shock, severe septic shock, severe haemorrhage and some nephrotoxins, such as ethylene glycol. Rare causes of cortical nephrocalcinosis include hyperoxaluria, Alport's syndrome (sensorineural hearing loss and congenital nephritis) and chronic transplant rejection.

Medullary nephrocalcinosis is relatively common and is characterised by calcification of the pyramids with sparing of the cortex. The commonest cause is medullary sponge kidney (Fig. 30.105). Pathologically this does not cause medullary nephrocalcinosis, as the calcification is in the form of tiny calculi within dilated collecting ducts. Radiologically, however, the calcification is seen in the region of the pyramids and it is convenient and accepted to include it in this category. Any cause of hypercalcaemia may produce medullary nephrocalcinosis and may be associated with urinary tract calculi and metastatic soft-tissue calcification. The most important cause from this point of view is hyperparathyroidism (Fig. 30.106). Disseminated malignancy causing hypercalcaemia is fairly frequently seen but it is unusual for it to persist long enough to cause medullary nephrocalcinosis. Sarcoidosis is worth bearing in mind as a cause of hypercalcaemia, and for completeness there



Fig. 30.106 Plain film showing extremely dense nephrocalcinosis due to hyperparathyroidism.

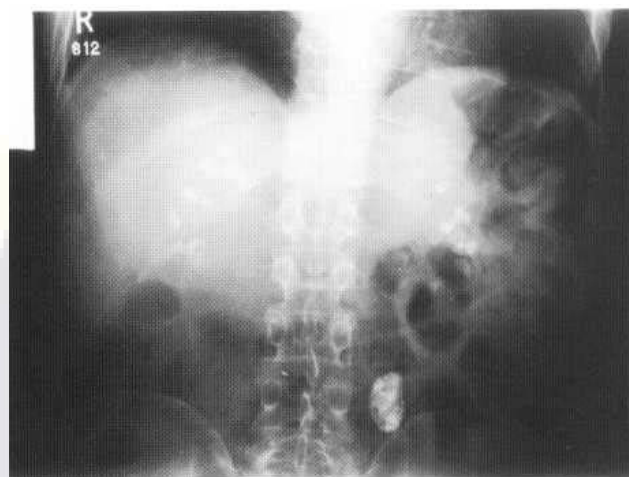


Fig. 30.107 Plain film showing moderately dense nephrocalcinosis due to secondary hyperoxaluria.

are some historical (milk-alkali syndrome, vitamin D overtreatment) and extremely rare (acromegaly, thyrotoxicosis) causes. Analgesic nephropathy/papillary necrosis may cause papillary necrosis at multiple sites and, although strictly speaking it produces multiple focal dystrophic calcific areas, it gives an appearance similar to medullary nephrocalcinosis.

There are two uncommon but important metabolic causes to consider. Type I (distal) renal tubular acidosis is associated with exceptionally dense medullary nephrocalcinosis, calculi and initially normal-sized kidneys and progressive renal failure. Hyperoxaluria may also produce fairly dense medullary nephrocalcinosis (Fig. 30.107), and on rare occasions also gives rise to cortical nephrocalcinosis, being the only condition to do this. Primary hyperoxaluria is a rare hereditary disorder and leads to renal failure and death in childhood or early adulthood. Secondary hyperoxaluria is much more common and has a more benign course. It is associated with extensive distal small-bowel disease (for example, Crohn's disease) and/or resection. The consequent malabsorption of fat allows fatty acids to combine with calcium in the intestine. Normally calcium is available to bind oxalate and prevent its absorption. With this mechanism ineffective, oxalate is absorbed in excess quantities, producing secondary hyperoxaluria. A final rare cause of medullary nephrocalcinosis is chronic furosemide use in premature infants with cardiovascular disease.

Papillary necrosis This condition is often listed as a cause of medullary nephrocalcinosis although it causes dystrophic calcification and strictly speaking should be excluded on that basis. However, radiologically calcification is seen over the pyramids and it is worth including in the differential diagnosis of medullary nephrocalcinosis. The disease is characterised by ischaemic necrosis of the papillae. The major causes are analgesic nephropathy (especially phenacetin but also aspirin and other non-steroidal anti-inflammatory agents), sickle-cell disease, diabetes mellitus, tuberculosis, acute severe pyelonephritis, renal vein thrombosis, cirrhosis, chronic heart failure and chronic obstruction (especially with infection). It is rarely seen in severely ill infants and neonates with dehydration, acidosis and respiratory distress. Presentation is usually insidious, with haematuria (usually microscopic), pyuria and symptoms of poor ability to concentrate the urine as medullary tissue is lost (frequency and polydipsia). Episodes of acute papillary necrosis are associated

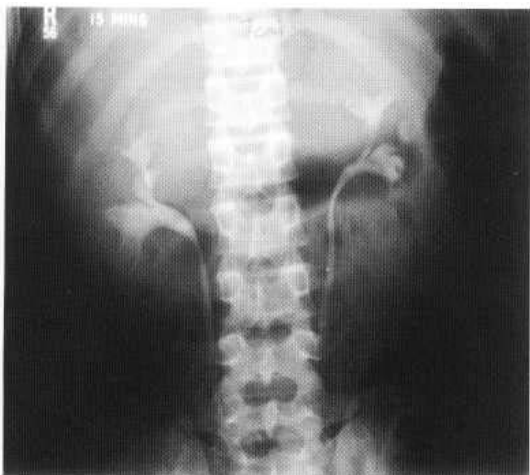


Fig. 30.108 Early papillary necrosis with erosions around the margins of some of the papillae.

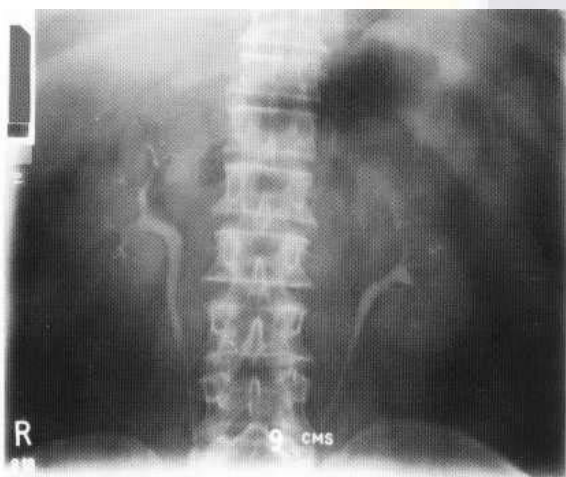


Fig. 30.109 Papillary necrosis with more widespread erosions into and around the papillae and a classic ball-in-cup configuration visible.



Fig. 30.110 Plain film of advanced papillary necrosis; small kidneys with papillary calcification.

with flank pain, haematuria and acute renal failure. The commonest cause is analgesic nephropathy when there is an association with an unstable urothelium and a predilection to the formation of multiple transitional cell carcinomas.

The classical features are described on IVU. Initially there are small necrotic areas which erode the tip of the papillae and irregularly excavate from the fornices into the pyramids (Fig. 30.108). As these excavations develop, the papilla becomes virtually surrounded by contrast (the so-called ball-in-cup appearance, Fig. 30.109) and may slough into the pelvicalyceal system, pass into the ureter and

present with colic. The defect left behind appears as flattening or concavity of the pyramidal tip (clubbing of the calyx). The necrotic papillae often calcify (Fig. 30.110). The disease is typically bilateral but asymmetrical and as it progresses there is parenchymal loss and the kidneys become small with smooth outlines and poorly functioning.

LESIONS OF THE URETER

It is useful to consider conditions of the ureter by the principal site affected, namely intraluminal, mural and extrinsic lesions. This is a convenient classification because there are significant differences in the radiological appearances and the investigative pathways for the different groups of diseases. However, some disease processes may affect more than one anatomical site and appearances may become mixed. For example, a polypoidal tumour of the wall will display some of the features of a mural lesion as well as a filling defect within the lumen.

Intraluminal lesions

Intraluminal lesions appear as filling defects largely surrounded by contrast material. Ureteric calculi represent over 99% of radiopaque filling defects and the vast majority of radiolucent filling defects. They are described under the section on calculi and obstruction above.

Where there is heavy haematuria, clots may form and appear on IVU as filling defects. They have a characteristic serpiginous appearance, effectively being partly retracted casts of the collecting system. They may cause obstruction but this is transient, urokinase within the urine causing lysis within a few hours and appearances usually returning to normal within a few days. There may be a demonstrable structural lesion causing the haematuria (such as a calculus or tumour) and this should be considered even if the patient has impaired coagulation, for example poorly controlled warfarinisation.

Occasionally in papillary necrosis a papilla is sloughed and appears as a filling defect. It may cause obstruction and is characteristically triangular, showing variable calcification (usually marginal) and is associated with a defect in the pyramid from which it is derived. Similarly a necrosing renal tumour that has invaded the collecting system may slough off fragments, which may pass into the ureter (Fig. 30.111).

Rarely inflammatory masses may be seen in the collecting system and have a configuration similar to thrombus. They consist

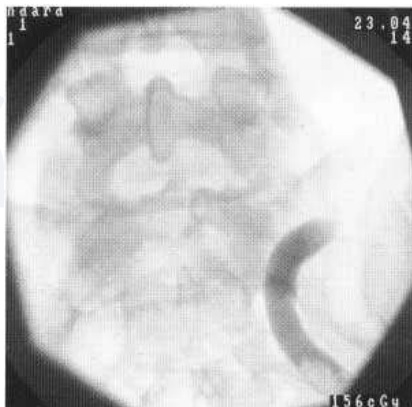


Fig. 30.111 Retrograde ureterogram showing a sloughed fragment of a large renal cell carcinoma seen lying within the ureter and causing obstruction above it.

of inflammatory debris, viscid pus and pathogens in varying proportion. They may be fungal in origin (usually *Candida* or *Aspergillus* spp) and associated with diabetes or other impaired immune state, or due to pyogenic bacteria.

Air bubbles may appear as well-defined mobile low-density filling defects on IVU, retrograde and antegrade pyelography and CT. They may be associated with urinary diversions such as conduits, instrumentation, gastrointestinal or cutaneous fistulas or infection with gas-producing organisms. The latter again are associated with diabetes and most commonly involve *E. coli*, *Proteus*, *Klebsiella* or yeasts.

Finally, it is worth reiterating that a polypoidal tumour of the ureteric wall will appear as a filling defect on IVU and retrograde pyelography. CT will differentiate it from a calculus because calculi essentially always appear radiopaque on CT and a lesion within the ureteric lumen that contains calcium is virtually always a calculus, rarely a calcified sloughed papilla and very rarely a tumour.

Other diseases of the ureteric wall may also demonstrate an exophytic pattern and appear as ureteric defects. They include oedema (for example, postinstrumentation or passage of calculus), pyeloureteritis cystica, leucoplakia, malacoplakia, endometriosis and schistosomiasis. An extrinsic prominent vessel (normal variant, collateral arteries or veins) may focally indent the ureter and appear as a well-defined filling defect.

Mural lesions

These lesions are connected to the ureteric wall. Some authorities differentiate between mucosal lesions that have acute angles at their margins with the wall and submucosal/intramural lesions that have obtuse angles. This may have some usefulness in stereotypical cases.

Ureteric tumours Ureteric tumours are uncommon, around 90% being transitional cell carcinoma; 5-10% are squamous cell carcinomas. Adenocarcinoma, sarcoma and metastases are rare. Transitional cell carcinomas classically appear in middle-aged or elderly adults and present as frank or microscopic haematuria, or occasionally loin pain due to clot colic or ureteric obstruction. Transitional cell carcinomas are multifocal in up to 20% and metachronous tumours in a further 20%, the additional tumours usually developing within the ipsilateral collecting system and the bladder. There is an increased risk of developing these tumours with smoking, analgesic abuse, chemotherapy (especially cyclophosphamide), marrow transplantation and the rare condition of Balkan nephropathy.

Approximately two-thirds of ureteric transitional cell carcinomas are papillary with a polypoidal configuration and are characteristically seen as radiolucent intraluminal filling defects, often irregular, with dilatation of the ureter above. When small, the lesion is often subtle and signs may appear on only one film of an IVU series (Fig. 30.1 12). As the tumour enlarges there may be some dilatation of the ureter below it as a result of chronic intussusception induced by ureteric peristalsis. One-third of transitional cell carcinomas are infiltrating and produce stricturing, often irregular. Patients with haematuria will often be investigated with ultrasound but this is usually normal until the tumour is large enough to cause a degree of hydroureter and hydronephrosis. Therefore patients with persistent unexplained haematuria should be investigated with IVU and, if this is equivocal, retrograde pyelography. CT or MRI will demon-

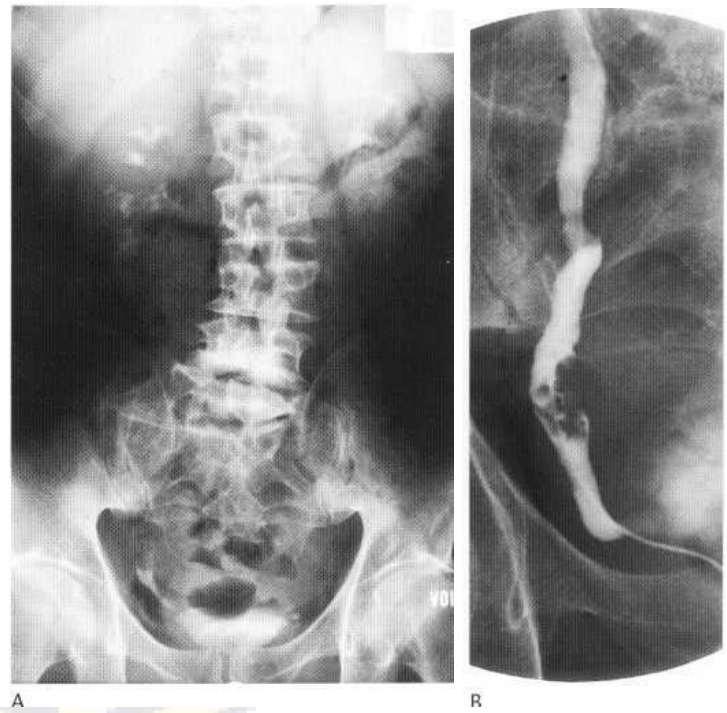


Fig. 30.112 IVU showing an irregular filling defect in the distal right ureter (A). This is better seen on the retrograde study (B).

strate soft-tissue extension out of the ureter into the retroperitoneum in advanced tumours.

Oedema Mucosal oedema may be associated with recent passage of a calculus or instrumentation. It may have the configuration of an annular, plaque-like or linear filling defect. The diagnosis is usually obvious from the history and its resolution over days or weeks after the initial presentation.

Leucoplakia This is a premalignant metaplasia of the urothelium which appears secondary to chronic irritation such as calculi, chronic urinary tract infection or schistosomiasis. It produces multiple flat plaques and is associated with squamous cell carcinoma in surrounding areas or developing subsequently. It is most often found in the bladder but occasionally in the ureter or pelvicalyceal system.

Pyeloureteritis cystica This is a relatively common condition in which multiple well-defined, rounded sterile submucosal fluid collections a couple of millimeters in diameter form in the ureter and renal pelvis. The condition is related to chronic urinary tract infection.

Intramural haemorrhage This is associated with abnormal coagulation, for example overzealous warfarinisation. It is usually associated with haematuria.

Malacoplakia This rare condition is also associated with chronic urinary tract infection. It consists of intramural plaques of defective macrophages and incompletely phagocytosed *E. coli*. It is benign and not premalignant. It may affect the bladder, the ureter, the pelvicalyceal system and the renal parenchyma. It resolves after treatment of the initiating urinary tract infection. It is thought it may represent a mild form of chronic granulomatous disease in which there is more severe defective macrophage phagocytosis.

Tuberculosis In the ureter this develops as a result of descending infection from renal tuberculosis. The characteristic features are seen on IVU and include ulceration in the early stages, followed by multifocal stricturing and calcification with hydroureter and hydronephrosis. The ureter may also shorten and straighten (pipestem ureter).

Schistosomiasis This condition involves the ureter in around one-third of cases. The distal ureter is particularly involved. In the early stages of the disease inflammatory polyps are common and may appear as filling defects. Later, multifocal strictures develop with proximal ureteric dilatation and hydronephrosis. Linear calcification may be seen in the ureteric wall.

Endometriosis Up to 10% of patients with endometriosis have urinary tract involvement due to endometrial tissue deposits over the bladder or retroperitoneally. Many of these lesions, particularly related to the bladder serosa, are clinically insignificant. Ureteric involvement can, however, lead to stricturing and obstruction. It is bilateral in 10%. Ureteric obstruction may be insidious but often presents with flank pain, which is cyclical, usually associated with other symptoms of endometriosis such as dyspareunia and dysmenorrhoea. IVU or retrograde pyelography shows a short smooth abruptly tapered stricture, usually in the distal third of the ureter, classically at the level of the uterosacral ligaments, which may be associated with some medial angulation of the ureter (Fig. 30.113).

Ureteric narrowing Many of the important causes of ureteric narrowing have been described above. They include ureteric and extrinsic tumours, endometriosis and inflammatory lesions (tuberculosis and schistosomiasis). Extrinsic inflammatory lesions, such as Crohn's disease and appendix or diverticular abscess, may lead to ureteric stricturing (Fig. 30.114). Ischaemic change in the ureteric wall is an important occasional cause of ureteric narrowing that is usually seen following aortic or radical pelvic surgery.

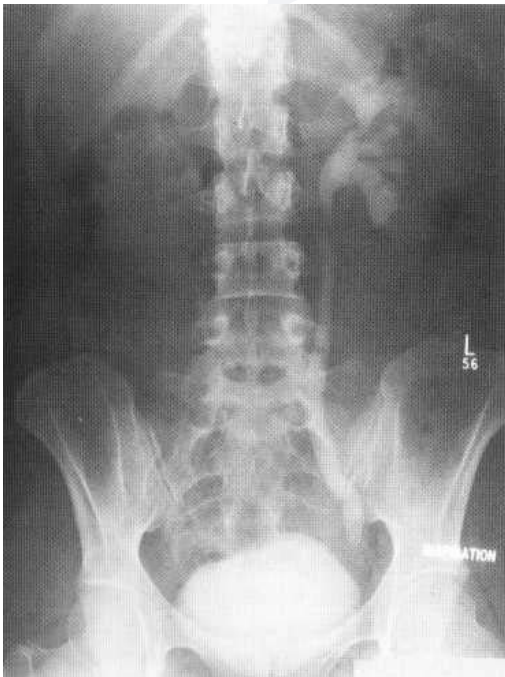


Fig. 30.113 Full length film from an IVU showing an abrupt smooth stricture in the distal ureter due to endometriosis.



Fig. 30.114 Short tight stricture in the distal left ureter due to involvement in a previous diverticular abscess.

Acutely the mucosa is swollen and scalloped and CT may demonstrate thickening of the wall. It is more commonly seen subacutely or chronically when an established fibrous stricture has developed. Postradiation stricturing is thought to be a particular variant of ischaemic stricturing. Characteristically it appears as a smooth abruptly narrowed segment that develops at least 1 year after radiotherapy.

Direct trauma to the ureter is an important cause of stricturing and is usually due to radical pelvic surgery. It may be associated with fistulas, particularly into the vaginal stump following hysterectomy. In the absence of a fistula it often leads to hydronephrosis and may result in insidious loss of the kidney, as the pain of the obstruction is obscured by postoperative pain. Other traumatic causes include difficult passage of ureteric calculi and/or ureteric instrumentation.

Extrinsic lesions

Purely extrinsic lesions are described as producing smooth ureteric narrowing with obtuse angles and ureteric deviation. Hypertrophic ureteric and other retroperitoneal arteries may cause notching of the ureters and develop in a number of conditions, including renal artery stenosis, hypervascular renal tumours, arteriovenous malformations and occlusive aortoiliac disease. Enlarged gonadal veins may also cause notching and have been reported with male or female varices, ovarian vein syndrome, gonadal thrombophlebitis and iliac venous occlusion.

A wide variety of retroperitoneal and pelvic mass lesions may impinge on the ureters, with the potential for displacement and obstruction. Aneurysms of the abdominal aorta characteristically deviate the upper two-thirds of the left ureter laterally. They are usually visible on plain films as a soft-tissue mass with linear wall calcification. Common iliac artery aneurysms have a similar appearance in the pelvis and may displace either ureter.

Hydronephrosis and hydroureters due to tumours that originate outside the ureter are frequently encountered. These commonly



Fig. 30.115 Bilateral medial deviation of the lower ureters due to physiological psoas muscle hypertrophy.

include gynaecological malignancies, lower urinary tract malignancies (carcinoma of the bladder or prostate) and anorectal cancers that directly involve the ureters, often bilaterally, with the production of obstructive renal failure. All of these may also provoke ureteric obstruction due to iliac and/or para-aortic/paracaval lymph node metastases, as may a variety of other malignancies including lymphoma and malignant teratoma.

Pathological causes of ureteric displacement should not be confused with bilateral medial deviation of the mid ureters in fit young males due to physiological psoas muscle hypertrophy (Fig. 30.1 15). There is often associated iliacus and obturator internus hypertrophy with inferomedial deviation of the distal ureters. Another benign cause of bilateral medial ureteric deviation is pelvic lipomatosis. This uncommon idiopathic condition is seen in overweight middle-aged men and is due to proliferation of fat within the pelvis. It may be asymptomatic or associated with lower tract symptoms such as dysuria or mild bladder outflow obstruction, which may progress to bilateral hydronephrosis and bladder compression (becoming pear-shaped). On plain radiographs (and more sensitively on CT) excess fat can be identified in the pelvis. Both IVU and CT show medial displacement of the distal ureters and upward displacement of the bladder, which appears laterally compressed (pear-shaped). Ultrasound demonstrates extensive echogenic perivesical fat. Severe cases may be associated with hydronephrosis and rectosigmoid obstruction.

Retroperitoneal fibrosis This is an uncommon condition in which fibrosis and chronic inflammatory cells infiltrate the retroperitoneal tissues. At least half of cases are idiopathic, although these may be associated with autoimmune conditions such as inflammatory bowel disease, sclerosing cholangitis and fibrosing mediastinitis. Retroperitoneal fibrosis may develop secondary to inflammatory aortic aneurysm, vascular grafts, retroperitoneal metastases (usually from lymphoma, carcinoma of the breast and colon and carcinoid), retroperitoneal haemorrhage,

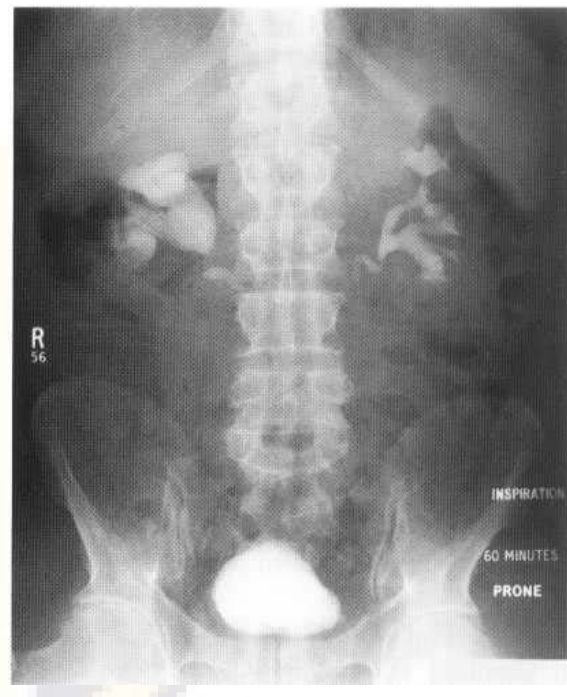


Fig. 30.116 Retroperitoneal fibrosis on IVU. There is marked abrupt deviation of both upper ureters with a right-sided hydronephrosis.

abscess, urinoma, diverticulitis, appendicitis, Crohn's disease and drugs (ergot alkaloids, hydralazine).

The disease process starts just lateral to the aorta and therefore affects the left ureter before the right. It spreads into the pericaval and intraaortocaval area. It occurs anywhere from the pelviureteric junction to the bladder but most commonly L3-L5. It is a slow process which encases the ureter and causes loss of peristalsis. There is rarely ureteric wall invasion. The mucosa is always spared. Consequently there is an insidious onset of obstructive symptoms with demonstrable hydronephrosis, considerably milder than the effect on renal function. Stems characteristically pass easily retrogradely (due to the absence of peristalsis and the ureters being fixed open by the process).

IVU shows variable medial deviation of the ureters (Fig. 30.1 16). In around half the cases the ureters are not significantly deviated. In the remainder of cases there is variable deviation, most often between the third and fifth lumbar vertebrae. Deviation is often asymmetrical and is unilateral in up to 25%.

CT and MRI demonstrate a smooth sheet of tissue around and over the aorta and inferior vena cava. It rarely extends between the



Fig. 30.117 CT demonstration of retroperitoneal fibrosis with classical appearance of the aorta as if taped down by a sheet of tissue.

aorta and the vertebrae, so the aorta has a taped-down appearance (Fig. 30.117). If the aorta is encased with soft-tissue material and displaced anteriorly off the spinal column, this suggests lymphoma or other widespread malignancy (Fig. 30.118). Image-guided biopsy (usually CT) should allow differentiation between benign and malignant retroperitoneal fibrosis.

Surgical treatment may involve freeing the ureter and positioning it markedly lateral within the abdomen, giving a characteristic post-operative appearance on IVU (Fig. 30.119).

Ureteric deviation Medial deviation of the ureter may be due to retroperitoneal fibrosis or tumours; in the upper abdomen these may arise from the lower pole of the kidney or the retroperitoneum, and in the pelvis from the iliac lymph nodes or the pelvic walls. Benign causes of medial deviation include iliopsoas hypertrophy and pelvic lipomatosis. Iliac artery aneurysms may also sometimes medially deviate the ureter. Following AP resection of rectal tumours the ureters are seen to lie medially and have a more directly inferior running course than normal. The cause is usually



Fig. 30.118 CT of malignant para-aortic and paracaval lymphadenopathy causing ureteric obstruction. Note the anterior displacement of the aorta off the spine.



Fig. 30.119 IVU showing the characteristic lateral displacement of the ureter following surgery for retroperitoneal fibrosis (only the right side has been operated on, as the left kidney was already severely damaged).

obvious in view of the low pelvic surgical clips and the history. On the right a retrocaval ureter may show an abrupt medial turn.

Ureters may take an unusually lateral course as part of renal malrotation or a horseshoe kidney. They may be displaced laterally by tumours, most frequently para-aortic/paraval lymphadenopathy. They may be deliberately displaced by surgery, classically for retroperitoneal fibrosis.

Ureters may also be displaced, often with part of the bladder, into femoral or inguinal hernias, where they may be at risk of surgical trauma during herniorrhaphy. Occasionally a short segment of distal ureter herniates into the sciatic notch. In all these hernias the ureter may become obstructed, but does not usually do so.

IMAGING IN RENAL TRANSPLANTATION

Carl Roobottom

Renal transplantation only became practical in the 1960s with the ability to perform tissue typing and the introduction of effective immunosuppressants. Since this time renal transplantation has established itself as the treatment of choice for the majority of patients with end-stage renal failure. Compared to dialysis it is more cost-effective, produces better survival and allows a more normal lifestyle.

Transplantation is achievable both with cadaveric or living related donor transplants. The latter afford greater graft survival (90% 2 year survival), less recipient morbidity and optimal timing for surgery, and are therefore the preferred option. Living donors must be assured of normal/near normal renal function following nephrectomy. Detailed assessment of both kidneys is therefore required to demonstrate two good kidneys and variations in normal vascular and collecting system anatomy. Previously this required a combination of ultrasound, IVU and arteriography. This, however, can now all be assessed via spiral CT, including arterial phase images to demonstrate arterial anatomy, followed by a single IVU film after CT to demonstrate the collecting system anatomy (Fig. 30.120). Donors are also screened for a variety of infections but the search for occult malignancy is usually confined in imaging terms to chest radiography.

For a great number of patients cadaveric transplants remain the only option for transplantation. Although results are not as good as related donor transplantation, 5 year graft survival in excess of 65% is achievable with good perioperative care and follow-up.

Renal transplant surgery

Understanding of the surgery performed is essential for accurate radiological evaluation. In adults and large children the donor kidney is placed extraperitoneally in the iliac fossa. Following dissection of the native vessels and lymphatics, the renal artery is usually anastomosed end-to-end to the internal iliac artery or via an end-to-side anastomosis of an aortic patch on to the external iliac in cadaveric transplants. An end-to-side venous anastomosis is performed with the iliac vein, and the urinary tract reconstruction is usually by an antireflux ureteroneocystotomy, either with or without separate cystotomy. Ureter length is kept short as the donor ureter has to receive all of its blood supply via the donor hilar vessels (the

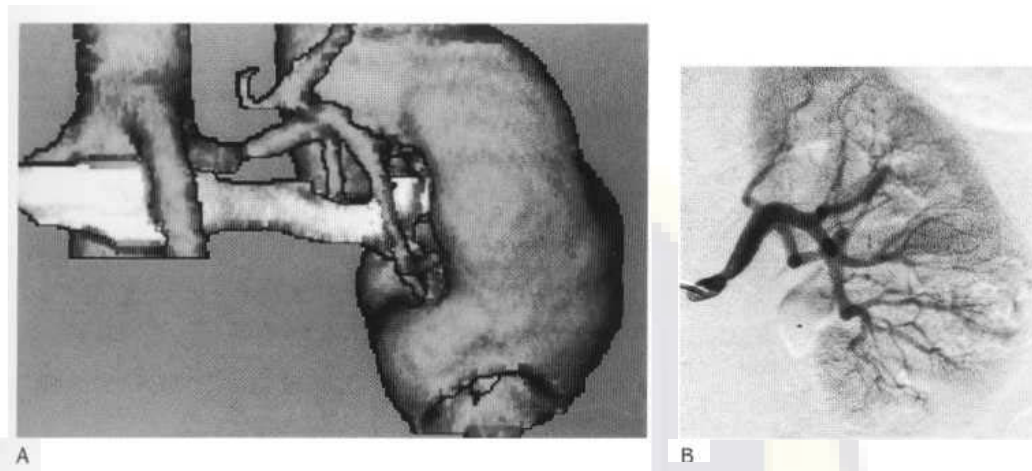


Fig. 30.120 (A) Surface-shaded 3D reconstruction of a spiral CT of the left kidney demonstrating renal morphology and vascular anatomy. The cortical defect seen caudally represented a renal cyst on axial images. Note the mild renal artery stenosis, which was confirmed angiographically (B).

remainder, out of necessity, are dissected away at the time of imaging and renal biopsy. Treatable causes must be excluded before harvest—placing the more distal ureter at risk of ischaemic damage). Variations of normal anatomy present technical problems to the surgeon and are therefore associated with an increased complication rate. All the sites of anastomosis and potential sources of problems are shown in Figure 30.121.

Early post-transplant Renal transplant recipients are immunosuppressed and have undergone major surgery; they are therefore susceptible to the usual postoperative risks, such as infection and deep vein thrombosis. The greatest risk, however, is early graft failure. Graft dysfunction is common with oliguria, occurring in nearly half of cadaveric transplant recipients. Clinical symptoms are often non-specific and the causes of failure are multiple and must be diagnosed early if they are to be reversed. This is best achieved by a routine policy of clinical surveillance and laboratory tests combined with

graft failure is attributed to rejection or acute tubular necrosis, and ultrasound, with colour flow and duplex Doppler imaging, is central in the diagnosis and sometimes treatment of graft failure.

Immediate graft dysfunction

When a renal transplant functions immediately or soon after surgery, obligate diuresis is usually seen and requires careful fluid balance management. In a significant percentage of patients, however, there is no immediate function. Causes can broadly be divided into mechanical and non-mechanical causes. This division is a useful one, as non-mechanical causes are either untreatable or treated by supportive means, whereas mechanical causes require prompt diagnosis and often immediate intervention.

Non-mechanical causes of graft dysfunction

Acute tubular necrosis Acute tubular necrosis (ATN) presents with anuria immediately or within the first few days post-transplant after an initial diuresis. Patients remain constitutionally well and urine sodium is usually high. ATN is the result of graft ischaemia and is therefore dependent on donor comorbid factors, the preservation technique used and the ischaemic time of the graft. It is almost exclusively seen in cadaveric transplants and is more frequent with difficult operations.

The main role of imaging is the exclusion of treatable causes. Ultrasound in ATN may show graft enlargement, most frequently with preservation of corticomedullary differentiation. Doppler studies usually show normal perfusion but in severe cases there is reduced perfusion globally. The duplex is either normal or shows reduced diastolic flow with an associated increase in resistive index (RI) and pulsatility index (PI). Appearances may overlap rejection and cyclosporin toxicity so biopsy is the most definitive investigation. Renal scintigraphy, which is now only infrequently used, usually shows normal or slightly decreased transplant perfusion, although again appearances may overlap with acute rejection.

Dead donor kidney This represents the extreme end of graft ischaemia and is therefore dependent upon donor factors, preservation and ischaemic times, as with ATN. Imaging is used to exclude treatable causes. All forms of imaging (nuclear medicine,

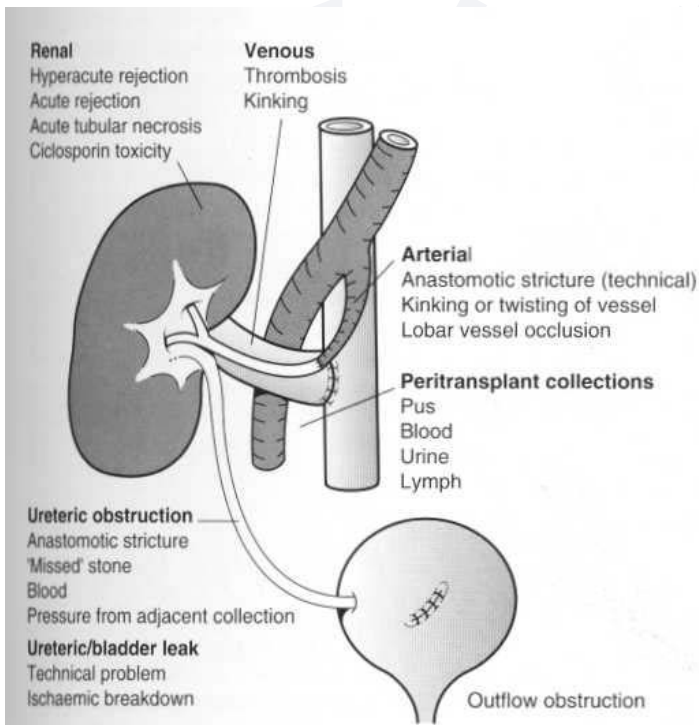


Fig. 30.121 Causes of acute rejection in the transplanted kidney.

angiography or Doppler imaging) show a global reduction in renal blood flow.

Acute rejection There are three forms of acute rejection. Hyperacute rejection is secondary to circulating antibodies present in the recipient at the time of transplantation. This causes immediate graft failure, with arterial thrombosis and cortical necrosis. It is usually evident at the time of surgery. It is now only rarely seen due to comprehensive immunological testing. Imaging plays no part in its management. It is treated by surgical excision of the graft.

Accelerated acute rejection is a combination of antibody and cell-mediated rejection that occurs within the first few days of transplantation. Imaging features overlap those of acute rejection (see below); however, prognosis for the graft is worse and rejection is frequently irreversible.

Acute rejection is mediated through cellular immunity. Although it can occur at any time, it is most frequent in the first 2 weeks post-surgery and is characterised by a sudden decline in graft function. This is usually associated with systemic symptoms of pyrexia and hypertension, with accompanying graft tenderness and enlargement. Oliguria is frequently accompanied by reduction in urinary sodium (cp-ATN). Although this is the most common cause of early graft failure, diagnosis must be assumed only after all treatable causes have been eliminated.

Ultrasound is the most useful investigation. Real-time imaging demonstrates swelling of the transplant with decreased echogenicity of the renal sinus fat and increased reflectivity of the cortex, producing conspicuous pyramids. Colour and power flow Doppler demonstrate reduction in perfusion of the cortex. Duplex is particularly useful and shows either reduced diastolic flow or flow reversal (Fig. 30.125). This gives a consequent increase in both the RI and PI. If the RI is greater than 0.8 and the PI greater than 1.6, these are strongly suggestive of acute rejection.

Renal scintigraphy is an alternative imaging modality. Serial examinations show perfusion initially to be normal but subsequent examinations will demonstrate decreasing renal perfusion with a prolonged excretory phase and a poor inhomogeneous nephrogram. Angiography has been used and demonstrates prolonged arterial opacification with multiple stenoses and occlusions but is rarely required.

Ciclosporin nephrotoxicity Ciclosporin is a major advance in immunosuppression in renal transplantation. Unfortunately, nephrotoxicity is a major side-effect and, as an early cause of graft dysfunction, has to be differentiated from ATN and acute rejection. It typically occurs with elevated serum levels, but as ciclosporin requirements vary widely between patients, levels serve only as a rough guide. There are no specific features either on imaging or biopsy.

Mechanical causes of graft failure

These can broadly be divided into vascular complications and obstructive complications (Fig. 30.122).

Vascular complications Early vascular complications are uncommon. Complete occlusion of the main renal artery is a rare cause of immediate anuria. It is usually observed when the anastomosis was technically difficult, usually because of multiple renal arteries. Segmental artery infarction is more common and

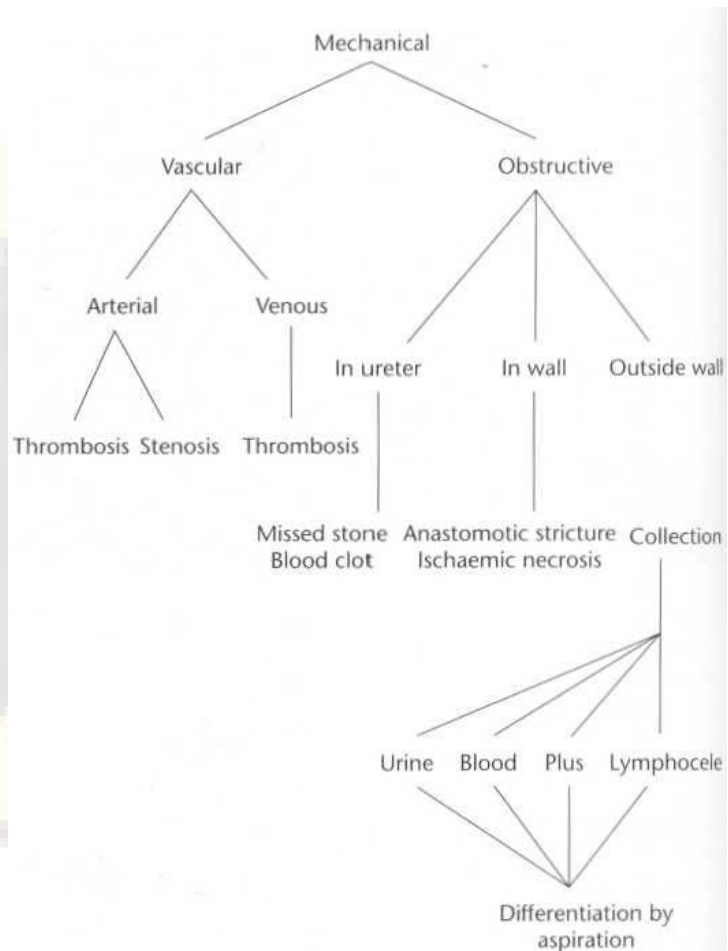


Fig. 30.122 Mechanical causes of renal failure.

can be due either to technical problems or to acute rejection. Diagnosis is usually made by colour/power Doppler imaging where there is global or segmental absence of perfusion. Confirmation has traditionally been with angiography but multi-slice spiral CT angiography is less invasive and quicker. Rapid diagnosis is the only potential chance of saving the graft with complete occlusions but is rarely successful.

Renal artery stenosis may occur at the anastomosis or within the graft and usually presents as a delayed cause of graft failure or hypertension. If stenoses are significant and are associated with hypertension or graft failure, they should be treated with renal artery stenting. If a renal artery stenosis presents in the early post-operative phase it is secondary to anastomotic problems at surgery and requires surgical correction (Fig. 30.123).

Other vascular problems Pseudoaneurysms, either due to percutaneous biopsy or faulty surgical technique, do occur and are picked up on colour Doppler imaging, where mixed arterial and venous pulsations are demonstrable within the mass. The majority spontaneously regress and are not a cause for graft failure. Arteriovenous fistulas have the same aetiology. Duplex demonstrates a high-velocity, low-resistance feeding artery on colour flow imaging. They may present with haematuria and are treated by embolisation if felt to be a cause of graft failure (Fig. 30.124).

Renal vein thrombosis This may be secondary to technical problems at the time of surgery, compression by adjacent collections, or secondary to the very slow flow associated with acute rejection.

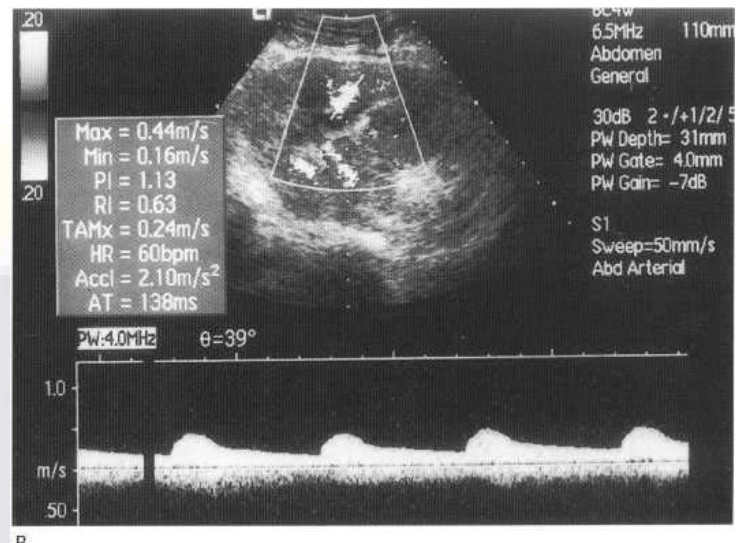
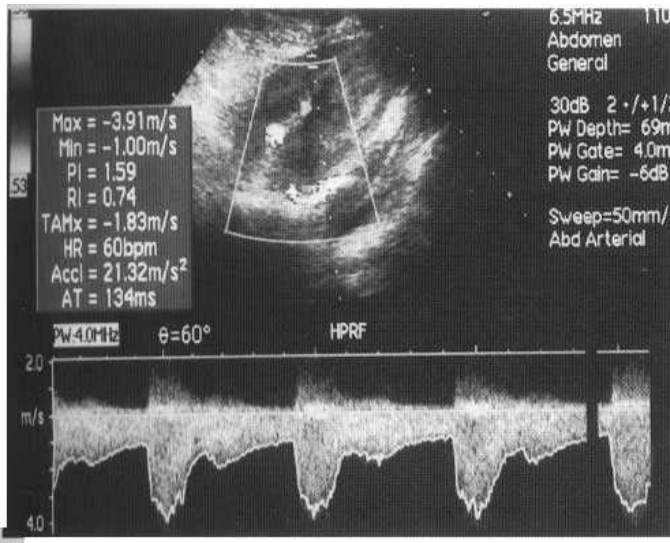


Fig. 30.123 Duplex demonstrates an increased and to turbulent flow at the origin of the renal artery (A) with associated damped flow at segmental level (B) indicating renal artery stenosis. This occurred early post-transplant and was secondary to anastomotic stricture confirmed at angiography (C).

this should be drained in the first instance. There should, however, be a low threshold for performing nephrostomy as there is a significant risk of rupture of the surgical ureteral anastomoses.

Early ureteral stenosis may occur. The majority are due to ureteral ischaemia with or without necrosis. They are therefore usually found at the ureterovesical anastomosis and require surgical treatment. More typically, stenosis occurs weeks or months after transplantation and can be secondary to ischaemia, injection or rejection. Treatment and diagnosis are as for early obstruction.

Fluid collections Fluid collections are common, occurring in nearly half the patients after surgery. The majority of fluid collections after transplant are, however, incidental findings on baseline ultrasound and require no intervention. When fluid collections are large, associated with increasing dilatation of the collecting

Clinical presentation is usually with an abrupt onset of renal dysfunction associated with pain over the graft and associated haematuria. Diagnosis can be made on duplex imaging. The graft appears very enlarged with loss of corticomedullary differentiation and subcapsular fluid collections. Colour flow imaging shows diminished cortical perfusion, absent venous flow and a duplex signal demonstrating a U-shaped pattern with reversal of diastolic arterial flow (Fig. 30.125).

Urinary obstruction Ureteral obstruction in the immediate post-operative period is due to unsuspected donor calculus, technical error, oedema, blood clot or perigraft fluid collection. A diagnosis of obstruction should be suggested by the demonstration of an increasing hydronephrosis on serial ultrasound scanning. A mild degree of dilatation of the renal pelvis is common and is probably due to denervation or vesicoureteric reflux, so a diagnosis cannot always be made on the initial scan. Serial scanning will, however, show progressive dilatation. If there is any uncertainty, a percutaneous nephrostogram can confirm the diagnosis and be followed by a nephrostomy if indicated. The most frequent cause is the presence of clots within the urinary tract, and bladder irrigation via the catheter should be performed before nephrostomy is considered. If the obstruction appears to be secondary to a collection,

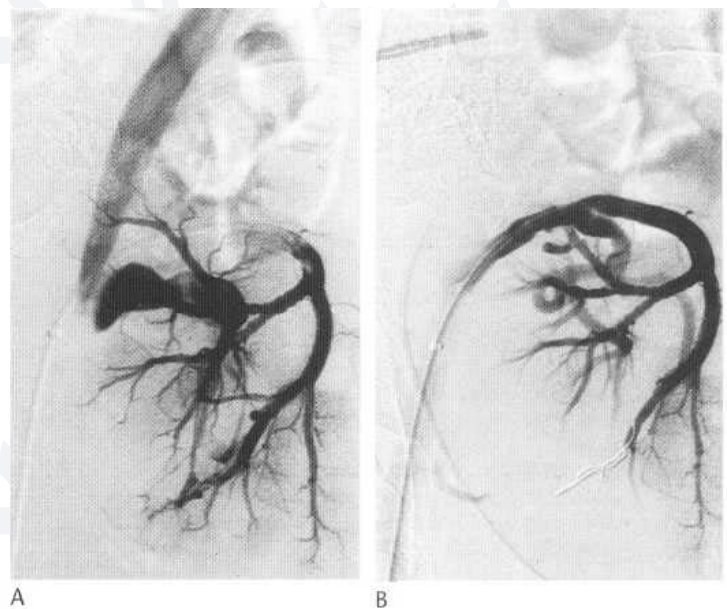


Fig. 30.124 (A) Selective angiography of the renal transplant demonstrates early iliac vein filling due to an arteriovenous fistula in the lower pole. (B) Supraselective embolisation with coils has occluded the arteriovenous fistula with very little infarction of renal cortex.

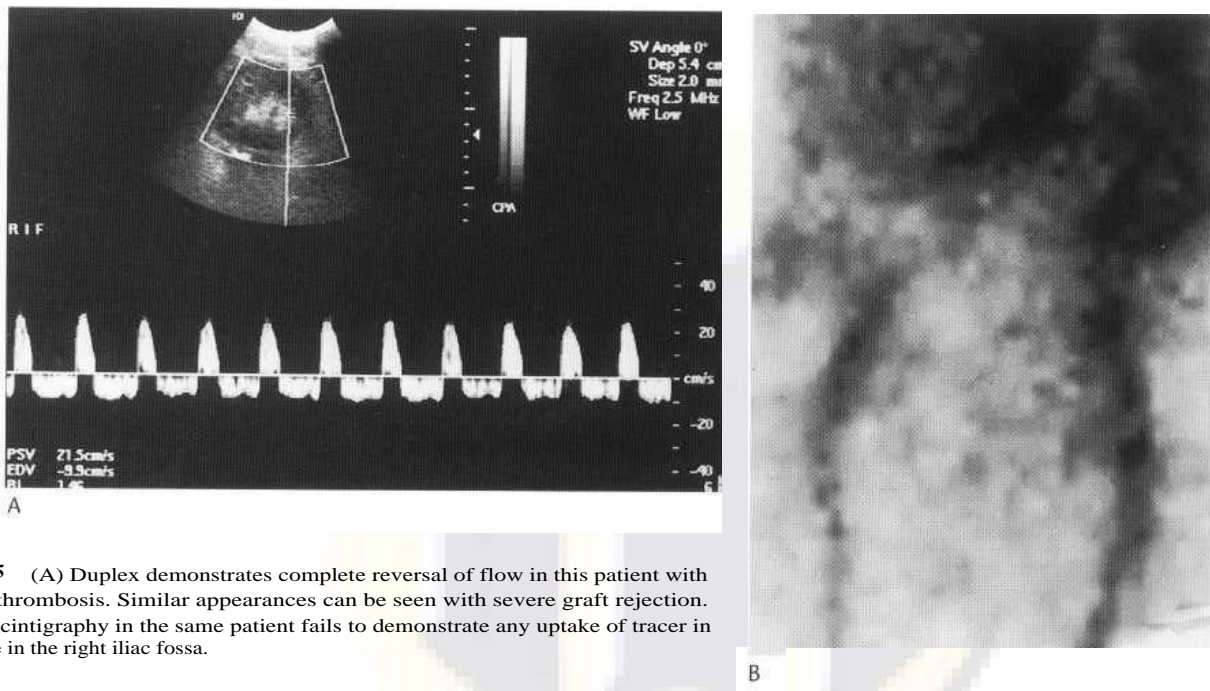


Fig. 30.125 (A) Duplex demonstrates complete reversal of flow in this patient with renal vein thrombosis. Similar appearances can be seen with severe graft rejection. (B) Renal scintigraphy in the same patient fails to demonstrate any uptake of tracer in the graft site in the right iliac fossa.

system or unexplained decline in renal function, ultrasound-guided aspiration is required. Simple drainage is all that is necessary unless frank pus is aspirated, when a drain should be inserted. The fluid should be sent for analysis to ascertain whether it is blood, urine, serum, lymph or pus. Recurrent collections, particularly abscess or lymphocele, usually require surgical intervention. Urinary extravasation in the presence of hydronephrosis or graft dysfunction requires further investigation to delineate the site of leak with contrast studies. Intravenous urography (if renal function allows) or retrograde cystography are the first-line investigations. If these are negative, percutaneous antegrade pyelography is performed to demonstrate the site of extravasation, either combined with nephrostomy or stent placement. Some leaks at the ureteroneocystostomy site may be managed by simple catheter drainage; however, open repair is frequently necessary. Haematomas are common and, unless causing graft compromise or increasing in size, are treated conservatively.

Lymphoceles can sometimes be problematical and recurrent. While these can be treated with percutaneous drainage, surgical fenestration into the peritoneal cavity is the most effective treatment.

REFERENCES AND SUGGESTIONS FOR FURTHER READING

- Bosniak, M. A. (1986) The current radiological approach to renal cysts. *Radiology*, **158**, 1-10.
- Bosniak, M. A. (1993) Problems in the radiologic diagnosis of renal parenchymal tumours. *Urologic Clinics of North America*, **20**, 217-230.
- Brown, M. A., Casola, G., Sirlin, C. B., Patel, N. Y., Hoyt, D. B. (2001) Blunt abdominal trauma: screening ultrasound in 2693 patients. *Radiology*, **218**, 352-358.
- Callahan, M. J. (2001) The drooping lily sign. *Radiology*, **219**, 226-228.
- Cass, A. S., Luxenberg, M., Gleich, P., Smith, C. S. (1986) Clinical indications for radiographic evaluation of renal trauma. *Journal of Urology*, **136**, 370-371.
- Charles, A. K., Vujanic, G. M., Berry, P. J. (1998) Renal tumours of childhood. *Histopathology*, **32**, 293-309.
- Charnsangavej, C. (1991) Lymphoma of the genitourinary tract. *Radiologic Clinics of North America*, **28**, 865-877.
- Choyke, P. L., Filling-Katze, M. R., Shawker, T. H., et al (1990) Von Hippel-Lindau disease: radiologic screening for visceral manifestations. *Radiology*, **174**, 815-820.
- Dal] Palma, L., Pozzi-Mucelli, F., Ene, V. (1999) Medical treatment of renal and perirenal abscesses: CT evaluation. *Clinical Radiology*, **54**, 792-797.
- Dalrymple, N. C., Casford, B., Raiken, D. P., Elsass, K. D., Pagan, R. A. (2000) Pearls and pitfalls in the diagnosis of ureterolithiasis with unenhanced helical CT. *Radiographics*, **20**, 439-447.
- Daneman, A., Alton, D. J. (1991) Radiographic manifestations of renal anomalies. *Radiologic Clinics of North America*, **29**, 351-363.
- Davidson, A. J., Choyke, P. L., Hartman, D. S., Davis, Jr. C. J. (1995) Renal medullary carcinoma associated with sickle cell trait. *Radiology*, **195**, 83-85.
- Evans, J. C., Curtis, J. (2000) The radiological appearances of tuberous sclerosis. *British Journal of Radiology*, **73**, 91-98.
- Federle, M. P. (1989) Evaluation of renal trauma. In: Pollack, H. M. (ed.) *Clinical Urography*, pp. 1422-1494. Philadelphia: Saunders.
- Fowler, C., Reznick, R. (2001) The indeterminate renal mass. *Imaging*, **13**, 27-43.
- Geller, E., Smergel, E. M., Lowry, P. A. (1997) Renal neoplasms of childhood. *Radiologic Clinics of North America*, **35**, 1391-1413.
- Greenwell, T. J., Woodhams, S., Denton, E. R. M., Mackenzie, A., Rankin, S. C., Popert, R. (2000) One year's clinical experience with unenhanced spiral computed tomography for the assessment of acute loin pain suggestive of renal colic. *British Journal of Urology International*, **85**, 632-636.
- Guinan, E., Saffrin, R., Stuldreher, D., Frank, W., Rubinstein, M. (1995) Renal cell carcinoma: comparison of the TNM and Robson stage groupings. *Journal of Surgical Oncology*, **59**, 186-189.
- Kabala, J. E., Gillatt, D. A., Persad, R. A., Penry, J. B., Gingell, J. C., Chadwick, D. (1991) Magnetic resonance imaging in the staging of renal cell carcinoma. *British Journal of Radiology*, **64**, 683-689.
- Kabala, J. E., Shield, J., Duncan, A. (1992) Renal cell carcinoma in childhood. *Paediatric Radiology*, **22**, 203-205.
- Kawashima, A., Sandler, C. M., Corl, F. M., et al (2001) Imaging of renal trauma: a comprehensive review. *Radiographics*, **21**, 557-574.
- Kawashima, A., Sandler, C. M., Ernst, R. D., Tamm, E. P., Goldman, S. M., Fishman, E. K. (2000) CT evaluation of reno-vascular disease. *Radiographics*, **20**, 1321-1340.
- Kawashima, A., Sandler, C. M., Goldman, S. M. (2000) Imaging in acute renal infection. *British Journal of Urology International*, **86**(Suppl. 1), 70-79.
- Ledcr, R. A., Dunnick, N. R. (1990) Transitional cell carcinoma of the pelviccalyces and ureter. *American Journal of Roentgenology*, **155**, 713-722.

- Levine, E. (1994) Acute renal and urinary tract disease. *Radiologic Clinics of North America*, 32, 989-1001.
- Levine, E. (1995) Renal cell carcinoma: clinical aspects, imaging diagnosis and staging. *Seminars in Roentgenology*, 30, 128-148.
- Loneragan, G. J., Martinez-Leon, M. I., Agrons, G. A., Montemarano, H., Suarcz, E. S. (1998) *Radiographics*, 18, 947-968.
- Loneragan, G. J., Rice, R. R., Suarcz, E. S. (2000) Autosomal recessive polycystic disease: radiologic-pathologic correlation. *Radiographics*, 20, 837-855.
- Lowe, L. H., Isuani, B. H., Heller, R. M., et al (2000) Paediatric renal masses: Wilms tumour and beyond. *Radiographics*, 20, 1585-1603.
- McAlinden, P., Chan, O. (2001) Imaging of renal trauma. *Imaging*, 13, 44-59.
- Mcgahan, J. P., Richards, J. R., Jones, C. D., Gerscovich, E. O. (1999) Use of ultrasonography in the patient with acute renal trauma. *Journal of Ultrasound in Medicine*, 18, 207-213.
- Maxwell, M. H., Blicifer, K. H., Franklin, S. S., Varady, P. O. (1972) Cooperative study of renovascular hypertension. Demographic analysis of the study. *AMA*, 220, 195-200.
- Miller, O. F., Kane, C. J. (1999) Time to stone passage for observed ureteral calculi: a guide for patient education. *Journal of Urology*, 162, 688-691.
- Minis, S. E. (1989) Diagnostic imaging of the urinary system following blunt trauma. *Clinical Imaging*, 13, 269-280.
- Mirvis, S. E. (1996) Trauma. *Radiologic Clinics of North America*, 34, 1225-1257.
- Mitsumori, A., Yasui, K., Akaki, S., et al (2000) Evaluation of crossing vessels in patients with ureteropelvic junction obstruction by means of helical CT. *Radiographics*, 20, 1383-1393.
- Moudouni, S. M., Patard, J. J., Manunta, A., Guiraud, P., Guille, F., Lobel, B. (2010) A conservative approach to major blunt renal lacerations with urinary extravasation and devitalised renal segments. *British Journal of Urology International*, 87, 290-294.
- Nicolaisen, G. S., McAninch, J. W., Marshall, G. A., Bluth, R. F., Carroll, P. R. (1985) Renal trauma: re-evaluation of the indicators for radiographic assessment. *Journal of Urology*, 133, 183-187.
- Nikken, J. J., Krestin, X. X. (2000) Magnetic resonance in the diagnosis of renal masses. *British Journal of Urology International*, 86(Suppl. 1), 58-69.
- Parienty, R. A., Prudel, J., Parienty, I. (1985) Cystic renal cancer. CT characteristics. *Radiology*, 157, 741-744.
- Rankin, S. C., Webb, J. A. W., Reznick, R. H. (2000) Spiral computed tomography in the diagnosis of renal masses. *British Journal of Urology International*, 86(Suppl. 1), 48-57.
- Reznick, R. (1998) Renal tumours. In *Imaging in Oncology*. pp. 191-214. Oxford: Isis.
- Ritchie, W. W., Whitely, V. C., Glocheski, S. K., Cook, D. E. (1988) Evaluation of azotaemic patients: diagnostic yield of initial ultrasound examination. *Radiology*, 167, 245-247.
- Robson, C. J., Churchill, B. M., Anderson, W. (1969) The results of radical nephrectomy for renal cell carcinoma. *Journal of Urology*, 101, 297-301.
- Roy, C., Pflieger, D. D., Tuchmann, C. M., Lang, H. H., Saussinc, C. C., Jacgmin, D. (2001) Emphysematous pyelitis: findings in five patients. *Radiology*, 218, 647-650.
- Sagalowsky, A. I., McConnell, J. D., Peters, P. C. (1983) Renal trauma requiring surgery: an analysis of 185 cases. *Journal of Trauma*, 23, 128-131.
- Shuman, W. P. (1997) CT of blunt abdominal trauma in adults. *Radiology*, 205, 297-306.
- Smith, R. C., Verga, M., McCarthy, S., Rosenfiel, A. T. (2000) Diagnosis of acute flank pain. Value of unenhanced CT. *American Journal of Roentgenology*, 166, 97-101.
- Smith, S. L., Somers, J. M., Broderick, N., Halliday, K. (2000) The role of the plain radiograph and renal tract ultrasound in the management of children with renal tract calculi. *Clinical Radiology*, 55, 708-710.
- Soulez, G., Oliva, V. L., Turpin, S., Lambert, R., Nicolet, V., Therasse, E. (2000) Imaging of renovascular hypertension: respective values of renal scintigraphy, renal Doppler US and MR angiography. *Radiographics*, 20, 1355-1368.
- Spencer, B. A., Wood, B. J., Dretler, S. P. (2000) Helical CT for renal colic—a time for change of practice in the new millennium? *Urologic Clinics of North America*, 27, 231-241.
- Spencer, J. A., Tomlinson, A. J., Weston, M., Lloyd, S. N. (2000) Early report: comparison of breath-hold MR excretory urography. Doppler ultrasound and isotope renography in evaluation of symptomatic hydronephrosis in pregnancy. *Clinical Radiology*, 55, 446-453.
- Strandness, D. E. (1994) Duplex imaging for the detection of renal artery stenosis. *American Journal of Kidney Diseases*, 24, 674-678.
- Studer, U. E., Scherz, S., Scheidegger, J. (1990) Enlargement of regional lymph nodes in renal cell carcinoma is often not due to metastases. *Journal of Urology*, 144, 243-245.
- Tomaszewski, J. E. (1995) The pathology of renal tumours. *Seminars in Roentgenology*, 2, 116-127.
- Urban, B. A., Fishman, E. K. (2000) Renal lymphoma: CT patterns with emphasis on helical CT. *Radiographics*, 20, 197-212.
- Van der Hulst, V. P. M., Van Baalen, J., Kool, L. S., et al (1996) Renal artery stenosis: endovascular flow wire study for validation of Doppler US. *Radiology*, 200, 165-168.
- Vivas, L., Nicholas, A. I., Velazquez, P., Elduayen, B., Fernandez-Villa, T., Martinez-Cuesta, A. (2000) Retroperitoneal fibrosis: typical and atypical manifestations. *British Journal of Radiology*, 73, 214-222.
- Wagner, B. J., Wong-You-Cheong, J. J., Davis, C. J. (1997) Adult renal hamartomas. *Radiographics*, 17, 155-169.
- Webb, J. (2000) Ultrasonography and Doppler studies in the diagnosis of renal obstruction. *British Journal of Urology International*, 86(Suppl. 1), 25-32.
- Working Party on Renovascular Hypertension (1987) Detection, evaluation and treatment of renovascular hypertension. *Archives of Internal Medicine*, 147, 820-829.
- Yousem, D., Gatewood, O. M. B., Goldman, S. M., Marshall, F. F. (1988) Synchronous and metachronous transitional cell carcinoma of the urinary tract: prevalence, incidence and radiographic detection. *Radiology*, 167, 613-618.



نشر الکترونیکی
موسسه انتشاراتی
نوردانش

THE BLADDER AND PROSTATE

Julian E. Kabala

with contributions from Gary N. Sibley, Jeremy P.R. Jenkins and Paul Hulse

THE BLADDER

Congenital lesions

Agensis Bladder agenesis is extremely rare and generally associated with urethral agenesis. There is usually marked upper tract dilatation and renal dysplasia.

Bladder duplication This is also rare and may be associated with urethral duplication. Each bladder receives the drainage from the ureter on that side. There are usually other associated anomalies of the genitourinary and/or gastrointestinal tract. In incomplete duplication the two moieties are fused caudally, there is only one urethra and associated anomalies are less common. Variations include partial or complete division of the bladder by a septum, which may be sagittal or transverse (hourglass bladder).

Bladder extrophy This is a rare condition in which the bladder is open anteriorly. It varies in severity from a small opening in the anterior abdominal wall to complete absence of the anterior bladder wall and overlying abdominal wall, which may be associated with exposure of bowel loops. There is usually separation of the symphysis pubis and there may be associated spinal and anorectal anomalies but with normal upper urinary tracts. There is a male to female predilection of 3:1 and a strong association with epispadias. Traditional treatment was implantation of the ureters into the sigmoid (ureterosigmoidostomy; Fig. 31.1) but this has been abandoned due to the high rate of complications of this procedure (infection, chronic pyelonephritis with progressive renal damage, adenocarcinoma at the anastomotic site and hyperchloaemic acidosis). Where bladder reconstruction is not possible a continent reservoir such as a Mitrofanoff procedure is performed, which preserves renal function. Although these procedures avoid anastomotic/colonic neoplasia there remains a high risk of carcinoma (usually adenocarcinoma) developing in the bladder or bladder remnant, which may be as high as 700 times the normal expected rate.

Urachal anomalies The fetal bladder tapers superiorly into the urachus, which in turn communicates with the allantois at the level

of the umbilicus. It closes around the middle of the second trimester, becoming the fibrous median umbilical ligament. It lies extraperitoneally between the transversalis fascia anteriorly and the peritoneum posteriorly. Varying degrees of failure of closure and obliteration of the urachus have been observed. They may be classified into four types: patent urachus (50%), umbilical-urachal sinus (15%), vesicourachal diverticulum (5%) and urachal cyst (30%).

Urachal remnants are usually lined with transitional cell epithelium, although up to one-third show columnar metaplasia. Patent urachus presents at an early age with urine leakage at the umbilicus. It is easily demonstrated with sinography or cystography. It may also be demonstrated as a fluid-filled tubular structure on ultrasound, CT or MRI. It



Fig. 31.1 Full-length film from an IVU series on a patient with bladder extrophy treated with ureterosigmoidostomies. There is characteristic separation of the symphysis pubis. The ureters have been anastomosed to the sigmoid colon close to the midline. Reflux has predisposed to dilatation of the distal ureters (black arrows) and the left kidney shows changes of chronic pyelonephritis with cortical loss and calyceal clubbing. Contrast-opacified urine has drained into the sigmoid colon and passed forwards into the rectum and retrogradely into the descending colon (white arrows).

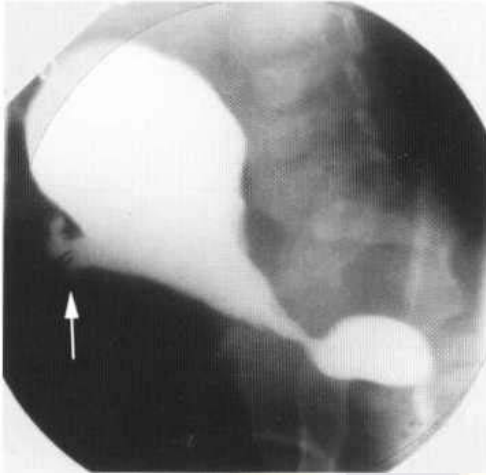


Fig. 31.2 Cystogram on an infant with prune-belly syndrome. There is a typical capacious flaccid bladder and absence of the prostate. A urachal diverticulum is demonstrated anteriorly (arrow).

is often associated with lower urinary tract anomalies such as posterior urethral valves, urethral atresia or diverticula.

The other anomalies are usually asymptomatic but may present at any age with infection. On rare occasions they are the origin of urachal carcinoma. Umbilicourachal sinus (urachus patent at the umbilicus but not at the bladder) may present with infection and/or periodic discharge. Sinography shows a blind-ending sinus and this also may be seen as a fluid-filled tubular structure on cross-sectional imaging.

Vesicourachal diverticulum (5% of urachal anomalies) is most often diagnosed incidentally on CT or ultrasound performed for some other condition. It sometimes presents with urinary tract infection and there is a strong association with bladder outflow obstruction and prune-belly syndrome (Fig. 31.2). It may predispose to calculus formation.

Urachal cyst is most often seen in the lower third of the urachal track. It is usually small but may enlarge and present as an abdominal mass. The commonest presentation is when supervening infection occurs. Characteristic appearances of a cyst are seen on ultrasound, CT or MRI, sometimes with delicate peripheral calcification (Fig. 31.3). Debris and increased echogenicity (or density) is seen in the presence of infection, often with wall thickening.

Prune-belly syndrome This is a syndrome of variable severity in which the anterior abdominal musculature is deficient. The upper tracts are dilated, with dysplastic kidneys. Classically the prostate

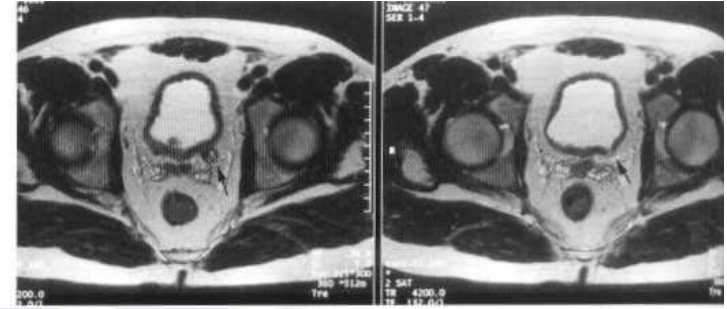


Fig. 31.4 MRI scan (transverse T₂-weighted images) showing a small left paraureteric congenital bladder diverticulum (arrows).

is deficient and the bladder is dilated and contracts poorly (Fig. 31.2). It is further described in Chapter 30.

Diverticula These are usually acquired (described below) but are occasionally congenital. In both cases they have no muscle in the wall, increase in size during bladder emptying and may become large. Congenital diverticula are usually narrow necked and originate just posterolateral to the ureteric orifice (paraureteric diverticula; Fig. 31.4). They may be asymptomatic or present with urinary tract infections. Occasionally they are large enough to obstruct the urethra or the meter.

Prostatic cysts and adnexal cysts The commonest cystic lesions of the prostate are acquired in association with benign prostatic hyperplasia and are located in the central gland. Occasionally, acquired isolated prostatic retention cysts are seen within any area of the gland. Acquired ejaculatory duct cysts are also seen within prostatic tissue at or close to the midline. They may be associated with calculi and ipsilateral seminal vesicle obstruction.

Congenital cysts of this area are uncommon but may be associated with infertility and/or other urinary tract anomalies. Congenital prostatic cysts may lie anywhere within the prostate but are often laterally placed. Utricular cysts originate from the verumontanum as a result of utricular dilatation. They lie close to the midline within the prostate and may be associated with hypospadias and cryptorchidism. Cysts may also originate from müllerian duct remnants. They lie adjacent to the prostate and may become large enough to impinge on the trigone and vesicoureteric junction. They may contain calculi and may be associated with ipsilateral renal agenesis. Seminal vesicle cysts (Fig. 31.5) may also be associated with ipsilateral urinary tract anomalies, including renal agenesis. They may be associated with calculi, infection (epididymitis) and occasionally extremely large size with mass effect.

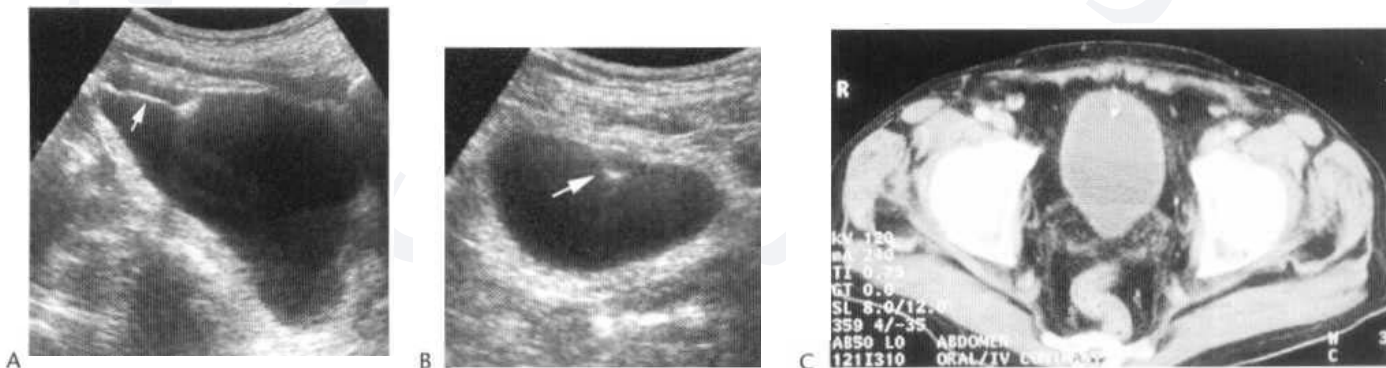


Fig. 31.3 Longitudinal (A) and transverse (B) ultrasound showing a urachal cyst as a thin-walled cylindrical echo-free area (arrow). The CT (C) demonstrates analogous features with a small area of calcification.

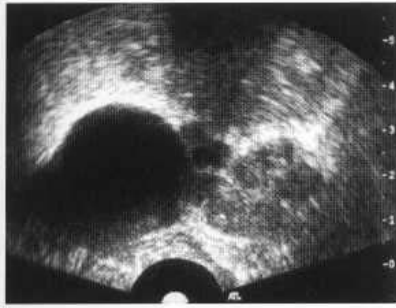


Fig. 31.5 Transverse image from a transrectal ultrasound examination showing a normal left seminal vesicle and a large right seminal vesicle cyst.

Inflammatory lesions

Acute bacterial cystitis Acute bacterial cystitis is extremely common and usually associated with Gram-negative coliforms, particularly *Escherichia coli*, *Klebsiella* and *Pseudomonas* species. It is seen most frequently in young and middle-aged adult females and may be associated with sexual activity. In these patients there is almost always a normal urinary tract, and investigation of the first episode of infection is unnecessary unless there are complicating features (childhood infection suggesting reflux nephropathy, associated pyelonephritis or analgesic abuse, unusual or persistent infecting organism etc). It is relatively uncommon in males of this age but is often seen in the older male

investigation of the first episode may therefore be appropriate. Bacterial cystitis itself usually has no imaging features unless it is severe, when there may be thickening and irregularity or nodularity of the mucosa apparent on IVU or ultrasound due to mucosal oedema. Ultrasound may also show some reduction in echogenicity of the mucosa and there may be some echogenic debris within the lumen of the bladder (Fig. 31.6). In extremely severe cases the mucosa may appear of reduced density on CT.

Chronic cystitis Chronic cystitis may result in a number of structural and pathological changes. There may be gross wall thickening, reduction in bladder capacity and the development of vesicoureteric reflux and/or ureteric dilatation. Histologically, clusters of hyperplastic urothelial cells may develop in the submucosa. These may progress to central necrosis, giving a pseudocystic appearance (cystitis cystica), which may be associated with a glandular appearance of the cell clusters (cystitis glandularis). These conditions may be regarded as a potentially reversible mucosal instability. An alternative reaction to chronic cystitis is the development of squamous metaplasia, which may be associated with white patches (leucoplakia), most commonly seen on the trigone and bladder base.



Fig. 31.6 Transverse ultrasound image showing bladder wall thickening and echogenic clumps of inflammatory debris within the urine in a patient with severe cystitis.

Emphysematous cystitis This rare condition is associated with diabetes mellitus and is usually due to *E. coli* (sometimes aerogenes or *Candida* sp., when there may be an associated fungus ball within the bladder). Mural and sometimes luminal gas develops; this appears linear or multicystic on imaging. Gas may ascend into the ureters and pelvic/lyceal systems.

Viral infection This is most often due to adenovirus 11 in childhood and influenza A in adults. It may be quite aggressive, leading to haematuria, dysuria and reduced bladder capacity, with multiple small polypoidal lesions of the mucosa visible on ultrasound or contrast examinations.

Malakoplakia Malakoplakia is thought to be a mild form of chronic granulomatous disease (a defect of cell-mediated immunity) in which there is defective lysosome function leading to a chronic ineffective response to urinary tract infections. It may affect any part of the urinary tract. It produces 5-10 mm diameter sessile plaques, particularly on the bladder base and in the lower ureters, where they may provoke stricturing.

Focal cystitis Focal cystitis may develop in response to chronic irritation, for example by a calculus, catheter or other foreign body or in association with paravesical disease, particularly diverticulitis, pelvic abscess and Crohn's disease. The resultant localised mural swelling may simulate a carcinoma (Fig. 31.7).

Tuberculosis This usually arises due to haematogenous spread from the lungs, rarely from the gastrointestinal tract or skin. It represents 10-20% of genitourinary tuberculosis and is virtually always associated with renal tuberculosis. It produces irregular mural thickening which subsequently proceeds to fibrosis (Fig. 31.8). This results in reduction in the bladder capacity and

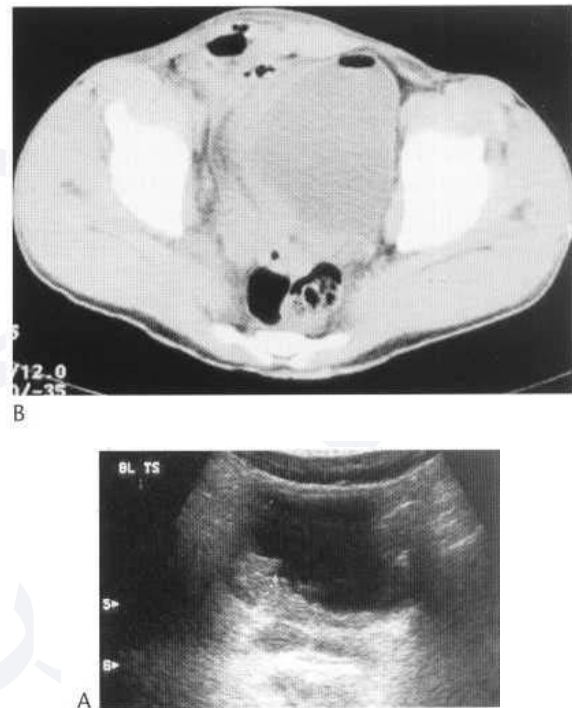


Fig. 31.7 Transverse ultrasound image (A) showing gross focal thickening of the right posterolateral bladder wall in a patient with acute Crohn's disease. Similar features are seen on CT (B), which also shows adherent swollen small bowel. An enterovesical fistula is present with gas seen in the bladder.

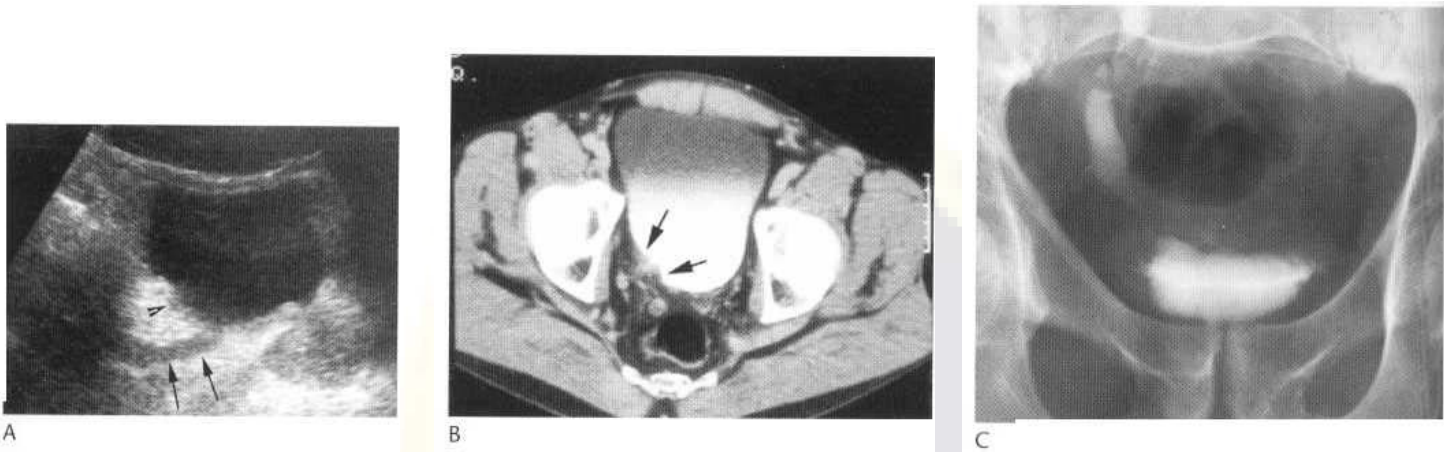


Fig. 31.8 Longitudinal ultrasound of the bladder (A) showing localised wall thickening in tuberculous cystitis (arrowhead) and dilated distal ureter (arrows). Similar heaped-up appearance of the bladder mucosa is seen on CT (B) around the ureteric orifice. The IVU (C) also demonstrates the localised bladder wall thickening, narrowing of the ureteric orifice and dilatation of the distal ureter.

may obstruct the ureters. Alternatively, traction on the ureteric orifices may lead to vesicoureteric reflux. Calcification is present in approximately 10%, especially where there is extensive tuberculosis throughout the urinary tract. There may be associated prostatic and seminal vesicle calcification.

Schistosomiasis Schistosomiasis (bilharzia) affects an estimated 200 million people worldwide. Infection is common in the tropics, particularly subSaharan Africa and the Middle East. This condition is due to a group of protozoan flukes, of which three species in particular affect humans: *Schistosoma haematobium*, *S. mansoni* and *S. japonicum*. *S. haematobium* particularly involves the genitourinary tract. Humans are the definitive host for the parasite and become infected by exposure to fresh water containing free-swimming schistosome cercariae, which invade the skin and enter the venous system. The larvae then migrate through the lungs into the systemic and subsequently portal circulation, and then into the veins of the bladder, prostate and lower gastrointestinal tract, where they mature. The adult female lays her eggs in the bladder wall. The eggs are released into the urine. The eggs hatch once

they have reached fresh water and infect the intermediate host, a freshwater snail, which in turn is responsible for the release of the infective larval stage. There is an acute pyrexial stage and a chronic stage. In endemic areas the disease is limited to individuals who are heavily infected. Although rare in the UK, occasional cases are seen in immigrants and increasingly in travellers (with more readily available adventure and long-distance holidays), when the disease is often acute.

In the bladder wall the eggs provoke oedema and granuloma formation. At this stage cystography may show flat polypoidal swellings. Clinical features of the acute stage include malaise, fever and dysuria. Haematuria may be seen but becomes more of a feature as the disease progresses. Ultrasound may be normal in early or mild cases but often shows wall thickening (up to 1 cm or more) and single or multiple polypoidal lesions, which may be sessile or wave-like and may protrude into the lumen of the ureter. Changes are most marked in the region of the bladder base and trigone. Later, fibrosis and calcification develops, which appears on plain films (visible in 50% of patients) and CT as eggshell or linear areas of calcification in the submucosa of the bladder and the distal ureters (Fig. 31.9). It may involve the entire bladder, particularly the base. The calcification is often fairly delicate but may become dense. In contrast to tuberculosis, bladder capacity and contractility are surprisingly well preserved.

The condition predisposes to bladder cancer of any histological sort, particularly squamous cell carcinoma. The development of tumour may be associated with interruption of the line of bladder wall calcification.

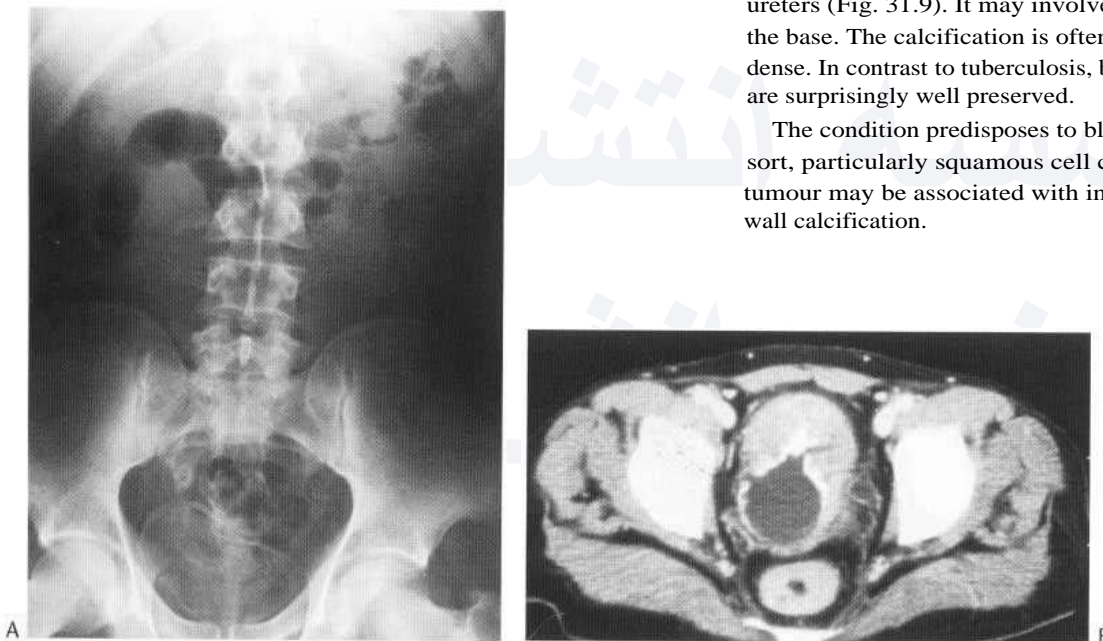


Fig. 31.9 Plain film (A) showing linear calcification along the bladder wall and distal left ureteric walls. CT (B, different patient) is highly sensitive for the demonstration of bladder wall calcification and will also show the soft-tissue wall thickening which may be gross and (as here) associated with rectal wall thickening. (Courtesy of Dr Shadley Fataar of the Royal Hospital, Muscat, Oman.)

The ureters are often involved and may show linear calcification (15% cases) and multifocal strictures with proximal dilatation. The distal ureter is affected first, but as the disease progresses the entire ureter may develop a beaded appearance. Other parts of the lower genitourinary tract are occasionally affected (urethra, prostate, vagina, cervix and uterus).

Haemorrhagic cystitis This condition develops following cyclophosphamide therapy. It may be gross and fulminant and appear within days. Thrombus is often visible within the lumen of the bladder and the wall becomes nodular. Later the bladder becomes contracted. Radiotherapy is well recognised as a cause of cystitis, which may also become haemorrhagic, sometimes intractably so.

Interstitial cystitis This condition is usually idiopathic but may be associated with atopy. It is characteristically seen in females and presents with suprapubic pain, frequency and urgency. It may appear with a number of autoimmune conditions, including polyarteritis nodosa, systemic lupus erythematosus and rheumatoid arthritis.

There are no imaging features in the early stages but later on the bladder becomes contracted and may have a nodular wall.

Encrustation cystitis Inflammatory lesions of the bladder wall severe enough to cause areas of necrosis may progress to areas of dystrophic calcification. This is particularly likely to occur when the urine has been alkalinised by the presence of urea-splitting organisms, particularly *Proteus* species, the higher pH predisposing to the precipitation of calcium. The resultant calcification may be focal or diffuse, depending on the distribution of the necrosis, and may be linear, coarse or nodular. It is likely to regress with resolution of the underlying cystitis. It is rare with straightforward bacterial cystitis and is more characteristically seen with haemorrhagic cystitis.

Mechanical problems of the bladder wall

Trabeculation On contrast films the normal bladder wall has a somewhat ridged internal aspect when virtually empty, due to the natural looseness of the mucosa. This pattern may be seen in exaggerated form even when the bladder is well filled, when the mucosa is intensely swollen (severe cystitis) or the underlying detrusor muscle strands are prominent. This latter condition occurs with bladder outflow obstruction and in the neurogenic bladder and is currently believed to be connective tissue infiltration of the muscle rather than hypertrophy. The bladder wall often appears thickened and its inner aspect shows an undulating or ridged pattern, features which are well seen on ultrasound (Fig. 31.10). Although bladder wall thickness may be within normal limits in mild outflow obstruction, it often rises with more severe and chronic disease. The mean bladder wall thickness on ultrasound is around 3.3 mm in males and 3.0 mm in females (maximum 7.6 mm in both). This does not change significantly with the degree of bladder filling.

The commonest cause of bladder outflow obstruction is benign prostatic hyperplasia. Other causes include prostatic neoplasia, bladder neck stenosis and urethral strictures and occasionally calculi. There is often a substantial postmicturition volume. Urodynamic studies may show high intravesical filling pressure (in



Fig. 31.10 Longitudinal ultrasound of the bladder showing wall thickening and trabeculation (replacement of normal smooth inner aspect by regularly undulating appearance).

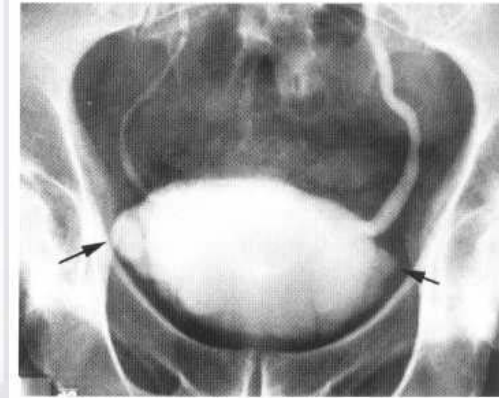


Fig. 31.11 Bladder view from an IVU series in a patient with bladder outflow obstruction due to prostatic hyperplasia. The bladder is trabeculated and sacculi (arrows) are beginning to develop. The distal ureters are showing some elevation in association with the prostatic enlargement and the bladder wall disease has provoked some fullness of the distal left ureter.



Fig. 31.12 Longitudinal ultrasound of the bladder showing gross sacculation, best seen along the posterior wall, in a patient with severe longstanding outflow obstruction.

excess of 15 cm HO). The prostate may be delectably enlarged, bulging into the bladder base. The distal ureters are often elevated and there may be some fullness of one or other ureter and sometimes the ipsilateral pelviccalyceal system, presumably related to bladder wall thickening interfering with efficient drainage through the intramural ureter (Fig. 31.11). In severe outflow obstruction sacculi and later diverticula may develop (Fig. 31.12).

Diverticula These are focal herniations of the urothelium and submucosa through weak sites in the bladder wall. Most are acquired due to chronic elevation of the intravesical pressure associated with bladder outflow obstruction or neurogenic bladder. They are therefore most frequently encountered in male patients above the age of 60. In the early stages, multiple (sometimes numerous) small protrusions of the bladder lumen appear between the trabeculae (sacculations). As they enlarge above 2 cm they become defined as diverticula (Fig. 31.13). Interestingly, usually only a small number of diverticula develop beyond this stage, presumably because they act to moderate the intravesical

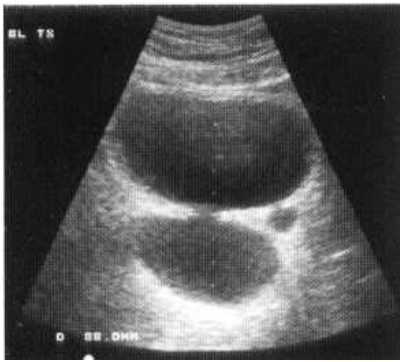


Fig. 31.13 Transverse ultrasound image of the bladder showing two posterior-lying diverticula.

pressure by filling with urine during bladder emptying. This may lead to the classical symptom of double micturition; when the patient empties the bladder a significant amount of urine is stored in the diverticulum, which then empties back into the bladder, causing a desire to micturate almost immediately after the first micturition. They are most frequently found close to the ureteric orifices (Fig. 31.14), and when large may displace both the bladder and the ureter (usually medially, occasionally laterally). They may provoke vesicoureteric reflux but rarely obstruct the ureter. Contrast examinations, ultrasound, CT and MRI will show a smooth inner wall of the diverticulum, often associated with a trabeculated bladder. They may become larger than the bladder itself. They are connected to the bladder by a narrow neck, which is often remarkably difficult to demonstrate. They frequently lie in among bowel loops, and preoperative assessment with CT is often desirable (Fig. 31.15). They are prone to calculus formation, infection and occasionally malignancy (Fig. 31.16).

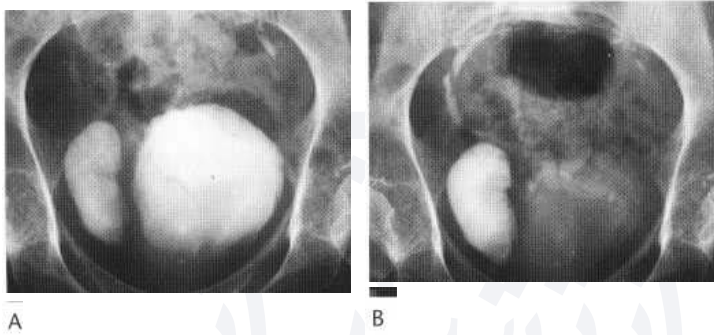


Fig. 31.14 Bladder image from an IVU examination showing a large right-sided diverticulum (A). On the postmicturition film the bladder has emptied but the narrow necked diverticulum remains contrast filled (B).



Fig. 31.15 CT scan demonstrating a large right posterolateral diverticulum.

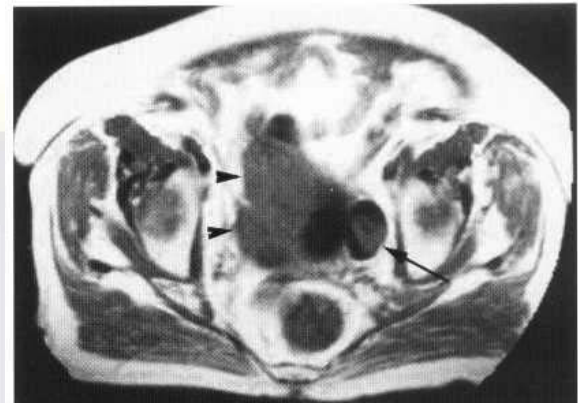


Fig. 31.16 T₁-weighted MRI showing a large right-sided bladder carcinoma (arrowheads) and a small left-sided diverticulum (arrow) containing a further deposit of carcinoma.

Cystocele This is a condition of abnormal bladder descent with prolapse into the vagina. Usually the bladder and urethra are involved but occasionally only the trigone prolapses. Descent of the bladder and urethra is associated with stress incontinence. Severe cases may be associated with bladder outflow obstruction or distal ureteric obstruction. The traditional means of diagnosing this condition is with the lateral standing cystogram, which is now performed as part of urodynamic studies. Descent of any part of the bladder that reaches the inferior pubic rami during straining indicates a cystocele.

Bladder herniation At least 95% of bladder herniation is into the inguinal or femoral canals, the former roughly twice as often as the latter. They are usually small (2-3 cm or so) and therefore asymptomatic (but vulnerable to damage at herniorrhaphy). They occasionally become big enough to act like a large diverticulum and result in double micturition, sometimes with the patient actively assisting emptying by pressing over the hernia. They generally have a narrow neck and fill poorly on routine contrast images and are therefore best seen on prone or erect films (Fig. 31.17).

Fistulas Fistulas from the bladder into the gastrointestinal tract are not uncommon. They are most frequently colovesical- and due to diverticulitis. Carcinoma of the large bowel (usually of the rectosigmoid region) is an important cause. Crohn's disease of the caecum is an occasional cause, carcinoma of the bladder a rare one. Presentation is with pneumaturia, faecuria and/or urinary



Fig. 31.17 Full-length film showing right-sided inguinal herniation of the distal right ureter and part of the bladder.

tract infections. The fistulous track may be demonstrated with cystoscopy or contrast studies, usually cystography or double-contrast barium enema, occasionally IVU. Cystoscopy, cystography and IVU may also demonstrate focal bladder wall thickening and irregularity due to the underlying disease. All these modalities, however, will miss at least 40% of fistulas. This is not necessarily important, as the diagnosis is largely based on the history and investigations are mainly directed towards diagnosing and staging the underlying cause. CT is often indicated for these purposes and may show a mass of tumour or inflammatory tissue, focal wall thickening and air within the bladder (Fig. 31.7). Gas is also seen in the bladder with recent instrumentation or catheterisation and infection with gas-forming organisms. These causes are usually easily distinguished clinically. Oral and rectal contrast are useful but intravenous contrast may be confusing and is best avoided in the investigation of vesicogastrointestinal fistulas.

Vesicoenteric fistulas are uncommon, usually associated with Crohn's disease and therefore predominantly right-sided. Small-bowel follow-through may demonstrate the fistula.

Vesicovaginal (Fig. 31.18) (*and ureterovaginal*) *fistulas* are usually due to surgery, mostly radical pelvic surgery for gynaecological malignancy. Less commonly they are found spontaneously in association with pelvic malignancy (cervix or bladder) and rarely due to obstetric injury, radiotherapy, long-term catheterisation, tuberculosis or schistosomiasis. Presentation is with continuous incontinence. IVU or cystography, ideally with lateral images, usually easily make the diagnosis.

Bladder neoplasia

Benign tumours

These are rare and usually mesenchymal in origin. These include leiomyoma, lipoma, neurogenic tumours (phaeochromocytoma and neurofibroma), vascular lesions (haemangioma, lymphangioma), hamartoma, and a range of fibrous tumours (fibroma, fibrous histiocytoma, fibromyoma and fibroepithelial polyp). All these tumours are generally submucosal and present with mass effect rather than haematuria, which is uncommon.

Leiomyoma appears as an isolated well-defined oval or spherical mural mass up to several centimetres diameter. Haemangiomas

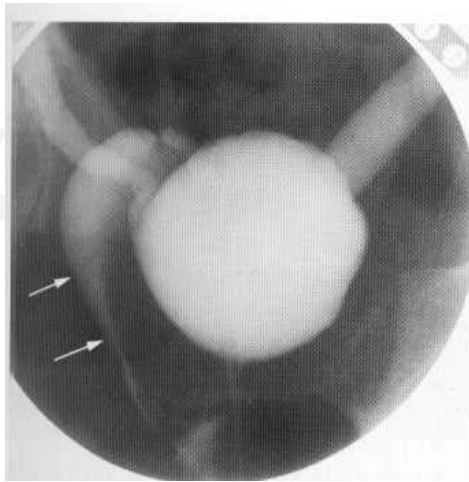


Fig. 31.18 Cystogram in a patient with gross ureteric reflux and vesicovaginal fistula following previous radiotherapy and pelvic surgery for pelvic malignancy. Arrows indicate contrast within the vagina.

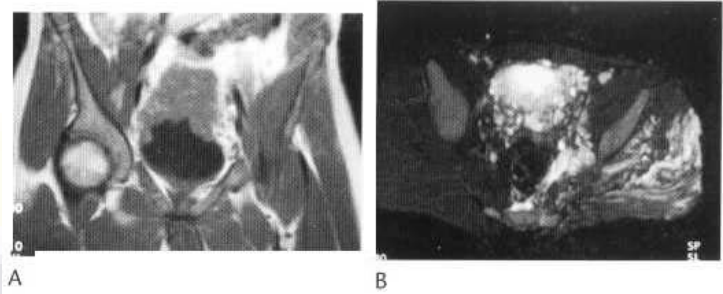


Fig. 31.19 Coronal T-weighted (A) and transverse STIR (B) images from an MRI scan of the pelvis of a patient with an extensive pelvic haemangioma in association with Klippel-Trenaunay syndrome. There is a large lobulated mass over the dome of the bladder which is continuous with further dilated vessels running posteriorly in the left hemipelvis and into the left buttock.

may be identifiable on plain films due to the presence of phleboliths. On MRI and CT they are seen as serpiginous vascular structures in the bladder wall (Fig. 31.19). They may be associated with Klippel-Trenaunay syndrome, when they may be extensive within the pelvis, perineum and leg.

Epithelial tumours include nephrogenic adenoma and transitional papilloma. This latter condition is usually a solitary polyp, around 5–20 mm with a stalk. Histologically it overlaps with low-grade papillary carcinoma, and 10% ultimately develop into carcinoma.

Malignant tumours

Bladder cancer is the commonest malignancy of the urinary tract and represents roughly 4% of all malignancies; 95% originate from the urothelium and 4% are of non-epithelial origin (leiomyosarcoma, rhabdomyosarcoma below the age of 6, and lymphoma). The remaining 1% include rarities such as carcinoid and metastases (especially from stomach and breast, occasionally kidney, melanoma or bronchus). Direct involvement of the bladder by cancer in adjacent pelvic organs (especially rectum, cervix and prostate) is not uncommon.

Urothelial carcinoma particularly affects adults from 50 to 69 years, although it may be encountered as young as the twenties; 95% are transitional cell carcinoma, 4% squamous cell carcinoma and 1% adenocarcinoma. There is a male to female predominance of 3:1 and a strong association with smoking, analgesic abuse, urothelial atypia or dysplasia (for example, cystitis glandularis), previous radiotherapy and a number of carcinogens, particularly encountered in rubber workers. Chronic irritation of any sort is associated with an increased risk of urothelial metaplasia and malignancy, particularly squamous cell carcinoma. This is seen in schistosomiasis, recurrent cystitis, especially with calculi, neurogenic bladders and long-term catheterisation. Adenocarcinoma is related particularly to urachal remnants and bladder extrophy.

The vast majority of bladder carcinoma presents with haematuria. Initial investigation of the urinary tract is with ultrasound, IVU or both (depending on local protocol). On ultrasound, superficial bladder tumours may be seen as mass lesions of intermediate echogenicity (Fig. 31.20). They may be sessile or papillary, the latter being easier to detect, sometimes down to 2–3 mm diameter. Tumour may be seen infiltrating the bladder wall and extending through it in advanced cases. There may be echogenic foci on the tumour surface due to calcific encrustation (Fig. 31.21). Small

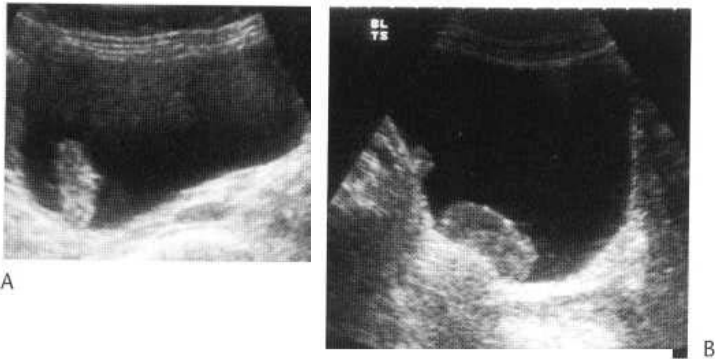


Fig. 31.20 Longitudinal ultrasound of the bladder showing a polypoidal bladder carcinoma (A). Transverse ultrasound of the bladder on a different patient (B) showing two sessile deposits of carcinoma.



Fig. 31.21 Transverse ultrasound of a large sessile bladder carcinoma with calcific encrustation appearing as intense superficial echogenicity with marked distal acoustic shadowing.

tumours are easy to overlook, especially when sessile, arising from the dome or when the bladder is poorly filled. With heavy haematuria, thrombus may be difficult to differentiate from tumour, although it should be possible to demonstrate the mobility of the former by changing the patient's position. Calcification in bladder cancer is visible on plain films in approximately 0.5% of bladder cancer, usually transitional or squamous cell carcinoma. It may be focal, linear, punctate or coarse (Fig. 31.22). On contrast films bladder cancer may be seen as irregular filling defects, which may be associated with focal or asymmetrical wall thickening (Fig. 31.23). Invasive tumours may be associated with ureteric obstruction.

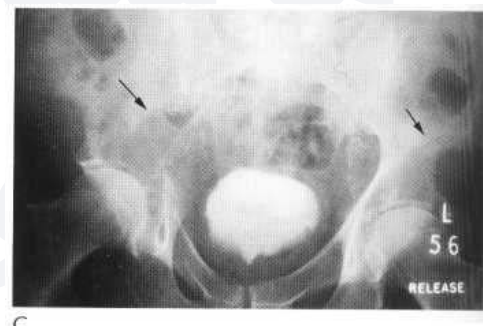
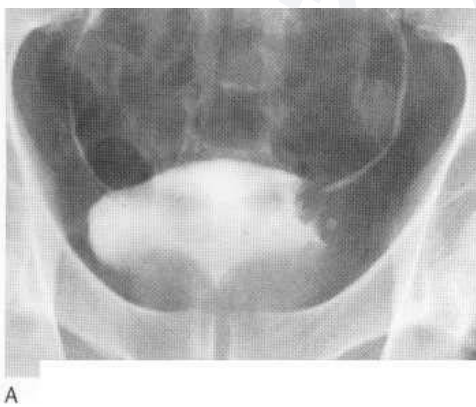


Fig. 31.23 Bladder images from IVU studies. Bladder carcinoma is seen as one or more filling defects with a variety of patterns. (A) A small slightly lobulated left-sided filling defect. (B) Multiple irregular filling defects are seen related to the dome and lateral walls of the bladder with a large basal filling defect. Bilateral ureteric obstruction is developing, worse on the right where tumour can be seen invading along the distal ureter. (C) Extensive irregular wall thickening is present, particularly along the bladder base. Lytic bone metastases are seen affecting the medial aspect of the right iliac bone and the lateral aspect of the left iliac bone (arrows).

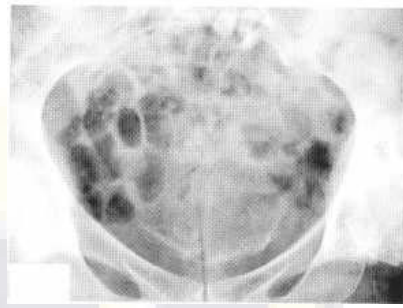


Fig. 31.22 Plain film of the bladder area showing irregular calcification over a bladder carcinoma.

It is important to be clear about the role of imaging in the diagnosis of bladder cancer. Both IVU and ultrasound will fail to diagnose a substantial proportion of cases (with a detection rate as low as 26% on IVU alone being quoted). All patients with haematuria should therefore have cystoscopy. Imaging may demonstrate the bladder tumour but, more importantly, will diagnose or exclude an alternative cause for the haematuria in the upper tract (renal cell carcinoma, calculi, etc.). An important consideration is the potential multiplicity of transitional cell carcinoma throughout the urothelium. The development of transitional cell carcinoma indicates potential instability of the entire urothelium and both synchronous and metachronous tumours may occur. Ureteric or pelvicalyceal transitional cell carcinoma is present

210 of patients with bladder cancer at the time of diagnosis. Upper tract transitional cell carcinomas are poorly seen with ultrasound and bladder cancer patients should be assessed with IVU (or retrograde pyelography). Approximately 3-4% of patients with bladder cancer develop subsequent upper tract transitional cell carcinoma within 5 years (roughly 60% within 2 years). These are often aggressive and nearly a third may be bilateral. Most are symptomatic and imaging may miss early asymptomatic cases. There is therefore some controversy about the usefulness of yearly IVU surveillance for 5 years, which nevertheless remains a standard protocol in many institutions.

Following the diagnosis of bladder cancer, staging is required to assist appropriate treatment selection. CT and MRI are the standard methods and are described below. Intravesical ultrasound has been utilised. Although it can sometimes offer very elegant demonstration of tumour extension through the bladder wall, it is difficult to interpret where there is coexistent bladder wall disease, such as trabeculation or infection, and it cannot stage regional lymph nodes. It is invasive and has fallen out of favour.

Urachel carcinomas are uncommon, accounting for less than 0.5% of bladder cancer. They are overwhelmingly adenocarcinoma (90%) and represent around one-third of all adenocarcinoma of the bladder. The vast majority arise in the urachus immediately adjacent to the bladder vault and extend superiorly in the perivesical space towards the umbilicus and inferiorly into the bladder. Classically they present late with local invasion because of their predominant extravascular and extraperitoneal position and consequently have a poor prognosis. They may present with blood or mucus in the urine and/or at the umbilicus. The considerable extravascular component and the position in the bladder vault should suggest the diagnosis of urachal rather than bladder carcinoma (which is predominantly intravesical and most frequently found on the posterior or lateral walls of the bladder). A minority of urachal tumours are found in the mid or superior part of the urachus towards the umbilicus, occasionally quite asymmetrically.

Urachal adenocarcinoma is often mucinous and around two-thirds show dystrophic calcification, which may be punctate or curvilinear. Around three-fifths show a substantial low-density cystic component. The cystic component is often echogenic on ultrasound because of the high protein content. CT will demonstrate the cystic and calcific components well, the classical vault location and the extravascular spread.

Primary lymphoma of the bladder is extremely rare (less than 1% of bladder primaries) and usually non-Hodgkin's. It typically presents with marked haematuria, frequency and dysuria in middle-aged to elderly female patients. Radiologically the appearances of the tumour are non-specific, usually a large lobulated mass or local wall thickening. There is usually good response to chemotherapy and radiotherapy. Secondary involvement of the bladder with lymphoma is common in advanced disease, being found in up to 13% of postmortem examinations in patients who die of lymphoma (two-thirds non-Hodgkin's and one-third Hodgkin's lymphoma).

Twenty per cent of *rhabdomyosarcoma* occurs in the lower genitourinary tract (bladder, prostate, vagina and paratesticular region). There is a biphasic age distribution with peaks at 2-6 years and 15-19 years. Characteristically the tumours grow rapidly, with early local invasion and lymphatic and haematogenous spread. Presentation may be with bladder outflow obstruction or incontinence, haematuria, infection or visible or palpable mass. On imaging the tumour appears as an infiltrating mass, often of considerable size. This is usually non-specific but the location of the mass (bladder base and/or lying between lower tract structures, leading to difficulty determining from which organ it has originated) may

offer a clue as to its nature (Fig. 31.24). It may appear as a large nodular mass that clinically bears some resemblance to a bunch of grapes (*sarcoma botryoides*).

Bladder calculi

Poorer populations have a lower incidence of upper tract calculi and a higher incidence of lower tract calculi than richer populations. Currently, therefore, in developed countries bladder calculi are much less common than renal calculi. They are almost always associated with a structural or functional abnormality of the urinary tract, most commonly stasis, usually from bladder outflow obstruction, which tends to provoke the development of initially poorly opaque orate calculi. Calculi may form as a result of infection (especially with proteus in an abnormally functioning bladder), when the calculi are magnesium ammonium phosphate and apatite. Foreign bodies such as a catheter tip may also provide the focus for calculus formation. Calculi are often asymptomatic but may present with haematuria, suprapubic pain, disruption of the urine stream or recurrent infection.

Most bladder calculi are visible on plain films and essentially all will be seen on CT. They may appear as radiopaque spiculated (jackstone), laminated or amorphous lesions (Fig. 31.25). As with upper tract calculi, on contrast investigations they are usually seen as filling defects, as they are mostly less radiopaque than contrast. Ultrasound reliably demonstrates them as highly echogenic mobile foci, especially when the bladder is full (Fig. 31.26).

Trauma

Rupture of the bladder is usually associated with pelvic trauma, although on rare occasions it occurs spontaneously. It may be associated with blunt or penetrating injury. It is most commonly seen in blunt injury in patients with severe multi-injury trauma. Bladder rupture is predisposed by having a full bladder at the time of trauma. Pelvic fractures are commonly associated, especially of the anterior ring. Seven per cent of symphysis pubis diastasis are associated with bladder injury. Bladder perforation is also seen following surgery, particularly caesarean section and transurethral bladder resection (usually for tumour). So-called spontaneous bladder rupture is associated with a pre-existing bladder wall abnormality and/or excessive straining, and causes therefore include bladder tumour, cystitis, perivesical inflammation, bladder outflow obstruction, neurogenic bladder and previous radiotherapy.

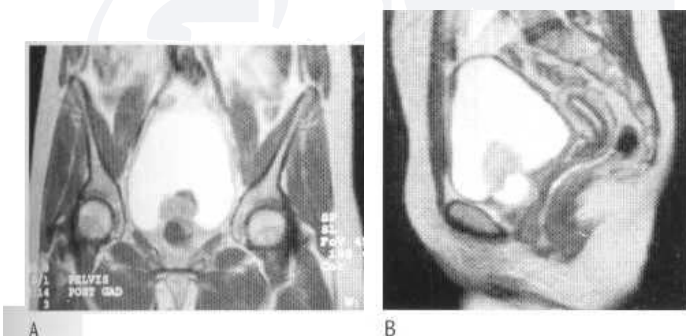


Fig. 31.24 MRI scan on a young adult female with a bladder base rhabdomyosarcoma. Coronal postcontrast T₁-weighted (A) and sagittal T₂-weighted images (B) show a large heterogeneous mass of tumour invading the anterior wall of the vagina.

Box 31.1 Bladder injuries

1. Contusion (incomplete or partial tear of the bladder mucosa; imaging findings usually normal)
2. Intraperitoneal rupture (contrast material seen around bowel loops and in the major peritoneal spaces)
3. Interstitial bladder injury (rare, contrast medium dissects into the bladder wall but not outside the bladder)
4. Extraperitoneal rupture (contrast seen within the perivesical space and a variable number of adjacent extraperitoneal spaces, depending on the severity of the injury)
5. Combined intraperitoneal and extraperitoneal rupture

From Sandler et al (1986).

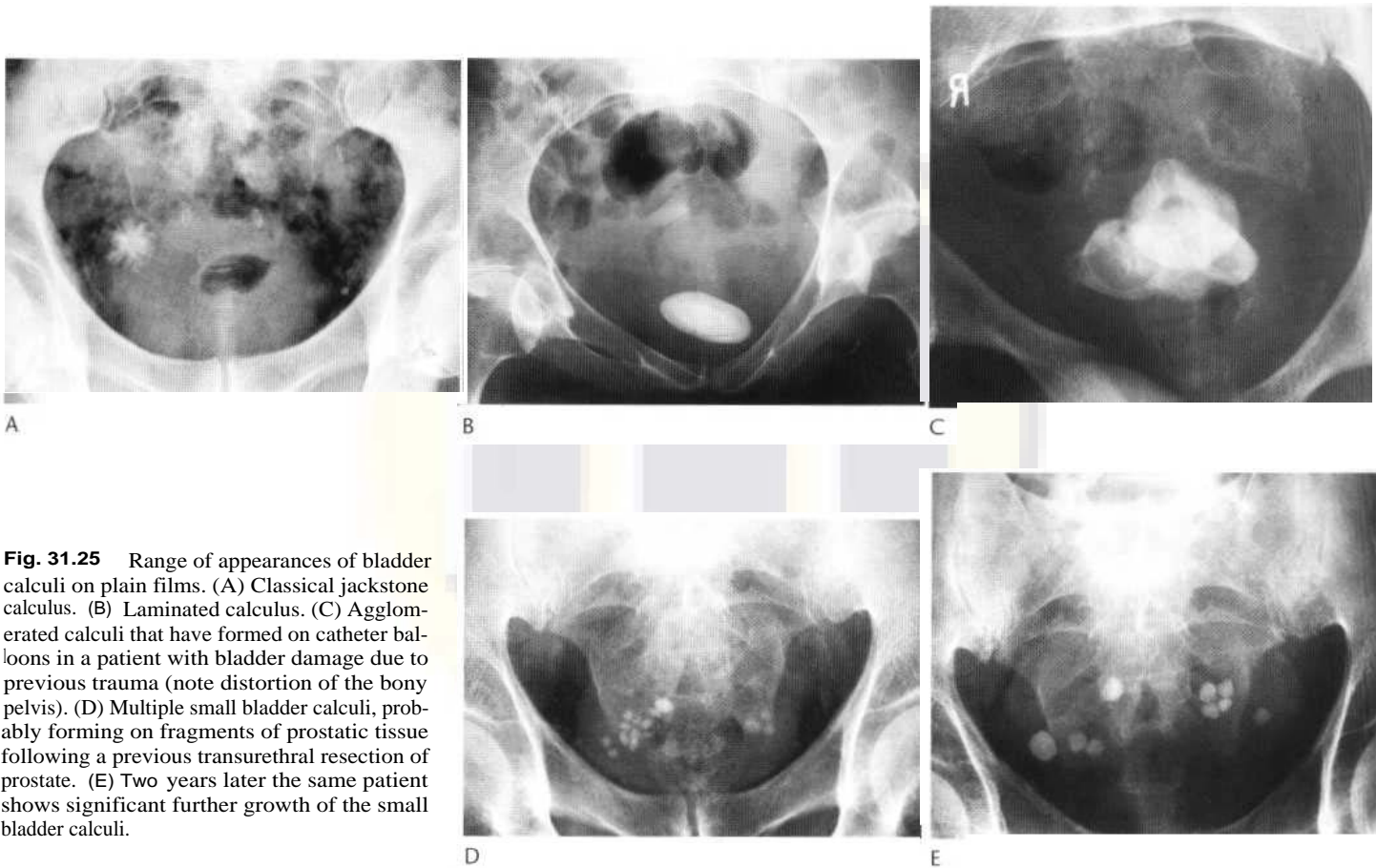


Fig. 31.25 Range of appearances of bladder calculi on plain films. (A) Classical jackstone calculus. (B) Laminated calculus. (C) Agglomerated calculi that have formed on catheter balloons in a patient with bladder damage due to previous trauma (note distortion of the bony pelvis). (D) Multiple small bladder calculi, probably forming on fragments of prostatic tissue following a previous transurethral resection of prostate. (E) Two years later the same patient shows significant further growth of the small bladder calculi.

Bladder injuries may be classified according to a formal system (Box 31.1) first described on cystography, modified for CT cystography. Although this includes contusions (type I) and interstitial bladder injury (type 3), the most important observation is the presence of a bladder tear or rupture. This may be intraperitoneal (type 2), extraperitoneal (type 4) or both (type 5). Extraperitoneal rupture is the commonest bladder injury (up to 90% of cases) and is treated conservatively with catheter drainage. Intraperitoneal (and combined infra- and extraperitoneal) rupture requires urgent surgical repair. The other forms of injury are also treated conservatively.

The diagnosis of bladder rupture and the distinction between intra- and extraperitoneal forms has traditionally been made with cystography. Extravasation of contrast into the perivesical space is seen with extraperitoneal rupture and is associated with anterior pelvic-ring fractures in 90% of cases. The defect in the bladder is usually anterolateral. If there is florid extravasation, contrast may extend anterosuperiorly along the anterior pelvic and abdominal wall as far as the umbilicus or posteriorly around the rectum into



Fig. 31.26 Transverse ultrasound of the bladder showing an echogenic spiculated calculus with distal acoustic shadowing.

the presacral space. There may be an associated tear of the urogenital diaphragm, allowing contrast to appear within the perineum, thigh and scrotum. With an extraperitoneal tear the extravasated contrast characteristically stays close to the bladder and has sharp irregular margins (Fig. 31.27).

When the tear is intraperitoneal, contrast extravasates into the peritoneal cavity and has a more cloudy nebulous appearance (Fig. 31.28). It is seen around small-bowel loops and may outline other structures projecting into the peritoneal cavity, such as the

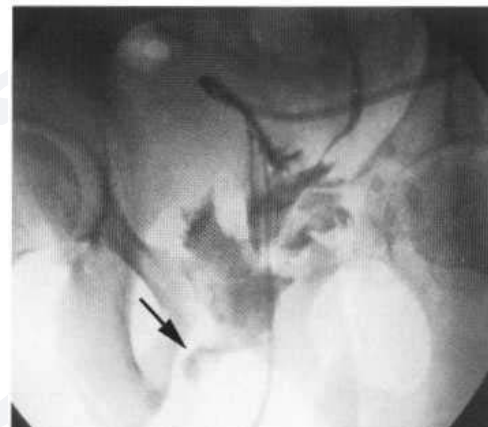


Fig. 31.27 Cystogram performed via a suprapubic catheter in a patient with major pelvic trauma and anterior pelvic fractures. There is florid extravasation from the bladder neck tear. Contrast remains extraperitoneal. There is associated trauma to the urogenital diaphragm and contrast extends inferiorly into the perineum (arrow). The line of the urethra is shown by the course of the urethral catheter.

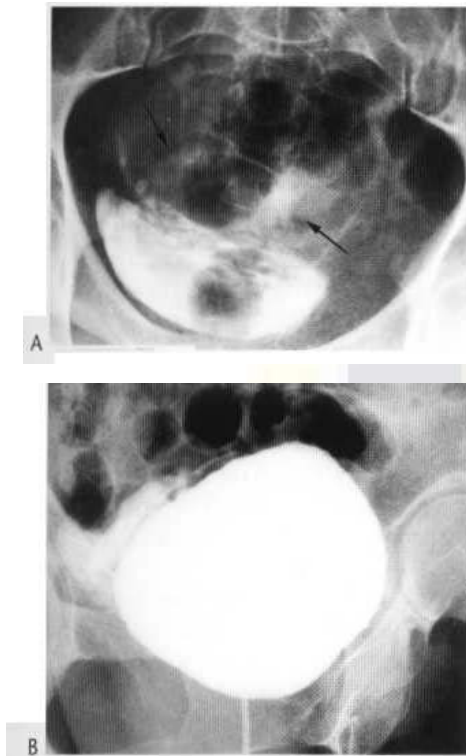


Fig. 31.28 (A) Intraoperative rupture, in this case visible on IVU. III-defined contrast extravasation is seen around bowel loops immediately superior to the bladder (arrows). (B) Cystogram showing intraperitoneal rupture with contrast outlining the caecal pole and the outer aspect of the right side of the bladder dome.

liver. Contrast also extends into the lateral pelvic recesses and the pouch of Douglas or rectovesical pouch (although this is better seen on CT). Usually the tear is along the dome of the bladder, which is the weakest part. Associated pelvic fractures are seen in approximately 75%. CT with intravenous contrast is often performed to investigate the abdomen and pelvis following significant trauma. CT cystography is a useful adjunct and can be performed by repeating the scan 15-30 minutes after the injection of contrast, keeping the bladder catheter clamped during this period. This is of comparable accuracy to conventional cystography and has the advantage of not requiring the patient to move to a separate table for a further investigation. It shows analogous features to those described above, often with better detail (Fig. 31.29). Conversely, contrast may be instilled via a urethral catheter immediately prior to CT scanning and this may increase the detection rate, particularly for subtle injuries. Adequate distension of the bladder is required for maximum sensitivity but this is sometimes impossible (and unnecessary) when the contrast escapes through a large tear.

Neuromuscular disorders

The neuromuscular control of voiding and continence is complex and may become abnormal as a result of numerous conditions at any site along the neuraxis, from cerebral cortex to detrusor muscle. Common causes within the brain include ischaemia, trauma, Parkinson's disease, Alzheimer's disease, hydrocephalus, head injury and multiple sclerosis. Within the spine, common causes include compressive lesions of the cord or cauda equina, such as prolapsed intervertebral disc or tumour.



Fig. 31.29 CT cystogram. There is an extensive bladder neck rupture. (A) The bladder cannot be distended, due to the size of the rupture, and remains collapsed (arrow). Contrast has flooded into the perivesical space anteriorly and shows florid extension superiorly (B) in the extraperitoneal space behind the anterior abdominal wall.

The detrusor muscle may become hyper-reflexic with frequency, urgency and urge incontinence. The bladder becomes heavily trabeculated (Fig. 31.30) and may develop the classical fir-tree appearance. Alternatively the detrusor muscle may become flaccid, with a smooth overdistended bladder. Investigation of the neuropathic bladder and other causes of bladder dysfunction is discussed in the section on urodynamics in Chapter 29.

Major bladder surgical procedures

Total cystectomy and associated techniques of urinary diversion or neobladder construction

Approximately 75% of bladder tumours are confined to the mucosa and submucosa (Ta and T1 tumours) and, as this group has a rela-



Fig. 31.30 Bladder image from an IVU study showing a heavily trabeculated neuropathic bladder.

tively low risk of metastases, they can be managed by regular endoscopic resection and/or diathermy. The remaining 25% invade the underlying bladder muscle (T2-T4) and are associated with a high risk of developing metastatic disease. Following the diagnosis of muscle-invasive disease at endoscopic resection, this group therefore requires more aggressive therapy; this may involve radiotherapy to the bladder, cystectomy and urinary diversion or a combination.

In many centres there is a trend towards aggressive initial surgical treatment of muscle-invasive bladder cancer by total cystectomy, which classically involves removal of the lower ureters, bladder, prostate and urethra in men, and the lower ureters, bladder, urethra and gynaecological organs in women. Although the results of cystectomy (either alone or following preoperative radiotherapy) are superior to radiotherapy alone, surgery has been less popular in the past because of the need for simultaneous urinary diversion (by ileal conduit or ureterosigmoidostomy: Fig. 31.31 A).

The ileal conduit is the classical urinary diversion procedure. A short segment of ileum, supplied by the ileocolic artery or a large branch of the superior mesenteric artery, is isolated. One end is closed and secured retroperitoneally near the aortic bifurcation. The other end is fashioned into the cutaneous stoma, usually in the right lower quadrant. End-to-side ureteroileal anastomoses are performed around 2 cm from the closed end. There is no antireflux mechanism. The left ureter usually has further to travel and is at risk of tension. However, with recent developments in reconstructive surgical techniques, it is now possible in suitable cases to avoid urinary diversion by construction of a bladder substitute from the intestine that is then anastomosed directly to the membranous urethra (orthotopic neobladder reconstruction). The intestinal neobladder may be constructed from ileum, the sigmoid colon or using an ileocolic segment.

Detubularisation and reconfiguration of the intestinal segment (Fig. 31.31B) eliminates coordinated contractions of the gut musculature, resulting in a low-pressure continent reservoir that is emptied by abdominal straining, although intermittent self-catheterisation may be required in some patients to achieve complete emptying. In men, potency may be retained by careful preservation of the neurovascular bundles innervating the corpora cavernosa.

Although initially the technique was only thought feasible in men, orthotopic neobladder reconstruction is increasingly being employed for female patients as well, the continence mechanism of the female urethral sphincter being maintained by preservation of the anterior vaginal wall and the neurovascular bundles that run in association with this. However, reconstruction onto the urethra is contraindicated in patients with multifocal tumours or widespread carcinoma in situ, owing to the risks of urethral recurrence, and in these patients urethrectomy is carried out at the same time as the bladder is removed.

When removal of the urethra is required or if anastomosis to the membranous urethra is not technically feasible, a urostomy may still be avoided by giving the bowel reservoir a continent catheterisable stoma instead. The continence mechanism can be provided by submucosal tunnelling of a narrow tube, such as appendix or ureter (with careful preservation of its blood supply), into the reservoir (Mitrofanoff principle), or by intussusception of a length of ileum to form a non-return valve (the Koek pouch). The patient then empties the reservoir at regular intervals by self-catheterisation of the cutaneous stoma opening onto the abdominal wall.

If radiotherapy is chosen as the initial treatment, cystectomy may still be necessary at a later stage either if tumour persists in the

bladder after completion of radiotherapy or if invasive tumour recurs at a subsequent date (salvage cystectomy). Salvage cystectomy may also be required for severe side-effects of radiotherapy (bleeding, contracted bladder, incontinence, fistulas). An ileal conduit is the most commonly employed urinary diversion technique used following salvage cystectomy, but with increasing experience of the orthotopic neobladder technique, reconstruction is being increasingly used in these post-radiation patients as well.

Augmentation and substitution cystoplasty Several bladder disorders may impair bladder capacity, either functionally or structurally, giving rise to frequency of micturition and nocturia. These symptoms may also be accompanied by urgency and incontinence. Symptomatic improvement may be obtained using agents with anticholinergic and/or smooth muscle relaxant properties (e.g. propantheline, oxybutynin) or by hydrostatic distension of the bladder under anaesthesia. For selected patients with intractable symptoms despite such measures, the bladder capacity can be increased by cystoplasty.

Augmentation or 'clam' ileocystoplasty involves incorporating a segment of detubularised ileum into the dome of the bladder after the bladder has been opened in either a transverse or anteroposterior plane (Fig. 31.31C). This technique has been particularly employed in the treatment of detrusor instability, a condition in which uninhibited contractions of the detrusor muscle impair the functional capacity of the bladder and cause frequency, urgency and urge incontinence. The success of the operation is believed to be the result of the relatively non-contractile tubularised bowel segment acting as a diverticulum to absorb any pressure surges from increased detrusor activity. The diverticulum effect is sometimes too effective and prevents complete bladder emptying, necessitating intermittent self-catheterisation.

In other disorders, changes occur in the bladder wall to restrict its structural capacity of the bladder. This includes the fibrosis of the wall seen following genitourinary tuberculosis, schistosomiasis and radiotherapy and the inflammation seen with interstitial cystitis. In these patients the diseased segment of the bladder is removed and replaced (substituted) with a segment of bowel (Fig. 31.31C). It is usually necessary to remove the whole of the bladder dome and body above the ureteric orifices, preserving just the latter and the trigone. The most commonly used segment of bowel used for substitution cystoplasty is caecum, which can either be anastomosed to the trigone as a tubular segment or as a detubularised ilco-caecal segment. As with clam ileocystoplasty, bladder emptying may be incomplete following substitution cystoplasty, again necessitating intermittent self-catheterisation.

Boari bladder flap If the lower ureter is damaged due to trauma or pelvic surgery, or if local excision is required to remove a low-grade tumour or stricture, there is often insufficient length to allow direct reimplantation of the ureter into the bladder. In these circumstances the deficit in length can be bridged by taking a vascularised flap from the anterior wall of the bladder, into which the ureter is reimplanted via a submucosal tunnel to prevent reflux (Boari flap; Fig. 31.31D). The anterior wall of the flap is then closed to form a tube leading down into the bladder. A ureteric stent is generally employed for a period of time to protect the ureteric anastomosis.

Radical prostatectomy The opportunity to consider curative treatment for carcinoma of the prostate has in the past been

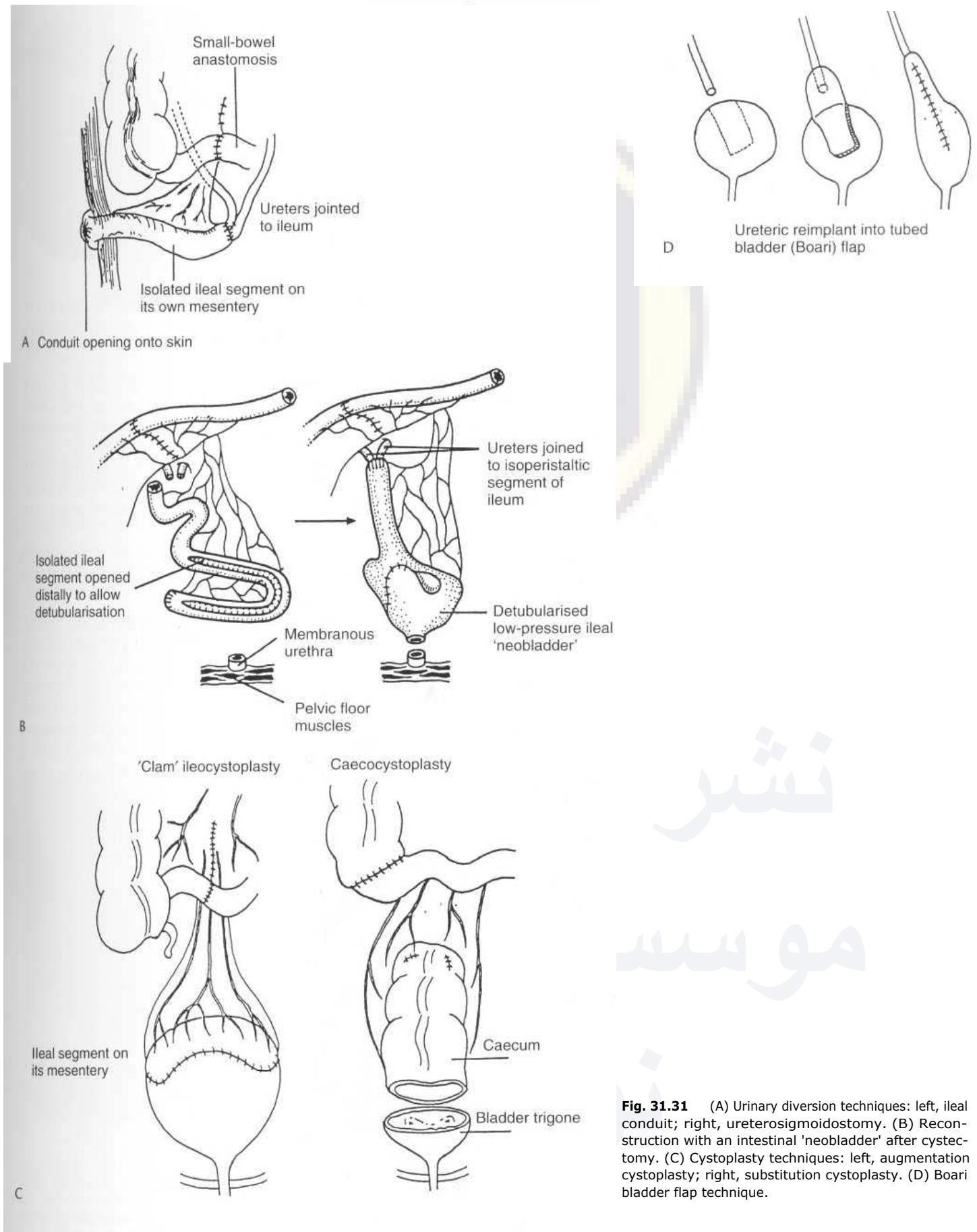


Fig. 31.31 (A) Urinary diversion techniques: left, ileal conduit; right, ureterosigmoidostomy. (B) Reconstruction with an intestinal 'neobladder' after cystectomy. (C) Cystoplasty techniques: left, augmentation cystoplasty; right, substitution cystoplasty. (D) Boari bladder flap technique.

hampered by the advanced stage of the disease at presentation in many patients. However, much earlier diagnosis has become possible in recent years using the tumour marker, prostate-specific antigen (PSA) and multiple ultrasound-guided prostate biopsies. If staging confirms localised disease, potentially curative treatment with radical radiotherapy or radical prostatectomy may be offered.

Radical prostatectomy involves total removal of the prostate and seminal vesicles en bloc. This may be achieved by either a low abdominal incision or a perineal incision. A number of centres are developing a transabdominal laparoscopic technique. Regardless of the approach, anastomosis of the bladder neck to the membranous urethra is required to reconstruct the urinary tract following radical prostatectomy, the urethral anastomosis being at the same site as described above when anastomosing a reconstructed neobladder to the urethra after total cystectomy (Fig. 31.31 B).

Imaging appearances of the postintervention bladder

Heal conduit The radiologist is routinely called upon to image urinary tract diversions and reconstructions of all types in the early postoperative period, to assess the state of the critical anastomoses and look for extravasation. Classically this is requested around 10 days following surgery when the surgeon will be contemplating removal of temporary stents routinely positioned across the anastomoses at the time of surgery. In the case of the ilea) conduit the typical site of extravasation is at the ureteroileal junctions (Fig. 31.32). Less commonly the anastomoses are too narrow and obstruction occurs.

Long-term complications include chronic pyelonephritis, calculus formation, obstruction and neoplasm.

By its nature the conduit predisposes to free bilateral reflux (Fig. 31.33) and there is a strong tendency for the ureters and pelvicalyceal systems progressively to dilate. Chronic infection is common and chronic pyelonephritis (adult reflux nephropathy) develops with cortical loss in up to one-third of patients. Ultimately after several years renal failure often develops. Routine assessment of the upper tracts is usually performed to monitor the state of the

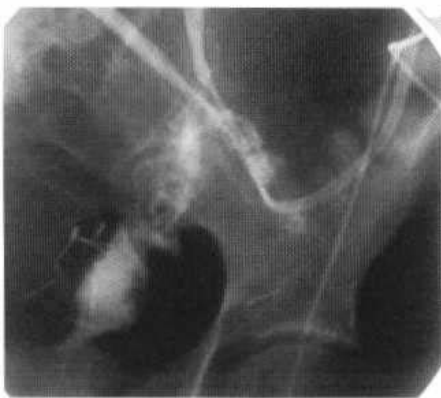


Fig. 31.32 Stentogram 10 days after fashioning an ileal conduit. Two stents have been positioned at the time of surgery, running through the conduit and then into the two ureters. Contrast has been injected via the stents to outline the ureters and then, as the contrast flows antegradely, the conduit. In this case very little contrast passes into the conduit, as most is seen to extravasate at the level of the ureteroileal junction inferiorly into the pelvis.



Fig. 31.33 Normal conduitogram (loopogram) showing typical small bowel mucosa in the conduit and free reflux into modestly dilated ureters.

kidneys, either with yearly ultrasound or IVU. If dilatation occurs it almost always represents reflux, rarely obstruction and a conduitogram (loopogram) will confirm this. Calculi may develop in around 5% of patients because of the infection and stasis.

Obstruction, usually due to benign stenosis at the ureteroileal anastomosis, is seen in approximately 5%, especially if radiotherapy was administered or if there was extravasation in the postoperative period.

Tumour recurrence occurs in up to 20% of postcarcinoma conduit patients and new metachronous urothelial carcinoma may be encountered in up to 33%.

Ureterosigmoidostomy Implantation of the distal ureters into the sigmoid colon has been performed historically in patients with severely abnormal bladders, particularly bladder extrophy. The advantage of the procedure was the avoidance of a cutaneous stoma. Numerous disadvantages have, however, been encountered, including diarrhoea and severe biochemical disturbances. In the long term two serious groups of problems are encountered (infection and neoplasia), which derive from the mixing of the Urinary and faecal streams. Patients suffer with recurrent or chronic urinary tract infection, leading to chronic pyelonephritis, renal cortical loss and failure (Fig. 31.1). There is a markedly increased risk of tumour development, most commonly in the

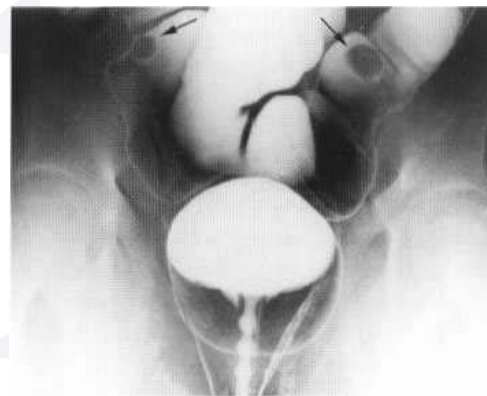


Fig. 31.34 Barium enema (prone angled view) showing the characteristic wide separation of the symphysis pubis seen in bladder extrophy. The patient was treated in childhood with bilateral ureterosigmoidostomies and has developed large colonic adenomas at the site of insertion of the ureters (arrows).

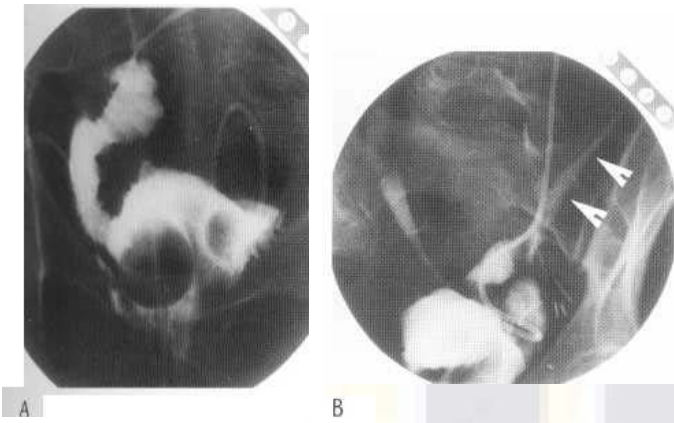


Fig. 31.35 (A) Early cystogram following fashioning of an orthotopic neobladder. Normal postoperative appearances. The two ureters are seen entering the afferent loop, which drains into the main body of the neobladder. No extravasation is seen, the anastomoses are intact. Both urethral and suprapubic balloon catheters are still present. (B) Early cystogram on a similar reconstruction. In this case the right ureter enters the afferent loop somewhat lower than the left. There is a stent still present in the left ureter running into the afferent loop because of concerns about the integrity of the left-sided anastomosis. This is justified because there is substantial extravasation from this anastomosis, running superiorly into the left retroperitoneum (arrowheads).

bowel mucosa at the ureterosigmoid anastomotic site. There is at least a one in three chance of developing colonic neoplasia with this type of operation, either adenomas or carcinoma, often highly aggressive (Fig. 31.34).

Orthotopic neobladder Because of the complexity of these procedures and the number of surgical anastomoses involved, bilateral ureteric stents and urethral and often suprapubic catheters are usually left in place for a week. Assessment with bilateral stentograms and a cystogram is then often performed to assess anastomotic integrity before removal of the ureteric stents first, followed over the next week or so by removal of the bladder

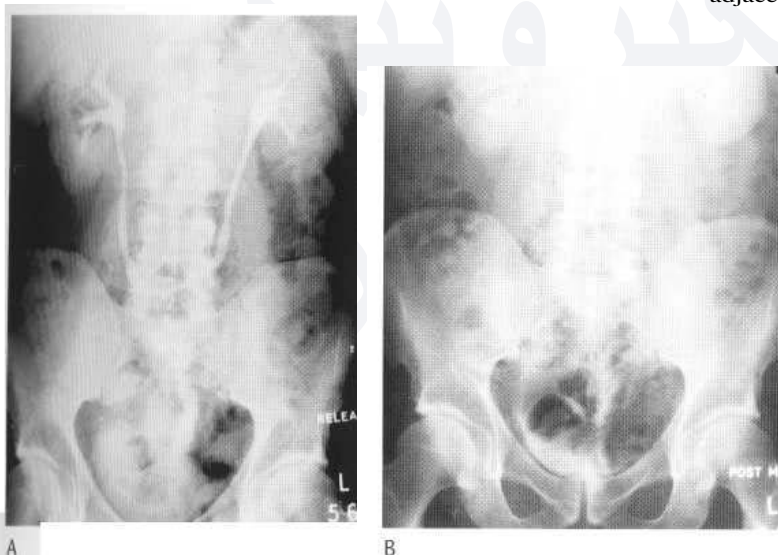


Fig. 31.36 *IVU* 1 year after fashioning an orthotopic neobladder. There is no upper tract dilatation and the ureters drain satisfactorily into the afferent loop; this drains into the neobladder, which is nicely seen on the full length film (A) and has a remarkably normal appearance. The postmicturition film (B) shows satisfactory emptying of the neobladder and reveals the characteristic mucosal pattern of the constituent small bowel.

catheters. The characteristic anatomy of the afferent loop and the neobladder with demonstrable small-bowel mucosa is easily seen on these contrast investigations (Fig. 31.35). Long-term follow-up of these procedures is performed to monitor postmicturition volume and the development of upper tract dilatation due to reflux or anastomotic stricturing (usually benign, occasionally due to tumour recurrence). Imaging protocols vary between centres but, although ultrasound is adequate for the detection of hydronephrosis and gross changes in postmicturition volume, many institutions prefer *IVU* to monitor the postoperative appearances (Fig. 31.36); it is likely to be more sensitive for the detection of metachronous upper tract urothelial tumours. Similar considerations apply to the early and late stages of imaging the Mitrofanoff and related continent diversions (Fig. 31.37).

Boari flap The length of the flap of bladder used varies depending on the distal ureteric deficit. The postoperative appearances range from a subtle angularity of the superolateral aspect of the affected side of the bladder to a very obvious tube of bladder extending superiorly to meet the ureter (Fig. 31.38).

Radical prostatectomy Following radical prostatectomy a urethral catheter is left in place to stent the surgical anastomosis to the urethra. Routine cystography is commonly requested 10-14 days after surgery to assess the state of the anastomosis. When this is intact, or shows only a tiny pouch of contrast projecting from the anastomotic line, the catheter may be removed, usually on the ward early in the day to permit several hours of observation before the patient is discharged. Substantial extravasation (Fig. 31.39) requires the catheter to remain in place for a further week or two before repeat cystography.

Extrinsic compression or displacement of the bladder

The underfilled bladder often shows some distortion of its shape by adjacent bowel loops, especially when they are loaded with gas or



Fig. 31.37 Full-length film from an *IVU* study on a patient 1 year after fashioning a Mitrofanoff reservoir. The appearances are satisfactory. The left pelvicalyceal system shows minimal fullness, which will require monitoring; the right-sided collecting system shows no dilatation at all. Incidental note is made of the complete duplex system on the right, which will have increased the complexity of the surgical procedure.

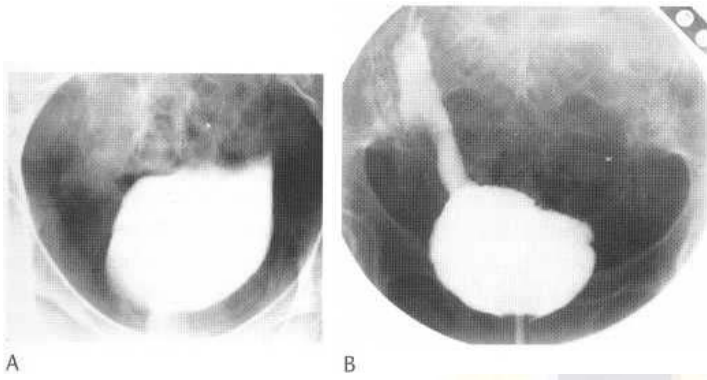


Fig. 31.38 Bladder images from IVU studies on two patients with Boari flap procedures: (A) shows only prominence of the right superolateral angle of the bladder in keeping with a small flap. (B) shows a patient who required resection of a substantial length of ureter and has a much longer flap reconstruction.

faeces. Superior indentation by the normal uterus in females of reproductive age is common. These appearances are usually easy to interpret correctly. Indentation of the bladder by a pathologically enlarged uterus (usually due to fibroids) is also relatively common and other gynaecological masses (ovarian cysts and tumours) will present this way from time to time and require ultrasound assessment

Compression of the bladder by urinoma or haematoma is seen after trauma (occasionally following surgery), the diagnosis being suggested by the history. Lateral compression of the bladder characteristically occurs when the source of bleeding is the iliac artery or the perivesical venous complex.

Other common causes of bladder indentation include adjacent diverticulum, pelvic abscess or pelvic tumours. Less commonly the bladder is compressed laterally by pelvic lymphadenopathy, psoas muscle hypertrophy, pelvic lipomatosis or venous collaterals due to inferior vena cava obstruction.

Pelvic lipomatosis is a rare condition in which there is excess formation of adipose tissue within the true pelvis. It is characteristically seen in overweight hypertensive males. It may present with abdominal or low back pain, urinary tract infections, frequency and constipation. Reduced density may be seen in the pelvis on plain radiographs. The bladder has an inverted pear shape on contrast investigations. The bladder base is elevated and the capacity reduced. There may be associated ureteric deviation and even obstruction. The rectum and sigmoid colon may also appear elongated and narrowed. CT is diagnostic, showing the excess of fat and excluding more sinister masses.

THE PROSTATE

Benign prostatic hyperplasia

Benign prostatic hyperplasia (BPH) is the development of nodular hyperplasia within the glandular tissue of the transitional zone of the prostate. It is essentially a disease of age, being present in 8% of males around the age of 40 years, up to 50% by the age of 60 years and around 90% at the age of 90. Presentation is usually with symptoms of bladder outflow obstruction, classically hesitancy, poor stream, postvoid dribbling and the sensation of incomplete empty-

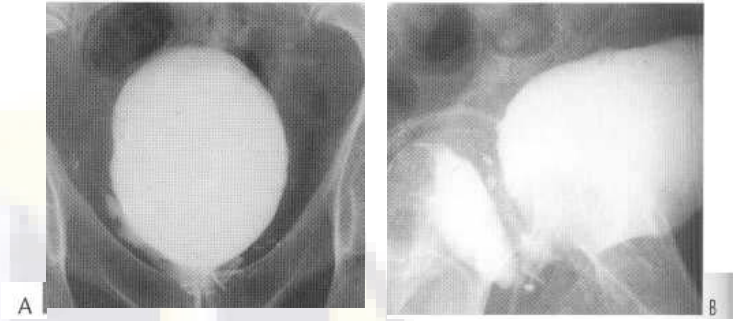


Fig. 31.39 Cystogram 10 days after radical prostatectomy. There is a substantial right posterolateral leak at the level of the anastomosis of the bladder on to the urethra, seen on the posteroanterior (A) and steep right anterior oblique (B) views. This requires conservative treatment with catheter drainage for 1-2 weeks and then repeat cystographic assessment

ing. The detrusor muscle often hypertrophies and leads to frequency, nocturia and urgency. The postmicturition urine volume may rise and lead to an increased incidence of cystitis and calculi. Chronic retention may occur, ultimately leading to upper tract distension with renal failure.

Transabdominal ultrasound with a full bladder usually allows some demonstration of the prostate and an approximate volume can be measured (Fig. 31.40). More accurate volume measurement can be obtained with transrectal ultrasound. Clinically, however, this is not terrifically useful because the symptoms, complications and treatment of BPH are not closely related to prostate volume. Occasionally the surgeon may ask for a volume measurement to assist with a decision to choose retropubic prostatectomy instead of the standard transrectal prostatectomy. Adenomatous nodules are seen as predominantly well-defined echo poor nodules, although they are sometimes hyperechoic. They are located centrally (originating in the transitional zone), expanding the central gland, displacing and compressing the hyperechoic peripheral zone. Frequently there are associated cysts of varying sizes due to dilatation of transitional zone glands by proteinaceous material (Fig. 31.41). Foci of calcification with dense shadowing are also frequently seen, characteristically with a periurethral distribution or at the junction of the central and peripheral glands. MRI is not routinely indicated to image BPH but the changes may be visible on scans performed for other indications, particularly staging carcinoma of the prostate when they may add to the difficulty of delineating the tumour accurately. Features analogous to those described on transrectal ultrasound are encountered. The central gland is enlarged and heterogeneous with visible nodules, usually of

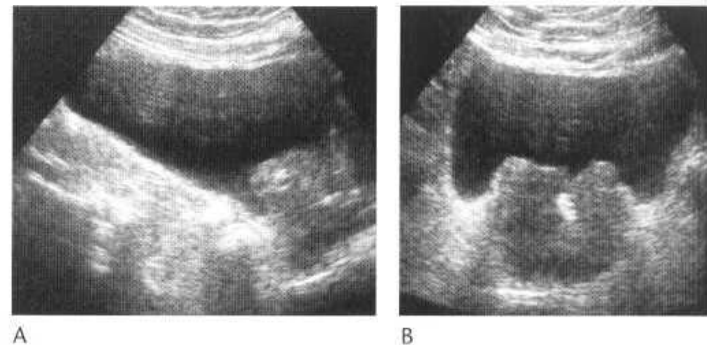


Fig. 31.40 Longitudinal (A) and transverse (B) ultrasound images of the bladder showing moderate lobulated benign prostatic enlargement with areas of calcification.

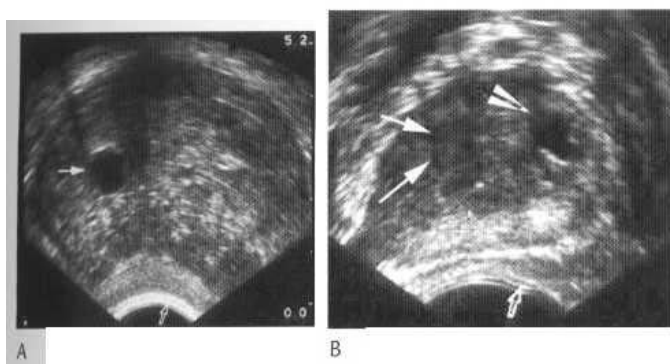


Fig. 31.41 Transrectal ultrasound (transverse images) on patients with benign prostatic hyperplasia. (A) shows marked prostatic enlargement. The central gland shows a multinodular appearance with a benign cyst (arrow) and gross enlargement. This has displaced and compressed the more echogenic peripheral zone. (B) shows more modest disease with less central gland enlargement. A benign cyst (arrowhead) and an adenomatous nodule (arrows) can be identified.

increased signal on the T₂-weighted sequence. Signal is more variable on the T₁-weighted sequence and may be high, medium or low. Stromal proliferation between the nodules is seen predominantly as low signal on both sequences, particularly the T₁ sequence. The peripheral zone is not directly involved but is usually compressed and displaced by the central hyperplasia.

Radiological investigation of BPH is more routinely targeted towards assessment of the effects of the disease on the rest of the urinary tract. Ultrasound will demonstrate the state of the bladder, notably increased wall thickness and the development of trabeculation, sacculations and diverticula. Bladder calculi may also be demonstrated. The postmicturition volume should be assessed. Although the patient may not have emptied the bladder as well as he could under less artificial circumstances, this should give at least some idea of the order of magnitude of the residual urine and whether or not chronic retention is present. This measurement is often combined with a urine flow-rate measurement. Upper tract ultrasound will demonstrate the presence of secondary hydronephrosis and cortical loss and detect any coincidentally present renal disease (calculi, scars, etc.). The IVU is not routinely indicated in the investigation of BPH but signs of the condition may be noted when this investigation is performed for other reasons. There may be a lobulated bladder-base mass (the enlarged prostate) associated with elevation of the trigone and distal ureters (Fig. 31.42). There may be upper tract distension ultimately with cortical loss, and the bladder wall may appear thickened and trabeculated. A substantial postmicturition residue may be seen on the preliminary film and the post micturition film, in which case demonstration of the bladder is often poor due to dilution of the contrast by the residual urine. Bladder calculi and diverticula may also be seen.



Fig. 31.42 Bladder image from an IVU series showing marked prostatic enlargement as a smooth bladder-base mass. Some trabeculation of the bladder wall is also visible.

Inflammation of the prostate may be acute or chronic. Strictly defined, the diagnosis rests on the demonstration of an infecting organism, usually Gram-negative bacilli in prostatic secretions or semen. More commonly it is inferred from the clinical picture. Acute prostatitis is frequently associated with cystitis. It causes fever, rigors, dysuria, frequency and perineal or rectal pain. On rectal examination the gland may be firm, swollen and tender. The onset may be remarkably acute and severe and may progress to septicaemia and abscess formation, when the gland becomes exquisitely tender. The disease usually responds well to antibiotics. Radiological investigations are not usually required, although it is reasonable to assess the urinary tract with ultrasound at some stage to look for predisposing or associated conditions, particularly bladder outflow obstruction. Transrectal ultrasound is rarely contributory and often extremely uncomfortable for the patient. The serum PSA often rises during an episode of prostatitis and, if this remains high and the gland remains clinically firm, patients may be referred for transrectal ultrasound because of concern about the presence of a carcinoma. Unfortunately, without biopsy transrectal ultrasound (Fig. 31.43) is non-specific (and biopsy is itself a cause of prostatitis). Ill-defined or geographical areas of reduced echogenicity may be seen throughout the prostate, but particularly centrally, and are indistinguishable from extensive carcinoma. Calcific areas are frequently present, especially in the periurethral area. Abscess formation is seen as an ill-defined area of cystic degeneration, often containing debris.

The clinical entity of chronic prostatitis includes dysuria and perineal or rectal pain. On transrectal ultrasound appearances are non-specific and may be virtually normal. Areas of reduced echogenicity as in acute prostatitis may be seen (moth-eaten prostate) with foci of calcification, particularly in the periurethral area, which may be dense. Positive bacteriology may be elusive and it has been suggested that similar organisms to those responsible for non-specific urethritis may be involved (*Chlamydia*, *Ureaplasma*, *Mycoplasma*, *Trichomonas spp.*, etc.). Treatment is often difficult, with little symptomatic relief in response to conventional antibiotics. It may be associated with recurrent urinary tract infections and epididymitis.

Haemospermia

Blood in the semen is overwhelmingly a benign and self-limiting condition. It usually affects middle-aged or young adult males. The

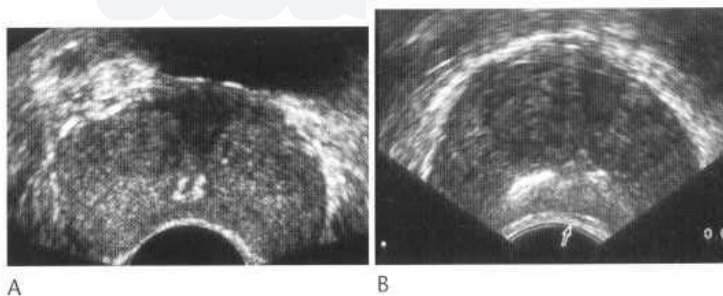


Fig. 31.43 Transrectal ultrasound (transverse images) on patients with clinical prostatitis. (A) shows periurethral calcification but an otherwise essentially normal young adult gland. (B) Older patient with some benign prostatic enlargement. There is calcification at the junction of the peripheral and central gland and a slightly moth-eaten appearance to the central gland.

cause is often unknown but sometimes it seems reasonable to ascribe it to the presence of infection or substantial calcific foci within the central prostate (prostatic calculi) or seminal vesicles. Rare causes include vascular malformations and prostatic cancer. With the appropriate clinical picture, transrectal ultrasound and biopsies (also a cause of haemospermia) may be indicated on occasion.

Malignancy

In males prostate cancer is the most common malignancy encountered and the second commonest cause of cancer-related deaths. A high proportion of prostate cancer appears to be clinically insignificant, being demonstrable at postmortem but failing to develop into significant disease during life. The vast majority of prostate cancer is adenocarcinoma and is classified histologically into five Gleason grades of increasing aggression from I to 5. Only the higher two grades are commonly associated with lymph node metastases. The tumour is often heterogenous and a Gleason score is employed to account for this, being derived from the sum of the grades of the two predominant histological patterns. This defines the categories of well, moderately and poorly differentiated (scores 2-4, 5-7 and 8-10, respectively). Tumour size is an independent predictor of aggressive behaviour such as metastases, seminal vesicle invasion being uncommon at a volume below 2.5 ml and the lymph node or other distant metastases being uncommon at volumes below 4 ml. Tumour differentiation also tends to deteriorate with increasing size.

Prostate cancer detected by digital rectal examination (DRE) is often advanced, roughly one-third already having metastasised and one-third of the remainder showing local extraprostatic spread.

Blood tests for PSA in urological patients (or more controversially in the general population) and transrectal ultrasound have been used to attempt to identify prostate cancer at an earlier stage, when it may be more amenable to radical treatment. PSA is a glycoprotein produced exclusively by glandular tissue of the prostate. It becomes elevated in the blood in prostatic disease, including benign prostatic hyperplasia, inflammation and cancer. The arbitrary upper limit of normal is often taken as 4 ng/ml; however, only 25% of patients with a value of 4-10 ng/ml are shown to have prostatic cancer. Above 10 ng/ml as many as 85% are shown to have cancer. A normal PSA value in the general population is usually associated with an absence of cancer, but does not exclude it. A small proportion of extremely undifferentiated cancers will not produce a demonstrable rise in the PSA, and very small cancers may not produce enough of a rise for the value to fall outside the normal range.

On transrectal ultrasound the peripheral zone is normally moderately hyperechoic. Roughly 85% of prostatic cancer originates from this zone and classically appears as a focal hypoechoic nodule or a more substantial ill-defined area of reduced echogenicity (Fig. 31.44). However, at least one-third are of similar echogenicity to normal peripheral zone tissue and cannot be identified on ultrasound alone, although they may be suspected if they are large enough to distort the prostatic outline. The remaining cancers originate within the central gland (transitional and central zones) and are extremely difficult to identify, as this area is often heterogeneous and nodular due to the development of benign prostatic hyperplasia from middle age onwards. Rarely cancers are hyperechoic and appear similar to areas of benign calcification which are commonly seen in the central gland. Up to 50% of cancers are multifocal and/or bilateral (Fig. 31.45). Cancers less than 1 cm diameter are difficult to detect with transrectal ultrasound, with approximately 80% not seen. Colour flow Doppler and ultrasound contrast medium have been reported to increase the sensitivity of transrectal ultrasound for the detection of cancers and their differentiation from benign lesions; however, a histological diagnosis is still required and the major use of transrectal ultrasound is to guide prostatic biopsies.

Routine antibiotic cover is required for transrectal biopsy; for example, ciprofloxacin 1000 mg orally 6-24 h prior to the procedure, metronidazole 1000 mg rectally immediately after the procedure, and ciprofloxacin 500 mg orally for 2 days afterwards. Multiple biopsies are performed with an 18 G cutting needle and a spring-loaded biopsy gun. The recommended number of biopsies to be taken continues to rise. Initially biopsies were targeted only to ultrasonographically suspicious areas. The realisation that many carcinomas cannot be detected ultrasonographically led to quadrant biopsies being routinely performed. Further work suggested that the detection rate of carcinomas would be increased by sextant biopsies. These can either be performed as high, middle and low biopsies on each lobe or as a fan shape (medial, middle and lateral on each side), with similar tumour detection rates or even better detection for the fan-shape protocol.

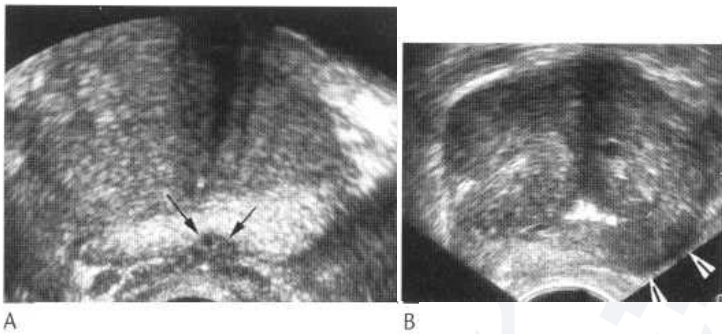


Fig. 31.44 Transrectal ultrasound (transverse images) on patients with prostatic cancer. (A) shows a tiny peripherally placed carcinoma as a hypoechoic nodule (arrows) easily seen against the remainder of the normal hyperechoic peripheral gland. (B) shows a larger area of reduced echogenicity (arrowheads) replacing much of the left peripheral gland and showing an ill-defined infiltrative margin towards the adjacent central gland. It currently, however, still appears confined by the prostatic capsule. (C) shows an extensive prostatic cancer seen as a sheet of echo-poor material that has replaced the normal peripheral gland and is infiltrating anteriorly into the central gland.

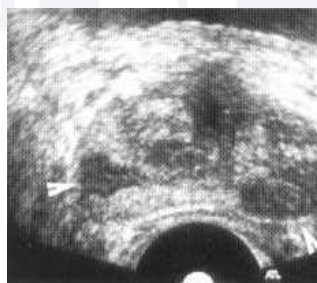
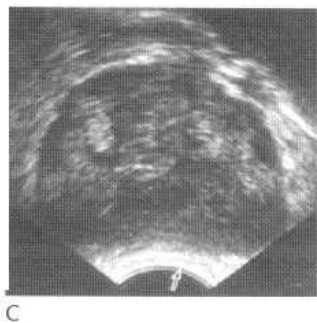


Fig. 31.45 Transrectal ultrasound (transverse image) showing multifocal echo-poor prostatic cancer (two nodules identified by arrowheads).



Fig. 31.46 Transrectal ultrasound (longitudinal image) showing echo-poor tumour in the peripheral gland extending anteriorly into the adjacent central gland and superiorly into the seminal vesicle.

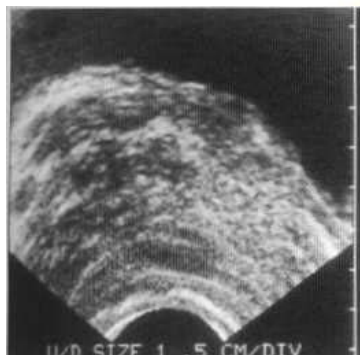


Fig. 31.47 Transrectal ultrasound (transverse image) showing echo-poor tumour infiltrating throughout the prostate, predominantly the right lobe, and extending laterally through the capsule on the right into the periprostatic fat.

Recently octant biopsies have been recommended and some centres are now advocating 12 or 13 routinely. It is still uncertain whether this increases the complication rate. The degree of discomfort associated with each biopsy varies between patients and has been described as similar to having a blood test taken; considerable discomfort or pain is reported by around 24% of patients. Low biopsies that catch the anal ring or the prostatic apex are extremely painful. Complications include haematuria (sometimes with retention), rectal bleeding, haemospermia and infection, which varies from cystitis to life-threatening septicaemia.

Prostate cancers can be locally staged with transrectal ultrasound. The size of the tumour, invasion of the seminal vesicles (Fig. 31.46) and the presence of multifocal tumours may be noted with variable accuracy and influence the prognosis. Extension of tumour through the capsule (Fig. 31.47) and beyond, particularly into the rectum, may also be demonstrated. The accuracy of ultrasound staging is debated and may be little better than digital rectal examination. Accuracies of around 78% for seminal vesicle invasion and 58–86% for extracapsular spread have been reported.

Regional lymph nodes are rarely visible on transrectal ultrasound. Recent work has examined the role of transrectal ultrasound in patients who have undergone radical prostatectomy for carcinoma of the prostate. The normal postoperative appearances are of a smooth tapered bladder neck with a symmetrical urethrovesical anastomosis. Recurrent disease may be seen as additional irregularly-shaped tissue which is usually hyp-echoic and in the area of the urethrovesical anastomosis.

MAGNETIC RESONANCE IMAGING OF THE BLADDER AND PROSTATE

Jeremy P. R. Jenkins

MRI is well suited to the evaluation of the pelvis, providing high soft-tissue contrast resolution and clear anatomical depiction of pelvic organs. Bladder musculature, zonal anatomy of the prostate

and uterus, tumours and other lesions can be demonstrated on T₂-weighted images. Vascular structures are easily distinguished from surrounding tissues and lesions on T₁- or proton density-weighted images without the need for intravenous contrast enhancement. Motion artefacts in the pelvis are less of a problem than with abdominal MRI. MRI is useful in the paediatric age group as it avoids the use of ionising radiation.

Transabdominal and transvaginal ultrasound are the techniques employed for the initial investigation of pelvic pathology and are usually sufficient for evaluation of benign disease, with MRI being used for problem-solving; however, MRI has become invaluable in the evaluation of malignant disease within the pelvis.

Normal appearances The bladder wall has low signal on T₁- and T₂-weighted images, whereas urine because of its very long T₁ and T₂, appears as low and high signal, respectively. Urine and bladder wall appears low signal on T₁-weighted scans and cannot be clearly distinguished. On T₂-weighted images, however, the bladder wall is demonstrated as a low-signal band, contrasting with the high signal from urine and perivesical fat. The fully distended bladder wall measures approximately 2 mm in thickness. A *chemical shift* artefact can occur between the water protons of the bladder wall and adjacent fat protons in the perivesical tissue (Fig. 31.48A). It produces a low-signal-intensity line at one edge of the bladder wall, with a high-signal band opposite, mimicking muscular hypertrophy or invasion, respectively. This artefact, which is more pronounced on high field strength systems, can be reduced by use of RF bandwidth adjust-

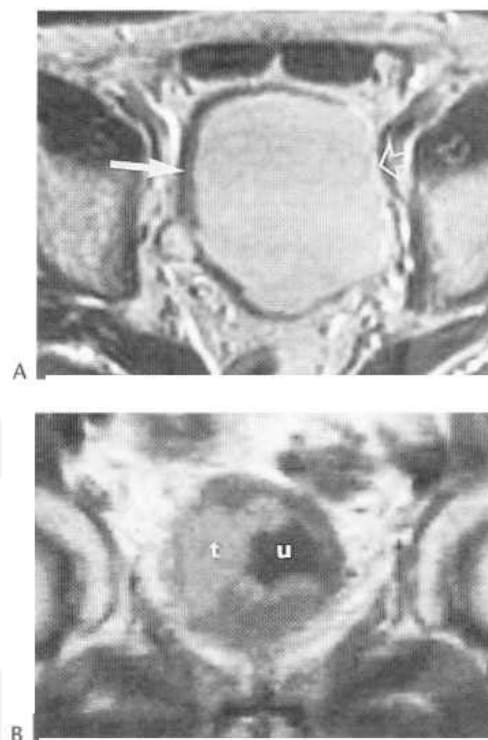


Fig. 31.48 (A) Transverse T₂-weighted spin-echo (SE 2000/80) image demonstrating a chemical shift artefact in the frequency direction (horizontal) with a low-signal-intensity line at one edge of the bladder wall (straight solid arrow) and a high-signal band in the opposite wall (open arrow). (B) Bladder tumour (histological stage T₂) with an intact low-signal bladder wall peripherally on a coronal intermediate-weighted spin-echo (SE 1200/26) image. t = tumour; u = urine.

Box 31.2 TNM staging of bladder carcinoma

T1	Invades subepithelial connective tissue
T2	Invades muscle
T2a	Invades superficial muscle (inner half)
T2b	Invades deep muscle (outer half)
T3	Invades perivesical tissue
T3a	Microscopically
T3b	Macroscopically (extravesical mass)
T4	Invades any of following: prostate, uterus, vagina, pelvic wall, abdominal wall
T4a	Invades prostate or uterus or vagina
T4b	Invades pelvic wall or abdominal wall
N1	Metastasis in a single lymph node 2 cm or less in greatest dimension
N2	Metastasis in a single lymph node >2 cm but < 5 cm in greatest dimension, or multiple lymph nodes, none >5 cm in greatest dimension
Mi	Distant metastasis

ment (i.e. increasing the bandwidth reduces the chemical shift artefact but the downside is a reduced signal to noise) or fat suppression techniques.

Bladder cancer

Purpose of imaging There are three main reasons for imaging patients with established bladder cancer: (i) to stage the tumour; (ii) to assess response to treatment; and (iii) to identify recurrent disease.

Staging In the United Kingdom and Europe, the TNM system is used to stage bladder cancer. The extent of spread within the bladder wall, the perivesical fat and adjacent organs (T stage), spread to pelvic and abdominal lymph nodes (N stage), and distant metastases (M stage) are assessed (Box 31.2).

Technique Prior to imaging it is essential to have a comprehensive and accurate clinical history. Recent endoscopic resection or biopsy gives rise to haemorrhage and oedema, which can produce misleading appearances on MRI.

The imaging technique is outlined in the Royal College of Radiologists' booklet *A Guide to the Practical Use of MRI in Oncology*. The patient should have a moderately full bladder in order to distend the bladder wall. An overfull bladder will result in

patients restlessness during the examination. An antiperistaltic agent such as glucagon can be administered to reduce bowel motion artefact. If available, a pelvic phased-array coil should be used for evaluation of the whole pelvis and abdomen. Transverse and coronal large field of view (typically 38–49 cm) T₁-weighted images of the abdomen and pelvis are obtained in order to evaluate the upper abdominal viscera, particularly the kidneys, for the presence of hydronephrosis, to identify any lymph node enlargement and the presence of bone metastases.

Transverse and coronal small field of view (typically 20–24 cm) T₁-weighted images of the pelvis are obtained in order to demonstrate the local and regional extent of tumour and to reconfirm the presence of lymph node metastases. Additional sagittal images can be obtained for tumours that are present in the bladder base or vault (Fig. 31.49). The use of intravenous gadolinium-chelate is not mandatory. It can be helpful to demonstrate small lesions and the extent of tumour spread through and beyond the bladder wall and invasion of adjacent organs, as the tumour enhances to a greater extent than the bladder wall (Fig. 31.50). A dynamic contrast-enhanced technique produces the best results, as tumour enhances during the early phase following injection, contrasted with the later

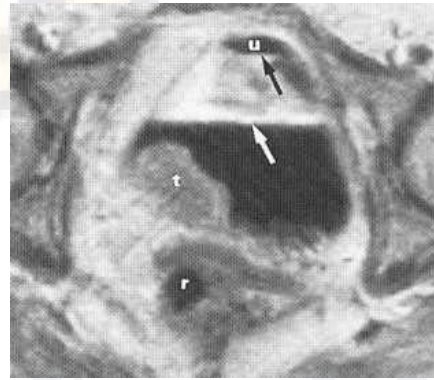


Fig. 31.50 Enhancing bladder carcinoma (t) in the posterolateral part of the bladder on a transverse T₁-weighted spin-echo (SE 740/40) post-gadolinium-DTPA image. Note the three layers—unopacified urine (u), signal void posteriorly in the bladder due to the superparamagnetic effect of high concentrations of gadolinium-DTPA, with a high-signal layer in between due to the paramagnetic effect of normal concentrations of gadolinium-DTPA. Also note the heterogeneity of signal within the middle layer due to urine flow. r = rectum; arrows = fluid levels.



Fig. 31.49 Extensive T_{3b} bladder tumour shown on (A) a transverse T₂-weighted spin-echo (SE 3000/100) image; (B) transverse (at the same anatomical level as (A)) and (C) parasagittal T₂-weighted spin-echo (SE 3000/100) images with fat suppression. The tumour (curved arrow) is infiltrating through the bladder wall (straight arrows), which is better appreciated on the fat suppression scans. p = prostate.

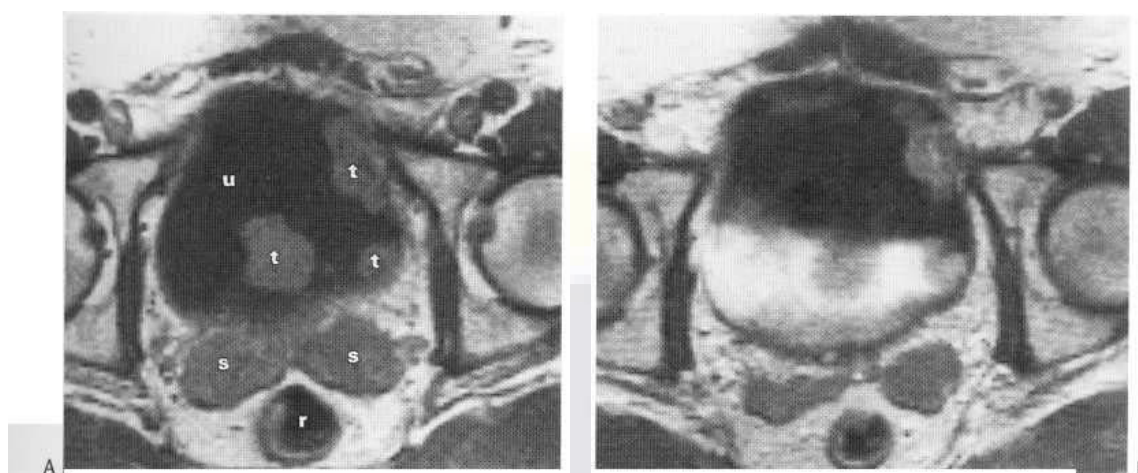


Fig. 31.51 Multiple confined bladder tumours (t) on transverse T_1 -weighted spin-echo (SE 740/40) (A) pre- and (B) early postgadolinium-DTPA images. Note the enhancing tumour anterolateral to the left is well visualised but the posterior-based lesions are obscured due to the high-signal effect of normal concentrations of gadolinium-DTPA. r = rectum; s = seminal vesicles; u = urine.

enhancement of normal structures (Fig. 31.51). Gadolinium-chelate is useful in the differentiation of enhancing tumour from non-enhancing intraluminal blood clots. The use of intravenous contrast has drawbacks. Enhancement within a tumour can make it more difficult to identify its outer margin separate from the high-signal perivesical fat. Enhancing pelvic lymph nodes and lytic bone metastases can become less conspicuous on postgadolinium-chelate T_1 -weighted images. The use of fat suppression sequences helps to rectify these drawbacks and increase the sensitivity for the detection of bone metastases.

MR findings in bladder carcinoma Lesions less than 1.0 cm in diameter cannot be reliably detected on MRI. On T_1 -weighted images the tumour is usually of medium signal intensity, higher than that of surrounding urine but lower than perivesical fat (Fig. 31.52). The tumour size, its intravesical component and extension into perivesical fat are best demonstrated on T_1 -weighted or fat-suppressed T_2 -weighted scans (Figs 31.49, 31.52). Tumours on T_2 -weighted images, particularly with fat suppression technique, show intermediate signal intensity lower than adjacent urine. T_2 -weighted images show extension through the bladder

wall and infiltration of adjacent organs, the former being recognised by disruption of the normal low-signal band (Fig. 31.53). Bladder carcinomas involving only the mucosa and submucosa (TNM stage T1) cannot be differentiated from those with superficial muscle infiltration (stage T2). It is sometimes possible to distinguish lesions involving only the superficial muscle layer (stage T2a) from those invading the deep muscle (stage T2b), based on the preservation of the integrity of the black line of the bladder wall remaining intact on T_1 -weighted images when the deep muscle layer is not involved. However, the important clinical question is whether sufficient bladder muscle is present deep to the tumour for endoscopic resection to be performed. The ability to obtain this information preoperatively can make some stage T3 lesions, at present treated by radiotherapy, amenable to endoscopic resection. Stage T3b tumour represents infiltration through the bladder wall into the perivesical fat, with stage T4a disease showing invasion of local organs and stage T4b indicated by pelvic or abdominal wall infiltration (Fig. 31.54).

As with CT, MRI relies on enlargement of lymph nodes to demonstrate the presence of metastatic disease within them. This has the drawback that metastatic tumour will not be identified in

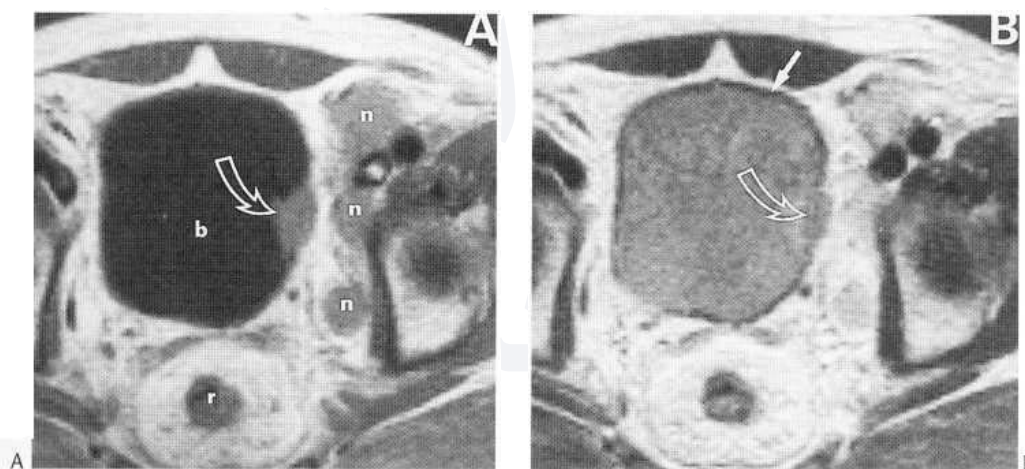


Fig. 31.52 Histological stage 13b bladder carcinoma (curved open arrow) on transverse (A) T_1 -weighted spin-echo (SE 700/40) and (B) moderately T_2 -weighted spin-echo (SE 1800/80) images. The intraluminal component of the tumour is well shown in (A) but the destruction of the low-signal bladder wall (straight arrow) is better demonstrated in (B). Left-sided pelvic lymphadenopathy (n) shown in (A) is obscured in (B). b = bladder; r = rectum.

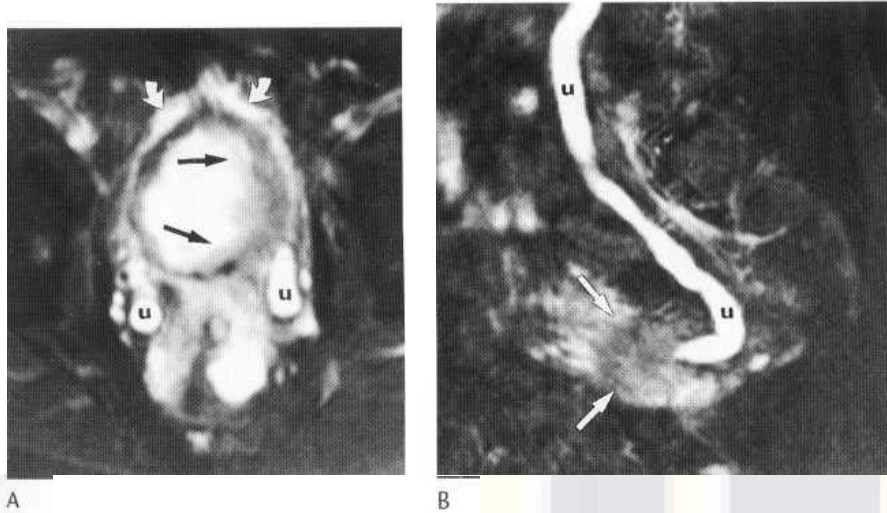


Fig. 31.53 Extensive stage T3b bladder tumour (straight arrows) with bilateral obstructive uropathy on (A) transverse and (B) parasagittal T₂-weighted spin-echo (SE 3500/100) images with fat suppression. The dilated ureters (u) are clearly shown to contain high-signal urine with no spread of the transitional cell carcinoma into the ureters. This was suggested on CT (not shown). There is also ascites (curved arrows) present.

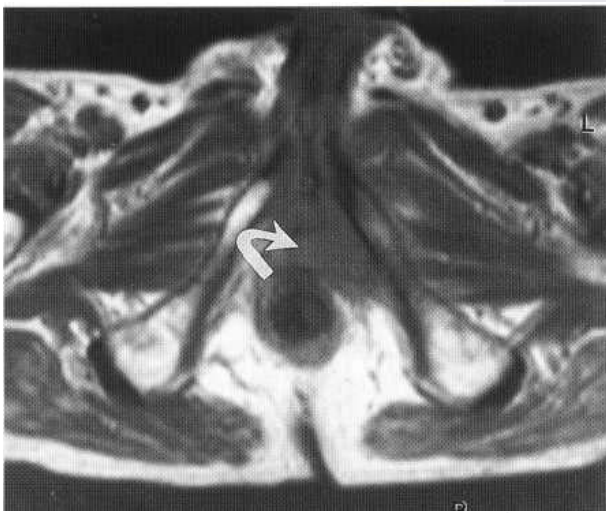


Fig. 31.54 Metastatic transitional cell bladder carcinoma on a transverse T₁-weighted spin-echo (SE 520/15) image showing a soft-tissue mass in the perineum (arrow) involving the left corpus cavernosum and left inferior pubic ramus.

normal-sized nodes, and tumour may be incorrectly diagnosed within enlarged hyperplastic nodes. In addition, in bladder cancer lymph nodes can frequently be completely replaced by tumour without becoming enlarged, resulting in high false-negative rates

for identification of metastatic disease. Ten millimetres is usually taken as the upper limit of normal for lymph nodes within the pelvis (with more refined measurements noted for certain nodal sites – common iliac 9 mm, internal iliac 7 mm, and obturator 8 mm). It should be noted that the maximum short axis diameter of the lymph node is used for measurement purposes, as it has been found that this measurement remains relatively constant irrespective of the orientation of the node in the vertical plane. Central and posterior pelvic nodes (paracervical, perirectal and presacral) are not usually visualised in normal individuals, therefore when they are identified they are highly suspicious of nodal metastases (Fig. 31.55).

Thorough scrutiny of the visualised portions of the lung bases, liver and bones should be performed to identify distant metastatic disease. Bone metastases are most conspicuous on T₁-weighted images and can be characterised by correlation with the accompanying T₂-weighted images.

Post-treatment appearances and recurrent disease Following treatment with radiotherapy or surgery, there is frequently oedema, inflammation and fibrosis, with consequent thickening of the bladder wall and distortion of the perivesical fat (Fig. 31.56). Radiotherapy change can persist for up to 2 years following treatment. Because of this, using MRI or CT to differentiate between post-treatment change and recurrent tumour is frequently unreliable. Comparison with pretreatment imaging is

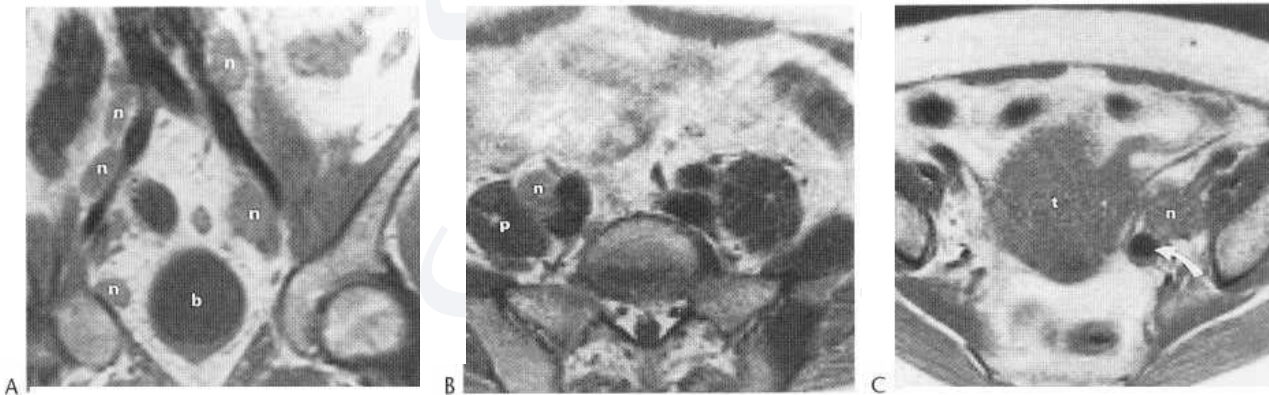


Fig. 31.55 Pelvic lymphadenopathy (n) demonstrated on T₁-weighted spin-echo (SE 740/40) images in (A) coronal and (B,C) transverse planes in different patients. The soft-tissue signal from the lymphadenopathy contrasts well with the signal void from flowing blood within adjacent vessels and high signal from surrounding fat. b = bladder; p = psoas muscles; t = bladder tumour; arrow = dilated left ureter filled with low-signal urine.

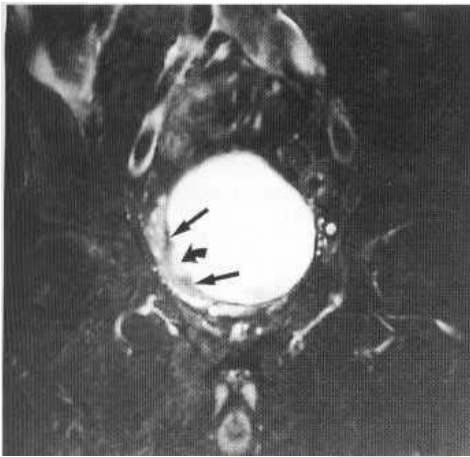
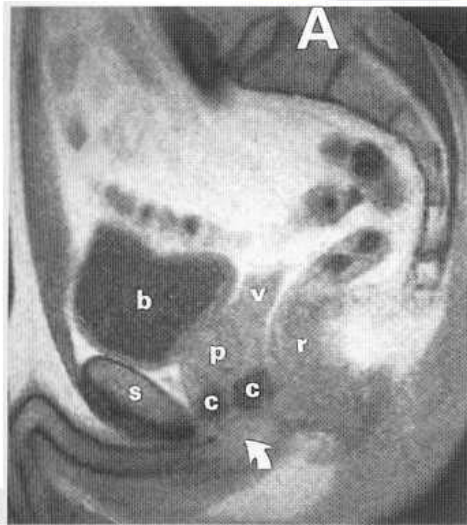
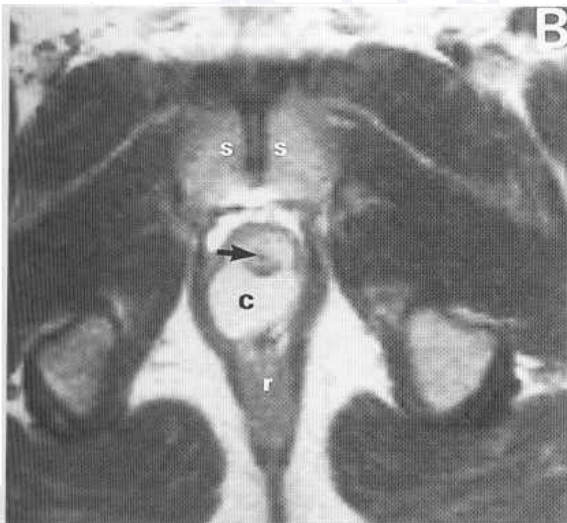


Fig. 31.56 Resected stage T1/T2 bladder tumour with a focal area of wall thickening (straight arrows) and ulcer crater (curved arrow) with no residual tumour on a coronal T₂-weighted spin-echo (FSE 3000/100) image with fat suppression. (1.5 T CE Horizon using a phased-array pelvic coil.)



A



B

Fig. 31.57 Cyst of Cowper's gland (c) on spin-echo (A) sagittal intermediate-weighted (SE 1100/26) and (B) transverse T₂-weighted (SE 2000/80) images. Note that the urethra is well visualised between the anterior and posterior parts of the cyst in (A). b = bladder; p = prostate; r = rectum; s = symphysis pubis; v = seminal vesicles; straight arrow = urethra; curved arrow = bulb of penis.

mandatory in order to identify a new soft-tissue mass at the site of suspected tumour recurrence, or the presence of new metastatic disease within lymph nodes or distant organs to indicate progressive disease. Dynamic imaging following gadolinium-chelate has been shown to help differentiate between radiotherapy change and recurrent tumour but it requires the construction and analysis of time-signal intensity curves and is not routinely employed in clinical practice.

MRI versus CT MRI has been consistently shown to be superior to CT in demonstration of tumour invasion of the deep muscle layer of the bladder (stage T2b) and early invasion of the perivesical tissues (stage T3a). In more advanced disease, CT and MRI are of similar accuracy for staging bladder cancer. However, while both CT and MRI rely on alterations in size and contour of adjacent organs in order to identify pathological changes, MRI has the advantage that changes in signal intensity also occur within those organs. MRI and CT both rely on lymph node enlargement to identify metastatic disease but MRI has the advantage over CT in that it can differentiate between ectatic pelvic vessels and enlarged nodes without the need for intravenous contrast enhancement. A recent advance of MRI is in the use of ultrasmall iron oxide particles (USIOP) (particle size of 20 nm), which are injected intravenously and taken up by normal and hyperplastic lymph nodes, producing a signal void (a superparamagnetic effect). Tumour-replaced nodes fail to take up the contrast and retain their signal characteristics (see p. 1007).

Prostate

Normal appearances The normal prostate has a homogeneous low-intermediate signal on T₁-weighted images (Fig. 31.57). Zonal anatomy is best demonstrated on T₂-weighted images. It comprises a low-signal central zone and a higher signal peripheral zone (Fig. 31.58). The transitional and central zones appear of similar signal intensity and are loosely termed the central gland. The prostate does not have a well-defined capsule but is enveloped by a variable band of condensed fibromuscular tissue. The periprostatic venous plexus can be visualised as a thin rim of high signal intensity anterolateral to the peripheral zone (Figs 31.59, 31.60). Denonvilliers' fascia can be resolved on sagittal images separating the prostate from the rectum. The neurovascular

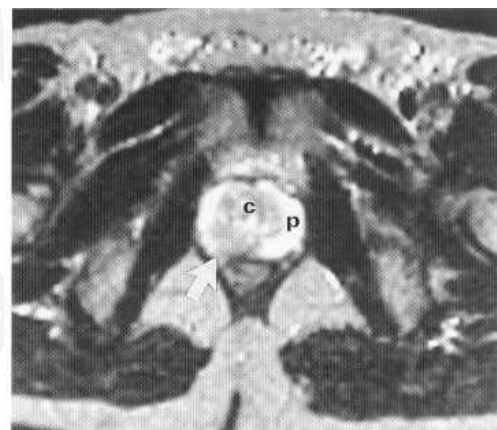


Fig. 31.58 Stage T3a prostate carcinoma (arrow) posterolateral to the right in the peripheral zone infiltrating through the capsule into the adjacent neurovascular bundle. p = peripheral zone; c = central gland.

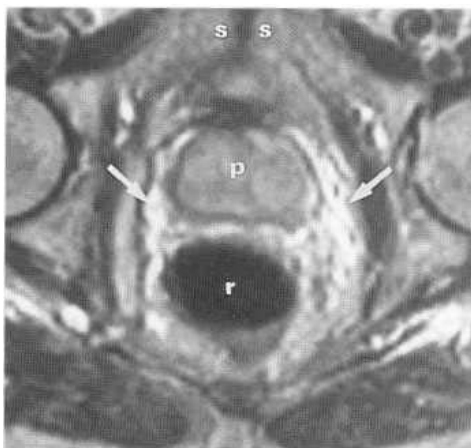


Fig. 31.59 Transverse T₂-weighted spin-echo (SE 2000/80) image through the prostate of an 80-year-old patient. Note that there is no differentiation between the central and peripheral zones due to benign prostatic hypertrophy. p = prostate; r = rectum; s = symphysis pubis; arrows, periprostatic venous plexus.



Fig. 31.60 Benign prostatic hypertrophy (p) on a fat-suppressed coronal T₂-weighted spin-echo (FSE 3500/100) image. Arrows = periprostatic venous plexus. (1.5 T IGE Horizon using a phased-array pelvic coil.)

bundles are sited posterolaterally at 5 and 7 o'clock positions on transverse sections of the prostate. Within this neurovascular bundle are the nerves supplying the corpora cavernosa of the penis and the external urethral sphincter, the preservation of which is critical for maintaining erectile function and urinary continence.

Prostate cancer

Purpose of imaging MRI is used to stage the extent of prostate cancer once the diagnosis has been established and to identify the presence of recurrent disease following treatment. It is important to realise that MRI is not used in the primary diagnosis of prostate cancer. This is usually established following biopsy at transrectal ultrasound.

The main role of MRI in staging prostate cancer is to determine whether disease is limited to the prostate gland. Debate still exists about the optimum treatment modality for limited disease, the choice being between nerve-sparing radical prostatectomy, radical external beam radiotherapy, or prostate brachytherapy. Patients with

Box 31.3 TNM staging of prostate carcinoma

T1	Clinically inapparent tumour not palpable nor visible by imaging
T2	Confined to the prostate
T2a	Involves one lobe
T2b	Involves both lobes
T3a	Extracapsular extension
T3b	Invades seminal vesicle
T4	Fixed or invades adjacent structure other than seminal vesicles: bladder neck, external sphincter, rectum, levator muscles, and/or pelvic wall
N1	Regional lymph node metastases
M1	Distant metastatic disease

more extensive disease are usually treated with external beam radiotherapy and hormone treatment.

Following treatment, monitoring of the serum prostate-specific antigen (PSA) is performed. Patients with rising PSA levels or others who are suspected of having recurrent disease have imaging evaluation of the skeleton using isotope bone scintigraphy, and of the lower spine and pelvis using MRI.

Staging The International Union Against Cancer (IUC) system is used to stage prostate cancer (Box 313). The usual pattern of spread is direct extension through the prostatic capsule into the bladder base and seminal vesicles. The presence of Denonvilliers' fascia prevents direct spread to the urethra and rectum unless there is extensive disease. The deficiency of the capsular condensation of fibromuscular tissue at the apex of the gland increases the likelihood of extracapsular extension occurring here.

Lymph node metastases initially occur in the local pelvic nodes, particularly the obturator nodes, and in the retroperitoneal nodes in more advanced disease. Distant metastases occur most frequently to bone, particularly that in the lumbar and thoracic spine because of the communication between the periprostatic venous plexus and the presacral veins. Bone metastases also occur in the appendicular skeleton, ribs and skull.

The majority (95%) of prostate cancers are adenocarcinomas, although other malignant tumour types do occur, notably transitional and squamous cell carcinoma. Within one gland, foci of tumour with different degrees of differentiation can occur. Poorly differentiated tumours tend to have a worse prognosis. The Gleason system of grading the degree of malignancy calculates the sum of the two predominant histological types within the gland and attributes each one a score out of 5, giving a sum of between 2 and 10. Glands with a score of 10 contain the most undifferentiated tumour and therefore these patients have the worst prognosis.

Technique Imaging technique is outlined in the Royal College of Radiologist booklet *A Guide to the Practical Use of MR in Oncology*. The patient should empty his bladder prior to the examination. If available, a pelvic phased-array coil should be used for evaluation of the whole pelvis and abdomen. An endorectal coil can be employed. This improves the spatial resolution within the area adjacent to the coil and can improve the accuracy in determining extracapsular extension of tumour: therefore, endorectal coils are most valuable in the evaluation of early stage disease. They have the drawback of a limited field of view and near-field artefacts, and being invasive. Some MRI systems combine pelvic phased-array and endorectal coils and, although not widely employed, these should help to resolve some of the drawbacks of endorectal coil imaging. Transverse and coronal

large field of view T₁-weighted images of the abdomen and pelvis are obtained in order to evaluate the upper abdominal viscera, particularly the kidneys, for the presence of hydronephrosis, to identify any lymph node enlargement and the presence of bone metastases.

Transverse, coronal and sagittal small field of view T₂-weighted images of the pelvis are obtained in order to demonstrate the local and regional extent of tumour and to reconfirm the presence of lymph node metastases. Sagittal and coronal images are particularly useful for evaluating the bladder base and extension of spread into the bladder neck and seminal vesicles.

As in bladder cancer, the use of gadolinium-chelate is not mandatory. Tumours in the central zone can appear more conspicuous following contrast enhancement. A dynamic examination may help to identify localised extracapsular spread as prostate cancer enhances earlier than normal tissue. In addition, work has shown that there is a correlation between enhancement characteristics and the grade of the tumour.

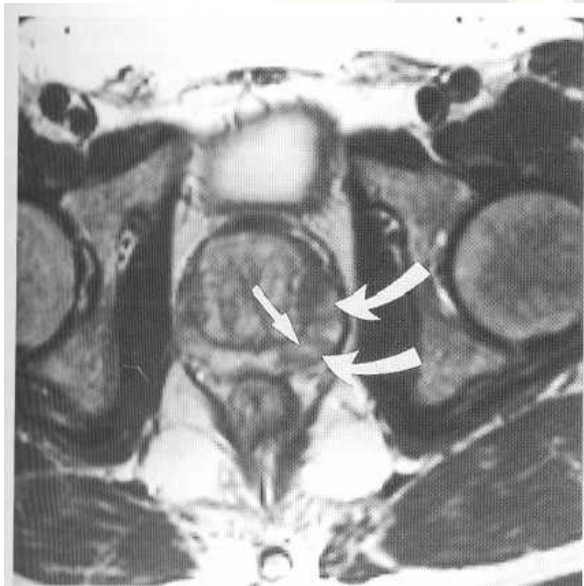


Fig. 31.61 Multifocal prostatic carcinoma (curved arrows) in the left peripheral zone with associated benign prostatic hypertrophy on a transverse T₁-weighted spin-echo (FSE 4000/104) image. Note the area of high signal (straight arrow) in the more posteriorly placed tumour due to haemorrhage from recent biopsy.



Fig. 31.62 Prostatic carcinoma (stage T₂) in the right peripheral zone (arrow) abutting onto the capsule on a fat-suppressed transverse T₂ prostatic hypertrophy. (1.5 T Philips Gyroscan using the body coil.)



Fig. 31.63 Stage T_{4a} prostatic carcinoma (arrow) infiltrating the bladder base on a fat-suppressed coronal T₂-weighted spin-echo (TSE 3500/100) image. This tumour was not detected on transrectal ultrasound examination (not shown). (1.5 T Philips Gyroscan using the body coil.)

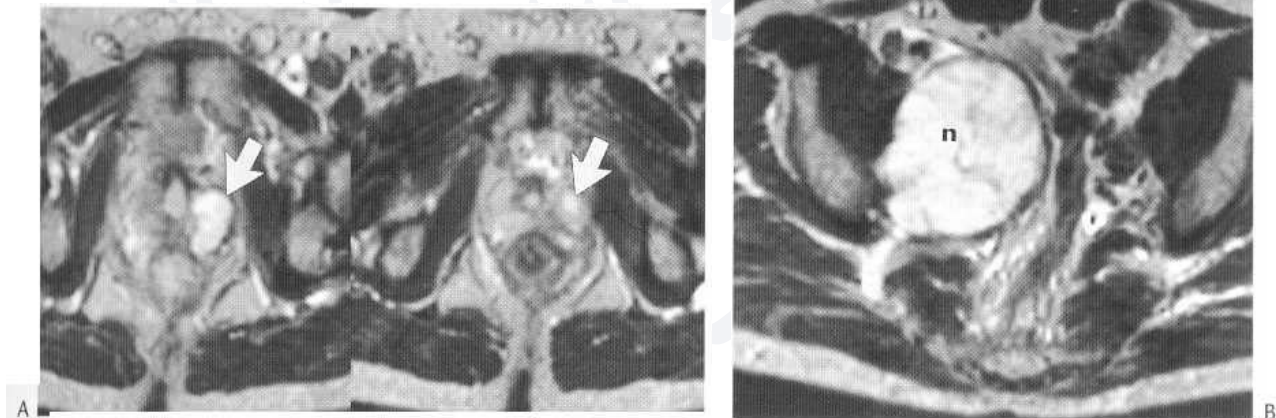


Fig. 31.64 (A,B) Mucin-secreting adenocarcinoma of the prostate (straight arrows) extending through the capsule with a large right pelvic nodal metastasis (n) on transverse T₂-weighted spin-echo (SE 2000/100) images. Note the similar high signal from the primary prostatic tumour and nodal disease.

MR findings in prostate cancer It is re-emphasised that MRI is not used for the diagnosis of prostate carcinoma. A normal-appearing prostate gland on MRI does not exclude the presence of a tumour. Conversely, a number of conditions can produce findings that mimic the presence of tumour. Benign prostatic hypertrophy which occurs in the transitional zone can be marked and give rise to a very heterogeneous appearance of the gland. Prostatitis and artefacts from haemorrhage and oedema, secondary to recent biopsies, can also cause confusion (Fig. 31.61).

Approximately 70% of tumours arise in the peripheral zone, 20% in the transitional zone, and 10% in the central zone. The usual pattern is of a single focus of low signal intensity on the T₂-weighted images seen within the peripheral zone but tumours can

be multifocal or diffusely infiltrating (Figs 31.61-31.63). Confusingly, up to a third of low-signal areas within the peripheral zone on T₂-weighted images may not be due to tumour and represent fibrosis or other benign pathology. In addition, the carcinoma may be isointense or hyperintense compared with the peripheral zone, the latter found in rare mucin-producing adenocarcinomas (Fig. 31.64). Tumour occurring in the transitional zone cannot be reliably distinguished from the heterogeneous signal due to benign prostatic hypertrophy.

Extension of the tumour through the capsule is usually adjacent to the neurovascular bundles, at the sites of nerve penetration of the capsule (perineural infiltration). Macrocapsular penetration (arbitrarily defined as tumour extending more than 2 mm beyond the capsule) can be assessed on MRI, and is shown as focal thickening and/or bulging of the capsule (Fig. 31.65). Periprostatic infiltration can be demonstrated on T₂-weighted images as a low signal within the periprostatic fat or as an intermediate signal using T₂-weighted fat-suppressed scans. Tumour extension into the seminal vesicles, recognised as an alteration of signal as well as surface contour, is

Extension of tumour into the bladder and rectum is best appreciated on transverse and sagittal T₂-weighted scans. Direct infiltration of



Fig. 31.65 Stage T3a prostatic carcinoma extending through the capsule (arrow) posterolaterally to the left with involvement of the adjacent neurovascular bundle on a fat-suppressed transverse T₂-weighted spin-echo (TSE 5000/117) image. (1.5 T IGE Horizon using a phased-array pelvic coil.)

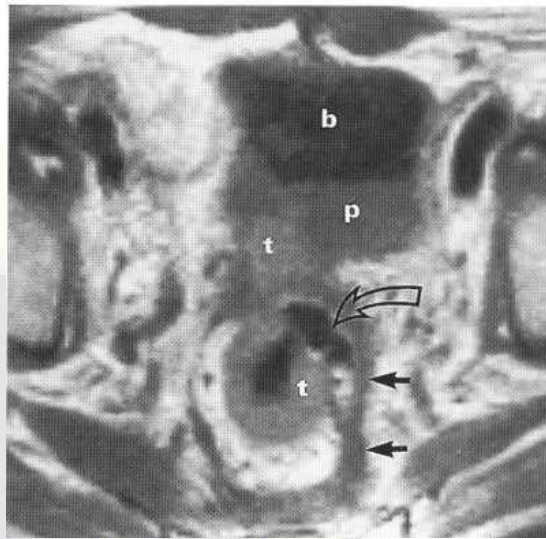


Fig. 31.66 Recurrent rectal carcinoma (t) infiltrating an enlarged prostate (p) from benign prostatic hypertrophy. b = bladder, curved open arrow = perforation into the perirectal fat space; straight arrows - thickened left perirectal fascia.

the prostate from primary tumours of the bladder or rectum can also be demonstrated (Fig. 31.66). T₁- and T₂-weighted images can be used for the detection of lymph node metastases. As with CT, MRI relies on enlargement of lymph nodes to demonstrate the presence of metastatic disease within them.

Thorough scrutiny of the visualised portions of the lung bases, liver and bones should be performed to identify metastatic disease and to evaluate the presence of hydronephrosis. Sclerotic bone metastases from prostate cancer are frequently of low signal on T₁-best demonstrated on transverse and coronal T₂-weighted images, and T₂-

post-treatment appearances and recurrent disease After irradiation or hormonal therapy, the prostate often becomes low signal on T₂-weighted images, an appearance that should not be confused with tumour recurrence. The seminal vesicles can also become deformed and show low-signal change but may retain small focal areas of high-signal fluid. After a time, the peripheral zone of the prostate may revert to its normal high signal on T₂-weighted images.

Following treatment, a patient with prostatic carcinoma is monitored for recurrent tumour by serial serum PSA levels. Patients with rising levels normally have evaluation with isotope bone scintigraphy, to identify disease in the skeleton, and MRI, to identify disease in the residual prostate or prostatic bed, and lymph node enlargement within the pelvis and retroperitoneum. The presence of an irregular new low-to-intermediate signal intensity mass on the T₂-weighted images is highly suspicious of recurrent disease.

Reference to previous imaging is, of course, very useful and recommended.

MRI versus transrectal ultrasound Transrectal ultrasound has established an essential role in the initial evaluation and biopsy of suspected prostate cancer; however, the results for its accuracy in staging, particularly predicting capsular penetration and seminal vesicle invasion, have been variable. Transrectal ultrasound has the limitation of being operator-dependent and dependent on the quality of the ultrasound machinery available. It cannot evaluate lymph node enlargement on the pelvic side-wall or retroperi-

toneum or identify the presence of distant metastatic disease. Because of this, MRI has been adopted as the imaging modality of choice in staging prostatic carcinoma, although with reported accuracies ranging from 70 to 90% improvements are required, particularly in the staging of early disease.

REFERENCES AND SUGGESTIONS FOR FURTHER READING

- Balaji, K. C., McGuire, M., Grotas, J. (1999) Upper tract recurrences following radical cystectomy: an analysis of prognostic factors, recurrence pattern and stage at presentation. *Journal of Urology*, 162, 1603-1606.
- Brossner, C., Bayer, G., Madersbacher, S., Kuber, W., Klingler, C., Pycha, A. (2000) Twelve prostate biopsies detect significant cancer volumes (>0.5 ml). *British Journal of Urology International*, 85, 705-707.
- Brossner, C., Madersbacher, S., Klingler, H. C., Pycha, A., Kuber, W., Marberger, M. (1998) A comparative study of a double-line versus a fan-shaped technique for obtaining transrectal ultrasound-guided biopsies of the prostate. *European Urology*, 33, 556-561.
- Charnsangavej, C. (1990) Lymphoma of the genitourinary tract. *Radiologic Clinics of North America*, 28, 865-877.
- Clements, R. (1996) The changing role of transrectal ultrasound in the diagnosis of prostate cancer. *Clinical Radiology*, 51, 671-676.
- Clements, R. (2001) Contemporary ultrasound guided biopsy in the diagnosis of prostate cancer. *Imaging*, 13, 18-26.
- Corrigan, N. T., Crooks, J., Shand, J. (2000) Are dedicated bladder films necessary as part of intravenous urography for haematuria? *British Journal of Urology International*, 85, 806-810.
- Crundwell, M. C., Cooke, P. W., Wallace, D. M. A. (1999) Patient's tolerance of transrectal ultrasound-guided prostatic biopsy: an audit of 104 cases. *British Journal of Urology*, 83, 792-795.
- Fontaine, E., Leaver, R., Woodhouse, C. R. J. (2000) The effect of intestinal urinary reservoirs on renal function: a 10 year follow-up. *British Journal of Urology*, 86, 195-198.
- Ganaway, W. M., Alexander, F. E. (1997) Prostate disease: epidemiology, natural history and demographic shifts. *British Journal of Urology*, 79(suppl. 2), 3-8.
- Grossfeld, G. D., Coakley, M. B. (2000) Benign prostatic hyperplasia: clinical overview and value of diagnostic imaging. *Radiologic Clinics of North America*, 38, 31-47.
- Hakenburg, O. W., Linne, C., Manseck, A., Wirth, M. P. (2000) Bladder wall thickness in normal adults and men with mild lower urinary tract symptoms and benign prostatic enlargement. *Neurology and Uroynamics*, 19, 585-593.
- Hall, T. B., MacVicar, A. D. (2001) Imaging of bladder cancer. *Imaging*, 13, 1-10.
- Halpern, E. J., Rosenberg, M., Gomella, L. G. (2001) Prostate cancer: contrast-enhanced US for detection. *Radiology*, 219, 219-225.
- Herman, T. E., McAlister, W. H. (1991) Radiographic manifestations of congenital anomalies of the lower urinary tract. *Radiologic Clinics of North America*, 29, 365-382.
- Hession, P., Flynn, P. N., Goodfellow, J., Murthy, L. N. S. (1999) Intravenous urography in urinary tract surveillance in carcinoma of the bladder. *Clinical Radiology*, 54, 465-467.
- Khadra, M. H., Pickard, R. S., Charlton, M., Powell, P. H., Neal, D. F. (2000) A prospective analysis of 1930 patients with haematuria to evaluate current diagnostic practice. *Journal of Urology*, 163, 524-527.
- Leventis, A. K., Shariat, S. F. (2001) Local recurrence after radical prostatectomy: correlation of US features with prostatic fossa biopsy findings. *Radiology*, 219, 432-439.
- Salah, M. A. (2000) Ultrasonography of urinary tract lesions caused by hilarziasis in Yemeni patients. *British Journal of Urology International*, 86, 790-793.
- Samuel, M., Misra, D., Larcher, V., Price, E. (2000) *Schi.stosoma haematohium* infection in children in Britain. *British Journal of Urology International*, 85, 316-318.
- Sandler, C. M., Hall, J. T., Rodriguez, M. B., Corriere, J. N. (1986) Bladder injury in blunt pelvic trauma. *Radiology*, 158, 633-638.
- Smeulders, N., Woodhouse, C. R. J. (2001) Neoplasia in adult exstrophy patients. *British Journal of Urology International*, 87, 623-628.
- Vaccaro, J. P., Brody, J. M. (2000) CT cystography in the evaluation of major bladder trauma. *Radiographics*, 20, 1373-1381.
- Wilkinson, B. A., Hamdy, F. C. (2001) State-of-the-art staging in prostate cancer. *British Journal of Urology International*, 87, 423-430.
- Yousem, D., Gatewood, O. M. B., Goldman, S. M., Marshall, F. F. (1988) Synchronous and metachronous transitional cell carcinoma of the urinary tract: Prevalence, incidence and radiographic detection. *Radiology*, 167, 613-618.
- Yu, J. S., Kim, K. W., Lee, H. J., Lee, Y. J., Yoon, C. S., Kim, M. J. (2001) Urachal remnant diseases: spectrum of CT and US findings. *Radiographics*, 21, 451-461.

MRI

- Aerts, P., Van Hoe, L., Bosmans, H., Oyen, R., Marchal, G., Baert, A. L. (1996) Breath-hold MR urography using the HASTE technique. *American Journal of Roentgenology*, 166, 543-545.
- Barentz, J. O., Berger-Hartog, O., Witjes, J. A., et al (1998) Evaluation of chemotherapy in advanced urinary bladder cancer with fast dynamic contrast-enhanced MR imaging. *Radiology*, 207, 791-797.
- Barentz, J. O., Lager, G. J., van Vierzen, P. B. J., et al (1996) Staging urinary bladder cancer after transurethral biopsy: value of fast dynamic contrast-enhanced MR imaging. *Radiology*, 201, 185-193.
- Bluemke, D. A. (ed.) (2000) Oncologic MR imaging. *Magnetic Resonance Imaging Clinics of North America*, 8, 691-963.
- Brawer, M. K., Deering, R. E., Brown, M. S., et al (1994) Predictors of the pathological stage in prostate carcinoma. The role of neovascularity. *Cancer*, 73, 678-687.
- Brown, G., MacVicar, D., Ayton, V., Husband, J. E. (1995) The role of intravenous contrast enhancement in MR staging of prostatic carcinoma. *Clinical Radiology*, 50, 601-606.
- Chan, T. W., Kressel, H. Y. (1991) Prostate and seminal vesicles after irradiation: MR appearance. *Journal of Magnetic Resonance Imaging*, 1, 503-506.
- Chen, M., Hricak, H., Kalbhen, C. L., et al (1996) Hormonal ablation of prostatic cancer: effects on prostate morphology, tumor detection, and staging by endorectal coil MR imaging. *American Journal of Roentgenology*, 166, 1157-1163.
- Clare, M. C., Tempany, M. D. (eds) (1996) The male pelvis. *Magnetic Resonance Imaging Clinics of North America*, 4, 439-587.
- Epstein, J. I., Carmichael, M. J., Pizov, G., Walsh, P. (1993) Influence of capsular penetration on the progression following radical prostatectomy: a study of 196 cases with long term follow-up. *Journal of Urology*, 150, 135-141.
- Fernback, S. K., Feinstein, K. A. (1994) Abnormalities of the bladder in children: imaging findings. *American Journal of Roentgenology*, 162, 1143-1150.
- Hamm, B., Laniado, M., Saini, S. (1990) Contrast-enhanced magnetic resonance imaging of the abdomen and pelvis. *Magnetic Resonance Quarterly*, 6, 108-135.
- Harris, R. D., Schned, A. R., Heaney, J. A. (1995) Staging of prostate cancer with endorectal MR imaging: lessons from a learning curve. *Radiographics*, 15, 813-829.
- Hawnaur, J. M., Johnson, R. J., Isherwood, L., Jenkins, J. P. R. (1990) Gd-DTPA in MRI of bladder carcinoma. In Bydder, G., et al (eds) *Contrast Media in MRI, International Workshop, Berlin*, pp. 357-363. Netherlands: Medicorn Europe.
- Hricak, H., Carrington, B. M. (1991) *MRI of the Pelvis--A Text Atlas*. London: Martin Dunitz.
- Hricak, H., White, S., Vigernon, D., et al (1994) Carcinoma of the prostate gland: MR imaging with pelvic phased array coils versus integrated endorectal-pelvic phased array coils. *Radiology*, 193, 703-709.
- Huch Boni, R. A., Boner, J. A., Debatin, J. F., et al (1995) Optimisation of prostate cancer staging: comparison of imaging and clinical methods. *Clinical Radiology*, 50, 593-600.
- Husband, J. E. (1992) Review: staging bladder cancer. *Clinical Radiology*, 46, 153-159.
- Husband, J. E. S., Reznick, R. H. (eds) (1998) *Imaging in Oncology*. Oxford: ISIS Medical Media.
- Husband, J. E., Padhani, A. R., MacVicar, A. D., Revell, P. (1998) Magnetic resonance imaging of prostate cancer: comparison of image quality using endorectal and pelvic phased array coils. *Clinical Radiology*, 53, 673-681.
- Jenkins, J. P. R. (1990) Magnetic resonance imaging in oncology. In Johnson, R. J., Eddleston, B., Hunter, R. D. (eds) *Radiology in the Management of Cancer*, Ch. 2, pp. 25-58. Edinburgh: Churchill Livingstone.
- Jenkins, J. P. R., Zhu, X. P., Isherwood, I. (1990) Magnetic resonance imaging: H: A quantitative approach. In Peeling, W. B. (ed.) *The Role of Imaging in Prostatic Cancer*, pp. 19-26. Oxford: Medicine Group (UK).

- Johnson, R. J., Carrington, B. M., Jenkins, J. P. R., Barnard, R. J., Read, G., Isherwood, I. (1989) Accuracy in staging carcinoma bladder by magnetic resonance imaging. *Clinical Radiology*, 41, 258-263.
- MacVicar, A. D. (2000) Bladder cancer staging. *British Journal of Urology International*, 86 (suppl. 1), 111-122.
- Mirowitz, S. A., Brown, D. G., Heiken, J. P. (1993) Evaluation of the prostate and prostatic carcinoma with gadolinium enhanced endorectal coil MR imaging. *Radiology*, 186, 153-157.
- Outwater, E. K., Petersen, R. O., Siegelman, E. S., et al (1994) Prostate carcinoma: assessment of diagnostic criteria for capsular penetration on endorectal coil MR images. *Radiology*, 193, 333-339.
- Padhani, A. R., Gapinski, C. J., MacVicar, J. A., et al (2000) Dynamic contrast enhanced MR of prostate cancer: correlation with morphology and tumour stage, histological grade and PSA. *Clinical Radiology*, 55, 99-109.
- Passe, T. J., Blumcke, D. A., Siegelman, S. S. (1997) Tumor angiogenesis: tutorial on implications for imaging. *Radiology*, 203, 593-600.
- Quinn, S., Franzini, J., Denlow, T., et al (1994) MR imaging of prostate cancer with endorectal surface coil technique: correlation with whole mount specimens. *Radiology*, 190, 323-327.
- Rifkin, M. D., Zerhouni, E. A., Gatsonis, C. A., et al (1990) Comparison of magnetic resonance imaging and ultrasonography in staging early prostate cancer-results of a multi-institutional cooperative trial. *New England Journal of Medicine*, 323, 621-626.
- Robinson, P., Collins, C. D., Ryder, W. J., et al (2000) Relationship of MRI and clinical stage to outcome in invasive bladder cancer treated by radiotherapy. *Clinical Radiology*, 55, 301-306.
- Rgrvik, J., Halvorsen, O. J., Albrektsen, G., Ersland, L., Deehlin, L., Haukaas, S. (1999) Use of pelvic surface coil MR imaging for assessment of clinically localised prostate cancer with histopathological correlation. *Clinical Radiology*, 54, 164-169.
- Saini, S., Modic, M. T., Hamm, B., Hahn, P. F. (1991) Advances in contrast-enhanced MR imaging. *American Journal of Roentgenology*, 156, 235-254.
- Scheidler, J., Hricak, H., Vigneron, D. B., et al (1999) Prostate cancer: localisation with three-dimensional proton MR spectroscopic imaging - clinicopathologic study. *Radiology*, 213, 473-480.
- Schnall, M. D., Bezzi, M., Pollack, H. M., Kressel, H. Y. (1990) Magnetic resonance imaging of the prostate. *Magnetic Resonance Quarterly*, 6, 1-16.
- Stark, D. D., Bradley, W. G. (eds) (1999) *Magnetic Resonance Imaging*, 3rd edn, Ch. 27 (Urinary bladder), Ch. 30 (Prostate and seminal vesicles). St Louis: Mosby.
- Tentpany, C., Zhou, X., Zerhouni, E., et al (1994) Staging of prostate cancer with MRI: results of Radiology Diagnostic Oncology Group project-comparison of different techniques including endorectal coil. *Radiology*, 192, 47-54.
- Vinniconi, S. J., Normal, A. R., Nicholson, V., Husband, J. E. (1995) Normal pelvic lymph nodes: evaluation with CT after hip pedal lymphangiography. *Radiology*, 194, 349-355.

نشر الکترونیکی
موسسه انتشاراتی
نور دانش

THE MALE GENITALIA AND URETHRA

Julian E. Kabala

with contributions from Philip J. A. Robinson, Raj Persad and Robert Jones

Congenital lesions of the urethra

Posterior urethral valves In this condition there is anomalous development of mucosal folds that obstruct the distal prostatic urethra in males. They manifest as bladder outflow obstruction of varying severity, the most extreme producing bilateral hydronephrosis, renal failure and Potter's syndrome. The milder forms present with lesser degrees of outflow obstruction and poor urinary stream. Micturating cystourethrography demonstrates dilatation of the prostatic urethra and a well-defined linear filling defect obstructing the urine flow.

Mullerian duct remnants The caudal part of the mullerian duct in the male becomes obliterated (apart from the caudal tip, which persists as the verumontanum). Incomplete obliteration may give rise to cysts between the bladder and the rectum. These may be asymptomatic or present with frequency, infertility, urinary obstructive symptoms or deep perineal pain on micturition or defecation. A cavity communicating with the posterior urethra derived from the caudal mullerian duct may be seen (prostatic utricle) and is considered the male homologue of the uterus. Again this may be asymptomatic but is often associated with maldevelopment of the genitalia (hypospadias, cryptorchidism, intersex, etc.) and may lead to urinary tract infection and calculi due to the presence of stagnant urine.

These lesions may be demonstrated as cystic structures on CT, MRI and transrectal ultrasound. Urethrography may demonstrate an extrinsic mass with a mullerian cyst or a communicating narrow-necked, often irregular, cavity within the prostate utricle.

Hypospadias In this congenital malformation the urethra terminates on the ventral surface of the penis, abnormally proximal. The meatus is found anywhere from just proximal to its normal site back as far as the perineum in severe cases. There is an association with other urinary tract anomalies and undescended testes. The anatomy is best demonstrated with urethrography but this may be difficult as the meatus is abnormal and usually narrowed, resulting in upstream urethral dilatation, often with secondary infection.

Cowper's glands These paired glands are embedded in the urogenital diaphragm and drain via ducts of variable length (from a few millimetres to a few centimetres), which run anteroinferiorly on to the ventral surface of the perineal part of the bulbar urethra. They may be opacified during urethrography in the presence of strictures or inflammation. The ducts to the glands may be congenitally dilated (Cowper's duct syringocele), usually asymptomatic but on rare occasions associated with urethral obstruction.

Other congenital urethral lesions The urethra is rarely duplicated congenitally, usually in the sagittal plane. The accessory urethra terminates along the shaft of the penis and is usually blind-ending, although if it communicates with the bladder it is associated with continuous incontinence. Variable narrowing of the urethra may occur, ranging from mild stenosis to complete atresia. The more severe forms are lethal, associated with obstructive renal failure and Potter's syndrome unless there is a persistent patent urachus or rectovesical fistula to decompress the system.

Urethral strictures

In developed countries these are most often traumatic in origin, sometimes inflammatory and rarely neoplastic.

Inflammatory Inflammatory urethral strictures may develop following urethritis. Classically it follows gonococcal urethritis but is occasionally seen following non-specific urethritis with organisms such as *Chlamydia trachomatis*. Urethrography should be avoided while there is active urethritis but on rare occasions the features of urethritis are observed on urethrography and include contrast filling of the periurethral glands and multiple small sessile filling defects due to polypoidal mucosal hyperplasia (urethritis cystica) especially with gonorrhoea.

The stricture is typically situated in the anterior urethra (Fig. 32.1), most commonly in the proximal bulbar urethra. Strictures may be multiple and of any length. Tuberculosis is a rare cause, being seen in the urethra in 2% or less of urinary tract tuberculosis. It almost always arises from a focus elsewhere in the

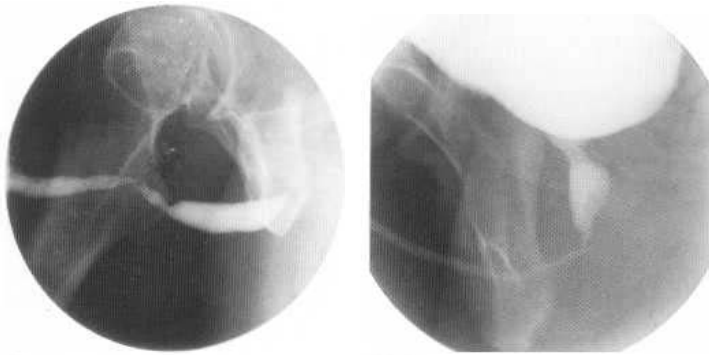


Fig. 32.1 Urethrogram demonstrating short postinflammatory stricture at the junction of the bulbar and penile urethra.

Fig. 32.2 Descending urethrogram in a male. The entire length of the urethra is demonstrated as the bladder empties. The prostatic urethra is a little distended in this example due to a short stricture at the junction of the membranous urethra and the bulbar urethra following a traumatic urethrosomy.

urinary tract, usually renal, sometimes as a result of direct extension of infection from the prostate or perineum. If severe, this may be associated with multiple urethroprincinal fistulas. Rarely strictures may be seen following severe, usually chronic, urethritis from almost any cause, including seronegative arthritides (Reiter's syndrome) and syphilitic and chemical urethritis. This latter condition arises from therapeutic instillation of chemicals into the urethra (for example, podophyllin or 5-fluorouracil for the treatment of condyloma accuminata). Formerly common, it is now rare.

Traumatic This may follow iatrogenic or accidental trauma. Iatrogenic strictures most commonly follow catheterisation (traumatic, failed or prolonged) and are usually at fixed narrowed areas, particularly the level of the membranous urethra and penoscrotal junction. They may also be seen following instrumentation and urethral surgery (Fig. 32.2). They may be single or multiple (Fig. 32.3) and of variable length but are usually short.

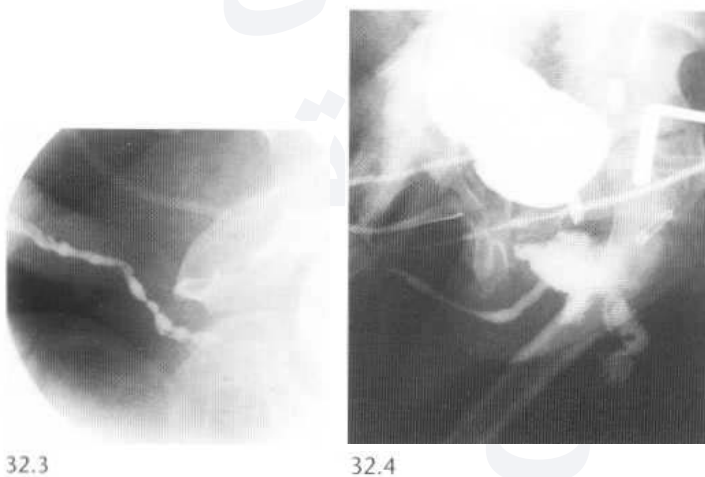


Fig. 32.3 Multiple short tight anterior urethral strictures following attempted self-catheterisation with a knitting needle and resultant gross urethritis.

Fig. 32.4 Micturating cystogram following extensive posterior urethral trauma showing gross urethral disruption at the level of the urogenital diaphragm and florid extravasation into the perineum.

Accidental injuries to the posterior urethra are frequently associated with subsequent stricture development, usually associated with complete transection of the urethra. They are generally short (less than 2 cm long) and solitary.

Strictures may be associated with pseudodiverticula and periurethral abscesses developing upstream. Fistulas, sinuses, urinary extravasation and false passages (especially following iatrogenic trauma) may also occur.

Urethral trauma

This is almost entirely restricted to the male, being exceptionally rare in the female urethra unless there is very major pelvic trauma. It should be suspected if pelvic trauma is associated with urinary retention or haematuria, especially blood at the urethral meatus. Investigation is with careful ascending urethrography, which will demonstrate the presence and extent of the injury and allow classification into trauma to the posterior or anterior urethra.

Posterior urethra This is traumatised in around 10% of anterior pelvic fractures. A formal classification for posterior urethral injuries has been described on the basis of urethrographic findings (Table 32.1).

In the mildest type of injury (I) there is only contusion or partial tear of the membranous urethra and no extravasation. The bulbar urethra appears normal or stretched if the bladder is elevated by haematoma. The commonest injury is the type II, with rupture at the prostatic apex (prostatomembranous junction) immediately above the urogenital diaphragm (UGD) with sparing of the UGD itself. Extravasation therefore occurs into the retro-pubic space but cannot extend into the perineum and the bulbar urethra is intact. In the type III injury the membranous urethra ruptures at the bulbomembranous junction below the UGD, which itself is disrupted. The bulbar urethra is often also ruptured. Contrast extravasation is in the direction of least resistance and into the perineum (Fig. 32.4).

There may be some bladder tilting on the retrograde urethrogram, allowing a diagnosis of partial or incomplete posterior urethral rupture to be made. Complete rupture is associated with absence of bladder tilting. Around two-thirds of type II injuries involve complete urethral rupture: one-third are partial. Type III are more severe and virtually always complete. While partial urethral tears usually heal uneventfully, complete tears are much more likely to be associated with adverse sequelae such as urethral strictures (usually less than 1 cm or so in length), impotence (up to around 10%) or incontinence (20%).

Table 32.1 Male posterior urethral injuries

Type	Membranous urethra	Bulbar urethra	Contrast extravasation	
			Perineum	Retropubic space
I	Contusion or partial tear	Normal or stretched	No	No
II	Rupture above urogenital diaphragm	Normal or stretched	No	Yes
III	Rupture below urogenital diaphragm	Ruptured	Yes	No



Fig. 32.5 Ascending urethrogram following a classical straddle injury showing marked extravasation of contrast from a partial anterior urethral tear.

Anterior urethra this is most commonly damaged during attempted catheterisation or instrumentation, usually iatrogenically (occasionally self-inflicted). In the community it is usually associated with blunt perineal trauma when the bulbar urethra and corpus spongiosum are compressed against the inferior aspect of the anterior pelvic ring (straddle injury). The injury is not usually associated with a fracture, then may be urethral contusion only or some degree of rupture, either partial or complete (Fig. 32.5). In partial rupture the proximal urethra is demonstrated, while in complete rupture there is an abrupt discontinuity at site of rupture. Extravasation is associated with both partial and complete rupture and contrast may enter the corpus spongiosum and veins. Even contusion alone may lead to subsequent stricture but this is more common with any degree of rupture, especially complete.

Urethral tumours

Benign tumours Fibroepithelial polyps are occasionally encountered, usually in children, sometimes in young adults. They appear as finger-like processes 1-2 cm long originating near the verumontanum and present with intermittent outflow obstruction.

Transitional and squamous cell papillomas are benign mesenchymal neoplasms lined with urothelium which may be metaplastic. In the male they may be seen in the prostatic urethra (and may be associated with bladder papillomas) but are most often situated in the fovea nasicularis and parametarial area. In the female they are usually found in the distal third of the urethra (urethral caluncles).

They usually present between 20 and 40 years of age with haematuria and/or discharge. They are seen as smooth solitary or multiple filling defects on urethrography.

Urethral carcinoma This rare tumour is also unusual in being encountered more frequently in females than males.

In the female it has a peak incidence around 40-60 years and is usually associated with chronic inflammation and may be associated with fibrous polyps and caruncles. It presents with blood appearing at the urethral meatus and symptoms of irritation and obstruction. Seventy-five per cent are squamous cell carcinomas and most of the rest are transitional cell carcinoma. Adenocarcinoma is occasionally encountered and arises from urethral diverticula, presumably reflecting the origin of the diverticulum from an infected paraurethral (Bartholin's) gland. Carcinoma appears as one or more serial irregular filling defects within the urethra on urethrography or as an irregular stricture. Lymph node metastases occur before blood-borne spread, the distal third of the urethra metastasising to superficial and deep inguinal lymph nodes, the proximal two-thirds to the external and internal iliac lymph nodes.

In the male the peak incidence is above the age of 50. It can be regarded as two different conditions. In the UK the commoner is carcinoma of the prostatic urethra, usually transitional cell carcinoma. It has a strong association with bladder transitional cell carcinoma, especially with previous resection. Carcinoma in the remainder of the urethra (membranous, bulbar and penile) is strongly associated with chronic urethral inflammation (including sexually transmitted disease) and strictures (present in up to 75% of patients). As with carcinoma of the female urethra, approximately 75% are squamous cell carcinoma, most of the rest are transitional cell carcinoma and adenocarcinoma is occasionally seen. Presentation is usually with insidious onset of poor urinary stream, haematuria and serosanguinous discharge. On urethrography carcinoma appears as a well-defined filling defect: it may be eccentric or circumferential and may be associated with irregular stricturing. Metastatic spread is virtually always via the lymphatics, the penile urethra metastasising to the deep inguinal and external iliac lymph nodes, the bulbar and posterior urethra to the internal iliac and obturator lymph nodes.

MRI is the favoured modality for staging urethral carcinoma in both sexes because of its better demonstration of the soft-tissue anatomy of the perineum. A formal TNM staging system is available, the salient features of which are: T1 tumour invading subepithelial connective tissue; T2 tumour invading any of periurethral muscle, corpus spongiosum or prostate; T3 tumour invading any of bladder neck, corpus cavernosum, anterior vagina; and T4 tumour invading any of the other adjacent organs, including the bladder (Fig. 32.6).

Urethral metastases Metastases from distant primaries to the urethelium of the urethra is excessively rare. The urethra is more

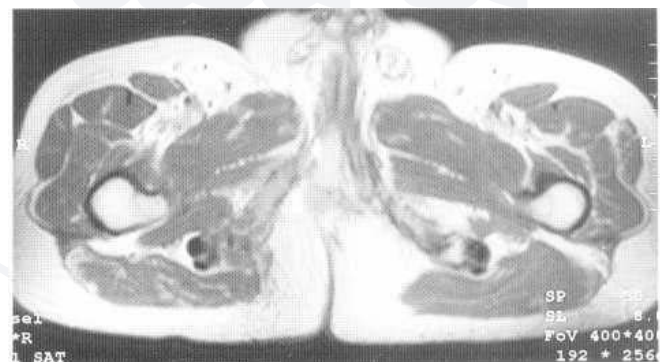


Fig. 32.6 Transverse post-gadolinium T₁-weighted image showing invasion of the penile bulb and muscles of the right side of the pelvic floor by urethral carcinoma.

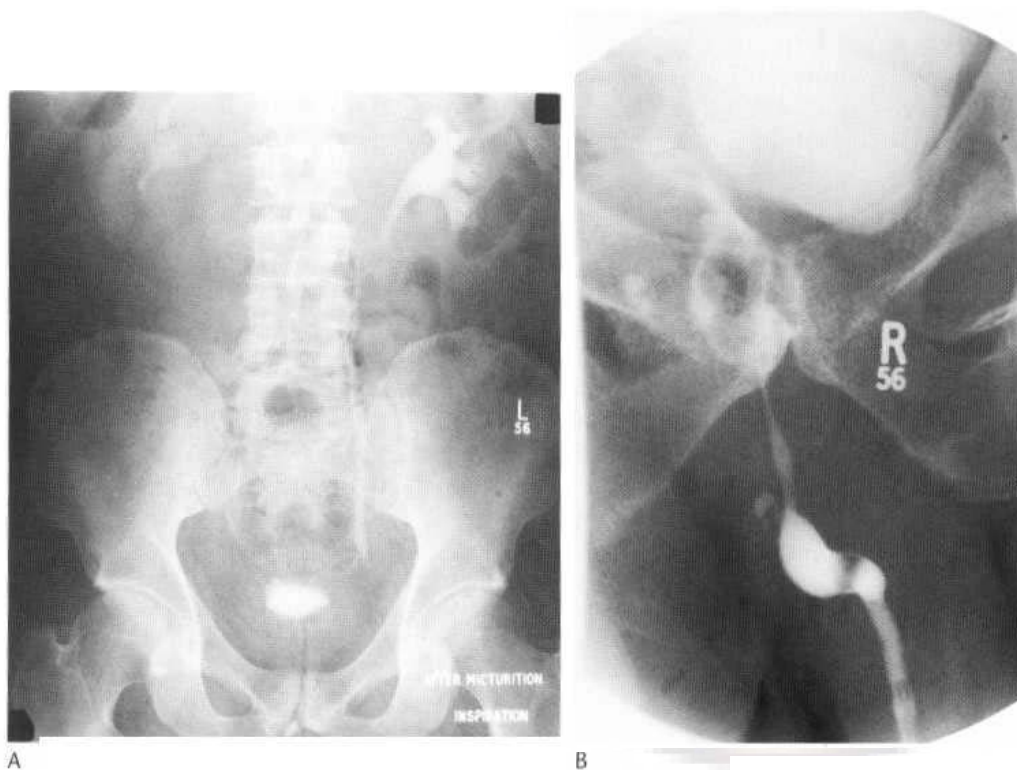


Fig. 32.7 (A) Postmicturition film from an iVU series showing a urethral calculus and gross detrusor hypertrophy due to secondary bladder outflow obstruction. (B) Urethrogram (different patient) showing a filling defect due to a urethral calculus within the prostatic urethra.

commonly involved by direct spread of turnout- from adjacent organs, most often carcinoma of the bladder or rectum, occasionally prostate, vagina or cervix.

Urethral filling defects

The commonest urethral filling defects are calculi and tumours (usually benign, occasionally carcinoma and rarely metastases). Other less common causes include the occasional urethral equivalent of inflammatory conditions seen elsewhere in the urinary tract (malacoplakia, urethritis cystica and the swollen mucosa of urethritis) and condyloma acuminata.

Condyloma acuminata (venereal wart) is due to a DNA papillomavirus and appears as a dermal wart on the genitals and around the anus. Condylomas may extend into the anterior urethra, where they appear as multiple sessile filling defects on urethrography. This procedure, however, may be associated with retrograde seeding of the infecting agent into the bladder and is best avoided if the diagnosis is suspected in advance (as is any form of urethral catheterisation). There is an association with squamous cell carcinoma of the vulva.

Urethral calculi Urethral calculi are uncommon and over 90% originate in the kidney or bladder. They may present with sudden obstruction of the urine flow or more chronic symptoms of urethritis, dysuria and poor stream. A minority originate in the urethra in association with a structural abnormality (usually strictures or diverticula). They enlarge slowly and present with symptoms of prostatism.

Although most urethral calculi are radiopaque, they are often overlooked as they are frequently not suspected and are situated over hone on radiographs, or even off the film entirely. In the female urethra they are usually seen in a midurethral diverticulum; in the male they are generally found around the junction of the prostatic and membranous urethra (Fig. 32.7).

Structural lesions of the urethral wall

Urethral diverticula These are rarely congenital, when they are classically saccular and situated in the midpenile urethra. They are associated with high-grade obstruction in children and are difficult to distinguish from urethral valves.

Acquired diverticula are strictly speaking pseudodiverticula, as they are lined with fibrous tissue or inflammatory cells rather than urothelium. They are inflammatory in origin and may develop from



Fig. 32.8 Cystourethrogram showing a substantial sinus from the posterior aspect of the urethra following rectal surgery.

an abscess in the paraurethral glands or within the prostate. Mechanical causes play a part and they may develop immediately upstream of a urethral stricture or following pressure necrosis with a long-term urethral catheter, usually on the inferior wall of the urethra at the penoscrotal junction. Stasis of urine may lead to secondary infection and calculus development. If they become large enough they may elevate the bladder base. They may be demonstrated on urethrography or ultrasound (transvaginally in the female), the latter having the advantage of avoiding radiation.

Urethral fistulas and sinuses These form if there is an impediment to closure after urethral rupture or laceration. They may be secondary to rectal or gynaecological surgery, obstetric injury, radiotherapy and some inflammatory lesions (Crohn's disease, periurethral abscess, tuberculosis) or with strictures or carcinoma. They may end in the soft tissues of the perineum or continue on to the skin of the perineum or penis. Alternatively they may communicate with the rectum, colon, vagina or uterus. Conventionally diagnosis is with sinography or micturating cystourethrogram



Fig. 32.9 Coronal T₂-weighted MR image showing a sinus from the base of the penile urethra down into the scrotum.

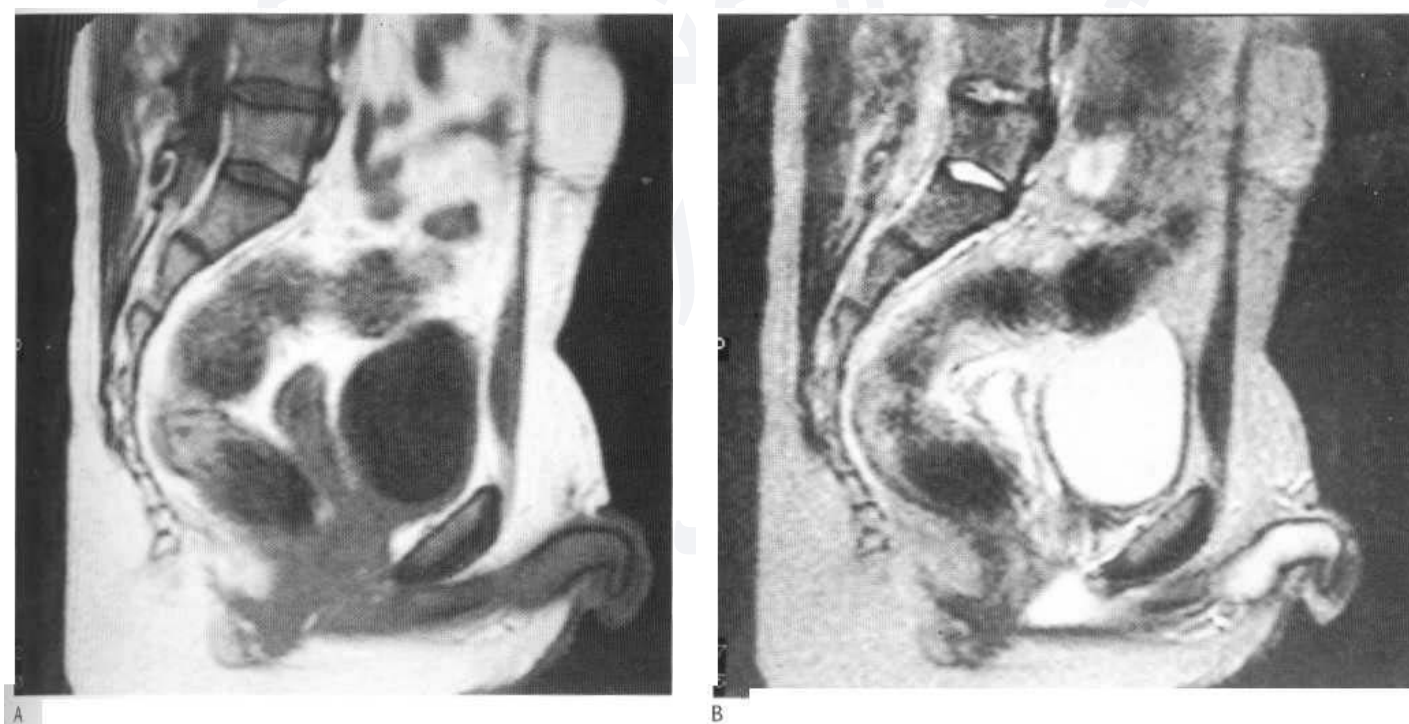


Fig. 32.10 Sagittal T₁-weighted (A) and T₂-weighted (B) MR images in a patient with Nunan's syndrome showing male external genitalia and a uterus.

(Fig. 32.8), which will show an irregular track that may lead into an irregular cavity or into another viscera. MRI is also useful to show the fistulous track (Fig. 32.9) and (together with CT) may demonstrate the underlying cause.

Congenital scrotal disorders

Ambiguous genitalia and intersex This is a complex situation with a wide variety of phenotypes. Specialist chromosomal, endocrine and clinical assessment are required and the radiologist's role is generally to assist with the determination of which internal pelvic structures are present and which associated congenital abnormalities exist, in particular within the urinary tract. Ultrasound and MRI (Fig. 32.10) are the preferred modalities, both to avoid ionising radiation and to demonstrate optimally the soft-tissue anatomy.

Undescended testicle (cryptorchidism) In the majority of prepubertal males the testes may normally be retractile into the groin because of the cremasteric muscle reflex. If, however, the testicle can never be located within the scrotum, it can be considered undescended. An undescended testicle most commonly lies in the inguinal canal (canalicular). Otherwise it may lie higher up along the normal line of descent (abdominal testicle) or in a site away from the normal line of descent (ectopic). Most abdominal testicles lie just proximal to the inguinal ring, although they may lie further cranially within the pelvis or retroperitoneum. Ectopic testicles are uncommon and are most often found in the superficial inguinal pouch, occasionally coming to lie in the femoral canal, suprapubic fat pad, the perineum and the opposite scrotum.

Failure of descent by the age of 2-3 years is associated with abnormal development of the testicle and this is particularly severe if it continues beyond puberty. Consequently undescended testes may be atrophic with poor spermatogenesis. A small proportion of undescended testes (5%) are not found even at Surgical exploration. While some of these may be true agenesis, it is distinctly possible that a number are so severely atrophic that they cannot be located.

Testes that remain undescended (especially abdominal testes) in boys above the age of 5 years also suffer from an increased incidence of malignant neoplasia, up to 40 times normal, usually with the development of seminoma. There is also an increased risk in the contralateral, normally descended testicle. Other associations of undescended testes include abnormalities of Wolfian duct-derived structures, for example seminal vesicle cysts and agenesis.

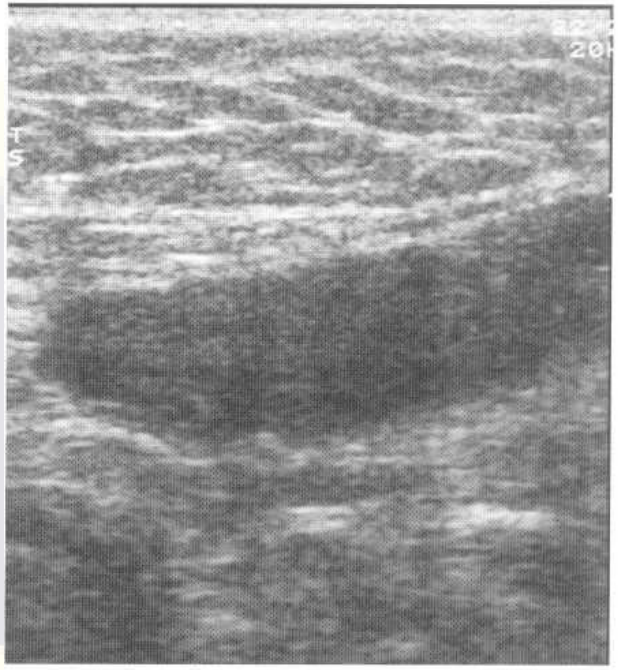


Fig. 32.11 Transverse ultrasound showing an atrophic undescended testicle (arrows) lying in the inguinal canal.

Ultrasound can be regarded as the first-line investigation to locate an undescended testicle, being quick and able to locate the testicle at its commonest sites (within the inguinal canal or just proximal to it). The testicle may look relatively normal, although the longer it has been undescended the more likely it is to be small, atrophic and echo poor (Fig. 32.11). If the testicle cannot be identified on ultrasound, a more extensive search may be performed with MRI. This is a better modality than CT as it avoids radiation and the testicle shows a conspicuous high signal on T weighted and STIR sequences (Fig. 32.12). Testicular phlebography or arteriography has been employed in the search for undescended testes. If both ultrasound and MRI are negative it is unlikely that these angiographic procedures will detect the missing organ, as it is probably absent or extremely atrophic. This is particularly the case if the patient is above 30 years old.

Patent processus vaginalis Failure of closure of the processus vaginalis after testicular descent results in a persistent communication between the peritoneal cavity and the scrotum. This may

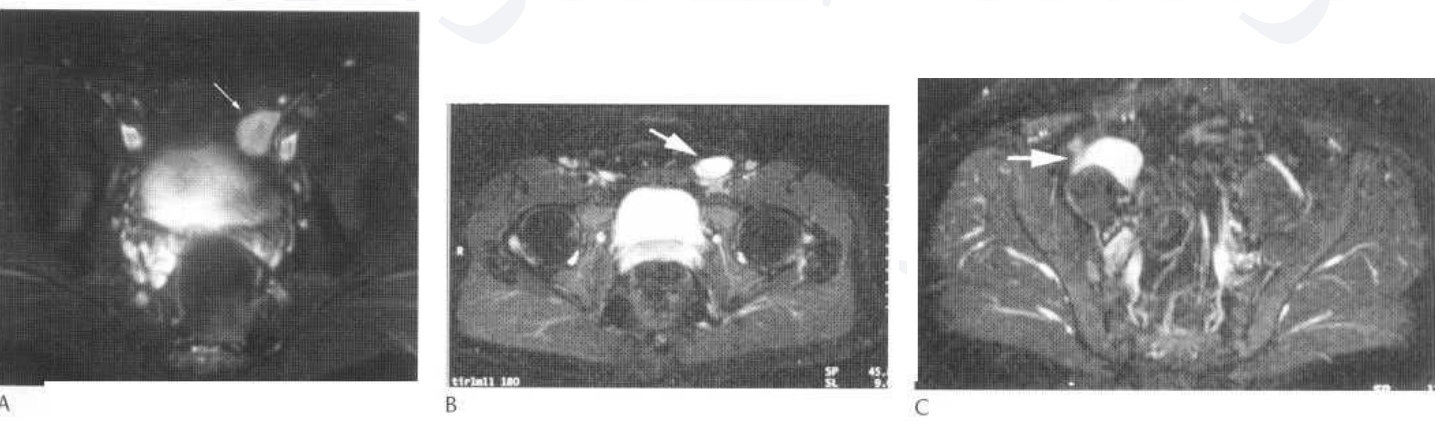


Fig. 32.12 Transverse STIR images from MRI examinations of patients with undescended testicles (arrow) in the proximal end of the inguinal canal (A), suprapubic pouch (B) and pelvis (C).

transmit disease processes (for example ascites) or become the site of a hernia. Incomplete closure of the processus may lead to a developmental cyst, usually in the upper scrotum or inguinal region.

Extratesticular scrotal disorders

Hydrocele A hydrocele is the formation of fluid between the two layers (visceral and parietal) of the tunica vaginalis. Ultrasonographically it is seen as an echo-free area (Fig. 32.13) partly surrounding the testicle (in comparison to cysts, which do not

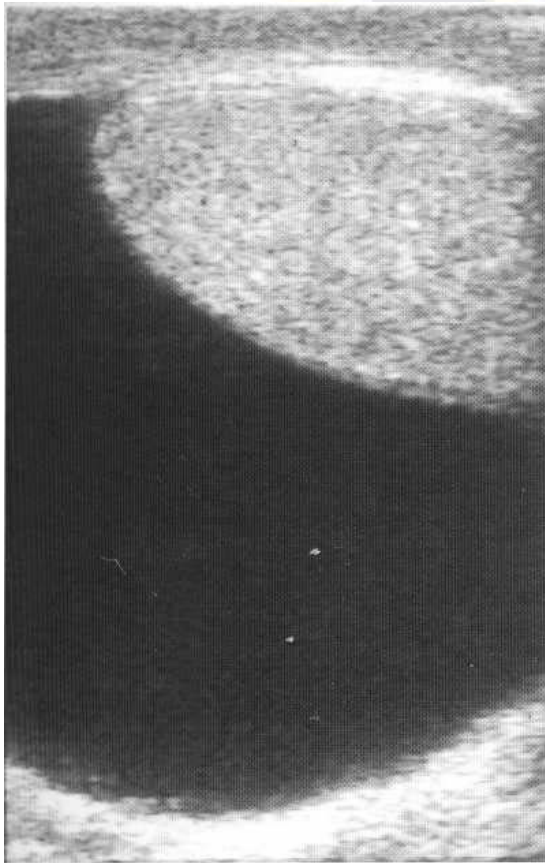


Fig. 32.13 Ultrasound demonstration of a hydrocele seen as an echo-free area partly surrounding a normal testicle.

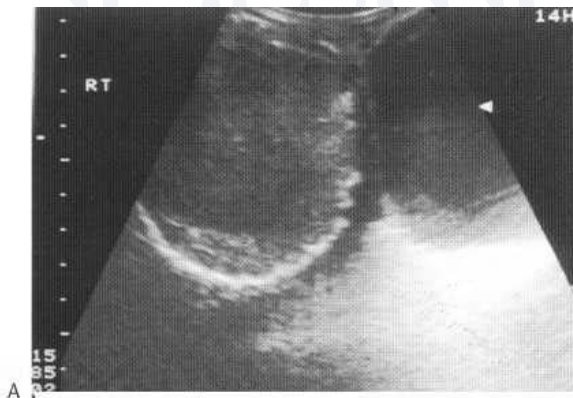


Fig. 32.15 Ultrasound (A) showing dense peripheral calcification around the exterior of a chronic inflammatory hydrocele. This is also visible on the plain film (B).

surround the testicle). A hydrocele may develop as a result of infection (epididymo-orchitis), trauma, malignant testicular tumour or infarction (including torsion). In most cases, however, an underlying cause for the hydrocele cannot be found.

When infection is a cause there are usually obvious clinical and radiological features of epididymitis. The hydrocele may demonstrate internal echoes (Fig. 32.14), especially on the rare occasions when infection is sufficiently severe for frank pus (pyocele) to develop. The commonest infective organisms are usually bowel-related Gram-negative bacilli but a variety of other agents may be responsible, although now tuberculosis is rare. Chronic infective hydrocele (especially tuberculous) may be associated with considerable calcification of the tunica (Fig. 32.15).

Following trauma a haematocele (haemorrhagic hydrocele) will also exhibit considerable echogenicity.

Cysts Simple cysts are extremely common in the scrotum. They may be seen at any age from adolescence onwards but are most common in the elderly. The majority are seen in the epididymis, particularly in the upper pole, and they may be single or multiple.

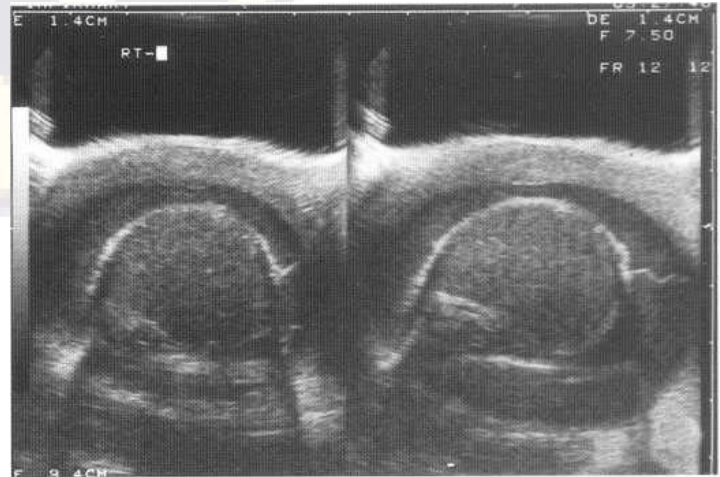
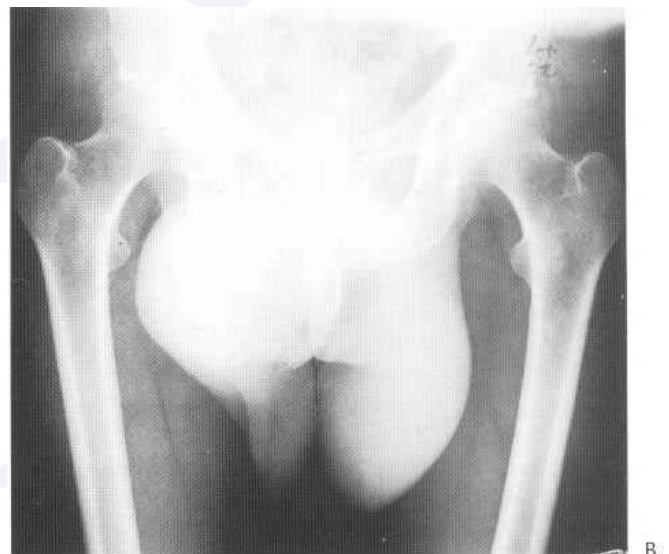


Fig. 32.14 Ultrasound showing an infected, partly septated echogenic hydrocele.



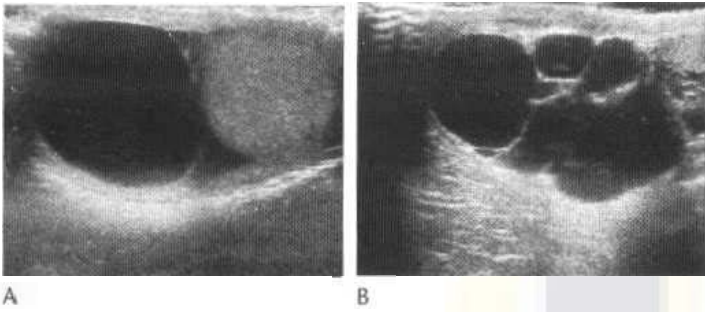


Fig. 32.16 Ultrasound showing (A) a classical echo-free well-defined thin-walled solitary epididymal cyst and (B) a cluster of simple cysts.

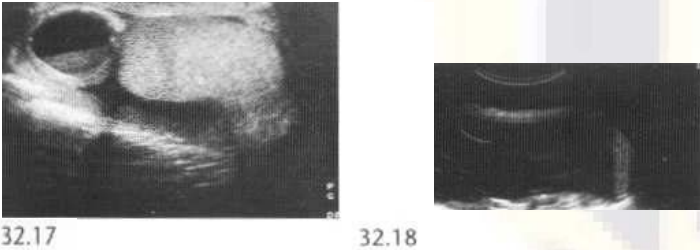


Fig. 32.17 Ultrasound of infected epididymal cyst showing debris and fluid level.

Fig. 32.18 Ultrasound of well-defined spermatocele with slightly echo-poor contents.

On ultrasound they show the classical features of cysts elsewhere in the body, being anechoic, showing distal acoustic enhancement and having no appreciable wall thickness (Fig. 32.16).

Haemorrhage or infection may alter the appearance of a pre-existing cyst to show some degree of echogenicity, occasionally with a visible fluid level (Fig. 32.17). Alternatively infection or trauma (including vasectomy) may provoke the creation of a cystic lesion with internal echoes, partly due to the presence of spermatozoa (spermatocele, Fig. 32.18). These again are more common in the upper pole of the epididymis.

Varicocele Dilatation of the network of veins draining the testicle is described as a varicocele. They are extremely common (up to 8-16% of the male population), and usually asymptomatic, often being discovered incidentally on clinical or ultrasonographic examination for other conditions. There is a possible association with subfertility, reported in 21-39% of males being investigated for subfertility. They are most frequent between 15 and 25 years of age, almost always left-sided and, when symptomatic, present with scrotal aching and/or soft scrotal mass. Classically these symptoms worsen during the day while the patient is upright. Occasionally they present relatively acutely as a manifestation of a renal carcinoma. Treatment may be offered for discomfort or as part of the management of subfertility.

On ultrasound varicoceles are seen as a leash of predominantly echo-free serpiginous structures measuring more than 2 mm maximum diameter (Fig. 32.19). Visible flow may be seen within larger varicoceles on conventional ultrasound. Confusion with cysts is unlikely, even when the varicocele is small, but confirmation of their nature can be obtained with slow-flow Doppler Ultrasound. Their prominence is increased in the upright position and with the Valsalva manoeuvre, although this is not routinely required to make the diagnosis.

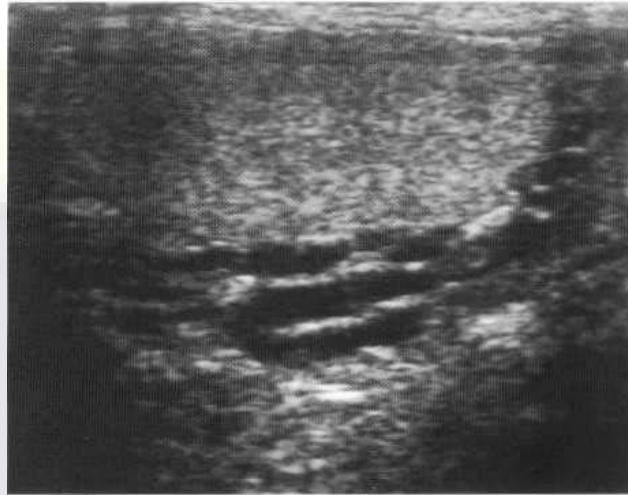


Fig. 32.19 Ultrasound of varicocele seen as echo-free serpiginous structures.

The vast majority of varicoceles are described as primary and are presumed to be due to developmental abnormalities of the valves and/or the veins themselves. This is far more likely on the left, where at least 95% are encountered. A minority occur secondary to a lesion compressing or occluding the testicular vein. The classical cause is a left-sided renal cell carcinoma extending along the renal vein as far as the termination of the testicular vein, but benign (for example, hydronephrosis) and other malignant conditions (including abdominal lymphadenopathy) can provoke a varicocele on either side. There is a higher risk of an underlying cause, particularly a tumour if the varicocele is of recent onset with an acute presentation, the patient is older than 40 years, it is right-sided and is unchanged with provocative manoeuvres.

Treatment of varicoceles is usually for persistent discomfort or as part of the treatment of subfertility and is by percutaneous embolisation or surgery. Direct surgical ligation of the testicular vein (by open operation or laparoscopy) should have a low primary failure rate (of the order of 1%) with a recurrence rate around 16%. Surgery, however, is more traumatic than percutaneous embolisation and is associated with specific risks not encountered with the alternative procedure, in particular damage to the testicular artery and resultant infarction.

The total failure rate for percutaneous embolisation (Fig. 32.20) is comparable with that for surgery, although the technical failure rate may be higher (6-12%) and the recurrence rate similar or lower (4-16%). Morbidity should be minor and infrequent, up to 10% experiencing transient discomfort in the loin or scrotum on the side of the varicocele, with few other symptoms.

Postvasectomy epididymis Numerous individuals have had a vasectomy and many will undergo subsequent scrotal ultrasound for one reason or other, often unrelated to the vasectomy. In these patients the epididymis often appears thickened and slightly echo-poor (Fig. 32.21). These findings can almost be regarded as variations of normal and are not usually related to any specific symptoms.

Epididymitis Inflammation of the epididymis, usually due to ascending infection with Gram-negative bacilli (*E. coli*, etc.) or *Chlamydia*, is extremely common. It is particularly seen in young adult males, with a second peak in late middle age and the elderly,

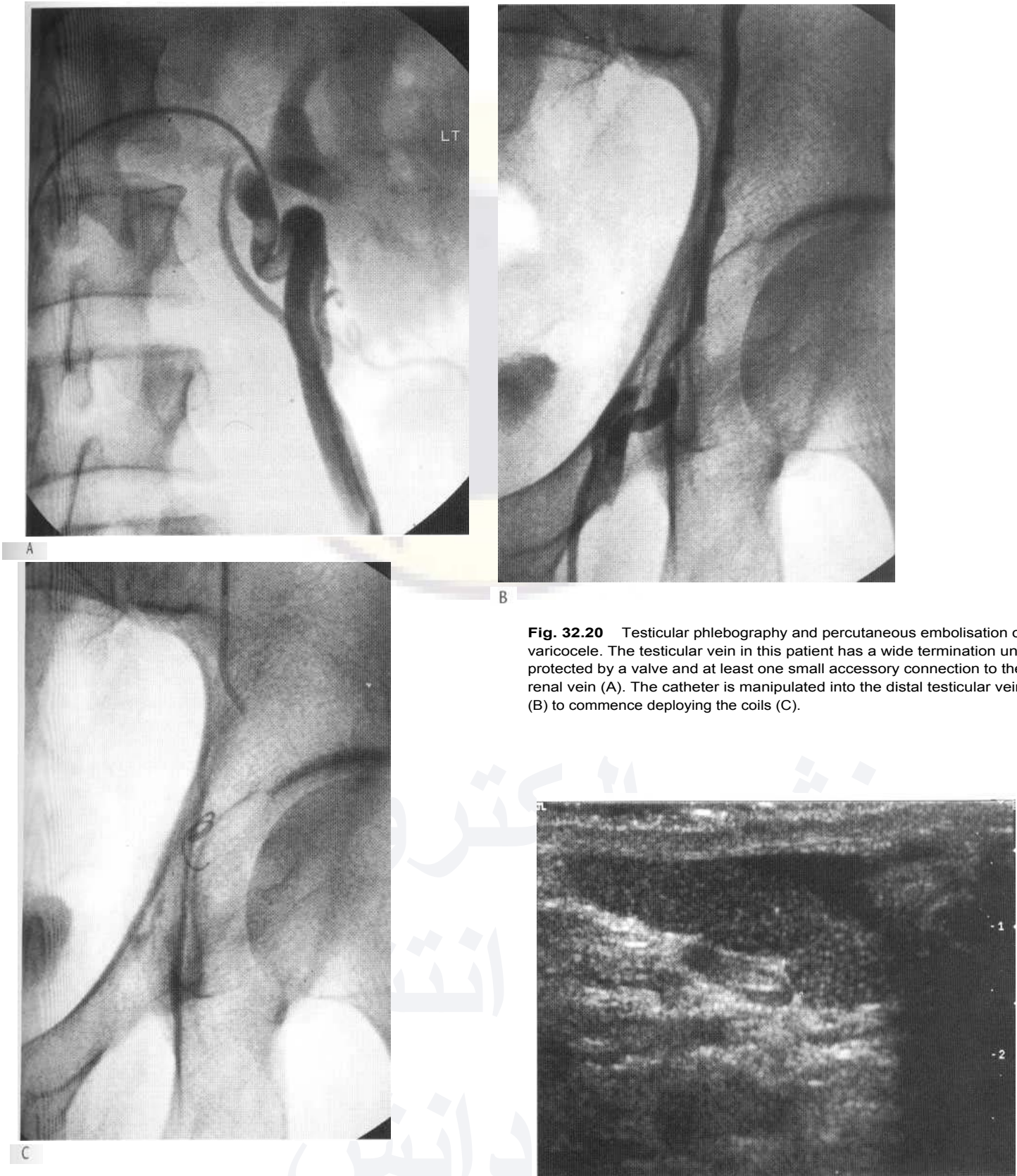


Fig. 32.20 Testicular phlebography and percutaneous embolisation of varicocele. The testicular vein in this patient has a wide termination unprotected by a valve and at least one small accessory connection to the renal vein (A). The catheter is manipulated into the distal testicular vein (B) to commence deploying the coils (C).

when it may be associated with cystitis and/or prostatitis in association with benign prostatic disease and bladder outflow obstruction. The clinical presentation varies in severity and acuteness from mild pain, tenderness and scrotal swelling to a severe pyrexial illness with marked scrotal pain and swelling. Although usually asymmetrical, epididymitis is not uncommonly bilateral.

Fig. 32.21 Ultrasound showing typical postvasectomy echo-poor epididymis.

On ultrasound the epididymis shows swelling, often nodular and particularly affecting the lower or upper pole. There is often diffuse or patchy reduction in echogenicity, although sometimes the epi-

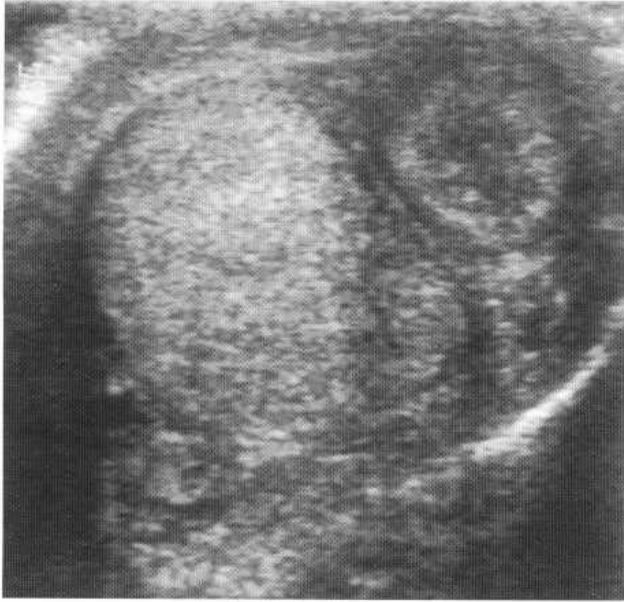


Fig. 32.22 Ultrasound of aggressive epididymitis showing a heterogeneous mass with areas of reduced and increased echogenicity adjacent to the lower pole of the testicle.



Fig. 32.23 Ultrasound of severe orchitis. The bulk of the testicle shows diffuse reduction in echogenicity. The heterogeneous area in the lower pole represents a developing abscess.

didymis shows considerable heterogeneity (Fig. 32.22) and even rarely a diffuse increase in echogenicity. A heterogeneous pattern of predominant increase in echogenicity is more frequently associated with chronic epididymitis. Doppler ultrasound often demonstrates hypervascularity. Rarely the condition progresses so that there is demonstrable abscess formation within the epididymis.

There is often an associated hydrocele of variable size, which may be septated and contain echogenic fluid. Severe cases may be associated with demonstrable oedematous thickening of the overlying skin and (in up to 20% of cases) there may be coexisting orchitis.

Orchitis Inflammation of the testicle itself may be seen in systemic viral illness (classically mumps) or in association with bacterial epididymitis. Up to 25% of postpubertal males with mumps will suffer some degree of orchitis, usually 7-10 days after the parotitis. Approximately two-thirds are unilateral. Other viruses implicated include echoviruses, group B arboviruses and the lymphocytic choriomeningitis virus. In the acute phase ultrasound may show testicular swelling with patchy or diffuse reduction in echogenicity. Following resolution the testicle may return to normal but in severe orchitis there may be atrophy, with reduction in size and echogenicity, usually apparent within 6 months of the acute insult.

Bacterial orchitis shows similar acute features (Fig. 32.23) but is usually with marked changes of epididymis. Doppler ultrasound may show increased vascularity but severe orchitis may be associated with ischaemia and infarction with reduced or absent vascularity. In particularly severe orchitis heterogeneous areas may develop with a potential for intratesticular abscess formation (irregular areas of liquefaction containing debris). Again there is a substantial risk of subsequent atrophy leading to a small echo-poor testicle with little or no spermatogenesis. The underlying organisms are usually the same as for epididymis, although rarely chronic epididymitis, especially with abscess formation, may be due to tuberculosis. Calcific scars may be seen following any form of orchitis.

Extratesticular tumours These are rare and usually benign; the most common is the adenomatoid tumour of the epididymis, which is a benign hamartoma, most frequently seen in the tail. It varies in size from about 5 to 50 mm and is of similar or slightly increased echogenicity compared with normal testicle.

Others include benign neoplasms, such as mesenchymal tumours (leiomyoma, fibroma, lipoma), adrenal rests and benign mesothelioma. This latter condition arises from the tunica vaginalis. It produces small paratesticular hyperechoic masses and a disproportionately large hydrocele.

Extratesticular malignancies are extremely rare. Although carcinoma and metastases have been described, the least rare malignant neoplasia in this site is sarcoma of the spermatic cord, most commonly embryonal rhabdomyosarcoma (in younger patients), but sarcomas of other mesenchymal tissue are seen occasionally, for example liposarcoma.

Torsion

Testicular torsion In this condition the spermatic cord becomes twisted as a result of testicular rotation, producing testicular ischaemia. It may occur at any age but is most frequent in the first year of life or in adolescence, when the testicle is rapidly enlarging.

Different patterns of torsion have been described. The loose attachment of the testicle and spermatic cord to the scrotum in infants and neonates predisposes to torsion of the entire cord above the level of the scrotum (extravaginal torsion). Rotation of the cord within the tunica vaginalis (intravaginal torsion) is the commonest situation in the older age group. This is most often due to poor testicular attachment to the posterior scrotal wall by an abnormally narrow mesentery, which predisposes to rotation of the cord. This anatomical situation has been referred to as the bell-and-clapper malformation and may be bilateral in up to 80% of cases, with simultaneous bilateral torsion in up to 5%. Surgical treatment of testicular torsion should therefore include detorsion

of the affected testicle and fixation of the contralateral testicle to prevent subsequent torsion.

Torsion may be complete (i.e. rotation of at least 360°) or incomplete and spontaneous torsion and detorsion may occur. The degree of torsion determines the severity of the ischaemia and the rapidity with which irreversible changes occur within the testicle. Surgical treatment of complete torsion within 5 h is associated with a testicular salvage rate of 80%, which falls to 20% or less after 12 h. If torsion is incomplete, the testicle remains viable longer: 80% up to 12 h and 40% up to 24 h. Even in this situation, however, viability falls to 10% after 24 h.

In the acute stage ultrasound may be normal or demonstrate a swollen testicle with patchy or diffuse hypoechogenicity (Fig. 32.24). The epididymis may also become swollen and echo-poor. There may be a reactive hydrocele and the overlying scrotal skin may be thickened and oedematous. Doppler ultrasound has a claimed sensitivity of upwards of 85% in the diagnosis of torsion by virtue of reduced vascularity (absence or poor colour flow, reduced peak systolic velocities) compared with the unaffected side. False positives (for example ischaemia associated with severe epididymo-orchitis) and false negatives (due to difficulty in obtaining an adequate colour flow, intermittent nature of torsion, etc.) are encountered and there is still considerable controversy as to the role of this investigation in the management of these patients. Given the importance of operating within a few hours of the onset of symptoms, it remains axiomatic that neither the performance nor interpretation of an ultrasound examination should delay surgical treatment. If there is doubt the urologist should operate on clinical grounds.

Appendix torsion The testicular appendix (often referred to as the hydatid of Morgagni) and rarely other vestigial scrotal appendices (such as the epididymal appendix) may undergo torsion. This is associated with acute scrotal pain and localised swelling and tenderness. On ultrasound there is a focal soft-tissue mass adjacent to the upper pole of the epididymis which is often heterogeneous with a central echo-poor area and an associated



32.24

Fig. 32.24 Ultrasound of an infarcting testicle. There are extensive areas of reduced echogenicity within the substance of the testicle. The adjacent epididymis is also markedly diseased and swollen.



32.25

Fig. 32.25 Ultrasound showing a classical highly echogenic scrotolith with marked distal acoustic shadowing and small hydrocele.

hydrocele. This may slough off and become calcified, giving rise to mobile highly echogenic shadowing foci between the layers of the tunica vaginalis (scrotoliths or scrotal pearls, Fig. 32.25).

Scrotal trauma

Blunt scrotal trauma most commonly results in haemorrhage around the testicle (haematocele) and intratesticular haematoma, which may be associated with a tear of the tunica albuginea. More significant trauma may be associated with demonstrable fragmentation of the testicle. The role of imaging depends on the surgical approach. Where there is substantial trauma, surgical exploration, drainage of haematoma and repair of testicular tears may enhance the subsequent viability of the testicle.

Ultrasound is the most appropriate imaging modality. The commonest finding is a complex haemorrhagic hydrocele (haematocele) with areas of intermediate and low echogenicity representing thrombus and liquid blood or serum. The underlying testicle may show areas of contusion or haematoma, visible as echo-poor, sometimes echogenic, areas, often with a relatively linear configuration. The testicle may be deformed by subcapsular haemorrhage. There may be rupture of the capsule (tunica albuginea) with disruption of the underlying testicle and associated haematoma (Fig. 32.26). The testicular tear may be linear or complex, and in severe trauma there may be fragmentation of the testicle.

Scrotal haematoma may be complicated by abscess formation, and severe testicular damage may be followed by subsequent atrophy.

Testicular masses

Testicular cysts As with cysts elsewhere in the body, testicular cysts are well-defined, thin-walled and anechoic on ultrasound, with distal acoustic enhancement. They vary in size from a millimetre or two to 1–2 cm and lie within testicular tissue (Fig. 32.27). They are occasionally multiple, are often situated at or close to the testicular hilum and may be associated with epididymal cysts. Cysts directly arising from the tunica albuginea have been described with similar ultrasound features (Fig. 32.28) and benign nature.

Multiple small cystic areas are not infrequently seen at the testicular hilum. These are often referred to as dilatation of the rete testes (Fig. 32.29) and again are often seen with epididymal cysts. All these lesions are entirely benign.



Fig. 32.26 Ultrasound showing traumatic disruption of upper pole of testicle and small adjacent haematocele.

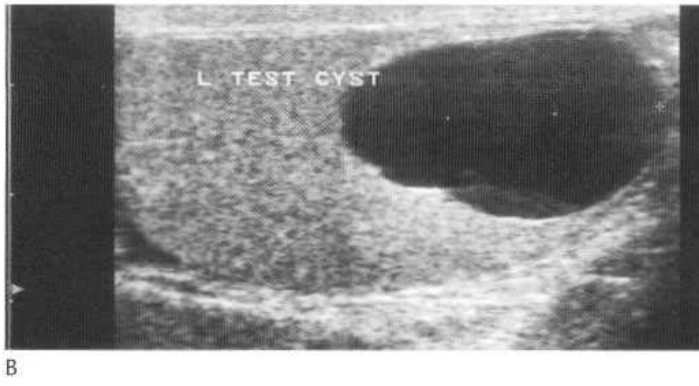


Fig. 32.27 Ultrasound of a small (A) and a large (B) testicular cyst, both showing an echo-free area without any significant solid elements.



Fig. 32.28 Ultrasound of a small echo-free tunica albuginea cyst.

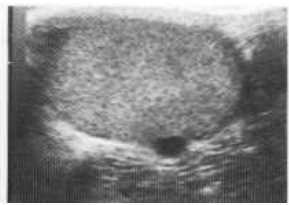


Fig. 32.30 Ultrasound of epidermoid cyst seen as a well-defined echo-poor nodule.

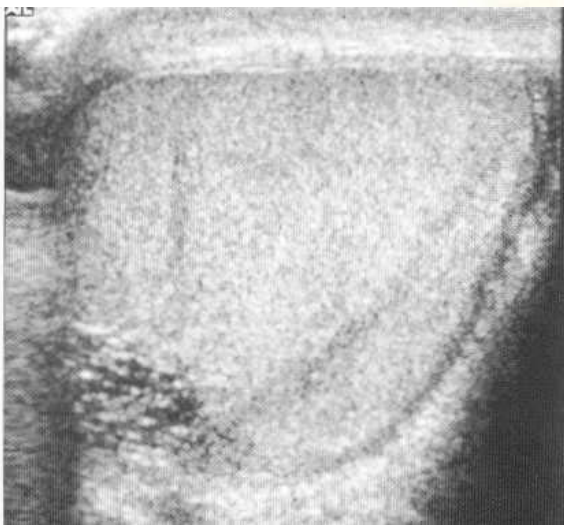


Fig. 32.29 Ultrasound showing multiple tiny echo-free areas at the testicular hilum (dilated rete testis).

Epidermoid cysts These uncommon benign tumours are thought to derive from epithelial rests or inclusions. They consist of layers of keratin within a fibrous capsule lined with squamous epithelium. On ultrasound they are well-defined auricular rounded lesions and may be solitary, multiple or bilateral. Calcification may be present and adopt a variety of patterns (multiple foci less

within the cyst, curvilinear along the wall or a target pattern of poor (Fig., 32.30). Occasionally they may appear highly echogenic, presumably if calcification becomes widespread throughout the lesion. If the typical ultrasound features are present, the urologist may be able to perform partial rather than total orchidectomy.

Testicular cancer Although uncommon (representing approximately 1% of cancers in males), testicular cancer is the commonest malignancy in males between 20 and 40 years of age, with the incidence apparently rising,

Approximately 95% of testicular neoplasms are of *germ cell* origin, 4% *lymphomas* and 1% rarities such as *metastases*, *Leydig cell* and *Sertoli cell tumours*. Approximately 50% of germ cell tumours are pure *seminomas*, which are less aggressive and present in an older age group (peak 30-45 years). The remaining 50% are classified as *non-seminomatous germ cell tumours* (NSGCTs), although up to a fifth of these may contain some seminomatous element. They present in the younger age group (peak 15-30 years) and a majority produce one or more biochemical tumour markers (beta-human chorionic gonadotrophin or alpha-fetoprotein). There are two main histological classifications of NSGCTs, the World Health Organization (WHO) and the British Testicular Tumour Panel systems, the former being more widely used in the North American literature. The two classifications are broadly similar. Both classify the yolk-sac tumours as a separate subgroup. In the British system, the rest are teratomas of varying pattern (differentiated, intermediate, undifferentiated, trophoblastic). In the WHO system, mixed germ cell tumours, embryonal carcinoma and choriocarcinoma are separated from the teratomas of varying histology.

Risk factors for the development of testicular malignancy include undescended testes, testicular atrophy, microlithiasis, previous testicular malignancy, infantile hernia, low birth weight and maternal exposure to diethylstilboestrol. There is a weak genetic tendency, with a family history of the disease seen in 2% of patients with testicular cancer. Testicular cancer most commonly presents as a painless scrotal mass inseparable from the testicle, although the patient may sometimes also complain of a dull ache or sensation of heaviness. Occasionally the condition presents with widespread pulmonary or abdominal metastases, rarely when the primary is no longer evident. The rare Leydig and Sertoli cell tumours may produce sex hormones, which can provoke premature virilisation (especially Leydig cell tumours) or gynaecomastia (especially Sertoli cell tumours).

Scrotal ultrasound is the investigation of choice, with a sensitivity approaching 100%. Tumours are seen as intratesticular lesions with replacement of the normal architectural pattern by material of predominantly low echogenicity. Small tumours may show no mass

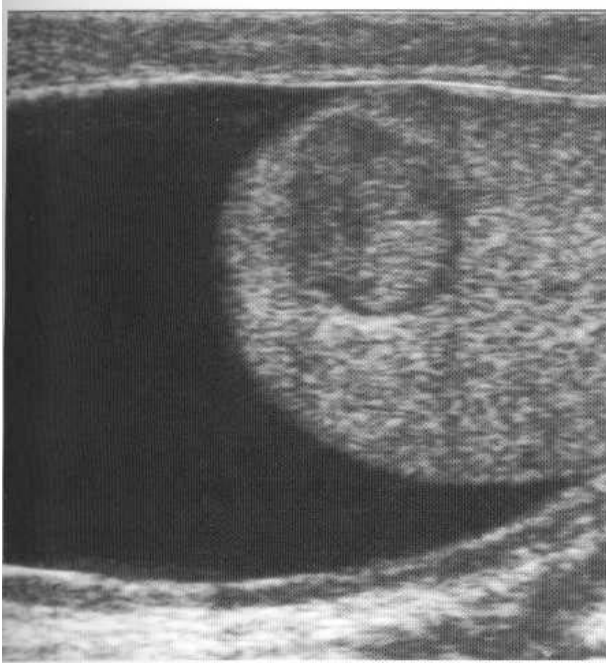


Fig. 32.31 Ultrasound of small testicular malignancy with hydrocele.

effect. When larger than 2-3 cm they are associated with deformity and expansion of the outline of the testicle. Occasionally there is an associated hydrocele (Fig. 32.31). The histology cannot be pre-



Fig. 32.32 Ultrasound of seminoma showing homogeneous reduction in echogenicity.

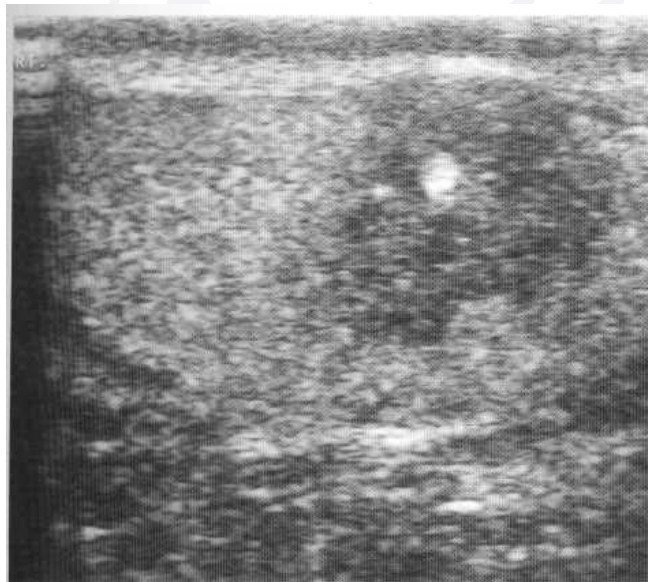


Fig. 32.33 Ultrasound of NSGCT which is echo-poor but relatively ill-defined and containing at least one area of prominent calcification.

dicted from the ultrasound appearances, which are usually non-specific. However, classically seminomas are well defined and uniformly modestly echo-poor (Fig. 32.32). NSGCTs more often show significant echogenic areas of fibrosis or calcification and echo-free cystic areas (Fig. 32.33). Larger tumours (above approximately 1.5 cm) may show increased vascularity on colour flow Doppler; smaller ones are more often hypovascular. The differential diagnosis includes focal or diffuse acute orchitis, abscess, infarct and haemorrhage. The clinical presentation and course usually permits differentiation. It is, however, important to exercise extreme caution, and an echo-poor lesion within the testicle must always be regarded as potentially representing a malignancy. Therefore, if an intratesticular lesion is not showing progressive resolution within a short time (a fortnight or less), consideration of orchidectomy would be recommended and the dilemma discussed with the patient. Occasionally a lesion of a centimetre or less is encountered within the testicle. Those that have been observed over a prolonged period of time appear to show a benign course. Again it would be prudent to ensure the patient is aware of the dilemma and seeks help at the slightest change.

The management of testicular cancer depends heavily on the detection and treatment of lymph node metastases. The lymphatic vessels from the testes follow the spermatic cord through the inguinal canal, cross the pelvis and ascend to drain into lymph nodes along the inferior vena cava and aorta in the lumbar region around the L2 level. Lymph node involvement virtually always starts on the side of the affected testicle. The first group of nodes affected are sometimes referred to as the sentinel nodes, being the nodes around the renal vessels (renal perihilar), the para-aortic nodes immediately below this level on the left and the paracaval nodes immediately below the renal vein on the right. Bilateral involvement is uncommon when the primary is left-sided, but is more often encountered when the disease starts in the right testicle. It does not usually occur until there is considerable ipsilateral disease. Contralateral lymphadenopathy with normal ipsilateral nodes is extremely rare. Following initial lymphadenopathy, disease may spread cranially and caudally along the para-aortic, paracaval and aortocaval nodes. Iliac and inguinal lymph nodes may be involved by retrograde spread, especially on the right, or directly in circumstances where the tumour gains access to the ilioinguinal lymphatic system. This may occur with disease originating from an intra-abdominal testicle, with disruption of the lymphatics following surgery or, if tumour is grossly invasive, within the scrotum (epididymal involvement may lead to external iliac nodal disease, skin invasion leading to inguinal lymphadenopathy). Tumour may also extend retrogradely into the mesenteric lymph nodes and antegradely into the retrocaval, mediastinal and supraclavicular lymph nodes. Drainage into the thoracic duct may occur, with subsequent haematogenous metastases to the lungs and, less often, the liver, brain and skeleton. Haematogenous spread is rare before lymphatic spread, except with choriocarcinoma. It is generally more common with non- seminomatous tumours.

Although a TNM staging system has been formulated for testicular malignancy, the Royal Marsden staging system is more widely used in routine practice (Box 32.1). Its importance is that it not only describes the site of metastases but also the volume of tumour, which is likely to be at least as important. In stage I there is no evidence of metastases. Abdominal lymph node metastases are seen in stage II, supradiaphragmatic in stage III. Distant metastases (extra-lymphatic) are present in stage IV.

Box 32.1 Royal Marsden staging system for testicular cancer

Stage I	No evidence of metastases
IM	Rising serum tumour markers
Stage II	Abdominal lymph node metastases
A	2 cm diameter or less
B	Between 2 and 5 cm diameter
C	5 cm diameter or above
Stage III	Supradiaphragmatic nodal metastasis
M	Mediastinal
N	Cervical or axillary
O	Without abdominal lymph node metastases
ABC	Relates to size as described in stage II
Stage IV	Extralymphatic metastases
Lung	
L1	3 metastases or less
L2	More than 3 metastases, all 2 cm diameter or less
L3	More than 3 metastases, at least one above 2 cm diameter
H	Liver metastases
Br	Cerebral metastases
Bo	Bone metastases

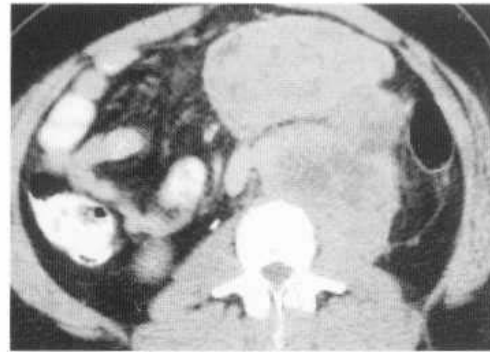


Fig. 32.35 CT demonstrating a huge left para-aortic mass of metastatic NSGCT showing areas of reduced density. The mass encases the aorta, which is displaced forward and invades posteriorly into the psoas muscle and anteriorly into the root of the mesentery.

visible node less than 1.0 cm in diameter is therefore best regarded as equivocal, especially if above 8 min, and the scan should be repeated in 3 months (or guided biopsy performed). Metastatic

CT is the conventional staging method (Fig. 32.34). CT detection of lymph node metastases depends on size. Lymph nodes above 1.0 cm are usually involved (specificity 87%–), and above 1.5 cm are almost always involved (specificity 98%). Most nodes less than 1 cm in diameter are uninvolved but the fact that 25–30% of untreated stage 1 disease develop subsequent metastases indicates that there is a significant number of lymph node micrometastases. A

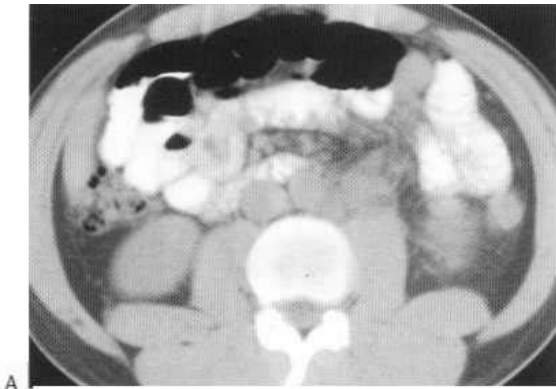


Fig. 32.34 CT demonstrating para-aortic metastases from a left testicular malignancy. (A) At this level a small lymph node deposit is seen immediately lateral to the aorta and a larger one is visible anterior to the left psoas muscle. Higher up (B), just below the level of the renal hila, there is a large left-sided metastatic mass partly encasing the aorta.

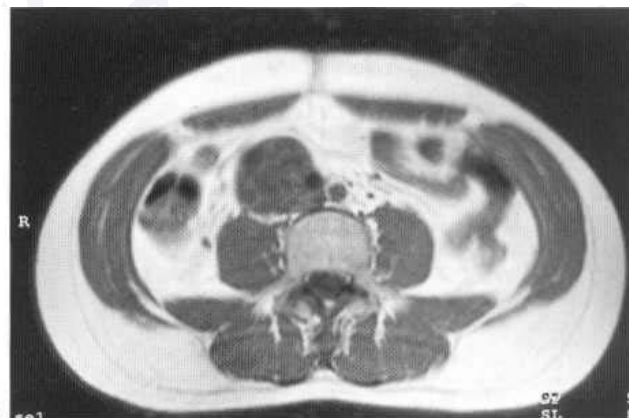
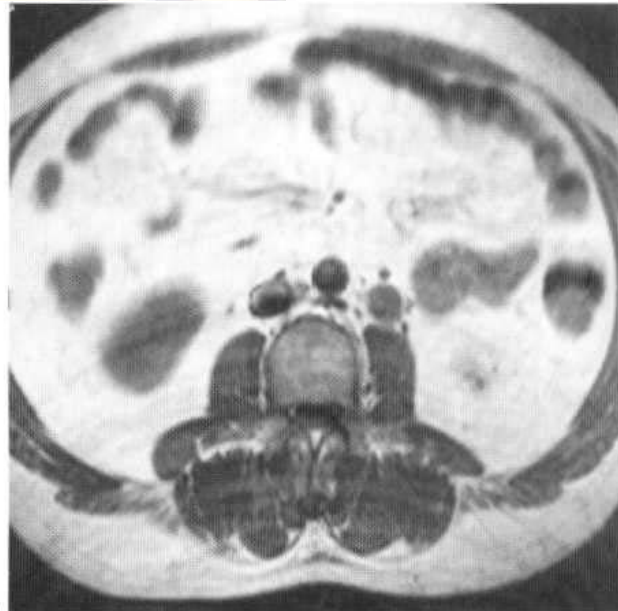


Fig. 32.36 Transverse T₁-weighted MR images on two different patients. (A) In this case there is a solitary left para-aortic lymph node tumour deposit from a left-sided testicular primary. (B) In this case there is a more substantial right-sided deposit from a NSGCT showing considerable heterogeneity. It has encased and displaced the inferior vena cava.

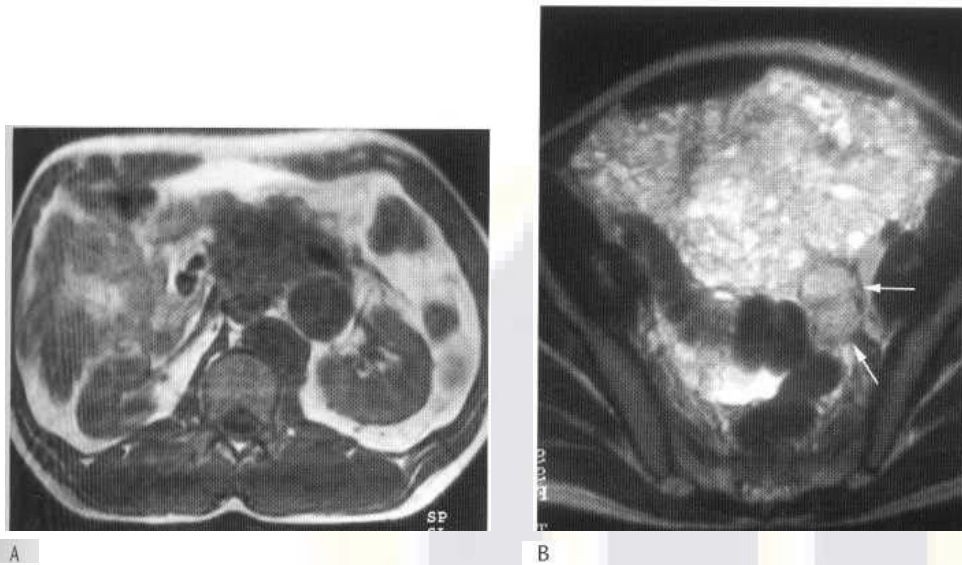


Fig. 32.37 Complex deposits of NSGCT in two different patients seen on MRI. (A) In the first case there are tumour deposits in the left retrocrural area, close to the left renal hilum, and a large mass invading into the mesentery. (B) In this case an undescended testicle is the site of grossly metastatic NSGCT which is seen throughout the pelvis on this T₂-weighted image. It is interesting to note that the pattern of spread is similar to ovarian cancer because of the atypical site of the primary.

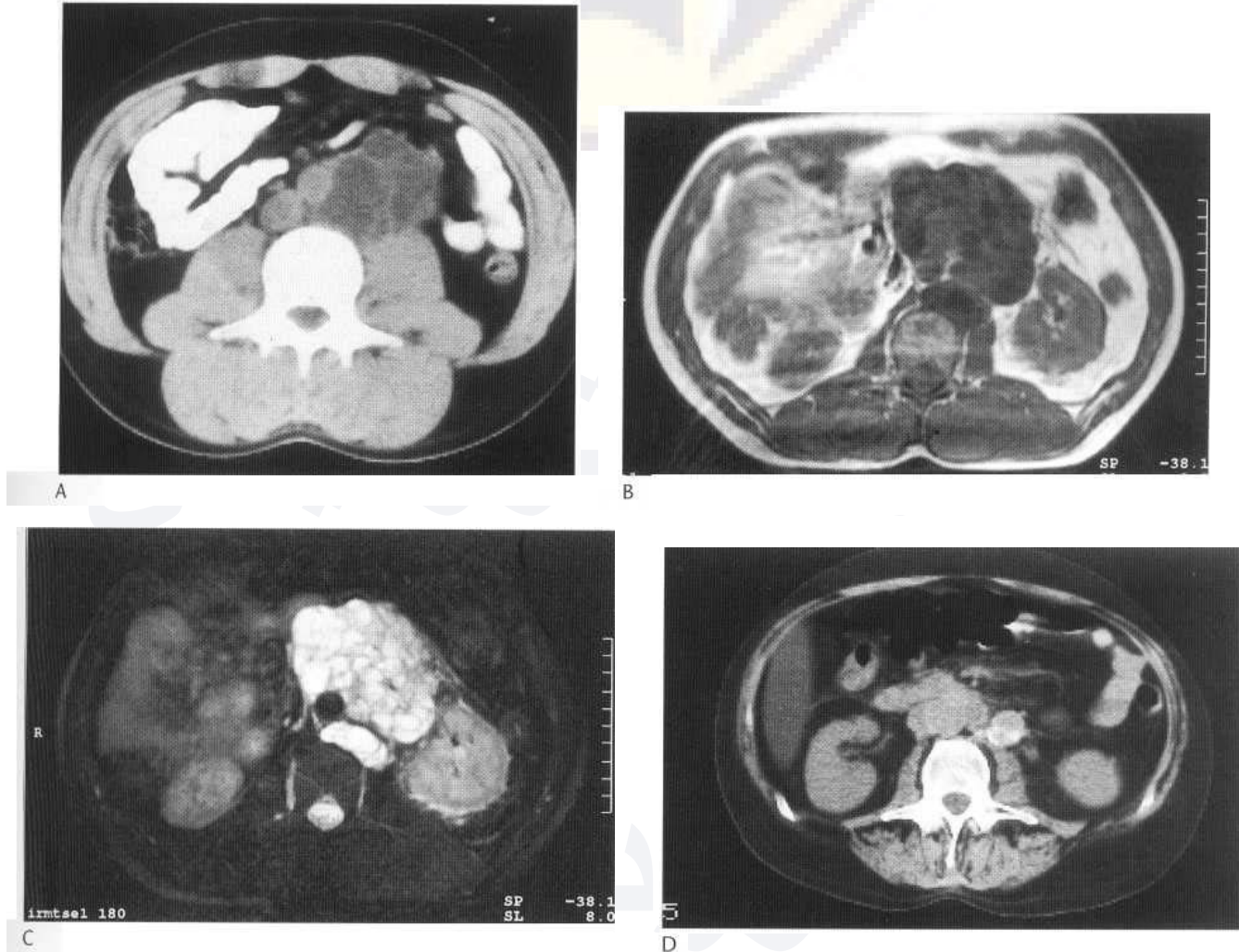


Fig. 32.38 Post-treatment lymph node masses. (A) CT showing substantial mass with substantial cystic (low-density) areas. (B) Transverse T₁-weighted MR scan showing a large predominantly cystic lymph node mass with extensive low-signal areas. These are seen on the transverse STIR sequence (C, higher level) as intensely high-signal areas. Note the tumour has displaced the aorta anteriorly and is extending into the left renal hilum associated with some renal obstruction, as demonstrated by the perinephric high signal. (D) CT showing an ill-defined lymph node mass between the aorta and inferior vena cava (and inseparable from both) and a second mass to the left of the aorta showing dense areas of calcification.

masses may become enormous but in the case of seminomas they usually remain of homogeneous soft-tissue density on CT, although they do occasionally demonstrate central necrosis. NSGCT deposits, however, often become heterogeneous as they enlarge, with lower density and even cystic elements (Fig. 32.35).

The role of MRI scanning is still a matter of controversy. The same size criteria for the detection of lymph node metastases described for CT apply to MRI scanning, and from that point of view the modalities are similar (Fig. 32.36). MRI has the advantage that it avoids ionising radiation but the disadvantage that it is probably inferior for the detection of pulmonary metastases and, especially with the advent of spiral and multislice CT, is significantly slower and hence prone to movement degradation. It does have better soft-tissue contrast and might have a role in difficult cases to assist differentiation of potential tumour deposits from native structures (large gonadal or ascending lumbar vessels, anomalous inferior vena cava or renal vessels, unopacified bowel loops), or areas of solid tumour from fibrosis or cystic degeneration (Fig. 32.37).

Approximately 75% of patients with seminomas have stage I disease. About 80% of these are cured with orchidectomy. The remainder are at risk of developing metastases. A surveillance policy is more difficult in this situation because of the absence of reliable biochemical tumour markers, so initial adjuvant radiotherapy to the para-aortic area can be offered, which raises the cure rate to 97%. Patients who present with metastatic disease are also treated with radiotherapy or chemotherapy (the latter particularly for bulky stage II disease).

Seventy per cent of stage I NSGCT patients are cured by orchidectomy alone; 30%, however, will demonstrate subsequent metastatic disease. This can be almost entirely prevented by retroperitoneal lymph node dissection at the time of staging (a policy pursued in North America). Alternatively, close radiological surveillance can be instituted to allow early detection of metastatic disease, with chemotherapy. Around 25% of NSGCT patients have metastases (stage II-IV) at presentation and these are also treated with chemotherapy, which is usually associated with a complete response. Around 25%, however, will demonstrate persistent lymph node masses following chemotherapy (Fig. 32.38). These often contain areas of fibrosis, haemorrhage, cystic degeneration and sometimes calcification, but some will contain mature teratoma and up to 10-30% of these will contain active malignancy. No imaging modality is currently completely reliable in determining which masses contain significant disease and generally these are treated with surgical excision (retroperitoneal lymph node dissection).

CT or MRI scanning should cover the pelvis, abdomen and chest. Follow-up scans should be performed relatively frequently for the first 2 years; for example, 3-monthly for the first year and 6-monthly in the second. Yearly scanning should be continued for at least 5 years for seminomas of all stages and stage I NSGCTs. There is an annual relapse rate of 1-2% for treated metastatic NSGCTs for more than 10 years and these tumours therefore require longer follow-up.

Sometimes a male patient presents with widespread metastases (which may include abdominal, pelvic and mediastinal lymphadenopathy and pulmonary metastases) that are confirmed histologically to originate from a malignant teratoma but without a palpable testicular tumour. In some of these patients the teratoma may have originated outside the testicle. In a proportion, however, a small primary lesion, with the classical echo-poor ultrasound appearances described above, is identified in a testicle on ultra-



Fig. 32.39 Testicular ultrasound showing a small echogenic area with distal acoustic enhancement. The patient presented with widespread abdominal and mediastinal lymphadenopathy and pulmonary metastases, histologically shown to be teratoma. The testicular lesion is presumed to be the site of a burnt-out primary.

sound. Rarely ultrasound demonstrates a small echogenic area within a testicle (Fig. 32.39), which is believed to represent the scar of a burnt-out primary, a situation that has been described with seminoma and NSGCT.

Metastases to the testicle are rare. The ultrasound appearance is of mixed, often predominantly reduced, echogenicity (Fig. 32.40); they are indistinguishable from primary malignancies except that they generally affect a significantly older age group. They often originate from cancer elsewhere in the urinary tract, especially the prostate. Occasionally carcinoma of the bronchus or malignant melanoma metastasise to the testicle. Others include lymphoma (the commonest testicular malignancy over the age of 60 years) and leukaemia (in childhood, the testicle being a classical sanctuary site for relapse).

Testicular lymphoma This condition is rare, accounting for less than 5% of malignancies of the testicle, although it is the commonest testicular tumour in men over the age of 60. It is bilateral in up to 25% and is associated with extranodal disease, especially in the pharynx, skin and central nervous system. It is virtually always non-Hodgkin's disease. The ultrasound appearances are of a well-defined mass of low echogenicity expanding the testicle. It



Fig. 32.40 Testicular ultrasound showing virtually complete replacement of normal testicular tissue by metastatic prostate cancer. An associated hydrocele is also demonstrated.

often extends to involve the epididymis and spermatic cord. The dominant feature of the mass is its homogeneity. Multiple nodules or foci of haemorrhage or necrosis are uncommon.

Testicular calcification

Coarse areas of calcification (above 3 mm diameter) that are relatively few in number are seen within some malignant testicular tumours, particularly non-seminomatous germ cell tumours. A solitary substantial focus may be associated with the so-called burnt-out primary tumour (Azzopardi tumour). Infection, trauma or infarct may also produce dystrophic calcific areas. They are usually solitary or few in number and vary from 1-2 mm in diameter to several millimetres.

Numerous small areas of calcification (1-2 mm diameter) seen throughout the testicle are referred to as testicular microlithiasis. These are thought to represent intratubular microcalcifications associated with degenerate cells within the seminiferous tubules and appear to be a primary process.

Testicular microlithiasis

This is usually bilateral but may be asymmetrical. It is associated with cryptorchidism, male pseudohermaphroditism, testicular atrophy and subfertility, as well as Down's syndrome and Klinefelter's syndrome. It appears to have an association with testicular cancer, although the strength of this association is still a subject of controversy. The mechanism is also still under investigation but there is a potential link with intratubular

germ cell neoplasia (GCN) (GCN formerly referred to as carcinoma in situ) is likely

to be the precursor of germ cell tumours. It is found adjacent to most tumours, and is seen in the contralateral testicle in up to 5% of cases. It is associated with testicular atrophy and infertility and progresses to carcinoma in approximately 50% of cases in 5 years. GCN itself is not identifiable on ultrasound but it is thought that it may be associated with testicular microlithiasis.

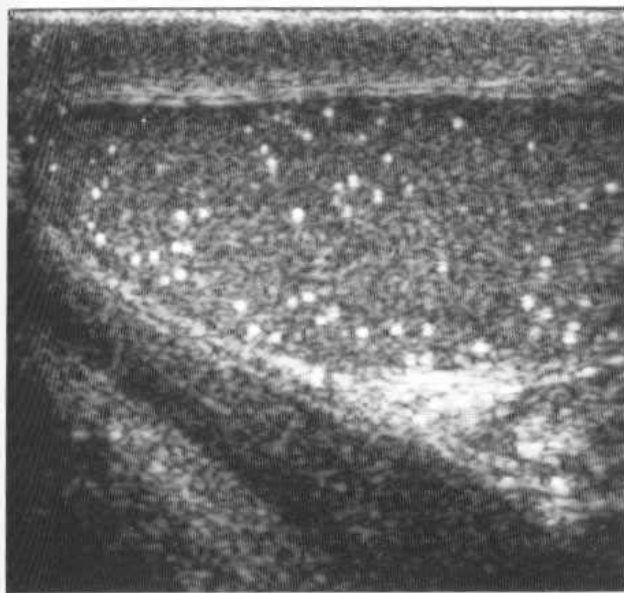


Fig. 32.41 Ultrasound of testicular microlithiasis showing numerous tiny calcific foci.

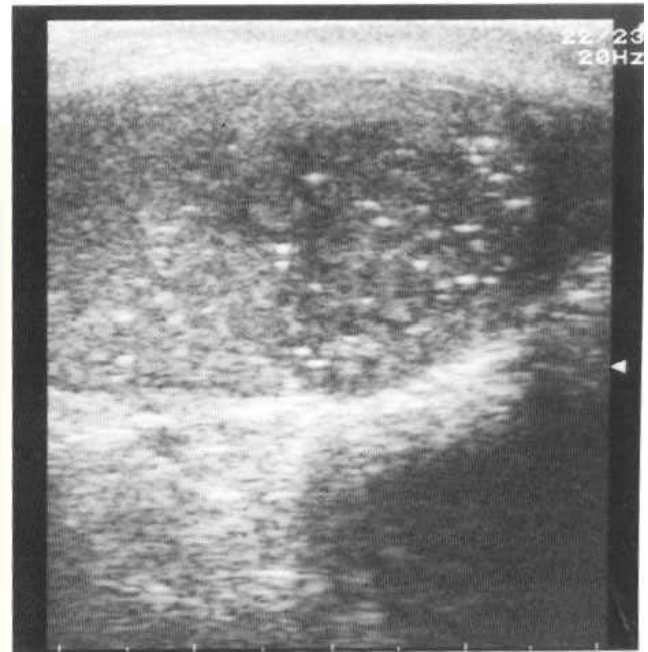


Fig. 32.42 Testicular ultrasound showing microlithiasis and the development of a seminoma.

Classical testicular microlithiasis (CTM) has been defined as five or more microliths visible on at least one ultrasound image (Fig. 32.41). More than one but less than five has been referred to as limited testicular microlithiasis (LTM). The frequency of tumour occurrence with microlithiasis (Fig. 32.42) and the risk of tumour development remains uncertain. Initial reports suggested a very high risk, with up to 40% of CTM associated with testicular cancer at the time of the initial ultrasound scan. More recently large studies have suggested a significantly lower range of 15-27%. Subsequent tumours have been reported as developing in CTM and LTM but the magnitude of the risk is still unclear. The most recent studies have not demonstrated any malignancies on limited follow-up of 3-4 years. It has become routine practice to suggest annual ultrasound surveillance of these patients, although regular testicular self-examination is probably more important and may even be sufficient.

Penile disorder

Carcinoma of the penis This uncommon malignancy is essentially a dermatological disease, being a keratinised squamous cell carcinoma (SCC), but with a urological presentation. It may be classified into three anatomical subsites (prepuce, glans penis and shaft). In practice it almost always starts in the sulcus and proceeds with local invasion into the glans and along the shaft. Advanced tumours invade into the urethra, penile shaft, prostate and perineum. There is a strong tendency, like all SCCs, to early lymph node metastases and late haematogenous spread.

The lymphatic drainage is to the superficial and deep inguinal nodes in the first instance. MRI is useful for assessing both the extent of the primary tumour and the regional lymph nodes (Fig. 32.43). Unfortunately these nodes are often hyperplastic due to inflammatory stimulus and may normally be up to 15 mm in maximum diameter, so unenlarged involved lymph nodes are easily overlooked. Nodes above 15 mm in diameter are highly likely to be

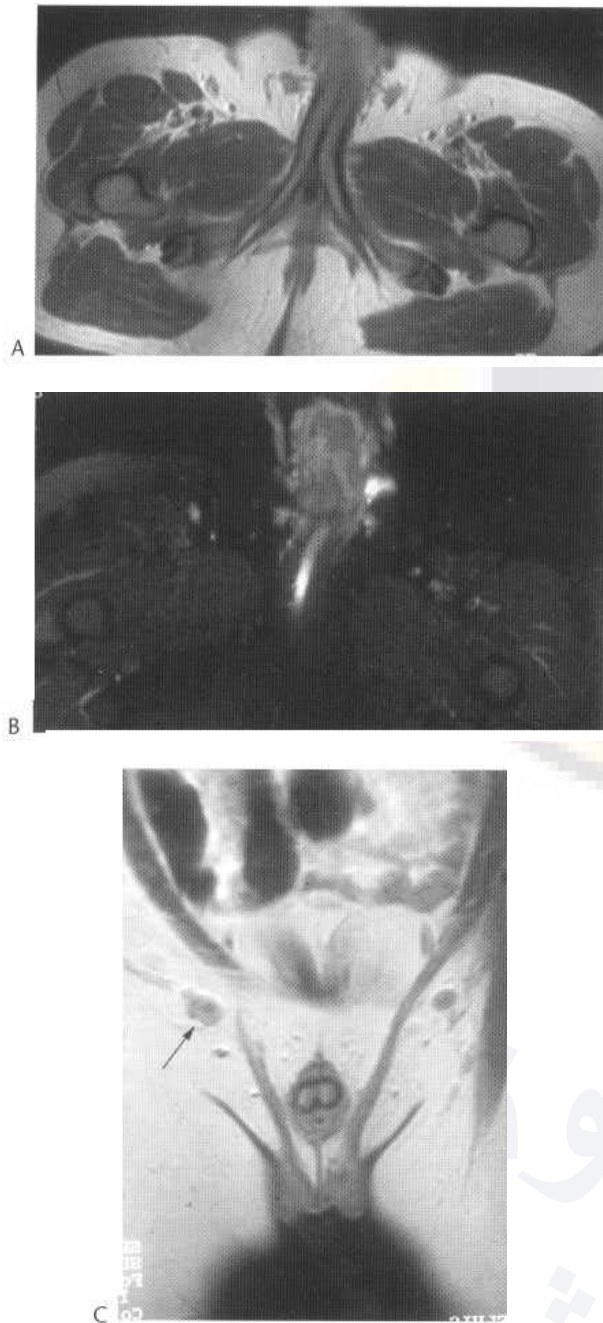


Fig. 32.43 MR scan of extensive penile carcinoma. Transverse post-gadolinium T₁-weighted image (A) shows destruction of the normal anatomy of the glans and shaft by the irregular enhancing mass of tumour. This is seen on the transverse STIR sequence (B), which also demonstrates upstream dilatation of the urethra, a finding generally only seen with advanced tumours. The coronal post-gadolinium T₁-weighted image (C) demonstrates the presence of inguinal lymph nodes. These are not particularly enlarged but the node on the right (arrow) shows central necrosis characteristic of squamous cell carcinoma metastasis.

involved by tumour. As with other SCCs, involved lymph nodes may develop irregular central necrosis, a finding highly suggestive of metastatic disease. This is seen as unenhancing areas on contrast MRI (or CT) or very high signal areas on T₁-weighted and STIR sequences.

Trauma Rupture of the tough fascia over the corpora cavernosa (the penile tunica albuginea) is a rare injury, referred to as fracture of the penis. It is usually due to lateral trauma during athletic or unusual sexual activity, generally presenting with a history of a sensation of

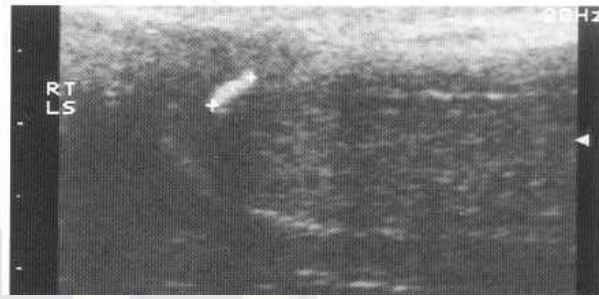


Fig. 32.44 Longitudinal ultrasound of a penis in Peyronie's disease showing a small calcified echogenic plaque with distal acoustic shadowing.

a snap at the time of injury, with immediate detumescence and marked ecchymosis. Ultrasound and cavernosography have been employed to image this condition but they contribute little, as the diagnosis is essentially clinical and the treatment (relatively acute surgical repair) is not affected by the imaging findings.

Peyronie's disease In this condition there is focal induration and fibrosis of the corpus cavernosum. It is of unknown aetiology and may present at any age, but particularly in middle age. It is of variable severity and often resolves spontaneously over a period of months or years. It presents with a palpable nodule and may be associated with painful erections and/or difficulty with sexual intercourse. It is seen on ultrasound as an echogenic plaque. Calcification may develop, leading to distal acoustic shadowing (Fig. 32.44). The disease may also be demonstrated on CT or MRI but imaging findings rarely alter the diagnosis or management, which again rests on the clinical picture.

RADIONUCLIDE IMAGING OF THE TESTIS

Scrotal scintigraphy

Scintigraphic demonstration of testicular perfusion offers a non-invasive approach for distinguishing between the ischaemia associated with testicular torsion and the hyperaemia associated with acute epididymo-orchitis (Figs 32.45, 32.46).

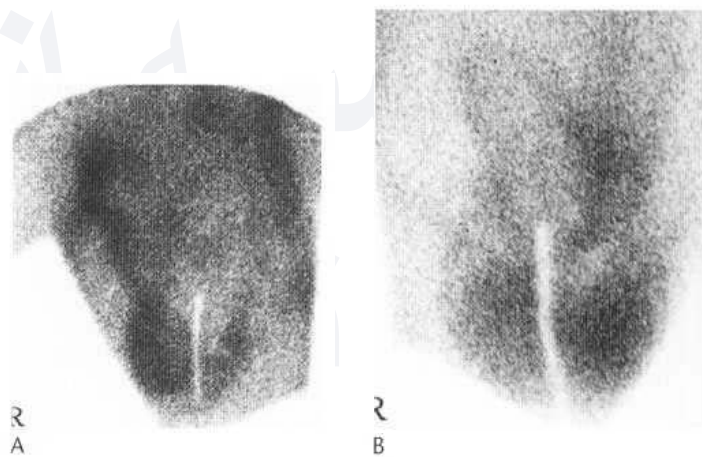


Fig. 32.45 Acute epididymo-orchitis (two cases). Anterior ^{99m}Tc images obtained 1 min after injection showing diffusely increased uptake in the right testis of case A and the left testis of case B. Case A also shows diffusely increased activity along the spermatic cord on the affected side. A lead marker has been used to indicate the midline of the scrotum.

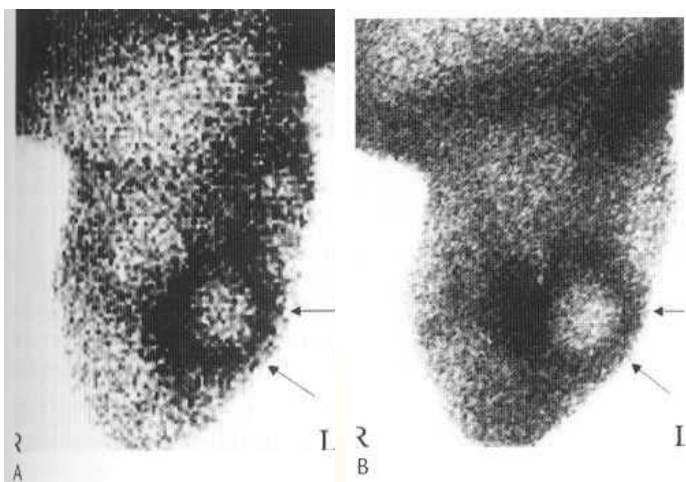


Fig. 32.46 Testicular torsion. Anterior view ^{99m}Tc pertechnetate study shows an intensely hyperaemic rim of tissue surrounding a photon-deficient area which represents the infarcted left testis (arrows).

Technique The patient is positioned supine, with the scrotum elevated by a towel placed between his legs, or better, a sling of adhesive tape placed across the thighs. It is also helpful to place a lead-rubber shield beneath the sling and the scrotum in order to block out activity from the patient's thighs. A rapid bolus injection of about 200 MBq of ^{99m}Tc -pertechnetate is given, and a rapid sequence of images of the scrotal region is obtained (e.g. one frame per second for 40 seconds). After the initial dynamic series, one or two further spot views with high count density should be obtained, but typically the most informative data are those derived from summing the first-pass frames to a single image.

Interpretation With torsion, the testis appears avascular or severely ischaemic. This is manifest on the images as a photon-deficient area, which is often surrounded by a rim of increased activity representing surrounding hyperaemia. The line of the spermatic cord also often shows increased activity. With acute epididymo-orchitis, activity within the testis itself is usually normal, but the inflammatory response in the epididymis produces a C-shaped margin of markedly increased activity, and in some cases this may appear to extend across the testis as well. The contralateral normal testis is used as a benchmark to indicate whether the affected side shows increased or reduced activity.

Application The main value of this test is as a supplement to Doppler ultrasound for those patients presenting acutely with unilateral testicular pain. Although the radionuclide procedure itself takes just a few minutes, its value can be fully realised only when a rapidly responding on-call service is provided, as the majority of patients with acute testicular problems present outside normal working hours.

RADIOLOGICAL PROCEDURES IN ANDROLOGY

Imaging in erectile dysfunction

Radiological assessment in erectile dysfunction is reserved for patients who have failed to respond to first-line therapy (oral sildenafil, intracavernosal injection of alprostadil, transurethral

Table 32.2 Radiological investigations of erectile dysfunction

Investigation	Indication	Comments
Duplex ultrasound	Screening test for vascular function	PSV >35 cm/s normal PSV <25 cm/s arterial insufficiency
Cavernosography	Suspected venous leakage (where surgery considered)	Declining use
Arteriography	Young men with traumatic arterial occlusion	Anatomical information for surgical planning

alprostadil or vacuum device) and in whom surgical intervention is contemplated. Imaging is used in the assessment of suspected vascular abnormality (arterial or venous), believed to be the commonest cause of organic erectile dysfunction.

Haemodynamic evaluation of these patients aims to detect arterial insufficiency and venous incompetence, for which surgical procedures are available. Penile revascularisation and venous ligation procedures have given disappointing long-term results, with rates of successful return to intercourse of around 60% and 40%, respectively. Successful outcome depends on careful selection of surgical candidates.

For many years assessment was based upon arteriography and cavernosography, which have now largely been replaced by duplex ultrasonography (Table 32.2). Duplex ultrasonography of the penis and cavernosal arteries was first described in 1985 and has now emerged as the investigation of choice for penile arterial screening, despite some debate regarding protocol and velocity thresholds (particularly for moderate reductions in systolic velocity). It has a more limited role in demonstrating impaired veno-occlusion.

Arterial blood supply to the penis originates from the internal iliac arteries via the internal pudendal arteries, which divide and form paired cavernosal arteries at the base of the penis. It has been estimated that penile arterial inflow may increase up to 30-fold during tumescence.

Tests of penile haemodynamics are performed following intracavernosal injection of a vasoactive agent to induce a pharmacological erection. Alprostadil (5–20 μg) is more effective than papaverine, with a lower incidence of priapism.

The ultrasound transducer (7.5 or 10 MHz) is positioned on the ventral surface of the base of the penis. Paired cavernosal arteries are found close to the septum. During the initial phase of erection, both systolic and diastolic flow is increased and continuous. The diastolic waveform decreases at an intracavernosal pressure over 40 mmHg and is reversed at an intracavernosal pressure over 80 mmHg. Above this, systolic flow is diminished and flow ceases if intracavernosal pressure approaches systolic blood pressure. Peak systolic velocity (PSV) and end-diastolic velocity (EDV) are recorded every 5 min for 30 min.

It is now generally accepted that PSV >35 cm/s predicts normal arterial inflow and that PSV <25 cm/s is a useful predictor of arterial insufficiency. Validation for these thresholds comes from studies correlating duplex ultrasonography with arteriography in patients with erectile dysfunction. For the intermediate PSV range of 25–35 cm/s, several parameters have been suggested to predict arterial insufficiency (using arterial waveform analysis) but none is widely accepted.

The relationship between EDV at duplex ultrasonography and venous incompetence at cavernosometry has also been examined. Although, overall, EDV correlates poorly with venous incompetence, EDV <5 cm/s in association with normal PSV (>35 cm/s) is believed to be an indicator that veno-occlusion is normal and further investigation (c.g. cavernosometry) is unnecessary. In patients with arterial insufficiency diagnosed by these duplex criteria, confirmation by arteriography is required if surgical intervention is planned (see below).

Erectile dysfunction may result from abnormal penile venous leakage in patients who have a failure of the veno-occlusive mechanism to provide adequate venous resistance during erection. This may be congenitally present or acquired (degenerative or traumatic). Venous drainage of erectile tissue occurs via the deep dorsal vein, which drains into the periprostatic plexus, and paired cavernosal veins, which drain via the internal pudendal veins. Commonly, incompetence originates in the deep dorsal vein. Pharmacocavernosography has been performed to investigate this. Both corpora cavernosa are cannulated with 19 gauge needles. A pump injection of 150 strength contrast medium is injected via one of the needles to demonstrate sites of abnormal venous leakage (Fig. 32.47). This is often combined with cavernosometry, to quantify the flow rate required to maintain a pharmacological erection. Synchronous pressure measurements are recorded through the other needle. Although this technique remains the best method of demonstrating venous incompetence as a cause of erectile dysfunction, poor results with venous ligation procedures have reduced their popularity and led to a dramatic reduction in the use of this test.

Although its use is now more limited, arteriography before and after a pharmacologically induced erection is still performed to demonstrate vascular anatomy prior to surgical intervention (arterial bypass or angioplasty). This is indicated only in a selected group of younger, otherwise healthy men with a history of blunt perineal or pelvic trauma who are suspected of having a focal arterial lesion

causing erectile dysfunction (rather than having diffuse atherosclerotic disease). Arterial injury is most commonly found in the distal internal pudendal artery at the level of the urogenital diaphragm. Anatomical variation in pudendal vasculature is not uncommon: in a series of 195 arteriograms, an accessory pudendal artery was demonstrated in 7% of patients.

Imaging in male infertility

Azoospermic men with a normal FSH level may be evaluated radiologically in an attempt to discover a treatable, obstructive cause for infertility. Traditionally this has been achieved via vasography; more recently there has been increased interest in the use of transrectal ultrasound (TRUS).

When both vasa arc clinically palpable in the scrotum, obstruction may be from congenital causes (most commonly midline cysts compressing the ejaculatory ducts) or acquired causes (commonly inflammatory or traumatic stenoses of the ejaculatory ducts or vasa). TRUS is useful in demonstrating distal obstruction at the level of the ejaculatory ducts, typically showing duct dilatation proximal to the obstruction and also congenital cysts, if present. Multifocal stenoses (which occur in up to 20% of obstructed vasa) or proximal stenoses of the vas deferens may be identified by vasography, with the vas cannulated just distal to the inguinal canal. Obstruction may be relieved surgically by epididymovasostomy in some patients.

Although its relevance is debated, the presence of scrotal varicoceles in association with oligospermia may represent a treatable cause of hypofertility. Treatment of varicoceles for subfertility has been the subject of controversy but at best it has been reported to improve consistently the semen analysis and be associated with demonstrable fertility in up to 40% of treated individuals.



Fig. 32.47 Cavernosogram showing opacification of the cavernosa and marked venous leakage.

REFERENCES AND SUGGESTIONS FOR FURTHER READING

- Atchley, J. T. M., and Dewbury, K. C. (2000) Ultrasound appearances of testicular epidermoid cysts. *Clinical Radiology*, **55**, 493-502.
- Azzopardi, J. G., Mostofi, J. K., Theiss, E. A. (1961) Lesions of testes observed in certain patients with widespread choriocarcinoma and related tumours. *American Journal of Pathology*, **38**, 207-225.
- Bach, A. M., Hann, L. E., Hadar, O., et al (2001) Testicular microlithiasis: what is its association with testicular cancer? *Radiology*, **220**, 70-75.
- Backus, M. I., Mack, L. A., Middleton, W. D., King, B. F., Winter, T. C., True, L. D. (1994) *Radiology*, **192**, 781-785.
- Bennett, H. F., Middleton, W. D., Bullock, A. D., Teefey, S. A. (2001) Testicular microlithiasis: US follow-up. *Radiology*, **218**, 359-363.
- Bockrath, J. M., Schaeffer, A. J., Kits, M. S., Neiman, H. L. (1983) Ultrasound identification of impalpable testicle tumour. *Journal of Urology*, **130**, 355-356.
- Bree, R. L., Hoang, D. T. (1996) Scrotal ultrasound. *Radiological Clinics of North America*, **34**, 1183-1205.
- Brown, D. L., Benson, C. B., Doherty, F. J., et al (1992) Cystic testicular mass caused by dilated rete testis: sonographic findings in 31 cases. *American Journal of Roentgenology*, **158**, 1257-1259.
- Charnsangavej, C. (1990) Lymphoma of the genitourinary tract. *Radiologic Clinics of North America*, **28**, 865-877.
- Clarke, B. G. (1966) Incidence of varicocele in normal men and among men of different ages. *JAMA*, **198**, 1121.
- Colapinto, V., McCallum, R. (1977) Injury to the male posterior urethra in fractured pelvis: a new classification. *Journal of Urology*, **118**, 575-580.
- Dearnaley, D. P., Huddart, R. A., Horwich, A. (2001) Managing testicular cancer. *BMJ*, **322**, 1583-1588.
- Dewbury, K. C. (2000) Scrotal ultrasound: an update. *British Journal of Urology International*, **86** (suppl. 1), 143-152.

- Fenley, M. R., Pat, M. K., Nockler, I. B., I lendry, W. F. (1997) Retrograde embolisation and causes of failure in the primary treatment of varicocele. *British Journal of Urology*, **80**, 642-646.
- Fowler, R. (1991) Review: Imaging the testis and scrotal structures. *Clinical Radiology*, **41**, 81-85.
- Gonda, Jr R. L., Karo, J. I., For et, R. A. (1987) Diagnosis of subclinical varicocele infertility. *American Journal of Roentgenology*, **138**, 973-675.
- Grantham, J. G., Charboneau, J. W., James, E. M., et al (1985) Testicular neoplasms: 29 tumours studied by high resolution US. *Radiology*, **157**, 775-780.
- Grey, A. C., Carrington, B. M., Hulse, P. A., Swindell, R., Yates, W. (2000) Magnetic resonance appearance of normal inguinal lymph nodes. *Clinical Radiology*, **55**, 124-130. h
- Gross, G. W., Rohner, T. J., Lomhard, J. S., Abrams, C. S. (1986) Metastatic seminoma with regression of testicular primary: ultrasonographic detection. *Journal of Urology*, **136**, 1086-1088.
- holm, M., Lenz, S., De Meys, E. R., Skakkehaek, N. E. (2001) Andrology Microcalcifications and carcinoma in situ of the testis. *British Journal of Urology International*, **87**, 144-149.
- Horenblas, S. (2001) Lymphadenectomy for squamous cell carcinoma of the penis. Diagnosis of lymph node metastasis. *British Journal of Urology International*, **88**, 467-472.
- howlet, D. C., Marchbank, N. D. P., Sahomi, D. F. (2000) Ultrasound of the testis. *Clinical Radiology*, **55**, 595-601.
- Husband, J., MacVicar, D. (1998) Testicular germ cell tumours. In *Imaging in Oncology*, pp. 259-276. Oxford: Isis.
- Keoghane, S. R., Kahala, J. E. (2001) Varicocele embolisation. *Imaging*, **13**, 11-17.
- Lien, H. H., Stenwig, A. E., Oils, S., Fossa, S. D. (1986) Influence of different criteria for abnormal lymph node size on reliability of computed tomography in patients with non-seminomatous testicular tumour. *Acta Radiologica*, **27**, 199-203.
- Linkowski, G. D., Avehane, A., Gooding, G. A. (1985) Scrotal calculi: sonographic detection. *Radiology*, **156**, 484-487.
- London, N. J. M., Smart, J. G., Kinder, R. B., Watkin, E. M., Rees, Y., Haley, P. (1989) Prospective study of routine scrotal ultrasonography in urological practice. *British Journal of Urology*, **63**, 416-419.
- Osier, J. (1971) Varicocele in children and adolescents. *Scandinavian Journal of Urology and Nephrology*, **5**, 27.
- Satchithananda, K., Beese, R. C., Sidhu, P. S. (2000) Acute appendicitis presenting with a testicular mass: ultrasound appearances. *British Journal of Radiology*, **73**, 780-782.
- Sheldon, C. A. (1985) Symposium on paediatric surgery. I. Undescended testes and testicular torsion. *Surgical Clinics of North America*, **65**, 1303-1329.
- Shlansky-Goldberg, R., Van Arsdalen, K. N., Rutter, C. M. (1997) Percutaneous varicocele embolisation versus surgical ligation for the treatment of infertility: changes in seminal parameters and pregnancy outcomes. *Journal of Vascular and Interventional Radiology*, **8**, 759-767.
- Sidhu, P. S. (1999) Clinical and imaging features of testicular torsion: role of ultrasound. *Clinical Radiology*, **54**, 343-352.
- Skakkehaek, N. E., Berthelsen, J. G., Muller, J. (1982) xxxxxx. *Urologic Clinics of North America*, **9**, 377-385.
- Skyrme, R. J., Fenn, N. J., Jones, A. R., Bowsher, W. G. (2000) Testicular microlithiasis in a UK population: its incidence, associations and follow-up. *British Journal of Urology International*, **86**, 482-485.
- Smith, W. S., Branamer, H. M., Henry, M., Frazier, H. (1991) Testicular microlithiasis: sonographic features with pathologic correlation. *American Journal of Roentgenology*, **157**, 1003-1004.
- Tackett, R. E., Ling, D., Catalona, W. L., et al. (1985) High resolution sonography in diagnosing testicular neoplasms: clinical significance of false positive scans. *Journal of Urology*, **135**, 494-496.
- Tammela, T. L. J., Karttunen, T. J., Mattila, S. I., Makarainen, H. P., ellstrom, P. A., Kontturi, M. J. (1991) Cysts of the tunica albuginea—more common testicular masses than previously thought? *British Journal of Urology*, **68**, 280-284.
- Benson, C. B., Aruny, J. E., Vickers, Jr, M. A. (1993) Correlation of duplex sonography with penile arteriography in patients with erectile dysfunction. *American Journal of Roentgenology*, **160**, 71-73.
- Cornud, F., Amar, E., Hamida, K., et al (2000) Imaging in male hypofertility and impotence. *British Journal of Urology International*, **86** (suppl. 1), 153-163.
- Furst, G., Muher-Matthcis, V., Cohnen, M., et al. (1999) Venous incompetence in erectile dysfunction: evaluation with color-coded duplex sonography and cavernosometry/-graphy. *European Radiology*, **9**, 35-41.
- Gonda, Jr R. L., Karo, J. I., Foret, R. A. (1987) Diagnosis of subclinical varicocele infertility. *American Journal of Roentgenology*, **138**, 973-975.
- Kropman, R. F., Schipper, J., van Oostayn, J. A., et al (1992) The Value of increased end diastolic velocity during penile duplex sonography in relation to pathological leakage in erectile dysfunction. *Journal of Urology*, **148**, 314-317.
- Linnet, O. I., Neff, L. L. (1994) Intracavernous prostaglandin E1 in erectile dysfunction. *Clinical Investigation*, **72**, 139-149.
- Littrup, P., Lee, F., McLeary, R., et al (1988) Transrectal US of the seminal vesicles and ejaculatory ducts: clinical correlation. *Radiology*, **168**, 625-628.
- Luc, T. F., Hricak, H., Marich, K. W., Tanagho, E. A. (1985) Vasculogenic impotence evaluated by high-resolution ultrasonography and pulsed Doppler spectrum analysis. *Radiology*, **155**, 777-781.
- Montague, D., Barada, J., Belker, A., et al (1996) Clinical guidelines panel on erectile dysfunction: summary report on the treatment of organic erectile dysfunction. *Journal of Urology*, **156**, 2007-2011.
- Rosen, M., Greenfield, A., Gregory-Walker, T., et al (1990) Arteriogenic impotence: findings in 195 impotent men examined with selective internal pudendal angiography. *Radiology*, **174**, 1043-1048.
- Schwartz, A. N., Wang, K. Y., Mack, L. A., et al (1989) Evaluation of normal erectile function with colour flow Doppler sonography. *American Journal of Roentgenology*, **153**, 1103-1100.
- Shirai, M., Ishii, N. (1981) Haemodynamics of erection in man. *Archives of Andrology*, **6**, 27-32.
- Valji, K., Bookstein, J. J. (1993) Diagnosis of arteriogenic impotence: efficacy of duplex sonography as a screening tool. *American Journal of Roentgenology*, **160**, 65-69.



نشر الکترونیکی
موسسه انتشاراتی
نوردانش

OBSTETRIC ULTRASOUND

Roger Chisholm

with contribution from Jeremy P. R. Jenkins

During the last 20 years ultrasound has revolutionised the practice of obstetrics. In some countries, including the UK, over 90% of women now have at least one ultrasound examination during pregnancy. In others, such as the USA, continuing concern about the possible harmful effects of ultrasound has limited the examination to those obstetric patients fulfilling certain criteria, in some cases less than 50% of the total. The intention of this chapter is to provide an overview of current practice and trends within obstetric radiology with, of necessity, an emphasis on diagnostic ultrasound,

an empty maternal bladder, the latter factor leading many women to prefer this technique to the transabdominal approach. Limitations include reduced beam penetration and the more invasive nature of the technique, which may make it less desirable in certain clinical situations.

Mechanical sector and phased-array systems are again available, frequencies being in the range 5-7.5 MHz.

Technique and equipment

Transabdominal sonography (TAS) Until 10 years ago TAS was used universally throughout pregnancy and continues to be the major technique for imaging in the second and third trimester. A full maternal bladder is frequently necessary to displace pelvic bowel loops, which otherwise obscure the field of view. Real-time ultrasound equipment for obstetric use includes:

- **Sector transducers**, which may be either mechanical or phased array systems. These are widely used and may be particularly useful where access is limited, for instance where the fetal head or placenta lies low within the pelvis.
- **Linear or curved array transducers**, which are suitable for most obstetric applications. They generally provide less distortion and a greater field of view than a mechanical sector transducer, but the larger surface area required for skin contact may occasionally prove a problem.

Frequencies for the above transducers lie between 3 and 5 MHz, the choice being a trade-off between beam penetration and resolution.

Transvaginal sonography (TVS) Initially described for ovarian follicle monitoring in 1984, TVS is now the method of choice for monitoring infertility disorders, the differentiation of the normal and abnormal first trimester pregnancy, and the diagnosis of ectopic pregnancy. Its major advantage is the ability to use a higher frequency transducer nearer to the organs of interest, thus facilitating higher resolution imaging of the uterus, ovaries, adnexa and eu de sac. Other advantages include the avoidance of subcutaneous fat and the fact that scanning can be performed with

Doppler ultrasound The routine use of *Doppler ultrasound* in pregnancy remains controversial, with concern about the increased power intensities when compared with imaging levels. This has become even more relevant with the widespread use of TVS. Despite this, many studies have shown that Doppler information may prove valuable in the assessment of pregnancy complications and the 'at risk' fetus. Thus *duplex Doppler waveforms* from the Uterine and umbilical arteries may give useful information in the assessment of intrauterine growth retardation (p. 1046), while *colour* and *power Doppler* may be invaluable in the assessment of the fetal heart and outflow tracts, as well as in looking at other fetal vessels such as intracerebral and renal arteries.

Tissue harmonic imaging (THI) Harmonic imaging involves the processing of the lower amplitude, higher frequency waveforms that accompany the fundamental frequency waveforms traditionally processed. The harmonic waveforms tend to have less clutter and scatter (reverberations and side lobe artefacts) than fundamental waveforms. Studies have confirmed better visualisation of fetal structures using THI, particularly in larger patients (Treadwell et al 2000).

Three-dimensional ultrasound (3D) The three-dimensional reconstruction of ultrasound images was first demonstrated nearly 15 years ago but has only recently become a clinical reality (Lees 2001). Ultrasound developments have led to 'cleaner' images with less speckle, clutter and other artefacts, while increases in computing power now allow real-time 3D rendering in the machine rather than on an offline workstation. Many of the early publications on 3D fetal ultrasound concentrated on the fetal face and skeleton. Several articles have shown significant improvements in the identification of cleft lips (Johnson et al 2000), while others have shown more information with skeletal dysplasias but no significant increase in overall diagnostic accuracy. The consensus

view at present would seem to be that, while state of the art 31) ultrasound produces excellent images, the value is still as an adjunct to the 2D image rather than as a stand-alone system.

Indications for an ultrasound examination

In the report of the Royal College of Obstetricians and Gynaecologists on the use of the ultrasound examination in pregnancy (1984), it was concluded that the benefits of a routine examination significantly outweighed any potential adverse effect from the dangers of the examination itself. The American position has remained substantially different, taking the view that, like any other medical test, ultrasound should only be performed where there are sound clinical indications (Box 33.1).

The normal ultrasound examination

Guidelines approved by the American Institute of Ultrasound in Medicine (Leopold 1986) serve as a useful summary of the

Box 33.1 Indications for an obstetric ultrasound examination

1. Estimation of gestational age for patients who are to undergo elective repeat caesarean section (over 25% of the total in some states), induction of labour or elective termination of pregnancy
2. Evaluation of fetal growth (where there is a genuine reason for believing that uteroplacental insufficiency, intrauterine growth retardation or macrosomia may exist)
3. Vaginal bleeding of undetermined aetiology
4. Determination of fetal presentation in labour
5. Suspected multiple gestation
6. Adjunct to amniocentesis
7. Significant uterine size/clinical dates discrepancy
8. Pelvic mass detected clinically
9. Suspected hydatidiform mole
10. Cervical cerclage
11. Special procedures
12. Suspected fetal death
13. Suspected uterine abnormality
14. IUCD localisation
15. Ovarian follicle development surveillance
16. Biophysical profile after 28 weeks of gestation
17. Observation of intrapartum events
18. Suspected poly- or oligohydramnios
19. Suspected abruptio placentae
20. Adjunct to external version from breech to vertex presentation
21. Estimation of fetal weight and/or presentation in premature rupture of the membranes or premature labour
22. Abnormal serum u-fetoprotein value for gestational age
23. Follow-up of identified fetal anomaly
24. History of previous congenital anomaly
25. Serial evaluation of fetal growth in multiple gestations
26. Estimation of gestational age in late registrants for prenatal care

*As agreed at a consensus conference of interested parties-The Use of Diagnostic Ultrasound During Pregnancy (1984).

questions to be answered by a normal antepartum obstetric ultrasound examination.

First trimester (commonly performed at 9-12 weeks of menstrual age)

1. *Identify the gestational sac and embryo.* Determine the sonographic age by measurement of the crown-rump length and other measurements if near the end of the first trimester. This provides a baseline for estimating the date of delivery, for assessing subsequent growth and for the timing of biochemical screening.

2. *Record the presence or absence of fetal life.* This can generally be accomplished by the sixth week (JAS) or fifth week (TVS) counting from the first day of the last menstrual period. Where there is reasonable doubt as to the viability of an embryo, repeat scanning within 7 days should resolve the dilemma.

3. *Document fetal number.* Multiple pregnancy should only be reported where multiple embryos (or yolk sacs) are seen (Fig. 33.1). Counting separate fluid collections within the uterus may result in false-positive diagnoses. Assess the chorionicity where multiple gestations are seen (see *Twin Pregnancies*, p. 1063)

4. *Examine the uterus and adnexal structures.* This allows identification of incidental findings which may be of clinical significance, e.g. uterine or cervical myomas.

5. *Measure the nuchal translucency* for the detection of chromosomal disease and other structural abnormalities (see *Genetic Screening*, p. 1048).

Second and third trimesters (but commonly performed at 18-20 weeks)

1. *Document fetal life, number and presentation.* Multiple pregnancies require the reporting of additional information, such as placental number, sac number and comparison of fetal size. Fetal malpresentations may be due to an associated fetal malformation, which should be sought.

2. *Estimate the amount of amniotic fluid* and assess whether it is increased, decreased or normal, while taking into account the normal physiological variation with the stage of pregnancy.

3. *Record the placental location* and its relationship to the internal cervical os.

4. *Assess gestational age* using the biparietal diameter, head circumference, femur length or a combination of these. Fetal weight may be assessed and expressed both in grams and also as a percentile based on the patient's menstrual age. The appropriateness of interval change should be given if previous studies are available. Finally, every obstetric ultrasound report should relate the calculated sonographic age to the patient's menstrual age.



Fig. 33.1 Two gestational sacs, each containing a yolk sac: transvaginal image.



Fig. 33.2 Profile face and upper thorax, early second trimester.

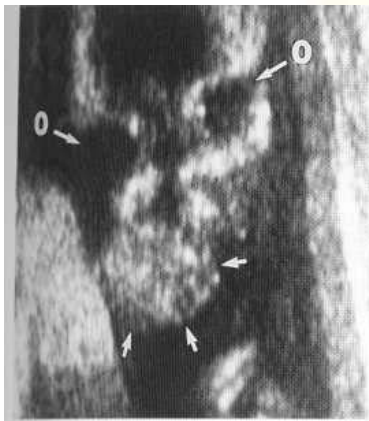


Fig. 33.3 Epignathus: corona image through the face showing soft-tissue mass (arrows) bulging from mouth. 18 week gestation. O = orbits.

5. Evaluate the uterus and adnexal structures, although it should be noted that this becomes more difficult later in pregnancy.

6. Assess the fetal situs by looking at fetal position and lie.

7. The following fetal anatomy should be demonstrated as a minimum: cerebellum, cerebral ventricles, spine, four-chamber heart and outflow tracts, stomach, kidneys and urinary bladder, umbilical cord insertion on the anterior abdominal wall, and all four limbs. Depending on the fetal position the face may be visible (Fig. 33.2) and associated abnormalities demonstrated (Fig. 33.3). The exact role of fetal anomaly scanning is debated and may be more appropriate in the high-risk pregnancy rather than in a routine screening population.

Computerised reporting systems are available on which all the above data can be recorded by a combination of menu-driven and free-form comment. Where sequential studies have been performed, growth curves and summary sheets can be printed.

Ultrasound assessment of fetal age

Gestational age may be estimated from the measurement of various fetal parameters. Different parameters are more reliable at different gestational ages (Table 33.1), as discussed below.

First trimester

1. The gestational sac may be identified by transabdominal scanning at 5 weeks and approximately a week earlier by transvaginal scanning. The mean sac diameter (MSD) correlates well with menstrual age during the early first trimester, with similar confidence limits to the crown-rump length during the early first trimester.

Table 33.1 Variability associated with fetal age: estimates derived from anatomical parameters

Parameter	Age variability (weeks)			
	6-14	12-18	24-30	36-42
CRL	±0.4			
BPD		±1.2	±2.2	±3.2
FL		±1.6	±2.8	±4.0
HC		±1.2	±2.1	±2.7
AC		±1.7	±2.2	±3.0
BPD, HC, AC, FL		±1.1	±1.8	±2.3



Fig. 33.4 Crown-rump lengths, with measurements on TVS of: 8 mm, corresponding to a gestational age of 7 weeks (A); 31 mm, corresponding to a gestational age of 10 weeks (B).

2. The embryo is consistently visualised from 6 weeks with TVS and a week later with TAS. Several published data sets are available for the estimation of the gestational age from the crown-rump length, generally regarded as the most accurate method of pregnancy dating between 6 and 10 weeks, when the variability is ± 5 days. The crown-rump length is measured along the longest axis of the embryo (Fig. 33.4), care being taken not to include the adjacent yolk sac. Later in the first trimester spinal flexion may produce a falsely low value and, in general, once the structure of the fetal head is apparent, the biparietal diameter should be used instead.

3. Nuchal translucency may be assessed towards the end of the first trimester. Increased values may be related to a range of fetal chromosome disorders as well as cardiac abnormalities. This will be considered further under Genetic Screening (p. 1048).

Second and third trimesters

1. The biparietal diameter can be measured from around 9 weeks until the end of pregnancy. Measurements are made on a

standard transverse axial plane passing through the widest portion of the skull, with both the thalamus and cavum septum pellucidum in the midline. By convention, the distance recorded is that between the leading edges of the two temporoparietal bones (Fig. 33.5). Figures 33.6-8 show various levels at which measurements would be incorrect. There are many tables and graphs that give the mean gestational age with confidence limits for each measured value of biparietal diameter.

2. *The head circumference* , measured on the same plane as the biparietal diameter, is a more accurate predictor of gestational age when the skull shape is abnormal. Computation is either by a

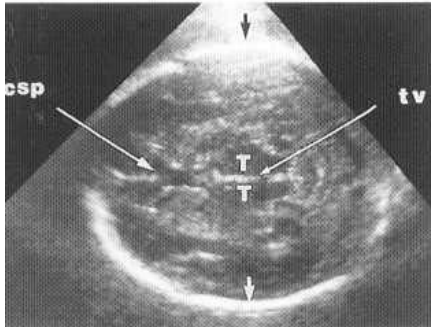


Fig. 33.5 The measurement of the biparietal diameter (leading edge to leading edge). csp = cavum septum pellucidum; tv = third ventricle, T = thalamus.

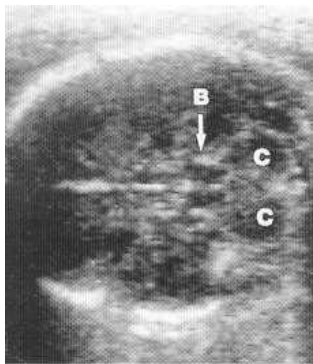


Fig. 33.6 Image oblique to transverse axial plane. B = brainstem; C = cerebellum.

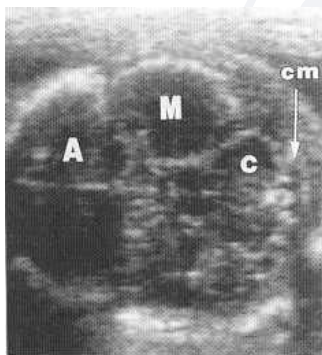


Fig. 33.7 Transverse image through skull base. A = anterior cranial fossa; M = middle cranial fossa; C = cerebellum; cm = cisterna magna.

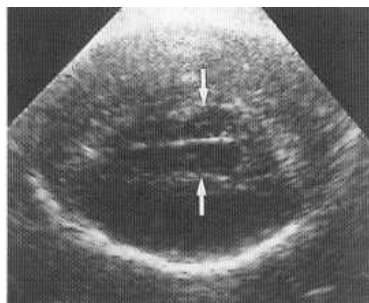


Fig. 33.8 Transverse image near vertex. The arrows delineate bright lines originally thought to be the ventricular wall but now accepted as venous structures in the periventricular white matter.

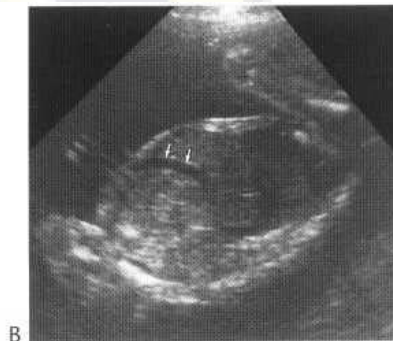
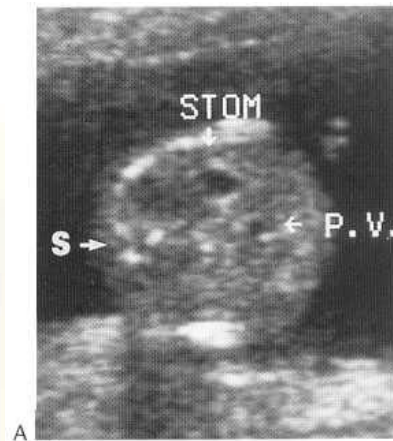


Fig. 33.9 (A) An appropriate level for measurement of the abdominal circumference: transverse image in a second trimester fetus. S = spine; STOM = stomach; P.V. = portal vein. (B) Longitudinal image through abdomen showing oblique course of portal vein through the liver (arrows). Measurement of the abdominal circumference from a section in the same plane as the portal vein will give a falsely elevated value.

trackball and cursor or by measurement of two orthogonal diameters, both methods giving similar accuracies. Variation in skull shape may also be documented with the cephalic index, a short:long axis ratio with a normal range of 0.7-0.86.

3. *The abdominal circumference* , measured in the same way as head circumference, is less accurate in establishing gestational age than the biparietal diameter. As the abdomen suffers first in asymmetric growth retardation, however, the ratio of head to abdominal circumference is a useful indicator of this condition. The abdominal section used should be approximately round and pass through the upper abdomen and liver. Suitable landmarks are the upper portion of the stomach and a short section of umbilical vein lying in the anterior portion of the abdomen and equidistant from the lateral walls of the abdomen (Fig. 33.9A). Care must be taken to measure the abdominal circumference in a plane perpendicular to the long axis of the fetus. A section incorporating a longer section of umbilical vein will necessarily be oblique (Fig. 33.9B) and therefore produce an artificially large abdominal circumference.

4. *The femur is* the only long bone routinely measured, although biometric tables exist for all the fetal long bones. Uses include the assessment of fetal age when the head is in a position unsuitable for measurement of the biparietal diameter and, less commonly, for the detection of microcephaly and fetal skeletal dysplasia. Measurement is made along the long axis of the diaphysis, disregarding the curvature of the medial border and also the non-ossified proximal and distal epiphyseal cartilages (Fig. 33.10). Various pitfalls in measurement exist, including foreshortening due to oblique imaging

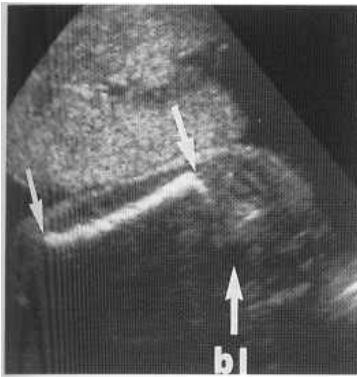
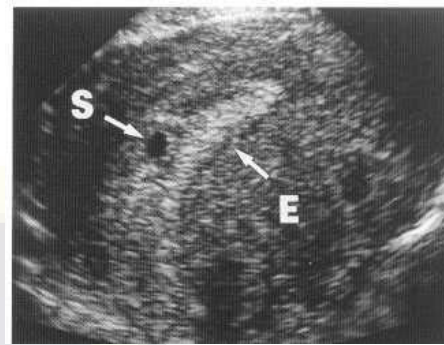


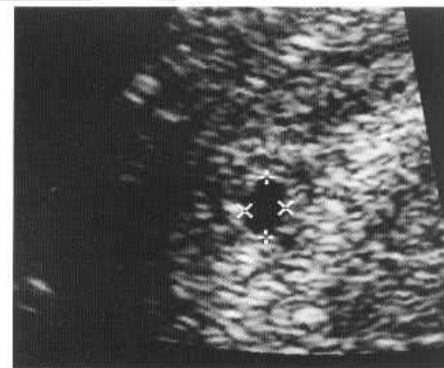
Fig. 33.10 Normal femur. Length of shaft (arrows). bl = fetal bladder.

and artefactual lengthening due to inclusion of the hyperechoic 'distal femoral point'.

5. Multiple fetal growth parameters. The well-known and progressive increase in variability known to occur in predicting gestational age from any one fetal measurement reaches a maximum of ± 3 weeks in the third trimester. Hadlock et al (1984) developed regression equations for predicting menstrual age throughout pregnancy using various combinations of the biparietal diameter, head circumference, abdominal circumference and femoral length. They demonstrated a significant reduction in overall variability and maximum error when using a combination of parameters rather than a single measurement. Such regression models are easily programmable into a microcomputer, so that optimum choices are made, depending on the number of technically satisfactory measurements made in any particular case. Commercial software can now be purchased which will analyse body proportionality (using the cephalic index, HC:AC, FL:AC and FL:BPD ratios) and will calculate age, weight and weight percentile, based on the appropriate measurements.



A



B

Fig. 33.11 (A) 42 week gestational sac (S) measuring 3 mm in diameter. Note the eccentric position in relation to the endometrium (E). (B) A magnified image, again demonstrating the gestational sac, demarcated by cursors.

Table 33.2 Detection of fetal structures by both transvaginal (TVS) and transabdominal (TAS) ultrasound

Sign or fetal structure	Menstrual age when detected (weeks)	
	TVS	TAS
Gestational sac	4 z	5
Double decidual sac sign (DDSS)	??	5
Double 'bleb' sign	??	6-7
Yolk sac	5	6-7
Fetal heartbeat	5 z	6 z
Head	8	9
Ventricles	8 2	11

Early pregnancy—the first trimester

Gestational sac The normal sac is round or oval with a smooth contour and is generally located in the fundus or middle uterus. TVS clearly demonstrates the normal eccentric location in relation to the endometrial cavity (Fig. 33.11). The sac may be first seen by TVS when the sac diameter is 2-3 mm, corresponding to a gestational age of approximately 4 weeks. The corresponding values with TAS are a diameter of around 5 mm and a gestational age of 5 weeks (Table 33.2).

Discriminatory gestational sac size The normal yolk sac, amnion and embryo can always be identified at a certain gestational age and therefore, by definition, when the gestational sac has reached a certain *discriminatory* size.

Different researchers have suggested that, on TAS, a living embryo should be seen once the gestational sac diameter exceeds values ranging from 17 to 30 mm, with corresponding values for TVS varying from 9 to 18 mm. Values can be established in a similar way for the appearance of the yolk sac, seen on TAS with sac diameters in excess of 20 mm and on TVS with diameters greater than 6-10 mm.

Once the relevant discriminatory sac size has been reached the normal embryo can be consistently seen as a discrete structure with a measurable crown-rump length and fetal heart (Fig. 33.12). The beating fetal heart has variously been demonstrated with crown-rump lengths of between 3 and 6 mm (with TVS and TAS, respectively),

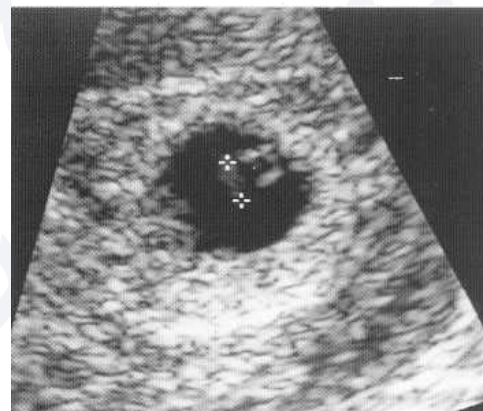


Fig. 33.12 A normal 6-week embryo (cursors). Note the adjacent yolk sac and thick echogenic ring of the normal gestational sac.

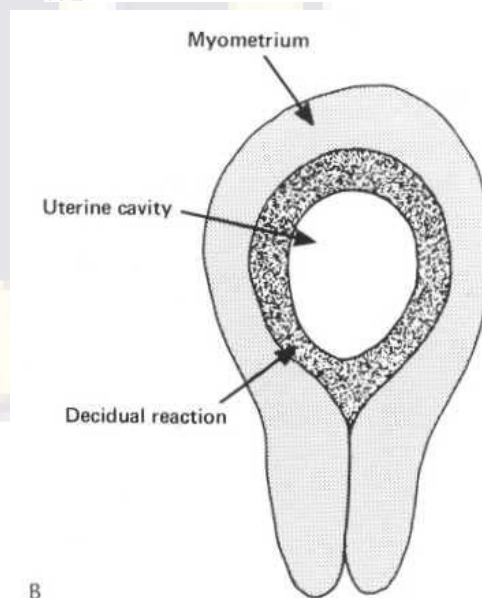
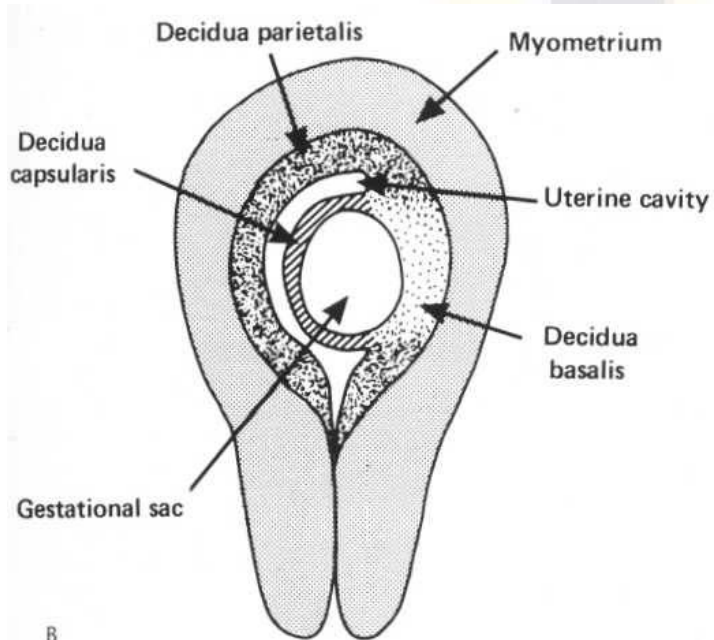
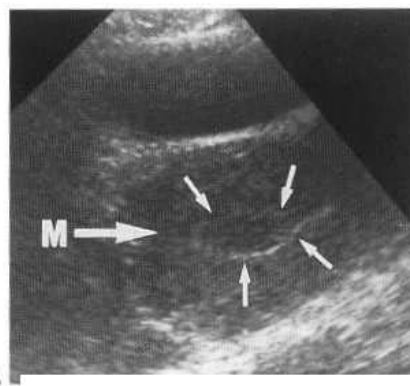
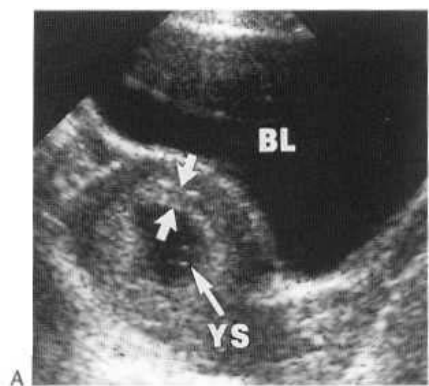


Fig. 33.13 (A) A normal intrauterine pregnancy: longitudinal image showing double decidual sac sign (arrows). YS = yolk sac; BL = bladder. (B) First trimester gestational sac. (Reproduced from Nyberg et al 1983).

Fig. 33.14 (A) Pseudogestational sac (arrows): longitudinal image in a patient with an ectopic gestation. M = myometrium. (B) Pseudogestational sac. (Reproduced from Nyberg et al 1983).

while others have claimed it may be seen as a discrete pulsation adjacent to the yolk sac even before the embryo itself is visible.

The double decidual sac sign (DDSS) This consists of two concentric echogenic rings surrounding at least a part of the gestational sac, and is thought to represent the decidua parietalis and adjacent decidua capsularis (Fig. 33.13). Described by several authors, this sign is thought to provide reliable distinction between the true gestational sac of an intrauterine pregnancy and the pseudogestational sac seen with an ectopic pregnancy, in which only a single echogenic layer of decidua surrounds an intraendometrial fluid collection (Fig. 33.14).

Once the embryo reaches 10 mm in crown-rump length the head may be differentiated from the body on TVS. The embryo technically becomes the fetus at 10 weeks after the last menstrual period, at which time the crown-rump length measures approximately 30-35 mm (Fig. 33.15).

Complications of early pregnancy

Bleeding in the first trimester, with or without associated uterine cramping, represents a fairly common problem in early pregnancy.

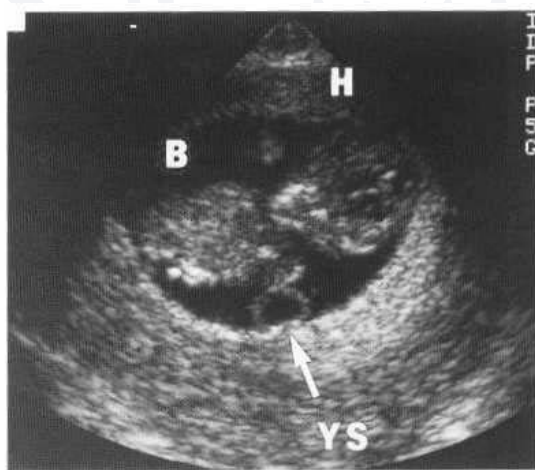


Fig. 33.15 Normal 10-week fetus with a crown-rump length of 32 mm. H = head; B = body; YS = yolk sac.

Although such symptoms may be caused by a cervical erosion or polyp, they more commonly suggest a threatened abortion.

Possible explanations include:

- *Intact intrauterine pregnancy* (50(k).
- *Missed abortion* (25-30(0)-a fetus without heart or limb motion which still remains within the gestational sac. The fetus

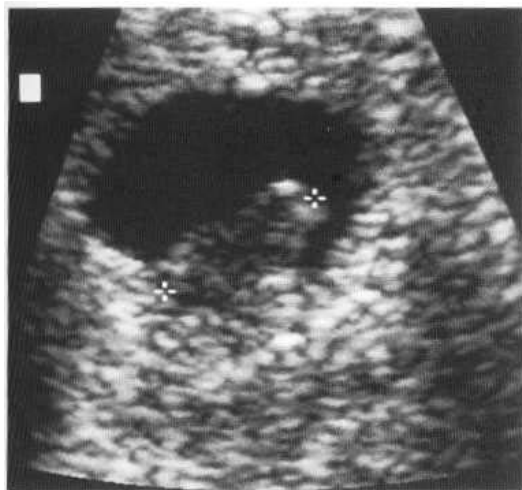


Fig. 33.16 A missed abortion. The rather amorphous embryo is marked by cursors. No fetal heart identified. Sonographic age 7 weeks, compared with a menstrual age of 10 weeks.



Fig. 33.17 Blighted ovum: transvaginal image showing empty gestational sac measuring 2.6 cm in length. No fetal pole or yolk sac identified. The menstrual age was 12 weeks.

may be merely smaller than expected for the sac size or may appear formless, depending on the length of time since demise (Fig. 33.16).

- **Blighted ovum (20-25%)**—an anembryonic pregnancy in which the gestational sac is present but empty (Fig. 33.17). Chromosomal abnormalities are present in approximately 50% of cases.
- **Incomplete abortion**, in which only a part of the products of conception remains within the uterus, the remainder having been expelled.
- **Inevitable abortion**, in which the gestational sac and fetus have become detached from the implantation site and lie in the lower uterine segment or vaginal canal. Once the cervix becomes dilated, abortion is inevitable, often within a matter of hours.
- **Complete spontaneous abortion**, in which all the products of conception have been expelled.
- **Ectopic pregnancy.**
- **Hydatidiform mole.**

Fifty per cent of patients with a threatened abortion will subsequently abort. Of those in whom a fetal heart is demonstrated, however, over 90% of pregnancies will continue and in these patients management is expectant. The priority for sonographic diagnosis is thus to determine the presence or absence of fetal life. Embryonic demise must be documented with care.

Table 33.3 The early diagnosis of non-viable pregnancy: correlation of gestational sac diameter with detection of yolk sac embryo

	Mean sac diameter (mm)	
	TVS	TAS
Yolk sac not detected	>8	>20
Embryo not detected	≥6	>25

From Levi et al (1988) and Nyberg et al (1986).

In many cases abnormal gestations cease development before the formation of a detectable embryo. Various authors have assessed the sonographic distinction between the gestational sac of an early normal intrauterine pregnancy and the sac of an abnormal gestation. Reference may be made to the discriminatory sac sizes, as documented above, and typical criteria are given in Table 33.3 for the detection of both the yolk sac and embryo by TVS and TAS. Using data from these authors an abnormal gestation may be reliably predicted if, for instance, a yolk sac is not identified by TVS when the sac measures greater than 8 mm across. More cautious criteria have been published by the Royal Colleges of Radiologists and Obstetricians and Gynaecologists *Guidance on Ultrasound Procedures in Early Pregnancy (1995)*. This Standing Joint Committee on Obstetric Ultrasound has indicated that, on TVS, a sac diameter of greater than 20 mm with no yolk sac or embryo is highly suggestive of a blighted ovum, and that, if an embryo greater than 6 mm in length has no evidence of cardiac pulsations, then this is highly suggestive of a missed abortion. Where these criteria are not met it is suggested that another examination should be performed after a further week to assess interval change. Other pointers to an abnormal gestation include an unusually small sac (Fig. 33.18) (Bromley et al 1991), a thin or weak decidual reaction, irregular contour (Fig. 33.19), absent double decidual sac, and low position. An abnormal shape or size to the yolk sac (Lindsay et al 1992) and an unusually thickened amniotic membrane (Fig. 33.20) (Horowitz 1992) have also been shown to be associated with a poor pregnancy outcome.

Human chorionic gonadotrophin

hCG, secreted by trophoblasts, shows an exponential rise after implantation, and serum levels can be detected by three menstrual

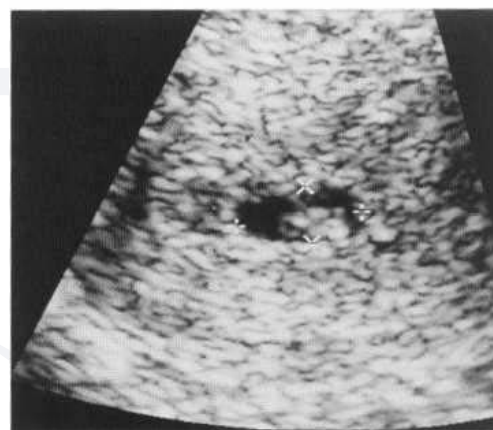


Fig. 33.18 A small gestational sac containing an embryo with beating heart. The menstrual age was 6 weeks 6 days and the crown-rump length was in agreement with this. Three days later there was a complete spontaneous abortion.

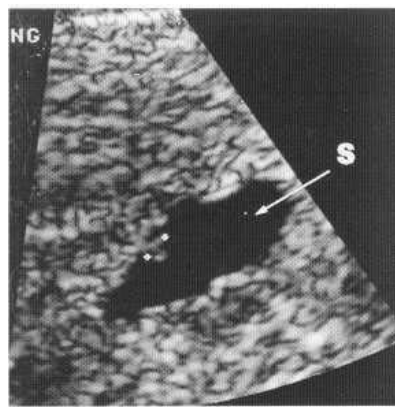


Fig. 33.19 An irregular gestational sac (S) with weak decidual reaction and embryonic remnants (cursors). No fetal heart identified. The menstrual age was 12 weeks.

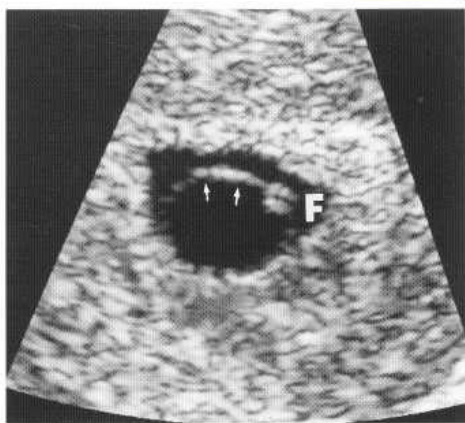


Fig. 33.20 Thickened amniotic membrane. A 2 mm fetal pole (F) was identified in this pregnancy with a menstrual age of 12 weeks. No fetal heart identified.

weeks. There is a strong correlation between hCG levels, menstrual age and gestational sac size before sonographic demonstration of the embryo. Thus, as with the MSD, there are *discriminatory* hCG levels above which the gestational sac, yolk sac and embryo should always be seen. Where the gestational sac is small or absent, these discriminatory levels may provide valuable additional information in differentiating between the normal and abnormal gestation.

Normal sac growth rates have been shown to be around 1.1 mm per day, while increases of less than 0.6 mm per day indicate abnormal development (Nyberg et al 1987a). These findings have practical implications for determining the optimum time interval between serial ultrasound examinations when an embryo or yolk sac is not seen on the initial study. Where a gestational sac appears abnormal on the initial study, a repeat study a few days later should show sub-normal sac growth and a failure of the normal 48 h hCG doubling time. Where a gestational sac appears sonographically normal, knowledge of normal sac growth rates allows re-examination to be scheduled when the sac size is expected to be 20-25 mm and an embryo and/or yolk sac present.

Once an unequivocal decision has been made about the non-viability of a pregnancy there is little point in delaying therapeutic evacuation of the uterus.

Fetal growth

Babies growing at under the tenth percentile for age constitute a heterogeneous population, some being growth retarded and some merely constitutionally small. Babies suffering genuine intrauterine

growth retardation (IUGR) who are born small for gestational age have a significantly higher perinatal morbidity and mortality than those in the normal weight range. For valid management decisions to be made, an attempt must be made to distinguish between these groups.

Types of IUGR

In *symmetric growth retardation* there is a uniform reduction in the weight of all organs, including the brain. It begins in the second trimester and affected fetuses show a higher incidence of chromosomal abnormalities, congenital malformations, intrauterine diseases and exposure to nicotine and other drugs. Genetically small but otherwise healthy babies are also included in this group.

Asymmetric growth retardation occurs primarily in the third trimester. The trunk is affected earlier and more severely than the head, and weight more than length. The major factor is uteroplacental insufficiency, due to maternal hypertension, renal disease, diabetes mellitus and idiopathic causes. This is the commoner form, accounting for 70-80% of all cases.

Diagnosis of IUGR

1. *Establish an accurate gestational age.* This value must be determined as early as possible in pregnancy (when the variability associated with age estimation is least) and becomes the reference for later studies.

2. *Various parameters (e.g. BPD, HC, AC, FL) measured in subsequent studies may be related by means of tables or graphs to the original estimation of gestational age and an assessment made as to whether values are smaller or greater than expected.*

Controversy exists as to the value of the various parameters in use for the estimation of IUGR. It is generally accepted that the size of the fetal trunk correlates most strongly with the overall size of the fetus and that an abdominal weight can be calculated from the measured *abdominal circumference*. Nevertheless, using the estimated fetal weight to identify babies born below the tenth percentile for weight gives a positive predictive value of only 24% at 25 weeks and 55% at 38 weeks. Better results are obtained using the ratio of head to abdominal circumference (62% positive predictive value) but even in this case 38% of fetuses with an abnormal test result will prove to be normal. The use of multiple sonographic parameters for the more accurate estimation of fetal weight is under evaluation and has been claimed to provide more reliable results (Benson et al 1990).

Doppler ultrasound analysis

Both the fetoplacental and uteroplacental circulations may be studied with Doppler ultrasound. As normal gestation progresses, blood flow through the placenta increases due to a reduction in placental vascular resistance. Conversely, an increased placental resistance may result in a reduction in blood flow, manifest as a diminished or absent end-diastolic flow. Various indices (systolic: diastolic ratio, resistive and pulsatility indices) have been used to quantify these changes. The umbilical and uterine (arcuate) arteries are the vessels most commonly studied, but use has also been made of the fetal aorta and carotid vessels.

Studies have shown that increased values for the above indices, associated with a reduction in end-diastolic flow in the relevant vessel, are associated with IUGR and poor fetal outcome (Rochelson et al 1987). Other associations include pregnancy-

induced hypertension, oligohydramnios, and caesarean section for fetal distress. Although the exact place of these techniques in routine screening remains a subject of debate, it is likely that they will continue to play an important role in the assessment of the high-risk fetus (Doubilet & Benson 1995).

The biophysical profile

Various fetal activities may be monitored with real-time ultrasound. These include body movement, breathing, fetal tone, sleep states, fetal heart rate, low in umbilical vessels, and the intrauterine environment, including amniotic fluid volume. Scoring systems incorporating a number of biophysical variables have been developed and these provide evidence of fetal risk and a basis for subsequent management.

Ectopic pregnancy

There have been several recent reviews of the role of ultrasonography in ectopic pregnancy.

The incidence of ectopic pregnancy is up to 1% of all pregnancies and is increasing. In the USA the condition is responsible for a quarter of all maternal deaths and is also a major cause of female infertility. Furthermore, 10% of subsequent pregnancies will also result in an ectopic gestation. Recently there has been a reduction in the attributable death rate, at least in part due to improvements in diagnosis made possible by improving real-time ultrasound equipment (and in particular by TVS) and also by the ability to readily quantify serum B-hCG levels.

Patients at risk These include those with:

- Previous ectopic pregnancy
- History of pelvic inflammatory disease
- Pregnant women with an IUCD in situ
- Previous tubal microsurgery or in vitro fertilisation
- Previous laparoscopic tubal coagulation.

Presenting symptoms The classic clinical triad of pelvic pain, abnormal vaginal bleeding and a palpable adnexal mass occurs in less than 50% of patients. In one series only 60% of patients reported missing a menstrual period, and in approximately 40% no pelvic mass was palpable.

Diagnosis

Pregnancy testing With the advent of β -hCG testing, pregnancy may now be confirmed at a menstrual age of only 3 weeks. Normal intrauterine gestations show a β -hCG doubling time of approximately 2 days, a rate not achieved by an ectopic pregnancy. Likewise, at any given gestational age B-hCG levels tend to be lower for an ectopic than for an intrauterine gestation. In those ectopic pregnancies with very low levels of β -hCG the fetus is probably already dead.

Ultrasonography (both TVS and TAS)

The **uterus** Coexistent intra- and extrauterine gestations occur approximately once per 30 000 pregnancies (although rather more frequently where the patient is undergoing ovulation induction). Demonstration of an intrauterine pregnancy is therefore valuable evidence against the existence of an ectopic pregnancy. Problems nevertheless arise in the assessment of the very early gestation

before specific findings of a normal intrauterine pregnancy are demonstrated.

Various authors have shown that the double decidual sac sign (DDSS) (Fig. 33.13) is both sensitive and specific as an indicator of a normal intrauterine pregnancy. It does not, however, completely exclude either an ectopic gestation or an abnormal intrauterine pregnancy. Hormonal stimulation from an ectopic gestation may also cause endometrial thickening similar to that seen in an early intrauterine gestation, and fluid collections within the endometrial canal may be seen in up to 20% of such cases. These 'pseudogestational sacs' are generally surrounded only by a single echogenic halo (Fig. 33.14), the result of decidual changes within the endometrial tissues.

Correlation with serum B-hCG levels is necessary where there is persisting doubt about whether the uterine contents represent a true or pseudogestational sac. Work by Nyberg et al (1987) showed that the absence of an intrauterine gestational sac when the β -hCG level exceeded 1800 mIU/ml was evidence for an ectopic pregnancy.

In addition, the normal gestational sac diameter/hCG correlation was not found with the pseudogestational sacs of those patients with an ectopic pregnancy.

In comparing normal and pseudogestational sacs, Doppler ultrasound has also been shown to be helpful in assessing peritrophoblastic blood flow in some patients, one study showing high-velocity low-impedance blood flow in all normal gestations over 36 menstrual days.

The adnexa With TVS, a live embryo may be seen in the adnexa in up to a quarter of patients with an ectopic pregnancy, significantly more than with TAS (Fig. 33.21). Almost as significant is the presence of an adnexal gestational sac, seen in up to 70% of patients with an ectopic pregnancy. These are usually small and thick-walled and may be empty or contain a yolk sac or embryo. They may sometimes be confused with a haemorrhagic corpus luteum cyst, with which they may coexist in up to a quarter of patients with an ectopic pregnancy.

Complex adnexal masses (Fig. 33.22) are seen with TVS in up to 90% of patients with an ectopic pregnancy, although rather less often if the mass is predominantly cystic rather than solid. Pelvic inflammatory disease with tubo-ovarian abscesses is an important differential diagnosis, as are other pelvic masses such as an endometrioma or dermoid. As described earlier, the ability to characterise trophoblastic tissue with Doppler analysis may prove useful in differentiating the various possibilities.



Fig. 33.21 Ectopic pregnancy noted in the right adnexa at a menstrual age of 7 weeks 3 days. A beating heart was noted in the embryo (E) and a yolk sac (Y) was present. There was surrounding haematoma.

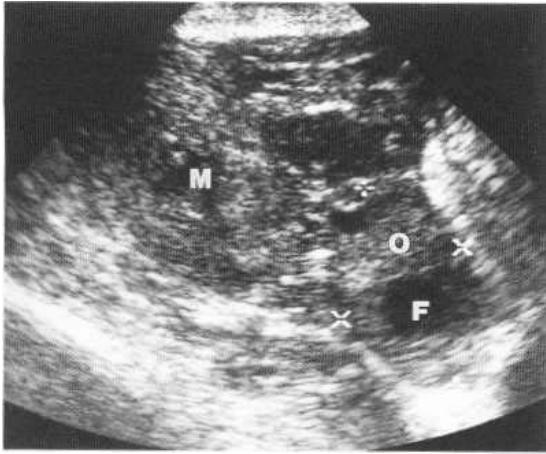


Fig. 33.22 Ectopic pregnancy. A complex adnexal mass (M) in a patient found at surgery to have a ruptured fallopian tube. The ovary (O) containing follicles (F) is seen adjacent to the mass.

The cul de sac Fluid in the cut de sac increases the probability that a pregnant patient has an ectopic gestation, although this may also be seen with a ruptured or haemorrhagic corpus luteum cyst or pelvic inflammatory disease. Clot, in association with haemorrhage, may cause the cul de sac fluid to become even more echogenic than the adjacent myometrium and so simulate a solid mass. This appearance is highly suggestive of haemoperitoneum and, in the appropriate clinical situation, a ruptured ectopic pregnancy.

Clinical management (positive pregnancy test assumed)

- The presence of a normal intrauterine pregnancy makes a coexistent extrauterine gestation very unlikely.
- The only certain evidence of an extrauterine gestation is visualisation of a viable embryo in an ectopic location.
- Patients with no intrauterine gestation and with the presence of an adnexal mass and/or cut do sac fluid are at substantial risk of an extrauterine gestation. TVS, in combination with discriminatory sac sizes and B-hCG levels, as well as duplex and colour Doppler ultrasound may all increase diagnostic accuracy.

Patients in whom the diagnosis remains in doubt, and where the delay of repeat sonographic and immunological studies is inadvisable, may require more invasive investigation. Conventionally, the possibilities included uterine dilatation and curettage, culdocentesis and laparoscopy. the last of these being the single most accurate method for confirming the presence of an ectopic gestation prior to surgery.

More recently it has been shown that between a quarter and two-thirds of ectopic pregnancies may resolve spontaneously, in particular where the B-hCG level is relatively low, the size of the gestation is small, and the vascularity of the adnexal mass is limited. Expectant management may therefore be possible in a clinically stable patient fulfilling these criteria. Other alternatives to operative management include systemic methotrexate, which has proved successful in the management of a high proportion of unruptured ectopic pregnancies, and local injection of either methotrexate or potassium into the ectopic gestation. Encouragingly, a high proportion of those treated with systemic methotrexate subsequently demonstrated tubal patency on hysterosalpingography and over half of these later achieved a normal intrauterine pregnancy.

Salpingectomy is the most common surgical treatment at Iaparo-tomy where there is tubal rupture or significant local haemorrhage.

Box 33.2 Indications for the prenatal diagnosis of genetic disorders

- Chromosomal abnormality (advanced maternat age or affected sibling)
- Single gene defects (sibling with metabolic disorder)
- Multifactorial disorders (including previous child with neural tube defect)
- Environmental defect (drugs, infectious agents)

Modified from Callen (1988).

Salpingostomy with expression of the ectopic from a tubal incision may be appropriate in some patients and may he performed laparoscopically, although occasionally a further operation may he neces-sitated by clinical status or elevated B-hCG levels.

Genetic screening

Many genetic disorders are now amenable to prenatal diagnosis (Box 33.2). Ultrasound plays a central role, not only in the primary diagnosis of fetal structural anomalies, but also in the guidance of amniocentesis needles and chorionic villous sampling catheters by which genetic material is made available for analysis. In recent years increasing weight has been given to the measurement of the fetal nuchal translucency in the first trimester and to a number of other ultrasonographically detected 'soft markers' of chromosome disease.

Amniocentesis Although amniocentesis is usually performed at around 16 weeks gestation, there have been recent suggestions that an earlier examination at 11-14 weeks may be technically satisfactory and offer advantages of earlier diagnosis. Amnio-centesis entails aspiration of amniotic fluid through a fine needle directed under ultrasound guidance. Ideally the chosen needle track avoids the placenta, but it has been shown that a needle traversing the placenta produces no increase in the expected abortion rate. The risk of fetal loss from amniocentesis is generally quoted as below 0.5%. Desquamated fetal cells within the amniotic fluid are grown in tissue culture and karyotyped or used for a variety of metabolic assays. These processes may take up to 3 weeks to pert orm, thereby allowing time for therapeutic abortion to be considered if clinically indicated.

Chorionic villous sampling (CVS) Ultrasound is also used to guide placement of the transcervical sampling catheters (and less commonly transabdominal needles) through which chorionic villous cells are aspirated from the trophoblast. This technique, which is performed at around 9-11 weeks gestation, has a fetal loss rate little different from that which would be expected in any case at this stage of pregnancy.

Fetal blood sampling Blood and, less commonly. tissue may be sampled under either direct fetoscopic or indirect percutaneous sonographic guidance. Analysis of fetal blood cells takes only 2-3 days.

Maternal serum a-fetoprotein (MSAFP) screening Generally performed at between 15 and 20 weeks, MSAFP detects up to 90% of fetal neural tube defects. Approximately 5% of screened pregnancies have a significantly elevated MSAFP level and are referred for detailed sonographic evaluation to rule out multiple gestation, demise or structural abnormality. In one large series (Anderson et al

1986) virtually all significant anomalies (neural tube defect, cystic hygroma and omphalocele) were detected by ultrasound, and those fetuses normal on sonographic examination proved to be normal at birth. Elevated MSAFP levels may occasionally (up to 1%) be seen with chromosome abnormalities but in the majority of these cases there will be either significant coexistent physical abnormalities or more subtle pointers to genetic disease (such as choroid plexus cysts), which will be detected by sonography. Although practice varies, ultrasound may obviate the need for subsequent amniocentesis in many of those patients with an elevated MSAFP.

Apart from the significance of a high MSAFP there is an association between a low value and trisomy 21. Detection of this condition may be further refined with the 'triple test', measuring the human chorionic gonadotrophin and serum oestriol as well as the MSAFP. These tests, as well as other sonographically detected soft markers (see below) may prove to be of use in routine screening for this condition.

Nuchal translucency This describes the maximum thickness of subcutaneous translucency between the skin and the soft tissue overlying the cervical spine of the fetus. When increased (>3 mm between 10 and 14 weeks gestation) there is a well-established association with chromosome abnormality (Nicolaidis et al 1992) as well as with other structural anomalies (in particular cardiac abnormalities, diaphragmatic hernia, omphalocele and body stalk abnormalities). In centres where first trimester nuchal translucency screening takes place, an abnormal result necessitates formal chromosomal analysis by either early amniocentesis or CVS. Where the chromosome complement proves normal there should be detailed transvaginal scanning in the first trimester, with further second trimester transabdominal scanning at around 21 weeks in the search for structural abnormalities.

The advantages of such screening are, of course, the earlier detection of abnormality and the possibility that suction termination may be possible in appropriate cases. One major disadvantage is the anxiety and grief caused to parents making decisions about whether or not to progress a pregnancy when there is already a high natural loss rate in fetuses with chromosomal abnormalities and major structural anomalies. Others include difficulties in obtaining a reliable nuchal measurement in a significant proportion of fetuses, determining the significance of minor abnormalities, and the absence of any pathological confirmation of the diagnosis.

'Soft markers' of chromosome abnormality There is some association of minor but relatively common sonographic abnormalities (including choroid plexus cysts, mild renal pyelectasis, nuchal thickening, shortened femur or humerus, echogenic bowel and mild ventriculomegaly) with chromosome abnormalities, although this has not been fully assessed in unselected populations (Chitty 1998). The majority of reported studies are based on selected populations and do not allow for known risk factors such as maternal age or serum markers. Uncertainty surrounds the value of these markers, with some units offering amniocentesis to affected individuals whereas others do not even mention or document the findings unless more than one marker is present.

In general, prior risk based on maternal age and serum markers may be modified by the presence of soft sonographic markers. Based on a detailed search for specific sonographic markers in patients at high risk of Down's syndrome, sensitivities and specificities in excess of 90% have been reported. Equally, where no markers were found, prior risk could be reduced by up to 50%.

Fetal gender This may be accurately determined at or after 20 weeks gestation in 95-100% of fetuses. More recent work has used both TAS and TVS for earlier assessment. Overall success at 12-14 weeks was 80% in one study (Whitlow et al 1999), identification increasing with gestational age and being highest at 14 weeks (90%). In relation to genetic screening, the clinical value of sex determination is in deciding whether to carry out prenatal invasive testing in pregnancies at risk of sex-linked genetic abnormalities, where testing would be necessary only with male fetuses.

Central nervous system

The brain The fetal brain was one of the first areas examined for abnormality, not only because the head was routinely imaged for the biparietal diameter, but also because CNS anomalies are among the commonest birth defects. Furthermore, such anomalies frequently carry severe clinical implications and their early recognition thus allows for the possibility of early therapeutic termination. With TVS it is possible to distinguish the fetal head and torso from 7 weeks gestation. At this time the fetal brain is seen as a single ventricle, while by the ninth week two lateral ventricles largely filled with choroid are apparent, surrounded by a thin cerebral mantle. The thalamus, third ventricle, midbrain, brainstem and cerebellar hemispheres have formed and change little throughout the rest of pregnancy, other than to enlarge progressively. Significant facial development takes place during the middle of the first trimester, with the bony elements of the mandible, maxilla and orbits being seen by 10 weeks (Fig. 33.23). By 18 weeks there has been marked thickening of the hypoechoic cerebral cortex and the ventricles appear less prominent.

The spine The earliest spinal structures may be seen at 7-8 weeks with TVS (Fig. 33.24). Although the spine is seen clearly with TAS as two parallel echogenic lines from 12 weeks on, developmental changes that take place during the first half of the second trimester make 18-20 weeks a more satisfactory time for the assessment of normality. The fetal vertebra is composed of three ossification centres: the anterior, which forms the vertebral body (centrum), and two posterior centres, which form the posterior neural arch. Full assessment requires imaging in three planes: the oblique coronal (Fig. 33.25 through the anterior centrum and one

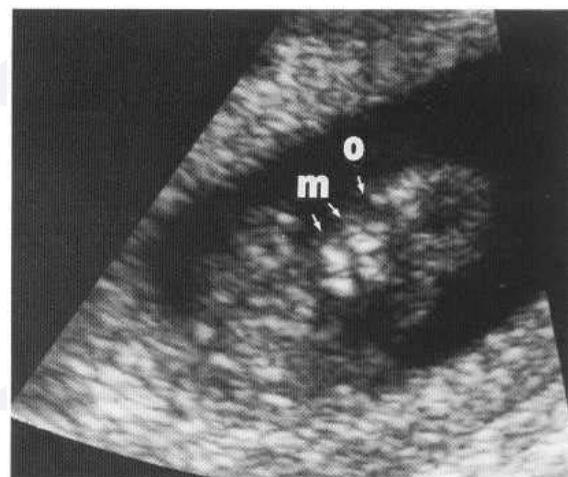
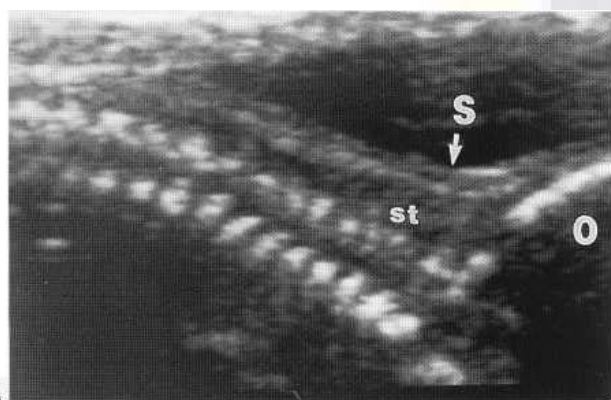


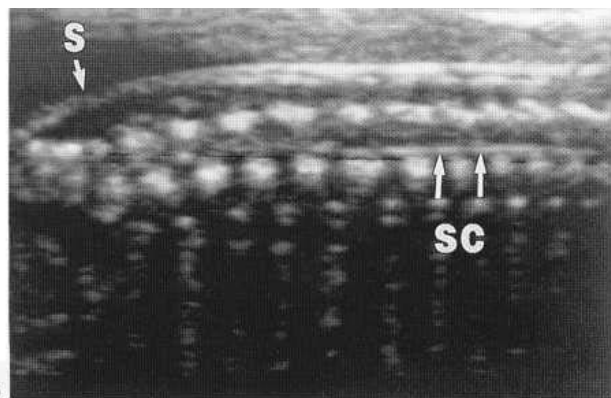
Fig. 33.23 A normal 10 week fetus. This coronal image of the face shows the orbits (o), maxilla and mandible (m).



Fig. 33.24 A normal fetus with a menstrual age of 8 weeks 3 days. The parallel echogenic lines of the developing spine (S) can be seen.



A



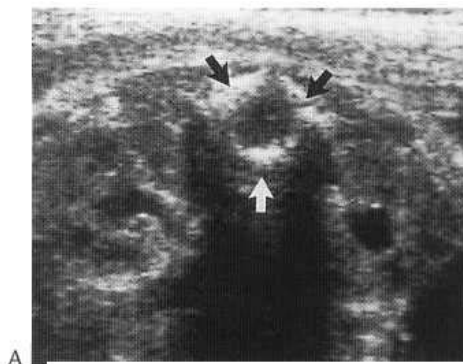
B

Fig. 33.25 Oblique coronal images: cervical (A) and lumbar (B) spines. O = occiput; S = intact skin surface; st = nuchal soft tissues; sc = spinal cord.

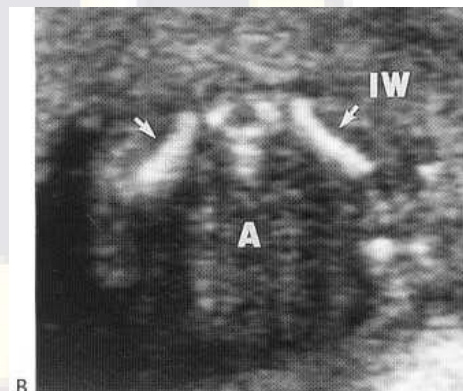
posterior centre), the true coronal (through both posterior centres) and the transverse (Fig. 33.26). The centra are ossified first in the lower thoracic and upper lumbar regions, followed by progressive ossification in both the cephalic and caudal directions. In contrast, ossification in the posterior centres follows sequentially in a cranio-caudal direction from the cervical region downward, and may not be seen in the lumbar spine until 22-24 weeks and in the sacral spine until 25 weeks or more. Awareness of these features is necessary to prevent false-positive diagnoses of spinal dysraphism.

Neural tube defects

Neural tube defects result from failure of the neural tube to close in early embryogenesis. These malformations include defects such as



A



B

Fig. 33.26 Transverse images. (A) Lumbar spine with three ossification centres forming a complete 'ring' (large arrows) in a third-trimester fetus. The two kidneys are seen on either side. (B) Lumbosacral junction. LW = iliac wings; A = lower abdomen.

the fatal condition anencephaly and various forms of spina bifida, ranging from the severe lumbar myelomeningocele to the potentially surgically correctable meningocele. Neural tube defects are disorders of polygenic multifactorial inheritance, with an overall incidence of 1-2 per thousand live births in the USA and as many as 4.5 per thousand live births in the UK. Not only are they relatively common compared with other fetal anomalies but they are also associated with a high rate of perinatal mortality, morbidity and long-term disability. Current technology, both immunological and sonographic, has meant that most neural tube defects can be recognised sufficiently early for therapeutic termination to be a realistic possibility.

Diagnosis A positive family history in either parent results in an increased risk of occurrence in the offspring (5%); in a couple with a prior affected child, the risk of recurrence is approximately 2%. Over 90% of neural tube defects occur in families without a positive family history.

Reference has already been made to the use of maternal serum a-fetoprotein screening and amniocentesis in the diagnosis of neural tube defects. If screening is applied to all pregnant women, few cases will be missed. Such a test works well for a very large group of fetuses with a low prevalence of disease, but there will be both false-positive and false-negative cases. Sonography subsequently provides an effective second-line test for discriminating the normal from the abnormal (and neural tube defects from other causes of a high MSAFP) in a small group of fetuses with a high prevalence of disease.

Anencephaly This accounts for 50-65% of all neural tube defects and is the commonest anomaly affecting the CNS. There is a failure of closure of the neural tube at its cephalic end between

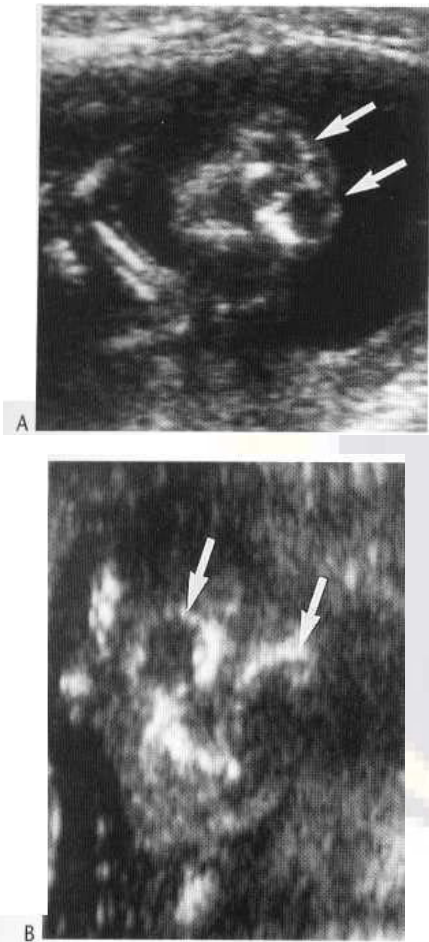


Fig. 33.27 (A,B) Anencephaly in two fetuses showing prominent orbits (arrows) and an absence of cerebral tissue more cranially.

the second and third weeks of development, which results in an absence of the cerebral hemispheres but relative preservation of the brainstem and portions of the midbrain. The main sonographic features are symmetric absence of the cranial vault and normal brain structures above large and prominent orbits (Fig. 33.27).

Polyhydramnios This may be seen in 40-50% of cases. Although the diagnosis may be suspected by 12-13 weeks, it is more reliable by around 15-16 weeks, at which time the ossification in normal calvarial bones is more obvious. Associated anomalies include spinal defects (in up to 50%) and midline facial defects.

Encephalocele The least common neural tube defect, encephalocele results in a bony calvarial defect which allows herniation of meninges alone (cranial meningocele) or both brain and meninges (encephalocele). Approximately 75% occur in the occipital midline, the remainder being divided between the frontal midline and parietal regions. Sonographically detected as a fluid- or solid-filled structure protruding from the calvarium, an encephalocele is usually fairly easy to demonstrate (Fig. 33.28). It may be more difficult conclusively to show a bony calvarial defect (necessary to distinguish an encephalocele from the commoner cystic hygroma) and conversely to guard against the possibility of producing bony defects by artefactual acoustic shadowing, a mistake which could lead to incorrect management decisions regarding the fetus.

Spina bifida This results from a failure of the neural tube to close at 3-4 weeks. Lesions may occur anywhere along the spine

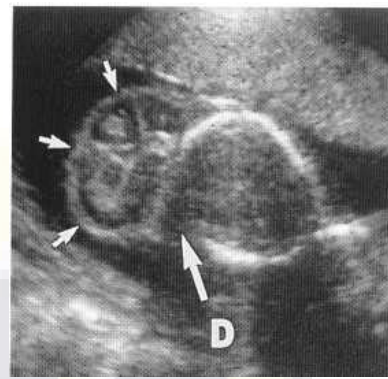


Fig. 33.28 Encephalocele (small arrows) with visible sulci. D = calvarial defect.

but are commoner in the lumbar or lumbosacral regions (90%) than in the thoracic (6%), or cervical (3%) spines. Isolated meningoceles are unusual compared with the commoner myelomeningocele. Prognosis tends to be worse for higher and larger lesions, or when there are other associated anomalies. Despite this, prediction of neurological deficit is frequently unreliable and demonstration of lower limb movement and bladder emptying in utero is no guide to function after birth.

Sonographic diagnosis may be difficult. The spine should be imaged in all three planes (sagittal, coronal and transverse), as any one of these may show abnormalities not demonstrated on the other two.

The spectrum of abnormality ranges from complete spinal disorganisation (Fig. 33.29), through isolated abnormalities at different levels (Fig. 33.30), to subtle splaying of the posterior neural arches demonstrated only on the coronal image. Classically, a divergence of the posterior neural arches on longitudinal imaging (Fig. 33.31 A) is

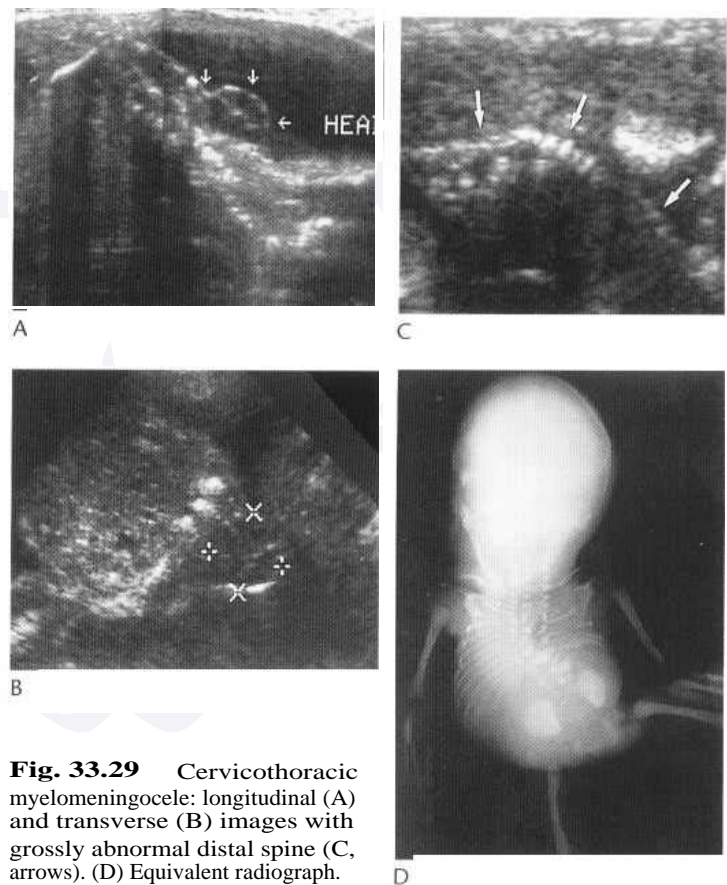


Fig. 33.29 Cervicothoracic myelomeningocele: longitudinal (A) and transverse (B) images with grossly abnormal distal spine (C, arrows). (D) Equivalent radiograph.

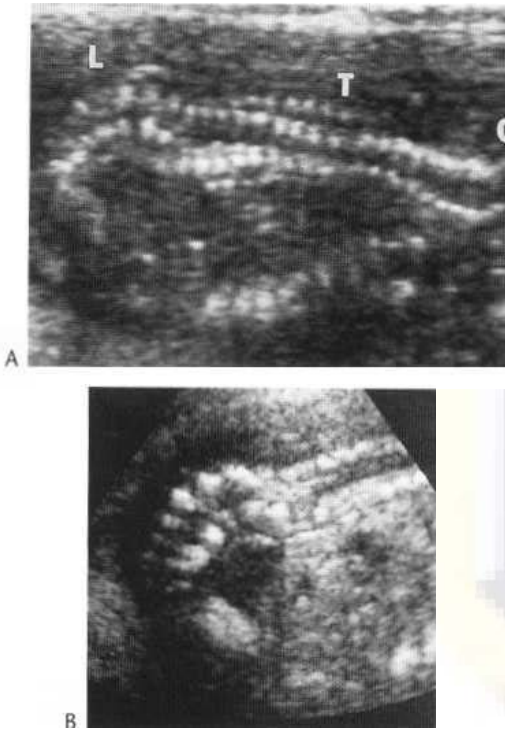


Fig. 33.30 Spina bifida with defects in the cervical (C), thoracic (T) and lumbar (L) spines. Longitudinal (A) and magnified (B) images.

accompanied by a 'V'-shaped profile on transverse imaging (Fig. 33.31 B), due to outward flaring of the two posterior ossification centres. The presence of an intact sae seen as an extension from the posterior aspect of the spine makes the diagnosis easier; conversely, when a sae is not seen, either because it has ruptured or is compressed against adjacent structures, the diagnosis must be made by demonstrating the 'bony' defect of spina bifida. With a simple

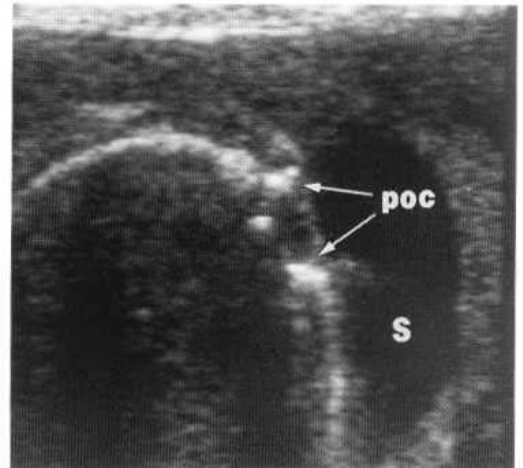


Fig. 33.32 Meningocele: transverse image. S = sac containing only fluid; poc = splaying of the posterior ossification centres.



Fig. 33.33 Meningomyelocele: transverse image. Short arrows = sac containing neural elements; poc = splaying of the posterior ossification centres.

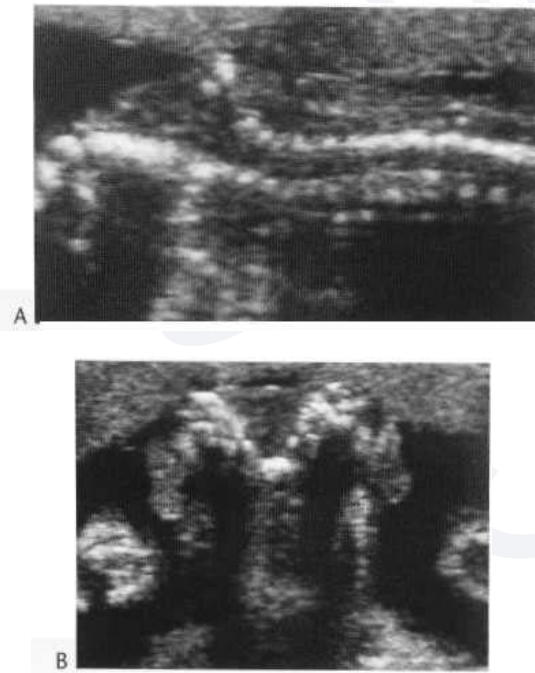


Fig. 33.31 Cervical spina bifida: longitudinal (A) and transverse (B) images. Note the 'V' shape rather than the normal 'ring' of ossification centres on the transverse image.

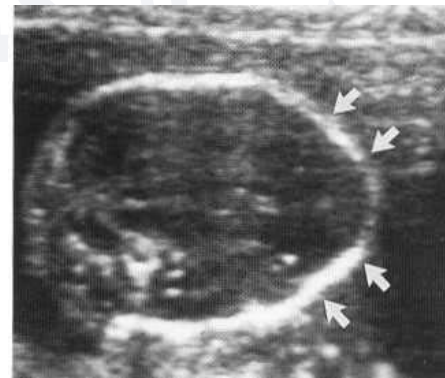


Fig. 33.34 The 'lemon sign'. There is flattening of the frontal bones (arrows) on this transverse image through the head.

meningocele the sae is fluid-filled (Fig. 33.32) but in the case of a myelomeningocele it also contains solid tissue (Figs 33.29, 33.33).

Other pointers to the diagnosis which have attracted interest recently include abnormalities of fetal cranial contour (the 'lemon sign'; Fig. 33.34) and of the cerebellum (the 'Banana sign' Fig. 33.35). Initially described by Nicolaides et al (1986), these signs have been shown to be useful predictors of spina bifida in a high-risk population, although in a routine screening population their positive predictive values are much less (Filly 1988). Effacement of the cisterna magna is another important pointer to the

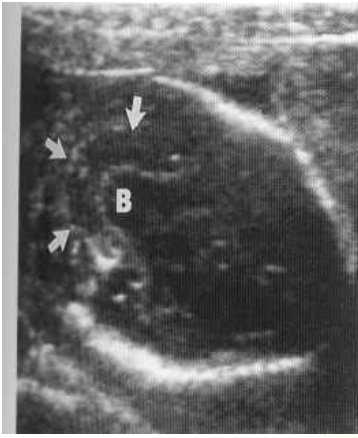


Fig. 33.35 The 'banana sign'. Note the cerebellum (arrows) stretched around the brainstem (B) with effacement of the cisterna magna.

Arnold-Chiari malformation, as is ventriculomegaly, seen in 80-90% of cases of spina bifida.

Full assessment of the fetal cranium after the first trimester thus requires imaging in the transcerebellar, transthalamic and transventricular planes.

Hydrocephalus

Fetal hydrocephalus has many causes and a variable, although generally poor, prognosis. Neonatal survival is less than 30% and many of these infants are mentally or physically handicapped. Although it may prove impossible to distinguish non-obstructive ventriculomegaly from hydrocephalus, in all cases a careful search should be made for other anomalies, both of the CNS and other organ systems.

Up to 30% of all cases of hydrocephalus may be associated with either a meningomyelocele or, less commonly, an encephalocele.

Nyberg et al (1987c) reviewed 61 fetuses with hydrocephalus over a 5-year period and found that 84% had one or more major CNS malformations or extra-CNS malformations. Fetal mortality was directly related to the presence of extra-CNS anomalies, which in this series was associated with a uniformly fatal outcome. Conversely, the prognosis for mild and occasionally transient lateral ventricular dilatation in the absence of other sonographically detected abnormalities (idiopathic ventricular dilatation) may be good. Accurate assessment is therefore essential.

The lateral cerebral ventricles become easily visible at around 13-14 menstrual weeks. The diagnosis of hydrocephalus has traditionally been based on the *lateral ventricular ratio* (Fig. 33.36) and a number of charts have been developed for normal fetuses which relate the ratio of the lateral ventricular width to the hemispheric width as a function of gestational age. Unfortunately the wide range of normality, particularly early in the second trimester, limits their usefulness.

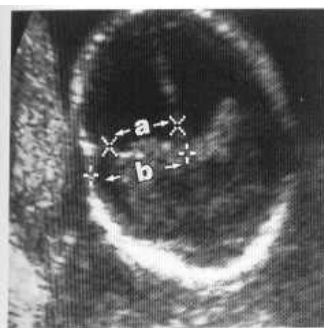


Fig. 33.36 Ventriculomegaly: transverse image through fetal head. a/b = lateral ventricular ratio.



Fig. 33.37 One of bilateral choroid plexus cysts (cursors), measuring 13 x 8 mm. There were additional forearm abnormalities and a small cystic hygroma in this fetus, which karyotyping showed to be a trisomy 18.

Other criteria for the diagnosis of ventriculomegaly have been suggested. An absolute measurement of *lateral ventricular width* (measured from the midline echo to the leading edge of the lateral wall of the lateral ventricle) of 1.1 cm or less and choroid plexus filling the body and atria of the lateral ventricle both suggest normality. Most commonly used today, the *ventricular atria/diameter* has been shown to be largely age independent through the second and third trimesters (Cardoza et al 1988), a value greater than 1.1 mm indicating significant ventriculomegaly. The attraction of this measurement is its simplicity, requiring neither a knowledge of the gestational age nor reference to charts relating ventricular size to gestational age to judge normalcy. Although the medial atrial wall is a better specular reflector than the lateral wall, the gravity dependent orientation of the choroid plexus serves as a useful pointer to the position of the latter interface. It has been suggested that assessment of the ventricular atrium, in combination with assessment of the posterior fossa and cisterna magna, constitutes the most appropriate sonographic screening procedure for major CNS malformations (Filly et al 1991).

Care must be taken not to confuse ventriculomegaly with choroid plexus cysts. These relatively common structures are almost always transient and of no clinical significance. Associated chromosomal abnormalities, in particular trisomy 18, have been reported but are uncommon (Fig. 33.37).



Fig. 33.38 Dandy-Walker syndrome. The posterior fossa cyst measures 12 x 9 mm in this fetus with a gestational age of 19 weeks. A hypoplastic cerebellum was identified and there was also ventriculomegaly with a ventricular atrium measuring 14 mm across.

Other intracranial anomalies

Dandy-Walker syndrome (DWS) This results from abnormal development of the cerebellum and fourth ventricle. Atresia of the foramina of Luschka and Magendie, with hypoplasia or aplasia of the cerebellar vermis, leads to dilatation of the fourth ventricle and expansion of the posterior cranial fossa (Fig. 33.38). Hydrocephalus is usually seen but is variable in extent. Associated anomalies include agenesis of the corpus callosum, encephaloceles, polycystic kidneys and cardiovascular defects. The sonographic appearances are characteristic, with separation of the cerebellar hemispheres by the enlarged fourth ventricle. Distinction must be made from a posterior fossa arachnoid cyst, in which case there is displacement but no separation of the cerebellar hemispheres by the cystic lesion.

Aqueduct stenosis This may be inherited as an X-linked recessive trait, but infectious, teratogenic and neoplastic causes have all been implicated. Although the diagnosis is suggested by the finding of dilated third and lateral ventricles with a normal fourth ventricle, these features are non-specific. Many other conditions of both non-obstructive ventriculomegaly and true hydrocephalus can give a similar sonographic appearance; even in the most experienced hands the diagnosis remains one of exclusion.

Holoprosencephaly This is a complex developmental abnormality of the forebrain occurring in early embryonic life. Chromosomal anomalies are frequent and there is both a familial tendency and also an association with teratogenic agents. The condition results from a failure of cleavage of the prosencephalon which gives rise to the cerebral hemispheres and diencephalon. Associated facial anomalies include cyclopia, cebocephaly and a median cleft lip. Three types are recognised alobar, semilobar and lobar depending on the degree of forebrain cleavage. Alobar holoprosencephaly, the most severe form, is associated with a

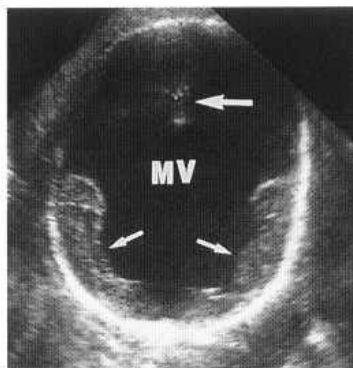


Fig. 33.40 Semilobar holoprosencephaly: transverse image. MV = monovertricle; small arrows = anterior cortex with no interhemispheric fissure; large arrow = posterior falx. On this image there is no distinction from the alobar form.

monoventricular cavity, fusion of the thalami, and absence of the corpus callosum, falx cerebri, optic tracts and olfactory bulbs (Fig. 33.39). In semilobar holoprosencephaly the two cerebral hemispheres are partially separated posteriorly but there is still a single ventricular cavity and partial fusion of the thalami (Fig. 33.40), whereas in the lobar variety the interhemispheric fissure is well developed and there is some separation of the thalami. In all types the posterior fossa is normal.

Reliable prenatal sonographic diagnosis is possible in cases of alobar and semilobar, but not usually lobar, holoprosencephaly. The prognosis for the first two of these is very poor.

Hydranencephaly This is the result of a destructive intrauterine insult rather than a developmental anomaly. Vascular occlusion of the internal carotid arteries has been postulated, leading to destruction of cerebral hemispheres, occasionally with some sparing

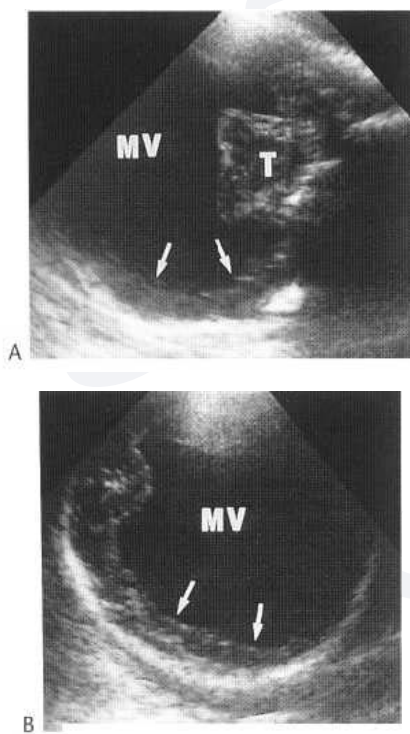


Fig. 33.39 Alobar holoprosencephaly: coronal (A) and transverse (B) images. T = fused thalami; MV = monovertricle; arrows = cortical mantle.

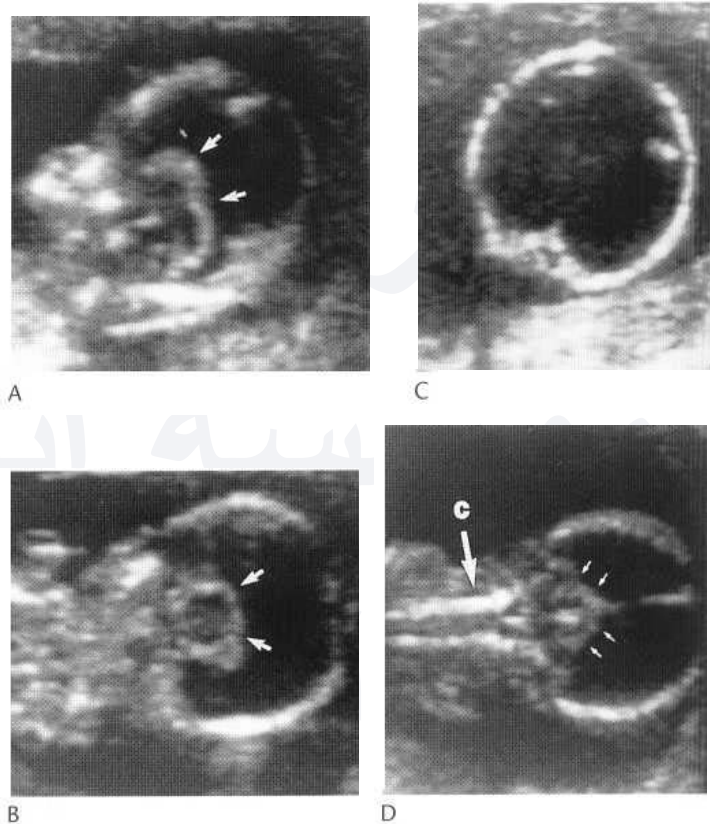


Fig. 33.41 Hydranencephaly: sagittal (A), anterior coronal (B), transverse (C) and posterior coronal (D) images. Note the brainstem surrounded by fluid (arrows, A,B) and an absence of cerebral cortex. In (D) the tentorium (small arrows) can be seen above a normal posterior fossa. c = cervical spine.

of the temporal and occipital cortex and basal ganglia. There is preservation of the brainstem, thalami and cerebellum, although these may be smaller than usual. The falx cerebri may be absent or incomplete and the choroid plexus is preserved, thus allowing secondary hydrocephalus and macrocrania to ensue. The head is filled with CSF, contained in a cavity lined with leptomeninges. The sonographic appearances of the brainstem protruding into this fluid-filled cavity are fairly characteristic (Fig. 33.41 A-C), but occasional confusion may occur with severe hydrocephalus (a thin rim of compressed cortical tissue would differentiate the two) or alobar holoprosencephaly (but the thalami are not fused in hydranencephaly). The posterior fossa appears normal (Fig. 33.41 D). Prognosis and management are as for holoprosencephaly.

Agenesis of the corpus callosum This may be associated with other CNS and non-CNS abnormalities, including holoprosencephaly, the Dandy-Walker malformation, microcephaly, macrocephaly, median cleft lip syndrome, and cardiovascular, gastrointestinal and genitourinary anomalies. Sonographic features include elevation of the third ventricle, an abnormal lateral ventricular axis, and localised dilatation of the atria and occipital horns. In addition, an abnormal pattern of gyral development occurs along the interhemispheric fissure, where sulci radiating toward the third ventricle may be seen as a wavy appearance of the midline in axial sections.

The prognosis is variable and is frequently determined by associated anomalies. In cases where the agcnesis is an isolated finding normal obstetric management applies.

Cardiovascular and respiratory systems

The heart

Congenital heart disease is the most common severe congenital anomaly found in neonates and may be associated with serious morbidity and mortality.

Examination of the fetal heart is an integral part of any prenatal obstetric ultrasound examination. Specific indications include the previous occurrence of congenital heart disease in mother or sibling (both with a recurrence risk of between 2 and 5%), a maternal disease known to affect the fetus, such as diabetes mellitus, and the use by the mother of drugs such as lithium or alcohol which are also known to affect the fetus.

Fetal heart activity has been reported at 40 days and should always be present at 46 menstrual days with TVS. Cardiac motion is generally seen as soon as the embryo is visualised and always

when the crown-rump length is greater than 5 mm. Normal cardiac rates vary with menstrual age, with values anywhere between 90 and 128 beats/min at 6 weeks, reaching a peak of up to 174 beats/min at 9 menstrual weeks, before declining to around 150 beats/min at 14 weeks.

The basic view of the fetal heart, and in many centres the only view obtained during the routine obstetric sonographic examination, is the *four-chamber view* (Fig. 33.42). This can be obtained in most fetuses older than 16 weeks but a more reliable assessment is possible between 18 and 22 weeks of gestation because the cardiac valves are then well developed and the size of the fetal heart and position of the fetus generally allow better visualisation at this stage.

Evaluation of the anatomical detail provided by this view may require several different approaches (McGahan 1991). The *apical four-chamber view* allows good visualisation of the atrioventricular valves, while the *subcostal view* will better demonstrate the integrity of the atrial and ventricular septa. The four-chamber view is also excellent for defining the comparative size of the cardiac chambers but does not demonstrate the aorta and pulmonary arteries. Other views are therefore necessary for establishing diagnoses such as transposition of the great vessels, tetralogy of Fallot, truncus arteriosus, aortic and pulmonary valve stenoses, and coarctation of the aortic arch (Allen 1986). Long-axis views may be obtained through both the left and right ventricles, allowing assessment of their respective outflow tracts, while the aortic arch is best imaged in the longitudinal axis of the fetus. A *short-axis view* allows for detailed assessment of the great vessels and can rule out a transposition.

Both M-mode and Doppler echocardiography have been used in the assessment of fetal cardiac anomalies. Not only can cardiac chambers and great vessels be measured but also *dysrhythmias* and *stenotic* and *regurgitant valvular lesions* may be diagnosed and quantified. With increasing experience of the technique, it is likely that fetal echocardiography for congenital heart defects and other cardiac anomalies will become an important part of fetal assessment.

In addition to the assessment outlined above, the first trimester nuchal translucency measurement should also be mentioned, as documented above (p. 1041). While important in the assessment of chromosomal abnormalities, an increased value may also be a strong pointer to major congenital cardiac defects. In one study (Hyett et al 1999), 55% of major abnormalities of the heart and great vessels were associated with an increased nuchal translucency thickness at 10-14 weeks gestation. They concluded that an increased thickness constituted an indication for specialist fetal echocardiography, even within the first trimester, where the relevant expertise exists.

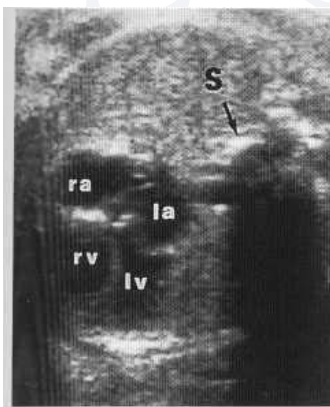


Fig. 33.42 Fetal heart: subcostal four-chamber image. S = spine; ra = right atrium; la = left atrium; rv = right ventricle with moderator band; lv = left ventricle.

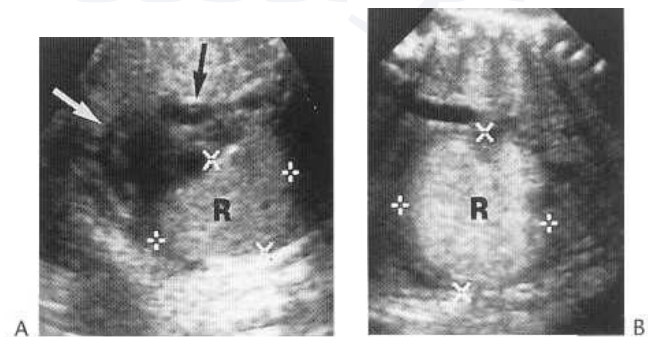


Fig. 33.43 Cardiac rhabdomyoma (R) in a 33 week fetus: oblique (A) and transverse (B) images. The tumour measured approximately 4 cm in diameter. Note small pericardial effusion (arrows).

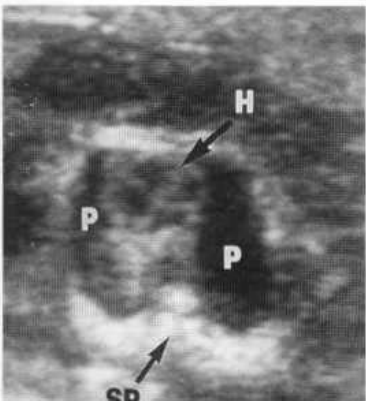


Fig. 33.44 Hydrops fetalis, transverse image. P = pleural effusions; H = heart; SP = spine.

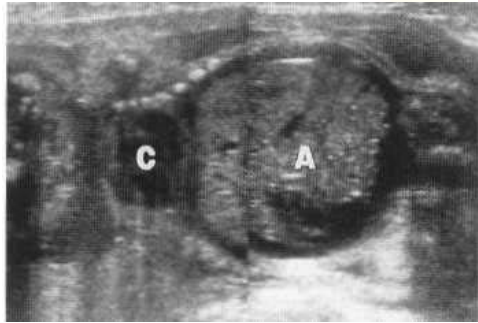


Fig. 33.45 Hypoplastic chest in a fetus with multiple abnormalities including hydrocephalus and short limbs. C = chest; A = abdomen (with ascites).

Apart from the anomalies mentioned above, ultrasound may also diagnose *congenital cardiac anomalies*. These are rare and generally benign. The commonest are *rhabdomyomas* (Fig. 33.43); less common lesions include *fibromas*, *neurofibromas* and *haemangiomas*. Although such tumours are generally isolated anomalies, there is a recognised association with *tuberous sclerosis* in up to 86% of cardiac rhabdomyomas.

The lung

Fetal lungs are non-aerated and demonstrate a homogeneous and solid appearance on ultrasound examination. Despite attempts to correlate the echogenicity and compressibility of lung with pulmonary maturity, the *lecithin:sphingomyelin ratio* within amniotic fluid remains the most reliable means of assessment at present. The fetal thorax can be scanned transversely from the clavicles at the lung apices to the echo-poor diaphragmatic crura, noting the shape and size of the chest, the size and position of the heart, and the appearance of the lungs. While small *pericardial effusions* have been reported in the normal fetus, *pleural fluid* is abnormal at any gestational age and may occur either in isolation or as part of a more general condition, such as fetal hydrops (Fig. 33.44) or urinary ascites secondary to posterior urethral valves. *Pulmonary hypoplasia* may be evident (Fig. 33.45) and is a common sequel to oligohydramnios of any cause.

The commonest thoracic abnormalities diagnosed with ultrasound are the following.

Congenital diaphragmatic hernia (CDH) The sonographic diagnosis of fetal CDH relies on the visualisation of abdominal organs in the chest (Fig. 33.46). Other pointers may be absence of a normally positioned stomach, mediastinal displacement, small abdominal circumference and polyhydramnios. Associated mor-

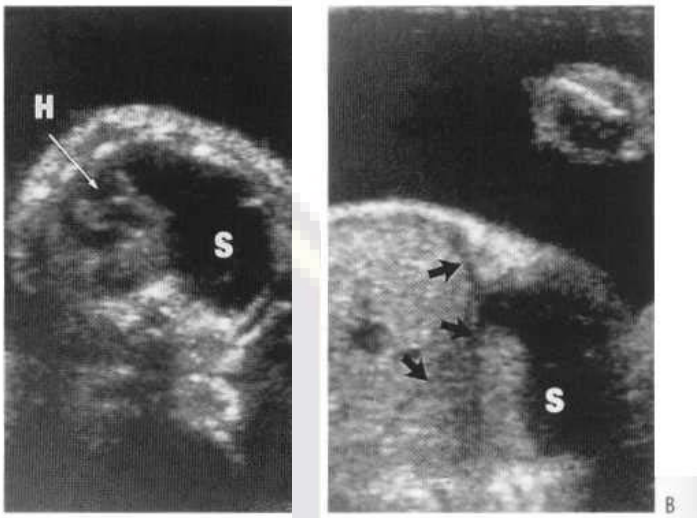


Fig. 33.46 Diaphragmatic hernia: transverse (A) and longitudinal (B) images. S = stomach, herniated into chest; H = heart; arrows - hypoechoic diaphragm. Note the polyhydramnios.

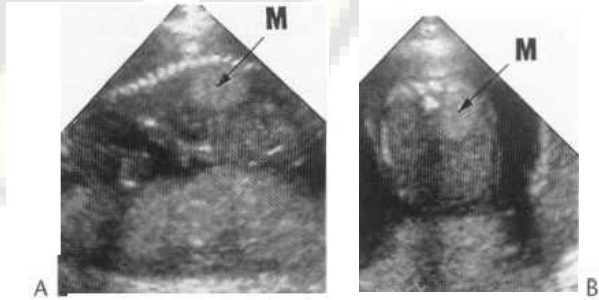


Fig. 33.47 Pulmonary sequestration: longitudinal (A) and transverse (B) images. M = hyperechoic mass lying at left lung base.

tality ranges from 50% to 80%, being due mainly to pulmonary hypoplasia arising secondary to the compression of the lungs by the adjacent hernia. Many anomalies may be associated with CDH, particularly in the central nervous and cardiovascular systems, and these are thought to account for many antenatal deaths. A detailed sonographic examination, together with chromosomal analysis, is essential in these patients.

pulmonary sequestration As with older patients, pulmonary sequestration in the fetus is divided into both extra- and intralobar forms, usually occurring in the posterobasal segments of the left lung. The extra-lobar variety is the only type to have been

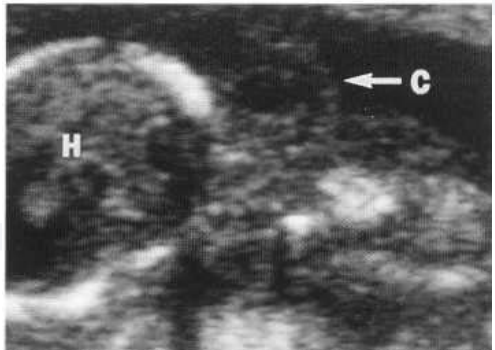


Fig. 33.48 Cystic hygroma: longitudinal image. H - head; C - small cystic lesion in occipitocervical region. Despite the relatively small size of this hygroma it was associated with extensive lymphoedema.

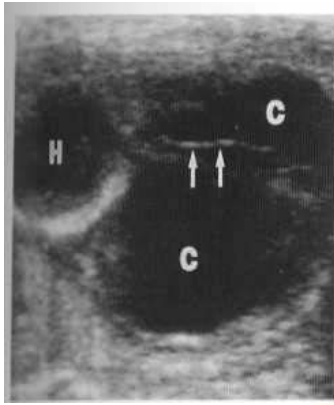


Fig. 33.49 Cystic hygroma: transverse image. H = head; C = large occipitocervical cysts with a prominent midline septation (arrows) corresponding to the ligamentum nuchae.

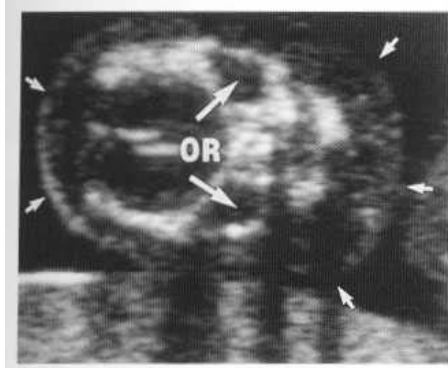


Fig. 33.50 Extensive lymphoedema (arrows) in a patient with a cystic hygroma: coronal image. OR = orbits.



Fig. 33.51 Hydrops fetalis: transverse image through abdomen. L = liver; A = ascites.

described antenatally and is associated with other foregut anomalies and also congenital diaphragmatic hernia. Sonographically the sequestration appears as an echogenic mass (Fig. 33.47) in the fetal thorax and, as with CDH, may be associated with fetal hydrops and polyhydramnios.

Congenital cystic adenomatoid malformation of the lung (CCAML) This is a rare hamartoma of the lung that has been demonstrated on antenatal ultrasound as a complex solid and cystic lung tumour, once again often associated with fetal hydrops and polyhydramnios.

Cystic hygroma

Cystic hygromas are multiseptate cystic structures usually located in the occipitocervical region of the fetus (Fig. 33.48). Large lesions usually demonstrate a thick septum dividing the cyst along the midline and corresponding to the nuchal ligament (Fig. 33.49).

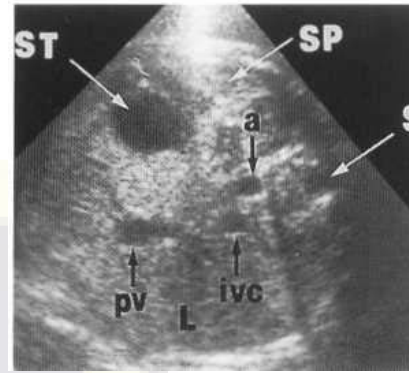


Fig. 33.52 Normal abdomen: transverse image in third trimester. ST = stomach; SP = spleen; S = spine; L = liver; a = aorta; ivc = IVC; pv = portal vein.

Arising as a result of failure of the normal communication between the fetal lymphatic system and jugular vein, there is initial distension of the jugular lymphatic sac (located in both sides of the neck), which may later progress to more generalised lymphoedema (Fig. 33.50) and non-immune hydrops (Figs 33.44, 33.51).

Up to 70% of cases may be associated with an abnormal karyotype, of which Turner syndrome is the commonest. The prognosis for prenatally diagnosed cystic hygroma is generally poor, even in the absence of chromosomal anomalies and fetal hydrops (Abramowicz et al 1989) but occasional reports have been made of documented regression.

Gastrointestinal system

Fetal bowel may be detected more frequently as gestation progresses. In one study (Nyberg et al 1987d), normal colon, appearing as a tubular structure located around the perimeter of the abdominal cavity, was demonstrated in all fetuses at 28 weeks and occasionally as early as 22 weeks gestation. Small bowel, lying centrally within the abdomen, was more difficult to visualise, being seen in only one-third of fetuses after 34 weeks. Unlike the colon, small bowel typically showed peristalsis and, although initially rather echogenic (producing a 'pseudomass' in the fetal abdomen), the appearances later give way to more usual anechoic fluid-filled loops. Meconium, which is hypoechoic when compared with the adjacent bowel wall accumulates within the colon from approximately 16 weeks onward, and causes a progressive increase in colonic diameter up to around 18 mm at term. Normal small-bowel calibre is less than for colon, with individual segments not exceeding 6 mm in diameter or 15 mm in length even at term.

Sonographically-detectable abnormalities in the fetal abdomen include the following.

Absent stomach The fetal stomach should be visualised in virtually all pregnancies from the start of the second trimester onward (Fig. 33.52). If it is not seen, abnormalities such as oesophageal atresia, diaphragmatic hernia or oligohydramnios should be considered. Oesophageal atresia is frequently associated with polyhydramnios, although in 90% of cases there is an associated tracheo-oesophageal fistula and fluid may then be seen within the stomach. There may also be associated anomalies in other organ systems and these must be looked for carefully.

Small-bowel atresia/obstruction Duodenal atresia is the commonest fetal small-bowel atresia. due to an aberration in

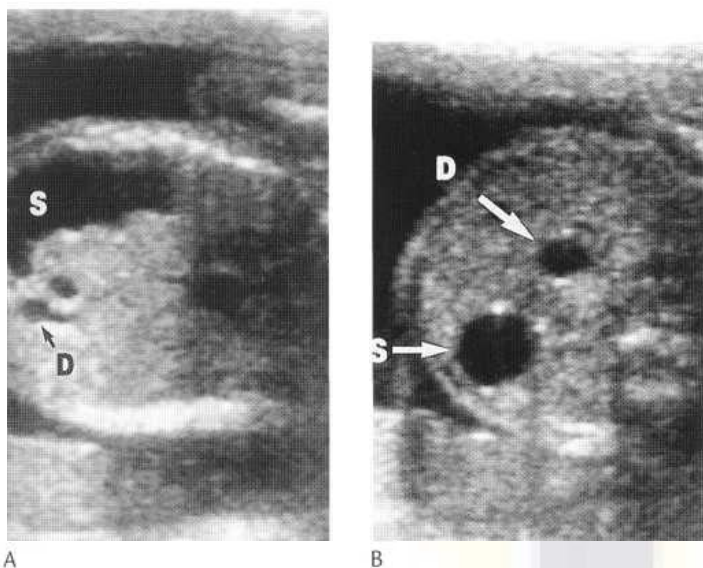
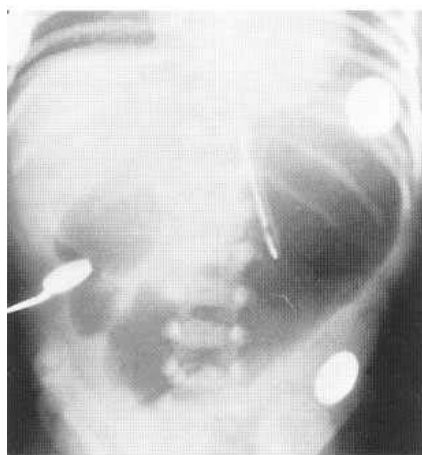


Fig. 33.53 Duodenal atresia: longitudinal (A) and transverse (B) images. (C) Postnatal radiograph. S = stomach; D = duodenum. Note the 'double bubble' in (B) and coexistent polyhydramnios.



embryogenesis and occurring in up to 1 in 10 000 births. Sonographically it is detected as a dilated stomach and proximal duodenum, producing a 'double-bubble' appearance (Fig. 33.53). As with other causes of intestinal obstruction, there is generally coexistent polyhydramnios, which is more marked the more proximal the level of obstruction. Thirty per cent of cases are associated with trisomy 21 so chromosomal analysis is advisable. Other associations include congenital heart disease and, less commonly, tracheo-oesophageal fistula, renal malformations, and hepatobiliary and pancreatic anomalies. Where more dilated bowel loops are demonstrated, a more distal site of obstruction should be considered. Possible causes include volvulus or intussusception, meconium ileus in patients with cystic fibrosis (Estroff et al 1992), or a jejunal or ileal atresia, usually secondary to vascular insult.

Large-bowel obstruction This is more difficult to diagnose than small-bowel obstruction because of the wide variation in the diameter of a healthy fetus's colon (Hertzberg 1994). The antenatal sonographic diagnosis of anorectal malformations, Hirschsprung's disease and meconium plug syndrome have all been described but are generally unreliable.

Ascites True ascites (Fig. 33.51) must be distinguished from the thin rim of pseudoascites which is seen in the normal fetus and is thought to be due to the hypoechoic abdominal wall

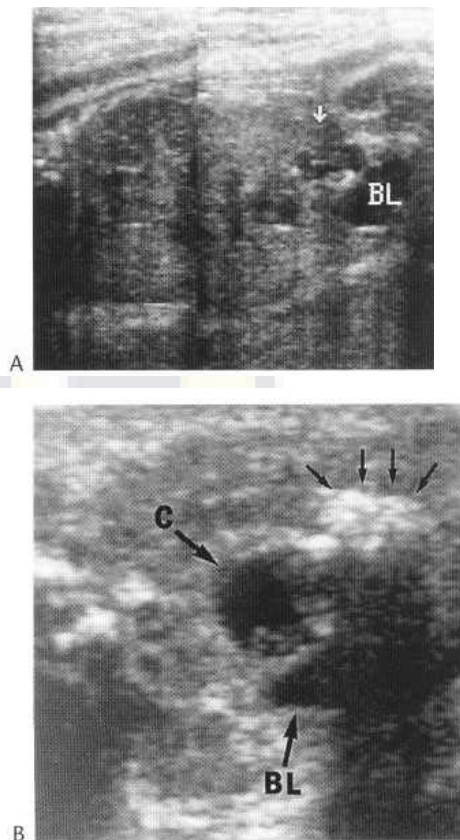


Fig. 33.54 Meconium peritonitis: longitudinal (A) and magnified (B) images. BL = bladder; C = cyst; small arrows = echogenic focus with distal shadowing.

musculature. It is always abnormal, being associated with *hydrops fetalis*, bowel perforation secondary to atresias or stenoses, and urinary ascites secondary to bladder outlet obstruction.

Calcification in the abdomen When localised to the peritoneum and unaccompanied by a solid mass lesion, most calcifications are secondary to *neonium peritonitis*, a sterile chemical peritonitis resulting from small-bowel perforation. Associated findings include pseudocyst formation as a result of the fibrinous peritoneal reaction (Fig. 33.54), polyhydramnios and bowel dilatation. In less than half of the cases of neonium peritonitis can a cause be found after delivery. Of these, a significant proportion are associated with obstructive bowel lesions such as atresias, volvulus and malrotations, and, less commonly, with neonium Hens and cystic fibrosis.

Abdominal wall defects Normal development midgut herniation occurs during weeks 9-11, after which the bowel returns to the abdominal cavity and undergoes its normal rotation. It is not possible to diagnose abdominal wall defects reliably before 14 menstrual weeks. After that time the two primary conditions which must be distinguished are omphalocele and gastroschisis.

Omphalocele Occurring in 1 of 5000 pregnancies, omphalocele is a ventral abdominal wall defect with herniation of the intra-abdominal contents into the base of the umbilical cord (Fig. 33.55). Bowel loops, stomach and liver are the most frequently herniated organs and are covered with a membrane of intact peritoneum into which the umbilical cord inserts.

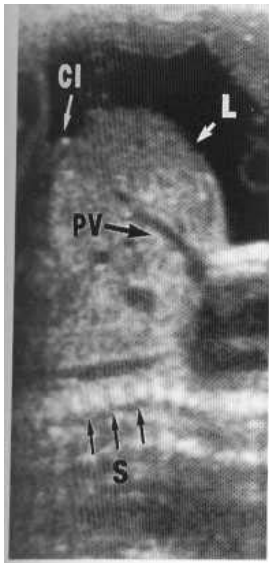


Fig. 33.55 Omphalocele: longitudinal image. L = herniated liver; PV = portal vein; CI - cord insertion; S = spine



Fig. 33.56 Gastroschisis, showing bowel loops floating freely within the amniotic fluid.

Gastroschisis This is less common, occurring in 1 in 12 000 pregnancies. It is a full-thickness defect of the abdominal wall, usually located to the right of the umbilical cord, which has a normal insertion. The defect is generally quite small and herniated organs include bowel loops, which may appear oedematous and which float freely within the amniotic fluid (Fig. 33.56). Liver herniation is less common than with omphalocele.

Associated anomalies occur with both conditions, but are much commoner with omphalocele, where they may be present in up to 88% of cases. These include *chromosomal anomalies* in up to 60% (particularly trisomy 13 and 18), *cardiac anomalies* (particularly septal defects and Fallot's tetralogy) in up to 47%, and *genitourinary anomalies* and *neural tube defects*, both in up to 40% of cases. Syndromes which include the presence of an omphalocele include *the pentalogy of Cantrell* (with diaphragmatic hernia, sternal cleft, ectopia cordis and a variety of cardiovascular malformations) and *the Beckwith-Wiedemann syndrome* (with gigantism, macroglossia and pancreatic hyperplasia).

Sonography can generally distinguish omphalocele from gastroschisis, although there are pitfalls, such as when the covering membrane of an omphalocele ruptures, thus allowing abdominal contents to spill into the amniotic fluid. In all cases a search must be made for other anomalies. With omphalocele this must include a detailed fetal echocardiographic examination and fetal karyotyping.

Genitourinary system

The prenatal sonographic assessment of the genitourinary system includes visualisation of the fetal kidneys and bladder and an assessment of the amniotic fluid volume. The appearance of the

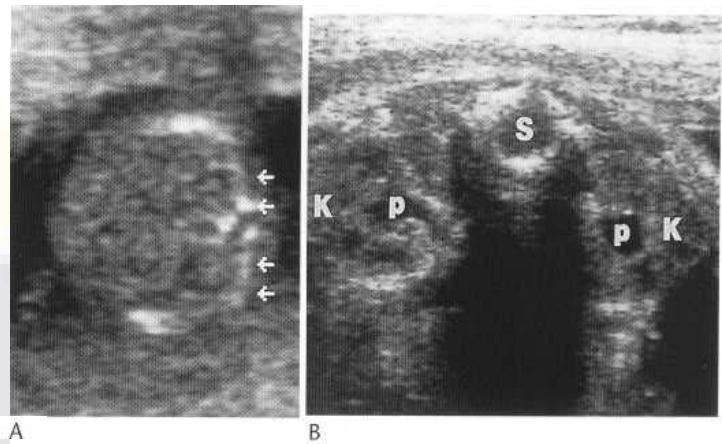


Fig. 33.57 Normal kidneys, transverse images: early second trimester (A) and late third trimester (B). K = kidney; p = normal renal pelvis, measuring less than 10 mm in diameter; S - spine.

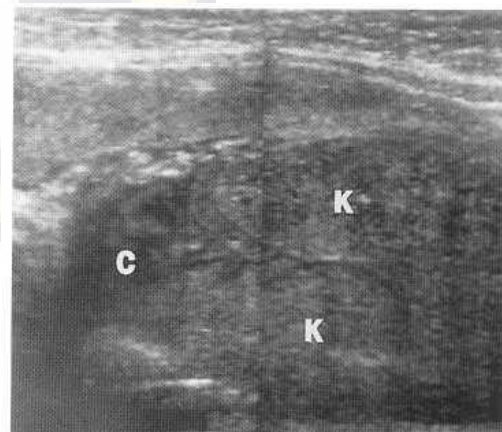


Fig. 33.58 Polycystic kidneys, Potter type I, longitudinal image. K = large hyperechoic kidneys; C = hypoplastic chest. Note oligohydramnios.

normal kidneys varies through pregnancy, the pelvicalyceal systems becoming relatively more prominent with increasing gestational age (Fig. 33.57). With TVS it is possible to demonstrate these organs at a gestational age of 12-13 weeks, provided the amniotic fluid volume is normal. The fetal kidneys contribute little to the amniotic fluid volume before 16 weeks gestation but are responsible for most of the production by the onset of the third trimester. Thus, although a normal amniotic fluid volume may be seen early in the second trimester in the absence of renal function, later in the pregnancy there will be inevitable oligohydramnios (Fig. 33.58). This in turn often makes detailed sonographic assessment of the fetus and fetal urinary tract more difficult.

Bilateral renal agenesis This may occur in isolation or may be associated with a characteristic facial anomaly, pulmonary hypoplasia and abnormalities of the extremities to give *Potter's syndrome*, or '*renofacial dysplasia*'. The condition is uniformly fatal. The sonographic diagnosis may be difficult, both on account of severe oligohydramnios and also because enlarged adrenal glands may take on a reniform shape in the absence of the kidneys. Colour and power Doppler may help, with a failure to demonstrate normal renal arteries. Absence of a visualised bladder on repeated examinations is a strong pointer to the diagnosis. The role of attempted fetal diuresis by administration of frusemide to the mother remains controversial. Associated anon-

alies may involve both adjacent structures (e.g. genital malformations) and also other organ systems.

Unilateral renal agenesis This is commoner than the bilateral form and, because of normal bladder function, is more difficult to diagnose. Fortunately the prognosis for these cases is good.

Infantile polycystic renal disease (Potter type I) This is inherited as an autosomal recessive disorder and results from a primary defect of the renal collecting tubules, which dilate to form tiny cysts 1-2 mm across. The nephrons are normal in number and morphology and, unlike multicystic dysplastic kidneys, show no connective tissue proliferation. The kidneys are symmetrically enlarged and have a rather echogenic appearance (Fig. 33.58), which is thought to result from a combination of through transmission behind the cysts and the multiple tissue interfaces presented to the ultrasound beam. Severe cases, where the typical renal appearances are combined with non-visualisation of the bladder and oligohydramnios, may be diagnosed by 16 weeks gestation. Those with less pronounced disease may not be recognised until after birth. Cases associated with bile duct proliferation and hepatic fibrosis tend to present later in infancy and have a generally better outlook than the commoner perinatal variety. These infants generally die soon after birth from a combination of pulmonary hypoplasia and renal failure.

Multicystic dysplastic kidneys (Potter type II) This condition may occur in isolation or as part of a syndrome (e.g. Meckel-

Gruber, Dandy-Walker, Apert). The disorder is congenital and characterised by cystic lesions which correspond to dilated renal collecting tubules. There is a wide spectrum of sonographic appearances, with cysts of varying size separated by residual strands of parenchyma causing lobulation of the renal margins. Involvement may be bilateral (Fig. 33.59A,B), unilateral (Fig. 33.59C,D) or segmental and the kidneys may be large (Potter type IIA) or small (type IIB). Where involvement is complete, the renal artery is usually small or absent and the renal pelvis and meter atretic. The renal pelvis is not usually seen, although it may occasionally be distended in cases of isolated ureteric atresia.

Bilateral multicystic dysplastic kidneys lead to severe oligohydramnios and the absence of a visible fetal bladder. Conversely a fetus with a unilateral dysplastic kidney may show no extracrnal abnormality. In up to 40% of these cases there will be a contralateral renal tract anomaly, including malrotation, ureteropelvic junction obstruction (in up to 10% -) and horseshoe kidney. Other associated anomalies may be seen in the CNS (anencephaly, hydrocephalus, spiny bifida), chest (diaphragmatic hernia) and abdomen (duodenal stenosis, imperforate anus).

Bilateral multicystic disease is generally easy to diagnose and the outcome is invariably fatal. The diagnosis of unilateral disease is more difficult. Not only must the contralateral kidney be checked for associated anomalies, but also the condition must be differentiated from a unilateral hydronephrosis, as perinatal management will clearly differ.

When the diagnosis of bilateral disease is made early in pregnancy, termination of pregnancy should be offered to the patient. Unilateral disease with no associated anomalies should not alter normal obstetric management.

Ureteropelvic junction obstruction This is the commonest cause of neonatal hydronephrosis. The condition is generally sporadic, although familial cases have been reported. A functional abnormality of renal tract musculature is the usual cause, although anatomical abnormalities such as adhesions, ureteric valves or aberrant lower pole vessels occasionally occur. Both kidneys may be involved in 10-30% of cases. Associated urinary tract anomalies are frequent. Extraurinary anomalies are seen in up to 20% of cases and include Hirschsprung's disease, cardiovascular abnormalities, neural tube defects, oesophageal atresia and imperforate anus.

The sonographic diagnosis depends on demonstrating a dilated pelvicalyceal system on the affected side. Severe cases may show a large fluid-filled structure with only a thin surrounding rim of parenchyma. Milder cases may be difficult to distinguish from normal physiological distension of the renal pelvis (Fig. 34.57B). Criteria indicating significant hydronephrosis include a renal pelvis to renal diameter ratio of greater than 50% and/or an antero-posterior diameter of the renal pelvis of greater than 10 mm (Grignon et al 1986). Pelvis diameters between 5 and 10 mm are mostly normal but merit follow-up.

The fetal bladder and amniotic fluid volume appear normal with unilateral ureteropelvic obstruction and a normal contralateral kidney. Where there is an associated anomaly of the contralateral kidney, or where the condition is bilateral, oligohydramnios may be present to a variable extent. A paradoxical polyhydramnios may occasionally occur, usually explained by a coexistent abnormality such as a gastrointestinal atresia. Obstetric management varies with the degree of obstruction and the presence of associated anomalies:

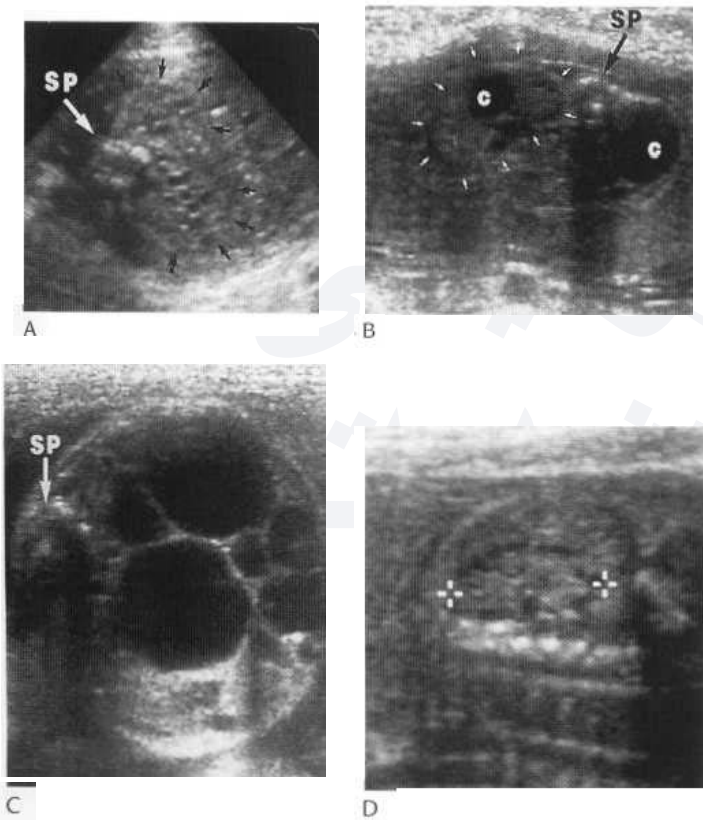


Fig. 33.59 (A-D) The spectrum of multicystic dysplastic kidneys, Potter type II: all are transverse images except (D), which is longitudinal. (A) Small cysts scattered throughout both kidneys. (B) A mixture of small and large cysts in both kidneys, right kidney arrowed. (C) Unilateral involvement with a large multicystic mass. The contralateral kidney was normal. (D) Unilateral involvement with small, peripheral cysts. All cases demonstrated oligohydramnios. SP = spine; c = cyst.

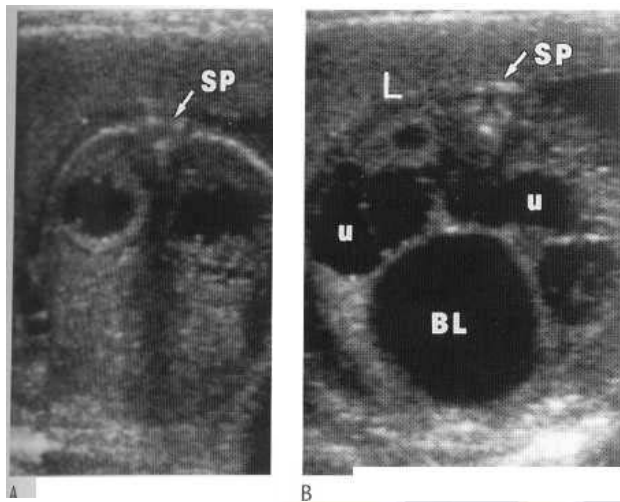


Fig. 33.60 Posterior urethral valves: transverse images through hydronephrotic kidneys (A) and more caudally (B). SP = spine; u = dilated ureters; BL = distended bladder. L denotes left side of fetus.

an isolated unilateral ureteropelvic obstruction should not alter standard practice.

Ureterovesical junction obstruction The reported frequency of this entity in neonates varies between 8 and 23% of urinary tract obstructions. Distal ureteric obstruction is usually functional, resulting in a primary megaureter, but may occasionally be due to a ureteric atresia. Non-obstructive causes of ureteral and renal dilatation may be difficult to distinguish from obstruction at the ureterovesical junction. Thus vesicoureteric reflux, or a duplex collecting system with ectopic ureterocele (classically giving an obstructed upper moiety with reflux into the lower moiety) may give a similar appearance.

Posterior urethral valves Almost always affecting male infants, the condition is characterised by obstruction of urinary flow by membranous 'valves' in the posterior urethra. Bladder wall thickening (of greater than 2 mm) and persistent dilatation of the fetal bladder are the two major signs of urethral obstruction. The dilated posterior urethra may be seen as an extension from the bladder base in up to 50% of cases, and gives the most direct evidence of urethral obstruction. Secondary dilatation of the ureters and renal pelvicalyceal systems (Fig. 33.60) may occur in up to 40% and oligohydramnios is seen in 50% of cases. Spontaneous bladder decompression may occur in up to 10% with the formation of urinary ascites or a perirenal urinoma.

The outlook is poor for patients with oligohydramnios and secondary pulmonary hypoplasia, with only 5% surviving the neonatal period. Other poor prognostic signs are the absence of dilated calyces (implying development of renal dysplasia with little urine production), extensive urinary ascites (leading to stenting and elevation of the diaphragm, again with pulmonary hypoplasia), and dystrophic calcification within the bladder wall at the site of previous rupture (Mahony et al 1985). Management of patients with good prognostic signs depends on the gestational age and pulmonary maturity of the fetus. Early delivery may be performed in a centre with access to neonatal urological care when biochemical markers indicate lung maturity. When this is not the case management is generally expectant unless oligohydramnios develops. The value of intrauterine bladder decompression is unproven. Termination of pregnancy may be offered where indicators suggest a poor prognosis

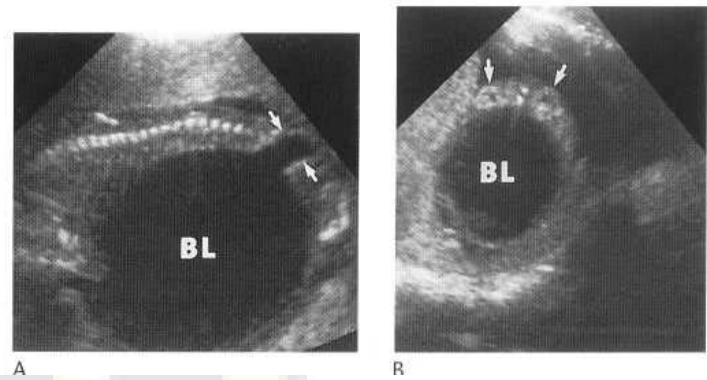


Fig. 33.61 Prune-belly syndrome: longitudinal image (A) and transverse image (B). BL = distended bladder; arrows (A) = dilated posterior urethra; arrows (B) = compressed kidneys.

before viability has been reached. After viability, aggressive intervention is inappropriate and normal obstetric care should continue.

Prune-belly syndrome The combination of a hypotonic abdominal wall, large hypotonic bladder with dilated ureters, and cryptorchidism forms the prune-belly syndrome. Although there is occasionally a primary aplasia of the abdominal wall muscles, more usually the defect is secondary to a variety of intra-abdominal space-occupying lesions. These include obstructive uropathy, polycystic kidneys, congenital cystic adenomatoid malformation of the lung and Hirschsprung's disease. The most common mechanism involves urethral obstruction from valves, leading to bladder hypertrophy and distension with dilated ureters, hydronephrosis and occasionally dysplastic kidneys (Fig. 33.61). Intestinal and skeletal anomalies may be present in up to 50% of fetuses.

There is a wide range of severity. As with posterior urethral valves, most infants with severe oligohydramnios die in the neonatal period from pulmonary hypoplasia, while others develop renal failure in infancy. Those with milder disease may suffer impaired but stable renal function. Surgery may be needed for relief of the obstructive uropathy, with bladder, ureteric and abdominal wall reconstruction.

Musculoskeletal system

Malformations of the fetal skeleton are seen either as a skeletal dysplasia, where there are abnormalities in multiple bones throughout the fetus, or as focal skeletal abnormalities with both variable distribution and extent of involvement (Bowerman 1995).

Skeletal dysplasias are a heterogeneous group of disorders of bone growth resulting in abnormal shape and size of the skeleton. The birth prevalence is around 2.4 per 10 000 births, with around 50% resulting in either stillbirths or fetal death within the first week of life. Major sonographic features associated with a generalised dysplasia are shortening, sometimes with bowing or fractures, of the extremity bones, demineralisation and a small thorax. Minor features, which may also be seen without a dysplasia, include polydactyly, abnormal calvaria, focal skeletal defects, spinal deformities, malalignment, midface hypoplasia, ventriculomegaly, polyhydramnios and hydrops fetalis. Preliminary work suggests a role for three-dimensional sonography in more reliably assessing the fetal skeleton.

The four major dysplasias are the following.

Thanatophoric dysplasia This is the most common lethal skeletal dysplasia in fetuses and neonates, characterised by rhizomelia, a narrow thorax and large head. As with other severe dysplasias,

the diagnosis may often be made in the second trimester, occasionally as early as 15 or 16 weeks.

Achondroplasia This is the most common non-lethal dysplasia, again with rhizomelia, limb bowing, lordotic spine and enlarged head. Unfortunately the abnormal long bone growth does not generally become apparent until the third trimester, so earlier antenatal diagnosis is rarely possible. Achondroplasia is inherited as an autosomal dominant condition: the homozygous state is lethal: heterozygotes may have a normal life expectancy.

Osteogenesis imperfecta This may be inherited as either an autosomal recessive or dominant condition, with varying degrees of severity. In the more severely affected fetuses antenatal diagnosis may often be made in the second trimester on the basis of shortened long bones with multiple fractures. The thorax tends to be short but not narrow. Along with hypophosphatasia and achondrogenesis, demineralisation of the skeleton may be a prominent feature and is usually most obvious in the fetal cranium.

Achondrogenesis This rare lethal disorder is characterised by micromelia, a short trunk and incomplete vertebral and cranial ossification. Sonographic features include short limbs, absent vertebral ossification, hydrops and polyhydramnios.

Focal skeletal dysplasias

Many conditions and syndromes, including chromosomal defects, may produce such abnormalities, ranging from extensive abnormalities to subtle features which may be difficult or impossible to detect sonographically. Extremities with short, absent, supernumerary or malaligned components are most often apparent (Fig. 33.62). Fetal karyotyping may be indicated, particularly with upper limb

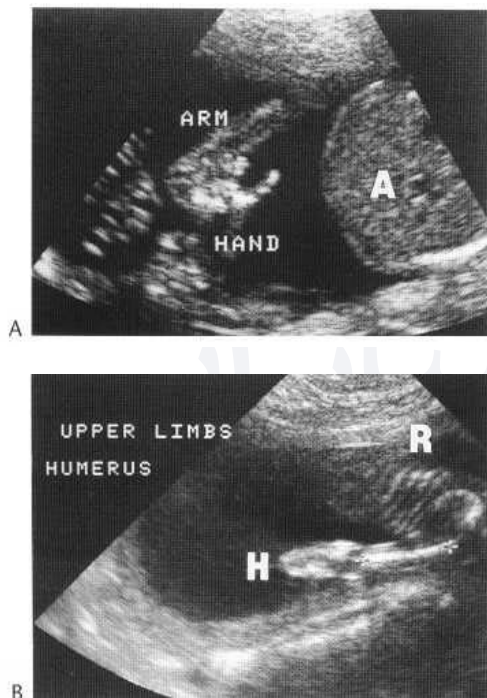


Fig. 33.62 Forearm abnormalities. (A) Persistent wrist flexion in both arms. This fetus with trisomy 18 also had a cystic hygroma and bilateral choroid plexus cysts. A = abdomen. (B) Absent radius and ulna, the hand being inserted onto the distal humerus (H). This fetus also had trisomy 18. Coexistent pleural effusions were noted. R = rib cage.

Box 33.3 Conditions associated with non-immune hydrops fetalis

I. Cardiovascular

Anatomical defects (septal defects, hypoplastic left heart, aortic valve stenosis, tetralogy of Fallot, premature closure of foramen ovale or ductus arteriosus)
Cardiomyopathy
Myocarditis

II. Chromosomal

Down's syndrome (trisomy 21)
Other trisomies
Turner syndrome

III. Malformation syndromes

Thanatophoric dwarfism, asphyxiating thoracic dystrophy, hypophosphatasia

IV. Twin pregnancy

Twin-twin transfusion syndrome

V. Hematological

Arteriovenous shunts (large vascular tumours)
Vena cava, portal vein or femoral obstruction
Haemolysis (G6PD deficiency or haemoglobinopathy)

VI. Pulmonary

Cystic adenomatoid malformation
Diaphragmatic hernia
Mediastinal teratoma
Pulmonary hypoplasia

VII. Gastrointestinal

Atresias of oesophagus, duodenum, ileum and anus
Meconium peritonitis
Malrotation of the intestine

VIII. Liver

Hepatic calcifications and fibrosis
Biliary atresia and cholestasis
Polycystic disease of the liver
Familial cirrhosis

IX. Genitourinary

Congenital nephrotic syndrome
Urethral obstruction with renal dysplasia
Polycystic kidneys
Prune-belly syndrome

X. Neurological

Fetal intracranial haemorrhage
Encephalocele

XI. Maternal

Severe diabetes mellitus, anaemia or hypoproteinaemia

XII. Placenta-umbilical cord

Chorioangioma
Fetomaternal transfusion
Placental and umbilical vein thrombosis

XIII. Medications

Antepartum indometacin taken to stop premature labour may cause fetal ductal closure

XIV. Infections

CMV, toxoplasmosis, syphilis, herpes simplex, rubella

XV. Miscellaneous

Congenital lymphoedema
Congenital neuroblastoma
Sacrococcygeal teratoma (Fig. 33.63)
Polysplenia syndrome
Tuberous sclerosis

Adapted from Holzgreve et al (1985).

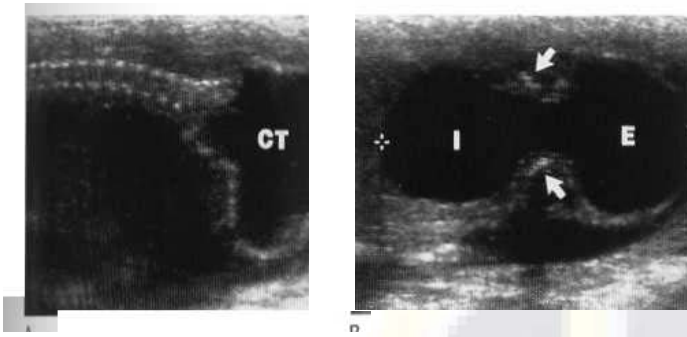


Fig. 33.63 Sacrococcygeal teratoma: longitudinal (A) and transverse (B) images. CT = cystic teratoma at lower end of spine; f and E = intra- and extrapelvic components respectively; arrows = pelvic bones.

and hand abnormalities, as chromosomal abnormalities (particularly trisomy 18 and 21) are associated.

Hydrops fetalis

Hydrops fetalis is characterised by an excess of total body water, causing soft-tissue oedema (Fig. 33.50) and fluid accumulation in body cavities (Figs 33.44, 33.5 I). In the absence of fetomaternal blood group incompatibility (isoimmunisation), the term non-immunological hydrops (NIHF) is used. Following the success of Rh-immune globulin therapy and the consequent reduction in the frequency of erythroblastosis fetalis, non-immunological causes predominate (Box 33.3).

Ultrasound is fundamental both to the initial diagnosis and also in identifying underlying fetal structural abnormalities and conditions which may be associated with non-immune hydrops fetalis.

These may be sonographically demonstrated in over 50% of cases, the cardiovascular being the commonest organ system involved. Where a structural abnormality is demonstrated, the prognosis is poor.

Sonographic features of hydrops fetalis are:

- Skin thickening greater than 5 mm
- Placental enlargement greater than 4 cm
- Ascites, pleural and pericardial effusions
- Polyhydramnios (in up to 75%)

Note that although the prognosis for non-immune hydrops fetalis is generally poor, the prognosis in individual cases with isolated pleural effusions or ascites may be much better. Other investigations necessary in elucidating causes of hydrops fetalis include:

- Maternal blood studies (including the indirect Coombs' test for immune hydrops)
- Amniocentesis for chromosomal analysis
- Fetal blood sampling if indicated, generally under ultrasound guidance.

Immune hydrops fetalis As mentioned previously, this condition is now far less common due to successful prevention of rhesus sensitisation by antibody administration. Diagnosis is largely a matter of immunology. Ultrasound may prove useful in monitoring fetal biometry where, for instance, early delivery is being considered, and in assessing the severity of disease. It may also be used to guide interventional procedures such as intraperitoneal or intravascular transfusion.

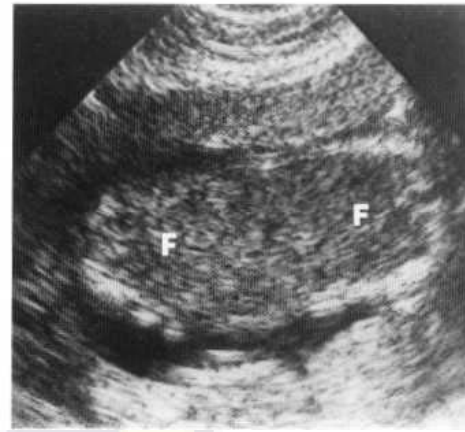


Fig. 33.64 Conjoined twins (F) joined at the chest and abdomen and sharing a common heart (thoraco-omphalopagus).

Twin pregnancies

Mortality and morbidity are significantly increased in twin gestations compared with singleton pregnancies. The degree to which these risks are raised is determined by the amnionicity and chorionicity of the fetuses. Dichorionic twins, each with their own placenta, are at the least risk. Monochorionic twins, sharing a placenta, have a higher risk of both growth retardation and death, while also being subject to specific syndromes (twin transfusion, twin embolisation, acardiac parabiotic and conjoined twins: Fig. 33.64).

A further problem seen with monochorionic monoamniotic twins is entanglement and knotting of the umbilical cords, which may lead to either sudden death of one or both fetuses in utero or vascular compromise during delivery.

In order to predict and anticipate potential problems later in pregnancy, much work has been directed to establishing the amnionicity and chorionicity of twin gestations (Filly et al 1990). The simplest and most reliable method is merely to count the number of gestational sacs (the echogenic 'ring' being comprised of chorion) early in the first trimester. One ring with two embryos equates to a monochorionic gestation, while two rings indicates dichorionicity (Fig. 33.65). Later in the second trimester differentiation is more difficult unless discrete placentas are identified or the fetuses are of differing sex. Studies have compared membrane thickness between the fetuses (thicker membranes indicating dichorionicity) and number of layers between fetuses (three or more indicating dichorionicity) but pitfalls and artefacts exist. A 'lambda sign' has been described with dichorionicity (Sepulveda 1997), although this is



Fig. 33.65 Twin pregnancy with a menstrual age of 8 weeks. Two sacs are seen, each surrounded by an echogenic ring of chorion and containing a live embryo. This is therefore a dichorionic gestation.

often not seen after 16 weeks gestation. In general, chorionicity can be established in a high proportion of pregnancies at less than 22 weeks gestation. To do so is important. If the twins are different in size, growth retardation of the smaller twin is likely with dichorionic twins, whereas with monochorionic twins a twin-twin transfusion syndrome is the most likely explanation.

Placenta

Demonstration and localisation of the placenta is an essential part of the routine obstetric examination. The placenta can generally be distinguished from surrounding portions of the chorion and the underlying myometrium from 12 weeks gestation onward.

Placenta praevia This occurs in 1 in 200 pregnancies at the time of delivery and may be subdivided into complete and partial forms. Although both cover the internal cervical os, the former shows attachments all around the placental margins, whereas the latter is only partially attached. When the lower margin of the placenta is within 2 cm of the internal cervical os it may be defined arbitrarily as low lying. False-positive diagnoses may result from:

- An overfilled bladder causing compression of the lower uterine segment and artefactual lengthening of the cervical canal
- Myometrial contractions, which can simulate placental tissue in an abnormally low location
- A low position early in pregnancy which may, by the third trimester, be entirely normal due to differential growth of the lower uterine segment.

Repeat scanning, either with an empty bladder or after an interval of 15-30 min, generally resolves the first two problems, while a further appointment for the mid-third trimester will demonstrate the

In cases where doubt persists, TVS should provide a definitive result, an approach recommended by the Royal College of Obstetricians and Gynaecologists (2001).

Predisposing factors include increasing maternal prior uterine operations and multiple pregnancies. Complications, apart from the painless haemorrhage that is characteristic of the condition, include premature delivery, intrauterine growth retardation and perinatal death.

Placental abruption patients with hypertension, vascular disease, trauma and drug abuse have a predisposition to premature separation of a normally positioned placenta. The location may be either retroplacental (Fig. 33.66A), resulting in high-pressure haemorrhage and high fetal mortality, or the more common marginal abruption (Fig. 33.66B), where lower pressure blood dissects beneath the placental membranes in a subchorionic plane and causes vaginal bleeding. Approximately 80% of subchorionic haematomas result in a normal term delivery, as compared with retroplacental haemorrhage where fetal mortality can be as high as 60%. The appearance of subchorionic haemorrhage (Fig. 33.67A) is quite distinct from that of separation of the amnion and chorion (Fig. 33.67B), which can be seen normally before 16 weeks and less commonly after that time.

Placental infarcts Systemic pathology within the mother, such as vascular disease or hypertension, can lead to uteroplacental insufficiency, the development of large hypoechoic placental infarcts (Fig. 33.68A) and a poor prognosis for the fetus

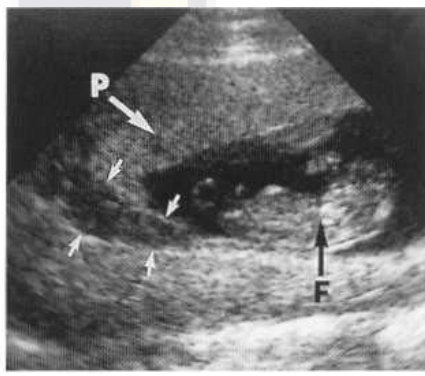
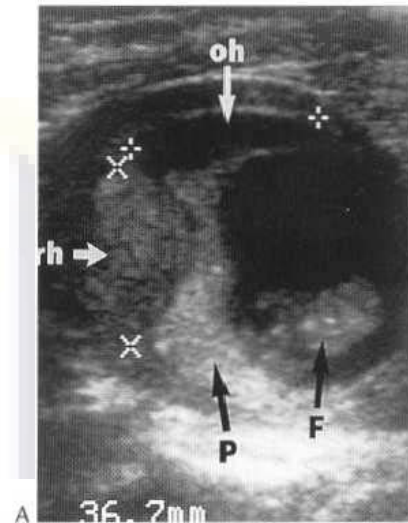


Fig. 33.66 F = fetus; P = placenta. (A) Haemorrhage in both a retroplacental (A) and marginal (B) location. Note yolk sac at caudal end of fetus.

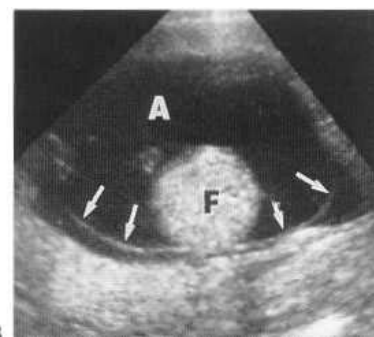
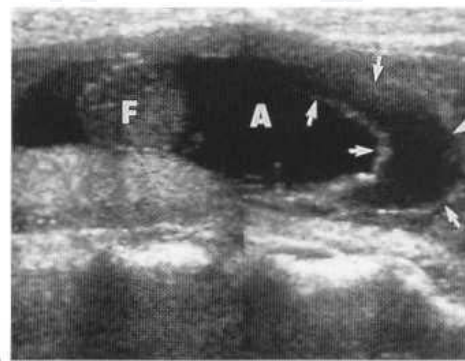


Fig. 33.67 F = fetus; A = amniotic fluid. (A) Subchorionic haemorrhage (arrows). (B) Amnion-chorion separation (arrows).

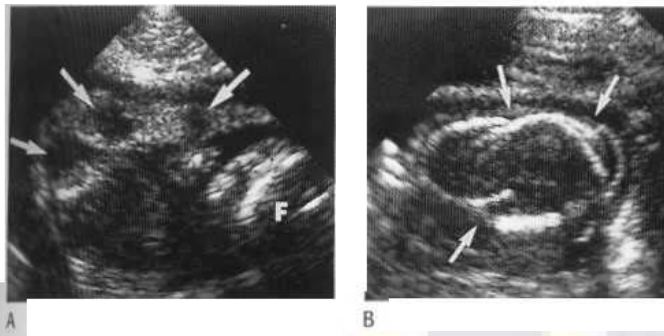


Fig. 33.68 (A) Multiple hypoechoic placental infarcts (arrows) in a patient with a systemic vasculitis. F = fetus. (B) Sonographic Spalding's sign following fetal death; same patient as in (A).



Fig. 33.69 Cervical fibroid (arrows) measuring 4 cm in length, longitudinal image. F = fetus; BL = bladder.

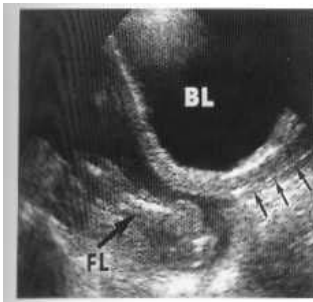


Fig. 33.70 Cervical incompetence. Longitudinal image showing cervical effacement. FL = fetal limbs; BL = bladder; arrows = vagina.

(Fig. 33.68B). The distinction between these and simple venous 'lakes' within the placenta rarely presents a problem. Small infarcts may be seen in up to 25% of normal placentas at term.

Cervix

Sonographic evaluation of the cervix is valuable, both to identify factors such as a large fibroid in the cervical canal (Fig. 33.69), which may influence the mode of delivery, and also for the assessment of cervical incompetence (Fig. 33.70). Not only can incompetence be demonstrated earlier than by clinical examination but serial measurements allow distinction between non-progressive shortening of the cervix and true progressive cases. It is also possible to check the placement of cerclage and monitor the success or failure of this technique.

Role of CT and MRI in obstetric practice

Pelvimetry This is more reliable and accurate in defining the margins of the bony pelvis than clinical examination. Although the improved information available from modern ultrasound has led to a decline in the use of pelvimetry, indications such as breech presentation or a suspected inadequate or deformed pelvis still exist. Conventional radiographic pelvimetry involves obtain-

ing anteroposterior and lateral radiographs of the pelvis together with numerical scales to allow for subsequent correction of inherent magnification errors. CT offers a more accurate method of pelvimetry, with the added advantage of a lower radiation dose to both mother and fetus. Anteroposterior and lateral 'scout' views are obtained, followed by a single axial section through the ischial spines. Standard measurements are then taken directly from the images using an electronic cursor. MRI provides similar accuracy, with the added advantage that ionising radiation is not involved.

Other uses CT has limited value in fetal evaluation. Administration of an intravenous radiographic contrast medium to the mother will cause enhancement of fetal kidneys and can rule out suspected renal agenesis, while contrast introduced into the amniotic fluid will allow subsequent imaging of the fetal bowel. The potential of MRI is greater, for imaging both the fetus and maternal pelvis. Applications range from the assessment of intrauterine growth retardation by the measurement of fetal body fat to the further investigation of suspected fetal anomalies not fully characterised by ultrasound. Faster scan times will reduce problems caused by fetal motion, and developments in spectroscopy may open new areas in the evaluation of metabolic processes. Many disadvantages remain, however, not the least of which are expense and resultant lack of availability. The flexibility, relative cheapness and effectiveness of obstetric ultrasound make it unlikely that there will be any significant switch to MRI in the foreseeable future.

Acknowledgments

The overall format of this chapter was adapted from Callen, *Ultrasonography in Obstetrics and Gynaecology*, 2nd edn, a text which covers the whole field in much greater depth.

Many of the illustrations were obtained while working on the Faculty of the University of Maryland School of Medicine in Baltimore. Particular thanks are due to Dr I. Kostrubiak, head of the department of ultrasound at that hospital, and also to Mrs J. Hindle, sonographer at Hope Hospital, Salford, who provided a number of the transvaginal images.

MRI IN OBSTETRICS

Jeremy P. R. Jenkins

The British National Radiological Protection Board (NRPB) recommend that, although there is no evidence to suggest that the fetus is sensitive to magnetic and radiofrequency (RF) fields at the levels encountered in MRI, it might be prudent to exclude pregnant women during the first 3 months of pregnancy, i.e. during rapid organogenesis. A similar recommendation has been given by the Food and Drugs Administration (FDA) in the USA. It should, however, be remembered that switching of gradients during the pulse sequence does introduce acoustic noise, which does raise concern on the developing ear (hearing develops after the 24th week of gestation). Women who will subsequently undergo abortion need not be excluded from examination.

In those women with cranial, spinal or neoplastic disease, and in whom CT or myelography is indicated, then MRI should be made available as the least invasive method of exclusion. Fetal and maternal anatomy can be displayed without the need for a distended

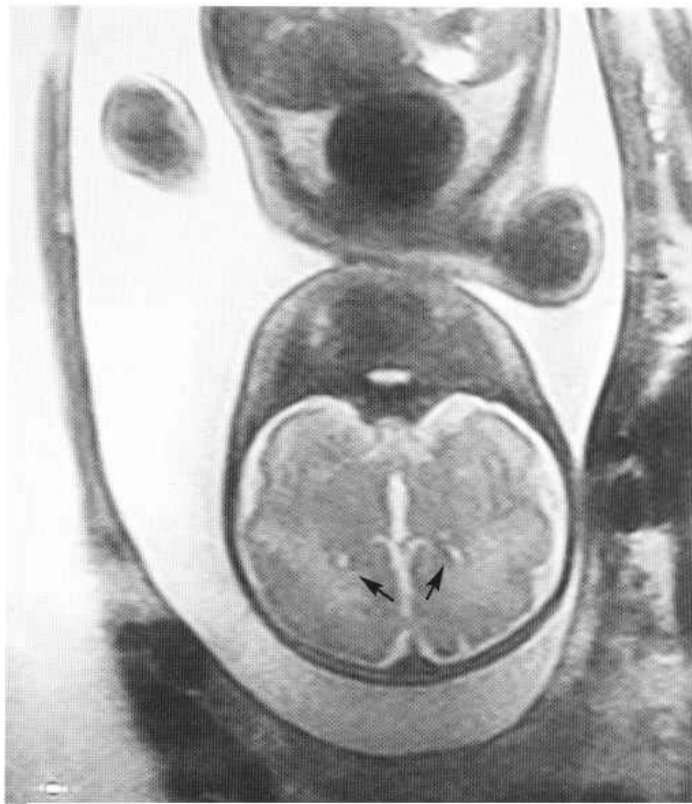
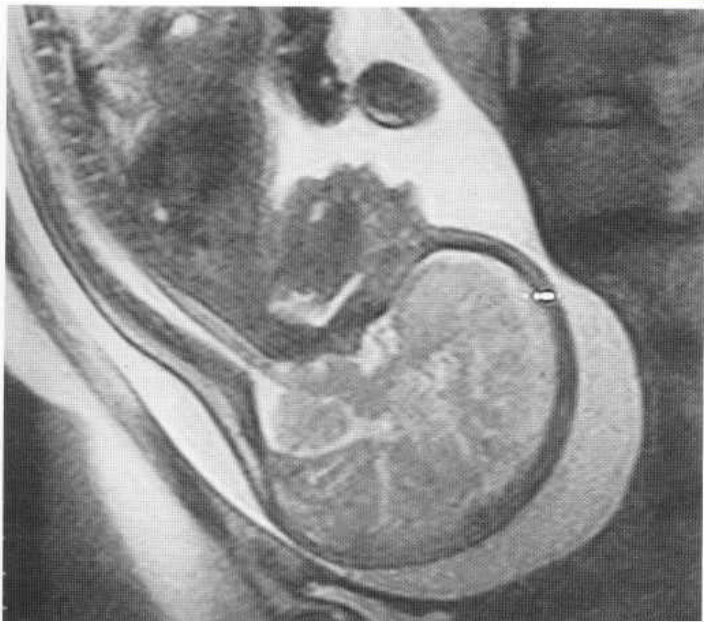


Fig. 33.71 Agenesis of the corpus callosum diagnosed in-utero using a single-shot fast spin echo sequence, on a 1.5T scanner, (A) sagittal and (B) coronal plane through the fetal head at 23 weeks gestation (the corpus callosum forms between 8 and 20 weeks gestation). The absent corpus callosum is arrowed in A. In B there is a high-riding third ventricle and crescentic lateral ventricles (arrowed) compressed by Probst bundles. (Courtesy of Professor Paul Griffiths, Sheffield)

bladder. Images are not affected by maternal bowel or adipose tissue or by the presence of oligohydramnios, which often degrades ultrasound scans. MRI can be of use in selected cases to identify suspected fetal abnormality, and is being increasingly used to clarify potential problems identified on ultrasound, and to confirm diagnosis. This is particularly relevant in the case of spinal and intracranial abnormalities, which can be more clearly defined on MRI (Fig. 33.71 A) than on ultrasound. Good fetal images can be obtained using rapid scanning techniques such as single-shot fast spin-echo or echo-planar sequences, which lessen the effect of fetal motion. Echo-planar sequences do have the advantage of lower RF values, with subsequent lower heating effect and power absorption.

MRI is safer than CT in the evaluation of patients with disease in the abdomen and pelvis and is preferable to contrast-enhanced CT in pregnant patients with suspected liver metastases. MRI can be used as an adjunct to ultrasound in separating a mass from the pregnant uterus and in the characterisation of pelvic masses. Cervical, uterine and ovarian masses can be differentiated.

Both T₁- and T₂-weighted images are required in order to identify and distinguish between fat, fluid and haemorrhage. Haemorrhage has a high signal on both T₁- and T₂-weighted scans, whereas fat, e.g. in a dermoid, has a high signal on T₁-weighted scans and an intermediate signal on T₂ weighted images. Ectopic pregnancy can be diagnosed with the uterus delineated as a separate mass.

The placenta can be demonstrated on MRI early in pregnancy as a low-intermediate signal and high signal on T₁- and T₂-weighted images, respectively. In the evaluation of placenta praevia the posi-

tion of the placenta in relation to the internal cervical os can be accurately measured. Haemorrhage between the placenta and uterine wall in an abruptio placentae can be depicted.

Gadolinium-DTPA has a molecular weight of 938 and does cross the placenta. It should only be administered to pregnant women in whom the possible benefits justify the potential risk to the fetus.

REFERENCES AND SUGGESTIONS FOR FURTHER READING

Indications

- Consensus Conference (1984) The use of diagnostic ultrasound imaging during pregnancy. *JAMA*, 252, 669-672.
- Leopold, G. R. (1986) Antepartum obstetrical ultrasound examination guidelines. *Journal of Ultrasound in Medicine*, 5, 241-242.
- Report of the Royal College of Obstetricians and Gynaecologists Working Party on Routine Ultrasound Examination in Pregnancy, December 1984. London: RCOG.
- US Department of Health and Human Services, Public Health Service (1984) *The Use of Diagnostic Ultrasound Imaging in Pregnancy*, NIH Publication No. 84-667. Washington, DC: National Institute of Health.

Techniques

- Johnson, D. D., Pretorius, D. H., Budorick, N. F., et al (2000) Fetal lip and primary palate: three dimensional versus two dimensional ultrasound. *Radiology*, 217, 236-239.
- Lees, W. R. (2001) Ultrasound imaging in three and four dimensions. *Seminars in Ultrasound, CT and MR*, 22, 85-105.
- Treadwell, M. C., Seubert, D. E., Zador, I., et al (2000) Benefits associated with harmonic tissue imaging in the obstetric patient. *American Journal of Obstetrics and Gynecology*, 182, 1620-1622.

Fetal age

- Defer, R. L. (1986) Determining fetal age with ultrasound. *The Female Patient*, 11, 100.
- Hadlock, F. P., Deter, R. L., Harrist, R. B., Park, S. K. (1984) Estimating fetal age: computer assisted analysis of multiple fetal growth parameters. *Radiology*, 152, 497-501.

Early pregnancy

- Bnmtlcy, B., Harlow, B. L., Laboda, L. A., Benacerraf, B. R. (1991) Small sac size in the first trimester: a predictor of poor fetal outcome. *Radiology*, 178, 375-377.
- Horrow, M. M. (1992) Enlarged amniotic cavity: a new sign of early embryonic demise. *American Journal of Roentgenology*, 158, 359-362.
- Levi, C. S., Lyons, E. A., Lindsay, D. J. (1988) Early diagnosis of nonviable pregnancy with endovaginal ultrasound. *Radiology*, 167, 383-385.
- Lindsay, D. J., Lovett, I. S., Lyons, E. A., et al (1992) Yolk sac diameter and shape at endovaginal US: predictors of pregnancy outcome in the first trimester. *Radiology*, 183, 115-118.
- Nyberg, D. A., Laing, F. C., Filly, R. A. (1986) Threatened abortion: sonographic distinction of normal and abnormal gestational sacs. *Radiology*, 158, 397-400.
- Nyberg, D. A., Mack, L. A., Laing, F. C., Patten, R. M. (1987a) Distinguishing normal from abnormal gestational sac growth in early pregnancy. *Journal of Ultrasound in Medicine*, 6, 23-27.
- Standing Joint Committee of the Royal Colleges of Radiologists and Obstetricians and Gynaecologists, *Guidance on Ultrasound Procedures in Early Pregnancy*, September 1995. London: RCR/RCOG.

Fetal growth

- Benson, C. B., Belville, J. S., Lentini, J. F., et al (1990) Intrauterine growth retardation: diagnosis based on multiple parameters - a prospective study. *Radiology*, 177, 499-502.
- Carroll, B. A. (1990) Duplex Doppler systems in obstetric ultrasound. *Radiologic Clinics of North America*, 28, 189-203.
- Douhilet, P. M., Benson, C. B. (1995) Sonographic evaluation of intrauterine growth retardation. *American Journal of Roentgenology*, 164, 709-717.
- Rochelson, B., Schulman, H., Farniakides, G., et al (1987) The significance of absent end-diastolic flow in umbilical artery velocity waveforms. *American Journal of Obstetrics and Gynecology*, 156, 1213-1218.

Ectopic pregnancy

- Filly, R. A. (1987) Ectopic pregnancy: the role of sonography. *Radiology*, 162, 661-668.
- Frutes, M. C., Laing, F. C. (1995) Sonographic evaluation of ectopic pregnancy: an update. *American Journal of Roentgenology*, 165, 251-259.
- Nyberg, D. A., Laing, F. C., Filly, R. A., et al (1983) Ultrasonographic differentiation of the gestational sac of early intrauterine pregnancy from the pseudo gestational sac of ectopic pregnancy. *Radiology*, 146, 755.
- Nyberg, D. A., Laing, F. C., Filly, R. A., et al (1987b) Ectopic pregnancy: diagnosis by sonography correlated with quantitative hCG levels. *Journal of Ultrasound in Medicine*, 6, 145-147.
- Stovall, T. G., Ling, F. W., Gray, L. A., et al (1991) Methotrexate treatment of unruptured ectopic pregnancy: a report of 100 cases. *Obstetrics and Gynecology*, 77, 749-753.

Genetic screening

- Anderson, R. L., Goldberg, J. D., Golbus, M. S. (1986) Findings at sonography in evaluation of elevated amniotic fluid alpha-fetoprotein. *Proceedings of the 7th International Congress of Human Genetics, Berlin*.
- Benacerraf, B. R. (1993) Should patients with elevated levels of maternal serum alpha fetoprotein always undergo amniocentesis? *Radiology*, 188, 17-18.
- Benacerraf, B. R., Frigoletto, F. D., Cramer, D. W. (1987) Down's syndrome: sonographic sign for diagnosis in the second trimester fetus. *Radiology*, 163, 811-813.
- Callen, P. W. (1988) *Ultrasonography in Obstetrics and Gynaecology*, 2nd edn, p. 11. Philadelphia: W. B. Saunders.
- Chitty, L. (1998) Prenatal screening for chromosomal abnormalities. *British Medical Bulletin*, 54, 839-856.
- Filly, R. A., Callen, P. W., Goldstein, R. (1993) Alpha fetoprotein screening programs: what every obstetric sonologist should know. *Radiology*, 188, 1-9.

- Nicolaidcs, K. H., Azar, G., Byrne, D., et al (1992) Fetal nuchal translucency: ultrasound screening for chromosomal defects in the first trimester of pregnancy. *BMJ*, 304, 867-869.
- Twining, P., Whalley, D. R., Lewin, E., et al (1991) Is a short femur length a useful marker for Down's syndrome? *British Journal of Radiology*, 64, 990-992.
- Whitlow, B., Azanakis, M. S., Economides, D. L. (1999) The sonographic identification of fetal gender from 11 to 14 weeks of gestation. *Ultrasound in Obstetrics and Gynecology*, 13, 301-304.

Fetal CNS

- Cardoza, J. D., Goldstein, R. B., Filly, R. A. (1988) Exclusion of fetal ventriculomegaly with a single measurement: the width of the lateral ventricular atrium. *Radiology*, 169, 711-714.
- Filly, R. A. (1988) The 'lemon' sign: a clinical perspective. *Radiology*, 167, 573-575.
- Filly, R. A., Goldstein, R. B., Callen, P. W. (1991) Fetal ventricle: importance in routine obstetric sonography. *Radiology*, 181, 1-7.
- Nicolaidcs, K. H., Campbell, S., Gabbc, S. G., Guidetti, R. (1986) Ultrasound screening for spina bifida: cranial and cerebellar signs. *Lancet*, ii, 72-74.
- Nyberg, D. A., Mack, L. A., Hirsch, J., Pagon, R., Shepard, T. H. (1987c) Fetal hydrocephalus: sonographic detection and clinical significance of associated anomalies. *Radiology*, 163, 187-191.

Fetal neck and thorax

- Abramowicz, J. S., Warsof, S. L., Doyle, D. L., et al (1989) Congenital cystic hygroma of the neck diagnosed prenatally: outcome with normal and abnormal karyotype. *Prenatal Diagnosis*, 9, 321-327.
- Allen, L. D. (1986) *Manual of Fetal Echocardiography*, pp. 13-47, 74-139. Lancaster: MTP Press.
- Hyett, J., Perdu, M., Sharland, G., et al (1999) Using fetal nuchal translucency to screen for major congenital cardiac defects at 10-14 weeks of gestation: population based cohort study. *BMJ*, 318, 81-85.
- McGahan, J. P. (1991) Sonography of the fetal heart: findings on the four chamber view. *American Journal of Roentgenology*, 156, 547-553.
- Romero, R., Pilu, G., Jeanty, P., Ghidini, A., Hobbins, J. C. (1988) *Prenatal Diagnosis of Congenital Anomalies*, pp. 125-197. New York: Appleton & Lange.

Fetal GI tract

- Bail, J. H., Russ, P. D., Prctorius, D. H., Manchester, D., Manco-Johnson, M. L. (1986) Fetal omphalocele and gastroschisis: a review of 24 cases. *American Journal of Roentgenology*, 147, 1047-1051.
- Eslroff, J. A., Parad, R. B., Benacerraf, B. R. (1992) Prevalence of cystic fibrosis in fetuses with dilated bowel. *Radiology*, 183, 677-680.
- hertzberg, B. S. (1994) Sonography of the fetal gastrointestinal tract: anatomic variants, diagnostic pitfalls, and abnormalities. *American Journal of Roentgenology*, 162, 1175-1182.
- Nyberg, D. A., Mack, L. A., Patten, R. M., Cyr, D. R. (1987d) Fetal bowel: normal sonographic findings. *Journal of Ultrasound in Medicine*, 6, 3-6.

The genitourinary system

- Grignon, A., Filion, R., Filiatrault, D., et al (1986) Urinary tract dilatation in utero: classification and clinical applications. *Radiology*, 160, 645-647.
- Mahony, B. S., Callen, P. W., Filly, R. A. (1985) Fetal urethral obstruction: US evaluation. *Radiology*, 157, 221-224.
- Romero, R., Pilu, G., Jeanty, P., Ghidini, A., Hobbins, J. C. (1988) *Prenatal Diagnosis of Congenital Anomalies*, pp. 259-277. New York: Appleton & Lange.

Musculoskeletal system

- Bowerman, R. A. (1995) Anomalies of the fetal skeleton: sonographic findings. *American Journal of Roentgenology*, 164, 973-979.
- Nelson, T. R., Prctorius, D. H. (1995) Visualization of the fetal thoracic skeleton with three-dimensional sonography: a preliminary report. *American Journal of Roentgenology*, 164, 1485-1488.
- Romero, R., Athanassiadis, A. P., Jeanty, P. (1990) Fetal skeletal anomalies. *Radiologic Clinics of North America*, 28, 75-99.

Hydrops fetalis

- Holzgreve, W., Holzgreve, B., Cury, J. R. (1985) Non-immune hydrops fetalis: diagnosis and management. *Seminars in Perinatology*, 9, 52.

Twin pregnancies

Filly, R. A., Goldstein, K. B., Callen, P. W. (1990) Monochorionic twinning: sonographic assessment. *American Journal of Roentgenology*, 154, 459-469.

Sepulveda, W., Schire, N., Hughes, K., et al. (1997) Evolution of the lambda or twin-chorionic peak sign in dichorionic twirl pregnancies. *Obstetrics and Gynecology*, 89, 439-441.

Placenta

Hertzberg, B. S., Bowie, J. D., Carroll, B. A., et al (1992) Diagnosis of placenta previa during the third trimester: role of transperineal sonography. *American Journal of Roentgenology*, 159, 83-87.

Royal College of Obstetricians and Gynaecologists (2001) *Placenta Praevia: Diagnosis and Management*, Guideline No. 27. London: RCOG.

MRI

Levine, D. (ed.) (2001) Fetal Magnetic Resonance Imaging. In: *Topics in Magnetic Resonance Imaging*, 12, 1-79.

نشر الکترونیکی
موسسه انتشاراتی
نوردانش

34

GYNAECOLOGICAL IMAGING

Mary Crofton

with a contribution from Jeremy P. R. Jenkins

ULTRASOUND

Ultrasound, either transabdominal or endovaginal, is the mainstay of imaging of the pelvis.

Transabdominal ultrasound (TAS) is usually performed with a 3-4 MHz sector or convex probe and requires the patient to have a full bladder. The distended bladder displaces small bowel out of the pelvis, pushes the uterus posteriorly and the ovaries laterally towards the pelvic side walls. The optimally distended bladder projects just beyond the fundus of a normal sized uterus. If the bladder is inadequately distended the pelvic structures may be obscured by bowel gas, but if overdistended the uterus becomes elongated and the ovaries displaced too far laterally. Longitudinal (sagittal) and transverse scans are performed using the bladder as a window. Endovaginal scanning (EVS) is best performed with an empty bladder and utilises a higher frequency sector/curvilinear probe (typically 5-7 MHz) giving improved resolution of structures

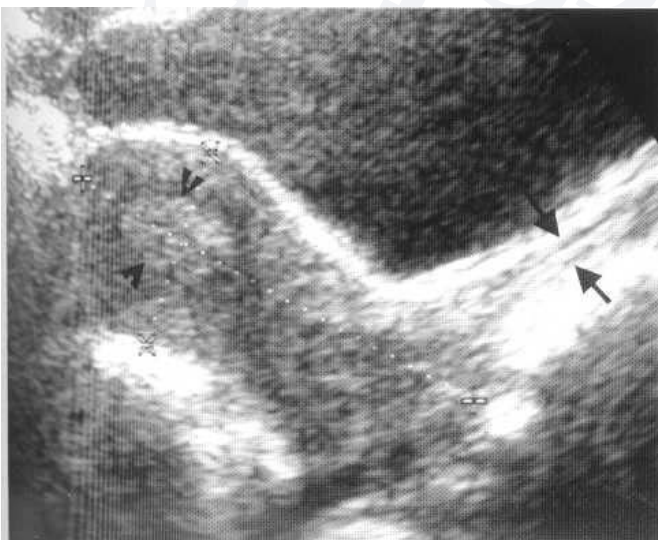


Fig. 34.1 Sagittal transabdominal scan (TAS) showing measurement of uterine size (white crosses) and a moderately thick luteal phase endometrium (arrowheads). Arrows indicate vaginal walls.

close to the probe but a limited field of view. Whereas many patients prefer endovaginal scanning, it is inappropriate in the very young, the very elderly and any patient who is virgo intacta. It is therefore important to be able to perform both types of scan with confidence.

Ultrasound anatomy of the pelvis

The pelvic side-walls are lined by iliacus and psoas muscles. Iliacus arises from the iliac wings and descends posterolateral to psoas into the pelvis. The two muscles run obliquely, passing posterior to the inguinal ligament to form a joint tendon that inserts onto the greater trochanter. These muscles are visualised on ultrasound as paired hypoechoic striated structures, separated by an echogenic fascial plane. The iliac vessels lie on psoas and can be used to define the normal position of the ovaries.

Vagina (Fig. 34.1) The vagina is visualised abdominally as two linear hypoechoic muscular walls around an echogenic mucosa. It is usually empty but may contain fluid or blood during menstruation or after bathing. A vaginal tampon can be visualised as a highly reflective structure with a strong acoustic shadow, often causing displacement of the cervix or bladder base (Fig. 34.2).

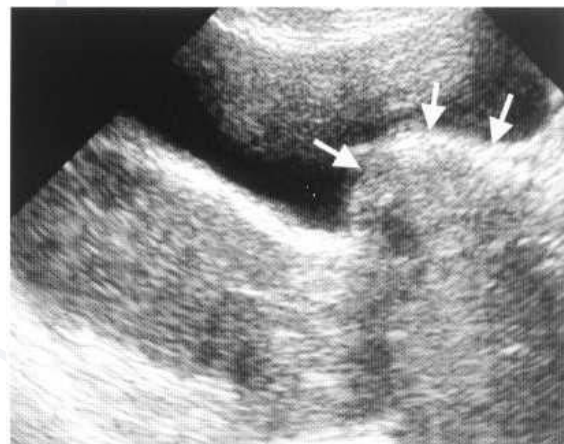


Fig. 34.2 Sagittal TAS. Deformity of the bladder base and acoustic shadowing due to a vaginal tampon (arrows).

The configuration of most endovaginal probes (end-firing and sector) limits their value in examining the vagina, although some visualisation is obtained by slowly withdrawing the probe and examining the vaginal walls as they collapse around the end of the probe. This technique can also be quite effective in examining the female urethra.

Cervix and uterus (Fig. 34.1) The uterus is a pear-shaped structure, which varies in size according to the age and hormonal status of the patient. Before puberty the cervix is large and the body of the uterus small, but following the menarche the uterine body increases in size to an overall length of 7-8 cm. Following the menopause the uterus and cervix slowly involute to 5-6 cm.

The uterus is variable in position and may lie straight or obliquely within the pelvis. The degree of anteversion or retroversion is of little consequence to the patient—indeed it changes in some patients with the degree of bladder filling. A retroverted, retroflexed uterus can be difficult to visualise with abdominal scanning but is easily seen with an endovaginal scan.

It should be possible to see the endometrium throughout the uterus and the endocervical canal. The endometrial thickness is conventionally measured as a double layer (Fig. 34.3). The deeper hypoechoic layer has been shown to represent the most superficial layer of myometrium and is not included in the endometrial measurement.

The uterus should have a homogeneous poorly reflective echotexture. Small blood vessels (arcuate veins and arteries) are frequently visible running around the periphery of the body and extending into the broad ligament. Prominent dilated veins in the broad ligament, extending into the uterus and around the cervix, are a feature of *pelvic congestion syndrome*. These veins are typically large (6 mm) and have very slow flow within them. Some patients with dilated veins (or varices) have a history of pelvic pain; however, many are completely asymptomatic so there is debate about their significance. Arterial calcification is seen in the elderly and those with diabetes or chronic renal failure. Tiny flecks of calcification at the endometrial-myometrial interface are occasionally seen following pregnancy (Fig. 34.4). These are usually of no significance but similar appearances can be caused by intrauterine adhesions. Small retention cysts (nabothian follicles) are also normally seen along the endocervical canal.



Fig. 34.3 Endovaginal scan (EVS). Measurement of the endometrium (black arrows). Note there are five layers included in the measurement but the deeper hypoechoic layer (white arrows) is not included. The central echogenic line (black arrowhead) is due to the interface of the two layers of endometrium.

Suspensory ligaments and fallopian tubes The uterus is suspended in the pelvis by the uterosacral and round ligaments. The uterosacral ligaments run posteriorly to the anterior surface of the sacrum and the round ligaments run laterally towards the inguinal canal. The round ligaments are invested in a double layer of peritoneum, known as the broad ligament. The fallopian tubes run in the broad ligament towards the ovary. Normally the suspensory ligaments and fallopian tubes cannot be visualised on ultrasound; however, they may be visualised in the presence of ascites or when a hydrosalpinx develops.

Ovaries (Fig. 34.5, 34.6) The ovaries are oval structures, usually closely related to the iliac vessels on the pelvic side-wall. They are less echogenic than the uterus and may contain a variable number of small cysts/follicles. Ovarian size varies according to the age and hormonal status of the patient. Less than 7.5 ml is considered normal in menstruating women but in postmenopausal women the volume should be less than 3 ml.

The ovarian volume is calculated using the formula for a prolate ellipse, i.e. $0.5 \text{ (length} \times \text{depth} \times \text{breadth)}$.

The position of the ovaries varies. They may be deep in the pouch of Douglas or high up on the pelvic side-wall. If the ovaries are not seen in the expected position it is therefore important to



Fig. 34.4 EVS. Small flecks of calcification (arrows) at the myometrial endometrial interface representing tiny insignificant fragments of retained placenta following pregnancy.



Fig. 34.5 EVS. Normal quiescent ovary lying on the iliac vessels.

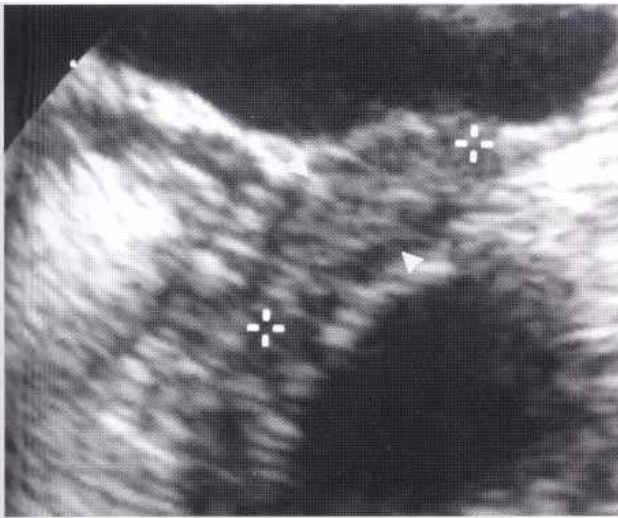


Fig. 34.6 EUS. Atrophic postmenopausal ovary (arrowheads).

continue scanning above the level of the distended bladder. In thin patients this may require scanning with a high-frequency linear probe. This is particularly true following Wertheim's hysterectomy if the surgeon moves the ovaries out of the pelvis (to avoid any subsequent radiation field and to help prevent dyspareunia). Ovaries can be seen in over 90% of normal menstruating women and approximately 60% of postmenopausal women, depending on age.

Doppler ultrasound The uterine arteries arise from the internal iliac arteries and ascend from the cervix in the broad ligament alongside the lateral surface of the uterine body. The main uterine arteries and their intrauterine branches can be seen with colour Doppler and spectral Doppler used to obtain waveforms from these vessels (Fig. 34.7). Similarly ovarian perfusion can be assessed. The ovaries obtain blood via the uterine arteries and also directly from the aorta. Flow in the uterine branches can usually be seen in the broad ligament superior to the uterus. Visualisation of intraovarian vessels depends on ovarian activity. The most commonly used indices to assess perfusion are the resistive index (RI) and the pulsatility index (PI).

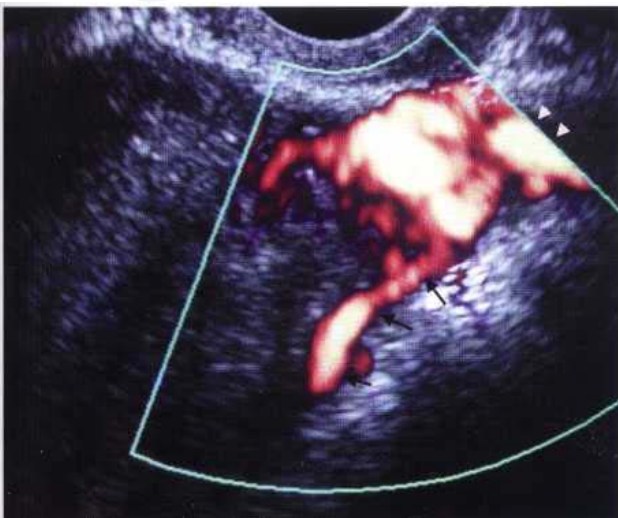


Fig. 34.7 EUS. Power Doppler showing uterine artery (arrows) running alongside the uterine body.



Fig. 34.8 EUS. Dominant follicle (arrows) developing in a normal ovary.



Fig. 34.9 EUS. Clot retraction within a normal corpus luteum (arrows). The angular margins and lack of blood flow within the solid triangular area confirm this is clot rather than a solid nodule.

The menstrual cycle (Figs 34.8-34.11)

Before puberty the uterine body is small, with a relatively large cervix and thin, barely visible endometrium. The ovaries are also small, with few or no cysts or follicles. At puberty the uterus changes in shape and several small cysts/follicles measuring 5-8 mm appear in the ovaries. These appearances are associated with low levels of circulating oestrogens and frequent anovulatory cycles typical of the menarche.

Once menstruation is established, regular cyclical changes occur in the appearance of the ovaries and uterus, reflecting the associated hormonal changes.

The *follicular phase* begins on day I of the menstrual cycle with the development of a small number of follicles. The endometrium is a thin echogenic line. From day 8-10 one follicle becomes dominant and continues growing at a rate of 2-3 mm/day, while the other follicles regress. This is accompanied by an increase in thickness and change in appearance of the endometrium to a five-layer appearance typical of midcycle (Fig. 34.3). About day 14, when the follicle measures 18-25 mm, ovulation occurs. *Ovulation* is indicated in 90% of cycles by disappearance of the follicle and escape of fluid around the ovary or into the pouch of Douglas. Other indicators of ovulation include a decrease in size, change in shape and the presence of internal echoes within the follicle.

The *luteal phase* commences following ovulation and lasts 14 days, unless pregnancy supervenes. The endometrium loses its multilayer appearance and becomes progressively more echogenic

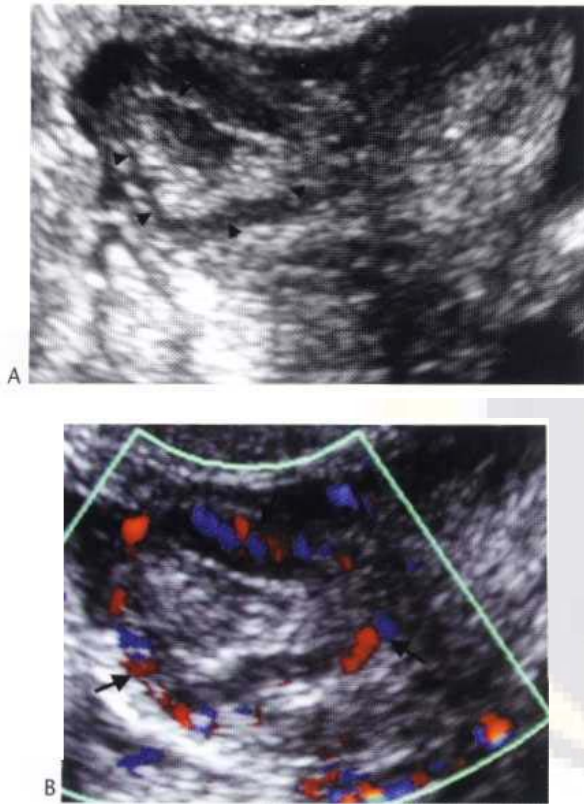


Fig. 34.10 (A) EVS. Irregularly shaped echogenic cyst (arrowheads) due to a collapsing corpus luteum. (B) Colour Doppler. Flow around the corpus luteum (arrows) due to neovascularisation.

(Fig. 34.1), with a normal thickness of 12-14 mm immediately prior to menstruation. The developing corpus luteum can be detected as an irregular cyst containing internal echoes due to blood or a hypoechoic area. Occasionally a well-defined luteal cyst develops and slowly increases in size to 25-40 mm. They usually resolve spontaneously over the next few months but can cause symptoms if they are large or undergo a complication such as haemorrhage, torsion or rupture.

Doppler studies During menstruation and the early follicular phase there is relatively high impedance flow in the ovary, i.e. the RI is approximately 0.7. Following ovulation and neovascularisation of the corpus luteum, diastolic flow increases, leading to lower impedance flow and typical values of less than 0.6 for the RI.

Menopause The menopause is characterised by involution of the uterus and ovaries over a period of about 5 years. Normal ovarian volume in postmenopausal women is less than 3 ml and normal endometrial thickness equal to or less than 4 mm. Doppler indices

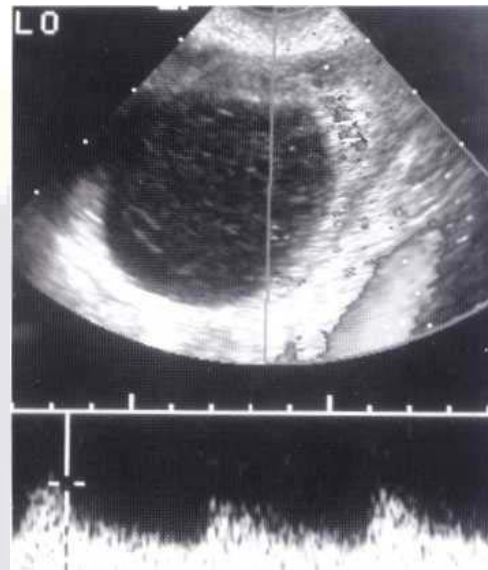


Fig. 34.11 Corpus luteum. Spectral Doppler shows low impedance flow with RI of 0.57.

in the postmenopausal patient are those of an inactive ovary, i.e. high impedance flow, such as is seen in the early follicular phase.

Ovulation disorders and ovarian morphology (Table 34.1)

Approximately 20% of menstruating women have *polycystic ovaries* (Figs 34.12, 34.13). This is an inherited condition with a wide spectrum of clinical features, ranging from the rare Stein-Leventhal syndrome, comprising amenorrhoea, obesity and hirsutism, to patients without any obvious symptoms. Many, but not all, patients have measurable hormonal abnormalities, the commonest of which is a raised LH:FSH ratio, thought to be responsible for excess androgen production by the ovaries. Clinical features of polycystic ovaries include:

- Oligomenorrhoea and other menstrual disorders including dysmenorrhoea and menorrhagia
- Hirsutism-90% hirsute patients have polycystic ovaries
- Acne
- Infertility (the commonest cause of anovulatory infertility)
- Recurrent miscarriage
- Obesity due to insulin resistance and impaired glucose tolerance
- Endometrial hyperplasia (and rarely endometrial carcinoma).

Multifollicular ovaries (Fig. 34.14) represent a reversion to the ovarian morphology seen at the menarche. They are a feature of low

Table 34.1 Distinguishing features of ovaries causing ovulation disorders

<i>Polycystic ovaries</i>	<i>Multifollicular ovaries</i>	<i>Primary ovarian failure</i>
Large; volume >7.5 ml	Normal size	Small
More than seven 2-5 mm follicles; mainly peripheral distribution	Several follicles of 5-10 mm	No evidence of follicular activity
Increased stroma	No increased stroma	No increased stroma
Large/normal uterus with thick endometrium	Normal/small uterus with thin endometrium	Small uterus with thin endometrium



Fig. 34.12 EVS. polycystic ovary with peripheral cysts.



Fig. 34.13 TAS. Polycystic ovary. Central and peripheral cysts.

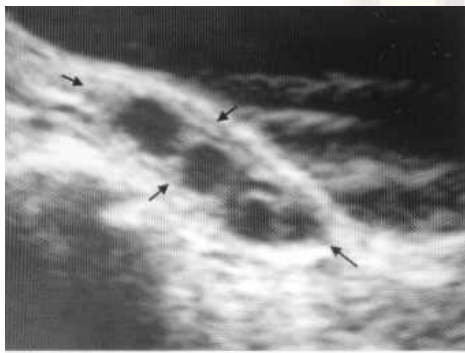


Fig. 34.14 TAS. Multifollicular ovary (arrows) in a patient with amenorrhoea due to anorexia nervosa.

levels of circulating oestrogens and are seen in athletes and in association with weight loss and anorexia nervosa.

Primary ovarian insufficiency or premature menopause is the onset of the menopause before the age of 35 years and is a rare cause of amenorrhoea.

Effect of hormones

Combined oral contraceptive pill The uterus and ovaries are suppressed. The endometrium should be thin and the ovaries small with no evidence of follicular activity.

Progesterone-only pill The progesterone-only pill does not necessarily inhibit follicular activity but the uterus should look small, with a thin endometrium.

Hormone replacement therapy (HRT) The effect of HRT on the uterus and ovaries depends on the type of HRT taken.

Unopposed oestrogen administration causes thickening of the endometrium due to endometrial hyperplasia. This is a precursor to endometrial carcinoma, therefore unopposed oestrogen regimens are only recommended if the patient has had a hysterectomy.



Fig. 34.15 TAS. Thickened irregular endometrium (arrows) due to tamoxifen. Note the small cysts (arrowheads) at the myometrial endometrial interface.

Sequential HRT i.e. oestrogens followed by progestones for at least 12 days/month, are usually prescribed for perimenopausal and early postmenopausal patients who have persistent but unpredictable ovarian function. Most patients have regular monthly bleeds on such a regimen so should have an endometrium that varies in thickness during the cycle. The maximum thickness should still be less than 8 mm. Any patient found to have a mildly thickened endometrium on sequential HRT should have a repeat scan following a withdrawal bleed.

Continuous combined hormone replacement involves taking oestrogen and progesterone together continuously and should result in endometrial atrophy within 6 months, i.e. endometrial thickness less than 4 mm.

Tamoxifen Tamoxifen, used in the treatment of breast cancer, has both antioestrogenic and oestrogenic effects and is associated with endometrial hyperplasia, an increased incidence of polyps and endometrial carcinoma. The uterus has a characteristic appearance with increased thickness of the cavity echo with multiple tiny cysts (Fig. 34.15). These cysts were originally thought to be part of the endometrium but recently it has been suggested that they are actually in the most superficial layer of the myometrium rather than the endometrium. Doppler studies in patients with endometrial thickening due to tamoxifen show low impedance flow, i.e. low values for the RI and PI.

Value of ultrasound screening for patients on HRT Routine screening is not indicated for patients on HRT but should be performed in those with abnormal vaginal bleeding.

Intrauterine contraceptive devices (IUCDs)

Conventional IUCDs An IUCD is a common incidental finding in patients undergoing pelvic ultrasound. They are easily visualised as highly echogenic structures with acoustic shadowing and should be entirely within the uterine cavity, not protruding into the myometrium or endocervical canal (Fig. 34.16). Large fibroids, particularly if calcified, can occasionally cause difficulty. Expulsion during menstruation does occur but most patients referred with 'missing coil' will have the IUCD present normally in the cavity, the threads having retracted into the cervical canal. Complications such as migration of the coil into or through the

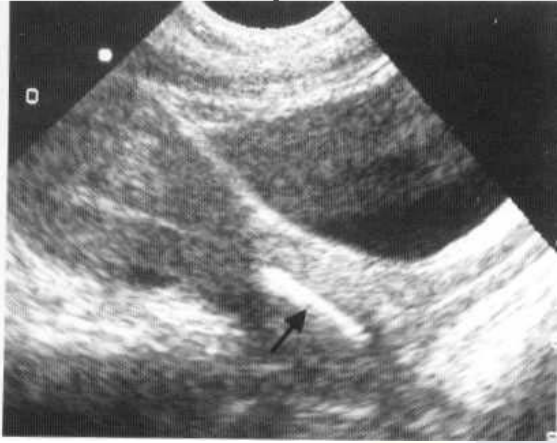
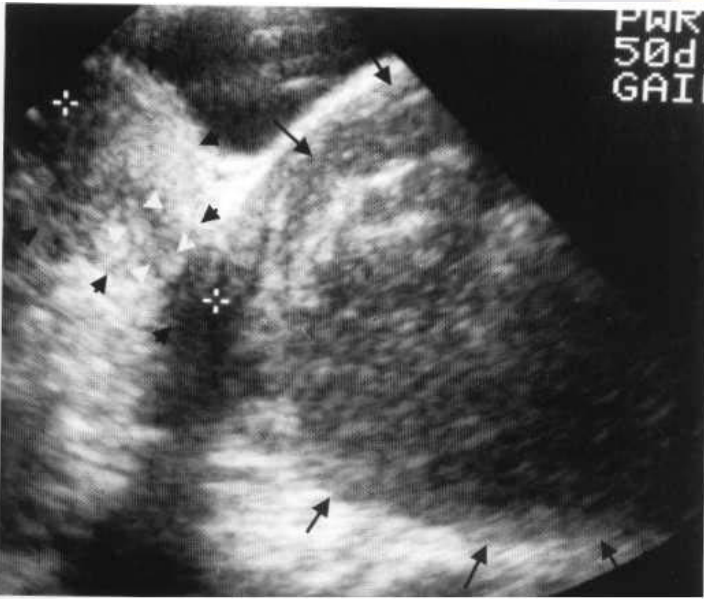


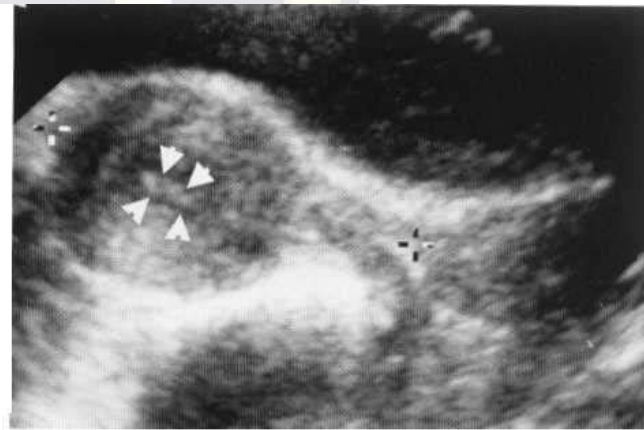
Fig. 34.16 TAS. IUCD (arrow) in the cervical canal.



Fig. 34.17 TAS. IUCD embedded in the myometrium (arrow), well outside the cavity (arrowheads).



A



B



C



D

Fig. 34.18 6-year-old girl with cyclical abdominal pain found to have a didelphys uterus with a complete vaginal septum and imperforate hymen on the left. (A) Longitudinal scan demonstrates a large heterogeneous mass (arrows) due to blood-filled distended vagina. A small uterus and cervix (arrowheads) can be seen at the upper margin of the mass. (B) Longitudinal scan to the right of (A) shows a further uterus (arrowheads mark the position of the endometrium). The normal right vagina is compressed and hence not visible. (C) Transverse scan confirming two uterine bodies. (D) Intravenous urogram. Solitary but duplex kidney on the left.

myometrium usually occur at the time of insertion and are associated with pain (Fig. 34.17). It is rarely possible to see an IUCD outside the uterus on ultrasound, so if there is doubt about the presence of an IUCD on the ultrasound a plain abdominal X-ray should be performed to exclude uterine perforation. Ultrasound is also indicated to look for causes of difficulty inserting a coil, e.g. large fibroid distorting the cavity or a severely retroflexed uterus.

The IUCD is associated with an increased incidence of pelvic infection. In particular colonisation with Actinomyces may occur with long-term use and may well be asymptomatic.

Mirena coil The Mirena IUCD contains progestogens and is used for both contraception and to treat dysfunctional uterine bleeding. Although similar in shape to most other coils, the Mirena coil is less echogenic than standard IUCDs and hence is harder to visualise on ultrasound, even when this is performed endovaginally. It is often seen by virtue of its acoustic shadow rather than direct visualisation of the coil itself.

Congenital uterine abnormalities

Minor duplication abnormalities of the uterus are only of relevance in the investigation of subfertility and recurrent miscarriage and are discussed in more detail in the section on hysterosalpingography. However, severe duplication anomalies with obstructed menstruation present in adolescence and early adulthood. Typical presenting symptoms are primary amenorrhoea, cyclical abdominal pain, pelvic mass and severe dysmenorrhoea. Ultrasound reveals a thick-walled cystic mass, owing either to an obstructed vagina (imperforate hymen) or an obstructed uterus (haematometrium), with

usually be reached if the possibility is considered and care taken to look for accessory pelvic organs. The examination must also include visualisation of the urinary tract as there is a high incidence of associated single kidneys (Fig. 34.18).

A non-obstructed double uterus (uterus didelphys) may simulate a solid adnexal mass on pelvic examination but can be differentiated on ultrasound due to the presence of a central endometrial echo (Fig. 34.19). The shape of the endometrial echo, particularly on a transverse scan, can also help diagnose the less severe duplication anomalies (Fig. 34.20). Differentiation of a septate uterus depends on identification of a fundal notch and requires visualisation of the uterus en face. This can be difficult with conventional ultrasound but is more easily achieved with 3D ultrasound.

Recognition of a unicornuate uterus is also difficult on ultrasound but can be inferred by its small size and abnormal lateral position.

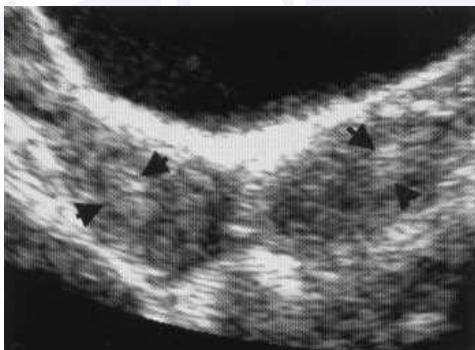


Fig. 34.19 TAS. Two separate uterine horns indicative of bicornuate uterus. Arrowheads indicate position of endometrium.



Fig. 34.20 EVS. Two endometrial echoes (arrows) within the uterus, suggestive of a uterine septum.

Uterine fibroids (leiomyomas)

Fibroids are present in up to 20-50% of women. They are particularly common and present at a younger age in black women. Although frequently asymptomatic, they may present with abnormal bleeding, pain, abdominal distension, subfertility or recurrent miscarriage, the symptoms depending to a certain extent on the location and size of the fibroids. Their location in the uterus is described as:

- Submucous-arising within the cavity. Rarely they can form a fibroid polyp and protrude through the os (Fig. 34.21).
- Mural within the myometrium. They may or may not abut or distort the shape of the cavity, depending on their precise location (Fig. 34.22).
- Subserosal arising deep to the serosa and causing a bulge on the surface of the uterus (Fig. 34.23).
- Pedunculated-on a pedicle usually from the serosal surface.
- Cervical rare, i.e. less than 5% fibroids.

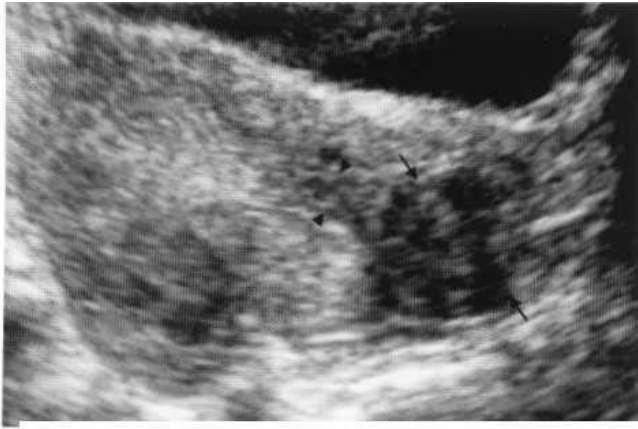
Fibroids are hormone-dependent, increasing in size and becoming less echogenic during pregnancy, and decreasing in size following the menopause. However, regression following the menopause is prevented and may be reversed in patients taking HRT.

On ultrasound, most fibroids are round, well-defined hypoechoic masses with a characteristic internal architecture showing recurrent shadowing (Fig. 34.24). They can be hyperechoic and may be calcified, particularly in postmenopausal patients. Degeneration within fibroids appears as either areas of increased echogenicity or irregular cystic areas (Fig. 34.25). Fibroids can be very vascular so Doppler studies may show very low impedance flow. Malignancy (leiomyosarcoma) is rare but should be suspected if a fibroid suddenly increases in size. There are no specific ultrasound features of malignancy.

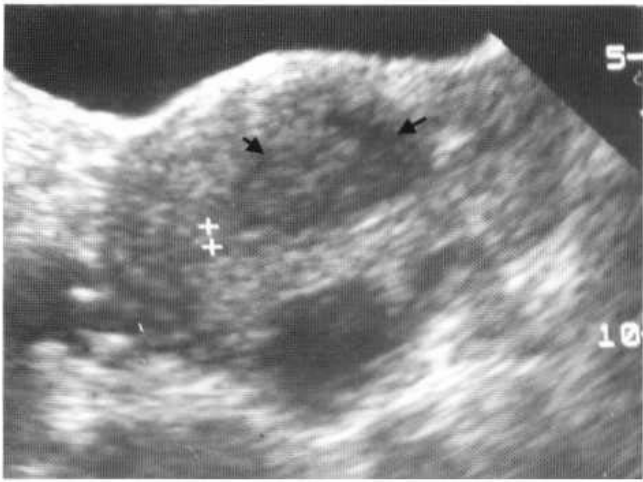
The role of ultrasound is to confirm the diagnosis and determine the number, size and location of fibroids, as this will help determine their likely significance and appropriate treatment. See Table 34.2 for differential diagnosis of fibroids.

Adenomyosis

Adenomyosis or endometriosis interna is the presence of endometrial glands within the myometrium associated with adjacent myometrial hyperplasia. It is usually a diffuse process but may form a localised mass or adenomyoma. Clinical findings are dysmenor-



A



B

Fig. 34.21 (A) TAS. Fibroid polyp (arrows) within the cervical canal. The stalk of the polyp (arrowheads) can be seen in the uterine cavity. (B) TAS. Same patient 6 months earlier. The fibroid polyp (arrows) is now seen within the uterine cavity.

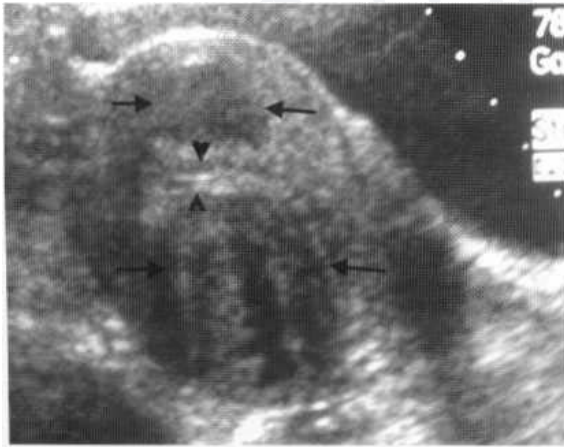


Fig. 34.22 TAS. Typical mural fibroids (arrows) abutting but not displacing the cavity (arrowheads). The larger fibroid shows typical recurrent shadowing.

rhoea and menorrhagia with a tender bulky uterus. Most cases are diagnosed following pathological examination of hysterectomy specimens: however, endovaginal ultrasound and MRI have been shown to be of value.

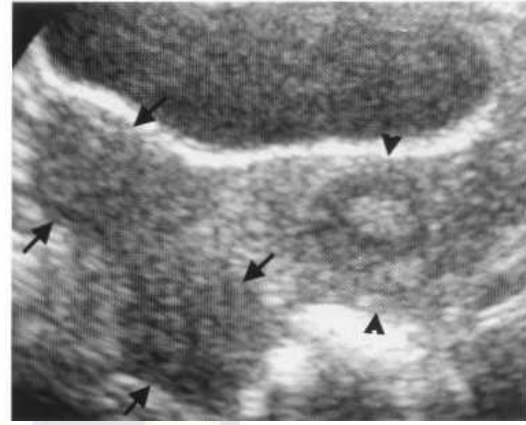


Fig. 34.23 TAS. Two subserosal fibroids (arrows). Arrowheads indicate position of uterine cavity.



Fig. 34.24 TAS. Fibroids. Typical recurrent shadowing (arrowheads).

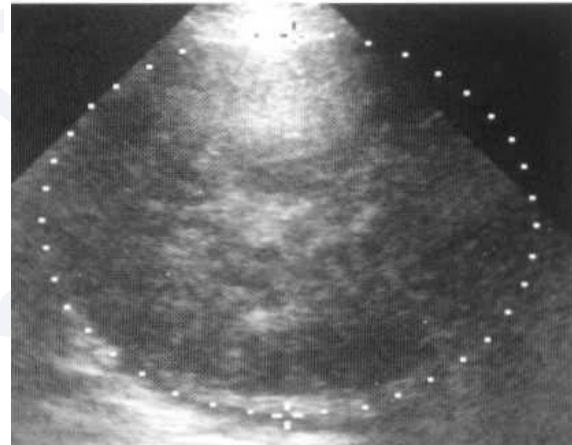


Fig. 34.25 TAS. Irregular area of increased reflectivity in the centre of a fibroid due to degeneration.

The ultrasound features of diffuse adenomyosis are poorly defined areas of decreased echogenicity and heterogeneity in the myometrium, associated in approximately 50% with small (2-5 mm) cystic spaces in the myometrium (Fig. 34.26). Using these criteria, sensitivities and specificities of 80-90% have been achieved.

Focal adenomyomas cause focal bulges in the myometrium and may be hyper- or hypoechoic. They are generally less well defined than fibroids but it is difficult to differentiate the two.

Table 34.2 Differential diagnosis of fibroids

Location	Differential diagnosis	Comments
Submucosal	Endometrial polyps Retained products of conception (RPC) Endometrial carcinoma	Usually hyperechoic, i.e. similar to endometrium History helpful. RPC usually of mixed echogenicity Postmenopausal patients. Less well defined, possibly with myometrial invasion
	Endometritis / fluid collection	Heterogeneous endometrium with little mass effect. Cavity may contain fluid (or gas if fistula present)
Mural/subserosal	Adenomyoma / area of adenomyosis	Less well defined area of heterogeneity with no recurrent shadowing effect
	Leiomyosarcoma	Rapid growth but otherwise impossible to differentiate. Very rare
	Myometrial contraction	Poorly defined virtually isoechoic mass; changes with time-rarely a problem
	Metastatic deposits	Very rare, no distinguishing features
Pedunculated	Any cause of solid adnexal mass	Usually possible to see connection with uterus. Doppler of no value



Fig. 34.26 EVS. Adenomyosis. Coarse myometrial texture with small cysts due to blood lakes.

Endometrial abnormalities

The endometrium is considered abnormally thick if it measures more than 14 mm in a premenopausal patient and more than 4 mm in a postmenopausal patient. Causes of thickening of the cavity include:

- endometrial polyps
- submucous fibroids
- endometrial hyperplasia
- endometrial carcinoma



Fig. 34.27 EVS. Multiple endometrial polyps. Note the midline echoes due to the endometrial interface (arrows) are displaced by the polyps. This is a useful feature when trying to differentiate hyperplasia from polyps.

- retained products of conception
- trophoblastic turnouts-usually following a pregnancy.

Fluid, including pus or blood, can also distend the cavity but should not be included in the endometrial measurement. A tiny amount of fluid (1-3 mm depth) is occasionally seen in a postmenopausal uterus and is of no significance; however, a cavity distended by fluid usually indicates an obstructed uterus. An attempt should be made to identify the underlying cause. e.g. cervical or uterine carcinoma, previous radiotherapy to the cervix, uterine synechiae due to Asherman's syndrome, previous cervical surgery, etc. A pyometrium due to a uterocolic or uterovesical fistula can cause a similar appearance.

Endometrial polyps are common and typically measure 5-15 mm (Fig. 34.27). There is an increased incidence in patients on tamoxifen or HRT. Most polyps are benign and cause intermenstrual bleeding, with or without pain.

Endometrial hyperplasia is a precursor to endometrial carcinoma so must be recognised and endometrial sampling performed. Causes of endometrial hyperplasia include polycystic ovaries, obesity, exogenous hormones, endogenous excess oestrogen production, e.g. due to functioning ovarian tumours.

Differentiation of endometrial polyps from hyperplasia can be difficult but can be helped by performing an endovaginal ultrasound examination during intrauterine injection of saline, so-called sonohysterography (Figs 34.28, 34.29).



Fig. 34.28 EVS. Endometrial thickening. This looks like hyperplasia but subsequent saline hystero-graphy demonstrated it to be a polyp.

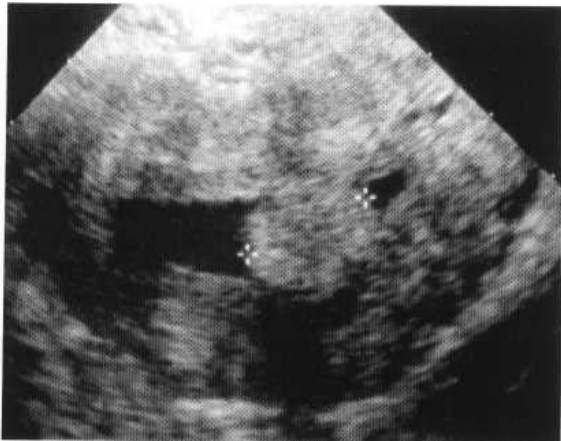


Fig. 34.29 Saline hystero-graphy. Endometrial polyp outlined by saline.

Endometrial carcinoma occurs mainly in postmenopausal women. The risk factors are the same as those described for endometrial hyperplasia, i.e. increased oestrogen levels, in addition to hypertension, diabetes and nulliparity. The most common presenting symptom is abnormal uterine bleeding.

Ultrasound appearances vary from moderate endometrial thickening, to an irregular hypoechoic intracavitary mass, to an enlarged diffusely infiltrated uterus (Figs 34.30, 34.31). Endovaginal ultrasound is said to be good at differentiating between stage I (less

than 50% myometrial invasion) and stage 2 disease (more than 50% myometrial invasion); however, MRI is far better at looking for extrauterine spread, so this is the preferred technique.

Doppler ultrasound of endometrial or intrauterine vessels is of little value in premenopausal patients because of cyclical changes and the effect of other uterine pathology, such as fibroids. However, measurement of Doppler indices may help in postmenopausal patients. It has been reported that malignancy is never found if the RI is greater than 0.83.

Cervix

The cervix is most effectively examined by direct inspection, Papanicolaou smears and colposcopy, so the role of ultrasound is very limited. It has no role in screening or routine staging of cervical carcinoma; however, occasionally patients present to the ultrasound department prior to vaginal examination so the radiologist needs to be aware of the appearances of cervical disease. Early tumours are undetectable but advanced tumours show an irregularly enlarged cervix (Fig. 34.32), with or without an area of highly reflective echoes due to necrosis. There may be an obstructed, distended uterine cavity. Advanced disease may also show invasion of the bladder wall and hydronephrosis due to ureteric involvement—either due to nodal involvement or direct ureteric invasion (Fig. 34.33).

Cervical polyps and cervical fibroids are also occasionally seen.



Fig. 34.30 EVS. Poorly defined intracavitary mass due to endometrial carcinoma.



Fig. 34.31 TAS. Obstructed uterus. The cavity (arrows) is distended by blood with a polypoid mass just above the internal os due to endometrial carcinoma.

Adnexal masses

Simple adnexal cysts Simple adnexal cysts are most commonly functional in origin. They vary in size, reaching up to 7 cm in diameter, and yet still resolve spontaneously. Haemorrhage into

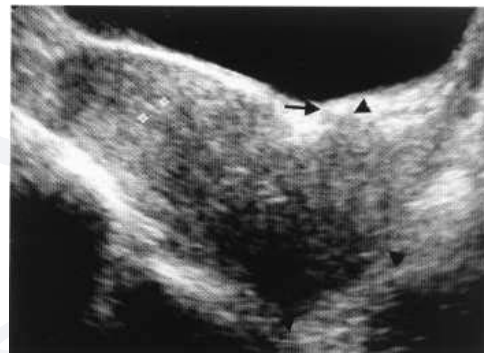


Fig. 34.32 TAS. Carcinoma of cervix. Large irregular cervix (arrowheads) with a small tongue of tumour (arrow) extending towards the bladder.



Fig. 34.33 TAS. Cervical carcinoma invading bladder base (arrows) and causing an obstructed uterus (arrowheads).

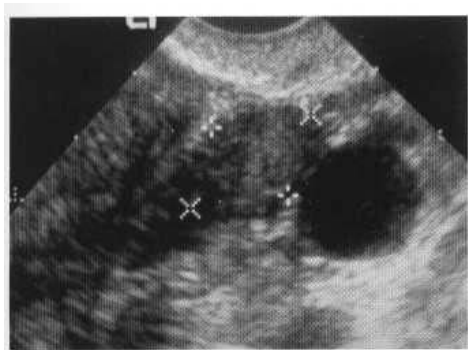


Fig. 34.34 eve. fimmoral cyst adjacent to ovary



Fig. 34.35 EVS. Hydrosalpinx (arrows) adjacent to the ovary (arrowheads).

the cyst may cause pain and give rise to diffuse internal echoes or a clump of solid echoes within the cyst due to clot. Follow-up ultrasound will show a reduction in the size of the cyst and a change in the appearance of the internal echoes confirming its benign nature.

Small simple cysts (1-3 cm) are also relatively common (3-5%h;) in post menopausal women. Doppler insonation should be performed to confirm high impedance flow and serum CA- 125 should be measured. If both these investigations are normal and the woman is asymptomatic, it is reasonable to follow the cyst with serial ultrasound scans to confirm no growth rather than proceed to laparoscopy.

The differential diagnosis of a simple adnexal cyst includes:

Paraovarian cysts may reach up to 10 cm, usually recognisable by the fact they are close to, but can be separated from, the ovary by gentle pressure with the ultrasound probe (Fig. 34.34).

- Endometriomas (chocolate cysts)-usually contain internal echoes and have a thick wall but may look entirely simple.
- Hydrosalpinx-a small hydrosalpinx may mimic an ovarian cyst but can be distinguished by its rather elongated shape, its position around or on the surface of the ovary and the presence of incomplete septations due to inucosal folds (Fig. 34.35).
- Neoplastic cysts-particularly benign cystadenomas and some borderline tumours.
- Peritoneal cysts or fluid trapped around the ovary due to adhesions. These may be asymptomatic or cause cyclical pain (*entrapped ovary s.vndrome*). The patients usually give a history of complicated pelvic surgery or infection.

Complex adnexal masses Complex adnexal masses can be due to complicated simple cysts; however, various inflammatory and neoplastic causes must be considered in addition to some non-gynaecological causes.



Fig. 34.36 EVS. Typical endometrioma with diffuse moderately high-level echoes (arrows).

The differential diagnosis of a complex adnexal mass should include:

- Haemorrhagic cyst-contains diffuse internal echoes or an irregular clump of echoes due to clot. Repeat scans helpful to show change.
- Ruptured cyst-typical history, irregularly-shaped cyst with surrounding fluid.
- Torsion of cyst or ovary-heterogeneous enlarged ovary with or without a thick-walled cyst with internal echoes. Presence of colour flow within the ovary is said to indicate viability of the ovary, hence laparoscopy is worthwhile to try and preserve function.
- Endometriosis.
- Acute / chronic tubo-ovarian abscess.
- Dermoid cyst-complex mass with cystic and solid areas, fat and/or calcification.
- Other neoplastic ovarian tumours, benign and malignant.
- Pedunculated fibroid differentiation from an ovarian mass depends on identification of the ovaries separately.
- Ectopic pregnancy-should always be considered in a patient of child-bearing age. Pregnancy test important.
- Other inflammatory masses-e.g. appendix or diverticular mass.
- Other neoplastic masses-e.g. arising from the bowel or peritoneum (benign peritoneal mesothelioma).

Endometriosis is an incidental finding in up to 25% of laparoscopies. Symptoms are variable but the most common is dysmenorrhoea. The majority (up to 90%) of endometriotic (chocolate) cysts contain diffuse internal echoes due to old blood. The echogenicity of these internal echoes varies from very low level, only discernible scanning endovaginally, to moderately high, which may cause some confusion with a dermoid cyst (Fig. 34.36). The echoes may show gravity-dependent layering creating a fluid-fluid level (Fig. 34.37). The wall thickness of the cysts varies and highly reflective foci or flecks of calcification may be seen within the wall. Septations, creating multilocular cysts, are common, the various locules containing echoes of differing densities, indicating haemorrhage of different ages (Fig. 34.38). Very large endometriotic cysts occasionally occur and may mimic a solid mass; however, compression of the mass with the probe will usually demonstrate the mass is deformable and the internal echoes move very slowly. Deposits are most easily recognised on the ovary and in the broad ligament; however, endometriotic deposits do occur anywhere in the pelvis or indeed outside the abdomen. Rarely nodules occur on the bowel, on the pleura and in the soft tissues, particularly at the sites of scars (Figs 34.39, 34.40). Adhesions and diffuse small endometriotic deposits cannot be

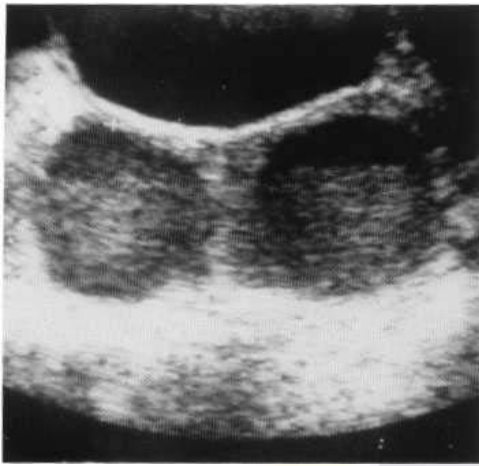


Fig. 34.37 TAS. Bilateral endometriomas. Note the fluid level on the left and the irregularly thickened wall.



Fig. 34.38 TAS. Endometriosis. Complex ovarian mass with internal septations and echoes of varying density. Differential diagnosis must include a malignant tumour.

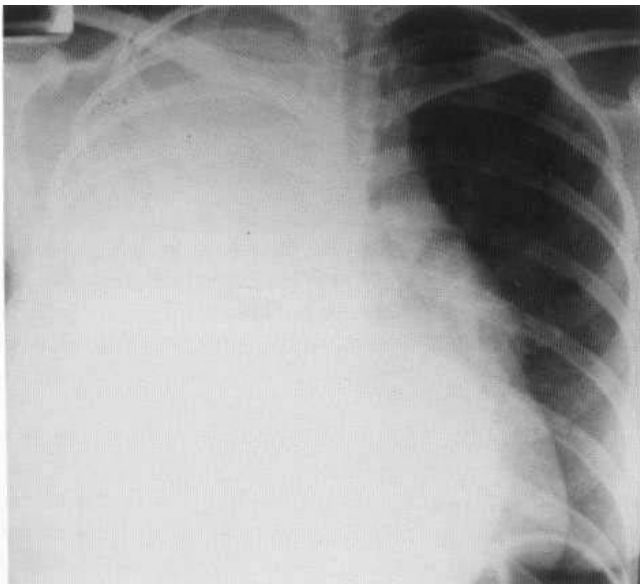


Fig. 34.39 Huge pleural effusion in a young girl. Aspiration revealed heavily blood-stained fluid with multiple macrophages typical of pleural endometriosis.

visualised with ultrasound so a normal ultrasound examination does not exclude endometriosis. Endometriosis normally resolves after the menopause but may be reactivated if the patient is taking HRT, hence endometriosis should still be considered as part of the differential diagnosis of a complex cyst in post menopausal patients taking HRT.



Fig. 34.40 TAS. Endometriosis in the bladder (cursors). Arrowheads mark position of the uterus.



Fig. 34.41 TAS. Acute pelvic infection with a thick-walled tubo-ovarian abscess (arrow) and free pus in the pouch of Douglas (arrowhead).



Fig. 34.42 EVS. Large thin-walled chronic hydrosalpinx.

Pelvic inflammatory disease is becoming increasingly common as a cause of adnexal masses, both in the acute and chronic phases. The ultrasound in acute infection may show free fluid (pus) in association with a complex adnexal mass, which comprises the ovary and thickened surrounding tube (Fig. 34.41). Doppler insonation shows low impedance flow due to a surrounding inflammatory reaction. In more chronic disease the ovary may be more easily definable (Fig. 34.35) with a thin-walled hydrosalpinx adjacent to the ovary.

The hydrosalpinx may contain internal echoes due to either blood or pus (Fig. 34.42) and the ovary may look like a polycystic ovary

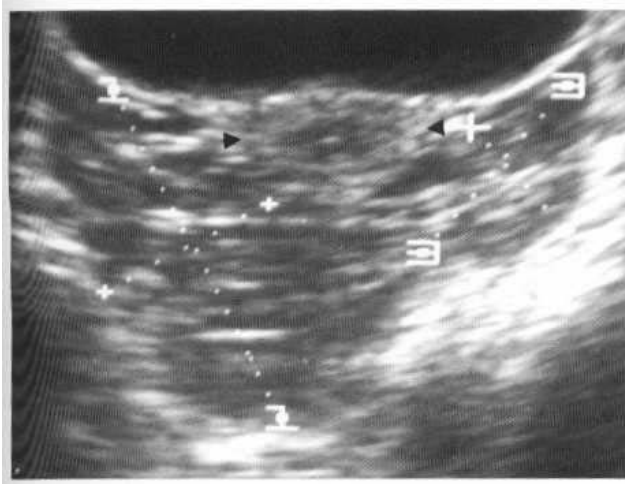


Fig. 34.43 TAS. Complex pelvic mass behind the uterus (arrowheads) due to peritoneal mesothelioma. Note multiple internal septations and how the mass conforms to the shape of the pelvis.

because of follicular fluid trapped by surface adhesions. Rarely patients present with right hypochondrial pain due to perihepatitis (Curtis-Fitz-Hugh syndrome). Adhesions around the liver have been described on ultrasound but it is rare to see any abnormality around the liver, and indeed the pelvic ultrasound may also be normal in even quite severe pelvic inflammatory disease.

Benign peritoneal mesothelioma is a slow-growing rare tumour that is difficult to treat because of its propensity to local recurrence (Fig. 34.43).

Ovarian tumours

Ovarian tumours are classified into three main types, according to their cells of origin: epithelial (60-70%), sex cord stromal (5-10%) and germ cell (15-20%) tumours. In addition, approximately 5% of significant ovarian tumours are metastatic in origin. Primary tumours can be associated with the production of various hormones, including oestrogens, progestogens and androgens. Calcification is seen in cystadenomas and cystadenocarcinomas, fibromas and dermoid cysts/teratomas.

In addition to classification as benign or malignant, some ovarian tumours are classified as borderline malignant, indicating that they have a better prognosis, with a low risk of local recurrence and even lower risk of metastatic disease.

Malignant ovarian tumours Carcinoma of the ovary is responsible for about 5000 deaths/annum in the UK: 80% of tumours occur in women over 50 years of age. Presenting symptoms (pain, abdominal distension, vaginal bleeding, bowel and urinary dysfunction) usually occur late in the disease with two-thirds of patients having spread outside the pelvis at the time of diagnosis. This late presentation is responsible for the overall high mortality rate of approximately 70% at 5 years. Metastatic spread occurs most commonly to the peritoneum, with multiple peritoneal nodules. Omental thickening and ascites. Lymphatic spread to the para-aortic nodes and liver metastases are also seen.

Risk factors for development of ovarian carcinoma include:

- Family history of ovarian, breast, endometrial or colorectal carcinoma. Women with a pathogenic mutation in the *BRCA1* or *BRCA2* genes have a lifetime risk of 40% or 25%, respectively.

- Increased number of episodes of ovulation, for example:
 - following treatment with ovulation induction agents
 - the nulliparous state.

Some protection is conferred by multiparity, breast-feeding and use of the contraceptive pill.

Epithelial ovarian tumours Eighty-five per cent of malignant ovarian tumours are epithelial in origin and the commonest epithelial carcinoma (60-80%) is a *serous cystadenocarcinoma*. Serous tumours are predominantly cystic masses. They may show wall thickening and nodularity, internal solid areas and septations. Malignant tumours tend to have more nodularity and solid areas than their benign counterparts (Figs 34.44-34.46).

Mucinous cystadenocarcinomas are also large predominantly cystic masses but tend to be multiloculated with multiple thick internal septations and diffuse internal echoes due to their high

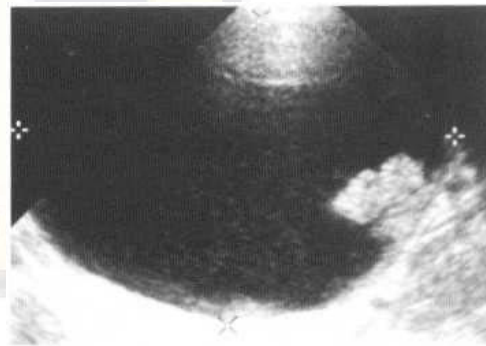


Fig. 34.44 TAS. Adnexal cyst with one solid area and some fine internal echoes suggestive of a serous cystadenocarcinoma. Histology confirmed a borderline malignant tumour.



Fig. 34.45 TAS. Malignant adnexal cyst with internal echoes and irregularly thickened wall (arrowhead).



Fig. 34.46 TAS. Solid tumour mass (white arrowheads) surrounding the posterior aspect of the uterus (black arrows).

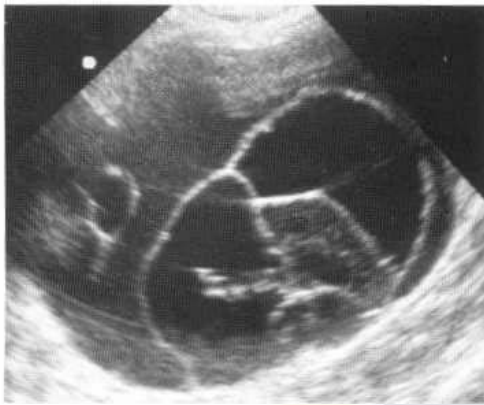


Fig. 34.47 TAS. Benign mucinous cystadenoma showing the typical multiloculated appearance-impossible to differentiate from a malignant tumour.

mucin content (Fig. 34.47). Benign mucinous cystadenomas similarly contain thick irregular septations such that, in the absence of ascites or lymphadenopathy, it is impossible to distinguish a benign from a malignant mucinous tumour. However, in spite of their worrying appearance, only 10% of mucinous tumours are actually malignant.

Between 60 and 70% of serous tumours and 5 and 10% of mucinous tumours are bilateral.

Other rarer epithelial tumours include *endometrioid carcinomas* (these are associated with endometrial thickening due to endometrial hyperplasia or carcinoma in approximately 20-30%), *clear cell carcinomas* and *Brenner's tumours*. *Brenner's tumours* are invariably benign, large at presentation and may be associated with a mucinous cystadenoma or dermoid cyst.

Sex cord tumours This group of tumours includes *Fibromas* and the hormone-secreting tumours such as *thecomas*, *granulosa cell tumours* and *Sertoli cell tumours (Leydig-stromal tumours)*. They are usually benign solid tumours. Patients with functioning tumours often present with the symptoms due to the excess hormone production, e.g. post menopausal bleeding (Fig. 34.48). *Fibromas* are benign slow-growing tumours which when large may be associated with ascites and pleural effusions, a condition known as *Meigs's syndrome*. Fibromas can be heavily calcified (Fig. 34.49).

Germ cell tumours *Dermoid cysts (or benign cystic teratomas)* are the commonest tumours in this group; 95% are benign-particularly in patients aged between 20 and 50 years. Dermoid



Fig. 34.48 TAS. Solid ovarian mass with a thickened endometrium (arrowheads) in a postmenopausal patient. Histology revealed a benign functioning thecoma.



Fig. 34.49 EUS. Ovarian fibroma. Homogeneous solid mass (arrows) arising from the ovary (arrowheads).

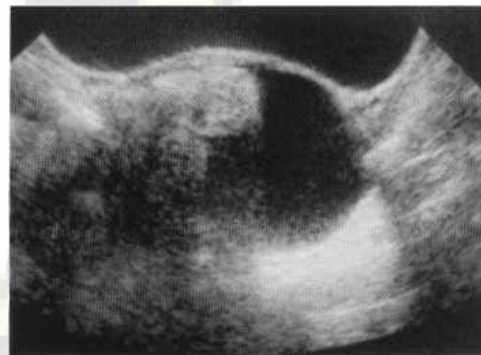


Fig. 34.50 TAS. Typical dermoid with a floating echogenic area with acoustic shadowing due to fat, with or without calcification.

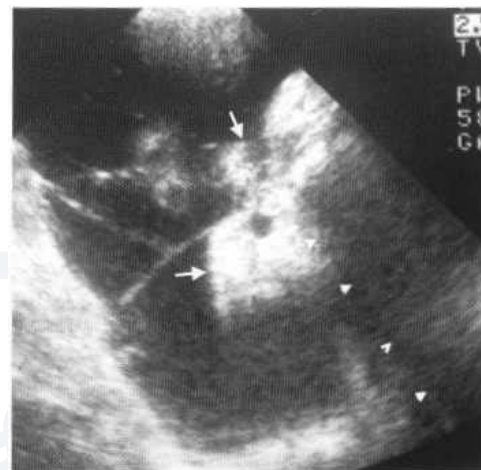


Fig. 34.51 TAS. Dermoid cyst in a pregnant patient. Note the echogenic nodule (arrows) and dense acoustic shadowing (arrowheads).

cysts are typically complex adnexal masses with variable amounts of cystic and solid areas. They typically show areas of markedly increased reflectivity and acoustic shadowing due to fat, calcification or teeth. Fat commonly floats at the top of the cyst, obscuring deeper structures and the true extent of the mass (Figs 34.50-34.52). The echogenic nature of the cyst can also make it difficult to differentiate from bowel (Fig. 34.53), hence the size of a dermoid cyst may be underestimated with ultrasound.

Approximately 25% are discovered incidentally. Management of asymptomatic dermoid cysts has changed over the last few years. Whereas previously all would have been removed, it is now considered acceptable not to operate on small (less than 5 cm), inciden-

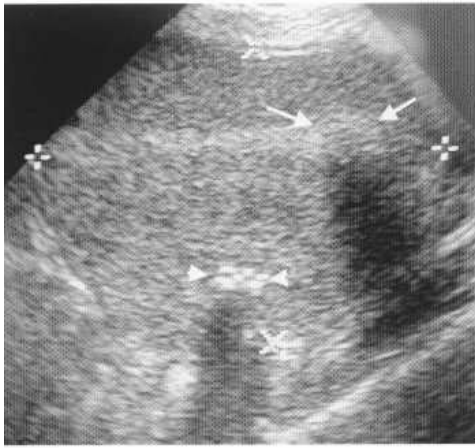


Fig. 34.52 EVS. Solid-appearing dermoid cyst. Note the thick septum and two nodules (arrows and arrowheads) casting shadows.

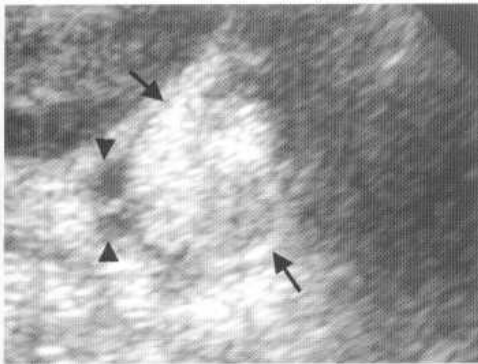


Fig. 34.53 EVS. Echogenic dermoid cyst (arrows). Note how the mass mimics a loop of bowel. The remainder of the ovary (arrowheads) is seen.

tally discovered dermoid cysts providing the ultrasound findings are typical and there is no growth on follow-up scans. Between 10 and 15% of dermoid cysts are bilateral.

Malignant germ cell tumours (dysgerminomas, immature teratomas) occur predominantly in young women (mean age of approximately 20 years). They are usually large solid tumours but typically only stage I at presentation. They are associated with raised levels of various tumour markers, e.g. hCG, AFP, CA-125.

Ovarian metastases (Krukenberg's tumours) Ovarian secondary tumours most commonly arise from primary tumours of the stomach, colon, pancreas or breast. They may be solid, cystic or complex ovarian masses, frequently bilateral and usually associated with ascites. Secondary tumours are less likely to be multi-jocular than primary ovarian tumours but otherwise there are no specific distinguishing features (Fig. 34.54).

Differentiation of benign from malignant masses A considerable amount has been written attempting to use ultrasound to differentiate benign from malignant adnexal masses with accuracy rates ranging from 50 to 98%! Clearly the presence of metastatic disease (Figs 34.55, 34.56) indicates malignancy but in earlier disease it is difficult to be sure.

Various scoring systems based on morphology and colour and spectral Doppler have been devised. A recent paper comparing the different schemes was able to show that a combination of both morphology and Doppler indices is more accurate than either used alone but there is no agreement as to which Doppler index is best and at which level the threshold should be set to distinguish



Fig. 34.54 TAS. Bilateral adnexal masses due to ovarian metastases. Note predominantly cystic mass on the right and partly solid mass on the left.

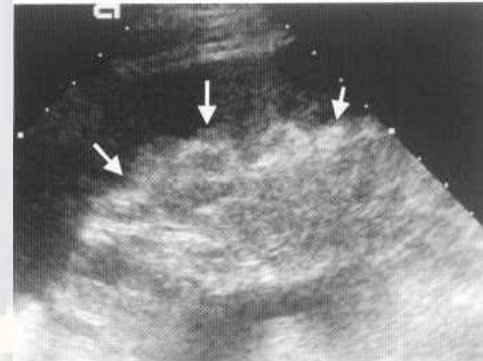


Fig. 34.55 TAS. Metastatic ovarian carcinoma causing omental thickening (arrows).

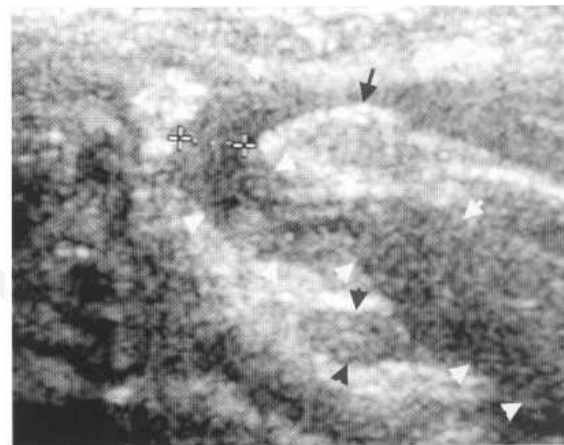


Fig. 34.56 TAS. Metastatic ovarian carcinoma showing serosal tumour (arrowheads) around a loop of bowel (arrow).

between high and low impedance flow. Current research is investigating the use of ultrasound contrast media in association with 3D ultrasound in the hope that assessment of the pattern of vessels within a mass will help, but to date this is unproven.

Features suggestive of malignancy are:

- Hypochoic solid area within the mass (highly echogenic solid areas due to fat or calcification are typical of dermoids).
- Thick (more than 3 mm) nodular septations.
- Size of mass greater than 7 cm, although very large but simple cysts are usually benign cystadenomas.
- Central rather than peripheral vascularity.
- RI less than 0.6 (Fig. 34.57). RI greater than 0.8 is suggestive of benign disease but there is an indeterminate range of 0.6-0.8;

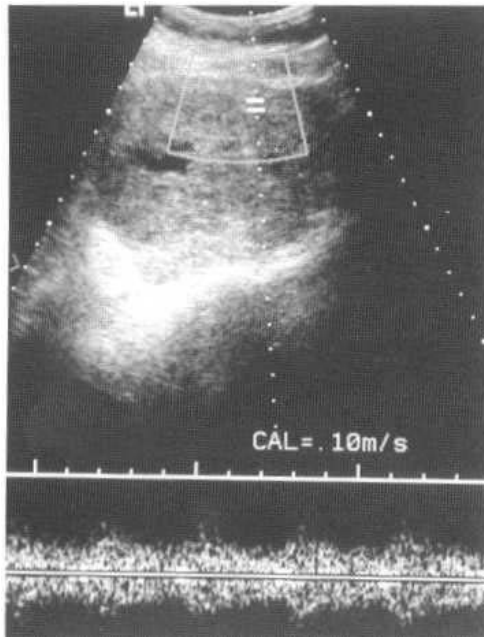


Fig. 34.57 TAS. Large malignant germ cell tumour in a 25-year-old. Doppler shows typical low impedance flow with RI of 0.5.

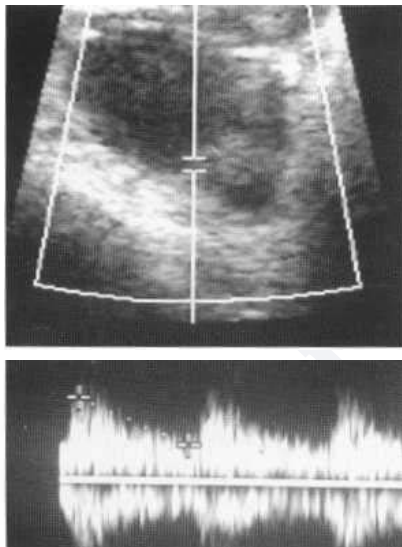


Fig. 34.58 EVS. Ovarian cyst with nodule in a 65-year-old. Doppler shows low impedance flow (RI 0.50) suggestive of a malignant tumour. Histology revealed a benign cystadenofibroma with a Brenner tumour. No evidence of malignancy.

however, low impedance [low can be seen with benign disease (Fig. 34.58) and high impedance [low with malignant disease.

Screening for ovarian cancer The 5 year survival for stage I disease is over 80%, hence there has been considerable interest in screening for early tumour. Serum CA-125 measurement, trans-abdominal and endovaginal ultrasound have all been investigated but found unreliable. CA-125 measurements are normal in up to 50% of stage I tumours, and abnormally high results are found in healthy controls and patients with endometriosis, cirrhosis and other abdominal malignancies. The difficulties in distinguishing benign from malignant masses on ultrasound also lead to a considerable number of false positives and unnecessary laparoscopies. Current recommendations are therefore that whole population screening is not justified. However, most authors agree there is benefit in screening patients known to be at increased risk of the disease, particularly those thought to have hereditary ovarian cancer.

Management of infertility

Ultrasound has a crucial diagnostic and therapeutic role in the management of infertility. Its main uses are:

- to confirm normal pelvic anatomy
- to assess ovarian morphology
- to look for pelvic pathology such as endometriosi s and hydrosalpinges
- cycle monitoring
 - to confirm ovulation in natural cycles
 - to monitor the response to ovulation induction agents, such as clomifene and Pergonal, and try and prevent ovarian hyperstimulation syndrome
 - to time hCG injections prior to assisted conception techniques such as IVF and donor insemination
 - to confirm development of the typical midcycle endometrium, as this has a bearing on conception rates
- to guide for procedures such as cyst aspiration and oocyte collection.

In some centres this initial ultrasound examination is combined with HyCoSy (hysterocontrastsonography) to confirm tubal patency.

Ovarian hyperstimulation syndrome (DHSS) results in very enlarged ovaries (up to 10 cm in length) with multiple follicles. It is associated with ascites and pleural effusions and, when severe, may lead to hypovolaemia, disseminated intravascular coagulation, venous thrombosis and even death. Mild forms are common and usually self-limiting.

HyCoSy (hysterocontrastsonography) is performed by inserting a small balloon catheter through the cervix into the uterine cavity. An endovaginal scan is performed while the ultrasound contrast agent Echovist is injected via the catheter. Tubal patency is confirmed when contrast is seen to flow along both fallopian tubes and around the ovary (Figs 34.59, 34.60). The technique is quite difficult to learn but in experienced hands accuracy rates of 80-90% for tubal patency can be achieved. Its obvious advantage over conventional hysterosalpingography is the lack of ionising radiation. Early reports claimed it was also less painful but this has not been substantiated and it has the disadvantage of not showing detailed tubal anatomy. Therefore its precise role is still to be determined. It is probably justified as a screening test for tubal patency in patients with a low probability of tubal disease.

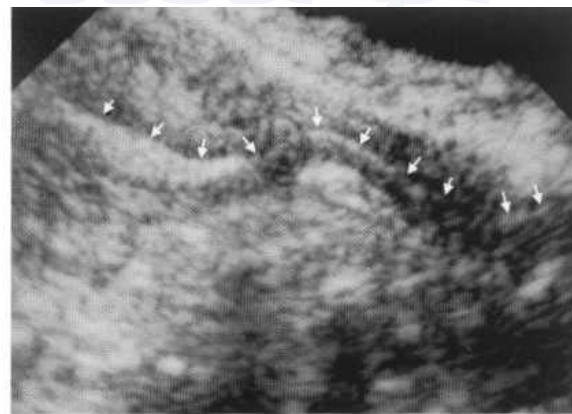


Fig. 34.59 HyCoSy. Contrast (Echovist) is seen outlining the cavity and entering the fallopian tube (arrows).

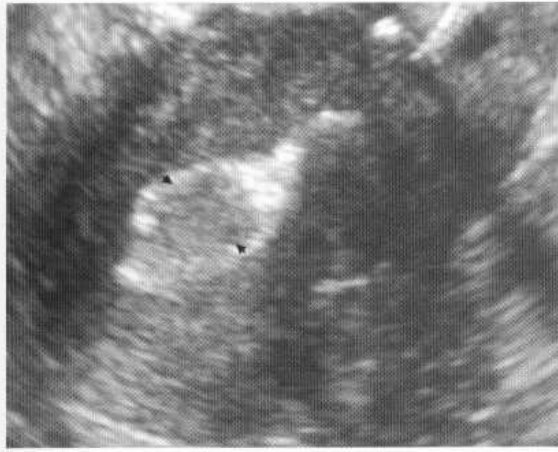


Fig. 34.60 HyCoSy. Echovist outlines a fibroid polyp (arrows) in the uterine cavity.

PLAIN FILM RADIOLOGY

The role of the plain radiograph in current gynaecological practice is very limited. However, it is clearly important to be able to recognise features of gynaecological disease on plain films and it is still necessary to perform a plain abdominal X-ray to look for an IUCD that cannot be found with ultrasound. Abdominal radiographs may also be requested to assess bowel dilatation in postoperative patients and to exclude bowel obstruction as a cause of abdominal distension in patients with advanced ovarian cancer. Rarely direct invasion by pelvic tumours may cause bone destruction.

Causes of pelvic calcification visible on a plain abdominal X-ray include:

- fibroids—typically coarse popcorn-type calcification
- dermoid cysts—commonest ovarian mass to calcify (teeth and/or a fat-fluid level pathognomonic; Fig. 34.61)
- other ovarian masses—cystadenomas /carcinomas, fibromas
- pseudomyxoma peritonei—from rupture of a mucinous tumour
- fallopian tube calcification—rare, should suggest tuberculosis
- uterine, i.e. endometrial ossification from chronic endometritis.

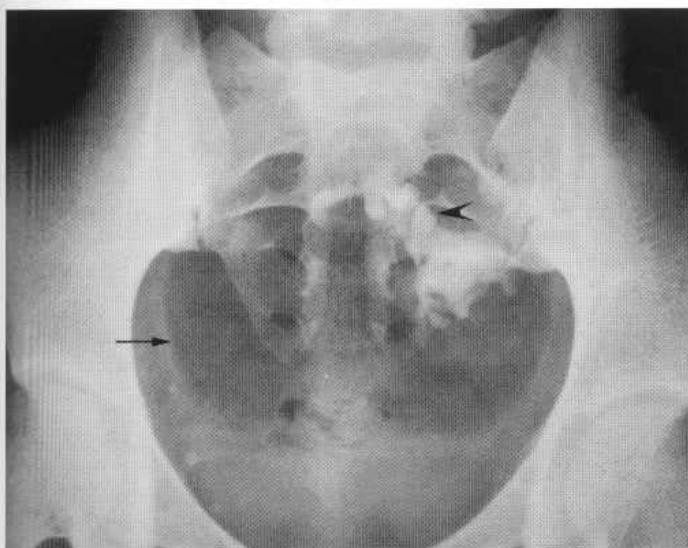


Fig. 34.61 Dermoid cyst. Note calcification and teeth with a fat-fluid level (arrow).

CONTRAST STUDIES

IUVUs, barium studies, cystograms and sinograms are all occasionally necessary in the investigation of gynaecological patients but have been largely superseded by ultrasound, CT and MRI. Cystograms and barium enemas are used to demonstrate vaginal fistula usually due to surgery or radiotherapy for malignant disease: the investigation of cyclical rectal bleeding and pain may require a barium enema to exclude the short smooth stricture typical of endometriosis and barium studies of the small and large bowel can be used to demonstrate the typical serosal metastases of ovarian carcinoma (Fig 34.62).

Hysterosalpingography

Hysterosalpingography (HSG) remains important in the investigation of infertility. It is an accurate means of assessing the uterine cavity and tuba) patency but has a low sensitivity for the diagnosis of pelvis adhesions so cannot replace laparoscopy. The main cut rent indications for HSG are infertility and recurrent miscarriage. Rare indications include checking the efficacy of tubal sterilisation and assessment of the tubes prior to attempted reversal of sterilisation.

Technique The procedure is performed in the first half of the menstrual cycle following cessation of bleeding. The patient is asked to refrain from unprotected sexual intercourse from the date of her period until after the investigation to be certain there is no risk of pregnancy. Examination in the second half of the cycle is avoided because the thickened secretory-phase endometrium increases the risk of venous intravasation, and may cause a false-positive diagnosis of cornual occlusion. Routine use of antibiotics is controversial but a recent consensus statement from the Royal College of Obstetrics and Gynaecology recommends that all non-pregnant women under 35 years of age undergoing uterine instrumentation should receive prophylactic antibiotics or be screened for relevant organisms. The suggested antibiotic regimen comprises metronidazole 1 g rectally at the time of the procedure plus doxycycline 100 mg twice daily for 7 days.

Numerous different types of cannula are available. All possess some means of preventing reflux of contrast through the cervix and ideally should allow traction on the uterus. Once the cannula is in place, water-soluble contrast medium is injected slowly under fluoroscopic control until the uterine cavity is distended, the tubes filled and contrast is seen to spill freely from the distal ends of the tubes. Spot films should be taken during the early filling phase to ensure small filling defects are not obliterated by contrast, during early tubal filling before the isthmic portions are obscured by contrast, and after complete filling of the tubes to demonstrate free peritoneal spill (Fig. 34.63). Additional oblique views help to demonstrate the position of the uterus and any fibroids. It is important that the uterine cavity is visualised en face. This is usually achieved by traction on the cervix, but if the uterus is retroverted it may be more effective to push the cervix so the uterine fundus tips back into the pelvis and is seen upside-down. Nowadays with modern fluoroscopic units it is also possible to angle the tube rather than manipulate the uterus.

Inadequate distension of the uterus (due to cervical reflux) and tubal spasm can give rise to a false-positive diagnosis of cornual occlusion. Intravenous hyoscine butylbromide (Buscopan) or

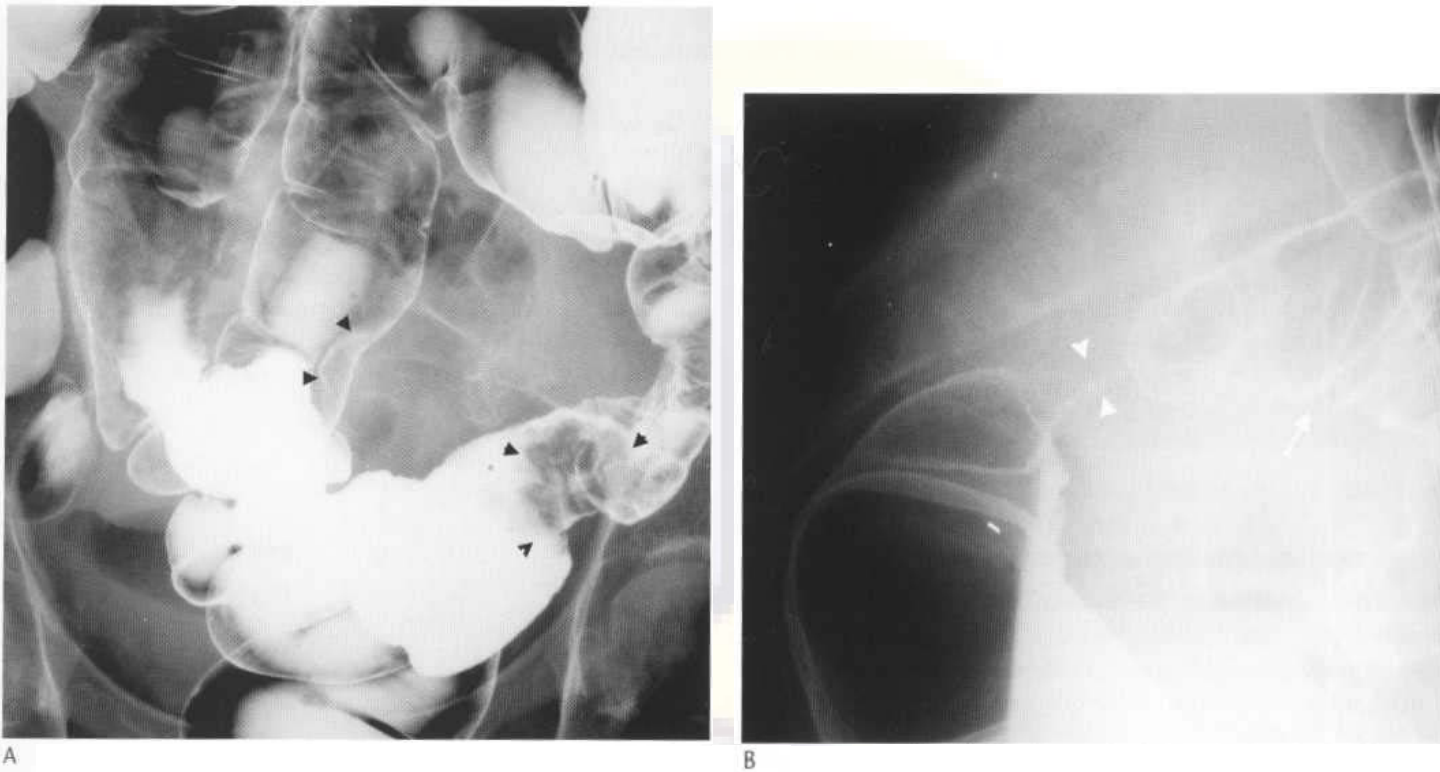


Fig. 34.62 Barium enemas. (A) Serosal metastases from ovarian carcinoma. (B) Short smooth stricture due to endometriosis (arrowheads). Note the puckering of the serosal surface due to adhesions (arrow).

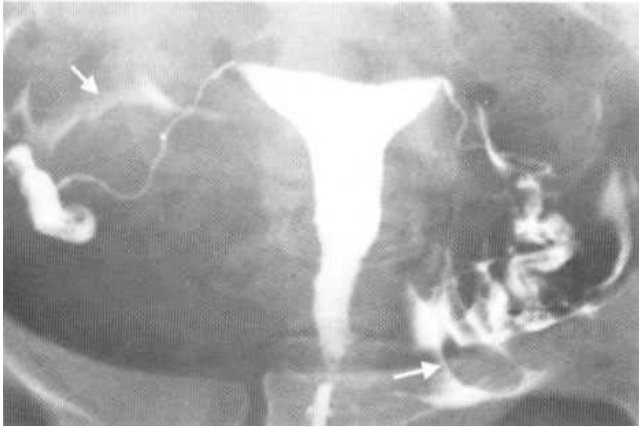


Fig. 34.63 HSG. Normal cavity. Both tubes visible with regular mucosal folds and free peritoneal spill. Note how the contrast flows around loops of bowel (arrows).



Fig. 34.64 HSG. Venous intravasation. The myometrial plexus is shown with drainage into the ovarian veins (arrowheads). Peritoneal spill is also seen.

glucagon have been suggested as treatment for this but a World Health Organization (WHO) study failed to confirm they were of any value. It is probably more important to avoid rough manipulation of the cervix and allow time for spasm to relax. Gentle traction on the uterus and change in position of the patient can also help. If there is doubt about the appearances distally, delayed films will help distinguish contrast flowing into a large hydrosalpinx from contrast spilling into the peritoneum and loculated spill.

Complications of HSG include:

- Pain—due to uterine distension or peritoneal spill. Minimise by slow injection of contrast and the use of isosmolar contrast agents.
- Infection—rare, but more frequent in patients with a past history of pelvic inflammatory disease and hydrosalpinges.

- Vasovagal reactions—usually from manipulation of the cervix or inflation of an occlusion balloon in the cervical canal.
- Venous intravasation of no clinical significance but can make interpretation of the images difficult. It occurs more commonly in the presence of fibroids or tubal obstruction (Fig. 34.64).
- Allergic reaction to contrast media—very rare.

Congenital uterine abnormalities The uterus develops by fusion of the paired müllerian duct systems. Complete or partial failure of fusion is estimated to occur in 3–4% of the general population. The range of resulting abnormalities is shown in Fig. 34.65.

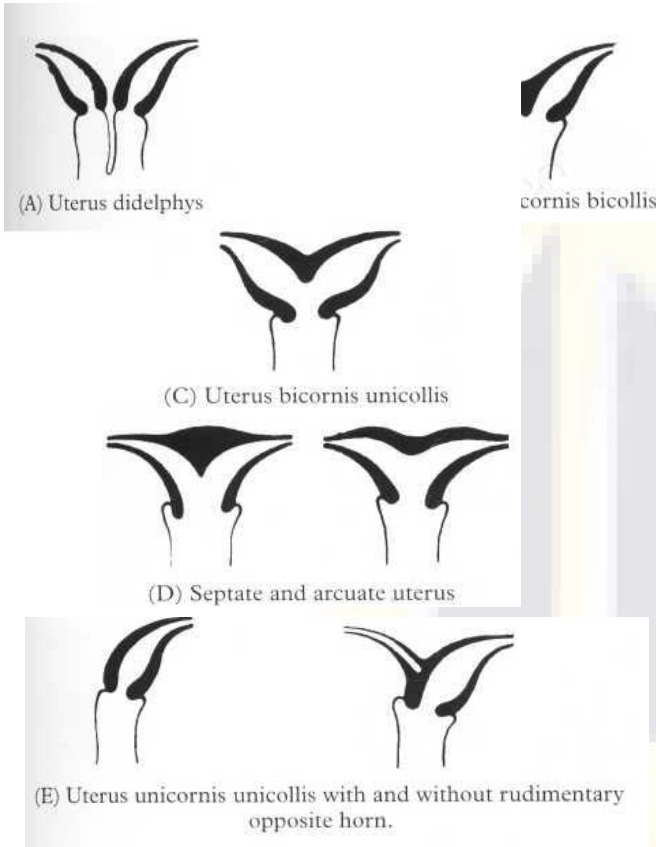


Fig. 34.65 Important congenital abnormalities of the uterus.

Minor degrees of abnormality are of no clinical significance; however, there is an increased incidence of recurrent miscarriage in patients with a septate uterus, so differentiation from a bicornuate uterus is important. On HSG an angle of $>90^\circ$ between the horns is suggestive of a bicornuate uterus but definite differentiation from a septate uterus requires further investigation to look for a fundal notch.

Truly unicornuate uteri are rare, so if an apparently unicornuate uterus is demonstrated on HSG care should be taken to look for a rudimentary horn or second cervix (Figs 34.66-34.68).



Fig. 34.66 HSG. Uterus bicornis bicornis. Note the completely separate cervical canals and uterine horns, both of which have patent tubes.

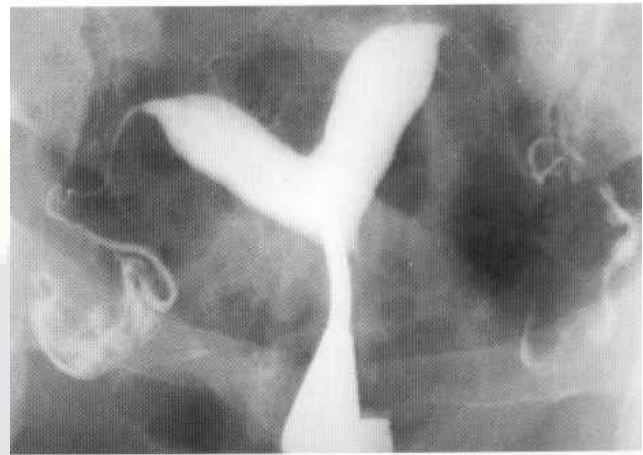


Fig. 34.67 HSG. Bifid uterine cavity. Impossible to be sure if this is bicornuate or septate.

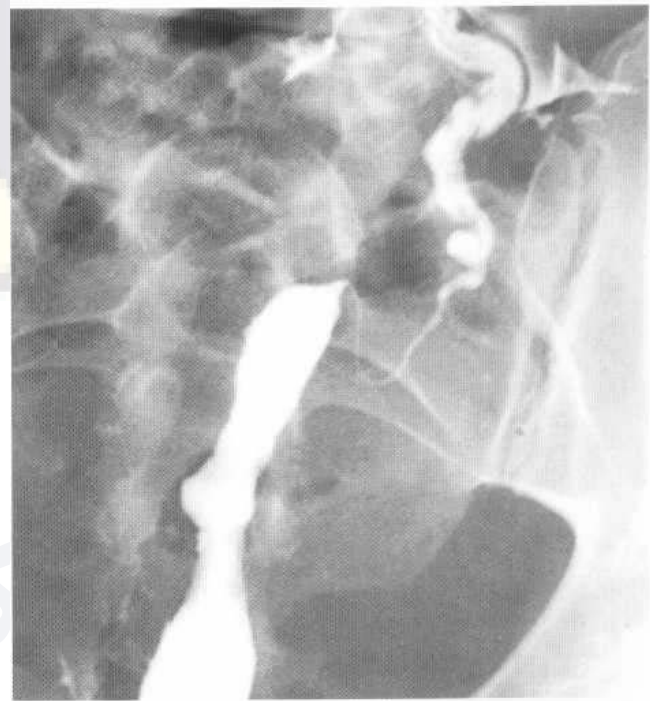


Fig. 34.68 HSG. Unicornuate uterus. No evidence of a rudimentary horn.

Other uterine abnormalities Filling defects in the uterus are caused by:

- fibroids (Figs 34.69-34.71)
- polyps / endometrial hyperplasia
- intrauterine adhesions, caused by dilatation and curettage (D&C), tuberculosis or following exposure to diethylstilboestrol (DES)
- pregnancy.

The effect of fibroids on an HSG depends on their position within the uterus. Subserosal fibroids may cause displacement of the cavity but are otherwise undetectable; mural fibroids enlarge the cavity and may or may not cause distortion; submucous fibroids appear as polypoid filling defects within the uterine cavity, indistinguishable from endometrial polyps. Early-filling films are necessary to demonstrate small fibroids and oblique views are helpful in confirming their exact location.

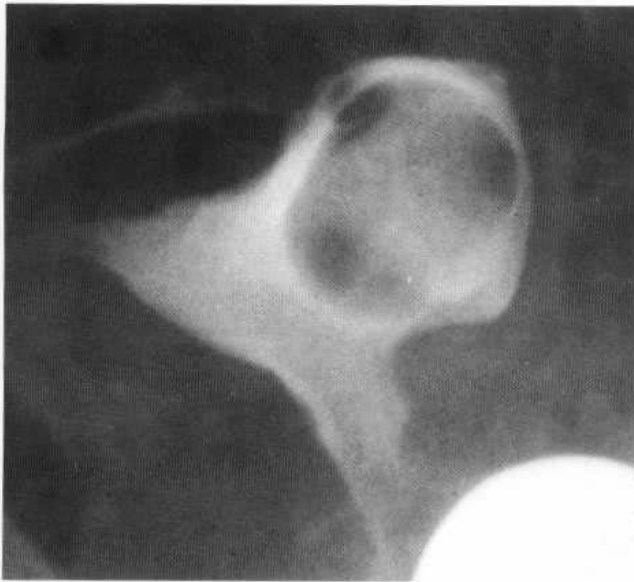


Fig. 34.69 HSG. Filling defect due to submucous fibroid.

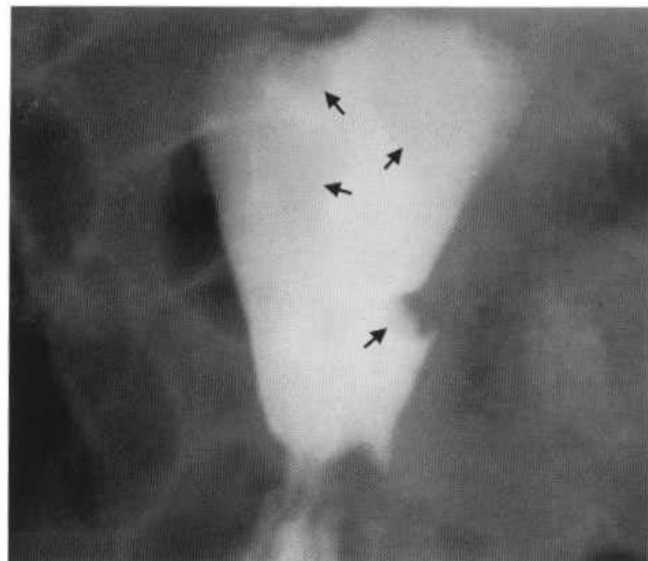


Fig. 34.72 HSG. Polypoid endometrium causing multiple filling defects (arrows) only seen on the early filling film.

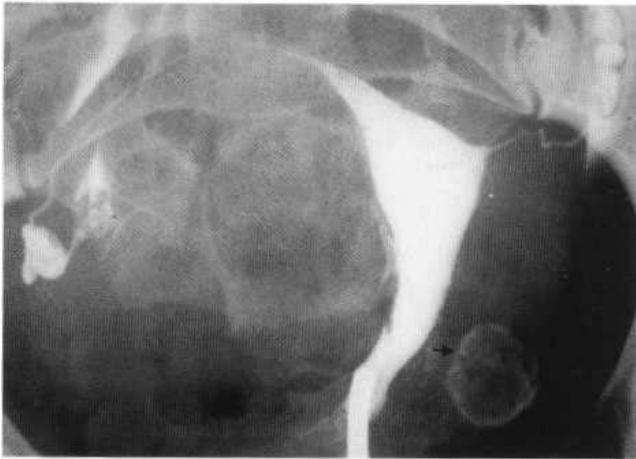


Fig. 34.70 HSG. Cavity and right fallopian tube being distorted by large mural fibroid. Note small calcified fibroid on the left (arrows).



Fig. 34.73 HSG. Linear filling defects in the uterine cavity due to adhesions.

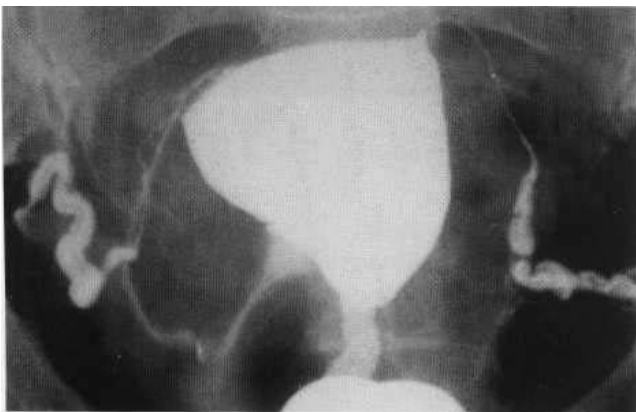


Fig. 34.71 HSG. Cavity enlarged by fibroids.

Multiple small filling defects causing an irregular lobulated outline to the uterine cavity are also seen with endometrial hyperplasia, for example in patients with polycystic ovary syndrome (Fig. 34.72). Intrauterine synechiae/adhesions cause linear or irregularly-shaped filling defects that are not obliterated by increasing amounts of contrast (Fig. 34.73). They are associated with recurrent miscarriage and,

if extensive, they can completely obliterate the uterine cavity, causing Asherman's syndrome (Fig. 34.74). *Asherman's syndrome* is amenorrhoea due to intrauterine synechiae, usually caused by dilatation and curettage for postpartum haemorrhage or retained products of conception. Rarely it follows a normal pregnancy. Treatment comprises hysteroscopic resection of the adhesions and insertion of an intrauterine device to separate the walls of the cavity.

Intrauterine adhesions and small irregularly-shaped cavities are also seen in patients with chronic endometritis due to tuberculosis (Fig. 34.75). *Genital Tuberculosis* primarily affects the fallopian tubes and 50% of patients with tubal disease will have a uterine abnormality. Tubal tuberculosis leads to a rigid abnormal tube with occlusion in the isthmus. The ends are frequently clubbed and there are diverticula-like projections from the tubal surface. Tubal (and very rarely ovarian) calcification can be seen.

A small irregular T-shaped cavity, with constrictions around the body, is also associated with *c.sposure to DES*, a drug that was used from 1940 to 1960 to treat recurrent miscarriage. It resulted in a range of genital abnormalities in the daughters of treated mothers and is associated with increased incidence of subfertility, ectopic pregnancy and pregnancy loss, as well as an increased incidence of clear cell carcinoma of the vagina.

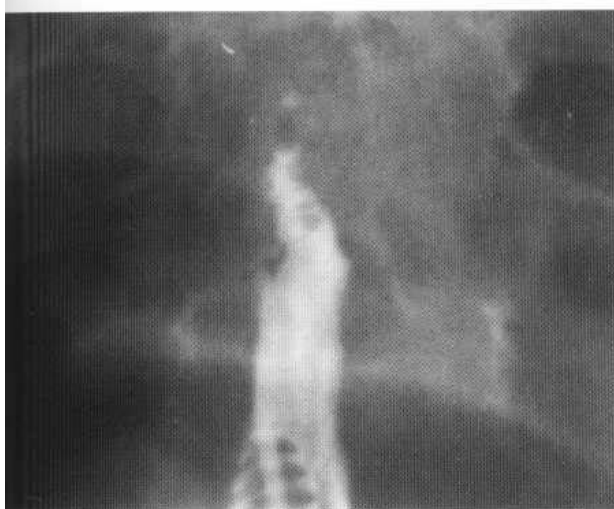


Fig. 34.74 HSG. Severe Asherman's syndrome with complete obliteration of the uterine cavity.

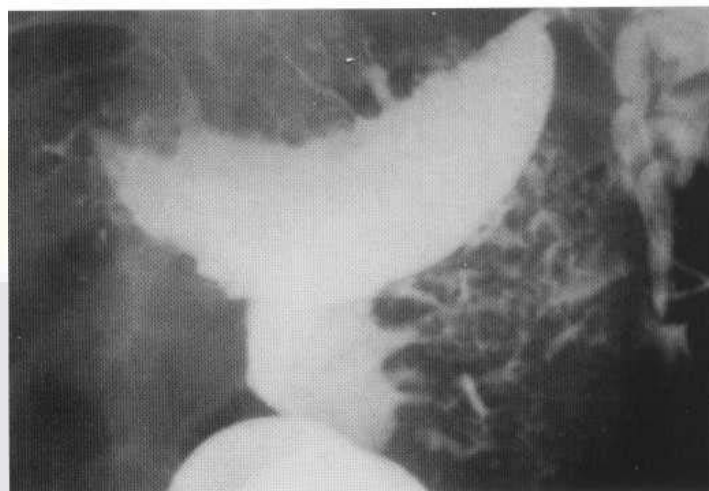


Fig. 34.76 HSG. Enlarged uterus with multiple diverticular-like projections of contrast into the myometrium typical of adenomyosis.

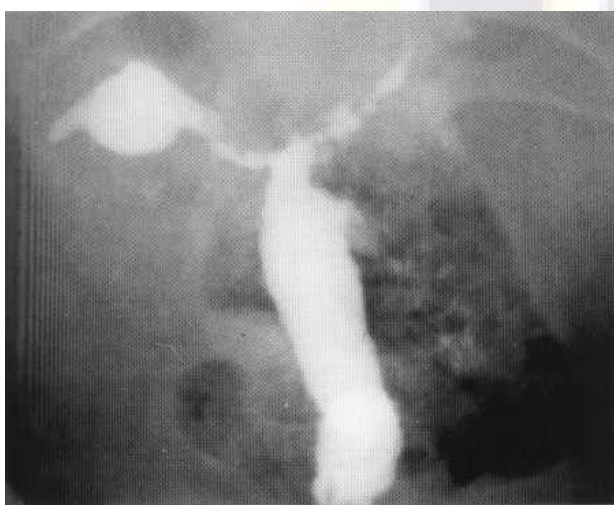


Fig. 34.75 HSG. Tuberculous endometritis leading to an irregular T-shaped uterine cavity.



Fig. 34.77 HSG. Normal right tube but a large left hydrosalpinx. Note the mucosal folds on the left have been obliterated and there is no distal spill.

Adenomyosis (endometriosis interna) is a rare cause of subfertility: it can be recognised by diverticula-like projections of contrast from the cavity into the myometrium, usually in association with an enlarged uterus (Fig. 34.76).

Tubal disease Pelvic inflammatory disease is the most common cause of both distal and proximal tubal occlusion. Preservation of mucosal folds within a hydrosalpinx is said to be associated with a good response to tubal surgery; however, nowadays patients are frequently referred directly for IVF rather than being considered for tubal surgery. Peritubal adhesions cannot be identified reliably on HSG but their presence can be inferred if contrast remains loculated around the tube instead of spreading freely in the peritoneum, and if the tube looks angulated or distorted. Delayed images may be of value in determining this (Fig. 34.77).

Other causes of tubal occlusion are endometriosis, postabortal or postpuerperal infection and tuberculosis.

Salpingitis isthmica nodosa (Fig. 34.78) is characterised by multiple diverticula-like collections of contrast projecting from the tubal lumen. It is usually due to pelvic inflammatory disease or endometriosis and is associated with an increased incidence of subfertility and ectopic pregnancy.



Fig. 34.78 HSG. Salpingitis isthmica nodosa (arrows). The right tube is patent but the left tube is very irregular and beaded and terminates in a hydrosalpinx (arrowhead).

Cornual polyps are occasionally seen as tiny filling defects at the cornua but they rarely cause obstruction and are of questionable clinical significance.

Selective fallopian tube catheterisation and recanalisation

Approximately 50% of proximal tubal occlusions have been shown to be due to spasm, amorphous debris and fine adhesions, rather than to a true histological occlusion, and these are amenable to treatment by selective fallopian tube catheterisation.

Following a conventional HSG a 5F catheter is manipulated into the origin of the tube. Contrast is injected to confirm tubal occlusion and then a guide-wire (0.35 in) is used to probe the tube and hopefully dislodge the obstruction. Success rates for tubal recanalisation of 70-80% have been achieved, with subsequent pregnancy rates of 10-45%. This compares favourably with success rates achieved by IVF. The technique is popular in the USA but has been slow to gain acceptance in the UK, most gynaecologists preferring to send their patients with tubal disease directly for IVF (Figs 34.79, 34.80).

Selective tubal catheterisation also allows measurement of *tubal filling pressures*. A pressure transducer is connected between the catheter and an injection pump. Once the catheter tip is positioned in the cornua, contrast is injected at a constant rate and the back-pressure monitored until tubal filling is achieved. Normal tubes fill with pressures less than 200 cm H₂O. A pressure rise of greater than

400 ChM before tubal filling has been associated with infertility and a poor response to tubal recanalisation.

COMPUTED TOMOGRAPHY

The role of CT in the evaluation of gynaecological diseases in the pelvis has declined since the advent of endovaginal scanning and MRI.

As a general rule, benign disease should be investigated initially by ultrasound and then MRI, rather than CT, which is used to solve specific problems. Staging of malignant disease requires CT or MRI, depending on the site of the primary tumour. MRI is superior to CT for staging cervical and uterine carcinoma, particularly with respect to local disease, but CT still has a role in ovarian carcinoma because of its ability to detect peritoneal deposits.

Currently CT and MRI have similar capabilities for detecting lymphadenopathy, although the use of different imaging planes and development of specific contrast suggest that MRI will eventually prove to be more accurate. However, CT is frequently used as an imaging modality in patients with non-specific lower abdominal symptoms such as pain, or to determine the site of origin of a mass, so it is clearly necessary to be aware of the CT appearances of gynaecological conditions.

CT of the pelvis is performed following opacification of the small bowel with oral contrast (given at least an hour before the scan) and with a moderately full bladder. Some institutions also use a vaginal tampon and rectal contrast. Intravenous contrast enhancement helps to distinguish lymphadenopathy from pelvic vessels, so is mandatory when CT is performed as a staging investigation.

CT anatomy of the pelvis The vagina is identified as a thin rectangular structure with a brightly enhancing mucosa. The cervix and uterus appear as soft-tissue masses, only distinguishable from each other by their shape, i.e. the cervix is round and the uterus oval or triangular in cross-section. The endometrium is not easily distinguished from the myometrium but distension of the cavity by fluid is discernible, particularly following enhancement with intravenous contrast.

The ovaries can usually be seen in adult premenopausal patients as soft-tissue masses posterolateral to the uterus; however, their position is variable and their precise appearance depends on whether or not there are cysts/follicles present. The atrophic ovaries of postmenopausal patients are frequently indistinguishable from surrounding structures.

Uterine fibroids Fibroids typically cause an enlarged lobulated uterus. They are usually isocchoic with the myometrium and show similar enhancement following intravenous contrast administration; however, they may contain calcification (up to 10%) or areas of reduced attenuation due to degeneration or necrosis. High-attenuation areas are also seen due to haemorrhage. Pedunculated fibroids may be difficult to distinguish from an adnexal mass and submucous fibroids may expand the cavity, mimicking an endometrial carcinoma. There are no specific features to differentiate fibroids from adenomyomas or other rare myometrial tumours, such as metastases or leiomyosarcomas (Figs 34.81, 34.82).

Endometrial carcinoma Endometrial carcinoma typically causes a hypodense, irregular mass expanding the uterine cavity, some-

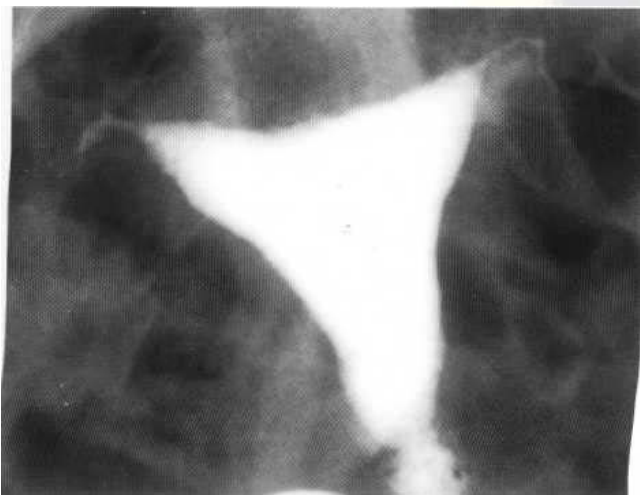


Fig. 34.79 HSG. Bilateral cornual occlusions.



Fig. 34.80 Selective salpingography. 5F catheter and wire manipulated into the right uterine cornua. Subsequent injection of contrast shows tubal patency with free peritoneal spill.



Fig. 34.81 CT. Bulky uterus with low-density areas due to fibroids. One small fleck of calcification.

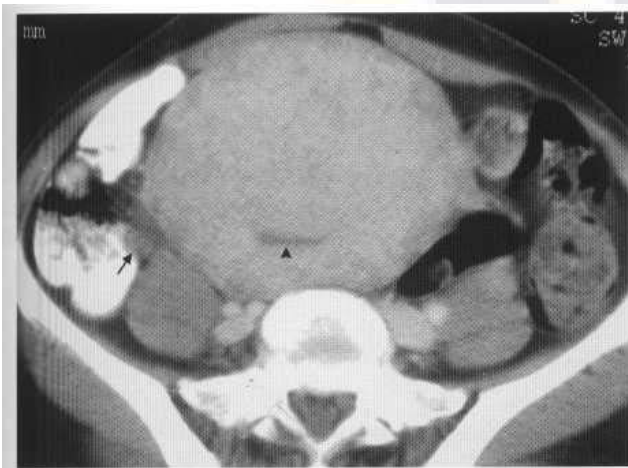


Fig. 34.82 CT. Bulky mildly heterogeneous uterus with posterior displacement of the cavity due to adenomyosis rather than fibroids.

times associated with blood, fluid or pus within the cavity. CT is good at determining the extent of extrauterine disease but cannot easily differentiate stage I from stage 2 disease, so formal staging is far better performed with MRI.

Cervical carcinoma Cervical carcinoma is suggested by the presence of an enlarged irregular cervix. The tumour enhances less than the surrounding normal cervical stroma, forming a relatively hypodense area following intravenous contrast. Fluid may be seen within a distended uterine cavity if the cervical canal is obstructed by tumour. Parametrial invasion is demonstrated by loss of clarity of the cervical margins, with an eccentric soft-tissue mass and stranding into the paracervical fat. However, minor soft-tissue stranding should be interpreted with caution as inflammatory changes and oedema following dilatation and curettage or cone biopsy can give similar appearances. Loss of the fat planes between the cervix and the ureters, rectum and/or bladder is indicative of advanced disease (i.e. stage 3 or greater). There is also strong correlation between cervical size and prognosis—a maximum anteroposterior depth greater than 4 cm is associated with a significantly higher incidence of nodal metastases and a poor prognosis.

Evaluation of a patient with cervical carcinoma must also include assessment of the iliac and para-aortic lymph nodes and both kidneys because of the propensity of the tumour to invade the

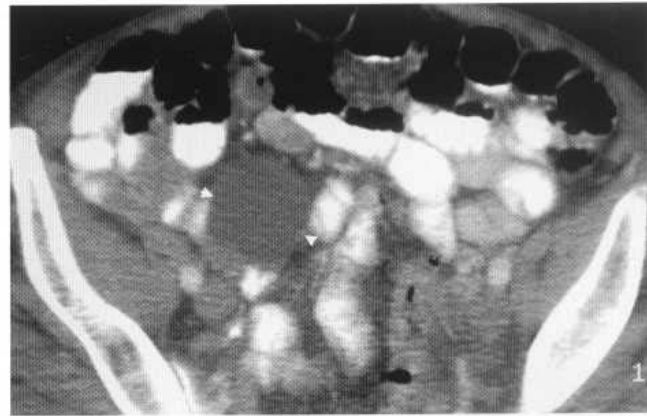


Fig. 34.83 CT. Small adnexal cyst (arrow) in postmenopausal patient. EVS confirmed a small simple cyst.



Fig. 34.84 CT. Complex mass in the pelvis typical of a dermoid cyst (arrows). The mass is of mixed attenuation but contains a large amount of fat. It has a calcified rim and a dense area of calcification (arrowheads) inferolaterally due to a tooth.

ureters. Short-axis measurements of greater than 0.8 cm in the

common iliac nodes is said to indicate a high likelihood of metastatic disease and this is particularly true if the nodes are relatively

hypoechoic following contrast enhancement, i.e. they possess the same enhancement characteristics as the primary tumour.

Adnexal masses Functional ovarian cysts are visible as thin-walled low-attenuation masses within the ovaries (Fig. 34.83). Pain can be due to rupture, haemorrhage or torsion. On CT haemorrhage may be recognised by the presence of high-attenuation fluid within a cyst. Acute torsion causes severe pain and most patients proceed to laparoscopy without CT; however, subacute torsion can be difficult to diagnose clinically. CT findings include deviation of the uterus to the side of the torsion and engorgement of adjacent blood vessels around a non-enhancing mass (the enlarged ischaemic ovary). Apparently simple functional cysts should be further evaluated with ultrasound to confirm their benign and transient nature.

The cause of complex (i.e. partly cystic and partly solid) adnexal masses is difficult to determine on CT. A dermoid cyst can be diagnosed with confidence if fat and calcification are seen within it (Fig. 34.84) (approximately 90%) but otherwise it is difficult to distinguish neoplastic from inflammatory masses. The same criteria

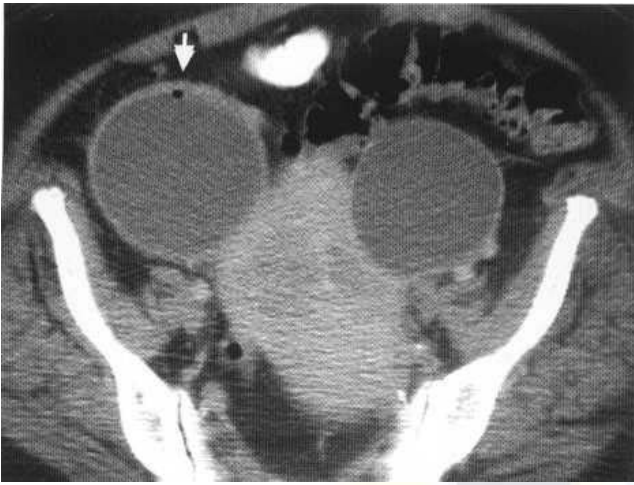


Fig. 34.85 CT. Bilateral cystic adnexal masses. Note the tiny gas bubble (arrow) seen in one of the masses. Laparoscopy confirmed bilateral hydrosalpinges with chronic infection.

are applied to adnexal masses on CT as for ultrasound, i.e. a complex mass with thick irregular septations and wall nodularity is strongly suggestive of a carcinoma. Rarely gas is seen within a mass and indicates a pelvic abscess (Fig. 34.85). Calcification may be seen in a pedunculated fibroid or a solid ovarian tumour such as a fibroma.

Endometriotic cysts have a very variable appearance on CT, with areas of high attenuation within them due to haemorrhage; however, both sensitivity and specificity for endometriosis are low on CT and quite extensive peritoneal implants can be missed.

Ovarian carcinoma

CT does, however, retain a role in staging of ovarian carcinoma, largely because of its ability to detect peritoneal and serosal deposits in addition to liver and nodal metastases. Typically there is diffuse thickening of the omentum—so-called omental cake—with nodular thickening of the peritoneum and serosal surface of the bowel (Fig. 34.86). Most ovarian carcinomas are already advanced at the time of presentation but surgery is still helpful to reduce tumour bulk. Preoperative staging of ovarian carcinoma is therefore performed to assess tumour bulk and detect those patients with

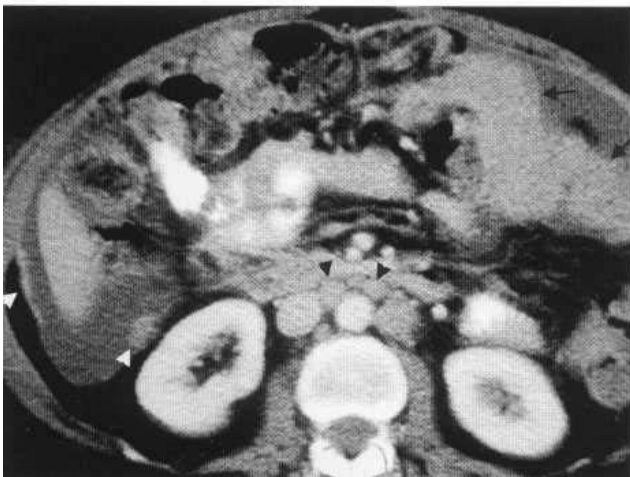


Fig. 34.86 CT. Patient with ovarian carcinoma, peritoneal deposits (white arrowheads), para-aortic lymphadenopathy (black arrowheads) and 'omental cake' (black arrows).

inoperable metastatic disease, e.g. liver metastases, for whom surgery may have little to offer.

INTERVENTIONAL RADIOLOGY

Angiography Arteriography as a purely diagnostic procedure is rarely indicated nowadays. However, embolisation of both uterine arteries can be performed safely with a high success rate and low complication rate, hence it can be used to treat intractable bleeding, such as may occur following childbirth, from pelvic tumours, following radiotherapy, following trauma and from the very rare uterine arteriovenous malformations. *Arteriovenous malformations* are suspected from a history of recurrent extremely heavy bleeds which usually follow a miscarriage or uterine intervention, such as dilatation and curettage or evacuation of retained products of conception. Colour Doppler ultrasound demonstrates an area of abnormal vascularity in the uterus with high flow rates and low impedance flow on spectral Doppler (Fig. 34.87).

More recently transcatheter embolisation of the uterine arteries has been advocated as a means of treating large fibroids in patients who wish to avoid hysterectomy. Embolisation of both uterine arteries is performed using polyvinyl alcohol (PVA) particles, with or without gel foam. Antibiotic cover is given, with sedation and analgesia as required. Results to date show a reduction in uterine size of 40-70% and a reduction in abnormal menstrual bleeding in 80-90% of patients. The complication rate is low, the most common complication being pain due to ischaemic necrosis. Postprocedural infection occurs in 1-2%. There are reports of successful pregnancy following embolisation but amenorrhoea, thought to be due to ovarian failure, has also been reported, so the technique should be considered very carefully in patients who are trying to conceive.

Percutaneous aspiration and drainage Follicular aspiration for oocyte retrieval is routinely performed with ultrasound guidance but there is reluctance to aspirate cysts because of fear of seeding malignant cells in to the peritoneal cavity. However, cysts that are

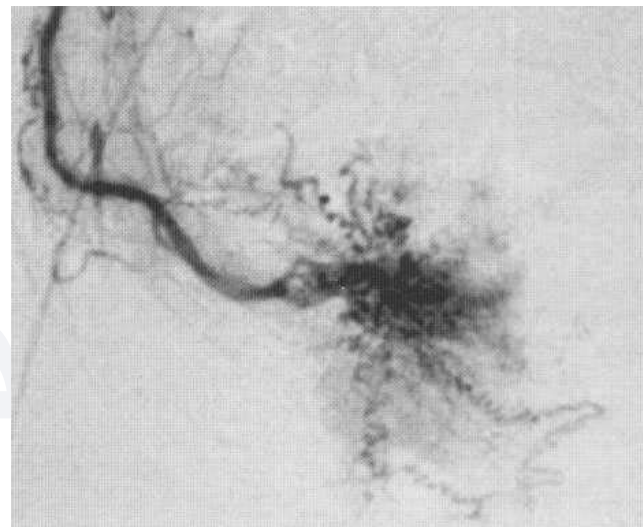


Fig. 34.87 Patient with a history of recurrent very heavy vaginal bleeding. Selective internal iliac artery injection shows an abnormal stellate collection of vessels on the right. Embolisation was performed, with good symptomatic relief.

likely to be benign can be safely aspirated—either trans-abdominally across a distended bladder or endovaginally. This is effective treatment for pain caused by functional cysts or adhesion-related peritoneal cysts, with a risk of recurrence of 15-20%.

Similarly patients with large tubo-ovarian abscesses may benefit from aspiration or drainage of the pus, the preferred route depending on the location of the abscess.

Ultrasound guidance can also help to guide drainage of an obstructed uterus.

MAGNETIC RESONANCE IMAGING

Jeremy P. R. Jenkins

MRI is an important technique in the evaluation of pelvic pathology due to its ability to obtain images with a high soft-tissue contrast resolution and discrimination in multiple planes. It is now the primary technique of choice in the staging of pelvic malignancy, with the exception of staging ovarian malignancy, where CT is the preferred technique. Advantages of MRI in the pelvis have been discussed in Chapter 31.

Uterus, cervix and vagina

Both sagittal and transverse imaging planes are required when assessing the uterine body, cervix and vagina. T₂-weighted scans display the characteristic zonal anatomy, with three distinct areas within the *uterine body* (Fig. 34.88). There is a hyperintense central zone representing the endometrium combined with secretions in the endometrial canal, an outer area of intermediate signal due to myometrium, and a low-signal functional zone between, from a layer of compressed myometrium. Changes in size and signal inten-

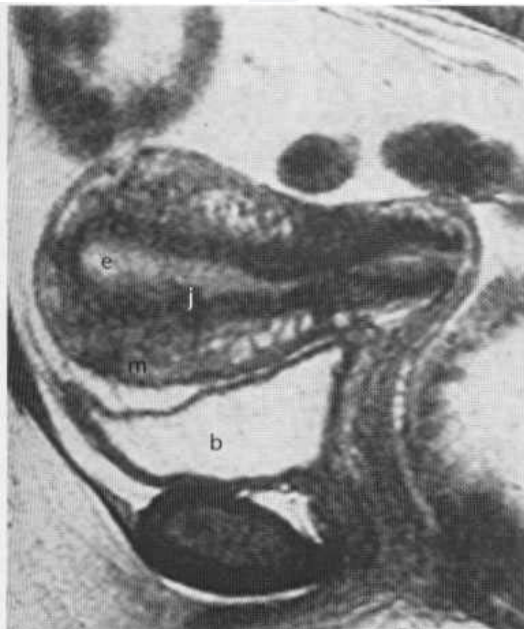


Fig. 34.88 Normal uterus on a sagittal T₂-weighted spin-echo (TSE 3500/100) image with normal zonal anatomy of central high-signal endometrium (e), the junctional zone (j) and the outer myometrium (m). urine-filled bladder.

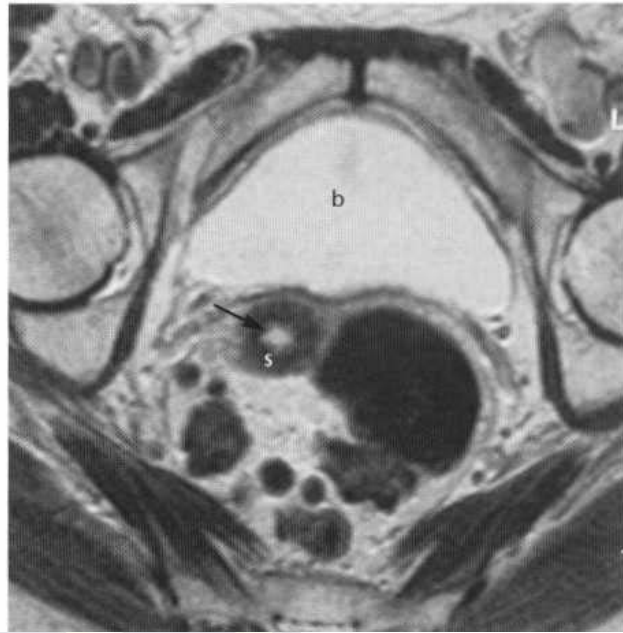


Fig. 34.89 Normal zonal anatomy of the cervix on a transverse T₂-weighted spin-echo (TSE 3500/100) image. b = bladder; s = cervical stroma; straight arrow = cervical mucus and epithelium.

sity of the three zones in the uterus occur during the menstrual cycle, with an increase in volume and signal of the myometrium in the secretory phase. Following intravenous gadolinium-chelate the endometrium and myometrium enhance, with the functional zone remaining low-signal on T₂-weighted images.

The *cervix* is a cylindrical-shaped structure measuring 2-4 cm in length, connecting with the body of the uterus at the isthmus. The level of the isthmus is approximately at the peritoneal reflection on the bladder. The cervix has two distinct layers: a hyperintense central zone representing cervical mucus and epithelium, with an outer zone of low signal, similar to the uterine functional zone, due to the fibrostromal wall (Fig. 34.89). A further peripheral layer of intermediate signal may be seen continuous with the myometrium. The *parametrium* has an intermediate signal on T₂-weighted images, with increase in signal on T₂-weighted scans. After intravenous gadolinium-chelate the compact cervical stroma retains its low signal, with enhancement of the paracervical tissue and inner cervical epithelium on T₂-weighted images. There are numerous glands lining the cervical canal and the ducts of these glands can become blocked, producing retention (nabothian) cysts (Fig. 34.90). These are commonly seen on MRI of the female pelvis.

The *vagina* can be identified as a high-signal central zone of mucus and epithelium surrounded by a low-signal muscular wall (Fig. 34.88). The vagina can be divided into three regions: an upper third is characterised by the lateral vaginal fornices, a middle third is at the level of the bladder base, and a lower third is at the level of the urethra. There is a high-signal venous plexus surrounding the cervix and vagina, best seen on transverse T₂-weighted images (Fig. 34.90).

Intrauterine contraceptive devices (IUCDs) are safely imaged with MRI, with no adverse heating or torque effects demonstrated. All IUCDs show a signal void, the extent depending on the type of device in situ, on all pulse sequences (Fig. 34.91). A contraceptive diaphragm will, however, produce a significant signal artefact.

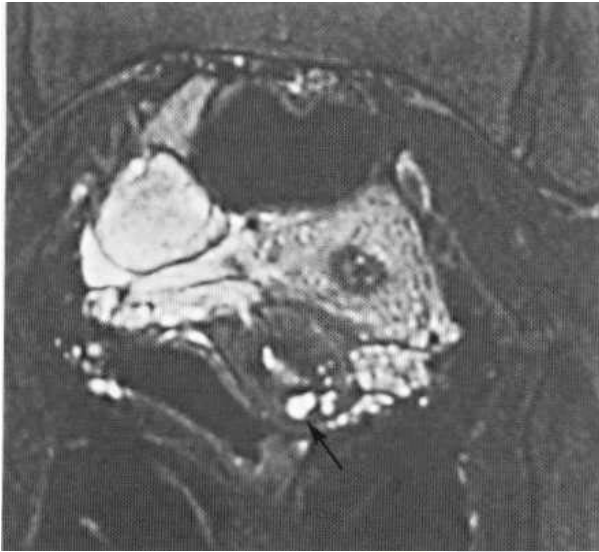


Fig. 34.90 Nabothian cysts (curved arrow) within the cervix on a fat-suppressed transverse T_2 -weighted spin-echo (FSE 3500/100) image.

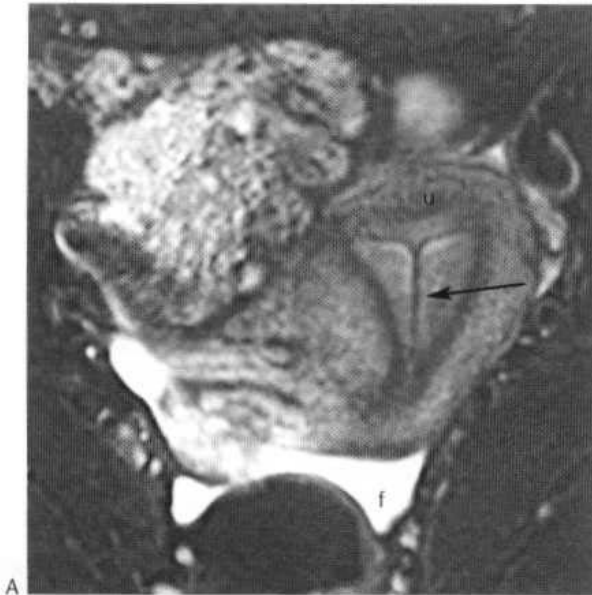


Fig. 34.91 An IUCD (arrow) within the uterus (u) on a transverse fat-suppressed T_2 -weighted spin-echo (FSE 3500/100) image. f = free fluid in the sacral cul de sac.

Congenital uterine anomalies

The upper two-thirds of the vagina, cervix, uterus and fallopian tubes develop from fusion and descent of paired müllerian ducts. The lower third of the vagina is derived from the urogenital sinus. Partial or complete failure of the ducts to fuse results in a spectrum of complex abnormalities. MRI is the technique of choice in assessment and evaluation of these congenital lesions. MRI can demonstrate *unicornuate*, *bicornuate* and *septate* uteri, and *uterine didelphys* (Fig. 34.92). A uterine didelphys is one in which two separate uteri and cervixes are visualized. A septate uterus is one in which the uterine septum fails to resorb, which results in failure of correct placental implantation and subsequent miscarriage. MRI is able, unlike other imaging techniques, to differentiate a septate from a bicornuate uterus. The importance of making this distinction is that the surgical approach for treating the two anomalies is dif-

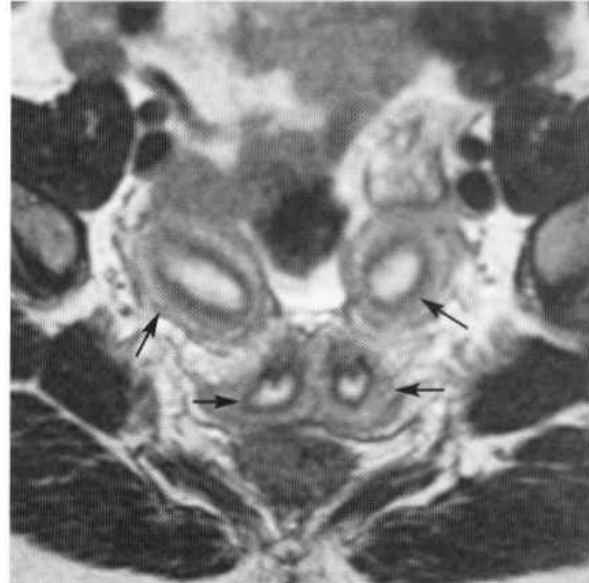


Fig. 34.92 (A,B) Uterine didelphys showing two separate uteri and cervixes (arrows) are demonstrated on transverse T_2 -weighted spin-echo (FSE 3500/100) images. Note the normal left ovary (o).

ferent: a bicornuate uterus requires abdominal surgery, whereas the septate uterus can be repaired hysteroscopically. MRI, as with other imaging methods, can be used to assess any renal tract abnormalities coexistent with these müllerian duct anomalies.

Uterine tumours

Leiomyoma This is the most common solid uterine tumour, being single or multiple. These tumours are composed of smooth muscle with varying amounts of fibrous tissue, and occur in 20-30% of premenopausal women. They are located in the submucosal, intramural and subserosal spaces of the uterus. Rarely they can occur along the broad ligament or be entirely separate from the uterus. Submucosal tumours project into the endometrial

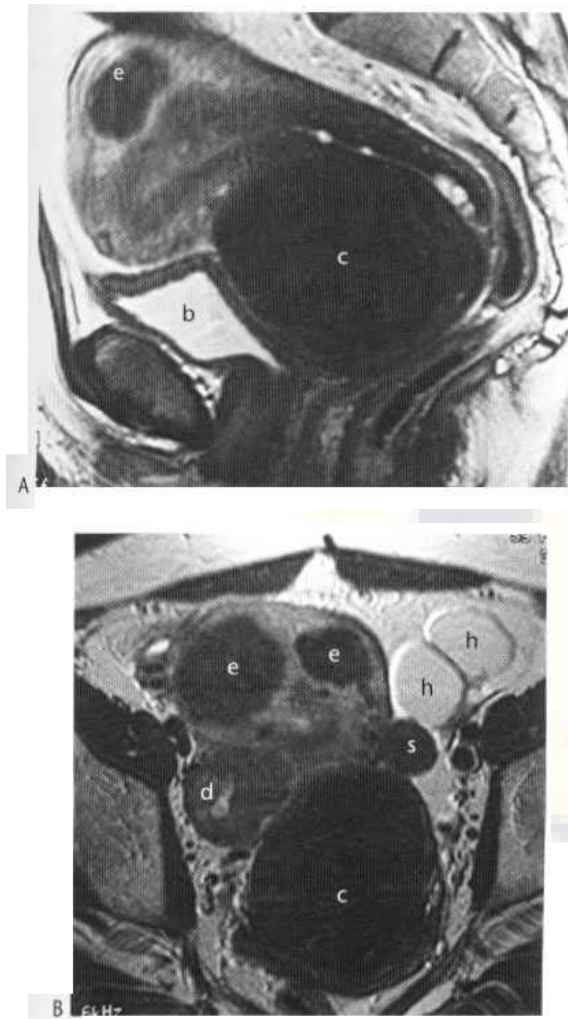


Fig. 34.93 Multiple leiomyomas (I) on (A) sagittal and (B) T_2 -weighted spin-echo (FSE 3500/100) images with a large cervical intramural leiomyoma (c) and smaller intramural tumours (e). There is a degenerating serosa leiomyoma (d) and a smaller serosal leiomyoma (s) adjacent to a loculated cystic collection due to an associated hydrosalpinx (h). b = bladder.

cavity, and intramural lesions arise within the myometrium. Subserosal leiomyomas occur along the serosal surface of the uterus. As the tumours are oestrogen-dependent they can grow rapidly during pregnancy, and tend to regress following the menopause.

MRI provides an accurate assessment of the site, size and number of uterine leiomyomas, with lesions as small as 3 mm diameter being detected. Leiomyomas are classified according to their position—submucosal, intramural, subserosal or cervical (Fig. 34.93). Non-degenerating leiomyomas have a characteristic uniform signal intensity, being indistinguishable from myometrium on T1-weighted images, with a lower signal on T₂-weighted scans (Fig. 34.93A). Occasionally calcification within these tumours produces a low signal on all pulse sequences. Degenerating tumours show a variable and non-specific signal appearance with an intermediate-high signal on T₁-weighted and a high signal on T₂-weighted images (Fig. 34.93B). Malignant transformation cannot be differentiated from benign degenerating tumours. The use of intravenous gadolinium-chelate does not improve the detection rate or characterisation of leiomyomas.

While the assessment of leiomyomas is usually by clinical examination and ultrasound, these techniques can be limited in the

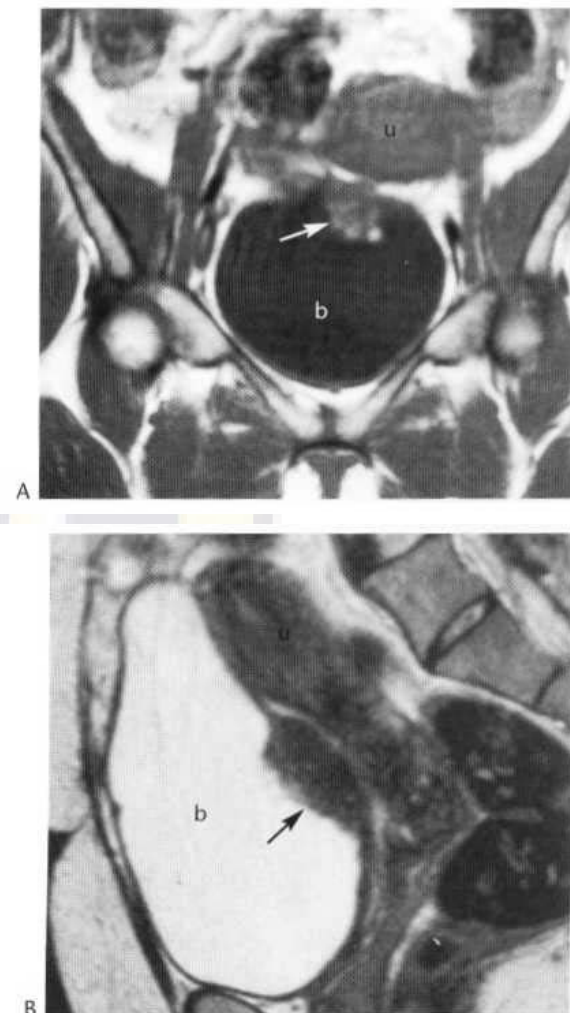


Fig. 34.94 Endometrioma deposit (arrow) within the bladder wall on (A) coronal T₁-weighted (SE 650/25) and (B) coronal T₂-weighted spin-echo (TSE 3500/100) images. Note the areas of high signal within the superficial margin of the deposit due to haemorrhage in (A), and the low signal on the T₂-weighted in (B). b = bladder; u = uterus.

presence of a retroverted or displaced uterus. In addition, difficulty can be encountered in discriminating between a uterine and an adnexal mass. False-negative rates of up to 20% for the detection of leiomyomas by ultrasound have been reported. Precise delineation of uterine leiomyomas can determine appropriate treatment. The relationship of these tumours to the endometrium and junctional zone is important in patients being considered for selective myomectomy. MRI is useful in demonstrating subserosal tumours and those submucosal lesions on a pedicle or stalk, as the presence of either of these precludes the use of uterine artery ablation as a treatment.

Endometriosis This is a condition of unknown cause in which endometrial glands and stroma (functioning endometrium) are found outside the uterine cavity and musculature. This ectopic endometrium, being influenced by circulating hormones, undergoes repeat haemorrhage and develops into blood-filled cysts (termed *endometriomas*). These haemorrhagic cysts are associated with adhesions and scarring. They can occur on any retroperitoneal surface, and have been found at distant sites (lymph nodes, lung and bone).

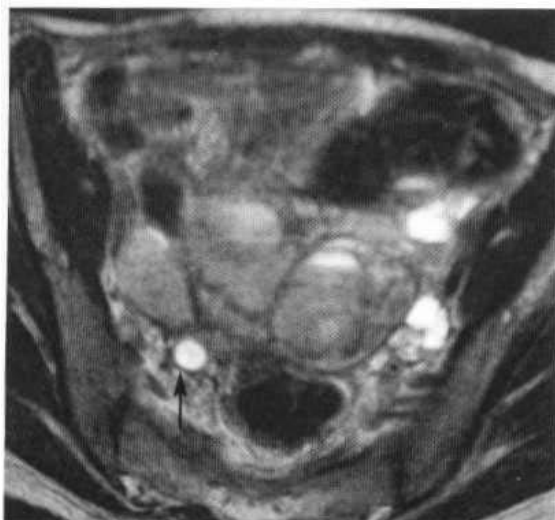


Fig. 34.95 Endometriosis on a transverse T_2 -weighted spin-echo (TSE 3500/100) image showing multiple fluid-fluid levels from haemorrhagic contents within multiloculated cysts filling the pelvis. There is dilatation of the right ureter (arrow).



Fig. 34.97 Diffuse adenomyosis on sagittal T_2 -weighted spin-echo (TSE 3500/100) image showing diffuse irregular low-signal thickening of the junctional zone. b = bladder.

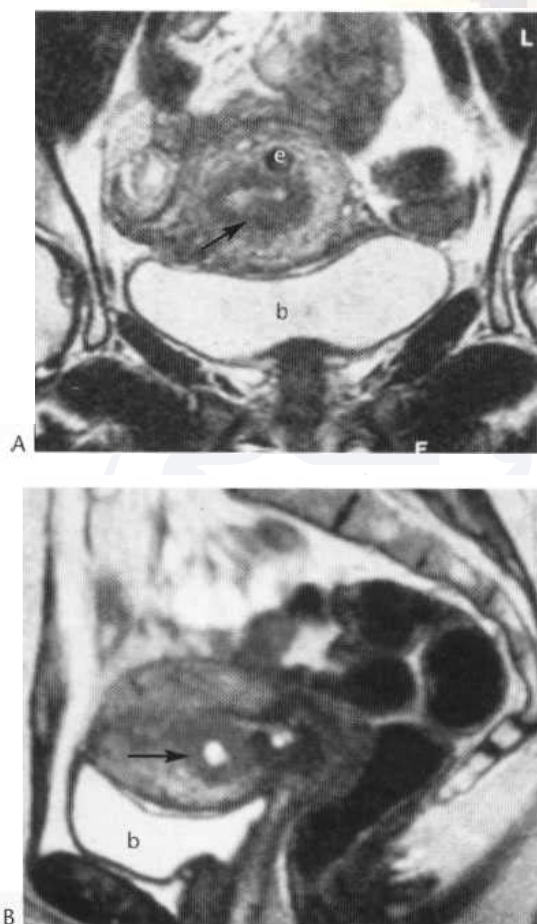


Fig. 34.96 Focal adenomyosis (arrow) on (A) coronal and (B) sagittal T_2 -weighted spin-echo (TSE 3500/100) images showing focal low-signal thickening of the junctional zone in (A) undergoing haemorrhage (arrowed in (B)) a year later. b = bladder; e = intramural leiomyoma.

MRI has been used in the detection of endometriomas (Fig. 34.94), with reported high levels of accuracy. However, small (<1 cm) endometrial implants, which may be the cause of symptoms, can easily be missed on MRI. Improved conspicuity in the

detection of these lesions can be achieved using high-resolution fat-suppressed T_2 -weighted imaging. MRI cannot be used for routine screening or staging because of limitations in sensitivity and specificity, and laparoscopy is still required. MRI is, however, useful in the assessment of patients with adnexal and other masses following a non-diagnostic ultrasound examination.

The characteristic appearance of endometriosis is of multiple, multiloculated cysts with thick walls and haemorrhagic fluid contents. On MRI the haemorrhagic component appears of high and low signal on T_1 - and T_2 -weighted images, respectively (Fig. 34.95). The low signal on the T_2 -weighted scans is due to the profound T_2 shortening from the haemorrhagic component. A less specific appearance, which is not uncommon in endometriomas, is of a high signal on both T_1 - and T_2 -weighted scans, and this is similar to haemorrhagic functional cysts of the ovary as well as malignant tumours. Some endometriomas are solid masses with low signal on T_2 -weighted images due to fibrosis (Fig. 34.94A), which can enhance following gadolinium-chelate injection. Small foci of haemorrhage may be seen in these masses. Solid endometriomas may invade deeply into bladder and bowel (Fig. 34.94).

Adenomyosis Adenomyosis, which represents heterotopic stratum basale of the endometrium interdigitating with the myometrium, cannot be distinguished from leiomyomas on clinical findings or by ultrasound. Each produces similar symptoms of pelvic pain and menorrhagia with uterine enlargement. Distinction between the two pathologies is important as treatment options are different: hysterectomy for adenomyosis versus myomectomy for leiomyoma. Adenomyosis can be focal, diffuse or microscopic. There is debate as to the normal thickness of the junctional zone, with the maximum limit suggested to be up to 12 mm, rather than 5 mm as indicated in earlier studies.

Adenomyosis can be diagnosed, and usually differentiated from leiomyomas, on MRI as a diffuse or focal thickening of the junctional zone, with or without focal areas of high signal on T_2 -weighted images (Figs 34.96, 34.97). On T_1 -weighted images focal adenomyosis appears as a poorly marginated low-signal mass within the myometrium contiguous with the endometrium. An ill-defined margin is the feature that distinguishes focal adenomyosis

Box 34.1 FIGO/TNM staging of cervical carcinoma

FIGO		TNM
0	In situ	Tis
I	Confined to uterus	T1
IA	Diagnosed only by microscopy	T1 a
AI	Depth <3 mm; width <7 mm	T1 al
IA2	Depth >3-5 mm; width <7 mm	T1 a2
IB	Clinically visible or microscopy >IA2	T1 b
IB1	Clinically <4 cm diameter	T1 b1
IB2	Clinically >4 cm	T1 b2
II	Beyond cervix but not to pelvic wall	T2
IIA	Involvement of vagina but not lower third	T2a
IIt	Parametrial extension but not to pelvic side-wall	T2b
III	Extension to pelvic wall/lower third vagina/hydronephrosis	T3
IIIA	Lower third vagina	T3a
IIIB	Extension to pelvic wall/hydronephrosis	T3b
IV	Extension beyond true pelvis/bladder/rectum	T4
IVA	Involvement of bladder/rectum	T4
IVB	Spread outside true pelvis/metastases to other organs	M1

from leiomyomas, although small leiomyomas can have ill-defined margins as well, which can lead to misdiagnoses.

Cervical carcinoma

A staging classification for *cervical carcinoma* has been described by the Committee of the International Federation of Gynaecology and Obstetrics (FIGO), based primarily on clinical findings and recently revised in 1995 (Box 34. 1, which also gives the TNM classification). This staging system was devised to assist in the assessment of different institutions and to aid in the evaluation of treatment planning and results. It should be noted that MRI and CT were not included as part of the staging classification, and nor was lymph node status, as these methods of assessment were not widely available. The FIGO staging classification is used in the assessment of cervical carcinoma.

FIGO stage I disease is tumour confined to the cervix and is subdivided according to the depth of stromal invasion. Current MRI usage is limited in its role in assessment of this stage of disease. The use of pelvic phased-array and/or endorectal/endovaginal coil technique with resultant improved resolution, possibly with contrast



Fig. 34.98 Carcinoma of the cervix (stage I1B2) showing exophytic tumour (arrows) within the vaginal canal on sagittal T₂-weighted spin-echo (TSE 3500/100) image. Note the intact low-signal vaginal wall. b = bladder.

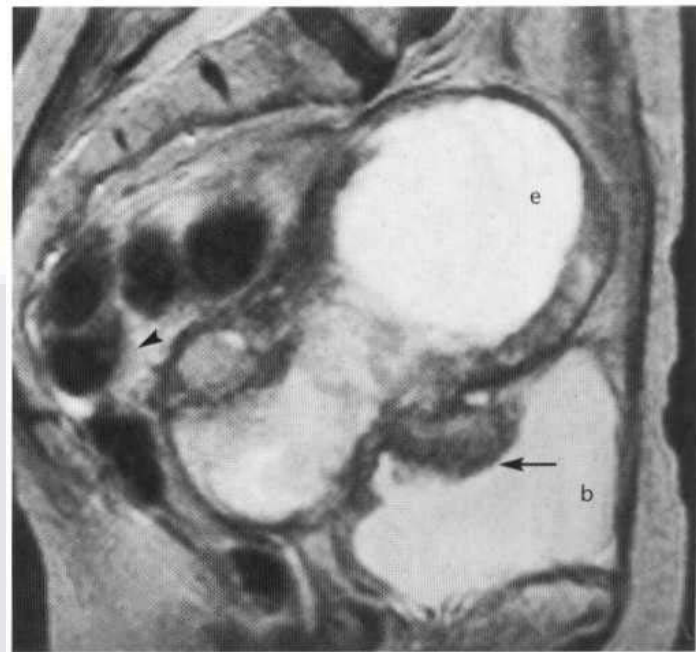


Fig. 34.99 Large cervical carcinoma (arrow) infiltrating into the bladder (b) with a separate tumour nodule in the posterior fornix (arrowhead) on a sagittal T₂-weighted spin-echo (FSE 3000/100) image. Note the endometrial obstruction (e). (Courtesy of Dr I. M. Hawnaur, Department of Diagnostic Radiology, University of Manchester.)

enhancement, should allow greater precision in measuring the depth of penetration of tumour into the cervical wall. Carcinoma confined within the cervix but with >5 mm depth of invasion or >7 mm in breadth (FIGO stage IB) can be demonstrated on MRI. Stage IB disease has recently been further subdivided into clinical tumours not exceeding 4 cm in diameter (stage IB1), and more bulky disease larger than 4 cm (stage IB2) (Fig. 34.98). Tumour volume is an important prognostic factor in stage I disease. Patients with early stage IB disease may have a survival of >90%, which reduces to 50-60% or less for those with bulky disease. This invasive cervical carcinoma is better demonstrated on MRI than CT and appears as an area of high signal contrasted against the low-signal cervical stroma on T₂-weighted images. The presence of a low-signal stromal ring around the high-signal tumour is good evidence (93-100% sensitivity) of a confined tumour. The absence of a low-signal stromal hand, however, is not certain evidence of parametrial spread due to limitation in spatial resolution using current MRI techniques. The use of high-resolution MRI, as indicated above, is likely to overcome this limitation. The cervix may enlarge, leading to obstruction of the endometrial canal with distension of the uterus from retained secretions (Fig. 34.99).

In FIGO stage II disease the tumour extends beyond the cervix. In stage IIA the tumour extends into the upper two-thirds of the vagina but not into the parametrium (Fig. 34.100), and stage IIB disease extends into the parametrium but not to the pelvic side-wall (Fig. 34.101). This distinction is critical, as most institutions treat lesions above stage IIA disease by radiation therapy. The reported accuracy of MRI in the demonstration of parametrial or vaginal spread is approximately 70-90%. On MRI T₂-weighted images extension into the parametrium is identified by the high-signal tumour breaching the low-signal cervical stromal wall on transverse, or transverse-oblique sections paralleling the short axis of the cervix. False-positive results on MRI are due to surrounding

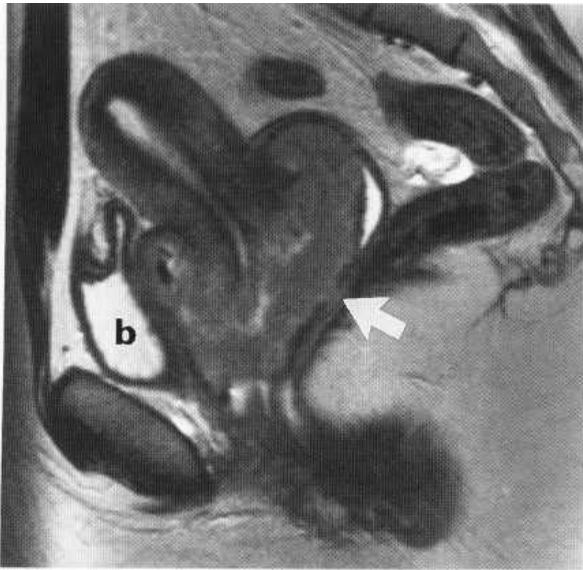


Fig. 34.100 Bulky exophytic cervical carcinoma confined within the cervix on a sagittal T₂-weighted spin-echo (TSE 5041/132) image. The low-signal vaginal wall remains intact apart from an area of tumour infiltration posteriorly (arrow). Within the tumour in the anterior fornix there is an area of necrosis. b = bladder. (Courtesy of Dr R. J. Johnson, Christie Hospital.)

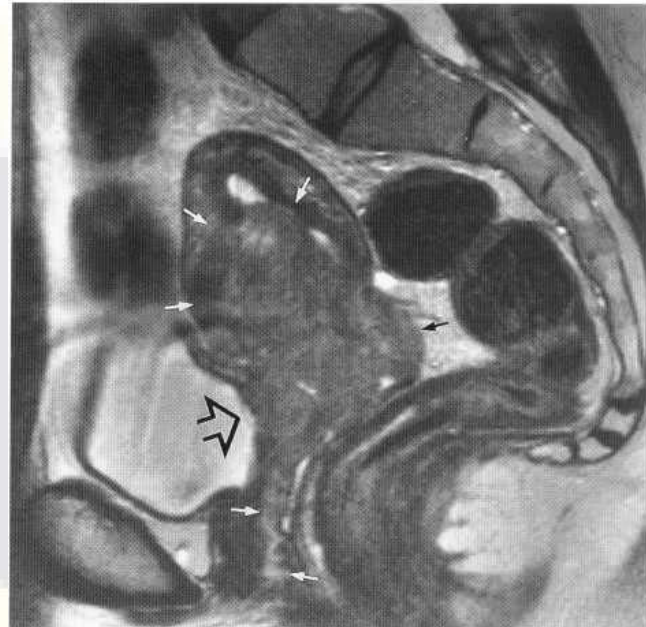


Fig. 34.102 Bulky carcinoma of the cervix extending into the body of the uterus, lower third of the vagina (small arrows) and bladder (open arrow) on a sagittal T₂-weighted spin-echo (TSE 5041/132) image. (Courtesy of Dr R. J. Johnson, Christie Hospital.)



Fig. 34.101 Carcinoma of the cervix (stage IIb) showing tumour (t) within the parametrium (arrows) on transverse T₂-weighted spin-echo (TSE 3500/100) image. Note the loss of the normal low signal from the cervical stroma. b = bladder.

oedema, vascular parametrium or an inflammatory reaction to the tumour. Vaginal extension is indicated on MRI by high-signal tumour replacing the normal low-signal vaginal wall (Fig. 34.100). Overstaging of disease occurs particularly from large exophytic tumours in the region of the anterior fornix. As direct inspection of vaginal infiltration can be easily performed, this assessment on MRI is not critical.

In FIGO stage III disease there is extension into the lower third of the vagina (stage IIIA) (Fig. 34.102), or to the pelvic side-wall with or without hydronephrosis, or a non-functioning kidney due to no known

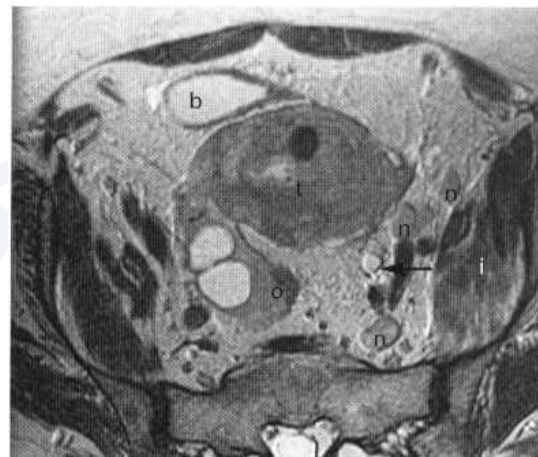


Fig. 34.103 Tumour (t) infiltrating the parametrium and left iliac muscle (i), with left-sided involved lymph nodes (n) and a right ovarian metastasis (o) on a transverse T₂-weighted spin-echo (TSE 3500/100) image. b = bladder.

other cause (stage IIIB) (Fig. 34.103). MRI criteria for pelvic side-wall invasion includes tumour within 1 cm of the muscles of the pelvic wall, vascular encasement or high-signal tumour replacement of low-signal adjacent muscles (levator am, piriformis, obturator internus) (Figs 34.103, 34.104). Overstaging of tumour can again occur due to surrounding oedema or inflammatory change.

In stage IV disease the tumour extends outside the reproductive tract, with tumour involvement of the mucosa of the rectum or bladder (stage IVA) (Fig. 34.105), or disease outside the true pelvis or distant metastases (stage IVB). Sagittal and transverse T₂-weighted scans allow assessment of tumour infiltration into the lower uterine segment, bladder, rectum and vagina, where high-signal tumour replaces the normal low-signal structures (Figs 34.106, 34.107). The use of dynamic contrast enhancement allows a clearer assessment of



Fig. 34.104 Cervical carcinoma (t) extending into the parametrium producing left hydronephrosis (straight arrow) and extending posteriorly through the perirectal fascia into the rectal mucosa (curved arrow) on a transverse T₂-weighted spin-echo (TSE 5041/132) image. b = bladder (Courtesy of Dr R.J. Johnson, Christie Hospital.)

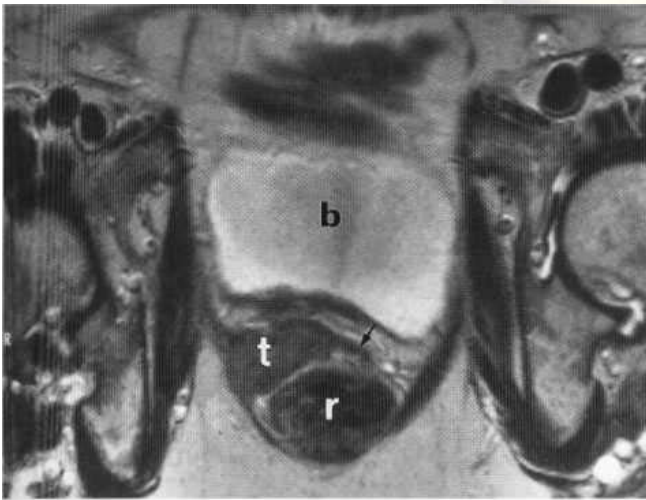


Fig. 34.105 Recurrent carcinoma of the cervix (t) infiltrating into the parametrium and right levator ani on a transverse T₂-weighted spin-echo (TSE 5041/132) image. Note the low-signal vaginal wall (arrow). b = bladder, r = rectum. (Courtesy of Dr R. J. Johnson, Christie Hospital.)

tumour extension into the bladder or rectal wall, compared with T₁-weighted images.

Although *sinph node* status is not part of the FIGO staging, the presence and extent of lymphadenopathy has important implications in treatment and prognosis. The presence or absence of pelvic lymphadenopathy is assessed on T₁-weighted images, with nodes greater than 7-10 mm in diameter being considered abnormal (see Ch. 31) (Fig. 34.103). Similar signal intensity appearances are, however, obtained from hyperplastic and metastatic nodes. A new MRI lymphographic contrast is now available using ultrasmall iron oxide particles (USIOP), which accumulates in normal nodes, producing a signal void while sparing metastatic nodes, which retain their abnormal signal (see Chapters 2, 59). The use of this agent

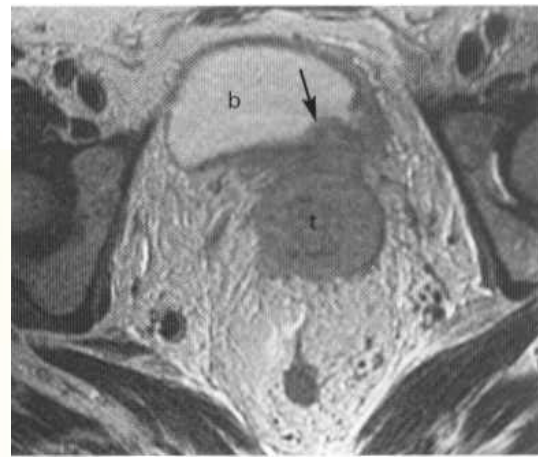


Fig. 34.106 Carcinoma of the cervix (t) infiltrating through the bladder wall (arrow) on a transverse T₂-weighted spin-echo (TSE 3500/100) image. b = bladder.

will increase the accuracy in the detection of nodal disease irrespective of size or anatomical distribution.

The treatment and prognosis of invasive cervical carcinoma is dependent on tumour volume, extent of disease, histological grade, depth of invasion and vascular and lymphatic involvement. Following histological diagnosis accurate staging is important in order to optimise treatment-demonstration of parametrial extension often precludes surgery and requires radiotherapy (Fig. 34.108). Clinical staging is often inaccurate, particularly in those with more advanced disease-two-thirds of these patients may be incorrectly staged. Imprecision in clinical staging is due to errors in assessment of size of endophytic tumours, uterine body extension, infiltration of parametria and pelvic side-wall and lymphadenopathy. X-ray, CT and ultrasound (including transrectal ultrasound) are used for staging and assessment of tumour volume but are limited due to poor tissue discrimination and difficulty in delineating adjacent organ involvement. MRI has an overall accuracy range in staging of approximately 78-92%, with improved accuracy in more advanced tumours. The accuracy of MRI for demonstrating extent of tumour invasion of the pelvic side-wall is over 90%, with a similar value for detecting bladder and rectal wall involvement. Good concordance has been achieved with tumour volume measurements on MRI when compared with data obtained by histological review. The advantages that MRI has over other imaging techniques include an improved tissue resolution and discrimination combined with a multiplanar facility, particularly with the use of phased-array coils, fast acquisition sequences with facility for fat suppression, and dynamic contrast enhancement methods. An advantage of dynamic contrast enhancement is in the assessment of neoangiogenesis of the tumour, which has a direct relationship to tumour growth rate and necrosis, but is not routinely used in staging tumours. T₁-weighted images remain superior in the evaluation of parametrial spread as the normal parametrium is well vascularised. The detailed imaging technique is outlined in the Royal College of Radiologists' booklet '*A Guide to the Practical Use of MRI in Oncology*'.

MRI is indicated in patients with tumours greater than 2 cm diameter on clinical examination, when the tumour is primarily in the endocervical canal, or if it is of an infiltrative type. MRI can be of particular value in assessing pregnant patients with invasive cervical carcinoma and in detecting concomitant uterine disease, e.g. Ictomy-

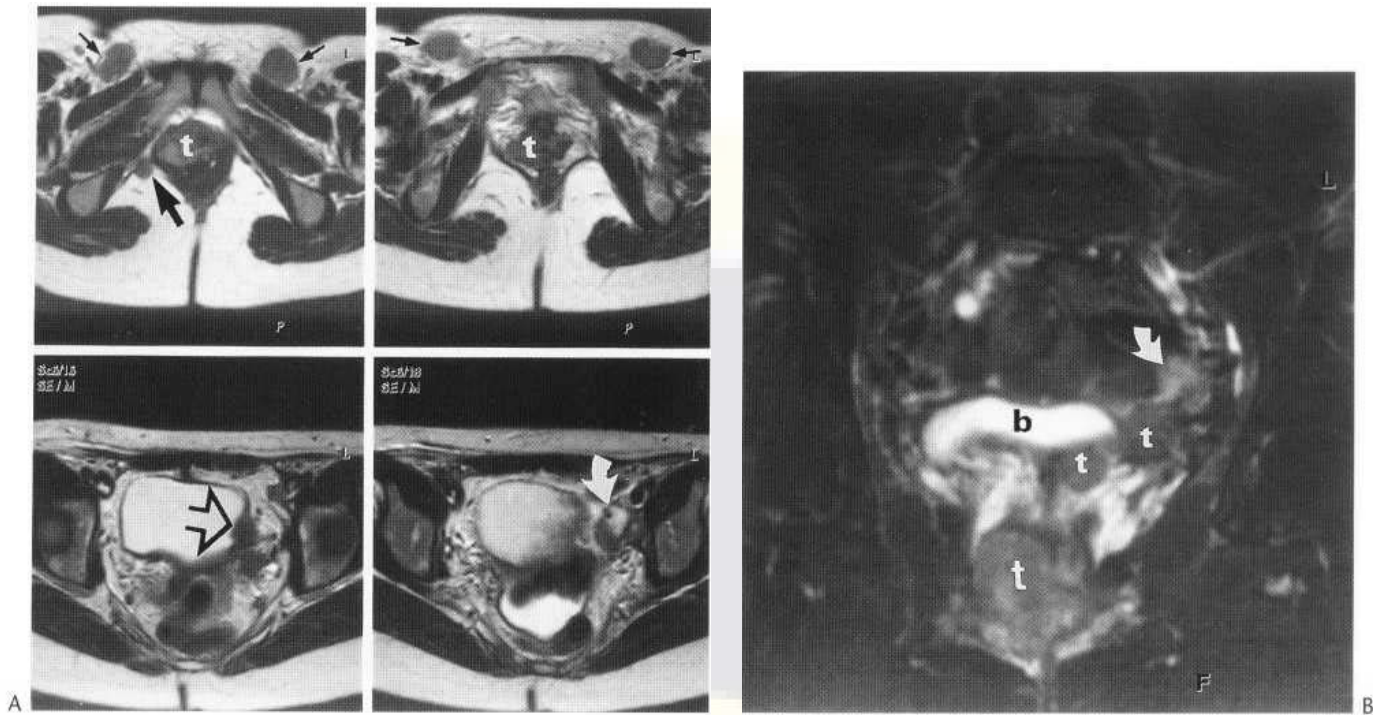


Fig. 34.107 Extensive recurrent cervical carcinoma (t) following a hysterectomy on (A) selected transverse T₂-weighted spin-echo (TSE 3500/100) images, and (B) coronal T₂-weighted spin-echo (TSE 3500/100) fat-suppressed image. There is a large tumour recurrence infiltrating through the lower two-thirds of the vagina into the pelvic floor and in the bladder wall (open arrow), with separate tumour nodules in the right ischial rectal fossa (straight arrow) and left parametrium. There is bilateral inguinal lymphadenopathy (small arrows). Note the mass of higher signal than tumour in the left adnexa from the native ovary. b = bladder.

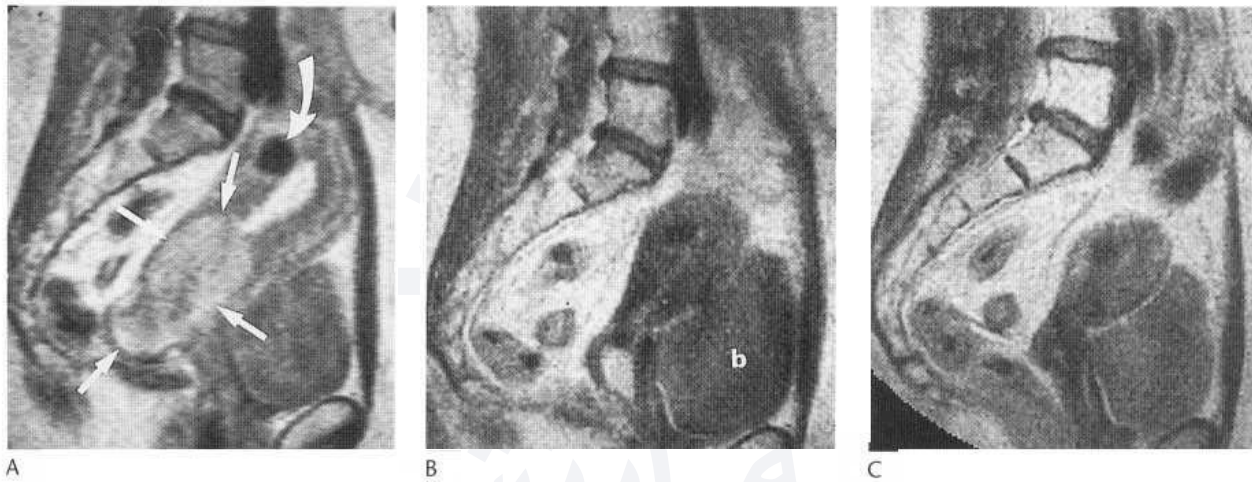


Fig. 34.108 Carcinoma of the cervix (straight arrows) on sagittal T₂-weighted spin echo (SE 1500/80) (A) before treatment, (B) 6 weeks, and (C) 6 months after radiotherapy. Note the rapid reduction in size of the tumour between (A) and (B). The small area of high signal in the cervix in (C) is due to either residual tumour or post-treatment change. Note the low-signal area in the uterus due to a non-degenerating leiomyoma (curved arrow), and the high mucosal signal in the posterior wall of the bladder (b) from radiotherapy change in (B) and (C).

omas (Fig. 34.108). MRI can be used in the diagnosis of recurrent disease and in aiding the distinction of tumour from post-treatment change (Fig. 34.109). *Tumour recurrence* is indicated by the presence of a soft-tissue mass which, on T₂-weighted images, exhibits a high signal compared with muscle and fat. Improved conspicuity of disease can be achieved using fat-suppressed sequences. Although longstanding post-treatment fibrosis can be of low signal on all pulse sequences, signal appearances otherwise may overlap with those obtained from tumour. Less than 6 months after radiotherapy both recurrent tumour and fibrosis exhibit hyperintensity on T₂-weighted

images, making distinction difficult. Six to 12 months post-radiotherapy the radiation fibrosis becomes lower in signal. The use of dynamic contrast enhancement with integration of signal intensity-time curves may allow separation of post-treatment fibrosis from recurrent tumour—the tumour neoangiogenesis allows a more rapid contrast uptake than in radiation fibrosis.

Significant overlap in measured T₂ values has been demonstrated between normal cervical tissue and tumour, although a reduction in tumour T₂ has been noted in cervical carcinomas following radiotherapy.

Endometrial carcinoma

Endometrial carcinoma is a common gynaecological malignancy, being the most prevalent invasive malignancy of the female genital tract in the USA. In 1998, 36 100 new cases of endometrial carcinoma were diagnosed, with approximately a sixth of patients dying from their disease. There has been a threefold increase in the incidence of endometrial carcinoma over the last 30 years, with a strong link to long-term oestrogen exposure without opposed progesterone. Risk factors include obesity, diabetes mellitus, hypertension, multiparity, late-onset menopause, polycystic ovaries, and the long-term use of tamoxifen for the treatment of breast cancer. In the UK this tumour is second in prevalence to ovarian malignancy.

Endometrial carcinoma may be localised or diffuse and mainly occurs in postmenopausal women. Over 90% present with postmenopausal bleeding. Approximately 90% of tumours are well differentiated adenocarcinomas arising within the uterine epithelium. *Localised* tumours are polypoidal with a superficial attachment to the endometrium, whereas *diffuse* lesions infiltrate the entire endometrium and invade the myometrium, spreading beyond the uterus and cervix to involve adjacent organs. The depth of infiltration of the myometrium relates to the presence of nodal metastases. Only a few per cent of patients have nodal involvement with superficial invasion, increasing to approximately 40% for deep myometrial infiltration.

The detailed imaging technique is outlined in the Royal College of Radiologists' booklet *A Guide to the Practical Use of MRI in Oncology*. On MRI endometrial carcinoma shows a signal intensity appearance similar to normal endometrium, which can cause difficulty in defining small lesions. Large lesions expand the endometrial cavity (Figs 34.110, 34.111) and can have a low signal on T-weighted images. Widening or signal heterogeneity on T-weighted images within the endometrial canal may be the only abnormal finding in early-stage disease (Fig. 34.116). Blood clot, adenomatous hyperplasia and degenerating submucosal leiomyoma can produce similar changes, making histological review essential. The most reliable criterion for the diagnosis of myometrial invasion is disruption of the junctional zone. Difficulty can occur in this

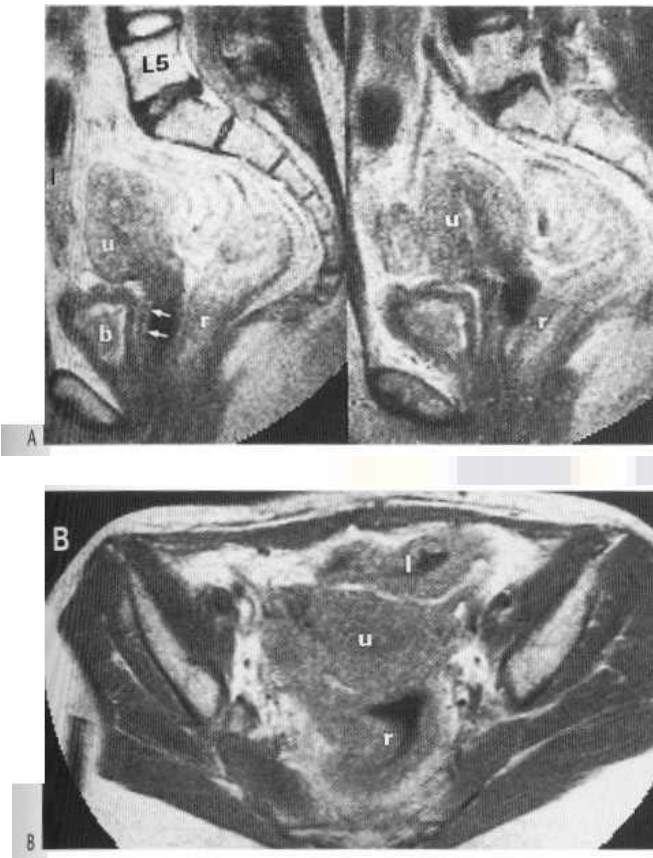


Fig. 34.109 Extensive radiation change involving the bladder, vagina, rectum and bowel loops on (A) sagittal T₂-weighted (SE 1500/80) and (B) transverse T₁-weighted (SE 800/40) images. In (A) the bladder (b) has a thickened wall with a high-signal-intensity mucosa around the posterior wall. The uterus (u) is enlarged and the vagina (arrows), rectosigmoid (r), and adjacent small bowel loops (l) show thickened walls with high signal. No evidence of recurrence of cervical carcinoma, which was confirmed on histological review. The high signal from the sacrum and L5 vertebra is due to radiation-induced fatty infiltration of the marrow spaces. The area of signal void within the vagina in (A) is due to a tampon in situ.



Fig. 34.110 Stage IC endometrial carcinoma (e) on a sagittal T₂ (TSE 3500/100) image. b = bladder.

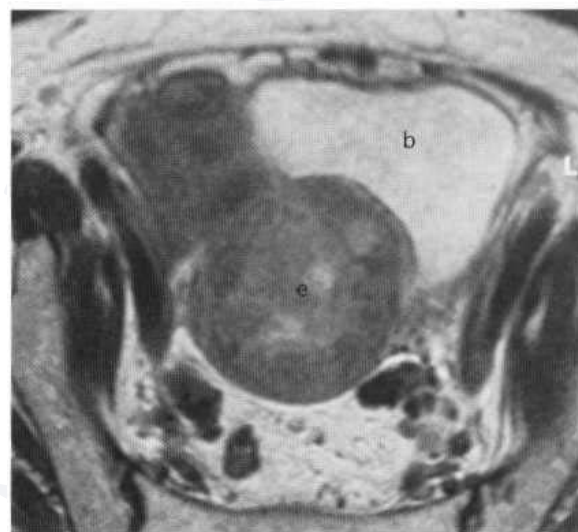


Fig. 34.111 Endometrial carcinoma (e) on a sagittal T₂-weighted spin-echo (TSE 3500/100) image with associated lymph node involvement (demonstrated on other sections) making this a stage III C tumour. b = bladder.

Box 34.2 FIGO/TNM staging for uterine corpus

FIGO		TNM
IA	Tumour confined to endometrium	T1 a
IB	Invasion < half depth of myometrium	T1 b
IC	Invasion > half depth of myometrium	T1 c
IIA	Extension to cervix, endocervical glands only	T2a
IIB	Invasion of cervical stroma	T2b
IIIA	Invasion of uterine serosa/adnexae/+ve peritoneal cytology	T3a
IIIB	Vaginal involvement (direct spread or metastasis)	T3b
IIIC	Pelvic and/or para-aortic lymph node metastases	N1
IVA	Invasion of bladder/bowel	T4
IVB	Distant metastases, including extrapelvic nodal disease	M1

assessment as the junctional zone may not be visible in some post-menopausal women. Following intravenous gadolinium-chelate the endometrial carcinoma enhances, increasing the contrast difference between tumour and normal endometrium and improving the conspicuity of smaller lesions. In addition, viable tumour can be differentiated from non-enhancing necrosis and blood clot. Dynamic contrast enhancement with integration of signal intensity-time curves allows separation of viable from necrotic tumour.

Staging of endometrial carcinoma is important in defining appropriate treatment, which is primarily surgical with or without pelvic radiotherapy (Box 34.2). Clinical staging is inaccurate: one-fifth of patients are understaged. As with the other imaging techniques, MRI cannot provide a histological diagnosis and is not indicated unless a positive histology has been obtained. The overall reported accuracy for MRI in staging is 85-92%; it has particular advantage in defining the depth of myometrial invasion and in demonstrating extrauterine extension. MRI is indicated in those patients in whom physical examination is difficult and there is a clinical suspicion of advanced disease, those who are unsuitable for surgical staging, or if the tumour is of high grade.

Ovaries

The normal-sized ovaries are best demonstrated on transverse or coronal scans, and can be identified in 96% of women of reproductive age. They measure 1.5-3 cm in diameter and have a variable signal on T₁- and T₂-weighted images. The premenopausal ovary shows a low-intermediate signal, similar to muscle, on T₁-weighted images. This appearance is altered if there is haemorrhage present. On T₂-weighted scans the ovary is usually of low signal, but it can be of high signal in some individuals. The cause of this high signal is unknown but is probably due to a looser vascular and connective tissue in the medulla of the ovary. A low-signal rim, in keeping with fibrous cortical tissue, can be observed on the T₁-weighted images. On high-resolution T₂-weighted imaging, numerous small peripheral cysts (follicles) are seen (Fig. 34.112), with a more intermediate-high signal from the central stroma of the ovary. This appearance must be distinguished from that of *polycystic ovarian disease*. The post-menopausal ovary demonstrates a low signal on T₁-weighted images, with few if any peripheral follicular cysts. On T₂-weighted images, difficulty can occur in identifying the ovaries separate from adjacent bowel and uterus. The use of bowel-specific oral contrast agents can be of help in this regard. After intravenous gadolinium-chelate the normal ovaries enhance, allowing improved detection of non-enhancing follicular cysts.

The vast majority of small ovarian cysts visualised on MRI are *ovarian follicles* in various stages of development. In women of reproductive years a cyst > 1 cm is usually a *corpus hemorrhagicum cyst*, occasions will be a follicular cyst. These simple ovarian cysts are thin-walled and tend to have a low-intermediate signal on T₁-weighted images and a high signal on T₂-weighted scans (Fig. 34.112). Simple ovarian cysts are not uncommon in post menopausal women.

The ovaries lie in the adnexa lateral to the uterus, maintaining a constant relationship with the pelvic ureter. The ureter courses posterior or lateral to the ovary, this relationship remaining constant irrespective of the position of an ovarian mass in the pelvis. Thus an ovarian mass will displace the ureter posteriorly or laterally

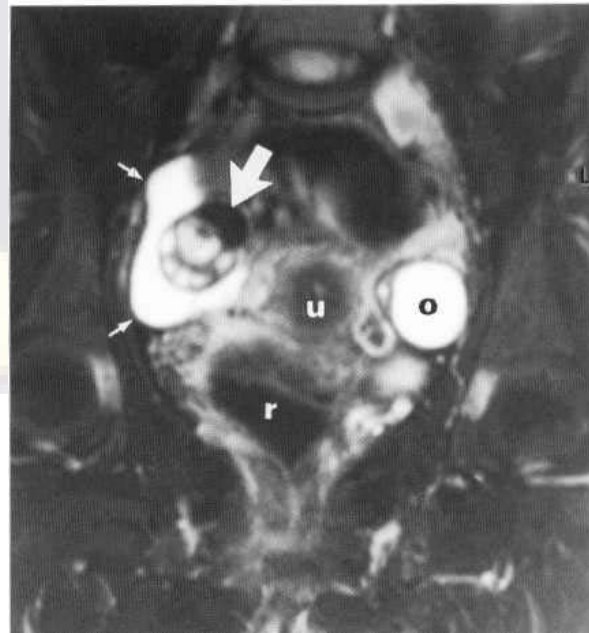


Fig. 34.112 Bilateral cystic ovaries (o) in a 25-year-old on a coronal fat-saturation T₂-weighted spin-echo (TSE 3500/100) image showing a low-signal haemorrhagic right ovarian cyst (large arrow-probably a corpus hemorrhagicum cyst) with some surrounding free intraperitoneal fluid (small arrows). r - rectum; u - uterus.

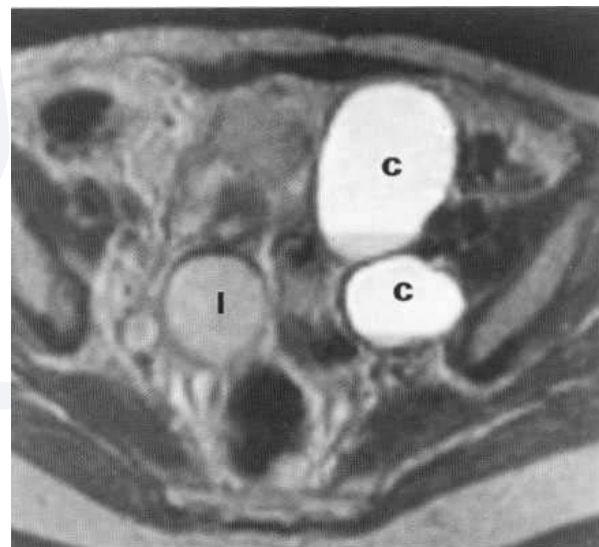


Fig. 34.113 Multiloculated thin-walled haemorrhagic benign ovarian cysts (c) showing fluid-fluid levels on a transverse T₂-weighted spin-echo (SE 2000/120) image. There is a coincidental uterine leiomyoma (l).

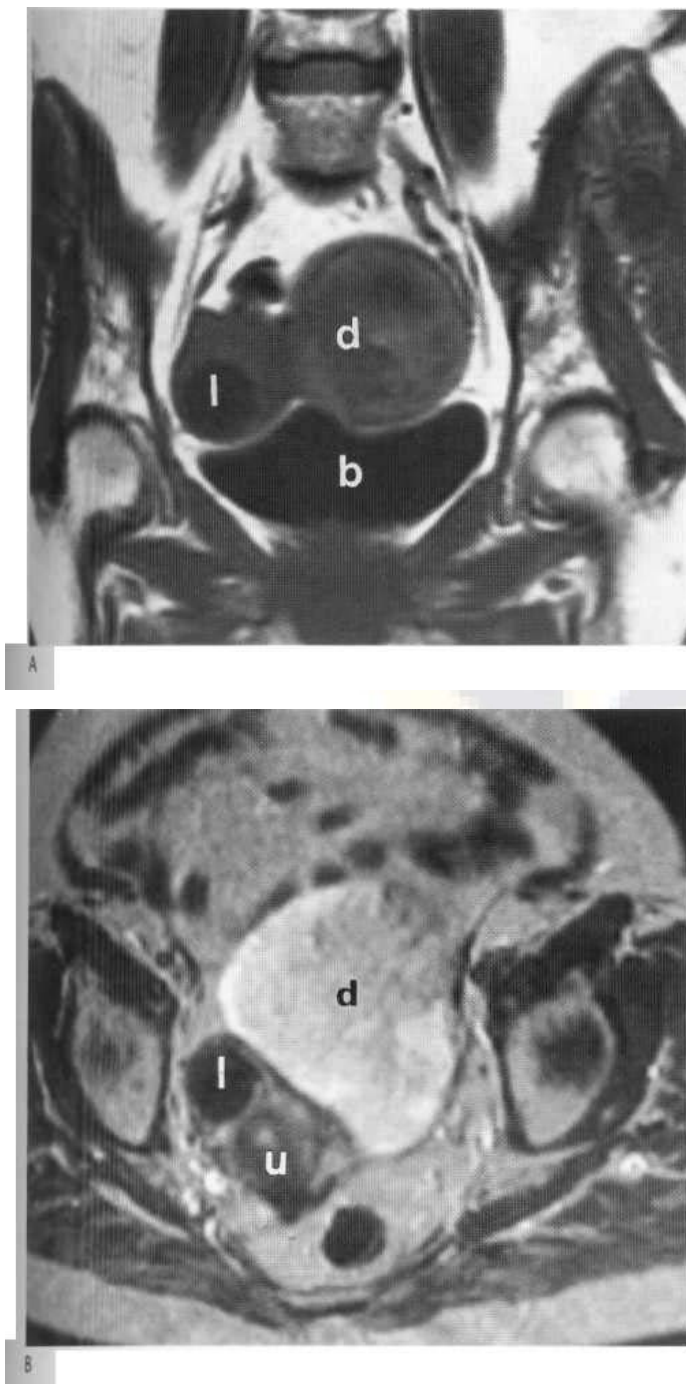


Fig. 34.114 Large left adnexal mass (d) due to an ovarian dermoid displacing the uterus which contains a coincident subserosal leiomyoma (l) on placing corona T₁-weighted (SE 720/25) and (B) transverse T₂-weighted spin-echo (TSE 2000/80) images. The dermoid cyst has solid and cystic components with some areas of intermediate-high signal noted in (A).

(Fig. 34.117B), in contradistinction to pelvic lymphadenopathy which lies on the pelvic side-wall lateral to the ureter.

Benign ovarian cysts These tend to be small (<3-4 cm diameter) and well margined with fluid contents and thin walls (<3 mm in thickness). They appear as low- and high-signal lesions on T₁- and T₂-weighted images, respectively. In the presence of haemorrhage, which shortens the T₁, leading to a high signal on T₁-weighted images, the cysts can appear similar to some endometriomas or ovarian teratomas (Figs 34.112, 34.1 13).

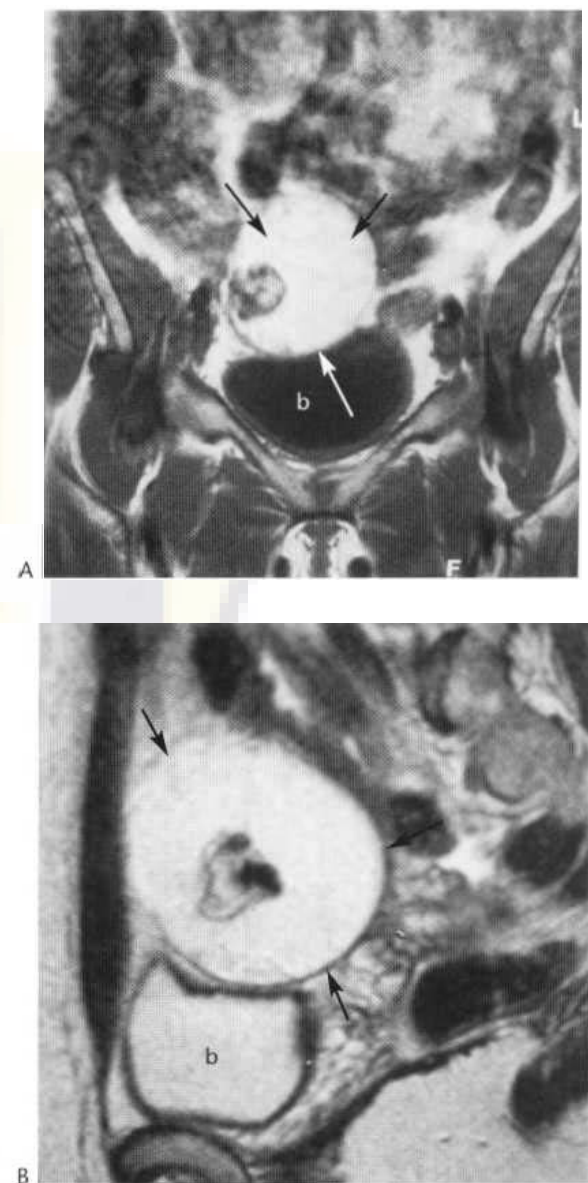


Fig. 34.115 Dermoid cyst (arrows) showing a unilocular mass with a nodule within high-signal fat on (A) coronal T₁-weighted spin-echo (TSE 700/12) image and (B) sagittal T₂-weighted spin-echo (TSE 3500/100) image. A fat-suppressed sequence (not shown) was also performed to confirm the fat contents of the cyst. b = bladder.

Dermoid cysts (mature cystic teratomas) These occur most commonly during the reproductive years, and account for 20% of all ovarian tumours. Approximately 12% are bilateral, with malignant degeneration in less than 2¹⁴. Typically they present as a unilocular cystic mass, with a few showing septa within the cystic component. The majority at presentation are 5-15 cm in diameter and are usually diagnosed on ultrasound. When confirmation or additional information is required, CT or MRI can be helpful (Fig. 34.1 14). Almost all dermoid cysts contain lipid material, either sebaceous or adipose tissue, which demonstrates a similar signal to subcutaneous fat (Figs 34.1 15). Hair, teeth, a mural nodule (Rokitansky's protuberance) or any combination can be demonstrated. Dermoid cysts and haemorrhagic adnexal masses show a similar MRI appearance, with a high signal on T₁-weighted images and a variable signal on T₂-weighted scans. A

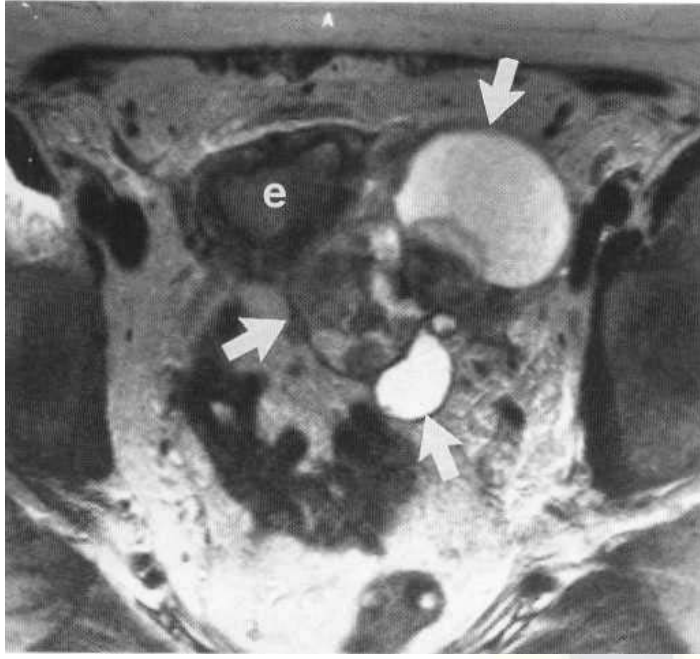


Fig. 34.116 Complex large left adnexal mass with solid and cystic components (arrows) compressing and displacing the uterus on transverse T_2 weighted spin-echo (TSE 5136/132) image. Note that there is distension of the endometrial cavity with intermediate to high signal due to a coexisting endometrial tumour (e). Endometrioid carcinoma of the ovary is associated in approximately a third of cases with endometrioid carcinoma of the uterus. (Courtesy of Dr R. J. Johnson, Christie Hospital.)

frequency-selective fat-suppressed sequence is useful in differentiating a haemorrhagic lesion from a dermoid cyst.

Cystadenoma and cystadenocarcinoma These can be difficult to distinguish unless lymphadenopathy, ascites or metastases are evident. The signal intensity appearance is dependent on the amount of solid and cystic tissue present (Figs 34.116, 34.117A). MRI is useful in defining and separating a uterine from an ovarian mass when ultrasound is equivocal.

X-ray CT is more accurate than MRI in staging ovarian carcinoma, being more sensitive in the detection of mesenteric and serosal metastases. The ovary does not have a true capsule and is only covered by a visceral peritoneum. This is the reason why ovarian carcinoma is frequently metastatic by the time of presentation. The most common site for metastases (90% of cases) is the peritoneum. Metastases to the ovaries (Krukenberg's tumours) show a similar signal intensity appearance to primary ovarian tumours.

Fallopian tubes The fallopian tubes are not seen routinely but may be visualised as low-signal structures within the high-signal fat. The use of high-resolution MRI may assist in their identification, together with the low-signal round and uterosacral ligaments. Following pelvic inflammatory disease scarring occurs within the fallopian tube, producing retention of fluid and leading to cystic dilatation, termed a hydrosalpinx. While readily identified on ultrasound, the serpentine paratubal cystic collection adjacent to the ovary can also be demonstrated on MRI (Fig. 34.93B). Pelvic inflammatory disease is an all-encompassing term describing all pelvic infections. Non-specific changes are demonstrated on MRI, and ultrasound is the preferred imaging method. MRI can be useful in some cases (Fig. 34.11713).

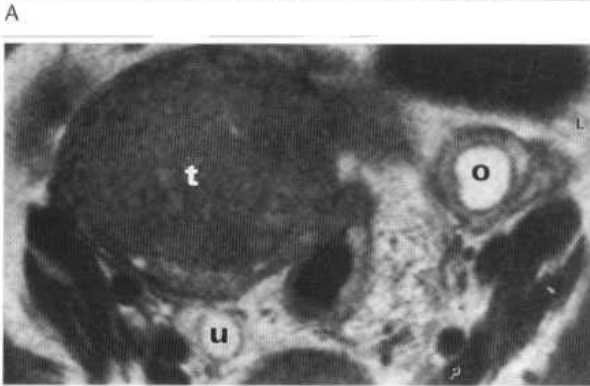
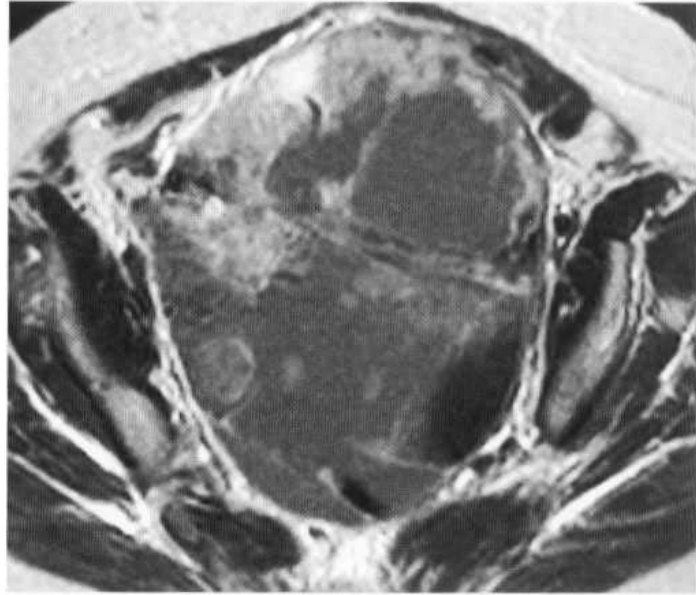


Fig. 34.117 (A) Mucinous cystadenocarcinoma of the ovary producing a large mass, with mixed contents, filling the pelvis on a transverse T_2 weighted (FSE 3000/100) image. The area of signal void within the tumour is due to either blood products or mucin. (Courtesy of Dr J. M. Hawnaur, Department of Diagnostic Radiology, University of Manchester.) (B) Large right ovarian inflammatory mass, proven actinomycosis (t) producing an obstructive uropathy with dilatation of the right ureter (u) on a transverse T_2 -weighted spin-echo (TSE 3500/100) image. Note the position of the ureter to the adnexal mass, and the normal left ovary (o).

REFERENCES AND SUGGESTIONS OF FURTHER READING

- Allan, P. L., Dubbins, P. A., Pozniak, M. A., McDicken, W. N. (2000) *Clinical Doppler Ultrasound*. New York: Churchill Livingstone.
- Brosens, I., Wamstekr, K. (1997) *Diagnostic Rouging and F_ndoscopyr in Gynecology: A Practical Guide*. London: W. B. Saunders.
- Brown, D. L., Doubilet, P. M., Miller, F. H., et al (1998) Benign and malignant ovarian masses: selection of the most discriminating gray scale and doppler sonographic features. *Radiolage*. **208**, 103-110.
- Fleischner, A. C., Javitt, M. C., Brooke Jeffrey Jr, R., Jones, H. W. (1997) *Clinical Gynecologic Imaging*. Philadelphia: Lippincott-Raven.
- Glicher, N., Parrilli, M., Redding, L., Pratt, D. E., Karandc, V. (1992) Standardisation of hysterosalpingography: a valuable adjunct to simple opacification studies. *Fertility and Sterility*, **58**, 1136-1141.
- Hunt, R. B., Alvin, A. M. (1990) *Hysterosalpingography Techniques and Interpretation*. New York: Year Book Medical.
- Kawamoto, S., Urban, B. A., Fishman, E. K. (1999) CT of epithelial ovarian tumours. *Radiographics*, **19**, S85-S102.
- Kinkel, K., Hricak, H., Lu, Y., Tsuda, K., Filly, R. A. (2000) US characterisation of ovarian masses: a meta-analysis. *Radiology*, **217**, 803-811.

- Levine, D. (1998) Review. Gynaecological ultrasound. *Clinical Radiology*, 53, 1-9.
- Reinhold, C., McCarthy, S., Bret, P. M., et al (1996) Diffuse adenomyosis: comparison of endovaginal US and MR imaging with histopathological correlation. *Radiology*, 199, 151-158.
- Royal College of Radiologists and Royal College of Obstetricians and Gynaecologists (2000) Clinical Recommendations on the Use of Uterine Artery Embolisation in the Management of Fibroids. Report of a Joint Working Party. London: RCR/RCOG.
- Scanlan, K. A., Propeck, A. P., Lee, F. T. (2001) Invasive procedures in the female pelvis: value of transabdominal, endovaginal and endorectal US guidance. *Radiographics*, 21, 491-506.
- Thurmond, A. S. (1994) Pregnancies after selective salpingography and tubal recanalisation. *Radiology*, 190, 11-13.
- Urban, N. (1999) (Editorial) Screening for ovarian cancer. *BMJ*, 319, 1317-1318.
- Wiener, Z., Beck, D., Rotten, S., Brandes, L. M., Thaler, I. (1993) Uterine artery flow velocity waveforms and colour flow imaging in women with perimenopausal and postmenopausal bleeding. Correlation to endometrial histopathology. *Acta Obstetrica et Gynæcologica Scandinavica*, 72, 162-166.
- MRI**
- Archer, S. M. (1998) MR imaging of the female pelvis: the time has come. *Radiographics*, 18, 93 1-945.
- Ascher, S. M., Imaska, I., Lage, J. M. (2000) Tamoxifen induced uterine abnormalities: the role of imaging. *Radiology*, 214, 29-38.
- Bluemke, D. A. (ed.) (2000) Oncologic MR Imaging. *Magnetic Resonance Imaging Clinics of North America*, 8, 691-963.
- Burn, P. R., McCall, J. M., Chinn, R. J., Vashisht, A., Smith, J. R., Healy, J. C. (2000) Uterine fibroid leiomyoma: MR imaging appearances before and after embolisation of uterine arteries. *Radiology*, 214, 729-734.
- Byun, J. Y., Kim, S. E., Choi, B. G., Ko, G. I., Jung, S. E., Choi, K. H. (1999) Diffuse and focal adenomyosis: MR imaging findings. *Radiographics*, 19, S161-S170.
- Creasman, W. T. (1995) New gynecologic cancer staging (editorial). *Gynecologic Oncology*, 58, 157-158.
- DeSouza, N. M., Scoones, D., Krausz, T., Gilderdale, D. J., Soutter, W. P. (1996) High-resolution MR imaging of stage I cervical neoplasia with a dedicated transvaginal coil: MR features and correlation of imaging and pathologic findings. *American Journal of Roentgenology*, 166, 553-559.
- Forstner, R., Hricak, H., Occhipinti, K. A., Powell, C. B., Frankel, S. D., Stern, J. L. (1995) Ovarian cancer: staging with CT and MR imaging. *Radiology*, 197, 619-626.
- Foshager, M. C., Hood, L. L., Walsh, J. W. (1996) Masses simulating gynecologic diseases at CT and MR imaging. *Radiographics*, 16, 1085-1099.
- Hawighorst, H., Knapstein, P. G., Weikel, W., et al (1996) Cervical carcinoma: comparison of standard and pharmacokinetic MR imaging. *Radiology*, 201, 531-539.
- Hawnaur, J. M. (1993) Review: staging of cervical and endometrial carcinoma. *Clinical Radiology*, 47, 7-13.
- Hawnaur, J. M., Johnson, R. J., Buckley, C. H., Tindall, V., Isherwood, I. (1994) Staging, volume estimation and assessment of nodal status in carcinoma of the cervix: comparison of magnetic resonance imaging with surgical findings. *Clinical Radiology*, 49, 443-452.
- Hawnaur, J. M., Johnson, R. J., Hunter, R. D., Jenkins, J. P. R., Isherwood, I. (1992) The value of magnetic resonance imaging in the assessment of carcinoma of the cervix and its response to radiotherapy. *Clinical Oncology*, 4, 11-17.
- Hricak, H., Carrington, B. M. (1991) *MRI of the Pelvis - A Text Atlas*. London: Martin Dunitz.
- Hricak, H., Yu, K. K. (1996) Radiology in invasive cervical carcinoma. *American Journal of Roentgenology*, 167, 1101-1108.
- Husband, J. E. S., Reznick, R. H. (eds) (1998) *Imaging in Oncology*. Oxford: ISIS Medical Media.
- Husband, J. E. S., Johnson, R. J., Reznick, R. H. (eds) (1999) *A Guide to the Practical Use of MRI in Oncology*. London: Royal College of Radiologists.
- IUCC (1999) *TNM Atlas: Illustrated Guide to the TNM/InTNM Classification of Malignant Tumours*, 4th edn. Berlin: Springer.
- Jenkins, J. P. R. (1990) Magnetic resonance imaging in oncology. In Johnson, R. J., Eddleston, B., Hunter, R. D. (eds) *Radiology in the Management of Cancer*, Ch. 2, pp. 25-58. Edinburgh: Churchill Livingstone.
- Johnson, R. J. (1993) Review: radiology in the management of ovarian cancer. *Clinical Radiology*, 48, 75-82.
- Kang, S., Turner, D. A., Foster, G. S., Rapoport, M. L., Spencer, S. A., Wang, J.-Z. (1996) Adenomyosis: specificity of 5 mm as maximum normal uterine junctional zone thickness in MR images. *American Journal of Roentgenology*, 166, 1145-1150.
- Kim, S. H., Kim, H. D., Song, Y. S., Kang, S. B., Lee, H. P. (1995) Detection of deep myometrial invasion in endometrial carcinoma: comparison of transvaginal ultrasound, CT and MRI. *Journal of Computer Assisted Tomography*, 19, 766-772.
- Kinkel, K., Kaji, Y., Yu, K. K., et al (1999) Radiological staging in patients with endometrial cancer: a meta-analysis. *Radiology*, 212, 711-718.
- Mezrich, R. (ed.) (1994) The female pelvis. *Magnetic Resonance Imaging Clinics of North America*, 2, 161-323.
- Murase, F., Sigelman, E. S., Outwater, E. K., Perez-Jaffe, L. A., Tureck, R. W. (1999) Uterine leiomyomas: histopathologic features, MR imaging findings, differential diagnosis, and treatment. *Radiographics*, 19, 1179-1197.
- Outwater, E. K., Dunton, C. J. (1995) Imaging of the ovary and adnexa: clinical issues and applications of MR imaging. *Radiology*, 194, 1-18.
- Pattani, S. J., Kier, R., Deal, R., Luchansky, E. (1995) MRI of uterine leiomyosarcoma. *Magnetic Resonance Imaging*, 13, 331-333.
- Schima, W., Mukerjee, A., Saini, S. (1996) Review: contrast-enhanced MR imaging. *Clinical Radiology*, 51, 235-244.
- Scoutt, L. M., McCarthy, S. M., Lange, R., Bourque, A., Schwartz, P. E. (1994) MR evaluation of clinically suspected adnexal masses. *Journal of Computer Assisted Tomography*, 18, 609-618.
- Siegelman, E. S., Outwater, E. K. (1999) Tissue characterisation in the female pelvis by means of MR imaging. *Radiology*, 212, 5-18.
- Siegelman, E. S., Outwater, E. K., Banner, M. P., Ramchandani, P., Anderson, T. L., Schnell, M. D. (1997) High Resolution MR imaging of the vagina. *Radiographics*, 17, 1183-1203.
- Stark, D. D., Bradley, W. G. (eds) (1999) Female pelvis. In *Magnetic Resonance Imaging*, 3rd edn. Ch. 28, pp. 557-590. St Louis: Mosby.
- Subak, L. L., Hricak, H., Powell, C. B., Azizi, L., Stern, J. L. (1995) Cervical carcinoma: computed tomography and magnetic resonance imaging for preoperative staging. *Obstetrics and Gynecology*, 86, 43-50.
- Szucs, R. A., Turner, M. A. (1996) Gastrointestinal tract involvement by gynecologic diseases. *Radiographics*, 16, 1251-1270.
- Takahashi, S., Murakami, T., Narumi, Y., et al (1998) Preoperative staging of endometrial carcinoma: diagnostic effect of T₂-weighted fast spin-echo MR imaging. *Radiology*, 206, 539-547.
- Tanaka, O. Y., Nishida, M., Yamaguchi, M., Kohno, K., Saida, Y., Itai, Y. (2000) MRI of gynaecological solid masses. *Clinical Radiology*, 55, 899-911.
- Tempny, C. M. C., Fielding, J. R. (1996) Female pelvis. In Edelman, R. E., Hesselink, J. R., Zlatkin, M. B. (eds) *Clinical Magnetic Resonance Imaging*, 2nd edn, Ch. 48, pp. 1432-1465. Philadelphia: W. B. Saunders.
- Vinnicombe, S. J., Normal, A. R., Nicholson, V., Husband, J. E. (1995) Normal pelvic lymph nodes: evaluation with CT after bipedal lymphangiography. *Radiology*, 194, 349-355.
- Weber, T. M., Sostman, H. D., Spritzer, C. E., et al (1995) Cervical carcinoma: determination of recurrent tumour extent versus radiation changes with MR imaging. *Radiology*, 194, 135-139.
- Woodward, P. J., Sohaey, R., Wagner, B. J. (1995) Congenital uterine malformations. *Current Problems in Diagnostic Radiology*, 5, 177-200.



نشر الکترونیکی
موسسه انتشاراتی
نوردانش

35

CONGENITAL SKELETAL ANOMALIES; SKELETAL DYSPLASIAS; CHROMOSOMAL DISORDERS

Peter Renton

with contributions from Ruth Green

CONGENITAL SKELETAL ANOMALIES

Very many congenital skeletal anomalies have been described. Some minor abnormalities are only discovered coincidentally or are never noticed. In many of these the skeleton is affected and often is the only system implicated. Many infective orthopaedic conditions acquired in childhood have been wholly or partially eradicated. Congenital abnormalities are therefore assuming increasing importance and present tremendous challenges to orthopaedic surgeons. However, only those of great importance to the radiologist will be dealt with in this section. Suggestions for further reading are given at the end of the chapter.

UPPER LIMB

Many congenital anomalies exist. A short glossary of descriptive terms in common use is presented here, but many are no longer used. Total or partial limb deficiencies are now described either as *longitudinal* or *transverse* (see below) (Day 1991).

Adactyly/v-absence of fingers

Amelia absence of limbs

Brachydactyly-short phalanges

Brachymesophalangy short middle phalanges

Clinodactyly incurving of a finger, usually the fifth, in the coronal plane

Hyper- or *hypophalangism*-the presence of a greater or lesser number of phalanges

Longitudinal defect-absence of part of a limb along its longitudinal axis; this may be pre-axial (radial), post-axial (ulnar) or central

- *Transverse* defect-normal development of a limb to a particular level, beyond which no skeletal elements are present, although there may be digital buds
- *Macrodactyly*-*enl*-enlargement of a digit
- *Polydactyly*-increased number of digits: may be pre- or post-axial
- *Symphalangism*-*fusion* of phalanges in one digit
- *Syndactyly* fusion of adjacent digits. May involve soft tissues and/or bone.

(After Poznanski 1984)

The lesions may be grouped into:

1. Failure of differentiation, e.g. syndactyly
2. Failure of development, which may be transverse or longitudinal
3. Duplications
4. Overgrowth as in neurofibromatosis
5. Generalised dysplasias
6. Congenital (Streeter's) hands.

Some lesions are solitary and of no significance, for example isolated clinodactyly, while others occur in combination so that clinodactyly is also seen as part of major syndromes, for example trisomy 21. Radial defects especially are associated with other anomalies, for example with atrial septal defects in the Holt-Oram syndrome. Some defects are attributable to drugs, such as thalidomide (Distaval) administered to the mother in the first 3 months of pregnancy. This may cause damage to the growing nerves and it may be that the sensory nerve is the tissue organiser (McCredic 1975). Epanutin, used in the treatment of maternal epilepsy, may cause hypoplasia of distal phalanges in utero. Many lesions are genetically inherited so that a harmless *congenital broad thumb* may be seen in different generations of the same family. Other defects may represent sporadic mutations of the gene.

Sprengel's shoulder

This deformity consists of an abnormally high scapula. The deformity is due to failure of the shoulder girdle to descend from its embryonic position in the neck, a process which is normally completed by the end of the third fetal month. The lesion is usually unilateral, though it may be bilateral. Other congenital anomalies are frequently associated.

Radiographs show the characteristic elevated scapula. The scapula may be normal in shape, but usually there is some shortening of its vertebral border with the result that its shape approaches that of an equilateral triangle. Rotation of the scapula may often be observed: generally the inferior angle rotates toward the spine, though rotation in the opposite direction may occur.

From the upper part of the vertebral border or from the superior angle, an accessory bone the omovertebral or suprascapular bone may be found uniting this part of the scapula to the spine (Fig. 35.1). This structure may be represented only by fibrous tissue or cartilage and, if bony, may vary greatly in size and radiopacity.

Other anomalies which frequently coexist include *cervical spine bifida*, the *Klippel-Feil anomaly*, *cervical ribs* and *oilier rib lesions*, *scoliosis* and *hemivertebrae*.

No difficulties in diagnosis should arise. In old *paralytic lesions*, the scapula may be raised. If not evident from the history, the correct diagnosis should be suspected by noting the hypoplasia of bone typical of a paralytic lesion.

Radius and ulna

Radial defects are much more common than ulnar and may occur in isolation or as part of major syndromes, in which case they are usually bilateral.

Radial defects may occur with:

- Ectodermal dysplasia
- Holt-Oram syndrome
- Fanconi's syndrome
- Thrombocytopenia-absent radius syndrome
- Trisomy 18
- Thalidomide embryopathy
- Renal, ear and oesophageal anomalies.

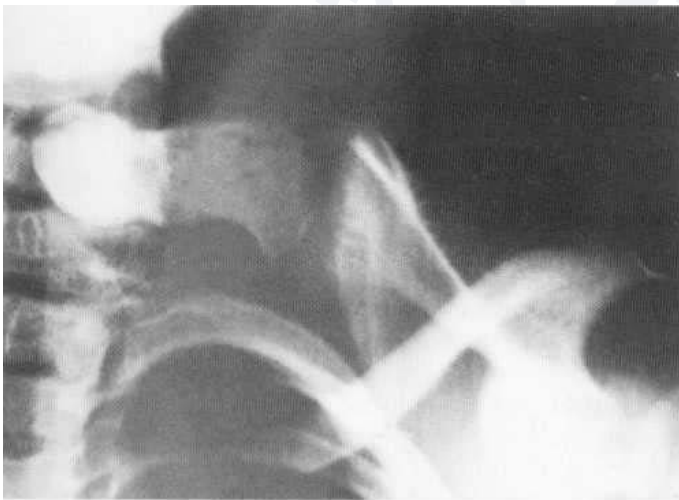


Fig. 35.1 The scapula is elevated and a large omovertebral bone is shown.

The defect may range from hypoplasia of the thumb to complete absence of radius, scaphoid, trapezium and thumb. The limb is shortened and a radial club hand results, with the hand deviated to the side of the absent bone.

Synostosis of the radius and ulna

This defect may be seen at the upper end and is usually associated with dislocation of the radial head. This lesion has marked hereditary tendencies.

Madelung's deformity

This lesion is much commoner in girls and it is generally bilateral. It usually presents during adolescence. The cardinal abnormality is defective development of the inner third of the epiphysis of the lower end of the radius. As a consequence the radial shaft is bowed, so increasing the interosseous space. The lower end of the ulna is subluxed backward. The hand and carpus project forward at the wrist joint to produce a bayonet-like appearance in a lateral view (Fig. 35.2).

The lesion may be part of the *Leri-Weill syndrome* (dyschondrosteosis see below) and *Turner's syndrome*. Similar appearances may follow trauma or infection to the growing epiphyseal plate (Fig. 35.3).

Hand and wrist

Very many congenital abnormalities (and normal variants) may be found in the hands and feet. Specialist monographs should be consulted (see 'References and suggestions for further reading').

Carpal fusions

Carpal fusions may occur in isolation or as part of a syndrome. In isolation they are usually transverse, for example lunate-triquetrum and capitale-hamate, and are much commoner in black-skinned



Fig. 35.2 (A,B) Madelung's deformity-defective development of the inner third of the radial epiphysis, increase in interosseous space, backward projection of the ulna and anterior displacement of the hand.



Fig.35.3 Trauma to the distal radius has resulted in partial fusion of the epiphyseal plate and partial growth arrest. Avulsion of the ulnar styloid occurred at the same time.

people. In syndromes they are usually proximodistal and occur in *Apert's syndrome*, *divschondrosteosis*, *chondroectodermal dysplasia*, *Holt-O rain syndrome* and *Turner's syndrome*. Similar appearances may follow trauma, infection and rheumatoid disease.

Polydactyly

Polydactyly is more common in black-skinned people. It may be *postaxial* (ulnar) and may range from a minor ossicle to complete duplication of the little finger. *Preaxial* lesions (radial) range from minor partial duplication of the thumb distal phalanx to complete thumb duplication. On occasion the hand may be duplicated. Syndactyly may be associated with polydactyly.

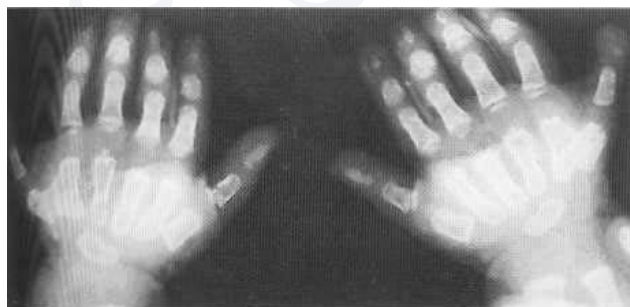


Fig. 35.4 Chondroectodermal dysplasia (Ellis-van Creveld syndrome). Polysyndactyly is demonstrated. In addition, the phalanges are abnormal in morphology.

Polydactyly may be associated with *Ellis-van Creveld syndrome* (chondroectodermal dysplasia) (Fig. 35.4). *Laurence-Moon-Biedl syndrome* (polysyndactyly, mental defect, obesity and retinitis pigmentosa), *trisomy 13* and *asphyxiating thoracic dysplasia-all postaxial-and with Holt-O rain syndrome* and *Fanconi's anaemia* (preaxial).

Syndactyly

Syndactyly Occurs in *Apert's syndrome*, *Fanconi's anaemia*, *Laurence-Moon-Biedl syndrome*, *trisomy 13* and *trisomy 18*. (For a fuller list consult specialist texts; see 'References and suggestions for further reading'.)

THE LOWER LIMB

Developmental dysplasia of the hip

(congenital dislocation of the hip)

This is a very important condition because success in its treatment depends upon early recognition. The incidence of hip instability at birth is 5-10/1000, and of frank dislocation 1-1.5/1000. One-third of cases of congenital dislocation of the hip are detected late, but these often have a family history of the disease.

Instability and dislocation is usually unilateral (L : R = 11 : 1) but both hips may be involved (unilateral : bilateral = 11:4). Females are more commonly affected (F : M = 5 : 1). Sixty per cent of affected children are first born. These children are far more likely to have been breech presentations (breech : vertex = 6 : 1), possibly because the abnormal lie does not permit reduction in utero. Children born by caesarean section are thus also more likely to have associated instability and dislocation. A family or twin history is also common; a subsequent child has a 6% risk of involvement.

Congenital dislocation of the hip is more commonly found in the winter (winter : summer = 1.5 : 1), possibly because of tight swaddling of children in a position of dislocation in winter.

Absolute indications

If any one of these is present, the hips should be examined by imaging:

1. Family history of congenital dislocation of hip
2. Neonatal hip instability
3. Limb shortening
4. Limitation of hip abduction in flexion.

Relative indications

If any two of these are present, the hips should be examined by imaging:

1. Breech presentation
2. First-born child
3. Caesarean section
4. Other congenital abnormalities
5. Excessive fetal moulding.

Imaging

Ultrasound (*Ruth Green*) Ultrasound is now the accepted method of primary investigation of suspected developmental dysplasia of

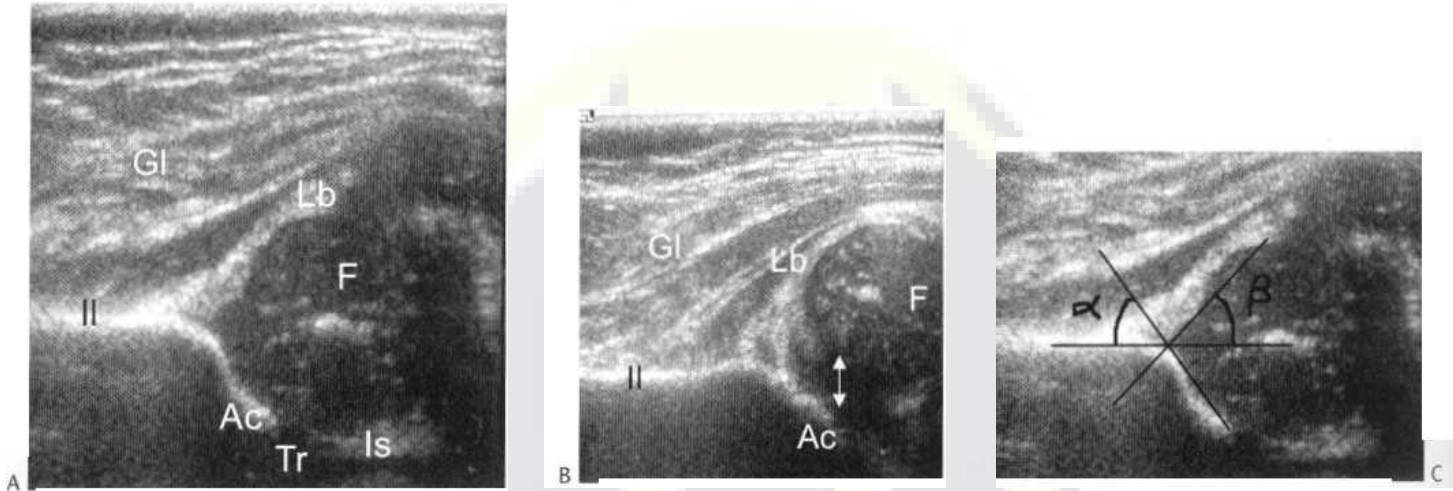


Fig. 35.5 (A) Coronal scan of a 3-month-old baby's hip. The ilium (Il) is parallel to the transducer. The femoral head (F) is round and of speckled low echogenicity with a central bright echogenic ossific centre. The bony acetabulum (Ac), cartilaginous labrum (Lb), triradiate cartilage (tr) and ischium (Is) should be seen if in the correct plane (gluteal muscle = Gl). (B) Coronal scan of developmental dysplasia of the hip. Note the shallow acetabulum (Ac) and displacement of the femoral head (F) (double-headed arrow). (C) Coronal scan of normal hip showing Graf angles (α = bony acetabular roof angle and β = the cartilaginous acetabular roof angle).

the hip. The image is obtained with the child on his/ her side with the hip slightly flexed, the transducer is parallel to the ilium and the image obtained is in the coronal plane (Fig. 35.5A). The measurement of Graf angles may be made in the assessment of hip dysplasia to determine the degree of dysplasia (Fig. 35.58) and plan management (Graf 1984a, b). The baseline is drawn as a straight-line extension from the ilium, a line drawn from the triradiate cartilage to the point where the bony acetabulum meets the baseline represents the alpha angle. The line drawn from the lateral aspect of labrum to the baseline where the lateral bony margin of the acetabulum meets the baseline represents the beta angle, a

measurement of the cartilaginous development (Fig. 35.5C). A simplified Graf classification is demonstrated in Table 35.1.

Plain film radiology The advent of neonatal hip ultrasound, especially if it can be carried out as a screening test and again at 3 months, has limited the use of conventional radiology. The indications for conventional radiographs given below (taken from Catterall's work (personal communication, 1990)) of course apply also to ultrasound.

At birth, neither femoral head is ossified but, occasionally, a notch above the acetabulum may be present (Fig. 35.6) and even in

Table 35.1 Simplified Graf classification

Type	Description	Alpha angle	Beta angle	Comment	Treatment
I	Good cartilaginous and osseous roofing of femoral head. Normal contact and centring of femoral head	$\gg 60$	< 55	Normal	None
IIa	Sufficient roofing of femoral head but poor osseous roof. No ossification of femoral epiphysis	50-60	55-77	< 3 months physiologically immature	Observe until mature
II b	Sufficient roofing of femoral head but poor osseous roof. No ossification of femoral epiphysis	50-60	55-77	> 3 months delayed maturity	Follow-up and consider (abduction) orthosis
IIIa	Cartilagenous roof pushed upward. Femoral head pushed cranially subluxing. No structural change of cartilage	$\ll 43$	> 77	Cartilage normal echogenicity	Reduce
IIIb	Progression of cartilagenous roof pushed upward. Femoral head subluxing. Structural change of cartilage	$\ll 43$	$\gg 77$	Cartilage increased echogenicity	Reduce
IV	Acetabulum empty and femoral head lying in soft tissues	Not measurable	Not measurable	Very shallow	Reduce Possible open reduction

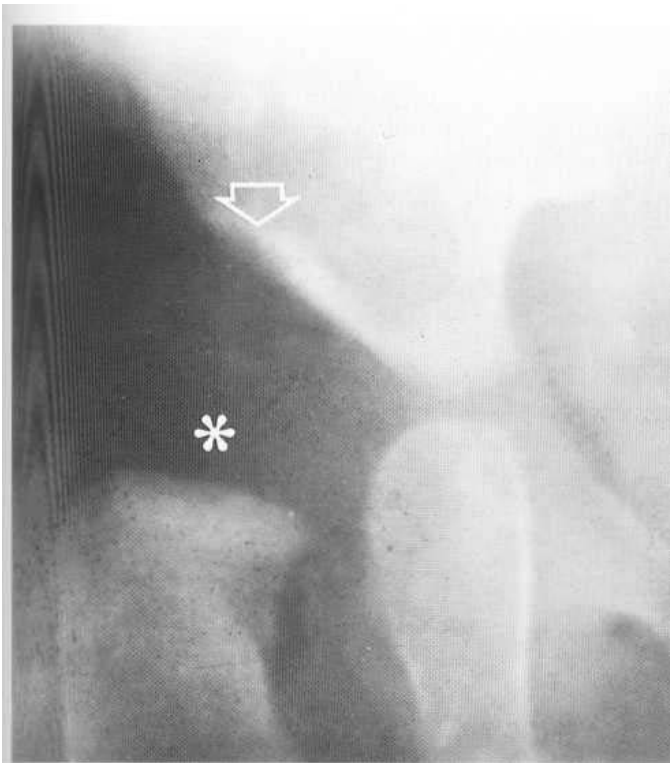


Fig. 35.6 A small defect with marginal sclerosis is seen above the acetabulum (arrow) in a neonate who later was shown to have a congenitally dislocated femoral head. * Marks the site of the projected femoral head.

the absence of the femoral head, congenital dislocation of the hip can then be diagnosed.

Retarded ossification of the femoral ossific nucleus is a traditional sign of congenital dislocation of the hip. In some early cases, however, the femoral ossific nucleus may appear to be larger on the dislocated than on the normal side. Some incongruous findings are probably explicable by the lesion being bilateral.

Sometimes poor development of the acetabulum is obvious in cases of congenital dislocation of the hip. In our experience the acetabular angle is increased in congenital dislocations even in the neonatal period. The *acetabular angle* is the angle subtended by a line drawn through the centres of both Y-cartilages (Hilgenreiner's line) and a line parallel to the acetabular roof.

The eventual position of the femoral head and its relationship to the acetabulum can often be inferred from a film of the hips in the neutral position. The site of the non-ossified epiphysis may be



Fig. 35.7 (A) Bilateral congenital dislocation of the hip. The initial radiograph demonstrates lateral subluxation of both femoral heads with dysplastic acetabula. The ossifying nucleus can be seen developing at the midpoint of the growth plate. Its eventual position could be predicted from the original plain film. (B) End-stage undiagnosed bilateral CDH. The femoral heads have molded in their new situation and articulate with the iliac blades.

inferred as lying superior to the epiphyseal plate. This in turn lies at right angles and proximal to the femoral neck (Fig. 35.6).

Seen later, from the age of 6 months onward, the radiological diagnosis is usually easy (Fig. 35.7). The femoral head will be displaced upward and outward and delayed ossification of its epiphysis will be observed. The acetabulum will be shallower than that of the normal hip and its roof will not be set horizontally but will slope upward and outward. Use of the many lines and coordinates described in this condition is not necessary, provided heed is paid to the possibility of a bilateral dislocation.

During management the radiologist will be asked to decide whether reduction has been attained or maintained. This decision may be very difficult to make on radiographs taken through plaster, but ultrasound may give the answer.

Arthrography of the infant hip Arthrography is of particular service in deciding whether complete reduction of a dislocation has been achieved. There are times when it is not possible to obtain this information from examination of plain films—especially when the femoral ossific nucleus appears to be set eccentrically on the femoral neck. Reduction may be impossible

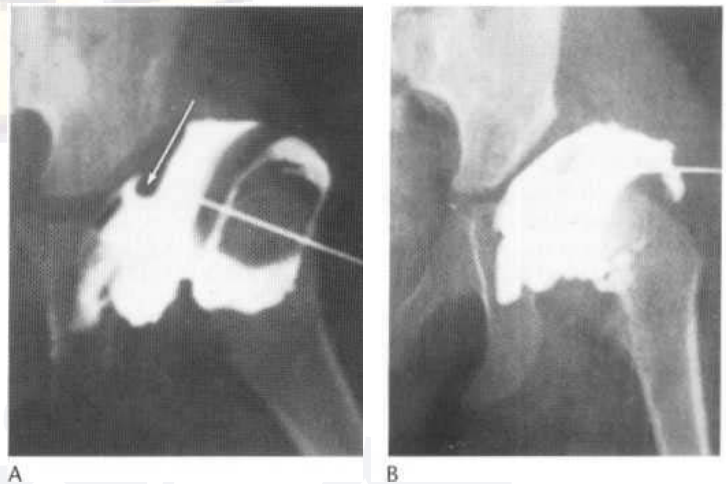
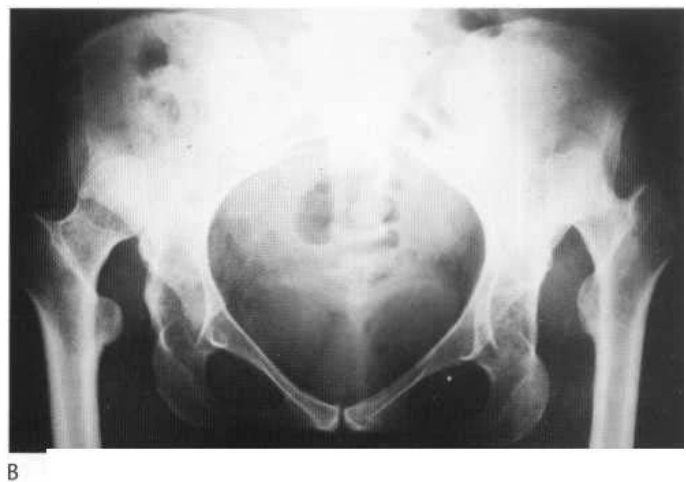


Fig. 35.8 (A) Arthrogram of the left hip shows filling defect caused by inverted limb (arrow). (B) Appearance following limbectomy. (Courtesy of Mr A. C. Clark.)



(B) End-stage undiagnosed bilateral CDH. The femoral heads have molded in their new situation and articulate with the iliac blades.

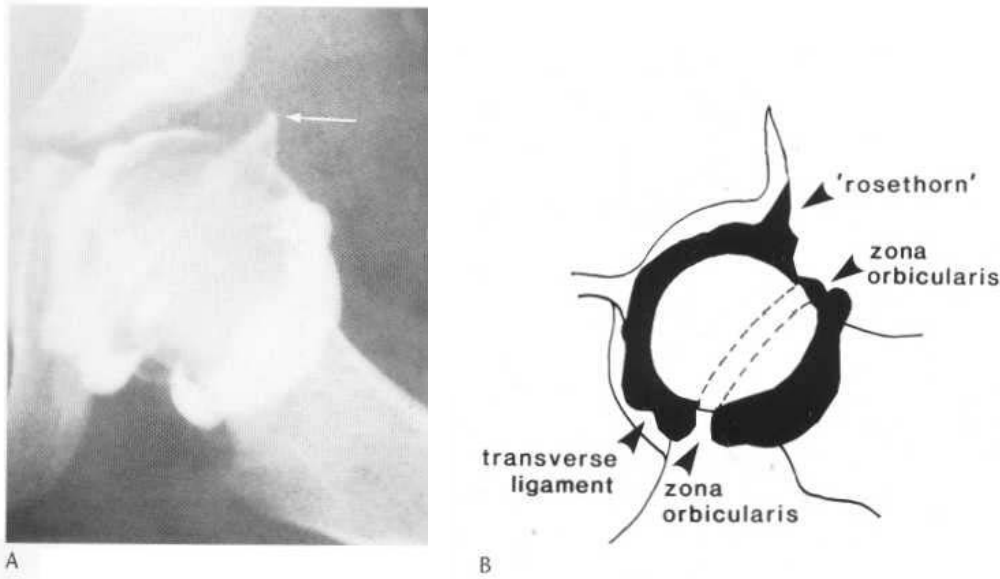


Fig. 35.9 (A) Arthrogram of the hip showing 'rose thorn' appearance of the normal limbus (arrow). The 'rose thorn' is larger than usual. (B) Diagrammatic representation of the normal hip arthrogram (see text).

to obtain or the hip may be unstable. In such cases arthrography may be used to study the disposition of soft-tissue structures of the joint.

Possible abnormal findings are:

1. The fibrocartilaginous rim of the acetabulum, called the *'limbus'* may become inverted into the joint and form a barrier to stable reduction. In an arthrogram of a normal hip a thorn-like projection marks a small gap between the outer part of the *limbus* and the capsular attachment. When the *limbus* is inverted, the 'thorn' is lost and the filling defect caused by the 'thorn' is seen (Fig. 35.8).
2. The *ligamentum teres* may become so large that it may offer a barrier to reduction. A hypertrophic *ligamentum fetes* may be visible on the arthrogram but estimation of its size by this means is unreliable.
3. The *psaos tendon* may become contracted and a notch for the tendon is seen inferiorly

The plain radiograph may show a shallow acetabulum and a small, or no, ossific nucleus for the proximal femoral epiphysis. The rest of the 'lucent' joint space is, of course, taken up by articular cartilage, and this is demonstrated after contrast medium has been injected. The ossific nucleus lies centrally within the spherical

The acetabular cartilaginous labrum deepens the acetabulum and has a triangular, sharply pointed prominence on its superolateral aspect, the *limbus*. This is covered by synovium and is 'lax'. If medially displaced into the joint, it prevents normal location of the femoral head.

The cartilage of the head should fit congruously within that of the acetabulum; contrast medium should be parallel with and evenly distributed between them, indicating that the joint space is even throughout (Fig. 35.9).

Hip arthrography in children should be performed under fluoroscopic control and, if possible, videotape recordings should be made during manipulation of the hip, as well as taking static films.

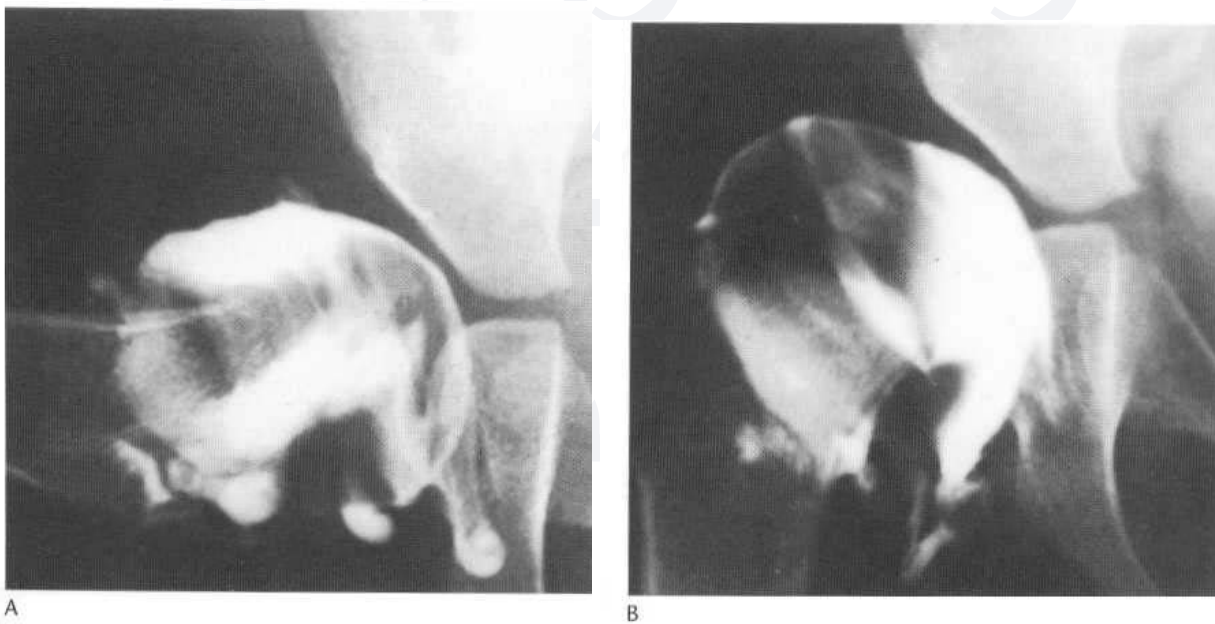


Fig. 35.10 Hip arthrogram in a child. The acetabulum is dysplastic. The ossific nucleus is seen within the largely cartilaginous head. (A) In abduction the femoral head is congruous with the acetabular cartilage. (B) In the neutral position the femoral head is incongruous, with pooling of contrast agent medially.

The head should be contained at all times within the congruous acetabulum and its movement not restricted.

With partial dislocation, or subluxation, movement is excessive and the lateral aspect of the head is uncovered. The limbus and 'rose thorn' are elevated and laterally displaced. Contrast medium pools medially with distention of the medial joint space. Manipulation of the hip under screen control in congenital dislocation of the hip shows the positions in which the femoral head and acetabular fossa are congruous (Fig. 35.1 OA) and incongruous (Fig. 35.1 OB). This information aids the surgeon in planning the operation required to facilitate joint development.

With total dislocation, the cartilaginous femoral head is totally uncovered; the limbus is medially and posteriorly displaced and may prevent reduction. Contrast medium again pools medially. Lateral subluxation of the head and medial displacement of the limbus narrows the capsule, giving a so-called 'hour-glass' constriction.

The primary cause of unstable reduction of a dislocated femoral head has long been debated. Excessive anteversion of the femoral neck is often seen and the condition often necessitates a de-rotation osteotomy for reduction to be maintained. The femoral neck of a normal baby is usually anteverted to 3.5°; this diminishes to 15° in the adult. In congenital dislocation, the femoral neck may be anteverted to 70-80°. CT is useful for measuring the degree of anteversion.

In neglected dislocations, the misplaced femoral head may produce a depression on the side of the ilium above the acetabulum, constituting a *false acetabulum* (Fig. 35.7B). This may vary in size from a shallow depression to a deep socket. The original acetabular socket becomes progressively more shallow.

Osteochondritis may complicate a congenital dislocation of the hip, particularly after vigorous methods of reduction or surgery. Not all cases of osteochondritis are attributable to the complications of treatment, for there does appear to be a true association between congenital dislocation and Perthes' disease of the hip.

Proximal femoral focal deficiency (PFFD) (congenitally short femur)

Torode & Gillespie (1991) classify PFFD into two groups. In Group I the patients have a congenitally short femur, coxa vara and a hypoplastic knee. The foot is (presumably) normal. In Group II the femur is very short and the head and neck may be absent. There may be a variable fibular deficiency, with a short fibula and valgus deformity at the ankle or, in severely affected cases, a deficient foot with absent rays. Deficiency of bony elements may only become obvious during skeletal maturation.

PFFD consists of failure of normal development of a lesser or greater part of the proximal femur. Some distal femur, by definition, is always present, thus distinguishing it from femoral agenesis.

In some cases which appear to have PFFD with no proximal femur in which to have coxa vara, arthrography of the hip may reveal a cartilaginous neck and head with varus deformity, as will ultrasound.

Radiographic findings (Fig. 35.11)

A short femur, which is laterally situated and proximally displaced, is demonstrated at birth. The distal femur is by definition present to a greater or lesser extent. A spectrum of proximal deficiencies exists. The radiological appearances of children with congenital femoral abnormality is a continuum from a minor defect to the most severe form with almost complete, or complete, absence of the femur.



Fig. 35.11 Proximal focal femoral deficiency. Only a hypoplastic portion of the distal right femur is apparent.

Idiopathic coxa vara of childhood

Two types of idiopathic coxa vara are recognised:

1. A congenital form, generally present at birth, sometimes associated with other congenital lesions
2. An infantile form, not present at birth, recognised around the age of 4 years and often bilateral (33%).

Coxa vara is included as part of the PFFD spectrum if the varus is associated with congenital femoral shortening present at birth, i.e. Group I above. If PFFD is severe, coxa vara cannot arise at all, even in congenital cases.

The mean angle of the neck of the shaft at 1 year of age is 148°, decreasing to 135° at 5 years, and 120° in the elderly. Coxa vara is present when the angle is less than normal, but certainly if below 110°.

Radiographic findings

The lesion is usually bilateral, though it may be unilateral. Coxa vara will usually be obvious. The femoral head will be situated low in the acetabulum and its outline may appear woolly. Secondary deformity of the acetabulum may result. A triangular fragment of bone may be seen at the lower part of the femoral neck. This wedge of bone, commoner in the infantile cases, is bounded by clear bands forming an inverted V (Fig. 35.12). The medial or inner band is the epiphyseal line. The outer one is, of course, abnormal. Some writers have regarded it as an area of osteochondritis, others as a stress fracture. In later cases the greater trochanter will be found to curve like a beak and it may articulate with the ilium. Not all these features are necessarily present in every case.



Fig. 35.12 Congenital coxa vara-extreme coxa vara with some slip of the epiphysis. A triangular fragment of bone is well shown.

Acquired coxa vara may be found in conditions where bone is softened, for example in *rickets*, *fibrous dysplasia*, *osteogenesis imperfecta* and *cleidocranial dysplasia*, as well as in *Perthes' disease* and following *slipped epiphysis*.



Fig. 35.13 Neurofibromatosis. Pseudarthroses are seen bilaterally. The fibulae are thin and bowed. Bony struts have been inserted at surgery.

Abnormalities of the patella

The patella is frequently *bipartite* and sometimes *multipartite*. The upper, outer part is always involved. The anomaly is often bilateral and well corticated all round, which helps to distinguish it from a fracture. Not all cases, however, are bilateral.

In the *nail patella syndrome* the patella may be rudimentary or hypoplastic and set laterally (Fig. 35.1 B).

The patella may be *dislocated* due to a variety of congenital causes, for example *hypoplasia of the lateral femoral condyle*, *external rotation of the tibia* and *malattachment of the iliotibial tract*. The displacement is invariably outward.

Congenital pseudarthrosis of the tibia and fibula

The pseudarthrosis of the tibia is seen at the junction of the middle and lower thirds. Often a similar lesion is found in the fibula.

Radiological examination of early cases may show a sclerotic or radiolucent zone in the affected area. This bows, resorbs and fractures and the severed ends of the bone become sclerotic. Still later, the proximal part becomes cupped and the distal part pointed, so forming a pseudarthrosis (Fig. 35.13). This uncommon lesion is notoriously resistant to treatment.

Neurofibromatosis is usually given as the most frequent cause of this condition. Other associations are with *fibrous dysplasia* and *idiopathic juvenile osteoporosis*. Occasionally, a similar lesion has been found affecting the forearm bones.

The foot and ankle

Accessory bones of the foot

Supernumerary centres of ossification are more common in the foot than in the hand. They should be identified to distinguish them from

fractures. They may themselves fracture and be a cause of pain, or may be involved in rheumatoid arthritis, osteochondritis, osteoarthritis, infections and hyperparathyroidism. More than 50 have been described but most of them are rarities. As they become radiologically visible in adults, the incidence rises to 30%. The *os tibiale externum* is found in some 7% of feet, the *os trigonum* in 5% and the *os peroneum* in 8%, but surveys differ as to their incidence.

Degenerative change, which may be painful, can occur between the os tibiale externum and the adjacent navicular. An overlying bursitis arises over the bony prominence.

The os trigonum may be entrapped between the calcaneus and posterior tibia in ballet dancers and footballers, and this bone becomes the site of osteochondritis. Change can be seen on plain films, where the ossicle becomes sclerotic and fragmented. The bone scan is positive, and change is also seen at MRI (Fig. 35.14).

The os peroneum may fracture.

Two sesamoids are regularly seen at the head of the great toe metatarsal. Sesamoids may on occasion be seen at all the metatarsal heads (Fig. 35.15). The medial is bipartite in one-third of cases, the lateral in only 5% of cases. A bipartite sesamoid is larger than its normal counterpart and corticated all round, while a fractured sesamoid shows non-corticated fracture parts. Pathology in metatarsal sesamoids can be demonstrated on axial views, and isotope bone scans will often be abnormal.

Talipes deformity (from the Latin: *ta/us* ankle: *pes* foot)

This is defined as a congenital abnormality of the foot, which is twisted out of shape. Talipes equinovarus accounts for 75% of these (see below). A number of foot deformities may be described.

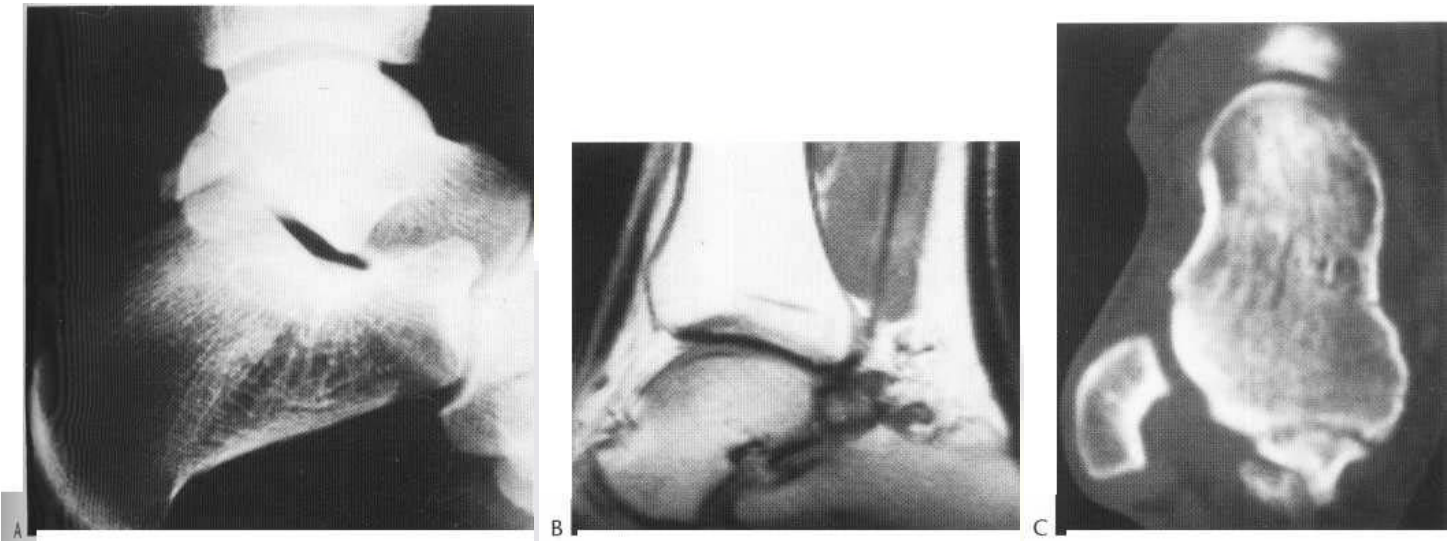


Fig. 35.14 Avascular necrosis of the os trigonum. (A) This bone is sclerotic and would be grossly abnormal on a bone scan. (B) MR scan. (C) CT scan.

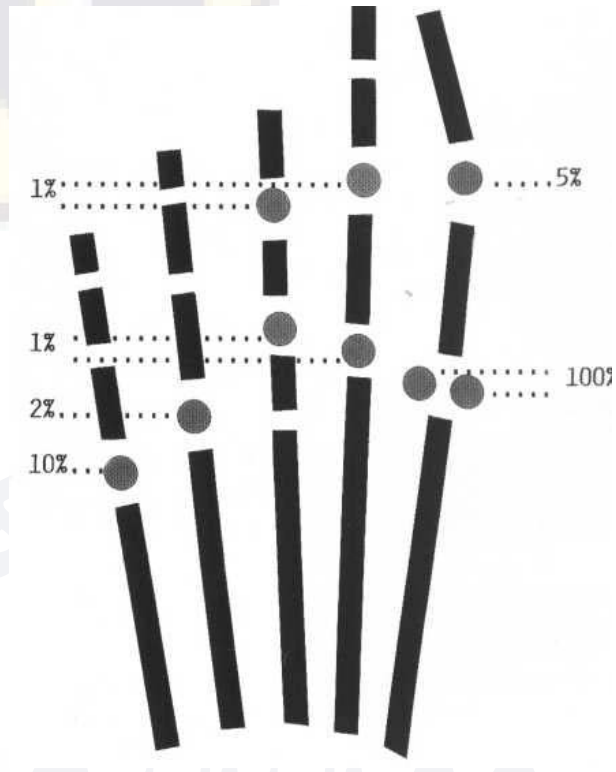


Fig. 35.15 (A) Sesamoids at the metatarsal heads. Apart from the usual medial and lateral sesamoids at the great toe metatarsal head, sesamoids are also seen at the second, third, fourth and fifth metatarsal heads. (B) To show the percentages of foot sesamoid incidence in Bizarre's (1921) series.

The heel may be in *valgus*, that is, the calcaneus is directed posteriorly away from the sagittal midline, or in *varus*, towards the midline. The calcaneus may be in *equinus*, distoplantariflexed, or in *cavus*, with an increased calcaneal pitch, or there may be *calcaneus*, when its anterior end elevates toward the vertical. There may be *pes planus*, with a flattened longitudinal arch. Metatarsus adductus or abductus may be seen.

Talipes equinovarus (club foot)

This was first described by Hippocrates in 400 BC. It has an incidence of around 1 : 1000 live births. There is a risk that further children may be affected (1 : 35). Clinically, the hindfoot is in equinus and varus, and the forefoot in equinus and varus (Fixen 1991).

Radiologically, on the AP view, the heel is in varus and the forefoot is also adducted in varus (toward the midline). The talocalcaneal angle is narrowed and the talus and calcaneum are parallel (Fig. 35.16). On the lateral view, the calcaneum is in equinus. The forefoot is plantarflexed and in cavus. The forefoot is also adducted.

The condition is nearly always idiopathic but club foot is sometimes associated with other bony abnormalities.

The idiopathic type is of limited interest to the radiologist. The three cardinal abnormalities are: (i) adduction of the forefoot; (ii) inversion of the foot; and (iii) plantarflexion of the foot. Radiologically, medial displacement of the navicular and cuboid in relation to the heads of the talus and calcaneus will be seen. The



A



B



C

Fig. 35.16 Congenital talipes equinovarus (clubfoot). (A) On the AP view the heel is in varus and the forefoot also. (B) There is extreme cavus on the lateral view. The foot bears weight laterally on the fifth metatarsal. (C) The oblique view of the foot shows the calcaneum in equinus.

calcaneus will rotate medially under the talus. Plantarflexion will be seen by posterior displacement of the calcaneus.

Ossification of the talus and navicular may be retarded. Usually secondary hypoplasia of the bones of the tarsus and of the soft tissue is seen.

Congenital vertical talus

This is a rare cause of congenital flat foot in children. The radiographic appearances are diagnostic. The talus is vertical, its long axis following that of the tibial shaft. The vertical displacement of the talus remains constant whether the patient is standing or recumbent. The bones of the forefoot and the calcaneus are raised and produce the typical rocker-bottom foot (Fig. 35.17). When the navicular becomes ossified its shape will be seen to appear normal except for a little constriction of its waist. It will be seen obviously dislocated and lying in contact with the body of the talus. The lateral view shows the heel in equinus with gross plantarflexion of the anterior calcaneus. A rocker-bottom foot results. The talus too is severely plantarflexed. The navicular articulates with its neck. The AP view shows gross heel valgus.

Flat foot

The heel is in valgus. The talus is no longer supported by the calcaneus and is plantarflexed. The calcaneus is flat and the longitudinal arch is flattened.

Ball and socket ankle joint

In this condition the ankle joint is abnormally shaped and its range of movement increased. It is usually found when the midtarsal and subtaloid joints are rigid, generally caused by tarsal fusions; in such cases inversion and eversion of the ankle compensate for the loss of these movements at the midtarsal and subtaloid joints.

Some cases are seen in patients with a short leg in a few no underlying cause is seen.

Radiographic features are characteristic. The trochlear surface of the talus, normally convex anteroposteriorly and concave from side to side, loses this concavity and approaches the shape of a sphere. The mortice of the talus becomes correspondingly moulded into a cup-like cavity to form a ball and socket articulation.

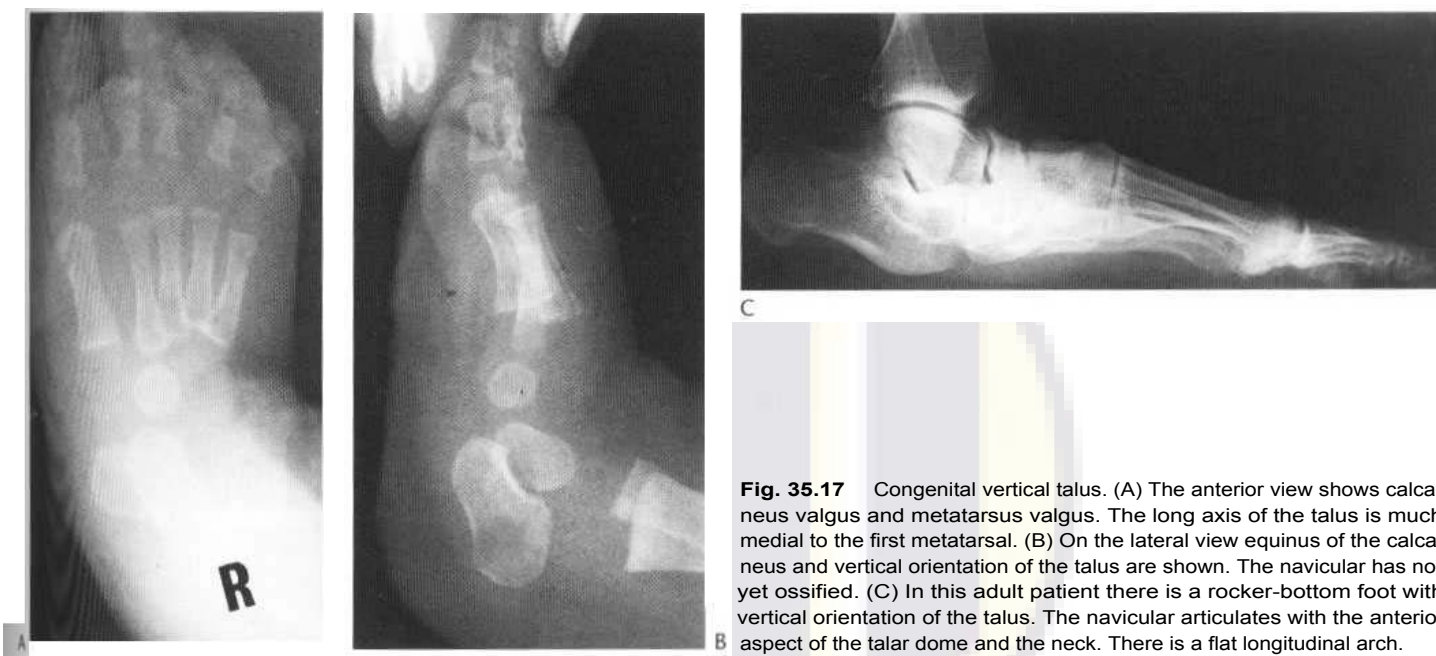


Fig. 35.17 Congenital vertical talus. (A) The anterior view shows calcaneus valgus and metatarsus valgus. The long axis of the talus is much medial to the first metatarsal. (B) On the lateral view equinus of the calcaneus and vertical orientation of the talus are shown. The navicular has not yet ossified. (C) In this adult patient there is a rocker-bottom foot with vertical orientation of the talus. The navicular articulates with the anterior aspect of the talar dome and the neck. There is a flat longitudinal arch.

Congenital fusions

Painful flat foot (the peroneal spastic flat foot) may be due to fusion of certain tarsal bones (Fig. 35.18). The lesion may be cartilaginous or fibrous, in which case the two bones are hypertrophic and closely approximated but not fused. Flattening of the longitudinal arch of the foot is seen. Bony union is not directly demonstrable before adolescence but appears with ossification of the cartilaginous link between the bones.

The most common form of hindfoot fusion is *talocalcaneal*, usually at the middle facet, or sustentaculotalar joint. The fusion is well seen on an axial or 'ski-jump' view of the foot or on oblique radiographs, but especially well at CT or MRI (Fig. 35.19). The isotope bone scan is also abnormal away from the fused area, due to stress changes around unfused joints.

The less common *calcaneonavicular* fusion is best seen on a conventional oblique radiograph of the foot (Fig. 35.18). Coalition has been described between all the bones of the hind foot. Restriction of movement at the subtalar joint causes abnormal movement of the hind foot, with lipping at the calcaneonavicular joint, seen together with longitudinal arch flattening and obliteration of subtalar joints on the lateral view of the foot.

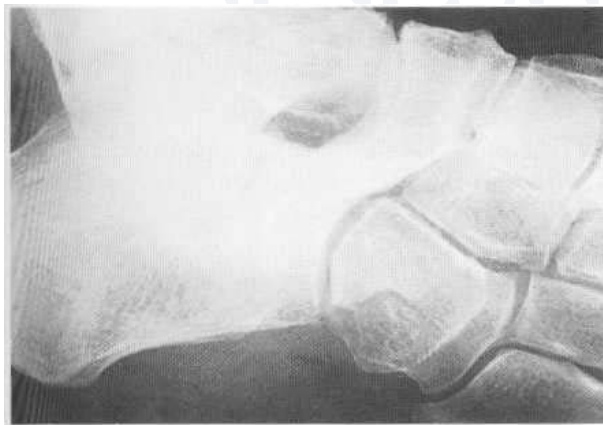


Fig. 35.18 Calcaneonavicular bar.

THE PELVIS

Iliac horns

These are bony processes projecting dorsally from the outer surface of the wings of the ilium. They may occur alone or be associated with the syndrome of rudimentary or absent patellae, deformity of the elbows (hypoplasia of capitellum and radial head) and dystrophy of the nails (*nail-patella syndrome-Fong's lesion* (Fig. 35.20).

THE SPINE

Spinal anomalies range from gross defects, incompatible with life, to minor anomalies which are no more than anatomical variants. Some of these may be mistaken for fractures, for example the unfused accessory ossification centres at the tips of inferior articular facets or those related to the anterosuperior part of the margins of vertebral bodies. Fractures are rarely seen at such sites and have ragged rather than smooth edges.

Coronal cleft vertebra

This anomaly is seen in vertebral bodies of newborn infants and is due to failure of fusion of two ossification centres. In about half the cases more than one vertebral body is affected. The abnormality has been seen on prenatal radiographs-it occurs more frequently in males.

The cleft is seen on a lateral radiograph as a linear or oval defect between a small posterior and larger anterior ossification centres. The anteroposterior diameter of the affected vertebral body is often increased. The cleft consolidates in a few months. These clefts are of no importance except that they are seen in some dysplasias (see *chondrodysplasia calcificans congenita*).

Butterfly vertebra

In the affected vertebra, the upper and lower surfaces are deeply concave or V-shaped, so that the vertical dimension of the vertebral

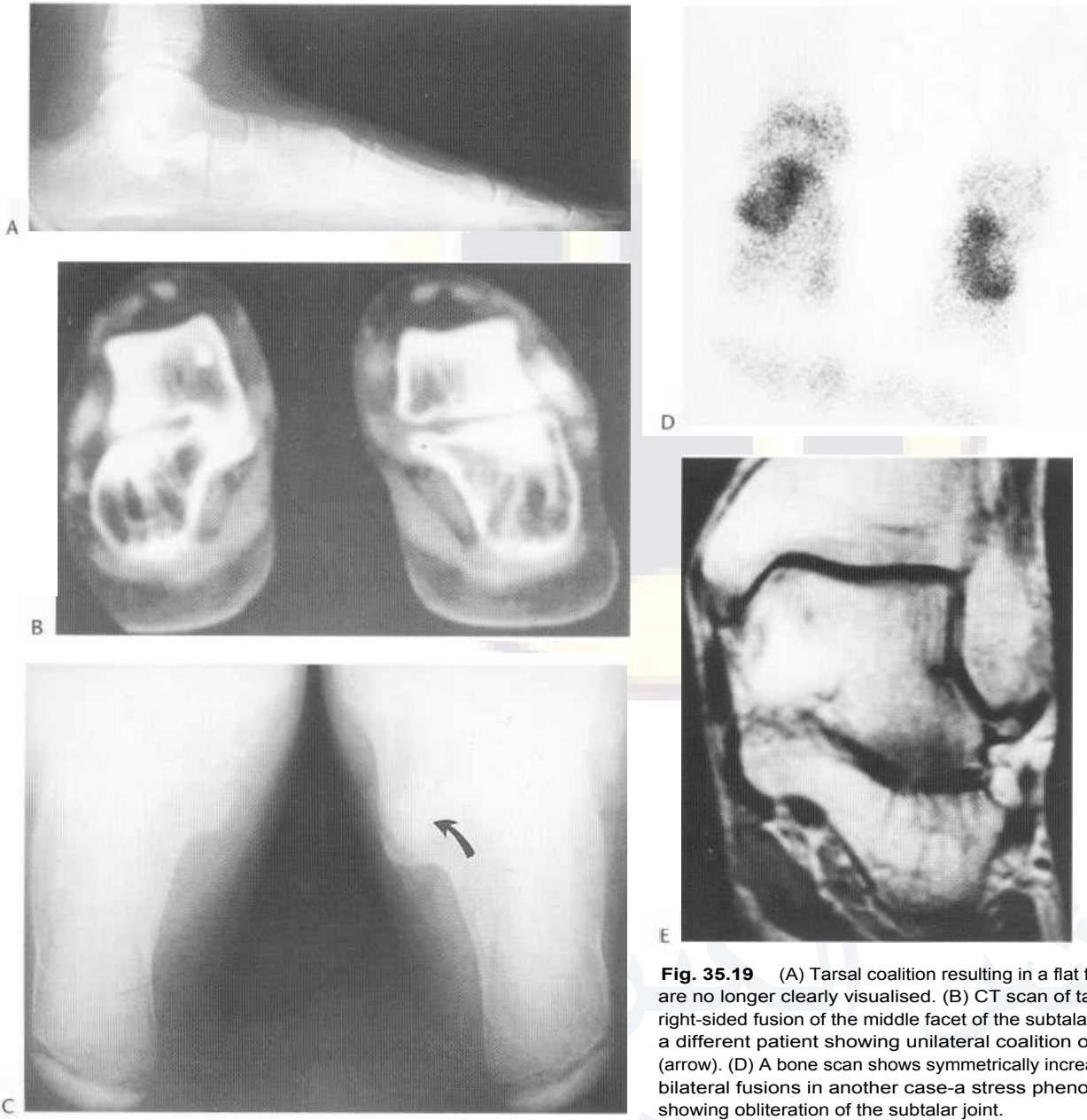


Fig. 35.19 (A) Tarsal coalition resulting in a flat foot. The subtalar joints are no longer clearly visualised. (B) CT scan of tarsal coalition showing right-sided fusion of the middle facet of the subtalar joint. (C) Axial view in a different patient showing unilateral coalition of the left middle facet (arrow). (D) A bone scan shows symmetrically increased uptake away from bilateral fusions in another case—a stress phenomenon. (E) MR scan showing obliteration of the subtalar joint.

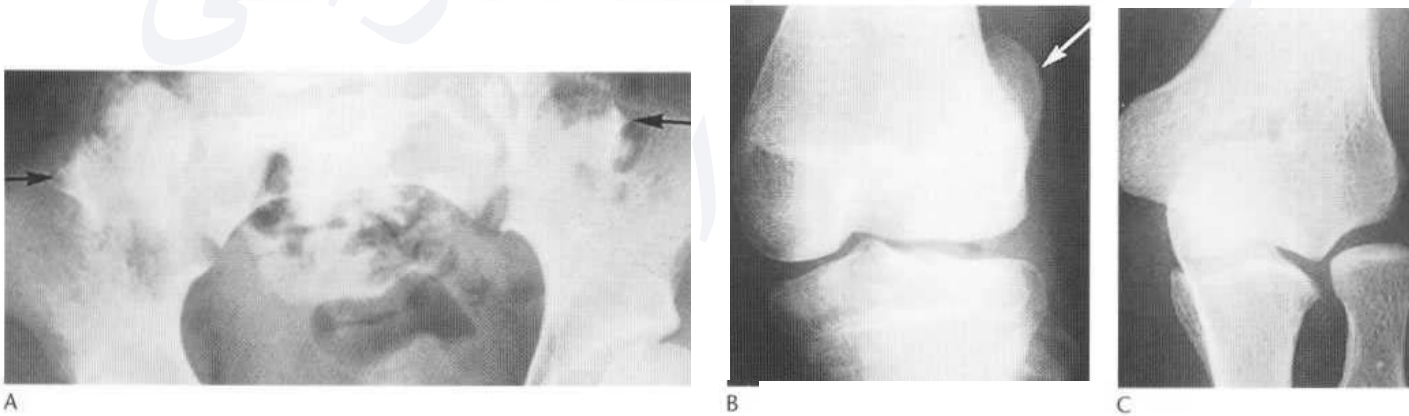


Fig. 35.20 Nail-patella syndrome. (A) Iliac horns are seen (arrows). (B) A small laterally placed patella is shown. (C) Hypoplasia of the capitellum is shown.

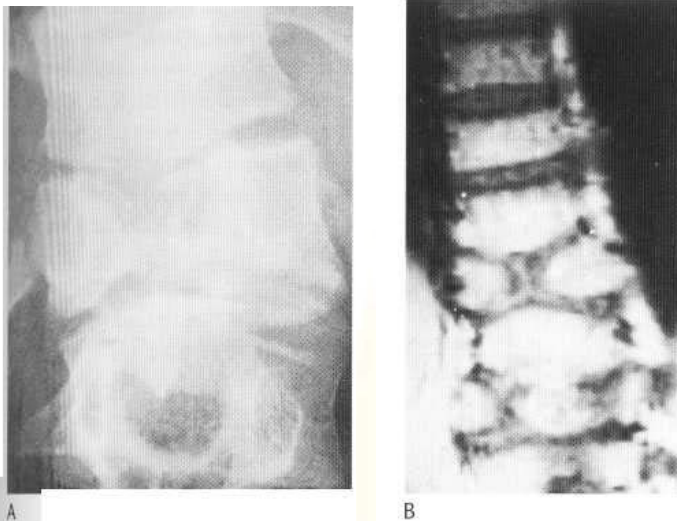


Fig. 35.21 Butterfly vertebra. (A) The upper and lower surfaces of affected vertebra are V-shaped, and contiguous vertebrae are moulded into the deficient centre. (B) MR image showing the same deformity.

body in the midline is much reduced. In the frontal projection, it is seen that vertebrae above and below are moulded into the deficient centres of the affected vertebra (Fig. 35.21).

Malfusions of appendages

Epiphyses of the spinous processes, transverse processes and articular facets may remain unfused. The abnormality is without importance except that it may mimic a fracture.

Hemivertebrae

They may cause scoliosis unless an equal number appear on each side (Fig. 35.22). In the thoracic region, a hemivertebra will bear a rib. Multiple hemivertebrae may cause dwarfism.



A



B



C

Fig. 35.22 Hemivertebra. (A) On the plain film there is a right-sided hemivertebra causing a significant osteogenic sclerosis concave to the left. (B) In another patient a thoracic hemivertebra is shown on the left, with an osteogenic scoliosis resulting. Deformity of the adjacent vertebral bodies is demonstrated. (C) In the same patient, the sagittal T_2 -weighted MR sequence shows the hemivertebra to be situated posteriorly and associated with an acute kyphosis.

Congenital vertebral fusion

Many forms of congenital vertebral fusion may be found. Complete fusion of the bodies and neural arches may occur, or the fusion may be limited to parts of the bodies or neural arches. At times it may not be possible to decide whether a fusion is developmental or postinflammatory. Fusion of neural arches, however, is almost always a developmental anomaly. The AP diameter of congenital block vertebrae may be reduced and an anterior concavity may be found. These features may also be found in old postinfective fusions or after juvenile chronic arthritis. A posterior concavity in addition may indicate a congenital lesion.

Complete vertebral fusions are often called 'block vertebrae'. They may be of no clinical significance but, frequently, disc degeneration develops above or below the fused vertebrae due to altered

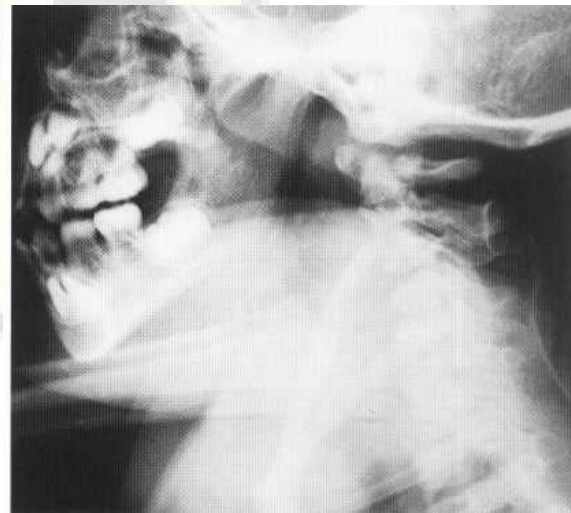


Fig. 35.23 Klippel-Feil deformity. Short neck with elevated shoulders and scapulae. Fusion is demonstrated at C2/3 level.

mechanics in the spine. Such lesions are relatively common in the cervical spine where a more severe anomaly, the *Klippel-Feil syndrome*, may be seen (Fig. 35.23). In this condition, many cervical vertebrae are fused, the neck is short and its movements limited, and hair grows low on the neck. Often there is torticollis and atrophy of facial musculature. Other congenital anomalies, such as spiny bifida, rib lesions and Sprengel's shoulder, usually coexist.

Vertebral fusions are also found in *fibrodysplasia ossificans progressiva* (see p. 1149).

Separate odontoid (*os odontoideum*)

The odontoid peg may sometimes be completely detached from the body of the second cervical vertebra, and be situated in the region of the foramen magnum (Fig. 35.24). Posterior fossa symptoms may result.

It has been shown that in some cases at least the separate ossicle results from a fracture in childhood of the base of the odontoid peg, with subsequent failure to unite. The lesion is thus not always 'congenital'.

Cervical rib

This is a common anomaly. The supplementary rib usually arises from the seventh cervical vertebra, rarely from the sixth and very rarely from the fifth.



Fig. 35.24 Os odontoideum. The odontoid peg is clearly separate from the body of C2 but retains a normal relationship with the arch of the atlas. These lesions usually follow trauma in childhood.

The diagnosis is straightforward, though it may be necessary to count all the ribs in order to distinguish a rudimentary first thoracic rib from a cervical rib. Cervical ribs arise from cervical transverse processes. Ribs slope downward from the neural arch in the cervical spine but upward in the thoracic spine. Cervical ribs vary greatly in size and shape, and clinical symptoms bear little relation to the radiographic abnormality. A very small cervical rib element may have a fibrous attachment to the first thoracic rib which causes much disability; this change may be seen at MRI (Fig. 35.25). A large cervical rib may be asymptomatic.

Sacralisation and lumbarisation

It is often difficult to give a definite level to a particular vertebral body in the lumbar region, especially if the lumbosacral region is transitional. Again, it may be necessary to count all the vertebral bodies from C I down. It has been said that the transverse processes of L3 are the lowest (most caudal) which lie transversely, while those for L4 are inclined upward. The transverse processes at L5 are the largest.

On axial MR images the iliolumbar ligaments link the L5 transverse processes to the iliac blade (Fig. 35.26).

Various permutations occur. Small, or absent, ribs on T12 may occur with large transverse processes on L5 which fuse with the sacrum (sacralisation of L5). This is known as cranial shift. Caudal shift implies the presence of ribs on L1 and lumbarisation of S1.



Fig. 35.26 Localisation of the L5 vertebral body at axial imaging by the presence of the iliolumbar ligament (arrow). This leads from the transverse process of L5 to the adjacent iliac blade.

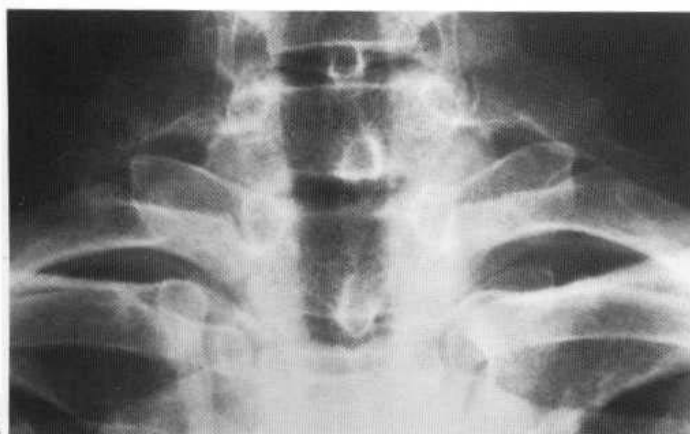


Fig. 35.25 Cervical rib. The cervical rib originates from a transverse process which points downwards. Thoracic ribs originate from upward-pointing transverse processes. (A) On the plain radiograph the well-corticated and ossified cervical ribs are shown originating from the C7 transverse processes. (B) At MR imaging the lesions are less well defined (arrows), but any associated fibrous attachments are seen with this imaging modality.

that is, it cones to bear free-floating transverse processes. A rudimentary disc is then seen between S1 and S2.

The sacralised transverse process may form a pseudarthrosis with the ilium and degenerative sclerosis may appear around the false joint. This may be a site of low back pain. In addition, the free disc above the pseudarthrosis shows early degeneration, especially if it lies high in relation to the iliac crest where it is said to be 'vulnerable' and susceptible to degeneration. Conversely, a low lumbosacral junction, buried deep between the crests, is less likely to degenerate. Similarly, a disc at the level beneath a transverse process-iliac blade fusion is 'protected' from early degeneration. The transverse process at L5 is usually the bulkiest and it may totally or partially articulate with the sacrum in 15-30%.

Anomalies of lumbosacral facets (*trophism*)

The facet joints in the lumbar spine may be clearly seen in the AP projection. They should be symmetrical but vary in their orientation. At L1 the facets have an almost vertical orientation but passing inferiorly are reorientated so that they face upward, inward and backward.

Facets are angled at around 52° in the sagittal midline at L5/S1 but 10° less at L4/5. The lower facets are asymmetrical in around 20-30% of patients. It has been said that the direction of disc degeneration and protrusion is related to the orientation of the facet-usually on the side of the more oblique facet.

Spina bifida

Incomplete fusion of neural arches is a common finding. In most cases only a minor midsagittal defect in the neural arch is seen. The rather misleading term 'spina bifida occulta' is applied to this condition. There is no true breach in such cases: the radiolucent area represents merely non-ossified cartilage. In children many of these areas become ossified as growth progresses.

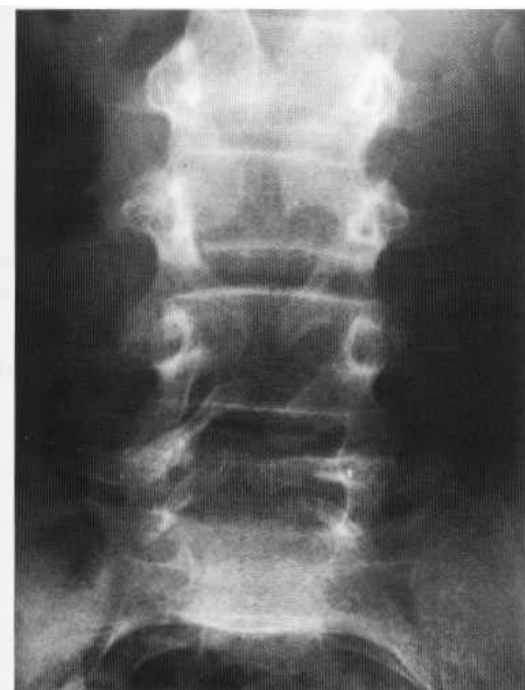


Fig. 35.27 Spina bifida. Central laminar defects are demonstrated throughout the lumbar spine. There is quite marked separation of the pedicles, which are hypoplastic.

True breaches in the neural arch do, of course, occur, and they may be accompanied by a meningocele protruding posteriorly and usually in the lumbar region. Occasionally, in the thorax and in the sacral region, the sac may protrude laterally and anteriorly through the intervertebral foramina and sacral foramina respectively (Fig. 35.27). Other vertebral and rib anomalies are very frequent in the severe forms of spina bifida. The presence of hydrocephalus is a common feature in marked spina bifida.

Foot deformities, such as *pes cavus*, may be associated with spina bifida. Likewise, *perforating ulcers* causing absorption of metatarsal heads, *neuropathic joints* and *spontaneous fractures* accompanied by excessive callus may all occur. *Metaphyseal fractures* are sometimes seen in this condition.

In cases of alimentary reduplications, the possibility of associated malformations of the spine should be borne in mind. The reduplications or *neurenteric cysts* may be associated with severe anterior and posterior *spina bifida*, *hemivertebra*, *absent vertebra* or *diastematomyelia*. In some cases no vertebral deformity is demonstrable.

Scoliosis

This term describes a lateral curvature of the spine. Usually, but not always, there is a primary curve with a compensatory curve above and below, unless the primary curve is lumbar.

Classification of scoliosis (after Cobb 1948)

1. Idiopathic (Fig. 35.28)
2. Osteogenic
 - a. congenital, e.g. hemivertebra (Fig. 35.22)
 - b. skeletal dysplasias, including neurofibromatosis (Fig. 35.29)

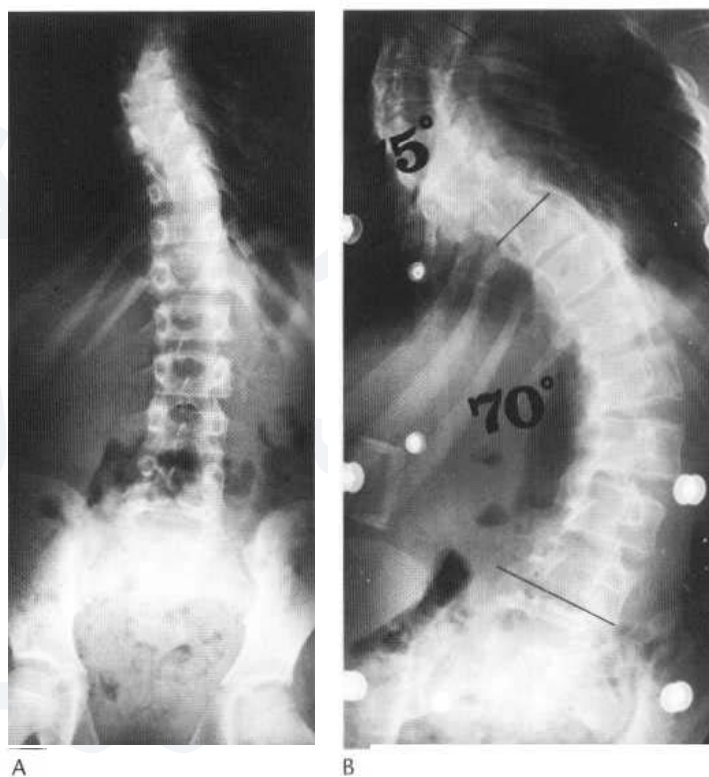


Fig. 35.28 Adolescent idiopathic scoliosis. (A) The initial radiograph shows a moderate thoracic scoliosis with compensation inferiorly. (B) Four years later the curves have increased in the coronal plane, as well as the degree of spinal rotation. This is especially apparent in the lumbar region.

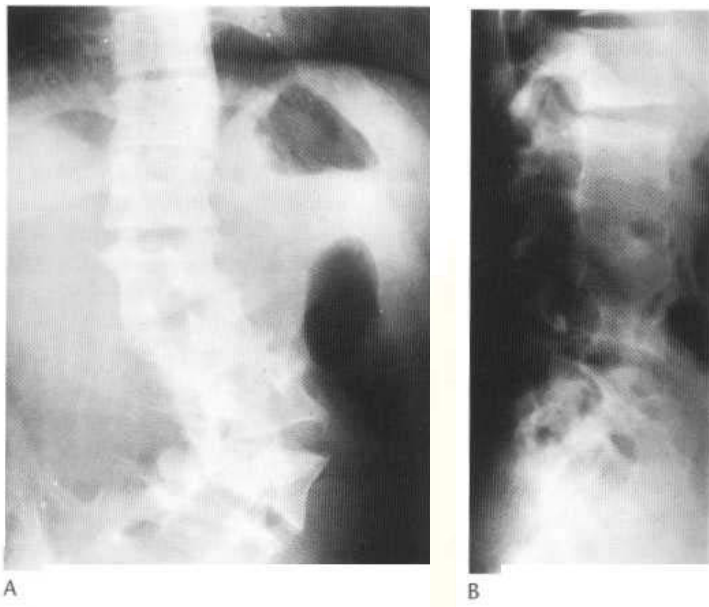


Fig. 35.29 Scoliosis in neurofibromatosis. (A) There is a very acute curve in the lumbar spine with marked rotation. (B) Dural ectasia is seen on the lateral view.

3. Neuropathic, e.g. polio, syringomyelia, Friedreich's ataxia
4. Hypopathic, e.g. Muscular dystrophy
5. Thoracogenic, e.g. post-pneumonectomy or thoracoplasty.

Idiopathic scoliosis

This is the most commonly seen form of scoliosis and may be further subdivided into the following groups:

- Infantile: age of onset 0-3 years
- Juvenile: age of onset 4-9 years
- Adolescent: age of onset 10 years, to the duration of growth.

In idiopathic scoliosis no other aetiology can be discerned and the diagnosis is made by exclusion. The earlier the onset of disease, the more marked the curve at the time of spinal skeletal maturity, after which little further deterioration is to be expected. Spinal skeletal maturity is reached when the apophysis for the iliac crest turns down toward and reaches that for the posterior superior iliac spine and, for this reason, films of the iliac crests are routinely obtained.

Idiopathic curves are associated with spinal rotation.

The curve can be measured by the method of Cobb (1948). The proximal and distal vertebrae at the margins of the curve do not show rotation of the spinous processes. Lines are drawn along the respective upper and lower end-plates at the margins of the curve and perpendiculars are drawn to these two lines (Fig. 35.30). The angles at which they meet is the angle of the curve. Severe curves are 100 or more, mild curves less than 69°, and moderate between 70 and 99°.

DYSPLASIAS OF BONE

The diagnosis of these lesions is mainly radiological and often entirely so. The radiologist will observe such features as alteration in bone density and in the size and shape of the bones. He or she will also observe the distribution of the lesion and the parts of the bones affected.

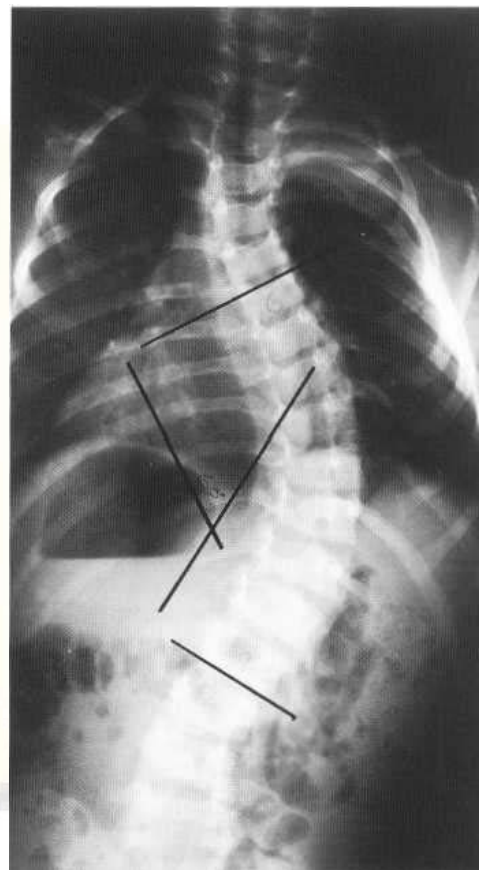


Fig. 35.30 Measurement of the curve by the method of Cobb. Perpendiculars are drawn to lines at the uppermost and lowest end-plates of the curve. The angle at which the perpendiculars meet is the angle of the curve.

Accurate diagnosis is now of prime importance and not merely an academic exercise. Genetic counselling is, of course, a well-established specialty depending on accurate diagnosis. In other fields, such as the *nu-copulvsaccharidnses*, new lines of therapy such as bone marrow transplantation are being evaluated.

Cleidocranial dysplasia (CCD) (synonym: cleidocranial dysostosis)

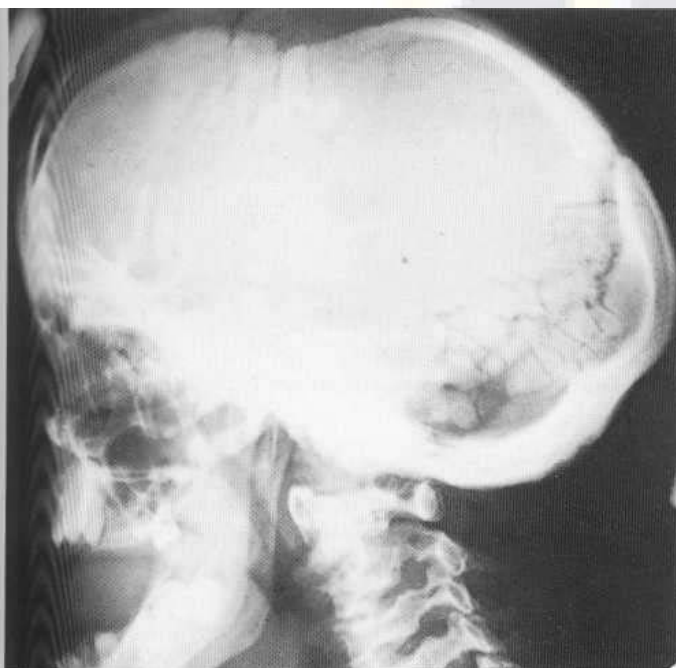
This is a benign hereditary condition, inherited as an autosomal dominant, which is recognised during childhood. The disease has considerable variation of expression. Thirty per cent of cases are due to spontaneous mutation.

Radiological features

Changes are widespread.

Clavicles There may be total (in 10% of cases) or partial absence of the clavicle (Fig. 35.31A). The outer end is absent more frequently than the inner, but both to an extremely variable extent. Central defects also occur. The clavicles may also be normal. The scapulae tend to be small and high, and the glenoid fossae are small.

Thorax The thorax is usually narrow, the ribs are short and directed obliquely downward. Respiratory distress may occur in the newborn. The sternum is incompletely ossified. Failure of fusion of neural arches occurs, with delay in maturation of vertebral bodies, which retain an infantile biconvex shape. Supernumerary or bifid ribs also occur.



C

Fig. 35.31 Cleidocranial dysplasia. (A) Clavicular defects are demonstrated, especially on the right side. (B) Note delayed mineralisation in the frontoparietal region and wormian bones posteriorly. Facial bones are small but the mandible is normal. Delayed dentition is also seen. (C) Failure of ossification of the symphysis pubis is demonstrated.

Skull In the newborn, mineralisation is delayed. The facial bones are small but the mandible is normal in size. The fontanelles remain open late and the sutures are widened. The bodies of the spheroids are hypoplastic. Many wormian bones are seen and frontal and parietal bossing may be present. Basilar invagination may also occur (Fig. 35.3 I B).

Pelvis Delayed and imperfect ossification of the pubic bones is a recognised finding (Fig. 35.3 IC) and congenital coxa vara is frequently seen.

Teeth See Chapter 50.

Hands Anomalies of the hand are very common. The second and fifth metacarpals are long and have supernumerary ossification centres at their bases. The middle phalanges of the second and fifth phalanges are short. Cone epiphyses and distal phalangeal tapering are found.

Short fibulae, congenital pseudarthrosis of the femur, genu valgum and obliquity of the articular space of the ankle joint are among many reported associations.

Pyknodysostosis

This condition has been confused with cleidocranial dysplasia (because of some similar clavicular and skull changes) and osteopetrosis (because of the generalised increase in diffuse bone density). It is inherited as an autosomal recessive disease, and

parents may be closely related. The patients are short (below 150 cm), which is not a prominent feature of CCD. The skeleton is susceptible to fractures. The disease is rare and found in all races. The French painter Toulouse-Lautrec is believed to have suffered from this disease.

Radiographic features

Skull There is brachycephaly with wide sutures and persistence of open fontanelles into adult life (Fig. 35.2A). Wormian bones are seen. The calvarium, base of skull and especially the orbital rims are very dense. The facial bones are small and the maxilla hypoplastic (Fig. 35.2A). The mandible has no angle—it is obtuse (see Ch. 50).

Limbs Normal modelling of long bones is usually seen. The cortices are dense but the medullary canals not completely obliterated.

Thorax Hypoplasia of the lateral ends of the clavicles is present to a varying degree. The ribs are dense overall.

Spine Failure of fusion of the neural arches and spondylolisthesis are found. In adults the vertebral bodies resemble spoons, with large anterior and posterior defects. The body dense (Fig. 35.2B). Vertebrae are uniformly

Hands Acro-osteolysis occurs, often with irregular distal fragments of the distal phalanges.

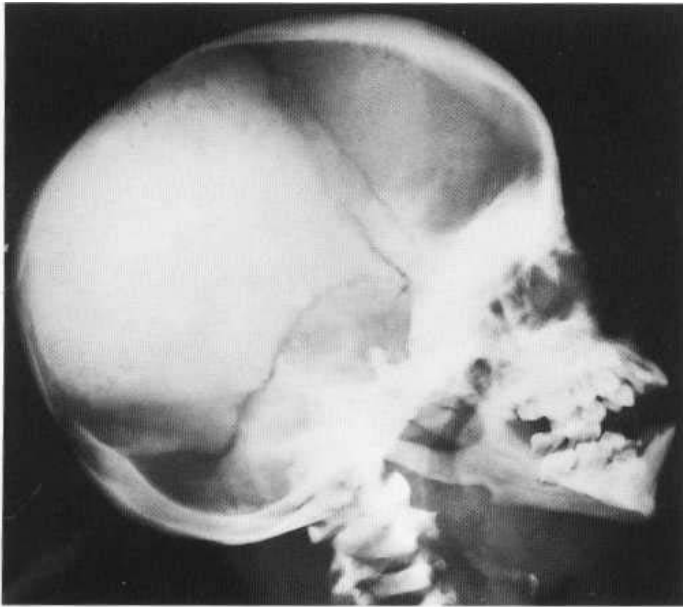


Fig. 35.32 Pyknodysostosis. (A) The skull shows failure of sutural fusion and sclerosis of the base. The angle of the mandible is obtuse and the maxilla hypoplastic (see Ch. xx). (B) The lumbar vertebral bodies show a spool shape with quite prominent anterior defects. Overall there is sclerosis.

Acro-osteolysis (eponym: Hajdu-Cheney syndrome)

Acro-osteolysis means disintegration of bone of the tips of the fingers and toes. This specific syndrome is inherited as an autosomal dominant. Other features include spinal osteoporosis, wormian bones in children and basilar invagination causing posterior fossa symptoms. Other types of inherited phalangeal resorption exist.

Box 35.1 Atrophic changes in distal phalanges

Atrophy of distal phalanges may be seen in disorders due to many causes

<i>Congenital</i>	Many forms of phalangeal agenesis may be found as congenital familial disorders
<i>Dysplastic</i>	Cleidocranial dysplasia Pyknodysostosis Acro-osteolysis
<i>Infective</i>	In acute infection usually only one digit affected—diagnosis obvious Leprosy-neurotrophic factors contributory Sarcoid
<i>Trauma</i>	Frostbite Electrical injuries
<i>Poisons</i>	Ergot-peripheral arterial spasm and gangrene Polyvinyl tank cleaners
<i>Metabolic</i>	Hyperparathyroidism
<i>Vascular</i>	Scleroderma with secondary Raynaud's phenomenon Occlusive vascular disease Pseudoxanthoma elasticum
<i>Neurotrophic</i>	Tabes, syringomyelia Diabetes-vascular and infective changes may be contributory
<i>Neoplastic</i>	Kaposi's sarcoma, where diffuse cutaneous and visual lesions are seen
<i>Miscellaneous</i>	Psoriasis, pityriasis rubra, epidermolysis bullosa, reticulohistiocytosis Ainhum Neurofibromatosis Progeria

There are many *other causes* of resorption of distal phalanges (Box 35.1). In some, resorption has a characteristic pattern and is accompanied by other features of the disease. Thus, in hyperparathyroidism, tuft resorption is accompanied by subperiosteal bone resorption around the cortices of middle phalanges.

Some patients have neurological lesions, for example in *syphilis, svingotnvelia* and *diabetes*. In some conditions, such as *rheumatoid arthritis* and *psoriasis*, peripheral vascular deficiency has been shown to occur in the region of tuft resorption.

Osteogenesis imperfecta (synonym: fragilitas ossium; eponyms: Vrolik = congenital recessive form, Lobstein = dominant form)

This is a relatively rare disorder manifested by increased fragility of bones and osteoporosis, as well as dental abnormalities (see Ch. 42), lax joints and thin skin. This disorder is due to an abnormality of Type I collagen, so that the sclera, cornea, joints and skin are also abnormal.

The original classification distinguished a severe recessive form and a milder and more common dominant type. The current classification (Sillence et al 1979) divides the disease into four basic types with further subtypes.

Type 1 This is the most common type; over 70% of cases of osteogenesis imperfecta fit into this category. It has *autosomal dominant* inheritance. Sclerae are blue. Bone fragility is mild. Stature is only mildly reduced. Deafness occurs in adult life.

This group is further divided into *Type 1A*—normal teeth, minor skeletal change—and *Type 1B*—dentinogenesis imperfecta (q.v.) and more severe skeletal change (Fig. 35.33A).

Osteoporosis occurs with cortical thinning with bowed, thin and gracile long bones (Fig. 35.338). In 10% fractures are seen at birth and in 1(Y' fractures never occur. Most fractures occur in young children. Wormian bones are seen in the skull (Fig. 35.34).



Fig. 35.33 Osteogenesis imperfecta. (A) There is osteopenia. A fracture has resulted in bowing and a periostitis. (B) The long bones are gracile and bowed. Marked osteopenia is also present.

Type 2 Ten per cent of cases of osteogenesis imperfecta are due to this *spontaneous dominant* new mutation which is usually lethal in utero or early infancy. The sclerae are dark blue.

Overall the bones are grossly demineralised with thin cortices. Numerous healed or healing rib fractures are seen at birth despite the protection of amniotic fluid. Fractures also occur during delivery.

This group is further divided into:

Type 2A. The long bones are bowed, short and *broad*. Numerous fractures are seen. The ribs are *broad* with continuous beading (Fig. 35.35).

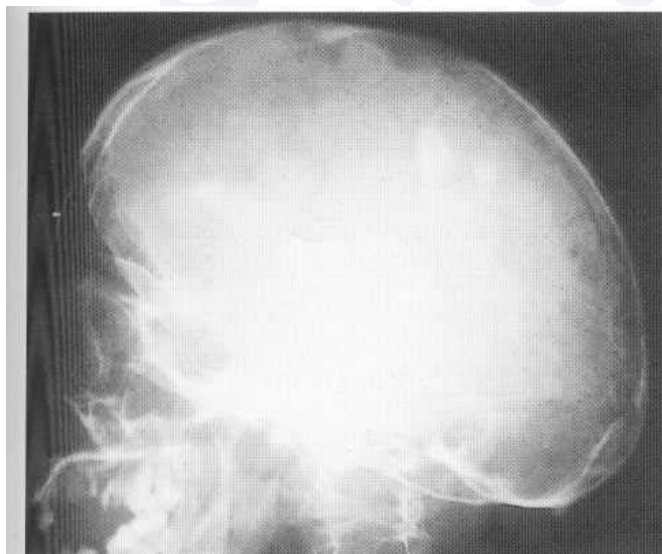


Fig. 35.34 Osteogenesis imperfecta. Persistence of wormian bones and basilar invagination are shown.

- *Type 2B.* The long bones are as in Type 2A, but the ribs show less or no beading.
- *Type 2C.* The long bones are *thinned*, show numerous fractures and the ribs too are *thin* and beaded.

Fairbank (1951) had already distinguished between a 'thick bone type' and a 'thin bone type'. Gross callus formation may be seen, but non-union may be present. Mineralisation in the skull may be severely retarded. Only the petrous bones may be clearly seen. The skull is enlarged and numerous wormian bones are seen.

Type 3 This occurs in 15% of patients, is a severe and progressively deforming type and is usually due to a new mutation. Sclerae may be blue at birth but are usually normal in adolescence.

Overall the bones are demineralised. Vertebral compression is seen and a kyphoscoliosis results. The long bones are osteoporotic and thin. Multiple fractures in childhood result in bowing (Fig. 35.36).

In the skull, ossification is again poor, sutures are wide and wormian bones persist. This type has associated dentinogenesis imperfecta.

Type 4 Again, there are two subtypes-4A with no dental lesion, 4B with dentinogenesis imperfecta. This group constitutes 5%. Sclerae are usually normal. Fractures are seen at birth in 30% and *bony fragility is mild*.



Fig. 35.35 Osteogenesis imperfecta. The child is stillborn. Multiple fractures are demonstrated in the short and broad long bones, which are cystic in appearance. Numerous rib fractures are seen.



Fig. 35.36 Osteogenesis imperfecta. The skeleton is immature. The femur is expanded and bowed at the site of previous fractures. The midshaft has a cystic, or soap-bubble, appearance.

Patients with a benign form of the disease may not present until adult life. Multiple fractures occur over a few years; eventually the diagnosis is made. Healing may be with excessive callus, so that a sarcoma is simulated. Sarcomatous degeneration is indeed described, but is rare. Occasionally, pseudarthroses are seen as in neurofibromatosis. Deafness is found in adults and may be due to ankylosis of ossicles and osteosclerosis.

The pelvis shows protrusio acetabuli, and further compression hinders childbirth. The ribs are so soft and thin that the downward pull of the intercostal muscles makes their posterior portion convex downward.

Differential diagnosis

Battered baby syndrome In osteogenesis imperfecta the fractures are often diaphyseal rather than metaphyseal, and the urinary hydroxyproline is often elevated. The differentiation is often of medicolegal significance.

Idiopathic juvenile osteoporosis This condition starts just before puberty and is usually self-limiting. Vertebral compression (Fig. 35.37) and characteristically *metaphyseal* fractures, especially of the lower limb long bones, occur (Fig. 35.38). The calcium balance is negative only in severe cases, otherwise the biochemical findings are normal.

Fibrogenesis imperfecta ossium

This is a rare condition which affects elderly patients and usually presents with pathological fractures. Radiologically, a gross

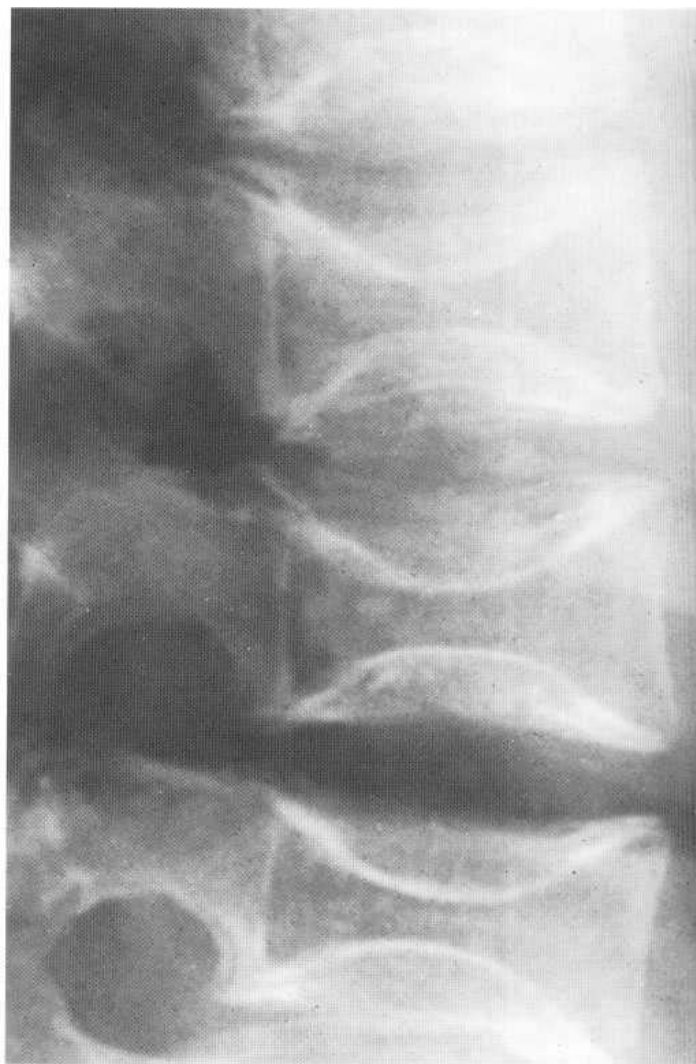


Fig. 35.37 Idiopathic juvenile osteoporosis. Gross vertebral compression affects mainly the central portions of the vertebral bodies.

coarsening of trabeculae is present so that the disease looks like Paget's disease (Fig. 35.39). All the bones are affected except the skull. Unlike Paget's disease, the bones retain their usual contour.

Osteopetrosis (synonym: marble bones; eponym: Albers-Schönberg disease)

As with osteogenesis imperfecta and many other dysplasias, there are many forms of this disease.

1. A severe, often fatal, early form, manifest in infancy or childhood and inherited in an autosomal recessive form. This has been diagnosed in utero (Figs 35.40, 35.41).
2. A more benign, tarda form, later in onset, inherited as a dominant. This autosomal dominant form can be further subdivided into:
 - a. Type I. Marked thickening of the sclerotic skull *vault* but with an almost normal spine
 - b. Type II. A sclerotic skull *base* and a 'rugger jersey' spine. Patients with Type II have a high risk of fracture; those with Type I do not.



Fig. 35.38 Metaphyseal fractures around the knee in idiopathic juvenile osteoporosis distinguish this condition from osteogenesis imperfecta.

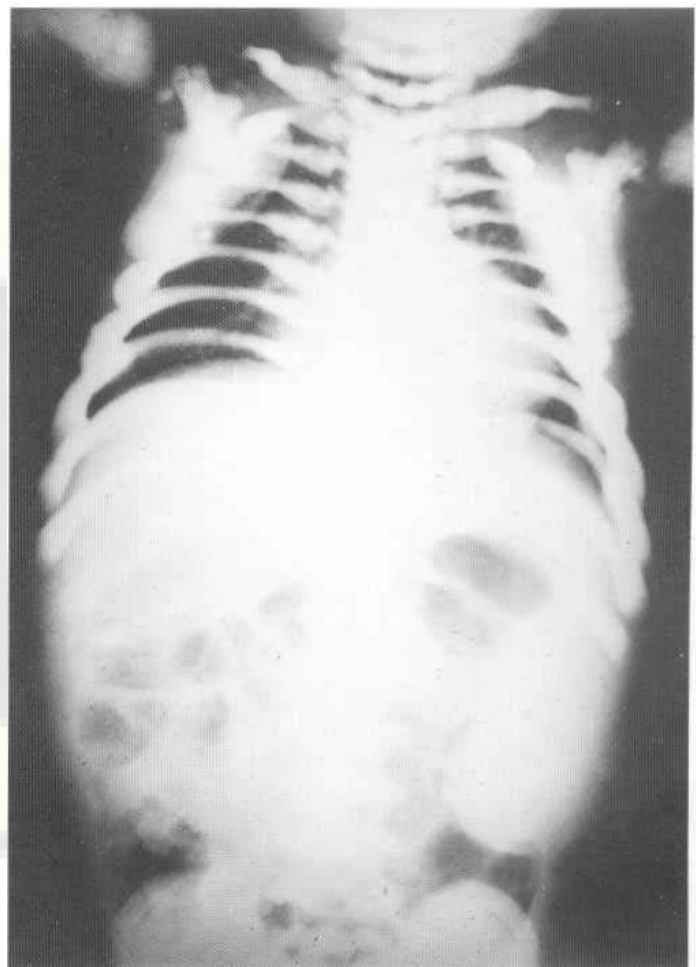
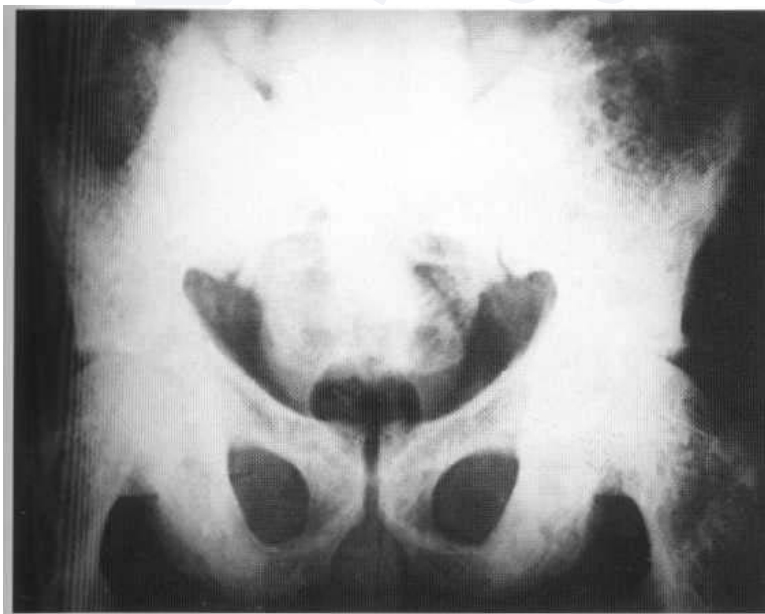


Fig. 35.40 Osteopetrosis. Bone density is uniformly increased apart from a small curved zone of normal bone at the iliac crest metaphysis. The spleen is the site of extramedullary haemopoiesis.

نشر الکترونیکی



موسسه نور

Fig. 35.39 Fibrogenesis imperfecta. Marked coarsening of trabeculation occurs throughout the skeleton but the bones retain their contour.

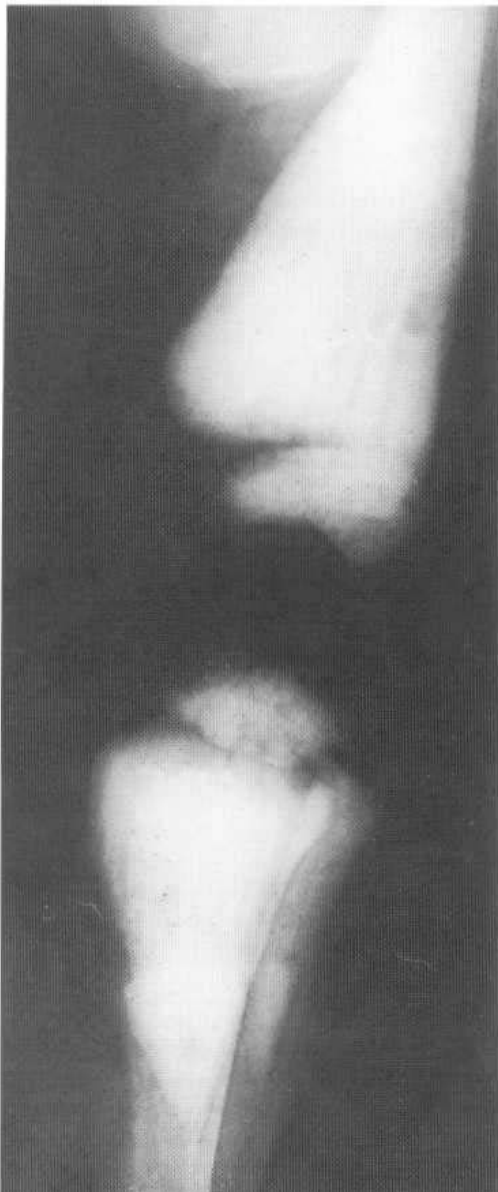


Fig. 35.41 Osteopetrosis-fine vertical lucencies are seen extending to the metaphyses, together with a 'bone within a bone' appearance at the tibial and fibular diaphyses.

3. An intermediate form with recessive inheritance.
4. A syndrome of *carbonic anhydrase 2 deficiency* associated with *renal tubular acidosis*.

Histology

There is failure of resorption of the primary primitive fetal spongiosa by the vascular mesenchyme. This primitive bone has a higher calcium content on ashing, and appears denser on radiology. The bone is brittle and fractures easily, but heals normally.

Normal bone may be laid down in episodes so that zones of normal and of denser bone may be seen, but the marrow is encroached upon and extramedullary haemopoiesis occurs (Fig. 35.40).

In the severe forms of the disease, anaemia and hepatosplenomegaly are found within months of birth and life expectancy is poor.

In the tarda form of the disease, the diagnosis is often made fortuitously when two or three fractures occur, perhaps in the space of a [year](#), in an adult patient. The bones may be slightly dense. Modelling abnormalities are seen with metaphyseal undertubulation.

Dental disease is common (see Ch. 38) with osteomyelitis occurring in the rather compact bone.

Radiological features

Increased density and thickening of long bones, especially metaphyses, can be seen in utero. The presence of a 'bone within a bone' differentiates osteopetrosis from the other sclerosing dysplasias. This is due to the cyclic nature of the disease, so that the dense shadow of, say, the tibia at the time of formation of abnormal bone is seen within the outline of the current normal or abnormal shadow. The timing of intrauterine onset of disease can thus be assessed. This 'bone within a bone' may be vertical in the long bone shafts and digits, transverse at the metaphyses or arcuate beneath the iliac crests.

Long bones Besides the 'Erlenmeyer flask' deformity due to failure of metaphyseal remodelling, giving gross distal undertubulation, and the presence of dense bone, vertical line lucencies extending to the metaphyses are also present (Fig. 35.41), probably due to vascular channels being better seen against dense bone.

Fractures are usually transverse (Fig. 35.42) and heal with normal callus. Residual varus results from proximal femoral fractures. Some diaphyseal remodelling is to be expected. Skeletal maturation is normal.

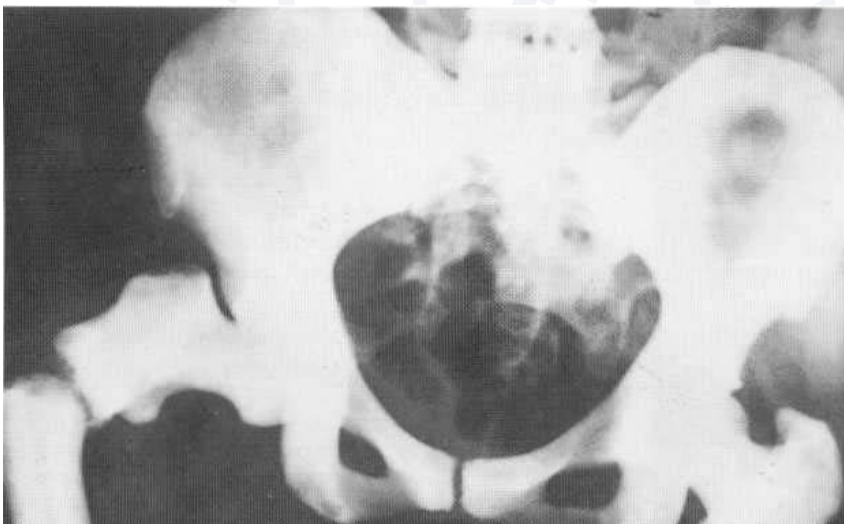


Fig. 35.42 Osteopetrosis-spontaneous fracture of upper end of right femur.



Fig. 35.43 Osteopetrosis—note inset of an earlier vertebra within each vertebral body.

Skull (for dental abnormalities, see Ch. 49) The bones of the skull base are initially affected with sclerosis and thickening, prominent in the floor of the anterior cranial fossa. The cranium is affected to a lesser degree. The sphenoid and frontal sinuses and mastoids are underpneumatised or not at all. Neural foramina are encroached upon and blindness results in serious cases. Bone softening with hydrocephalus does not appear to be a problem.

Spine Platyspondyly does not seem to occur, but spondylolisthesis does. In vertebral bodies, an appearance like a 'rugger jersey' spine may be seen due to the inserted shadow of an earlier, more dense body (Fig. 35.43), especially in Type 2-II.

In the adult form of the disease, the bones are roughly normal in shape. The medulla in the proximal skeleton is primarily involved and the periphery spared. Mild, uniform increase in density may be seen.

There is an association with renal tubular acidosis and dense cerebral calcification in patients with carbonic anhydrase 2 deficiency.

Melorheostosis (eponym: Léri's disease)

This is a very rare lesion affecting both sexes; no familial trend has been reported. Though the condition has not been observed in a child under the age of 3 years, there is strong presumptive evidence that it is present at birth.

Patients may complain of pain and of restricted movements of joints but the condition is often asymptomatic. Some cases are associated with skin lesions, such as scleroderma, and with vascular anomalies; joint contractures may be found in some patients.

The condition is characterised by the presence of dense irregular bone running down the cortex of a long bone. Both the internal and external aspects of the cortex may be affected. Dense areas tend to be overgrown and bowing may result. Murray & McCredie (1979) have pointed out that the distribution of the new bone corresponds to a sclerotome, the segmental root nerve innervation of a bone.

The new bone has been likened to molten wax running down the side of a burning candle (Fig. 35.44). The lesions tend to be segmental and unilateral, though both limbs may be affected. Occasionally the condition is bilateral but never symmetrical. Some lesions are progressive. The lower limbs are most commonly affected. Premature epiphyseal fusion may result, so that an affected limb may be larger or smaller than normal.

The skull, spine and ribs are rarely affected. Ectopic bone may be found in soft tissues around joints between affected bones.

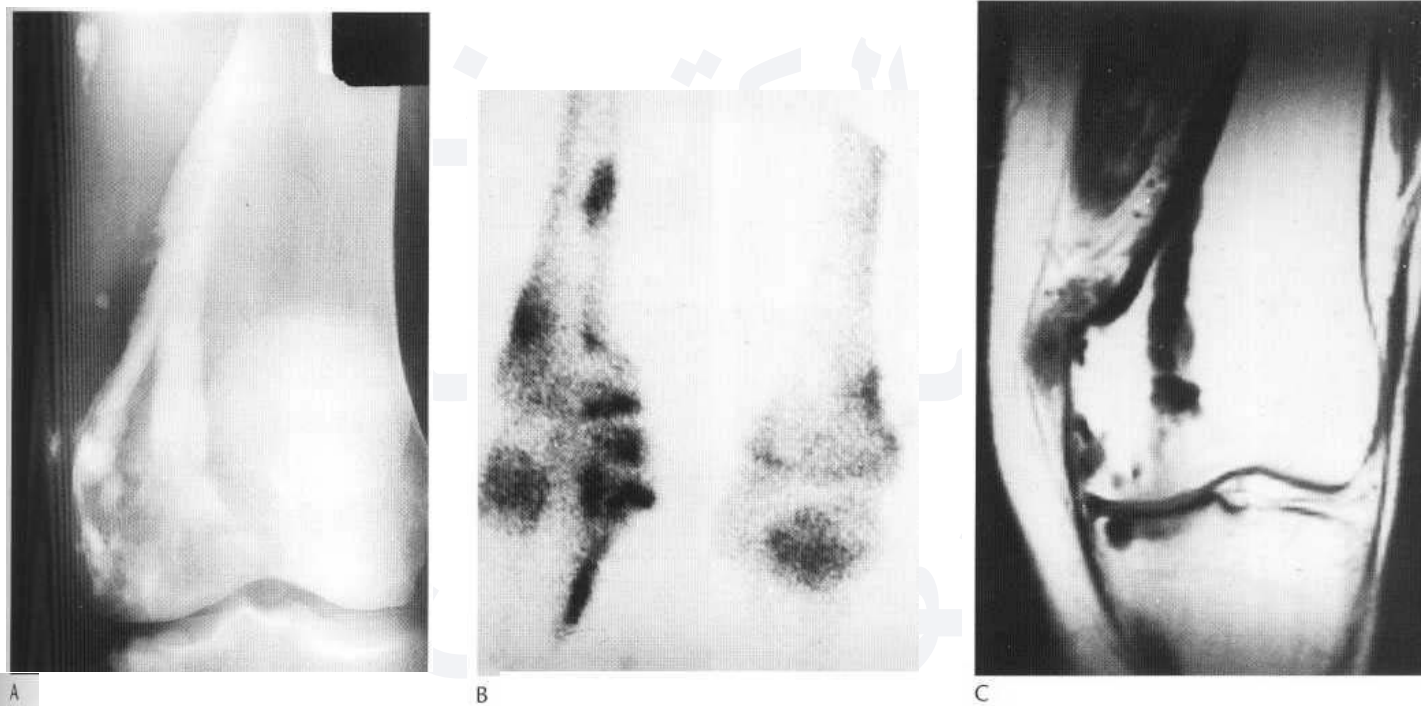


Fig. 35.44 Melorheostosis. (A) The plain film shows eccentric and irregular sclerosis along the medial aspect of the distal femur, crossing the joint into the adjacent tibia. There is new bone on the outer aspect of the cortex and also in the soft tissues. (B) On the radioisotope bone scan increase in uptake is demonstrated in the areas of bone sclerosis. (C) The coronal T₁-weighted MR sequence shows sclerotic bone, as expected, as areas of low signal lying within the marrow, on the periosteum and in the soft tissues.

Osteopoikylisis (synonym: osteopathia condensans disseminata)

This is usually an incidental radiological finding but some patients have associated skin nodules. The lesions are familial. It affects both sexes equally and is characterised by the presence of multiple, dense, radiopaque spots which are round, oval or lanceolate, and tend to be situated parallel to the axis of the affected bone. They are usually uniform in density but may have relatively clear central zones. Any bone may be affected. They occur especially frequently in the ends of long bones and around joints, in the carpus and tarsus, and in the pelvis (Fig. 35.45). This lesion must be differentiated from serious conditions such as tuberos sclerososis and metastases, but their distributions around joints, and the fact that the nodules rarely increase in size or number under observation, distinguish this benign condition from metastases.

Osteopathia striata (eponym: Voorhoeve's disease)

In this asymptomatic disorder sclerotic striations are found in the long bones, especially of the lower limbs, affecting both bone ends and diaphyses (Fig. 35.46).

Fibrous dysplasia

This is a disease of unknown aetiology. It is probably more common in women. The disease is found in two forms, monostotic and polyostotic. With polyostotic disease, over 50% of the skeleton may be involved, but symmetry is unusual and the lesions tend to be unilaterally distributed. The lesions are usually found incidentally or following pathological fracture. Deformity may occasionally be marked. The alkaline phosphatase is elevated but does not correlate with the extent of the disease. The age of onset is usually between 10 and 30, but polyostotic disease may present in the first decade. The lesions often

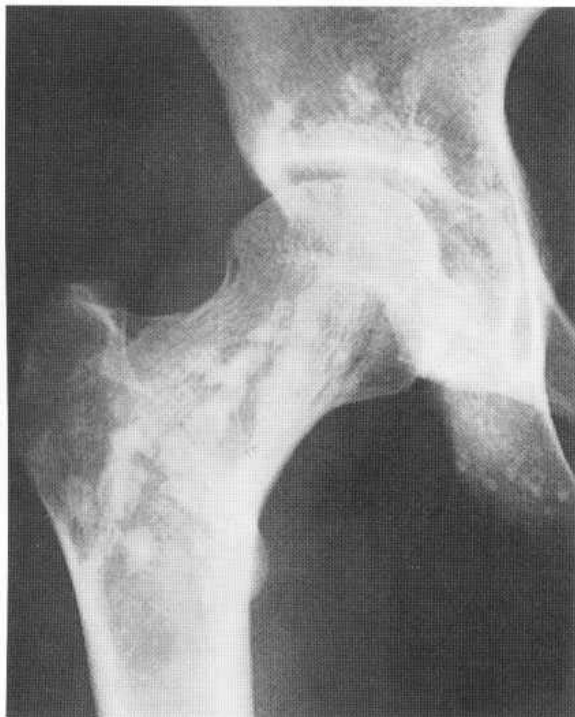


Fig. 35.45 Osteopoikylisis.

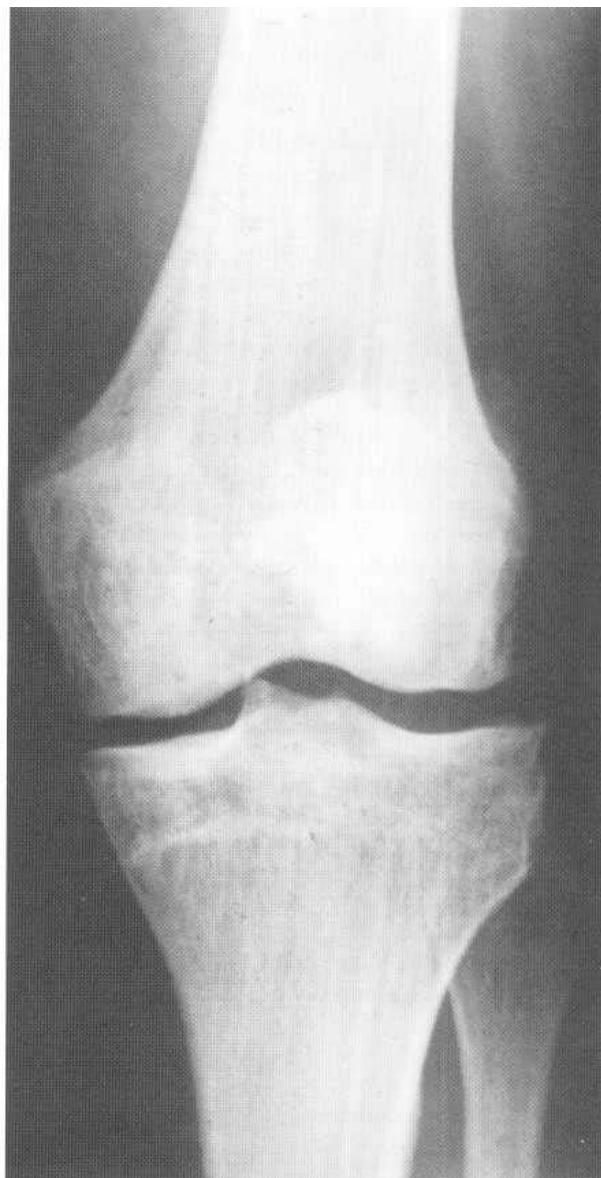


Fig. 35.46 Vertical striation extends to the articular surfaces in osteopathia striata.

cease growing with skeletal maturity but may be seen in old age. Monostotic lesions are more likely to enlarge in adult life. Prognosis is worse when the lesions occur early in life.

Pathology

Medullary bone is replaced by well-defined areas of fibrous tissue, and cysts containing blood or serous fluid. These appear similar on radiographs. The fibrous tissue then undergoes varying degrees of abnormal ossification so that some of the lesions show an increase in density, dependent on the extent of ossification. This increase in density may thus be patchy, giving a cottonwool appearance, or homogeneous giving a ground-glass appearance.

Radiological features The lesions have a smooth dense margin of varying width, often so wide as to resemble the rind of an orange (Fig. 35.47). The bone is expanded and the cortex scalloped and thinned but intact (Fig. 35.48). Lesions tend to be multilocular and expand down the medulla rather than cause great cortical expansion. Unlike Paget's disease, the bone ends are not necessarily



Fig. 35.47 Four examples of quiescent fibrous dysplasia in the proximal femur. The lesions are well defined, often with a very thick 'rind' around them, and show various degrees of central mineralisation. The site is typical for fibrous dysplasia.

affected and lesions tend to be diaphyseal. Bone ends may be involved after fusion, and epiphyses may be involved in the child.

Any bone may be affected, though involvement of the spine is uncommon and vertebral collapse is unusual. Lesions do not really need to be diagnosed by biopsy as the appearances are usually characteristic.

The pelvis (Fig. 35.49), femur and ribs are commonly involved. In the femur, deformity due to softening, expansion and fracture gives an appearance likened to a 'shepherd's crook' (Fig. 35.50) and discrepancies in limb length result. Lesions are well defined and may be expanded with well-defined margins. These may be lucent, dense or a mixture of the two, with small flecks of density due to ossification (Fig.35.50).

In the skull, the frontal, sphenoid, parietal and maxillary bones and mandible are often affected (Fig. 35.51). A grossly expanded sclerotic hyperostosis of the sphenoid may resemble a meningioma. Orbital fissures may be encroached upon and proptosis may result. Obliteration and bony expansion of the facial sinuses make the face appear grotesque and mask-like. In the vault, lesions tend to be grossly expansile, sclerotic, but localised (blister lesion) (Fig. 35.52).



Fig. 35.48 Fibrous dysplasia. A multilocular, partly cystic, expansile lesion of the midshaft femur is surrounded by a thick rim of reactive sclerosis.



Fig. 35.49 Fibrous dysplasia-large expanding lesion in superior pubic ramus and sclerosis in upper end of the femur.

The lesions show increased uptake on *racliorucclide scanning* (Fig. 35.53). The degree of increase depends on the nature of the underlying lesion-whether fluid-filled cysts, non-mineralised matrix, or sclerotic, ground-glass or patchily mineralised.

On *MRI* cysts will show features of fluid, i.e. grey on T₁-weighted images, bright on T₂-weighted or STIR sequences. The greater the degree of mineralisation, the lower the signal, either homogeneous or spotty. Hypocellular fibrous tissue is generally of low signal on T₂-weighted images (Fig. 35.54).

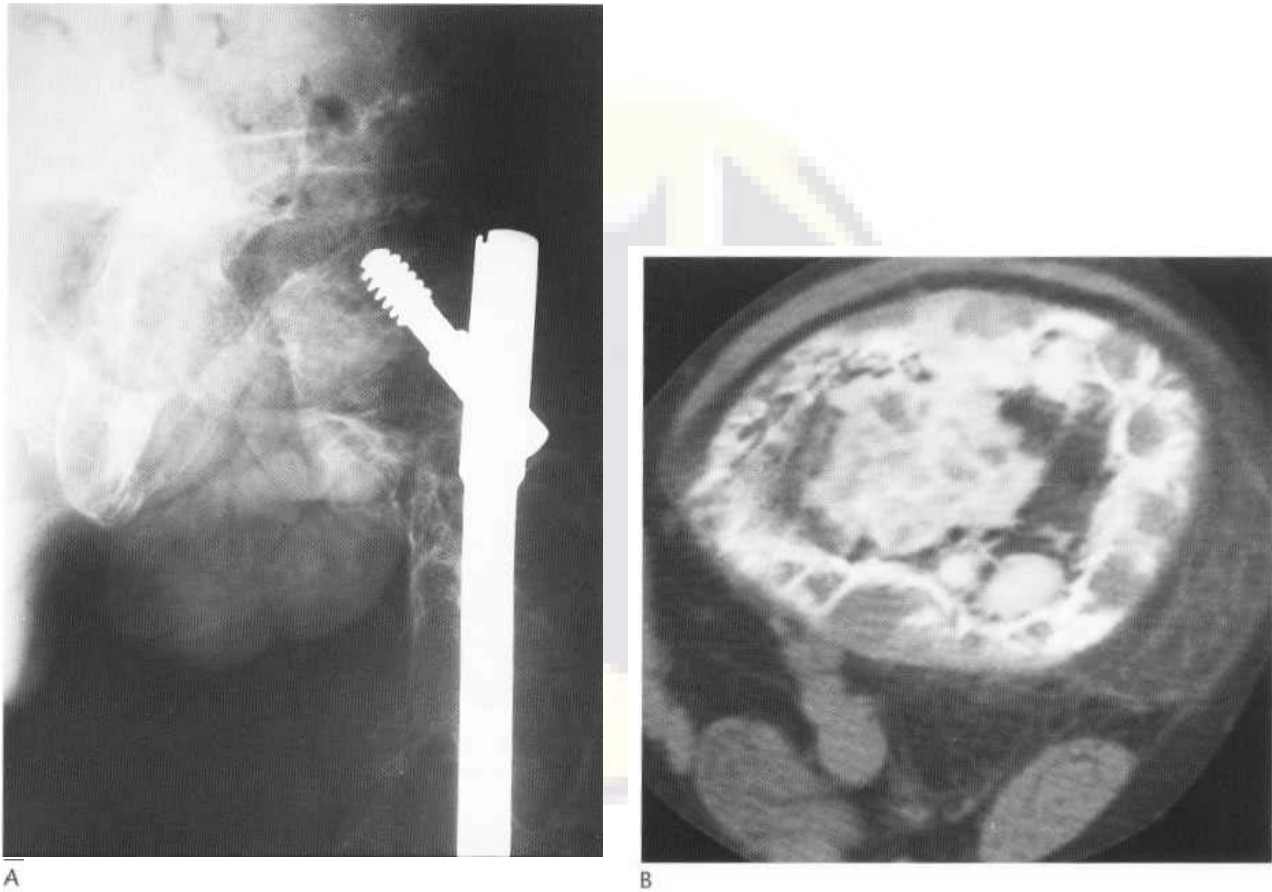


Fig. 35.50 Fibrous dysplasia. (A) The plain film in this much more severe polycystic case shows marked enlargement and deformity of the pelvis and proximal femur. There is marked bony expansion with extensive cyst formation. The shepherd's crook deformity has been stabilised. (B) The CT scan shows the mixed pattern of tissues seen in fibrous dysplasia, ranging from cystic through ground-glass to heavily mineralised tissue.

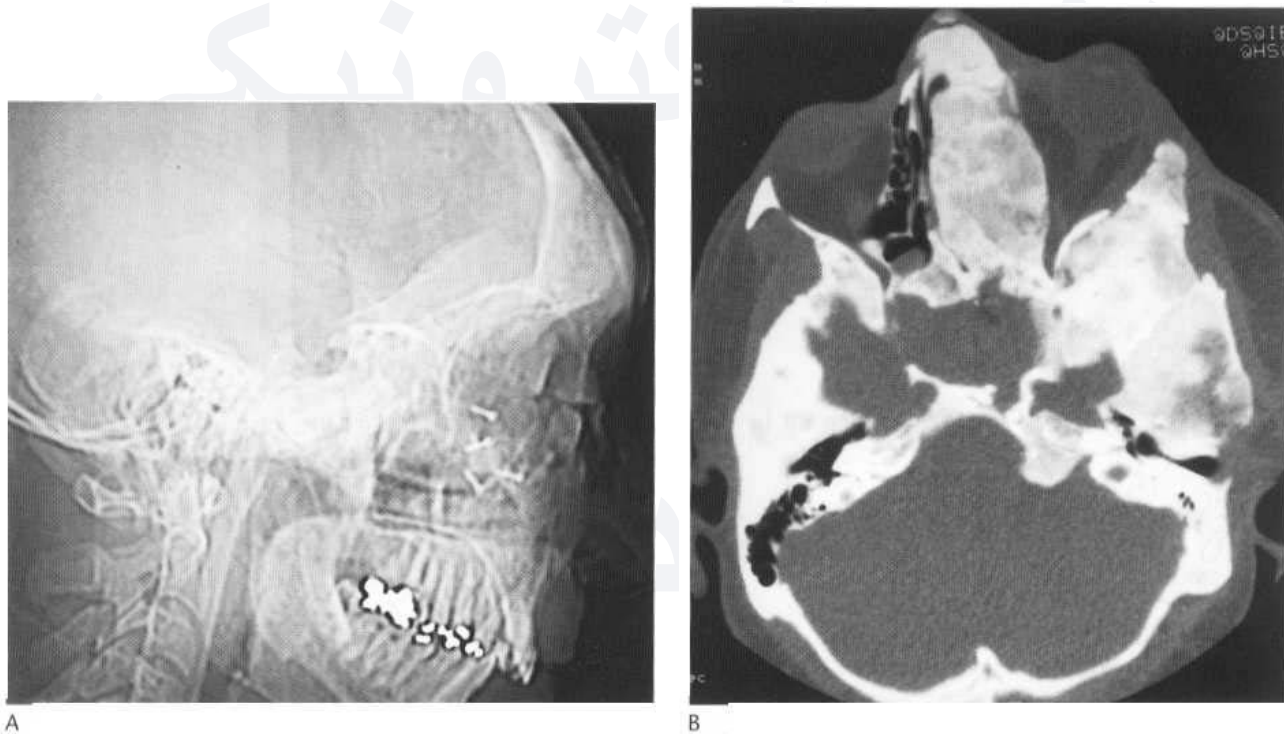


Fig. 35.51 Fibrous dysplasia. (A) There is thickening with sclerosis of the frontal bone, the floor of the anterior cranial fossa and the base of the skull extending back to the sphenoid sinus, which is replaced by dense amorphous bone. (B) The CT scan shows expanded and abnormally mineralised bone occupying mainly the left side of the skull base. Considerable facial deformity is present.

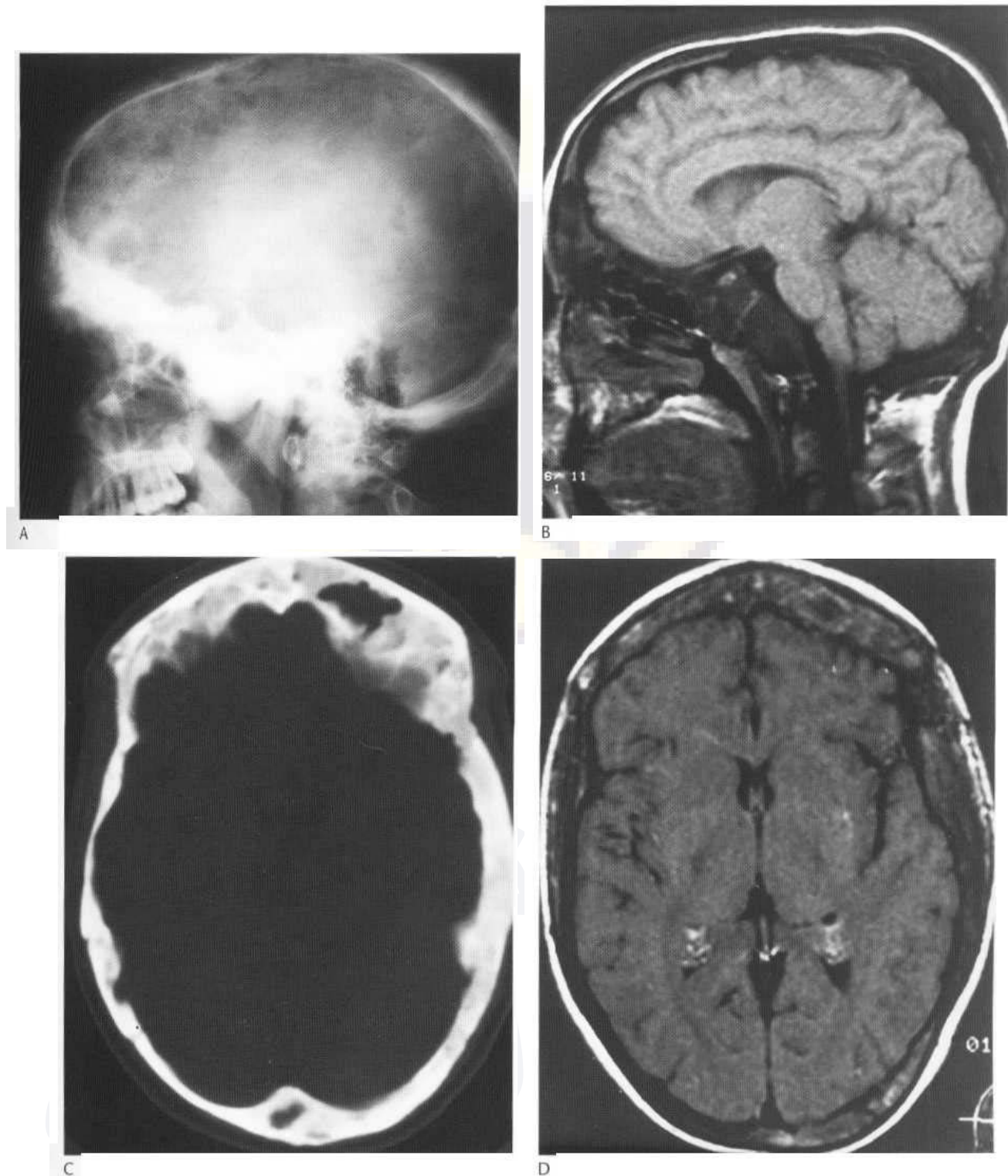


Fig. 35.52 Polyostotic fibrous dysplasia. (A) The plain film shows extensive involvement of the skull base which is sclerotic and thickened, but a rather more patchy and diffuse involvement of the vault, which shows areas of normal bone interspersed with areas of thickened bone. (B) On the sagittal T₁-weighted MR sequence the appearances exactly mirror the changes seen on the plain film. The skull base is thickened and shows extensive low signal with loss of marrow. Marrow is only to be seen in part of the frontal bone. The region of the frontal sinus, which is obliterated, shows a mixture of low and intermediate signal. The low signal indicates mineralisation, the intermediate fibrous tissue, and the subcutaneous fat shows uniform bright signal. (C) An axial CT scan through the vault shows a typical mixed pattern of fibrous tissue which is partially mineralised. Cysts are shown. (D) The same skull at MR imaging. On the T₁-weighted sequence the bright outer band represents fat beneath the skin; the thickened skull vault is seen as a mainly low-signal area anteriorly.

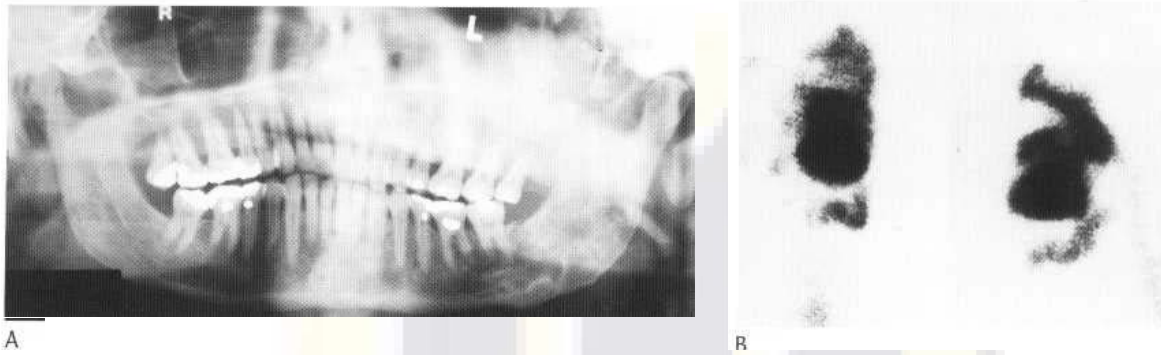


Fig. 35.53 Fibrous dysplasia. (A) In this patient the left antrum shows increased density and the left maxillary alveolus is enlarged by a sclerotic area of fibrous dysplasia. In the left side of the mandible, the expansile lesion is more radiolucent. (B) On the radioisotope bone scan, the anterior and lateral scans show a gross increase in uptake in the left maxillary antral region. Expansion is also confirmed. The abnormality extends to the base of the skull at the anterior cranial fossa. The lytic mandibular lesion seen on the plain radiograph is also seen as an area of increased uptake but, as expected, is not as prominent.

Complications

Fractures, deformity and irregularity Of limb length have been mentioned. Nerve palsies may occur in the skull.

Endocrine complications. *Albright's syndrome* consists of skin pigmentation, usually on the side of the bone lesions, fibrous dysplasia (usually polyostotic) and precocious puberty. This occurs usually in girls, and only rarely in boys. Most patients with skin pigmentation and polyostotic disease do not have associated endocrine disease and, in girls, only 50% have precocious puberty. *Hyperthyroidism, acromegaly, Cushing's syndrome, gynaecomastia* and *parathyroid enlargement* have all been reported in association with polyostotic fibrous dysplasia.

Sarcomatous degeneration occurs in less than 1% of patients, usually to *fibrosarcoma* (Fig. 35.55). Some, but not all, of these patients give a history of previous irradiation.

Chondrodystrophia calcificans congenita (synonyms: *chondrodysplasia punctata, dysplasia epiphysealis punctata, stippled epiphyses*)

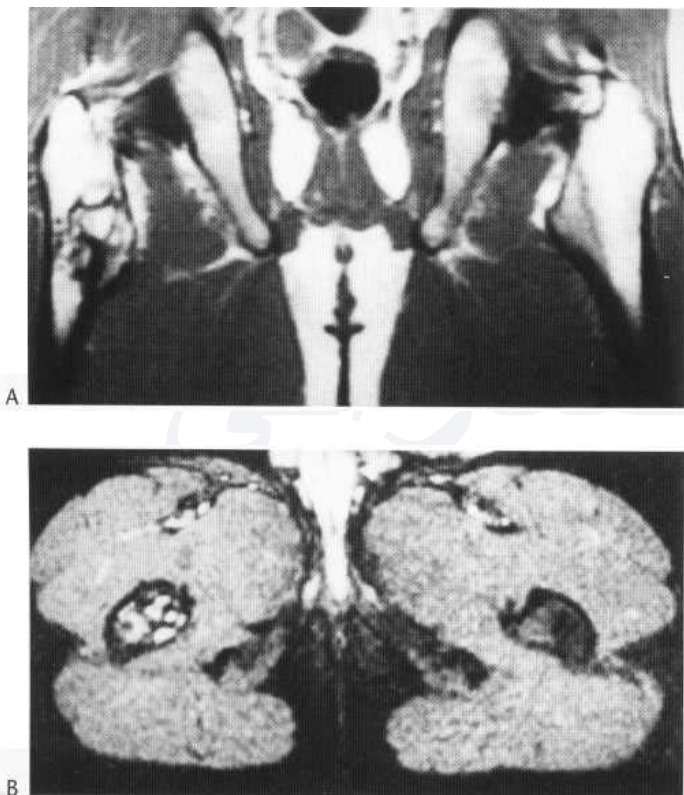


Fig. 35.54 Fibrous dysplasia, right femur: MR scans. (A) There is a localised well-defined expansile lesion with an intact cortex showing areas of mixed signal on the T₁-weighted coronal image. (B) The axial fat-suppression study confirms the expansion of the bone and shows fluid within well-loculated cysts in the lesion.

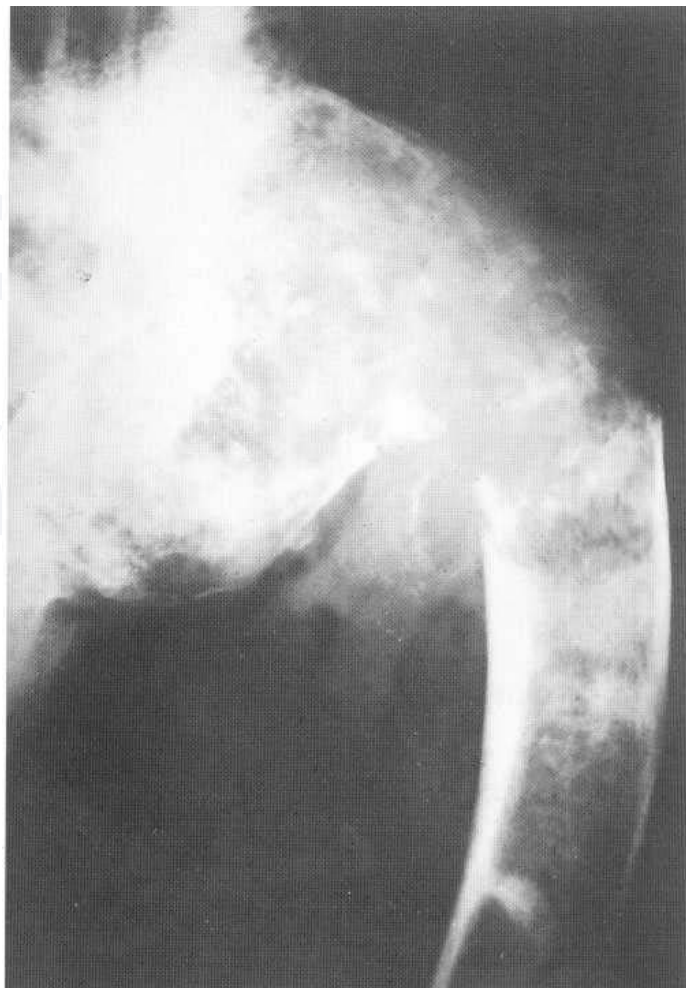


Fig. 35.55 A pathological fracture with irregular bone destruction due to malignant degeneration is superimposed upon fibrous dysplasia.

This disease exists in at least three types, inherited differently:

1. *Rhizomelic* type (recessive) usually lethal; the most common fatal type
2. *Non-rhizomelic* types (Conradi-Hiinermann)
 - a. Dominant-common, usually mild
 - b. X-linked dominant lethal in males.

These have similar radiographic changes. Ichthyosis may be seen in the rhizomelic and X-linked forms.

The less severe Conradi form of the condition is characterised in infancy by stippling or punctate calcification of the tarsus and corpus, long bone epiphyses, vertebral transverse processes and the pubic bones. The resulting epiphyses in later life are often misshapen, and deformities with asymmetrical limb shortening result. The spine often ends up scoliotic but, if the infants survive, life expectancy is normal but with an appearance resembling multiple epiphyseal dysplasia (see below).

The more severe forms usually result in death in the first year; survivors are likely to be mentally defective. Stippling is present as above but is, if anything, more gross, also occurring in the trachea. Long bones show gross symmetrical shortening and metaphyseal irregularity (Fig. 35.56). In this form the vertebral bodies show a vertical radiolucency on the lateral view which does not occur in the dominant type. In survivors, there is marked retardation of epiphyseal development.

Multiple epiphyseal dysplasia (synonym: *dysplasia epiphysealis multiplex*)

This condition, which is transmitted as an autosomal dominant, primarily affects the epiphyses. Dwarfism of the short-limb type may be seen. The condition may express itself in various ways, so much so that some writers subdivide the disease into a severe form (*Fairbank*) characterised by small epiphyses, and a mild type (*Ribbing*) characterised by flat epiphyses.

In order of frequency, the epiphyses affected are those of the hips, shoulders, ankles, knees, wrists and elbows. Epiphyses tend to appear late and are fragmented and flattened (Figs 35.57-35.60); the deformities persist throughout life and cause premature osteoarthritis. The femoral capital epiphyses show symmetrical flattening and fragmentation in the immature skeleton, the symmetry distinguishing this from bilateral Perthes' disease (Fig. 35.61). Symmetrical fragmentation is also seen in *m_vxoedaina* in association with skeletal retardation.

No characteristic changes are found in the metaphyses but they may be widened to conform to the deformed contiguous epiphyses. Secondary changes in contour are often seen in glenoid and acetabular fossae. The carpal and tarsal bones may be affected and digits and toes may be 'stubby'. The skull is not affected. Sonic features may be characteristic but none is constant:

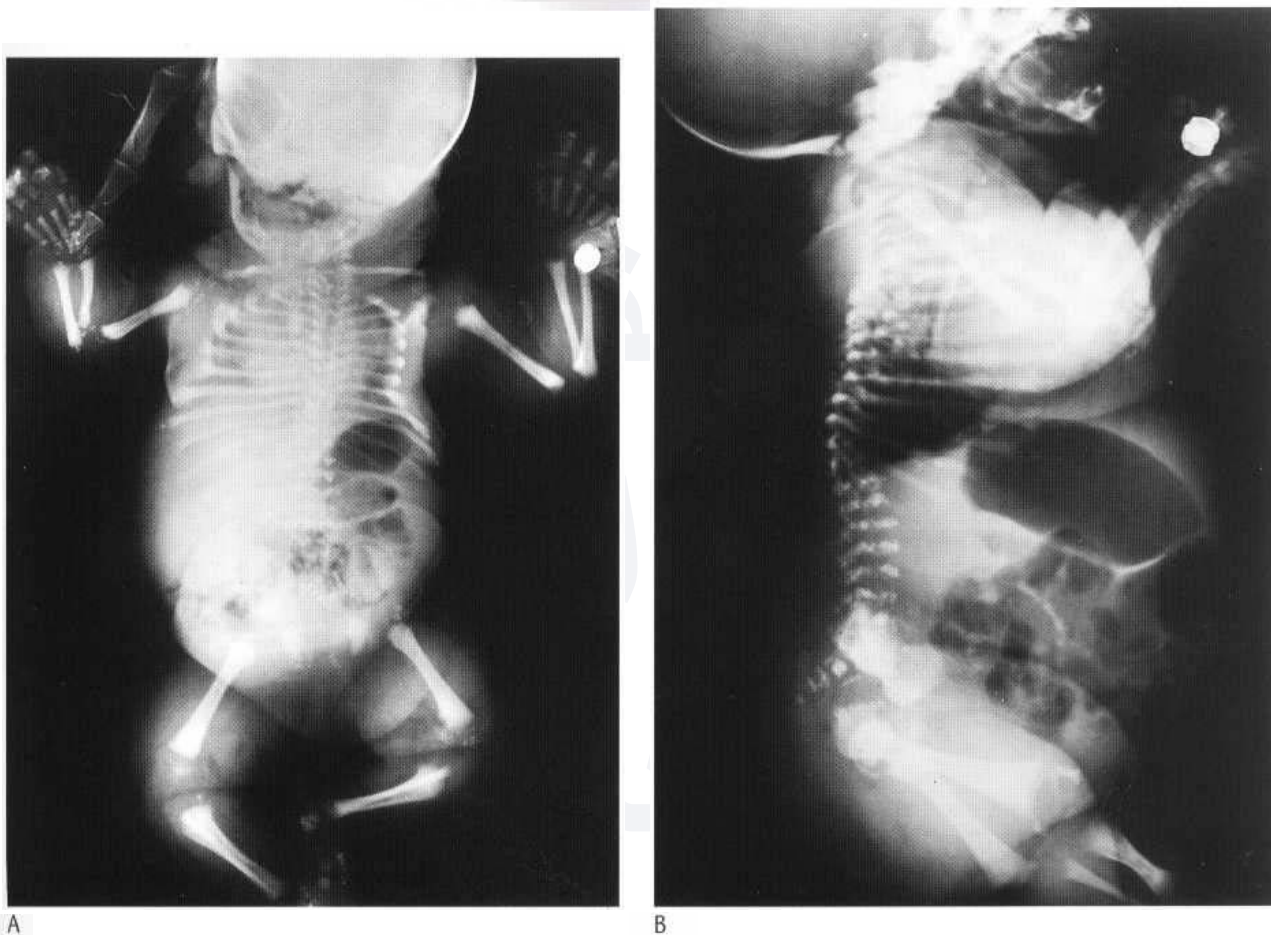


Fig. 35.56 (A,B) *Chondrodystrophia calcificans congenita*. There is irregularity of vertebral bodies and of the neural arches and spinous processes in association with soft-tissue stippled calcification. These changes are also seen at the joints. The long bones are markedly shortened. The humeral metaphyses are irregular.

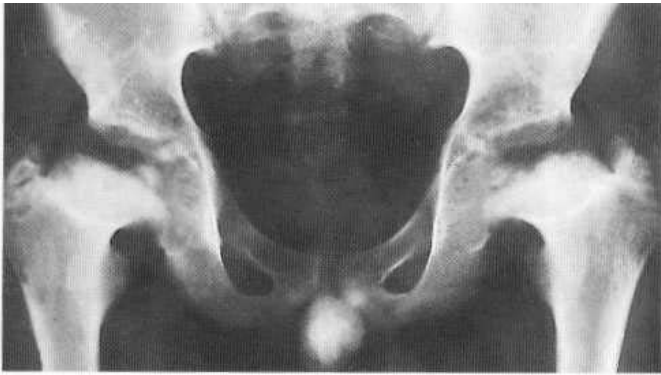


Fig. 35.57 Dysplasia epiphysealis multiplex. Both femoral heads are hypoplastic and fragmented. The femoral necks are irregular and broad. Similar changes are seen at the greater trochanteric apophyses. Dysplastic acetabula are demonstrated.

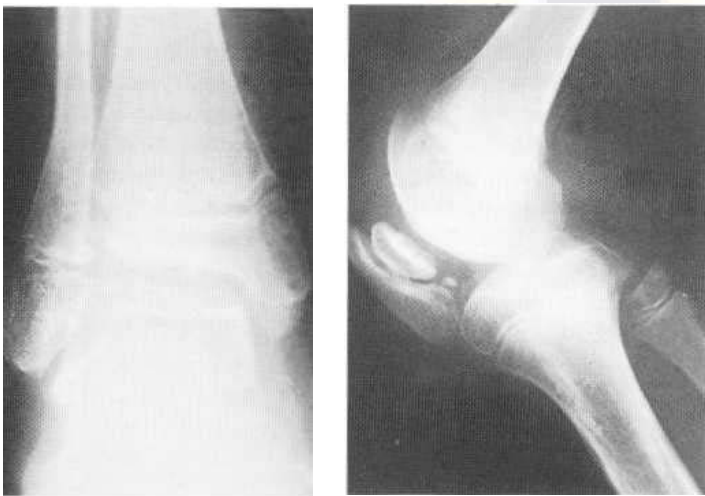


Fig. 35.58 Dysplasia epiphysealis multiplex, showing thinning of the outer part of the lower tibial epiphysis; this is seen in about half of all cases.

Fig. 35.59 Knee of same patient as in Fig. 35.58. Marked fragmentation of the patella.

1. *Lower tibial epiphysis*-the lateral part of the lower tibial epiphysis is thinner than the medial part; the trochlear part of the talus is shaped to conform to the abnormal mortise. A tibiotalar slant results (Fig. 35.58).
2. *The double-lowered patella* (Fig. 35.59) is characteristic but is found in few cases.
3. *The femoral and tibial condyles* may be hypoplastic and the intercondylar notch shallow (Fig. 35.60). Flattening of the femoral and tibial condyles makes the joint look widened.

Spinal changes are seldom pronounced and may be absent. The appearances in the spine, if present, resemble *osteochondritis*.

Some cases of *chondrodystrophia calcificans congenita* may survive and their pattern may later resemble that of multiple epiphyseal dysplasia.

Dysplasia epiphysealis hemimelica

(synonym: tarsoepiphyseal aclasis; eponym: Trevor's disease)

In this rare condition, irregular overgrowth of part of an epiphysis or epiphyses lying on one side of a single limb is seen (Fig. 35.62).

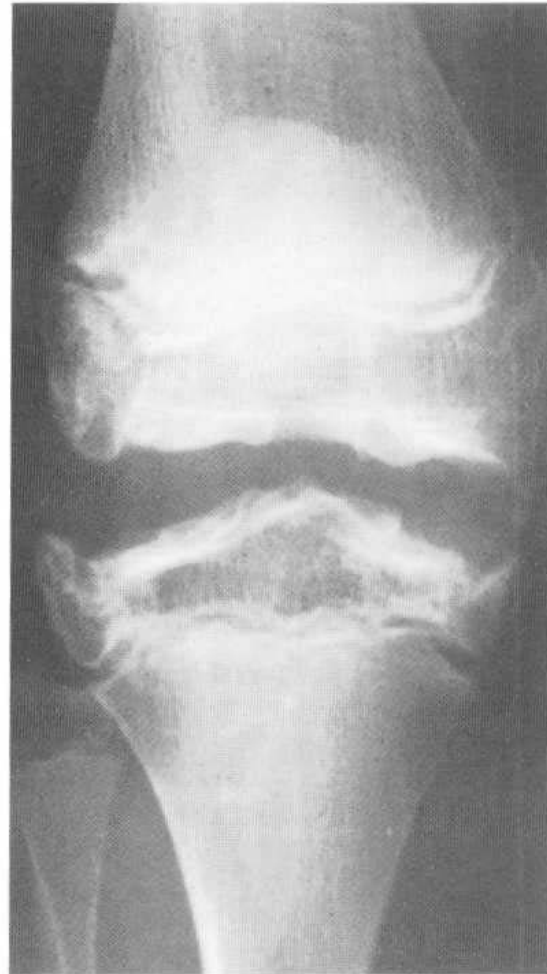


Fig. 35.60 Dysplasia epiphysealis multiplex-angular condyles and flat intercondylar notch. This is a characteristic appearance though not always present.

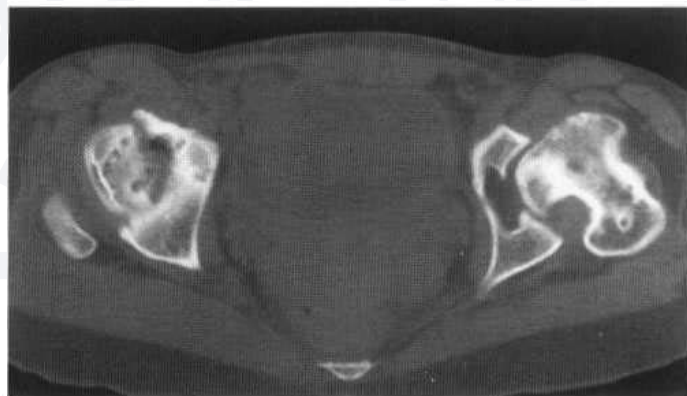


Fig. 35.61 Dysplasia epiphysealis multiplex. At CT scanning the flattening of the femoral heads is confirmed in association with marked irregularity and fragmentation. There is substantial anteversion and uncovering on the left. Muscle atrophy is evident.

The epiphysis is enlarged and an irregularly ossifying cartilage mass further arises on it. The leg is commonly affected but the arm may be. Sometimes both an arm and a leg may be involved and bilateral lesions have been recorded. If more than one epiphysis is affected, then the same parts. i.e. the medial or lateral, of the other epiphyses are abnormal.

Hyperplasia of the affected epiphysis may lead to a lesion that is indistinguishable radiologically and histologically from an osteochondroma. The lesions may be easily palpable. Such a feature is relatively common in the lower end of the fibula and adjacent talus (Fig. 35.63). All the epiphyses around the ankle enlarge, even those not affected by a superimposed osteochondroma, and abnormalities of fusion of growth plates occur; a 'chevron' deformity can result.

Metaphyseal chondrodysplasia (synonyms: metaphyseal dysplasia, metaphyseal dysostosis)

1. Schmid described a mild type that is relatively common (Fig. 35.64). Metaphyses of long bones are cupped and resemble rickets. No biochemical changes are found. The patient may be wrongly diagnosed as suffering from *vitamin D-resistant rickets* and consequently and injudiciously given large doses of vitamin D.
2. *Jansen's enetaphyseal chondrodysplasia*. Grossly irregular mineralisation is seen in the metaphyses of tubular bones (Fig. 35.65). A large gap is also seen between the epiphyses and the disordered metaphyses.



Fig. 35.62 Dysplasia epiphysealis hemimelica. Marked overgrowth of the femoral head. It is subluxed laterally. The superior portion resembles a partially calcified cartilaginous tumour.



Fig. 35.64 Metaphyseal chondrodysplasia, type Schmid; mild changes only in upper femoral metaphyses. Other metaphyses were similarly affected.



Fig. 35.63 (A) At the knee there is overgrowth of the epiphyses with premature fusion centrally resulting in a chevron deformity. There is a large osteochondromatous growth on top of the proximal tibial epiphysis laterally and also affecting the lateral femoral condyle. (B) Premature fusion is demonstrated at the distal tibial growth plate laterally and osteochondromatous overgrowth is demonstrated at the epiphysis and also at the adjacent talus. The distal fibular epiphysis is abnormal in shape and quite markedly overgrown.

3. Other types named after *Pena* and *Vaandrager* show intermediate involvement of metaphyses, less than in the Jansen type but more than in the Schmid type. Such lesions may resemble *Ollier's disease*.
4. Some cases of metaphyseal chondrodysplasia are associated with *pancreatic insufficiency* and *neutropenia*.
5. *McKusick* described a syndrome of sparse hair, metaphyseal lesions and dwarfism in Amish *families-cartilage-hair hypoplasia*.
6. Sometimes metaphyseal changes are associated with lesions of the spine—such conditions should be designated *spondylometaphyseal (Ivsostosis)*.

Diaphyseal aclasis (synonym: hereditary multiple exostoses)

This disease is inherited and familial. Sixty per cent of those affected have an involved parent. The remainder are presumably

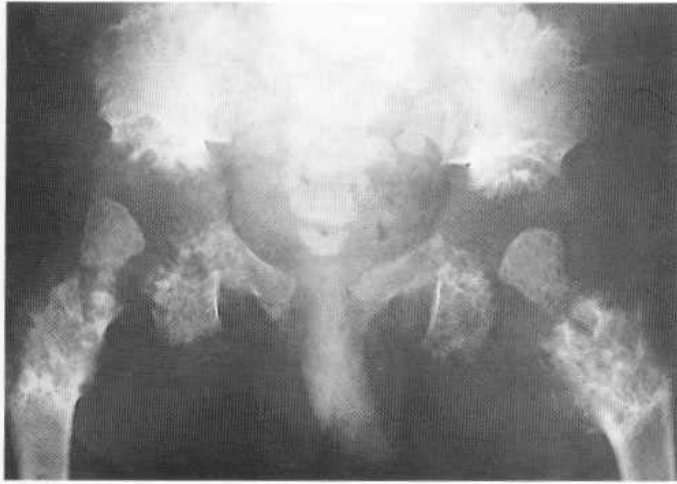


Fig. 35.65 Metaphyseal chondrodysplasia, type Jansen.

mutants to the gene. The sex incidence is equal and lesions within the family are not necessarily of the same severity.

The bones chiefly affected are the long bones, especially in the *metaphyseal* regions of the shoulders, hips, knees and ankles, which become irregularly expanded and club shaped. Upon these local enlargements of the shaft are projected osseous excrescences—exostoses—which are round or pointed. Their cortex merges with that of the shaft and their cancellous bone merges with the cancellous bone of the shaft, that is, they do not lie upon the cortex. Exostoses are also found on the vertebral bodies and on the medial border of the scapula. The epiphyses are not involved.

Exostoses may be seen as small metaphyseal projections in infants and their growth may be observed. With growth, they come to point away from the adjacent joint (Fig. 35.66). During skeletal growth, the bony exostoses are covered by a cartilage cap which undergoes spotty calcification, and with increasing maturity the cartilaginous mass becomes increasingly dense and a smooth margin



A

Fig. 35.66 Growing lesions in multiple exostoses (diaphyseal aclasis). (A) Initial radiograph taken at 3 months of age shows small metaphyseal spurs. (B) Left humerus at 3.5 years of age. (C) Left knee at 10 years of the same child.

can be discerned. By the time growth ceases, the cartilage has usually completely ossified. The exostoses and the metaphyseal clubbing are separate lesions though the former may be superimposed on the latter.

Increase in transverse width is often accompanied by shortening so that deformities result. These changes are especially common at the radius and ulna, resulting in Madelung's deformity (Fig. 35.67). Metacarpal bowing, radioulnar synostosis and radial head dislocation may also be found. *Ollier's disease* gives a similar appearance.

Lesions may be apparent early in life, especially if it is known that one parent is affected, or a lesion may affect a subcutaneous bone such as the tibia. Nerve compression may occur and paraplegia may result if the vertebral column is affected (Fig. 35.68). Some lesions may present with a dull ache, but pain and rapid growth raise the possibility of malignant degeneration. The incidence of *chondrosarcoma* in diaphyseal aclasis is said to be about 10% and these are often around the hip (Fig. 35.69).

Achondroplasia

This is the most common type of disproportionate dwarfism. In sufferers, one part of a limb shows relatively greater shortening. If proximal, *rhizomelia* is present; if medial, *mesomelia*; if distal, *acromelia*. In recent years many conditions, such as *thanatophoric dwarfism*, have been split off from achondroplasia so that a truly homogeneous picture now emerges. Inheritance is autosomal dominant, but most cases (85%) seem to be due to mutation of the gene, probably in older fathers. The patients have normal intelligence though a lack of muscle tone at birth suggests retardation.

The children have characteristic features at birth. *Trident hands* with short, stubby fingers, a *depressed nasal bridge* with a prominent forehead and a disproportionately *large skull*, and *prominent buttocks* due to lumbar lordosis are all seen. The large head can obstruct labour. Limb bones are short with a rhizomelic pattern.



B



C



Fig. 35.67 Diaphyseal aclasis—typical deformity of bones of the forearm.

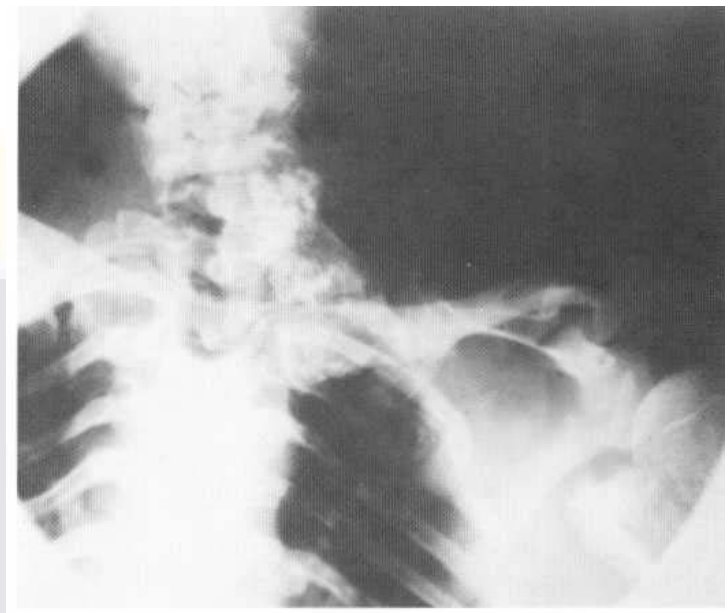


Fig. 35.68 Diaphyseal aclasis. Exostoses are seen associated with the spine in this patient who developed paraplegia.

Radiological findings

Long bones The tubular bones are short, appear relatively widened and have prominent muscle insertions. The humeri and femora are affected more than distal bones (rhizomelia). The fibulas are long and bowed. The epiphyses are deformed by their insertion into V-shaped defects at the metaphyses. The epiphyses themselves have V-shaped distal ends with deep intercondylar notches the 'chevron' sign. The appearances are similar to



A



B

Fig. 35.69 Malignant degeneration of cartilage-capped exostosis. (A) The initial radiograph shows the exostosis with a large soft-tissue mass lying peripheral to it; the margin of the exostosis is irregular. (B) The sagittal T₁-weighted MR sequence demonstrates a large irregular soft-tissue mass containing only a little mineralised bone. There is invasion of the underlying marrow by the tumour.

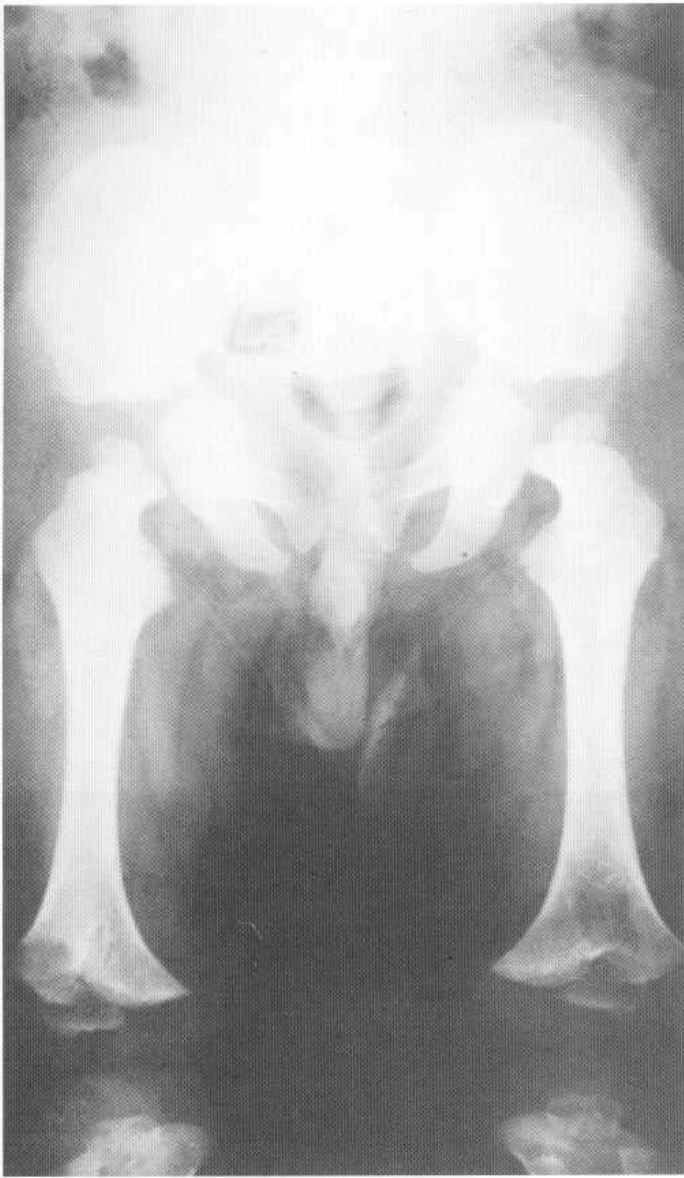


Fig. 35.70 Achondroplasia. Square iliac blades with horizontal acetabular roofs. Note also the narrow interpedicular distances in the lumbosacral region and the defects at the distal femoral metaphyses into which the epiphyses insert.

those seen with local premature fusion after infection, trauma or irradiation. The joint spaces appear widened owing to the proximity of epiphyses and metaphyses.

Retardation of ossification and a reduced AP diameter cause the upper ends of the femora of babies to appear relatively radiolucent. A defect is present in older children at the site of the epiphysis of the tibial tubercle due to an excess of uncalcified cartilage at this age.

Pelvis The pelvis is small and its diameters reduced. The iliac blades are particularly small and rather square—the 'tombstone' appearance. The acetabula are set posteriorly and the acetabular roofs are horizontal (Fig. 35.70). L5 is deeply set and excessive pelvic tilt causes prominence of the buttocks and an illusion of lordosis. The sacrosiatic notch is narrow, with a prominent medially directed spur. The pelvic inlet resembles a champagne glass.

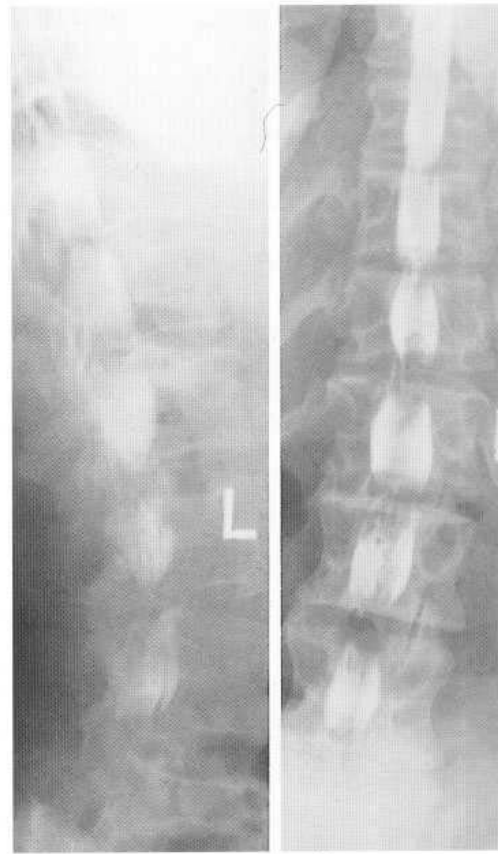


Fig. 35.71 Achondroplasia. Canal stenosis is demonstrated at radiculography. Posterior scalloping of vertebral bodies is shown between areas of distal indentation upon the opacified theca.

Spine The AP diameters of vertebral bodies are often short but the height of vertebral bodies is insignificantly reduced. In the thoracolumbar region a vertebral body or two may appear wedged or bullet-nosed. In some, a thoracolumbar vertebral body may resemble that found in Hurler's syndrome. Scalloping at the back of vertebrae may be seen (Fig. 35.71).

The spinal canal in the lumbar region tapers caudally so that the interpedicular distances decrease from L1 to L5 (Figs 35.70, 35.71). The lateral view will also show the small spinal canal. Severe symptoms from disc protrusions are liable to develop in later life—the spinal stenosis in the lumbosacral region is an important predisposing factor and can be confirmed by radiculography, CT or MRI (Fig. 35.72).

Skull changes These changes are mandatory to the diagnosis of achondroplasia. The calvarium is large but the base is shortened. The sella may be small. The foramen magnum is characteristically small and funnel-shaped; hydrocephalus may occur and has been attributed to this mechanical cause.

Chest The ribs are short, the anterior ends widened and the sternum short and broad. The scapulae have peculiar shapes, losing their sharp angles; the glenoid fossae are small in relation to the humeral heads.

Hands and feet Tubular bones of the hands and feet appear short and wide, but carpal and tarsal bones are little affected (Fig. 35.73). The *trident hand*, in which all the fingers are almost of equal length and diverge from one another in two pairs plus the thumb, is often found.

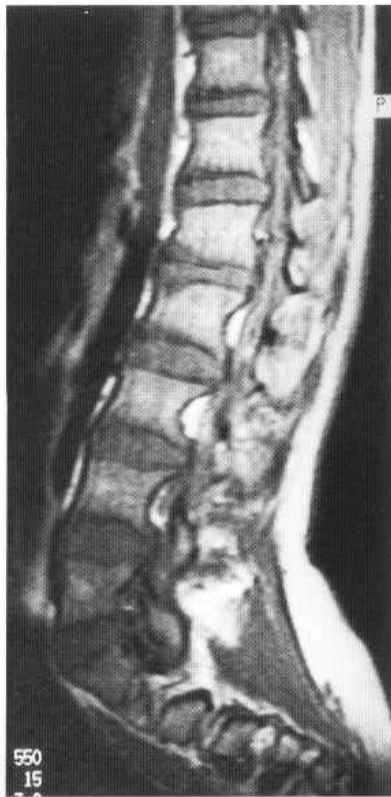


Fig. 35.72 Achondroplasia. (A) This sagittal T1-weighted MR sequence shows vertebral scalloping as a prominent feature in the lumbar spine. (B) The axial image shows short, broad pedicles and severe associated canal stenosis.



Fig. 35.73 Trident hand in achondroplasia.

Hypochondroplasia

This condition has been separated from classic achondroplasia, though there are some features in common. The skull is never affected, and the patients are either normal or mildly reduced in



Fig. 35.74 Overgrowth of the distal fibula in hypochondroplasia.

height. The disease is inherited as a dominant. The abdomen and buttocks are prominent, as in achondroplasia, and the legs are bowed in childhood.

Radiological features

There is rhizomelia with a short, broad femoral neck. The distal fibula is overgrown compared with the distal tibia (Fig. 35.74). The iliac bones are smaller than normal but not as markedly reduced as in achondroplasia. The interpedicular distances narrow from L1 to L5 and the pedicles are short, so that spinal stenosis results (Fig. 35.75). The lumbar lordosis is increased.

Pseudoachondroplasia

This condition is a short-limbed dwarfism occurring in both recessive and dominant forms of mild or marked severity, so that some patients are barely affected and some are grossly deformed. In all patients, however, the skull is normal, distinguishing this condition from achondroplasia. Also, no changes are seen in the first year of life.

Radiological features

Spine Vertebral bodies may be flat and irregular with central anterior 'tongues' (Fig. 35.76A). In adult life, appearances vary from near normal to platyspondyly and scoliosis. The spine in multiple epiphyseal dysplasia is barely affected.

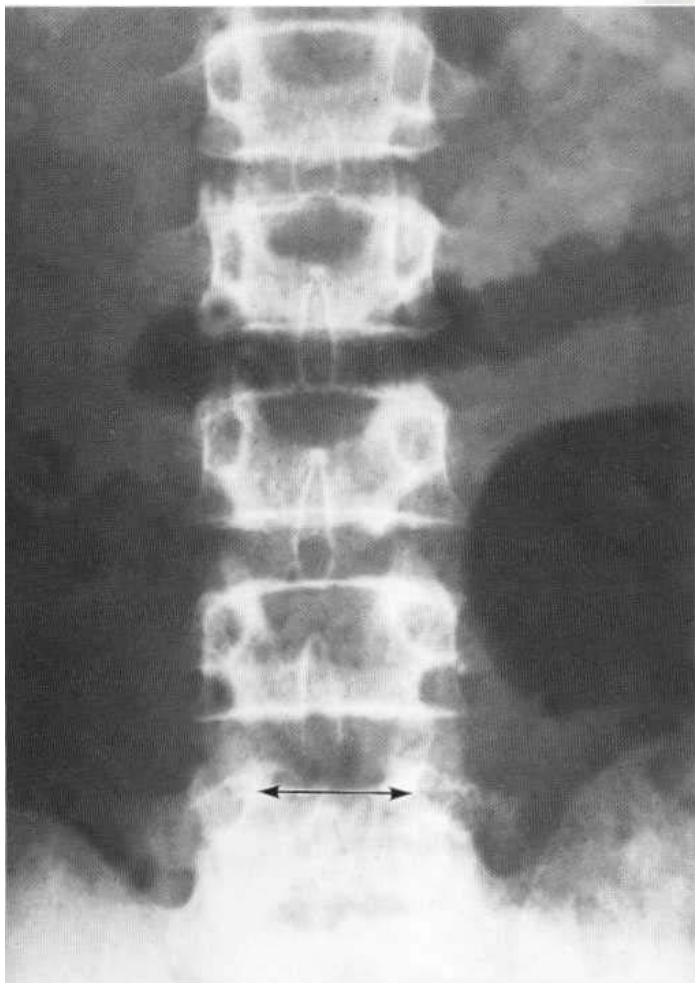


Fig. 35.75 Hypochondroplasia. A narrowed interpedicular distance at L5 in the same patient as Fig. 35.74.

Long bones The epiphyses are delayed in appearance and markedly irregular (Fig. 35.76B), again differing from achondroplasia. Metaphyses are broad and spurred. After fusion, epiphyseal dysplasia of varying degrees of severity is found.

Pelvis The acetabulum is irregular and premature osteoarthritis of the hips occurs. The ilia are large and the pubes and ischia short.

Hands In severe cases, the tubular bones are short and stubby with delay in ossification of irregular epiphyses and carpal bones (Fig. 35.76C). In the adult, the metacarpals end up shortened. Shortening of the radius and ulna may be marked and both bones at the wrist may be hypoplastic centrally, giving a 'V' appearance.

Thanatophoric dwarfism

This has relatively recently been separated from achondroplasia and is the commonest fatal neonatal dysplasia.

Radiological findings

Limbs There is rhizomelic dwarfism but the long bones are bowed. The metaphyses are irregular. Epiphyses of the knee are absent at birth. Short, wide metacarpals and phalanges are shown.

Axial skeleton There is marked platyspondyly but the posterior vertebral elements are normal so that, on an anterior view, the vertebral bodies resemble the letter H (Fig. 35.77). The pelvis shows poor mineralisation of the ischium and pubis, and small square iliac blades. The skull often shows lateral temporal bulging ('cloverleaf skull') due to craniostenosis. The ribs are short and flared anteriorly.

The infants are stillborn or die shortly after birth.

Asphyxiating thoracic dystrophy (eponym: Jeune's disease)

Most, but not all, patients with the disease die in infancy from respiratory distress. In contradistinction to thanatophoric dwarfism, the spine is normal and the long bones are not curved and only a little shortened.

The thorax is stenotic. The ribs are short and horizontal and the clavicles highly placed (Fig. 35.78).

Polydactyly is present in many cases and epiphyses are present at the knee.

Inheritance is autosomal recessive. In those patients who survive, renal failure may result even if bone changes revert to normal.

Chondroectodermal dysplasia (eponym: Ellis-van Creveld syndrome)

Fifty per cent of patients have congenital cardiac defects which may be fatal. The inheritance is autosomal recessive.

Radiographic features

Limbs In the limbs, the paired long bones are short and the metaphyses dome-shaped (Fig. 35.79); the dwarfism is mesomelic. At the proximal tibia the developing epiphysis is situated over the



Fig. 35.76 Pseudoachondroplasia. (A) Tongue-like projections of the vertebral bodies with superior and inferior defects. (B) Long bones-irregular epiphyses and metaphyses with tilt deformities. (C) Hands-the radius and ulna are flared at the metaphyses, the carpal bone epiphyses delayed and irregular, and the metacarpals short. The phalanges are stubby and the epiphyses angular and irregular.

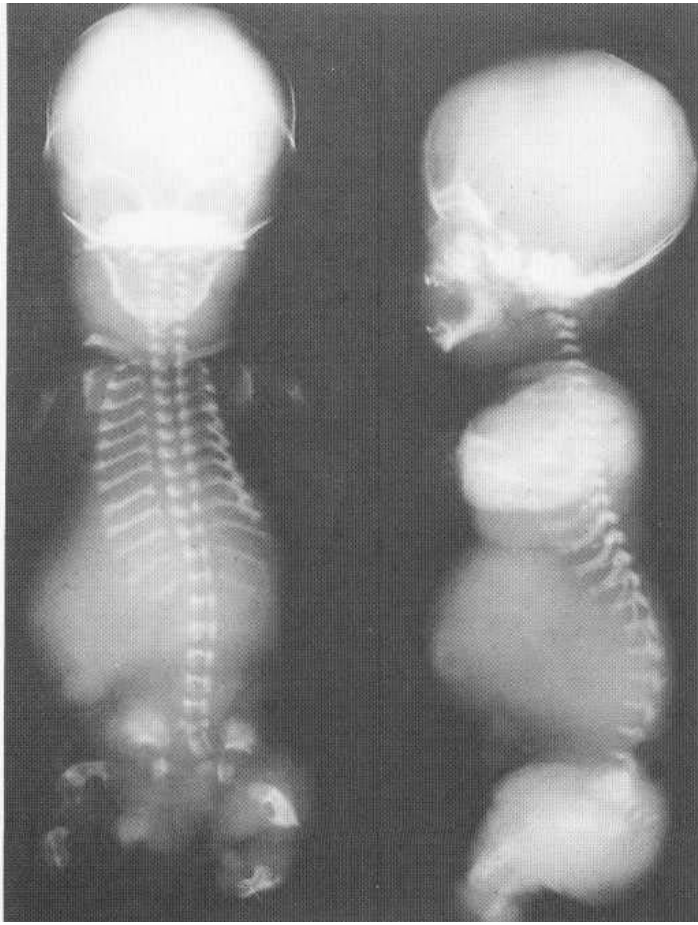


Fig. 35.77 Thanatophoric dwarfism. A cloverleaf skull is present. The scapulae are hypoplastic and the clavicles high. Platyspondyly is shown, resulting in H-shaped vertebral bodies. The bones are short and bowed.

abnormal medial tibial plateau and is defective laterally, so that valgus deformity results. Postaxial polysyndactyly is also present (Fig. 35.80). Carpal development is delayed and carpal fusions are seen, especially between capitate and hamate.



Fig. 35.79 Chondroectodermal dysplasia. Hypoplasia of the lateral portion of the upper tibial epiphysis is present and the metaphysis is dome-shaped. Incidental fractures are demonstrated.

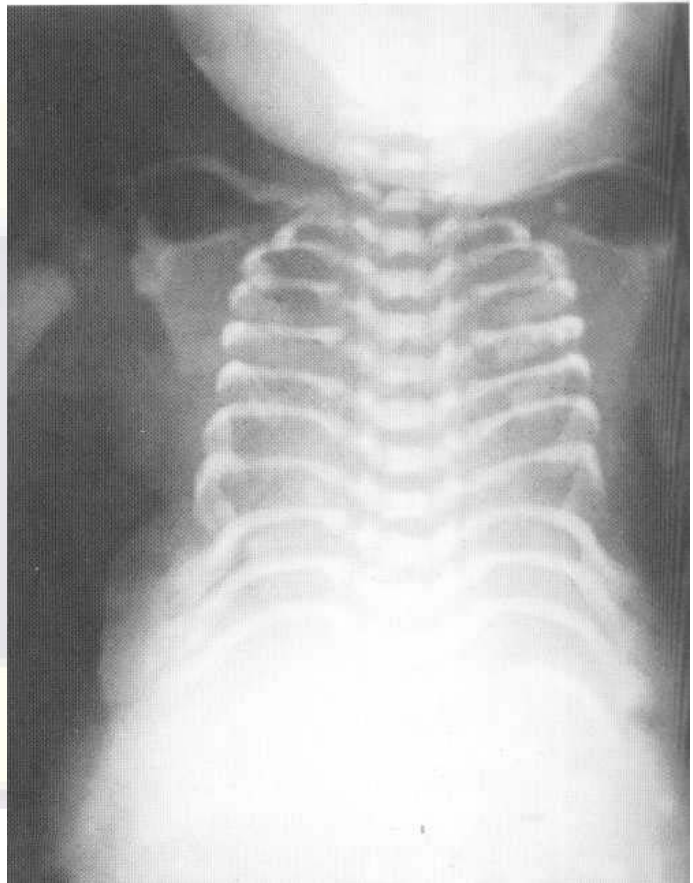


Fig. 35.78 Asphyxiating thoracic dystrophy—short horizontal ribs with high clavicles but a normal spine. The scapulae are hypoplastic.

Axial skeleton The skull and spine are normal. The rib cage resembles that seen in asphyxiating thoracic dystrophy. The acetabulum has a medial spur in the region of the triradiate cartilage.

The ectodermal dysplasia, with partial or total absence of teeth, and abnormal hair and nails, is not seen in asphyxiating thoracic dystrophy.

Dyschondrosteosis (eponym: Léri–Weill syndrome)

This is inherited as an autosomal dominant. The patients are often female, short in stature with a mesomeric type of dwarfism. There is hypoplasia of the inner aspect of the distal radius; the ulna is therefore prominent and is subluxated dorsally (Madelung's deformity). The carpal bones herniate proximally into the deficiency caused by the hypoplastic radius (Fig. 35.81).

The medial aspect of the proximal/distal tibia is similarly defective, and the fibula may be hypoplastic.

THE MUCOPOLYSACCHARIDOSES AND MUCOLIPIDOSES

The above terms embrace an extremely complex group of disorders. All members of the group are associated with an abnormality in mucopolysaccharide or glycoprotein metabolism. The most that can be expected of the radiologist is to suggest a diagnosis of mucopolysaccharidosis (MPS), and niceties of nosology are the province of the clinician, geneticist and biochemist. The same considerations apply to the mucolipidoses.



Fig. 35.80 Chondroectodermal dysplasia. Polysyndactyly is present together with anomalies of carpal segmentation.



Fig. 35.81 Dyschondrosteosis. (A) There is separation of the hypoplastic distal radius and ulna with proximal herniation of the carpus. (B) The lateral view shows the posterior situation of the ulna and hypoplasia of the proximal radius.

Types of mucopolysaccharidoses are:

- MPS I-H (Hurler's syndrome; gargoylism)
- MPS II (Hunter's syndrome)
- MPS III (Sanfilippo's syndrome)
- MPS IV (Morquio-Brailsford syndrome)
- MPS I-S (Scheie's syndrome)
- MPS VI (Maroteaux-Lamy syndrome).

The *Hunter* type is inherited as an X-linked recessive, the rest as autosomal recessives. Some are severe, others relatively mild. Sufferers have various degrees of mental retardation, corneal clouding and skeletal changes.

MPS I-H (synonym: gargoylism; eponym: Hurler's syndrome)

Radiological features

Changes include macrocephaly, J-shaped sella, thickened calvaria, oar-shaped ribs and hook-shaped vertebral bodies (Fig. 35.82). The ilia are widely flared, the femoral ossific nuclei fragmented, and



Fig. 35.82 MPS I-H (Hurler's syndrome). Hypoplasia of L2 body with a pronounced inferior beak and a resulting angular kyphosis.



Fig. 35.83 MPS I-H (Hurler's syndrome). Undertubulation is associated with demineralisation. The metacarpals are pointed proximally. The distal radius and ulna are angulated.

coxa valga is usual. The proximal ends of the metacarpals taper and in older children the distal ends of the radius and especially the ulna slope toward each other (Fig. 35.83).

MPS IV (eponym: Morquio–Brailsford syndrome)

This condition presents with dwarfism, due mainly to shortness of the spine and to a marked kyphosis. The tubular bones are also widely affected. The lesion may be familial. Intelligence is unimpaired.

Radiographic features

Spinal changes are the dominant feature. The vertebrae are flat, and in childhood tend to have a characteristic form. The upper and lower surfaces of the vertebral body are defective and a central tongue of bone protrudes forward (Fig. 35.84). This appearance is best seen in the lower thoracic and upper lumbar region. Later, as growth proceeds, the defect becomes repaired. One thoracolumbar vertebra may be smaller than its fellows and displaced posteriorly, causing a marked kyphosis.

As a rule, tubular bones are not markedly affected but may be short and rather wide with somewhat irregular metaphyses. The epiphyses are markedly irregular and fragmented, notably those of the femoral heads. The joint spaces are increased and the joint surfaces, for example of the acetabulum and glenoid, are shallow and irregular.

The pelvis tends to be narrow, or shaped like that of an ape (Fig. 35.85). In the hands and feet the tubular bones are short and stubby, and some irregularity of the carpal and tarsal bones is also found.



Fig. 35.84 MPS IV (Morquio-Brailsford syndrome). The lateral view of the spine shows osteopenia and platyspondyly with anterior beaking. There is a thoracolumbar kyphosis. The hip joints appear irregular, even on the lateral view.

Spondyloepiphyseal dysplasia

The term 'spondyloepiphyseal dysplasia' (SED) is used to embrace a group of conditions characterised by platyspondyly and dysplasia of other bones. The degrees of spinal and tubular bone involvement and the amount of dwarfism vary between the different groups.

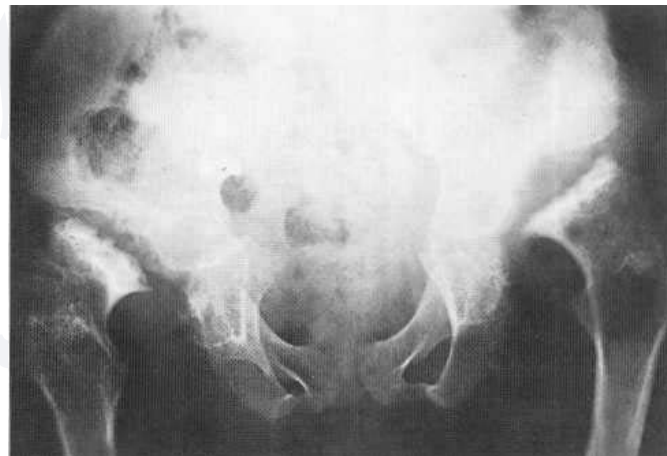


Fig. 35.85 MPS IV. Simian pelvis, fragmented, maldeveloped femoral capital epiphyses with associated metaphyseal irregularity. Shallow acetabula with dislocation of both femoral heads shown also—a feature sometimes seen in this condition.



Fig. 35.86 Spondyloepiphyseal dysplasia (X-linked recessive form) showing characteristic platyspondyly. Mounds of bone are seen on the superior and inferior parts of the posterior parts of the vertebral bodies. Gas is seen in the prematurely degenerate discs.

1. X-linked variety-SED tarda. This type has a distinctive spinal lesion. Mounds of dense bone are found on the superior and inferior surfaces of the posterior parts of the vertebral end-plates (Fig. 35.86). The tubular bones are not much affected and may resemble those in mild cases of dysplasia epiphysealis multiplex. The iliac wings are characteristically small. Hip degeneration frequently occurs prematurely (Fig. 35.87).



Fig. 35.87 Pelvis of patient in Fig. 35.86. Some (but not gross) osteoarthritis is seen, with some bilateral acetabular protrusion. The iliac wings are characteristically small in this condition.

2. *Dominant variety SED congenita.* In these patients the platyspondyly is maximal in the thoracic spine. Lesions of tubular bones are severe and early osteoarthritis may be expected. The hands are unaffected. Retinal detachment is common.
3. *Recessive variety.* The platyspondyly is generalised and the severe wedging of the dominant form is not found.

Hypophosphatasia

This is a genetically determined metabolic disease, included in this section on account of its manifestations. Several subgroups have been described, dependent on the age of onset and severity of symptoms. They are characterised by: (i) low or absent serum alkaline phosphatase; (ii) phosphoethanolamine in the urine and plasma; and (iii) hypercalcaemia in severe forms.

In the severe type, gross general failure of ossification of the skeleton is seen (Fig. 35.88). These babies do not survive. Some less severe forms present as severe rickets. If they survive, the radiographic picture may resemble that of Ollier's disease. An adult form of this condition is characterised by osteoporosis and a tendency to fractures.

Arachnodactyly (eponym: Marfan's syndrome)

This condition is inherited as an autosomal dominant. Clinically, the long bones are lengthened and muscle weakness, hypermobility and lens dislocations are found. A high arched palate, depressed sternum and scoliosis also occur. Cardiovascular lesions include aortic dissections, atria) septa) defects and mitral valve lesions.

Radiographic features

The tubular bones are elongated and slender, the distal bones being much more affected than the proximal ones. The hands and feet are especially elongated (Fig. 35.89) and occasionally their bones have extra epiphyses. Kyphosis and scoliosis are frequent findings. Some scalloping of the back of the vertebral bodies may be seen.



Fig. 35.88 Hypophosphatasia in an infant. The appearances resemble a very severe form of rickets, changes especially affecting the metaphyses, but proceeding further into the shaft of the long bone than is normal with rickets. The growth plates are widened but the ossification centres at the epiphyses are far better defined than would be usual in rickets.



Fig. 35.89 Marfan's syndrome -elongation of metacarpals and phalanges is demonstrated.

The diagnosis is usually straightforward. Estimation of the *metacarpal index* will aid the diagnosis in doubtful cases. This index is estimated by measuring the lengths of the second, third, fourth and fifth metacarpals and dividing their breadths taken at the exact midpoint. The resulting figures, from each of the four metacarpals, are added together and divided by four. In normal adult subjects the metacarpal index varies from 5.4 to 7.9; in arachnodactyly the range varies from 8.4 to 10.4.

Homocystinuria

This lesion has some similarity to Marfan's syndrome but is inherited as an autosomal recessive. A definite biochemical abnormality has been demonstrated. Absence of the enzyme cystathionine (3-synthase results in an excess of urinary homocystine. The most important feature is that thrombosis of arteries and veins is liable to occur, especially after catheterisation, and fatalities have been reported.

Osteoporosis in the spine, with posterior scalloping of the vertebral bodies (Fig. 35.90), differentiates this condition radiologically from Marfan's syndrome. Epiphyses and carpal bones tend to be enlarged and metaphyses broadened (Fig. 35.91), but arachnodactyly is less marked. Also these patients tend to have pes

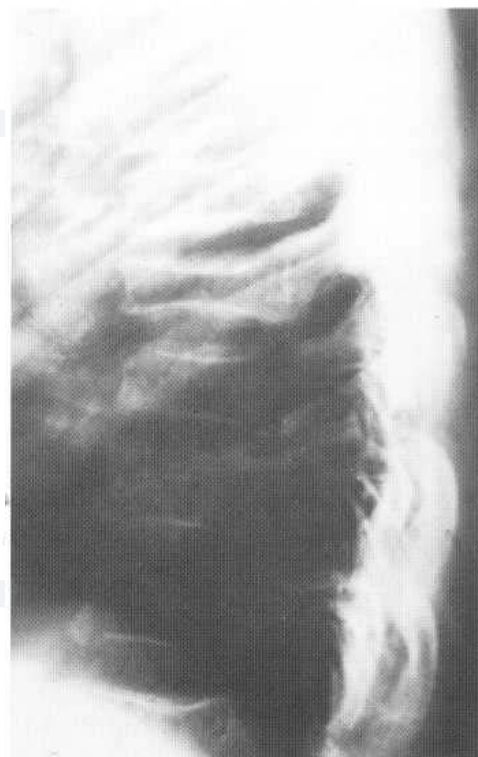


Fig. 35.90 Homocystinuria. Osteoporosis is associated with platyspondyly of the thoracic spine.



Fig. 35.91 Homocystinuria. Overgrowth of carpal epiphyses is present.

cavus and grosser sternal lesions than in Marfan's syndrome. Cardiac and aortic lesions are less common.

Achondrogenesis

This is an uncommon lethal form of infantile dysplasia characterised by a large deformed head with gross underdevelopment of the limbs and a large squat abdomen.

Radiological features

The long bones are extremely short, irregular and grossly undermineralised (Fig. 35.92). The pelvis is barely visualised at birth or in utero (Type I). In Type II, the limb bones are still short and metaphyses irregular, but slightly better mineralised. The vertebral bodies, however, may not be mineralised, especially caudally.

The diseases are both inherited as autosomal recessives.

Fibrodysplasia ossificans progressiva

(synonym: myositis ossificans progressiva; eponym: Munchmeyer's disease)

The disease process primarily involves the connective tissues rather than muscle fibres. Soft-tissue swellings begin in utero or early in life. These painful swellings affect the neck and upper trunk. *Ossification* commences in the lumps within months and is aggravated by surgical biopsy. Large masses of bone form in voluntary muscles which may extend to the normal skeletal structures and resemble exostoses (Fig. 35.93). Movements become restricted.

A skeletal dysplasia is present at birth. Seventy-five per cent have involvement of the *great toe*, with fusion and microdactyly or hallux valgus (Fig. 35.94), and 50% have thumb hypoplasia and

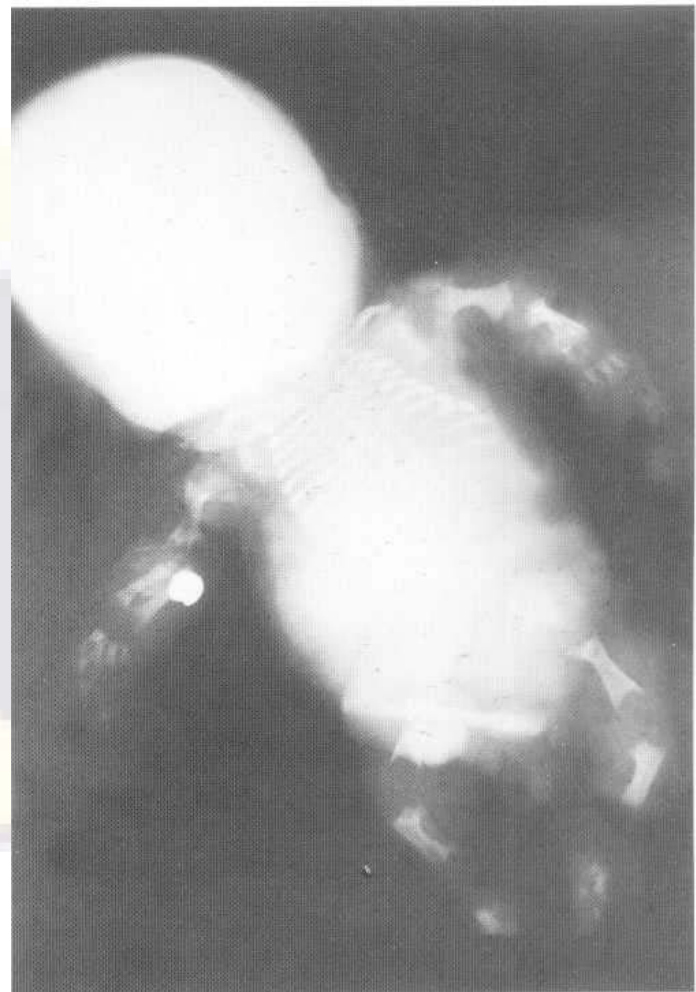


Fig. 35.92 Achondrogenesis. Gross shortening of the long bones is seen. The metaphyses are irregular and the epiphyses around the knee delayed in appearance. Poor mineralisation of the caudal vertebral bodies, sacrum and pubic bones characterise Type II achondrogenesis.

little finger clinodactyly. The femoral necks and mandibular condyles are broad and the cervical vertebral bodies are hypoplastic and fused (Fig. 35.95).

Inheritance is probably autosomal dominant but most cases are sporadic as few patients survive to reproductive age.

CHROMOSOMAL DISORDERS

Down's syndrome (synonyms: mongolism, trisomy 21)

This condition is associated with an extra chromosome in the 21-22 group. The clinical diagnosis of older children suffering from mongolism is usually easy. In a baby the diagnosis may not be evident clinically but it is, of course, of great human importance. The newborn Down's syndrome baby has a large ilium with a flat acetabular roof; an elongated tapering ischium develops after a few months.

Many other skeletal and visceral anomalies have been described in this disease, though none of them is invariably present. Some of the following anomalies have been recognised relatively recently:

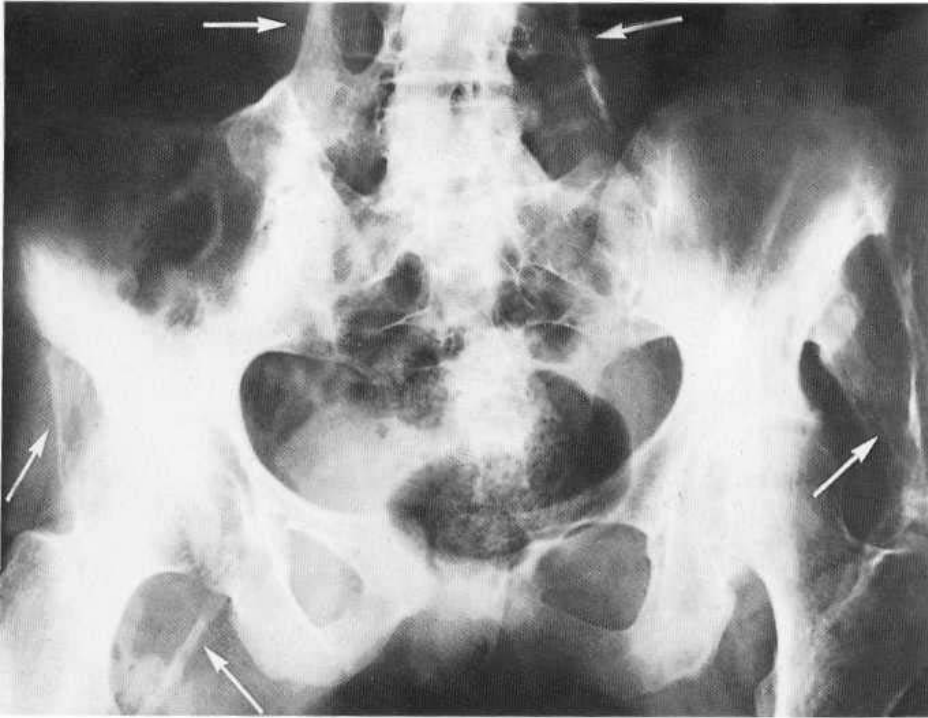


Fig. 35.93 Fibrodysplasia ossificans progressiva-soft-tissue ossification (arrows).



Fig. 35.94 Fibrodysplasia ossificans progressiva. Dysplastic changes are demonstrated in the great toe in 75% of patients.

1. Brachycephaly, hypoplasia of the nasal bones, maxillae and sphenoids, and absent frontal sinuses. Instability of the atlanto-axial joint and abnormalities in the upper cervical spine may be found in 20%.
2. The interorbital distance is decreased in most cases, indicating orbital hypotelorism.
3. Extra ossification centres for the manubrium sterni are found in 90% of cases between the ages of 1 and 4 years, this sign is



Fig. 35.95 Fibrodysplasia ossificans progressiva. There is partial fusion of the vertebral bodies and laminae and, in addition, ossification of ligamentum nuchae. The cervical canal is slightly widened. Mandibular hypoplasia is also shown, perhaps because of interference with the growth plate at the mandibular condyle.

seen in 20% of normal children of the same age group. The calcaneus may ossify in two centres.

4. Many Down's syndrome children have only 11 pairs of ribs.
5. The middle and distal phalanges of the fifth digits are often hypoplastic and curve inward-clinodactyly. The proximal phalanx of the thumb may be small and triangular or delta shaped.
6. The lumbar vertebrae are often greater in height than in width, a reversal of the normal ratio, and they show concave anterior surfaces. Thus a lateral view of the lumbar spine may be of

diagnostic help. This is not diagnostic of Down's syndrome but may be found in many children with delayed motor development.

7. Congenital heart disease is frequently found in Down's syndrome children, as is an aberrant right subclavian artery.
8. An increased incidence of duodenal stenosis and atresia and of Hirschsprung's disease may be found.

Turner's syndrome

Not all patients with Turner's syndrome have an abnormal sex chromosome pattern, nor do all individuals with the characteristic chromosomal pattern have Turner's syndrome. The essential components of this condition are: *agenesis of the gonads*, *webbing of the neck* and *cubitus valgus*. The syndrome is confined to females. Mental deficiency, congenital cardiac and aortic lesions and anomalies of the kidneys such as malrotation are often associated. Sometimes males are found with a similar body configuration, viz. short stature and a webbed neck. However, these boys have a normal chromosomal pattern and they tend to get auricular septa defects and pulmonary stenosis rather than coarctation of the aorta which may be associated with Turner's syndrome.

Radiological findings

The skeletal features are inconstant and non-specific. Density of the skeleton, especially of the hands and feet, is reduced. General osteoporosis is frequent in older patients. The metacarpals may be short (Fig. 35.96) and accelerated fusion of the epiphysis may be found. The so-called 'metacarpal sign' is an expression of gross shortening of the fourth metacarpal. Minor shortening may be seen in some normal subjects.

The increase in the carrying angle of the elbow is better assessed clinically than radiologically. The medial tibial condyle is depressed and beak-like, and the medial femoral condyle may project downward (as in *Blount's disease*) (Fig. 35.97).

Maldevelopment of the clavicles and slender ribs are often seen. Kyphosis and scoliosis are frequently found. Hypoplasia of the atlas and odontoid peg may be seen. In many females the pelvic inlet is android, the pubic arch narrowed and the sacroscliotic notches small.

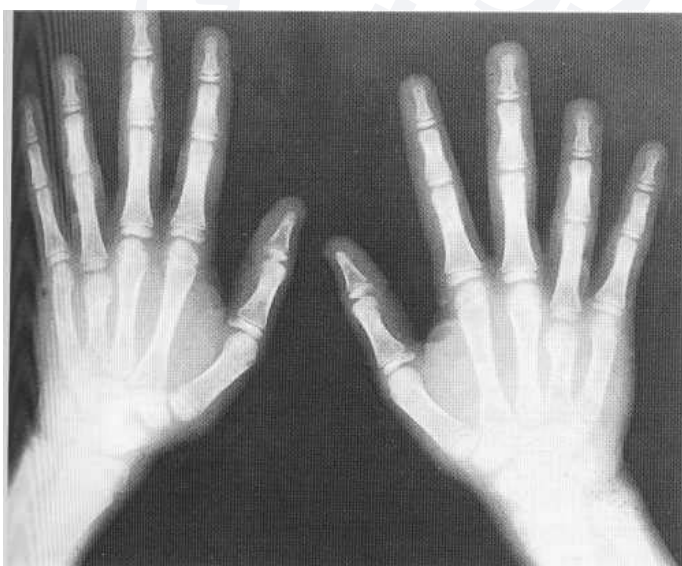


Fig. 35.96 Turner's syndrome-typical shortening of fourth metacarpals.



Fig. 35.97 Turner's syndrome. The medial tibial plateau is depressed and the adjacent femoral condyle enlarged.

REFERENCES AND SUGGESTIONS FOR FURTHER READING

- Anderson, Jr. P. E., Bo Ilerslev, J. (1987) Heterogeneity of autosomal dominant osteopetrosis. *Radiology*, **164**, 223-225.
- Baker, S. L., Dent, C. E., Friedman, M., Watson, L. (1966) Fibrogenesis imperfecta ossium. *Journal of Bone and Joint Surgery*, **48B**, 804-825.
- Beighton, P., Cremin, B. J. (1980) *Sclerosing Bone Dysplasias*. Berlin: Springer.
- Bizarro, A. H. (1921) On the sesamoid and supernumerary bones of the limbs. *Journal of Anatomy (Cambridge)*, **55**, 256-268.
- Blockley, N. J. (1969) Observations on infantile coxa vara. *Journal of Bone and Joint Surgery*, **51B**, 106-111.
- Carty, H., Shaw, D., Brunelle, F., Kendall, B. (eds) (1994) *Imaging Children*. Edinburgh: Churchill Livingstone.
- Clarke, N. M. P., Harcke, H. T., McHugh, P., Lee, M. S., Boruns, P., MacEwen, G. (1985) Real time ultrasound in the diagnosis of congenital dislocation of the hip. *Journal of Bone and Joint Surgery*, **67B**, 406-412.
- Cobb, J. R. (1948) *Outline for the Study of Scoliosis*. American Academy of Orthopedic Surgeons, Instructional Course Lectures, vol. 5. p. 261.
- Day, H. J. B. (1991) The ISO/ISPO classification of congenital limb deficiency. *Prosthetics and Orthotics International*, **15**, 67-69.
- El-Tawil, T., Stoker, D. J. (1993) Benign osteopetrosis: a review of 42 cases showing two different patterns. *Skeletal Radiology*, **22**, 587-593.
- Fairbank, T. (1951) *An Atlas of General Affections of the Skeleton*. Edinburgh: Livingstone.

- Fixen, J. A. (1991) The foot in childhood. In: Klenerman, L. (ed.) *The Foot and Its Disorders*, 3rd edn. Oxford: Blackwell Scientific.
- Freiberger, R. H., Hersh, A., Harrison, M. O. (1970) Roentgen examination of the deformed foot. *Journal of Bone and Joint Surgery*, 70A, 341-353.
- Gibson, M. J., Middlemiss, H. (1971) Fibrous dysplasia of bone. *British Journal of Radiology*, 44, 1-13.
- Graf, R. (1984a) Fundamentals of sonographic diagnosis of infant hip dysplasia. *Journal of Pediatric Orthopedics*, 4, 735-740.
- Graf, R. (1984b) Classification of hip joint dysplasia by means of sonography. *Archives of Orthopaedic and Trauma Surgery*, 102, 248-255.
- Hernandez, R. J., Poznanski, A. K. (1985) CT evaluation of pediatric hip disorders. *Orthopedic Clinics of North America*, 16, 513-541.
- Heselson, N. G., Cremin, B. J., Beighton, P. (1978) Lethal chondrodysplasia punctata. *Clinical Radiology*, 29, 679-684.
- Houang, M. T., Brenton, D. P., Renton, P., Shaw, D. (1978) Idiopathic juvenile osteoporosis. *Skeletal Radiology*, 3, 17-23.
- James, J. I. P. (1959) Structural scoliosis. In: Nassim, R., Jackson Burrows, H. (eds) *Modern Trends in Diseases of the Vertebral Column*. London: Butterworth.
- Jarvis, J. L., Keats, T. E. (1974) Cleidocranial dysostosis: a review of 40 new cases. *American Journal of Roentgenology*, 121, 5-16.
- Kaufmann, H. J. (1973) Progress in pediatric radiology. In: *Intrinsic Diseases of Bone*. Basel: Karger.
- Langer Jr., L. O., Baumann, P. A., Gorlin, R. J. (1967) Achondroplasia. *American Journal of Roentgenology*, 100, 12-26.
- Levinson, E. D., Ozonoff, M. B., Royen, P. M. (1977) Proximal femoral focal deficiency. *Radiology*, 125, 197-203.
- McCredie, J. (1975) Congenital fusion of bones radiology, embryology and pathogenesis. *Clinical Radiology*, 26, 47-75.
- Murray, R. O., McCredie, J. (1979) Melorheostosis and the sclerotomes. *Skeletal Radiology*, 4, 57-71.
- Murray, R. O., Jacobson, H. G., Stoker, D. J. (1990) *The Radiology of Skeletal Disorders*, 3rd edn. Edinburgh: Churchill Livingstone.
- Neuhauser, E. B. D., Wittenborg, M. H., Dehlinger, K. (1950) Diastematomyelia. *Radiology*, 54, 659-664.
- Poznanski, A. K. (1984) *The Hand in Radiologic Diagnosis*, 2nd edn. Philadelphia: Saunders.
- Renton, P. (1998) *Orthopaedic Radiology: Pattern Recognition and Differential Diagnosis 2nd edn*. London: Dunitz.
- Risser, J. C., Ferguson, A. B. (1936) Scoliosis: its prognosis. *Journal of Bone and Joint Surgery*, 18, 667.
- Sillence, D. O., Senn, A., Danks, D. M. (1979) Genetic heterogeneity in osteogenesis imperfecta. *Journal of Medical Genetics*, 16, 101-116.
- Solomon, L. (1963) Hereditary multiple exostoses. *Journal of Bone and Joint Surgery*, 45B, 292-304.
- Spranger, J. (1976) The epiphyseal dysplasias. *Clinical Orthopaedics and Related Research*, 114, 46-60.
- Torode, I. P., Gillespie, R. (1991) The classification and treatment of proximal femoral deficiencies. *Prosthetics and Orthotics International*, 15, 117-126.
- Wynne-Davies, R., Hall, C. M., Apley, A. G. (1985) *Atlas of Skeletal Dysplasias*. Edinburgh: Churchill Livingstone.

نشر الکترونیکی
موسسه انتشاراتی
نور دانش

36

PERIOSTEAL REACTION; BONE AND JOINT INFECTIONS; SARCOID

Peter Renton

PERIOSTEAL NEW BONE FORMATION (Periosteal Reaction)

New bone is laid down in many conditions with different aetiologies (Box 36.1). In some the periosteum is physically elevated by tumour, haemorrhage or infection. Vascular abnormalities, viruses and autoimmune diseases may all cause new bone deposition. New bone may be deposited locally, around a solitary focus of disease, or may be generalised. In some systemic conditions, new bone is laid down in characteristic sites.

In its simplest form the new bone is seen as a linear density separated from the bony shaft by a clear zone, often later obliterated as

the new bone merges with the cortex. Difficulty is caused by bones such as the fibula which have naturally irregular outlines. Insertions of interosseous membranes, ligaments and tendons in other bones also cause confusion.

There are a wide variety of types of periosteal reaction and often certain patterns can be discerned. However, the type of periosteal reaction cannot always be correlated with the underlying disease.

TUMOURS AND PERIOSTEAL NEW BONE

Plain film appearances

A tumour, having broken through the cortex, elevates the periosteum and new bone forms beneath it. If the tumour grows slowly,

Box 36.1 Causes of periosteal new bone formation

Physiologic	In neonates, especially in prematurity	Vascular	Haemophilia and other bleeding disorders. Myeloid metaplasia probably due to associated thrombocytopenia. Erythroblastic anaemias.
Congenital	Tuberous sclerosis		Leukaemias. Varicose veins (before ulceration occurs).
Dysplastic	Melorheostosis, Engelmann's disease		Hypertrophic pulmonary osteoarthropathy (probably of vascular aetiology) and pachydermoperiostosis
Traumatic	Local subperiosteal trauma; fracture, including march fracture. Unrecognised skeletal trauma (Caffey's 'battered baby syndrome')	Collagen diseases	Polyarteritis nodosa
Infective	Acute: osteomyelitis-staphylococcal, streptococcal, pneumococcal, etc. Chronic: Brodie's abscess, tuberculosis, syphilis (congenital and acquired), yaws; also from nearby infection, e.g. varicose ulcer; ribs in pulmonary and pleural infections	Reticuloses	Hodgkin's disease, etc.
Hypo- and hypervitaminosis	Rickets, scurvy, hypervitaminosis A	Neoplastic	Primary: <i>benign</i> —meningioma, angioma, osteoid osteoma; <i>malignant</i> —osteogenic sarcoma, fibrosarcoma, Ewing's sarcoma, etc. Secondary: any metastatic bony deposit may be associated with periosteal reaction
Endocrine	Thyroid acropachy, hyperparathyroidism healing phase; secondary hyperparathyroidism in renal osteodystrophy	Primary joint lesions	Ankylosing spondylitis, juvenile chronic arthritis (Still's disease), Reiter's syndrome, rheumatoid arthritis, osteoarthritis (femoral neck only)
		Miscellaneous	Infantile cortical hyperostosis (Caffey), histiocytosis

Trauma and inflammation are the commonest causes of periosteal reaction both in adults and in children. Primary malignant neoplasms are rare but nearly always cause periosteal reaction. Periosteal reaction is occasionally seen in metastases. In adults, less common causes such as reticuloses, hypertrophic pulmonary osteoarthropathy and varicose ulceration may cause diagnostic difficulty. In neonates, congenital syphilis and infantile cortical hyperostosis must be remembered. Later, scurvy, leukaemia and erythroblastic anaemias (in immigrants) are possible causes. Ewing's sarcoma and metastases from neuroblastoma are other childhood causes which may prove diagnostically elusive.

the elevated periosteal new bone may remain intact and even take over the function of the destroyed cortex. If tumour growth is cyclic, as in Ewing's sarcoma, successive layers of periosteal new bone are laid down, giving a lamellated or onion-skin appearance. If tumour growth is rapid, the periosteal new bone becomes disorganised and remains intact at the tumour margins only. Buttressing and elevation of periosteal new bone at tumour margins leads to a so-called Codman's triangle which is usually indicative of a malignant tumour, though in an aneurysmal bone cyst Codman's triangle really indicates rapidity of progression.

In Ewing's sarcoma and in hypertrophic osteoarthropathy (see Ch. 49), the layers of new bone are characteristically fine, and thinner than the spaces between them. New bone in osteogenic sarcoma, parosteal osteosarcoma and secondary deposits tend to be coarser and less well defined, so that the spicules are thicker than the intervening spaces. In osteogenic sarcoma, also, new bone may be perpendicular to the shaft and, originating from a finite focus of disease, resembles a sunray-so-called 'sunray spiculation'. This may also be found with angioma and thalassaemia, but is then generally more orderly and better organised. Meningioma may resemble osteogenic sarcoma more closely, but the site is characteristic. Vertical spicules ('hair-on-end') are also found in Ewing's sarcoma but, in keeping with the more diffuse nature of the underlying tumour, are not usually 'sunburst' but extend for a considerable distance along the bone and are more delicate. Vertical spiculation may result from bony deposition along the elevated and stretched fibres connecting periosteum to bone, the Sharpey's fibres.

Isotope scans

Increase in uptake may be seen early, in the blood-pool phase, reflecting increased blood flow, and in the delayed scan, reflecting increase in bone turnover. Any displacement of cortex and periosteum and involvement of soft tissues further increases the size of the abnormal area of increase in uptake, which is seen superimposed on the pre-existing cortical image.

CT

CT demonstrates cortical thickening. By altering the windows, changes within the periostitis may be better defined-lamellation, cloacae, stress fractures or tumour, for example osteoid osteoma.

MRI

This is generally not as good at showing cortical bone as is CT. Cortical signal is normally low because of the nature of compact bone. Periosteal new bone is seen as an accretion of low signal mass but oedema, haemorrhage and tumour are especially bright on T₂-weighted and STIR sequences and better delineate the periosteal new bone and cortical changes.

VASCULAR INSUFFICIENCY AND PERIOSTEAL NEW BONE

Venous stasis causes changes in the lower limb, especially at the diaphysis and distal metaphysis of the tibia and fibula. The periosteal new bone which is formed may be lamellar or irregular. Changes may be seen in the presence of chronic ulceration (Fig. 36.1), but also in its absence, so that an ulcer is not essential. Indeed, the periosteal new bone often extends far proximally from an ulcer. Phleboliths may be present and varicosities may also be seen in subcutaneous tissues, which appear thickened and oedematous.



Fig. 36.1 Irregular periosteal new bone is demonstrated in a patient with varicose veins.

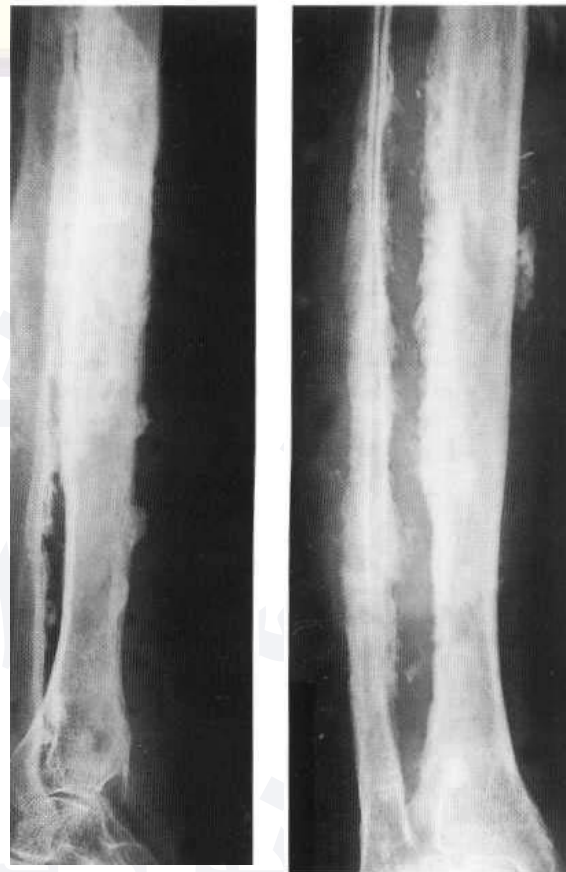


Fig. 36.2 Polyarteritis nodosa. An exuberant periostitis is seen along both tibia and fibula-much more florid than that seen in hypertrophic osteoarthropathy.

A florid and exuberant periosteal reaction occurs infrequently in *polyarteritis nodosa*. Arterial occlusion and skin ulceration are found and the periosteal reactions often occur around affected parts and in relation to skin lesions (Fig. 36.2).



Fig. 36.3 Thyroid acropathy. Marked cortical thickening is demonstrated at the midshafts of the tubular bones of the hands (see Ch. 42).

THYROID ACROPACHY

Literally 'thickening of the extremities', this occurs in patients who have been treated for thyrotoxicosis and end up myxoedematous. The hands are more commonly affected than the feet. The distal ends of paired long bones are less often affected. The distribution is similar to that of hypertrophic osteoarthropathy but the new bone is more likely to be shaggy, spiculated and perpendicular to the shaft rather than lamellar. The overlying soft tissues are often grossly thickened (Fig. 36.3).

INFECTION

OSTEOMYELITIS

An invading organism may attack bone by direct invasion from an infected wound, or from an infected joint, or it may gain access by haematogenous spread from distant foci, usually in the skin. Haematogenous osteomyelitis usually occurs during the period of growth, but all ages may be affected and cases are even found in old age. In infants, *Streptococcus* usually causes osteomyelitis. In adults, *Staphylococcus* is more common.

It is important to understand the blood supply to bone before describing blood-borne infection. The blood supply to a long bone is via:

1. *The nutrient artery.* This is the major source of blood supply throughout life. It supplies the marrow and most of the inner cortex.
2. *Periosteal vessels.* These supply the outer cortex.
3. *Metaphyseal and epiphyseal vessels.*

In the *infant*, vessels penetrate the epiphyseal plate in both directions. Metaphyseal infections can thus pass to the epiphysis and then the joint. Acute pyogenic arthritis is therefore a relatively common sequel of osteomyelitis in infants. The periosteum in infants is very loosely attached to underlying bone. Pus easily elevates periosteum and so can extend to the epiphyseal plate along the shaft. In situations where the metaphysis is intracapsular, such as the hip, metaphyseal infection also results in septic arthritis.

In *childhood*, between 2 and 16 years, few vessels cross the epiphyseal plate though the periosteum is still relatively loosely attached. The epiphysis and joint are thus less frequently infected. The metaphyseal vessels terminate instead in slow-flowing sinusoids which promote blood-borne infective change (Figs 36.4, 36.5).

In the *adult*, after the epiphyseal plate has fused, metaphyseal and epiphyseal vessels are again connected so that septic arthritis can recur. Periosteum, however, is well bound down and articular infections via a metaphyseal route are less likely.

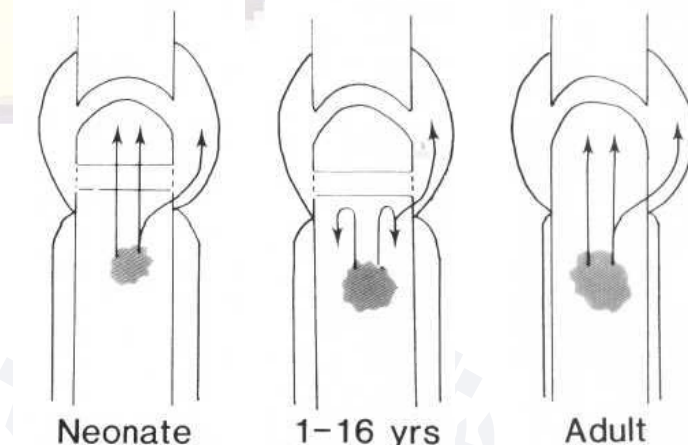


Fig. 36.4 Osteomyelitis. The three ages of infection and how change involves the joint.

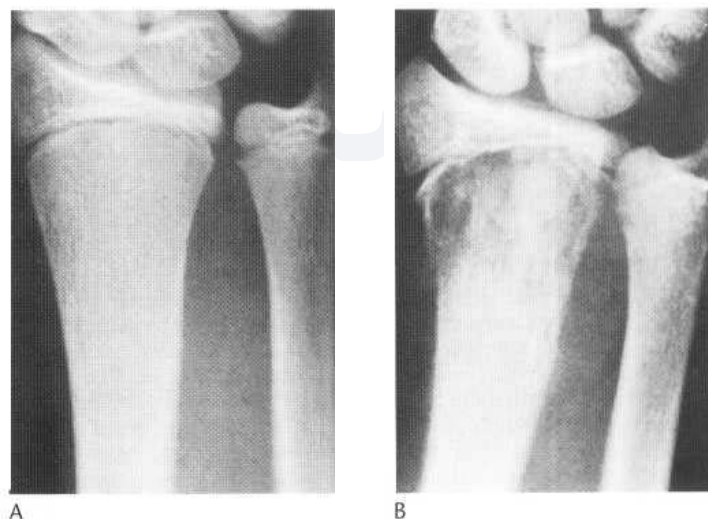


Fig. 36.5 (A) Early metaphyseal infection. There is very minimal focal bone destruction at the distal radial metaphysis. (B) With progressive bone destruction, metaphyseal abnormality is now very evident.



Fig. 36.6 Advanced osteomyelitis involving the whole of the right tibia and lower end of fibula. Note sequestrum in tibia (arrow) and further sequestrum being extruded from the fibula (arrow).

The formation of pus in the bone deprives local cortex and medulla of its blood supply. Dead bone is resorbed by *granulation tissue*. Pieces of dead bone, especially if cortical or surrounded by *pus*, are not resorbed and remain as *sequestra* (Fig. 36.6). As sequestra are devitalised they remain denser than surrounding vital bone, which becomes demineralised due to hyperaemia and immobilisation. Absorption of sequestra is also facilitated by the presence of an *involucrum*. The involucrum forms beneath vital periosteum which has been elevated by pus. As periosteum is poorly attached in infants, involucrum formation is greater and so is the resorption of dead bone, and healing.

In areas of dead periosteum, defects in the involucrum occur. These *cloacae* allow pus and sequestra to escape, sometimes to the skin via a sinus. The track and its deep connection to bone can then be demonstrated by sinography using water-soluble contrast medium (Fig. 36.7).

Radiological findings

These depend to some extent on the age of the patient.

Soft-tissue changes may be immediately apparent, especially in infants. Swelling, with oedema and blurring of fat planes is seen in distinction to the soft-tissue masses around tumours. Where the displaced fat planes are preserved. Osteoporosis may be visualised within 1014 days of onset of symptoms. In children this is usually metaphyseal.

An involucrum is usually visualised after 3 weeks and is more prolific in infants and children than in adults (Fig. 36.8). The rapid escape and decompression of pus which results prevents vascular compression and infarction, and promotes healing. Computed and conventional tomography are invaluable in detecting sequestra. These are seen as fragments of dense bone within an area of local bone destruction. Treatment by antibiotics and/or surgical decompression affects the course of the disease so that often little apart from new bone may be found during the course of the disease.



Fig. 36.7 Chronic osteomyelitis. (A) The preliminary radiograph shows a deformed right femur. There is cortical thickening with evidence of intramedullary cavitation and angulation. Linear calcified densities in the soft tissues may represent extruded sequestra. (B) Coronal fat-suppression MR image shows muscle wasting; the deformity of the bone is again demonstrated. There is extensive increase in signal within the medulla, indicating a fluid collection. A band of high signal can be seen extending from the medulla superiorly, through the cortex laterally and into the adjacent soft tissues. There is an effusion in the knee joint and oedema of the subcutaneous soft tissues. (C) The sinogram shows contrast medium in the same distribution as the fluid in B.



Fig. 36.8 Osteomyelitis of femur and septic arthritis of the hip in neonate. Note dislocation of hip, involucrum, cloaca and sequestrum.

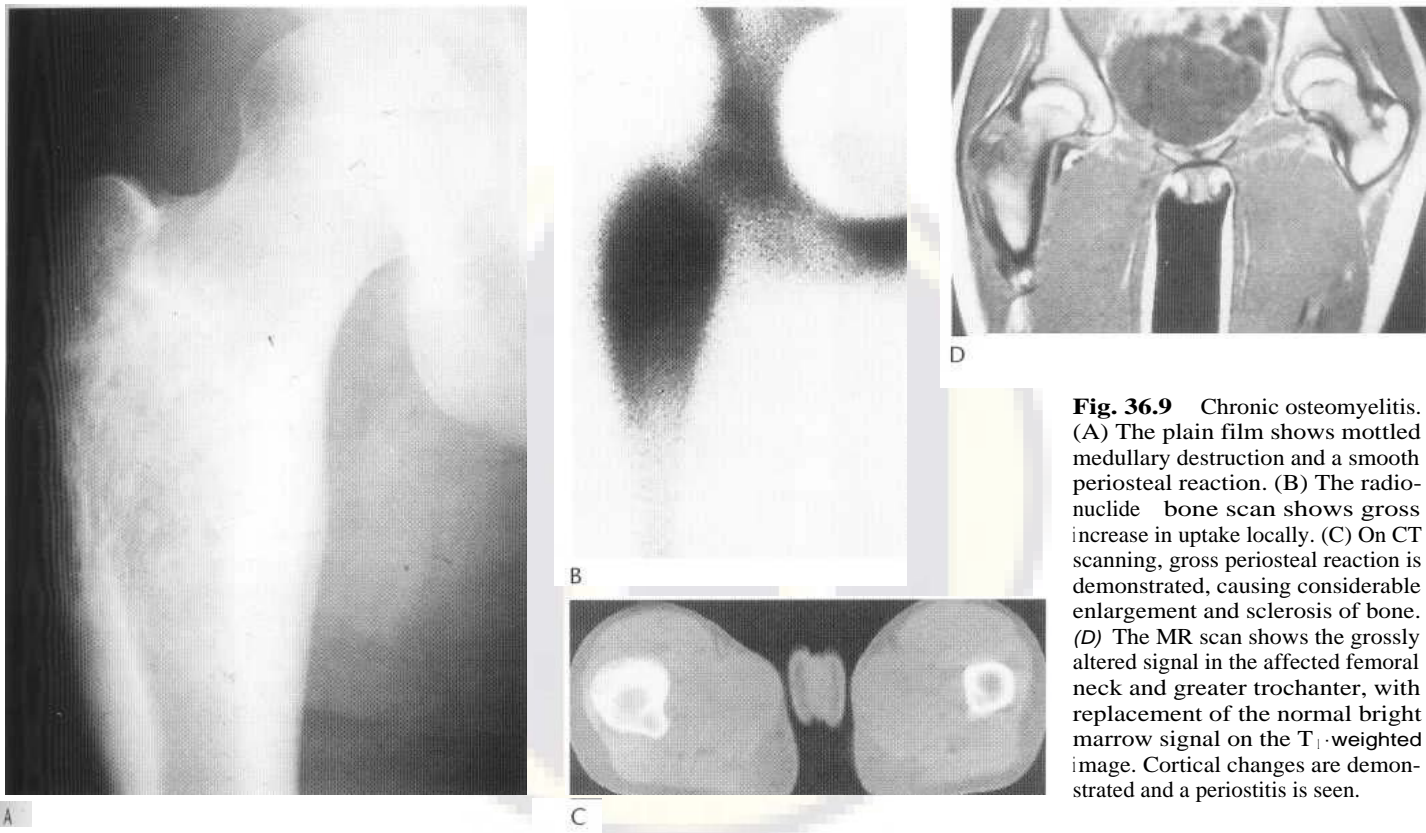


Fig. 36.9 Chronic osteomyelitis. (A) The plain film shows mottled medullary destruction and a smooth periosteal reaction. (B) The radionuclide bone scan shows gross increase in uptake locally. (C) On CT scanning, gross periosteal reaction is demonstrated, causing considerable enlargement and sclerosis of bone. (D) The MR scan shows the grossly altered signal in the affected femoral neck and greater trochanter, with replacement of the normal bright marrow signal on the T₁-weighted image. Cortical changes are demonstrated and a periostitis is seen.

With adequate treatment in infants and children, a return to more or less normal appearances with growth is to be expected unless the epiphyseal plate and epiphysis have been damaged, in which case growth abnormalities may result. In adults, the affected bone often remains sclerotic and irregular in outline (Fig. 36.9). Should chronic sepsis persist, tomography may reveal persistent cloacae and sequestra. The radiographic picture never returns completely to normal in cases discovered late (Table 36.1).

Radionuclide scanning in bone infection

Skeletal scintigraphy in suspected bone infection should rightly precede plain film examination. Plain radiographic changes cannot be seen for up to 10-14 days with simple infections, though in tuberculous disease changes are usually present at first presentation. Using scintigraphy, however, the diagnosis of osteomyelitis can be confirmed as early as 48 hours after the onset of the disease, even if clinical signs are equivocal. Early aggressive treatment may prevent

gross bone destruction and, indeed, if given early enough on the basis of a positive scan, need never develop (Fig. 36.10).

Standard techniques involve the use of *technetium 99m-labelled phosphonate* and phosphate compounds. The accretion of radionuclide in bone is related to blood flow as well as to local bone turnover. This allows two separate sets of images to be obtained in osteomyelitis:

1. A 'blood-pool' image of the painful area immediately after injection. This shows increased local radioactivity, if positive, in areas of increased blood flow.
2. Delayed skeletal scintigraphic images at 3-4 hours. By this time the radionuclide has been absorbed onto bone crystal. This gives a skeletal image with local accentuation in areas of increased blood flow and bone turnover. This also differentiates osteomyelitis from cellulitis.

Using these techniques it can safely be said that not only is scanning more sensitive in detecting infective foci earlier, but it is nearly always accurate-positive or negative. It is however non-specific, because tumours and infection may give similar appearances. Technetium uptake is limited if blood vessels are occluded in the infective process by tamponade or thrombus; thus, in neonates, up to 30% of scans may be negative because of this. Difficulty may also arise because the metaphysis is always the site of increased uptake in the growing skeleton. With metaphyseal infection, however, the depth of increase in uptake is greater.

Gallium 67-labelled citrate scans may be used when the technetium scan is negative in patients with clinical osteomyelitis, or even in conjunction with a technetium scan. Gallium concentrates avidly at the site of infection following local accumulation of leucocytes and proteins which are labelled in vivo. The radiation dose is higher however and the image poorer. Gallium scans are also

Table 36.1 Haematogenous osteomyelitis of tubular bones

Features	Infant	Child	Adult
Localisation	Metaphyseal with epiphyseal extension	Metaphyseal	Epiphyseal
Involucrum	Common	Common	Not common
Sequestration	Common	Common	Not common
Joint involvement	Common	Not common	Common
Soft-tissue abscess	Common	Common	Not common
Pathological fracture	Not common	Not common	Common*
Fistulas	Not common	Variable	Common

* in neglected cases

(Reproduced from *Diagnosis of Bone and joint Disorders*, by courtesy of Drs D. Resnick and G. Niwayama, and W. B. Saunders, publishers.)

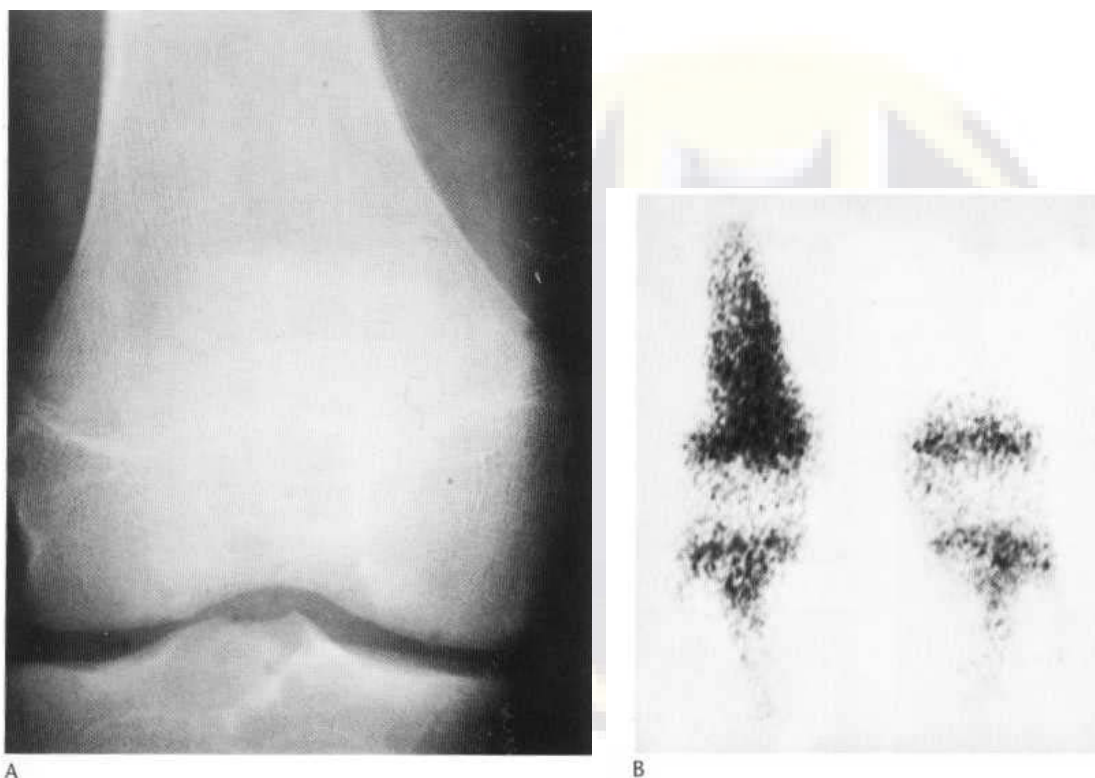


Fig. 36.10 Early osteomyelitis. (A) There is a barely discernible radiolucency affecting the distal shaft of the femur, but an early periostitis is demonstrated medially and laterally. (B) The radioisotope bone scan shows the extent of the pathological change.

probably more helpful in follow-up of active osteomyelitis, as such scans are negative earlier than technetium scans when disease becomes quiescent. Technetium scans remain positive for some time even in inactive disease, as the mode of uptake depends on a different physiological process. Gallium scans cannot distinguish with accuracy between cellulitis and osteomyelitis.

Similar results may be obtained with *in vitro* indium-labelled leucocytes which are reinjected into the patient.

CT scanning

Though of less value in the diagnosis of acute infection, CT demonstrates changes in subacute or chronic osteomyelitis well, especially those related to cortical bone or periosteum (Fig. 36.11). Sequestra, as on conventional films, are shown as areas of dense or high attenuation spicules of bone lying in areas of osteolysis (Fig. 36.12). Cloacae, periostitis and local soft-tissue masses are shown. These may enhance with intravenous contrast medium.

CT-guided biopsy can be used to obtain material for culture.

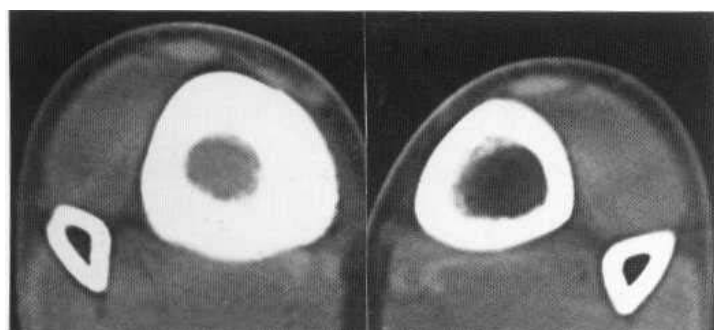


Fig. 36.11 Chronic osteomyelitis. The CT scan shows the left side to be normal, while on the right there is extreme cortical thickening and marrow oedema of the tibia.



Fig. 36.12 Osteomyelitis of the clavicle with an involucrum and sequestrum, demonstrated at CT scanning.

MRI

MRI demonstrates osteomyelitis as early as isotope scanning and, where available, is the modality of choice in the diagnosis of musculoskeletal infection. Using appropriate weightings, or paramagnetic enhancement, changes in bone and soft-tissue oedema may be identified early on. Ischaemia and destruction of cortex or marrow. Subsequent soft-tissue extension of pus through cloacae and para-osseous abscesses may be seen. Central necrosis in abscesses may be shown. Images can be obtained in all planes (Fig. 36.9D).

Weightings in common usage are T₁, T₂, and fat suppression. Fatty marrow is bright in signal on T₁ studies, while the compact cortex, having less fluid, has a low signal. Oedema and inflammatory changes increase signal dramatically on T₂-weighting and especially on STIR sequences (Table 36.2).

Areas that become devitalised or necrotic will show loss of signal, and will not enhance after intravenous gadolinium.

Table 36.2 Signal changes with different weightings

	<i>T₁-weighting</i>	<i>T₂-weighting</i>	<i>STIR</i>
Normal cortex	Low signal	Low signal	Low signal
Normal medulla	Very bright	Less bright	Low signal
Oedematous cortex	Low signal	Bright	Very bright
Oedematous medulla	Lowered signal enhancing with gadolinium	Bright	Very bright

Calcified tissues are generally better defined with CT but soft-tissue changes are better seen at MR scanning. While density changes in marrow infection can be assessed at CT, MR is much better at demonstrating the extent of pathology in bone and surrounding soft tissues and is at least as sensitive as isotope scanning. The latter has the advantage of showing other possible foci of disease outside the area of interest.

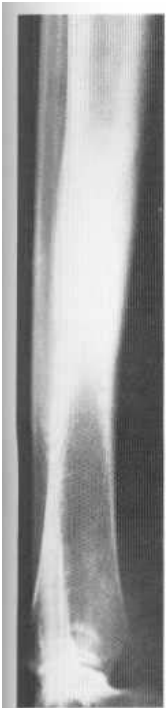
Bone biopsy in infection

Bone biopsy by needle is performed in the diagnosis of both infections and tumours. In our radiological practise, the spine is the area most frequently biopsied: open biopsy for tissue and bacteriological diagnosis is clearly a much more serious procedure and is generally not the first technique to be used.

As far as infection is concerned, the aims of biopsy are:

1. To confirm the presence of infection and exclude tumour or other causes of a radiological lesion.
2. To distinguish the organism, both by direct microscopic examination of the aspirate and after culture.
3. To allow correct antibiotic treatment after appropriate sensitivities have been established.

General anaesthesia is unnecessary except in infancy or if non-cooperation is expected. Sedation and analgesia are adequate. Analgesia should be both intravenous and local, including infiltration of local anaesthesia down to the periosteum.

**Fig. 36.13** Garre's type of osteomyelitis.

Closed or open biopsy can be performed using for guidance fluoroscopy, ultrasound, CT or even MR scanners. Many types of biopsy needle are available. Some are of very large bore and consist of pointed trochars in a cannula which are used to enter bone, when the pointed trochar is replaced by a trephine with a cutting edge. Certainly, hard bone needs a rigid biopsy needle. Infected bone or disc, however, tends to be soft and, in practice, a fine aspiration needle is often all that is needed. Complications using a fine needle are usually minor. Pneumothorax and bleeding in the chest, or bleeding from abdominal organs, are not usually serious problems. The preference of the histologist governs the size of the sample the radiologist needs to obtain.

SPECIAL FORMS OF OSTEOMYELITIS

Sclerosing osteomyelitis of Garré

This condition is manifested by gross sclerosis in the absence of apparent bone destruction (Fig. 36.13). True examples of this condition are found occasionally, but some of the cases described in the past were probably examples of *osteoid osteoma*.

Brodie's abscess

This localised form of osteomyelitis is usually found in the cancellous tissue near the end of a long bone (Fig. 36.14). A well-circumscribed area of bone destruction has a surrounding zone of reactive sclerosis, sometimes accompanied by a periosteal reaction. It may have a finger-like extension into neighbouring bone toward the epiphyseal plate, which, when present, is pathognomonic of infection.

**Fig. 36.14** Brodie's abscess demonstrated at MR. On this fat-suppression image, the localised abscess is demonstrated as an area of extremely high signal.

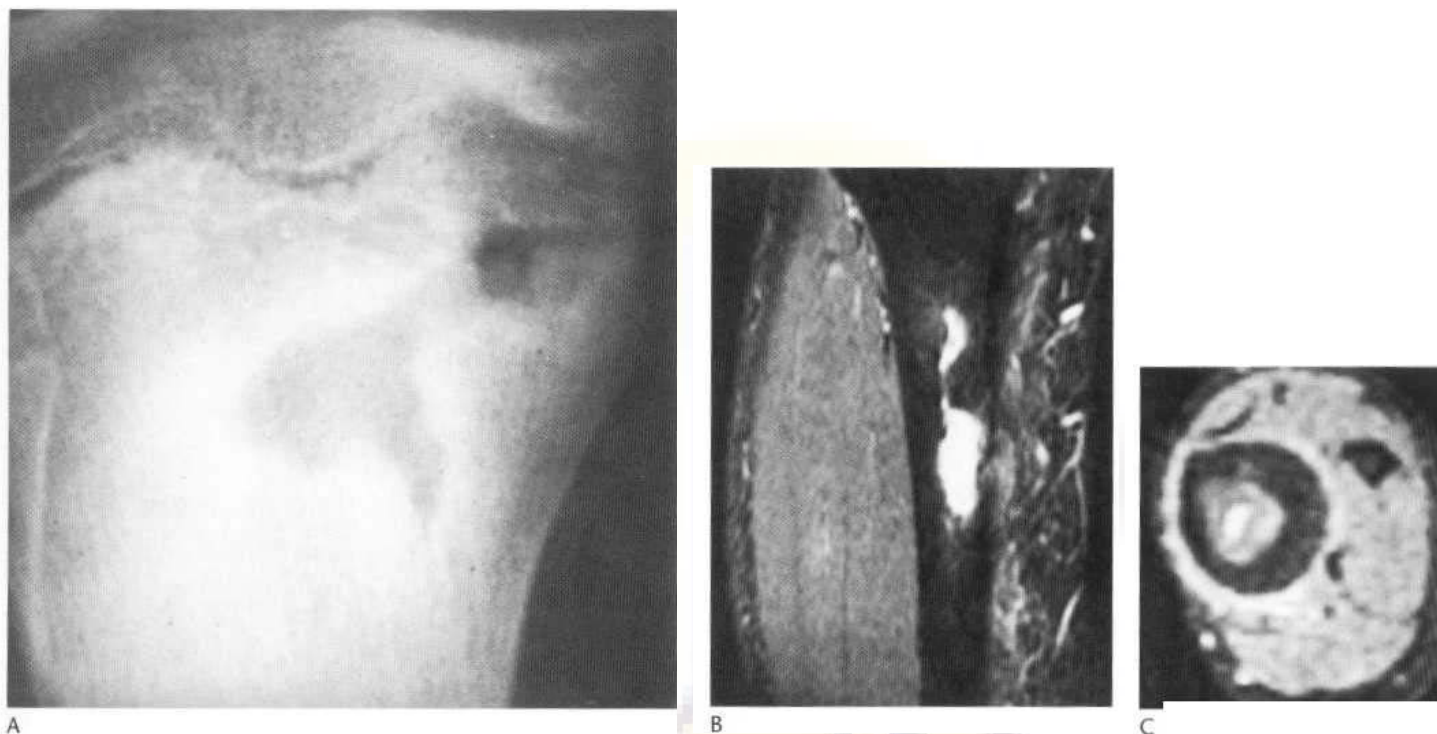


Fig. 36.15 'Tunnelling' in osteomyelitis. (A) A finger-like process of osteomyelitic bone destruction extends from the main focus. This is tunnelling, which usually indicates the presence of chronic infection. (B) In another patient, the sagittal fat-suppression MR sequence shows a vertically orientated and fluid-filled cavity in the proximal tibia. It is well defined and has all the features of a chronic infective lesion. (C) The chronically thickened cortex together with the central fluid-filled cavity lying within the medulla are demonstrated on this axial fat-suppression MR image.

('tunnelling') (Fig. 36.15). If a sequestrum is present an osteoid osteoma may be simulated.

Brodie's abscess typically enhances on the delayed isotope scan. An osteoid osteoma enhances centrally, both on the blood-pool and delayed scan due to its central vascularity. CT demonstrates central necrosis and sequestration of the Brodie's abscess, even in the presence of significant local surrounding sclerosis, much as would conventional linear tomography. At MR1, it is to be expected that the central vascular material in the osteoid osteoma will exhibit brighter signal and enhancement, while necrotic tissue in the Brodie's abscess will not (Fig. 36.16).

OSTEOMYELITIS IN SPECIAL SITES

Skull

Lesions occur secondary to scalp infection or frontal sinus suppuration (Fig. 36.17).

Mandible

Infection may complicate a fracture into the mouth, or it may follow dental extraction. Infection via the pulp canal is probably most common and follows poor oral hygiene and dental decay.



Fig. 36.16 Brodie's abscess. The plain film was not helpful. (A) The radioisotope bone scan confirms the presence of a focal lesion in the upper cervical spine. (B) The CT scan shows an appearance which could represent either an osteoid osteoma or a Brodie's abscess, that is, an area of osteolysis with central sclerosis and surrounding it a well-demarcated zone of reactive sclerosis. (C) Changes at MR mirror those seen at CT in the lateral mass of C2.



Fig. 36.17 Multiple areas of bone destruction and reactive sclerosis (arrow) are seen in a patient with chronic osteomyelitis.

Pelvis

The sacroiliac joint is occasionally affected. It may be difficult radiologically to differentiate pyogenic from tuberculous lesions. Ankylosis of the sacroiliac joint may result from either cause.

Osteitis pubis is a low-grade infection around the symphysis pubis which may complicate operations on the prostate and bladder or, occasionally, other pelvic operations.

Hands

Bone infection may follow perforating injuries to the pulp space. The distal phalanx may be involved by osteomyelitis, or local pressure may cause ischaemia and avascular necrosis.

A bizarre form of osteomyelitis, often due to oral organisms, follows bite wounds on hands or after punching the face and teeth, with resulting perforations and implantation (Fig. 36.18).

Feet

Puncture wounds of the feet are common in children and in those societies where walking barefoot is common. Soft-tissue infections may lead to osteomyelitis, often with destruction of joints. In the tropics, direct implantation by mycetoma results in 'Madura foot' (see 'Mycetoma' below). Implantation by thorns leads to a particular lesion.

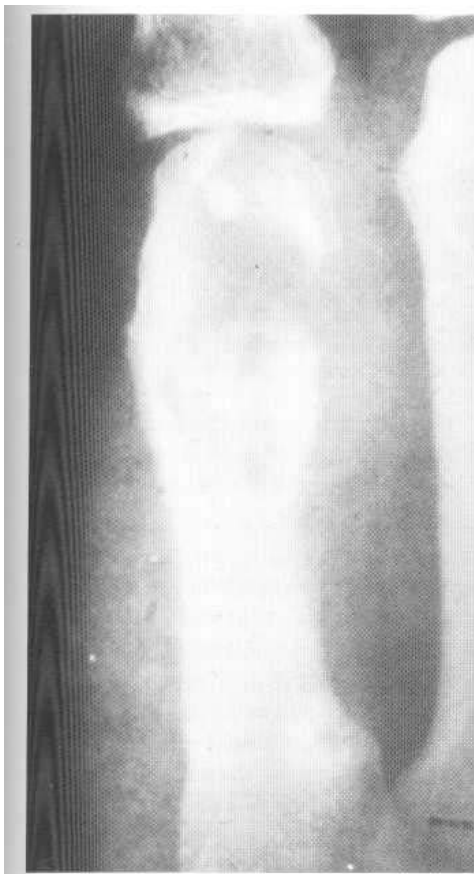


Fig. 36.18 Bone destruction, sequestrum formation and periostitis follow implantation of oral organisms after a bite.

COMPLICATIONS OF OSTEOMYELITIS

1. *Amyloid disease* infrequently complicates chronic osteomyelitis.
2. *Malignant changes* can follow longstanding suppurative osteomyelitis with draining sinuses. Increasing severity of symptoms with rapid osteolysis raises the possibility of a tumour, either an *epithelioma* of the sinus tract or, less frequently, an *osteosarcoma*.

OSTEOMYELITIS OF THE SPINE

Spinal osteomyelitis is not common, comprising less than 10% of bone infections (Epstein 1976), and can occur at any age. Patients

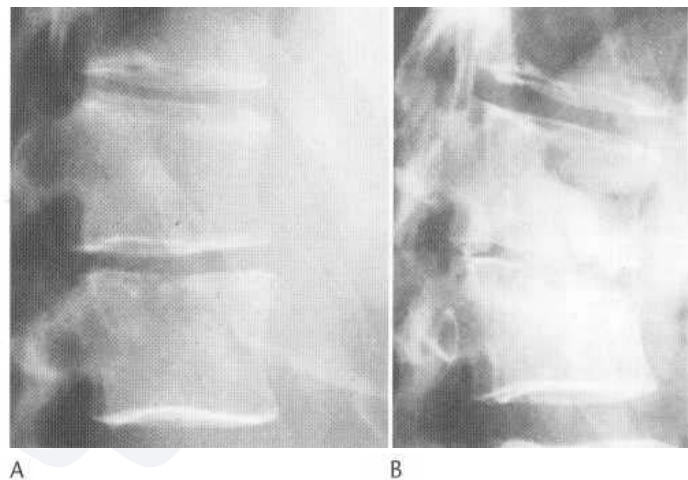


Fig. 36.19 Infective discitis. (A) The initial film shows early bone destruction beneath the end-plates around a narrowed disc. (B) The later film shows progressive destruction of disc and bone with surrounding reactive sclerosis.

often have a history of skin or pelvic infections. Spread of infection is usually to the vertebral body rather than to appendages and is mainly blood-borne, though osteomyelitis may follow spinal surgery. Spread of disease from the pelvis is facilitated through Batson's vertebral venous plexus which is a valveless system of veins joining the pelvis with the rest of the axial skeleton via the spinal canal. Flow in this valveless system ebbs back and forth with changes in intra-abdominal pressure. Vertebral bodies are very vascular, especially below end-plates where large sinusoids with a sluggish blood flow potentiate infection. Spinal osteomyelitis is most common in the lumbar region and least common in the cervical and sacral spines.

Infective discitis (infective spondylitis)

Perforating blood vessels still supply the disc in children and young adults so that in these age groups a primary infection of the discs can occur. Changes are most common in the lumbar spine.

Radiological findings

Infection usually starts anteriorly beneath the end-plate. Plain film changes lag behind symptoms by 2-3 weeks, when a focus of osteolysis becomes visible and the cortex becomes blurred or vanishes. Infection may be beneath the anterior longitudinal ligament, facilitating vertical spread, or into the disc, which is then rapidly destroyed and loses height (Figs 36.19, 36.20). The adjacent end-plate then also loses density and vertebral destruction begins in the body above or below. In most patients only two bodies are involved, and only rarely is the infection confined to one vertebral body.

Collapse of a vertebral body is accompanied by soft-tissue masses which are easily seen against air in the larynx, trachea or lung (Fig. 36.21). Blurring or displacement of the psoas shadows also occurs. Kyphosis and cord compression may also follow.



Fig. 36.20 Infective discitis. The sagittal T₁-weighted MR sequence shows vertebral body destruction at L3/4 and replacement of marrow-fat signal by soft tissue. There is also expansion of the vertebral body mass posteriorly into the canal.



Fig. 36.21 End-plate destruction with distal loss and a kyphosis is associated with facet subluxation and a large anterior soft-tissue mass (arrow).

Reparative processes can begin as early as 4-6 weeks after the onset of radiological change if treatment is effective. Sclerotic new bone is formed around the disc, in the bodies and at vertebral margins (Fig. 36.22). Dense spurs bridge discs peripherally. Ankylosis across discs may result in fusion of bodies. If this occurs after skeletal maturity, the sagittal diameters of vertebral bodies are not likely to be reduced. Ivory vertebrae and soft-tissue calcification are occasionally found.

Isotope scanning

Here, as elsewhere, isotope scanning detects infection of bone and surrounding soft tissues before plain film changes are visible; further confirmation can be obtained with indium or gallium white-cell-labelled scans.

CT

CT is of value in showing established disease and demonstrates trabecular destruction, soft-tissue masses and encroachment on the canal and cord. Intrathecal contrast may be used in conjunction with CT to show the relationship of a mass in the canal to the cord.

MRI

This is the most sensitive technique and is now the investigation of choice. Cortical destruction is seen on T₁-weighted studies; disc and marrow inflammation are well shown on T₁- and T₂-weighted and STIR sequences (Fig. 36.20). Soft-tissue extension is particularly well demonstrated, as is abscess formation.

With treatment, the increase in signal on T₂-weighted studies seen early on declines so that, when the disease is inactive, the discal remnant is seen as a narrowed dehydrated structure of low intensity. Persistence of increase in signal implies continuing inflammation.

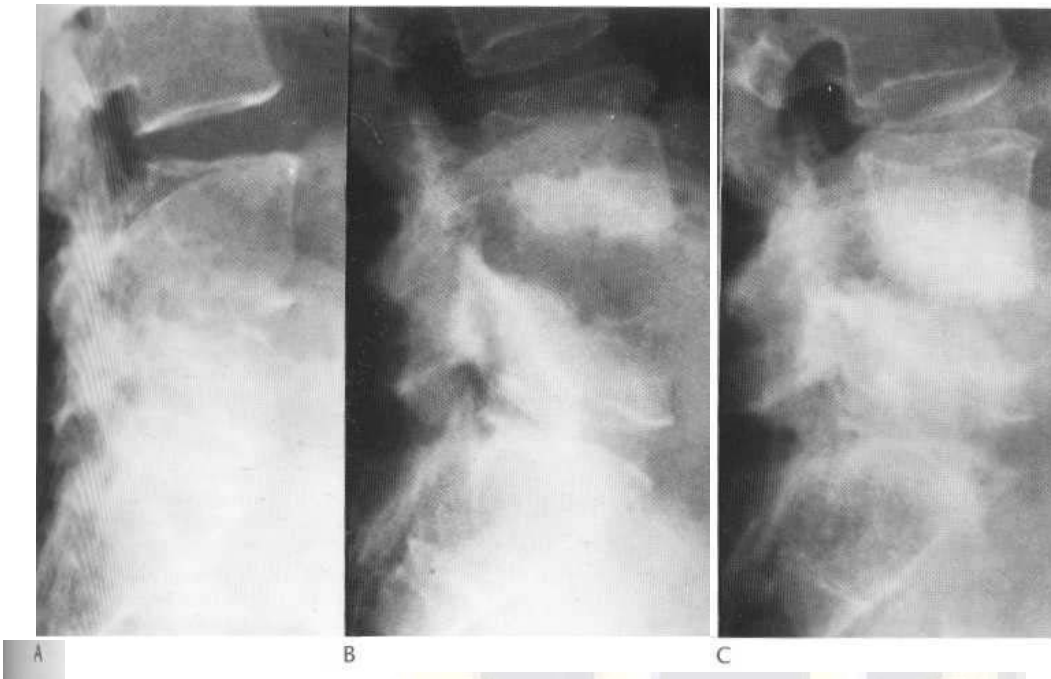


Fig. 36.22 Infective discitis with progressive healing and reactive sclerotic change: (A) September; (B) October; (C) subsequent January.



Fig. 36.23 Diabetic ulcer. Gas is seen in the defect adjacent to the fifth metatarsal head. The phalanges are subluxed and there is a reactive periostitis around the shaft of the proximal phalanx of the little toe.

OSTEOMYELITIS IN DIABETES

Infection occurs in both soft tissue and bone. Soft-tissue infection may follow a puncture through anaesthetic skin and presents with swelling and loss of fat planes due to oedema. In the presence of gas-producing organisms, spherical lucencies are seen extending proximally. Anaesthetic ulcers show as soft-tissue defects, usually over pressure points such as the metatarsal heads, and over the tips and proximal interphalangeal joints of the commonly associated claw toes. Initially painless, the ulcers involve underlying bones with the development of osteomyelitis (Fig. 36.23). Sepsis may be superimposed on a neuropathic lesion, so that osteoporosis and destruction are accelerated. If skin ulceration is absent, osteomyelitis is unlikely to be seen.

CHRONIC GRANULOMATOUS DISEASE OF CHILDHOOD

This is a group of disorders in which the leucocytes are unable to respond normally to infections, especially to those organisms that cause chronic low-grade infections. Leucocytes are able to engulf bacilli but cannot destroy them so that toxins are still produced. A chronic inflammatory process results. Bones are commonly affected. Widespread small foci of osteolysis may be found, often abutting on to epiphyseal plates (Fig. 36.24). The lesions heal with florid formation of new bone, both endosteally and superficially, so that sclerosis and expansion result, often resembling malignant tumours (Fig. 36.25). The lesions are usually multifocal and isotope scans of the whole body are needed to show all the infective foci.

MRI demonstrates the inflammatory changes well on T₂-weighted and STIR sequences. Oedema is shown to be extensive in the surrounding bone, including the epiphysis, and adjacent soft tissues. The destructive metaphyseal lesion is well demonstrated.

SEPTIC ARTHRITIS

Joint infections occur at any age, but especially in children. *Staphylococcus*, *Streptococcus* and *Pneumococcus* are common causative organisms. Usually only one joint is affected. If more than one joint is infected, an immune defect should be suspected or the possibility of steroid administration queried.

A joint may be contaminated by:

1. direct intervention-following surgery, aspiration or perforating injury
2. spread from adjacent bone (see above)
3. haematogenous spread-direct infection of synovium by septic emboli.

Radiological features

Initially synovial thickening and effusion distend the joint. Fat lines are displaced but may be blurred by oedema. Demineralisation follows hyperaemia and immobilisation. When infection begins to destroy cartilage, joint narrowing becomes apparent (Fig. 36.26).

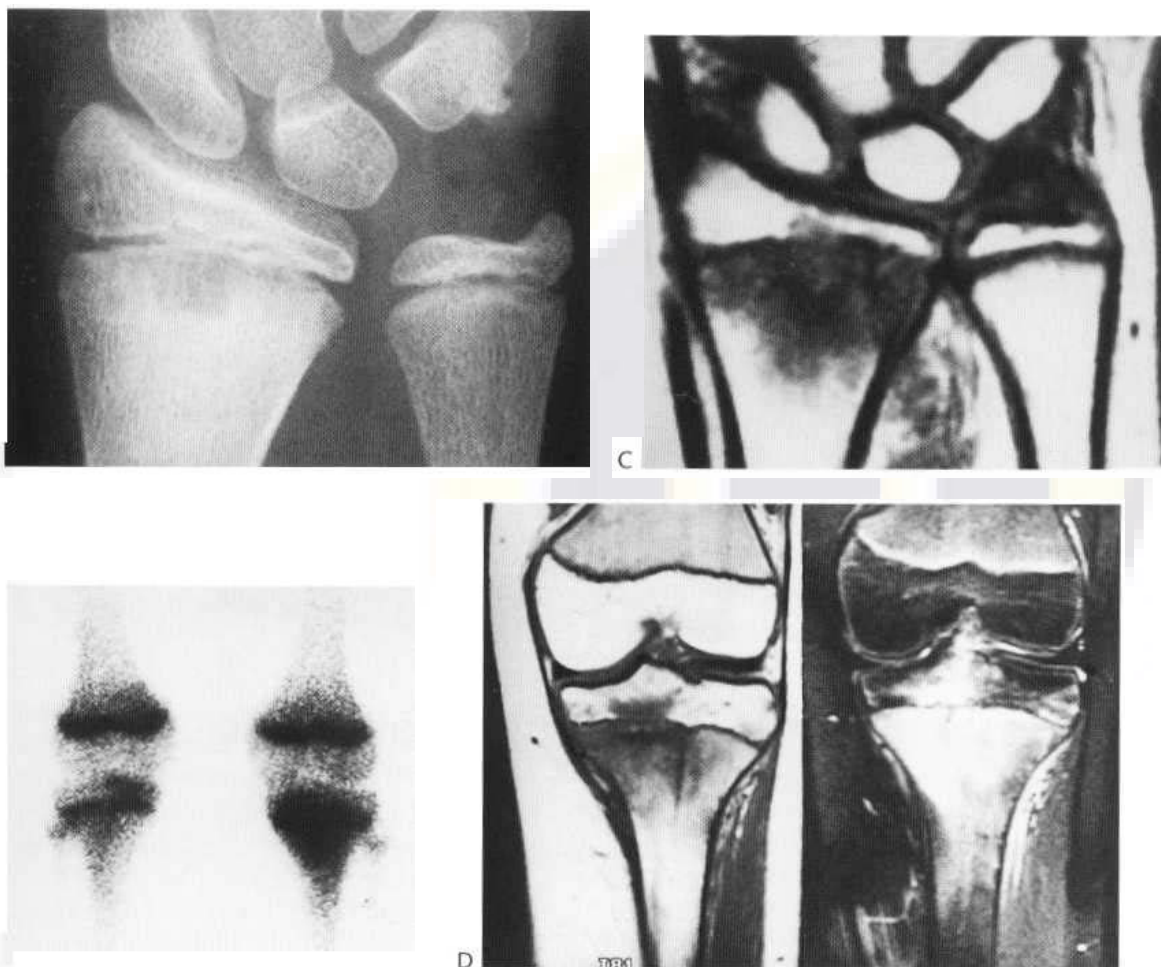


Fig. 36.24 Chronic granulomatous disease. (A) There is a localised metaphyseal defect surrounded by sclerosis. These features are characteristic of chronic infection in a child. (B) The MR scan confirms the presence of localised metaphyseal abnormality with replacement of the local fat. There is a mixture of destruction of bone, oedema and reactive new bone formation at the margin of the lesion. (C) Same patient. The radioisotope bone scan shows increase in uptake in the proximal tibial metaphysis of the left knee. (D) Coronal T₁ and STIR sequences confirm the presence of change, not merely in the metaphysis but also in the epiphysis. Fluid replaces fat on both sequences. (Courtesy of Dr R. Phillips.)

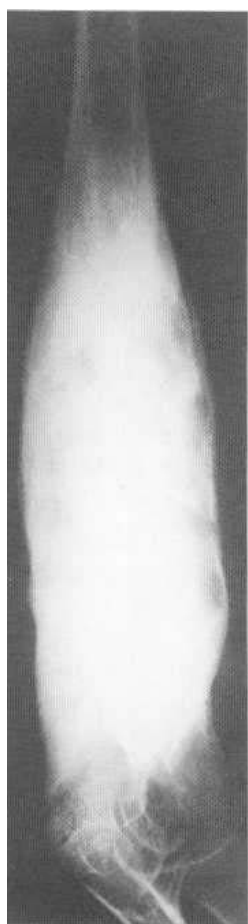


Fig. 36.25 Gross reactive sclerosis with new bone formation at multiple sites is found in chronic granulomatous disease.

The articular cortex becomes blurred and then eroded, both peripherally and centrally, and subarticular bone is later destroyed. Severe cases are characterised by massive destruction, separation of bone ends, subluxation and dislocation.

During recovery, bones recalcify and in severe cases fibrous and bone ankylosis may result. Dystrophic calcification may be seen on occasion following pyogenic arthritis. Marginal erosions persist but their outlines become well demarcated and sclerotic.

Arthritis of the hip in infants (Tom Smith arthritis)

The hip joint in infants is especially susceptible to infection as explained above. In neonates sepsis may be transmitted via the umbilical vessels, often due to *Streptococcus*, but infection may be directly introduced following blood sampling at the groin. In infants, because of lax muscles around the hip and the cartilaginous nature of the acetabulum, an effusion may dislocate the hip (Fig. 36.27). This can be assessed even if the ossific nucleus has not appeared. Failure to recognise acute dislocation may result in permanent deformity. In any case, gross metaphyseal destruction is soon apparent with cortical and medullary erosions. Gross sequestration rapidly occurs and an involucrum may involve the entire femur. The femoral shaft generally heals, but the femoral head and neck may be totally destroyed, never to appear. Deformity and shortening inevitably result. In older children, such change is less likely as the epiphyseal plate is not crossed by vessels. The femoral head, even if severely affected, then reconstitutes with a flattened mushroom-like appearance similar to old Perthes' disease or slipped epiphysis. Because of vascular compression, osteonecrosis may actually complicate infection.



Fig. 36.26 (A-C) Pyogenic arthritis of the hip-rapid progression of the lesion during a period of one month.

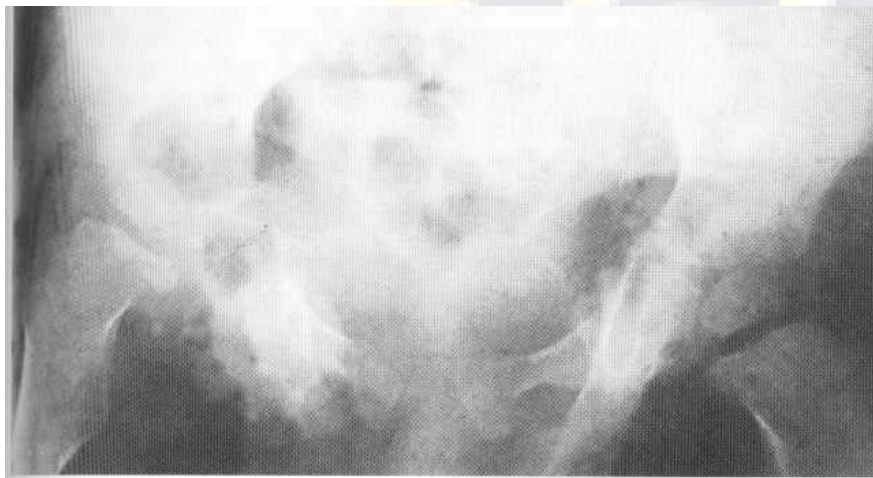


Fig. 36.27 Septic dislocation of the right hip.

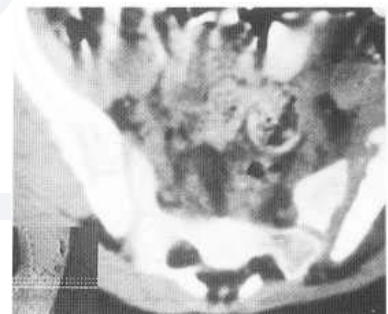
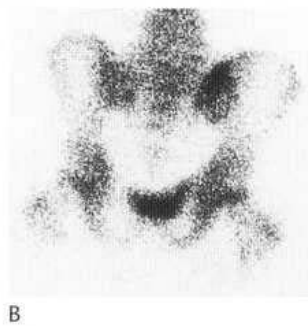
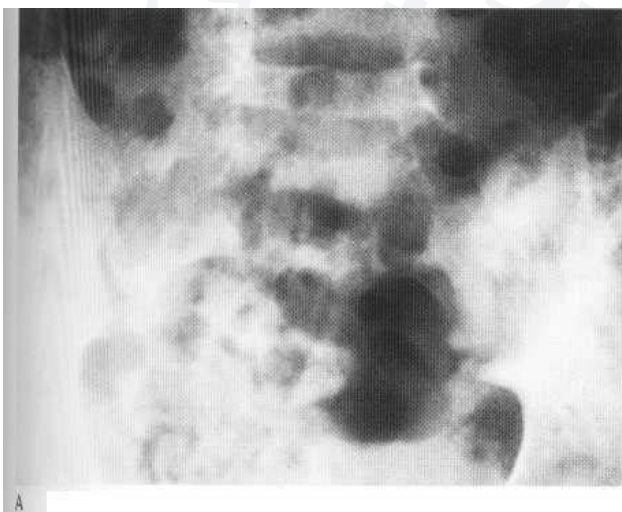


Fig. 36.28 Infective sacroiliitis. (A) There is resorption of bone and sclerosis around the left sacroiliac joint. The radioisotope bone scan (B) shows the increase in uptake, and the CT scan (C) shows the widened joint with areas of irregular bone destruction and soft-tissue swelling. (Courtesy of Professor H. Carty.)

Infection at major joints may show widening of the joint and distension of the capsule by effusion or pus. This can be assessed by plain film or ultrasound, which has the advantage that it can be followed by needle aspiration of fluid, microscopy and culture.

An isotope scan will be positive at an early stage. CT can be used for biopsy but patients should not be overinvestigated or treatment delayed because of a desire to use all imaging modalities. A diagnostic specimen should be obtained prior to instituting antibiotic therapy (Fig. 36.28).

MRI is probably the investigation of choice in the early diagnosis of septic arthritis, where effusion and bone oedema are clearly seen.

TUBERCULOSIS OF BONES AND JOINTS

Though the incidence of skeletal tuberculosis has fallen markedly in recent years, the disease has not yet been eradicated. One-third of our present-day patients are immigrants to Britain; they tend to produce unusual disease patterns which will be described later.

Haematogenous spread of infection to the skeleton is assumed to be from the lung and may occur at the time of primary infection or later from postprimary foci. Chest radiography, however, shows active disease in less than 50% of cases, the organism presumably having laid dormant and become active later. The bacillus lodges in the spongiosa of the metaphysis of a long bone, but the vertebral



Fig. 36.29 Tuberculosis of femur—large metaphyseal focus.



Fig. 36.30 Tuberculous focus in greater trochanter. This type is less common than a surface erosion.

column is affected in 50% of cases. Lesions are usually single, though multifocal cystic osseous tuberculosis is described.

Certain features are relatively common. The tuberculous reaction is destructive and accompanied by pus which may later become calcified. Calcification of abscesses is rarely seen currently if antibiotic treatment is adequate. In contradistinction to pyogenic osteomyelitis, neither sequestration nor periostitis is a prominent feature. Abscesses often point to the skin and a sinus track may be demonstrated after injection of contrast medium.

Radiographic appearances

The diagnosis is usually made after considerable delay and radiographic changes are seen at presentation, in contrast to pyogenic infections where radiographic changes occur 2-3 weeks after clinical presentation.

The metaphysis is the site of election: an oval or rounded focus will be found which soon crosses the epiphyseal line (Fig. 36.29). No surrounding sclerosis is to be expected. Sequestra are small and are absorbed by granulation tissue. Though slight periosteal reaction may be found if the local lesion is subcortical, this is not a prominent feature. The initial focus may sometimes be sited in the epiphysis.



Fig. 36.31 Tuberculous discitis. (A) The changes on the plain film are really quite similar to those that would be seen with a simple infection. There is distal destruction associated with irregularity of the overlying end-plates and some reactive new bone formation. There is perhaps a suggestion on the plain film that a soft-tissue mass is demonstrated anterior to the vertebral bodies. (B) The MR T₁-weighted axial image shows the end-plate defect seen so well on the plain film but, in addition, psoas abscesses with central necrosis are demonstrated.

Lesions of the diaphysis are rare, and even rarer is the multiple cystic type of lesion.

Lesions of individual bones

Greater trochanter

This is a common site, particularly in adolescents and young adults. The lesion may start in the bone or in the overlying bursa. The erosion may be deep, but often it is superficial and difficult to detect: sometimes it may be cystic (Fig. 36.30).

Spine

Roughly half the cases of osteoarticular tuberculosis seen in the UK occur in the spine. Most lesions occur in or below the midthoracic spine and involvement of the cervical and upper thoracic spine is uncommon. All ages may be affected.

Radiographic appearances (Fig. 36.31)

Vertebral bodies may be first affected in three places—at the upper or lower disc margin, in the centre, and anteriorly under the periosteum. The disc substance is often eroded. Two or more vertebrae may be attacked. Tomography may show the lesion to be more extensive than it appears from examination of plain films. Since the anterior parts of the vertebrae are most affected, a local *kyphosis* or

gibbus will appear, and some scoliosis may also occur. Abscesses form early and are easily seen in the thoracic region in contrast to the radiolucent lungs (Fig. 36.32). In the lumbar region, lateral bulging of the psoas outlines may be demonstrable. Abscesses may track widely and may become calcified. They may sometimes be intraosseous and subsequently calcify (Fig. 36.33). Rib crowding may be seen, even on a chest radiograph, if vertebral bodies collapse.

It is often difficult to differentiate between tuberculous and pyogenic spondylitis, especially if the patient is Caucasian. Clearly, tuberculosis must always be suspected if the patient is of African or Asian origin. Reactive new bone formation is much less pronounced in tuberculous disease, so that sclerotic osteophytes are unusual. Discs are destroyed early with simple infections and later in tuberculosis. Calcification, where present, indicates tuberculosis.

The lesions generally respond rapidly to antibiotics, but before antibiotics were introduced, gross destructive lesions were common, and the affected vertebral bodies frequently became fused.

The subperiosteal type of infection begins anteriorly under the periosteum and spreads under the anterior common ligament. Disc destruction may be late and the anterior erosions difficult to detect.

Aortic pulsation, transmitted through an anterior paraspinal abscess between T4 and T10, may cause the vertebral bodies to become deeply concave anteriorly (Fig. 36.34). This process does not affect the intervertebral discs. An *aneurysm* causes similar changes by direct pulsation.

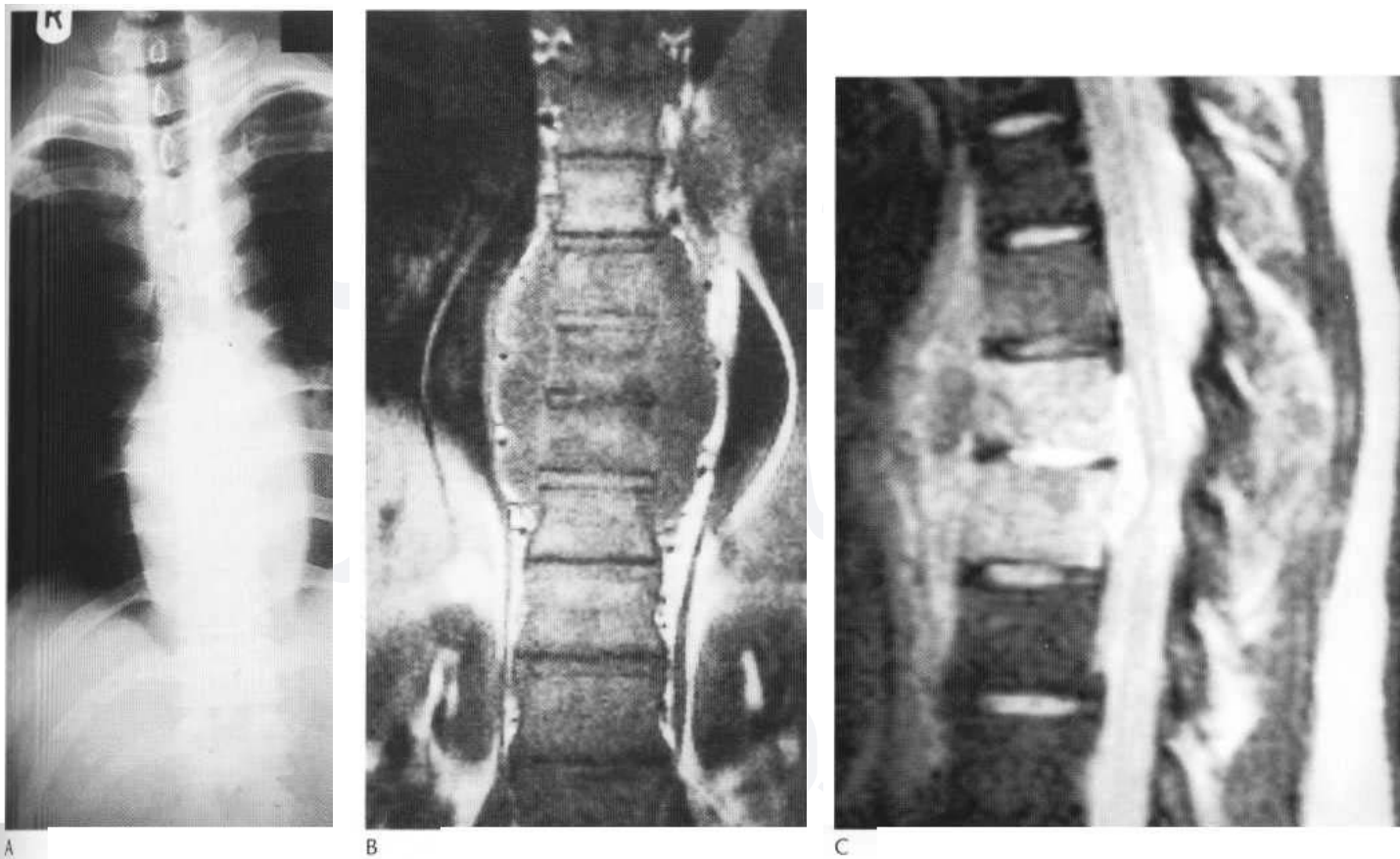


Fig. 36.32 (A) The plain film shows features which are typical for spinal tuberculous disease. There is an extensive paraspinal soft-tissue mass. Detail in the underlying spine is poor but there is early crowding of ribs posteriorly, indicating early vertebral collapse. (B) Coronal MR image of the thoracic spine demonstrates destruction of the intervertebral disc at the point where the paraspinal widening is maximal and this change is associated with alteration of signal from the vertebrae. (C) The sagittal fat-suppression image shows increase in signal in adjacent vertebral bodies together with anterior and posterior soft-tissue masses, the latter indenting the spinal canal and compressing the adjacent cord.

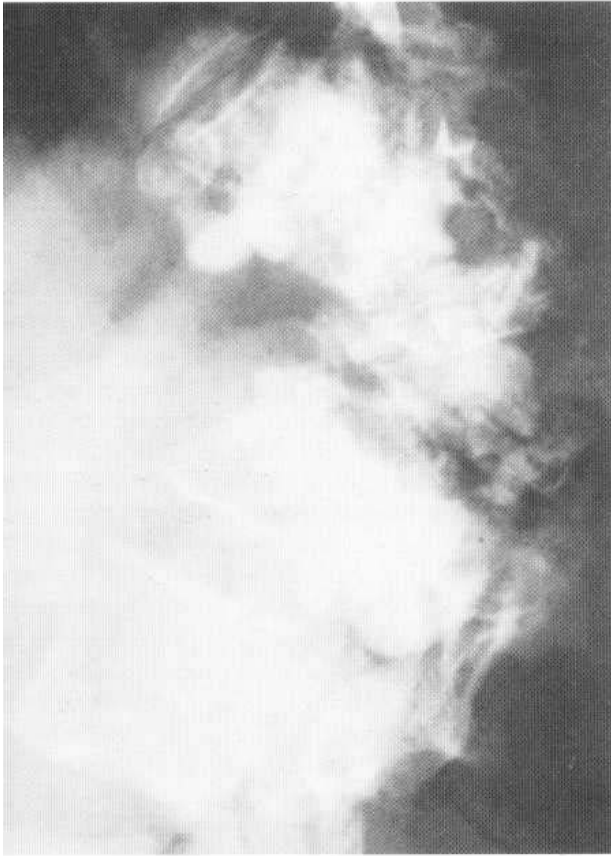


Fig. 36.33 Tuberculous spondylitis has healed with calcifying psoas abscesses and angular kyphosis.

In black-skinned patients, tuberculous spondylitis has a somewhat different presentation. Often, only one vertebra is involved, with conspicuous preservation of adjacent discs, even if the body is totally destroyed or flattened. Occasionally, *vertebra plana* results (Fig. 36.35). Sclerosis and new bone formation is a feature of the disease in black-skinned patients, as in pyogenic spondylitis. More importantly, the posterior elements are frequently involved, especially in the lumbosacral and thoracolumbar junctions, often with huge abscesses (Fig. 36.36). The cervical spine is also more frequently involved than in white-skinned patients, with dysphagia or paraplegia as complications. Multiple lesions are also more common. Additionally, involvement of the spinal column follows gibbus formation or extrusion of granulation tissue into the canal.

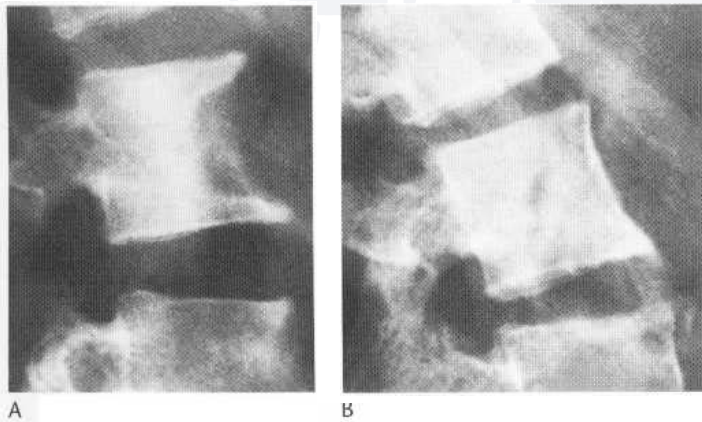


Fig. 36.34 (A, B) Anterior subperiosteal type of Pott's disease.

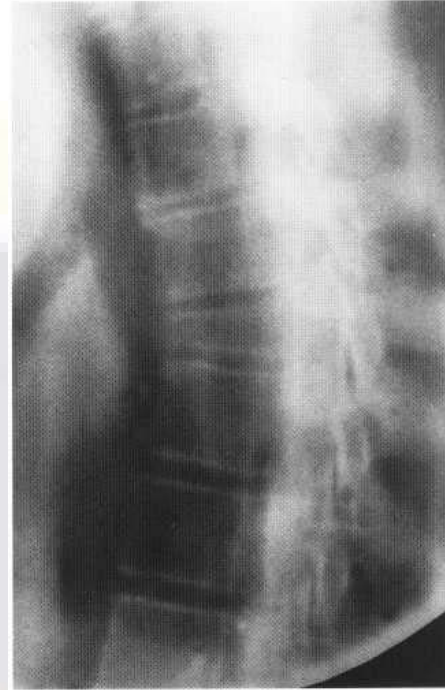


Fig. 36.35 Spinal osteomyelitis in a Saudi Arabian patient showing vertebra plana with preservation of the disc and end-plates.

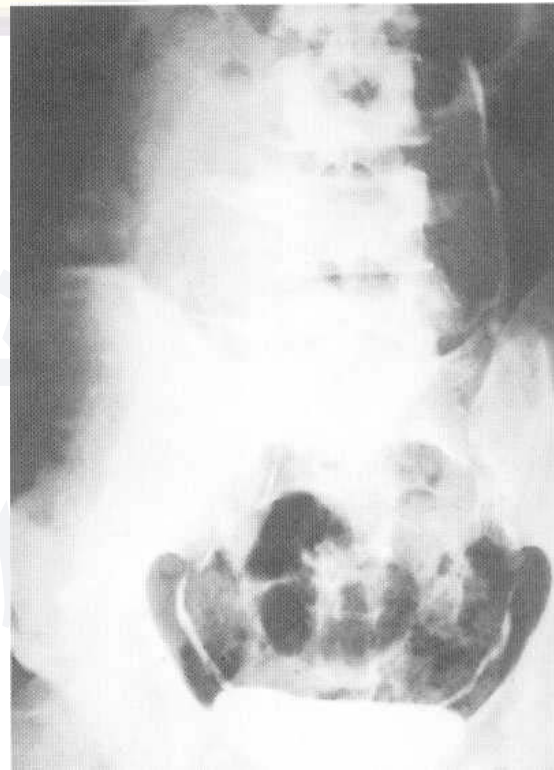


Fig. 36.36 A large abscess displaces the right ureter medially and destroys the right transverse process and adjacent part of the body of L5. Two and a half pints of tuberculous pus were removed at operation.

Tuberculous dactylitis

This lesion is sometimes seen in the UK immigrant population. The affected phalanx is characteristically widened by medullary expansion (*spiny ventosa*), whereas in syphilitic dactylitis the bone is widened by the production of cortical new bone (Fig. 36.37).



Fig. 36.37 Typical spina ventosa of the proximal phalanx of the forefinger. (Courtesy of Dr D. J. Mitchell.)



Fig. 36.38 Tuberculosis of the skull vault. The fairly well defined lytic lesion was a solitary finding but these changes are often multiple. Note the gross tunnelling.

Skull

Tuberculous lesions are rare in the skull, except in UK immigrants. They may be localised and well defined, resembling *eosinophilic granuloma*, or they may be more diffuse (Fig. 36.38). Overlying cold abscesses are generally associated.

Joint lesions

Tuberculous arthritis usually affects major joints—the hip and knee especially. Multifocal infection is rare. Infection may be synovial or secondary to bony disease. The latter is facilitated as the epiphyseal plate apparently offers little resistance to tuberculosis.



Fig. 36.39 Synovial tuberculosis of left knee—note synovial effusion, osteoporosis, blurring of trabeculae and accelerated maturation of bone ends (normal right knee for comparison).

Early radiographic signs in synovial lesions are non-specific and will be manifested by capsular thickening, synovial effusion and surrounding osteoporosis. Later, continued hyperaemia will cause accelerated maturation of bone ends and epiphyses if infection occurs in children. Bony trabeculae become blurred and the cortex thinned (Fig. 36.39).

The bone ends eventually become affected. Local marginal or surface erosions may appear (Fig. 36.40). Loss of joint space will ultimately occur, but this is not as prominent a feature as it is in pyogenic arthritis. Sometimes one-half of a joint will be affected and bony erosions seen on contiguous bony surfaces.

The advent of antibiotics has changed the picture considerably. Patients usually respond well to treatment so that only the earlier phases are now seen. Formerly such sequelae as subluxation and ankylosis of joints, severe bone atrophy and tracking abscesses were common.

Joint tuberculosis is now rare in Caucasian patients in the UK, but still occasionally seen in immigrant groups in whom a destructive lesion of bone and joints is more likely to be due to tuberculosis than simple infection. Diagnostic aspiration should be performed. In Africa and Asia, however, the lesions are treated



Fig. 36.40 Tuberculous erosions of margins of medial tibial condyle and lateral femoral condyle (arrows).

immediately by chemotherapy as osteoarticular destruction is assumed to be tuberculous (Martini 1988).

Hip

This is a common site: lesions may arise in the acetabulum, synovium, femoral epiphysis or metaphysis. Sometimes infection spreads to the hip from foci in the greater trochanter or ischium. All degrees of bone loss of the femoral head and neck could be found (Fig. 36.41). A frequent finding was the pointed 'bird's beak' appearance with intrapelvic protrusion.

Knee

With synovial infection in childhood, effusion, osteoporosis and accelerated skeletal maturation are seen (Fig. 36.39). Overgrowth leads to modelling abnormalities, with big bulbous squared epiphyses, so that the appearance resembles that seen in *juvenile chronic arthritis* and *haemophilia*.

Shoulder

The humeral head, the glenoid, or both, may be affected (Fig. 36.42). Sometimes a lesion in the humeral head is large and cystic in appearance and may resemble an osteoclastoma.

Some tuberculous shoulder lesions run a relatively benign course without pus formation-*caries sicca*. In such cases a relatively small pitted erosion is seen on the humeral head. These may resemble degenerative changes.

Wrist and carpus (Fig. 36.43)

All carpal bones tend to be attacked in the adult, whereas more localised lesions are the tendency in children. This is possibly due

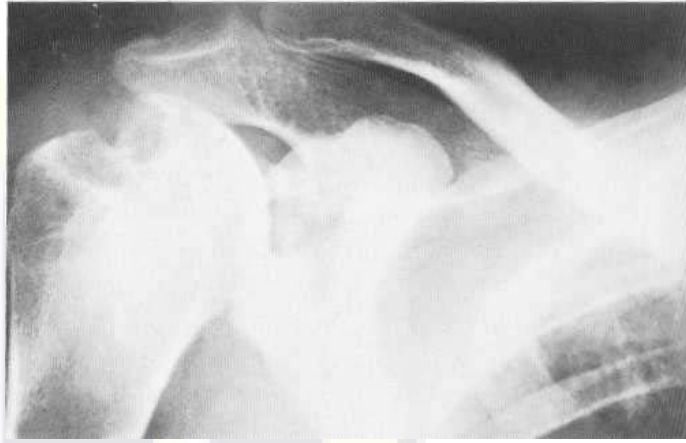


Fig. 36.42 Tuberculosis of shoulder-note lesions of humerus and glenoid and also lung.



Fig. 36.43 Soft-tissue swelling around the wrist with evidence of a widespread synovial abnormality. Bone and cartilage are destroyed. Osteoporosis is seen at the metacarpophalangeal joints. The metacarpal shafts however remain normal in density. The fifth metacarpal shaft has a periosteal reaction.



A



B

Fig. 36.41 Tuberculous arthritis. (A) The plain film shows destruction of the articular surfaces on both sides of the hip joint, with narrowing of the joint space and subarticular cyst formation. (B) At arthrography the presence of an irregular and shrunken synovial capsule is demonstrated. Defects are shown in the acetabulum and on the femoral head. Infection has resulted in a restrictive capsulitis and destruction of cartilage and bone.



Fig. 36.44 Old tuberculosis of the carpus. No doubt this occurred relatively early on in life as the metacarpals are shortened. The carpal bones are fused following widespread osteoarticular destruction. The tuberculous origin of the lesion is shown by soft-tissue and bone calcification on the lateral view.

to the relatively thicker articular cartilage in the latter. With cartilage destruction the carpal bones become crowded, and even if initially one bone is the focus of irregularity, the destructive process soon involves adjacent bones. Intense demineralisation is found throughout the carpus and distal radius and ulna, within the confines of synovium. Demineralisation is often also pronounced at distal small joints of the hand, with relative preservation of metacarpal and phalangeal shaft density. However, these joints are not eroded as in rheumatoid arthritis.

End-stage disease is often shown by total bony fusion and the presence of foci of dystrophic calcification, either within the bone or in the adjacent soft tissues (Fig. 36.44).



Fig. 36.45 Tuberculous sacroiliac joint-extensive destructive lesion.

Sacroiliac joints (Fig. 36.45)

This joint is affected more often in young adults than in children. Only occasionally is the condition bilateral. Subarticular erosions cause widening of joint space. The infection is usually associated with abscess formation over the back of the joint and, later, pus may calcify. Tuberculous infection of the spine is a frequent accompaniment.

SYPHILIS OF BONES AND JOINTS

Very few cases of syphilis of bone are now seen in the UK, yet up to the time of the Second World War it was a condition that merited serious consideration in the differential diagnosis of most conditions of bone. In this section merely a summary of the findings is presented, and illustrations are selected with a view to emphasising the protean pattern of the lesions.

CONGENITAL SYPHILIS

Lesions may be found in infants whose serological reactions are negative, especially when the mother is receiving treatment. They may appear early, i.e. from birth to 4 years, or later, i.e. between the ages of 5 and 15 years.

Radiographic appearances

The lesions may be widespread and usually symmetrical. Generally they are best shown in the lower ends of the radius and ulna and around the knee. Changes are:

1. *Periostitis*. This is the commonest feature and is seen either as a thin layer or as more marked laminated layers. Marked thickening on the convexity of a diaphysis may be seen in later cases as, for example, in the so-called 'sabre tibia'.
2. *Metaphysitis*. There may be irregularity of metaphyses, and metaphyseal fractures may occur (Fig. 36.46).



Fig. 36.46 Congenital syphilis—some increased density with sub-adjacent translucent zones at lower ends of femora. Metaphyseal fractures are shown.

3. *Osteitis* or *osteomyelitis*. Erosions on the upper medial surfaces of the tibiae are very characteristic of congenital syphilis. Sometimes more diffuse osteomyelitis of single bones is seen. Syphilis is a productive lesion, so sclerosis will be found frequently in such lesions.
4. *Syphilitic dactylitis* is rare; it resembles tuberculous dactylitis.
5. *Skull lesions* may be purely sclerotic or may present as a combination of sclerosis and osteolysis. In purely sclerotic lesions, new bone may be laid down in the frontal and parietal regions, so producing the 'hot cross bun' skull.



Fig. 36.48 Syphilitic osteomyelitis of the humerus. (Courtesy of Dr W. Fowler.)

ACQUIRED SYPHILIS

Any bone may be affected by this condition. Radiological manifestations comprise periostitis and osteomyelitis.

Periostitis

This sign may be seen as a simple laminated periosteal reaction or as a more exuberant lace-like appearance. Bony spiculation at right angles to the shaft is rare, but when it occurs, it may mimic a neoplastic lesion.

Osteomyelitis

This may occur as a localised or as a diffuse lesion. The localised lesion is termed a *gumma* (Fig. 36.47), but a more diffuse lesion is often referred to as 'gummatous osteitis' (Figs 36.48, 36.49). Sclerosis is generally found; irregularity of bone trabeculation is often apparent. Syphilis causes a combination of destruction and proliferation of bone.

It is important to remember the possibility of syphilis when presented with an atypical bone lesion.

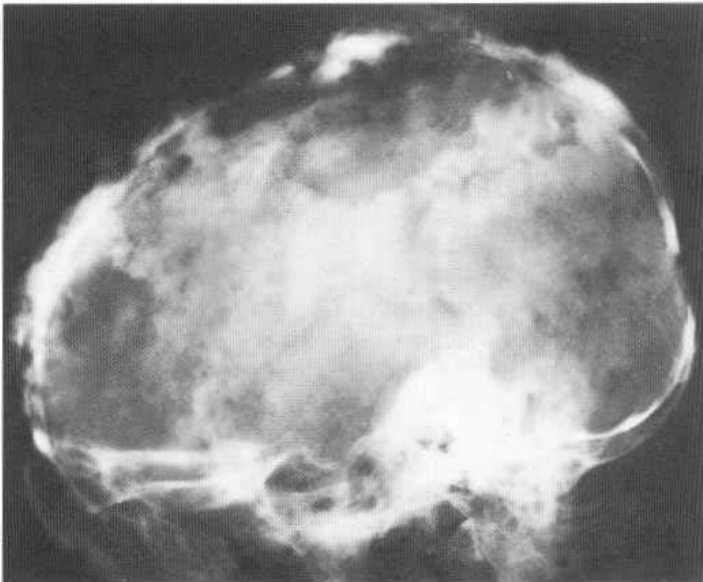


Fig. 36.49 Gummatous osteomyelitis of the skull.

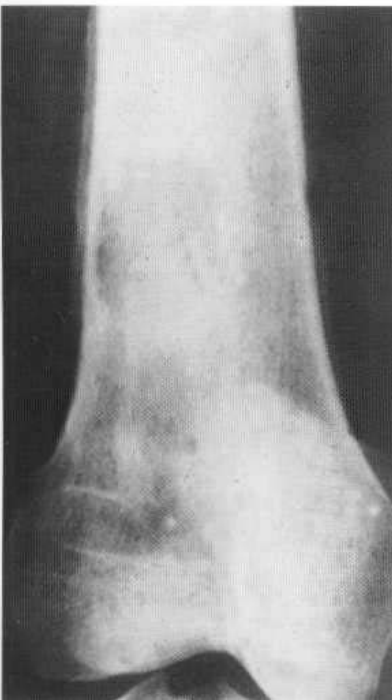


Fig. 36.47 Gumma of the lower femoral shaft. Note bone destruction and periosteal reaction.

SARCOIDOSIS

This disease is a non-caseating granulomatous disorder commoner in young adult males and especially in patients of black African descent. Changes in the skeleton are moderately common, occurring in up to 15% of cases. The hands and feet are far more commonly affected but any bone may be involved; lesions in the skull, vertebrae and long bones have all been described. Though the granulomas usually cause lysis of bone, often resembling tuberculosis, sclerosis occasionally results. Radionuclide scanning detects early bone lesions with greater sensitivity than plain radiographs.

Radiological findings

The changes in the bones include:

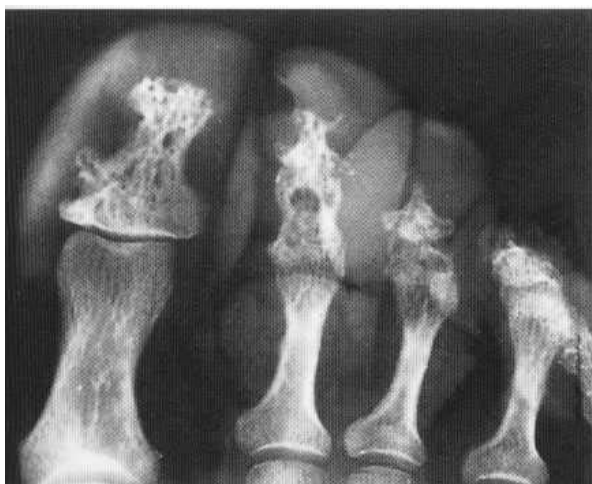


Fig. 36.50 Sarcoid-foot showing typical pseudocysts and absorption of tufts of distal phalanges.

1. Punched-out, well-defined areas of lucency in the phalanges. These are probably due to deposition of sarcoid tissue but, as in granulomatous *leprosy* (see below), the nutrient foramina are also said to be enlarged.
2. A more diffuse, reticular, lace-like pattern of resorption permeating the bone, described as a lattice-like appearance (Fig. 36.50).
3. Resorption of distal phalanges and of cortical bone along phalangeal shafts. Cortical resorption vaguely resembles that seen in *hyperparathyroidism*.
4. Sclerosis, which may be widely disseminated (Fig. 36.51).
5. Periosteal reaction.
6. Soft-tissue nodules far commoner than bone changes.
7. Periarticular calcification due to hypercalcaemia, which occurs in 20-45% of cases of Sarcoid.

SARCOID ARTHRITIS

An arthritis is a common manifestation of sarcoid, occurring in up to 37% of patients, most commonly in females. In the acute form, joint destruction does not occur but, in chronic disease, a destructive arthropathy of large joints does rarely occur due to local granulomas.

RARE BONE INFECTIONS

BRUCELLOSIS (synonyms: undulant fever, Malta fever)

This disease is more prevalent in the UK than was once thought. Transmission is from unpasteurised milk or by direct contact with

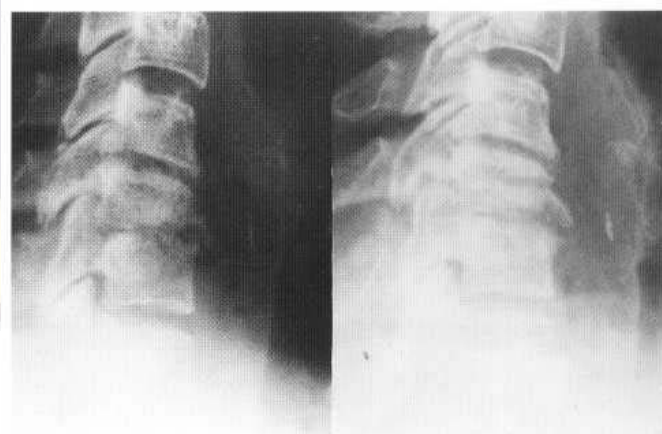


Fig. 36.52 Brucellosis. Vertebro-distal destruction with florid new bone formation are characteristic features of this disease.

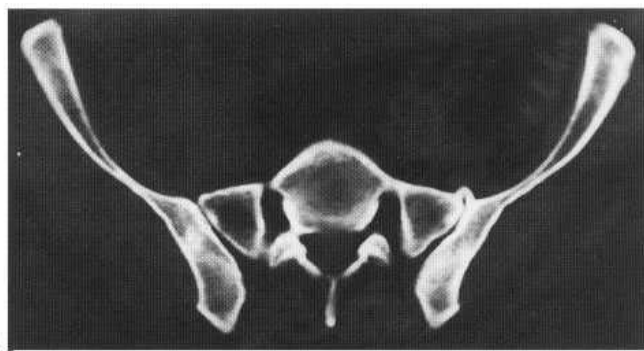


Fig. 36.51 Sarcoid. (A) Multiple foci of sclerosis are a recognised, if uncommon, feature of sarcoid. (B) Sclerotic change in sarcoidosis demonstrated at CT scanning.

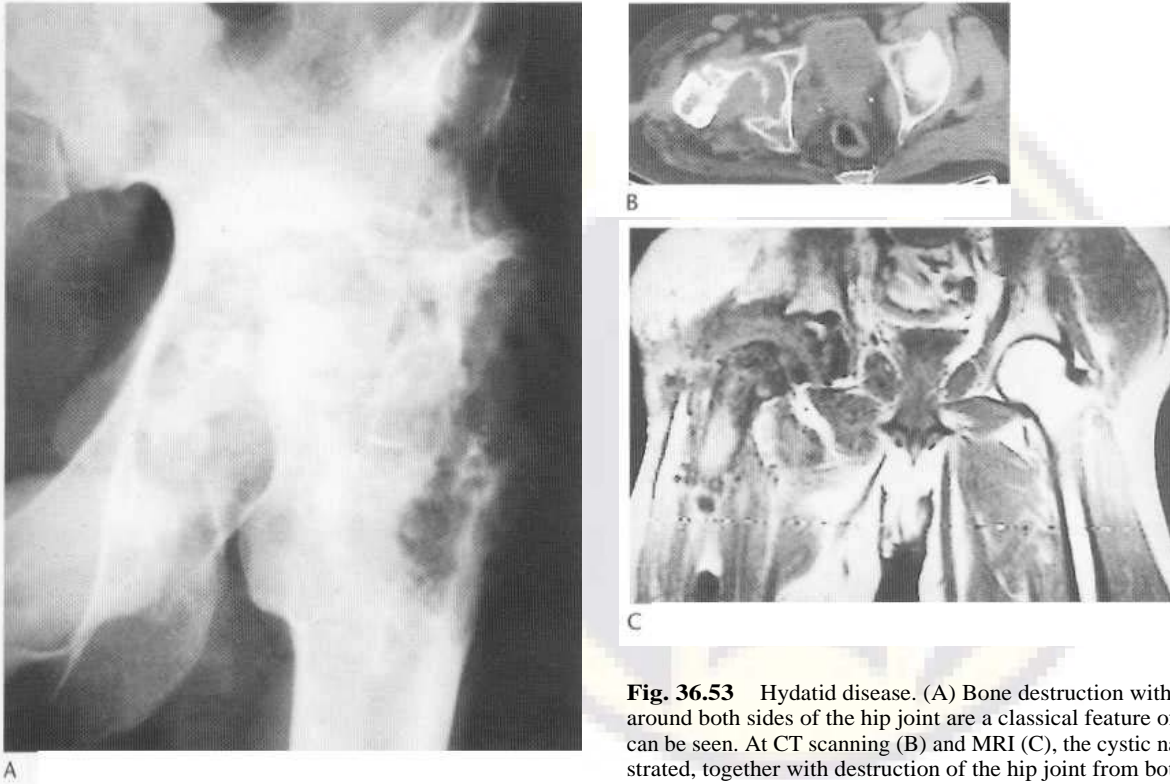


Fig. 36.53 Hydatid disease. (A) Bone destruction with the formation of large cysts around both sides of the hip joint are a classical feature of osseous hydatid. Sequestra can be seen. At CT scanning (B) and MRI (C), the cystic nature of the lesions is demonstrated, together with destruction of the hip joint from both sides.

affected animals. *Bruce/lus melitensis* infects sheep, *Br abortus* infects cattle and *Br suis* pigs.

The hones are affected in 10% of cases, most often the spine and especially the lumbar region. Widespread granulomatous lesions may be present:

1. **Spinal lesions.** These bear a marked resemblance to other forms of osteomyelitis. Focal sclerosis develops to a marked degree around the end-plate (Fig. 36.52). The disc is rapidly destroyed and adjacent vertebrae rapidly affected. Healing is by the production of extremely large, coarse and shaggy bridging osteophytes.
2. **Changes in other hones.** The radiographic appearances resemble those of subacute osteomyelitis.
3. **Changes in Joints.** These resemble the changes of *synovial tuberculosis*. In advanced cases erosive lesions may be seen.

In obscure and atypical bone infections, it is always advisable to test samples of the blood and of the synovial fluid of affected joints for agglutination reaction for brucellosis, and also for the typhoid and paratyphoid group of bacilli.

ACTINOMYCOSIS

Bony lesions due to this disease are rarely seen. They usually result from direct extension of soft-tissue lesions. Manifestations may be seen in the following sites:

1. **Mandible.** Chronic osteomyelitis arises by direct spread from oral infections and infected cervical glands. The lesion appears to be irregularly destructive.
2. **Ribs and thoracic spine.** Destructive foci and periosteal reaction in these bones arise from pleuropulmonary lesions.

3. **Right side of the pelvis and lumbar spine.** Infection spreads to these bones from ilioacetal foci. Spinal lesions are usually accompanied by paravertebral abscesses. The disc is usually spared.

Very rarely, destructive metastatic foci are found in other hones.

HYDATID DISEASE (Echinococcus)

Hydatid disease is rare in the UK and in less than 2% of affected patients is hone involved. The pelvis, spine and proximal long hones are usually involved. The disease is found in sheep-farming areas.

The enlarging cysts in bone absorb trabeculae and spread along the medulla, thinning the cortex and expanding the bone. Later, the cystic lesions become well defined, so that *fibrous dysplasia* may be simulated in long hones.

Around the hip joint, both the acetabulum and femoral head and neck are destroyed by large cystic lesions (Fig. 36.53). Fusion may result.

In the spine, the cysts break out of the cortex, forming large paraspinous masses which do not calcify but do cause paraplegia (Fig. 36.54). The appearance may resemble dumb-bell tumours in *neurofibromatosis*.

TROPICAL CONDITIONS

YAWS (Treponematosis)

This disease, which has more or less been eradicated, may still be seen in chronic cases. It was prevalent in the Caribbean, Indonesia and parts of tropical Africa and South America, and is due to a non-

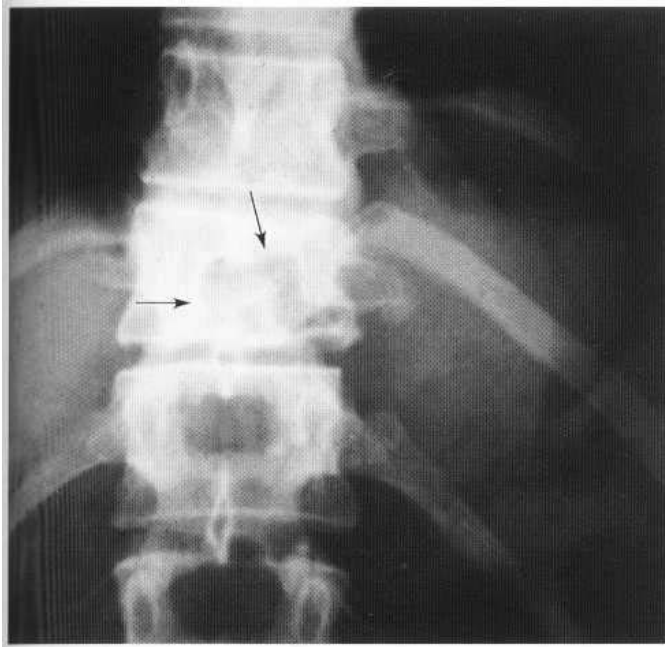


Fig. 36.54 This patient had never been outside England but had hydatid disease of the spine. Note the large paraspinal soft-tissue mass.

venereal infection by *Treponema pertenue*. As the disease is not transmitted to the fetus, congenital yaws does not occur, but children become infected. Infection usually occurs through a cut or abrasion. Bony changes are seen in the secondary and tertiary stages: these are usually indistinguishable radiologically.

Any bone may be involved. The distribution may be random, but there is a tendency to symmetry. In the early stages, multiple, small, rarefied areas of bone destruction are shown with overlying peri-

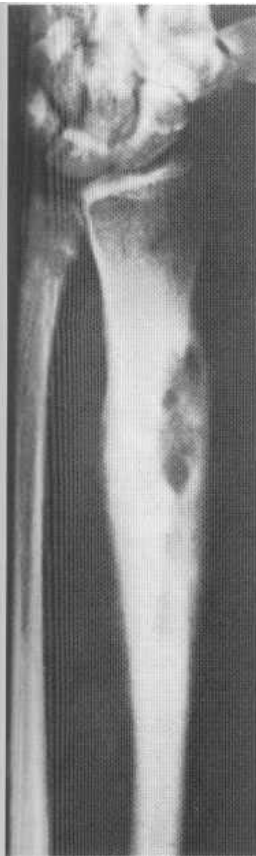


Fig. 36.55 Yaws-moderately early stage, showing destructive areas and much periosteal new bone formation. The appearances of the small destructive foci in yaws have been likened to the effects of a borer beetle. (Courtesy of Dr A. G. Davies.)

osteal new bone (Fig. 36.55). The hand may be especially affected. Larger areas of destruction occur in the skull and long bones, often with marked surrounding reactive sclerosis and new bone formation. Periostitis along the shaft, and softening of bone due to osteitis, lead to the sabre tibia deformity.

In the skull, gummatous lesions cause foci of osteolysis while slowly growing masses arising from the premaxilla produce a dense hyperostosis known as *goundou*. *Gangosa*, another manifestation of yaws, is an ulceration of the face causing severe necrosis of sub-jacent bone.

LEPROSY

This disease has a widespread geographical distribution, occurring in Egypt, Africa, Asia, the Caribbean and Pacific Islands. It is also seen in the UK's immigrant population. The lesions seen radiologically mostly affect the hands, feet and face, and are caused by infection by *Mycobacterium leprae*. This bacillus is of low infectivity and prolonged exposure is needed. The nature of the disease depends on host resistance. The incidence of bony change in leprosy may be around 15%.

Three types of bony lesions are found:

1. *Specific changes of osteitis leprosa* (15%). Granulomas cause areas of focal cortical or medullary bone destruction. The lesions may be rounded or may infiltrate, giving a lacy pattern



Fig. 36.56 Leprosy. Some small 'cysts' are seen, e.g. in the head of the proximal phalanx of the fifth finger-this condition is sometimes called 'osteitis multiplex cystica leprosa'. The end-results of lepra granulomas are seen in the heads of the proximal phalanges of the third and fourth fingers. (Courtesy of Dr. D. E. Paterson.)

just as in sarcoid. In addition, medullary nutrient foramina enlarge (Fig. 36.56).

2. *Non-specific leprous osteitis* (50%). In these patients Hansen bacilli are rarely found in the marrow. Neuropathic resorption gives a 'licked candy stick' appearance with bone loss both longitudinally and circumferentially (Fig. 36.57). In addition, Charcot-like changes take place in the tarsus. These patients have abnormal, thickened nerves and arterial occlusions. An abnormal stance potentiates this bone resorption in the denervated weight-bearing foot.

With anaesthesia, plantar ulceration and bone and soft-tissue infections are superimposed, so that pyogenic osteomyelitis is common in these patients. These changes are superimposed upon those of the neuropathic osteopathy.

3. A *diffuse osteoporosis* is seen which is non-specific. Nerve calcification is occasionally seen.

TROPICAL ULCER

This common lesion found throughout the tropics may also be seen in immigrants to the UK. Chronic indolent skin ulcers cause secondary bone changes, usually in the tibia or fibula. Periostitis is seen early in various forms, for example linear, onion-layer, lace-work and spicular. In very chronic cases, much dense cortical new bone is deposited and the final picture resembles that of an *ivory osteoma* (Fig. 36.58).

COCCIDIOIDOMYCOSIS

This is a chronic granulomatous condition caused by a fungus and found in the south-western parts of the USA. The lesions are



Fig. 36.57 Leprosy. 'Cup and pencil' or 'licked candy stick' appearances demonstrated associated with thickening and irregularity of the soft tissues, presumably the result of chronic infection in the soft tissues.



Fig. 36.58 Tropical ulcer. (A) Extensive osteomyelitis is seen in the underlying tibia. (B) Osteoma-like lesion on the front of the tibial shaft—a late sequel of tropical ulcer.

multiple and are most commonly found in the spine, pelvis, hands and feet. The bone lesions have the appearances of *acute* and *chronic osteomyelitis*; the joint lesions are similar to those found in *tuberculous arthritis*. The more frequent intrathoracic lesions of *coccidioidomycosis* are described in Chapter 5.

MYCETOMA

Mycetoma implantation occurs mainly in the (bare) feet in semi-desert regions throughout the tropics. The skull and knees may also be implanted, usually by thorns. Different organisms are found in different regions—*M. mycetoma* in the Middle East, Africa and India, and *S. somaliensis* and *pelletieri* in the Sudan. Lesions due to *M. mycetoma* are usually localised as large, well defined black fungus balls, which can be seen on soft-tissue radiographs. These erode the cortices and cause cystic defects in the medulla. Madura foot results (the lesions were first described in that region of India). With superadded infection via the implantation track, gross bone destruction results (Fig. 36.59). Reactive sclerosis and a shaggy periostitis with bone resorption give an appearance likened to 'melting snow'. With *S. pelletieri*, diffuse infection occurs earlier

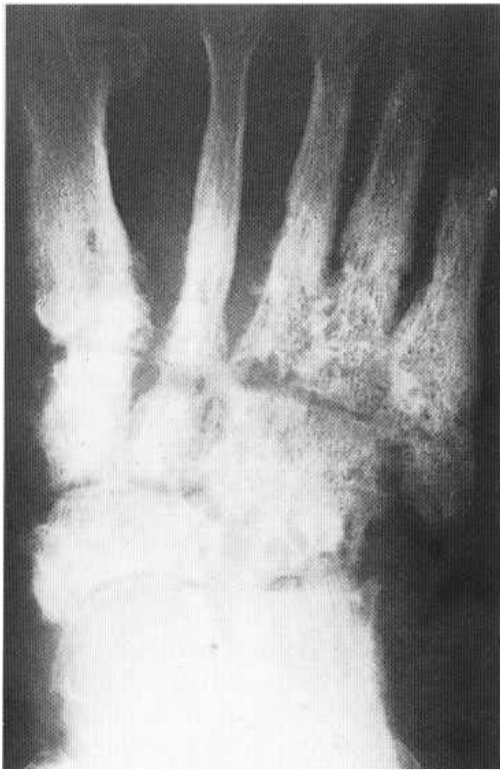


Fig. 36.59 Mycetoma (Madura foot)-diffuse infiltrating destruction affecting the whole tarsus and proximal ends of the metatarsals.

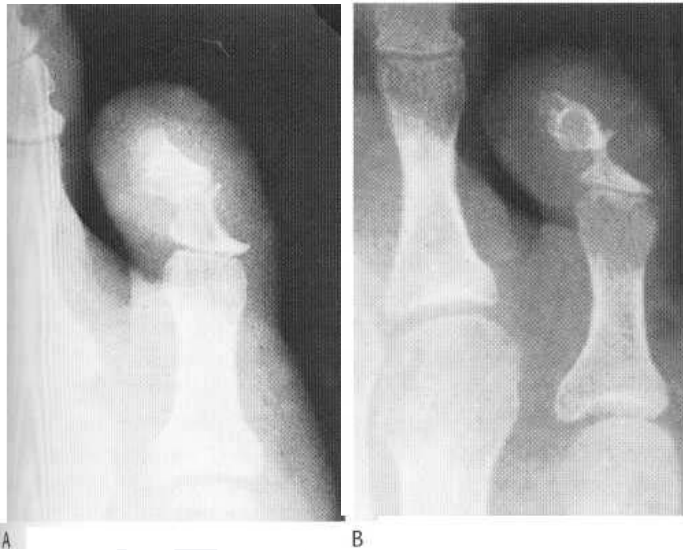


Fig. 36.60 Ainhum, showing progression of the lesion in an African immigrant. (B) was taken two years after (A).

but the end-stage appearances after secondary infection are usually similar.

AINHUM (Dactylosis Spontanea)

This is seen in 2% of the Nigerian population. The local word *avan*, from which ainhum is derived, means to saw or file-and a pointed fifth or, less commonly, fourth toe is found (Fig. 36.60).

A groove begins on the medial side of the base of the toe which deepens. This can be identified radiologically. As the constriction deepens, autoamputation occurs, leaving a pointed proximal phalanx of the little toe.

CONSTRICTION RINGS (Streeter's bands)

These rings cause similar congenital lesions of hands and feet, often in association with club foot.

REFERENCES AND SUGGESTIONS FOR FURTHER READING

- Chapman, M., Murray, R. O., Stoker, D. J. (1979) Tuberculosis of the bones and joints. *Seminars in Roentgenology*, 14, 266-282.
- Coekshott, P., Middlemiss, J. H. (1979) *Clinical Radiology in the Tropics*. Edinburgh: Churchill Livingstone.
- Enna, C. D., Jacobson, R. R., Rausch, R. O. (1971) Bone changes in leprosy: correlation of clinical and radiographic features. *Radiology*, 100, 295-306.
- Epstein, B. S. (1976) *The Spine*, 4th edn. Philadelphia: Lea & Febiger.
- Gohel, K., Dalinka, M. K., Edeiken, J. (1973) The serpiginous tract: a sign of subacute osteomyelitis. *Journal of the Canadian Association of Radiologists*, 24, 337-339.
- Golimbu, C., Firooznia, H., Ralii, M. (1984) CT osteomyelitis of the spine. *American Journal of Roentgenology*, 142, 159-163.
- Kolawole, T. M., Bohrer, S. P. (1970) Ulcer osteoma: bone response to tropical ulcer. *American Journal of Roentgenology*, 109, 611-618.
- Martini, M. (ed.) (1988) *Tuberculosis of the Bones and Joints*. Berlin: Springer.
- Modic, M. T., Feiglin, D. H., Piraino, D. W., et al (1985) Vertebral osteomyelitis: assessment using MR. *Radiology*, 157, 157-166.
- Murray, R. O., Jacobson, H. G., Stoker, D. J. (1990) *The Radiology of Skeletal Disorders*, 3rd edn. Edinburgh: Churchill Livingstone.
- Renton, P. (1991) Radiology of the foot. In: Klenerman, L. (ed.) *The Foot and its Disorders*, 3rd edn. Oxford: Blackwell Scientific.
- Resnick, D. (1995) *Diagnosis of Bone and Joint Disorders*, 3rd edn. Philadelphia: Saunders.
- Sharif, H. S., Aideyan, O. A., Clark, D. C., et al (1989) Brucellar and tuberculous spondylitis: comparative imaging features. *Radiology*, 171, 419-425.
- Smith, A. S., Weinstein, M. A., Mizushima, A., et al (1989) MR imaging characteristics of tuberculous spondylitis versus vertebral osteomyelitis. *American Journal of Roentgenology*, 153, 399-405.
- Unger, E., Moldofsky, P., Gatenby, R., Hartz, W., Broder, G. (1988) Diagnosis of osteomyelitis by MR imaging. *American Journal of Roentgenology*, 150, 605-610.
- Weaver, P., Lifeso, R. M. (1984) The radiological diagnosis of tuberculosis of the adult spine. *Skeletal Radiology*, 12, 178-186.



نشر الکترونیکی
موسسه انتشاراتی
نوردانش

37

AVASCULAR NECROSIS; OSTEOCHONDRITIS; MISCELLANEOUS BONE LESIONS

Peter Renton

with contributions from Ruth Green

OSTEONECROSIS (synonyms: aseptic necrosis, avascular necrosis, bone infarction)

The term 'osteonecrosis' implies that a segment of bone has lost its blood supply so that the cellular elements within it die. The phrase 'aseptic necrosis' indicates that infection generally plays no part in the process, though a sequestrum is also necrotic and avascular.

Pathology

Ischaemia of bone follows occlusion of arteries or veins and is therefore dependent on the anatomy of the blood supply to a given bone (a rise in venous pressure eventually arrests arterial supply). Anaemia results in death of haemopoietic tissue within 6-12 hours of the osteoclasts, osteoblasts and osteocytes within 12-48 hours; and of marrow fat in 2-5 days. Empty osteocyte lacunae indicate death of bone. Dead bone at this stage is radiologically normal since the trabecular framework remains intact.

Revascularisation is seen at the live marrow-dead marrow interface. The necrotic zone is invaded by capillaries, fibroblasts and macrophages. Fibrous tissue replaces dead marrow and in time may calcify. New osteoblasts lay down fresh woven bone on the devitalised trabeculae. This advancing front of neo-vascularisation and ossification has been termed 'creeping substitution' (Pheister).

At bone ends, cartilage receives nutrition from synovial fluid. Cartilage and subcartilaginous bone are not therefore necessarily affected.

Radiological changes

Stage 1 No changes are visible.

Stage 2 Disuse, for instance following immobility, leads to osteoporosis, except in devitalised avascular bone which is now devoid of osteoclasts and osteocytes. Avascular areas are of

normal or increased density, while immobile but vascular bone loses density. The avascular proximal pole of the scaphoid is dense after waist of scaphoid fractures.

Stage 3 At large joints—hips, shoulder, knee—a subcortical necrotic zone of translucency and trabecular loss beneath a thin and sclerotic cortex is shown (Fig. 37.1). This results in structural failure in subarticular bone at areas of maximal stress with cortical microfractures followed by collapse and trabecular compression (Fig. 37.2).

Stage 4 A flattened articular surface results with increased subarticular density as trabeculae are compressed (Fig. 37.3).

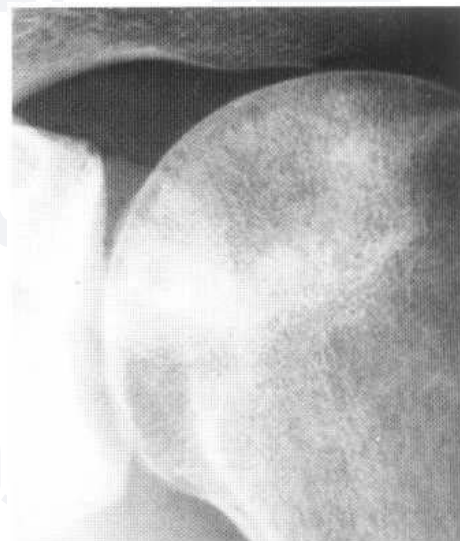


Fig. 37.1 Avascular necrosis. The cortex is thin and dense. There is a subcortical zone of demineralisation. The head also shows a zone of creeping substitution, seen as a serpiginous area of increase in density around the infarcted area.



Fig. 37.2 Early collapse of the right femoral head is demonstrated. The superior contour shows flattening. Creeping substitution is also demonstrated here.



Fig. 37.3 Avascular necrosis. Structural failure with fractures of both femoral heads. There is subarticular cyst formation and sclerosis resulting from trabecular compression.

Stage S Osteoarthritis with joint space narrowing follows later.

In the diaphysis and subarticular regions, the infarcted area is surrounded by a serpiginous line of sclerosis, representing the advancing front of new bone laid down on the old trabecular framework. The central area within the infarct may look relatively lucent, or may actually be the site of osteoclastic resorption, but it may also contain foci of added density representing dystrophic calcification in debris (Figs 37.2, 37.3).

In some diseases following infarction, a 'hone within a bone' or split cortex' is seen as a linear density lying within and parallel to the healthy cortex. This probably represents the old infarcted cortex left behind by processes of growth and remodelling beneath the vital periosteum. This change is seen in *Gaucher's* and *sickle cell disease*, and following *osteomyelitis* (Fig. 37.4).

Epiphyseal abnormalities Infarcts at growth plates, for instance in the hands and at the vertebral end-plates in sickle cell disease (Fig. 37.5), cause local arrest of growth or may result in 'cone' epiphyses or premature fusion. The latter also occurs after irradiation, infection or trauma.

Infarcted bone, for example following irradiation, is susceptible to fractures. This is seen in the ribs following irradiation for breast cancer and in the femoral necks after pelvic irradiation, though it is less common nowadays.



Fig. 37.4 Sickle cell disease. There is widespread sclerosis of bone following infarction. The hip joint space is narrowed and the femoral head has migrated superolaterally. This may be the result of infection. A split cortex or bone-within-a-bone appearance is seen within the proximal femur (arrows).

Isotope scanning

Changes in the isotope scan reflect the stages of the disease from photopenia in early avascular necrosis to increase in uptake when healing with vascular ingrowth takes place (Fig. 37.6).

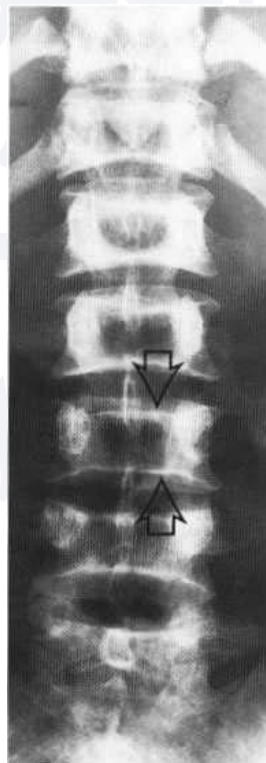


Fig. 37.5 End-plate infarcts in sickle cell disease. Failure of growth following infarction of end-arteries in the vertebral body results in horizontally aligned defects (arrows), as opposed to the more usual concave defects seen as a result of bone softening.

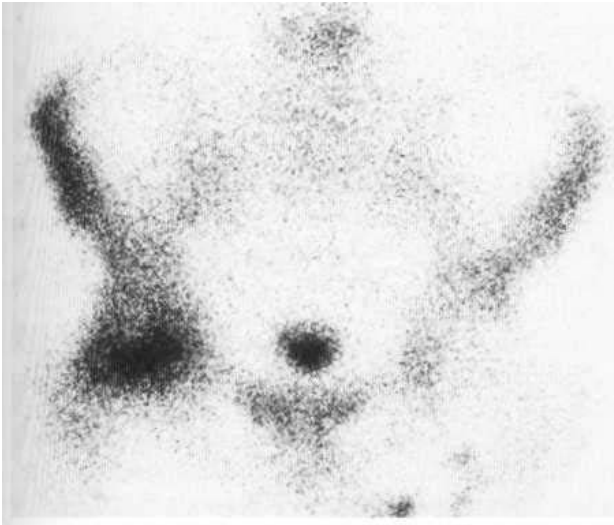


Fig. 37.6 Radioisotope bone scan in avascular necrosis. Increase in uptake is demonstrated around the infarcted area, indicating healing at the margins of the infarct.

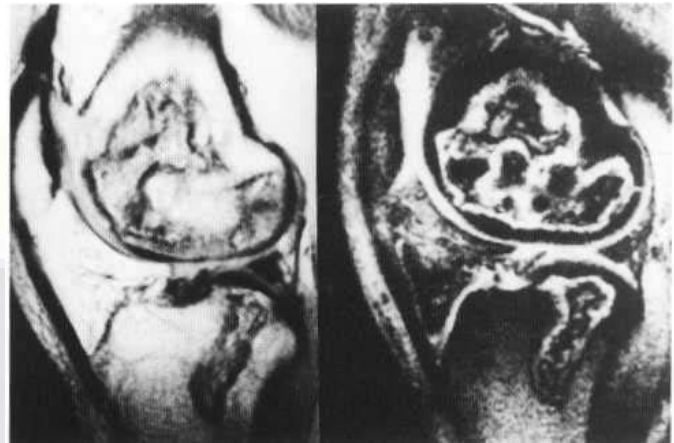


Fig. 37.8 Avascular necrosis. Changes are demonstrated on T₁- and T₂-weighted images on both sides of the joint. Areas of infarcted bone are demonstrated surrounded by fluid. There is also an effusion in the joint.



Fig. 37.7 Avascular necrosis. Coronal T₁-weighted images of the hip showing a serpiginous zone of low signal around the avascular areas.

MRI

MR scanning is the most sensitive and accurate means of detecting changes in avascular necrosis. Sensitivity and specificity for avascular necrosis approach 100%, while false-negative isotope scans occur early on in the disease.

Changes at MRI are usually seen in the anterosuperior segment of the femoral head. Initially, bright signal remains in the affected area but subsequently, after a week, this decreases corresponding to progressive lymphocytic infiltration and fibrosis. Radiographs remain normal.

A serpiginous zone of low signal on T₁- and T₂-weighted images develops around the avascular area, internal to which a zone of bright signal may be seen on T₂-weighted images; this represents oedema or vascularity (Fig. 37.7). Haemorrhage, cyst formation, fibrosis and collapse of bone alter the shape and signal in the femoral head. Haemorrhage and cysts are of intermediate signal on T₂-weighting, but bright on T₂-weighted and STIR sequences. Sclerotic bone radiologically is of low signal on all sequences.

Anatomical changes of bone collapse and deformity may be seen on plain radiographs, CT and MR scans, but MRI is the most sensitive modality in the diagnosis of early disease. Sagittal, coronal and axial images allow optimal assessment of the extent of the disease. The vascular response in healing can also be assessed (Fig. 37.8).

Causes of osteonecrosis (Box 37.1)

Vascular insufficiency to bone is of three types.

1. *Interruption to the flow of blood* to bone most commonly follows trauma with tearing of blood vessels.
2. *Emboli or studging*. This occurs in *sickle cell disease* where abnormal red cells aggregate; in *pancreatitis* where fat emboli obstruct vessels; and in *decompression disease* where possibly gas bubbles occlude small vessels. Vasculitis, in collagen disorders and following irradiation, also occludes small vessels.
3. *Intraosseous compression of vessels* occurs in *Gaucher's disease*, where masses of Gaucher cells pack marrow spaces.

The role of drugs in avascular necrosis

Steroids and non-steroidal anti-inflammatory drugs are associated with bone necrosis.

Pain relief and euphoria associated with prolonged dosage lead to overuse of often already damaged joints and a Charcot-type lesion results with bone loss and eburnation. Similar changes may follow alcohol abuse. In addition, steroids cause vasculitis and marked sub-cortical osteoporosis which further potentiates bone collapse.

OSTEOCHONDRITIS (osteochondrosis)

Osteochondritis is a disease of epiphyses, beginning as necrosis and followed by healing. The term 'osteochondritis' is used to describe

Box 37.1 Conditions associated with spontaneous aseptic bone necrosis

Alcoholism**	Hyperlipaemia**
Arthropathy	Hypertension
Rheumatoid arthritis**	Hypertriglyceridaemia**
Psoriasis	Hyperuricaemia**
Neuropathic	Immobilisation
Osteoarthritis	Immunosuppressive therapy*
Clotting defects	Irradiation*
Convulsive disorders	Microfractures
Cushing's syndrome*	Mitral insufficiency
Decompression syndrome*	Myxoedema
Diabetes**	Obesity
Endocarditis	Pancreatitis**
Fat embolism**	Peripheral neuropathy
Giant cell arteritis	Peripheral vascular disease
Gout**	Periarthritis nodosa
Haemoglobinopathy*	Pregnancy
Haemopoietic disorders*	Systemic lupus erythematosus**
Haemophilia	Thermal injuries*
Gaucher's disease	Burns
Histiocytosis	Electrical
Polycythaemia	Frostbite
Hyperadrenocorticism*	Trauma*
Hypercholesterolaemia	

*General accepted contributory factor.
 **Commonly reported associated factor.
 Reproduced from 1. K. Davidson (ed.), *Aseptic Necrosis of Bone*, by kind permission of Excerpta Medica, Amsterdam.

the lesions but is a misnomer, as: (i) there is no inflammation; and (ii) cartilage is not primarily involved. Over 40 sites have been described and all have eponyms which are too closely associated with the lesions to be currently abandoned (Table 37.1).

The mechanism of pathological change is not identical at all sites. Some changes, such as in Perthes' disease, are generally regarded as being due to vascular occlusion. The mechanism for this is not clearly understood, especially as in some patients an osteochondritis affects more than one epiphysis. At other sites—the tibial tubercle and the lower pole of patella—tendons avulse bone which subsequently necroses. Vertebra plana follows eosinophilic granuloma. Adolescent kyphosis may follow distal herniation into end-plate defects.

Table 37.1 Types of eponymous osteochondritis

Disease	Cause	Site
Legg-Calve-Perthes	Primary aseptic necrosis	Femoral head
Kohler's	? Primary aseptic necrosis ? Necrosis following fracture	Tarsal navicular
Freiberg's	? Primary aseptic necrosis ? Necrosis following fracture	Metatarsal head
Kienbock's	? Necrosis following fracture ? Primary aseptic necrosis	Lunate
Osgood-Schlatter	Necrosis following partial avulsion of patellar tendon	Tibial tubercle
Sinding-Larsen	Necrosis following partial avulsion of patellar tendon	Lower pole of patella
Sever's	Necrosis following partial avulsion of tendo-Achillis	Calcaneal apophysis
Calve's	Eosinophilic granuloma	Vertebral body epiphysis
Scheuermann's	Disc herniation through defective end-plate	Ring-like epiphysis of vertebra

Reproduced from J.K. Davidson (ed.), *Aseptic Necrosis of Bone*, by kind permission of Dr. Mary Catto, and Excerpta Medica, Amsterdam.

Epiphyseal areas of necrosis eventually heal and are converted into normal bone. In some sites, especially at the femoral head, prominent metaphyseal changes are also present.

The irritable hip syndrome

A few patients with this syndrome (up to 7%) develop changes of Perthes' disease. The affected children present with acute hip pain and often fever and a raised ESR. Most cases resolve with simple bed rest, but prolonged immobilisation and traction may be necessary. Other causes of acute hip pain—infection or juvenile arthritis—must be excluded.

The initial examination of the painful hip in a child should be an AP radiograph. This will exclude gross pathology, but may show an effusion with joint space widening and fat plane displacement. A 'frog' or lateral view may exclude early avascular necrosis or slipped femoral capital epiphysis. Ultrasound should be performed to exclude effusion or infection and, if necessary, can be followed by hip aspiration.

Osteochondritis of the femoral capital epiphysis (synonym: *coxa plana*; eponyms: *Waldenström* (1909), *Legg* (1910), *Calvé* (1910), *Perthes* (1913))

This condition is commoner in boys than girls (M : F = 4 : 1) and most cases present between 4 and 9 years of age. The age of onset is earlier in girls and the prognosis worse.

Bilateral disease is even more common in boys (M : F = 7 : 1) but the disease is rarely symmetrical. If symmetry is present, *hypoplvroidism* or *multiple epiphysal dysplasia* should be excluded. There is no increased familial incidence, but parents of affected children are often elderly. Many of the affected children have a below-average birthweight and, at presentation, show skeletal growth retardation in the hands. This is especially seen in boys. There is an increased incidence of associated congenital anomalies, including congenital heart disease, pyloric stenosis, hernia, renal anomalies and undescended testes.

Following ischaemia, the ossific nucleus of the epiphysis necroses, causing growth arrest. The overlying cartilage, which is supplied by synovial fluid, survives and thickens especially in the non-weight-bearing regions, medially and laterally. Dense, necrotic bone resorbs and is slowly replaced by vital bone. The pre-disease

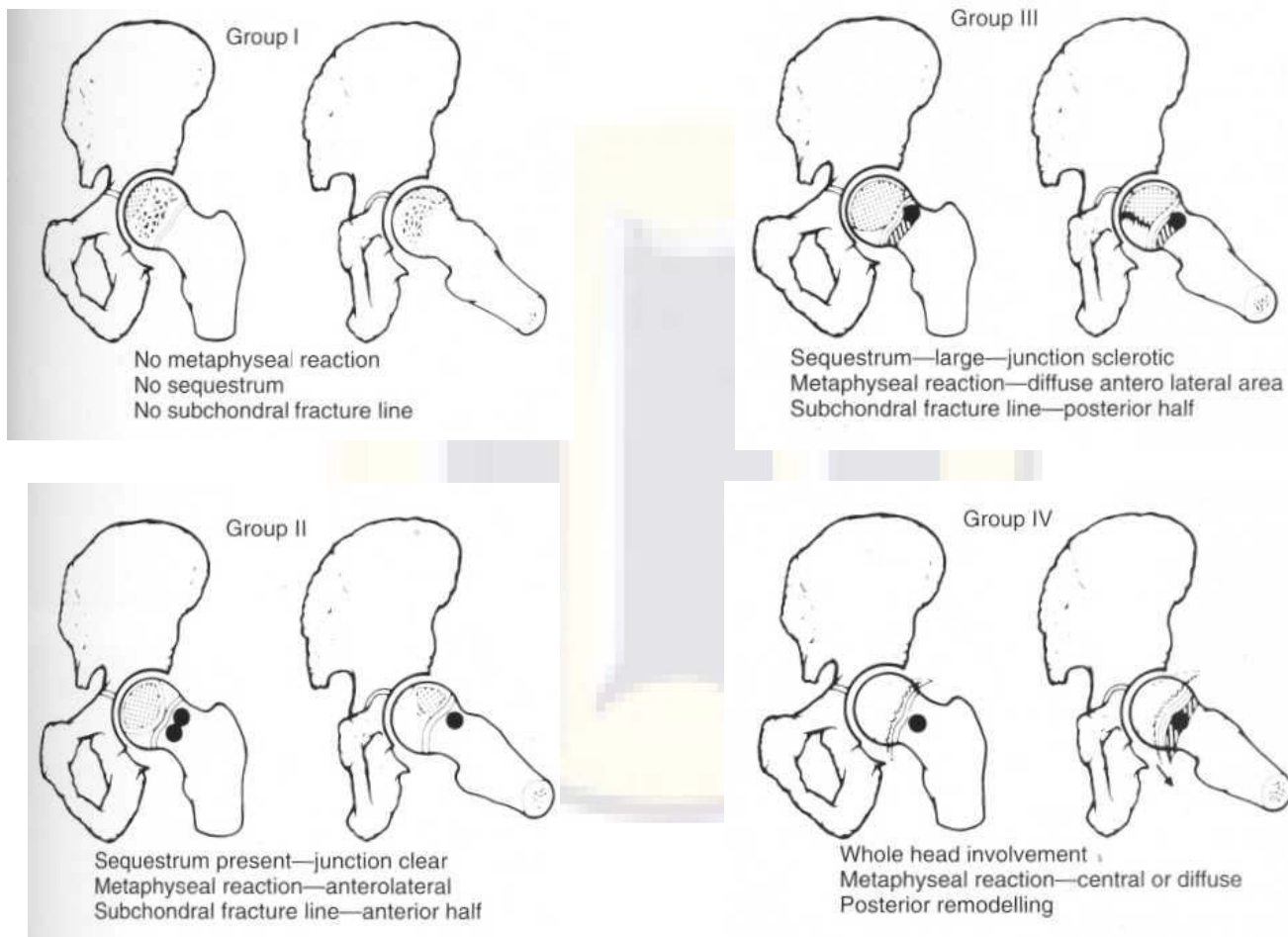


Fig. 37.9 Catterall classification of Perthes' disease. (Reproduced by courtesy of Mr A. Catterall, FRCS; see list of Further reading.)

shape of the necrotic nucleus does not return to normal and the nucleus ends up flat in whole or in part.

Catterall (1971) has grouped Perthes' disease according to the degree of epiphyseal involvement as assessed radiologically (Fig. 37.9). Prognosis depends on the degree of radiological involvement.

Stages of the disease

These occur within each group. There is an *initial* phase of onset, with widening of the joint space and increased density of all or part of the ossific nucleus, which is followed by collapse of part or all of the nucleus, according to group. *Repair* removes the fragmented, crushed necrotic bone. *Healing* shows as an increase in size and re-ossification (Fig. 37.10). *Remodelling* then occurs and is aided when the femoral head is completely contained within the acetabulum. Uncovering of the lateral margin of the femoral head has a bad prognosis.

The metaphyseal lesion leads to an abnormal femoral neck (Fig. 37.11). The most severely involved cases have a broad, short neck, that is, the neck length/width ratio is lower than normal (Fig. 37.10).

Prognosis

The prognosis in untreated disease is proportional to the degree of epiphyseal involvement. Thus, Group I and Group II patients have a good prognosis.

Radiological features

1. *Lateral displacement of the femoral head.* Early on, and in the irritable hip syndrome, displacement of the femoral head (Waldenstrom's sign) is seen (Fig. 37.12A), possibly due to effusion or to thickening of the ligamentum teres. Later, the superior part of the joint may also be widened. These changes may be seen on ultrasound.

2. *A subcortical fissure in the femoral ossific nucleus.* This sign is seen early in the disease but is transient. It is best seen in the 'frog' lateral view (Fig. 37.12B).

3. *Reduction in size of the ossific nucleus of the epiphysis.* This is found in some 50% of cases and is due to growth retardation. The medial joint space then seems wider.

4. *Increase in density of the femoral ossific nucleus.* This is due to trabecular compression, dystrophic calcification in debris and creeping substitution repair, with laying down of new bone on the pre-existing trabeculation (Fig. 37.10).

5. *Metaphyseal broadening and irregularity.* The neck may end up shortened (Fig. 37.11).

Arthrography

It must be understood that the ossific nucleus is not the entire femoral head and, in Perthes' disease, the cartilaginous outline of the femoral head is essentially normal and not flat, irregular and fragmented, as the ossific nucleus may be. Arthrography does not diagnose Perthes' disease but determines: (i) the size and shape of

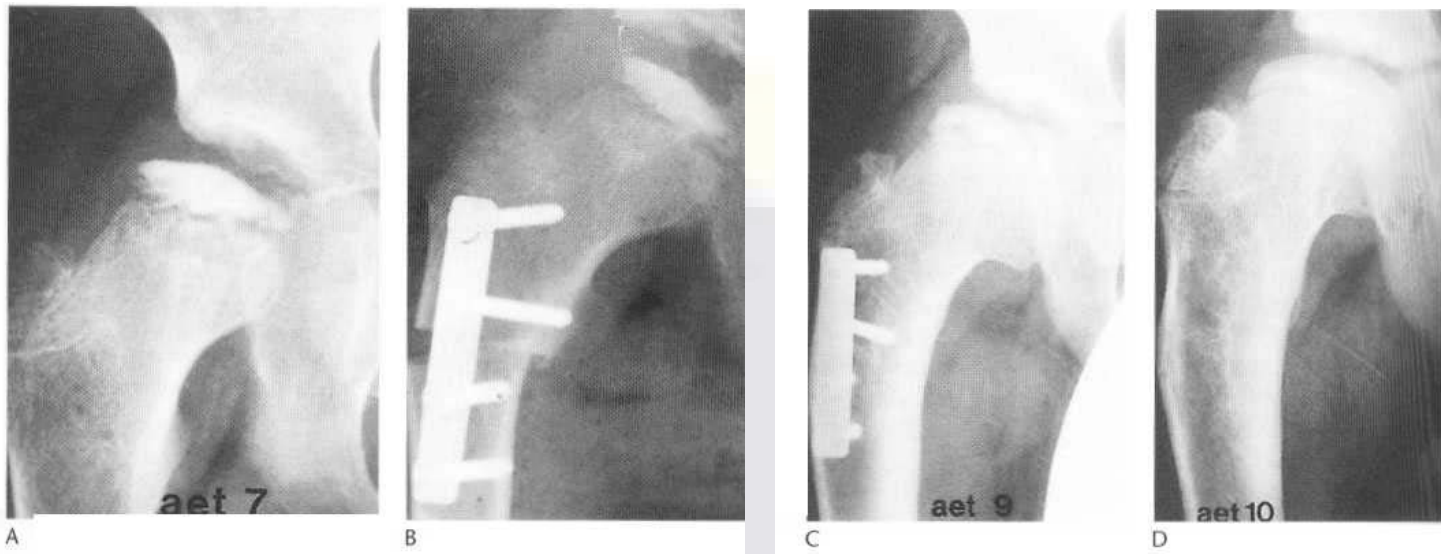


Fig. 37.10 Perthes' disease. A series of radiographs showing the stages of healing. (A) The initial radiograph shows a flattened, sclerotic femoral head. (B) An osteotomy is performed. (C, D) Later films show resorption of the sclerotic dead bone and its replacement with vital bone, resulting in a mushroom-shaped femoral head.



Fig. 37.11 The left femoral neck is broadened, the metaphysis sclerotic with focal areas of lucency, the growth plate irregular and the femoral head flattened and sclerotic. It is uncovered laterally. The joint space appears widened.

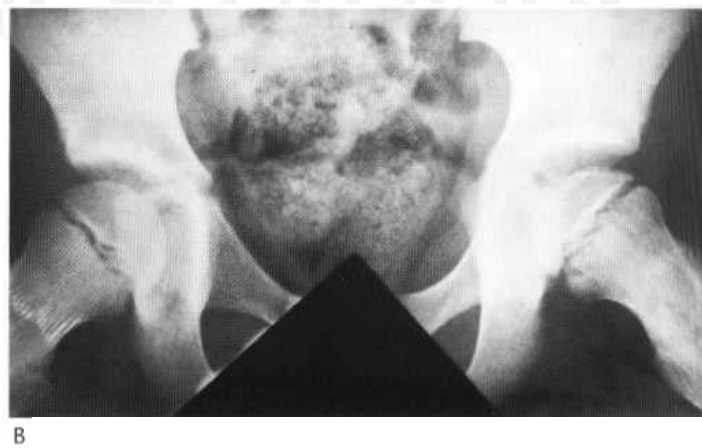
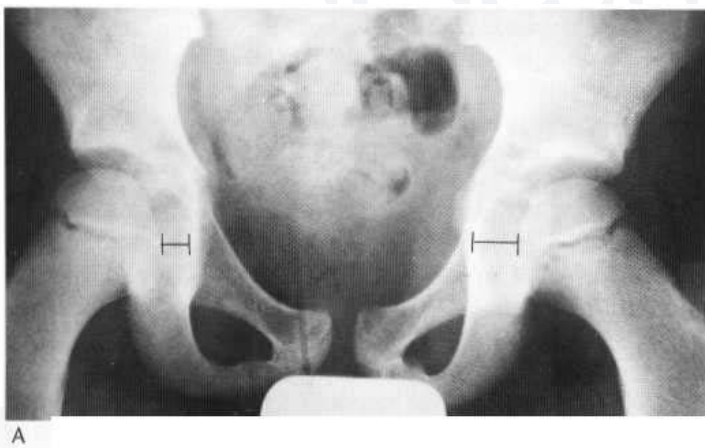


Fig. 37.12 (A) In this patient with an irritable hip, there is widening of the medial joint space. (B) A later film in the frog lateral position shows a vacuum phenomenon in the normal right hip but, on the left, elevation of the fragmented anterosuperior articular cortex of the femoral head. The femoral head also appears flattened locally.

articular cartilage; and (ii) the presence or absence of congruity (Fig. 37.13).

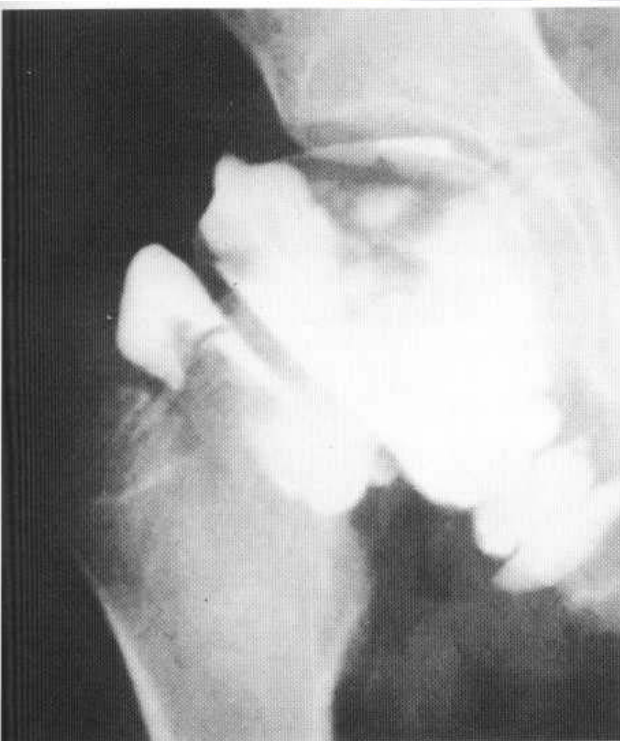
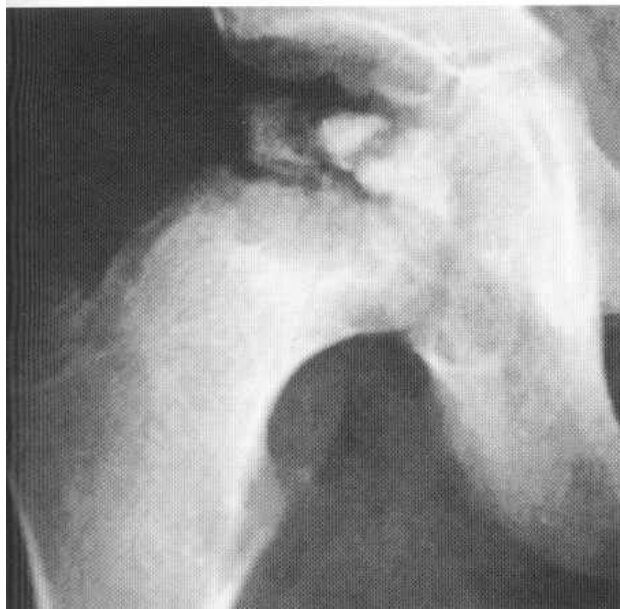
Ultrasound

This can also be used to assess hip joint effusions in children. By scanning in the sagittal plane from the front of the patient an image of the hip is obtained (Fig. 37.14). If there is at least 3 mm of fluid depth, a difference between the two sides of 2 mm, and convexity of the capsule, then a decision can be made to aspirate fluid, so excluding infection and relieving pain (Marchal et al 1987).

Radionuclide bone scanning

Technetium scan images of bone depend in part on blood flow to bone. Avascular areas therefore are seen as scan defects. Nuclide scanning of a painful hip distinguishes a 'cold' area in infarction from an area of increased uptake in infective or inflammatory disease. It seems logical to scan all children with acutely painful hips.

In the early stage, when no radiological abnormality is yet visible in the child with an avascular lesion, a defect is seen in the femoral head image on radionuclide scanning. In the early case, the size of the defect on the scan correlates well with the eventual size of the



A

B

C

Fig. 37.13 (A) Gross Perthes' disease of the femoral head. (B) The outline of the cartilaginous epiphysis is somewhat dome shaped with slight flattening and broadening laterally. The lateral aspect of the femoral head is uncovered but in the neutral position is in congruity. (C) In abduction there is pooling of contrast agent medially within the joint.

defect on radiography, which only becomes assessable some 6-9 months after the initial nuclide scan (Fig. 37.15).

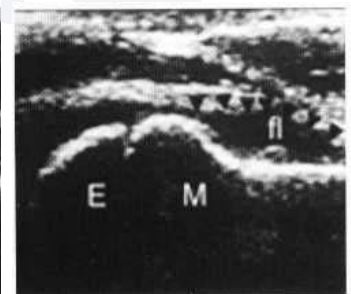
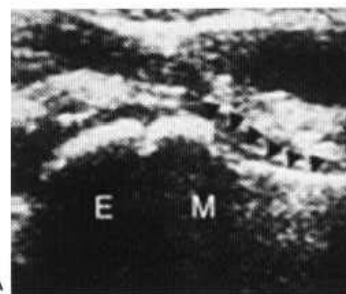
In cases of established disease, correlation of the scan defect with radiological change is less helpful, as revascularisation gives a local increase in activity, so that the defect size is underestimated.

MRI

MRI changes are seen in bone and cartilaginous structures of the femoral head and acetabulum.

The ossific nucleus flattens and the normal bright signal related to marrow fat diminishes following loss of the normal circulation. The signal seen from this region varies with the stage of disease and healing, and may range from low early on in the disease to a mixture of high and low when revascularisation occurs or if cysts are present. The bone deformity is visualised. Metaphyseal irregularity is seen and an abnormal relationship of the entire head to the acetabulum shown (Fig. 37.16).

MRI also shows thickening of the non-ossified cartilage of the femoral head, especially laterally, and of the acetabulum, especially the labrum. This change of cartilaginous hypertrophy is reproducible experimentally after ligation of the epiphyseal arterial supply, and is seen at arthrography, which is invasive, as well as at MRI. The degree of acetabular covering of the developing femoral head, as well as articular congruity, is seen both at MRI and arthrography, though arthrography allows the relationship between the head and socket to be assessed dynamically as a precursor to surgery (Fig. 37.17).



A

B

Fig. 37.14 Sagittal scan of a child's hip. In (A) and (B) the high echogenicity of the cortical bone of the epiphysis (E) and metaphysis (M) are noted. The (VV) indicate the joint capsule, in (A) this is concave along the femoral neck but in (B) this is convex to the femoral neck beneath which there is anechoic fluid (fl).

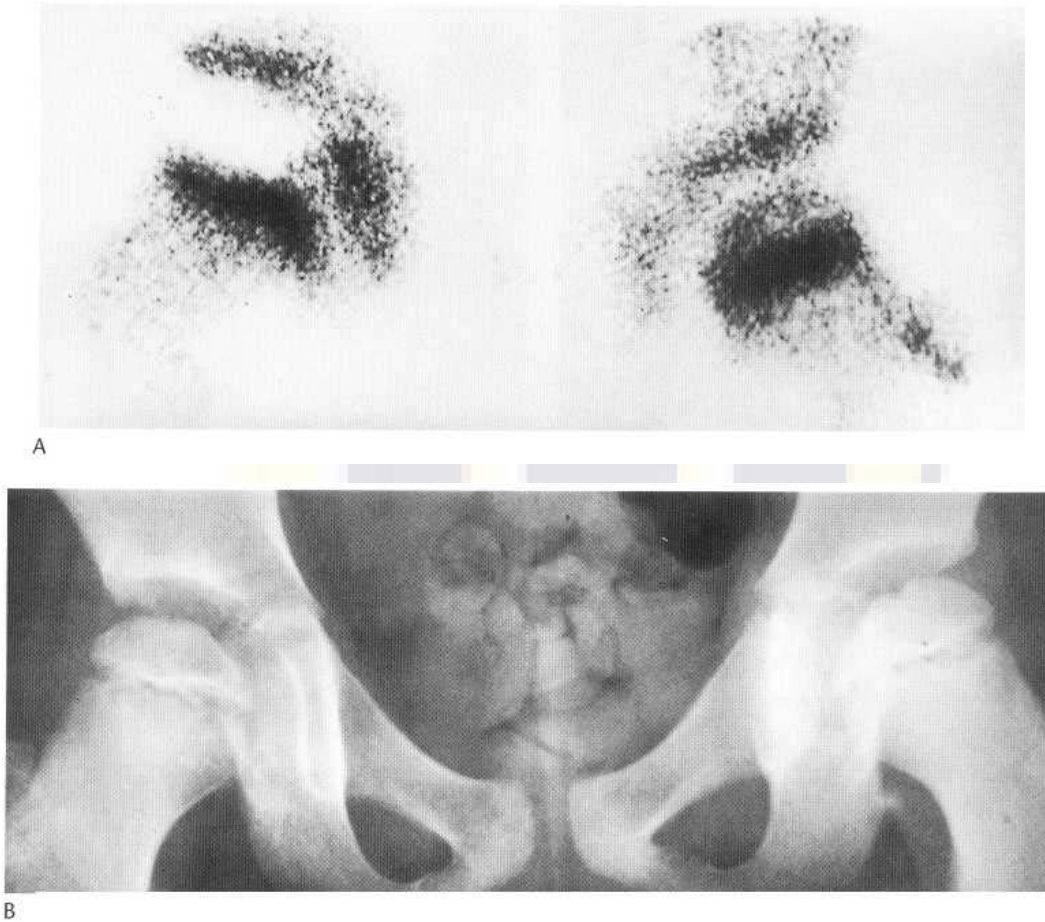


Fig. 37.15 Perthes' disease. (A) The lateral aspect of the right femoral head does not show up on radionuclide scanning. (B) On X-ray, the involved area looks smaller than on the scan. The right ossific nucleus is flattened, irregular and smaller than that on the normal left side. It shows collapse. The growth plate and metaphysis are irregular.

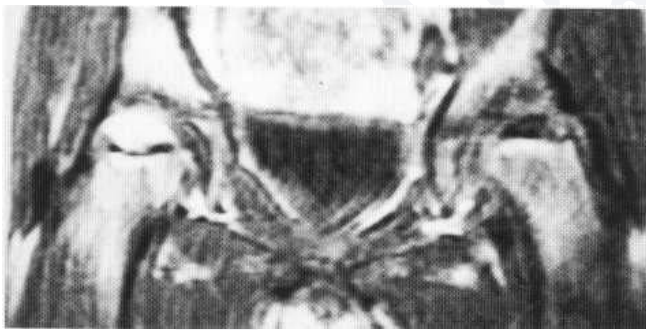


Fig. 37.16 Perthes' disease. A T₁-weighted MR scan showing collapse of the left femoral head with avascular changes. The head is subluxated laterally in addition, and is uncovered laterally. Note the movement artefact.

Osteochondritis of the tibial tubercle

(eponyms: Osgood's disease, Schlatler's disease)

The diagnosis is essentially clinical and is confirmed radiologically by a soft-tissue lateral film of the area. This demonstrates local soft-tissue swelling over an often fragmented and dense tuberosity (Fig. 37.18). The other knee should also be examined radiologically, especially to compare the soft tissues. The condition is usually self-limiting and rest brings relief of symptoms.



Fig. 37.17 Left hip arthrogram in Perthes' disease. The flattened fragmented ossific nucleus of the femoral head is shown to lie within the capital cartilage. This flattens as a result of the central ossific nuclear flattening. In abduction there is substantial incongruity with pooling of contrast superomedially.



Fig. 37.18 Osgood-Schlatter disease. Fragmentation of the tibial tuberosity with thickening of the ligamentum patellae.



Fig. 37.20 Osteochondritis of the second metatarsal head. (A) Minimal change of increased density of the epiphysis. (B) Later stage of flattening of the epiphysis, increased joint space and loose body separation.



Fig. 37.21 Calve's disease (vertebra plana) (arrows) of a midthoracic vertebral body. Complete regeneration occurred. No evidence of histiocytosis was found on biopsy.



Fig. 37.19 Osteochondritis of the tarsal navicular.

The tubercle fuses to the shaft at 15 years, but occasionally remains unfused and fragmented. Examination of soft tissues will rule out ongoing disease.

Osteochondritis of the tarsal navicular

(eponym: Köhler's disease I)

As in Osgood-Schlatter disease, the combination of pain and radiological change is needed for the diagnosis to be made. The disease is much more common in boys. The age incidence is 3-10 years, with the peak between 5 and 6 years, and the disease appears earlier in girls—as does the ossific nucleus itself. The process is thought to be ischaemic in origin. Between 15 and 20% are bilateral.

Radiographic appearances

Irregularity of the outline of the navicular and fissure formation are early signs. The bone may appear later as a mere dense disc (Fig. 37.19). No loss of cartilage on either side of the bone occurs. The onset of regeneration is shown by the production of new bone around the compression disc.

Osteochondritis of the metatarsal head

(eponyms: Freiberg's infraction, Köhler's disease II)

The second metatarsal head is most frequently involved. The condition is commoner in girls. Its usual incidence is between 10 and 15 years. There is a history of chronic trauma, for example girls wearing high-heeled shoes for the first time.

Radiographic appearances

Condensation, increased density (Fig. 37.20) and fragmentation of the epiphysis are seen. The joint space may be increased in size and the opposing bone surfaces greatly splayed. Gradual thickening of the metatarsal neck and shaft occurs.

Osteochondritis of the vertebral body

(synonym: vertebra plana; eponym: Calvé's disease)

This condition is manifested by collapse and increased density of a vertebral body; the adjacent disc spaces are normal or increased in width (Fig. 37.21). Recovery to normal shape follows, but it may be incomplete.

Most cases may be shown to be a manifestation of *histiocytosis*. Regeneration is expected but histiocytosis may be associated with paraplegia. *Leukaemia*, *Ewing's sarcoma*, *metastases*, *tuberculosis*, etc. may cause similar appearances and should always be excluded before a diagnosis of Calve's disease is accepted.

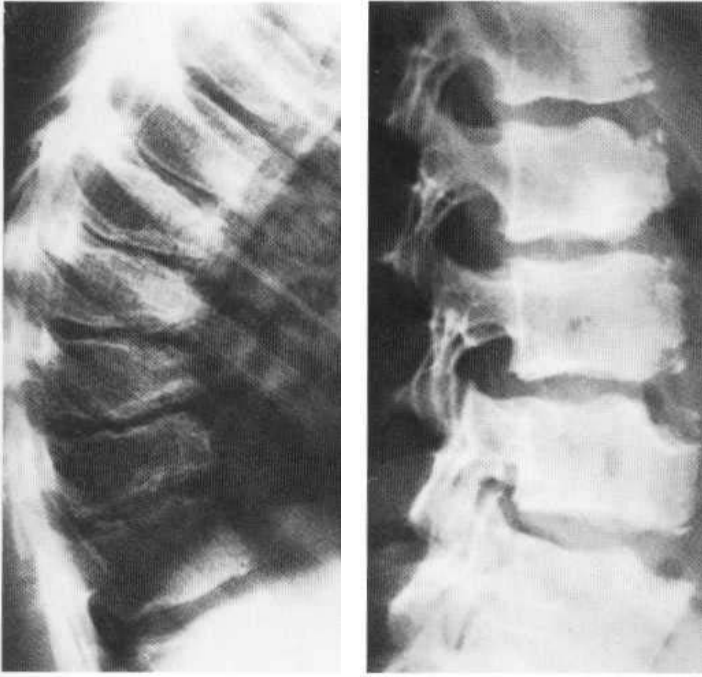


Fig. 37.22 Adolescent kyphosis (advanced case). **Fig. 37.23** Osteochondritis of lumbar vertebral bodies.

Adolescent kyphosis (synonyms: vertebral epiphysitis, osteochondritis of vertebral epiphyseal plates; eponym: Scheuermann's disease)

The condition affects both sexes; it usually begins at puberty, having peak incidence from 15 to 16 years. The mid and lower thoracic spine is the region most commonly affected and usually several adjacent vertebrae are involved (Fig. 37.22). Less frequently, the lesion may be found in the lumbar spine (Fig. 37.23) and in the upper thoracic spine. Sometimes changes are confined to a single vertebra.

Radiographic appearances

Irregularity is seen affecting the superior and inferior parts of the vertebral bodies. Later, wedging of vertebral bodies and kyphosis appear. Some scoliosis may also be present. Schmorl's nodes are seen and disc spaces become narrowed. Sometimes a small paraspinal bulge is observed at the level of the lesion.

The radiographic picture tends to remain static for a while. Improvement is slow and consolidation may take several years. Radiographic recovery is often incomplete: various degrees of irregularity and wedging of thoracolumbar vertebrae may be permanent. Indeed, evidence of old adolescent kyphosis is one of the most frequent abnormalities seen in spinal radiographs.

No constitutional effects are found in adolescent kyphosis and the vertebral defects are bounded by sclerotic rims, which are not seen in tuberculous lesions.

Residual wedging in late cases may be indistinguishable from that caused by a previous compression fracture. The ring apophysis may be displaced by discal herniation, never to unite. It is then seen as a triangular fragment of bone adjacent to the end-plate. Discography shows a disc filled with contrast medium which extends between the vertebral body and the detached fragment of bone.

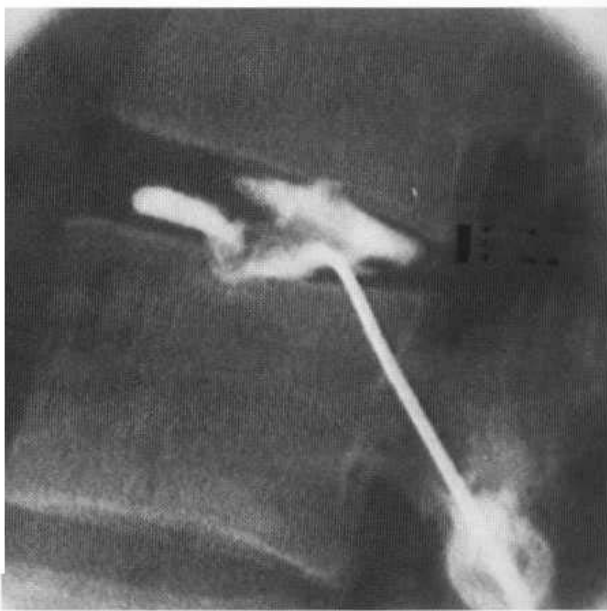


Fig. 37.24 (A) T₂-weighted sagittal MR scan of the lumbar spine showing rounded, fairly central end-plate defects into which distal material is herniated. (B) The discogram of the same patient shows the distal herniation into the defects.

Changes at MRI reflect changes seen on the plain film (and at discography) (Fig. 37.24). The affected disc is narrowed and usually shows a loss of signal, indicating dehydration. The disc is seen to herniate into the end-plate defect and beneath the non-fused ring apophysis.

Osteochondritis at other sites

Most osteochondritis is found in the hip or spine. Other sites include:

1. *Capitellum*.
2. *Patellaprimary centre* (Kbhl'er's disease) (Fig. 37.25).
3. *Patella-secondary centre* (Sinding-Larsen disease). Some cases are associated with Osgood-Schlatter disease. This condition



Fig. 37.25 Osteochondritis of the patella-primary centre. Irregularity, fragmentation and sclerosis of the body of the patella in an immature skeleton.

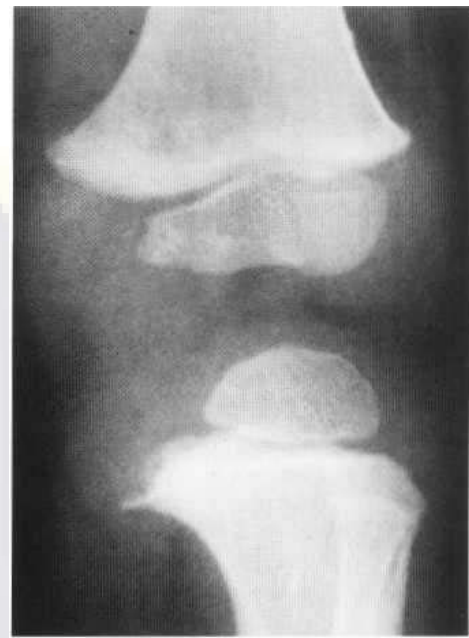


Fig. 37.27 Blount's disease. There is a large medial spur at the upper tibial metaphysis with irregularity of the bone adjacent to the growth plate.



Fig. 37.26 Sinding-Larsen disease. A good plain film will demonstrate thickening of the ligamentum patellae origin, together with irregularity of the bone from which it originates. The lower pole seems irregular and lengthened. In later life, elongation of the patella inferiorly is probably the result of this disease in adolescence.

is also almost always due to an avulsion strain by the patellar ligament (Fig. 37.26).

4. *Tibia Vara* (osteochondritis of the medial tibia) condyle-Blount's disease). This change may be seen from the first to the 12th year of age, but is most common in the earlier age group. As the name implies, the abnormality is usually to be seen on the medial aspect of the knee joint. An irregular defect is often present on the medial aspect of the proximal tibia metaphysis beneath which a large and prominent spur sticks out, almost at right angles (Fig. 37.27). The adjacent aspect of the tibia epiphysis may be defective, and a local femoral spur may also be seen. The overall effect is a varus deformity. The lateral aspect of the proximal tibia metaphysis is straight, and not bowed as in physiological bow-legs. The changes are possibly related to early onset of walking.

Osteochondritis in adult bones

Often a closer link with trauma is seen in adult osteochondritis than in juvenile cases, but this is not always so. Sites subject to trauma include the *scaphoid*, the *carpal lunate* (Kienbock's disease) (Fig. 37.28), the *tarsal navicular* and the *medial sesamoid bone of*

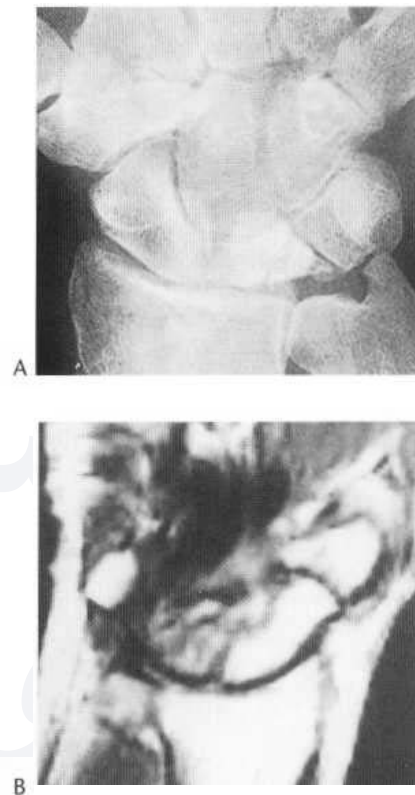


Fig. 37.28 (A) osteoarthritis of the lunate bone (Kienbock's disease). (B) Avascular necrosis of the lunate. On MR scanning the lunate shows a mixed signal, with patchy areas of low and high density. Compare with the normal signal coming from the scaphoid.

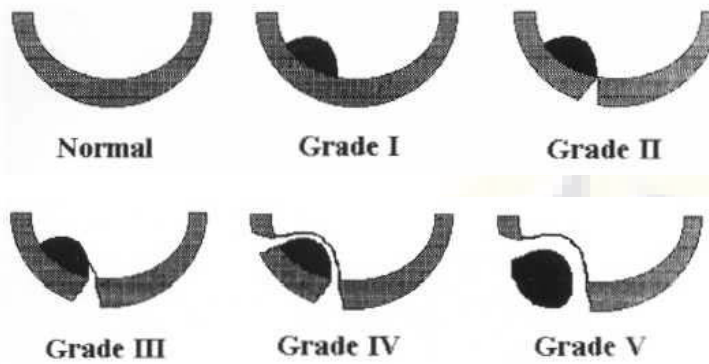


Fig. 37.29 Classification of osteochondral lesions. Grade I-the dissected fragment is shown in black; the overlying cartilage is intact. Grade II-there is a small localised cartilage defect. Grade III-the defect extends through the cartilage and around the bone, but is only partial. Grade IV-there is a total defect around cartilage and bone, but no displacement of fragments. Grade V-a loose detached fragment is seen.

the great toe, as well as the *os trigonum*. Fragmentation, collapse and sclerosis, perhaps with cyst formation, are seen on the plain film. CT demonstrates these changes and allows reconstruction in any plane. MR scans show the changes in anatomy and a mixture of low signal indicating collapse, bone condensation and sclerosis as seen on the plain film, as well as the bright signal of fluid or cyst formation and vascularity indicating healing.

Osteochondritis dissecans

In this condition fragments of articular cartilage, with or without subchondral bone, become partially or completely detached at characteristic sites (Fig. 37.29). The separated fragment is avascular, in contradistinction to that at an osteochondral fracture, and the 'bed' of the defect remains vital, in contradistinction to avascular necrosis.

Sites of election are convex articular surfaces; for example, the medial femoral condyle, the capitellum of the humerus and the trochlear surface of the talus. The lesion is twice as common in males as in females and about one-third of all cases are bilateral. In some patients several epiphyses are affected. The condition is not always symptomatic. The lesion characteristically occurs in adolescence and early adult life. It is the commonest cause of a loose body in the joint of a young adult. The present tendency is to emphasise the role of trauma in the aetiology of this lesion.

Radiographic features

In early cases it may be necessary to take several views of the joint in different degrees of obliquity in order to demonstrate the lesion adequately. Conventional topography is often helpful, and arthrography is sometimes useful.

When separation of the fragment is being established, one will see a radiolucent ring surrounding the bony fragment when viewed from the front; the loosening fragment may be seen opposite a pit in the bone when viewed in profile (Figs 37.30, 37.31). The loose

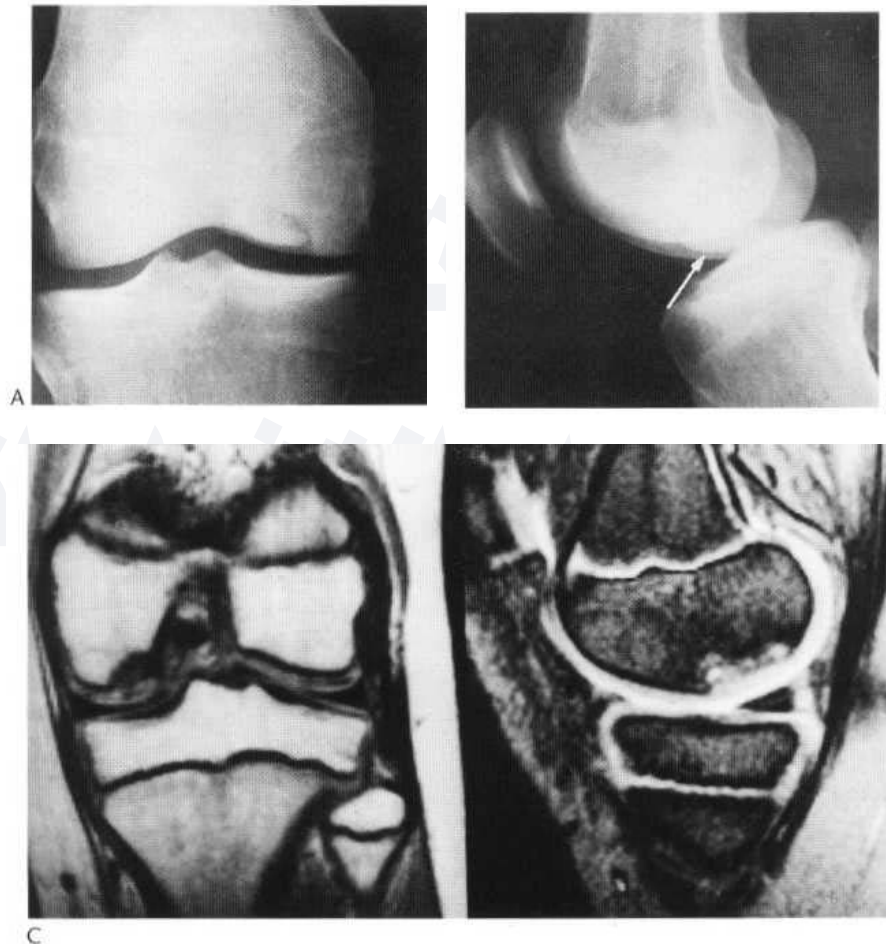


Fig. 37.30 (A,B) Osteochondritis dissecans of the medial femoral condyle (arrow). (C) T, coronal and sagittal fat-suppression images of the knee demonstrating osteochondritis dissecans at a typical site. On the latter image, the defect is seen to contain fluid.



Fig. 37.31 Osteochondritis dissecans of the medial part of the articular surface of the talus.

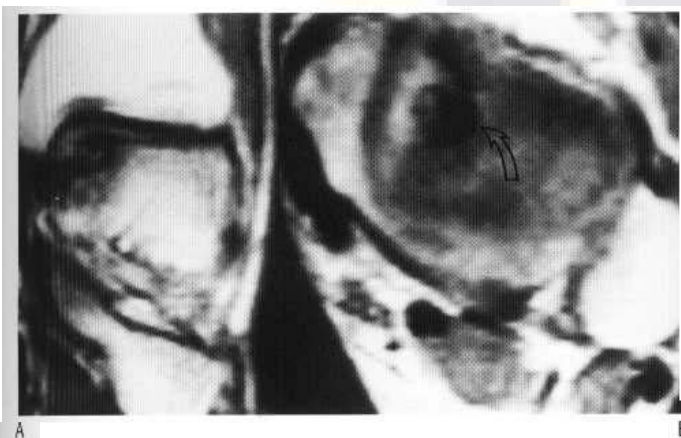


Fig. 37.32 Osteochondritis of the talar dome. (A) The medial corner of the talus is a very common site for osteochondral defects, seen as a low signal change on this coronal T₁-weighted MR sequence. (B) The lesion is also seen on the adjacent axial image (arrow).

fragments are usually small and ovoid in shape though they may be larger and irregular.

The fragment may become completely separated and form an intra-articular loose body. If entirely cartilaginous in content, the image of the loose body will not be seen on routine radiographs but it may be demonstrable by arthrography or at MRI (Fig. 37.32). If not removed surgically, the loose body may grow and calcify later; it is able to obtain adequate nourishment from synovial fluid even when it is completely detached from its parent bone. However, the fragment may not become free, but may become absorbed leaving a residual gap in the underlying bone.

CT is, as elsewhere, a good imaging modality for showing cortical defects and loose bodies. The defects can thus be seen in the axial plane at the elbow, knee and talar dome and the appropriate coronal or sagittal reconstruction views obtained.

MR images are obtained in all planes. The vitality of the underlying bone can be confirmed, as well as the integrity of the overlying cartilage. A thin film of fluid, bright on T₂-weighted images, separates the dissected fragment from the underlying bone. STIR sequences will also show this feature as well as any bone oedema.

Caisson disease (synonym: dysbaric osteonecrosis)

Exposure to a hyperbaric atmosphere may result in decompression sickness - 'the bends' - and in the late complication of osteonecrosis.

The lesions are liable to appear if the worker is too rapidly decompressed. It is thought that nitrogen becomes liberated from bone marrow and causes bone infarcts by occluding small blood vessels.

A history of previous decompression sickness is not necessary for the occurrence of osteonecrosis.

Radiographic findings

1. *Juxta-articular lesions.* They are recognised as:
 - a. a transradiant subcortical band that may underlie as much as two-thirds of the articular cortex (Fig. 37.33)
 - b. collapse of part of the articular cortex
 - c. sequestration of part of the cortex
 - d. secondary osteoarthritis.

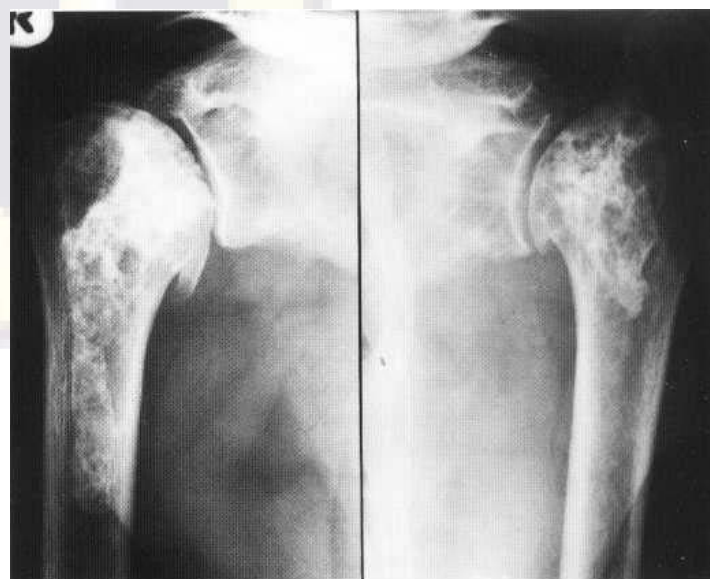


Fig. 37.33 Caisson disease of both shoulders. Medullary infarcts are demonstrated. These are well defined. There is a split cortex on the right. The humeral heads are flattened and irregular. Secondary osteoarthritic change is shown. Widespread metaphyseal infarction is demonstrated. The infarcted areas have well-defined margins that are symmetrically metaphyseal.



Fig. 37.34 Caisson disease. Well-defined metaphyseal infarcts are shown around both knee joints.

2. *Neck and shaft lesions.* They cause the following appearances:
- dense areas—small, multiple, bilateral, ill-defined opacities resembling hone islands in the upper ends of the femoral and humeral shafts and in the femoral neck
 - irregular calcified areas—typically in the distal part of the femoral shafts (Fig. 37.34) and in the proximal parts of the shafts of the humeri and tibiae
 - Malignant changes have occasionally been reported in such infarcts, usually in the form of *malignant fibrous histiocytoma* (Fig. 37.35).

Infantile cortical hyperostosis (eponym: Caffey's disease)

The cause of this disease is unknown. Many affected children have high fever, most have raised sedimentation rates and occasionally pleural exudates are found. However, an infective agent has never been identified. Occasionally, the disease has been reported in siblings, cousins and twins.

The condition has been diagnosed in utero. Usually, however, the babies are well for several weeks before the onset. The average age of onset is 9 weeks, and cases do not apparently start after the age of 5 months.

Three features common to all these patients are hyperirritability, soft-tissue swelling and bony cortical thickening. The soft-tissue swellings may be very painful, but are deeply situated and not accompanied by surface warmth or discoloration. Such swellings appear before bony changes are demonstrable and they disappear long before the bone lesions resolve. Sometimes the swellings may recur at their original site or new swellings may appear at other sites. The disease is characterised by the patchy distribution of the lesions and by remissions and relapses.

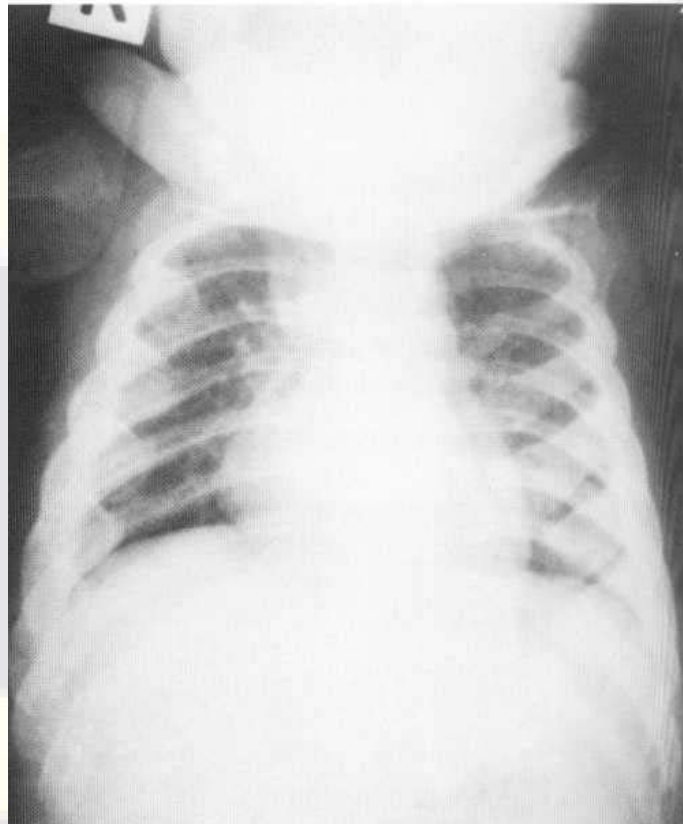


Fig. 37.36 Caffey's disease. Gross periostitis affects the ribs and the mandible is also thickened. (Courtesy of Dr Ann Barrington, Sheffield.)

Bones commonly affected are the *mandible, ribs* (Fig. 37.36), *clavicle, scapula* and the *ulna*, but any tubular bones except the phalanges may be affected. The condition may also be found in the *skull* and *pelvis*, but not in the spine. Lesions are confined to the shafts of the bones, and the epiphyses and metaphyses are not affected. This distribution affords a ready differentiation from rickets, scurvy and congenital syphilis.

Radiological features

Marked periosteal proliferation and cortical thickening are seen in bones beneath the soft-tissue swellings. The cortical hyperostosis may be massive. Patients usually recover after several weeks or months; in about 12 months, bones will usually have returned to normal.

Paget's disease (synonym: osteitis deformans)

Sir James Paget first described this disease in 1876. Its origin is not definitely known. Nonetheless, current thinking is that a 'slow' virus may be the initiating factor. Although no virus has been isolated, histological changes are seen that are present in viral infections.

There is variation in the distribution of the disease. It is common in the UK, parts of the USA, Australia and New Zealand, but uncommon in the Far and Middle East and Scandinavia. Within Britain, there appear to be some regional differences in the incidence.

The incidence of the disease as judged by pathological and radiological surveys is 3-4% of the population. Slightly more men are affected than women. Paget's disease is predominantly found in the



Fig. 37.35 Changes of medullary infarction are associated with an area of osteolysis due to fibrosarcoma.

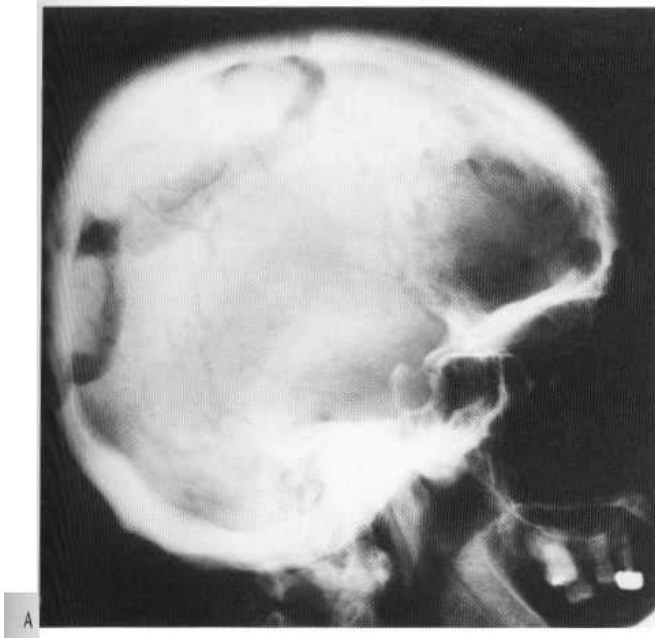


Fig. 37.37 Osteoporosis circumscripta. Two circular focal areas of active osteolysis in Paget's disease (A) are reflected as areas of increased uptake on the radioisotope bone scan (B).

elderly. Monostotic disease is not common (10-20%). Overall, the condition is found most commonly in the *sacrum* and *lumbar spine*, followed by the *skull*, *pelvis* and *femur*. Apart from the skull, the weight-bearing and persisting red marrow areas are most commonly involved, though multiple rib and upper limb lesions are uncommon. No bone is exempt. Lesions of the fibula are very rare.

The radiographic appearances are explained by the underlying pathological processes.

1. An *initial phase* of increased osteoclastic activity results in bone resorption. This early phase is osteolytic and is not commonly seen radiologically, still less in established disease. It may persist in the skull, as *osteoporosis circumscripta* (Fig. 37.37).

2. *Mixed phase* (spongy type with coarse, irregular trabeculation). Increased resorption of bone is followed by increased formation of abnormally coarsened trabeculae of increased volume (Figs 37.38, 37.39). Haversian systems are destroyed and replaced by new bone with a characteristic mosaic pattern. The margin between cortex and medulla is lost.

3. *Sclerotic phase* (amorphous appearance). Osteoclastic activity declines and osteoblastic activity proceeds, so that disorganised new bone of increased density replaces lytic areas. Eventually the disease becomes quiescent.



Fig. 37.38 (A) Paget's disease of the skull vault and mandible. There is bone expansion, loss of trabecular differentiation and an overall pattern of sclerosis. (B,C) Paget's disease demonstrated by radionuclide and CT scanning. The vault is thickened and there is increased isotope uptake.

Radiological features

Long bones Paget's disease starts at a bone end and, as it extends to the other bone end, it is demarcated from normal bone by a V shaped zone of transition (Fig. 37.40).

Long bones increase in cortical width and the femur and tibia may be bowed. Bones also increase in length; this may result in bowing if only one of a pair of long bones is affected. Paget's disease may cause more bony enlargement than is seen in any other disease.

Pelvis In the early stages loss of some trabeculae with coarsening of those remaining may be seen. Thickening and loss of clarity of the ileopectineal line and the teardrop also indicate the disease.

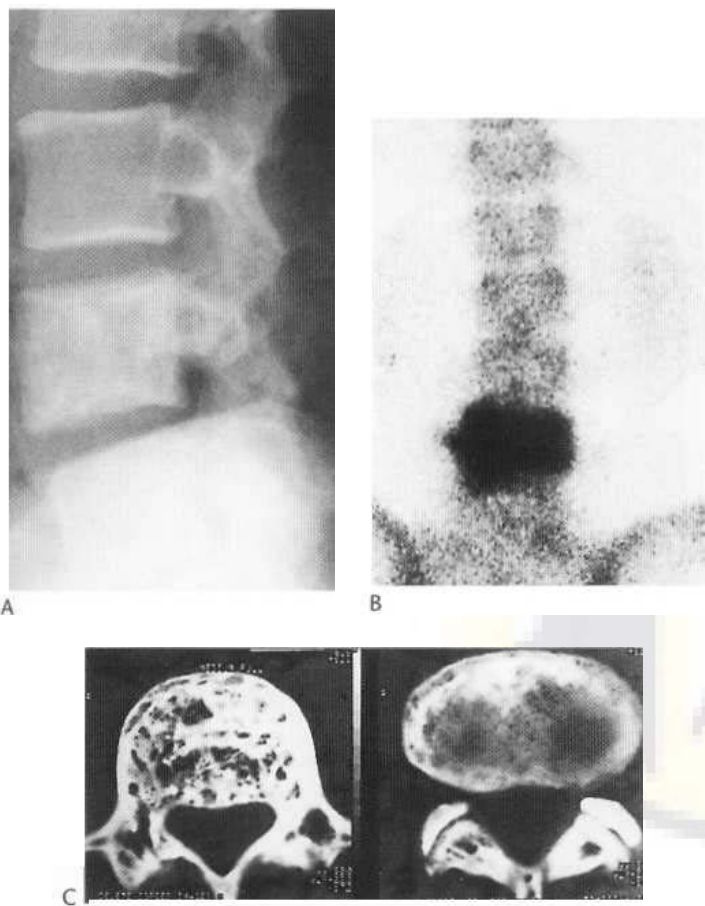


Fig. 37.39 Paget's disease. (A) The affected vertebral body is expanded as well as showing abnormal texture. (B) The bone scan confirms the increase in uptake in the expanded vertebral body. (C) The CT scan shows the rather spongy texture of the abnormal body, extending into the pedicles and laminae.

Narrowing of the hip joint space, especially in a medial direction, leads to protrusio with deformity of the pelvic brim. Secondary osteoarthritis then develops (Fig. 37.41).

Vertebrae All three forms of the disease may be found in the vertebrae. The neural arch and pedicles may be involved as well as the vertebral body, and all parts are enlarged. The width of the body is increased so that the interpedicular distance is also increased, even if the pedicles are enlarged. A characteristic, if infrequent, finding is a 'picture-frame' appearance with condensed, thickened end-plates and vertebral margins enclosing a cystic spongiosa (Fig. 37.42). The condensed end-plates are not seen with haemangiomas and involvement of posterior elements is also less common. Enlargement is unusual in both haemangiomas and metastatic disease.

Collapse is common and may cause spinal nerve compression. Vertebral enlargement distinguishes this from osteoporotic or malignant disease.

Skull In the skull, the disease begins as a destructive process affecting the outer table and sparing the inner table (Fig. 37.37). The full picture of osteoporosis circumscripta is rarely seen. In the reparative stage, sclerosis of the inner table is pronounced, and later the diploic spaces and the outer table become thickened. A classical, widespread 'cottonwool' effect results (Fig. 37.38A). The cranial cavity is not encroached upon.



Fig. 37.40 Paget's disease. (A) The initial radiograph shows a zone of resorption due to active disease. The distal end of the process has a flame- or V-shape. (B) A film taken a year later shows a mixed phase, perhaps proceeding on to quiescence in the same area. The lesion does not apparently reach the proximal articular surface of the tibia but, in this long bone, it does not always do so. It seems in this patient to be related to the fused growth plate for the tibial tuberosity.

Dental abnormalities include loss of lamina dura and hypercementosis (see Ch. 49).

Radionuclide bone scanning

This technique is of value during early activity, when it will pick up lesions which may not be radiologically detectable, while in the quiescent phase the presence of disease is best shown by conventional means. The total body scan detects disease in sites not routinely examined, such as the foot, but such sites are not commonly affected. The scan does however provide a quick overview of the skeleton and is useful in assessing change or malignant degeneration, so that follow-up is probably best performed by scanning (Fig. 37.43).

CT

Because changes are in mineralised tissue, they are well reflected at CT scanning. Bone resorption, expansion, cysts or sclerosis are seen (Fig. 37.39). Lesions in long bones are more easily imaged on plain films, but lesions of the skull involving optic foramina and the middle ear are well shown on CT scans. Three-dimensional reconstruction in particular can show skull deformity, but is generally of value only if reconstructive surgery is contemplated.

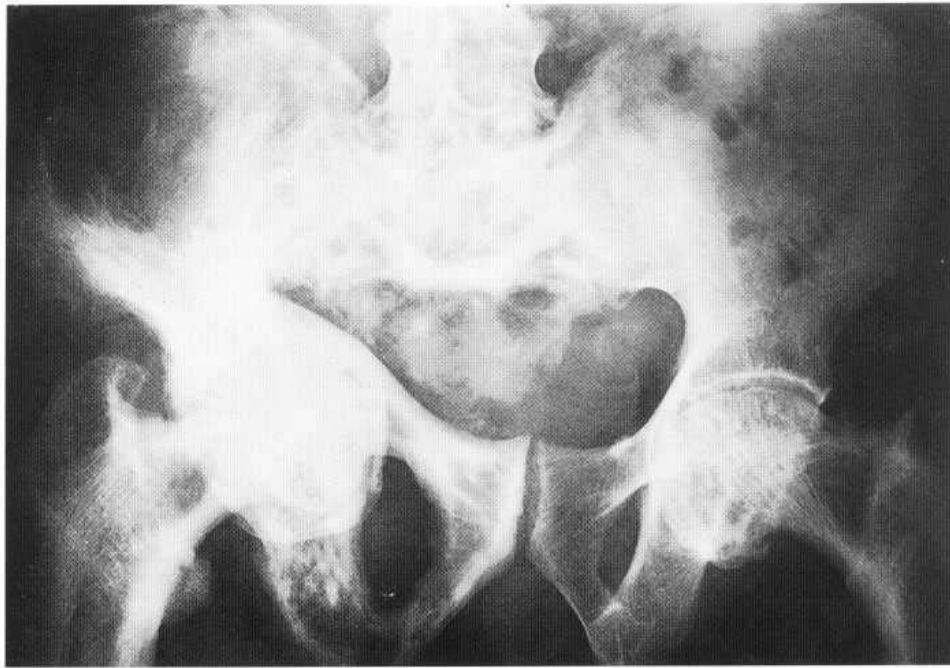
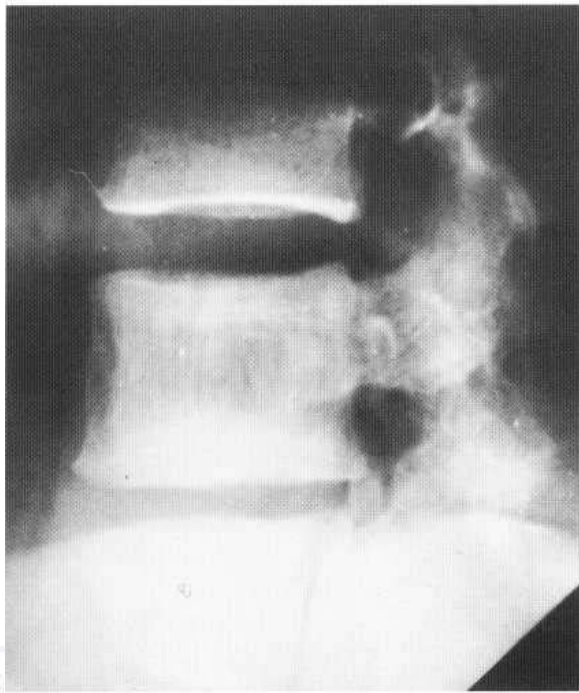
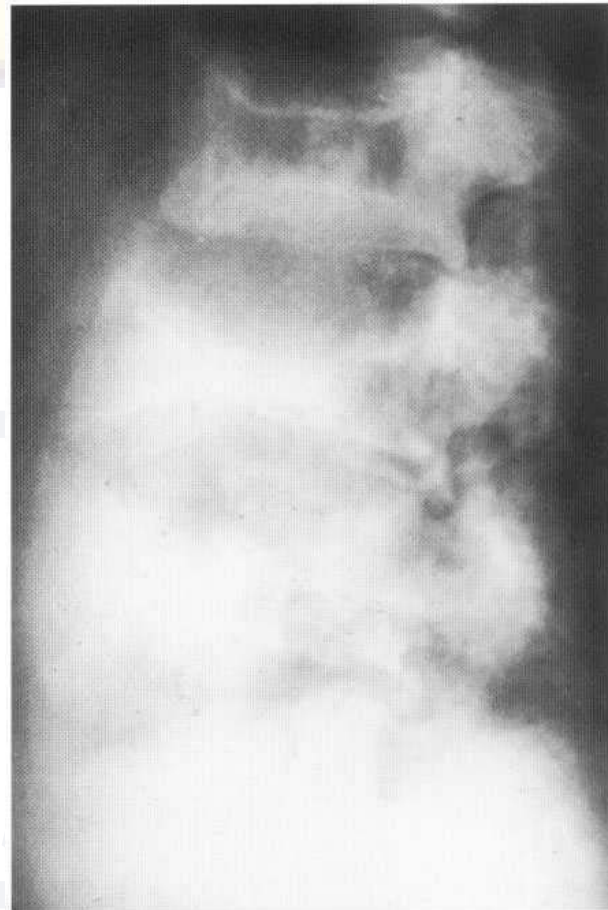


Fig. 37.41 Pelvis in Paget's disease. There is a combination of spongy and amorphous bone. Note the striated appearance of the left femoral head and neck. Marked deformity of the pelvic inlet and acetabular protrusion on the right are shown. There is enlargement of the right pubis and ischium.



A



B

Fig. 37.42 Paget's disease of the spine. (A) Picture-frame appearance in a vertebral body. The appendages are also enlarged. (B) Vertebral collapse and expansion together with abnormal bone texture in another patient.

MRI

Because the changes of Paget's disease vary with the stage of the disease, and because these are so well recognised on plain films, MRI is probably better used to assess the complications of Paget's disease related to bone expansion (Fig. 37.44) and subsequent

relation to compromised soft tissues, for example nerves, and fractures. Malignant degeneration and expansion into soft tissues are especially well demonstrated.

With uncomplicated disease, the bone is seen to be expanded. An excess of sclerotic or woven bone will be seen as an area of low

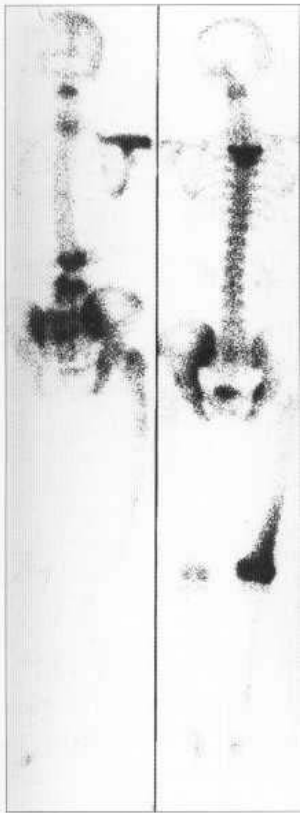


Fig. 37.43 Radioisotope bone scan (anterior and posterior scans) in Paget's disease showing multifocal areas of increase in uptake related to active disease.

signal with thickened, irregular trabeculae interspersed with fat. Cortical thickening is especially well shown. Hypervascular tissue in expanded bone might suggest malignant change in this age group. Soft-tissue change would occur with fractures or sarcomatous degeneration. Correlation with plain films is thus always indicated to avoid erroneous diagnosis.

Complications of Paget's disease

1. *Marginal (incremental) or incomplete transverse fractures.* These fractures are usually found on the thickened convex surface of the bowed bone where they may be multiple (Fig. 37.45). Occasionally, such a fracture may become complete (see below).
2. *Pathological fractures* are the commonest complication of Paget's disease and are most often seen in the early stages of the disease. Usually transverse, they are more common in women. Often multiple, they are most common in the upper femur and upper tibia. Healing is poorer in Paget's disease than in normal bone. Sarcoma may follow a pathological fracture. Bone may also be avulsed at sites of muscle insertions.
3. *Osteoarthritis* occurs at major joints (see above).
4. *Skull complications.* Cranial nerve palsies result when foramina are encroached upon. Vascular compromise also causes blindness. Deafness may result from involvement of the ossicles or cochlea or compression of the eighth nerve. Basilar invagination may cause brainstem compression. CSF obstruction can lead to hydrocephalus. Stretching of vertebral arteries may give rise to vertebrobasilar insufficiency.
5. *Cardiovascular complications.* Cardiac output is increased and, if much of the skeleton is actively involved, cardiomegaly, cardiac ischaemia and high output failure may result. Systemic hypertension and calcification of the media of the arteries also result, not purely due to age but related to the extent of the disease and its activity.
6. *Malignant degeneration.* Osteogenic sarcoma and, to a lesser extent, fibrosarcoma, chondrosarcoma and malignant fibrous histiocytoma may arise as complications of Paget's disease (Fig. 37.46) (see Ch. 39).

Differential diagnosis

Most difficulties arise in monostotic cases. Sometimes a full bone survey will reveal evidence of Paget's disease elsewhere. A solitary

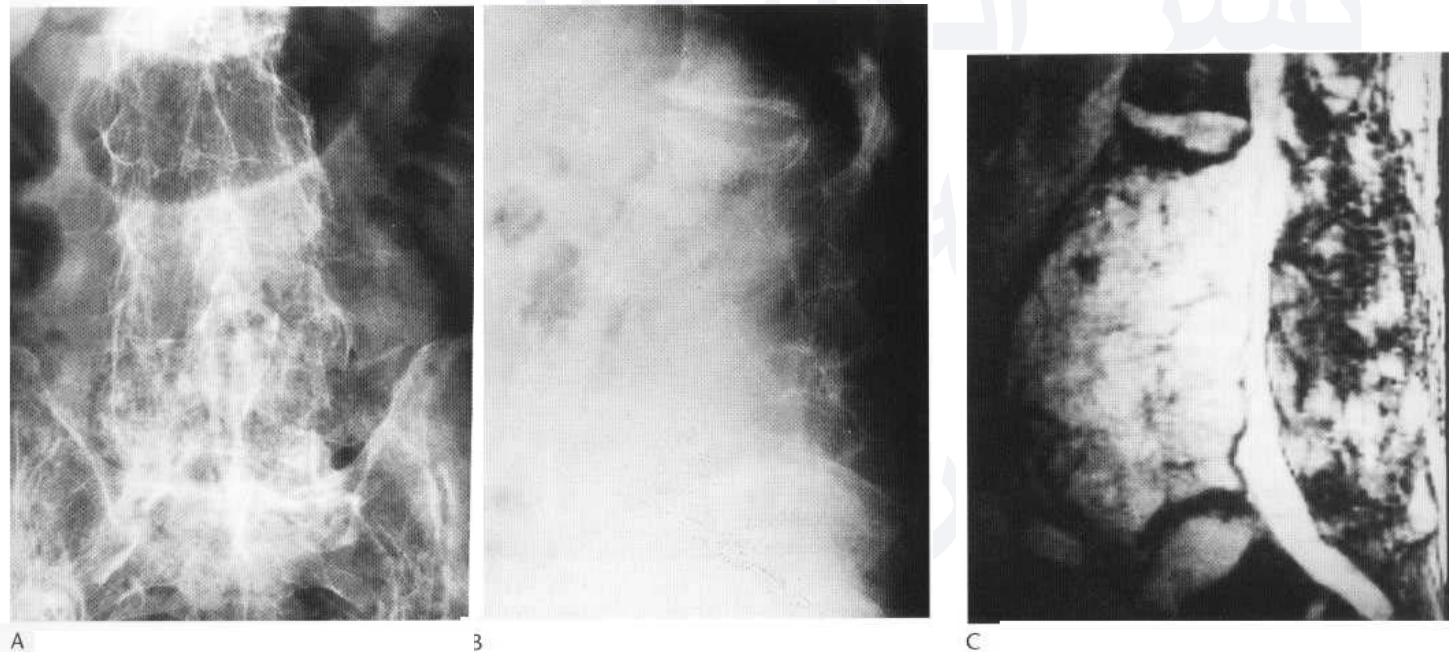


Fig. 37.44 Paget's disease. (A,B) The radiographs show three expanded and apparently fused vertebral bodies in the lumbar spine, which are demineralised. The appearances are those of a highly vascular form of Paget's disease in an active phase. (C) The MR scan confirms the presence of expansion and fusion with encroachment upon the canal, and confirms the presence of vascularity.

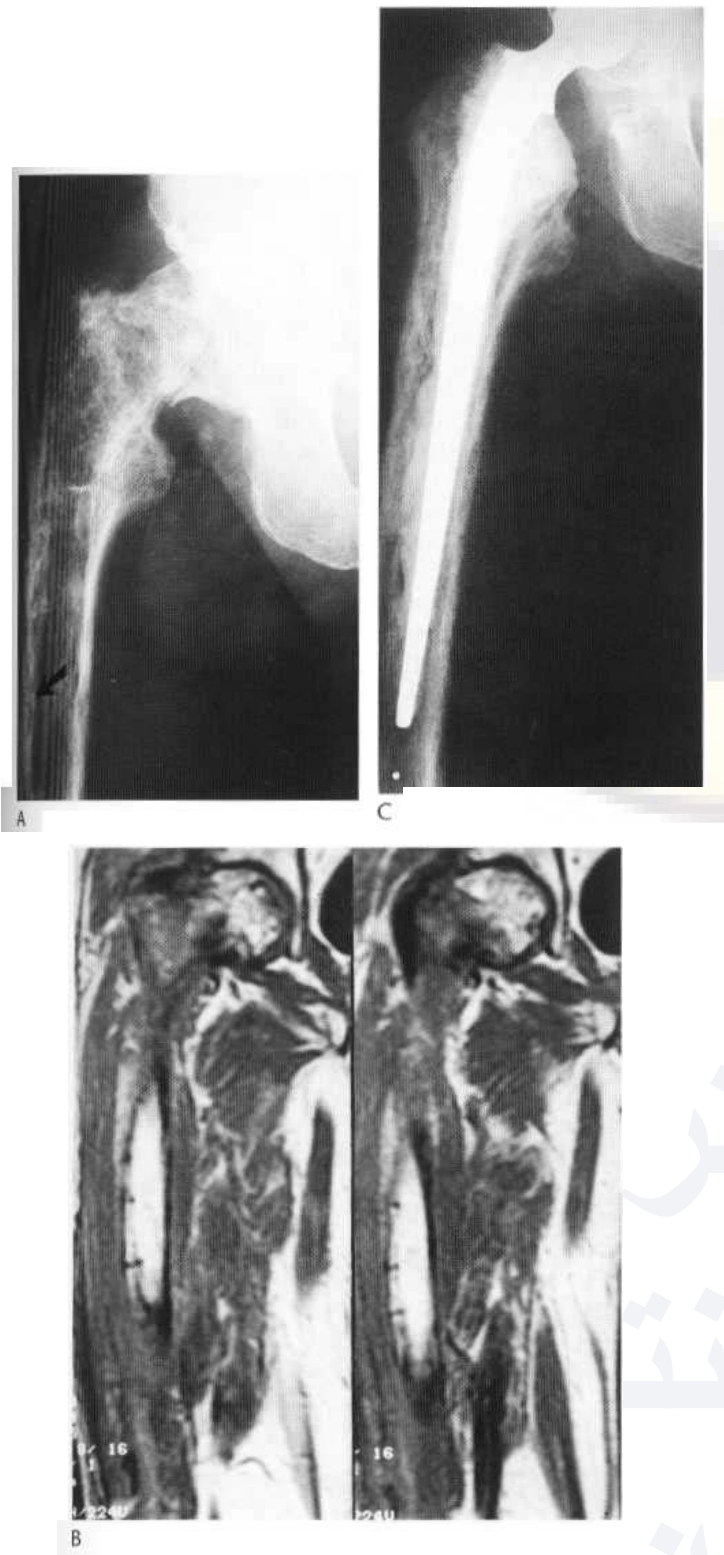


Fig. 37.45 Pathological and insufficiency fractures in Paget's disease. (A) The proximal femur shows all the changes of Paget's disease and a transcervical fracture has occurred. A transverse insufficiency fracture (arrow) is shown in the lateral femoral cortex. (B) Coronal T₁-weighted MR images of the right femur demonstrate changes related to the fracture of the femoral neck—there is varus deformity and quite marked alteration of fatty marrow signal due to haemorrhage. In addition, multiple insufficiency fractures are demonstrated in the lateral femoral cortex. (C) The insufficiency fractures are very well seen in the postoperative film.

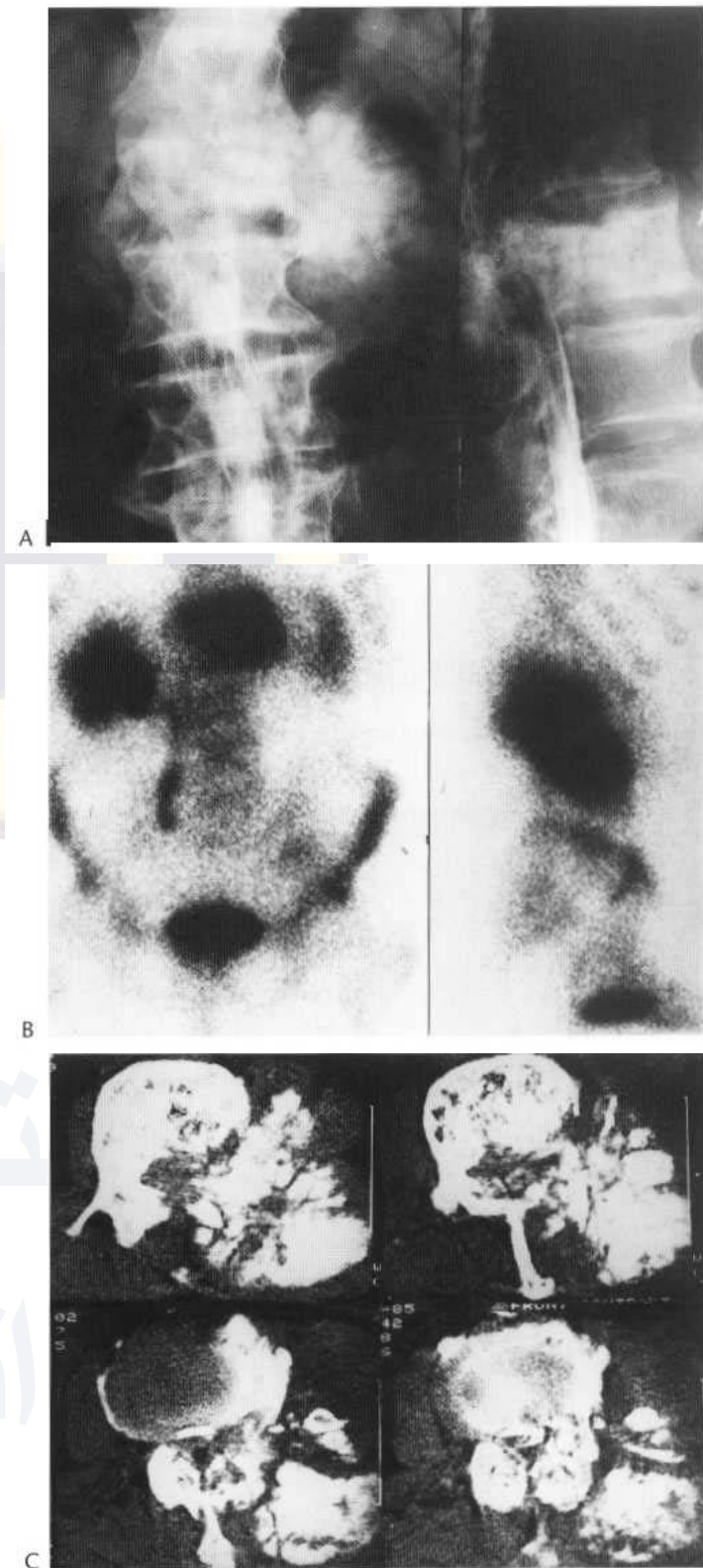


Fig. 37.46 Osteogenic sarcoma in Paget's disease. (A) The radiologram shows an ossifying mass in the soft tissues adjacent to the abnormal vertebral body at L2. This in turn shows expansion with sclerosis. There is hold-up of contrast medium at that level. The pathology extends into the neural arch. (B) The radioisotope bone scan confirms the presence of change at this level and also shows ureteric obstruction, presumably by pathologically enlarged lymph nodes in the pelvis. (C) The CT scan confirms the presence of sclerotic Paget's disease within the vertebral body but also demonstrates the ossifying sarcomatous mass in the soft tissues. The spinal canal is encroached upon. (Courtesy of Dr K. Walmsley.)

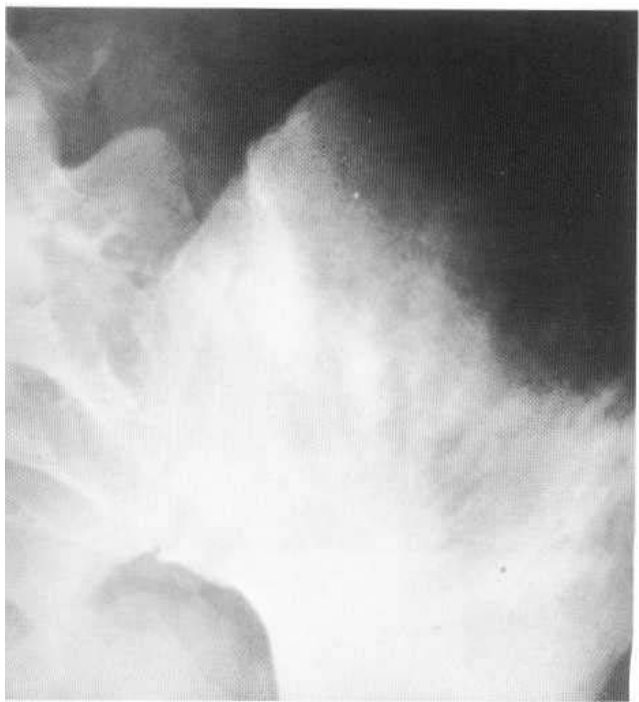


Fig. 37.47 Tuberous sclerosis. Flame-shaped areas of sclerosis in the iliac blades.



Fig. 37.48 Tuberous sclerosis in the hands. Cyst-like defects are seen in the bones, both beneath the fingernails and more proximally. Cortical defects and periostitis are also present.

dense vertebra or *vertebra nigra* may cause diagnostic difficulties because *osteoblastic metastases* and *reticulos* can cause identical appearances. The amorphous type of Paget's disease in the pelvis may be difficult to differentiate from *prostatic secondaries*, especially if little bone enlargement is evident. Elevation of the serum acid phosphatase will be found in the latter lesion.

An *angioma* of a vertebral body may resemble Paget's disease, but an angioma will not produce the typical widening of the bone seen in Paget's disease. The remaining trabeculae in an angioma are well defined and are surrounded by (vascular) marrow. Angiomas, especially affecting only part of the body, are commonly seen at MRI and should not be confused with malignant tumours.

Leontiasis ossea

This term is used in two senses: *specifically*, for an isolated progressive sclerosing hyperostosis of the skull, and *descriptively* when diseases such as Paget's disease and fibrous dysplasia affect the skull and facial bones. Whether or not the condition is ever a specific entity is debatable. It could well be that the isolated lesion is really a form of fibrous dysplasia.

Tuberous sclerosis (synonym: epiloia; eponyms: von Recklinghausen (1862), Bourneville (1880))

The classical clinical manifestations are a triad of epilepsy, mental retardation and adenoma sebaceum. The disease is inherited as an autosomal dominant condition but most cases are sporadic. Pathologically, hamartomas are formed in many of the body tissues—brain, eyes, lungs, kidneys and gastrointestinal tract.

In the skeleton, the commonest finding is that of poorly defined areas of sclerosis, affecting the skull, spine and pelvis. In the *skull*, woolly areas of density may be due to osteosclerosis, or to tuberous calcifications within the brain. CT scanning rapidly differentiates between the two. Sclerosis also affects the *vertebral bodies*. In the *pelvis*, the iliac blades are the sites of flame-shaped densities which do not resemble metastases (Fig. 37.47), or more nodular densities which do simulate malignancy.

Periostitis may be found on long bones, metatarsals and, to a lesser extent, metacarpals. In the *hands*, rather than the feet, cysts occur in phalanges (Fig. 37.48). These may be related to subungual fibromas and are well demarcated (Fig. 37.49).



Fig. 37.49 Tuberous sclerosis. Note periosteal thickening of fifth metacarpal, cysts in head of proximal phalanx and pressure erosion of distal phalanx by subungual tumour. (Courtesy of Dr L. Langton.)

REFERENCES AND SUGGESTIONS FOR FURTHER READING

- Aichroth, P. (1971) Osteochondritis dissecans of the knee -a clinical survey. *Journal of Bone and Joint Surgery*, **55B**, 440-447.
- Berquist, T. H. (ed.) (1995) *MRI of the Musculoskeletal System*, 3rd edn. New York: Raven Press.
- Bush, B. H., Bramson, R. T., Ogden, J. A. (1988) Legg-Calvd-Perthes' disease: detection of cartilaginous and synovial changes with MR imaging. *Radiology*, **167**, 473-476.
- Catterall, A. (1971) The natural history of Perthes' disease. *Journal of Bone and Joint Surgery*, **53B**, 37-53.
- Catterall, A. (1982) *Legg-Calve-Perthes' Disease*. Edinburgh: Churchill Livingstone.
- Davidson, J. K. (ed.) (1975) *Aseptic Necrosis of Bone*. Amsterdam: Excerpta Medica.
- Ficat, R. F. (1983) Treatment of avascular necrosis of the femoral head. *Hip*, **2**, 279-295.
- Fisher, R.L., Roderique, J.W., Brown, D.C., Danigelis, J.A., Ozonoff. M.B., Sziklas, J.J. (1980) The relationship of isotopic bone imaging guiding the prognosis in Legg-Perthes' disease. *Clinical Orthopaedics*, **150**, 23-29.
- Hamdy, R. C. (1981) *Paget's Disease of Bone*. New York: Praeger.
- Markisz, J. A., Knowles, R.J.R, Altchek, D. W., Schneider, R., Whalen, J. P., Cahill, P. T. (1987) Segmental patterns of avascular necrosis of the femoral heads: early detection with MR imaging. *Radiology*, **162**, 717-720.
- Marchal, G. J., Van Holsbecek, M., Racs, M. et al (1987) Transient synovitis of the hip in children: Role of US. *Radiology* **163**: 825-828.
- Mitchell, M. D., Kunkel, H. L., Steinberg, M. E., Kressel, H. Y., Alavi, A., Axel, L. (1986) Avascular necrosis of the hip: comparison of MR, CT and scintigraphy. *American Journal of Roentgenology*, **147**, 67-71.
- Murray, R. O., Jacobson, H. G., Stoker, D. J. (1990) *The Radiology of Skeletal Disorders*, 3rd edn. Edinburgh: Churchill Livingstone.
- Resnick, D., Niwayama, G. (1995) *Diagnosis of Bone and Joint Disorders*, 3rd edn. Philadelphia: Saunders.
- Ryan, P.J., Fogelman, I. (1994) The role of nuclear medicine in orthopaedics. *Nuclear Medicine Communications*, **15**, 341-360.

نشر الکترونیکی
موسسه انتشاراتی
نوردانش



نشر الکترونیکی
موسسه انتشاراتی
نوردانش

DISEASES OF JOINTS

Peter Renton

with a contribution from Ruth Green

RHEUMATOID ARTHRITIS

This disease is seen at all ages, but especially from 20 to 55 years, with small peaks in childhood and in the elderly. Women are more commonly affected (M : F = 1 : 3).

The joints most typically involved are the small joints, especially the metatarsophalangeal and metacarpophalangeal and carpal joints, but any joint, including the temporomandibular and cricoarytenoid, may be affected. The axial skeleton is later and less often affected, with the exception of the cervical spine. Sites of ligamentous and tendinous insertions (entheses) are less frequently involved. The tendency at the peripheral joints is to symmetry, and often identical digits on either side of the body arc affected. Asymmetry of distribution may follow unilateral paralysis or weakness, when underutilisation of a limb may prevent the onset of rheumatoid disease in that limb. Conversely, asymmetry may follow overuse of a limb which often is more severely involved. This is seen especially in men and in those performing heavy manual work. In general, excess physical activity leads to more severe forms of joint disease.

Rheumatoid arthritis is a systemic disease, and other body systems may be involved, for example lung parenchyma and pleura.

Radiological findings

The plain film Joint changes may be summarised as follows:

1. Soft-tissue changes
2. Osteoporosis
3. Joint space changes and alignment deformities
4. Periostitis
5. Erosions
6. Secondary osteoarthritis.

Changes 1, 2, 4 and 5 may be seen at entheses, that is, metabolically active sites of ligamentous and tendinous insertions into bone.

1. Soft-tissue changes

These changes are best assessed clinically but may also be shown radiologically in the hand and wrist (Fig. 38.1), knee or foot and at other small joints. Soft-tissue swelling is due to oedema of periarticular tissues and to synovial inflammation in bursae, joint spaces

and along tendon sheaths. Joint distension also follows an increase in synovial fluid.

In the hand, fusiform swelling due to capsular distension and local oedema may be seen over the interphalangeal joints and over the metacarpophalangeal joints, especially the first, second and fifth. Soft-tissue swelling over the third and fourth metacarpophalangeal joints is seen as a local increase in density and occasionally as a soft-tissue projection into adjacent web spaces. Soft-tissue swelling over the ulnar styloid can be due to local involvement of the extensor carpi ulnaris tendon sheath. Changes at the radial styloid are related to local radiocarpal joint synovial hypertrophy.

Soft-tissue changes are less well demonstrated in the foot. Changes over the first and fifth metacarpophalangeal joints reflect synovitis in the bursae over the first and fifth metatarsal heads, but swelling over the remaining metacarpophalangeal joints may be seen as fusiform increases in density.

The Achilles tendon inserts into the back of the calcaneus 1-2 cm below its upper margin. It is sharply demarcated anteriorly by the pre-Achilles fat pad and, more inferiorly, by the retrocalcaneal bursa. When local synovitis thickens the bursa, oedema obliterates the local fat and blurs out margins of the tendon, which also thickens (Fig. 38.2). Similar changes occur inferiorly, at the plantar fascial origin at the base of the calcaneus.

Distension of the capsule of the knee joint is shown on the anteroposterior radiograph as a lateral displacement of the normally barely visualised fat planes adjacent to the distal femur. On a lateral view of the knee the suprapatellar pouch is distended and its surrounding fat planes blurred. Posteriorly, a distended joint capsule may give a local increase in density and in this way a Baker cyst is often identified. This can be confirmed by ultrasound, arthrography or MRI.

On the lateral view of the elbow, the anterior and posterior fat planes are displaced in a direction vertical to the long axis of the joint, but may be obliterated by local oedema.

Swelling around an affected joint is symmetrical, while in gout the swelling is eccentric. In rheumatoid arthritis, however, a rheumatoid nodule may cause a localised eccentric swelling, and these often occur at pressure points, for example over the olecranon.



Fig. 38.1 Rheumatoid arthritis. Bilateral changes are fairly symmetrical. Soft-tissue swelling is demonstrated, especially over the ulnar styloids. Erosions are demonstrated at the carpus, distal radius and ulna, with joint space narrowing and collapse of bone. Metacarpophalangeal erosions are also seen associated with joint space narrowing. There is a swan-neck deformity of the right fifth distal interphalangeal joint.



Fig. 38.2 Retrocalcaneal bursitis in association with thickening of the tendo Achilles and a retrocalcaneal erosion. A soft-tissue mass is demonstrated in the angle normally filled by fat between the insertion of the tendon and the upper calcaneus.

2. Osteoporosis

Assessment of osteoporosis depends in part on film quality, and comparison between normal and abnormal joints in the same patient may be helpful. Interpretation is subjective and changes are seen only after loss of 25-50% of mineral. Differences in assess-

ment of osteoporosis may exist, both between different observers and between the same observer at different times.

Osteoporosis in rheumatoid arthritis is of two types:

a. **Generalised** This may be due to steroids or limitation of movement due to pain, or muscle wasting, and occurs later in the course of the disease. It may also reflect coincidental bone loss in postmenopausal women, who are commonly affected by this disorder.

b. **Localised** Local osteoporosis around joints occurs earlier and is due to synovial inflammation and hyperaemia.

Osteoporosis increases in incidence with the duration of the disease and the age of the patient. Some 30% of patients show it at presentation but, two years after, 80% are affected.

Osteoporosis is a precursor of erosive disease and may mask early erosions (Fig. 38.3).

Generalised or solitary *sclerosis* of one or more distal phalanges (terminal phalangeal sclerosis) is often rendered more prominent because of osteoporosis elsewhere. This phenomenon occurs in some 35% of patients with rheumatoid arthritis and other arthropathies and may be present before any other abnormality. In a woman, especially, it may prognosticate future disease, but it is seen in some normal patients (Fig. 38.4).

3. Joint space changes and alignment deformities

In the early stage a joint space may be widened by synovial hypertrophy and an effusion. Later in the disease, joint spaces narrow due to cartilage destruction by pannus (Fig. 38.5). Narrowing of joint spaces may, however, be apparent rather than real in the presence of flexion deformities, so that an oblique view may help to assess the joint space width. Alignment abnormalities at joints may result from local synovitis weakening the capsule and tendinitis preventing



Fig. 38.3 Rheumatoid arthritis. (A) The initial radiograph shows a hint of early trabecular loss around the proximal interphalangeal joint of a finger with preservation of the joint space and early marginal cortical loss at the base of the middle phalanx. (B) The subsequent radiograph shows established erosive change in the area of ill-defined demineralisation in association with joint space narrowing. (Courtesy of Dr. A. Larsen, Oslo.)

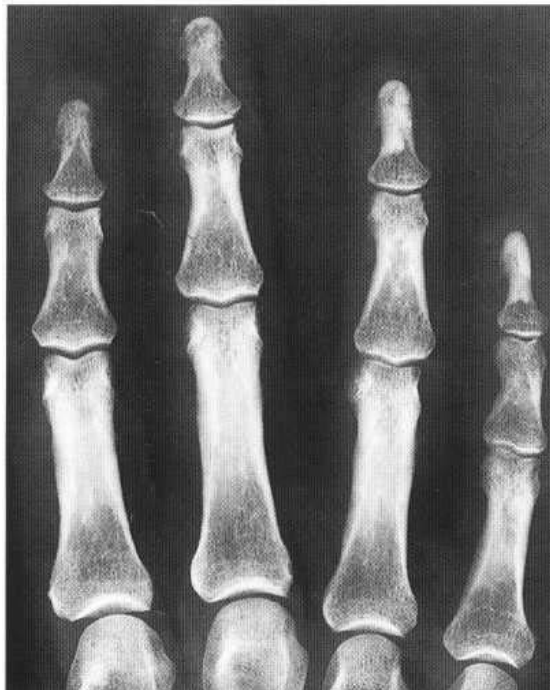


Fig. 38.4 Terminal phalangeal sclerosis in rheumatoid arthritis. Obliteration of the medullary cavity of the distal phalanges is demonstrated in this patient. The new bone is very dense and well defined. The change is especially marked at the little and ring fingers.

normal musculotendinous action. Tendons may also rupture in the region of roughened bone. Thus, rotator cuff tears allow upward subluxation of the eroded humeral head.

Many changes of alignment in the rheumatoid hand are irreversible but, if due to local soft-tissue laxity, may be corrected by applied pressure. Subluxations at metacarpophalangeal joints lead to ulnar deviation (Fig. 38.6), which occurs in up to 50% of those with chronic disease. This is also associated with increasing palmar flexion. This change may result from ulnar deviation of extensor tendons.

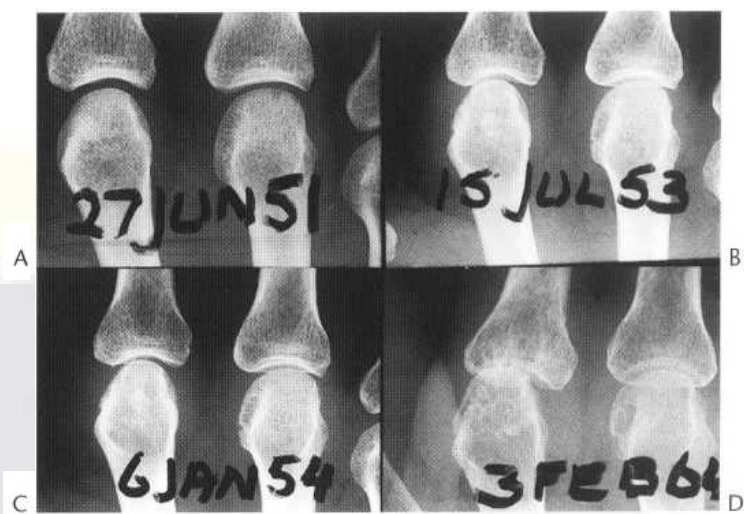


Fig. 38.5 Progressive narrowing of a joint in rheumatoid arthritis. (A) *Year 1*. The metacarpophalangeal joint looks normal. (B) *Year 3*. There is narrowing of the metacarpophalangeal joint of the index finger with associated local soft-tissue swelling. Erosive change is demonstrated at the metacarpal head. (C) *Year 4*. Little change over the year. (D) *Year 13*. On this late film the soft tissues remain thickened. The joint space is obliterated. Erosive change is demonstrated, especially at the metacarpal head. There is ulnar drift.

An erosive change is also now evident at the third metacarpal head on films B, C and D.



Fig. 38.6 Gross rheumatoid arthritis at the carpus with ulnar deviation, subluxation and joint narrowing at the metacarpophalangeal joints. Boutonniere deformities are present at the index and little fingers.

The boutonniere deformity results from proximal interphalangeal joint flexion and distal interphalangeal joint extension, and the swan-neck deformity from the reverse (proximal interphalangeal joint extension and distal interphalangeal joint flexion) (Fig. 38.1). The boutonniere deformity is the more common.

Similarly, lateral deviation of the toes may be found. Hallux valgus is especially common. The hallux sesamoids sublux between the first and second metatarsal heads and the transverse arch flattens as local inflammation causes ligamentous laxity.

4. Periostitis

Local periosteal reactions occur either along the midshaft of a phalanx or metacarpal as a reaction to local tendinitis, or at the metaphysis near a joint affected by synovitis. Such changes are less common in rheumatoid arthritis than in the seronegative arthropathies. They are difficult to identify, may be mistaken for lumbrical impressions, and are commoner in the feet (Fig. 38.7). Periostitis in the form of fluffy calcaneal spurs, plantar and posterior, is ^{also} less common in rheumatoid arthritis than in the seronegative arthropathies (Fig. 38.8). When present, they are larger and more irregular than the normal small well-corticated spurs of the elderly. Spurs may arise ab initio or may follow healing of erosions.

5. Erosions

These are the most important diagnostic change but are not necessarily present when the patient first attends. Their incidence rises



Fig. 38.8 Rheumatoid arthritis. A lateral view of the heel shows irregular erosive change along the base of the heel in association with a small plantar spur. Erosive change is also demonstrated posteriorly at the insertion of the tendo Achillis.



Fig. 38.7 Rheumatoid arthritis with narrowing of the metatarsophalangeal joint of the great toe and a fine periostitis on the adjacent shafts (arrows).



Fig. 38.9 Rheumatoid arthritis. (A) The initial radiograph shows demineralisation of bone at the second and third metacarpals heads with preservation of local joint spaces. (B) The second film shows that the areas of demineralisation at the second metacarpal head hid erosions. The erosions are marginal. The joint space narrows slightly.

from less than 40% of patients at 3 months to up to 90% or 95% at 10 years.

Classic periarticular erosions occur at the so-called 'bare areas' of bone between the edge of the articular cartilage and the attachment of the joint capsule (Fig. 38.9).

Erosions in rheumatoid arthritis should be sought for at the common sites. Supplementary views, such as the 'ball-catcher' (supine 25° oblique view), may be needed. Erosions appear earlier and are more often seen in the feet, 90% of which will eventually be affected, than in the hands (75%), and most often at the fifth metacarpophalangeal joint. The hallux metatarsophalangeal is the least



Fig. 38.10 Rheumatoid arthritis. Marked soft-tissue swelling is demonstrated over the ulnar aspect of the carpus in association with erosion at the distal ulna and the related carpal bones. The joint space between the carpus and the ulna is narrowed.

often involved of the metatarsal joints. Erosions affect typically the lateral side of the fifth metatarsal but the medial side of the others.

The metatarsal head erodes before the base of the distal phalanx. In the hand, the second and third metacarpophalangeal joints are the earliest affected, initially on the radial aspects. More distal erosions are inconstant. Erosions occur at the ulnar styloid, at the radial styloid and at the proximal compartment of the distal radioulnar joint (Fig. 38.10). Carpal erosions occur throughout the wrist. An erosion is, for example, commonly seen on the lateral scaphoid at its waist. Carpal disease may be followed by fusion, but this is uncommon elsewhere in adult rheumatoid arthritis, although it does occur in the cervical spine. On occasion, massive carpal destruction may be found in the presence of virtually normal peripheral joints (Fig. 38.10).

Tarsal erosions, other than at the posterior and inferior surfaces of the calcaneus, are uncommon and are also less common in rheumatoid arthritis than in the seronegative spondyloarthropathies (Fig. 38.11). In rheumatoid arthritis, erosions are usually seen at or above the insertion of the tendo Achilles into the back of the calcaneus.

Erosions arise in an area of local demineralisation beneath the cortex, which is progressively resorbed, leaving irregular underlying trabeculae. The destroyed area increases in size and, as pannus spreads over articular surfaces, the entire articular cortex may be destroyed, leaving a destroyed bone end (Fig. 38.12). Chronic trauma, in weight-bearing or due to abnormal tendon alignment, may further collapse articular surfaces. Steroids and analgesics also modify the disease so that neuropathic-type destructive changes may result. Healing rarely reverses erosions and so it is not often that a normal appearance returns. Usually the margins of healed erosions become corticated and they do not enlarge on follow-up.

Erosive change is less common at the larger joints but often bone destruction is greater owing to the greater stresses placed on knees, elbows and shoulders. On occasion, intraosseous defects-cysts or



Fig. 38.11 Rheumatoid arthritis very pronounced destructive changes in the tarsus and in metatarsal heads.



Fig. 38.12 Rheumatoid arthritis. Progressive films taken over 6 years, showing marginal erosions and joint space narrowing followed by collapse of articular surfaces. A small geode is demonstrated in the proximal phalanx of the third ray.

geodes-2-3 cm or more in diameter, may be seen beneath joint surfaces (Fig. 38.13); when these collapse, marked deformity results. An alternative form of change at large articular surfaces is a superficial surface irregularity with a little reactive sclerosis in the presence of much joint narrowing. This change is seen at the elbow, knee and hip; in the hip joint it is characteristically the medial joint



Fig. 38.13 Geodes in rheumatoid arthritis. There is joint space narrowing. Osteoporosis is demonstrated. An effusion is present. There are large distal femoral geodes which reach the patellofemoral articulation.

space, which is narrowed and eroded (as opposed to the superior in osteoarthritis). Medial migration of the femoral head and anterior resorption results in protrusio acetabuli (Fig. 38.14). This is classic but not pathognomonic of rheumatoid arthritis, as it also occurs in osteoarthritis in conditions with bone softening, and in an idiopathic inherited form. Gross loss of bone, especially at the femoral head, may result in a 'bird's beak' appearance (Fig. 38.14). Marked loss of bone around articular surfaces is also common at the elbow (Fig. 38.15) and shoulder, and deformities of alignment follow. Bone loss at the acromioclavicular joint may often be seen on a chest radiograph, with pointing of adjacent bone ends. Upward subluxation of the humeral head results in scalloping of the undersurface of the acromion (Fig. 38.16). Erosions of the superior aspects of the upper ribs are seen in patients with longstanding disease and muscle wasting, and are probably due to the adjacent scapula rubbing on the rib rather than synovial hypertrophy.

Rheumatoid changes in the axial skeleton

Sacroiliac joints Changes are less common and less severe than in seronegative disease but may be seen in up to 30% of those with longstanding disease. The changes are more common in women (cf. ankylosing spondylitis) and rarely end in fusion.



Fig. 38.15 Rheumatoid arthritis of the elbow showing marked resorption of all the articular surfaces with marginal erosions, especially well seen at the radial neck and trochlea.



Fig. 38.16 Rheumatoid arthritis-widening of the acromioclavicular joint. Erosion of the third and fourth ribs superiorly is also seen in this condition.

Spinal changes Rheumatoid changes are common in the cervical spine but uncommon in the thoracic and lumbar regions.

Osteoporosis, disc narrowing and end-plate irregularity are seen with only a little reactive new bone formation at the upper cervical



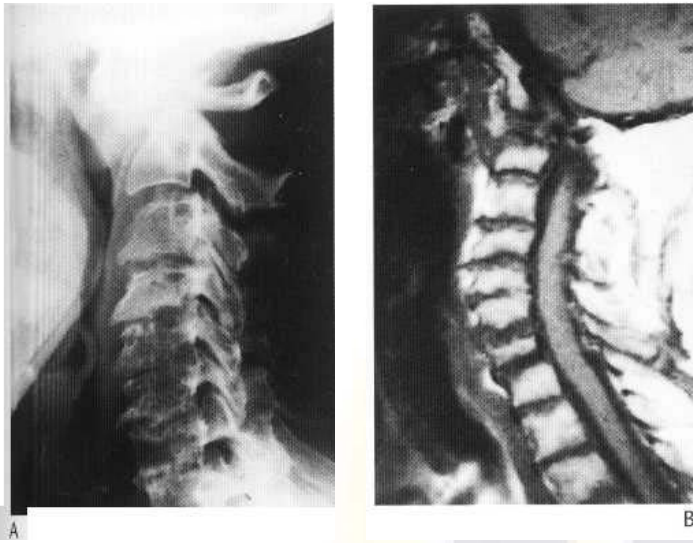


Fig. 38.17 Rheumatoid arthritis of the cervical spine. (A) The plain film shows subluxation of C1 and loss of the odontoid peg. The disc spaces from C3 down are narrowed and the end-plates irregular and eroded. Fusion is demonstrated at C5/6 and C7/T1 levels. There is no soft-tissue swelling, but deformity results from the forward subluxation of C1 upon C2. (B) In the same patient the sagittal T₂-weighted MR sequence demonstrates that the odontoid peg is no longer visible. End-plate irregularity is again demonstrated with narrowing of disc spaces.

vertebrae. Osteoarthritis, in distinction, is seen more inferiorly. Facet joint erosions may result in subluxation (Fig. 38.17), so that nerve entrapment follows. Subluxation and erosion also occur at the synovial joint between the odontoid peg and arch of atlas (Fig. 38.18), and are potentiated by laxity of ligaments around the peg. Separation in flexion of more than 2.5 mm in adults or 5 mm in children is held to be abnormal. This instability can be seen in up to 30% of patients with chronic rheumatoid arthritis and is best seen in flexion. The eroded odontoid may also fracture.

Resorption of bone at non-articular surfaces occurs in the cervical spine at the spinous processes, which become short, sharp and tapered in patients with chronic disease.

6. Secondary osteoarthritis

Weight-bearing joints affected by rheumatoid arthritis often develop secondary osteoarthritis. Indeed, at the hips, osteoarthritic change may be superimposed on a previously unrecognised rheumatoid



Fig. 38.18 Rheumatoid arthritis of cervical spine-tomographic section showing erosions of the left atlanto-axial articulation. Similar changes affect the right side and also the occipito-atlanto joints and the odontoid peg.

arthritis. Reactive sclerosis and new bone formation in osteoarthritis is not marked in those whose underlying disease has characteristic features of osteoporosis and bone destruction.

Arthrography

Following joint aspiration a single or double air-contrast technique can be used to demonstrate the status of synovium, cartilage and bone. Synovial proliferation and irregularity may be present in a distended capsule. Marginal and articular cartilage loss can be confirmed. Loose bodies are shown in the joint. Cysts or geodes may fill with contrast (Fig. 38.19).



A



B

Fig. 38.19 Rheumatoid arthritis. (A) Erosions and upward subluxation of the humeral head. (B) Arthrogram showing numerous 'millet seeds' floating freely within the joint. There is also a rotator cuff tear.

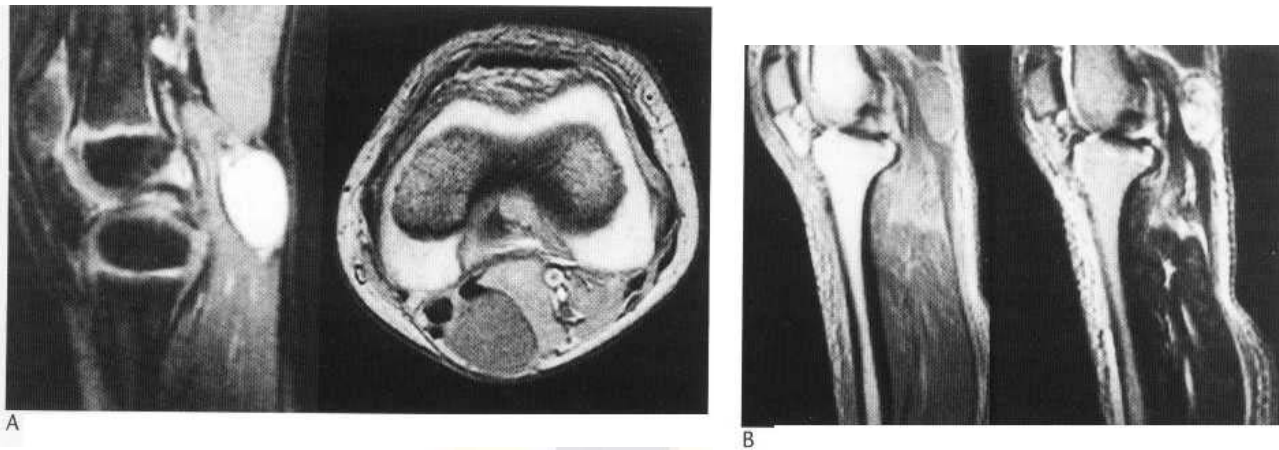


Fig. 38.20 Baker's cyst. (A) Sagittal fat-suppression (left) and axial T₁-weighted gradient-echo (right) MR sequences. The sagittal image demonstrates a well-defined and intact Baker's cyst posterior to the knee joint in this child. The axial image shows the medial situation of the Baker's cyst and demonstrates its origin between the tendons of the medial gastrocnemius head and distal semimembranosus muscles. (B) T₁- and T₂-weighted MR images showing a posteriorly situated cyst, seen to contain debris. The leak disrupts the adjacent musculature.

The technique is now infrequently employed, but rupture of the capsule or a Baker cyst shows leak of contrast into adjacent muscles. Here, the pain may simulate a deep vein thrombosis. Arthrography

confirms the leak; ultrasound can be used to show either a deep vein thrombosis or a normal vein, which may be displaced by a large cyst. MRI of course shows the cyst (Fig. 38.20A) and leak (Fig. 38.20B).

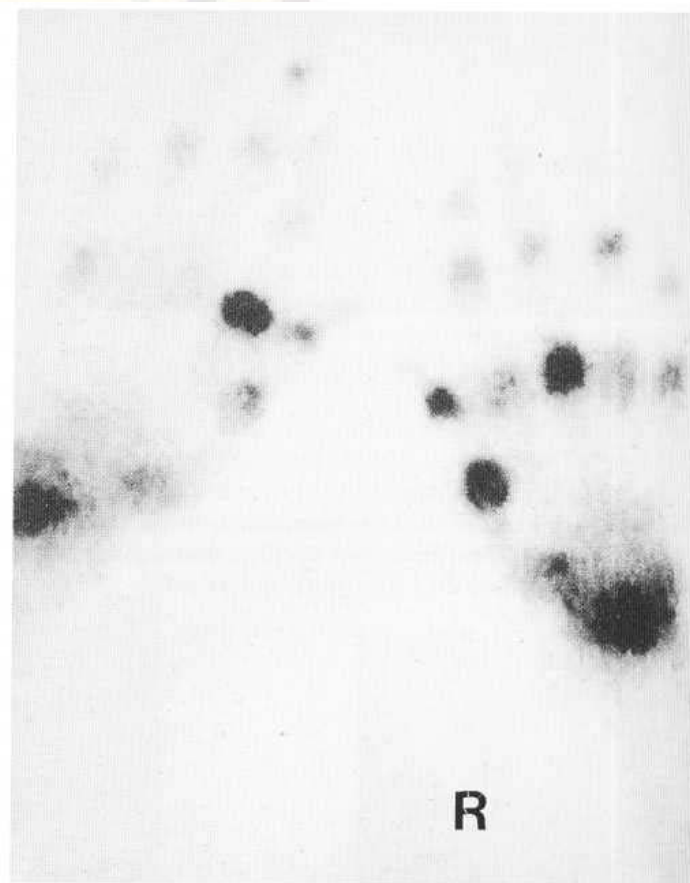


Fig. 38.21 Rheumatoid arthritis. (A) Whole-body radioisotope scan showing areas of increase in uptake in the neck, both shoulder joints, the elbow joints, the left hip, both knees and ankles in a patient with rheumatoid disease. The distribution of disease is shown, but the changes on this scan are not specific. (Courtesy of Dr A. Hilson.) (B) Localised images of the hands showing changes of a more specific distribution. (Courtesy of Dr A. Saifuddin.)

CT scanning

In the axial plane CT can be used to demonstrate erosions with considerable clarity, especially in the carpus and tarsus, and to show joint space narrowing and erosive change. Joint fusion is especially well shown with CT.

Radionuclide scanning

⁹⁹Te-MDP images show increased blood flow to synovium in the early or blood-pool phase of the scan; on delayed images obtained at 3 hours, increased uptake is shown at sites of increased bone turnover. Isotope scanning is highly sensitive in the arthritides but shows poor specificity for individual diseases, relying on distribution of abnormal foci to make a specific diagnosis (Fig. 38.21). In rheumatoid disease, isotopes are at least 70% more sensitive than conventional films and also are a good prognosticator for subsequent erosions. Inactive erosions may be negative at isotope bone scanning. Spatial discrimination is improved by the use of single photon emission computed tomography (SPECT).

Periosteal reactions show up as a generalised increase in uptake and thickening of the cortical image.

Ultrasound

Ruth Green

Bone is refractory to sound waves, although joint margins can be assessed for erosions (Fig. 38.22). Structures deep in joints cannot be completely assessed by ultrasound; however, ultrasound can be used as an adjuvant to MRI in demonstrating the fluid nature of cystic structures, for example meniscal cysts arising in conjunction with a meniscal tears (Fig. 38.23).

Soft tissues around joints may also be assessed using ultrasound to differentiate between subcutaneous oedema, synovial reaction and/or joint effusion (Fig. 38.24). Loose bodies may also be demonstrated in joints or bursa if fluid is present within these (Fig. 38.25).

With the advent of high-resolution linear ultrasound transducers of at least 7.5 MHz, and preferably 12-15 MHz variable frequency, we are able to assess the internal structure of tendons and evaluate their integrity. Ultrasound is real time and therefore dynamic scan-

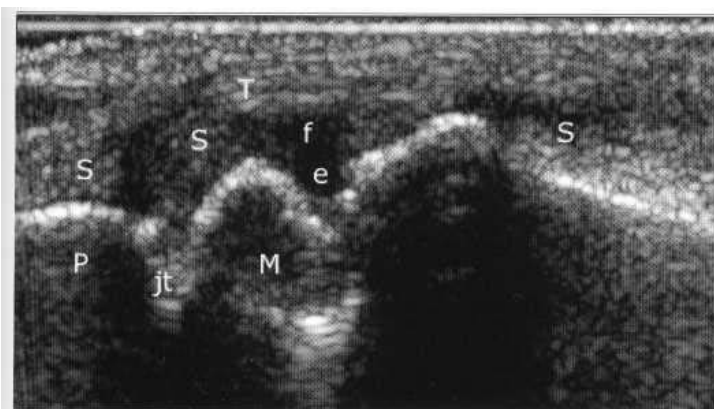


Fig. 38.22 Sagittal scan of metacarpophalangeal joint affected by rheumatoid arthritis. The irregular echogenic margin of an erosion (e) is shown in the distal high echogenic cortical margin of the head of the second metacarpal (M) with adjacent low echogenic synovial proliferation (S) and anechoic fluid (f). The fibrillar extensor tendon (T) and echogenic cortex of proximal phalanx (P) and metacarpophalangeal joint (jt) are shown.

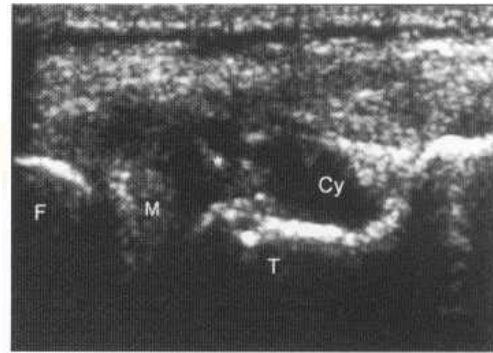


Fig. 38.23 Coronal scan of lateral meniscal tear. Echogenic margin of lateral femoral condyle (F) and tibial plateau (T), intermediate lower echogenicity of meniscus (M) with torn fragment (*), areas of anechoic fluid of the meniscal cyst (Cy) arising from the tear.

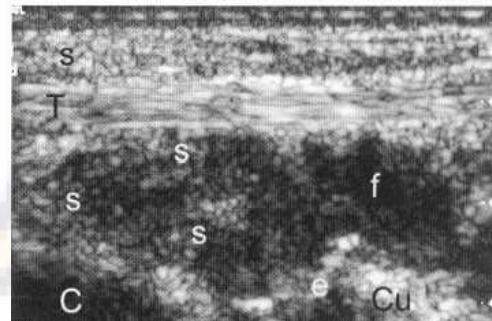


Fig. 38.24 Longitudinal scan of synovial thickening around the lateral mid foot. Echogenic margins of the calcaneum (C) and cuboid (Cu). Irregular margin of cuboid representing erosion (e). Synovial thickening (black S) of intermediate echogenicity around peroneus brevis tendon (T) which has a bright fibrillar structure. Irregular fingers of synovium (white S) associated with calcaneocuboid joint with associated anechoic synovial fluid and low echogenicity (f).

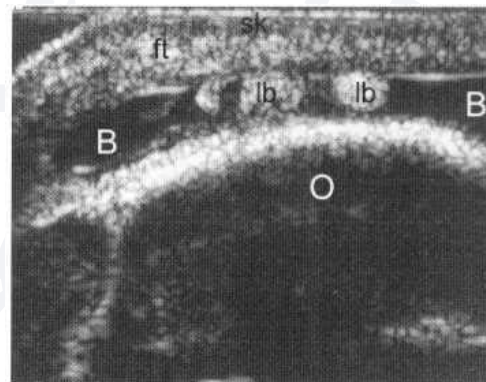


Fig 38.25 Transverse scan through olecranon bursa. Deep to the skin (sk) and subcutaneous fat (ft), an anechoic fluid-filled bursa (B) is shown with echogenic foci within, these representing loose bodies (lb) adjacent to the echogenic cortical margin of the olecranon (O).

ning of the tendons is also possible, especially in the hand where tendon rupture may be suspected clinically in rheumatoid disease.

Tendons are fibrillar structures and the ultrasound beam must be held perpendicular to the fibres, whether in a transverse or longitudinal plane, with the tendon under tension in order to avoid anisotropic or reflective artefact. This is where low echogenicity occurs in an area where there are intact tendon fibrils. This artefact is seen normally at the insertion of the tendon as the fibres curve away from the trans-

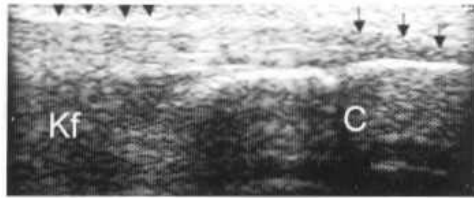


Fig. 38.26 Longitudinal scan of the normal Achilles tendon. Echogenic fibrillar structure of the tendon, with bright linear echogenicity of the paratenon (arrows) and anisotropic effect of tendon fibrils (tailed arrows) as they curve into the insertion point in the calcaneum (C). Karger's fat pad (Kf) is of low heterogeneous echogenicity.

ducer into the bony insertion (Fig. 38.26). Tendons may be surrounded by synovium, for example in the hands and feet, or loose areolar connective tissue called paratenon, for example the Achilles and patella tendon. Ultrasound may be helpful in differentiating between the causes of pain around a joint, localising it to pathology in the tendon itself (Figs 38.27, 38.28), paratenon or synovium

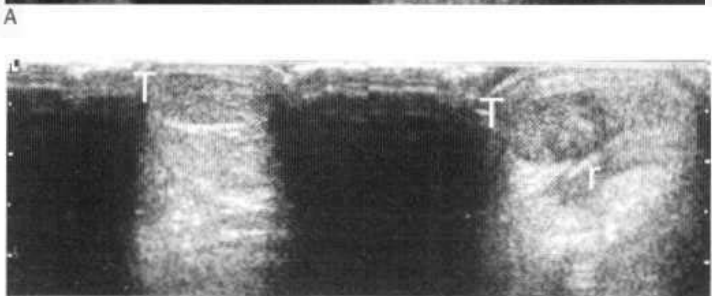
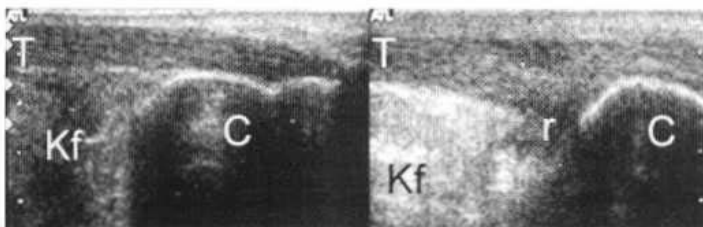


Fig. 38.27 (A) Longitudinal scans of the Achilles tendon. On the left, normal tendon (T), Karger's fat pad (Kf) and insertion of tendon into calcaneum (C). On the right the tendon (T) is swollen and has focal low echogenicity near the insertion into the calcaneum (C) consistent with focal tendinosis. A small area of low echogenicity deep to the tendon (r) is a retrocalcaneal bursa. Also, note the increased echogenicity of Karger's fat pad on the right associated with the inflammatory change. (B) Transverse scans of the Achilles tendon. On the left normal tendon (T) and on the right the focal area of tendinosis (T) in the medial aspect of the tendon.

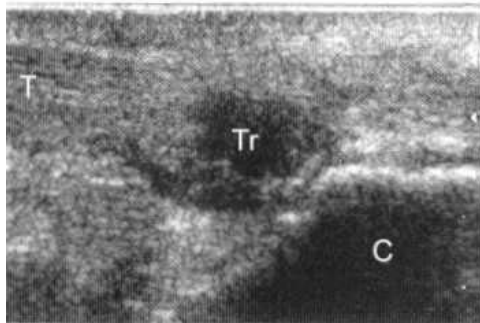


Fig. 38.28 Longitudinal scan of partial tear in the distal Achilles tendon (T) where torn fibrils of the tendon extend into a liquefied anechoic haematoma (Tr) adjacent to insertion in calcaneum (C).

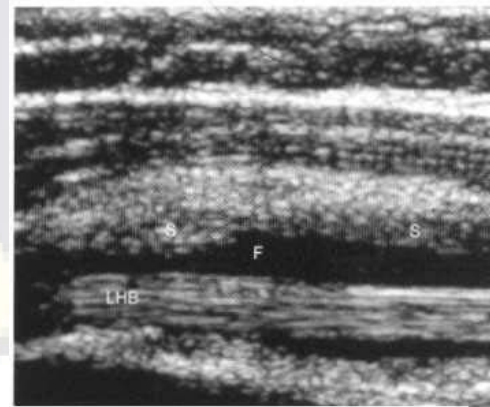
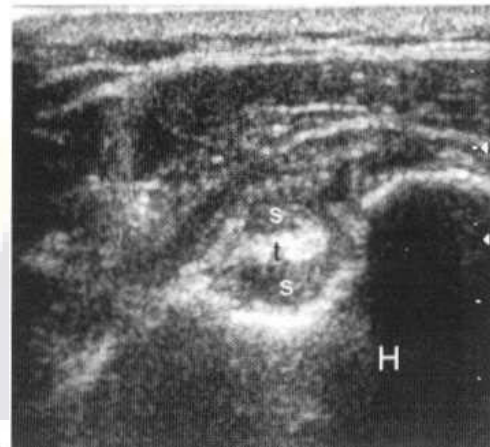


Fig. 38.29 (A) Transverse scan through the bicipital groove of the humerus (H), which contains a normal brightly echogenic long head of biceps tendon (t) surrounded by low echogenic synovial thickening (s). (B) Longitudinal scan through the long head of biceps (LHB) surrounded by anechoic fluid (F) and synovial thickening (S).

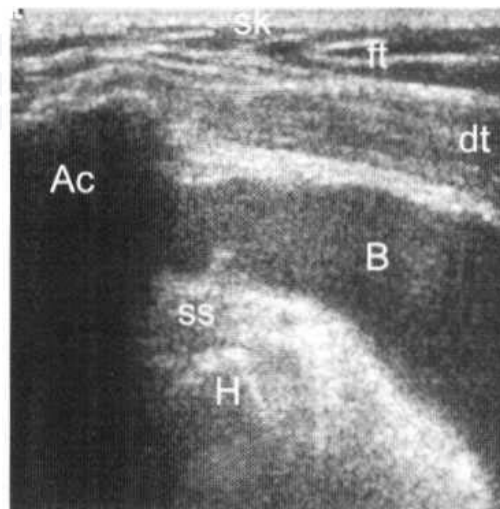


Fig. 38.30 Coronal scan through the shoulder showing the tip of the acromion (Ac) casting acoustic shadow, the layers of tissue superficial to the supraspinatus tendon (ss) as it inserts into the greater tuberosity of the humerus (H), namely: skin (sk), fat (ft), deltoid muscle (dt) and a large subacromion bursa (B) of hypoechogenicity, the cause of the patient's symptoms.

(Fig. 38.29), a bursa (Fig. 38.30), or even the subcutaneous tissues, such as in Huglund's disease—a thickening of dermis and hypodermis. Ultrasound may also show the local extent of a tendon

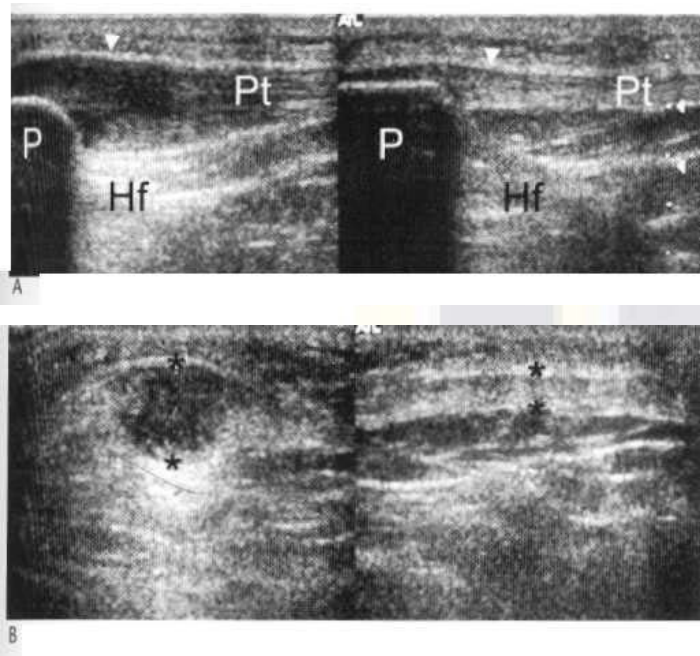


Fig. 38.31 'Jumper's knee'. (A) Longitudinal scan. A focal central tendinosis of the patella tendon (Pt) at the proximal insertion in the lower pole of the patella (P). There is increase in the echogenicity of the related Hoffa's fat pad (Hf) adjacent to the area of swelling and low echogenicity in the patella tendon on the left compared to the normal tendon on the right. Arrowheads indicate the paratenon. (B) Transverse scan showing the patella tendon between *. On the left the central focal area of swelling and low echogenicity can be compared to the wide thin high echogenicity of the normal tendon on the right.

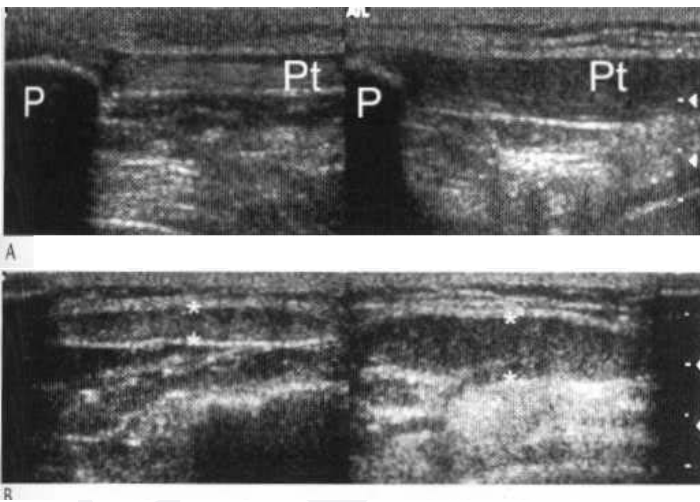


Fig. 38.32 (A) Longitudinal scan through diffuse/global patella tendinosis; the patella tendon (Pt) on the right is swollen and of generally low echogenicity compared to the normal tendon on the left. (B) Transverse scan through diffuse/global patella tendinosis, showing the patella tendon between * on the right being diffusely swollen compared to Fig. 38.31B and the normal tendon on the left (P) = patella.

problem, such as a focal (Fig. 38.31) versus a diffuse (Fig. 38.32) tendonopathy, which may precede rupture. Leakage of synovial fluid may also be demonstrated using ultrasound, for example a ruptured Baker's cyst (Figs 38.33, 38.34) which needs to be differentiated from other causes of calf pain, such as muscle tear (Fig. 38.35) or deep vein thrombosis.

It should be noted that MRI is more useful in the assessment of overall anatomy around a joint. However, if a joint has been

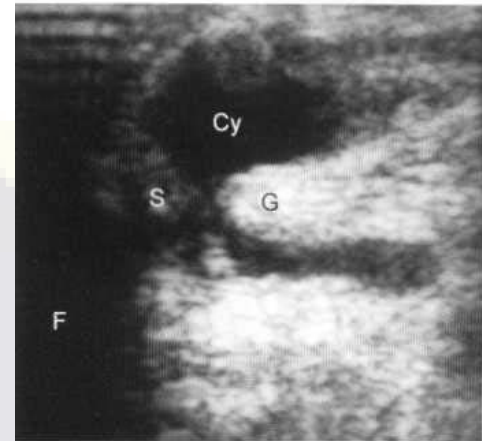


Fig. 38.33 Transverse scan through Baker's cyst, an anechoic collection of fluid (Cy). This is a bursa communicating with the knee joint sited behind the medial femoral condyle (F), the neck of the cyst has formed between the medial head of gastrocnemius (G) and the semimembranosus tendon (S)

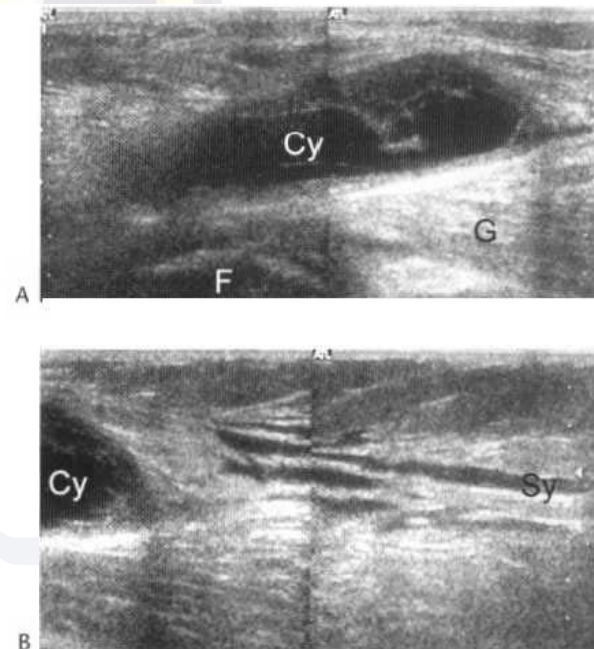


Fig. 38.34 Ruptured Baker's cyst. (A) Longitudinal scan of the ruptured Baker's cyst (Cy) posterior to the medial femoral condyle (F) and gastrocnemius muscle (G) with a mixture of anechoic synovial fluid and synovial thickening and debris extending into the cystic cavity which may relate to haemorrhage. The tapered inferior end of the cyst indicates that there has been rupture. (B) Longitudinal scan of the tip of the ruptured cyst (Cy); the streaks of low echogenicity extending into the muscle (sy) represent synovial fluid that has leaked into the surrounding fluid.

replaced, ultrasound may be more helpful in defining the state of tissues around the replacement as it will be unaffected by metal artefact.

MRI

Using MRI, synovium, synovial fluid, cartilage, ligaments, tendons and bone can all be identified (Fig. 38.36).

Erosions are seen both earlier and more often at MRI than on plain films and are seen as defects in bone. Pannus is seen as a soft-tissue signal mass adjacent to the erosion. When synovial proliferation is

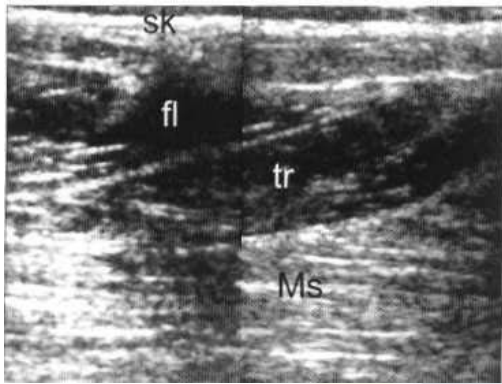


Fig. 38.35 Longitudinal scan of lower leg and a muscle tear (tr) associated with liquefied haematoma (fl) just below the skin (sk). In comparison with Fig. 38.34B, the area of low echogenicity is more heterogeneous and has a more irregular contour than the muscle oedema. Note normal muscle (Ms)

vascular, it is even better demonstrated after the use of intravenous gadolinium (Fig. 38.37).

MRI is not only sensitive (as is isotope scanning) but also specific (unlike scanning). MRI is superior in showing not only erosions but also subarticular cysts and bone oedema. Effusions and tendinous change as well as extra-articular collections of fluid are seen with MRI so that, where available, this is the investigation of choice in the initial diagnosis of disease and its progression. MRI is also superior to any other modality in demonstrating cartilage loss in both osteoarthritis and rheumatoid disease (Fig. 38.38).

Changes in the tendo Achilles and its insertion into the hind foot are better seen at MRI than on plain films (Fig. 38.2). The tendon is of low signal and stands out clearly against the fat that surrounds it. In tendinitis, the tendon is thickened, often grossly so, and is surrounded by (bright-signalled) oedema. Central areas of cystic necrosis in this or any other tendon are always bright on T₂-weighted or STIR sequence images. Erosions in the insertion are seen as cortical defects, often with surrounding local oedema. The enlarged retrocalcaneal bursa is also clearly demonstrated at MRI (Fig. 38.39).

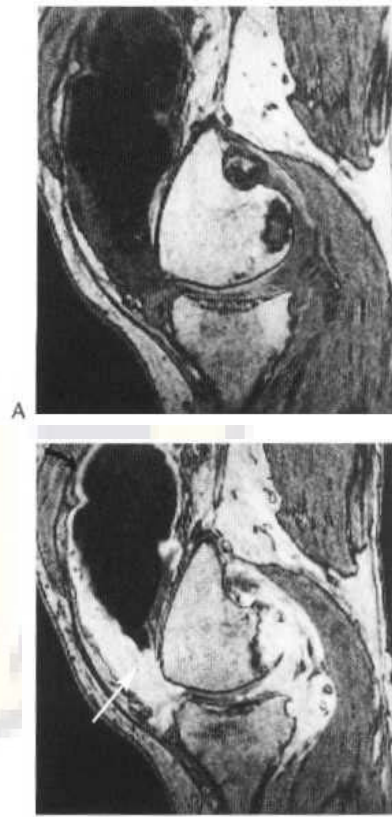


Fig. 38.37 Pannus in rheumatoid arthritis. Thickened synovium demonstrated (A) pre- and (B) post-gadolinium enhancement. The effusion exhibits a low signal, while the surrounding area of bright signal (arrow) represents hypertrophic vascular synovium. (Courtesy of Dr G. Clunie, UCL Hospitals.)

C1/C2 lesions

Changes at C1 and C2 were better shown by linear tomograph) than on conventional plain films and, subsequently, by CT in both the axial plane and with sagittal and coronal reconstruction.

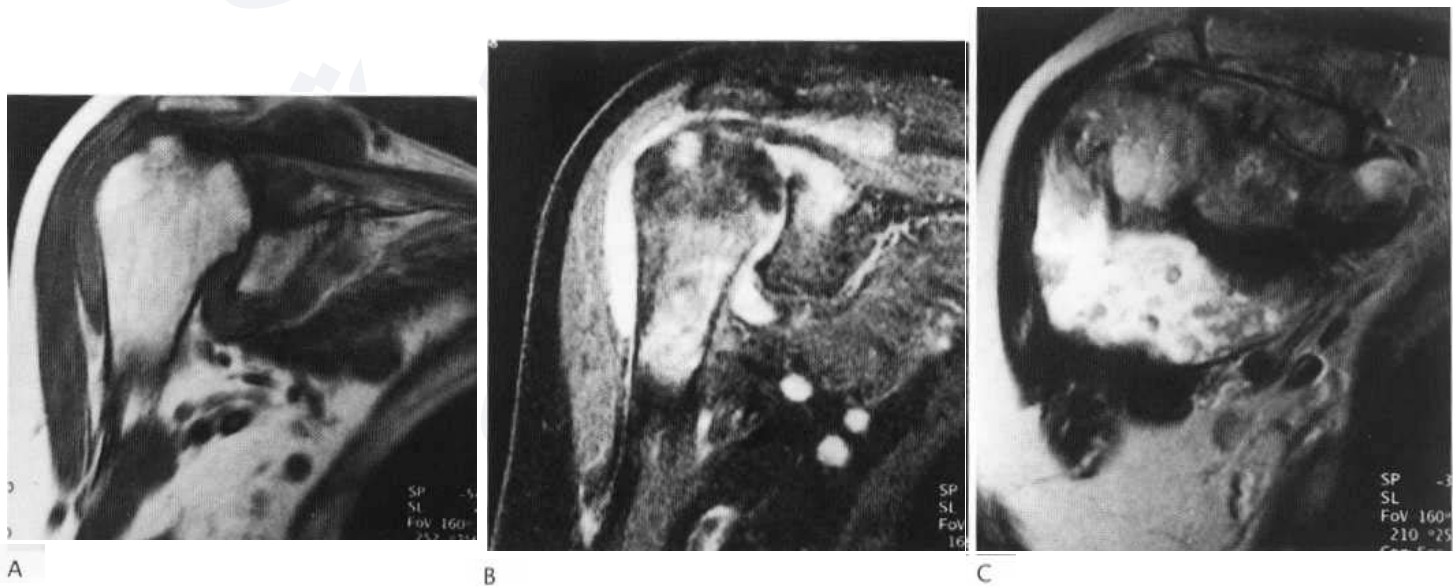


Fig. 38.36 Rheumatoid arthritis at MRI. (A) Coronal T₁-weighted sequence. (B) Coronal fat-suppression images. There is a large effusion in the shoulder joint and in the subacromial bursa. There is upward subluxation of the humeral head but the rotator cuff tendon is in part intact. Erosive changes are demonstrated in the humeral head with the appropriate signal change. (C) A more anterior scan shows the distended subacromial bursa containing numerous loose bodies. See also Fig. 38.19.



Fig. 38.38 Rheumatoid arthritis at MRI (corona (A) and sagittal (B) T₂-weighted sequences). There is loss of meniscal and articular cartilage, irregularity of articular surfaces and subchondral cysts filled with fluid. There is also debris within the joint.

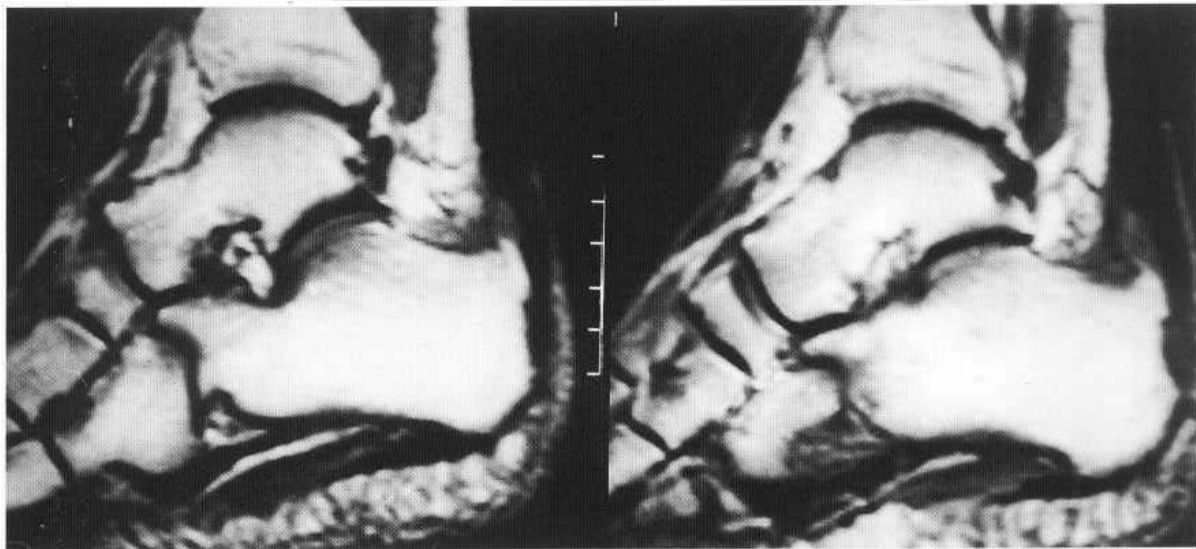


Fig. 38.39 Retrocalcaneal bursitis with an erosion. The tendo Achilles is thickened distally; the bone is eroded at its insertion and there is also an erosion on the upper aspect of the calcaneus associated with a local bursitis.

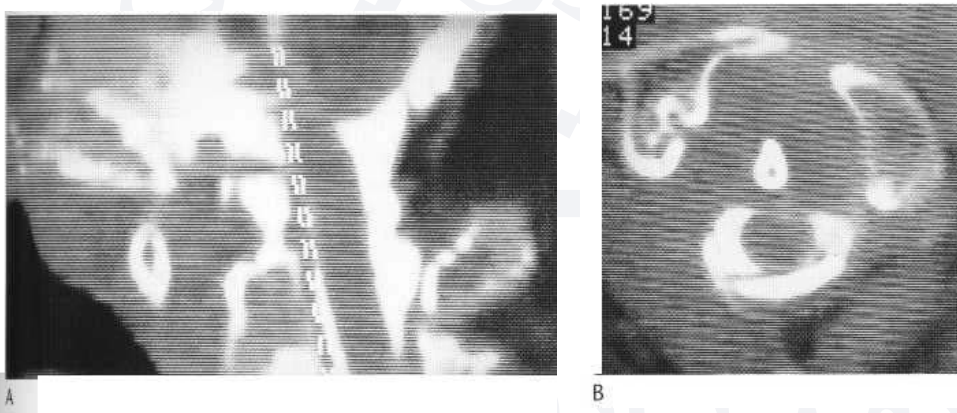


Fig. 38.40 (A) Sagittal CT reconstruction showing odontoid peg erosion and separation of the space between the peg and arch. There is a soft-tissue mass interposed between the two structures. The peg is upwardly subluxated. (Courtesy of Dr J. Stevens.) (B) CT radiculography in rheumatoid arthritis. The odontoid peg is eroded and separated from the arch of the atlas by a soft-tissue mass. (Courtesy of Dr J. Stevens.)

Opacification of the CSF at radiculography renders both the cord and soft-tissue pannus visible and allows changes in flexion and extension to be visualised during the examination (Fig. 38.40).

MRI is now the investigation of choice for imaging the cranio-cervical junction, and the status of the cord can be assessed simultaneously (Fig. 38.41). Bone, pannus, cord and CSF are all

simultaneously imaged. Changes in flexion and extension are also assessed, but are equally well seen on a plain film.

ARTHRITIS IN CHILDREN

There are many causes of polyarthritis in children, the most common being viral infections. It is now recognised that chronic



A



B

Fig. 38.41 Rheumatoid arthritis at MR scanning. (A) T₁-weighted axial image. (B) T₁-weighted sagittal image. A soft-tissue mass is seen in the region of the eroded odontoid peg and this indents the cord. Note distal changes at all levels in the cervical spine.

childhood polyarthritis is a heterogeneous group of disorders, the generic term for which is *juvenile idiopathic polyarthritis* (Box 38.1). Some 10% of the total eventually have a *seropositive* form of disease similar to, or identical with, adult rheumatoid arthritis, that is, an essentially peripheral erosive polyarthritis. The remaining patients have *seronegative* juvenile chronic arthritis for which definite clinical and histological diagnostic criteria exist.

Children with seronegative juvenile chronic arthritis may be further subdivided:

1. *Acute systemic onset type* (true Still's disease) with constitutional symptoms and hepatosplenomegaly, but little or no joint involvement.

Box 38.1 Classification of juvenile idiopathic arthritis

1. Adult-type rheumatoid arthritis (with IgM rheumatoid factor)
2. Polyarthritis with ankylosing spondylitis-type sacroiliitis
3. Still's disease
 - a. systemic
 - b. polyarticular
 - c. pauciarticular, with or without chronic iridocyclitis
4. Psoriatic arthropathy
5. Arthritis associated with ulcerative colitis or regional enteritis (as in adults)
6. Polyarthropathies associated with other disorders, such as systemic lupus erythematosus or familial Mediterranean fever, etc

(Reproduced by kind permission of Dr B.M. Ansell.)



Fig. 38.42 juvenile chronic arthritis. Accelerated skeletal maturity with modelling abnormalities of the carpal bones and osteoporosis.

2. *Pauci-articular* (not more than four joints involved) affecting especially the knees, wrists and ankles. This usually ends up as:

3. *Polvarticular disease*, which may also present at the onset. Radiological changes are late and the disease is non-erosive.

In the carpus and tarsus the bones show accelerated maturation due to hyperaemia, crowding of bones with joint space narrowing and an abnormal angular shape (Fig. 38.42). In general, early overgrowth of epiphyseal centres (Fig. 38.43) with squaring or angulation (Fig. 38.44) leads to premature fusion and eventual hypoplasia. This occurs at metacarpal and metatarsal epiphyses and around the knees, hips, elbows and shoulders. The abnormally modelled bone ends cannot be easily distinguished from the similar changes of synovial tuberculosis or haemophilia. Osteoporosis may result from



Fig. 38.43 Juvenile chronic arthritis. Monarticular arthritis with soft-tissue swelling, osteoporosis and overgrowth of the epiphyses at the right knee. Normal left knee.

hyperaemia or steroid administration which, in large doses, also causes undergrowth. Pathological fractures may result. Residual trabeculae along lines of stress are rendered very prominent. At the elbow, marked radial head enlargement may be seen and the paired long bones may bow. The cervical spine is often affected and indeed is the cause of presentation in 2% of cases. Diminution of neck movement is followed by apophyseal joint changes, maximal at C2-3, where erosions lead to ankylosis. The associated vertebral bodies fail to develop (Fig. 38.45). Atlanto-axial subluxation is said to occur only rarely in those patients with seronegative disease, and neurocentral joint lesions do not occur in seronegative disease.

Juvenile ankylosing spondylitis

This disease has a characteristic onset at about 10 years of age. It is five times more common in boys and presents initially with an asymmetrical peripheral arthropathy. Sacroiliac changes develop some 5-15 years later.

SERONEGATIVE SPONDYLOARTHROPATHIES

This is a group of non-rheumatoid seronegative disorders that have clinical, radiological and familial interrelationships. There are definite criteria for their diagnosis. These features include:

1. Absence of rheumatoid factors
2. Peripheral arthropathy
3. Sacroiliitis with or without ankylosing spondylitis



Fig. 38.44 Juvenile chronic arthritis. There is overgrowth of the epiphyses around the knee with associated soft-tissue swelling. The tibial epiphysis in particular shows a rather square shape with marked angulation of its margins, which never occurs in the normal.

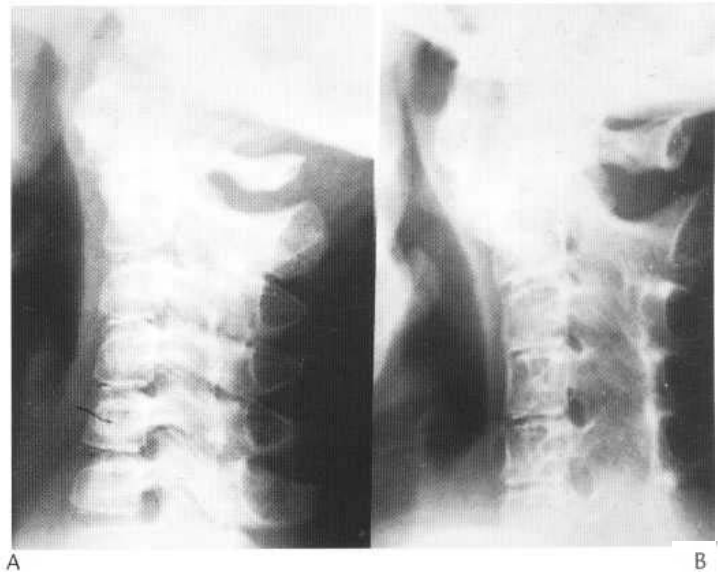


Fig. 38.45 Juvenile chronic arthritis. (A) The early radiograph in this patient shows hypoplasia of the vertebral bodies and a widened cervical canal. (B) Subsequently the vertebral bodies and facet joints ankylose, with failure of development.

4. Clinical overlap, including two or more of the following features-psoriatic skin or nail lesions; conjunctivitis; ulceration of mouth, intestines or genitals; genitourinary infections; erythema nodosum
5. Increased incidence of the same or any other of these diseases in families.

The diseases which fit into these categories are:

1. Ankylosing spondylitis
2. Psoriatic arthritis
3. Reiter's syndrome
4. Ulcerative colitis
5. Crohn's disease
6. Whipple's disease
7. Behcet's syndrome.

The interrelationships between the diseases are seen in Figure 38.46. Chronic inflammatory bowel disease can, for instance, be seen to be linked to spondylitis and uveitis, while spondylitis is further linked to aortitis, seronegative arthritis and psoriasis.

This genetic and clinical overlap accounts for the marked radiological overlap of these syndromes, so that spondylitis is seen in many of these conditions. Nonetheless, differences in the type of spondylitis seen in these diseases also exist.

Psoriatic arthritis

An association between psoriasis and arthritis was described as long ago as 1822. Some 10% of patients develop arthritis before the skin lesions appear, in 25% the two develop simultaneously and, in 65%, psoriasis precedes arthritis, often by up to 3.5 years. It seems that about 5% of patients with psoriasis develop an arthritis, but 15-30% of these are seropositive and have a radiological

appearance identical with that of rheumatoid disease. The remainder has a 'pure' pattern of psoriatic arthropathy, or a mixture of the two types. Normal bone mineralisation is regarded as a solid diagnostic criterion for psoriatic arthritis, but is not in fact particularly common, especially in chronic or severe disease.

The hands are as frequently affected by erosive change as are the feet in psoriatic arthropathy, in contradistinction to the patterns of Reiter's syndrome. Nail changes are related to resorption of the distal phalanges but no definite correlation exists between nail lesions and interphalangeal joints erosions. Erosions have a predilection for the distal interphalangeal joints, and especially the interphalangeal joint of the great toe (Fig. 38.47). Erosive changes are asymmetrical, even late in the disease, unlike rheumatoid arthritis, and especially if the metacarpophalangeal joints are involved. Joint narrowing may never occur.

Erosions are modified by proliferation of new bone at the interphalangeal joints and especially around erosions on the calcaneus, where large, irregular fluffy painful spurs form both posteriorly and inferiorly. Such change is more common in Reiter's syndrome, but is uncommon in rheumatoid arthritis. Late changes in the hands include osseous *fission* of the interphalangeal joints (Fig. 38.48) and a 'cup-and-pencil' appearance at affected joints, leading to arthritis mutilans, but not ulnar deviation.

Periostitis in psoriatic arthritis occurs along the shafts of the tubular bones on hands and feet, which become sclerotic and expanded and, in association with soft-tissue swelling, gives a 'sausage digit' (Fig. 38.49).

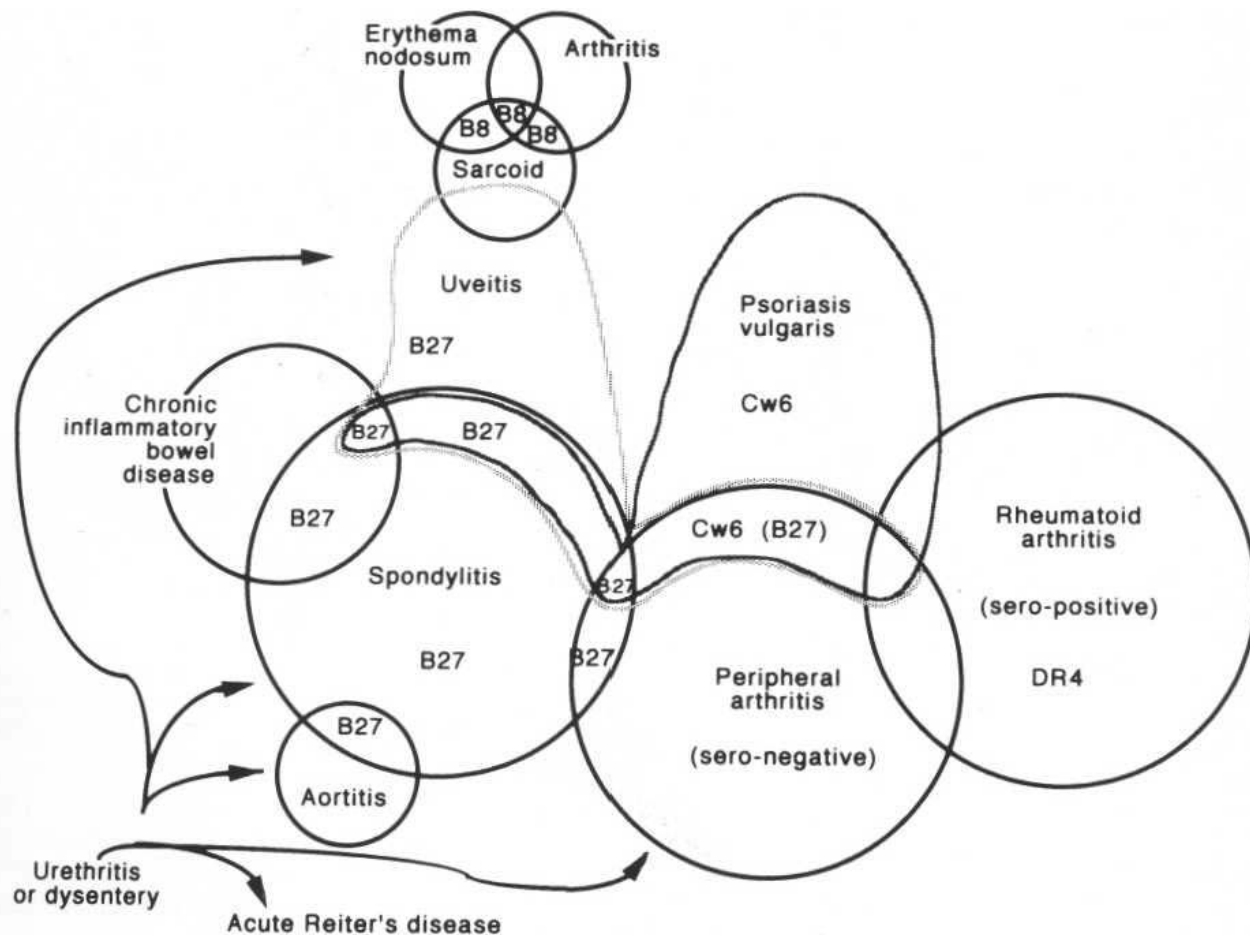


Fig. 38.46 The relationship between the different manifestations of arthritis is shown, together with the appropriate tissue markers. (Courtesy of Dr D. A. Brewerton.)



Fig. 38.47 Psoriasis. Soft-tissue swelling is seen over the great toe and the erosions at the bases of the distal phalanges are on the articular, rather than the periarticular, surface, producing a 'gull's wing' appearance.

Involvement of the larger joints is not common, but *sacroiliitis* may be seen in up to 50% of those with psoriatic arthritis. Often, but not inevitably, symmetrical erosions, joint widening and sclerosis are seen but fusion is less common than in ankylosing spondylitis.

Paravertebral ossification may be the only feature of an osteopathy, even occurring in the absence of sacroiliac or digital disease. These *syndesmophytes*, which may be vertically directed and are not always attached to vertebral margins, should be distinguished from the more horizontally directed degenerative osteophytes. Vertebral squaring is uncommon in psoriatic spondylitis (Fig. 38.50).

Reiter's syndrome

This occurs most commonly in young men and is usually sexually transmitted. The classic triad in the UK consists of a male patient with arthritis, urethritis and conjunctivitis. Gonococcal arthritis may thus cause confusion. In continental Europe, the similar syndrome, originally described by Reiter in 1916, occurs in association with bacillary dysentery in both sexes.

Skeletal abnormalities will eventually be found in up to 80% of patients. Initial attacks of pain subside, but later recur, leaving progressive change at joints and entheses (the sites of musculotendinous insertion into bone). Reiter's syndrome affects the feet rather than the hands, and also in a more severe form. In the foot, erosions occur at the metatarsophalangeal joints and the interphalangeal joint



Fig. 38.48 Psoriasis. The distal interphalangeal joints are involved in this condition. Bone density is often preserved. Erosions proceed along the bases of the distal phalanges and there is splaying of bone locally. Despite the erosive change, the joints may be increased in width or, alternatively, fused. These changes are totally unlike those seen in rheumatoid arthritis both in appearance and distribution. There is also a neurotrophic change at the distal and middle phalanges, with longitudinal and concentric bone resorption, producing a 'licked candy stick' appearance.

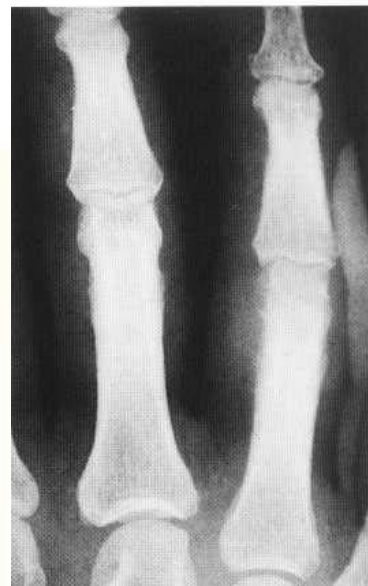


Fig. 38.49 A 'sausage digit' in psoriatic arthritis. There is soft-tissue swelling. Periostitis is demonstrated. The bone shows an apparent increase in density.

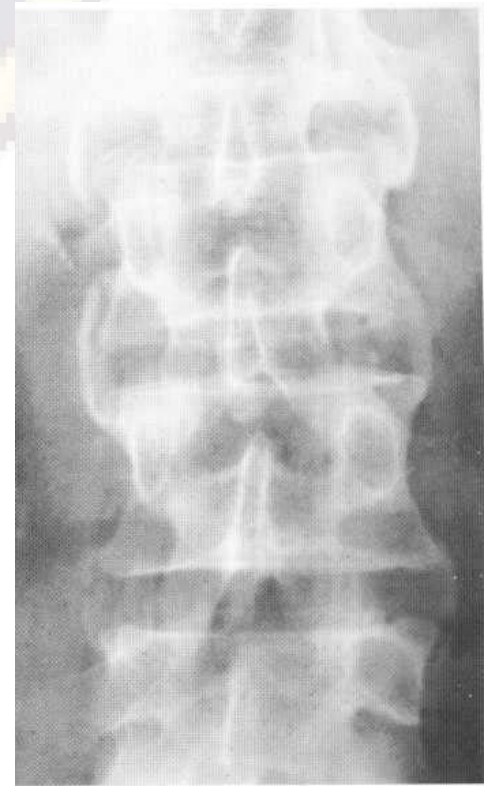


Fig. 38.50 Psoriatic spondylitis. Non-marginal vertical floating syndesmophytes are more typical of psoriasis and are less often seen in ankylosing spondylitis. (Courtesy of Dr J. T. Patton.)

of the great toe. Osteoporosis is not a prominent feature of the disorder. It can be asymmetrical, unlike rheumatoid arthritis.

Irregular erosions occur at entheses. Periostitis may be fine and lamellar in acute cases (Fig. 38.51), or fluffy and irregular in chronic disease. Painful erosions (Fig. 38.52) and reactive spurs are very common around the calcaneus, probably more so than in any other arthropathy, occurring in 20% of patients. In contrast to ankylosing spondylitis, the feet are severely affected. Sacroiliitis develops late in Reiter's syndrome but may be seen in about half of all cases. The changes may be asymmetrical or unilateral (Fig. 38.53). Fusion is also less frequent than in ankylosing spondylitis. Spinal

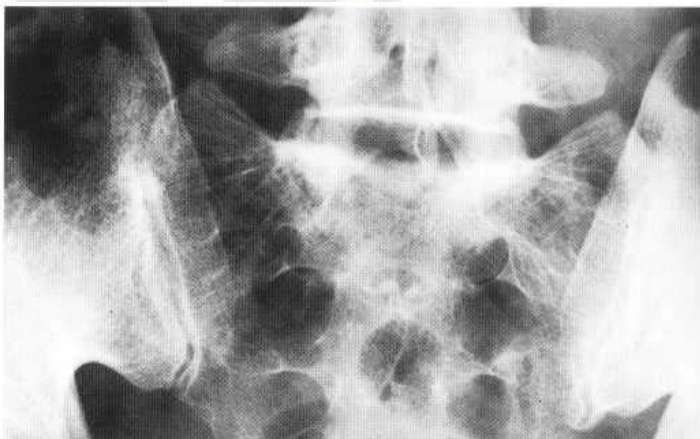
non-marginal syndesmophytes, identical to those seen in psoriatic arthritis, occur especially around the thoracolumbar junction but less frequently than in psoriatic arthritis.

Ankylosing spondylitis

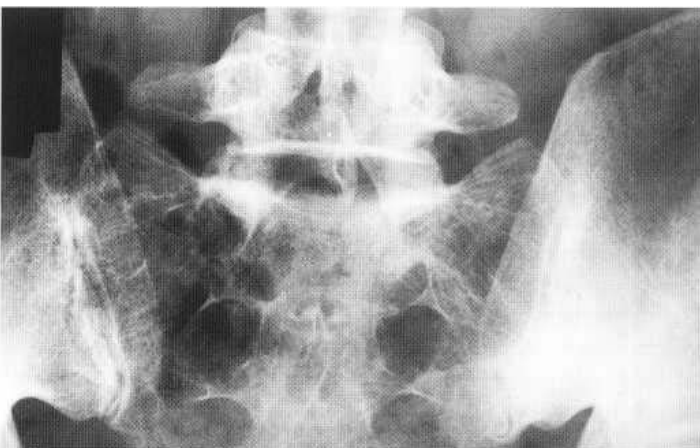
Ankylosing spondylitis (Marie Strumpell arthritis, Bechterew's disease) is a seronegative spondyloarthropathy. Some 90% of patients with this disease have the HLA-B27 antigen or, to put it another way, an individual with this antigen is 300 times as likely to have ankylosing spondylitis as is a person without the antigen. Sixty-five per cent of patients with psoriasis and spondylitis, or inflammatory bowel disease and spondylitis, have HLA-B27, but in



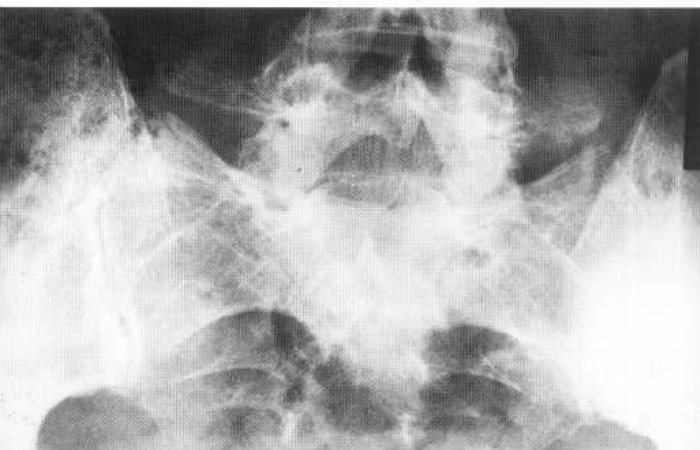
Fig. 38.51 Reiter's syndrome-acute form, showing marked osteoporosis and periosteal reaction (arrows).



A



B



C

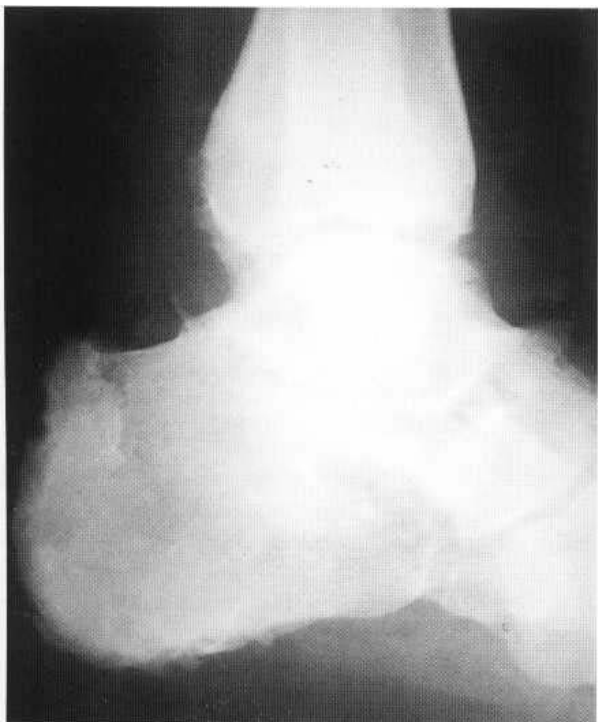


Fig. 38.52 Reiter's syndrome. Periostitis and erosive changes on the plantar and posterior aspects of the calcaneus and of the distal tibia.

Fig. 38.53 (A,B,C) Reiter's syndrome. The three radiographs taken over a 12-year period demonstrate the progression of a unilateral sacroiliitis.

psoriasis with a peripheral arthropathy there is only a weak association if spondylitis or sacroiliitis are not present. Thus the antigen is essentially related to the presence of spinal changes.

Histologically, the synovitis of ankylosing spondylitis is identical with that of rheumatoid arthritis: the enthesopathy consists of destruction of ligaments, tendons and local bone with sub-jacent inflammatory infiltrates. The destructive lesion heals by deposition of new bone at the local tendon or ligament interface, causing healing with bone proliferation at non-articular sites, syndesmophytes at vertebral margins and ossification of joint capsules.

Though the disease may affect children, it is said to occur more commonly in young men in their late teens and twenties, but recently it has been realised that women may be affected in equal numbers. The onset is often insidious so that sacroiliitis is usually seen at presentation. Spondylitis need not be present but develops subsequently, often at the thoracolumbar region initially, but sometimes affecting the cervical spine in females. Spinal changes without sacroiliac changes are very rare in this disease.

Sacroiliac joints Symmetrical change is almost inevitable (Fig. 38.54A). Erosions, often worse on the iliac side, widen the joint and its hazy margins may resemble the normal adolescent joint. The erosions later show considerable sclerosis, and the joint narrows as irregular new bone bridges the joint space, so that fusion eventually occurs.

Joint changes are assessed using the *prone* view of the sacroiliac joint, though oblique views are helpful. Linear tomography gives good images of the sacroiliac joints, but was superseded by CT scanning, which defines cortical bone well (Fig. 38.54B). Images are free of overlying gut shadows. Small and early erosions can be visualised. This is probably the examination of choice.

Radionuclide scanning shows non-specific increase in uptake unilaterally or bilaterally. Bilateral change may be more difficult to assess if increase in uptake is symmetrical. An increase in the ratio of counts between sacroiliac joints and the sacrum of more than 1.4 : 1 was held to indicate the presence of sacroiliitis (Fig. 38.55). MRI is probably not as helpful in showing the cortical and joint changes in the sacroiliac region.



A



B

Fig. 38.54 Ankylosing spondylitis-early. (A) Serrated margins of sacroiliac joints and periarticular sclerosis. (B) CT scanning demonstrates bilateral sacroiliitis.

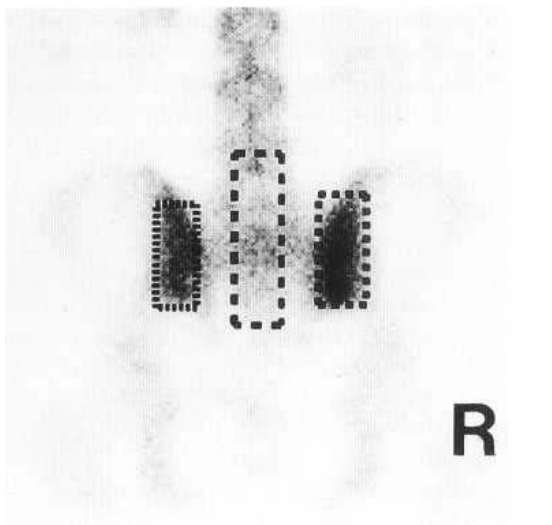


Fig. 38.55 Ankylosing spondylitis. Increase in uptake is demonstrated at both sacroiliac joints, greater on the right, in this posterior scan. (Courtesy of Dr A. Hilson.)

Spinal changes Erosions of vertebral margins heal by proliferation of sclerotic bone, which stands out in marked contrast to the rest of the vertebral body (the Romanus lesion) (Fig. 38.56). These healed erosions of vertebral margins may account for vertebral 'squaring'; an alternative cause is the laying down of new bone anteriorly beneath the longitudinal ligament. Both mechanisms may be operative (Fig. 38.57).



Fig. 38.56 Ankylosing spondylitis. Discal narrowing and adjacent erosions heal with prolific new bone formation. Sclerosis and vertebral squaring result.

Further bony outgrowths in a later stage of healing lead to neat, vertically disposed marginal syndesmophytes, which may extend all the way up the spine (Fig. 38.58). The ossification lies in the annulus. Similar well-defined bands of ossification may be seen in the interspinous ligaments and around minor and major joints. If the intervertebral disc is intact at the time of syndesmophyte formation, it often never narrows, but may undergo central calcification. This phenomenon often follows vertebral fusion from any cause. Should the disc bulge, the syndesmophytes may be displaced. Syndesmophytes give the spine a knobbly appearance (Fig. 38.58), likened to a bamboo stick. Erosions at costotransverse and apophyseal joints also end in fusion. A cauda equina syndrome may result from arachnoiditis when large posterior dural diverticula are occasionally seen at radiculography, with osseous defects in the laminae.

A scoliosis is often seen in the chronically diseased spine.

If the patient falls forward onto the head or chest, the rigid spine may snap, often through the porotic bone just beneath the end-plate. Hypermobility may be demonstrated on fluoroscopy. A sclerotic pseudarthrosis may result. Fractures may also occur through discs (Fig. 38.59). An associated pseudarthrosis is usually present at the neural arch at the same level as the discal or paradiscal fracture.

Occasionally, localised destructive lesions of adjacent end-plates are seen, with disc narrowing and marked reactive sclerosis (the Andersson lesion) (Figs 38.57B, 38.60). This lesion resembles an infective discitis or a neuropathy.

Peripheral joints Osteoporosis, erosions and joint space narrowing are less prominent than in rheumatoid arthritis, but shaggy periostitis and ankylosis are more common. At the hip, a prominent fringe of new bone may form at the capsule-bone junction. Bony ankylosis may precede or follow prosthetic joint replacement (Fig. 38.61).



Fig. 38.57 Ankylosing spondylitis. (A) Squaring of vertebral bodies is demonstrated, much of which is due to ossification in the line of the anterior longitudinal ligament. Longstanding fusion has resulted in calcification of the discal nucleus. There is also quite marked ankylosis of the posterior spinal elements. (B) A T₂-weighted MR sequence showing vertebral squaring with fusion across the narrowed intervertebral discs. There is prominence both of the anterior and posterior longitudinal ligaments, which may relate to ligamentous ossification.

There is marked abnormality too at the L1/2 disc space, which remains patent, the end-plate surfaces are irregular and there is surrounding bone oedema. See also Fig. 38.60.

Enthesopathies at iliac, ischial and calcaneal sites of ligamentous and tendinous insertions cause erosions followed by marked sclerotic periostitis.

Enteropathic spondyloarthropathies

Ulcerative colitis, regional enteritis and Whipple's disease may be associated with joint disease of two distinct types.

Peripheral arthropathy Episodes of fleeting asymmetrical peripheral arthritis follow the cyclic course of the gut disease and its severity is also proportional to the extent of the lesion. Radiographic change is usually confined to soft-tissue swelling and local periostitis. These patients are seronegative and HLA-B27 negative.

Sacroiliitis and spondylitis Pelvic and spinal changes identical to those of ankylosing spondylitis are seen. These do not correlate with gut disease activity but may precede its onset and continue to

worsen even if, for instance, the colon is totally removed. These patients (usually male) have a high level of HLA-B27 antigen.

gus. This florid exuberance is grosser than that seen in degenerative change. While continuity might also be seen following spinal infections, in DISH it is superimposed on a background of normal vertebrae and discs. Osteoarthritis, however, shows underlying bone and disc disease.

The sacroiliac joints may appear symmetrically fused on a plain film of the pelvis (Fig. 38.63). CT scanning demonstrates ligamentous and osteophytic ankylosis around the joint in the absence of erosions (Fig. 38.64). The patients may complain of spinal stiffness and low back pain. Florid neo-ossification is also seen at extraspinal sites, around the iliac crests, ischia and above the acetabulum, and at the sites of ligamentous or tendinous insertions into bone.

Similar changes are found in the foot, especially on the calcaneus, where florid spur formation is sometimes seen. The new bone is generally well defined and not related to local erosive or degenerative change. Fusion between the paired long bones may occasionally occur.

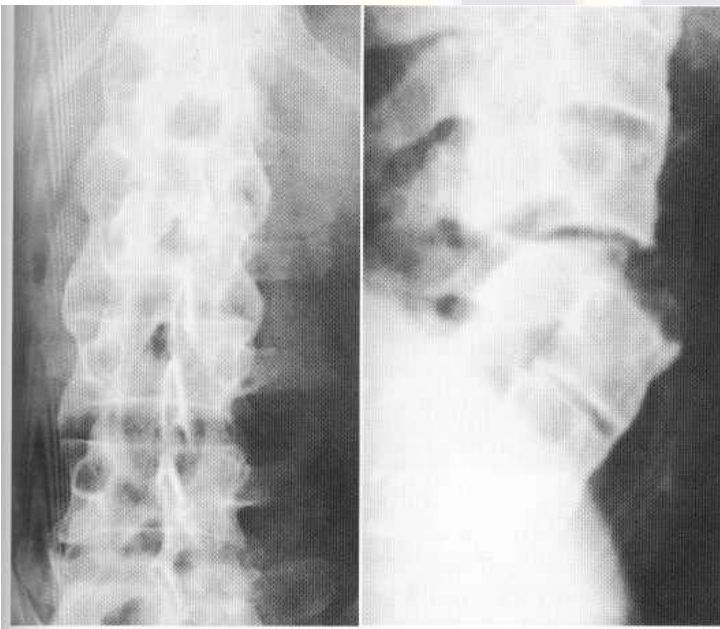


Fig. 38.58 Ankylosing spondylitis - 'bamboo spine' with marginal syndesmophytes.

Fig. 38.59 Cervical spine in ankylosing spondylitis, with fractures through the C4/5 and C5/6 discs.

worsen even if, for instance, the colon is totally removed. These patients (usually male) have a high level of HLA-B27 antigen.

Diffuse idiopathic skeletal hyperostosis

(Forestier's disease, senile ankylosing spondylitis)

This condition was originally thought to affect the spine only. The current title clearly indicates that the condition is a generalised one, in which extensive ossification is found at many sites. It is usually seen in elderly men (M:F=3:1). Some studies show an increased incidence of HLA-B27 in patients with diffuse idiopathic skeletal hyperostosis (DISH).

In the spine, dense ossification is found in the cervical (Fig. 38.62) and especially lower thoracic regions. Bone is laid down often in continuity anteriorly and, in the thoracic region, on the right side, as the left-sided aortic pulsation prevents its deposition. The thick, flowing, corticated plaques may indent the oesophagus.

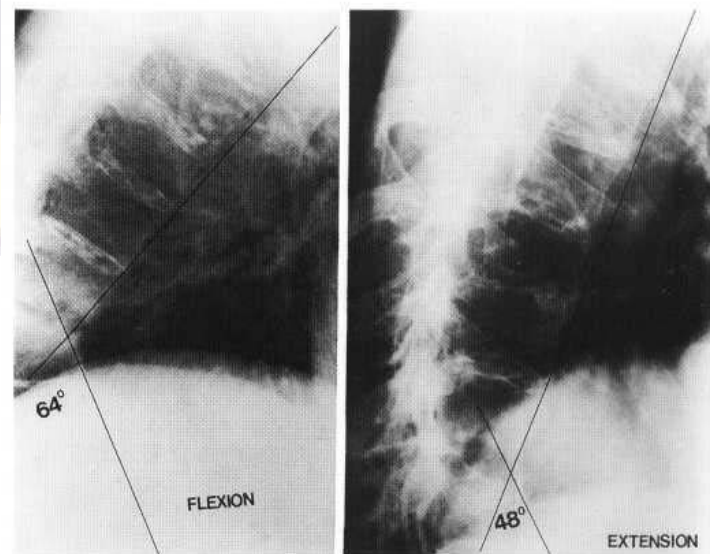


Fig. 38.60 Ankylosing spondylitis (Andersson lesion). End-plate irregularity is demonstrated together with reactive sclerosis in the underlying bone in this patient with ankylosing spondylitis. There is also instability at this level.

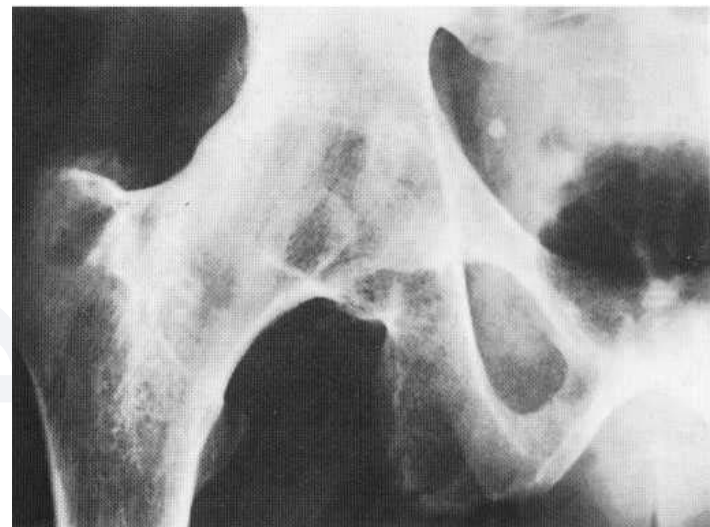


Fig. 38.61 Ankylosing spondylitis-note bony ankylosis across joint cartilage. Irregularity of the surface of the ischium is also shown.



Fig. 38.62 Senile ankylosing hyperostosis-this is an extreme example of this common lesion. A tremendous amount of new bone has formed. The outlines of the original vertebral bodies and disc spaces are preserved.

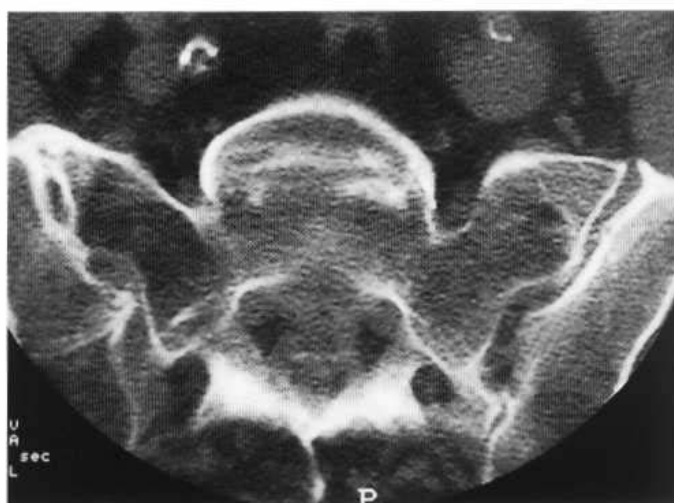


Fig. 38.64 Diffuse idiopathic skeletal hyperostosis. The CT scan shows that the joint spaces are still patent but there is ankylosis anteriorly.



Fig. 38.65 Diffuse idiopathic skeletal hyperostosis with ossification of the posterior longitudinal ligament. New bone is seen anteriorly on this cervical vertebral body and posteriorly in the canal along the line of the posterior longitudinal ligament.



Fig. 38.63 Diffuse idiopathic skeletal hyperostosis. The plain radiograph of this patient demonstrates new bone formation at the iliac crests and ischia as well as fusion of the sacroiliac joints superiorly. There is also faget's disease in the right femur.

Rarely, posterior ligamentous ossification (OPLL) encroaches on the theca and produces cord compression (Fig. 38.65).

Ossification of the posterior longitudinal ligament

New bone formation is seen in the posterior longitudinal ligament as an isolated phenomenon, often in Japanese patients, or in DISH or ankylosing spondylitis. The new bone is well shown on CT or MR scans (Fig. 38.65). Radioisotope scans show an increase in uptake in the spine if enough new bone is present in ankylosing spondylitis or DISH.

OSTEOARTHRITIS (osteoarthritis, degenerative arthritis, hypertrophic arthritis)

Osteoarthritis is a degenerative condition affecting articulations, especially those which bear weight or those subjected to much 'wear and tear'. The disease may be considered *primary* when no underlying cause can be discerned, or *secondary* if the joint is abnormal in form ab initio or is subjected to unusual stresses. In terms of end-stage appearances and treatment, the difference is probably academic.

Though there may be differences in the radiological appearances of osteoarthritis at different joints, degenerative disease has a number of specific features wherever it occurs.

Joint space narrowing The width of a joint space seen radiologically is due to the radiolucent cartilage; joint space narrowing is therefore the result of cartilage destruction. Often in a given joint a predictable pattern of joint narrowing may be expected. This change characteristically occurs in areas of excessive weight-bearing.

Joint space remodelling Joint narrowing due to cartilage destruction is followed by loss of underlying bone in stressed areas, and

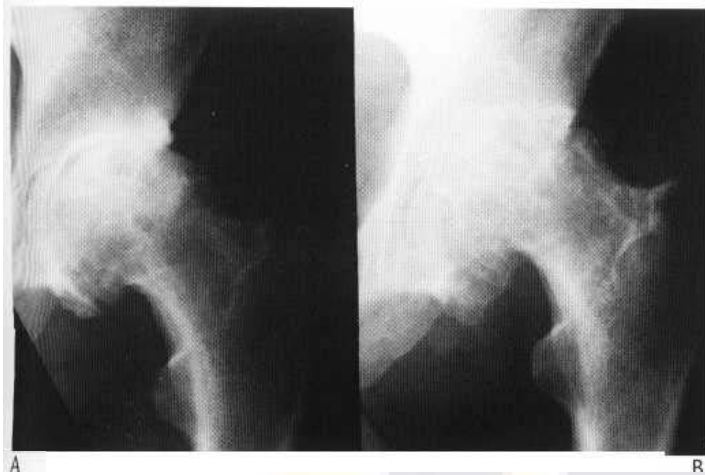


Fig. 38.66 (A) The initial radiograph shows lateral migration of the femoral head with obliteration of the superior joint space. There is accretion of new bone medially within the joint. (B) The subsequent radiograph shows collapse of the femoral head and of the acetabulum. There is now more new bone both on the femoral head and on the acetabulum medially. A new joint space often results. Buttressing of the medial cortex of the femoral neck (the calcar) is a common finding in degenerative disease of the hip.

formation of new bone and cartilage in non-stressed area and at joint margins, so that joint alignment alters (Fig. 38.66).

Beneath areas of cartilage destruction, eburnation results (Figs 38.66, 38.67). Localised increase in density is presumably due to: (i) stress-induced new bone formation; and (ii) trabecular collapse. Flattening and sclerosis result. New bone is formed in areas of low stress at joint margins—peripheral osteophytosis—or within the joint—central osteophytosis. Osteophytic new bone is formed in response to new lines of force and prevents further malalignment. Buttressing osteophytes may thus be seen on the narrower side of a degenerate disc.

Cyst or geode formation in subarticular regions occurs in osteoarthritis as well as in rheumatoid arthritis and is found in the weight-bearing areas, often associated with joint narrowing, eburnation and collapse of bone (Fig. 38.68).

Loose bodies These are formed by detachment of osteophytes, crumbling of articular surfaces or ossification of cartilage debris (Fig. 38.69). Osteoporosis and bony ankylosis are not manifestations of degenerative disease. Indeed, hypertrophic new bone is seldom seen in patients who are osteoporotic. Osteoporotic patients often fracture their femoral necks, but do not have masses of new bone about their hips. Conversely, patients with florid osteophytosis tend to have good bone density and fewer femoral neck fractures. When osteoarthritis results in pain and immobility, osteoporosis and soft-tissue wasting may result secondarily.

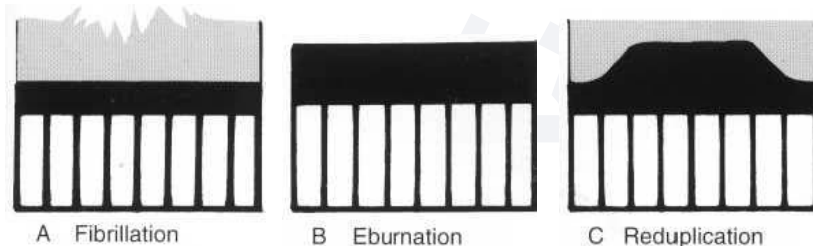


Fig. 38.67 (A,B,C) Patterns of degeneration (see text). Key: Grey = cartilage; black = cortex; stripes = medulla. (D) Reduplication with new bone laid down on the articular surface.

As so many of the changes in osteoarthritis relate to cortical bone, they are well imaged on plain films and CT scans, the latter showing osteophytes, erosions and cysts especially well. MRI is, however, the preferred imaging modality for osteoarthritis in the major joints. As in rheumatoid arthritis, changes of cartilage loss and subcartilaginous bone, oedema, cysts and bone necrosis are well demonstrated, together with loose bodies in the joint space and effusions. Osteophytes are especially well shown. Capsular thickening and plicae, and extracapsular changes in collateral ligaments and tendons, are all probably better seen than by any other means (Fig. 38.70).

Osteoarthritis in particular joints

The hip joint

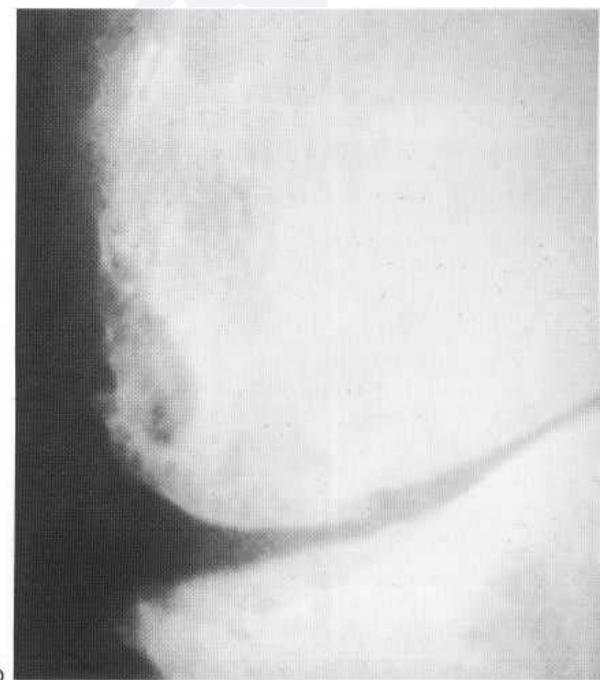
Murray (1965) has shown that only 35% of cases have no underlying radiologically determinable abnormality. Many patients who develop premature osteoarthritis in their forties are found to have a pre-existing abnormality. Some result from childhood-congenital dysplasias, congenital dislocation of the hip, acetabular dysplasia, Perthes' disease or slipped epiphysis. The underlying cause is often recognisable. Others occur later—Paget's disease, scoliosis, rheumatoid arthritis and variants and aseptic necrosis from any cause.

There is no 'typical' appearance for osteoarthritis of the hip; rather, groups of different patterns may be defined. The appearances are complicated by analgesic therapy, which may result in a neuropathic-type appearance with eburnation and rapid loss of bone (Fig. 38.71).

Patterns of osteoarthritis of the hip

These depend on the direction of migration of the femoral head which may be displaced superiorly (78%) (Fig. 38.72A) or medially (22%) (Fig. 38.72C). Superolateral migration may occur (Fig. 38.66), medially, or in an intermediate direction with narrowing of the appropriate segments of the joint.

Medial migration may lead to protrusio acetabuli (Fig. 38.72B), lateral migration to lateral acetabular restraining osteophytes and new bone within the medial aspect of the acetabulum (Fig. 38.66). Capsular traction leads to buttressing new bone formation, usually



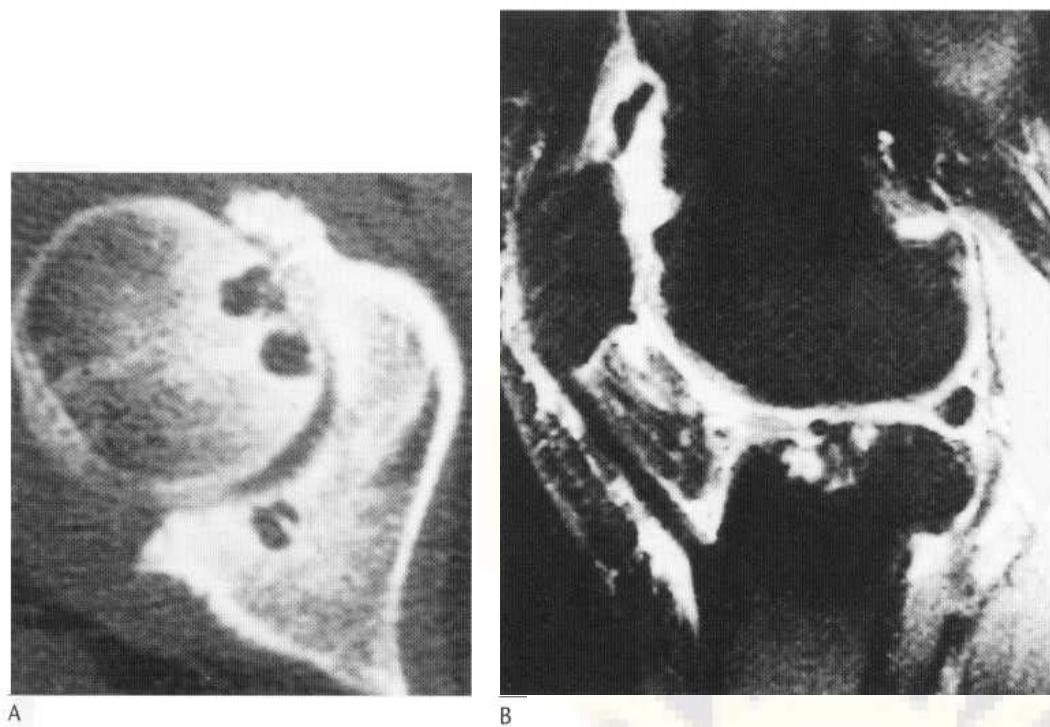
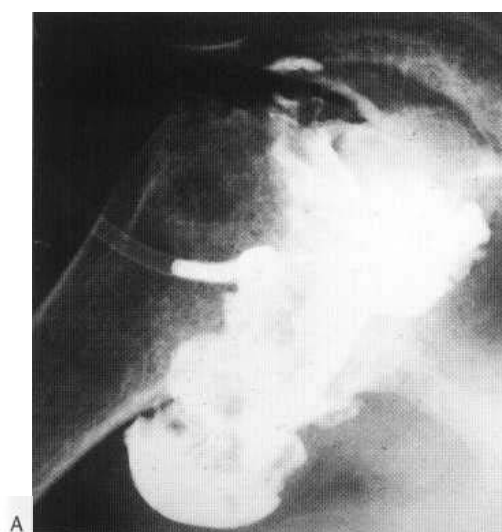


Fig. 38.68 (A) CT scan of osteoarthritis showing new bone formation within the acetabulum and cyst formation at the articular surface. (B) Osteoarthritis demonstrated at MRI: sagittal STIR (fat-suppression) sequence showing loss of joint space, subarticular cyst formation in the tibia with oedema of the peritibial soft tissues, as well as an effusion in the joint.



on the medial, rather than the lateral, aspect of the femoral neck (Fig. 38.66).

The end result is often a femoral head which shows bone loss in weight-bearing areas and bone proliferation in non-weight-bearing areas (Fig. 38.66). The acetabulum may be deepened following medial migration or show new bone medially and superolaterally following lateral migration of the femoral head.

The shoulder joint

Osteoarthritis does not usually occur at the glenohumeral articulation in the absence of a predisposing factor, for example the use of crutches, or secondary to acromegaly, or with the malalignment that follows a chronic rotator cuff tear. Golding (1962) has shown that degenerative changes in the shoulder joint are closely linked with soft-tissue degeneration. Radiological manifestations include erosion, cysts and sclerosis of the greater tuberosity, cysts or irregular sclerosis along the anatomical neck (at the site of the capsular inser-

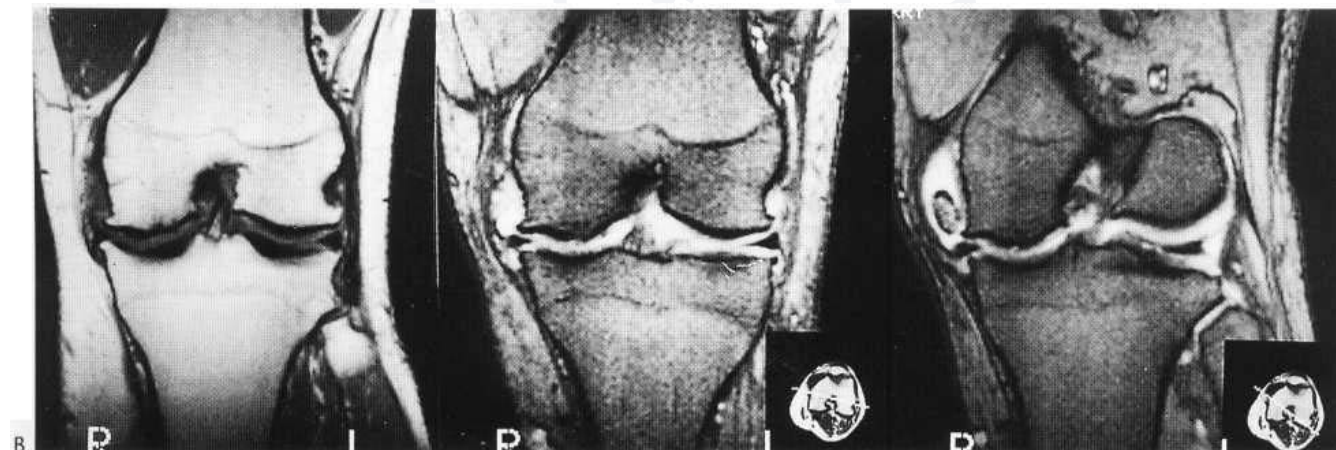


Fig. 38.69 Osteoarthritis. (A) Right shoulder arthrogram. There is irregularity of the synovium and numerous loose bodies are demonstrated within the joint space. There is also a small rotator cuff tear. (B) MRI demonstrates degenerative changes of the knee with an effusion, loss of the medial meniscus, marginal osteophytosis and a large loose body lying medially within the joint.

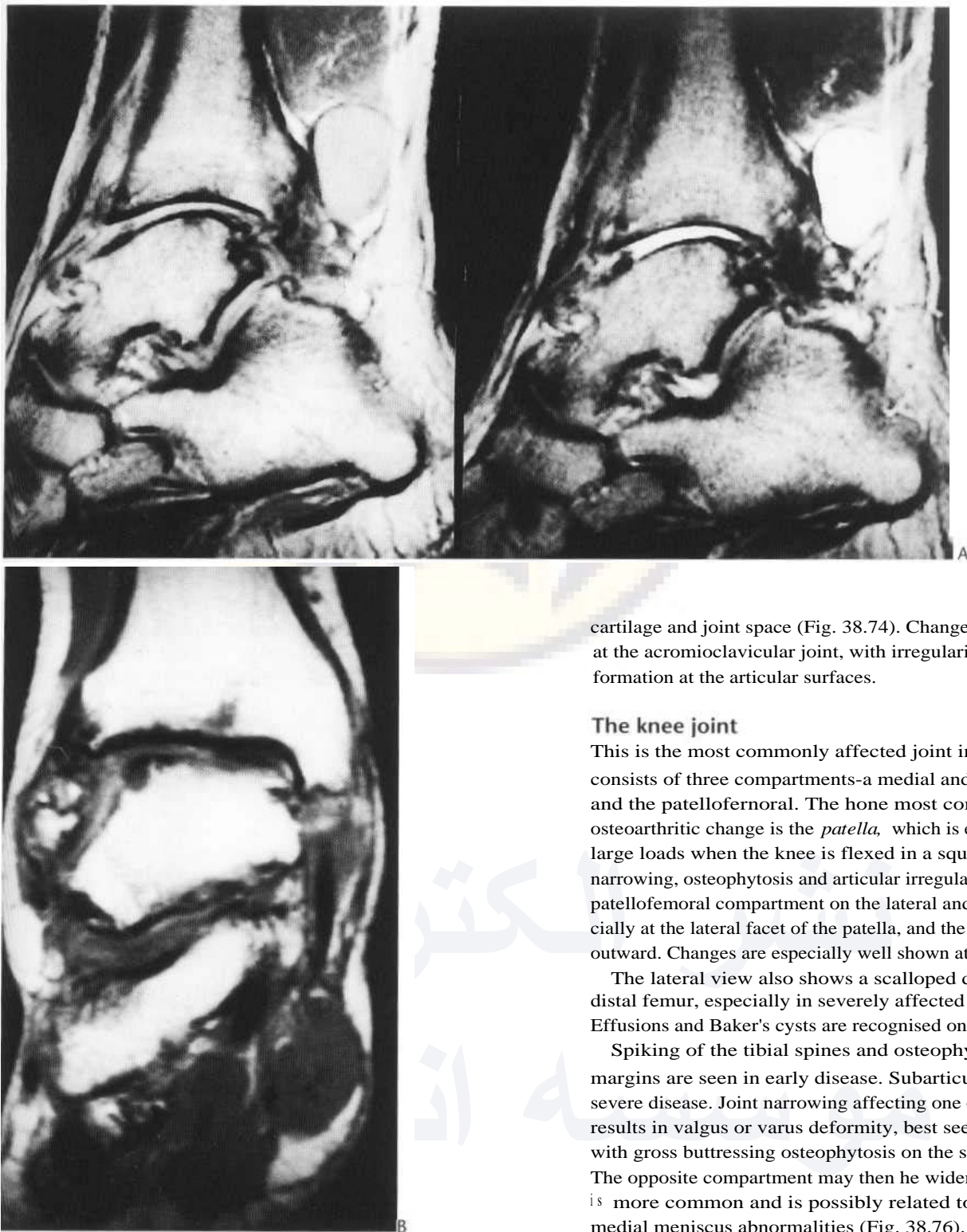


Fig. 38.70 (A,B) Osteoarthritis of the ankle. Articular irregularity with synovial thickening and effusions as well as synovial diverticula are demonstrated. Loss of articular cartilage is seen and erosive changes are demonstrated, especially on the upper surface of the talus. Osteophytes are demonstrated at the malleoli. There is a very large anterior osteophyte associated with local synovial proliferation, seen on the sagittal images.

Lion (Fig. 38.73); later upward subluxation of the humeral head occurs in association with rotator cuff tears. Occasionally, however, examples of the more classical type of osteoarthritis are seen in the shoulder, manifested by osteophytosis, sclerosis and marked loss of

cartilage and joint space (Fig. 38.74). Changes are commonly seen at the acromioclavicular joint, with irregularity, sclerosis and cyst formation at the articular surfaces.

The knee joint

This is the most commonly affected joint in clinical practice. It consists of three compartments—a medial and lateral tibiofemoral, and the patellofemoral. The bone most commonly involved in osteoarthritic change is the *patella*, which is especially subjected to large loads when the knee is flexed in a squatting position. Joint narrowing, osteophytosis and articular irregularity can be seen at the patellofemoral compartment on the lateral and skyline views, especially at the lateral facet of the patella, and the patella often migrates outward. Changes are especially well shown at CT and MRI.

The lateral view also shows a scalloped defect of the anterior distal femur, especially in severely affected women (Fig. 38.75). Effusions and Baker's cysts are recognised on the lateral view.

Spiking of the tibial spines and osteophytes on the articular margins are seen in early disease. Subarticular cysts occur with severe disease. Joint narrowing affecting one or other compartment results in valgus or varus deformity, best seen in erect AP views, with gross buttressing osteophytosis on the side of the narrowing. The opposite compartment may then be widened. Varus deformity is more common and is possibly related to the more common medial meniscus abnormalities (Fig. 38.76). Osteoarthritis of the knees is also more common in the obese. The *fabella* may also be enlarged and irregular in osteoarthritis.

The hands

The carpometacarpal joint of the thumb and the trapezioscapoid joint are commonly affected, especially in women (Fig. 38.77). These joints are seldom involved in rheumatoid arthritis. In osteoarthritis, in contrast to the changes in rheumatoid arthritis, the distal interphalangeal joints are most commonly affected, but any joint may be involved. Narrowing may affect all, or a few, distal



Fig. 38.71 Loss of the femoral head and deepening of the acetabulum may be the end-stage of osteoarthritis.

interphalangeal joints, with large osteophytes on the distal phalangeal bases and overlying soft-tissue swelling. There may be small periarticular ossicles in the adjacent soft tissues (Fig. 38.78).



A



B



C

Fig. 38.72 Patterns of osteoarthritis. (A) Superior migration of the femoral head. There is new bone on the medial aspect of the acetabulum. (B) Osteoarthritis associated with protrusio acetabuli. (C) Migration of the femoral head is in a superomedial direction.

Erosive osteoarthritis

Patients are typically seronegative and complain of episodic pain due to a symmetrical arthritis of the interphalangeal joints and, less commonly, metacarpophalangeal and carpometacarpal joints. Bone density remains good but the joints show a mixture of marked joint narrowing and erosion with florid base-of-phalanx new bone formation. The erosions spread across the entire joint surface, which then collapses (Fig. 38.79). Fusion at interphalangeal joints or marked deformity may result. Pathologically, the synovium is inflamed and some patients seem to develop rheumatoid arthritis later.

Spinal degenerative disease

Though the structure of a disc and its surrounding vertebral end-plates differs anatomically from that at a synovial articulation, the radiological appearance of degeneration at both sites is similar. The space between two opposing bones becomes narrowed and marginal new bone formation, 'articular' irregularity and sclerosis appear. Later, malalignment may result. In the spine the marginal new bone results from elevation of the paraspinal ligaments following disc narrowing. New bone forms beneath the displaced and elevated ligaments. The outgrowth s-osteophytes-are generally laterally directed. Osteophytes also develop on the concavity of a scoliosis, no doubt also secondary to ligamentous redundancy, but act as a buttress, similar to the restraining osteophytes in hip degeneration.

Disc degeneration alters mobility at the apophyseal joints, where degenerative changes become manifest by joint space narrowing and sclerosis. Facet slip at these joints results in encroachment on exit foramina, and new bone around them may narrow the spinal canal. Compressive symptoms result. Degenerative instability, scoliosis and spondylolysis may also result.

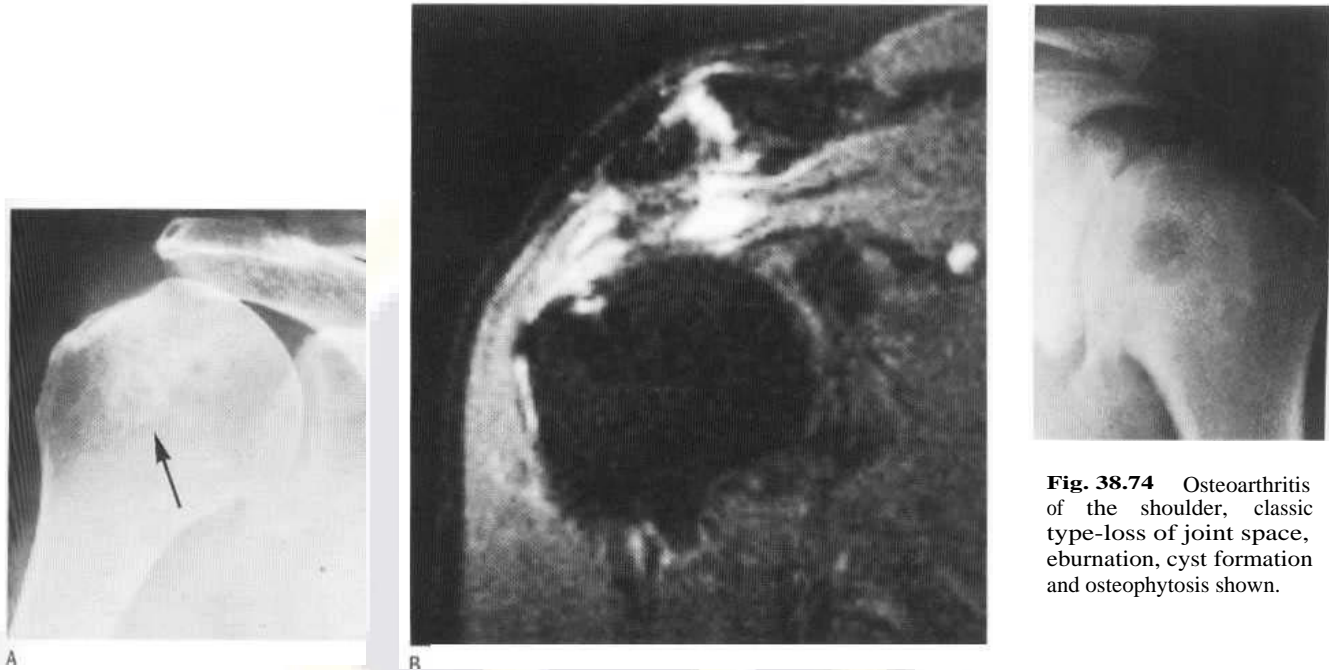


Fig. 38.73 (A) Osteoarthritis of the shoulder-note excavation of the upper part of the anatomical neck with local sclerosis, and cysts seen en face (arrow). (B) Widespread abnormalities are present on this coronal image of the shoulder. There is degeneration with an effusion around the acromioclavicular joint, a subacromial bursitis and considerable thickening of the rotator cuff, which shows a cyst in its body. In addition, there is a distal tendinitis associated with an erosion of the greater tuberosity.

Fig. 38.74 Osteoarthritis of the shoulder, classic type-loss of joint space, eburnation, cyst formation and osteophytosis shown.



Fig. 38.75 Osteoarthritis of patellofemoral joint. There is a groove on the lower anterior part of the femoral shaft (arrow).

Cervical spine

Additional synovial joints, the uncovertebral or neurocentral joints of Luschka, are found from C3 down and are easily recognised on the AP view. As elsewhere, disc degeneration results in narrowing of these joints with osteophytic lipping. In the adult, maximal movement between flexion and extension occurs around the level of the disc between the fifth and sixth cervical vertebral bodies and it is here that the earliest and also the most severe degenerative

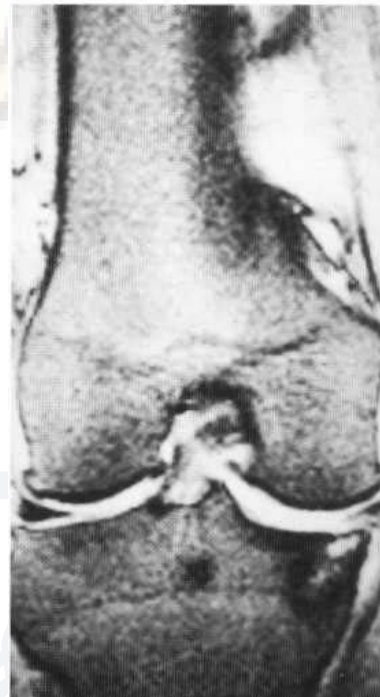


Fig. 38.76 Osteoarthritis. A degenerate and torn medial meniscus is associated with marginal osteophytosis and a subarticular cyst in the tibia. In addition, there is spiking of the tibial spines and at the intercondylar notch. An effusion is also present.

changes are to be found. The next most common site of changes is around the C6/7 disc, but degeneration is less common superiorly (Fig. 38.80).

In established osteoarthritis, spinal movement is restricted between flexion and extension. The normal lordosis is lost and the spine is straightened in affected segments. A lateral view in flexion demonstrates functional change with lack of movement at affected levels.

Oblique views confirm the level of degeneration, and show encroachment on exit foramina at levels affected by disc narrowing (Figs 38.81, 38.82).

Posterior vertebral body osteophytosis, disc narrowing and protrusion, and longitudinal ligament displacement may all cause cord compression (Fig. 38.83).



Fig. 38.77 Severe osteoarthritis of the carpometacarpal joint of the thumb.

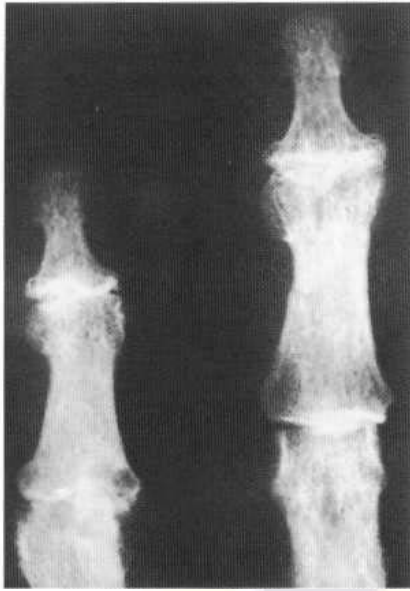


Fig. 38.78 Osteoarthritis, joint narrowing and osteophyte formation, with broadening of the joint underlying the Heberden's nodes.



Fig. 38.79 Erosive osteoarthritis of the interphalangeal joints. Appearance of destruction around some proximal and distal interphalangeal joints.

Thoracic spine

Degeneration in the thoracic spine is common, but not usually severe or significant, though girdle-type pain may result, or even long tract signs if disc material herniates posteriorly.

Minor disc narrowing and osteophytosis is usually present anteriorly, especially in the elderly, often in association with a smooth kyphosis.

Lumbar spine

Disc narrowing most commonly affects the L4/5 and L5/S1 discs. When the radiograph is initially inspected the number of lumbar-type vertebral bodies should be noted. The first sacral body may be totally or partially lumbarised, with a narrow disc between S1 and S2, or L5 may be sacralised. If the lowest free disc is 'high' with respect to the iliac crest, it is subjected to greater stress, and is more liable to degeneration. Any departure from normal anatomy alters the distribution of stresses and renders the local disc liable to premature degeneration. A unilateral pseudarthrosis between S1 transverse process and the iliac crest may be the seat of local degeneration. Disc degeneration may result in fissuring and gas is seen in the disc space—a 'vacuum' phenomenon—as well as calcification on occasion.

The lower lumbar facet joints cease to be symmetrical, so that often one joint is seen and the other at that level is not (Fig. 38.84A). This rotational change is associated with much new bone around the narrowed facet joints and adjacent laminae, often with symptoms of nerve root impingement. The changes are well demonstrated with CT scanning (Fig. 38.84B), when the acquired asymmetry of the entire neural arch is seen as well as the local new bone formation (trochism). Slip at the facets narrows the exit foramina further.

Facet and disc degeneration may result in vertebral slip without pars defects. With an excessive lordosis, contact between 'kissing' spinous processes may result in soft-tissue entrapment and local pain (Fig. 38.85). As in the cervical spine, degeneration results in loss of the curve, rigidity and loss of movement between flexion and extension.

Discography

The insertion of opaque contrast medium into the nucleus of the disc is used to demonstrate the integrity of the nucleus and annulus. Pain reproduction during injection confirms the level of abnormality prior to surgery (Fig. 38.86) and can demonstrate that a disc, which is abnormal at MRI, may be pain free. Conversely, a disc that is normal at MRI may be abnormal at discography (Fig. 38.80).

MRI in discal disease

Possibly the earliest change in degeneration is circumferential fissuring and radial tearing of the annulus. These changes, occurring in the third and fourth decades, are associated with an abnormal discogram. The MRI scan, however, may be normal, if loss of disc height and dehydration have not yet occurred. Subsequent dehydration and fissuring in the disc are associated with loss of signal, so that the disc is no longer bright on T₂-weighted images (Fig. 38.87). Loss of disc height and of the lordosis occurs. Osteophytes develop, especially anteriorly in association with anterior annular tears. In the underlying vertebral body, oedema, cysts or reactive new bone formation—so-called Modic changes—are seen (Modic et al 1988). Posterior and anterior annular fissures, initially partial, which are intrinsically painful, extend to the distal margins as full-thickness tears. The abnormal disc may show a *high-intensity zone* (HIZ) (Fig. 38.88). This is a focus of high signal, usually seen in association with severe degenerative change in the posterior aspect of the disc, and often in its protruded segment. This area fills with contrast medium at discography. The presence of Modic changes and a HIZ are often associated with concordant pain at discography (Braithwaite et al 1998).

Disc material herniates into the canal, centrally or peripherally, or into the exit foramina, or laterally. At all these sites nerve compression can result in a radiculopathy (Fig. 38.89).

MRI demonstrates disc degeneration and protrusion well. Often multiple areas of unsuspected disease may be seen. Not all,

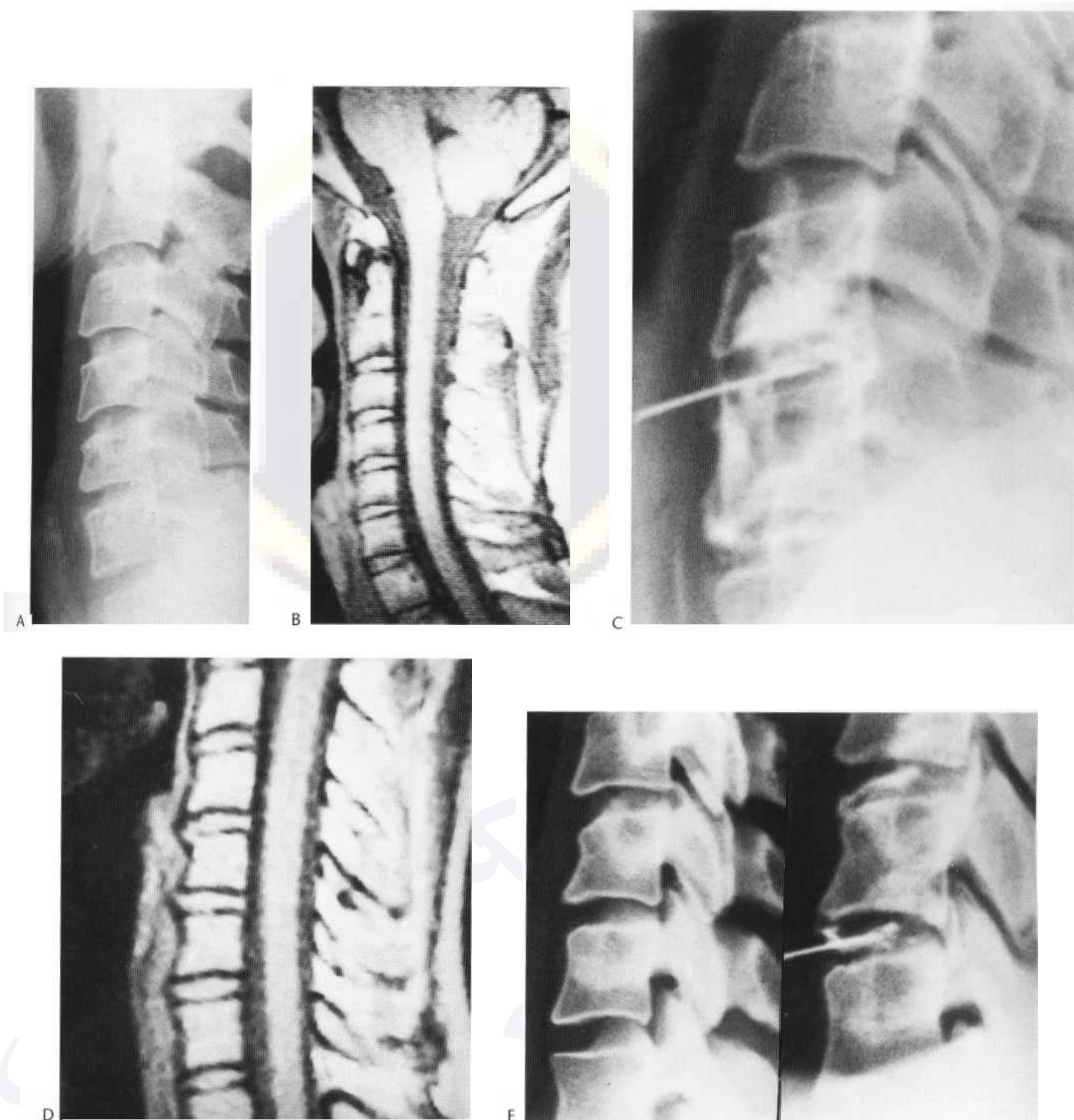


Fig. 38.80 Early cervical spondylosis. (A) The plain film shows slight loss of the normal curve centered around the C5/6 disc which is also minimally narrowed. (B) MR scan shows anterior discal bulging and marginal osteophytosis at the C4/5 and C5/6 levels. (C) Cervical discogram confirms the presence of an annular tear with substantial leak of contrast. (D) Cervical discogram in a more advanced form. The MR scan is abnormal with anterior discal bulging and marginal osteophytosis at C4/5 and C5/6 levels. (E) In the discogram of the same patient anterior and posterior annular tears are demonstrated with dorsal bulging. The anterior annular tears are shown to extend to the osteophytes.

however, will be symptomatic. Almost all elderly patients will have evidence of spondylosis at one or more levels, but few are symptomatic.

Gout

Radiographic findings

1. *Erosions.* These are caused by deposition of *sodium hyaluronate* and are typically punched out in appearance. They tend to appear



Fig. 38.82 Oblique projection of cervical spine showing large osteophytic protrusions into the C5/6 intervertebral foramen (arrow).



Fig. 38.83 MRI of the cervical spine. Dorsal osteophytosis and distal protrusion indent the thecal sac and cervical cord.

Fig. 38.81 Cervical spondylosis. (A) There is early narrowing of the C5/6 disc and the beginnings of anterior osteophytosis. (B) Disc degeneration is now pronounced, with both anterior and posterior osteophytes.

near joint margins. As they enlarge, they tend to involve more of the cortex of the shaft rather than the articular surface (Fig. 38.90). Large erosions extend to the articular cortex and enlarge diffusely

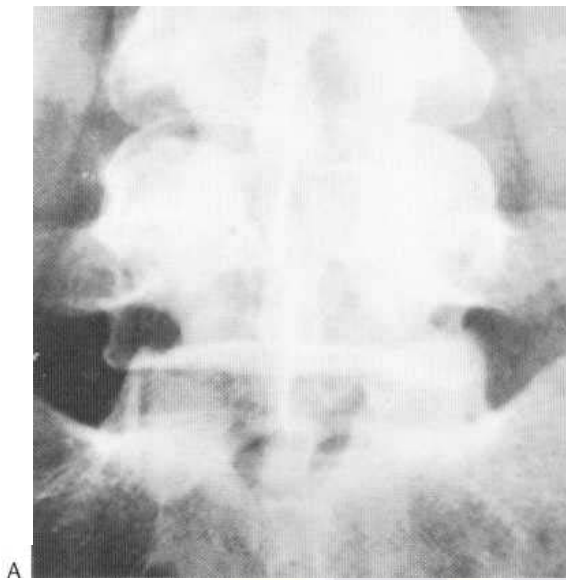
in the shafts (Fig. 38.91). Cartilage destruction is a relatively late manifestation. Usually much bony destruction is seen before cartilage loss supervenes. In the hand, gout tends to attack the distal and proximal interphalangeal joints, whereas rheumatoid arthritis affects the metacarpophalangeal and proximal interphalangeal joints.

2. *Osteoporosis* is not seen except in advanced cases which have been immobilised.

3. *Tophi*. These are shown as soft-tissue swellings eccentric in distribution, in contradistinction to the fusiform soft-tissue swellings of rheumatoid arthritis (Fig. 38.91). Eventually, both soft-tissue and intraosseous tophi may become calcified (Fig. 38.92), but this is uncommon,

Differential diagnosis

Differentiation between gout and *multiple enchondromas* may be difficult radiographically. The tendency of multiple enchondromas to spare bone ends is an important diagnostic point. The clinical findings and history readily differentiate the two conditions.



A



B

Fig. 38.84 (A) The facet joints are no longer symmetrical and show features of degeneration. (B) The CT scan shows gross new bone formation around narrowed facet joints. There is marked bony encroachment upon the exit foramina, especially the left. Gas is seen in the disc (vacuum phenomenon).

In practice, the most frequent difficulty is in differentiating gout from *rheumatoid arthritis*. Important points are: the longer latent period of gout; its eccentric, often gross soft-tissue swellings; and tendency to attack distal interphalangeal joints. Osteoporosis is found much more frequently in rheumatoid arthritis. Rheumatoid erosions are not so sharply defined as those of gout. Calcified tophi are, of course, diagnostic of gout. In difficult cases, differentiation will be made by laboratory tests revealing a raised uric acid level in blood.

Hypertrophic (pulmonary) osteoarthropathy

This condition was originally thought to be associated solely with intrathoracic disease, but it is now known to be associated with intra-abdominal and other diseases. The word 'pulmonary' is best avoided in the title. The vast majority of cases are associated with intrathoracic neoplasms, mainly bronchogenic carcinoma, up to 12% of

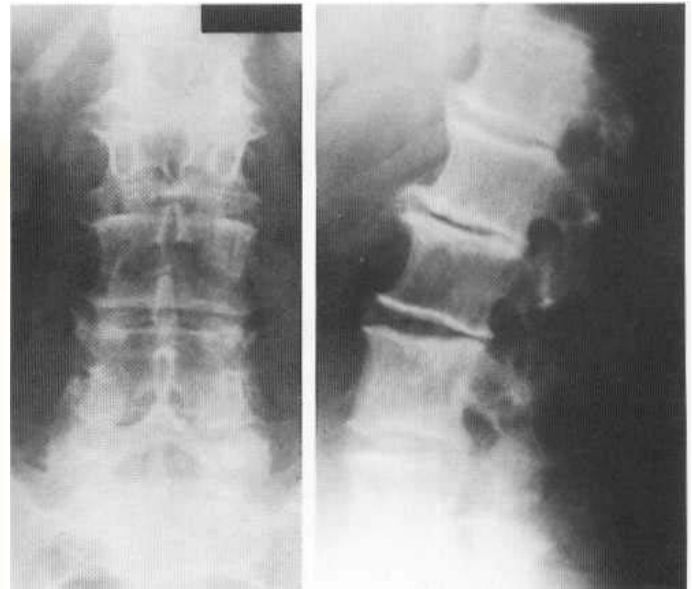


Fig. 38.85 Lumbar spondylosis. There is distal narrowing and a vacuum phenomenon is present in the degenerative discs. Marginal osteophytes are present. Inferiorly the facet joints show features of degeneration and, with the increase in lordosis, the spinous processes are in contact.

which have hypertrophic osteoarthropathy, with the exception of oat cell carcinomas. Hypertrophic osteoarthropathy is also associated with secondary lung tumours. Its highest incidence is found with fibrous mesothelioma of the pleura. Hypertrophic osteoarthropathy is more common with peripherally seated tumours.

Hypertrophic osteoarthropathy is also observed with bronchiectasis, rarely with tuberculosis, and congenital cyanotic heart disease, and may also be found with chronic liver and gut inflammatory disorders. Even though hypertrophic osteoarthropathy is usually accompanied by clubbing, the latter should be separated on clinical, radiological and pathological grounds.

Periostitis is seen earliest at the distal third of the radius and ulna (Fig. 38.93), then the tibia and fibula, and then the humerus and femur, metacarpals, metatarsals and proximal and middle phalanges (Fig. 38.94). Distal phalanges are rarely affected. Radiologically, soft-tissue swelling may be seen over distal phalanges if clubbing is present, but the underlying bone is normal.

In the long bones, periostitis affects the distal diaphyses but the bone ends are uninvolved. A single fine layer, or multiple layers, of periosteal new bone, giving an onion-skin appearance, may be seen. On occasion the periostitis may be shaggy. The new bone merges with the cortex in longstanding cases. Endosteal new bone is not seen. The axial skeletal is rarely affected.

Occasionally joint pain and swelling are related to an underlying arthritis, usually of larger joints. Radiologically, osteoporosis and effusions may be recognised but erosions do not apparently occur.

Radionuclide scanning in hypertrophic osteoarthropathy

Hypertrophic osteoarthropathy is a disease in which blood flow to the limb is increased and new bone is formed. As expected, scanning is an accurate and sensitive means of detecting disease, and the changes are seen before those on the plain films. Increased uptake is seen symmetrically along the shafts of affected long bones paralleling the cortices and thus differing from focal or widespread metastatic foci. With treatment of the underlying condition, the changes evident on both film and scan regress. Increased uptake on scan is also seen around affected joints (Fig. 38.95).

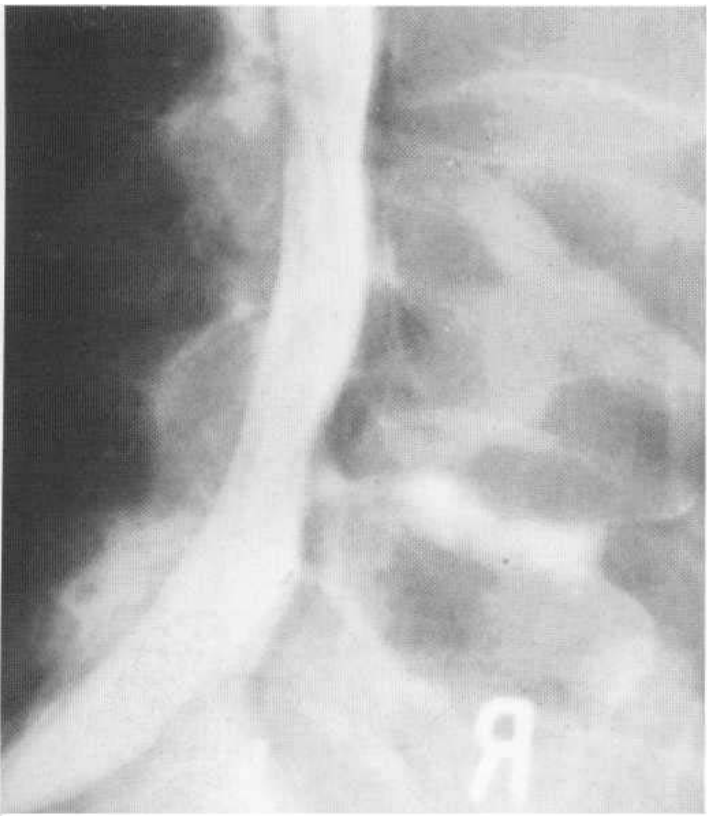


Fig. 38.86 (A) Simultaneous discography and radiculography demonstrate a torn annulus, through which contrast medium escapes and impinges upon the opacified theca. **(B)** The CT scan shows, in the axial plane, the site of the annular tear and the displacement of the nucleus. Indentation of the opacified thecal sac is demonstrated.

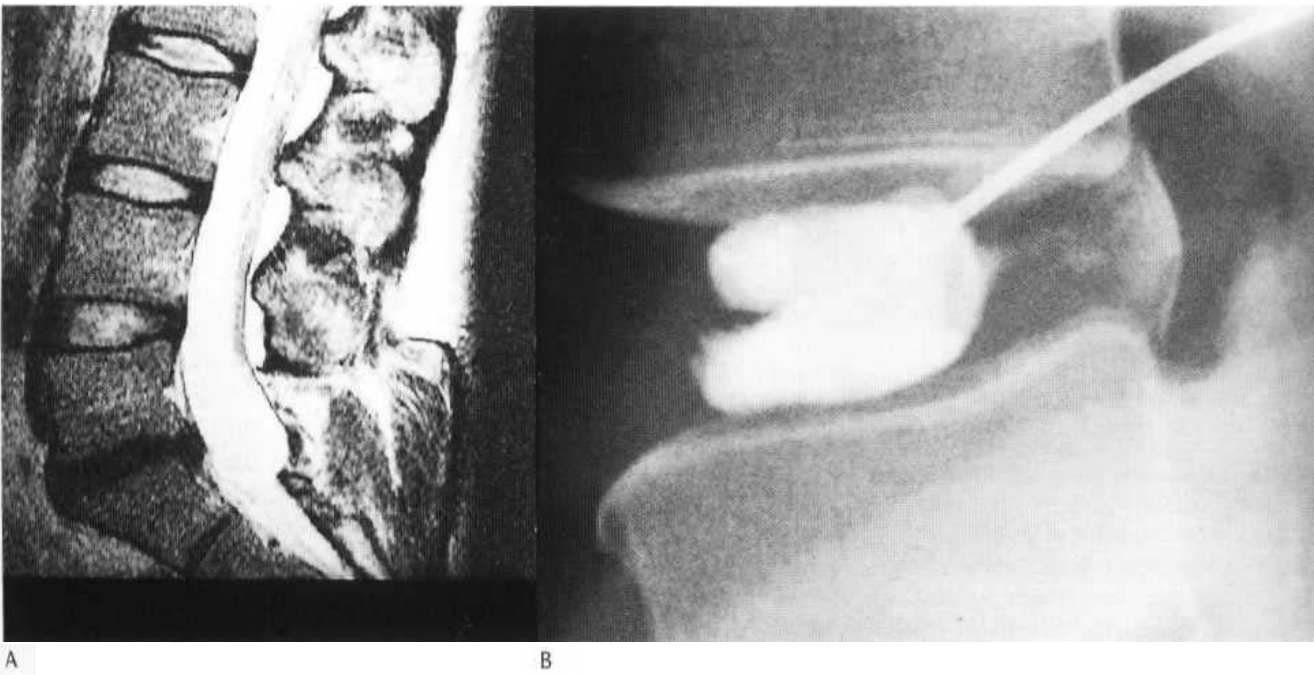


Fig. 38.87 Lumbar degeneration. **(A)** The L5/S1 disc is clearly grossly abnormal showing loss of height and signal, together with a dorsal distal protrusion. At L4/5 there is early loss of signal. **(B)** The discogram at L4/5 shows an essentially normal nucleus, but there is a fine annular tear which is associated with a bulge. No extraneous leak. This injection was extremely painful.

Pachydermoperiostosis

In this condition radiological changes similar to those seen in hypertrophic osteoarthropathy present early in life, often after puberty. Though the periosteal new bone is like that seen in hypertrophic osteoarthropathy, it is often coarser and may extend further

along the shafts to the epiphyses. A familial history is present in over 50% of cases and males are said to be more commonly affected. No related chest disease is found. The skin of the face, especially the forehead, becomes thickened and greasy with acne and hyperhidrosis.



Fig. 38.88 The HIZ T₂-weighted MR sequence showing the posterior high-intensity zone.

Systemic lupus erythematosus

This disorder is more common in young females and in black Africans. It is associated with a 'butterfly' skin rash over the cheeks, with pleurisy, pericarditis, glomerulonephritis and psychiatric disorders. It may be precipitated by drugs.

Systemic lupus erythematosus may present with a symmetrical peripheral arthropathy. Soft-tissue swelling and osteoporosis are seen, but erosive change is minimal and uncommon. Soft-tissue calcification also occurs around the joints and in blood vessels. Alignment deformities of the hands are more typical, so that ulnar deviation and swan-neck deformities are seen, which are reversible, voluntarily and involuntarily.



Fig. 38.91 Very advanced gout. Note eccentric soft-tissue swellings, intraosseous tophi extending to bone ends and lack of osteoporosis.

Avascular necrosis is common, being found in the hips, knees and shoulder joints. It probably follows steroid therapy but, in view of the high incidence (10°G-), may be due to the disease [alone](#). [C1/C2](#) subluxation may be found.

Progressive systemic sclerosis

This is a widespread disorder of connective tissue, which often presents with Raynaud's phenomenon due to small vessel occlusion. Fibrosis of the skin, especially over distal phalanges, leads to resorption of the distal phalanges and then progressively of the middle and proximal phalanges. Soft-tissue calcification is seen,

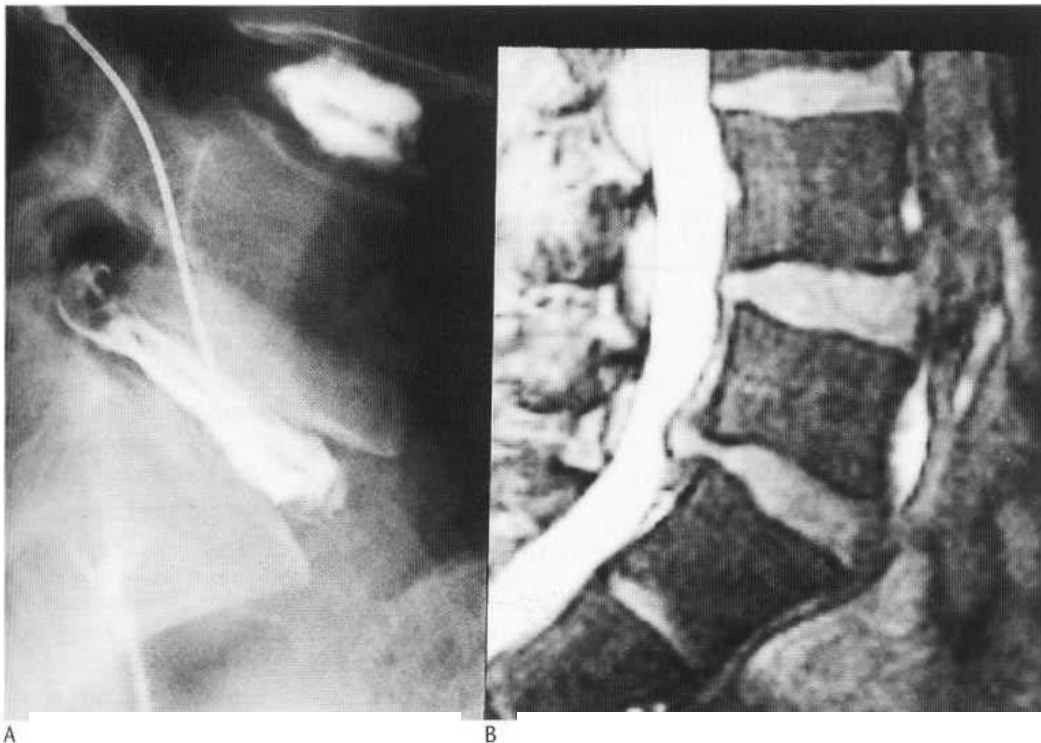


Fig. 38.89 (A,B) MRI and discography demonstrate a dorsal distal protrusion with narrowing of the canal at that level.



Fig. 38.90 Gout-erosion on the medial part of the first metacarpal extends away from the joint surface.

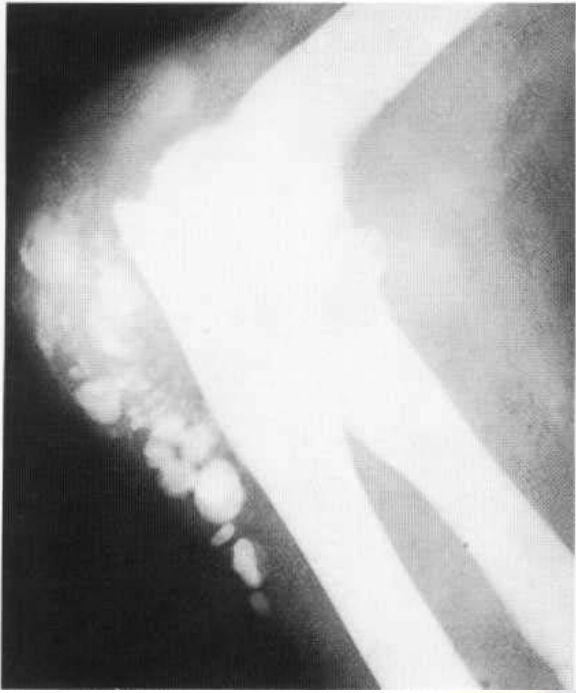


Fig. 38.92 Gout-large calcified tophi in olecranon bursa.



Fig. 38.94 Hypertrophic osteoarthropathy secondary to pulmonary neoplasm.



Fig. 38.93 Hypertrophic osteoarthropathy-exuberant periosteal reaction of the radius and ulna. In this patient, changes in the bones of the hands were minimal.

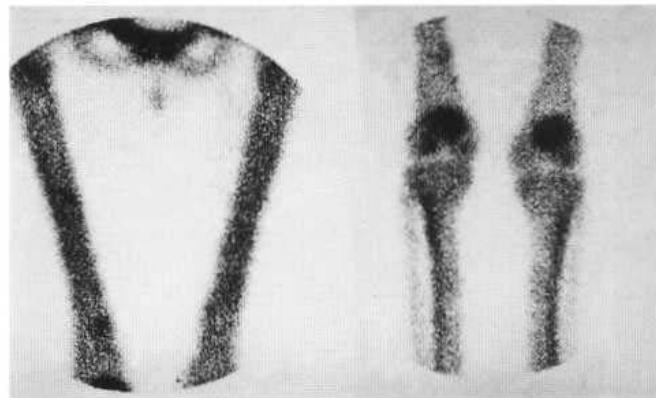


Fig. 38.95 Hypertrophic osteoarthropathy. Generalised and symmetrical diffuse increase in uptake is associated with thickening of the bony image at isotope scanning.

especially over distal phalanges and around joints. Fibrosis may lead to contractures (Fig. 38.96). These changes may be preceded or accompanied by a polyarthritis similar to rheumatoid arthritis in at least 10% of patients. Osteoporosis, joint space narrowing, erosions and subluxations may be seen. Changes of an erosive arthropathy in association with calcification should suggest the presence of progressive systemic sclerosis.

Jaccoud's arthropathy

This arthropathy does not involve synovium but causes capsular fibrosis. Deformities of the hands and feet that are initially reversible occur. Lateral deviation of the hands and feet may be

seen when these parts are examined without weight-bearing. When the hands are pressed down onto the cassette surface, the deformities vanish. The joint spaces are mainly preserved. True erosions are not found, but so-called 'hook' erosions of the metacarpal heads are produced, possibly because of local capsular pressure (Fig. 38.96). The patients are seronegative for rheumatoid arthritis.

Mixed connective tissue disease

This is a so-called 'overlap syndrome' comprising a mixture of features of rheumatoid arthritis, dermatomyositis, systemic lupus erythematosus and progressive systemic sclerosis.

Osteoporosis, soft-tissue swelling and joint space narrowing are found at affected joints. The distribution also may mimic rheumatoid arthritis, but distal interphalangeal joints may be affected and the peripheral arthropathy may be asymmetrical. Erosive change is not



Fig. 38.96 Scleroderma. Contractures result in pressure resorption of bone at metacarpal necks. Para-articular calcification is prominent, as is distal phalangeal sclerosis.

inevitably present in these situations, which are a mixture of the sites of rheumatoid arthritis and psoriasis. The distal phalanges show soft-tissue loss, distal tuft bone resorption and calcification suggesting progressive systemic sclerosis. Ulnar drift, as in systemic lupus erythematosus or rheumatoid arthritis, is also seen. Pericardial and pleural effusions may be shown by chest radiography.

IMAGING OF JOINTS

Arthrography involves the injection of iodine-based water-soluble contrast media, or air, or both, into a joint. It has become less commonly used for two main reasons:

1. *Arthroscopy* is used as a primary diagnostic modality by the surgeon who can proceed directly on to surgery. The knee, shoulder and temporomandibular joints are all routinely examined by this mode. Arthrography was as accurate in the diagnosis of meniscal lesions as arthroscopy, but far less accurate for diagnosis of cruciate ligament change as well as abnormalities of cartilage.

2. *MRI* has become more generally available. Changes can be seen both in the joint, for example the menisci, cruciate ligaments and cartilage at the knee, and also in the subarticular bone and in the extrasynovial tissues. Changes of bone marrow, for example oedema or haemorrhage, or in the adjacent ligaments and tendons, can be assessed. Where MRI is available, the use of arthrography has declined dramatically.

Knee joint

Arthrography

The normal meniscus is triangular in cross-section. The lateral meniscus has a posterior peripheral defect for a synovial tunnel in which runs the popliteus tendon. In utero, the menisci are larger, bisecting the joint. Rarely, this large bulbous fetal structure persists into adult life as a discoid meniscus, usually on the lateral side, well seen at arthrography and MRI, and on the plain film by widening of the lateral compartment (Fig. 38.97).

Tears are seen as fissures containing air or contrast. They are more common in the medial meniscus, especially posteriorly (Fig. 38.98). They may be partial, or extend from the top to the bottom of the meniscus, which may be partially or totally peripherally detached.

Baker's cysts and loose bodies may be seen, and the state of the articular cartilage in the region of the meniscal section under examination fairly well assessed (Fig. 38.99).

Optimal arthrography needs an experienced operator. It is advantageous to have a fine-focus tube in the fluoroscopy unit. Only the superficial surfaces of the internal structures of the joint are well seen. Cruciate ligaments are not consistently well seen.

MRI

MRI shows not only the surfaces of the intra-articular structures but also change *within* the menisci and cruciate and other ligaments, and in adjacent structures—bone and muscle.

Changes in the menisci have been graded 0-3 (Fig. 38.100). Fluid or myxoid degeneration in the meniscus is seen as a band of increased signal on T₂-weighted and STIR images in the body of the meniscus (Grades 1-2) (Fig. 38.97). If the signal extends to the meniscal surface (Grade 3), a tear is present (Fig. 38.101). Grade 1-2 changes can, with time, become Grade 3 lesions. Recurrent tears post meniscectomy are also easily diagnosed. Cysts at the periphery of the meniscus extend into the adjacent soft tissues as adventitial bursae (Fig. 38.102).

The cruciate ligaments are especially well shown. The posterior is thick and easily seen and it is not often damaged (Fig. 38.103). The anterior is thinner, runs obliquely to the sagittal plane and is less well seen, but is more easily damaged (Fig. 38.104), often in association with a medial meniscal tear. Fluid may be seen in the ligament following acute injury or there may be total retraction. Chronic changes are of fibrosis and deformity.

The collateral ligaments are well seen on coronal images and tears, especially of the medial, can be identified following injury (Fig. 38.105).

STIR weightings show oedema in the articular cartilage and oedema, bruising or cysts in the underlying bone (Fig. 38.106). Degenerative changes are best seen at MRI, often in the presence of local meniscal abnormalities (Fig. 38.68B).

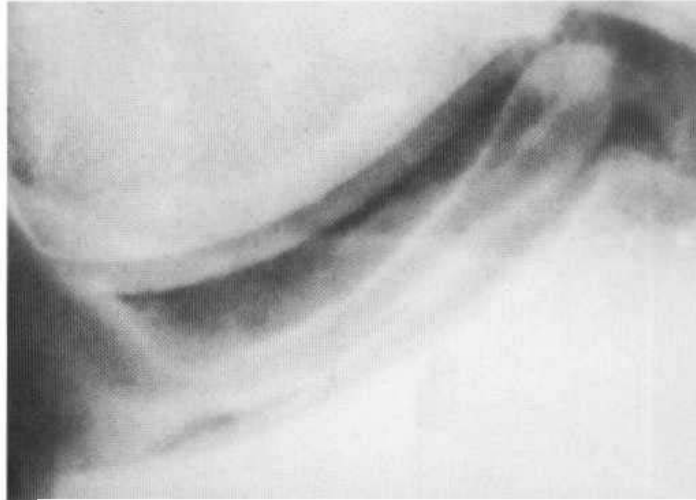
Baker's cysts may rupture, causing symptoms similar to those of a deep vein thrombosis. These cysts can be seen on occasion on a plain film, but are well shown with ultrasound (Figs 38.33, 38.34), arthrography (Fig. 38.107) or MRI (Figs 38.20, 38.99), as is the leak. A negative venogram rules out a deep vein thrombosis, but the popliteal vein may be displaced by the cyst.

Ultrasound

Ultrasound is of limited value in the knee, as the vulnerable structures are contained deep in the joint. The sound waves cannot pass



A



B



C

Fig. 38.97 Discoid meniscus. (A) The plain film shows dishing of the lateral tibial plateau. (B) Arthrography. The meniscus extends medially to the midline of the joint and has a bulbous internal aspect. (C) The MR scan shows the same external contour of the meniscus as the arthrogram but shows cystic degeneration within the structure of the meniscus. Note also the increase in signal at the metaphysis—a normal feature.

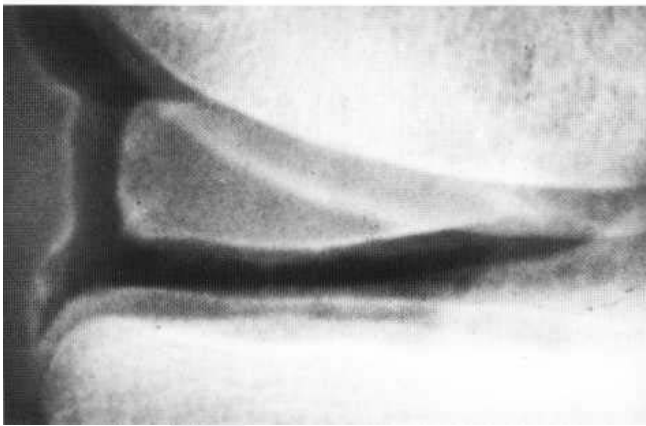


Fig. 38.98 Double-contrast arthrography of the knee showing total peripheral detachment.

through bone and so deep structures cannot be visualised. Nonetheless, superficial soft tissues can be seen, including the patellar tendon (Figs 38.31, 38.32), collateral ligaments and superficial meniscal parts (Fig. 38.23), as well as effusions.

Radioisotope scanning

Single photon emission computed tomography (SPECT) can be used to show meniscal abnormalities by demonstrating increase in uptake in the condyles and tibial plateau. Changes at SPECT are said to have both high sensitivity and specificity (Fig. 38.108).



Fig. 38.99 Sagittal T₁-weighted image of the knee. The medial meniscus is torn. There is a large Baker's cyst which contains loose bodies.

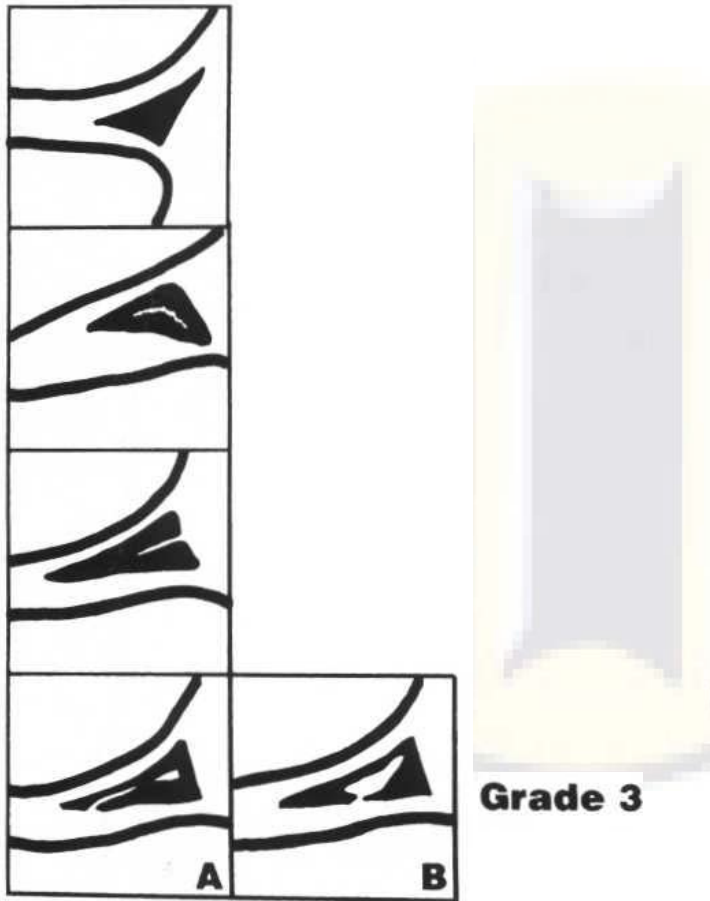


Fig. 38.100 Classification of meniscal change at MRI from normal to tear, according to Mink et al (1993).

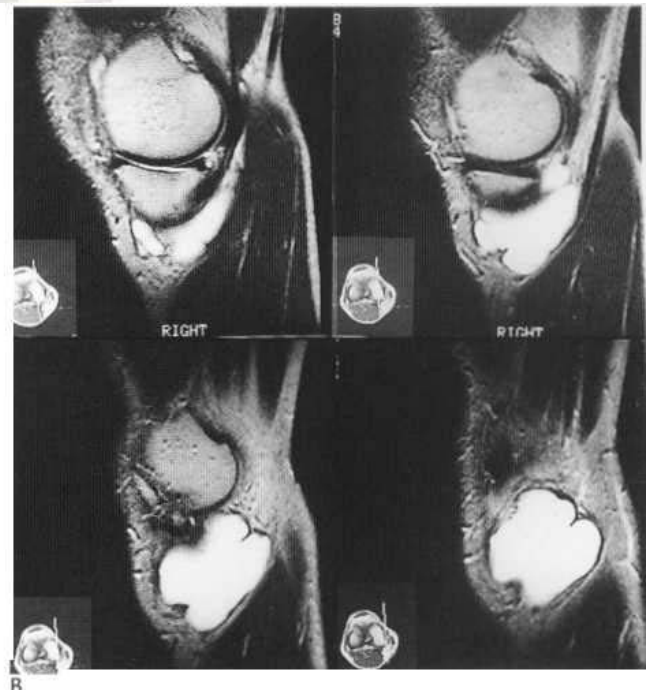


Fig. 38.102 (A,B) A medially directed cyst related to an abnormal posterior horn is shown in coronal, axial (A) and sagittal (B) images. The cyst is palpable beneath the skin and serial images track its communication to the interior of the joint.

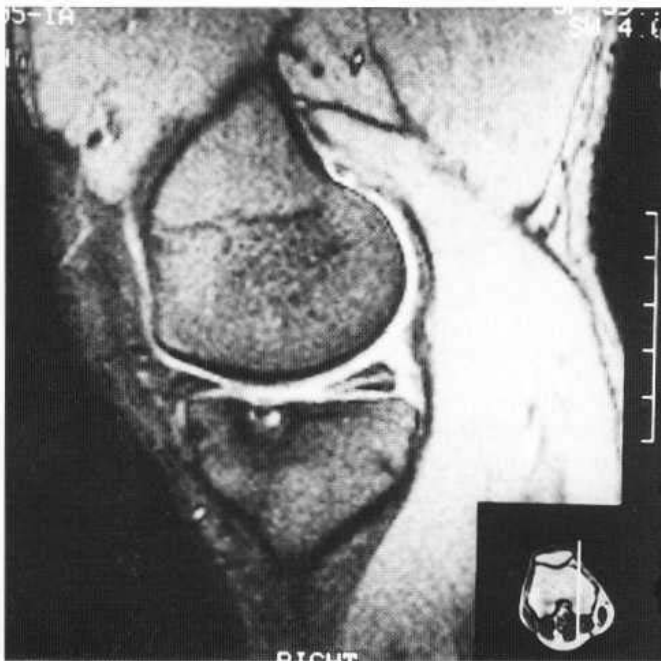


Fig. 38.101 Tear of the posterior horn of the medial meniscus associated with a tibial cyst. Peripheral meniscal cysts originating from degenerate menisci are seen on sagittal, axial and coronal images at MR scanning.

Shoulder joint

Arthrography

This is used especially to demonstrate tears of the rotator cuff and the long head of biceps, but also to demonstrate loose bodies and to assess joint volumes in restrictive capsulitis.

The normal shoulder has an intact Mahoney's line (cf. Shenton's line) and a space of 1-1.5 cm between the humeral head and the acromion. This space consists (from above downward) of the sub-acromial bursa, the rotator cuff, the long head of biceps and the shoulder joint space proper. The two synovial spaces are thus sepa-



Fig. 38.103 A disrupted posterior cruciate ligament surrounded by effusion.



Fig. 38.104 Sagittal T₁-weighted MR sequence of the knee showing an irregular and ruptured anterior cruciate ligament (arrow).

rate (Fig. 38.109). The normal joint also shows a normal Subcoracoid recess and an axillary recess.

With chronic rotator cuff tears, the defect in the tendon allows the humeral head to sublux upward, that is, it comes to lie beneath

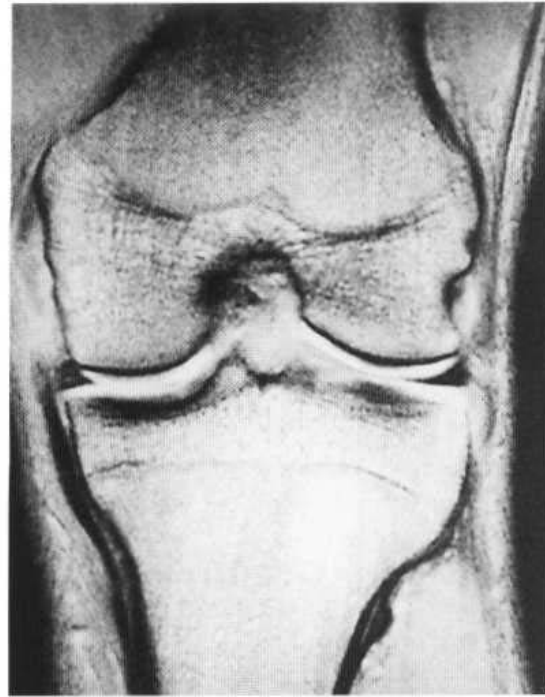


Fig. 38.105 Coronal T₂-weighted image of the knee demonstrates a tear of the medial collateral ligament.

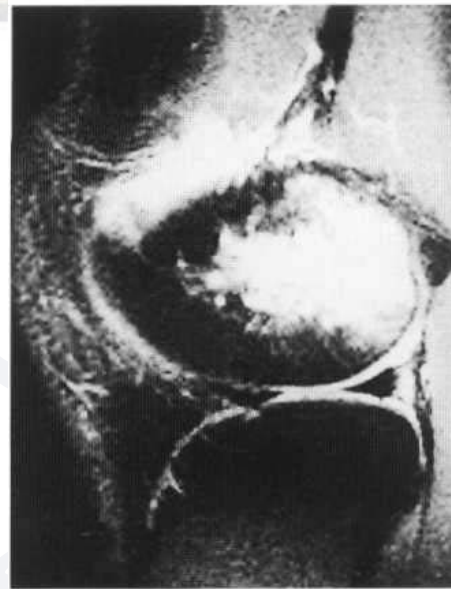


Fig. 38.106 Bone bruising in the medial femoral condyle well demonstrated on a sagittal fat-suppression image of the knee.

the acromion, which may be scalloped by the elevated humeral head (Fig. 38.110) (see also Fig. 38.19A). Contrast medium fills the Subacromial bursa from the glenohumeral joint and lies lateral to the shoulder joint capsule and humeral head.

Double-contrast arthrography may be combined with CT scanning. This especially demonstrates the presence or absence of articular cartilage at the glenoid labrum and humeral head, as well as showing the presence or absence of a hatchet defect following recurrent dislocation (Fig. 38.111). The hatchet or Hill-Sachs deformity is usually a posterior defect of the humeral head. It follows chronic dislocation of the humeral head in the commoner anterior direction, so that the anterior glenoid impacts upon the pos-

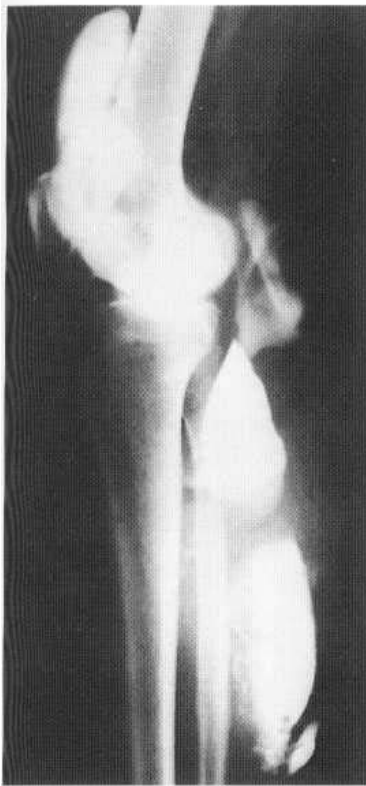


Fig. 38.107 Rupture of a Baker's cyst is demonstrated. This is probably chronic, as the cavity in the calf has a smooth margin. (Courtesy of Dr A. R. Taylor.)

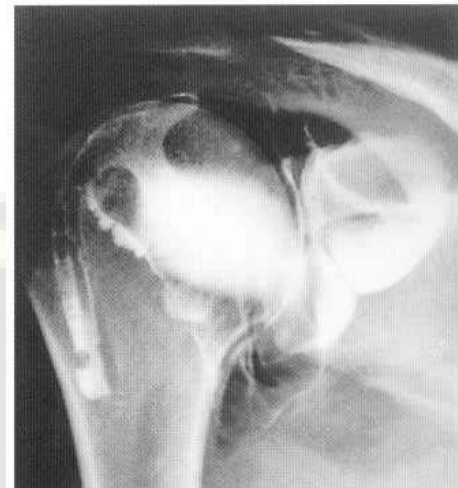


Fig. 38.109 A normal shoulder arthrogram showing the extent of the glenohumeral synovium. There is no contrast beneath the acromion. The synovial reflection around the long head of biceps tendon is shown.

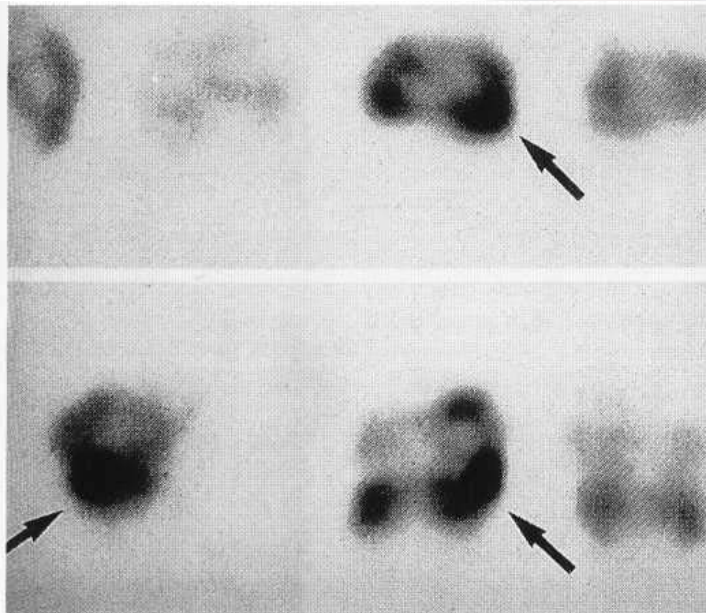


Fig. 38.108 Radioisotope bone scan (SPECT) of the knee shows focal areas of increase in uptake (arrows) at sites of proven abnormality of the menisci. (Courtesy of Dr I. Fogelman.)

terior aspect of the femoral head. Labral and bony defects of the anterior glenoid also result.

In addition, the long head of biceps tendon is well demonstrated in its sheath. Foreign bodies are especially easily shown in the shoulder.

Here again, 'however, where available, MRI has largely superseded arthrography and CT arthrography, largely because it is non-invasive.



Fig. 38.110 A rupture of the rotator cuff is seen at shoulder arthrography, with contrast medium filling the subacromial space.

MRI

MRI shows changes within the tendons. Attention should be directed to the acromioclavicular joint on coronal images as bone and soft-tissue hypertrophy cause compression and oedema of the underlying supraspinatus muscle.

The presence of a subacromial osteophyte has been shown to lead to changes in the underlying rotator cuff tendon. This important spur of bone causes first pressure atrophy and subsequent rupture of the tendon (Fig. 38.112). Tendinitis is seen as an increase of signal in the normally low signal of the tendon. Tears may be partial and superior or inferior, or total (Fig. 38.113). Tendon retraction occurs, and the humeral head subluxes upward.

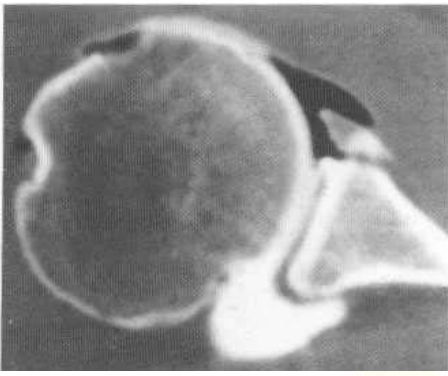


Fig. 38.111 CT arthrotomography showing a labral and glenoid fracture.

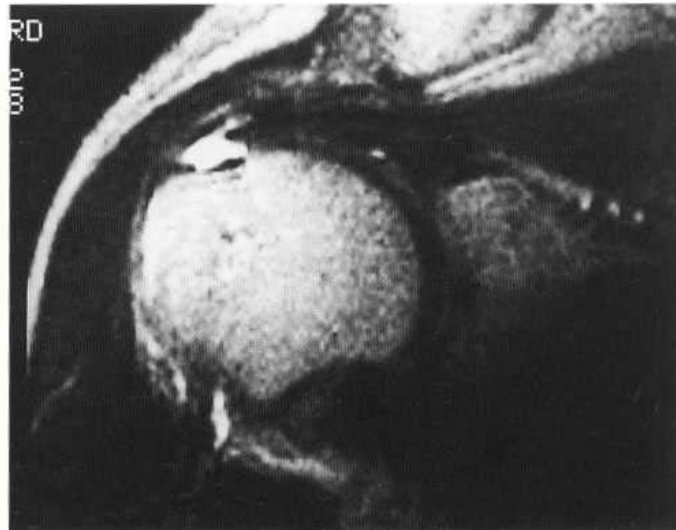


Fig. 38.113 Total rotator cuff tear with retraction. Axial CT of the shoulder demonstrates an anterior labral tear.

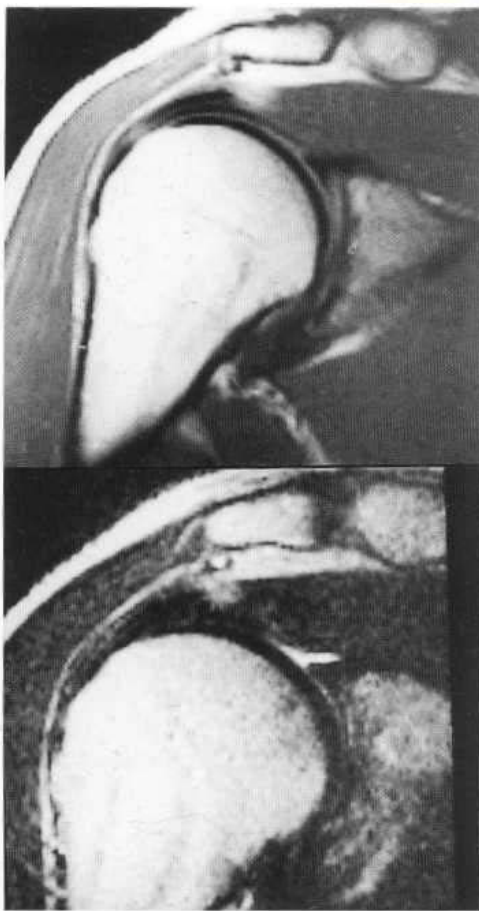


Fig. 38.112 A subacromial osteophyte is associated with local tendinitis (T₁- and T₂-weightings).

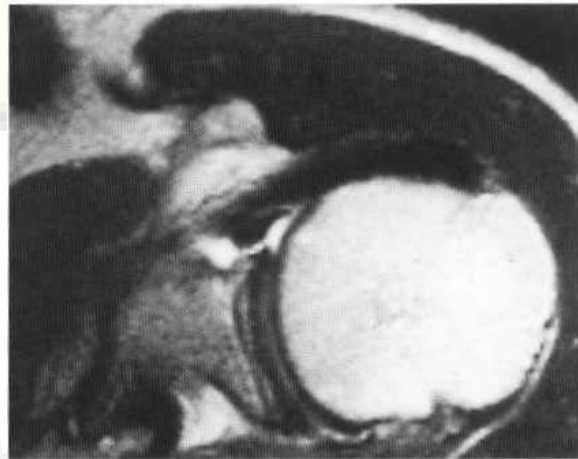


Fig. 38.114 A tear of the labrum glenoidale anteriorly shown at MR scanning. Fluid provides the contrast medium on the T₁-weighted image.

Ultrasound

This is fast becoming the first investigation of choice for rotator cuff tear and long head of biceps pathology, but requires operator skill with a significant learning curve in carrying out the technique, as well as a cooperative patient, who is able to achieve satisfactory positions for assessment of each tendon of the rotator cuff. Ultrasound gives more detail of the internal structure of the tendons making up the rotator cuff than does MRI (Figs 38.115-38.118), and can differentiate between synovial thickening and/or the presence of synovial fluid (Fig. 38.29). The real-time nature of ultrasound enables dynamic assessment of the rotator cuff for impingement and the biceps tendon for subluxation (Fig. 38.119). In addition, the acromioclavicular joint can also be assessed for degenerative change, the presence of effusion or erosion and also dynamically of subluxation. Hill-Sachs deformities may also be demonstrated (Farm et al 1996, Cica et al 1998).

Ankle joint

Investigation of ligamentous injuries is the main indication, but *arthrography* is seldom used in practice in studying this joint. In the

Degenerative cysts are often seen at the rotator cuff insertion, and are well seen on STIR or T₂-weighted images. Axial scans show the long head of biceps tendon in its sheath; tenosynovitis may be present with a distended sheath. The labrum is usually seen as a triangular structure arising from the anterior and posterior glenoid margins on axial scans, and the upper and lower margins on coronal images. Tears or detachments are shown on T₂ or STIR weightings, giving an appearance similar to those seen after the introduction of contrast medium into the joint and CT scanning (Fig. 38.114).

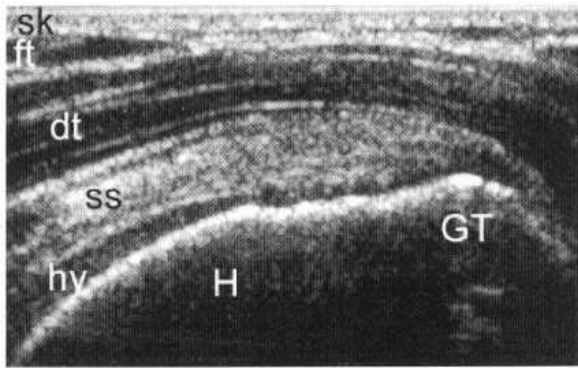


Fig. 38.115 Coronal oblique scan of a normal supraspinatus tendon. The layers of tissue that should be seen are: skin (sk), fat (ft), deltoid muscle (dt), brightly echogenic supraspinatus tendon (ss), low echogenic hyaline cartilage (hy), high echogenicity of the cortex of the humerus (H) and greater tuberosity (GT).

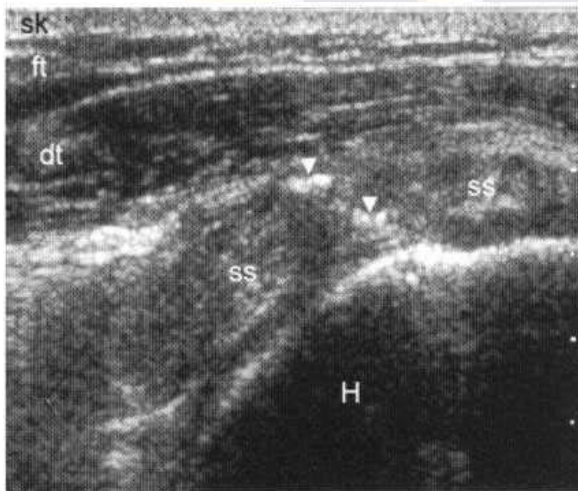


Fig. 38.116 Coronal oblique scan of supraspinatus calcific tendonitis. The supraspinatus tendon (ss) is of heterogeneous low echogenicity with foci of high echogenicity (arrowheads), some of which cast acoustic shadow consistent with calcification. Skin (sk), fat (ft), deltoid muscle (dt) and humeral head (H) are shown.

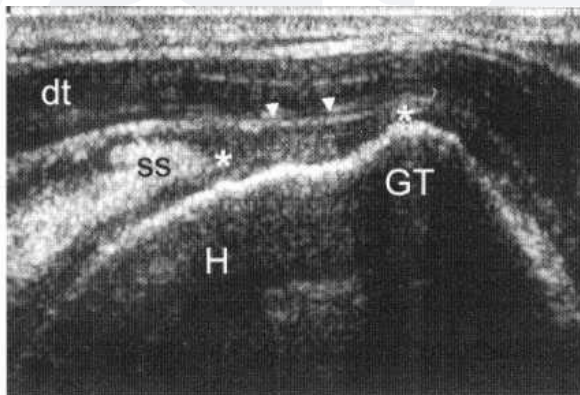


Fig. 38.117 Coronal oblique scan of supraspinatus full-thickness tear. There is an area of low echogenicity between the two points indicated (*), which contains a mixture of low-echogenic debris. Note how the deltoid muscle (dt) dips into the defect in the supraspinatus tendon (ss). GT = greater tuberosity; H = humeral head.

normal arthrogram, contrast medium may extend upward for 1 cm into the inferior tibiofibular joint. In ligamentous and capsular ruptures, contrast medium will seep into adjacent tissues and into tendon sheaths.

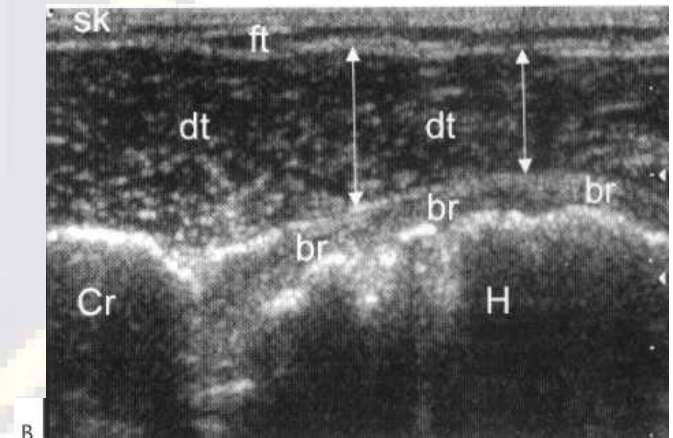
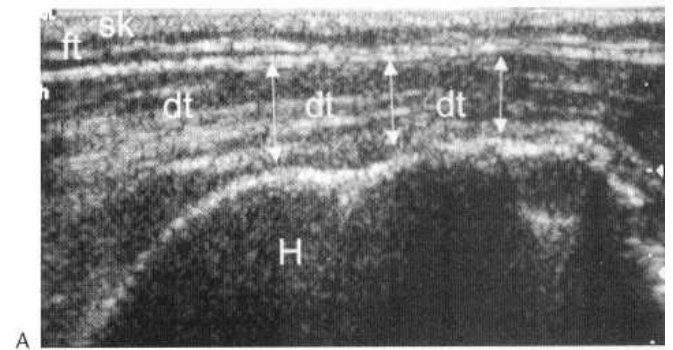


Fig. 38.118 Coronal oblique (A) and axial (B) scans of massive full-thickness rotator cuff tear. The skin (sk), fat (ft) and deltoid muscle (dt) between the double-headed arrows and synovium of subdeltoid bursa (br) are the only layers of soft tissue seen between the subcutaneous fat and humeral head (H). Note the irregularity of the humeral head contour in B. Cr = coracoid process.

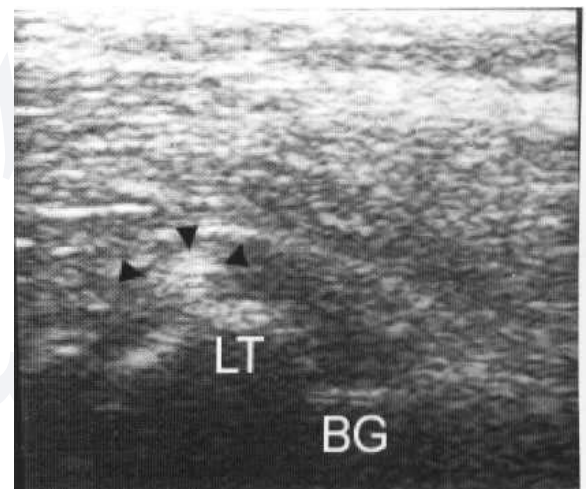


Fig. 38.119 Axial scan showing the long head of biceps (arrowheads) subluxed onto the lesser tuberosity (LT), and an empty low echogenic bicipital groove (BG), indicating tear of the transverse humeral ligament.

MRI

MRI has proved to be of great value in the ankle. Effusions are seen, as in other joints. Tendons around the joint arc assessed. Thickening, loss of clarity and increase in signal are especially well seen in the tendons behind the malleoli, with distension of the sheaths (Fig. 38.120). *Tenosynography* need no longer be performed.

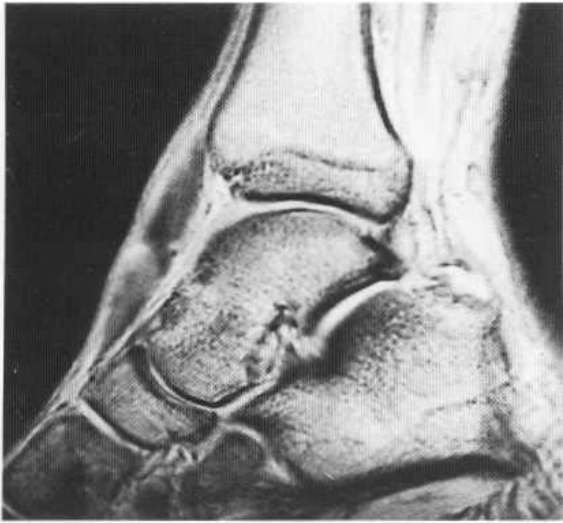


Fig. 38.120 Thickening of the tibialis anterior tendon demonstrated at MRI.

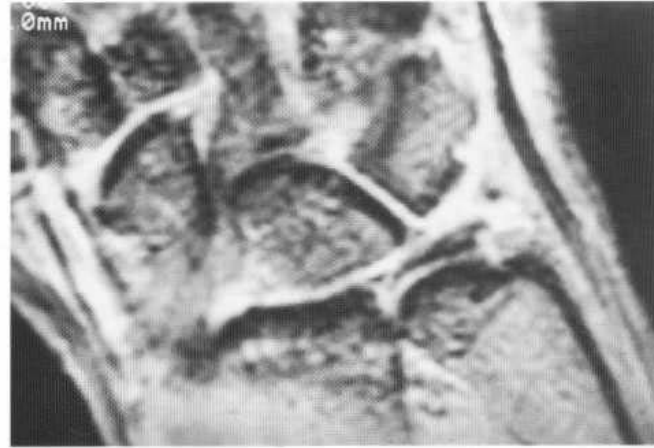


Fig. 38.123 MRI of the triangular cartilage. There is bright signal within the bulk of the triangular cartilage extending to its distal surface.



Fig. 38.121 Total rupture of a thickened tendo Achilles demonstrated at MRI. Fluid fills the space between the retracted parts.

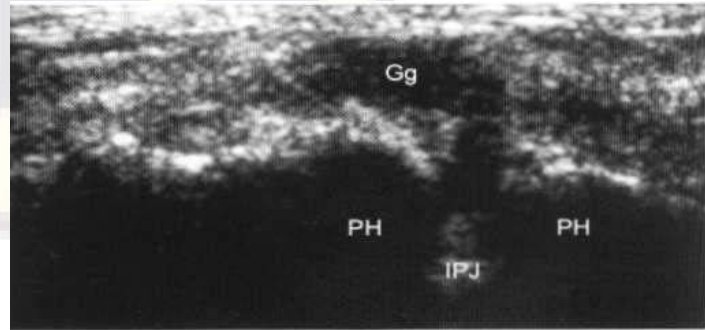


Fig. 38.124 Sagittal scan of a ganglion (Gg) arising from an interphalangeal joint (IPJ). The ganglion is anechoic consistent with being fluid filled, and has a 'speech bubble' shape, the tail extending between the phalanges (PH) into the joint.

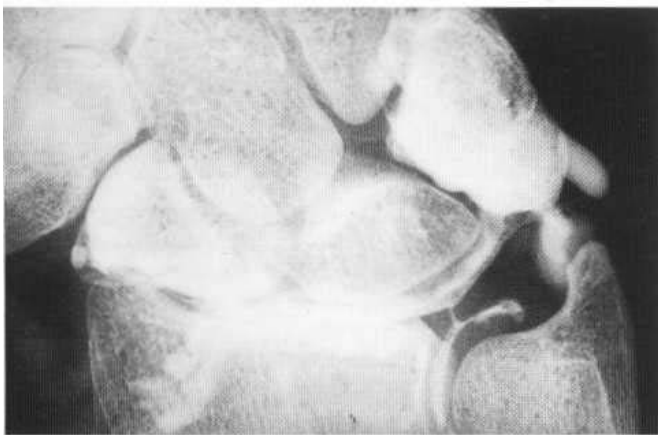


Fig. 38.122 Injection of the radiocarpal joint space has demonstrated a tear of the triangular cartilage and filling of the distal radioulnar joint at arthrography.



Fig. 38.125 Loosening of the hip prosthesis is demonstrated at arthrography. Contrast medium surrounds the acetabular component and tracks down the femoral stem. There is also a defect in the bone through which contrast medium escapes into the soft tissues.

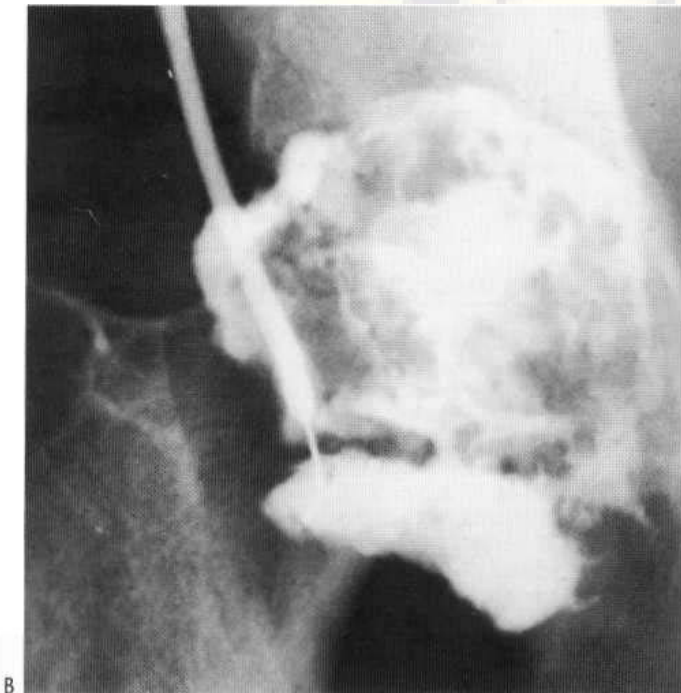
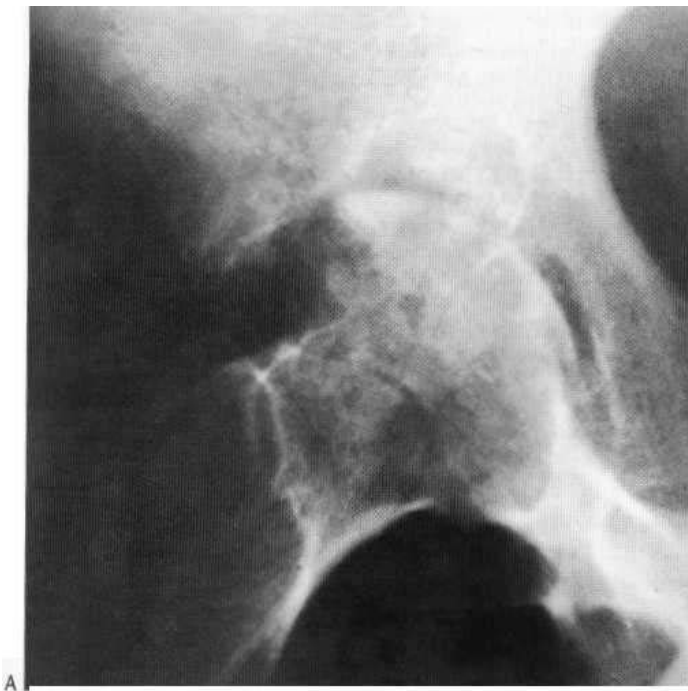


Fig. 38.126 Synovial tuberculosis. (A) The plain film shows bone and cartilage destruction on both sides of the joint. (B) The arthrogram shows gross irregular synovial hypertrophy. The geode does not fill.

The Achilles tendon is especially well shown. Tendinous thickening and central necrosis may be followed by rupture (Fig. 38.121). These changes are all seen in ultrasound scans too (Figs 38.26-38.28).

Ultrasound

As described above 'ultrasound', shows the internal structure of the tendons around the ankle and is useful in the assessment of integrity of the tendon, synovial sheaths and also dynamically con-

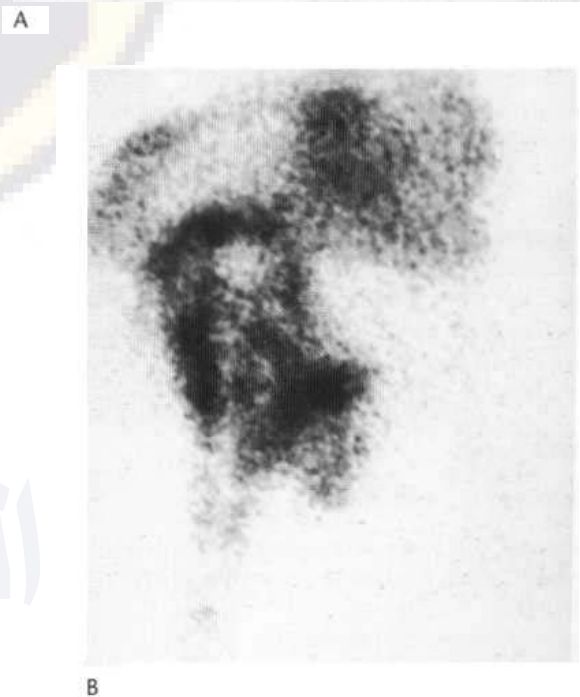


Fig. 38.127 Technetium bone scan. (A) Anterior scan of pelvis. (B) Oblique scan of right hip. The prosthesis can be seen as a defect on the scan and there is increased uptake around it, especially at the femoral component.

firms the presence of subluxation, for example of the peroneal tendons.

Changes in bone-avascular necrosis, osteochondritis of the talar dome, stress fractures, degeneration and bruising-are all well shown by MRI.

The deltoid, talofibular and spring ligaments can all be seen at MRI.

Elbow joint

Arthrography

Arthrography of the elbow is usually performed in the search for loose bodies. Capsular ruptures are shown by spreading of contrast

medium into adjacent soft tissues. Intra-articular loose bodies are outlined by contrast medium, but are better seen at CT scanning.

Wrist Joint

Arthrography

This technique has been used to demonstrate the integrity of the triangular cartilage. Injection of the radiocarpal joint at fluoroscopy shows a tom cartilage and filling of the distal radioulnar joint (Fig. 38.122). Unfortunately this can occur as a normal variant in up to 15%. The joint spaces around the proximal row of carpal bones fill during this injection, but the distal intercarpal joint spaces should not if the local ligaments are intact.

MRI

MRI demonstrates the triangular cartilage well in coronal images, and oedema, tears and detachments are seen (Fig. 38.123).

Collateral ligaments around small joints are demonstrated as well as the deep and superficial tendons in the hand.

Axial images of the wrist are also used in the *carpal tunnel syndrome*. Bowing of the flexor retinaculum and compression of the intermediate signal median nerve in the tunnel are associated with local oedema.

Ultrasound

This investigation may also be used to assess tendons and synovial reactions. In addition ultrasound has the advantage of assessing the ganglia (which are thought to be secondary to protrusions of encapsulated synovial tissue) and confirming the fluid nature of these and their origin from a joint or tendon (Fig. 38.124).

Hip joint

Indications for investigation include:

1. Evaluation of hip dysplasias-congenital dislocation of the hip, proximal focal femoral deficiency, epiphyseal dysplasias (see Ch. 35)
2. Evaluation of Perthes' disease (see Ch. 37)
3. Assessment of synovial infection, inflammation or tumours
4. Localisation of loose bodies
5. Assessment of pain following total hip replacement.

Hip arthrography in adults

Indications Most adult hip arthrograms are performed to assess either loosening or infection of a prosthesis. These patients complain of pain of increasing severity, often years after hip replacement. Such complications arise in up to 20% of patients, and 5% are infected.

Methyl methacrylate cement causes thermal necrosis of bone. A 1-mm zone of lucency is thus to be expected at the cement-bone interface, especially around the cup of the acetabular prosthesis. Lucency between cement and metal is less prominent and may result from movement during insertion of the prosthesis, pressure on weight-bearing or osteoclastic stimulation. Excessive or progressive widening of the interface lucency, or settling of the prosthesis into bone or cement, may indicate loosening or infection with resorption of bone.

Loosening is shown at arthrography by tracking of contrast medium between interfaces (Fig. 38.125). This is especially seen at the femoral component, but a thin (less than 1 mm) smear of contrast medium around the cup does not necessarily indicate loosening, especially if it covers the entire cup.

Infection also causes bone resorption at interfaces, but occasionally sinuses develop. Sinograms then show a connection with the prosthesis. Bone resorption is usually more severe and focal.

Synovial lesions or loose bodies may also be demonstrated by arthrography (Fig. 38.126). The needle is again inserted vertically over the central part of the femoral neck.

Radionuclide bone scanning and prosthetic loosening

Following insertion of a prosthesis, increased uptake of tracer is to be expected in the surrounding bone. This is uniformly distributed and lasts for up to 1 year, after which no increase is seen. No conclusion about the abnormality can be drawn in this early stage. After this *in me.*, focal increase in uptake using ^{99m}Tc -labelled MDP tracers can be assumed to represent infection or loosening or both. Such uptake is most commonly found at the tip of the femoral prosthetic stem and along its lateral margin (Fig. 38.127).

Differentiation between loosening and infection cannot be made using ^{99m}Tc scans, though a negative technetium scan probably rules out these factors as a cause of hip pain. Differential scanning using ^{67}Ga -citrate in addition to technetium is said to differentiate between loosening and infection. Gallium localises well in leukocytes at the site of infection. This change is best seen 24 hours after injection, when the vascular phase of increased local uptake is over. A positive technetium but negative gallium scan indicates loosening alone; if both are positive, infection is probably present.

REFERENCES AND SUGGESTIONS FOR FURTHER READING

- Aisen, A. M., Martel, W., Ellis, J. H., McCune, W. J. (1987) Cervical spine involvement in rheumatoid arthritis. *Radiology*, **165**, 159-163.
- Ansell, B. M. (1990) *Rheumatic Disorders in Childhood*. London: Butterworths.
- Ansell, B. M., Kent, P. A. (1977) Radiological changes in juvenile chronic polyarthritis. *Skeletal Radiology*, **1**, 129-144.
- Borlaza, G. S., Seigel, R., Kuhns, L. R., Good, A. E., Rapp, R., Martel, W. (1981) Computed tomography in the evaluation of sacroiliac arthritis. *Radiology*, **139**, 437-440.
- Braithwaite, I., White, J., Saifuddin, A., Renton, P., Taylor, B. A. (1998) Vertebral end-plate (Modic) changes on lumbar spine MRI: correlation with pain reproduction at lumbar discography. *European Spine Journal*, **7**, 363-386.
- Burk, D. L. Jr, Karasick, D., Mitchell, D. G., Rifkin, M. D. (1990) MR imaging of the shoulder: correlation with plain radiography. *American Journal of Roentgenology*, **154**, 549-553.
- Cica, N., Bilic, R., Delimar, D. (1998) Hill-Sachs lesion in recurrent shoulder dislocation: sonographic detection. *Journal of Ultrasound Medicine*, **17**(9), 557-560.
- Farm, P. U., Kaukanen, E., Jaroma, H., Harju, A., Vaatainen, U. (1996) Hill-Sachs lesion: sonographic detection. *Skeletal Radiology* **25**(6): 559-562.
- Fletcher, D. E., Rowley, K. A. (1952) The radiological features of rheumatoid arthritis. *British Journal of Radiology*, **25**, 282-295.
- Freiberger, R. H., Kaye, J. J. (1979) *Arthrography*. New York: Appleton-Century-Croft.
- Golding, F. C. (1962) The shoulder-the forgotten joint. *British Journal of Radiology*, **35**, 149-158.
- Golimbu, C. N., Firooznia, H., Melone, C. P., Rafii, M., Weinreb, J., Leber, C. (1989) Tears of the triangular fibrocartilage of the wrist: MR imaging. *Radiology*, **173**, 731-733.
- Goodman, N. (1967) The significance of terminal phalangeal sclerosis. *Radiology*, **69**, 709-712.

- Graf, R. (1984a) Fundamentals of sonographic diagnosis of infant hip dysplasia. *Journal of Pediatric Orthopedics*, 4, 735-740.
- Graf, R. (1984b) Classification of hip joint dysplasia by means of sonography. *Archives of Orthopaedic and Trauma Surgery*, 102, 248-255.
- Greenfield, G. B., Schorsch, H., Shkolnick, A. (1967) The various roentgen appearances of pulmonary hypertrophic osteoarthropathy. *American Journal of Roentgenology*, 101, 927-931.
- Grenier, N., Grdselle, J. F., Douws, C., et al (1990) MR imaging of foraminal and extraforaminal lumbar disk herniations. *Journal of Computer Assisted Tomography*, 14, 243-249.
- Hall, F. M. (1989) Sonography of the shoulder. *Radiology*, 113, 113-130.
- Hendrix, R. W., Fisher, M. R. (1986) Imaging of septic arthritis. *Clinics in Rheumatic Diseases*, 12, 459-487.
- Kieft, G. J., Dijkmans, B. A. C., Bloem, J. L., Kroon, H. L. (1990) Magnetic resonance imaging of the shoulder in patients with rheumatoid arthritis. *Annals of Rheumatic Disorders*, 49, 7-11.
- Lazarus, J. H., Galloway, J. K. (1973) Pachydermoperiostosis. *American Journal of Roentgenology*, 118, 308-313.
- Lee, B. C. P., Kazam, E., Newman, A. D. (1987) Computed tomography of the spine and the spinal cord. *Radiology*, 128, 95-102.
- Maddison, P. J., Isenberg, D. A., Woo, P., Glass, D. N. (eds) (1993) *Oxford Textbook of Rheumatology*. Oxford: Oxford University Press.
- Marchal, G. J., Van Holsbeeck, M., Raes, M., et al (1987) Transient synovitis of the hip in children: role of US. *Radiology*, 163, 825-828.
- Martel, W., Stuck, K. J., Dworin, A. M., Hyland, R. G. (1980) Erosive osteoarthritis and psoriatic arthritis: a radiologic comparison in the hand, wrist and foot. *American Journal of Roentgenology*, 134, 125-135.
- Mesgarzadeh, M., Schneck, C. D., Bonakdarpour, A., Mitra, A., Conaway, D. (1989) Carpal tunnel: MR imaging. Part II. Carpal tunnel syndrome. *Radiology*, 171, 749-754.
- Middleton, W. D., Kneeland, J. B., Carrera, G. F., et al (1987) High resolution MR imaging of the normal rotator cuff. *American Journal of Roentgenology*, 148, 559-564.
- Mink, J. H., Reicher, M. A., Cruess, J. V. (1993) *MRI of the Knee*, 2nd edn, pp. 100-103. New York: Raven Press.
- Modic, M. T., Steinberg, P. M., Ross, J. S., Masaryk, T. J., Carter, J. R. (1988) Degenerative disk disease: assessment of changes in vertebral body marrow with MR imaging. *Radiology*, 166, 193-199.
- Murphey, M. D., Wetzel, L. H., Bramble, J. M., Levine, E., Simpson, K. M., Lindley, H. B. (1991) Sacroiliitis: MR imaging findings. *Radiology*, 180, 239-244.
- Murray, R. O. (1965) The aetiology of primary osteoarthritis of the hip. *British Journal of Radiology*, 38, 810-824.
- Neer, C. S. (1983) Impingement lesions. *Clinical Orthopaedics*, 173, 70-77.
- Park, W. M., O'Neill, M., McCall, I. W. (1979) The radiology of rheumatoid involvement of the cervical spine. *Skeletal Radiology*, 4, 1-7.
- Patton, J. T. (1976) Differential diagnosis of inflammatory spondylitis. *Skeletal Radiology*, 1, 77-85.
- Peter, J. P., Pearson, C. M., Marmor, L. (1966) Erosive osteoarthritis of the hands. *Arthritis and Rheumatism*, 9, 365-387.
- Resnick, D. (1995) *Diagnosis of Bone and Joint Disorders*, 3rd edn. Philadelphia: Saunders.
- Resnick, D., Shaul, R., Robins, J. M. (1975) Diffuse idiopathic skeletal hyperostosis: Forestier's disease with extraspinal manifestations. *Radiology*, 115, 513-524.
- Reynolds, H., Carter, S. W., Murtagh, F. R., Rechtine, G. R. (1987) Cervical rheumatoid arthritis: value of flexion and extension views in imaging. *Radiology*, 164, 215-218.
- Ryan, P. J., Taylor, M., Grevitt, M., et al (1993) Bone single-photon emission tomography in recent meniscal tears: an assessment of diagnostic criteria. *European Journal of Nuclear Medicine*, 20, 703-707.
- Seminars in Musculoskeletal Radiology*, (1998) 2(3).
- Sholkoff, S. D., Glickman, M. G., Steinbach, H. L. (1970) Roentgenology of Reiter's syndrome. *Radiology*, 97, 497-503.
- Thould, A. K., Simon, G. (1966) Assessment of radiological changes in the hands and feet in rheumatoid arthritis. *Annals of the Rheumatic Diseases*, 25, 220-228.
- Van Holsbeeck M., Introcaso J. H. (1991) *Musculoskeletal Ultrasound*. Chicago: Mosby Year Book.
- Yulish, B. S., Lieberman, J. M., Newman, A. J., Bryan, P. J., Mutopoulos, G. P., Modic, M. T. (1987) Juvenile rheumatoid arthritis: assessment with MR imaging. *Radiology*, 165, 149-152.
- Zinberg, E. M., Palmer, A. K., Coren, A. B., Levinsohn, E. M. (1988) The triple injection wrist arthrogram. *Journal of Hand Surgery (Ain)*, 13, 803-809.

نشر الکترونیکی
 موسسه انتشاراتی
 نور دانش



نشر الکترونیکی
موسسه انتشاراتی
نوردانش

39

TUMOURS AND TUMOUR-LIKE CONDITIONS OF BONE (1)

Mark Cobby and Iain Watt

Bone tumours present radiological problems that vary from simple to impossible. Whilst benign and innocuous lesions such as fibrous cortical defects are common, and may occur in up to 30% of normal children, primary malignant tumours of bone are relatively rare and are responsible for only 1% of all deaths from neoplasia. Consequently most radiologists will see comparatively few cases and, even in referral centres, considerable difficulty often arises in making an exact diagnosis.

When presented with a lesion in a bone, three important questions require to be answered:

- Is the lesion neoplastic or infective?
- Is it benign or malignant?
- Is it a primary or secondary neoplasm?

In many cases, these problems can be resolved without hesitation. In others, notably those in which cartilaginous tissue is involved, great difficulty may be experienced. It must never be forgotten that it is much more common for malignancy in bones to be metastatic rather than primary. It is important that a radiological diagnosis should be made before biopsy. An apparently simple radiological diagnosis may not be confirmed histologically and vice versa. Biopsy itself may significantly alter radiological features. It is also important to remember that although the pathologist may be regarded as the final arbiter, fully representative material must be available for opinion, and this may require sectioning the whole lesion. On the one hand, in some benign conditions, such as non-ossifying fibroma or an osteochondroma, it may be considered unnecessary to resort to pathological confirmation, and a conservative attitude or treatment by a minor surgical procedure may be adopted. On the other hand, if a more radical course is being considered, radiology serves not only to provide a diagnosis but also to delineate soft-tissue and bony involvement, thereby permitting procedural planning. Inadequate investigations have occasionally been responsible for erroneous diagnoses of benign lesions as malignant, resulting in unnecessary surgical procedures, including such iatrogenic disasters as amputation.

Many different types of bone tumour are now recognised, varying greatly in their mode of clinical presentation, pathology and behaviour. Their aetiology remains obscure. Some appear to be superimposed upon a pre-existing disease such as Paget's disease or

bone infarction. An increased incidence of both benign and malignant neoplasms is known to follow radiation therapy.

Classification of bone tumours

It would be convenient to classify bone tumours according to their cell of origin or histogenesis. However, histologically the exact cell of origin of a tumour is not always certain and typing may depend only on the cell or cells that predominate in the developed lesion. In some cases, a single tumour may produce several major different types of cell line (e.g. osteosarcoma); in others, undifferentiated small round cells may be a predominant histological feature, permitting only a broad collective diagnosis of malignant round cell tumour. A number of interrelated connective tissue cells are present in bone, and from this skeletal connective tissue, the majority of bone tumours appear to arise. Other bone tumours are related to non-osseous components of the skeleton, including blood vessels and nerves. Those associated with haematopoietic and lymphoreticular elements are discussed elsewhere (see Ch. 41).

A classification of bone tumours is suggested in Table 39.1. Non-neoplastic tumours (the word tumour is synonymous with a swelling), abscess, haematoma and so forth, have been included since they must feature in the differential diagnosis. Never forget that a radiologically unusual metastasis is commoner, particularly in older patients, than a primary tumour.

GENERAL PRINCIPLES OF DIAGNOSIS

Before attempting to interpret the radiological features of a bone tumour, consider the age of the patient and the clinical history. Many tumours are found in fairly constant age groups. The history may be less useful as many lesions present with non-specific features of pain, swelling or pathological fracture. However, lesions are not infrequently discovered by chance. The sex incidence in primary bone tumours is of little diagnostic value, although of relevance in skeletal metastasis.

The conventional radiograph is vital in establishing the diagnosis or differential diagnosis of a bone lesion and is supplemented here

Table 39.1 Classification of primary tumours of bone

	Benign	Malignant
A. Presumed to arise from skeletal tissue		
Bony origin?	Bone island Ivory osteoma Osteoid osteoma Osteoblastoma	Osteosarcoma Parosteal osteosarcoma
Cartilaginous?	Chondroma Chondroblastoma Chondromyxoid fibroma	Chondrosarcoma Dedifferentiated chondrosarcoma Mesenchymal chondrosarcoma
Fibrous?	Fibrous cortical defect Non-ossifying fibroma Desmoplastic fibroma Fibromatosis Atypical Paget's disease	Fibrosarcoma Fibrous histiocytoma Paget's sarcoma
Giant cell containing?	Giant cell tumour Aneurysmal bone cyst Hyperparathyroid brown tumour	Malignant giant cell tumour
B. Presumed to arise from other tissues in bones		
Blood vessels?	Hemangioma Cystic angiomatosis Haemangiomas [Massive osteolysis/ vanishing bone disease] Glomus tumour [Haemangiopericytoma]	Angiosarcoma
Nerves?	Neurofibroma Neurilemmoma	Neurofibrosarcoma Neuroblastoma
Fat?	Lipoma [Intraosseous and parosteal]	Liposarcoma
Notochord?		Chordoma
Epithelium?	Implantation dermoid	Adamantinoma
Lymphoid/haematopoietic? (see Ch. 41)		Leukaemias Lymphomas Plasmacytoma Myelomatosis
C. Presumed to arise from joints		
	Intraosseous ganglion Pigmented villonodular synovitis Synovial chondromatosis (Differentiate from: osteoarthritic cyst rheumatoid geode)	Synovioma Synovioma
D. No known origin		
	Solitary bone cyst	Malignant round cell tumours (including Ewing's, neuroblastomas, reticulosarcoma)
E. Non-neoplastic tumours (a tumour is a swelling!)		
	Brodie's abscess Hydatid Haematoma Infarction Flistiocyctosis	

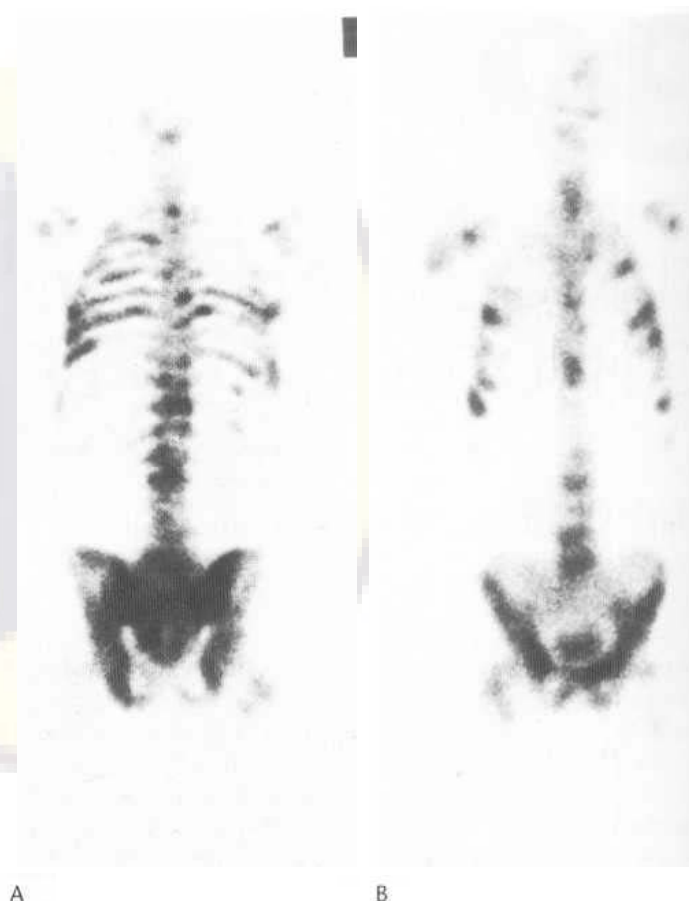


Fig. 39.1 Multiple skeletal metastasis is demonstrated on a whole-body radionuclide bone scan. The primary tumour was carcinoma of the breast in a middle-aged woman. Note the predominantly axial distribution of the lesions, many of which were not apparent on conventional radiographs. (A) PA view. (B) AP view.

necessary by CT, scintigraphy, angiography and MRI. Questions to consider include:

1. Is the lesion solitary or multiple?

With the exception of multiple osteochondromas of diaphyseal aclerosis and multiple cartilage tumours in dyschondroplasia, most primary bone tumours are solitary.

⁹⁹ *"Tc-HDP scintigraphy is commonly used to establish whether or not the lesion is unifocal (Fig. 39.1). Other abnormal foci may then be subjected to radiographic examination. Difficulties will be experienced in myelomatosis when most lesions are photon deficient, or with metastasis from some primary carcinomas, such as cholangiocarcinoma or primary pelvic lesions, including cervix uteri. The high false-negative detection rate in these tumours may justify the more time-consuming and expensive radiographic skeletal survey. Never forget to take a radiograph of the chest, whether or not a skeletal survey has been undertaken. The diagnosis becomes easier if a bronchial carcinoma or an obvious metastasis can be detected.*

2. What type of bone is involved?

It is of some value to differentiate between flat bones and tubular bones because, for example, lesions in the axial skeleton or proximal ends of long bones are in the sites of persistent haematopoietic tissue and should always raise the possibility of a metastasis or

lymphoma. Osteoid osteoma is very rare in membrane bone. A radiolucency in the mandible is more likely to be myeloma than metastasis. Although no part of the skeleton is exempt from involvement by a primary bone tumour, a large proportion is found in the pelvis and long bones, particularly around the hips and knees.

3. Where is the lesion within the bone?

Many benign tumours tend to appear in characteristic sites: for example, non-ossifying fibroma and fibrous cortical defects are by definition in the cortex, eccentrically toward the metadiaphysis of a long bone. Chondroblastoma occurs in an epiphysis or apophysis. Giant cell tumour is almost invariably immediately subarticular and eccentric in location. Most tumours of cartilaginous origin, except those that are associated with an osteochondroma, have a medullary location.

4. Conventional radiographic features

Never settle for anything less than perfect plain films. It is important that soft tissue detail is not lost on an overexposed film, because soft-tissue tumour extension typically presents a well-defined margin, whereas soft-tissue swelling associated with inflammation has ill-defined margins. Similarly, soft-tissue calcification or ossification may be overlooked. Do not settle for underpenetrated films as the inner texture of a tumour may be overlooked, for example the ground-glass quality of fibrous dysplasia, or the radiolucent focus of an osteoid osteoma may not be visualised. Take films 'around the clock'. Simply because periosteal new bone cannot be visualised on a standard AP and lateral film does not mean that it will not be present on an oblique projection. Is the pattern of bone change destructive, proliferative or both? Correlating the size of the lesion with the length of history may be a guide as to its rapidity of growth and, similarly, follow-up films permit an assessment of its aggressive potential or malignancy. Tumours of osteoblastic origin are commonly, but not always, bone producing. Consequently, areas of increased density and/or surrounding new bone formation extending into soft tissue are likely to be evident. Cartilaginous tumours are mainly radiolucent but small loci of calcification represent an important hallmark.

5. What do the margins of the lesion look like?

Is there a narrow or wide zone of transition between apparent tumour and normal bone? A wide zone of transition suggests a lesion that is rapidly growing, such as an aggressive malignancy or infection. Is the zone of transition marked with bone reaction or not? A thin rim of sclerosis is present characteristically around a non-ossifying fibroma, whereas extensive sclerosis is typical of a cortical osteoid osteoma. Of course, these findings are not constant and ill-defined sclerosis with a widened zone of transition may occur in such benign conditions as histiocytosis. Examine the cortex: is it resorbed from within, indicating a medullary lesion such as a cartilaginous tumour or myelomatosis? Peripheral cortical lesions are more commonly caused by pressure or direct invasion from abnormalities in adjacent soft tissues. Exceptions to this are the 'saucerisation' of Ewing's sarcoma and metastasis. If the margins of such a cortical defect are smooth the lesion is usually benign, for example a neurofibroma, or non-neoplastic, as in the case of anterior erosion of vertebral bodies by an aortic aneurysm. Conversely, an irregular margin may suggest invasion by a malignant soft-tissue lesion, for example metastasis, or direct invasion by carcinoma of the antrum or lymphoma. Finally, is there an associated soft-tissue mass? The

presence of a soft-tissue mass frequently can be shown in relation to malignant bone tumours, although oblique views may be necessary to delineate it. An ill-defined soft-tissue mass is almost invariably associated with an inflammatory lesion. Examine the margin of the soft-tissue lesion to see whether or not there is a thin shell of bone as occurs in some aggressive types of aneurysmal bone cysts, particularly those arising in the spine.

Further imaging investigations

All further investigations are performed in order to delineate or elicit differential characteristics of a lesion already demonstrated on conventional radiographs, to precisely define the local extent of the lesion and to exclude the presence of metastasis. Where appropriate, imaging studies are required to monitor preoperative (neoadjuvant) chemotherapy and to detect recurrent disease.

Tomography

Tomography has been largely superseded by CT and MRI. The object of a tomogram is either to delineate the characteristic radiological features summarised above or to assist demarcation of the intra- and extra-osseous extent of the abnormality.

Scintigraphy

This procedure may be performed as the first additional investigation in most instances, depending on the availability of MRI or CT. High-resolution gamma camera images using ^{99m}Tc -labelled diphosphonate compounds provide optimal images. Two phases of the bone scan should be recorded. First, by counting the first 300 000 events after the injection a blood-pool scan is obtained while the radiopharmaceutical is still largely in the intravascular or perivascular extracellular fluid space. Two to three hours later the skeleton is imaged, when the radiopharmaceutical has localised in bone and is in the delayed or bone-scan phase. The blood-pool phase is vital and should never be overlooked. Scintigraphy may be used to assess the primary presenting lesion and to detect whether it is monostotic or accompanied by other skeletal lesions, such as metastasis.

Examine the blood-pool phase: is the lesion vascular, as in an aneurysmal bone cyst, or avascular, as in most cartilage tumours? Does the lesion itself accumulate radiopharmaceutical, suggesting that it is being bound into a fibrous, cartilaginous or bone-forming matrix, or is the lesion essentially photon deficient with increased activity surrounding it, suggesting either a heterogeneous tumour or a host reaction? Does the lesion extend beyond the confines demonstrated by plain film, remembering that the apparent extent of intraosseous involvement can be slightly greater because the scan may not distinguish between bone-forming tumour and a rim of reactive host response? If the lesion is photon rich, check the lungs since metastases from an osteosarcoma are occasionally detectable by bone scanning. Finally, are there any lesions elsewhere? If so, radiograph them.

CT

CT has an important part to play both in the assessment of the primary presenting lesion and in the detection of potential metastatic dissemination. CT will give an impression of the predominant variety of tissue present, particularly if there is fat or calcification. It will not necessarily indicate whether those tissues are benign. Examine the intraosseous extent of the tumour, looking for subtle

changes in medullary fat. Examine also extraosseous extent and soft-tissue relationships. Contrast medium enhancement is of little value, because most tumours do not enhance in a diagnostically useful fashion. However, the vascular nature of a tumour may be detected and the relationship of the soft-tissue component of the tumour to blood vessels can be assessed. CT detects more pulmonary metastasis than is possible with a conventional chest radiograph.

Angiography

Angiography has been the subject of fashion but in recent years has fallen into disrepute. The initial hope that it would, in isolation, distinguish reliably between benign and malignant lesions has foundered. No characteristic angiographic feature of malignancy exists. However, two signs—encasement and tumour vessels occur with much greater frequency in malignant tumours. Encasement results from the vessel being surrounded by tumour and hence is shown by a localised segment of narrowing. Tumour vessels are defined as structures pursuing a random course with an irregular branching pattern.

Angiography should be used in the differential, rather than in the absolute, diagnosis of a lesion, as for example to distinguish between tumour and infection. A malignant round cell tumour has an intrinsically abnormal vascular pattern, whereas osteomyelitis is characterised by an increased number of normal arterial branches and enlarged periosteal veins. Similarly, angiography may be used to distinguish between tumours, since osteosarcomas are highly vascular, whereas most chondrosarcomas are hypovascular. It is arguable, however, whether angiography now contributes significantly to the assessment of primary tumours and their extent, as much of the information obtainable on angiogram may be obtained by scintigraphy, CT and MRI.

Angiography, however, may still be necessary in order to delineate the involvement of major vessels by extension of a tumour into soft tissues when prosthetic or other limb conservation surgery is being considered. Interventional angiography has also enjoyed a

vogue. Very vascular tumours may be infarcted before resection or intra-arterial chemotherapy given.

MRI

MR images have come to be of prime importance in the assessment of bone and soft-tissue contrast, with the ability to distinguish between various soft tissues by altering pulse sequences. Not only is a superb delineation of intra- and extra-osseous extent of tumour possible, but also the flexibility of imaging planes permits advantageous visualisation for tumour staging and planning of surgery. Intraosseous oedema and extra-osseous inflammatory response may be demonstrated. The relationship between tumour masses, inflammatory response, blood vessels and other important structures such as joints may be demonstrated very accurately. This information is of prime importance in planning limb-salvaging procedures and assessing whether or not soft-tissue compartments are breached. Small foci of calcification and fine osseous detail may not be visualised however. CT remains valuable for this purpose. Similarly, current images of the lungs are not yet of high enough resolution to confidently detect the presence of a small metastasis. Again, CT is recommended for this purpose.

A measure of tumour aggressiveness may be obtained by measuring the rate of enhancement following intravenous contrast medium; well-perfused, often cellular tumours, accumulate a high concentration of gadolinium, the rate at which this accumulates correlating well with biological activity. MRI is also invaluable in monitoring tumour response to neoadjuvant chemotherapy, as in osteogenic sarcoma, before limb-salvage surgery. Also it may help determine the appropriate adjuvant (postoperative) chemotherapy. An indication of the tissue content of a lesion such as fat, haemorrhage, fibrosis or fluid may be evident from the MR images. Fluid-fluid levels characteristically are seen in aneurysmal bone cysts due to suspended solid old haemorrhage material creating a layering effect within the fluid. Highly cellular tumours, such as those containing chondroid material,

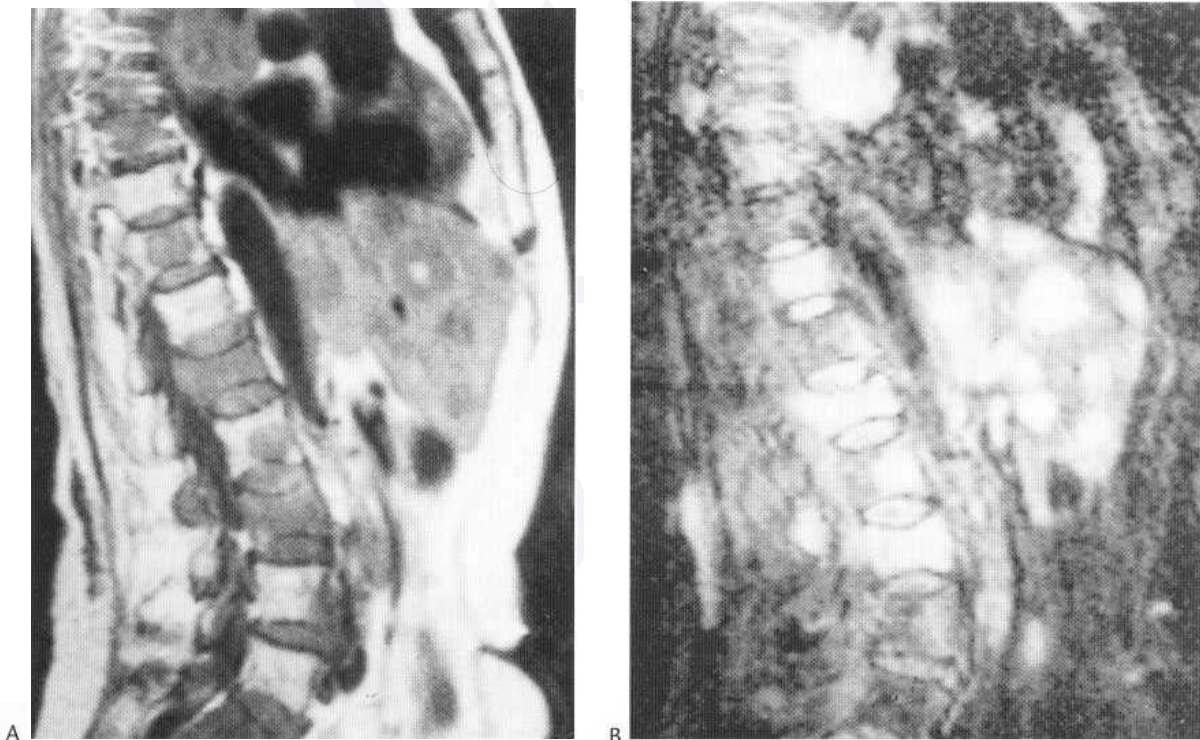


Fig. 39.2 Metastatic carcinoma of the bronchus. Sagittal T_1 -weighted (A) and STIR (B) MRI sequences obtained in the body coil demonstrate extensive metastasis throughout the thoracolumbar spine and liver. The primary bronchial carcinoma is also evident.

have particularly high signal intensity on T_0 -weighted images and may have a lobulated appearance. By comparison, relatively acellular tumours with a high collagen content show low signal intensity on all sequences, including T_2 -weighted and STIR sequences. Gadolinium-enhanced images can help to differentiate between viable tumour, reactive oedema and necrosis, and can be used to guide the biopsy site.

METASTATIC TUMOUR INVOLVEMENT OF BONE

The later stages of many malignant neoplasms are associated almost inevitably with metastasis, and the skeleton is very commonly affected. The radiographic presence of such lesions very often lags behind their detectability by scintigraphy, CT or MRI (Fig. 39.2). Bony metastasis is present in approximately 25% of all deaths from malignant disease. Any primary tumour may metastasise to bone, but in women the most important carcinoma is breast, from which secondary deposits develop in about two-thirds of cases. In men, approximately 80% of cases of carcinoma of the prostate and a quarter of lung and kidney tumours may be expected to produce bone metastasis. A metastasis, indeed, may be the presenting feature of the disease.

While a bone metastasis may present as a pathological fracture, usually it produces only vague pain or is entirely occult. Biopsy of a metastasis may indicate the site of origin of a previously unsuspected primary tumour. Usually, the more malignant the primary tumour, the more rapidly does secondary spread occur. Some tumours, however, may present with a metastasis years before the primary lesion is clinically apparent and indeed the metastasis itself may remain virtually unchanged radiologically for a long time. This may be observed particularly with carcinoma of the thyroid. A latent period often separates the removal of a primary tumour, particularly from the breast, and the subsequent development of skeletal metastasis.

The *spine, pelvis* and *ribs* are the most common sites of involvement together with the proximal ends of the *humeri* and *femora* and, less often, the *skull* (Fig. 39.1). These areas correspond to sites of persistent haematopoiesis in the adult, malignant spread usually occurring by a haematogenous route. Local spread to the lumbar spine and pelvis may be expected from tumours arising in the pelvis, notably carcinoma of the cervix. Some metastasis have a predictable distribution, the majority of renal cell carcinoma metastasis occurring in the lumbar spine and pelvis. They have a rather characteristic radiological appearance (see below). Metastasis distal to the knee and elbow is rare and usually arises from a primary tumour of the bronchus or pelvic organs, particularly colon and bladder.

Blood chemistry studies may be of some value. The *serum alkaline phosphatase* is always raised in the presence of multiple bony metastasis, but remains normal in myelomatosis. With widespread osteolytic destruction the *serum calcium* is usually elevated. In the case of carcinoma of the prostate a marked rise in the *serum acid phosphatase* and *prostate specific antigen* (PSA) levels is characteristic, the latter being now the marker of choice.

Some metastases respond to treatment with, for example, hormone therapy. Under these circumstances, both radiography and scintigraphy are needed to monitor the progress of such lesions. Remember that it is inadequate simply to document the number and

extent of metastases. It is a radiologist's duty to draw the clinician's attention to those that may be considered hazardous—for example, associated with significant vertebral body collapse (and the possible development of cord compression) or in long bones of the lower limb (with the potential for disabling fracture). In the latter circumstance, prophylactic nailing of the femur or femoral neck will be considered if 50% or more of the cortex is destroyed.

Radiological features

The majority of metastases is predominantly osteolytic. Typically they arise in the medulla and progressively extend in all directions, destroying the cortex, usually without the development of much periosteal reaction. Soft-tissue extension is relatively uncommon. Some metastases, particularly from bronchial carcinoma, may appear eccentric and primarily destroy cortex, especially in the femur. Others are predominantly osteoblastic, including those derived from the prostate, stomach and carcinoid. They produce dense and often well-circumscribed areas of increased radiopacity. Such lesions are less subject to pathological fracture. A small group of metastases is accompanied by tumour bone formation; this includes osteosarcoma, liposarcoma, transitional cell carcinoma (of either bladder or kidney) and some adenocarcinomas of the colon (Fig. 39.3).

The diagnosis of metastasis is usually simplified by the multiplicity of lesions. Difficulty may arise when a lesion is apparently solitary. Unusual primary tumours are often responsible for unusual metastasis and, further, a metastasis can simulate closely almost any known primary bone tumour!



Fig. 39.3 Two examples of solitary metastasis producing bone in the adjacent soft tissues. (A) Carcinoma of the colon in a great toe metatarsal. (B) Transitional cell carcinoma of the bladder in the mid tibia.

Breast

Not only is this the most common primary tumour in women but its metastases shows an unusual affinity for bone. Bone scanning demonstrates a significant incidence of bone metastasis at the time of diagnosis, roughly in proportion to the degree of malignancy. The lesions are usually osteolytic and commonly multiple. Diffuse infiltration, however, may cause an apparently coarse trabecular pattern without an obvious area of bone destruction. The condition should be suspected in the presence of vertebral compression fractures in older women. Differentiation of these from osteoporotic collapse may be difficult, although, in the latter, evidence of focal areas of bone destruction is usually lacking. MRI may be extremely helpful in the difficult case, recent attention being focused on diffusion weighted imaging. Multiple lytic lesions also may resemble myelomatosis, but in that condition, the margins of the lucencies are sharply defined with endosteal scalloping and the serum alkaline phosphatase is usually normal.

About 10% of metastases from carcinoma of the breast produce osteoblastic lesions and in another 10% the lesions are mixed (Fig. 39.4). Sclerosis may occur in lytic lesions following successful hormone or radiation therapy.

Difficulty may be experienced in differentiating between intense disuse osteoporosis following radiotherapy and metastatic disease. This problem arises particularly around the shoulder where the bones have been included in the radiation field. The lesions of intense disuse osteoporosis tend to be sharply defined and ellipsoid in the long axis of bone. Similarly, multiple rib fractures secondary to radiation therapy should not be mistaken for metastasis. Often such fractures occur at the edge of the radiation field and conse-



Fig. 39.4 Mixed skeletal metastasis from carcinoma of the breast in a middle-aged woman.

quently tend to be in a line, a distribution observed also in acute trauma and osteoporosis.

Prostate

This is the commonest secondary bone tumour in men and, in contrast to breast deposits, almost all these metastases are osteoblastic (Fig. 39.5). They appear as round or oval areas of increased density, particularly in the pelvis and spine, growing slowly and merging so that widespread and diffuse increase in bone density may ensue. Periosteal new bone formation and/or apparent expansion of bone may occur, so that the differentiation from Paget's disease may be difficult. The deposits may be shown to regress with hormone therapy. In some patients metastases from the prostate may be osteolytic and expansile (Fig. 39.6). They may be solitary. If the carcinoma involves the base of the bladder some metastases may be associated with new bone formation in the adjacent soft tissue, resembling an osteosarcoma.

Kidney

Renal cell carcinoma characteristically presents with a solitary bone metastasis and has a marked predilection for the pelvis and lumbar spine. Even when multiple their number seldom exceeds six. These lesions are typically expansile with a crenellated margin and usually have a typical radiological appearance (Fig. 39.7). They are richly vascular, as demonstrated scintigraphically or angiographically. These tumours are often slow growing and may have a ret-



Fig. 39.5 Carcinoma of prostate—extensive sclerosis is present in the ribs and clavicle due to widespread metastasis in an elderly man.

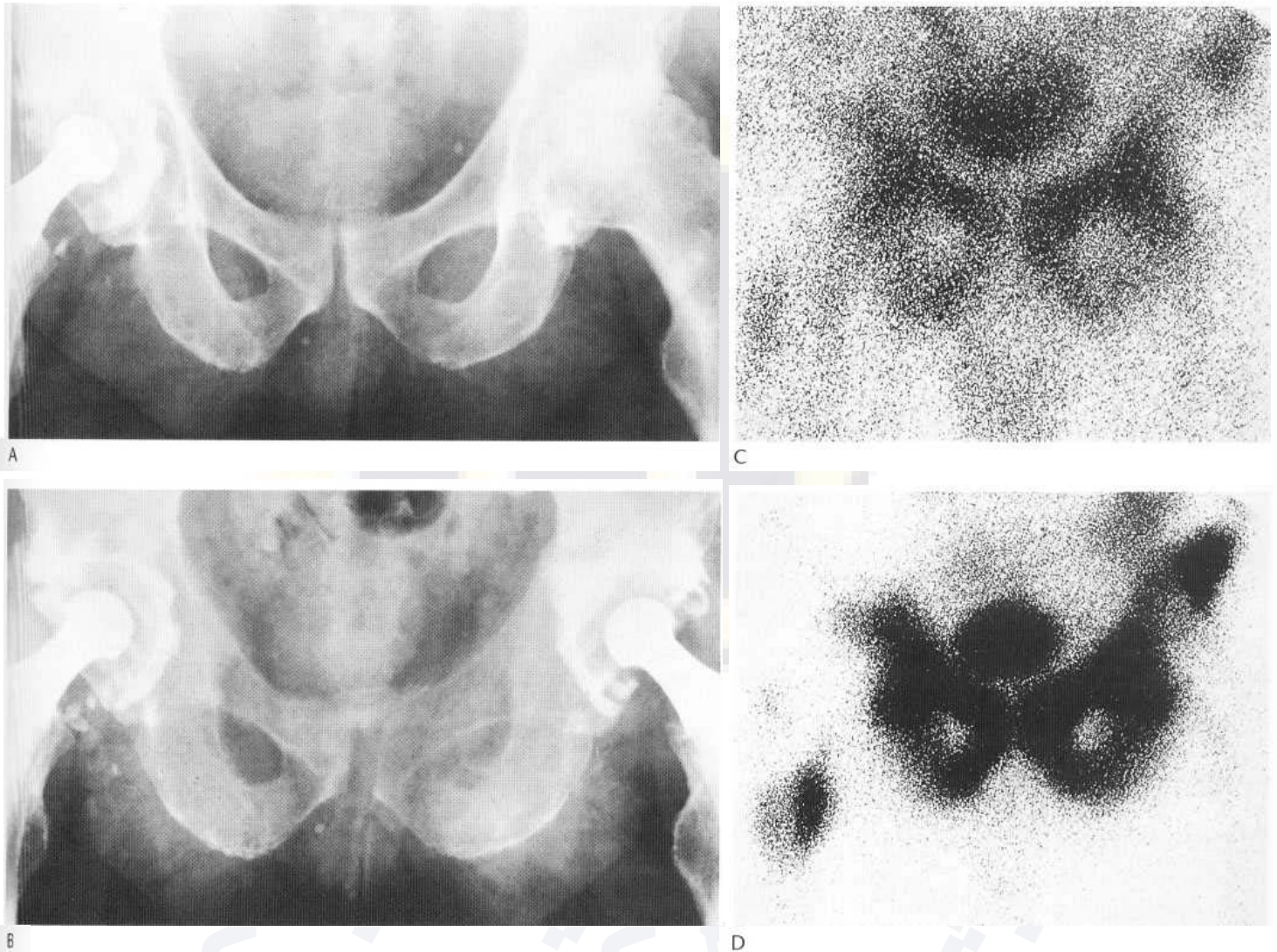


Fig. 39.6 Carcinoma of the prostate with expansile lytic metastasis. (A) A view of the pelvis before the onset of symptoms reveals no abnormality in the pubic rings. (B) Five years later the patient was complaining of severe pain in the groin. Note the ill-defined trabecular pattern, expansion of bone and ill definition of cortex that has developed since the previous examination. (C) Blood-pool phase of a bone scan and (D) delayed image reveals a marked increase in activity. Note the abnormality in the lesser trochanter of the right femur. These features could not be distinguished from active aggressive Paget's disease on purely scintigraphic grounds except that the lesion in the right femur has not started at a joint. The diagnosis was established by biopsy and the presence of a very high acid phosphatase level in the blood.

Lively good prognosis, particularly following excision of the affected kidney and a solitary deposit. Transcatheter embolisation may prove a useful addition to management.

Lung

In men this tumour is second only to the prostate in causing a high proportion of cases to develop skeletal metastases, such bone lesions occurring eventually in about a third. These metastases are almost always osteolytic and can be unusual, occurring in the small bones of the hand or eccentrically in the cortex of a long bone.

Alimentary tract

Carcinoma of the stomach and colon, and carcinoid, may metastasise to bone in both sexes. Metastases from the stomach and carcinoid are often osteoblastic and may be multiple. The bone-forming characteristic of colonic metastases has been already emphasised.

Other primary tumours

These often produce bizarre and atypical radiological patterns. In particular the metastases from thyroid carcinoma are classically expansile, osteolytic and often solitary (Fig. 39.8).

Invasion and destruction by extrasosseous primary malignant tumours

Lesions of this type are rare compared with skeletal metastases, but may be observed in association with direct spread of such lesions as carcinoma of the cervix or bladder, and from carcinoma of the paranasal sinuses. Malignant tumours adjacent to bone may cause resorption of the cortex with a permeative pattern, but lower grade malignancies, including tendon sheath abnormalities, may produce well-defined cortical defects suggesting pressure erosion. Destruction of adjacent bones should suggest a lesion originating in

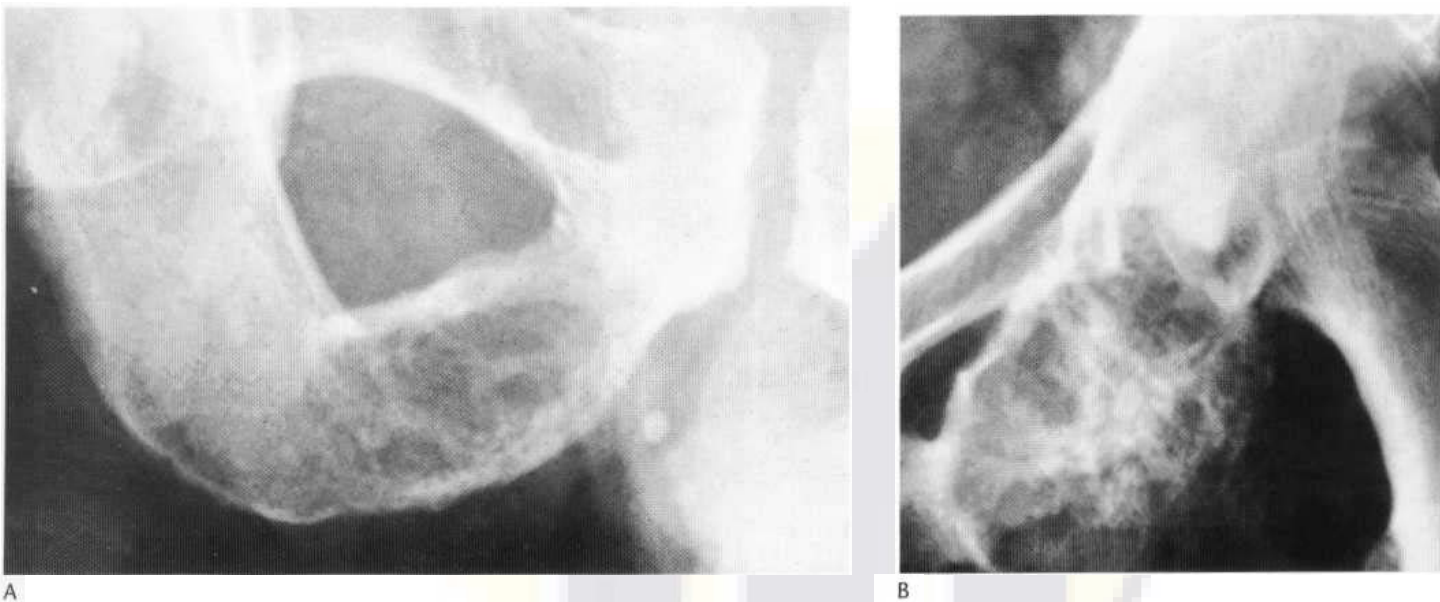


Fig. 39.7 (A,B) Two examples of solitary metastasis from renal cell carcinoma. In both cases, these metastases were the presenting abnormality. Both are expansile and have crenellated margins, with trabeculation in the lesion.

soft tissues. An important example is involvement of the upper ribs by bronchial carcinoma (Pancoast's tumour) in patients being assessed for neck, brachial plexus or shoulder pain (Fig. 39.9).

BONE-FORMING TUMOURS

Bone Island (also known as enostosis)

Although no evidence exists to suggest that this is a true bony neoplasm, confusion may arise on occasions. The lesions may be single or multiple, are always medullary in location and consist of normal, compact lamellar bone. The lesion is uniformly dense, round or oval, and characteristically has radiating thorn-like spicules extending into the surrounding medullary cavity with a narrow zone of transition (Fig. 39.10). They usually measure less than 15 mm in diameter, but occasionally can be as large as 4 cm in size. Bone islands may grow in size up to the age of skeletal maturity but only rarely thereafter. Exceptionally they may regress. Periosteal new bone and cortical expansion do not occur. On a radionuclide bone scan, they may show a slight increase in activity, the degree being related to their size. No blood-pool abnormality becomes evident. In elderly patients, it may be necessary to differentiate these sclerotic lesions from osteoblastic metastases.

Osteoma

True osteomas are rather rare, arising principally from skull, paranasal sinuses and mandible (Fig. 39.11). They are benign, slow-growing tumours consisting entirely of well-differentiated bone. They have a broad base with a smooth well-defined margin. Two types are recognised: the dense variety, the so-called ivory osteoma; and the trabeculated or spongy variety more commonly occurring in the cranial vault. While varying in size, few are larger than 2.5 cm in diameter. The tumour itself is asymptomatic, but growth from the inner table of the skull may produce raised intracranial pressure or other symptoms similar to those of a meningioma. Growth

within the paranasal sinuses may interfere with nasal drainage, causing a mucocele. The rarer, spongy variety is shown histologically to contain moderate quantities of fibrous tissue and may be a variant of fibrous dysplasia.

Further investigation is rarely necessary apart from documenting the secondary effects of the lesion. Scintigraphical activity reflects the size of the lesion as in the case of a bone island.

When craniofacial osteomas are detected, the possibility of Gardner's syndrome should be considered, particularly if lesions are present in the mandible. The presence of osteomas elsewhere in the skeleton, soft-tissue tumours of connective tissue origin and polyposis coli establish the diagnosis.

Osteoid osteoma

Unlike other bone tumours this lesion has a definite male preponderance of the order of three to one. The majority of cases present in the second and third decades. The typical history is of localised, intermittent bone pain of several weeks' or months' duration, occurring especially at night, with dramatic relief by aspirin. Pain may be sufficient to provoke muscle wasting from limitation of movement. Growth disparities may develop in the immature skeleton, including failure of tubulation and leg-length discrepancy. Difficulty in diagnosis sometimes causes these patients to be referred to psychiatrists in the belief that their symptoms are functional. The natural history of this tumour is uncertain because most cases are treated by immediate surgical excision but it appears probable that untreated lesions eventually undergo spontaneous involution. The diaphyses of long bones are the sites of predilection with at least half of all cases occurring in the femur, especially its proximal end, and the tibia, although virtually any bone may be affected. When the spine is involved, the tumour is usually situated in the neural arch and not the vertebral body. The symptoms of spinal involvement may mimic those of an adolescent disc protrusion, and indeed painful scoliosis in a child or adolescent demands careful scrutiny of the neural arches at the apex of the concavity to exclude the presence of this tumour.

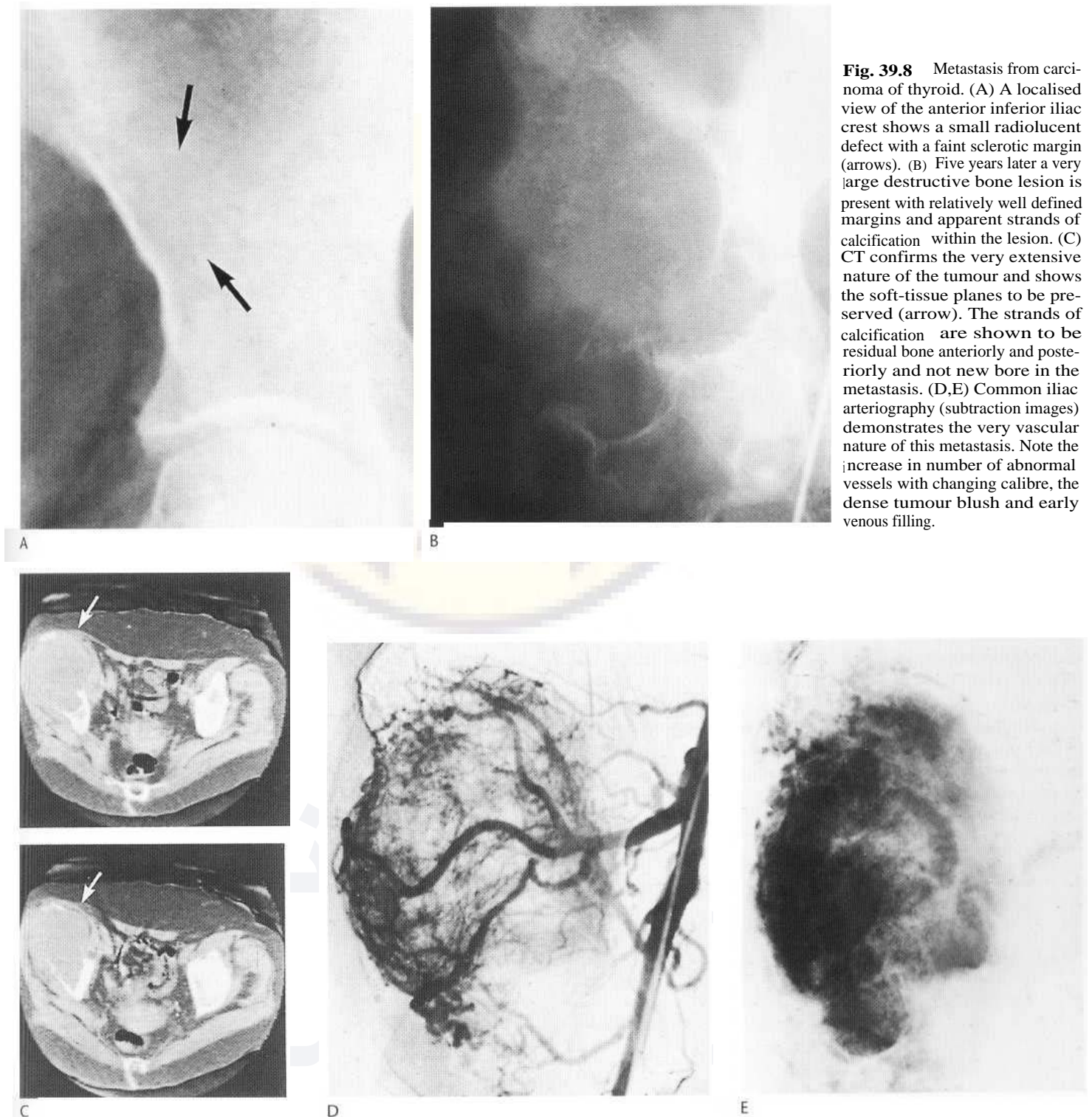


Fig. 39.8 Metastasis from carcinoma of thyroid. (A) A localised view of the anterior inferior iliac crest shows a small radiolucent defect with a faint sclerotic margin (arrows). (B) Five years later a very large destructive bone lesion is present with relatively well defined margins and apparent strands of calcification within the lesion. (C) CT confirms the very extensive nature of the tumour and shows the soft-tissue planes to be preserved (arrow). The strands of calcification are shown to be residual bone anteriorly and posteriorly and not new bone in the metastasis. (D,E) Common iliac arteriography (subtraction images) demonstrates the very vascular nature of this metastasis. Note the increase in number of abnormal vessels with changing calibre, the dense tumour blush and early venous filling.

Radiological features

The lesion comprises a round or oval area or radiolucency with a sclerotic margin. This radiolucency usually contains a small dense opacity known, on the east side of the Atlantic, as the *nidus* (Fig. 39.12). In North America the word *nidus* (meaning nest) is employed more correctly for the whole radiolucency itself. While the overall size of the lesion varies up to about 2.5 cm in diameter, the width of the central density rarely exceeds 1 cm. The lesion is surrounded by a variable degree of dense sclerosis. The extent of this density depends on the site of the tumour within the affected

bone. It is minimal when the tumour lies in the spongy bone of the medulla, particularly close to joints (Figs 39.13, 39.14).

Occasionally no peripheral density may be evident and the small central opacity appears to lie within an area of radiolucency. More commonly, the lesion is sited in relation to cortical bone and is surrounded by dense sclerosis that may be extensive and extend into the medulla. When the lesion is adjacent to the periosteum in children new bone formation is particularly florid. The reactive new bone may be so dense that the lesion itself is obscured on conventional radiographs.

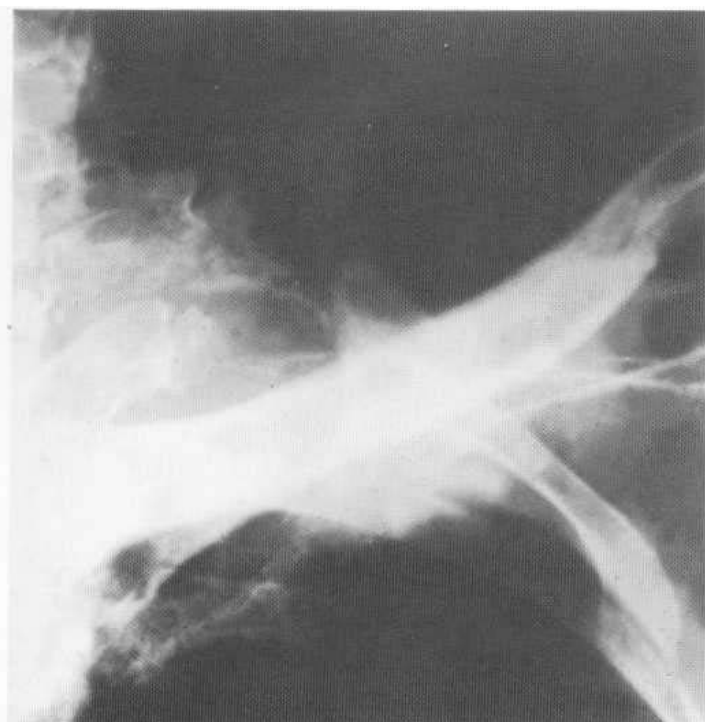


Fig. 39.9 Pancoast tumour-carcinoma of the apex of the lung invading and destroying the first and second ribs.

If the essential features of the radiolucency and its central density are demonstrated, the diagnosis is established radiologically with little difficulty. Those lesions arising in an intra-articular location (Fig. 39.14) or within the small bones of the hand and foot (Fig. 39.15) can have a very variable appearance, commonly resulting in a delayed diagnosis. When the lesion is surrounded by dense sclerosis further investigation is necessary, requiring overpenetrated films, tomography (either conventional or CT) and bone scintigraphy.

Because of the extensive sclerosis it is important not to overcount the bone scan which characteristically shows an intense focal area of increased activity due to the osteoid osteoma surrounded by less intense activity from the reactive sclerosis (Fig. 39.12). In the case of a medullary osteoid osteoma with little or no radiological abnormality on conventional films, bone scintigraphy remains the most important means of detecting the presence of a lesion. An intense focal abnormality is evident in the blood-pool image and intense activity persists in the delayed image. Scintigraphy should be undertaken in any young person with bone pain and apparently normal radiographs. These scintigraphic abnormalities correspond to the highly vascular nature of the neoplasm that may be demonstrated by angiography, particularly by the tumour blush evident in the late venous phase.

The presence of the lesion and its exact site may require localisation with CT (Figs 39.12, 39.14). Extensive bone marrow oedema may be seen on MRI, although it is frequently difficult to identify the nidus unless contrast enhancement is used and sufficiently thin sections are obtained (Fig. 39.14).

The pain produced by these tumours is relieved immediately by surgical excision and the reactive new bone slowly undergoes remodelling. If, however, removal of the tumour is incomplete, not only will the pain persist but also the lesion will recur. On rare occasions, osteoid osteoma may be multifocal, more than one opacity being contained within a single area of radiolucency. Some lesions near joints in childhood may be associated with synovitis, with resulting diffuse hyaline cartilage thinning and disuse osteoporosis. Delay in establishing a diagnosis often results due to the atypical clinical presentation and lack of characteristic radiological appearances. Subsequent deformity of the joint and other growth disturbances may occur.

Osteoid osteoma must be differentiated from osteoblastoma (described below) and other causes of chronic cortical thickening. These include stress fracture, chronic sclerosing osteomyelitis, foreign body granulomas ('blackthorn'), polyarteritis nodosa and

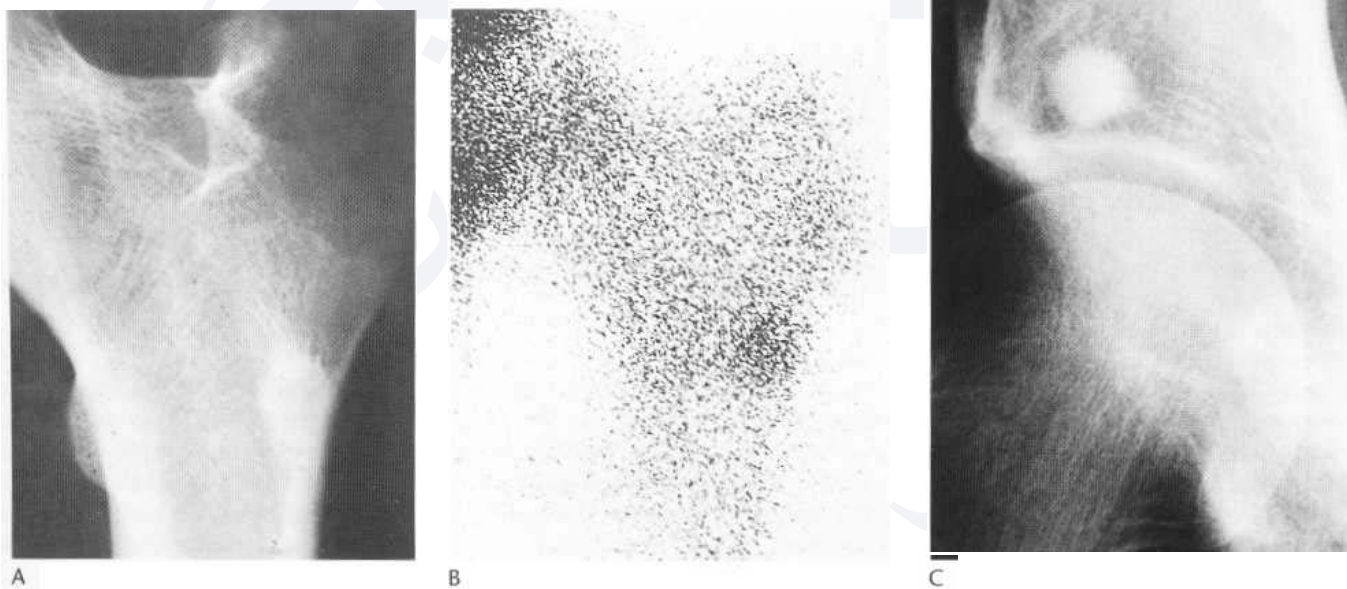


Fig. 39.10 Bone island-enostosis. (A) A dense area of endosteal sclerosis present in the upper femoral shaft, discovered by chance following injury. (B) A bone scan reveals slight increase in activity localised to the area of sclerosis. Biopsy confirmation. (C) Enostosis, acetabular roof. Uniformly dense circular lesion with characteristic radiating spicules extending into the adjacent bone.

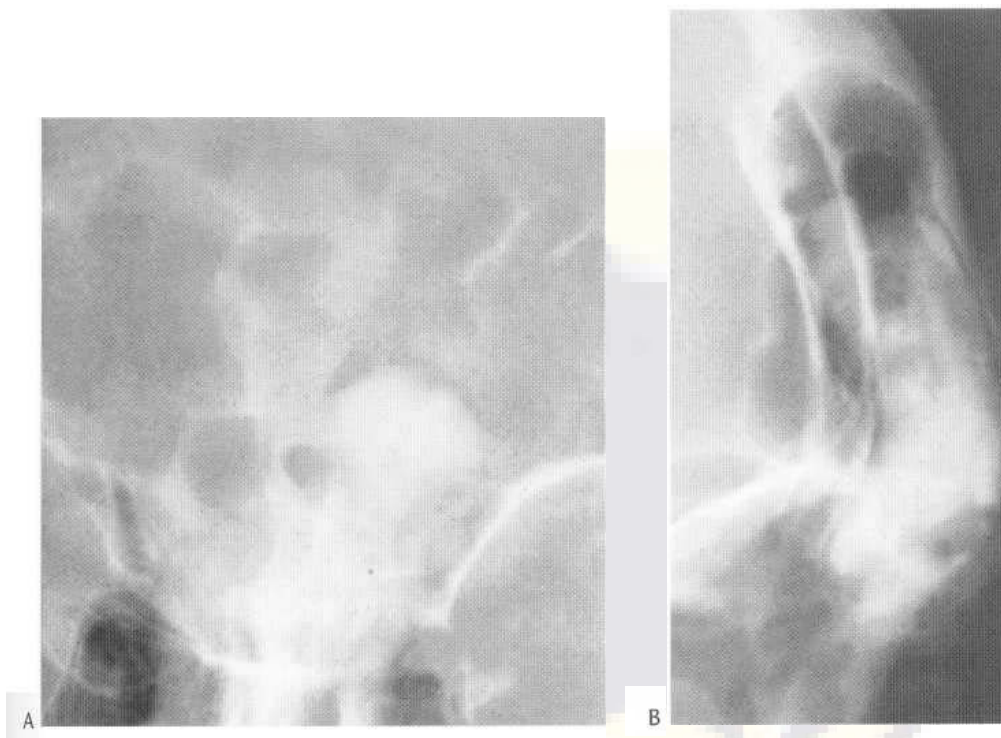


Fig. 39.11 Ivory osteomas of the frontal sinus. (A) A typical, compact, rounded, dense opacity is demonstrated on the frontal view. (B) In another patient a larger lesion has moulded to the shape of the sinus.

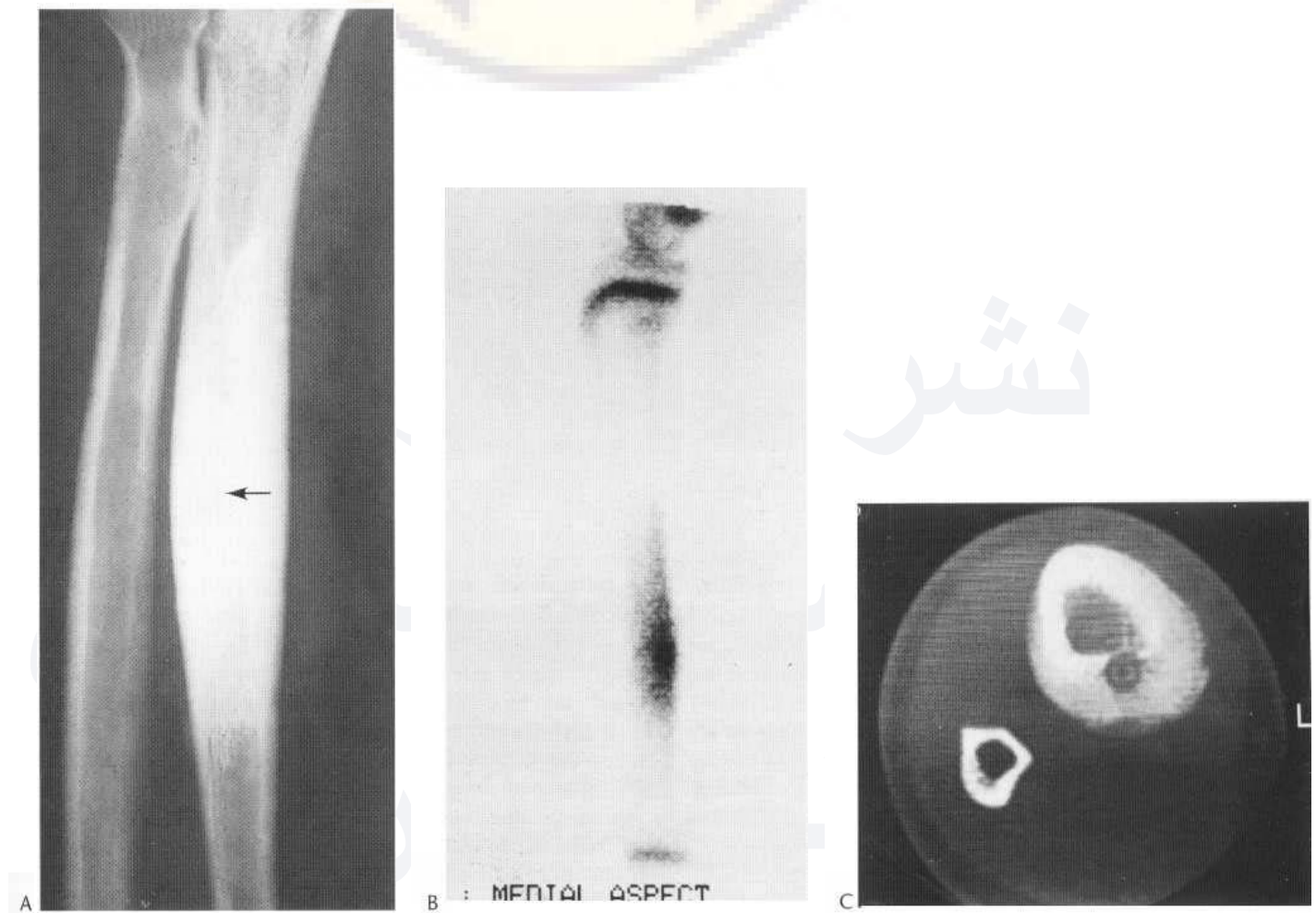


Fig. 39.12 Osteoid osteoma. (A) Involving the ulna in a 13-year-old boy. The appearances are typical, with a well-defined area of radiolucency (arrow) containing a dense nidus. Extensive cortical sclerosis is present around the lesion. (B) Radioisotope bone scan in another patient demonstrating intense focal increased scintigraphic activity in the distal tibia surrounded by a more diffuse area of less intense activity, typical of an osteoid osteoma. (C) CT section of the tibial lesion elegantly demonstrating the cortically located nidus.

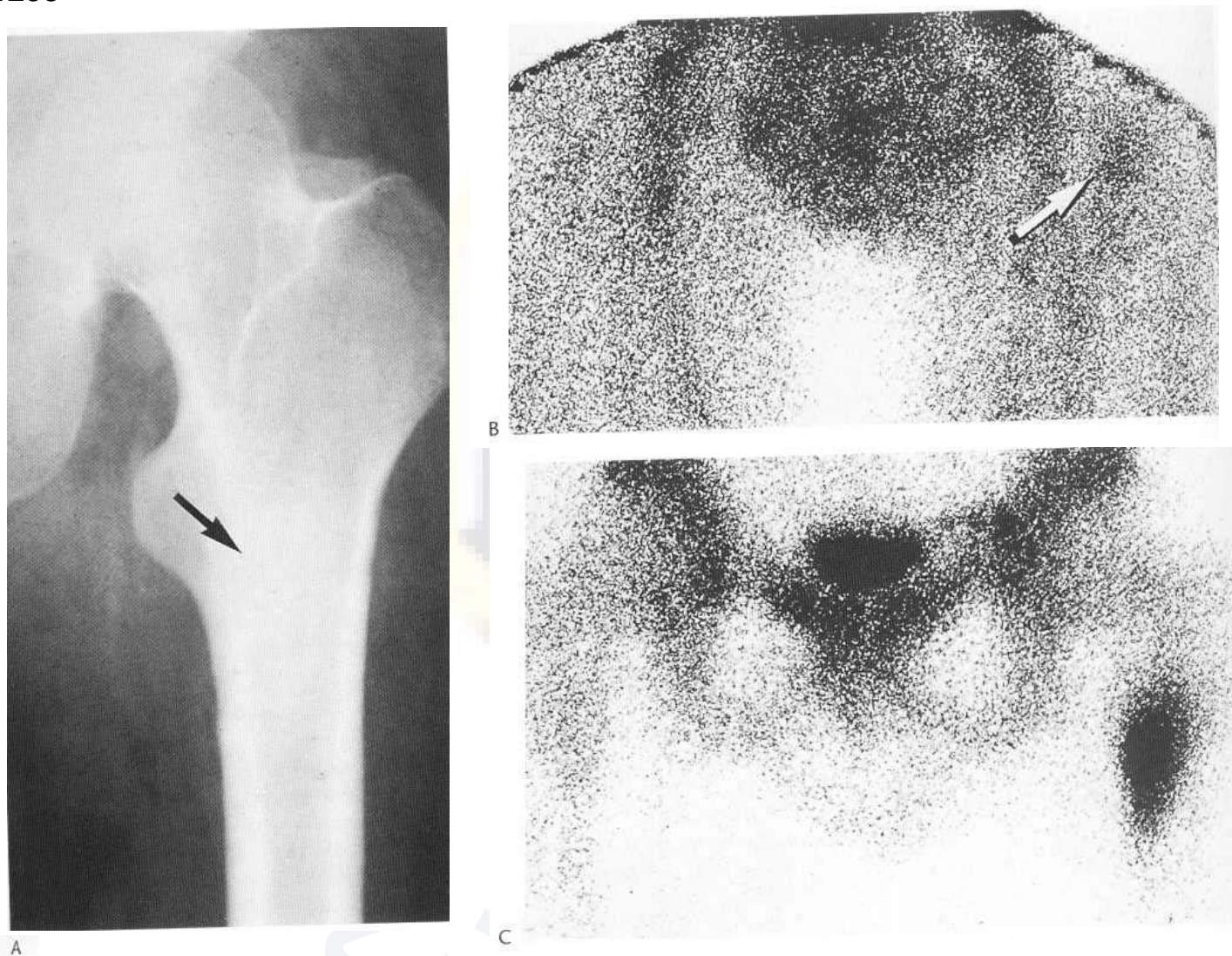


Fig. 39.13 Osteoid osteoma—a young man complaining of groin pain. (A) Initially it was thought the X-rays were normal; however, in retrospect, a small radiolucency (arrow) is present. A bone scan was performed in order to detect any occult cause of pain. (B) A localised focus of increased vascularity is shown on the blood-pool film (arrow). (C) Extensive abnormality on the delayed film. (D) CT demonstrates the radiolucent defect anteriorly (closed arrow) with associated, consolidated periosteal new bone. A nutrient artery is shown posteriorly (open arrow) and is an incidental finding.

subperiosteal haematoma, particularly along the shin. In general, the distinction between osteoid osteoma and chronic osteomyelitis is straightforward. In osteomyelitis, the area of radiolucency tends to be more irregular, although a sequestrum may be confused with a nidus. Whereas the central opacity of an osteoid osteoma is usually round or slightly oval, the majority of osteomyelitic sequestra are irregular and often linear in shape. Scintigraphy shows a diffuse increase in activity both in the blood-pool and the delayed phases. MRI may demonstrate considerable bone oedema in both cases but a fluid collection clearly indicates infection.

Osteoblastoma

This tumour is now accepted as a distinct entity, although a considerable overlap undoubtedly exists with osteoid osteoma. Indeed the situation is confused by the occasional osteoid osteoma that is

larger than usual and may be referred to as giant osteoid osteoma. Both osteoblastoma and osteoid osteoma superficially have similar histological characteristics. The tumour is, in almost all circumstances, benign, but may be aggressive (see below). It is accompanied often by a long insidious history of pain, one in ten patients suffering worsening of the pain at night. Aspirin relief is not a feature. No definite sex incidence has been recognised but at least 80% of the patients are under the age of 30.

While any bone may be involved, the majority of lesions occur in the spine and flat bones, particularly the vertebral appendages. Again, as in the case of osteoid osteoma, the last location may stimulate a scoliosis; indeed in one series as many as 50% of the patients had a scoliosis, some with positive neurological signs.

Pathologically the lesion is larger than an osteoid osteoma, irregular in shape, friable and haemorrhagic. Abundant osteoid tissue is present with broad, widely spread trabeculae, in relation to

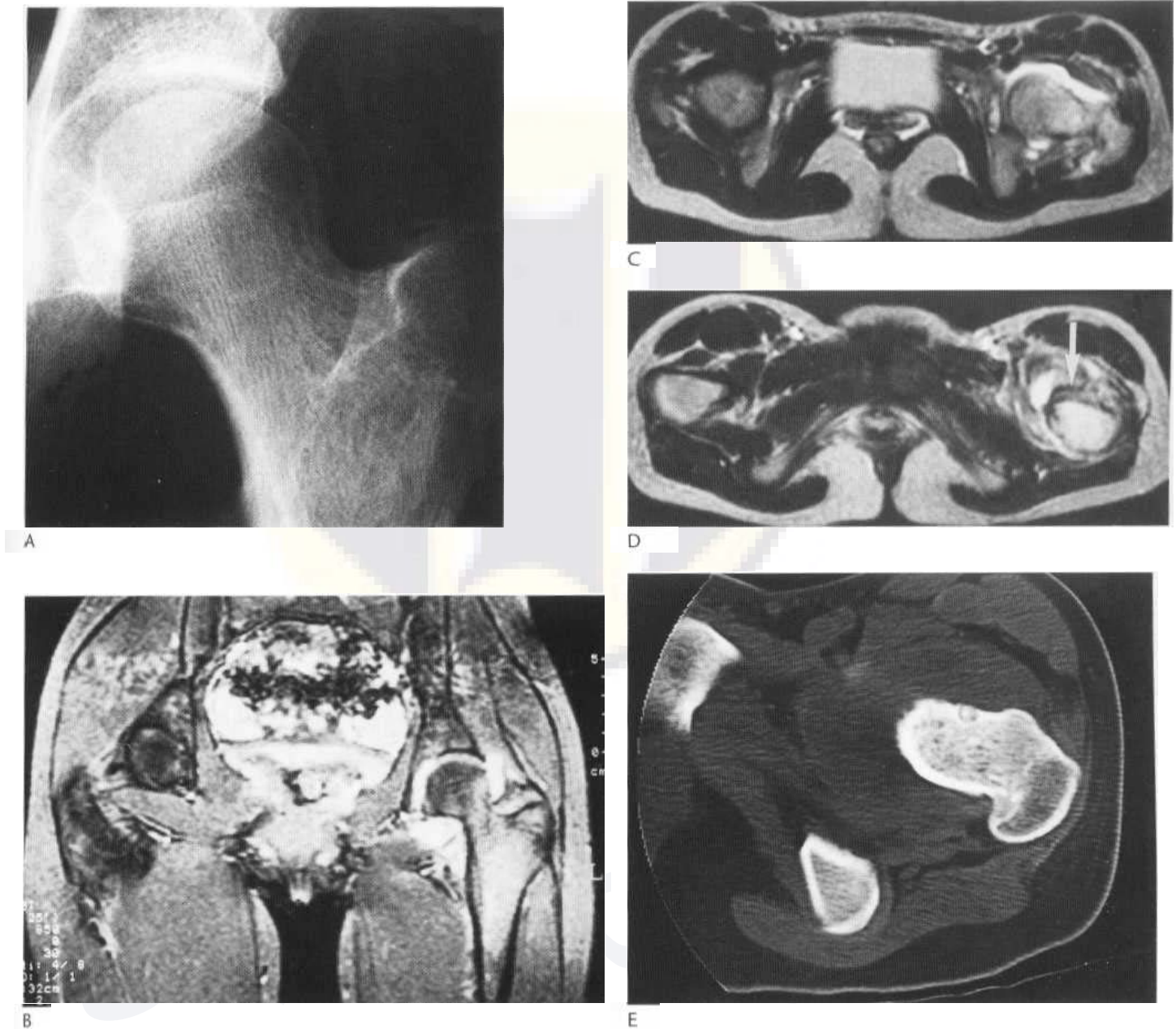


Fig. 39.14 Osteoid osteoma in a young girl complaining of left hip and knee pain, initially thought to be due to juvenile onset rheumatoid arthritis. (A) A subtle radiolucency with a central density is shown in the basi-cervical region of the left femur. (B) Coronal FFE-T₂ MR section demonstrating high signal intensity within the proximal left femur due to considerable bone marrow oedema. A joint effusion is evident also together with some surrounding soft-tissue oedema. (C) Axial T₂-weighted MRI showing a prominent left hip joint effusion and bone marrow oedema within the femoral neck. The nidus, however, is not evident. (D) Axial T₂-weighted image through the proximal femur demonstrating more striking bone marrow oedema distal to the joint capsule and level of the osteoid osteoma. Periosteal new bone formation is also shown anteriorly (arrow). (E) Thin section CT showing the anteriorly located calcified nidus within the cortex of the femoral neck and the large joint effusion.

which are numerous osteoblasts and osteoclasts. Many thin-walled capillaries account for the marked vascularity of the tumour.

Radiological features

An area of radiolucency is typical, being considerably larger than that of an osteoid osteoma and of the order of 2-10 cm in diameter (Fig. 39.16). Difficulty may arise on occasions in distinguishing this appearance from an exceptionally large osteoid osteoma. The margins of the radiolucency show considerable irregularity, although they are usually sharply demarcated. This margin, however, may sometimes be ill defined and not easily distinguishable from a malignant lesion, par-

ticularly an osteosarcoma. A giant cell tumour may be considered when the lesion is subarticular in location. Cortical expansion and exquisite thinning is common so that only a fine opaque shell may remain. This appearance simulates the cortical expansion caused by an aneurysmal bone cyst, but may be distinguished by the total absence of bone reaction and the poorly defined margin of the latter tumour.

The majority of osteoblastomas enlarge slowly, with consequent remodelling of bone around the lesion. The degree of associated bone sclerosis varies considerably but may be profound. Calcification or ossification of osteoid tissue within the tumour may cause a punctate or amorphous increase in density (Fig. 39.17), best

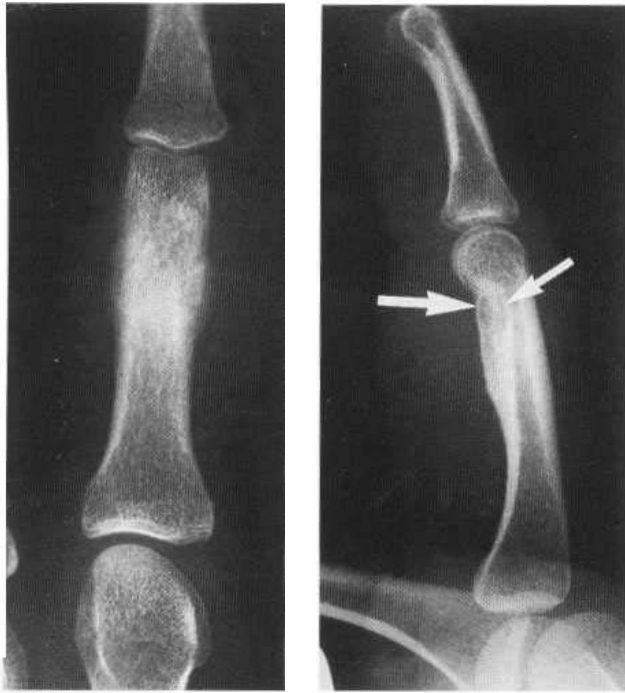


Fig. 39.15 Osteoid osteoma in the proximal phalanx of the index finger. (A) The AP radiograph shows ill-defined periosteal new bone formation and some sclerosis involving the proximal phalanx. Marked soft-tissue oedema is also evident. (B) The lateral radiograph demonstrates apparent expansion and scalloping of the distal anterior cortex of the proximal phalanx with trabecular sclerosis distal to the radiolucent nidus (arrows).



Fig. 39.16 Osteoblastoma of the right transverse process and pedicle of L3. An ill-defined radiolucency is shown within a sclerotic and expanded transverse process and pedicle.

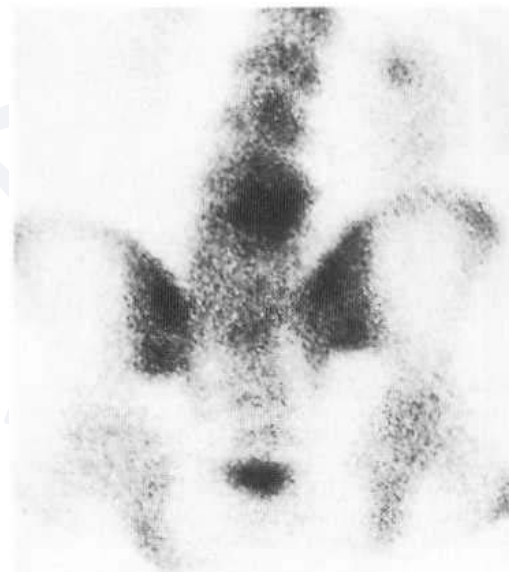
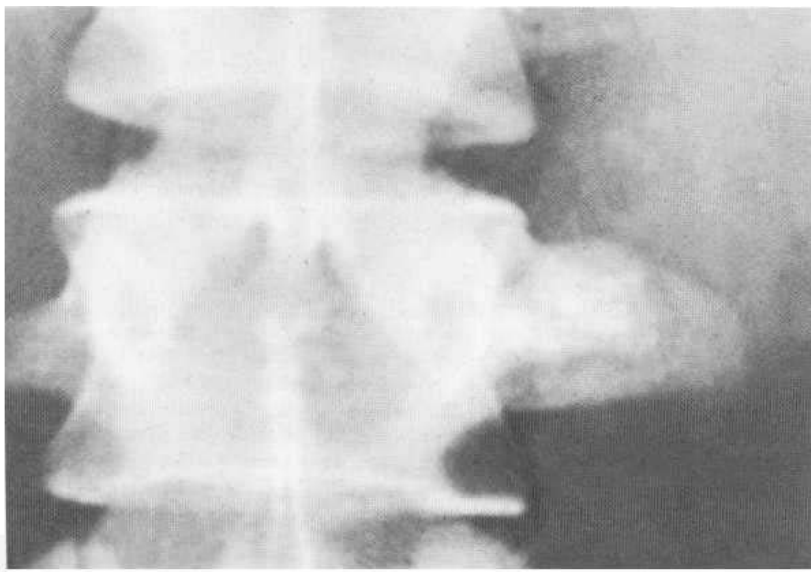


Fig. 39.17 Osteoblastoma of the left transverse process of L3. (A) In this example the central area exhibits calcification. Expansion is present with diffuse sclerosis. (B) Note on the bone scan (which has been reversed for ease of comparison) the extensive area of increased activity corresponding to the whole of the osteoblastoma on the plain film. Note also the scoliosis, with which these patients may present.

appreciated on tomography or CT (Fig. 39.18). Calcification is never annular as in a cartilage tumour.

Scintigraphically these lesions are extremely active both in the blood-pool and delayed phases of a bone scan. On the delayed phase, the lesion may seem very extensive, reflecting the secondary bone sclerosis. If angiography is undertaken the radiolucency may be shown to contain an increased number of vessels with a blush

and small lakes of contrast medium, but encasement and other features suggestive of malignancy are not present. As with osteoid osteoma, MRI demonstrates considerable bone, and often soft-tissue, oedema surrounding a lesion.

In the vast majority of patients, the prognosis is excellent once total excision of the tumour has been achieved. On some occasions, however, an osteoblastoma behaves in an aggressive fashion, particu-

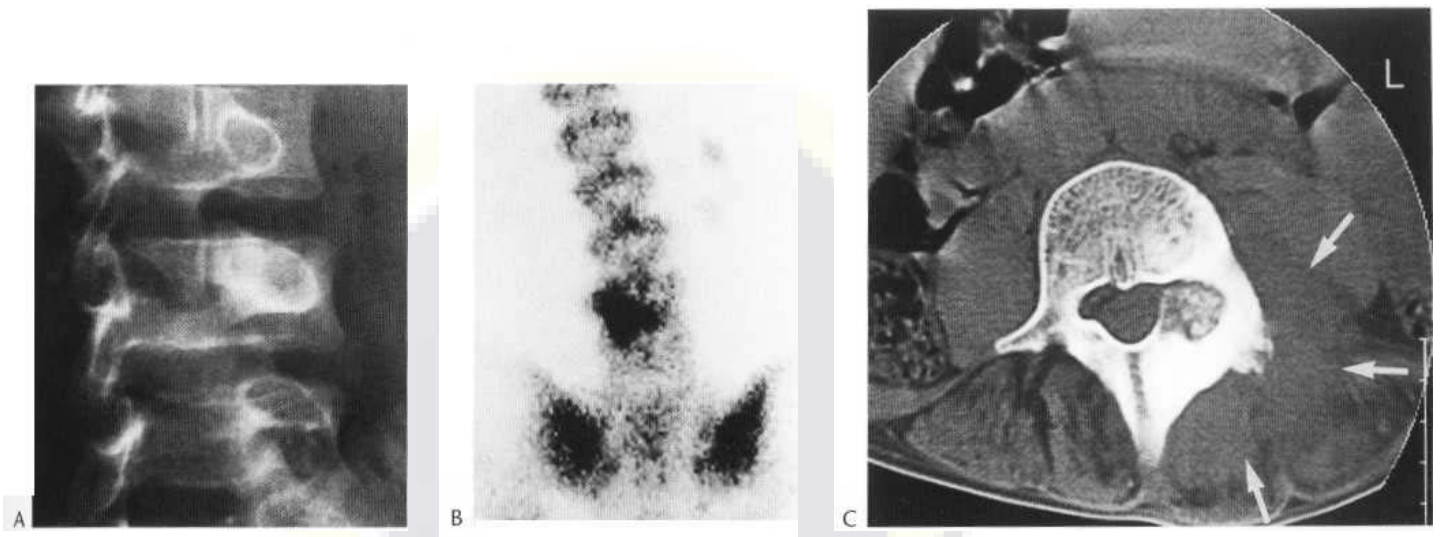


Fig. 39.18 Osteoblastoma of the left pedicle and lamina of L3. (A) Conventional oblique radiograph showing expansion and sclerosis. (B) Radionuclide bone scan demonstrating extensive and marked increase in activity and a scoliosis. (C) CT section showing punctate calcification of the lesion with expansion of the pedicle and lamina and prominent dense sclerosis. Considerable soft-tissue oedema is also evident (arrows).

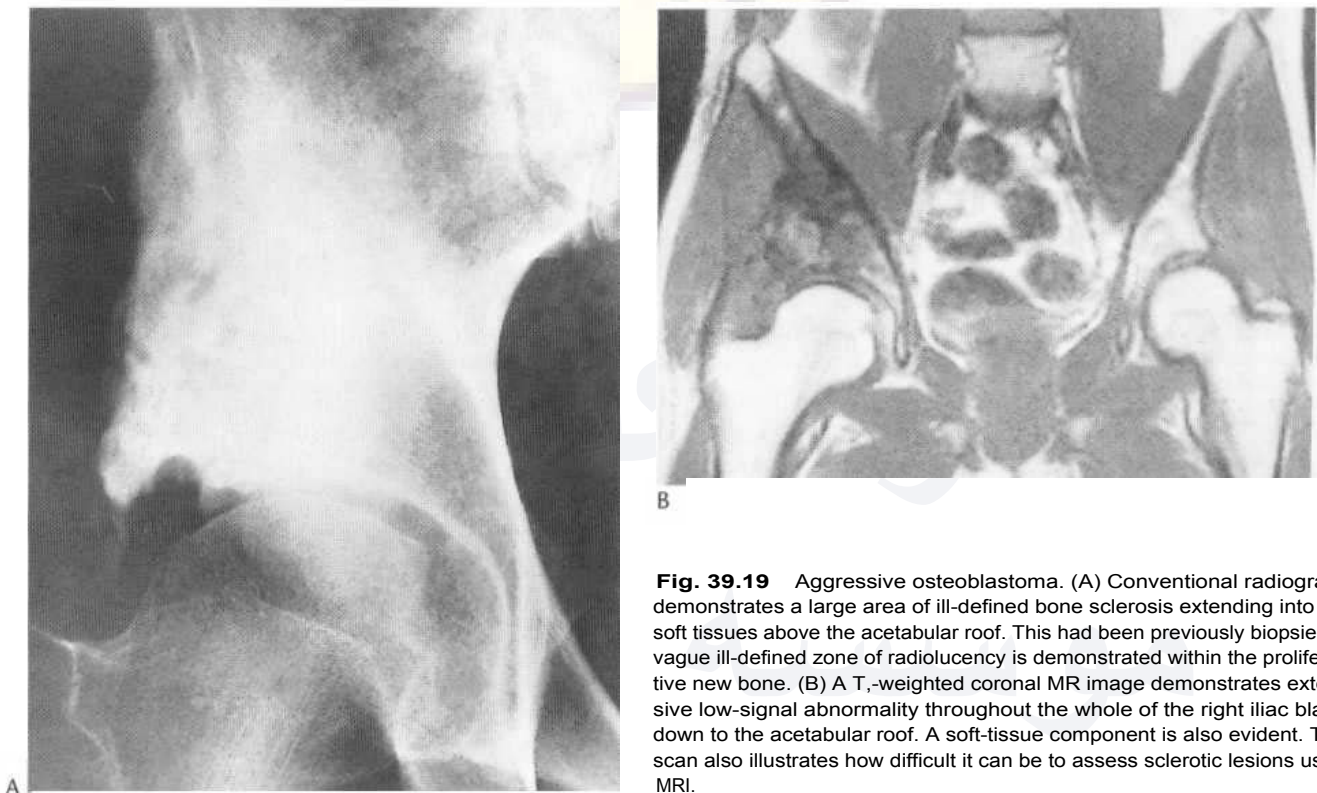


Fig. 39.19 Aggressive osteoblastoma. (A) Conventional radiograph demonstrates a large area of ill-defined bone sclerosis extending into the soft tissues above the acetabular roof. This had been previously biopsied. A vague ill-defined zone of radiolucency is demonstrated within the proliferative new bone. (B) A T₁-weighted coronal MR image demonstrates extensive low-signal abnormality throughout the whole of the right iliac blade down to the acetabular roof. A soft-tissue component is also evident. This scan also illustrates how difficult it can be to assess sclerotic lesions using MRI.

larly after incomplete removal. Not only is the lesion radiographically aggressive, with soft-tissue masses containing ill-defined calcification and ossification, but a similar pattern of aggression is visible also under the microscope. On rare occasions, the lesion behaves frankly as an osteosarcoma with pulmonary metastasis (Fig. 39.19).

Osteosarcoma

Osteosarcoma is the commonest primary malignant bone tumour, accounting for 25% of all primary bone tumours. Characteristically it is histologically pleomorphic, but two diagnostic features are: (i)

its ability to produce osteoid tissue, without necessarily the development of a cartilaginous precursor, and (ii) the presence of abundant alkaline phosphatase histochemically within the tumour cells. The osteoid tissue may undergo some degree of ossification. However, because of the pleomorphic nature of the sarcoma a dominant cell line may modify the appearance. If osteoblasts predominate, tumour bone formation will result, whereas if cells of cartilage origin are present, extensive calcification may be a presenting feature. Terms such as osteoblastic (Fig. 39.20), chondroblastic (Fig. 39.21), fibroblastic, and anaplastic or telangiectatic (Fig. 39.22) are often applied. No convincing evidence has been

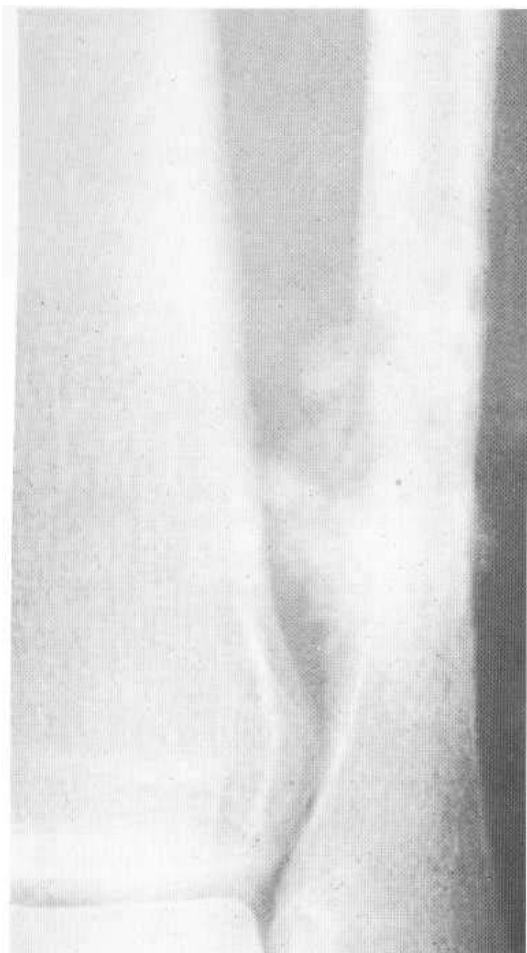


Fig. 39.20 Osteosarcoma of the distal fibula—predominantly osteoblastic. Amorphous calcification/ossification is present in the soft tissues with cortical destruction and a little periosteal new bone formation.



Fig. 39.21 Osteosarcoma of the distal femur—predominantly chondroblastic. Note the well-defined soft-tissue mass and radiating spiculation of calcification within it. Sclerosis and lysis are present within the medullary cavity that is slightly expanded.

established that these pathological subgroups have much influence on prognosis. Nonetheless, each has slightly different radiological characteristics. Osteosarcoma arising in relation to the periosteum and secondary to other conditions is considered below.

Osteosarcoma presents usually with localised pain or swelling, particularly around the knee, in an adolescent or young adult. Not infrequently, the lesion may present with a pathological fracture (Fig. 39.23). A slight male preponderance exists, the peak incidence occurring between 10 and 25 years of age. Many of the tumours occurring in older age groups are associated with Paget's disease (see below). Although any bone may be involved, rather more than half of all osteosarcomas are located around the knee, involving the metadiaphyses of the distal end of the femur and the proximal end of the tibia. Indeed the vast majority of osteosarcomas arise in those sites in long bones that are exhibiting the greatest longitudinal growth. Osteosarcomas are infrequently found in the pelvis and spine (Fig. 39.24). Involvement of the clavicle, ribs, scapula and the small bones of the hands and feet is rare. About 10% of tumours arise in the diaphysis. These have a similar age and sex incidence to ordinary osteosarcoma (see below). Orthodox teaching suggested that epiphyseal involvement occurs late, metaphyseal cartilage acting as a temporary barrier to spread of the tumour. Although this appears to be supported by the evidence of plain films, investigation

by scintigraphy, angiography and MRI has indicated that in many cases epiphyseal involvement occurs earlier.

The lesion commonly arises eccentrically in the medullary cavity, with ill-defined cortical destruction and soft-tissue involvement. The pleomorphic nature of the histology may cause misleading biopsy results, because if the sample is taken from areas rich in cartilaginous elements, a misdiagnosis of chondrosarcoma may occur. Metastatic spread occurs by the haematogenous route so that a search for pulmonary metastasis should be undertaken. Pulmonary metastasis is associated with an unusually high incidence of pneumothorax (Fig. 39.25). Any lung lesion arising in a patient with osteosarcoma should be regarded with suspicion (Fig. 39.26). Lymphatic spread is relatively rare. In the later stages, metastasis may develop in bone, population surveys have suggested that these deposits are themselves metastatic from the pulmonary lesions.

Imaging features

Typically, *conventional radiographs will* show an eccentric area of permeative bone destruction in the metadiaphysis adjacent to the knee joint, associated with cortical erosion and a well-defined soft-tissue mass. Elevation of the periosteum is associated with new bone formation, the so-called Codman's triangles. The epiphysis usually appears normal. The soft-tissue mass may contain calcifica-

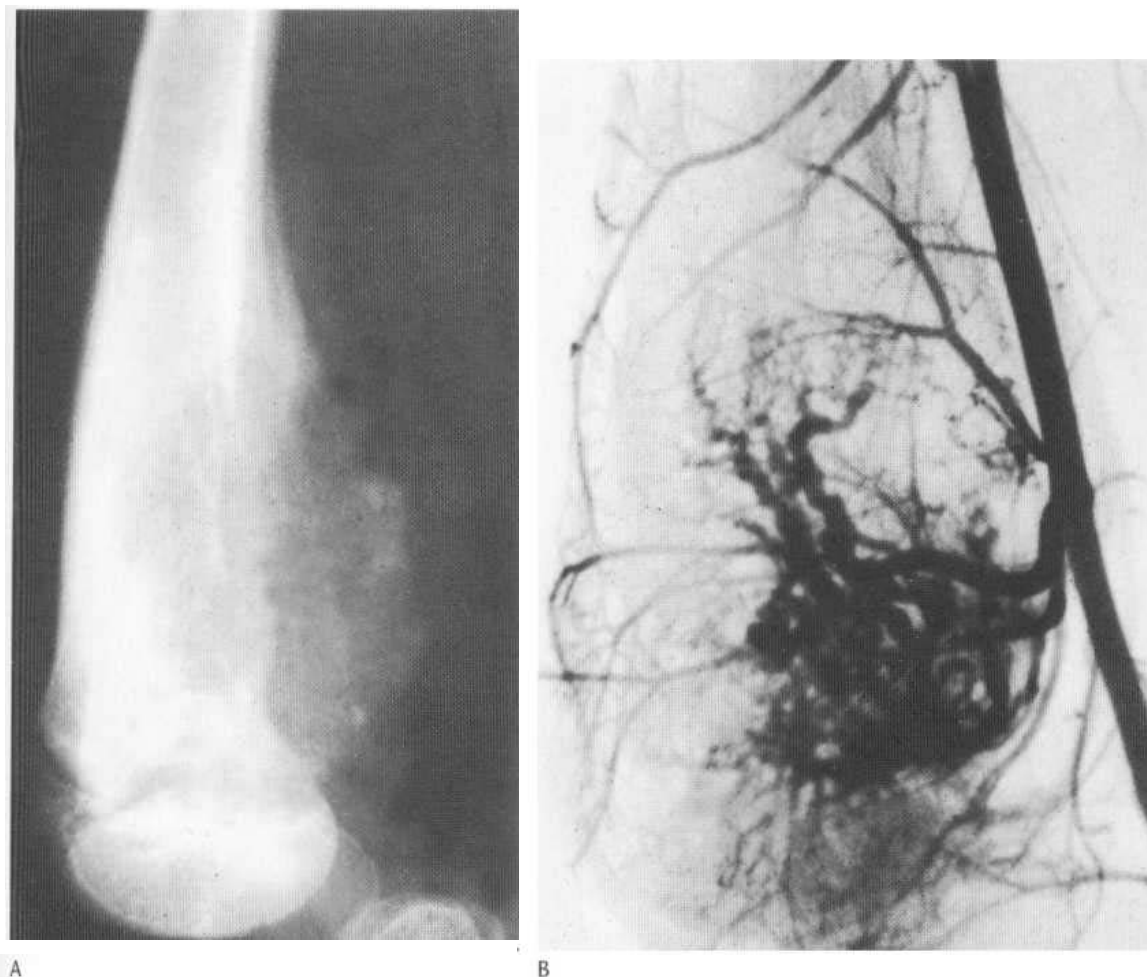


Fig. 39.22 Telangiectatic osteosarcoma of the distal femur. (A) A predominantly radiolucent defect is shown on conventional radiograph which angiographically (B) is shown to contain large, tortuous, pathological vessels. Well-marked Codman's triangles are present together with sclerosis in the shaft of the bone, surrounding the lesion.

tion that may show either an amorphous or a spiculated appearance. A mixture of sclerosis and bone destruction is usually present within the bony lesion. Occasionally the lesion may be purely lytic.

Scintigraphically, increased vascularity is constant in the blood-pool phase of a bone scan with an extensive abnormality on the delayed images (Fig. 39.27). The extent of the tumour, as delineated by a bone scan, may be greater than that shown on conventional radiography, due to a surrounding ring of reactive bone. Scintigraphy may confirm epiphyseal spread of the tumour, but an apparent increase in activity in an adjacent joint should not be mistaken for synovial involvement. Scintigraphy also may detect the presence of lung metastases, although this procedure is not reliable if purely fibroblastic lesions are present or if the metastases have been treated.

CT demonstrates to advantage those features evident on conventional radiographs and can delineate the intra- and extra-osseous extent of tumour (Figs 39.27C, 39.28D). It is the most sensitive means of detecting pulmonary metastasis (Fig. 39.26B).

The *angiographic features* suggest an aggressive tumour and again may be used to establish the extent of tumour, if treatment by prosthetic replacement is being considered (Figs 39.28, 39.29).

MRI is the prime investigation of choice for osteosarcoma following conventional radiographs. An obvious heterogeneous tumour is demonstrated with surrounding bone and usually a soft-tissue mass. Areas of calcification and ossification are shown as low signal, but even within the sclerotic component within the medullary canal there is usually high signal associated with tumour

bulk. Careful delineation of the lesion and assessment of relationships between it and adjacent blood vessels and joints are essential in preoperative planning (Figs 39.30-39.33). Marked enhancement is shown following contrast administration, particularly in non-ossified regions. Intramedullary skip lesions may also be identified (Fig. 39.34).

Differential diagnosis is either from other neoplasms, including malignant round cell tumours and metastasis, or from chronic bone infections, including tuberculosis and mycetoma. In the case of infections the aetiology may be suggested by diffuse ill-defined swelling of soft tissues, disproportionately extensive new bone formation and widespread activity on bone scintigraphy.

Special types of osteosarcoma

Diaphyseal Approximately 10% of tumours arise in the diaphyses of long bones and may cause diagnostic confusion. While most resemble those of osteosarcoma elsewhere (Fig. 39.35), others are purely lytic or indeed sclerotic (Fig. 39.36) and an accurate pre-biopsy diagnosis may not be possible.

Central osteosarcoma Similar difficulty may arise when a lesion presents in the metadiaphysis as an area of dense sclerosis that may be thought to represent a large bone island (Fig. 39.37). Specific characteristics on plain films to suggest malignant disease are absent. Scintigraphy, MRI and angiography, however, will demonstrate features that are much more aggressive.



Fig. 39.23 An advanced osteosarcoma of the proximal humerus presents with a pathological fracture. A large well-defined soft-tissue mass contains calcification and ossification. Codman's triangles are present. Extensive tumour in the medulla has caused both bone destruction and bone formation.

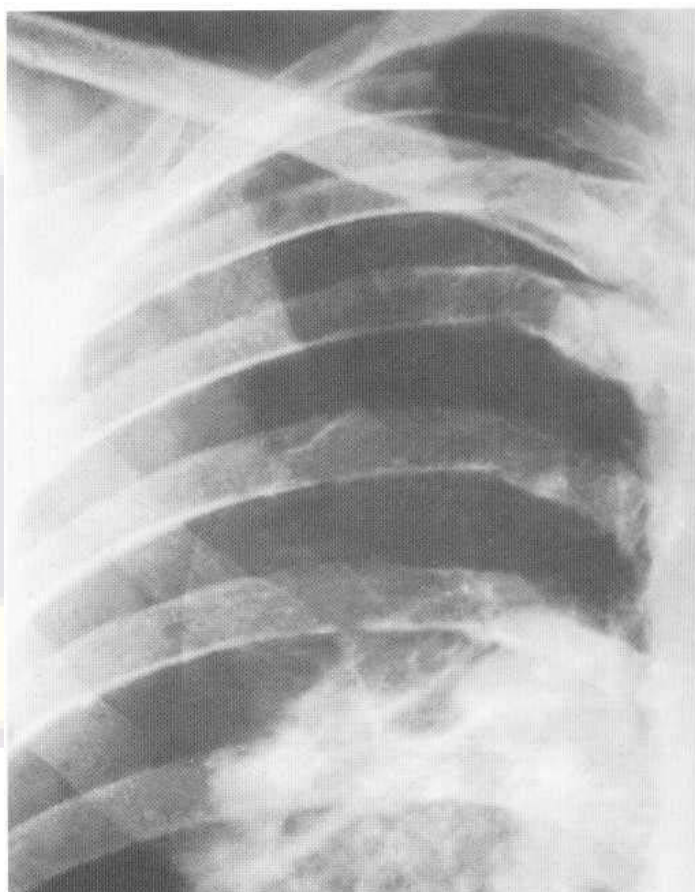


Fig. 39.25 Osteosarcoma—metastasis in the lungs presents with a pneumothorax.



A



B

Fig. 39.24 Osteosarcoma of the spine. (A) A conventional radiograph of the upper lumbar spine shows an extensive area of tumour new bone formation arising from the lamina of L1 and extending into the paravertebral soft tissues. (B) The CT section demonstrates the origin and extent of the tumour. Marked compression of the dural sac results from extension onto the spinal canal.

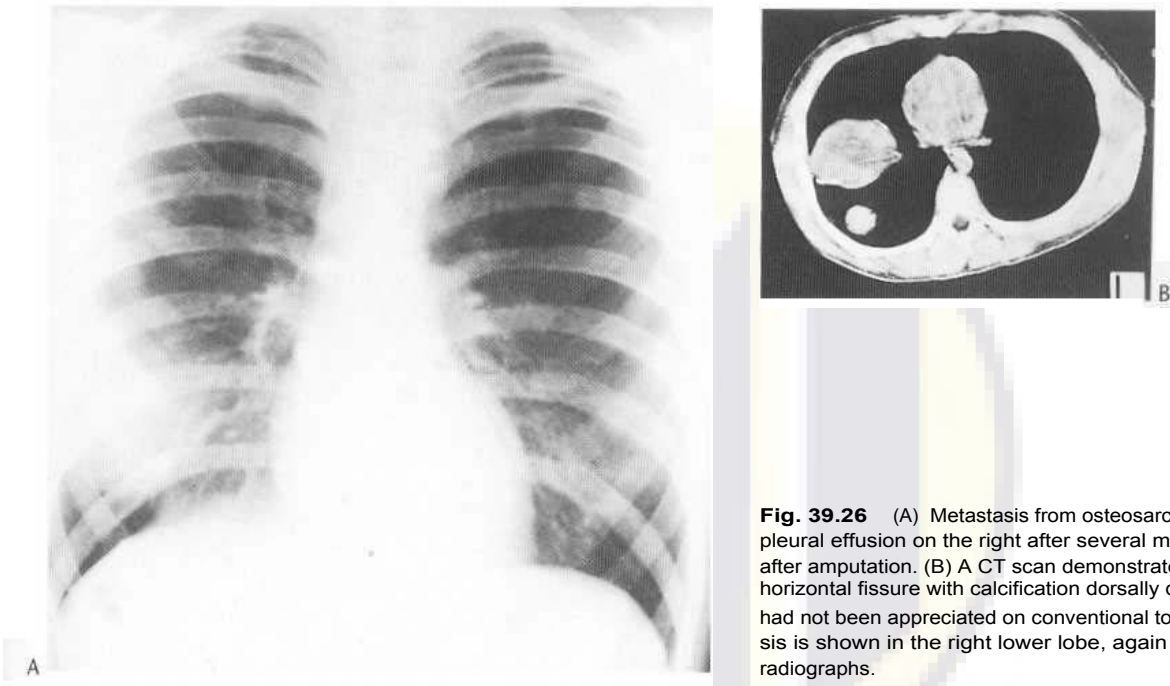


Fig. 39.26 (A) Metastasis from osteosarcoma presents with an encysted pleural effusion on the right after several months apparently disease free after amputation. (B) A CT scan demonstrates the encysted effusion in the horizontal fissure with calcification dorsally due to metastasis. This feature had not been appreciated on conventional tomography. A second metastasis is shown in the right lower lobe, again not obvious on conventional radiographs.

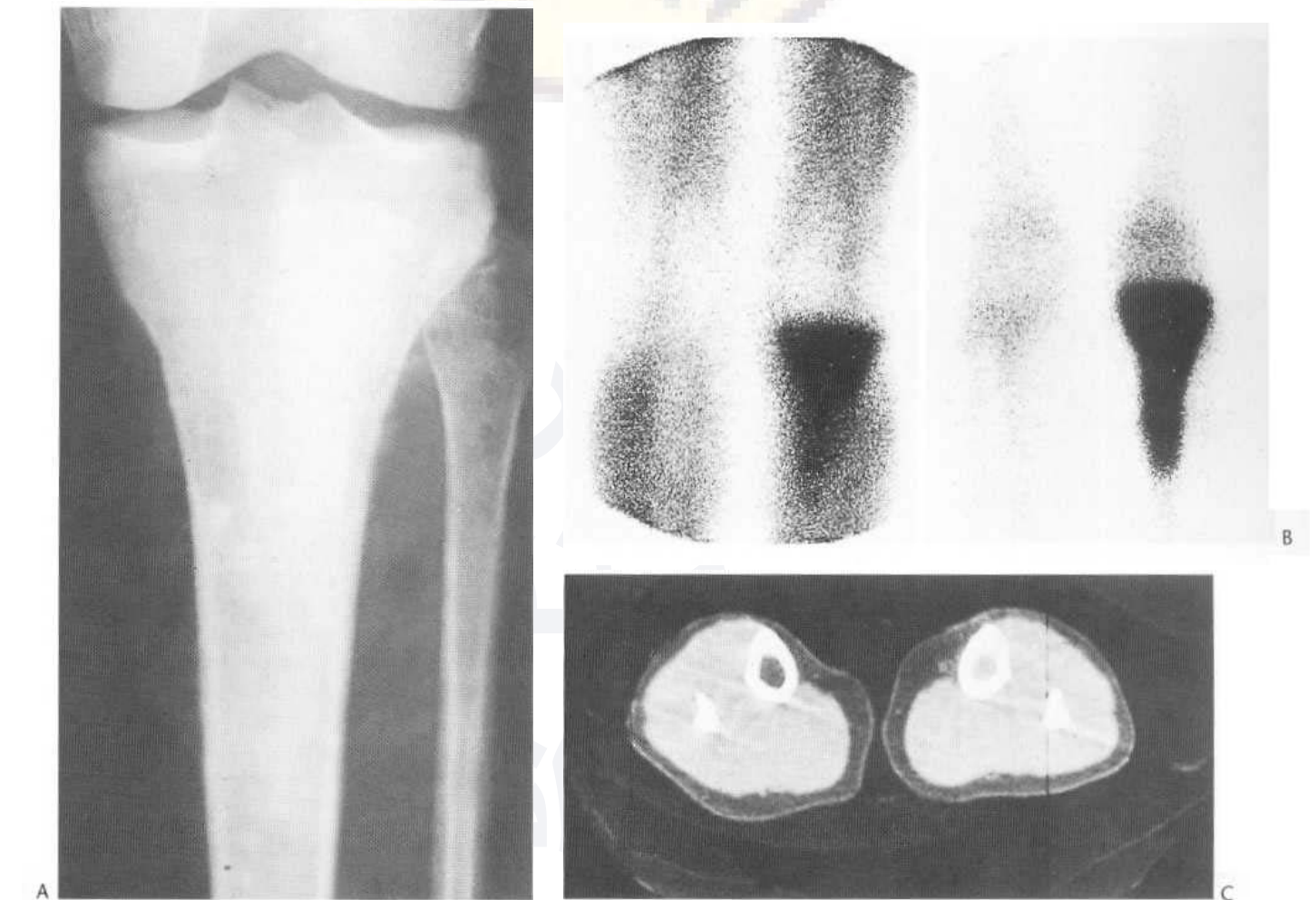


Fig. 39.27 Osteoblastic osteosarcoma of the proximal tibia. (A) The conventional radiograph reveals patchy increased density in much of the upper tibia. Note a little new bone laterally. (B) A scan in the early blood-pool (left) and delayed phases (right) demonstrates an extensive abnormality. Note the activity is more uniform and extensive than the apparent involvement shown on the plain film. The distal extent of the tumour is confirmed however by (C), a CT scan which shows a subtle change in marrow attenuation below the level of the apparent tumour on plain film, an example of how CT may be used to gauge the extent of marrow involvement.



Fig. 39.28 Osteosarcoma of the distal femur of a young woman. (A) The full intraosseous extent is difficult to assess on the plain film. (B) An arteriogram demonstrates a very extensive pathological circulation and on the late capillary phase (C) note that the tumour extends into the epiphysis, almost to the articular surface, and that there is a satellite or 'skip' lesion in the proximal femoral shaft (arrow). This latter lesion is confirmed by CT (D), and is shown to be bone forming (the upper image shows an attenuation of 188 HU in the lesion).

Multifocal osteosarcoma is extremely rare and occurs only in childhood. The condition is rapidly fatal, with pulmonary metastasis, and is characterised by a marked elevation of serum alkaline phos-

phatase. Radiologically symmetrical and densely sclerotic lesions have a predilection for metaphyses and flat bones. Unlike ordinary osteosarcoma, epiphyseal and soft-tissue involvement occurs early.



Fig. 39.29 Osteoblastic osteosarcoma. A middle-aged woman presented with pain and swelling in the mid ulna. (A) A radiograph shows ill-defined sclerosis and cortical destruction. (B) An angiogram demonstrates an egg-shaped soft-tissue mass with displacement of both the ulnar and interosseous arteries. The extraosseous extent of the tumour was thereby delineated.

Soft-tissue osteosarcoma On rare occasions the tumour arises purely in soft tissue (Fig. 39.38). Various sites of origin have been described, including breast and kidney. Usually, however, the lesion is para-articular. The ill-defined amorphous nature of the soft-tissue opacification may suggest tumour bone rather than calcification. The differential diagnosis is from post-traumatic myositis ossificans that can also produce markedly abnormal features with scintigraphy and angiography, particularly early in its evolution. Histological examination of both entities can be fraught with diagnostic pitfalls in inexperienced hands.

Radiation-induced sarcoma

Radiation therapy Sarcomas arise in bone following radiation, typically when the total dose has exceeded 30 Gy (3000 rad), often after a latent interval of 7-10 years. While most are fibrosarcomas, a few osteosarcomas occur. The diagnosis is not difficult radiologically but they often have a predominantly lytic nature and are markedly aggressive. They arise in predictable



Fig. 39.30 Osteosarcoma. Coronal T₁-weighted (A) and STIR (B) sequences demonstrate an extensive osteosarcoma of the lateral femoral condyle. The pleomorphic nature of the tumour can be appreciated by the more superficial main neoplasm with subadjacent marrow oedema. Note the overlying abnormal vessels shown as a signal void and the joint effusion on the STIR sequence. Clear extension across the metaphysis is also shown. These features confirm an extracompartmental osteosarcoma.

sites, based on radiation fields, for example in the pelvis following the treatment of gynaecological cancer (Fig. 39.39).

The ingestion of radioactive material Radium and radiomethorium were introduced in America in 1914 in the preparation of luminous paint. In applying this to watch dials, ingestion of the radioactive material occurred through pointing the paintbrush with the lips. The subsequent development of osteosarcoma was first reported in 1931, although more usually areas of bone destruction and sclerosis are due to infarction. A long latent interval between ingestion and tumour development is typical. Thorium was associated with abdominal neoplasia and is no longer used (see Ch. 15).

Parosteal osteosarcoma

Some confusion in nomenclature relates to osteosarcomas arising in or near the periosteum. For practical purposes these may be divided into two groups: parosteal osteosarcoma which will be described; and periosteal osteosarcoma which is similar in most ways to an ordinary osteosarcoma except that it arises close to the periosteum.

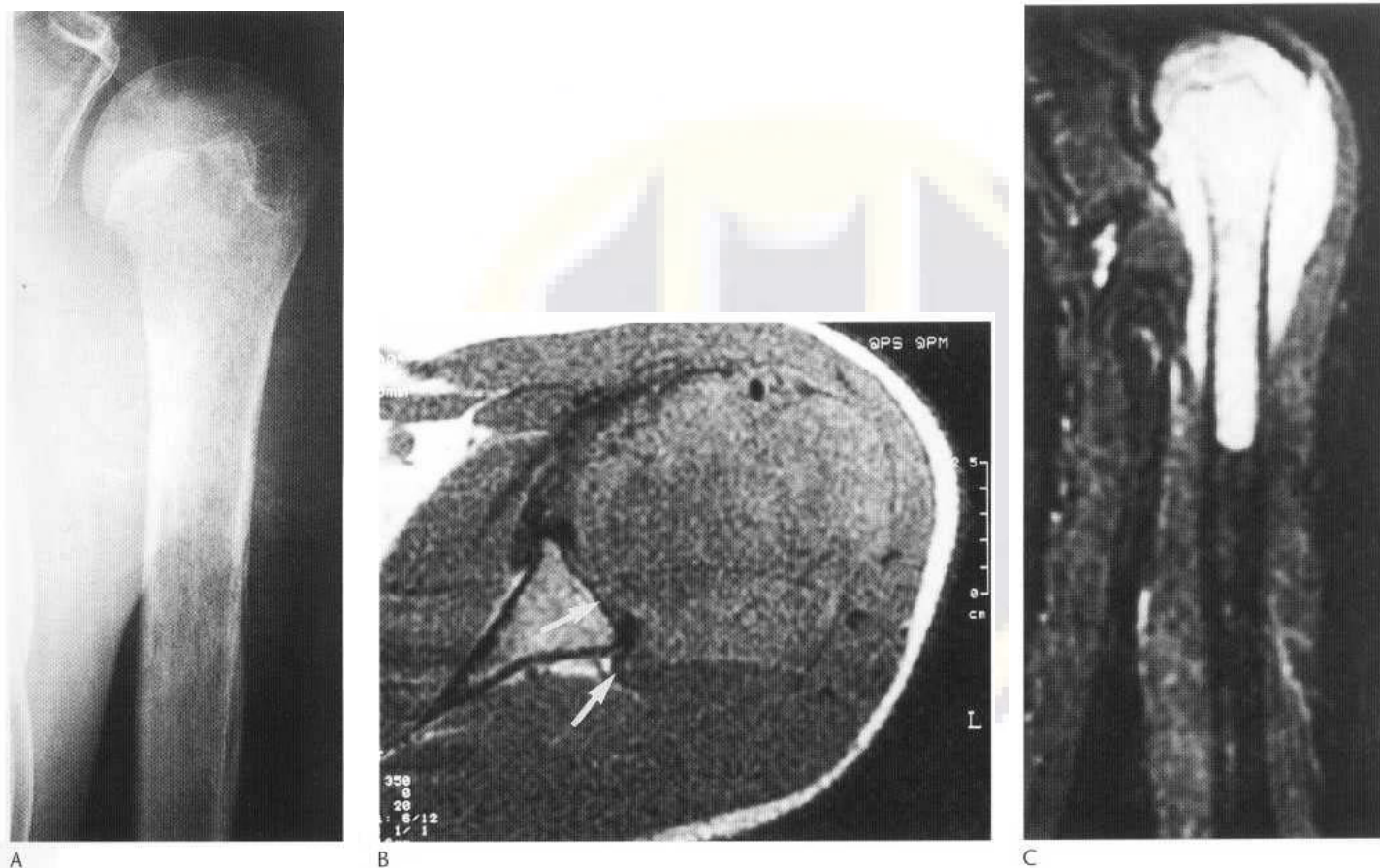


Fig. 39.31 Osteosarcoma of the proximal humerus. (A) Conventional radiograph showing permeative bone destruction and focal areas of intramedullary sclerosis. A spiculated periosteal reaction is also evident. Axial T₁-weighted (B) and coronal STIR (C) images demonstrate the longitudinal extent of the tumour within the medullary canal and the extrasosseous involvement, including extension into the shoulder joint (arrows).

Parosteal osteosarcomas comprise some 1% of all malignant primary bone tumours and about 4% of osteosarcomas. Clinically they occur in older patients, at least 50% being over the age of 30. The tumour is slow growing by comparison and has a much better prognosis. In low-grade lesions, the histology may not immediately suggest a neoplasm at all. Parosteal osteosarcomas occur most commonly on the distal femur and proximal humerus.

Radiological features

Typically dense tumour surrounds a long bone, particularly a femur or a tibia. The tumour bone may be extensive, ranging between 2 and 10 cm in length and as much as 5 cm in breadth. The margins are sharply defined but tend to undulate. The tumour is denser centrally and at the base than peripherally. Characteristically there is a radiolucent zone between the ossified outer margins of the tumour and adjacent host bone (Fig. 39.40). Penetrated films, tomography or CT may be required in order to demonstrate this sign, which may be obscured if the tumour is very large or has invaded the cortex. Usually, the tumour appears to be attached to the cortex by a broad pedicle. Endosteal sclerosis may occur. Marrow invasion is usually only seen in longstanding cases, following local recurrence or in high-grade lesions. Scintigraphically the blood-pool image is usually unremarkable, although considerable increase in activity is evident in the delayed phase. Some evidence suggests that the malignancy of this tumour is reflected by the degree of abnormal vascularity on an angiogram (Fig. 39.41). MRI serves to confirm

tumour localisation and extent, but is frequently confusing as much of the tumour is a low signal mass. Hence, the aggressive potential of the lesion may be underassessed.

The condition must be differentiated from subperiosteal haematoma and other benign causes of periosteal new bone formation.

Sarcoma in Paget's disease

Malignant tumours are said to arise in bone affected by Paget's disease in about 1% of cases. It is difficult to gauge the exact incidence, because many cases of Paget's disease are asymptomatic or diagnosed by chance. Clinically the possibility of a sarcoma arising in Paget's disease should be considered when alteration occurs in the character of bone pain, either an increase in severity or more precise localisation and if a pathological fracture develops. The presence of a soft-tissue mass and a further rise in the serum alkaline phosphatase may be observed. Sarcomas may occur in the polyostotic or monostotic disease though there seems to be a particular predilection for the humerus in the latter. Overall, the skull, pelvis and long bones are typical sites (Fig. 39.42). Men are more commonly affected, even allowing for the increased male incidence of Paget's disease.

Histologically the tumours may be classified as osteosarcoma, fibrosarcoma and chondrosarcoma. However, the tumour is very aggressive and the outlook is very poor. Radiologically, in order of frequency, the lesion is lytic, mixed or sclerotic. The tumour grows



Fig. 39.32 Osteosarcoma of the proximal tibia. (A) Conventional radiograph demonstrating an osteosclerotic lesion with Codman's triangles and a pretibial soft-tissue mass. (B) Sagittal T₁-weighted image showing intramedullary involvement throughout the whole of the tibia included in the illustration and extension into the proximal epiphysis. Both posterior and anterior extraosseous involvement is evident. (C) Axial turbo T₁-weighted image demonstrating circumferential soft-tissue involvement with radiating spicules of new bone within the soft-tissue component.

rapidly with an extensive soft-tissue mass. The margins of the lesion within bone are usually ill defined, frequently with extensive cortical destruction. Periosteal new bone formation is relatively uncommon.

CARTILAGE-FORMING TUMOURS

Benign cartilage lesions divide into two main groups, central and peripheral. The former includes chondroma (with which must be considered the generalised dysplasia of bone-dyschondroplasia), benign chondroblastoma and chondromyxoid fibroma. The malignant counterpart of chondroma is a central chondrosarcoma. There are no reports of the malignant transformation of chondroblastoma and chondromyxoid fibroma. The peripheral lesion to be considered is an osteochondroma, or cartilage-capped exostosis, which in its multiple form also constitutes a general bone dysplasia (diaphyseal aclasia). The cartilage cap of these lesions is a potential site for the development of chondrosarcoma. The majority of chondrosarcomas, however, arise without evidence of a pre-existing benign tumour.

Chondroma

Nearly all of these tumours are benign in their clinical presentation and in their radiological and histological appearances, yet all must be regarded as the site of potential malignancy. It is very unusual for the common chondromatous lesions that occur in the hands and feet to become malignant, but every flat or long bone cartilage tumour should be regarded as a potential risk. The complaint of increasing pain, the demonstration, on serial films, of alteration in the radiological appearances or the late development of a patho-

logical fracture are in themselves sufficient to justify anxiety. The transition from benign to malignant in the histological spectrum may be very difficult and contentious.

These tumours are notoriously insensitive to therapy. Local recurrence is very high unless there is meticulous surgical removal, and cartilage tumours have the habit of becoming more aggressive with each subsequent episode of surgical or therapeutic interference. It must be emphasised that the exact time of change from benign to malignant is extremely hard to establish and it is possible that those tumours that are frankly malignant have been so since their inception. While most cartilage tumours arise in conjunction with bone it is important to note that they may occur in soft tissues, particularly tendon sheaths and in relation to synovium. They may even occur intracranially, and when present at the base of the skull should be considered in the differential diagnosis of chordoma.

Single tumours are common. Approximately half are found in the hands, in the medullary cavity of the phalanges, less commonly in metacarpals. About 10% occur in the small bones of the feet. Long bones, particularly the femur, humerus and tibia, are involved in 20% of cases, the remainder occurring in flat bones, particularly the pelvis, scapula and vertebral bodies. It is in these areas that the potential danger of malignant transformation is greatest.

Clinical features

The age of onset is usually later than with bone-forming tumours. Since these lesions grow slowly, they are rarely symptomatic and are often uncovered through examinations for other indications, particularly trauma. However, on direct questioning the patient

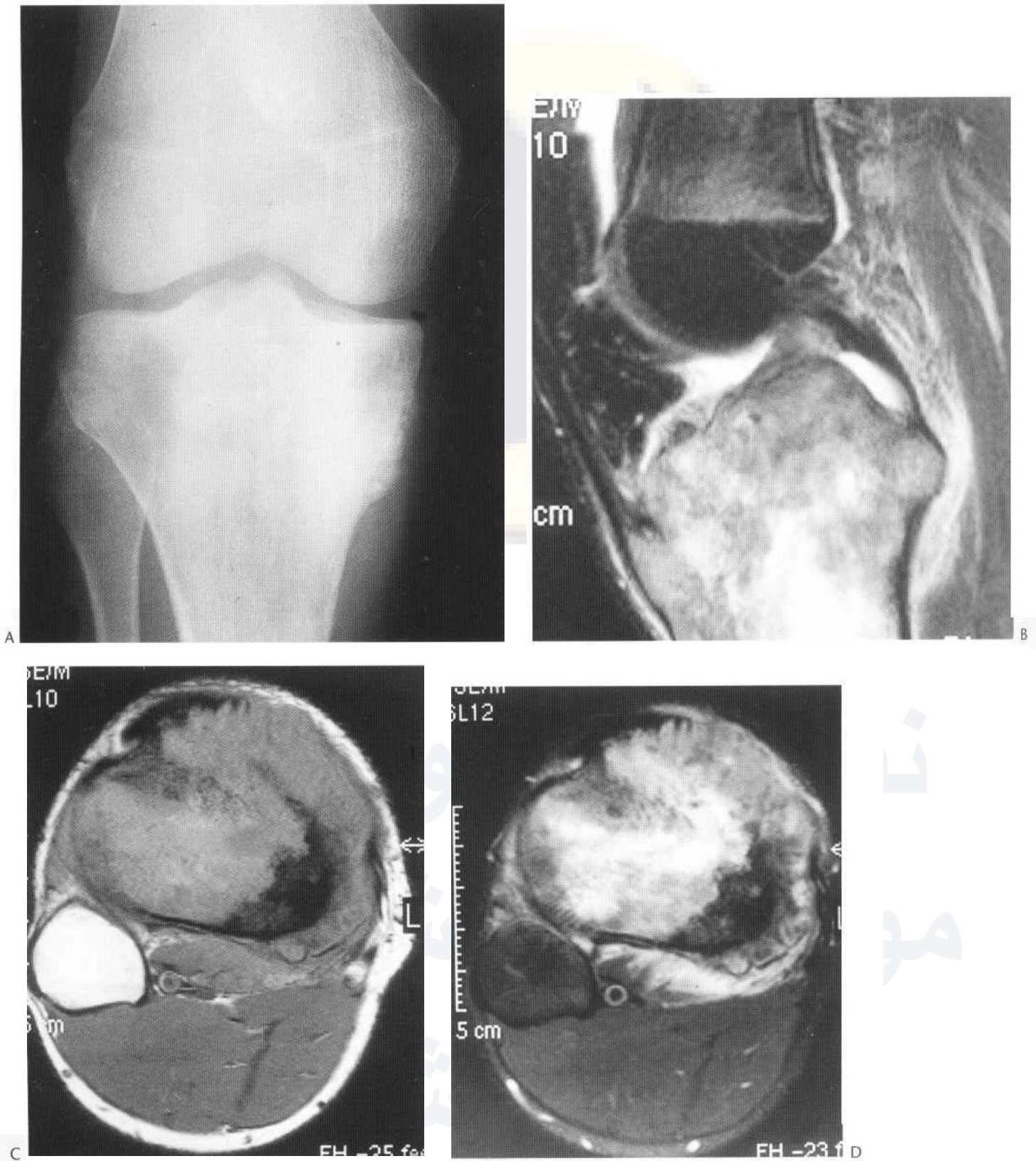


Fig. 39.33 Osteosarcoma of the proximal tibia. (A) Conventional radiograph showing an osteoblastic lesion with periosteal new bone medially. (B) Sagittal turbo T_1 -weighted image with fat suppression. (C) Axial T_1 -weighted image with fat suppression. (D) Axial turbo T_2 -weighted image with fat suppression. The MR images elegantly demonstrate the heterogeneity of the tumour, the intramedullary involvement (note the normal fatty marrow within the distal femur and proximal fibula), periosteal new bone and involvement of the tibia origin of the patellar tendon. Perilesional oedema and a joint effusion are also evident.



Fig. 39.34 Coronal T₁-weighted (A) and coronal T₂-weighted (B) images of a distal femoral osteosarcoma and mid-diaphyseal skip lesion.

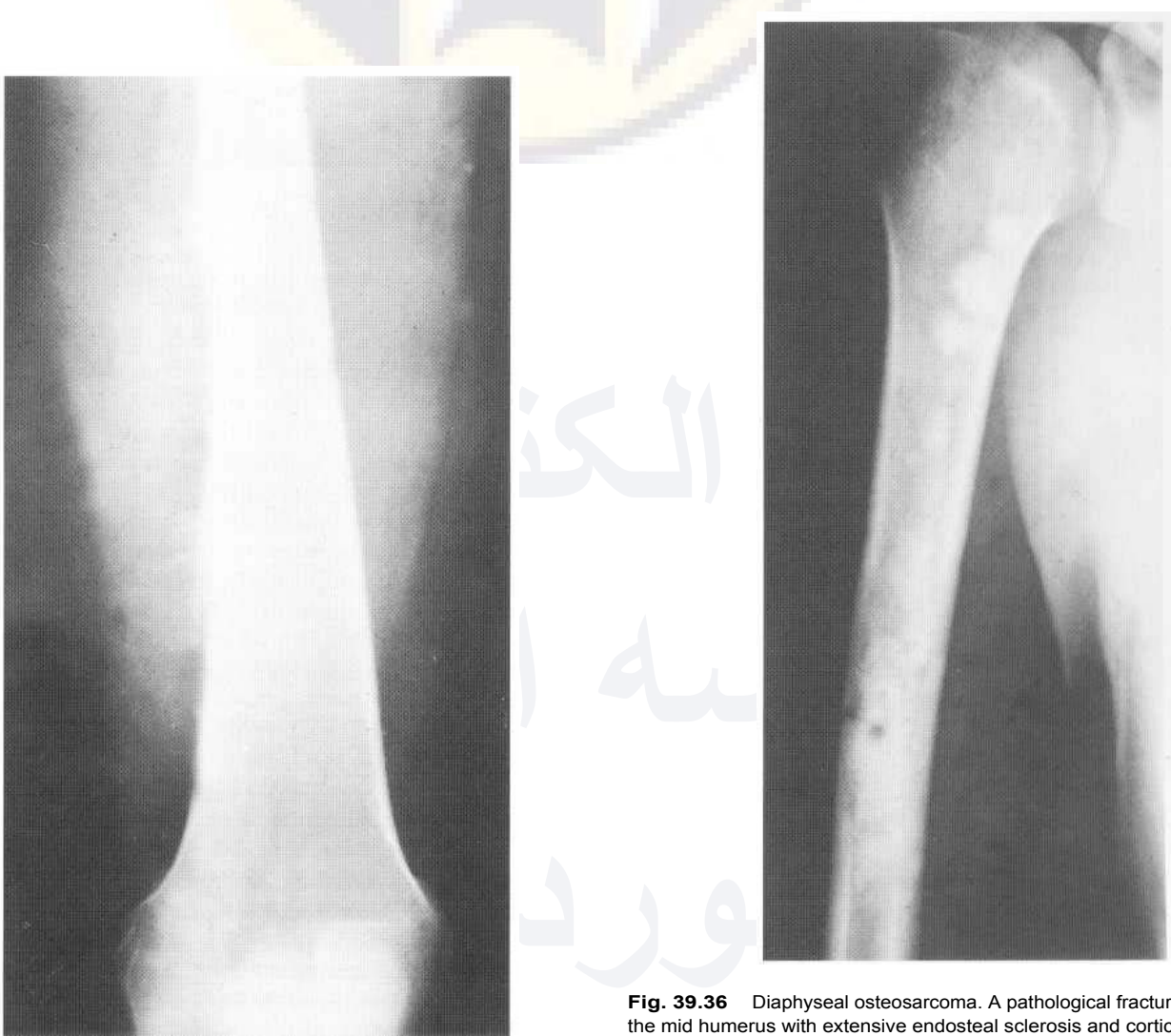


Fig. 39.35 Diaphyseal osteosarcoma of the midshaft of the femur. Note the radiating spiculation of bone, Codman's triangles and well-defined soft-tissue mass.

Fig. 39.36 Diaphyseal osteosarcoma. A pathological fracture is present in the mid humerus with extensive endosteal sclerosis and cortical destruction from the medullary aspect. Tumour is present to the neck of the humerus with areas of dense sclerosis and surrounding faint radiolucency. These 'skip' lesions do not represent isolated tumour; the shaft was involved continuously. This variety carries a poor prognosis.

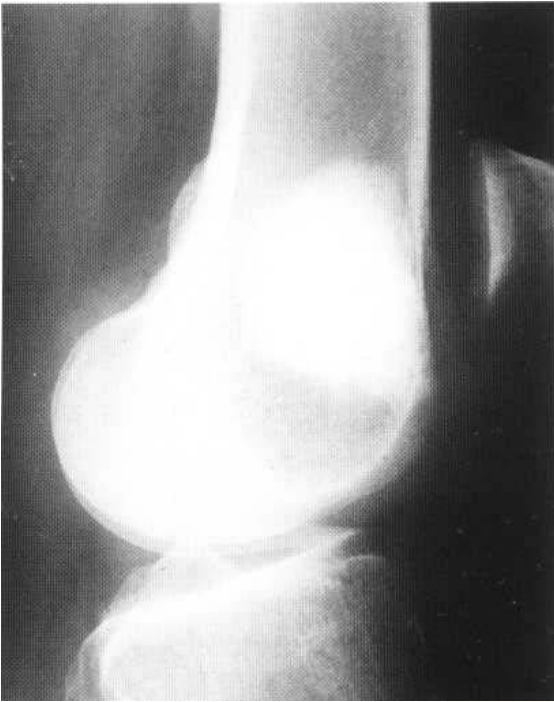


Fig. 39.37 Central osteosarcoma of the distal femoral metaphysis presenting as a dense area of sclerosis with ill-defined margins.



Fig. 39.38 Soft-tissue osteosarcoma. An elderly vicar complained of an enlarging soft-tissue mass adjacent to the medial malleolus of his right ankle. Note the amorphous soft-tissue ossification and calcification and normal bone underlying the lesion.

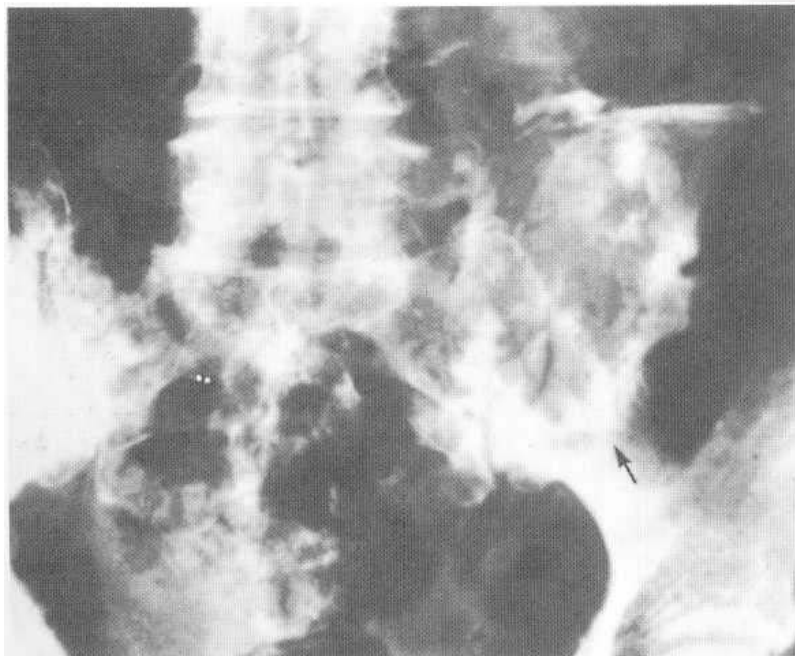


Fig. 39.39 Radiation sarcoma arising in the posterior iliac crest on the left, in an elderly woman treated 6 years previously for carcinoma of the cervix. The lesion is purely osteolytic with ill-defined surrounding sclerosis (arrow).

may admit to having noted a localised hard swelling for many years. Pathological fracture is not uncommon. To restate, low-grade pain or swelling of recent onset should cause the possibility of chondrosarcoma to be considered.

Radiological features

Cartilaginous tissue is not radiopaque. The characteristic feature is of a single well-defined demarcated zone of radiolucency in the medulla. In the small bones of the hand and feet tumours are particu-

larly likely to expand and thin the overlying cortex (Fig. 39.43), but without its destruction or the development of a periosteal reaction other than that following a fracture. The zone of transition is narrow and sclerotic. The endosteal margin may be scalloped. As in all neoplasms of cartilaginous origin, flecks of calcification are frequently present within the tumour, especially as they become more mature, and may assume a pathognomonic 'popcorn' or annular configuration. Calcification also may be observed, together with ossification, in healing callus following a pathological fracture. Lesions rarely

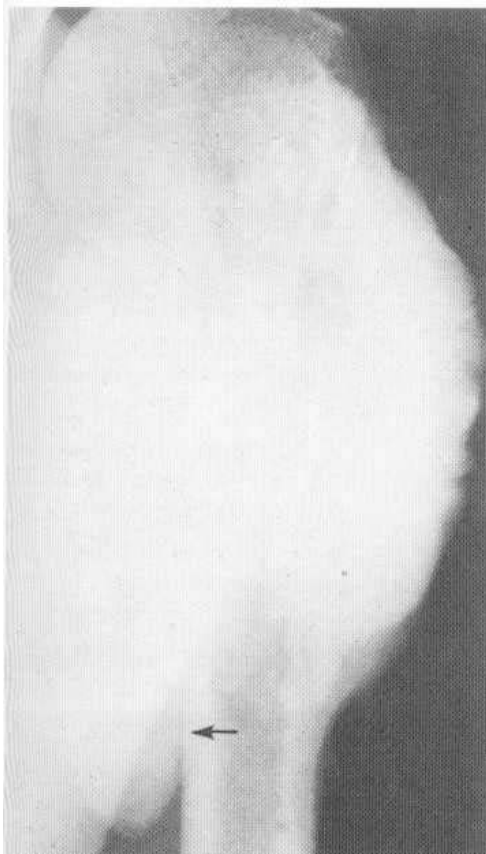


Fig. 39.40 Parosteal osteosarcoma of the proximal humerus. A well-defined mass of dense tumour bone surrounds the humeral shaft. A typical radiolucent line is present between the tumour bone and the proximal shaft inferomedially (arrow). The underlying bone appears normal.

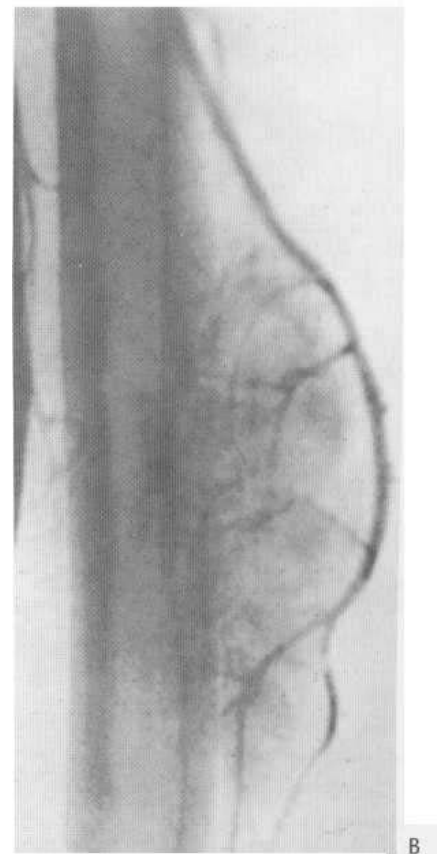
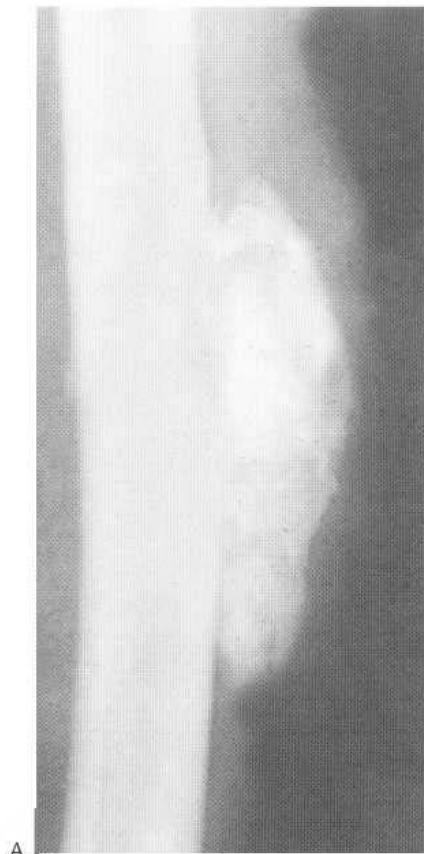


Fig. 39.41 Parosteal osteosarcoma arising from the anterior aspect of the femur (A) is shown angiographically (B) to be unremarkable apart from a slight increase in the number of branches going into the tumour. The lesion was found at biopsy to be of very low-grade malignancy.

extend to the ends of the affected bones and are often situated in the distal portions. Very few other osteolytic lesions in the bones of the hands are likely to cause diagnostic difficulty, apart from the rare implantation dermoid cyst in a terminal phalanx or perhaps fibrous dysplasia. These cartilaginous tumours are unremarkable scintigraphically, and angiographically their low vascularity is readily demonstrated; a marked increase in photon activity on a bone scan should raise the possibility of a pathological fracture or chondrosarcoma. The high water content of the hyaline cartilage matrix results in particularly high signal intensity on T₂-weighted MR images that often have a lobulated contour. MRI, like other radiological techniques, cannot distinguish between a benign enchondroma and a low-grade chondrosarcoma with certainty (Fig. 39.44).

Less commonly chondromas develop in the medullary cavities of long bones and must be distinguished from other medullary osteolytic lesions. Here again the presence of calcification is a great help, but is not entirely specific. The tumour margin is usually sharply defined and accompanied by some evidence of sclerosis. The tumour erodes the cortex from within with a clear-cut edge. The cortex, however, remains intact and the development of an enlarging lesion may cause eccentric expansion of bone due to organised periosteal new bone. Most of these tumours are discovered in adult life and therefore differentiation from other osteolytic lesions, such as bone cysts and non-ossifying fibromas, offers less difficulty because of the patient's age. Evidence of extension of the lesion or irregularity of the margin (particularly in the presence of periosteal

new bone formation or a soft-tissue mass) will immediately suggest a chondrosarcoma. Further investigation is unrewarding, although CT may identify or confirm cartilage calcification and both CT and MRI may serve to delineate the extent of the intramedullary lesion.

It is necessary to distinguish the central variety of chondroma from unimportant areas of amorphous calcification arranged in a roughly linear fashion in the medullary canal, often described as 'cartilage rests'. The localised stippled nature of these opacities and the absence of any other radiological abnormality indicates the latter diagnosis. These lesions are scintigraphically inert. However, differentiation of a central chondroma from a medullary bone infarct may be more difficult. A helpful feature is the curvilinear peripheral calcification around the infarct rather than the annular calcification with a true cartilage tumour. Both lesions may be associated with subsequent malignant complications, differentiated chondrosarcoma from chondroma (see below) and fibrosarcoma or malignant fibrous histiocytoma from the wall of an infarct.

Special types of chondroma

Juxtacortical chondroma is a rare benign cartilage tumour usually arising in young adults and related to the cortex of a long bone, most commonly the humerus or femur. The presenting complaint is of a slowly enlarging hard mass which may not be tender (Fig. 39.45). Radiologically a well-defined soft-tissue mass may

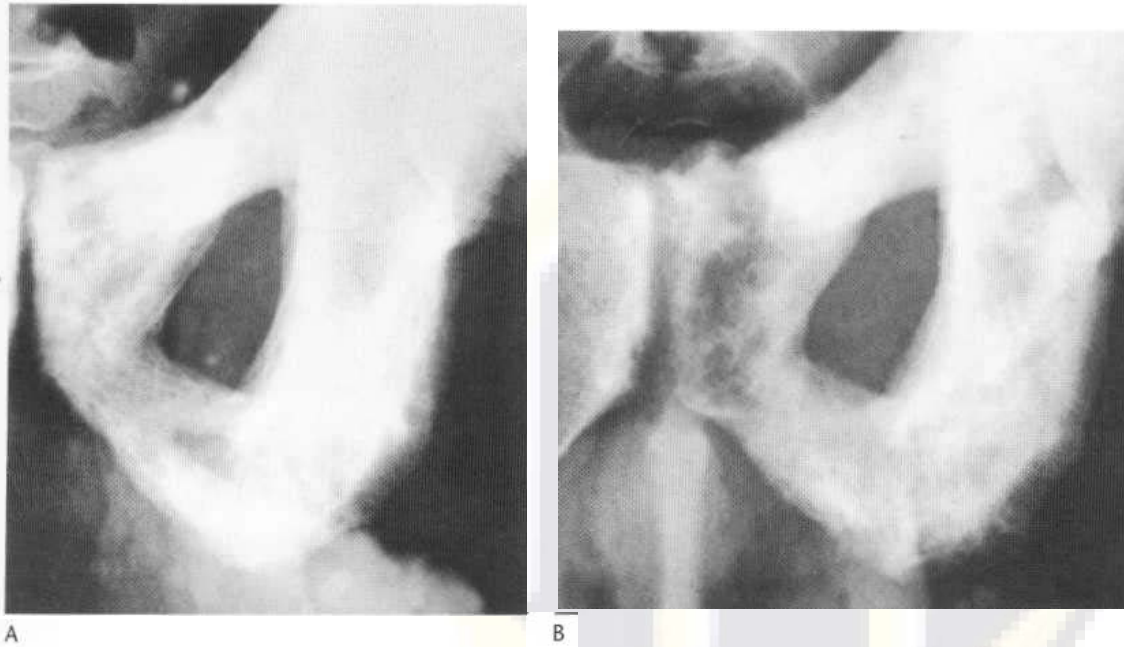


Fig. 39.42 Paget's sarcoma of the body of the pubis. (A) No malignancy was seen in this man at initial presentation with polyostotic Paget's disease. (B) Three years later, however, he complained of local pain with the development of a purely lytic destructive lesion involving the body of the pubis.

contain calcification and be bordered by a thin, but usually incomplete, shell of overlying bone. Pressure erosion produces scalloping of the underlying cortex and usually provokes a variable sclerotic reaction. The presence of calcification within the lesion makes the diagnosis of a cartilage-containing tumour relatively easy, but if calcification is absent the mass may have to be distinguished from non-ossifying fibroma, periosteal lipoma or neurofibroma.

Multiple enchondromas The individual lesions of the bone dysplasia described by Olier are now known as dyschondroplasia and are essentially neoplastic in type, corresponding to the descriptions already given. Cartilage tumours found in dysplasias may be extremely gross and cause complete destruction of the bones of the hand. In addition to the multiple cartilage tumours, columns of dysplastic cartilage frequently cause considerable tabulation anomalies and growth deformities of limbs. Although recognised in the literature to be subject to chondrosarcomatous change, this complication has been uncommon in the experience of the authors.

Maffucci's syndrome is the rare association of dyschondroplasia with cavernous haemangiomas in the soft tissues, the latter being characterised radiologically by soft-tissue masses containing phleboliths (Fig. 39.46). Chondrosarcomatous metaplasia is a recognised hazard of this entity and probably develops in about 20% of cases.

Chondroblastoma

This relatively rare tumour arises almost always in an epiphysis or apophysis, 50% occurring in the second decade of life. Presentation is of pain around the joint, usually of mild proportions, and of months' or even years' duration. Joint movement often is limited. Most of these tumours occur in epiphyses of long bones, especially around the hips, knees or shoulders, but some have been observed in apophyses. Histologically the appearances are distinctive, cartilage cells being interspersed with foci of calcification and giant cells. This lesion has been considered as a giant cell tumour variant.



Fig. 39.43 Multiple chondromas in the hand. This child presented with painless swelling. Note the cortical expansion and thinning, well-defined defects, patchy amorphous calcification and moulding abnormalities indicating slow growth.

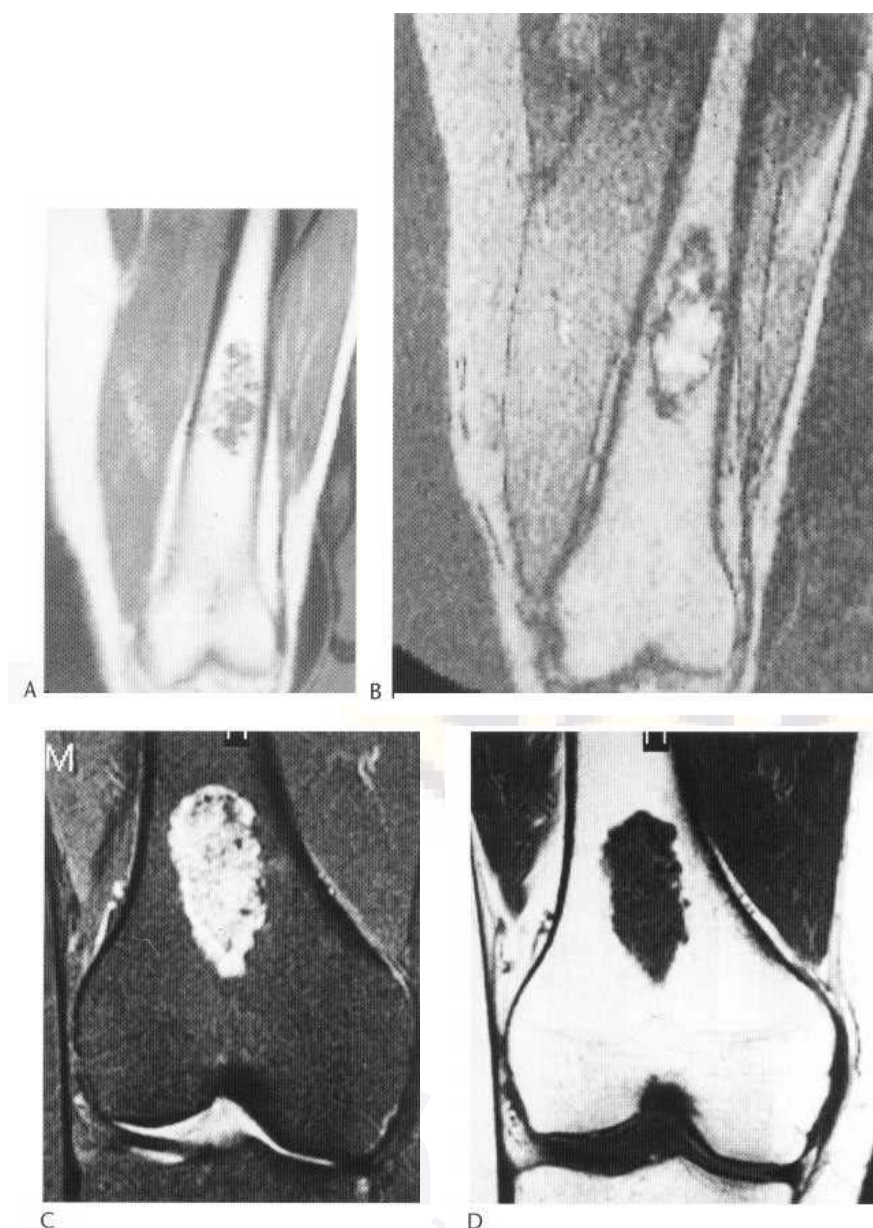


Fig. 39.44 Cartilage tumour. This patient presented with a longstanding ache in the thigh. Coronal T_1 -weighted (A) and STIR (B) sequences demonstrate a mixed lesion within the femoral shaft. Note that the cartilage has high signal on the STIR sequence. A surrounding rim of sclerosis is shown by deficient signal on both images. Histologically, this tumour was considered benign, in spite of giving rise to symptoms and to increased activity on a radionuclide scan and showing a high water content on MRI. In a different patient, presenting with signs of internal derangement, a similar lesion is shown on coronal T_1 -weighted (C) and STIR (D) images.

Radiological features

A well-defined, radiolucent, oval lesion within an epiphysis is characteristic, often with a thin rim of sclerosis and cortical expansion (Figs. 39.47, 39.48). The endosteal margin is well defined. Not infrequently, the tumour extends into the metaphysis. Stippled calcification occurs in about a quarter of examples (Fig. 39.49) and in a smaller number, an adjacent periosteal reaction may be present. The extreme vascularity of these lesions is confirmed by the blood-pool phase of the bone scan or by angiography. The delayed phase of a bone scan is not helpful. CT or MRI may be of value in assessing the extent of those few lesions that expand rapidly into the soft tissues. No incidence of spontaneous malignant transformation, however, has been recorded.

Chondromyxoid fibroma

This tumour is predominantly chondroid, but contains myxomatous tissue and giant cells. It may be mistaken for a chondrosarcoma. The presenting complaints are non-specific, usually localised pain

and swelling, often of many months' duration. The peak age incidence is between 20 and 30, with no particular sex incidence. Typically, the lesion occurs around the knee joint in two-thirds of cases, with an especial affinity for the proximal end of the tibia. Flat bones and short bones have been affected.

Radiological features

The predominant feature is a radiolucent, eccentric, space-occupying lesion that is situated in the metaphysis. The margin within bone is usually well defined, with surrounding sclerosis (Fig. 39.50). The sharpness of the margin between the lesion and the sclerosis contrasts with the rather ill-defined margin between the sclerosis and the host bone. In many cases, the cortex is expanded considerably (Fig. 39.51), the peripheral bony margin often becoming hazy and poorly defined. This aggressive appearance may be so marked that the possibility of malignant change may be considered. Unlike other cartilaginous neoplasms, calcification within the lesion is very uncommon.

While *scintigraphy* in the blood-pool phase of a bone scan, or *angiography*, may reveal a slight increase in perfusion to the lesion,



Fig. 39.45 Juxtacortical chondromas arising on the volar aspect of the proximal and middle phalanges of the index finger. Obvious pressure defects are present with new bone formation at the margins. Punctate calcification is present in the middle of the proximal lesion.



Fig. 39.46 Maffucci's syndrome (woman aged 23). Numerous chondromas in this case of dyschondroplasia are accompanied by soft-tissue swelling which contains phleboliths indicating haemangiomas. These skeletal lesions are more liable than ordinary chondromas to undergo malignant transformation.

the vascular pattern is unremarkable. When the bone scan does show increased activity it is usually localised to the reactive sclerosis rather than to the lesion itself. *CT* may be necessary to delineate a cortical margin in the expanded soft-tissue mass.

This tumour is undoubtedly very closely related to benign chondroblastoma and indeed aneurysmal bone cyst, since all three contain giant cells. Histological differentiation is usually easy, but unrepresentative biopsy material may create confusion. Radiologically, confusion will only occur when these lesions occur in childhood, although the typical location of a chondroblastoma and the ill-defined endosteal margin of an aneurysmal bone cyst will normally suggest the correct diagnosis.

OSTEOCHONDROMA (cartilage-capped exostosis)

This lesion is essentially an osseous outgrowth arising from bony cortex. Usually it grows slowly during childhood and adolescence with endochondral ossification, the central spongiosa merging with that of the bone from which it is derived. Very occasionally the lesion involutes with increasing age and finally results only in a minor abnormality of tubulation. It is usual for growth to cease with



Fig. 39.47 Chondroblastoma in the proximal epiphysis of the tibia. The tumour has thinned the overlying cortex and extends across the growth plate into the upper metaphysis.

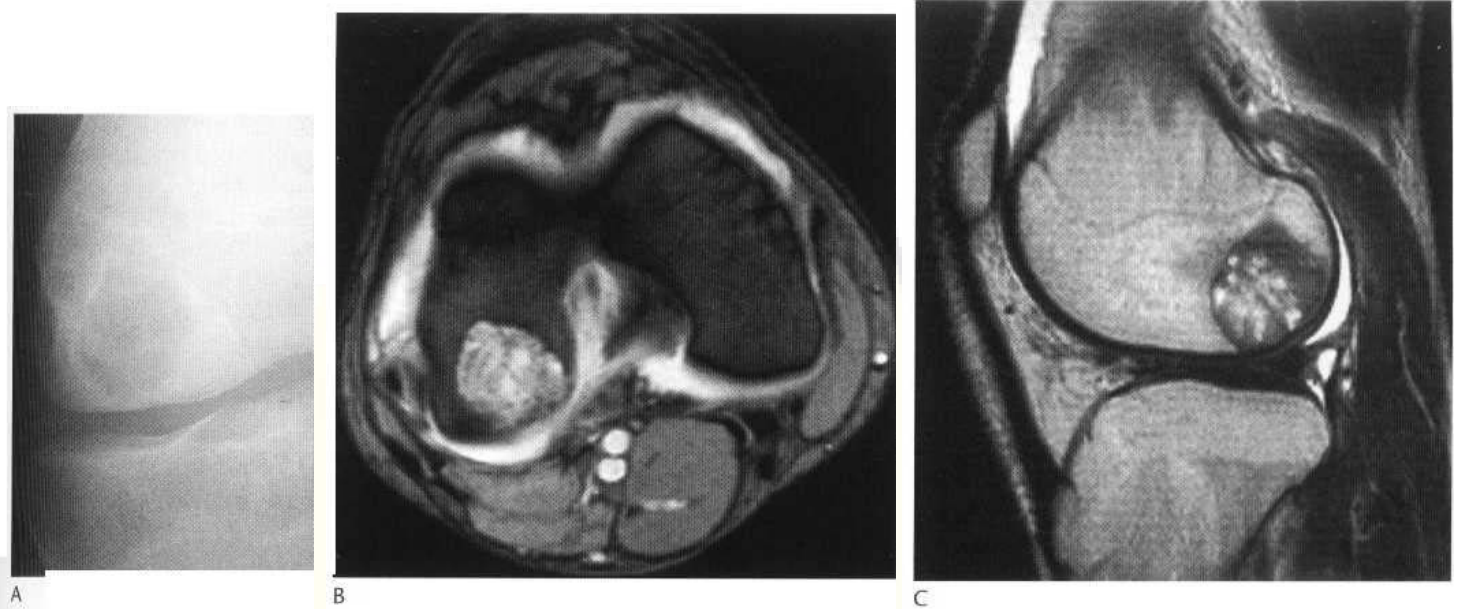


Fig. 39.48 Chondroblastoma. (A) A lytic lesion with a thin rim of sclerosis is shown in the distal femoral epiphysis. Axial gradient echo-image (B) and sagittal T_2 -weighted image (C) showing speckled areas of high-signal intensity within the subchondral lesion.

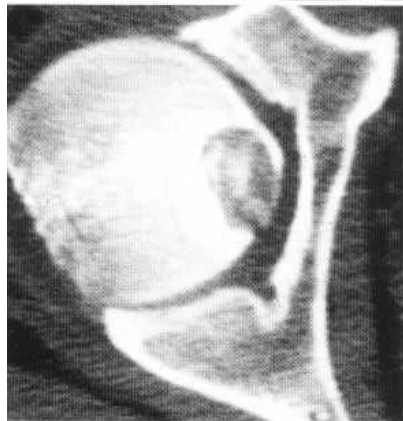


Fig. 39.49 Chondroblastoma of the femoral head. The CT image demonstrates a destructive subchondral lesion containing areas of calcification within it and bordered by a sclerotic rim.

skeletal maturity. Although commonly solitary, the tumours may be multiple, when the condition is recognised as the deforming congenital bone dysplasia known as diaphyseal aclasia (see Ch. 35). The importance of this relatively common benign tumour, and its place among bone tumours, relates to the cartilage cap with which it is covered. This structure may be very prominent and in this tissue lies the very small risk of malignancy in the form of chondrosarcoma. This risk is probably less than 1% but may be significantly higher (of the order of 10%) in diaphyseal aclasia.

These tumours arise mainly in tubular bones near the metaphyses related to the sites of tendinous attachments. They are particularly common around the knee and the proximal end of the humerus. They may be either sessile or pedunculated. The latter type always grows away from the metaphysis, being directed toward the diaphysis. Flat bones also may be affected, the pelvis and scapula being equally involved. In the pelvis, these lesions are almost invariably of the sessile type. Rare lesions related to the laminae of vertebral bodies may produce neurological signs.

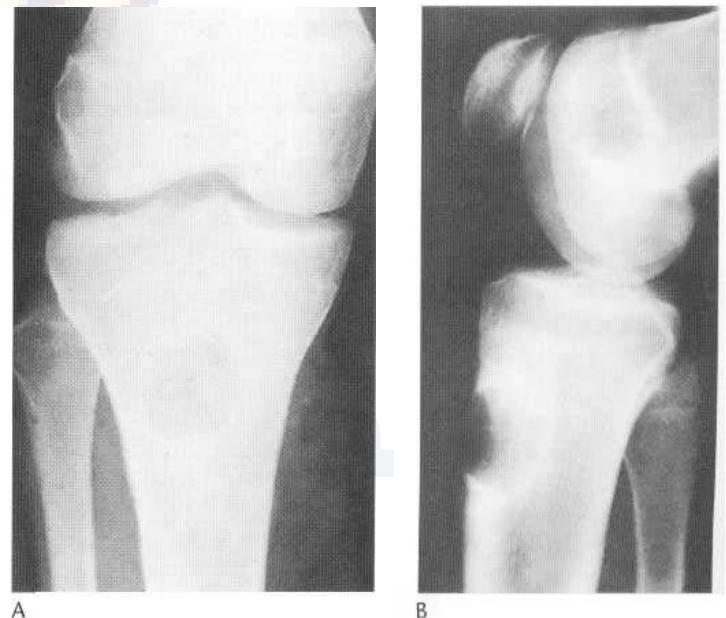


Fig. 39.50 Chondromyxoid fibroma of the proximal tibia. Note the extremely well defined radiolucent defect with a sclerotic margin on the endosteal aspect. (A) AP view. (B) Lateral view.

Both types occur equally in the sexes and may be entirely asymptomatic, apart from their cosmetic effect. Presentation usually follows minor trauma. They may interfere with footwear comfort and can cause localised neural or vascular compression. Such symptoms are unlikely to develop until the later stages of growth, at or around puberty. Surgical removal should be undertaken if any increase in pain or size of the lesion occurs, particularly after growth has ceased. Features of this type may indicate chondrosarcomatous change in the cartilage cap.

Radiological features

Osteochondromas have a characteristic appearance. With a pedunculated tumour it is particularly easy to identify the continuation of

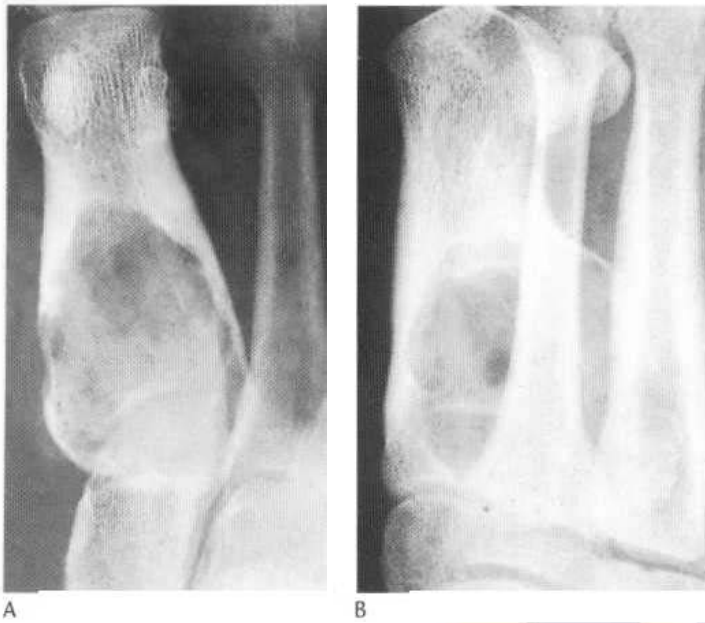


Fig. 39.51 (A, B) Chondromyxoid fibroma-great toe metatarsal. The tumour is eccentric in position with extreme cortical expansion and thinning. The endosteal margin is well defined and faintly sclerotic. No calcification is present.

its cortex with that of the underlying bone from which it arises and the merging of its trabecular pattern into the medullary cavity through the cortical defect (Fig. 39.52). In young adults, the cartilage cap may not be visualised on conventional radiographs, although seen clearly on CT and MRI. As age progresses calcification becomes apparent within the cartilaginous element of the tumour, causing an increase in punctate or curvilinear radiodensity. Thus, the developed lesion in the adult is likely to show irregular calcification. Growth of osteochondromas usually occurs until skeletal maturation is complete (Fig. 39.53), ceasing thereafter. Rarely osteochondromas may be shown to regress (Fig. 39.54). Pedunculated tumours vary in size, but may be up to 8 or 10 cm in length and are typically directed away from the nearest joint. Flat and sessile types are more commonly related to flat bones, particularly the pelvis, and may grow to a substantial size, be of considerable irregularity and become very dense. In such cases the resemblance to a cauliflower may be striking! If the sharply defined peripheral margin is preserved, and serial examinations reveal no increase in size, their benign nature may be assumed.

Any change in radiological appearance, particularly with the development of poor definition of the margin, even in one part of the lesion, is highly suggestive of chondrosarcoma, particularly if accompanied by a history of an insidious increase in local pain. Local resection and histological studies then become essential because of the shortcomings of further radiological investigation in detecting chondrosarcoma (see below). *MRI* may be of assistance in suggesting the presence of sarcomatous change by showing the thickness of the cartilaginous cap (greater than 1 cm should be viewed with suspicion), changes in the cartilage cap in an adult, and any infiltration of adjacent soft-tissue structures. The individual lesions of diaphyseal aclasia are those of any osteochondroma. However, their multiplicity results in considerable moulding abnormality and deformity (Fig. 39.55).

Chondrosarcoma

Differentiation of this malignant member of the group of cartilage-forming tumours is to be made from osteosarcoma, with which it may be confused. Chondrosarcoma forms a spectrum of malignancy, but usually develops later in life than osteosarcoma and carries a much better prospect of survival because metastasis often occurs late. A high-grade (aggressively malignant) chondrosarcoma, however, behaves in a fashion very similar to an osteosarcoma.

The *clinical problem*, therefore, is not so much that of metastatic dissemination but of local recurrence. Failure to provide adequate and early excision is attended by the subsequent necessity of further and more difficult surgical procedures. Some evidence exists that each surgical insult causes the tumour to become even more aggressive. Certain pleomorphic osteosarcomas demonstrate cartilage formation, but the established chondrosarcoma is associated with cartilage that is mature in its development. Although some of this cartilaginous tissue may ossify, no direct ossification (unlike an osteosarcoma) takes place in the absence of a chondroid precursor. In addition, these cells are histochemically negative for the production of alkaline phosphatase.

Chondrosarcomas may develop in a cartilaginous lesion previously thought to be benign. Malignancy may arise in the cartilage cap of an osteochondroma or in a long or flat bone (Fig. 39.56). Chondrosarcoma of the hand or foot is distinctly unusual. The lesions of dyschondroplasia, particularly if associated with the haemangiomas of Maffucci's syndrome, are also subject to malignant change. Nonetheless, the incidence of what might be called secondary chondrosarcoma is far less common than that apparently



Fig. 39.52 Osteochondroma of the distal femur. The cortex is continuous with that of the underlying bone and trabecular bone merges with that of the femur. A well-defined cartilage cap contains calcification and is directed away from the joint.

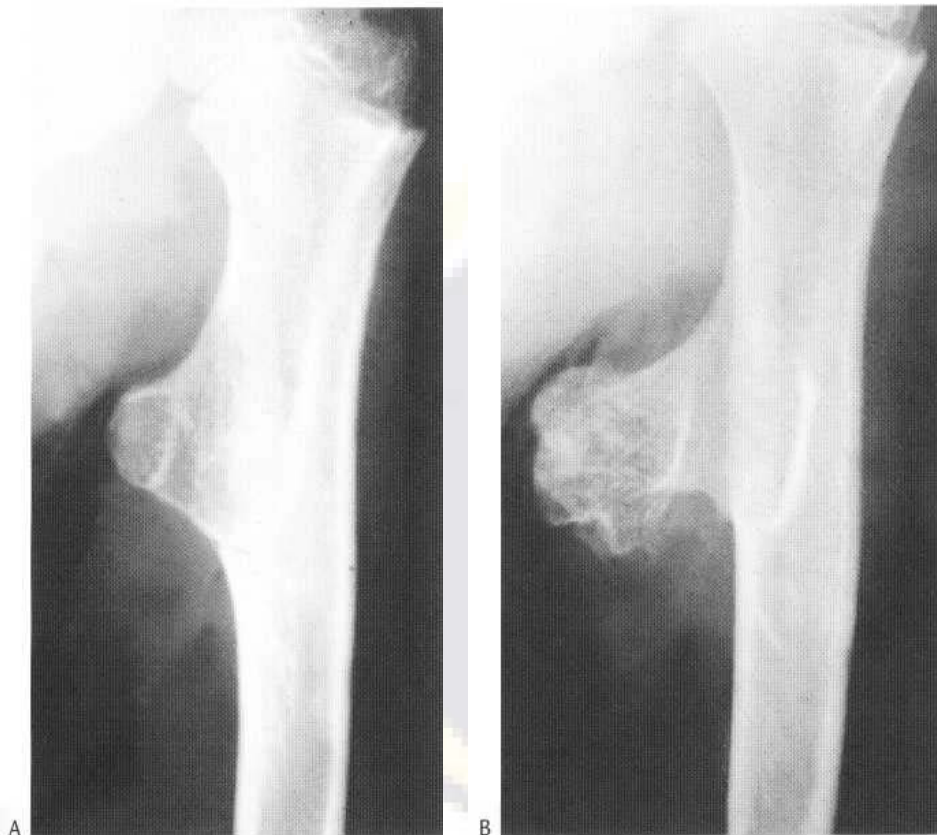


Fig. 39.53 (A,B) A pedunculated osteochondroma exhibits growth over a 2-year period in the humerus of a child. Such growth is common and stops usually at, or soon after, puberty.

arising de novo. Indeed only 10% of these neoplasms arise from a recognisable precursor, usually the cartilage cap of an osteochondroma, especially in patients suffering from diaphyseal aclasia.

Primary chondrosarcoma occurs mainly between the ages of 30 and 70 years and is relatively rare distal to the elbow and knee joints, the pelvis and ribs being the most common sites, followed closely by the proximal end of the femur. Because of this distribution, virtually all chondromas arising in flat and long bones should be regarded as potentially malignant ab initio. Diagnosis may be delayed because of slow growth or relatively mild symptomatology. The tumour, therefore, may be very large when it is first recognised.

Prognosis for chondrosarcoma is relatively good if complete surgical excision is possible before dissemination, metastasis only occurring in the later stages by the haematogenous route. Because of the risks of local recurrence, it may be necessary to undertake amputation. The histological spectrum of chondrosarcoma varies widely. Difficulties with differentiation arise, at the benign end of the spectrum, from a benign chondroma and, at the aggressive end, from an osteosarcoma. In consequence, interpretation by a highly skilled pathologist is essential. Particularly in a case of less aggressive chondrosarcoma situated in a site of easy access, such as the proximal end of the femur, prosthetic replacement is an effective and cosmetic surgical treatment.

Radiological features

When a chondrosarcoma arises from a previous cartilaginous lesion the diagnosis is usually straightforward. In the case of osteochondroma, particular attention should be paid to areas of local cortical destruction with ill-defined margins. In addition, it may be possible to demonstrate an associated soft-tissue mass representing abnormal cartilage growth. MRI demonstrates these features more the proximal humerus cannot be visualised 6 years later.

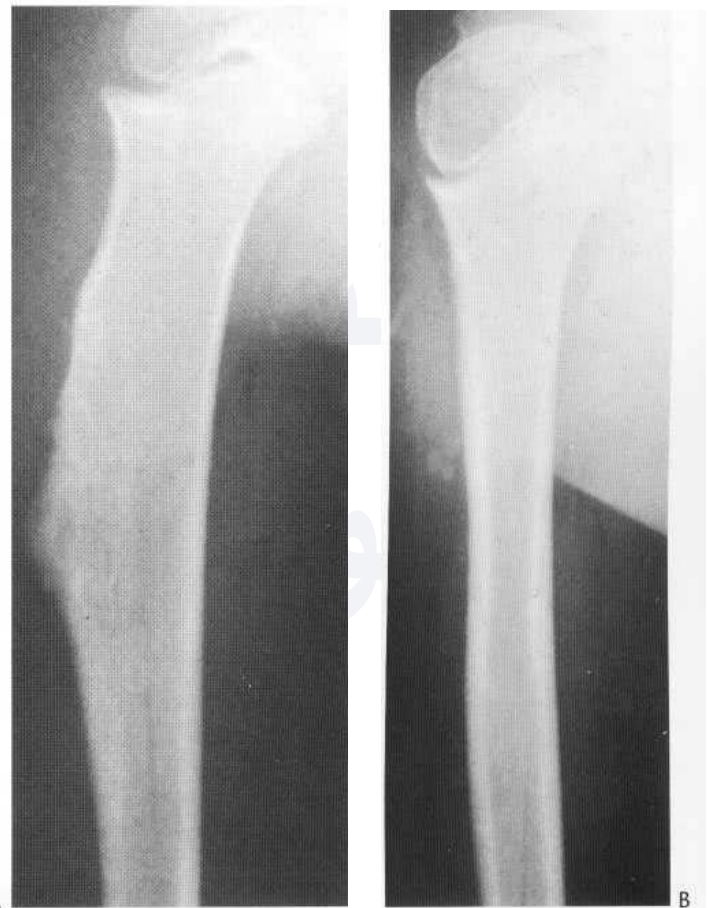


Fig. 39.54 (A,B) Osteochondromas may rarely be shown to regress, remodelling resulting in normal appearances. Here an osteochondroma of the proximal humerus cannot be visualised 6 years later.



Fig. 39.55 Diaphyseal aclasia. (A) Multiple osteochondromas are present in the proximal tibia and fibula. A large sessile lesion of the proximal tibia has caused widening of the interosseous space and secondary moulding abnormalities of both the tibia and fibula. In another patient (B), similar modelling abnormalities are shown. On MRI, following ligamentous injury, only a minimal cartilage cap can be identified on the medial osteochondroma, and a slightly thicker cap on the laterally projecting osteochondroma: (C) coronal T₁-weighted, (D) coronal FFE-T₂ and (E) axial T₁-weighted images.



Fig. 39.56 Chondrosarcoma arising from the superior pubic ramus on the left. A huge mass is present containing extensive calcification. The femoral artery is displaced by the mass but note the absence of any pathological circulation. This is typical of a low-grade chondrosarcoma.

clearly. The conventional radiological demonstration of cartilage within such a mass by punctuate or curvilinear calcification may be absent, as this characteristic feature tends to occur in the more mature parts of these tumours. Similarly, the central chondroma that becomes malignant tends clinically to grow silently, spreading within the medullary cavity to produce irregular medullary destruction. Uneven infiltration makes it difficult to determine the margin between normal and abnormal tissue. Irregular calcification is likely to be present in the older and central parts of the tumour. These more organised zones may be destroyed by newer malignant infiltration, indicating the dedifferentiated form of chondrosarcoma.

As growth proceeds slowly, the tumour causes smooth, scalloped erosions on the endosteal aspect of the cortex. An overlying lamellar periosteal reaction is not rare, especially if the malignancy is low grade. In consequence, the ultimate thickness of the cortex around the tumour may exceed that in the unaffected portion of the bone, the appearance then being that of a localised fusiform expansion (Fig. 39.57). Pathological fractures are quite common and may draw initial attention to these tumours.

The malignant nature of the lesion is unequivocally established when penetration of the cortex is shown together with an associated and clearly defined soft-tissue mass, within which calcification, or even ossification, may occur (Fig. 39.58).

Primary chondrosarcoma

Particularly in its early stages, this chondrosarcoma presents difficult diagnostic problems as the presenting symptoms of minor

pain or discomfort may be accompanied by only minimal radiological change. This may be a poorly defined area of medullary translucency with possibly a little periosteal reaction or the presence of an abnormal soft-tissue mass. The acetabulum is sometimes the site of the development of these rather nebulous and difficult lesions (Figs 39.59, 39.60). The first radiological evidence of its presence may be a soft-tissue mass projecting into the pelvic cavity. The cortex of flat bones tends to be thinner than that of long bones, and chondrosarcomas of the ribs or the pelvis penetrate it at an early stage. This feature may be demonstrated more clearly by CT. Hence these tumours are especially liable to grow to a substantial size over a prolonged period, particularly if in a clinically occult area. Rapid growth naturally indicates a more aggressive type of malignancy.

As may be expected, the more mature cartilage elements frequently progress to calcification and ossification, and larger tumours often have a lobulated or cauliflower appearance. Very rarely a chondrosarcoma may arise in soft tissues, including tendon sheath and meninges. Cranial lesions also can arise from the sphenoid (Fig. 39.61) and clivus where they require differentiation from chordoma.

Radiologically no criterion of malignancy is absolute. The demonstration of increase in size and ill-defined margins on plain film is highly suggestive. Destruction of organised existing cartilage calcification is indicative also of local infiltration. The demonstration of cortical disruption is helpful.

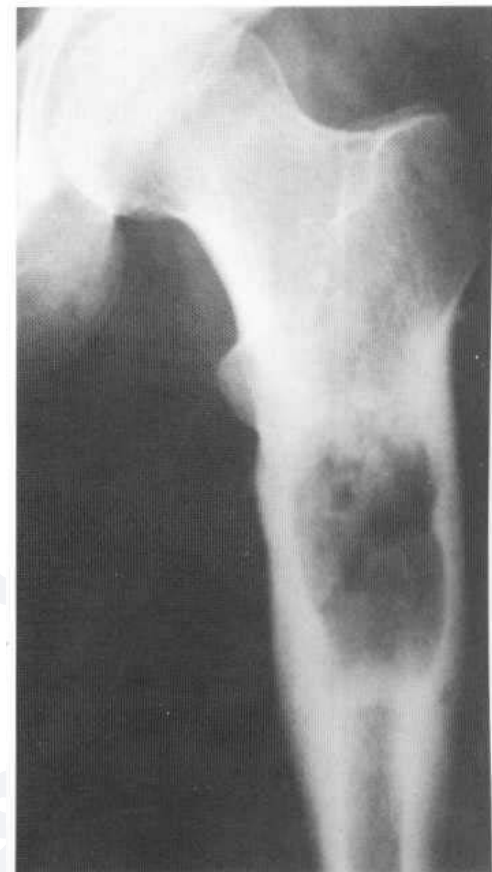


Fig. 39.57 Central chondrosarcoma. The destructive lesion in the femoral shaft has smooth well-defined margins, but in the upper portion, some characteristic punctate calcification is visible. The tumour is of a slow-growing type because organised periosteal new bone has thickened the cortex around the lesion.

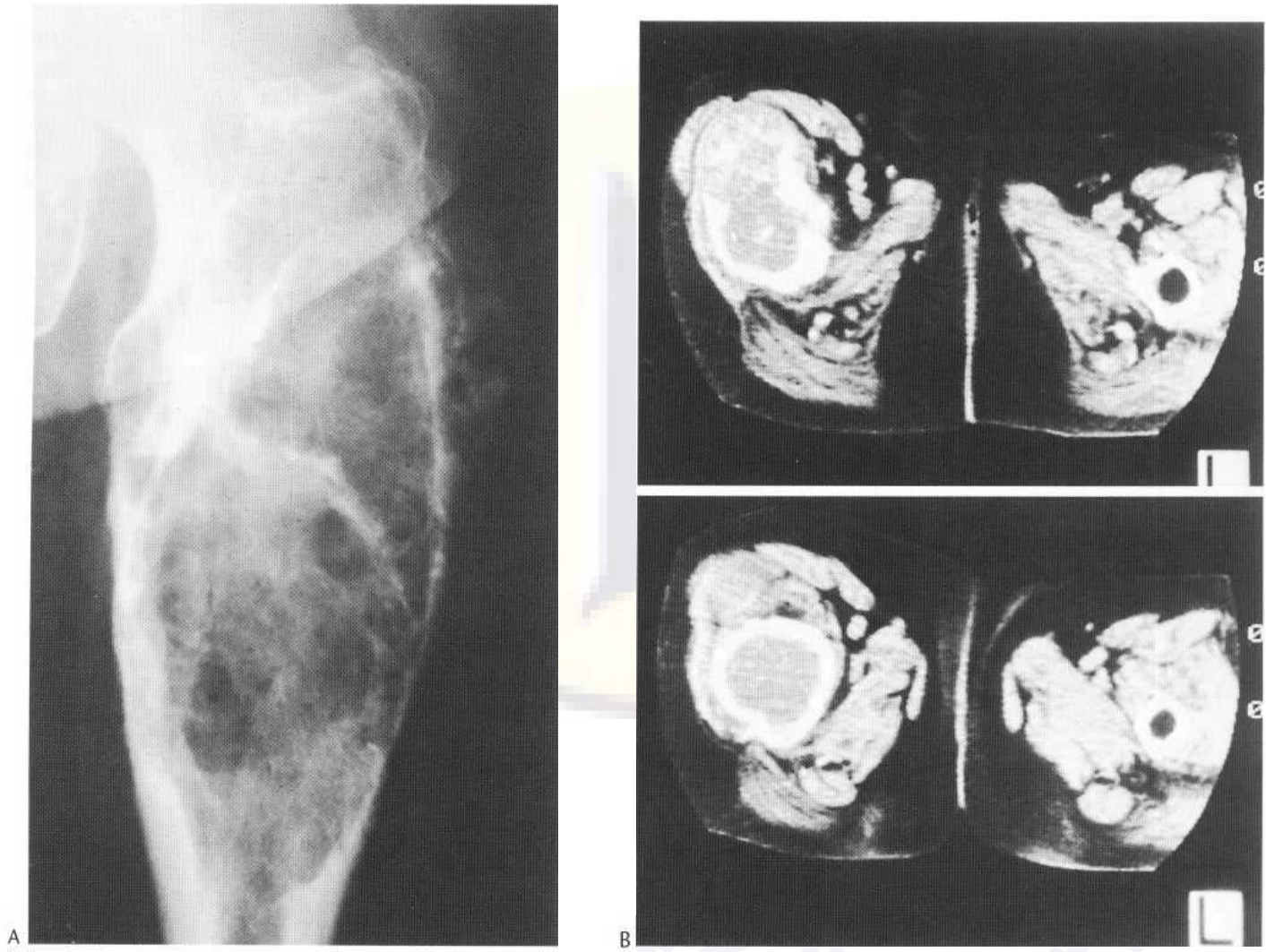


Fig. 39.58 Central chondrosarcoma. (A) The tumour is more aggressive than that in Fig. 39.57, and has extended into soft tissues. This is confirmed by CT (B), showing extension anterior to the femoral shaft. Calcification is present both in the soft-tissue mass and within the shaft lesion.

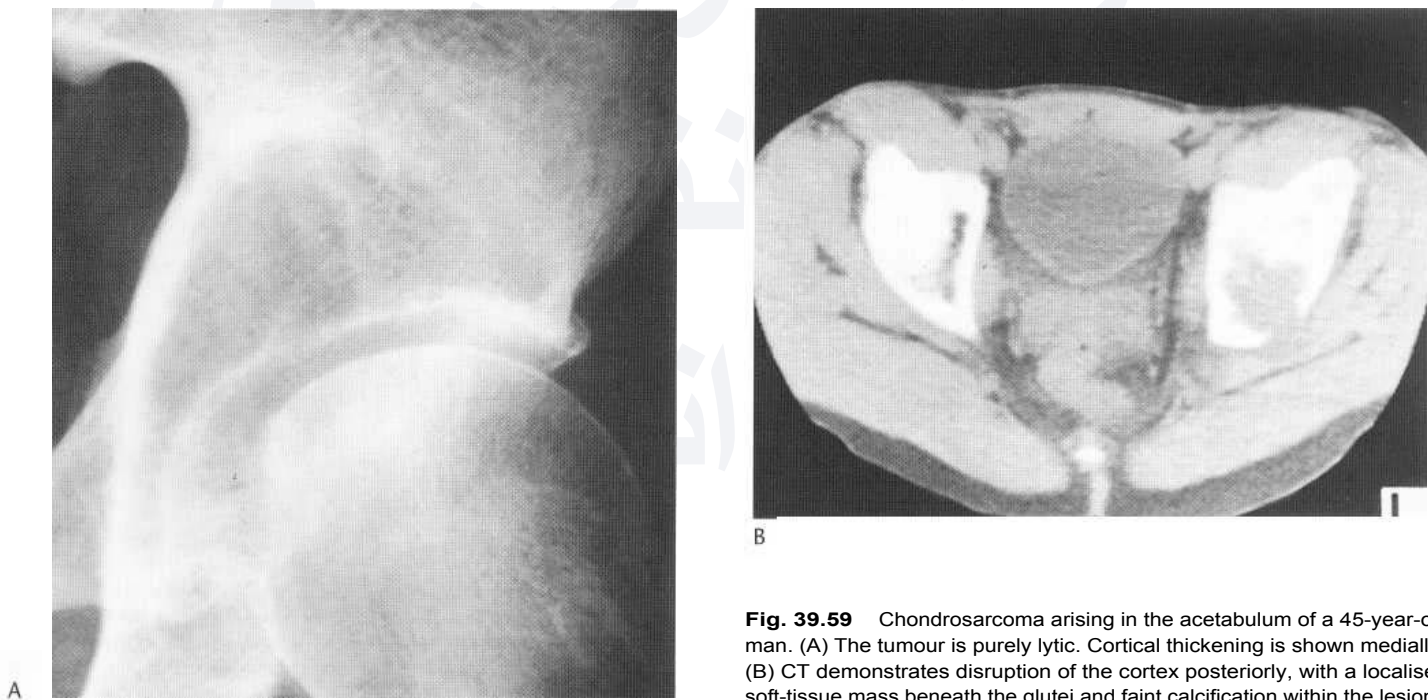
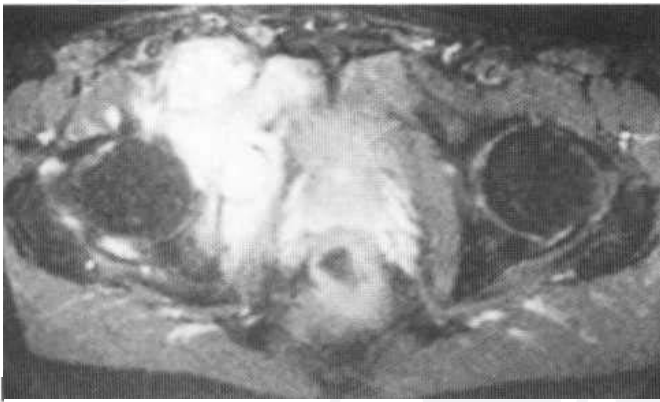


Fig. 39.59 Chondrosarcoma arising in the acetabulum of a 45-year-old man. (A) The tumour is purely lytic. Cortical thickening is shown medially. (B) CT demonstrates disruption of the cortex posteriorly, with a localised soft-tissue mass beneath the glutei and faint calcification within the lesion.

Scintigraphically most of these neoplasms tend to have a slight increase in activity only on the delayed phase of a bone scan, but high-grade chondrosarcomas may demonstrate an increase in the blood-pool image. *Angiographical/v*, minor vascular displacement is usually evident, with scanty new vessels in the majority. Only when the tumour is of particularly high-grade malignancy is the type of increased perfusion and new vessel formation similar to that associated with an osteosarcoma. While *MRI* may infer a cartilage tumour, by virtue of the high water content of cartilage, only the direct infiltration of adjacent soft tissues will definitely suggest malignancy (Fig. 39.60). Reference has been made above to malignant cartilaginous tumours of relatively low-grade malignancy undergoing relatively rapid deterioration. In such instances the radiological diagnosis of dedifferentiation may be suggested when an area of osteolytic destruction develops adjacent to the original tumour (Fig. 39.62) and which may destroy part of the pre-existing calcified portion of the tumour. These dedifferentiated forms may exhibit the microscopic appearance of a frank osteosarcoma, fibrosarcoma or, not uncommonly, malignant fibrous histiocytoma with its characteristic storiform pattern of the tumour cells (see below). The age, sex and clinical features otherwise are comparable to those of an orthodox chondrosarcoma.



A



B

Fig. 39.60 Chondrosarcoma. Arising primarily in the region of the acetabulum. A coronal T_1 -weighted (A) and axial STIR (B) sequences demonstrate a large lobulated mass occupying the floor of the acetabulum and extending through into the pelvis and the obturator foramen. Note the high signal on STIR, suggesting aggressive tumour, with also some increased signal surrounding the lesion due to oedema (secondary response). There is obvious involvement of the hip joint.

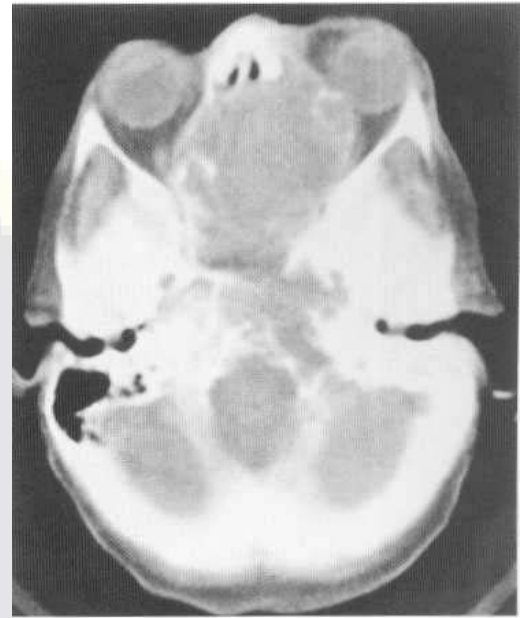


Fig. 39.61 Chondrosarcoma arising in the sphenoid bone of an adult woman. A large soft-tissue tumour extends from the nasal cavity to the middle fossa. A thin sclerotic margin outlines the mass, which contains faint punctate calcification. Note the displacement of the globe.



Fig. 39.62 Dedifferentiated chondrosarcoma. A chondrosarcoma is present centrally within the distal femoral shaft, characterised by slight expansion and amorphous calcification. In addition, an area of osteolysis is present with cortical destruction around the lower half of the tumour. The latter represents a high-grade malignancy arising in conjunction with a pre-existing relatively low-grade tumour.

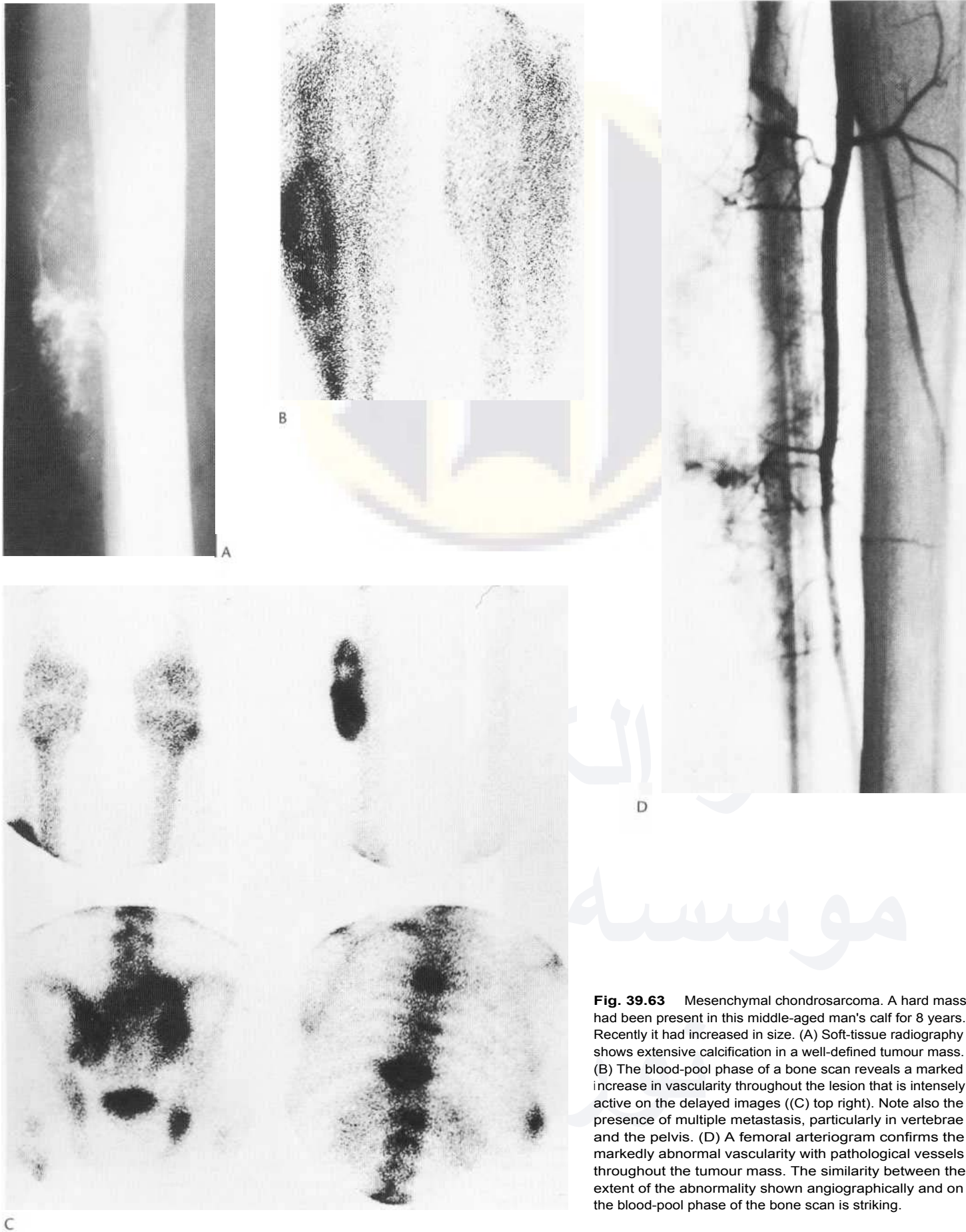


Fig. 39.63 Mesenchymal chondrosarcoma. A hard mass had been present in this middle-aged man's calf for 8 years. Recently it had increased in size. (A) Soft-tissue radiography shows extensive calcification in a well-defined tumour mass. (B) The blood-pool phase of a bone scan reveals a marked increase in vascularity throughout the lesion that is intensely active on the delayed images ((C) top right). Note also the presence of multiple metastasis, particularly in vertebrae and the pelvis. (D) A femoral arteriogram confirms the markedly abnormal vascularity with pathological vessels throughout the tumour mass. The similarity between the extent of the abnormality shown angiographically and on the blood-pool phase of the bone scan is striking.

Mesenchymal chondrosarcoma

This malignant cartilage tumour is rare. Histologically it is characterised by the presence of more or less differentiated cartilage together with highly vascular spindle cell or round cell mesenchymal tissue. About a third of these tumours arise in the soft tissues, especially in the extremities (thigh and calf). The soft-tissue mass frequently shows irregular calcification (Fig. 39.63).

Radiological/v this lesion shows a rapid increase in size with highly aggressive features and the early detection of metastasis. The condition affects adults at an earlier age than most chondrosarcomas, although in general the age group is older than that of osteosarcoma.

Clear cell chondrosarcoma

This is an uncommon variant of chondrosarcoma that is typically located within the epiphysis, usually occurring within the proximal humerus, femur or tibia.

Radiological/v clear cell chondrosarcoma resembles chondroblastoma, resulting in a well-defined osteolytic lesion in the epiphysis that may have a sclerotic border. A periosteal reaction is not seen although calcification within the lesion may occur.

REFERENCES AND SUGGESTIONS FOR FURTHER READING

See end of Chapter 41.

نشر الکترونیکی
موسسه انتشاراتی
نوردانش



نشر الکترونیکی
موسسه انتشاراتی
نوردانش

40

TUMOURS AND TUMOUR-LIKE CONDITIONS OF BONE (2)

Mark Cobby and Iain Watt

BONE TUMOURS PRESUMED TO ARISE FROM SKELETAL TISSUE—FIBROUS TUMOURS

1. Fibrous cortical defect

Fibrous cortical defects are extremely common, occurring in up to a third of normal children between the ages of 2 and 15 years. Characteristically they occur around the knee, especially in the distal posteromedial femoral cortex. They are usually discovered by chance and are not known to be symptomatic.

Radiologically they are blister-like expansions of the cortex with a thin shell of overlying bone (Fig. 40.1). They may be slightly lobulated, but are always sharply defined (Fig. 40.2) and have a fine sclerotic margin, particularly when seen in profile. Because of their characteristic site they are radiolucent when observed in a frontal view of the knee. An oblique projection will always show the cortical location. With increasing skeletal maturity the lesion may appear to migrate toward the diaphysis before becoming progressively sclerotic and involuting completely. *Bone scans* are unremarkable, revealing only a minimal increase in activity on the delayed phase in proportion to the size of the lesion.

The differential diagnosis, when the lesion occurs in its typical site, is from a cortical desmoid or cortical avulsion syndrome that occurs at the insertion of the adductor magnus muscle or the origin of the medial head of the gastrocnemius muscle. This abnormality is attributed to chronic low-grade traction resulting in irregularity of the femoral cortex, sometimes with a radiolucency, but often with irregular calcification. Because these lesions are almost certainly of traumatic origin, an abnormal increase in activity is evident on a bone scan and a slight increase in vascularity is seen on an angiogram. The typical site and lack of endosteal abnormality should prevent the misdiagnosis of a sarcoma.

2. Non-ossifying fibroma

This lesion is similar to a fibrous cortical defect except that it is much larger and characteristically occurs in a slightly older age

group, between 10 and 20 years. The vast majority is found around the knee joint, the distal end of the femur being the most common location. The lesion occasionally presents with a pathological fracture (Fig. 40.3). Usually it is asymptomatic.

The radiological findings reveal an area of increased radiolucency which is sharply defined in the metadiaphysis, the margins are smooth and sharp, with a rather lobulated appearance, and are defined by a thin zone of reactive sclerosis. In larger bones such as the tibia and fibula the lesion may be eccentric and appropriate oblique views will show its relationship to one of the cortices. However, in more slender bones, such as the fibula, the whole width of the bone may be involved. On the outer margin the cortex is usually slightly expanded but remains intact and thinned. Scintigraphically only a minimal increase in activity can be detected on the delayed phase scan, the degree of increased activity solely reflecting the size of the lesion, unless there has been a pathological fracture. As in fibrous cortical defect, the natural history is for the lesion to regress, initially by an increase in the surrounding zone of sclerosis and latterly by replacement with normal bone (Fig. 40.4). There is a debatable association of multiple non-ossifying fibromas with neurofibromatosis.

The differential diagnosis, particularly when the whole width of the bone is involved, is from a solitary bone cyst or monostotic fibrous dysplasia. Differentiation from the former may be very difficult on all radiological grounds whereas distinction from monostotic fibrous dysplasia is relatively straightforward, due to the avidity of the latter for bone-seeking radiopharmaceuticals and the obvious textural difference on MRI between a cyst and a solid lesion.

3. Desmoplastic fibroma

This rare tumour exhibits dense fibrous tissue, simulating desmoid tumours of the abdominal wall. Relatively few occur in bone and then usually in young adults. Pain is a constant presenting feature. The lesion is often tender. The majority arises in the metadiaphysis of long bones (Fig. 40.5), although the pelvis and spine are other sites of predilection.

Radiologically these tumours tend to be large, solitary and destructive, with an expanded and irregular sclerotic margin and

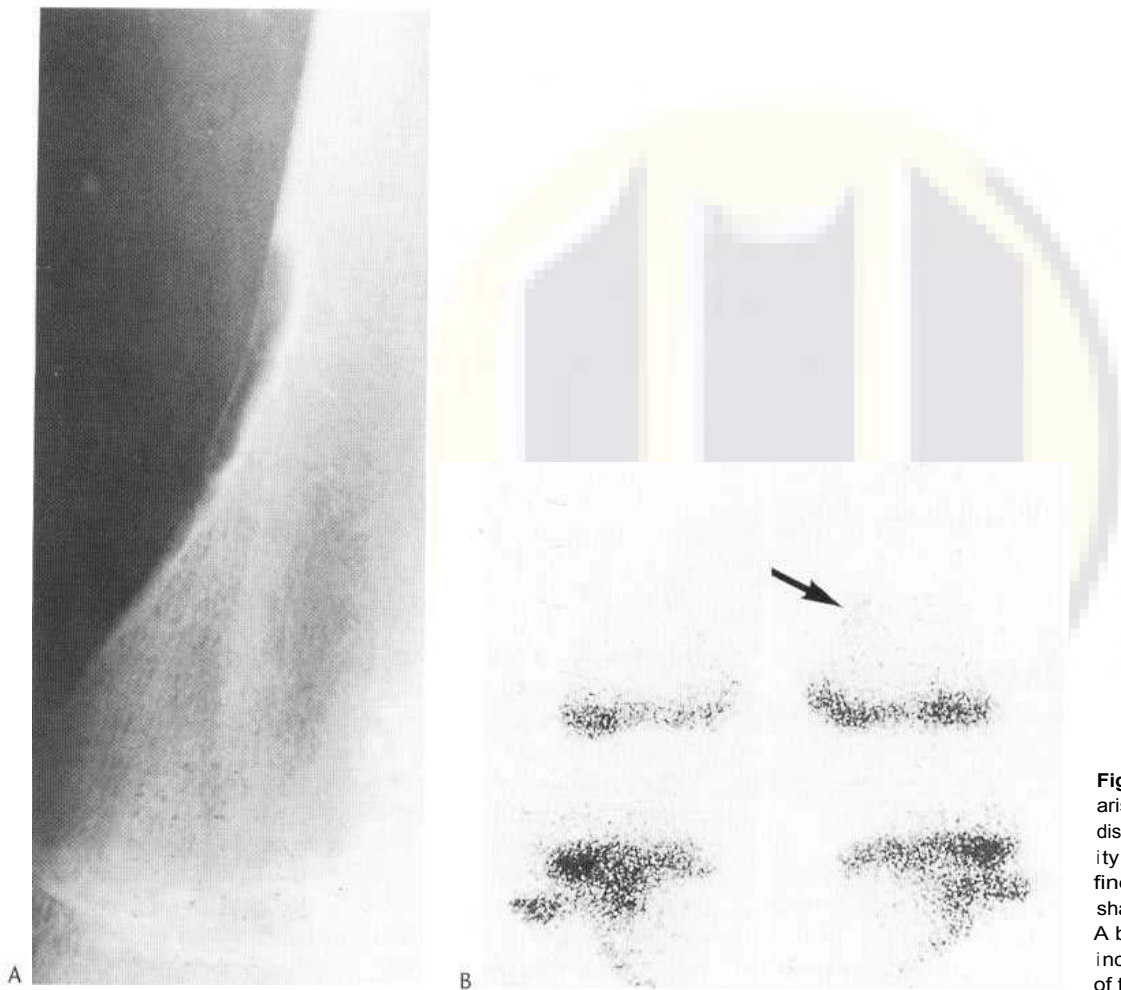


Fig. 40.1 Fibrous cortical defect arising in posteromedial aspect of the distal medial femur. (A) The abnormality is confined to the cortex with very fine shell of overlying bone and a sharply defined endosteal margin. (B) A bone scan demonstrates a slight increase in activity (arrow) at the site of the lesion.

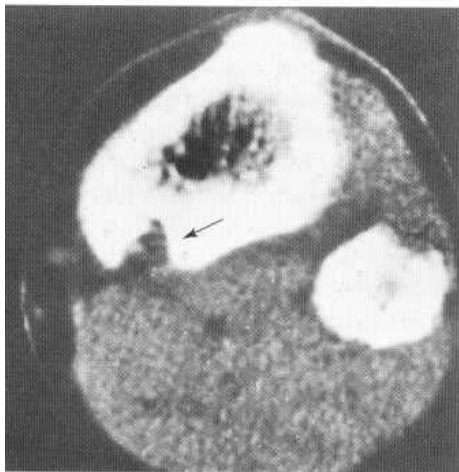


Fig. 40.2 Fibrous cortical defect in the upper medial tibia is shown on CT (arrow). Note the purely cortical position of the defect and its sharply defined margin. The thin shell of overlying bone is not seen completely because of the partial volume effect.

often with a trabeculated pattern. There may be a slight increase in density within the lesion, so that superficially it may resemble monostotic fibrous dysplasia. Slight irregularity of the margin may suggest an aneurysmal bone cyst when the lesion is purely osteolytic.

Multiple fibromatous tumours are present in *congenital multiple fibromatosis*, in which half the patients have associated bony abnormalities. This rare childhood condition demonstrates multiple,

rounded, corticated, cystic metaphyseal lesions, often with sharply defined sclerotic margins. These fibromatous foci tend to regress with increasing age and have an excellent prognosis. In *infantile myofibromatosis (congenital generalised fibromatosis)* similar multiple nodular fibroblastic lesions of the soft tissues, frequently associated with multiple lytic bone lesions, occur with disseminated involvement of muscle, heart and lungs; the outlook in this group is poor.

4. Fibrosarcoma

Although this is the least common of the malignant primary tumours arising in skeletal connective tissue, representing about 5% of all, individual lesions vary widely in their appearances and to this extent can create diagnostic difficulties. This variation corresponds to a wide range of histological characteristics, but the degree of malignancy and the radiological features correlate reasonably well. Many of the characteristics lie between those of osteosarcoma and chondrosarcoma.

Fibrosarcoma occurs most commonly in the third to sixth decades, with no sex difference. Presentation is usually due to low-grade pain, sometimes swelling, usually present for less than a year. In many, the precipitating factor may be a pathological fracture (Fig. 40.6). While a few of these tumours arise primarily in soft tissue and cause secondary bony changes, the majority develop primarily in bone and may be either medullary or periosteal in location. A medullary lesion is considerably more common and usually arises in the metaphyseal area. Approximately 80% occur around

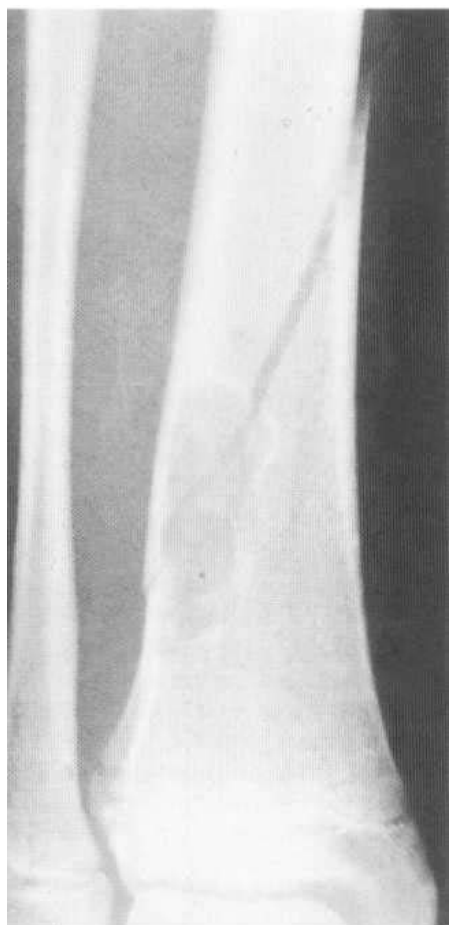


Fig. 40.3 Non-ossifying fibroma of the distal tibia presenting with a fracture. The well-defined outline and eccentric position of the tumour are demonstrated together with sharply defined sclerotic margins.



Fig. 40.5 Desmoplastic fibroma. A destructive, lobulated lesion is present in the distal metadiaphysis of the humerus. Bone expansion is present with sclerotic margins around the tumour. A soft-tissue component has caused consolidated periosteal new bone formation.

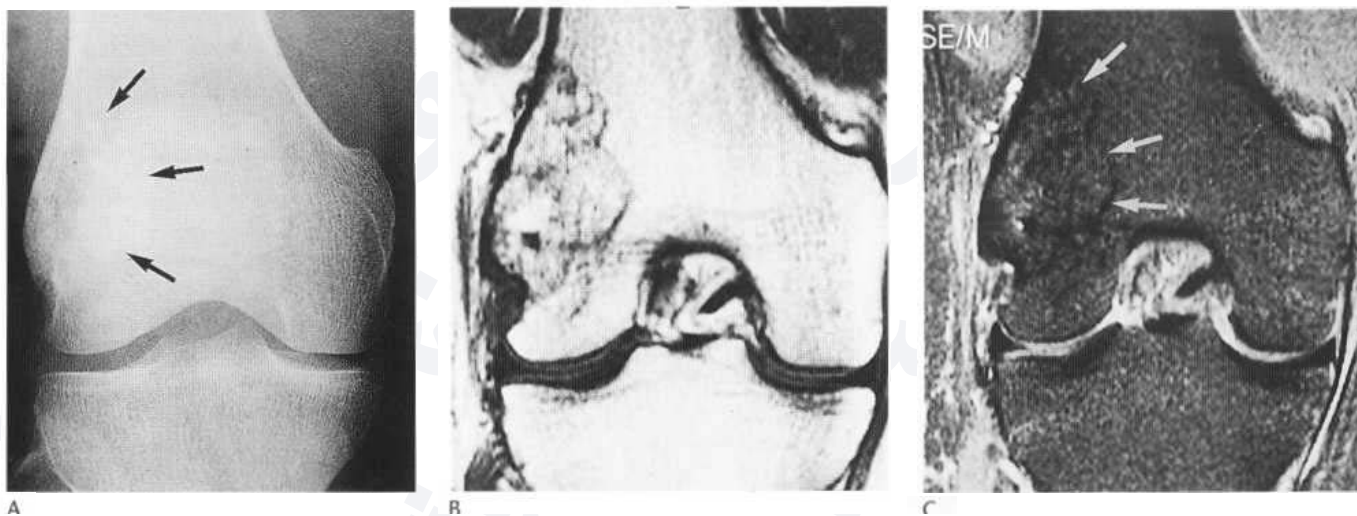


Fig. 40.4 Sclerosis of a non-ossifying fibroma. Incidental finding following multiple ligamentous injuries to the knee. (A) Conventional radiograph. Only a faint band of sclerosis is shown around the margins of the fibroma (arrows). Coronal T-weighted (B) and STIR (C) MR images showing mixed fibrous and normal marrow replacement (arrows) within the involuted lesion. Tears of the anterior cruciate and medial collateral ligaments are also evident.

the knee. It is less usual for a flat bone to be involved. The rarer periosteal type has a more widespread distribution, but still has a predilection for long bones, where any portion of the shaft may be affected. This type tends to develop a clinically palpable mass in the earlier stages.

Radiological features

The tumour is essentially osteolytic, provokes little new bone formation and usually lacks calcification or ossification. The medullary variety is characterised usually by an irregular area of radiolucency. The zone of transition may vary from being relatively narrow,



Fig. 40.6 Fibrosarcoma presenting with pathological fracture of the femur in a woman of 50. Ill-defined bone destruction, particularly of the medulla, is associated with very minor periosteal new bone formation and no sclerosis. The cortex has been thinned on the endosteal surface.

indicating a well-differentiated tumour, to being diffuse and permeative, suggesting a highly aggressive tumour (Fig. 40.7). With very low grade tumours a minimal degree of sclerosis may surround the radiolucency. Slowly growing tumours may thin and expand the cortex, but with a diffuse infiltrative pattern it is more usual for cortical destruction to occur. The subsequent soft-tissue extensions are without calcification or ossification, and periosteal new bone forma-

tion is unremarkable. This feature may differentiate the tumour from osteosarcoma or chondrosarcoma.

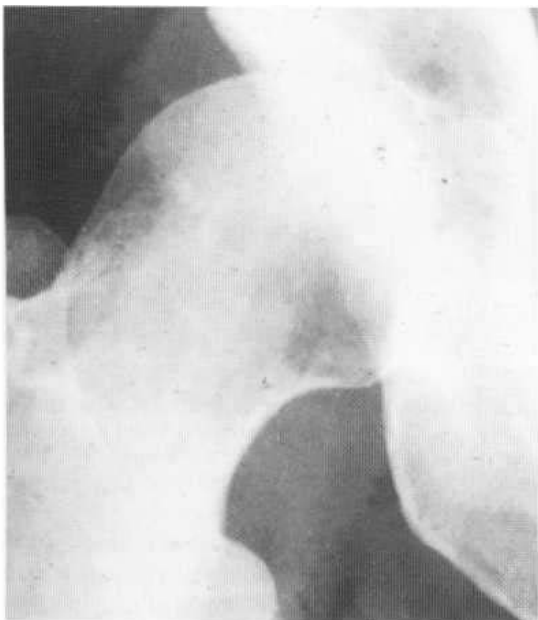
Periosteal tumours, however, frequently exhibit shaggy ill-defined periosteal new bone formation. Destruction of the outer side of the cortex frequently takes place, but the erosion is usually clearly defined, almost as though a piece of bone has been removed surgically. In this respect considerable variance is shown from the poor definition of the edge of most malignant tumours. Consequently the impression may be gained of a benign periosteal tumour, such as a lipoma. Secondary involvement of bone may result also from a fibrosarcoma arising in soft tissue.

As with the conventional radiographic appearances, angiography roughly mirrors the degree of malignancy of the tumour. CT and MRI will define the extent of the tumour and its relationship to neurovascular structures. The success of a bone scan is variable, as it depends on the degree of bone response and the amount of periosteal new bone formation. Metastatic dissemination from fibrosarcoma is not usually detectable with a bone-seeking agent.

Fibrosarcoma may also arise in the fibrous wall of a medullary infarct, following irradiation or secondary to chronic osteomyelitis, and is one of the histological patterns associated with Paget's sarcoma. To differentiate fibrosarcoma of bone from other malignancies is by no means straightforward. The major differential is from osteosarcoma and chondrosarcoma. Moreover, the more aggressive, ill-defined varieties may be indistinguishable from malignant round cell tumours, particularly non-Hodgkin's lymphoma.

5. Malignant fibrous histiocytoma

A group of tumours has been separated, mainly from fibrosarcomas, based on histological and clinical findings. These aggressive, often metastasising, tumours are probably of histiocytic origin. They occur in an older population, usually around 55 years of age, affected individuals complaining chiefly of pain, swelling or of a slowly enlarging mass. The majority develops in soft tissues. The relatively small number arising in bone has a predilection for the femur and the ends of the tibia and humerus; others arise in the pelvis and ribs.



A



B

Fig. 40.7 Fibrosarcoma arising in the medulla of the femoral head and neck. This 35-year-old man presented with poorly localised pain in the hip. (A) At presentation an ill-defined area of bone destruction on the medial aspect of the femoral head and neck. The cortex is preserved with no new bone formation. (B) Three months later a pathological fracture has occurred through the destructive lesion.

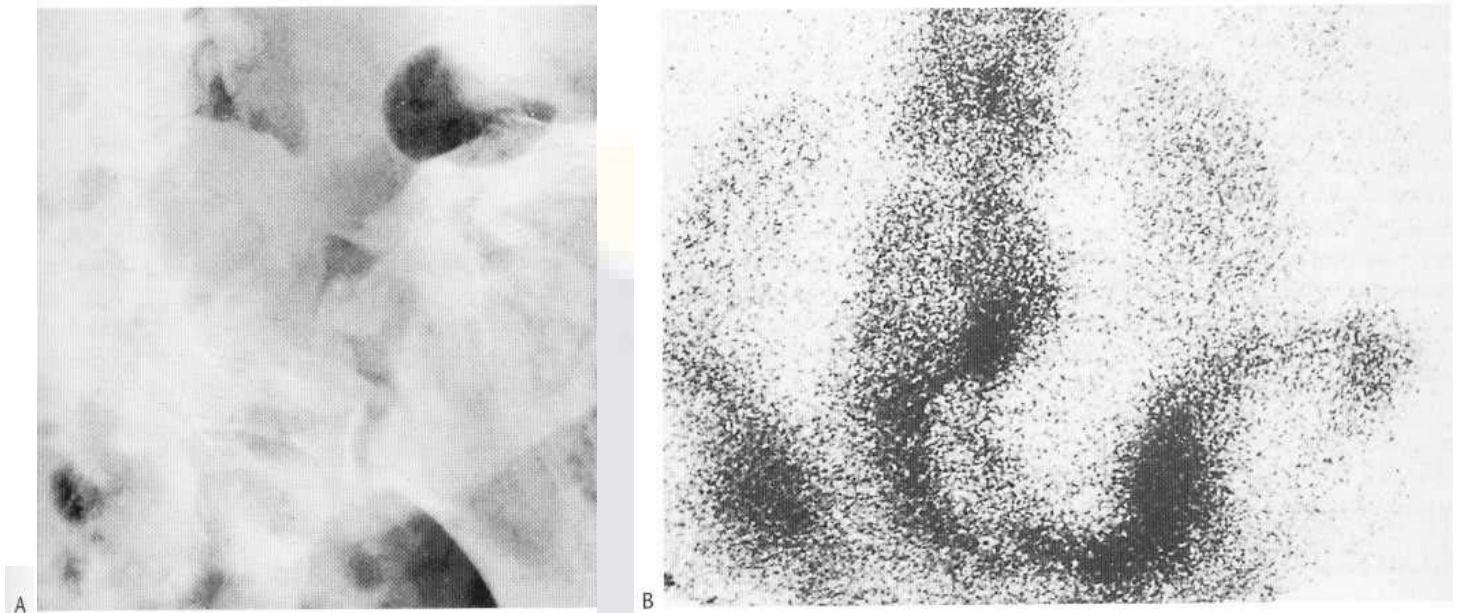


Fig. 40.8 Malignant fibrous histiocytoma arising in the sacral ala of a 60-year-old woman. (A) A purely destructive, lytic lesion is present with slight sclerosis around its margins. Note that the lower border of L5 has also been destroyed together with part of the iliac wing. (B) A radionuclide bone scan shows the tumour to be photon deficient but a rim of increased activity corresponds to reactive bone sclerosis.

The radiological features are primarily those of an ill-defined, purely osteolytic lesion with early cortical destruction, frequently in a permeative fashion, often with some expansion. To this extent, they resemble fibrosarcomas of an aggressive type. Occasionally punctate, soft-tissue calcification is present and a small proportion exhibit periosteal reaction and endosteal sclerosis (Fig. 40.8). A soft-tissue mass often develops early. Angiographically, areas of avascularity and hypervascularity are typical, including the demonstration of new vessels and encasement. Scintigraphy is not usually informative. Many cases present with multiple skeletal lesions and the initial impression is of skeletal metastases rather than of a primary or multifocal bone tumour. As with fibrosarcoma, malignant round cell tumours require consideration in the differential diagnosis.

6. Adamantinoma of long bone

This rather unusual neoplasm is almost invariably located in the tibial shaft. Clinically, localised pain and swelling have usually been present for several years. The age range varies from 15 to 55 years. On examination a soft-tissue, possibly cystic, swelling is palpated. Histologically, difficulty may arise in differentiating this lesion from metastatic adenocarcinoma or squamous cell carcinoma, since the glandular and fibrous component of the tumour may suggest an epithelial derivation.

Radiologically an eccentric area of destruction usually involves the anterior portion of the tibia shaft. Slight expansion and cortical thinning, with a cystic or multiloculated appearance, are usual (Fig. 40.9). Periosteal reaction is not marked, but cortical destruc-

Fig. 40.9 Adamantinoma of the tibia. Eccentric areas of bone destruction are present anteriorly with thinning of the cortex. The cortex is expanded. In addition to this abnormality, sclerosis and ill-defined cortical thickening are present throughout the whole of the tibia, which is also bowed. These features are due to associated fibrous dysplasia (or a close variety sometimes known as ossifying fibroma which occurs only at this site). (A) AP view. (B) Lateral view.



tion may be extensive. The margin of the tumour varies from being sharply and clearly defined, with a slight sclerotic margin, to a hazy zone of transition several millimetres in width, comparable to that observed in giant cell tumours. Some of these tumours may be 15 cm long or more, with satellite lesions.

Adamantinoma probably has a relationship to ossifying fibroma, which may be itself a localised form of fibrous dysplasia in which it has been observed to develop as a late complication. While the radiological appearances of adamantinoma are not pathognomonic, the location and the clinical history suggest the diagnosis. The tumour continues to grow at a slow rate, but is characterised by local recurrence and eventual metastasis to lung. Extensive local resection is the usual form of treatment.

BONE TUMOURS PRESUMED TO ARISE FROM SKELETAL TISSUE: GIANT CELL CONTAINING

A group of turnouts rich in giant cells, formerly confused in the literature, has now been subdivided, on histological and radiological grounds, into giant cell tumour ('osteoclastoma') and the giant cell tumour variants. The latter include chondroblastoma (see Ch 39), chondromyxoid fibroma (see Ch 39) and aneurysmal bone cyst (see below). However, all these variants exhibit some areas that are identical histologically. In consequence, while broadly clear-cut radiological and histological categorisation is possible, a definite overlap exists. The 'brown' tumours of hyperparathyroidism have also been included in this category as they may be indistinguishable histologically.

1. Giant cell tumour (osteoclastoma)

These tumours conform to a fairly constant clinical and radiological pattern. As with many other tumours, the initial presentation is of localised pain and swelling, some presenting following trauma or as an incidental finding. Histologically, richly vascular tissue contains plump spindle cells and numerous giant cells containing 50-100 nuclei. The tumour forms neither bone nor cartilage.

It is locally aggressive and likely in more than half of instances to recur in spite of extensive curettage or excision with or without radiotherapy.

A small proportion is allegedly malignant. Malignancy may be mistaken in those that are initially extremely aggressive and others that become so following surgical or therapeutic intervention. Sometimes confusion arises because the extreme aggressiveness of the tumour, histologically and radiologically, does not correlate with the subsequent development of distant metastases to the lung. A small group of undoubtedly malignant, metastatic giant cell tumours has been recognised, often with a dominant fibrosarcomatous stroma. Attempts at histological and radiological grading have had only limited prognostic value.

The majority of patients present between the ages of 20 and 40 years. Only about 3% of cases develop in immature skeletons, distinguishing these patients from those with aneurysmal bone cysts, in whom the tumour maximally occurs before epiphyseal fusion. Giant cell tumours are multifocal in about 0.5% of cases, often in the hands. The solitary lesion shows a predilection for bones adjacent to the knee joint and the distal end of the radius. Histological

review of a number of cases in which spinal lesions have been detected has indicated that the correct diagnosis is much more commonly an aneurysmal bone cyst. Facial bones appear to be exempt.

Radiological features

A zone of radiolucency is typically situated immediately beneath the articular cortex, sited eccentrically at the end of a long bone (Fig. 40.10). The exception to this rule is when the lesion arises in a former apophysis, notably the greater trochanter. Unless complicated by a fracture, the lesion does not contain calcification or ossification, although in about 40% of cases it is characterised by a 'soap-bubble' pattern of trabeculation. The margins are purely osteolytic; a sclerotic margin is rarely evident. Characteristically, therefore, the margin is hazy and ill defined with no bone reaction (Fig. 40.11).

Lesions that are more aggressive are associated with widening of the zone of transition. The overlying cortex may be expanded and exquisitely thinned, without the development of periosteal new bone formation, except as a response to a pathological fracture (Fig. 40.12). The tumour may produce a well-defined extension into the adjacent soft tissues, without evidence of calcification or new bone formation. The presence of such a soft-tissue mass does not, of necessity, indicate a sarcoma. This complication is inferred by a rapid change in size or character of the tumour on sequential radiographs.

Angiographically, and on the blood-pool phase of a bone scan, vascularity is markedly increased, typically with an increased number of vessels, arteriovenous shunting and tumour staining. Many exhibit encasement. These features do not correlate with either clinical aggressiveness or sarcomatous change and may be extremely difficult to distinguish from those observed in other giant cell-containing



Fig. 40.10 Giant cell tumour arising in the distal radius of an adult man. A characteristic, eccentric, immediately subarticular position makes this diagnosis very probable. The margins are ill defined with no sclerotic reaction.



Fig. 40.11 Giant cell tumour of the patella. Giant cell tumours can arise in almost any bone but those around the knee are particularly affected. Note the immediately subarticular, eccentric position of the tumour which is purely osteolytic with no sclerotic reaction. The epiphyses have fused.

tumours, particularly aneurysmal bone cysts. The delayed phase of a bone scan is usually normal. CT or MRI (Fig. 40.13) may be necessary to delineate fully the soft-tissue extent of the tumour.

Many of the rather more aggressive giant cell-containing tumours in the younger age group may in fact be giant cell-rich osteosarcomas (Fig. 40.14). It is possible that some of the reported metastasising malignant giant cell tumours may be of this type. Usually, however, little difficulty arises in differential diagnosis, the eccentric, purely lytic and subarticular location of the tumour being characteristic. Differential diagnosis includes aneurysmal bone cysts and chondroblastoma. The 'brown' tumours of hyperparathyroidism and monostotic fibrous dysplasia require consideration (Fig. 40.15). Occasionally an intraosseous ganglion or large subarticular geode may cause confusion (Fig. 40.16).

In spite of apparently successful curettage and packing with bone chips, these tumours have a tendency to recur, even years after initial treatment. Intraosseous recurrence results in osteolysis adjacent to the previous surgery. Occasionally soft-tissue deposits implanted at the time of surgery will appear as enlarging ossified masses. Secondary sarcomatous change may also occur following radiotherapy after intervals of several years. On rare occasions the tumour may cross a joint or extend from one bone to another.

2. Aneurysmal bone cyst

The exact aetiology of this tumour is unknown, but the descriptive name is derived from the macroscopic appearances of a blood-filled, expansile, sponge-like tumour containing numerous giant cells. Aneurysmal bone cyst has been shown to arise in association with other abnormalities of the skeleton, particularly non-ossifying fibroma, fibrous dysplasia and chondromyxoid fibroma. Such lesions



Fig. 40.12 Giant cell tumour of the distal femur. AP (A) and lateral (B) radiographs showing a large immediately subarticular osteolytic lesion with apparent trabeculation and a wide zone of transition proximally. A localised area of cortical expansion is demonstrated posteriorly with a thin overlying shell of bone. (C, D) CT sections through the lesion demonstrating the localised dorsal expansion and intact overlying cortex. The apparent trabeculation demonstrated on the conventional radiographs is shown to be due to unresorbed ridges of cortical or trabecular bone at the margins of the lesion.

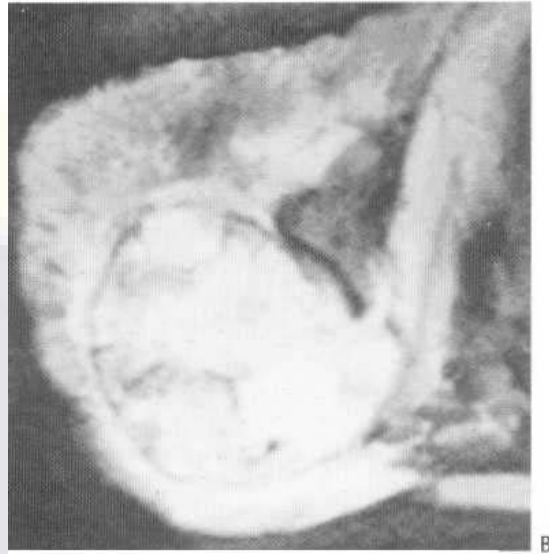
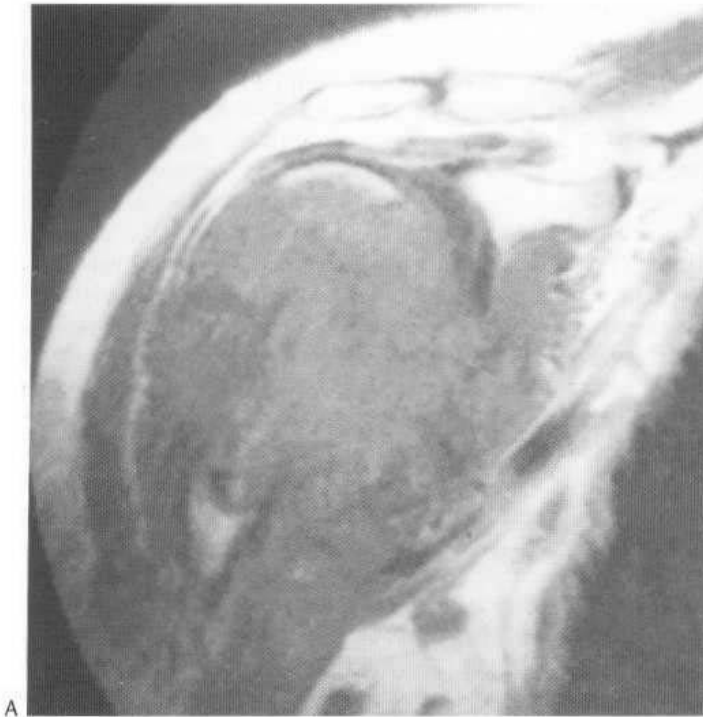


Fig. 40.13 A giant cell tumour of humerus. Coronal T₁-weighted (A) and axial STIR (B) sequences demonstrate a large lobulated mass in the humeral head and neck replacing all normal bone structures. Note the close approximation to the articular surface and the displaced axillary vessels.



Fig. 40.14 Giant cell-rich osteosarcoma. (A) A radiograph of this boy at presentation demonstrates an eccentric, purely osteolytic lesion in the upper tibial metaphysis. The cortex has been breached but there is no periosteal new bone and only very faint surrounding sclerosis. (B) Six months later, following curettage and packing with bone chips, the flagrantly aggressive nature of this tumour is obvious. Note now the Codman's triangle on the lateral aspect of the tibial shaft and a substantial soft-tissue mass that contains ossification.

B

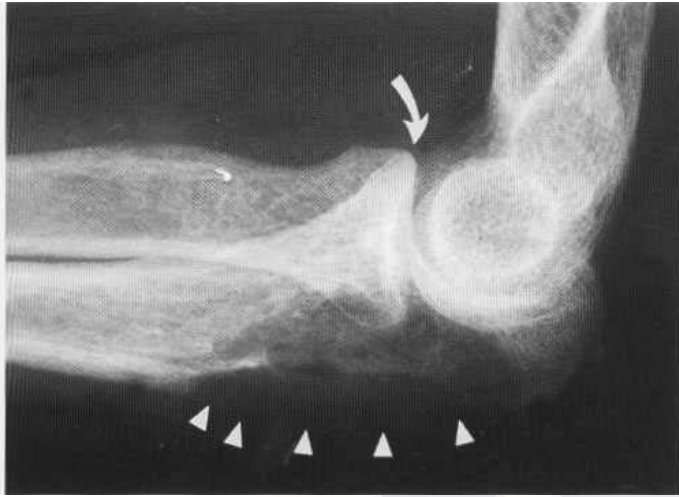


Fig. 40.15 Brown tumour of hyperparathyroidism simulating the appearance of a giant cell tumour. An osteolytic lesion in the proximal ulna is shown extending to the immediate subarticular region. The margins are poorly defined and there is marked thinning and expansion of the dorsal cortex (arrowheads). A clue to the correct diagnosis, however, is provided by the subtle chondrocalcinosis of the articular surface radial head (curved arrow).

have been described as 'secondary' aneurysmal bone cysts. They have also been recorded following a fracture.

These tumours present in childhood or early adolescent life, with a predilection for the long bones and the lumbar spine. Those arising in the spine occur slightly later, between 10 and 20 years of age. The neural arch is more commonly involved than the body (Fig. 40.17), half of these cases involving more than one vertebra. The prognosis is entirely benign apart from secondary neurological lesions due to spinal canal compression.

Radiological features

Typically an area of bone resorption occurs with slight or marked expansion (Fig. 40.18), the size of the lesion varying between 2 cm and, in gross examples, as much as 20 cm in diameter. The overlying cortex is thinned and may be expanded (Fig. 40.19) to such a degree that in places it can be identified only by tomography or CT. The endosteal margin is relatively well defined against cortex, and an ill-defined zone of transition is usual between the lesion and medullary bone, occasionally with slight sclerosis. A margin of this type is similar to that observed in giant cell tumour. Sometimes it is scalloped or irregular. Angiographically many features are common to giant cell tumour, in particular a rich increase in vessels with diffuse opacification and early venous filling. This appearance may be shown in the blood-pool phase of a bone scan. Both CT and MRI may show fluid levels in the vascular spaces (Fig. 40.20).

Most lesions evolve slowly. However a few show a highly aggressive radiological pattern and may increase alarmingly in size, even doubling in a few weeks. The possibility of a very malignant vascular tumour such as an angiosarcoma may then be entertained.

Differentiation from giant cell tumour is aided by the age of the patient, as three-quarters of aneurysmal bone cysts occur before epiphyseal fusion has occurred, and their widespread anatomical distribution contrasts with the majority of giant cell tumours occurring around the knee and wrist. Therefore, difficulty is likely to arise only when the abnormality occurs after epiphyseal closure or when it is situated at the end of a long bone. Aneurysmal bone cyst rarely extends to the articular surface and is often central, compared to the subarticular eccentric nature of giant cell tumour. The spinal lesions need to be differentiated from osteoblastoma and osteoid osteoma. The bone-forming nature of these latter two tumours, together with their associated sclerotic reactions, provides valuable differential diagnostic signs.

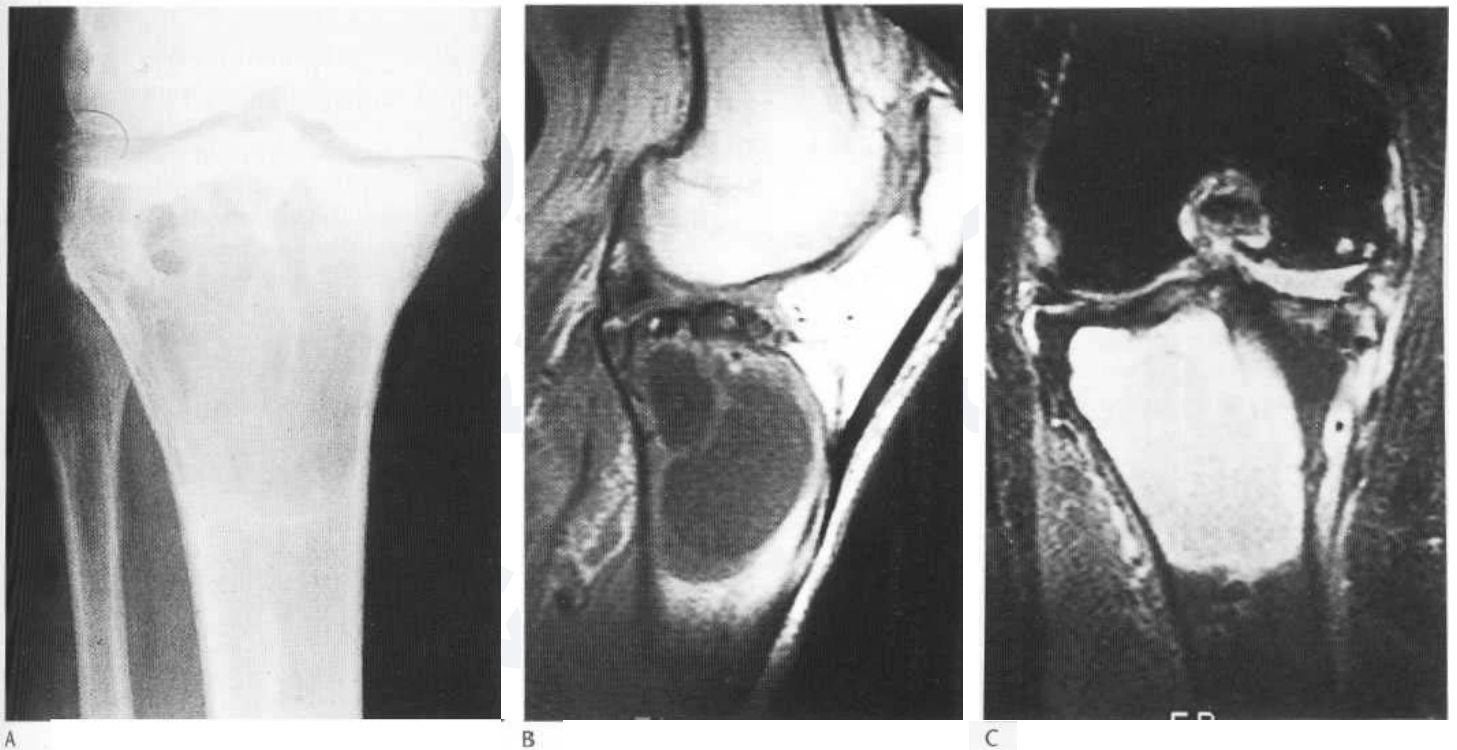


Fig. 40.16 Large subarticular geode mimicking a giant cell tumour. (A) Conventional AP radiograph showing a large subarticular osteolucency with well-defined distal margins in the proximal tibia. Prominent medial compartment osteoarthritis is shown. Sagittal T₁-weighted (B) and coronal STIR (C) MR images showing the multiloculated cystic nature of the tibial geode and the well-marked knee joint osteoarthritis.



Fig. 40.17 Aneurysmal bone cyst arising from lamina and internal mass of C6 resulting in a unilateral dislocation of the facet joints in a 10 year old girl. Some extension into the adjacent vertebra of C7 is evident.

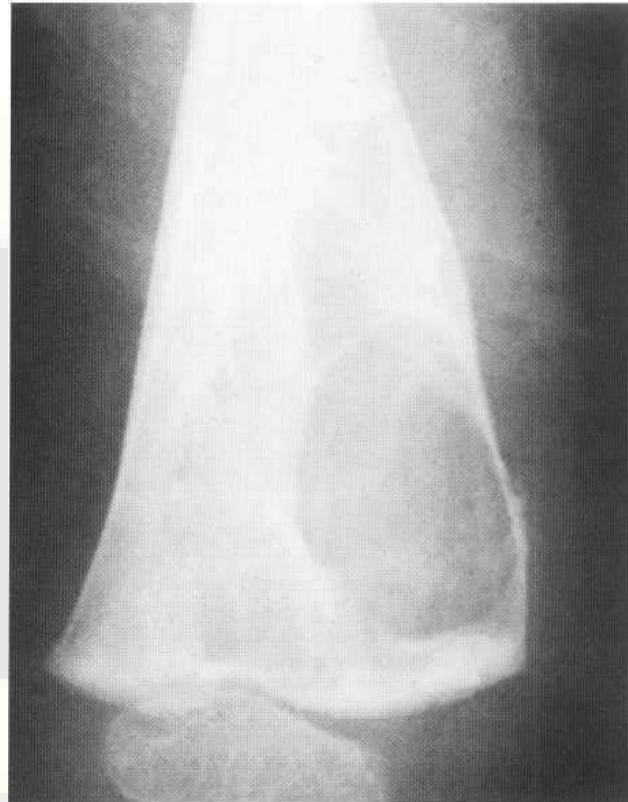


Fig. 40.18 Aneurysmal bone cyst (boy aged two). This film was taken because of an asymptomatic swelling and shows the characteristic features of metaphyseal involvement, cortical expansion and thinning, with a relatively well defined endosteal margin.

logical deficits may occur secondary to the collapse of an involved vertebral body with or without an extraosseous soft-tissue tumour component. The age of presentation is between 10 and 45 years. /

Haemangiomas are either cavernous, with large thin-walled vessels occurring particularly in vertebrae and the skull, or capillary, tending to spread in a sunburst pattern. Typically, the tumour is solitary, the commonest site being a thoracic or lumbar vertebral body.

Radiologically, conventional radiographs show increased translucency with a characteristic fine vertical striation (Fig. 40.22). Half the lesions involve purely the vertebral body, the other half extending into the posterior elements. A small proportion has an associated soft-tissue mass (Fig. 40.23). The overall size of the vertebral body is often within normal limits, a helpful differential feature from Paget's disease.

The remainder of the skeleton is affected in approximately half of cases, with the skull and long bones being sites of predilection, although other areas may uncommonly be involved (Figs 40.24, 40.25). Although these tumours may present a striated appearance in long bones and ribs, as in the vertebral lesions, the radiological changes in these other areas are usually very different, tending to be osteolytic with sclerotic margins and often causing some cortical expansion. The osteolytic component has a soap-bubble appearance within which a sunburst or stippled radiodensity may be evident, possibly extending into the soft tissues with radiating spicules of bone. This pattern may be encountered with a capillary haemangioma, particularly in the skull and pelvis (Fig. 40.26). In some cases localised cortical thickening, from which peripheral bone spicules may extend, simulates an osteosarcoma. However, scrutiny and appropriate further investigation resolves any difficulty.

Aneurysmal bone cysts are treated by curettage or radiotherapy, the latter being particularly valuable in spinal lesions where surgery may be considered hazardous. An increasing role, however, has developed for transcatheter embolisation in the management of these tumours. Aneurysmal bone cyst is a particularly good example of the importance of radiological investigation being complete before biopsy is undertaken, because these lesions, not surprisingly, bleed considerably and the preoperative demonstration of the vascular nature of this tumour may save some embarrassment!

TUMOURS PRESUMED TO ARISE FROM OTHER TISSUES IN BONE: BLOOD VESSELS

1. Haemangioma

Intraosseous haemangiomas are benign and slow growing. Malignancy is virtually unknown. Many of these benign vascular neoplasms are asymptomatic, their presence being detected incidentally.

They are not infrequently shown on MR studies of the spine, particularly lumbar (Fig. 40.21). The autopsy incidence is about 10%. A few cause swelling and mild pain. Occasionally, significant neuro-

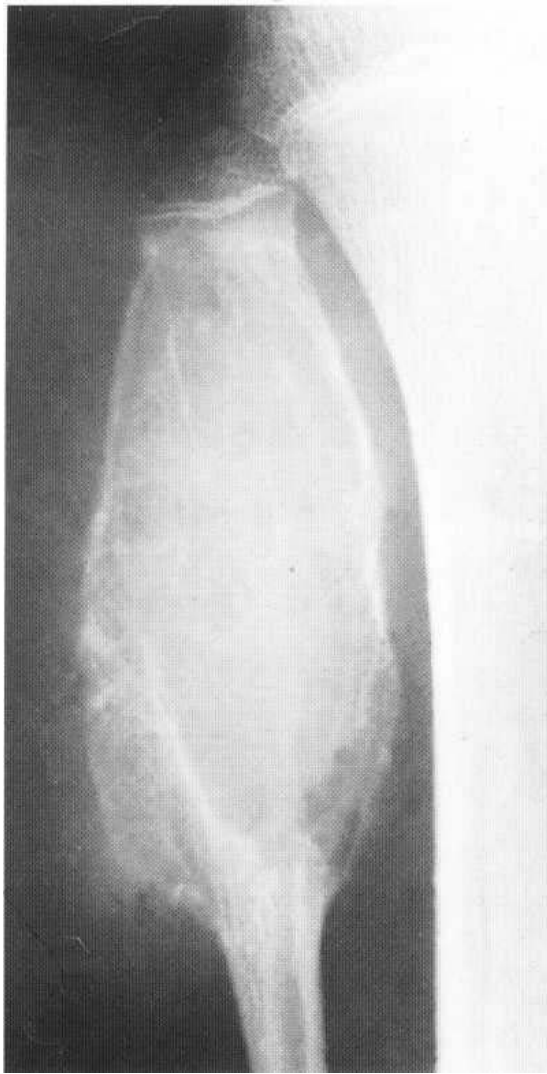


Fig. 40.19 Aneurysmal bone cyst of the proximal fibula. Considerably greater expansion has occurred in this example. The cortex is now very thin though apparently intact. The zone of transition between the lesion and adjacent bone is narrow but ill defined. Note apparent multiple septa within the lesion.

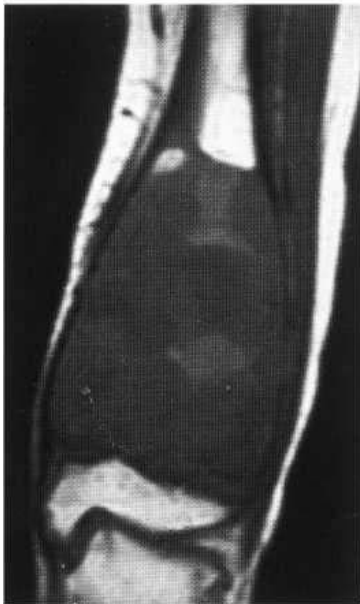


A

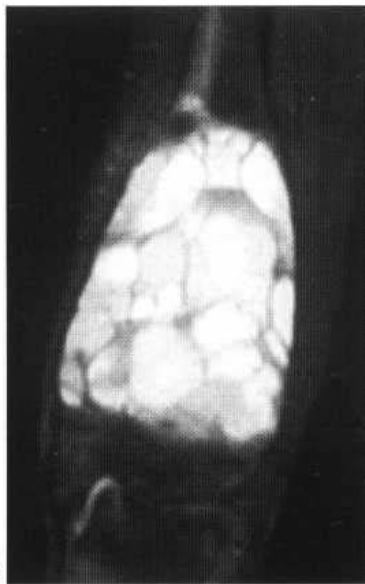


B

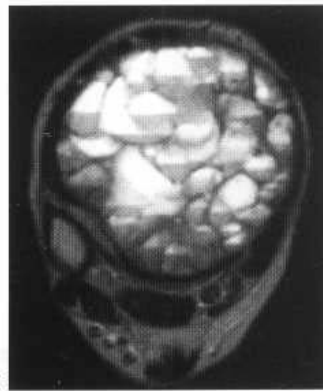
Fig 40.21 Vertebral haemangioma showing characteristic high signal intensity due to the associated fatty matrix on both the T₁-weighted (A) and T₂-weighted (B) images of the upper lumbar spine. The circular nature and speckled low-signal areas within the lesion are typical features.



A



B



C

Fig 40.20 Aneurysmal bone cyst of the distal tibia. (A) Coronal T₁-weighted image showing an expansile lesion of the distal metaphysis containing heterogeneous areas of low signal intensity. (B) Coronal T₂ multiloculated high-signal-intensity expansile lesion of the metaphysis. (C) Axial T₂ levels are demonstrated in the vascular spaces.

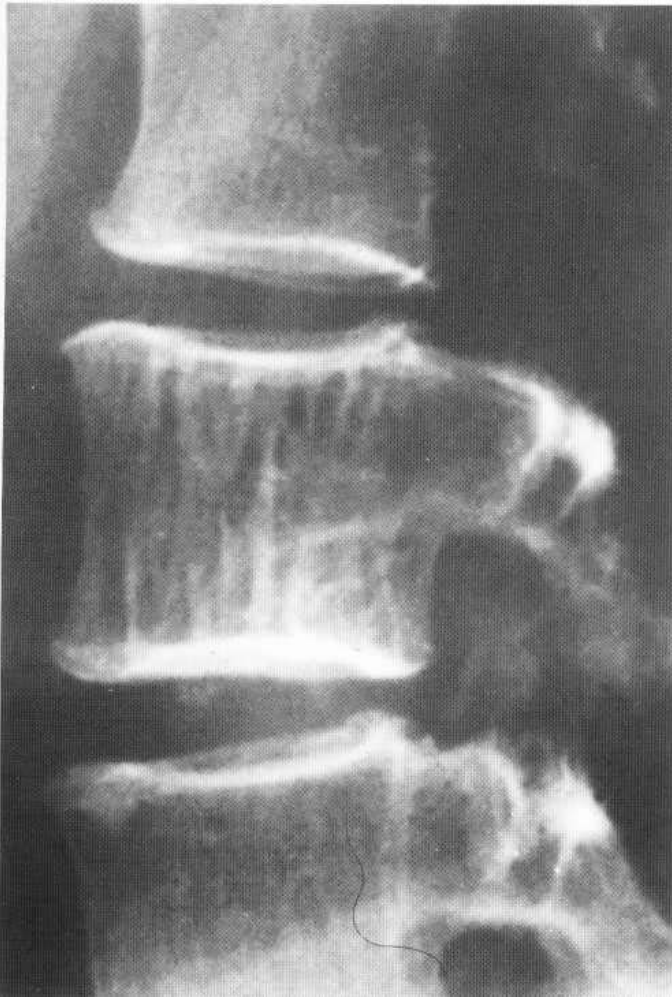


Fig. 40.22 Haemangioma of the vertebral body of L3. The whole body is marked by the characteristic vertical striation, which in this example does not extend into the pedicles.



Fig 40.23 Axial T_2 -weighted image through the lumbar spine showing a vertebral haemangioma with a substantial extraosseous component. This results in considerable compromise to the thecal sac and widening of the right neural foramen.

Soft-tissue cavernous haemangiomas may be recognised by well-defined circular calcifications due to phleboliths (Fig. 40.27). This is one component of Maffucci's syndrome, the other being multiple chondromas (see Fig. 39.46).

Scintigraphically, the bone lesion shows increased activity on the delayed phase of a bone scan (Fig. 40.28). Both bone and soft-tissue lesions may be detected by a blood-pool scan (Fig. 40.29). The appearance of increased activity in a vertebral tumour cannot therefore be used to distinguish between Pallet's disease, a sclerotic metastasis or a haemangioma. MRI will demonstrate any soft-tissue mass arising from a vertebral lesion. If surgical excision or transcatheter embolisation is required, it may be important to demonstrate the artery of Adamkiewicz with spinal arteriography to avoid paraplegia. Some lesions respond well to radiotherapy, particularly those in vertebrae.

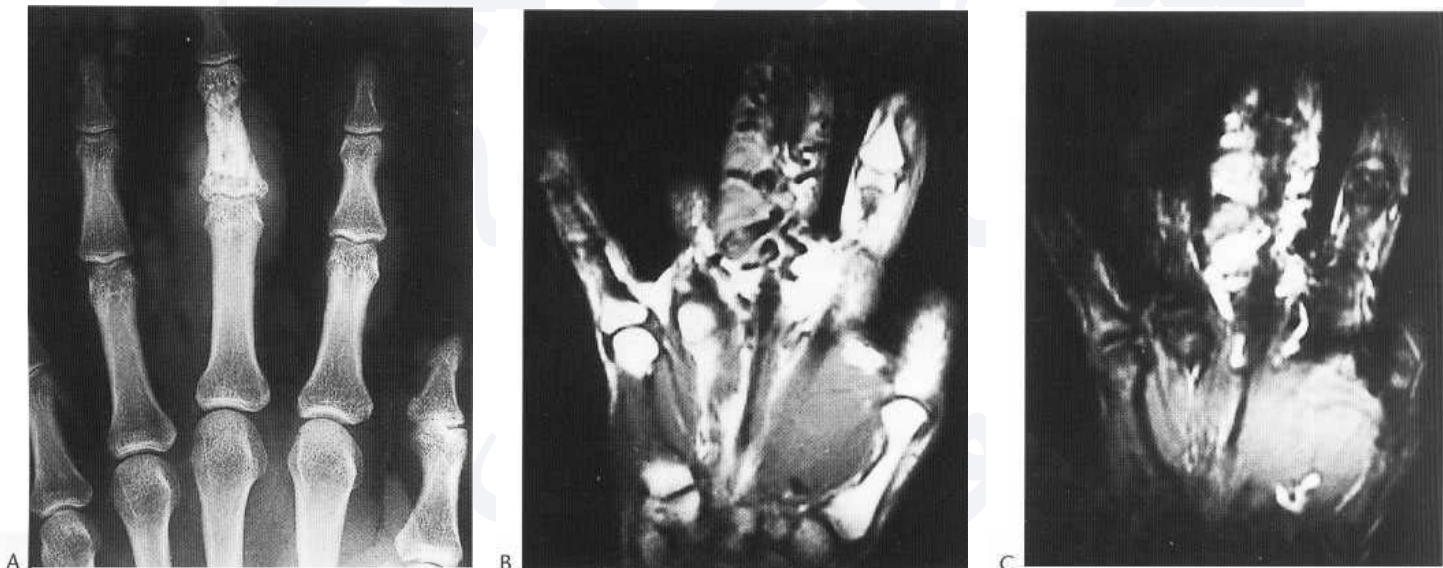


Fig. 40.24 Haemangioma of the middle finger middle phalanx with associated prominent soft-tissue component. (A) Conventional radiograph showing sclerotic striated phalanx of the middle finger and soft-tissue swelling. Coronal T_1 -weighted (B) and gradient-echo (C) MR images showing the extensive soft-tissue component of the cavernous haemangioma. The dilated abnormal vessels and vascular spaces appear as characteristic low-signal serpiginous channels on the T_1 -weighted sequence but have a high signal intensity on the gradient-echo image.

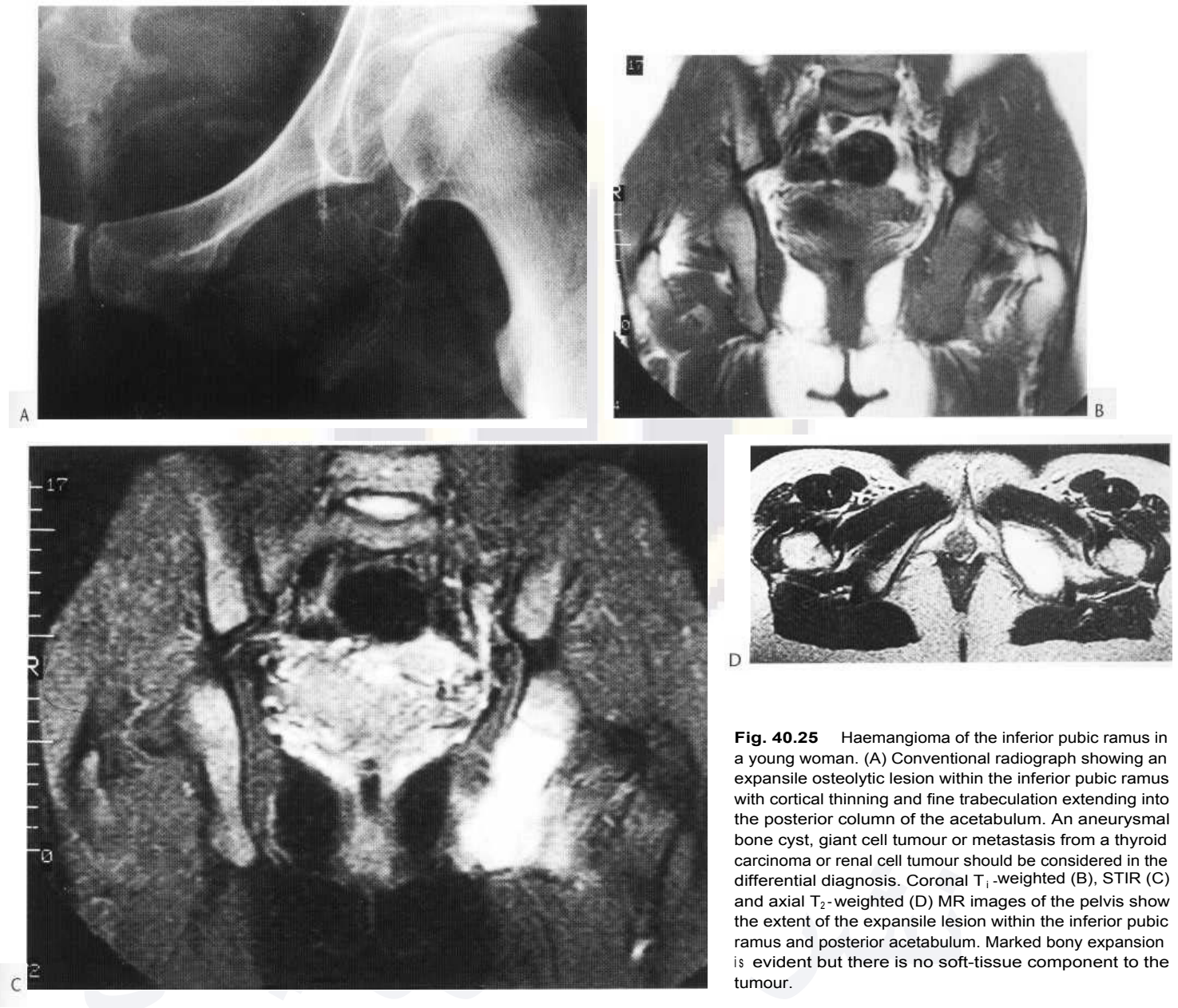


Fig. 40.25 Haemangioma of the inferior pubic ramus in a young woman. (A) Conventional radiograph showing an expansile osteolytic lesion within the inferior pubic ramus with cortical thinning and fine trabeculation extending into the posterior column of the acetabulum. An aneurysmal bone cyst, giant cell tumour or metastasis from a thyroid carcinoma or renal cell tumour should be considered in the differential diagnosis. Coronal T_1 -weighted (B), STIR (C) and axial T_2 -weighted (D) MR images of the pelvis show the extent of the expansile lesion within the inferior pubic ramus and posterior acetabulum. Marked bony expansion is evident but there is no soft-tissue component to the tumour.

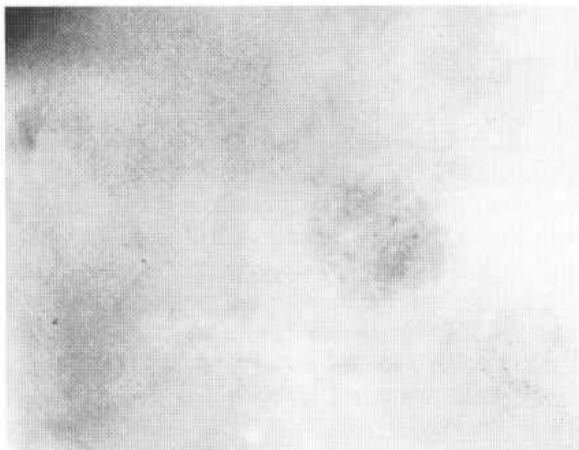


Fig. 40.26 Haemangioma of the skull is shown on a localised view of the temporal fossa. Note the purely osteolytic lesion with stippled radiodensities.

2. Vanishing bone disease (Gorham's disease)

This relatively rare syndrome is a variant of angiomas of bone in which vascular proliferation predominates. Its origin is unknown. It is recognised usually in childhood, but more than one-third of patients is over the age of 35. Progressive weakness and limitation of movement of the affected area characterise the onset. Pain is not an early feature, although obviously occurring with a pathological fracture. After a period of months or years the limb becomes useless or flail. The course is unpredictable, either stabilising or progressing fatally with the development of chylothorax.

Radiologically an ill-defined area of radiolucency may be observed in a single bone, but this destructive process progresses slowly to involve adjacent bones without respect for intervening joints (Fig. 40.30). Symptoms, however, may be so insidious that extensive absorption of many adjacent bony structures may be revealed at the initial examination. Arteriography and lymphography have shown no connection of these lesions to either the vascular or lymphatic circulations.

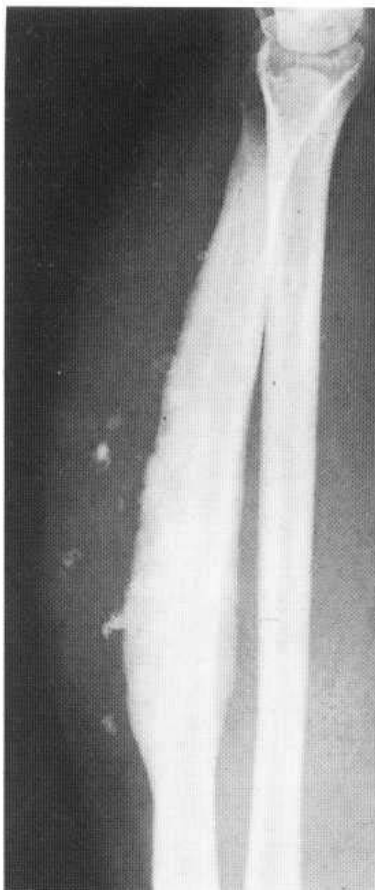


Fig. 40.27 Cavernous haemangioma of the soft tissues of the forearm is diagnosed by the presence of soft-tissue swelling within which there are phleboliths. The presence of extensive consolidated periosteal new bone and bowing of the ulna suggest an intimate relationship with the periosteum.

The radiological appearance is consequently that of a diffuse increase in translucency with progressive absorption of the affected structures. In the course of the process, deformity is likely to develop and may be crippling. Although local recurrence is a major hazard, slow progression is the rule.

Similar massive osteolysis may occur with tumorous masses of lymphatic origin (*lymphangiomas*). Histological differentiation of the cavernous spaces that are found may be difficult and the radiological features are virtually identical.

3. Cystic angiomatosis of bone

This rare entity is probably due to a hamartomatous malformation of primitive vessels. It may be difficult to distinguish the tissue of origin. Some lesions are clearly related to blood vessels, others to lymphatics. Among numerous synonyms, cystic angiomatosis is the most descriptive.

The condition may be recognised in childhood or adolescence in the virtual absence of symptoms, other than mild bony swellings or, occasionally, a pathological fracture. The diagnostic radiological abnormalities may be discovered incidentally. Broadly, two groups of patients are affected, those with and those without visceral and/or cutaneous involvement. The former has multiple angiomatous lesions in abdominal viscera, brain, muscle, lungs and lymph nodes, and although these lesions are histologically innocent, death may be caused from anaemia or bleeding. The prognosis in the latter group is excellent.

Radiologically, multiple sharply defined radiolucent lesions surrounded by a narrow sclerotic margin involve both cortex and medulla (Fig. 40.31). An initial impression of myeloma may be

given. The skull, flat bones and proximal ends of long bones are affected particularly. Scintigraphically, activity may be increased around the lesions. Angiography is usually normal, but in those cases that have differentiated more closely along lymphatic lines a connection with deep lymphatics may be demonstrated by lymphography.

4. Glomus tumour

This rare, highly differentiated, benign vascular tumour affects soft tissues more than bone. It creates, however, pressure erosion, usually of a terminal phalanx, particularly the subungual portion (Fig. 40.32). A few lesions may originally arise in bone. Typically, an extremely sharp margin is associated with a well-marked sclerotic rim.

Clinically the tumours are exquisitely tender and have many episodes of stabbing pain, particularly with the rarer and less differentiated haemangiopericytoma. Angiographically, the lesion is richly vascular, and so may be detected on a blood-pool scan or on the early phase of a bone scan. The classic triad of pain, tenderness and sensitivity to cold usually establishes the correct clinical diagnosis with little difficulty.

5. Angiosarcoma (haemangioendothelial sarcoma)

Primary malignant vascular tumours in bone are rare. None has been observed to arise from a benign precursor.

Radiologically the lesions are purely lytic and rapidly fatal, with metastatic spread to the lungs often being present at the time the diagnosis is made. The destructive areas have irregular endosteal margins with slight expansion or coarse loculation occasionally giving a rather soap-bubble appearance. Distinction of this lesion from a highly vascular (telangiectatic) osteosarcoma may be very difficult. A clue may be derived from the sometimes multifocal nature of angiosarcoma, occurring in about one-third of cases.

TUMOURS PRESUMED TO ARISE FROM OTHER TISSUES IN BONE: NERVE TISSUE

1. Neurofibroma and neurilemmoma

There is no clear distinction between these two tumours. It is thought that neurilemmoma or schwannoma arises from a specific cell, the Schwann cell, whereas neurofibromas come from non-specific cells in nerve sheath. The essential difference is that a schwannoma is eccentric in relation to the nerve with which it is associated, whereas a neurofibroma is an expansile mass through which the nerve passes. When these lesions enlarge in intimate relation to bone, the latter undergoes pressure erosion resulting in an osseous defect. Radiological differentiation between such lesions is not possible. However there is some histological importance, as neurilemmomas are usually solitary and never undergo malignant change, whereas neurofibromas are often multiple and may become sarcomatous. Tumours arise at any age, and in either sex, usually giving rise to symptoms only as the result of nerve pressure or occasionally pathological fracture. Nerve pressure arises typically when the tumour is located within an osseous canal. Neurilemmomas have a predilection for the mandible whereas neurofibromas are more closely related to the spinal canal.

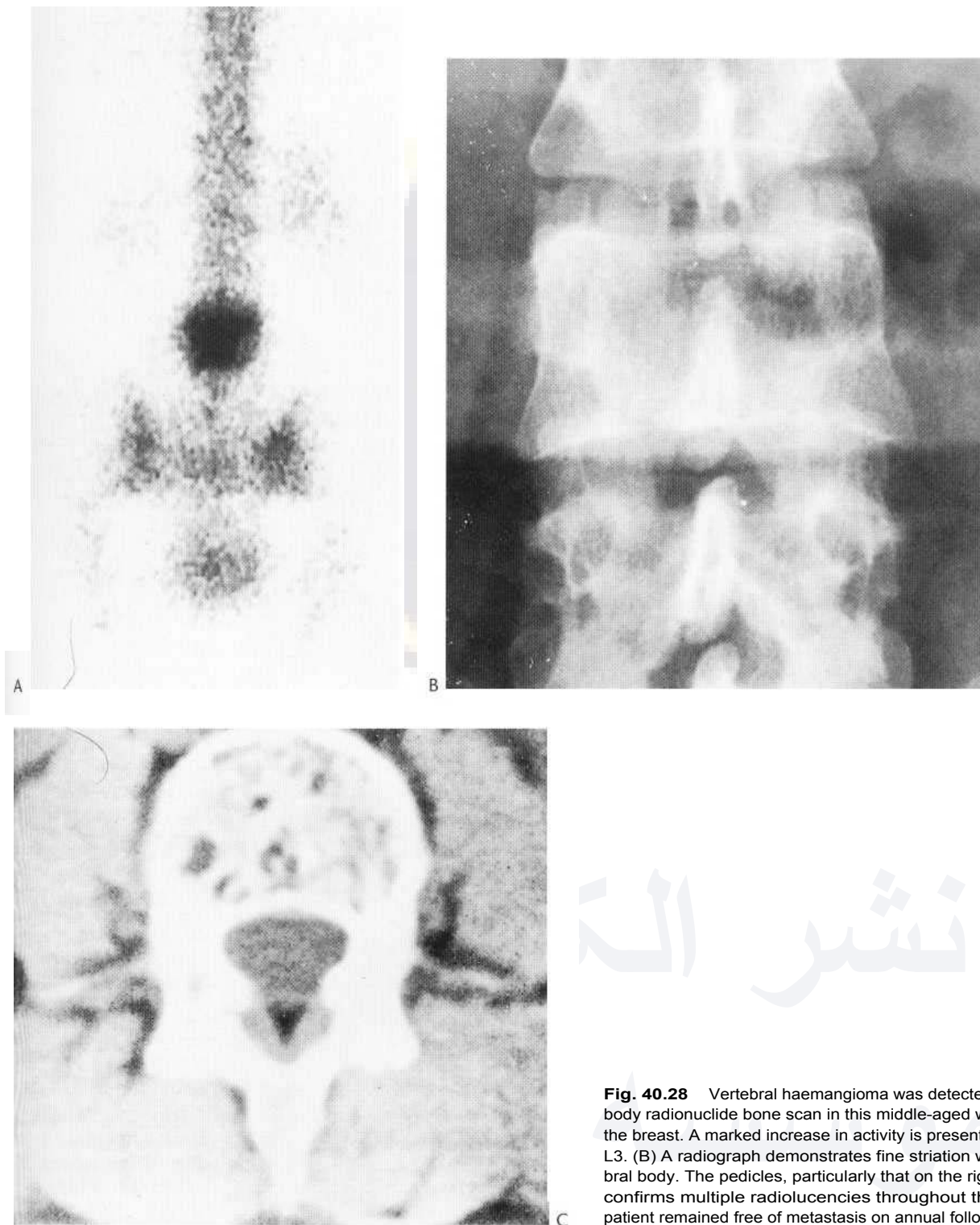


Fig. 40.28 Vertebral haemangioma was detected initially (A) on a whole-body radionuclide bone scan in this middle-aged woman with carcinoma of the breast. A marked increase in activity is present throughout the whole of L3. (B) A radiograph demonstrates fine striation within an enlarged vertebral body. The pedicles, particularly that on the right, are enlarged. (C) CT confirms multiple radiolucencies throughout the vertebral body. This patient remained free of metastasis on annual follow-up for 5 years.

Radiological features

The presence of a benign lesion within the spinal canal may be evident from erosion of a pedicle or widening of an exit foramen (Figs 40.33, 40.34). The width of the interpedicular distance may also be increased. A soft-tissue mass projecting through the enlarged foramen is typical of the so-called *dumb-bell tumour*. Discrete pressure erosions on the surface of bone may be observed elsewhere in the skeleton (Fig. 40.35), but as these tumours are able to grow away from bone they are usually not symptomatic. Neurofibromas cause notches at the inferior surface of ribs but should

not be confused with those in coarctation of the aorta because they vary both in size and in distribution, not principally affecting the fourth to eighth ribs. All erosive lesions are rounded and clearly defined with a discrete sclerotic margin. CT or MRI, however, may be necessary to demonstrate that they have predominantly a soft tissue origin.

On MRI neurofibromas have intermediate signal intensity on T₁-weighted images, and very high signal intensity on T₂-weighted images and following gadolinium enhancement. Sometimes areas of lower signal intensity centrally may be seen due to the presence

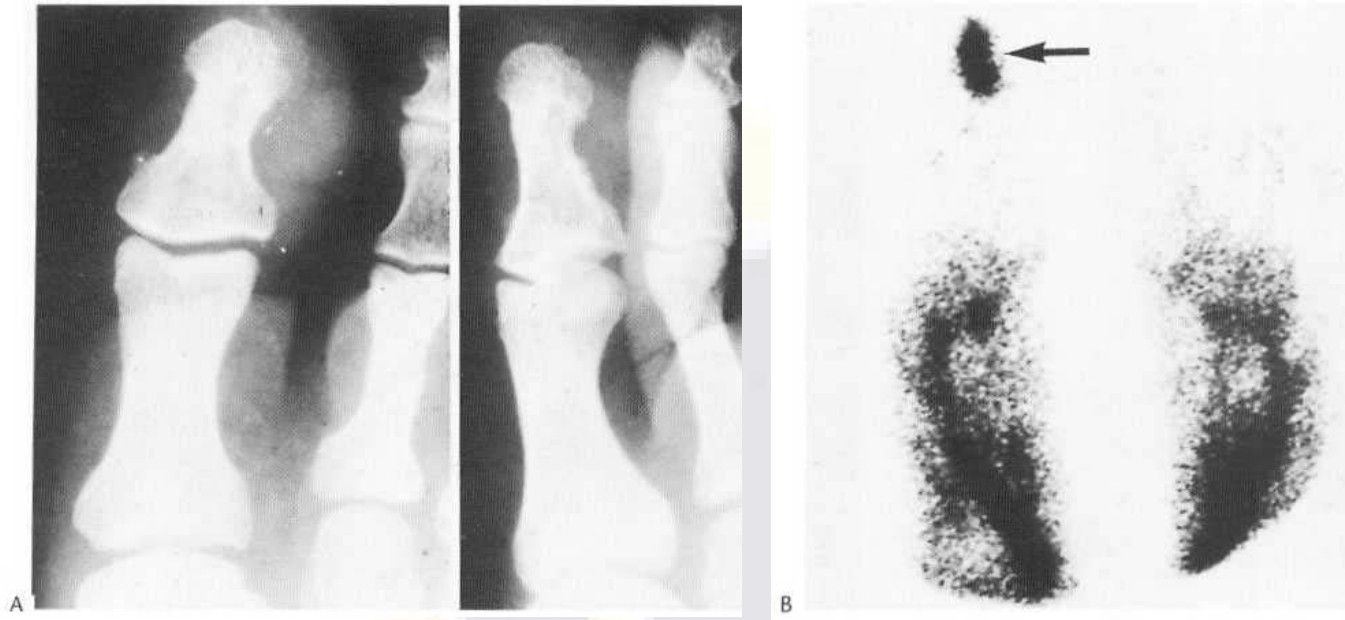


Fig. 40.29 Soft-tissue haemangioma of the great toe. This patient complained of a swollen great toe with a purple area of discoloration. (A) A plain film reveals soft-tissue swelling and pressure erosion of the plantar aspect of the distal phalanx. (B) A blood-pool scan confirms an intense focus of activity (arrow) corresponding to the cavernous haemangioma.

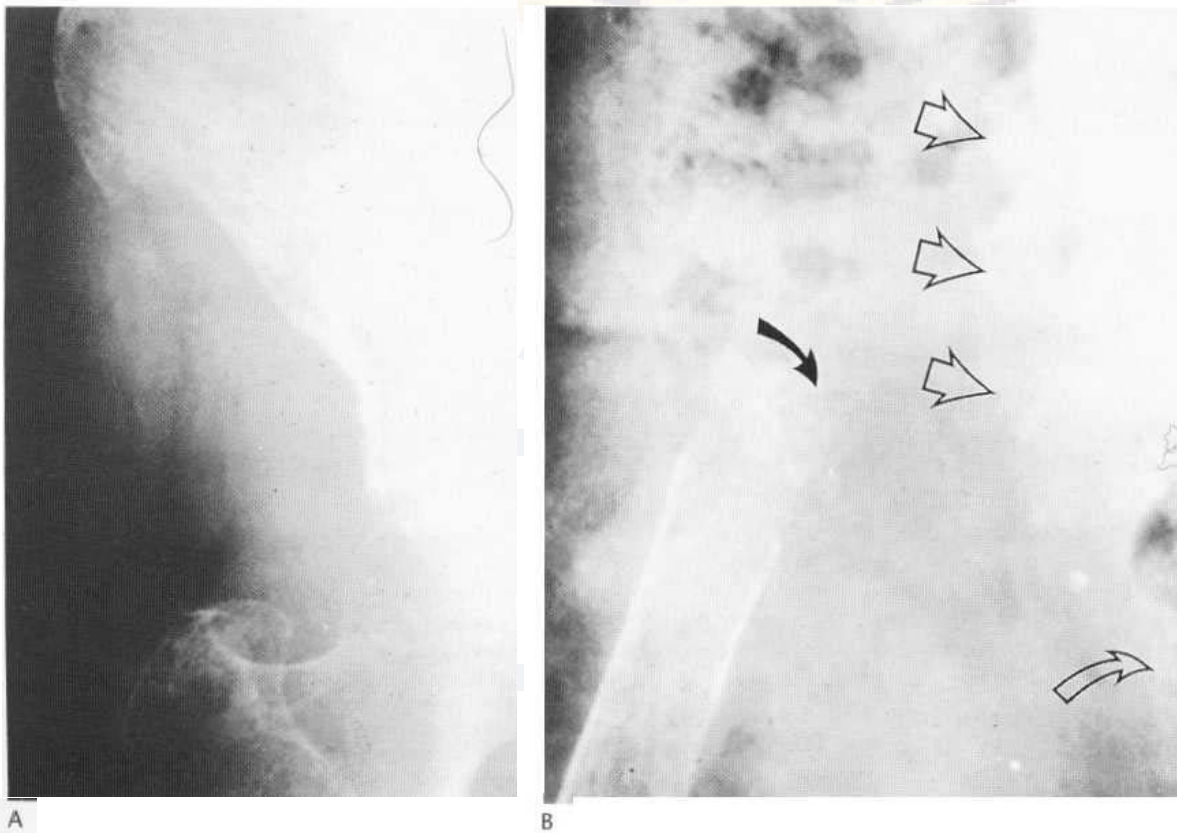


Fig. 40.30 Vanishing bone disease. A 70-year-old woman presented with poorly localised pain in her right hip. (A) A radiograph at presentation reveals ill-defined destruction of the anterior inferior iliac spine. (B) Nine months later there is total destruction of the whole of the hemipelvis and hip joint. Note the faint outline of the residual femoral head (curved arrow), pathological fracture of the femoral neck and the articular surfaces of the sacrum and symphysis pubis which no longer articulate with bone (open arrows).

of collagen and fibrous tissue. Because of the predilection of neurofibromas to arise in nerve roots, many appear in the lumbosacral area and are detected during the investigation of low back pain and sciatica (Figs 40.36, 40.37). MRI also allows easy recognition of plexiform neurofibromas as they extend in a lobulated infiltrating pattern along neural bundles.

Peripheral lesions may be assessed readily with ultrasound, again the feature being a rounded or lobulated mass, usually echo poor, arising in conjunction with a nerve.

2. Neurofibromatosis

Neurofibromatosis is often noticed at birth or soon after. Typical clinical manifestations are *cafe-au-lait spots* and *multiple cutaneous tumours*. Larger soft-tissue masses or growth disparities may also become apparent. These include scoliosis, pseudoarthrosis of long bones (particularly the tibia) and hemihypertrophy. Scoliosis, usually of short segment distribution, often occurs in the thoracic spine. In addition numerous abnormalities arise related to the neural



Fig. 40.31 Cystic angiomas of bone. Shortly before taking his university entrance examination this young man complained of a vague discomfort in his right shoulder. Note multiple well-defined radiolucencies involving the acromion, coracoid, glenoid and upper humeral shaft. The latter has a rather 'woodworm'-like appearance. Lesions were present elsewhere in the skeleton but he had no soft-tissue abnormality.

canal, including generalised dilatation (dural ectasia) with scalloping of vertebral bodies (Fig. 40.37), internal meningoceles and dysraphic anomalies (see Ch. 54). Abnormal rib tubulation results in a 'ribbon-shaped' appearance. A particularly common abnormality is defective ossification of the posterior superior wall of the orbit. Pseudarthrosis of the tibia is characterised by marked absorption of the fracture margins, so that they become pointed (Fig. 40.38). Similar lesions may occur in the radius or clavicle. A number of published reports suggest that malignant sarcomatous change is relatively common, of the order of 5-12% of affected patients. The radiological appearances then become those of an infiltrating diffuse destructive process.

Many extraskeletal manifestations of neurofibromatosis occur because of the neuroectodermal and mesodermal derivation of the tissue (Fig. 40.39). Gliomas of the optic nerves, pheochromocytomas, aneurysms of cerebral and renal arteries, and acoustic neurilemmomas are well recognised. Similarly, the incidence of fibrous tumour of bone is increased, particularly around the knee



Fig. 40.32 Glomus tumour. Intermittent swelling of the index finger had been present for many years and had, intermittently, been exquisitely painful. A discrete soft-tissue mass caused pressure erosion on the radial side of the terminal phalanx.

where radiologically they seem identical to non-ossifying fibromas and fibrous cortical defects.

TUMOURS PRESUMED TO ARISE FROM OTHER TISSUES IN BONE: FATTY TISSUE

Lipoma and liposarcoma

Although fat represents one of the normal connective tissue elements within bone, intraosseous lipomas are exceedingly rare. The few that have been observed usually cause an oval lytic lesion within a long bone of the lower limb or the calcaneum. In a long bone the appearances may bear a distinct resemblance to non-ossifying fibroma. A sharply defined discrete sclerotic margin is associated with bone expansion and trabeculation. Periosteal new bone formation is not a feature. Within the calcaneum an intraosseous lipoma has a characteristic appearance, presenting as an osteolytic lesion with a central focus of ossification and sclerotic margins (Fig. 40.40). It invariably occurs in the same location as a simple bone cyst within the triangular radiolucent zone between the major trabecular groups.

Parosteal lipomas, by contrast, present a much more characteristic appearance with strands of ossification forming around the radiolucent fatty lobules of this rare tumour (Fig. 40.41). They tend to be very slow in growth and produce minor symptoms. Marked periosteal new bone formation does occur, with an obvious, but well-defined, soft-tissue mass.

A more aggressive nature, however, must be considered when the soft-tissue element fails to contain fatty lucencies, possibly

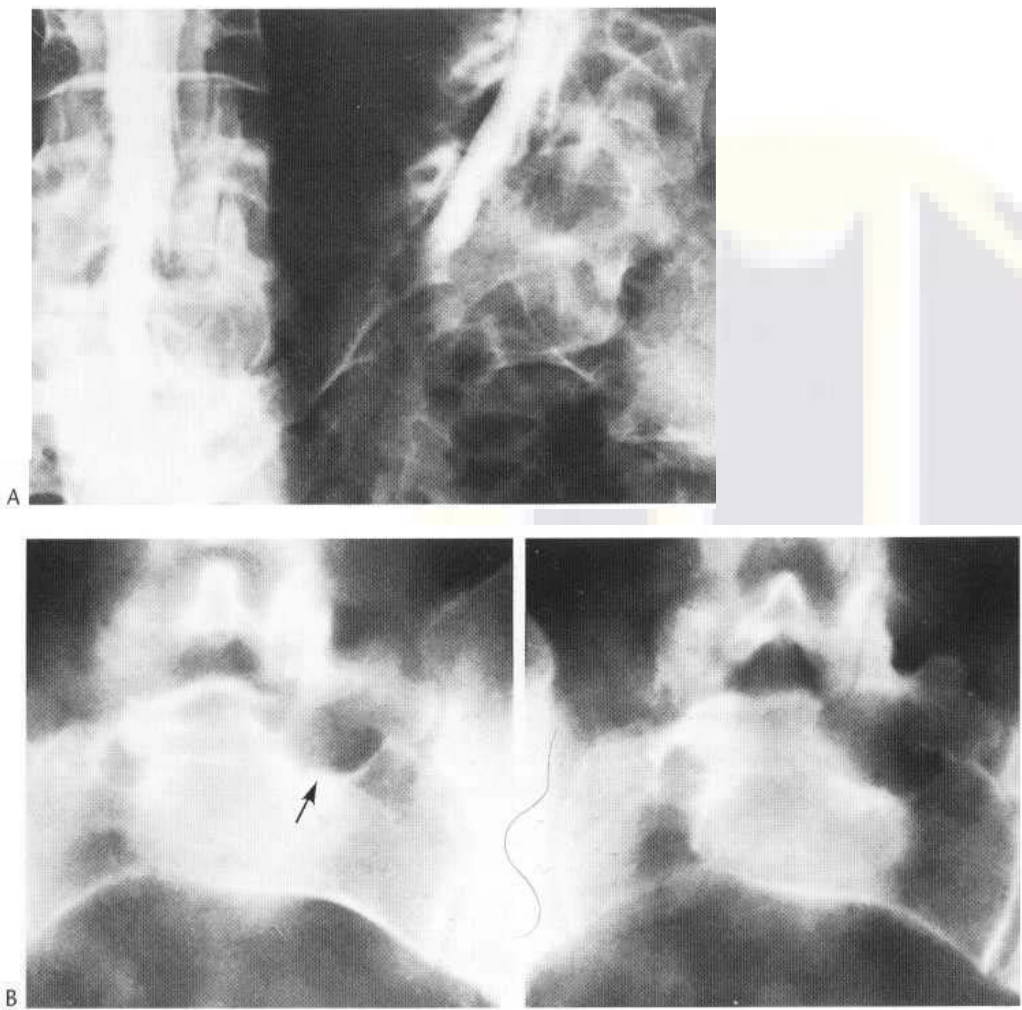


Fig. 40.33 Neurofibroma arising in the exit foramen of the first sacral segment. The patient presented with sciatic pain and two views (A) from a water-soluble radiculogram reveal amputation of the S1 nerve root sheath, displacement of the S1 and S2 roots and a large well-defined rounded radiolucency with sclerotic margins in the exit foramen. (B) Frontal tomograms confirm a large bony defect (arrow), compared with the normal right foramen.

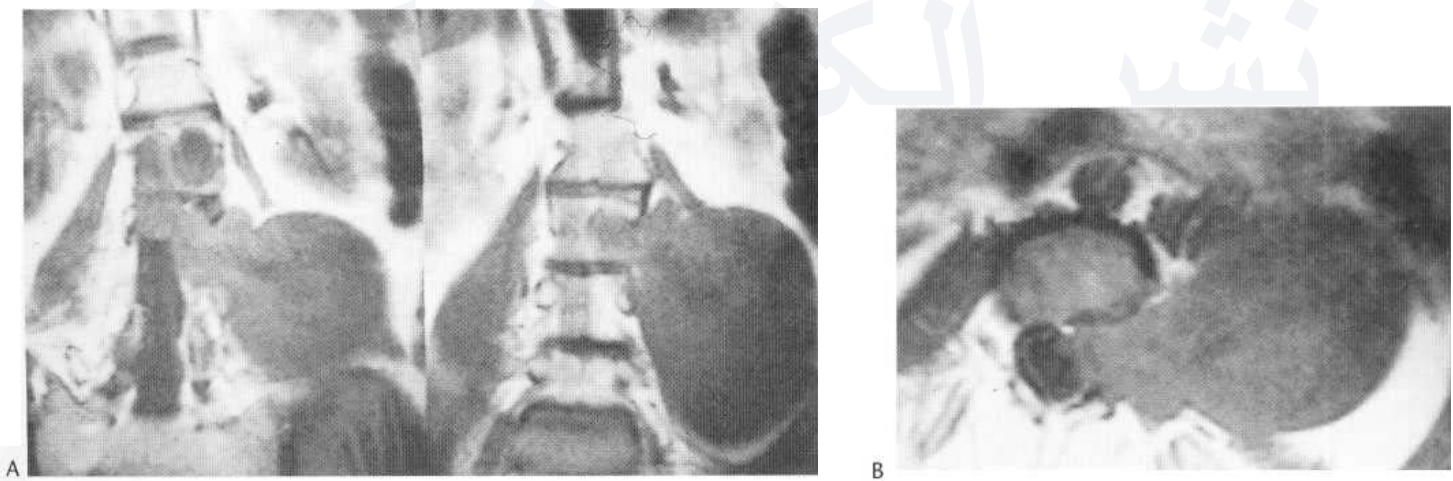


Fig. 40.34 Neurofibroma demonstrated by coronal T₁-weighted (A) and axial (B) MR images. A typical dumb-bell tumour is shown with large extra-neural component. Note, however, there is extension into the exit foramen and other intrathecal abnormalities.

indicating the presence of a *parosteal liposarcoma*. *Intraosseous liposarcoma* has been described but is exceedingly rare and produces an ill-defined lytic area, usually in the femur or tibia, which is extremely vascular. Rapid extension into the soft tissues, and early pulmonary metastasis, is usual.

The characteristic radiolucencies of soft-tissue lipomas are discussed in Chapter 45, and *lipomas in the lumbar canal* are considered in Chapter 54. *Macrodystrophia lipomatosa* is a rare form of localised gigantism of a hand or foot accompanied by an over-growth of the associated mesenchymal elements, particularly fat.



Fig. 40.35 Neurofibroma arising in the obturator ring has caused considerable pressure erosion of both right pubic rami, particularly the superior one. The margins of the pressure defect are sharply defined.

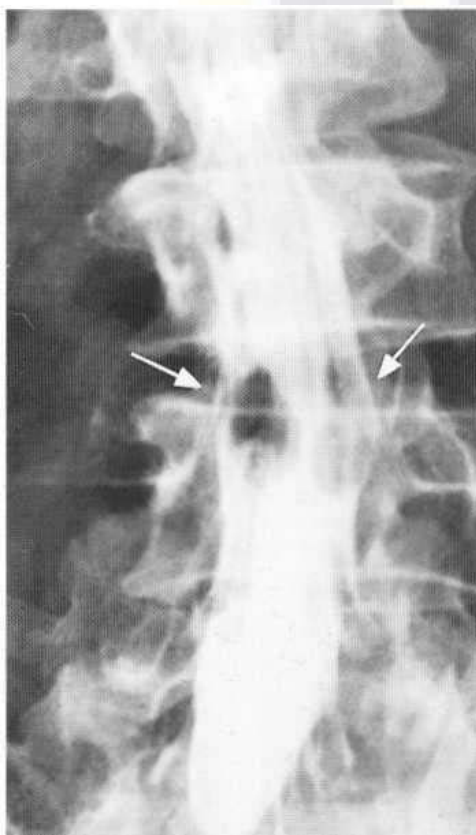


Fig. 40.36 Multiple neurofibromas in the cauda equina. This middle-aged patient was investigated for low back pain by radiculography. Two large ovoid neurofibromas (arrows) are shown as filling defects within the thecal sac at the L4/5 level.

TUMOURS PRESUMED TO ARISE FROM OTHER TISSUES IN BONE: NOTOCHORD

Chordoma

The notochord extends, during embryological development, from the coccyx to the buccopharyngeal membrane and is the precursor of the vertebrae and intervertebral discs. Chordoma is a destructive



Fig. 40.37 Neurofibromatosis. Pseudarthroses of the tibia and fibula shown in an infant. Bowing of bone and absence of any evidence of bone repair are typical.

bone tumour believed to arise from notochord cell rests. All are locally malignant with a strong tendency to recur after attempted excision. The lesions are slow growing and become apparent due to pressure symptoms, with or without localised pain. The extreme ends of the axial skeleton are mainly involved, approximately half the lesions arising in the sacrum and/or coccyx, the others in the basioccipital and basisphenoid regions of the skull. A vertebral origin is found only in 1.5% of patients. Adjacent vertebrae may be involved. A fatal outcome results from a local extension, metastatic spread being unusual.

The usual clinical presentation is of a roan between 40 and 70. The clinical symptoms and signs depending on the site of obstruction. Constipation is often a feature of those arising from the sacrum.

Radiological features

In the sacral area the tumour typically arises in the midline and involves the fourth or fifth sacral vertebra (Fig. 40.42). The lesion is purely lytic, relatively well defined, usually being oval or slightly lobulated. It may contain areas of calcification. The sacral margins may occasionally be sclerotic. The soft-tissue structures within the pelvis are displaced anteriorly. Tumours arising at the basioccipital or hypophyseal regions are accompanied by erosion and destruction of the dorsum sella and clivus. Again, a lobulated or rounded area of bone destruction is associated with a large soft-tissue mass displac-

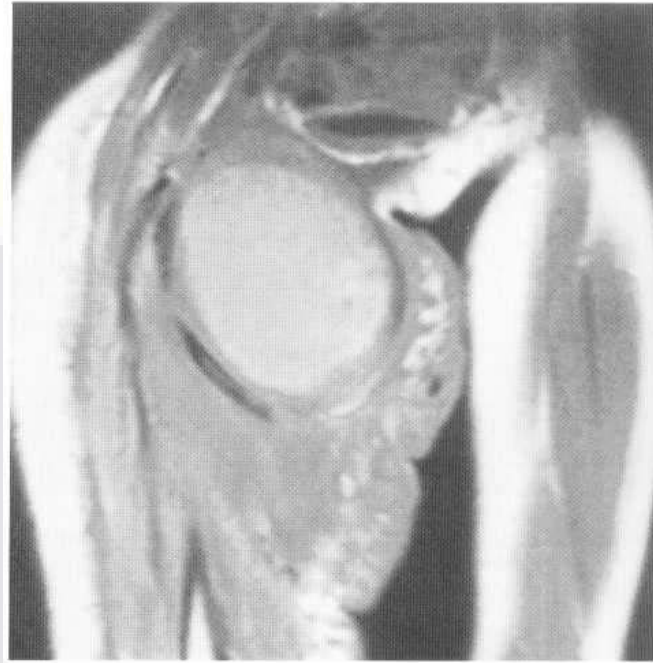


Fig. 40.39 Neurofibromatosis. A coronal T₁-weighted sequence of the thighs demonstrates an obvious abnormality on the right. In addition to a solitary neurofibroma displacing the femoral vessels (shown by a signal void), there is clear mesenchymal dysplasia, with extensive abnormalities of subcutaneous tissue and hemihypertrophy.

Fig. 40.38 Neurofibromatosis. A lateral tomogram of the lumbar spine demonstrates typical posterior scalloping, part of the general dysplasia of the neural canal and its contents found in this condition.

in- nasopharynx anteriorly and sometimes containing amorphous calcification. Here the differential diagnosis is from chondrosarcoma, whereas in the sacrum the possibility of plasmacytoma or a giant cell tumour should be considered.

TUMOURS PRESUMED TO ARISE FROM OTHER TISSUES IN BONE: EPITHELIAL ORIGIN

Implantation dermoid cysts

These rare lesions usually follow a penetrating wound associated with a crush fracture, when it is assumed that epithelial cells are carried into the underlying bony structure. Typically, they arise in



Fig. 40.40 Intraosseous lipoma within the calcaneum. Lateral (A) and axial (B) conventional radiograph showing an osteolytic lesion characteristically located between the major trabecular groups of the bone. A thin sclerotic margin surrounds the lesion that contains an eccentric stellate calcified focus. (C) Coronal CT of the hindfoot establishing the fat content of the lesion.

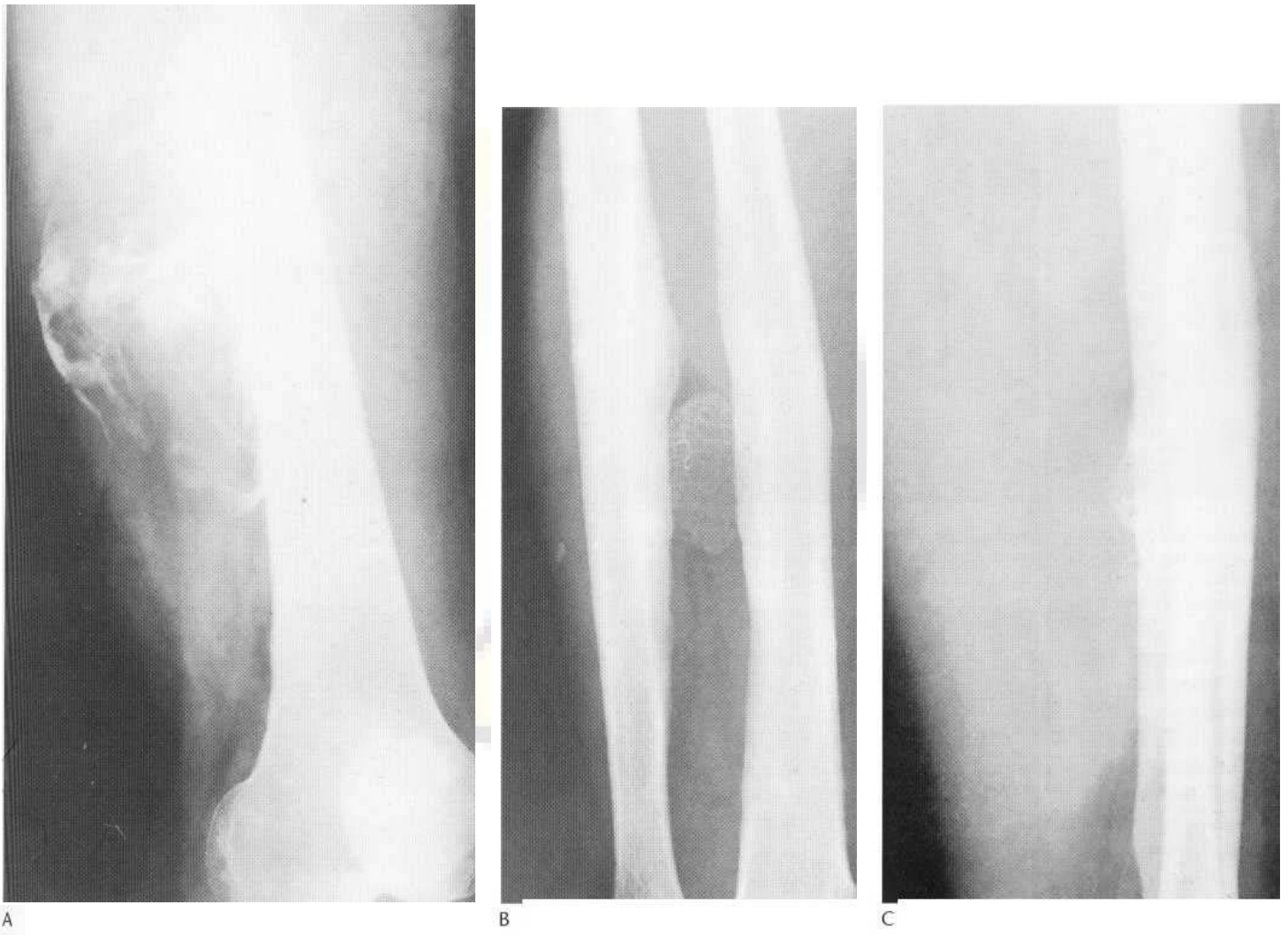


Fig. 40.41 Parosteal lipoma. Two examples are shown of parosteal lipomas arising in middle-aged patients. Both presented with a painless, rather firm mass, apparently attached to bone. (A) A large lesion arising on the lateral aspect of the femur. Note the strands of ossification surrounding the radiolucent areas of fat. (B, C) A more discrete tumour arises from the interosseous membrane of the forearm. A fatty radiolucency is present, together with ossification in the soft tissues and some periosteal new bone formation.

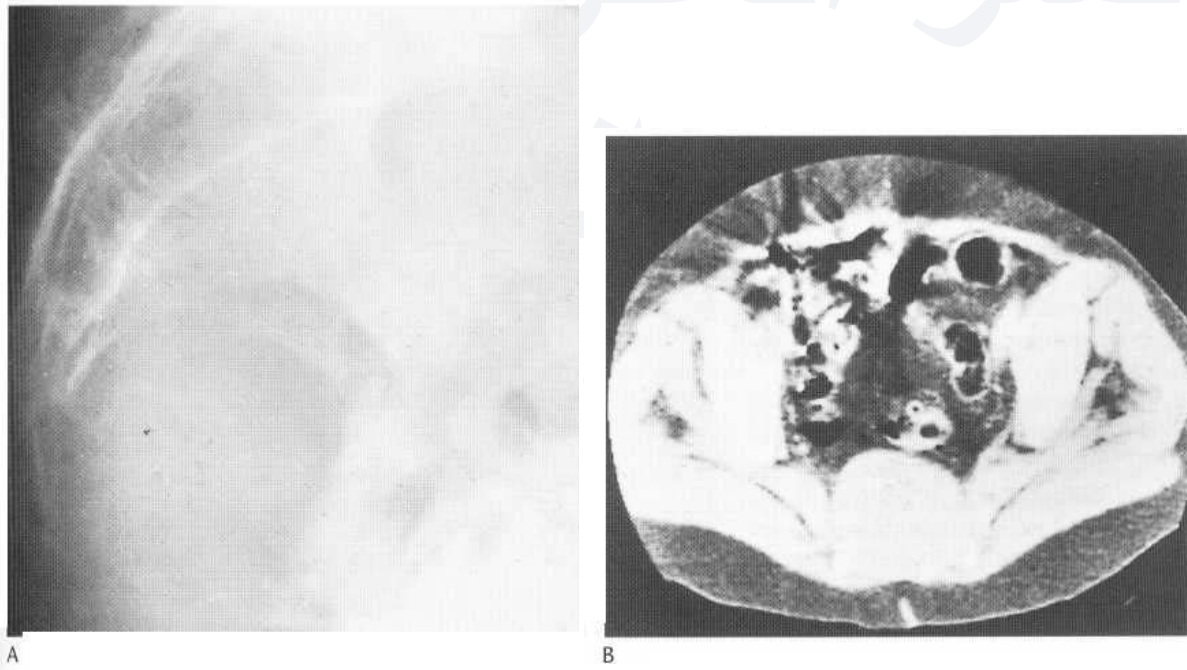


Fig. 40.42 Chordoma of the distal sacrum. (A) A lateral film demonstrates a large soft-tissue mass displacing bowel anteriorly. The anterior cortex of the distal sacral vertebrae is ill defined and the coccyx is not seen. (B) CT demonstrates the typical well-defined soft-tissue mass extending anteriorly from the sacrum. The anterior cortex of the sacrum has been destroyed. Chordomas usually exhibit an apparent disproportion between the size of the soft-tissue mass and the extent of the bony involvement.



Fig. 40.43 Implantation dermoid cyst. A cystic lesion in the terminal phalanx of the thumb was found in an elderly woman many years after a penetrating injury. The sharp definition of its margins and the location of the lesion are characteristic.

distal phalanges of adolescents or young adults, the left middle finger being the single commonest site. The lesion grows slowly over many years.

Radiologically a well-defined translucency results, with slight expansion and sharply defined margins around which a minimal sclerotic reaction may be visible (Fig. 40.43). Subungual fibromas represent the only serious differential diagnostic possibility. A glomus tumour is almost invariably extraosseous.

TUMOURS RELATED TO JOINTS

1. Synovial chondromatosis (osteochondromatosis)

This is a relatively unusual synovial disease, commonly regarded as a benign neoplasm, in which metaplastic cartilage formation occurs throughout the synovium. Typically, young and middle-aged adults are affected, with a male preponderance and an affinity for large joints, in particular the knee, hip and elbow. Minimal pain, swelling and limitation of movement are the usual presenting complaints. Cartilaginous lesions develop throughout the synovium, later becoming pedunculated and separating into the joint space. When large enough they undergo ossification. This condition undoubtedly progresses in phases, with episodes of synovitis and the shedding of loose bodies (Fig. 40.44).

In the early stages the only abnormality which may be detected on conventional radiographs is an apparent joint effusion. CT may delineate this, when a slight increase in density may be observed.

Arthrography, however, demonstrates not only an irregular, nodular synovium but also cartilaginous loose bodies. The unenhanced *MRI appearances* may be non-specific, particularly in the absence of cartilage calcification, demonstrating only homogeneous high-signal intensity on T₂-weighted images, mimicking a joint effusion. However, the mass and proliferative effects of the lesion may be evident with erosion of bone, hyaline cartilage and normal intra-articular structures, such as the pulvinar fat pad within the acetabular fossa. Calcification and ossification of the cartilaginous

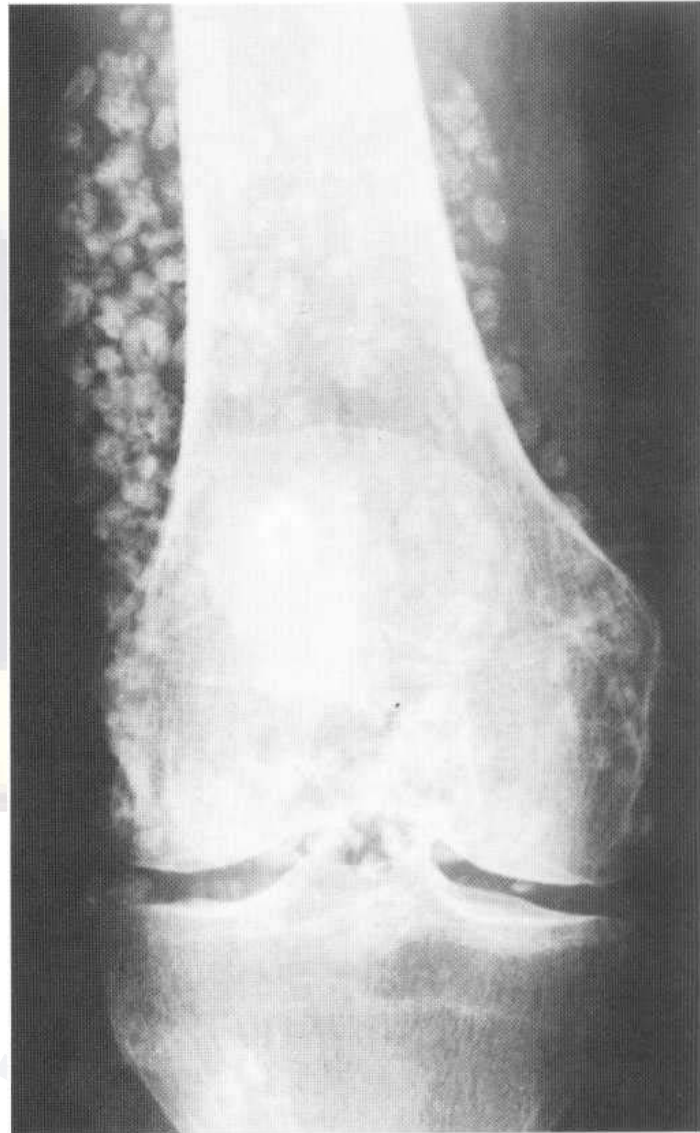


Fig. 40.44 Synovial chondromatosis. Hundreds of calcified lesions are shown in relation to the synovium, all of them approximately the same size. Nearly all were loose bodies at arthroscopy.

masses result in numerous oval or rounded opacities, often of similar size, demonstrated on conventional radiographs (Fig. 40.45). Serial examination may show these to be fairly constant in position. Scintigraphy using a bone-seeking radiopharmaceutical often demonstrates an appreciable increase in activity localised particularly in the larger masses, suggesting that active ossification and calcification are occurring. Eventually extensive capsular distension may result in marginal bony erosions occurring characteristically at the insertion of joint capsule, with clearly defined margins. Synovial chondromatosis also occurs in tendon sheaths, usually in the hand, wrist or foot, and bursae. Chondrosarcoma is an extremely rare complication.

2. Pigmented villonodular synovitis

The aetiology of this disorder of synovium is not known. It is generally regarded as a benign neoplasm. The disease may be mono-articular or polyarticular, the latter being very rare. Adolescents and young adults are affected, usually complaining of local pain and swelling, occasionally with cystic masses related to a large joint,



Fig. 40.45 Synovial chondromatosis of the knee. (A) Axial T_2 -weighted fat-suppressed image showing numerous low-signal-intensity filling defects within the joint and thickened nodular synovium due to intrasynovial calcification. (B) In another patient a number of ossified masses of uniform size are present in a popliteal cyst. Medial compartment osteoarthritis is evident.

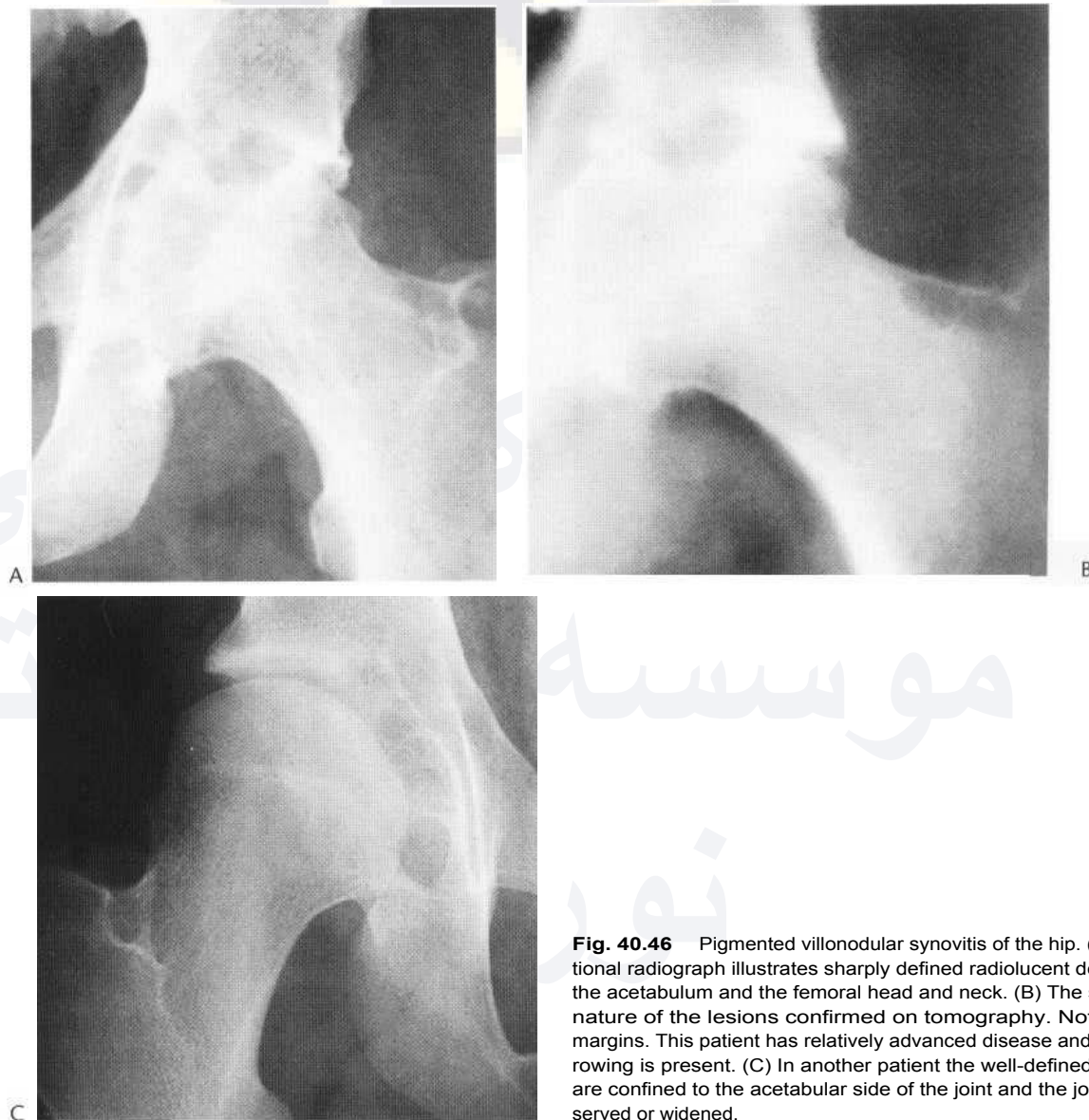


Fig. 40.46 Pigmented villonodular synovitis of the hip. (A) The conventional radiograph illustrates sharply defined radiolucent defects involving the acetabulum and the femoral head and neck. (B) The sharply defined nature of the lesions confirmed on tomography. Note the sclerotic margins. This patient has relatively advanced disease and joint space narrowing is present. (C) In another patient the well-defined radiolucencies are confined to the acetabular side of the joint and the joint space is preserved or widened.

usually the knee or hip. Histologically the appearances show considerable variation, with proliferation of villonodular masses of synovial tissue associated with the deposition of haemosiderin, a feature that may be detected by increased tissue attenuation on CT and low-signal-intensity masses on MRI due to the paramagnetic effect of haemosiderin.

Radiologically, synovial thickening is usually evident, particularly with soft-tissue exposures. Features which suggest the diagnosis are sharply defined para-articular erosions with sclerotic margins, particularly if these lesions are present on both sides of the affected joint (Figs 40.46, 40.47). As in gout, integrity of the articular surfaces and preservation of the width of the joint space are maintained until relatively late in the disease. Disuse osteoporosis is not an initial feature. Calcification within the synovial mass is exceedingly rare, unlike malignant synovioma. Arthrographically the thickening of the synovium is confirmed, usually being diffuse in larger joints, such as the knee, whereas in small joints, particularly metacarpophalangeal joints, the thickening is nodular (Fig. 40.48).

Characteristic appearances on MRI are often seen with a diffuse heterogeneous signal intensity mass, traversed by low-signal-intensity septa, containing clumps of tissue with variable signal intensity. The exact appearances will depend on the relative proportions of fat, haemosiderin, fibrous stroma, synovitis and cellular elements making up the lesion (Fig. 40.49). Pigmented villonodular synovitis is one of a group of disorders to produce low-signal masses in synovium on all pulse sequences. The other causes include chronic bleeding disorders (e.g. haemophilia, see Ch. 41), synovial chondromatosis and amyloid

(see below). Bone erosions are also well demonstrated. The synovium of tendon sheaths and bursae may also be affected by this disease (also called giant-cell tumour of tendon sheath) (Fig. 40.50).

3. Lipoma arborescens

This condition occurs most commonly in the knee and is characterised by a mass of numerous fat-laden synovial villous projections



A



B

Fig. 40.47 Pigmented villonodular synovitis of the hip. Coronal T₁-weighted (A) and STIR (B) sequences demonstrate a lobulated synovial mass on the right with modestly high signal on the STIR sequence, though less so than the joint effusion associated with it. Note the replacement of the pulvina on the T₁-weighted sequence by tumour.



A



B



C

Fig. 40.48 Pigmented villonodular synovitis of the index finger metacarpophalangeal joint. (A) An arthrogram confirms an enlarged joint space and thickened nodular synovium. In another patient the corresponding MR features are shown on coronal T₁-weighted contrast-enhanced (B) and T₂-weighted fat-suppressed (C) images.

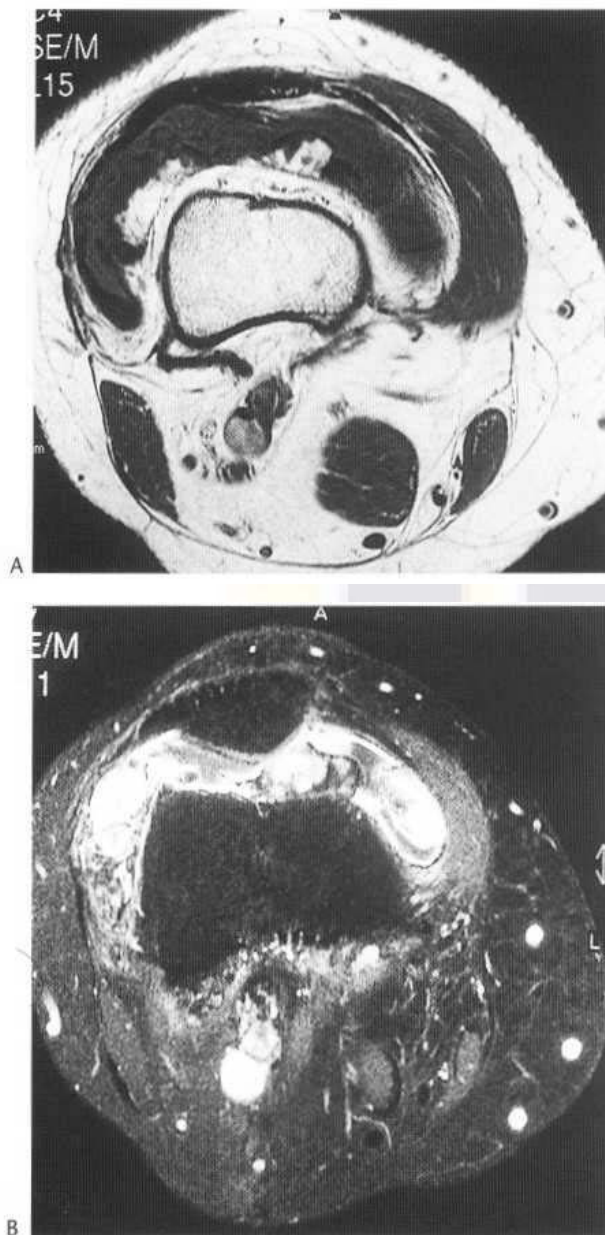


Fig. 40.49 Pigmented villonodular synovitis of the knee joint. Axial T₁-weighted (A) and T₂-weighted fat-suppressed (B) MR images through the patella and suprapatellar recess showing a heterogeneous mass within the joint made up of fat, haemosiderin, fibrous tissue and cellular elements.

(lipomatosis of the synovium). On conventional radiographs the radiolucent arborising fatty projections may be evident as a soft-tissue mass originating from the joint. The lesion can be elegantly demonstrated on MRI which will confirm the fatty nature of the tumour (Fig. 40.51).

4. Dialysis-related amyloidosis

This is a relatively recently recognised complication of long-term haemodialysis. It is due to the deposition of a unique form of amyloid derived from circulating Beta-2 microglobulin. The condition is characterised by painful stiff joints, usually first involving the shoulders and less often the hands, wrists and other large joints. The carpal tunnel syndrome is a common presentation. The disease is seldom seen before 5 years of treatment.



Fig. 40.50 (A,B) Pigmented villonodular synovitis of the flexor tendon sheath of the middle finger. A sharply circumscribed soft-tissue mass has caused slight pressure erosion of the middle phalanx.

Radiologically the conventional radiographic findings may mimic pigmented villonodular synovitis with well-defined pressure-like erosions, often with sclerotic margins, involving both sides of the joint (Fig. 40.52). On MRI a characteristic appearance is demonstrated with bony erosions and synovial masses exhibiting a predominately low signal intensity on both T₁- and T₂-weighted images (Fig. 40.53).

5. Synovioma

This is a highly malignant tumour growing rapidly with early metastases to lymph nodes, unlike most other musculoskeletal tumours. Young adults are most commonly affected, the mean age being 35. The lesion arises in soft tissue adjacent to, but probably not from, synovial structures of joints, tendon sheaths and bursae. The tumour is so called, as the two predominant cell lines are reminiscent histologically of synovium. Seventy per cent of cases involve the lower extremities, particularly around the knee. Clinically, a soft-tissue mass or ill-defined swelling associated with local pain, is present in nearly three-quarters of patients.

Radiologically, a soft-tissue mass is shown associated with a joint, about one patient in five demonstrating calcification of an amorphous nature (Fig. 40.54). Ossification does not occur, unlike the later stages of synovial chondromatosis. About 10% of cases are associated with bone involvement, shown radiologically by irregular bone destruction, particularly at capsular attachments (Fig. 40.55).

This tumour may occasionally arise in the synovial lining of tendon sheaths, producing a similar soft-tissue mass. Secondary involvement of adjacent bone has been observed, particularly in the feet.

5. Intraosseous ganglion

This is a relatively uncommon lesion, representing ganglion material within a long tubular bone, the origin of which is unclear. Direct

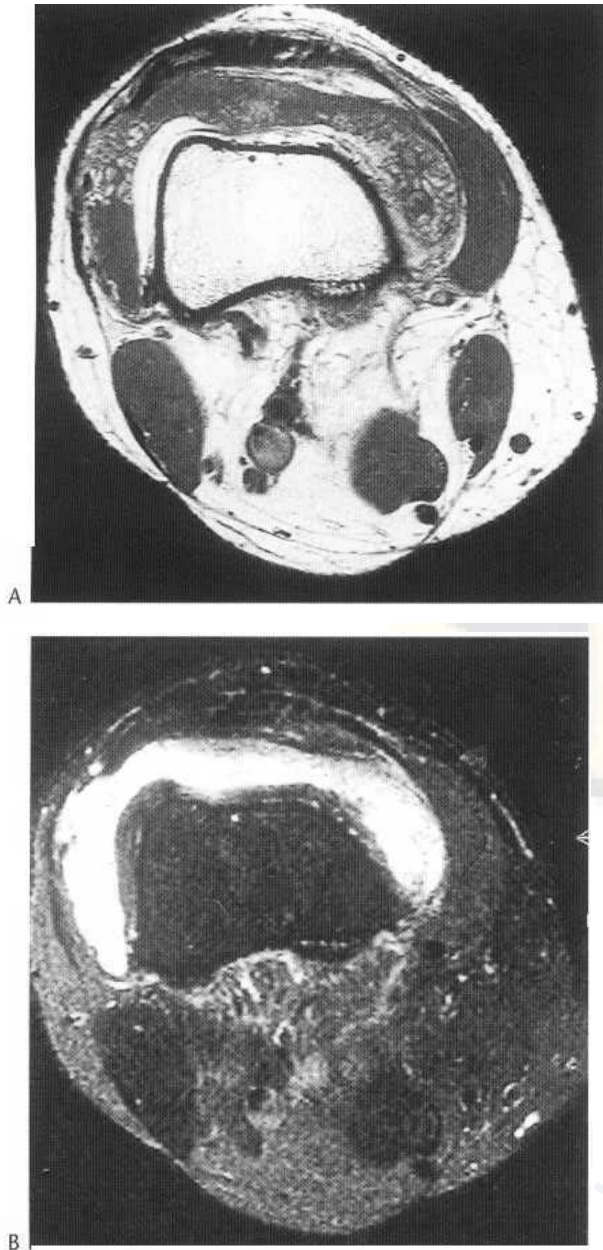


Fig. 40.51 Lipoma arborescens of the knee joint. Axial T_1 -weighted (A) and T_2 -weighted (B) fat-suppressed MR images through the suprapatellar recess showing numerous fatty fronds of synovium and a large joint effusion. Note how the high signal intensity villous projections on the T_1 -weighted image are suppressed on the T_2 -weighted fat-suppressed sequence.

communication with a joint is demonstrated rarely. It may be shown occasionally to extend from an extraosseous lesion. Patients are between 30 and 60 years of age and two-thirds complain of local joint pain, often related to exercise. Most commonly the lesion occurs around the knee or ankle; hips and carpus are also common sites.

Radiologically, an oval or circular eccentric osteolytic lesion is shown, which is often expansile, with a thin sclerotic rim. These may appear multilocular, varying between 1 and 5 cm in size (Figs 40.56, 40.57).

6. Subarticular arthritic cyst and geode

Although not neoplasms, these space-occupying lesions may occasionally cause confusion. Described in detail elsewhere (see Ch. 38),

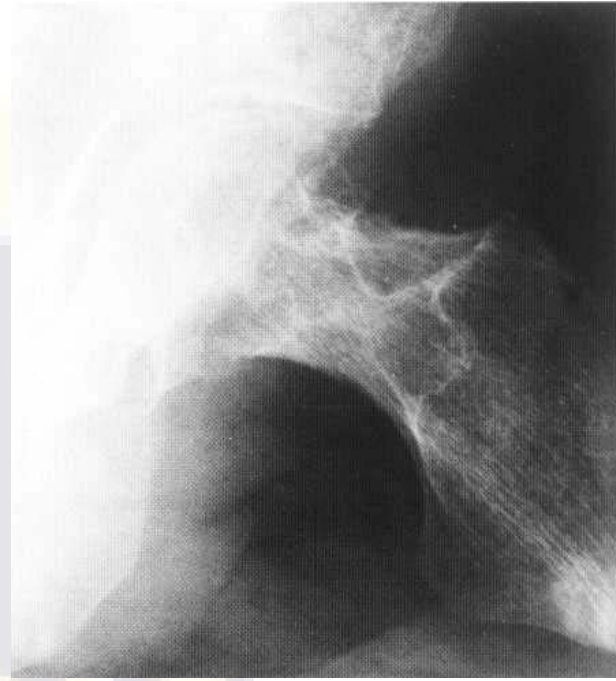


Fig. 40.52 Dialysis-related amyloidosis of the hip resulting in pressure-like erosions of the femoral neck. Note the coarsened quality of the trabecular bone due to secondary hyperparathyroidism.

they most usually accompany rheumatoid disease, particularly with secondary degenerative change and osteoarthritis. The knee and hip are classic sites; the latter may present with a pathological fracture. The historical and radiological features of a pre-existing arthropathy should assist the diagnosis, together with the discrete sclerotic margins and close relationship with a joint (Fig. 40.58).

TUMOURS OF NO KNOWN ORIGIN

1. Solitary bone cyst (unicameral bone cyst)

This entirely benign lesion is unlikely to be a true neoplasm, but is considered here because its diagnosis depends largely on radiological findings which can resemble those of known neoplastic conditions, and because of its predilection to recur after treatment.

Solitary bone cysts are always unilocular. The site of origin depends on the patient's age: before epiphyseal fusion the majority occur in the proximal humeri and femora (Figs 40.59, 40.60) with the former being the most usual site. Following skeletal maturation some lesions occur in such bones as the calcaneum (Fig. 40.61). Solitary bone cysts are commoner in males and develop during skeletal growth. Childhood and early adolescence is therefore the usual time for them to be discovered. More than half present due to a pathological fracture, a few may produce minor discomfort, others are found incidentally.

During the stage of skeletal development the lesion lies close to the metaphysis and is often situated in the midline, extending across the whole shaft. With further skeletal growth, normal bone develops between the cyst and metaphysis so that the lesion is seen to be carried toward the diaphysis. Hence, those that develop early eventually lie in the middle of the shaft of a bone. The cyst contains clear liquid unless there has been contamination by bleeding following a fracture. It is lined by a thin layer of connective tissue.

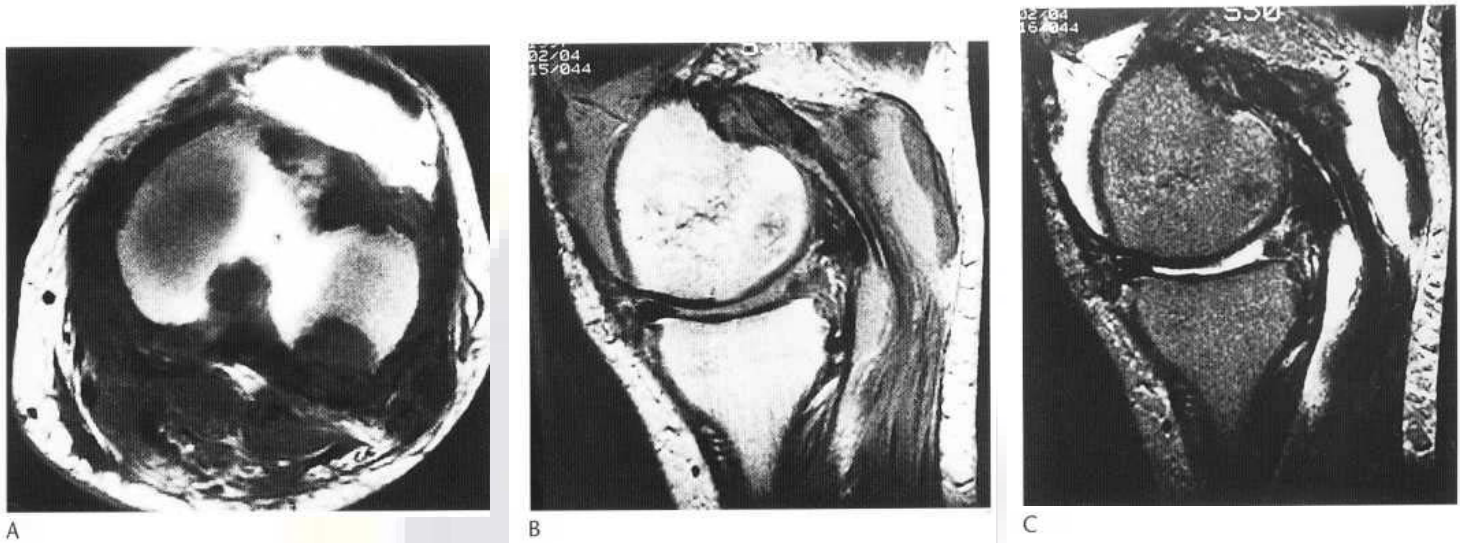


Fig. 40.53 Dialysis-related amyloidosis of the knee. Axial T_1 -weighted (A), sagittal proton density (B) and T_2 -weighted (C) MR images showing numerous erosions of the margin of the tibia and characteristic low-signal-intensity masses within the synovium, most evident posteriorly within the popliteal cyst. A large joint effusion is also present.

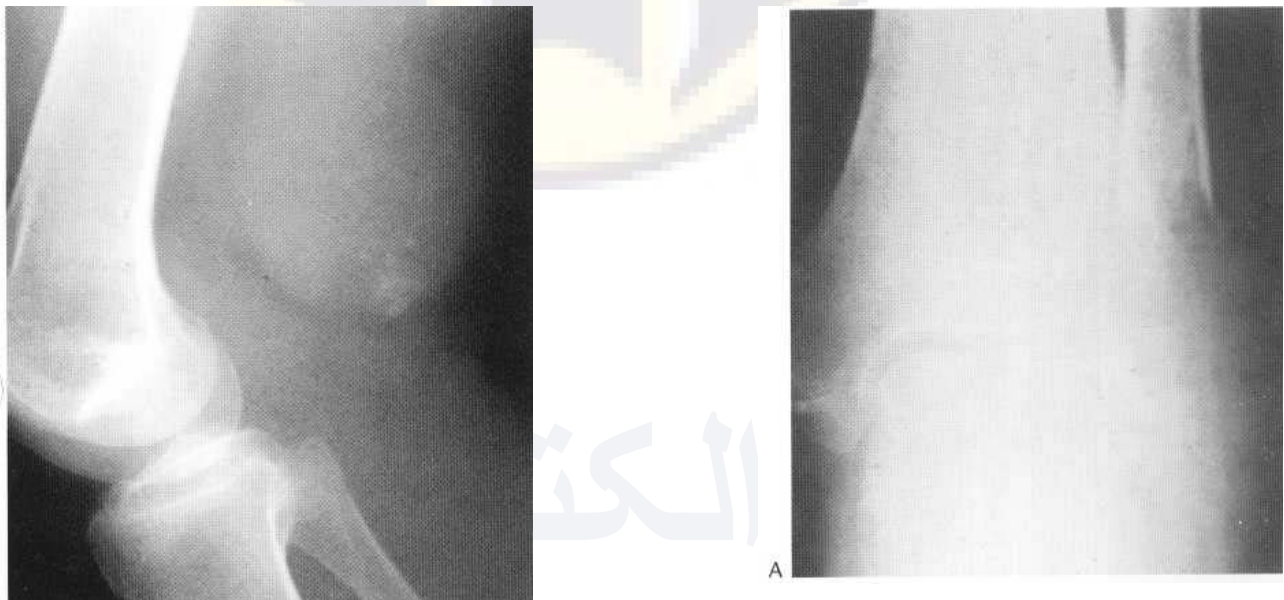


Fig. 40.54 Synovioma. A large soft-tissue mass is present posterior to the distal femur within which there is some amorphous eccentrically located calcification.

Radiologically, an area of translucency centrally in the metadiaphysis is characteristic. The overlying cortex is often thinned and slightly expanded with no periosteal reaction unless a fracture has occurred. The lesion may develop in relation to an apophysis, particularly the greater trochanter of the femur. In the earlier stages of growth, metaphyseal cysts tend to have a continuous rounded, sharply defined margin on the metaphyseal side but perhaps slightly less demarcation on the diaphyseal side. Sclerotic reaction is usually present around the margin but may be discrete. A serpiginous margin may cause the cyst to appear multilocular. As normal

Fig. 40.55 Malignant synovioma of the ankle. Gross synovial thickening was present with hazy erosion of the capsular attachment. (A) AP view. (B) Lateral view.

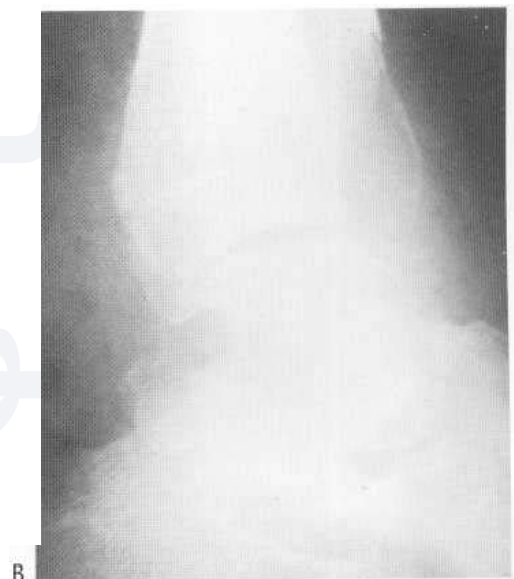




Fig. 40.56 Intraosseous ganglion of the proximal fibula shown at a typical location. A slightly expansile lytic lesion is evident with endosteal thinning of the cortex and a well-defined margin.



Fig. 40.57 Intraosseous ganglion. An oval, eccentric, osteolytic lesion arises from the medial malleolus with a thin sclerotic margin.

bone grows in the metaphysis, subsequent examination demonstrates the apparent migration of the lesion along the shaft of the affected bone, with an increasing sclerotic reaction around its margins. On bone scanning no abnormality develops in the blood-pool phase, in contrast to aneurysmal bone cysts. The delayed image demonstrates increased activity only around the margins of the lesion, unlike fibrous dysplasia (Fig. 40.62). The only serious differential diagnostic possibility is a chondroma, but no calcification occurs in a simple bone cyst unless callus has formed from a fracture. MRI is seldom required to assist in the diagnosis. However, distinction between pure chondroid matrix and cyst fluid may be difficult.

The prognosis depends partly on the patient's age. Before the age of 10 recurrences are frequent, whereas after that age primary healing usually occurs even after fractures. Because of the risk of pathological fracture the majority of patients are treated by curettage and packing with bone chips. Some lesions have been reported to regress satisfactorily after injection with steroids.

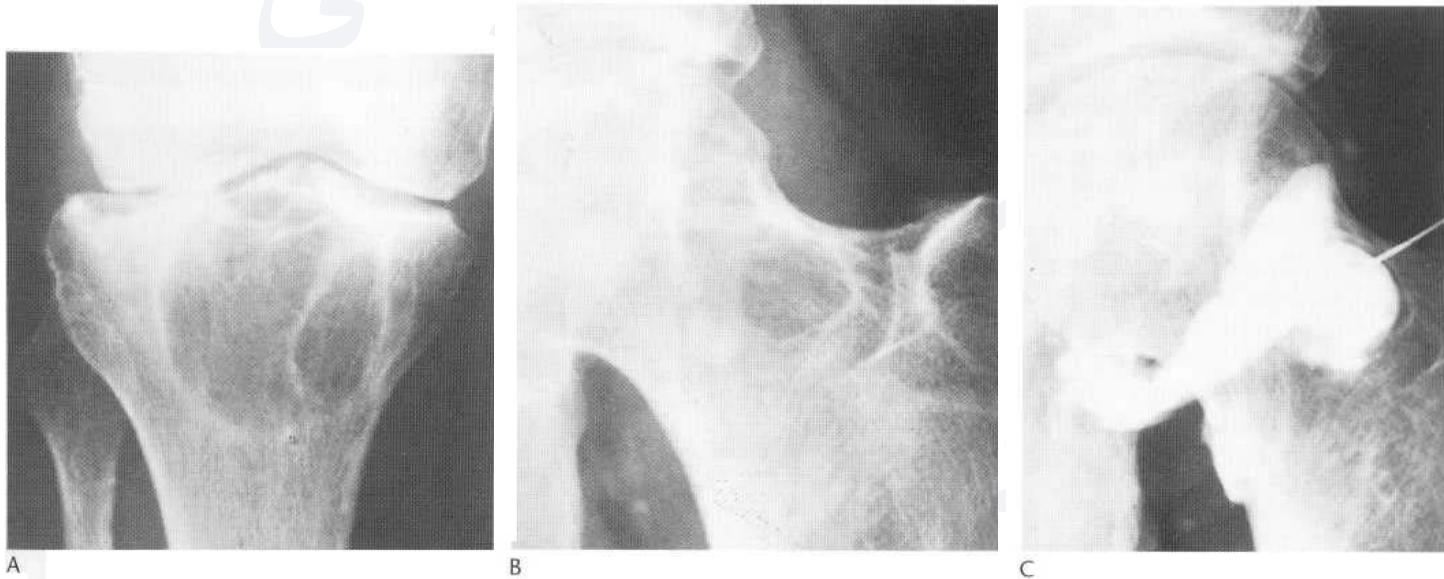


Fig. 40.58 Subarticular geodes. (A) An elderly female with rheumatoid arthritis and secondary degenerative arthritis has a typical, large geode immediately beneath the articular surface of the tibia. (B) A younger male with rheumatoid disease has an oval, well-defined defect in the upper femoral neck. This too has a sclerotic margin. (C) Aspiration of the defect yielded synovial fluid and injection of contrast medium confirmed communication between the sub-articular geode and the joint cavity.

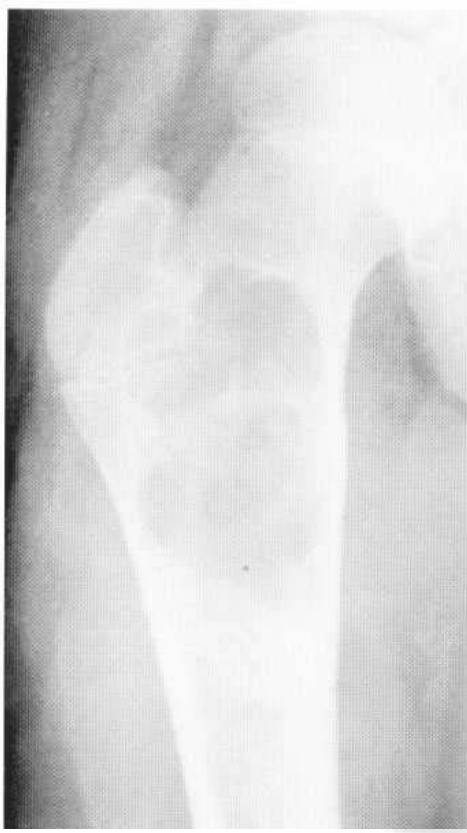


Fig. 40.59 Solitary bone cyst of the proximal femur showing expansion and thinning of the cortex, clearly defined endosteal margins but no calcification or periosteal new bone formation.

2. Ewing's sarcoma: malignant round cell tumours

A group of highly malignant tumours involving bone is characterised histologically by numerous small round cells. Within this group are included Ewing's sarcoma, metastatic neuroblastoma, non-Hodgkin's lymphoma and undifferentiated tumours. Pathological distinction may be extremely difficult, even with the benefit of electron microscopy and histochemical techniques. While it is clear that these entities show considerable overlap, Ewing's sarcoma is sufficiently distinctive to require definitive description.

Clinically, pain of several weeks' or months' duration is accompanied by localised tender swelling. The majority of patients are between 5 and 30 years of age. This rapidly progressive malignant tumour is characterised by pyrexia, anaemia and a raised ESR. These clinical symptoms and signs may closely simulate osteomyelitis but occur also in non-Hodgkin's lymphoma. It should be emphasised that the child with a Ewing's tumour is ill, in contrast to those with such benign lesions as eosinophilic granuloma that may cause similar radiological appearances.

Histologically the malignant round cells typically contain glycogen granules. The lesion is most often found in a long bone, the diaphysis being more commonly affected than a metaphysis. In about 40% of cases, however, the axial skeleton is involved, particularly the pelvis and ribs. Metastatic spread occurs early to lungs and to other bones where the radiological and histological findings are virtually identical. The time delay between the discovery of the primary lesion and the development of secondary deposits suggest



Fig. 40.60 Solitary bone of the cyst proximal humerus. (A) This child presented with a pathological fracture through this long centrally located lytic lesion. Endosteal thinning and slight expansion is evident. There is no periosteal reaction and the distal extent of the lesion is well defined. Some 'fallen fragments' are present near to the fracture site. Coronal T₁-weighted (B), T₂-weighted (C) and T₁-weighted (D) contrast-enhanced fat-suppressed images. The extent of the lesion is well shown and is confined to the medullary canal of the humerus. Only the margins enhance consistent with a fluid-containing lesion. Some adjacent soft-tissue enhancement results from the fracture.

that this tumour does indeed originate in bone, unlike some other malignant round cell tumours.

Radiologically the appearances are inconclusive. The lesion is essentially destructive, ill defined and principally involves the medullary cavity. Cortical erosions and overlying periosteal reactions occur early; indeed a periosteal reaction may be the only sign of abnormality (Figs 40.63, 40.64). Although the onion-peel lamellar

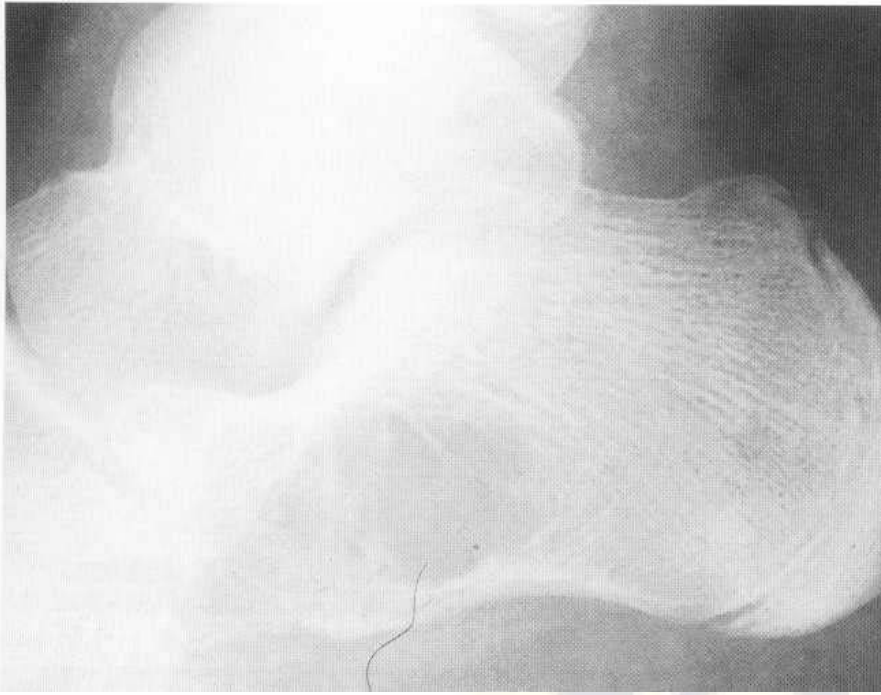
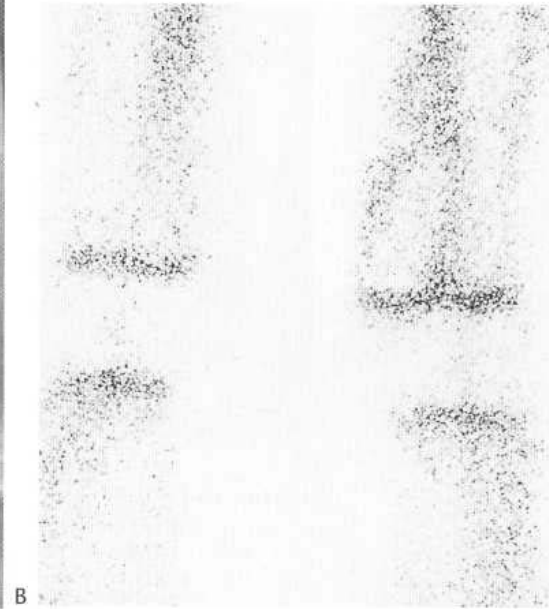


Fig. 40.61 Solitary bone cyst arising in a typical site in the os calcis. The margins in this bone tend to be less well defined.



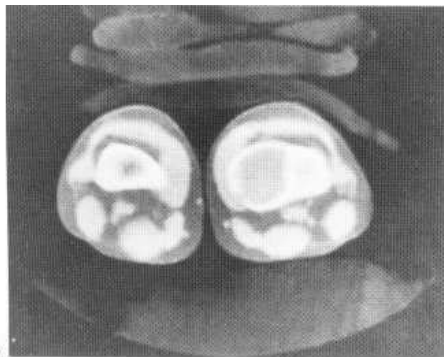
A



B



C



D

Fig. 40.62 Solitary bone cyst of the distal femur. The lesion is rather atypical (A), and plain film diagnosis is not easy. However, it illustrates how further investigations can help in differential diagnosis. A bone scan in the blood-pool phase (B) and in the delayed phase (C) shows increased activity around the margin of the lesion corresponding to sclerosis on plain film. (D) A CT scan demonstrates a soft-tissue density expansile lesion with no calcification. The differential diagnosis includes aneurysmal bone cyst, fibrous dysplasia (monostotic) and a chondroma. Aneurysmal bone cyst is vascular in the blood-pool phase of a bone scan, fibrous dysplasia markedly so on the delayed scan. Calcification may be expected on CT in a chondroma.

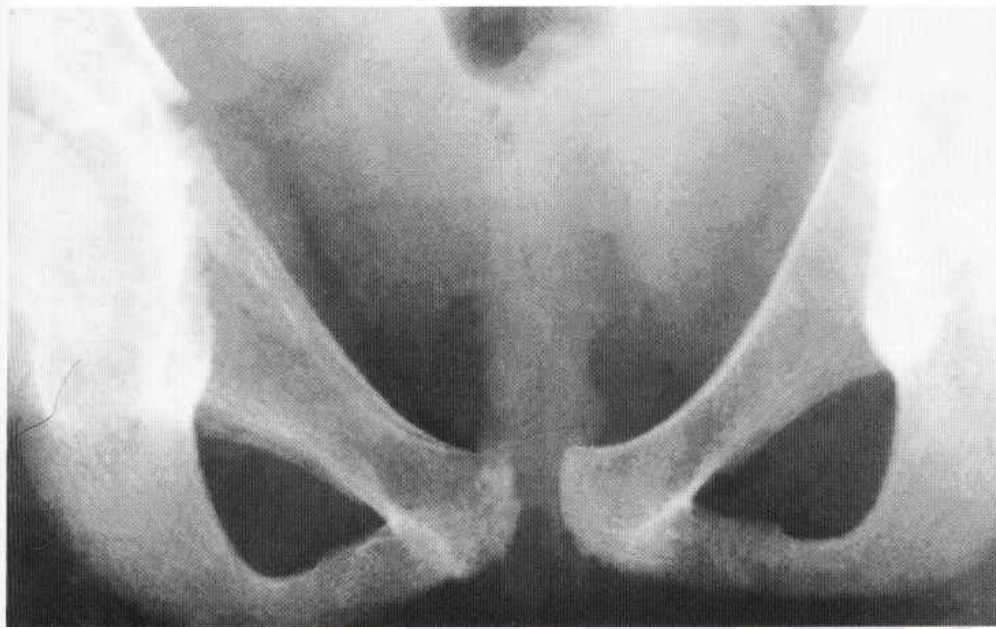


Fig. 40.63 Ewing's sarcoma. The only abnormal sign here is of lamellar periosteal new bone arising from the superior pubic ramus on the right.

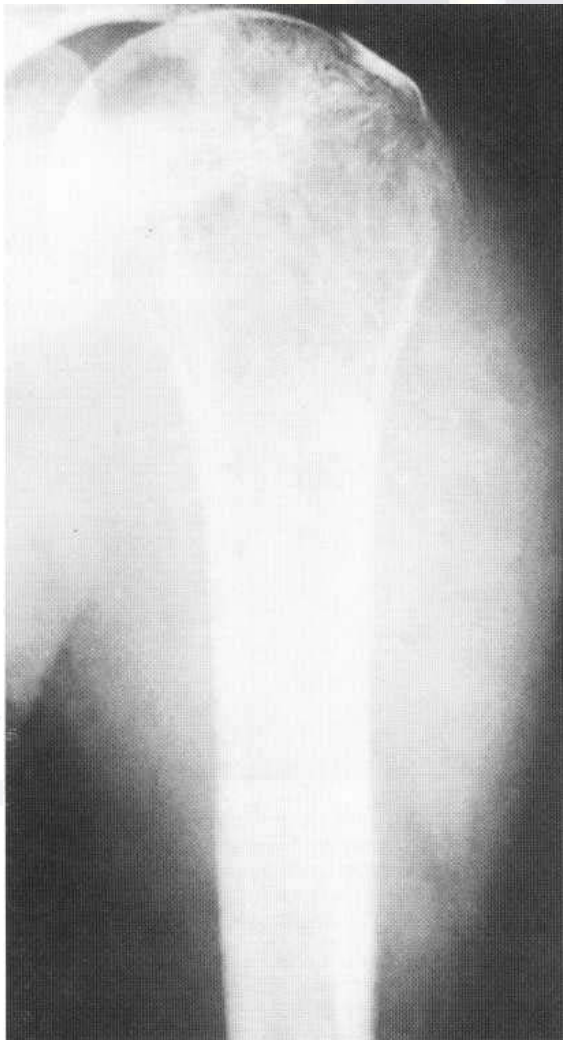


Fig. 40.64 Ewing's sarcoma. This tumour is much more advanced, with a well-defined soft-tissue mass, Codman's triangles, ossification and calcification in the soft tissues and ill-defined bony destruction. The radiological distinction from osteosarcoma is difficult.

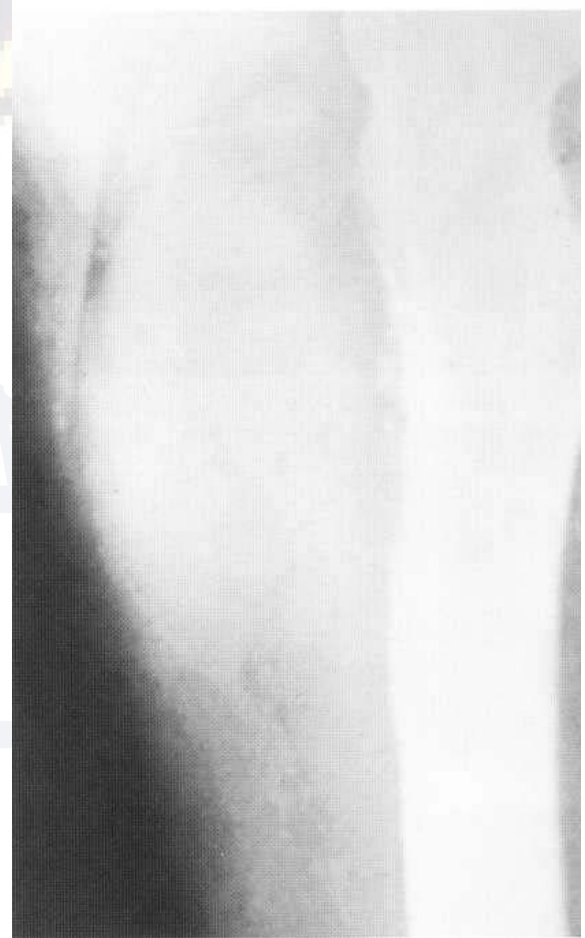
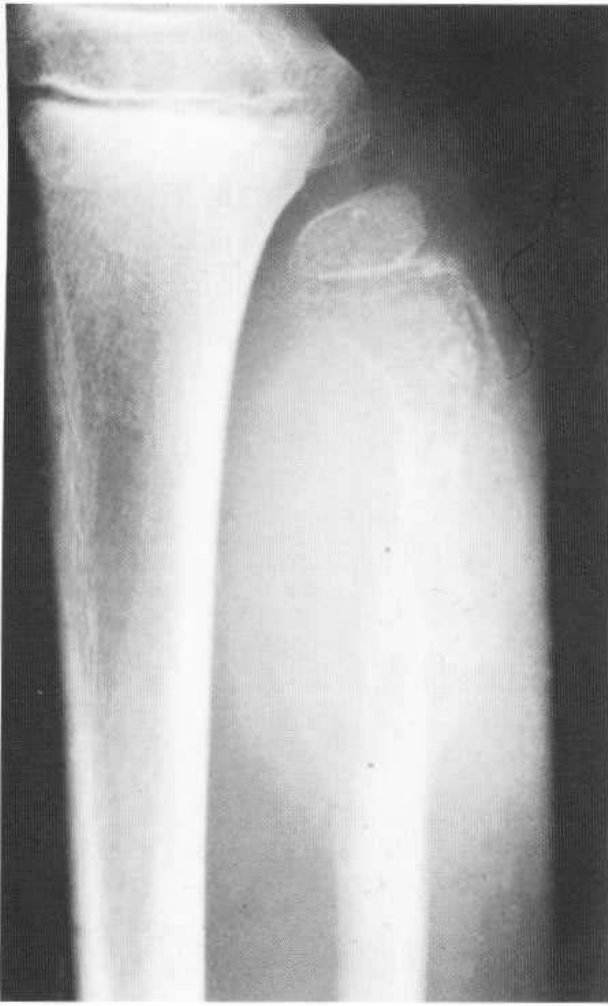
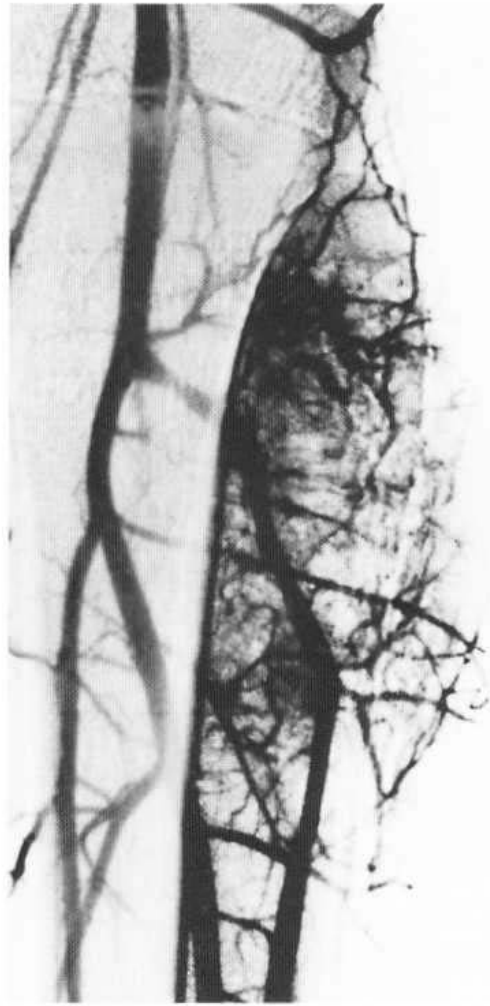


Fig. 40.65 Ewing's sarcoma arising primarily in the soft tissues of the thigh. A well-marked erosion ('saucerisation') defect has been caused with periosteal new bone formation.

type of periosteal reaction is classically associated with this lesion, it is observed only infrequently. Onion-peel periosteal reaction occurs in many other lesions, including osteosarcoma and infection. Elevation of periosteal new bone at the margins of cortical erosions



A



B



C

نشر الکتبر
موسسه اند
نور داد

Fig. 40.66 Ewing's sarcoma of bone arising in the proximal fibula of an 8 year old. (A) An advanced tumour is shown on plain films, with Codman's triangles, a soft-tissue mass and ill-defined bone destruction. (B) The subtraction print of a femoral arteriogram demonstrates a very abnormal circulation with a large soft-tissue mass. (C) A bone scan, in the delayed phase, demonstrates increased activity where new bone formation is present on plain films. The lesion itself is photon deficient. Osteosarcoma may present similar appearances.

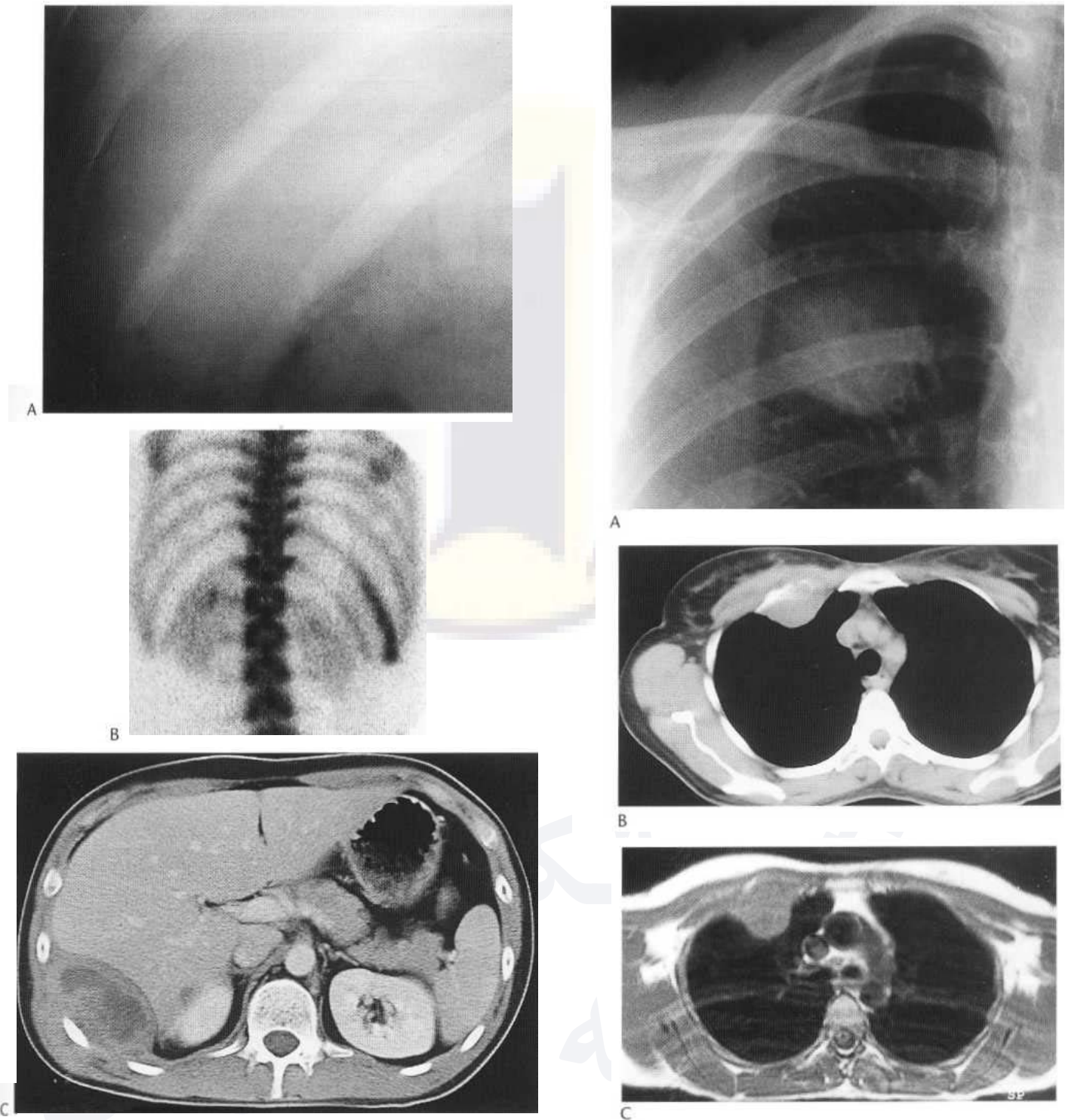
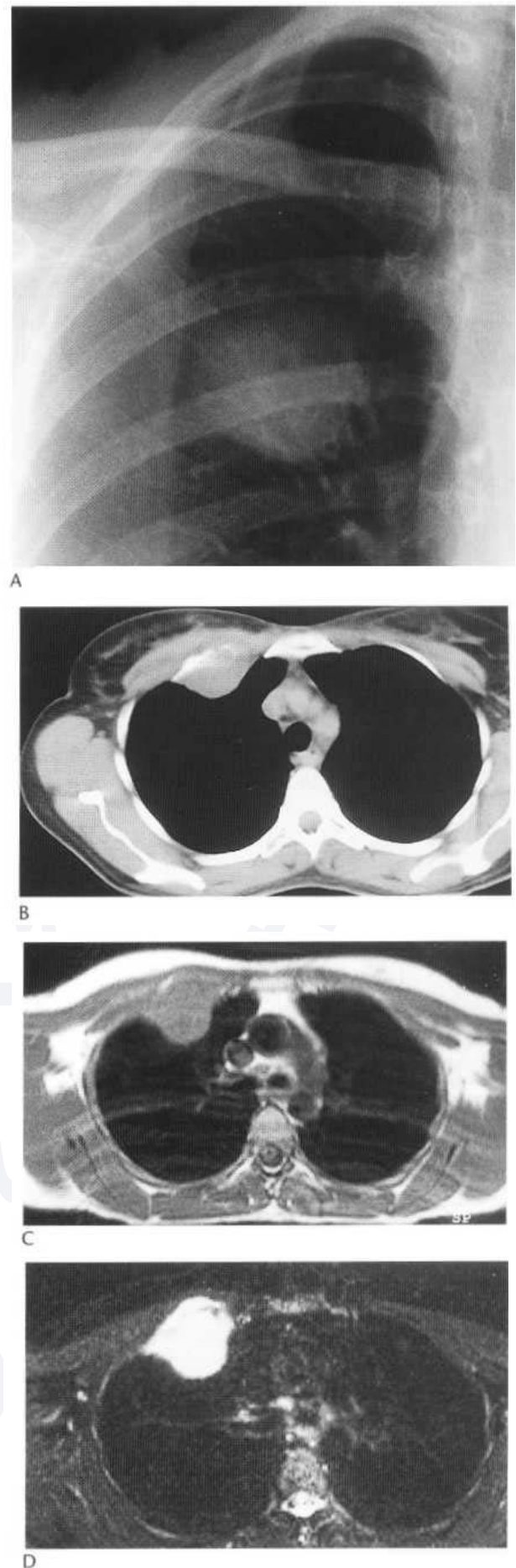


Fig. 40.67 Ewing's sarcoma of a lower rib. The conventional radiograph (A) shows a long moth-eaten lesion of the eleventh right rib which demonstrates prominent increased scintigraphic activity on the posterior bone scan (B). The extent of the associated soft-tissue mass, however, is best demonstrated on the CT (C) of the upper abdomen (dynamic enhanced scan).

Fig. 40.68 Ewing's sarcoma of the anterior aspect of the right second rib. (A) On the conventional radiograph the appearances simulate an intrapulmonary lesion. (B) CT section showing destruction of the second rib and associated soft-tissue mass. (C) On the axial T₁-weighted image the soft-tissue component of the lesion has an intermediate signal intensity, and with the STIR sequence (D) an extremely high signal intensity.



(Codman's triangles) may emphasise the shallow cortical erosions; known as 'saucerisation' defects, they offer a highly suspicious diagnostic feature (Fig. 40.65). The tumour is highly vascular and grows rapidly.

Angiographically, the extensive soft-tissue component and abnormal circulation is obvious (Fig. 40.66). The blood-pool phase of a bone scan also demonstrates increased vascularity, but, in the delayed phase, an increase in activity is evident only at the margins of the tumour within bone and in periosteal new bone.

CT or MRI will optimally delineate the osseous and soft-tissue extent of the tumour, which is often much greater than may be

appreciated on conventional radiographs (Figs 40.67, 40.68). A whole-body radionuclide bone scan is also of value in detecting recurrences and metastasis. The differential diagnosis may be difficult. Osteosarcoma may present almost identical radiological features, and non-malignant conditions such as histiocytosis and aggressive osteomyelitis (particularly from *Staphylococcus*) require consideration.

REFERENCES AND SUGGESTIONS FOR FURTHER READING

See end of Chapter 41.

نشر الکترونیکی
موسسه انتشاراتی
نوردانش

41

DISORDERS OF THE LYMPHORETICULAR SYSTEM AND OTHER HAEMATOPOIETIC DISORDERS

Mark Cobby and Iain Watt

This important group of disorders is responsible for some of the most bizarre radiological abnormalities encountered in the skeleton and may be subdivided conveniently into diseases affecting:

1. Red blood cells
2. White blood cells
3. Lymphoreticular system
4. Coagulation mechanism.

DISEASES PRIMARILY INVOLVING RED BLOOD CELLS

In the infant, red marrow extends throughout the medullary cavities of the whole skeleton with the exception of the epiphyses and apophyses. During the first few months of life, red blood cells are also produced by the spleen and liver, this function being described as extramedullary erythropoiesis. As the physiological requirement for erythrocyte production diminishes progressively during the years of growth, a cessation of this function occurs in the liver and spleen and later by regression of the red marrow areas in the peripheral skeleton. By the age of 20 years, red marrow is normally confined to the proximal ends of the femora and humeri and to the axial skeleton. Residual areas of fatty non-haematopoietic marrow in the appendicular skeleton, as well as the liver and spleen, may be reactivated should the need arise. Such a response occurs normally after a severe haemorrhage. These episodes are insufficiently prolonged to cause conventional radiographic changes although this reconversion from fatty to red marrow is readily identified on MRI.

Chronic haemolytic anaemias

These anaemias, in which red blood cells suffer extensive destruction, are followed in many instances by such a degree of marrow hyperplasia that striking skeletal abnormalities result. The great majority of these diseases are congenital and hereditary in origin. The red blood cells are abnormal in shape, in fragility and in the

type of haemoglobin that they contain. The clinical picture is that of any chronic anaemia. Dyspnoea, pallor, fatigue and weakness are often accompanied by jaundice due to erythrocyte destruction. If extramedullary haematopoiesis occurs, the liver and spleen may be enlarged, particularly the latter, especially when the anaemia is profound. Cardiac enlargement and failure may occur, and many of the more severely affected patients die before puberty.

Radiological changes

Radiological changes in the skeleton resulting from marrow hyperplasia, vary greatly with disease severity. In children, the changes are widespread and are usually demonstrated most easily in the extremities and the skull. To some degree, marrow hyperplasia causes destruction of many of the medullary trabeculae. This is followed by thinning and expansion and even perforation of the overlying cortex. In many patients this hyperplasia achieves its compensatory object, so that a state of erythrocytic balance is reached. The areas of bone destruction show features of repair, by formation of fibrous tissue and the development of reactive bone sclerosis. The latter thickens the remaining trabeculae and, in some, the endosteal aspect of the cortex, to produce an overall increase in bone density. As age advances, the peripheral bones, now in a state of balance, tend to revert to a normal appearance, but some residual increase in density may remain. Evidence of continued erythropoiesis to a greater degree than normal is then confined to the physiological red marrow areas.

Extramedullary haematopoiesis, in addition to producing evidence of hepatosplenomegaly, may be revealed by the presence of sharply defined paravertebral soft-tissue masses of haematopoietic tissue, especially around the thoracic spine (Fig. 41.1).

Thalassaemia (Cooley's anaemia)

Described by Cooley in 1927, this condition, known also as Mediterranean anaemia, is by no means confined to Mediterranean countries or races. The geographical distribution of this condition

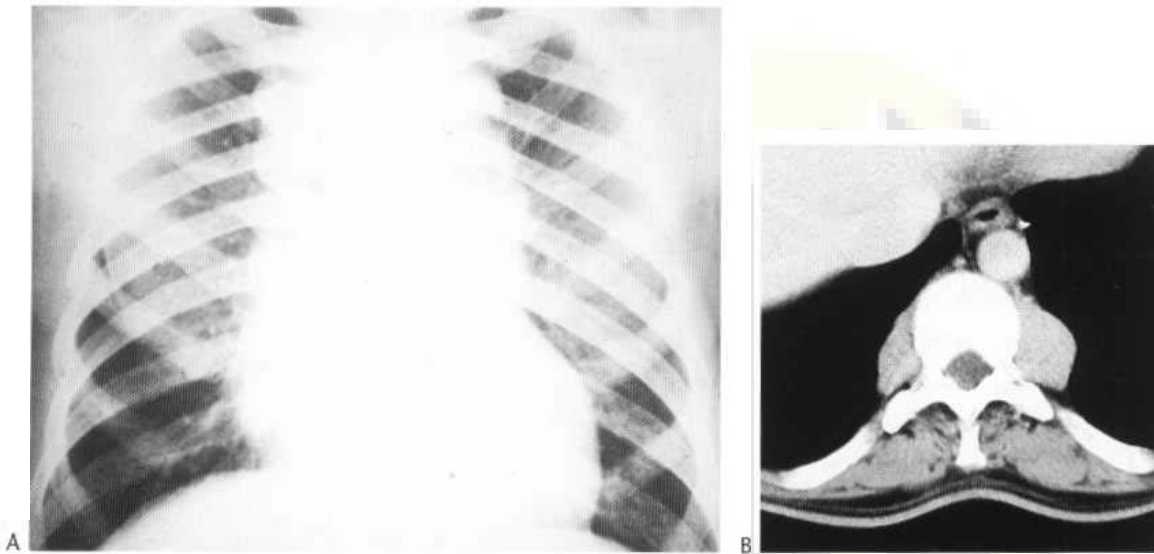


Fig. 41.1 Thalassaemia. (A) Lobulated soft-tissue masses due to extramedullary haematopoiesis are present adjacent to the thoracic spine. (B) In another patient, paravertebral extramedullary haematopoietic tissue is shown in the lower sections of a CT examination of the thorax.

extends eastward in a broad band through Asia and West Africa. In such areas it is commonplace. It may be encountered anywhere in the world in individuals having a heredity originating from these areas.

The disease is due to abnormalities of the haemoglobin molecule, of which many have been established. Homozygous subjects, who have inherited the trait from both parents, develop the more severe form of the disease, known clinically as thalassaemia major, whereas heterozygous subjects develop a minor form. Both may vary greatly in severity, so that the distinction between them and other haematological variants is of relatively little radiological importance. Severe forms usually become manifest in the first two years of life. Although the majority of these patients die before puberty, some survive to early adult life. Those with less severe disease live correspondingly longer and minimal manifestations may be found only by examination of the blood of individuals who otherwise appear entirely normal. The important clinical features, in addition to those of other anaemias, are dwarfing, delay in development of secondary sexual characteristics, and either 'mongoloid'

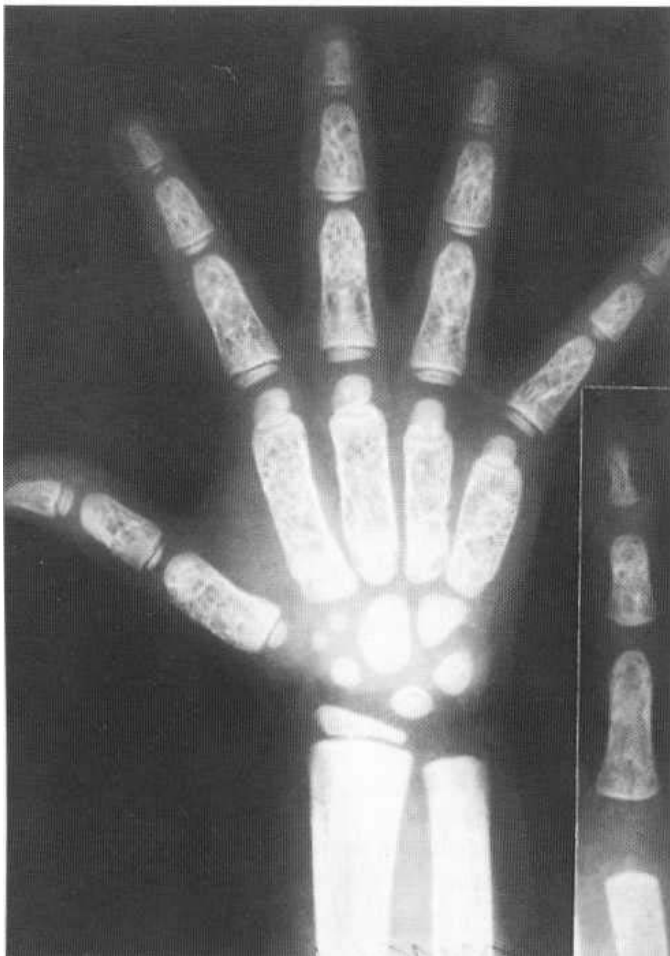


Fig. 41.2 Thalassaemia (boy aged 7). Gross marrow hyperplasia has expanded and thinned overlying cortical bone. Medullary trabeculae have been destroyed and the residual ones are coarsened. Inset—early changes of the same type in a finger of a child aged 4.



Fig. 41.3 Thalassaemia (boy aged 15). A chest film shows gross expansion of bone structures due to marrow hyperplasia. Note particularly involvement of the ribs and scapulae.

or 'rodent' facies clue to expansion of the underlying facial bones because of erythroblastic hypertrophy.

Radiological changes

Hyperplasia of the marrow destroys many of the medullary trabeculae and expands and thins the overlying cortex. In children this is evident especially in the hands, when the shafts of the phalanges and metacarpals become biconvex instead of being biconcave (Fig. 41.2). The feet are affected in the same way. Similar abnormalities in the ribs (Fig. 41.3) and long bones (Fig. 41.4) may produce apparent failure of modelling with, for example, flask-shaped femora (Fig. 41.5). In the skull the diploic space is widened and gross thinning of the outer table may be followed by marked diploic thickening, starting in the frontal region, but usually exempting the occipital bone in which the marrow content is minimal (Fig. 41.6). The 'classical' appearance of the 'hairbrush' spicules is relatively uncommon. These changes appear considerably later than those in the short bones of the extremities. Development of the air spaces of the skull, especially the maxillary antra and the mastoids, is impaired because of hyperplasia of the marrow, accounting for the clinical manifestation of 'rodent' facies, with malocclusion. The spine shows only diffuse demineralisation with the same generalised coarsened trabecular pattern as that observed in the appendicular skeleton. Vertebral collapse is uncommon.

Osseous abnormalities of this type may be observed also in a number of lesser forms of thalassaemia and its variants, including those associated with other abnormal haemoglobins and the sickle cell trait. In all these conditions, however, the changes tend to be very much less prominent than in thalassaemia major.



Fig. 41.4 Thalassaemia. Considerable bone expansion, cortical thinning and simplification of trabecular pattern are demonstrated in the forearm of a boy of 15.



Fig. 41.5 Thalassaemia. Considerable marrow expansion has produced a flask shape of the distal femur. The coarsened trabecular pattern and cortical thinning are obvious.

Sickle cell disease

This chronic haemolytic anaemia is congenital and hereditary in origin. The erythrocytes, when hypoxic, become abnormal in shape, being unusually long and slender. The abnormal haemoglobin that they contain has a reduced oxygen-carrying capacity. The disease occurs almost exclusively in black-skinned races, especially those in Central Africa or their descendants, who are homozygous for the sickling trait. This trait may be crossed with normal or abnormal haemoglobins, including thalassaemia. In these crossed types, the patient is less severely affected, both clinically and radiologically. Differentiation of the true homozygous state from the variants (of which combination with haemoglobin C is the most common) is of some importance. The former group rarely survives after the age of 30, whereas the latter may have a normal lifespan. The former is characterised clinically by early onset of the severe anaemic picture, with frequent skeletal and abdominal crises. These acutely painful episodes, lasting for several days, are due essentially to infarction, attributed to vascular blockage by collections of erythrocytes which have undergone sickling in areas of capillary stasis with resultant hypoxia.

Infarcts may affect many systems. The fundamental skeletal abnormalities consist of hyperplasia of marrow with superimposition of areas of bone necrosis due to infarction and subsequent growth disparities. A further clinical complication is the develop-

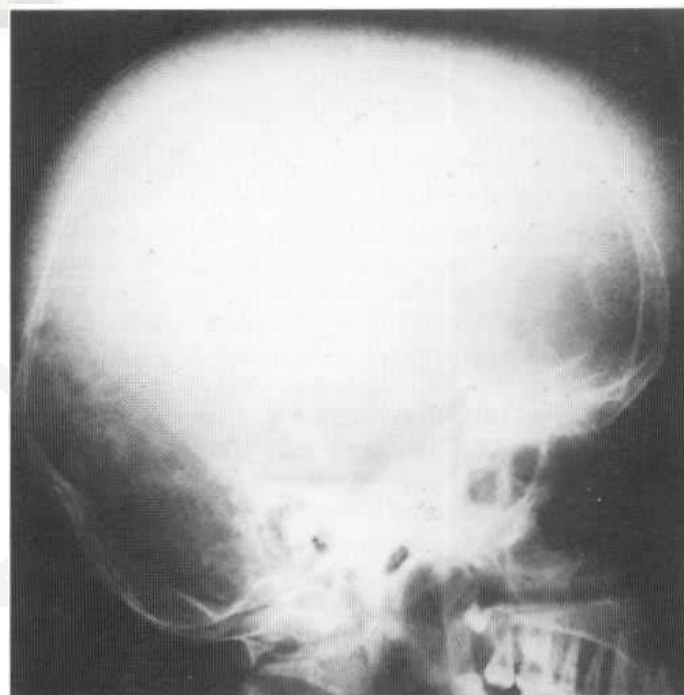


Fig. 41.6 Thalassaemia. Thickening of the outer table of the skull in the frontal area with perpendicular striation-'hairbrush sign'.

ment of infection within these infarcts, particularly in lesions developing in the long bones of children.

Radiological changes

The chronic haemolytic state is reflected by the development of characteristic and diagnostic radiological abnormalities, affecting primarily the erythropoietic skeleton, and also the soft tissues involved by extramedullary haematopoiesis. The frequency with

which abnormalities are discovered increases with age. All variants of sickle cell disease produce essentially similar radiological abnormalities.

1. *Marrow hyperplasia* is fundamental. In this disease, however, the effects on the skeleton, which are so prominent in thalassaemia major, occur in modified form, even in its worst clinical manifestations being less severe. A generalised osteoporotic appearance is evident throughout the haematopoietic areas of the skeleton, but even in infants and children it is recognised more easily in the axial than in the peripheral skeleton. This feature is not diagnostic, but in a black-skinned child should arouse suspicion. Unlike severe thalassaemia, significant modelling abnormalities are uncommon so that the air spaces of the paranasal sinuses are rarely affected. The diploic space of the skull may be widened, with consequent bossing. If a state of erythrocytic balance is achieved, diffuse trabecular thickening is likely to develop.

Such an appearance may be shown incidentally in an asymptomatic adult sickle cell trait carrier. In more advanced cases, a coarse medullary pattern is associated with enlarged vascular channels in bone, especially in proximal or middle phalanges.

2. *Endosteal apposition of bone*. Inward cortical thickening is separated occasionally by a thin zone of translucency, to result in the appearance in the long bones of 'a bone within a bone'. This sign may be observed in other conditions, including Gaucher's disease (see below). The medullary cavities, in severe cases, may ultimately be grossly narrowed and almost obliterated, so that a diffuse and generalised increase in bone density results. This does not occur in the axial skeleton, which is a persistent red marrow area, and this provides an important diagnostic feature even in the absence of other signs.

3. *Infarction of bone* provides the diagnostic hallmark of this disease. Infarction of various tissues is considered the cause of the classic clinical episodes of sickle cell crises. Unlike thalassaemia, in which infarction is virtually unknown, this type of involvement of the skeleton is common. The consequent radiological abnormalities are comparable to those observed in other systemic disorders such as dysbaric osteonecrosis (caisson disease) and Gaucher's disease. Such infarcts are usually multiple and most commonly affect the femoral and humeral heads (Fig. 41.7), and, in particular, medullary bone. Medullary infarcts may be of two varieties, with either sharply defined margins or producing diffuse sclerosis. In their mildest form they may be recognised in an asymptomatic patient. The classic 'snowcap' sign refers to the subarticular area of increased density, particularly in a humeral head, which reflects the revascularisation of an area of bone that has been necrotic (Fig. 41.8). At this phase of development bone scans are usually abnormal with increased activity. Nevertheless, in acute infarction a photon deficiency is often present within 24 hours of the insult (Fig. 41.9). Repairing bone is brittle, however, and fractures easily—varying from 'osteochondritis dissecans' to complete collapse.

Femoral heads affected in childhood present an appearance exactly comparable to Perthe's disease (Fig. 41.7). In young black-children the areas of predilection for infarctions are the small tubular bones of the hands and feet (Figs 41.10, 41.11), causing destructive changes accompanied by massive and painful soft-tissue swellings and periosteal reactions which may be florid and reflect associated infarction of cortical bone (sickle cell dactylitis or 'hand-foot' syndrome). These findings may indicate the correct diagnosis, but other causes of infantile periosteal reactions such as cortical hyperostosis

of the infantile or traumatic types, tuberculous dactylitis, or possibly hypervitaminosis A, may require consideration. The formation of perpendicular bony spicules on the skull, uncommon even in thalassaemia, is distinctly unusual. More important is the possibility of superadded infection, which is discussed below.

Infarcts of vertebral bodies are another characteristic radiological stigma. Generalised depressions of the central portions of the vertebral end-plates are common, and may be demonstrated in an asymptomatic patient. The depressions are often concave and rounded, initially simulating an ordinary nucleus pulposus impression on a bone that is already porotic. Infarction may be diagnosed when the centre of the depression is flat and the sides slope obliquely, producing characteristic H-shaped vertebrae (Fig. 41.12).

The diaphyses of the long bones, especially in the older child and the adolescent, are sites of predilection for infarction. Typically they involve the zones between the mid diaphysis and the metaphysis, the so-called 'intermediate fifths'. When the metaphysis is involved significant deformity may occur due to growth arrest. *Central metaphyseal defects* and lucencies are typical. These in turn may produce fragmentation and deformity of the epiphyses. They may also be the sites of pathological fractures. Infarcts may be massive, causing bone destruction, sequestration, reactive sclerosis and even the formation of involucrum. The pattern may suggest acute pyogenic osteomyelitis.

4. *Superadded infection*. The areas of bone necrosis caused by infarction are especially susceptible to infection, classically by salmonella organisms of the paratyphoid B group. Differentiation between the pure infarct and those that have been infected in this



Fig. 41.7 Sickle cell disease. Infarction in the proximal femoral metaphysis has produced a large defect with avascular necrosis of the femoral head. These features are similar to those of Perthe's disease.

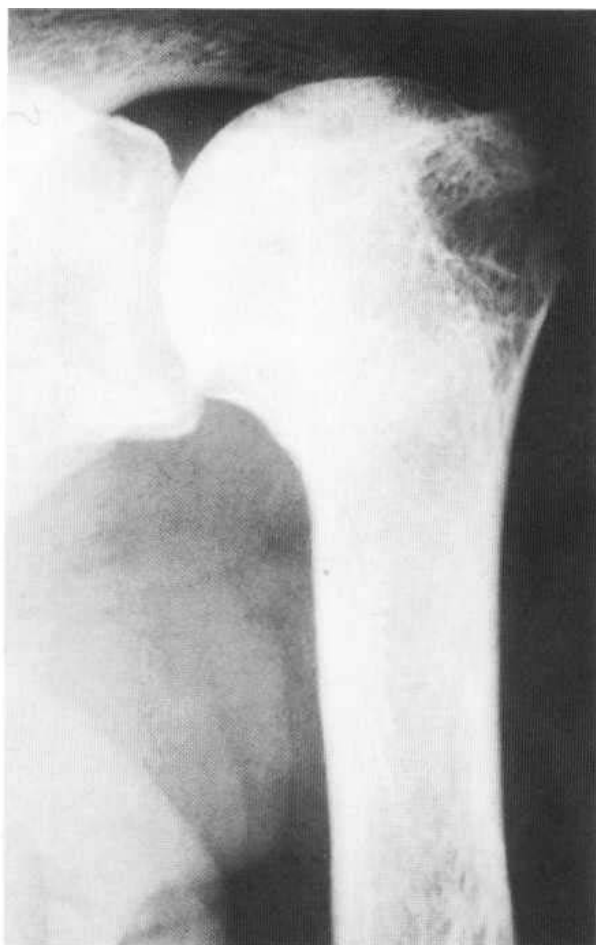


Fig. 41.8 Sickle cell disease. Endosteal bone deposition has resulted in diffuse sclerosis beneath the articular surface (the 'snow-cap' sign) due to medullary infarction. Note the lack of distinction between cortical and medullary bone in the upper humeral shaft, again due to endosteal deposition of bone.



Fig. 41.10 Sickle cell disease. Soft-tissue swelling surrounds an expanded proximal phalanx. Medullary expansion is present with simplification of trabecular pattern and penetration of the cortex. The distinction between these changes and osteomyelitis is extremely difficult.

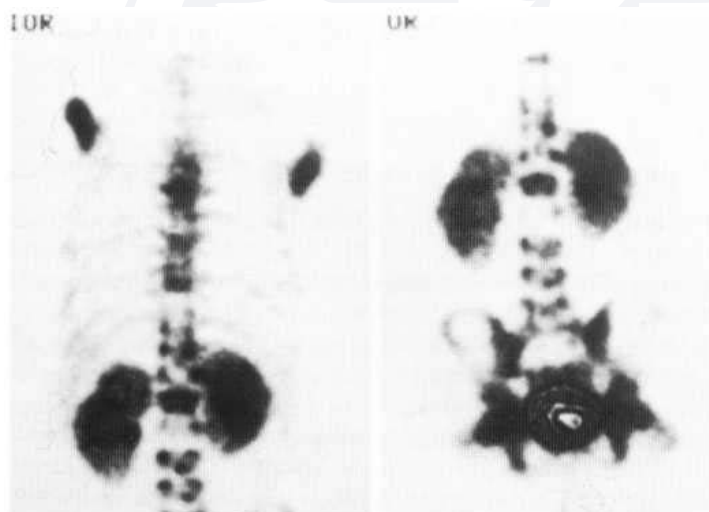


Fig. 41.9 Sickle cell disease. A bone scan performed 16 hours after the onset of severe pain in a boy with known sickle cell disease. Acute infarction of L2 has resulted in a relative photon deficiency in this area. Previous infarctions, in varying phases of evolution, are shown as areas of increased activity (see particularly L1 and midthoracic vertebrae).

way may be extremely difficult (Fig. 41.13) both radiologically and pathologically, since cultures are often sterile. Such lesions are liable to occur especially in the tubular bones of the hands and feet in infants and in the long bones and the spine of older children (Fig. 41.12). In the adult, septic arthritis may be superimposed on an adjacent infarct. With appropriate treatment, either by conservative antibiotic therapy or by active surgical measures, including sequestrectomy, healing usually takes place with remarkable rapidity.

5. Soft-tissue involvement may be seen as in other chronic haemolytic anaemias and such disorders of the marrow as Gaucher's disease. These may consist of heterotopic masses of haematopoietic tissue in the dorsal paravertebral areas as well as hepatosplenomegaly. Heterotopic masses of haematopoietic tissue may develop in the dorsal paravertebral areas. Release of iron pigments by accelerated destruction of erythrocytes may hasten the formation of biliary calculi.

Erythroblastosis fetalis (haemolytic disease of the newborn)

Haemolytic anaemia occurring in the fetus and newborn results from immunological incompatibility between the blood of the

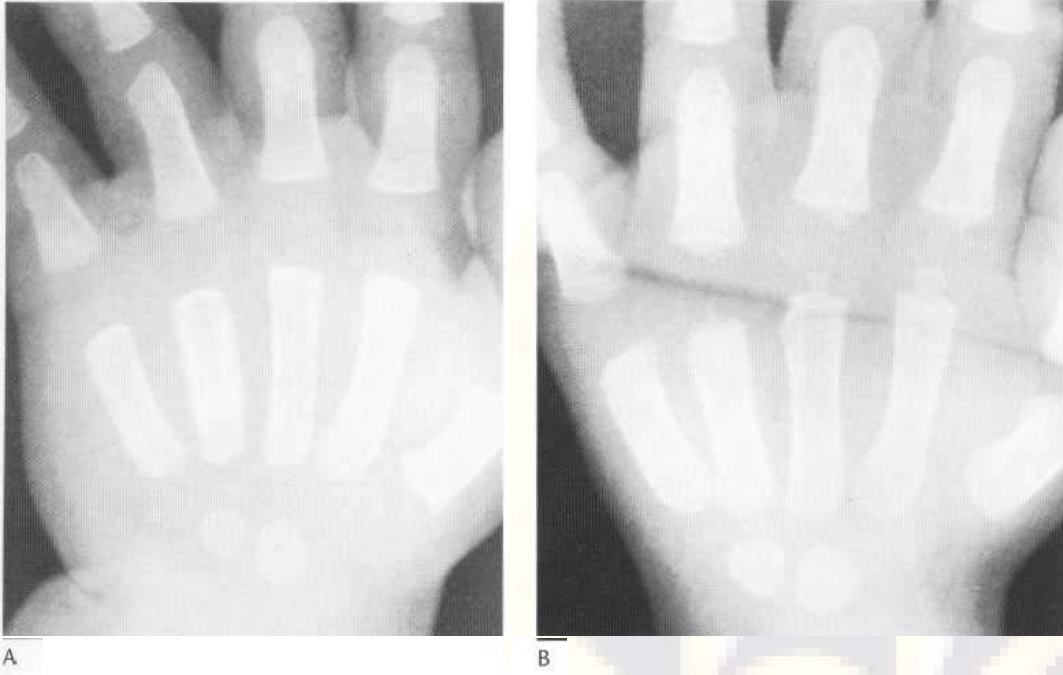


Fig. 41.11 Sickle cell disease, infarction in childhood. (A) At presentation, periosteal new bone formation surrounds the diaphysis of the fourth finger metacarpal. (B) Ten months later resolution has occurred and growth has proceeded normally. The distinction between infarction and infection may be very difficult. In this case no specific treatment was given.



Fig. 41.12 Sickle cell disease. Flat depressions within the vertebral bodies with sloping sides typify metaphyseal infarct ('the vertebral step sign' or H-shaped vertebra). Frank destruction of the vertebral body with narrowing of the contiguous disc spaces is due to associated salmonella osteomyelitis.

mother and the fetus, most commonly due to Rh factor, although other haematological errors of this type are known. The severity of the affection of the infant may vary widely, from a mild anaemia to icterus neonatorum and fetal hydrops.

The Rh-positive erythrocytes of the fetus, crossing the placental barrier in a mother without Rh antigen, stimulate maternal formation of anti-Rh antibodies that traverse the placenta to enter the fetal circulation, there to haemolyse the fetal red blood cells. The danger of infants being affected by this incompatibility increases with the number of conceptions, but early recognition of the disorder and the adoption of prophylactic measures has greatly reduced its incidence.

Radiological changes

The only skeletal abnormality is the development of transverse metaphyseal translucencies in the long bones. These translucencies are non-specific, as they may occur also with other severe maternal illnesses during pregnancy and in congenital syphilis. With successful treatment the translucent areas ossify with residual growth lines. In the spine, such growth lines often cause 'ghost shadows' within the vertebral bodies. Fetal hydrops may be diagnosed sonographically (see Ch. 33) by the detection of growth retardation, effusions and subcutaneous oedema. The fetus is displaced by enlargement of the placenta.

Other chronic anaemias

The anaemia of infants suffering from *iron deficiency* may produce radiological changes in the skull due to marrow hyperplasia similar to those of the less severe congenital anaemias. An inadequate diet is the usual cause, but malabsorption or abnormal loss of iron may be important factors. The widening of the diploic space and the subsequent bossing of the skull vault are again characteristic, but the disease has never been reported to cause changes sufficiently severe to involve the long bones and facial bones.

Hereditary spherocytosis

This is an inherited defect in which the red blood cells are of an abnormal round shape. The anaemia which results may produce mild changes comparable to the other congenital anaemias. Removal of the spleen permits the bone structures to revert to a normal appearance.

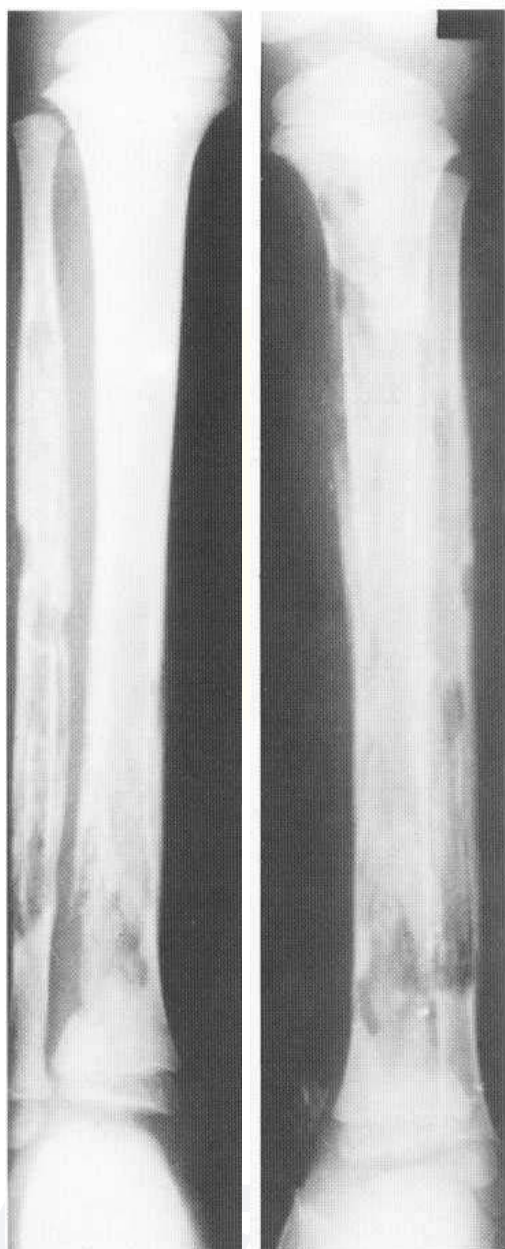


Fig. 41.13 Sickle cell disease with salmonella osteomyelitis. (Nigerian boy aged 4). Extreme destructive changes in the long bones have been caused by infection superimposed upon infarction. Numerous sequestra are present. (Courtesy of Mr Geoffrey Walker.)

Fanconi's syndrome

This syndrome of congenital aplastic anaemia with multiple congenital anomalies (not to be confused with the other syndrome described by the same author and concerned with osteomalacia and an abnormal renal tubular mechanism) is of interest in that the haematological changes are unlikely to appear before the age of 2 years. These consist of hypoplastic anaemia, marrow hypoplasia and skin pigmentation. The defect is inherited and congenital abnormalities of the skeleton are associated, such as deficient formation of the bones of the thumb, first metacarpal and radius; other abnormalities, including congenital dislocation of the hip and club foot, have also been observed. These are evident long before the haematological abnormalities become apparent, and the latter are not responsible for any skeletal abnormalities. Some cases have terminated in leukaemia.

Polycythaemia

This condition is due to overproduction of red cells. Although occasionally responsible for bone infarction, it produces no characteristic radiological changes in the skeleton. Transition to myeloid metaplasia is common. Pulmonary abnormalities in polycythaemia may occur in the form of increased reticulation or fine mottling.

DISEASES PRIMARILY INVOLVING WHITE BLOOD CELLS

Leukaemia

Children are most commonly affected, almost invariably by an acute form. In adults the disease may also be acute, but it is more commonly chronic. Haematopoietic tissue is widely distributed throughout the skeleton of a child but is confined in the adult to the 'red marrow' areas of the axial skeleton and the proximal ends of the humeri and femora. Thus, radiological changes in the bones are commonly in the younger age groups. More than half the children affected show skeletal abnormalities, while in adults these are found in fewer than 10% of cases. While the diagnosis is usually confirmed by examination of the blood and sternal marrow, bone changes may precede the development of a grossly pathological blood picture, especially in the so-called *leukemic* type.

Differentiation between myeloid and lymphatic types of leukaemia cannot be made by radiological examination.

Radiological changes

These are observed mainly in *children* and consist of the following:

1. *Metaphyseal translucencies.* In children the most characteristic sign, occurring in 90% of cases, is the presence of bands of translucency running transversely across the metaphyses (Figs 41.14, 41.15). Such bands may be narrow and incomplete in the early stages of the disease, but in the course of a few weeks they may be found to traverse the metaphyses completely and be as much as 5 mm in width. The most rapidly growing areas—knees, wrists and ankles—are commonly affected first, but later the metaphyses of the shoulders, hips and vertebral bodies also may be involved. With treatment, remission may occur, and the bands of translucency resolve.

2. *Metaphyseal cortical erosions* on the medial side of the proximal ends of the humeral (Fig. 41.16A) and tibial shafts sometimes occur as an early feature. They are usually bilateral.

3. *Osteolytic lesions* develop in over half the cases. Usually they are punctuate and diffusely scattered, though solitary and larger lesions may occur. While any portion of the skeleton may be involved by such leukaemic deposits, they are commonest in the shafts of the long bones (Fig. 41.17). When the vertebral bodies are involved, collapse often takes place before specific areas of rarefaction can be identified (Fig. 41.16B).

4. *Periosteal reactions* are usually associated with underlying bony lesions.

5. *Osteosclerosis of the metaphysis* is a rare but well recognised primary manifestation. It may develop during treatment.

In *metastatic neuroblastoma* skeletal changes take place which may be indistinguishable from leukaemia. Separation of the sutures of the skull in the former condition is a helpful differentiating sign.



Fig. 41.14 Acute leukaemia. Extensive metaphyseal radiolucencies are present with adjacent periosteal new bone formation.

In *adults* skeletal lesions are rare. As has been stressed before, the deposits occur essentially in red marrow areas. Changes include *porosis*, *translucent areas* of leukaemic bone destruction (which tend to be oval with the long axis parallel to the shaft), and *vertebral destruction* and *collapse*. Periosteal reactions are unusual. Occasionally, generalised *osteosclerosis* of the marrow area is evident. This is likely to be caused by trabecular thickening during periods of remission and may be patchy in type. In some instances, however, the leukaemic changes may be a secondary and terminal process in myeloid metaplasia.

Myeloid metaplasia (myelofibrosis and myelosclerosis)

This syndrome is characterised by the triad of myelofibrosis, myeloid metaplasia and features in the peripheral blood film which simulate leukaemia. The relationship between myeloid metaplasia, myelosclerosis and other diseases, including polycythaemia rubra vera and chronic myeloid leukaemia, is intimate. The typical patient is a middle-aged or elderly adult, the primary disorder being metaplasia of the marrow cells to fibrous tissue. The usual presenting complaints are fatigue and abdominal fullness due to hepatosplenomegaly. Obliteration of the haematopoietic tissue results in progressive anaemia, the appearance of immature red and white cells in the peripheral blood and compensatory splenomegaly. In the later stages of the disease, the fibrous tissue becomes converted to bone, and endosteal cortical thickening develops. Polycythaemia may be followed by myeloid metaplasia and it appears probable that nearly half of the developed cases of myeloid metaplasia previously had some form of this blood disorder. Purine hypermetabolism may manifest itself as secondary gout.

Radiological changes

In the sclerotic stage of the disease increased density of the hones may be diffuse or patchy in nature. Areas of relative translucency

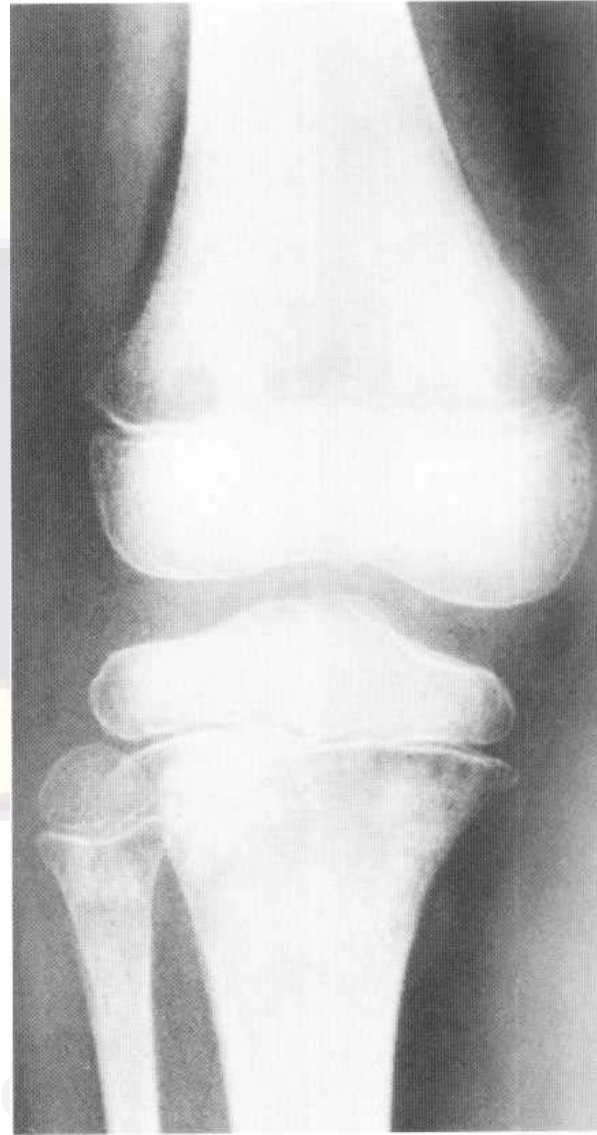


Fig. 41.15 Lymphatic leukaemia. Metaphyseal radiolucencies are present around the knee. Endosteal sclerosis is present adjacent to these lesions, obscuring the corticomedullary junction. Minor periosteal new bone formation is present in the upper tibia and fibula.

due to fibrosis may persist (Figs 41.18, 41.19). The increased density is due to new bone deposition on the trabeculae and to the endosteal cortical thickening with loss of the normal cortico-medullary distinction. Narrowing of the medullary space becomes clearly visible and resembles, in the long bones, the later stages of sickle-cell anaemia. Irregular periosteal reactions may occur, particularly near the ends of long bones. These may be well organised and continuous with the cortex or separated from it by a zone of translucency. While the red marrow areas (particularly the pelvis) are especially subject to these pathological changes, the whole skeleton may be affected. Density of the skull is associated with obliteration of the diploic space, though some persistent areas of fibrosis may remain translucent. Splenomegaly is almost invariably evident (Fig. 41.20).

Differentiation must be made from other conditions causing a generalised increase of bone density. The congenital sclerosing dysplasias, including osteopetrosis, are likely to be encountered in adult life only as an incidental finding or in association with a pathological fracture. Fluorosis is likely to occur in an endemic area.

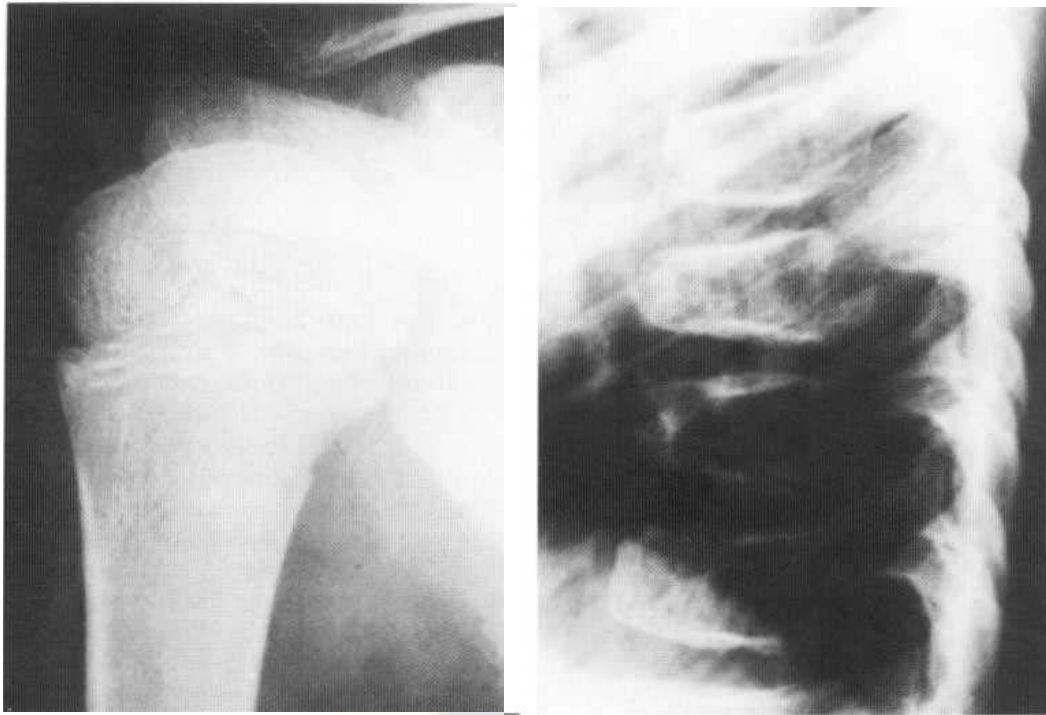


Fig. 41.16 Lymphatic leukaemia. (A) Erosions of the medial side of the proximal metaphyses of both humeri were present in this 8 year old. The disease was in an aleukaemic phase, not an uncommon finding even when skeletal changes are present. (B) The same child complained of back pain. Multiple vertebral collapse is shown with the preservation of disc-space height. Overall bone density is reduced with a simplified trabecular pattern.

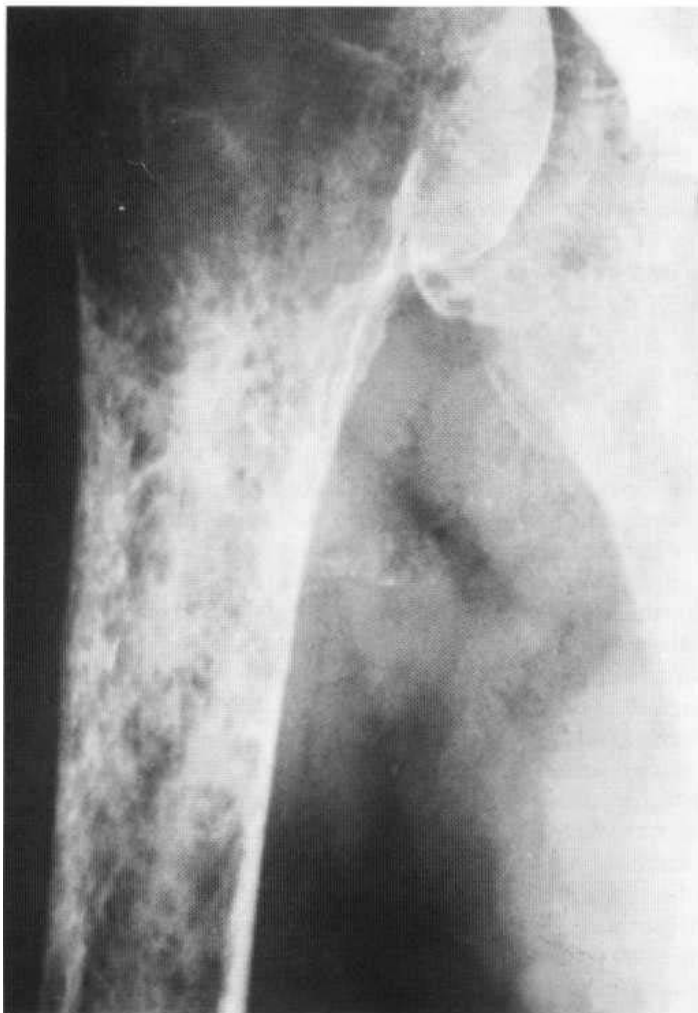


Fig. 41.17 Chronic lymphatic leukaemia-adult type. Diffuse medullary infiltration is shown in the humerus and scapula with cortical erosion.



Fig. 41.18 Myeloid metaplasia. Widespread but patchy areas of sclerosis are shown throughout the pelvis and lumbar spine.

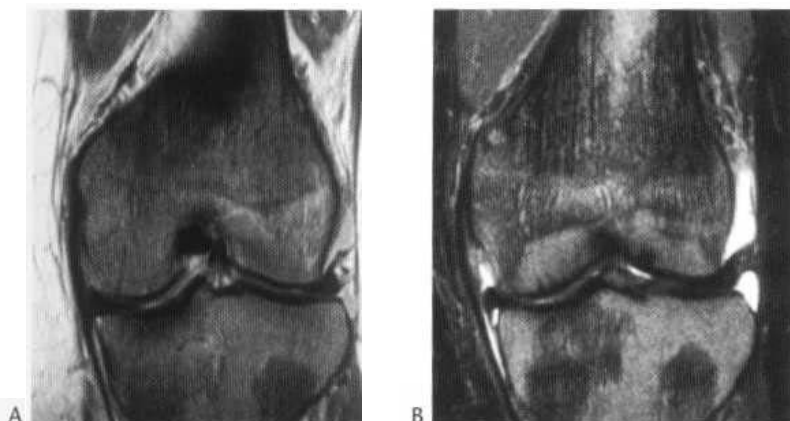


Fig. 41.19 Coronal intermediate weighted (A) and T₂-weighted (B) MR images of the knee in a patient with myelofibrosis showing replacement of the normal high-signal-intensity fatty marrow by fibrosis. This, and the abnormal bone deposition around the trabeculae, results in the diffuse low signal intensity from the medullary cavity.

Mastocytosis may cause some confusion, but the lesions are usually less diffuse and are accompanied by urticaria pigmentosa. Sclerosing and widespread metastasis, particularly prostatic, should not be forgotten.

- A. Lymphomas: including Hodgkin's and non-Hodgkin's lymphomas
- B. Plasma-cell disease: plasmacytoma and multiple myeloma
- C. Histiocytosis
- D. Storage disorders: Gaucher's disease and Niemann-Pick disease.

DISORDERS OF THE LYMPHORETICULAR SYSTEM

Four main groups of disorder will be considered, divided for convenience as follows:

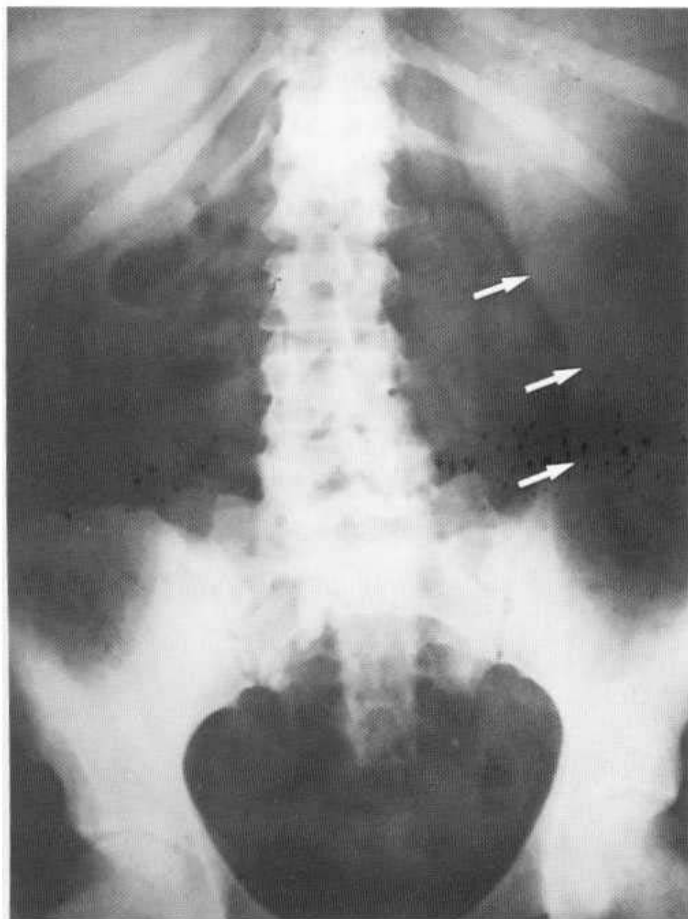


Fig. 41.20 Myeloid metaplasia (woman aged 63). All the bones are diffusely dense with lack of distinction between cortical and medullary bone. The spleen is grossly enlarged (arrows).

THE LYMPHOMAS

The classification of the proliferative disorders of the lymphoreticular system is changing constantly and is based essentially upon histological features detected in lymph nodes. Consequently, caution is necessary in extending such classifications to bone or bowel lymphoma. Malignant lymphoma is a generic term embracing all previously named tumours, including Hodgkin's disease, lymphadenoma, lymphosarcoma, reticulum cell sarcoma and others.

Malignant lymphomas

These may be subdivided into two groups: Hodgkin's disease and a group of non-Hodgkin's lymphomas.

Hodgkin's disease

This defined tumour has an agreed classification on histological grounds, named after Rye. This comprises nodular sclerosing Hodgkin's disease, a complaint of young women involving int athoracic lymph nodes, and three categories, lymphocyte-predominant Hodgkin's disease, mixed cellularity Hodgkin's disease and lymphocyte-depleted Hodgkin's disease. The last three comprise a spectrum with, in order listed, worsening outlook. Bone involvement always implies a less favourable prognosis. It is a feature of widespread disease and has been found at postmortem in more than half of cases. Skeletal lesions at presentation are far less common. Primary Hodgkin's disease of bone probably does not occur. There is no correlation between the variety of Hodgkin's disease and the nature of the individual bony lesions it produces.

The age of onset varies widely from childhood to old age but the diagnosis is most commonly made in young adults. The red marrow areas are the most frequent sites of presentation, the majority of lesions being found in the spine, thoracic cage and pelvis. Bone pain may precede, by several months, the development of these lesions and the importance of serial radiological examination, either radiographic or scintigraphic, must be stressed.

Radiological changes

In the skeleton the majority of early lesions are destructive and often large at the time they are first observed, either from direct involvement from affected soft tissues, particularly lymph nodes, or from infiltration of bone marrow. About a third are essentially osteolytic in type (Fig. 41.21). The majority is however of mixed type with patchy sclerosis and destruction (Fig. 41.22). Diffuse trabecular thickening causes sclerotic lesions in the remainder (Fig. 41.23).

Such an appearance may develop in a few months, being preceded by bone pain, and may well show no preliminary bone destruction. It may also follow treatment of a formerly osteolytic lesion.

Conversely, some sclerotic lesions may be observed to become osteolytic or normal following treatment (Fig. 41.23). Whereas the osteolytic lesions may thin, displace and erode the overlying cortex and develop associated soft-tissue masses, the primary sclerotic lesion does not cause enlargement of the affected bone. Skeletal scintigraphy is a sensitive means of detecting the presence of bony lesions, particularly when sclerotic deposits have developed. The method is less reliable when purely lytic lesions are present. MRI is extremely sensitive (Fig. 41.24).

The spine is by far the most frequently involved area. A feature that is almost diagnostic is anterior erosion of a vertebral body (Fig. 41.25). This may or may not present reactive sclerosis in its margin and is attributed to involvement of adjacent paravertebral lymph nodes. Several vertebrae may be affected and the osteolytic lesions are likely to collapse. Soft-tissue masses will stimulate paravertebral abscesses. The sclerotic type shows a diffuse increase of density, possibly also with some anterior erosion but without increase in size of the affected body. A solitary dense vertebra, especially in young adults, is suggestive of this disease. In all these types the intervertebral discs are usually spared, aiding differentiation from an infection. Even in the rare cases where a disc space does become narrowed, preservation of density of the vertebral end-plates usually permits differentiation from an infective discitis where loss of this density is an early diagnostic sign. Lesions in the ribs may be found by themselves, sometimes being observed in a chest radiograph. They are usually osteolytic and expanding in type.

The sternum is also a not-infrequent site for a lesion to appear, again usually osteolytic, but sometimes mixed in type with perpendicular spicules of new bone. Presternal and retrosternal soft-tissue swelling is not uncommon (Fig. 41.21). In the pelvis, mixed or sclerosing types tend to predominate. The medial portions of the innominate bones are often dense. Osteolytic lesions, rather non-specific in appearance, are not uncommon in the ischia and change from either type to the mixed pattern may be observed in serial examinations.

In the long bones the sites of predilection are the red marrow areas in the proximal portions of the femora and humeri. These are usually of the osteolytic type and many small translucencies, oval in the long axis of the bone, extend throughout the marrow cavity associated with endosteal scalloping of the cortex. While such an appearance is a feature of this disease, it may be seen also in non-Hodgkin's lymphoma, leukaemia and Gaucher's disease. Fusion of such areas may produce a honeycomb pattern, with coarse residual trabeculation, very like the medullary changes of Gaucher's disease. Organised periosteal reactions are not infrequent. Such a feature is rare in Gaucher's disease.

The skull, clavicles and scapulae are sometimes affected. Pathological fractures are uncommon. With sclerosing lesions in

elderly individuals, confusion with Paget's disease may easily arise, but the characteristic enlargement of the affected bone in that disease will probably be absent. Differentiation, in all these lesions, must be made from metastasis. Intrathoracic disease may present with hypertrophic osteoarthropathy.

Non-Hodgkin's lymphoma

This forms a much more difficult spectrum of disease with a continually evolving classification. That commonly used is based on lymph node histology and cytoimmunohistochemistry. As a simplification, non-Hodgkin's lymphomas (NHL) are categorised according to the histological architecture of the tumour into follicular or diffuse forms, and according to their cell type into B-cell and T-cell tumours. As a working formulation the tumour is then classified as low, medium or high grade. In general, low-grade tumours tend to be follicular B-cell lymphomas and high-grade tumours tend to be diffuse T-cell lymphomas.

It is difficult to assess how many patients present with primary skeletal non-Hodgkin's lymphoma; the proportion is probably less than one-third, the majority of patients having diffuse disease at diagnosis. Experience suggests that low-grade NHL may present as a primary bone tumour, although in older patients particularly it can



Fig. 41.21 Hodgkin's disease. An expanding, destructive lesion involves the body of the sternum, with anterior and posterior soft-tissue masses. Bizarre changes in this bone should always arouse suspicion of a lymphoma.

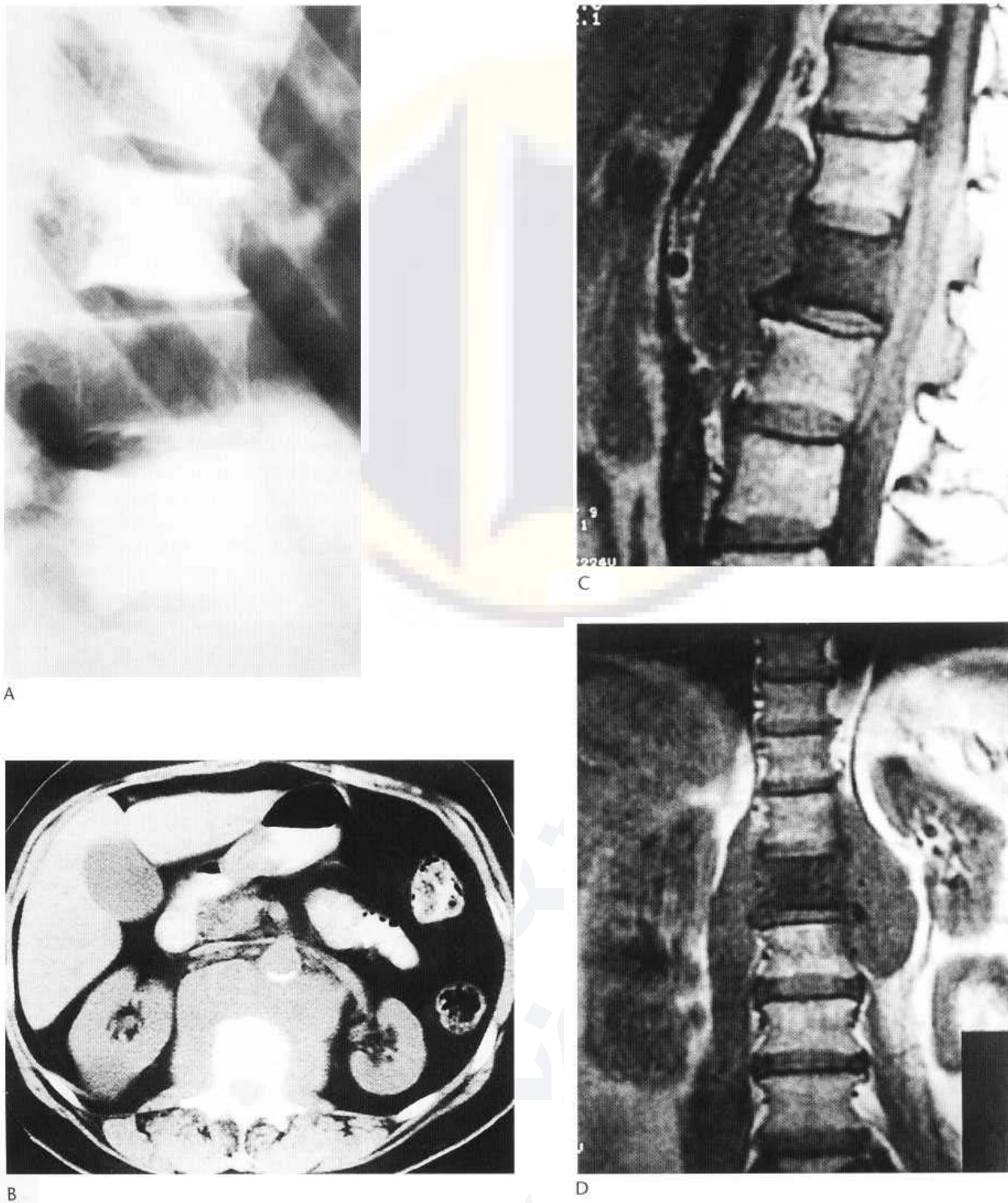


Fig. 41.22 Hodgkin's disease. (A) The common pattern of endosteal sclerosis and patchy bone destruction is shown in the vertebral body of T9 in an adult man. Similar changes are also present at T11. These features are virtually diagnostic. (B) In another patient, an intravenous enhanced CT section of the abdomen demonstrates a densely sclerotic lumbar vertebral body associated with a large paravertebral soft-tissue mass. Sagittal (C) and coronal (D) T₁-weighted images show low signal intensity within the upper lumbar vertebral body due to diffuse sclerosis and the extent of the soft-tissue mass. This extends into the central spinal canal and circumferentially around the thecal sac.

be multifocal and systemic. It is unlikely that high-grade NHL ever presents primarily in the skeleton.

Low-grade non-Hodgkin's lymphoma

Skeletal involvement by low-grade NHL may be with localised pain and swelling, often over a protracted period. The tumour may be

asymptomatic, lesions presenting with pathological fracture. Males are affected twice as commonly as females. The majority is observed in the third and fourth decades although presentation during later years is not unusual. The lesions may be multifocal in the older age group. These tumours may be confused with other malignancies including *osteosarcoma*, *metastasis* and *malignant*

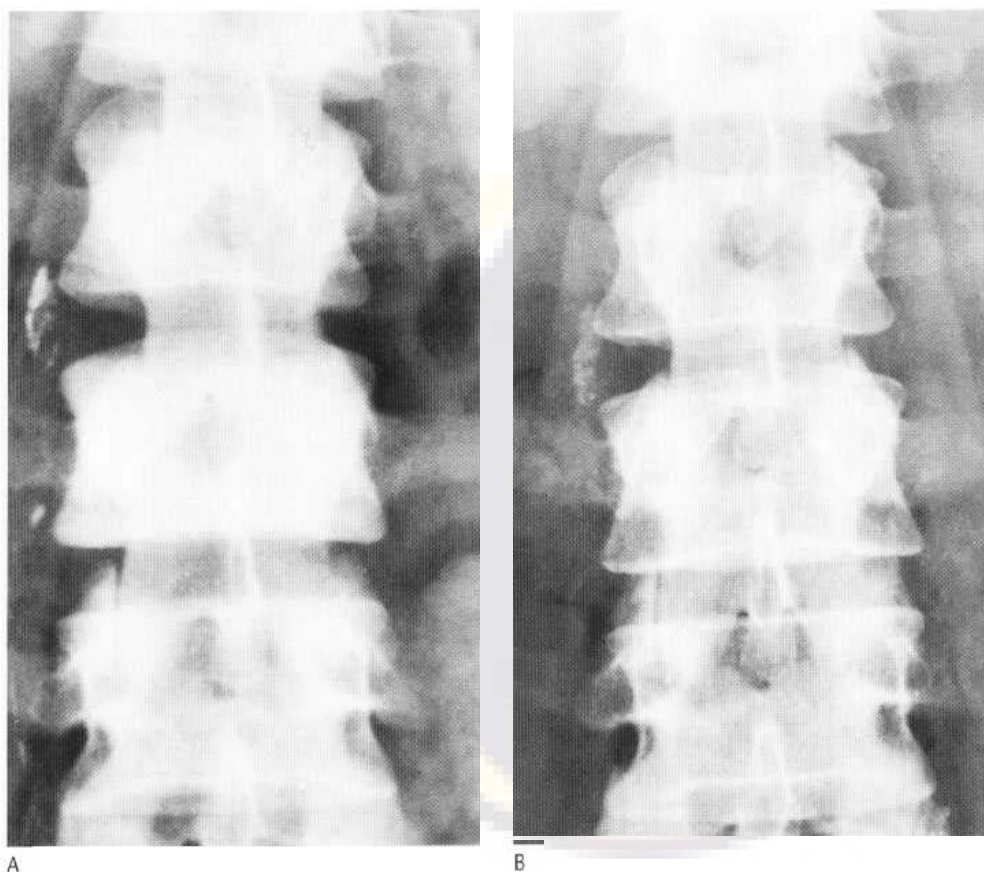


Fig. 41.23 Diffuse sclerotic changes in the bodies of L2 and L3 in a young woman at presentation with the disease. (B) Two years later, following treatment, the appearances have reverted to normal. (Lymphographic contrast medium is present in para-aortic nodes.)

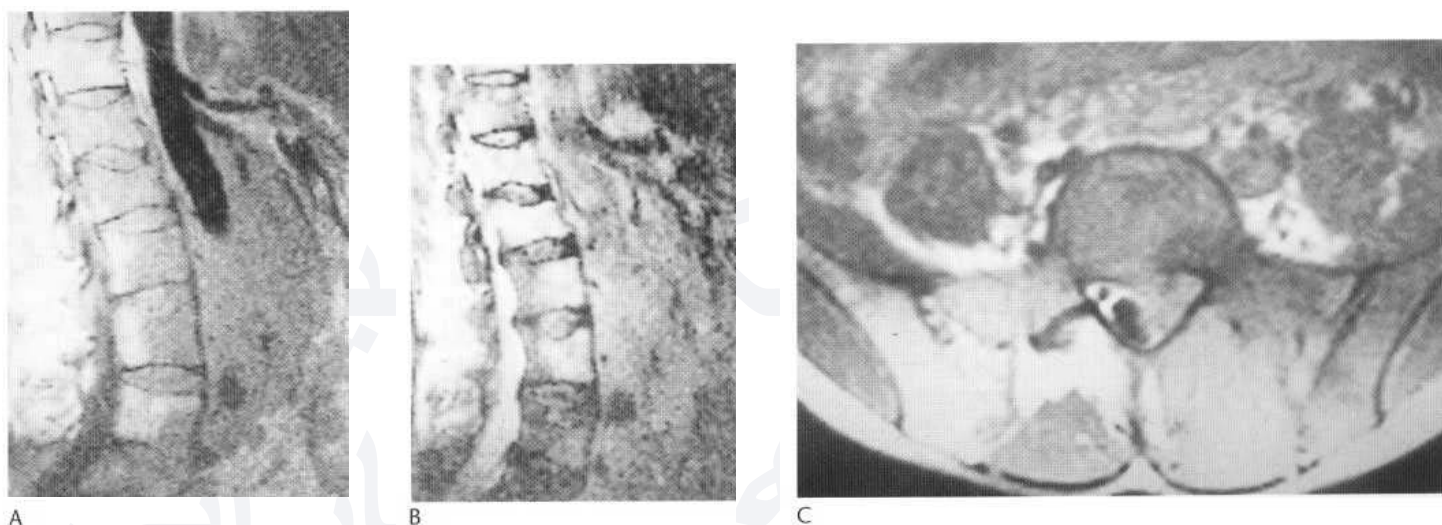


Fig. 41.24 Hodgkin's lymphoma. T-weighted (A) and STIR (B) sagittal images demonstrate extensive abnormality of the marrow of the lumbar spine. In addition, a huge mass of lymph nodes is demonstrated anteriorly, wrapped around the abdominal aorta and displacing the superior mesenteric artery. An axial image (C) demonstrates not only body and left ala involvement of the sacrum, but also subcutaneous and spinal canal extension of the tumour. The thecal sac is displaced to the right.

round cell tumours. Indeed differentiation between these tumours in a young adult may be extremely difficult, not only on clinical and radiological grounds but also histologically.

The lesion may arise as an apparently primary tumour within bone marrow tending to remain confined to the skeleton, although it may spread to other bones and only at a later stage to lymph nodes and viscera.

In its primary form, the condition is localised to a single bone with a marked predilection for the long bones (Fig. 41.26). Nearly

half the cases occur near the knee (Fig. 41.27), often with an associated synovial effusion. The proximal end of the humerus is another common site and about a third of cases are found in the flat bones of the axial skeleton. Spinal, rib and pelvic involvement tends to occur with the extraskeletal form, and in the older age group.

The tumour may be extremely radiosensitive, and radiotherapy alone or in combination with surgery has resulted in many long survivals (Fig. 41.28). Although a primary lesion may have regressed

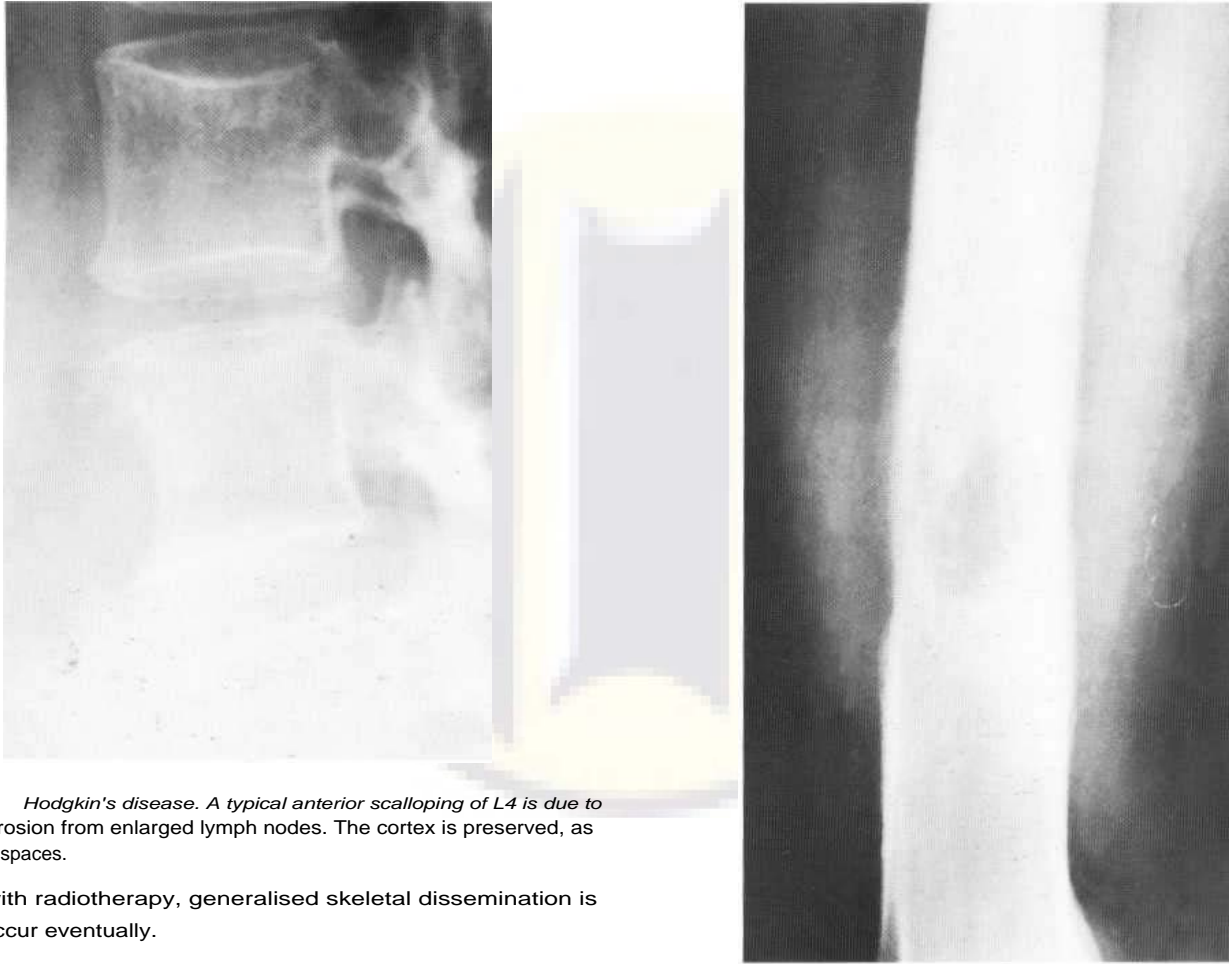


Fig. 41.25 Hodgkin's disease. A typical anterior scalloping of L4 is due to pressure erosion from enlarged lymph nodes. The cortex is preserved, as are the disc spaces.

entirely with radiotherapy, generalised skeletal dissemination is likely to occur eventually.

Radiological changes The earliest evidence of the tumour is diffuse medullary destruction or sclerosis of a patchy nature with very poorly defined margins (Figs. 41.26, 41.29, 41.30). At this stage it may be impossible to differentiate the lesion radiologically from any other aggressive neoplasm. In particular, an oste-

Fig. 41.27 Non-Hodgkin's lymphoma. A purely destructive lesion is present in the distal femur of a woman patient. The margins are ill defined with cortical destruction. Periosteal new bone formation is present adjacent to this destruction. These appearances resemble metastasis and osteosarcoma.

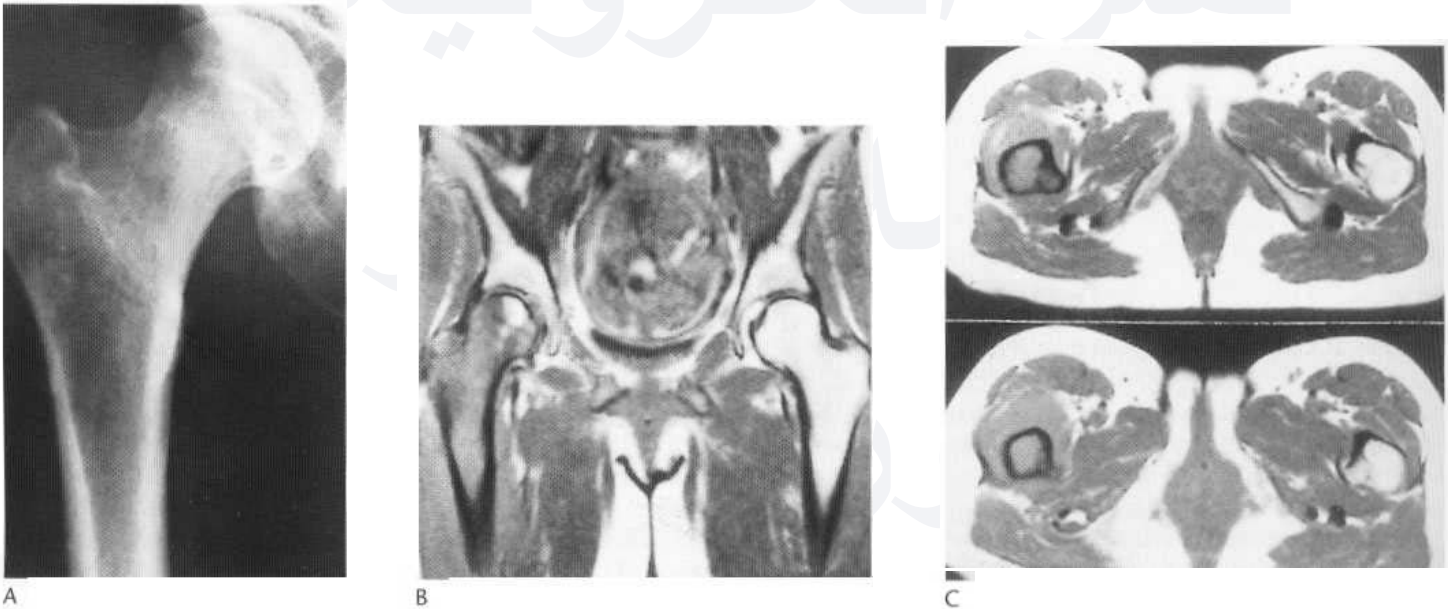


Fig. 41.26 Non-Hodgkin's lymphoma. A conventional radiograph (A) is virtually normal save for the slight suggestion of patchy ill-defined bone destruction. Subsequent T₁-weighted coronal (B) and axial (C) MR images demonstrate not only extensive marrow replacement but also a substantial enveloping soft-tissue mass. The degree and extent of tumour involvement of bone was virtually impossible to appreciate from the radiographic examinations.

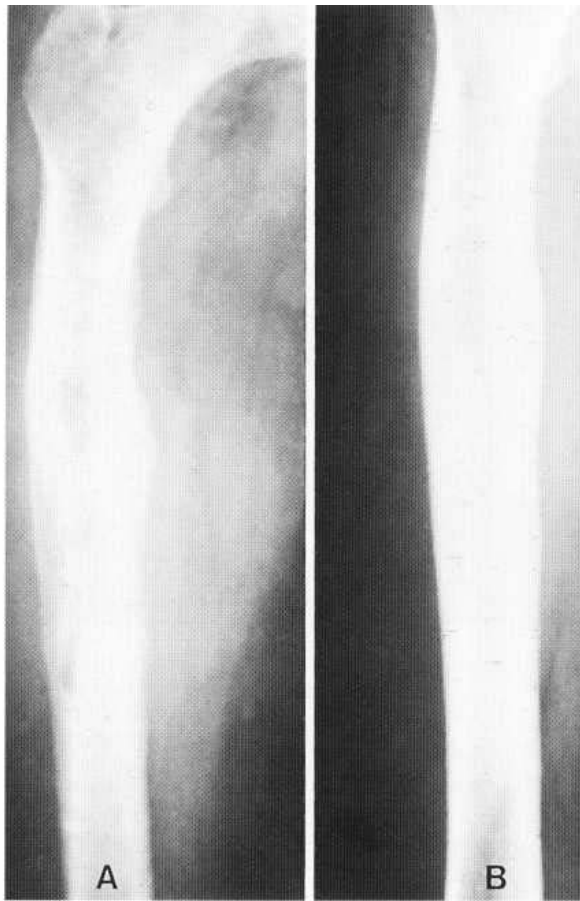


Fig. 41.28 Non-Hodgkin's lymphoma. Advanced changes are shown in the femoral shaft, with dramatic resolution 11 months later following local radiotherapy.

olytic metastasis is likely to present the greatest difficulty. The lesion may resemble other primary malignant neoplasms stimulating little or no reactive bone formation such as Ewing's tumour, fibrosarcoma or malignant fibrous histiocytoma. Radiological confusion with osteomyelitis may also arise, particularly as overlying periosteal reaction is present in half the cases (Fig. 41.27). Indeed periosteal reaction may be present before medullary changes become evident. Scintigraphically the features are unremarkable. Usually increased activity is detected. Multifocal lesions may be found. Radiologically the area of destruction spreads widely through the marrow cavity and remains patchy in nature. Much of the adjacent cortex undergoes resorption with the development of well-defined soft-tissue swelling from soft-tissue tumour extension. Cortical thickening and reactive sclerosis are not prominent features, although they may occur exceptionally.

In the generalised form of the disease, lesions may be detected throughout the skeleton and each presents the same characteristics as a solitary focus (Fig. 41.31). The patient is likely to be over the age of 40. The ultimate degree of osseous destruction may be extreme.

High-grade non-Hodgkin's lymphoma

This malignant tumour is rarer than Hodgkin's disease and mainly affects an older age group: patients in the fifth and sixth decades. Nonetheless a number of cases have been observed in children and in these male sex preponderance has been found. A proportion of these patients develops frank *lymphocytic leukaemia*.

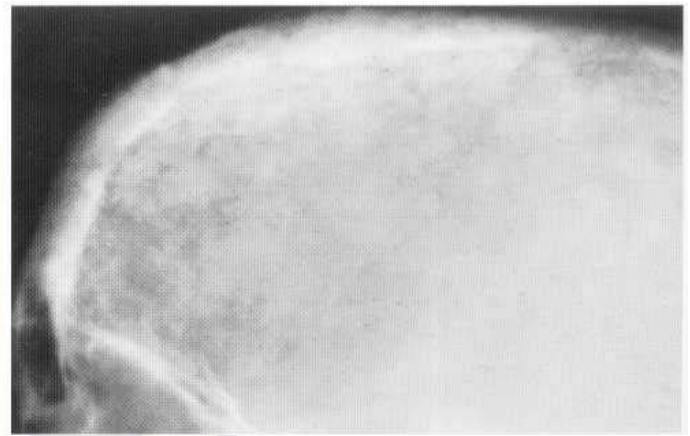


Fig. 41.29 Non-Hodgkin's lymphoma. Extensive patchy destruction of the cranium was present in this adult patient with generalised disease.

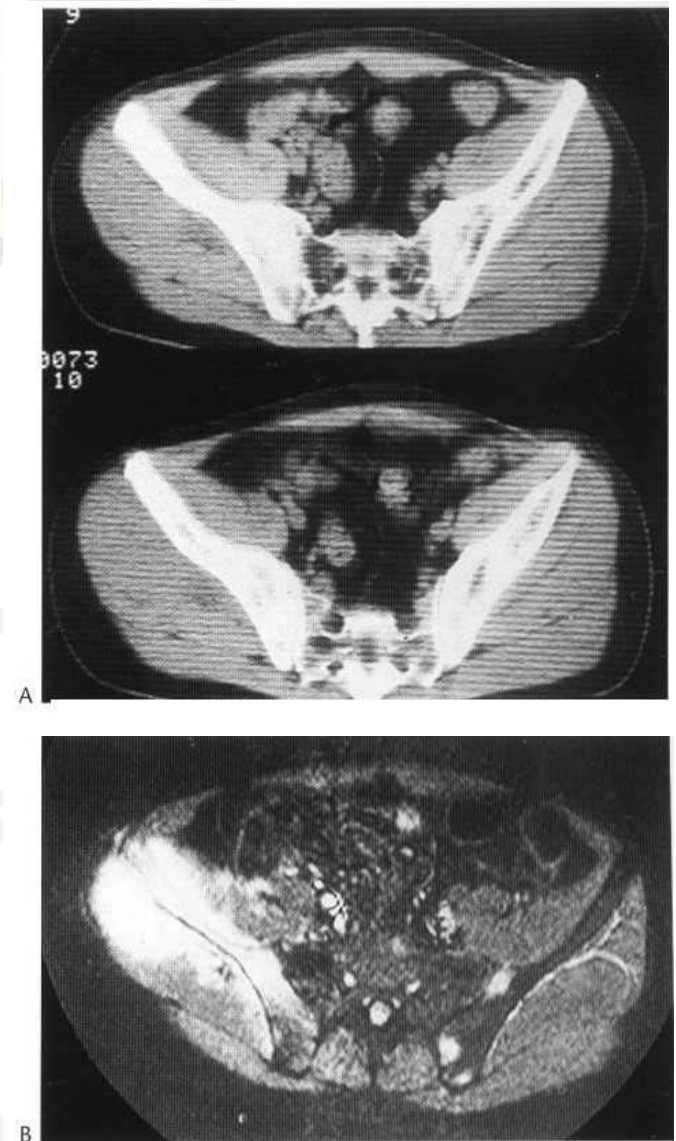


Fig. 41.30 (A) CT of the pelvis in non-Hodgkin's lymphoma showing diffuse sclerosis within the right innominate bone, with ill-defined periosteal bone formation on the inner surface. A soft-tissue mass is evident. (B) The extent of these changes is easier to appreciate on the axial STIR image, where additional lesions within the left innominate bone are also evident.

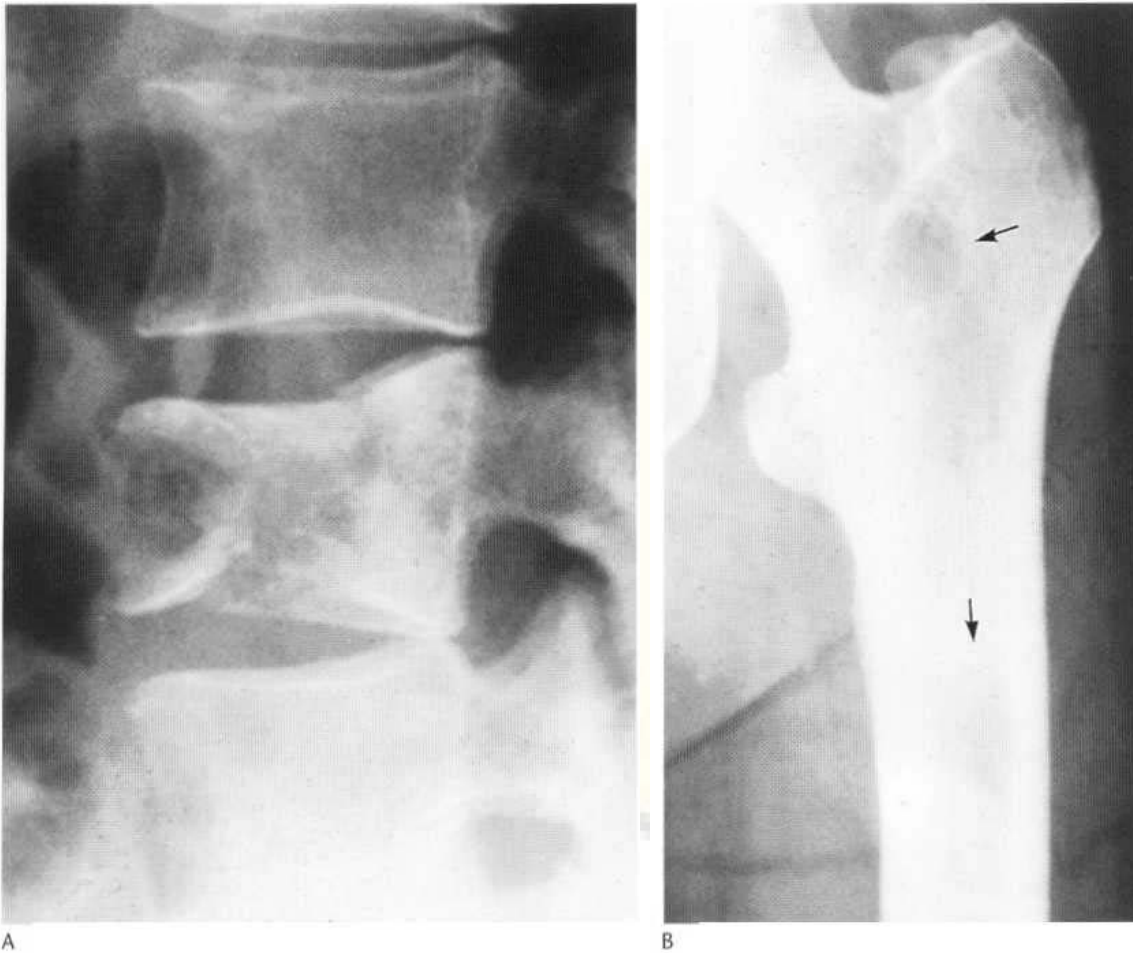


Fig. 41.31 (A,B) Non-Hodgkin's lymphoma. Multifocal disease was found at presentation in an elderly patient with low back pain. In addition to a pathological fracture of a lumbar vertebral body, ill-defined endosteal defects are present in the femoral shaft (arrows).

The incidence of bone lesions is of the order of 10-20%, although more are detected at postmortem. Prognostically bone lesions imply a poor outcome. Primary skeletal involvement is probably extremely rare.

Radiological changes In the skeleton these resemble those very closely those of Hodgkin's disease; other lesions grow more rapidly and are almost always osteolytic in type. Areas of destruction, commonly in red marrow areas, may be large with diffuse and irregular margins, and with scalloping of the inner aspects of the cortex. They may be solitary or multiple and, because of their osteolytic nature, pathological fractures are common. The latter affect especially the femoral and humeral necks and may cause collapse of vertebral bodies. When the lesions are multiple they all tend to be of the same osteolytic type, unlike Hodgkin's disease when all the different types of bone change may be present. Erosion of the cortex is likely to be followed by the formation of large associated soft-tissue masses with relatively little periosteal reaction. Such erosions usually take place through an area of cortex that has already been thinned and expanded by underlying pathological process, emphasising the radiological similarity of the individual lesions to Ewing's sarcoma.

Burkitt's tumour

An exceptional and particularly aggressive form of non-Hodgkin's lymphoma is common in African children and has been reported in

other parts of the world. Large, destructive lesions develop especially in the mandible and maxilla (Fig. 41.32).

Radiologically these lesions are purely osteolytic and grow rapidly. The jaw lesions are characterised by the resorption of the lamina dura with multiple lytic foci that eventually coalesce with radiating spicules of bone. Spinal lesions are characterised by lytic, ill-defined destructive foci with paravertebral masses. In long bones the permeative lytic nature of the turnout, particularly with cortical erosions, may resemble a Ewing's sarcoma. Foci develop in soft tissues, particularly the kidneys, ovaries and abdominal lymph nodes.

The disease is associated with a virus (Epstein-Barr) and is especially prevalent in endemic malarial areas. Regression can occur following the use of cytotoxic drugs.

Mastocytosis

The rare condition of urticaria pigmentosa is associated with enlargement of the liver, spleen and lymph nodes due to the proliferation of mast cells. The disease is relatively benign, but a few instances of leukaemic termination have been recorded. Bone changes are usually identified in early adult life.

Radiological changes

In probably a third of cases, generalised skeletal changes are present. These are diffuse or circumscribed areas of increased density, apparently due to thickening of the medullary trabeculae (Fig. 41.33). It may be difficult to identify the endosteal margin of

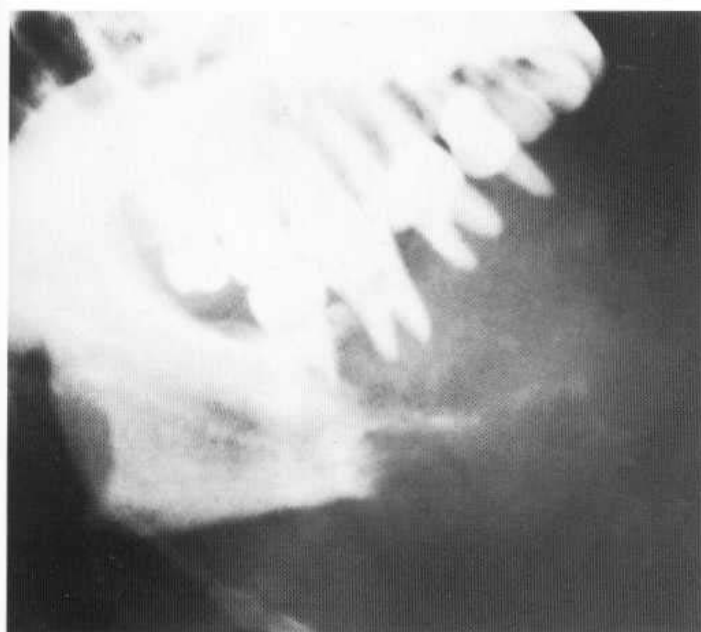


Fig. 41.32 Burkitt's tumour. A large destructive lesion in the mandible of this African child is typical of this form of lymphoma.

the cortex. The absorption of some trabeculae and the thickening of others may cause the osseous structures to have a coarse pattern (Fig. 41.34) but the generalised increase in density predominates usually. Any bone may be affected. At this stage it is possible to demonstrate only a few mast cells in the bone marrow. The appearance may closely resemble *osteosclerosis*, the *sclerosing types of leukaemia*, *chronic anaemias* and *osteopetrosis*. Occasionally the dense areas are sharply defined, of considerable size and localised to a few areas. Particularly in young adults, differentiation from Hodgkin's disease must be made.

PLASMA CELL DISEASES

Plasma cells represent the end product of B-lymphocyte maturation. Pathological proliferation produces either a local tumour (plasmacytoma) or disseminated disease (myelomatosis).

Plasmacytoma

This condition is unifocal, causing a localised destructive lesion in the skeleton, in a red marrow area. Many other descriptive terms (such as solitary myeloma) for this localised lesion have been used. Although for many years it may remain localised, and without health disturbance, ultimately it undergoes transition to generalised myelomatosis. A latent interval of 5-10 years is usual: consequently, the outlook is better than multiple myelomatosis. In comparison with the latter these lesions are uncommon, but the exact incidence is difficult to assess as they are frequently asymptomatic. For example, a plasmacytoma in a rib may be noted incidentally on a routine examination of the chest.

When symptoms occur they are commonly those of bone pain, particularly backache. The vertebral bodies, especially in the thoracolumbar and lumbar regions, are the most common sites for these lesions and are likely to undergo partial collapse. The pelvis, especially the ilium, femur and humerus, are the next most commonly involved sites.



Fig. 41.33 Mastocytosis (man aged 34). A localised area of endosteal sclerosis is present in the body of L1. In addition, ill-defined thinning of trabeculae is demonstrated in L2 and patchier changes in the upper surface of L3.



Fig. 41.34 Mastocytosis. A coarse pattern of generalised sclerosis is shown.

The vast majority of affected individuals are between 30 and 60 years of age so that this is almost entirely a disease of late middle age. The differential diagnosis always includes a solitary osteolytic metastasis.

Radiological changes

These lesions arise in areas of red marrow function. Bone expansion, which may be considerable with thinning of the overlying cortex, is common but, when a vertebral body is affected, collapse may precede such apparent expansions. The margins are usually well defined and sharply demarcated and characteristically without a sclerotic reaction (Fig. 41.35). Coarse trabecular strands of increased density may give a network appearance in the area of destruction, and exceptionally the lesion may be entirely sclerotic. Large lesions in flat bones may assume a soap-bubble appearance (Fig. 41.36).

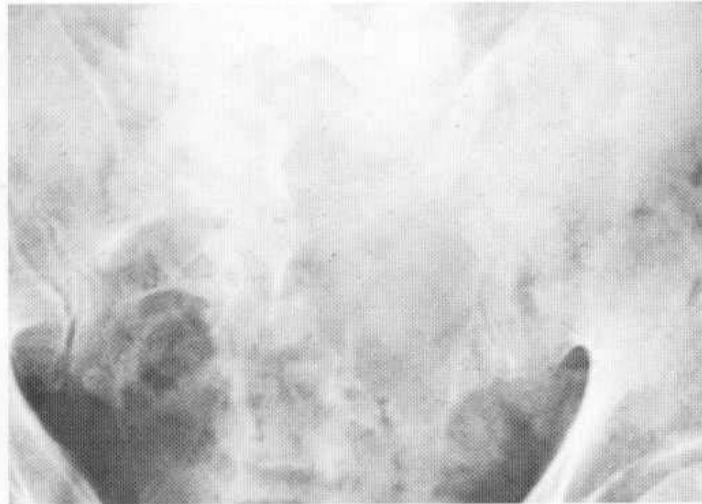
Differential diagnosis of these tumours may be difficult. In view of the age group concerned the most important is an *osteolytic metastasis*. In vertebrae, such metastases are likely to involve the pedicles more commonly. Metastatic disease apart, the development

of a solitary osteolytic lesion in a vertebral body in a patient in late middle age should always be considered as a plasmacytoma (Figs 41.37, 41.38). *Chordoma* may produce similar features. Other differential diagnoses to be considered, especially with an expanding lytic focus in a rib, are *fibrous dysplasia*, a 'brown' tumour of *hyperparathyroidism* and, particularly when the lesion is adjacent to an articular surface, a *giant cell tumour*. Resemblance to a giant cell tumour may be close; however, these lesions are found in early adult life and furthermore have a different distribution, commonly affecting the appendicular skeleton, whereas plasmacytoma is more likely to be axial.

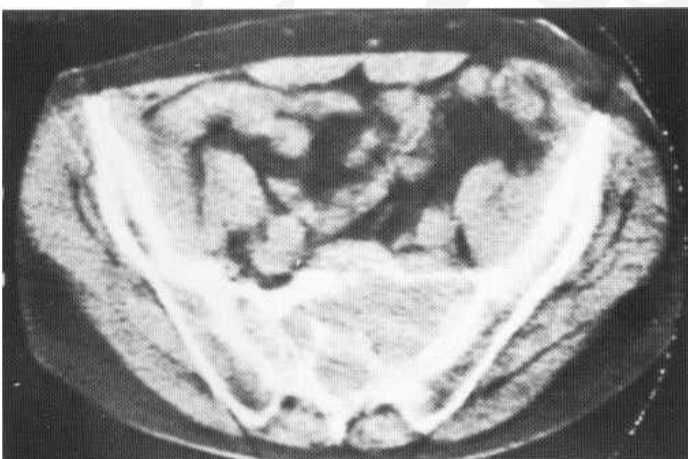
Scintigraphy and *CT* afford no specific diagnostic features. Increased activity is observed on the blood-pool phase of a bone scan, while the delayed phase shows increased activity around the margins. *CT* confirms the extent of these tumours but does not afford tissue-specific information.

Multiple myelomatosis

The disseminated or generalised form of plasma cell infiltration of bone marrow is known as multiple myelomatosis. This entity may be preceded by a solitary plasmacytoma or arise de novo.



A



B

Fig. 41.35 Plasmacytoma of sacrum. (A) An adult man exhibits a well-defined radiolucent defect involving the left sacral ala. (B) A CT scan demonstrated the extensive destructive nature of the tumour, seen clearly to cross the midline. Note the marked cortical thinning with absence of sclerosis or periosteal new bone formation.

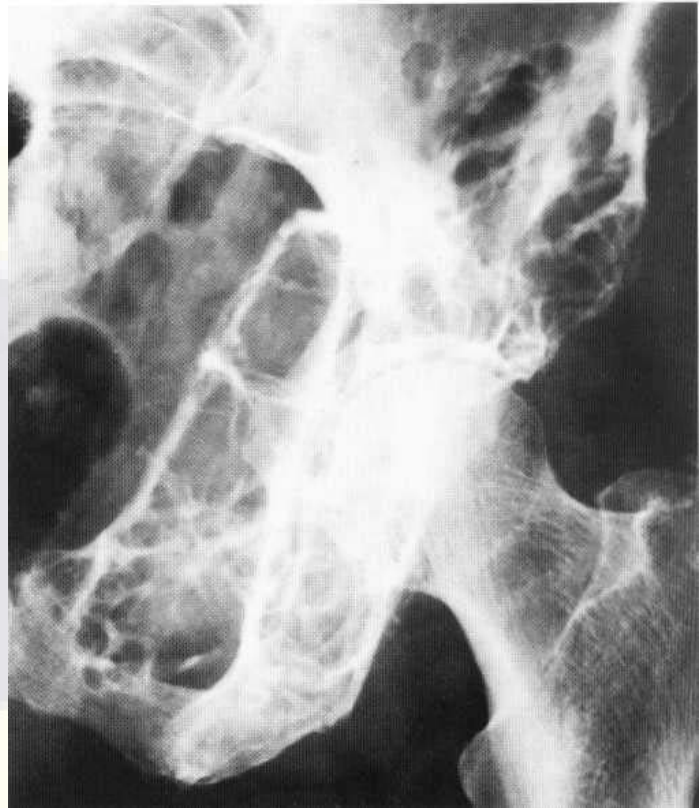
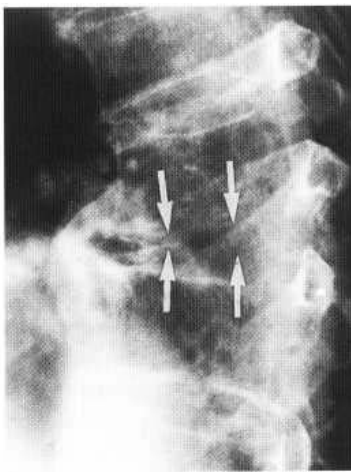


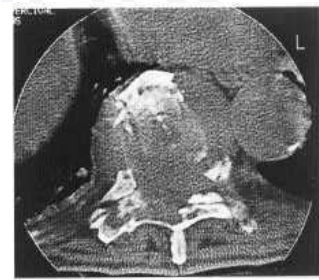
Fig. 41.36 Plasmacytoma of pelvis. This very extensive lesion was unaccompanied by any systemic abnormality. Bone expansion is associated with coarse trabeculation, producing a soap-bubble appearance.

It is much more common for the widespread form to present radiologically as a fully developed entity in the over-40 age group. Men are affected twice as often as women. Persistent bone pain or a pathological fracture are usually the first complaints.

Plasma cell proliferation causes elevation of the total serum proteins, due to the production of abnormal immunoglobulins. Such proliferation eventually takes place at the expense of all other marrow functions so that a non-specific leukopenia and secondary



A



B

Fig. 41.37 Plasmacytoma presenting with paraparesis. (A) Conventional radiograph of the thoracic spine showing vertebra plana (arrows). (B) CT demonstrating the degree of bony destruction, associated paravertebral mass and marked posterior extension into the spinal canal resulting in severe cord compression.

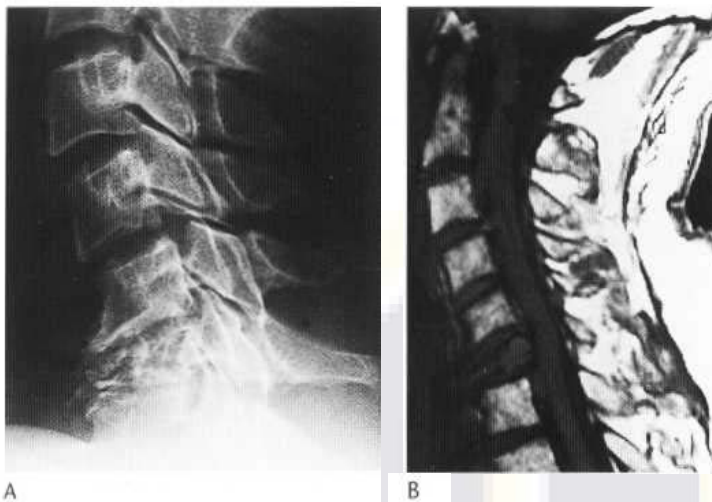


Fig. 41.38 Plasmacytoma. (A) Conventional cervical spine radiograph showing osteolytic destruction of C6 with pathological collapse of the vertebral body. (B) Sagittal T₁-weighted MR image showing the intermediate-signal-intensity lesion of C6 resulting in focal extradural compression of the spinal cord.

anaemia develop. In about half of cases, presence of an abnormal urinary protein constituent, Bence Jones proteose, may be demonstrated. Abnormal proteinuria causes cast formation in the renal tubules with impairment of renal function. Hypercalcaemia, hypercalcuria and amyloidosis occur, the last in about 10% of all cases, and resemble the distribution of primary amyloidosis. The hypercalcaemia and hypercalcuria are unassociated with an elevation of either the serum alkaline phosphatase or phosphate levels.

The pattern of bone destruction may vary from diffuse osteoporosis, through small and almost insignificant areas of translucency, to rounded or oval defects with sharply defined margins. The last, regarded as characteristic, develops relatively late. Frequently the defects coalesce to produce even larger areas of osteolysis.

Radiological changes

The two cardinal features are generalised reduction in bone density and localised areas of radiolucency in red marrow areas. The axial skeleton, therefore, is affected predominantly. Lesions may be observed also in the shafts of long bones and in the skull. In spite of positive bone marrow aspiration, radiological features may be absent in as many as one-third of cases, at least at initial presentation. This group of patients tends to develop generalised osteoporosis.

Radiology plays an important part in the initial diagnosis of the disease. Whether a skeletal survey is relevant or not will depend on the clinician's approach to therapy, many will rely solely on the level of abnormal immunoglobulin to monitor treatment. If necessary, a radiographic skeletal survey is superior to scintigraphic investigation using a bone-scanning agent, because the lesions are essentially osteolytic with no bone reaction. A bone scan is superior, however, in detecting lesions in the ribs because the associated fractures are demonstrated more easily.

Diffuse osteoporosis alone can cause suspicion of the disease in an elderly patient. Even though age-related osteoporosis may be expected, the possibility of myelomatosis always merits consideration, particularly when symptomatic bone pain is present (Fig. 41.39). The smaller areas of radiolucency are poorly demarcated and appear to be irregular accentuations of the generalised osteoporotic process (Fig. 41.40). The rounded and oval defects that

develop are characterised by the sharp definition of their edges. Reactive marginal sclerosis is absent. Typically, the cortex is eroded from within sharply defined margins (Fig. 41.41).

Exceptionally, however, sclerosing changes have been reported. These have varied, some resembling focal lesions of prostatic metastases, some the spiculation of osteosarcoma and some a generalised diffuse increase in density. This very rare form of multiple myelomatosis occurs in probably 2-4% of cases, and is frequently accompanied by a peripheral neuropathy.

Treatment, as in other conditions, may alter these appearances and, during its course, it is common to observe some lesions resolving while others evolve.

The *distribution of lesions* is very widespread and destructive foci are commonly located in the long bones in addition to the axial skeleton. Involvement of the skull is variable. Diffuse and irregular translucencies with generalised osteoporosis are not uncommon. Such changes eventually become pronounced and extensive. The disease will not always be evident by the presence of the classic 'raindrop' lesions, circular defects varying in diameter from a few millimetres to 2 or 3 cm. Indeed, the skull may be normal, even in the presence of many lesions elsewhere in the skeleton. Areas of osteolysis may be observed also in the mandible, a site only rarely affected by metastasis. Myelomatous lesions may erode the cortex and extend into the adjacent soft tissues. The resulting soft-tissue masses are helpful in differentiating the advanced forms of the disease from the lesions of metastatic carcinoma, which much less commonly produce extension into the soft tissues. The spine is often merely osteoporotic, but as the disease advances, multiple foci of destruction, almost invariably accompanied by some degree of collapse of the affected bodies, are likely to be present. With such collapse, paravertebral soft-tissue shadows are common. Differentiation from inflammatory lesions can be made, as the intervertebral disc spaces and the articular surfaces are not affected. The pedicles and posterior elements are involved less frequently and at a later stage than occurs with metastases. In the thorax, a destructive rib lesion with a large associated soft-tissue mass is much more suggestive of myelomatosis than of a plasmacytoma. Diffuse involvement,



Fig. 41.39 Multiple myeloma. Sagittal T₂-weighted image of the thoracolumbar junction showing multiple foci of high signal intensity within the vertebral bodies.

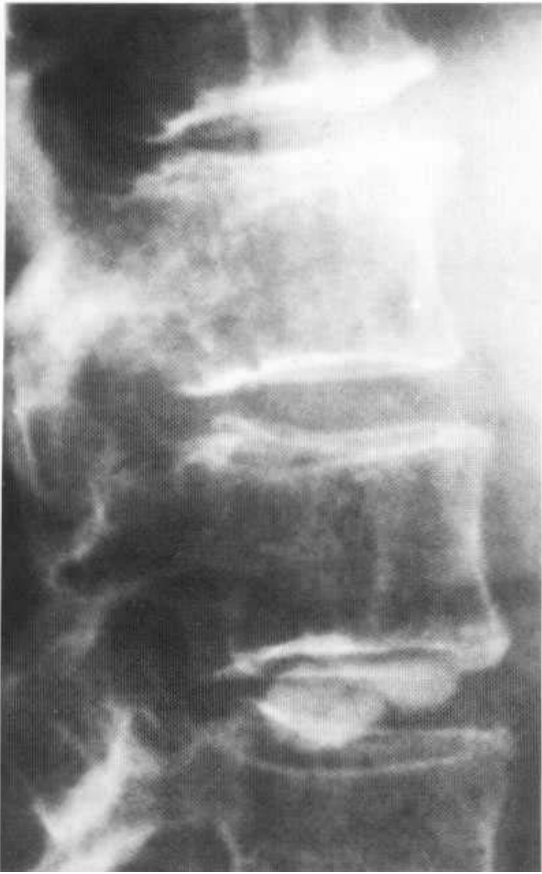


Fig. 41.40 Myelomatosis. Diffuse marrow involvement has resulted in an overall reduction in bone density similar to that seen in osteoporosis. However, the rather patchy nature of radiolucencies should raise the possibility of myeloma.

however, is more usual, numerous characteristic lytic lesions being present. The clavicles and scapulae may also show these destructive changes, indeed such a lesion in the clavicle is far more likely to be due to myeloma than metastasis.

The long bones are affected most commonly in the persistent red marrow areas of the proximal ends of the humeri and femora. Lesions, however, are by no means found only in such areas, and irregular or punched-out fractures in the shafts of other bones may be the first radiological manifestation of disease. In some advanced cases lytic defects may be due also to secondary amyloidosis, which can complicate many chronic disorders such as rheumatoid disease and longstanding infections.

Pathological fractures are very often the initiating factor in the diagnosis of the disease. These fractures heal remarkably quickly and soundly with massive callus and new bone formation. This response is somewhat surprising in view of the numerous cystic lesions and widespread osteoporosis which are likely to be present without any evidence of reactive sclerosis.

POEMS syndrome

An uncommon condition with the acronym POEMS is characterised by a chronic progressive Polyneuropathy, Organomegaly (hepatosplenomegaly), Endocrinopathy (commonly diabetes mellitus), M-proteins (plasma-cell dyscrasia) and Skin changes (hirsutism, pigmentation, oedema). It is usually seen in young men and



Fig. 41.41 Typical localised lesions of myeloma are demonstrated in the upper femur of an adult woman. The sharply defined rounded defects with endosteal erosion of the cortex are characteristic.

radiologically presents with multiple sclerotic lesions, most commonly in the spine and pelvis.

HISTIOCYTOSIS

The basic pathological abnormality in this group of diseases is a proliferation of histiocytic cells occurring particularly in the bone marrow, the spleen, the liver, the lymphatic glands and the lungs. In the more chronic forms these cells become swollen with lipid deposits, essentially cholesterol (though the blood cholesterol level remains normal) and they present the pathological appearances of 'foam cells'. Some of these become necrotic and are replaced by fibrous tissue.

Various forms of the condition have been regarded in the past as separate entities. These forms are outlined below but it must be emphasised that this subdivision is entirely arbitrary since histiocytosis essentially presents a spectrum of disease.

Eosinophilic granuloma

This is the mildest expression of histiocytosis. Pathological changes are predominantly bony, although occasionally pulmonary involve-

meat may occur. Children, especially boys, between 3 and 12 years are most commonly affected, although these lesions may be observed in adolescents, young adults and exceptionally the middle aged. Any bone may be affected. A quarter of cases occurs in the skull. The skull, pelvis and femora between them account for nearly two-thirds of all cases.

Clinically pain and swelling may be accompanied by mild fever. Histologically the eosinophilic infiltration is found around collections of histiocytes. In this relatively mild form necrosis and fibrosis are rare and the appearance of foam cells suggests a more serious variety.

Radiological changes

Translucent areas of bone destruction, with sharply defined margins and often of considerable size, are characteristic. The round or oval defects may have scalloped margins (Fig. 41.42). Although in the active phase they provoke no sclerotic margin, the healing phase, which usually develops by spontaneous regression, is marked by peripheral sclerosis round the lesion and slow reconstitution of the bony structure (Fig. 41.43). This healing phase may be accelerated by biopsy, radiotherapy or steroid injection. True expansion is uncommon except in ribs and vertebral bodies. Apparent expansion may result from thickening of the overlying periosteum, especially if the cortex has been partially eroded (Fig. 41.44) or infarction has occurred. In approximately two-thirds of patients the lesions are *solitary*. Differential diagnosis of a solitary lesion of this type may be extremely difficult and is from either osteomyelitis or Ewing's tumour, which has a similar age incidence. Skeletal survey, scintigraphic or radiographic, may disclose the presence of other asymptomatic lesions, facilitating the diagnosis. *Multiple* eosinophilic granulomas are usually found to be in different phases of evolution (Fig. 41.43). As one lesion resolves another may appear in a different part of the skeleton. In the skull particularly, new lesions



Fig. 41.42 Histiocytosis. A purely osteolytic lesion is present in the mandible, with well-defined, slightly scalloped margins. The lamina dura has been destroyed. The teeth seem to 'float in air'.

several centimetres in diameter may appear in as many weeks. Button sequestra may be observed.

Solitary lesions in the spine may collapse, partially or completely, the latter presenting the classic appearance of *vertebra plana* (Fig. 41.45). The most commonly affected site is the thoracic spine. The lesions at one time were considered to represent an 'osteochondritis' and were named *Calve's disease*. During the phase of collapse, the walls of the affected vertebral body tend to bulge laterally and paravertebral soft-tissue shadows may be evident. The disc spaces on either side remain intact and may appear widened. As healing occurs, remarkably good reconstitution of these vertebral bodies may take place if sufficient years of growth remain. The vast majority of vertebral plana lesions, especially in a relatively healthy child, are caused by an eosinophilic granuloma, and confirmatory biopsy is usually unnecessary. The differential diagnosis of collapse of a single vertebral body includes

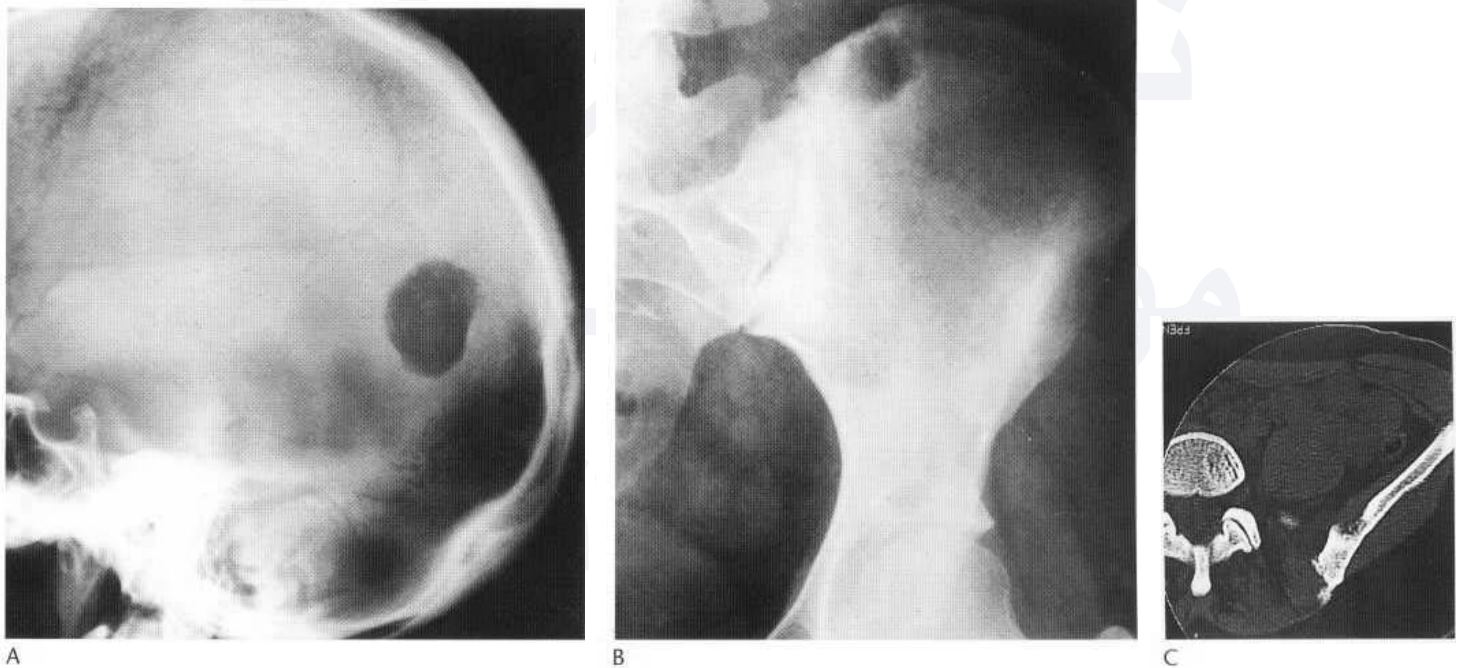


Fig. 41.43 Histiocytosis. (A) Lateral skull radiograph showing a well-defined osteolytic lesion with a narrow zone of transition and no sclerosis in the posterior parietal region. (B) Osteolytic lesion of the innominate bone with ill-defined peripheral sclerosis. (C) CT of the innominate lesion showing destruction of the anterior cortex of the iliac wing and the ill-defined surrounding sclerosis of this healing lesion.

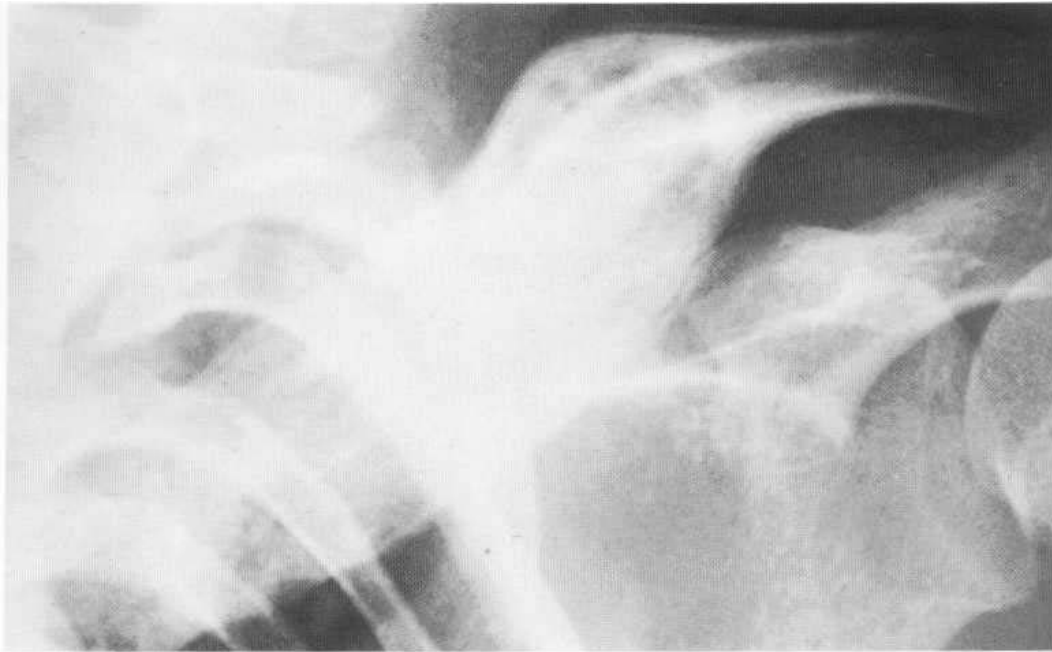


Fig. 41.44 Histiocytosis. Extensive involvement of a bone, here the clavicle, is often associated with layered periosteal new bone causing bony expansion. Ill-defined areas of resorption may be visualised in the lesion. This was the only abnormality found in a young girl over several years' follow-up.

the relative rarities of Ewing's tumour, metastasis from a neuroblastoma, benign osteoblastoma or an atypical tuberculous focus. Tuberculosis is becoming commoner in the 'Western' world again.

This benign form of histiocytosis occasionally affects long bones and initially has a predilection for the diaphysis (Fig. 41.46). However, metaphyseal involvement may occur again, causing confusion with a pyogenic infection. A rare entity, *chronic granulomatous (Langerhans-cell) disease*, tends to cause skeletal lesions, including those in the metaphyses, which simulate closely the radiological appearance of multiple eosinophilic granulomas. This condition is usually due to inherited and inadequate responses of leucocytes to infection.

Hand-Schüller-Christian disease

This is a more chronic form of the disease, with dissemination of lesions in the lungs, lymph nodes, liver and spleen, in addition to virtually constant and early involvement of the skeleton.

The early case reports drew attention to a syndrome consisting of skull defects, exophthalmos and diabetes insipidus, the last two being associated with lesions round the orbit and the hypophysis



Fig. 41.45 Histiocytosis. Vertebral lesions in the thoracic spine are shown on a lateral tomogram. The bodies of T7 and 8 have collapsed with a slight increase in bone density. Note the relative preservation of the disc spaces.



Fig. 41.46 Histiocytosis. A healing diaphyseal lesion exhibits periosteal new bone formation and minimal sclerosis around the margins of the radiolucency.

respectively. Children below the age of 5 years are most frequently affected, though sporadic cases occur at later ages up to middle life. The course of the disease is chronic, often extending over 10 or more years. It is characterised by soreness of the mouth and loose teeth, due to deposits in the gums and jaws, and skin lesions. Abnormalities in the temporal bone are common, with an associated otitis media. The eventual prognosis is good, since spontaneous remission, possibly initiated or accelerated by radiotherapy, takes place in the majority of cases. Over 107 however, terminate fatally.

Radiological changes

The bone defects are essentially the same as those of eosinophilic granulomas. They are far more numerous and particularly affect the flat bones. In the skull they often coalesce to produce widespread irregular defects usually likened to a map and described as the 'geographical skull', both tables often being involved (Fig. 41.47). Lesions in the mandible and maxilla begin around the tooth roots, so that the teeth, which are never affected, remain dense and appear to 'float in air' (Fig. 41.42). Several vertebrae may be completely or partially collapsed and extensive lesions may develop in the scapulae, ribs and pelvis. Osteolytic pelvic lesions or vertebral collapse in a child are suggestive of this disease. Long bone involvement is less common (Fig. 41.48).

In a relatively early stage, sclerotic reaction around the sharply defined margins of these lesions is absent. When healing occurs the lesions fill in by sclerosis in the same way as eosinophilic granulomas. New lesions may appear after the original ones have begun to heal, emphasising again the wide spectrum of radiological change in histiocytosis.

The lungs show a fine nodular infiltration in the acute phase. With healing, these fibrose and persist as linear strands of increased density, but the presence of pulmonary changes in histiocytosis indicates a worse prognosis (Fig. 41.49).

Letterer-Siwe disease

This is an acute or subacute disseminated form of the disease, occurring very rarely in infants below the age of 2 years and pre-

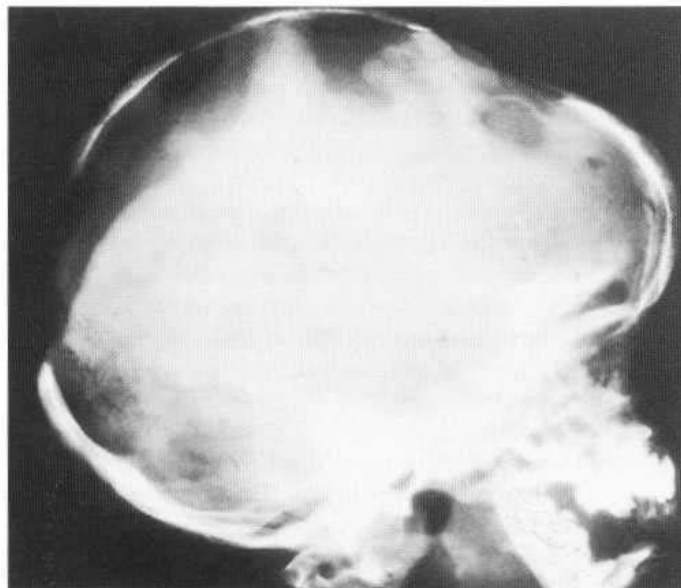


Fig. 41.47 Histiocytosis. Extensive skull involvement in a child with the Hand-Schuller-Christian type of lesion. The areas of destruction in the flat bones of the skull have a map-like configuration.

sensing a much more severe clinical picture. It is characterised by pyrexia, with a rash and mouth sores, bleeding gums, respiratory symptoms and failure to thrive. Particular involvement of the extraskletal tissues occurs with enlargement of the liver, spleen and lymph nodes. The disease usually ends fatally, often in a few months and at the most in 2 years. In those cases with a rapidly fatal outcome, skeletal lesions are unlikely to be demonstrated radiologically, having insufficient time to develop. Nevertheless, histological change may be present in the bone marrow, with widespread masses of histiocytes and eosinophilic infiltration, comparable with the early histological picture of the benign eosinophilic granuloma. Only in the rare cases that survive do fibrosis and cholesterol-containing foam cells become apparent.

Radiological changes

gone lesions, when they occur, are indistinguishable from those of Hand-Schuller-Christian disease and are purely lytic. However, they tend to be even more widely spread both in the flat bones and especially in the metadiaphyseal areas of the long bones (Fig. 41.50). Diffuse pulmonary infiltration is common. This may closely resemble miliary tuberculosis and is a variety of honeycomb lung.



Fig. 41.48 Histiocytosis: Hand-Schuller-Christian type. Very extensive radiolucencies are present both in the metaphysis and diaphysis of this child's femur. A healed pathological fracture is present. Histiocytosis should always be considered in the differential diagnosis of bizarre bone lesions.

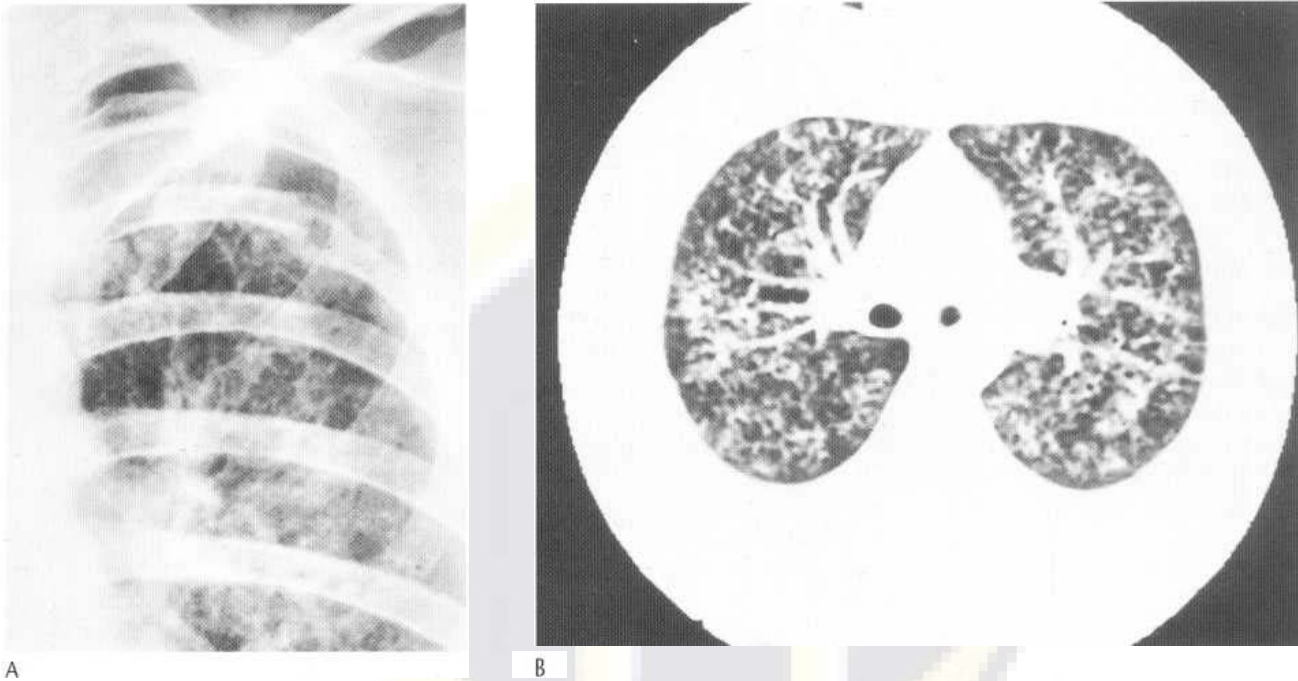


Fig. 41.49 Histiocytosis. Adult pulmonary involvement (man aged 20). (A) A localised view from a chest radiograph demonstrates a coarse interstitial pulmonary fibrosis. Note also a pathological fracture of the left fourth rib due to a bony deposit. (B) A CT scan demonstrates peripheral interstitial pulmonary fibrosis with thickened interlobular septa and irregular honeycombing.

In summary, histiocytosis is a disease primarily of childhood, although exceptionally its more benign manifestations may be observed in early adult life. The older the child, and the more the lesions are confined to the skeleton rather than other tissues, the better the prognosis. It must be appreciated that the benign eosinophilic granuloma may deteriorate to a chronic, multifocal form of the spectrum, and rarely vice versa.

STORAGE DISORDERS OF THE LYMPHORETICULAR SYSTEM

A number of conditions have been described in which the lymphoreticular system is the site of abnormal deposition of lipoproteins, usually as a result of inborn errors of metabolism. The commonest of these rare disorders are Gaucher's disease and Niemann-Pick disease.

Gaucher's disease

Young Jewish females are particularly susceptible to this hereditary condition caused by deficiency of β -glucosidase. It is not confined to this ethnic group or sex. Although manifestations of the condition commonly become apparent in the later years of childhood and in early adult life, the disease may be so chronic, and of such insidious onset, that it may be recognised for the first time only in middle age or even later life. In infancy, the rapidly fatal course of this systemic disease is characterised by gross neurological changes and pulmonary infiltration.

In the juvenile and young adult variety, the principal complaint is of weakness and fatigue with progressive dementia. On clinical examination splenic enlargement is detected in 95% of cases. Bone pain may be present, sometimes severe. In the chronic form of the disease characteristic and diagnostic bone changes may be expected.

Histological examination reveals numerous large histiocytes within which an abnormal lipoprotein, kersin, is present. These cells are disseminated throughout the marrow of the haematopoietic skeleton, in addition to the spleen and liver.

Radiological changes

Diffuse infiltration of the bone marrow causes widespread and irregular medullary radiolucency. When collections of the abnormal histiocytes occur destructive medullary lesions become visible and abnormal modelling of the long bones may be evident. Expansion of the distal ends of the femora begins with a loss of the normal concavity of the medial sides. Eventually this justifies the classic description of 'flask-shaped', on the analogy of the contour of the Erlenmeyer flask (Fig. 41.51). This feature is, however, not diagnostic of Gaucher's disease and may be seen in other conditions including haemolytic anaemias (thalassaemia), leukaemia and osteopetrosis. Other bones, notably the tibia and humerus, may be similarly affected.

Destructive lesions cause localised endosteal cortical erosions, with sharply defined scalloped borders. As these lesions increase in size and coalesce, the areas of bone abnormality may become exceedingly widespread, both in the individual bone and in the skeleton as a whole. *Infarction of bone* is not uncommon (Fig. 41.52). The femoral and humeral heads, especially the former, are often involved in this way. In a child such infarction may simulate Perthe's disease. In an adult the destructive changes in the femoral head that develop cannot be differentiated from avascular necrosis of other origin. *Bone scintigraphy* may be helpful in the assessment of acute bone pain in order to detect early infarction (Fig. 41.53). Subsequent disruption of articular surfaces promotes osteoarthritis (Fig. 41.54).

Pathological fractures may follow relatively minor trauma. While fractures may occur through any affected bone, compression of a vertebral body is the usual lesion. As in many other conditions,

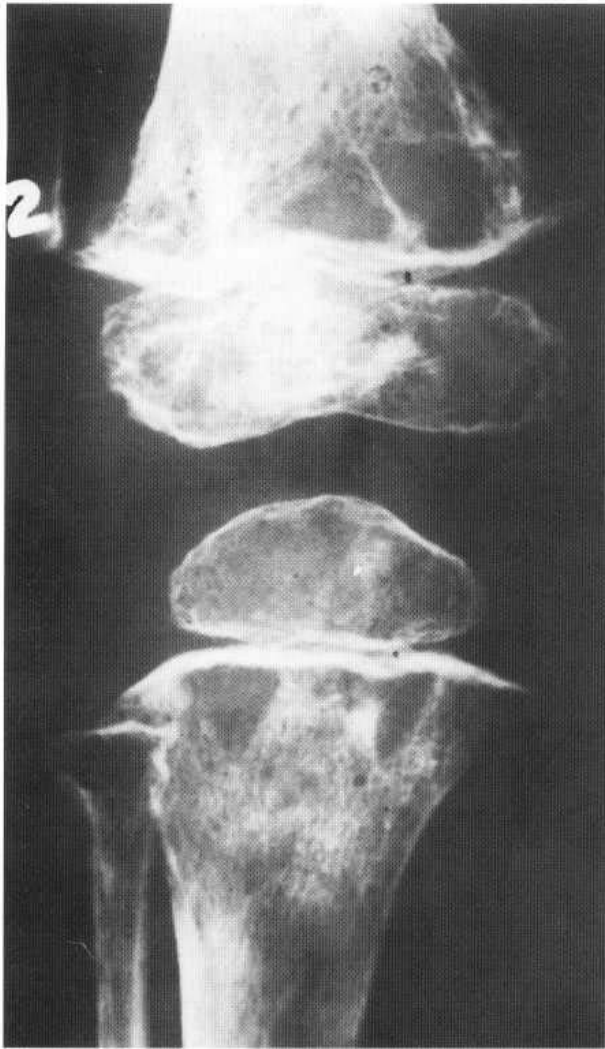


Fig. 41.50 Histiocytosis: Letterer-Siwe type. Massive destructive lesions are present throughout the skeleton, but affect particularly the metadiaphyseal areas of the long bones. A similar appearance could be produced by metastases from a neuroblastoma or the advanced stages of leukaemia.

these compression fractures are most likely to be found in the lower dorsal or lumbar regions, the areas of greatest loading. Frank zones of osteolysis in the spine are rare in Gaucher's disease, but generalised osteoporosis is common. Pathological fractures also occur in the femoral neck causing coxa vara, and in sites where no concomitant radiological abnormality can be identified.

Usually bone trabeculae are destroyed, but the chronic form of the disease may be characterised by sclerotic reaction within the bone. A coarse network of dense medullary strands results that may give the appearance of a honeycomb. In addition, endosteal thickening may develop, as in the later stages of sickle cell disease and myelosclerosis, the appearances again being suggestive of a 'bone within a bone'. On the outer surface, diffuse periosteal reactions may develop, usually overlying an intact cortex.

Because of these reactive changes in the later stages of the disease, the radiological picture may be confusing. It is particularly important for differentiation from chronic osteomyelitis to be made, as misguided surgical intervention has sometimes been followed by chronic and resistant infection with persistent discharging sinuses.



Fig. 41.51 Gaucher's disease (woman aged 20). Abnormal modelling of the distal ends of the femora has resulted in a typical flask-shaped appearance. An osteolytic lesion with a coarse trabecular pattern is present in the right femur.

Unlike some of the other diseases in this group, notably the chronic haemolytic anaemias, the distribution of these lesions tends to be peripheral rather than central. The chronic form of the disease may cause characteristic changes in the first decade: the diffuse medullary osteoporosis and abnormality of modelling in the distal ends of the femora are likely to be the first radiological manifestations. The changes may be widespread and may resemble thalassaemia, except that the bones of the hands and feet are usually completely or relatively exempt.

In the adult, the long tubular bones are usually the sites of lesions, destructive processes in the pelvis and thoracic cage being rarely evident. Nevertheless involvement of the axial skeleton does occur, as shown by the frequency of spinal osteoporosis and occasional vertebral collapse, which may be apparent even in the absence of other radiological evidence of this disease. No characteristic lesions are recognised in the skull, but diffuse osteoporosis has been reported. Frank cystic areas of destruction have been noted around the tooth roots in the mandible.

In the radiological assessment of any skeletal abnormality, appreciation of associated abnormalities of soft tissue is important. In this instance the combination of the changes described above, with a patient with an appropriate ethnic background and with splenomegaly, provides a strong diagnostic triad. Enlargement of the spleen, and often the liver, is almost constant in this disease. Pulmonary involvement is unusual, but an appearance suggestive of interstitial fibrosis may be observed, particularly in young children, even in the absence of skeletal involvement.

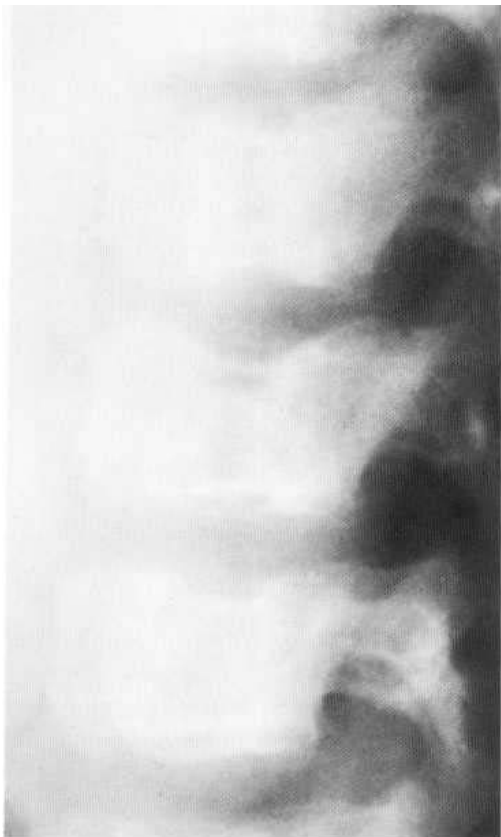


Fig. 41.52 Gaucher's disease. Infarctions in vertebral bodies have produced the 'bone within a bone' appearance throughout the lumbar spine in this child.

Niemann-Pick disease

This rare disorder of the lymphoreticular system, of a type similar to Gaucher's disease, has, in its classic form, a predilection for Jewish girls under the age of 2 years. The abnormal lipoprotein in

the 'foam cells' in this instance is *sphingomyelin*. Osseous changes are less severe than in Gaucher's disease. Nevertheless, careful study may disclose generalised osteoporosis, minor coarsening of the trabeculae and minor modelling abnormalities.

Overt areas of osteolysis do occur, but are unusual and may resemble the lesions of histiocytosis. However interstitial pulmonary infiltration, causing a 'honeycomb' lung appearance, and hepatosplenomegaly are common in classic cases, for which the prognosis is grave. Other types of the condition have been recognised in older children.

DISORDERS OF THE COAGULATION MECHANISM

Haemophilia and its variants

The normal process of blood coagulation depends on a number of factors, individual deficiencies of which have led to descriptions of several disease entities within the haemophiliac group.

From the radiological aspect the most important of these disorders are classic *haemophilia*, due to deficiency of factor V III, and the rarer *Christmas disease*, due to deficiency of factor IX. These hereditary diseases primarily affect males, being X-linked, usually recessive disorders. The degree of affliction is related to the level of deficiency.

The bleeding tendency is observed usually during the first year of life and may affect any tissue system. Christmas disease is usually less severe. Bleeding results from trauma, possibly very slight, rather than being spontaneous. Bleeding into joints is characteristic. Such episodes become more frequent during the later years of childhood and adolescence. Milder forms of the disease may cause the formation of large, soft-tissue haematoma without significant joint involvement. This is true of *Von Willebrand's disease*, which affects both sexes equally and is transmitted in an autosomal dominant manner. If, however, the factor VIII level is low, bleeding into joints can occur in this condition.

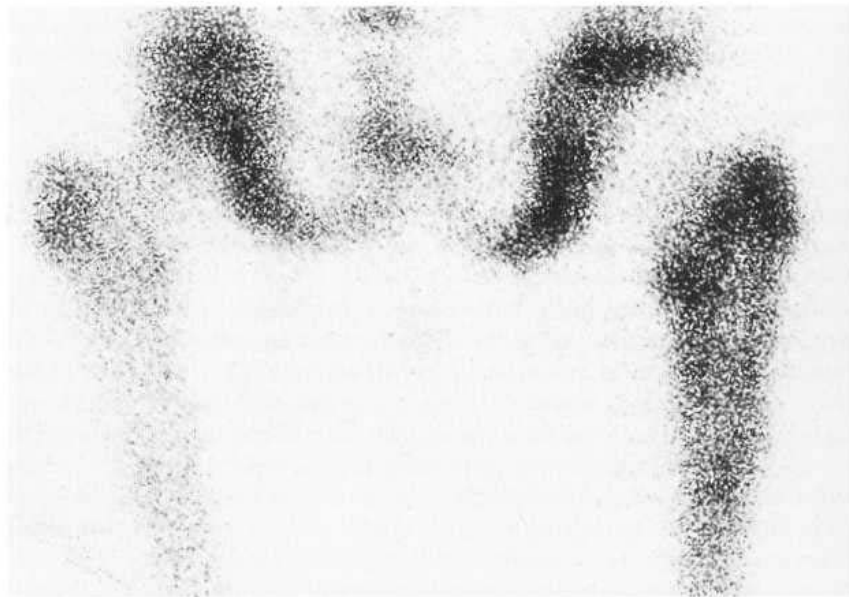


Fig. 41.53 Gaucher's disease-acute bone infarction. (A) A radiograph of a 13-year-old girl, with known Gaucher's disease, presenting with acute hip pain of 12 hours' duration. Slight endosteal sclerosis is shown in the inferior pubic ramus and an area of ill-defined radiolucency in the intertrochanteric region. (B) The delayed phase of a bone scan reveals the femoral head and neck to be markedly photon deficient consistent with acute infarction. Abnormally increased activity is present also at site of previous disease.

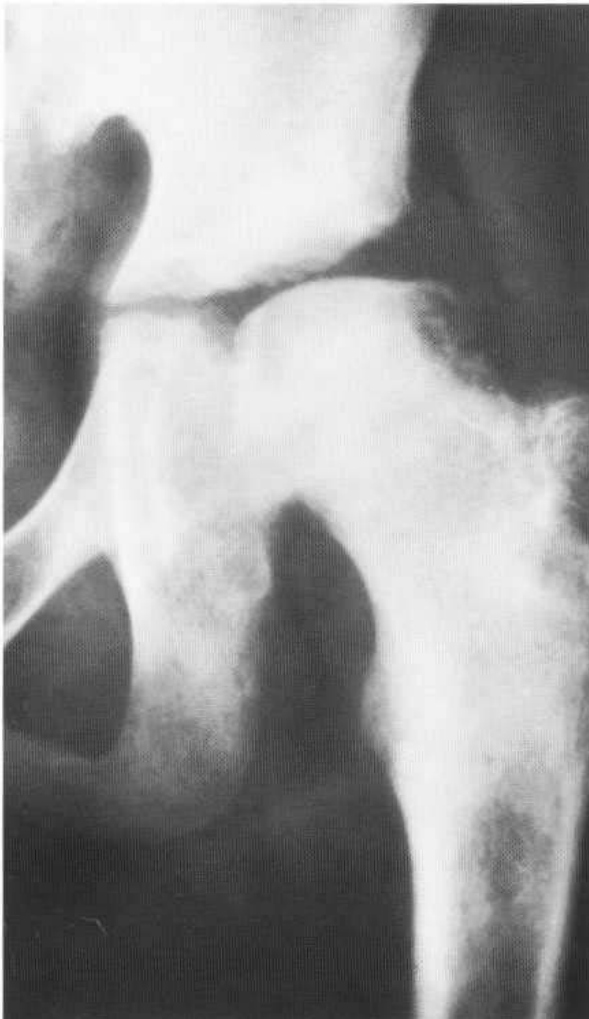


Fig. 41.54 Gaucher's disease. This adolescent has considerable deformity of the femoral head and acetabulum secondary to episodes of infarction. Evidence of degenerative arthritis is already present.

Radiological changes

In the skeleton these are caused by bleeding into joints, within bony structures and beneath the periosteum. Frequent repetition of such episodes, particularly at an early age, increases their severity.

Intra-articular haemorrhage In the early stages of the disease, the soft-tissue distension of a joint due to a haemarthrosis cannot be distinguished radiologically from a frank traumatic or inflammatory synovial effusion. Frequent repetition of haemorrhagic incidents results in synovial thickening and articular erosions. Initially these erosions tend to be marginal in distribution. At the same time the bony structures near an affected joint are likely to become porotic, partly through disuse, but particularly through persistent hyperaemia associated with organisation of the haemarthrosis. This latter factor, as with hyperaemia of any other cause, commonly causes enlargement of the growing epiphyses (Fig. 41.55). Such epiphyses may become abnormal in shape and often fuse prematurely. Differentiation from a chronic inflammatory synovitis, particularly tuberculous, may present radiological difficulty. The trabecular pattern of the bone becomes coarse and often has a lattice appearance. Secondary degenerative changes large,

The knee is affected almost invariably, involvement being frequently bilateral. The intercondylar notch becomes wide and deep. The patella may develop an unusually rectangular shape and its proximal articular surface is a common site of an erosion.

The elbows and ankles also are commonly affected. A characteristic abnormality in the former joint is an enlarged and deformed radial head. The shoulders and wrists are less frequently involved. Bleeding into the hip is unusual, but when this does occur avascular necrosis of the femoral head causes an appearance comparable to Perthe's disease. Distended joint capsules, particularly those of the elbows, may become radiologically dense by deposition within them of haemosiderin (Fig. 41.57). This too produces low signal on MR images of diseased synovium (Fig. 41.58).

Intraosseous haemorrhage Juxta-articular cystic lesions may be observed in the later stages of the disease, with a peculiar predilection for the proximal humeral epiphyses and the olccranon processes. While many are comparable to the post-traumatic sub-articular cysts of degenerative joint disease, the fact that some of these cysts are remote from the articular surfaces has led to the belief that they may be caused by haemorrhage within the bone itself.

Subperiosteal haemorrhage Large osteolytic lesions, haemophilic pseudotumours, occur in about 1 or 2 % of severely affected patients. They arise especially in the iliac wings and in the shafts of the long bones of the lower limb, although other bones, including the calcaneum, have been involved (Fig. 41.59). These destructive lesions have been attributed to bleeding below the periosteum, or muscle attachments, and often are accompanied by large swellings, sometimes relatively painless,



Fig. 41.55 Haemophilia. The former epiphyses are disproportionately enlarged, presenting a 'squared' appearance. Hyaline cartilage thickness at the ankle joint is reduced.



Fig. 41.56 (A,B) Haemophilia. Typical appearances in an adult patient subject to recurrent haemarthroses since childhood. As well as the enlarged, squared appearance of the former epiphyses, hyaline cartilage width is reduced, and osteophytes are present due to secondary osteoarthritis. Areas of radiolucency within medullary bone probably represent old intraosseous haemorrhages.

of the soft tissues. Relation to a former traumatic incident may occasionally be established. Absorption of the underlying cortex and medulla with elevation of the periosteal margins results in an appearance that may be highly suggestive of a malignant bone tumour. Calcification is not uncommon within the space-occupying lesions. A diagnostic clue, however, may be



A



B

Fig. 41.57 (A,B) Haemophilia. Repeated intra-articular haemorrhages have caused overgrowth of the epiphyses, particularly the head of the radius. The joint capsule is distended and the synovium is amorphously dense due to the deposition of haemosiderin from recurrent haemarthroses. A subarticular cyst is present in the olecranon fossa, and degenerative changes, in the form of hyaline cartilage thinning and osteophyte formation, are present.

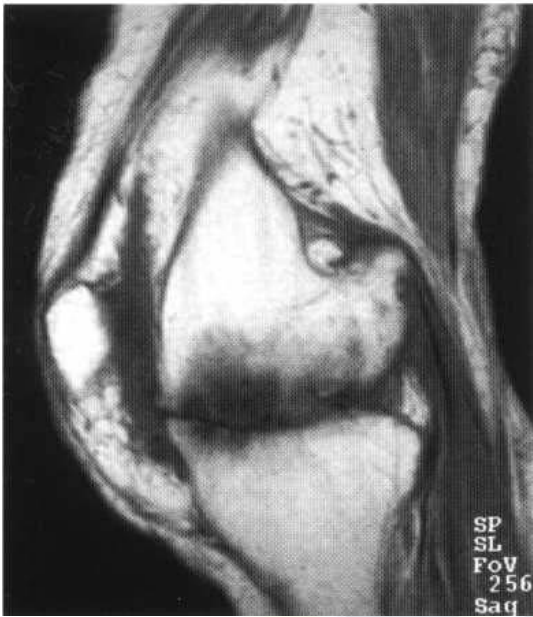


Fig. 41.58 Haemophilia. Sagittal T₁-weighted image showing loss of hyaline cartilage over the medial compartment and very low signal intensity synovium due to haemosiderin deposition.

provided by evidence in an adjacent joint of a haemophilic arthropathy. Failure to appreciate the nature of this entity, nevertheless, has resulted in iatrogenic disasters by inappropriate treatment.

The diagnosis of haemophilia is likely to be made clinically, but the radiologist must be aware of its skeletal manifestations, including not only the typical arthropathics and bone cysts, but also and importantly the rare haemophilic pseudotumours.

REFERENCES AND SUGGESTIONS FOR FURTHER READING (CHAPTERS 39–41)

- Bullough. P. G. (1997) *Bullaugli and Vigorita's Orthopaedic Pathology*, 3rd Ed. Mosby.
- Dahlin, D.C., Krishnan, K. U. (1986) *Bone Tumours*, 4th edn. Springfield: C. C. Thomas.
- Resnick D. (2000) *Diagnosis of Bone and Joint Disorders*. 4th Ed. Saunders.
- Wilner, 1). (1982) *Radiology of Bone Tumours and Allied Disorders*. Philadelphia: W. B. Saunders.



Fig. 41.59 Haemophilic pseudotumour. A huge destructive lesion in the tibia, with relatively well-defined margins, is associated with some periosteal reaction. Although an initial impression may be of a malignant tumour, changes of haemophilic arthropathy can be seen in the knee and ankle.

موسسه انتشاراتی
نور دانش



نشر الکترونیکی
موسسه انتشاراتی
نوردانش

42

METABOLIC AND ENDOCRINE DISORDERS AFFECTING BONE

Jeremy W. R. Young

with contributions from Leonie Gordon

In general, metabolic bone disease affects the skeleton in one of two ways: there is either too much or too little calcified bone. The latter change, which comprises the majority of metabolic bone disease, is due either to a decrease in the amount of bone formed, or to excessive resorption of bone. In turn this may be due to a variety of causes but most commonly to abnormalities of vitamin D and calcium metabolism, which in turn arise from abnormality of diet or renal function, endocrine abnormalities (particularly of the parathyroid gland), drug therapy or poisoning.

For the most part metabolic processes involve the skeleton as a whole. The radiographic changes of metabolic bone diseases are therefore predominantly diffuse or at least multifocal, involving many areas of the skeleton, although on occasion isolated lesions may be found, such as brown tumours in hyperparathyroidism. Another feature of metabolic bone disease is the tendency to involve specific locations, and to be symmetrical in the body, as seen in the 'Looser's zones' of osteomalacia (see below). Radiographic evaluation of metabolic disease, and in particular the evaluation of changes in bone density, is difficult, as up to 40% of bone mass has been devised for the measurement of bone density. The more important ones are described below.

BONE DENSITY MEASUREMENTS

There are a variety of techniques for non-invasive assessment of the skeleton.

Radiographic absorptiometry

Radiographic absorptiometry (RA), also known as photodensitometry, was one of the first quantitative techniques used to assess trabecular and cortical bone mass. Although, it is an inexpensive and readily accessible technique, it is characterised by high-precision errors of about 9-10%. Computer-assisted methods have reduced operator errors and improved precision. Accuracy error is about 4.5% and it is suitable for measurements of the bone mineral density of the phalanges and metacarpals.

Single photon and X-ray absorptiometry

Single photon absorptiometry (SPA) was introduced in the 1960s and was superseded by the introduction of single X-ray absorptiometry (SXA). Both methods make a quantitative assessment of bone mineral content (BMC) at peripheral sites of the skeleton (e.g. distal radius, calcaneus). A highly collimated photon beam from a radioactive source or a small X-ray tube is used to measure improved attenuation at the measurement site. Placing the radioactive source with an X-ray tube has improved the precision and spatial resolution of the systems. The problem with this method is that separate measurements of trabecular and cortical bone are not possible. There is also some question whether bone mineral content of the appendicular skeleton correlates with peripheral bone mineral density.

Dual photon and X-ray absorptiometry

Dual photon absorptiometry (DPA) technique uses a gadolinium-153 source, which emits photons at different energy levels, allowing differentiation between soft tissue and bone. This method has been replaced by dual X-ray absorptiometry (DXA) where the radioactive source is replaced by an X-ray beam. DXA measurements are mainly performed at the lumbar spine, proximal femur and whole body, but can be used for assessment at peripheral sites such as the forearm and calcaneus. Using the current generation of DXA systems, images may be obtained in about 2 minutes and there is a sufficiently high resolution to measure geometrical features as well as bone mineral density (BMD). Radiation doses are very low and precision errors are small. The range of these errors is 1-1.5% for the lumbar spine, 2-3% for the lateral spine, 1.5-3% for the femoral neck and 1% for the total body and forearm scanning. DXA of the lumbar spine hip can predict osteoporotic vertebra and proximal femur fractures and these measurements show age-related changes as well as response to therapy. DXA bone mineral density readings may be elevated in patients with aortic calcifications, osteophytes and disc space narrowing.

Quantitative ultrasound

Ultrasound properties are primarily assessed in calcaneal trabecular bone. Two parameters are assessed: speed sound (SOS) and broad band ultrasound attenuation (BUA). SOS is a measure of the transmission velocity in the bone where BUA reflects the frequency dependence of the ultrasound attenuation. Calcaneal ultrasound is significantly but modestly correlated with bone mineral density assessed at the calcaneus and other sites. Its role may be in providing structural information independent of bone mineral density and bone strength. The advantage of ultrasound devices is that they are compact, inexpensive and free of ionising radiation. It is generally believed that quantitative ultrasound is affected by both the material and structural properties of bone, i.e. the number, orientation and connectivity of the trabecular. The calcaneus, precision for SOS and BUA are in the range of 0.59% and 1.59% and 0.9% and 6.3% respectively. Information provided by this technique should be used to complement information obtained on bone mineral density.

CT and high-resolution MRI

Using CT and MRI, it is possible to obtain three-dimensional images at a range of skeletal sites with direct examination of trabecular and cortical properties. These systems allow for assessment of factors other than bone mineral density, such as trabecular structure and cortical geometry, which are determinates of bone strength.

Spinal quantitative CT

Standard body CT scanners with slices of 5-10 mm are obtained through the midvertebral body and a region of interest placed inside the metabolically active vertebral trabecular bone. Quantitative CT (QCT) is widely employed for assessment for osteoporosis, as it can assess trabecular bone mineral density which is important for vertebral strength. Peripheral QCT are also table-top available for the assessment of the distal radius. Radial measurements are taken in trabecular, integral and cortical regions of interest, and they can measure the radial area of cortex. It is an expensive way to assess peripheral bone density and its correlation with central (axial) bone density is questionable.

Volumetric QCT

Volumetric QCT approaches have been developed for improved precision for assessment of the spine and, more importantly, for

densitometric assessment of the hip, the complex architecture of which hinders assessment using single-slice approaches. An approach recently developed for assessment of the proximal femur analyses the three-dimensional (3D) architecture of the hip and uses anatomical features to place 3D regions of interest in the trabecular femoral neck and trochanteric regions with excellent precision. Using this type of approach, it is not only possible to obtain serial data, but it is also possible to examine the regional variation in bone density.

High-resolution MRI

In applications in osteoporosis, high-resolution MRI may be employed to depict changes in trabecular structure at several sites in the peripheral skeleton. For the distal radius, in-plane image resolutions of 156 µm can be obtained using a standard 1.5-tesla imager. Although this resolution is significantly higher than that of high-resolution spinal CT, there is partial volume averaging and the result is still dependent on the thresholding process used. A recent study has shown that apparent histomorphometric parameters show age-related changes, modest correlations to bone mineral density, and significant differences between osteoporotic and age-matched normal subjects.

BASIC BIOCHEMISTRY OF BONE METABOLISM

Biochemical findings in metabolic and endocrine disease of the bone are variable, but can be extremely helpful in making the diagnosis. They are summarised in Table 42.1.

Changes due to vitamin D abnormalities

Vitamin D is derived from the diet, and as a result of the action of ultraviolet light on the skin. After hydroxylation of cholecalciferol in the liver, further hydroxylation occurs in the kidney to generate the active form of vitamin D, 1,25-dihydroxycholecalciferol (1,25 DHCC), which has several modes of action. In bone, homeostasis is maintained by two effects of 1,25 DHCC: mobilisation of calcium and phosphorus, and promotion of mineralisation and maturation. The former requires the presence of both 1,25 DHCC and parathormone. Also, 1,25 DHCC absorption of calcium and phosphorus

Table 42.1 Laboratory changes in metabolic bone disease

	Serum levels			Urine levels		
	Calcium	Phosphorus	Alkaline phosphatase	Urea or creatinine	Calcium	Hydroxy praline
Osteoporosis	N	N	N	N	N	N or
Hyperparathyroidism						
Primary	↑	↓	N or ↑	N or ↑	N or ↑	↑
Secondary	N or ↓	↑	↑	↑	↓	↑
Tertiary	↑	N or ↓	N or ↑	↑	N or ↑	N or
Hypoparathyroidism	↓	↑	N	N	↓	N
Pseudohypoparathyroidism	↓	↑	N	N	↓	N
Hyperthyroidism	N or ↑	N	N	N	↑	↑
Rickets/osteomalacia						
Vitamin D deficiency	↓	↓	↑	N	↓	N
Vitamin D refractory	N	↓	↑	N or	↓	N
Hypophosphatasia	N or ↑	N	↓	N	N or ↑	↓

N = normal; ↑ = elevated; ↓ = lowered.

is promoted in the intestines. In addition, it affects the kidney, both directly, on proximal renal tubular function, and indirectly, by stimulating production of relatively inert 24,25 dihydroxycholecalciferol, which has a negative feedback effect, limiting 1,25 DHCC production. Finally, there are receptors in other organs, particularly the pituitary, placenta and breast, which are thought to reflect the increased demand for calcium during growth, pregnancy and lactation.

Rickets and osteomalacia (vitamin deficiency)

Rickets and osteomalacia are the same basic disorder, occurring in children and adults respectively. The pathological changes result from an interruption of development and, in particular, mineralisation of the growth plate in the developing skeleton, or from lack of mineralisation of osteoid in the mature skeleton. They occur as a result of a lack of the actions of vitamin D, which in turn may be due to dietary lack, lack of production by the body, failure of absorption or defective metabolism. In practice, as the body can normally generate sufficient vitamin D when there is adequate ultraviolet light, nutritional deficiency only occurs when there is a dietary lack together with too little exposure to ultraviolet light. This is most commonly seen in black-skinned immigrants who make their homes in the colder and less sunny areas of Northern Europe. It may also occur in the neglected elderly, particularly in larger cities in the higher latitudes,

Malabsorption states, including Crohn's disease and scleroderma, can result in osteomalacia (Box 42.1). Liver disease, whether ductal or hepatocellular, is also a cause of osteomalacia, although osteoporosis is also found histologically. The osteomalacia of liver disease is multifactorial, but appears largely due to malabsorption of vitamin D, as bile salts are necessary for vitamin D absorption in micelle form. In coeliac disease, the small bowel is less responsive to the action of vitamin D in calcium transport.

Drug therapy may produce osteomalacia, particularly long-term anticonvulsant therapy (phenytoin/dilantin). A similar effect has also been reported with rifampicin and glutethimide.

Finally, many toxins have been found to cause osteomalacia by causing tubular damage and phosphate deficiency. These include aluminum hydroxide, magnesium sulphate and cadmium, the latter being associated with alkaline battery manufacture, or the painful condition of 'itai-itai' (ouch, ouch) reported in Japan in patients drinking cadmium-polluted water.

Rickets

There are many causes of rickets in childhood. In general, however, the radiological features are similar, although varying in severity and location. The skeletal effects are due to a lack of calcification of osteoid. Consequently the most obvious changes are at the metaphysis, where the most rapid growth is occurring. The initial abnormality is a loss of the normal 'zone of provisional calcification'

Box 42.1 Malabsorption states causing osteomalacia

- Crohn's disease
- Celiac disease
- Lymphoma
- Amyloidosis
- Small bowel fistula
- Postoperative states (bowel resection)
- Hepatobiliary disease



42.1

Fig. 42.1 Rickets. There is obvious 'fraying' of the visible metaphyseal margins.



42.2

Fig. 42.2 Rickets. There is splaying of all of the visible metatarsals, with widening of the epiphyseal plates. In addition, there is so characteristic bowing of the femora and bones of the lower leg.

adjacent to the metaphysis, although usually by the time radiographs are obtained, significant metaphyseal abnormality is seen. This begins as an indistinctness of the metaphyseal margin, progressing to a 'frayed' appearance with a widening of the growth plate, due to lack of calcification of metaphyseal bone (Fig. 42.1). Weight-bearing and stress on the uncalcified bone give rise to splaying, and cupping of the metaphysis and distortion of the bone architecture (Fig. 42.2).

A similar but less marked effect occurs in the subperiosteal layer, which may cause lack of distinctness of the cortical margin. Eventually a generalised reduction in bone density is seen, and in longstanding cases fractures may occur. Looser's zones are not seen as often as in osteomalacia (see below). In the epiphysis, there may be some haziness of the cortical margins.

With treatment, mineralisation occurs, giving rise to a dense white line at the zone of provisional calcification adjacent to the metaphysis, but becoming contiguous with the metaphysis during the healing process. In cases of intermittent dietary vitamin deficiency, or inadequate treatment, the metaphysis will show patchy sclerosis. In severe cases of rickets additional deformities of the bones occur, with bowing of the long bones (particularly of the lower limbs) (Fig. 42.2), thoracic kyphosis with a 'pigeon chest', enlargement of the anterior ribs, causing the 'ricketic rosary' (Fig. 42.3), and bossing of the skull. Rickets may be seen in low-birthweight and premature infants, and may be severe, causing spontaneous fractures and respiratory difficulty. Affected infants are usually below 1000 g in weight, or less than 28 weeks' gestation.

Vitamin D-resistant rickets (familial hypophosphatasia)

This condition is usually inherited in a dominant sex-linked fashion. Affected women pass the disease on to half of their sons and daugh-

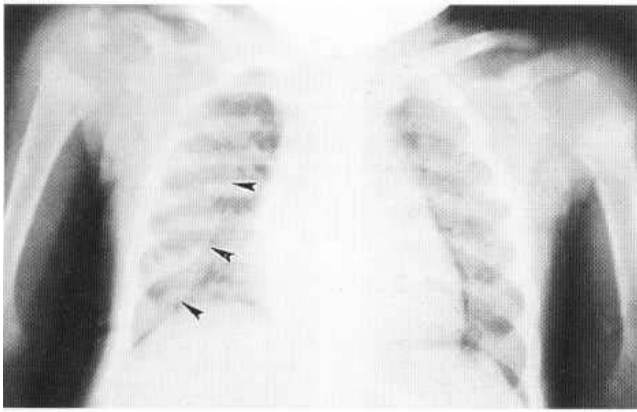


Fig. 42.3 Rickets. Widening of the anterior ribs is clearly demonstrated (arrows). The classic metaphyseal changes of rickets are also seen in the proximal humeri.

ters, while affected men pass the disease on to none of their sons and half of their daughters. The disease is similar to rickets in radiographic appearance, but it is refractory to vitamin D therapy, and growth retardation may be marked. The radiographic changes are variable from mild to severe, and may be similar to the metaphyseal dysplasia of the Schmid variety (see Ch. 35).

Acquired hypophosphataemic rickets

Rarely, hypophosphataemia has been seen in association with tumours of bone or soft tissues, frequently fibrous in origin. It has also been reported in association with prostatic carcinoma, and oat cell carcinoma of the lung, and a similar condition has also been reported with other conditions, for example neurofibromatosis, fibrous dysplasia.

Vitamin D-resistant rickets associated with renal tubular disorders

A variety of renal dysfunction syndromes produce rickets and osteomalacia. These include hypercalcaemia, renal phosphate loss and secondary hypophosphataemia, amino aciduria and renal tubular acidosis. In renal tubular acidosis affected patients demonstrate retarded growth and short stature. As well as the changes of osteomalacia, nephrocalcinosis and nephrolithiasis are seen (Fig. 42.4).

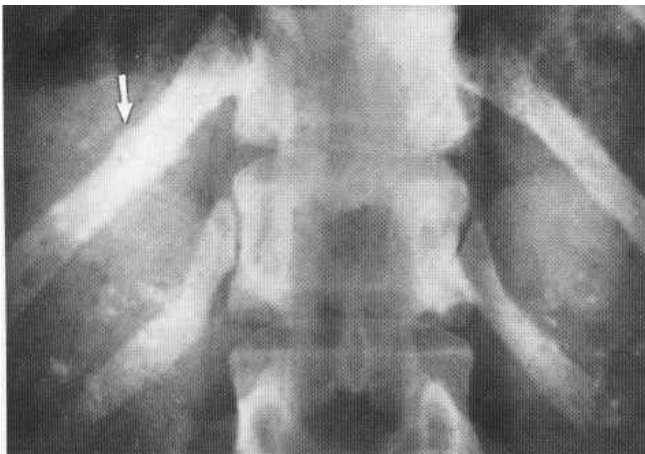


Fig. 42.4 Renal tubular acidosis. The combination of nephrocalcinosis and osteomalacia (Looser's zone-arrow) in the right 11th rib is characteristic, although symptomatic bone disease affects only a minority of patients. (Courtesy Dr. DI Stoker and Institute of Orthopaedics.)

Osteomalacia

This refers to the changes resulting from vitamin D deficiency in the mature skeleton. Bone pain is a frequent complaint. Serum alkaline phosphatase is elevated, and serum phosphorus is low. The hallmark of osteomalacia is the pseudofracture or 'Looser's zone'. This is a narrow zone of lucency, usually running perpendicular or nearly perpendicular to the bone cortex (Fig. 42.5). Initially poorly defined, these zones become progressively more prominent, with sclerotic margins (Fig. 42.6). They are generally accepted as occurring at sites of stress as subclinical stress fractures that are repaired by unossified osteoid. They are frequently bilateral and symmetrical, and occur at regular sites (Fig. 42.7) such as the pubic rami, proximal femur (Fig. 42.8), scapula (Fig. 42.6), lower ribs and ulna (Fig. 42.5). Osteopenia develops with 'pencil-in' of the vertebral bodies, and loss of vertebral height in a characteristic 'codfish vertebra' pattern (Fig. 42.9).

Bowing of the long bones may occur. Compression wedge fractures of the vertebra are less common than in osteoporosis. The histopathology of osteomalacia is characteristic, with excessive osteoid and/or failure of ossification of new bone.

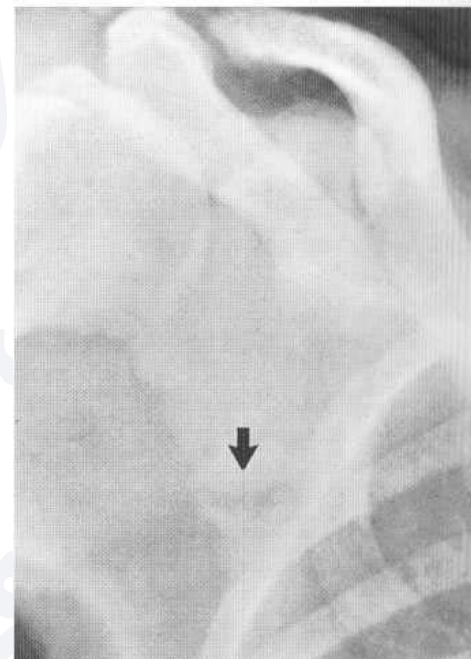
Hypophosphatasia

Inherited as an autosomal recessive trait, this rare disorder presents with a radiographic picture which varies from a mild to a very



42.5

Fig. 42.5 Looser's zone. The characteristic lucency of the mid ulna is seen.



42.6

Fig. 42.6 Looser's zone. There is lucency with surrounding sclerosis in the lateral border of the scapula-a common site.

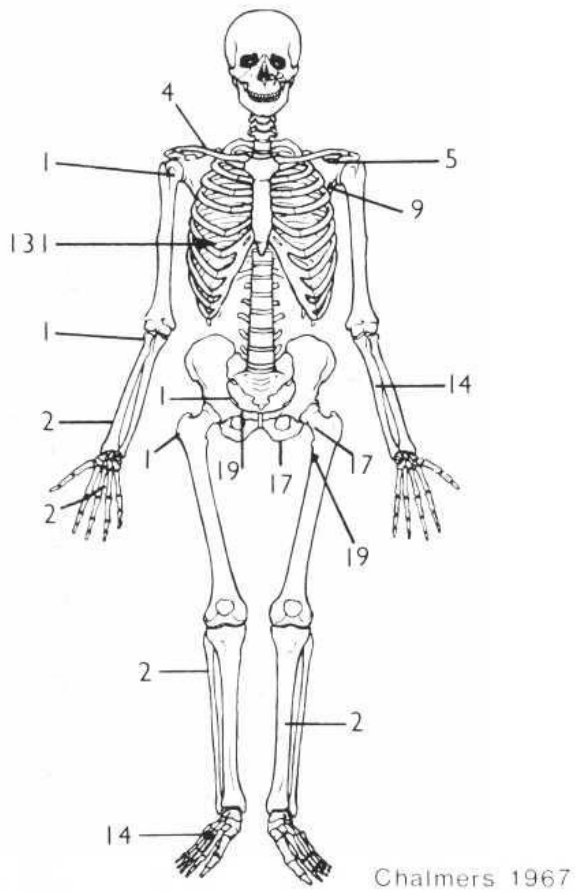


Fig. 42.7 Sites of incidence of Looser's zones in osteomalacia. In a group of middle-aged and elderly patients with dietetic osteomalacia. (Courtesy of Dr D. J. Stoker and Institute of Orthopaedics.)

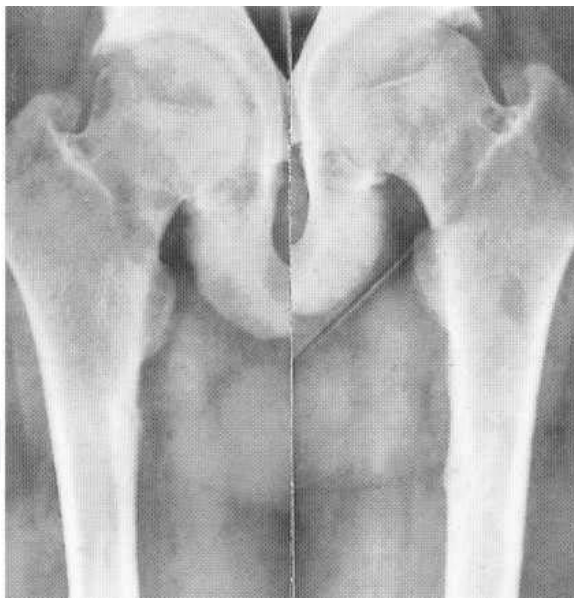


Fig. 42.8 Looser's zones. Symmetrical lucencies are seen involving the medial cortex of the proximal femur bilaterally—another characteristic site.

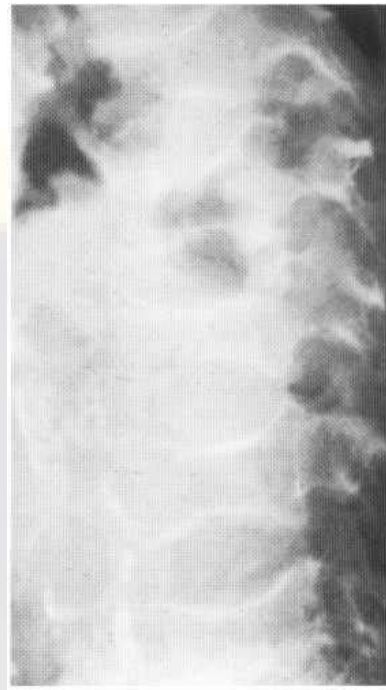


Fig. 42.9 Osteomalacia. Marked biconcavity of the vertebral bodies (codfish vertebrae). (Courtesy of Dr D. J. Stoker and Institute of Orthopaedics.)

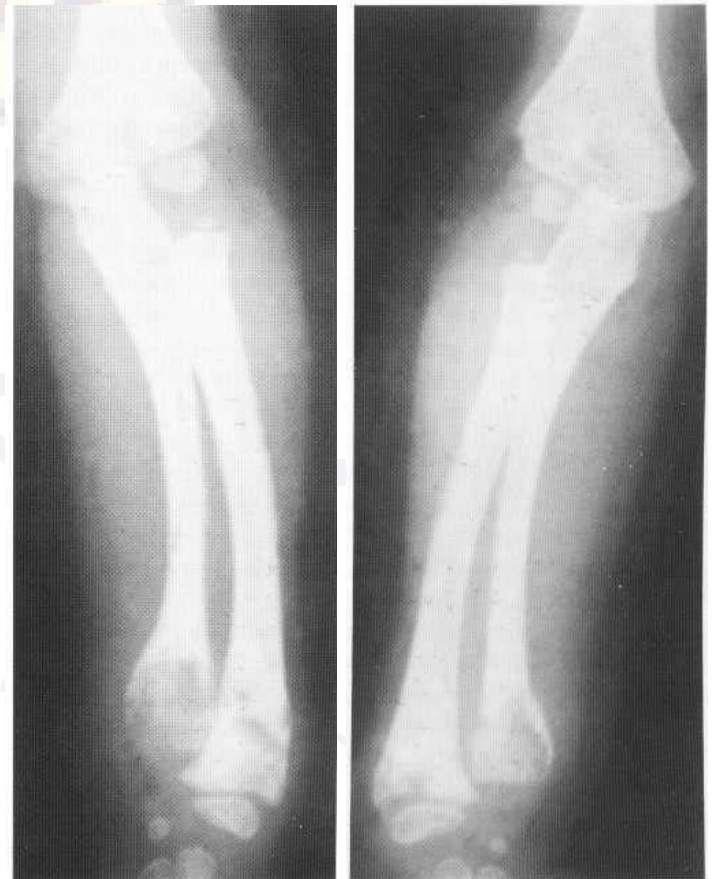


Fig. 42.10 Hypophosphatasia. In this child metaphyseal ossification is delayed in the ulnae while the distal radii contain islands of non-ossified tissue. (Courtesy of Dr D. J. Stoker and Institute of Orthopaedics.)

severe form of rickets, depending upon the age of onset, the neonatal variety being most severe, and generally lethal. There is a low serum alkaline phosphatase, and increased urinary phosphoethanolamine. In severe cases an exaggerated fraying of the

metaphysis is seen, with uncalcified osteoid extending into the metaphysis (Fig. 42.10). Craniostenosis and nephrocalcinosis may occur, and deformities, particularly of the distal phalanges and tibia, are seen.

Familial hyperphosphataemia

This extremely rare condition of autosomal recessive inheritance presents in early infancy. The radiographic appearance is similar to that of Paget's disease, but occurring in infancy and demonstrating more symmetry; the conditions however are unrelated. The skull vault is thickened and the long bones are tubular, enlarged and bowed, but with cortical irregularity (Fig. 42.11). Serum alkaline phosphatase is elevated.

Fibrogenesis imperfecta ossium

This rare disorder presents with coarsening of the trabecular pattern of the bones, and in particular the ends of the long bones. Multiple fractures are seen. Serum alkaline phosphatase is elevated.

Axial osteomalacia

This rare condition is characterised by a coarsening of the bony trabeculae, similar to that seen in fibrogenesis imperfecta ossium, but only involving the vertebra, pelvis and ribs. Histologically osteomalacia is found, but serum alkaline phosphatase levels are normal.

VITAMIN C DEFICIENCY

Vitamin C deficiency leads to a deficiency in the formation of bone matrix, as it is necessary for the formation of hydroxyproline, which is vital for collagen. About 90% of the matrix of mature bone is collagen, and hence a lack of collagen will have a severe effect on bone formation. In childhood, this gives rise to scurvy. The adult counterpart is osteoporosis.

Scurvy

Scurvy is rare before 6 months of age since the storage of vitamin C in the neonate is generally adequate. Children present with limb pain and irritability. Radiographically, four characteristic signs are seen: (i) the epiphysis is small, and sharply marginated by a sclerotic rim (Wimberger's sign) (Fig. 42.12); (ii) the zone of provisional calcification at the growing metaphysis is dense, giving a white line (Frankel's line); (iii) beneath this is a lucent zone, due to lack of mineralization of osteoid (Trummerfeld zone); (iv) finally, as this area is weakened, it is prone to fractures which manifest themselves at the cortical margin, giving rise to (Pelkan's) spurs (Fig. 42.13).

In addition, due to capillary fragility, subperiosteal haemorrhages occur (Fig. 42.13), which may give rise to periosteal elevation and subsequent new bone formation, particularly following treatment. This dense periosteal new bone should be differentiated from that found in battered infants.

Following treatment, dense bands of bone may be left, resembling growth arrest lines.

OSTEOPOROSIS

Osteoporosis is the most frequent metabolic bone disease, and is due to a decrease in bone mass. It is the result of many underlying causes (Box 42.2). In general, the loss of bone mass gives rise to increased incidence of fractures, particularly in the femoral neck, spine (compression fractures), distal radius and pubic symphysis. In osteoporosis the microstructure of the bone is normal, but the quantity of bone is diminished. This eventually gives rise to a clear loss of bone density, radiographically best described as osteopenia. This radiographic appearance of generalised osteopenia however is

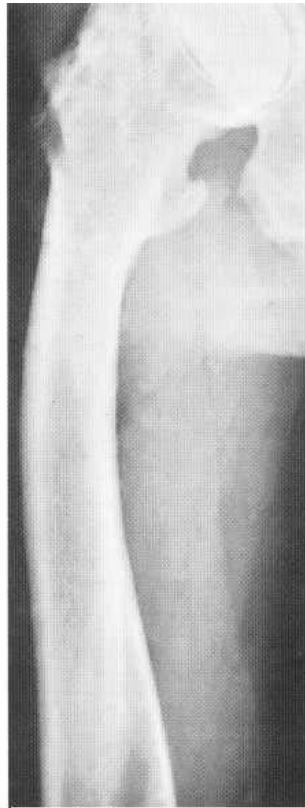
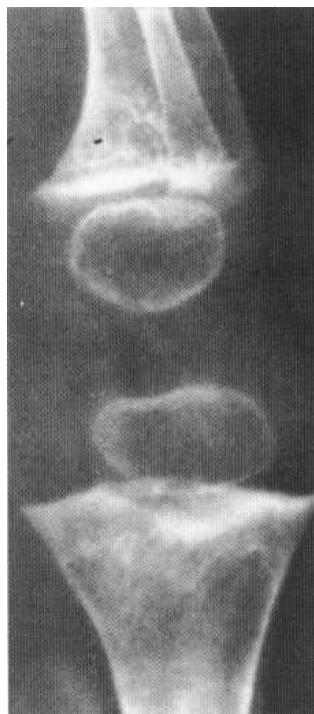


Fig. 42.11 Familial hyperphosphataemia. (A) The femur is abnormal with some bowing, increased width, and prominent but irregular cortex, somewhat resembling Paget's disease. (Courtesy of Dr C. S. Resnik.) (B) The radiological appearances in this child are diagnostic. The bones are widened with loss of differentiation of cortex and medulla. A coarse trabecular pattern and bowing are also evident. Again, these features resemble those of Paget's disease. (Courtesy of Dr D. J. Stoker and Institute of Orthopaedics.)





42.12

Fig. 42.12 Scurvy. The margins of the epiphyses are sclerotic (Wimberger's sign). There is a narrow epiphyseal plate, with increased density of the zone of provisional calcification (Frankel's line). The lucent zone beneath this is due to lack of mineralized osteoid (Trummerfeld zone).



42.13

Fig. 42.13 Scurvy. Subperiosteal haemorrhage has elevated the periosteum. The healing stage shows marked periosteal new bone formation. The metaphyseal lucency (Trummerfeld zone) is again visible, as is Pelkan's spur, at the medial border of the proximal tibial metaphysis.

Box 42.2 Causes of generalised osteoporosis

Age-related conditions (senile and postmenopausal states)
 Deficiency states
 Malnutrition
 Calcium deficiency
 Scurvy
 Drugs
 Steroids
 Heparin
 Metabolic
 Hyperthyroidism
 Hyperparathyroidism
 Cushing's disease
 Acromegaly
 Pregnancy
 Diabetes mellitus
 Hypogonadism
 Alcoholism
 Chronic liver disease
 Anaemias
 Idiopathic

Box 42.3 Major causes of diffuse osteopenia

Osteoporosis
 Osteomalacia
 Hyperparathyroidism
 Neoplasia (particularly multiple myeloma)

Box 42.4 Major causes of localised osteoporosis

Immobilisation
 Post-fracture
 Sudeck's atrophy
 Arthritis
 Infection

not specific to osteoporosis and can be seen in a variety of conditions (Box 42.3). In addition there are many conditions that can give rise to localised osteopenia (Box 42.4).

In osteoporosis trabecular loss is most evident radiographically in the spine, where there is a loss of density, which may be appreciated as 'pencil-ing in' of the vertebrae by the more radiographically dense end-plates (Fig. 42.14). Biconcave vertebral bodies (cod-fish vertebrae) may occur. In the femoral neck the osteopenia is manifested by an apparent increase in density of the residual trabecula (Fig. 42.15). Endosteal and intracortical resorption of bone is prominent, producing cortical thinning most evident in the appendicular skeleton.

Postmenopausal and senile osteoporosis (involutional osteoporosis)

Postmenopausal osteoporosis occurs in women typically aged 50-65. There is a disproportionate loss of trabecular bone, giving rise to rapid bone loss, and a proportionate increase in fractures, particularly of the vertebrae and distal radius. In the vertebra, loss of height and anterior wedging occur, which may lead to a marked kyphotic deformity (Fig. 42.14). The changes of osteoporosis have been linked to reduced oestrogen levels, although additional factors such as skeletal size, level of activity, nutritional status and genetic determinants have been proposed. In general, once osteoporosis is established, oestrogen therapy does not affect the radiographic density of the bone. Blood chemistry is usually normal, although urinary hydroxyproline levels may be elevated in the acute stage.

Senile osteoporosis differs from postmenopausal osteoporosis in that there is proportionate loss of cortical and trabecular bone. Fractures occur most commonly in the femoral neck, proximal humerus, tibia and pelvis. There is no dramatic increase in bone loss in the postmenopausal stage, and patients tend to be older. The ratio of affected women to men is approximately 2:1. The aetiology is uncertain, but reduced intestinal absorption, diminished adrenal function and secondary hyperparathyroidism may play a role.

Idiopathic juvenile osteoporosis

This disorder is a rare self-limiting disease that affects both sexes and occurs typically before puberty. Patients present with bone pain, backache or limp related to fractures, characteristically of the metaphysis of the long bones with minimal trauma. Compressions of the vertebrae with kyphosis may result. The diagnosis is one of exclusion, particularly from leukaemia, lymphoma and hypercorti-

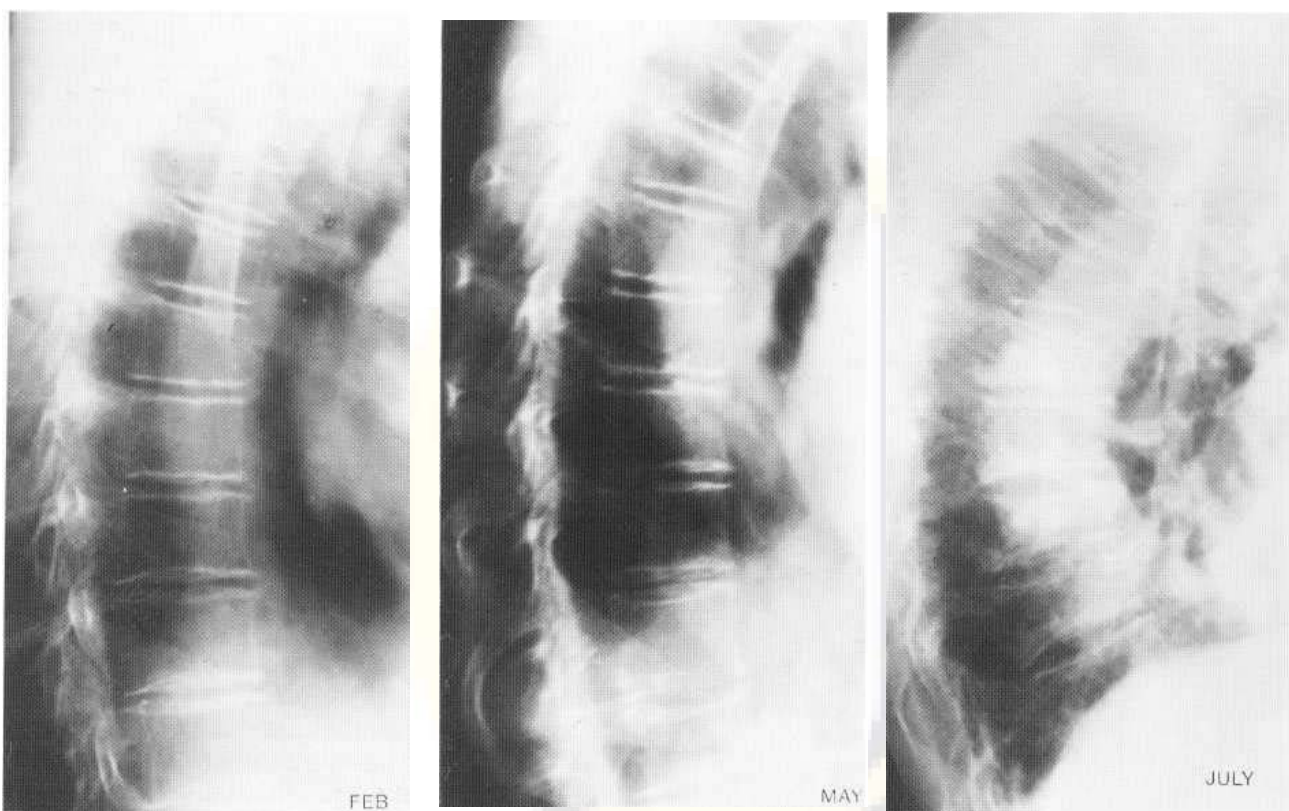


Fig. 42.14 Postmenopausal osteoporosis. Serial films in this patient show the progressive development of kyphosis as a result of anterior wedging of the thoracic vertebral bodies during the course of 6 months. (Courtesy of Dr D. J. Stoker and Institute of Orthopaedics.)



Fig. 42.15 Osteoporosis. In this patient, resorption of the secondary trabeculae has left the primary trabeculae to delineate the lines of stress within the femoral neck.

costeroid states. Another radiographic diagnostic consideration is osteogenesis imperfecta (see Ch. I), as this also presents with diffuse osteoporosis and multiple fractures. Blood chemistry is normal.

Idiopathic male osteoporosis

A number of male patients present with generalised osteopenia before the age of 60. No definite predisposing factors have been found. Hypercalciuria and increased calcium absorption seem to be

constant findings, and the condition may be an acquired defect in bone metabolism. Again, this is a diagnosis of exclusion.

ENDOCRINE-INDUCED OSTEOPOROSIS

Abnormality of function of the adrenal, pituitary and thyroid glands, hyperfunction of the parathyroids and hypofunction of the pancreas and gonads have all been linked with osteoporosis. As well as osteoporosis, other skeletal abnormalities are associated with particular endocrine disorders.

Steroid-induced osteoporosis (Cushing's disease)

(Glucocortical excess may be related to therapy, but can be due to a number of causes, although it is usually secondary to Cushing's disease. Histological studies have revealed decreased bone formation and increased resorption. Biochemically there is a negative calcium balance and hypercalciuria. Exuberant callus formation at fractures is seen, particularly in long bones, ribs (Fig. 42.16) and vertebral bodies. In the latter case, a characteristic increased density of the end-plates occurs (Fig. 42.17). Avascular necrosis may occur, particularly of the femoral head. In children, growth may be retarded. Rib fractures may be multiple, painless and unsuspected.

Hypogonadism

In boys, this results in delayed closure of the epiphyseal plates. As a result, the patients have long limbs in relation to their trunks. A similar hypogonadal disorder in girls (Turner's syndrome) results in short stature, increased carrying angle at the elbow, a short fourth metacarpal and changes of Blount's disease at the knee. Congenital cardiovascular anomalies also occur, most commonly coarctation of the aorta.



Fig. 42.16 Cushing's disease. Excessive callus formation is seen at multiple fracture sites in the ribs. The patient had functional adrenal carcinoma.



Fig. 42.17 Cushing's disease. Generalised reduction in bone density simulates postmenopausal osteoporosis in this patient. The compression fracture of the superior border of the body of L4 has characteristically produced dense callus. This feature is almost, but not entirely, pathognomonic of glucocorticosteroid excess. (Courtesy of Dr D. J. Stoker and Institute of Orthopaedics.)

The thyroid gland

Hyperthyroidism

In hyperthyroidism, a generalised osteoporosis may be seen. There is an increased metabolic ratio, with an increase in both bone formation and resorption. Increased cortical striations of the long bones are seen. Thyroid acropachy is a rare condition which usually follows therapy for previous hyperthyroidism or occurs in patients who have been on thyroid for many years. There is a characteristic periosteal thickening in the extremities and particularly in the hands, although it can be seen in the feet. In the extremities, the commonest and most characteristic site of involvement is the



Fig. 42.18 Thyroid acropachy. A dense periosteal reaction is seen along the first metatarsal. Although this can occur in any of the digits, the first is a characteristic site.

first metacarpal or metatarsal (Fig. 42.18). It must be distinguished from hypertrophic osteoarthropathy, which is also found in the extremities (Figs 42.19, 42.20), but is usually exquisitely painful. Exophthalmos and pretibial myxoedema are frequently present. Rarely, hyperthyroidism appears in childhood, when accelerated skeletal maturation occurs.

Hypothyroidism

Although it is not associated with osteoporosis, it is appropriate to discuss this condition at this point. In children, skeletal maturation is delayed and growth is retarded. Epiphyses are late in appearing (Fig. 42.21) and fragmented, although when they do appear, the sequence is normal. This may cause an appearance in the hip that must be differentiated from (Legg) Perthes' disease. Wormian bones are seen in the skull, and the sella is either small and bowl-shaped (young children), or of large rounded 'cherry sella' configuration (older children). The paranasal sinuses are underdeveloped. In the spine, bullet-shaped vertebral bodies are seen, especially at the thoracolumbar junction, where kyphosis may develop. All the long bones are short. In the pelvis the incidence of slipped capital femoral epiphysis is increased, and the pelvis itself is often narrow, with coxa vara deformities. In the adult the changes are exaggerated (Fig. 42.22).



Fig. 42.19 Hypertrophic (pulmonary) osteoarthropathy. There is marked periosteal reaction along most of the visualised bones, with, in addition, some periarticular osteoporosis, most likely secondary to disuse, resulting from the severe pain experienced in this condition.

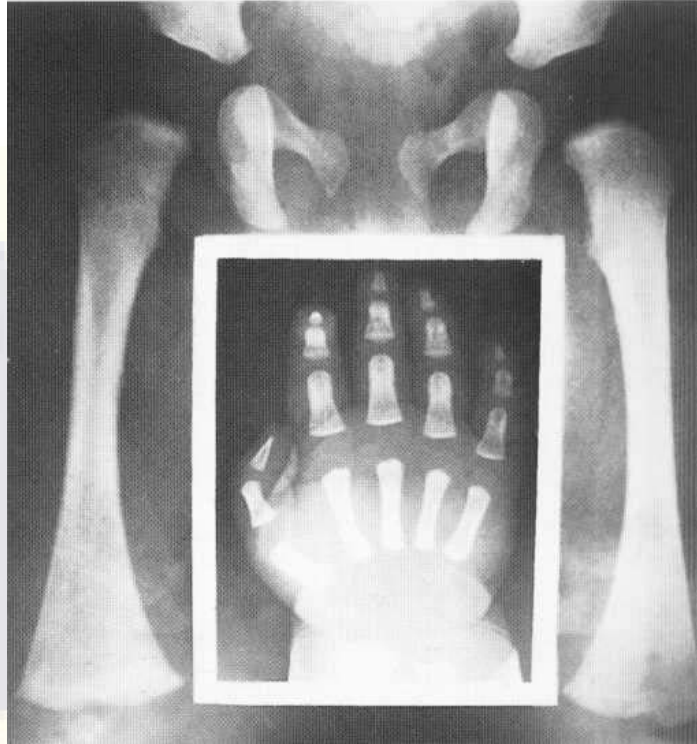


Fig. 42.21 Cretinism. Marked skeletal retardation was present in this 12-month-old child. Note that the carpal and proximal femoral centres have not yet appeared. (Courtesy of Dr D. I. Stoker and Institute of Orthopaedics.)



Fig. 42.20 Hypertrophic osteoarthropathy: periosteal reaction is identified along the medial aspect of the distal femur.

Hyperpituitarism (acromegaly)

It is questionable whether acromegaly is a cause for true osteoporosis. It will however be included in this section. Gigantism in the immature skeleton, and acromegaly in the adult, result from excessive growth hormone production by an eosinophilic adenoma. The radiographic features of acromegaly include enlarged mastoid air cells and sinuses, frontal bossing and prognathism (Fig. 42.23). Pituitary fossa enlargement may be seen on the plain film (Fig. 42.23), although CT or MRI are more helpful in evaluating for a pituitary adenoma (see Ch. 58). In the spine, enlargement of the vertebral bodies with posterior scalloping is seen (Fig. 42.24). The hands show characteristic enlargement of the bones and soft tissues with spade-like terminal tufts, or arrowhead distal phalanges (Fig. 42.25). Widening of the joint spaces due to overgrowth of articular cartilage may be seen. The feet show evidence of increased thickness of the heel pads, although this is no longer regarded as an infallible sign of acromegaly (Fig. 42.26). The long bones of the feet are elongated, although the feet usually remain slender. Prominence of muscle attachments, and premature or exaggerated degenerative change may be seen (Fig. 42.27). Calcification of the pinna of the ear occurs. Chondrocalcinosis has been reported as a rare variation, although crystal arthropathy has been suggested as the underlying cause by some authors.

The parathyroid glands

Hypoparathyroidism

Rarely, osteoporosis is seen in patients with hypoparathyroidism. The most common cause for hypoparathyroidism is parathyroid gland removal at thyroid surgery, or ^{131}I -labelled thyroid therapy.

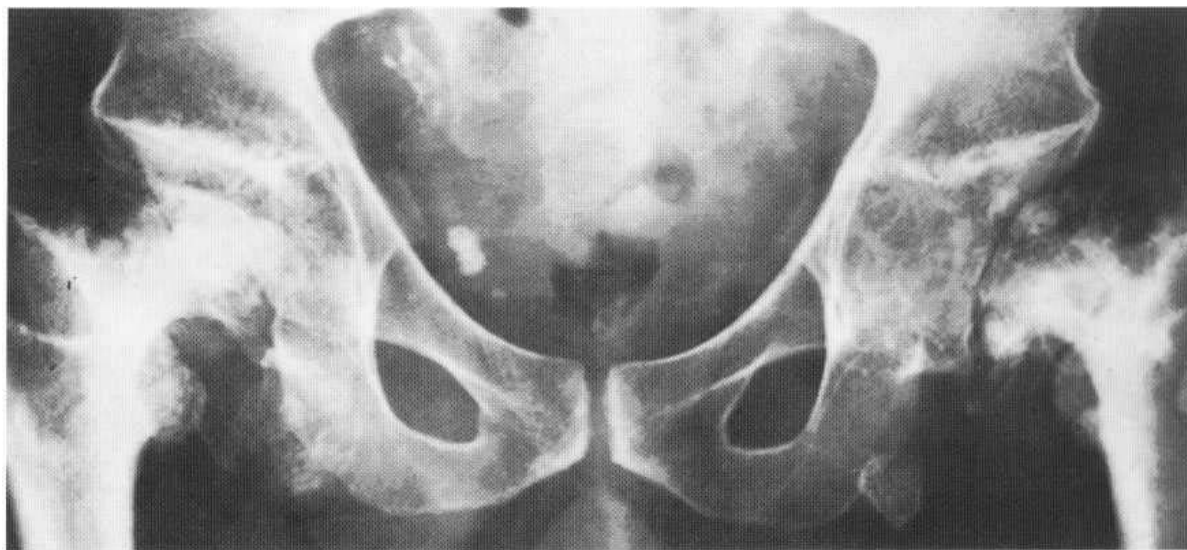


Fig. 42.22 Adult cretinism. This 39-year-old man received no therapy until 4 years before this film was obtained. Coxa vara is present, while the femoral heads are deformed and irregularly ossified in the absence of thyroid hormone during development. (Courtesy of Dr D.J. Stoker and Institute of Orthopaedics.)

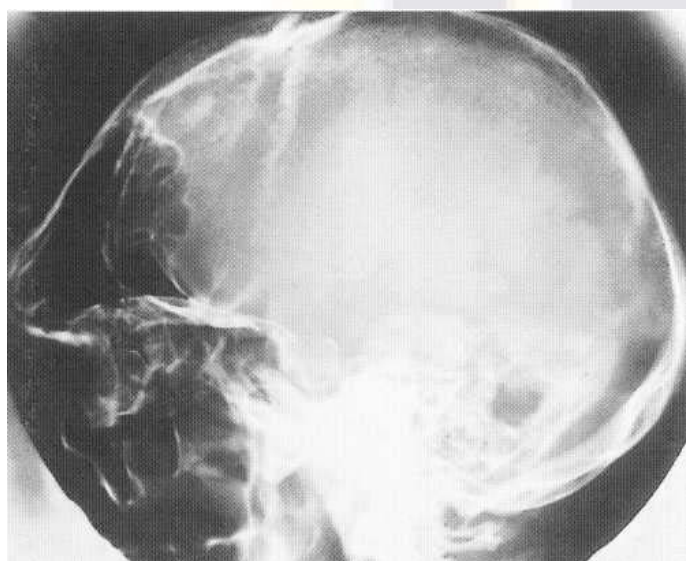


Fig. 42.23 Acromegaly. The frontal sinuses are markedly enlarged, and there is frontal bossing. A double floor is seen in the pituitary fossa with 'ballooning'.

Rarely it can result from excessive therapeutic radiation, haemorrhage, infection, tumour deposition in the thyroid gland or iron deposition in iron overload conditions. Idiopathic hypoparathyroidism, either autoimmune or familial, can occur without atrophy of the glands. It is associated with a variety of endocrine and immune deficiency states including Addison's disease, ovarian dysgenesis, hypothyroidism and chronic mucocutaneous candidiasis. Circulating antibodies to the parathyroid, thyroid and adrenal glands have been found. Calcium deposition in the basal ganglia occurs and osteosclerosis, particularly of the pelvis, inner table of the skull, proximal femur and vertebral bodies can be seen, as well as abnormal tooth development. Serum calcium is low, and phosphate diuresis follows parathormone administration.

Pseudohypoparathyroidism

This is inherited in a dominant fashion and is characterised by hypocalcaemia and hyperphosphataemia which are unresponsive to parathormone. The parathyroid glands are normal, but there is 'end-

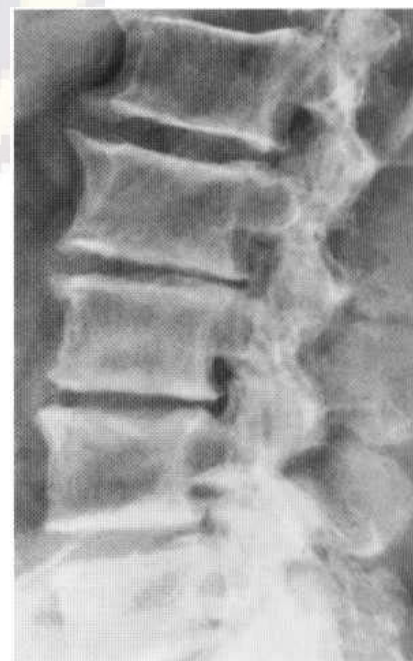


Fig. 42.24 Acromegaly. The vertebral bodies show bony overgrowth. Mild posterior scalloping is also seen at several levels. (Courtesy of Dr. C. S. Resnik.)

organ' resistance to parathormone. This may be due to a defect in the adenylyl-cyclase-cyclic AMP system in the renal tubules and bones. Basal ganglia calcification is more common than in idiopathic hypoparathyroidism. Short metacarpals are seen, particularly the fourth and fifth (Fig. 42.28). Abnormal dentition is also seen, with hypoplasia and cranial defects, and there may be calcification in the connective tissues of the skin, ligaments, tendons and fascial planes. Coxa vara, coxa valga, cone-shaped epiphyses and bowing of long bones are also reported. Secondary hyperparathyroidism is a feature of this disorder.

Pseudopseudohypoparathyroidism

This condition presents with the same clinical and radiographic appearances as pseudohypoparathyroidism, but with normal blood chemistry.



Fig. 42.25 Acromegaly. There is obvious enlargement of the soft tissues and phalanges with prominent joint spaces due to increased cartilage thickness. The distal phalanges show the characteristic 'arrowhead' configuration.

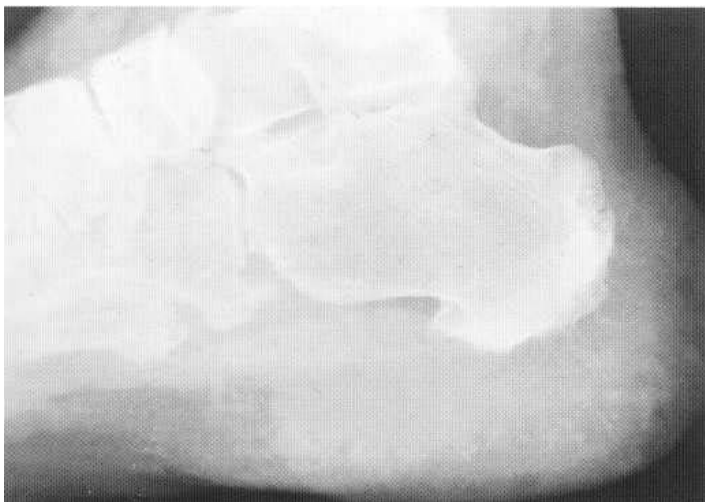


Fig. 42.26 Acromegaly. There is marked prominence of the soft tissues of the heel pad which measures approximately 35 mm.

Hypoparathyroidism

This condition is divided into the primary, secondary and tertiary forms. In the *primary* form, increased hormone production occurs as a result of parathyroid adenomas (75%), hyperplasia or carcinoma. It occurs most commonly in middle-aged and elderly people, and is more common in women (2:1). Symptoms include weakness, lassitude, constipation, polydipsia, polyuria, peptic ulceration, renal calculi and psychiatric problems. Radiographically, bone resorption is seen, and although frank osteopenia is difficult to detect radiographically in early cases, bone mineral content mea-

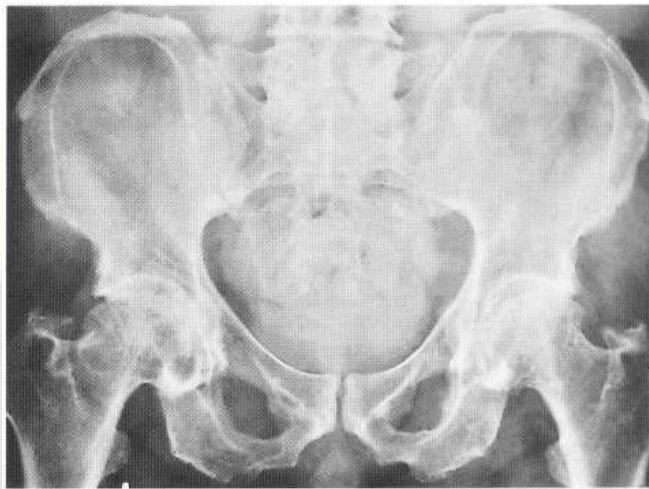


Fig. 42.27 Acromegaly. There is overgrowth of the bone in the iliac crests and irregular bony prominence of the sites of muscle attachments throughout the pelvis.



Fig. 42.28 Pseudohypoparathyroidism. A markedly short fourth metacarpal bone is seen. Although not specific for pseudohypoparathyroidism, this is a characteristic finding. (Courtesy of Dr C. S. Resnik.)

surements confirm bone mineral loss in approximately 50% of cases. More advanced cases demonstrate bone density loss, and sometimes a ground-glass appearance.

Subperiosteal erosion of bone, particularly along the radial aspect of the middle phalanx of the middle and index finger, is virtually pathognomonic (Fig. 42.29), although fine-grain film or magnification views may be required to detect it. Other sites include the medial aspect of the proximal tibia (Fig. 42.30), femur and humerus, and the ribs. Loss of the lamina dura around the teeth occurs, although this is not specific for hyperparathyroidism.



Fig. 42.29 Hyperparathyroidism. There is marked subperiosteal resorption of the radial aspect of several of the phalanges and erosion of the tufts.

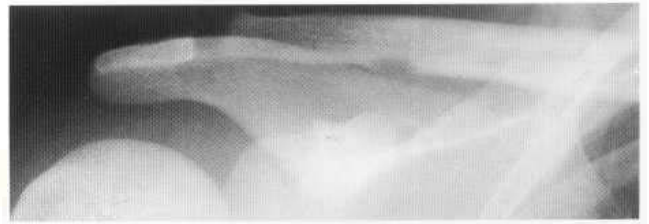


Fig. 42.31 Hyperparathyroidism. There is subperiosteal erosion of the distal end of the clavicle, as well as on the inferior surface at the site of the attachment of the coracoclavicular ligament.

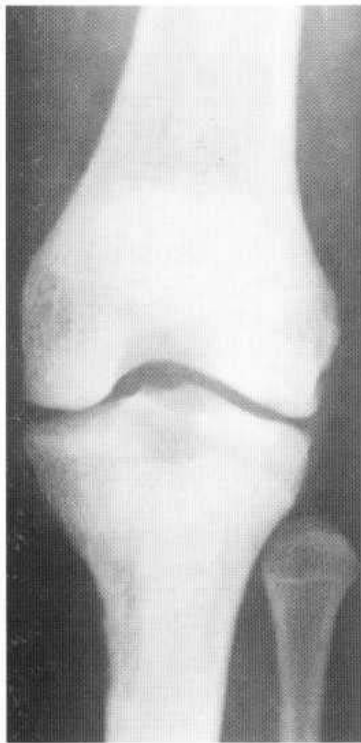


Fig. 42.30 Hyperparathyroidism. There is subperiosteal erosion of the medial side of the proximal tibia.



42.32

Fig. 42.32 Hyperparathyroidism. Intracortical bone resorption is seen, with multiple small oval lucencies within the cortical bone. A brown tumour is seen in the proximal femur.



42.33

Fig. 42.33 Severe disuse osteoporosis. There is marked intracortical bone resorption, particularly evident in the tibia.

Subchondral bone resorption is another common occurrence, being found at the distal and sometimes proximal end of the clavicle (Fig. 42.31), symphysis pubis and sacroiliac joints. This may also occur at the vertebral end-plates, which may permit disc herniation (Schmorl's nodes).

Intracortical bone resorption is another feature of hyperparathyroidism, resulting from osteoclastic activity within the Haversian canals. This gives rise to small (2-5 mm) oval or cigar-shaped lucencies within the cortex (Fig. 42.32). This is a feature of rapid bone

turnover, and is also seen in other conditions, such as hyperthyroidism, osteomalacia and acute (focal) osteoporosis (Fig. 42.33). Loss of the corticomedullary junction may occur with a 'basket-

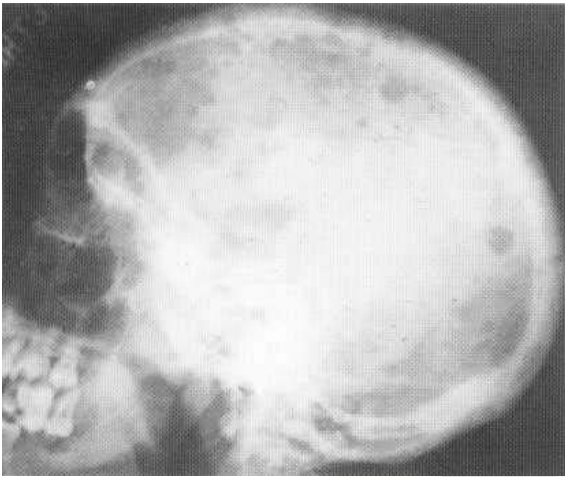


Fig. 42.34 Hyperparathyroidism. 'Pepper-pot' skull. There are multiple characteristic lucencies throughout the skull.

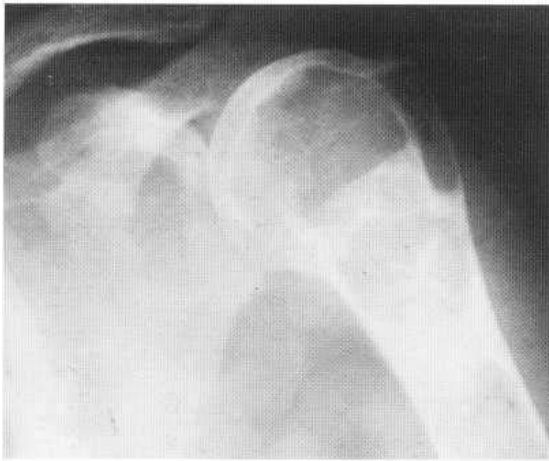


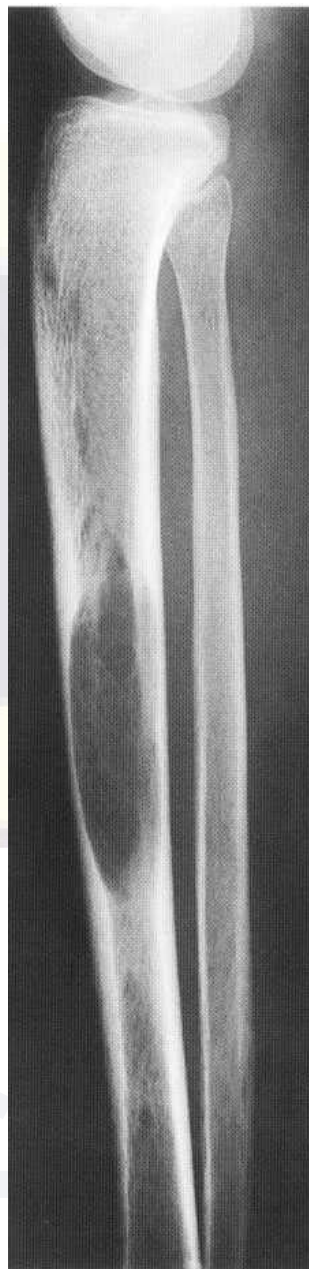
Fig. 42.35 Brown tumour of hyperparathyroidism. There is a well-defined, lytic, mildly expansive lesion of the proximal humerus.

work' appearance to the cortex. In the skull, a characteristic granular or mottled appearance may occur, giving rise to the so-called 'pepper-pot' or 'salt-and-pepper' (USA) skull (Fig. 42.34).

Subligamentous resorption occurs at sites of ligament or tendon insertions, and is seen in the ischial tuberosity, greater and lesser trochanters, inferior calcaneus and inferior surface of the distal clavicle (Fig. 42.31).

Brown tumours are locally destructive areas of intense osteoelastic activity. They present as a lytic lesion which may be expansive (Figs 42.33, 42.35, 42.36), and may destroy the overlying cortex. Pathological fractures may occur. The lesions are generally well defined, and may be multilocular. Following treatment, they may resolve, but can persist for many years.

Rarely, an erosive arthropathy may also occur. This usually involves the hands, wrists and shoulders. It may simulate the appearance of rheumatoid arthritis, but subperiosteal resorption is usually a concurrent feature, and the distal interphalangeal joints are often involved, unlike rheumatoid arthritis. Renal calculi have been reported in as many as 50% of patients. The majority are



42.36

Fig. 42.36 Brown tumour of the mid tibia. The patient was found to have a parathyroid adenoma.



42.37

Fig. 42.37 Renal osteodystrophy. Rugger-jersey spine of renal osteodystrophy. Typical end-plate sclerosis is seen with alternating bands of lucency (Courtesy of Dr D. J. Stoker and Institute of Orthopaedics.)

calcium oxalate, although a minority are uric acid stones. Nephrocalcinosis also occurs, but is less common.

Secondary hyperparathyroidism

Parathyroid hyperplasia involving all of the glands occurs in response to persistent hypocalcaemia. This can be seen in rickets, osteomalacia and chronic renal failure. The skeletal changes are similar to those of primary hyperparathyroidism although brown tumours are less frequently seen. Nevertheless, as secondary hyperparathyroidism is so much more common than primary hyperparathyroidism, in practice brown tumours are more commonly

seen as a result of the former. Calcification of arteries and soft tissues occurs, but is most common in the secondary hyperparathyroidism of renal osteodystrophy.

Chronic renal failure

This can result from numerous diseases, the most common of which is glomerulonephritis. Musculoskeletal manifestations are increasingly recognised, due to improving long-term patient survival, secondary to haemodialysis. The radiographic appearances fall into two distinct categories; those associated with renal osteodystrophy itself, and those relating to aluminum toxicity, amyloid deposition, crystal deposition, infection and avascular necrosis.

Renal osteodystrophy is of particular interest as it combines the findings of osteomalacia, hyperparathyroidism and bone sclerosis. As in hyperparathyroidism, the commonest finding in secondary hyperparathyroidism of renal osteodystrophy is subperiosteal absorption, although all manifestations may be seen. The reported prevalence of osseous resorption has been shown to increase from 10% in the early stages of disease, to 50-70% of patients after 3-9 years of dialysis. With improving techniques of haemodialysis, however, and the use of parathyroidectomy, bone resorption (excluding subchondral resorption in the hands) often shows resolution. Calcification of arteries, articular cartilage and periarticular tissues also occurs in renal osteodystrophy. Osteomalacia is identified predominantly by the presence of Looser's zones.

Osteosclerosis occurs in 9-34% of patients, and may occasionally be the only manifestation of renal osteodystrophy. It has a predilection for the axial skeleton, favouring the vertebral endplates ('rugger-jersey' spine, Fig. 42.37), the pelvis, ribs and clavicles. It also involves the metaphyses (rarely epiphyses) of long bones and the skull.

Osteopenia has been reported in up to 85% of patients, and is the end result of the effects of osteomalacia, bone resorption and a decrease in bone quantity (osteoporosis). This is due to a combination of factors including chronic metabolic acidosis, poor nutrition, azotaemia, steroid use, hyperparathyroidism and low levels of vitamin D.

In children, metaphyseal changes resembling rickets are seen, which together with cortical erosions can give rise to the so-called 'rotting fence-post' appearance, particularly at the femoral neck (Fig. 42.38). Slipped capital epiphyses are also seen as a complication, most commonly involving the proximal femur.

Other manifestations

A form of arthropathy has been associated with chronic renal failure, and is seen in patients on long-term haemodialysis. This consists of changes resembling Charcot joints, but without the extensive bone debris. The most common sites are the shoulder and spine (Fig. 42.39). The aetiology is most likely crystal deposition and amyloidosis.

Aluminium accumulation occurs in long-term haemodialysis patients, resulting most commonly from the ingestion of aluminium salts in phosphate-binding antacids used to control hyperphosphataemia. The effects are mostly cerebral and musculoskeletal. Many of the changes are identical to those of osteomalacia, but the characteristics of aluminium toxicity are lack of osteosclerosis, less evidence of subperiosteal resorption, avascular necrosis, and more than three fractures not associated with trauma. The ribs, vertebra,



Fig. 42.38 Uraemic osteodystrophy in childhood. In this child with chronic renal failure, the combination of rickets and secondary hyperparathyroidism affects the skeleton. The femoral metaphysis is irregular and the capital epiphysis shows considerable displacement. This has been likened to a rotting fence post.

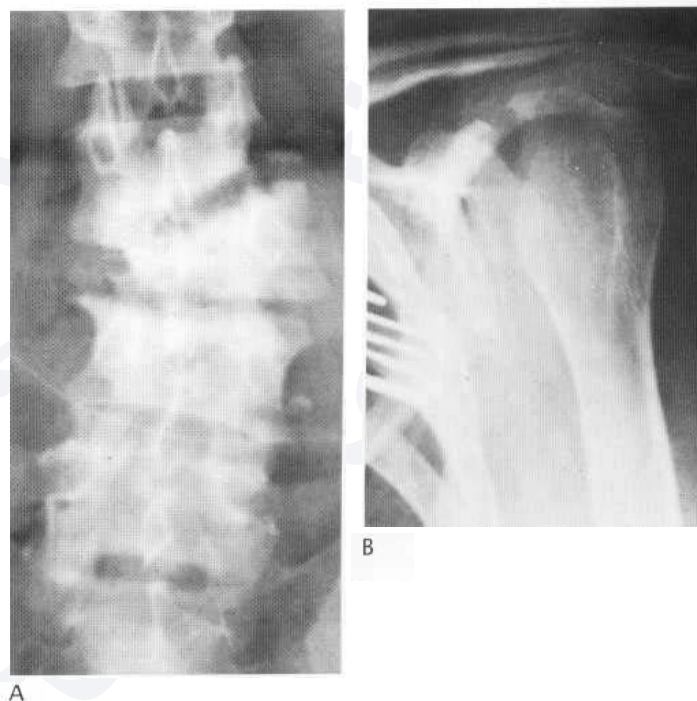


Fig. 42.39 Chronic renal failure: haemodialysis patient. (A) There is an appearance resembling a Charcot spine, or even infection. (B) A destructive arthropathy of the shoulder is also seen, without evidence of infection or neuropathy.

hips and pelvis are the commonest sites, although the extremities, particularly the long bones, may be involved.

Crystal deposition also occurs in chronic renal failure patients. The crystals involved are calcium hydroxyapatite (CPPD), monosodium urate and calcium oxalate. These can induce synovitis and bursitis. Interestingly, however, the typical arthritic changes of CPPD are unusual.

Osteomyelitis and septic arthritis with bacteria or fungi are well-recognised complications, particularly after long-term haemodialysis and transplantation. Predisposing fractures are immunosuppressive therapy, long-term debilitation, and dialysis, arteriovenous fistulas, providing an entry site for the organisms.

Avascular necrosis, most likely resulting from steroid therapy, is common, occurring in up to 40% of patients after renal transplantation. This most commonly involves the femoral head, although the humeral head, knee and talus are involved frequently.

Tertiary hyperparathyroidism

This term applies to cases in which secondary hyperparathyroidism give rise to autonomous hyperparathyroidism. Treatment of the underlying disorder fails to control the [hyperparathyroidism](#). Surgical removal of the autonomous parathyroid tissue is necessary.

Drug- and toxin-induced osteoporosis

Heparin, immunosuppressants and alcohol have all been implicated in osteoporosis, as well as corticosteroids. The development of osteoporosis has been reported in patients who receive large doses of heparin (usually greater than 15 000 units per day), although the mechanism is uncertain. The activity of mast cells may be an important factor.

In alcoholics, the cause is not known, but it may well be, at least in part, dietary or due to concurrent osteomalacia, secondary to associated liver disease.

Pregnancy and related conditions

Rarely, osteoporosis may be observed during pregnancy, although the cause for this has not been determined.

Other causes of osteoporosis

Other causes of generalised osteoporosis included multiple myeloma, glycogen storage diseases, marrow packing disorders such as Gaucher's disease, chronic liver disease, nutritional deficiency states, and chronic anaemias. Osteogenesis imperfecta exhibits marked osteoporosis, wormian bones, and fractures which heal with marked callus formation (see Ch. 35). Blue sclera and deafness are also found. Homocystinuria is another cause of osteoporosis.

Oxalosis

Primary hyperoxaluria is inherited as an autosomal recessive trait. The main feature is recurrent urinary calculi, progressing to renal failure. Calcium oxalate deposition in bone and soft tissues occurs in those who survive with dialysis (Fig. 42.40).

Ochronosis (alkaptonuria)

This rare hereditary disorder of tyrosine metabolism is inherited as an autosomal recessive trait. Due to a lack of homogentisic acid oxalate, homogentisic acid accumulates in the tissues, particularly



Fig. 42.40 Oxalosis. There is a generalised but slightly patchy increase in density of much of the visualised skeleton, due to calcium oxalate deposition.

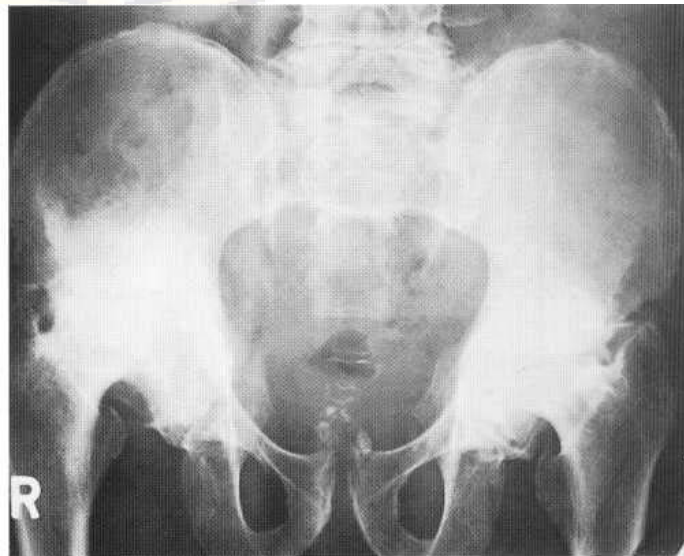


Fig. 42.41 Ochronosis. Gross narrowing of the joint spaces of both hips is associated with other evidence of severe degenerative disease. The intervertebral disc spaces are calcified and narrowed. (Courtesy of Dr D. J. Stoker and Institute of Orthopaedics.)

connective tissue. The radiographic features are mainly those of degenerative disease of the peripheral joints (Fig. 42.41) and calcification of spinal disc spaces (Fig. 42.42). In the spine, advanced changes may lead to an appearance resembling ankylosing spondylitis. Although kyphoscoliosis may occur in the spine, in the major joints there may be considerable joint-space narrowing without marked osteophyte formation or sclerosis until the later stages.

Miscellaneous conditions

Wilson's disease (hepatolenticular degeneration) is a rare autosomal recessive disorder of copper metabolism that produces skeletal



Fig. 42.42 Ochronosis. The intervertebral disc spaces are narrowed and calcified. Such widespread change is uncommon in uncomplicated degenerative spondylosis. (Courtesy of Dr D. J. Stoker and Institute of Orthopaedics.)

changes of osteomalacia, and a form of arthritis. Other metabolic disorders, such as haemochromatosis and calcium pyrophosphate dihydrate deposition disease, also mainly produce joint disease.

Haemochromatosis may also give rise to a generalised osteopenia.

Copper deficiency in infants is rare, but is reported in severely malnourished infants, and in infants on long-term parenteral nutrition. There is reduction in bone density, cortical thinning and metaphyseal irregularity, with delayed maturation. However, unlike rickets, the zone of provisional calcification is preserved.

Homoeystia nuria

This is a rare disorder inherited in an autosomal recessive manner and due to a deficiency in the activity of the enzyme cystathionine synthetase, which converts homocysteine to cystathionine and cysteine. In one form of the disease (pyridoxine-resistant), changes in the skeleton include osteoporosis, arachnodactyly, epiphyseal enlargement, scoliosis, sternal deformity, and valgus deformity of the knees and hips. Being pyridoxine resistant, this requires a low methionine diet. The other form of the disease is responsive to pyridoxine, and normal skeletal development follows.

LOCALISED OSTEOPOROSIS

On occasion a localised osteoporosis may occur. The commonest cause for this is disuse osteoporosis, which may result from pain

following trauma, severe vascular disease, infection or enforced immobilisation. A rapid, aggressive-looking resorption of bone occurs, most marked in the cortical and subarticular areas of the bones (Fig. 42.33).

Reflex sympathetic dystrophy syndrome

(Sudeck's atrophy, algodystrophy, reflex neurovascular dystrophy)

This is regarded as a distinct entity, including terms such as causalgia, Sudeck's atrophy, shoulder hand syndrome and reflex sympathetic dystrophy. The condition has been reported in association with prior trauma, surgery or infectious states, as well as vasculitis, calcific tendonitis, neoplasia, disc herniation, myocardial infarction, degenerative cervical spine disease and cardiovascular disorders. Symptoms usually include pain, swelling, stiffness and weakness, but may be associated with hyperaesthesia, vasomotor changes and disability. It is thought to be related to abnormal neural reflexes. Endosteal bone resorption is the most prevalent form of demineralisation in this condition, although subperiosteal resorption, periarticular porosis, intracortical resorption and subchondral erosions are also seen (see Fig. 43.28). Despite the superficial similarities, of pain and osteoporosis seen with transient osteoporosis and regional migratory osteoporosis (see below), the pattern of bone marrow oedema seen in these conditions is not identified in patients with reflex sympathetic dystrophy.

Transient (regional) osteoporosis

This is a rare condition of large joints where gross focal osteoporosis and pain occur. The femoral head is the commonest site. It occurs typically in young and middle-aged adults, and is more common in men. Interestingly, when it occurs in women, the left hip is almost exclusively affected, and the disease occurs in the third trimester of pregnancy. There is no history of trauma or infection. Some authors believe that it is a form of Sudeck's atrophy. Synovial biopsy may show mild chronic inflammation. Symptoms resolve spontaneously in 4-10 months.

Regional migratory osteoporosis

This condition is migratory in nature, and the hip is involved less frequently than other areas, such as the knee, ankle and foot. It is commoner in men than in women, and is most evident between 30 and 50. Clinically it is similar to transient osteoporosis of the hip, the involvement of each joint lasting approximately 9 months. Recurrences in other bones may occur successively, or be separated by up to 2 years or more.

Idiopathic chondrolysis of the hip

This is a rare disorder of unknown aetiology. It affects predominantly adolescent girls and young women, particularly black-skinned patients, and gives rise to localised pain and marked osteoporosis. Early degenerative change results.

TOXIC EFFECTS ON THE SKELETON

Many toxins and poisons may affect the skeleton. Some common conditions are discussed below.

Hypervitaminosis A

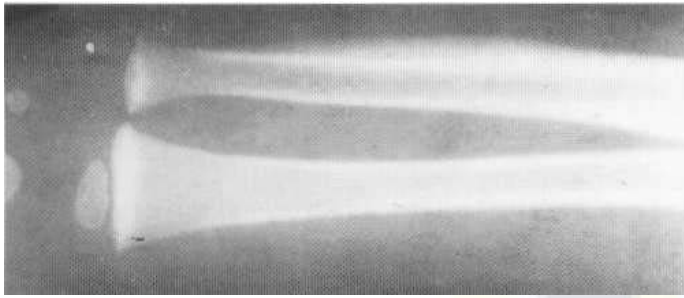


Fig. 42.43 Hypervitaminosis A. There is increased cortical density, most marked in the ulna.



Fig. 42.46 Vinyl chloride poisoning. Inhalation or ingestion of vinyl chloride may produce this characteristic resorption of the central portions of the terminal phalanges. (Courtesy of Dr D. J. Stoker and Institute of Orthopaedics.)



42.44

Fig. 42.44 Lead lines: metaphyseal bands of increased density.



42.45

Fig. 42.45 Bismuth poisoning: dense metaphyseal lines are present, similar to those seen in lead poisoning.

Overdosage of vitamin A may occur in children, but is rare in adults. It gives rise to hypercalcaemia, and an increase in periosteal new bone. Tender swellings of the limbs may occur. Radiographically, dense periosteal new bone is identified (Fig. 42.43), which, in contrast to infantile cortical hyperostosis, is not seen usually until

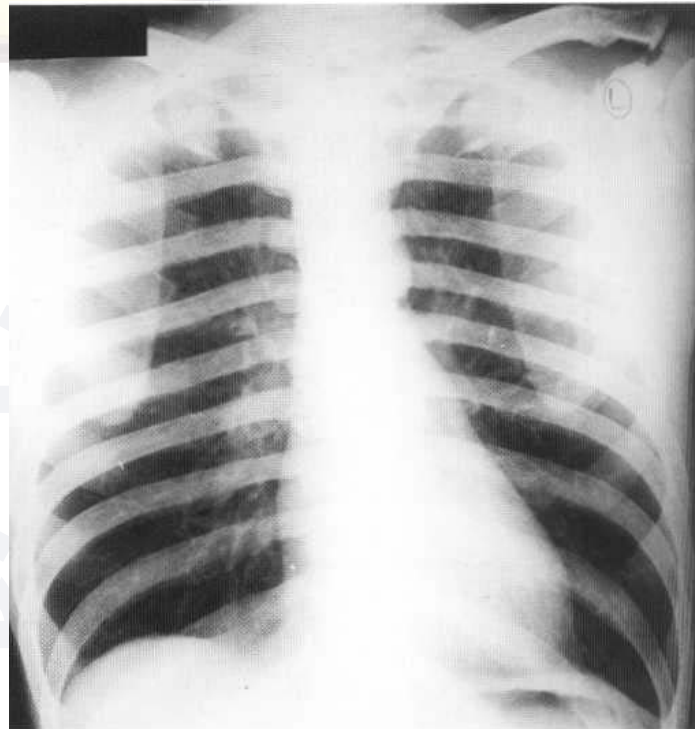


Fig. 42.47 Fluorosis. There is markedly increased density of all the visualised bones.

after the first year of life. Withdrawal of vitamin A supplements results in remodelling of the bone.

Lead poisoning

Lead poisoning occurs in children who ingest lead-containing paint or water from lead-containing pipes and leads to lead deposition in the growing metaphyseal regions. This may cause modelling deformities

and increased bone density, although most of this is due to reactive change (Fig. 42.44). Lead encephalopathy is a serious complication.

Bismuth intoxication

Bismuth intoxication (often following treatment for syphilis in the past) causes a similar appearance to that of lead poisoning (Fig. 42.45).

Vinyl chloride poisoning

Vinyl chloride poisoning found in workers in PVC manufacture causes Raynaud's phenomenon, and a characteristic form of acro-osteolysis (Fig. 42.46). Sacroiliitis is also seen, and haemangiosarcoma of the liver has been reported.

Fluorosis

Fluorosis, due to chronic fluoride poisoning, is endemic in some parts of the Middle and Far East, but may also occur in aluminum smelting industries, and from drinking wine when fluorine is used as a preservative. A generalised increased bone density is seen (Fig. 42.47), which is again due to osteoclastic response to the fluorine rather than to fluorine deposition per se. Cortical thickening occurs, causing encroachment upon the medullary cavity, and ossification of ligamentous and musculotendinous attachments is seen. Endemic fluorosis is rare in children, unless there are exceptionally high levels of fluorine; it may be associated with crippling stiffness and pain.

REFERENCES AND SUGGESTIONS FOR FURTHER READING

Bone density

- Funke, M., Kopka, L., Vosshenrich R., et al (1995) Broad hand ultrasound attenuation the diagnosis of osteoporosis: correlation with osteodensitometry and fracture. *Radiology*, *194*, 77-81.
- Genant, H. K. (1998) Current state of bone densitometry for osteoporosis. *Radiographics*, *18*, 913-918.
- Genant, H. K., Black, J. E., Steigler, P., et al (1987) Quantitative computed tomography in assessment of osteoporosis. *Seminars in Nuclear Medicine*, *17*, 316-323.

- Herd, R. J., Blake, G. M., Ramalingam, T., et al (1993) Measurements of postmenopausal bone loss with a new contact ultrasound system. *Calcified Tissue International*, *53*, 153-157.
- Pacifici, R., Rupich, R., Griffin, N., et al (1990) Dual energy radiography versus quantitative computer tomography for the diagnosis of osteoporosis. *Journal of Clinical Endocrinology and Metabolism*, *70*, 705-710.

General

- Fogelman, L. Carr, I. (1980) A comparison of bone scanning and radiology in the evaluation of patients with metabolic bone disease. *Clinical Radiology*, *31*, 321-326.
- Genant, H. K., et al (1980) Computed tomography of the musculoskeletal system. *Journal of Bone and Joint Surgery*, *62A*, 1088-1011.
- Pitt, M. J. (1981) Ricketic and osteomalacia syndromes. *Radiologic Clinics of North America*, *19*, 581-599.
- Resnick, D. (ed.) (1989) *Bone and Joint Imaging*. Philadelphia: W. B. Saunders.
- Sartoris, D. J. (1996) Metabolic bone diseases. In *Musculoskeletal Imaging*, pp. 286-318. St Louis: Mosby.

Osteomalacia and rickets

- Callenbach, J. C., Shennan, M. B., Abramson, S. J., Hall, R. T. (1981) Etiologic factors in rickets of very low-birth-weight infants. *Journal of Pediatrics*, *98*, 800-805.
- Swischuk, L. E., Hayden Jr., C. K. (1979) Rickets: a roentgenographic scheme for diagnosis. *Pediatric Radiology*, *8*, 203-208.

Poisons and toxins

- Betts, P. R., Watson, S. M., Astley, R. (1973) A suggested role of radiology in lead poisoning. *Annales de Radiologie*, *16*, 183-187.
- Caffey, J. (1951) Chronic poisoning due to excess of vitamin A. *American Journal of Roentgenology*, *65*, 12-26.
- Christie, D. V. (1980) The spectrum of radiographic bone changes in children with fluorosis. *Radiology*, *136*, 85-90.
- Harris, D. K., Adams, W. G. F. (1967) Acro-osteolysis occurring in polymerization of vinyl chloride. *British Medical Journal*, *iii*, 712-714.

Renal failure/haemodialysis

- Griffin, C. N. (1986) Severe erosive arthritis of large joints in chronic renal failure. *Skeletal Radiology*, *12*, 24-33.
- Kaplan, P., Resnick, D., Murphey, M., et al (1986) Destructive noninfectious spondyloarthropathy in hemodialysis patients: a report of four cases. *Radiology*, *162*, 241-247.
- Murphy, M. D., Sartoris, D. J., Quale, J. L., et al (1993) Musculoskeletal manifestations of chronic renal insufficiency. *Radiographics*, *13*, 357-379.
- Naidich, J. B., Massey, R. T., McHeffey-Atkinson, B., et al (1988) Spondyloarthropathy from long-term hemodialysis. *Radiology*, *167*, 761-766.

Miscellaneous

- Caffey, J. (1972) Familial hyperphosphatasemia with ateliosis and hypermetabolism of growing membranous bone. *Bulletin of the Hospital for Joint Diseases*, *33*, 81-110.
- Houang, M. T. D., Brenton, D. P., Renton, P., Shaw, D. G. (1978) Idiopathic juvenile osteoporosis. *Skeletal Radiology*, *3*, 17-23.
- Kozlowski, K., et al (1976) Hypophosphatasia. Review of 25 cases. *Pediatric Radiology*, *5*, 103-117.



نشر الکترونیکی
موسسه انتشاراتی
نوردانش

43

SKELETAL TRAUMA: GENERAL CONSIDERATIONS

Jeremy W.R. Young

Skeletal trauma is one of the most important aspects of orthopaedic radiology, being by far the commonest problem presented to the musculoskeletal radiologist. Despite this fact however, trauma radiology continues to be a neglected aspect of this subspecialty, particularly in teaching institutions. This may reflect an illogical approach to skeletal trauma historically, whereby fractures and dislocations were presented as a confusing list of unassociated injuries, often better known by eponyms. More recently there has been a trend towards classifying fractures by the force of injury causing them. This allows a more logical and thoughtful approach, and enhances understanding of fracture patterns, and associated injuries.

A fracture of a bone occurs when there is a break in the continuity of bone, which may be either complete or incomplete. When a loading force is applied to bone, it initially deforms elastically, and as the load is removed, the deformity of the bone is reversed and the bone returns to normal. As the loading force is increased, however, the elasticity of the bone is overcome, and a plastic 'fracture' occurs, with the bone remaining deformed after cessation of the load. Finally, complete failure of the bone will occur, giving rise to a true fracture. Repetitive loading of a bone at 'subfracture' levels may lead to the development of stress fracture (see below). Fractures are described in many different ways, as discussed below.

Terminology

The descriptive terms *open* or *closed* refer to whether the bone fragments communicate with the outside environment or not. If bone fragments penetrate the skin, the fracture is open (Fig. 43.1). If the fracture remains covered with intact skin, it is called closed. Although apparent on clinical inspection, various radiographic signs will suggest an open fracture (Box 43.1).

The nature of the fracture lines also describes the fracture. Generally a single fracture line follows one of three major types: *transverse*, *oblique* or *spiral*, although a combination of these may be present. In addition, if the injury produces more than one fracture line, the fracture is said to be *comminuted*. Comminuted fractures will often produce a minor triangular fragment of bone, known as a 'butterfly' fragment (Fig. 43.2). A segmental fracture is one in which a segment of bone is isolated by fractures at each end (Fig. 43.3).



Fig. 43.1 A comminuted fracture of the tibia, with medial displacement and overriding of the distal fragment. Because of the proximity of the skin surface to the antero-medial aspect of the tibia, penetration of the skin is likely, and in fact, air is seen in the soft tissues, indicating that penetration has occurred. There is medial displacement, but lateral angulation of the distal fragment. A segmental fibula fracture is noted.

Box 43.1 Radiographic signs of open fracture

- Obvious protrusion of bone fragments beyond the soft-tissue margins
- Absence of portions of the bone
- Gross soft-tissue disruption extending to the bone surface
- Subcutaneous gas
- Foreign material within the fracture

Fractures may also be termed *incomplete* or *complete*. Incomplete fractures occur most commonly in children, when bone resilience is greater, and are of three types. As mentioned above, plastic fractures occur when there is bending of the bone without cortical disruption, or acute angulation; a 'torus' or 'buckle' fracture is the term applied to a fracture of the cortex on the *compressive* side of the bone with

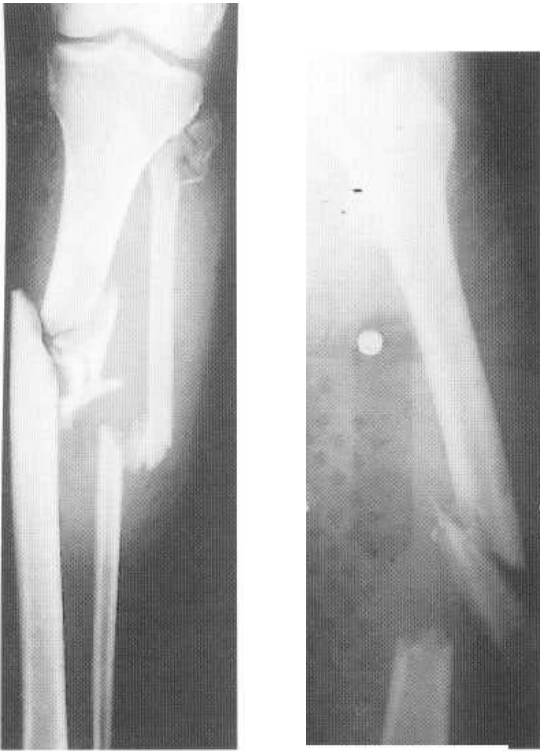


Fig. 43.2 A comminuted fracture of the tibia, with a triangular 'butterfly' fragment.

Fig. 43.3 Segmental fracture of the femur: by definition a comminuted fracture. In this case the isolated segment is clearly malaligned.

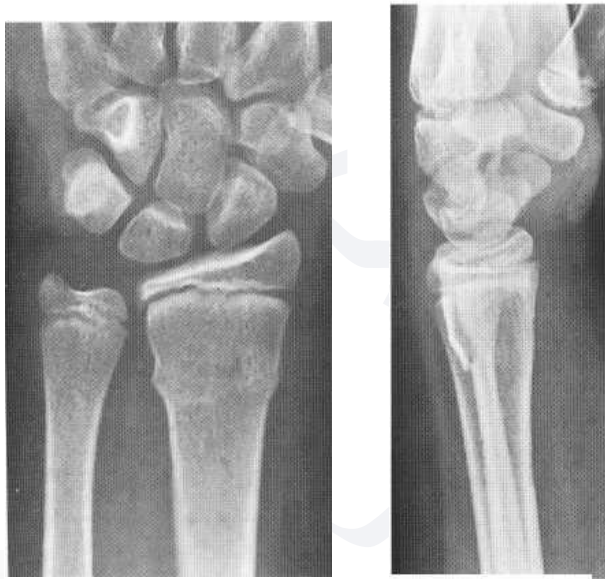


Fig. 43.4 (A,B) Torus fracture of the radius. The cortex is buckled on the dorsal surface. Apart from minor plastic deformity, the volar surface is intact.

an intact cortex on the tension side (Fig. 43.4): *greenstick* fracture is the converse of the torus fracture, occurring only on the tension side, with cortical interruption.

Fractures should also be evaluated for continuity and proximity of the fracture fragments. The term *apposition* refers to the position of the major fragments with respect to each other. Fragments which are not apposed are described as being distracted if the displacement is along the long axis of the bone, or displaced, away from the long axis. In such cases, the fracture should be described according

to the direction of displacement of the distal fragment relative to the proximal bone.

Alignment refers to the relationship along the axis of major fragments. Abnormality of alignment may be described in two ways. The most logical description refers to the alignment of the distal fragment with respect to the proximal (Fig. 43.1). This has the additional advantage of following the same 'rules' as apply to displacement. The alternative method, commonly used by orthopaedic surgeons, is to describe the angulation as the direction of the apex of the angle at the fracture site.

Varus and *valgus angulation* are terms that are commonly used, particularly by orthopaedic surgeons—they refer to the alignment of the distal fragment with respect to the midline of the body, with varus indicating angulation of the distal fragment towards the midline and valgus the reverse.

Impaction is the descriptive term for fractures in which the bone fragments are driven into each other.

Abnormality of rotation of the distal fragment is an important finding and should always be assessed. This requires visualisation of both ends of the bone on the same radiograph, so that the orientation of the proximal and distal joints can be assessed.

Associated soft-tissue abnormalities

Although the majority of fractures are readily identified, on occasion they may be difficult or impossible to see on initial radiographs. Additional clues may be helpful in such cases. For



Fig. 43.5 Elbow effusion: elevation of the anterior fat pad (arrow). Although not pathognomonic for fracture, anterior fat pad elevation indicates significant effusion, and is frequently associated with a fracture. Careful inspection of the unfused radial head shows a minor cortical step-off of the metaphysis, indicating a fracture.



Fig. 43.6 A fat-fluid level (lipohaemarthrosis) is seen in the knee joint on this cross-table lateral view. This indicates intra-articular bone injury.

example, fractures around a joint may provide evidence of a joint effusion or haemarthrosis, providing the joint capsule remains intact. This can be particularly useful at the elbow, where elevation of the fat pads, either anterior or posterior, is good evidence of injury (Fig. 43.5). In such cases, lack of obvious bone injury should

be regarded with caution, and delayed views after immobilisation will often reveal a fracture.

A fat-fluid level (lipohaemarthrosis) within a joint, most commonly seen in the knee with the radiograph made with a horizontal beam, is also firm presumptive evidence of an intra-articular frac-

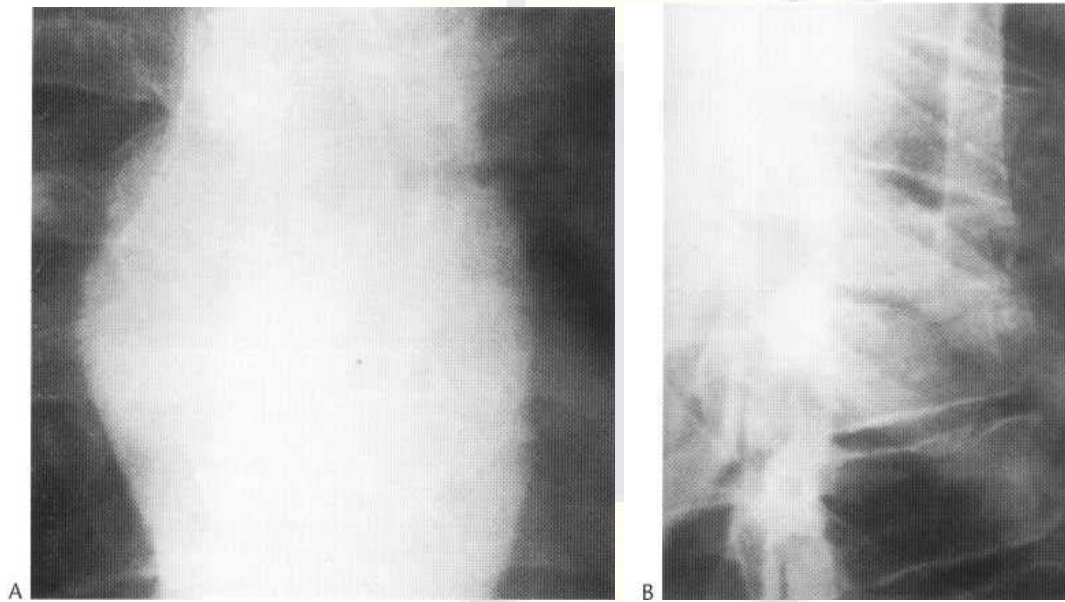


Fig. 43.7 (A,B) Compression fractures of the vertebral bodies of T7, T8 and T9 with large paraspinal haematoma, which took many months to absorb, still being visible after the fracture had consolidated. (Courtesy of Dr D. J. Stoker and Institute of Orthopaedics.)

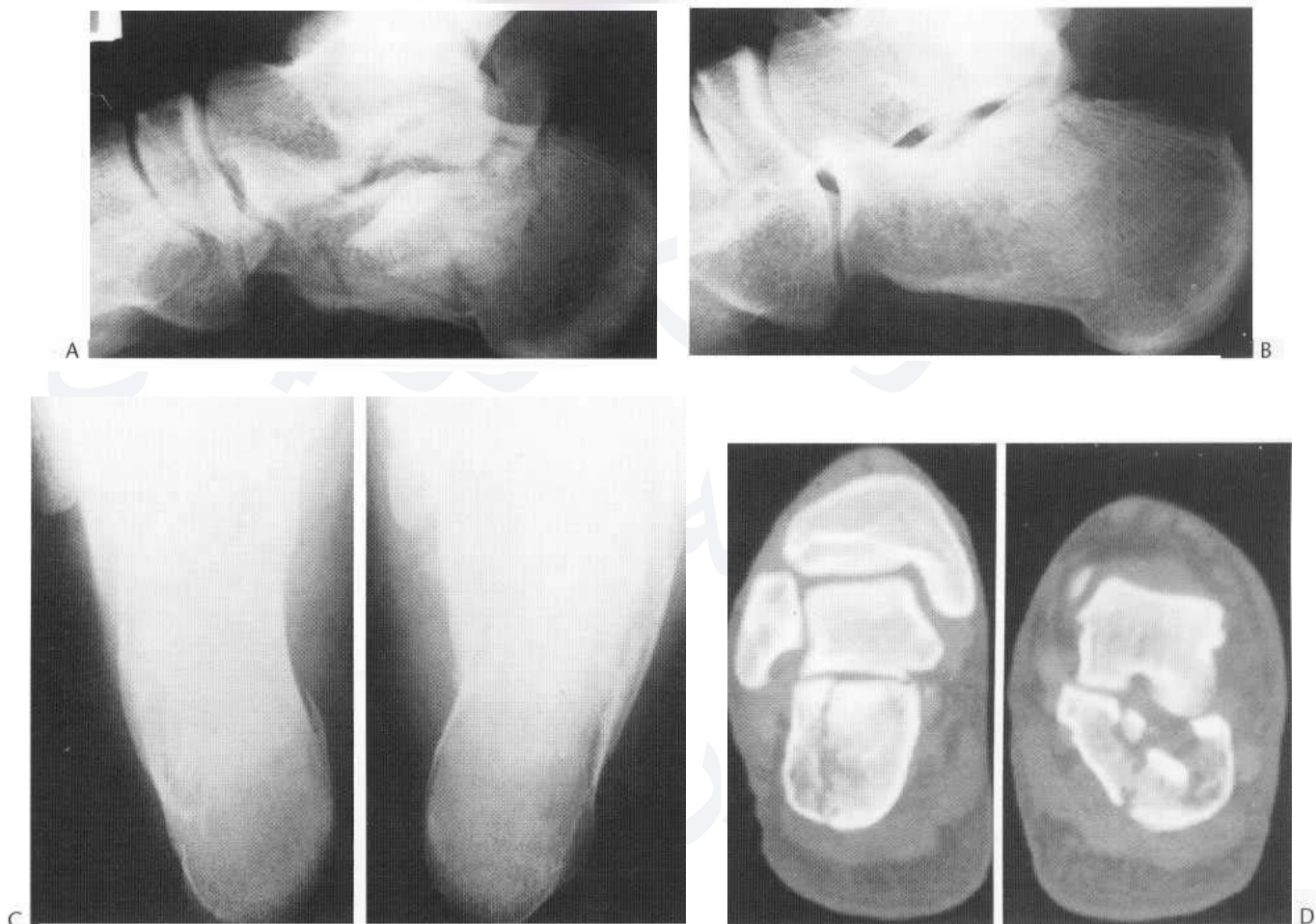


Fig. 43.8 Comminuted fractures of both calcanei. The extent of the injury, and in particular of the articular involvement, is poorly displayed by the plain radiographs (A-C) particularly on the right. (D) CT images, however, demonstrate that there is an obvious disorganisation of fragments at the articular surface on the left, and a mildly depressed segment on the right.

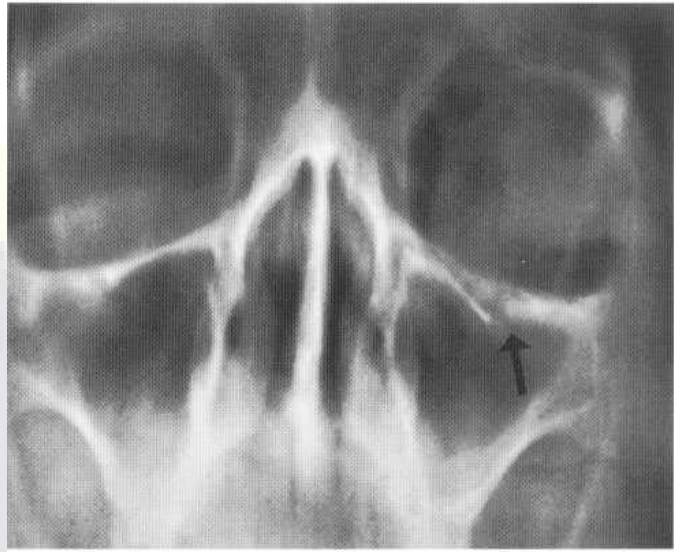
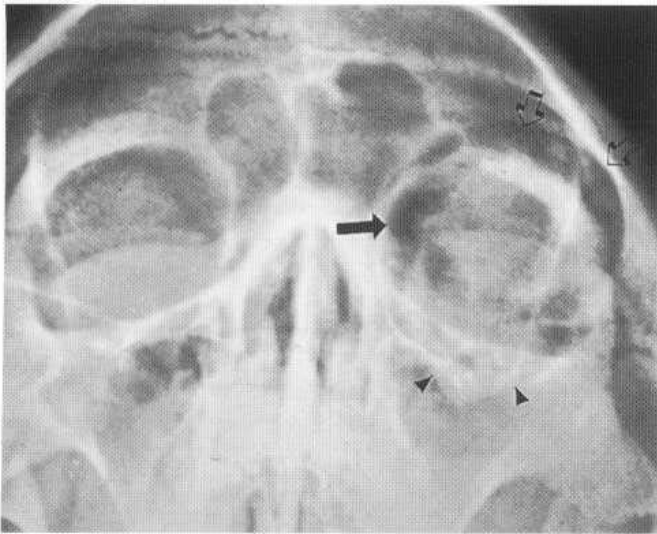


Fig. 43.9 (A) Note orbital emphysema on the left, with air surrounding the eyeball (arrow), and beneath the eyelid (open arrows). This is highly suggestive of a blowout fracture. In this case there is irregularity of the inferior orbital rim (arrowheads), with an apparent soft-tissue density projecting into the maxillary sinus. (B) Tomography confirms the fracture of the orbital floor (arrow).

lure, the fat being derived from the bone marrow (Fig. 43.6). In the thoracic spine, haemorrhage from a vertebral fracture can be seen as a localised paravertebral soft-tissue mass, giving an appearance similar to that seen in cases of abscess (Fig. 43.7).

Soft-tissue swelling in the retropharyngeal space has also been cited as being a reliable sign of cervical spine trauma, although the value of this sign has been questioned.

Fracture healing

After a fracture has occurred, the process of healing begins. In the normal healing process, a haematoma initially forms between the bone ends, occasionally causing periosteal elevation. Granulation tissue then forms between the fracture fragments, with immature osteoid (callus) laid down on the bone surface acting as an early bridge. This first becomes calcified, but eventually woven bone is laid down, leading to firm bone union.

The early stages of bone formation are not visible radiographically, but in a healthy person, new bone formation is visible within 4-6 weeks, with the healing process complete in 4-6 months for a single fracture in a large tubular bone. Delay in union however may be evident by a delay in the appearance of new bone, and can occur from a variety of causes (see below).

Evaluation of skeletal trauma

The vast majority of injuries can be adequately visualized by *plain radiographs*. On occasion however, other methods may be needed. *Tomography* has traditionally been used to assess fractures which are not visible, or poorly seen on plain radiographs. However, in modern departments, tomography has been abandoned in favour of other techniques, such as CT or, occasionally, nuclear medicine bone scan. Arguments that tomography is superior to CT in the evaluation of fractures in the horizontal plane (cervical spine), or of structures that lie parallel to the beam of the CT scanners (floor of orbit), are negated by the use of thin slice spiral CT scanners, with coronally reconstructed images. This is particularly true of modern,

multislice CT scanners, where information is gathered rapidly, and reconstructed into 2D or 3D images at will.

In practice, the advent of the multislice scanners raises new questions about how best to image our patients a scanner that produces many hundreds of thin 'slices' in less than a minute requires changes in philosophy as to how to best view the resulting information. With computer workstations capable of producing multiplanar 2D or 3D images in a matter of seconds, it may be appropriate to re-evaluate whether axial sections are the best way to evaluate the information. Realistically, the scanners provide a volume of information, and even the term computer tomography may not be appropriate. The term *computerised volume imaging (CVI)* would appear to make more sense.

Tomography was often used historically to evaluate depression of bone fragments in tibial plateau fractures, or to determine the position of fragments in fractures of the tibial plafond, talus and calcaneus. Even in such cases however, it can be argued that modern CT scanners provide information that is at least as good as, if not better (Fig. 43.8). If CT is available, particularly of the helical variety, there are few if any indications for tomography. However, tomography may be helpful in suspected blowout fractures of the orbit (Fig. 43.9).

Nuclear medicine can be helpful in detecting occult fractures, for example of the scaphoid or femoral neck, although a positive scan may not be seen for 24 hours following injury, especially in older patients. Nuclear medicine can also delineate stress fractures of bone, often with a characteristic appearance (Fig 43.10).

In many centres, *MRI* has become the method of choice for evaluating injuries of and around the joints. It has the ability to detect not only injury to the surrounding soft tissues, but also it can identify occult injury to the bones themselves, such as 'bone bruising' (see Fig. 44.83), osteochondral fractures (Fig. 43.11) and post-traumatic avascular necrosis (Fig. 43.24). Among its advantages are its ability to demonstrate soft-tissue detail, its capability of multiplanar imaging and its lack of ionising radiation. These features are responsible for the rapidly increasing use of MRI in musculoskeletal radiology. Injuries to ligaments and tendons are readily identi-

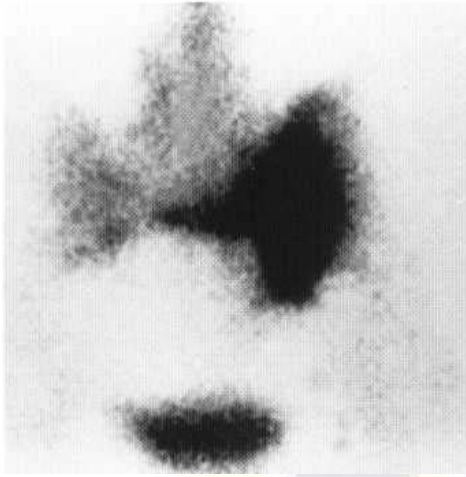


Fig. 43.10 Stress fractures of the sacrum. This elderly patient underwent nuclear medicine bone scan for pain in the lower back. A characteristic pattern of increased tracer uptake indicates a stress fracture in the osteoporotic sacrum.

fied by MRI (see relevant sections below), and muscle trauma can be appreciated (Figs 43.12, 43.13). This has greatly expanded the role of the radiologist in the traumatised patient.

Complications of fracture

There are potential problems in all fractures. Although most uncomplicated fractures heal readily, in open fractures there is an increased potential for infection at the fracture site and careful scrutiny of the healing process is warranted.

The tibia has long been singled out as a bone liable to *delayed union* or *non-union*. The reasons for this are obscure, but poor vascular supply and lack of immobilisation have been cited. In practice, however, it would appear that the reason for the high incidence of cases of delayed or non-union may be due to the large number of 'high-energy' injuries seen in the tibia, particularly from pedestrian 'bumper' injuries, with a large amount of resulting necrosis of soft tissue and bone at and around the fracture site.

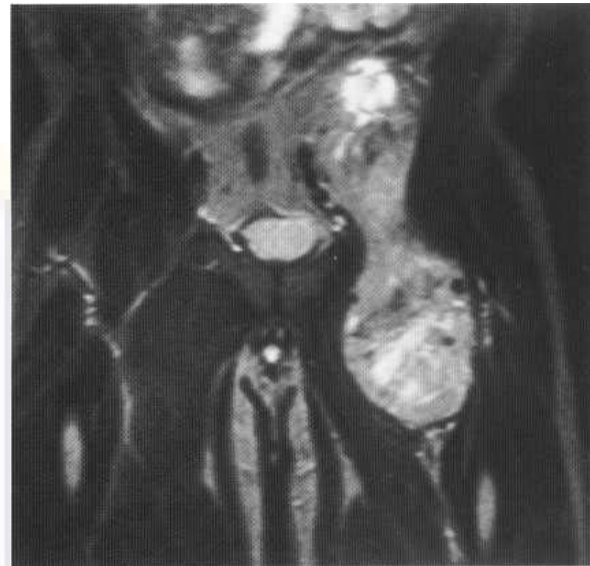


Fig. 43.12 Coronal MRI (T₂-weighted) of the pelvis and thighs of a young gymnast, who complained of pain and swelling in the groin. A well-defined lesion of mixed signal intensity occupies the region of the iliopsoas. The mixed signal pattern is common in haematoma, indicating the complexity of the haematoma, and variations in haemoglobin, deoxyhaemoglobin, methaemoglobin and haemosiderin levels.

Delayed union may occur from many causes (Box 43.2).

Non-union is the absence of bony union over a prolonged period (Box 43.3). The radiographic appearance is usually of a persistent fracture line, usually with sclerotic margins, and marked surrounding sclerosis (Fig. 43.14). MRI may have a role to play in the assessment of non-union with its ability to detect infective causes (Fig. 43.15).

Malunion is the term given to a fracture which heals in an unsatisfactory anatomical position, either with excessive overlap of fragments, giving rise to shortening of the bone, or unsatisfactory angulation or displacement of the distal fragment (Fig. 43.16).

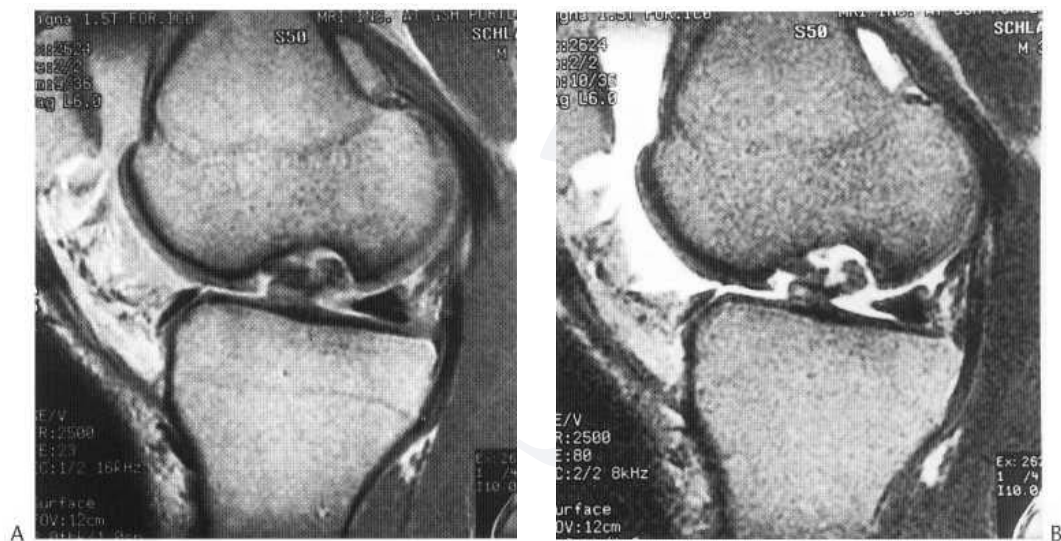


Fig. 43.11 Sagittal T₁-weighted image (A) and T₂-weighted image (B) demonstrate a well-defined osteochondral fracture of the femoral condyle. A large joint effusion (bright on T₂-weighting) is seen.

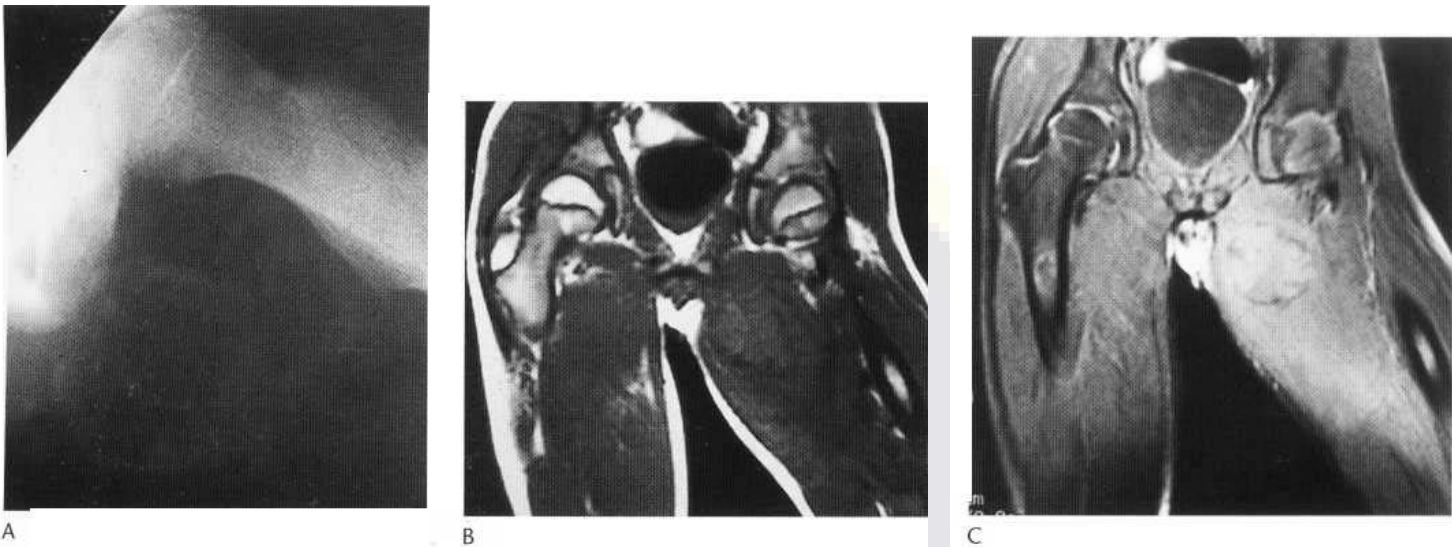


Fig. 43.13 (A) A calcified 'mass' in the thigh of this 16 year old was worked to exclude tumour. (B) T₁-weighted coronal MR images demonstrate a mass of low signal intensity, with surrounding low-signal-intensity oedema, with increased signal intensity on T₂-weighted images (C). There is also a well-defined, low-signal-intensity 'ring' of calcification. Their appearances are characteristic of post-traumatic myositis ossificans.

Box 43.2 Causes of delayed union

- Mechanical* Poor apposition
Inadequate stabilisation
- Pathological* Age-decreased osteoblastic activity
Dietary-vitamin deficiency (C and D)
Pathological fracture (underlying abnormality);
Infection

Box 43.3 Causes of non-union

1. Idiopathic (particularly tibia)
2. Poor stabilisation
3. Infection
4. Pathological fracture
5. Massive initial trauma



Fig. 43.14 Non-union of the tibia despite interosseous bone grafting and surgical wiring. There is sclerosis around the fracture line, without firm evidence of bone bridging, 1 year after the fracture.

Special types of trauma

Stress (fatigue) fractures

These fractures result from chronic repetitive forces which by themselves are insufficient to cause fracture, but over the course of time lead to the classical changes of a stress fracture. They occur in many bones, and usually at characteristic sites, often as the result of athletic activity: for example the 'march' fracture of the second and third metatarsal head, the stress fracture of the mid and distal tibia and fibula in long-distance runners and ballet dancers, and fractures of the proximal fibula in paratroopers.

The earliest diagnosis can be made by nuclear medicine scanning or MRI. A nuclear medicine bone scan will show increased activity before radiographic signs appear. When radiographic signs appear, they may take several forms, depending upon the stage of healing or the chronicity of the stress. A hairlike lucency may be seen traversing the bone. New bone formation around the fracture may be the only radiographic sign, or may accompany the cortical fracture (Fig. 43.17). MRI may also be useful in making the diagnosis before any changes are seen radiographically. If the patient con-

tinues the activity, a form of chronic fracture will occur, with abundant sclerotic periosteal new bone and a persistent lucent fracture line, with surrounding sclerosis (Fig. 43.18).

A type of stress fracture is said to account for the pars interarticularis defects seen in spondylolysis (Fig. 43.19), whereby the continuance of the stress leads to a complete fracture, followed by non-union. Alternatively a congenital hypoplasia of the articular processes, or degenerative change within the posterior joints, may be the underlying cause. The defect in the pars is known as *spondylolysis*. When anterior displacement of the superior vertebral body on its neighbour is seen *spondylolisthesis* is said to have

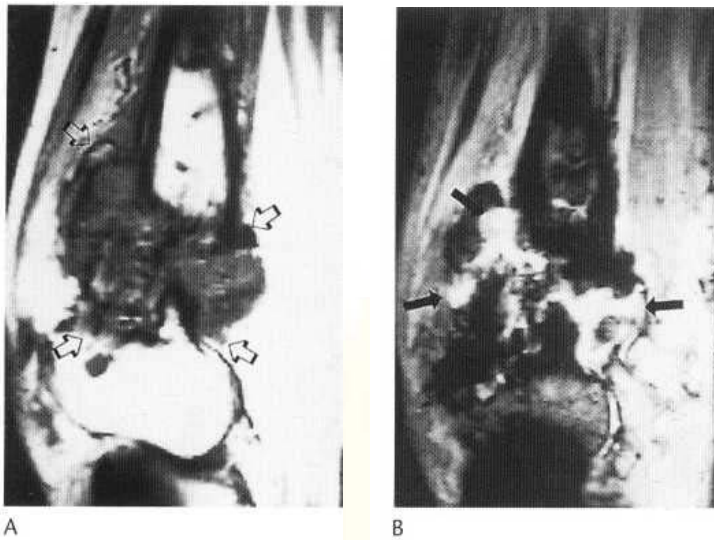


Fig. 43.15 (A) MRI scan demonstrates tissue of mixed signal intensity in the fracture gap of non-union of the distal femur (arrows) on T₁-weighted images. (B) Areas of increased signal intensity are shown on T₂-weighted images (dark arrows), indicating foci of infection.

occurred. Mild degrees of spondylolisthesis can occur when there is loss of articular cartilage at the posterior intervertebral joints as in degenerative disease. More severe spondylolisthesis results from pars interarticularis defects, and is graded according to severity: Grade I up to 25% displacement of the vertebral body; Grade II up to 50%; Grade III up to 75%; and Grade 100% displacement.

Avulsion fractures

These occur from avulsion of bone fragments at the site of ligamentous or tendinous attachments throughout the skeleton. Of

note are abnormalities which have previously been classified as osteochondritis, but which represent avulsion fractures from chronic or repeated trauma. This includes *Osgood-Schlatter disease* (Fig. 43.20) and *Sinding-Larsen disease* of the tibial tubercle and inferior patella respectively.

The diagnosis of Osgood-Schlatter disease is made clinically, although it can be suggested radiographically when there is clear elevation of fragments of the tibial tubercle separated from the underlying bone (Fig. 43.20). Apparent fragmentation alone without displacement does not constitute Osgood-Schlatter disease, and merely represents multiple unfused ossification centres.

Common avulsion injuries at the origin of muscle tendon insertions are seen at the inferior border of the ischium (hamstrings) (Fig. 43.21), anterior inferior iliac crest (rectus femoris; Fig. 43.22) and lesser trochanter (iliopsoas) (Table 43.1).

Pathological fractures

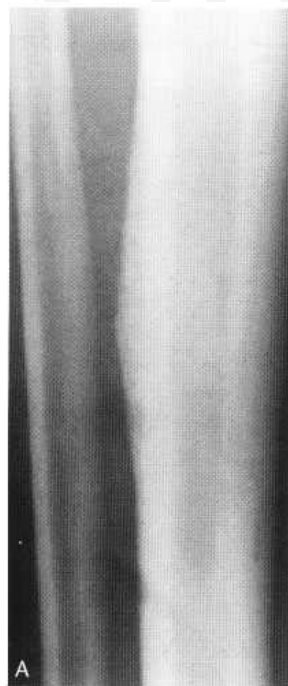
Pathological fractures occur through bone that has been weakened by an underlying disease. This does not necessarily mean an underlying malignancy, although the term 'pathological fracture' tends to suggest it. Pathological fractures occur through bone that is weakened by such conditions as osteoporosis or osteomalacia, bone tumours (whether benign (Fig. 43.23) or malignant) or even tumour-like lesions of bone. In elderly patients underlying malignancy should be considered, especially if the fracture occurs in a site other than those usually seen in osteoporosis such as the femoral neck, or in cases in which the severity of the injury is inappropriate to the fracture created.

Post-traumatic avascular necrosis

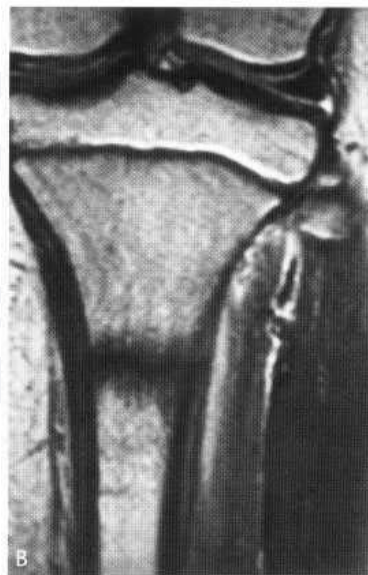
This occurs from a traumatic severance of the blood supply to the bone or a fragment thereof. There are several bones in the body in which this is likely to happen in areas when the blood supply is easily



43.16



43.17



43.18



43.18

Fig. 43.16 Malunion of the tibial fracture, which has healed well, but shows lateral angulation of the distal fragment.

Fig. 43.17 Stress fracture. (A) An area of increased sclerosis, with some dense periosteal new bone in the mid tibia. (B) MRI may be helpful in early diagnosis before the plain radiographic signs become apparent.

Fig. 43.18 Multiple stress fractures are seen, some with obvious horizontal lucencies running perpendicular to the bone cortex. The patient was a jogger who refused to give up jogging despite the pain!

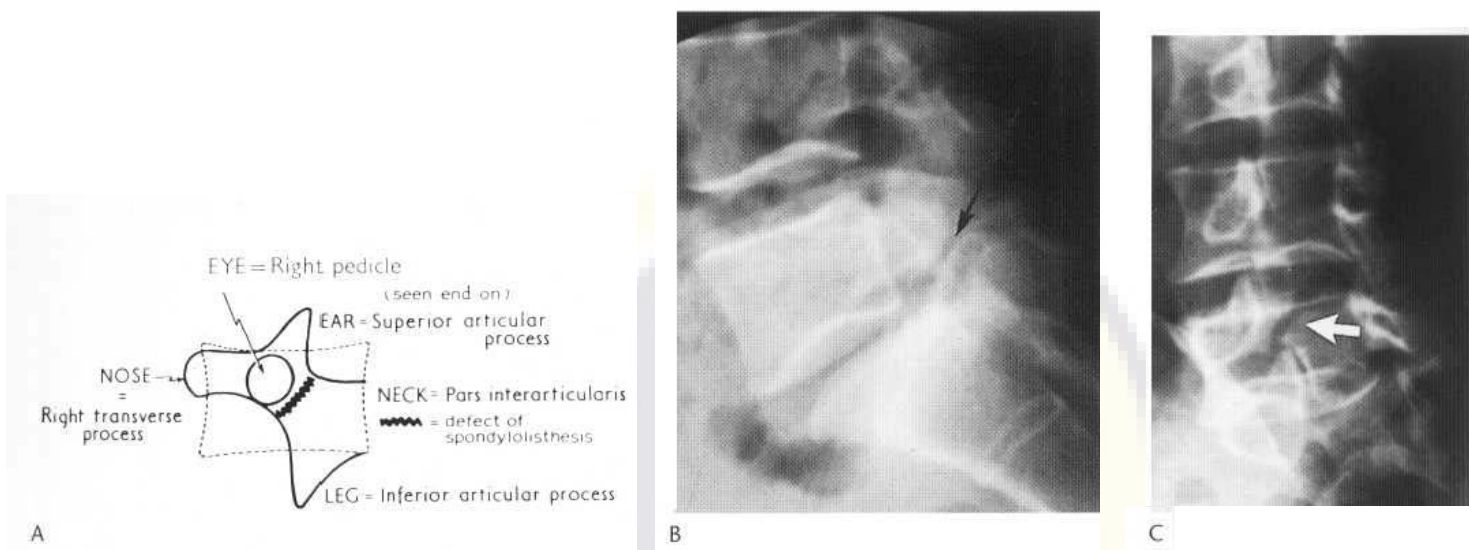


Fig. 43.19 (A) Diagrammatic representation of an oblique view of a lumbar vertebra, presenting the 'scotty dog' appearance. The pars interarticularis defect corresponds to the dog's collar. (B, C) Pars defect: oblique radiograph demonstrates the same appearances as in (A). (Courtesy of Dr D. J. Stoker and Institute of Orthopaedics.)

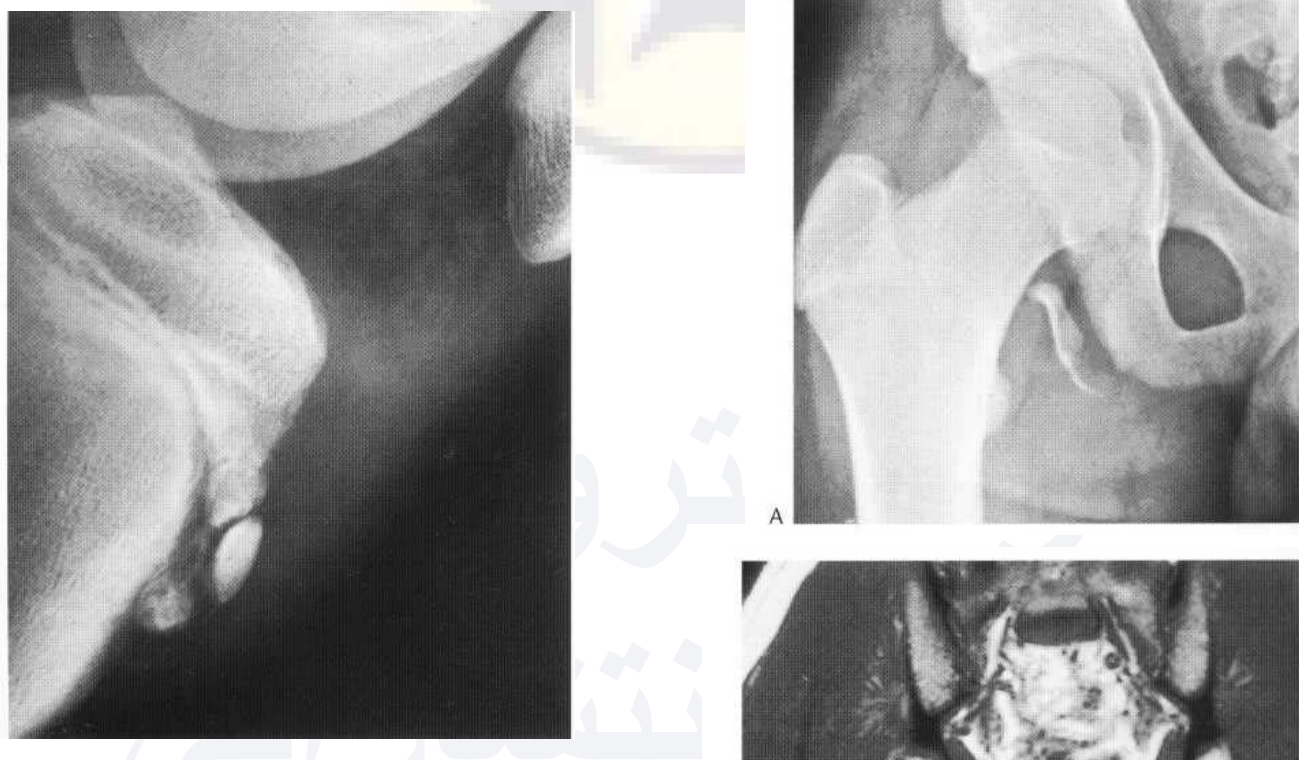


Fig. 43.20 Osgood-Schlatter disease. Fragmentation may be seen and a portion of the tibial tubercle ossification centre is elevated.

compromised. Femoral neck fractures may interrupt the vascular supply to the femoral head, as can posterior dislocation of the femoral head, with or without overt fractures of the head or acetabulum (Fig. 43.24). In fractures of the wrist involving the scaphoid, the proximal pole is at risk as the vascular supply enters the bone more distally (Fig. 43.25). Similarly, talar waist fractures threaten the proximal fragment. Post-traumatic avascular necrosis may occur in part of a bone as described above, but may also involve the growing epiphysis such as the head of the second or third metatarsal (*Friberg's disease*) or even the whole of a small bone, for example Innate (*Kienhock's disease*) (Fig. 43.26). Frequently there is no clear history of predisposing fracture. However there is evidence that even conditions such as *Pertus*

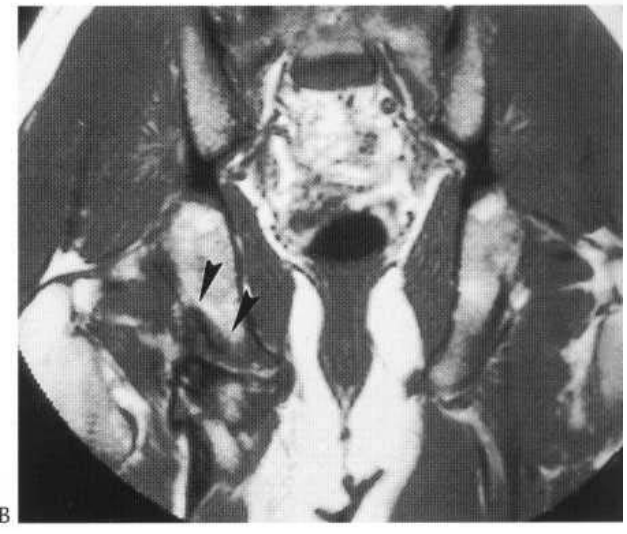


Fig. 43.21 (A) Note an avulsion of the inferior border of the ischium at the site of insertion of the hamstrings. MRI of this injury (B) indicates the extent of injury to the underlying bone (arrowheads), not seen on the plain radiographs.

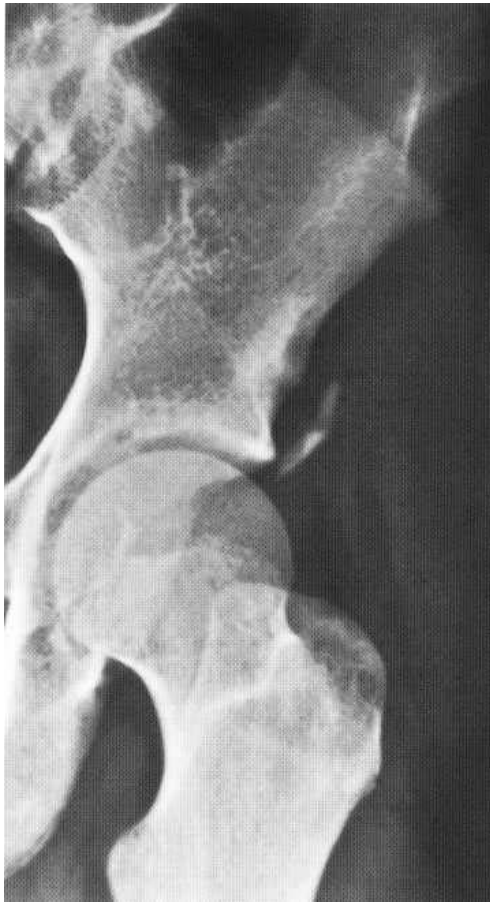


Fig. 43.22 Avulsion fracture of the anterior inferior iliac crest: This is the origin of the rectus femoris muscle.



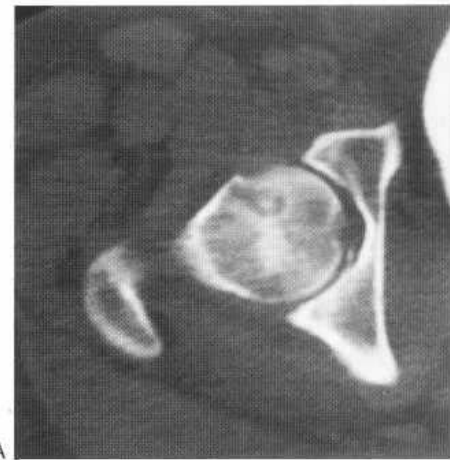
Fig. 43.23 Pathological fracture through a simple bone cyst of the proximal humerus.

Table 43.1 Sites of avulsion fractures with muscle origin

Site of avulsion fracture	Muscle origin
Anterior superior iliac crest	Sartorius
Anterior inferior iliac crest	Rectus femoris
Iliac tuberosity	Hamstrings
Greater trochanter	Gluteals
Lesser trochanter	Iliopsoas
Posterior calcaneus	Achilles tendon
Olecranon process	Triceps
Superior patella	Quadriceps
Inferior patella (Sinding-Larsen)	Patella ligament
Tibial tuberosity (Osgood-Schlatter)	Patella ligament

disease may result from trauma, and a traumatic effusion, which may also be responsible for the widening of the joint space that may be seen in the condition. This radiographic abnormality may be seen in the 'irritable hip syndrome' of children, which may progress to frank necrosis of the femoral head. This has been attributed to interruption of the vascular flow, possibly on the venous side, by the formation of granulation tissue. A similar scenario has been suggested for septic arthritis (pus within the joint) and haemophilia (blood within the joint).

In avascular necrosis, the necrotic bone usually becomes denser than the surrounding bone (Fig. 43.2.5), which in turn may become more osteopenic due to disuse. Studies on the femoral heads removed following fracture in the process of hip prosthesis



A



R

Fig. 43.24 (A) CT shows a cortical fracture of the femoral head from previous posterior hip dislocation. A small intra-articular fragment is seen. (B) MRI scan performed several weeks later, indicates the typical findings of avascular necrosis.



43.25



43.26

Fig. 43.25 Post-traumatic avascular necrosis of the proximal pole of the scaphoid. Although the fracture of the waist of the scaphoid has 'healed', avascular necrosis has occurred, with resulting sclerosis.

Fig. 43.26 Kienbock's disease: in fact, a form of traumatic avascular necrosis of the lunate.

implantation show that this is due to revascularisation, when a thin layer of calcifying osteoid is laid down on the necrotic trabecula. This feature may occur anytime from 2 months to 2 years following injury. Eventually collapse and fragmentation are likely to occur. MRI scan may be useful in the diagnosis.

Drillers' disease (vibration syndrome)

Drillers' disease is seen in workers using vibrating machinery, usually after five or more years of use. Degenerative cysts are found in the bones of the wrist, and occasionally the hand (Fig. 43.27). They are however indistinguishable from the cysts also seen that result from heavy manual labour, and the exact aetiology is uncertain.



Fig. 43.27 Vibration syndrome. Fragmentation and flattening of the lunate due to avascular necrosis is typical of Kienbock's disease, accompanied by extensive cystic changes in the surrounding bones. These abnormalities occurred in a worker using compressed-air drills, who had been exposed to this repeated trauma for many years. (Courtesy of Dr D. J. Stoker and Institute of Orthopaedics.)

Sudeck's atrophy (post-traumatic reflex dystrophy, reflex sympathetic dystrophy)

This is a rare condition in which, following injury to a limb, intense pain and swelling occur, resulting in severe disuse osteoporosis. Interestingly, the initial injury may be relatively minor; the effects however are dramatic, with loss of function which is often protracted (Fig. 43.28). An associated neurovascular reaction may be present.

Transient osteoporosis

This is a rare condition which usually affects the hip. Although this may represent a type of Sudeck's atrophy, a history of trauma is rare. Massive subarticular osteoporosis occurs, but this is self-limiting, however, with spontaneous resolution within 4-10 months.

Myositis ossificans (post-traumatic)

This usually occurs without overt underlying bone injury. The exact aetiology is uncertain, but it may be due to ossification of a haematoma or reactive periosteal elements which have been displaced into the soft tissues. The thigh is the commonest site. Hazy density in the soft tissues gives way to frank new bone formation, which may extend to the bone surface (Figs 43.13, 43.29). This may cause difficulty in distinguishing the lesion from



Fig. 43.28 Sudeck's atrophy: there was minor trauma to the forearm some weeks earlier. Note gross osteoporosis of the bones of the hand, wrist and forearm, most marked at the bone ends, but also causing cortical 'thinning' and resorption.

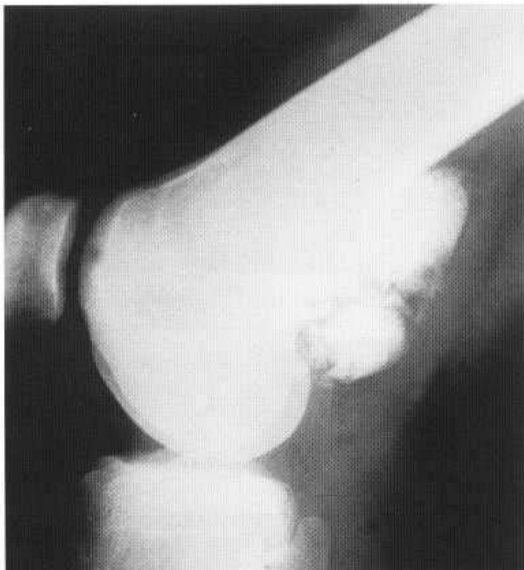


Fig. 43.29 Post-traumatic myositis ossificans. A well-defined bone density arises from the cortex of the distal femur and extends into the soft tissues. There was a history of blunt trauma, but even so, this lesion needs to be differentiated from parosteal osteosarcoma.

parosteal osteosarcoma. Furthermore, unless adequate biopsy material is obtained, including the central and peripheral components of the lesion, histological differentiation may also be difficult.

MRI has been shown to be a useful tool in the diagnosis of post-traumatic myositis ossificans, due to its ability to define the characteristic soft-tissue abnormality (Fig. 43.13), which also may be seen before the changes are evident radiographically. A similar type of calcification or ossification may occur around joints following dislocation, and in cases of severe closed head injury (Fig. 43.30). Ligamentous avulsions or chronic ligamentous trauma may also result in calcification, such as calcification of the medial collateral ligament of the knee in cases of chronic subclinical trauma (Fig. 43.31 Pellegrini-Stieda lesion).

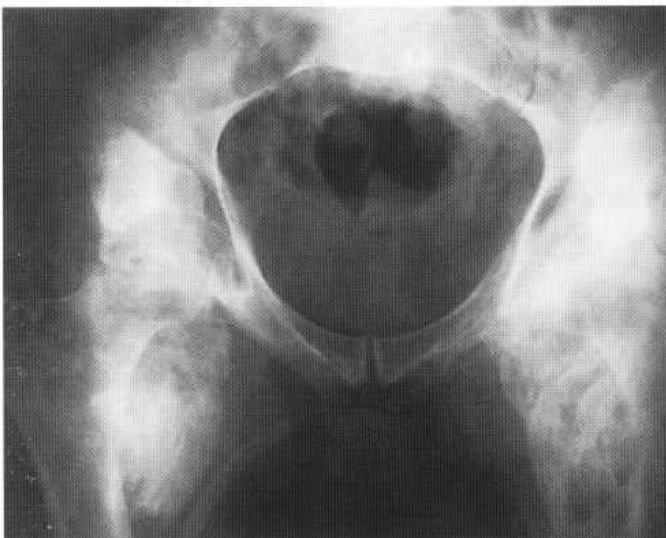


Fig. 43.30 Myositis ossificans associated with paraplegia. Very extensive soft-tissue ossification is visible around both hip joints. (Courtesy of Dr D. J. Stoker and Institute of Orthopaedics.)

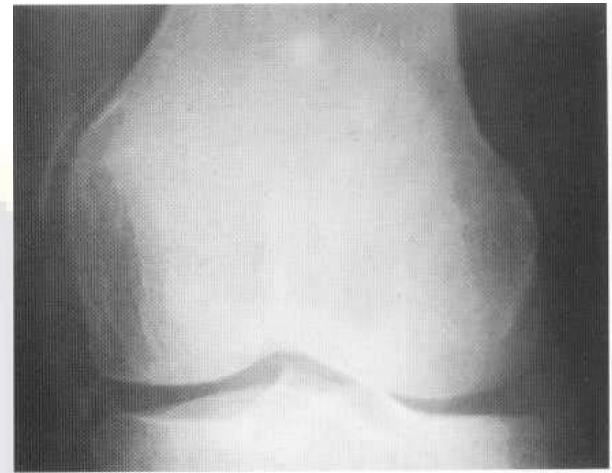


Fig. 43.31 Pellegrini-Stieda lesion. Post-traumatic calcification is shown in relation to the medial femoral condyle following a tear of the medial collateral ligament. (Courtesy of Dr D. J. Stoker and Institute of Orthopaedics.)

Compartment syndrome

Rarely, trauma to a limb will give rise to a potentially devastating situation whereby the tissue pressure within a closed 'compartment' causes progressive ischaemia and ultimately necrosis. The compartments of the limbs consist of areas surrounded by rigid osseous and fascial planes. Tissue oedema or haemorrhage may be the initiating factor and result from direct trauma and/or vascular interruption. The result of oedema within a closed compartment is to raise the tissue pressure, thereby further decreasing vascular perfusion. Prompt fasciotomy is required. Volkmann's ischaemia and contracture of the forearm, following fracture of the elbow, is probably a form of the compartment syndrome. Today the syndrome is most commonly seen in the leg as the result of road traffic accidents.

Arterial injury

Vascular trauma generally occurs as the result of penetrating injury, although it may be caused by sharp bone fragments from a frac-

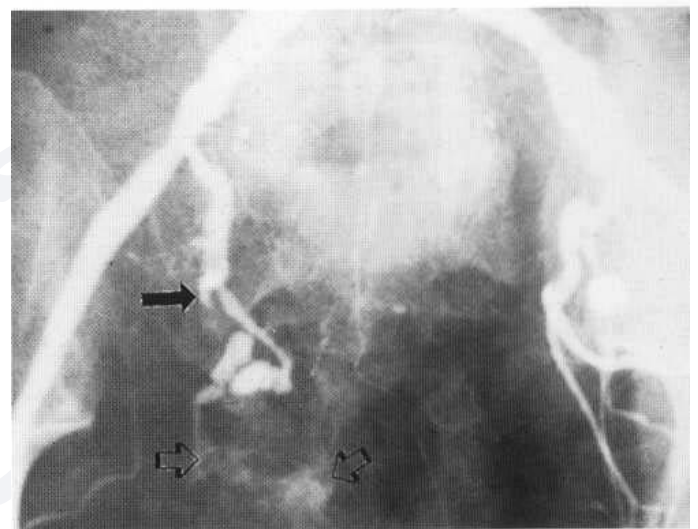


Fig. 43.32 Traumatic avulsion of the right superior gluteal artery (arrow) from pelvic trauma. Bleeding from branches of the internal iliac artery is also seen (open arrows). Marked diastasis of the right sacroiliac joint has occurred.

lure, either at the time of injury or during manipulation. The popliteal artery is commonly injured from fractures or dislocations around the knee. Brachial artery injury may also result from supracondylar fractures of the humerus or elbow dislocations, particularly in children. Branches of the internal iliac artery, especially the superior gluteal, pudendal and vesical, are at risk in pelvic ring fractures (see below), and are responsible for the massive blood loss and associated high mortality rates (Fig. 43.32).

Traditionally, vascular injury has been evaluated almost exclusively by angiography. Spiral CT, particularly if using multislice technology, has the ability to provide high-quality angiographic images, and often far more rapidly, and more effectively than angiography (Fig. 43.11). Advantages of CT over angiography are the fact the patient does not have to be sent to the angiographic suite and that the images are obtained in a matter of seconds, with an intravenous injection rather than arterial catheterisation. Also, with a variety of post-processing capabilities, 31) or multiplanar representations can be obtained easily

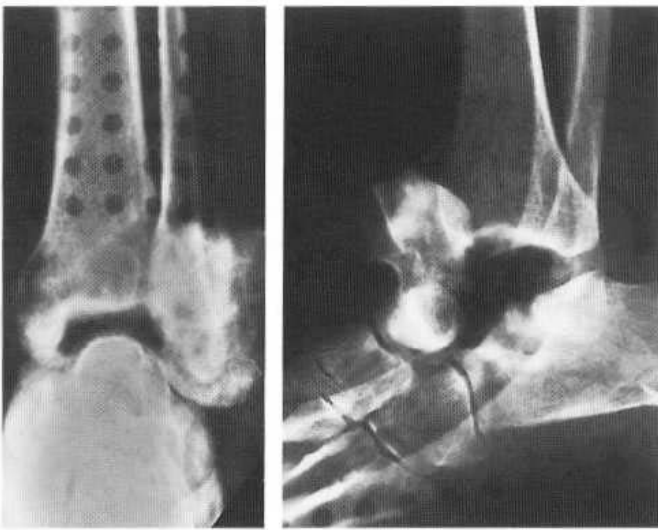


Fig. 43.33 Complete dislocation of the talus.



Fig. 43.34 CT image demonstrates complete diastasis of the right sacroiliac joint.

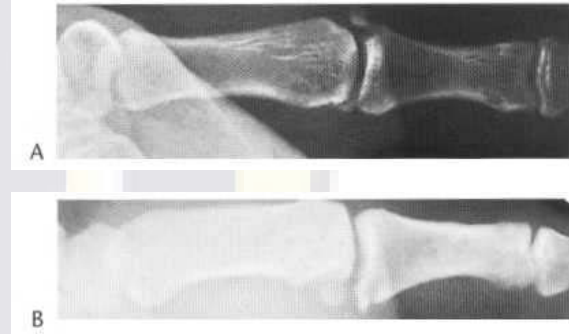


Fig. 43.35 Avulsion fractures of the proximal phalanx of the thumb. (A) Fracture at the site of attachment of the radial collateral ligament. (B) Fracture at the site of the attachment of the ulnar collateral ligament. In practice, the adductor of the thumb inserts in the same area, and may also be avulsed.

and rapidly. Although conventional spiral scanners have not been universally accepted for peripheral work, the new multislice scanners show early promise, even in the periphery.

Joint injuries

Dislocations occur when there is a complete loss of normal articular contact between the bones comprising the joint (Fig. 43.33). Subluxation refers to a partial loss of articular contact. Diastasis refers to separation of fibrous joints, for example symphysis pubis, sacroiliac joint (Fig. 43.34).

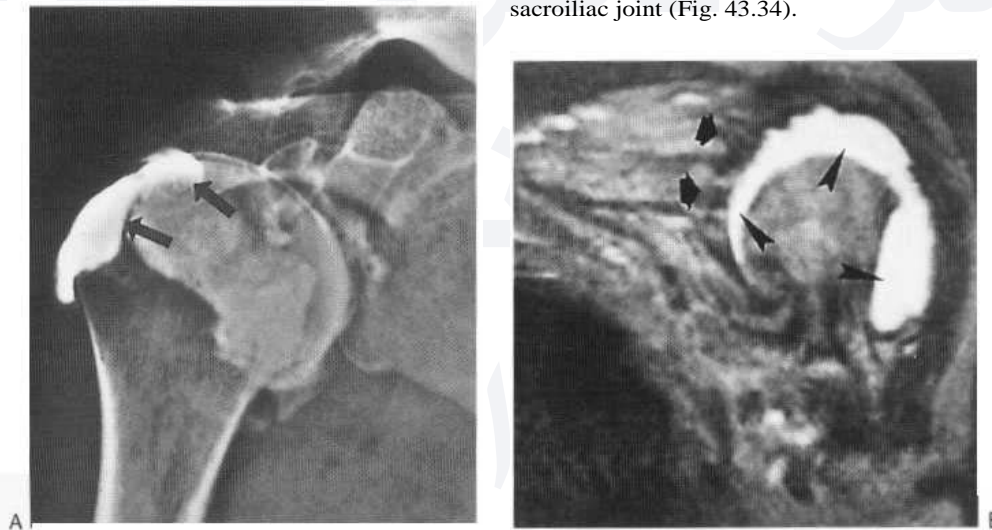


Fig. 43.36 Rotator cuff tear. (A) Arthrography is performed by injecting contrast medium, with or without air, into the shoulder joint. Leakage of contrast into the subdeltoid bursa (arrows) indicates a rupture of the rotator cuff which normally separates the bursa from the joint. (B) MRI demonstrates a large joint effusion, shown as high signal on this FLASH image. The effusion, which shows markedly increased signal intensity on this sequence, has tracked into the subdeltoid bursa (arrowheads), indicating rotator cuff rupture. In this case the subscapularis is seen to be retracted, with an irregular lateral margin (large arrows).

Joint injuries may be difficult to diagnose radiographically, as they frequently comprise ligamentous injury without obvious bone involvement. In addition, subtle avulsion fractures adjacent to joints may be the only indicator of gross ligamentous injuries. These are most commonly encountered around the ankle, where avulsions of the medial and lateral malleoli indicate collateral ligament disruption. Other important areas are the base of the proximal phalanx of the thumb (Fig. 43.35) and corner avulsions of the tibia] plateau. Plain radiographic signs of injury such as effusion or haemarthrosis may be helpful. Stress views of the involved joint have been advocated, but this may require the patient to be sedated as they may be extremely painful to obtain.

Assessment of joints

Arthrography has traditionally been used to assess joint abnormalities (Fig. 43.36). Ultrasound has also been used, particularly to assess the shoulder joint for injuries to the rotator cuff (see below), and CT is also useful in the shoulder, especially when combined with arthrography, when injuries of the glenoid labrum may be seen.

Most recently however, MRI has made immense progress with its ability to define the soft tissues, ligaments and tendons. Although originally finding favour for its ability to diagnose meniscal tears in the knee (Fig. 43.37), it can be useful for a variety of soft-tissue abnormalities around the knee (Fig. 43.38), shoulder (Fig. 43.36), ankle and wrist, where ligamentous and tendinous abnormalities may be demonstrated.

Fractures in childhood

Fractures in children differ from those in adults in several ways. They are often incomplete (torus or greenstick fractures) (Fig. 43.4), and 'plastic' fractures, without any cortical disruption, may occur. Children's bones have a greater capacity for remodelling than adult's bones, which allows for less exact corrective reduction, although rotational anomalies cannot be corrected by remodelling. Because



Fig. 43.37 Tear of the posterior horn of medial meniscus. MRI image (T₂-weighted) demonstrates a linear area of higher signal extending to the articular surface.

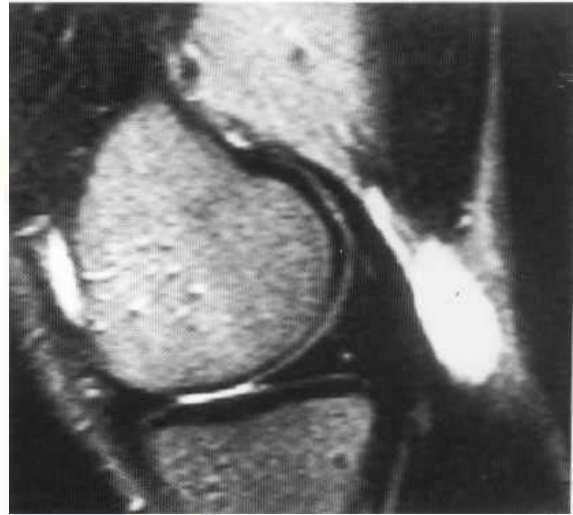


Fig. 43.38 Baker's cyst. T₂-weighted sagittal image of the knee demonstrates a well-defined high-signal-intensity lesion posterior to the knee joint.

of the hyperaemia associated with fracture healing, there may be increased growth in the affected limb. This helps to restore length when overlap of the main fragments occurs, but on occasion also can cause unwanted increased length in a limb.

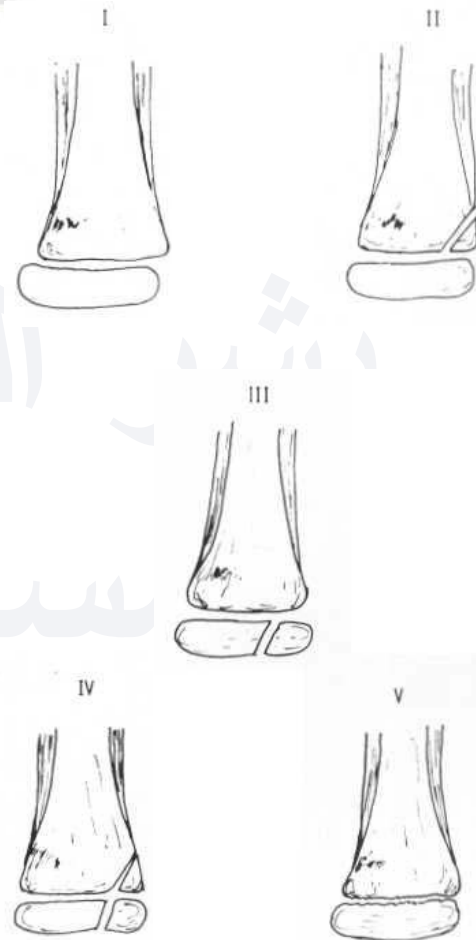


Fig. 43.39 Salter-Harris classification. I, Injury through the epiphyseal plate only. II, Fracture through the epiphyseal plate and metaphysis. III, Fracture through the epiphyseal plate and epiphysis. IV, Fracture through the epiphyseal plate, metaphysis and epiphysis. V, Crush fracture of the epiphyseal plate.

Finally, because of the relatively weak epiphyseal plate, fractures through this region are common. Damage to the epiphyseal plate may result in partial or even complete growth arrest. The Salter-Harris classification of fractures of the epiphyseal plate is most commonly used (Figs 43.39, 43.40). Under this system, the potential for growth arrest increases with increasing type number, Types IV and V having the greatest potential for growth arrest (Fig. 43.41). However, it must be remembered that in a small child with uncalcified epiphysis, it may be difficult or impossible to accurately determine damage to the epiphyseal, and what may appear to be a simple Type I or II fracture may indeed represent a Type IV or V injury, with the increased potential for growth arrest.

Growth arrest may take several forms, which have been classified by Bright. Type I and II growth arrests, which involve less than 25% of the area of the growth plate, can be treated by resection and implanting of inert material, but the more complex types may

require radical resection and fusion with subsequent osteotomies or limb-lengthening procedures.

Slipped femoral capital epiphysis

This occurs in adolescent children and is probably related to trauma, which may be chronic. It represents a variety of Salter-Harris Type I fracture of the epiphyseal plate. It is commonly seen in boys approaching puberty, particularly those who are overweight and sexually immature. The incidence in girls however is rising, possibly as a result of an increase in sporting and physical activity. It may be bilateral (30-40%).

The epiphysis is displaced from the metaphysis, usually in a posterior and slightly inferior direction reflecting an anterior and superior slip of the femoral neck with respect to the epiphysis. 'Frog's-leaf' views as well as anteroposterior views may be needed to make the diagnosis and both hips should be examined because of the high incidence of bilateral involvement (Fig. 43.42).

Radiographic signs include: (i) blurring of the epiphyseal/metaphyseal junction due to superimposition; (ii) increased width of the epiphyseal plate; (iii) so-called elongation of the superior neck of the femur, whereby a line drawn along the superior neck fails to cut the epiphysis or cuts only a small portion (in normal patients this line usually cuts approximately one-fifth to one-fourth of the epiphysis); and (iv) loss of height of the epiphysis when compared to a normal contralateral hip. Careful follow-up of the contralateral hip is mandatory due to the high incidence of bilateral involvement.

A rare late complication of congenital slipped epiphysis is chondrolysis (*Waldenstrom's disease*), which ultimately causes joint-space narrowing and early degenerative arthritis.

The battered child

In 1946 Caffey described a syndrome of subdural haematoma, associated with multiple fractures of the long bones, often in various stages of repair. This is the condition known today as the battered infant. In addition, clinical inspection of such cases may demonstrate bruises, burns, evidence of malnutrition and signs of neglect. Inconsistencies in the history given by the parents or guardian are usual.



Fig. 43.40 Fracture-separation of the distal femoral epiphysis in an anteromedial direction, carrying with it a large fragment of the femoral metaphysis—the relatively common Salter-Harris Type II injury.

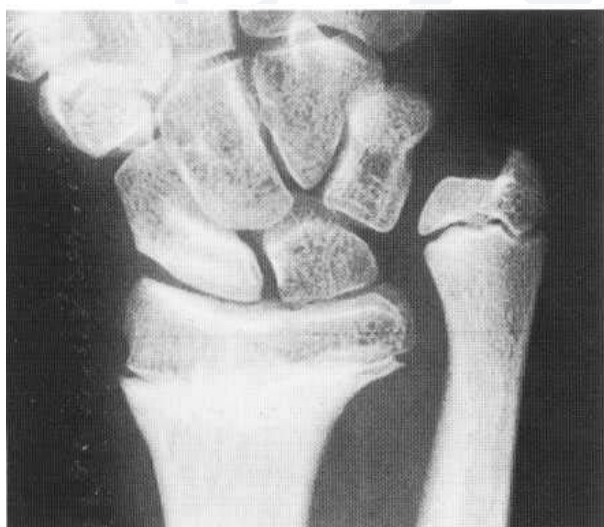


Fig. 43.41 Premature fusion of the distal radial epiphysis, following a fracture-separation 7 years before, with relative overgrowth of the ulna.

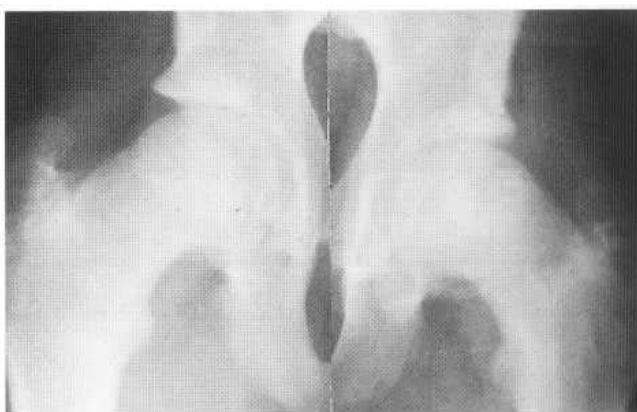


Fig. 43.42 Bilateral slipped capital femoral epiphyses. The diagnosis is more difficult when there is such symmetrical abnormality. There is, however, obvious blurring of the epiphyseal line, and elongation of the femoral neck. The femoral head does not project above the line of the femoral neck on either side.

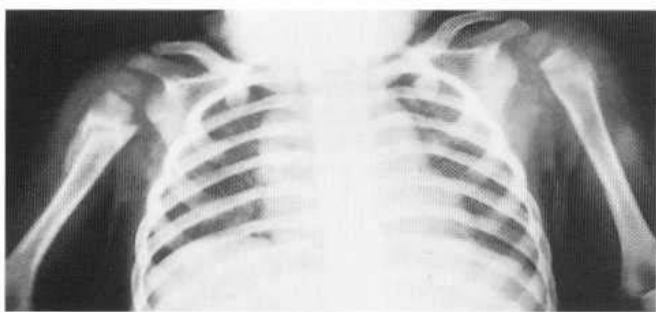


Fig. 43.43 Battered child. Healing fractures are seen in both proximal humeri.

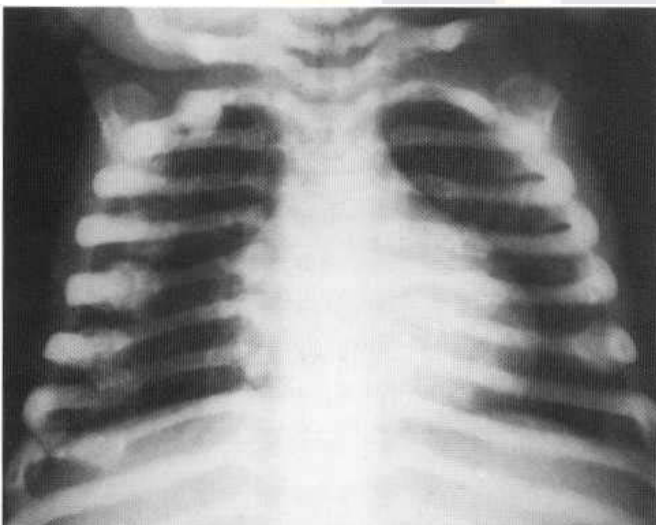


Fig. 43.44 Non-accidental injury. The radiograph shows multiple rib fractures at different stages of healing, probably the result of repeated compression injuries to the thorax. The child was admitted with a recent skull fracture. (Courtesy of Dr D. J. Stoker and Institute of Orthopaedics.)

Radiographic findings include fractures in different stages of healing, periosteal reactions (Fig. 43.43) particularly in the bones of the distal forearm or leg, multiple growth recovery lines, and injuries to the skull and ribs (Fig. 4.3.44). Epiphyseal separations and metaphyseal infractions are particularly common. Fractures in unusual sites (e.g. femoral shaft), and from apparently minor trauma, should also alert the physician to the possibility of non-accidental injury. Such findings warrant a complete skeletal survey and communication to the referring physician immediately, as many children subjected to battering die at a subsequent assault.

Other forms of trauma

Trauma may occur from a variety of other causes, including *ionising radiation*, *frostbite* and rarely *electrical burns* and *decompression osteonecrosis (caisson disease)*.

Ionising radiation may cause an area of osteonecrosis at the site of the insult, whether from radiation therapy or other causes, for example the mouth in radium dial workers in the past. The affected bone generally exhibits a patchy sclerosis, and may fracture spontaneously. Secondary malignant degeneration may occur, usually to osteosarcoma after a latent period of more than 5 years.



Fig. 43.45 Frostbite. Note acro-osteolysis of the toes, with almost complete resorption of the distal phalanges.

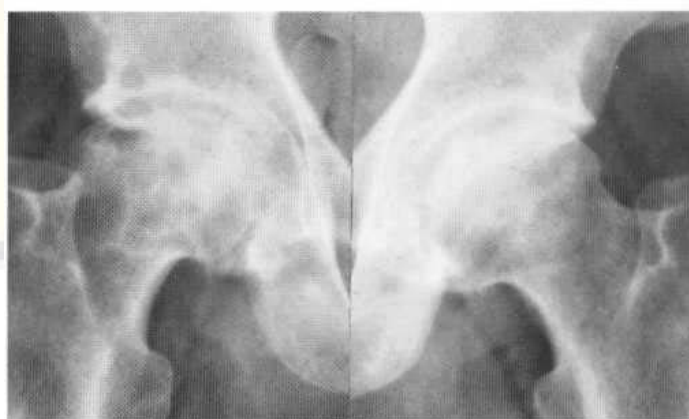


Fig. 43.46 Avascular necrosis of the hips. Note mixed sclerosis and lucency of the femoral heads, with collapse of the weight-bearing surface but maintenance of the joint spaces, indicating intact articular cartilage.

Box 43.4 Causes of subarticular bone infarction—avascular necrosis

- Caisson disease
- Sickle cell disease
- Gaucher's disease
- Pancreatitis
- Chronic alcoholism (? pancreatitis)

Frostbite may give rise to acro-osteolysis (Fig. 43.45), and in children, premature epiphyseal closure and growth arrest.

Caisson disease is found in deep-sea divers and tunnel workers, and is due to poor decompression giving rise to bubbles of nitrogen in the blood. These may block capillaries, causing avascular necrosis. Bone changes include areas of irregular bone density, usually in the long bones, and due to medullary infarction, and subarticular infarctions, particularly in the humeral and femoral heads (Fig. 43.46). A similar pattern of subarticular bone infarction is seen in a variety of other conditions (Box 43.4). The changes of avascular necrosis are visible on nuclear medicine bone scan and MRI long before they can be seen radiographically.

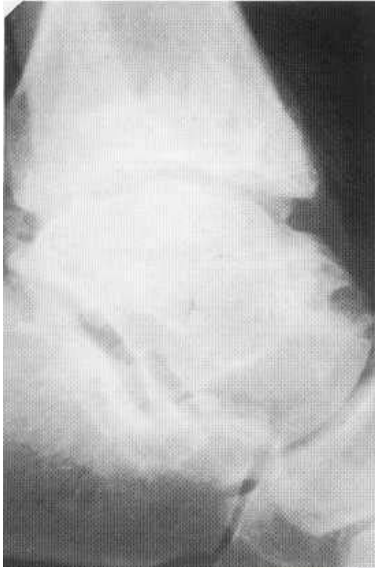


Fig. 43.47 Early Charcot joint, diabetic patient. Note irregularity of the talar dome, with increased density seen around the ankle joint.

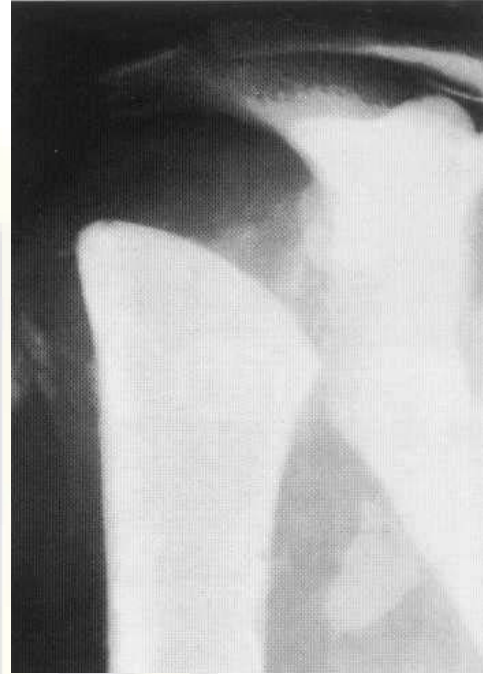
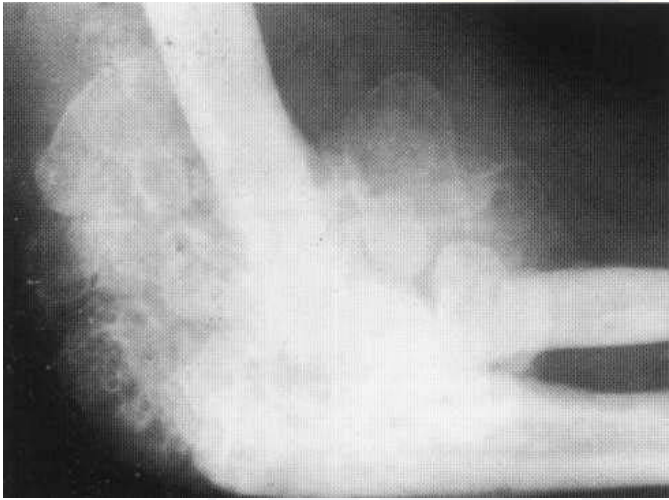


Fig. 43.48 Charcot joint: syringomyelia. The elbow joint shows marked irregularity, with abundant sclerosis, deformity and bone debris. On initial examination, the appearance resembles synovial osteochondromatosis. However, the generalised sclerosis and joint destruction indicate the diagnosis.



Box 43.5 Causes of Charcot joints

- Diabetes (Fig. 43.47)
- Neurosyphilis
- Syringomyelia (Figs 43.48, 43.49)
- Spina bifida
- Leprosy
- Congenital indifference to pain

Osteochondritis dissecans (osteochondral fractures)

Osteochondritis dissecans is really a misnomer, as the lesions clinically referred to as osteochondritis are usually the result of trauma, and indicate an osteochondral or chondral fracture occurring at an articular surface. After injury the detached portion of the bone may remain in situ, may be mildly displaced or may become loose within the joint (Fig. 43.50; see Fig. 44.81).

The most common site of osteochondritis dissecans is the distal femur. The medial condyle is involved in 85% of cases with the lesion classically on the lateral aspect of the medial femoral condyle (Fig. 43.50). Other forms of osteochondral fractures involve the weight bearing surface of the joint (Fig. 43.11), or the site of intra-articular ligamentous disruption (Fig. 43.51). Other sites of osteochondritis dissecans include the posterior patella and talar dome.

Other forms of osteochondral fractures occur, with direct trauma to the articular surface, as seen in the Hill-Sachs deformity of the humeral head (see Ch. 44), from anterior dislocations, and the anterior femoral head defect following posterior dislocation of the hip (Fig. 43.24).

Fig. 43.48 Charcot joint: syringomyelia. The elbow joint shows marked irregularity, with abundant sclerosis, deformity and bone debris. On initial examination, the appearance resembles synovial osteochondromatosis. However, the generalised sclerosis and joint destruction indicate the diagnosis.

Chronic trauma to the joints (neuropathic arthropathy)

Brief mention will be made of this entity, although it is covered more fully in Chapter 44. Repeated trauma to the joints in the absence of normal pain and proprioceptive sensation will give rise to a severe destruction arthropathy, first described by Charcot (Figs 43.47-43.49). Although seen originally in cases of neurosyphilis, there are a variety of causes (Box 43.5).

Most joints show evidence of *disorganisation*, increased bone density, debris within the joint capsule and bone destruction, giving rise to *deformity*-the so-called '5Ds'. On occasion however, a characteristic clear-cut destruction of the metaphysis of the bone is seen suggesting, at least superficially, a surgical procedure (Fig. 43.49).

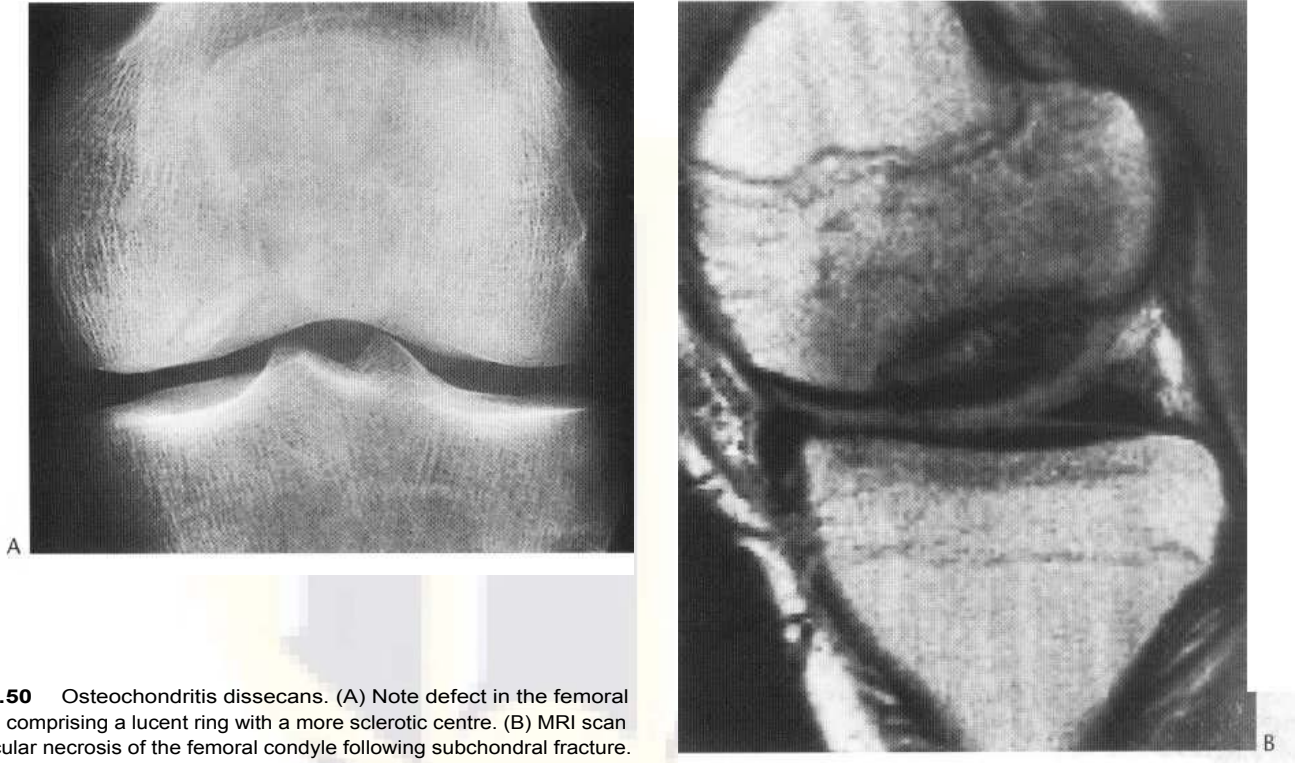


Fig. 43.50 Osteochondritis dissecans. (A) Note defect in the femoral condyle, comprising a lucent ring with a more sclerotic centre. (B) MRI scan of avascular necrosis of the femoral condyle following subchondral fracture.

REFERENCES AND SUGGESTIONS FOR FURTHER READING

See end of Chapter 44.

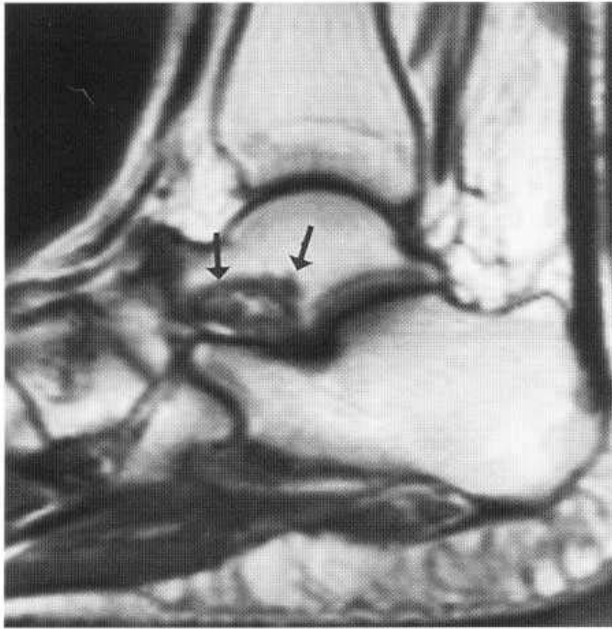


Fig. 43.51 Osteochondral fracture. Sagittal T_1 -weighted MRI of the ankle. There is a well-defined area of abnormal signal in the inferior border of the talus at the insertion of the interosseous ligament (arrows). The ligament itself cannot be seen, indicating disruption.



نشر الکترونیکی
موسسه انتشاراتی
نوردانش

SKELETAL TRAUMA: REGIONAL

Jeremy W.R. Young

The skull

Head trauma, whether accidental or intentional, is a common event with an incidence of almost 8 million cases each year in the USA. Of these injuries approximately 500 000 are considered major, and half of those require emergency treatment. Overall, mortality rates are reported from 57 to 50% and the majority of deaths in motor vehicle accidents are the result of head trauma.

Despite the large number of publications refuting the clinical value of plain radiographs of the skull, they continue to be widely requested, although thankfully common sense is beginning to be applied in many centres. The logical approach would be that if there has been sufficient injury to necessitate examination, CT should be performed, as whether a fracture is present or not, intracranial haemorrhage may have occurred (Fig. 44.1).

Although not as sensitive as CT, if plain radiograph is performed it will demonstrate most skull fractures, although clearly radiographs are inadequate to evaluate the intracranial structures. The

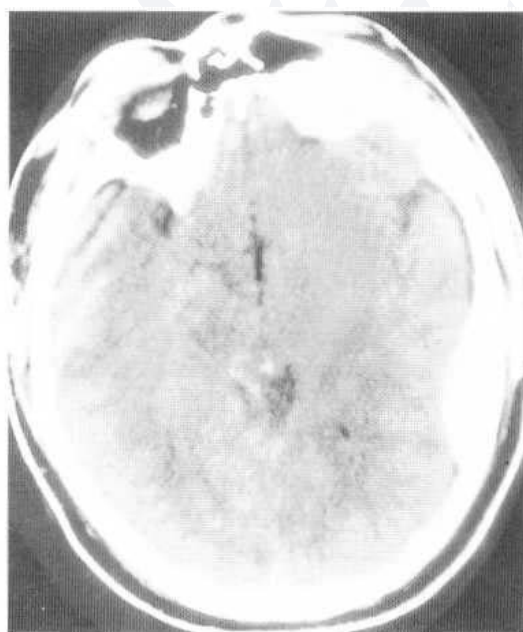


Fig. 44.1 Extradural haematoma: CT scan. A well-defined area of increased density is seen. The clear-cut convex inner margin is diagnostic of an extradural collection.

majority of fractures are linear and on occasion these can cause a diagnostic problem when they may simulate or be simulated by vascular grooves (see Ch. 53). In general, vascular grooves are less lucent and less sharply marginated, and are seen to branch and make curves rather than sharp angles.

Fractures which extend to the base of the skull may extend into the sphenoid sinus and an air-fluid level may be identified. Otorrhoea or rhinorrhoea may occur. In the temporal bones, there are generally two varieties of fracture: longitudinal (along the axis of the temporal bone) or transverse. Both may cause damage to the auditory or facial nerve, but longitudinal fractures are more likely to cause injury to the tympanic membrane and ossicles.

Depressed fractures of the skull may be readily apparent clinically but can be missed. In general, however, they have a typical radiographic appearance of a crescent of dense bone, due to overlapping fragments (Fig. 44.2). Tangential views provide the conclusive diagnosis in these cases. Intracranial haemorrhage may be suggested by shift of the calcified pineal gland on the frontal views of the skull.

CT is effective in detecting most skull fractures, particularly if 'bone windows' are used, although occasionally on older scanners a fracture may be missed due to 'volume averaging'. These may be clinically insignificant however, unless (here is concomitant intracerebral haemorrhage, which usually is readily recognised (Fig. 44.3).

Several studies suggest that MRI is not only more sensitive at detecting intracerebral trauma than conventional CT, but also may demonstrate lesions earlier (Fig. 44.4). On the whole, however, MRI is less available than CT at this time, particularly in the trauma centre, and is also more problematical to use. The advent of multi-slice spiral CT also allows for much improved contrast and spatial resolution than conventional CT scanners.

The facial bones

Usually the result of automobile accidents or assaults, facial bone injury generally involves one of four areas: mandible, zygomatic arch and orbit, nasal bones, or complex fractures of the Le Fort varieties. Le Fort defined lines of weakness within the facial bones, leading to the classification system based on the type of fracture pattern (Figs 44.5, 44.6). In practice, pure symphyseal Le Fort

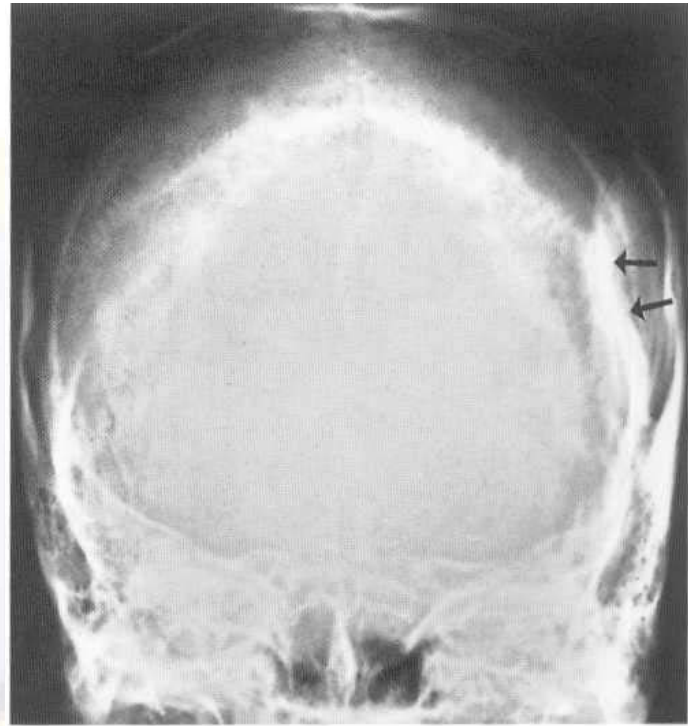
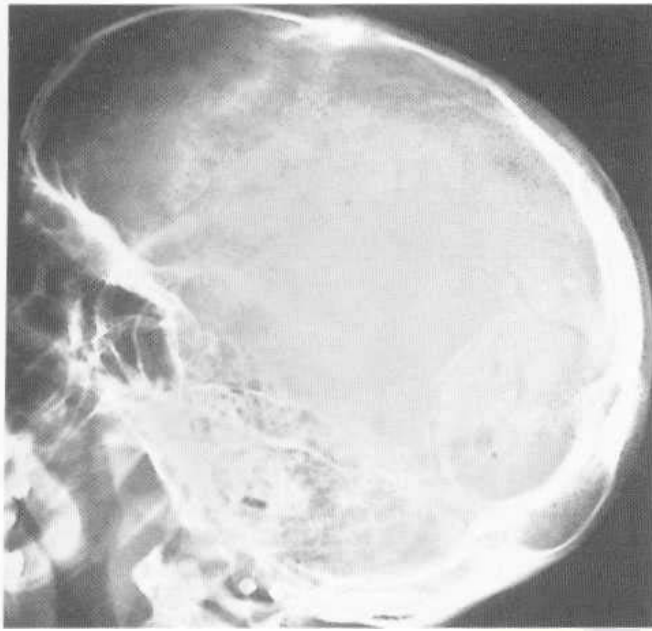


Fig. 44.2 Depressed skull fracture. (A) A curvilinear density overlies the posterior parietal region on the lateral view. (B) On the Townes' view, the depressed nature of the defect can be appreciated (arrows).

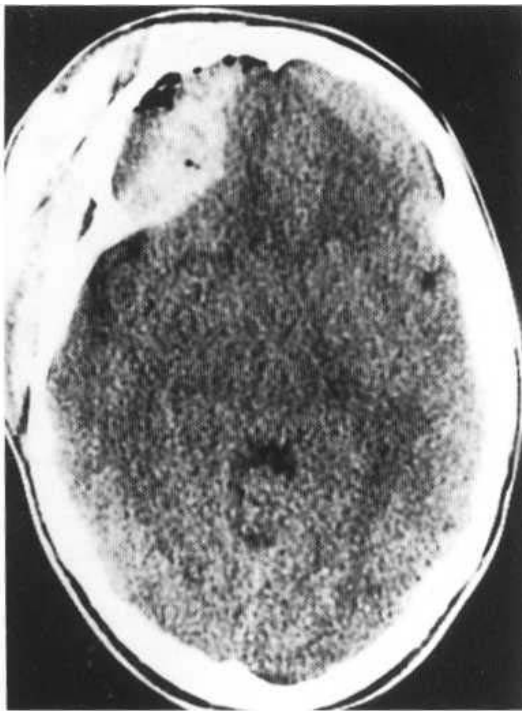


Fig. 44.3 Skull fracture: CT scan demonstrates a large extradural haematoma with, in addition, obvious high-density blood in the right frontal lobe. Low-density air 'bubbles' are also seen, indicative of fracture communicating to the outside environment, most likely via the frontal sinuses.

fractures of any one variety are rare, and a combination of the injuries usually occurs (Fig. 44.6).

Conventional radiographic examination of the facial bones will include lateral, PA (occipito-frontal) and Waters (occipito-mental) views. Although these provide moderately good information, over-



Fig. 44.4 MRI of right temporal lobe contusion (T,-weighted). There is irregular high signal intensity within the temporal lobe, following trauma to the tempoparietal region of the skull.

lying soft-tissue swelling can obscure detail considerably. Additional views such as obliques may be helpful, but CT has proved to be vastly superior to the plain film in the evaluation of facial trauma, and is invariably used to define the nature and extent of injuries. Furthermore, modern high-quality 3D reconstruction capabilities are now readily achievable, providing the surgeons with far better information than can be achieved by plain radiographs (Figs 44.7-44.9).

The modern multislice CT scanners, with their ability to scan a complete body part in a matter of seconds, have the opportunity to revolutionise our approach to trauma evaluation. It is reasonable to

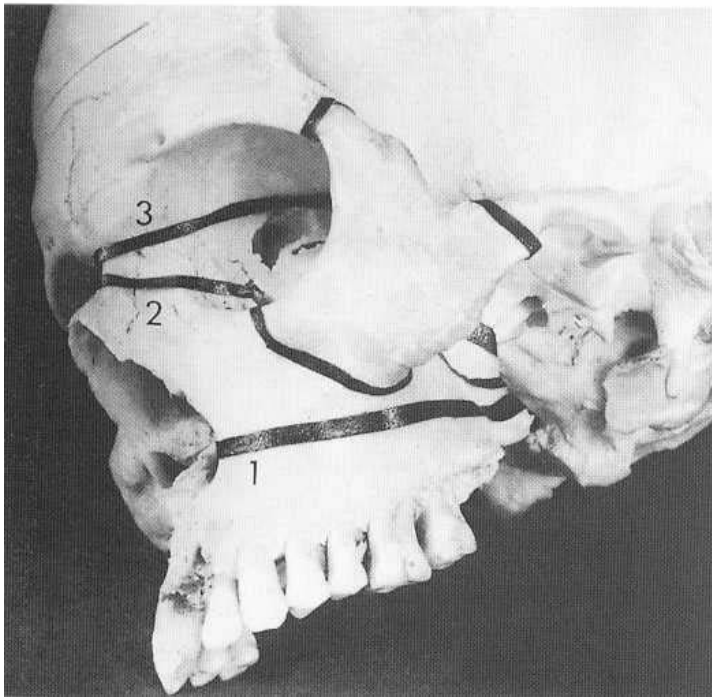


Fig. 44.5 Facial fracture lines. The lines of the common fractures are marked on the skull: 1 = low transverse fracture; 2 = pyramidal fracture; 3 = high transverse fracture. The numbers also relate to the Le Fort lines of weakness.

expect a complete scan of the skull, brain, spine, chest, abdomen and pelvis to be completed in only 1 or 2 minutes, thus allowing for a complete reading, with 2D or 3D reformatting, and without having to perform difficult, time-consuming plain radiographs on compromised, or combative patients, with only limited diagnostic potential. However, as multislice spiral CT is, as yet, only in its infancy, this text will concentrate on the more traditional imaging techniques.

On plain radiographs, the zygomatic arch and orbital rim are best seen on the occipito-mental (Waters) view, although the submento-vertical and Townes' views are good for assessing the zygoma for depression. Fluid levels or opacification of the maxillary sinus are important hints of fractures extending into the sinus and may be the only sign of 'blow-out' fractures of the orbital floor. Blow-out fractures may also involve the ethmoid sinus walls, and air may penetrate the periorbital space, giving rise to orbital emphysema (see Ch. 43).

The mandible is most commonly fractured at its weak spot, adjacent to the canine tooth (Fig. 44.9). However, as it forms a 'ring'

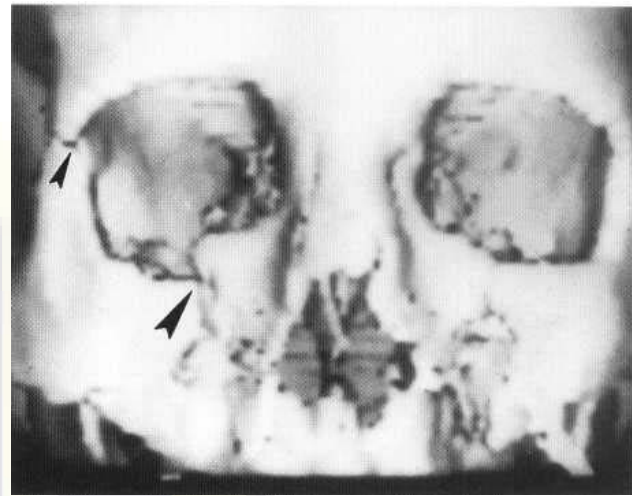


Fig. 44.7 Zygomatic inferior orbital rim fracture: 3D CT. The zygomatic arch and inferior orbital rim are depressed on the right, with a comminuted fracture involving the inferior orbital rim (large arrowhead) and frontozygomatic suture (small arrowhead).

structure with the skull, there is a strong possibility of two fractures occurring, and this should always be excluded (Fig. 44.10).

The nasal bones are best identified on the lateral view, although the frontal views or occlusal film will determine displacement of the nasal septum. Again, CT is considerably more accurate than plain film radiography.

The spine

Spinal trauma is a common cause of disability, with approximately 150 000 persons suffering from spinal injury in the USA each year. It is predominantly an affliction of the young, with 80% occurring below the age of 40. Spinal injuries are common in multitrauma patients, predominantly from motor vehicle accidents and from falls. Cervical spine injury occurs in over 20% of such cases.

Examination of the patient in the acute setting may be difficult due to combative or uncooperative behaviour, which may be the result either of head trauma or intoxication. Plain films are still the primary method of evaluation and will detect abnormalities of alignment, as well as the majority of fractures. Additional methods of examination include tomography, CT and MRI. CT is able clearly to identify small bone fragments not seen on plain radiographs and has the advantage of better definition than tomography, as well as an ability to visualise the soft tissues. It also involves

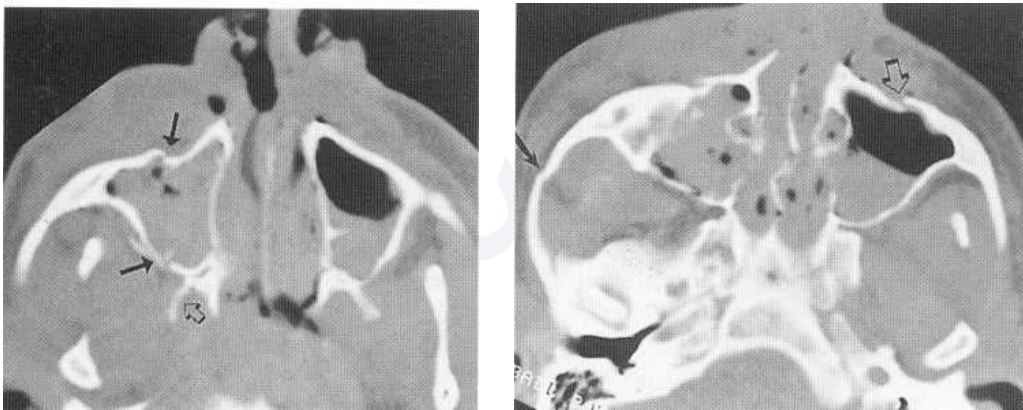


Fig. 44.6 CT of facial fracture. (A) Fractures are identified through the anterior and lateral walls of the right maxillary sinus (arrows), and pterygoid plate (open arrow). There is complete opacification of the right antrum and nasal passage from haematoma, and a fluid level in the left antrum due to a maxillary fracture (not seen on this image). On another cut (B) the zygomatic arch fracture is also seen (arrow), and there is obvious depression of the zygoma. The left maxillary fracture is also seen (open arrow).

A

B

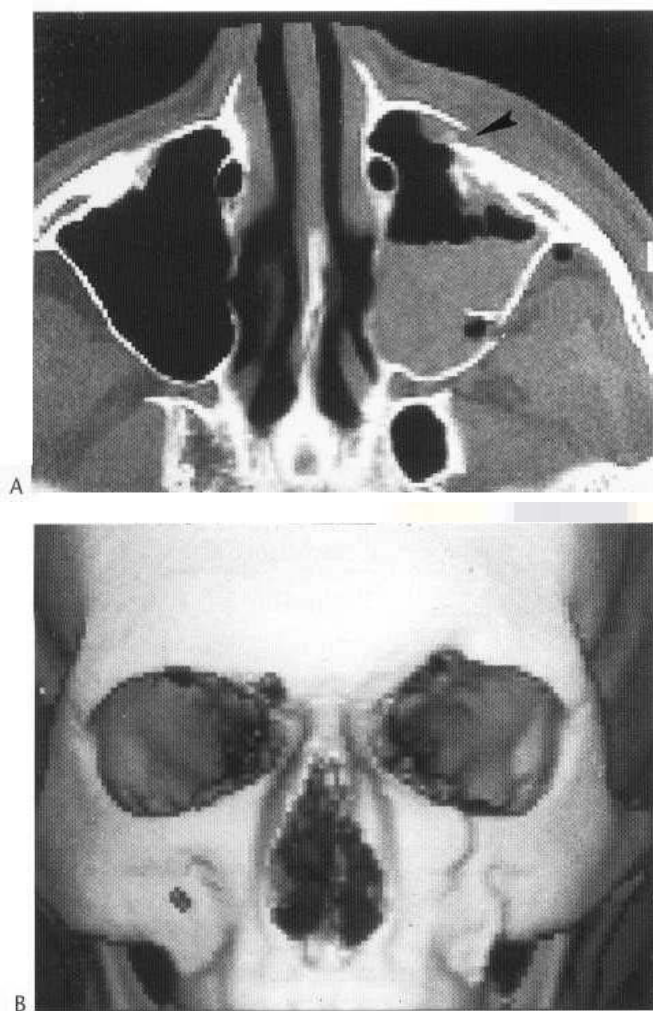


Fig. 44.8 (A) CT scan demonstrates an air-fluid level in the left maxillary antrum, and a fracture of the anterior wall (arrowhead). (B) 3D reconstruction of the face, showing the fracture.

less radiation and is quicker than tomography. With the newer scanners, high-quality reconstruction in virtually any plane, and 3D images may also be obtained (Fig. 44.11).

MRI is becoming increasingly utilised in the spine, and has the advantage of detecting injury to the substance of the spinal cord, intervertebral discs and supporting ligaments, which cannot be evaluated by other techniques (Figs 44.12, 44.13). Also, it can easily define the later changes of post-traumatic syringomyelia.

Cervical spine

Normal radiographic anatomy

An understanding of the anatomy of the normal cervical spine is obligatory for correct evaluation. The anatomical features are identified in Figure 44.14. Alignment should be assessed along several anatomical lines as shown. These are: the anterior and posterior spinal lines, joining the anterior and posterior aspects of the vertebral bodies along the line of the longitudinal ligaments; the spinolaminar line, which joins the anterior margins of the junction of the lamina and spinous processes; and the spinous process line, joining the tips of the spinous processes. In addition, a fifth line should be drawn between the posterior margins of the articular pillars. This line defines the posterior aspect of the articular pillars and allows

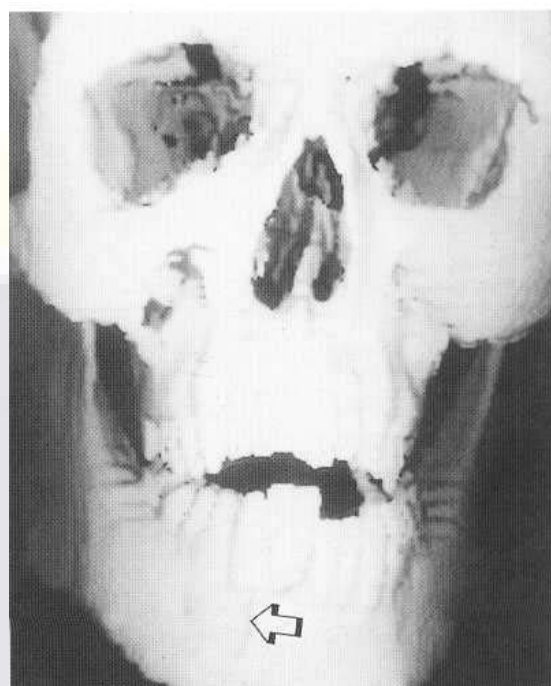


Fig. 44.9 Mandibular fracture (arrow): 3D CT. Fine detail is provided by the 3D reconstruction.

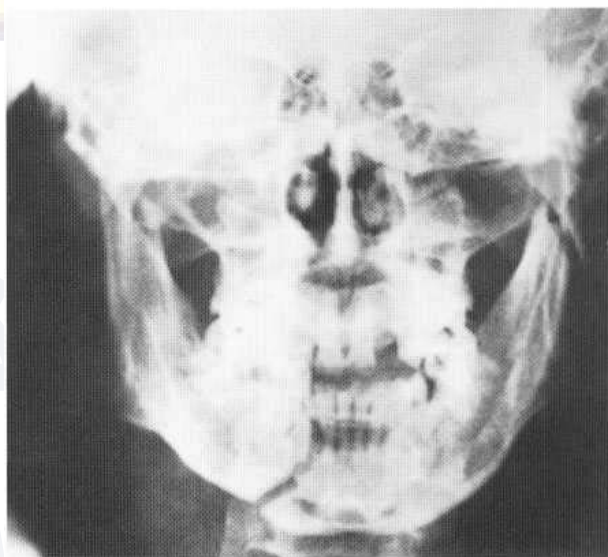


Fig. 44.10 Fractures of the mandible following direct injury. As with other bony rings, fractures in two places are common. Fractures involve the right canine region and the neck of the left condyle.

assessment of the laminar space between the posterior pillar and spinolaminar line. Abrupt variation in this space has been shown to be an accurate method of determining rotational abnormality of a vertebral column, either with or without a fracture of the articular pillar (Figs 44.15, 44.16). Prevertebral soft-tissue measurements have traditionally been regarded as being a valuable indicator of injury or normality. However, Templeton et al (1987) have shown these to be of limited value, with the statistical likelihood of underlying injury occurring only at measurements above 7 mm at the C3 and C4 level, and a significant shift towards abnormality occurring only at measurements above 10 mm.

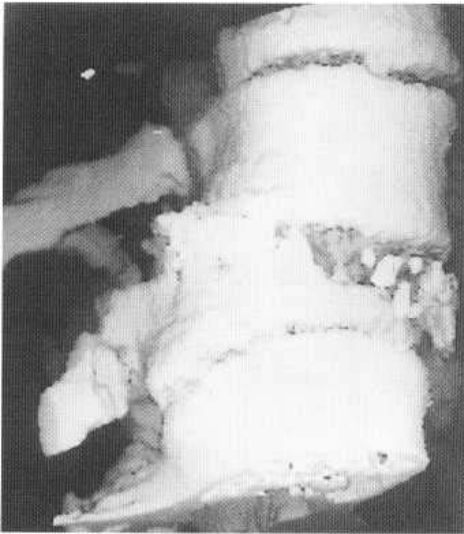


Fig. 44.11 3D CT of the spine. Note crush fracture of the body of L1, with anterior subluxation of T12 on L1.

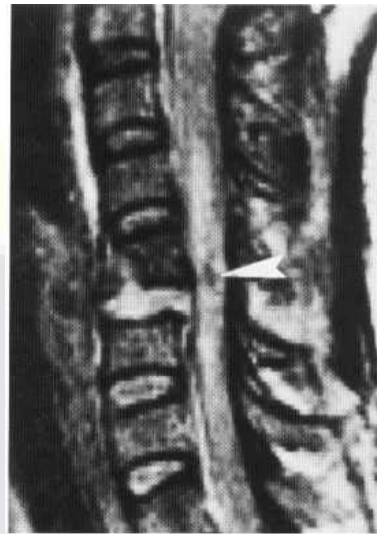


Fig. 44.13 MRI: spinal cord contusion. This gradient-echo sequence shows a focal area of decreased signal in the cord posterior to the hyperflexion teardrop fracture of C5 (arrow-head), compatible with intracellular deoxyhaemoglobin. There is surrounding high signal oedema.



Fig. 44.12 MRI of the cervical spine: T₂-weighted image. There has been a fracture of C6, with mild posterior displacement of the dorsal fragment of the vertebral body (curved arrow). A focal area of high signal within the spinal cord at this level (straight arrow) indicates a focal cord injury.

Radiographic evaluation

The condition of the patient will determine to a large extent the type and detail of the initial radiographic examination. The cross-table lateral view, with the patient supine, is the single most important radiographic examination. The cross-table lateral view, with the patient supine, is the single most important radiographic examination and should be made as soon as the patient is stabilised. Evaluation of this film alone by an expert in the field will allow diagnosis of abnormality in the vast majority of cases. All seven vertebral bodies should be included on the radiographs. A normal cervical spine will demonstrate a gentle lordosis, but although lack of lordosis may be due to muscular spasm and indicate spinal injury, age, prior trauma, radiographic positioning, flexion of the spine and the wearing of a hard collar (so commonly seen today) can all cause alteration in the natural lordosis.

In the lateral radiograph of the resting cervical spine, as well as a normal lordosis, there should be no disruption of the anterior spinal line. In flexion, the mid and upper segments of the spine move forwards over the next inferior segment with concurrent sliding of each inferior articular facet over the superior facet of the level below, up to approximately 30% of the length of the articular surface. A unique phenomenon is seen in children up to the age of 8, approximately 25% of whom will demonstrate a 'pseudosubluxation' at the C2/C3 level, attributed to laxity of the ligaments. This can be confirmed by examining the spinolaminar line, which will maintain a normal relationship in cases of pseudosubluxation. In addition, in approximately 20% of patients in this age group, over half of the anterior arch of the atlas lies above the tip of the dens. This should not be misinterpreted as atlanto-axial dislocation. Furthermore, the space between the posterior surface of the anterior arch of C1 and the anterior surface of the dens may widen in flexion by up to 6 mm in children, although it remains constant in adults.

Kyphosis, or a localised flexion angulation, may be mild or severe, and can occur as a result of narrowing of the vertebral bodies anteriorly, as in a wedge compression fracture. Alternatively, widening of the interspinous distance and/or interfacet joints posteriorly indicates posterior ligamentous disruption, as seen in hyperflexion sprains (Fig. 44.17) (see below). Both of these appearances indicate a hyperflexion force as the cause of injury, and they may occur together. Asymmetry of the disc space is also a useful sign,



Fig. 44.14 Normal cervical spine. Five lines should be drawn in the mind. A and P are the anterior and posterior longitudinal lines respectively. These run along the margin of the anterior and posterior longitudinal ligament. L is the spinolaminar line, which runs between the anterior margin of the dorsal spines, outlining the posterior margin of the spinal canal. The asterisks represent the spinous line, along the posterior margin of the dorsal spines. F is the posterior pillar line, along the posterior margins of the articular pillars. Note divergence of the posterior pillar line in the upper and mid spine, due to mild positional rotation.

and may indicate ligamentous damage to the longitudinal ligament at the site of widening.

Additional plain radiographic examination of the patient with a suspected spinal injury may include an AP view, and an open-mouth AP odontoid view. The incidence of injury to C7 in cervical injuries has been reported at 30%, although in the author's experience this figure would appear to be on the high side. Because of difficulty in demonstrating this region, in some patients, additional evaluation with CT may be needed in the symptomatic or compromised patient. Oblique views are reported to be useful for defining

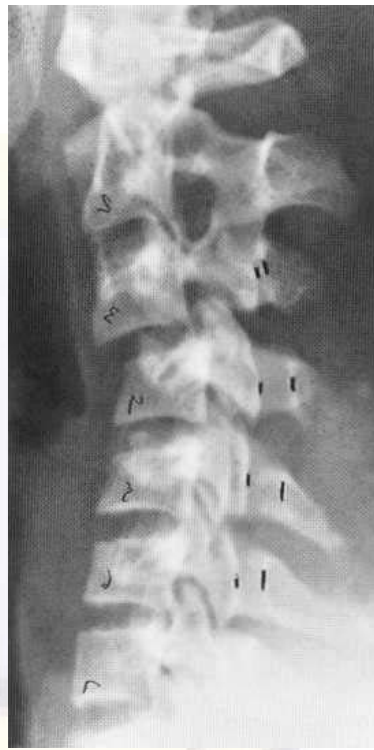


Fig. 44.15 Unilateral facet dislocation. There is an abrupt change in the laminar space (between the spinolaminar line and the posterior articular pillar line) at the C3-C4 level, indicating rotation. There is also a mild anterior subluxation of C3 on C4.



Fig. 44.16 Unilateral facet fracture-dislocation. There is a mild anterior subluxation of C5 on C6; also there is overlap of the posterior articular pillar lines at C6, but separation at C5, indicating rotation. The superior facet of C6 has been fractured, and rotated forwards with the anteriorly displaced inferior facet of C5 (arrow).

the neural foramina, and may clarify a fracture of the articular pillars or a unilateral facet dislocation. 'Pillar views' of the cervical spine are also advocated by some authors. However, it can be argued that these additional views are superfluous; if an abnormality is not seen by routine plain film evaluation in a clinical setting suggestive of a fracture or dislocation, more definitive additional studies are mandatory in any case. These will include flexion-extension lateral radiographs, CT or MRI. These methods will

provide additional information of abnormality, or confirm normality, and are indicated in the symptomatic patient, whether the oblique and pillar views demonstrate abnormality or not.

Classification

Most classification systems for cervical spine injury are based on the classic paper by Whitley and Forsythe (1960). These regard the forces acting on the spine as flexion, extension, rotation, compression or a combination of the above. Each fracture force will be covered below.

Hyperflexion injuries

These include hyperflexion sprain, flexion compression fractures, flexion teardrop fractures, bilateral facet dislocation, and if rotation also occurs, unilateral facet lock.

Hyperflexion sprain

These injuries usually involve anterior subluxation of a vertebral body, with respect to the vertebra located inferiorly. Flexion extension views are invaluable in cases in which injury is expected but not immediately visible, or when minor abnormality such as asymmetry of a disc space or questionable 'fanning' of the spinous processes is seen. However, they should never be obtained when there is clear radiographic evidence of vertebral displacement or ligamentous injury. Also, in the acute setting, muscular spasm may prohibit movement of the spine, thus invalidating the technique.

Pure hyperflexion injuries are associated with posterior ligamentous injury of the spine. Depending upon the severity, the ligaments will be involved in the following order:

1. *Interspinous ligaments*, giving rise to widening of the interspinous distance.
2. The *ligamentum flavum* and *capsular ligaments*, which gives rise to more marked widening of the interspinous distance, and widening or subluxation of the facet joints (Fig. 44.17).
3. The *posterior longitudinal ligaments*, allowing widening of the posterior disc space (Fig. 44.18).
4. Disruption, or stripping of the *anterior longitudinal ligaments* allowing subluxation of the facets and ultimately *bilateral dislocation/facet* (Fig. 44.19). This is usually associated with anterior subluxation of 50% or more of the vertebral body above the injury, and will cause stripping or rupture of the anterior longitudinal ligament.

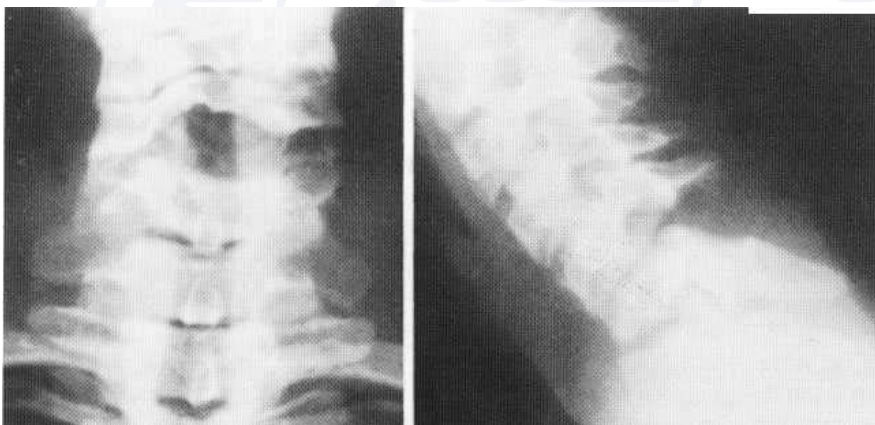


Fig. 44.18 Hyperflexion sprain. Note widening of the interspinous distance at C5/6, with additional widening of the facet joints, and superior subluxation of the facets of C4 on C5 and posterior intervertebral joint. This picture indicates severe ligamentous disruption.

Flexion teardrop fracture

This occurs with flexion injuries when there is a compression fracture of the anterior aspect of the vertebral body inferior to the level of the injury (Fig. 44.20), caused by a compression force on the anterior vertebral body, as the fulcrum of the rotational force on the vertebra is in a central position in the vertebral body, allowing distraction posteriorly but compression anteriorly. This may also be associated with a posterior displacement of the posterior portion of the affected vertebral body, causing spinal cord compression.

Wedge fractures

These occur when there is wedging of the anterior aspect of the vertebra, without ligamentous injury or posterior displacement of fragments. This usually means less than 30% compression of the anterior vertebra, and is associated predominantly with axial loading as well as hyperflexion.

Fig. 44.17 Hyperflexion sprain/wedge compression fracture. There is a wedge compression fracture of C6 with marked widening of the interspinous distances of C5-6; also, widening of the facet joint at C5-6, with near 'perching' of the inferior facets of C5 on the superior facets of C6.

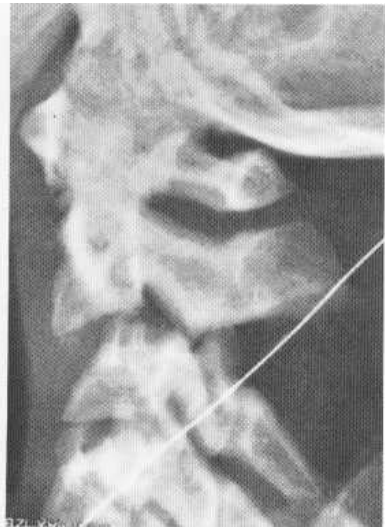


Fig. 44.19 Bilateral locked facet. C2 has leap-frogged over C3, and now lies with its inferior facets anterior to the superior articular facets of C3.



Fig. 44.21 Hyperextension fracture of the articular pillar of C3. (A) There is obvious bone disruption of the posterior elements of C3, involving both the articular pillars, (closed arrow) and lamina (open arrow). (B) Tomography demonstrates the crush fracture of the articular pillar, with posterior displacement of the posteroinferior fragment (arrow).



Fig. 44.20 Flexion teardrop fracture of C5. Note anterior compression of C5, with a fracture of the anterior inferior aspect. A very small avulsion is also seen at the anterior, inferior aspect of C4.

Unilateral facet dislocation

When a rotational force is combined with hyperflexion, unilateral facet dislocation occurs. In such cases, the facet on the abnormal side rotates up and over the subjacent facet. The contralateral side acts as the fulcrum and is not involved in the injury. On the abnormal side, there is either 'locking' of the inferior articulation of the facet of the rotated vertebra, anterior to the superior articulation of the facet of the normally positioned lower vertebral body, or—as occurs in approximately 30% of cases—there is a fracture through one of the articular facets, usually the superior facet of the lower vertebral body. In general this fracture is horizontally orientated, indicating the rotational shearing nature of the force. Radiographically, the vertebral body of the rotated vertebra is displaced anteriorly, varying in degree up to approximately 20% of the vertebral body. Change in the lamina/facet interspace is an accurate assessment of rotational anomaly (Fig. 44.15). An apparent shift of

the spinous process may be identified on the frontal view, due to its being 'rotated' away from the midline.

Hyperextension injuries

In general, hyperextension injuries are associated with rupture of the anterior longitudinal ligament. This causes widening of the anterior disc space, and may cause prevertebral soft-tissue swelling. It must be remembered, however, that positioning of the head in the neutral position by a well-meaning passer-by, or the placement of a cervical collar at the scene of the accident, may largely restore any displacement, so that on initial inspection the radiograph can appear grossly normal. Hyperextension teardrop fractures may occur, usually at the anterior inferior aspect of the vertebral body involved, indicating the site of avulsion of the anterior longitudinal ligament. A further effect of hyperflexion, however, may be to cause an axial load on the posterior elements, giving rise to crush fractures of the articular pillars (Fig. 44.21) and narrowing of the interspinous distance. Fractures through the spinous process may also occur, due to axial compression. Facial injuries are often associated with these fractures.

Hangman's fracture

This injury, misnamed because of a superficial resemblance to fractures seen in victims of hanging, occurs with hyperextension of the head, and therefore a form of axial loading on the posterior elements of the upper cervical spine caused by posterior rotation of the head in the sagittal plane (Fig. 44.22). The injurious force is in effect delivered by the occiput as it moves in an inferior and anterior direction, as a result of the posterior rotation of the skull. This causes the injury force vector to be delivered in an inferior and anterior direction, giving rise to a corresponding oblique fracture through the posterior arch of C2, which may extend into the body of C2. This fracture may be extremely unstable, although the spinal cord is usually spared due to the large AP diameter of the spinal canal at this level. The fracture may also extend into the vertebral

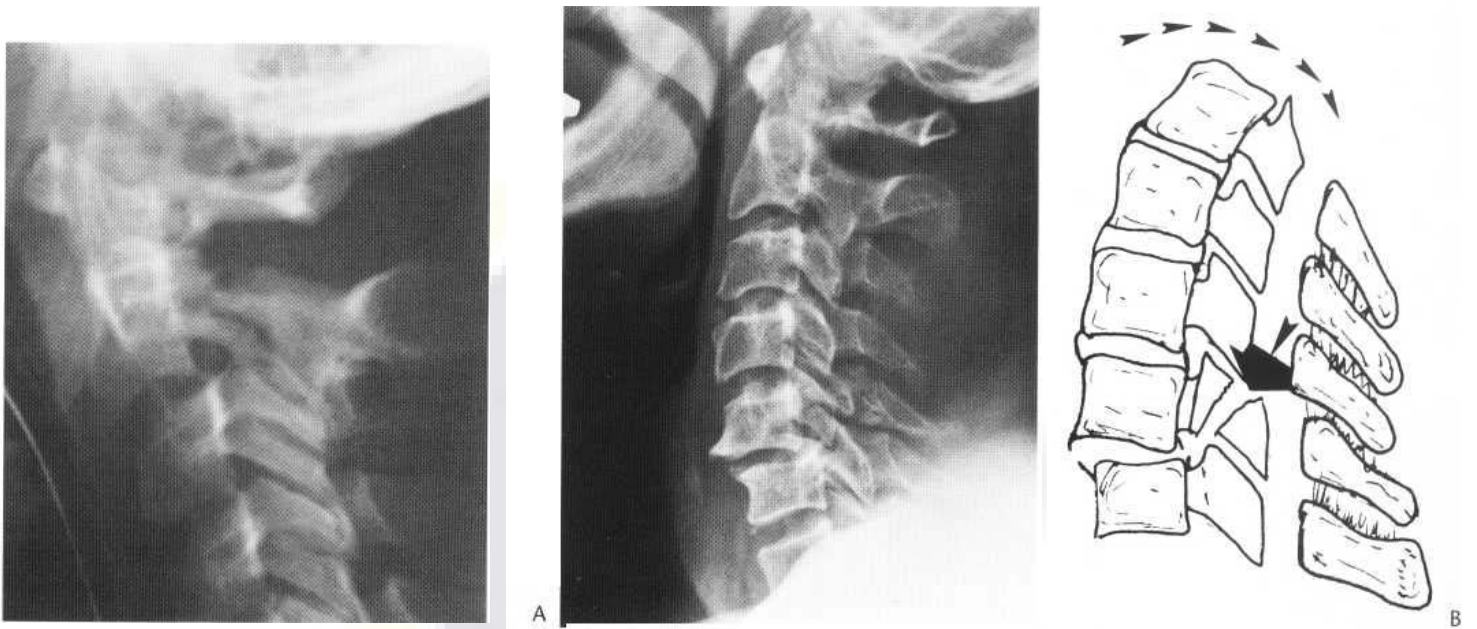


Fig. 44.22 Hangman's fracture. Classical oblique fractures through the pars interarticularis of C2 are associated with anterior subluxation of the body of C2.

Fig. 44.23 Low Hangman's fracture. Note the similarity to the Hangman's fracture pattern, but at a lower level. (A) There is anterior subluxation of C5 on C6, with an oblique fracture through the posterior arch of C5, indicating the anterior/inferior direction of the force vector, from the posterior elements of C5, caused by massive hyperextension. This is a fracture pattern typical of the hangman's fracture at C2. (B) Diagrammatic representation of the 'low hangman's' fracture. The extension force has a rotary configuration (small arrow heads), with an inferior/anterior component to the vector (large arrow), as in the true hangman's fracture.

canals, risking injury to the vertebral arteries. A similar fracture pattern may occasionally be seen at lower levels in the spine (Fig. 44.23), a so-called 'low hangman's' fracture.

Axial loading

Jefferson fracture: burst fracture of C1

In these injuries, axial loading causes compression of the lateral masses of C1 between C2 and the occipital condyles. Because of

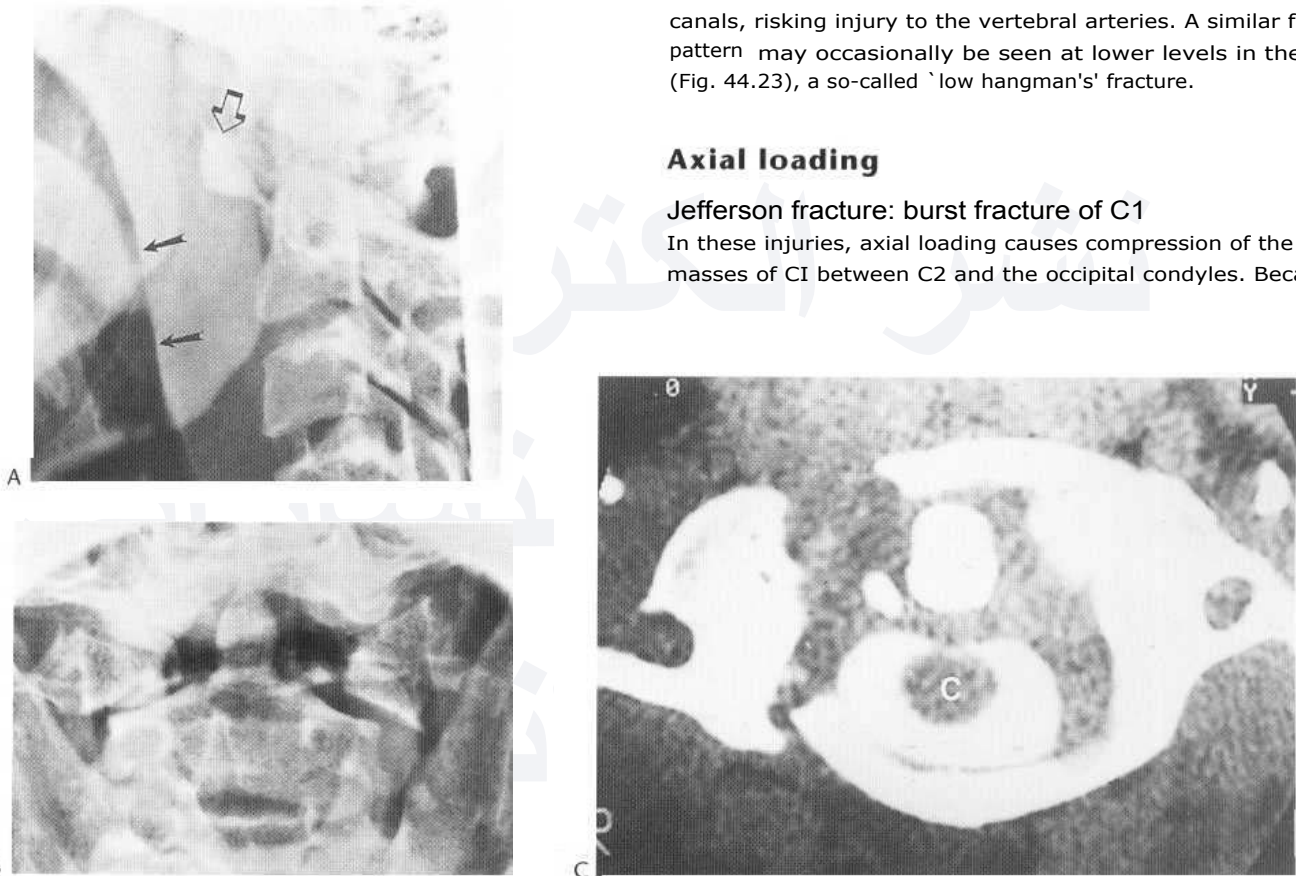


Fig. 44.24 Jefferson burst fracture of C1. (A) The lateral view indicates anterior displacement of the anterior arch of C1 with respect to the odontoid process (open arrow). There is marked prevertebral soft-tissue swelling (closed arrows). (B) The AP view demonstrates lateral displacement of the lateral masses of C1. (C) Axial CT of Jefferson fracture of atlas. Contrast in subarachnoid space outlines cord.

the anatomy of the region, and wedge shape of the lateral masses, a laterally directed force vector is produced, giving rise to lateral displacement of the masses of C1 (Fig. 44.24), thus disrupting the ring. This can be appreciated on the AP odontoid view, but usually gives rise to anterior displacement of the atlas relative to the odontoid process. Prevertebral soft-tissue swelling is usual.

Burst fracture

This is caused by axial loading and the vertebra is shattered, often in all directions. The importance of this injury lies in the possibility of posterior displacement of fragments into the spinal canal.



Fig. 44.25 Low (Type II) odontoid fracture. The fracture passes through the base of the odontoid process with slight separation, and anterior displacement of the odontoid process and ring of C1.



Fig. 44.27 Os odontoideum. The tip of the odontoid process is separated from the body, with smooth, well-corticated margins (arrows).

Miscellaneous

Spinous process fracture

This most commonly occurs at C7, and is often seen as an avulsion injury (clay shoveller's fracture). However, it may occur in direct trauma, or from compressive hyperextension (see above), or as the result of forced hyperflexion.

Odontoid fractures

Fractures of the odontoid have traditionally been divided into three types; Type I, in which the fracture is through the upper aspect of the odontoid process; Type II, in which the fracture occurs through the base of the odontoid (Fig. 44.25); Type III, where the fracture extends into the body of C2 (Fig. 44.26). More recently there has been a move towards classifying them as either high or low, the latter fractures extending into the body of C2, and hence representing the Type III fractures of the past. Non-united Type I fractures involving the superior aspect of the odontoid process are arguably the cause of the so-called *os odontoideum*, although a congenital non-union has also been suggested (Fig. 44.27). Odontoid fractures may be seen on the AP odontoid view, but should not be confused with artefacts from the posterior arch of the atlas (Mach effect) (Fig. 44.28) or overlying teeth. Type III (low) fractures extending into the body of C2 may cause disruption of the cortical 'ring' of the lateral aspect of the body of C2, seen on the lateral view (Fig. 44.26). There may also be an anterior tilt of the dens and hence anterior displacement of C1 with respect to the ring of C2.

Rotational injuries

Pure rotational injuries are rare, but may give rise to rotational (rotatory) subluxation. This is usually at the C1/C2 level, and in children may give rise to torticollis. Although the condition may be self-limiting, occasionally it persists. It is best appreciated on open-mouth odontoid views, in the AP and both oblique projections, although tomography may be needed for full evaluation (Fig. 44.29).

Additional rotational injuries are those associated with axial loading or hyperextension, both of which can give rise to unilateral facet dislocation (see above).



Fig. 44.26 Low (Type III) odontoid fracture. (A) The lateral radiograph demonstrates interruption of the radiographic 'ring' of the body of C2 (arrows). (B) CT demonstrates the nature of the fracture, through the body of C2.

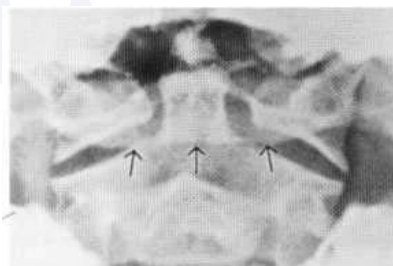


Fig. 44.28 Mach effect. An apparent fracture through the base of the odontoid process is due to the overlying posterior ring of C1 (arrows).

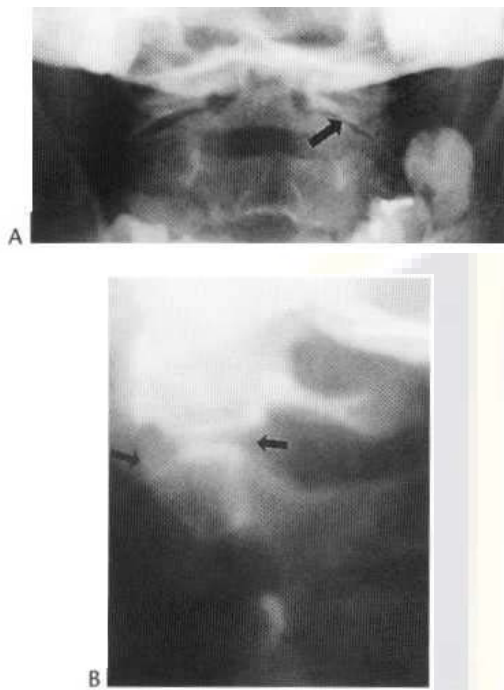


Fig. 44.29 Rotatory subluxation of C1 on C2. Despite a nearly perfect AP view (A), there is asymmetry of the C1 /C2 articulation with narrowing of the left (arrow), which cannot be attributed to patient positioning. This suggests a rotation of C1 on C2, confirmed (B) by lateral tomograms, which indicate subluxation of the articular surfaces (arrows).

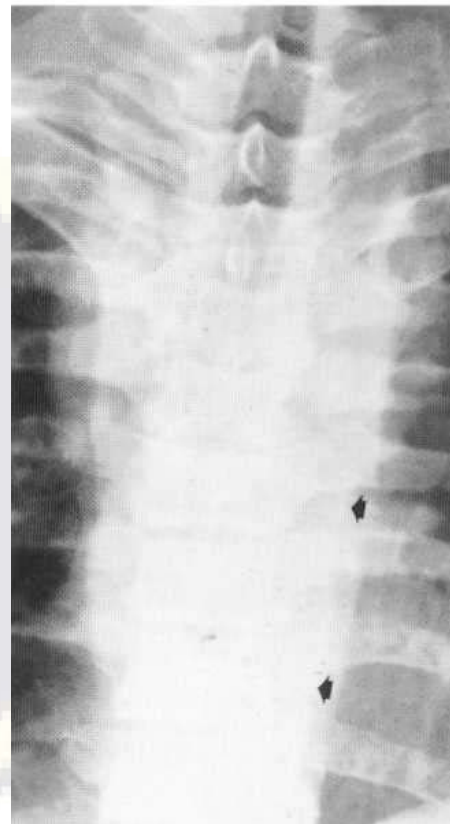


Fig. 44.31 Compression fracture: mild crush fracture of the body of T5, with a paraspinal soft-tissue 'mass' (arrows) due to haemorrhage.

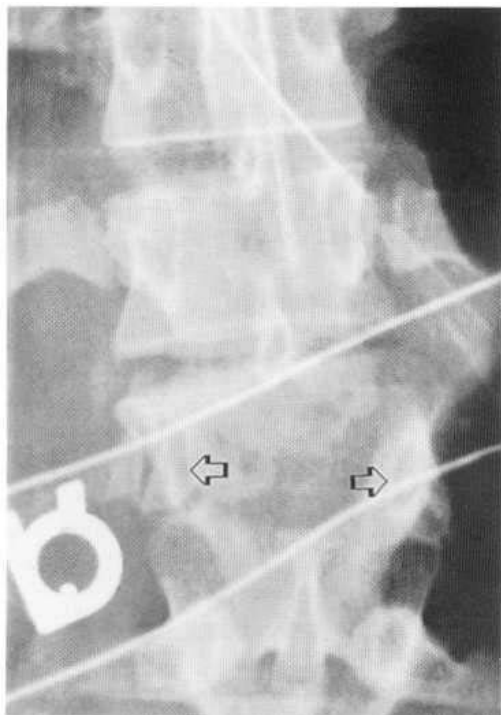


Fig. 44.30 Crush fracture L1. The interpedicular distance is widened, indicating lateral displacement of the pedicles, and hence 'bursting' of the ring formed by the vertebral body and posterior elements. Water-soluble contrast medium is present in the subarachnoid space.

Thoracolumbar spine

Fractures in the thoracolumbar spine are generally the result of severe flexion and axial loading, as in falls from a height (crush

fractures), or acute flexion injuries, although rotation, and shearing may also play a role as in the cervical spine. The thoracic spine is somewhat less prone to injury than the lumbar spine, due to the additional protective effect of the ribs and thoracic cage. However, it must be remembered that the large size and stability of the vertebrae relative to the cervical spine, mean that large forces are generally required to cause injury to the thoracic and lumbar spine. Additional injuries, both skeletal, and to the soft tissues and internal

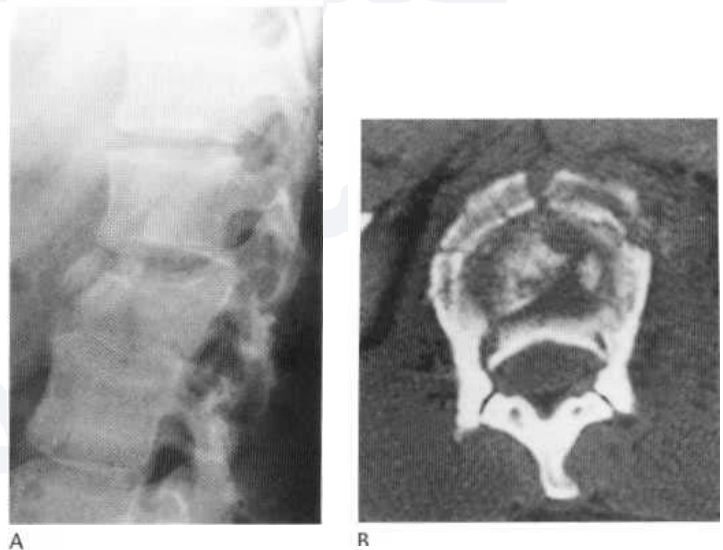


Fig. 44.32 Compression fracture of L2. (A) Plain lateral radiograph indicates wedging of L2, with posterior bulging of the dorsal margin. (B) CT scan demonstrates the extent of the impingement of the dorsal fragment upon the spinal canal.

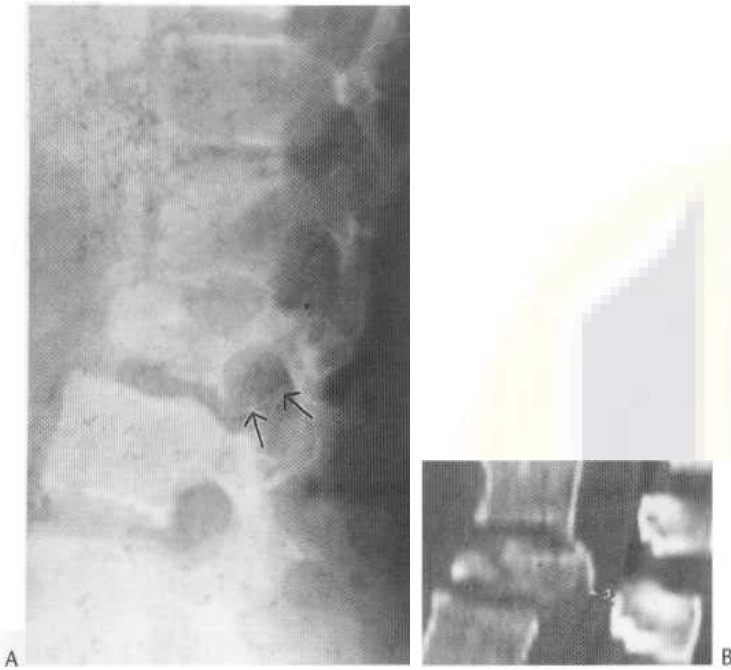


Fig. 44.33 Compression fracture L2. (A) Again there is wedging and compression of L2, with evidence of body debris overlying the spinal canal (arrows). (B) CT reconstruction indicates the position of the bone fragments and narrowing of the canal.

organs, therefore, are frequently present. A special type of flexion injury is also commonly seen in seat-belt injuries in car accidents (see below). As in the cervical spine, ligamentous injury can usually be appreciated by subluxation, either anterior or lateral. Widening of the interpedicular distance or disc space, as well as paravertebral swelling in the thoracic region, are signs of injury which should be sought on plain radiographs (Figs 44.30, 44.31).

Compression injuries cause 'burst fractures' or, when associated with flexion, wedge compression fractures, usually more marked at the anterior margin (Figs 44.32, 44.33). Lateral compression may also occur, but is less common. Crush fractures are common in victims of falls, and in the lumbar spine are associated with fractures of the calcaneus, 'piton' fractures of the tibia and vertical shear pelvic fractures (see below). Conversely, these injuries to the pelvis and lower limb should warn of possible spinal trauma, particularly of the upper lumbar region. All forms of compression fracture require CT to evaluate for posterior displacement of fracture fragments, and impingement upon the spinal cord (Figs 44.32,

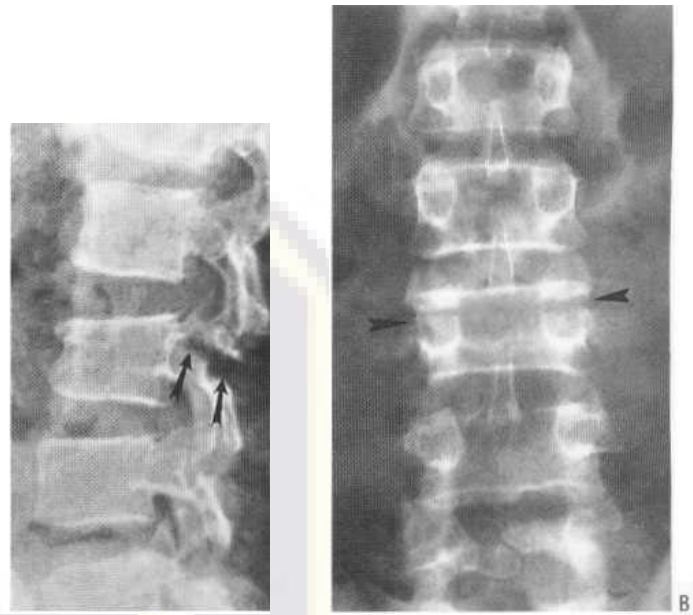


Fig. 44.34 Lap-belt injury: Smith fracture. (A) There are horizontal fractures extending posteriorly from the dorsal surface of the vertebral body, through the pedicles (arrows). (B) The AP view demonstrates the characteristic 'horizontal' defects in the pedicles (arrowheads).

44.33), as plain films are inadequate to assess this parameter, and the extent of injury.

Seat-belt injuries

These are caused by massive localised hyperflexion, typically the result of sudden deceleration, in a car accident, when the occupant is restrained by a lap seat belt. In general there is very little, or no, anterior wedging of the vertebral body, suggesting a distracting hyperflexion force. The fractures are subdivided into three groups. Type I, the 'Chance fracture', extends horizontally from the spinous process into the vertebral body, passing through the articular pillars and pedicles; Type II, the Smith fracture, is similar, but does not involve the spinous process (Fig. 44.34); Type III involves one side only, due to a rotational component of the force responsible.

The pelvis and hip

Much confusion has arisen over pelvic fractures, due to a lack of a logical and meaningful classification system. Traditionally, pelvic

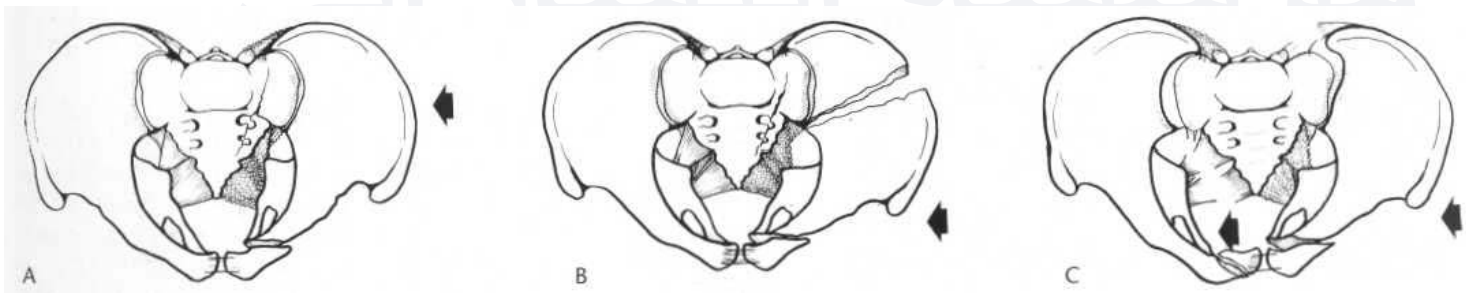


Fig. 44.35 Lateral compression pelvic fracture classification. (A) Type I. Posteriorly positioned lateral force causes compression of the sacrum, and 'horizontal' or buckle fractures of the pubic rami. (B) Type II. The force is delivered more anteriorly, causing inward rotation of the anterior pelvis around the anterior aspect of the sacroiliac joint. Either disruption of the posterior sacroiliac ligaments or fracture of the iliac wing (shown here) results. (C) Type III. The lateral force on one side is transmitted to the contralateral side, causing an externally directed force to 'open' the contralateral pelvis. Disruption of the major anterior ligamentous groups (anterior sacroiliac, sacrotuberous and sacrospinous) occurs. (Reproduced with permission of Urban and Schwarzenberg from Young and Burgess (1987).)

fractures were classified by reference to historical descriptions of individual fractures, without any connection between them. These classifications included single fractures of the pelvis and thus were largely outdated by the work of Gertzbein and Chenoweth (1977) who demonstrated that there was always a second site of injury even in apparently single pelvic fractures. This is due to the fact that the pelvis is a bony ring, held together by ligamentous groups posteriorly and anteriorly. A search for a second site of injury should therefore always be made in fractures involving the pelvic ring.

The classification system of Young and Burgess (1987) developed from work by Pennal and Tile, which describes fractures relative to the force of injury, will be used in this text.

Lateral compression fractures

These are subdivided into three types, depending upon the severity of the injury, and progressive involvement of the posterior pelvis (Fig. 44.35). Pubic rami fractures are invariably present, and generally run 'horizontally', or in the coronal plane. Alternatively they may present as a 'buckle' fracture. A common association is a crush fracture of the sacrum (Fig. 44.36). Fracture of the medial wall of the acetabulum with or without central dislocation of the femoral head is also associated (Fig. 44.36). In Type I fractures, there is no ligamentous damage, and no posterior pelvis instability. However, with Type II injuries, there is medial displacement of the anterior pelvis on the side of injury, with either a fracture through the sacroiliac joint and iliac wing, or rupture of the posterior sacroiliac ligaments (Fig. 44.37). This allows some posterior instability. In Type III fractures, the lateral force on one side of the pelvis is transmitted through to the contralateral side, so that the force is directed outward (Figs 44.35, 44.38). This causes 'opening' of the pelvis on the contralateral side, with associated posterior ligamentous disruption.

AP compression fracture

The damaging force in the AP (or PA) direction tends to cause 'opening' of the anterior pelvis (Fig. 44.36), with splaying of the symphysis pubis and/or fractures of the pubic rami, which, how-

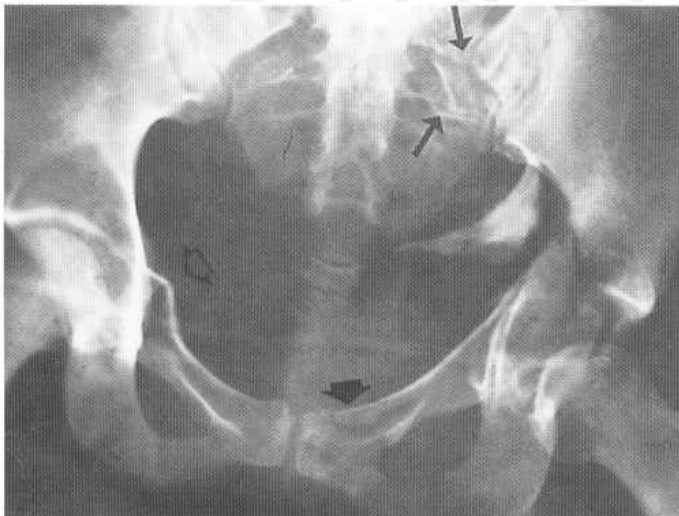


Fig. 44.36 Type I lateral compression fracture. A horizontal fracture of the left (closed arrow) and a buckle fracture of the right (open arrows) superior pubic ramus are seen. There is a crush fracture of the left sacrum (long arrows), and a fracture predominantly of the medial wall of the left acetabulum. (Reproduced with permission of Urban and Schwartzberg from Young and Burgess (1987).)

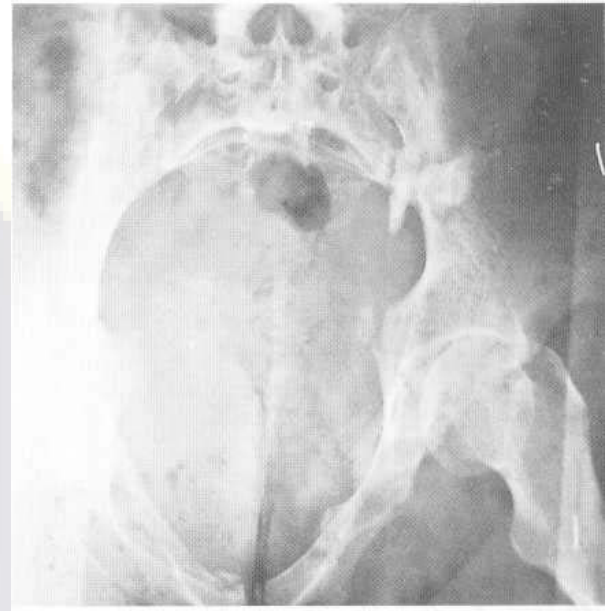


Fig. 44.37 Type II B lateral compression fracture. 'Horizontal' fracture of the right symphysis, and oblique fracture of the left iliac wing, arising from the sacroiliac joint. There is moderate medial displacement of the left anterior pelvis. (Reproduced with permission of Urban and Schwartzberg from Young and Burgess (1987).)

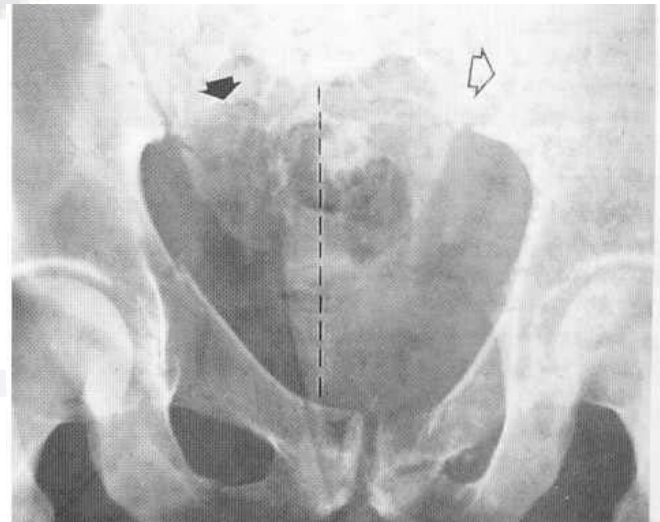


Fig. 44.38 Lateral compression Type III. There are crush fractures of the right sacrum (closed arrow) and left pubic rami. Note diastasis of the left sacroiliac joint (open arrow) and lateral displacement of the whole of the anterior pelvis to the left. Fractures of the right pubic rami are also seen.

ever, are in the vertical plane, in contrast to lateral compression fractures. This is demonstrated diagrammatically in Figure 44.30.

The more severe Types II and III fractures relate to increasing posterior ligamentous injury, and hence increasing instability (Figs 44.39-44.41). In Type II fractures, the anterior sacroiliac, sacrospinous and sacrotuberous ligaments are disrupted, allowing wide splaying of the anterior pelvis (Figs 44.39, 44.40). In Type III fractures, there is total disruption of the sacroiliac joint (Fig. 44.41). Fractures of the anterior and posterior acetabular pillars are common, and posterior hip dislocations are also associated, in contrast to lateral compression fractures, when the medial wall of the acetabulum is at risk (see above).

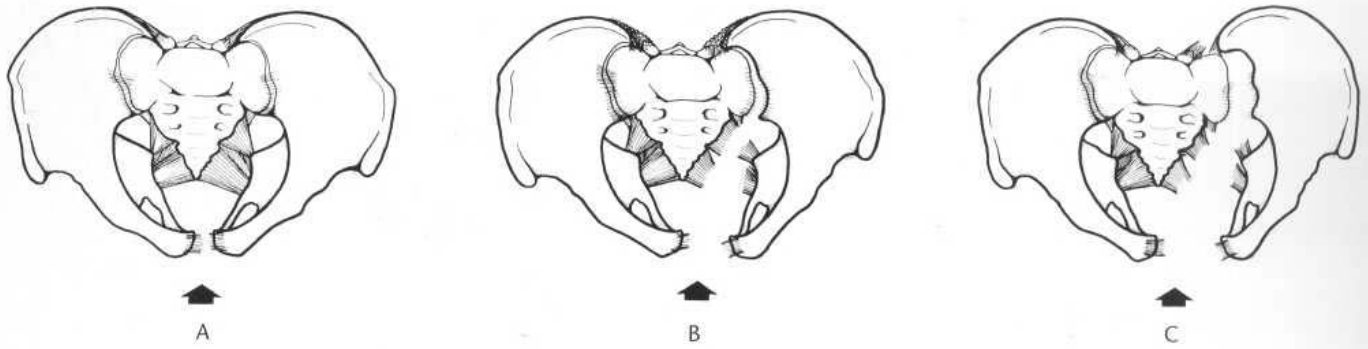


Fig. 44.39 Anteroposterior (AP) compression fracture classification. (A) Type I. Diastasis of the symphysis pubis only. (B) Type II. Diastasis of the symphysis pubis, disruption of the sacrospinous and sacrotuberous ligaments, and anterior sacroiliac ligament. (C) Type III. Total ligamentous disruption, including the posterior sacroiliac ligaments. (Reproduced with permission of Urban and Schwartzberg from Young and Burgess (1987).)

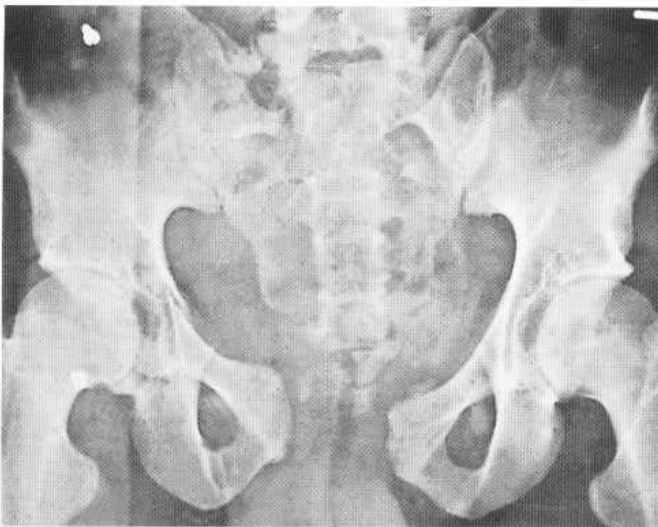


Fig. 44.40 Type II AP compression fracture. There is wide diastasis of the symphysis pubis and anterior left sacroiliac joint.



Fig. 44.41 Type III AP compression fracture. CT scan demonstrates complete diastasis of the left sacroiliac joint.

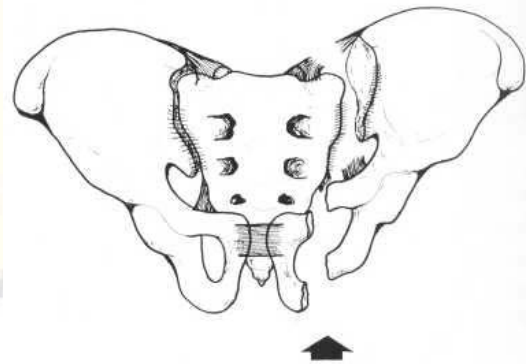


Fig. 44.42 Vertical shear fracture pattern. A superiorly directed force disrupts the left hemipelvis, with diastasis (or fracture) through the left sacroiliac region, and fractures of the pubic rami (or symphysis diastasis). The separated pelvic fragment containing the acetabulum is displaced superiorly. (Reproduced with permission of Urban and Schwartzberg from Young and Burgess (1987).)

Vertical shear fractures

These commonly result from falls from a height. Fractures occur through the pubic rami and posterior pelvis, and are vertically oriented (Fig. 44.42). The large lateral hemipelvic fracture fragment containing the acetabulum is displaced superiorly.

Fractures of the posterior and superior acetabula are often associated with superior displacement of the femoral head. These injuries are associated with fractures of the lumbar vertebrae and calcaneus.

Mixed fracture pattern

These arise from a combination vector of the forces causing injury, and give rise to a mixed pattern of fracture, the commonest being a mixed anterolateral pattern (Fig. 44.43), with signs of both AP and lateral compression.

Straddle fractures

It is questionable whether this term should be used at all, as it gives no useful indication about the underlying mechanism of injury. Multiple fractures of the pubic rami can occur from lateral, AP compression or vertical shear fractures and clues should be sought to the likely force vector, and to associated injuries (Fig. 44.44).

Isolated fractures

Isolated fractures of the sacrum, iliac crest or inferior pubic ramus may occur, as these do not violate the integrity of the pelvic ring. Such sacral fractures are usually transverse and may be difficult to diagnose without a lateral view. Single fractures of a pubic ramus can be seen, resulting from a direct blow. However this is a rare occurrence, and additional injury to the pelvis should always be excluded.

Avulsion injuries

Avulsion injuries of the pelvis occur most commonly as the result of the muscular exertion during sporting activities. The anterior superior iliac spine (sartorius), anterior inferior iliac spine (rectus femoris) and the ischial tuberosity (hamstrings) are the commonest sites.

Acetabular fractures

Acetabular fractures in general involve one or more of four regions: the posterior rim, the posterior pillar, the anterior pillar or the



Fig. 44.43 Combined fracture pattern. (A) AP and lateral compression. This type of injury gives fracture patterns of both AP and lateral compression, such as in (B), where there are 'horizontal' fractures of the left pubic rami, indicating lateral compression, but disruption of the left sacroiliac joint, indicating AP compression.

quadrilateral plate. As expected, fractures of the posterior ring are usually caused by posterior dislocation of the femur (Fig. 44.45). These are commonly associated with cortical fractures of the ante-



Fig. 44.44 The so-called 'straddle' fracture is not due to straddling, but, in this case, to AP compression. Diastasis of the left sacroiliac joint indicates a Type III AP compression fracture.



A



B

Fig. 44.45 (A) Posterior acetabular rim fracture shown on CT. There has been a posterior hip dislocation. A characteristic defect described by Richardson et al (1990) is seen in the anterior femoral head (arrow): it is similar to the Hill-Sachs deformity of the humeral head in anterior humeral dislocations. (B) This type of dislocation may lead to post-traumatic avascular necrosis, as shown on this coronal MRI image.

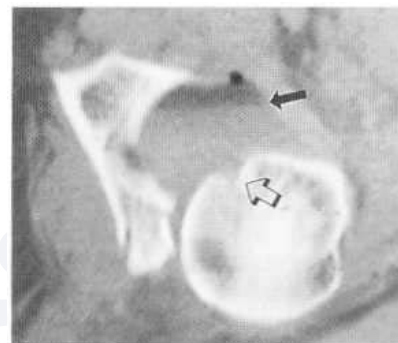


Fig. 44.46 Posterior acetabular pillar fracture. CT scan demonstrates an extensive fracture of the posterior acetabular pillar, again usually associated with posterior hip dislocation. A fat-fluid level is seen in the joint (arrow), with a small collection of air anteriorly, probably a 'vacuum' phenomenon. The cortical femoral head defect is again seen (open arrow).



Fig. 44.47 Comminuted right acetabular fracture. CT indicates involvement of predominantly the quadrilateral plate, with disruption of the medial articular surface. A fracture through the anterior rim of the left acetabulum is also seen.

rior femoral head. Fractures of the posterior pillar may also be seen with posterior dislocations of the femur (Fig. 44.46), and, together with fractures of the anterior pillar, are common in AP compression fractures of the pelvis. By contrast, fractures involving the quadrilateral plate are usually associated with lateral compression forces (Fig. 44.36). Undoubtedly CT provides the most detailed information about the fracture (Fig. 44.47), and there is a trend

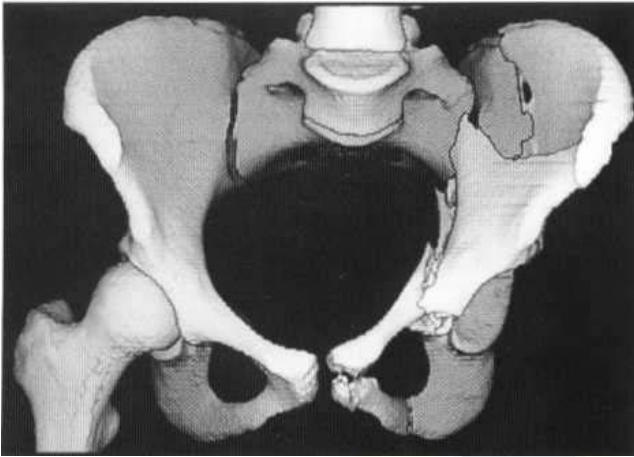


Fig. 44.48 Three-dimensional reformatting of a fracture of the left pelvis and acetabulum, with computerised disarticulation.

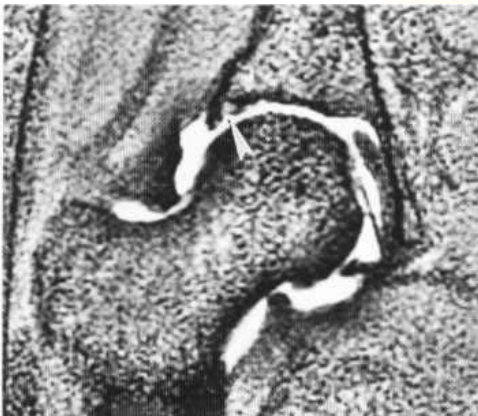


Fig. 44.49 MR image of a superior labral tear of right acetabulum. T₁-weighted image (fat suppression and intra-articular gadolinium) demonstrates irregularity of the superior labrum (arrowhead). (Courtesy of William Conway, MD.)

towards 3D imaging of these fractures. The real advantage of conventional CT over plain radiography lies in its ability to detect small bone fragments within the joint space. 3D CT has been shown to miss small undisplaced fracture lines and intra-articular fragments, although it provides a dramatic representation of the overall fracture and orientation of fragments (Fig. 44.48).

MRI also has a role to play, particularly with its ability to detect avascular necrosis (see Chapter 9) (Fig. 44.45), or injury to the internal structures, such as labral tears (Fig. 44.49).

It should be reiterated that ultra-fast multislice CT scanning may have a significant role to play in the management of acute trauma. A single multislice scan through the pelvis, particularly if done in conjunction with IV contrast, will not only provide rapid assessment of the pelvic ring, but can provide a high-quality CT angiogram, and evaluate the pelvic soft-tissue structures, in less than 10 seconds, thus potentially diagnosing not just bone, but vascular and soft-tissue injury.

The lower ribs are commonly fractured, often from relatively minor trauma. Pneumothorax and haemothorax may be associated, although they may be missed on supine radiography, which is often performed initially in the trauma setting. An upright film is preferred and should be obtained if possible, as pneumothorax or effusion are the important diagnostic features of rib fractures. Plain radiographic evaluations of the ribs themselves is of doubtful clinical value.

Fractures of the first and second rib arc usually from major trauma, and serious associations including pneumothorax, haemopneumothorax, ruptured subclavian artery, pneumopericardium and tracheobronchial fistula may be seen.

The shoulder and upper arm

The clavicle

Fractures of the clavicle involve the middle third in 80%, the outer third in 15% and the medial third in 5% of cases. Overriding of fragments and inferior displacement of the lateral fragment are common. Specific views however may be necessary to visualise the fracture. Fractures of the outer third are divided into two types, those in which disruption of the coracoclavicular ligaments does not occur (Type I) and those in which it does (Type II). Type II fractures are associated with greater displacement and a higher incidence of non-union.

The scapula

Fractures of the scapula are relatively rare, comprising only 1% of all fractures. They usually occur from major direct blows, and thus are commonly associated with other injuries, frequently of the ribs and clavicle. They may occur in any of the anatomical regions of the scapula, but are most common in the body (50-70%). They are



Fig. 44.50 Anterior dislocation of the shoulder. (A) The humeral head lies medial and inferior to the glenoid in the subscapular fossa. (B) MR scan (T₁-weighting) following anterior dislocation demonstrates an area of decreased signal, indicating subarticular bone 'bruising', possibly leading to the later radiographic appearances of a Hill-Sachs deformity.

not always appreciated clinically in the multitrauma setting, and may be difficult to see on a supine chest radiograph, even with careful inspection. Fractures of the glenoid rim occur in approximately 20% of shoulder dislocations. Isolated fractures of the spinous process are rare. Fractures of the coracoid process may occur from anterior humeral dislocations, or from avulsion injuries (coracoclavicular ligament, coracobrachialis), and may also be seen from shotgun or rifle recoils.

Dislocations

Dislocations around the shoulder are relatively common and usually involved the humeral head or acromioclavicular joint. The humerus is most commonly dislocated anteriorly (95%), or in practice, anteriorly, medially and inferiorly, coming to lie inferior to the coracoid process (Fig. 44.50). This may cause a cortical impaction both of the superior posterior aspect of the humerus (hatchet or Hill-Sachs deformity) (Fig. 44.51), and inferior aspect of the glenoid, or may give rise to injury of the anterior portion of the glenoid labrum (Bankart lesion) (Fig. 44.52). Although more common after multiple or recurrent dislocations, the Hill-Sachs defect can occur after a single episode, and merely represents an osteochondral fracture. Anterior dislocations present no diagnostic difficulty.

Posterior dislocations, however, may be difficult to appreciate, although they should not be missed. In general, they can be appreciated on the AP view by persistent internal rotation of the humerus

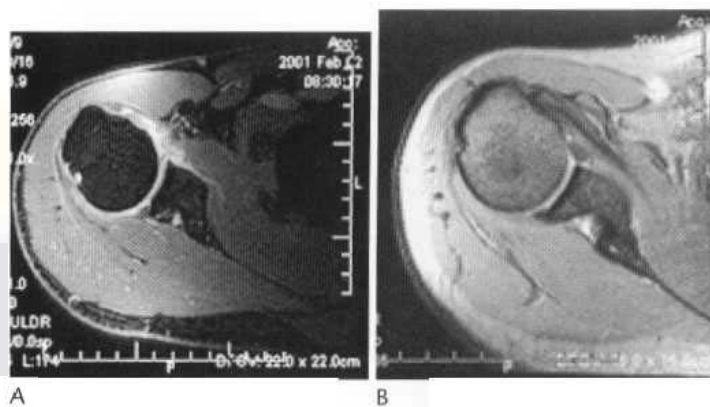


Fig. 44.52 (A) Axial fat saturated sequence shows labral disruption as well as an osseous defect in the posterior humeral head, indicating a mild Hill-Sachs deformity not to be confused with the rate Buford complex (B) where the labrum is absent, with a hypertrophied middle glenohumeral ligament.



Fig. 44.53 Posterior dislocation of the shoulder. Note the circular appearance of the humeral head and the lack of parallelism between this and the glenoid fossa. The injury followed a severe electric shock causing muscle spasm, which had also precipitated compression fractures of the fifth and sixth thoracic vertebral bodies.



A



B

Fig. 44.51 Recurrent anterior dislocation of the shoulder. The characteristic defect is well shown in the axial projection (A). A large defect of this nature can even be visualised clearly in the AP projection, but it is rarely possible to identify small defects on a simple frontal projection; a film in 60° internal rotation or a Stryker view (B) is required.



Fig. 44.54 Luxatio erecta. An unusual inferior dislocation of the humerus, which is 'locked' in abduction.

and asymmetry of the glenohumeral joint (Fig. 44.53). An axillary view may be impossible to obtain, but a transthoracic or 'swimmers' view or oblique (Y) view will confirm the diagnosis.



Fig. 44.55 Dislocation of the acromioclavicular joint following a fall on the point of the shoulder. The deformity is accentuated by examination in the erect position with weights being carried in both hands.

An unusual inferior dislocation (*luxatio erecta*) is caused by severe hyperabduction of the arm, whereby the humeral head impinges upon the acromion, which in turn acts as a fulcrum and causes an inferior displacement of the humeral head with the arm 'locked' in abduction (Fig. 44.54).

Acromioclavicular separation is usually the result of a fall on the outstretched arm or point of the shoulder. The importance of acromioclavicular dislocation lies in the trauma to the coracoclavicular ligament. This injury has been classified as sprain (Grade I), subluxation (Grade II) and dislocation (Grade III) (Fig. 44.55). Grade III injuries are in general obvious on plain radiography, with both acromioclavicular, and coracoclavicular separation. In Grade II injuries, stress views with weight bearing may be needed. In



Fig. 44.56 Fracture of the surgical neck of the humerus: axial view. There is marked displacement of the distal humerus, with the comminuted fracture extending into the humeral head.

Grade I injuries, mild widening of the acromioclavicular space, but not the coracoclavicular space, may be seen on stress views.

Humerus

Most injuries result from falls on the outstretched arm, particularly in elderly (osteopenic) women. Fractures of the surgical neck or greater tuberosity are the commonest injuries. Spiral and oblique fractures are common, usually with displacement or angulation of the distal fragment (Fig. 44.56), often requiring open fixation. Radial nerve injury occurs in up to 30% of cases.

Intra-articular fractures may be mild, as in the Hill-Sachs lesion, or severe, leading to fragmentation and intra-articular bone fragments. A 'drooping' shoulder may be seen, possibly as a result of capsular, muscular and neurological factors. Osteonecrosis has been reported in up to 50% of cases.

Rotator cuff and labra

Rotator cuff and labral injuries

This is the term applied to the conjoined tendons of the supraspinatus, infraspinatus, subscapularis and teres minor muscles. The rotator cuff passes between the humeral head and acromion before inserting into the greater tuberosity of the humerus. It separates the glenohumeral joint from the subdeltoid bursa. Ruptures, either partial or complete, may be diagnosed by arthrography, although ultrasound and MRI are gaining popularity as diagnostic tools, and where available, are the method of choice for evaluating the rotator cuff (Fig. 44.57).

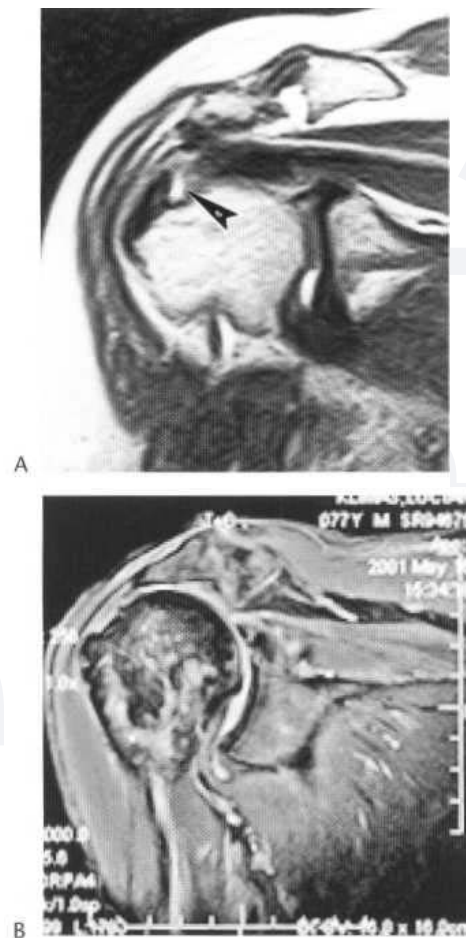


Fig. 44.57 MRI rotator cuff injury. Paracoronal (A) and parasagittal (B) Complete tear of supraspinatus, with retraction of the muscle belly and loss of acromiohumeral joint space.



Fig. 44.58 SLAP injury: T₂-weighted coronal image from MR arthrography demonstrates high signal contrast penetrating a defect in the superior labrum (small arrowhead). Not to be confused with a normal, sublabral recess, into which the tear extends (large arrowhead).

MRI has also become the most acceptable non-invasive way with which to examine the internal structure of the shoulder, with its ability to define disruptions of the internal ligaments and even small tears of the labra, whether involving the commonly injured anterior labrum, the posterior labrum, or even the superior labrum, as in the SLAP (superior labrum anterior posterior) injury (Fig. 44.58). However, care must be taken not to misinterpret areas of increased signal that represent normal structures, as tears. This is particularly

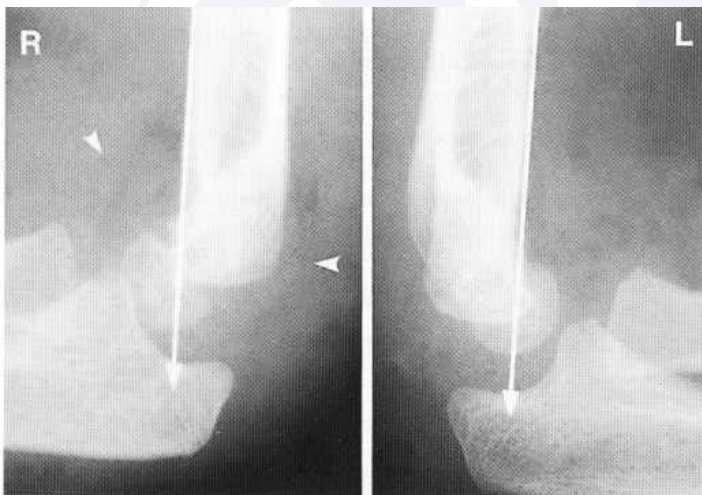


Fig. 44.59 Supracondylar fracture of humerus. The left humerus is normal; the line extending from the anterior cortex of the shaft passes through the middle third of the capitellum. A similar line on the right cuts the posterior third of the capitellum, indicating the anterior displacement of the fragment. A haemarthrosis of the right elbow joint displaces both fat pads.

true of the normal recesses that may be found between the labra, and articular cartilage in the anterior, and superior labra. Developmental absence of a portion of the anterior labrum is also seen in the *Beuford complex*.

The elbow

Fracture of the radial head is the commonest elbow injury in adults, usually occurring as a result of a fall on the outstretched arm. The fracture line may not be seen initially, but an elbow effusion is a good warning sign, warranting immobilisation and repeat radiograph in 7-10 days.

Olecranon fractures result from falls onto the point of the elbow, or avulsions of the triceps insertions. They must be distinguished from the unfused ossification centre in children and young adults.

Supracondylar fractures

Supracondylar fractures are the commonest elbow injury in children (60%), resulting from a fall on the outstretched hand. No fracture line may be seen initially on the radiograph, but haemarthrosis with elevation of the anterior and/or posterior fat pads is highly suggestive. Volar displacement of the capitellum is also a helpful sign (Fig. 44.59). These fractures, with associated vascular damage, may be of importance in the development of *Volkman's ischaemia* of the forearm. The second most common elbow fracture in children is that of the lateral epicondyle, although medial epicondylar fractures are also seen (Fig. 44.60).

Forearm fractures

Fractures of the bones of the forearm are extremely common, particularly of the radial head, olecranon process, distal radius and ulna. The forearm effectively acts as a ring structure and apparent single fractures may be associated with additional injury, either ligamentous or bony. This 'closed ring' concept explains double forearm fractures (Fig. 44.61), i.e. Galeazzi fractures of the radius with distal ulnar dislocation (Fig. 44.62), and Monteggia fractures of the ulna with radial head dislocation (Fig. 44.63). It is therefore essential to examine the wrist and elbow carefully for additional injury in 'single bone' forearm fractures.



Fig. 44.60 Avulsion of medial epicondyle of the humerus. The centre for the lateral epicondyle has ossified in this child, therefore the medial epicondyle should also have appeared. It is not in its normal location but lies within the medial compartment of the elbow joint.



Fig. 44.61 Fractures through both forearm bones are seen. Apparent 'shortening' of the distal ulna, with marked angulation, suggests distal radioulnar joint injury.



Fig. 44.62 Galeazzi fracture. Dislocation of the distal ulna accompanies the radial fracture.



Fig. 44.64 Fracture of the distal radius with dorsal angulation of the distal fragment. Although frequently referred to as Colles' fracture, the extension of the fracture to the articular surface, seen on the AP view, indicates that this is a Barton's fracture.



Fig. 44.63 Monteggia fracture-dislocation. There is a comminuted fracture of the ulna with dislocation of the radial head.



Fig. 44.65 Although commonly referred to as a Smith's fracture, the involvement of the articular surface indicates that this should more correctly be called a reverse Barton's fracture.

Injuries around the wrist

As mentioned above, injuries of the distal radioulnar joint are commonly associated with fractures of the radius and ulna, either alone or in combination. Injury to the wrist, and in particular disruption of the triangular fibrocartilage complex (TFCC), should be excluded in forearm fractures. TFCC disruptions may also be seen following a fall onto the outstretched hand. Arthrography is commonly used in evaluating TFCC disruptions, although MRI is gaining in popularity as a method of evaluating the wrist joint. The TFCC is, in general, well seen on MRI, although consistent visualisation of the intercarpal ligaments has been less successful, and requires the highest quality of images.

The distal forearm is one of the commonest sites of fracture in the entire body, and most fractures are associated with eponyms. In *Colles' fracture*, the distal radius is fractured and angulated dorsally, giving rise clinically to the 'dinner-fork' deformity of the wrist (Fig. 44.64). The ulnar styloid is fractured in over 50% of cases, and there is almost invariably distal radioulnar dissociation.

Smith's fracture is the reverse of the Colles' fracture, with volar angulation of the distal fragments of the radius. In *Barton's fractures*, the fracture line extends through the dorsum of the distal radius to involve the articular surface. If the volar radial rim is involved, this is a reverse Barton's fracture (Fig. 44.65).

Fractures of the carpus

The scaphoid bone is the most common carpal bone to be fractured. Once again, initial radiographic examination may be negative and a follow-up X-ray should be performed in 7-10 days after immobilisation if there is a clinical suspicion (Fig. 44.66). Alternatively, a radionuclide bone scan may be helpful. Non-union and osteonecrosis of the proximal fragment are important complications, particularly in fractures of the proximal scaphoid, as the vascular supply enters in the middle of the bone. Dorsal avulsion fractures of the triquetrum are the second most common and may be appreciated best on the lateral view. The other carpal bones



Fig. 44.66 Scaphoid fracture. There is a mild cortical irregularity of the radial side of the waist of the scaphoid. A faint fracture line extends through the waist.

are only rarely injured, except for the hamate, the hook of which may be detached acutely by blows on the proximal palm of the hand, or by chronic trauma, such as from holding a tennis racquet or golf club.

Dislocation of the carpus

Dislocations of the carpus are complex, but are best appreciated by understanding two important concepts.

1. On the postero-anterior view, two major areas define the carpal relationship (Fig. 44.67): the proximal and distal carpal lines, following the proximal and distal margins of the scaphoid, lunate and triquetrum respectively. These lines should be roughly parallel, and the intercarpal joint spaces should be approximately equal.



Fig. 44.67 Normal carpal relationship. The proximal and distal carpal lines define the normal carpal relationship on the PA projection.

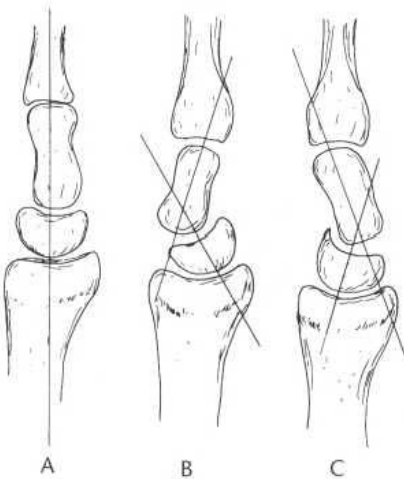


Fig. 44.68 (A) Normal alignment of the wrist allows a continuous line to be drawn through the radius, lunate and capitate. (B) Abnormal alignment: palmar flexion instability (VISI). The lunate is rotated towards the palmar surface of the wrist, with the capitate rotated towards the dorsal surface. (C) Dorsi-flexion instability (DISI)-the converse of B.

2. On the lateral view of the normal wrist in its neutral position, a straight line can be drawn through the long axis of the radius, lunate and capitate (Fig. 44.68). This should intersect a line drawn along the long axis of the scaphoid at 30-60° (Fig. 44.69). A variation of the angle of any of these lines indicates carpal instability. Other patterns of instability are triquetrohamate instability (dissociation) and triquetrolunate dissociation, usually diagnosed by abnormal motion on fluoroscopy.

Examination of carpal trauma has led to the concept of two 'injury arcs' in the wrist (Fig. 44.70), enabling a sequence of injuries to be predicted. The sequence usually begins on the radial side with rotary subluxation of the scaphoid and scapholunate dissociation (see below). Stage I is the perilunate dislocation (see below), following failure of the radiocapitate ligament. In Stage III, injury to the radiotriquetral ligament and dorsal radiocarpal ligaments gives rise to triquetral malrotation and triquetrolunate dissociation, and in Stage IV injury, there is disruption of the dorsal radiocarpal ligament, allowing complete dislocation of the lunate.

In lunate dislocation, the normal anatomy of the proximal carpal row is lost, and the lunate is usually seen to overlap the capitate, hamate and triquetrum on the PA view, also taking on a triangular, rather than a rectangular shape (Fig. 44.71). On the lateral projection, the lunate is seen overlying the volar aspect of the wrist, in an abnormal orientation.

In perilunate (± transcapitoid fracture) dislocation, the whole of the carpus (minus the proximal scaphoid pole in trans-scaphoid

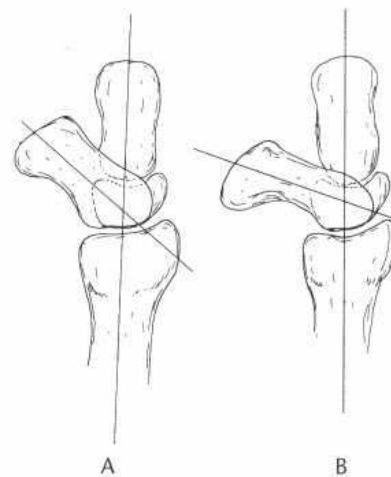


Fig. 44.69 (A) In the normal wrist, the scaphoid long axis at approximately 45° (30-60°). (B) Rotary subluxation: the long axis of the scaphoid is tilted in a volar direction.



Fig. 44.70 Arcs of injury of the wrist. 1 = The greater arc: pure injury of the greater arc gives rise to a transcapitoid, transcapitate, transhamate and triquetrolunate dislocation. 2 = The lesser arc: injury here gives rise to lunate or perilunate dislocation.

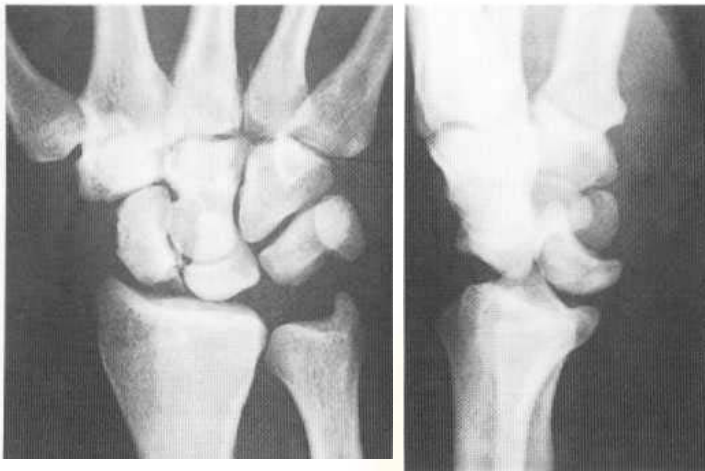


Fig. 44.71 Dislocation of the lunate. In the anteroposterior projection the lunate bone appears to be triangular instead of quadrilateral in shape, and the lateral projection shows clearly that it is displaced forwards. The distal concavity no longer contains the base of the capitate. Because this appearance is perhaps intermediate between a lunate and a perilunate dislocation, it is better referred to as a dorsal midcarpal dislocation. A chip fracture of the proximal scaphoid is also present.



Fig. 44.72 (A,B) Perilunate dislocation of the carpus. With the exception of the lunate, the whole of the carpus has been dislocated dorsally in relation to the radius. Both the radial and ulnar styloid processes have been fractured. Note loss of articulation between lunate and adjacent carpal bones.

injuries) is dislocated posteriorly with respect to the lunate. This is usually evident on the PA view, but again is clear on the lateral projection (Fig. 44.72).

Scapholunate dissociation is identified by widening of the scapholunate joint, often exacerbated on clenching the fist (Terry-Thomas sign) (Fig. 44.73). This may be seen in rotational (rotatory) dislocation of the scaphoid.

Although arthrography has traditionally been the method of choice for examining the intercarpal ligaments, high quality MRI scanning is gaining acceptance. When arthrography is performed, some authors advocate injection of all three wrist compartments, although careful examination with video fluoroscopy after injection of the radiocarpal joint alone will define the vast majority of injuries (Fig. 44.74).



Fig. 44.73 Scapholunate dissociation: 'Terry-Thomas' or 'tooth gap' sign. There is wide separation of the scaphoid and lunate.



Fig. 44.74 Intercarpal ligament disruption: arthrogram. Injection of the radiocarpal joint has resulted in filling of the intercarpal joint as well. Contrast medium is seen passing between the lunate and triquetrum (arrowhead), indicating ligamentous disruption.



Fig. 44.75 Bennett's fracture-dislocation. The articular surface of the base of the first metacarpal is involved and the main portion of the bone is displaced proximally in relation to the trapezium.

The hand

Hand injuries are common and usually present no diagnostic difficulty.

'Bennett's fracture' is a fracture-dislocation of the base of the first metacarpal with involvement of the articular surface, usually associated with 'dislocation' of the major fragment (Fig. 44.75).

Another important injury in the thumb is avulsion of the ulnar aspect of the base of the proximal phalanx, clue to forced radial or posterior hyperextension. This injury is due to avulsion of either the ulnar collateral ligament or the adductor pollicis and creates instability.



Fig. 44.76 Boxer's fracture: a fracture of the distal aspect of the fifth metacarpal, with volar angulation of the distal fragment.

ity and loss of forceful adduction if left untreated. Although named the 'mechanical bull' thumb, this is more common in skiing injuries, from falling into snow without releasing the ski pole. The 'boxer's' fracture of the fifth metacarpal is a common injury presenting in accident and emergency departments (Fig. 44.76).

The lower limb

Fracture of the femoral neck and intertrochanteric fractures are common injuries following a fall, particularly in the elderly when osteoporosis is present (Fig. 44.77). Nevertheless, because of the age of many of the patients, underlying pathology such as metastasis should always be excluded. These fractures may be extremely difficult to define radiographically and radionuclide bone scan may be indicated, particularly with a strong clinical suspicion. A faint ill-defined linear density across the femoral neck, interruption of trabecular lines, and subtle cortical disruptions may be the only radiological signs.



Fig. 44.77 A fracture of the femoral neck may be identified as a lucency interrupting the trabecular pattern, and the femur is externally rotated distal to the fracture.

Fractures of the femoral shaft are almost always a sign of significant trauma, often in multitrauma victims (see Fig. 43.3). In trivial trauma, underlying pathology should always be suspected.

Fractures of the distal femur are frequently intra-articular and give rise to angulation of the distal fragments and disruption of the knee joint.

The knee and lower leg

Fractures around the knee include femoral fractures (see above), patellar fractures and tibial plateau fractures (Fig. 44.78). The only difficulty with patellar fractures may be in differentiating them from a bipartite patella when the fracture is single and involves the

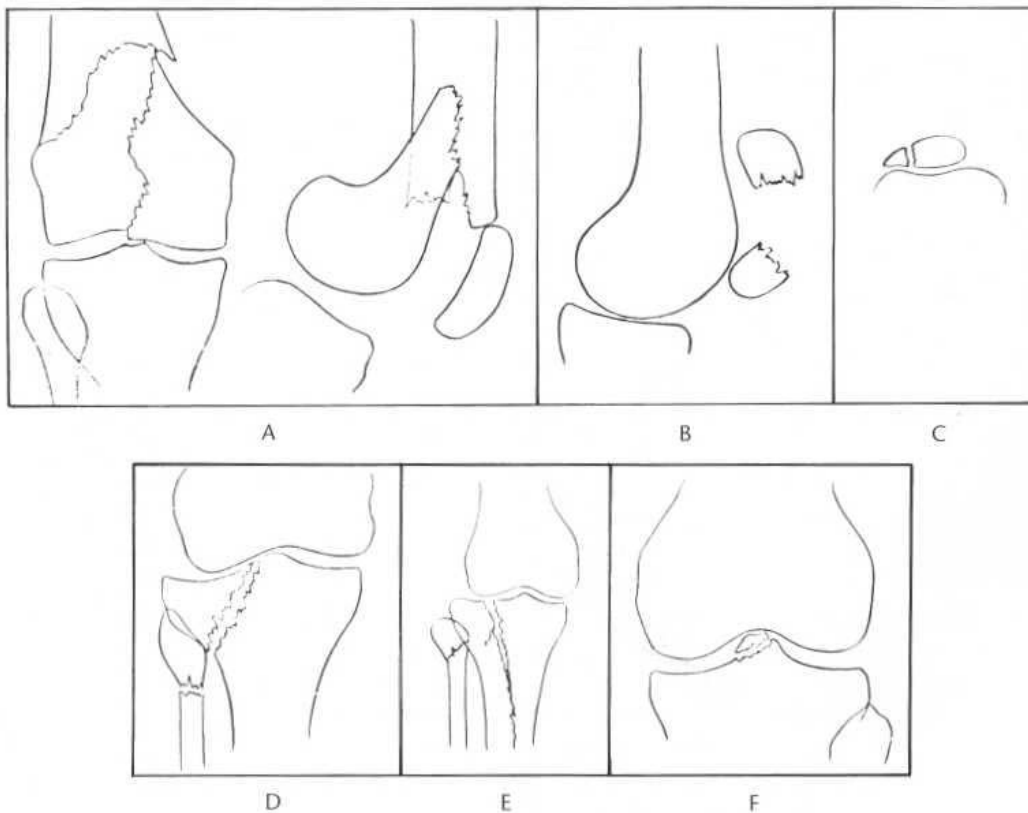


Fig. 44.78 Injuries of the knee and leg. (A) Supracondylar fracture of the femur with extension to involve the articular surface. (B) Transverse fracture of the patella with wide separation of fragments. (C) Vertical fracture of the patella visible only in the axial projection. (D) Fracture of the lateral condyle of the tibia and neck of fibula. This injury has resulted from forced abduction, with impact of the surface of the lateral femoral condyle upon the tibia. Involvement of the articular surface is minimal and this injury carries a good prognosis. (E) A more severe fracture of the lateral tibial condyle with a crack running downwards into the tibial shaft. This has been caused by complete rupture of the internal lateral ligament and the cruciate ligaments, so that the lateral margin of the femur has impacted upon the surface of the lateral tibial condyle to produce the injury. The articular surface is involved. The neck of the fibula is also fractured. (F) Avulsion injury to extrasynovial intercondylar region of tibia.

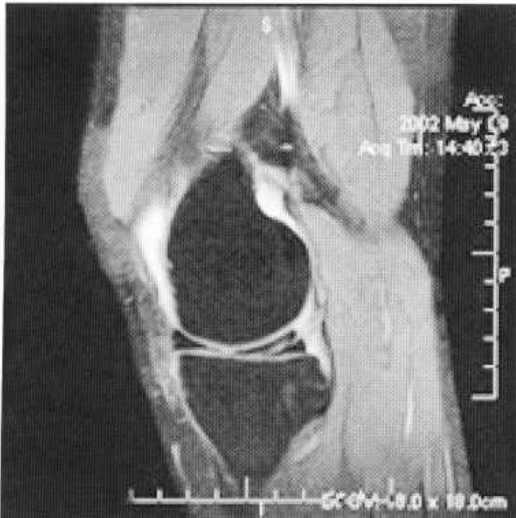


Fig. 44.79 MRI of tear. There is a linear area of increased signal extending through the meniscus to the inferior surface. These changes indicate a complete tear.

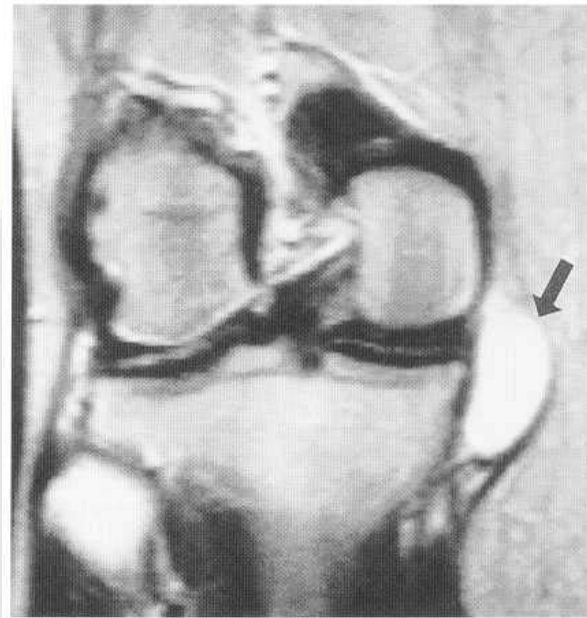


Fig. 44.82 Meniscal cyst: MRI (T₂-weighted). There is increased signal in a well-defined fluid collection (arrow) arising from the medial meniscus.



Fig. 44.80 MRI of anterior cruciate tear: There is loss of detail of the ligament, which is replaced by an amorphous collection of haematoma and debris.

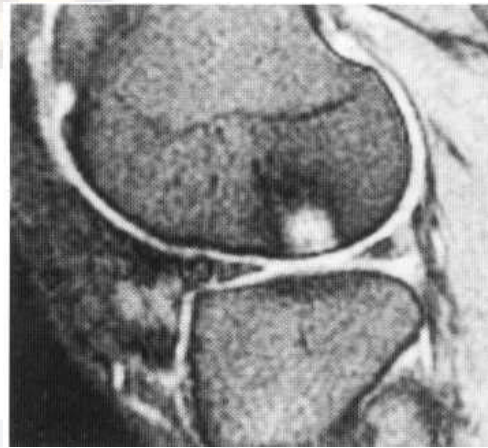


Fig. 44.83 Bone 'bruising' of the femoral condyle, following knee dislocation. MRI gradient-echo image, showing the typical appearances of a focal area of increased signal.

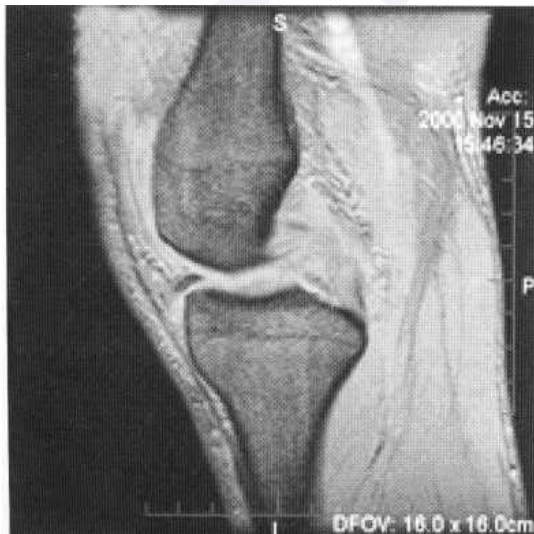


Fig. 44.81 Posterior cruciate tear: There is loss of detail, and structure of the ligament.

superior margins. This should be evident clinically and is usually clear radiographically although confusion may arise.

Fractures of the tibial plateau are obvious in general cross-table lateral radiograph which demonstrate a fat-fluid level of

lipohaemarthrosis in the suprapatellar bursa, indicating an intra-articular process (see Fig. 43.6). Tomograms may be needed in tibial plateau fractures to determine any depression of fragments. CT is also gaining popularity as a method of evaluating the extent of injury. Injuries to the menisci traditionally have been examined by arthrography. However, in most centres MRI has superseded arthrography by virtue of its improved sensitivity and patient comfort. Not only can it define abnormality of the menisci (Fig. 44.79), but it can also identify abnormality of the supporting ligaments (Figs 44.80, 44.81), surrounding soft tissues (Fig. 44.82) and bony structures (Fig. 44.83).

Fractures of the shaft of the tibia are usually oblique or spiral, although transverse fractures also occur. There is invariably an associated fracture of the fibula, again indicating the association of double injuries with bony 'ring' structures. Complications of tibia] fractures include a high incidence of open injuries and delayed union, usually the result of high-energy impact forces.

Stress fractures

These are found in those who inflict chronic stress on the leg (joggers, ballet dancers, etc.). The proximal shaft is the commonest site, but they may occur at any site. Pain and increased uptake on bone scan are the earliest signs. Periosteal reaction follows. Chronic stress fractures exhibit abundant surrounding sclerosis (see Fig. 43.18). Early diagnosis can be made by MRI, before radiographic changes become apparent (see Fig. 43.17).

The ankle and foot

The most detailed (and complex) classification of ankle fractures, that of Lauge-Hansen, is based on classifying the injury according to the nature of the causative force, much as in the pelvis and spine. However, as well as using the parameters of external rotation, abduction, adduction and dorsiflexion, the classification is complicated by whether the foot is in pronation or supination at the time of injury. A similar system regards ankle injuries as being the result of forced supination or pronation, and forced adduction or abduction with some variation being imparted by external (or rarely internal) rotation (Fig. 44.84) when injuries to the tibial plafond (usually posterior) may result. In practice, the injury patterns obtained using this less complicated system are the same as those described in the Lauge-Hansen classification.

Radiographically, symmetry of the ankle mortise should be sought, as asymmetry may be the only indication of significant ligamentous injury. In addition, the nature of the injury to the

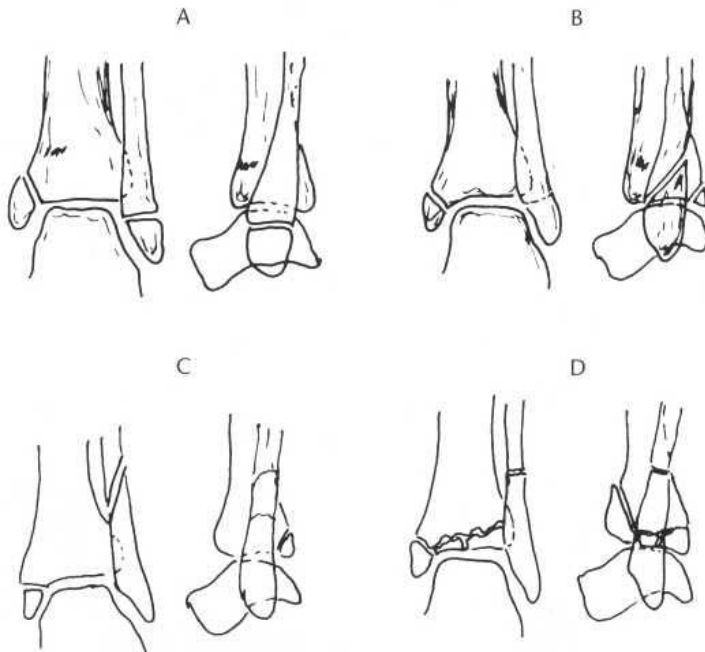


Fig. 44.84 Diagram of the major varieties of injuries of the ankle. (A) Adduction/inversion injury of the ankle. The fracture on the tension side (lateral malleolus) is transverse. The medial malleolar fracture is oblique. (B) Additional external rotation gives rise to an oblique or spiral fracture of the fibula ± fracture of the posterior aspect of the tibial plafond. (C) Abduction (eversion) injury. The fracture on the tension side (medial malleolus) again is transverse; with external rotation, fracture of the posterior aspect of the tibial plafond may occur, as shown. (D) Forced dorsiflexion. Comminution of the tibial plafond is expected, particularly involving the anterior aspect.

malleoli (i.e. whether horizontal or oblique) will indicate the side from which the force of injury was derived, the horizontal fracture occurring on the side of injury, and the oblique fracture on the opposite side. If no fracture is present, stress views may be indicated, to evaluate for ligamentous damage. Again, however, MRI is gaining in popularity for evaluating the ankle, due to its ability to demonstrate ligamentous injury, particularly the internal ligaments, and injuries to the surrounding tendons (Fig. 44.85).

MRI is also the method of choice for evaluating the tendons around the ankle and foot. Although injury to the Achilles tendon is usually readily seen, injury to the smaller tendons may also be appreciated.

Talar fractures are generally avulsions or fractures through the waist, usually as a result of forced dorsiflexion. These are often



Fig. 44.85 MRI of the ankle: rupture of the Achilles tendon. There is gross irregularity, and widening of the tendon above its insertion, with areas of increased signal, within and surrounding the tendon sheath. Normal low-signal-intensity tendon is not present in the expected region, due to muscle retraction.



Fig. 44.86 (A,B) Fracture-dislocation of the talus. There is a fracture through the waist of the talus, with complete dislocation of the posterior fragment.

Included in the first group are fractures of the ribs, scapula, Lisfranc joint, cervicothoracic junction and posterior spinal elements. All of these regions can be overlooked, particularly if the clinical details are sketchy, or if the radiographs are suboptimal. This is particularly true in multitrauma patients, where optimal imaging may be extremely difficult technically.

The thumb is also a notoriously overlooked area, and care must be taken to identify correct alignment (Fig. 44.89) and integrity of the bones. Avulsion injuries of the base of the proximal phalanx, at the attachment of collateral ligaments or tendons, are often missed. These usually involve the ulnar aspect as in avulsions of the adductor tendon in ski pole or steering wheel injuries, but can also involve the radial aspect (Fig. 44.90). These are potentially serious injuries, as if left untreated, stabilisation and power of the actions of the thumb may be lost.



Fig. 44.90 Radial collateral ligament avulsion of the thumb. Lateral radiograph shows some irregularity of the radial aspect of the base of the proximal phalanx of the thumb, missed on initial interpretation, possibly being mistaken for a sesamoid bone.



44.91



44.92

Fig. 44.91 Scaphoid fracture, not seen on the initial radiographs (A). Dedicated scaphoid view (B) clearly demonstrates the fracture.

Fig. 44.92 Minor stress fracture in the ankle: T₁-weighted coronal images (A/A and T₂-weighted image B demonstrate areas of linear abnormal signal within the inferior talus and superior calcaneus of this young gymnast with ankle pain. These are areas of linear decreased signal intensity on T₁ sequences, with markedly increased intensity on the T₂ sequences, indicating acute focal oedema.

Simple rib fractures are only of importance from the point of view of the associated pain, and undisplaced fractures without associated complications such as pneumothorax or haemothorax are of little additional significance. Pneumothorax and haemothorax however, may be a significant clinical problem, an indication of severe chest trauma, especially in multitrauma patients. They may also be missed on initial supine radiographs, and unless normality is clearly defined additional erect films should be obtained once the spine has been 'cleared'. These will prove more effective in defining the presence or absence of a pneumothorax or haemothorax, and will help to 'clear' the aorta if this was obscured on the supine film. As in so many areas, CT, especially multislice, may assume an even greater role in the diagnosis of chest injury.

Scapula fractures are frequently missed on initial radiograph, and may require special oblique views. Even so, non-displaced fractures can be difficult to see, and again, CT is the method of choice for evaluating the scapula if there is clinical suspicion of fracture.

Fractures and dislocations at C1, T1 and T2 can be very difficult to image with plain radiographs, especially in a multitrauma setting, where it may be impossible to see adequate bone detail due to technical difficulties in demonstrating the cervicothoracic junction adequately. In such settings, CT may be needed to fully evaluate the region, and is mandatory in any clinical setting where injury is suspected, or the patient's mental status is compromised and the region is not seen clearly.

As a rule, CT is becoming more and more valuable, not just for 'clearing' difficult areas, but, as the speed and capabilities increase, as a primary diagnostic tool. Modern multislice scanners can more reliably provide a greater detail than plain radiography, in a much faster time, and with greater patient comfort, and it is only a matter of time before they will become the primary method of investiga-

tion in many cases. Even today, however, in cases of skeletal trauma, a good rule is that in the event of clinical signs of injury, such as pain, loss of motion or neurological deficit, if the plain radiographs are normal, CT scanning should be performed.

In the second group of potential missed fractures, Scaphoid, radial head and femoral neck fractures may be difficult or even impossible to see initially, even on adequate radiographs. Scaphoid fractures and radial head fractures can easily be missed on conventional films, and in the correct clinical setting, appropriate 'special' views should be obtained (Fig. 44.91). Stress fractures are also

usually occult initially, and careful correlation with a good clinical history is important. Secondary signs may be particularly useful in occult fractures in and around a joint, such as elevated fat pads caused by effusion in the elbow in fractures of the radial head or in supracondylar fractures of the humerus, and the pronator fat pad sign in injuries to the distal forearm and wrist. As mentioned in the relevant section above, additional studies such as further views, radionuclide bone scan, delayed radiographs (24 or 48 hours) or MRI may be needed, and should always be suggested in the appropriate clinical setting.

REFERENCES AND SUGGESTIONS FOR FURTHER READING

- Ashnian, C. J., Yu, J. C., Chung, C. B. (1997) Chance fractures; anteroposterior radiographic signs. *Emergency Radiology*, **14**, 320-325.
- Berquist, T. H. (1996) *MRI of the Musculoskeletal System*, 3rd edn. Philadelphia: Lippincott-Raven.
- Bloomberg, T. J., Nuttall, J., Stoker, D. J. (1978) Radiology in early slipped femoral capital epiphysis. *Clinical Radiology*, **29**, 657-667.
- Bohdort, K. (1996) Injuries at the articulating surface of bone. *European Journal of Radiology*, **22**, 22-29.
- Breitseher, M. J., Gaebler, C. (1997) Trauma of the wrist. **25**, 129-135.
- Bright, R. W. (1982) Partial growth arrest: identification, classification, and result of treatment. *Orthopedic Transactions*, **6**, 65-73.
- Daffner, R. H., Deeb, Z. L., Rothfus, W. E. (1986) Fingerprints of vertebral trauma—a unifying concept based on mechanisms. *Skeletal Radiology*, **15**, 518-525. Specially recommended.]
- Daffner, R. H., Deeb, Z. L., Rothfus, W. E. (1987) Posterior vertebral body line: importance in the detection of burst fracture. *American Journal of Roentgenology*, **148**, 93-98.
- Deutsch, A. L., Resnick, D., Mink, J. H., et al (1984) Computed tomography of the glenohumeral joint: normal anatomy and clinical experience. *Radiology*, **153**, 603-608.
- Deutsch, A. L., Klein, M. A., Mink, J. H., et al (1997) MRI imaging of miscellaneous disorders of the shoulder. *MRI Clinics Of North America*, **5**, 881-889. Specially recommended.]
- Dias, J. J., Stirling, A. J., Finaly, D. B. L., Gregg, P. J. (1987) Computerized axial tomography for tibial plateau fractures. *Journal of Bone and Joint Surgery*. **69B**, 84-89.
- Fernbach, S. K., Wilkinson, R. H. (1984) Avulsion injuries of the pelvis and proximal femur. *American Journal Of Roentgenology*, **137**, 581-586.
- Fielding, J. W., Hawkins, R. J. (1977) Atlanto-axial rotatory fixation (fixed rotatory subluxation of the atlanto-axial joint). *Journal Of Bone and Joint Surgery*, **59A**, 37-44.
- Foster, S. C., Foster, R. R. (1976) Lisfranc's tarsometatarsal fracture-dislocation. *Radiology*, **120**, 79-85.
- Gertzbein, S. D., Chenoweth, D. R. (1977) Occult injuries of the pelvic ring. *Clinical Orthopaedics*. **128**, 201-207.
- Gilula, L. A., Weeks, P. M. (1978) Post-traumatic ligamentous instabilities of the wrist. *Radiology*, **129**, 641-647.
- Goldberg, A. L., Rothfus, W. E., Deeb, Z. L., et al (1988) Impact of magnetic resonance on the diagnostic evaluation of acute cervicothoracic spinal trauma. *Skeletal Radiology*, **17**, 39-95.
- Greaney, R. B., Gerber, F. H., Laughlin, R. I., et al (1983) Distribution and natural history of stress fractures in US marine recruits. *Radiology*, **146**, 339-346.
- Harris, Jr, J. H., Harris, W. H. (1975) *The Radiology of Emergency Medicine*. Baltimore: Williams & Wilkins.
- Johnson, B. A., Tanenbaum, L. W. (1998) Contemporary spinal CT applications. *Neuroimaging Clinics Of North America*, **8**, 559-565.
- Judet, R., Judet, J., Letournel, E. (1964) Fracture of the acetabulum: classification and surgical approaches for open reduction. *Journal Of Bone and Joint Surgery*, **46A**, 1615-1631.
- Kosling, S., Dietrich, K., Steinecke, R. (1997) Diagnostic value of 3D CT surface reconstruction in spinal fractures. **7-1**, 61-66.
- Lauge-Hansen, N. (1954) Fractures of the ankle: genetic roentgenologic diagnosis of fractures of the ankle. *American Journal of Roentgenology*, **71**, 456-462.
- Milgram, J. W., Rogers, L. F., Miller, J. W. (1978) Osteochondral fractures: mechanisms of injury and fate of fragments. *American Journal of Roentgenology*, **130**, 651-656.
- Mirvis, S. E. (1989) Applications of MRI and 3-D CT in emergency medicine. *Annals of Emergency Medicine*, **18**, 1315-1321.
- Mirvis, S. E., Young, J. W. R. (1992) *Imaging in Trauma and Critical Care*. Baltimore: Williams & Wilkins.
- Mirvis, S. E., Young, J. W. R., Lim, C., Greenberg, J. (1986) Hangman's fracture: radiologic assessment in 27 cases. *Radiology*, **163**, 713-717.
- Pennal, G. F., Tile, M., Waddell, J. P., Garside, M. (1980) Pelvic disruption: assessment and classification. *Clinical Orthopaedics*, **151**, 12-23.
- Rajii, M., Firooznia, H., Golimbu, C. (1997) MR imaging of glenohumeral instability. *MRI Clinics Of North America*, **5**, 787-795.
- Reckling, F. W. (1982) Unstable fracture-dislocations of the forearm (Monteggia and Galeazzi lesions). *Journal of Bone and Joint Surgery*, **64A**, 857-863.
- Resnick, D. (ed) (1996) *Bone and Joint Imaging*, 2nd edn. Philadelphia: W. B. Saunders.
- Resnik, C. S., Gelberman, R. H., Resnick, D. (1983) Transscaphoid, triscapitate, perilunate fracture dislocation (scaphocapitate syndrome). *Skeletal Radiology*, **9**, 192-197.
- Richardson, P., Young, J. W. R., Porter, D. (1990) CT detection of cortical fracture of the femoral head associated with posterior inferior dislocation. *American Journal Of Roentgenology*, **155**, 93-94.
- Rogers, L. R. (1992) *Radiology of Skeletal Trauma*, 2nd edn. Edinburgh: Churchill Livingstone.
- Rosen, R. A. (1970) Transitory demineralization of the femoral head. *Radiology*, **94**, 509-514.
- Ryan, M. D., Taylor, R. F. K. (1982) Odontoid fractures. *Journal of Bone and Joint Surgery*. **64B**, 416-421.
- Salter, R. B., Harris, W. R. (1963) Injuries involving the epiphyseal plate. *Journal Of Bone and Joint Surgery*. **45A**, 587-622.
- Scott, W. J. R., Fishman, E. K., Magid, D. (1987) Acetabular fractures: optimal imaging. *Radiology*, **165**, 537-539.
- Sherman, O. H. (1997) MR imaging of impingement and rotator cuff disorders: surgical perspective. *MRI Clinics Of North America*, **5**, 721-727.
- Stoller, D. W. (1999) *MRI arthroscopy, and surgical anatomy of the joints*. Philadelphia: Lippincott-Raven.
- Templeton, P. A., Young, J. W. R., Mirvis, S. E., Buddemeyer, E. U. (1987) The value of retropharyngeal soft tissue measurement in trauma of the adult cervical spine. *Skeletal Radiology*. **16**, 98-104.
- Thomason, M., Young, J. W. R. (1984) Os odontoidem. Case report 261. *Skeletal Radiology*, **11**, 144-146.
- Tile, M. (1986) *Fractures Of the Pelvis and Acetabulum*. Baltimore: Williams and Wilkins.
- Waddell, J. P., Johnston, D. W. C., Neidre, A. (1981) Fractures of the tibial plateau: a review of ninety-five patients and comparison of treatment methods. *Journal of Trauma*, **21**, 376-381.
- Wang, S. C., Grattan-Smith, A. (1987) Thoracolumbar burst fractures: two 'new' plain film signs with CT correlation. *Australasian Radiology*, **31**, 404-409.
- Whitley, J. E. N., Forsythe, H. F. (1960) Classification of cervical spine injuries. *American Journal of Roentgenology*, **83**, 633-641. Specially recommended.]
- Young, J. W. R., Burgess, A. R. (1987) *Radiologic Management of Pelvic Ring Fractures*, Baltimore: Urban-Schwartzberg.
- Young, J. W. R., Resnik, C. S., DeCandido, P., Mirvis, S. E. (1989) The lamina space in the diagnosis of rotational flexion injuries to the cervical spine. *American Journal of Radiology*, **152**, 103-107.



نشر الکترونیکی
موسسه انتشاراتی
نوردانش

45

THE SOFT TISSUES

Jeremy P. R. Jenkins

with contributions from Janet Murfitt and Fritz Starer, Richard W. Whitehouse and W. Gedroyc

MRI IN SOFT TISSUES

MRI is the modality of choice for the evaluation of the musculoskeletal system, being particularly useful in the evaluation of trauma and infection and in the investigation of an indeterminate soft-tissue mass. It is superior to all other imaging techniques for the detection and characterisation of soft-tissue lesions, but should be combined with a plain radiograph for assessment of calcification/ ossification, adjacent cortical destruction/periosteal reaction. MRI has a multiplanar facility with high soft-tissue contrast resolution and discrimination, being able to differentiate muscle, tendon, cartilage, disc, menisci, synovium, nerves, vessels, fat, fluid, cortical bone and bone marrow on signal intensity appearances. The technique is painless and non-invasive, uses non-ionising radiation, and is particularly of value in patients with acute injury and in the assessment of children. The ability of MRI to show normality, including normal variants (Fig. 45.1), and exclude a soft-tissue mass with certainty is not to be underestimated.

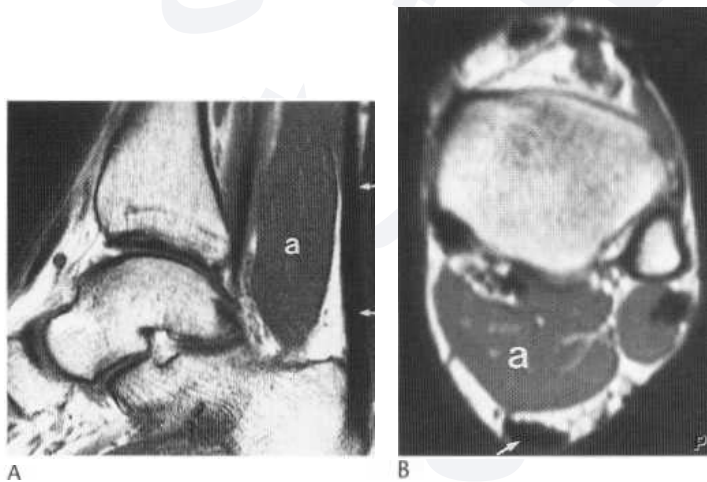


Fig. 45.1 Accessory soleus muscle (a) on (A) sagittal T₁-weighted SE and (B) transverse intermediate-weighted SE images. This accessory muscle is producing a soft-tissue mass anterior to the Achilles tendon (arrows) and was referred as a potential sarcoma. Symptoms of pain on exercise were due to claudication within the accessory muscle from poor vascular supply.

Technical aspects

The patient can be positioned supine, decubitus or prone in the magnet bore. The prone position can be used when pathology is suspected in the posterior compartment of the limb or body in order to prevent anatomical distortion. Positioning can be difficult when imaging the upper limb as it is important to try to place the part to be imaged as close to the centre of the field of view (magnet bore) where the magnetic field is most uniform (homogeneous). Newer magnet systems allow a greater off-centre field-of-view scanning for imaging the upper limb by the side of the patient, a more comfortable position than with the arm above the patient's head.

The image field of view is inversely proportional to spatial resolution, and should be optimised for the area of interest. It should be remembered, however, that a reduction in the field of view, although improving spatial resolution, is accompanied by a reduction in the signal-to-noise ratio and thus a surface coil should be utilised to offset this effect. The smallest surface coil should be used in order to achieve maximum signal-to-noise ratio with the highest spatial resolution. One proviso is in the assessment of soft-tissue tumours where the relationship of the mass to the adjacent joint should be ascertained. Some tumours are multiple or form satellite nodules usually confined to the compartment of origin. In these instances it is important that the whole limb or compartment be screened initially with further surface coil imaging of the presenting mass. Evaluation of lesions in the pelvis, thigh and shoulder girdle usually requires body coil imaging but surface coils can be utilised in addition to obtain higher spatial resolution images. Newer coil designs with multiple coil (phased) array allow the use of several coils simultaneously with consequent improved signal-to-noise ratio and a greater anatomical area of coverage than can be achieved by a single surface coil (Fig. 45.2).

There is a wide array of pulse sequences available utilising spin-echo (SE), inversion recovery (IR) and gradient-echo (GE) techniques, with or without fat suppression/saturation. In the majority of cases both T₁- and T₂-weighted images are obtained in at least two different imaging planes.

Fat suppression/saturation techniques are advantageous in the assessment of the musculoskeletal system. There are two different ways in which the fat signal can be suppressed-short tau inversion

recovery (STIR) and frequency specific (spectral) presaturation sequences. STIR is a complete sequence, and displays additive T₁ and T₂ contrast with fat suppression. being highly sensitive for the

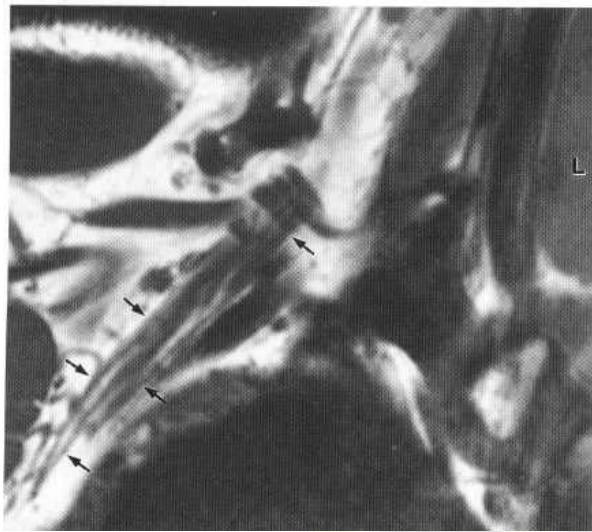


Fig. 45.2 Normal brachial plexus (arrows) on coronal-oblique T₁-weighted SE image.

detection of pathology and useful for characterising soft-tissue tumours of fatty origin (Fig. 45.3). The additive T₁ and T₂ contrast is a particular advantage with long T₁ tissues (e.g. cerebrospinal/joint fluid) appearing bright, which is opposite to that with conventional SE and GE sequences where long T₁ tissues are of low-signal intensity. A number of disadvantages, however, are apparent when using STIR imaging. The specificity for characterisation of a lesion is reduced when compared with T₁- and T₂-weighted images. The fat suppression is based on relaxation time values, and lesions with a similar relaxation time also show a suppression of signal. This includes haemorrhage and an enhancing lesion following gadolinium-chelate injection. Therefore STIR imaging should not be used following a contrast injection. Also, the fat relaxation values do also vary in different locations within the magnetic field and suppression of the fat may not be even throughout the area of interest, although STIR is preferable compared with spectral presaturation imaging if any susceptibility artefact (e.g. from post-surgical change or a prosthetic implant) is present (Fig. 45.4).

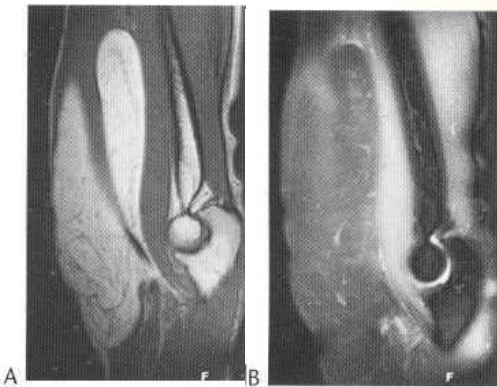


Fig. 45.3 Inter- and intramuscular lipoma between biceps brachii (superficial) and deeper brachialis muscles on sagittal (A) T₁-weighted SE and (B) fat-suppressed proton density-weighted TSE images.

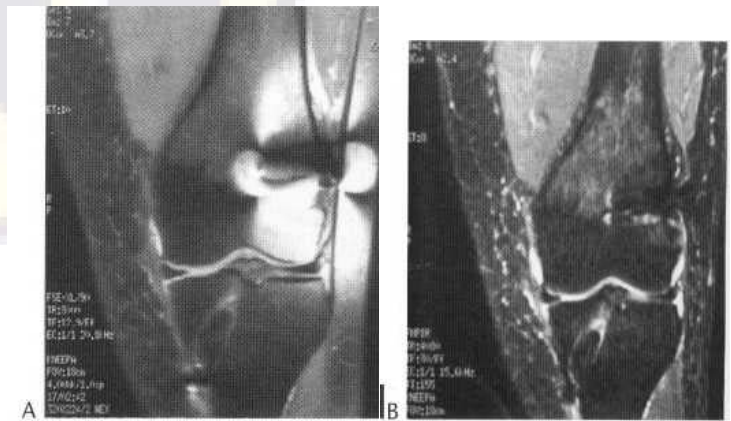


Fig. 45.4 Postsurgical artefacts from an ACL reconstruction on coronal (A) spectral fat-suppressed proton density FSE and (B) STIR images. Note the more pronounced artefacts in A compared with B.

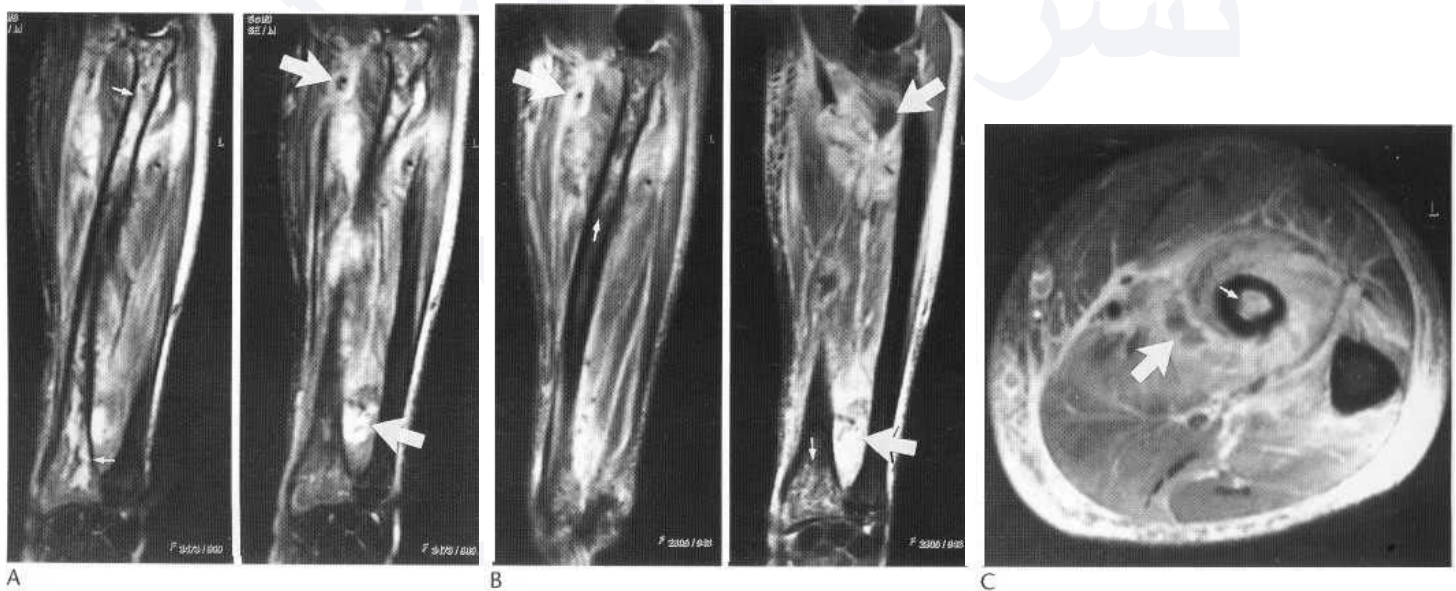


Fig. 45.5 Soft-tissue infection with abscess formation (straight arrows) and osteomyelitis of the radius (small arrows) in a 23-year-old male on (A) coronal-oblique T₂-weighted TSE, (B) coronal oblique, and (C) transverse post gadolinium-chelate T₁-weighted SE image with fat suppression. There is extensive diffuse high signal throughout the flexor and extensor muscle compartments, subcutaneous tissues of the forearm and radius. Note the similar appearance of the T₂- and, post contrast, T₁-weighted images.

Spectral presaturation imaging is frequency specific (dependent on the fact that fat and water protons precess at slightly different frequencies) and can be applied as a preparatory pulse to conventional T₁- and T₀-weighted SE and GE sequences. Spectral presaturation imaging has the advantages of STIR without the above-mentioned disadvantages, although problems can occur in the complete saturation of fat over a large volume of tissue such as in the body, particularly where physiological motion occurs, and at the edge of the field. It is not a complete sequence and has to be added to other sequences with a consequent time penalty, particularly when used with the T₁-weighted sequence, although with adjustment of the repetition time of the sequence this can be minimised. It may also lead to inadvertent suppression of water protons within the image, particularly along curved regions that are off-centred, such as the shoulder and ankle. This can lead to erroneous areas of high signal that can mimic pathology. Therefore, spectral presaturation requires good water-fat separation achieved in highly homogeneous magnet systems (usually 1 Tesla or greater), whereas STIR can be utilised with all magnet field strengths across a wide range of homogeneities. As the reduction in the fat signal is based on a frequency difference and not the relaxation time value, the spectral presaturation technique is more specific for the diagnosis of haemorrhage, and can be used following gadolinium-chelate injection (intravenous or intra-articular). It is important that the spectral presaturation technique is used with gadolinium-chelate enhancement for lesions in the subcutaneous fat and bone marrow (Fig. 45.5), as without its use an enhancing lesion is less conspicuous and can be missed. Fat suppression techniques are particularly useful in the demonstration of inflammation, infection, post-traumatic changes (including bone-bruise and muscle tear/contusion), tenosynovitis, tendinopathy and tendon tear (especially in the rotator cuff of the shoulder) (Fig. 45.6). They also provide for improved conspicuity of pathology compared with conventional T₁- and T₂-weighted sequences alone.

Dynamic scanning techniques have been used to assess lesions before and after treatment. Rapid sequential imaging up to 3 minutes following a bolus injection of gadolinium-chelate provides signal intensity curves, which can be helpful in distinguishing between a malignant and a benign lesion. An early steep slope of the signal intensity curve is indicative of a malignant tumour. Further work is required to refine this methodology for routine use.

Further advances of MRI are to be expected with new contrast agents, real-time scanning (MR fluoroscopy), and the development of new generation magnet systems allowing open access for minimal invasive biopsy and treatment (see p 1445 and Ch. 59). MR fluoroscopy will allow for the kinematic study of joints in real time, providing a platform for the dynamic assessment of ligaments, tendons and muscle with stress studies of joints.

Trauma

In addition to demonstrating the bone marrow changes secondary to bone injury (the so-called 'bone-bruise') and stress fractures (without the need to remove a POP cast if present), MRI has become the primary method for evaluating the integrity of ligaments, tendons and muscles, allowing early diagnosis of injury. MRI is the first non-invasive technique for the detection and assessment of excess muscle usage patterns. *Injury to ligaments and tendons* produces an increase in signal intensity (due to oedema, inflammation, haemorrhage) within these structures on both T₁- and T₂-weighted images. Chronic repetitive damage leads to thickened tendons and

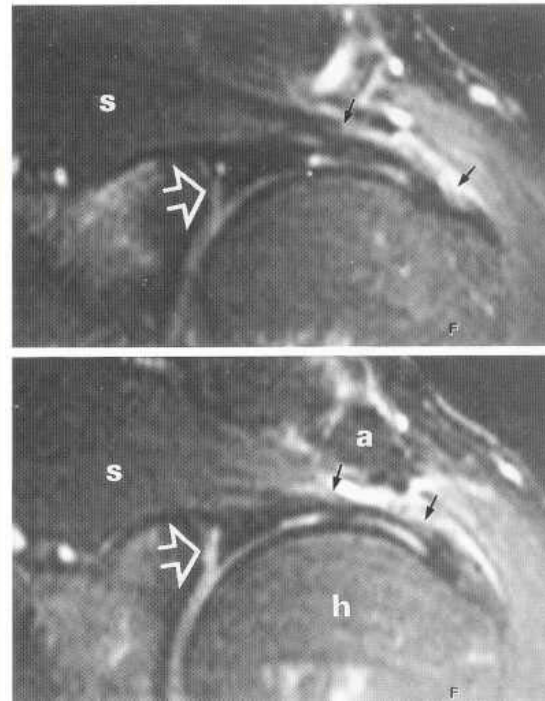


Fig. 45.6 SLAP tear (superior labral tear from anterior to posterior; open arrow) on contiguous coronal-oblique fat-suppressed T₂-weighted TSE images in a 40-year-old man who fell on an outstretched hand. There is also an associated and extensive partial tear on the bursal surface of supraspinatus tendon (small arrows) from bony impingement from a laterally down-sloping acromion (a). Note the excess fluid in the subacromial/subdeltoid bursa. h = humeral head; s = supraspinatus muscle.

ligaments. *Muscle* contusion, haemorrhage, haematoma, necrosis and fatty replacement can be diagnosed and differentiated.

Ligaments are bands of paucicellular fibrous tissue that connect two or more bones and have low-signal intensity on all pulse sequences. The MRI criteria for a recently torn ligament include disruption and irregular contour of the ligament associated with a high signal within the ligament on either T₁- or T₂-weighted images. Tears are more obvious on T₂-weighted images due to the higher signal intensity of fluid within the tear. In the acute stage MRI can overdiagnose a partial tear as complete due to intra-substance haemorrhage and oedema. The MRI appearance, however, does depend on the age and degree of disruption. Partial tears can be diagnosed by attenuation of the ligament. A partial tear can heal with fibrosis—this produces thickening of the ligament, which appears low signal on all sequences.

Tendons Normal tendons are relatively acellular structures composed of dense collagen fibres aligned within an amorphous ground substance. A normal tendon appears as low signal on all pulse sequences. There are exceptions with an increase in signal intensity at insertion sites of certain tendons producing a multistriated appearance (e.g. quadriceps and triceps tendon) due to several tendons fusing together to form a conjoined tendon. In addition, many tendons fan out at their distal insertions (Fig. 45.7A,B). Another pitfall in interpretation is the so-called 'magic angle' effect, in which signal artefact is seen within tendons that are orientated 55° to the main magnetic field (e.g. supraspinatus, tibialis posterior and peroneal tendons) (Fig. 45.8). This artefact is seen on short TE images (T₁- or intermediate-weighted) images but is not evident on T₂-weighted scans and can therefore be differentiated from significant tendon degeneration/partial tears.

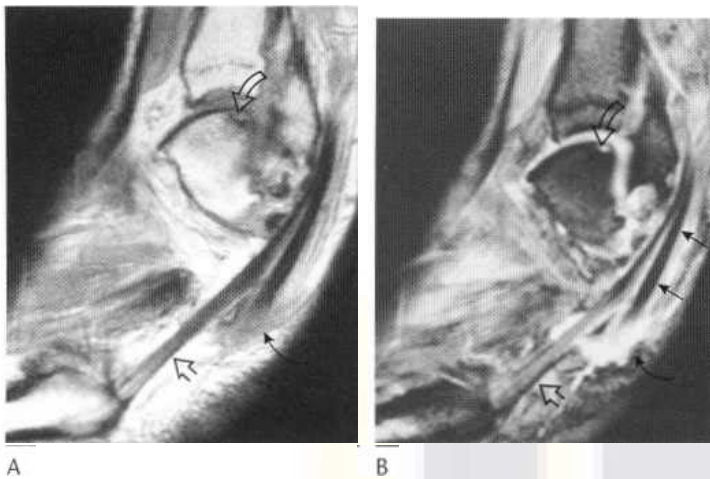


Fig. 45.7 Complete disruption of peroneus longus tendon (curved arrow) as it passes underneath the cuboid on parasagittal (A) T₁-weighted SE and (B) T₂-weighted GE images. There is fluid signal from tenosynovitis surrounding the more proximal part of this tendon (small arrows). There is intermediate signal from the distal part of peroneus brevis tendon (open straight arrow) close to its insertion onto the base of the fifth metatarsal, which is a normal finding. Note that there is an associated osteochondral defect of the lateral talar dome (curved open arrow).



Fig. 45.8 Focal increased signal (arrow) within the distal tendon of supraspinatus due to magic angle effect on a coronal-oblique proton density-weighted TSE image. The T₂-weighted image (not shown) confirmed a normal appearance to the tendon throughout its length.

Tendon abnormalities can be classified as tendinopathy, tear/rupture, tenosynovitis, subluxation/dislocation or entrapment. A fat-suppressed sequence (STIR or preferably spectral presaturation with intermediate or T₁-weighted scans) is the optimum imaging technique for the assessment of tendon abnormalities. The *nonseulotendinous junction* is the weakest part of a normal muscle-tendon complex. A tendon can be injured due to repetitive, blunt or penetrating trauma. A tendon is frequently already weakened from prior injury or intrinsic degeneration that can lead to partial tear or rupture when excessive force is applied. The Achilles, quadriceps, patellar and rotator cuff tendons are frequent sites of intrinsic degeneration/ tendinopathy. Tendon damage can also occur from chronic abrasion at susceptible sites, for example supraspinatus tendon from bony impingement (Fig. 45.6), long head of biceps tendon in the bicipital groove (Fig. 45.9) and the tibialis posterior and peroneal tendons around the ankle (Fig. 45.7). It requires approximately 30% loss of function of a tendon for it to be clinically apparent.

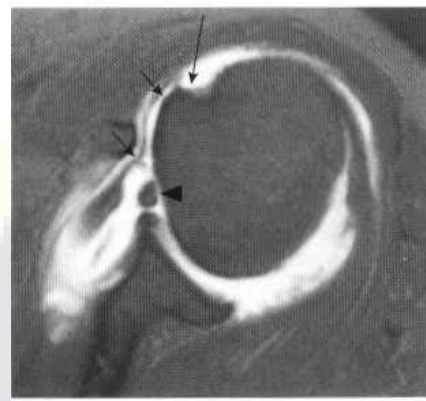


Fig. 45.9 Medially displaced long head of biceps tendon (arrowhead) abutting onto the anterior glenoid labrum on a transverse fat-suppressed T₁-weighted post-arthrographic SE image. The intra-articular gadolinium-chelate returns a bright signal and highlights the torn and attenuated subscapularis tendon (short arrows). Note the empty bicipital groove (long arrow).

Myxoid degeneration of a tendon (called 'tendinopathy' or 'tendinosis') is a chronic condition slowly worsening over years, weakening the tendon. It leads to tendon rupture with minimal trauma (e.g. quadriceps and Achilles tendon disruption in the middle-aged individual). It is rarely an acute inflammatory condition, and thus it is best not to use the terms 'tendonitis'. Tendinopathy occurs with ageing and chronic overuse. Intermediate to high signal within a tendon on T₁- or intermediate-weighted images, which remains intermediate signal on T₂-weighted scans, is recognised as a highly sensitive predictor of early tendinopathy. The tendon can be normal, thickened or attenuated in calibre (Fig. 45.10A).

Tendon tears Certain factors and conditions are associated with weakening of a tendon predisposing to its rupture (Box 45.1). Intrinsic high signal within a tendon on T₂-weighted images (particularly well seen with fat suppression) indicates a partial tear, which tends to coexist with degeneration. Tendons can tear vertically producing longitudinal defects-termed partial intrasubstance/cleavage tears (Fig. 45.10B). A high signal noted on all sequences indicates an acute tear within a tendon, due to haemorrhage and oedema; chronic tears lead to fibrosis with the morphology of the tendon, or the surrounding fluid in the tendon sheath, being the only clues as to the ongoing pathology. A complete tear is diagnosed when there is separation of the tendon by intervening high signal and retraction of the torn tendon. When a complete full thickness tear of a tendon is recognised, it is important to measure the gap between the tendon ends and to describe the appearance of the retracted tendon and muscle, as these are criteria used in the management of the patient. The MRI diagnosis of a full thickness tear, for example of the rotator cuff of the shoulder, is relatively easy with a high degree of accuracy, whereas more difficulty is noted in the diagnosis of partial tears of the tendon. Fatty atrophy of the muscle indicates that the changes are longstanding and irreversible.

Box 45.1 Factors associated with tendon rupture

- Ageing-degeneration/tendinopathy
- Trauma-acute or chronic (repetitive strain/overuse)
- Medication-systemic steroids
 - quinolone derivative antibiotics (e.g., ciprofloxacin)
- Disease processes-diabetes mellitus
 - inflammatory arthropathies (rheumatoid arthritis, gout)
 - chronic renal failure
 - hyperparathyroidism
 - systemic lupus erythematosus
- Infection of tendon sheath (infective tenosynovitis)

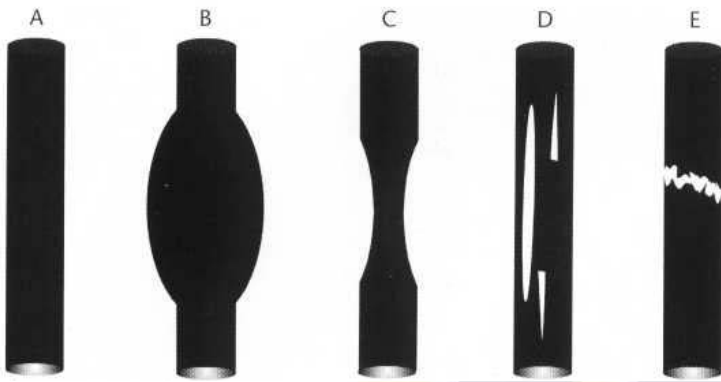


Fig. 45.10A Diagram of tendon abnormalities: (A) normal; (B) thickened tendinopathy; (C) thinned tendinopathy; (D) intrasubstance longitudinal splitting-cleavage tears; (E) complete full thickness tear ((B) to (D) are partial tendon tears).

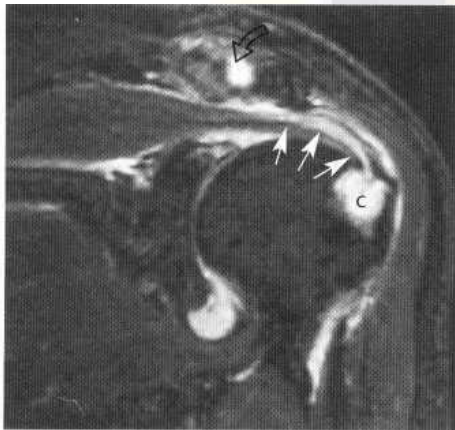


Fig. 45.10B Cleavage tear (small arrows) in supraspinatus tendon on a coronal fat-suppressed T_2 -weighted FSE image. There is fluid signal within the tendon extending into a large impingement cyst (C) on the lateral head of the humerus. Note the excess fluid within the glenohumeral joint and subacromial-subdeltoid bursa. Curved arrow = degenerative acromioclavicular joint.

A grading system has been described for tendon tears. Three types of tear are recognised, with a type I lesion demonstrating thickening and associated longitudinal splitting of the tendon (Fig. 45.11). In a type II lesion the tendon is markedly attenuated (Fig. 45.12), whereas with a type III tear it is discontinuous (Figs 45.7B, 45.8). One can also get a normal-sized tendon with longitudinal splitting of the tendon fibres. Associated peritendinous inflammatory changes (termed 'tenosynovitis') can be seen in all three types.

In *tenosynovitis* there is fluid distension of the tendon sheath with or without thickening or abnormality of the tendon tendons (Fig. 45.10). Fluid is not demonstrated within normal tendon sheaths except for small amounts around the ankle and wrist tendons, which is of no consequence. Certain tendon sheaths, however, connect with the adjacent joint (long head of biceps and flexor hallucis longus tendons), and fluid within these tendon sheaths does not necessarily indicate tenosynovitis unless there is no associated joint effusion. Stenosis of a tendon sheath (e.g. flexor hallucis longus in the os trigonum syndrome, and the first compartment extensor tendons in de Quervain's stenosing tenosynovitis) is recognised by loculated fluid collections separated by thin linear septations within the fluid. It is important to note that the Achilles tendon (the longest and thickest in the body) does not have a tendon sheath but has a surrounding loose connective tissue (termed

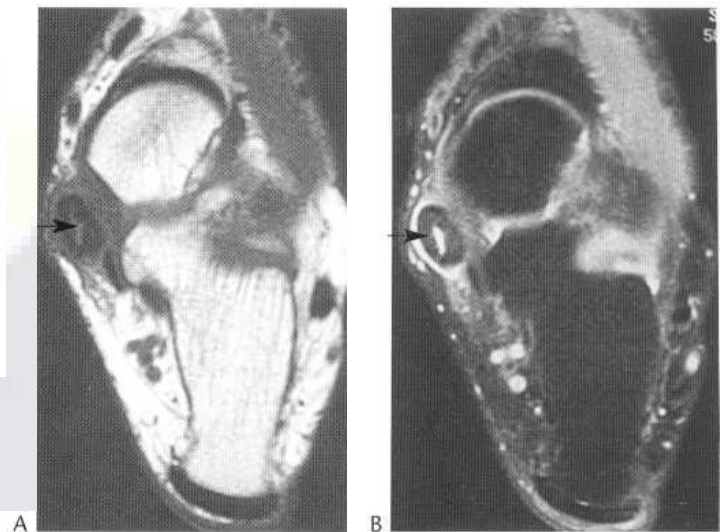


Fig. 45.11 Type I tendinopathy of tibialis posterior tendon (arrows) with intrasubstance cleavage tear (longitudinal splitting) and surrounding tenosynovitis on transverse (A) T_1 -weighted SE and (B) fat-suppressed proton density-weighted FSE images.



Fig. 45.12 Type II tendinopathy of peroneus longus tendon (arrows) with surrounding tenosynovitis on sagittal fat-suppressed proton-density TSE image. The peroneus brevis tendon with surrounding tenosynovitis is noted anterior to the peroneus longus tendon.

paratenon). The paratenon can become inflamed which is demonstrated as oedema signal around the tendon.

Subluxation/dislocation of a tendon can be demonstrated when the tendon is not in its correct anatomical location, and is frequently associated with tenosynovitis. Certain tendons (e.g. long head of biceps, extensor carpi ulnaris, peroneal and tibialis posterior tendons) are prone to subluxation and dislocation (Fig. 45.8). *Compression* and flattening of a tendon by entrapment from callus formation or scar tissue following a fracture can be diagnosed. Tendinopathy and tenosynovitis frequently occur with entrapment.

Calcific deposits can occur in and around any of the rotator cuff tendons, or in any tendinous or ligamentous insertion. The calcification, in the form of calcium hydroxyapatite crystals, occurs most frequently in and around supraspinatus tendon (usually best visualised on a plain radiography with the humerus in external rotation). Unusually for calcification it is well demonstrated on MRI as a signal void on all pulse sequences (Fig. 45.13). It is usually discovered because of local pain and periartthritis but may be in its silent phase and clinically unsuspected prior to rupture into the adjacent bursa. Soft-tissue apatite deposition may ultimately, however, prove to be a manifestation of a wider syndrome that can declare itself in other ways, such as crystal-induced synovitis and destructive arthritis (e.g. Milwaukee shoulder). Pannus from rheumatoid arthritis may present in a tendon sheath producing filling defects within the fluid signal mimicking infective (TB) tenosynovitis and synovial osteochondromatosis of the tendon

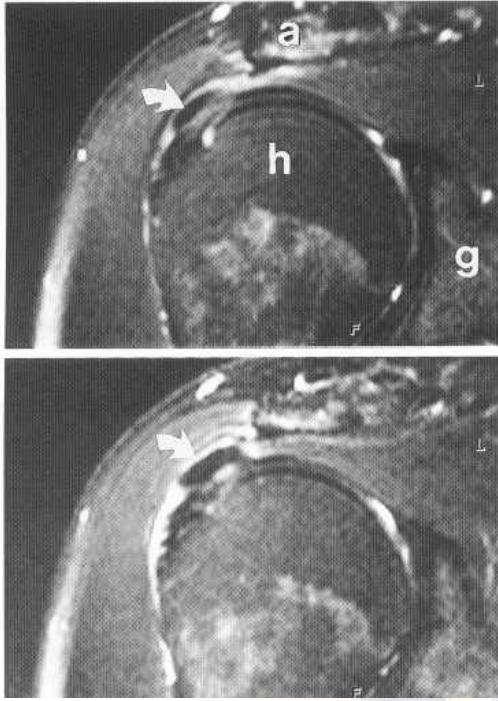


Fig. 45.13 Extensive calcific tendinopathy (curved arrow) of supraspinatus tendon previously undiagnosed on contiguous coronal-oblique fat-suppressed T₂-weighted TSE images. Note the fluid in the subacromial/subdeltoid bursa. a = acromion; g = glenoid; h = humeral head.

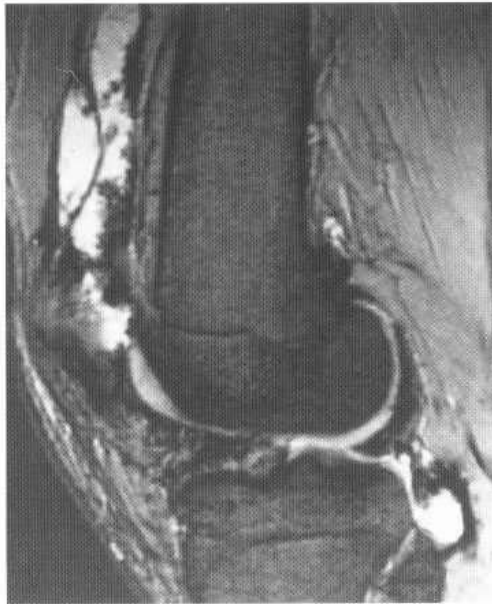


Fig. 45.14 Pigmented villonodular synovitis (PVNS) on a sagittal GE image. There is a joint effusion with multiple areas of signal void from haemosiderin deposition and thickening of the synovium and plical fold within a distended suprapatellar bursa. Note the similar appearance as in Fig. 45.15.

sheath. Giant cell tumour of tendon sheath is the extra-articular form of pigmented villonodular synovitis and is a common mass in the feet and hands. It presents as a painless soft-tissue mass usually with a characteristic focal area of signal void (best demonstrated on a T₂-weighted GE sequence) from haemosiderin deposition (Figs 45.14, 45.15) closely related to a tendon.

Muscles Normal muscle is used as the reference tissue for assessment of signal intensity changes in the musculoskeletal

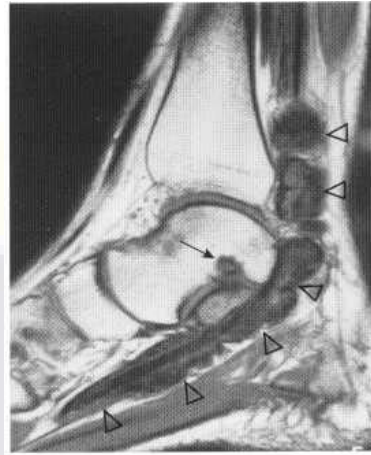


Fig. 45.15 Pigmented villonodular synovitis involving flexor hallucis longus tendon sheath (arrowheads) with involvement of the sinus tarsi (arrow) and subtalar joints on a sagittal T₁-weighted image. Note the haemosiderin deposition. Similar appearance may be seen with chronic haemarthrosis (as in haemophilia), chronic rheumatoid arthritis, chronic TB arthritis, amyloidosis and gout.

system. There appears to be good correlation between the MRI findings and the degree of muscle injury. A mild muscle strain (clinical grade I) represents a minor intrasubstance partial disruption (contusion) of muscle fibres. This degree of injury is commonly recognised on MRI by a patchy high signal within the muscle on T₂-weighted images. In an MRJ study of athletes, a cross-sectional area of involvement of less than 50% of a hamstring injury was associated with a recovery within 5 weeks. A clinical grade II strain represents a more severe degree of injury with damage to the musculotendinous region from a partial muscle or myofascial tear. On MRI this grade II injury has a 50% or greater cross-sectional area of involvement of the affected muscle, detected as a diffuse high signal on T₂-weighted images (Fig. 45.16). There is no large fluid collection to suggest complete separation of the muscle but small areas of haemorrhage/haematoma may occasionally be visible. A clinical grade III injury is associated with loss of muscle function with or without a palpable defect. This degree of injury is well recognised on both T₁- and T₂-weighted images as fluid (low and high signal respectively) and haemorrhage (high signal on both) filling the defect in the muscle. There is tendon retraction with enlargement of the proximal part of the muscle. It is important to diagnose this severe type of muscle injury as rapid atrophy can occur without operative repair.

It should be noted that the MRI changes remain apparent for many weeks following even minor muscle injury, and after symptoms have resolved. This can lead to difficulty in the correct interpretation of the MRI changes, as the patient may not remember a previous traumatic episode. Muscle and tendon retraction, muscle herniation through a fascial defect (Fig. 45.17), compensatory hypertrophy of adjacent uninjured musculature (Fig. 45.18) and accessory muscles (Fig. 45.1) can lead to the clinical suspicion of a soft-tissue tumour.

Haematofnas can occur in subcutaneous tissues and muscle, being well-defined collections of blood and blood products. The MRI appearance is variable and is dependent on the age of the lesion (Table 45.1). A haematoma follows a similar but more protracted course compared with an intracranial bleed due to the lower oxygen tension outside the central nervous system. A hyperacute haematoma (within the first few hours) contains oxyhaemoglobin and serum, returning an intermediate signal on T₁-weighted images (similar to muscle) and a high signal on T₂-weighted scans. After a few hours and days (acute haematoma) the blood products degrade to deoxyhaemoglobin with oedema and show an intermediate signal on both T₁- and T₂-weighted sequences. After a week to 3 months (subacute



Fig. 45.16 Grade II tear of rectus femoris muscle (arrows) on transverse (A) intermediate-weighted SE, (B) T₂-weighted SE, and (C) T₂-weighted GRE images. Note that there is a perifascial rim of high signal together with diffuse signal within the rectus femoris muscle, best shown in C.



Fig. 45.17 Muscle hernia of vastus lateralis (arrows) through a defect in the deep fascia of the right thigh demarcated by cod liver oil capsules on (A) coronal and (B) transverse T₁-weighted images.



Fig. 45.18 Denervation atrophy of semimembranosus muscle (straight arrow) following removal of a lipoma on a transverse fat saturation T₂-weighted spin echo (TSE 3000/100) image. The muscle is of high signal reduced in size. There is associated hypertrophy of gracilis muscle which accounted for the clinical referral as a possible tumor recurrence. There is incomplete fat saturation.

Table 45.1 Changes in signal in an evolving haematoma

Stage	Blood product	T ₁ signal intensity	T ₂ signal intensity
Hyperacute	Oxyhaemoglobin	Intermediate	High
Acute	Deoxyhaemoglobin	Intermediate	Low
Subacute-early	Methaemoglobin (intracellular)	High	Low
Subacute-late	Methaemoglobin (extracellular)	High	High
Chronic-late	Haemosiderin	Low (void)	Low (void)

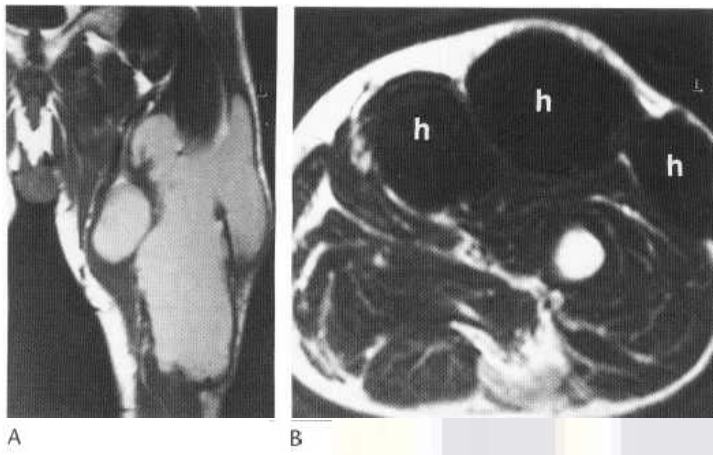


Fig. 45.19 Large multiloculated early subacute haematoma (h) in the proximal thigh with high signal in (A) coronal T₁-weighted SE and signal void in (B) transverse T₂-weighted TSE images due to intracellular methaemoglobin (short T₁ and T₂).

haematoma) methaemoglobin (short T₁) is formed which produces a high signal, similar to fat, on the T₁-weighted images. Initially the methaemoglobin remains intracellular, which produces a low signal on T₁-weighted scans from its short T₂ effect (Fig. 45.19), but eventually it becomes extracellular where it has a lesser paramagnetic effect and then returns a high signal on T₂-weighted images (long T₂) (Fig. 45.20). Chronic haematomas (>3 months) show a high

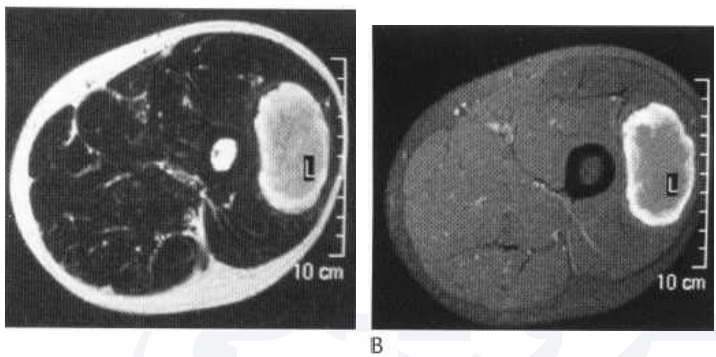


Fig. 45.20 Late subacute haematoma within the thigh with a peripheral signal appearance due to extracellular methaemoglobin (short T₁ and long T₂) on transverse (A) T₂-weighted TSE and (B) fat-suppressed T₁-weighted SE images.

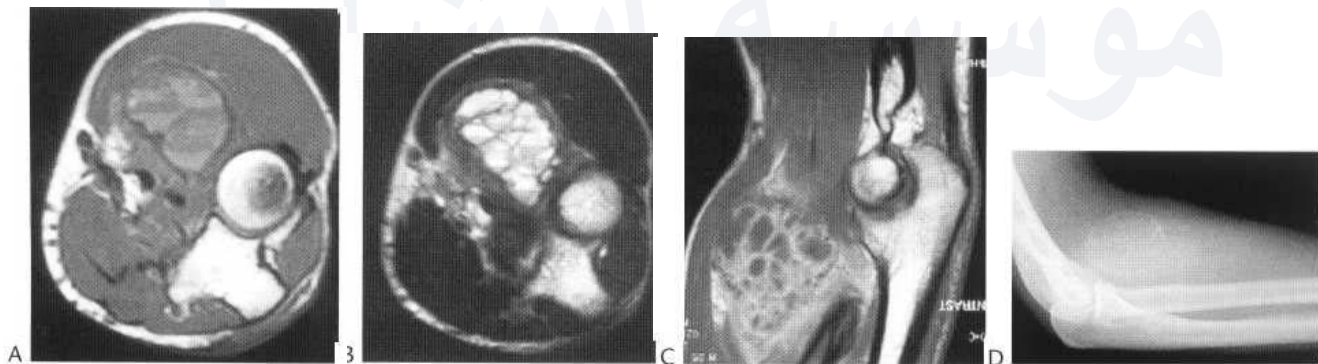


Fig. 45.22 Subacute myositis ossificans in the antecubital fossa in a 25 year old referred with a potential diagnosis of a desmoid/sarcoma (prior trucut biopsy was reported as being inconclusive) on (A) transverse T₁-weighted SE, (B) transverse T₂-weighted FSE, (C) sagittal postcontrast T₁-weighted SE images and (D) lateral radiograph of the elbow. The plain radiograph shows the characteristic peripheral ossification and multiple high-signal fluid-fluid levels from haemorrhage on the MR images.



Fig. 45.21 Chronic haematoma, with heterogeneity in signal, involving the deep fascia of the medial calf indenting the medial gastrocnemius muscle on a coronal T₁-weighted SE image. Note the peripheral signal void due to haemosiderin deposition.

signal on all sequences similar to late subacute lesions with a rind of signal void from haemosiderin deposition (Fig. 45.21). Eventually the haematoma reduces in size with a low signal similar to surrounding muscle.

Myositis ossificans is heterotopic bone (sometimes cartilage) forming in muscles, tendons and fascia following trauma, although a history of previous injury may not be forthcoming. Following muscle damage, what initially may appear to be a haematoma can subsequently show fine, lacy calcification. During the first 2 weeks following trauma a warm and painful soft tissue mass develops. Fluid fluid levels can be seen as a result of the haematoma, and there is marked enhancement with gadolinium-chelate injection as a consequence of the marked vascularity of this condition (Fig. 45.22). In the subsequent 2 weeks amorphous densities develop in the mass, possibly with periosteal reaction. During this initial 4-week period the process histologically resembles a parosteal osteosarcoma, and the MRI features are non-specific; however, there is usually a thin line of separation between the ossification and adjacent bone, which aids in the differentiation. One characteristic feature of myositis ossificans in its acute and intermediate stages (<8 weeks) is the marked degree of surrounding oedema. This is an unusual appearance in the majority of primary soft-tissue sarcomas that have not been biopsied or undergone internal haemorrhage. Subsequently the post-traumatic myositis ossificans matures (ossifies) in a peripheral to central pattern (with fatty marrow) (Fig. 45.23) and there is a reduction in size of the mass, factors that also help to distinguish it from a malignant

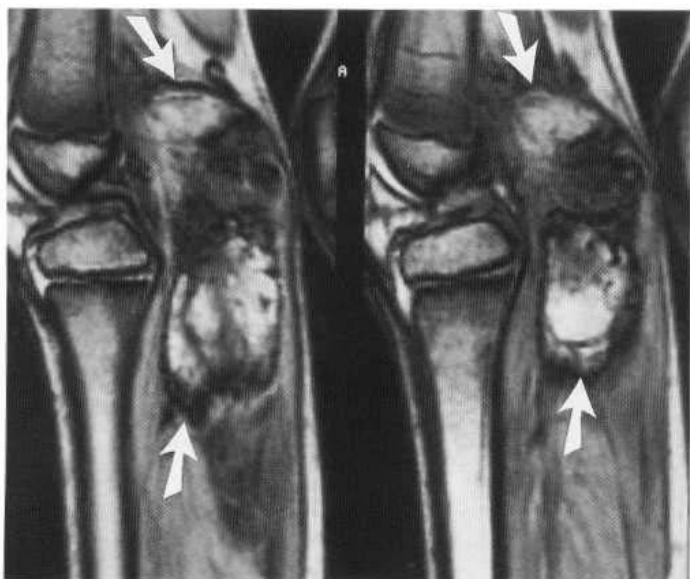


Fig. 45.23 Mature myositis ossificans (arrows) within gastrocnemius muscle in a 9-year-old girl on contiguous sagittal T_2 -weighted GE images. This mass was resected 2 years previously and referred as a possible osteosarcoma. Note the low-signal corticated rim with the central areas showing fatty marrow signal (same case as 45.85).

process. Surgical resection is best left until after maturation is complete, as determined by isotope bone scanning or MRI, otherwise a high recurrence rate is to be expected. The soft tissues around the elbow and in the thigh are common sites for the development of this complication. Brachialis muscle is particularly prone to this; radiographs following elbow injury merit careful scrutiny for this complication, which the unwary could mistake for a malignant process. The quadriceps muscle group is another common site.

Compartment syndrome within the forearm and calf, which in its chronic form is often difficult to diagnose clinically, can be delineated on MRI as a diffuse area of abnormal signal within the musculature confined to that compartment. A compartment syndrome occurs when the pressure within an osteomuscular compartment exceeds normal capillary pressures, producing a reduction in tissue perfusion. There are two forms of compartment syndrome, induced by trauma or exercise. The *post-traumatic* type produces acute symptoms related to haemorrhage and inflammation into a

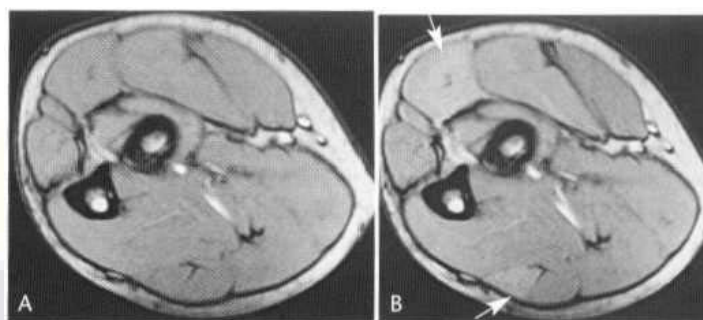


Fig. 45.24 Exercise-induced compartment syndrome in the forearm musculature (arrows) involving the flexor and extensor compartments in a 43-year-old weight-lifter on (A) pre- and (B) post-exercise proton density-weighted spoiled GE (FLASH) images.

muscle within a confined space following injury with a fracture. The increased pressure within the compartment leads to a reduction in circulation and subsequent muscle necrosis. This is a surgical emergency and MRI generally plays no role in making the diagnosis. Chronic changes, with atrophy and dense fibrosis, can occur within the affected muscles. Rarely the muscle compartment (e.g. peroneal compartment) calcifies (termed calcific myonecrosis). MRI is useful to show the extent of muscle damage.

Exercise-induced compartment syndrome is more chronic in onset and difficult to assess clinically. It should be noted that intensive exercise normally leads to a transient rise in the relaxation times, due to an increase in the extracellular free water within the muscles, producing a change in signal intensity compared with the resting state. The signal change occurs diffusely within the muscles and resolves within 10 minutes of the exercise. Exercise-induced compartment syndrome is diagnosed when oedematous muscles fail to return to a normal appearance after 15-25 minutes post-exercise (Fig. 45.24). On MRI few other pathologies have a diffuse complete, or almost complete involvement of muscles in one or more muscle compartments. The main differential diagnosis is infection, which should be easily excluded. Myositis ossificans has a more focal and patchy distribution of signal change.

Inflammatory myopathies Inflammatory myopathies (pyomyositis, necrotising fasciitis, sarcoidosis and autoimmune inflammatory polymyopathies) are relatively uncommon conditions that can affect muscle (Fig. 45.25). Necrotising fasciitis is a rare rapidly progressive infection of the intermuscular fascia accompanied by

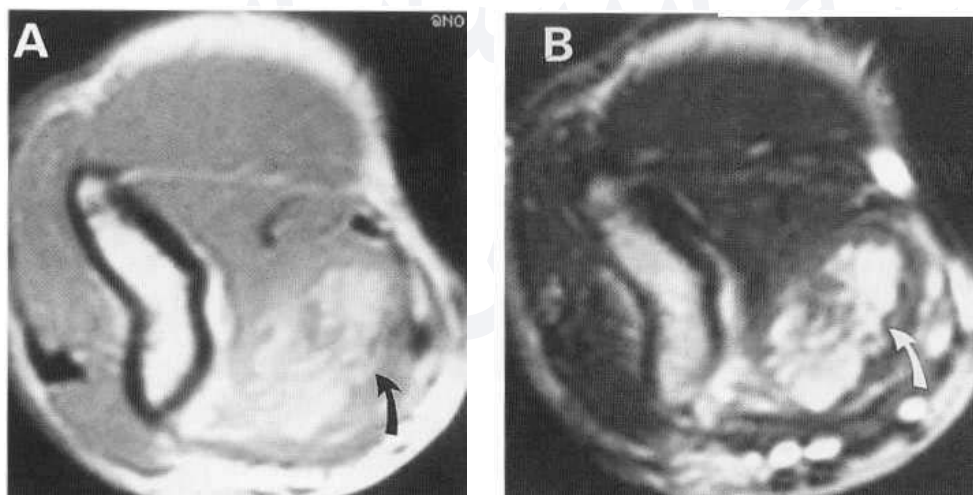


Fig. 45.25 Haemorrhagic pyomyositis (arrows) in brachialis muscle on transverse spin-echo (A) proton-density-weighted and (B) T_2 -weighted SE images. Note the more infiltrative pattern with little mass effect, as compared with the soft-tissue sarcoma in Fig. 45.32. The high signal from the lesion on the T_2 -weighted image is not as intense as adjacent vessels, differentiating this from a haemangioma.

severe systemic toxicity with a high mortality rate. The early clinical diagnosis is difficult and inseparable from cellulites. Cellulitis involves the subcutaneous tissues and can be treated by antibiotics, whereas necrotising fasciitis requires early surgical debridement and fasciotomy. MRI is very useful in differentiating the two conditions. Cellulitis shows a reticular pattern of oedema signal limited to the subcutaneous space. In necrotising fasciitis there is increased signal on T₂-weighted images, and soft-tissue thickening in the deep fascia between the muscles. The adjacent muscles may have increased signal secondary to hyperaemia and oedema from the inflammatory process. Although the appearances on MRI are non-specific, the clinical context of the case allows the diagnosis to be made.

Muscle denervation produces atrophy, fatty infiltration and oedema. Cerebral palsy, amyotrophic lateral sclerosis, and hereditary sensorimotor neuropathy lead to muscle atrophy with little fatty infiltration, whereas poliomyelitis produces atrophy with marked fatty change.

Regional pain syndrome (old terminology reflex sympathetic dystrophy, Sudek's atrophy or algodystrophy) can involve all compartments, including bone marrow, muscles, synovium and subcutaneous tissue, in a heterogeneous pattern. It is mediated by the sympathetic nervous system and is characterised by an aggressive osteopenia, soft-tissue swelling with hyperaemia and hyperaesthesia leading to muscle atrophy and contracture. Trauma is implicated in the majority of cases.

Cystic lesions

Cystic lesions such as bursae, ganglia and parameniscal cysts are commonly occurring masses in the musculoskeletal system. A pure cyst demonstrates a uniform low and high signal on T₁- and T₂-weighted images.

Bursae are synovial-lined closed sacs usually found over bony prominences. They contain minimal lubricating fluid to reduce friction between tendons and adjacent tissue. The subdeltoid and subacromial bursae are in continuity. The ulnar bursa is associated with the flexor tendons of the wrist and the radial bursa with the flexor pollicis longus tendon. A distended semimembranosus/gastrocnemius bursa is a common finding in individuals with a joint effusion as it connects with the knee joint. The iliopsoas bursa may communicate with the hip joint and, if distended, (in cause pain on

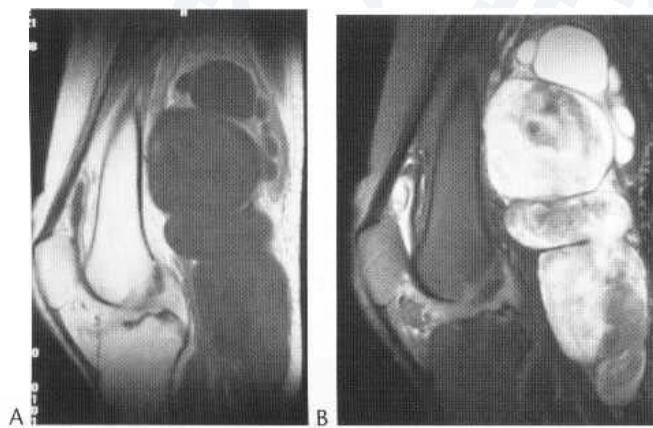


Fig. 45.26 Large benign haemorrhagic popliteal cyst on sagittal (A) post-contrast T₁-weighted SE and (B) T₂-weighted TSE images demonstrating peripheral enhancement in (A) around the multiloculated cysts superiorly.

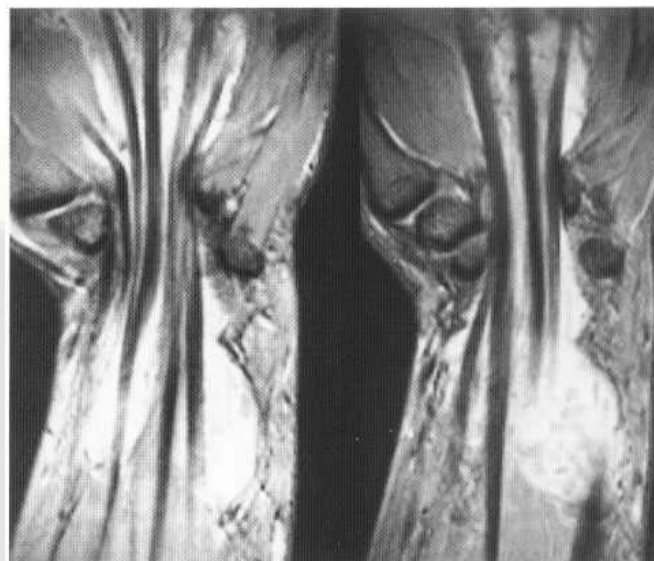


Fig. 45.27 Synovial osteochondromatosis within the flexor tendon sheaths of the wrist on contiguous coronal T₂-weighted GRE images. Note the multiple loose bodies of similar size within the fluid of the distended tendon sheaths.

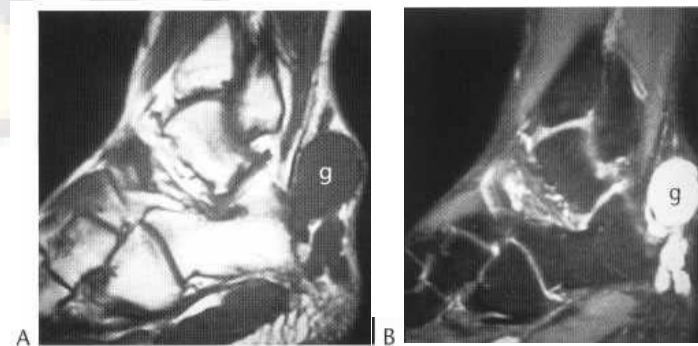


Fig. 45.28 Multilobulated ganglion (g) in the retrocalcaneal soft tissues on parasagittal (A) T₁-weighted SE and (B) T₂-weighted TSE images.

hip movement. Fluid can accumulate with subsequent bursal enlargement from inflammatory, infective or post-traumatic causes. An enlarged bursa usually demonstrates homogeneous low and high signal on T₁- and T₂-weighted images, but may contain proteinaceous tissue from inflammation or trauma mimicking a soft-tissue tumour (Fig. 45.26). Common locations include around the knee (prepatellar, infrapatellar and pes anserinus bursitis), shoulder (subdeltoid/subacromial bursitis) and hip (greater trochanter bursitis). Occasionally 'melon-seed' loose bodies (synovial osteochondromatosis-Fig. 45.27) may be visible within the bursa.

Ganglia and parameniscal cysts have a characteristic appearance being usually multilocular with low signal stranding/septae within the fluid spaces (Fig. 45.28). The thin peripheral wall and internal septae do enhance following contrast administration but with no enhancement of the fluid spaces.

Cystic hygroma is a congenital disorder in which the lymphatic spaces are markedly dilated. The abnormality is predominantly in the neck but may involve the axilla, mediastinum and pleural spaces (Fig. 45.29).

Intramuscular myxomas are well-circumscribed lesions containing a thick gelatinous material which can mimic a cyst on MR. Following contrast administration heterogeneous enhancement may

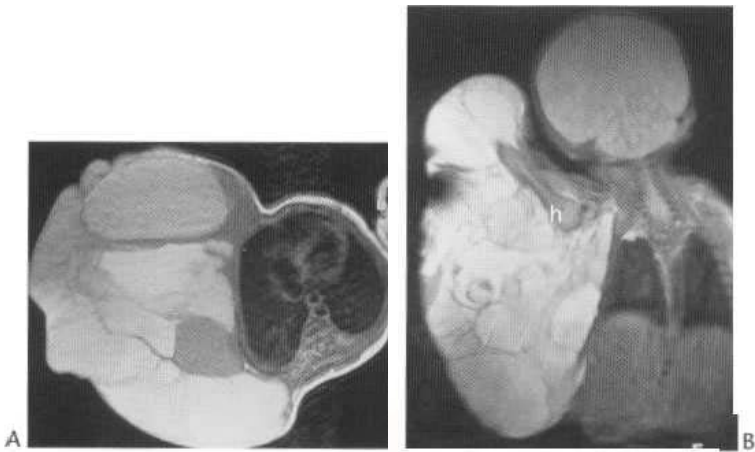


Fig. 45.29 Extrathoracic cystic hygroma wrapping around the right humerus (h) and involving the chest wall axilla in a 3-day-old neonate showing a multiloculated cystic lesion with fluid-fluid levels (arrows) due to haemorrhage on (A) transverse T_1 -weighted SE and (B) coronal T_2 -weighted TSE images. This tumour was subsequently successfully removed.

be seen either within the lesion or limited to the periphery and septae. They are usually solitary (if multiple are associated with fibrous dysplasia in Mazabraud's syndrome) most commonly occurring in the thigh. Solid tumours that contain myxoid elements (c.g. myxoid liposarcoma, myxoid malignant fibrous histiocytoma, myxoid chondrosarcoma) may appear cystic on unenhanced MRI (Fig. 45.30) but will demonstrate diffuse enhancement. If a cyst-like structure does not have the typical appearances of a ganglion, or is in an atypical location, then contrast enhancement should be performed to exclude a myxoid tumour.

Soft-tissue tumours

MRI is the method of choice in the assessment and staging of tumours of the musculoskeletal system but does not provide histological diagnosis. Soft-tissue involvement is often underestimated by CT. Recent surgery or biopsy gives rise to haemorrhage and oedema, which can produce misleading appearances on MRI.



Fig. 45.30 Benign myxoma (m) within deltoid muscle mimicking a cyst (uniform low signal) on (A) coronal pre-contrast T_1 -weighted SE image but demonstrating in (B) heterogeneous soft-tissue enhancement on postcontrast injection. Small myxoid liposarcoma within lateral abdominal wall musculature on (C) T_1 -weighted SE and (D) T_2 -weighted FSE images. The myxoid lesion is mimicking a cyst. Note it is not possible to differentiate between a benign or malignant tumour on MR characteristics, and although it was histologically a liposarcoma no fatty elements are demonstrated on MRI.

Indeterminate lesions will require biopsy and/or careful follow-up. Once histology has confirmed that a lesion is malignant then CT scanning of the thorax is required to determine the presence or absence of intrapulmonary metastases. There are three basic components for the staging of musculoskeletal tumours—(i) histological grade of the tumour which dictates potential for the lesion to metastasise (a low-grade tumour is less biologically active compared with a high-grade lesion); (ii) local extent of the tumour, (iii) presence or absence of metastases.

Prior to imaging it is essential to have a comprehensive and accurate clinical history available as this can have a significant bearing on the radiological interpretation and may provide a specific diagnosis when the imaging is indeterminate (Box 45.2). A slow-growing tumour does not necessarily indicate a benign process and can occur with certain malignant tumours (e.g. synovial sarcomas).

Purpose of imaging

The objectives of imaging are to confirm the presence, precise site (including compartmental spread) and extent of soft-tissue tumour; to detect neurovascular invasion, cortical infiltration and regional nodal metastases (Box 45.3); and to aid biopsy. Following treatment it is useful to obtain a baseline MRI examination (usually at 6 months) with contrast enhancement, and further follow-up scans depending on the grade of the initial tumour, to identify any tumour recurrence. If recurrent tumour is demonstrated then repeat staging is required including a CT thorax.

Box 45.2 Clinical information required in the assessment of a soft-tissue tumour

- Is the lesion painful? (*suspect on inflammatory lesion*)
- Is there a history of trauma?
- Has the lesion remained stable over a long period, or is it growing?
- Has the lesion varied in size over time or activity? (*suspect ganglion or haemangioma*)
- Is there a history of a previous lesion or malignancy?
- Has there been previous surgery or radiotherapy?
- Is the lesion solitary or multiple?

Box 45.3 Imaging criteria in the assessment of a soft-tissue mass

Size (growth rate)
 Location (include measurement to nearest joint)
 Compartment spread
 Tumour margin
 Signal intensity (SI)
 Enhancement characteristics
 Neurovascular invasion
 Bone infiltration/destruction
 Adjacent soft-tissue SI

A *compartment* is an anatomical structure or space bounded by natural barriers to tumour extension. An example of a compartment is the anterior compartment of the thigh, containing the quadriceps group of muscles, bounded by fascia including the medial and lateral intermuscular septa and proximally by the femoral triangle and distally the knee joint. The interfascial planes containing the major neurovascular bundles are not compartments as they have no proximal or distal barriers. Extracompartmental spread implies aggressive behaviour of the tumour and is associated with a poorer prognosis. It should be noted that some benign tumours (e.g. intermuscular lipoma, cavernous haemangioma) can extend across more than one compartment.

Technique

The imaging technique is outlined in the Royal College of Radiologists' booklet 'A guide to the practical use of MRI in oncology'. I prefer to use coronal or sagittal T₁-weighted SE and fat-suppressed intermediate (proton density)-weighted TSE with a relative large field of view to include the lesion, adjacent joint and regional lymphatic site. Higher resolution smaller field of view transverse T₁-weighted TSE and fat suppressed T₁-weighted SE, the latter being repeated following gadolinium-chelate injection. A STIR sequence can be used if susceptibility artefact (e.g. from postsurgical change or a prosthetic implant) is present. Cod liver oil capsules taped to the skin to the side of a suspected soft-tissue lesion is a useful technique to confirm that the correct area has been imaged, particularly if no lesion is subsequently identified. If an indeterminate soft-tissue mass is confirmed on MRI then a plain radiograph of the affected area should be obtained if not already performed. A radiograph is frequently unrewarding but maybe diagnostic by showing calcification, callus, exostosis, bone involvement. Remember that calcification is usually poorly visualized on MRI - its identification and appearance can be diagnostic (Fig. 45.22).

Contrast enhancement

Intravenous gadolinium-chelate is helpful if a mass lesion is not pure blood, water or fat. As noted above fat-suppressed T₁-weighted images are used for optimum enhancement. Soft-tissue tumours (benign and malignant) show *nodular* enhancement, and biopsy can be targeted to this area of the lesion for histological grading of viable tumour. Haematomas do not usually enhance, except very occasionally when organising fibrovascular tissue is formed. Gadolinium-chelate enhancement is useful in distinguishing between a simple haematoma from a haemorrhagic sarcoma (Fig. 45.31). In myositis ossificans enhancement is diffuse and different to that of a soft-tissue sarcoma. A myxoma and myxoid sarcoma can mimic a cyst (being low and high signal in relation to muscle on T₁- and T₂-weighted

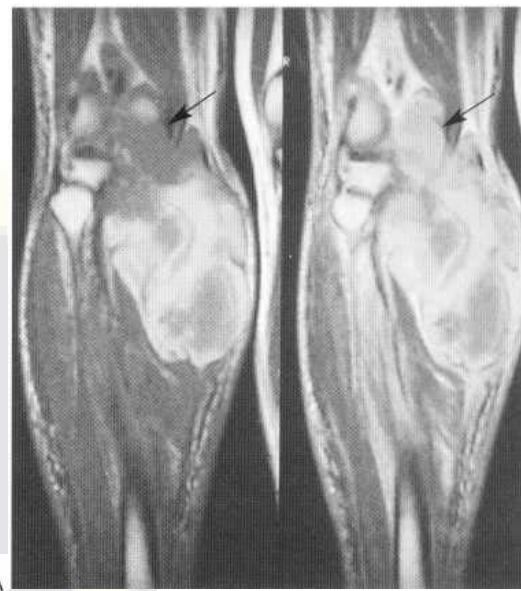


Fig. 45.31 Haemorrhagic malignant fibrous histiocytoma (MFH) on corona) (A) pre-contrast and (B) postcontrast T₁-weighted SE images. Note a soft tissue tumour nodule (arrows) enhancing in (B) proximal to the major haemorrhagic component.

images respectively) on unenhanced images but shows soft-tissue enhancement. A cyst does not enhance except for its wall.

Soft-tissue sarcomas

Soft-tissue sarcomas are uncommon lesions, representing approximately 1% of all malignant tumours. They are, however, twice as common as primary malignant bone tumours. The annual incidence of soft-tissue sarcomas is approximately 1-2/100 000 population, increasing with age up to 8/100 000 in individuals over 80 years of age. It has been estimated that there are around 800 new cases per year in the UK. It should be noted that benign soft-tissue tumours far outnumber malignant tumours, the incidence of the former being estimated to be 300/100 000 population.

Soft-tissue tumours arise from mesenchymal tissue and are classified according to which adult tissue they resemble on histology. Many soft-tissue sarcomas are poorly differentiated but can be further differentiated using immunohistochemical stains. Despite this approximately 5-15% remain unclassified. The commonest soft-tissue sarcomas in middle aged and elderly individuals, in order of frequency, are malignant fibrous histiocytoma (MFH), liposarcoma, leiomyosarcoma and malignant peripheral nerve sheath tumour (MPNST-this term is used rather than the previous nomenclature of malignant schwannoma or neurofibrosarcoma.). In younger individuals (first to the third decade of life) fibrosarcoma, rhabdomyosarcoma, synovial sarcoma and MPNST are the commoner sarcomas found. The common benign soft-tissue tumours include lipoma, and its variants, haemangioma, fibromatosis, neurofibroma, schwannoma, giant cell tumour of tendon sheath, glomus tumour and pigmented villonodular synovitis (PVNS).

A large (>5 cm) heterogeneous painless mass within a deep compartment should be regarded with a high suspicion of malignancy. The majority (95%) of benign soft-tissue tumours have a size <5 cm. It should be emphasised, however, that size on its own is not a good discriminator (Fig. 45.30). In addition, some benign lesions (e.g. haematomas) show heterogeneity in structure (Figs 45.21, 45.26). When sarcomas arise in the superficial tissues they tend to

he less aggressive compared with the deep-seated tumours. Sarcomas tend to be painless without limb dysfunction, unless adjacent to neurovascular structures. A previously painless mass that becomes painful should, however, arouse suspicion of malignancy (a useful criterion when assessing patients with neurofibromatosis and multiple nerve sheath tumours).

MRI

It is useful to assess the MRI findings in terms of the various criteria given in Box 45.3. It is important that the location and full extent of any soft-tissue mass, together with its relationship to the adjacent joint and surrounding anatomical structures, be clearly demonstrated. This requires the use of multiple imaging planes using a variety of pulse sequences as described above. It was originally hoped that MRI would correctly characterise different tissues on the basis of signal intensity appearances on T₁- and T₂-weighted images. Subsequent work has shown that signal intensity patterns are not a good discriminator between benign and malignant tumours, but some soft-tissue tumours can be diagnosed with certainty. A well-defined soft-tissue mass with homogeneous signal intensity cannot be assumed to be benign, neither is a mass with a heterogeneous signal intensity necessarily malignant. The variable specificity of MRI is also compounded by the relative inexperience of the general radiologist in reviewing such cases. One aspect of this technique not to be underestimated, however, is that it is highly accurate as a negative predictor of a clinically suspected soft-tissue mass, defining normality with certainty.

The majority of malignant soft-tissue tumours have well-defined margins with a so-called 'pseudocapsule'. It should be noted that the pseudocapsule does contain tumour cells and these extend outside this structure on histological review. Soft-tissue lesions that have ill-defined margins with infiltration of surrounding structures are usually inflammatory (c.g. acute myositis ossificans or soft-tissue infection). The majority of malignant soft-tissue tumours have a non-specific low and high signal on T₁- and T₂-weighted images respectively (Fig. 45.32).

There are some soft-tissue tumours that have characteristic signal intensities on T₁- and T₂-weighted images (Boxes 45.4, 45.5). The differential diagnosis of lesions containing high signal on T₁-weighted images is limited to either fatty tissue or blood products (Figs 45.3, 45.20, 45.31). Lipomas have well-defined margins with a

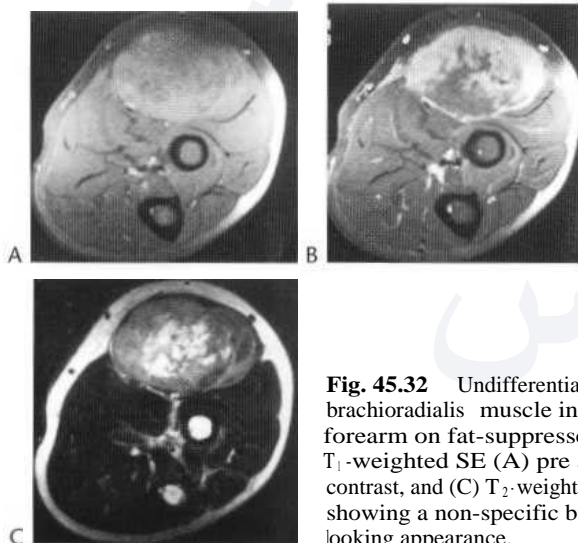


Fig. 45.32 Undifferentiated sarcoma in brachioradialis muscle in the proximal forearm on fat-suppressed transverse T₁-weighted SE (A) pre and (B) post contrast, and (C) T₂-weighted TSE images showing a non-specific but malignant-looking appearance.

Box 45.4 Signal intensity on T₁-weighted images (reference tissue—muscle)

Homogeneous low SI

- Cyst
- Ganglion
- Lymphocele
- Cystic hygroma
- Myxoma
- Myxoid sarcoma

Moderate to high SI

- Lipoma
- Subacute haematoma
- Haemangioma
- Well-differentiated liposarcoma
- Intralesional haemorrhage
- Lipoma arborescens
- Elastofibroma
- Fibrolipohamartoma
- Melanoma

Slight increased SI

- Neurofibroma/schwannoma
- Haemangioma
- Abscess
- Solid malignancies

Box 45.5 Low-signal intensity on T₂-weighted images

- Fibrous lesions—plantar fibroma
- Morton's neuroma
- aggressive fibromatosis (desmoid)
- Some malignant fibrous histiocytoma (MFH)
- Some malignant peripheral nerve sheath tumour (MPNST)
- Pigmented villonodular synovitis (PVNS)
- Giant cell tumour of tendon sheath
- Aneurysms/vascular malformation
- Chronic haematoma
- Amyloid
- Gouty tophus

uniform signal intensity of fat on all sequences (best confirmed using fat-suppressed sequences) (Fig. 45.3). Even when soft-tissue masses have characteristic appearances, such as lipomas, problems can still occur. Most lipomas tend to interpose themselves between tissues but some, for example intramuscular lipomas, may involve both muscular and intramuscular tissue. Some lipomas may also have internal septa, an appearance mimicking a well-differentiated liposarcoma (termed atypical lipoma) (Fig. 45.33). The use of contrast-enhanced fat-suppressed T₁-weighted images can be helpful in separating between enhancing nodular tumour and non-enhancing linear septae. Other lesions return a characteristic low signal or signal void on T₂-weighted images (Box 45.5) (Figs 45.14, 45.15, 45.34, 45.35). Haematoma and malignant melanoma can demonstrate variable signal due to their paramagnetic contents.

Certain tumours have a characteristic morphology in addition to their signal intensity appearance. Soft-tissue (subcutaneous and intramuscular) cavernous haemangiomas have a typical appearance with serpentine (*not* 'serpiginous' as this is an incorrect term) vascular channels surrounded by excess fatty tissue (Fig. 45.36). The vessels can demonstrate high-signal intensity on T₂-weighted images, but may also return a signal void depending on the flow

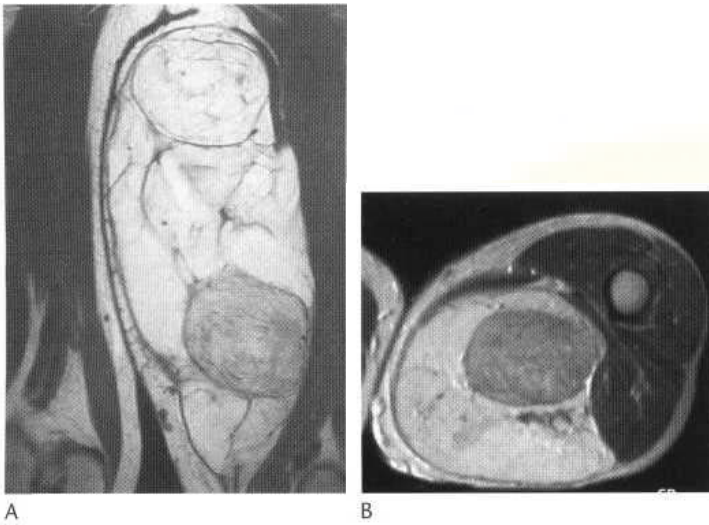


Fig. 45.33 Well-differentiated liposarcoma (atypical lipoma) in the medial thigh compartment on (A) coronal T₁-weighted SE and (B) transverse T₂-weighted TSE images.

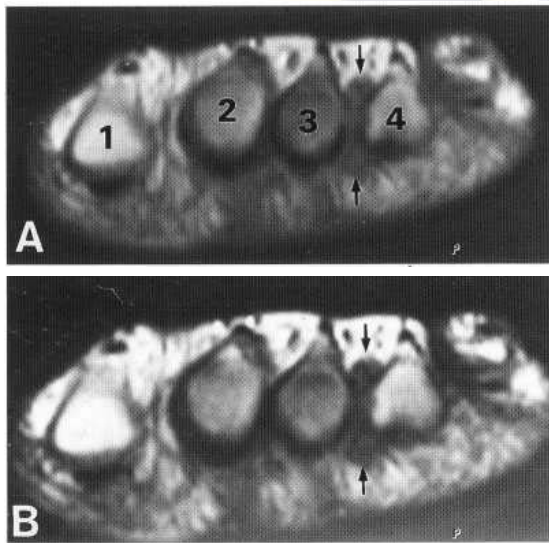


Fig. 45.34 Morton's neuroma (arrows) in the web space between the third and fourth metatarsal heads on coronal (short-axis) (A) intermediate- and (B) T₂-weighted dual echo images. This interdigital tumour is not a true neoplasm but a post-traumatic, degenerative fibrosing process around the plantar digital nerves. It is the most common entrapment syndrome in the foot and is frequently bilateral. The dense fibrous tissue making up this lesion is reflected in its low signal in (B).

rate within the vessels. Cavernous haemangiomas are usually well defined with lobular contours, but may also appear infiltrative crossing fascial boundaries and involve adjacent bone. Neurogenic tumours usually show a characteristic morphological appearance being often related to a neurovascular bundle particularly in the extremities. These tumours usually have a fusiform shape with the nerve often seen entering and exiting the mass (Fig. 45.37). The presence of this sign is pathognomonic but it is not always seen with neurogenic tumours of small nerves or those in the subcutaneous tissues/retroperitoneum. A target sign can be present with a central hypointensity surrounded by high signal on T₁-weighted images this sign, however, can also be found in an acute haematoma (Fig. 45.38). Intermediate (proton density) and T₁-weighted scans often reveal small ring-like areas of intermediate to low

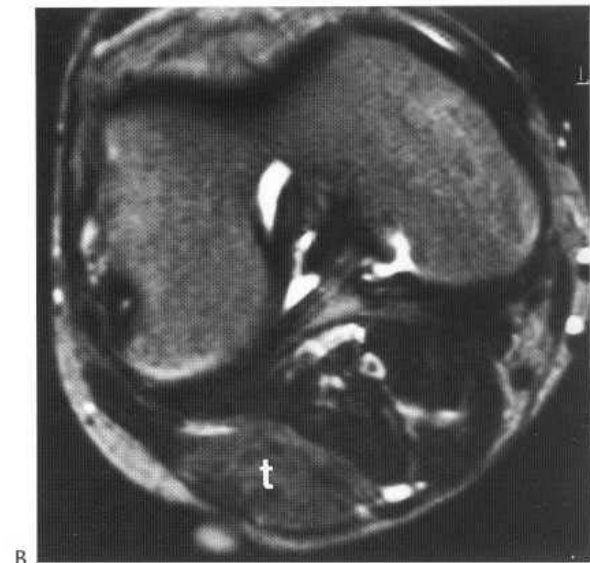


Fig. 45.35 Aggressive fibromatosis (desmoid) (t) in a 26-year-old male on (A) sagittal intermediate-weighted and (B) transverse T₂-weighted TSE images. Note the characteristic multiplicity and mixed composition of this tumour with an area of signal void from fibrosis together with more cellular soft-tissue components. There is a cod liver oil capsule (c) in place as a marker.

signal surrounded by slightly higher signal intensity on the periphery (Fig. 45.38). This has been termed the 'fascicular sign' and is thought to reflect the fascicular bundles of tissue seen within neurogenic tumours and normal nerves. This fascicular sign is usually seen in benign lesions although occasionally can be seen in MPNST. The enhancement patterns following gadolinium-chelate injection are non-specific. Many neurogenic tumours also have a peripheral rim of fat. The distinction between neurofibromas (being central within the nerve) and schwannomas (eccentric to the nerve but within its sheath capsule) can be difficult but may be made if the lesion involves a large nerve.

There are a few specific soft-tissue tumours that have a propensity to be multiple (Box 45.6). Careful follow-up and/or biopsy are required for indeterminate lesions.

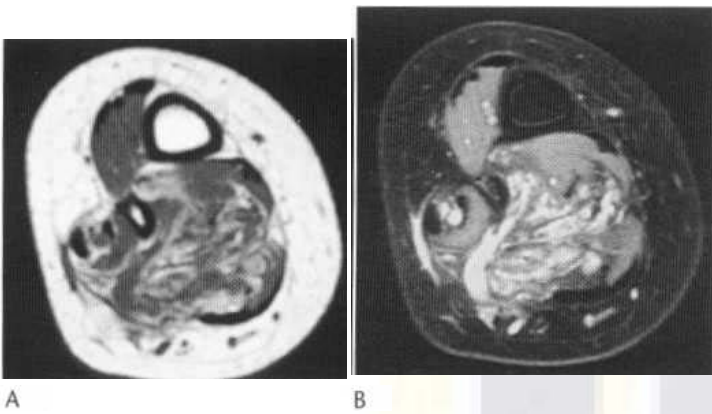


Fig. 45.36 Soft-tissue cavernous haemangioma in an 11-year-old girl with 18-month history of a soft-tissue swelling exacerbated by exercise on transverse (A) T_1 -weighted SE and (B) fat-suppressed proton density-weighted FSE images. Note the serpentine appearance of the vascular spaces infiltrating the muscles of the posterior and lateral compartments and subcutaneous tissues, together with some fat content typical of this lesion.



Fig. 45.37 Malignant peripheral nerve sheath tumour (MPNST) in the posterior compartment of the thigh on a sagittal fat-suppressed T_2 -weighted TSE image showing the sciatic nerve (arrow) entering and exiting the heterogeneous mass.

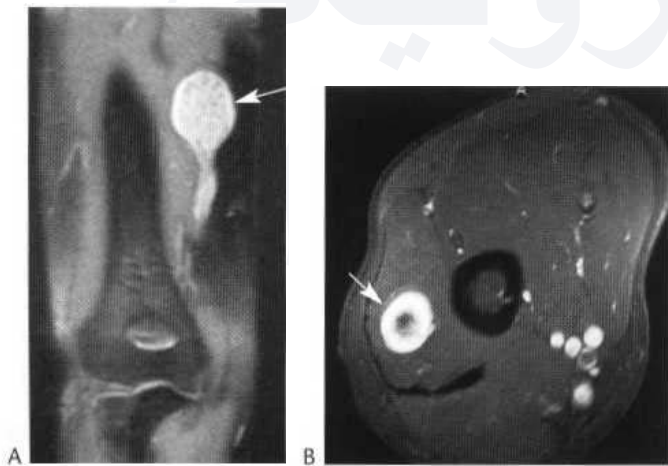


Fig. 45.38 Ulnar nerve neuroma (arrows) within the medial triceps muscle on (A) coronal fat-suppressed proton density-weighted FSE and (B) transverse fat-suppressed T_1 -weighted SE postcontrast image. In A the neuroma demonstrates a thickened exiting ulnar nerve together with small ring-like areas with a higher periphery signal reflecting the fascicular bundles (termed the fascicular sign). The fascicular sign, optimally appreciated on proton density images, is usually seen in benign tumours, but if present in MPNST is only focal. In B the target sign is shown.

Box 45.6 Multiple soft-tissue tumours

- Lipomas (5-15% of patients presenting with a soft-tissue mass)
- Nerve sheath tumours (neurofibromatosis)
- Aggressive fibromatosis (desmoids)
- Angiomatous lesions
- Myxomas (association with polyostotic fibrous dysplasia-Mazabraud's syndrome)
- Secondaries (multiple myeloma, melanoma)

Tumour recurrence

MR1 plays a major role in the detection of tumour recurrence. In the postoperative patient, most metallic surgical clips or prosthetic implants produce only minimal localised image artefact, and diagnostic scans can often be obtained. Some metallic implants such as bone screws are ferromagnetic, however, and produce significant image artefact. Problems can arise in separating high-signal tumour from radiation change or early postoperative appearances due to inflammation, haemorrhage or infection, although some discrimination can be made with careful review of signal intensity appearances on T_1 -weighted images, and fat-suppressed T_1 -weighted post enhancement (Fig. 45.39). A low-signal lesion on T_1 -weighted images following radiation therapy or surgery for a malignant soft-tissue sarcoma most likely indicates that the patient does not have active tumour. A possible tumour recurrence is shown as a high-signal-intensity mass on T_1 -weighted images. However, there can be difficulty in separating the changes related to recent treatment, particularly radiotherapy, from tumour. Nodular enhancement following contrast injection should be

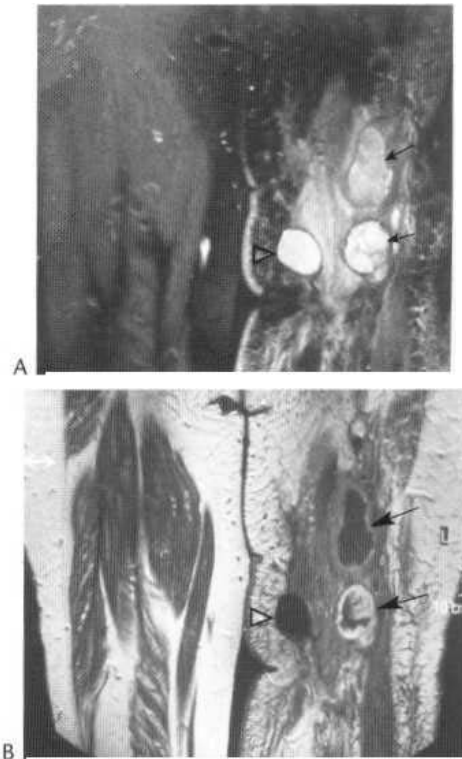


Fig. 45.39 Two separate recurrent sarcoma masses (arrows) and a benign seroma (arrowhead) in the posterior compartment of the thigh on coronal (A) fat-suppressed T_2 -weighted TSE and (B) postcontrast T_1 -weighted SE. The patient had undergone prior surgery and post-radiation treatment for a malignant fibrous histiocytoma. The post-treatment change is producing the diffuse infiltrative abnormal signal with the tumour recurrences showing cystic nodular enhancing masses.

regarded as tumour recurrence. Dynamic gadolinium-chelate enhancement (obtaining images within 6 seconds of the injection) has been found to be helpful in distinguishing recurrent tumour (early enhancement from neoangiogenesis) from radiation-induced inflammation and necrosis (later enhancement via the normal vascular supply).

Infection

MRI is more sensitive than radionuclide scanning in the demonstration of soft-tissue infection without bone involvement. Soft-tissue cellulitis, abscess formation, sinus tracts, septic arthritis and osteomyelitis can be differentiated using contrast enhancement (Figs 45.5, 45.40, 45.41). Cellulitis shows an ill-defined area, whereas an abscess is a well-defined mass, of low and high signal on T_1 - and T_2 -weighted images respectively, in the presence of normal bone marrow. A joint effusion is the first sign of septic arthritis progressing to chondrolysis and bone erosion. Distinction between infected and non-infected joint fluid cannot be made on MRI even with contrast enhancement. MRI is, however, useful in a patient with signs of infection, allowing a number of sites of infection to be imaged simultaneously, to demonstrate any coincidental osteomyelitis and for guidance for percutaneous aspiration. Osteomyelitis demonstrates abnormal bone marrow with an associ-

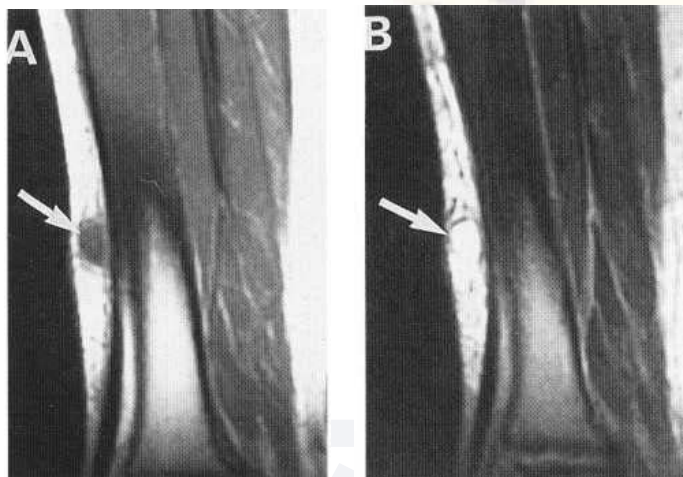


Fig. 45.40 Soft-tissue abscess (arrow) with surrounding oedema and radiating linear strands (due to dilated lymphatics) on coronal spin-echo (A) proton density-weighted and (B) T_2 -weighted SE images. The absence of bone marrow involvement excludes osteomyelitis.

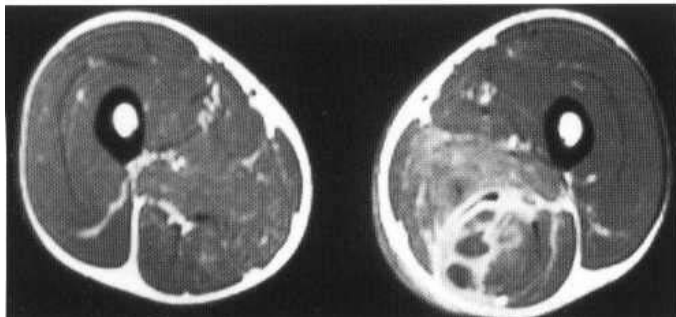


Fig. 45.41 Soft-tissue infection within the posterior and adductor compartments of the left thigh in 37-year-old woman with no associated symptoms on a transverse postcontrast T_1 -weighted SE image. There is replacement of musculature with abscess formation and infiltrative oedematous signal, appearances different to that of a soft-tissue sarcoma.

ated surrounding soft-tissue mass (Fig. 45.5). The infiltrative homogeneous morphological pattern of soft-tissue infection can be differentiated from the well-delineated heterogeneous appearance found with the majority of soft-tissue tumours (Fig. 45.41). MRI is of value in the evaluation of the growth plate in the growing skeleton where isotope scanning shows a normal high uptake, obscuring abnormality. MRI may also have a useful role in the detection of infection in the diabetic foot, although difficulties arise in the differentiation from neuropathic changes. The presence of secondary signs of cortical interruption, skin ulceration and a sinus tract can increase specificity for infection. Soft-tissue infection cannot be differentiated from non-infective inflammation, soft-tissue trauma or postoperative changes on MRI, alone.

Inflammation

Inflammatory arthropathies can be demonstrated early during the course of the disease and, although not used in routine evaluation, MRI can be of value in making the diagnosis in a clinically unsuspected case and in monitoring treatment. A finding of widespread tenosynovitis around the ankle or wrist points to a diagnosis of seronegative arthropathy. MRI can demonstrate joint effusions, tenosynovitis, hyaline and fibrocartilage destruction, and pannus formation. It is of particular value in the assessment of involvement of the cervical spine, clearly depicting erosions, synovial overgrowth and pannus formation, atlanto-axial subluxation and cord compression.

In the evaluation of patients with recurrence of symptoms following previous lumbar disc surgery, MRI is considered to be the most accurate technique in differentiating between a recurrent/residual disc and postoperative granulation/scar tissue. The use of contrast enhancement allows enhancing granulation tissue to be differentiated from non-enhancing disc.

PLAIN FILMS

Janet Murfitt and Fritz Starer

The soft tissues can always be visualised on a plain film. The majority of films are taken to visualise bony structures and bright lighting is needed to see the soft tissues satisfactorily. Soft-tissue-specific films require a low kV and low filtration. Fat has a sufficiently different coefficient of absorption to muscle to allow the normal fat planes to be seen. In particular the subcutaneous fat outlines the skin and fat pads are present around joints. Fat within a muscle can give a faint herringbone pattern.

It is well recognised that the soft tissues can cause artefacts, particularly the pinna on the lateral skull film and skin folds in the neonate overlying the chest. Superficial cutaneous nodules, for example the nipple shadow on the chest film, are surrounded by air and are sharply demarcated. When two soft-tissue shadows overlap the mach effect results in a thin dark line which may suggest a fracture if overlying a bone.

Foreign bodies

Both metallic (Fig. 45.42) and glass foreign bodies are usually visible on a plain film whereas wood and plastic (Fig. 45.43) are rarely identifiable but may be demonstrated by ultrasound and CT. The site of entry of the suspected foreign body should be indicated on the plain films without the marker overlying the soft tissues. Views in two planes are necessary to confirm a density is lying

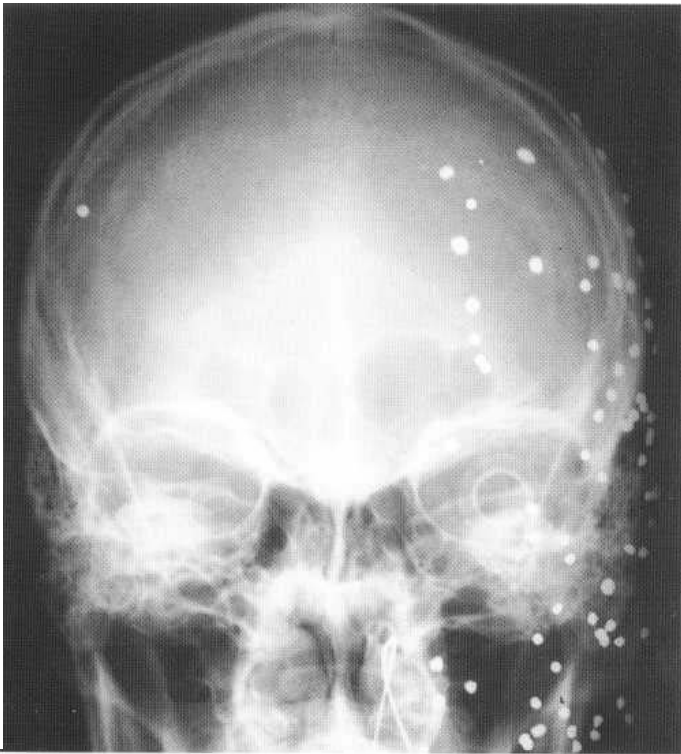


Fig. 45.42 Multiple shot-gun pellets. Note the left glass eye as the result of a previous encounter.



Fig. 45.43 Tendon implant.

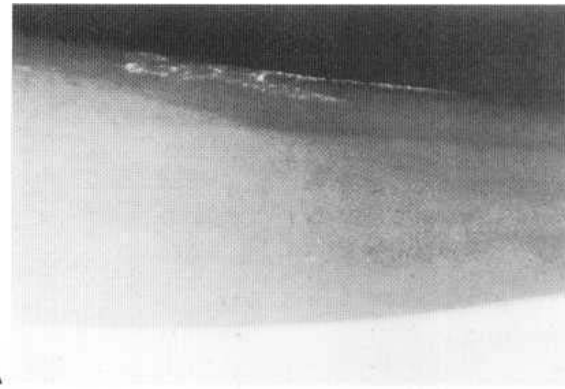
within the tissues and is not an artifact or on the skin surface. Over a period of years foreign bodies often migrate, sometimes over significant distances.

Tattoos (Fig. 45.44) may show as superficial densities. Injection sites are frequently seen particularly in the buttocks. Bismuth (Fig. 45.45) and other heavy metal injections may result in opaque needle tracks or rounded sterile abscesses. Quinine causes soft-tissue necrosis which shows as calcified ring shadows.

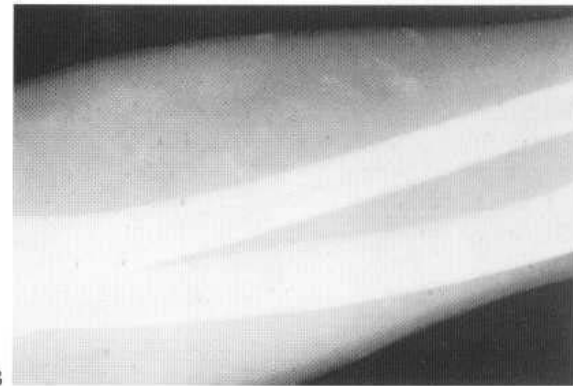
Gas

Air in the soft tissues appears as bubbles or linear streaks of transparency less dense than fat. Gas may be seen in bowel lying within a hernia most commonly in the groins or periumbilical region. Occasionally gas can be identified within a sinus track.

Gas-forming organisms, particularly *Clostridium perfringens*, cause gas gangrene with superficial bubbles and/or linear streaks of gas lying subcutaneously or along the muscle fibres (Fig. 45.46). A focal collection of gas may be seen within an abscess. When there



A



B

Fig. 45.44 (A,B) Mercury and iron compounds in pigments of a tattoo.

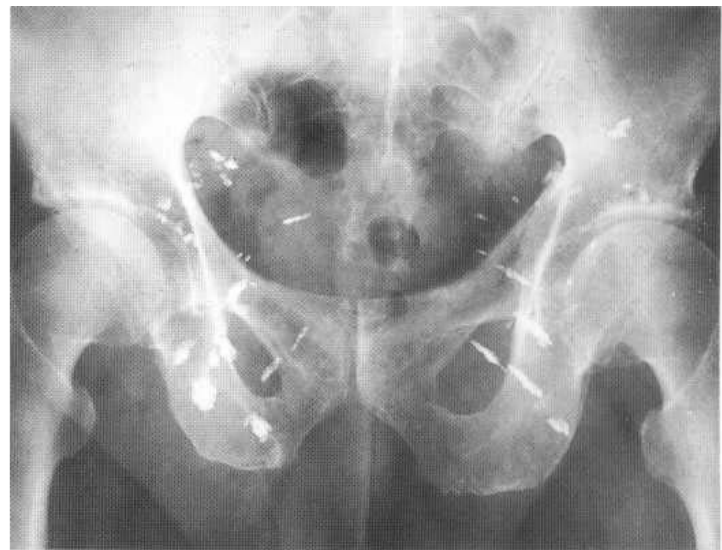


Fig. 45.45 Bismuth injection sites in the buttocks.

has been a penetrating injury, any increase in the amount of gas present on serial films is indicative of gas gangrene. Diabetics are particularly prone to such infections.

Following penetrating trauma or open wounds, gas may be introduced into the soft tissues, both subcutaneously and in the fascial planes, or into a joint (Fig. 45.47). Surgical emphysema may follow thoracic surgery or occur as a result of trauma with rib fractures, lung parenchymal injury or rupture of the airways or oesophagus. Air will track up from the mediastinum to the neck. Following rib fractures, surgical emphysema may occur in the absence of a pneumothorax. The emphysema usually resolves within a few days.



45.46

Fig. 45.46 Gas gangrene.



45.47

Fig. 45.47 Major trauma with soft-tissue disruption. Fractured ankle with air in the joint and soft tissues.

Fat

The *lipoma* is one of the commonest of the soft-tissue benign tumours. Its high fat content contrasts with the surrounding soft tissues and it appears as a well-defined lucency (Fig. 45.48). Sometimes a lipoma has a high fibrous content and is less translucent. Calcification is rare and forms centrally within an area of ischaemic necrosis.

With *muscular dystrophy* (Fig. 45.49) there is loss of normal muscle bulk. Initially there is infiltration of the muscle with fat accentuating the normal herringbone pattern to give a striated appearance with translucent streaks. Ultimately the muscle is totally replaced by fat so that the muscle sheath is clearly outlined as a linear density. In the *Duchenne type muscular dystrophy*, the muscles appear bulky although replaced by fat. *Arthrogryposis multiplex congenita* is a hereditary disorder with poor muscle development replaced by a relative excess of fat. The bones are osteopenic and slender. There are multiple associated abnormalities including contractures, fractures, congenital amputations and hip dislocation.

Following a fracture of the bone involving a joint, blood and fat is released from the bone marrow into the joint creating a *lipoma arthrosis*. With a horizontal beam film a fat-fluid level may be seen with the fat floating on the blood. The shoulder (Fig. 45.50) and the knee are the most common sites. Displacement of the fat planes around a joint, especially the elbow, is another sign suggesting bleeding into a joint due to a fracture.

If it persists or increases in volume this implies a persistent leak, for example a bronchopleural fistula. Surgical emphysema in the lower abdominal wall and thigh may follow rupture of a diverticular pelvic abscess.

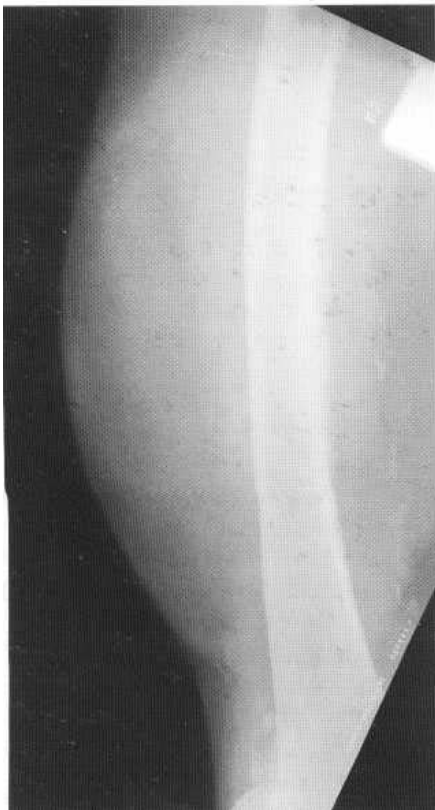
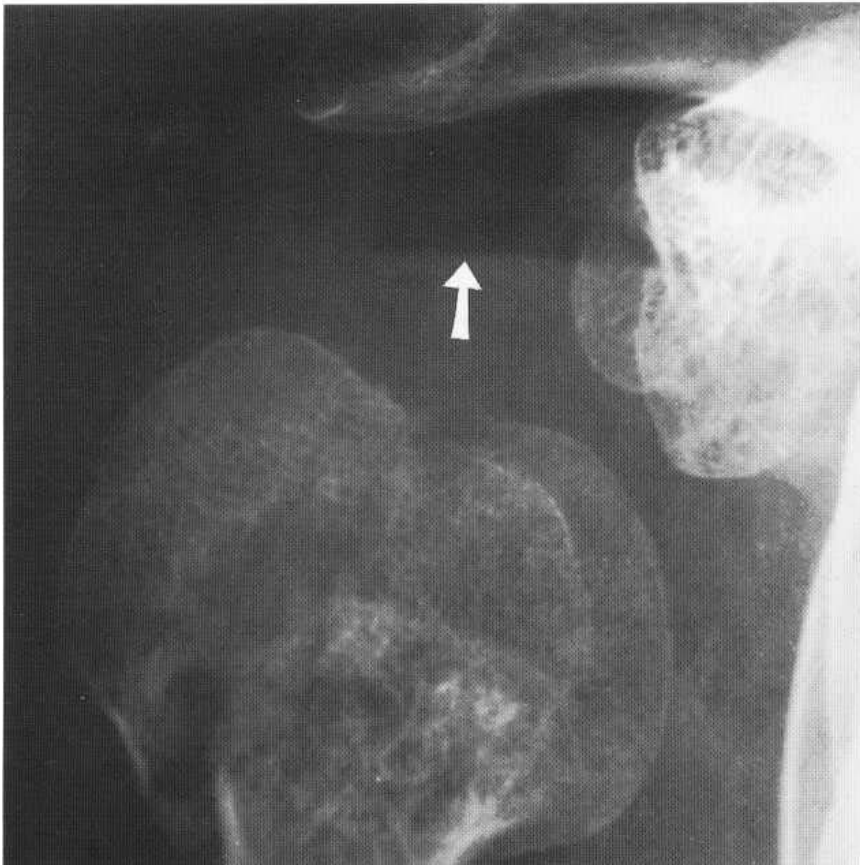


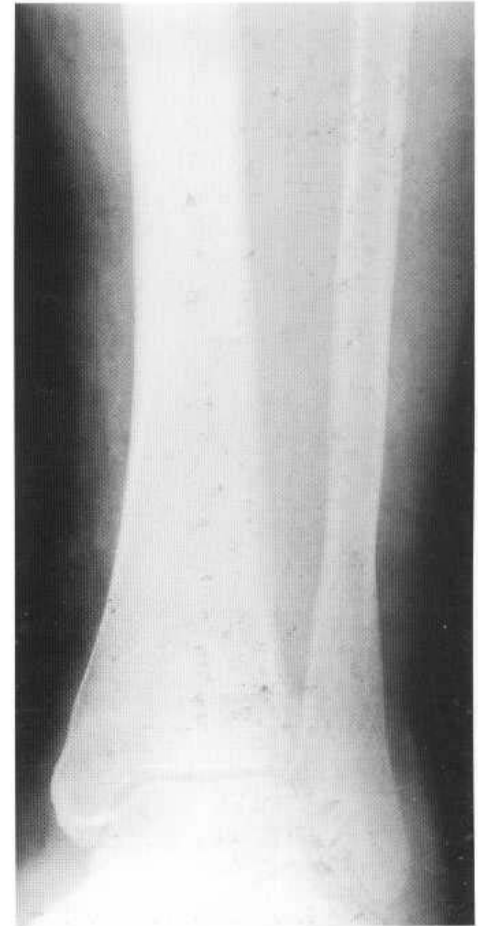
Fig. 45.48 Large well-defined lipoma of the thigh.



Fig. 45.49 Peroneal muscular dystrophy. Atrophied muscle replaced by fat.



45.50



45.51



45.52

Fig. 45.50 Lipohaemarthrosis of the shoulder. Fracture-dislocation of the humeral head. (Courtesy of Dr F. Starer.)

Fig. 45.51 Cellulitis of the lower leg. Oedema and loss of tissue planes.

Fig. 45.52 Calcified popliteal aneurysm..

Oedema

Oedema of the soft tissues causes increased thickness with prominence of the fibrous septa giving a coarse reticular pattern, and obliteration of the tissue planes (Fig. 45.51).

Thickening of the soft tissues occurs in acromegaly and is most obvious in the hands and the heel pad. The heel pad thickness is measured from the tip of the os calcis to the plantar skin surface of the heel. The upper limit of normal is 23 mm.

Ossification and calcification

Calcification in the soft tissues may be classified as *metastatic* as a result of abnormal calcium metabolism, *calcinosis* with a normal calcium metabolism or *dystrophic* related to tissue damage. Ossification can be recognised by the presence of trabeculae within the calcified area.

Arteries Calcification of the aorta, iliac and femoral arteries is a common finding due to irregularly calcified atheromatous plaques. The extent of the calcification does not correlate with the severity of the disease. Curvilinear calcification in a soft-tissue mass adjacent to a vessel is a typical finding of an aneurysm (Fig. 45.52).

With Monckeberg's medial atherosclerosis there is calcification of the media without narrowing of the lumen giving a pipestem ring-like pattern. Calcification in the small vessels of the feet is characteristic of diabetes mellitus and hyperparathyroidism. Calcification of the vessels is not a feature of Buerger's disease.

Veins A phlebolith is calcified thrombus in a vein and is typically 3-5 mm in length with a central lucency. They are a normal finding in the uterine and prostatic veins in the pelvis but when a focal collection of phleboliths is seen elsewhere it is characteristic



Fig. 45.53 Cavernous haemangioma of forearm with multiple phleboliths.

Fig. 45.54 Chronic venous stasis with calcification.

Fig. 45.55 Neural calcification in leprosy.

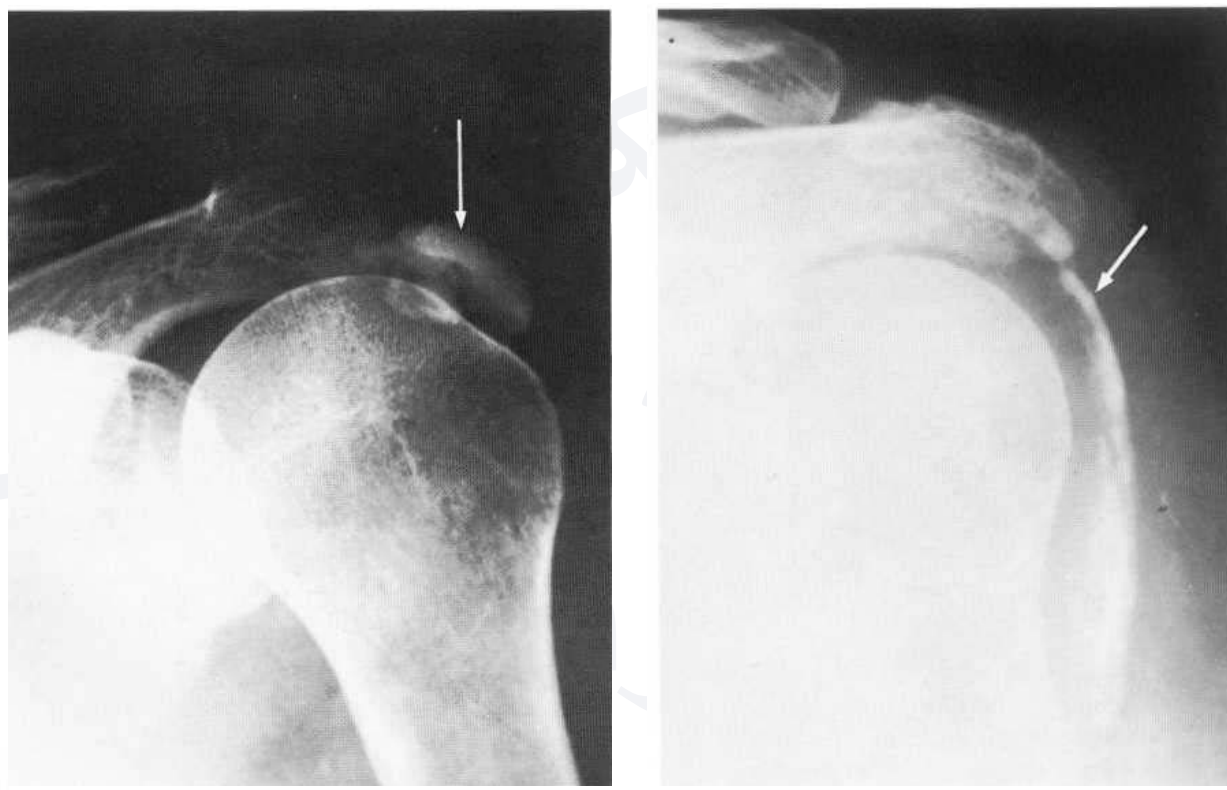


Fig. 45.56 (A) Calcification in the supraspinatus tendon (arrow). (B) Same patient. Following sudden cessation of pain there has been extrusion of calcareous material (arrow) from the tendon.

of a cavernous haemangioma (Fig. 45.53). Chronic venous stasis of the legs may cause subcutaneous calcification in a linear, branching or plaque-like pattern (Fig. 45.54). Ulceration, phleboliths and well-organised periosteal reactions may also be present. Occasionally a thrombus in a vein may calcify along its length.

Nerves Neural calcification is very rare but has been reported in leprosy and neurofibromatosis (Fig. 45.55).

Lymph nodes

Calcified mediastinal and hilar nodes are a frequent finding, in the majority of cases following tuberculosis. Nodes in the cervical chain may also be involved. The calcification is typically coarse and mottled.

Tendons

The tendons, particularly the patella and Achilles tendons, are often outlined by fat. Calcific tendonitis develops following chronic trauma and inflammation. The supraspinatus tendon is most commonly responsible for a frozen shoulder, although other tendons of the rotator cuff may be affected. Calcification lies directly over the humeral head in a crescentic distribution (Fig. 45.56) and may be present in asymptomatic patients. Other common sites are the flexor carpi radialis in violinists and the medial collateral ligament of the knee, known as the Pellegrini-Stieda lesion (Fig. 45.57). Ossification may also occur particularly in the Achilles tendon (Fig. 45.58). This is probably related to previous trauma and is four times more common in males than females. Ossification of tendons and ligaments is also more frequent in diffuse skeletal hyperostosis (DISH) mainly involving the axial skeleton and foot. Prominent muscle attachments in the pelvis are a feature of fluorosis with sclerosis, a coarse bony trabecular pattern and calcification of the pelvic sacrotuberous and sacrospinous ligaments. Bursae appear as soft-tissue swellings related to the joints but calcification is uncommon.

Parasites

The ova of the pork tapeworm, *Taenia solium*, are ingested by eating undercooked infected meat with the pig being the intermedi-

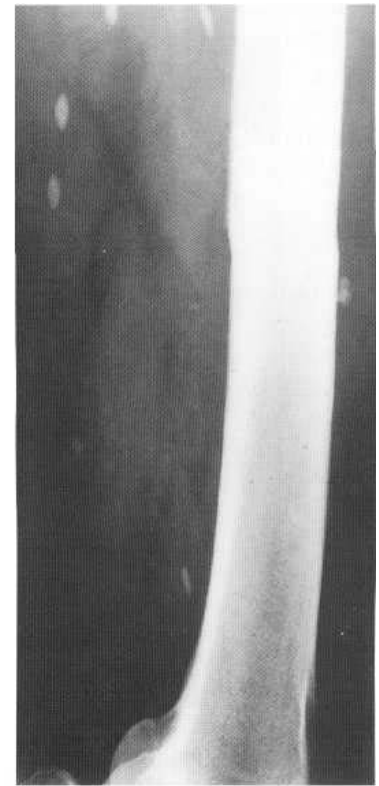


Fig. 45.57 Pellegrini-Stieda lesion of medial femoral condyle.



45.58

Fig. 45.58 Ossification in the Achilles tendon.



45.59

Fig. 45.59 Cystercicosis.

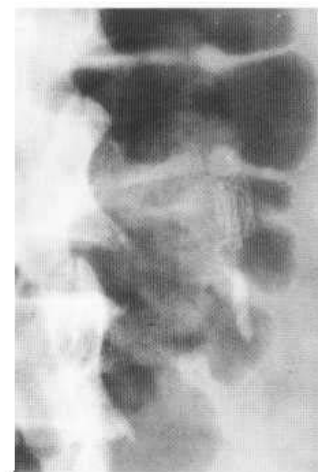
ate host. The embryo enters the bloodstream and the parasite, *Cysticercosis cellulosa*, becomes encysted within the soft tissues, brain and meninges. In muscle the parasite calcifies forming ellipsoid masses 10-15 mm long often with a translucent centre and which lie in the direction of the muscle fibres (Fig. 45.59). This infection is most frequent in Mediterranean countries, and the Middle and Far East.

The guinea worm, *Dranunculus medinensis*, dies in the muscles forming a spherical calcified mass (Fig. 45.60) or a long string-like



45.60

Fig. 45.60 Calcified guinea worm mass.



45.61

Fig. 45.61 Calcified guinea worm.



Fig. 45.62 *Loa loa*.

calcified worm 10-12 cm in length (Fig. 45.61). This infestation occurs in India, Africa and the Middle East. *Loa loa*, or microfiliariasis, is a small parasite which is common in West Africa. It dies and calcifies appearing as coiled threads in the hands and feet (Fig. 45.62). *Armillifer armillatus* is a parasite which infests snakes and infects humans who eat them. It appears as C-shaped calcifications less than 1 cm in length in the serosa of the chest and abdomen (Fig. 45.63).

Hydatid cysts in the soft tissues are rare and the calcification is usually atypical and non-specific.

Metabolic

Metabolic or metastatic calcification is the result of abnormal calcium or phosphate metabolism, in particular any cause of hypercalcaemia. This occurs more commonly with secondary hyperparathyroidism rather than the primary form with calcification of the menisci and arteries. Periarticular calcinosis develops as well as metastatic calcification in the soft tissues (Fig. 45.64). This may

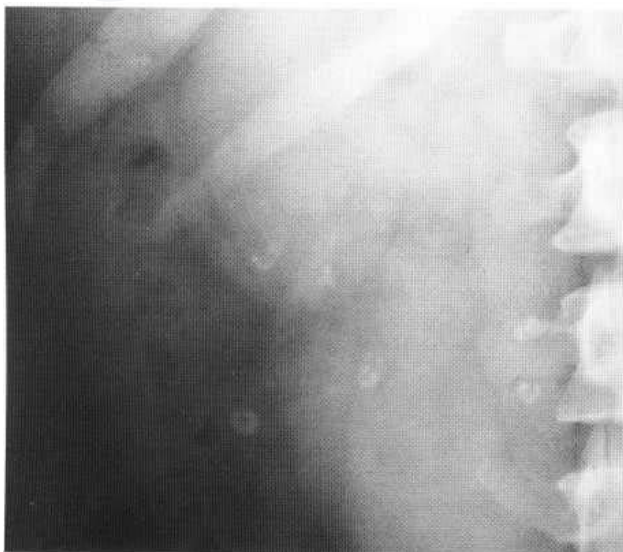


Fig. 45.63 *Armillifer armillatus*.

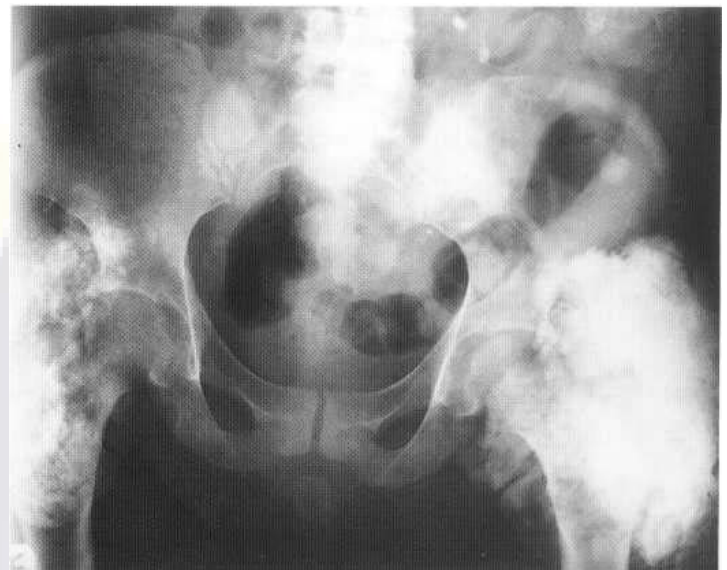


Fig. 45.64 Extensive metastatic calcification in renal failure.

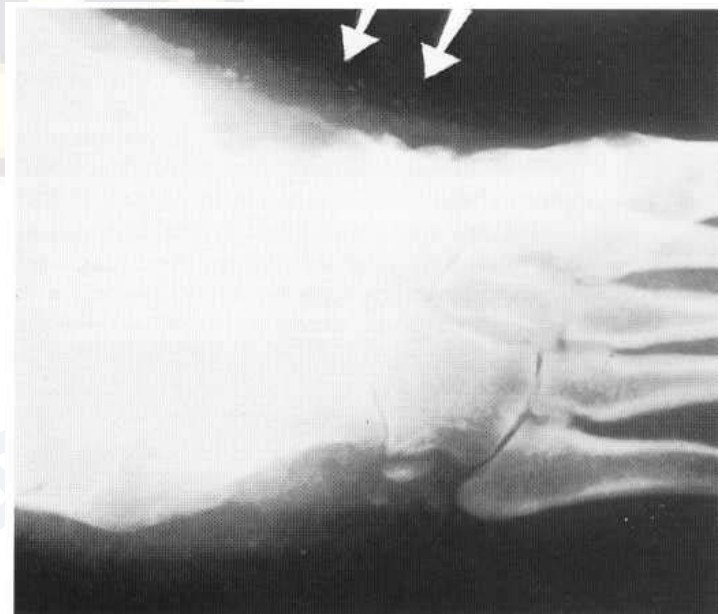
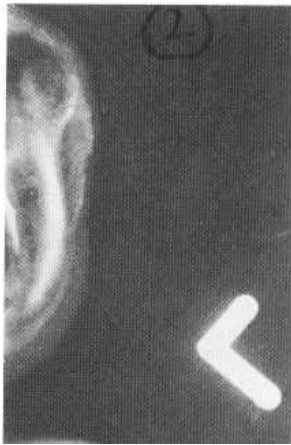


Fig. 45.65 Pseudohypoparathyroidism causing nodular soft-tissue calcification.

be so extensive that layering of the calcium is seen. Following treatment of the hypercalcaemia the soft-tissue calcification may resolve.

Periarticular and interstitial calcinosis may be seen with hypoparathyroidism. In pseudohypoparathyroidism there may be punctate or nodular areas of soft-tissue calcification (Fig. 45.65). In pseudopseudohypoparathyroidism calcification of the skin, subcutaneous tissues, fascia) planes and tendons is present in 30-50% of cases. Other associations are calcification of the dentate nuclei and basal ganglia and cataracts. Calcification of the pinna is a feature of alkaptonuria, Addison's disease (Fig. 45.66) and frostbite. With gout, deposits of calcium urate in the soft tissues form calcified, juxta-articular masses, or tophi, with associated para-articular erosions.



45.66



45.67

Fig. 45.66 Calcification and ossification of the pinna in Addison's disease.

Fig. 45.67 Calcified and ossified haematoma of the upper arm with an associated periosteal reaction.

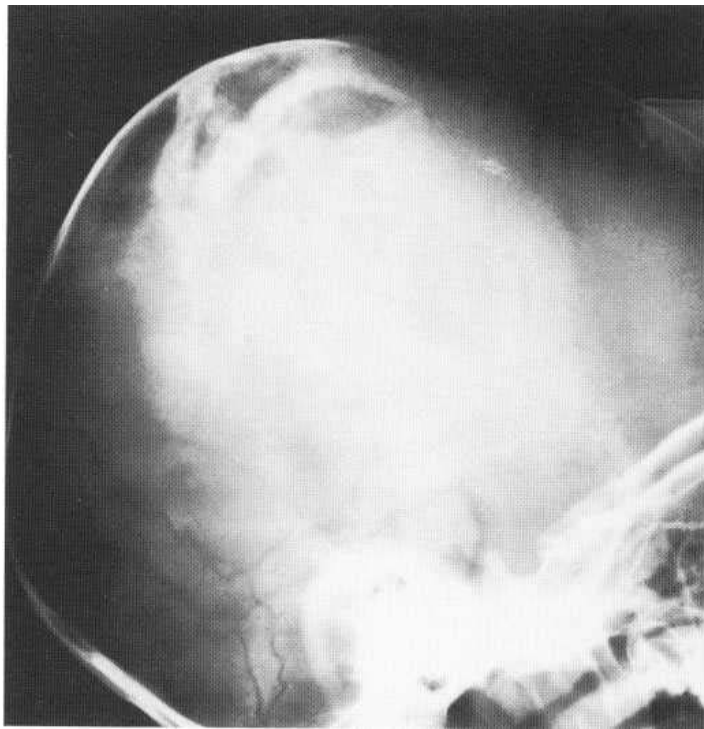


Fig. 45.68 Persistent irregular density in the parietal bone following a previous cephalhaematoma.

Haematomas

Initially there is an increase in soft-tissue density at the site of injury. Calcification is rare but may appear within a few days in children. It usually forms in the periphery of the haematoma. At this stage an isotope bone scan will show increased uptake. If the

trauma has caused an associated periosteal reaction, the resulting appearance can be difficult to differentiate from a parosteal sarcoma on the plain film (Fig. 45.67).

In neonates a subperiosteal bleed in the parietal bone results in a cephalhaematoma which may calcify. This slowly absorbs and disappears with time although an irregular bone density may persist for years (Fig. 45.68).

Soft-tissue necrosis

Necrosis of the soft tissues may follow injections (as previously described) and other forms of trauma, frostbite and burns. Post-traumatic fat necrosis results in coarse spheroid calcified masses. Frostbite typically affects the pinna. Burns occasionally calcify, particularly in children.

Calcinosis circumscripta

This is associated with scleroderma (Fig. 45.69) and Raynaud's disease. Dense areas of calcification develop in the hands and occasionally affect the large joints over the pressure areas. There is loss of the soft tissues of the tips of the fingers and associated bone changes including acro-osteolysis.

Calcinosis interstitialis universalis or dermatomyositis

This is a condition where there is degeneration of collagen tissue resulting in diffuse subcutaneous plaques or nodules of calcium or reticular calcification often with overlying ulceration. In addition with progression, calcified masses or sheets of calcium form in the deeper tissues and lie in the direction of the limbs (Fig. 45.70). There is normal calcium and phosphate metabolism. Those affected have pain and muscle weakness. If progressive the disease may be fatal. In adults there is an association between dermatomyositis and an increased incidence of malignancy.

Ehlers-Danlos syndrome is a hereditary disorder with findings including lax joints, fragile and elastic skin and blood vessels, acro-osteolysis and subcutaneous nodules which calcify. The nodules occur predominantly over the bony prominences and are oval or round, often ring-like and 2-10 mm in length. They need to be distinguished from phleboliths and parasites. Thickening of the skin of

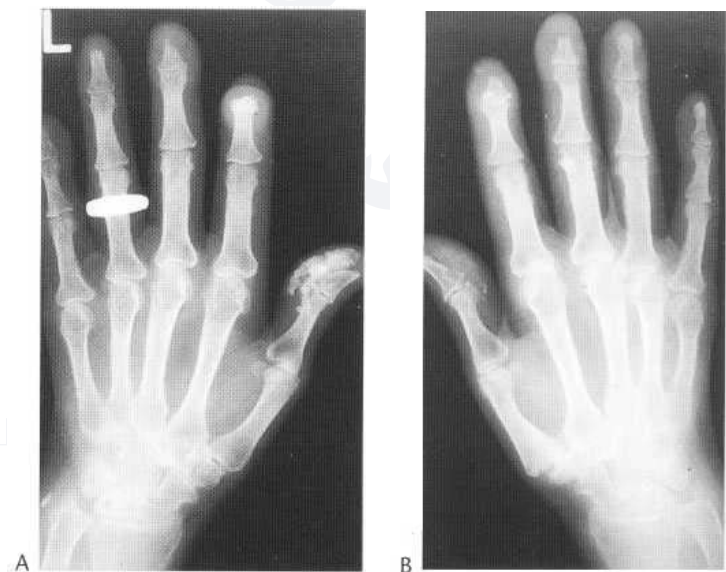
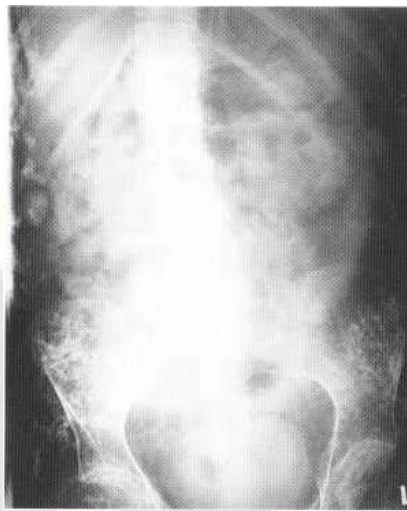


Fig. 45.69 Scleroderma. (A) Acro-osteolysis and (B) calcinosis circumscripta.



A



B

Fig. 45.70 (A,B) Dermatomyositis.

the hands and feet with loss of muscle bulk and premature ageing are features of *Werner's syndrome*. Arterial calcification in the hands and feet and calcification over the bony prominences are frequent findings.

Tumoral calcinosis

Tumoral calcinosis typically presents in young African men with swellings, which may be painful, around the large joints and predominantly affecting the extensor surfaces. The hips are most frequently involved followed by the elbows and the shoulders (Fig. 45.71). The joints themselves are normal. These masses arise in the fascial planes between the muscles and calcify or ossify, usually appearing well circumscribed, lobulated and solid, although the calcification may be of a lacy or linear pattern. Occasionally fluid levels are evident within the masses with the calcium lying inferiorly. Rarely there are associated periosteal reactions of the greater trochanter, ischium and elbow. There is often hyperphosphataemia with normal renal function, calcium and parathyroid hormone levels.

Pseudoxanthoma elasticum

This presents with similar calcified masses, arterial calcification and cutaneous xanthoma.

Ossification

Myositis ossificans

This condition is classified into three types: progressive, post-traumatic and paraplegic. The */progressive form*, myositis ossificans congenita, is a hereditary disease which is usually autosomal dominant or an isolated mutation and commoner in boys. It presents with ossification of the perimuscular fascia within one year and is associated with many congenital bone lesions such as phalangeal and metacarpal hypoplasia of the thumbs and big toes. Initially there is ill-defined hazy calcification of the soft tissues over the neck and back with soft-tissue masses. The swellings resolve and this is followed by the formation of irregular plates of bone with trabeculation and cortex formation which in the limbs lies along the axis of the muscles (Fig. 45.72). The joints become ankylosed. The condition is usually fatal. In the limbs the appearance needs to be distinguished from a parosteal sarcoma.



Fig. 45.71 Tumoral calcinosis. A large soft-tissue swelling with calcification.

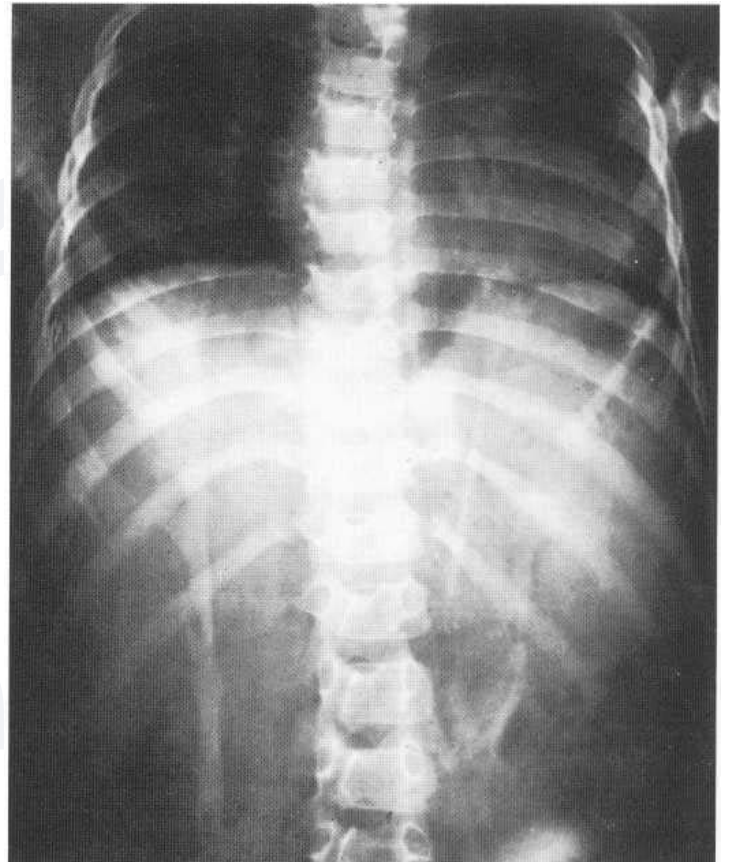


Fig. 45.72 Myositis ossificans congenita. Note the plates of bone formed in the soft tissues of the back.



Fig. 45.73 (A) Dislocated elbow. (B) Post-traumatic myositis.



Fig. 45.75 Calcified neural tumour.



Fig. 45.74 Paraplegic myositis around the hip.

Post-traumatic myositis results in a soft-tissue mass which ossifies with a lacy pattern by 4-8 weeks. Common sites are the elbow (Fig. 45.73) and knee. The ossification may resolve. Paraplegic myositis develops in paraplegics within 3-4 weeks below the level of the paralysis. There is heterotopic periarticular calcification and ossification around the joints particularly the hip with irregular plaques of bone forming (Fig. 45.74).

Tumours

The plain film is frequently non-contributory but there may be a soft-tissue swelling with a diffuse increase in density and distortion of the fat planes with bone destruction if malignant, or displacement of the fat planes and a bony pressure defect and sclerosis if benign. MRI is the investigation of choice in conjunction with a plain film or CT to demonstrate the presence of calcification.

The lipoma is the commonest soft-tissue tumour. Malignant tumours are rare, usually develop in the elderly and comprise less than 1% of all cancers. With neurofibromatosis there are multiple superficial skin nodules which are usually sharply demarcated by the surrounding air.

Various types of calcification may develop within both benign and malignant tumours (Fig. 45.75). Phleboliths occur in haemangiomas. Central calcified necrosis may be seen within a lipoma, but calcification is more commonly a feature of a liposarcoma.

A liposarcoma usually develops in the middle aged and elderly in the deep soft tissues of the thigh, buttocks and retroperitoneum. They are more opaque than the benign lipoma and less well defined with calcification forming between the fatty lobules (Fig. 45.76). Large irregular calcified areas may be found with a soft-tissue osteogenic sarcoma or a synovial sarcoma. Only 10% of synovial



Fig. 45.76 Calcified liposarcoma.

sarcomas arise primarily from the joint and they may develop in tendon sheaths. The majority occur in the lower limb. Calcification occurs in one-third of synoviomias and is associated with a better prognosis. Primary soft-tissue chondrosarcomas are rare and associated calcification may be amorphous, spotty or streaky. Similar calcification is described with other sarcomas.

Juvenile fascial or aponeurotic fibroma is a rare benign tumour which presents as a painless mass in infants and children. It arises from the aponeurosis of the palm of the hand but also the lower leg and foot. It is often very large with stippled calcification appearing late. It is locally invasive.

CT OF SOFT TISSUES

Richard W. Whitehouse

Technical considerations

CT of the *chest and abdominal walls* can be performed using similar techniques to those for routine chest and abdominal scanning and is thus familiar to most CT departments. Routine assessment of the chest or abdominal wall should be a part of all CT scans of these regions (Figs 45.77, 45.78). Scanning of the *limbs* is much less frequently performed. Careful technique and consideration of patient positioning is required to obtain optimal results. Reducing the volume of tissue within the scan plane will allow scans at a lower mA with better signal-to-noise ratio, lower patient radiation dose, less beam hardening and less streak artefact. Therefore, it is generally better to scan only one limb at the site of pathology rather than both limbs together.

For the lower limbs, it is feasible to lie the patient supine, flex the normal hip and knee, and place the normal foot on the table at the level of the contralateral knee. Scanning of the affected leg alone is then possible from the knee downward. Above the knee it is necessary to scan both lower limbs together. In the upper limb, scanning from the elbow downward is possible with the patient standing or sitting by the scanner table with the affected forearm placed centrally along the long axis of the table. Scanning of the arm from shoulder to elbow is possible with the patient lying on the affected side, with the arm abducted over a large triangular foam pad and the scanner gantry tilted away from the patient's head. The alternative-scanning with the arm by the patient's side-results in the entire chest being irradiated, with consequent massive increase in effective dose and reduction in image quality.



Fig. 45.77 CT thorax. Atrophy of the right serratus anterior muscle is evident (arrow), secondary to previous lateral thoracic nerve damage.



Fig. 45.78 Abdominal wall hernias. (A) Inguinal hernia (arrows). (B) Spigelian hernia (lateral to the rectus sheath) (*). (C) Lumbar hernia (arrows).

Images should be obtained targeted to the region of interest and using a high-resolution algorithm (commensurate with acceptable image noise in the soft tissues) to give the greatest possible spatial resolution. Not all patients will tolerate these positions for long, and a rapid scan technique is thus essential. If contrast enhancement is required, placement of a venous catheter prior to patient positioning may be necessary. Lesions may extend beyond the obvious compartment involved, and care must be taken to ensure that the full extent of an abnormality is demonstrated (e.g. a proximal thigh lesion may extend into the pelvis). While magnetic resonance imaging (MRI) is the method of choice for imaging most soft-tissue lesions. CT can demonstrate many lesions adequately and with careful technique gives a low effective radiation dose to the patient.

Anatomical considerations

The soft-tissue planes of the limbs are demonstrated by CT due to the presence of fat between the muscles and fascia. The amount of fat within and between muscles generally increases with increasing age, increasing the number of individual muscles separately identifiable. The density of muscle tissue is not significantly different between the sexes nor is it markedly affected by age or pathology, though muscle bulk may change and fatty infiltration between muscle fibre bundles may be appreciated.

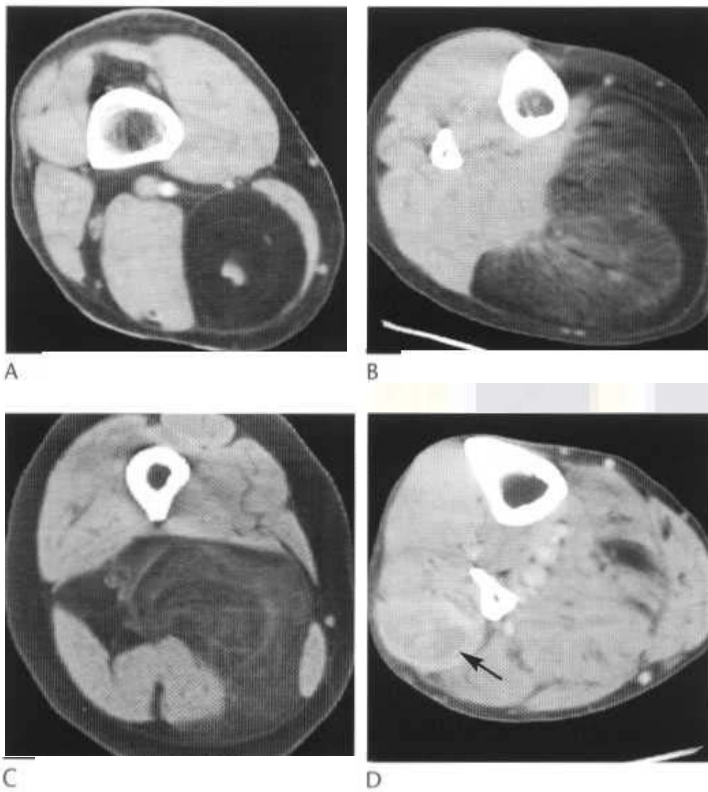


Fig. 45.79 (A) Simple intramuscular lipoma with a central vascular structure. (B) Intramuscular lipoma interdigitating between the muscle fibres of gastrocnemius. (C) Atypical lipoma with irregular soft-tissue densities in the tumour, indistinguishable from a low-grade liposarcoma but histologically due to myxoid changes. (D) Intramuscular sarcoma (arrow).

Clinical applications

CT will demonstrate the site, size and extent of soft-tissue masses and may identify characteristic fat or calcific density in some lesions. CT is used in radiotherapy treatment and planning. The determination of body composition (fat lean ratio) can be performed using CT but this is a relatively high radiation dose research method. The degree of peripheral oedema in chronic lymphoedema can be measured and monitored by CT. This technique can also demonstrate the distribution of muscle atrophy and fatty replacement in intrinsic and neuromuscular disease.

Benign soft-tissue masses

Lipoma The characteristic attenuation of fat identifies lipomas. A thin soft-tissue capsule may be seen surrounding a subcutaneous lipoma. Within the lesion there should be homogeneous fat density with few, if any, internal septa. Larger lesions may contain blood vessels. A significant soft-tissue element or heterogeneity of attenuation within a fatty lesion raises the possibility of liposarcoma. Lipomas most commonly arise in the subcutaneous fat but intermuscular and intramuscular lipomas can occur (Fig. 45.79).

Haemangioma Intramuscular haemangiomas are uncommon. They characteristically contain calcifications (phleboliths) and areas of fatty tissue between and around the abnormal vessels within the lesion. The CT appearances may therefore be diagnostic. The vascular spaces may enhance after intravenous contrast but the timing of the enhancement is variable, depending



Fig. 45.80 Soft-tissue haemangioma. Multiple punctate and serpentine calcifications (arrow).



Fig. 45.81 Sural nerve neuroma (arrow).

upon the site of the lesion and the rate of blood flow through it (Fig. 45.80).

Neurofibroma Peripheral neurofibromas are soft-tissue density, well-defined oval or rounded masses, typically lying with their long axis along the course of a nerve. They are usually of lower density than adjacent muscle (Fig. 45.81).

Desmoid Desmoid tumours may contain dense fibrous tissue which can result in a CT number higher than other soft tissues (100-200 HU). CT scanning of the hand and wrist for soft-tissue pathology is unusual (Fig. 45.82). The commonest solid soft-tissue mass in the hand is a giant cell tumour of the tendon

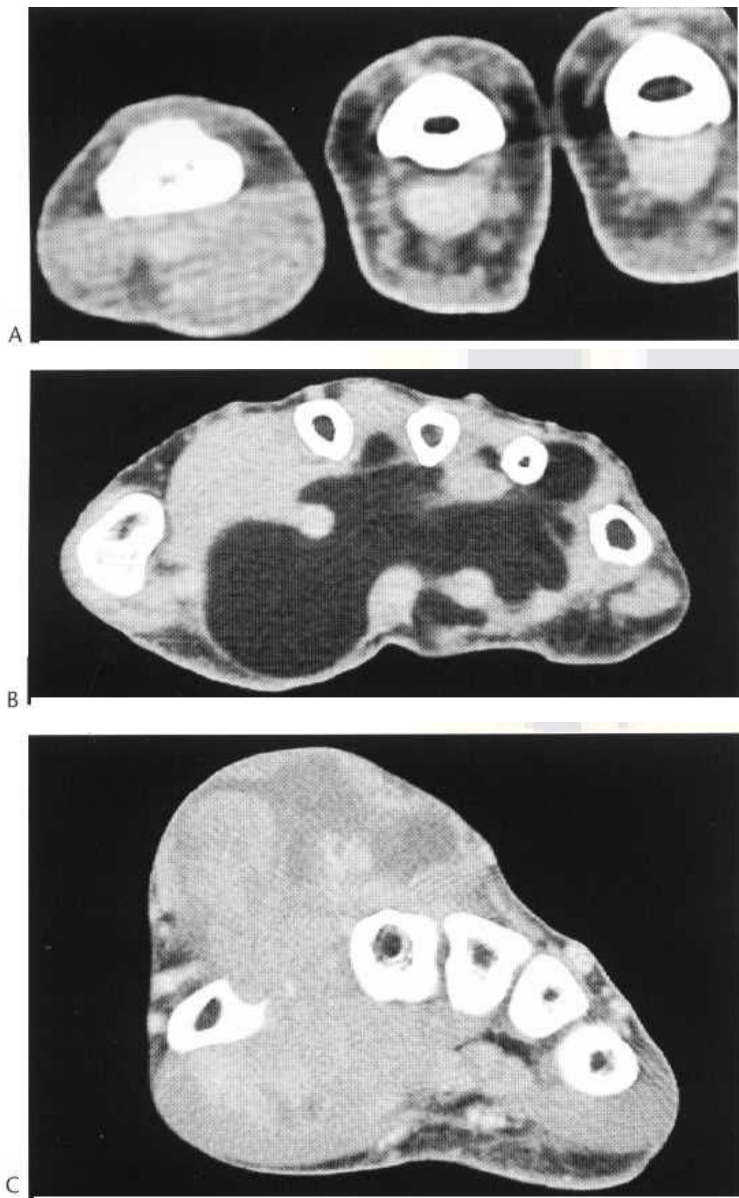


Fig. 45.82 CT images of the hand. (A) Giant cell tumour encasing the flexor tendon of the little finger. (B) Lipoma of the palm, interdigitating between the flexor tendons and metacarpals. (C) Soft-tissue sarcoma arising in the hand.

sheath, while the commonest cystic lesion is a ganglions. CT is not usually indicated for the evaluation of either of these lesions.

Malignant soft-tissue masses

Primary soft-tissue *sarcomas* are rare; the commonest is *malignant fibrous histiocytoma*. With the exception of *liposarcoma*, which may contain identifiable fat density on CT, the histological type of a soft-tissue sarcoma cannot be reliably identified on CT. Although infiltration of adjacent soft-tissue structures might be anticipated, most soft-tissue sarcomas are lobulated, well-defined masses on CT (Fig. 45.79).

Areas of necrosis or haemorrhage may result in heterogeneous attenuation within the lesion. Contrast enhancement is variable. Biopsy of a suspected soft-tissue sarcoma should only be performed after discussion with the surgeon planning definitive management, as inappropriate biopsy can adversely affect subsequent surgery. CT

scanning of the thorax is an important staging procedure for sarcoma to identify pulmonary metastatic disease.

Soft-tissue involvement with *lymphoma* may occur. Infiltration of muscle may produce increase in bulk and distortion of muscle outline but the tumour itself may be indistinguishable from muscle in density, making some lesions undetectable on CT.

Soft-tissue *metastatic deposits* are rare except in advanced disease.

Soft-tissue infection

Abscesses in the soft tissues have appearances typical of abscesses elsewhere, with a central low-attenuation (fluid) area and a surrounding denser wall which may show enhancement after contrast. Inflammatory changes surrounding this may make adjacent fat appear indistinct or infiltrated. *Gas* may occasionally be seen in the soft tissues; differentiation of intramuscular gas (seen in gas gangrene) from interstitial/subcutaneous gas (seen in other gas-forming infections) is important.

Haematoma

The size, site and progression of intramuscular haematoma can be identified on CT; this may be of value in hemophiliac patients (Fig. 45.83).

Muscle rupture

Muscle rupture is best identified on MRI but may present as a soft-tissue mass (due to muscle bunching adjacent to the tear). CT may demonstrate a defect in the muscle adjacent to the mass of muscle

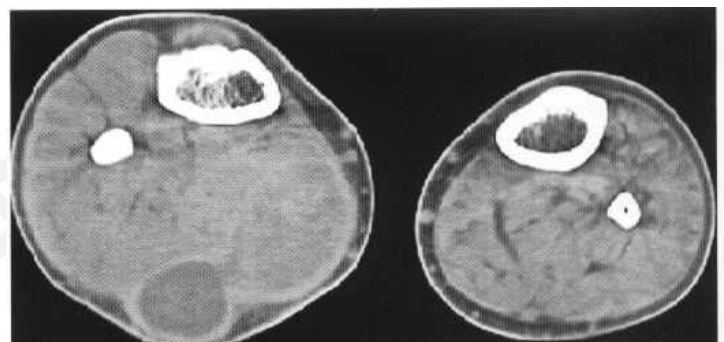


Fig. 45.83 Chronic haematoma in the calf (haemophiliac).



Fig. 45.84 Partial rupture of the right rectus femoris; note reduction in bulk of the right muscle and focal high- and low density areas centrally, representing fibrosis and fat infiltration (arrows).

density. The defect may contain fat or soft tissue from haematoma or fibrosis (Fig. 45.84).

Myositis ossificans

Post-traumatic myositis ossificans has characteristic appearances on CT, with calcification or ossification most dense around the periphery of the lesion, often with a linear or striated appearance as it extends between muscle bundles (Fig. 45.85). By contrast, most calcifying tumours are most densely calcified centrally. Correct identification of myositis ossificans is important as recurrence and progression of the lesions may occur if surgical resection is attempted. Soft-tissue calcification from other causes can also be demonstrated on CT (Fig. 45.86) as on plain film.

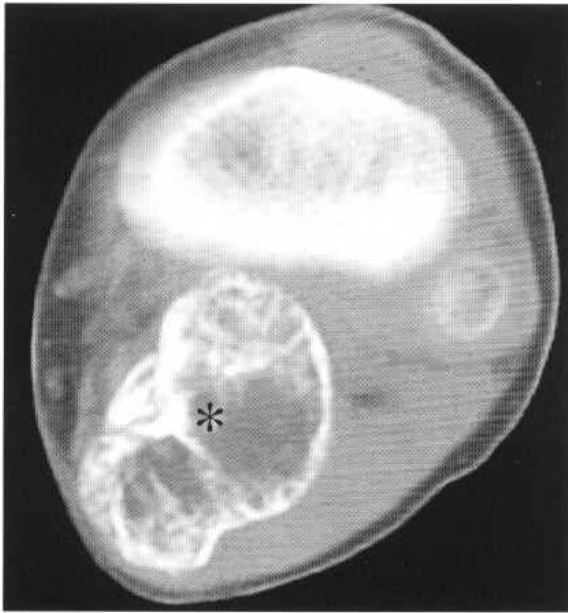


Fig. 45.85 CT Post-traumatic myositis ossificans behind the knee.

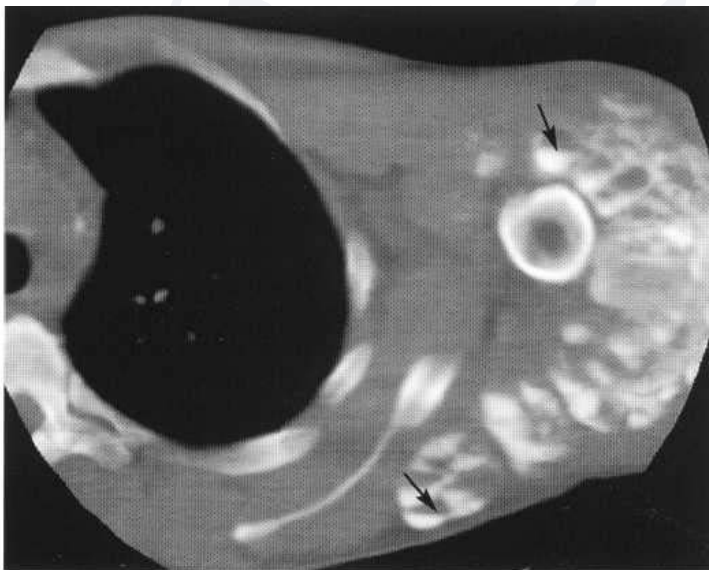


Fig. 45.86 Tumoral calcinosis, calcium-fluid levels (arrow) in a multi-loculate collection around the shoulder in a patient in renal failure. (Courtesy of Professor J. E. Adams.)

INTERVENTIONAL MRI OF SOFT TISSUES

W. Gedroyc

Interventional work is rarely performed on MRI machines because it is awkward to carry out and time consuming in the normal conditions that apply in a regular diagnostic magnet. Despite this MRI has many theoretical advantages in the interventional field which, if they could be correctly harnessed, would make it a very powerful technique bringing many new strengths.

Advantages

1. No ionising radiation is involved in MRI: this is obviously a very advantageous situation. The patient does not receive a significant dose of ionising radiation and it is also much safer for the operator and any procedural assistants. Imaging can be potentially carried out over long periods, and needles, catheters, etc., can all be moved during imaging from within the field, which is not possible during conventional imaging of interventional procedures. An example of this is CT, where needle movements are carried out blind with movements interspersed with images. In addition, pregnant patients (second and third trimester) may be safely examined under this form of imaging.

2. The high soft-tissue sensitivity inherent to MRI is much greater than that of all other imaging modalities. MRI can therefore discriminate between areas of pathology and normal tissue, even if there is no change in the size of the organ involved, allowing excellent discrimination of the margins of the lesions. As a result MRI provides the best possible visualisation of a lesion, allowing it to be biopsied, punctured, etc., in an optimal fashion.

3. MRI allows multiplanar operator-independent images to be readily obtained, enabling complete assessment of any lesion and how it can be approached. If an oblique paracoronal or parasagittal approach is the best plane in which a lesion may be approached, then such an image can be readily set up and intervention monitored in this plane using repeated MR scans without having to move the patient.

4. Some metabolic changes in the tissues can be monitored in real time by MRI. This is potentially the single most important aspect of interventional MRI. The most common example of such changes is that seen secondary to heat or cold application to tissues, with the result that the signal intensity of the tissues is significantly decreased. Destructive thermal energy can be applied to tissue lesions and the effect and extent of this energy on the target tissue can be imaged by MRI in real time. This application has been studied in the greatest depth with Nd-YAG laser fibres applying heat to tissue, but much the same effect is seen with cryofibres applying cold energy. This aspect of MR scanning will permit the development of many new procedures in this area which will allow the use of localised destructive energy in pathological lesions without damaging adjacent tissues (see below).

Disadvantages

1. *Access to patients.* Conventional MR machines enclose patients in a long tunnel in the centre of the machine, preventing all access to the patient during scanning. Conventional diagnostic MR

machines are therefore awkward for interventional work. This problem is being addressed by the design of a new range of open MR machines which have a gap where the imaging volume is to be placed so that access can be obtained to the patient to allow such procedures.

2. *Speed of imaging.* The speed at which MRI can be carried out has increased greatly over the last 5 years. Many conventional scanners, however, cannot routinely carry out the rapid imaging which is required in interventional procedures. Fast gradient-echo scanning, echo planar scanning, etc., have all increased the rapidity with which MR machines can acquire images, so that currently many machines have the capability of producing near real-time results. Exact details of these vary immensely between machines, but these newer sequences will allow the development of 'MR fluoroscopy'.

3. *MR-compatible instrumentation.* Conventional ferromagnetic instruments cannot be used in an MR machine. Such instruments are strongly attracted into the centre of the magnet and may become missiles themselves. Even a small amount of iron which may be present within a tool may often make movement within the magnetic field very problematical. In addition ferromagnetic substances produce very substantial artefact in the imaging field so that little of the target image will be seen if such an instrument is inadvertently placed within the imaging volume. A completely new field of MR-compatible instrumentation is developing using a variety of new materials. Non-ferromagnetic metals such as titanium and other alloys are being introduced in many areas, and non-metallic components such as plastics, ceramics, carbon fibre, etc., are being developed to replace iron and overcome the above problems.

Apparatus

A variety of more open MR scanners are being developed by most of the major MR imaging manufacturers. Their capabilities vary as does their field strength, with the most powerful open scanner currently available being at 0.5 tesla. As technology develops these field strengths will increase, permitting faster sequences and easier monitoring of interventional procedures as a result.

Role of interventional MRI

The range of new procedures that interventional MRI will initially develop can be categorised into the following main areas:

1. Thermal ablation procedures
2. Accurate biopsies in difficult/unusual places
3. Endoscopic monitoring
4. Guidance of open surgery
5. Upright biomechanical imaging.

Thermal ablation procedures

These have been briefly described above. As heat or cold is applied to tissue its signal intensity is lowered on MR images of the area. The amount of signal loss is broadly proportional to the amount of heat or cold applied until cell necrosis occurs. This property allows MRI to be used as an *in vivo* thermometer. As a result thermal ablation procedures where destructive heat or cold energy is applied to a pathological lesion such as a secondary tumour can be closely controlled. Thermal ablation procedures are used without MR guidance but they suffer from a substantial unpredictability in terms of the

extent of tissue destruction produced. MR guidance of these procedures will overcome this unpredictability and allow such therapies to be safely and effectively applied in many areas of the body.

The ability to utilise this form of localised destructive energy in many different areas of the body under close image guidance will open up a wide range of new procedures, potentially replacing many operative surgical procedures by simple minimally invasive day-case interventions. This combination of technologies therefore allows the targeting of closely controlled destructive energy without damaging adjacent tissues.

Complex biopsy:

The more advanced open scanners have integral sophisticated tracking and localising facilities which allow very accurate placement of biopsy needles, etc., in target tissues. With on-line near real-time images available, this will allow biopsy of a variety of complex areas within the body under continuous imaging control. The most obvious area to benefit from this form of approach is the brain. Conventional CT guided stereotactic biopsy is very time-consuming and requires the use of applied metal frames. Frameless stereotactic biopsies will be possible with the more sophisticated open magnets guided by real-time imaging (Figs 45.87, 45.88), allowing a massive improvement in speed, safety and efficacy of such procedures since the needle would actually be able to be guided into the lesion in question under direct imaging which is not currently possible with conventional stereotactic biopsy.

Endoscopic monitoring

Minimally invasive endoscopic procedures are becoming much more popular, and larger and larger interventions are being carried

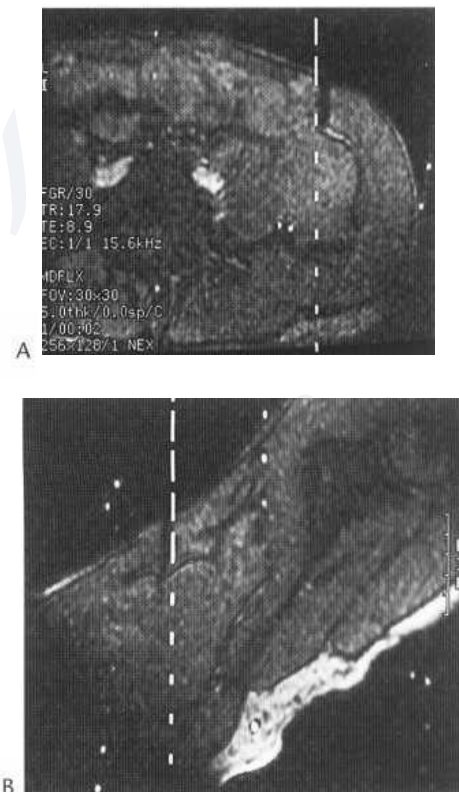


Fig. 45.87 Percutaneous biopsy of lung in right iliac fossa under MR control. Axial (A) and sagittal (B) views. Dotted lines represent computer-generated tracks of titanium biopsy needle. Histology-carcinoma of the colon.

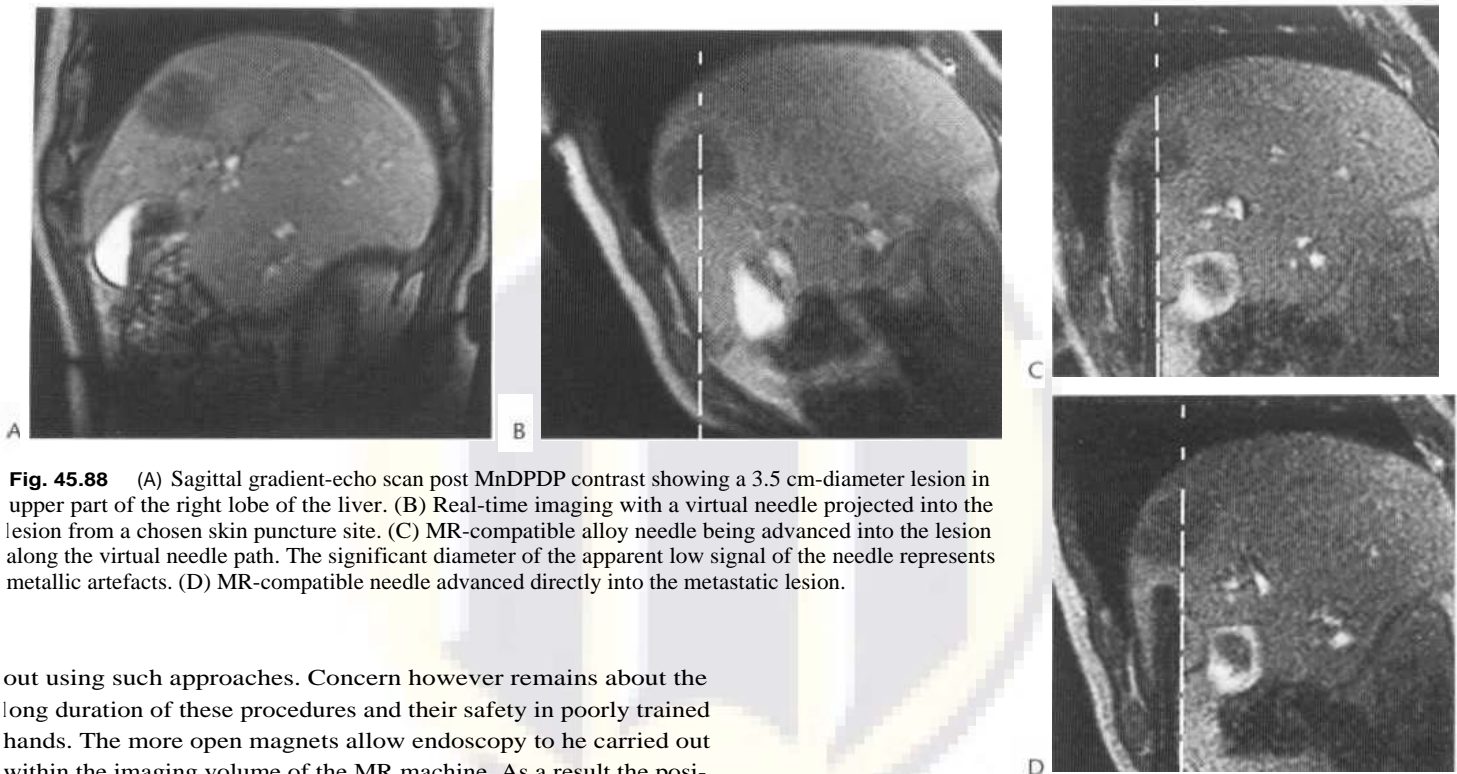


Fig. 45.88 (A) Sagittal gradient-echo scan post MnDPDP contrast showing a 3.5 cm-diameter lesion in upper part of the right lobe of the liver. (B) Real-time imaging with a virtual needle projected into the lesion from a chosen skin puncture site. (C) MR-compatible alloy needle being advanced into the lesion along the virtual needle path. The significant diameter of the apparent low signal of the needle represents metallic artefacts. (D) MR-compatible needle advanced directly into the metastatic lesion.

out using such approaches. Concern however remains about the long duration of these procedures and their safety in poorly trained hands. The more open magnets allow endoscopy to be carried out within the imaging volume of the MR machine. As a result the position of the endoscope can be monitored on MR images and the surgeon can be guided by repeated MR scans to the target tissue or informed as to the nature of the tissue that he or she is visualising" This is particularly important as the use of microendoscopes with a much smaller field of view becomes more popular. These new flexible scopes can be placed in many more difficult and unusual parts of the body but because of their small field of view they are more difficult to manoeuvre through the body to the target [area](#). MR can overcome this problem. Further localisation devices are available which will allow the endoscope to trigger the MR machine to scan to its tip as it is moved through the target volume, thus allowing continuous monitoring of the site of the endoscopy. It is hoped that

the use of such endoscopic guidance will shorten the duration of these procedures and make them more effective, and, as a result, improve their safety.

Guidance of open surgery (Figs 45.89, 45.90)

The open access to the imaging volume in newer open scanners, particularly in the vertical orientation, allows surgical procedures to be performed in MR scanners. In many instances surgery is performed in circumstances where the operator cannot visualise

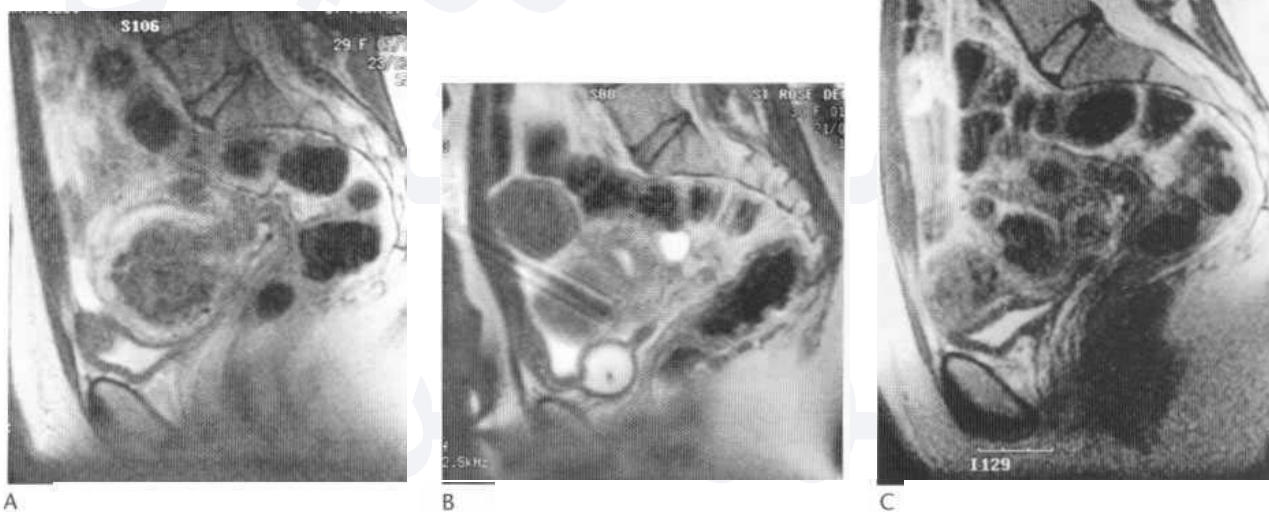


Fig. 45.89 (A) Fibroid pre-5-cm fibroid arising from the anterior lower uterine wall. Sagittal T_2 -weighted image. (B) Fibroid with needles. T_2 -weighted image showing MR-compatible needles placed into the fibroid seen in Fig. 45.90 under MR guidance. Laser fibres are subsequently placed via these needles and heat is applied directly to the target fibroid using MR thermal mapping to control position and extent of healing. (C) Fibroid post. Same patient 4 months later showing marked subsequent reduction in fibroid size.



Fig. 45.90 (A) Liver thermal ablation. Real-time MR thermal map produced by a subtraction process using T₂ signal loss. Red area indicates the extent of necrosis in this liver. Images are updated every 4 seconds providing an approximate *in vivo* thermometric read out which is used to control the (ablation). (B, C) Print outs at 4 second intervals.

the proximity and position of adjacent vital structures. This means that the extent of the surgical procedure may unwittingly damage adjacent structures or often the procedure is limited at a relatively early stage because of fear of causing such collateral local damage. If a surgeon had the means of imaging the resection margin and adjacent soft tissues these inherent surgical problems could be potentially reduced. Using MRI to provide to such monitoring may solve these problems in many situations. MRI can provide excellent anatomical and pathological depiction of the whole surgical field and will allow the full extent of the resection target to be clearly visualised in most cases, and can show how the resection margins are positioned with respect to the target. Similarly adjacent vital structures such as blood vessels, sphincters, etc. are easily visualised using MRI and surgery can be adjusted appropriately to ensure that they are not inadvertently damaged. The disadvantage of this type of approach is that surgery must be carried out within the very hostile environment of a high magnetic field. Instrumentation must be modified because normal surgical materials are predominantly iron based and as a result instruments can become dangerous missiles within the MR environment. In addition the movement of surgeons in the magnetic field is much more limited because of the enclosed nature of a magnet. However the advantages that this type of approach bring counterbalance many of these problems. Most surgical instrumentation is now available in MR-compatible materials such as plastic and ceramics and titanium.

Neurosurgery has pioneered this approach particularly within the brain. The intention here is to try and resect the maximum amount of abnormal tissue while damaging the least amount of normal brain. Early reviews of this type of work suggest that this approach may reduce the incidence of early significant recurrences of brain tumours. Similar principles are also starting to be applied to general surgical procedures. Early work has been performed in breast surgery and anorectal surgery with the same overall goals as neurosurgical procedures.

Biomechanical investigations

The space around patients in open MR scanners allows images to be obtained in a variety of joint positions with the whole limb moving between images. This means that for the first time changes in soft-tissue positions induced by movement within joints can start to be appreciated. Conventional soft-tissue imaging is entirely static and while it has allowed massive gains in our understanding of musculoskeletal diseases, it is very likely that dynamic motion imaging will allow us to gain significant further insights into how joints work in normal patients and how such function is altered by disease. The predominance of open MR scanners have horizontal access to the patient and therefore cannot image patients in an erect weight bearing position. It is not yet completely clear how much influence the erect position has but it seems likely that this is a very important factor. A significant amount of work is therefore being driven towards trying to mimic these loading stresses on joints within horizontal magnetic environments by a variety of pulley-systems, etc. Scanners that have a more vertical access can carry out images easily in the direct erect weight-bearing position and it is likely both these approaches will provide us with a new appreciation of how joints really move in everyday life.

Summary

Interventional MRI has great potential in the development of a whole new range of minimally invasive therapeutic procedures. It marries MR monitoring with other technologically advanced modalities, improving the results of both and raising the prospect of carrying out extensive therapeutic procedures as day cases. This will provide substantial improvements in patient mortality and morbidity and will allow significant overall cost benefits to health services. The emergence of this field points the way towards the methods we will be using to treat patients in the next century.

REFERENCES AND SUGGESTIONS FOR FURTHER READING**MRI**

- Beltran, J. (1995) MR imaging of soft tissue infection. *Magnetic Resonance Imaging Clinics of North America*, 3, 743-751.
- Berquist, T. H. (1996) *MRI of Musculoskeletal System*. Philadelphia: Lippincott/Raven.
- Bloem, J. L., et al (1997) Does MRI make a difference for patients with musculo-skeletal sarcoma? *British Journal of Radiology*, 70, 327-337.
- Bluemke, D. A. (ed.) (2000) *Oncologic MR Imaging. Magnetic Resonance Imaging Clinics of North America*, 8, 691-963.
- Boutin, R. D., et al (1998) Update on imaging of orthopaedic infections. *Orthopedic Clinics of North America*, 29, 41-66.
- Davies, A. M., Vanel, D. (1998) Follow-up of musculo-skeletal tumours. *European Journal of Radiology*, 8, 791-799.
- De Schepper, A. M., et al (1997) *Imaging of Soft Tissue Tumours*. Heidelberg: Springer Verlag.
- Enzinger, F. M., Weiss, S. W. (1988) *Soft-tissue Tumors*. St Louis: Mosby.
- Firooznia, H. F., Golimbi, C., Rafii, M., Rauschnig, W., Weinreb, J. (1992) *MRI card CT of Musculoskeletal System*. St Louis: Mosby Year Book.
- Gordon, B. A., et al (1995) Pyomyositis: characteristics at CT and MR imaging. *Radiology*, 197, 279-286.
- Hawnaur, J. M., Whitehouse, R. W., Jenkins, J. P. R., Isherwood, I. (1990) Musculoskeletal haemangiomas: comparison of MRI with CT. *Skeletal Radiology*, 19, 251-258.
- Ho, C. P. (ed.) (1999) MR imaging of sports-related injuries. *Magnetic Resonance Imaging Clinics of North America*, 7, 1-205.
- Husband, J. E. S., Reznick, R. H. (eds) (1998) *Imaging in Oncology*. Oxford: ISIS Medical Media.
- Husband, J. E. S., Johnson, R. J., Reznick, R. H. (eds) (1999) *A Guide to the Practical Use of MRI in Oncology*. London: The Royal College of Radiologists.
- Kaplan, P. A., Helms, C. A., Dussault, R., Anderson, M. W., Major, N. M. (2001) *Musculoskeletal MRI*. Philadelphia: W. B. Saunders.
- Kransdorf, M. J., Murphy, M. D. (eds) (1997) *Imaging of Soft Tissue Tumours*. Philadelphia: W. B. Saunders.
- Kransdorf, M. J., Murphy, M. D. (2000) Radiologic evaluation of soft-tissue masses: a current perspective. *American Journal of Roentgenology*, 175, 575-587.
- Laorr, A., Helms, C. A. (1997) *MRI of Musculoskeletal Masses: a practical text and atlas*. Iagaku-Shoin, New York.
- Loh, N. N., et al (1997) Deep fascial hyperintensity in soft tissue abnormalities as revealed by T₁-weighted MR imaging. *American Journal of Radiology*, 168, 1301-1304.
- Ma, L. D., Frassica, F. J., Scott, W. W., Fishman, E. K., Zerhouni, E. A. (1995) Differentiation of benign and malignant musculoskeletal tumors: potential pitfalls with MR imaging. *Radiographics*, 15, 349-366.
- Ma, L. D., et al (1997) CT and MRI evaluation of musculoskeletal infection. *Crit Rev Diagn Imaging*, 38, 535-568.
- Marcus, C. D., Ladam-Marcus, V. J., Leone, J., Malgrange, D., Bonnet-Gausserand, F. M., Menanteau, B. P. (1996) MR imaging of osteomyelitis and neuropathic osteoarthropathy in the feet of diabetics. *Radiographics*, 16, 1337-1348.
- Mirowitz, S. A. (1996) *Pitfalls, Variants, and Artifacts in Body MR Imaging*. Chicago: Mosby Year Book.
- Multi authors (1997) Mini-symposium: soft tissue tumors of the musculoskeletal system. *Current Orthopedics*, 11, 75-113.
- Pettersson, H. (ed.) (1999) *The Encyclopaedia of Medical Imaging. Musculoskeletal and soft-tissue imaging*. Oslo: Isis Medical Media, The Nicer Institute.
- Pomeranz, S. J. (1993) *Gamuts and Pearls in MRI*, 2nd edn. Cincinnati: MRI-EFI Publications.
- Pomeranz, S. J., Kim, T. W. (1995) *Pitfalls and Variations in Neuro-orthopedic MRI*. Cincinnati: MRI-EFI Publications.
- Reeder, M. M., Bradley, W. G. (1993) *Reeder and Nelson's Gamuts in Radiology*, 3rd edn. London: Springer-Verlag.
- Resnick, D. (1996) *Diagnosis of Bone and Joint Disorders*, 3rd edn. Philadelphia: W. B. Saunders.
- Sartoris, D. J. (ed.) (1994) Advances in musculoskeletal imaging. *Radiologic Clinics of North America*, 32, 201-411.
- Sartoris, D. J. (1996) *Musculoskeletal Imaging-the Requisites*. St Louis: Mosby.
- Schima, W., Mukerjee, A., Saini, S. (1996) Review: contrast-enhanced MR imaging. *Clinical Radiology*, 51, 235-244.
- Seltzer, S., Macht, S. D., Davis, D. O., Javitt, M. C. (1990) MRI of soft-tissue masses of the extremities. *MRI Decisions*, 4, 12-23.
- Stark, D. D., Bradley, W. G. (eds) (1999) Musculoskeletal section. In: *Magnetic Resonance Imaging*, vol. III, 3rd edn. St Louis: Mosby.
- Stoller, D. W. (1996) *Magnetic Resonance Imaging in Orthopaedics and Sports Medicine*. Philadelphia: J. B. Lippincott.
- Sundaram, M., McLeod, R. A. (1990) MR imaging of tumor and tumorlike lesions of bone and soft tissue. *American Journal of Roentgenology*, 155, 817-824.
- Towers, J. D. (1997) The use of intravenous contrast in MRI of extremity infection. *Seminars in Ultrasound CT and MR*, 18, 269-275.
- Vanel, D., Shapeero, L. G., De Baere, T., Gilles, R., Tardivon, A., Genin, J., Guinebretiere, J. M. (1994) MR imaging in the follow-up of malignant and aggressive soft-tissue tumours: results of 511 examination. *Radiology*, 190, 263-268.
- Weissman, B. N. (ed.) (1993) Syllabus: A Categorical Course in Musculoskeletal Radiology. Advanced Imaging of Joints: Theory and Practice. Presented at the 79th Annual Meeting of the Radiologic Society of North America.
- Weatherall, P. T. (ed.) (1995) Musculoskeletal soft-tissue imaging. *Magnetic Resonance Imaging Clinics of North America*, 3, 563-793.

Plain film

- Diethelm, L. (ed.) (1968) Roentgen diagnosis of the soft tissues. In: *Encyclopaedia of Medical Radiology*, vol. VIII, pp. 124-177. Berlin: Springer.
- Griiffiths, H. J. (1976) *Radiology of Renal Failure*. Philadelphia: W. B. Saunders.
- Kuhns, L. R., Berger, P. E., Roloff, D. W., Poznanski, A. K., Holt, J. F. (1974) Fat thickness in the newborn infant of a diabetic mother. *Radiology*, 111, 665-671.
- Meema, H. E., Oreopoulos, D. G., de Veber, G. A. (1976) Arterial calcifications in severe chronic renal disease and their relationship to dialysis treatment, renal transplant and parathyroidectomy. *Radiology*, 121, 315-321.
- Middlemiss, J. H. (ed.) (1961) *Tropical Radiology*. London: Heinemann.
- Murray, R. O., Jacobson, H. E., Stoker, D. J. (1990) *Textbook of Skeletal Disorders*, 3rd edn. Edinburgh: Churchill Livingstone.
- Sutton, D., Al-Kutoubi, M. A., De Silva, R. D. D., Thomas, D. (1985) Computed tomography in deep-seated peripheral neurofibromas. *Clinical Radiology*, 36, 19-22.
- Wolfe, J. N. (1969) Xeroradiography of bones, joints and soft tissues. *Radiology*, 93, 583-587.

CT

- Hawnaur, J. M., Whitehouse, R. W., Jenkins, J. P. R., Isherwood, I. (1990) Musculoskeletal haemangiomas: comparison of MRI with CT. *Skeletal Radiology*, 19, 251-258.
- Wegener, O. H. (1992) *Whole Body Computed Tomography*, pp. 491-509. Massachusetts: Blackwell Scientific.



نشر الکترونیکی
موسسه انتشاراتی
نوردانش

46

THE BREAST

Michael J. Michell

with contributions from Chris Lawinski, Will Teh and Sarah Vinnicombe

Radiological examination of the breast is established as an essential part of the modern multidisciplinary approach to effective investigation and management of breast disease. The more widespread use of X-ray mammography in breast cancer screening programmes has been accompanied by further development of both invasive and non-invasive radiological techniques used for establishing the diagnosis of palpable and non-palpable lesions. The standard techniques used for breast imaging are *screen film X-ray mammography* and *real-time ultrasound*. Other new techniques which are either under development or for which the indications for use are being evaluated include MRI, colour Doppler and contrast ultrasound, scintimammography and digital mammography.

Technical aspects of mammography

Effective mammography requires consistent high-quality images with optimum film density and contrast, high resolution and low radiation dose. This is particularly important for the detection of small cancers because the radiological signs may be very subtle. The mammography equipment and technique used therefore have to take into account wide variation in breast size, variation in the relative amounts of fat, glandular and stromal tissue which are present, and the low contrast between normal breast tissue and common pathological lesions. The current physical criteria for an acceptable mammographic image are:

- Mean optical density = 1.4-1.8 (measured by imaging a 4 cm perspex block using the AEC at standard clinical settings)
- High-contrast spatial resolution = 10 line pairs per mm
- Low-contrast spatial resolution = 3.2 line pairs per mm
- Minimum detectable contrast: 5-6 mm details = 1%, 0-5 mm details = 5%
- Mean glandular dose = 2 mGy per view (1.5 mGy or less per view is currently achieved by about 75% of UK screening centres).

Dedicated mammography X-ray equipment is necessary for producing high-quality images and should have the following features:

1. *Generator*. Most modern high-voltage generators produce a near constant potential output using medium- or high-frequency converter technology. A high output rate is desirable in order to reduce exposure time and therefore minimise movement unsharpness.

2. *X-ray tube*. The most commonly used target-filter combination is a molybdenum (Mo) target with 0.03 mm Mo filter. The peak kilovoltage is normally in the range 26-30 kV and typically 28 kV. The resultant X-ray spectrum exhibits characteristic X-rays at 17.4 and 19.4 keV, with a sharp cut-off above 20 keV due to the absorption edge for molybdenum. The remaining lower energy photons, mainly in the range 17-20 keV, are well suited for producing maximum contrast from the radiographically similar soft tissues of the breast.

The Mo/Mo target-filter combination is well suited to the average or small-sized breast. Large breasts or breasts containing a high proportion of dense glandular tissue may require a higher energy spectrum of radiation to provide sufficient penetration and prevent excessive dose. Certain modern mammography machines therefore have a choice of target-filter combinations including Mo/Mo, Mo/rhodium, Mo/palladium, rhodium/rhodium so that the optimum X-ray spectrum can be selected for different types of breast.

A small focal spot is necessary for high-resolution images. However, the size is limited due to thermal considerations. Typically, an X-ray tube with a nominal focal spot size of 0.3-0.35 mm is used for normal mammography. A fine focal spot of 0.1 mm is used for magnification techniques. The focus to film distance is in the range 60-65 cm.

The X-ray tube needs efficient heat dispersal characteristics to allow short exposure times with a high tube current while allowing high patient throughput.

3. *Automatic exposure control (AEC)*. The AEC automatically controls the exposure duration so that the optimum optical density of the mammograms is maintained over a wide range of different breast sizes and densities. The AEC device, either a photo-timer or ionisation chamber, is normally positioned 3-5 cm posterior to the nipple, where the most dense glandular tissue is likely to be situated.

4. *Secondary radiation grid.* The use of a moving grid system results in improved resolution and contrast by decreasing scattered radiation. The potential increase in dose due to use of a grid can be offset by use of faster film-screen combinations. A grid is not necessary for magnification mammography where the scattered radiation is removed by the air gap.

5. *Compression.* Firm compression is essential for high-quality mammograms and is applied using a powered system operated by a foot control. It is important that there is even compression of the entire breast. The effects of compression are:

- (i) reduced dose;
- (ii) reduced scatter-improved contrast;
- (iii) reduced geometric unsharpness;
- (iv) reduced movement unsharpness;
- (v) reduced range of breast thickness;
- (vi) reduced tissue overlap improved resolution.

6. *Film-screen combination.* Single side emulsion film is used with a single intensifying screen in order to ensure optimum resolution. Specially designed cassettes ensure good film-screen contact and have a front face constructed of low radiation absorption material. Modern screens use rare earth materials, e.g. gadolinium oxysulphide, which increase the speed of the film-screen combination, allowing a decrease in the radiation dose required while maximising contrast.

7. *Processing.* Dedicated processing facilities should be available for mammography film to obtain consistently highest quality images. The chosen processing conditions and chemistry need to be matched to the film-screen combination in use. In general, optimum film density and contrast are achieved by an extended processing time of up to 3.5 minutes together with a lower developer temperature (34°C) than for general radiography.

Digital imaging for mammography

Recent developments in diagnostic imaging technology have resulted in the gradual replacement of film-screen imaging systems by digital devices. In mammography, digital technology was first applied to small field imaging devices. More recently, full field digital imaging systems have been developed.

Digital imaging provides a higher dynamic range and improved contrast resolution when compared to film-screen imaging. This may improve diagnostic capability and for mammography should outweigh the potential loss in limiting spatial resolution. The greater dynamic range should also reduce the number of retakes required and lead to a greater consistency of quality. Currently, digital imaging results in a similar breast dose to that of a modern mammographic film-screen combination. However, developments in detector design may eventually result in a reduction in radiation dose. Additionally, the improved contrast performance may also allow imaging at higher kV values and with higher atomic number filters with consequent reduction in breast dose.

Digital mammography systems have an associated computer workstation with controls for image acquisition, display, processing and handling. Ideally reporting should be directly from the workstation monitor (softcopy). Alternatively, the image can be printed onto film (hard copy).

Small field digital imaging

The primary application of small field digital systems (field sizes ranging from 5 x 5 cm to 4.9 x 8.5 cm) is for stereotactic biopsy

procedures. All the current units are based on charge coupled device (CCD) technology in which the CCD camera is coupled to a phosphor screen. X-ray photons are converted to light by the phosphor and then to an electronic signal by the CCD. Spatial resolution, in terms of pixel size, is between 2.5 and 100 µm, depending on the design of the system.

The benefits of rapid image acquisition can significantly reduce the time taken for a similar examination using film-screen imaging. Other advantages of this technique are the benefits to the patient of a reduced time under compression, less chance for movement of the breast and a saving of radiologist's waiting time. Thus it may be possible to perform the procedure on an 'as and when' basis rather than needing to recall the patient for a stereotactic session. Clinical experience has suggested that the use of digital imaging can improve the performance of upright stereotactic core biopsy of microcalcifications giving a significantly increased success rate in accurately obtaining calcifications (Whitlock et al 2000).

Certain of the systems can be used for spot imaging in addition to stereotactic localisations. Magnification techniques may also be possible although the zoom/magnify facility in the image processing software may replace the necessity for acquisition of a magnified image. Small field digital imaging systems are also available as part of dedicated breast biopsy units. The patient lies on a horizontal tabletop in a prone position, an aperture is provided for the breast. The table is designed to comfortably support the patient in a stable fixed position while allowing maximum access to the breast. The X-ray tube and detector assembly are mounted below the tabletop.

Full field digital imaging

Computed radiography

Computed radiography (CR) systems, using laser-stimulated phosphor technology, are widely used for general radiography. An advantage of CR is that the imaging plate is contained in a cassette that can be loaded into a conventional bucky assembly or cassette holder.

Initially, for mammographic imaging, high-resolution plates designed for general radiography were processed in a standard image reader using special algorithms for breast imaging. Resolution is typically 100 µm. More recently, CR systems designed specifically for mammography, with improved plate/phosphor design providing increased spatial resolution (50 µm) and dedicated image readers, have been developed.

The CR image can be presented on film using a high-resolution laser imager or displayed on a monitor at a suitable workstation. Data from centres using CR suggests that the sensitivity for carcinoma detection with CR imaging is at least equal to that of conventional film-screen mammography.

Direct digital detectors

Image acquisition in CR is a two-stage process requiring transfer of the CR plate to the readout device. Direct digital radiography (DDR) is a single-stage process in which the image is transferred directly from the detector to the workstation. Two approaches to the design of full field direct digital detectors have been considered.

CCD devices One manufacturer has produced a full field imaging system based on a tiled array of CCD detectors. After exposure the image is 'stitched' together from the individual sections from each detector element. Stitching artefacts or narrow strips

between the sections that are lost from the image (typically 80-100 μm in width) may occur but the manufacturer suggests that these are so small as not to be of significance in clinical practice. Spatial resolution is superior to current flat panel detectors at approximately 40 μm . An alternative approach is a scanning system in which a moving slit collimator scans a fan beam of X-rays across the breast. The detector comprises a linear array of CCD devices and its movement is synchronised with the scanning X-ray beam. The scanning beam technique provides high scatter rejection resulting in improved image quality. Radiation dose is reduced as a secondary radiation grid is not required. An image resolution of 55 μm or better may be possible. However, the time for a typical scan is approximately 4-5 seconds.

Flat panel detectors Two designs of flat panel detector have been considered.

Amorphous silicon detectors Currently, one manufacturer offers a full field digital imaging system using an amorphous silicon-based flat panel detector that provides an image resolution of 100 μm . A caesium iodide phosphor screen converts X-ray photons to light. The phosphor is coupled directly to an amorphous silicon panel that incorporates a photodiode/thin film transistor (TFT) array. Each of the photodiodes represents a pixel, these absorb and convert the light to electronic charge which is then read by the associated transistor array.

Amorphous selenium detectors These detectors are similar to the amorphous silicon devices but without the requirement for a phosphor screen. The X-ray photons are converted directly to electronic charge in a selenium layer that is then read by the TFT array. This design has the potential to improve image quality (primarily in terms of sharpness) as there is no light spread associated with the use of a phosphor. A number of selenium-based systems are in development, resolution is projected to be between 80 and 100 μm .

Image display modes

Display of digital mammography images will be by high-quality monitors at a workstation for softcopy reporting or printed on to film using a high-resolution device, such as a high-resolution laser film printer, for hardcopy reporting. A lower specification printer may be considered if images are only required for patient records.

Small field digital imaging systems are supplied with a single workstation that provides the operating system for image acquisition plus a range of image-processing tools for image display. Due to the limited image field size, a single monitor can be used to display single images or stereo pairs.

Full field digital imaging systems are provided with an acquisition workstation with a single monitor and a limited range of image-processing and handling tools. The reporting workstation will require two high-quality monitors mounted next to each other in portrait format to allow the display of pairs of digital mammograms at full resolution. A comprehensive range of image processing and handling tools will be provided. Some manufacturers are developing advanced features for digital imaging such as computer-aided detection (CAD), telcmammography (transmission of images) and 3D reconstruction.

Digital images comprise a large amount of data that need to be stored both in the short and long term. Short-term storage is generally provided on the workstation computer hard disk. For long-term

storage, a separate archive facility is required and may take several forms. Data compression may be used to improve the efficiency of storage.

Mammography projections and normal appearances

Mammography projections (Box 46.1)

The standard examination for women undergoing either symptomatic mammography or their first screening examination consists of a lateral oblique and a cranio-caudal view of each breast. The *lateral oblique* view is usually obtained with the tube angled at 45° to the horizontal, but tube angulation from 30° to 60° may be needed depending on the build of the woman. More breast tissue is demonstrated on the lateral oblique projection than on any other projection.

Careful positioning is essential for satisfactory demonstration of the breast. The criteria for adequate positioning for the oblique view are shown in Figure 46.1. The nipple should be seen in profile; the anterior surface of the pectoralis muscle should be visible down to

Box 46.1

Standard views:
Lateral oblique
Craniocaudal

Supplementary views:
Lateral (lateromedial or mediolateral)
Extended craniocaudal (medially or laterally related)
Magnification
Localised compression (may be combined with magnification)
Cleavage view

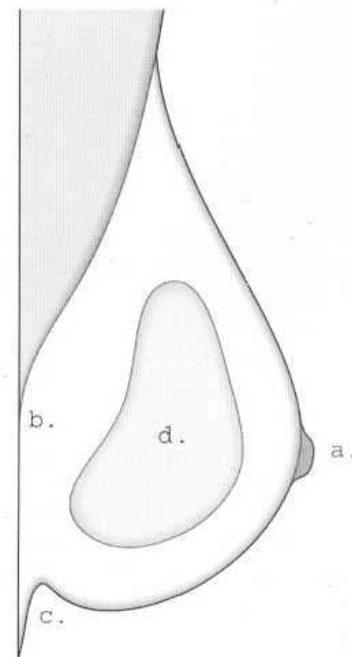
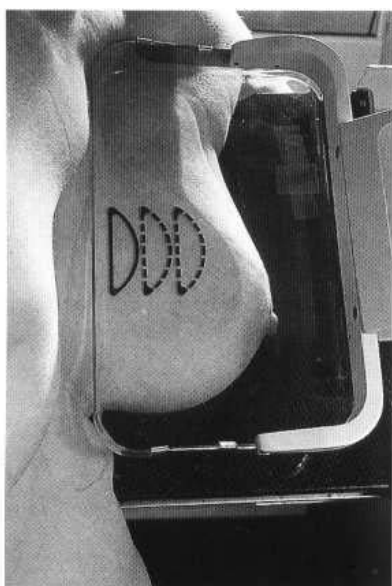


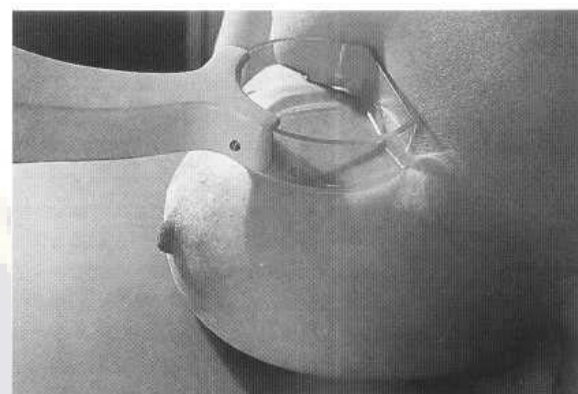
Fig. 46.1 Correct positioning for mediolateral oblique view. a = Nipple in profile. b = Pectoralis muscle visible down to level of the nipple. c = Inframammary fold visible. d = Glandular tissue evenly compressed and adequately penetrated.



46.2



46.3



46.4

Fig. 46.2 Positioning for the lateral oblique view.

Fig. 46.3 Positioning for the craniocaudal view.

Fig. 46.4 Positioning for a localised compression view.

the level of the nipple; the inframammary skin fold should be visible; the breast should be lifted sufficiently and compression applied so that the breast tissue is spread evenly between the compression plate and the film holder; there should be no skin folds superimposed on the breast (Fig. 46.2). In order to achieve a satisfactory position, the radiographer should enable the patient to be as relaxed as possible.

The standard *craniocaudal film* is obtained with a vertical X-ray beam and the nipple should be in profile (Fig. 46.3). The craniocaudal projection demonstrates the subareolar, medial, and lateral portions of the breast. However, tissue in the posterolateral aspect of the breast may be incompletely demonstrated.

Supplementary views

For demonstration of tissue in the most posterolateral part of the breast, an extended craniocaudal view is used with the patient rotated medially to bring the lateral aspect of the breast and axillary tail over the film. When the posteromedial portion of the breast is not satisfactorily demonstrated, an extended craniocaudal view with lateral rotation of the patient is obtained.

Magnification views are obtained by increasing the object-film distance, producing an 'air gap', and using a fine focal spot to increase resolution. A magnification factor of 1.5 is usual and the increased resolution obtained is particularly helpful for detailed analysis of microcalcifications and the margins of small mass lesions.

Localised compression views are obtained by using a small paddle compression device (Fig. 46.4) and may be used together with magnification. By compressing one area of the breast, tissue overlying a small lesion is displaced, allowing better demonstration of its features. The technique is also very helpful in analysing asymmetrical soft-tissue shadows, either by confirming that the shadow has the appearance of normal glandular tissue or by demonstrating that an underlying lesion is present.

Normal mammographic anatomy

The breast contains 15-20 lobes, each with a duct opening in the nipple. The main duct branches repeatedly within the breast and the

most distal branches of the duct system are called the terminal ducts. The terminal duct consists of extralobular and intralobular portions. The intralobular portion, together with the acini, forms a lobule. The extralobular terminal duct and the lobule form a terminal ductal lobular unit (TDLU). The TDLU is the site of origin of most malignant and benign diseases of the breast.

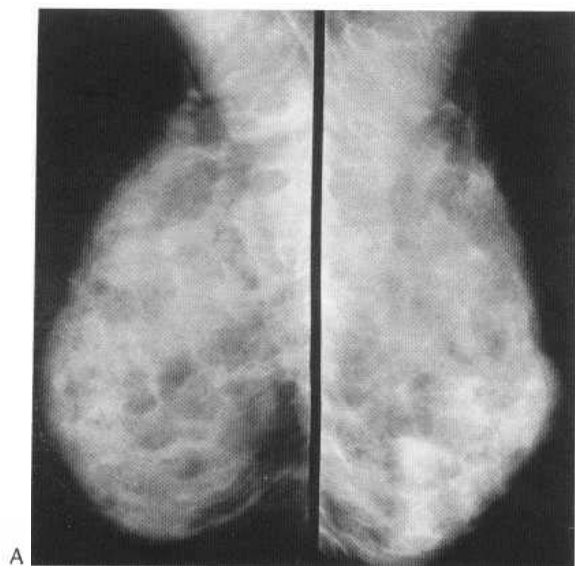
The mammographic appearance of the breast depends on the relative amounts of fat and glandular tissue which are present (Fig. 46.5). The young woman's breast contains a large proportion of glandular tissue which appears as soft-tissue density on the mammogram; in older women, when involution of the glandular tissue has occurred, most of the breast tissue appears of fatty density. During involution, there is a mixture of soft-tissue and fat density present. The junction between the subcutaneous and retro mammary fat layers and the glandular tissue should consist of a series of curved margins. Straightening or distortion of these margins may indicate the presence of underlying pathology in the glandular tissue. Other normal structures visible on the mammogram include nipple and skin, blood vessels, ducts, Cooper's ligaments and axillary lymph nodes.

Normal variants

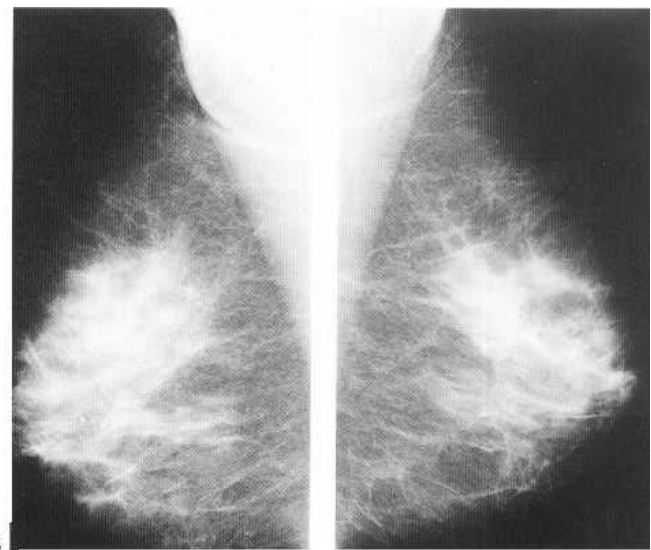
The normal anatomical variants of the breast result from the embryological development of the breast from the band of ectoderm on the ventral surface of the embryo extending from clavicle to groin, the 'nipple line'. An area of accessory breast tissue is commonly seen in the axillary tail, or occasionally in the inframammary fold. An accessory nipple may occur at any site along the nipple line. Congenital absence or hyperplasia of the pectoralis muscle may occur and is seen in Poland's syndrome (Fig. 46.6).

The dense breast

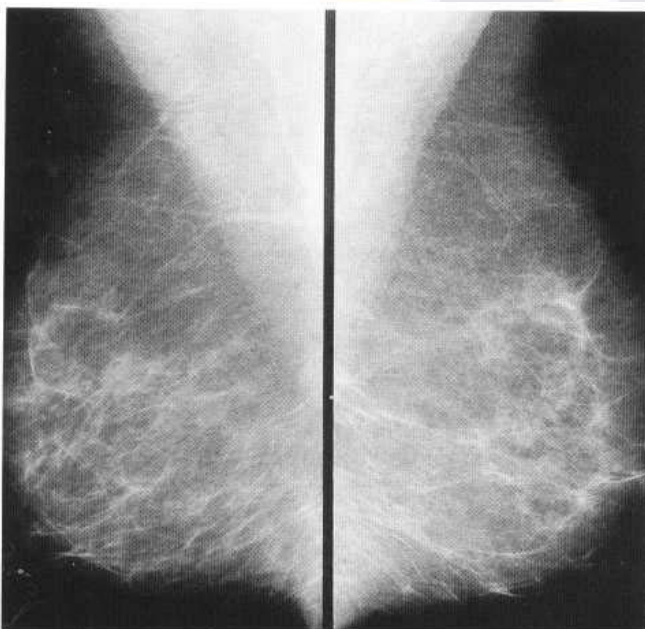
Diffuse increase in the density of the breast tissue is caused by oedema (see the 'Oedematous breast' below) or by an increase in the glandular tissue and/or fibrous tissue. This is commonly seen in benign breast change, and may be accompanied by evidence of cysts, and in women who are taking hormone replacement therapy (HRT) for menopausal symptoms. The increased density of the parenchyma seen as a result of HRT has been shown to be associ-



A



B



C

Fig. 46.5 Lateral oblique views. (A) Glandular breasts. (B) Involuting breasts. (C) Adipose breasts.

ated with a decrease in the sensitivity of screening mammography for cancer detection. Diffuse increase in parenchymal density is also occasionally seen due to loss of fat due to severe weight loss or cachexia, or lack of fat due to lipodystrophy.

Breast ultrasound

Technique

High-quality images of the normal and abnormal breast can be obtained with modern ultrasound equipment. At the minimum, a 7.5 MHz linear array probe should be used, though digital broadband-width transducers using higher frequency (mid-range exceeding 7.5 MHz) are now widely available and allow higher resolution imaging. The patient is examined in the supine oblique position. The side being examined is raised and the arm placed above the head to ensure that the breast tissue is evenly distributed over the chest wall. In addition to conventional orthogonal scanning directions, scanning in the radial and antiradial planes are of value in demonstrating ductal abnormalities.

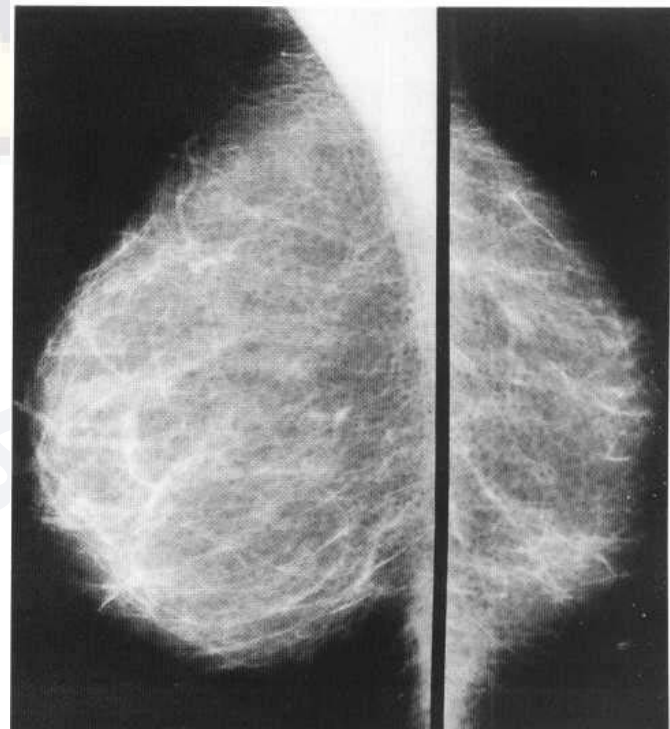


Fig. 46.6 Congenital absence of the left breast pectoralis muscle.

Indications for breast ultrasound

The original role of breast sonography is in the differentiation of cystic and solid lesions. Though this is still a major role, the role of ultrasound complements both clinical examination and mammography. It is also successfully used as a 'second-look' procedure where an abnormality has been identified using MRI or scintimammography. Because it does not use ionising radiation, it is the examination of choice in young women and is valuable in the assessment of the mammographically 'dense' breast. Ultrasound plays an important role in the triple assessment of symptomatic lesions. Being the only 'real-time' imaging modality also means it

can be used to accurately localise or biopsy breast lesions. The main indications are summarised in Box 46.2.

Ultrasound interpretation

The subcutaneous fat layer is demonstrated superficially as hypo-echoic tissue compared to the glandular tissue from which it is separated by a well-defined scalloped margin (Fig. 46.7). Normal ducts are often visible, particularly in the subareolar region, as anechoic tubular structures. Deep to the glandular tissue, a retromammary fat layer is usually visible and, behind this, the structures of the chest wall. The ultrasound appearance of breast tissue depends on how much involution of the glandular tissue has taken place. The young glandular breast contains a well-defined layer of glandular tissue, within which round or oval well-defined echo-poor

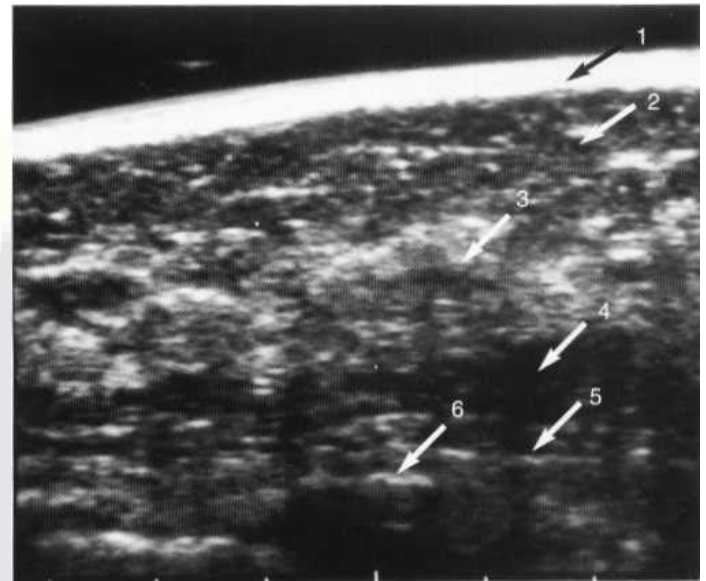


Fig. 46.7 Normal breast ultrasound: 1 = skin; 2 = subcutaneous fat; 3 = glandular tissue; 4 = retromammary fat; 5 = pectoralis muscle; 6 = rib.

Box 46.2 Indications for mammography and breast ultrasound

Mammography

- Screening asymptomatic women aged 50 years and over
- Screening asymptomatic women aged 35 years and over who have a high risk of developing breast cancer:
 - women who have one or more first degree relatives who have been diagnosed with premenopausal breast cancer
 - women with histologic risk factors found at previous surgery, e.g. atypical ductal hyperplasia
- Investigation of symptomatic women aged 35 years and over with a breast lump or other clinical evidence of breast cancer
- Surveillance of the breast following local excision of breast carcinoma
- Evaluation of a breast lump in women following augmentation mammoplasty
- Investigation of a suspicious breast lump in a man

Breast ultrasound

- Symptomatic breast lumps in women aged less than 35 years
- Breast lump developing during pregnancy or lactation
- Assessment of mammographic abnormality (± further mammographic views)
- Assessment of MRI or scintimammography detected lesions
- Clinical breast mass with negative mammograms
- Breast inflammation
- The augmented breast (together with MRI)
- Breast lump in a male (together with mammography)
- Guidance of needle biopsy or localisation
- Follow-up of breast cancer treated with adjuvant chemotherapy

fat lobules may be present. As involution takes place, more of the breast is composed of fat: in the completely involuted breast, ultrasound shows fat lobules separated by line curvilinear septa of increased echogenicity. The pregnant or lactating breast is almost entirely composed of highly echogenic glandular tissue due to the glandular proliferation. The echotexture of any lesion is compared relative to the echotexture of the intramammary fat.

Cysts are typically well-defined rounded anechoic lesions with posterior acoustic enhancement, though the presence of debris can increase the overall internal echogenicity. Wall thickening, irregularity or mural nodules should be treated with suspicion and aspiration should be performed. Needle biopsy should be performed if there is a residual mass or bloody aspirate. The typical characteristics of benign and malignant mass lesions are summarised in Table 46.1. It is however important to be aware of the shortcomings and limitations of relying purely on morphological appearances. The presence of posterior acoustic enhancement and well-defined margins that occurs with benign masses such as fibroadenomas

Table 46.1 Typical ultrasound characteristics of solid breast lesions

	<i>Benign</i>	<i>Malignant</i>
Shape	Oval/ellipsoid	Variable
Alignment	Wider than deep; aligned parallel to tissue planes	Deeper than wide
Margins	Smooth/thin echogenic pseudocapsule with 2-3 gentle lobulations	Irregular or spiculated; echogenic 'halo'
Echotexture	Variable to intense hyperechogenicity	Low-level Marked hypoechogenicity
Homogeneity of internal echoes	Uniform	Non-uniform
Lateral shadowing	Present	Absent
Posterior effect	Minimum attenuation/posterior enhancement	Attenuation with obscured posterior margin
Other signs		Calcification Microlobulation Intraductal extension Infiltration across tissue planes and increased echogenicity of surrounding fat

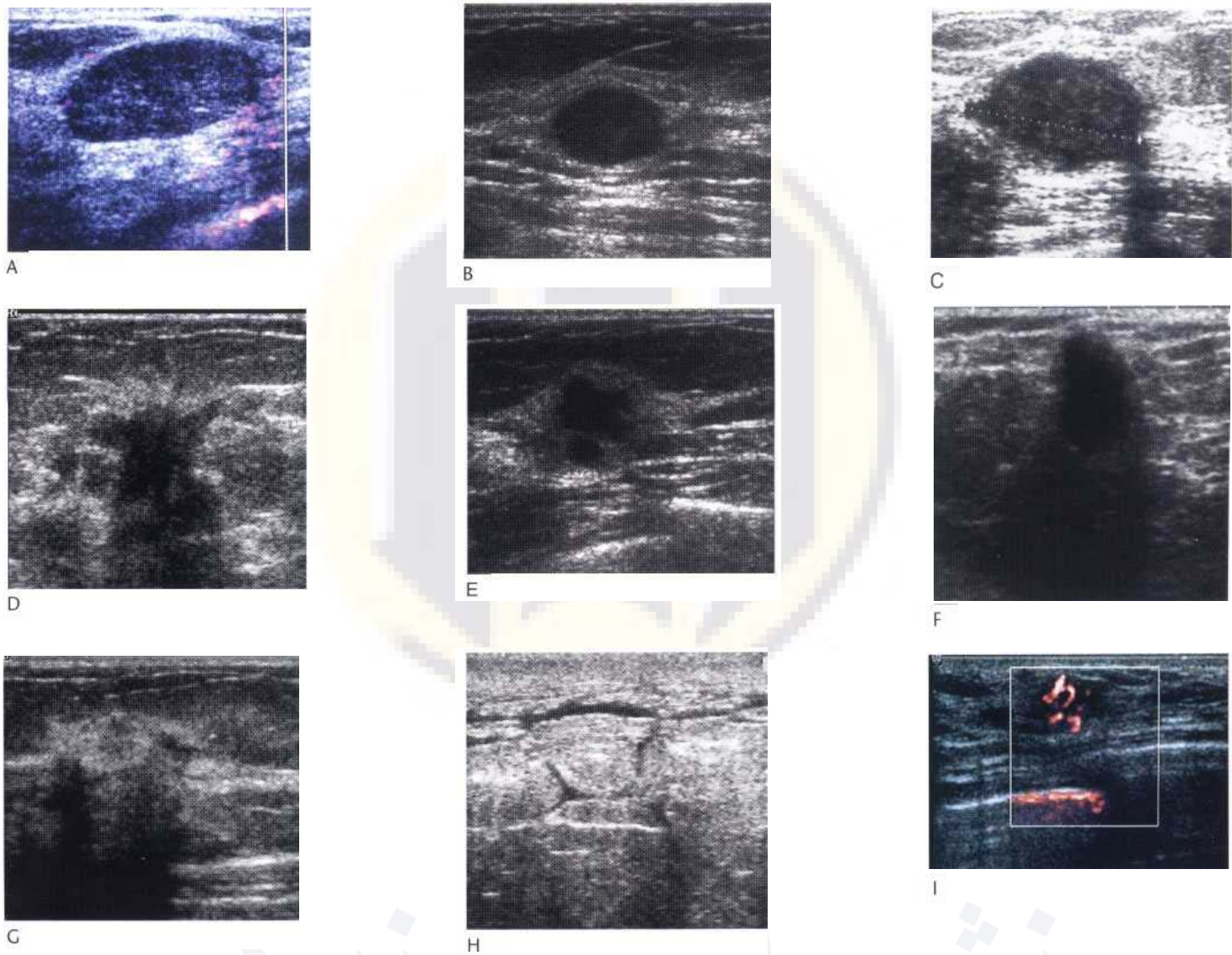


Fig. 46.8 (A). A typical fibroadenoma with homogeneous internal echoes with an ovoid shape and circumscribed margins. There is posterior acoustic enhancement. (B,C) Examples of malignant breast masses with 'benign' ultrasound characteristics. The medullary carcinoma in B has a smooth well-defined margin and is 'wider than tall'. The grade 3 invasive ductal carcinoma in C has marked posterior acoustic enhancement; however its margins are irregular and microlobulated. (D) A typical 'tall' irregular spiculated hypoechoic attenuating mass in keeping with a malignant breast tumour. (E,F) Two examples of fat necrosis mimicking malignant lesions. The case in E shows two hypoechoic areas with irregular outlines. The case in F shows a 'tall' hypoechoic lesion with posterior acoustic shadowing. (G) An invasive lobular carcinoma presenting as areas of scattered indeterminate attenuation. There is also increased hyperechogenicity of intramammary fat on the right side. (H) Inflammatory breast cancer with secondary signs. Note the loss of the normal glandular adipose differentiation due to increased hyperechogenicity of the intramammary fat. Lymphatic dilatation is also apparent under the thickened subcutaneous layer. (I) A power Doppler image of an invasive grade 3 breast cancer. Note the high density of irregular tortuous and branching vessels penetrating into the centre of the tumour.

(Fig. 46.8A) is also associated with high-grade malignancy as well as mucinous or medullary carcinoma (Fig. 46.8B). Conversely, hypoechoic attenuating lesions with irregular margins typical of malignant disease (Fig. 46.8D) can also be demonstrated in benign pathology such as fat necrosis, scarring or fibrosis (Fig. 46.8F). In practice, needle biopsy should be performed as part of triple assessment in the presence of a discrete solid mass. Not all breast pathology presents as a discrete lesion. Inflammatory or lobular cancers may present as areas of scattered indeterminate attenuation (Fig. 46.8G). There may be other associated secondary signs such as increased hyperechogenicity of the intramammary fat, lymphatic dilatation or skin thickening (Fig. 46.8H). The use of colour and power Doppler has also been exploited in aiding the benign-

malignant differentiation of solid masses. In general, malignant masses tend to show an increased number of vessels that penetrate deep into the tumour with a branching morphology (Fig. 46.8I).

Applications

The use of ultrasound to assess symptomatic lumps has already been discussed. In the absence of a suspicious clinical lesion, a negative ultrasound and mammographic examination has a very high negative predictive value for malignant disease. Though ultrasound is successfully used to aid assessment of abnormalities detected by mammography, it should not be used as a sole modality for screening as ultrasound does not always detect cancers that are visualised mam-

mographically. Conversely, used in conjunction with mammography, ultrasound can detect clinically and mammographically occult cancers particularly when there is a higher possibility of cancer (for instance in women who have already been diagnosed as having cancer). With new high-frequency transducers, it is also possible to detect malignancy associated with mammographically detected clustered microcalcifications especially where the clusters are larger than 10 μ m. These lesions may be evident as irregular masses, abnormal dilated ducts or clustered foci of increased echogenicity with increased Doppler vascularity (Fig. 46.9).

Viewing mammograms

Mammograms should be viewed in optimum lighting conditions, with light from around the films and extraneous light in the viewing room excluded as far as possible. The films should be checked for correct identification labelling and for radiographic quality. The overall parenchymal pattern of the breasts is assessed. The standard lateral oblique and craniocaudal views are studied with the right and left breast films 'back to back' so that symmetry of the breast tissue can be examined. A systematic search for abnormal mammographic signs is made and any abnormal signs are analysed to decide, for screening examinations, whether the woman should be recalled for assessment, and, for symptomatic/assessment examinations, what the nature of the abnormality is and whether further views or other tests are indicated.

Abnormal signs on mammography and ultrasound

Spiculate mass (synon: stellate mass)

A spiculate mass is the commonest mammographic appearance of invasive breast carcinoma. It consists of a central soft-tissue tumour mass from the surface of which spicules extend into the surrounding breast tissue (Figs 46.10, 46.11). The larger the tumour mass, the longer the spicules tend to be. There is often associated distortion of

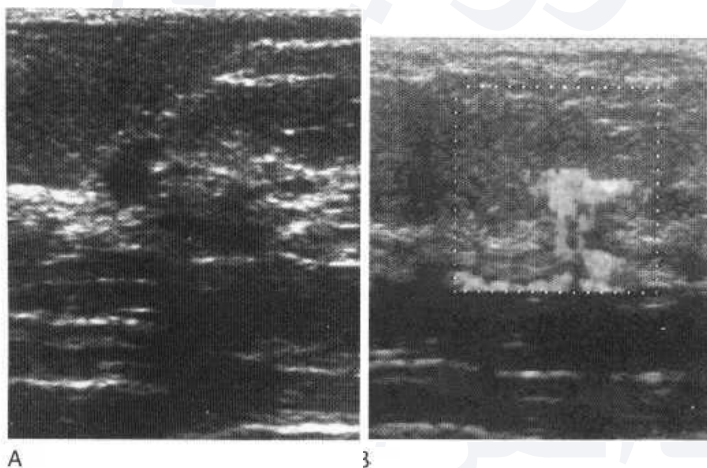


Fig. 46.9 (A) This image shows a focus of high signal corresponding to a fleck of microcalcification lying within an irregular hypoechoic mass with intraductal dilation. (B) The corresponding power Doppler image demonstrates associated neovasculation. This corresponded to a small focus of invasive carcinoma lying within an area of high-grade ductal carcinoma in situ.

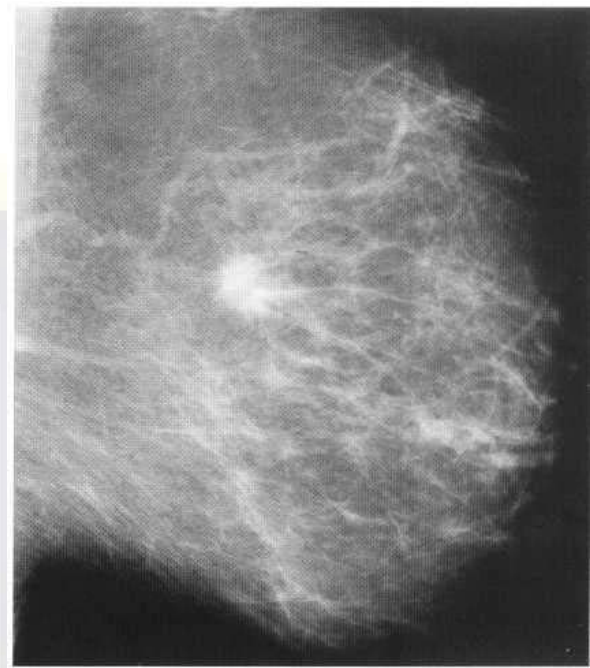


Fig. 46.10 Spiculate mass due to an invasive carcinoma.

the surrounding breast tissue with straightening of the trabeculae due to retraction. This distortion may cause localised loss of the normal curvilinear outline of the anterior or posterior borders of the glandular tissue close to the tumour resulting in a 'V' shape, the 'tent' sign. Large or superficially positioned tumours may be associated with localised skin thickening and retraction. Deeply positioned tumours may be associated with tethering of the pectoralis muscle. Irregular microcalcifications due to associated ductal carcinoma in situ may be found within the tumour or in the surrounding breast tissue, sometimes extending to the nipple. Observation of the extent of the microcalcification is important because this may influence the type of surgery performed. Coarse calcifications may be associated with large tumours due to necrosis.

Masses in adipose breasts are easy to detect because of the high contrast between the mass and the surrounding tissue. In more dense glandular breasts, however, abnormal masses can be more difficult to perceive because they may be partially obscured by glandular tissue. It is very important, therefore, to look carefully for indirect signs of malignancy, particularly parenchymal distortion, retraction and straightening of the breast trabeculae.

Differential diagnosis and management

Differential diagnosis

- Invasive carcinoma
- Non-invasive carcinoma
- Complex sclerosing lesion/radial scar
- Surgical scar
- Fibromatosis
- Granular cell tumour.

Approximately 95% of spiculate masses seen on mammography are due to invasive breast cancers. Complex sclerosing lesions may show an identical appearance to a small spiculate carcinoma (Fig. 46.12). Diagnosis of most malignant lesions can be confirmed preoperatively by fine needle aspiration cytology (FNAC) or core biopsy (CB), and definitive surgical treatment can be planned. In

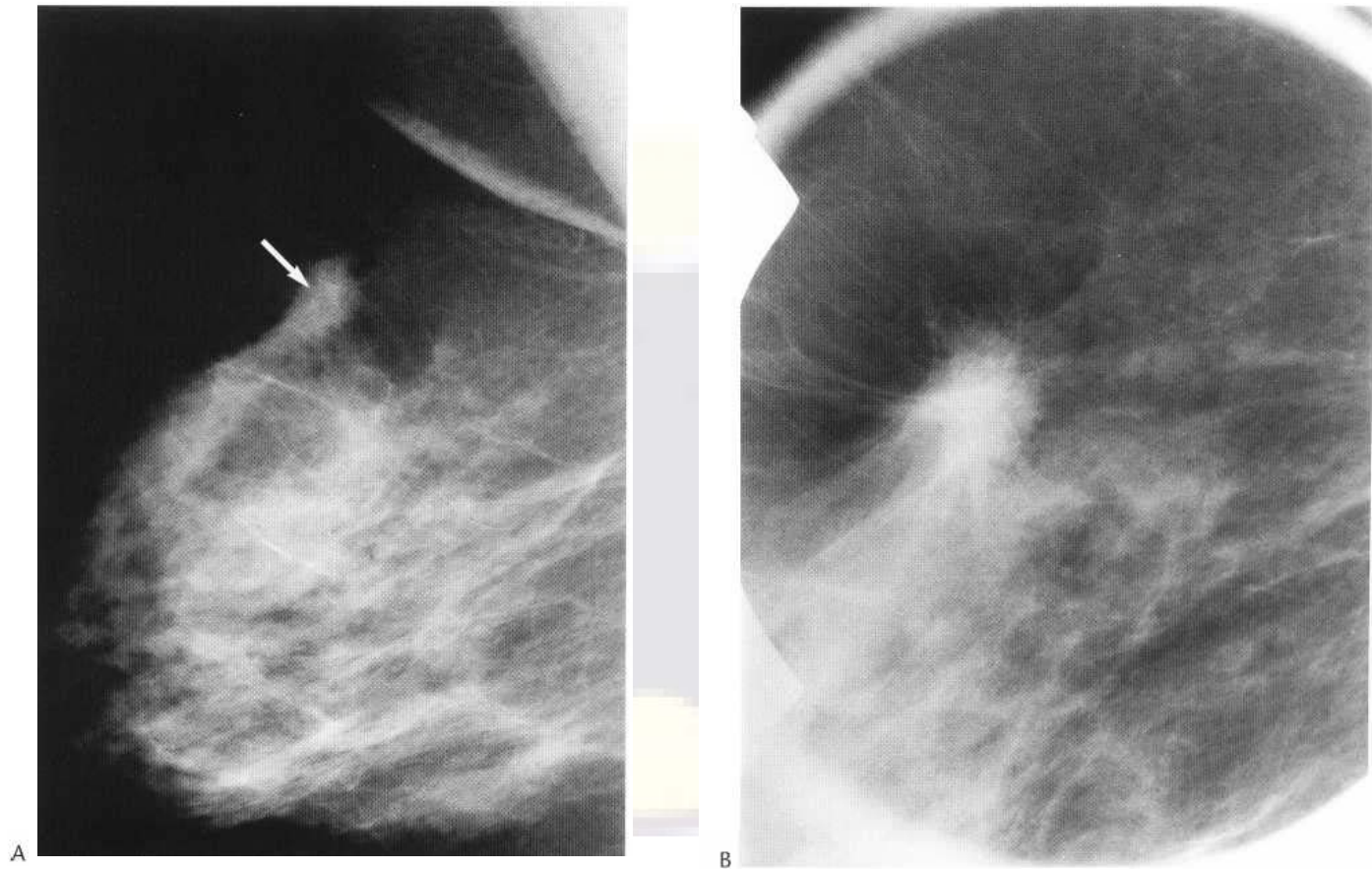


Fig. 46.11 Spiculate mass (arrow) due to an invasive carcinoma on: (A) lateral view; (B) localised compression magnification view.

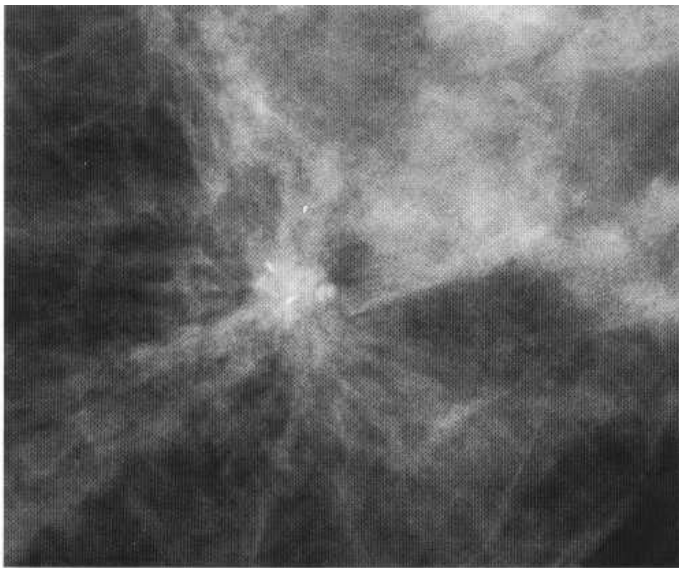


Fig. 46.12 A spiculate mass with microcalcification due to a complex sclerosing lesion/radial scar (magnification view)

those cases where cytology or core biopsy does not confirm the diagnosis, a diagnostic surgical excision should be performed with radiological preoperative localisation and operative specimen radiography for non-palpable lesions.

Most spiculate carcinomas of 1 cm diameter or more can be demonstrated by *ultrasound*. The typical ultrasound features are of an echo-poor mass, with poorly defined margins and posterior

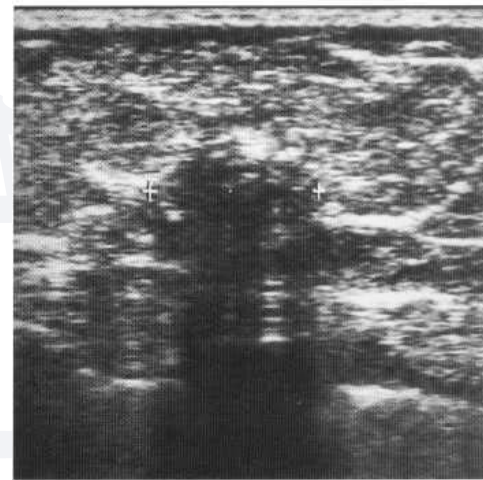


Fig. 46.13 Ultrasound showing an echo-poor mass with irregular margins and posterior acoustic shadowing due to a carcinoma.

acoustic shadowing (Fig. 46.13). Distortion of the surrounding breast tissue may be visible and a rim of increased reflectivity around the tumour mass may be seen. The presence of these signs, however, is variable: acoustic shadowing may be absent; an echo-poor mass may not be visible with very small tumours. Similar suspicious ultrasound appearances may be caused by a sclerosing fibroadenoma or benign complex sclerosing lesion

(radial scar).

Ultrasound may be used to guide diagnostic needle biopsy or preoperative needle/hookwire insertion for non-palpable lesions.

Fibromatosis (Fig. 46.14) is a rare condition which has the same histology characteristics as abdominal desmoid tumours. It may be locally invasive but does not metastasise. Local recurrence may occur if surgical excision is incomplete. The mammographic appearance mimics carcinoma.

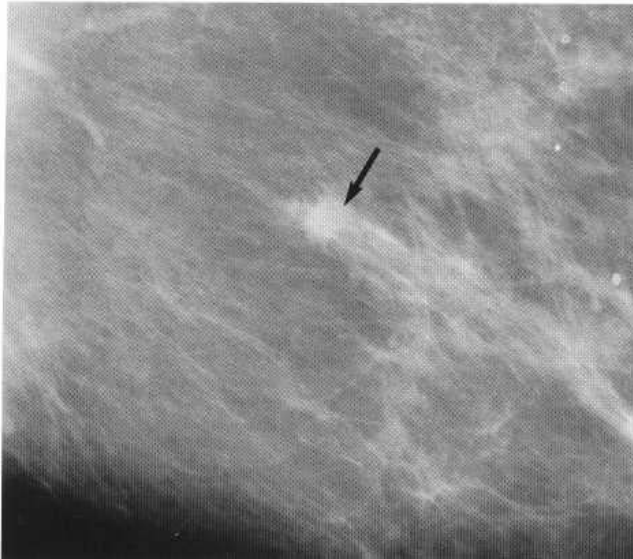


Fig. 46.14 A small mass (arrow) due to fibromatosis.

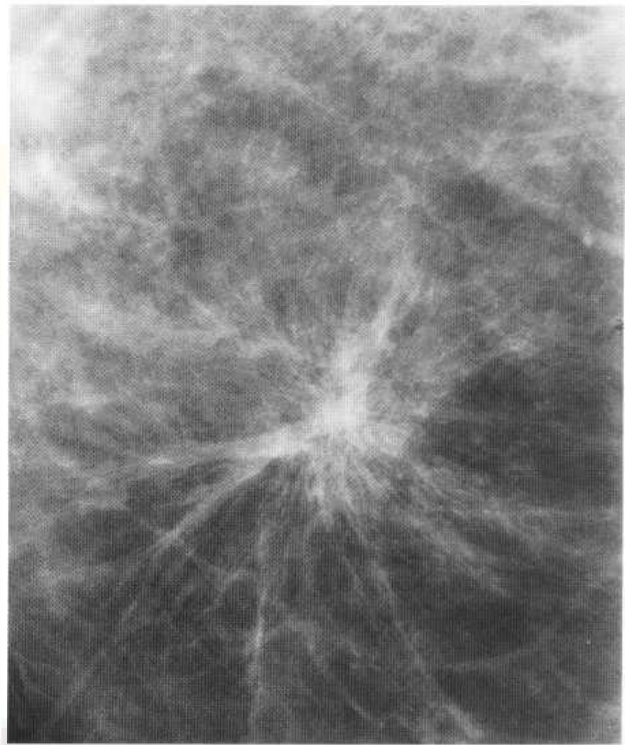


Fig. 46.15 Magnification localised compression view showing an architectural distortion (stellate lesion) due to a benign complex sclerosing lesion/radial scar.

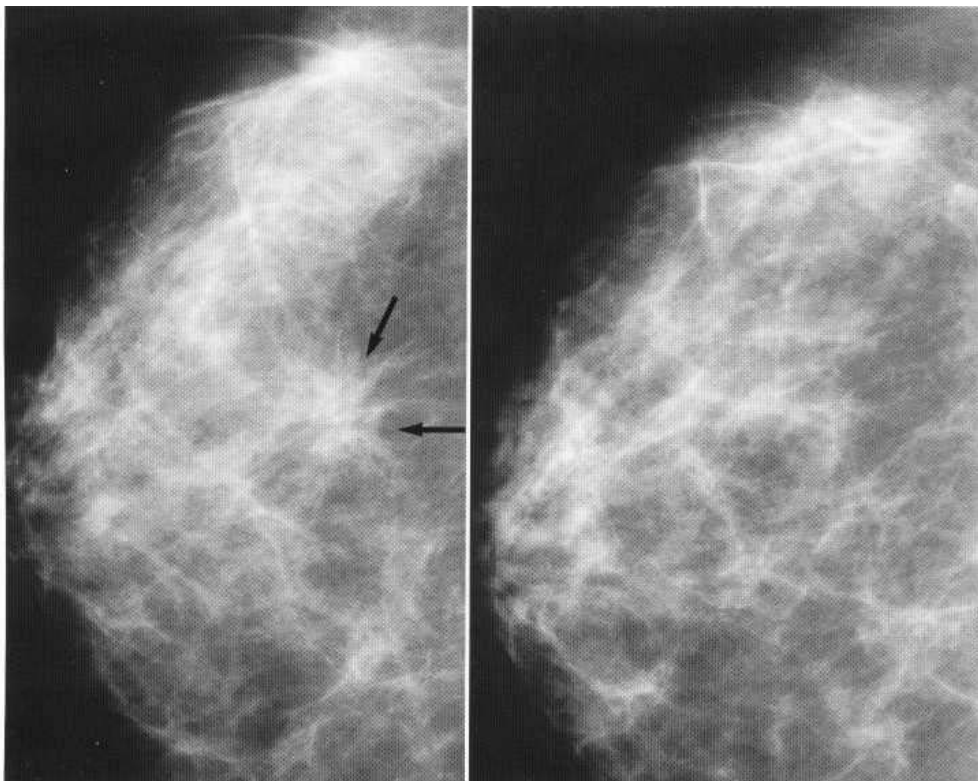


Fig. 46.16 (A) Stellate appearance (arrows) due to summation of overlying stromal shadows. (B) Repeat film shows that no lesion is present.

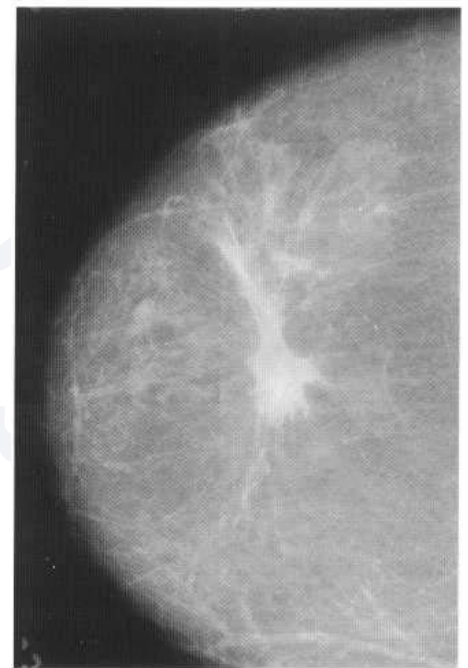


Fig. 46.17 Stellate opacity due to a surgical scar.

Architectural distortion (synonym: parenchymal distortion, stellate lesion)

An area of architectural distortion of the breast is seen mammographically as numerous straight lines usually measuring from 1 to 4 cm in length radiating toward a central area (Fig. 46.15). The central part of the lesion typically shows no central soft-tissue mass either on standard or localised compression views. A mammographic work-up including repeat standard views and, where necessary, localised compression views should be performed to confirm that a stellate lesion is present rather than a density with apparent architectural distortion caused by summation of normal overlying stromal shadows (Fig. 46.16), and to look for associated signs such as microcalcification.

Differential diagnosis and management

Differential diagnosis:

- Complex sclerosing lesion/radial scar
- Carcinoma
- Surgical scar.

Surgical scar (Fig. 46.17) can be diagnosed from the appropriate clinical history and physical examination showing that the position of the scar corresponds to the position of the stellate lesion, if necessary by carrying out mammograms with skin markers on the scar. Surgical scars, because they are discoid in shape, will often show a difference in size and shape on orthogonal views.

Complex sclerosing lesion (CSL) (synonyms: radial scar, infiltrating epitheliosis) is characterised histologically by a fibroelastic centre surrounded by ducts and lobules arranged in a radiating fashion. Areas of simple or atypical ductal hyperplasia are often found in the periphery of CSLs. The radiological features of these lesions reflect the underlying histological architecture. Microcalcifications may be found, usually in association with the areas of epithelial hyperplasia.

Having excluded surgical scars, 50-60% of architectural distortions are due to *carcinoma* (Figs 46.18, 46.19), often of special type, e.g. tubular, tubulo-lobular. It is not possible using mammographic features alone to distinguish those due to carcinoma from

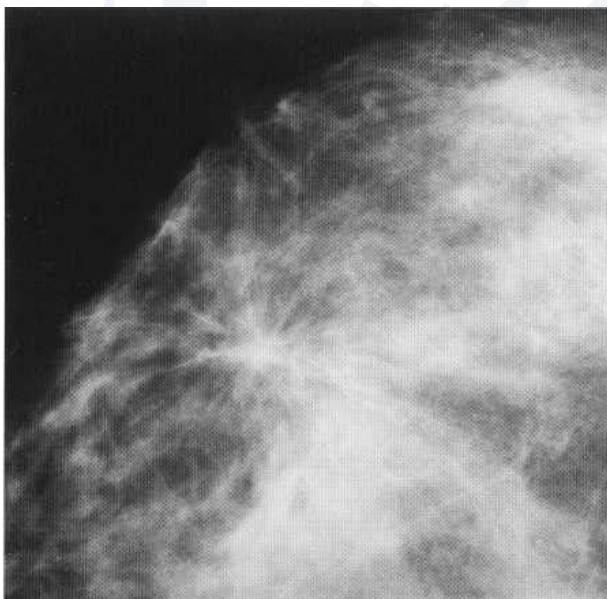


Fig. 46.18 Stellate lesion due to an invasive tubular carcinoma.

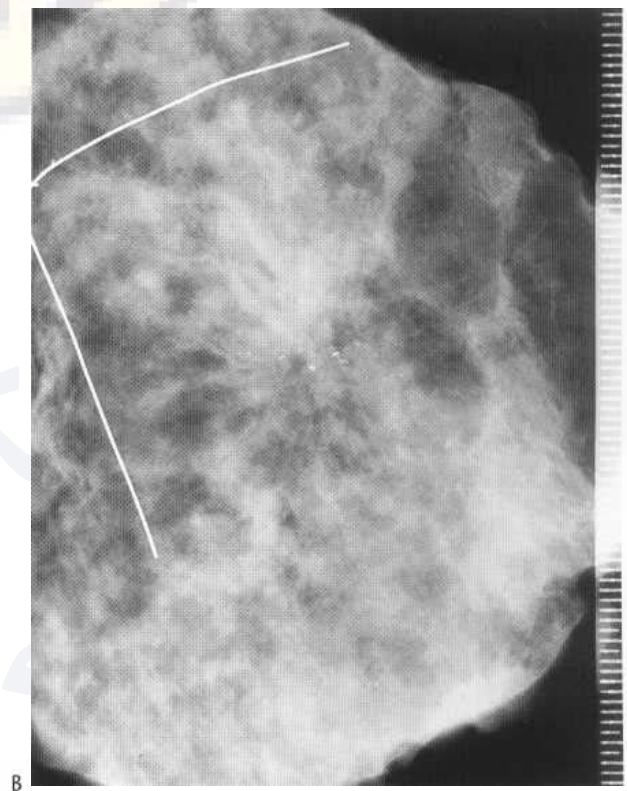
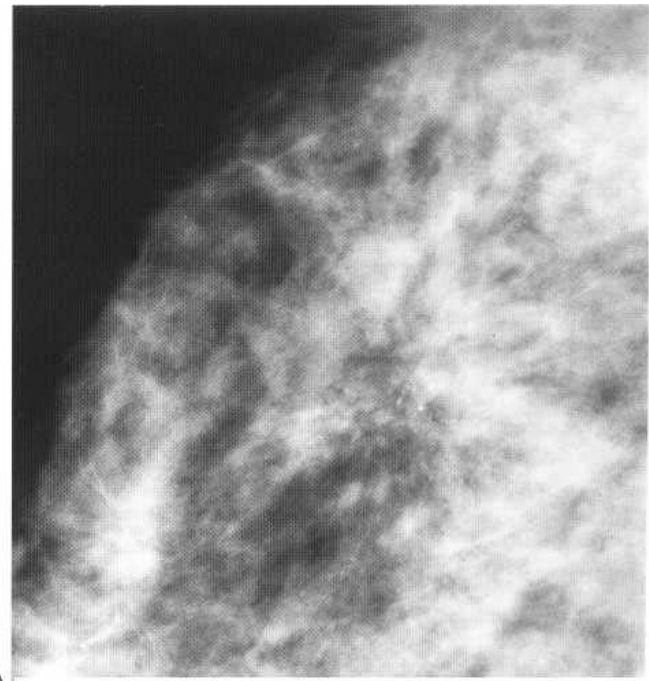


Fig. 46.19 Stellate lesion with microcalcification due to a Grade 1 invasive ductal carcinoma. (A) Magnification view. (B) Specimen radiograph.

those due to benign complex sclerosing lesions/radial scars, although radiological and clinical features may indicate which is the most likely diagnosis. Spicule length is related to the size of the tumour in cancers but the spicules tend to be long with no central mass in CSLs. A benign CSL is usually not associated with a palpable mass even though the mammographic abnormality may be 4-5 cm in diameter. Both benign and malignant causes of architectural distortion may be associated with microcalcification,

either within or near the periphery of the lesion. Ultrasound is not helpful in the differential diagnosis of benign CSL from carcinoma. CSLs may show a variety of ultrasound features including shadowing alone, a mass with shadowing, parenchymal distortion or no abnormality.

Localised areas of architectural distortion, with the exception of those due to Surgical scars, require a histological diagnosis. This may be obtained by image-guided needle core biopsy or diagnostic surgical excision. In most malignant cases a positive diagnosis will be obtained using core biopsy allowing planning of definitive surgery. For cases in which a benign core biopsy is obtained, diagnostic surgical excision with radiological localisation is recommended because of the risk of invasive or in situ malignancy at the periphery of the lesion.

Asymmetrical soft-tissue density

Asymmetry of the glandular tissue is a common finding on normal mammograms and can often be diagnosed confidently-analysis of the radiological features of the asymmetry shows areas of low soft-tissue density, lucency and curvilinear margins with no evidence of straightened breast trabeculae or distortion. Diagnostic difficulty may occur because some carcinomas, particularly small tumours found in screening practice, may not show typical features of malignancy such as an irregular or spiculate outline. These tumours may appear on basic screening films as asymmetrical soft-tissue opacities (Fig. 46.20).

The site of an asymmetrical density may be helpful both in detecting some small tumours and in deciding whether further work-up is necessary. The following review areas should be systematically examined.

- A 3-4 cm wide area anterior to the edge of the pectoralis muscle on the lateral oblique view (Fig. 46.21).
- The retroglandular clear space between the posterior margin of the parenchyma and the chest wall on both the lateral oblique and craniocaudal projections.
- The medial half of the breast on the craniocaudal views.
- The retroareolar area-perception of carcinomas in this site may be difficult because of superimposition of ductal structures and stroma.
- The inferior part of the breast.

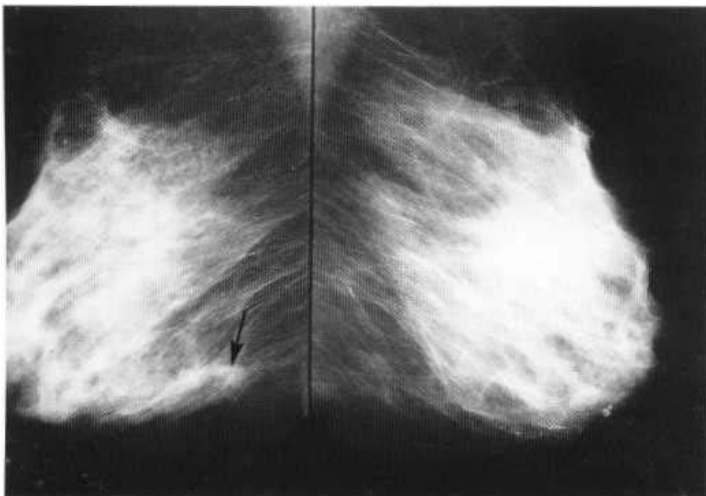


Fig. 46.20 MLO views showing a right asymmetrical density (arrow) due to a carcinoma.

Asymmetrical soft-tissue densities observed in these areas should be carefully analysed including, when possible, a comparison with previous films. Where the features are not typical of normal glandular tissue, further assessment should be carried out using clinical examination, mammography and ultrasound.

Circumscribed mass

A circumscribed mass is analysed according to the following features:

1. **Density:**
 - (i) radiolucent
 - (ii) mixed density
 - (iii) radiopaque (soft-tissue density)
2. **Contour:**
 - (i) sharply outlined capsule
- 'halo' sign
 - (ii) ill-defined outline
3. **Interval change**
4. **Number:**
 - (i) single
 - (ii) multiple.

Radiolucent lesions

Differential diagnosis

- Lipoma
- Oil cyst
- Galactocele.

Lipomas are solitary lesions, often have a thin capsule and, although they are frequently large at the time of diagnosis, may be difficult to palpate on clinical examination because they are soft (Fig. 46.22).

Oil casts may be single or multiple, are usually 2-3 cm in diameter, and result from trauma which is usually surgical but they may be seen following seat-belt injuries in automobile accidents (Fig. 46.23). Oil cysts may develop mural curvilinear calcifications.

Galactoceles develop during lactation and are usually 2-3 cm in diameter.

Mixed density lesions

Differential diagnosis

- Adenolipoma/hamartoma
- Galactocele
- Haematoma
- Lymph node.

Adenolipomas are often large when diagnosed, measuring 6 cm in diameter or more, but are either impalpable or feel soft on clinical examination. Their mammographic appearance is determined by the relative amounts of fat and glandular tissue which are present (Fig. 46.24). There may be a thin soft-tissue density capsule visible.

Galactoceles are more frequently seen as mixed density lesions than radiolucent lesions (Fig. 46.25). They may be managed by simple needle aspiration but in some cases this is difficult due to the thick consistency of the contents.

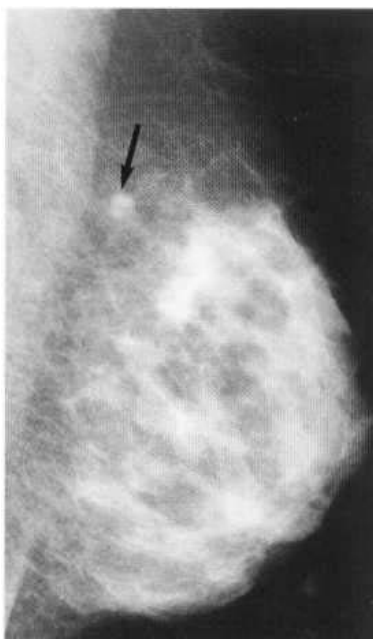


Fig. 46.21 A small soft-tissue density with irregular margins due to a carcinoma is present just anterior to the left pectoralis muscle (arrow).

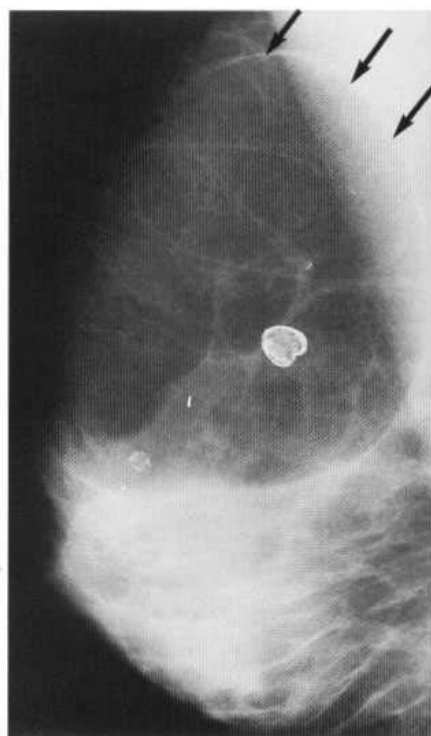


Fig. 46.22 Lipoma—large circumscribed radiolucent mass with a thin capsule (arrows) and coarse calcification.

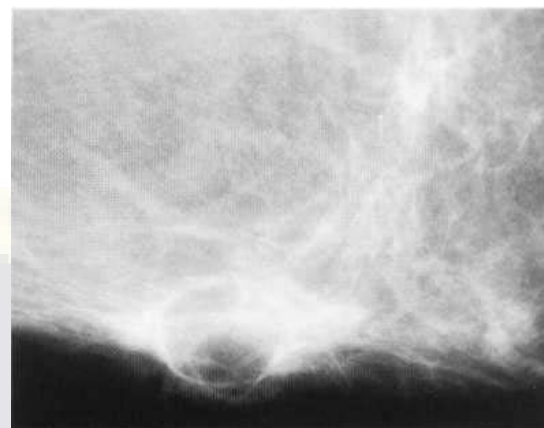


Fig. 46.23 Oil cyst. A round radiolucent lesion is present at the site of a previous surgical excision; clinically a firm lump was present.

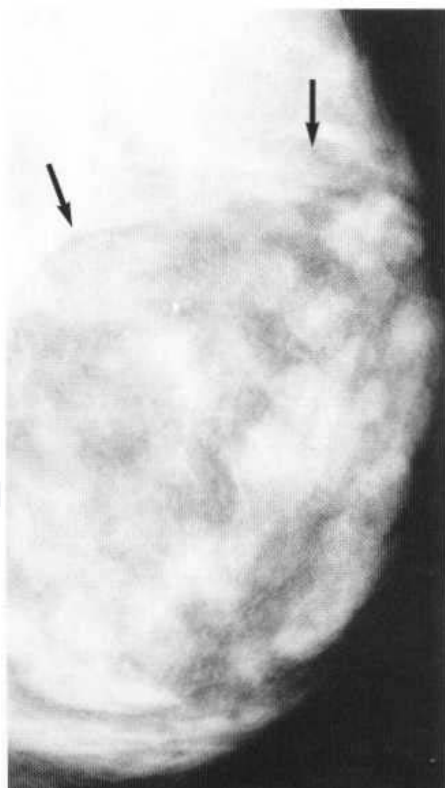


Fig. 46.24 Adenolipoma. A large circumscribed mixed density mass is present (arrows). Clinically only a soft swelling was present.



Fig. 46.25 Galactocele. A circumscribed mixed density lesion with a capsule (arrows).

Following trauma, mammograms may demonstrate an ill-defined or circumscribed area of increased density due to *hnenratotna*.

Normal axillary *lymph nodes* are commonly seen on mammograms and are well defined, have a peripheral area of soft-tissue density and a central radiolucent area. Intramammary lymph nodes most commonly occur in the upper outer quadrant and show the same features.

Radiopaque (soft-tissue density) lesions

Differential diagnosis

Benign lesions

- Cyst
- Fibroadenoma
- Papilloma
- Phyllodes tumour
- Abscess
- Lymph node
 - rheumatoid arthritis
 - sarcoidosis
- Sebaceous cyst

Malignant lesions

- Mucinous carcinoma
- Medullary carcinoma
- Papillary carcinoma
- Invasive ductal carcinoma
- DCIS-intracystic carcinoma
- Metastasis
 - melanoma
 - lung
 - ovary
- Lymphoma
- Sarcoma
- Pathological lymph node
 - breast cancer
 - Phyllodes tumour
 - lymphoma
 - metastasis
- Recurrent breast cancer

The *contour* of circumscribed soft-tissue density lesions should be carefully analysed, if necessary using localised compression and magnification techniques.

The *density* should also be analysed according to whether normal breast structures superimposed on the lesion are visible (low soft-tissue density) or not (high soft-tissue density). Ultrasound is particularly helpful in differentiating cysts from solid lesions and can show the presence of an intracystic tumour.

In practice, the commonest cause of a circumscribed mass arising in a woman aged 40 years or more is a *simple cyst* (Fig. 46.26). Cysts appear on mammography as sharply outlined (sometimes with a thin, radiolucent 'halo'), low soft-tissue density lesions, measuring most commonly 1-3 cm in diameter although they are occasionally much larger and are often multiple and bilateral. The diagnosis is confirmed by ultrasound, which demonstrates a round or oval echo-free lesion with smooth, well-defined walls. If the cyst is symptomatic, it can be treated by needle aspiration of the contents. *Pneumocystography* can be performed at the time of aspiration and has been used to decrease the rate of recurrence.

Between 1 and 2% of cysts will be found to contain an intracystic tumour on ultrasound (Fig. 46.27). The tumour may be benign or malignant. Diagnostic needle aspiration and/or core biopsy should be performed and surgical excision considered. Internal echoes within a cyst may be due to turbid cyst contents or haemorrhage. Diagnostic needle aspiration should be performed and intracystic carcinoma suspected if a blood-stained aspirate is obtained (Fig. 46.28). It may be difficult to distinguish between a small echogenic cyst and a solid lesion. If the mammographic or ultrasound features are suspicious, diagnostic needle biopsy should be performed.

Fibroadenomas are characteristically sharply outlined, low soft-tissue density lesions, sometimes with a lobulated outline; they are usually solitary but may be multiple (Fig. 46.29). With increasing age, they may undergo calcification which is typically coarse in appearance (Fig. 46.30) and eventually an area of dense calcification with little evidence of a soft-tissue mass may be the only sign that remains mammographically. A circumscribed soft-tissue lesion with coarse calcification therefore presents no diagnostic problem. Fibroadenomas can, however, show very fine calcifications with

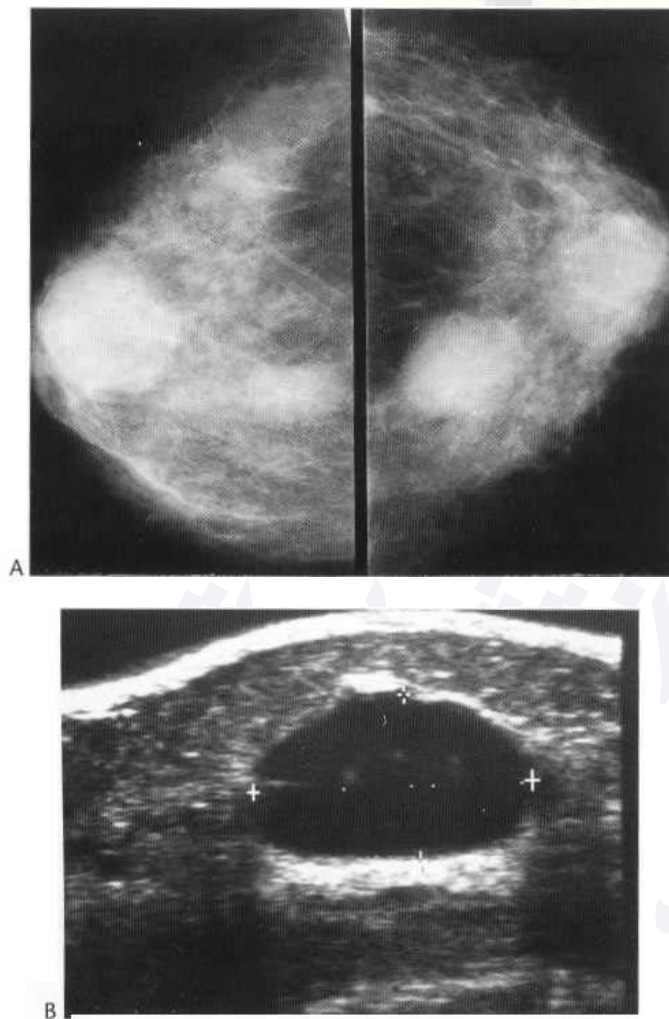


Fig. 46.26 Simple cysts. (A) Multiple circumscribed low soft-tissue density lesions are seen in both breasts. (B) Ultrasound shows the typical features of a simple cyst—a well-defined anechoic lesion with posterior acoustic accentuation.

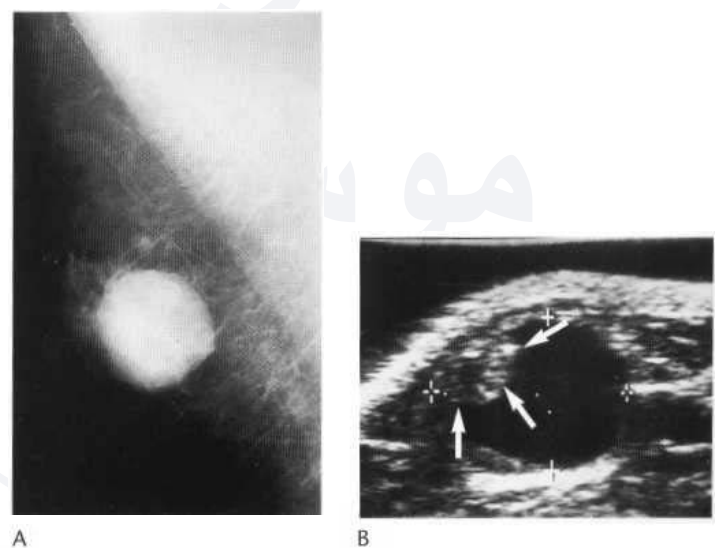


Fig. 46.27 Intracystic carcinoma in a male presenting with a mass. (A) The mammogram shows a circumscribed soft-tissue-density mass. (B) Ultrasound shows a lobulated intracystic mass (arrow) with calcification. Histology—non-invasive carcinoma.

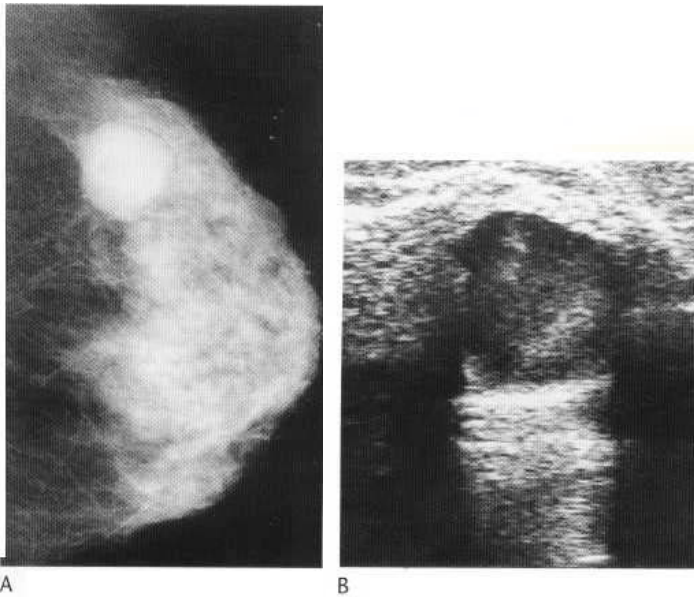


Fig. 46.28 Intraductal carcinoma. (A) The mammogram shows a circumscribed soft-tissue mass. (B) Ultrasound shows internal echoes within a cyst. Needle aspiration—blood-stained fluid containing malignant cells. Histology—non-invasive carcinoma.

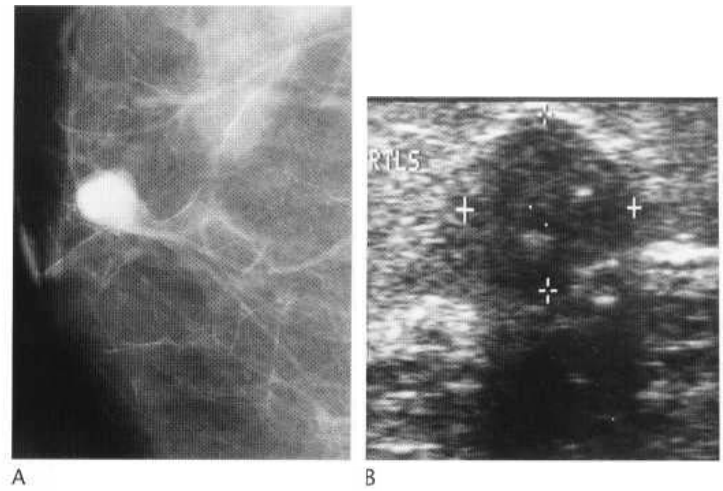
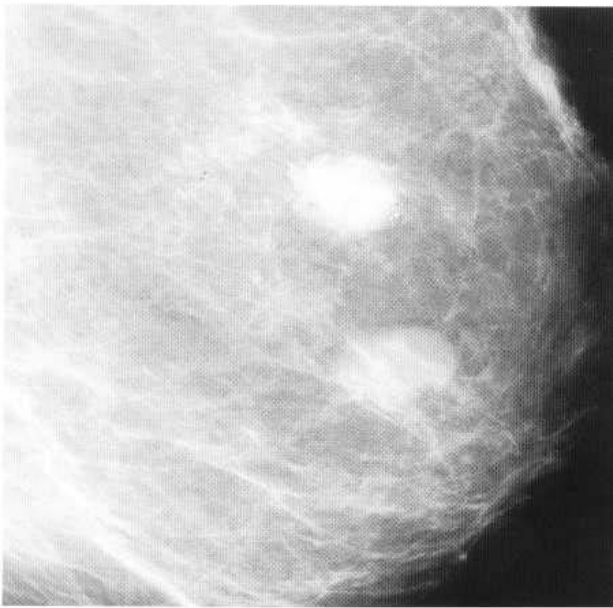


Fig. 46.29 Fibroadenoma. (A) Mammogram—a circumscribed soft-tissue-density lesion. (B) Ultrasound—a circumscribed solid low reflectivity mass with posterior acoustic shadowing. A focus of calcification is seen.

Fig. 46.30 Fibroadenomas. (A) First screening mammogram. (B) Second round screening mammogram. Two circumscribed lobulated masses are present. The superior lesion shows progressive coarse calcification.

some pleomorphism which can raise the suspicion of malignancy. Magnification views may be helpful by demonstrating calcifications of similar density and a sharply defined soft-tissue mass. Fibroadenomas do not arise *de novo* in women aged 40 years or more but may grow in menopausal women who are taking HRT (Fig. 46.31). The typical ultrasound appearance of a fibroadenoma is a well-circumscribed round or oval mass showing posterior acoustic enhancement and with a homogeneous internal echo pattern, usually of low reflectivity compared to the surrounding breast tissue. However, the appearances are variable: posterior acoustic shadowing and a heterogeneous internal echo pattern are frequent findings with or without associated calcification. The ultrasound findings alone therefore cannot be used to confirm the diagnosis of a circumscribed solid lesion found on mammography.

Papillomas are less common than fibroadenomas but show similar characteristics. They may be single or multiple and are frequently found in the anterior third of the breast. They often develop coarse calcification.

Phyllodes tumour is a fibroepithelial tumour which is usually large when diagnosed. Most phyllodes tumours are benign but they may recur locally if not completely excised: rarely they may metastasise to the lungs or pleura. The typical mammographic appearance is a large, lobulated high soft-tissue density lesion with a moderately well-defined outline (Fig. 46.32). Phyllodes tumours may develop plaque-like calcifications.

Circumscribed malignant lesions are most commonly medullary, mucinous (Fig. 46.33), papillary or intracystic carcinomas (Fig. 46.34), rarely invasive ductal carcinoma (Fig. 46.35), or sarcoma (Fig. 46.36). *Medullary carcinomas* may grow rapidly and

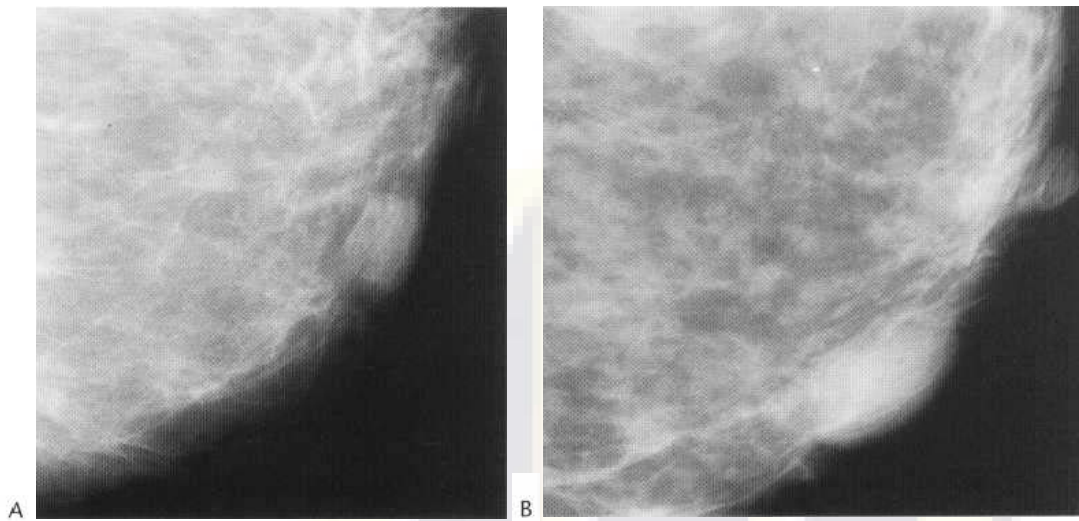


Fig. 46.31 Fibroadenoma. Growth while on hormone replacement therapy. (A) First screening mammogram. (B) Second round screening mammogram.

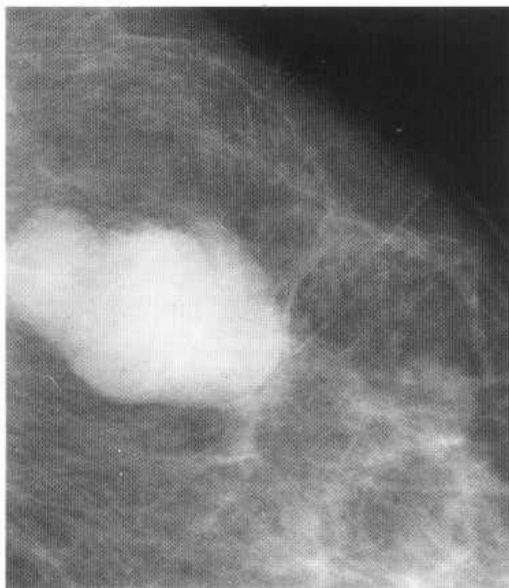


Fig. 46.32 Phyllodes tumour-mammogram. A circumscribed soft-tissue mass with a lobulated outline.

most occur in women less than 50 years old. *Mucinous and papillary carcinomas* have a favourable prognosis and most occur in women over 50 years. The outline of these lesions is usually less sharply defined than benign circumscribed masses and malignant lesions are typically of high soft-tissue density. Magnification and localised compression views are of great value in analysis of the margin of the lesion.

Metastases to the breast are unusual and may be single or multiple. They are well defined on mammography; the commonest primary sites are melanoma, lung and ovary. *Lymphoma deposits* in the breast may show the same features.

Management of solid circumscribed soft-tissue mass

The imaging work-up and analysis of the signs enables lesions to be categorised according to the probability of a benign or malignant diagnosis. Lesions which are considered moderately or highly suspicious for malignancy should be considered for surgery; the

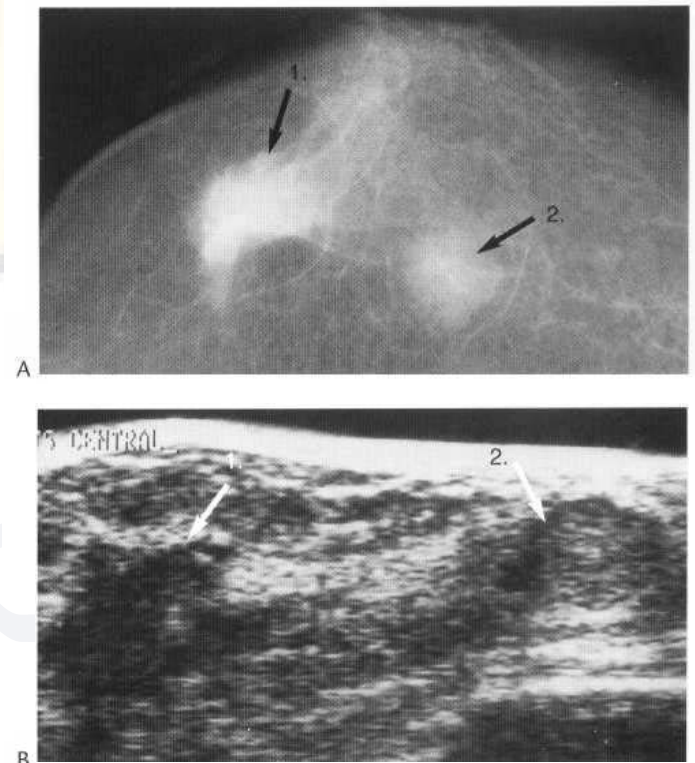


Fig. 46.33 Mucinous carcinoma and invasive ductal carcinoma. (A) Mammogram shows a poorly defined spiculate mass: (1) due to invasive ductal carcinoma and a circumscribed soft-tissue mass; (2) due to a mucinous carcinoma. (B) Ultrasound shows a typical low reflectivity mass: (1) due to invasive ductal carcinoma, and a circumscribed mass with posterior acoustic accentuation due to the mucinous carcinoma (2).

purpose of preoperative needle biopsy is to confirm the diagnosis of malignancy so that definitive treatment can be planned.

Circumscribed solid masses considered on imaging and clinical evaluation to be probably benign are likely to be fibroadenomas or papillomas. In many of these cases, the diagnosis can be confirmed by needle biopsy and the patient spared diagnostic surgery. Core biopsy is more likely to be diagnostic because of the hypocellular nature of fibroadenomas in the older age group.

If a diagnosis is not obtained by needle biopsy on a lesion considered to have suspicious imaging findings, diagnostic surgical

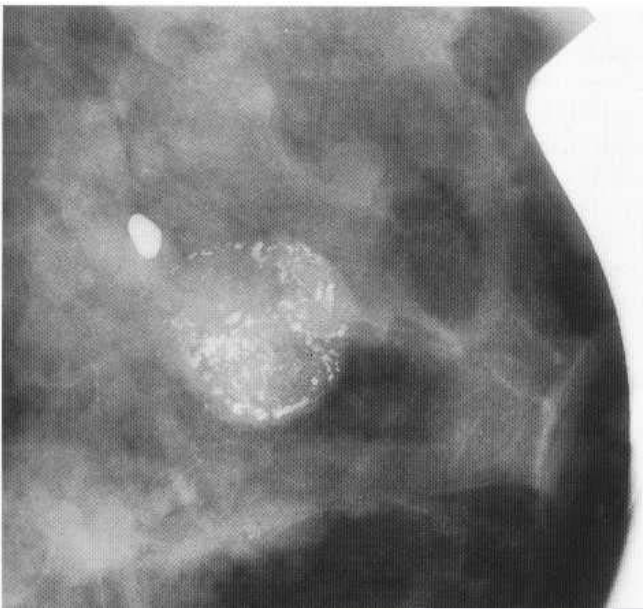


Fig. 46.34 Non-invasive intracystic carcinoma. Mammogram-magnified localised compression views shows a circumscribed mass with irregular microcalcification.



Fig. 46.36 Sarcoma. A round soft-tissue mass with homogeneous internal echoes and normal glandular tissue anteriorly.

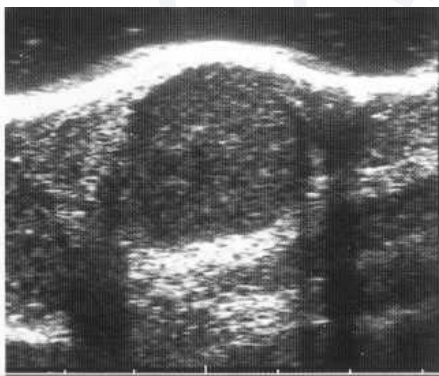
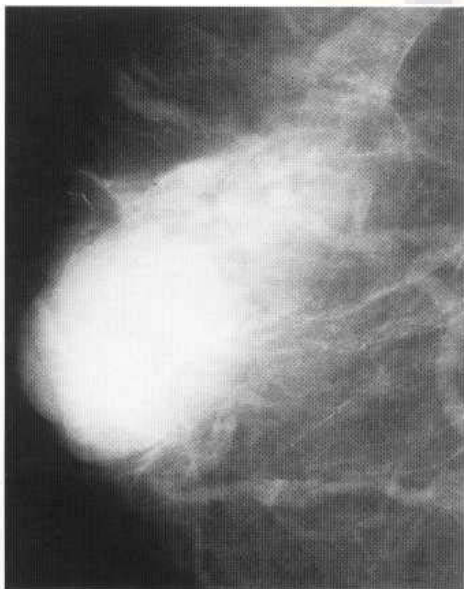


Fig. 46.35 Invasive ductal carcinoma. (A) Mammogram -a circumscribed retroareolar mass with poorly defined posterior margins. (B) Ultrasound-a circumscribed mass with a homogeneous internal echo pattern and through transmission of sound.

excision is indicated. For lesions which have benign imaging features, repeat imaging-guided core needle biopsy may be considered as an alternative to surgical biopsy.

Circumscribed mass in women aged below 35 years

Ultrasound is used if imaging is required for investigation of a breast lump in this age group. The commonest cause of a lump is a fibroadenoma; this appears as a well-defined mass with a homogeneous internal echo pattern and posterior acoustic accentuation. Fibroadenomas may be single or multiple and show an internal echo pattern which is characteristically of lower reflectivity than surrounding glandular tissue (Fig. 46.37). FNAC or core biopsy should be performed in such lesions in women aged 25 and over to confirm the diagnosis. Fibroadenomas occasionally undergo rapid growth in teenagers and may appear to occupy the whole breast-giant Fibroadenoma' (Fig. 46.38). Ultrasound, however, demonstrates normal compressed glandular tissue surrounding the mass. If there are atypical ultrasound or clinical features, solid lesions should be further investigated and mammography may be helpful in making a diagnosis. Imaging findings should be taken together with clinical features and results of needle biopsy when deciding on management. Cysts are rarely found in women aged less than 30 years.

Abnormal axillary nodes

Pathological lymph nodes in the axilla are recognised because of loss of the central fatty tissue and enlargement. Enlarged axillary lymph nodes may be due to benign conditions such as rheumatoid

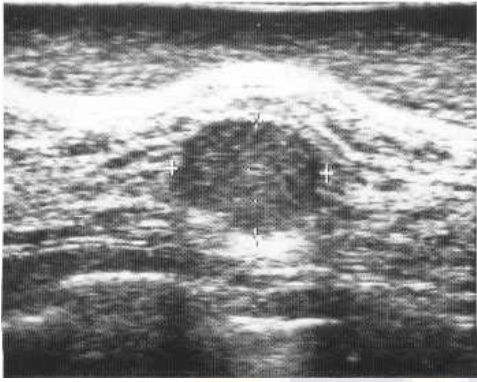


Fig. 46.37 Fibroadenoma—an oval well-defined low reflectivity lesion with posterior acoustic accentuation.

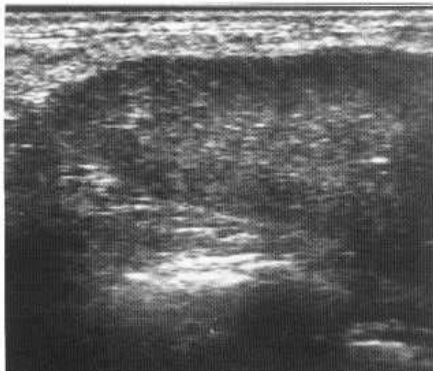


Fig. 46.38 Giant fibroadenoma. Ultrasound shows a well-defined mass with a homogeneous internal echo pattern and normal glandular tissue anteriorly.

arthritis (Fig. 46.39), sarcoidosis and infection, e.g. tuberculosis, or malignant conditions such as leukaemia (Fig. 46.40), lymphoma, metastases from the breast or, rarely, another primary site such as ovary (Fig. 46.41). Pathological lymph nodes from breast cancer or ovarian cancer may contain irregular microcalcifications. Coarse calcification is seen in nodes previously affected by tuberculosis. Fine, punctate calcification may be seen in nodes to sarcoidosis. This appearance may be mimicked in patients who have been on long-term gold therapy for rheumatoid arthritis who may develop fine, dense gold deposits.

Skin lesions

Mammograms may show single or multiple soft-tissue opacities due to skin lesions such as sebaceous cyst, wart, neurofibromatosis (Fig. 46.42) or keloid scar (Fig. 46.43). The diagnosis should be clear from the clinical details. The mammographic opacity is usually very well defined because it is outlined by air.

Microcalcification

Mammographically detected microcalcification is the sole radiological abnormality in up to 25% of screening-detected carcinomas. Microcalcification, however, has also led to many open surgical excision biopsies for benign breast change. Combined assessment of microcalcifications with high-quality magnification mammography and mammographically guided needle biopsy, together with a thorough understanding of the histological changes associated with



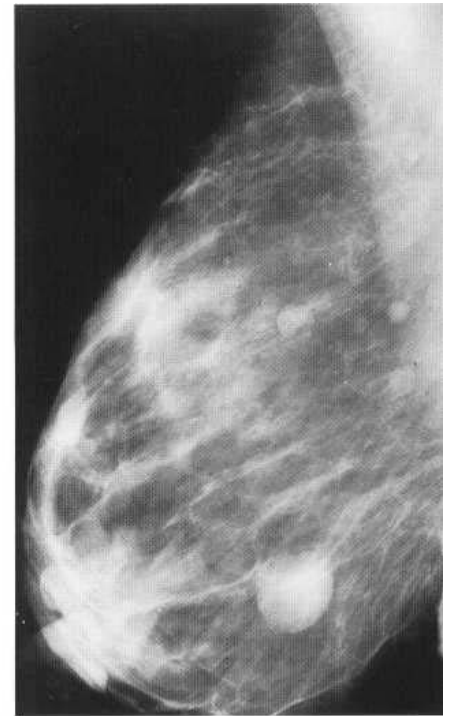
46.39



46.40



46.41



46.42

Fig. 46.39 Axillary lymphadenopathy due to rheumatoid arthritis.

Fig. 46.40 Axillary lymphadenopathy due to chronic lymphatic leukaemia.

Fig. 46.41 Axillary lymphadenopathy with calcification due to ovarian carcinoma.

Fig. 46.42 Neurofibromatosis. Multiple round soft-tissue opacities are seen overlying the breast tissue due to neurofibromas.

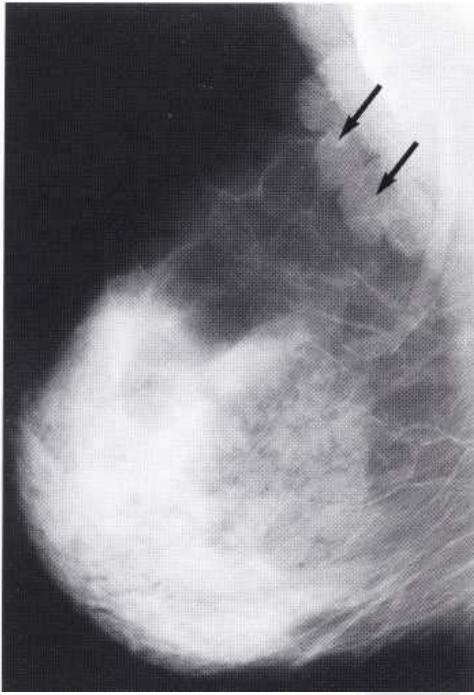


Fig. 46.43 Keloid. A lobulated soft-tissue opacity is demonstrated overlying the upper part of the breast (arrows).

microcalcification, now allow a definitive diagnosis to be made for most women with both benign and malignant disease without surgical biopsy.

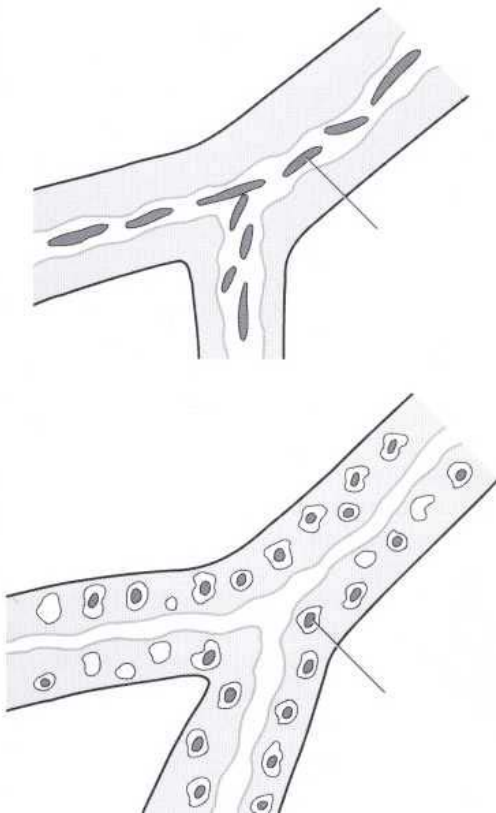


Fig. 46.44 Microcalcification in ductal carcinoma in situ. (A) Comedo type. (B) Cribriform type.

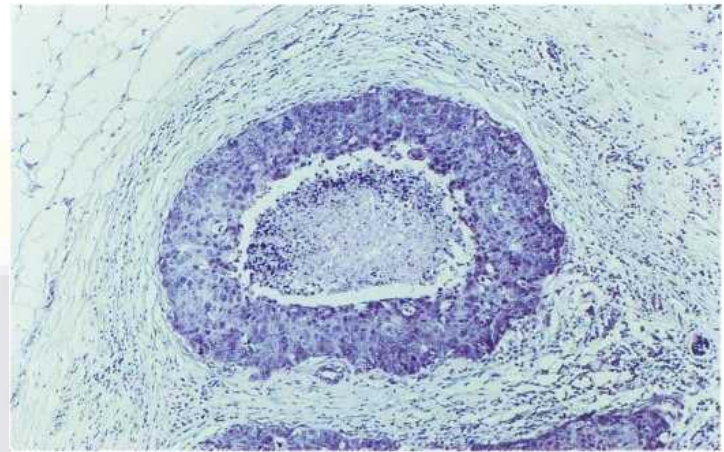


Fig. 46.45 Ductal carcinoma in situ-comedo type. Transverse section through a duct showing central necrosis and calcification. (Courtesy of Dr S. Humphreys.)

Ductal calcifications

1. Ductal carcinoma in situ (DCIS) Ductal carcinoma in situ is a malignant transformation of the epithelial cells lining the ducts which may extend into the lobules and in which the proliferating cells are confined by an intact basement membrane. DCIS subtypes can be classified according to cytological and histological characteristics and these features determine the mammographic appearances.

The histological appearance of DCIS is defined by:

- (i) *Nuclear grade*: high; intermediate; low.
- (ii) *Growth pattern*: solid; micropapillary; cribriform.
- (iii) Presence or absence of necrosis.

Predominantly high nuclear grade DCIS is associated with polymorphic nuclei, solid or micropapillary growth pattern, and necrosis. Calcification of the necrotic material within the duct occurs (Figs 46.44, 46.45). On mammography, this typically appears as linear, fragmented, branching, irregular and 'casting type' calcifications (Fig. 46.46). It is often distributed extensively within a lobe, or may be confined to a small area. This type of DCIS is often called 'comedo type' because when the tissue is examined macroscopically, necrotic material can often be squeezed out of the ducts.

Intermediate/low nuclear grade DCIS is characterised by monomorphic nuclei, a solid growth pattern and necrosis. The calcifications appear as single or multiple clusters of coarse, granular type or polymorphic particles like fragments of crushed stone or broken needle tips (Figs 46.47, 46.48). The differential diagnosis for this type of microcalcification is fibroadenoma, papilloma or focal fibrocystic change.

Predominantly low nuclear grade DCIS is associated with small cells, micropapillary or cribriform growth pattern (Fig. 46.49), and little necrosis. The calcifications appear as fine particles, sometimes giving a powderish appearance, arranged in single or multiple clusters (Fig. 46.50). This type may be difficult to distinguish from lobular calcifications seen in fibrocystic change.

Less common mammographic appearances of DCIS. 70-80% of cases of DCIS are detected by microcalcification alone. The remainder appear mammographically as a circumscribed mass (see 'Circumscribed mass' above), an area of architectural distortion or stellate lesion with or without microcalcification (see

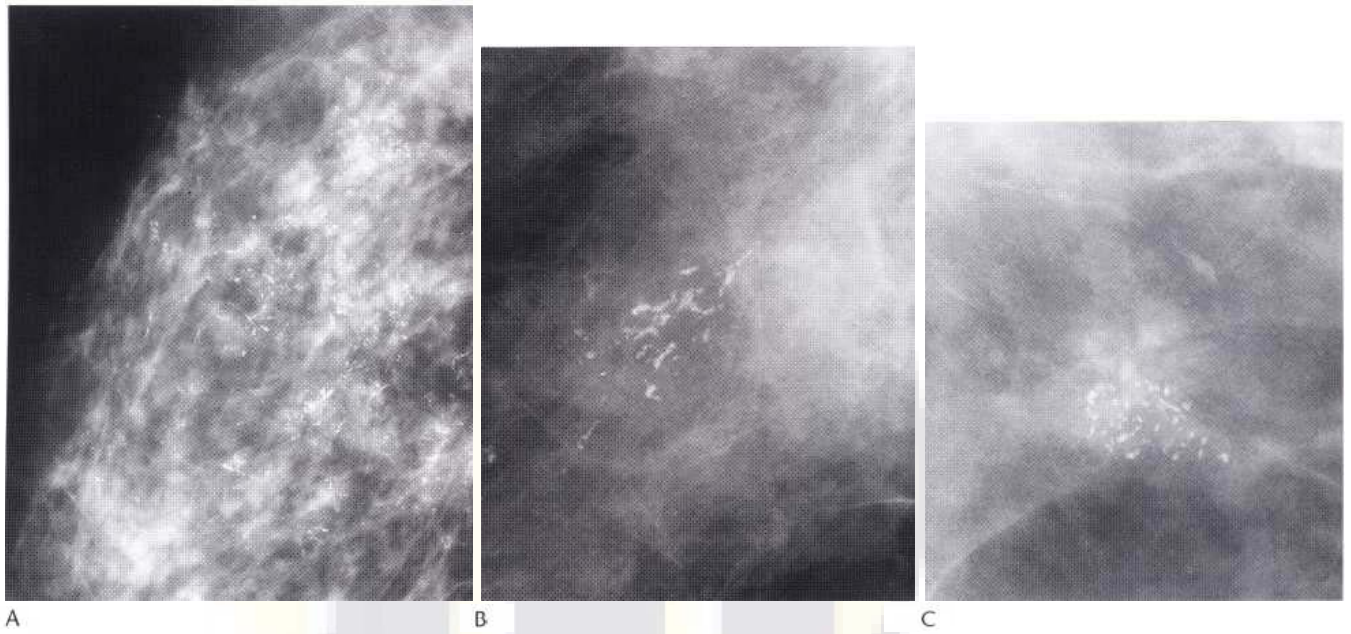


Fig. 46.46 Ductal carcinoma in situ-high-grade comedo type. (A-C) Irregular linear branching microcalcification.

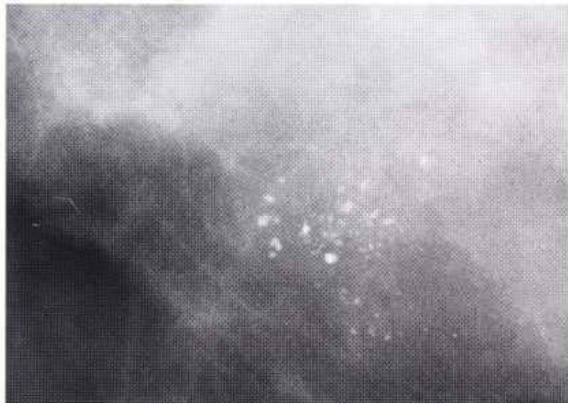


Fig. 46.47 Ductal carcinoma in situ. Intermediate/low grade. Magnification view-irregular polymorphic particles of microcalcification.

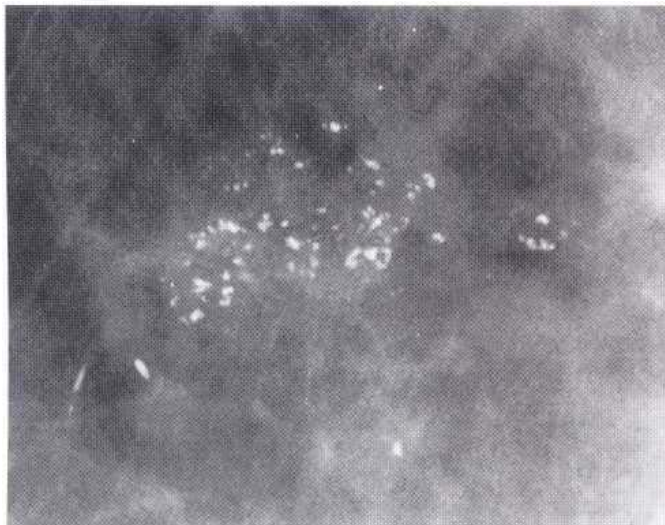


Fig. 46.48 Ductal carcinoma in situ. Irregular pleomorphic microcalcification.

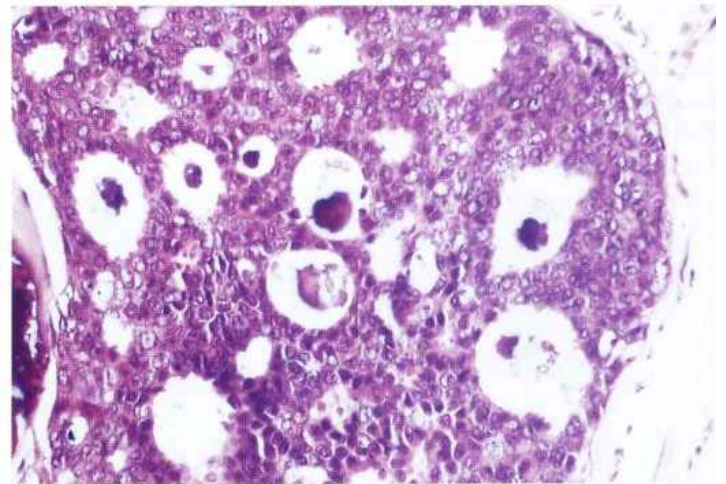


Fig. 46.49 Ductal carcinoma in situ. Cribriform architecture. The particles of calcification are in the small spaces within the thickened duct wall. (Courtesy of Dr S. Humphreys.)

'Architectural distortion' above), or as a filling defect on galactography.

2. Secretary change (plasma cell mastitis, duct ectasia)

Calcification may occur in inspissated secretions in dilated ducts and this may be associated with a periductal inflammatory reaction. Calcification may occur within the lumen of the duct, in the duct wall, or may be periductal. It is characteristically distributed bilaterally and in the anterior third of the breast. The particles are linear or tubular, dense, and have well-defined smooth outlines (Fig. 46.51), which allows this type of calcification to be readily distinguished from linear calcification due to DCIS.

Lobular calcifications

Most calcifications within the lobules are due to benign processes. The mammographic appearance of the calcifications reflects the histological changes that occur within the lobules (Fig. 46.52).

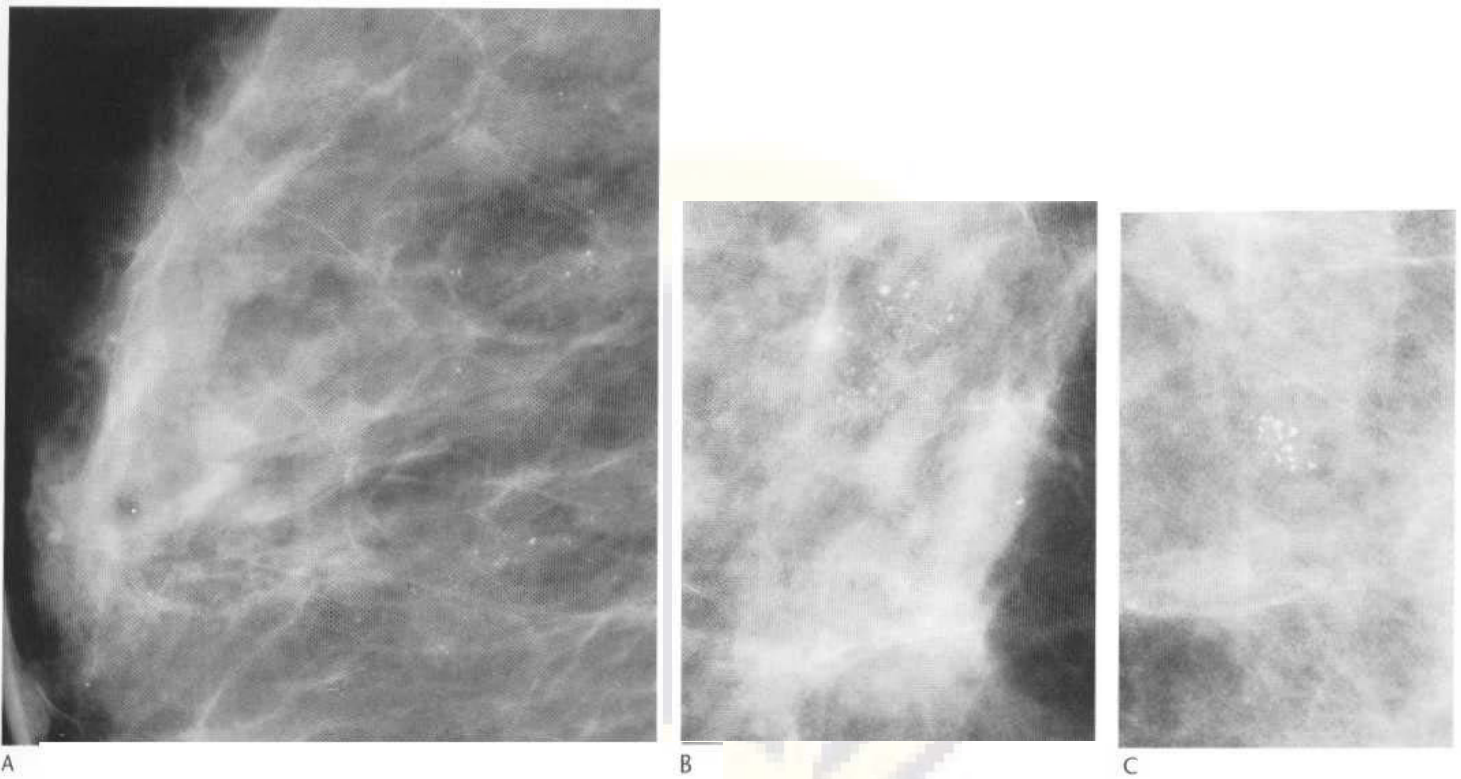


Fig. 46.50 Ductal carcinoma in situ. Low-grade, cribriform architecture. (A) Multiple clusters of punctate microcalcification distributed throughout one quadrant. (B, C) Solitary clusters of slightly pleomorphic microcalcifications.

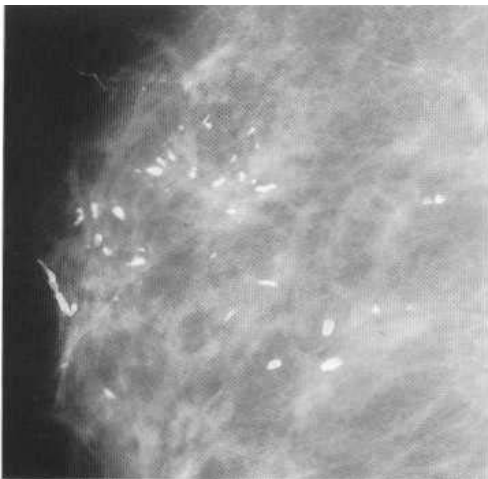


Fig. 46.51 Well-defined calcifications associated with secretory change.

1. *Microcystic change (blunt duct adenosis)*. There is an increase both in the number of acini and their size. Calcium may be deposited in the enlarged acini or microcysts (Fig. 46.53) and the characteristic mammographic appearance is of multiple round, discrete particles of similar density, 0.1-0.3 mm diameter, often distributed widely in both breasts (Fig. 46.54). They may be arranged in multiple rounded clusters.

2. *Sclerosing adenosis*. There is proliferation of the fibrous tissue surrounding the lobules in addition to the epithelial proliferation of adenosis. This causes deformity of the lobular spaces. Thus, the calcifications which occur in the distorted lobular spaces may show considerable pleomorphism and irregularity compared to simple microcystic change (Fig. 46.55). This type of microcalcification may be difficult to distinguish from some types of DCIS.

3. *Microcystic change with milk of calcium*. The lobular spaces enlarge further to form small cysts within which numerous minute calcific particles (psammoma bodies) are in solution. These form a

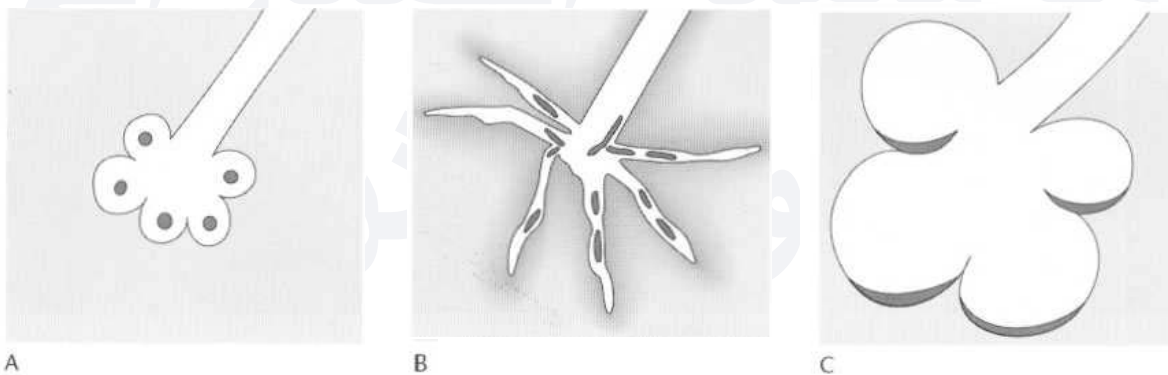


Fig. 46.52 Lobular calcifications. (A) Adenosis. (B) Sclerosing adenosis. (C) Microcystic change.

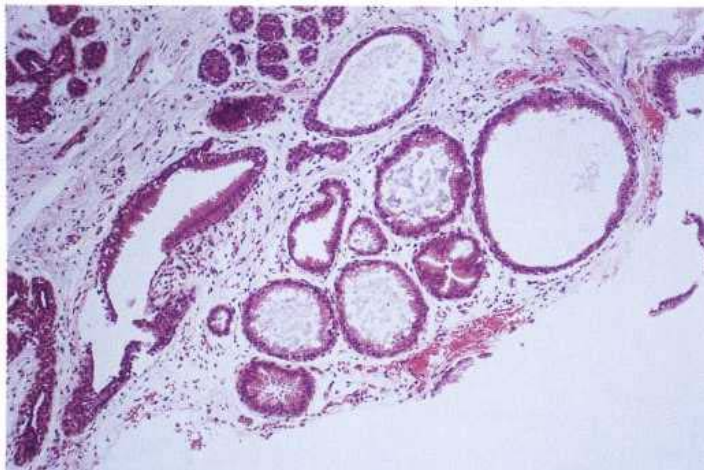


Fig. 46.53 Microcystic change. Calcifications in enlarged lobular spaces.

layer in the dependent part of the cyst due to gravity. Thus a horizontal beam lateral view will demonstrate a calcium-fluid level or meniscus (the 'tea cup' sign) while a craniocaudal view will show a round 'smudge' shadow. These signs are best demonstrated using high-quality magnification views in lateral and craniocaudal projections (Fig. 46.56).

Differential diagnosis and management

Differential diagnosis of a cluster of microcalcifications

- Ductal carcinoma in situ
- Sclerosing adenosis/fibrocystic change
- Atypical ductal hyperplasia
- Simple epithelial hyperplasia
- Microcystic change
- Fibroadenoma
- Papilloma.

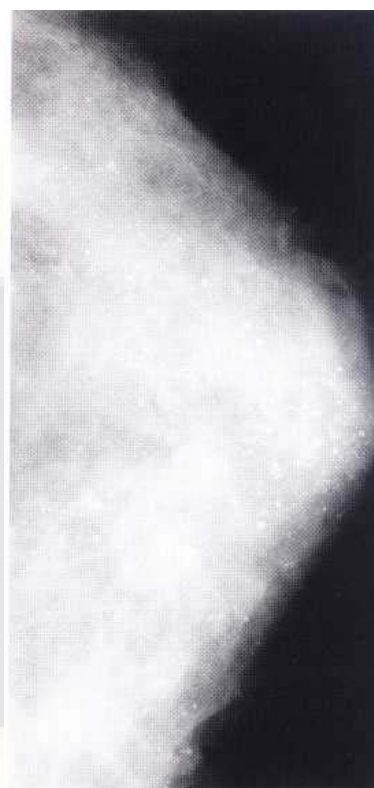


Fig. 46.54 Microcystic change. Multiple rounded calcifications of similar density.

The level of suspicion for malignancy is assessed from analysis of the mammographic signs on magnification views. The key features that are analysed are:

- Particle shape
- Particle density
- Cluster shape
- Distribution.

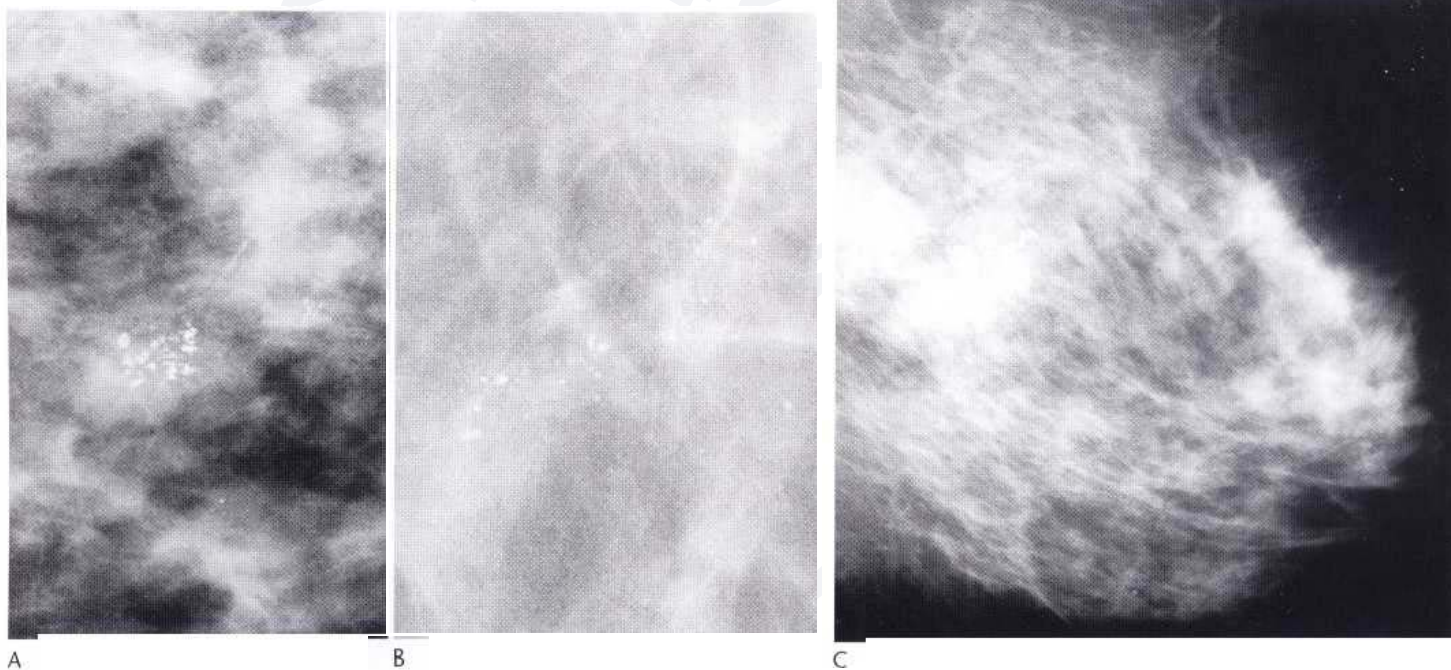


Fig. 46.55 Sclerosing adenosis. (A,B) Clusters of fine granular pleomorphic calcifications. (C) The calcifications are coarser and are associated with a soft-tissue opacity.

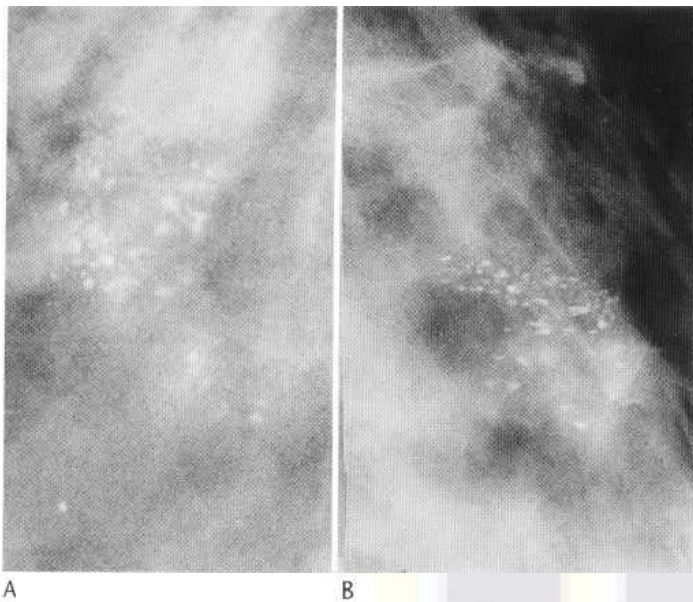


Fig. 46.56 Milk of calcium in benign cystic change. On the craniocaudal view the calcifications appear as round 'smudge' shadows (A). On the lateral view the calcifications show a straight upper border, the 'tea cup' sign (B).

The calcification particles of ductal carcinoma in situ are typically variable in density and shape: linear, casting, branching, and irregular shapes may be present, with variation of the density from particle to particle. Benign calcifications are more often punctate or round and of similar density. The cluster shape of malignant microcalcifications is typically irregular or triangular, pointing towards the nipple, while a cluster of benign calcifications tends to be round or oval. Malignant microcalcification is usually distributed within a lobe or segment of the breast, although occasionally a quadrant or the whole breast may be involved. Benign microcalcification is often bilateral or involves multiple quadrants.

For cases in which the mammographic signs are highly suspicious for malignancy, needle biopsy (FNAC or core biopsy) is carried out to confirm the diagnosis of malignancy so that definitive surgery may be planned. If the needle biopsy (FNAC) is acellular or equivocal, or core biopsy shows atypical ductal hyperplasia or other suspicious features, either repeat needle biopsy or diagnostic surgical excision should be performed. For cases in which the mammographic signs indicate a low level of suspicion for malignancy, needle biopsy is carried out to confirm the diagnosis. If a satisfactory needle biopsy specimen is obtained, and the needle biopsy findings are consistent with the mammographic features, the patient need not undergo diagnostic surgical excision.

Miscellaneous calcifications located outside the glandular tissue

Arterial: curvilinear, parallel line calcifications along the course of a blood vessel.

Skin:

- Sebaceous gland calcification-1-2 mm diameter ring-shaped calcifications (Fig. 46.57). Tangential views may demonstrate that they lie within the skin.
- Pseudoxanthoma clasticum-may cause multiple irregular fine skin microcalcifications.

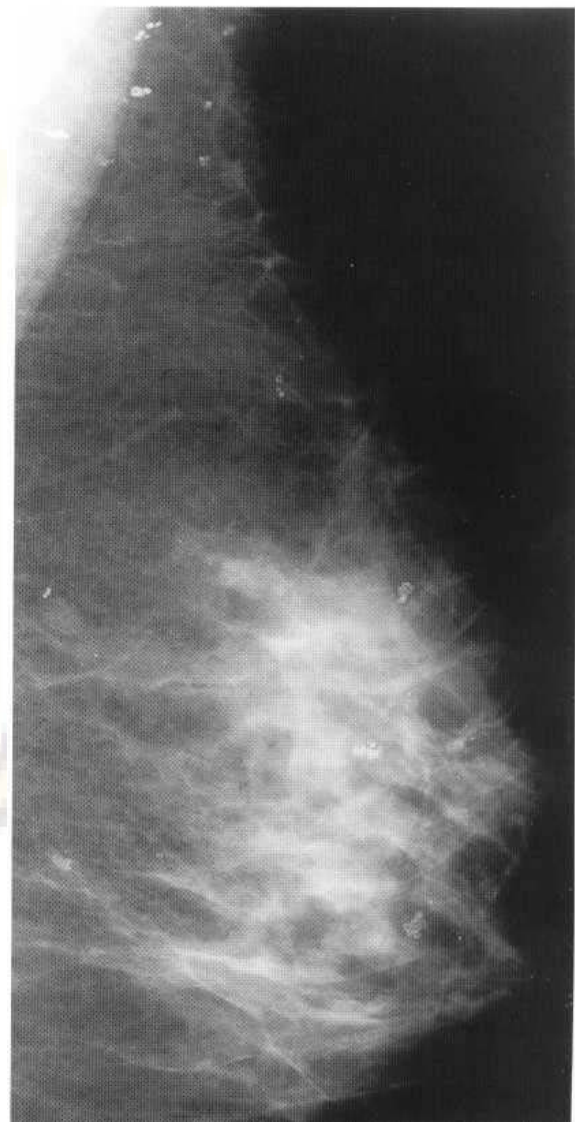


Fig. 46.57 Skin calcification. Multiple small ring-shaped calcifications.

Papilloina: coarse or fine, irregular calcifications associated with a lobulated soft-tissue opacity.

Fat necrosis:

- Liponecrosis macrocystica coarse, curvilinear calcification associated with radiolucent centre: usually following surgery (Fig. 46.58).
- Liponecrosis microcystica-1-4 mm diameter round calcifications with a radiolucent centre.

Fibroadenoma: coarse 'popcorn' type calcification associated with a soft-tissue mass. Less commonly the calcifications may be fine, irregular or curvilinear 'eggshell' type related to the periphery of the lesion (Fig. 46.59).

Cyst: curvilinear calcification may occur in the wall of a cyst (Fig. 46.60).

Calcified suture material: dense, curvilinear.

Cavernous haemangioma: coarse and punctate calcifications within a lobulated soft-tissue mass.

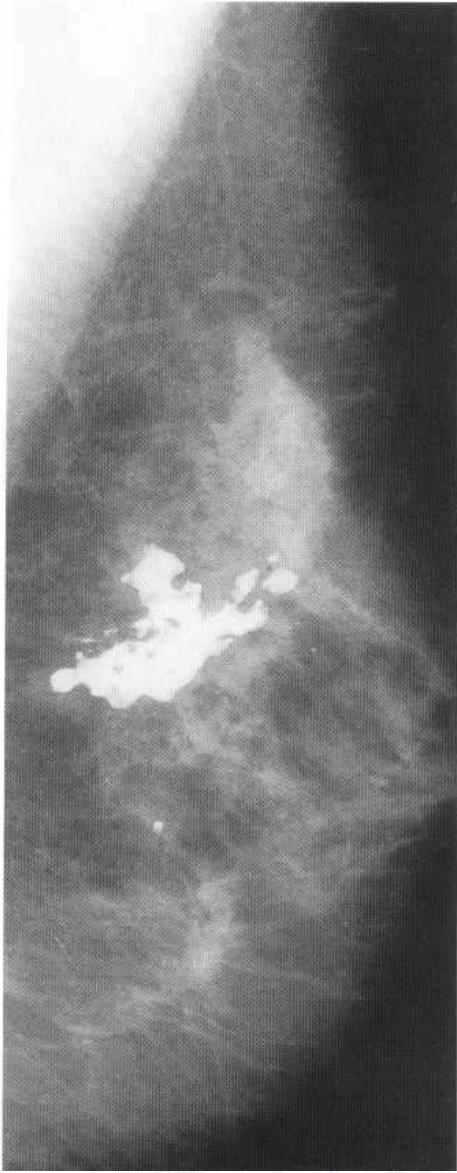


Fig. 46.58 Coarse calcification due to fat necrosis from previous surgery.

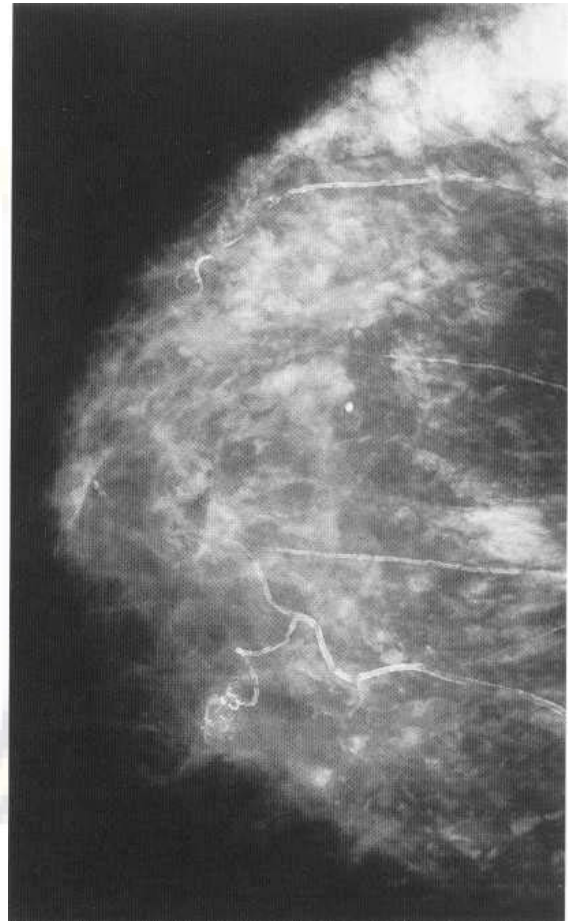


Fig. 46.61 Renal failure. Extensive stromal and vascular calcification.

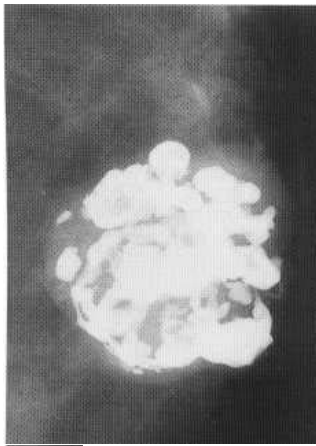
Postsurgical scar: punctate and coarse stromal calcifications associated with a scar.

Renal failure: extensive stromal calcification may occur (Fig. 46.61).

Breast augmentation:

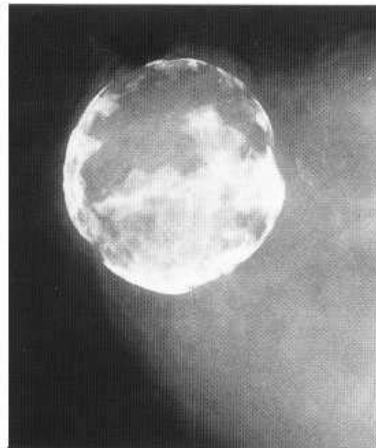
- Silicone implant-eggshell type calcification, may occur on the surface of the implant.
- Direct silicone injection may result in extensive fibrosis and calcifications (see 'Breast augmentation' below).

Parasites: filariasis may cause single or multiple curvilinear or 'coiled' calcifications due to calcium deposition around the dead parasites (Fig. 46.62).



46.59

Fig. 46.59 Coarse 'popcorn' calcification in a fibroadenoma.



46.60

Fig. 46.60 Curvilinear mural calcification of a cyst.

The oedematous breast

The mammographic features are:

- Thickened skin initially affecting mainly the lower part of the breast
- Diffuse increased density
- Coarse trabecular pattern
- Enlargement of the breast.

The causes of an oedematous breast are:

1. *Primary breast carcinoma.* An oedematous breast may be caused either by an advanced primary tumour, lymphatic spread



Fig. 46.62 Calcifications due to filariasis.

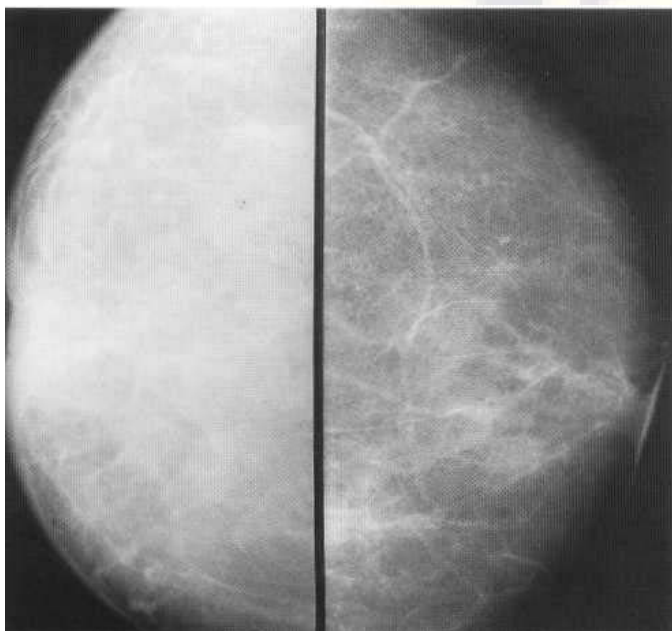


Fig. 46.63 Oedematous right breast due to right heart failure.

from a primary tumour or inflammatory carcinoma. Diffuse involvement by high nuclear grade comedo carcinoma may cause extensive irregular microcalcifications.

2. *Axillar.v lymph node metastases* secondary to a carcinoma of the contralateral breast.

3. *Breast abscess.*

4. *Congestive cardiac failure and renal failure* may cause either unilateral or bilateral oedematous breast (Fig. 46.63).

5. *Axillar.v lymph node metastases* from advanced gynaecological malignancy, e.g. ovarian carcinoma, cervical carcinoma.

6. *Radiotherapy.* The features of oedema develop progressively following radiotherapy treatment, reach a maximum at about 6 months, and have resolved approximately 18 months following treatment.

An integrated approach to the use of imaging in breast diagnosis

The indications for mammography and breast ultrasound are shown in Box 46.2. In women with symptomatic breast disease, imaging is most effectively used if the clinical findings are fully taken into account. This is particularly important because, although mammography is the most sensitive examination available for detecting small breast carcinomas, the false-negative rate for mammography in the detection of symptomatic breast carcinoma is 5-10%. A delay in the diagnosis of symptomatic breast carcinomas with negative mammograms can be avoided if radiologists ensure that their clinical colleagues who are referring women for mammography are fully aware of the false-negative rate and will therefore continue the investigation of patients with suspicious clinical findings.

The correct diagnosis in both symptomatic women and in women with screening-detected abnormalities is most likely to be achieved by adopting a combined multidisciplinary approach to investigation and assessment using information from:

- Clinical history and examination
- Imaging - mammography, ultrasound
- Needle biopsy-FNAC or core biopsy.

The combination of imaging investigations used (standard views, localised compression views, magnification views, ultrasound) should be chosen according to the clinical findings and age of patient (Figs 46.64, 46.65). Supplementary mammographic views are obtained if indicated from the findings on standard views.

The aim of the imaging investigations is to assess the probability of a lesion being benign or malignant. Terms indicating the level of suspicion are:

- Normal
- Benign
- Probably benign
- Malignant
- Suspicious.

Departments offering a breast diagnostic service should have a clearly defined protocol for deciding on further investigations (e.g. FNAC, core biopsy) and management of breast lesions based on both clinical and imaging findings.



Fig. 46.64 Ultrasound of a 48-year-old woman with a palpable left breast mass. The mammogram did not demonstrate a mass. Ultrasound shows a solid mass. FNAC - malignant cells. Final diagnosis - invasive breast carcinoma.

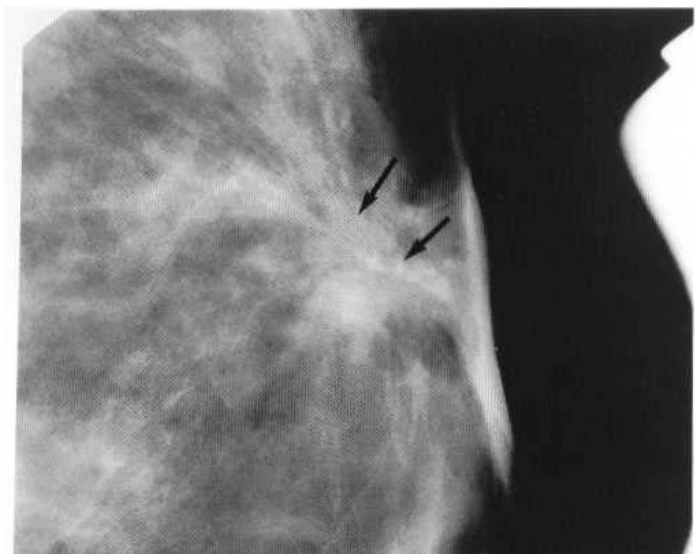


Fig. 46.65 Localised compression magnification view of a 56-year-old woman with a palpable left subareolar mass. The standard views showed no subareolar abnormality. The localised compression view, however, shows a spiculate mass (arrows) due to an invasive carcinoma.

Breast MRI

Since early studies first demonstrated that MRI was exceptionally sensitive in the detection of breast cancer, there has been a huge volume of research into the use of MRI in the evaluation of breast disease. This has been made possible through the development of high-resolution surface coils, fast imaging sequences and software capable of handling large volumes of data in a suitable timescale.

Technique

The requirement for high-resolution scans (in-plane resolution of 1 mm or less) with an adequate signal-to-noise and contrast-to-noise ratio necessitates the use of high-quality dedicated surface coils, preferably capable of imaging both breasts. The patient is positioned prone with the breasts pendent in the 'cups' of the coil, with judicious padding to minimise patient motion and transmitted vibration. Since intrinsic contrast between normal and abnormal breast parenchyma is low on standard spin-echo sequences, contrast-enhanced T1-weighted gradient-echo sequences are essential. Prior to positioning in the breast coil, a 20 or 22 gauge cannula is placed in an antecubital vein. This is attached to a long connecting tube primed with gadolinium-DPTA (0.1-0.2 mmol/kg). A 20 ml normal saline flush is attached to this via a three-way tap, enabling a fast bolus injection of contrast, preferably with an injector pump, without disturbing the patient.

The standard sequence is a T1-weighted 2D or 3D gradient-echo sequence (FLASH or FSPGR), before and after dynamic injection of contrast material (supplemented by T2-weighted spin-echo sequences as necessary). 3D sequences allow coverage of both breasts in their entirety in under 90 seconds if a coronal plane is used, so that five postcontrast scans can be acquired in under 8 minutes. Volume acquisitions enable re-formatting in other planes and maximum-intensity projections. 2D sequences allow repeated interrogation of a limited area of one breast in a few seconds for quantitative studies of known lesions. The precise technique used

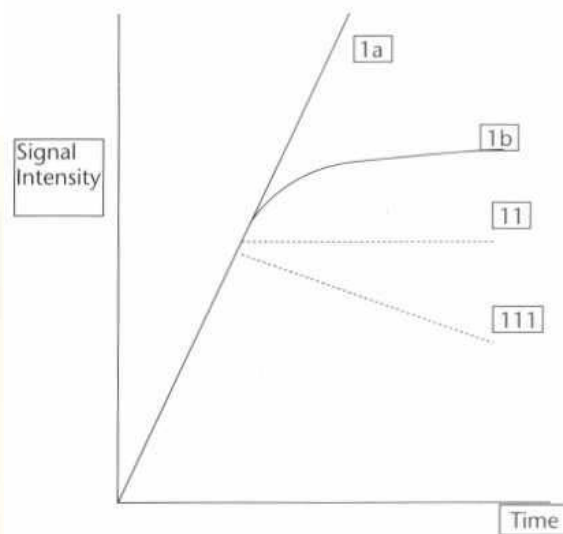


Fig. 46.66 Breast MRI: time-signal intensity curves following IV contrast. In type I, enhancement continues through the duration of the study. In type II, there is a plateau, whereas in type III, signal intensity diminishes (washout).

depends on the clinical question to be addressed. Image analysis is facilitated by fat suppression, but if uniform fat suppression is not possible, computer-generated fat-subtracted images should be routinely obtained. Time-signal intensity curves should be generated for any areas of enhancement (Fig. 46.66). In patients with breast implants, a combination of T1- and T2-weighted spin-echo sequences in orthogonal planes are supplemented by a combination of sequences with water or fat suppression, or 'silicon-selective' sequences can be used to increase the conspicuity of extra-capsular silicon. This can be followed by a standard dynamic contrast-enhanced sequence as indicated. Image evaluation should include assessment of the distribution, degree and rapidity of any enhancement together with evaluation of the morphology of any masses, particularly shape, border characteristics, homogeneity, the presence of septations and rim enhancement.

Normal appearances

Normal glandular parenchyma has intermediate signal intensity on T1- and T2-weighted sequences, whereas fat is of high signal. The fibrous trabeculae are readily appreciated as fine low-signal-intensity structures traversing the subcutaneous fat. Low axillary and intramammary lymph nodes can be recognised through their characteristic bean shape and central fatty hilum. The skin is of intermediate signal and uniformly thin except in the areolar region, where it may approach a few millimetres in thickness. After intravenous gadolinium, the nipple, blood vessels and lymph nodes normally enhance. The glandular parenchyma can also enhance gradually especially in the second half of the menstrual cycle, reflecting normal hormonal-induced glandular proliferation. This enhancement is often diffuse and rather patchy. The appearance of an implant depends upon the nature of the contents and whether it is a single- or double-lumen implant. Saline and silicon are high signal on T2-weighted sequences but silicon is higher signal than saline on T1-weighted sequences. The surrounding capsule is low-signal intensity on all sequences. Radial folds, normal infoldings of

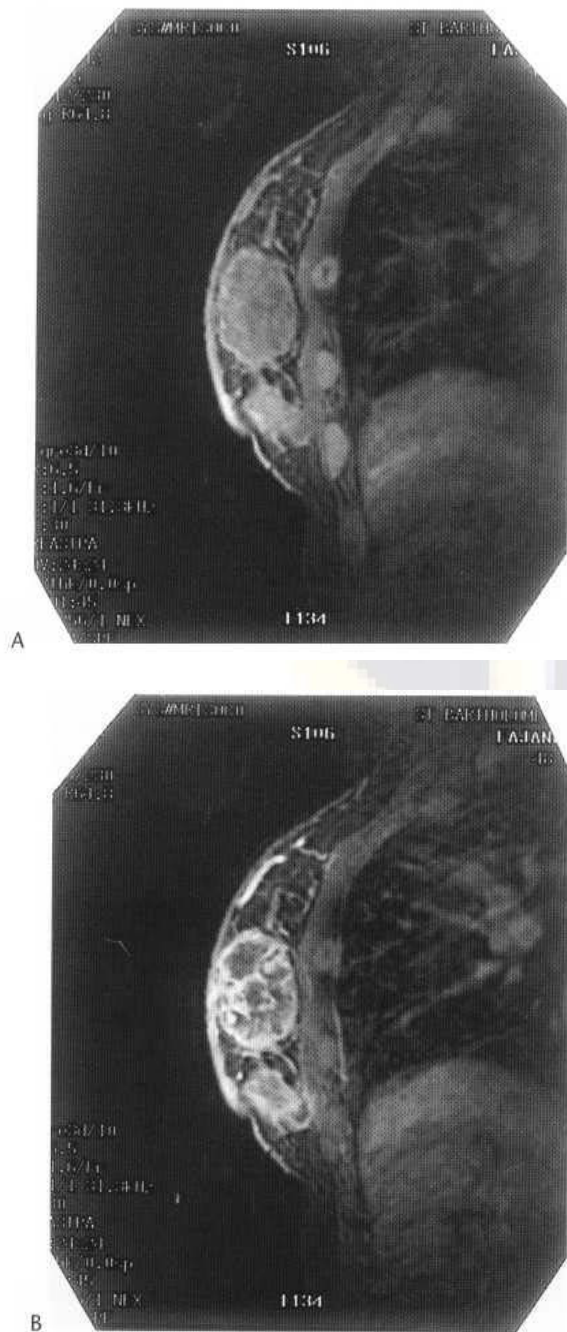


Fig. 46.67 Sagittal T₁-weighted gradient-echo images with fat saturation pre (A) and post (B) intravenous gadolinium-DTPA. Two malignant masses are demonstrated. Note typical heterogeneous and rim enhancement of the larger mass and clear demonstration of involvement of the prepectoral fascia, pectoralis major muscle and skin by the inferior mass.

the implant envelope, are seen as thin low-signal folds invaginated into the implant contents.

Abnormal findings

Though MRI is rarely indicated in the assessment of benign disease, cysts are often seen as well-defined non-enhancing masses of low signal on T₁- and high signal on T₂-weighted images. In premenopausal women, it is common to see tiny foci of intense and rapid enhancement, in addition to the normal gradual parenchymal enhancement. These often change from cycle to cycle, enabling dif-

ferentiation from small malignant lesions. Incidental fibroadenomas are common. They are usually well-defined ovoid or lobulated low-signal-intensity masses on T₁-weighted scans. Myxoid fibroadenomas are often high signal on T₂-weighted scans. The amount and rapidity of enhancement depends upon the composition of the fibroadenoma. Thus hyalinised ones may not enhance at all, whereas myxoid fibroadenomas in young women can enhance as quickly and markedly as carcinomas. Usually, enhancement is uniform, gradual and moderate with a type I or orb curve (Fig. 46.66). The presence of non-enhancing internal septations strongly predicts benignity. Papillomata appear very similar, though without septations.

Typically, ductal carcinomas are irregular poorly margined masses that are low T₁ and intermediate to low T₂ signal. Distortion may be evident. Enhancement is a function of tumoral neoangiogenesis and is usually marked and rapid with signal intensity more than doubling. Rim enhancement and centripetal enhancement are common and have a high positive predictive value for malignancy (Fig. 46.67). Time-intensity curves often demonstrate a plateau effect (type 2) or washout (type 3), the latter having a relatively low sensitivity but high specificity for malignancy (Fig. 46.66). Some carcinomas behave atypically, enhancing only little and gradually (lobular carcinomas) or being well defined (papillary and mucinous carcinomas). Ductal carcinoma in situ (DCIS) has a variable appearance depending on the degree of neoangiogenesis, but the presence of linear and nodular enhancement in a ductal or segmental distribution is highly suggestive. Inflammatory carcinomas result in generalised skin and trabecular thickening, often with generalised moderate enhancement, but it is not possible to differentiate inflammatory carcinoma from other causes of inflammation such as infection or early postradiotherapy change. In patients with implants, the presence of a collapsed infolded silicon shell lying within the implant contents (the linguine sign) is diagnostic of intracapsular rupture (Fig. 46.68), whereas collections of silicon lying outside the ruptured fibrous capsule indicate extracapsular rupture. A small amount of free fluid around the implant can be a normal finding.

Current indications and possible future applications

Breast MRI is the technique of choice in the differentiation between postoperative scarring and local recurrence, provided enough time has elapsed to allow treatment-related enhancement to settle. It has an important role in the assessment of the indeterminate mass because of its very high sensitivity for malignancy, though at present, core biopsy is a more cost-effective approach. It is very accurate in the local staging of breast cancer in difficult cases (very dense breasts, mammographically occult tumours, suspected multifocality or multicentricity and suspected chest wall involvement). It is the technique of choice in the evaluation of implant integrity and detection of cancer in the augmented breast. It is also accurate in the differentiation of axillary recurrence and brachial plexopathy post radiotherapy.

Breast MRI appears highly accurate in the assessment of response to neoadjuvant and primary chemotherapy, predicting ultimate response before changes in tumour volume and differentiating between residual tumour and fibrosis. Its role in this area is likely to grow. The place of breast MRI in screening high-risk patients has yet to be established and the results of the MRC trial addressing this (the MARIBS study) are awaited with interest.

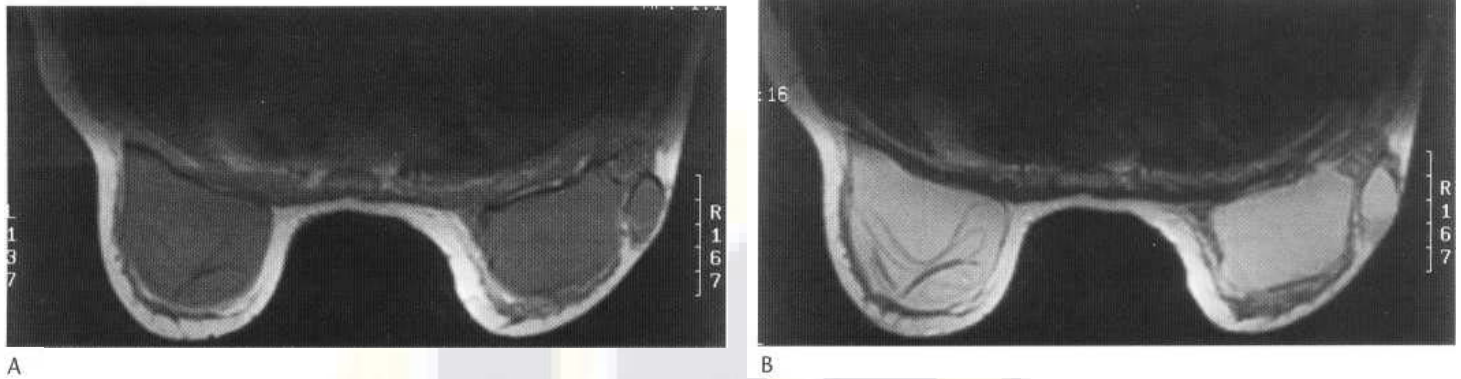


Fig. 46.68 Axial T₁-weighted (A) and T₂-weighted (B) images in a patient with bilateral single lumen silicon implants. Note extracapsular rupture of the right breast implant, with a collection of silicon lying in the lateral aspect of the breast. There is intracapsular rupture of the left breast implant, with a classical linguine sign.

The exceptional sensitivity of breast MRI for the detection of breast cancer makes it a potentially very effective diagnostic technique, but the relatively low specificity, highly variable diagnostic criteria and limited availability are such that its precise role in routine practice has yet to be established. The development of dedicated magnets, tissue-specific contrast agents, standardised techniques and reporting systems and MR-guided biopsy systems should help overcome these problems.

Imaging in the follow-up of patients with breast cancer

Patients who have been treated for breast cancer may develop locally recurrent tumour and are at increased risk of developing a second primary breast cancer (6 x lifetime risk). The aim of follow-up is to detect recurrence or a new primary tumour as early as possible when the tumour is likely to show better prognostic features. Local tumour recurrence which is more common in young patients and in those with cancer showing poor prognosis features may be expected to affect 5% of women in the first 5 years and 10-15% of women within 10 years of breast-conserving treatment. Recurrent tumour is likely to show the same mammographic features as the primary tumour. Routine mammographic surveillance imaging of the breast following breast-conserving treatment and of the contralateral breast is therefore recommended every 1-2 years following treatment and should be carried out in conjunction with clinical examination. The duration of follow-up should take into account that the majority of recurrences and 80% of contralateral breast cancers will arise within 10 years of the primary diagnosis. Any abnormality detected on routine surveillance should be further assessed using the triple diagnostic approach. MRI has been shown to be useful in cases where the results of the triple approach are not diagnostic.

The breast following augmentation

Imaging is carried out following insertion of breast prostheses for the following reasons:

- To diagnose the cause of symptoms arising from complications related to the prosthesis.
- To diagnose symptomatic disease in the tissue surrounding the prosthesis.
- Breast cancer screening in women aged 50 years and over.

Standard oblique and craniocaudal views can be obtained without damage to the prosthesis. Exposure factors have to be adjusted so that the tissue surrounding the prosthesis is not overexposed. The Eklund technique is suitable for breasts where there is a relatively large volume of breast tissue overlying the implant and involves posterior displacement of the implant so that only the breast tissue is compressed and imaged.

Ultrasound is particularly helpful in the examination of the augmented breast because areas of breast tissue which may be partially obscured by the implant on mammography can be satisfactorily demonstrated.

MRI is the most sensitive technique for the assessment of implants and should be used if mammography and ultrasound are non-diagnostic or equivocal.

Calcification overlying the surface of the implant is commonly seen. Features of internal and external implant rupture may be demonstrated. External rupture with siliconoma formation may cause a firm palpable lump and shows a characteristic appearance on mammography and ultrasound-mammography shows a soft-tissue opacity with multiple 3-4 mm diameter round nodules associated with it due to granuloma formation in response to the presence of silicone (Fig. 46.69A). Ultrasound shows dense acoustic shadowing (Fig. 46.69B).

Augmentation has in the past been performed by injecting silicone directly into the breast. The long-term results of this treatment produce a characteristic mammographic and ultrasound appearance due to fibrosis and siliconoma formation. The breast tissue is dense and contains many round calcifying nodules (Fig. 46.70) ultrasound shows acoustic shadowing.

Imaging-guided practical procedures

Imaging is used to ensure accurate needle positioning for the following diagnostic and therapeutic procedures:

- Simple cyst aspiration (therapeutic)
- Complex cyst aspiration (diagnostic)
- Abscess aspiration
- Fine needle aspiration cytology (FNAC)
- Core biopsy/wide-bore needle biopsy
- Vacuum-assisted core biopsy
- Preoperative localisation of non-palpable lesions.

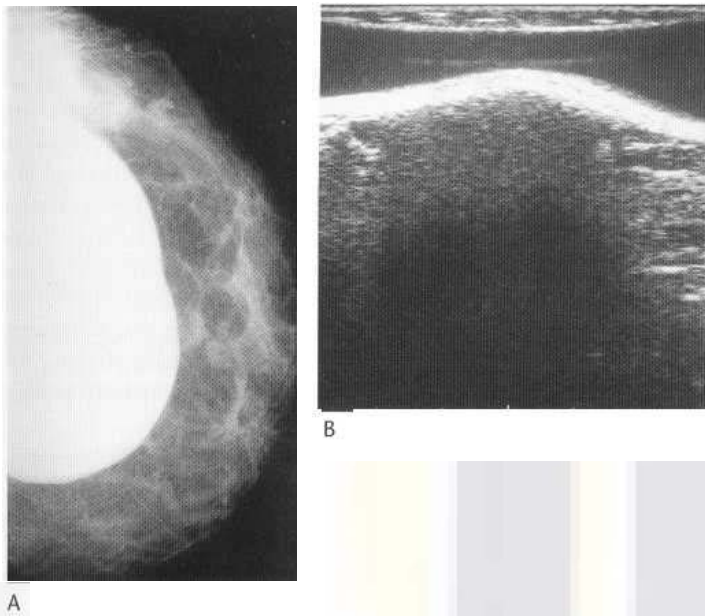


Fig. 46.69 (A) Implant with silicoma formation. A firm mass was palpable adjacent to the lateral aspect of the implant. The craniocaudal view shows a soft-tissue opacity with irregular margins adjacent to the lateral aspect of the implant. There are several small round nodules in the adjacent breast tissue. (B) Ultrasound at the site of the mass shows acoustic shadowing only.

The type of imaging chosen depends principally on which method (ultrasound or mammography) shows the lesion clearly. Ultrasound is used for cysts and most soft-tissue lesions; mammography is used for microcalcification and for soft-tissue lesions, particularly distortions, which are not sufficiently well visualised on ultrasound.

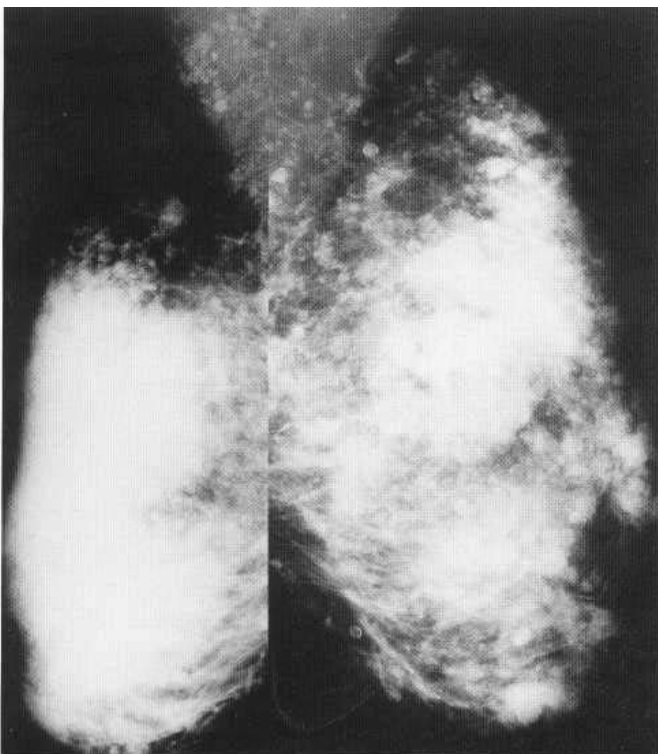


Fig. 46.70 Siliconoma due to direct injection of silicone into both breasts.

Ultrasound-guided procedures

Cyst aspiration

Simple cysts are most commonly aspirated because they are causing symptoms, e.g. a tender breast lump. Asymptomatic cysts found on imaging do not need to be aspirated unless there are imaging features present which suggest that the lesion may not be a simple cyst but may contain an intracystic tumour.

Abscess aspiration

Most simple, unilocular breast abscesses can be effectively managed by percutaneous needle aspiration and oral antibiotics. The needle aspiration may need to be repeated and should be carried out using local anaesthetic. Large multilocular abscesses (Fig. 46.71) require surgical incision and drainage.

Ultrasound-guided FNAC

Solid lesions which are visible on ultrasound can be biopsied using a fine needle (21–23G) in order to obtain an aspirate containing cellular material which is analysed to provide a cytological diagnosis. Local anaesthetic infiltration of the skin may be used and two or three separate passes are made to increase the chance of obtaining a cellular aspirate. Visualisation of the needle in relation to the lesion is easiest if the needle is introduced as parallel to the surface of the probe as possible, so that the long axis of the needle is perpendicular to the direction of the ultrasound beam. The needle is moved to and fro within the lesion with simultaneous rotation and with negative pressure applied. The negative pressure is most easily applied by an assistant using a syringe connected to the needle by a short extension tube. Aspiration is continued until material is seen within the hub of the needle; the aspirate is then delivered onto slides and dry and wet preparations made in accordance with instructions from the local cytopathologist. If local circumstances allow, it may be helpful to have the cellularity of the specimens checked by a cytology technician immediately following the procedure.

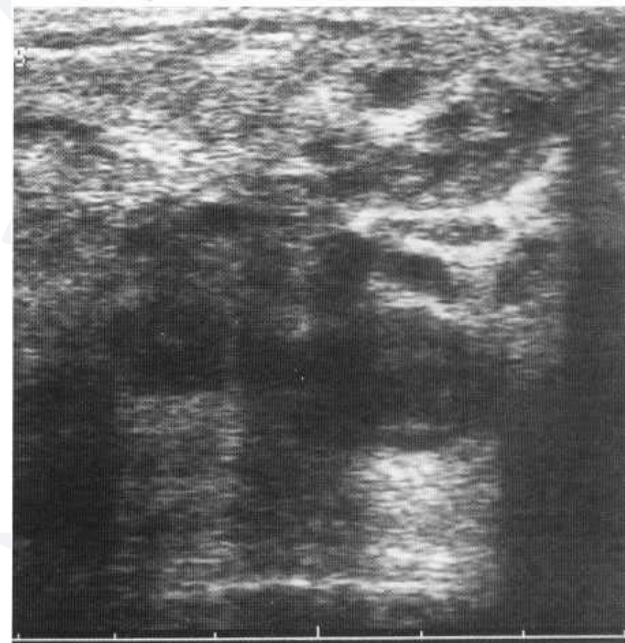


Fig. 46.71 A complex multilocular abscess requiring surgical drainage.



Fig. 46.72 14G needle and automated biopsy device used for ultrasound and stereotactic core breast biopsy.

Ultrasound-guided FNAC is used for the diagnosis of non-palpable lesions but can also be used to increase the accuracy of FNAC of small masses which are difficult to palpate clinically.

Ultrasound-guided core biopsy

Small solid lesions can also be effectively biopsied using ultrasound guidance for core biopsy. A 14G needle is used together with an automated biopsy device (Manon/Kimal) (Fig. 46.72). The biopsy device rapidly advances the central trochar through the lesion; the outer cutting sheath of the needle is then rapidly advanced over the central portion of the needle, cutting a core of tissue which lies within a 17mm biopsy 'port'. The needle is withdrawn and the core of tissue delivered into formal saline. This procedure is carried out under local anaesthetic and a small 3-4 mm skin incision is necessary to allow easy passage of the 14G needle. The biopsy needle should be introduced as parallel as possible both to the ultrasound

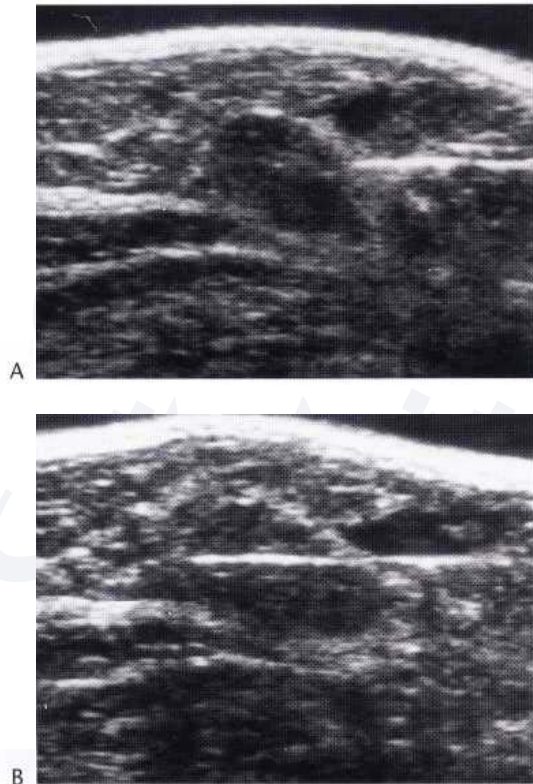


Fig. 46.73 Ultrasound-guided 14G core biopsy of a solid mass. (A) The tip of the needle is positioned just proximal to the lesion prior to firing the biopsy device. (B) The needle is demonstrated within the lesion after firing the biopsy device. Note that the needle is parallel to the chest wall.

probe, to optimise visualization of the needle, and to the chest wall to prevent any risk of the needle tip passing posteriorly into the chest. The 22 mm 'throw' of the needle tip on firing must be considered when deciding whether the needle is satisfactorily positioned. The tip of the needle should be positioned just proximal to the edge of the lesion. Manoeuvring the needle into the correct position for biopsy is easiest if the needle is passed through the breast tissue in a radial direction in relation to the nipple-in this way, fewer tissue planes need to be traversed. The needle can be observed passing through the lesion during the biopsy (Fig. 46.73). Several passes are carried out through the same skin incision to ensure that representative material has been obtained. Following the procedure, firm pressure should be applied to the area for at least 5 minutes to prevent haematoma formation.

X-Ray guided procedures

Stereotactic-guided FNAC

For lesions that are not seen or are poorly visualised on ultrasound, mammographic guidance is required for needle biopsy. The most common method currently in use is an add-on stereotactic device which is used with a conventional upright mammography machine (Fig. 46.74). With the patient seated a superior approach with the breast positioned for a craniocaudal view is suitable for most lesions but lateromedial, mediolateral or oblique approaches may be needed for lesions that are inferiorly positioned or are situated laterally in the axillary tail region. The lesion is demonstrated on paired stereotactic views obtained with the X-ray tube angled 15° either side of the central tube position. Measurements defining the position of the lesion on the stereotactic views are used to determine the position of the needle guide in the X, Y and Z axes. When the needle, of specified length, has been inserted through the guide into the breast, check stereotactic views are obtained to ensure that the tip of the needle is correctly positioned in relation to the lesion (Fig. 46.75). If the position is not correct, the needle can be repositioned and further check films obtained. When the needle position is correct, the remainder of the aspiration procedure is similar to that for ultrasound-guided FNAC. Different areas of the

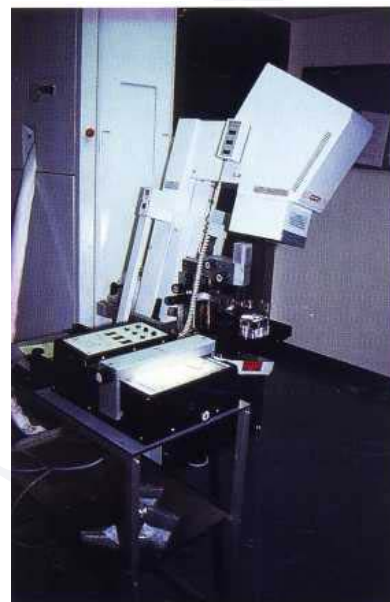


Fig. 46.74 Conventional stereotactic device.

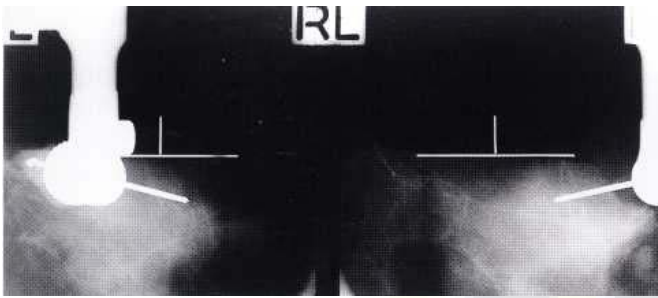


Fig. 46.75 Stereotactic-guided fine needle aspiration. The check pair of films shows the tip of the needle positioned within the small cluster of microcalcification on both views.

lesion are sampled by moving the needle guide 2-3 mm in the X and Y axes. Up to five aspirates are usually obtained.

Stereotactic-guided core biopsy

Conventional mammography apparatus with add-on stereotactic equipment and analogue imaging can be used for stereotactic core biopsy, but more accurate results have been obtained using either add-on digital imaging or dedicated prone stereotactic biopsy equipment with digital imaging (e.g. Fischer Imaging) (Fig. 46.76). Using this equipment, the patient lies in the prone or prone oblique position and the breast passes through an aperture in the table. The direction of the X-ray beam is horizontal and stereotactic views are obtained by rotating the tube 15° either side of the central position. The digital X-ray images obtained are displayed on a computer screen within approximately 5 seconds of exposure, and the com-



Fig. 46.76 Dedicated prone stereotactic breast biopsy apparatus.

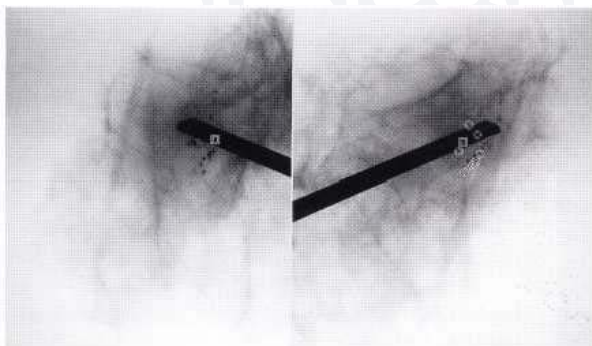


Fig. 46.77 Stereotactic core biopsy. Stereo film pair showing 'post fire' position of needle during biopsy of microcalcification.

puter offers rapid contrast adjustment and zoom facilities. Target areas for biopsy are selected on the computer screen and the position and angulation of the biopsy needle/gun holder are adjusted automatically. A 14G needle is used; after insertion under local anaesthetic, check films are taken to ensure correct positioning (Fig. 46.77). Check films can also be taken after firing the biopsy gun to ensure that the lesion has been traversed by the needle. Five or more core biopsies are usually obtained. Core biopsy specimen radiographs are taken when sampling areas of microcalcification to ensure that representative tissue has been obtained (Fig. 46.78). Problems which may occur with 14G core biopsy include:

- Suspicious core biopsy result-the pathologist is unable to make a specific diagnosis on the material provided or atypical ductal hyperplasia (ADH) is found. At surgical excision, 40-50% of such cases will prove to be malignant.
- Under diagnosis of invasive cancer-a small focus of invasive cancer within an area of malignant microcalcification may not be sampled.
- Targeting of small lesions - accurate sampling of very small 2-3 mm diameter clusters of microcalcification may be difficult.

Vacuum-assisted core biopsy

Vacuum-assisted core biopsy allows a larger tissue sample to be obtained and overcomes some of the problems of 14G core biopsy,



Fig. 46.78 (A) Core biopsy specimen radiograph demonstrating microcalcification within the core samples. (B) Core biopsy showing ductal carcinoma in situ with calcification.

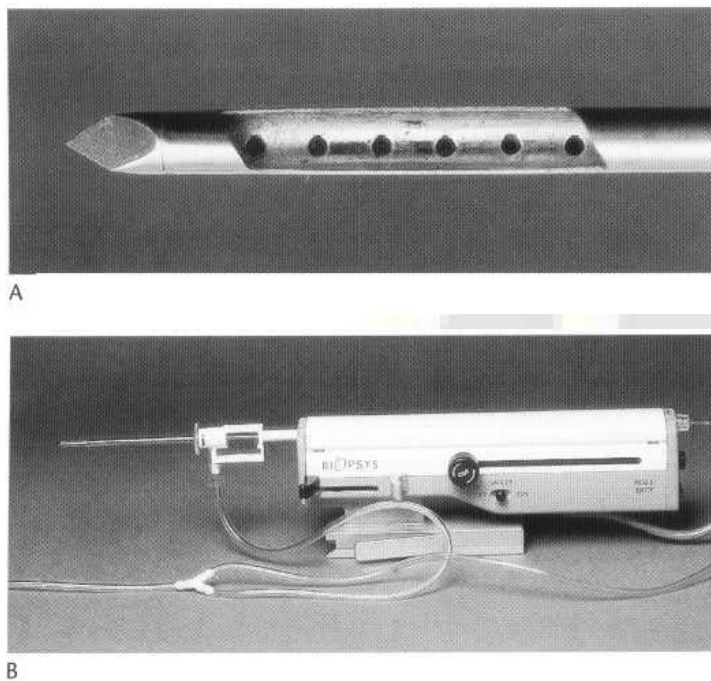
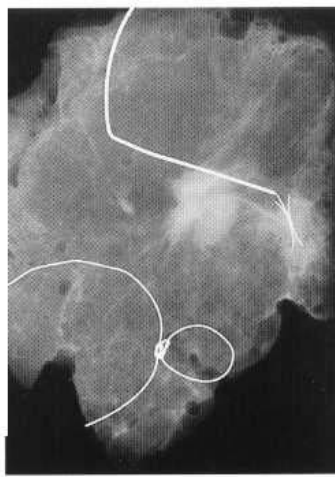
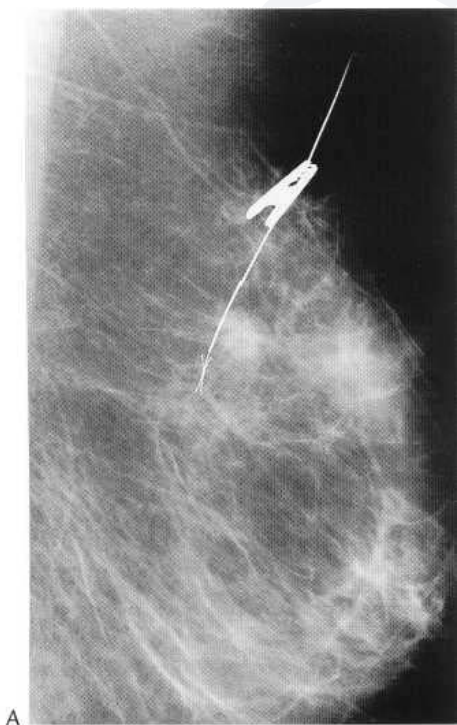


Fig. 46.79 Vacuum-assisted core biopsy. (A) Probe showing biopsy port with holes leading to vacuum-producing apparatus. (B) Biopsy probe and driver unit.

particularly targeting of very small lesions. An IIG probe with a biopsy port attached to a vacuum-producing device (Fig. 46.79) is inserted into the breast under local anaesthetic and stereotactic guidance. Tissue from the target area is sucked into the biopsy port by the vacuum and is then separated from the surrounding breast by a rotating cutting cylinder which passes down within the probe. The tissue sample is then delivered by withdrawing the cutting cylinder—the probe is left in position in the breast and is rotated so that the biopsy port is aligned with the next site for sampling. In



this way multiple samples are taken and small clusters of microcalcification will usually be completely removed. If the mammographic marker is removed, a small metal clip is deployed at the site of the biopsy to allow accurate localisation should subsequent surgical excision be necessary. Vacuum-assisted core biopsy has also been used under ultrasound guidance for sampling of soft-tissue lesions, and under MRI guidance for lesions which are not visible using either mammography or ultrasound.

Preoperative localisation of non-palpable lesions

Prior to surgical excision of non-palpable lesions, information from the combined imaging/needle biopsy work-up is used to determine whether the surgery is to be therapeutic, in cases where a diagnosis of malignancy has been confirmed, or diagnostic, for cases where the diagnosis remains uncertain. The position of the lesion in the breast is marked using a wire with a hook or barb on the end to prevent movement of the wire within the breast. The wire is contained within a needle which is inserted into the breast under local anaesthetic, using either X-ray or ultrasound guidance. When X-ray guidance is used, a simple perforated compression plate or aperture compression plate is satisfactory and stereotaxis is not usually required. When the tip of the needle has been shown to be satisfactorily positioned within 10 mm of the lesion, the needle sheath is withdrawn leaving the wire in situ. Check craniocaudal and lateral views are obtained to show the final position of the wire in relation to the lesion. Peroperative specimen radiography is mandatory to ensure that the excised breast tissue contains the mammographic abnormality (Fig. 46.80).

Ductography

Ductography may be performed in the investigation of patients with unilateral blood-stained nipple discharge to identify the site of pathology within the duct. The duct orifice from which the discharge is occurring is identified by squeezing the breast tissue to express the discharge. The duct orifice is then cannulated using a fine 30G cannula, e.g. sialogram cannula, the tip of which is passed into the lactiferous sinus. Approximately 3 ml of water-soluble contrast is then injected, the cannula is taped to the nipple, and lateral and craniocaudal views are obtained. Ductal filling defects may be caused by papilloma or carcinoma in situ (Fig. 46.81).

Fig. 46.80 Wire localisation and surgical excision of a non-palpable carcinoma. (A) The position of a spiculate mass in the upper part of the left breast is marked with a localising wire. (B) Peroperative specimen radiography confirms that the mass has been excised.

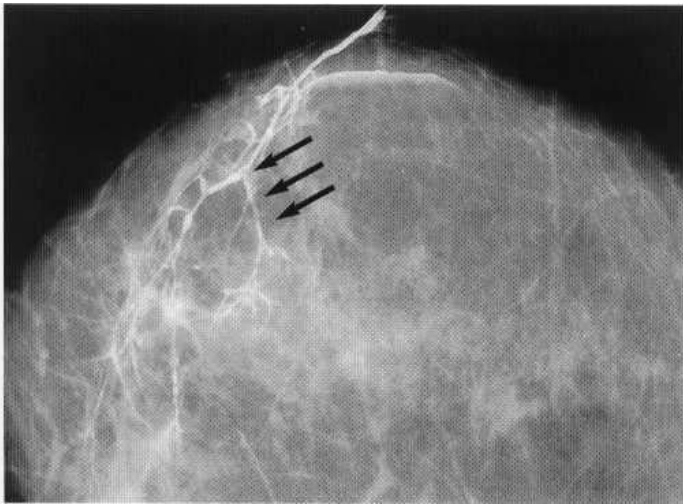


Fig. 46.81 A ductogram showing small filling defects due to an intraductal carcinoma (arrows).

Breast cancer screening

The aim of screening by mammography is to reduce mortality from breast cancer by detecting cancers when they are small, before they have spread and for which the prognosis following treatment is better than for larger tumours. National breast screening programmes have been implemented in many countries using high-quality X-ray mammography, the only screening test for breast cancer which has been shown to be effective in reducing mortality.

The effectiveness of screening

The effect of screening is to bring forward the time of diagnosis of breast cancer by the lead time. The following biases have to be taken into account when assessing the effectiveness of screening:

- **Lead time bias:** in some women, the prognosis will not be altered by detecting the tumour earlier. The effect of screening in such cases is to lengthen the time during which a woman lives with a diagnosis of breast cancer.
- **Length bias sampling:** some slow-growing invasive or non-invasive cancers detected by screening may not have become clinically apparent during a woman's natural lifespan. The effect of screening in such cases is to detect and treat what may have remained occult disease.

Lead time bias and length bias sampling reflect the heterogeneity of breast cancer. In order to demonstrate the effect of mammography screening, large-scale prospective randomised trials have been conducted in Europe and the USA. Long-term follow-up results from the Swedish Two Countries Trial demonstrate a 30% (95% CI 18-40%) reduction in breast cancer mortality in women aged 40-74 years. Combined data from the published results of prospective trials show that breast screening reduces mortality by 24% (95% CI 13-33%; $P < 0.01$) for women invited for screening aged 50-74 years assuming a 70% acceptance rate. The reduction in mortality for women aged 40-49 years invited for screening is estimated from the combined data to be 15% (95% CI 8-32%; $P = 0.2$).

Organisation of screening

A national mammography screening programme was implemented in the UK following publication in 1986 of the findings of an expert committee chaired by Sir Patrick Forrest.

The current policy for mammography screening in the UK is:

1. All women aged 50 years and over are offered screening.
2. Women aged 50-64 years are invited for screening once every 3 years. This age range is currently being extended to 50-70 years. Women who are older than the invitation age range may arrange screening by self-referral.
3. The screening test is a lateral oblique and craniocaudal mammogram for the prevalent screen and a lateral oblique mammogram for incident screens. The programme is currently in the process of implementing two-view mammography for all screens.

The main stages of the screening process are

1. Invitation
2. Basic screen
3. Assessment and diagnosis
4. Treatment.

1. Invitation Eligible women in the age range for invitation are identified from health authority computerised records of women registered with general practitioners. Women are offered their first invitation for screening before their 53rd birthday and are sent further invitations every 3 years while they are within the age range for invitation.

2. Basic screen The basic screening mammogram is carried out in static units, particularly in urban areas or on mobile units used in many rural areas. The screening films are read to identify any which show an abnormality suspicious for cancer. Screen film reading is carried out by radiologists, and appropriately trained clinicians and radiographers. Double reading is carried out where possible because this has been shown to increase the sensitivity for cancer detection.

Factors which influence sensitivity of screening mammography:

(i) **Film quality:** high-quality films are essential for the detection of small cancers. Careful positioning is required to ensure that as much of the breast as possible is demonstrated with the tissue adequately compressed. High film density has been shown to be associated with high small cancer detection rates—a target film density of 1.4-1.8 is recommended.

(ii) **Number of views:** studies have shown that two-view mammography increases the cancer detection rate by up to 24%.

(iii) **Number of readers:** double reading has been shown to increase cancer detection rates. The effect is seen in both prevalent and incident screens and appears to be due particularly to improved detection of small <15 mm diameter invasive cancers. The SDR (standardised detection ratio) is increased by 32% (95% CI 3-69%) for prevalent screen small invasive cancer detection and by 73% (95% CI 40-113%) for incident screen small invasive cancer detection.

3. Assessment and diagnosis Women are recalled following the basic screen because:

- (i) The screening films show an appearance suspicious for cancer.

- (ii) A significant clinical symptom or sign, e.g. a lump, is indicated by the woman to the radiographer at the time of screening.
- (iii) The screening films are technically unsatisfactory.

Women whose films are technically unsatisfactory may have repeat films carried out at the basic screening unit. Women who have been recalled because of a mammographic or clinical abnormality are recalled to a specialist multidisciplinary clinic where facilities are available for clinical examination, standard and supplementary mammography views, ultrasound needle biopsy (FNAC and core biopsy) and counselling. The combination of tests in a particular case is chosen according to the type of abnormality present.

At assessment:

- (i) The triple diagnostic approach is used to confirm the diagnosis in women with breast cancer so that treatment can be planned together with appropriate counselling.
- (ii) Women who are found to have normal breasts or benign change are reassured and discharged until their next routine screening examination.
- (iii) Women who have a suspicious lesion in whom a definitive diagnosis cannot be achieved using the triple diagnostic approach are advised to undergo diagnostic surgical excision. This includes cases where atypical ductal hyperplasia has been diagnosed on image-guided core biopsy because of the risk of associated invasive or in situ carcinoma being found at surgical excision.
- (iv) Women who have a low suspicion lesion, in whom a definitive diagnosis cannot be made using the triple diagnostic approach, may be followed by repeating the mammograms earlier than the routine 3-year recall e.g. early recall at 1 year: the number of women on early recall should be kept to a minimum because of the anxiety that this may cause.

4. Treatment

Surgical biopsy and treatment For the majority of women with screening-detected cancer, it is now possible to confirm the diagnosis preoperatively and treatment is planned accordingly using combined information from clinical examination, imaging and needle biopsy.

Open surgical excision will still be required for some cases where the mammographic findings are suspicious for malignancy but the findings from needle biopsy are not diagnostic. Between 50 and 60% of screening-detected lesions requiring surgery are non-palpable and require preoperative radiological localisation. In all such cases, preoperative mammography of the excised tissue is mandatory to ensure that the mammographic abnormality has been removed. Preoperative 'frozen-section' pathological examination in such cases is contraindicated because of the difficulty of accurately diagnosing some screening detected lesions using this method.

Quality assurance: targets for radiological performance in breast screening

Standards for radiological performance in breast screening which have been set for each stage of the screening process have been adjusted since the beginning of the programme following review of the results and as more epidemiological information has become available. The purpose of the quality assurance programme is to ensure that by delivering a high-quality service, the benefit of screening, a reduction in breast cancer mortality, is maximised while the adverse effects of

screening such as anxiety due to recall for assessment and the trauma of surgical biopsy for benign breast conditions are minimised.

The Current Quality Assurance Standards for the UK screening programme together with recent results are shown in Tables 46.2 and 46.3.

Interval cancers

Interval cancers in a screening programme are those cancers which are diagnosed in the interval between a negative screen and the next routine screen. Analysis of the number and type of interval cancers provides an important indication of the effectiveness of the screening service and review of their mammographic features has enabled film readers to improve their ability to detect small cancers with subtle mammographic features. Interval cancers are an inevitable part of any screening programme, but their number should be kept as low as possible. The expected interval cancer rates are derived using an underlying incidence of breast cancer of 21.6 per 10,000 for women aged 53-64. The observed rates of interval cancers in the Swedish Two Counties study indicate that the number of interval cancers should not exceed 20% of the underlying incidence in the first year (4.5 per 1000), 30.4 in the second year (6.5 per 1000) and 60% in the third year (13 per 1000). In the UK screening programme, the standard for the expected interval cancer rate is <12/1000 in the first 24 months following screening and <13/1000 screened for the subsequent 12 months (these figures exclude DCIS).

Interval cancers are classified radiologically as follows:

1. True interval: there is no evidence of the cancer on the screening films but the cancer is demonstrated on clinical mammograms at presentation.
2. Occult: there is no evidence of the cancer either on the screening mammograms or on the clinical mammograms.
3. False negative: there is evidence of the cancer on the original screening films which corresponds with the abnormal signs shown on clinical mammograms at the time of diagnosis.
4. Minimal sign: there are subtle features on the screening mammograms which correspond to the position of the carcinoma shown on the clinical films but are only recognisable on retrospective review or for which recall would not have been indicated.
5. Unclassified: mammography was not performed at the time of diagnosis and therefore the presence of mammographic signs of malignancy on the previous screening films cannot be verified.

Breast screening research

1. The age trials Screening for women aged 40-49 years-women in the study group have been offered yearly mammography screening from the age of 40 years. The mortality from breast cancer in the study group will be compared to that in the control group in order to assess the effect of screening this age group.

Screening for women aged over 64 years-pilot studies have been carried out to measure the results of inviting women for screening aged 65-70 years. As a result of these studies, the upper age limit for routine invitations for screening in the UK is being extended to 70 years.

Table 46.2 Quality assurance target for breast screening

Objective	Criteria	Minimum standard	Target
1. To maximise the number of eligible women who attend for screening	The percentage of eligible women who attend for screening	>70% of invited women to attend for screening	
2. To maximise the number of cancers detected	a. The rate of invasive cancers detected in eligible women b. The rate of cancers detected which are in situ carcinoma c. Standardised detection ratio (SDR)	Prevalent screen >2.7 per 1000 Incident screen >3.0 per 1000 Prevalent screen >0.4 to >0.9 per 1000 Incident screen >0.5 to >1.0 per 1000 >0.75	Prevalent screen >3.6 per 1000 Incident screen >4.0 per 1000 <1.0
3. To maximise the number of small invasive cancers	The rate of invasive cancers less than 15 mm in diameter detected in eligible women invited and screened	Prevalent screen >1.5 per 1000 Incident screen >1.65 per 1000	Prevalent screen >2.0 per 1000 Incident screen >2.2 per 1000
4. To achieve optimum image quality	a. High contrast spatial resolution b. Minimal detectable contrast (approx.) 5-6 mm detail 0.5 mm detail c. Standard film density	>10p/mm >% <5% 1 4-18	
5. To limit radiation	Mean glandular dose per film to standard breast using a grid	<2 mGy	
6. To minimise the number of women undergoing repeat examinations	The number of repeat examinations	<3% of total examinations	<2% of total examinations
7. To minimise the number of women screened who are referred for further tests	a) The percentage of women who are referred for assessment. b) The percentage of women screened who are placed on early recall	Prevalent screen <10% Incident screen <7% <1%	Prevalent screen <7% Incident screen <5% <0.25%
8. To ensure that the majority of cancers, both palpable and impalpable, receive a non-operative tissue diagnosis of cancer	The percentage of women who have non-operative diagnosis of cancer by cytology or needle histology	>70%	>90%
9. To minimise the number of unnecessary operative procedures	The rate of benign biopsies	Prevalent screen <3.6 per 1000 Incident screen >2.0 per 1000	Prevalent screen <1.8 per 1000 Incident screen <1.0 per 1000
10. To minimise the number of cancers in women screened presenting between screening episodes	The rate of cancers presenting in screened women . a. in the 2 years following a normal screening episode b. In the third year	Expected standard 1.2 per 1000 screened 1.3 per 1000 screened	
11. To ensure that women are recalled for screening at appropriate intervals	The percentage of eligible women whose first offered appointment is within 36 months of their previous screen	>90%	100%

2. One-view vs. Two-view Mammography The results of the prospective study show that two-view mammography improves the sensitivity, particularly for the detection of small breast cancers, by up to 24%. As a result of this study, two-view mammography is now offered to all women attending prevalent screens and will soon be offered to women attending for incident screens.

3. The frequency trial This study is designed to identify the optimum interval between routine examinations. Women in the study group are offered 1 year screening; women in the control group undergo routine yearly screening. The prognostic features of cancers detected in the study group are compared to those of cancers detected in the control group.

Table 46.3 Recent results of the UK Breast Screening Programme: 1990–2000

	90/91	91/92	92/93	93/94	94/95	95/96	96/97	97/98	98/99	99/00
Number invited	996 086	1 443 914	1 612 450	1 608 948	1 507 605	1 517 033	1 558 955	1 668 476	1 699 727	1 811 541
Number screened	709 091	1 059 703	1 165 726	1 220 135	1 260 609	1 282 933	1 340 172	1 350 104	1 406 317	1 489 790
Screened >65 years			22 036	24 406	39 193	57 535	66 889	86 214	103 476	113 558
Uptake (%)	71.2	71.3	71.3	72.0	76.0	75.8	75.8	75.1	75.5	75.4
Recall rate (% women screened)										
Prevalent	7.0	6.2	5.9	6.5	7.2	7.3	7.6	7.8	8.2	8.3
Incident			3	3.1	3.4	3.4	3.6	3.3	3.9	3.9
Cancer detection/ 1 000 screened										
invasive + DCIS										
Prevalent	6.2	6.2	5.7	6.0	5.9	6.3	6.2	6.5	6.8	6.7
Incident			3.8	3.8	4.3	4.3	4.7	4.8	5.3	5.6
Invasive cancer detection/1 000 screened										
Prevalent							4.8	5.0	5.2	5
Incident							3.7	3.8	4.3	4.4
SDR										
Prevalent	0.74	0.78	0.81	0.87	0.97	1.10	1.17	1.22	1.29	1.26
Incident					0.85	0.87	0.94	0.98	1.06	1.10
Invasive carcinoma										
All sizes					5348	5518	5710	6214	7038	7516
<15 mm dia					2680	2807	3156	3381	3722	4041
<15 mm % of all invasive cancers					49.7	50.9	55.3	54.4	52.9	53.8
DCIS										
DCIS total					1 308	1 328	1 431	1 718	1 733	2 009
DCIS					19.6	19.4	20	21.6	19.7	21.09
Preoperative diagnosis (%)							62	71	81	85
Surgery										
Total	6981	9433	9129	9188	9033	9297	10 409	10 144	10 804	11 453
Benign	2597	2828	2532	2456	2377	2451	3268	2212	2033	1 928
Cancer	4384	6605	6597	6732	6656	6846	7141	7932	8771	9525
B/M ratio	1 : 1.7	1 : 2.3	1 : 2.6	1 : 2.7	1 : 2.8	1 : 2.8	1 : 2.2	1 : 3.6	1 : 4.3	1 : 4.94
Benign biopsy/ 1 000 screened										
Prevalent					2.8	3.8	5.1	3.3	2.9	2.7
Incident					0.8	1.0	1.3	0.8	0.8	0.7

REFERENCES AND SUGGESTIONS FOR FURTHER READING**Textbooks**

- Council, The Royal College of Radiologists (1995) *The Use of Imaging in the Follow-up of Patients with Breast Cancer*. London: The Royal College of Radiologists.
- Dixon, J. M. (1995) *ABC of Breast Diseases*. London: BMJ Publishing.
- Heywang-Kobrunner, S. (1990) *Contrast Enhanced MRI of the Breast*, 2nd edn. Berlin: Springer.
- Lanyi, M. (1986) *Diagnosis and Differential Diagnosis of Breast Calcifications*. Berlin: Springer-Verlag.
- Lee, L., Strickland, V., Wilson, R., Roebuck, E. (1995) *Fundamentals of Mammography*. London: Saunders.
- Parker, S. H., Jobe, W. E. (1993) *Percutaneous Breast Biopsy*. New York: Raven Press.
- Roebuck, F. J. (1990) *Clinical Radiology of the Breast*. Oxford: Heinemann Medical.
- Stavros, A. T. (1998) *Breast Ultrasound*. Philadelphia: Lippincourt.
- Tabar, L., Dean, P. B. (2001) *Teaching Atlas of Mammography*, 3rd edn. Stuttgart. Thieme.
- Tohno, E., Cosgrove, D. O., Sloane, J. P. (1994) *Ultrasound Diagnosis of Breast Diseases*. New York: Churchill Livingstone.

Clinical breast imaging

- Adler, D. D., Hevic, M. A., Obernian, H. A., Ikeda, D. M., Bhan, A. O. (1990) Radial sclerosing lesion of the breast: mammographic features. *Radiology*, 176, 737-740.
- Baker, J. A., Soo, M. S., Rosen, E. L. (2001) Artifacts and pitfalls in sonographic imaging of the breast. *American Journal of Roentgenology*, 176, 1261-1266.
- Britton, P. (1999) Fine needle aspiration or core biopsy. *Breast*, 8, 1-4.
- Ciatto, S., Cataliotti, L., Distanto, V. (1987) Non palpable lesions detected with mammography: review of 512 consecutive cases. *Radiology*, 165, 99-102.
- Cornford, E. J., Poller, D. N., Ellis, I. O., Wilson, A. R. M. (1993) The mammographic appearances of fibromatosis of the breast. *Breast*, 2, 175-179.
- Cornford, E. J., Wilson, A. R. M., Athanassiou, E., et al (1995) Mammographic features of invasive lobular and invasive ductal carcinoma of the breast: a comparative analysis. *British Journal of Radiology*, 68, 450-453.

- Cosgrove, D. O., Bamber, J. C., Davey, J. B., McKinna, J. A., Sinnett, H. D. (1990) Color Doppler signals from breast tumors. *Radiology*, **176**, 175-180.
- DeBruhl, N. D., Gorczyca, D. P., Ahn, C. Y., et al (1993) Silicone breast implants: US evaluation. *Radiology*, **189**, 95-98.
- Denton, E. R. E. Ryan, S., Beaconsfield, T., Michell, M. J. (1999) Image guided breast biopsy: analysis of pain and discomfort related to technique. *Breast*, **8**, 257-260.
- Finlay, M. E., Liston, J. E., Lunt, L. G., Young, J. R. (1994) Assessment of the role of ultrasound in the differentiation of radial scars from stellate carcinomas of the breast. *Clinical Radiology*, **49**, 52-55.
- Frouge, C., Tristant, H., Guinebretiere, J. M., et al (1995) Mammographic lesions suggestive of radial scars: microscopic findings in 40 cases. *Radiology*, **195**, 623-625.
- Garstin, W. I. H., Kaufman, Z., Michell, M. J., Baum, M. (1991) Fibrous mastopathy in insulin dependent diabetics. *Clinical Radiology*, **44**, 89-91.
- Gawne-Cain, M. L., Smith, F., Darby, M., Given-Wilson, R. (1995) The use of ultrasound for monitoring breast tumour response to pro-adjuvant therapy. *Clinical Radiology*, **50**, 681-686.
- Guyer, P. B., Dcwbury, K. C., Rubin, C. M., et al (1992) Ultrasonic attenuation in fibroadenoma of the breast. *Clinical Radiology*, **45**, 175-178.
- Hashimoto, B. E., Mantel, D. J. (2001) High detection rate of breast ductal carcinoma in situ calcifications on mammographically directed high-resolution sonography. *Journal of Ultrasound in Medicine*, **20**, 501-508.
- Hayes, R., Michell, M. J., Nunnerley, H. (1991) Acute inflammation of the breast—the role of breast ultrasound in diagnosis and management. *Clinical Radiology*, **44**, 253-256.
- Hayes, R., Michell, M. J., Nunnerley, H. B. N. (1991) Evaluation of magnification and paddle compression techniques in the assessment of mammographic screening detected abnormalities. *Clinical Radiology*, **44**, 158-160.
- Holland, R., Hendriks, J. H. C. L., Verbeck, A. L. M. (1990) Clinical practice: extent, distribution and mammographic/histological correlations of breast ductal carcinoma in situ. *Lancet*, **335**, 519-522.
- Ikedo, D. M., Helvic, M. A., Frank, T. S., et al (1993) Paget's disease of the nipple: radiologic pathologic correlation. *Radiology*, **189**, 89-94.
- Kaufman, Z., Garstin, I., Hayes, R., Michell, M. J., Baum, M. (1991) The mammographic parenchymal patterns of women on hormone replacement therapy. *Clinical Radiology*, **43**, 389-392.
- Kedar, R. P., Cosgrove, D. O., Bamber, J. C., Bell, D. S. (1995) Automated quantification of color Doppler signals: a preliminary study in breast tumours. *Radiology*, **197**, 39-43.
- Kirwan, S. E. M., Denton, E. R. E., Nash, R., Michell, M. J. (2000) Multiple 14G stereotactic core biopsies in the diagnosis of mammographically detected stellate lesions of the breast. *Clinical Radiology*, **55**, 763-766.
- Kolb, T. M., Lichy, J., Newhouse, J. H. (1998) Occult cancer in women with dense breasts: detection with screening US diagnostic yield and tumor characteristics. *Radiology*, **207**, 191-199.
- Liberian, L. (1999) Advanced breast biopsy instrumentation (ABBI). *American Journal of Roentgenology*, **172**, 1413-1416.
- Liberman, L. (2000) Percutaneous image guided core breast biopsy: start of the art at millennium. *American Journal of Roentgenology*, **174**, 119-121.
- Liberman, L., Giess, C. S., Denshaw, D. D., et al (1994) Non Hodgkins lymphoma of the breast: imaging characteristics and correlation with histopathologic findings. *Radiology*, **192**, 157-160.
- Lister, D., Evans, A. J., Burrell, H. C., et al (1998) The accuracy of breast ultrasound in the evaluation of clinically benign, discrete, symptomatic breast lump. *Clinical Radiology*, **53**, 490-492.
- Lundgren, B., Jacobssen, S. (1976) Single view mammography. *Cancer*, **38**, 1124-1129.
- Mitnick, J. S., Vasquez, M. F., Marris, M. D., et al (1989) Differentiation of radial scar from scirrhous carcinoma of the breast: mammographic-pathological correlation. *Radiology*, **173**, 697-700.
- Memis, A., Ozdemir, N., Parildar, M., Ustun, E. E., Erhan, Y. (2000) Mucinous (colloid) breast cancer: mammographic and US features with histologic correlation. *European Journal of Radiology*, **35**, 39-43.
- O'Toole, M., Caskey, C. I. (2000) Imaging spectrum of breast implant complications: mammography, ultrasound, and magnetic resonance imaging. *Seminars in Ultrasound, CT & MR*, **121**, 351-361.
- Reiff, D. B., Cooke, J., Griffin, M., Given-Wilson, R. (1994) Ductal carcinoma in situ presenting as a stellate lesion on mammography. *Clinical Radiology*, **49**, 396-399.
- Rich, P. M., Michell, M. J., Humphreys, S., Howes, G. P., Nunnerley, H. B., (1999) Core biopsy of non palpable breast cancer: what is the relationship between the number of core samples taken and the sensitivity for detection of malignancy. *Clinical Radiology*, **54**, 384-389.
- Sibbering, D. M., Burrell, H. C., Evans, A. J., et al (1995) Mammographic sensitivity in women under 50 years presenting symptomatically with breast cancer. *Breast*, **4**, 127-129.
- Sickles, E. A. (2000) Breast imaging: from 1965 to the present. *Radiology*, **215**, 1-16.
- Stuhrmann, M., Aronius, R., Schietzel, M. (2000) Tumor vascularity of breast lesion: potentials and limits of contrast-enhanced Doppler sonography. *American Journal of Roentgenology*, **176**, 1585-1589.
- Tabar, L., Chen, H. H., Duffy, S. W., et al (2000) A novel method for prediction of long term outcome of women with T1a, T1b and T1c mm invasive breast cancers: a prospective study. *Lancet*, **355**, 429-433.
- Teh, W. L., Wilson, A. R. M., Evans, A. J., Burrell, H., Pinder, S. E., Ellis, I. O. (2000) Ultrasound guided core biopsy of suspicious mammographic calcifications using high frequency and power Doppler ultrasound. *Clinical Radiology*, **55**, 390-395.
- Wallis, M. G., Walsh, M. T., Lee, J. R. (1991) A review of false negative mammography in a symptomatic population. *Clinical Radiology*, **44**, 13-15.
- Warren, S. L. (1930) A roentgenologic study of the breast. *American Journal of Roentgenology*, **24**, 113-124.

MRI

- Boetes, C., Strijk, S. P., Holland, R., Barentsz, J. O., Van Der Sluis, R. F., Ruijs, J. H. J. (1997) False negative MR imaging of malignant breast tumours. *European Radiology*, **7**, 1231-1234.
- Friedrich, M. (1998) MRI of the breast: state of the art. *European Radiology*, **8**, 707-725.
- Heywang-Kobrunner, S. H., Schlegel, A., et al (1993) Contrast-enhanced MRI of the breast after limited surgery and radiation therapy. *Journal of Computer Assisted Tomography*, **17**, 891-900.
- Heywang-Kiibrunner, S. H., Heinig, A., Schaumloffel, U., et al (1999) MR-guided percutaneous excisional and incisional biopsy of breast lesion. *European Radiology*, **9**, 1656-1665.
- Kuhl, C. K., Mielcarek, P., Klaschik, S., et al (1999) Dynamic breast MR imaging: are signal intensity time course data useful for differential diagnosis of enhancing lesions? *Radiology*, **211**, 101-110.
- Mumf, D. F., Farria, D. M., Gorczyca, D. P., et al (1993) MR imaging of the breast in patients with silicon-gel implants: spectrum of findings. *American Journal of Roentgenology*, **161**, 773-778.
- Orel, S. G., Schnall, M. D., Powell, C. M., et al (1995) Staging of suspected breast cancer: effect of MR imaging and MR-guided biopsy. *Radiology*, **196**, 115-122.
- Orel, S. G., Weinstein, S. P., Schnall, M. D., et al (1999) Breast MR imaging in patients with axillary nodal metastases and unknown primary malignancy. *Radiology*, **212**, 543-549.
- Piccoli, C. W., Grccc, J. G., Mitchell, D. G. (1996) Breast MR imaging for cancer detection and implant evaluation: potential pitfalls. *Radiographics*, **16**, 63-75.
- Weinreb, J. C., Newstead, G. (1995) MR imaging of the breast. *Radiology*, **196**, 593-610.

Breast cancer screening

- Andersson, I., Aspegren, K., Janzen, L., et al (1988) Mammographic screening and mortality from breast cancer: the Malmo mammographic screening trial. *British Medical Journal*, **297**, 943-948.
- Baker, L. H. (1982) Breast cancer demonstration project. Five-year summary report. *Cancer*, **32**, 194-225.
- Blanks, R. G., Day, N. E., Moss, S. M. (1996) Monitoring the performance of breast screening programmes: use of indirect standardisation in evaluating the invasive cancer detection rate. *Journal of Medical Screening*, **3**(2), 79-81.
- Blanks, R., Wallis, M. G., Moss, S. M. (1998) A comparison of cancer detection rates achieved by breast cancer screening programmes by number of readers, for one and two view mammography: results from the UK NHS breast screening programmes. *Journal of Medical Screening*, **5**(4), 195-201.
- Blanks, R. G., Moss, S. M., Patrick, J., (2000) Results from the UK NHS breast screening programme 1994-1999. *Journal of Medical Screening*, **7**(4), 195-198.

- Chamberlain, J., Moss, S. M., Kirkpatrick, A. E., Michell, M. J., Johns, L. (1993) National Health Service breast screening programme results for 1991-2. *British Medical Journal*, *307*, 353-356.
- Colette, H. J. A., Day, N. E., Rombach, J. J., De Waard, F. (1984) Evaluation of screening for breast cancer in a non-randomised study (the DOM project) by means of a case control study. *Lancet*, *i*, 1224-1226.
- Duncan, A. A., Wallis, M. G. (1995) Classifying interval cancers. *Clinical Radiology*, *50*, 774-777.
- Forrest, P. (1986) *Breast Cancer Screening: Report to the Health Ministers of England, Wales, Scotland and Northern Ireland*. London: HMSO.
- Moss, S., Blanks, R., for the Interval Cancer Working Group (1998) Calculating appropriate target cancer detection rates and expected interval cancer rates for the UK NHS breast screening programme. *Journal of Epidemiology and Community Health*, *52*, 111-115.
- NHS Breast Screening Radiologists Quality Assurance Committee (1977) *Quality Assurance Guidelines for Radiologists*. NHS BSP Publication No. 15, Sheffield.
- NHS Cancer Screening Programmes (2001) *Guidelines for Non-operative Diagnosis Procedures and Reporting in Breast Cancer Screening*. NHS BSP Publication No. 50, Sheffield.
- On, G., Austroker, J., Brett, J. (1997) Breast screening: adverse psychological consequences one month after placing women on early recall because of a diagnostic uncertainty. A multicentre study. *Journal of Medical Screening*, *4*, 158-168.
- Patrick J. (ed.) (2000) *NHS Breast Screening Programme Review 2000*. NHS BSP Publications, Sheffield.
- Peters, P. H. M., Verbeek, A. L. M., Hendricks, J. H. C. L., et al (1989) The occurrence of interval cancers in the Nijmegen Screening Programme. *British Journal of Cancer*, *59*, 929-932.
- Quinn, M., Allen, E., on behalf of the United Kingdom Association of Cancer Registries (1995) Changes in incidence of and mortality from breast cancer in England and Wales since introduction of screening. *British Medical Journal*, *311*, 1391-1395.
- Roberts, M. M., Alexander, F. E., Anderson, T. J., et al (1990) Edinburgh trial of screening for breast cancer: mortality at seven years. *Lancet*, *i*, 241-246.
- Screening brief, breast cancer (1994) *Journal of Medical Screening*, *1*, 73.
- Shapiro, S., Venet, W., Stax, P., et al (1982) Ten to fourteen year effect of breast cancer screening on mortality. *Journal of the National Cancer Institute*, *69*, 349-355.
- Tahar, L., Fagerberg, G., Duffy, S. W., Day, N. E., Gad, A., Grontoft, O. (1992) Update of the Swedish two county program of mammographic screening for breast cancer. *Radiologic Clinics of North America*, *30*, 187-210.
- Tahar, L., Duffy, S. W., Vitak, B., et al (1999) The natural history of breast carcinoma. What have we learned from the screening? *Cancer*, *86*, 449-462.
- Tahar, L., Vitak, B., Chen, H. H., et al (2000) The Swedish two county trial twenty years later. *Radiologic Clinics of North America*, *38*, 625-651.
- UK Trial of Early Detection of Breast Cancer Group (1993) Breast cancer mortality after 10 years in the UK trial of early detection of breast cancer. *Breast*, *2*, 13-20.
- Verbeek, A. L. M., Hendriks, J. H. C. L., Holland, R., Mravunac, M., Sturmans, F., Day, N. E. (1984) Reduction in breast cancer mortality through mass screening with mammography. First results of the Nijmegen Project, 1975-1981. *Lancet*, *i*, 1222-1224.
- Wald, N. J., Hackshaw, A., Chamberlain, J. (1994) The efficacy and safety of periodic mammographic breast cancer screening: summary of report of the European Society of Mastology. *Clinical Radiology*, *49*, 592-593.
- Wald, N. J., Murphy, P., Major, P., Parkes, C., Townsend, J., Frost, C. (1995) UKCCCR multicentre randomised control trial of one and two view mammography in breast cancer screening. *British Medical Journal*, *311*, 1189-1193.
- Werdman, C. B. J., Threlfall, A. G., Boggis, C. R. M., Prior, P. (1995) Is the three year breast screening interval too long? Occurrence of interval cancers in NHS breast screening programmes North Western Region. *British Medical Journal*, *310*, 224-226.
- Wilson, A. R. M., Asbury, D., Cooke, J., et al (eds) (2001) *Clinical Guidelines for Breast Cancer Screening Assessment*. NHS cancer screening programmes, NHS BSP publication No 49, Sheffield.
- Young, K. C., Wallis, M. G., Ramsdale, M. L. (1994) Mammographic film density and detection of small breast cancers. *Clinical Radiology*, *49*, 461-465.

نشر الکترونیکی
موسسه انتشاراتی
نور دانش

47

THE PHARYNX AND LARYNX: THE NECK

Peter D. Phelps

with contributions from Philip J. A. Robinson, Richard W. Whitehouse and Andrew R. Wright, and Julie F. C. Olliff.

Radiological investigation of the upper air and food passages has a relatively minor role and is subsidiary to clinical investigations. Inspection may be direct or by use of a mirror and may be performed under a general anaesthetic, when suspicious areas can be biopsied. Imaging techniques are required to show foreign bodies, the lower limit of a tumour when this cannot be assessed endoscopically, and sometimes for dynamic studies of deglutition and soft-palate function.

Traditionally the radiographic techniques used have been:

- Plain films to show the air/soft-tissue interface and surrounding bony structures
- Intraluminal contrast examinations.

High-kV techniques are used to give a better demonstration of the outlines of these air-filled cavities by partially eliminating the overlying bony structures from the image.

Computed tomography (CT) has greatly improved and extended the imaging capabilities in this region. Not only is the clearest demonstration of the air/soft-tissue interface given in axial sections but the surrounding fascial planes, muscles and vessels in the parapharyngeal region can be shown. The ability of CT with contrast enhancement to show neoplastic involvement of lymph nodes is increasing its use in staging neoplasms of the head and neck.

Magnetic resonance imaging (MRI), with its superior soft-tissue discrimination and facility of three-plane imaging, is now the investigation of choice for neck masses. MRI is also useful for neoplasia of the tongue and for showing the pre-epiglottic space and floor of the mouth.

Barium swallow remains the most important radiological examination of the oro- and hypopharynx, especially when combined with cineradiography and video fluoroscopy.

Radiography technique

Plain film

The best plain film view is given by the lateral projection with the pharynx and larynx clear of the cervical spine (Fig. 47.1). The film is placed against the shoulder and the incident beam is centred on the angle of the jaw if the nasopharynx is the region of interest, or the thyroid cartilage if the larynx is being examined.

Barium swallow

This is a simple and easy means of examination, although obviously of more value for lesions below the cricopharyngeus which cannot be assessed with a laryngeal mirror. Tumours of the pharynx will be well outlined by a coating of barium, and masses demonstrated in the piriform fossae, which are sometimes difficult to see with a mirror. The normal larynx will appear as a 'filling defect' in the frontal projection with contrast in the piriform fossa on either side. This is well shown on the oblique projection, obtained with the patient swallowing while the head is turned to one side. When the larynx fails in its primary function as a protective sphincter for the lungs, 'spill-over' will occur to give a 'barium laryngogram'. This problem is seen more and more in an ageing population where dysphagia is often the result of a mild stroke.

Cineradiography

At four frames per second, cineradiography gives a good demonstration of deglutition. Passage of the bolus across the back of the tongue with elevation of the larynx and tilting of the epiglottis down over the closed larynx is shown (Fig. 47.2). Contrast then passes through the open cricopharyngeus into the oesophagus. Minor functional disorders of swallowing can only be shown by this technique (Fig. 47.3). *Videofluoroscopy* is an alternative means of assessing swallowing function and a technique for assessment of oral or pharyngeal dysphagia is described in detail in Chapter 18.

Computed tomography

CT is now the optimum method of imaging the outlines of the nasopharynx but also shows the soft-tissue structures of the infratemporal fossa and parapharyngeal space, which lie alongside the naso- and oropharynx. Formerly this region could be studied radiologically only in an indirect way by examination of surrounding bony structures or by invasive contrast examinations such as sialography and angiography. The infratemporal fossa is situated below the skull base and is bounded by the pharyngeal musculature medially and the mandible laterally. The most prominent and easily recognised structures within the infratemporal fossa are the pterygoid muscles. The anatomy of this region is depicted in Fig. 47.4.

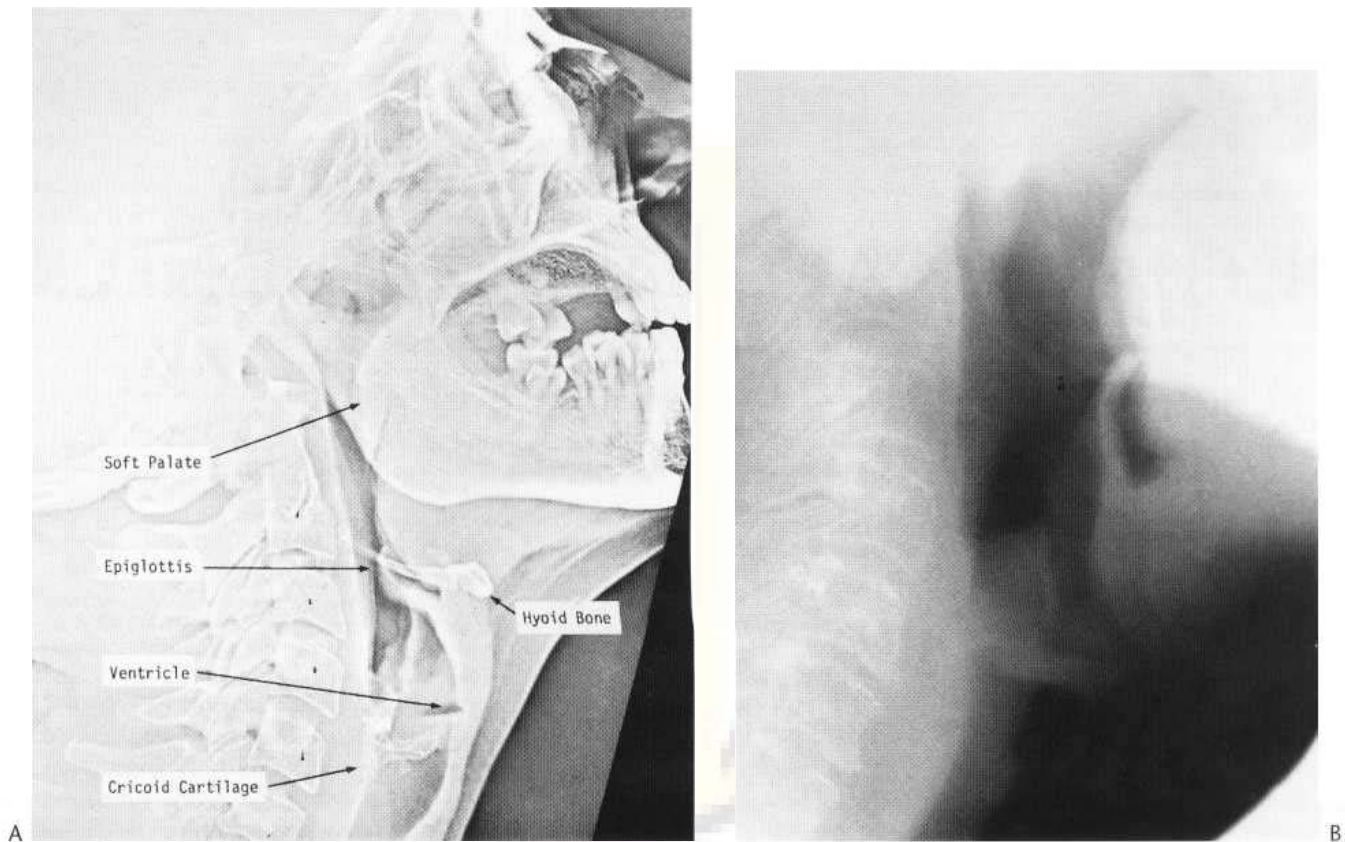


Fig. 47.1 (A) Some of the structures demonstrated on a plain lateral view of the neck. Xerography, although giving an excellent demonstration of the air-soft-tissue interface, is no longer available because of the high radiation dose used. (B) High-kV lateral neck gives an adequate demonstration of the soft tissue anatomy.

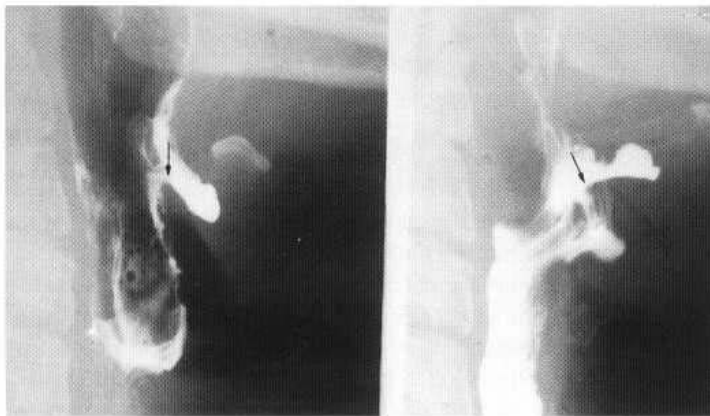


Fig. 47.2 Lateral views of a normal barium swallow. The epiglottis (arrow) folds down over the larynx as barium passes down into the oesophagus.

Below, the infratemporal fossa is continuous with the parapharyngeal space.

The role of CT for lesions in this region may be defined as:

- To complement direct examination of lesions in the postnasal space.
- To assess the size and situation and relations of a well-defined mass for prospective surgical removal, or the extent of local deep infiltration for radiotherapy planning.
- To assess the relation of the mass to the great vessels and the parotid gland: by combining CT with contrast enhancement

more accurate differentiation becomes possible. Contrast enhancement should be assessed in the vascular phase by intravenous infusion or bolus injection. Further sections in the coronal plane may give more information. Respiratory movement is less of a problem with the new fast scanners.

Scanning is begun at the level of the thyroid bone and sequential scans of 5 min slices are made in a caudal direction. The shape of the airway alters as sequential scans are viewed. Above the rounded hypopharynx it is bisected by the crescentic epiglottis. Further down, the median and lateral glossoepiglottic folds delineate the valleculae. Below this the airway assumes a triangular shape and the pyriform sinuses are seen as two lateral appendages separated by the aryepiglottic folds. At the level of the cords the shape changes to the characteristic glottic chink or boat shape with the sharp anterior commissure extending right up to the thyroid cartilage in the midline (Fig. 47.5). In the subglottic area there is an even, symmetric oval shape which gives way at the level of the first tracheal ring to an oval flattened posteriorly, which may be likened to the shape of a horseshoe.

CT provides a non-invasive, quick and effective radiological investigation of the larynx, and is not uncomfortable for the patient. It can be done without risk in the face of respiratory obstruction, or after suspected laryngeal injury. It gives an accurate assessment of laryngeal anatomy and involvement by tumour, particularly at the glottic level. The value of such an assessment is greatly increased if partial laryngectomy is contemplated, but this is an unusual operation in the UK where carcinoma of the larynx is treated by radiotherapy and/or total laryngectomy.

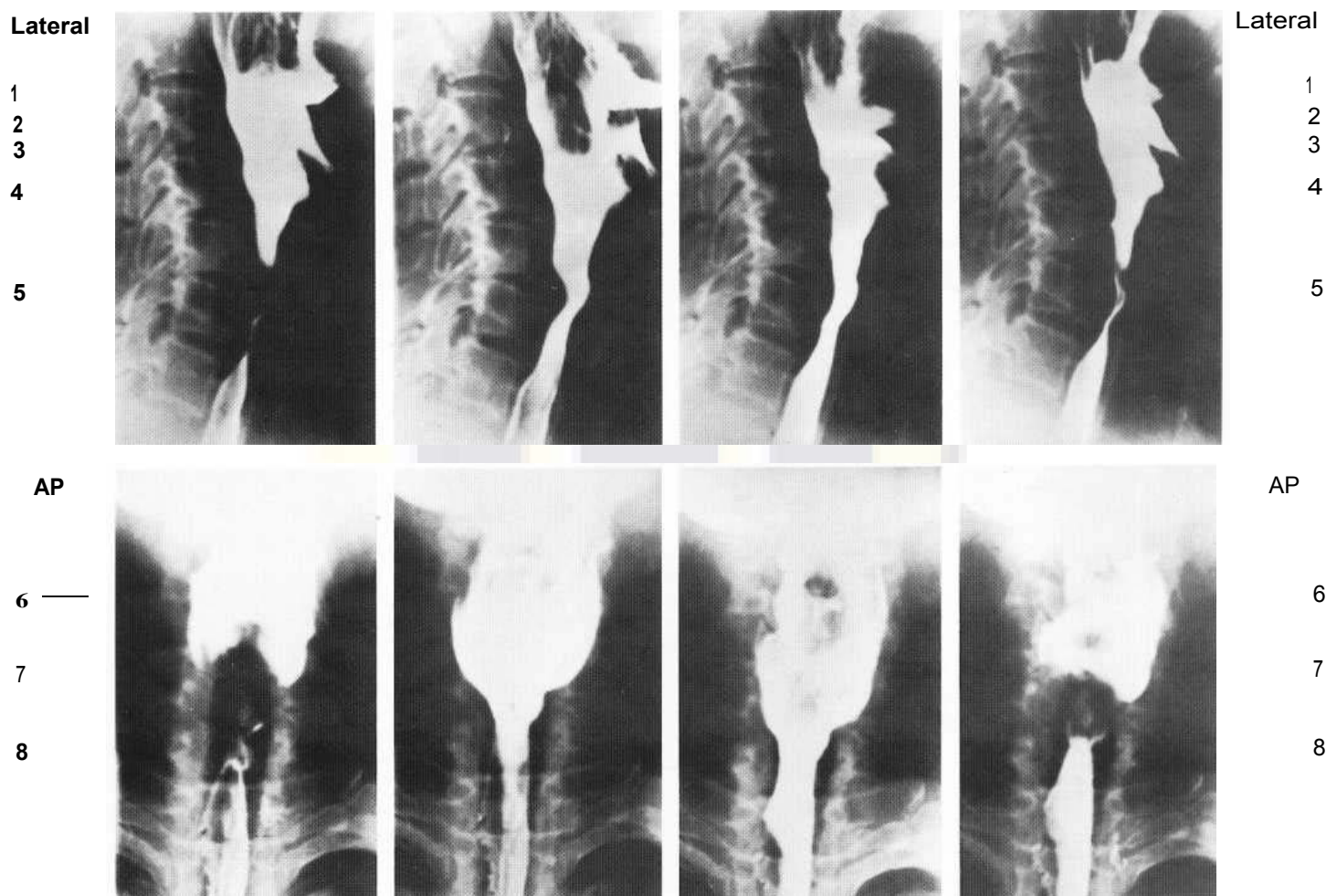


Fig. 47.3 Cine barium swallow. Four frames in 1 s, frontal and lateral views. The patient had mild dysphagia due to unilateral vagal paralysis. Various normal and abnormal features are demonstrated. **Lateral view.** 1. The vallecula fills with barium and is then partially effaced by the normal backward compression of the tongue. 2. The epiglottis is partially immobile and only tilts down to the transverse position, not fully covering the laryngeal inlet. 3. Barium enters the vestibule of the larynx. This may occasionally be observed in asymptomatic subjects but is usually an indication of failure of the laryngeal sphincters ('spill-over'). 4. At the same time the relation of the postpharyngeal wall to the cervical spine does not change, indicating paralysis of the middle pharyngeal constrictor. 5. Cricopharyngeus contracts and relaxes normally. **AP view.** 6. The epiglottis shows little movement. 7. The right side of the pharynx contracts normally but the left remains flaccid and filled with barium. 8. Cricopharyngeus contracts and releases normally.

Magnetic resonance imaging

MRI has acknowledged advantages over CT for neck masses and is now the imaging investigation of choice, but careful clinical assessment and use of needle biopsy should avoid the need for MRI for inflammatory or superficial masses in the parotid. MRI shows clearly the major vessels of the neck without added contrast. T₁-weighted sequences have the best spatial resolution and give a strong signal from fat in the tissue planes (Fig. 47.6). However T₂-weighted protocols are most useful for showing muscle invasion by carcinoma, especially in the tongue base. A standard headcoil is satisfactory for the nasopharynx but the changing contours of the neck make development of suitable coils difficult. Image degradation by movement and failure to depict calcification or fine bone detail are disadvantages of MRI. Evaluation of cervical lymphadenopathy for the staging of lymph node metastatic disease is probably best done by contrast-enhanced CT at the present time. Ring enhancement, capsular penetration and extranodal spread into fat are well shown by CT but MRI appears more promising for distinguishing end-stage fibrosis from recurrent tumour. Neither technique can differentiate with certainty nodal neoplasia from

inflammatory hyperplasia, but recently metabolic imaging, such as FDG-PET or SPECT, has been shown to be of value in differentiating continent or recurrent neoplasia from radiation damage.

Below the skull base the presence of fat with its characteristically high signal on T₁ images provides inherent contrast outlining soft-tissue structures; however, this fat may obscure lesions, especially when contrast enhancement has been used. Fat suppression techniques can therefore be very useful in detecting and defining the extent of abnormalities. The STIR protocol, the first and most reliable means of fat suppression, shows increased signal intensity from most tumours, especially in the parotid gland, but cannot be used with gadolinium enhancement. Chemical shift fat suppression can show recurrent tumour after gadolinium enhancement, especially perineural spread, but one must beware of artefacts.

Recently fat suppression techniques that may be used either with the T₁-weighted fast spin-echo sequence or with a postgadolinium T₂ protocol have proved useful for defining lesions in the neck, although artefacts such as bulk and magnetic susceptibility effects can be a problem (Barakos 1994).

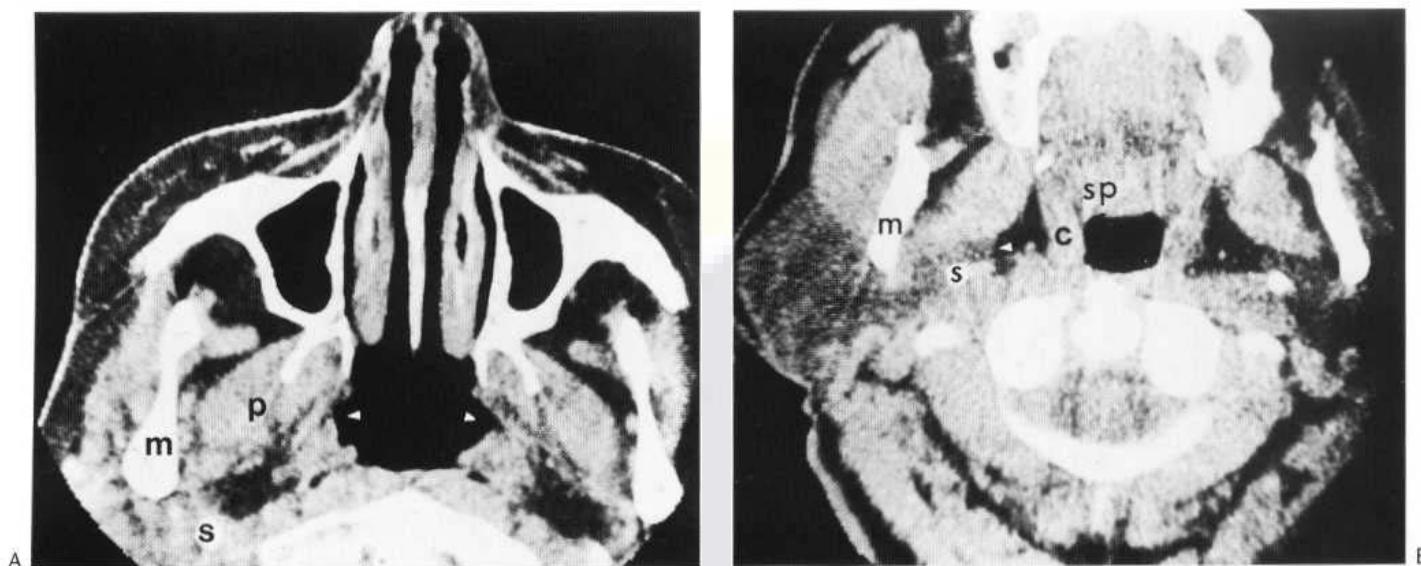


Fig. 47.4 Axial CT of soft tissues below the skull base. (A) Normal section through antra and postnasal space. The arrowheads indicate the openings of the eustachian tubes. m = ramus of mandible; s = styloid process; p = pterygoid muscles. (B) Section at a slightly lower level passes through the soft palate (sp). Tensor and levator palatini blend with the pharyngeal constrictors (c) to give a dense muscle mass. The enlarged but otherwise normal parotid gland has a lower attenuation, i.e. appears darker, than the masseter muscle in front of it but not as dark as the fatty tissue in the parapharyngeal space. Thus the medial limit of the deep parotid lobe can be defined (arrowhead). These features are best shown by MRI.

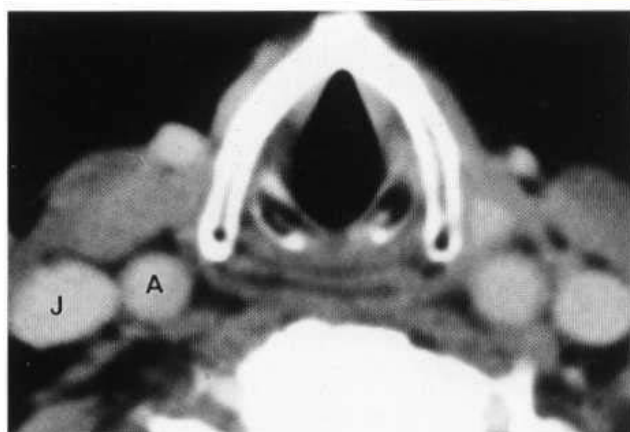


Fig. 47.5 Axial CT of the normal larynx at the level of the true vocal cords. Note the diamond shape of the airway with the cords in abduction. Intravenous contrast has been given and so the common carotid artery (A) and internal jugular vein (J) are well shown.

LESIONS OF THE NASOPHARYNX

Developmental and other lesions

Meningoceles

These are rare manifestations in the postnasal space. They are usually associated with a defect in the skull base and are best shown by coronal section CT or MRI, which will differentiate a meningocele from an encephalocele.

Adenoid hyperplasia

The value of demonstrating the size of the adenoid pad by lateral plain films is controversial, and even the necessity for adenoidectomy in all but a handful of cases has now been questioned. Nevertheless a significant correlation exists between the absolute adenoid volume as found at surgery, the nasal obstruction score and

the radiological assessment of adenoid size. However, cephalometric methods, with careful measurement of radiological adenoid area and the width of the postnasal space airway, are necessary, as well as considerable observer experience.

Antrochoanal polyps

These appear as smoothly outlined pear-shaped soft-tissue masses in the postnasal space on plain lateral films. They are associated with complete or partial opacity of the antrum but not with bone erosion, which helps to distinguish them from juvenile angiofibromas. They have high homogeneous signal on T₂-weighted MRI (Fig. 47.7).

Benign tumours

Juvenile angiofibroma

This is the commonest benign tumour of the nasopharynx, occurring in pubescent males. It presents clinically with epistaxis and nasal obstruction and a dark red or ulcerated mass in the nasal cavities and postnasal space, but its situation and extent are best assessed by CT or MRI.

Studies by CT and observations at surgery confirm that the mass arises at or close to the base of the pterygoid lamina; bone erosion in this site is probably a pathognomonic feature (Fig. 47.8). As well as expanding into the nose and postnasal space, these tumours have a tendency to spread laterally through the pterygomaxillary fissure into the infratemporal fossa. This causes widening of the fissure and an important sign of the tumour, namely anterior bowing of the posterior wall of the antrum, although other slow-growing masses will produce the same effect. Involvement of the orbit with proptosis is a late feature. Extension into the sphenoid sinus or rarely into the cranial cavity is best assessed by coronal CT section. There is usually considerable contrast enhancement after bolus injection and this helps to delineate the limit of lateral extension in the infratemporal fossa (Fig. 47.9). Carotid angiography, although diagnostic.

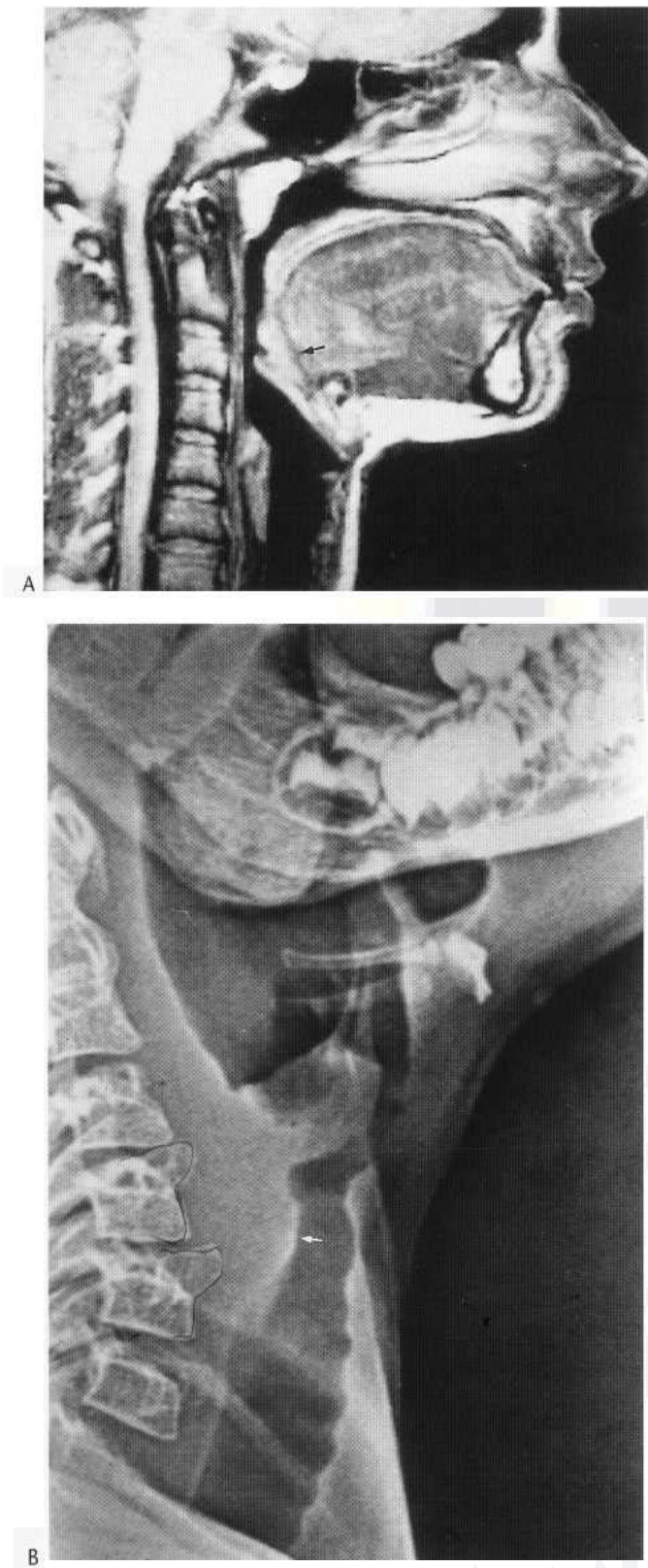


Fig. 47.6 (A) Sagittal MRI, T₁-weighted, shows good differentiation between the tongue muscles, the genioglossi in the floor of the mouth and the surrounding fat, especially in the pre-epiglottic space (arrow). (B) Sagittal film in a child revealing subglottic stenosis (arrow).

is not usually necessary. The presence of flow voids by MRI as well as marked enhancement with gadolinium is characteristic of juvenile angiofibroma and is required to show intracranial extension.

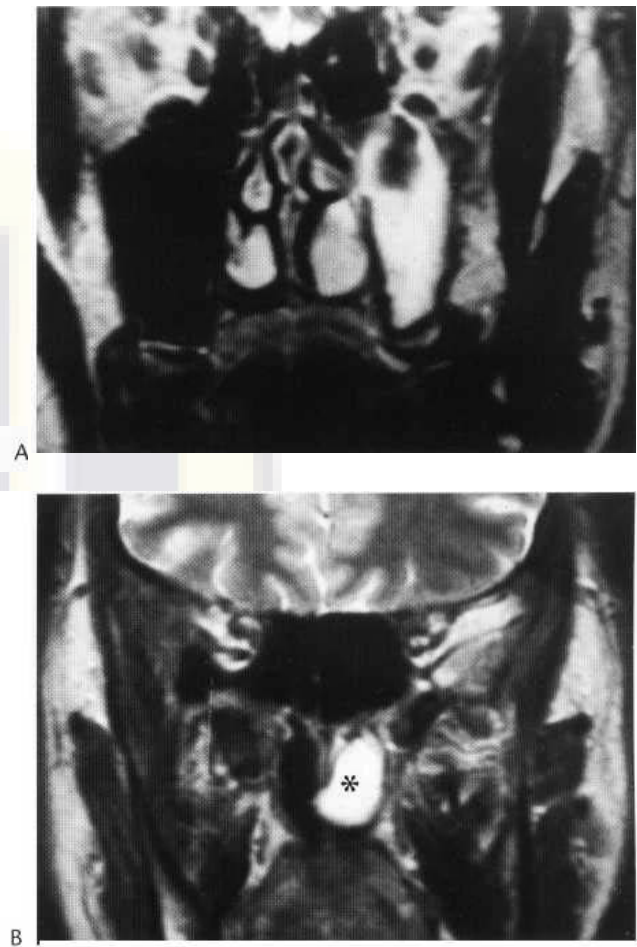


Fig. 47.7 Coronal T₂-weighted MR sections showing high signal from the mucosa over the nasal turbinates and the antrochoanal polyp (asterisk).

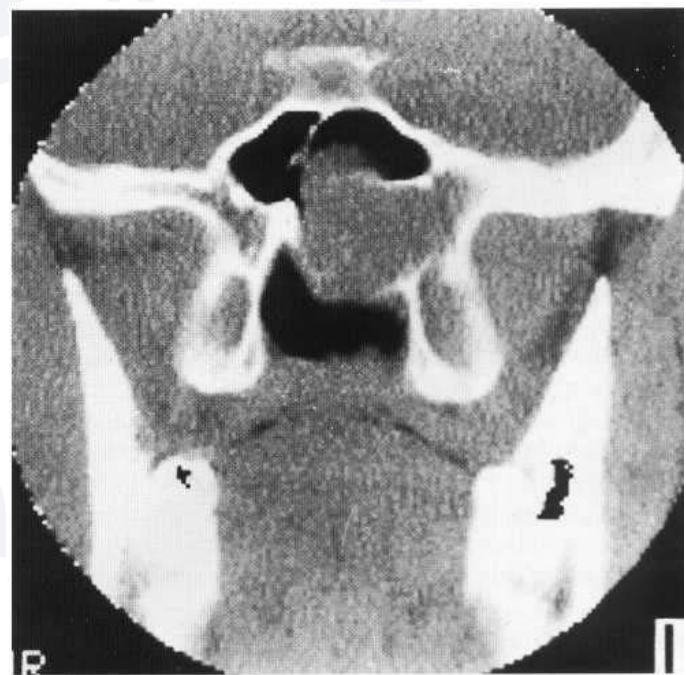


Fig. 47.8 A small juvenile angiofibroma arising from and eroding the pterygoid lamina. Coronal CT scan showing the pterygoid plates.

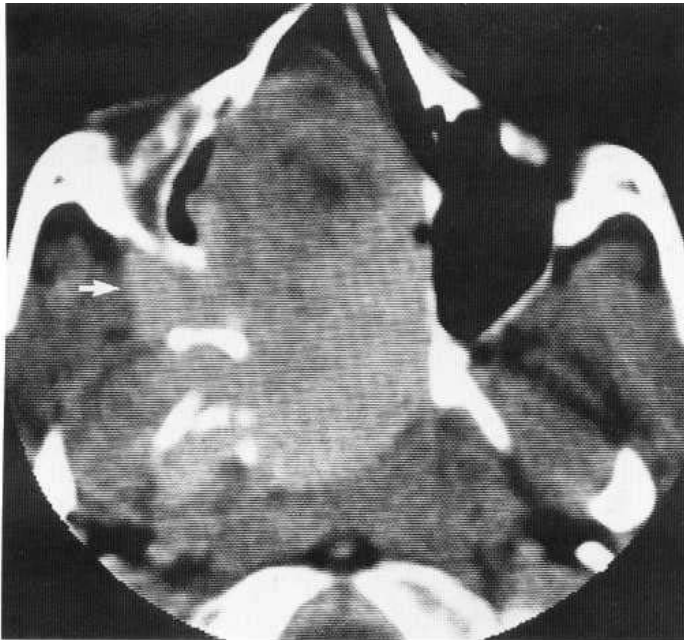


Fig. 47.9 A large juvenile angiofibroma which has displaced the back of the right antrum anteriorly. After contrast enhancement the lateral extension of the tumour into the infratemporal fossa is well shown on this axial scan (arrow).

Chordomas

These are predominantly midline tumours occurring in an older age group. A large soft-tissue mass in the postnasal space is associated with destruction of the basisphenoid and sometimes flecks of calcification, best shown by CT. There is usually an associated intracranial mass. MRI is the imaging investigation of choice (Fig. 47.10, see also Ch. 57).

Malignant tumours

Squamous-cell carcinomas

These constitute 80% of cancers of the postnasal space. Occasionally they are large and exophytic, in which case a soft-tissue mass may be seen in the postnasal space. More usually the tumour infiltrates directly through the base of the skull, so that the patient presents with cranial nerve lesions, or spreads via lymphatics, so that enlarged neck glands are the first manifestation. Serous otitis media with deafness from obstruction of the eustachian tube by the tumour is another presenting feature. Formerly, careful study of the base skull view for bone erosion of the middle cranial fossa floor (Fig. 47.11) was the only basic radiological investigation. Such erosion can be assessed by high-resolution CT, which will also show the common obliteration of the lateral pharyngeal recess (fossa of Rosenmiiller) by tumours arising in this area. Obliteration of the soft-tissue planes as shown by CT is another indication of spread of a postnasal space carcinoma (Fig. 47.12), especially in that small but well-recognised group where the tumour grows submucosally and is not evident on examination or even initial biopsy.

Lymphoid tumours

In the postnasal space these tumours tend to grow in a bulky circumferential pattern without early invasion of the parapharyngeal spaces. Magnetic resonance with three-plane imaging is now

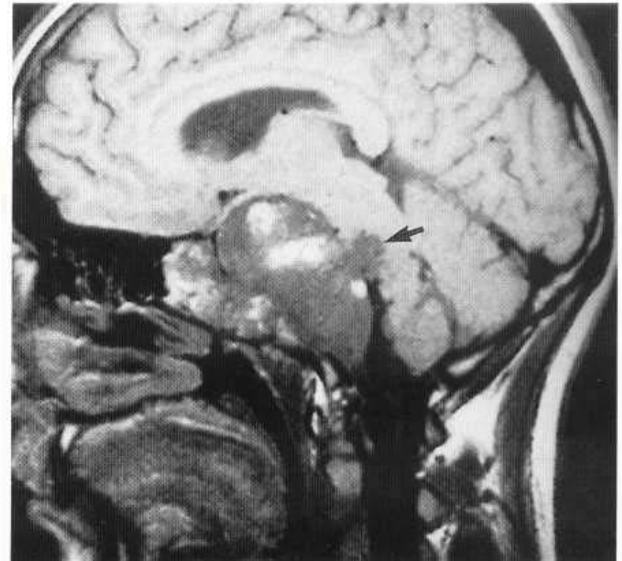


Fig. 47.10 Chordoma. Sagittal MR section, T₁-weighted, shows a non-homogeneous mass in the nasopharynx and replacing the basisphenoid. The tumour has burst out of its capsule and is displacing the brainstem posteriorly.

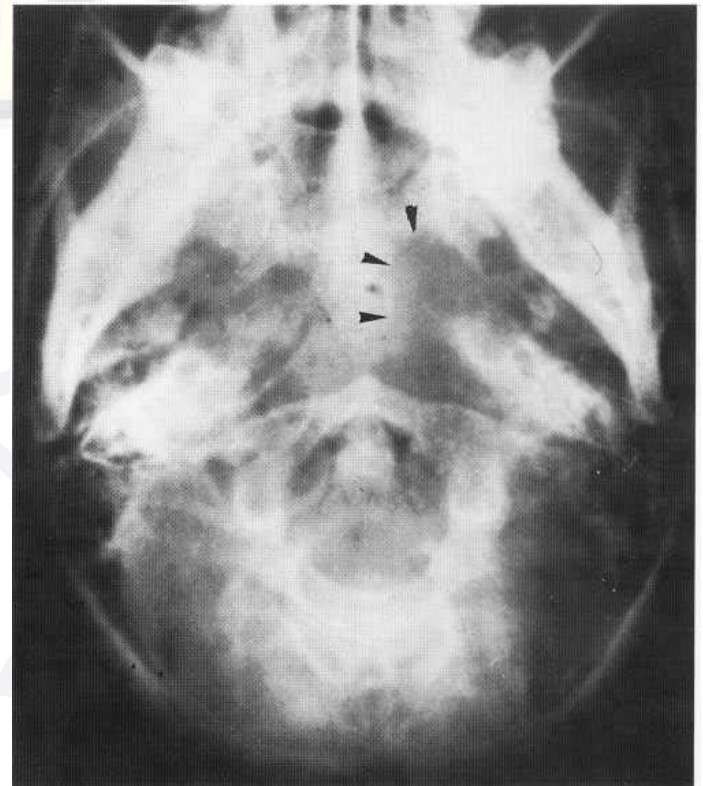


Fig. 47.11 Plain base view of the skull, showing erosion of the skull base in the region of the basisphenoid and foramen lacerum (arrows) by a postnasal space carcinoma.

becoming the investigation of choice for nasopharyngeal neoplasia, especially for *adenoid cystic carcinomas* where sometimes the characteristic perineural infiltration can be shown (Hamlin & Hasso 1994), as well as any intracranial extension (Fig. 47.13). Enhanced MRI in the coronal plane is necessary to define these T₄ lesions but fat suppression techniques best show extension laterally into the soft-tissue planes of the nasopharyngeal region (Fig. 47.14).

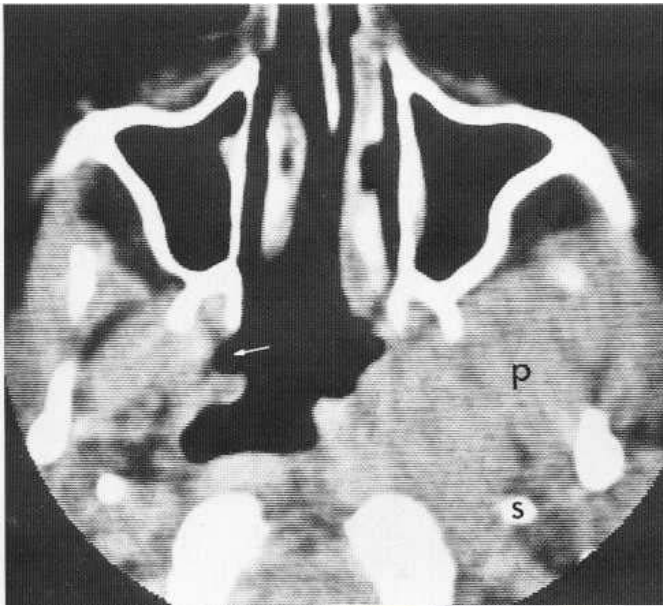


Fig. 47.12 A mucoepidermoid carcinoma obliterates the soft-tissue planes medial to the styloid process (s) on the left side. Although the mass bulges into the postnasal space, the mucosa appeared normal on examination and a positive biopsy was only obtained through the base of the antrum. Note the obliteration of tissue planes and eustachian orifice by this poorly delineated mass. p = pterygoid muscles. The arrow points to the eustachian orifice on the opposite side.

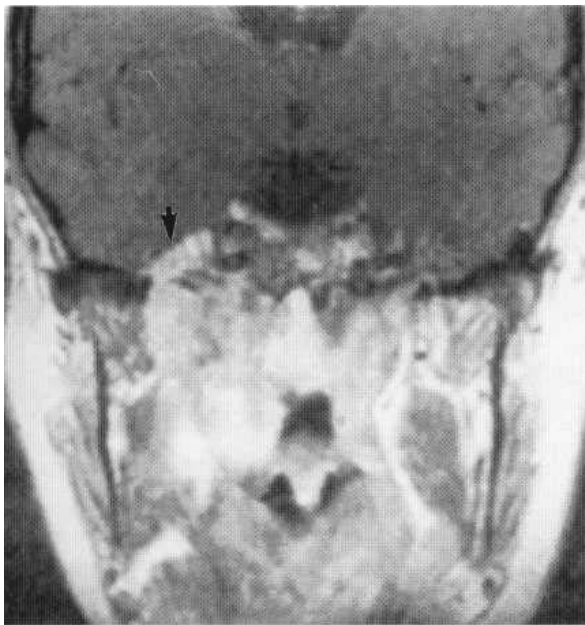


Fig. 47.13 Coronal Gd-MRI section showing an adenoid cystic carcinoma of the nasopharynx which has eroded the skull base in the region of the foramen lacerum and extended up into the parasellar area (arrow). This intracranial extension could only be fully appreciated on the enhanced scan but discrimination of the lower part of the tumour from fat and enhanced mucosa is less certain.

LESIONS OF THE PHARYNX AND LARYNX

Functional disorders

Velopharyngeal dysfunction, the inability of the soft palate to close off the nasopharynx by apposition to the posterior pharyngeal wall,

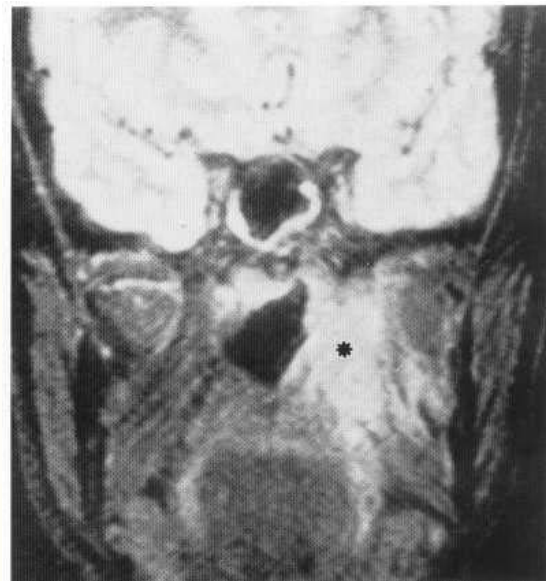


Fig. 47.14 Coronal fat-suppressed (STIR) section showing infiltration of the pterygoid muscles by a carcinoma of the nasopharynx (asterisk). The patient had severe tinnitus.

can be shown by videofluoroscopy or by high-kV lateral radiographs with the patient articulating 'K' (Fig. 47.15). A good account of pharyngeal deglutition in patients with functional disorders of the act of swallowing, compared with a group of volunteers with no complaint of dysphagia, is contained in two papers from Malmo (Ekberg & Nylander 1982a,b). These authors, using cineradiography at 50-100 frames per second, found a high incidence of epiglottic dysmotility and cricopharyngeal incoordination in the patient with dysphagia. Although only a small percentage had severe disturbance, such as complete paralysis of the pharyngeal constrictors or aspiration into the trachea, nevertheless contrast was frequently seen to enter the vestibule of the larynx (Fig. 47.3). Incoordination of contraction in the inferior constrictor of the pharynx is thought to be responsible for the common pharyngeal pouch, which consists of a protrusion of mucosa through a weak area above cricopharyngeus; so the pouch becomes more and more a direct continuation of the pharynx (Fig. 47.16). It should not be forgotten that carcinoma may develop in a pharyngeal pouch.

Traumatic lesions

Foreign bodies in the upper aerodigestive tract are usually fish or meat bones lodged in the upper oesophagus (Fig. 47.17). It may be difficult to differentiate the foreign body from ossification in the laryngeal cartilages. The presence of air in the soft tissues or in the oesophagus held open by a non-opaque foreign body is an important sign. Further investigation by barium studies is not often required, but pledgets of cotton wool soaked in barium may become caught on the foreign body and indicate the site if this is not revealed by a conventional barium swallow. Less often, objects such as pins, coins, dentures, buttons, etc. may lodge in the piriform fossa, the nasopharynx or between the cords. Stridor is the presenting feature in such cases. Perforation, either by the foreign body or by instrumentation, can lead to inflammatory changes in the para- and retropharyngeal tissue planes. Widening of the retropharyngeal soft-tissue space is seen in such cases, sometimes with surgical emphysema or an abscess cavity. Fractures of the larynx, as from direct contact with the steering wheel of a motor

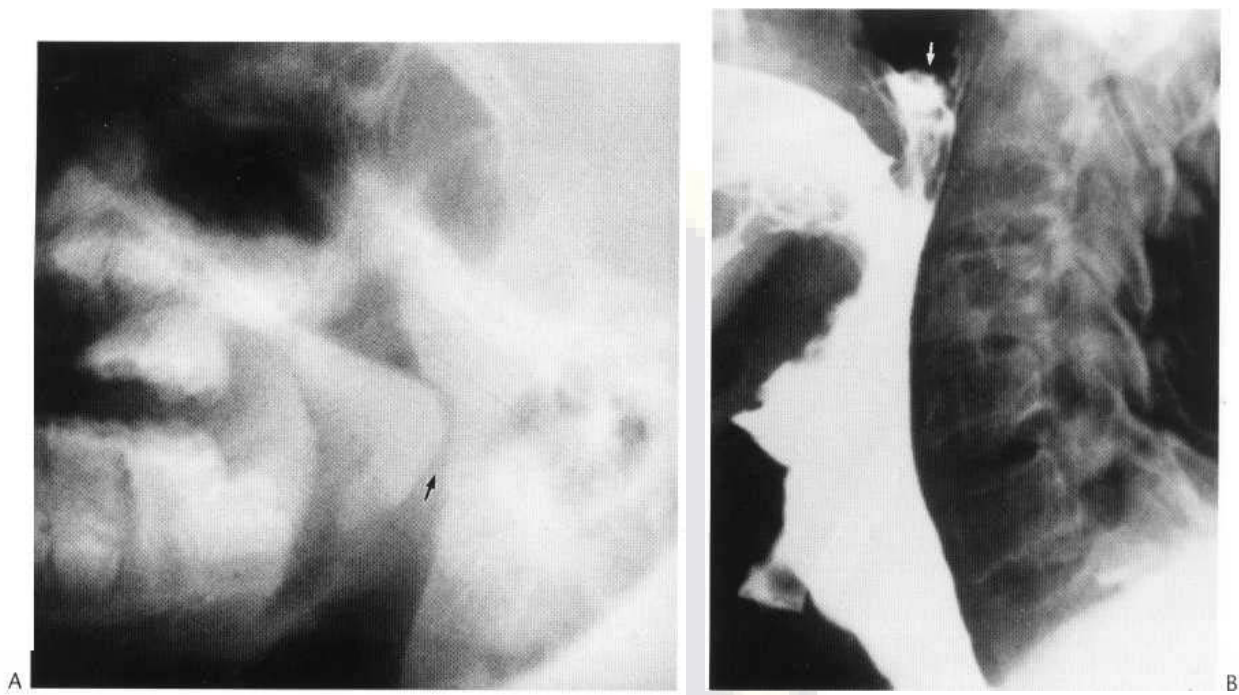


Fig. 47.15 (A) High-kV view lateral neck with the patient articulating 'K'. There is a small gap between the soft palate and the posterior pharyngeal wall (arrow). (B) A barium swallow showing velopharyngeal dysfunction.

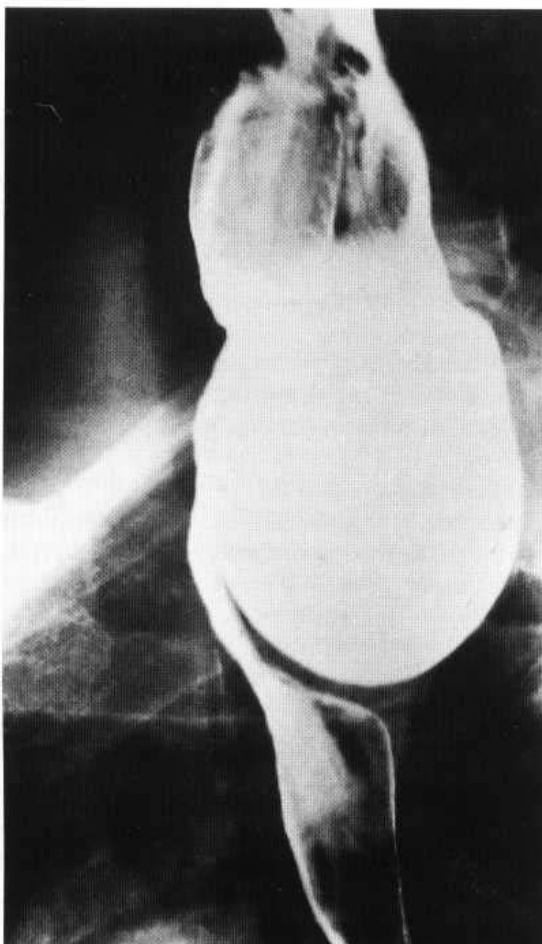


Fig. 47.16 A large pharyngeal pouch with the oesophagus displaced anteriorly and to one side.

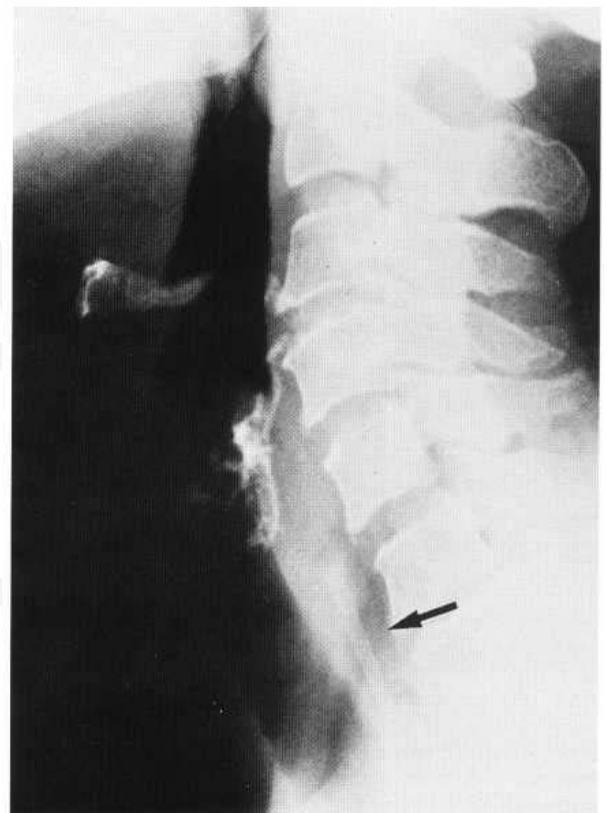


Fig. 47.17 A fish bone impacted in the upper oesophagus (arrow).

vehicle, are difficult to demonstrate radiologically and even harder to assess clinically. CT is now the optimum method for showing fractures of the thyroid cartilage, displacement of the arytenoids, and the size and state of the airway.

Infections

Radiological examination is seldom necessary to demonstrate inflammatory disease of pharynx, larynx and epiglottis, but may be required to exclude pulmonary disease. In a child, narrowing of the trachea may point to the presence of a laryngotrachobronchitis, or forward displacement of the trachea to a retropharyngeal abscess. Following surgical incision or spontaneous rupture, small pockets of air with air-fluid levels may be visible in the abscess.

Laryngoceles

An air-filled sac arising from the laryngeal ventricle and sacculae constitutes a laryngocele. It is sometimes bilateral and may be congenital in origin, but expiration against resistance, as in glass blowers and trumpeters, probably encourages its formation. It gives a characteristic radiological appearance, especially with forced expiration. Laryngoceles may be internal or external, depending on whether they lie inside or outside the thyroid lamina. Internal laryngoceles may cause obstructive respiratory symptoms, whereas external laryngoceles produce soft-tissue swellings of the neck. Films taken in the anteroposterior position are more useful than lateral films in outlining the laryngocele. In the lateral position a small laryngocele may be superimposed on the normal laryngeal air shadow and may be overlooked. High-kV studies in the anteroposterior plane are essential for the clear demonstration of small internal laryngoceles that have not extended outside the thyroid cartilage. Alternatively a good demonstration in cross-section is given by axial CT.

Cysts

Cysts of the pharynx and larynx are either congenital or retention in origin. They can be recognised on plain lateral films of the neck.

TUMOURS OF THE PHARYNX AND LARYNX

Malignant tumours of the oro- and hypopharynx

Such tumours are almost invariably *carcinomas*. They present as either ulcerative or proliferative lesions and are usually diagnosed clinically. Radiologically tumours of the oro- and hypopharynx present as:

- Soft-tissue tumours encroaching on normal air-filled spaces, e.g. vallecula or piriform fossa
- Filling defects in a barium swallow when the lesion is advanced
- Changes in the mucosal relief pattern.

Although CT or an orthopantomogram (OPG) will best show minor erosion of cortical bone of the mandible, carcinomas of the tongue and floor of the mouth can only be assessed adequately from an imaging point of view by MRI. The basic MR examination is axial T₁-weighted sections to show loss of fat signal from the lesion. Fat is present in the normal floor of the mouth and the tongue, as well as in yellow bone marrow in the mandible. Further views using a gradient-echo sequence after gadolinium enhancement will define better the extent of the lesion (Fig. 47.18). The STIR fat suppression sequence is particularly good for demonstrating cancers of the hypopharynx (Fig. 47.19).

Growths in the hypopharynx usually occur in the retrocricoid region. The *Paterson-Brown Kelly syndrome* and *oesophageal Weh*

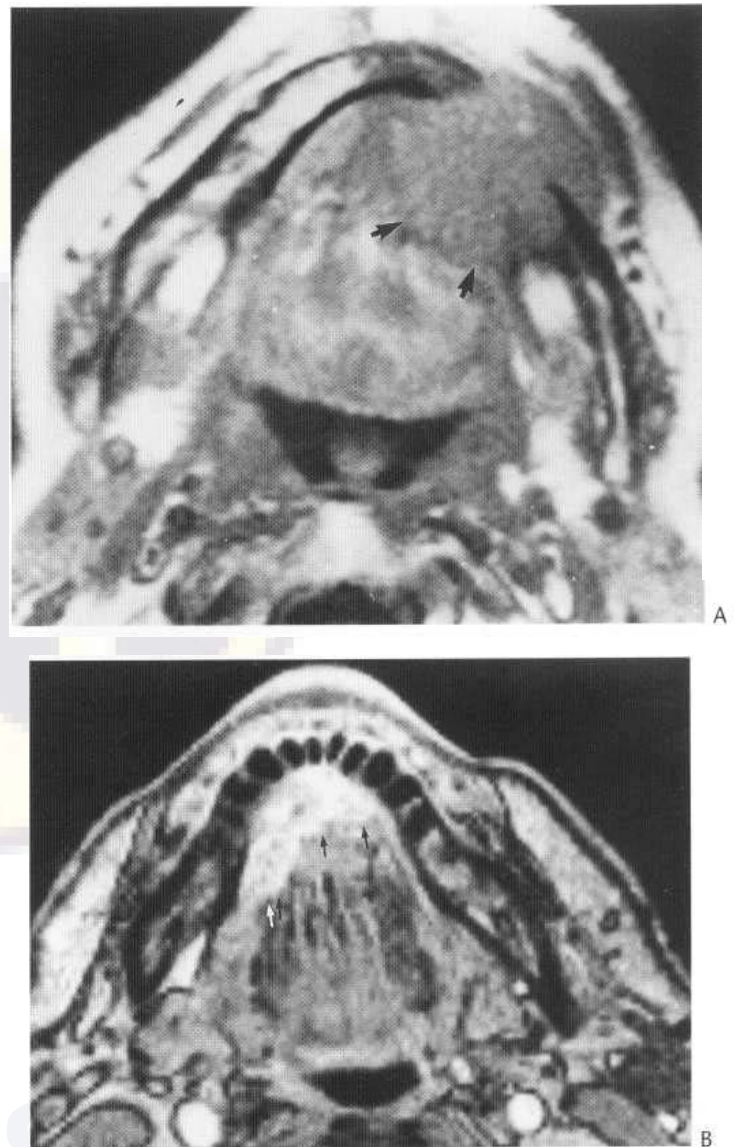


Fig. 47.18 Carcinoma of the floor of the mouth. (A) Axial T₁-weighted MRI showing the lesion as an area of low signal (arrows) extending through the mandible into the buccal sulcus. (B) Gradient-echo FLASH sequence of another case after gadolinium enhancement showing high signal from the tumour (arrows).

(Fig. 47.20) predispose to this type of carcinoma, which is common in women than in men. The radiological features are:

- Widening of the postcricoid space. Determination of what can be accepted as normal is the greatest problem in diagnosis, but an increase of the postcricoid space to over 1 cm must be regarded with suspicion.
- Irregularity and hold-up in the barium swallow. The Outline of the pharynx is irregular and the mucosal folds are destroyed (Fig. 47.21).

Benign tumours of the larynx

Papillomas These are common in adults and are premalignant. They are usually single and may be sessile or polypoid. A pedunculated papilloma may be blown up and down through the vocal cords. Juvenile papillomas are not premalignant but are usually multiple.



Fig. 47.19 The STIR sequence in the sagittal plane showing a hypopharyngeal carcinoma extending into the base of the tongue (arrows).



Fig. 47.21 Retrocricoid carcinoma affecting the upper 4 cm of the oesophagus as well as the hypopharynx (arrows). Note the spill-over of barium into the larynx and trachea.

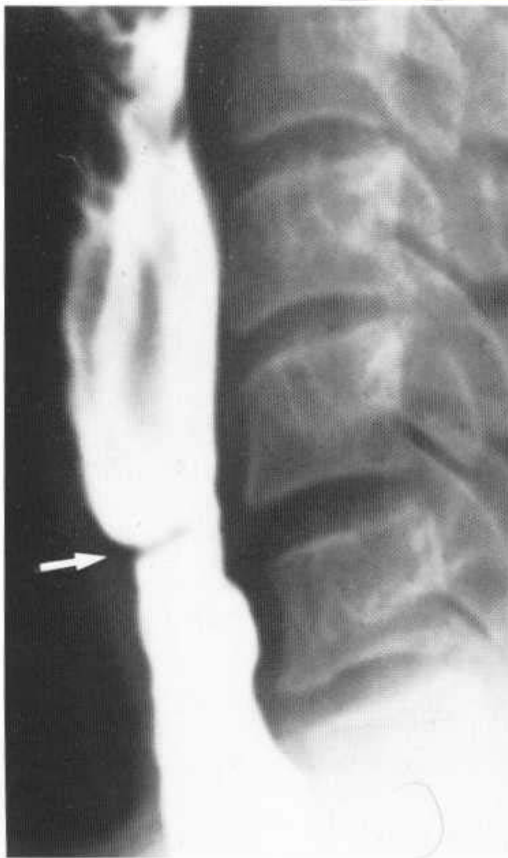


Fig. 47.20 An anterior web in the upper oesophagus in a patient with the Paterson-Brown Kelly syndrome.

Chondromas These arise from one of the laryngeal or tracheal cartilages and show a typical appearance on CT with speckled calcification (Fig. 47.22).

Plasmacytoma This appears radiologically as a smooth, rounded tumour, homogeneous in consistency and often indistinguishable from carcinoma of the larynx. The larynx and upper air passages are the commonest site for extramedullary plasmacytoma to develop.

Malignant tumours of the larynx

Carcinomas are customarily classified into supraglottic, glottic and subglottic, depending on the site of origin of the tumour.

Glottic tumours

Carcinoma of the true cord is the commonest form of intralaryngeal growth. It presents early with hoarseness, is easily assessed by direct examination, and has the best prognosis. However, involvement of the anterior commissure with spread to the other side worsens the prognosis. More extensive involvement of the thyroid or arytenoid cartilages or subglottic spread are even worse prognostic features and may require total laryngectomy at an early stage.

Supraglottic tumours

These are best assessed endoscopically, but may be shown by their ragged appearance on a plain lateral neck view. Growths arising in the vallecula or in the ventricle of the larynx may be apparent on endoscopy or confirmed by biopsy. CT or MRI may

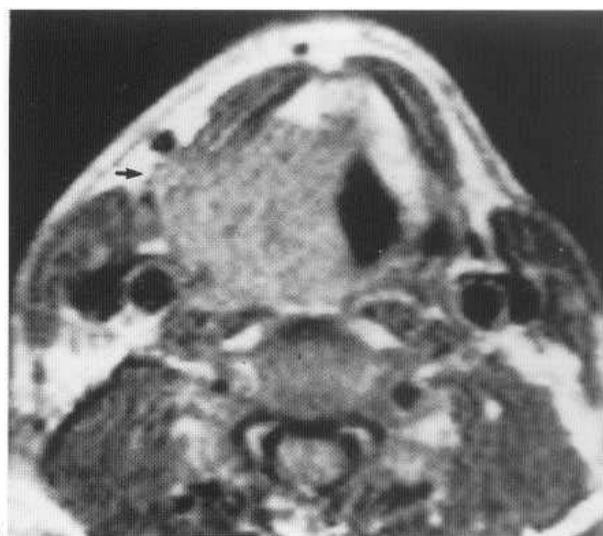


Fig. 47.22 A chondroma arising from the tracheal cartilage and obstructing the airway, well shown on this sagittal T₁-weighted MR section.

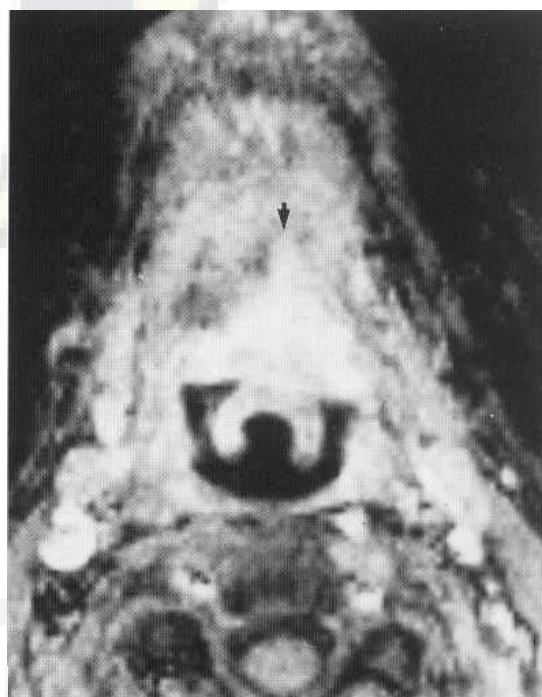
he of help by demonstrating invasion of the base of the tongue, obliteration of the ventricle, and erosion through the thyroid cartilages into the thyroid gland (Fig. 47.23). Supraglottic cancers tend to spread directly to the upper deep cervical lymph nodes (Fig. 47.24).

Subglottic tumours

These are the least common type. The undersurface of the cord is the usual site of origin and subsequent involvement of the vocal cord occurs. This region is difficult to assess endoscopically; MRI and CT may help by showing asymmetry (Fig. 47.25). Immobility of the cord results from neoplastic infiltration or from paralysis of the nearby recurrent laryngeal nerve. The most important role for CT is to show invasion of the cartilaginous skeleton of the larynx by the tumour. Such involvement is a strong indication for total laryngectomy. Gross involvement of the thyroid laminae is usually obvious on CT, but minor degrees of destruction by tumour invasion may be difficult to evaluate, as normal thyroid laminae may show considerable unevenness of density. This may give rise to both false positives and also false negatives in interpretation. Another feature, which has been associated with invasion of the cartilages confirmed after surgical excision of the larynx, has been the presence of increased density and ossification. This may involve the arytenoid, cricoid and thyroid lamina. Extension of tumour into the soft tissues, laterally to the larynx or into the base of the tongue, is shown best with MRI. As with lesions of the oropharynx, T₁ axial sections are followed by a fat suppression sequence. Lymphomas and reticulosarcomas are also best shown by fat-suppressed sequences and usually show extensive lesions (Fig. 47.26).



A



B

Fig. 47.23 (A) Carcinoma of the larynx eroding the thyroid cartilage and extending into the soft tissue of the neck shown on an axial T₁ section (arrow). (B) A gradient-echo FLASH section with gadolinium enhancement showing extension of a laryngeal carcinoma into the base of the tongue (arrow).

LESIONS OF THE INFRATEMPORAL FOSSA AND PARAPHARYNGEAL REGION

The low-density fascia] planes around the upper aerodigestive tract are readily identified by CT and provide important clues to the situation, extent and occasionally the diagnosis of benign and malignant lesions. The normal anatomy of this region is shown in Figure 47.4.

Magnetic resonance

This provides an alternative, probably better, means of imaging the soft tissues of the neck. MRI (either spin-echo or gradient-echo pulse sequences) readily demonstrates most vascular struc-

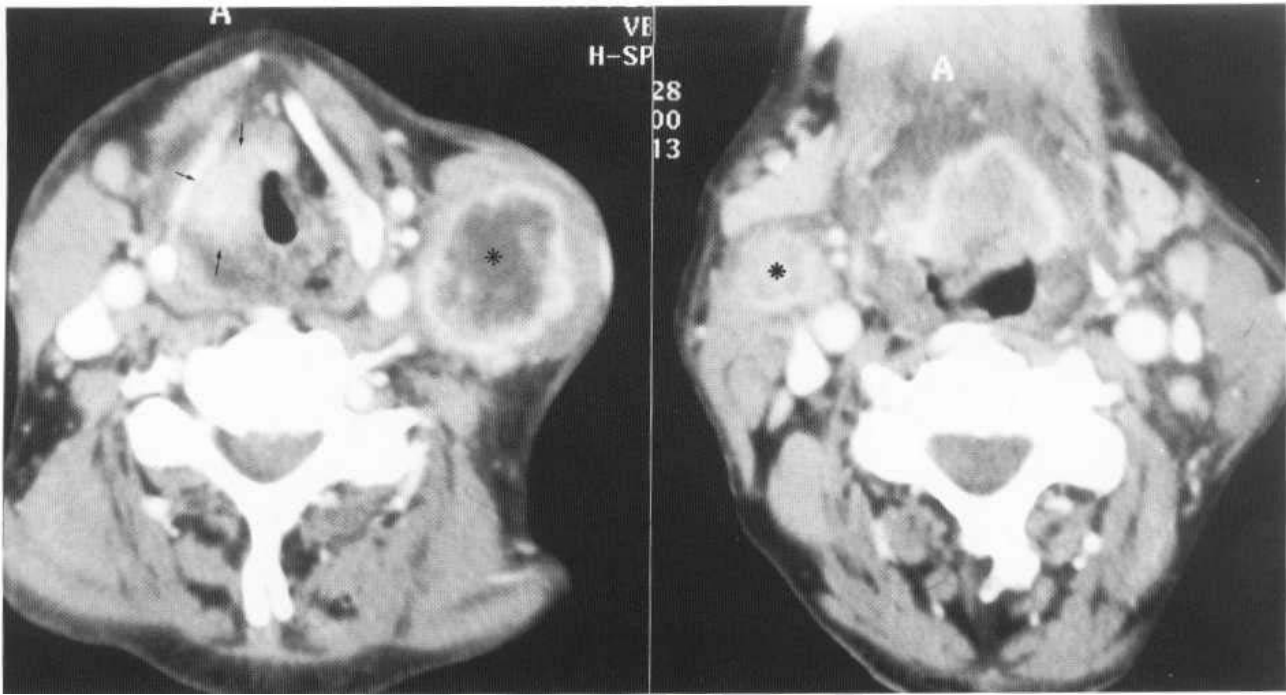


Fig. 47.24 Two axial CT sections after contrast enhancement showing a supraglottic carcinoma (arrows) with bilateral neck nodes (asterisks).



Fig. 47.25 CT section just below the true cords shows a squamous carcinoma distorting the normal oval shape of the subglottic airway and eroding the thyroid cartilage anteriorly (arrows).

tares as well as tumour vascularity. Differentiation of the parotid from extraparotid masses is also more reliable by MRI. A head-coil is usually satisfactory and T₂-weighted axial views are used in the first instance. T₂-weighted protocols usually give a stronger signal from the tumour and are better able to differentiate tumour from muscle. Coronal images are best for demonstrating any intracranial extension of tumour, especially with gadolinium (Fig. 47.12). Sagittal and coronal views are helpful in discerning the position of the mass in relation to the carotid and jugular vessels.

Congenital and developmental anomalies

1. *Bronchial cleft c.v.ct.c.*, usually of second arch origin and appearing deep to or along the anterior border of the sternomastoid muscle in young patients, characteristically can be shown by ultra-



Fig. 47.26 Axial STIR section showing a lymphoma involving both tonsils and neck nodes bilaterally.

sound or T₂-weighted MRI to contain fluid (Fig. 47.27). Sometimes, however, the branchial cyst is filled with proteinaceous material and may then be indistinguishable from neuroma on CT or MRI.

2. *Lymphangioma (cystic hygroma)*. Abnormal lymphatic channels and cysts in the neck of an infant show typical appearances of large fluid-filled spaces on CT or MRI.

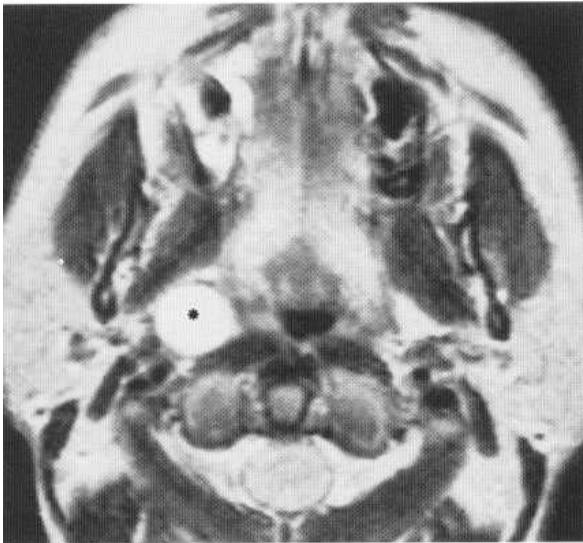


Fig. 47.27 A small fluid-filled branchial cyst (asterisk) gives high signal on a T_2 -weighted axial section of the neck.

3. *Haemangiomas*, like lymphangiomas, are usually present at birth or appear within the first few years of life. Although the presence of phleboliths in cavernous haemangiomas shows as typical round opacities on CT, nevertheless large well-defined areas of high signal on T_1 -weighted MR pictures in any area of the neck or salivary tissue are characteristic of haemangioma (Fig. 47.28).

Parapharyngeal masses

Parapharyngeal masses in the anterior compartment anterior to the styloid process and styloid muscles are usually *salivary* in origin. They arise in the deep lobe of parotid, from a minor pharyngeal salivary gland or from ectopic salivary cell rests. In such cases we have found coronal CT particularly useful for showing a cleavage plane between a deep lobe tumour and the pharyngeal musculature



Fig. 47.28 High signal on T_2 -weighted axial section of haemangioma of the infratemporal fossa with a component extending into the pharyngeal airway (arrow).

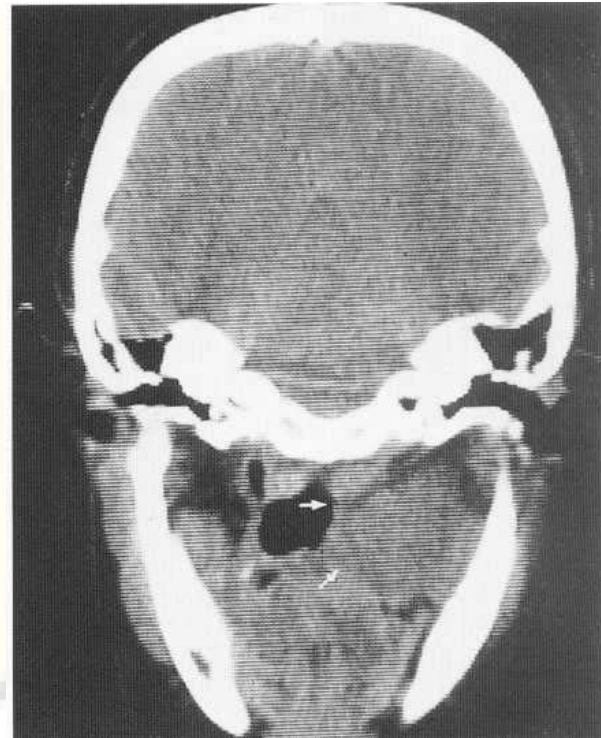


Fig. 47.29 Coronal CT section showing a pleomorphic salivary adenoma of the deep parotid lobe bulging into the nasopharynx and depressing the soft palate (arrows). Note the way the pharyngeal muscles are displaced medially by a well-defined mass, indicating that this adenoma did not arise from an accessory pharyngeal salivary gland.

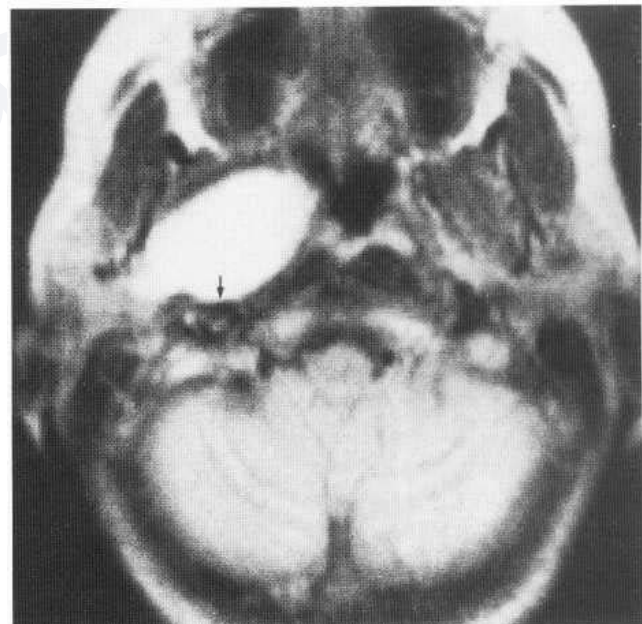


Fig. 47.30 MR axial section of the skull base shows a pleomorphic adenoma of the deep lobe of the parotid displacing the carotid artery posteriorly (arrow). Note the absence of a fat plane between the gland and the tumour. The very bright signal on this T_2 protocol gave the lesion the MR appearance of a mucocele (see Ch. 48) and was the result of mucoid degeneration in the tumour.

the parotid gland, although this sign is unreliable if the tumour is very large. All these masses in the anterior compartment tend to push the carotid artery posteriorly (Fig. 47.30).

Post-styloid/carotid lesions

Lesions of the post-styloid or carotid space typically separate carotid artery and jugular vein, with the artery pushed forward and the vein displaced backward and laterally. The rare *glomus vagale tumour* is the only tumour of the glomus and carotid body group, also called chemodectoma or paraganglioma, which arises primarily in the parapharyngeal region. A *glomus jugulare tumour* may, however, extend down from an eroded jugular fossa, or a *carotid hods' tumour* may extend up from the carotid bifurcation. (Fig. 47.31). These tumours, arising within the carotid sheath, are



Fig. 47.31 Sagittal T₁ section showing a typical carotid body tumour at the bifurcation of the internal and external carotid arteries. Note the flow voids showing that this is a very vascular tumour.

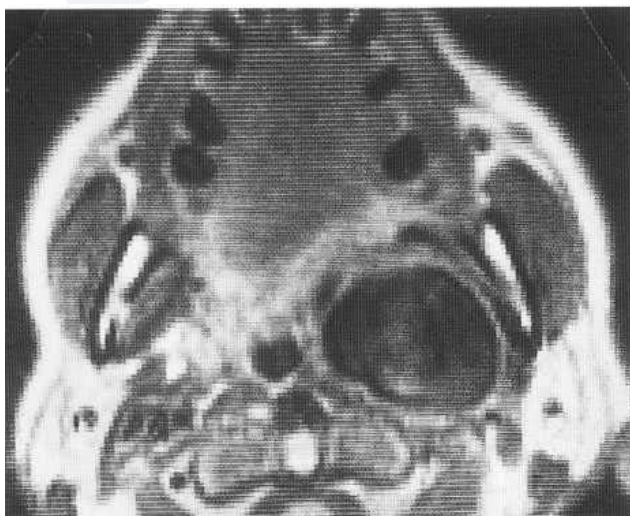


Fig. 47.32 Aneurysm within the carotid space appears as a well-circumscribed round mass, mostly black from flowing blood but with areas of high signal representing blood clot.

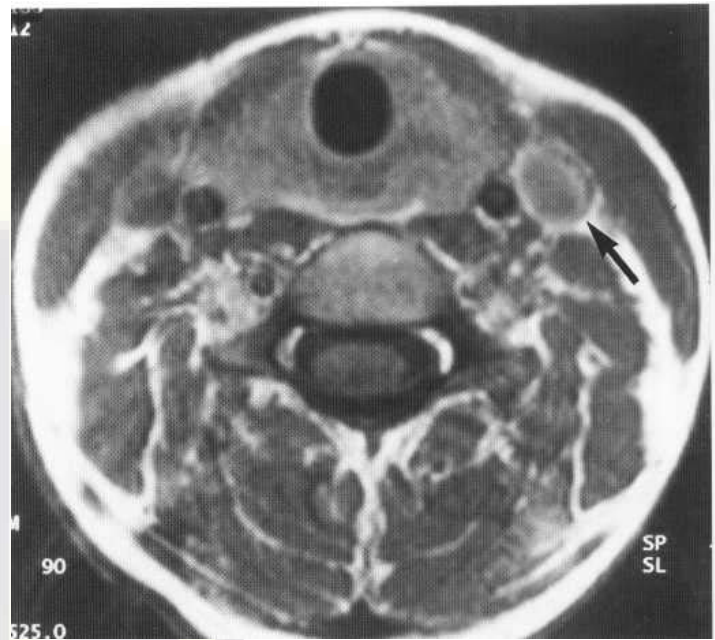


Fig. 47.33 Axial enhanced T₁ section at the level of the thyroid gland showing a peripherally enhancing typical small neuroma (arrow) lateral to the carotid artery.

usually large at the time of examination and have obliterated the surrounding fat planes on CT. MRT is diagnostic for rare aneurysms within the carotid sheath (Fig. 47.32).

Neurogenic tumours (neuromas and ganglioneuromas) are the other masses which arise within the carotid sheath. Typically they separate carotid and jugular, with the vein displaced backward and laterally. Differentiation from glomus tumours is important. Characteristically neuromas shown by CT have some degree of enhancement, often with a low-density centre (Fig. 47.33). Branchial cysts also have a typical low-density centre unless they are filled with proteinaceous material, when they can be indistin-



Fig. 47.34 Axial MR of an invasive malignant lymphoma infiltrating the parotid, back of the masseter (large arrow) as well as the muscle of the back of the neck (T₁-weighted image). Note the slight anterior displacement of the carotid artery (small arrow) and obliteration of the internal jugular vein when compared with the normal side.

guishable from neurofibromas on CT or MR. It is rarely possible to predict the type of tumour occurring in the parapharyngeal region. Sometimes very low attenuation values will suggest a lipoma or teratoma containing much fat, while calcification within the tumour indicates a probable meningioma, presumably extending from the skull base.

Obliteration of the fascial planes is established as the most important contribution of CT to the investigation of malignant tumours of this region, especially those arising in the nasopharynx and not identified by endoscopy and biopsy. Guidance for the surgeon as to the best approach for a positive biopsy is a new and important contribution CT makes to the management of these difficult cases. In one series (Mancuso & Hanafee 1983) there were 19 mucosally inapparent carcinomas of the upper aerodigestive tract out of more than 160 cases examined. The same authors found

that the parapharyngeal spaces were obliterated in over 80% of the malignant tumours. Moreover, these become visible again following successful radiotherapy in some cases. Thus CT may provide a

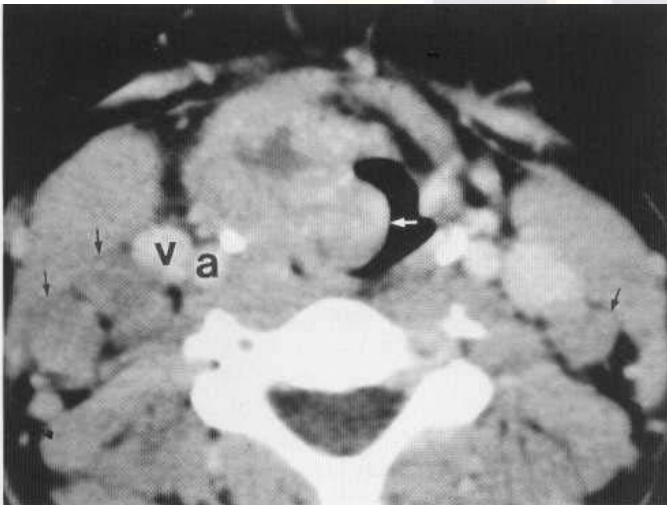


Fig. 47.35 Axial enhanced CT section of a supraglottic laryngeal carcinoma (white arrow) with multiple nodal metastases (black arrows). a = carotid artery; v = internal jugular vein.

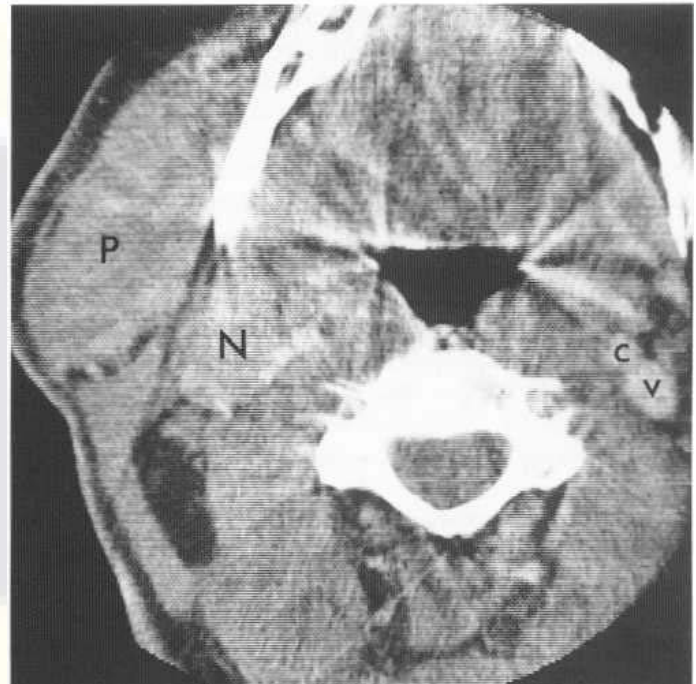


Fig. 47.36 This axial CT section with contrast enhancement illustrates several points. The patient has an anaplastic carcinoma from an unknown primary. On the left the bolus injection has demonstrated the normal carotid (c) and internal jugular vein (v). On the right the parotid gland (P) has been largely replaced by an affected node which is isodense with the surrounding musculature. Another large, clinically inapparent, node lies medially with compressed vessels surrounding it, thus indicating that this is a node lying within the fascial sheath surrounding the neurovascular bundle. A neuroma of the vagus or accessory nerves will produce similar vessel displacement.

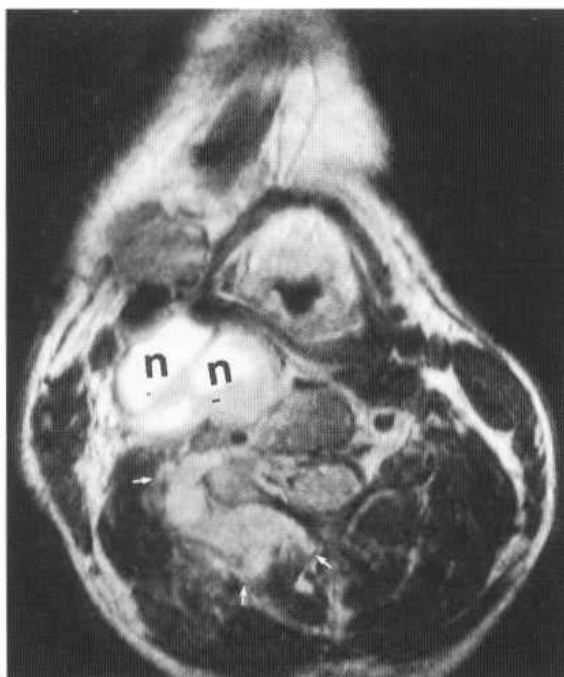


Fig. 47.37 Tuberculosis affecting the soft-tissue planes of the neck with necrotic lymph nodes (n). The inflammatory tissue shows high signal on the T₂-weighted fast spin-echo image (A) and the gadolinium-enhanced T₁ pictures (B) (arrows).

tool for monitoring tumour response. As with benign lesions, malignant tumours of the neck are best imaged by MR with its superior density resolution. Carcinoma tends to have a low signal (long T₁) on T₁-weighted images and may be difficult to differentiate from surrounding muscle, although it will be clearly outlined by adjacent fat planes (Fig. 47.34). On T₂-weighted images the tumour has varying degrees of high-intensity signal and is better differentiated from muscle. This is especially important for the tongue.

Staging of neoplasms of the neck is dependent on assessing evidence of metastatic spread to the lymph nodes and at present CT is preferred to MRI for this (Fig. 47.35). Most authorities recommend the administration of large doses of iodine-containing contrast medium when assessing lymph node involvement, but enhancement is variable and prominent nodal rim enhancement may indicate spread outside the capsule of the node. An enhanced scan at parotid level of a patient with an anaplastic carcinoma from an unknown primary is shown in Figure 47.36 and illustrates some of the advantages and limitations of this technique.

Inflammatory disease

Infection of the soft-tissue spaces of the neck, and particularly the mastication space, is usually of dental origin. The infection may be localised initially but the disruption of fat planes, multispace involvement, or fluid collections suggestive of necrosis and abscess formation soon occur. These features are best demonstrated by MRI (Fig. 47.37) but accompanying osteomyelitis needs to be shown by CT.

RADIONUCLIDE IMAGING OF THE THYROID

Philip J. A. Robinson

Thyroid disorders present either with disturbances of function, or with abnormal local anatomy lumps or nodules in the neck. Radionuclide imaging is used to demonstrate the functional attributes of anatomically normal or abnormal tissue in the neck and to characterise abnormal thyroid tissue elsewhere.

Techniques

Which agent?

Certain anions are selectively trapped by the thyroid (and also by the salivary glands, gastric and colonic mucosa, and the choroid plexus of the brain). After trapping, only iodide is organified—the other anions are released by the gland without being further metabolised, and this discharge can be promoted by giving potassium perchlorate. One of the anions treated in this way is pertechnetate (TcO₄⁻) so ^{99m}Tc in the form of sodium pertechnetate is suitable for thyroid imaging, as a substitute for iodine. Iodine has 2.5 isotopes, only one of which (¹²⁷I) is stable—the rest are radioactive. ¹³¹I is favoured for therapeutic purposes because of its beta emission and a half-life of 8 days. For imaging, ¹²³I has the most favourable properties, including a half-life of about 13 h, no beta emission, and a principal gamma emission at 159 keV.

Pertechnetate is widely used for routine thyroid imaging as a substitute for iodide because ^{99m}Tc is readily available and inexpensive,

and the radiation dose delivered is relatively low. Pertechnetate is less suitable for assessment of thyroid function than it is for imaging, as uptake measurements cannot reliably separate normal from hypofunctioning glands, although hyperfunction can be recognised. Iodine-123 is preferred for imaging retrosternal or ectopic thyroid tissue, in neonatal or childhood hypothyroidism, and in the follow-up of patients who have had surgery for thyroid malignancy.

Indications

Thyroid scintigraphy may be valuable:

- in thyrotoxicosis, to distinguish diffuse toxic goitre (Graves' disease) from autonomous toxic nodule (Plummer's disease)
- with a mass in the neck, tongue or mouth, to identify its relation to the thyroid
- in the presence of a goitre or nodule, to determine the number and activity of thyroid nodules
- to detect ectopic, lingual or mediastinal thyroid
- to monitor the progress of thyroiditis
- to find functioning thyroid metastases
- when occult thyroid malignancy is suspected; for example, in patients presenting with metastatic disease of uncertain origin.

Because of the greater sensitivity of the child's thyroid to radiation, studies in children are performed with particular caution. Both iodide and pertechnetate cross the placenta and they are both secreted in milk, so thyroid imaging is relatively contraindicated during pregnancy and lactation.

Preparation

Imaging may be severely impaired if the patient is undergoing treatment with thyroid supplements or has received a high iodine load. Use of radiographic contrast media may depress the uptake of iodine by the thyroid for up to a month, so imaging studies should be scheduled accordingly. Patients on thyroxine should be switched to T₃ about a month before the study is scheduled, and the T₃ stopped for a few days immediately before the study. Carbimazole and related antithyroid drugs need not be stopped, as they do not interfere with the uptake of iodide, only with its organification. Long-term treatment with amiodarone may also impair thyroid imaging because of the iodide loading it induces.

Image acquisition

Either ¹²³I-labelled sodium iodide (20 mBq) or ^{99m}Tc-sodium pertechnetate (80 mBq) is given intravenously. With ¹²³I images are obtained 2–3 h later, while with ^{99m}Tc-pertechnetate images are obtained about 20–30 min postinjection, using a high resolution or pinhole collimator. Markers indicating the position of the thyroid cartilage and sternal notch are helpful and additional markers may be used to indicate the site of palpable nodules in the neck. Oblique views may clarify dubious nodules and a lateral view of the neck should be added if ectopic thyroid is suspected.

Normal appearances

The left and right lobes are approximately equal in size, although a minor degree of asymmetry is acceptable (Fig. 47.38). Each lobe measures up to 7 cm in craniocaudal length, and up to 3 cm in width. Uptake of the tracer is uniform, and at least equal to (^{99m}TcO₄⁻) or slightly more (1.3) than uptake in the parotid and submandibular glands. In occasional cases, a small pyramidal lobe is visible, close to the midline.

Applications

Thyrotoxicosis

The main contribution of scintigraphy is to discriminate between diffuse toxic goitre (Graves' disease), which accounts for over 80% of cases of thyrotoxicosis, and autonomous toxic nodule (Plummer's disease), which accounts for 10-15% of cases. In Graves' disease the gland shows diffusely increased uptake of either $^{99m}\text{TcO}_4$ or ^{131}I , and a pyramidal lobe is more often apparent than in euthyroid patients (Fig. 47.39), while autonomous toxic nodules appear as intensely active foci within a thyroid which is partly or totally suppressed (Fig. 47.40). Scintigraphy may also demonstrate the small proportion of patients in whom Graves' disease arises in a pre-existing multinodular goitre (Fig. 37.41). In those cases where the gland is not enlarged, scintigraphy may also demonstrate an impalpable nodule, or Graves' disease in a normal-sized gland.

The importance of establishing the underlying cause is related to the different treatment chosen. Surgery is much more likely to be considered for a solitary nodule. The therapy for a solitary nodule requires a larger dose of activity than is used for Graves' disease, and in either condition the calculation of the therapeutic dose can be guided by measurement of the uptake of a diagnostic (imaging) dose. Finally, the demonstration of a cold nodule within a toxic gland is an indication for fine-needle aspiration (FNA) biopsy, as

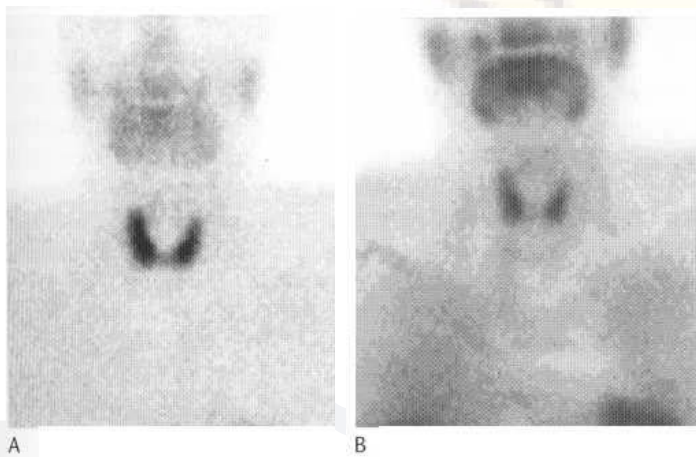


Fig. 47.38 Thyroid/parathyroid scintigraphy. Normal thyroid uptake of $^{99m}\text{TcO}_4$ (A) and $^{99m}\text{Tc-MIBI}$ (B). (Note: the normal parathyroids are not visible.)

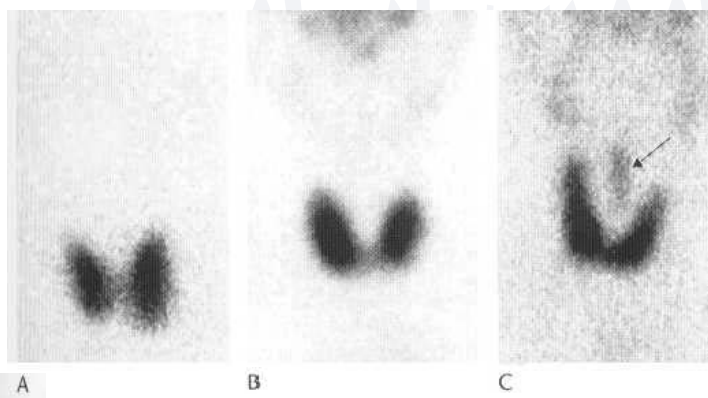


Fig. 47.39 Graves' disease. Three patients showing diffusely increased thyroid uptake with ^{131}I (A) and with $^{99m}\text{TcO}_4$ (B, C). A pyramidal lobe (arrow) is also shown in (C).

such nodules have a higher incidence of malignancy than similar nodules in a non-toxic gland.

In patients with a solitary autonomous nodule, the remaining thyroid tissue may be suppressed to the degree that it is invisible on scintigraphy. If surgery is contemplated in such cases, it is wise first to perform repeat scintigraphy after 3-4 days stimulation with daily doses of thyroid stimulating hormone (TSH) in order to confirm that the residual thyroid is functionally intact.

Thyroid nodules

The object of imaging is to discriminate between the vast majority of innocent nodules and the small proportion that are malignant. Their incidence increases with age, such that 5-6% of patients over 60 have clinically apparent nodules, and autopsy or careful ultrasound examination will show that many more older patients have nodular changes that are clinically occult. More than 80% of thyroid nodules show reduced or absent activity on scintigraphy, and most of the remainder, which show normal or mildly increased activity, are non-toxic. Malignancy is more likely in male patients, in those under 20 or over 60 years, in those with a family history of thyroid cancer, and in patients who have previously undergone irradiation to the head and neck. Solitary nodules are thought to have a higher incidence of malignancy than multiple nodules, and other pointers to malignancy include hardness to palpation, rapid growth, laryngeal nerve involvement causing hoarseness, and the enlargement of lymph nodes in the neck. About half of patients with nodules that appear clinically to be solitary will have multinodular thyroids shown by imaging.

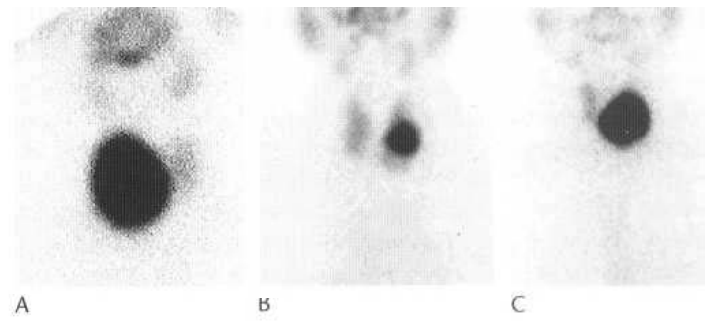


Fig. 47.40 (A-C) Autonomous nodules. Three patients with solitary 'hot' nodules of overactive thyroid tissue and relative suppression of the remainder of the gland.

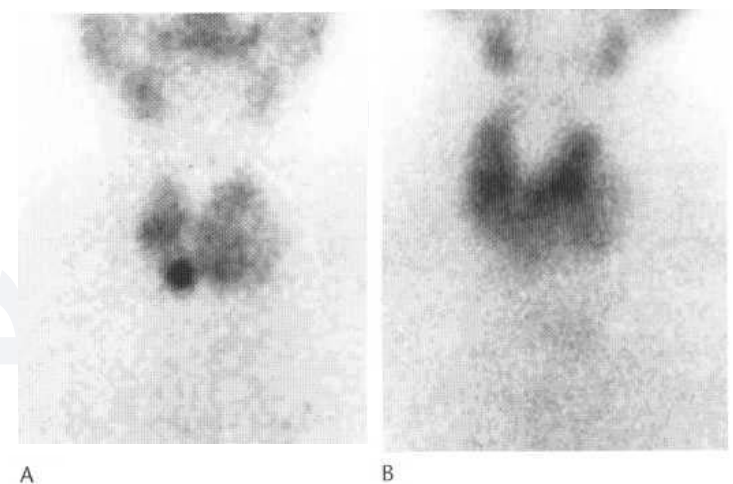


Fig. 47.41 (A,B) Multinodular goitre. Two patients with enlarged thyroids showing areas of increased and reduced activity.

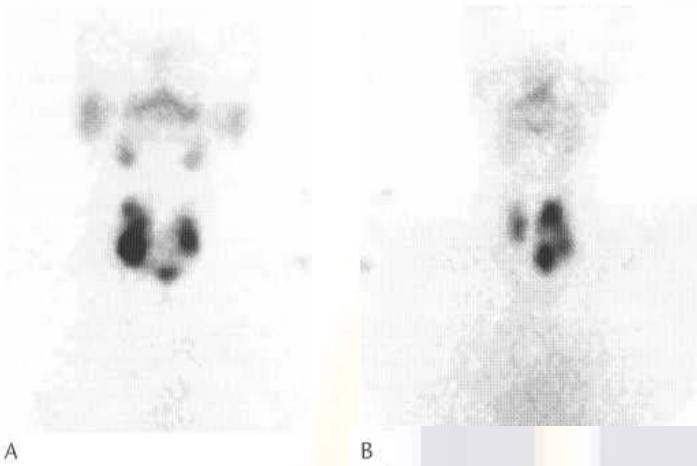


Fig. 47.42 (A,B) Multinodular goitre with hyperactive nodules. Two patients with multiple nodules of increased activity.

Scintigraphy, ultrasonography and FNA biopsy are used in conjunction to discriminate between solitary and multiple nodules, between solid and cystic nodules, and between active and inactive nodules (Fig. 47.42). Solid inactive nodules have the highest risk of malignancy, so these should be biopsied, but some current approaches suggest that FNA biopsy should be the first procedure for all nodules that are clinically apparent in the euthyroid patient (Fig. 47.43).

Ectopic thyroid

Ectopic thyroid tissue may lie along the line of the thyroglossal duct or adjacent to it. The presence of a normally situated thyroid gland does not exclude the possibility of ectopic thyroid, although in other cases the ectopic tissue may be the only functioning thyroid, and in such cases its removal is undesirable. Most commonly, ectopic thyroid presents in childhood as a nodule or mass at the base of the tongue, but it may also present in adult life (Fig. 47.44). For imaging, ¹²³I is preferable to ^{99m}Tc because it shows greater uptake in the thyroid compared with the salivary glands.

'Retrosternal' thyroids are commonly posterior to the trachea in the superior mediastinum, and are usually extensions of a multinodular goitre in the neck. Again, ¹²³I is superior to ^{99m}Tc for imaging, this time owing to the much lower background activity in the rest of the mediastinum when iodine is used. Most mediastinal thyroids will show moderately reduced or normal levels of activity, but occasionally they are inactive and biopsy is needed for diagnosis.

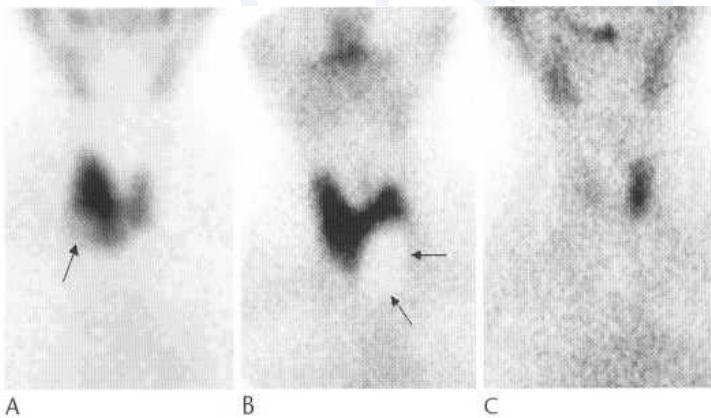


Fig. 47.43 Solitary 'cold' nodules in three patients subjected to FNA. (A) Benign non-functioning adenoma (arrow); (B) carcinoma (arrows); (C) chronic thyroiditis affecting only the right lobe.

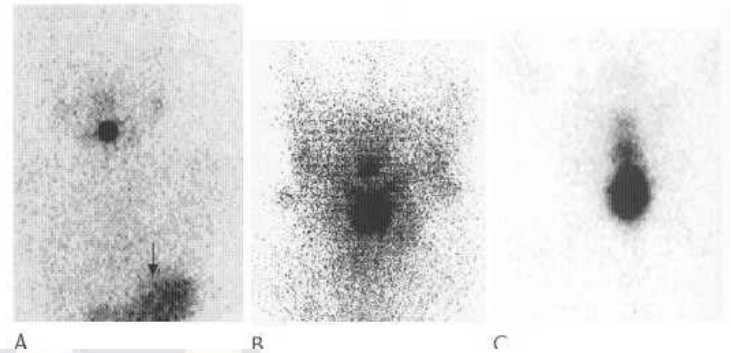


Fig. 47.44 Ectopic thyroid. Three patients with no functioning thyroid in the neck: (A) a typical lingual thyroid in a child—the arrow indicates gastric mucosal uptake; (B) submandibular ectopic thyroid which presented as a mass in adult life; (C) ectopic thyroid tissue developing in the line of the thyroglossal duct.

Neonatal hypothyroidism

Scintigraphy is helpful to show the presence of ectopic thyroid tissue, which is seen in 40-50% of cases, or to demonstrate the absence of thyroid tissue, which is the underlying problem in 30-40% of cases. In a small minority the thyroid may be shown to be anatomically normal. The presence of either orthotopic or ectopic thyroid tissue is of prognostic value, as in such infants the functional deficit may be transient rather than permanent.

Perchlorate discharge test

Imaging does not discriminate between iodide that is trapped in the thyroid and that which has been both trapped and organified. Disorders characterised by a failure to organify the trapped iodide (of which the most common is Pendred's syndrome) can be recognised by obtaining serial images of the thyroid, giving first the usual diagnostic amount of I¹²³I, and 2 h later giving sodium or potassium perchlorate, which rapidly discharges the unbound iodide from the gland. The normal gland will retain that proportion of the iodide which has been bound, whereas with an organification defect most of the thyroid activity will be eliminated.

Thyroiditis and colloid goitre

Diagnosis of both Hashimoto's disease and subacute (de Quervain's) thyroiditis is primarily clinical and biochemical. Scintigraphy provides supplementary anatomical and functional definition of the condition, and may be used to monitor changes in the size or activity of the gland which occur either in response to treatment or during the natural history of the disease.

Subacute thyroiditis is a self-limiting condition in which pain, tenderness and swelling of the thyroid are accompanied by a mild degree of thyrotoxicosis, caused by the leakage of stored hormones within the thyroid rather than by excess production. Scintigraphy shows a large thyroid with diffuse activity, which may be normal, mildly increased or mildly decreased. Increased activity usually returns to normal after a few months.

Hashimoto's disease is a long-term condition which does not show the more acute symptoms and signs seen with de Quervain's thyroiditis. The thyroid is usually enlarged but tracer uptake may be diffusely increased or reduced, may show a nodular distribution, a focal defect, or unilaterally reduced function (Fig. 47.43C).

In 'simple' colloid goitre, scintigraphy typically shows diffuse enlargement with normal or mildly reduced activity throughout.

Multinodular goitres show a patchy distribution of normal and reduced activity. Excessive iodine intake may produce a mildly toxic diffuse goitre, and long-term administration of amiodarone can produce a similar condition.

Carcinoma

Well-differentiated papillary and follicular tumours usually take up radio-iodine, but to a much lesser degree than normal thyroid. Scintigraphically, thyroid cancer may present as a solitary cold nodule within an otherwise normal gland, as a dominant cold nodule in a multinodular goitre, as reduced or absent function of an entire lobe, or as diffusely reduced function affecting the whole of the gland. Carcinoma should be suspected when a cold thyroid nodule appears solitary, enlarges rapidly, is hard on palpation and is associated with nodes in the neck. Poorly differentiated carcinomas take up little or no radio-iodine but otherwise show similar features to the above (Fig. 47.43B). After surgical removal of the primary tumour, surveillance for recurrent disease in the neck and for distant metastases can be carried out using whole-body imaging with ^{123}I . For whole-body studies, the activity of iodide given is increased to 80 mBq. Metastases from well-differentiated thyroid carcinomas, which take up diagnostic doses of radio-iodine, may be treated with a much larger dose of ^{131}I , following a diagnostic study to detect and localise the lesions. In such cases it is important to confirm that all the normal thyroid tissue has already been removed from the neck, otherwise both the diagnostic and therapeutic doses will accumulate preferentially in the residual normal tissue and the diagnostic sensitivity for metastatic disease will be much less (Fig. 47.45).

Medullary thyroid cancer (MTC)

This uncommon tumour, which accounts for about 10% of thyroid malignancies, arises in the C cells of the thyroid, which originate in neural crest tissue and belong to the APUD series. In the majority of cases they secrete calcitonin but occasionally produce ACTH, somatostatin, substance P or carcinoembryonic antigen. In about 20% of cases, MTC is part of the familial multiple endocrine neoplasia (MEN2) syndrome, along with pheochromocytoma and hyperparathyroidism. Diagnosis is usually made by biopsy, together with measurement of circulating calcitonin levels. Scintigraphy with iodide or pertechnetate shows one or more non-functioning nodules, similar to the appearances of the adenocarcinomas. Imaging with the somatostatin analogue ^{111}In -octreotide shows increased activity in MTC, but possibly the most sensitive technique is to use penta-valent $^{99\text{m}}\text{Tc}$ -DMSA. This agent shows fairly

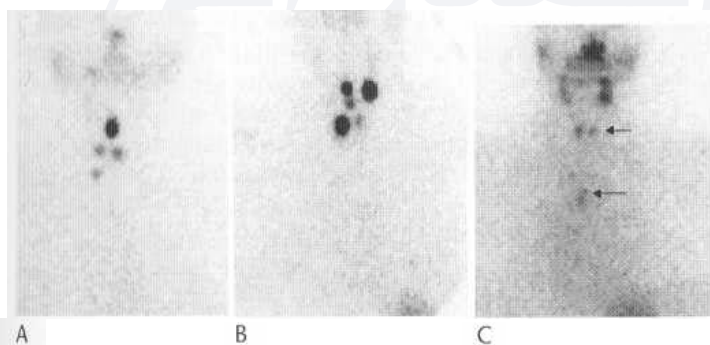


Fig. 47.45 Carcinoma of the thyroid. Postresection appearances in two patients with small nodules of residual thyroid tissue (A,B), and (C) a patient with metastases in cervical and mediastinal lymph nodes (arrows).

specific uptake in MTC, with no uptake in follicular or papillary tumours. Images 2-3 h after injection may show primary and metastatic sites of MTC. The main role of this technique is in the follow-up of patients after surgical resection of the primary tumour.

RADIONUCLIDE IMAGING OF THE PARATHYROIDS

Imaging is used to localise parathyroid adenomas, hyperplastic glands or ectopic sources of excessive parathyroid hormone secretion. Primary hyperparathyroidism results from a single adenoma in about 80% of cases, from hyperplasia of all four parathyroids in about 15%, and rarely from multiple adenomas or from carcinoma. Secondary hyperparathyroidism is most commonly the result of chronic renal failure, and occasionally arises in patients with chronic gastrointestinal disorders associated with calcium wasting or chronic vitamin D deficiency. Tertiary hyperparathyroidism describes patients with chronic renal failure and secondary hyperparathyroidism, whose glands remain overactive after kidney transplantation has restored good renal function.

Why localise?

Hyperparathyroidism is defined as persistent hypercalcaemia with raised parathyroid hormone levels. If serum calcium is only mildly elevated, renal function is normal and the patient has no related symptoms, surveillance may be the most appropriate management, particularly for elderly patients, but if active treatment is indicated, surgery or image-guided alcohol ablation is performed. Experienced surgeons should find and remove 95% of parathyroid adenomas at the first operation. None of the imaging methods can improve on this, so preoperative imaging is not recommended as a routine. Imaging for localisation is now usually restricted to those patients whose first surgical procedure fails to cure the disease, i.e. those with residual or recurrent parathyroid lesions. An alternative view is that preoperative localisation simplifies and shortens the operative procedure, with potential benefits for both patient and surgeon.

Techniques

The preferred radiopharmaceutical for parathyroid imaging is currently $^{99\text{m}}\text{Tc}$ -methoxyisobutyl-isocitronate (MIBI), an agent which is specifically extracted by myocardial tissue and also by the parathyroids. Like all other radioactive tracers that are known to be taken up by the parathyroids, MIBI is also taken up by the thyroid, but the tracer is retained more avidly in parathyroid tissue. Thallium-201, as thallos chloride, was also widely used in the past but $^{99\text{m}}\text{Tc}$ -MIBI is preferred because it has a lower radiation dose. The cardiac agent $^{99\text{m}}\text{Tc}$ -tetrafosmin also produces good results but has no particular advantage over MIBI.

After intravenous injection, $^{99\text{m}}\text{Tc}$ -MIBI is taken up rapidly in both thyroid and parathyroid glands, but washes out of the thyroid over the next few hours, whereas parathyroid uptake is retained. Images obtained within the first 10 min after injection of 200 mBq of $^{99\text{m}}\text{Tc}$ -MIBI may be compared with images obtained 3-4 h later. After appropriate scaling for differences in count rate, subtraction of the early from the delayed images will highlight parathyroid lesions, as these retain the activity for longer than the thyroid tissue. A better approach is to carry out a conventional pertechnetate image of the thyroid after the MIBI images have been obtained,

without moving the patient. This then allows the thyroid to be more effectively subtracted from the parathyroid plus thyroid combination that is shown on the MIBI images. A further technical refinement is to obtain serial dynamic images after the MIBI injection, and to generate time activity curves from the thyroid and from nodules suspected of being parathyroid adenomas, in order to demonstrate the difference in washout rates between thyroid and parathyroid. It is important to use a high-resolution collimator, and to include the superior mediastinum within the field of view, in order that ectopic parathyroid adenomas may be recognised. Anterior views are routine, obliques of the neck may be helpful in dubious cases, and SPECT images may help to localise ectopic sites.

Findings

Normal parathyroid glands measure about 6 x 3 x 2 mm and weigh 20-30 mg each. The smallest adenomas currently detected by imaging are in the region of 150-200 mT, so normal parathyroid glands are not shown (Fig. 47.38B). Adenomas are usually demonstrated as areas of persistently increased activity adjacent to or overlapping the thyroid (Fig. 47.46). Differential clearance of MIBI on early and delayed images, or on a dynamic sequence, helps to differentiate parathyroid

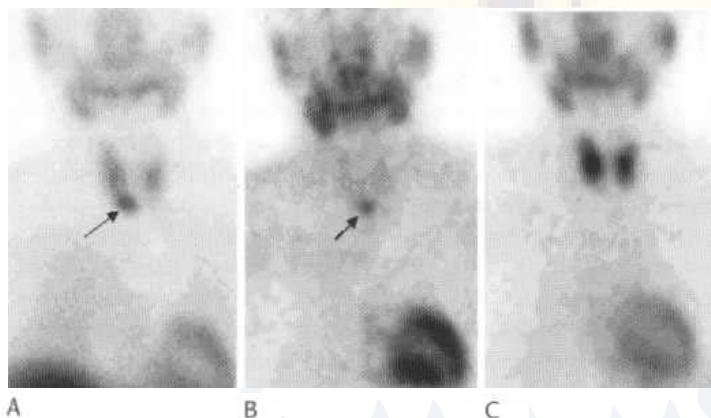


Fig. 47.46 Parathyroid adenoma. ^{99m}Tc-MIBI images at 10 min (A) and 3 h (B) showing a persistent focus of activity inferior to the right lobe of the thyroid; ^{99m}TcO₄ image (C) shows normal thyroid uptake but the adenoma is not visualised.

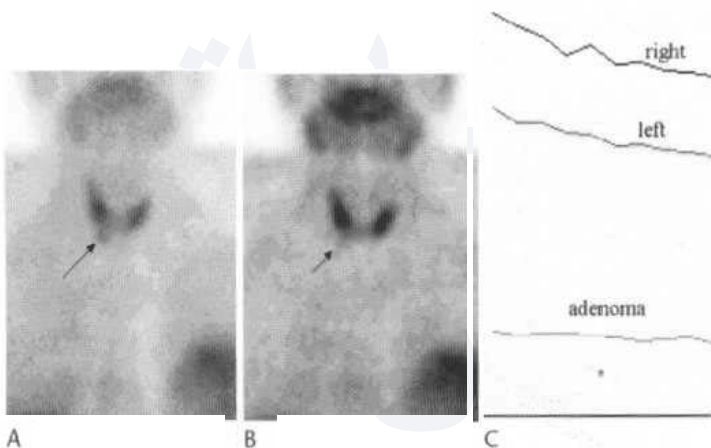


Fig. 47.47 Parathyroid adenoma. Early ^{99m}Tc-MIBI image (A) and 3 h combined ^{99m}Tc-MIBI and pertechnetate image (B) showing a small parathyroid adenoma (arrows); time-activity curves from the 5-30 min dynamic images (C) show gradual wash-out of activity from right and left thyroid lobes while activity in the adenoma remains stable.

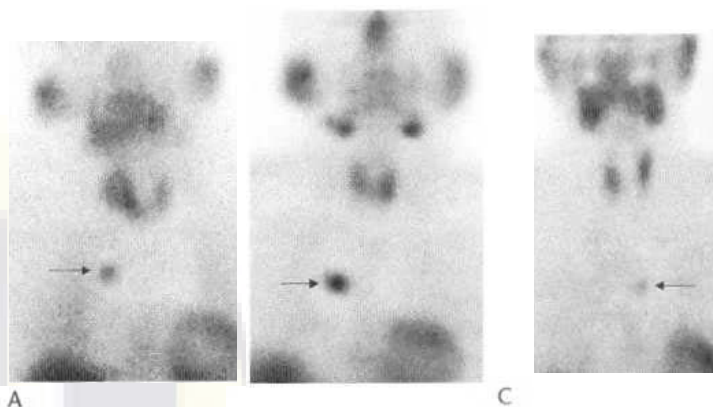


Fig. 47.48 (A-C) Mediastinal parathyroid adenomas. Three patients with mediastinal adenomas shown on ^{99m}Tc-MIBI imaging.

adenomas from normal thyroid tissue (Fig. 47.47), and subtraction of an additional thyroid image is also helpful, particularly in cases where the thyroid is itself abnormal. Hyperplasia is shown as multiple warm or hot nodules distinguishable from adjacent thyroid tissue. Ectopic adenomas are usually sited in the superior mediastinum, often adjacent to the aortic arch (Fig. 47.48).

Results

The accuracy of radionuclide localisation of adenomas that are subsequently removed surgically is in excess of 90%. Since surgical localisation is at least as good as this, the main contribution of imaging is in patients with persistent or recurrent disease in whom the difficulties of localisation are greater. The results of parathyroid scintigraphy are affected by the following:

- Adenomas are easier to find than hyperplasia.
- Preoperative patients are easier to image than postoperative patients.
- Localisation is more successful in primary than in secondary hyperparathyroidism.
- The presence of a multinodular goitre reduces the chance of successful localisation.

Finally, there is a rough correlation between the size of adenomas and the severity of the biochemical disturbance they produce. Large adenomas are more readily identified than small ones, so patients with only marginal biochemical disease are less likely to benefit from imaging than those with more marked disease.

New approaches

Initial studies with positron emission tomography (PET) suggest that imaging with ¹⁸F-fluorodeoxyglucose (FDG) or with ¹¹C-methionine is likely to be more accurate than the conventional single-photon agents in locating parathyroid lesions. The possibility of intraoperative localisation using a hand-held gamma probe is also being explored.

COMPUTED TOMOGRAPHY OF THE NECK

Richard W. Whitehouse and Andrew R. Wright

Technical considerations

Cervical anatomy is clearly demonstrated by axial CT scanning. A modified Valsalva manoeuvre during scanning will improve identification of the airways and structures in the larynx. Angulation

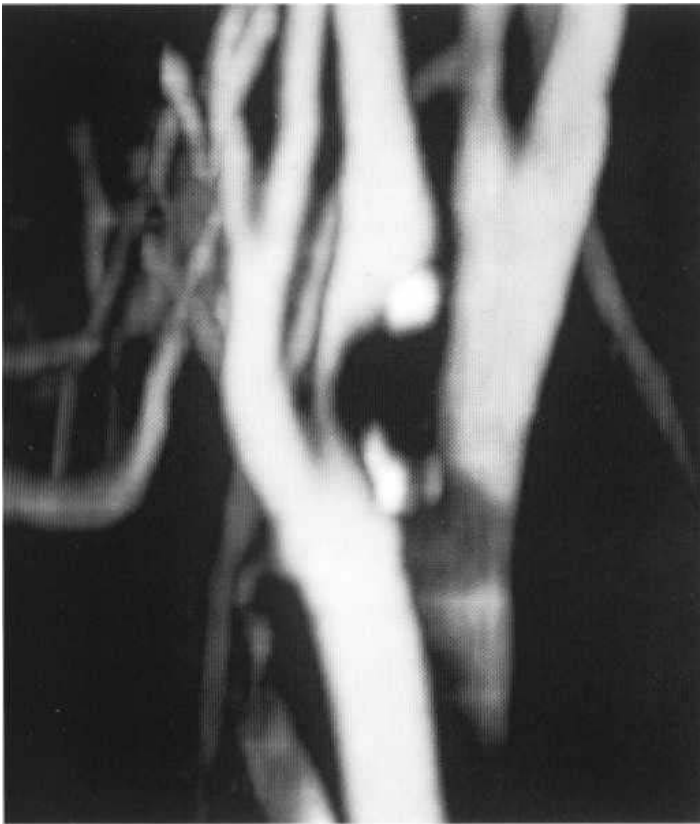


Fig. 47.49 Maximum-intensity projection image from spiral CT dataset showing severe stenosis of proximal internal carotid artery. The calcification within the plaque is clearly seen.

of the scanner gantry toward the feet anteriorly can improve scans through the tipper neck by removing the anterior mandible from the scan plane and will also demonstrate the anterior lower neck with less streak artefact from the shoulders. With multislice CT, however, best results are obtained with a straight gantry and thin-slice collimation (typically 1.0-2.5 mm). Coronal, sagittal and oblique-axial reformats can then be constructed from the dataset in postprocessing. Intravenous contrast enhancement is best achieved with a lower iodine concentration (around 200-250 mg I/ml) to reduce streak artefact from undiluted contrast in the brachiocephalic vein. Contrast reflex into small cervical veins is commonly seen and a small air bubble in these veins from intravenous cannulation is also common. Spiral or multislice acquisition with narrow collimation during contrast infusion will allow subsequent workstation reconstruction of vascular images, e.g. maximum intensity projections of the carotid arteries (Fig. 47.49). Since skin entry radiation doses from a single CT scan of the neck are typically in the region of 20-40 mGy, a clear clinical indication for the examination is required to justify the consequent thyroid radiation dose.

Anatomical considerations

The neck is anatomically described as a series of triangles, the major anterior and posterior triangles being separated by the sternomastoid muscle. The anterior triangle is further divided into supra- and infrahyoid parts by the hyoid bone. The suprahyoid part is subdivided by the anterior belly of the digastric muscle into submental and submandibular triangles; this part of the neck contains the sublingual and submandibular salivary glands and is further described in Chapter 18. The infrahyoid neck is divided by the

superior belly of the omohyoid muscle into an anterior muscular triangle and a posterolateral carotid triangle.

The posterior triangle is divided by the inferior belly of the omohyoid muscle into an inferior subclavian triangle and a superoposterior occipital triangle. These triangles are used clinically to identify the sites of pathology and surgical approaches. The boundaries of the triangles are apparent on CT scanning and should be referred to when localising lesions. In addition to the triangles described above, the neck is divided into spaces by several fascial planes. These planes form boundaries which may confine or guide the extension of disease, and the space involved may also indicate the likely site of origin and differential diagnosis of a lesion. The *carotid space* contains the carotid artery, jugular vein, Xth nerve, sympathetic chain and deep cervical lymphatics. It is surrounded by the carotid sheath from the deep cervical fascia. This space extends from the skull base to the arch of the aorta. The *visceral space* lies medial to this and crosses the midline. It is invested by the middle layer of the deep cervical fascia and contains the larynx, trachea, thyroid and parathyroid glands, hypopharynx and oesophagus, paratracheal lymph nodes and the recurrent laryngeal nerves. The visceral space extends from the hyoid to the mediastinum. The *posterior cervical space* is posterior to the carotid space and corresponds largely to the posterior triangle. It extends from the skull base to the clavicle and contains the XIth nerve, lymphatics and the brachial plexus. The *renopharyngeal space* lies between the middle and deep layers of the deep cervical fascia, posterior to the visceral space. It extends from the skull base to the mediastinum and contains a layer of fat. The *prevertebral space* lies within the deep layer of the deep cervical fascia and therefore includes the cervical spine, its contents, the emerging cervical roots (including the phrenic nerve) and adjacent (prevertebral, scalene and paraspinous) musculature from the skull base to the mediastinum.

Clinical applications

The **thyroid gland** is well seen on CT due to its higher than average soft-tissue attenuation, caused by the physiologically high iodine content of the gland. Thyroid *adenomas* and *carcinomas* are seen as soft tissue masses within the gland: calcification and cyst formation



Fig. 47.50 (A) Large goitre with an unusually extensive posterior component surrounding the trachea. (B) The coronal reconstruction shows the goitre extending down to the level of the aortic arch. There is only mild narrowing of the trachea.

is seen in both types of lesion and CT cannot reliably distinguish benign from malignant thyroid masses unless metastatic disease, bone or cartilage destruction or neurological involvement is identified in the latter. Iodine-containing contrast enhancement may prevent subsequent radioactive iodine treatment of thyroid carcinoma for up to 6 months: CT is therefore not recommended for staging thyroid carcinoma. Thyroid carcinoma or lymphoma may be seen as an infiltrating soft-tissue mass extending from the thyroid. The retrosternal extent of thyroid goitres can be demonstrated (Fig. 47.50).

Parathyroid adenoma

Parathyroid adenoma can be localised on CT (Fig. 47.51), but MRI, ultrasound or radionuclide imaging are the preferred techniques when preoperative imaging is required. CT can identify ectopic parathyroid adenomas in the neck or upper mediastinum.

Proximal oesophageal and laryngeal carcinoma are usually diagnosed though barium studies (in the former) or endoscopic techniques. CT, however, is useful for overall tumour staging, including demonstration of local involvement, nodal status and metastatic disease (Figs 47.52, 47.53).

Masses in the carotid space

Masses in the carotid space are usually closely applied to the carotid or jugular vessels. *Inflammatory adenopathy; abscess* or *tuberculous oedema* can develop here, as will *metastatic adenopathy* to the

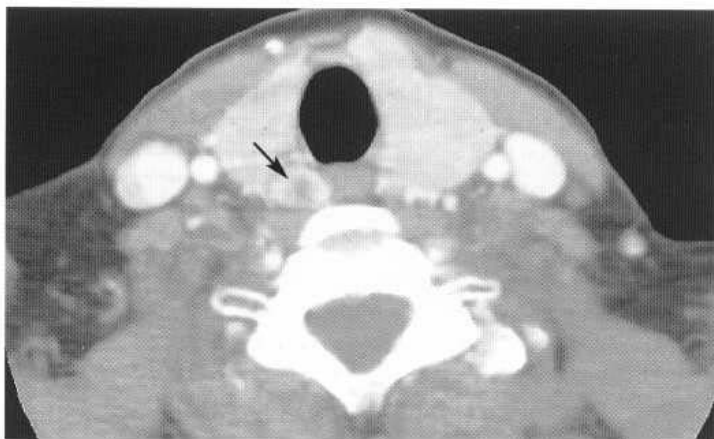


Fig. 47.51 Cystic parathyroid adenoma (arrow).



Fig. 47.52 Axial (A) and sagittal (B) views of extensive proximal oesophageal carcinoma. Ring-enhancing lymph nodes are seen displacing the left thyroid lobe anteriorly.

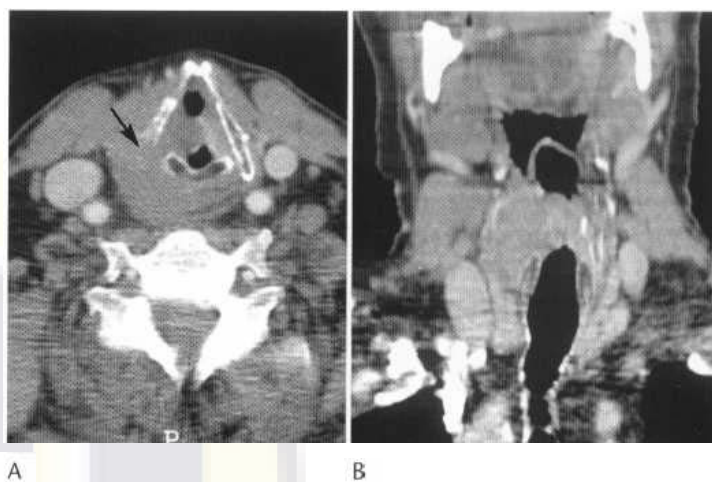


Fig. 47.53 (A) Carcinoma of the larynx eroding through the right thyroid cartilage (arrow). (B) The coronal reconstruction shows the superior-inferior extent well.

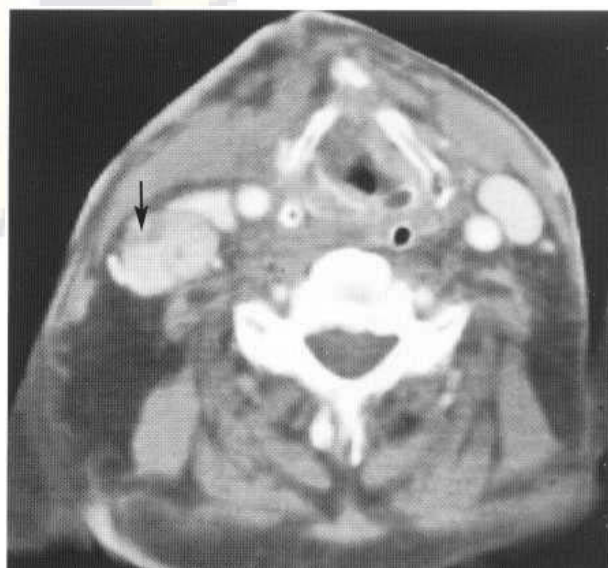


Fig. 47.54 Markedly enhancing metastatic node from a follicular carcinoma of the thyroid (arrow). The primary tumour has already been treated by surgical resection and local radiotherapy.

deep cervical chain from squamous carcinoma, thyroid carcinoma (Fig. 47.54), lymphoma or other primary tumours. Metastatic nodes are diagnosed by size, being over 1-1.5 cm in diameter.

Micrometastases within normal-sized nodes cannot be identified but cystic change within a metastatic lymph node is typical of a squamous-cell carcinoma metastasis (Fig. 47.55). Primary benign tumours in this space include the *carotid body tumour* or *paraganglioma* (Fig. 47.56), which characteristically shows marked contrast enhancement, and neural sheath tumours. *Second bronchial cleft cysts*, although rare, may also be in the carotid space (Fig. 47.57). As previously noted, spiral or multislice CT is a non-invasive way of directly imaging the carotid arteries and assessing severity of stenosis. Unlike Doppler ultrasound or MR angiography, CT is sensitive to plaque calcification.

Inflammatory adenopathy

Inflammatory adenopathy in the posterior cervical chain of the **posterior cervical space** may occur from similar pathologies to

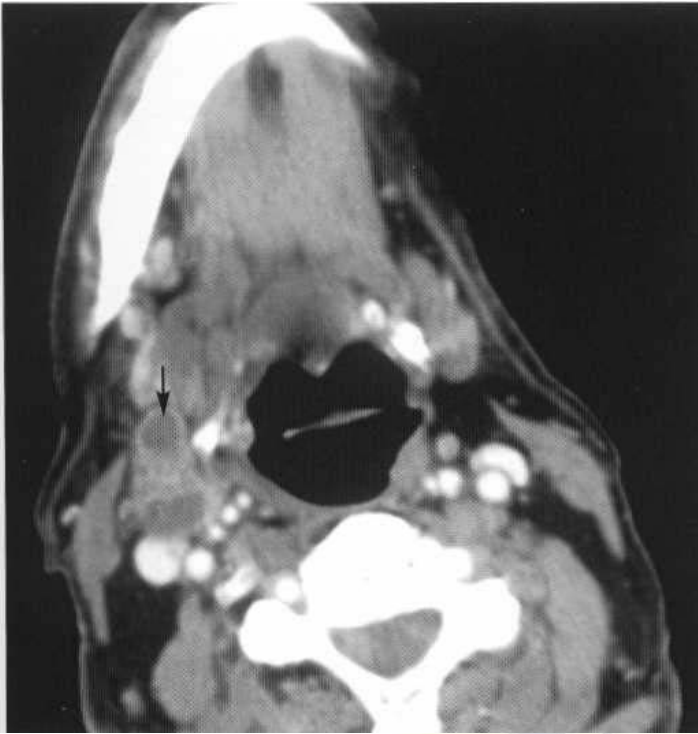


Fig. 47.55 Metastatic squamous carcinoma in right-sided cervical lymph node. Note the central cystic change, characteristic of squamous carcinoma metastasis (arrow).

those in the carotid space. *Malignant adenopathy* also occurs here, with nasopharyngeal squamous-cell carcinoma metastasizing to these nodes. Lymphoma may also involve these nodes. The posterior cervical space is the commonest site for a *lipoma* to develop in the head and neck, with characteristic internally featureless fat density on CT. Cystic *hygroma* is seen as a water density, multiloculate lesion in this space (Fig. 47.58).

The retropharyngeal space

The **retropharyngeal space** below the level of the hyoid contains only fat: primary tumours of this region are therefore rare but the

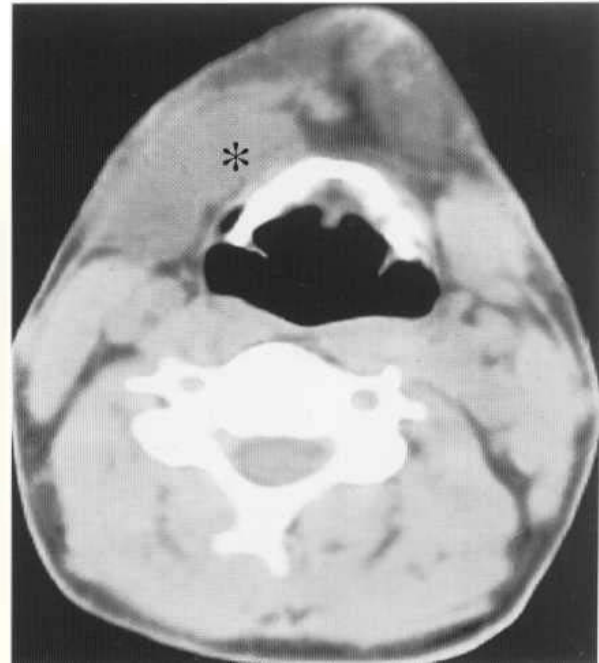


Fig. 47.57 Second branchial cleft cyst (asterisk).

space can act as a channel for the spread of tumour or infection from the neck to the mediastinum.

The prevertebral space

The **prevertebral space** is most commonly affected by pathology extending from a cervical vertebral body or intervertebral disc-metastatic disease and infections are the most likely lesions. Assessment of the CT images on appropriate bone and soft-tissue windows is therefore necessary.

The *brachial plexus* crosses several spaces in its development from roots through to branches. Careful tracking of the anatomical site of the plexus through contiguous sections from the level of the hyoid bone down to the level of the aortic arch is needed if a brachial plexus lesion is suspected.

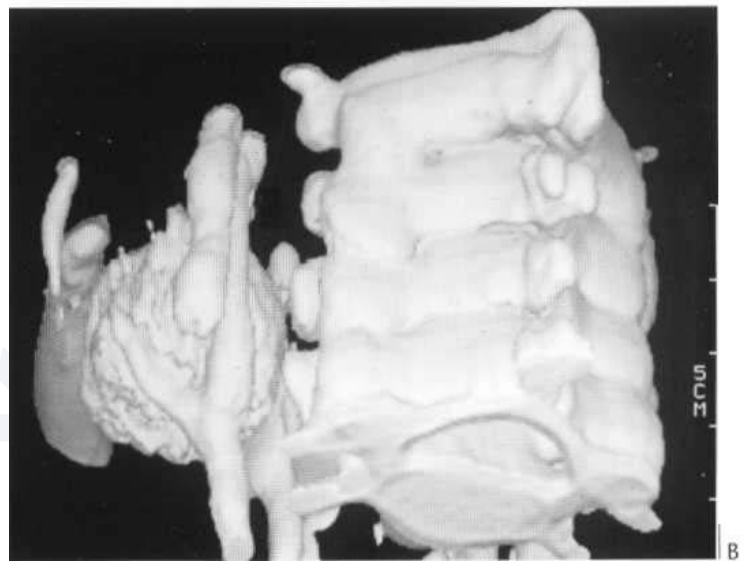


Fig. 47.56 (A) Carotid body tumour showing marked contrast enhancement (arrow). (B) Surface-shaded reconstruction with posterior oblique viewpoint showing anatomical relationship of the tumour.

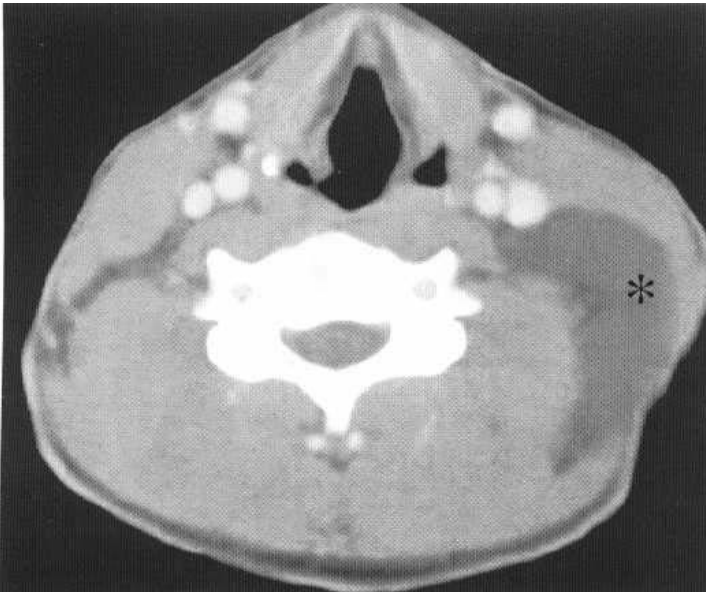


Fig. 47.58 Multiloculate cystic hygroma lying posterior to the sternomastoid muscle (asterisk).

ULTRASOUND OF THE NECK

Julie F. C. Olliff

Ultrasound of the neck should be performed using a linear probe. A 7.5-10 MHz probe is appropriate for most examinations but a 5 MHz probe may be necessary for deeper structures, such as the deep lobe of the parotid, or for the well-built patient.

Thyroid

The thyroid consists of a right and left lobe joined by a narrow isthmus. A further lobe, the pyramidal lobe, is seen in approximately one-third of the population. Arising from the isthmus, it extends upwards either in the midline or to the left of the midline, lying anterior to the thyroid cartilage. It is small and rarely appreci-

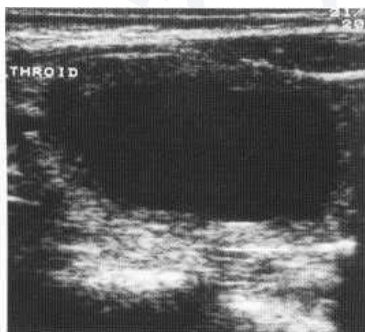


Fig. 47.59 Longitudinal ultrasound scan through the left lobe of the thyroid demonstrates a simple cyst.

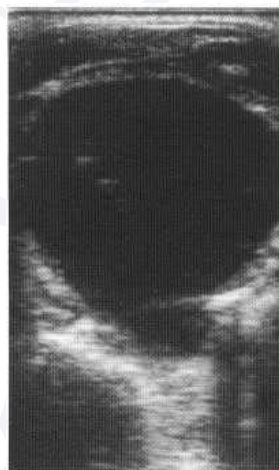


Fig. 47.60 Ultrasound of a large cystic mass within the right lobe of the thyroid demonstrates small focal regions of increased reflectivity with 'comet tails' due to a colloid cyst.

aged on ultrasound. The normal thyroid appears of uniform reflectivity. Adjacent muscles are of lower reflectivity and the thyroid capsule of higher reflectivity. Vessels within the gland are well seen. Ultrasound may be used to assess a thyroid swelling, giving information about size, number and nature (solid or cystic). There are, however, no absolute criteria which allow differentiation of benign from malignant lesions. Cystic areas occur in 24% of thyroid masses, with 38% of malignant lesions having a cystic component. Well-defined margins are seen in 16% of malignant lesions, with irregular or ill-defined margins seen in approximately 45% of benign lesions. Calcification and haemorrhage occur in both benign and malignant conditions.

Benign cysts

True epithelial thyroid cysts are rare. Most cysts are due to cystic degeneration of thyroid adenomas and as such a simple cyst (Fig. 47.59) on ultrasound is very uncommon. Most cystic lesions on ultrasound will have irregular thick walls with solid components. The presence of a comet-tail sign on ultrasound has been said to be a highly specific sign of a benign colloid nodule (Fig. 47.60).

Thyroid adenoma

These can be divided into functioning and non-functioning nodules using radionuclide imaging but no such distinction can be made using ultrasound. Toxic adenomas rarely cause clinical symptoms until they are greater than 3 cm in size. There are no specific imaging signs and nodules may be solid or cystic (as described above) and may be heterogeneous, containing calcification and/or haemorrhage. Peripheral and coarse calcification is more frequently seen in benign nodules (Fig. 47.61). Generally, vessels will be seen on colour flow Doppler around nodules (Fig. 47.62), with some flow being appreciated within most nodules.

Multinodular goitre

A goitre is an enlarged thyroid gland. A multinodular goitre is the commonest pathological condition of the thyroid. The incidence of malignancy in a multinodular goitre is low but cytology should be performed of any nodule that is large, dominant or hard or is growing. The characteristic ultrasound appearance of a multinodular goitre is of mixed solid and cystic areas within an enlarged gland, with or without calcification. Multinodular goitres may reach an enormous size, extending well into the mediastinum and up into the neck, causing airway and oesophageal compression.



Fig. 47.61 Ultrasound scan of the thyroid in a patient with thyrotoxicosis reveals a multinodular gland with an area of coarse calcification.

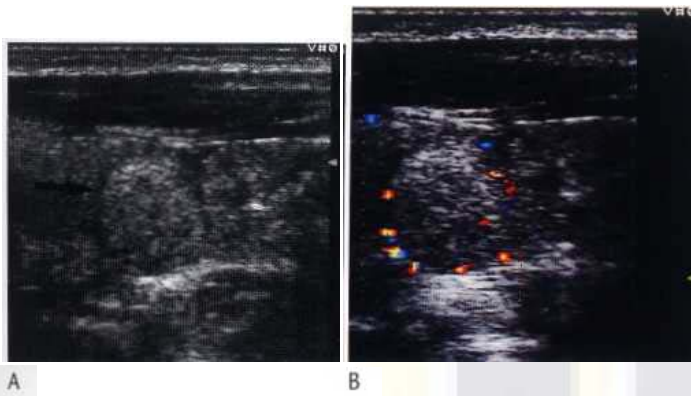


Fig. 47.62 (A) A solid nodule seen within the thyroid. (B) Colour flow is seen around the periphery of this benign nodule.

Graves' disease is the commonest cause of hyperthyroidism. It affects women more commonly than men. It is due to thyroid-stimulating immunoglobulins such as long-acting thyroid stimulator (LATS). These simulate the function of thyroid-stimulating hormone (TSH), resulting in an enlarged homogeneous thyroid gland.

Thyroid malignancy

The most common thyroid malignancy is *papillary cell carcinoma*, which accounts for 55-80% of all thyroid malignancies. The majority of patients are young females and it has a good prognosis. Papillary carcinoma is often (77%) solid and hypoechoic on ultrasound (Fig. 47.63) but may be isoechoic (14%). The presence of calcification or haemorrhage, which is not uncommon, causes areas of increased reflectivity and there may be areas of cystic degeneration (20-30%) within the tumour (Fig. 47.64). The tumour may be multifocal. Colour flow imaging frequently demonstrates vascularity within the tumour (Fig. 47.64) with multiple chaotically arranged vessels. Nodal metastases occur in up to 50% at presentation. Like the primary tumour, these may show cystic degeneration and calcification (Fig. 47.62).

Follicular carcinoma is relatively uncommon. It is not possible to differentiate between follicular adenoma and carcinoma on imaging, fine needle aspiration cytology (FNAC) or biopsy. The only definitive sign for the histopathologist is microinvasion of the capsule, and this is not seen by ultrasound. It accounts for 2-5% of

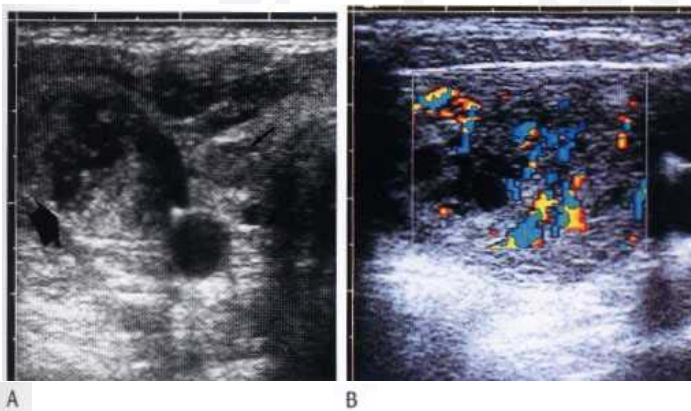


Fig. 47.63 (A) Transverse ultrasound scan of the lower pole of the right lobe of the thyroid with a small hypoechoic mass (arrow). There is an adjacent level four nodal metastasis which is larger than the primary papillary cancer and shows cystic change and abnormal vascularity (B).

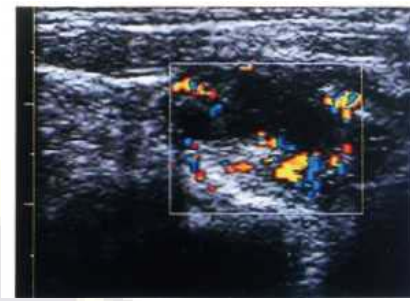


Fig. 47.64 Abnormal partially cystic mass within the thyroid in another patient with abnormal vascularity proved to be a papillary carcinoma.

thyroid cancers. It is a predominantly solid tumour which is commonly hyperechoic and homogenous. Calcification is rare and a halo is commonly present. It usually demonstrates a chaotic internal vascular pattern on colour flow Doppler. Nodal involvement is much less common but patients present more frequently with metastatic spread to bone, lung, brain and liver. *Anaplastic thyroid cancer* is very aggressive. It represents 15-20% of all thyroid cancers. It usually presents with a rapidly growing thyroid nodule, often with signs and symptoms of airway and oesophageal compression. The mass is often hypoechoic, with areas of calcification seen in over half of patients. It often has ill-defined margins and areas of necrosis are frequently seen. There may be evidence of extracapsular spread and adjacent vascular invasion. The outlook is dismal with nodal spread and distant metastatic disease present in 80%.

Medullary carcinoma accounts for 5% of thyroid cancers. The tumour arises from the parafollicular C-cells, which secrete calcitonin. The tumour is associated with multiple endocrine neoplasia (MEN) type 2a. The other conditions associated with this disorder are pheochromocytoma and parathyroid adenomas and/or hyperplasia. There is a familial incidence of 10-20%. These tumours are more likely to be multifocal and more aggressive than the non-familial type. The thyroid tumours are usually solid on ultrasound, with echogenic foci due to the presence of calcification in 80-90%. Intratumoral vessels are seen on ultrasound and have a disorganised pattern. Lymph node involvement occurs in over 50%. These also frequently demonstrate calcification. There is a tendency for bony metastatic disease.

Lymphoma

Lymphoma more commonly presents as a solitary mass (80%) but multiple nodules are seen. A previous history of Hashimoto's thyroiditis is almost always present. Non-Hodgkin's lymphoma is more common than Hodgkin's disease. Extracapsular extension is common (50-60%) and vascular invasion is seen in one-quarter of patients. Focal nodules are usually hypoechoic but may have a pseudocystic appearance. Diffuse involvement may cause thyroid enlargement with little detectable abnormality, or a heterogenous pattern may be seen (Fig. 47.65A). There may be cervical lymphadenopathy (Fig. 47.65B).

Hurthle cell tumours

Hurthle cell tumours are very rare. They have been considered benign lesions in the past but may exhibit malignant characteristics with metastatic spread to lymph nodes and lung. This is seen more frequently (80%) in lesions measuring greater than 4 cm in diameter. The tumours are of mixed echogenicity on ultrasound, usually solid and often ill defined with no calcification.

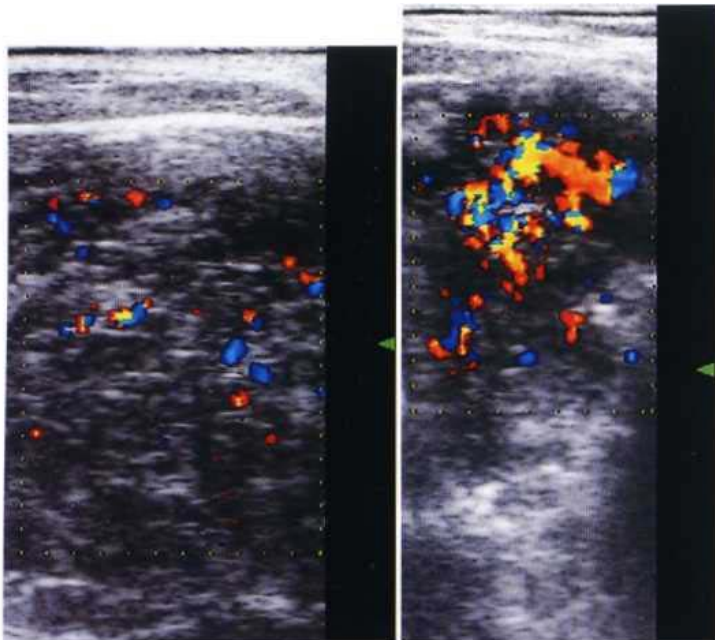


Fig. 47.65 (A) Longitudinal scan through the left lobe of the thyroid in a patient known to have Hashimoto's thyroiditis reveals a loose heterogeneous echotexture with abnormal colour flow. There are enlarged neck nodes (B), again with abnormal colour flow in this patient who has developed lymphoma.

Metastatic disease

Metastatic disease involving the thyroid is uncommon. The common primary sites include melanoma, breast and renal cell carcinoma.

Inflammatory lesions

There are no specific imaging features to differentiate the varying inflammatory processes that affect the thyroid gland. Acute suppurative thyroiditis is rare, particularly affecting children. It may be associated with a fourth branchial cleft anomaly. The patient will present with painful thyroid swelling and fever. Abscess formation is common and the role of ultrasound is to confirm this, demarcate its boundaries and its relationship to the major neck vessels.

Hashimoto's thyroiditis

Hashimoto's thyroiditis is the most common chronic thyroiditis. It is much commoner in women and reaches a peak incidence between the ages of 40 and 60 years. The disease is due to an autoimmune process, with hypothyroidism at presentation or developing later in 50% of cases. The gland is enlarged and tender. Acutely there may either be diffuse involvement of the gland, which appears of decreased vascularity with multiple small nodules within it, or there may be focal nodular thyroiditis with small hypoechoic ill-defined nodules. In the chronic state the thyroid may be enlarged and hypervascular, with multiple ill-defined hypoechoic areas separated by echogenic fibrous septa. A small atrophic gland is seen in end-stage disease.

Riedel's thyroiditis

Riedel's thyroiditis is rare. The disease may be uni- or bilateral and is commoner in women. The presentation is usually with a rapidly enlarging thyroid mass with compressive symptoms and the patient is usually hypothyroid. The thyroid is diffusely hypoechoic on

ultrasound. It may spread beyond the thyroid, obliterating soft-tissue planes. It is associated with mediastinal and retroperitoneal fibrosis, sclerosing cholangitis and orbital pseudotumour.

De Quervain's thyroiditis

De Quervain's thyroiditis occurs more commonly in women following an upper respiratory tract infection. In the acute state there is usually a tender ill-defined hypoechoic nodule and the adjacent thyroid is heterogeneous. There may be diminished vascularity of the thyroid. In the subacute phase the thyroid is swollen, tender and hypoechoic. Enlarged neck nodes may be seen in both phases. Patients usually recover within 6 months with medical treatment.

Parathyroid glands

The parathyroid glands are derived from the third (lower pair of parathyroid glands) and fourth (upper pair) pharyngeal pouches. The majority of people have four glands but 25% have more than this. The superior glands are more constant in position, lying along the dorsal aspect of the superior pole of the thyroid laterally near the recurrent laryngeal nerve. The lower glands have more varied positions, lying along the dorsal aspects of the lower poles of the lobes of the thyroid, but they can lie further away at the cervicothoracic junction and even within the superior mediastinum. The normal parathyroids are difficult to visualise with ultrasound.

The main indication for imaging the parathyroid glands is during the investigation of hyperparathyroidism, which is either caused by an adenoma, usually affecting one gland, parathyroid hyperplasia, in which all glands are involved, or parathyroid carcinoma. Primary hyperparathyroidism is caused by an adenoma in 80%, hyperplasia in approximately 20% and carcinoma is rare, occurring in P/c. In many institutions the parathyroids are not routinely imaged before the first surgical exploration. In good hands this will have a success rate of over 90%.

Scanning should be performed with the patient's neck hyperextended, as many parathyroid adenomas lie low in the neck. Generally the abnormal parathyroid gland is of lower reflectivity than the normal thyroid (Fig. 47.66) and the echogenic capsule will separate one from the other. Calcification is rare in parathyroid adenomas but may be seen in hyperplastic parathyroid glands and in parathyroid carcinomas. Cystic change may be seen. Most lesions



Fig. 47.66 Ultrasound scan of the neck demonstrates a rounded mass of lower reflectivity than the adjacent lower pole of the thyroid in a patient with hyperparathyroidism. This was removed and shown to be a parathyroid adenoma.

(90%) are hypervascular unless they are small, measuring less than 1 cm in diameter, or show cystic change. It has been suggested that a combination of ^{99m}Tc scintigraphy and ultrasound may be the best diagnostic tool for the preoperative diagnosis of primary hyperparathyroidism, with improved sensitivity and specificity and positive and negative predictive values. Other authors have suggested that power Doppler may demonstrate prominent vessels feeding parathyroid adenomas and can be used as 'road maps' to the abnormal glands.

Salivary glands

The major salivary glands consist of paired parotid, submandibular and lingual glands. Multiple minor salivary glands occur elsewhere but especially in the hard palate and lateral pharyngeal wall. The *parotid* is the largest gland and the palpable superficial lobe of the gland lies over the ascending ramus and angle of the mandible. It rarely extends as far cranially as the zygomatic arch. The smaller deep lobe extends through the stylomandibular tunnel between the posterior edge of the mandibular ramus and the anterior borders of the sternocleidomastoid muscle and posterior belly of the digastric muscle. The deep portion of the gland is anterior to the styloid process and the carotid sheath and thus lies in the prestyloid compartment of the pharyngeal space. The facial nerve runs through the gland from the styloid foramen superiorly, dividing the deep from the superficial lobe. The nerve cannot be identified on ultrasound but it is important when examining a parotid mass to determine whether the mass lies within the deep or superficial lobe because this may well alter the surgical approach. The retromandibular vein is an important anatomical landmark, lying medial and parallel to the nerve. There are usually three or four lymph nodes within the parotid gland. The gland itself appears of homogeneous, fairly bright reflectivity. Intraparotid nodes are well defined, measuring less than 5 mm in diameter with a reflective hilum. Stenson's duct is about 7 cm long and is seen on ultrasound as parallel reflective lines. It should not measure more than 3 mm in diameter. The normal duct is generally not visualised on ultrasound beyond the parotid gland itself. Intraglandular ducts may be seen as short reflective thin lines.

The *submandibular* and *lingual* glands have a similar reflectivity to the parotid glands. Wharton's duct is about 5 cm long but has thinner walls than Stenson's duct and may not be seen in the normal individual.

Ultrasound may be used to determine whether a mass lies within or outside the salivary glands and whether the mass is solid or cystic. It may be used to guide FNAC, which will be needed to suggest histological type. Benign lesions tend to have well-defined margins on ultrasound. Pleomorphic adenomas, which are the commonest parotid tumours, are often homogeneous and hyporeflective on ultrasound, often displaying through transmission. Some will display colour Doppler flow within the lesion. Adenolymphoma (Warthin's tumour) is rarely seen in the submandibular gland. It is usually well defined with solid and cystic areas and may have a multiseptated appearance. Lipomas can be more confidently diagnosed using CT or MRI but will appear well defined and hyperreflective on ultrasound. Malignant tumours are more commonly seen in the smaller salivary glands. They have similar appearances on ultrasound, with ill-defined margins and are hyporeflective (Fig. 47.67) with a heterogeneous texture. Some low-grade malignancies may develop a pseudocapsule and thus appear well defined.



Fig. 47.67 Ultrasound scan of a carcinoma ex pleomorphic adenoma of the left parotid gland demonstrates a hyporeflective mass with scanty colour flow within it.

Neck nodes

The inaccuracies in physical examination of cervical lymph nodes are well documented and all diagnostic imaging modalities have been shown to have superior diagnostic accuracy. Ultrasound is being increasingly used to assess cervical nodes. It has the benefits of not using ionising radiation or intravenous contrast medium but it is generally accepted that it is less able to stage most primary tumours at the same time, and deep lymph nodes, for example in the retropharyngeal region, cannot be assessed by ultrasound. The optimal size criteria to define pathological lymph nodes at ultrasound are minimum diameters of 9 mm for level 2 nodes and 8 mm for the remaining levels. These measurements offer a sensitivity of 74% and specificity of 78%. The ratio of minimal to maximal axial diameter has been reported to be a valuable predictor of malignancy, a ratio of greater than 0.55 indicating malignancy, with a specificity of 63% and sensitivity of 92%.

Ultrasound has potential advantages over MRI and CT in the evaluation of nodal shape, with its ability to rotate the probe at ultrasound and select true minimal and maximal diameters. Ultrasound also has the advantage of demonstrating the normal nodal architecture with the presence in the normal node of an echogenic lymph node hilum and surrounding hypoechoic cortex. This has been shown to be helpful in distinguishing malignant from benign normal-sized nodes. Central necrosis will be identified by



Fig. 47.68 There is an abnormal neck node with a thick irregular wall (arrow), cystic necrosis centrally with through transmission and abnormal vascularity on power flow Doppler.



Fig. 47.69 Ultrasound scan of the left supraclavicular fossa demonstrates an abnormal node with peripheral flow in a patient with oesophageal cancer.

areas of low echogenicity with posterior acoustic enhancement. The rim of the node will usually be thick and irregular (Fig. 47.68). Coagulative necrosis can also give the appearance of a very heterogeneous nodal architecture, with areas of increased reflectivity within the nodes. The distribution of blood flow in lymph nodes has also been evaluated using Doppler ultrasound. It has been shown that areas of vascular sparing and isolated peripheral flow (Fig. 47.69) are suggestive of malignancy. Ultrasound contrast medium may contribute to such Doppler assessments in the future. Nodes involved by lymphoma may appear of very low reflectivity with through transmission and thus mimic cysts. Increasing the gain settings will demonstrate low-level echoes within the node (Fig. 47.70) and colour flow can be demonstrated within the node to differentiate it from a cyst (Fig. 47.71).

The most promising contribution of ultrasound is in the guidance of FNAC. This increases the specificity of ultrasound detection of lymph node metastases to 100% but reported sensitivities remain between 50 and 98%. These results do depend on whether the study population includes patients with No necks (those patients who clinically have no palpable disease), as these nodes will be smaller and more difficult to aspirate. Some papers performing direct comparison of ultrasound-guided FNAC with CT and MRI have shown

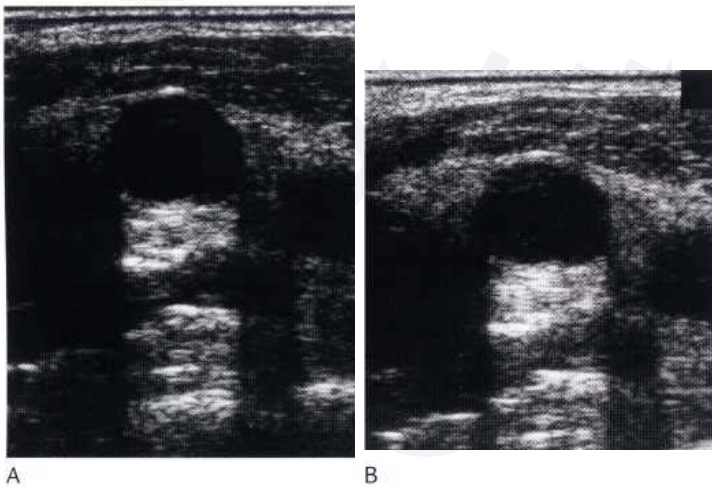


Fig. 47.70 (A) Ultrasound scan of a neck node involved by lymphoma initially demonstrates a cystic-appearing mass. (B) The scan has been performed with increased gain settings and now some low-level internal echoes are seen.



Fig. 47.71 Abnormal colour flow is seen within this lymphomatous neck node.

it to be the most accurate technique in staging both the clinically metastatic and normal neck. The major drawback of using ultrasound in the staging of nodal metastases in the neck is the inability in most cases to stage the primary site of disease. The presence of extracapsular spread of disease does have major prognostic implications but is also less well seen with ultrasound than with CT.

REFERENCES AND SUGGESTIONS FOR FURTHER READING

- Barakos, J. A. (1994) Advances in magnetic resonance imaging of the head and neck. *Topics in Magnetic Resonance Imaging*, 6(3), 155-165.
- Campbell, R. S. D., et al (1995) MRI T staging of squamous cell carcinoma of the oral cavity: radiological-pathological correlation. *Clinical Radiology*, 50, 533-540.
- Duhin, M. D., et al (1995) Conspicuity of tumors of the head and neck on fat-suppressed MR images. *American Journal of Roentgenology*, 164,1213-1221.
- Ekberg, O., Nylander, G. (1982a) Cineradiography of the pharyngeal stage of deglutition in 150 individuals without dysphagia. *British Journal of Radiology*, 55, 253-257.
- Ekberg, O., Nylander, G. (1982b) Cineradiography of the pharyngeal state of deglutition in 250 patients with dysphagia. *British Journal of Radiology*, 55,258-262.
- Hamlin, J. A., Hasso, A. N. (1994) Magnetic resonance imaging of the skull base. *Topics in Magnetic Resonance Imaging*, 6, 183-201.
- Lloyd, G. A. S. (1988) *Diagnostic Imaging of the Nose-Paranasal Sinuses*. Berlin: Springer-Verlag.
- Lloyd, G. A. S., Michaels, L., Phelps, P. D. (1981) The demonstration of cartilaginous involvement in laryngeal carcinoma by computerized tomography. *Clinical Otolaryngology*, 6, 171-177.
- Mancuso, A. A., Dillon, W. P. (1989) The neck. *Radiologic Clinics of North America*, 27, 407-434. (See also other relevant chapters.)
- Mancuso, A. A., Hanafee, W. N. (1983) *Computed Tomography of the Head and Neck*. Baltimore: Williams & Wilkins.
- Valvassori, G. E., Mafee, M. F., Carter, B. L. (1995) *Imaging of the Head and Neck*. New York: Thieme.

Radionuclide imaging

- Cases, J. A., Surks, M. I. (2000) The changing role of scintigraphy in the evaluation of thyroid nodules. *Seminars in Nuclear Medicine*, 30, 81-87.
- Castellani, M., Reschini, E., et al (2001) Role of Tc^{99m} sestamibi scintigraphy in the diagnosis and surgical decision-making process in primary hyperparathyroid disease. *Clinical Nuclear Medicine*, 26, 139-144.
- Freitas, J. E., Freitas, A. E. (1994) Thyroid and parathyroid imaging. *Seminars in Nuclear Medicine*, 24, 234-245.
- Krausz, Y., Lebenshart, P. D., Klein, M., et al (2000) Preoperative localisation of parathyroid adenoma in patients with concomitant thyroid nodular disease. *World Journal of Surgery*, 12, 1573-1578.
- Lind, P. (1999) ^{131}I scintigraphy in thyroid cancer patients. *Quarterly Journal of Nuclear Medicine*, 43, 188-194.

NIH Conference (1991) Diagnosis and management of asymptomatic primary hyperparathyroidism: consensus development conference statement. *Annals of Internal Medicine*, 114, 593-597.

CT

- Baum, U., Gress, H., Left, M., Nomayr, A., Lenz, M. (2000) Imaging of head and neck tumors-methods: CT, spiral-CT, multislice-spiral-CT. *European Journal of Radiology*, 33, 153-160.
- Bransteler, B. F., Weissman, J. L. (2000) Normal anatomy of the neck with CT and MR imaging correlation. *Radiologic Clinics of North America*, 38,925-940.
- Council, The Royal College of Radiologists (1994) *The Use of Computed Tomography in the Initial Investigation of Common Malignancies*, pp. 12-15. London: Royal College of Radiologists.
- Ginsberg, L. E. (2000) Contrast-enhanced spiral CT of the head and neck. *American Journal of Neuroradiology*, 21, 1365.
- Harnsherger, H. R. (1995) The infrahyoid neck. In: *Handbook of Head and Neck Imaging*. pp. 150-199. St Louis: Mosby Year Book.
- Sumi, M., Ohki, M., Nakamura, T. (2001) Comparison of sonography and CT for differentiating benign from malignant cervical lymph nodes in patients with squamous cell carcinoma of the head and neck. *American Journal of Roentgenology*, 176, 1019-1924.

Ultrasound

- Ariji, Y., Kimura, Y., Hayashi, N., et al (1998) Power Doppler sonography of cervical lymph nodes in patients with head and neck cancer. *American Journal of Neuroradiology*, 19, 303-307.
- Atula, T. S., Varpula, M. J., Kurki, T. J., Klemi, P.-J., Grenman, R. (1997) Assessment of cervical lymph node status in head and neck cancer patients: palpation, computed tomography and low field magnetic resonance imaging compared with ultrasound guided fine needle aspirate cytology. *European Journal of Radiology*, 25, 152-161.
- Baatenburg de Jong, R. J., Rongen, R. J., Verwoerd, C. D., et al (1991) Ultrasound guided fine needle biopsy for neck nodes. *Archives of Otolaryngology and Head and Neck Surgery*, 117, 402-404.
- Barakos, J. A. (1994) Advances in magnetic resonance imaging of the head and neck. *Topics in Magnetic Resonance Imaging*, 6(3), 155-165.
- Bruncton, J. N., Balu-Maestro, C., Marcy, P. Y., Melia, P., Mourou, M. Y. (1994) Very high frequency (13 MHz) ultrasonographic examination of the normal neck: detection of normal lymph nodes and thyroid nodules. *Journal of Ultrasound Medicine*, 13, 87-90.
- De feo, M. L., Cholagrande, S., Biagini, C., et al (2000) Parathyroid gland: combination of ^{99m}Tc MIBI scintigraphy US for demonstration of parathyroid glands and nodules. *Radiology*, 214, 393-402.
- Dubin, M. D., Teresi, L. M., Bradley Jr, W. G., et al (1995) Conspicuity of tumors of the head and neck on fat-suppressed MR images. *American Journal of Roentgenology*, 164, 1213-1221.
- Lane, M. J., Desser, T. S., Weigel, R. J., Jeffroi Jr, R. D. (1998) Use of color and power Doppler sonography to identify CD arteries associated with parathyroid adenomas. *American Journal of Roentgenology*, 171, 891-823.
- Righi, P. D., Kopecky, K. K., Caldemeyer, K. S., et al (1997) Comparison of ultrasound guided fine needle aspiration and computed tomography in patients undergoing elective neck dissection. *Head and Neck*, 19, 604-610.
- Rubaltelli, L., Proto, E., Salmaso, R., et al (1990) Sonography of abnormal lymph nodes in vitro: correlation of sonographic and histologic findings. *American Journal of Roentgenology*, 155, 1241-1244.
- Steinkamp, H.-J., Mueffelmann, M., Bock, J. C., et al (1998) Differential diagnosis of lymph node lesions: a semiquantitative approach to colour Doppler ultrasound. *British Journal of Radiology*, 71, 828-833.
- Takashima, S., Sone, S., Nomura, N., et al (1997) Non-palpable lymph nodes of the neck: assessment with US and US guided fine needle aspirate biopsy. *Journal of Clinical Ultrasound*, 25, 283-292.
- Takes, R. P., Knegt, P., Manni, J. J., et al (1996) Regional metastasis in head and neck squamous cell carcinoma: revised value of US and US guided FNAB. *Radiology*, 198, 819-823.
- Valvassori, G. E., Mafee, M. F., Carter, J. L. (1995) *Imaging of the Head and Neck*. New York: Thieme.
- Van den Brekel, M. W., Castelijns, J. A., Stel, H. V. (1993) Modern imaging techniques and ultrasound guided aspiration cytology for the assessment of neck node metastases: a prospective comparative study. *European Archives of Otorhinolaryngology*, 250, 11-17.
- Van den Brekel, M. W., Castelijns, J. A., Snow, G. B. (1998) The size of lymph nodes in the neck on sonograms as a radiologic criterion for metastasis: how reliable is it? *American Journal of Neuroradiology*, 19,695-700.
- Vassallo, P., Wernecke, K., Roos, N., Peters, P. E. (1992) Differentiation of benign from malignant superficial lymphadenopathy: the role of high resolution ultrasound. *Radiology*, 183, 215-220.

نشر الکترونیکی

موسسه انتشاراتی

نور دانش



نشر الکترونیکی
موسسه انتشاراتی
نوردانش

48

THE SINUSES

Swarupsinh V. Chavda, Julie F. C. Olliff

IMAGING

Plain films The indication and the need for plain X-rays in diagnosis and further management has declined over the last decade. Most patients require a CT scan. There is still a limited role for plain films of the paranasal sinuses in acute infection. The X-rays are limited to a single occipitomental (OM) view, which is considered adequate for the basic assessment of the maxillary antra, the frontal sinuses and the sphenoid sinus but is poor at excluding pathology of the ethmoid air cells or providing fine bony detail.

OM view The patient sits facing the film and the radiographic baseline is tilted 45°. The incident beam is horizontal and is centred on the occipital bone, 3 cm above the external occipital protuberance. This view shows the maxillary antra free of the overlap of the petrous bones, and if the mouth is kept open during the examination the sphenoid sinuses and the nasopharynx can be seen through it.

CT CT is the imaging modality of choice since the advent of functional endoscopic sinus surgery (FESS). It is now mandatory and a medicolegal requirement to evaluate the paranasal sinuses and nose before FESS, as this provides a 'roadmap'. Excellent detail is available regarding the anatomy, anatomical variants and pathology.

Technique Coronal sections are used ideally for full evaluation of the nose and paranasal sinuses, especially as most present-day CT scanners allow postprocessing reformat for further views in different planes if required.

There are occasions when axial reformat views are required to help define the posterior ethmoid complex, the walls of the frontal sinuses and the distance between the nasal aperture and the sphenoid sinus ostium, and when parasagittal views are required to assess the frontoethmoid recess. The coronal scans have the added benefit of reduction in radiation dose to the eyes.

The advent of multislice scanning has enabled the acquisition of a 3D volume block with isotopic voxels. This allows multiplanar reconstruction.

Coronal scans are performed by hyperextension of the patient's head and angulation of the gantry, preferably with the patient in the prone position with the chin resting on a pad. This keeps the free fluid out of the infundibulum. In patients unable to attain this because of age or neck pathology, the 'hanging-head' supine position may be acceptable. The gantry should be angled perpendicular to the hard palate.

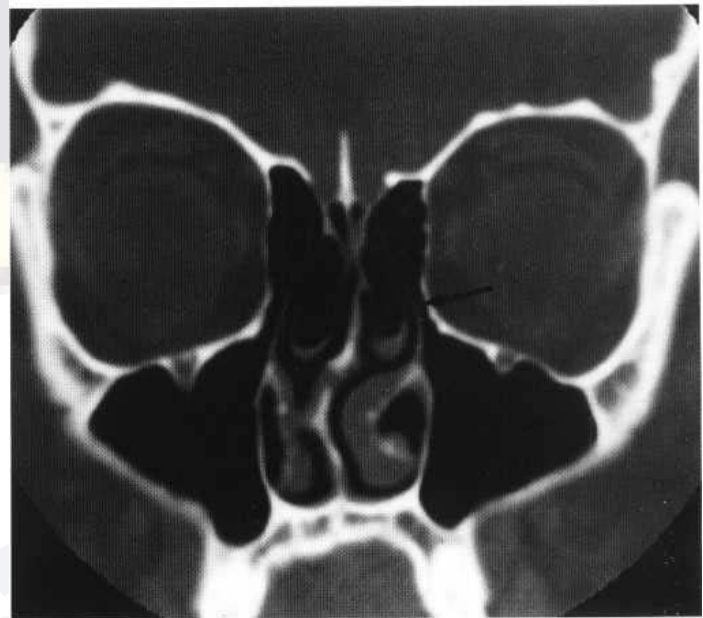


Fig. 48.1 SSCT showing the normal ostiomeatal complex. Incidental bilateral concha bullosa. The arrow points to the infundibulum and ostium.

The ideal scan thickness varies from centre to centre but we prefer to use 3-5 mm slice thickness to cover from the anterior margin of the frontal sinus to the posterior margin of the sphenoid sinus. Thinner slice thickness of 2-3 mm reconstructed at 1 mm with various reformat can be utilised when helical CT is available. There is no need for intravenous contrast (Fig. 48.1).

The radiation dose is kept to the minimum by use of low mA with peak kV of 120. Images should be obtained at an intermediate setting of about 2000-2500 HU window width, 200-350 HU window level, as this provides details of bone and soft tissues on a single set of films.

MRI MRI is predominantly used for the pre- and postoperative assessment of nasosinus malignancy. Other conditions, including inflammatory disease and benign tumours, are in most cases adequately demonstrated by CT. The chief disadvantage of MRI is its inability to show the bony details of the sinuses, as both air and bone give no signal; for the same reason it cannot show calcification or hyperostosis caused by, or associated with, a neoplasm. The multiplanar imaging facility, the excellent soft-tissue detail and the lack of X-ray radiation give some advantage over CT.

The standard quadrature headcoil is used for MR imaging. Most commonly used sequences are the T₁ and T₂ weighted in the axial/coronal plane. The availability of the new fast pulse sequences has led to the use of fast spin echo (FSE) instead of the conventional spin echo (CSE) imaging. It is important to note that fat remains bright on T₁ images on FSE. The ability to obtain fat-suppressed imaging without significant time penalty is used to obtain pre- and postcontrast fat-suppressed T₁ scans. Most centres tend to settle for axial pre- and post-fat-suppressed T₁ scans because of the possibility of asymmetric fat saturation. Fat suppressed T₂ scans are also excellent at delineating pathology, and STIR images are used at most centres.

Sinonasal physiology and anatomy

The normal secretions (approximately 2 litres of serous secretions daily) produced by the sinuses are cleared by the cilia lining the mucosa. These drain the secretions towards the natural sinus ostia. This occurs despite the presence of any other openings. Each sinus has its own opening and hence its own pattern of mucociliary clearance. Adequate normal secretions, normal ciliary action and patent ostia are necessary for normal physiological function, and any alteration in any one will result in pathology.

The nose and the paranasal sinuses have to be considered as a unit because of the common embryology. The lateral wall of the nose is an undulating surface with superior, middle and inferior turbinates. These are C-shaped structures that curl inferolaterally and define channels termed meati.

The frontal sinuses drain into the frontoethmoidal recess, through the anterior ethmoid air cells, into the anterior frontal recess of the middle meatus; the anterior ethmoid air cells drain into the anterior aspects of hiatus semilunaris; the middle ethmoid air cells drain through the ethmoid bulla; the posterior ethmoids drain into the superior meatus.

The maxillary sinus drains via the infundibulum into the ostium, which lies on the posterior aspect of the hiatus semilunaris of the middle meatus. The sphenoid sinus drains into the sphenoid recess posterior to the superior meatus. The *ostiomeatal complex* or *unit* is the region where the frontal, anterior and middle ethmoid and maxillary sinuses drain. This includes the frontoethmoidal recess, uncinete process, hiatus semilunaris, ethmoid bulla, the maxillary infundibulum and ostium and the ethmoid infundibulum. Disease at the ostiomeatal complex is the major cause of recurrent acute or chronic sinusitis.

Inflammatory sinus disease

Acute sinusitis

Acute sinusitis is often due to secondary bacterial infection following an upper respiratory tract infection of viral origin or from local infection, e.g. an infected tooth. The infection causes swelling of the mucosa, which appears as an opaque rim around the periphery of the sinus. Acute sinusitis is accompanied by an outpouring of the mucus into the sinus cavity, causing an opaque sinus on plain X-ray. This is a non-specific sign, and although in most cases it denotes infection, a sinus filled with blood or new growth can give a similar appearance. If there is any doubt about the presence of fluid a tilted view should be obtained-this will confirm the presence of a fluid level (Fig. 48.2).

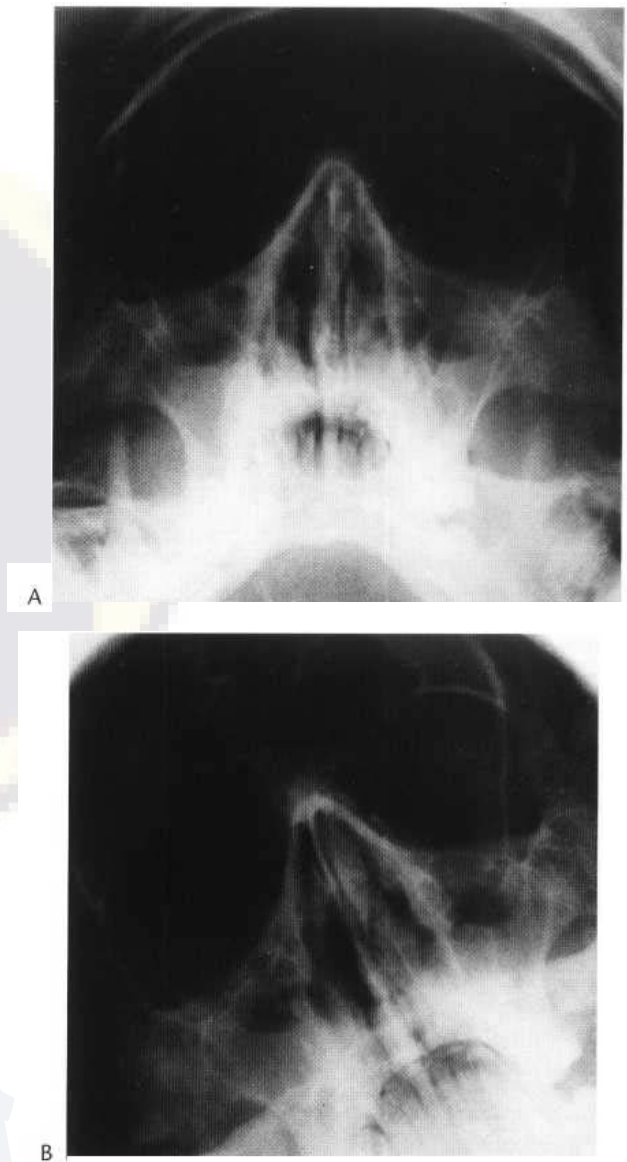


Fig. 48.2 (A, B) Plain X-ray. Note opacification due to acute sinusitis and the fluid levels on tilted view (B).

Complications of acute sinusitis

Osteomyelitis This has become rare since the advent of antibiotics. It may follow empyema, which may rarely lead to bone involvement. This results in loss of outline of the sinus wall followed by frank osteolysis and bone sequestration.

Intracranial abscess Spread of infection from the frontal or sphenoid sinuses may result in an intracranial abscess or, subdural or extradural empyema. CT or MRI will show the characteristic ring enhancement. It is imperative that thrombosis of the superior ophthalmic vein (Fig. 48.3) or the cavernous sinus is looked for and excluded.

Orbital cellulitis This commonly follows an ethmoiditis and may result in abscess formation, often situated outside the periorbital adjacent to the infected sinus. The abscess may be demonstrated on the CT scan as a soft-tissue mass in the medial or superomedial orbit, sometimes accompanied by the presence of gas or a fluid level.

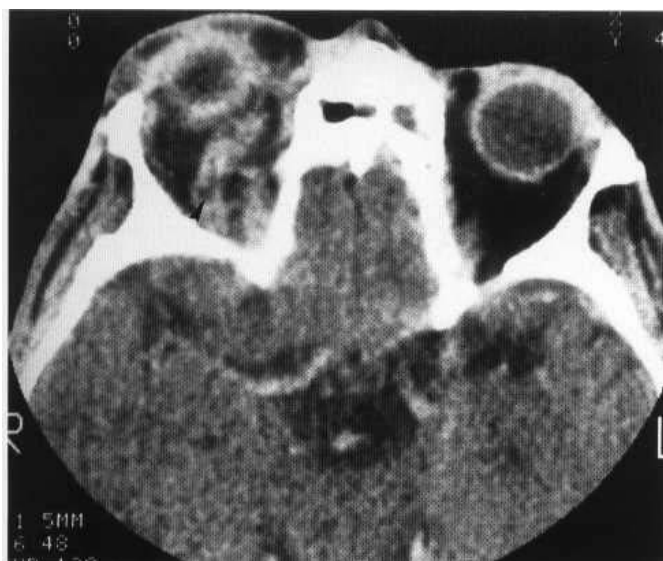


Fig. 48.3 CT scan showing infection in the sinuses with orbital cellulitis and superior ophthalmic vein thrombosis (arrowhead).

Chronic rhinosinusitis Chronic inflammatory disease of the paranasal sinuses and nasal cavity clinically represents recurrent acute sinusitis or a prolonged episode that has failed to respond to conservative management. CT is the investigation of choice as this defines the degree and extent of involvement of the paranasal sinuses and also provides the surgeon with the 'roadmap' of the anatomy before surgery. Functional endoscopic sinus surgery is usually the treatment for patients with chronic rhinosinusitis.

Imaging for functional endoscopic sinus surgery (FESS) Coronal CT scans are obtained according to the protocol described earlier. Particular attention is paid to the ostiomeatal complex, as most chronic rhinosinusitis is associated with disease in the middle meatus. The scans will show the extent of mucosal thickening and the number of sinuses affected, and help confirm that the pathology is due to an inflammatory process. Chronic disease will manifest with thickening and sclerosis of the bones. Acute-on-chronic sinus secretions have a CT density that is less than muscle but higher than fat, usually in the range of 10-25 HU, referred to as watery or mucoid density. These have a low T₁ and high T₂ on MRI. Once the secretions have become chronically thickened and concentrated, the CT density will rise to 60-80 HU. The MR appearances depend on the protein content of the secretions and can therefore be quite variable. Chronic desiccated sinus secretions may lead to an erroneous diagnosis, as this is of low signal intensity on T₁- and T₂-weighted scans and may be reported as a well-aerated sinus. If contrast enhancement is used, the periphery of the sinus mucosa will enhance, not the secretions.

The modality of choice is therefore the CT scan, referred to as screening sinus CT (SSCT), while MRI is reserved for difficult cases, especially where there is doubt about the pathology on SSCT. MRI is also useful to assess any intracranial or orbital involvement.

The second and more important use of SSCT is to help the surgeon avoid the known hazards of endoscopic surgery. Major complications, such as blindness, ocular motility dysfunction, orbital haematoma, CSF leak and carotico-cavernous fistula, have been reported. The function of SSCT is to show the important

anatomical landmarks and the anatomical variants. The commonly encountered variants include septa deviation, spur formation, concha bullosa, paradoxical curve of the middle turbinate and the unusually low position of the roof of the ethmoid air cells (fovea ethmoidalis).

Chronic rhinosinusitis tends to present in certain recognisable patterns on CT. Five distinct patterns of sinonasal disease are easily identified on SSCT. The first three are due to obstruction to the known mucociliary drainage. In the infundibular pattern (I) there is obstruction of the maxillary infundibulum resulting in isolated maxillary sinusitis. In the ostiomeatal unit pattern (II) there is middle meatus obstruction resulting in ipsilateral sinusitis affecting the frontal, anterior and middle ethmoids and the maxillary antrum. The sphenothmoid recess pattern (III) of obstruction results in posterior ethmoid and sphenoid sinusitis. In the sinonasal polyposis pattern (IV) sinonasal polyps are evident, with opacification of various sinuses. The sporadic or unclassifiable pattern (V) includes retention cysts, mucocoeles and mild mucosal thickening without obstruction.

Sinonasal polyposis

The polyps in sinonasal polyposis are soft-tissue pedunculated masses of oedematous hyperplastic upper respiratory mucosa. The specific polysaccharide material within the ground substance attracts excess fluid and electrolytes. The commonest site of sinonasal polyposis is the ethmoids, followed by the maxillary antra and then the sphenoid sinus.

The cause remains unclear but there is an association with atopic rhinitis (allergic and non-allergic), asthma, infection, cystic fibrosis, aspirin intolerance and Kartagener's syndrome.

Multiple polyps give rise to a characteristic pattern. Plain X-rays and SSCT confirm the presence of polypoidal masses in the nasal cavity, with widening of the infundibulum, opacification of the sinuses, and thinning of sinus walls and the nasal and ethmoid septa (Fig. 48.4). There may be bulging of the lamina papyracea, leading to displacement of the eyeballs and hypertelorism. Antrochoanal



Fig. 48.4 Extensive nasal polyposis with pansinus opacification. The septa and sinus walls are thinned and eroded.

and sphenochoanal polyps arise from mucosa lining the maxillary or sphenoid sinus and pass through an ostium into the nose.

Mucocele The term 'mucocele' is defined as the end-stage of a chronically obstructed sinus—an obstructed, airless, mucoid-filled expanded sinus. The most commonly affected sinus is the frontal (66%); about 25% occur in the ethmoids and 10% in the maxillary antra. Mucocele of the sphenoid sinus is rare.

On CT mucoceles have mucoid attenuation collection with remodelling of the wall. The bone may be locally thinned or eroded but the overall picture is of remodelling and bone preservation.

MRI is the optimum imaging modality as any intracranial and intraorbital extension can be assessed before surgery. On MRI the contents will have varying signal intensities on T₁- and T₂-weighted images, according to the protein content. Postcontrast scans typically show peripheral enhancement of the mucosa with no enhancement of the secretions (Figs. 48.5, 48.6).

Frontal sinus mucocele The principal sign on plain X-ray is an expansion of the sinus cavity with loss of the scalloped margin of the normal sinus. In most patients the sinus is more opaque than normal, due to secretions, but may on occasions appear more radiolucent if bone destruction is marked. CT will show the full extent of the expansion and is usually enough to make the diagnosis. MRI may be used to assess intracranial extension.

Ethmoid mucoceles The majority are found in the anterior ethmoid air cells. Expansions of the posterior ethmoid air cells are less common and are associated with sphenoid mucoceles. Ethmoid mucoceles are usually more obvious clinically, as most present with a palpable mass at the medial canthus. Other important features are the presence of proptosis and, in some patients, epiphora, when the expansion impinges the lacrimal sac (Fig. 48.5).

Sphenoid mucoceles Only a very small percentage occur in the sphenoid sinus. Imaging plays a key role in the diagnosis of sphenoid mucoceles, and it is important that the condition be recognised by the radiologist at an early stage and dealt with surgically before vision is seriously compromised. Involvement of the optic nerve, cavernous sinus and oculomotor nerve is common due to the proximity of these structures to the sinus. The patient commonly presents with headache combined with eye symptoms such as blurred vision or diplopia.

CT and MRI show rounded or partially rounded expansion of the sinus, as opposed to the destruction of bone in situ caused by malignancy (Fig. 48.6).

Fungal disease Fungal disease of the paranasal sinuses is usually diagnosed when an apparent routine infection fails to respond to normal antibiotic treatment. A number of mycotic agents are capable of infecting the nose and paranasal sinuses; the most common of these is the saprophyte aspergillus. It is found in the soil, dust and decaying organic matter, and can be pathogenic in humans, animals and birds. The usual point of entry is the nose, from where it may spread to the sinuses and bronchi or disseminate in the lung. The condition may occur in the immune compromised host or in those debilitated by other primary conditions; it may affect otherwise healthy subjects. *Aspergillus fumigatus* is the species which most often causes paranasal sinus disease; *A. flavus* is less common but in the Sudan, where the disease is endemic, it is the predominant organism. The ethmoids and the maxillary antra are commonly involved; the sphenoid sinus may be occasionally involved; and the frontal sinuses are rarely affected.

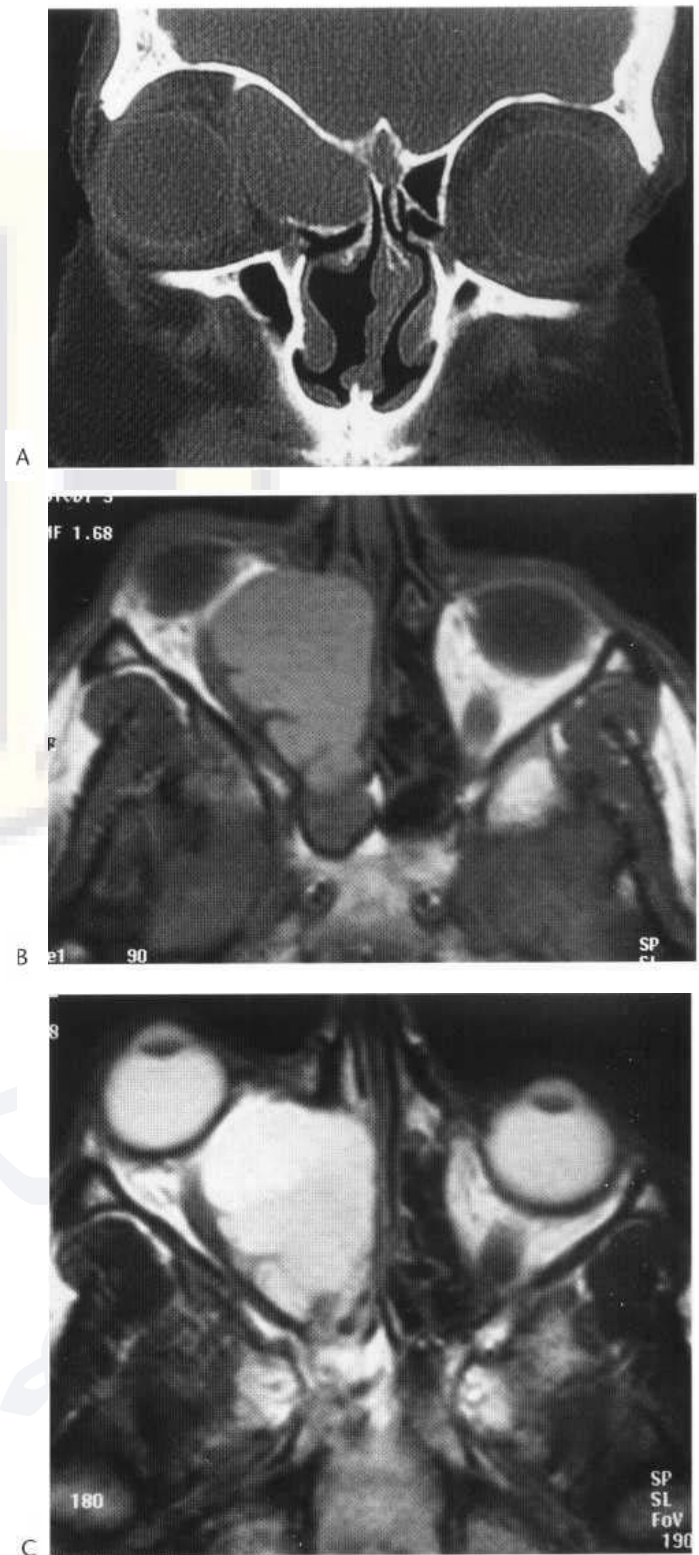


Fig. 48.5 Frontoethmoid mucocele. (A) Direct coronal CT scan demonstrates expansion of the right ethmoid cells with bony expansion and a mass which extends into the right orbit. (B) Axial T₁-weighted and (C) axial T₂-weighted MRI scans show expansion and scalloping of the bony margins with extension into the right orbit.

The findings vary from non-specific mucosal thickening without bone involvement to an opacified sinus with a central mycetoma with reactive new bone formation or even erosions.

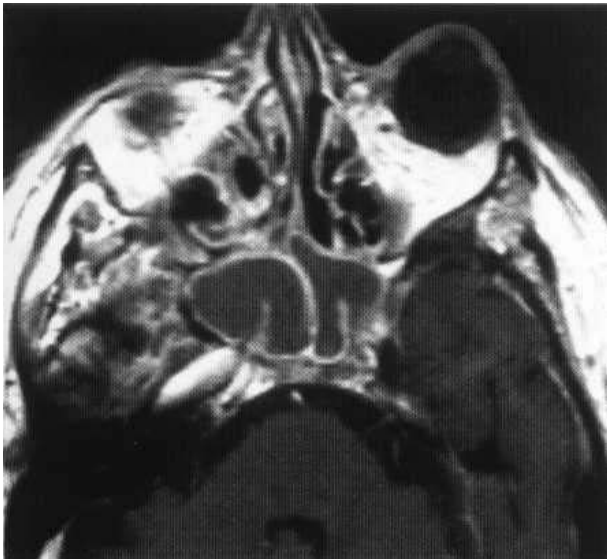


Fig. 48.6 Axial T₁-weighted gadolinium-enhanced MRI of a sphenoid mucocele demonstrates an expanded rim enhancing sphenoid sinus containing fluid-density material.

On CT fungal disease appears as a high-density central mass separated by mucoïd secretions. Areas of calcification may be present. The calcification may be diffuse, nodular or linear and may be accompanied by bone expansion and bone destruction in the invasive form of the disease (Fig. 48.7A).

Signal hypointensity is the distinctive feature of aspergillosis on MRL either low signal on T₁ and T₂, when there is fibrosis, or a total absence of signal on all sequences due to the paramagnetic effect of heavy metals present in the fungal ball (Fig. 48.7).

Granulomatous disease The majority of these are infectious and include tuberculosis, syphilis, leprosy, rhinoscleroma and actinomycosis. Other causes include Wegener's granulomatosis, midline granuloma, sarcoidosis and now the nasal granuloma due to cocaine abuse.

There are non-specific findings on imaging. Most start in the nasal cavity with soft-tissue masses and chronic non-specific pansinusitis. A diagnosis of granulomatous disease should be considered when there is evidence of a nasal septal mass with septa erosion on imaging.

Retention cysts These occur as a result of obstruction of the ducts of the mucosal glands. They are usually small, have a well-defined outline and are seen in approximately 10% of the population. They may occasionally enlarge to fill the sinus. CT appearance is of a smooth, broad-based soft-tissue mass with a well-defined outline (Fig. 48.8). On MRI these are usually of low intensity on T₁ and bright on T₂, but may appear bright on T₁, depending on the concentration of entrapped secretions.

Tumours of the paranasal sinuses

Benign tumours

Osteoma These are benign, slowly growing tumours containing mature compact or cancellous bone. They occur most frequently in

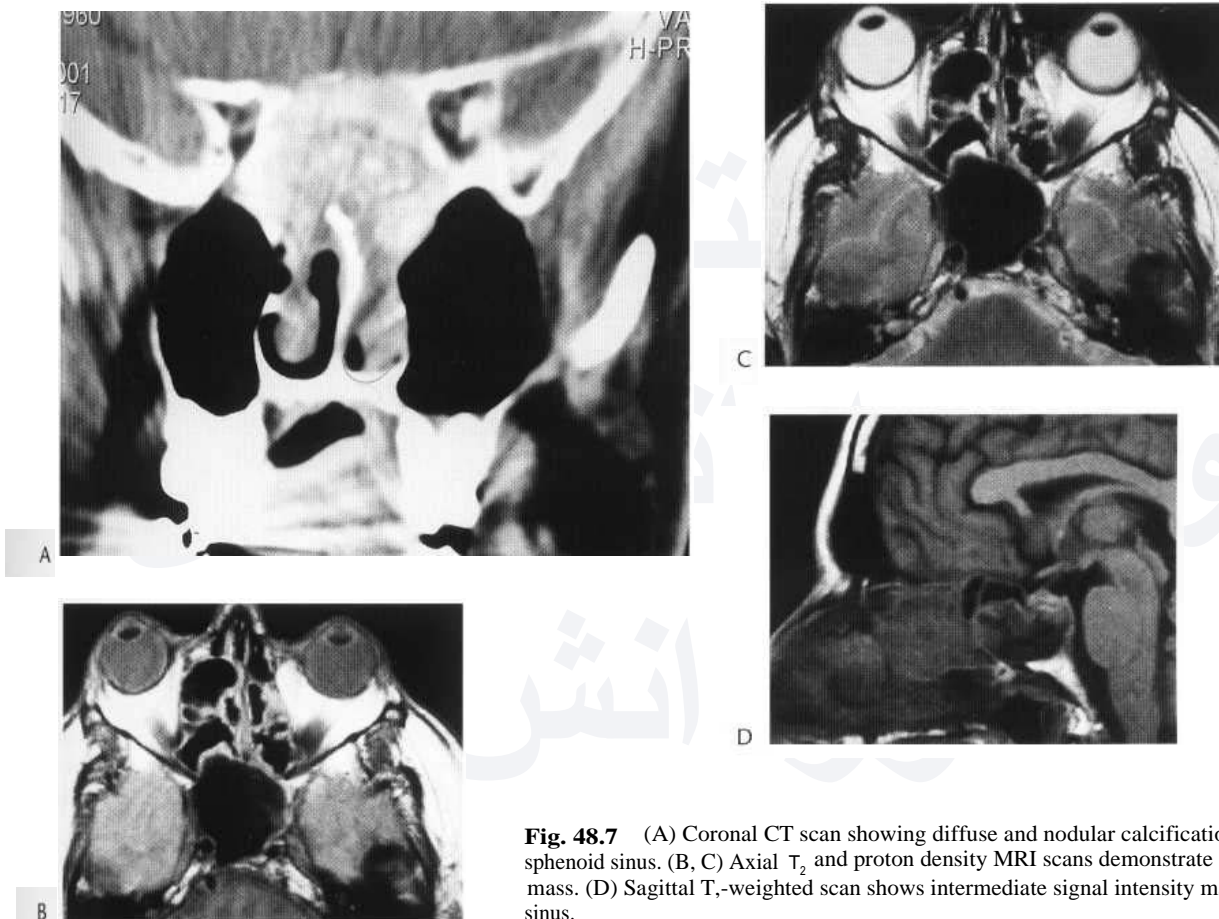


Fig. 48.7 (A) Coronal CT scan showing diffuse and nodular calcification in the fungal mass in the sphenoid sinus. (B, C) Axial T₂ and proton density MRI scans demonstrate signal void from the fungal mass. (D) Sagittal T₁-weighted scan shows intermediate signal intensity material within the sphenoid sinus.

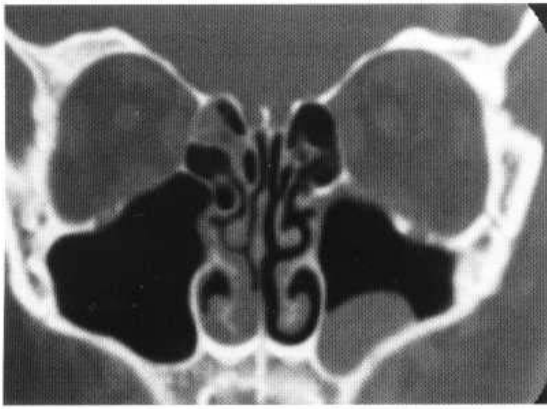


Fig. 48.8 Coronal CT scan demonstrates the typical appearance of a retention cyst within the right maxillary antrum.

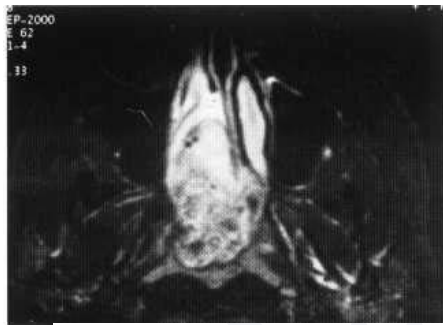
the frontal sinus, followed by the ethmoid and maxillary sinuses. They are usually asymptomatic but may block the drainage of a sinus, resulting in recurrent infection and/or mucocoele. Large frontal sinus osteomas can erode the inner table to the frontal bone, which in turn will allow sinus infection to spread intracranially and pneumocephalus will be seen. Osteomas in the ethmoid frequently cause proptosis. Posterior extension may lead to compromise of the optic nerve. Osteomas are seen in patients with Gardner's syndrome.

Plain film and CT findings are those of a well-defined very dense lesion if the osteoma comprises compact mature bone, but an osteoma containing cancellous bone will be less ossified. If these lesions are histologically predominantly filled with fat, fibrous tissue or haemopoietic elements, they may appear of almost soft-tissue density and can potentially be confused with retention cysts or polyps.

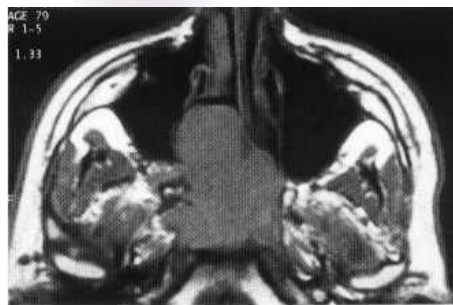
A wide variety of benign and malignant tumours affect the paranasal sinuses. The mucosal lining of the nose is derived from ectoderm and is called the schneiderian membrane. This mucosa may give rise to three different types of **papillomas**: the *fungiform*, the *inverted* and the *cylindrical cell* papilloma.

The fungiform variety arises almost always from the nasal septum, usually anteriorly. The other two varieties usually originate from the lateral nasal wall. *Inverted papillomas* are the commonest. Characteristically they arise from the lateral nasal wall near the middle turbinate and extend into the sinuses, usually involving the maxillary and ethmoid sinuses. The most common presenting symptoms are nasal obstruction, epistaxis and anosmia. Recurrence following local surgical excision can be common, occurring in up to 73% of patients.

On imaging, the appearances of all of these papillomas can vary from a small nasal polypoid mass to an expansile nasal mass with remodelling of the nasal cavity and extension into the sinuses with secondary obstructive sinusitis. The nasal septum usually remains



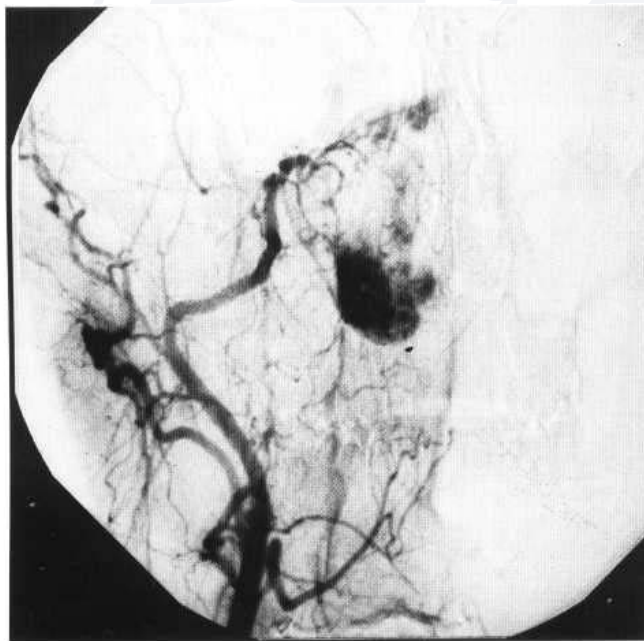
A



B



C



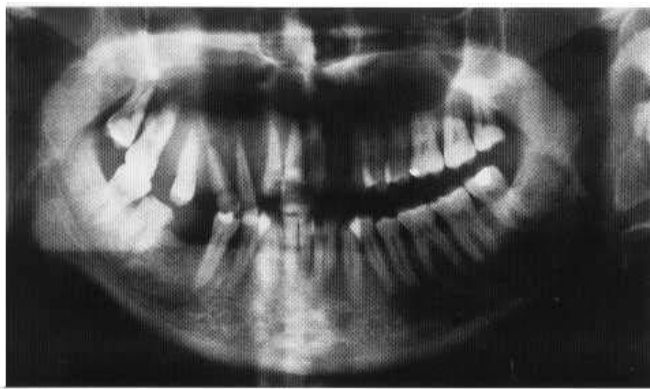
D

Fig. 48.9 MRI scans and angiogram of nasopharyngeal angiofibroma. (A) Axial STIR-weighted MRI scan shows a predominantly high signal intensity mass within the posterior nose and extending into the nasopharynx. Areas of flow void are seen within this highly vascular mass. (B) Axial T₁-weighted MRI scan demonstrates the intermediate signal intensity mass within extension into the pterygopalatine fossa (arrow). This shows intense enhancement following gadolinium (C). This is confirmed on the angiogram (D), which preceded embolisation of this nasopharyngeal angiofibroma.

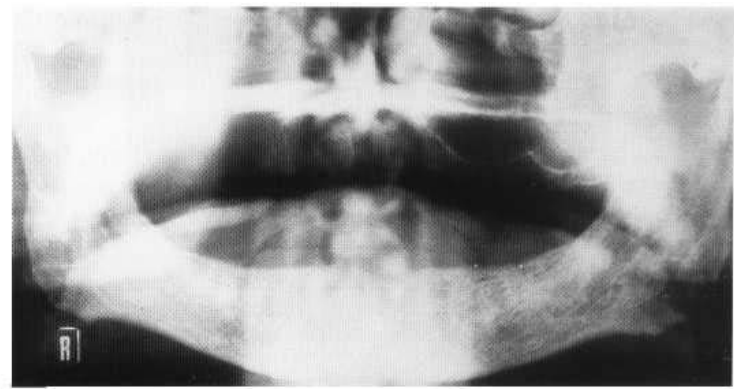
intact but may also be remodelled with bowing of the septum. Inverted papillomas are frequently multicentric. Carcinoma ex inverted papilloma, usually of squamous cell variety, has been reported in up to 24% of patients.

Adenomas may simulate a nasal polyp but are locally invasive and local recurrence occurs if they are not completely excised.

Nasopharyngeal angiofibroma (juvenile angiofibroma) is a rare histologically benign but locally aggressive tumour. It is a highly vascular polypoid mass which occurs almost always in males, usually between the ages of 10 and 18 years. Almost all tumours originate from the posterior choanal tissue near the pterygopalatine fossa and sphenopalatine foramen. They fill the entire nasopharynx and frequently extend into the pterygopalatine fossa, resulting in widening of



A



B



C

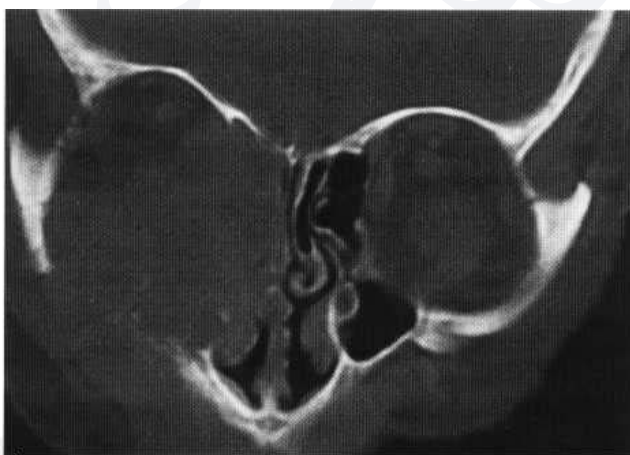
Fig. 48.10 (A) Orthopantomogram (OPG). There is abnormal bony texture and destruction of the right side of the maxilla. (B) OPG shows bony destruction of the right side of the maxilla with an abnormal opacity within the right maxillary antrum. This was due to a squamous cell carcinoma with adjacent bone invasion. (C) Occipitomental (OM) view demonstrates an opacity of the right maxillary antrum with destruction of the lateral wall of the maxillary antrum. An abnormal opacity is also seen within the nasal cavity.

the fossa and anterior bowing of the posterior ipsilateral antral wall (Fig. 48.9). Although other tumours may widen the pterygopalatine fossa, antral bowing is seen uncommonly in these conditions. The sphenoid sinus is involved in over half of cases, with spread in the maxillary and ethmoid sinuses in less than a half of cases. Intracranial extension occurs uncommonly in 5-20%, usually involving the middle cranial fossa. This arises from extension from the pterygopalatine fossa through the inferior orbital fissure and into the orbits and then intracranially through the superior orbital [fissure](#).

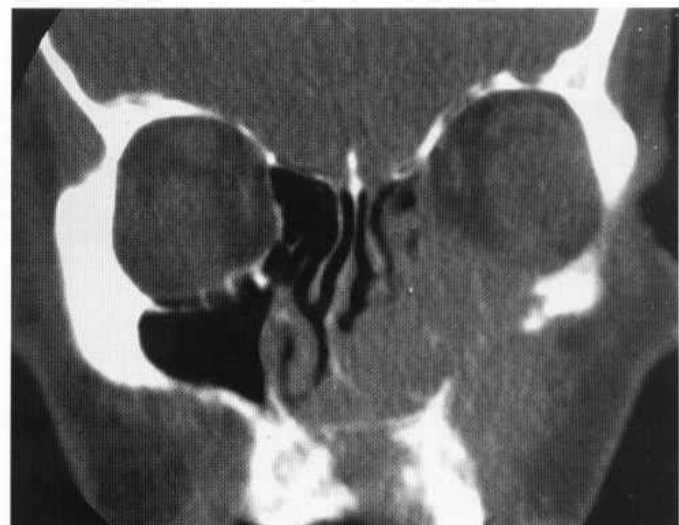
The bowing of the posterior antral wall may be appreciated on a lateral film of the sinuses. In addition, a soft-tissue nasopharyngeal

mass and opacification of the sphenoid sinus may be seen. Superior orbital fissure widening is seen as an indication of intracranial extension. Cross-sectional imaging will demonstrate an avidly enhancing mass (Fig. 48.9B,C). Intraorbital and intracranial extension will be much better visualised on cross-sectional imaging than on plain films. Multiple flow voids will be seen within the tumour on T₁- and T₂-weighted spin-echo sequences (Fig. 48.9A). The internal maxillary artery and ascending pharyngeal artery are the major feeding vessels which will be demonstrated on angiography, and a preoperative embolisation may be used to aid subsequent surgery (Fig. 48.9D).

An **angiomatous polyp** may be mistaken for a nasopharyngeal angiofibroma, in that it is a fibrosed and vascularised nasal polyp but it is located primarily in the nasal fossa and not in the nasopharynx. It does not extend into the pterygopalatine fossa or intracranially. The vascular supply of these lesions is less extensive than that of



A



B

Fig. 48.11 (A) Direct coronal scan on bone window settings demonstrates a large abnormal soft-tissue mass (squamous cell carcinoma) extending from the right maxillary antrum, destroying the inferior orbital wall and extending into the orbital fat on the right side, with destruction of the medial orbital floor and lateral maxillary antral floor, and abnormal soft tissue is seen within the ethmoid air cells and within the soft tissues of the cheek. (B) Large soft-tissue mass (squamous cell carcinoma) based upon the left maxillary antrum. It has involved and destroyed the floor of the maxillary antrum, with destruction of the maxilla and the lateral maxillary antral wall and spread of soft tissue into the cheek and the floor of the orbit. There is extension into the orbital fat, through into the medial maxillary antral wall and the nasal cavity.

angiofibromas. They therefore do not enhance avidly following intravenous contrast and vascular flow voids are not seen on MRI.

Malignant tumours

Plain radiographs are no longer recommended for screening for sinonasal malignancy (Fig. 48.10). Cross-sectional imaging is required to stage these tumours in order to visualise the extent of tumour beyond the sinuses.

The areas of particular concern are the intraorbital cavity (Fig. 48.11), pterygomaxillary fossa, pterygopalatine fossa (Fig. 48.12), infratemporal region (Fig. 48.13) and intracranial extension (Fig. 48.14). CT and MRI are often complementary. CT acquisition is much faster with helical and multislice scanners. CT is sensitive to bone destruction and is more readily available.

Direct coronal and axial scans should usually be performed. MRI, however, has the advantage of multiplanar imaging. It is better able to differentiate tumour from secretion than CT. Dental amalgam artefact also raises less of a problem.

Gadolinium-enhanced MRI is better than CT for the detection of intracranial and perineural tumour extension. Nodal disease may be assessed by either CT or MRI. Intravenous contrast enhancement allows identification of rim enhancement and central necrosis, which is often seen in squamous cell carcinoma. Extracapsular spread of nodal disease is better assessed by CT than MRI.

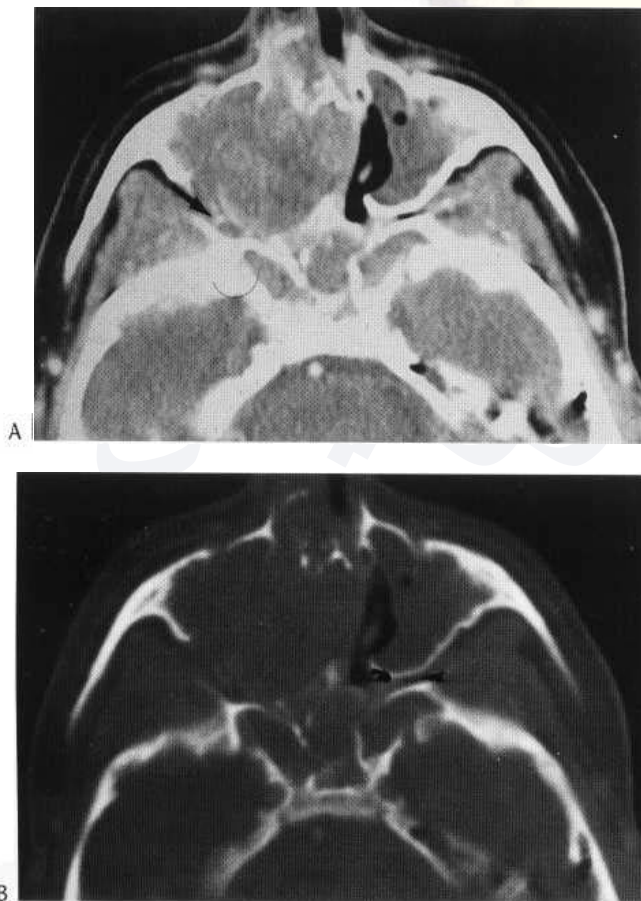


Fig. 48.12 Axial CT scans displayed on soft tissue (A) and bone (B) window settings show a large soft-tissue mass involving the right maxillary antrum. There is destruction of the posterolateral wall of the right maxillary antrum and abnormal soft tissue is seen extending into the infratemporal fossa and right pterygopalatine fossa (arrow). Note the normal-appearing left pterygopalatine fossa (arrowhead).

The role of positron emission tomography has been established for the detection of unknown primaries and is useful in patients who have undergone previous surgery or radiotherapy. It is very limited in its availability and much more expensive than either MRI or CT.

Ideally scans should include the first and second oral draining nodes. Tumours involving the maxillary antrum drain initially to the retropharyngeal nodes but level 2 (upper internal jugular) and level I (submandibular) groups may be involved and these should therefore be included within the scan. Collimation should be 5 mm or less. Direct coronal and axial scans should be obtained with both bone and soft-tissue algorithm. On MRI a slice thickness of 4 mm or less should be used. T₁- and T₂-weighted scans should be obtained with scans following intravenous contrast obtained using T₁-weighted fat-saturated sequences in the axial and coronal plane. Sagittal T₁-weighted fat-saturated scans after gadolinium enhancement may also be useful in assessing perineural and intracranial extension.

Carcinomas of the sinuses and nasal cavity account for 0.2-0.8% of all carcinomas and only 3% of those in the upper aerodigestive tract (Osguthorpe 1994). There are multiple risk factors for sinonasal cancer, including exposure to hardwood dust (adenocarcinoma), soft-wood dust (squamous carcinoma), nickel refining, chromium working, boot, shoe and textile working, isopropil oil, volatile hydrocarbons and snuff taking. There is a male to female predominance of 2 to 1. Human papilloma virus may be a cofactor.

These tumours often present at an advanced stage. The commonest tumour is squamous cell carcinoma, which accounts for 80% of all sinus malignancies. Approximately 50-65% arise in the maxillary sinuses (Figs 48.11-48.13), 10-25% in the ethmoid sinuses (Fig. 48.14) and 15-30% in the nasal cavity. CT and MRI often have complementary roles to play in the staging of these tumours. The location and extent of disease is important in deciding treatment.

The maxillary antrum is divided, by lines drawn on a coronal view of the sinuses through the antral floor and antral roof, into an infrastructure, mesostructure and suprastructure. Tumours limited to the mesostructure and infrastructure will be treated with a partial or total maxillectomy (Fig. 48.15). Most tumours involving the suprastructure will need a total maxillectomy and orbital exenteration (Fig. 48.11). It is thus important to include coronal views in the staging examination. Axial views are also necessary to determine posterior and anterior extension of disease (Fig. 48.16).

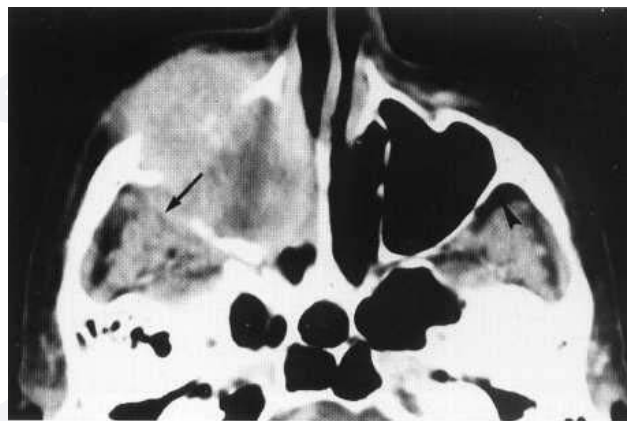


Fig. 48.13 Soft-tissue mass (squamous cell carcinoma) involving the right maxillary antrum. There is destruction of the posterolateral maxillary antral wall, where abnormal soft-tissue is seen extending into the fat of the right infratemporal fossa (arrow). Note normal low-attenuation fat in the left infratemporal fossa (arrowhead).

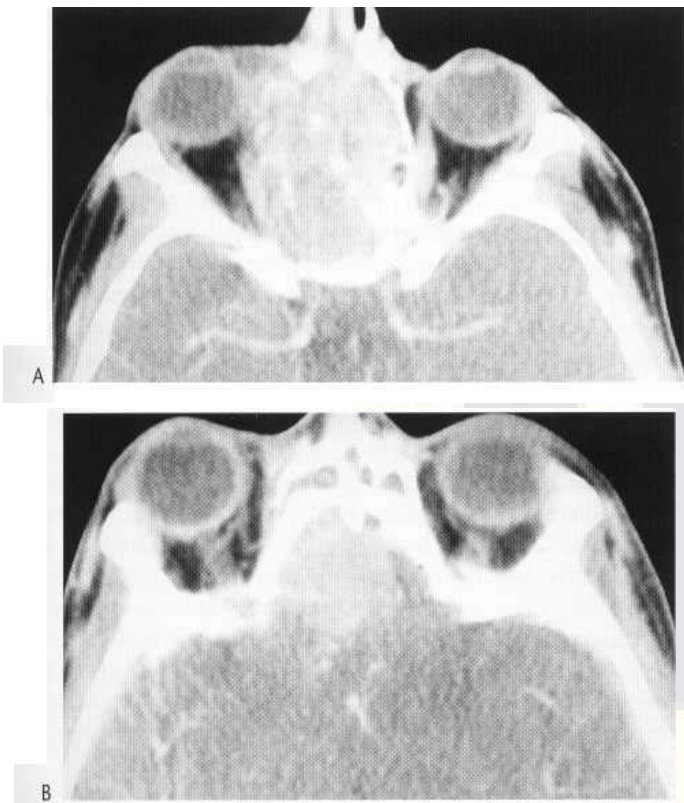


Fig. 48.14 (A, B) Axial contrast-enhanced CT scans of an extensive ethmoid carcinoma showing abnormality extending up through the cribriform plate and involving the inferior aspect of the frontal lobes bilaterally (B).

Small tumours will mimic the appearances of chronic sinusitis and nasal polyposis, thus many patients will be diagnosed at a late stage of their disease. Curative surgery is not usually possible if

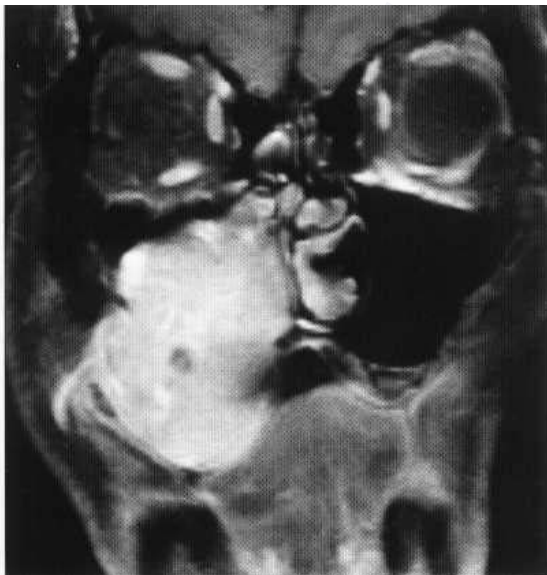


Fig. 48.15 T₁-weighted fat-saturated scan after intravenous gadolinium enhancement in the coronal plane in a patient with a maxillary antral carcinoma demonstrates an enhancing mass seen within the mesostructure and infrastructure of the right maxillary antrum, with abnormality involving the right maxilla and soft tissues of the cheek. Note that the suprastructure of the right maxillary antrum is not involved, with a normal-appearing right orbit and orbital floor.

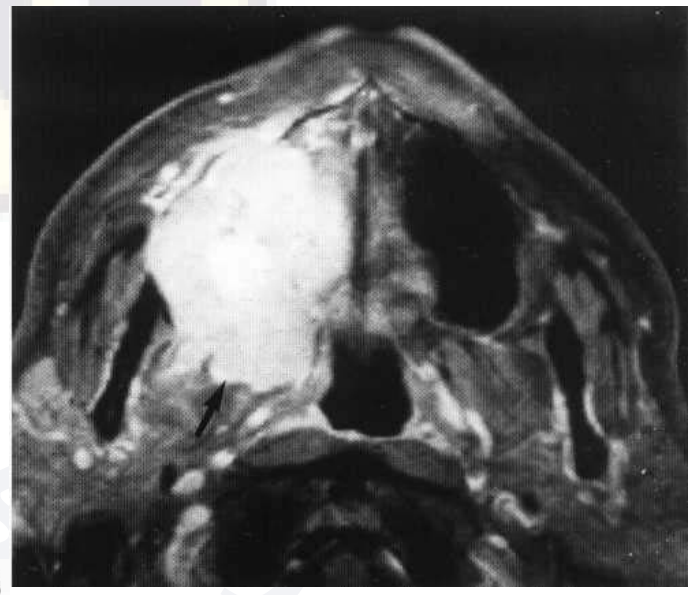
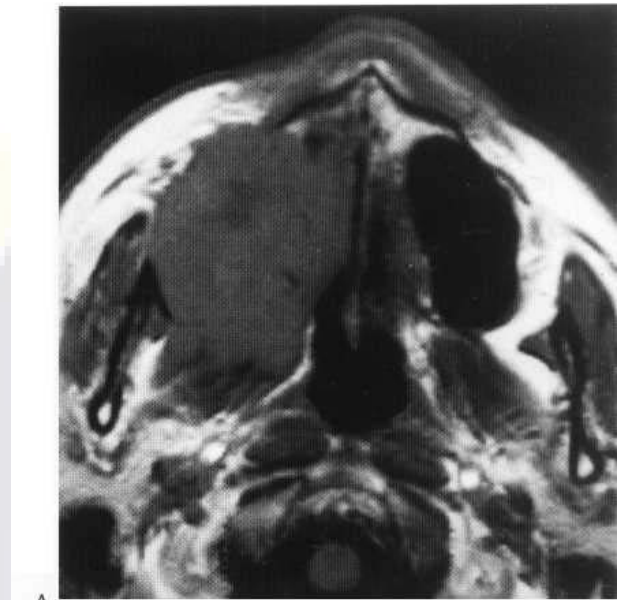


Fig. 48.16 (A) T₁-weighted axial MRI scan of a patient with a maxillary antral carcinoma before gadolinium enhancement. (B) Axial T₁-weighted fat-saturated scan in the same position after gadolinium enhancement. Both scans demonstrate a large mass, which shows enhancement following intravenous gadolinium, filling the right maxillary antrum and extending posteriorly into the infratemporal fossa on the right (arrow).

there is central skull base obstruction, tumour extension into the pterygopalatine fossa or tumour extension into the nasopharynx. Nodal metastatic disease also confers a poor prognosis. Primary frontal sinus carcinoma and sphenoid sinus carcinoma are rare. Bone destruction is commonly seen.

The primary tumour shows little if any enhancement on CT following intravenous contrast. On MRI, the tumours are of intermediate T₁ signal intensity and slightly higher signal intensity on T₁-weighted images. Larger tumours may have areas of necrosis and haemorrhage altering the signal intensities within them. They also enhance slightly following intravenous gadolinium.

Approximately 10% of sinonasal tumours are adenocarcinomas, being due to adenocystic carcinomas (minor salivary gland origin), mucoepidermoid carcinomas, ascinic carcinomas and benign and

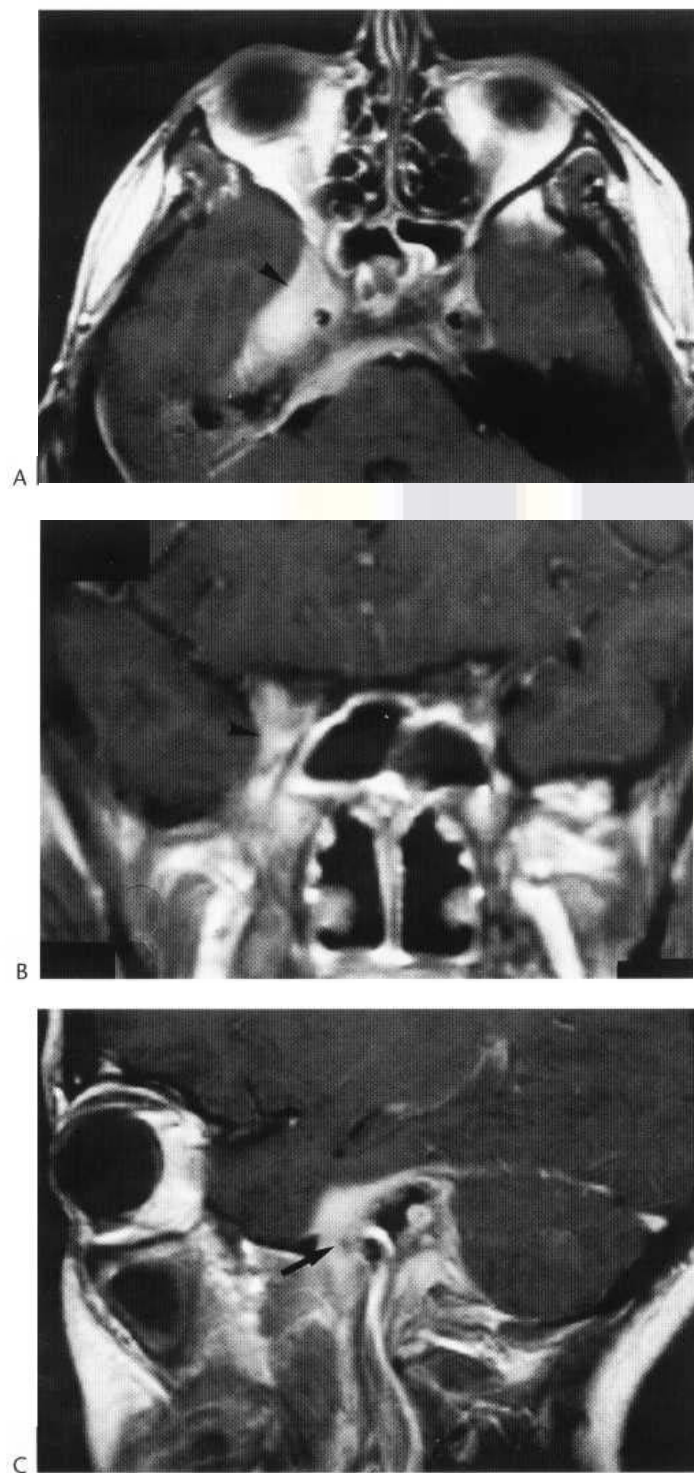


Fig. 48.17 Axial (A), coronal (B) and sagittal scans (C) of a patient with a recurrent adenoid cystic carcinoma of minor salivary gland origin. There is abnormal enhancing soft tissue extending superiorly through the foramen lacerum (arrow in C) and filling the right cavernous sinus (arrowheads in A and B).

malignant pleomorphic adenomas. Minor salivary gland tumours can arise anywhere within the sinonasal cavities but the commonest site is within the palate with extension into the nasal fossa and paranasal sinuses. The most common tumour to affect the minor salivary gland is adenoid cystic carcinoma. Disease recurrence is common following surgery, due to the presence of 'skip' lesions within nerves. Perineural spread is best identified using gadolinium-enhanced MRI (Fig. 48.17).

Mucoepidermoid carcinoma and adenocarcinoma not otherwise specified are less common tumours of the minor salivary glands. Most of these tumours involve the antrum and nasal cavity. Benign mixed tumours of the sinonasal cavities are rare. Most cases arise from the nasal septum. Malignant change within a sinonasal pleomorphic adenoma is rare but an entity known as benign metastasising pleomorphic adenoma is a very uncommon tumour that metastasises to the lungs and soft tissues, despite having a benign histology.

Intestinal-type adenocarcinomas of the sinonasal cavities are especially common in individuals with a previous exposure to hardwood dust and to people who have worked in the shoe industries. The histology of the high-grade tumours resemble colonic and gastric carcinomas. In these patients metastatic disease from gastrointestinal primaries should be ruled out before making the diagnosis, but this is a rare occurrence.

Malignant melanomas occur more commonly in the sinonasal cavities. When they do occur, involvement of the nose is more common than the sinus. Local recurrence or metastatic disease within the first year is seen in up to 65% of patients, metastases affecting the lungs, nodes, brain, adrenal glands, liver and skin. Nasal melanomas have a better prognosis than tumours originating in the paranasal sinuses. These tumours enhance more avidly than squamous cell carcinomas on postcontrast scans. Some lesions will exhibit high signal intensities on T₁-weighted sequences owing to the presence of haemorrhage and/or melanin.

Olfactory neuroblastoma arises from the olfactory epithelium of the nasal cavity and is a tumour of neural crest origin. There is a bimodal age distribution, with the tumour occurring most frequently in patients aged 11-20 years and 51-60 years. Epistaxis and nasal obstruction are the most common presenting symptoms. The prognosis is related to the extent of disease at presentation. These lesions are hypointense to brain on T₁-weighted images and hypointense to brain on T₂-weighted images. Coronal and sagittal scans are usual to determine the relationship of the tumour to the cribriform plate and intracranial extension. Microscopic intracranial spread can, however, occur with an intact and normal-appearing cribriform plate on imaging. The tumours enhance with intravenous contrast on both CT and MRI. Metastatic disease is seen in up to 38% of patients, with involvement of cervical lymph nodes, parotid glands, skin, lung, liver, eye, spinal cord and spinal canal.

Non-Hodgkin's lymphoma within the neck most frequently involves Waldeyer's ring but primary nasal and paranasal disease may occur. **Hodgkin's lymphoma** rarely presents in extranodal sites within the head and neck. Lymphomas may mimic sinusitis, polyposis and other benign and malignant neoplasms on CT and MRI, with no specific imaging features. They are often seen as bulky masses causing expansion, erosion or infiltration. **Lethal midline granuloma** is a prelymphomatous state generally occurring in a population younger than those patients with sinonasal lymphoma. Sinonasal lymphomas can occur with or without associated cervical or systemic nodal disease.

Prognosis is worsened by the presence of adenopathy with extranodal lymphoma. Disease is most often located within the nasal fossae, maxillary sinuses, with the ethmoid sinuses less often involved, and very rare involvement of the sphenoid and frontal sinuses. The soft-tissue masses tend to have an intermediate signal intensity on both T₁- and T₂-weighted sequences. **Burkitt's lymphoma** is the most common childhood malignancy in central Africa. It is strongly associated with the Epstein-Barr virus. This disease can involve head and neck structures, such as the jaw,

orbits, meninges, extradural spaces, nasopharynx and lymph nodes, but rarely involves the **sinonasal** cavity.

Leukaemic infiltrates rarely infiltrate the paranasal sinuses. Involvement of the paranasal sinuses in these patients is more likely to be due to opportunistic infection and haemorrhage.

Granulocytic sarcoma is a rare malignant tumour composed of immature myeloid elements. The bony lesions have been reported in the skull base, orbit and paranasal sinuses and extramedullary lesions have been reported in the nasal cavity, paranasal sinuses and nasopharynx.

Almost one half of patients have an associated myeloproliferative disease, which is most commonly **acute myeloid leukaemia**. The appearances are of enhancing masses on CT and MRI. Intermediate to high signal intensity is seen on both T₁- and T₂-weighted sequences on unenhanced MRI.

Multiple myeloma is most commonly seen in the form of skeletal lytic lesions and/or osteoporosis. An extraosseous tumour is rare as the initial appearance of multiple myeloma. In the head and neck **plasmacytomas** occur usually in the nose, paranasal sinuses, nasopharynx and tonsils.

Extramedullary plasmacytoma is a rare malignancy but 80% of these tumours occur in the head and neck and represent 3-4% of all sinonasal cavity tumours. These tumours are usually seen as homogeneous enhancing polypoid masses that remodel surrounding bone. They have an intermediate signal intensity on all MR sequences. Vascular flow voids may be seen in the lesions due to their highly vascular nature.

Rhabdomyosarcoma is a malignant tumour of skeletal muscle and usually occurs in the paediatric age group, with just over three-quarters occurring in children under 12 years of age. Alveolar rhabdomyosarcomas usually occur in an older age group (15-25 years old). The orbit is the commonest site for rhabdomyosarcoma in the head and neck but the nasopharynx and sinonasal cavities are involved in 15% and 8%, respectively. Cervical lymph node involvement occurs in 42%, with 58% having distant metastases. These tumours cause both bone remodelling and bone destruction. They appear homogeneous with intermediate signal intensity on MR imaging sequences and show little to moderate enhancement.

REFERENCES AND SUGGESTIONS FOR FURTHER READING

- Babbal, R., Harnsberger, H. R., Nelson, B., et al (1991) Optimization of techniques in screening CT of the sinuses. *American Journal of Neuroradiology*, **12**, 849-854.
- Earwaker, J. (1993) Anatomic variants in sinonasal CT. *Radiographic*, **13**, 381-415.
- Jones, R. L., Chavda, S.V., Violaris, N., Pahor, A. L. (1995) Infra-cranial complications of sinusitis-the need for aggressive management. *Journal of Laryngology and Otolaryngology*, **109**, 1061-1062.
- Osguthorpe, D. (1994) Sinus neoplasia. *Archives of Otolaryngology and Head and Neck Surgery*, **120**, 19-25.
- Patel, K., Chavda, S. V., Violaris, N., Pahor, A. L. (1996) Incidental paranasal sinus inflammatory changes in a British population. *Journal of Laryngology and Otolaryngology*, **110**, 649-651.
- Sam, P. M., Brandwein, M. (1996) Sinonasal Cavities. Inflammatory Diseases, Tumours, Fractures, and Postoperative Findings in Head and Neck Imaging. Eds Peter M. Sam, Hugh D. Curtis. Third Edition. Mosby.

نشر الکترونیکی
موسسه انتشاراتی
نور دانش



نشر الکترونیکی
موسسه انتشاراتی
نوردانش

49

TEETH AND JAWS

Peter Renton

Diseases of the mandible and maxilla often present in different ways from those of bone lesions elsewhere. In addition, the jaws bear specialised organs – the teeth-whose abnormalities, congenital and acquired, may affect the bone around them.

Radiography Dental radiographic techniques in common use include:

1. Intraoral views
2. Occlusal views
3. Panoramic views
4. View of the temporomandibular joints
5. View of the facial bones.

Anatomy

The bulk of a tooth is formed of *dentine*, which is sensitive to temperature change and other stimuli. In the centre of the tooth crown, and down the root to the tooth apex, is a hollow space occupied by the *pulp*, which is soft tissue containing nerves and vessels. The crown projects from the gingiva and is protected by a layer of *enamel* in the form of a thimble or cap (Fig. 49.1). Enamel is insensitive and hard, like ivory (= elephant enamel) but is susceptible to caries. Beyond the crown there is a thin layer of *cementum* covering the dentine of the root, and this layer forms the anchorage for the

periodontal membrane or *ligament* which slings the tooth in its bony socket. The bony anchorage for the fibres of the periodontal membrane is a thin layer of compact bone lining the socket called the *lamina dura*. Beyond the lamina dura is the cancellous bone of the *alveolar process* (the tooth-supporting bone) of the jaw, and this is covered with a thin layer of compact bone beneath the gingiva.

Enamel is denser to X-rays than dentine, which is comparable in density to compact bone, while the pulp space is more lucent than dentine.

The thin layer of cementum covering the root beneath the gingiva is radiographically indistinguishable from dentine. The cancellous bone forming the alveolar process surrounds the sockets on at least three sides and so the shadow of its trabecular network is superimposed on those of the periodontal membrane and the roots of the teeth.

Tooth charting Teeth are conventionally labelled thus for the primary dentition:

e d c b a	a b c d e
e d c b a	a b c d e

and thus for the secondary:

8 7 6 5 4 3 2 1	1 2 3 4 5 6 7 8
8 7 6 5 4 3 2 1	1 2 3 4 5 6 7 8

Dental eruption is shown in Table 49.1.

Infection

Caries is a bacterial invasion of the tooth which first liquefies a narrow track through the enamel and then causes more extensive softening and staining of the adjacent dentine. It attacks the occlusal surface of molars, the neighbouring surfaces, and the necks of the teeth where carbohydrate food residues have been allowed to remain. Dental pulpitis resulting from caries is by far the commonest cause of pain near the mouth. The pain of toothache may be referred to the ear and also to the opposite teeth on the same side, but not across the midline, and is often not well localised to the decayed tooth.

Deep caries will kill the pulp, which tends to be strangled by the inflammatory exudate in the rigid space in the tooth. In young teeth, before the apex is closed, and for some years after this while the apical canal is still wide, the pulp is more tolerant of carious

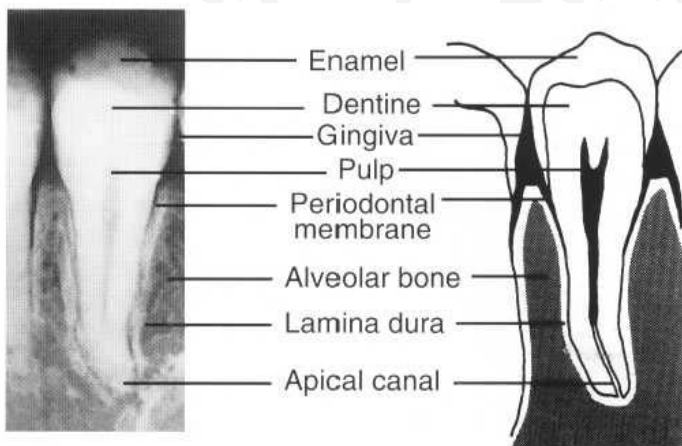


Fig. 49.1 X-ray and diagram of normal tooth.

Table 49.1 Chronology of tooth development*

Tooth	Formation of crown complete	Appearance in mouth cavity
<i>Deciduous</i>		
Incisors	2-3 months	6-9 months
Canines	9 months	16-18 months
1st molars	6 months	12-14 months
2nd molars	12 months	20-30 months
<i>Permanent</i>		
Incisors	4-5 years	Lower: 6-8 years Upper: 7-9 years
Canines	6-7 years	Lower: 9-10 years Upper: 11-12 year,
Premolars	5-7 years	10-12 years
1st molars	2yr3 years	6-7 years
2nd molars	7-8 years	11-13 years
3rd molars	12-16 years	17-21 years

* Teeth appear earlier in girls than in boys.

involvement. Once the pulp has died, infection may spread to the periapical region. Root treatment after removal of all infected and dead pulp tissue is aimed at avoiding this or enabling the periapical infection to heal.

When infection has spread beyond the apex, the effect depends on the severity of the inflammation. An acute **abscess** is the most marked reaction, with throbbing pain and a very tender tooth. There may be swelling of the gingiva and of the face and, if the tooth is related to the antrum, of the antral mucosa also. The earliest change in apical infection is oedema of the periodontal membrane, and this is shown radiologically as widening of the periodontal membrane space. Infection and hyperaemia combined then result in ill-defined trabecular destruction about the apex, and blurring and loss of the lamina dura. If adequate treatment is instituted, trabeculae return to normal.

A **subacute abscess** or gumboil results if the lesion is not treated. There is further evidence of bone destruction around the apex and, clinically, swelling of the gingiva, usually on the outer side and near the root of the affected tooth. There will be a sinus with a purulent discharge, and the opening is often on a rather sac-like projection of the oral mucosa. The bone destruction shows a diffuse area of radiolucency at the tooth apex, including the lamina dura of the socket in this region. The lamina dura is the thin layer of compact bone lining the socket and is the first bone to be destroyed near the tooth apex when infection has spread to this region (Fig. 49.2). Lucency due to natural thinning of the bone is associated with an intact lamina dura round the normal tooth apex.

Chronic apical infection may be present without clinical signs. The X-ray changes then are those of a discrete peripheral lucency, sometimes outlined by a white line which is continuous with the lamina dura of the socket at the margin of the lesion (Fig. 49.3). Chronic infection of a tooth at the antral floor lifts the mucoperiosteum over the granuloma and this can develop a bony halo surrounding it. Commonly, recurrent subacute infection leads on to chronic infection. Stimulation and proliferation of local squamous-cell



Fig. 49.2 Early periapical infection beneath the lower second molar in a youth of 16. The lamina dura is destroyed round the apical thirds of its roots with widening of the dark line around the roots. Compare with the normal first molar and the incompletely formed roots of the third molar.



Fig. 49.3 There is a granuloma at the apex of the second premolar surrounded by a thin halo of bone formed by the antral mucoperiosteum. There is a similar pattern over the mesial root apex of the first molar.

rests, normally present in the periodontal ligament, converts chronic apical granulomas into radicular cysts (see under Cysts, below).

Root treatment is used to preserve accessible teeth whose pulps would otherwise die or are already dead. Sometimes *apicectomy* is performed to remove the chronic periapical granuloma and infected apex after treatment of the root canal, but efficient modern root canal treatment will also lead to eradication of such an apical area. The periapical bone, including lamina dura, will be reformed over a period of 1-2 years once all the necrotic pulp tissue has been removed. Root fillings are almost always radiopaque, due to zinc oxide or other metal salts. Inadequately treated dead teeth can be a source of acute or chronic infection, and low-grade infection can cause the formation of a radicular cyst.

Periodontal disease is initially a gingivitis; this may be acute, as with a Vincent's infection. If the inflammation persists, resorption of the peaks of the underlying interdental bony papillae can result and this may be demonstrated radiologically. The interdental bony papilla is blunted and shortened and has a broader top, while its edge will be ragged and poorly defined in the active stage of the disease. There are often deposits of calculus (tartar) around the

neck of the tooth; this opaque material will show in the films (Fig. 49.4) and will aggravate the chronic or subacute gingival inflammation. Cervical caries can occur beyond the edge of the enamel after gingiva and bone have receded.

The pattern of bone loss in periodontal disease takes two forms, horizontal loss and vertical loss. In horizontal loss (Fig. 49.5) there is general all-round recession: this is a slow but steady progression of the disease, with deeper loss of the supporting bone than in the normal recession with age. In vertical loss, there is irregular and deep local loss which may reach the tooth apex in some regions, and thus some teeth are lost.

Chronic dental infection, both periapical and periodontal, used to be blamed for general ill-health, and teeth were too easily condemned and removed. A transient bacteraemia can result from ordinary masticatory forces on inflamed gums or on teeth with apical infection. In otherwise fit people, this does not usually cause



Fig. 49.4 Alveolar bone recession is associated with calculus around the necks of the teeth and periapical bone loss,

trouble, but it can give rise to subacute bacterial endocarditis in hearts with previous damage or in those who have had operations involving the endocardium. In these subjects dental infection must be eliminated and this may mean condemning teeth unless the infection can be cleared by treatment. Extensive dental sepsis can also cause pyrexia, with a raised ESR and constitutional upset, yet with little by way of local symptoms. Distal septic foci may occur.

A more widespread form of infection of bone may occur in the mandible and only rarely affects the maxilla. This *subacute osteomyelitis* usually extends from a tooth socket, either after extraction or from an apical abscess, when conditions are unfavourable. The early radiographic pattern, from about 3 weeks after onset, is of patches of lucency with islands of normal-looking bone between them (Fig. 49.6). The lamina dura is destroyed in this process.

Some of these patches of normal-looking bone will develop into sequestra, and sooner or later there may be evidence of periosteal new bone formation, but periosteal new bone formation is not a prominent feature of healing in the mandible. It appears as a soft fusiform opacity along the lower border or on the outer or inner margin of the jaw (Fig. 49.7). In the later stages, the area of bone destruction becomes sharply defined and the periosteal new bone becomes consolidated. More acute and extensive osteomyelitis of the mandible is rare nowadays but is sometimes of blood-borne origin, particularly in those rare examples which occur in infancy before teeth have erupted. The appearances may simulate those seen with eosinophilic granuloma.

Radiation changes in the jaw

Radiation and chemotherapy cause damage to developing teeth. If the fetus or infant is irradiated, damage to the developing tooth germ can cause either absence of the tooth or gross hypoplasia, both of primary and secondary dentition. In addition, mandibular growth is retarded and hypoplasia results (Fig. 49.8).

Irradiation of the oral tissues (e.g. for soft-tissue sarcoma) affects the salivary glands and the nature of their secretions, which diminish and become more acid. Caries is potentiated in a dry mouth and can result in apical infection. For this reason, immaculate oral hygiene is indicated in those undergoing therapeutic irradiation.



Fig. 49.5 A Panoramic film showing general horizontal loss of supporting bone with deposits of calculus.



Fig. 49.6 Irregular bone destruction in the mandible of a man of 41 some 6 weeks after onset of osteomyelitis.

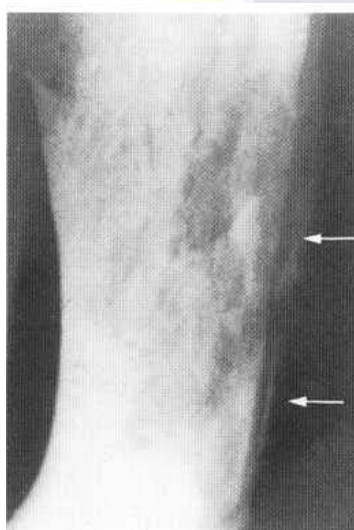


Fig. 49.7 A few weeks later than Fig. 49.6, periosteal new bone has formed on the buccal aspect of the jaw (arrows).

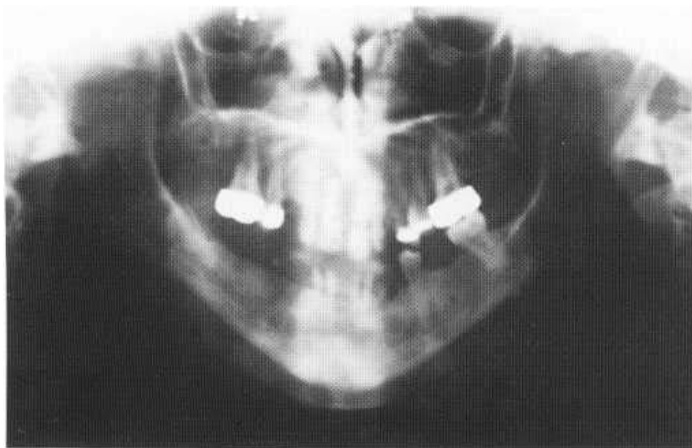


Fig. 49.8 Radiation damage to the mandible and teeth is evident in this 25-year-old patient who was irradiated at the age of 6 months for a cutaneous haemangioma. The mandible is hypoplastic, many of the teeth have not formed, and a few dwarfed deciduous teeth may be seen.

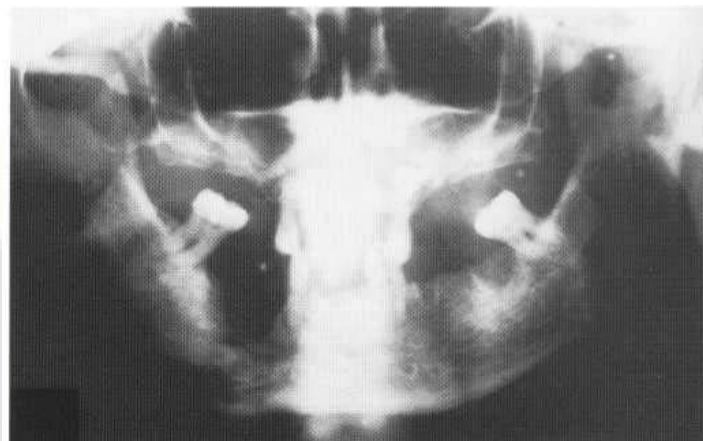


Fig. 49.9 Radiation necrosis. A pathological fracture has occurred through an area of bone necrosis.

Radionecrosis Radiation directly causes cell death and also induces local ischaemia by endarteritis. Ischaemia further potentiates infection (see above).

Initially, osteoporosis is seen, but the end-stage is a pattern of mixed sclerosis and lysis. Pathological fractures and bone resorption as well as sequestra are seen. Periosteal new bone is not prominent in the mandible. The appearance is complicated by the presence of superadded infection (Fig. 49.9). The prophylactic removal of diseased teeth may be indicated before radiotherapy to reduce the possibility of radionecrosis.

Sclerosing lesions of the jaws

Bone sclerosis may occasionally be generalised. Paget's disease and fibrous dysplasia may cause such change. Widespread sclerotic metastases are not common in the jaws.

Localised areas of sclerosis are more common, and are usually benign.

Hypercementosis (Fig. 49.10). Excessive cement is laid down over the apex and body of the root so that the root has a bulbous expansion. The expanded root is still surrounded by a lamina dura



Fig. 49.10 Apical bone resorption with loss of the lamina dura is associated in this patient with hypercementosis and obliteration of the root canals.

and periodontal membrane space, which are of course displaced sideways. Removal of such teeth may be difficult.

Cementoma These dense areas of coarse trabeculation are found at the apices of teeth, especially in the mandible. They are fibrous outgrowths of the periodontal membrane space, so that the initial radiographic appearance is of multiple apical lucencies, often on normal teeth. The lamina dura is destroyed locally, simulating cysts of dental origin. Usually the fibrous tissue becomes calcified, so that a woolly central density is surrounded by a lucent halo of fibrous tissue. The lesions may safely be left alone (Fig. 49.11).

Postinflammatory sclerosing osteitis (Fig. 49.12) An increase in bone density is seen in the apical and interdental regions of patients with chronic gingival and dental sepsis. Caries and apical resorption of bone are prominent features in these patients, who often have poor oral hygiene. The local periodontal membrane space is widened and the lamina dura lost due to chronic sepsis. The bone may revert at least partly to normal after treatment of the underlying dental condition.

Benign osteosclerosis This common lesion usually has no underlying aetiology, but may follow surgery, dental extraction or a bridge. Small areas of sclerosis are seen between teeth or adjacent to roots. They lie up against, and may be continuous with, the lamina dura. Surrounding trabeculae blend into the lesion, which

thus has a 'spiky' contour. The lesions are common and benign, and should be left alone (Fig. 49.13).

Odontomes These are hamartomas or abnormalities of tooth development containing enamel, dentine, cement and connective tissue, i.e. all the elements of normal teeth. There are two types:

Complex odontome These are common in the molar region and usually in the secondary dentition. Females are more commonly affected. The tumour consists of a lobulated density surrounded by a radiolucent zone. A thin zone of reactive sclerosis separates this from normal bone.

Compound odontome This lesion shows better differentiation, into multiple small united denticles, in which individual cusps may be recognised. This lesion is also surrounded by a zone of lucency. It is more commonly found in the canine region and often prevents normal dental eruption (Fig. 49.14).

Localised fibrous dysplasia This occurs typically as an enlargement of one side of the maxilla (less often of the mandible) with an increase in its radiodensity. The lesion is usually homogeneous, fully replacing the normal architecture of the region and, with enlargement of the affected part of the jaw, the lesion is usually denser than normal bone (Fig. 49.15).



Fig. 49.11 Cementoma. A well-demarcated radiolucent lesion extends to the alveolar margin and shows irregular calcification within it. This does not happen with radicular cysts.



Fig. 49.13 A well-defined radicular cyst is related to the right lower canine. Benign sclerosing osteitis is seen between the right lower 5 and the right lower 6.

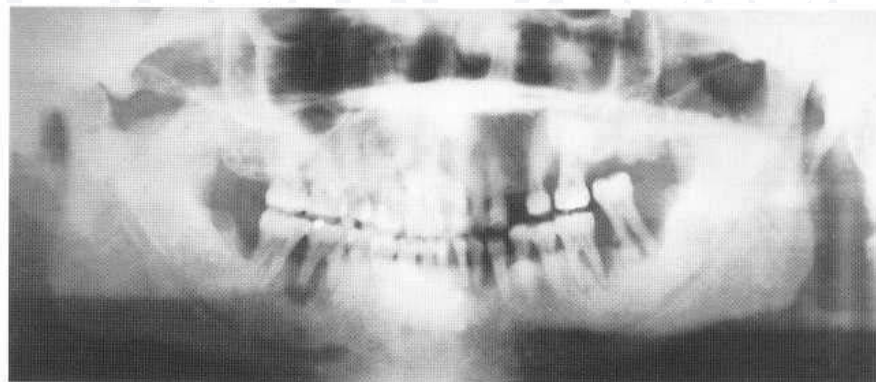
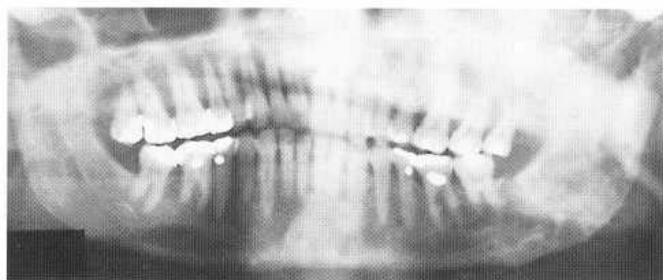


Fig. 49.12 Reactive sclerosis is related to the chronic apicitis. Note the bone resorption around the molar teeth. The inferior dental canals stand out in sharp relief.



Fig. 49.14 Compound odontome. A large aggregate of rudimentary dental elements prevents eruption of a normal tooth.



A



B

Fig. 49.15 Fibrous dysplasia. (A) The radiograph shows expansion with altered bone texture in the left ascending ramus and mandible. A ground-glass pattern is demonstrated. Similar changes are seen in the left antrum. (B) The radio-isotope bone scan shows the extent of the facial, antral and mandibular disease.

It arises in the second decade or just before and is painless and easily overlooked, but a developing tooth may be displaced and fail to erupt. Small or moderate-sized lesions are often discovered years later when the dental surgeon finds the gingiva and bone are thickened, but the phase of active enlargement does not extend much into the third decade.

Paget's disease (*osteitis deformans*) (see Ch. 37). Patients often have neuralgic pain in an enlarging alveolar ridge, and an artificial denture may become too tight.

In the jaw, bone enlargement and sclerosis are usually seen (Fig. 49.16). Irregular dense sclerotic patches may form on teeth, if any are present, or merely in what had been the tooth-bearing bone.



Fig. 49.16 Paget's disease. The mandible shows expansion, loss of corticomedullary differentiation, and a coarsened texture throughout. These appearances are typical of Paget's disease.

The mandible often remains normal but it may be affected, with or without the other bones. Either jaw can become very large indeed.

Of the three complications to which Paget's bone is liable, infection is relatively common and may be the presenting lesion, especially in the mandible. Fracture and neoplasm are rare in the Paget's jaw, but infection from a recent socket, from a dead tooth, or perhaps from a denture ulcer finds little resistance in the abnormal bone. A large sequestrum is likely to form and to separate slowly.

Trauma

A blow on a tooth may cause no disruption of the X-ray pattern, and yet the blood supply to the pulp may have been interrupted. The pulp may then die and become infected, with the effects already described. Less commonly, the pulp vessels are only damaged and the response is obliteration of the pulp space by dentine over a period of perhaps a year. In either case, the crown can become darkened clinically by blood pigments in the dentine.

A less common effect of pulp damage by trauma or even by caries is a *pulp granuloma*—internal resorption of the dentine. External resorption of the root at the neck of the tooth also occurs sometimes following trauma, and also when the pulp is dying from carious infection (Fig. 49.17).

Injuries to the teeth may be classified as follows:

- Class 1 Traumatized tooth without fracture:
 - a. with loosening
 - b. without loosening
 Loosening is shown as widening of the periodontal membrane space.
- Class 2 Fracture of the crown:
 - a. involving enamel
 - b. involving dentine
- Class 3 Fracture of the crown, exposing pulp
- Class 4 Fracture of the root, either
 - a. without crown fracture
 - b. with crown fracture
- Class 5 Avulsion of the tooth.

In any case the pulp may be killed but, if the teeth are young and still have a large apical foramen or a frankly incomplete root, the pulp has a better chance of surviving. The damaged pulp of such a severed tooth will react by becoming partly obliterated (Figs. 49.18, 49.19).



Fig. 49.17 Extensive external root resorption in a man of 62. This erosion reaches into the crown as well as halfway down the root, but the outline of the pulp persists, although it must have been breached. Infection from the gingival margin has reached the pulp and led to an apical abscess.

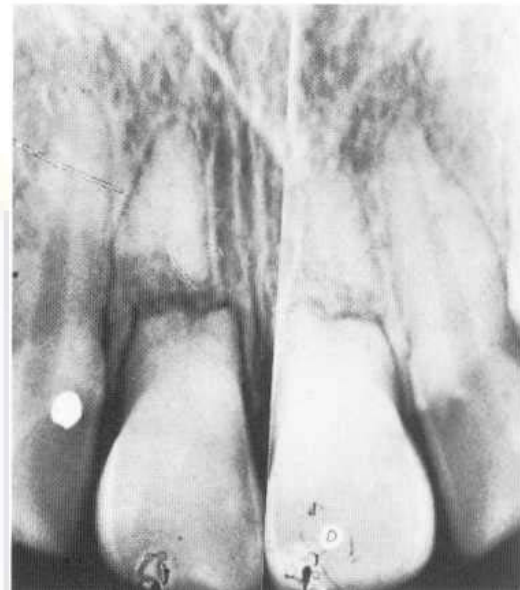


Fig. 49.19 Two years later, the vital but damaged pulps have partly calcified up in root as well as in crown portions of the teeth. A layer of bone has formed between the root ends, separated by a dark line like periodontal membrane from the root and with an intact lamina dura beyond this.

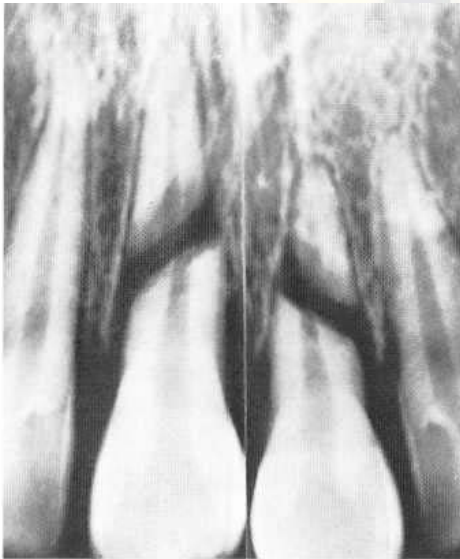


Fig. 49.18 Fracture of both upper central incisor roots occurred 1 week before this film was taken in a girl of 14. The pulp survived in both portions of each tooth, as it often will in young jaws.

When an upper first molar is removed from a patient with a large antrum, the bony floor of the sinus may be fractured. Sometimes the tooth is broken instead. A root may remain in the socket with lamina dura intact around it or, in an attempt to remove it, the root may be pushed up through the socket into the antrum, when it may act as a nidus for concretions, forming an antrolith. An *oroantral fistula* may be formed from a large bony breach; this may not necessarily give rise to complications but is nevertheless better repaired early.

Developmental errors

Absence of teeth Teeth may be absent in the Ellis-van Creveld and Down's syndromes (see Ch. 35). Isolated absence of teeth is common and often familial. The permanent third molar teeth are

most commonly missing, but premolar and lateral incisors can also be deficient.

Supernumerary teeth These are more common in the maxilla and usually do not erupt, being found on radiographic examination only. Supernumerary teeth are generally smaller than normal teeth (Fig. 49.20) but may resemble the other teeth in that region. They may retard normal dental eruption.

Various types of supernumerary tooth arise in the upper incisor region. The most common is the *mesiodens*, which develops close to the midline and at a time between the first and second dentitions (Fig. 49.21).

Small teeth Dental hypoplasia (microdontia) is often familial and commonly affects those teeth which are often absent in other patients (see above). The crown or the root, or both, may be affected. Microdontia occurs following irradiation (see above) and also in chondroectodermal dysplasia.

Fusion of teeth Teeth may unite at the crown, the root, or both. Often supernumerary teeth are involved.

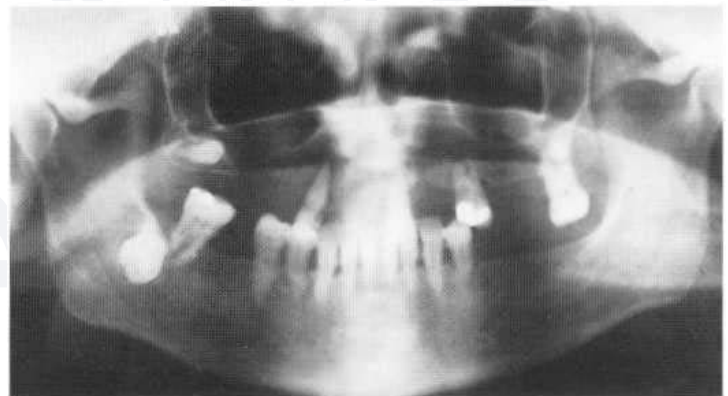


Fig. 49.20 Supernumerary upper 9s. Note how small and conically shaped these teeth are.



Fig. 49.21 Bilateral mesiodentes with normal eruption.



Fig. 49.22 Dens in dente. The tooth is also carious and shows apical bone resorption, with loss of the lamina dura due to ascending infection.

Dens in dente A defect exists on the crown and leads to an invagination into the body of the tooth. This is lined by dense enamel and has a central lucency. The 'tooth in a tooth' may be confined to the crown or may reach the apex of the root (Fig. 49.22).

Taurodontia Here the teeth resemble those seen in oxen, with large pulp chambers and abnormally short roots. The condition is probably atavistic.

Cleft of the hard palate This is a defect in the floor of the nose just lateral to the midline; it may be bilateral. It usually extends forward through the alveolar process medial to the canine. The premaxilla between the two canines may be very distorted or rudimentary, containing small misshapen denticles. It is usually necessary to keep all possible teeth as an anchorage for an obturator; they are difficult teeth to radiograph. The orbiting panoramic film



Fig. 49.23 Cleft palate. The occlusal view demonstrates the defect and shows the resulting dental anomalies.

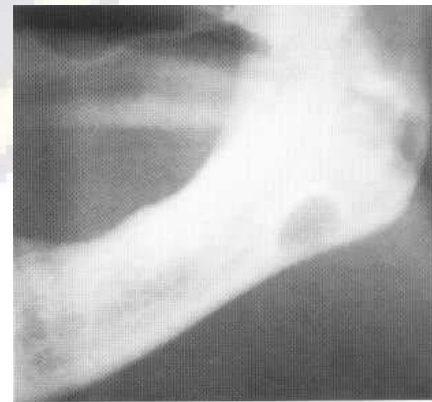


Fig. 49.24 Stafne cyst. The lesion represents salivary gland inclusion in bone.

is usually of very little help and occlusal views are more helpful (Fig. 49.23).

Salivary inclusion defect (Stafne's defect) Localised, well-demarcated defects at the angle of the mandible are often seen on sialography to communicate with the local salivary gland. They contain salivary gland tissue as a developmental error (Fig. 49.24).

Generalised diseases involving teeth and jaws

Endocrine disorders

Aeromegaly Excess of growth hormone after skeletal maturity results in a characteristic coarsened and enlarged facies. The mandible especially increases in size in both the body and ascending ramus, so that the lower border of the body lies more inferiorly in relation to the cervical spine than is normal. The increase in size of the mandible results in separation of the teeth. Dental separation may also result from the increased size of the tongue.

The angle of the mandible becomes more obtuse, i.e. there is straightening, and the lower border becomes more curved, as seen on the lateral view.

Gigantism Dental separation again results from jaw enlargement, but the skull in gigantism does not resemble that seen in

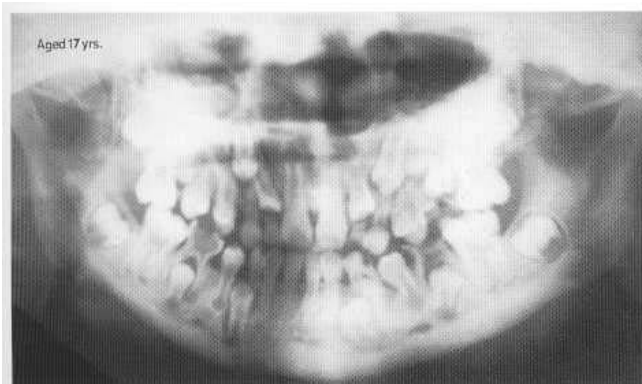


Fig. 49.25 Cretin, showing gross retardation of dental maturity.

acromegaly. Mandibular lengthening may be even more pronounced. As the disease precedes the onset of skeletal maturity, the dental age is advanced. The teeth that develop after onset of disease show hypercementosis.

Hypopituitarism Hypoplasia of the jaws and teeth and delayed dental age arc found, as would be expected.

Cretinism This childhood condition is far more common than childhood thyrotoxicosis, which is rare.

In cretinism there is a generalised delay in skeletal and dental maturity, so that the facial bones are hypoplastic and dentition is delayed. Shedding of deciduous teeth is retarded, as is formation and eruption of secondary dentition. The small jaws thus show gross dental crowding (Fig. 49.25). Thyrotoxicosis, on the other hand, causes acceleration of dental maturity and bone demineralisation.

Hyperparathyroidism Subperiosteal bone resorption is the pathognomonic bony change in this disease.

The lamina dura of the dental socket represents the cortical bone and is resorbed in hyperparathyroidism. The change is not common, however, and not all sockets are affected, so that its value as a radiodiagnostic tool in hyperparathyroidism is poor. Patients with radiological bone disease will always have hand changes.

In the past, *osteoclastomas* and *brown tumours* were not uncommonly seen in the jaws and were often multiple, occurring alone or accompanied by resorption of the lamina dura (Fig. 49.26). As

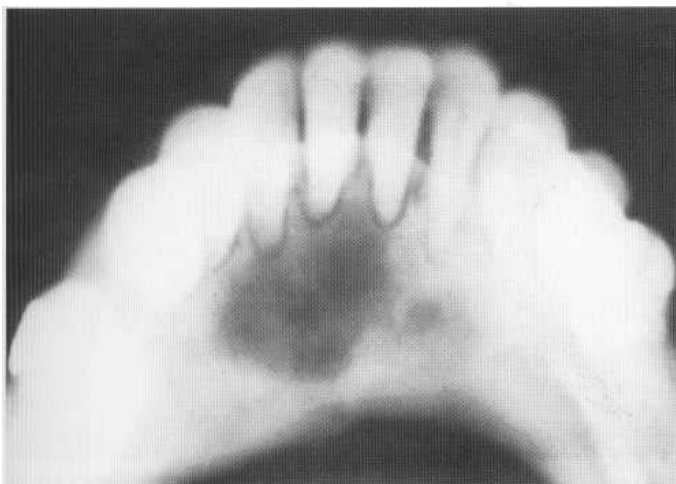


Fig. 49.26 Hyperparathyroidism. A brown tumour is associated with resorption of the lamina dura.

hyperparathyroidism is now usually diagnosed early on routine blood analysis, large skeletal cysts and jaw lesions are not often seen.

Hypoparathyroidism Oral candidiasis is commonly found. The crowns of the teeth are irregular, with deficient enamel. The lamina dura is quite dense and thickened, around roots which may be hypoplastic. There is also retardation of dental age.

Cushing's syndrome Osteoporosis may be seen in the jaws, and the lamina dura may be poorly visualised or absent.

Dysplasias

Cherubism (*hereditary fibrous dysplasia of the fuses*) Although histologically indistinguishable from fibrous dysplasia, this entity has a definite familial incidence. Involved patients do not have the disease outside the jaws. Changes affect the mandible primarily, but the maxillary tuberosity may also be involved.

The mandible is enlarged by radiolucent areas of cystic and fibrous change, so that the jawline of the patient becomes prominent. Affected children come to resemble winged angels-cherubs-with the chubby faces seen in classical paintings.

Agenesis of the teeth occurs in the involved areas, and the teeth that do form become displaced, separated from each other, and unerupted (Fig. 49.27).

Changes take place from 1 year of age onward, but from puberty onward they regress, so that by middle age the jawline may appear normal.

Cleidocranial dysplasia Almost all patients with this disease have abnormal dentition. The maxillae are underdeveloped so that the cheeks are small, and the teeth of the upper jaw appear crowded. This appearance is further accentuated by the almost inevitable failure of eruption of the secondary teeth. In addition, multiple supernumerary teeth are also present: up to 13 have been shown in one patient. The small jaws thus show a large number of crowded supernumerary, primary and secondary teeth, which may even be displaced into the orbits (Fig. 49.28).

Cement formation is also deficient in this disorder, and hypercementosis is not seen.

Ectodermal dysplasia The ectodermal abnormality is characterised by abnormal hair, defective or absent finger and toenails, and a paucity of sweat glands. In addition, there is partial or total absence of the teeth (anodontia), so that often only the central teeth are present, and their crowns are conical (Fig. 49.29).

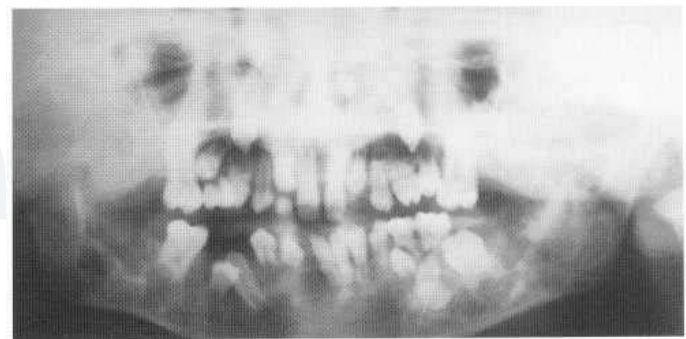
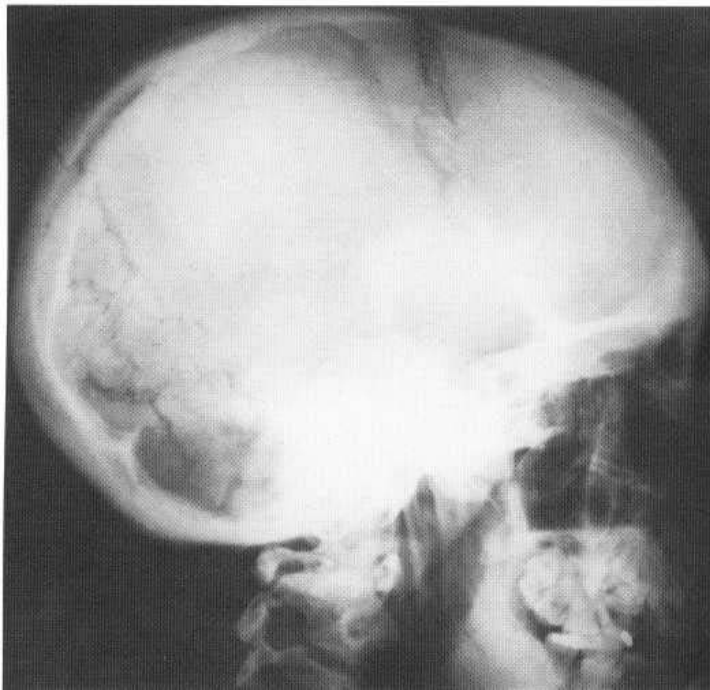
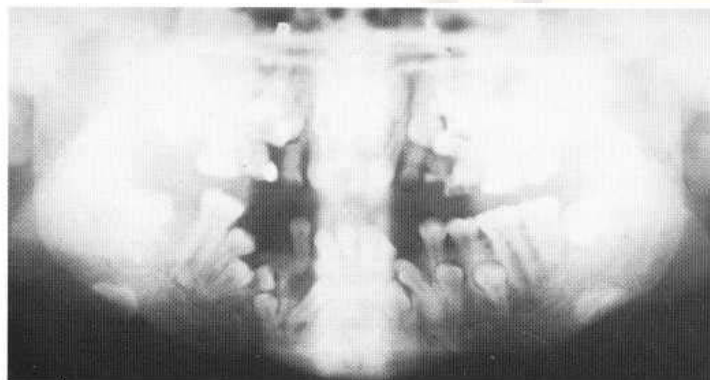


Fig. 49.27 Cherubism. Fibro-osseous lesions of the mandible prevent the formation of some teeth and displace others.



A



B



C

Fig. 49.28 Cleidocranial dysplasia. (A,B) There is persistence of wormian bones with maxillary hypoplasia, and a large number of primary and unerupted secondary teeth with supernumerary tooth formation. (C) A midline defect is present at the symphysis mentis.

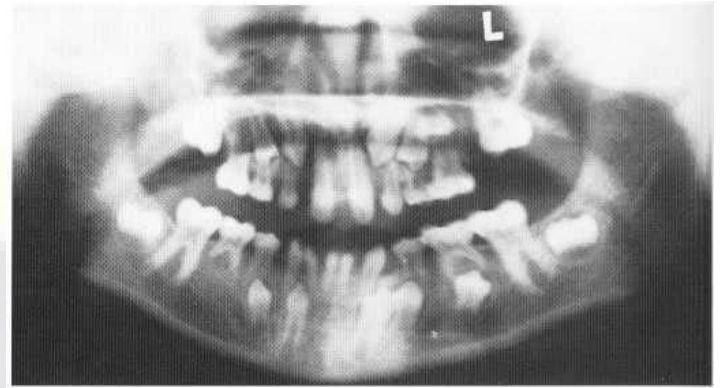


Fig. 49.29 Ectodermal dysplasia. Much of the secondary dentition is absent.

In some patients, the ectodermal dysplasia is associated with a mesenchymal dysplasia, e.g. the *Ellis-von Creveld s.yndrome* (chondroectodermal dysplasia).

Gardner's syndrome (*osteomotosis-intestinal polyposis svndrome*) This syndrome is inherited as an autosomal dominant. The features include:

1. **Multiple osteomas.** These benign osseous excrescences appear around puberty and arc found on the vault and mandible and in the facial sinuses. Facial deformities result. Facial osteomas are larger and much more common than those elsewhere, but they are seen on the radius, ulna, tibia and fibula. Radiologically, dense areas of bone are also seen in the vault; these lie within bone and are distinguishable from the exostoses (Fig. 49.30).
2. **Other dental lesions.** Compound odontomes and unerupted supernumerary teeth are found in up to 50% of patients.
3. **Skin lesions.** Epidermoid inclusion cysts arise in 50% of cases, around puberty. They are found anywhere on the body. Other dermal lesions found are lipomas, fibromas and desmoid tumours. The last arise in muscle, arc particularly prone to recur after surgery for their removal, and may grow to a large size, especially in the abdomen. Ureteric obstruction may result.
4. **Polypsis coli.** Multiple adenomatous polyps arise around puberty in the colon and rectum, and occasionally in the small bowel. In view of their almost inevitable malignant transformation, treatment is usually by prophylactic colectomy.



Fig. 49.30 Gardner's syndrome. Multiple osteomas are seen on the mandible and in the paranasal air sinuses, together with areas of sclerosis in the mandible.

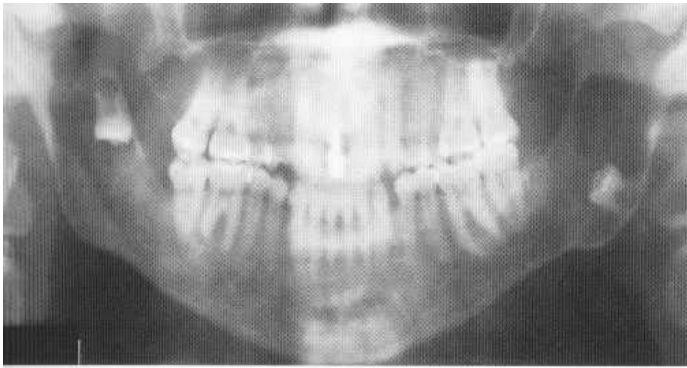


Fig. 49.31 Gorlin syndrome. Multiple dentigerous cysts are seen in the mandible.

Multiple naevoid basal-cell carcinoma and jaw cyst syndrome (Gorlin-Coltz, syndrome) This syndrome is inherited as an autosomal dominant and consists of widespread skeletal and dental abnormalities and jaw lesions. Consequently some patients present to the dermatologist, some to the dentist, and some to the orthopaedic surgeon.

1. **Jaws and face.** Large dental cysts occur in 75% of cases. They are multiple, occurring in both maxilla and mandible, but more commonly in the latter, often in the region of the third molar teeth. The cysts usually start after puberty and present as a swelling in the mouth, or with a pathological fracture. Radiologically, the cysts resemble either odontogenic keratocysts or dentigerous cysts (see below) and may also expand into the antra (Fig. 49.31). Histologically, the cysts resemble odontogenic keratocysts and so are prone to recurrence. On occasion, transformation to ameloblastoma and squamous-cell carcinoma has been reported.

2. **Face and skull.** Patients have bossing of the frontal and parietal regions, giving a pagetoid appearance, with hypertelorism and prognathia. The sella turcica is often bridged over. The falx cerebri and adjacent meninges show heavy plate-like calcification.

3. **Other skeletal anomalies.** Rib abnormalities are common. They are usually bifid, and this change may be bilateral. Synostosis also occurs. Cervical ribs are found. Thoracic scoliosis and spiny bifida occulta are seen. Sprengel's shoulder occurs less commonly, as do short fourth and fifth metacarpals. This is an interesting association with intracranial calcification (see above), which also occurs in hypoparathyroidism.

4. **Multiple naevoid basal-cell carcinomas** occur with increasing frequency from the second decade on. These lesions are identical with basal-cell carcinomas and are distributed over face, neck, thorax and upper abdomen.

Neurofibromatosis (von Recklinghausen's disease) This syndrome is a complex one, with a combination of cutaneous and deep neural tumours. Local overgrowth of a nerve (plexiform neurofibroma) is often associated with bony and soft-tissue hypertrophy in the innervated segment. The mandible is an unusual bone in that a nerve actually runs within it, in the inferior dental canal. With a neurofibroma of the inferior dental nerve, the canal and its opening are widened and the hemimandible may be enlarged. Erosion of the mandible may also result from extrinsic pressure by a superficial neurofibroma (Fig. 49.32).

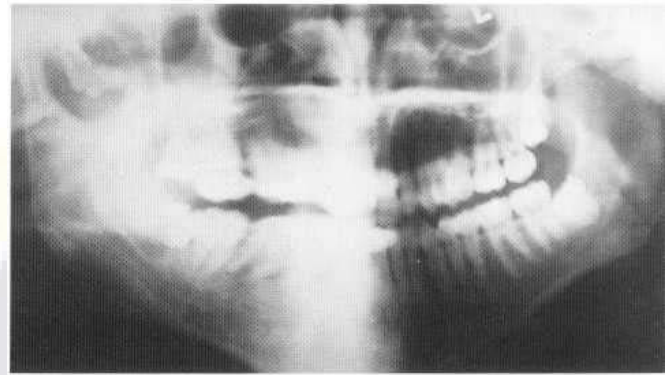


Fig. 49.32 Neurofibromatosis. The right side of the mandible is enlarged. The right condyle is scalloped due to a local neurofibroma, while the origin of the inferior dental canal is widened-also because of the local neurofibroma.

Osteopetrosis Increased density of bone is seen in the mandible and maxilla, so that the roots of the teeth may barely be visible. The abnormal bone is highly susceptible to infection, and osteomyelitis of the jaw is a recognised complication which may lead to loss of the mandible if not treated. Dental sepsis is also more common, as the enamel is defective and the crowns pits easily. The lamina dura around the roots is grossly thickened but the periodontal membrane space is preserved.

Haemoglobinopathies

Thalassaemia When severe, this causes the greatest amount of marrow hyperplasia of all the haemoglobinopathies. The bones are expanded, cortices are thinned, and trabeculae resorbed, so that those remaining trabeculae are thrown into prominence. In the facial skeleton, expansion of the mandible may be marked, causing separation of the teeth. The paranasal sinuses, with the exception of the ethmoids, are obliterated by marrow (Fig. 49.33). Gross thickening of the diploe affects all the bones of the cranium with the exception of the basiocciput.

Sickle-cell disease Marrow hyperplasia causes changes similar to those seen in thalassaemia, but generally of lesser severity. In addition, infarcts may cause local areas of bone sclerosis. A 'rodent facies' may also be seen in severe cases, due to overgrowth of maxilla and mandible, with forward displacement of anterior teeth.

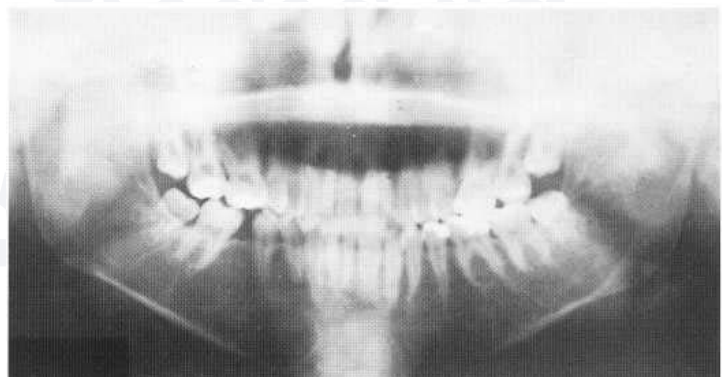


Fig. 49.33 Thalassaemia. The mandible is enlarged, the cortex thinned and the trabeculae resorbed. The paranasal air sinuses contain marrow.

Histiocytosis X

Lesions around the jaws are common, and both bone and soft tissues are involved in as many as 50% of cases.

Localised destructive lesions of bone occur, especially in the peripheral regions. The socket becomes destroyed and the tooth 'floats free'. Forming tooth-buds may be destroyed. Lesions are often multiple, so that teeth either do not form or are rapidly exfoliated. The bony defects heal well with radiotherapy (Fig. 49.34).

Cysts of the jaws

Not only can the jaws be sites of bony lesions which occur throughout the skeleton, but since they also bear specialised organs the teeth they have their own special local anomalies. In addition, because of the nature of facial development in utero, abnormalities of growth and fusion can occur.

Cysts of the jaws may conveniently be classified into:

1. Cysts of *denial origin*, developmental or post inflammatory
2. *Non-dental*, developmental or fissural cysts
3. *Non-epitheliated cysts* of bone, which may also be seen elsewhere.

Mandibular and maxillary cysts often seem to present a problem to the medical radiologist, yet their diagnosis is essentially simple. There are three commonly seen cystic lesions (Fig. 49.35):

- a. The *apical* or *radicular* cyst. This is by far the most common. It sits on the very apex of the root of a tooth, which is usually carious.

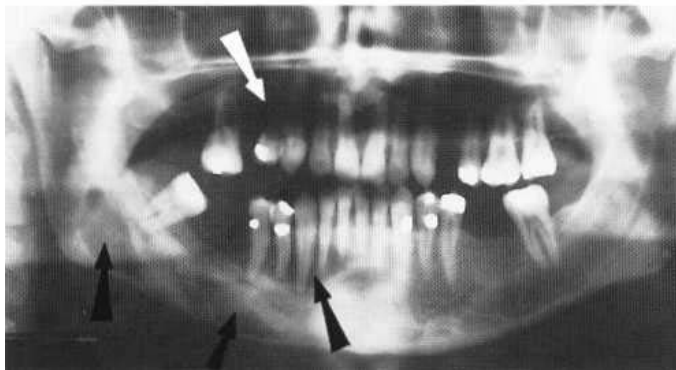


Fig. 49.34 Eosinophilic granuloma. Arrows point to the multiple osteolytic lesions, which are well defined.

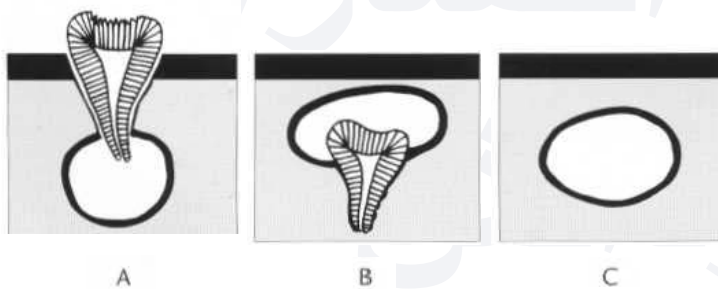


Fig. 49.35 The three common types of dental cyst. (A) Radicular cyst. The tooth is carious, the cyst sits at the apex of the bone and absorbs the local lamina dura. (B) Dentigerous cyst. The cyst is related to the crown of an unerupted tooth. (C) A large cyst which is not related to a dental element - a primordial cyst.

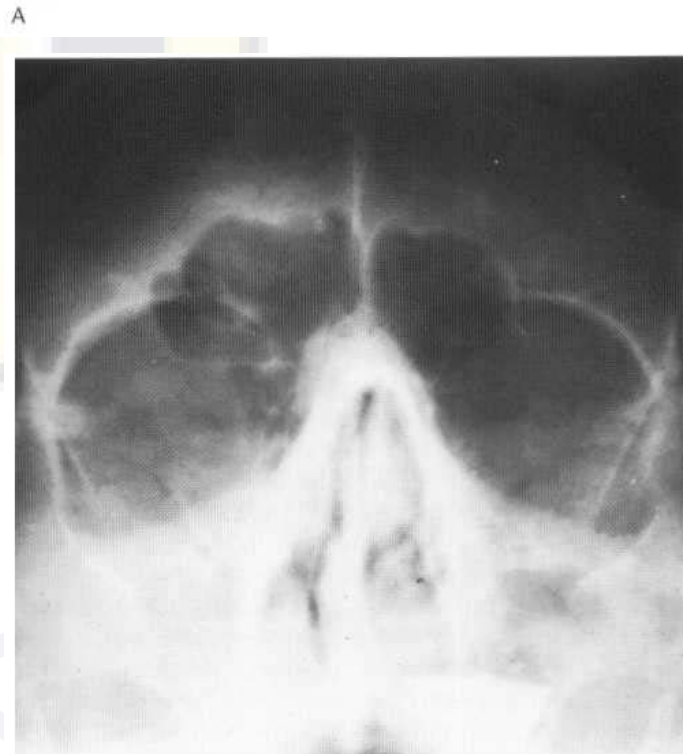


Fig. 49.36 Cyst of the antrum. (A) The dental lesion expands into the antrum and has a well-corticated superior margin. (B) Aspiration of contents and installation of contrast medium confirms the true nature of the cyst.

- b. The *dentigerous* or *parulis* cyst, which is a cyst related to the crown of an unerupted tooth.

- c. The *primordial* or *odontogenic keratocyst*. This often develops in place of a tooth and may reach a very large size, but is not as common as the dentigerous cyst.

In addition, *central* or *midline* cysts tend to be fissural or developmental in origin.

When a cyst arises on a tooth related to the floor of the maxilla, the cyst extends into the maxillary antrum and appears rather like a polyp. The floor of the antrum is displaced upward by the cyst, however, and its upper surface is thus a thin dense line, unlike a polyp. Aspiration of the contents and insertion of contrast medium confirms the cystic nature of the lesion (Fig. 49.36).

1. Cysts of dental origin

a. Developmental

(i) **Odontogenic keratocyst (primordial cyst)** These may follow cystic degeneration of the enamel organ before the tooth is formed, so that the cyst replaces the tooth, but they may also arise from ectopic odontogenic epithelium. Should a normal complement of teeth be present, the cyst is assumed to have replaced a supernumerary tooth. Primordial cysts are more common in young men, but may be seen at all ages. They are slow-growing but may reach a very large size and may occupy the entire ascending ramus (Fig. 49.37). The cortex becomes thinned and an axial view also demonstrates expansion in the buccal-lingual plane. They are most commonly seen in the posterior mandible and are usually monolocular. These cases present either because a critical size is reached and the patient feels a fluctuant swelling of the mandible, or because of secondary infection and purulent discharge.

Because of their growth potential, they may abut against an initially unrelated and unerupted tooth. A dentigerous cyst is then simulated, although the size and location may help in differentiation. The diagnosis is in any case confirmed by enucleation and histological examination.

These cysts are almost inevitably re-attained and are very likely to recur unless removed completely. Long-term follow-up is therefore advisable.

(ii) **Dentigerous cyst (follicular cyst)** Cystic degeneration of the enamel organ may occur after the tooth has been formed but before it has erupted. This results in a cyst related to the crown of an unerupted tooth. Cysts enlarge in part because of local hydrostatic imbalance. If the pressure within the cyst exceeds the eruptive pressure of the tooth, that tooth is prevented from erupting. It becomes displaced, often for some distance. Part of the crown always remains in contact with the cyst (Fig. 49.38).

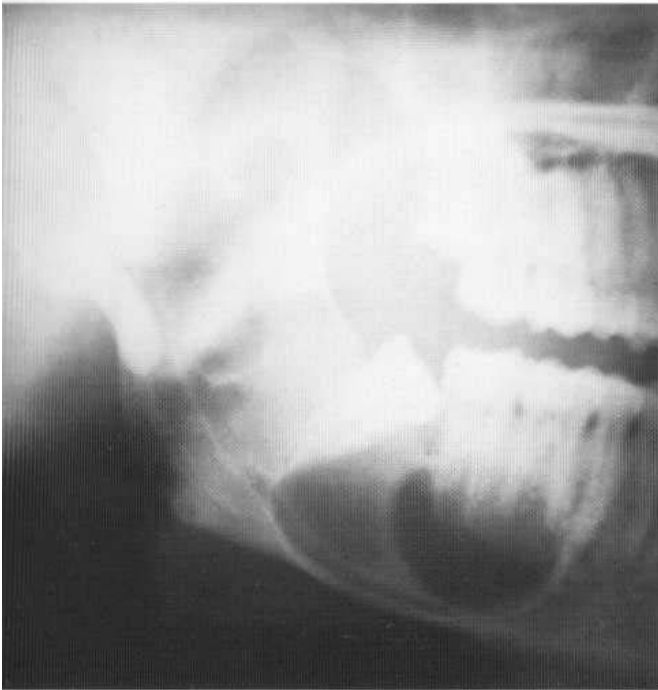


Fig. 49.37 Odontogenic keratocyst. A large cystic lesion extends to the base of the condyle and expands the bone. It is not related to caries or to the crown of an unerupted tooth.



Fig. 49.38 Dentigerous cyst. The cyst is related to the crown of an unerupted tooth.

These cysts are found primarily in adolescents and young adults. The permanent mandibular third molar and maxillary canine are especially affected. The cysts are usually unilocular. If multiple, they may be associated with Gorlin's syndrome. On occasion, small cysts are seen at the crown of a normally situated tooth which is erupting. These *eruptive* cysts vanish when the crown reaches the surface.

b. Postinflammatory Radicular (apical) cysts Most cysts of the jaws are radicular. They lie directly upon the apex of a tooth, which is usually diseased. They follow inflammation of the pulp and apical bone, when a local apical area of chronic inflammation, the granuloma, may result. This is seen radiologically as a poorly defined para-apical area of bone loss rather like a Brodie's abscess. Chronic inflammation stimulates local epithelial-cell rests at the dental apex, and the granuloma becomes epithelialised. The well-defined radicular cyst results. Its dense opaque margin is continuous with the lamina dura at the periphery of the cyst, but within the cyst the lamina dura is destroyed. These cysts are generally less than 1.5 cm in diameter and in grossly carious mouths may be multiple (Fig. 49.13).

Treatment is by removal of the tooth and curettage. This should result in bony healing with gradual obliteration of the cavity. Should the cyst persist after dental extraction, it is known as a *residual* cyst and its origin cannot be inferred from a radiograph (Fig. 49.39).



Fig. 49.39 Residual cyst. A well-defined cyst is all that remains of a radicular cyst following dental extraction. Note reactive sclerosis elsewhere.

2. Developmental (fissural) cysts

These presumably occur at sites of fusion of embryonic processes. Such cysts are:

- a. *Medial mandibular* (Fig. 49.40).
- b. *Medial maxillary, Nasopalatine.*

The nasopalatine ducts connect the nasal cavity with the palate behind the central incisors. Four ducts are present in utero, two on either side of the midline. Failure of normal ductal obliteration may result in local epithelial remnants undergoing cystic degeneration.

d. *Globulomaxillary.* These cysts look like an inverted pear and lie between the upper lateral incisor and canine, the roots of which are diverged. There is some doubt as to whether these are fissural or inflammatory. The majority are odontogenic keratocysts (Fig. 49.41).

3. Non-epithelialised bone cysts

a. *Simple bone cyst.* These may follow trauma and are thus also known as traumatic cysts. They appear in young patients, usually boys, in the posterior aspect of the body of the mandible. Like other types of cyst, they are vaguely spherical, well-defined, and surrounded by a thin dense zone of reactive sclerosis. These features

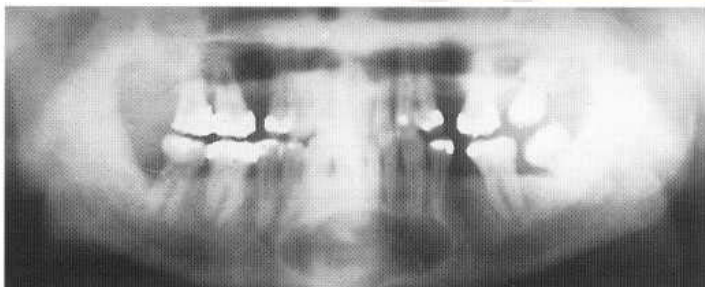


Fig. 49.40 Midline mandibular cyst. This could be a radicular cyst but the local teeth are normal radiologically and vital.

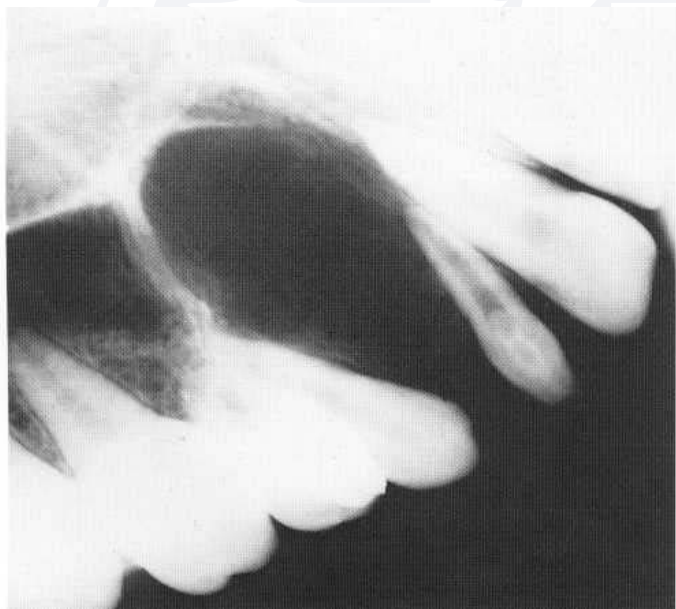


Fig. 49.41 Dens in dente and a globulomaxillary cyst.

are non-specific and the diagnosis is essentially histological. There is a tendency for the lesion to extend upward, between the teeth, to the alveolar margin.

b. *Aneurysmal bone cyst.* These present as a well-defined expansile radiolucency, displacing teeth. Again, the lesion is not common in the jaws, and histology is usually needed to confirm its identity. They may be secondary to other tumours (Fig. 49.42).

Neoplasms

Benign neoplasms

Benign tumours of bone do occur in the jaws but are not common. Any of the local elements of bone-osteoid, fibrous tissue, blood vessels, etc.-can give rise to benign tumours. There is some doubt as to whether cartilaginous tumours can arise in the jaws, which are formed in membrane. Such lesions as have been described may have arisen from 'rests'. Enchondroma, osteochondroma and chondrosarcoma have all been (rarely) described.

Osteoma Both osteoid osteoma and 'simple' osteoma have been described. An osteoma may be seen as a dense, well-defined lobular mass, e.g. in Gardner's syndrome (Fig. 49.30), and may be attached to the outside of the bone or lie within it. Central sclerosing lesions, however, may also be due to old sepsis or trauma or may be fibro-osseous in origin (see Sclerosing Lesions, above).

Torus palatinus is an exostosis of cortical origin in the midline of the palate. *Torus mandibularis* presents as an exostosis on the lingual aspect of the mandible in the premolar region. It is best seen on occlusal views. The lesions are probably genetically inherited.

Osteoelastoma A true osteoclastoma is rare in the jaws but a Giant-cell lesion can arise in young jaws (from 7 years to the early 20s) called, after Jaffe, a *giant-cell reparative granuloma*. It is a central soft-tissue mass replacing bone, and may look clear-cut like a cyst, or have a much less well-defined margin. It arises in the tooth-bearing part of the jaw, and will displace developing teeth and expand the bone (Fig. 49.43).

Fibrous lesions Fibrous dysplasia, cherubism and cementomas (see above) are common fibro-osseous lesions which all have their origins in fibrous tissue.

Fibromatous and cartilaginous lesions both cause localised areas of osteolysis which have a tendency to ossify.

Malignant neoplasms

Oral cancers only comprise up to 2% of all malignant tumours in England but are very common in Asia. Most of these lesions are *squamous-cell carcinomas*. Precipitating factors include poor oral hygiene, cigar and pipe smoking, alcohol, and possibly syphilis. Betel-nut chewers in India and England also have a high incidence of oral cancers, as do people with leucoplakia. Oral squamous-cell carcinoma is more common in men.

The lesion readily becomes attached to bone, but X-ray evidence of bone destruction by the invading neoplasm is less frequent. The bone destruction has an ill-defined irregular margin.

Carcinomas also occur in the antra and may cause dental symptoms, with swelling, loss of teeth, and bone destruction. The antra are opaque and the tumour breaches the antral walls to extend into local soft tissues (Fig. 49.44).

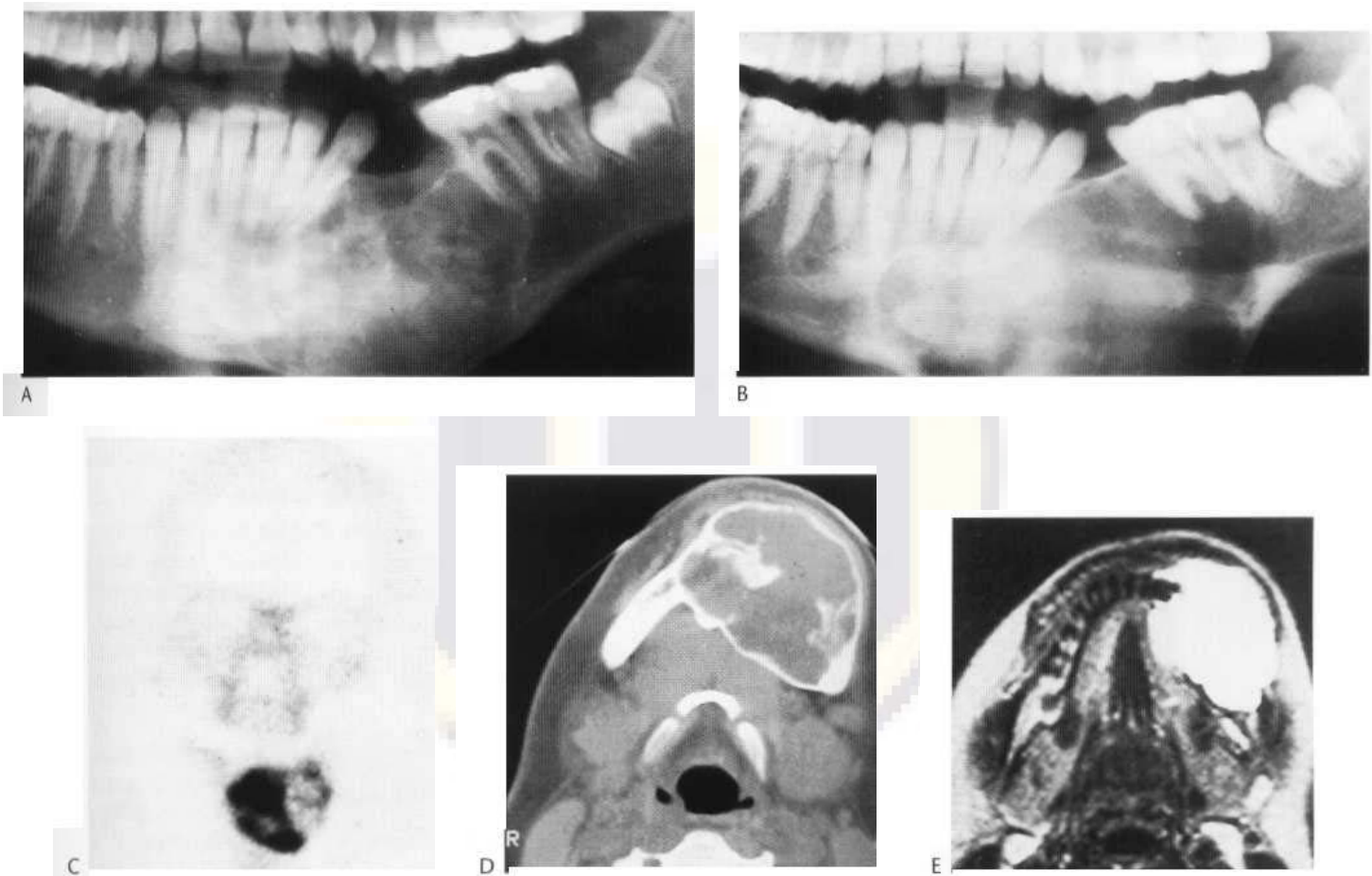


Fig. 49.42 Fibrous dysplasia and resulting degeneration into aneurysmal bone cyst. (A) The initial radiograph shows an expansile, well-demarcated lesion displacing teeth; there is a mixed pattern of lysis and sclerosis. These changes are typical of fibrous dysplasia. Subsequently expansion took place (B) and the lesion became more cystic. (C) The bone scan at this time shows a mixed pattern with a central cold area. (D) The CT scan shows the expanded mandible and the now essentially cystic nature of the lesion. (E) MRI confirms the change in the nature of the lesion from a solid to a fluid-filled tumour.

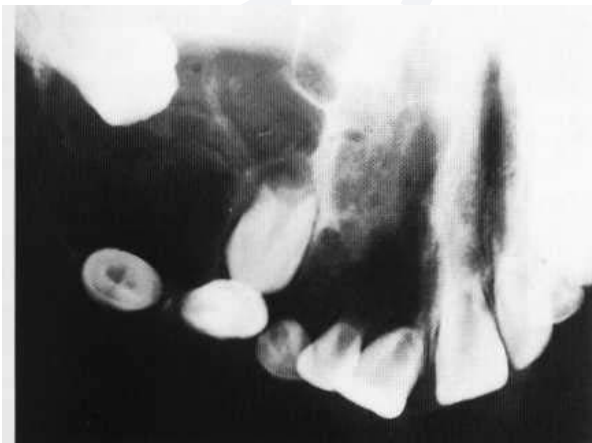


Fig. 49.43 Boy aged 8. An occlusal view of a large giant-cell lesion expanding the right maxilla which has displaced several teeth.

Ameloblastoma This is a not uncommon lesion. It accounts for 1% of oral tumours in Europe but has a much higher incidence in Africans (0.3% of all tumours). Most lesions present in middle age, but they may occur at all ages. Men are more commonly affected. Ameloblastoma occurs mainly in the molar region of the mandible.

Radiologically, the lesions are expansile, with thinning of the cortex in the buccal-lingual plane. The lesions are classically multilocular

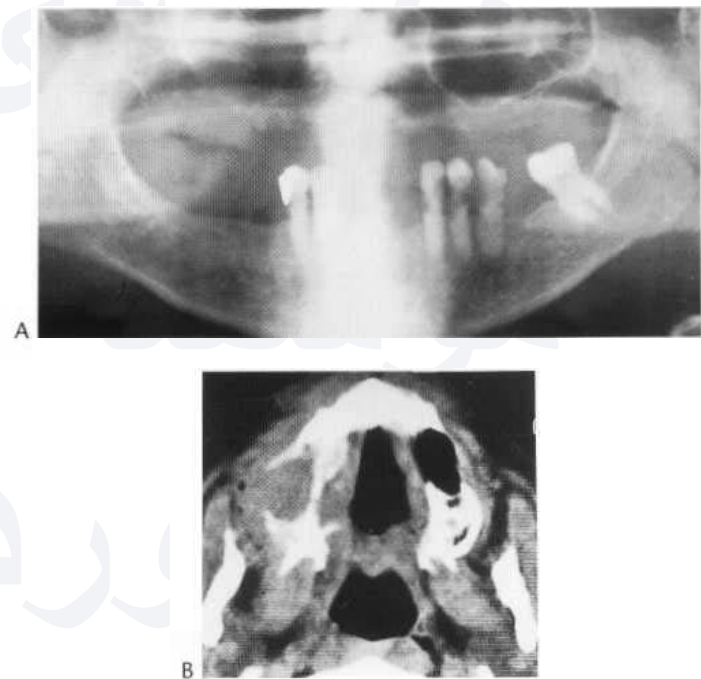


Fig. 49.44 Carcinoma of the maxillary antrum. (A) The radiograph shows a soft-tissue mass invading the floor of the right antrum. (B) CT confirms the change and shows the highly invasive nature of the tumour.

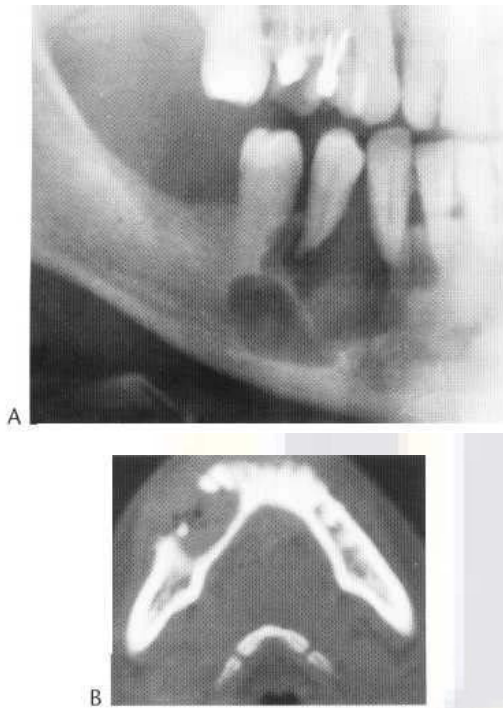


Fig. 49.45 Ameloblastoma. (A) The radiograph shows a well-defined multilocular lesion which characteristically reaches the alveolar margin and erodes teeth. This latter feature is unusual in lesions other than ameloblastoma. (B) The CT scan demonstrates the marked expansion caused by these tumours in the axial plane.

cystic 'soap-bubble' or 'honeycomb' in appearance, with peripheral satellite defects which are well demarcated (Fig. 49.45). On pathological examination, the defects may be found to be truly cystic, or cellular. On occasion, unilocular ameloblastomas are seen, resembling dentigerous cysts or odontogenic keratocysts (Fig. 49.46) (similarly, the latter may also be multilocular).



Fig. 49.46 Ameloblastoma. A multilocular cystic lesion erodes the root of a molar but also prevents eruption of a wisdom tooth. The ameloblastoma may be secondary to a dentigerous cyst.

If the diagnosis is likely radiologically, block excision of bone should be carried out so that no satellite lesions are left behind: if the tumour is completely excised, recurrence is unlikely. Following incomplete excision and re-exploration, however, the lesion may be spread both locally and to the lungs. The probable route of pulmonary spread is by cellular aspiration.

Osteosarcoma This is an uncommon tumour in the jaws and has a higher age of incidence than classic osteosarcoma elsewhere, being seen in the third and fourth decades. The radiological appearances are no different from those found elsewhere, but the lesions have a better prognosis, with a higher 5 year survival rate (Fig. 49.47). Occasionally, sarcomatous changes develop following irradiation or Paget's disease, but reported cases are few.

Ewing's tumour This lesion affects the same age group in the jaws as elsewhere. It is predominantly lytic, as elsewhere, and the prognosis is poor (Fig. 49.48).

Metastases Secondary deposits may be blood-borne but because the jaws are low in marrow, the incidence of secondaries is not as high as in the axial skeleton (Fig. 49.49). In the mandible they may cause anaesthesia of the lip if the inferior dental nerve is compressed. Metastases are not commonly seen either radiologically or on radionuclide scans, even if they are present elsewhere in the skeleton.

Myeloma This is seen more often in the mandible than are secondary deposits, apparently in up to 30% of cases, although lesions of the mandible are not as common as those of the skull vault. The radiological appearances are as elsewhere.

Burkitt's lymphoma This condition occurs throughout the world but especially in equatorial Africa, where it accounts for 50% of all childhood malignancies. The jaws are frequently affected by massive tumours that deform the face, but the lesions are multifocal. The antrum and orbits are involved more often than the mandible. Destruction of bone often starts around the roots of the teeth, which are then exfoliated. The area of destruction increases in size and massive tumours form, deforming the face, invading the orbits, and enlarging the mandible. New bone forms in these lesions, giving a coarse, spiculated, sunray appearance.

Temporomandibular joints (TMJ)

The temporomandibular joint is the site of the usual afflictions of joints. It is eroded by local synovial or osseous tumours. Up to 50% of patients with rheumatoid arthritis have symptoms referable to the joint but not all have erosive change (Fig. 49.50). Hyperparathyroidism in renal osteodystrophy occurs locally, with cortical resorption and demineralisation (Fig. 49.51). Dysplasias of bone, especially the mucopolysaccharidoses, cause abnormal condylar shapes. Ankylosis is seen in fibrodysplasia ossificans progressiva.

Most radiological examinations of the temporomandibular joints are undertaken for local pain, limitation of movement, clicking joints or crepitus. Patients often have a history of bruxism. On clinical examination the joint may be tender and its excursion limited. Masseteric hypertrophy and pterygoid tenderness are often present, and sometimes dental malocclusion. These patients are often young to middle-aged women who may be aided by minor tranquillisation, which relaxes the muscles of mastication and inhibits bruxism.

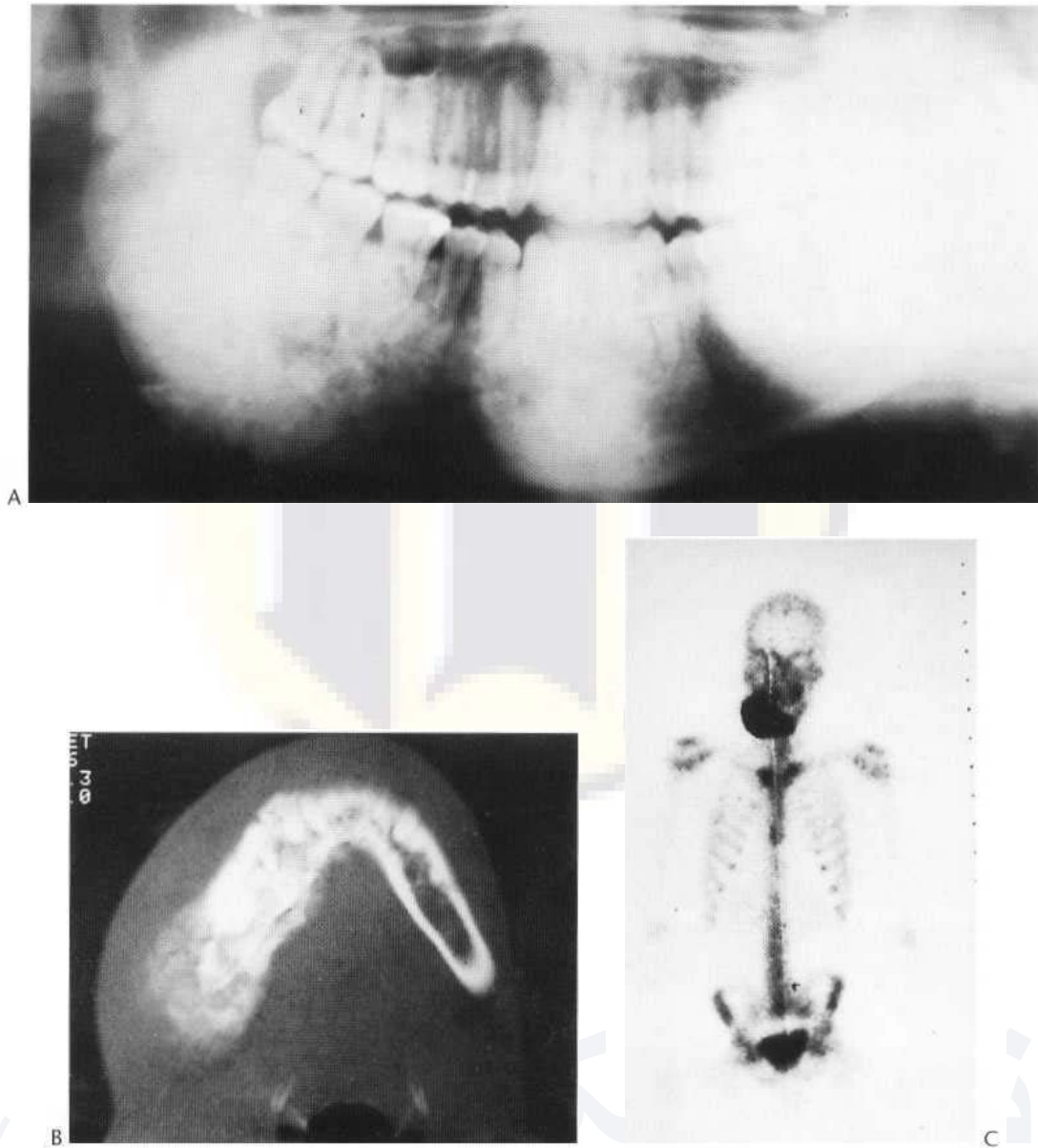


Fig. 49.47 Osteogenic sarcoma in a 26-year-old man. (A) Panoramic view shows a large bone-forming tumour affecting the right hemimandible and crossing the midline. (B) CT scan confirms the extent of involvement. (C) Radioisotope bone scan also delineates the affected area.



Fig. 49.48 Ewing's tumour. These lesions are uncommon in the mandible. (A) In this patient an osteolytic lesion is present in the left ascending ramus and condyle; it is expansile and shows slight residual trabeculation. (B) The CT scan shows a large soft-tissue mass associated with bone destruction in the left ascending ramus.

and jaw clenching at night. Radiologically, some of these patients have changes which are similar to those of osteoarthritis elsewhere, with flattened condyles, a narrow joint space and limitation of movement. At arthrography and MR scanning, meniscal deformity

is often found to be present. The meniscus is usually thinned posteriorly and bunched forward anteriorly. This acts as an obstruction to mouth opening. If the condyle can traverse the mass, an audible and palpable click is produced (Figs 49.52-49.54).

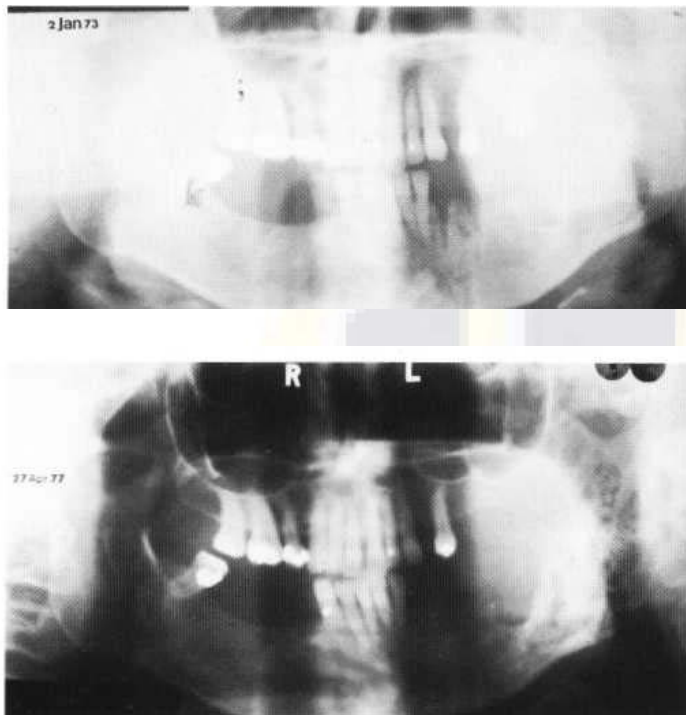


Fig. 49.49 Carcinoma of the breast with metastases to the mandible. The initial film shows gross bone resorption of the left hemimandible. The lower illustration shows the appearances following radiotherapy.



Fig. 49.51 Hyperparathyroidism in renal osteodystrophy with medullary and cortical bone resorption. (Courtesy of Dr R. Dick, Royal Free Hospital, London.)

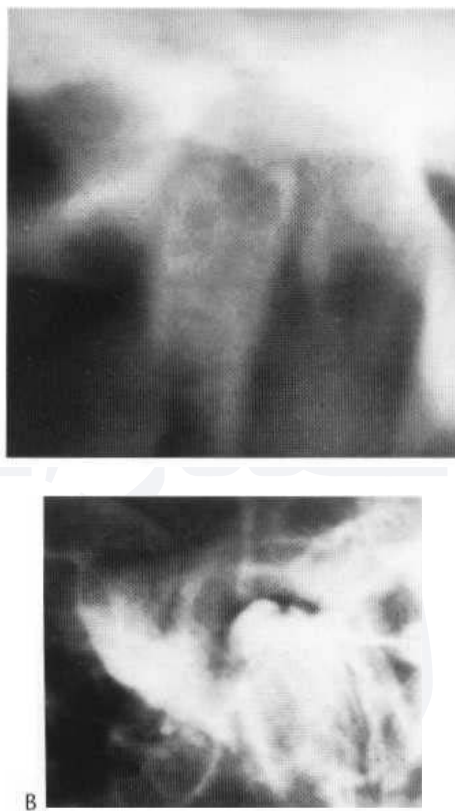


Fig. 49.50 Rheumatoid arthritis. (A) Erosion of the condyle is marked. (B) Injection of the lower joint space shows the hypertrophic synovium associated with rheumatoid arthritis.



Fig. 49.52 Deformity of the meniscus is shown at injection of the lower compartment. There is a large anterior meniscal mass. The condyle passes over it with an audible 'clunk'.



Fig. 49.53 TMJ malfunction syndrome (A-C). The preliminary tomogram shows narrowing of the posterior portion of the joint with widening of the anterior. This usually implies anterior displacement of the meniscus. These changes are confirmed at arthrotomography and the deformed anteriorly displaced meniscus prevents significant forward movement of the condyle.

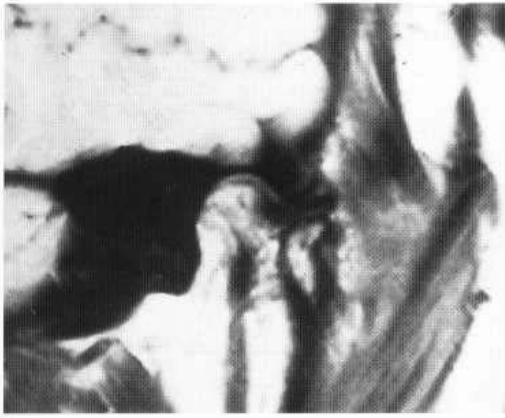
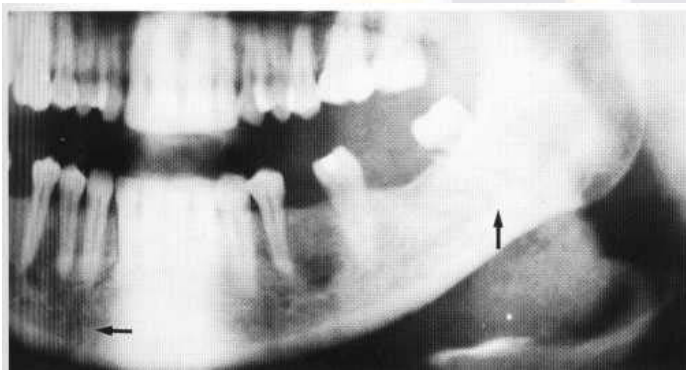
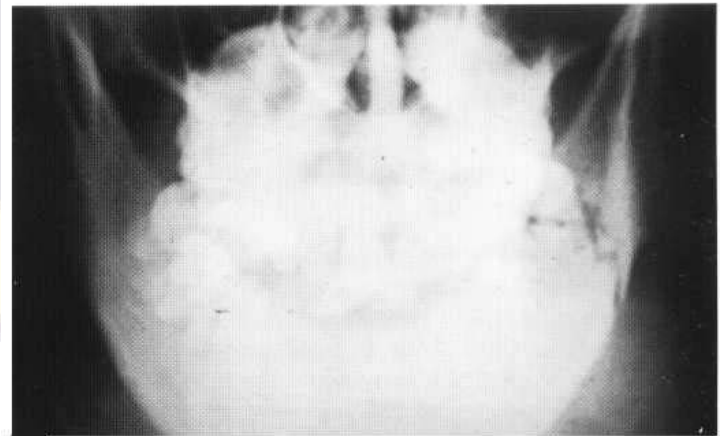


Fig. 49.54 The anteriorly displaced meniscus is shown on MRI as a low-signal mass anterior to the bright signal of the condyle.

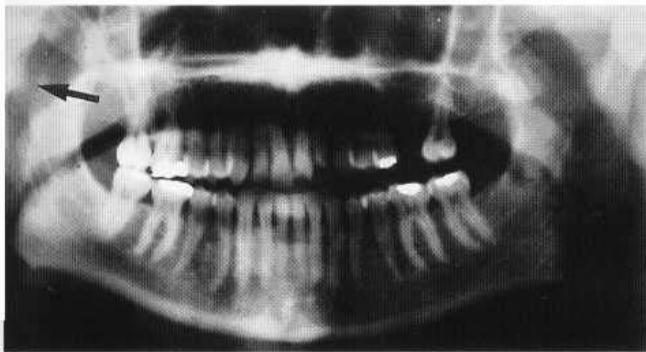


A



B

Fig. 49.55 Fracture of mandible. (A) As is often the case, the mandible has fractured in two places. One fracture extends through the wisdom tooth. (B) The AP view demonstrates normal alignment at the angle of the mandible.



A

Fig. 49.56 Condylar fracture. (A) The right condyle now overlaps the ascending ramus in part. The subsequent film (B) shows union with malalignment.

The mandible is shaped like a hemisphere which is fairly rigidly attached to the base of the skull at the temporomandibular joints. Ring-like structures in general fracture in two places, not just one, and the mandible is no exception. If a fracture line is clearly visible on one side, the other side must be closely inspected for a fracture or temporomandibular joint dislocation. Following fracture, the mandible must be radiologically examined in two planes (Fig. 49.55). A panoramic view should be accompanied by an anterior view and a Towne's view to visualise the condyles and zygomatic arches. Lateral oblique

views are not generally as helpful or as easy to take as panoramic views. Base or occlusal views assess displacement around the symphysis mentis but may not be possible because of local pain or trismus.

Fractures occur in the midline following a blow to the point of the jaw and may be accompanied by unilateral or bilateral condylar fractures or dislocations. A fracture line often extends into a tooth socket, loosening or fracturing the tooth (Fig. 49.56). Fractures of the body are usually vertical or oblique, but transverse fractures of the alveolar processes also occur. Following mandibular and, especially, condylar fractures, unopposed muscle pull can cause significant displacement of fragments. Condylar fractures are usually low and extracapsular (Fig. 49.56A), and the condyle is usually displaced medially on an anterior view radiograph (Fig. 49.56B). It then fuses at its base in the abnormal position.

REFERENCES AND SUGGESTIONS FOR FURTHER READING

- Gorlin, R. J., Pindborg, J. J., Cohen, M. M. (1976) *Syndromes of the Head and Neck*, 2nd edn. New York: McGraw Hill.
- Lucas, R. B. (1976) *Pathology of Tumours of the Oral Tissues*, 3rd edn. Edinburgh: Churchill Livingstone.
- Manson-Hing, L. R. (1980) *Panoramic Dental Radiography*. 2nd edn. Springfield, IL: Charles C. Thomas.
- Murray, D., Whyte, A. (2002) Dental panoramic tomography: what the general radiologist needs to know. *Clinical Radiology*, 57, 1-7.
- Stafne, F. C. (1983) *Stafne's Radiographic Diagnosis*, 5th edit. Philadelphia: Saunders.
- Trapnell, D. II., Bowerman, J. E. (1973) *Dental Manifestations of Systemic Disease*. London: Butterworths.



نشر الکترونیکی
موسسه انتشاراتی
نوردانش

50

ULTRASOUND OF THE EYE AND ORBIT

J. A. Fielding

THE EYE

Ultrasound images of the eye give an accurate 2D representation of the normal anatomical structures (Fig. 50.1). The cystic structure and superficial position make the eye ideal for ultrasound examination. Knowledge of the anatomy and firm structural anchoring points of the vitreous, inner and middle coats enables the pathological appearances of the detached vitreous, retina and choroid to be understood. Ultrasound is the most practical method of obtaining images of the posterior segment of the eye when the light-conducting media are opaque, and this is the most useful investigation prior to vitrectomy.

The skilled practitioner is able to study characteristics of the notion and topography of pathological intraocular structures, differentiating retinal detachment and vitreous membrane, or tumour and haemorrhage. Ultrasound contributes more to tissue diagnosis than CT or MRI, as these cannot scan in real time and lack spatial resolution. For most diagnostic purposes real-time B-scanning is the mainstay technique. The 2D B-scan image displays ocular structures much more effectively than the one-dimensional A-scan, but variations in echo amplitude from tissue interfaces are not as clearly demonstrated by grey-scale imaging as with the A-scan. Although combined B- and A-scanning is used in some centres, and standardised A-scan systems provide quantitative data on intra-

ocular echoes, they seldom yield information which usefully supplements that of the B-scan.

Anatomy and ultrasound features

The eyeball

The globe is the principal structure in the anterior orbit, embedded in fat but separated from it by a membranous sac termed the fascia bulbi or Tenon's capsule (Fig. 50.2). The eyeball is composed of segments of two different-sized spheres. The transparent anterior segment forms about one-sixth of the eyeball, and is part of a small sphere. The opaque posterior segment forms about five-sixths of the eyeball and is part of the larger sphere. The optic axis is a line joining the anterior pole—the central point of the anterior curvature of the globe, to the posterior pole—the central point of its posterior curvature. The normal axial length of the eye is 24 mm.

Sclera and cornea

The wall of the eyeball is constructed of three coats which enclose the transparent media (Fig. 50.3). The outer coat is tough and fibrous,

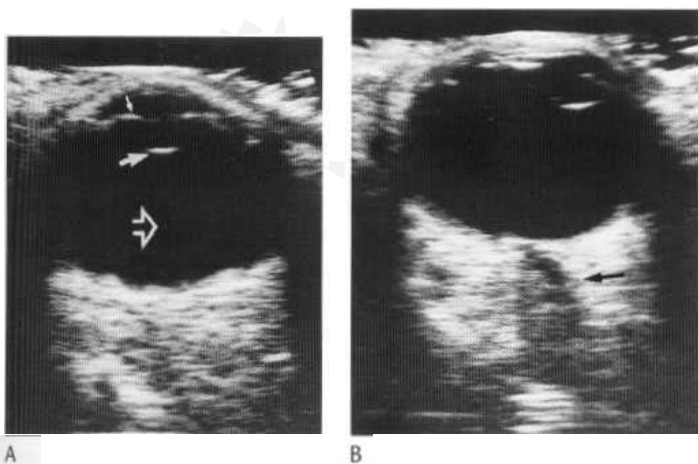


Fig. 50.1 (A) Normal eye showing iris (small arrow), posterior lens surface (arrow) and clear vitreous (open arrow). Horizontal scan. (B) Normal eye deviated left, showing optic nerve (arrow). Horizontal scan.

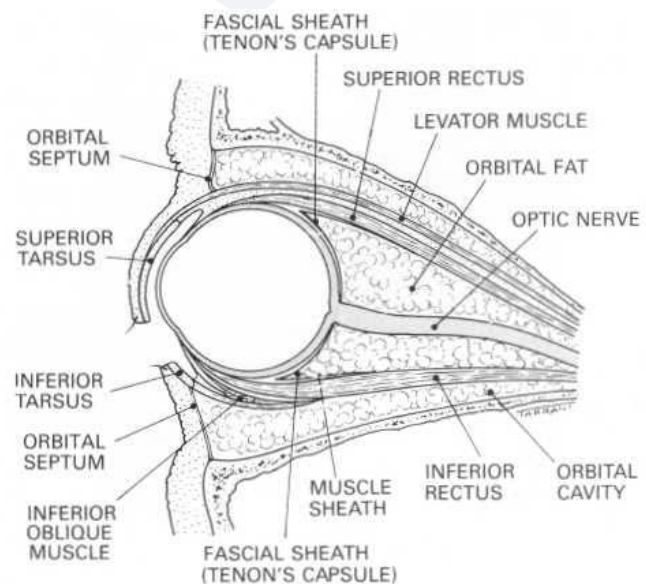


Fig. 50.2 Vertical section of the eye and orbit. (From Cosgrove et al 2001.)

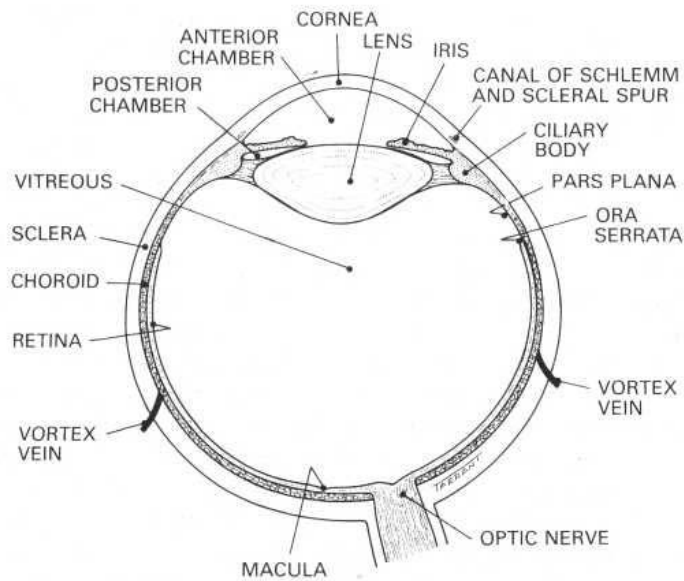


Fig. 50.3 Horizontal section through eye. (From Cosgrove et al 2001.)

comprising the sclera and cornea, which are almost avascular. The bulbar conjunctiva is attached to it by loose connective tissue. The sclera is a cup-like expansion of the dural sheath of the optic nerve and is resolvable from the inner layers of choroid and retina (Fig. 50.4). It is thicker posteriorly (1 mm) than anteriorly (0.6 mm) or at the equator (0.5 mm). The optic nerve pierces the sclera posteriorly, 3 mm to the nasal side of the posterior pole and slightly above the horizontal meridian. Near the equator there are four apertures the exit foramina of the vortex veins, one in each posterior quadrant.

The cornea is continuous with the sclera, but its laminae of fibrous tissue are transparent instead of opaque white. It bulges forward from the sclera and is slightly thicker. The corneoscleral junction is circumscribed by the sinus venosus sclerae (canal of Schlemm), at the periphery of the anterior chamber. Aqueous humour at the iridocorneal angle drains into the canal, which communicates with the anterior scleral veins.

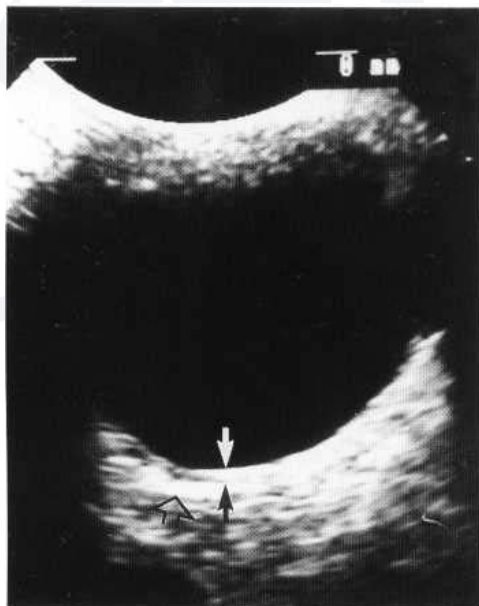


Fig. 50.4 Normal retina-choroid (arrows) and sclera (open arrow). Horizontal scan.

Choroid ciliary body, and iris

The intermediate coat is a continuum of vascular tissue comprising the choroid, the ciliary body and the iris, and is an expansion of the arachnoid and pia of the optic nerve. The choroid is a thin, erectile vascular layer which may be up to 1 mm thick and is of lower reflectivity than the retina and sclera. It lines the posterior part of the sclera, from which it is separated by the suprachoroidal space, a thin connective tissue layer across which the ciliary arteries, veins and nerves pass. A few loose connective tissue fibres hold most of the choroid in position. However, anteriorly, the choroid ends at the ora serrata, where it merges into the pars plana of the ciliary body, the latter being firmly attached to the scleral spur. Posteriorly, the choroid is firmly attached to the exit foramina of the vortex veins and point of entrance of the optic nerve. The basal lamina (membrane of Bruch) is a transparent membrane which separates the vascular layer of the choroid from the pigmented layer of the retina, to which it is firmly adherent.

The periphery of the iris is attached halfway along the short anterior side of the triangle made by the ciliary body. The iris is a contractile diaphragm up to 1 mm in thickness situated in front of the lens, obscuring the anterior lens surface on ultrasound scans, and the pupil is a circular aperture positioned slightly toward the nasal side of the centre of the iris. The iris partially divides the space between the cornea and lens into two sections which are filled with aqueous humour the anterior and posterior chambers of the eye.

Retina

The retina is the innermost, nervous membrane of the eyeball. Its anterior surface is clearly identifiable on ultrasound examination but the posterior surface of the retina merges with the choroid and is difficult to resolve separately. It is an expansion of the neural substance of the optic nerve, whose fibres arc spread out in the nervous layer of the retina. There are two layers: an outer pigmented layer attached to the choroid, and an inner nervous layer—the retina proper—in contact with the vitreous body. The retina originates from the entrance of the optic nerve, from which it spreads out to end at the posterior edge of the ciliary body in a dentate line named the ora serrata. The thickness of the retina is 0.4 mm near the entrance of the optic nerve, but reduces to 0.1 mm at the ora serrata. Around the optic disc and at the ora serrata the retina is more firmly adherent to the choroid than elsewhere. The optic disc has a diameter of about 1.5 mm, and its circumference is slightly raised. It is situated about 3 mm to the nasal side and slightly above the level of the posterior pole, and is important as the site of entry of the retinal arteries and exit point for retinal nerves and veins. The macula is positioned 4 mm lateral to the centre of the optic disc and 1 mm inferiorly. Its central part, the fovea centralis, is a shallow depression. The macula is the area of the most acute vision, but the optic disc is insensitive to light, and is known as the 'blind spot'.

During scanning, the well-recognised artefacts 'Baum's humps' are sometimes seen on the retina, named after the first documenter of B-scanning (Fig. 50.5). These are caused by refraction and increased propagation velocity of ultrasound in the lens.

Refracting media

The transparent or refracting media of the eyeball comprise the cornea, the aqueous humour, the lens and the vitreous body. The aqueous humour is a dilute saline solution, secreted into the posterior chamber from the vessels of the iris and the ciliary processes.



Fig. 50.5 Baum's bumps (arrows) refraction artefact.

The *lens* is a transparent biconvex body enclosed in a transparent elastic capsule. It is 10 mm in diameter and 3-4 mm in thickness. Its posterior surface, which rests on the vitreous, is more convex than the anterior surface. The interior of the normal lens is anechoic, but echoes arise from the central part of the posterior lens cortex as a fine curve. The *vitreous body* is a transparent gel, occupying the posterior four-fifths of the eyeball. It comprises a collagenous matrix containing mucopolysaccharides and water, the latter making up over 98% of the substance of the gel. The vitreous is indented anteriorly by the posterior convexity of the lens, and is adherent to the ciliary processes behind the iris. It is also attached to the optic disc, but more firmly at the pars plana, just in front of the ora serrata. Elsewhere it lies free, in contact with the retina. The normal gel is acoustically clear, but its posterior surface is sometimes seen undulating off the retina during dynamic scanning.

Examination technique

B-scan

The high resolution of images produced by currently available general purpose ultrasound scanners has made eye scanning a practical proposition for all departments possessing a short-focus, 10 or 12 MHz real-time, small-parts probe. Sector scanning is carried out with the patient lying supine, which gives stability and support to the head, making it easy for the patient to remain motionless. In this position, the pull of gravity is exerted in the direction of the optic axis, enabling a detached vitreous still suspended from the vitreous base, or the sedimentation of blood, to be readily assessed. However, some operators prefer the patient to be sitting in the erect position. The main method of examination is the 'contact' method, when the probe is placed directly on the closed eyelid, with an intervening coupling gel. Alternatively, some purpose-built probes require direct contact with the topically anaesthetised eyeball. A stand-off facility, with a small fluid-filled compartment, has the advantage of improving visualisation of anterior structures.

The aim is to image the globe while static, and during rapid eye movements with the patient deviating the eyes to the right and left

side, during which the motion of intraocular structures is observed. Complete visualisation of the ocular contents is achieved by careful movement and orientation of the transducer, with the eye in the primary (straight ahead) position and in all directions of gaze. The mobility of the eye enables up to 50° of movement in any direction from the primary position, and the structure of the coats of the eye (the sclera, choroid and retina) resists deformation during these movements. The vitreous, however, is an elastic body which lies in free contact with the retina over most of its [area](#). So distortion of the gel occurs with each eye movement. Mobility of the pathological vitreous and retina may be observed during dynamic scanning, together with vitreoretinal adhesions: following an ocular excursion, after-movements may continue for approximately a second. The gel moves as a complete body, but the detached retina undulates as a membrane, unless fixed by fibrosis. Choroidal tumours appear solid, and their attachment to the ocular wall is apparent, whereas vitreous, retrohyaloid or subretinal haemorrhage may swirl and sediment during eye movements. When vitreoretinal microsurgical techniques are being considered, information provided by these methods of scanning about the structure and mobility of the ocular contents is of great importance for assessing surgical approach and prognosis.

Doppler techniques

These may be applied to intraocular structures, both normal and pathological, to the eye itself, and to the ophthalmic and carotid vessels which supply the blood. Doppler studies rely upon a frequency shift in the signal returning from sound scatterers (erythrocytes) in blood to determine blood flow through a vessel. Pulsed Doppler is required to discriminate between blood flow at different depths (range resolution).

Orbital vascular disease and amaurosis fugax (transient ocular ischaemia) are closely associated with carotid arterial disease and stenosis. Doppler studies can determine the degree of stenosis by demonstrating the flow velocity in the carotid and degree of turbulence, the flow in superficial temporal vessels, and the direction of flow in supraorbital vessels (reverse flow occurs in severe internal carotid disease and in the presence of an anastomotic circulation). Flow has also been studied in the ophthalmic artery and its branches and in pathological structures within the orbit, including quantification of vitreous mobility in posterior vitreous detachment. Problems encountered in imaging a vessel as small as the ophthalmic artery (0.7-1.4 mm linear diameter) are overcome by employing duplex scanning, where a real-time B-scan is displayed simultaneously with the Doppler spectrogram (Fig. 50.6). The situation is further clarified by **triplex scanning** which includes the superimposition of *colour coding*. The latter is done on the basis of

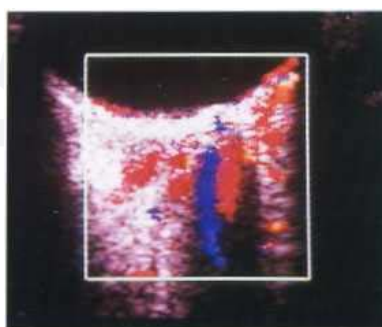


Fig. 50.6 Colour Doppler scan showing normal central retinal artery (red) and vein (blue).

direction of flow; traditionally arteries are coded red and veins blue. Positioning of a variable width gate on the B-scan helps to locate accurately the origin of the Doppler signals. Although the position of the ophthalmic artery itself is variable, its most common anatomical position is known to be inferonasal to the optic nerve, behind the globe. The choroid receives most of the blood supply to the eye via the posterior ciliary branches of the ophthalmic artery. Examining the artery close to the globe, therefore, excludes blood flow to branches supplying extraocular structures and gives an accurate estimation of blood flow to the eye itself. Changes in systemic blood pressure and intraocular pressure have a direct effect on ocular blood flow as there is no autoregulation of the choroidal vasculature.

Flow velocities measured in the central retinal artery (CRA) and central retinal vein (CRV) at the optic nerve head may indicate whether CRA or CRV occlusion has occurred if the examination is carried out within days of the onset. Although Baxter concluded that no routine application had emerged for colour Doppler imaging (CDI) in the orbit, it is this author's experience that CDI is a useful supportive method of diagnosing intraocular tumours such as melanomas, metastases and retinoblastomas, tumour vessels showing vividly as pulsating channels or lakes of colour. Melanoma is occasionally mimicked by benign conditions such as disciform lesions, subretinal haemorrhage or choroidal folds. In this situation the demonstration of tumour vasculature by CDI is a considerable aid to differential diagnosis.

Indications

The indications for eye scanning are:

- Opacity of light-conducting media, making direct vision by ophthalmoscopy difficult
- Suspected intraocular tumour-solid lesions are readily diagnosed, sited and measured by ultrasound
- Differentiation of serous and solid retinal detachment; a detachment may conceal a tumour-the subretinal area is clearly demonstrated by ultrasound
- Examination of the vitreous
- Localisation of foreign bodies
- Ocular measurements (biometry by calibrated A-scan)
- Proptosis (CT and MRI are usually more helpful)
- Doppler investigation of orbital vascular disease and tumours.

Patients with opaque light-conducting media form the majority of referrals, especially those with cataracts and haemorrhages. It is not necessary to scan every patient with a cataract, but if other symptoms develop, for example inflammation, pain, rapidly worsening vision or the development of glaucoma, then a scan must be performed to determine any coexistent pathology.

When vitreoretinal surgery is contemplated, ultrasound assessment of the globe is mandatory. The information required includes:

- The state of the vitreous
- The position and extent of any intraocular lesion visible by ultrasound
- The condition of the retina, and particularly the macula
- The motility of the contents of the globe, which has a direct influence on operability
- The relation between the vitreous and retina, mapping out any vitreoretinal adhesions.

Pathology

Lens

Cataract

Cataracts are usually seen incidentally when scanning the posterior segment of an opaque eye. The lens outline is seen particularly well if there is a senile subcapsular cataract which leaves a deposition of reflective material below the lens capsule (Fig. 50.7). Immature cataract is one in which scattered opacities are separated by clear zones. Mature cataract forms a totally opaque cortex, which results in a very dense lens on scanning.

Intraocular lens implant

These prostheses impede scanning; knowledge of the presence of an implant is important prior to undertaking the examination. Cataract extraction is frequently followed by intraocular lens implantation posterior chamber implants lie behind the iris, and anterior chamber implants in front. The artificial lenses are manufactured from plastics, which cause a dense artefact in the anterior vitreous during scanning if the incident sound beam passes through the implant (Fig. 50.8). A plane of examination to the side of the lens must therefore be sought.

Ectopia lentis

The lens without cataract is less easy to image, but it is possible to identify the ectopic lens in congenital disorders. *Bilateral lens subluxation* in an upward direction is a feature of *Marfan's syndrome*, which is also a cause of retinal detachment due to retinal degeneration. *Homo(cystin)uria* is an inborn error of metabolism giving rise to high levels of homocystine in the plasma and urine. In this condition lens subluxation is typically downward (Fig. 50.9). *Glaucoma* may result from pupil block, due to lens incarceration in the pupil, or from a total dislocation into the anterior chamber. Retinal detachment is also a complication.



Fig. 50.7 Subcapsular cataract. Horizontal scan.

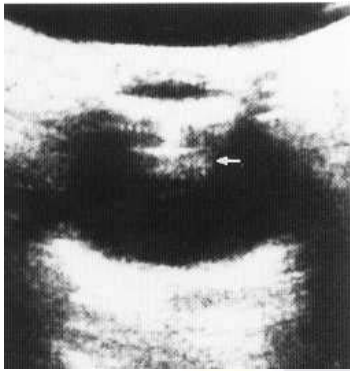


Fig. 50.8 Reverberation artefact (arrow) from plastic lens implant.



Fig. 50.10 Retinal tear (arrow) and total retinal detachment. Horizontal scan.

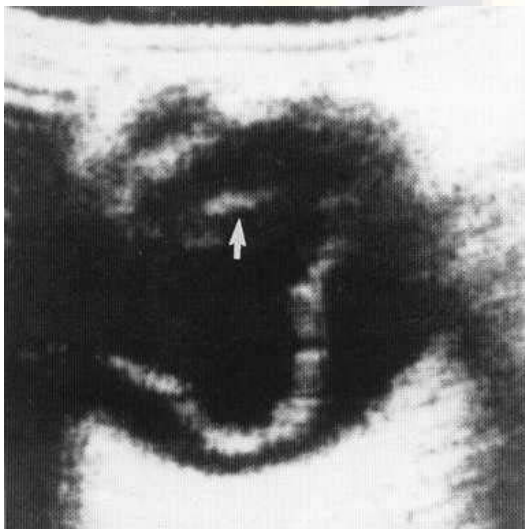


Fig. 50.9 Ectopic lens (arrow) and retinal detachment in homocystinuria. Horizontal scan. (From Cosgrove et al 2001.)

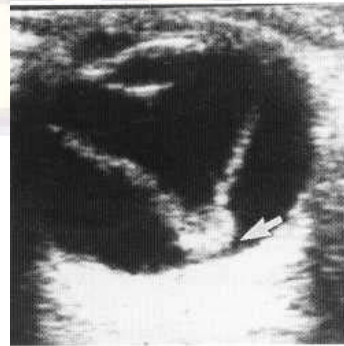


Fig. 50.11 Total retinal detachment, firm anatomical attachment posteriorly at optic nerve head (arrow), and anteriorly at ora serrata. Horizontal scan.

Retina and vitreous

Pathological conditions affecting the retina and vitreous are interrelated, and will therefore be considered together.

Retinal detachment

Retinal detachment (RD) may be due to a break or tear (*rhegmatogenous detachment*) from degeneration or trauma, resulting in the entry of subretinal fluid (Fig. 50.10). *Non-rhegmatogenous detachment* is caused by either vitreoretinal traction from contracting membranes or subretinal exudate. Detachments do not normally extend beyond the firm anchoring points of the ora serrata anteriorly, and optic nerve head posteriorly. A total detachment therefore shows a funnel-shaped appearance (Fig. 50.11) and, particularly in recent, rhegmatogenous detachment, dynamic scanning reveals an undulating, sinuous or whiplash motion of the retinal membrane. Although a minority of RDs remain stationary for some years, if untreated most RDs become total and progressively immobile due to the development of preretinal fibrosis (Fig. 50.12). The retina contracts to form a taut membrane stretched between the optic disc and periphery.

The aim of ultrasound is to diagnose RD early so that surgery may be carried out to seal the break by laser or cryotherapy and re-establish contact between the RD and retinal base.

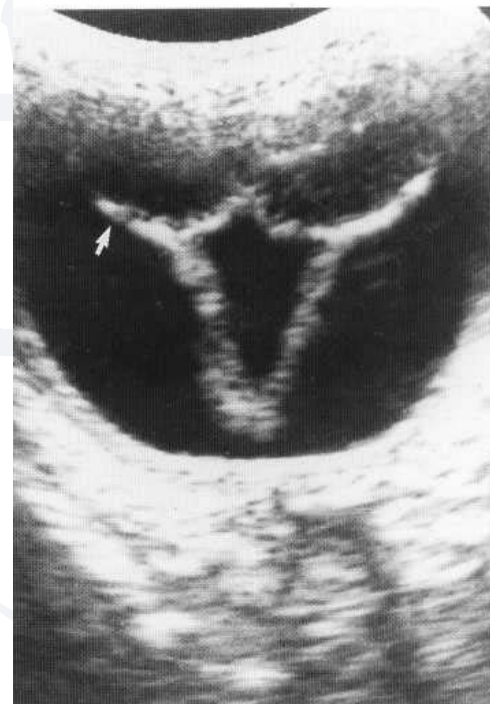


Fig. 50.12 Proliferative vitreoretinopathy showing triangular retinal detachment and transvitreal membrane (arrow). Horizontal scan.

Acquired retinoschisis

This condition is prevalent in hypermetropes, when the sensory retina splits into two layers: it is present in about 5% of the population above 20 years of age. The inferotemporal periphery of both fundi is affected initially (Fig. 50.13), but the lesions may progress circumferentially to involve the whole periphery of the fundus. The usual (plexiform) type remains anterior to the equator, but the reticular form may progress posteriorly and encroach upon the fovea. Scanning demonstrates a focal, dome-shaped membrane which is thinner than a retinal or choroidal detachment. Serial scanning monitors the development of this complication. Retinal detachment is a rare complication of acquired retinoschisis.

Disciform lesions

These are a manifestation of senile macular (or paramacular) degeneration (SMD), giving rise to an elevated collection of subretinal exudate and fibrosis. The early changes are rupture of Bruch's membrane by the penetration of a neovascular membrane derived from the choroid. The neovascular tissue may bleed or leak, producing subretinal exudate which subsequently absorbs or heals by fibrosis. Macular degeneration is usually bilateral, but the severity and progression are often asymmetric. Subretinal elevation caused by SMD may therefore mimic a choroidal tumour. On ultrasound, the lesions are frequently dome-shaped but are sometimes irregular in outline with a heterogeneous appearance, ranging from low to high reflectivity. Serial scans may document a decrease in size over a period of weeks, which may be the most significant feature to differentiate a disciform lesion from a small melanoma or other tumour (Fig. 50.14). Colour Doppler imaging may be of help in the diagnosis of lesions over 3 mm in size, if the presence of tumour vasculature is demonstrated.

Drusen (*hyaline bodies*)

This congenital optic disc anomaly manifests as hyaline, calcific deposits within the substance of the optic nerve head. These lie in size and number, and secondary calcification occurs. Often they are localised to the macular or extramacular region and may elevate the retina without impairing vision. Many patients with drusen have normal vision throughout life, but a significant number of elderly patients develop progressive impairment of central vision due to AMD.



Fig. 50.13 Retinoschisis (arrow). Horizontal scan.



Fig. 50.14 Disciform lesion (arrow), small subretinal haemorrhage. Horizontal scan.

in the second decade they become visible on the surface of the optic disc as bright, pearl-like nodules, and scanning demonstrates a collection of calcific material in the optic nerve head, sometimes standing proud and casting a dense acoustic shadow (Fig. 50.15). Congenital drusen usually remain asymptomatic throughout life, but occasionally cause visual impairment due to haemorrhage or neovascularisation.

Drusen are also a manifestation of *age-related macular degeneration* (AMD). Small globular collections of hyaline material are situated between the basal lamina of retinal pigment epithelium, and the inner, collagenous layer of Bruch's membrane. They are distributed symmetrically at the posterior pole of both fundi and are rarely visible before the age of 45 years. With advancing age they increase in size and number, and secondary calcification occurs. Often they are localised to the macular or extramacular region and may elevate the retina without impairing vision. Many patients with drusen have normal vision throughout life, but a significant number of elderly patients develop progressive impairment of central vision due to AMD.



Fig. 50.15 Drusen of optic nerve head (arrow). Horizontal scan. (From Cosgrove et al 2001.)

Choroidal detachment

A complete choroidal detachment shows fluid in the suprachoroidal space, limited by the attachments of the choroid— anteriorly to the ciliary body and hence the scleral spur, posteriorly at the exit foramina of the vortex veins. A complete detachment therefore appears on scanning as convex indentations of the globe (Fig. 50.16). If the vortex veins are absent or avulsed, the detachment may extend to the optic disc. Choroidal detachment in association with RD is not pathognomonic for an exudative detachment, because many rhegmatogenous detachments have an associated choroidal detachment (Fig. 50.17). Scanning may reveal choroidal tumour (melanoma, secondary deposit or retinoblastoma) as the cause of exudative RD, but the aetiology also includes endogenous uveitis and infection.

Choroidal haemorrhage may follow trauma or surgery and occasionally occurs spontaneously. These lesions are dome-shaped and the suprachoroidal blood is solid-looking when clotted. However, it may liquefy over a period of time and start to absorb (Fig. 50.18).



Fig. 50.16 Choroidal detachment. Horizontal scan.



Fig. 50.17 Choroidal and retinal detachments with vitreous collapse. Horizontal scan.



Fig. 50.18 Suprachoroidal haemorrhage (arrow). Horizontal scan.

Vitreous

The vitreous is a transonic gel in the young person but with advancing age fine points of low reflectivity may develop within its structure. With careful adjustment of the scanner's sensitivity, dynamic scanning shows some undulations of the posterior hyaloid surface with eye movements, and the posterior surface of the gel is seen transiently when correctly aligned to the incident sound. The vitreous is more readily imaged if it is occupied or surrounded by reflective pathological material, and with movement the gel is a deformable, elastic body.

Persistent hyperplastic primary vitreous (PHPV)

This is a serious unilateral developmental disorder of the vitreous and a cause of leucocoria, or white pupil. Embryologically, the vitreous develops from the primary vitreous, which occasionally persists in a microphthalmic eye. In the more common anterior type, PHPV is characterised by the presence of a retrolental membrane and the lens is thinner than normal. In the rarer posterior type, a dense membrane containing the hyaloid artery extends from the retrolental region to the optic disc (Fig. 50.19) and may cause tractional retinal detachment.



Fig. 50.19 Persistent hyperplastic primary vitreous showing linear membrane (arrow). Horizontal scan, eye deviated left.

Vitreous haemorrhage

This is one of the commonest findings when scanning the eye. Haemorrhage in the vitreous cavity may occur inside the gel, within the retrohyaloid space (retrohyaloid or subvitreal haemorrhage) or into both compartments. Causes include tearing from vitreoretinal traction, diabetic retinopathy, age-related macular degeneration, vasculitis, retinal vein thrombosis, subarachnoid haemorrhage (*Terson's syndrome*) and blunt trauma. Initially, small haemorrhages may be difficult to demonstrate and usually resolve after an interval, but larger bleeds increase in density over the first day or so and are more easily seen as widespread low-reflective areas, with marked movement on dynamic scanning. In vitreous haemorrhage resulting from subarachnoid haemorrhage (*Terson's syndrome*) or from blunt trauma, the red blood cells sediment and compact near the posterior hyaloid surface of the detached vitreous, and scanning shows echoes of increasing density in the posterior gel (Fig. 50.20). Degenerating blood cells give rise to lower density echoes and colour the posterior vitreous cortex to give the clinical feature known as 'ochre membrane'. Subvitreal haemorrhage may sediment to form a fluid level behind the collapsing gel (Fig. 50.21). Haemorrhage within the vitreous cavity may therefore persist for some considerable time as widely dispersed echoes in the gel or subvitreal space. Sometimes, however, fibrinous membranes develop and give rise to mobile, linear structures (Fig. 50.22),



Fig. 50.20 Intragel haemorrhage with lacuna. Horizontal scan.



Fig. 50.21 Subvitreal haemorrhage in a diabetic.

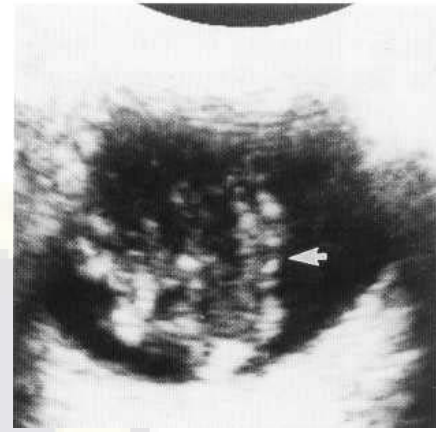


Fig. 50.22 Dense vitreous haemorrhage arranging into thick mobile fibrinous membranes (arrow). Horizontal scan.

which may progressively become immobile. This is known as 'arrangement' as true 'organisation' is not involved.

The presence of blood has a destructive effect on gel structure, including PVD, liquefaction of the gel, and the formation of vitreous bands and an ochre membrane. The inflammatory response to the erythrocytes is low grade, with unphagocytosed cells remaining intact for several weeks. Fibrosis or organisation is an unusual sequel to vitreous haemorrhage, and is usually associated with severe ocular trauma or ocular disease in which vitreous haemorrhage is an incidental finding, for example diabetic proliferations or retinal vasculitis.

Asteroid hyalosis

This is a senile, degenerative disorder of unknown origin, occurring in otherwise healthy eyes; it is unilocular in 75% of cases. Calcium soaps form asteroid bodies, scattered through the vitreous and remaining in suspension, and there is no associated liquefaction. An area of clear vitreous remains between the posterior boundary of the opacities and the posterior hyaloid surface, mimicking a shallow posterior vitreous detachment. The calcified bodies show multiple, high-amplitude echoes and demonstrate considerable after-movement on dynamic scanning, creating a shimmering effect (Fig. 50.23).



Fig. 50.23 Asteroid hyalosis. Horizontal scan.

Synchysis scintillans

This is another degenerative condition, frequently bilateral, occurring after longstanding uveitis or following vitreous haemorrhage. The vitreous is liquefied and contains cholesterol crystals which sink under the action of gravity. Eye movements stir up the crystals, seen ophthalmoscopically as glittering particles, and ultrasonically as multiple, high-amplitude echoes similar to asteroid hyalosis. However, the cholesterol crystals sediment, leaving an echo-free vitreous if the eye is still. Asteroid hyalosis and synchysis scintillans do not reduce visual acuity but have a striking ultrasound appearance, whereas vitreous haemorrhage reduces visual acuity but has much subtler ultrasound features.

Posterior vitreous detachment (PVD)

In the elderly, alterations in the micromolecular structure of the vitreous cause gel liquefaction (synchysis senilis). The resultant fluid enters the subvitreous space and detaches the gel as far as the vitreous base. The result of synchysis senilis is a gel of reduced volume and increased mobility, suspended from the vitreous base and surrounded by synchytic fluid. Most cases remain uncomplicated and the condition is frequently seen when scanning cataractous eyes. If, however, vitreous traction causes a retinal tear or avulsion of a peripheral blood vessel, then intragel and subvitreous haemorrhage may occur. Under these circumstances dynamic scanning may demonstrate a surprisingly marked mobility and elasticity of the detached vitreous, the gel assuming mirror-image configurations when the eye is deviated to one side and then the other (Figs 50.24, 50.25). Failure to move in this way, or asymmetric suspension, may indicate immobilisation of part of the gel by an adhesion or by a restriction from a penetrating injury (Fig. 50.26). Subvitreous haemorrhage in the presence of a posterior vitreoretinal adhesion may incarcerate the gel, resulting in little mobility on dynamic scanning.

Incomplete PVD

In the normal eye the vitreous cortex is loosely attached to the internal limiting membrane of the sensory retina, but there are stronger anchoring points at the vitreous base and optic disc margin. Weak attachments exist around the fovea and at the site of peripheral blood vessels. In the abnormal eye, strong vitreoretinal adhesions may occur at the posterior border of retinal lattice degeneration, at congenital cystic retinal tufts, retinal pigment clumps, vitreous base anomalies, or at the impaction site of a foreign body. In diabetics, strong adhesions are present if



Fig. 50.26 Vitreoretinal adhesion (arrow). Haemorrhage within gel.

fibrovascular membranes form in proliferative vitreoretinopathy (Fig. 50.27). Retinal vein occlusion may result in adhesion at sites of neovascularisation at the posterior pole. If vitreous haemorrhage occurs with complete PVD, the likely cause is a retinal tear requiring prompt interventional treatment. However, if haemorrhage is seen in association with a posterior vitreoretinal adhesion, the likely cause is a retinal vein occlusion, which requires a more conservative approach. Confusion may occasionally arise if a posterior vitreoretinal adhesion causes a retinal tear, or if complete PVD is prevented by a strong posterior adhesion.

When scanning the moderately collapsed gel, sites of vitreoretinal adhesion are not always obvious until dynamic testing is employed and positions of restricted movement identified. Similarly, fine vitreous strands, usually joining the gel mass to the posterior pole, are not seen until eye movement demonstrates gel tethering (Fig. 50.28).

Occasionally, a thickened PVD which remains attached to the optic disc may be confused on ultrasound with an RD. The characteristic motion of vitreous and retina normally enables these structures to be distinguished, and very careful observation during dynamic scanning may be required to differentiate the unified motion of gel mass from the membranous behaviour of a detached retina. If the vitreous contains pathological material this distinction is made easier. Also, RD may be ruled out if the membrane inserts



Fig. 50.24 PVD, eye deviated to right side. Horizontal scan.



Fig. 50.25 PVD, eye deviated to left side. Horizontal scan.



Fig. 50.27 X membranes. Horizontal scan.

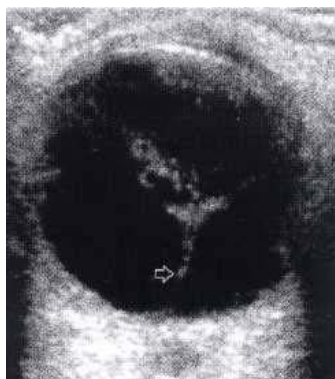


Fig. 50.28 Fine vitreoretinal adhesion (arrow). Horizontal scan.

into the peripapillary region rather than the optic disc. The presence of another membrane either in front or behind may give a strong clue to the identity of the lesion in question.

OCULAR TUMOURS

Characterisation of tissue with ultrasound has been an aim zealously pursued by practitioners involved in the diagnosis of ocular tumours. Although claims have been made for almost 100% accuracy in the diagnosis of these from the ultrasound features alone, some workers have failed to appreciate that conventional scanning (which utilises only time delay and echo amplitude) is incapable of demonstrating microscopic rather than macroscopic structures, preventing 'ultrasound histology'. In addition, there is wide histological and structural variability even in one tumour type (e.g. melanoma), giving rise to a spectrum of ultrasound features.

However, other tissue interactions of ultrasound contain some useful data to improve diagnostic accuracy. The frequency shift in returning echoes may be examined by spectral analysis, a technique developed by Lizzi and coworkers, which gives consistent, reproducible spectral features of ocular tumours. This method distinguishes between certain cell types of choroidal melanoma, and between melanoma and metastasis. Unfortunately, the equipment is not generally available.

Metastatic carcinoma

Choroidal metastases are commoner than primary malignancies and are usually located posteriorly in the fundus, appearing as diffuse lesions with mild to moderate elevation. The usual site of the primary is the breast in females, and the bronchus in males. Less common primary sites are the testis, kidney and gastrointestinal tract. Metastases may be single or multiple, and are sometimes shown on ultrasound to be more extensive than is appreciated clinically. The tumours infiltrate laterally and are therefore low undulating masses with a broad base (Fig. 50.29). Ultrasonography shows a diffuse choroidal thickening with either high or medium amplitude echoes, occasionally developing a globular shape which mimics amelanotic melanoma. The history gives a strong indication of the tumour's origin. Exudative retinal detachment may complicate choroidal deposits, and careful examination of the opposite eye is important as metastases are frequently bilateral.

Choroidal and ciliary body melanoma

Ultrasound is extremely valuable in the diagnosis, assessment and measurement of ocular melanomas, especially in the presence of

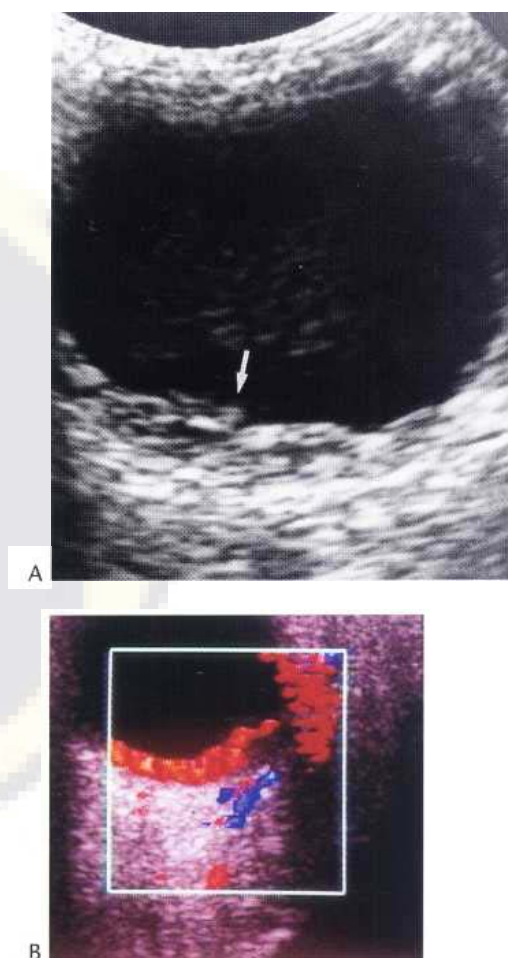


Fig. 50.29 (A) Choroidal metastases (arrow). Vertical scan. (B) Colour Doppler scan.

opaque media. With transparent media it provides a reliable confirmatory diagnosis. Previously the diagnosis of melanoma has not always been easy. In 1964, Ferry stated that approximately 20% of eyes removed because they were thought to contain a melanoma were subsequently found to be negative for this condition. Recently the rate of misdiagnosis has fallen to 0.48%. *Malignant melanoma of the choroid* is the commonest primary intraocular tumour in adults; 85% of ocular melanomas arise from the choroid, and 15% from the ciliary body. It occurs most frequently between the ages of 50 and 60 years, and is rare below the age of 30 and above 80 years. The tumour is rare in black populations, but patients with ocular melanosis are at increased risk. Most tumours arise posterior to the equator and are usually single and unilateral, occasionally developing from a pre-existing naevus.

Recently, there has been a move away from the traditional treatment of enucleation of the eye, especially for small tumours, as tumour dissemination during surgery has been considered a possible cause of increased death rates in the following 2 years. A more conservative approach has given ultrasound an important role in management, particularly in eyes with hazy media, as information about size, position, extent and growth of a tumour is readily obtained.

The ultrasound features of choroidal melanoma are well described. Typically there is a lenticular-shaped mass, deeply embedded in and arising from the choroid. The mass is usually moderately reflective and its high acoustic absorbancy shows a

dense tumour, with some attenuation of the beam (Figs 50.30, 50.31). Less commonly, the tumour is low-reflective and there may be a cystic component. Calcification is rare.

A serous or exudative retinal detachment may conceal an underlying melanoma from ophthalmoscopic examination, but scanning reveals the solid nature of the hidden tumour (Fig. 50.32). Some melanomas have a collar button- or mushroom-shaped appearance caused by waisting as they break through Bruch's membrane (Fig. 50.33). If the membrane remains intact, the tumour is lenticular or dome-shaped. Some tumours demonstrate choroidal excavation, the presence of low-amplitude tumour cell echoes replacing and enlarging the choroid. However, this finding is not pathognomonic as other tumours may show this feature. Small melanomas may be relatively echo-free, making differentiation from retinal degenerative or disciform lesions difficult. However, a clue is given if the situation of the lesion is identified as being deep in the choroid, and serial examinations may show growth. Colour Doppler scanning is a simple method of differentiating melanoma from subretinal haemorrhage by positioning the Doppler window on the tumour and demonstrating blood flow within it (Fig. 50.34). Tumour vessels show as pulsating channels or lakes of colour. Care must be taken that blood flow in the overlying retina is not mistaken for tumour circulation. Not all tumours show vascularity on Doppler, especially if they are under 3 mm in size. In future the intensifying effect of ultrasound contrast agents on the Doppler signal may prove a useful diagnostic aid in the above situation.

Melanoma may be complicated by intraocular haemorrhage, subretinally or into the vitreous compartment. The resulting ultrasound appearances are confusing, but dynamic scanning clarifies the situation. With rapid eye movements, the tumour shows itself fixed to the wall of the eye, whereas subretinal haemorrhage shows some movement and sedimentation, the fluid appearing more transonic than the associated tumour (Fig. 50.35). The retina elevated over



Fig. 50.30 Lenticular-shaped melanoma. Power Doppler scan.



Fig. 50.31 Cottage-loaf shaped melanoma below retinal detachment (arrow). Horizontal scan.



Fig. 50.32 Melanoma showing vascularity. Power Doppler scan.



Fig. 50.33 Melanoma bursting through Bruch's membrane (white arrows). Choroidal excavation (black arrow).



Fig. 50.34 Colour Doppler scan showing vessels in melanoma.

the area of haemorrhage also shows movement as a membrane restraining a fluid collection. Bleeding into the vitreous usually causes degeneration, detachment and loss of gel volume. The resultant mobile reflective gel is identified on dynamic testing. B-



Fig. 50.35 Melanoma (arrow) and associated subretinal haemorrhage (open arrow).

scanning is useful in the assessment of scleral erosion and extraocular extension of a melanoma, the extraocular component showing as a low-reflective area within the orbital fat (Fig. 50.36).

Information gained from ultrasound aids management when a varied range of therapies is available. If local resection (choroidectomy) is considered, the location of the tumour in relation to the optic disc and macula is required, also the elevation, base diameter, presence of scleral erosion and whether there is extraocular extension. For photocoagulation, the lesion should not be greater than 10 mm at its widest point, with no more than 3 nun elevation, and the location should be 1.5 mm away from the fovea (to avoid burn damage). Observation is considered for small or asymptomatic lesions in which the diagnosis is equivocal. Melanomas less than 3 mm thick and 10 mm in diameter have an excellent prognosis and remain dormant for many years, with a low likelihood of metastasis. Radioactive plaques, attached to the globe for a set period of time, deliver a fixed dose of radiation. They are suitable for small tumours (less than 3 mm thick and 10 mm in diameter) and inations are necessary to demonstrate that a haemorrhage is regressing or static, rather than increasing in size, which implies a tumour. Occasionally, ultrasound-guided tissue biopsy is used to obtain cellular aspirates for cytological diagnosis.

Unfortunately, radiation-induced complications include retinopathy, vitreous haemorrhage and cataract. Colour Doppler imaging is of value in assessment of the effects of radiotherapy, which causes flow velocities in tumour vessels to decrease, supporting the concept that radiation causes sclerosis of these vessels. Enucleation is indicated for very large melanomas, particularly if vision has been lost. However, enucleation does not improve the prognosis in patients over 65 years with slowly growing tumours and normal vision. Cyclotron-generated, heavy charged particle irradiation is a new approach which may prove an alternative to enucleation, but is still only available in a few centres.

Ciliary body melanomas are more difficult to see clinically than posterior tumours, unless the pupil is widely dilated. They are also less easy to image with ultrasound, particularly if small, unless a stand-off is used. The scan demonstrates a solid tumour with features similar to a choroidal melanoma; the dimensions and posterior extent should be determined (Fig. 50.37). There is also an annular form of melanoma, which is differentiated from serous choroidal detachment by the fluid content of the latter. Posterior extension of ciliary body melanoma may cause retinal detachment. Pressure exerted by the tumour upon the lens may cause anterior displacement.



Fig. 50.36 Extraocular extension of melanoma (arrow). Horizontal scan.

The diagnosis of choroidal melanoma is not always straightforward, and occasionally confusion may occur with other choroidal conditions. Degenerative disease or trauma may cause choroidal defects or tears, which bleed into the subretinal space. The haemorrhage is followed by neovascularisation, the formation of a (fibrovascular disciform lesion. These lesions are known as Fuchs* spots; they are highly echogenic even at low gain, but sound absorption is minimal. This condition occurs at the macula, in myopic eyes, and in the elderly. Disciform lesions can have the same appearance as a small melanoma, and serial ultrasound examinations are necessary to demonstrate that a haemorrhage is regressing or static, rather than increasing in size, which implies a tumour. Occasionally, ultrasound-guided tissue biopsy is used to obtain cellular aspirates for cytological diagnosis.

Osseous choristoma (choroidal osteoma)

This is a rare benign tumour affecting young women, and is rarely bilateral. Most cases are focal, unilateral, slightly elevated lesions

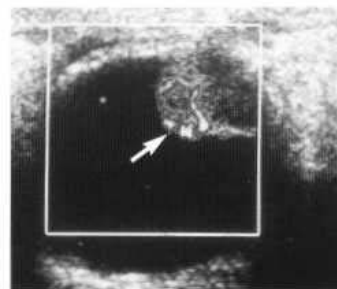


Fig. 50.37 Ciliary body melanoma (arrow). Horizontal scan.



Fig. 50.38 Osseous choristoma (arrow).

with well-defined borders, situated in the peripapillary region. Ultrasonography reveals a dense, highly reflective lesion due to bone formation, with marked acoustic shadowing (Fig. 50.38). Confusion may arise with drusen, but the clinical features should indicate the true nature of the condition.

Choroidal haemangioma

This is a rare congenital tumour, usually presenting at adulthood and often associated with *cutaneous angiomas* and with *Sturge-Weber syndrome*. The lesions are mildly elevated and dome-shaped with a broad base, situated at the posterior fundus temporal to the optic disc. The tumours show high internal reflectivity on ultrasound, being composed of multiple small vascular channels and blood-filled spaces. Doppler scanning may show blood flow within the lesion, and serous retinal detachment may occur at the margins. *Calcification* is sometimes seen on the surface of a haemangioma (Fig. 50.39).

Retinoblastoma

Ultrasound is useful for detection and diagnosis of retinoblastoma and for its differentiation from other intraocular masses. It is the commonest primary malignant intraocular tumour of childhood and comprises about 30% of all ocular tumours (about 40% are malignant melanomas). Nevertheless it is rare, occurring in about 1 in 20 000 live births. It arises from cells derived from the embryonic retinal epithelium of the primary optic vesicle. As modern treatments increase the survival rate, the chance of hereditary transmission is increased. Retinoblastoma has the best prognosis of all childhood tumours, with over 80% survival. Both sexes are equally affected, and although initially presenting in one eye, the tumour is bilateral in about one-third of cases. Most tumours become apparent before the age of 3 years, and the average age of diagnosis is 18 months. Only 6% of cases have a positive family history of retinoblastoma, and here the mode of inheritance is autosomal dominant, with a high but incomplete penetrance. The remaining 94% of cases are sporadic; of these, 25% are germinal mutations which may be inherited.

Retinoblastomas normally present at a late stage with *leucocoria* or 'amaurotic cat's eye', but earlier stages are seen if the fundus is being kept under observation in an 'at risk' patient. Endophytic tumours project from the retina into the vitreous cavity as a white or pinkish mass, and are sharply demarcated in the presence of secondary calcification. Several tumours may be present in one eye

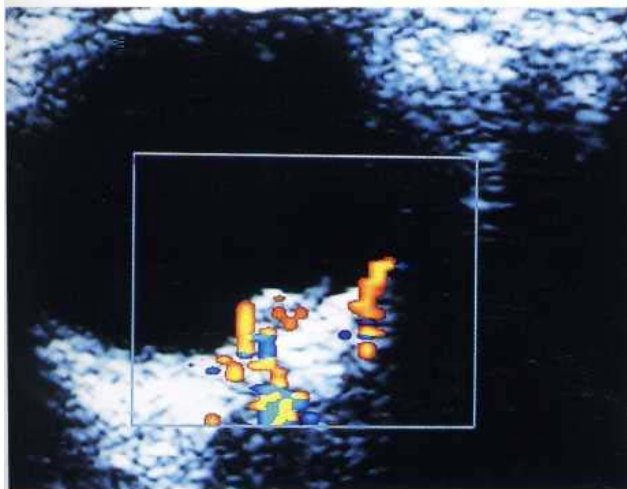


Fig. 50.39 Colour Doppler scan showing choroidal haemangioma.



Fig. 50.40 Retinoblastoma with calcium deposits (arrow).

from seedling deposits. Exophytic tumours grow in the subretinal space, causing a total retinal detachment. Ultrasound will reveal the hidden tumour in this situation.

When scanning retinoblastoma, the tumour may be seen to be localised in one area of the globe and have a dome-shaped appearance, but frequently it has an irregular outline (Fig. 50.40). Calcium deposits are commonly present and are a helpful aid to diagnosis. The amount and distribution of calcification varies the internal reflectivity, and may be seen as a few dense foci or numerous widely distributed deposits. Non-calcified retinoblastomas are more difficult to diagnose and may be associated with signs of inflammation. It is important to recognise invasion of the optic nerve, a long segment of which must be excised when the eye is enucleated. However, CT or MRI scanning more clearly demonstrates extraocular and optic nerve involvement, and is necessary to show CNS spread or pineal involvement. Optic nerve involvement beyond the point of surgical transection is associated with a 65% mortality rate, but if the nerve is uninvolved the mortality rate is only about 8%.

Differential diagnosis

Retinoblastoma is only one of several differential diagnoses to be considered when an infant or child presents with leucocoria. The other conditions are: *Coats' disease retinopathy of prematurity*, *toxocariasis* and *PHPV*. *Coats' disease* is the most severe form of retinal telangiectasia, characterised by large areas of intraretinal and



Fig. 50.41 Coats' disease with total retinal detachment and subretinal exudate. (Courtesy of H. Atta.)

subretinal exudate, progressing to retinal detachment, subretinal cholesterol crystals, and uveitis. The cholesterol in Coats' disease typically gives rise to lower amplitude echoes than retinoblastoma (Fig. 50.41). The condition is unocular, and is commoner in boys. Although it presents in the first decade of life, presentation is at a later age than with retinoblastoma.

Retinopathy of prematurity causes retrolental fibroplasia with the development of dense retrolental membranes. The condition is usually bilateral and associated with a history of prematurity and oxygen therapy (Fig. 50.42). It is seen in normal, or larger than normal-sized eyes, and neovascularisation from the retinal periphery results in fibrotic changes in the anterior vitreous. In severe cases the retina is detached and funnel-shaped, sometimes with peripheral loops. Eyes may be shorter than normal in the severest stages.

Toxocariasis is an infestation caused by ingestion of the intestinal roundworm of cats and dogs, which may result in larvae travelling in the bloodstream to the eyes. Young children who eat dirt or who are in close contact with puppies are at greatest risk of contracting the disease. In ocular toxocariasis, the commonest ocular lesions are chronic endophthalmitis, vitreous membranes, a peripheral or a posterior pole granuloma, and traction retinal detachment.

Persistent hyperplastic primary vitreous (PHPV) is the most serious development disorder of the vitreous, caused by failure of regression of the primary vitreous, and typically occurring unilaterally in a microphthalmic eye. Features of this condition have already been discussed.

TRAUMA

Evaluation of the ocular contents with ultrasound is the best practicable method of examination of the eye following major ocular trauma, as direct vision is frequently hampered by opaque media. Even if severe injuries preclude complete ultrasound examination, useful information is frequently obtained. A very gentle technique is required, occasionally with the use of a sterile sheath over the



Fig. 50.42 Retrolental fibroplasia showing retinal loop (arrow).

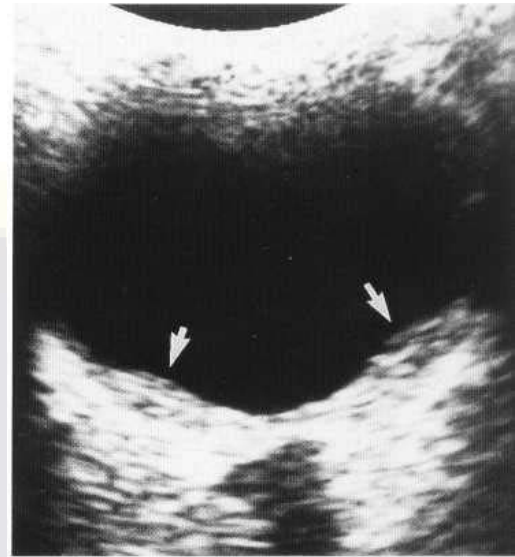


Fig. 50.43 Choroidal thickening (arrows) following penetrating injury.

probe. Early assessment of intraocular damage enables vitrectomy and other microsurgical techniques to be carried out before chronic internal structural changes develop.

Blunt trauma often causes more severe ocular damage than is clinically evident. Compression of the anteroposterior diameter of the eye and corresponding expansion of the equatorial plane occurs. Differential elasticity of the vitreous gel causes traction at the posterior aspect of the vitreous base, with retinal tearing (dialysis). Traumatic dialyses occur in any quadrant but are commoner in the upper nasal quadrant. Many cases of trauma occur in young patients with healthy vitreous gels, with the result that progression to retinal detachment is slow, taking several months. Oedema may cause marked thickening of the retinochoroidal layer, resulting in visual loss if the macula is involved (Fig. 50.43). Blows to the lateral aspect of the orbit, striking the eye just anterior to the lateral wall, may cause rupture of the globe.

Penetrating ocular trauma involving the posterior segment results in retinal detachment in about one-fifth of cases. The detachment may be rhegmatogenous if the retina is breached by a foreign body, or tractional following vitreous incarceration in the wound.

Ultrasound findings

The *lens contents* are normally anechoic and therefore lens subluxation is difficult to evaluate. Complete dislocation is more easily demonstrated, particularly if the lens is cataractous or if the complete lens lies within an area of vitreous haemorrhage (Fig. 50.44).



Fig. 50.44 Displaced lens (arrow). Horizontal scan. (From Cosgrove et al 2001.)

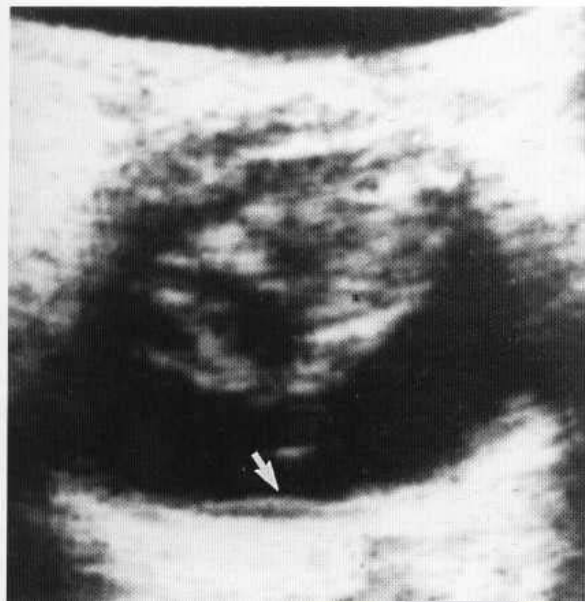


Fig. 50.45 Traumatic vitreous haemorrhage and collapse, with lacuna and vitreoretinal adhesion causing shallow traction retinal detachment (arrow). Vertical scan. (From Cosgrove et al 2001 .)

Haemorrhage in the vitreous compartment may be confined within the vitreous gel, the retrohyaloid space, or both. Small haemorrhages are difficult to demonstrate, but larger bleeds are easy to detect and aid delineation of lacunae, whose formation indicates impending posterior vitreous detachment. Dynamic scanning is important in the detection of vitreoretinal adhesions, which result in traction retinal detachment and must therefore be divided during vitrectomy (Fig. 50.45). If post-traumatic retinal detachment is left untreated, proliferative vitreoretinopathy develops, resulting in the formation of epiretinal membranes and the typical triangle sign on scanning. Penetrating injuries may cause vitreous incarceration at the point of injury. This results in incomplete PVD, with asymmetric suspension of the gel (Fig. 50.46).

Post-traumatic retinal holes are not usually detectable by ultrasound but occasionally giant tears and dialyses may be identified

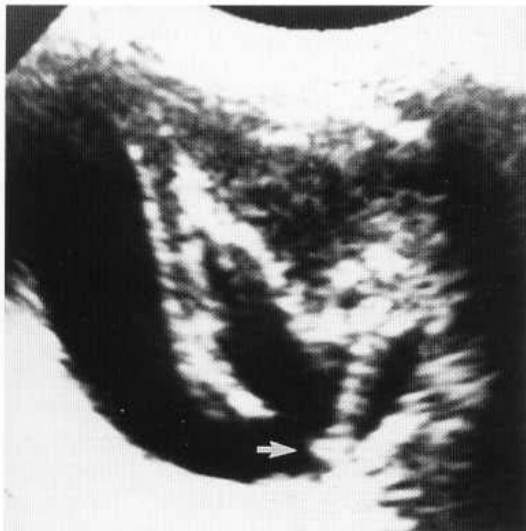


Fig. 50.46 Vitreous laceration by shotgun pellet, and incarceration into retina (arrow). Horizontal scan. (From Cosgrove et al 2001 .)



Fig. 50.47 Direct blow causing extensive haemorrhage outlining lens, retinal dialysis (arrow), and rupture of globe at equator. Vertical scan. (From Cosgrove et al 2001.)

(Fig. 50.47). Subretinal haemorrhage is seen as high-amplitude mobile echoes in the subretinal space, associated with retina detachment. Penetrating injury in the region of the pars plana sometimes results in traction between the gel incarcerated at the injury site and the vitreous base, causing the ora serrata to be pulled along behind the lens. This is the so-called 'purse-string retinal detachment, whose recognition is important so that surgical incision is not made into the subretinal space instead of the vitreous cavity.

Rupture of the globe usually occurs in the equatorial region following an anterolateral blow (Fig. 50.48). Signs of rupture include distortion of the normal shape with loss of ocular volume, intravitreal haemorrhage and intraocular air, particularly if there is communication with an ethmoid sinus.

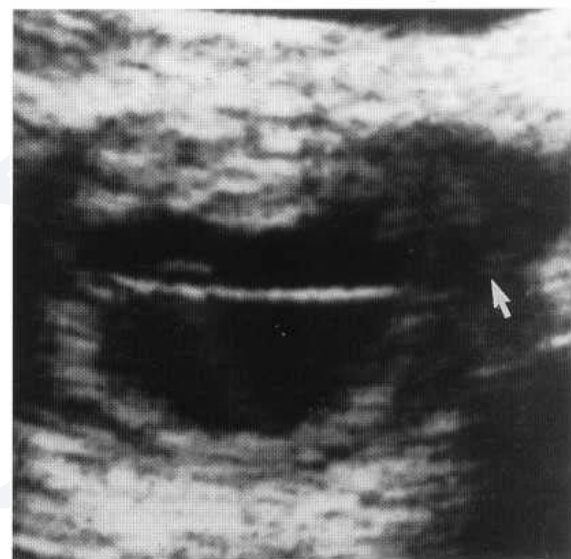


Fig. 50.48 Direct blow causing intravitreal blood-fluid level, thickening of inner coats, and rupture of globe (arrow). Horizontal scan. (From Cosgrove et al 2001.)



Fig. 50.49 Phthisis bulbi. Calcified lens and globe.

Phthisis bulbi is an end-stage condition, following trauma and ocular haemorrhage. The eye is blind, small and contains extensive calcification (Fig. 50.49).

Foreign bodies

Small *metal* or *glass* fragments travelling at high speed cause penetrating injuries and remain within the globe. Most intraocular foreign bodies are detectable by ultrasound, but some objects made of low-density material, such as *wood* or *organic matter*, may be difficult to identify, particularly if surrounded by haemorrhage. Dense materials like metal, glass or stone are highly reflective and therefore easier to demonstrate (Fig. 50.50). Following penetration by a foreign body, a track of haemorrhage may be seen crossing the vitreous, outlining the trajectory of the object and indicating its position. Frequently though, intragel haemorrhage obscures the pathway. The entry or exit sites of a foreign body may cause vitreous incarceration, and some injuries allow entry of air into the globe. Small bubbles of intragel gas show as highly reflective spots which may be confused with foreign bodies, but the latter are usually more highly reflective, with denser acoustic shadowing (Fig. 50.51). Air bubbles may move when the head is tilted and usually disappear after a couple of days. If any doubt exists, CT scanning will clarify the situation.

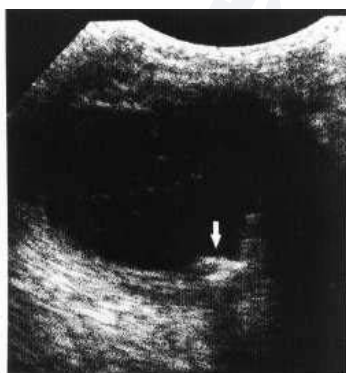


Fig. 50.50 Metallic foreign body (arrow). Horizontal scan. (From Cosgrove et al 2001.)



Fig. 50.51 Penetrating injury with intragel haemorrhage and air bubble (arrow). Vertical scan. (From Cosgrove et al 2001.)

Ultrasound locates intraocular foreign bodies precisely prior to removal, unless the object is very small and linear, when it may be difficult to align the beam perpendicular to its long axis. Because some foreign bodies may be missed with ultrasound examination, it is important to utilise plain radiography and CT scanning, but ultrasound is superior in detection of associated intraocular abnormalities.

THE ORBIT

Computed tomography and magnetic resonance imaging of the retrobulbar structures have several advantages over ultrasound, including high-resolution images with thin sections, magnification techniques, and the capability of imaging in the coronal plane. Lesions are demonstrated in the posterior and apical parts of the orbit, and the adjacent sinuses and intracranial structures are also seen. For these reasons, these modalities are now the methods of choice in investigating orbital disease. Disadvantages include: (i) the delivery of a radiation dose to the lens with CT; (ii) subtle lesions of the posterior sclera and optic nerve are missed; and (iii) the examination may be time-consuming. In addition, CT and MRI require sedation in small children. Ultrasound has the advantage of rapidity and accessibility, and its ability to identify the orbital walls, optic nerve, extraocular muscles and orbital masses makes it a useful first-line investigation in proptosis (Figs 50.52, 50.53).

The aims of orbital investigation are the demonstration and establishment of an orbital lesion and its position within the orbit. The pathological nature of the lesion may be less easy to determine as some ultrasound features are non-specific, and the clinical history must be taken into account. A patient with malignancy raises the possibility of an orbital metastasis; concomitant thyroid disease suggests thyroid ophthalmopathy. A gradually developing proptosis is suggestive of a slowly growing benign tumour, for example of neural origin. Ultrasound is useful in the follow-up of lesions that may previously have been more fully investigated by the other modalities when serial examination is required, for example to document progress or regression of pseudotumour, tumour, haematoma or thyroid ophthalmopathy.

The contact method is suitable for orbital scanning, and frequencies between 5 and 10 MHz are needed for good penetration of the sound beam. Scanning is more readily carried out in a horizontal

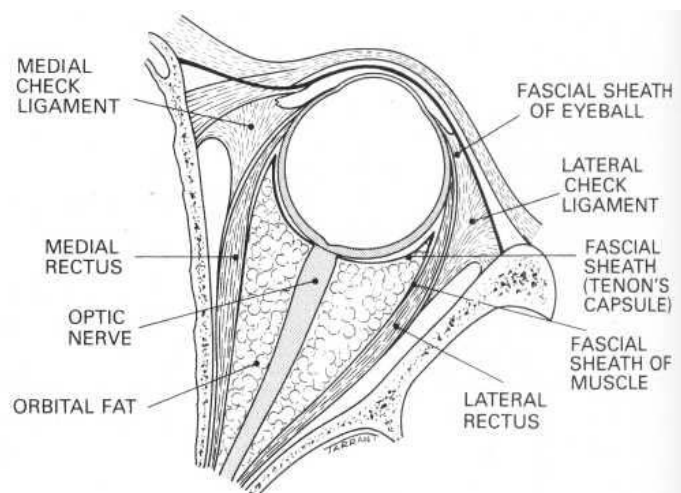


Fig. 50.52 Horizontal section through eye and orbit. (From Cosgrove et al 2001.)

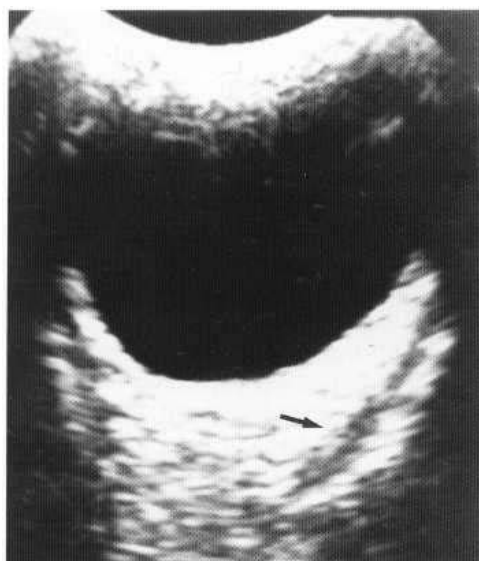


Fig. 50.53 Normal orbit, with medial rectus and lateral rectus (arrow). Horizontal scan.

than a vertical plane, due to better access of the sound beam to the orbit horizontally, and interpretation is easier. A vertical scanning plane is used to examine the upper anterior orbit and inferior rectus muscle, but, although the probe may be angled in an oblique plane for examination of the lacrimal fossa, this area is more easily demonstrated on CT or MRI.

Pathology

Thyroid ophthalmopathy

Graves' disease is the commonest cause of extraocular muscle enlargement: most patients develop changes of thyroid ophthalmopathy at some stage. It is typically bilateral, but patients are frequently referred for investigation of unilateral proptosis and do not always have supportive biochemical findings, which gives ultrasound a useful role in confirmatory diagnosis. The mid and posterior part of the muscle belly is enlarged but not the tendon. The involved muscles have medium to high reflectivity due to separation of muscle fibres by inflammatory cells and oedema. Only 3-5% of patients develop the sight-threatening complication of optic neuropathy due to optic nerve compression by enlarged extraocular muscles. Although CT is a sensitive imaging technique for demonstrating these changes, it cannot be used repeatedly because of radiation dose to the lens. All the extraocular muscles may be enlarged but severity of involvement is assessed by ultrasound measurements of medial rectus width, which correlate with CT measurements. Ultrasound measurements are made with the electronic calliper as the subject maintains forward gaze. The upper limit of normal maximum medial rectus width is about 4 mm using real-time scanning, and measurements above this level are suggestive of Graves' disease. Serial scans may be carried out to monitor advancement of the disease and the effect of therapy. Patients with ophthalmoplegia but normal medial rectus width require assessment of the inferior rectus, which is sometimes selectively enlarged (Fig. 50.54). This muscle requires a vertical scanning plane and is more difficult to image with ultrasound, sometimes making CT necessary.

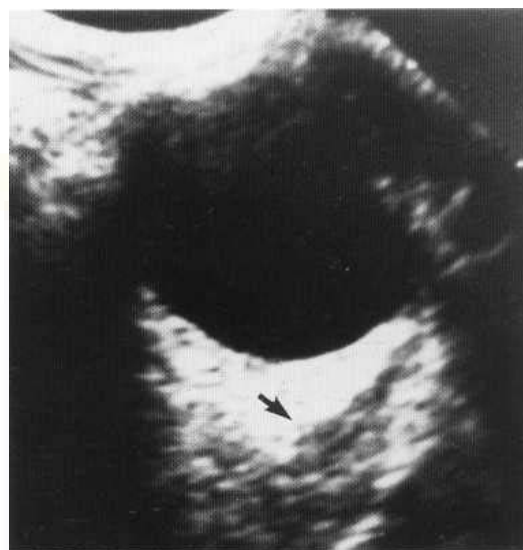


Fig. 50.54 Thyroid ophthalmopathy, enlarged belly of inferior rectus (arrow). Vertical scan. (From Cosgrove et al 2001.)

Other features of thyroid ophthalmopathy include increased orbital fat and orbital oedema. This is seen as fluid within Tenon's capsule and low-reflective areas within the orbital fat, sometimes with encysted spaces.

Inflammatory orbital disease (pseudotumour)

This is the name given to a group of relatively rare, idiopathic, non-neoplastic orbital lesions, including myositis, dacryoadenitis, periscleritis, perineuritis and the diffuse condition. The disease may affect any of the soft-tissue components of the orbit in any age group, but the majority of patients are middle-aged. The onset is usually acute and unilateral, mimicking the presence of an orbital tumour with proptosis, hence the term 'pseudotumour'. Sometimes the presence of a discrete inflammatory mass makes differentiation from a true neoplasm difficult, but pseudotumour usually responds well to steroid therapy. The ultrasound appearance of the mass is a low-reflective lesion with features similar to those of a metastasis or lymphoma deposit (Fig. 50.55). The mass may be smooth in outline or, more commonly, irregularly shaped. In the diffuse form involvement of the orbital fat predominates, causing a mottled appearance on scanning. Myositis is seen as enlargement of the whole of an extraocular muscle, including origin and insertion, differing from the selective muscle belly enlargement of thyroid ophthalmopathy.

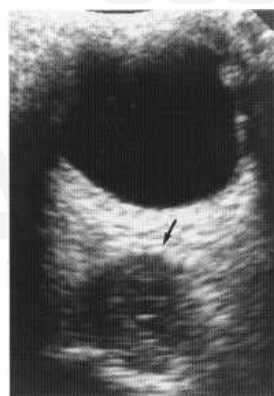


Fig. 50.55 Orbital pseudotumour (arrow).

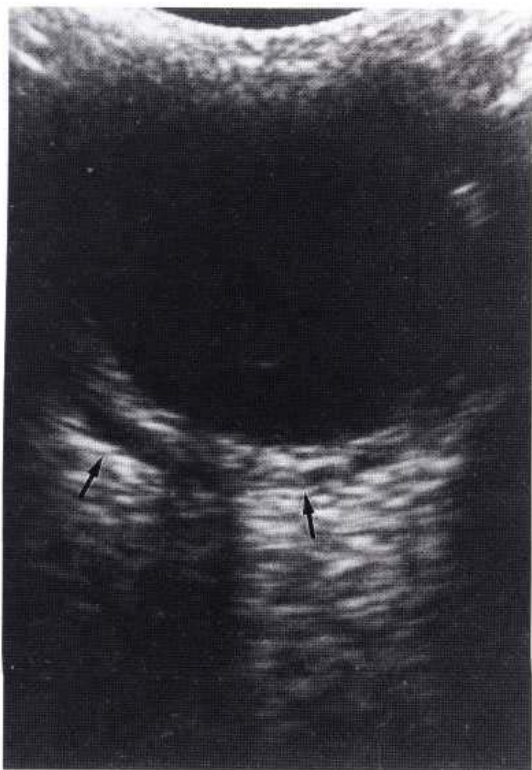


Fig. 50.56 'T' sign (arrows). Fluid in Tenon's capsule.

Oedema in the retrobulbar fascia (Tenon's capsule) tracks along the optic nerve sheath to form the 'T' sign (Fig. 50.56). In children, about one-third of idiopathic pseudotumour is bilateral, but in adults bilateral involvement raises suspicion of systemic disease, for example lymphoma, sarcoidosis, Wegener's granulomatosis, or other autoimmune disease. Chronic cases of inflammatory orbital disease develop firm, fibrous stroma which replaces the orbital fat, termed sclerosing orbital pseudotumour.



Fig. 50.57 Colour Doppler scan showing arterialised blood flow in dilated superior ophthalmic vein. Vertical scan.

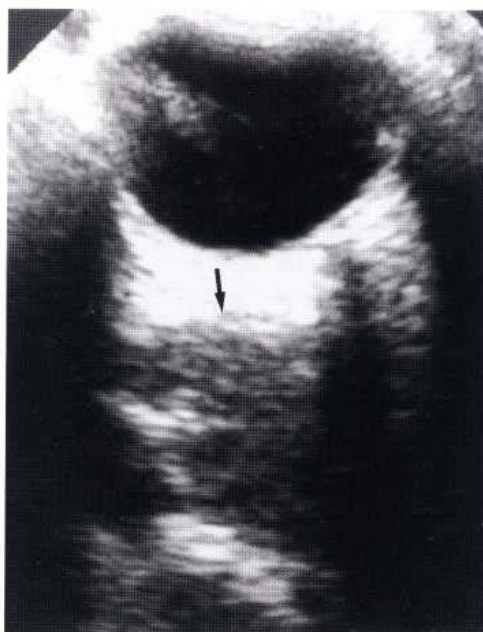


Fig. 50.58 Orbital metastasis (arrow) displacing optic nerve.

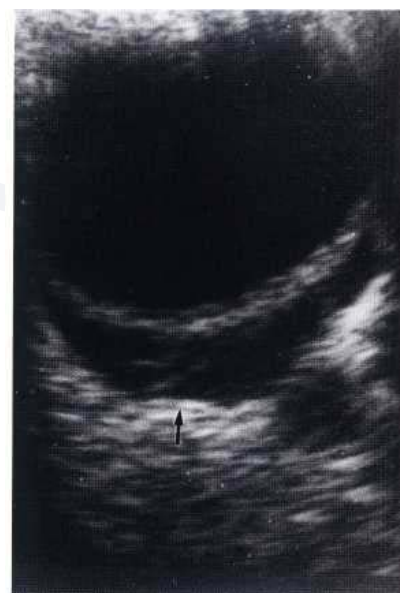


Fig. 50.59 Lymphoma cupping globe.

Vascular lesions

Orbital haemangioma

Cavernous haemangioma is the commonest benign orbital tumour in adults, occurring most frequently in the second to fifth decades of life, and characterised by a slowly progressive unilateral proptosis. The tumours comprise dilated, endothelium-lined vascular channels, surrounded by a fibrous pseudocapsulc. The majority are located within the muscle cone, and may occasionally compress the optic nerve, while causing little proptosis.

The ultrasound appearance is that of a transonic mass containing echoes of medium to strong reflectivity, emanating from the vascular surfaces within the lesion and connective tissue stroma. There is poor attenuation of the sound beam and a negative Doppler phenomenon due to stagnant blood within the vascular spaces. Occasionally, calcified phleboliths are seen.

In infancy, orbital haemangiomas are of the capillary type, usually presenting in the anterior orbit at birth or soon afterwards. They undergo periods of growth, then stabilisation, and eventual regression, usually at about 5 years of age. Ultrasonically, the lesion is less reflective than the cavernous type, due to small vascular channels and scant stroma. The prominent arterial supply to the lesion produces a positive Doppler phenomenon.

Varices

The diagnosis is made by observing the blood-filled spaces on 13-scan while the jugular veins are compressed, causing the varices to increase in size. Doppler may also be used; these techniques enable differentiation from orbital cysts. The diagnosis is often made clinically from the sign of intermittent exophthalmos.

Arteriovenous fistula

These may develop spontaneously or after head injury, and are often not diagnosed clinically unless large. Carotid-cavernous sinus fistula (CCSF) and dural cavernous arteriovenous malformations

(DCAVM) are readily diagnosed and monitored by colour Doppler imaging (CDI). The superior ophthalmic vein conveys blood from the orbit posteriorly to the cavernous sinus. However, in CCSF and DCAVM, arterial blood enters the cavernous sinus and blood flow in the superior ophthalmic vein is reversed or arterialised, resulting in proptosis with dilated conjunctival vessels (Fig. 50.57). CDI may be the only investigation required if symptoms are mild in DCAVM, which is a low-flow condition, and is used to assess progression. In CCSF, which is a high-flow lesion, orbital haemodynamics are assessed by CDI prior to carotid angiography and the results of therapeutic embolisation followed up.

Orbital tumours

The ultrasound features of many orbital malignancies are very similar, and unless there are clear indications of the likely nature of the tumour from the clinical history, the ultrasound report may have to be confined to a description of the topographical features of the lesion, and a comment on the likelihood of malignancy. Similar scan appearances in a 7-year-old child and 65-year-old adult would be diagnosed as rhabdomyosarcoma in the former, and metastasis or lymphoma in the latter (Fig. 50.58). The demonstration of a low-reflective irregular orbital mass, with good penetration of the sound beam, is a strong indication of orbital malignancy. However, these appearances are not pathognomonic, as shown by the above descriptions of pseudotumour and other inflammatory lesions.

Lymphoproliferative disorders

Orbital lymphoma is usually of the non-Hodgkin's type, and appears on ultrasound as an elongated, low-reflective, oval mass typically affecting patients above the age of 60 years. The lesions may occur in any part of the orbit, are sometimes bilateral, and occasionally exclusively involve the lacrimal gland. Sometimes there is a mass cupping the back of the globe (Fig. 50.59). Histological studies usually make a distinction between malignant lymphomas and inflammatory conditions, but there is also an intermediate group, some of which have a benign outcome, resolving with steroid therapy, but others developing systemic lymphoma several years later. Thorough systemic evaluation is therefore necessary in all patients with both benign and malignant lymphoid lesions of the orbit. *Ultrasound-guided biopsy* is a useful technique for accurate retrieval of lymphoma tissue, and serial scans demonstrate the response to therapy.

Rhabdomyosarcoma

This is the commonest primary malignant orbital tumour of childhood. Presentation is usually at around the age of 7 years, with a rapidly progressive proptosis. The tumour may involve any part of the orbit arising from an extraocular muscle, but usually occurs in the superonasal quadrant, appearing as a low-reflective mass (Fig. 50.60). Metastatic neuroblastoma should be considered as a differential diagnosis.

Metastases

Orbital metastases occur in about 40% of **children** with *neuroblastoma*. Presentation is usually with a rapid onset proptosis, and deposits may be bilateral. *Ewing's sarcoma* of bone, *Wilms'tumour* and *leukaemia* can also give rise to orbital deposits.

Adults Orbital metastases most commonly arise from primaries in the *bronchus, breast, prostate, kidney* and *gastrointestinal tract*



Fig. 50.60 Orbital rhabdomyosarcoma. Vertical scan. (From Cosgrove et al 2001.)

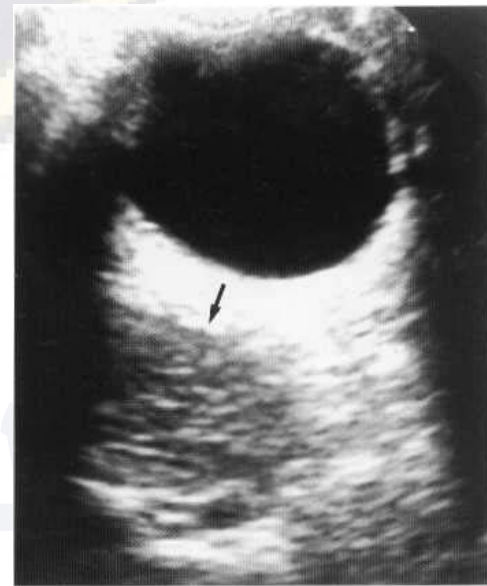


Fig. 50.61 Orbital metastasis (arrow).

(Fig. 50.61). Orbital invasion may also occur from adjacent malignancy in the paranasal sinus (Fig. 50.62).

Optic nerve tumours

Neurilemmoma

Usually arising in the superior orbit, either intraconally or extraconally, these rounded masses contain low to medium amplitude echoes and occasionally cystic areas. They transmit sound less well than cavernous haemangiomas (Fig. 50.63).

Glioma

This is a benign congenital hamartoma which presents between the ages of 4 and 8 years with visual loss and proptosis. Over half of these patients have neurofibromatosis. On ultrasound, a fusiform or irregular expansion of the optic nerve is demonstrated, but CT and MRI are better at showing extension into the optic

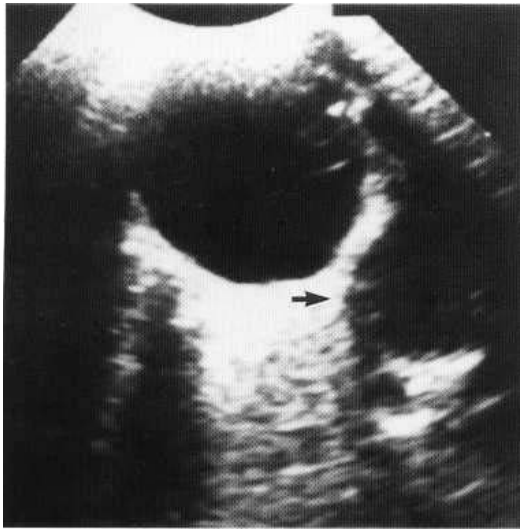


Fig. 50.62 Antral carcinoma invading orbital floor (arrow) and elevating inferior rectus muscle. Vertical scan. (From Cosgrove et al 2001.)

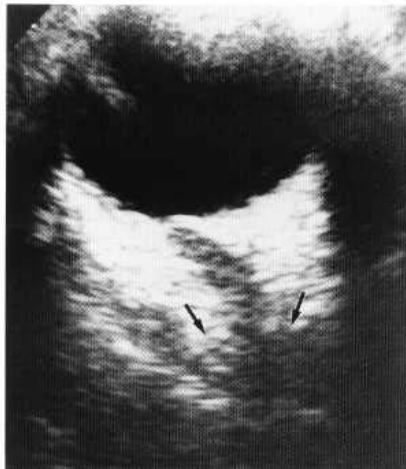


Fig. 50.64 Optic nerve sheath meningioma (arrows). Horizontal scan.

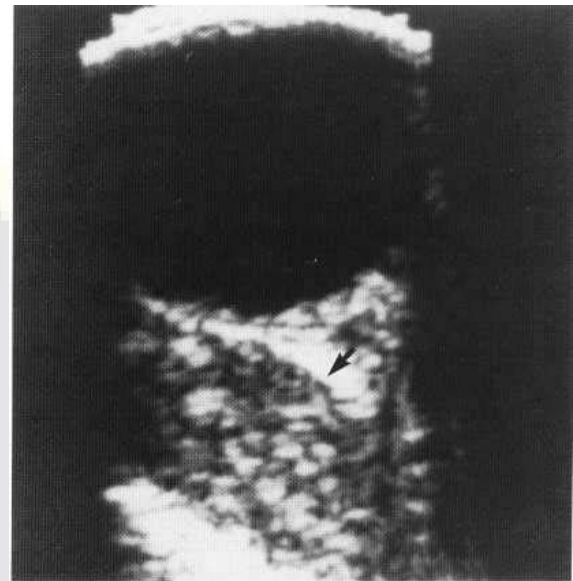


Fig. 50.63 Orbital neurilemmoma (arrow). Horizontal scan. (From Cosgrove et al 2001.)

canal. Although the lesion is low-reflective, there is poor acoustic transmission.

Meningioma

Optic nerve sheath meningiomas arise from arachnoid villi and present with unilateral, slowly devolving impairment of vision. This results from optic nerve compression as the tumour grows within the dural sheath. When the tumour enlarges and ruptures through the dura, it forms an intraconal mass resulting in proptosis. Ultrasound shows a diffuse or focal broadening of the optic nerve, with high reflectivity (Fig. 50.64). Meningiomas are invasive tumours, typically affecting middle-aged women. They also arise en plaque' in the greater and lesser wings of the sphenoid, and involve the orbit secondarily.

REFERENCES AND SUGGESTIONS FOR FURTHER READING

- Baxter, G.M., Williamson, T.H. (1993) Colour Doppler flow imaging in central retinal vein occlusion: a new diagnostic technique? *Radiology*, 187, 847-850.
- Baxter, G. M., Williamson, T. H. (1994) Colour flow imaging of the orbit—concept or diagnostic tool? *Clinical Radiology*, 49, 845-846.
- Byrne, S. F., Green, R. L. (1992) Optic nerve. In *Ultrasound of the Eye and Orbit*, pp. 393-429. St Louis: Mosby Year Book.
- Cennamo, G., Rosa, N., Vallone, G.F., et al (1994) First experience with a new echographic contrast agent. *British Journal of Ophthalmology*, 78, 823-826.
- Char, D. H. (1984) Therapeutic options in uveal melanomas. *American Journal of Ophthalmology*, 98, 796-799.
- Coleman, D. J., Abramson, D. H., Jack, R. L., Franzen, L. A. (1974) Ultrasonic diagnosis of tumours of the choroid. *Archives of Ophthalmology*, 91, 344-354.
- Collaborative Ocular Melanoma Study Group (1990) Accuracy of diagnosis of choroidal melanomas in the collaborative study group. *Archives of Ophthalmology*, 108, 1268-1273.
- Cosgrove, D., Meire, H., Dewbury, K. (2001) *Clinical Ultrasound*, 2nd edn, vol.2: *Abdominal and General Ultrasound*. Edinburgh: Churchill Livingstone.
- Etherington, R. J., Hourihan, M. D. (1989) Localisation of intraocular and intraorbital foreign bodies using computed tomography. *Clinical Radiology*, 40, 610-614.
- Felepa, E. J., Lizzi, F. L., Coleman, D. J., Yaremko, M. M. (1986) Diagnostic spectrum analysis in ophthalmology: a physical perspective. *Ultrasound in Medicine and Biology*, 12, 623.
- Ferry, A. P. (1964) Lesions mistaken for malignant melanomas of the posterior uvea. *Archives of Ophthalmology*, 72, 463-469.
- Fielding, J. A. (1993) *Imaging the eye with ultrasound*. MD thesis, University of Liverpool.
- Fielding, J. A. (2001) The eye and orbit. In: Cosgrove, D., Meire, H., Dewbury, K. (eds) *Clinical Ultrasound*, 2nd edn., vol. 1 1, pp. 659-695. Edinburgh: Churchill Livingstone.
- Foos, R. Y. (1974) Vitreous base, retinal tufts, and retinal tears. In: Regan, C. D. J. (ed.) *Retina Congress*, pp. 259-280. New York: Appleton-Century-Crofts.
- Forrester, J. V., Lee, W. R., Williamson, J. (1978) The pathology of vitreous haemorrhage. *Archives of Ophthalmology*, 95, 703-710.
- Fuller, D. G., Snyder, W. B., Hutton, W. L., Vaiser, A. (1979) Ultrasonographic features of choroidal malignant melanomas. *Archives of Ophthalmology*, 97, 1465-1472.
- Garner, A., Rahi, A. H. S., Wright, J. E. (1983) Lymphoproliferative disorders of the orbit: an immunological approach to diagnosis and pathogenesis. *British Journal of Ophthalmology*, 67, 561-569.
- Gass, J. I. M. (1977) Problems in the differential diagnosis of choroidal naevi and malignant melanomas. *American Journal of Ophthalmology*, 83, 299-32
- Given-Wilson, R., Pope, R. M., Mitchell, M. J., Cannon, R., McGregor, A. M. (1989) The use of real-time orbital ultrasound in Graves' ophthalmopathy: a comparison with computed tomography. *British Journal of Radiology*, 62, 705-709.

- Green, R.L. (1987) The echographic evaluation of spontaneous vitreous haemorrhage. In: Ossoinig, K.C. (ed.) *Ophthalmic Echography*, pp. 233-238. Dordrecht: Martinus Nijhoff/W Junk.
- Hayrehh, S. S. (1962) The ophthalmic artery and its branches. *British Journal of Ophthalmology*, 46, 212-214.
- Hughes, J. R., Byrne, S. F. (1987) Detection of posterior ruptures in opaque media. In: Ossoinig, K.C. (ed.) *Ophthalmic Echography*, pp. 333-341. Dordrecht: Martinus Nijhoff/W Junk.
- Hungerford, J. (1985) Recent advances in the understanding of retinoblastoma. *Transactions of the Ophthalmic Society of the United Kingdom*, 104, 832-835.
- Lizzi, F. I., Mortimer, A. J. (1988) Bioeffects considerations for the safety of diagnostic ultrasound. *Journal of Ultrasound in Medicine*, 7 (suppl.). 1-38.
- Passani, F., Barco, L., Venturi, G. (1983) Pre-vitreotomy examination of the traumatised eye. In: Hillman, J.S., Le May, M.M. (eds.) *Ophthalmic Ultrasonography*, pp. 121-125. The Hague: Martinus Nijhoff/W Junk.
- Richardson, J., Wood, C.M., Mackay, L.J., Gardner, E.S. (1989) A vitreoretinal service. *BMJ*, 299, 241-245.
- Rootman, J., Nugent, R. (1982) The classification and management of acute orbital pseudotumours. *Ophthalmology*, 89, 1040-1048.
- Williamson, T. H., Baxter, G. M., Dutton, G. N. (1993) Colour Doppler velocimetry of the optic nerve head in arterial occlusion. *Ophthalmology*, 100, 312-317.
- Wong, D., Restori, M. (1988) Ultrasonic Doppler studies of the vitreous. *Eye*, 2, 87-91.

نشر الکترونیکی
موسسه انتشاراتی
نوردانش



نشر الکترونیکی
موسسه انتشاراتی
نوردانش

51

THE ORBIT

Michael I. Rothman, Gregg H. Zoarski

Techniques of examination

The orbit forms only a small part of the skull but pathology of this region assumes critical importance because of the high value placed on vision. The evaluation of orbital pathology has progressed rapidly with the development and more widespread availability of computer assisted imaging. Plain radiography, ultrasound (US), computed tomography (CT) and magnetic resonance imaging (MRI), as well as fluoroscopy and nuclear medicine, have all been used in the evaluation of orbital pathology. Imaging must be directed by the clinical history and physical examination, and should include orthogonal views of the orbit and adjacent regions of the skull, face and sinuses, and intracranial structures.

Plain radiography this is usually the primary procedure of choice in the assessment of orbital trauma, including evaluation for radiopaque foreign bodies. X-ray examination should consist of standard skull projections posteroanterior, lateral and half axial (Towne's) views. An optic canal view may be useful to evaluate the optic canal and fissures, although patients will usually receive a CT scan for full evaluation (Fig. 51.1).

Lacrimeography This is used in the evaluation of congenital and acquired disorders of the lacrimal drainage apparatus. After cannulation of the superior or inferior punctum with a small-bore rounded-lip needle, water-soluble contrast material is injected into the canaliculus during fluoroscopy, with subtraction images

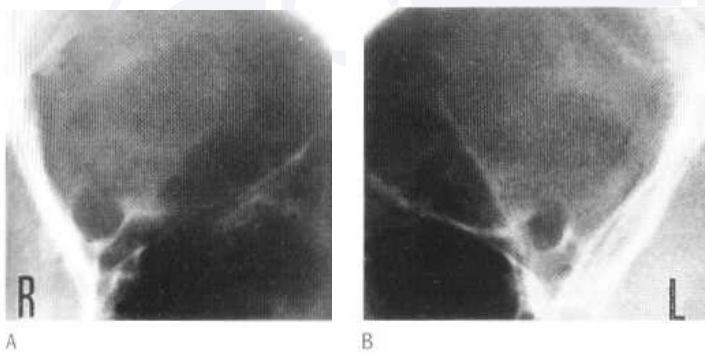


Fig. 51.1 Optic nerve glioma. Right (A) and left (B) optic canal views show a large right canal, confirming extension of the tumour to this portion of the nerve.

obtained to improve visualisation of subtle pathology. Intubation of both sides is usually performed simultaneously due to the high incidence of bilateral abnormalities. The canaliculi fill initially, followed by the lacrimal sac, with subsequent opacification of the nasolacrimal duct. Spill into the nasal cavity indicates patency of the drainage system (Fig. 51.2).

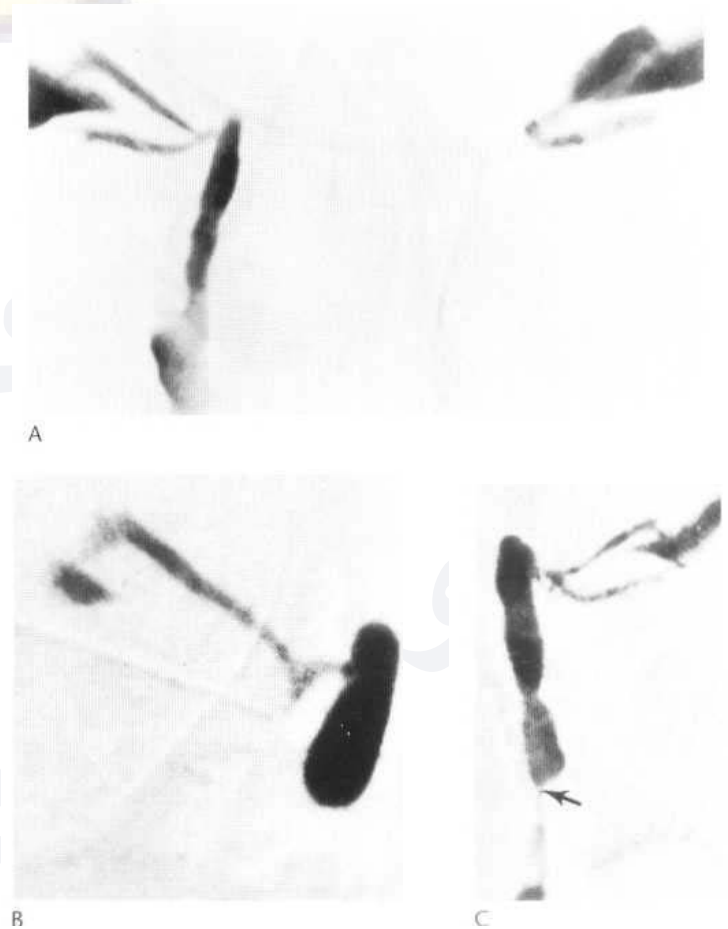


Fig. 51.2 (A) Left common canaliculus block (proximal end). Normal right side for comparison. (B) Subtraction macrodacryocystogram showing a lacrimal sac mucocele. (C) General dilatation of the lacrimal sac and duct due to an incomplete obstruction at the lower ostium (arrow).

Angiography This is now rarely used in the evaluation of the orbit. It is performed principally on those patients with suspected or proven vascular anomalies of the orbit or middle cranial fossa such as carotid-cavernous fistula or dural arteriovenous malformation. Both diagnostic examinations and therapeutic interventions may be carried out.

US Ultrasound may be used to evaluate the globe for intrinsic pathology but the remainder of the orbit is poorly seen due to the marked echogenicity of the postseptal fat. It is discussed in detail in Chapter 50.

CT If proptosis is present, a mass is expected, and *CT scans* are preferred due to the speed and easy availability of this modality. Subtle or small calcifications are well shown, and artefact from eye motion is minimised. Iodinated intravenous contrast may be used to assist in characterising a mass, although it is not usually necessary as intraorbital fat provides excellent natural contrast. CT scans should be performed with contiguous thin section

(2-3 mm) axial, and thicker section (4-5 mm) coronal images, displayed in both soft-tissue and bone windows. Alternatively, coronal and oblique sagittal projections may be reformatted from axial images; the resultant image quality is improved by using overlapping sections to avoid 'stair-step' artefact (e.g. 3 mm thick, 2 mm table increments). Evaluation of the orbital apex may require very thin section overlapping coronal images (1.5 mm thick, with 1 mm table motion), so that 3D reconstructions may be made. *Spiral CT scanning*, if available may also be used to provide the same dataset for subsequent reconstructions.

MRI Due to the lack of bony artefact and improved conspicuity of subtle lesions, MRI is the procedure of choice in the evaluation of visual loss or suspected cranial nerve dysfunction. Complete evaluation should include the entire course of the affected nerve, including the brainstem, with the use of intravenous contrast (gadolinium chelates). Contrast is required to visualise subtle abnormalities of the globe and cranial nerves, and to further characterise a lesion. However, patient cooperation is necessary due to the length of most sequences (2-9 min) and the need to minimise eye motion during this time. Eye makeup may contain iron-based pigment which must be removed to avoid artefact. Additionally, patients with ferromagnetic foreign bodies within the globe or implanted on their person (e.g. pacemaker, cochlear implant, insulin or morphine pumps, aneurysm clips) may not enter the MRI suite due to deflection forces and subsequent torque and dislodgement, possibly with catastrophic consequences. The use of MRI on pregnant patients is relatively contraindicated, as no systematic studies of its effects have yet been performed.

MRI of the orbit should include both T₁ (short T_R and T_O and T₂ (long T_R and T_E) weighted thin section (3 mm) contiguous (or with small interscan gap) axial images obtained prior to contrast, usually preceded by sagittal T₁-weighted images of the brain. After the administration of intravenous contrast material, axial, coronal and possibly oblique parasagittal (parallel to the course of the optic nerve) T₁-weighted images are obtained. The use of fat suppression combined with the postcontrast sequences significantly improves visualisation of subtle masses and lesions of the optic nerve, and is highly recommended. A T₁-weighted axial sequence, performed after contrast administration, of the entire brain is useful as a supplement to the evaluation of the orbit, because of the possibility of spread of pathology to or from the subarachnoid space or along the

course of the cranial nerves. Magnetic resonance angiography (MRA) may be used in the same session for evaluation for pathology of the adjacent arterial and venous systems. Two-dimensional and 3D time of flight or phase contrast techniques are available and may be tailored to the suspected abnormality.

Anatomy (see Figs 50.2, 50.3)

The bony orbit is a pyramid placed on its side, loosely lined by periosteum (periorbita) which is continuous with the parietal layer of the intracranial dura. The orbit contains the globe and optic nerve, blood vessels, extraocular muscles and lacrimal gland, all of which are surrounded by fatty fibroareolar tissue. The *roof* of the orbit is formed by the frontal bone anteriorly and the lesser wing of the sphenoid bone posteriorly. The *lateral wall* is composed of the zygoma anteriorly and the greater wing of the sphenoid bone posteriorly. The *orbital floor* and *medial wall* are more complex in structure, formed by components of the maxilla, zygoma and palatine bones, and the maxillary, ethmoid, sphenoid and lacrimal bones, respectively. The orbital rim is thicker and strong, while the medial wall (lamina papyracea) and orbital floor are thinner and are most prone to fracture with trauma. Grooves in the roof and floor of the orbit transmit the supra- and infraorbital nerves and vessels. These exit the orbit anteriorly through foramina.

The orbital apex is located posteriorly, at the point of the pyramid, and is fenestrated to allow transit of the ophthalmic artery and veins and cranial nerves 11, III, IV, V (branches I and 2) and VI via the optic canal superomedially, superior orbital fissure laterally, and inferior orbital fissure inferolaterally. The superior and inferior fissures are continuous and form a V on its side with the apex directed medially. The optic canal and superior orbital fissure are separated by the optic strut, which also forms the base of the anterior clinoid process.

The *extraocular muscles* are: the superior, lateral, inferior and medial recti, the superior and inferior obliques, and the levator palpebrae. The rectus muscles are bridged by connective tissue fascia to form the 'muscle cone', while the two oblique muscles are separate and located in the superomedial and inferomedial orbit, respectively. The recti join posteriorly in a dense fibrous band (the *annulus of Zinn*), which surrounds the optic nerve, ophthalmic artery, cranial nerves III, V (1st division) and VI, and related structures, and attach in front of the globe equator anteriorly (*Tenon's capsule*). The fibrous septum is also anchored here, and extends in all directions to connect peripherally to the periosteum of the orbital rim. The effect is to create three spaces: a preseptal space contiguous with the face, and two postseptal spaces—one intracanal and one extraconal. The levator palpebrae muscle is external to the superior rectus and attaches to the upper eyelid. The lateral rectus muscle is innervated by cranial nerve VI (abducens) and the superior oblique muscle by cranial nerve IV (trochlear). All of the remaining extraocular muscles are supplied by cranial nerve III (oculomotor).

The spherical globe is composed of three layers: a fibrous outer layer or sclera, an inner layer of neural tissue or retina, and a middle layer that provides vascular flow and support. This intervening layer of choroid, iris and ciliary body is collectively termed the uvea. The globe transmits light via the cornea and through the lens, which focuses the light with the assistance of the ciliary body upon the retina posteriorly. The lens separates the anterior chamber of the globe, which contains aqueous humour, from the thin posterior

chamber and larger vitreous chamber containing vitreous humour. The iris expands or contracts to regulate the amount of light that reaches the retina.

The optic nerve (cranial nerve II) is a tract within the central nervous system (CNS) surrounded by meninges which are continuous with the visceral layer of the dura (optic nerve sheath), with varying amounts of cerebrospinal fluid seen within the perioptic subarachnoid space. The nerve emerges from the posterior globe at the papilla, and extends intracranially to the optic chiasm. Inside the globe, axons from the retina pierce the sclera and choroid layers to connect with the optic nerve.

The ophthalmic artery enters the orbit adjacent and inferior to the optic nerve within the optic canal, then courses anteriorly and medially, crossing over the midsegment of the optic nerve. Terminal branches supply the lacrimal gland, eyelid, muscles, nerve sheath and globe. Small vessels pierce the sclera circumferentially posterior to the equator of the globe to supply the choroid layer. The superior ophthalmic vein extends from the facial venous plexus through the orbit and joins with the inferior ophthalmic vein in the orbital apex, exiting via the superior orbital fissure to empty into the cavernous sinus.

The ovoid lacrimal gland is located in the superior lateral orbit in the postseptal extraconal space (lacrimal fossa), and supplies lubrication to the visible portion of the globe. Fluid (tears) is spread across the globe by blinking, with the excess accumulating inferomedially in the lacrimal sac through the superior and inferior canaliculi. The sac is preseptal and empties via the nasolacrimal duct into the nasal cavity beneath the inferior turbinate.

Trauma

The orbit may be injured directly or indirectly, with both blunt and penetrating trauma occurring with equal frequency. Soft-tissue swelling often obscures direct clinical evaluation of the globe, its motion and vision. Plain film evaluation of the orbit accurately depicts the presence of bony injury and its associated sequelae, as well as the presence of radiopaque and radiolucent foreign bodies. CT shows both soft-tissue and bony injury, and more clearly defines the location and orientation of displaced bony fragments, foreign bodies and air, although US has been shown to be more sensitive for the sequelae of such injuries. MRI may be complementary to CT scanning in certain patients, particularly with injuries involving the globe or optic nerve, but is contraindicated in the presence of a metallic foreign body. Ultrasound is being used more often in this setting, although direct pressure on the globe is painful, and may be contraindicated in globe disruption.

Blow-out fractures occur when direct blunt force is applied to the globe and orbit, with disruption of the inferior floor or medial wall allowing decompression. Herniation of orbital fat and periorbita into the adjacent maxillary or ethmoid sinuses may occur, and is easily seen on both CT and MRI (Figs 51.3–51.4). Related air-fluid levels or sinus opacification may be noted. These injuries may be associated with displacement of the inferior or medial rectus muscles or their connective tissue attachments and limitation of range of motion of the globe (*entrapment syndrome*). Fractures may also allow communication of air or herniation of soft tissue into the orbit (Fig. 51.4).

More complex fractures of the midface are also well defined by CT, including: tripod fractures (the zygomatic arch, floor of the orbit, lateral wall of the maxillary sinus and zygomaticofrontal

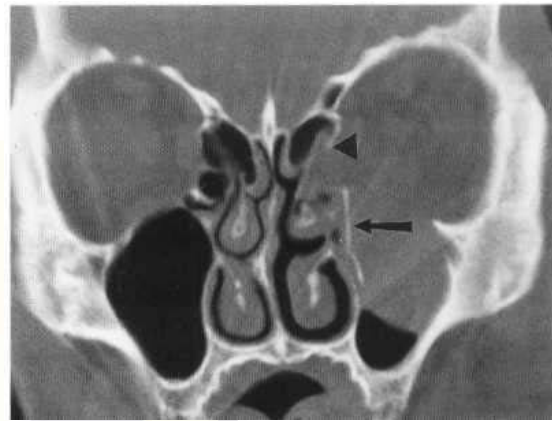
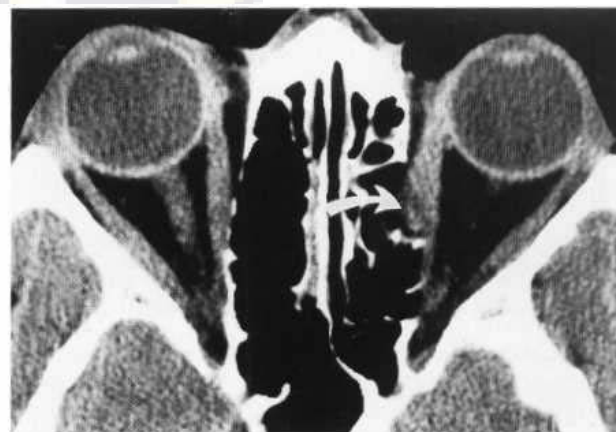
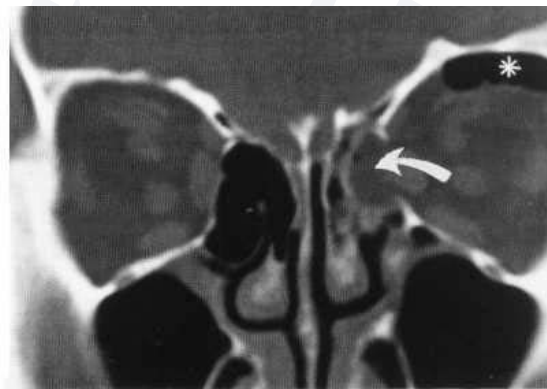


Fig. 51.3 Inferior and medial blow-out fractures. Coronal CT image demonstrates inferomedial displacement of bony fragments of left orbital floor (arrow) as well as accompanying fracture of left lamina papyracea (arrowhead). (Case courtesy of Orlando Ortiz, M.D.)



A



B

Fig. 51.4 Medial blow-out fracture. Axial (A) and coronal (B) CT images demonstrate partial herniation of medial rectus muscle and orbital fat into left ethmoid air cells through fractured lamina papyracea (arrow). There is associated intraorbital emphysema (asterisk).

process), Le Fort type II and III fractures (involvement of the pterygoid plates, nasal cavity and orbit walls) and skull base fractures extending through the optic canal. MRI may be helpful in directly evaluating the intracanalicular portion of the optic nerve.

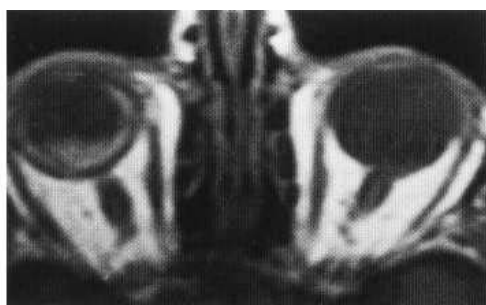
Damage to the globe may be minor to severe, with laceration and rupture well seen on CT as deformation of the globe with decreased ocular volume (Fig. 51.5). Enucleation may occur, and is more



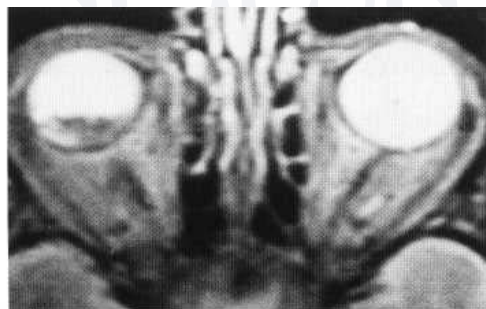
Fig. 51.5 Ruptured globe. Opacification of ethmoids with blood and fluid secondary to extensive comminuted nasal and ethmoid fractures. Bilateral fractures of lateral orbital wall (arrows). Hyperdense blood fills ruptured and misshapen left globe. There is contusion of retro-orbital fat as well as preseptal soft-tissue swelling.



Fig. 51.6 Dislocated lens. Axial T_2 -weighted MR image demonstrates dislocated right lens dependently within the vitreous chamber. Dislocation is also seen on axial non-contrast CT.



A

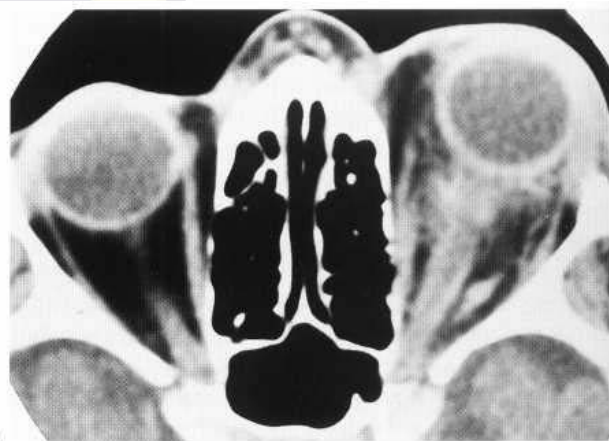


B

Fig. 51.7 Vitreous haemorrhage. Axial T_1 - (A) and T_2 -weighted (B) MR images demonstrate layering of blood within the dependent portion of the right globe. High signal on T_1 -weighted image and low signal on T_2 -weighted image represents haemorrhage.

common following trauma to the lateral border of the orbit. Lens dislocation is well seen by CT or MRI (Fig. 51.6). Haemorrhage appears as amorphous soft-tissue density within the anterior or posterior chambers, or in the orbital fat at the site of injury (Figs 51.7, 51.8).

Retinal detachments may occur in any setting, and appear as peripheral biconvex areas of increased CT density or MRI signal intensity within the globe (Fig. 51.9). The detached retina is tethered to the insertion of the optic nerve posteriorly and to the anterior border of the sclera/retina anteriorly (ora serrata). Choroidal detachments have a similar appearance, except that an additional site of attachment is present at the midglobe where the choroidal arteries pierce the sclera (Fig. 51.10). Retinal and choroidal detachments may be present concurrently.



A



B

Fig. 51.8 Retro-orbital haemorrhage. Axial (A) and coronal (B) CT images demonstrate hyperdense lesion adjacent to left optic nerve. There is proptosis due to infiltration of the retro-orbital fat.

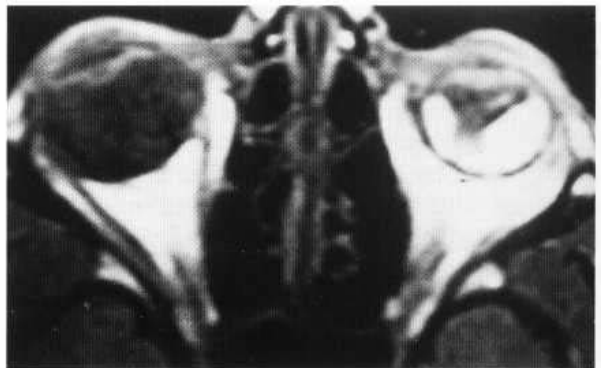


Fig. 51.9 Haemorrhagic retinal detachment. T_1 -weighted MR image demonstrates elevation of retina by hyperintense haemorrhage. Retinal attachment anteriorly to the ora serrata and posteriorly to the macula creates a characteristic V-shaped configuration.

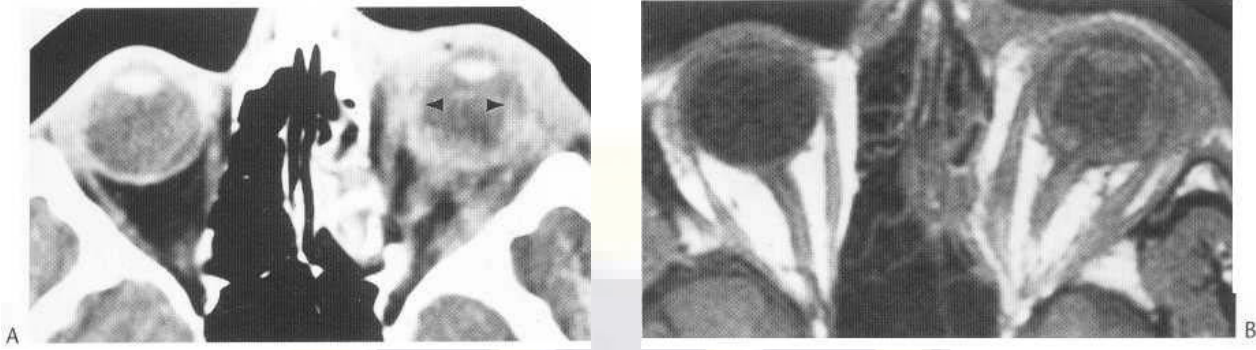


Fig. 51.10 Trauma with blow-out fracture and choroidal detachment. Axial CT image (A) demonstrates preseptal soft-tissue swelling as well as infiltration of retro-orbital fat representing contusion. Elevation of choroid (arrowheads) is due to hyperdense suprachoroidal haemorrhage. Opacification of left ethmoid sinuses is related to medial blow-out fracture. Axial T₁-weighted MR (B) confirms presence of suprachoroidal blood.

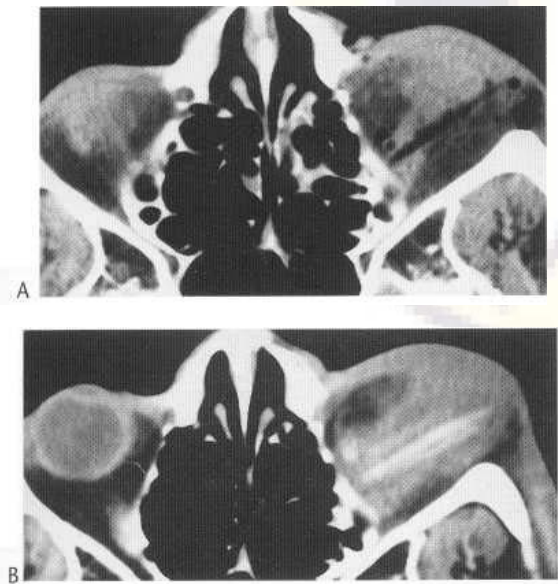


Fig. 51.11 Intraorbital wooden foreign body. Axial CT image (A) performed immediately after injury demonstrates large radiolucent splinter penetrating left globe, simulating appearance of intraorbital emphysema. Follow-up examination (B) performed 3 weeks later demonstrates increased density of foreign body as the interstices have become filled with fluid.

Optic nerve damage may be seen directly as discontinuity, but more often must be inferred from the clinical findings and presence of perineural haematoma. MRI may demonstrate focal injury as an

area of increased T₂ signal intensity, which may enhance with contrast administration on T₂-weighted sequences.

Foreign bodies may be deposited with penetrating injury, and must be localised prior to surgical debridement. X-rays may provide sufficient information, but CT demonstrates smaller fragments and their relationship to the globe and optic nerve. Wood is generally seen as air density, while glass is usually hyperdense (Fig. 51.11). Plastics vary in their composition and CT appearance. Metals are hyperdense, and may cause streak artefact (Figs 51.12, 51.13). Either study may be used with confidence in excluding the presence of ocular metal foreign bodies prior to MRI.

Diffuse processes

Most diffuse processes involving the orbit are inflammatory or infectious in origin. Patients often present with restriction of motion of the globe, proptosis and pain. Systemic symptoms and signs may be present. Imaging is performed to define the aetiology and extent of disease, and to assess the response to therapy.

Infection

Infection, the most common orbital pathology in children, usually occurs secondary to direct injury or spread from an adjacent focus, particularly the paranasal sinuses or face (Fig. 51.14). Most are bacterial in origin, but immunocompromised and diabetic patients are prone to devastating fungal infections. The septum and muscle cone

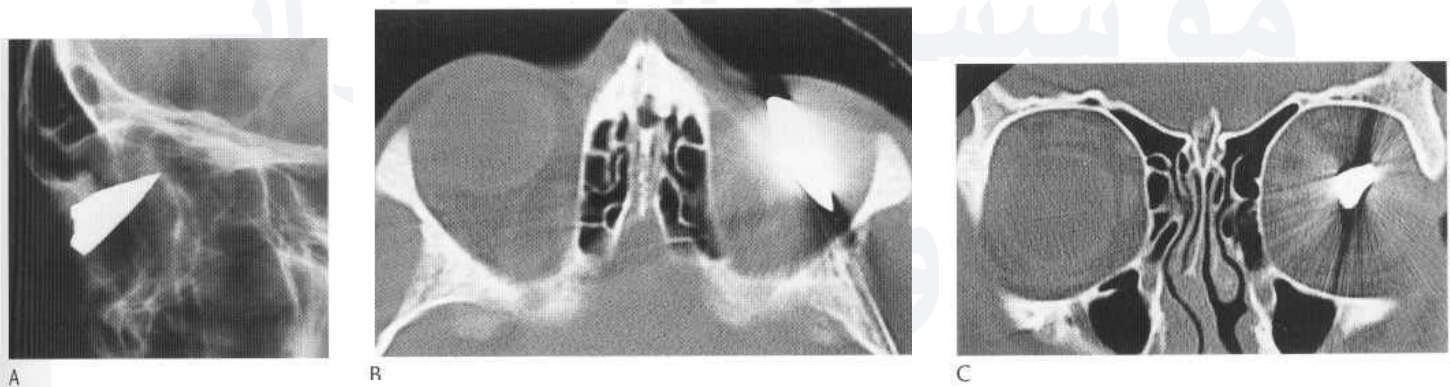


Fig. 51.12 Intraorbital metallic foreign body. Fractured tip of knife blade demonstrated on lateral plain film (A) is well localised to left intraconal compartment by axial (B) and coronal (C) CT images. Retro-orbital haematoma obliterates the normal intraconal fat. There is rupture of the globe. (Case courtesy of Orlando Ortiz, M.D.)

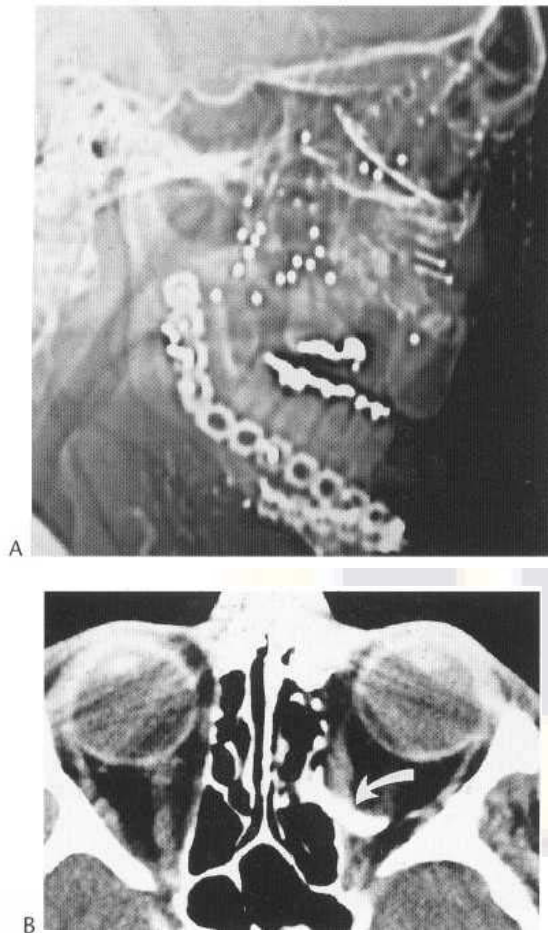


Fig. 51.13 Displaced metallic orbital floor prosthesis. Lateral scout radiograph (A) demonstrates operative fixation of previous mandible fracture and orbitonasal injuries. Punctate densities represent projectiles from recent shotgun blast. Axial CT image (B) demonstrates upward displacement of metallic orbital floor prosthesis (arrow).

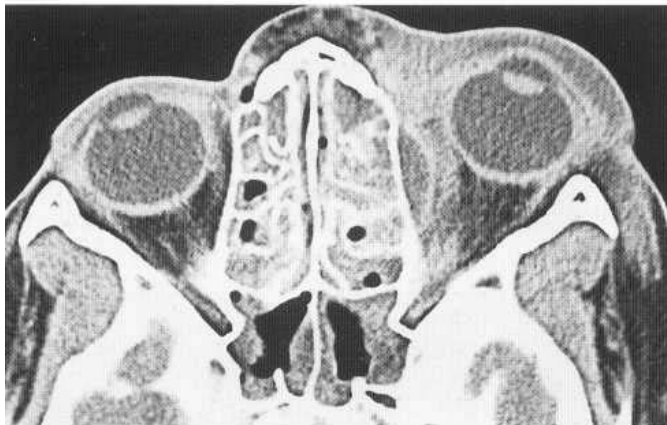


Fig. 51.14 Extraconal orbital abscess from sinusitis. Enhanced axial CT image demonstrates opacification of ethmoid sinuses and mucosal thickening within the sphenoid sinus. There is preseptal cellulitis on the left, with thickening of the eyelid. Low-attenuation subperiosteal abscess in the medial extraconal compartment causes proptosis.

provide strong barriers to the spread of infection, although the valveless veins of the face and orbit allow the spread of thrombophlebitis across these planes. Coronal imaging is extremely useful, as most infections are extraconal and broad-based against the bony orbital wall.

Cellulitis is seen as a poorly defined area of increased CT density or T₂ signal intensity within the fat. There is amorphous enhancement following contrast infusion. *Abscesses* are more discrete and mass-like, and may contain central low CT density or higher T₂ signal intensity, with peripheral enhancement following contrast administration on CT and T₂-weighted sequences. Air may rarely be seen within the abscess. Fungal infections often demonstrate aggressive bony destruction, which is best seen on CT.

Prompt identification, treatment and drainage are required, as life-threatening complications may occur due to intracranial spread of infection. Asymmetric size or enhancement or bowing of the lateral wall of the cavernous sinus may indicate septic thrombosis and must be reported as an emergency. MRI may be most sensitive in this setting.

Orbital pseudotumour

The most common cause of orbital mass in adults is idiopathic inflammatory pseudotumour. Most patients with the acute form present with pain, proptosis and diminished ocular mobility, with histological changes similar to vasculitis. The chronic form may mimic infection or lymphoma both clinically and histologically. No underlying cause has been identified, although autoimmune aetiologies are suspected. Unilateral presentation is most common, but findings can be bilateral. All compartments of the orbit may be affected—lacrimal gland, muscle cone, optic nerve and sclera in a diffuse pattern (Fig. 51.15). A rapid response to the administration of steroids is helpful in confirming the clinical and radiographic diagnosis. Biopsy is reserved for those patients with atypical features such as bony involvement or lack of response to medication; lymphoma will often be diagnosed in these situations.

Imaging usually shows heterogeneous poorly margined increased CT density and decreased T₁ and T₂ MRI signal intensity (versus fat and muscle) within the intraconal fat surrounding a thickened sclera or enlarged optic nerve, sometimes simulating a mass. The diffuse form shows these changes throughout the orbit (Fig. 51.16), or may present as a discrete mass lesion. The lacrimal gland may be enlarged. Enhancement occurs following contrast infusion.

Muscle cone involvement has been well studied, but remains difficult to separate from thyroid ophthalmopathy. Enlargement of one or more muscles may occur unilaterally or bilaterally (Fig. 51.17). Pseudotumour is more likely than Graves' myositis if the tendinous insertions are also involved. Lack of insertion involvement has no predictive value. Isolated lateral rectus muscle thickening

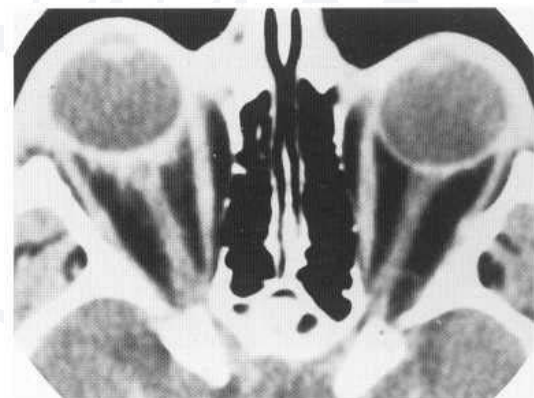


Fig. 51.15 Scleral pseudotumour. Marked thickening and irregularity of the sclera of the right globe involves the adjacent retro-orbital fat.

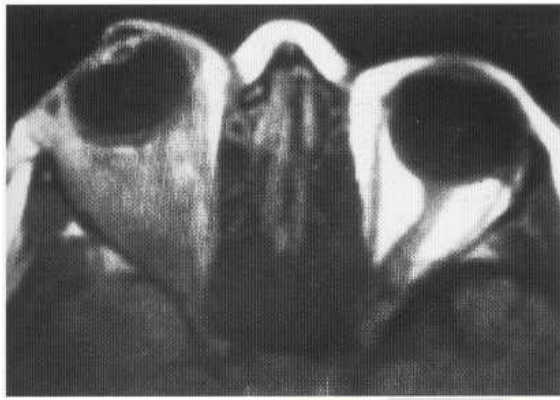


Fig. 51.16 Diffuse pseudotumour. Axial MR T₂-weighted image showing a diffuse mass in the right orbit due to pseudotumour.



Fig. 51.17 Myositic pseudotumour. Enhanced axial (A) and coronal (B) CT images demonstrate fusiform enlargement of right lateral rectus muscle (arrowheads).

favours pseudotumour, especially if the lacrimal gland is also enlarged.

Graves' ophthalmopathy

Patients with Graves' disease present with proptosis and eyelid retraction, ophthalmoplegia and scleral injection. Hyperthyroidism may not be apparent clinically at presentation. Conversely, ophthalmopathy may occur in patients who are currently euthyroid, but who have previously been hyperthyroid. Bilateral symmetrical enlargement of the extraocular muscles is most frequent, usually involving the inferior, medial and superior recti, in that order, with the lateral rectus least often affected. Inflammatory enlargement of the extraocular muscles occurs acutely, and is the cause of symptoms. In the chronic phase, inflammatory cells are replaced by fibrous and fatty tissue, at which time treatment with steroids and/or radiation therapy is poorly effective and surgical decompression may be required. If thyrotoxicosis is also present, increased intra-orbital fat may be seen. This increase in orbital contents is responsible for the proptosis and may cause visual loss due to corneal ulceration or optic nerve compression.



Fig. 51.18 Thyroid ophthalmopathy. Unenhanced axial (A) and coronal (B) CT images demonstrate massive enlargement of the rectus muscles, including fusiform enlargement of the lateral rectus with relative sparing of the distal muscle insertion.

Imaging demonstrates that enlargement is confined to the muscle belly, sparing the tendinous insertion (Fig. 51.18). CT density measurements of affected muscles may not vary from normal, but areas of increased T₂ MRI signal intensity are often noted. Patients with these findings have a more favourable response to treatment. Enhancement of the affected muscle groups occurs acutely, but may be diminished in the chronic phase.

Rhabdomyosarcoma

Rhabdomyosarcoma is the most common primary orbital malignancy in the paediatric age group, with most patients presenting below 6 years of age. One half are metastases to the orbit from primary tumours located elsewhere; one half arise primarily within the superior orbit, probably from undifferentiated cell rests. Patients present with rapidly progressive exophthalmos that may mimic orbital infection. Bone destruction and extension into the paranasal sinuses may further confuse the imaging appearance (Fig. 51.19). Spread of tumour beyond the orbit, particularly intracranially, portends a worse prognosis. The tumour is very sensitive to chemotherapy and radiotherapy, and may respond to treatment quickly.

Both CT and MRI will typically show a mass involving an extraocular muscle. Lesions are isodense on CT and isointense on T₂-weighted images when compared to muscle. There may be associated bony destruction and contiguous extraorbital spread. The tumour involves the globe less often, but when involvement is present, MRI is the preferred imaging modality. Marked enhancement throughout the mass is seen after contrast administration.

Miscellaneous muscle lesions

Lymphoma uncommonly involves the orbit, but may infiltrate the extraocular muscles in any pattern (Fig. 51.20). Systemic disease is

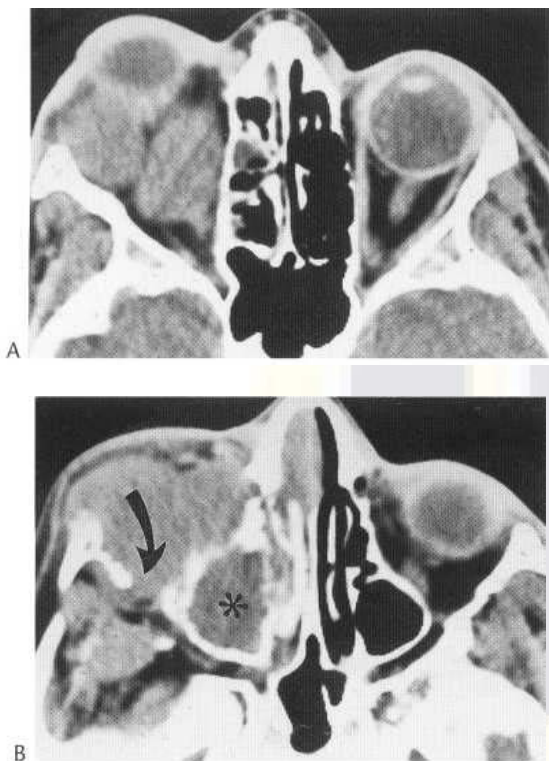


Fig. 51.19 Rhabdomyosarcoma. Contrast-enhanced axial CT image (A) through orbits demonstrates right proptosis due to large, lobular, intra-orbital mass. Image at lower level (B) demonstrates invasion of right maxillary sinus (asterisk) as well as extension through lateral orbital wall (arrow), consistent with the aggressive nature of this tumour. (Case courtesy of Orlando Ortiz, M.D.)

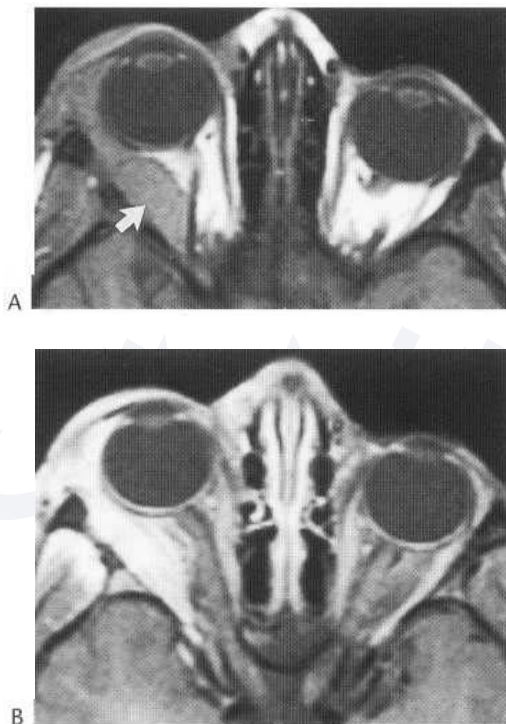


Fig. 51.20 Lymphoma. T₂-weighted MR image (A) demonstrates proptosis of right globe due to a large intermediate signal intensity lesion that involves the lacrimal fossa and the right lateral rectus muscle (arrow), with extension posteriorly in the extraconal compartment. Postcontrast image (B) demonstrates homogeneous enhancement.

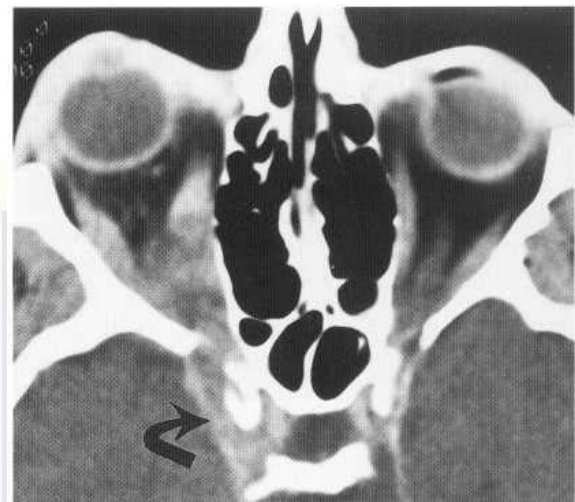


Fig. 51.21 Lymphoma. Enhanced axial CT image demonstrates extension of right orbital apex mass to the right cavernous sinus (arrow) via the superior orbital fissure. There is right proptosis. Enlargement and abnormal enhancement of right medial and lateral rectus muscles could represent infiltration by tumour, but are more likely due to venous congestion from cavernous sinus obstruction. (Case courtesy of Orlando Ortiz, M.D.)

uncommon at initial presentation, but develops subsequently in one third of patients, particularly those with bilateral disease. There is female predominance. *Non-Hodgkin's lymphoma* is most common (Fig. 51.21).

Muscle enlargement may be seen with *granulomatous disease*, such as Wegener's granulomatosis, sarcoidosis or histiocytosis X. They may be symmetric, and difficult to differentiate from pseudo tumour. Concurrent sites of involvement elsewhere in the head neck or chest may be present.

Secondary swelling and oedema of the extraocular muscles may also be associated with *vascular lesions* that result in increased venous pressure, such as carotid-cavernous fistulas (Fig. 51.22). Apical masses that produce compression of the ophthalmic vein may also cause the same findings.

Orbital masses

Most masses present with proptosis due to mass effect within the closed space of the orbit. They are usually benign and are infrequently associated with systemic illness or symptoms, particularly in adults. Imaging is utilised to evaluate the location and extent of the abnormality.

Haemangioma These benign masses composed of dilated vessels with endothelial linings may be divided into the capillary type, which occur in childhood, and the cavernous type, occurring in adults. Both forms have a female predominance.

Capillary haemangiomas These present in infancy with chemosis of the eyelid and injection of the sclera. They may grow quickly, plateau, and then gradually involute. They have no surrounding capsule, and therefore may grow large and appear infiltrative, similar to rhabdomyosarcoma. Concurrent preseptal and postseptal involvement may occur. Secondary remodelling and enlargement of the orbit may occur but bone destruction is not seen. CT shows an infiltrative mass of homogeneous intermediate density, while heterogeneous T₂ signal intensity similar to muscle is noted on

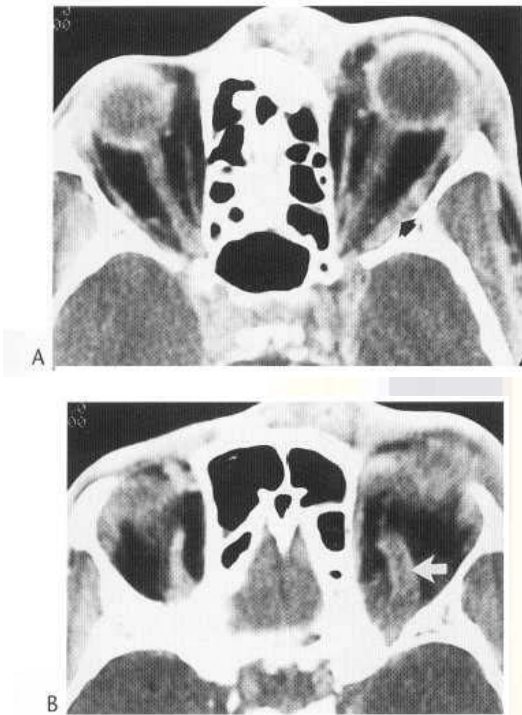


Fig. 51.22 Cavernous sinus thrombosis. Axial CT image (A) demonstrates proptosis with preseptal soft-tissue swelling and enlargement of the left lateral rectus muscle (arrowhead). There is subtle enlargement of the left cavernous sinus, with areas of diminished enhancement. Image at a higher level (B) demonstrates massive distension of the left superior ophthalmic vein (arrow).

MRI. Marked enhancement occurs following contrast infusion. Pooling of contrast may be seen on CT, with flow voids noted on MRI corresponding to dilated vessels. Phleboliths are rarely seen.

Cavernous haemangiomas These are the most common benign orbital tumours in adults. These masses grow slowly, with most located intraconally. Patients present with proptosis or diminished range of ocular motion and diplopia. When the tumour is located in the apex, optic nerve compression may occur and the patient may have a history of acute proptosis and ocular pain. Cavernous haemangiomas have a fibrous pseudocapsule, and are homogeneous and sharply margined in appearance. T₁-weighted MRI sequences demonstrate high signal intensity within this lesion. Dense contrast enhancement with pooling and flow voids is also seen (Fig. 51.23).

Lymphangioma Lymphangiomas are hamartomas that arise embryologically from the primitive vascular tree, as the postseptal orbit has no normal lymphatic tissue. They are composed of varying amounts of solid and cystic material, including fibrous tissue, dilated lymphatic channels, dysplastic vessels and lymphoid tissue. Haemorrhagic products of different ages are noted on MRI. Patients present in childhood with slowly progressive exophthalmos or with sudden proptosis due to intratumoral haemorrhage and expansion.

These lesions are largely extraconal but commonly cross boundaries to show simultaneous intraconal and preseptal involvement. CT shows a poorly defined lobulated mass of mixed attenuation with variable enhancement (Fig. 51.24). MRI more clearly shows trans-fascial spread as well as the heterogeneous cystic and haemorrhagic components, especially on T₂-weighted sequences (Fig. 51.25). Enhancement on MRI is minimal, and occurs in the venous compo-

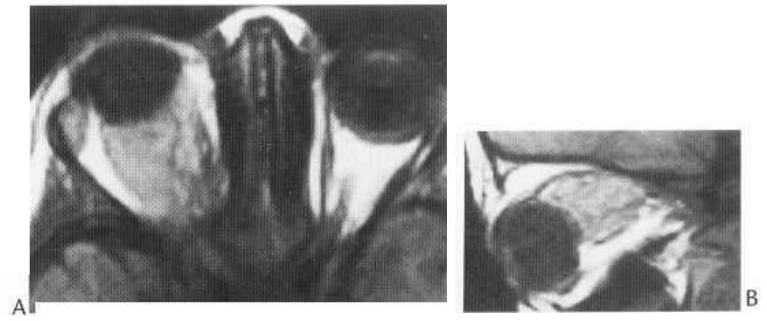


Fig. 51.23 Cavernous haemangioma. T₁-weighted axial (A) and sagittal (B) MR images demonstrate proptosis of right globe due to well-circumscribed, mid to high signal intensity intraconal mass.

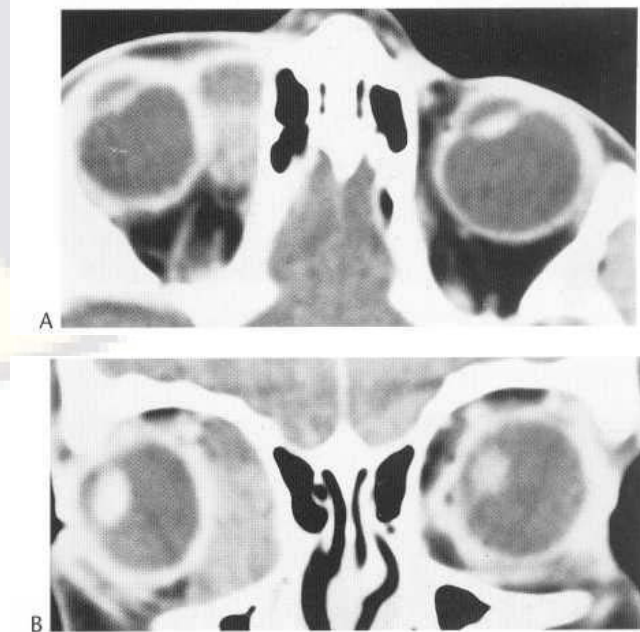


Fig. 51.24 Lymphangioma. Supine axial (A) and prone corona (B) enhanced CT images demonstrate a complex intraorbital mass medial to the right globe. Fluid-fluid level is characteristic for haemorrhage, and consistent with the clinical history of acute proptosis and ocular pain. (Case courtesy of Orlando Ortiz, M.D.)

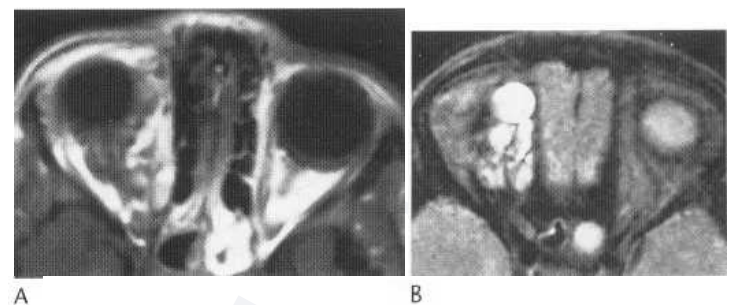


Fig. 51.25 Lymphangioma. Axial T₁-weighted (A) and T₂-weighted (B) MR images demonstrate mild right proptosis due to complex, multi-lobulated, cystic, extra-axial lesion in the superomedial aspect of the right orbit.

ponents that bleed. MRI is preferred for preoperative planning as it most clearly delineates the boundaries of the lesion.

Haemangiopericytoma Haemangiopericytoma is a vascular tumour occurring in adults. Clinical presentation and appearance are very similar to cavernous haemangiomas: both are encapsulated with generally homogeneous density and signal intensity,

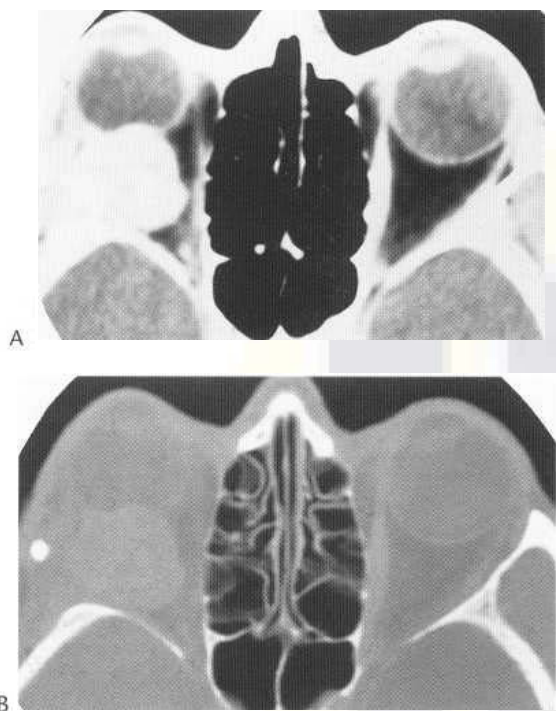


Fig. 51.26 Haemangiopericytoma. Axial CT image (A) demonstrate well-circumscribed enhancing retro-orbital lesion. Bone window, (B) demonstrate erosion of adjacent lateral orbital wall.

and marked contrast enhancement. However, haemangiopericytomas may demonstrate bone destruction and muscle invasion and recur following incomplete excision (Fig. 51.26). Distant metastases may also be seen.

Neurofibromas/neurinomas In addition to the cranial nerves there are sympathetic, parasympathetic, and sensory and motor nerves that traverse the orbit; these may be the source of isolated neurinomas and plexiform neurofibromas. The isolated variety presents itself in adulthood with proptosis. The plexiform type is strongly associated with neurofibromatosis, and is most often seen in younger patients with known disease. In patients with neurofibromatosis, the ipsilateral greater wing of the sphenoid bone may be dysplastic, which may result in pulsatile exophthalmos (Fig. 51.27).



Fig. 51.27 Encephalocele. Axial T-weighted MR image demonstrates marked proptosis of right globe with stretching of attenuated right optic nerve (arrowhead) due to herniation of dura and temporal lobe through a large sphenoid defect in this patient with neurofibromatosis.

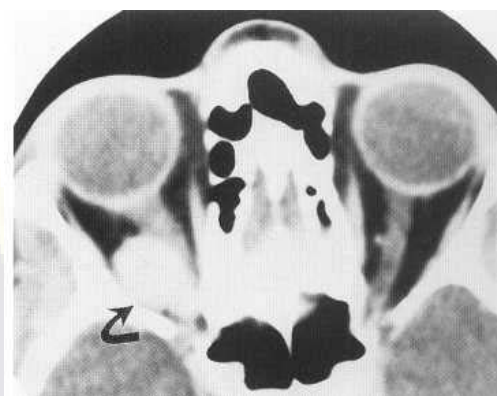


Fig. 51.28 Neurinoma. Contrast-enhanced CT demonstrates medial displacement of right optic nerve by a well-circumscribed, homogeneously enhancing VIth nerve neurinoma. Note adjacent scalloping of sphenoid bone (arrow).

Non-plexiform neurofibromas and neurinomas are ovoid, well-defined, homogeneous and hypovascular, with mild uniform enhancement (Fig. 51.28). Cystic degeneration may occur, and will appear hypodense on CT, and hyperintense on T₂-weighted MR sequences. Plexiform neurofibromas are poorly defined, crossing fascial planes and surrounding normal structures (Fig. 51.29). Contiguous extension to the face or cranium may be seen, and is best evaluated by MRI. Signal intensity and enhancement patterns are heterogeneous and variable, as the cellular composition is inconstant.

Metastases and lymphoma Although rarely discovered clinically, metastases to the orbit may occur from systemic primaries, particularly neuroblastoma and leukaemias in children (Fig. 51.30), and breast, lung, prostate (Fig. 51.31) and stomach cancer in adults. Patients present with pain and proptosis, sometimes without a history of known primary malignancy. These lesions are poorly defined, infiltrative and demonstrate marked contrast enhancement on CT and MRI. Most often the primary source of the tumour cannot be differentiated prospectively based on imaging appearances. Primary lymphoma of the orbit represents 1% of lymphoma patients, and is most often of non-Hodgkin's variety (Fig. 51.32). Metastatic lymphoma to the orbit is even less common, and is usually indistinguishable from other malignancies.

Histiocytosis X Histiocytosis X is a chronic granulomatous disorder of unknown cause that primarily affects the reticuloendothelial system. Multiple eosinophilic granulomas occur, usually near the lacrimal fossa, often associated with lytic bone defects. The intermediate variety, Hand-Schuller-Christian disease, affects children; the infantile form, Letterer-Siwe disease, may produce additional intracranial or calvarial lesions. CT and MRI show a poorly defined homogeneous soft-tissue mass, generally with sharply marginated bony erosion, with marked enhancement following contrast administration (Fig. 51.33). A diffuse infiltrative pattern that mimics pseudotumour occurs less often.

Dermoid/epidermoid These are congenital lesions that result from sequestration of primitive ectoderm in the region of the orbit, usually presenting during childhood as a discrete mass or with proptosis. They are most often located near the lacrimal fossa or nasal bone and are homogeneous in appearance. They grow slowly, often remodelling adjacent bone or sutures. The presence of fat is clearly seen on CT and MRI, allowing accurate

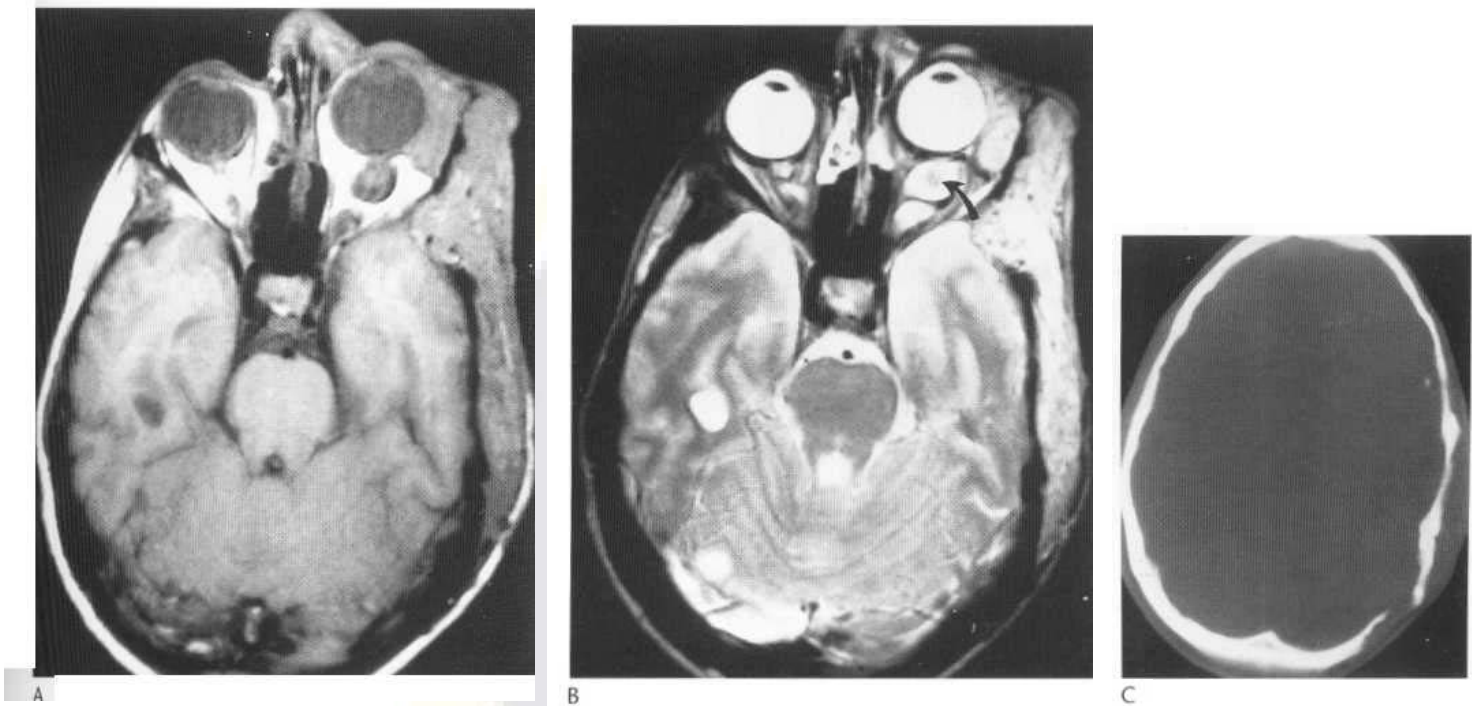


Fig. 51.29 Plexiform neurofibroma. T_1 -weighted (A) and T_2 -weighted (B) MR images demonstrate extensive left temporal scalp lesion with extension to the left orbit resulting in mild proptosis. MR also demonstrates ectatic left optic nerve (arrow). CT image at bone windows (C) demonstrates associated bony defect of left lambda suture.



Fig. 51.30 Leukaemic chloroma. Enhanced axial CT image in 12-year-old female with ALL demonstrates left proptosis due to well-circumscribed, homogeneous extraconal mass. (Case courtesy of Orlando Ortiz, M.D.)

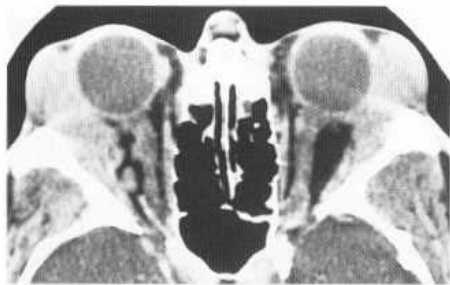


Fig. 51.32 Lymphoma. Bilateral, symmetric, enhancing soft-tissue masses occupy the lacrimal gland fossa. There is posterior extension in the extraconal compartment with bilateral proptosis.

prospective differentiation from other orbital masses (Fig. 51.34). They do not enhance. Variation in cyst contents will result in a less typical imaging appearance.

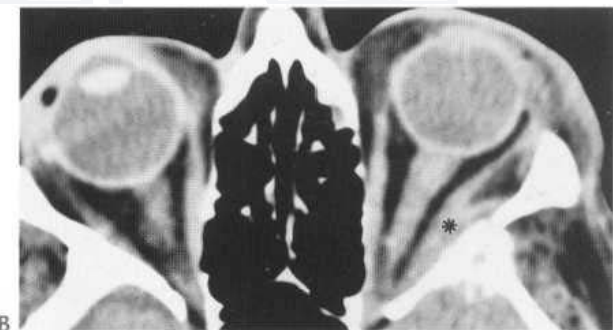
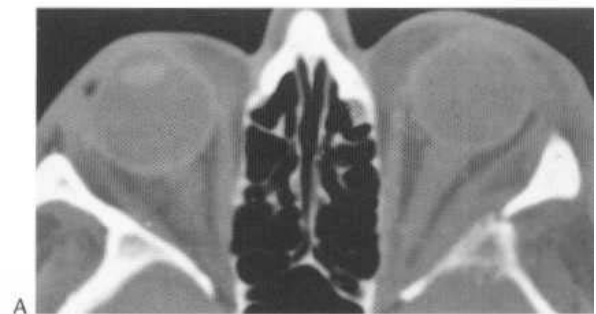


Fig. 51.31 Metastatic prostate carcinoma. Axial CT image (A) through orbits demonstrates small lytic lesion of left lateral orbital wall in a patient with prostate carcinoma. Soft-tissue windows (B) demonstrate contiguous extension of soft tissue into lateral extraconal compartment (asterisk) with medial displacement of the lateral rectus muscle.

Trochlear apparatus calcification Calcification of the trochlear apparatus (superior-medial quadrant of the orbit) is commonly seen in patients over 50 years of age as a benign finding. When present at an earlier age, it is highly associated with diabetes mellitus. The cause is unknown. Differentiation from tendon sheath

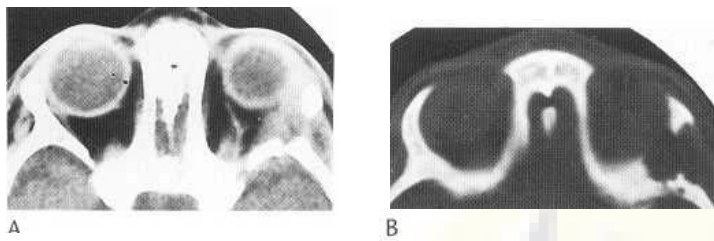


Fig. 51.33 Histiocytosis. Axial CT image (A) demonstrates soft-tissue mass in superolateral aspect of left orbit. Bone window (B) shows associated bony erosion.

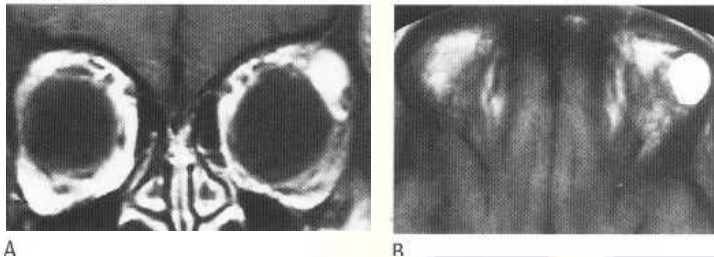


Fig. 51.34 Lacrimal gland dermoid. Coronal (A) and axial (B) T₁-weighted images demonstrate a well-circumscribed lesion located in the upper outer quadrant of left orbit. High signal intensity is consistent with fat.

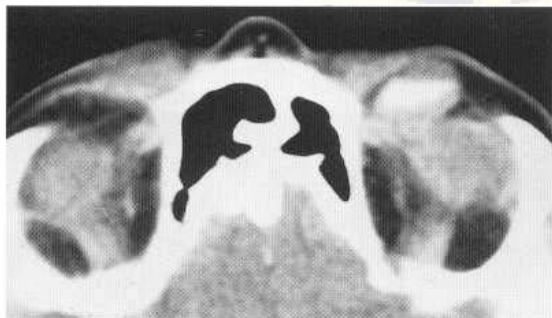


Fig. 51.35 Varix. Contrast-enhanced CT demonstrates fluid-contrast level within preseptal varix of left orbit.

syndrome (Brown's syndrome) is based on the presence of ocular motility restriction in symptomatic patients.

Varix Mild asymmetry or prominence of the superior ophthalmic veins is common in normal patients. An increase in systemic venous pressure, such as with the Valsalva manoeuvre, coughing or dependent head position, may result in dilatation and proptosis. Differentiation from venous dilatation due to other causes is mandatory, as masses in the orbital apex may compress and distend the vein. Haemorrhage can occur, and repeated episodes of proptosis may result in blindness. Ultrasound with colour Doppler imaging, CT and MRI will all demonstrate the vein and its status, and show dilatation on dynamic imaging with straining, confirming the diagnosis (Fig. 51.35). Phleboliths are rarely present.

Ophthalmic vein thrombosis This may occur as a result of stasis and compression, infection, or extension of cavernous sinus thrombosis. Lack of normal flow void within the vessel is seen on MRI sequences. Aetiological causes within the orbit, orbital apex or cavernous sinus are usually seen, particularly on MRI after contrast enhancement. Coronal images may best demonstrate the pathology. MRA of the venous system may also demonstrate absence of flow within the vein. Colour Doppler imaging may also be employed in this setting to confirm the diagnosis non-invasively.

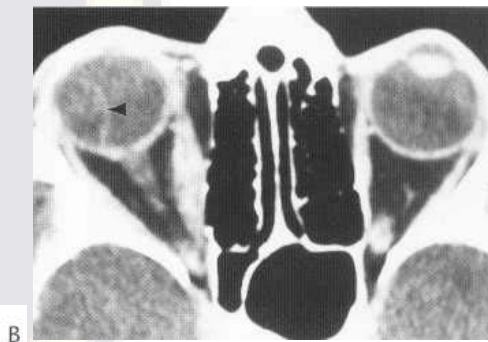


Fig. 51.36 Carotid-cavernous fistula. Enhanced axial CT image (A) demonstrates enlargement of right superior ophthalmic vein (arrow). Image at lower level (B) demonstrates engorgement of right medial rectus muscle as well as elevation of choroid (arrowhead) by suprachoroidal effusion resulting from orbital venous hypertension.

Carotid-cavernous fistula Direct communication between the internal carotid artery and the cavernous sinus, resulting in transmission of arterial pressure to the venous system, is termed a fistula. It may occur following trauma (skull base fracture, penetrating injury), or develop spontaneously due to an underlying vascular disorder (fibromuscular dysplasia, atherosclerosis, aneurysm rupture, dural arteriovenous malformations). Patients present acutely with unilateral injection of the sclera, chemosis of the eyelids and pulsatile exophthalmos. Bilateral orbital findings can be present due to transmission of increased venous pressure to the contralateral cavernous sinus via the circular sinus. Visual loss may accompany severe venous congestion.

Venous distension is apparent on US, CT and MRI (Fig. 51.36), although muscle enlargement may be seen only with CT and MRI. Carotid arteriography is still the diagnostic procedure of choice (Fig. 51.37). Early filling of the cavernous sinus and jugular veins is seen, with the superior ophthalmic vein providing an important collateral channel to the external jugular system. Neuro-interventional treatment may be employed to close the fistula site directly.

Optic nerve-sheath complex

Patients with abnormalities of the optic nerve and its coverings present with proptosis, visual loss and papilloedema. As symptoms are non-specific and clinical examination of the postseptal space is limited, imaging is required for diagnosis. Expansion of the tubular-shaped optic nerve and sheath is well demonstrated on both CT and MRI, especially with coronal sections where direct comparison to the uninvolved side may be made. Imaging of the intracranial space is required because the optic nerve and its coverings are contiguous

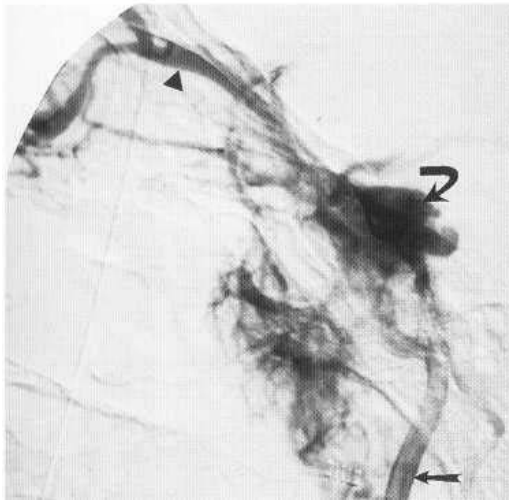


Fig. 51.37 Carotid-cavernous fistula. Right internal carotid injection (straight arrow), lateral view, opacities cavernous sinus (curved arrow) as well as dilated superior ophthalmic vein (arrowhead). Note absence of filling of intracranial carotid circulation.

with the brain and dura mater, and other portions of the visual pathway are often involved.

Optic nerve glioma

Optic nerve gliomas are uncommon tumours, occurring almost entirely in children. They are most often low-grade pilocytic astrocytomas in the paediatric population. There is a high degree of association with neurofibromatosis type 1, especially when bilateral masses are present. Tumours in adults are rare and are usually higher in grade and extend from a primary lesion involving the optic chiasm. The optic nerve may expand uniformly and diffusely, or may be fusiform. Exophytic growth through the sheath occurs less commonly. Plain films may show asymmetric widening of the optic nerve canal. CT density and MRI signal intensity is generally homogeneous, with only mild uniform enhancement seen after contrast administration (Figs 51.38, 51.39). The coronal cross-section density is also uniform, distinguishing this tumour from those of the meningeal sheath. Haemorrhage and calcification are rare. MRI is preferred for evaluation for evaluation of the intracranial visual pathways.

Optic nerve meningiomas

Tumours of the sheath are demographically and histologically similar to those seen intracranially. Meningiomas are most often seen in middle-aged women who present with visual loss, papilloedema and pallor of the optic nerve head. The tumour originates from the sheath itself, circumferentially encasing and spreading

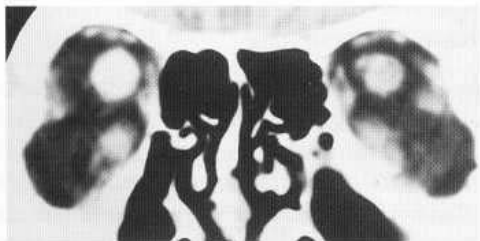


Fig. 51.38 Optic nerve glioma. Enhanced coronal CT image demonstrates homogeneous enhancement of enlarged right optic nerve.

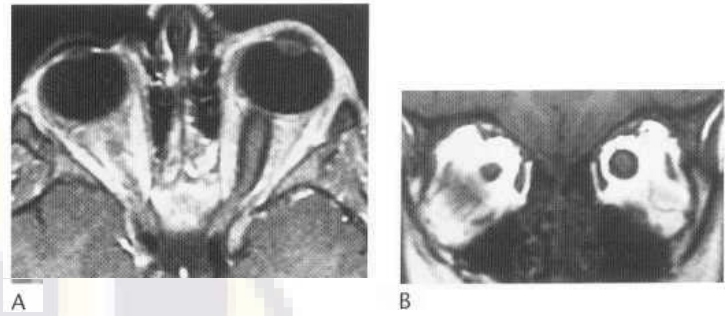


Fig. 51.39 Optic nerve glioma. Enhanced fat-saturated axial T₁-weighted image (A) demonstrates mild enhancement and enlargement of intra-orbital and canicular segments of left optic nerve as well as dilated low signal intensity perioptic space. Coronal image (B) confirms enlargement of nerve and surrounding perioptic space.



Fig. 51.40 Optic nerve meningioma. Enhancement of thickened right optic nerve with elevation of optic disc (arrowhead).

along the nerve. With continued progression, exophytic growth is seen. Ectopic meningiomas also occur infrequently, arising from rests found within the orbit.

Meningiomas are dense fibrous tumours with a high degree of cellularity and little extracellular fluid. Calcification is common. Plain films may show widening of the optic canal, or hyperostosis of the sphenoid wing. CT generally shows a dense, sharply defined tubular mass surrounding and paralleling the course of the optic

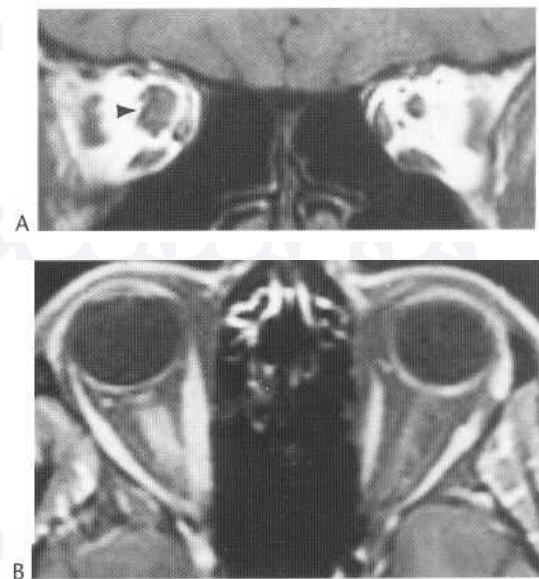


Fig. 51.41 Optic nerve meningioma. Coronal T₁-weighted MR image (A) demonstrates marked thickening of right optic nerve sheath (arrowhead). Axial T₁-weighted postcontrast fat-saturated image (B) demonstrates peripheral enhancement of the thickened right optic nerve sheath. Non-enhancing soft tissue within represents the encased optic nerve.

nerve, with marked enhancement after contrast administration ('tram track') (Fig. 51.40). Kinking of the nerve may be seen. MRI will show a homogeneous mass of decreased T₁ and T₂ signal intensity, with strong enhancement, especially with the use of fat suppression sequences. Coronal images are preferred, as the encased optic nerve will be seen in relief against the densely enhanced tumour. Extension through the optic canal is best demonstrated by MRI (Fig. 51.41).

Dilated perioptic subarachnoid space

Approximately half of normal individuals will demonstrate prominent subarachnoid space surrounding the optic nerve as a normal finding, usually bilaterally. Intrathecal enhancement is often seen following myelography or cisternography.

Elevated intracranial pressure may be transmitted through a patent perioptic space and may result in progressive visual loss if untreated. Gross distension and tortuosity of the complex is characteristic, with convex bulging of the optic nerve head at the papilla seen on axial or sagittal images of the globe. CT and MRI show the space between the meningeal coverings and nerve as isodense and isointense to CSF, respectively. These findings are often seen in

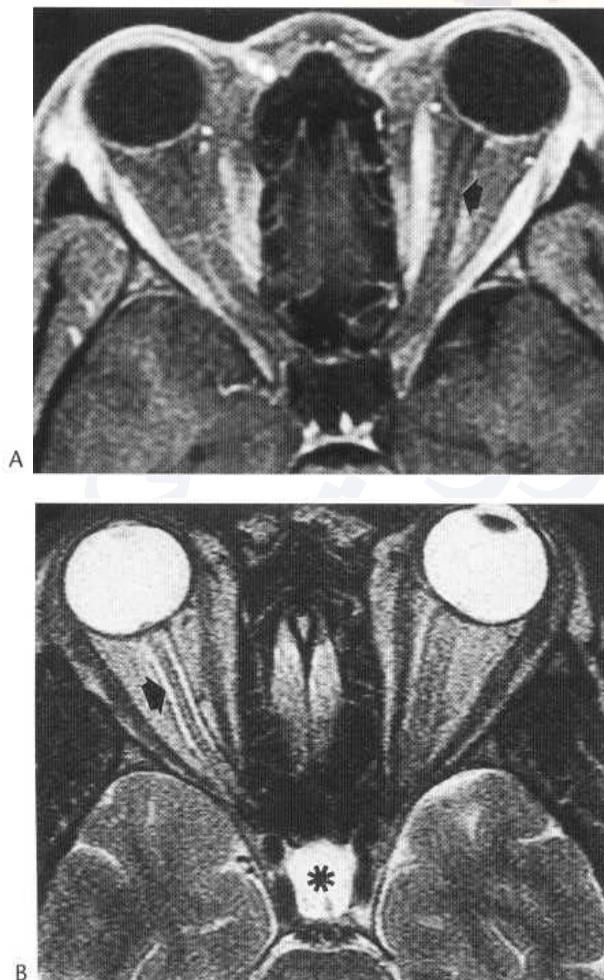


Fig. 51.42 Pseudotumour cerebri. Enhanced, fat-saturated axial T₁-weighted (A) and T₂-weighted (B) MR images demonstrate dilated optic nerve sheath surrounding optic nerves (arrowheads). Papilloedema (seen on right in (B) and fluid-filled empty sella (asterisk) are frequent accompanying findings.

symptomatic cases of pseudotumour cerebri, but are not specific for this entity (Fig. 51.42).

Hydrops, or focal accumulation of fluid within the perioptic space, may occur following compression from any extrinsic mass, particularly if located in the orbital apex. Symptoms are unilateral and referable to the compression of the nerve rather than to intracranial causes.

Optic neuritis

Acute inflammation of the optic nerve may occur as an isolated event or in association with multiple sclerosis. Oedema and inflammatory cells infiltrate the nerve, resulting in uniform swelling and focal demyelination. Because of strong similarities in demographics, laboratory studies and imaging appearances, isolated optic neuritis is thought to be a *forme fruste* of multiple sclerosis. Patients are most often young women who present with painful visual loss, without ophthalmoplegia. Steroids may be used in therapy, although most patients will improve spontaneously.

MRI is the imaging test of choice due to the high sensitivity to fluid and oedema seen with T₂-weighted sequences. Contrast-enhanced T₂-weighted fat suppression sequences will usually demonstrate focal enhancement at sites of increased T₂ signal intensity representing changes characteristic of multiple sclerosis arc seen within the brain in one-third of patients. CT is relatively insensitive to these subtle changes, and may show only minimal enhancement (Fig. 51.45).

Radiation-induced optic neuropathy This may have a similar imaging appearance. MRI will show areas of increased T₂ signal intensity and enhancement on T₂-weighted images within the optic nerve confined to the field of irradiation for head and neck, pituitary or cavernous sinus malignancies. A direct dose-response curve is seen for doses over the tolerance level of 50-55 Gy. Correlation of the history, images and radiation port and dosage confirms the diagnosis.

Ischaemic optic neuropathy This condition is well shown on T₂-weighted MRI sequences, and is indistinguishable on imaging from optic neuritis due to multiple sclerosis and radiation therapy. However, patients with this diagnosis are usually elderly, with sudden and painless loss of vision in one eye, associated with pallid swelling of the disc. Both eyes may eventually be involved. The cause of the ischaemia is unknown, although giant-cell arteritis may be identified in a small subpopulation. Surgical decompression had been recommended in the past, but has recently been shown to be ineffective or dangerous. Currently, no treatment is considered proven effective.

Miscellaneous expansions of the optic nerve-sheath complex

Enlargement of the optic nerve and sheath can occur due to secondary involvement from a variety of orbital and systemic abnormalities. *Pseudotumour* may result in a mild increase in size of the complex, particularly near the insertion on the globe, with indistinct margins and enhancement. Other portions of the sclera or orbit are often also abnormal. *Graves' disease* may demonstrate a similar appearance. *Sarcoidosis* may also present with enlargement of the optic nerve-sheath complex, most often with concurrent involve-

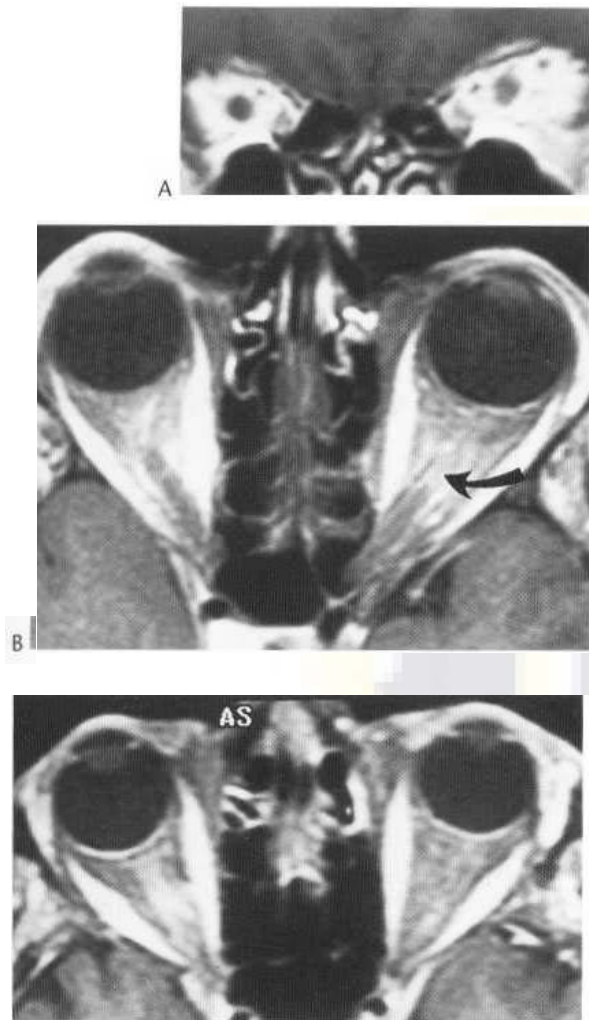


Fig. 51.44 Optic neuritis. Axial T₁-weighted postcontrast MR image with fat saturation demonstrates enhancement of the intraconal portion of the right optic nerve. Normal left optic nerve is indistinguishable from surrounding intraconal fat. Note normal bright enhancement of extraconal muscles.



Fig. 51.45 Optic neuritis. Straightening and thickening of right optic nerve. Similar but less severe changes on left.

ment of the proximal visual pathway, especially the optic chiasm (Fig. 51.46).

Metastases from solid organ tumours may result in focal or diffuse nodular enlargement, particularly in children, while leukaemias and lymphomas may result in smooth tubular expansion due to infiltration throughout the sheath and nerve. The clinical findings and history will usually assist in arriving at the diagnosis. Intraocular malignancy may also extend along the optic nerve.

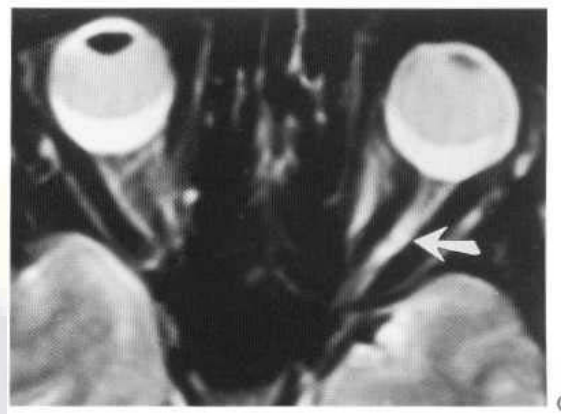


Fig. 51.43 Optic neuritis. Contrast-enhanced T₁-weighted coronal (A) and fat-saturated axial T₁ (B) MR images demonstrate subtle enlargement and enhancement of the left optic nerve (curved arrow). T₂-weighted axial image (C) demonstrates corresponding increased signal intensity (straight arrow).

Haemorrhage in and around the complex may cause apparent expansion and alteration of the appearance of the normal perioptic fat, but enhancement is uncommon, and clinical indications of tumour are absent.

'*Tenting of the globe*' is seen as a secondary sign of increased orbital tension due to an acute or subacute mass that produces proptosis and stretching of the nerve. The degree of posterior scleral angulation correlates well with the severity of proptosis. A posterior globe angle of less than 120° with acute proptosis is an indication for urgent surgical intervention.

The globe

Disorders of the globe in adults usually present with visual field deficits. Children may present with alterations of ocular shape and size that are often apparent clinically, or with a lack of the normally observed red reflex on fundoscopic examination (leucocorrea). In other patients, ocular pathology may be discovered incidentally. Imaging is required to define the specific lesion and exclude additional abnormalities. Ocular masses may be equally well evaluated by US, CT or MRI, but associated extraocular abnormalities are better defined by MRI.

Disorders of shape and size

Colobomas Failure of normal globe development resulting in a defect in closure of the fetal optic stalk is termed a coloboma. This abnormality is inherited in an autosomal dominant pattern, and bilateral defects are common. Any portion of the globe may be involved; variable extension into the optic nerve may cause dilatation. Other CNS anomalies may be present. Most patients present in childhood with visual field defects, or with a 'keyhole' defect in the iris noted on clinical examination. Imaging demonstrates an elongated globe, occasionally with posteroinferior retinal cysts (Fig. 51.47).

Axial myopia/staphyloma Elongation of the anteroposterior diameter of the globe may be congenital or acquired. A history of

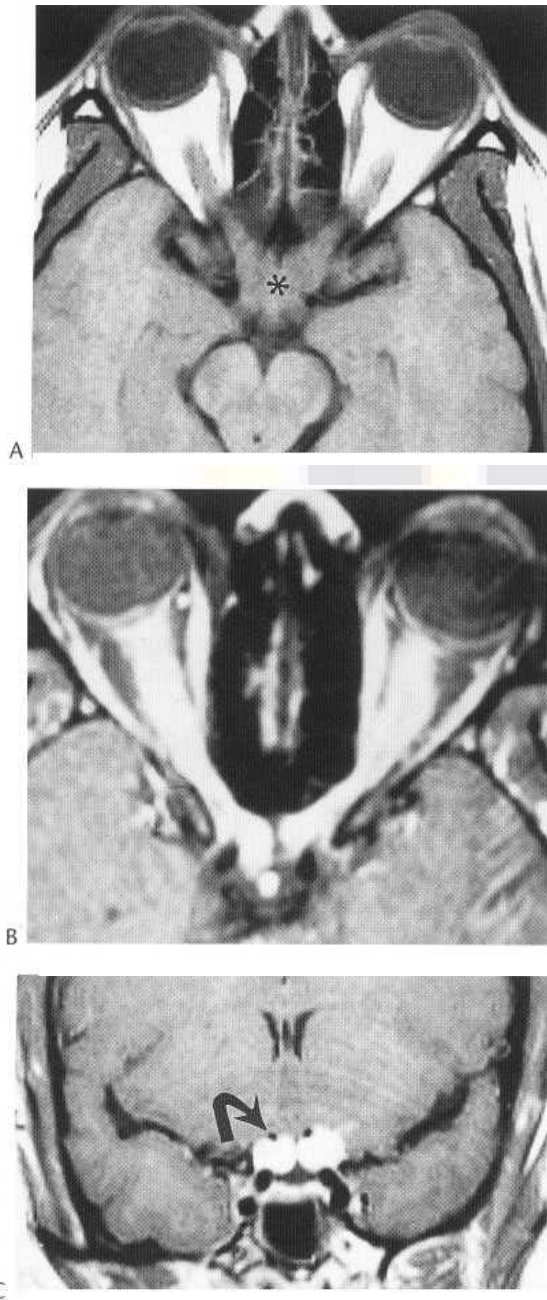


Fig. 51.46 Sarcoidosis. Axial T₁-weighted MR image (A) demonstrates thickening of optic nerves and chiasm (asterisk). Fat-saturated contrast-enhanced axial (B) and coronal T₁-weighted enhanced (C) images demonstrate marked enhancement of the optic nerves and chiasm.

parental myopia is highly associated with the development of juvenile onset myopia in children. These patients present with blurry vision. The underlying problem is a mismatch between the location of the focal zone produced by the cornea and lens, and the retina. Optometric correction is required. Imaging is rarely used in the evaluation unless additional clinical findings are noted. Elongation of the globe is seen, normally with a smooth contour. Focal bulges of the sclera may be found, and are termed staphylomas. These acquired defects are due to an area of focal thinning of the sclera.

Buphthalmos Defects in the pattern of flow of aqueous humour from the anterior chamber through the ciliary body result in increased intraocular pressure and congenital glaucoma. The

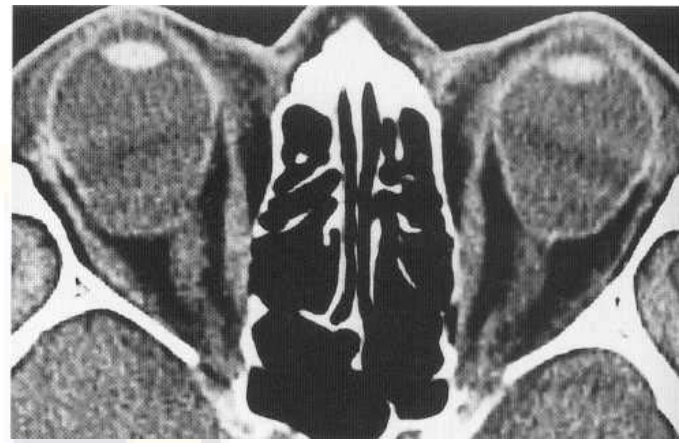


Fig. 51.47 Coloboma. Axial CT image demonstrates bilateral retinal defects with outpouching in the region of the optic nerve head.

globe is enlarged and poorly sensitive to light. The process is almost always bilateral. Differentiation from other causes of macrophthalmos with normal intraocular pressures is required. Clinical examination will usually confirm the diagnosis.

Micropthalmia Failure of the optic stalk to form properly may result in failure of induction and subsequent lack of identifiable external eye structures. The resultant disorganised tissue may be minimally evident, or result in a sizable cyst. Complete failure of development is rare. The bony orbit is generally small, but may be enlarged if a cyst is present. Identification of a lens and the ciliary mechanism differentiates an abnormal globe from an

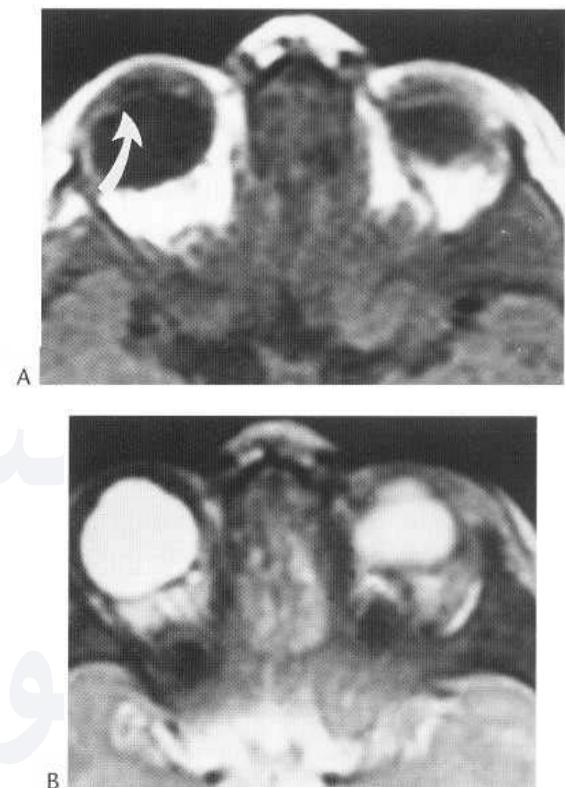


Fig. 51.48 Congenital absence of the lens. Axial T₁- (A) and T₂-weighted (B) MR images demonstrate bilaterally mis-shaped globes, with micropthalmia, on left. Lens is not visualised. Presence of the ciliary mechanism (arrow) differentiates congenital absence of the lens from ocular cyst in this case.



Fig. 51.49 Phthisis bulbi. CT image showing calcification of shrunken and irregularly thickened left globe.

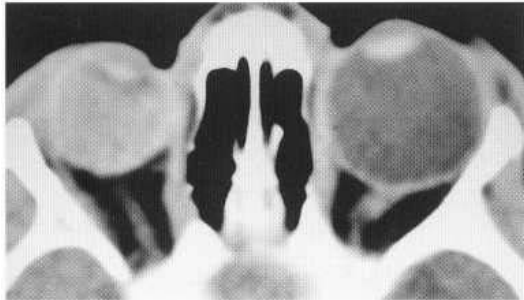


Fig. 51.50 Retrolental fibroplasia. Left globe is enlarged; there is right microphthalmos with abnormally increased attenuation throughout the posterior vitreous chamber.

ocular cyst (Fig. 51.48). There is a high association with genetic disorders and other CNS malformations.

Phthisis bulbi The end-result of many destructive orbital processes is a small, shrunken, misshapen globe that is insensitive to light. The sclera is thickened and redundant, with dense calcification. The imaging appearance is characteristic (Fig. 51.49).

Retinopathy of prematurity Retrolental fibroplasia occurs in premature infants with respiratory distress syndrome treated with high concentrations of inspired oxygen for prolonged periods of time. An asymmetric bilateral presentation is common. Globe atrophy or enlargement is seen, with or without retinal detachment. Retinal damage results in scarring and visual loss. Imaging demonstrates size abnormalities in globes of patients with appropriate histories (Fig. 51.50).

Ocular masses

Melanoma Melanomas arise from the choroid layer of the globe, and are the most common primary ocular malignancy of adults. African Americans are rarely affected. Most patients are older; childhood cases are uncommon. Patients present with decreased visual acuity, retinal detachment or ocular pain. Tumours may be classified as melanotic or amelanotic, although histological staining invariably demonstrates cytoplasmic melanin granules. Melanomas are highly invasive, and recurrence is common once extraocular spread develops. Metastases may happen early or after along disease-free interval, with hepatic, pulmonary, osseous and cutaneous secondary sites involved most often.

US typically shows a raised homogeneously echogenic focus along the posterior wall of the vitreous chamber ('collar button'). En plaque tumours also occur and are more difficult to identify.

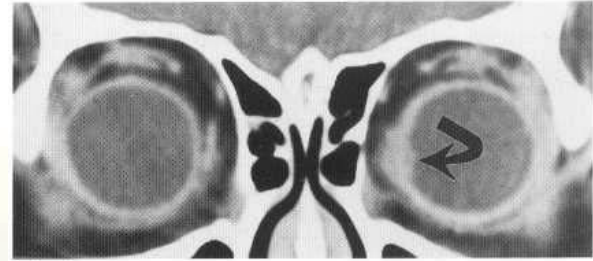


Fig. 51.51 Choroidal melanoma. Contrast-enhanced coronal CT image demonstrates enhancing lesion of the medial retina of the left eye with trans-scleral invasion (arrow). (Case courtesy of Orlando Ortiz, M.D.)

Less often, the majority of the globe may be involved. Retinal detachments are frequently noted, and may be haemorrhagic. Echogenic foci representing calcification are rare initially, but are common following treatment. Doppler imaging usually shows a low resistance flow pattern with little systolic/diastolic [change](#). US cannot evaluate the postseptal compartment well.

CT demonstrates a homogeneously dense soft-tissue mass extending into the vitreous cavity. Moderate enhancement is seen following contrast administration (Fig. 51.51). Extrascleral spread to the post-septal or perineural spaces is also well demonstrated. The MRI appearance is highly dependent on the amount of melanin pigment present. Melanotic tumours will be hyperintense on T₁-weighted sequences and hypointense on T₂-weighted sequences due to the paramagnetic effect of melanin (Fig. 51.52), while the amelanotic variety will be identical in signal characteristics to any other soft-tissue mass such as a metastasis. Contrast enhancement is typically marked, and as a result T₁-weighted postcontrast infusion thin section images are most sensitive for the presence of subtle lesions. MRI is also the procedure of choice for evaluation of trans-scleral and perineural spread.

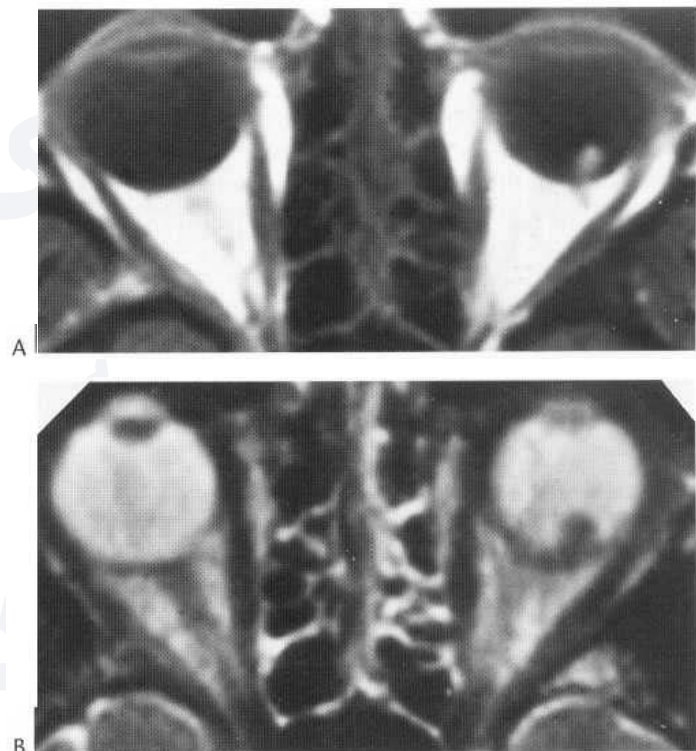


Fig. 51.52 Choroidal melanoma. T₁- (A) and T₂-weighted (B) MR images demonstrate well-circumscribed broad based lesion of posterior left retina. High signal intensity on T₁-weighted images and low signal intensity on T₂-weighted images is due to characteristic paramagnetic effect of melanin.

Metastases Secondary tumours of the globe are more common than primary malignancies in adults. Most patients have a known primary malignancy elsewhere, with breast, lung and renal primary sites accounting for the majority of such lesions. The choroid is usually affected due to the vascular pattern of spread of most tumours. Retinal detachments occur frequently, but associated haemorrhage is uncommon.

Both US and CT show a globular or polypoid mass extending into the vitreous cavity, sometimes associated with subretinal fluid and partial retinal detachment. Echogenicity and density are variable. Contrast enhancement on CT helps to differentiate tumour from associated effusions, when present. MRI signal patterns are non-specific, but MRI is better able to characterise the soft-tissue component.

Haemangiomas Although they are uncommon lesions, haemangiomas may occur within the globe. *Cavernous haemangiomas* affect the choroid layer, usually during adolescence. They are benign lesions which are histologically similar to the much more common intraorbital variety. Spontaneous haemorrhage or retinal detachments occur infrequently. There is a strong association with Sturge-Weber syndrome. Cavernous haemangiomas appear as soft-tissue masses on CT and MRI, often with marked [enhancement](#). [US](#) may be able to characterise them correctly by their Doppler flow pattern.

Capillary haemangiomas affect the retina; one-half of patients are known to have von Hippel-Lindau syndrome. They are histologically similar to cerebellar haemangiomas and may be bilateral or multiple in one-half of patients. Retinal detachments and haemorrhage are common, and are often the reason such patients seek ophthalmologic evaluation. US, CT and MRI demonstrate inhomogeneous soft-tissue masses of variable echogenicity, density and signal intensity, respectively, extending into the vitreous space. Enhancement is marked following contrast administration. Due to the associated haemorrhage, MRI signal intensity patterns can mimic melanotic melanoma quite closely.

Retinoblastoma Retinoblastoma is the most common intraocular malignancy in childhood. Most patients are diagnosed in early childhood due to the presence of an abnormal light reflex on fundoscopic examination (leucocoria). Alternatively, visual loss, strabismus or non-specific symptoms may be noted. Approximately one-third of patients present with bilateral tumours and a history of autosomal dominant inheritance. Rare cases of trilateral retinoblastoma demonstrate a concomitant primitive neuroectodermal tumour of the pineal region.

Retinoblastomas are highly malignant and aggressive primitive neuroectodermal tumours with frequent intraocular, trans-scleral or haematogenous spread. In the absence of dissemination, enucleation and radiation therapy may be curative, but extension into the vascular spaces of the orbit or to the subarachnoid space predicts a very poor prognosis. Recurrence rates are high; most patients present within 1 year of initial diagnosis and treatment with a recurrent enlarging intraorbital mass. Approximately one-fifth of successfully treated patients will develop a second neoplasm regionally, especially those treated with radiation therapy.

US demonstrates a highly echogenic mass with shadowing in the posterior globe, possibly with increased flow seen on Doppler imaging. CT is the diagnostic procedure of choice due to the dense calcification almost invariably observed within the retinal-based soft-tissue mass (Figs 51.53, 51.54). Only 10% of retinoblastomas lack calcification on CT. Any calcification seen within the globe on

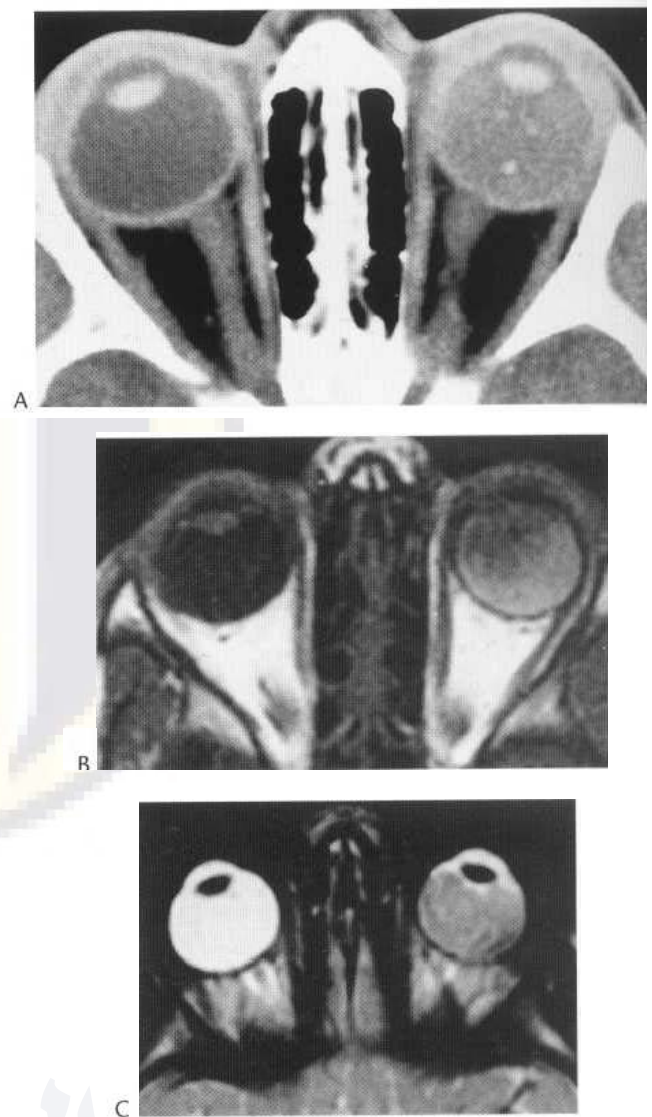


Fig. 51.53 Retinoblastoma. Non-contrast axial CT (A) demonstrates punctate foci of calcification within hyperdense left globe. Axial T₁-weighted (B) and T₂-weighted (C) MR images demonstrate full extent of large lesion within left globe. High signal intensity on T₁-weighted images, and low signal intensity on T₂-weighted images is consistent with the dense cellular nature of this tumour.

Fig. 51.54 Retinoblastoma. Non-contrast axial CT (A) demonstrates bilateral partially calcified intraocular masses. Enhanced image (B) demonstrates spread through sclera and into intraconal compartment (arrow), predicting poor prognosis.

CT scans in paediatric patients should be considered retinoblastoma until proven otherwise. MRI shows the tumour as mildly hyperintense to the extraocular muscles on T₁-weighted sequences, with increased signal intensity on T₂-weighted sequences. Gradient-echo sequences may show hypointensity within the mass due to the mag-

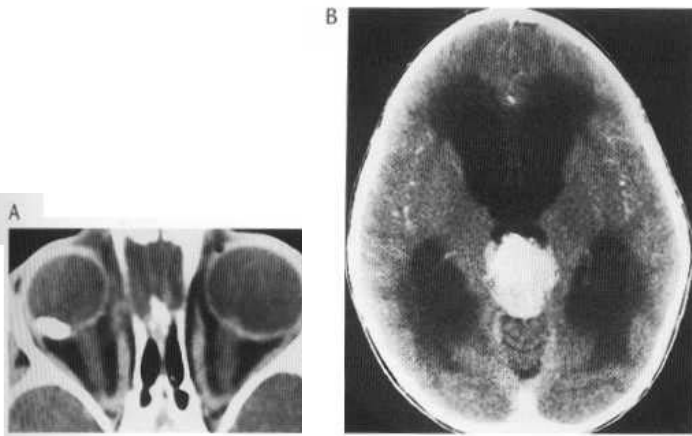


Fig. 51.55 Trilateral retinoblastoma. Enhanced axial CT image (A) demonstrates large lobular calcification based on right retina. A second, smaller, retinal lesion can be seen overlying the left optic nerve head. Axial image at higher level (B) demonstrates hydrocephalus due to large enhancing mass in the region of the posterior third ventricle/pineal cistern representing pineoblastoma.

netic susceptibility changes associated with calcifications. Marked enhancement of the non-calcified soft-tissue component occurs after contrast infusion.

Due to its improved sensitivity and multiplanar capability, MRI may be superior to CT in the evaluation of trans-scleral or perineural spread, and in the evaluation of the pineal region for additional masses (Fig. 51.55). However, the retinal calcifications so easily seen with CT are poorly noted on MRI, and these two examinations are often performed together.

Coats' disease Coats' disease, benign retinal telangiectasia, is generally associated with complete retinal detachment and massive subretinal exudates, resulting in unilateral leucocoria. No aetiological cause is identified. Males are most often affected, usually presenting between 6 and 8 years of age. Calcification is rare, allowing differentiation from retinoblastoma.

CT shows homogeneous increased density within the vitreous chamber, retinal detachment and lack of enhancement after contrast administration (Fig. 51.56). MRI demonstrates homogeneous hyperintense signal intensity on both T₁- and T₂-weighted sequences, again without enhancement following contrast infusion.

Persistent hyperplastic primary vitreous Persistent hyperplastic primary vitreous (PHPV) is the result of lack of regression of the embryonic hyaloid vascular system. These vessels are fragile and prone to haemorrhage. Affected children may present with leuco-

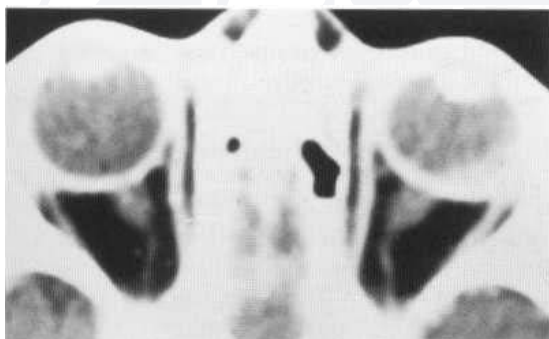


Fig. 51.56 Coats' disease. Contrast-enhanced CT demonstrates [hyperdensity in](#) posterior portion of left globe.



Fig. 51.57 Persistent hyperplastic primary vitreous. Non-contrast axial CT demonstrates hyperdensity throughout the posterior compartment of the right eye.

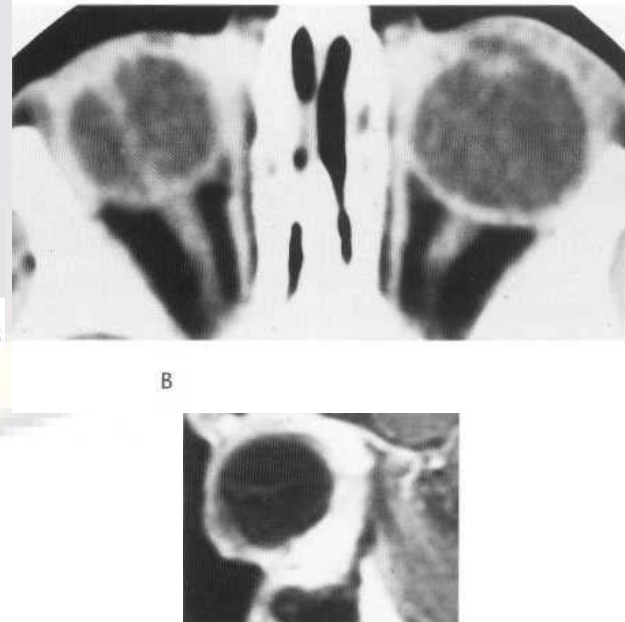


Fig. 51.58 Persistent hyperplastic primary vitreous. Axial CT (A) demonstrates central linear density within smaller right globe. Sagittal T₁-weighted MR (B) confirms finding of PHPV.

coria or following acute vitreous haemorrhage. Seizures, mental retardation and hearing loss may be associated. If bilateral, PHPV may be part of the diagnosis of Norrie's disease (congenital progressive oculoacoustic cerebral degeneration), an X-linked genetic disorder.

US, CT and MRI will all show a well-defined linear or triangular structure representing the persistent hyaloid artery extending from the lens to the optic disc (Figs 51.57, 51.58). The lens may be abnormally placed or shaped, and the globe may be small in severe forms. Vitreous haemorrhage may occur, but retinal detachments are uncommon. Enhancement of the fibrovascular pedicle may occur following contrast administration. Calcification is rare.

Infection

Toxocara canis Infection may present with leucocoria, often bilateral. Intracranial infection may also be present, possibly resulting in seizures. The infection results in a sclerosing endophthalmitis and replacement of the normal vitreous humour with a proteinaceous exudate and larval granulomas. The diagnosis is usually made on clinical grounds and confirmed by blood assays for *T. canis* antibodies. CT demonstrates a hyperdense vitreous

cavity, sometimes with retinal detachment. No enhancement is seen. MRI shows this process as increased T₁ and T₂ signal intensity within the vitreous humour.

Toxoplasma gondii The globe may be infected, with an imaging appearance almost identical to *T. canis*. Infection is thought to be acquired in utero or immediately postnatally, with few cases occurring later in life. It begins as a retinitis, with subsequent spread of the inflammatory changes into the vitreous chamber. Although usually self-limited, severe scarring of the retina may occur, resulting in a dense visual field defect. Multiple lesions occur more often in the immunocompromised patient, leading to progressive visual loss. Recurrence is also more common in this latter population.

Cytomegalovirus (CMV) Infection of the globe is the most common infection occurring in the immunocompromised patient. Immunocompetent patients are rarely infected. Symptoms of visual loss are due to proliferative haemorrhagic retinal exudates. Treatment with antiviral medications is usually successful. Blindness occurs if the infection is left untreated. CT findings are usually non-specific, with changes due to retinal haemorrhage. MRI findings may reflect the same process, but high-resolution

T₂-weighted images may show moderate retinal enhancement following contrast infusion. Concurrent CNS involvement may also be present and is best evaluated by MRI.

Ocular infection with syphilis, herpes virus, *Pneumocystis carinii* and human immunodeficiency virus may occur in the immunocompromised patient. Diagnosis is generally made on clinical grounds, or after vitreous aspiration and laboratory examination.

Optic nerve drusen

Optic nerve drusen are the most common causes of ocular calcification in adults. They represent deposits of hyaline material with secondary calcification, and are probably degenerative. Most patients will have a subtle visual field defect even though the site of the defect does not correlate with the location of the calcification. Drusen are usually found incidentally on imaging, and are often bilateral. There may be an inherited tendency to develop these lesions. Fundoscopic evaluations may confuse their appearance with true papilloedema. US and CT show a punctate calcification centred on the optic nerve head (Fig. 51.59).

Orbital implants

A wide range of materials and constructs may be found within the orbit as replacements for the globe after enucleation. Glass or

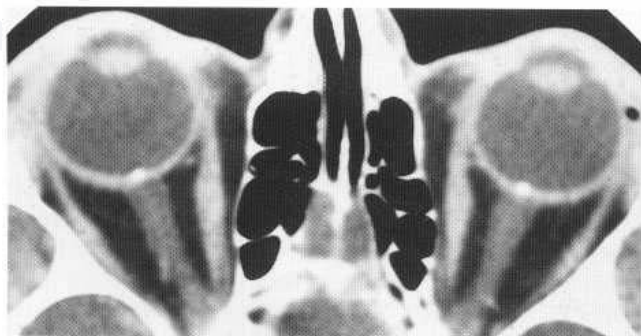


Fig. 51.59 Drusen. CT shows bilateral punctate calcifications, located centrally over the optic nerve head.

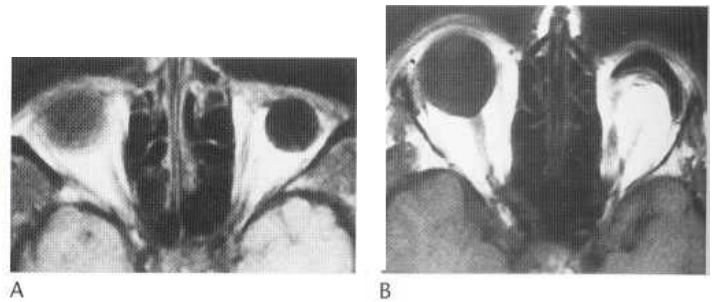


Fig. 51.60 (A,B) Ocular prosthesis. Axial T₁-weighted images demonstrate left ocular prostheses in two different patients.

plastic spheres or shields may be used in this role. They are generally all hyperdense on CT, and demonstrate signal void on MRI (Fig. 51.60). The exception to this pattern is the integrated hydroxyapatite implant made of denatured coral. This implant has an improved cosmetic appearance and mobility because the extraocular muscles may be directly surgically attached to the implant. Successful integration of the implant occurs due to fibrovascular growth. Assessment of implant acceptance may be demonstrated by uptake of nuclear medicine bone scan tracers or by enhancement on T₁-weighted MRI studies.

Lacrimal gland masses

The lacrimal gland is a minor salivary gland and therefore demonstrates pathology similar to salivary glands found elsewhere in the head and neck. One-half of all lacrimal gland disorders are due to epithelial tumours, of which one-half are benign. The remainder of the processes that affect the gland are inflammatory or lymphoid in origin. Patients present with a superolateral orbit mass, inferomedial proptosis, or a dry eye. The fascial planes surrounding the gland within the lacrimal fossa provide a resistant barrier to the spread of pathology from this area. Abnormalities of the lacrimal gland are the most common primary extraconal masses.

Benign tumours Benign mixed-cell tumours (*pleomorphic adenoma*) are well-defined homogeneous soft-tissue masses of the deep lobe that distort the remainder of the gland and may cause minor remodelling of the adjacent bony wall. Distortion of the adjacent globe may also be present, but is usually minor. They grow slowly and are often present for 1 or 2 years before the patient seeks clinical attention. Calcification is infrequently seen. Enhancement is mild and variable on both CT and MRI. Treatment is surgical removal of the entire gland. Recurrence is uncommon. Malignant transformation may rarely occur in patients with benign disease who remain untreated for extended periods of time.

Dermoid and *epidermoid tumours* may also occur within the lacrimal fossa, and result in proptosis. These benign tumours are well defined and encapsulated, and are typically homogeneous and non-enhancing. CT may show density approaching that of fat (Fig. 51.34), while MRI may demonstrate hypointense T₁ and hyperintense T₂ signal intensity relative to the normal intra-orbital fat. *Epithelial cysts* may occur within the lacrimal gland, but are uncommon. CT density and MRI signal intensity parallel water, although partial volume averaging may interfere with direct measurements (Fig. 51.61).

Malignancy *Carcinomas* present with an accelerated clinical course. Adenoid cystic carcinoma is the most common malignancy of the lacrimal gland, and middle-aged females are most frequently



Fig. 51.61 Lacrimal gland cyst. Axial CT image demonstrates non-enhancing cystic lesion lateral to the globe in upper outer quadrant of left orbit.



A



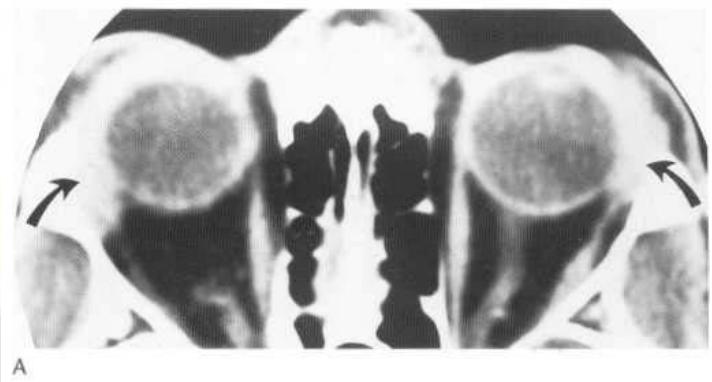
B

Fig. 51.62 Adenoid cystic carcinoma. Axial T₁-weighted (A) and T₂-weighted fat-saturated (B) MR images demonstrate enlargement of the posterior lobe of the left lacrimal gland by heterogeneously enhancing lesion. Note adjacent remodelling of sphenoid bone, indicating longstanding presence of lesion.

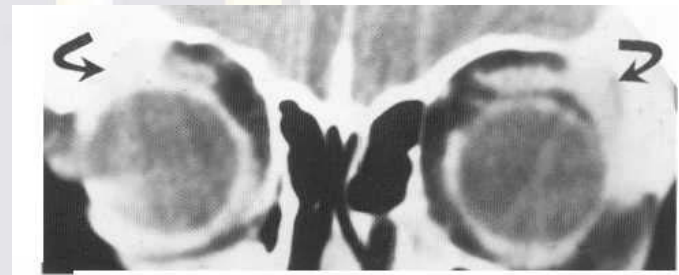
affected. Spread to the adjacent lateral rectus muscle or globe may result in pain or restriction of motion. Erosion of the lateral wall of the orbit may be seen on plain film or CT (Fig. 51.62). CT and MRI demonstrate a poorly defined inhomogeneous soft-tissue mass, often with marked focal enhancement. Spread of tumour along muscles and nerves is characteristic, and predicts a poor prognosis. Recurrence is common following surgical removal.

Inflammatory masses Inflammatory and lymphoid masses of the lacrimal gland constitute a diverse and overlapping group of disorders. Most patients are of late middle age, and often present with dry eyes due to diminished gland function, or with painless proptosis of less than 1 year's duration. Bilateral involvement is common.

The lacrimal gland has true lymphoid tissue within it, and therefore may harbour primary lymphoma, usually of the non-Hodgkin's type (Fig. 51.20). Pseudolymphoma or reactive lymphomatoid hyperplasia may also occur. Both masses are soft and tend to conform to the orbit wall and globe: they rarely result in bony



A



B

Fig. 51.63 Sarcoidosis. Axial (A) and coronal (B) T₁-weighted images demonstrate prominent bilateral enhancement of lacrimal glands (arrows).



A



B



C

Fig. 51.64 Squamous-cell carcinoma of lacrimal sac. Axial (A) and coronal (B) CT scans demonstrate a large enhancing mass in the inferomedial portion of the left orbit. There is proptosis and lateral deviation of the left globe. Bone windows (C) demonstrate destruction of medial orbital wall and nasolacrimal duct canal. Normal bony canal is seen on right (arrow).

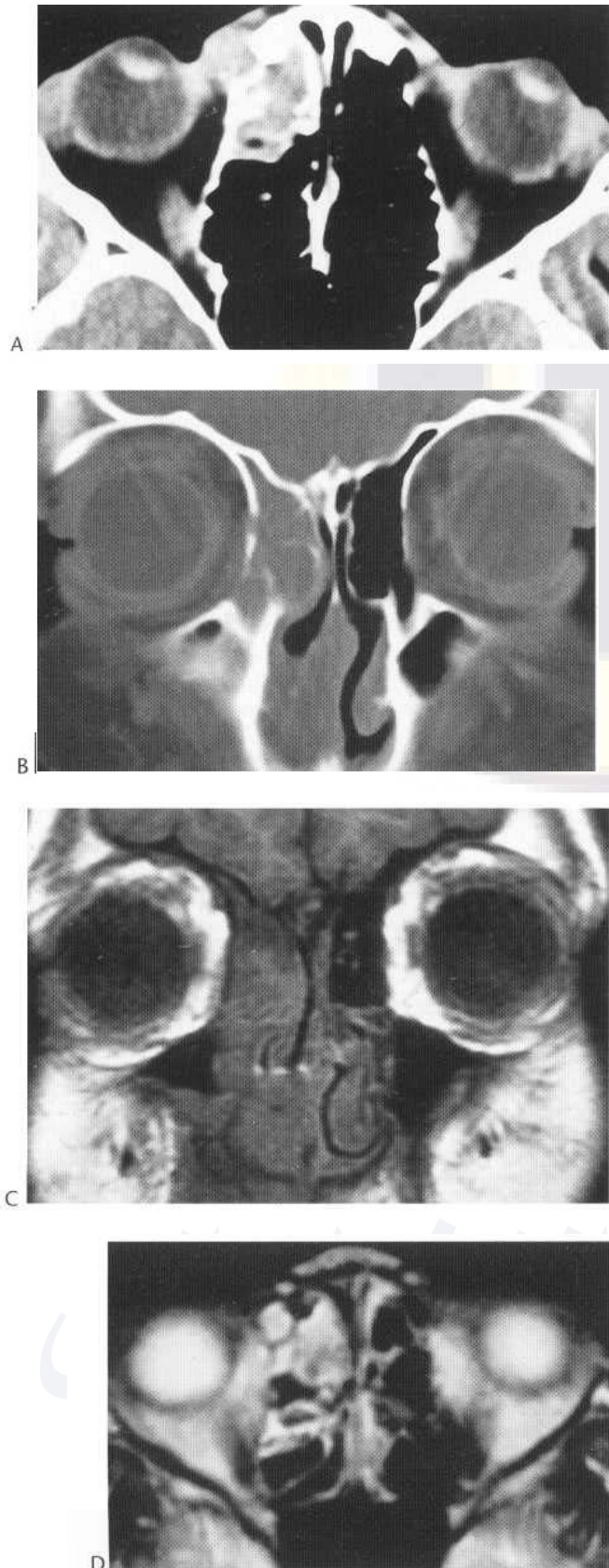


Fig. 51.65 Nasolacrimal lymphoma. Enhanced axial (A) and coronal (B) CT images demonstrate right ethmoid mass extending to the lacrimal sac in the region of the right medial canthus. Non-enhanced coronal T_1 -weighted MR image (C) shows extensive involvement of right ethmoids and right nasal cavity; axial T_2 -weighted MR image (D) shows abnormal increased signal in right anterior ethmoid region.

destruction or marked proptosis. They are difficult to differentiate radiographically and pathologically.

Dacryoadenitis This may be seen as a result of numerous processes such as sarcoidosis (Fig. 51.63), Graves' disease, Sjogren's syndrome, inflammatory pseudotumour, or following radiation therapy for regional malignancies. Rarely, infection may also affect the lacrimal gland. Most causes of dacryoadenitis result in a non-specific homogeneously enlarged appearance of the gland, with significant enhancement seen only with Sjogren's syndrome or subacutely following radiation therapy treatment. CT and MRI are employed to define the location and extent of the clinically suspected mass, with particular attention directed to features suggesting invasion and extraorbital extension.

Lacrimal drainage apparatus

The nasolacrimal drainage system is responsible for the removal of excess fluid from the preseptal space. Patients with abnormality of the nasolacrimal system present with tearing (epiphora), commonly with cellulitis and swelling. A mucocele may occur in infants due to embryologic failure of canalisation of a valve in the distal nasolacrimal duct. Cross-sectional imaging is performed to evaluate postseptal extension of infection, rather than the primary diagnosis of infection itself. Dacryocystography is employed to define the lacrimal sac and nasolacrimal duct system anatomically in a search for sites of stenosis or obstruction (Fig. 51.2). Treatment may consist of cannulation of the nasolacrimal duct with dilatation and stenting, rather than surgery, although recurrent symptoms due to restenosis are common. Using helical CT, topical administration of contrast media into the eye, with rapid-sequence cross-sectional imaging and retrospective sagittal and coronal reconstructions, may be used to image the drainage apparatus non-invasively.

Primary or secondary involvement by malignancies is uncommon. Squamous-cell carcinoma is the most frequent primary tumour of this area (Fig. 51.64), although basal-cell carcinoma has also been reported. Lymphoma is rare (Fig. 51.65). Spread to the medial canthus from sinonasal tumours may also occur. Malignant features are often apparent clinically, with bone destruction and invasion seen on CT and MRI.

REFERENCES AND SUGGESTIONS FOR FURTHER READING

- Azar-Kia, B., Mafee, M. F., Horowitz, S. W., Fine, M., Raofi, B. (1988) CT and MRI of the optic nerve and sheath. *Seminars in Ultrasound, CT and MR*, 9, 443-454.
- Beck, R. W., Arrington, J., Murtaugh, F. R., Cleary, P. A., Kaufman, D. I. (1993) Optic Neuritis Study Group. Brain magnetic resonance imaging in acute optic neuritis, experience of the Optic Neuritis Study Group. *Archives of Neurology*, 50, 841-846.
- Belden, C. J., Abbitt, P. L., Beadles, K. A. (1995) Color Doppler US of the orbit. *Radiographics*, 15, 589-608.
- Bilaniuk, L. T., Farber, M. (1992) Imaging of developmental anomalies of the eye and orbit. *American Journal of Neuroradiology*, 13, 793-803.
- Bond, J. B., Haik, B. G., Taveras, J. L., et al (1992) Magnetic resonance imaging of orbital lymphangioma with and without gadolinium contrast enhancement. *Journal of Ophthalmology*, 99, 1318-1324.
- Burns, B. J., McHugh, K., McDowell, I. P., et al (2001) Localized paediatric orbital rhabdomyosarcoma: influence of imaging on treatment. *Clinical Radiology*, 56, 959-964.
- Campbell, W. (1964) The radiology of the lacrimal system. *British Journal of Radiology*, 37, 1.

- Carmody, R. F., Mafec, M. F., Goddwin, J. A., Small, K., Hacry, C. (1994) Orbital and optic pathway sarcoidosis: MR Findings. *American Journal of Neuroradiology*, 15, 775-783.
- Dalley, R. W., Robertson, W. D., Rootman, J. (1989) Globe tenting: a sign of increased orbital tension. *American Journal of Neuroradiology*, 10, 181-186.
- De Potter, P., Shields, O. L., Shields, J. A., Flanders, A. E., Rao, V. M. (1992) Role of magnetic resonance imaging in the evaluation of the hydroxyapatite orbital implant. *Journal of Ophthalmology*, 99, 824-830.
- Depper, M. H., Truweit, O. L., Dreishach, J. N., Kelly, W. M. (1993) Isolated abducens nerve palsy: MR imaging findings. *American Journal of Radiology*, 160, 837-841.
- Dervin, J. E., Beaconsfield, M., Wright, J. E., Moseley, I. F. (1989) CT findings in orbital tumours of nerve sheath origin. *Clinical Radiology*, 40, 475-479.
- de Smet, M. D., Nussenbatt, R. B. (1991) Ocular manifestations of AIDS. *JAMA*, 266, 3019-3022.
- Etherington, R. J., Hourain, M. D. (1989) Localisation of intraocular and intraorbital foreign bodies using computed tomography. *Clinical Radiology*, 40, 610-614.
- Flanders, A. F., Mafee, M. F., Rao, V. M., Choi, K. H. (1989) CT characteristics of orbital pseudotumors and other orbital inflammatory processes. *Journal of Computer Assisted Tomography*, 13, 40-47.
- Font, R. L., Patipa, M., Rosenbaum, P. S., Smith, S., Berg, L. (1990) Correlation of computed tomographic and histopathologic features in malignant transformation of benign mixed cell tumor of the lacrimal gland. *Surveys of Ophthalmology*, 34, 449-452.
- Friedman, D. P., Rao, V. M., Flanders, A. E. (1993) Lesions causing a mass in the medial canthus of the orbit: CT and MRI features. *American Journal of Radiology*, 160, 1095-1099.
- Froula, P. D., Bartley, G. B., Garrity, J. A., Forbes, G. (1993) The differential diagnosis of orbital calcifications as detected on computed tomographic scans. *Mayo Clinic Proceedings*, 68, 256-261.
- Gibby, W. A., Cohen, M. S., Goldberg, H. I., Sergott, R. C. (1993) Pseudotumor cerebri: CT findings and correlation with visual loss. *American Journal of Radiology*, 160, 143-146.
- Glover, A. T., Grove, A. S. (1989) Orbital invasion by malignant eyelid tumors. *Journal of Ophthalmological, Plastic and Reconstructive Surgery*, 5, 1-12.
- Goldberg, R. A., Hannani, K., Toga, A. W. (1992) Microanatomy of the orbital apex. computed tomography and microcryoplaning of soft and hard tissue. *Journal of Ophthalmology*, 99, 1447-1452.
- Hanafee, W. N. (1972) Orbital venography. *Radiologic Clinics of North America*, 10, 63.
- Handler, L. C., Davey, I. C., Hill, J. C., Laurysse, C. (1991) The acute orbit: differentiation of orbital cellulitis from subperiosteal abscess by computed tomography. *Journal of Neuroradiology*, 33, 15-18.
- Hart, B. L., Spar, J. A., Orrison, W. W. (1992) Calcification of the trochlear apparatus of the orbit: CT appearance and association with diabetes and age. *American Journal of Neuroradiology*, 159, 1291-1294.
- Hayman, L. A., Maturi, K. K., Pflieger, M. I., et al (1995) MR imaging of the eyelids: normal and pathologic findings. *American Journal of Radiology*, 165, 639-644.
- Hilborn, M. D., Munk, P. L., Lin, D. T. C., Vellet, A. D., Poon, P. Y. (1993) Sonography of ocular choroidal melanomas. *American Journal of Radiology*, 161, 1253-1257.
- Hopper, K. D., Sherman, J. L., Boal, D. K., Egli, K. D. (1992) CT and MR imaging of the pediatric orbit. *Radiographics*, 12, 485-503.
- Hoslen, N., Sander, B., Cordes, M., Schubert, C. J., Schorner, W., Felix, R. (1989) Graves' ophthalmopathy: MR imaging of the orbits. *Radiology*, 172, 759-762.
- Ilankov, V., Hadley, D., Moos, K., et al (1991) A comparison of imaging techniques with surgical experience in orbital injuries, a prospective study. *Journal of Cranio-Maxillo-Facial Surgery*, 19, 348-352.
- Lines, R. K., Hoyt, W. F. (1991) Magnetic resonance imaging signs of optic nerve gliomas in neurofibromatosis 1. *American Journal of Ophthalmology*, 111, 729-734.
- Ischemic Optic Neuropathy Decompression Trial Research Group (1995) Optic nerve decompression surgery for nonarteritic anterior ischemic optic neuropathy (NAION) is not effective and may be harmful. *JAMA*, 273, 625-632.
- Jenkins, J. R. (1987) Optic hydrops: isolated nerve sheath dilation demonstrated by CT. *American Journal of Neuroradiology*, 8, 867-870.
- Klucznik, R. P., Carrier, D. A., Pyka, R., Haid, R. W. (1993) Placement of a ferromagnetic intracerebral aneurysm clip in a magnetic field with a fatal outcome. *Radiology*, 187, 855-856.
- Lorigan, J. G., Wallace, S., Mavligit, G. M. (1991) The prevalence and location of metastases from ocular melanoma: imaging study in 110 patients. *American Journal of Radiology*, 157, 1279-1281.
- McNicholas, M. M. J., Brophy, D. P., Power, W. J., Griffin, J. F. (1995) Ocular trauma: evaluation with US. *Radiology*, 195, 423-427.
- McNicholas, M. M. J., Power, W. J., Griffin, J. F. (1991) Idiopathic inflammatory pseudotumour of the orbit: CT features correlated with clinical outcome. *Clinical Radiology*, 44, 3-7.
- McNicholas, M. M. J., Power, W. J., Griffin, J. F. (1994) Sonography in optic disk drusen: imaging findings and role in diagnosis when fundoscopic findings are normal. *American Journal of Radiology*, 162, 161-163.
- Mark, A. S., Blake, P., Kolsky, M. (1993) MRI evaluation of the third nerve. *MRI Decisions*, Mar/Apr, 23-31.
- Mihara, F., Gupta, K. L., Murayama, S., Lee, N., Bond, J. B., Haik, B. G. (1991) MR imaging of malignant uveal melanoma: role of pulse sequence and contrast agent. *American Journal of Neuroradiology*, 12, 991-996.
- Mills, P., Parsons, C. A. (1989) Primary orbital lymphoma: staging by computed tomographic scanning. *British Journal of Radiology*, 62, 287-289.
- Moran, C. C., Buckwalter, K., Caldemeyer, K. S., Smith, R. R. (1995) Helical CT with topical water-soluble contrast media for imaging of the lacrimal drainage apparatus. *American Journal of Radiology*, 164, 995-996.
- Munk, P. L., Vellet, A. D., Levin, M., Lin, D. T. C., Collyer, R. T. (1991) Sonography of the eye. *American Journal of Radiology*, 157, 1079-1086.
- Novelline, R. A., Leibig, T., Jordan, F., Bilyk, J. R., Rubin, P. A. D. (1994) Computed tomography of ocular trauma. *Journal of the American Society of Emergency Radiologists*, 1, 56-67.
- Nugent, R. A., Belkin, R. L., Neigel, J. M., et al (1990) Graves' orbitopathy: correlation of CT and clinical findings. *Radiology*, 177, 675-682.
- Nussenbatt, R. B., Belfort, R. (1994) Ocular toxoplasmosis: an old disease revisited. *JAMA*, 271, 304-307.
- Ohnishi, T., Noguchi, S., Murakami, N., et al (1994) Extraocular muscles in Graves' ophthalmopathy: usefulness of T2 relaxation time measurements. *Radiology*, 190, 857-862.
- Shellock, F. G., Morisoli, S., Kanal, E. (1993) MR procedures and biomedical implants, materials and devices: 1993 update. *Radiology*, 189, 587-599.
- Song, H., Ahn, H., Park, C., Kwon, S., Kim, C., Choi, K. (1993) Complete obstruction of the nasolacrimal system. Part I. Treatment with balloon dilation. *Radiology*, 186, 367-371.
- Song, H., Jin, Y., Kim, J., Sung, K., Han, Y., Cho, N. (1994) Nasolacrimal duct obstruction treated non-surgically with the use of plastic stents. *Radiology*, 190, 535-539.
- Templeton, P. A., Rao, K. C. V. G. (1987) Computed tomography of *Toxocara* (anis) endophthalmitis. *Journal of Computer Assisted Tomography*, 11, 99-101.
- Tien, R. D., Chu, P. K., Hesselink, J. R., Szumowski, J. (1991) Intra and paraorbital lesions: value of fat-suppression MR imaging with paramagnetic contrast enhancement. *American Journal of Neuroradiology*, 12, 245-253.
- Tonami, H., Yamamoto, I., Matsuda, M., et al (1991) Orbital fractures: surface coil MR imaging. *Radiology*, 179, 789-794.
- Westcott, S., Garner, A., Moseley, I. F., Wright, J. E. (1991) Orbital lymphoma versus reactive lymphoid hyperplasia: an analysis of the use of computed tomography in the differential diagnosis. *British Journal of Ophthalmology*, 78, 722-725.
- Young, W. C., Thornton, A. F., Gebarski, S. S., Cornblath, W. T. (1992) Radiation-induced optic neuropathy: correlation of MR imaging and radiation dosimetry. *Radiology*, 185, 904-907.
- Zadnik, K., Satariano, W. A., Mutti, D. O., Sholtz, R. I., Adams, A. J. (1994) The effect of parental history of myopia on children's eye size. *JAMA*, 271, 1323-1327.



نشر الکترونیکی
موسسه انتشاراتی
نوردانش

52

THE PETROUS TEMPORAL BONE

Peter D. Phelps

The petrous temporal bone is a complex structure with tiny bony objects such as the crura of the stapes and canals like the vestibular aqueduct which are less than 1 mm in diameter. These are close to the limits of resolution by imaging. Thus the best possible spatial resolution is essential and discrimination of 24 line pairs per centimetre can be achieved on the latest CT scanners. This imaging is mostly by CT, for showing bone detail, and MRI, for the inner ear and its central connections. Conventional angiography has been almost entirely replaced by MR angiography or contrast CT angiography. Metabolic imaging such as FDG-PET is being used to overcome the problem of distinguishing recurrent tumour from radiation damage. Isotope studies have an occasional role to assess activity in malignant otitis externa.

Imaging techniques

Plain radiography of the temporal bone

Plain mastoid views are now almost entirely obsolete except for postoperative assessment of the position of a cochlear implant electrode array in the inner ear. For this either the Stenver's or the perorbital view may be used.

Oblique posteroanterior (Stenver's) view In this view, the whole length of the petrous bone is demonstrated by placing it parallel to the X-ray film with the incident ray passing at right angles to it. With the radiographic baseline horizontal, the sagittal plane of the skull is rotated through 35° and tilted 15° away from the side to be examined. The incident ray is inclined at an angle of 12° cranially and is centred on a point 2 cm medial to the tip of the mastoid process. A radiograph in Stenver's position should demonstrate the petrous tip and internal auditory meatus (IAM), the semicircular canals (superior and lateral), the middle ear cleft, the mastoid antrum and the mastoid process (Fig. 52.1).

Perorbital view This is the best view of the IAM if tomography is unavailable; it should be done in the postero-anterior position to reduce radiation to the eyes. The orbitomeatal line is at right angles to the film. The tube is angled 5–10° caudally, centring between the orbits. The petrous pyramids and IAM are thus projected through the orbits (Fig. 52.2).

Coronal sections by CT to show the state of the bony outlines of the IAMs as a screening test for acoustic neuroma have also

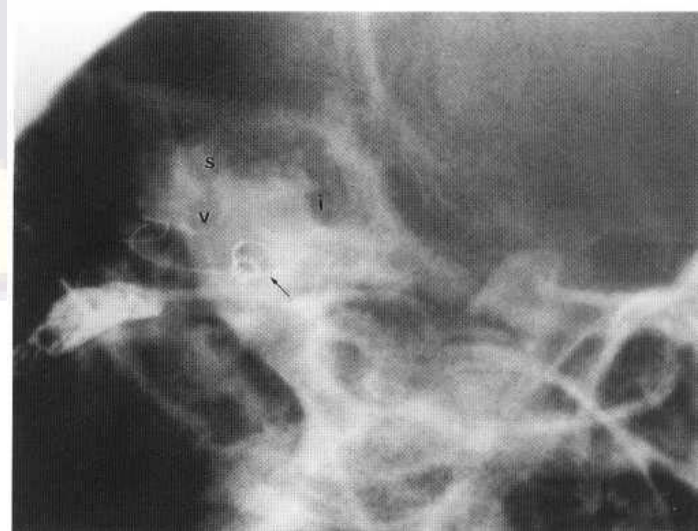


Fig. 52.1 Stenver's view of the petrous temporal bone with an extended electrode array in the first and second coils of the cochlea. v = vestibule; s = superior semicircular canal; i = internal auditory meatus.

become obsolete as MRI is now available for exclusion of acoustic neuroma in all suspected cases.

Computed tomography

The ability of CT to show intracranial lesions has been its first and most important contribution to diagnostic imaging. For the otologist this is the demonstration of intracranial complications of suppurative ear disease, such as brain abscess, and the intracranial extension of tumours of the petrous temporal bone, such as glomus and acoustic neuroma. Normal brain scan techniques with contrast enhancement are required. In the high-resolution mode CT can be used for the study of the middle and inner ears. Thin sections, 1 mm thick, are viewed on a wide window setting of 3000 or 4000 HU. Contrast enhancement is almost never used if lesions are confined to the petrous pyramid.

The routine CT examination of the petrous temporal bone begins with a lateral scout view showing the sections required for the examination in the axial plane (Fig. 52.3). This is the natural plane for CT and the most comfortable for the patient. It also gives the maximum information regarding the middle and inner ears, especially the coils

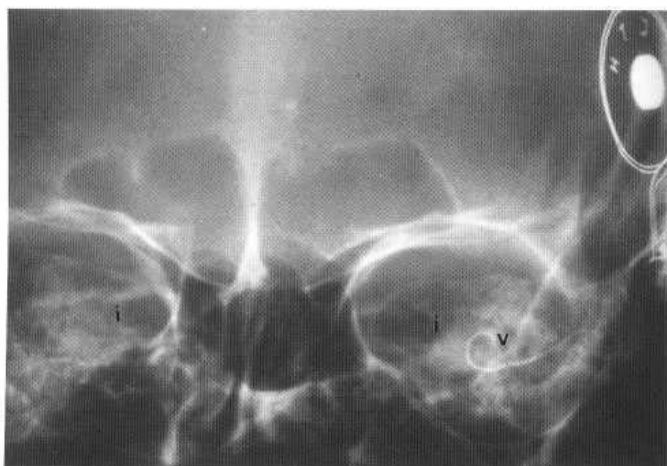


Fig. 52.2 Periorbital view showing an electrode array in the basal cochlear coil. There is extensive pneumatization to the petrous apex. v = vestibule; i = internal auditory meatus.

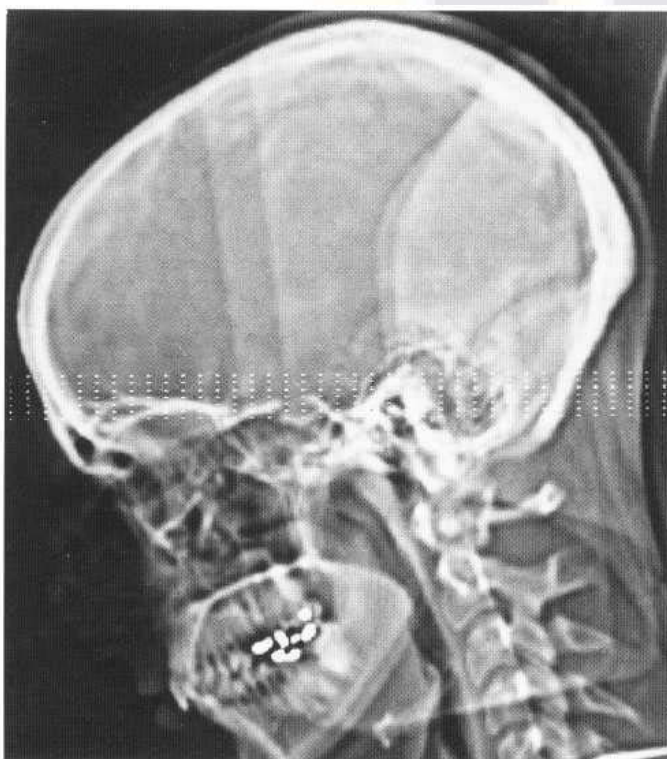


Fig. 52.3 The sections for a routine axial CT examination of the temporal bone shown on a sagittal scout view.

of the cochlea. The plane is not strictly speaking a true axial but a plane at 30° to the radiographic baseline, which is the orbitomeatal line drawn from the centre of the external meatus to the outer canthus of the eye. This is to limit the radiation dose to the eye although some sections will pass through the orbit, the centre of the globe is not in the direct X-ray beam. The pictures are viewed on a wide window setting of 4000 HU using the bone algorithm.

Sections in the axial plane start just below the external auditory meatus and show the basal turn of cochlea and round window niche: midmodiolar sections show the individual coils of the cochlea and incudostapedial region; the section through the vestibule and loop of the lateral semicircular canal, at right angles to each other. Sections at the level of the vestibule best show the IAM. The head of the malleus

and body and short process of incus are also shown at this level. The three parts of the facial nerve canal can be identified, although the base plane is least satisfactory for the descending portion, which is seen in cross-section behind the middle ear cavity. The most important cochlear and vestibular sections in axial and coronal planes are illustrated in Figure 52.4. Other important features in the axial plane are the round window niche and the pyramid on the posterior wall of the middle ear and the jugular fossa (Fig. 52.5).

Coronal sections (Fig. 52.6) begin at the level of the carotid canal and curl of the central bony spiral of the cochlea; the malleus is well shown at this level. Further back the section at the level of the vestibule shows the internal auditory meatus as well as the stapes and oval window. Further back still, at the most prominent part of the lateral semicircular canal, the pyramidal eminence is shown between facial recess and sinus tympani. The descending facial canal and jugular fossa are assessed and the examination finishes at the posterior semicircular canal, although further sections may be necessary to show the mastoid air cells.

Reformatted images

These can be obtained from multiple thin contiguous axial sections (Fig. 52.7). Reformatted images can be made in any plane but the quality is always inferior to a direct examination and depends on two factors:

1. The number of sections and therefore the amount of raw data available for the reconstruction process
2. Absolute immobility of the patient while these sections are being obtained, although this is less of a problem with the new very fast scanners.

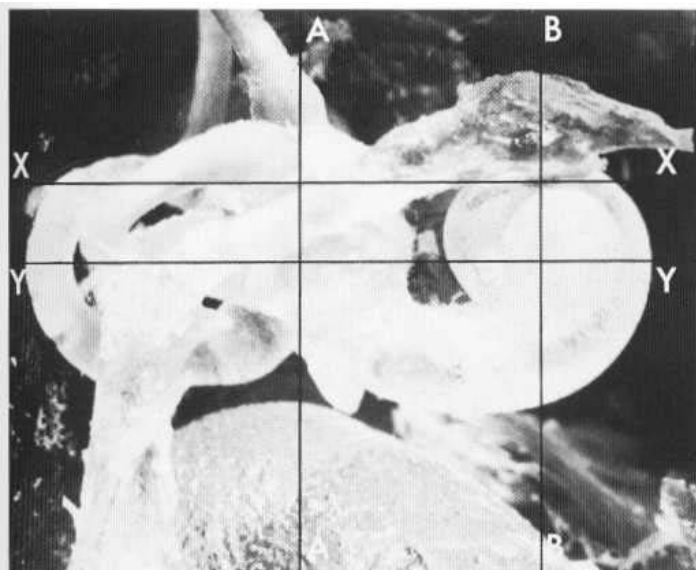
Magnetic resonance imaging

Sectional magnetic resonance pictures in the region of the skull base are a valuable adjunct to CT, provided suitable scanning parameters are chosen to produce optimum signal strength and contrast and to enable lesions to be distinguished from surrounding structures. Bone produces a negligible signal on MR scans, and so both the bone of the petromastoid and the air in the middle ear cleft and mastoid cell system appear as black areas, devoid of any of the bone detail so well demonstrated by high-resolution CT. Thus, only soft-tissue structures within the petrous temporal bone are imaged and this can be an advantage for the demonstration of the cranial nerves passing through the skull base, as the nerve itself will be shown, and not the canal in which it lies.

In contrast to the absence of signal from compact bone, T_1 -weighted images give an intense signal from yellow bone marrow with its high fat content, especially in the petrous apex (Fig. 52.8). Cerebrospinal fluid and the labyrinthine fluids have low signal intensity on T_1 -weighted spin-echo sequences and high signal on T_2 . Flowing blood gives no signal and thus blood vessels normally appear black.

Formerly a standard investigation usually used T_1 - and T_2 -weighted protocols. The T_1 images show better spatial resolution. The T_2 images show poorer spatial resolution and take longer. but there is higher signal from water-containing soft tissues. Thus cysts are particularly well shown, but also tumours, as neoplasms usually have a higher than normal water content.

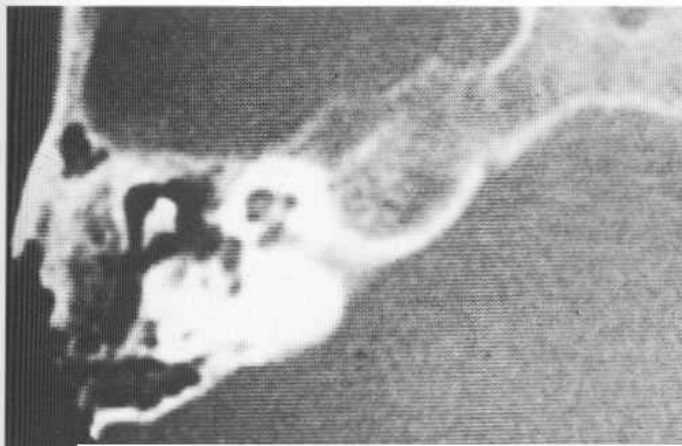
Contrast enhancement using the paramagnetic agent gadolinium DTPA is used with a T_1 protocol and most tumours show a significant



52.4A



52.4B1



52.4B2



52.4C1



52.4C2

Fig. 52.4 The four most important sections in the study of the petrous temporal bone by CT: the cochlear and vestibular cuts in both coronal and axial planes. (A) The position of these cuts is shown on a cast of the labyrinth of the inner ear viewed from the lateral aspect. (B) Axial plane. (C) Coronal plane. The internal auditory meatus and oval window are well shown in both planes.

Gadolinium-enhanced T₁-weighted images of the labyrinthine fluids in labyrinthitis or of the intratemporal facial nerve in Bell's palsy can also be shown (Fig. 52.11).

Angiography

Angiography now has only a very limited place in the investigation of lesions of the petrous temporal bone, as its traditional role for vascular anomalies and tumours has been largely superseded by CT and MR. The extent of glomus tumours is better shown by MRI, although angiography may be required to show the detailed blood supply of large tumours. Angiography is therefore used rarely as a diagnostic procedure, but more as a preoperative assessment for glomus jugulare tumours, when it can be combined with therapeutic embolisation to reduce operative bleeding from large tumours.

Aneurysms and vascular malformations obviously need selective angiography for their full assessment, although they can be shown initially by MRI. Likewise an *aberrant carotid artery* should be apparent on the CT examination, although confirmation by angiography is almost always sought.

degree of enhancement: this became the definitive investigation for acoustic neuromas. Now, however, the latest MR scanners using either spin-echo or gradient-echo 3DFT constructive interference in steady state (CISS) can produce thin section T₁-weighted images for the study of the inner ear and its central connections (Fig. 52.9).

The cranial nerves are demonstrated in the IAM and cerebello-pontine angle against the high signal from cerebrospinal fluid and the fluids in the labyrinth of the inner ear (Fig. 52.10).

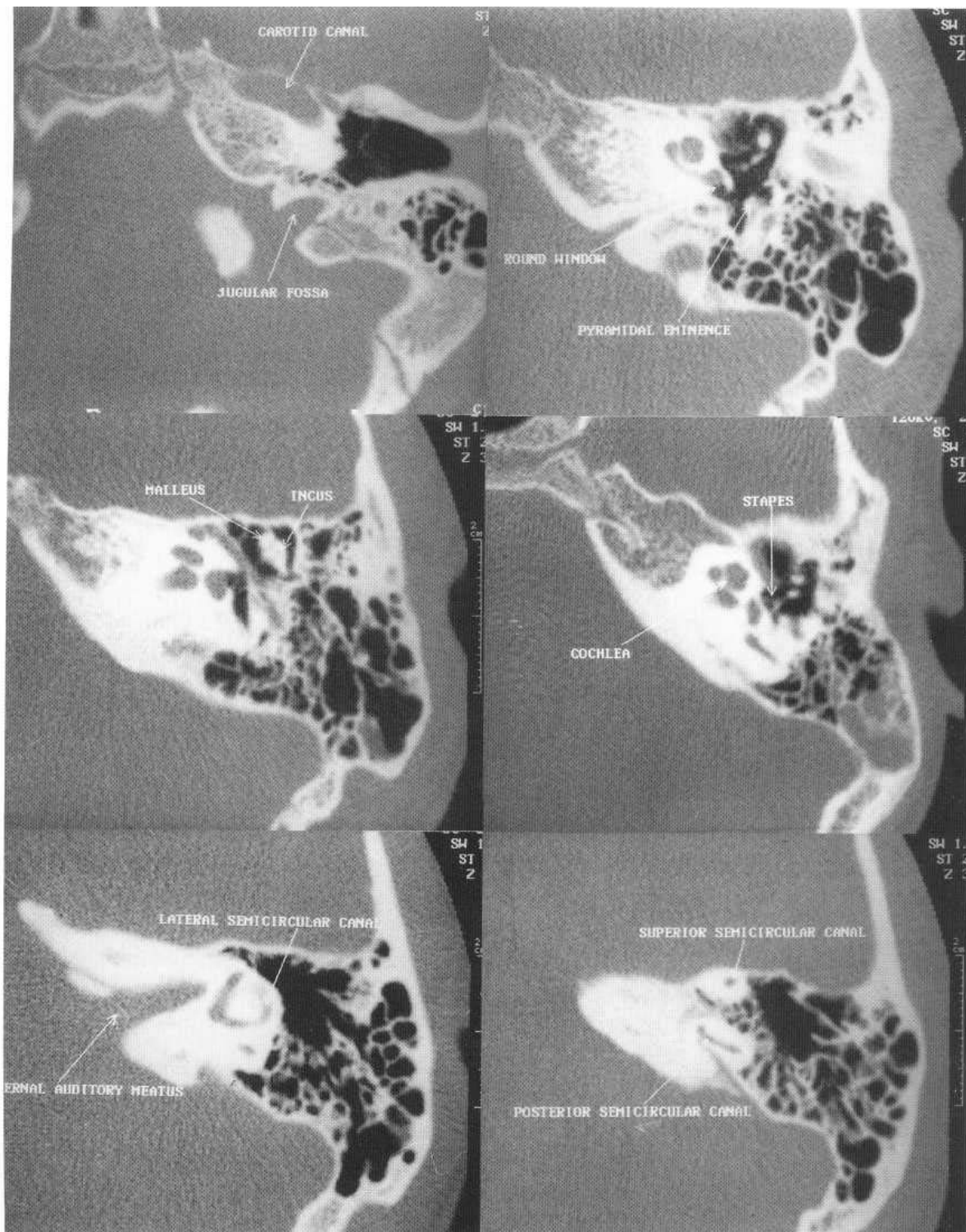


Fig. 52.5 Six labelled axial sections of the petrous temporal bone. Note that the oval window is shown in the same section as the second part of the facial nerve and the bodies of malleus and incus and above the section showing the crura of the stapes.

The role of magnetic resonance angiography (MRA) continues to increase and to supplant conventional angiography. The technique involves gradient-echo sequences to give flow-related enhancement which can demonstrate arterial abnormalities, such as aneurysms, or lesions of the nervous system, such as sigmoid sinus thrombosis. The most important single parameter for visualisation of the vasculature in MRI is the flow velocity, as the demonstration of vessels depends on selection of proper sequences which are predefined for imaging either fast- or slow-flowing blood (Fig. 52.12). Laminar and turbulent flow continue to pose problems.

CONGENITAL EAR DEFORMITIES

Many congenital abnormalities of the hearing organ do not involve bony structures and therefore cannot be shown by radiological methods. Nevertheless, structural abnormalities of the inner, middle and external ear can be shown in considerable detail by tomographic techniques. Unfortunately, affected children are usually referred between the ages of 2 and 4 when the deafness is first confirmed, and sedation or a general anaesthetic is required for the examination. If, after careful consideration, it is felt that the results

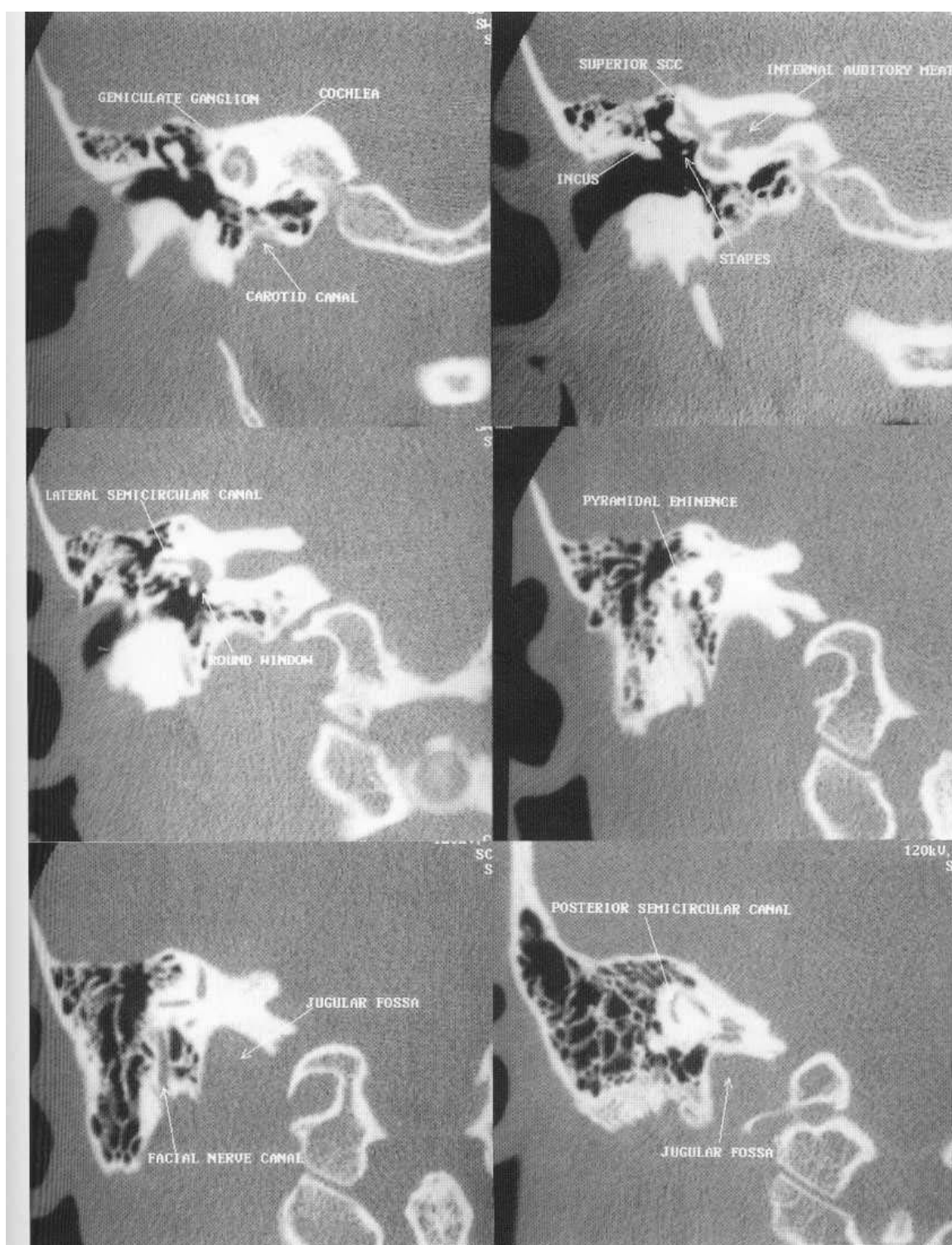


Fig. 52.6 Six labelled coronal sections.

of the investigation are unlikely to affect patient management, it may be reasonable to defer the examination until the child can co-operate. In the neonatal period a few sections can usually be obtained after a large feed, and this is recommended for those infants with relevant external deformities or syndromes in which temporal bone abnormalities are a feature. Plain films will also give much information at this age before full ossification of the petrous pyramids takes place, but at a later stage are only really useful for showing the degree of pneumatization.

The purpose of imaging is to demonstrate firstly any bony abnormality of the inner ear and particularly of the cochlea. This is

complementary to the audiological assessment, and ideally evoked-response audiometry may be done under the same sedation.

Congenital abnormalities of the middle and external ear are shown much more often than deformities of the inner ear, although combined deformities occur in about 20% of cases. The study of the outer ear relates to the prospects for surgical intervention to improve the sound-conducting mechanism, and is mandatory before any exploration of congenital atresia. Surgery is now, however, rarely performed for unilateral lesions. In fact the success of bone-anchored hearing aids has meant that only the most minor deformities of the conducting mechanism now warrant surgical exploration.

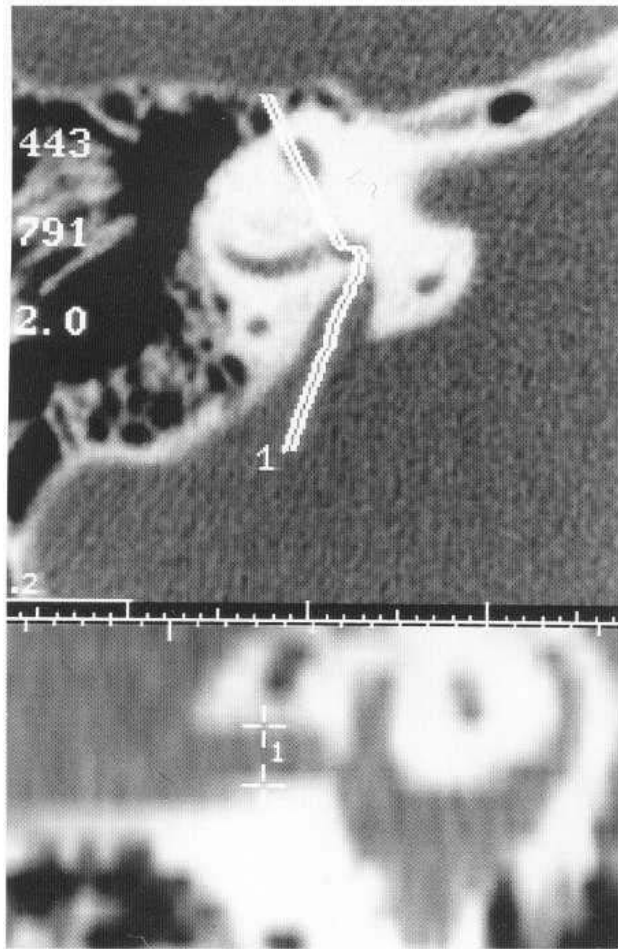


Fig. 52.7 An axial CT section showing a large vestibular aqueduct with a line depicting the plane of reformatting, enabling a measurement to be made in the midportion of the descending limb (labelled 1 and measuring 2.0 mm in diameter).

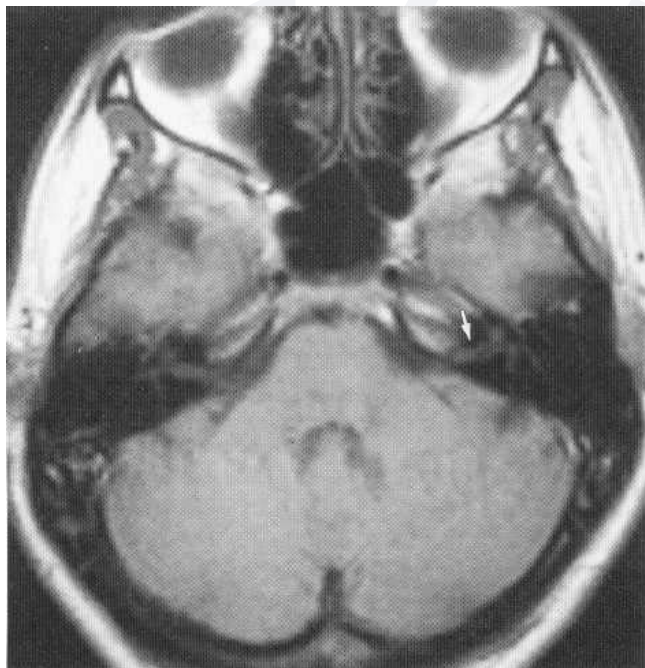


Fig. 52.8 An axial MR section through the posterior cranial fossa at the level of the IAM. The arrow points to the nerves in the IAM on this T₁-weighted protocol. Note the high signal from fat in the petrous apex.



Fig. 52.9 (A) A similar section to that in Figure 52.8 but T₂ weighted using a fast spin-echo sequence, giving greatly improved spatial resolution. The open arrow points to the basilar artery, the small arrow to the spiral ganglion of the cochlear nerve. (B) Tiny presumed acoustic neuroma on the superior vestibular nerve (arrow) in another patient.

A discussion of the indications for imaging and the syndromes in which it is likely to be useful is outside the scope of this book and the reader is referred to Chapters 3 and 4 of Phelps and Lloyd's *Diagnostic Imaging of the Ear* (1990). The following is a brief account of some of the great variety of lesions which occur and which defy adequate classification. The series of diagrams (Figs 52.13, 52.15) depict some examples.

Inner ear lesions

The *Michel* (total aplasia) and *Mondini* deformities (Fig. 52.14) are the two classically described inner ear lesions which can be shown by imaging. A limited amount of hearing is possible with the Mondini deformity because of the normal basal turn of the cochlea. A most important deformity is that of a dysplastic and dilated labyrinth or common cavity lesion, first described by Cock in 1838. Although no hearing is possible with this deformity, there is a very real risk of a spontaneous cerebrospinal fluid fistula developing via the abnormal IAM and the oval window to the middle ear. There is a risk of a 'stapes gusher' with any dilatation of the vestibule. The standard axial view is not the optimum one for showing the vestibular aqueduct but nevertheless a large vestibular aqueduct, the commonest structural malformation of the inner ear, is easily recognised on axial CT (Fig. 52.9). This anomaly may occur alone or with other deformities and characteristically is associated with progressive and fluctuant deafness. However, it would seem more pertinent to show an enlarged endolymphatic sac in the vestibular aqueduct.

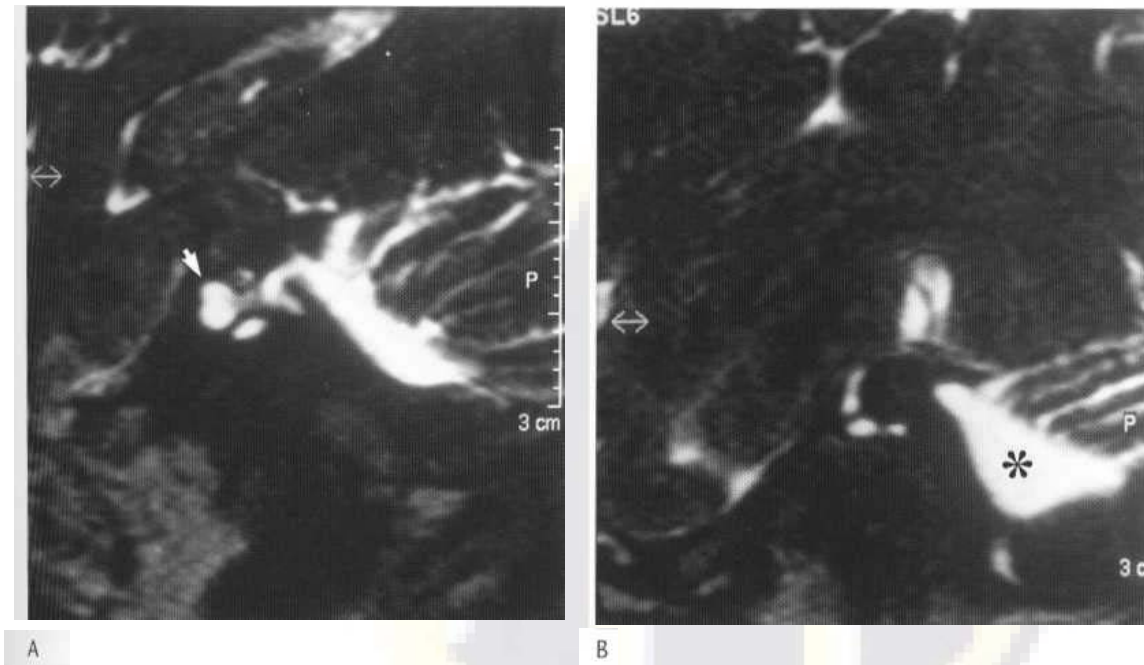


Fig. 52.10 (A,B) Sagittal MR sections T₂-weighted showing a grossly dilated endolymphatic sac (asterisk) in a typical case of Pendred's syndrome. Note also the sac in place of the distal 1.5 coils of the cochlea, i.e. a typical Mondini deformity (arrow).

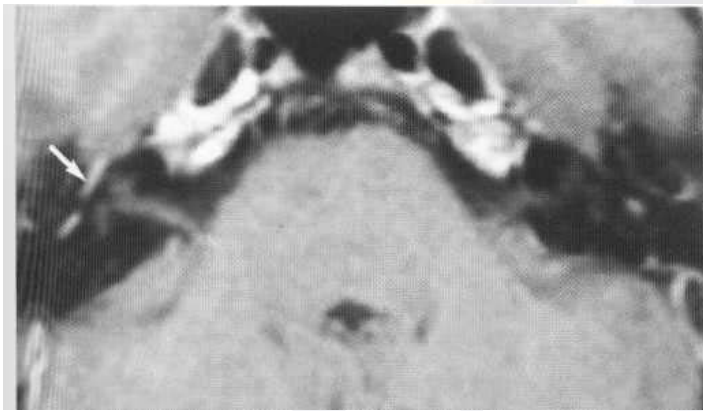


Fig. 52.11 Axial T₁-weighted image at the level of the IAM but after contrast enhancement. The arrow points to the second part of the facial nerve.

This can be done easily by MRI (Fig. 52.10). The relationship between an enlarged duct and sac has not as yet been assessed but does not seem to be constant. The normal endolymphatic sac is small and can be seen in approximately 50% of normal axial MR scans. The second commonest anomaly of the labyrinth is a solitary dysplastic lateral semicircular canal. On its own, this anomaly is not very significant and may accompany normal cochlear function. The IAM is very rarely absent with congenital deafness but it may be

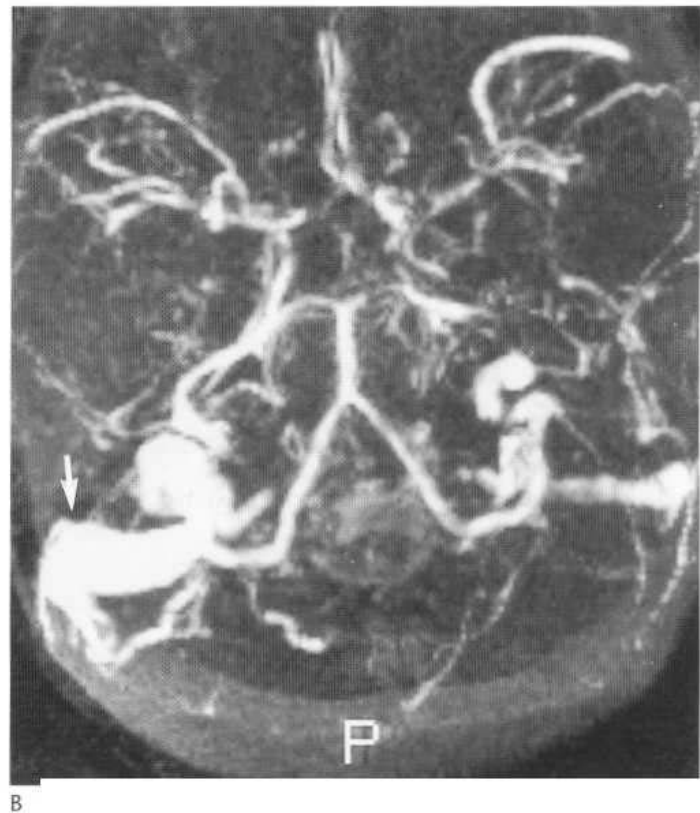
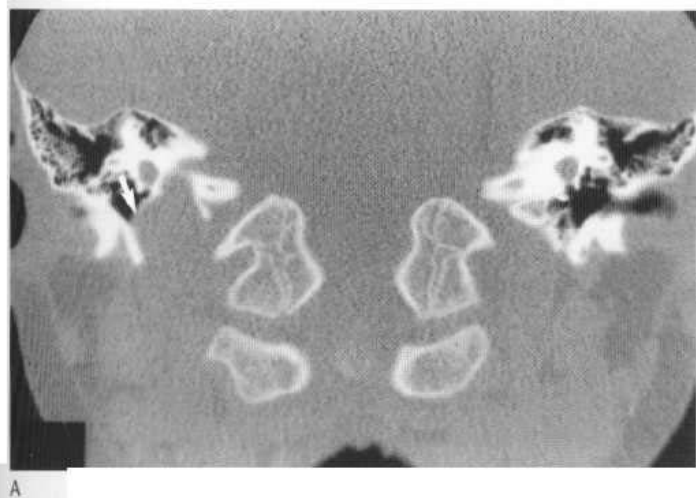


Fig. 52.12 (A) Coronal CT section showing high jugular fossa on one side with diverticulum. The arrow points to the thin bone separating the jugular bulb from the hypotympanum of the middle ear. (B) MRA shows the large jugular bulb (arrow).

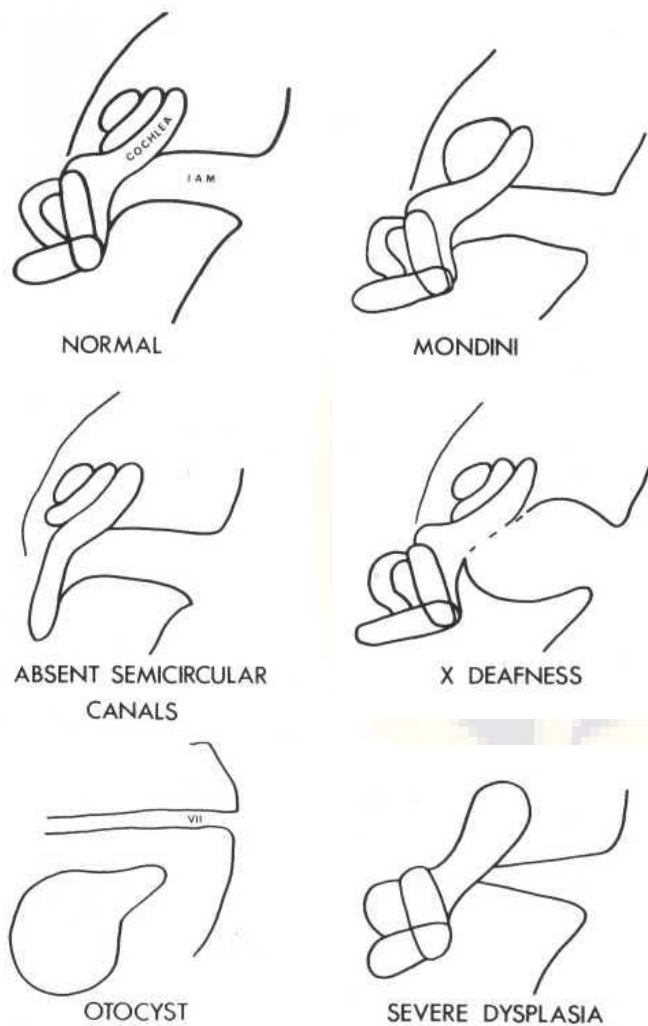


Fig. 52.13 Line drawings based on axial CT sections of the types of labyrinthine deformity. (From Phelps & Stansbie 1993, with permission.)

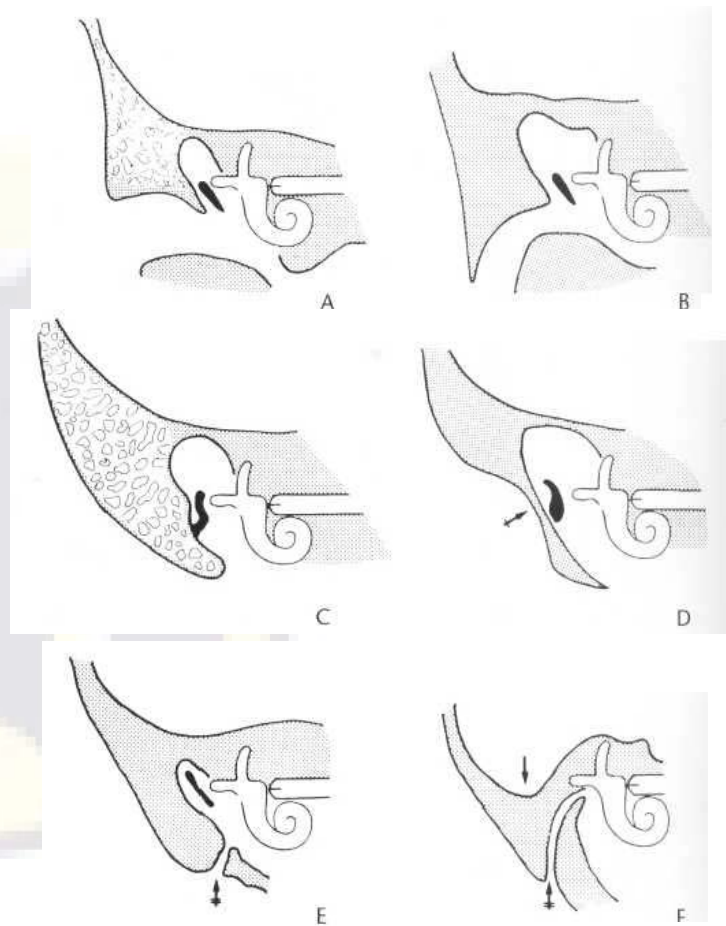


Fig. 52.15 Congenital malformations of the middle and external ears, based on coronal section tomograms. (A) Normal. (B) Sloping external meatus. (C) Pneumatised atretic plate with ossicular mass fixed to it. (D) Thin atretic plate. (E) Small middle ear cavity, spidery ossicles, and facial nerve canal exits through the atretic plate (arrow). (F) Depressed tegmen (arrow), lower part of middle ear only present, and anterior position of the facial nerve (crossed arrow). (From Phelps et al 1977.)

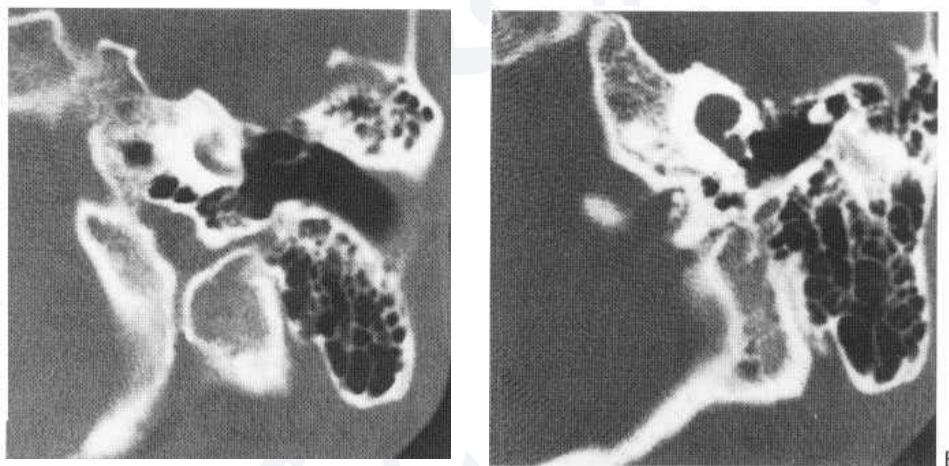


Fig. 52.14 Two basal CT sections showing a normal basal turn of cochlea (A) and distal sac (B), i.e. a true Mondini deformity. Some hearing was present and the normal basal turn suggests no risk of fistula or meningitis.

narrow (when it must be assessed tomographically in two planes), wide, ballooned, tapered, double or run in an abnormal direction.

Middle and external ear lesions

The most important assessment is the state of the middle ear cavity. In most unilateral atresias of the external auditory meatus with

associated deformity of the pinna there is good pneumatisation in a normally formed mastoid and the middle ear cavity is of relatively normal shape. Even in the most severe deformities there is rarely complete absence of the middle ear. In mandibulofacial dysostosis (*Trencher Collins syndrome*) the mastoid is unpneumatised and the attic and antrum are typically absent or slit-like, being replaced in



Fig. 52.16 Coronal CT section at the level of the cochlea showing typical appearances of hemifacial microsomia on the left with depression of the floor of the middle cranial fossa (open arrow), anterior descending portion of the facial nerve (black arrow), and deformity of the left temporomandibular joint.

varying degrees by solid bone. Descent of the tegmen to give a gutter-shaped depression in the floor of the middle cranial fossa (Fig. 52.15B) is typical of *craniofacial microsomia* (Fig. 47.16). The ossicles may be deformed, hypoplastic, absent or malpositioned. Malleus and incus are often represented by a fused mass, which may be fixed to the atretic plate.

The course of the facial nerve should be demonstrated, as the descending part is often more anteriorly situated than normal (Fig. 52.17). Some of the middle ear abnormalities that may be encountered are represented in Figure 52.15. Atresia of the external auditory meatus is usually due to a bony plate in place of the tympanic ring, but soft-tissue obstruction is also present.

Congenital vascular anomalies

The jugular fossa and intrapetrous carotid canal are well shown by tomographic techniques. Very rarely an *ectopic carotid artery*, or more commonly a *large jugular bulb*, may appear in the middle ear and cause not only symptoms but problems in differential diagnosis from glomus tumours (Fig. 52.18). Aberrant carotid in the middle ear becomes apparent on CT if comparison is made with the course of the normal artery on the opposite side.

There is great variation and asymmetry in the size of the normal jugular bulb. It may project into the lower part of the middle ear cavity, with or without a bony covering, but the outline of the lossa will appear smooth, with an intact septum between the carotid canal and jugular foramen on axial CT. An excessively large jugular bulb may affect not only the middle ear, causing conductive deafness, but also parts of the inner ear may be exposed to the bulb, especially if there is a 'diverticulum' from the jugular fossa extending upon the medial side of the labyrinth. This may even reach the superior surface of the petrous bone.

Trauma

Fractures of the petrous temporal bone, ossicular dislocations and foreign bodies can be demonstrated by radiological techniques.

Fractures

Although fractures of the petrous temporal bone follow no set pattern, they are usually classified with reference to the axis of the petrous pyramid as longitudinal and transverse. The fracture line in the commoner longitudinal type is in the long axis of the petrous bone; typically, it extends from the squama across the posterior

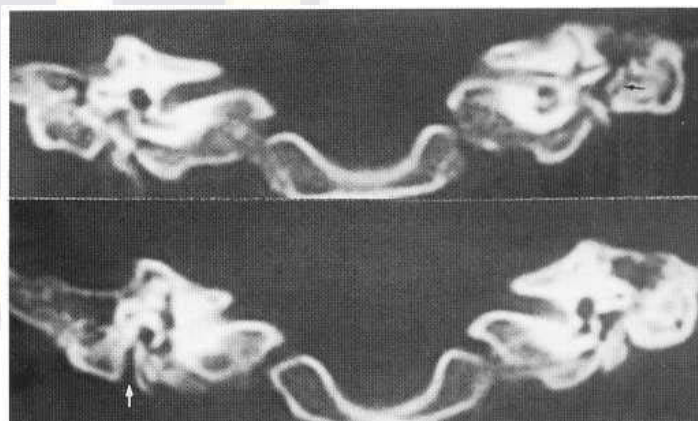


Fig. 52.17 Bilateral metal atresia shown by two coronal CT sections. There are small middle ear cavities, and some hypoplastic ossicles can be identified (black arrow). The tegmen is depressed unilaterally and the descending facial canal (white arrow) is at the level of the oval window.

aspect of the bony external auditory meatus and through the tegmen, which forms the roof of the middle ear cavity (Fig. 52.19). Longitudinal fractures are associated with facial nerve injury in 20% of patients. Anterior longitudinal fractures tend to involve the horizontal portion of the facial nerve canal in the region of the genicular ganglion. Posterior fractures may involve the vertical portion of the canal or the posterior gems. In the transverse type the fracture line runs at a right angle to the long axis of the petrous bone, often passing across the labyrinth or IAM and producing facial palsy and sensorineural deafness (Fig. 52.20).

The radiological investigation should relate to and depend upon the clinical picture. To demonstrate a fracture the X-ray beam must be in or close to the plane of the fracture line. Thus, several projections in different planes are necessary to show fractures of the temporal bone. High-resolution CT will show more fractures than will plain films and is valuable for demonstrating more precisely the path and extent of the fracture. The examination may need to be performed in at least two planes. However, thin sections in the base plane will show the majority of fractures and such an examination can be made as a continuation of the standard brain scan if damage to the ear is suspected.

Ossicular dislocations

When a head injury is followed by conductive deafness, it is most commonly due to a simple haemotympanum or to a traumatic rupture

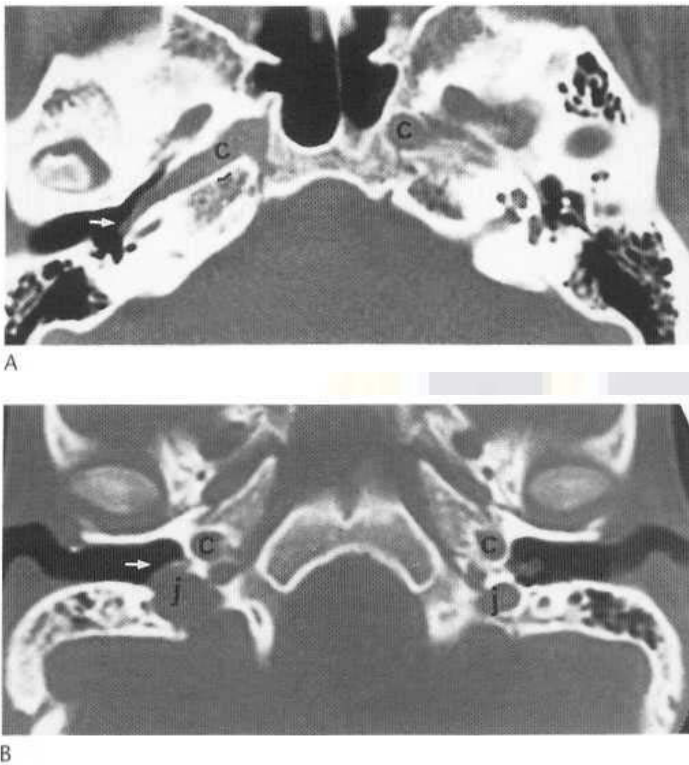


Fig. 52.18 Two different but important vascular anomalies which can be diagnosed on base CT sections, although further imaging in the coronal plane is desirable. (A) Aberrant internal carotid artery (c) in the middle ear (arrow). (B) Large jugular bulb (j), partially dehiscent, in the middle ear cavity. Compare with the normal side in each case.

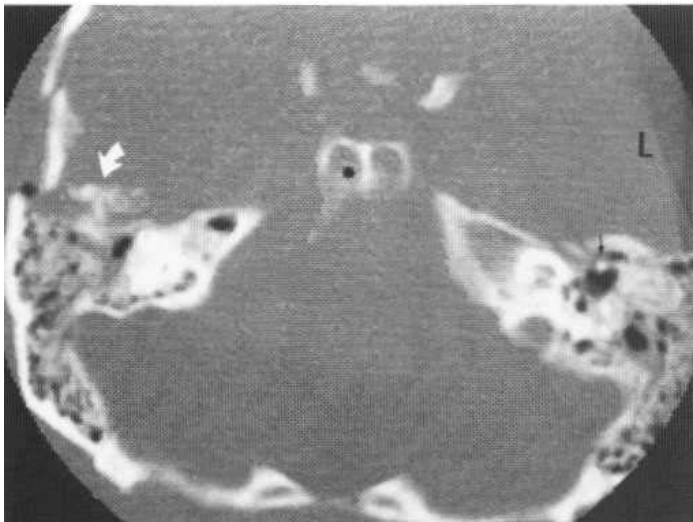


Fig. 52.19 Longitudinal fracture of the petrous temporal bone with a depressed fragment of squamous temporal. The fracture line runs along the roof of the external meatus and middle ear with a small fragment of bone in the region of the genicular ganglion (white arrow). The fracture passed through the sphenoid sinuses which are filled (asterisk). On the left side the black arrow indicates the malleus in normal position; the incus was displaced. Axial CT scan.

of the drum. However, if hearing loss remains after the drumhead has healed then disruption of the ossicular chain must be suspected.

Unfortunately the commonest dislocation, namely of the incudostapedial junction, is not always satisfactorily demonstrated by tomographic methods. Displacement of the incus, rarely the malleus,

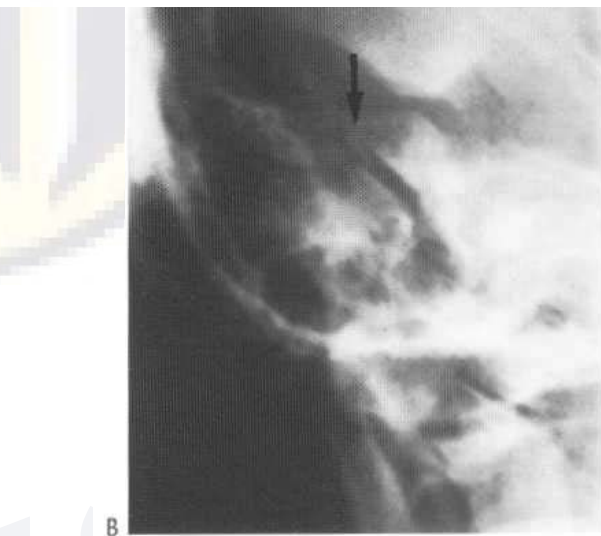
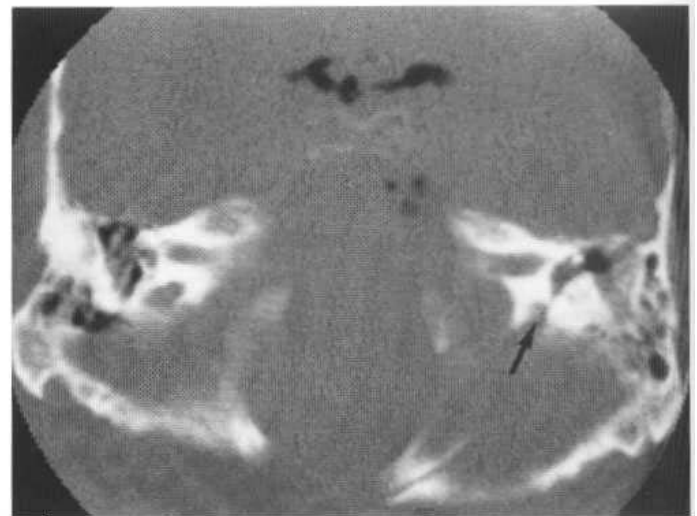


Fig. 52.20 (A) Transverse fracture of the pyramid passing through the vestibule (arrow). Note the air in the cranial cavity and the CSF level in the middle ear. (B) Plain Stenver's view showing the fracture line (arrow).

and separation of the incudomalleolar joint can be demonstrated by axial and coronal high-resolution CT (Fig. 52.21). Loss of the normal 'molar tooth' sign on sagittal reformatted CT is another important sign of major ossicular displacement.

Inflammatory disease

Acute mastoiditis is the most common complication of acute otitis media and results from the spread of the infective process beyond the mucosal lining of the middle ear cleft into the underlying bone. Because of the anatomical arrangement of the region this phenomenon occurs primarily and predominantly in the mastoid air cell system and produces clinical signs and symptoms accordingly. As with acute otitis media, the diagnosis of acute mastoiditis is essentially a clinical one, but radiology may provide supporting evidence. Radiologically, the dominant finding is breakdown of the cell wall trabeculations in addition to the loss of translucence found in acute otitis media. The improved resolution of the air, soft-tissue and bone boundaries in CT makes interpretation of the precise state of the mastoid air cell system easier but such an examination is very rarely justified (Fig. 52.22). If



Fig. 52.21 Coronal CT scan showing massive incus displacement following a road traffic accident. The images of the ossicles are completely separate and the incus is lying inverted in the attic (arrow).

there is extensive breakdown of the cell walls, the resultant abscess cavity may be shown radiologically with irregular margins.

Two main types of *chronic suppurative otitis media* are recognised. For the safe *lubotympanic (vpe)* with central perforation radiology is of very limited use. *Atticoantral disease* is most likely to be due to the acquired form of cholesteatoma, which because of its erosive nature carries a significant risk of complications. *Tuberculous otitis media* produces extensive ragged bone destruction. Adhesive otitis media or *Rvmpanosclerosis* produces calcified plaques as the end-result of suppurative ear disease. These may cause some confusion when demonstrated by CT. If the suppurative process involves the labyrinth a 'dead ear' results and granulation tissue within the labyrinth may ossify to give so-called *labyrinthitis obliterans* (syn. labyrinthitis ossificans). Usually CT shows that parts of the lumen of the bony labyrinth have 'disappeared' (Fig. 52.23) or been narrowed. Such cases with 'reduced hearing' are good candidates for cochlear implantation but the ossified cochlea makes insertion of the electrode array difficult or impossible. Moreover CT is not always reliable for demonstrating tubular obstruction and MRI is therefore necessary to confirm, by higher signal on T₂-weighted images, that the coils of the cochlea are fluid-containing (Fig. 52.24). Differentiation from congenital malformations of the inner ear or advanced otosclerosis may be difficult.

The intracranial complications of suppurative ear disease, particularly abscess in the temporal lobe or cerebellum, are most important and are now easily shown by CT brain scan. They are considered in Chapter 55.

Cholesteatoma

The aetiology of the characteristic epidermoid cyst containing keratin is not fully understood. Two types are recognised, although they do not differ histologically.

- Congenital cholesteatoma originating from ectodermal cell rests - this may arise in any of the cranial bones, the petrous temporal being the most commonly affected, or within the cranial cavity.

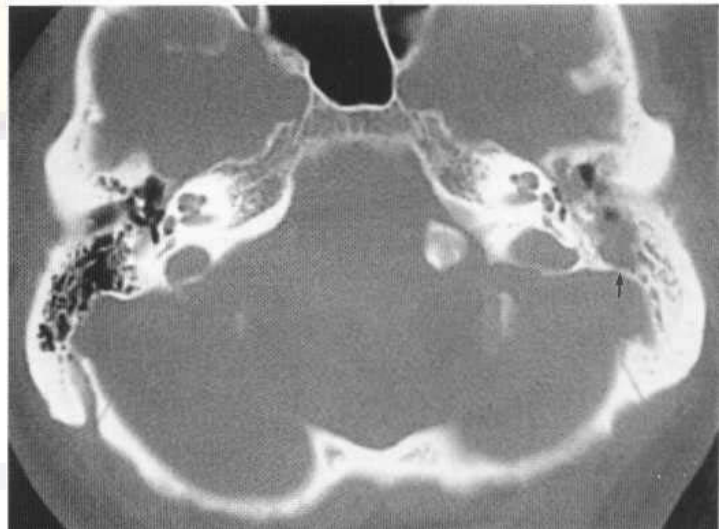


Fig. 52.22 Axial CT scan showing fluid in the mastoid cell system on the left (arrow), with cell wall breakdown.

- Acquired cholesteatoma, associated with disorders of the middle ear cleft and involving the attic, with or without preceding infection.

Congenital cholesteatoma

Congenital cholesteatoma, which involves the middle ear cleft, cannot certainly be differentiated from the acquired type, but the middle ear may be normal clinically and radiologically, and the cholesteatoma, usually in the petrous apex, produces a clearly defined 'punched-out' area of bone destruction. It has been realised recently that such a lesion is as likely to be a cholesterol granuloma containing golden or brown fluid as a cholesteatoma. Differentiation is only important for the type of surgery required and can be made by MRI. *Cholesterol granuloma* gives a strong signal on all protocols (Fig. 52.25). Cholesteatoma only on L-weighted sequences, when it can be difficult to distinguish from cerebrospinal fluid.

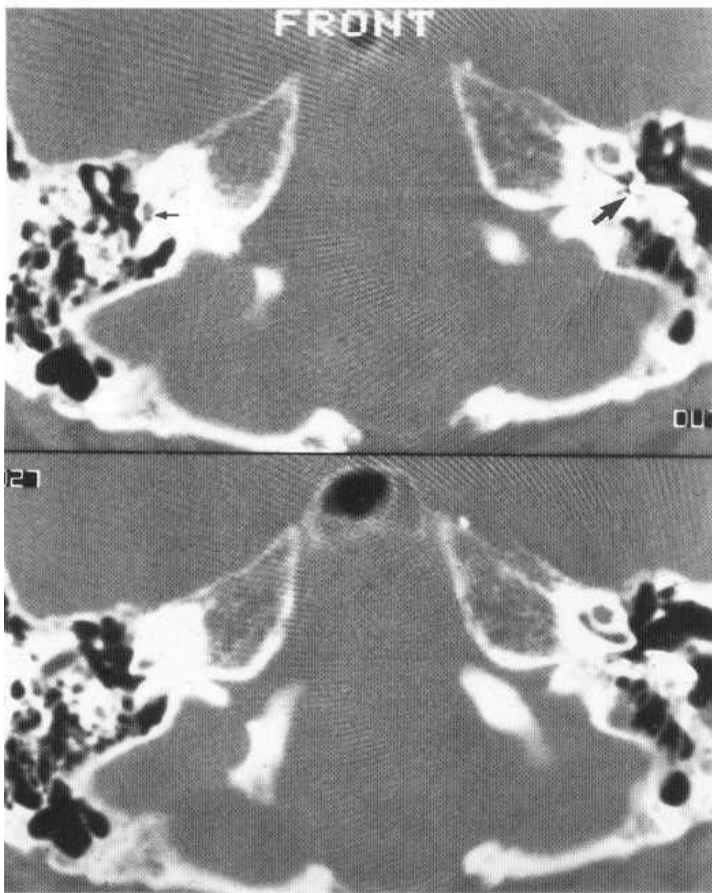


Fig. 52.23 Axial CT scan through the basal turn of the cochlea. On one side a single channel cochlear implant has been inserted in the round window (large arrow); on the other side there is labyrinthitis obliterans with only the hook of the basal turn readily apparent (small arrow).



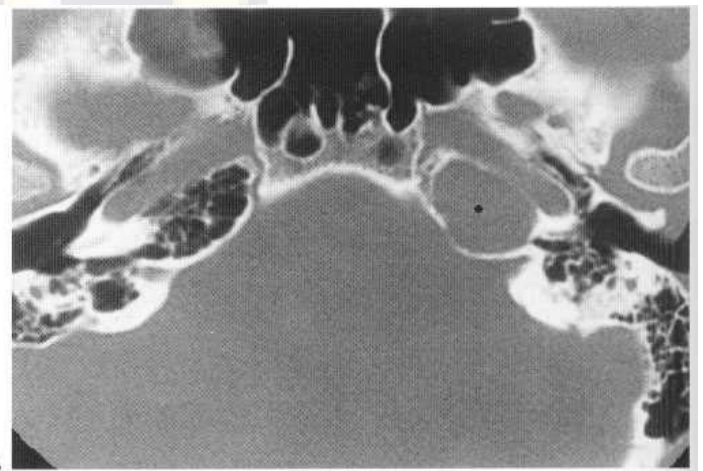
Fig. 52.24 Axial T₂-weighted MR section of the inner ear in a patient for cochlear implantation. The basal coil of the cochlea on the right shows high signal from the medial part but low signal laterally, presumably due to fibrosis (arrow) so insertion of the electrode was unsuccessful. The basal turn on the left shows uniform high signal and was subsequently implanted without difficulty.

The vast majority of *acquired cholesteatomas* arise in the posterosuperior part of the middle ear. From here they extend into other parts of the middle ear cleft, into the rest of the tympanic cavity,

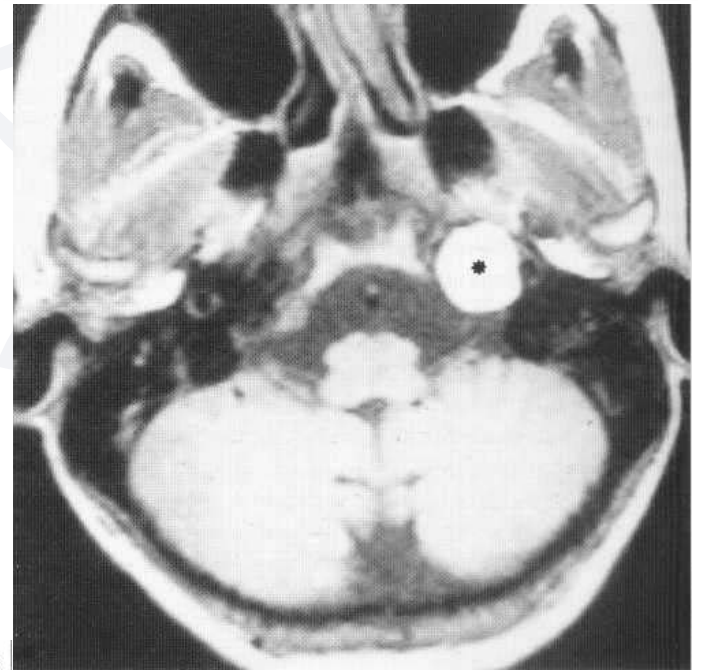
and backward into the mastoid antrum and air cells. There is associated erosion of the wall of the cleft. Typically, there is a marginal perforation in the posterior superior aspect of the eardrum.

Pneumatisation is usually poor or absent. CT in the coronal plane is the optimum method for demonstrating small cholesteatomas in the attic and antrum, and the presence of a soft-tissue mass in that part of the middle ear cleft is characteristic (Fig. 52.26). Unfortunately, attenuation measurements are not sufficiently accurate to differentiate cholesteatoma from granulation tissue or other opacities. The detection of atticointral bone erosion, in particular blunting of the spur or outer attic wall, is more important. The ossicles may be eroded or slightly displaced. Extension medially erodes the labyrinth, the lateral semicircular canal usually being the first part affected, although all cochlear function may not be lost in the early stages, even when the cochlear capsule is itself eroded (Fig. 52.27).

The CT appearances of cholesteatoma, both congenital and acquired, differ from those of the ragged infiltrative lesions produced



A



B

Fig. 52.25 (A) Axial CT section showing an expansile lesion in the petrous apex (asterisk). This was a presumed cholesterol granuloma following trauma. Note the good pneumatization of the petrous apex on the other side. (B) High signal on both T₁- and T₂-weighted MR protocols confirmed that this was a cholesterol granuloma.

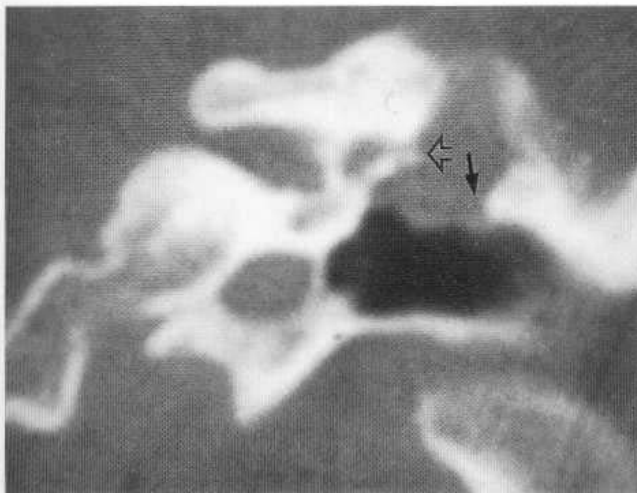


Fig. 52.26 Coronal CT section at the level of the vestibule showing a typical acquired cholesteatoma which has eroded both the outer attic wall (arrow) and the apex of the lateral semicircular canal (open arrow) to give a positive fistula sign clinically.

by other infective and neoplastic processes, which tend to affect the labyrinth capsule only at a very late stage. Nevertheless it should be stressed that the majority of cholesteatomas are diagnosed clinically by inspection of an eardrum perforation. Exploratory surgery is nearly always required when squamous epithelium is found in the middle ear cavity. The radiological findings are unlikely to influence the type or the course of the operation in straightforward cases, and CT should therefore only be employed to assist the otologist with specific problems, for instance when a cholesteatoma is suspected although the eardrum is intact, or where features such as sensorineural deafness suggest a more extensive disease process.

Benign neoplasms

Osteoma

A compact osteoma appears as a well-defined, usually single although occasionally lobulated, bony mass of high density (Fig. 52.28). It may arise from any bony surface and will cause conductive deafness if it blocks the external auditory meatus or middle ear.

Glomus tumours

The diagnosis of *jugulotympanic glomus tumours*, also called chemodectomas or paragangliomas, can usually be made from the otoscopic appearance of a red mass behind the lower part of the eardrum. Less commonly these tumours arise as a haemorrhagic polyp in the external auditory meatus, as a mass in the cerebellopontine angle, or with lower cranial nerve signs. They should not be biopsied; imaging is crucial for confirming the diagnosis and assessing their situation and extent. Glomus bodies are situated in the top of the jugular bulb and in the middle ear, thus a tumour in the middle ear may be a glomus tympanicum confined to the tympanum or a jugulare tumour that has come up from below. This differentiation cannot be made clinically but is of the utmost importance to the surgeon.

Tympanicum tumours can be removed by normal middle ear surgical techniques but a *jugulare mass* needs an infratemporal fossa approach and special expertise. Radiotherapy may be the preferred treatment for larger tumours, especially in the elderly. The most important feature of a glomus jugulare tumour on the initial radio-

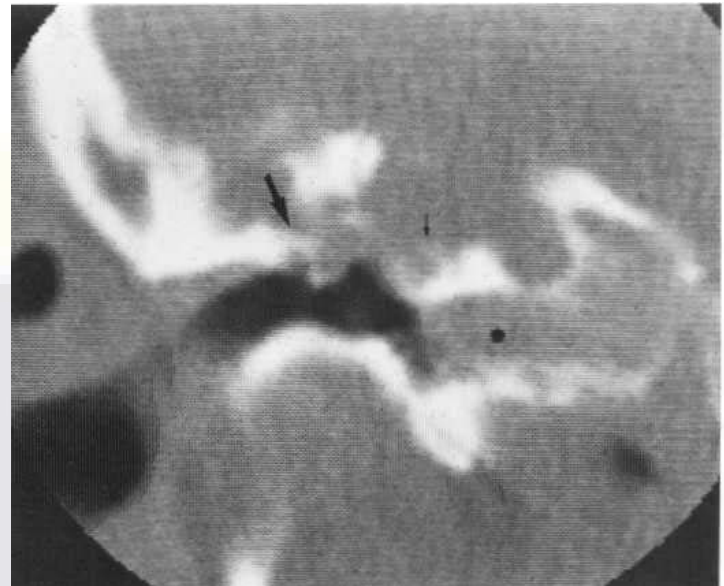


Fig. 52.27 Coronal CT section showing an attic cholesteatoma which has pushed the malleus (large arrow) against the lateral attic wall, but also eroded around the labyrinth and into the top of the cochlea. The exposed central spiral of the cochlea is shown. The asterisk marks the carotid canal.

graphs is erosion of the margins of the jugular foramen (Fig. 52.29), and in particular the crest of bone between the jugular fossa and the carotid canal. This is a far more important sign than enlargement as the two fossae are rarely symmetric and expansion may be difficult to assess. The typical ragged erosion of the undersurface of the petrous bone is better demonstrated by high-resolution CT. Although contrast-enhanced CT gives a good demonstration of intracranial extension of glomus tumours, we have not found it very satisfactory in the middle ear or neck. We prefer MRI to demonstrate the soft-tissue extent of the mass, both intracranially and downward in the neck. Large tumours have a characteristic appearance of serpiginous areas of signal void representing blood vessels. Gadolinium enhancement helps further to delineate the limits of the tumour (Fig. 52.30).

Glomus tympanicum tumours arise within the middle ear cavity and, although when large they are indistinguishable from glomus jugularis tumours, they may nevertheless present with a mass behind the eardrum when the tumour is confined to the hypotympanum. The small soft-tissue mass on the promontory shown by coronal CT (Fig. 52.31 A) is virtually diagnostic. The importance of showing an intact floor to the middle ear to exclude a jugulare tumour is stressed, but further confirmation is provided by the Gd-MR scan, which shows a bright tumour in the middle ear distinct from the jugular bulb, represented as a large area of signal void so long as the bulb is filled with flowing blood (Fig. 52.31 B). Gd-MRI will also show the relation of the tumour to the carotid artery and differentiate tumour from the serous otitis which results from obstruction to the eustachian tube (Fig. 52.29B).

Angiography is no longer a mandatory or primary investigation and is not required for small glomus tympanica or large tumours to be treated by radiotherapy. However, the angiographic appearances of large vascular spaces and dense tumour stain are characteristic and may be needed to confirm the diagnosis. The role of angiography is in preoperative assessment, combined with therapeutic embolisation in selected areas. Angiography is also well suited to assess multiple chemodectomas of the carotid body, glomus vagale

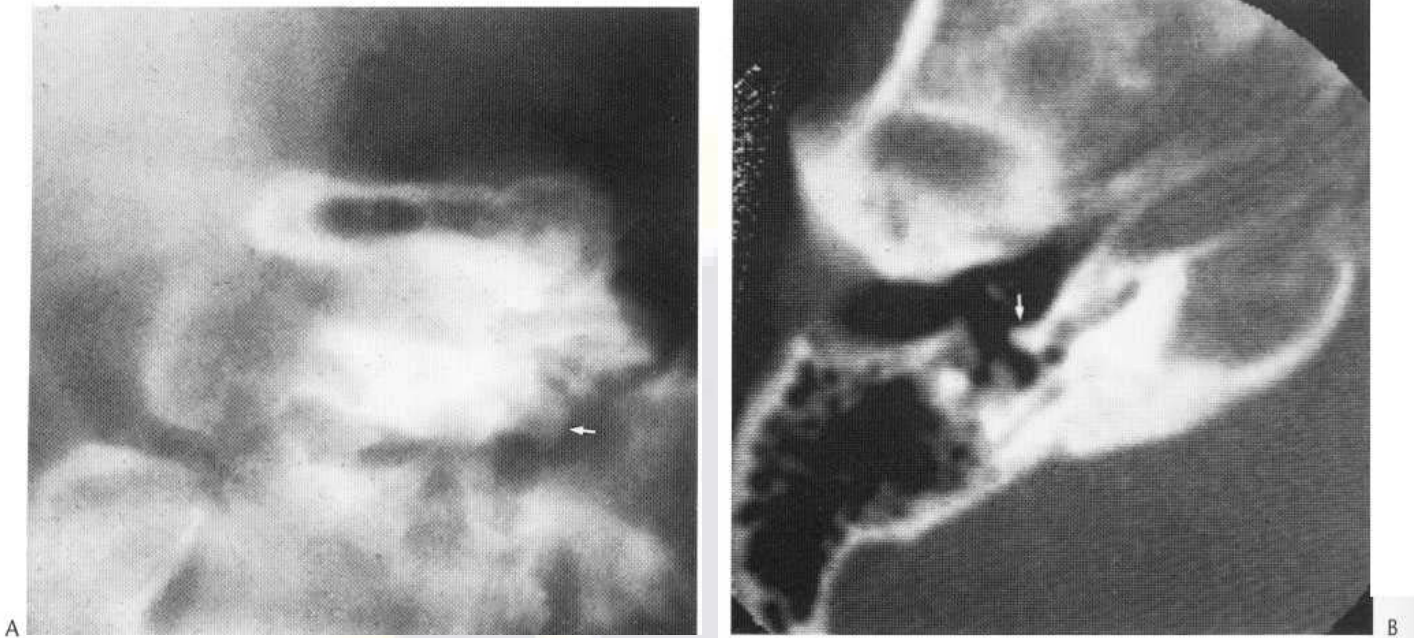


Fig. 52.28 A small osteoma of the middle ear arising from the posterior aspect of the promontory close to the round window. (A) Coronal tomogram shows the osteoma just below the incudostapedial joint. (B) Axial CT also shows the relation to the basal turn of the cochlea.

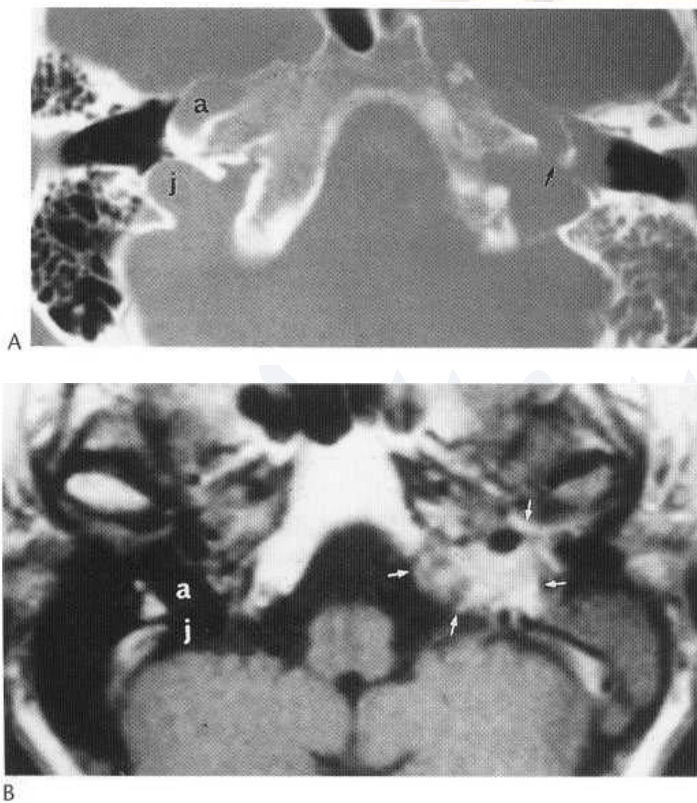


Fig. 52.29 (A) Base CT at the level of jugular fossa (j) and horizontal carotid canal (a). On the right the crest of bone between them is apparent. On the left this part of the jugular fossa is eroded by a glomus jugulare tumour (arrow), which has also extended into the middle ear. (B) Base Gd-MR scan at the same level, showing the tumour surrounding the carotid artery and quite distinct from the fluid in the mastoid.

and jugulare types, which may occur together, although these can usually be fully demonstrated by Gd-MRI or magnetic resonance angiography (MRA). MRA and MR phlebography combined with

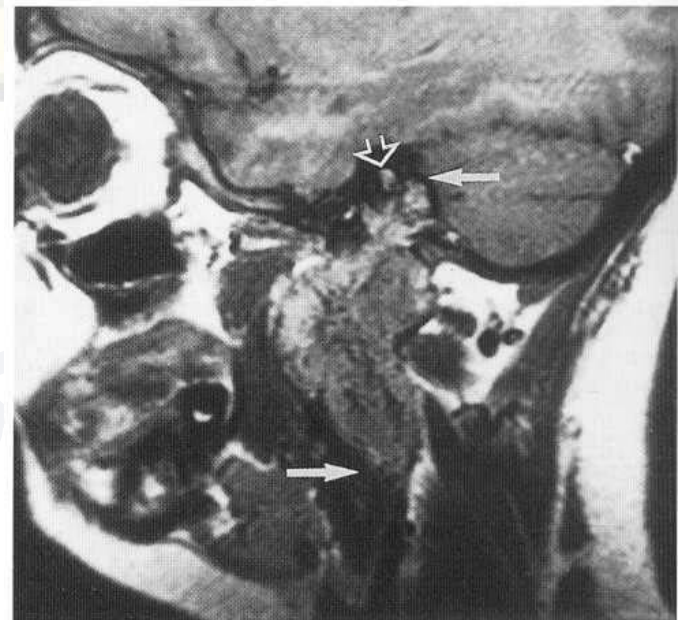


Fig. 52.30 Sagittal Gd-MR scan showing a large glomus jugulare tumour and its upper and lower limits in the posterior cranial fossa and neck (arrows). The black streaks representing blood vessels are characteristic. Gadolinium enhancement, although giving improved differentiation in the mastoid and cranial cavity, is not such an advantage in the neck, where adjacent fat also gives a bright signal on a T_1 -weighted image. The open arrow points to the IAM.

spin-echo MRI have been recommended for ruling out tumour in patients with pulsatile tinnitus (Vogl et al 1994).

Neuromas

These tumours arise from Schwann cells which invest the cranial nerves; they are therefore more correctly called schwannomas, although the term neuroma is more widely used. The temporal bone may be affected by tumours arising from the Vth, VIIth, XIth or

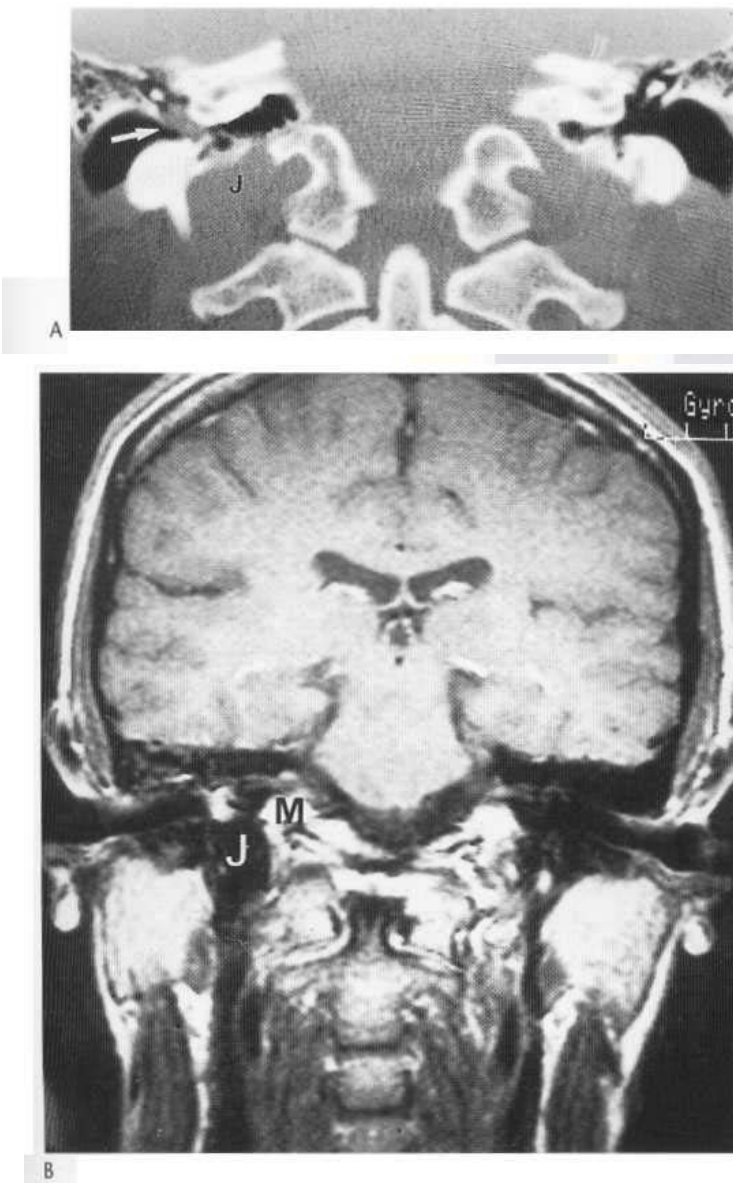


Fig. 52.31 (A) Coronal CT showing a small glomus tympanicum in the lower middle ear cavity (arrow). J = jugular bulb. (B) An equivalent MR section confirms that this is quite separate from flowing blood in the jugular bulb (J). Note the confusing proximity of marrow fat (M).

XIIth cranial nerves. These are all very rare, except in patients with neurofibromatosis type 2 (NF2). Marked gadolinium enhancement of a mass in the course of the appropriate cranial nerve is the distinguishing feature (Fig. 52.32). However, VIIIth nerve tumours, are the commonest tumours affecting the petrous pyramid: 80% arise within the IAM (Fig. 52.33), usually from one of the vestibular nerves. The less common tumours of extrameatal origin are considered in the differential diagnosis of masses in the posterior cranial fossa in Chapter 57.

Imaging investigation of acoustic neuromas

Despite a variety of clinical tests for acoustic tumour, a definitive diagnosis can only be made by imaging. Bone studies of the IAM are obsolete and thin section T, MRI is the standard investigation to demonstrate or exclude the presence of an acoustic neuroma (Fig. 52.34). However, gadolinium is usually used to confirm by enhancement that a mass in the cerebellopontine angle is a neuroma

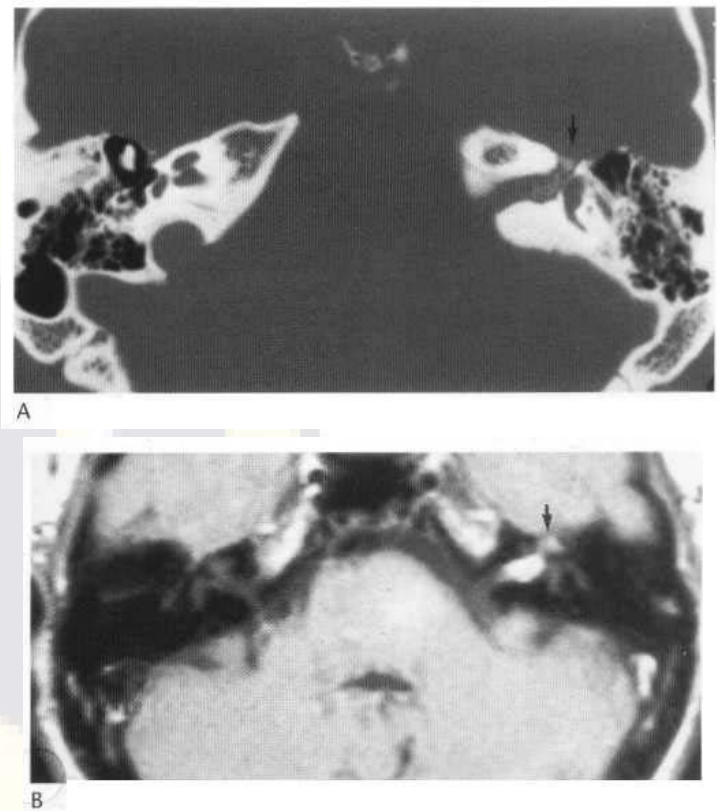


Fig. 52.32 (A) Axial CT section through the IAM showing expansion of the first part of the facial nerve canal (arrow). Note the calcification which should have suggested that this was a haemangioma rather than a neuroma. (B) Axial MR section, T₁-weighted with gadolinium enhancement, shows the mass (arrow).

and is also required in cases of NF2 (Figs 52.35, 52.36). Gadolinium enhancement is also required for 'follow-up' after removal of an acoustic neuroma, either in total or partially (Fig. 52.37). Enhanced CT is only used for those patients who for various reasons are unable to be examined by MRI.

Meningioma

Meningiomas are the next most common tumours that occur in the cerebellopontine angle. Several differentiating features have been described. Unlike neuromas, meningiomas often calcify. They tend to have a broad attachment to the petrous ridge, which may show characteristic hyperostosis. Intense contrast enhancement occurs with Gd-MR (Fig. 52.38).

Malignant neoplasms

Carcinoma Carcinoma of the ear, arising in the external auditory meatus, middle ear cleft or a mastoid cavity, is a rare but distressing disease which is seldom diagnosed early. The prognosis is very poor. Sclerosis of the mastoid and clouding of the cells are radiological signs of little value but the presence of ragged erosion, usually extensive or in an unusual site, suggests neoplastic change. An important sign on the lateral mastoid view of CT is erosion of the articular fossa of the temporomandibular joint. The hard avascular bone of the labyrinthine capsule is relatively unaffected by carcinoma of the ear, and erosion of the capsule with direct invasion of the inner ear is a late radiological feature. There are two important modes of

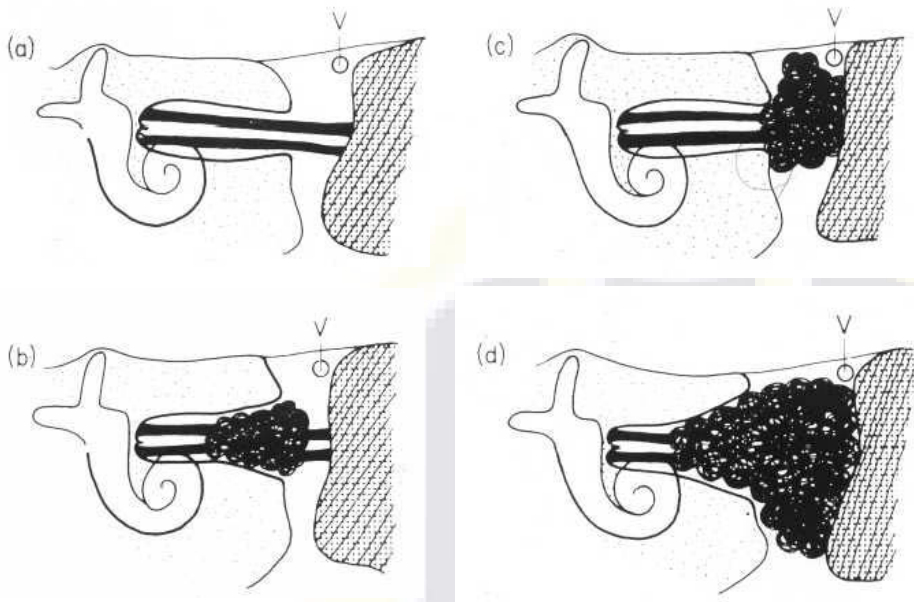


Fig. 52.33 Diagrams based on coronal section tomograms. (a) The nerves in the normal IAM passing from brainstem to labyrinth; (b) intrameatal, (c) extrameatal, and (d) large acoustic neuromas. V = trigeminal nerve. (From Phelps & Lloyd 1983.)

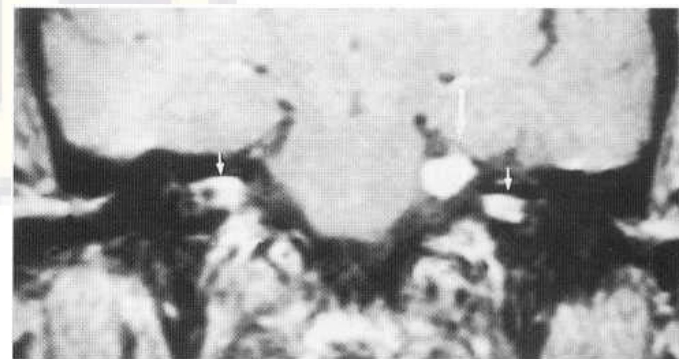
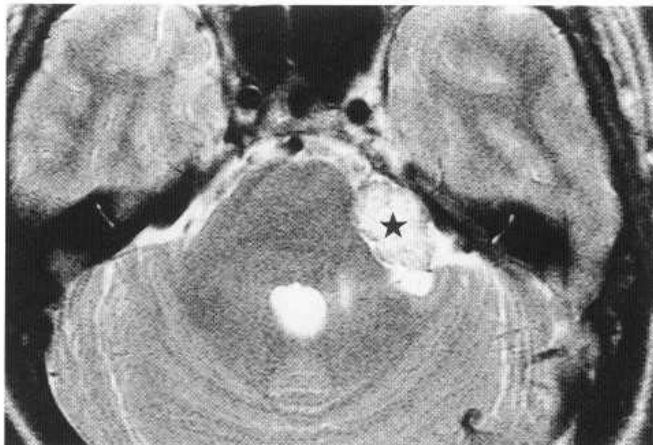


Fig. 52.35 Corona) Gd-MRI showing bilateral intrameatal acoustic neuromas (small arrows) and a trigeminal neuroma (large arrow) in a patient with neurofibromatosis (NF2).

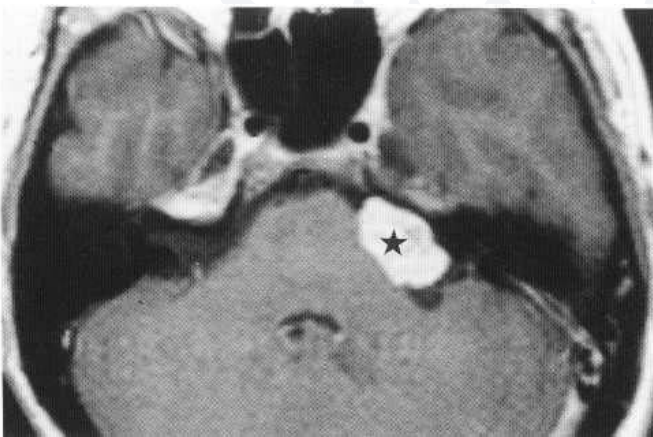


Fig. 52.34 Large acoustic neuroma in the left cerebellopontine angle (asterisk). (A) Fast spin-echo T_2 axial section. (B) Equivalent T_1 section after gadolinium enhancement.

spread of carcinoma of the middle ear. First, the tumour extends anteriorly and penetrates the bony septum separating the middle ear cavity from the carotid artery. It then spreads around the artery and extends down around the eustachian tube toward the

postnasal space. Second the tumour may spread upward through the tegmen tympani and backward through the mastoid air cells (Fig. 52.39). Erosion of these thin bony structures may be demonstrated by CT; the soft-tissue extension is best shown by MRI with gadolinium.

Malignant otitis externa This term is rather confusingly applied to a non-neoplastic condition—a severe infection of the external auditory meatus occurring usually in elderly diabetics. Massive bone destruction around the meatus and obliteration of soft-tissue planes in the infratemporal fossa are best shown by high-resolution CT but isotope studies assess the activity of the disease process.

A mixture of bone destruction and sclerosis of the skull base may be seen (Fig. 52.40).

Bone dysplasias

Otosclerosis is a localised disease of unknown aetiology in which new bone replaces the endochondral bone of the otic capsule. The French term 'otospongiose' is better as it describes the active phase of the disease characterised by rarefaction with which imaging is mostly concerned. The otic capsule is the densest bone in the body and cannot become denser, therefore otosclerosis can only be

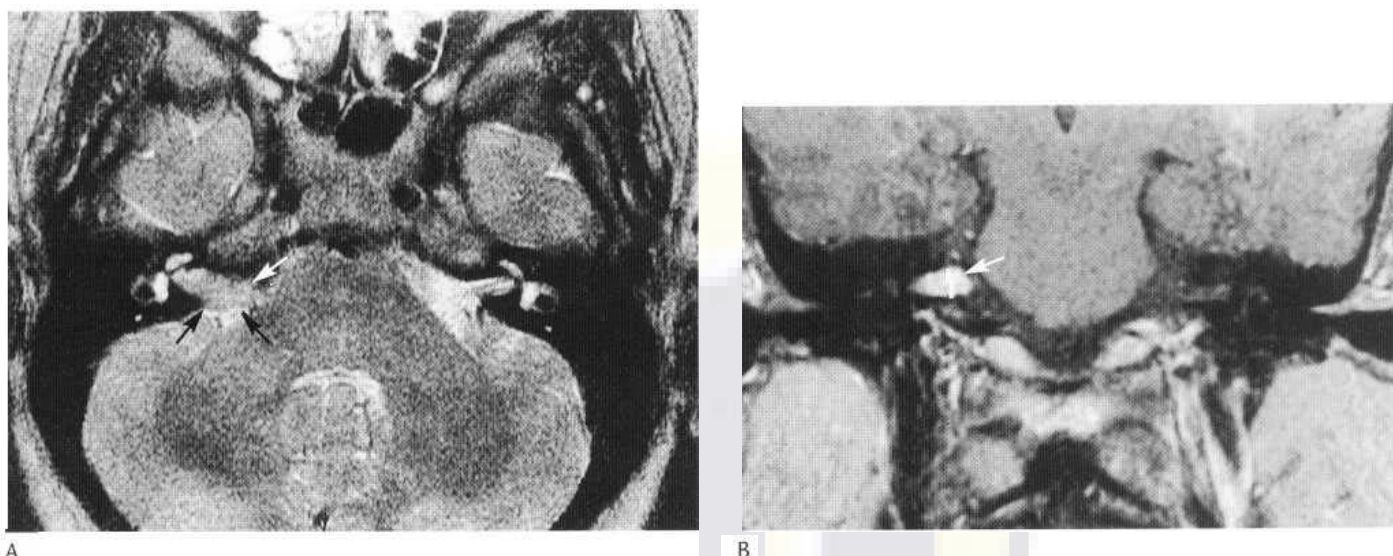


Fig. 52.36 (A) Axial FSE section showing a small acoustic neuroma in the right IAM just protruding into the cerebellopontine angle. Note the normal nerves in the left IAM. (B) Equivalent coronal T₁ section after gadolinium enhancement.

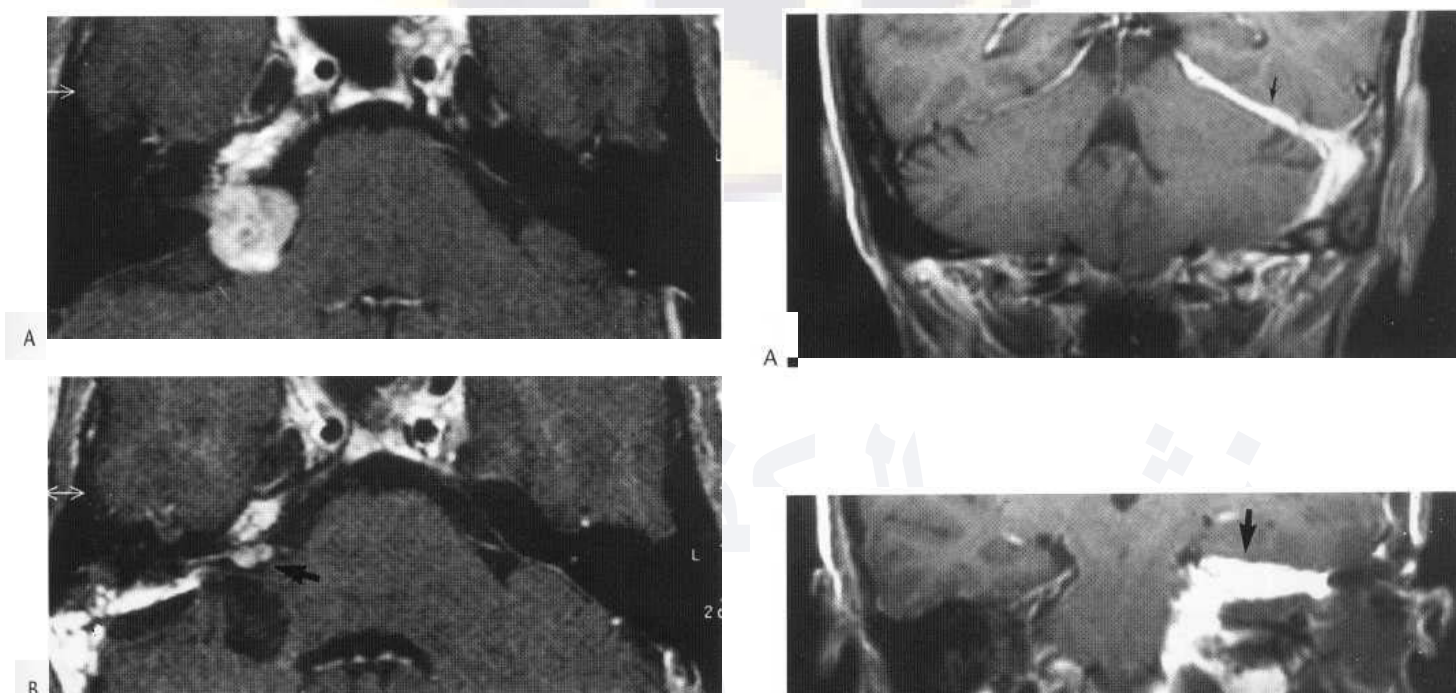


Fig. 52.37 (A) Axial Gd-MRI showing a large acoustic neuroma in the cerebellopontine angle and medial part of the IAM. (B) The bulk of the tumour has been removed but a small segment adherent to the facial nerve has been left deliberately (arrow) to preserve facial nerve function and will be monitored for growth on subsequent scans. Note the 'hole' in the posterior cranial fossa.

detected by imaging when it is far advanced and blocks the oval window or distorts the outline of the cochlear coils. Otospongiosis on the other hand may be seen as patchy or ring rarefaction around the cochlear coils or adjacent to the oval window. But lesser degrees of rarefaction, not apparent to the naked eye, can be shown by densitometry (Fig. 52.41). Such an assessment is important to the differential diagnosis and if fluoride therapy is contemplated. We have found *cochlear otospongiosis to be much more common than is generally realised and consider it to be a relative contraindication to stapedec-*

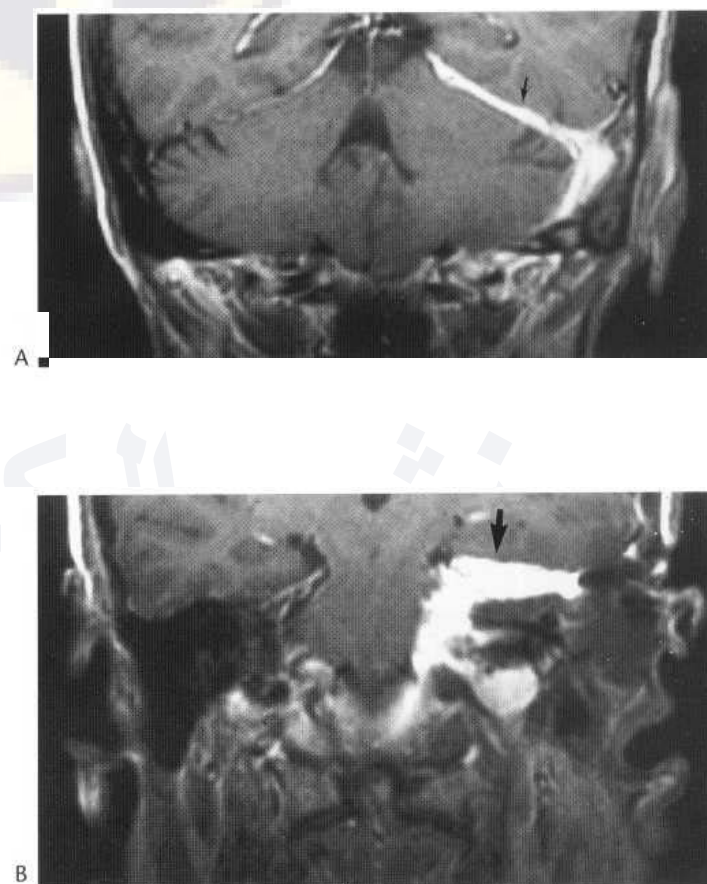


Fig. 52.38 (A,B) Coronal T₁-weighted MR with gadolinium enhancement showing a meningioma of the posterior cranial fossa extending into the IAM and jugular fossa as well as onto the superior surface of the petrous pyramid and into the tentorium (arrows).

omy. We believe that densitometry should be done prior to any stapedectomy procedure, even if there is a favourable air-bone gap'.

Fenestral otosclerosis This is harder to assess but thickening of the stapes footplate or even obliteration of the oval window can be

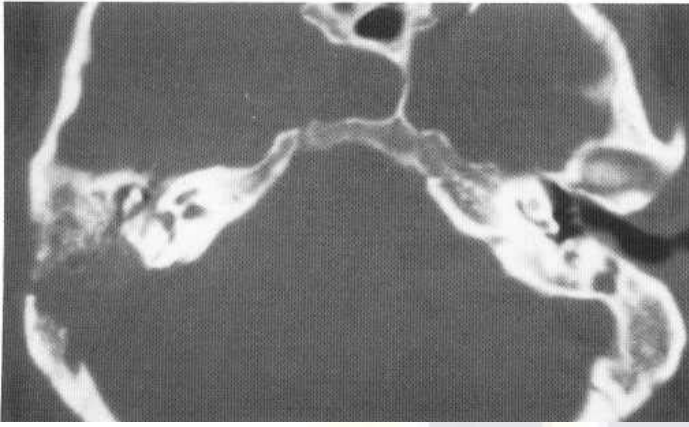


Fig. 52.39 Ragged erosion of the right mastoid region by a carcinoma shown on this axial CT section.

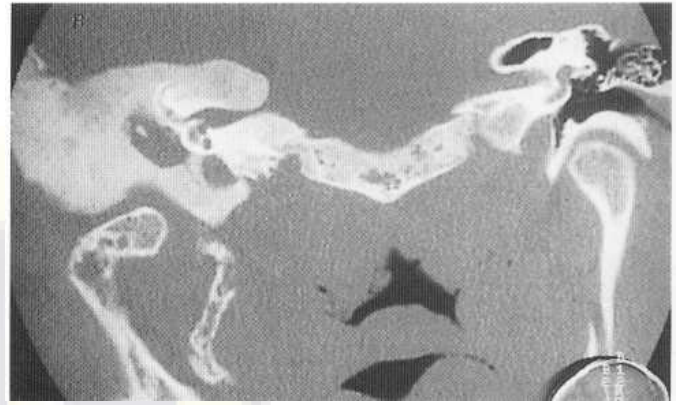


Fig. 52.42 Fibrous dysplasia, also affecting the right mandible, is narrowing the right IAM and external meatus. Such expansion of abnormal bone may lead to cholesteatoma formation behind the obstruction as here, but unlike Paget's disease the otic capsule does not appear to be affected by fibrous dysplasia.



Fig. 52.40 Malignant otitis externa. Bone destruction in the region of the mastoid (arrow) around the internal carotid artery (a) and temporomandibular joint (T) as well as sclerosis of the basisphenoid (s) are shown on this axial CT scan.

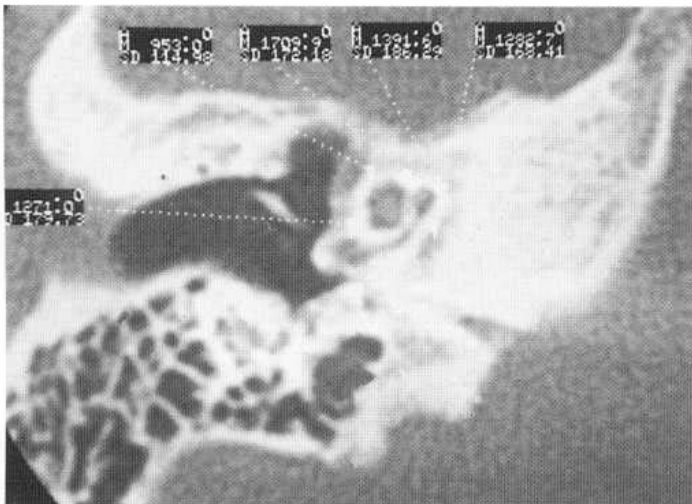


Fig. 52.41 Axial CT with densitometry, showing otospongiosis as a ring of rarefaction around the cochlear coils. The densitometry readings are mostly around 1200 HU. The normal range is 1800-2400 HU.

shown by coronal section CT at 1 mm intervals. Such an examination can also be used to reveal complications after stapedectomy, such as a prosthesis that is too long or has become displaced. Otosclerosis affects only the labyrinthine capsule, unlike widespread bone dysplasias which either affect the capsule not at all, like fibrous dysplasia (Fig. 52.42), or at a late stage as in Paget's disease (Fig. 52.43). Both diseases can result in encroachment of bone on the middle ear cavity and on the internal and external auditory meatus. Congenital sclerosing bone dysplasias cause greatly increased density of the petrous pyramid but this seems to be due to an abnormality of surrounding periosteal bone and not a change in the labyrinthine capsule itself.

Demineralisation of both the otic capsule and the surrounding bone is a feature of osteogenesis imperfecta, which radiologically is often indistinguishable from, and indeed may accompany, otospongiosis. The increasing use of cochlear implants necessitates good demonstrations of the cochlear coils and oval and round windows. Complete or partial obliteration of these structures is often due to severe, often undiagnosed, otosclerosis and labyrinthitis obliterans. The latter condition may be the end-result of a meningitic episode or infective labyrinthitis (Fig. 52.23).

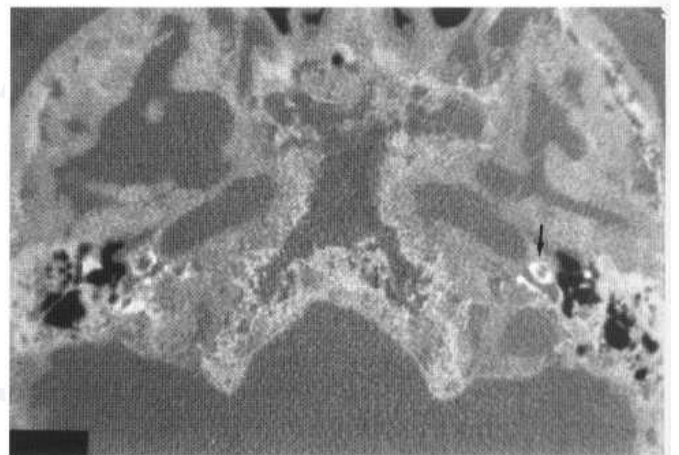


Fig. 52.43 Gross Paget's disease of the skull base which is encroaching upon the labyrinthine capsule on both sides. Only remnants of normal capsular bone surround the membranous labyrinth in the cochlea (arrow).

REFERENCES AND SUGGESTIONS FOR FURTHER READING

- Phelps, A. P., Lloyd, G. A. S. (1983) *Radiology of the Ear*. Oxford: Blackwell Scientific.
- Phelps, P. D., Lloyd, G. A. S. (1990) *Diagnostic Imaging of the Ear*. Berlin: Springer-Verlag.
- Phelps, P. D., Stansbie, J. M. (1988) Glomus jugulare or tympanicum? The role of CT and MR imaging with gadolinium DTPA. *Journal of Laryngology and Otology*. 102. 766-776.
- Phelps, P. D., Stansbie, J. M. (1993) *Clinical FNT Radiology*. Oxford: Butterworth Heinemann.
- Phelps, P. D., Wright, A. (1990) Imaging cholesteatoma. *Clinical Radiology*, 41, 156-162.
- Phelps, A. P., Lloyd, G. A. S., Sheldon, P. W. E. (1977) Congenital deformities of the middle and external ear. *British Journal of Otolaryngology*, 50, 714-727.
- Schwartz, J. D. (1986) *Imaging of the Temporal Bone*. New York: Thieme.
- Schwartz, J. D., Harnsberger, H. R. (1992) *Imaging of the Temporal Bone*. New York: Thieme.
- Valavanis, A., Seuhiger, O., Naidich, T. P. (1987) *Clinical Imaging of the Cerebello-Pontine Angle*. Berlin: Springer-Verlag.
- Valvassori, G. E., Mafee, M. F., Carter, B. L. (1995) *Imaging of the Head and Neck*. New York: Thieme.
- Vogl, T. J., Juergens, M., Balzer, J. O., et al (1994) Glomus tumors of the skull base: combined use of MR angiography and spin-echo imaging. *Radiology* v. 192, 103-110.

نشر الکترونیکی
موسسه انتشاراتی
نوردانش



نشر الکترونیکی
موسسه انتشاراتی
نوردانش

53

THE SKULL

David Sutton

The skull is a very complex structure, composed of more than 20 different bones. A thorough radiological survey of the skull to demonstrate all anatomical features is impractical as a routine procedure, as it would require too many different projections and too many films to be cost-effective. In the past, and when skull surveys were more widely practised, it was considered a reasonable compromise to take four standard views of the skull. The four standard projections are illustrated in Figure 53.1 and the resulting films are illustrated in Figures 53.2-53.5.

The student should be familiar with these four standard projections, even though they are no longer routinely practised, since they illustrate so many important anatomical features, and, as will be apparent later in this chapter, certain abnormalities may only be shown in one projection.

The **standard projections** are:

1. The *lateral view*, taken as shown in Figure 53.1A with the side of the suspected lesion against the film. The centring point is over the pituitary fossa—1 cm above the orbitomeatal line and 2.5 cm anterior to the external auditory meatus with the head in the true lateral position.

2. The *PA view*. This should be taken with the orbitomeatal line vertical and the central ray tilted 20° caudally and centred on theinion in order to project the dense petrous bones clear of the orbits (Fig. 53.1 B).

3. The *Towne's view* obtained by tilting the central ray 30° caudally and centring as shown in Figure 53.1 C.

4. The *basal view* obtained by placing the patient's head in the 'hanging head' position with the anatomical baseline horizontal, and centring vertical to it and between the angles of the mandible (Fig. 53.1 D).

The decline in the routine use of the four standard projections applies particularly to the investigation of suspected intracranial tumours and followed the introduction of CT scanning in 1972. It soon became clear that in the diagnosis of intracranial tumours CT had an accuracy approaching 100% in confirming and localising a lesion, and the tumour was also characterised in a high proportion of cases. By contrast, the skull survey identified fewer than 50% of patients with intracranial tumours and had an even poorer record in localisation and characterisation. This led many workers to dispense with routine skull surveys in the investigation of suspected cerebral tumours. Where skull films are taken it is now standard practice to take only a *lateral* film unless there is clinical evidence to suggest that a lesion may be shown in other views. Several series have demonstrated that the single lateral view is as likely to show a lesion as a full skull survey in patients with no clinical evidence of a localised lesion.

Although plain films of the skull are now relatively unimportant in the diagnosis of cerebral tumours and other cerebral lesions, they remain essential in the investigation of lesions affecting the bony skull, including fractures, bony tumours (both primary and secondary), and inflammatory lesions. In addition to the standard views, many cases may require extra projections to define specific anatomical landmarks.

The special views in general use include:

1. Optic foramen
2. Sinuses
3. Mastoids
4. Petrous bones
5. Coned pituitary fossa.

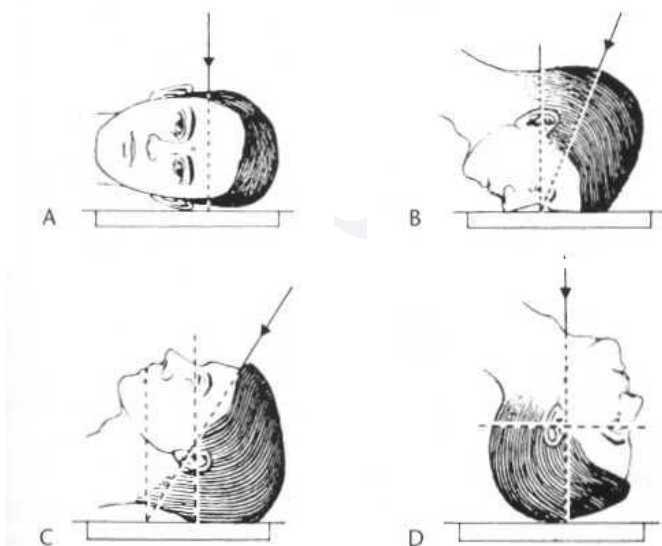
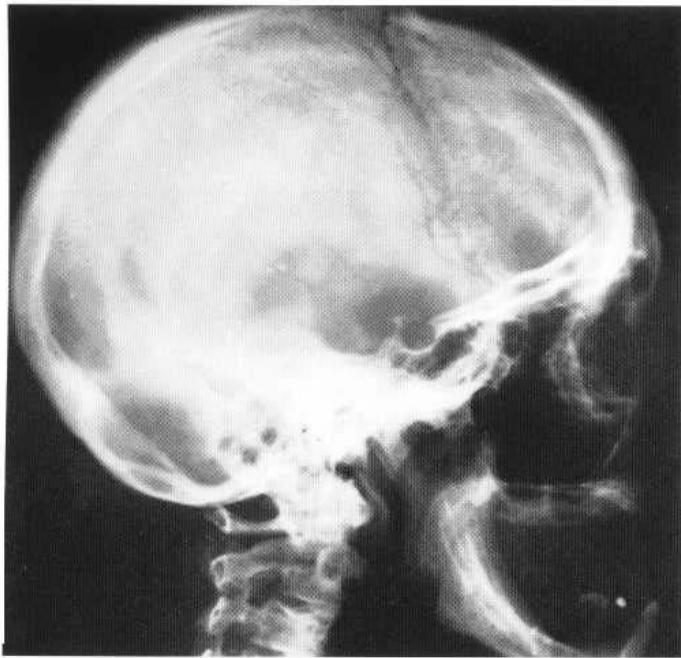
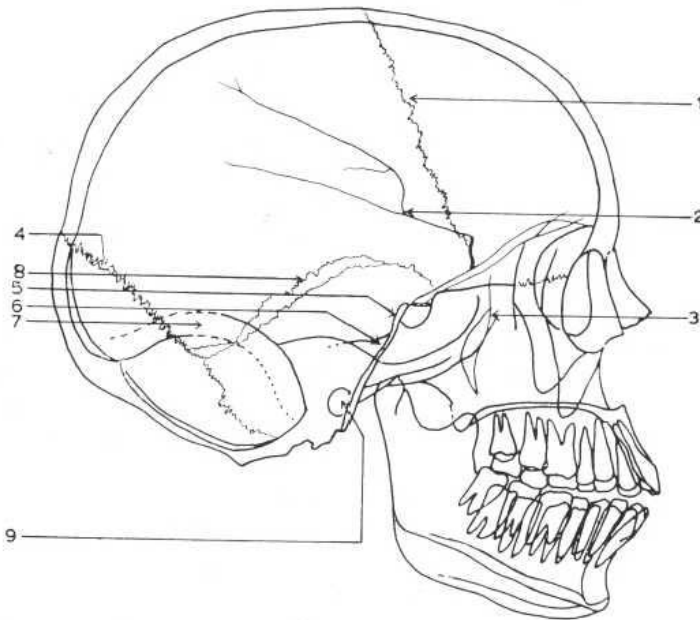


Fig. 53.1 The four standard skull projections: (A) lateral; (B) PA; (C) Towne's; (D) basal.



A

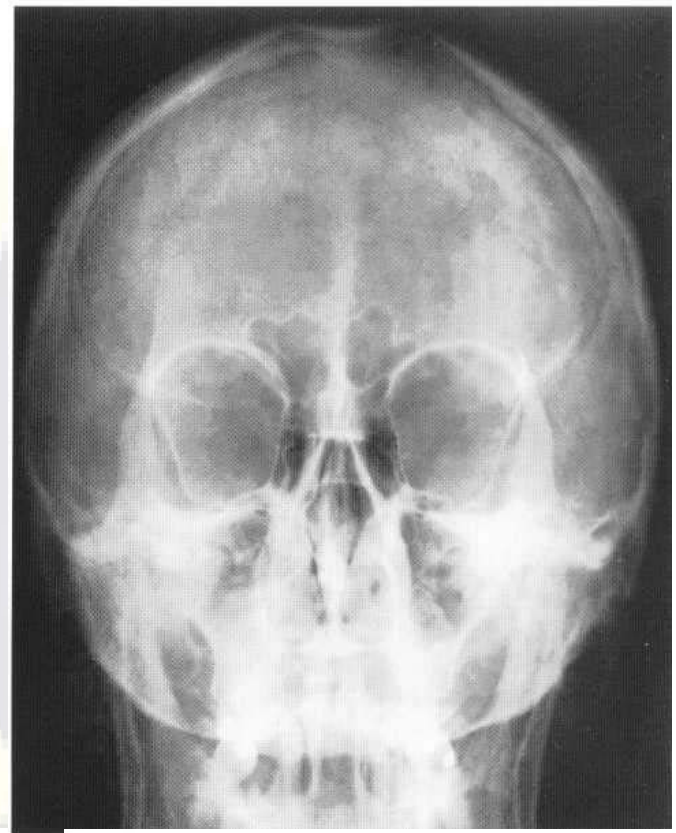


B

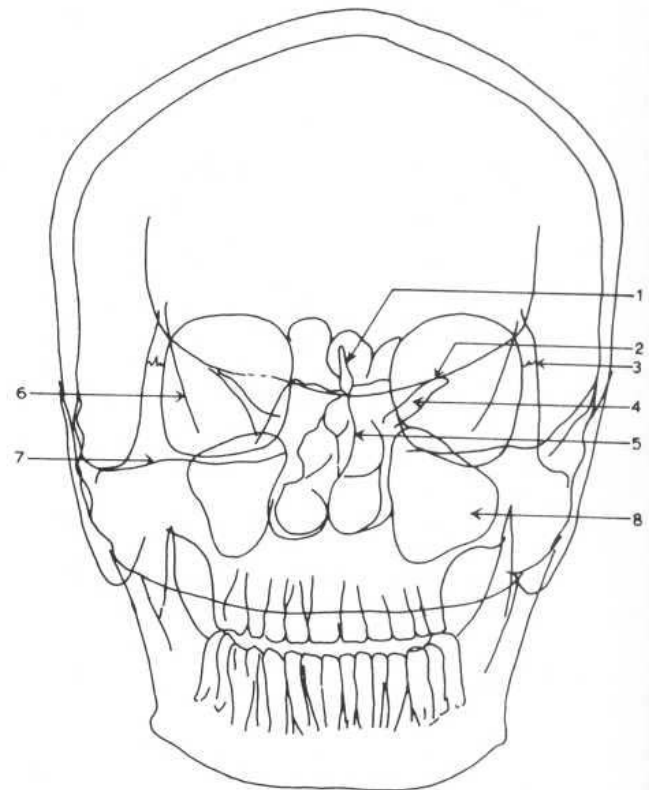
Fig. 53.2 (A) X-ray film of skull taken in standard lateral projection. (B) Diagram to illustrate the standard lateral view. 1 = coronal suture; 2 = meningeal vascular marking, anterior branch; 3 = anterior border of middle fossa; 4 = lambdoid suture; 5 = dorsum sellae; 6 = clivus; 7 = lateral sinus; 8 = squamosoparietal suture; 9 = external auditory meatus.

The projections used for the optic foramina, sinuses, petrous bones, and mastoids are described in detail in the appropriate chapters devoted to these structures (Chs 51, 48, 52).

The optic canal In adults this appears in the standard oblique optic foramen view as a ring shadow projected over the superolateral part of the orbit (Fig. 53.6); in infants and children it is more pear-shaped. The canal passes from the middle fossa (sulcus chiasmaticus) to the back of the orbit and carries the optic nerve and ophthalmic artery. It is 4-9 mm long and 4-6.5 mm in maximum diameter as measured on the film.



A



B

Fig. 53.3 (A) X-ray film taken in standard AP projection. (B) Diagram to illustrate (A) 1 - crista galli; 2 = lesser sphenoidal wing; 3 = zygomaticofrontal suture; 4 superior orbital fissure; 5 nasal septum; 6 innominate line formed by inner wall of temporal fossa; 7 = superior margin of petrous ridge; 8 = maxillary antrum.

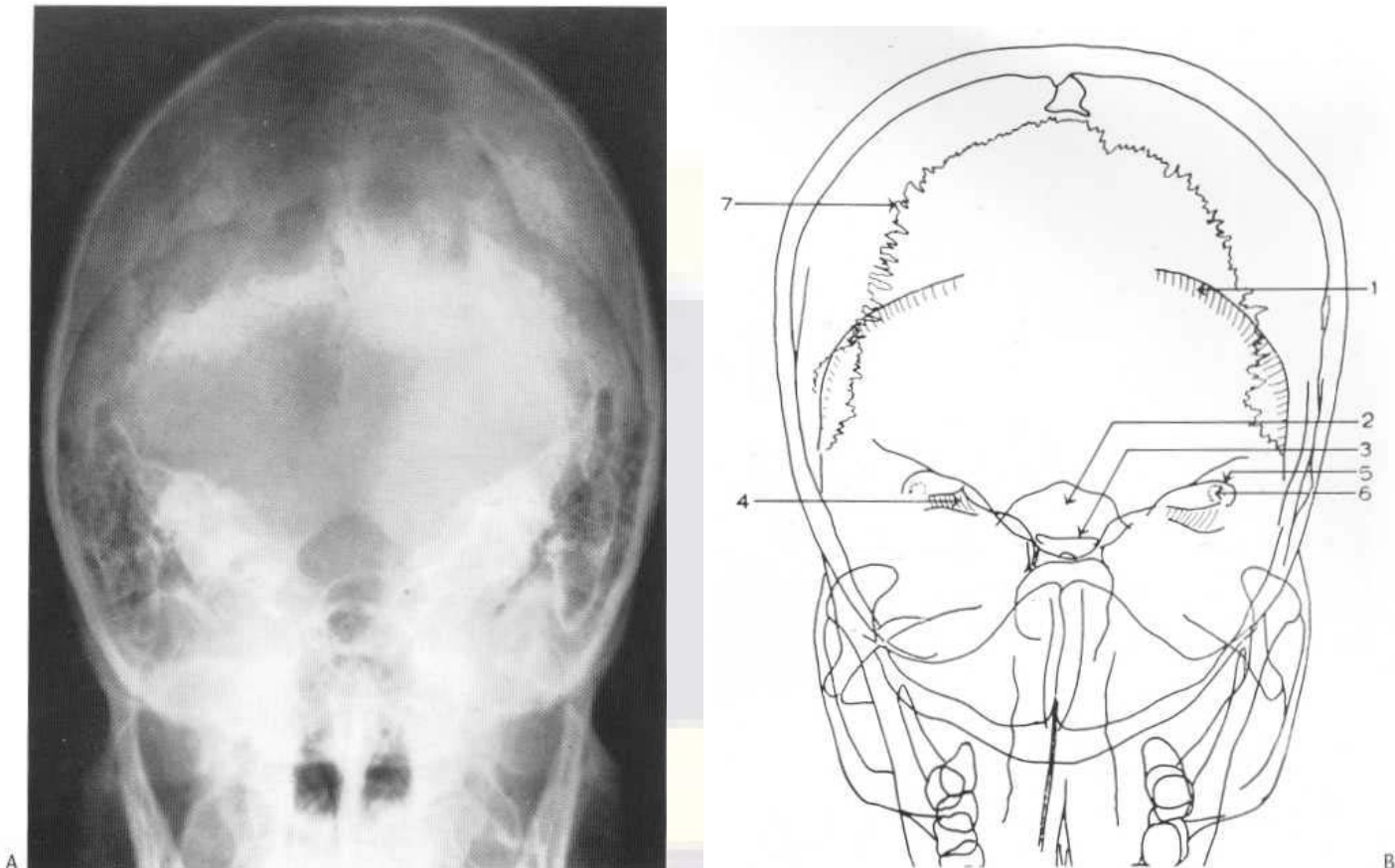


Fig. 53.4 (A) X-ray film taken in standard Towne's projection. (B) Diagram to illustrate (A) 1 = lateral sinus; 2 = foramen magnum; 3 = dorsum sellae; 4 = internal auditory meatus; 5 = acuate eminence; 6 = superior semicircular canal; 7 = lambdoid suture.

A so-called 'keyhole' optic foramen is encountered as a congenital anomaly in 4% of people and may be unilateral. Rarely, the keyhole is divided into two separate foramina by a fine bony strut ('figure-8' foramen). In these cases the larger upper foramen carries the optic nerve and the lower foramen the ophthalmic artery.

The inferolateral border of the optic canal is also a bony strut, known as the 'optic strut', which separates it from the top of the sphenoidal fissure. Both the optic strut and the anterior clinoid may be pneumatised, further complicating the appearances. Large retro-orbital aneurysms, usually involving the origin of the ophthalmic artery, can produce a characteristic erosion of the optic strut.

The paranasal sinuses These are discussed in detail in Chapter 48. They are rudimentary at birth and increase in size with age, reaching full development in the adult skull. There is a wide variation in adult size, particularly of the frontal sinuses, ranging from the rudimentary to frontal sinuses reaching the lateral aspect of the skull. Such large sinuses are a particular feature of *acromegaly*, and are of importance to the neurosurgeon as they can be unintentionally perforated in frontal craniotomy if no preliminary skull radiograph is taken.

The mastoids These are discussed in more detail in Chapter 52. Like the sinuses they are absent or rudimentary at birth and reach full development in the adult, where they can also vary greatly in size and extent.

The petrous bones These are fully discussed in Chapter 52. The internal auditory meatus is well shown in the standard Towne's view, or in the Stockholm C or transorbital views (Figs 53.7-53.9).

Vascular markings The *meningeal* markings are easily recognised by their constant position and course, following the anterior and posterior branches from the skull vault to the skull base and foramen spinosum. They increase gradually in size from above downwards, resembling the outline of a river and its tributaries on a map (Figs 53.2, 53.10). The meningeal vascular markings are also easily identified on the internal surface of a dried skull.

The supraorbital and middle temporal arteries which lie on the outer surface of the skull are occasionally associated with vascular grooves which can be mistaken for fractures (Fig. 53.10).

The *diploic* vascular markings, on the other hand, are extremely variable in size, number and position. They may be extremely numerous or completely absent and are most prominent in the parietal region. Characteristically their course seems random and purposeless. They may run a short course, widening and narrowing, or they may be star-shaped. Although easily seen on the skull radiograph, they are not identifiable on the dried skull as they lie in the diploic between the skull tables.

The pituitary fossa The normal pituitary fossa as shown in a lateral skull film can vary considerably in size. A length of 11-16 mm and a depth of 8-12 mm are regarded as within normal limits. However, the question of the upper limit of normal remains largely subjective and few experienced workers rely on such measurements to assess abnormal enlargement; as with all human measurements, the upper limit of normal overlaps the pathological.

An unusually small pituitary fossa as seen in a lateral radiograph has no particular significance, although a small sella is said to be a common finding in *mn0lonia congenita*.

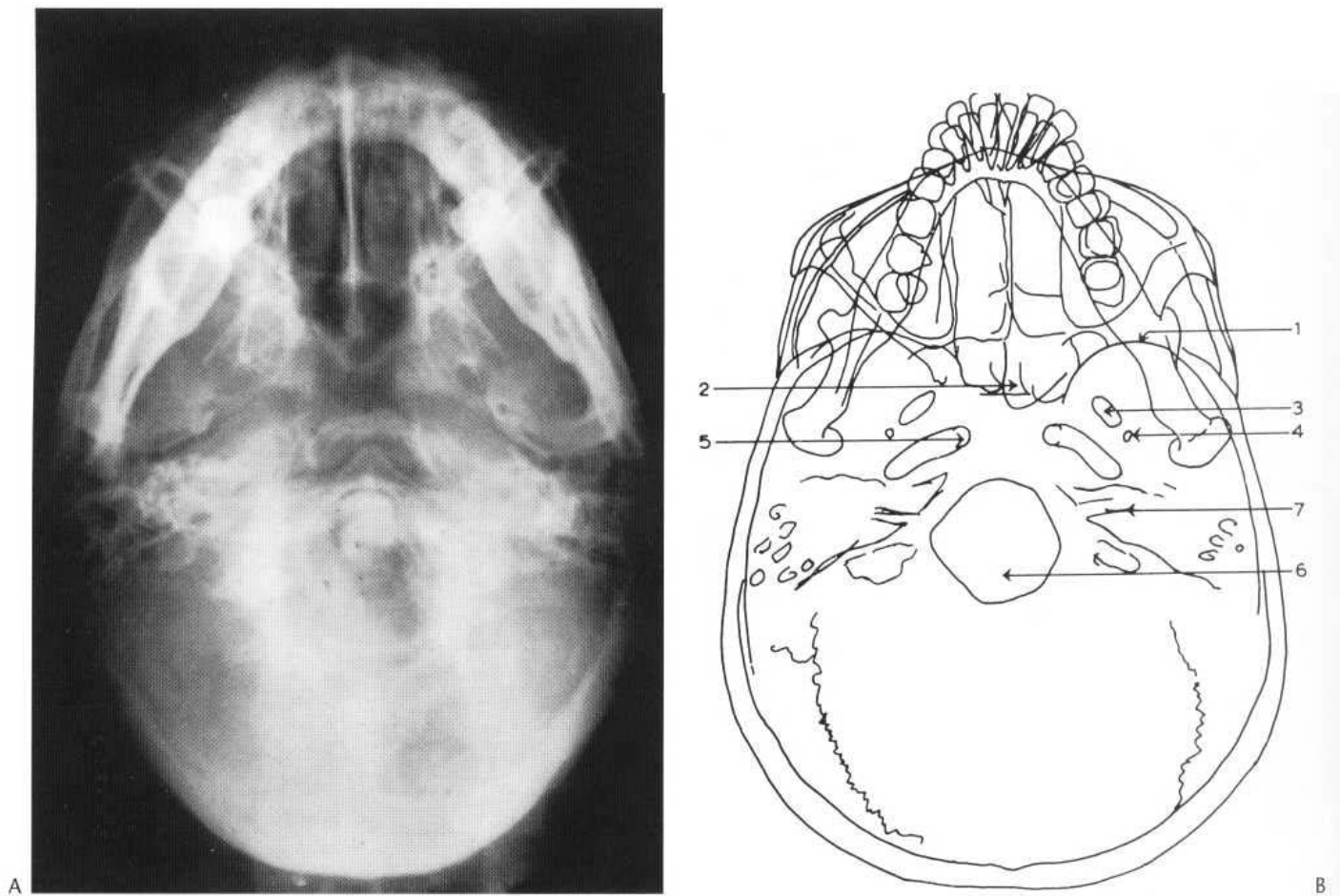


Fig. 53.5 (A) X-ray film taken in standard basal view. (B) Diagram to illustrate (A) 1 = greater sphenoidal wing; 2 = sphenoidal sinus; 3 = foramen ovale; 4 = foramen spinosum; 5 = foramen lacerum medium; 6 = foramen magnum; 7 = internal auditory meatus.

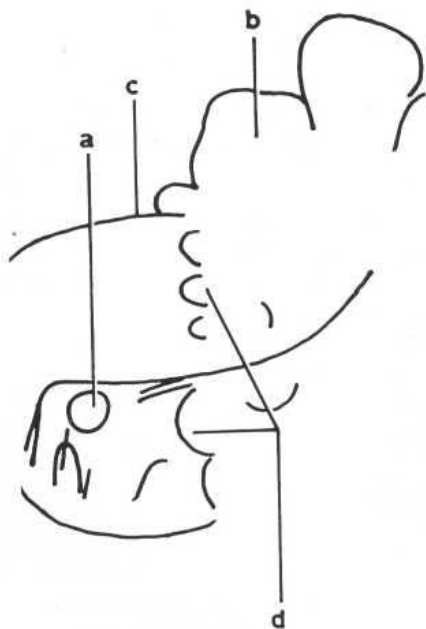


Fig. 53.6 Structures seen in optic foramen view. a = optic foramen; b = frontal sinuses; c = roof of orbit; d = ethmoid sinuses. See also Fig. 53.54.

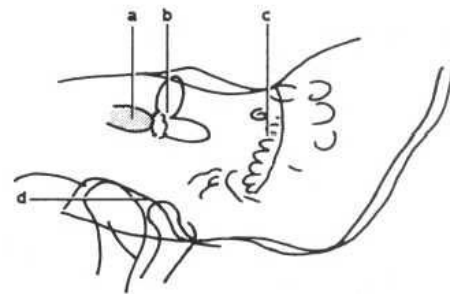


Fig. 53.7 Structures seen in oblique (Stockholm C) view of petrous bone. a = internal auditory meatus; b = internal ear and semicircular canals; c = mastoid air cells; d = temporomandibular joint.

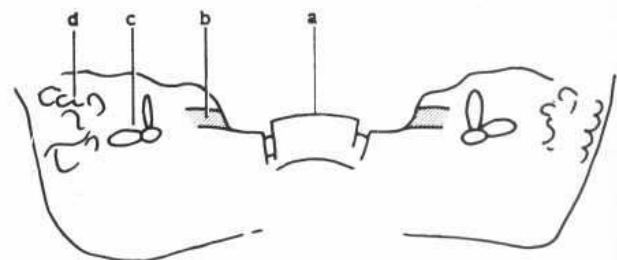


Fig. 53.8 Internal auditory meatuses as seen in the Towne's view. a = dorsum sellae; b = internal auditory meatus; c = internal ear; d = mastoid air cells.

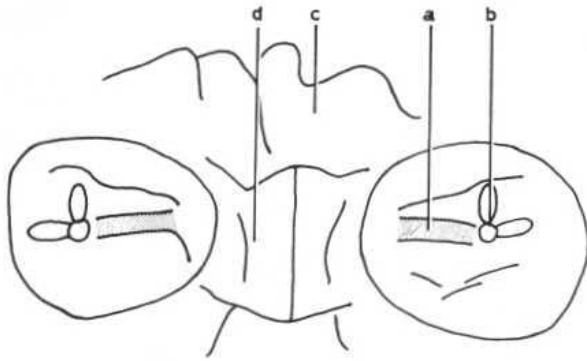


Fig. 53.9 Internal auditory meatus as seen in transorbital view. a = internal auditory meatus; b = internal ear and semicircular canals; c = frontal sinuses; d = ethmoid sinuses.

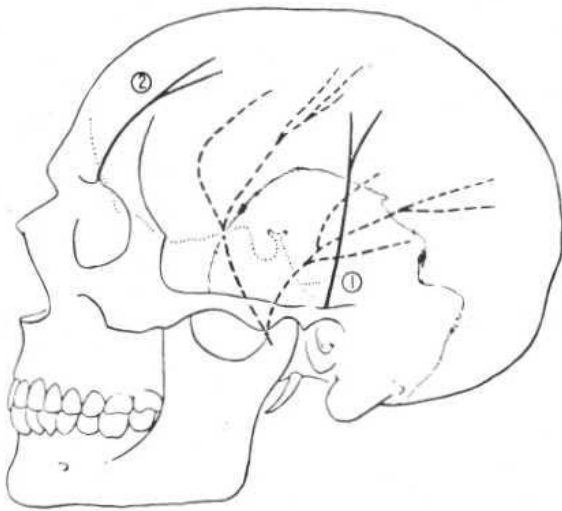


Fig. 53.10 Two vascular markings on the outer surface of the skull which may resemble fractures and are due to: (1) the middle temporal artery; (2) the supraorbital artery. The meningeal vascular markings are shown by dotted lines. (After Schunk & Marayama 1960.)

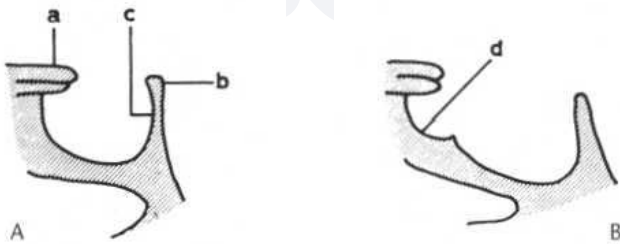


Fig. 53.11 (A) Diagram of normal sella. a = anterior clinoids; b = posterior clinoids; c = cortex or 'lamina dura' of dorsum and floor of sella. (B) J-shaped sella. d = sulcus chiasmaticus.

The appearance of the *dorsum sellae* is of considerable importance. In a healthy young adult the dorsum has a well-defined bony cortex outlining its anterior and posterior surfaces (Fig. 53.11 A). Beneath the cortex the bone has a spongy texture and varies in thickness. Occasionally the sphenoid sinus extends into the dorsum (pneumatisation of the dorsum).

Loss of definition of the dorsum sellae may occur as a normal finding in the *elderly* in association with generalised osteoporosis, and it is also seen commonly in association with *prolonged hypertension*. In both cases it is important to distinguish such causes

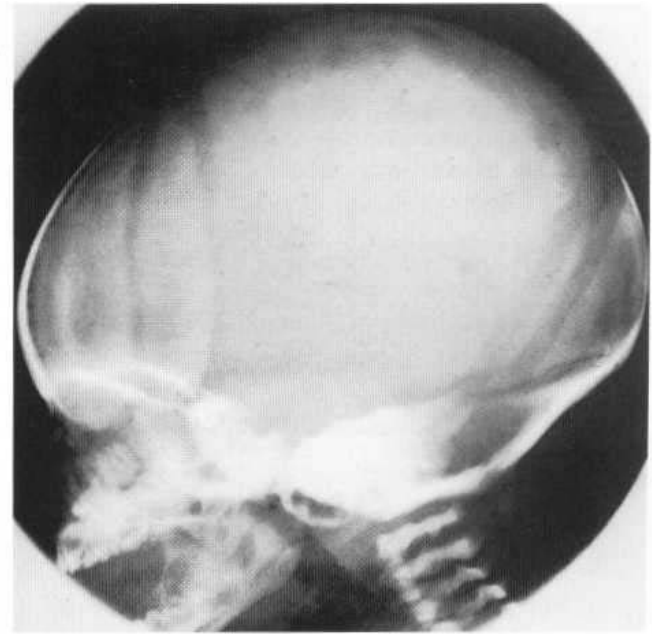


Fig. 53.12 Neonate skull. Note the wide fontanelles and sutures.

from the similar changes seen in patients with chronic raised intracranial pressure (see below).

The *J-shaped sella* (synonyms: 'omega-shaped', 'shoe-shaped' or 'hour-glass' sella) is an elongated sella with a shallow anterior convexity (Fig. 53.11 B) which represents an exaggeration of the normal slight impression of the sulcus chiasmaticus. The latter is rarely seen in films of an adult skull, but is sometimes well shown in those of children (about 5%). This odd-shaped sella has also been described in glioma of the optic chiasm, in children with 'gargoylism', and in those with chronic hydrocephalus.

The sutures These are readily recognised on films of the adult skull and their serrated appearances are illustrated in Figures 53.2-53.5. The serrations visualised lie on the outer table: the suture is linear on the inner table but this is not identified except occasionally when the rays are vertical to the suture. The superimposition on the serrated suture should help to differentiate it from a fracture.

In infants the sutures appear quite different and are easily recognisable as radiolucent linear bands running to and from the wide-open fontanelles (Fig. 53.12).

Skull vault The inner and outer tables of the vault are visible in most projections, as is the diploe in between. *Pacchionian impressions* are produced on the inner table by the pacchionian bodies and appear as relative translucencies suggesting small bone defects. Tangential views confirm that they are due to small depressions on the inner table. They are most numerous in the parasagittal region but may be seen in other sites, particularly around the torcular, where they can simulate pathological bone defects due to metastases.

Normal intracranial calcification

Intracranial calcification regarded as physiological can occur at various sites. These are listed in Box 53.1.

Pineal calcification is rarely seen in radiographs of children's skulls but is shown in most adult skulls, the percentage increasing

Box 53.1 Normal intracranial calcification

1. Pineal
2. Habenula
3. Choroid plexuses
4. Dura (falx; tentorium; over vault)
5. Ligaments (petroclinoid and interclinoid)
6. Pacchionian bodies
7. Basal ganglia and dentate nuclei
8. Pituitary gland
9. Lens

with age. It usually occupies an area 3-5 mm in diameter but can be more extensive (Fig. 53.13A).

The *habenular commissure* lies directly anterior to the pineal at the back end of the third ventricle. It is frequently calcified but is often mistaken for the pineal, although its characteristic shape should readily distinguish it. The calcification is typically C-shaped with the open part of the letter facing backward (Fig. 53.13B).

The *choroid plexuses* are frequently calcified, mainly in the glomus as it lies in the region of the trigone. Calcification varies from a few punctate dots to a larger dense calcification extending over an area more than 1 cm in diameter (Fig. 53.14). The calcification is usually bilateral and symmetric as seen in the Towne's view.

Dural calcification is common in the middle-aged and elderly and is most easily recognised in the falx (Fig. 53.15) or tentorium.

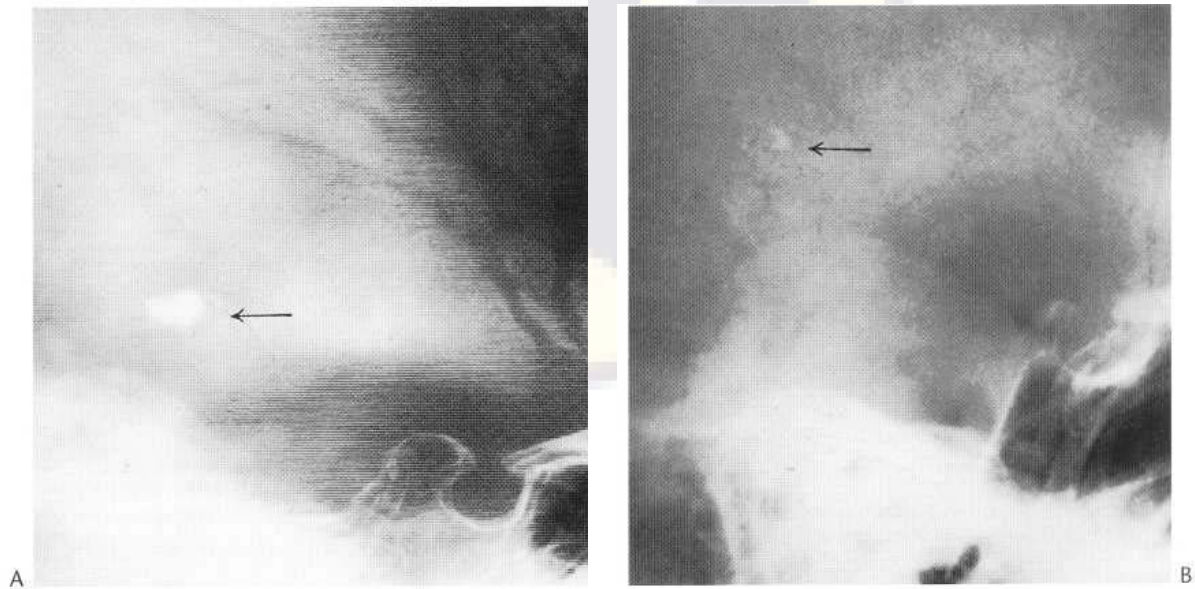


Fig. 53.13 (A) Heavily calcified but normal pineal (arrow). (B) Calcification in the habenular commissure (arrow).

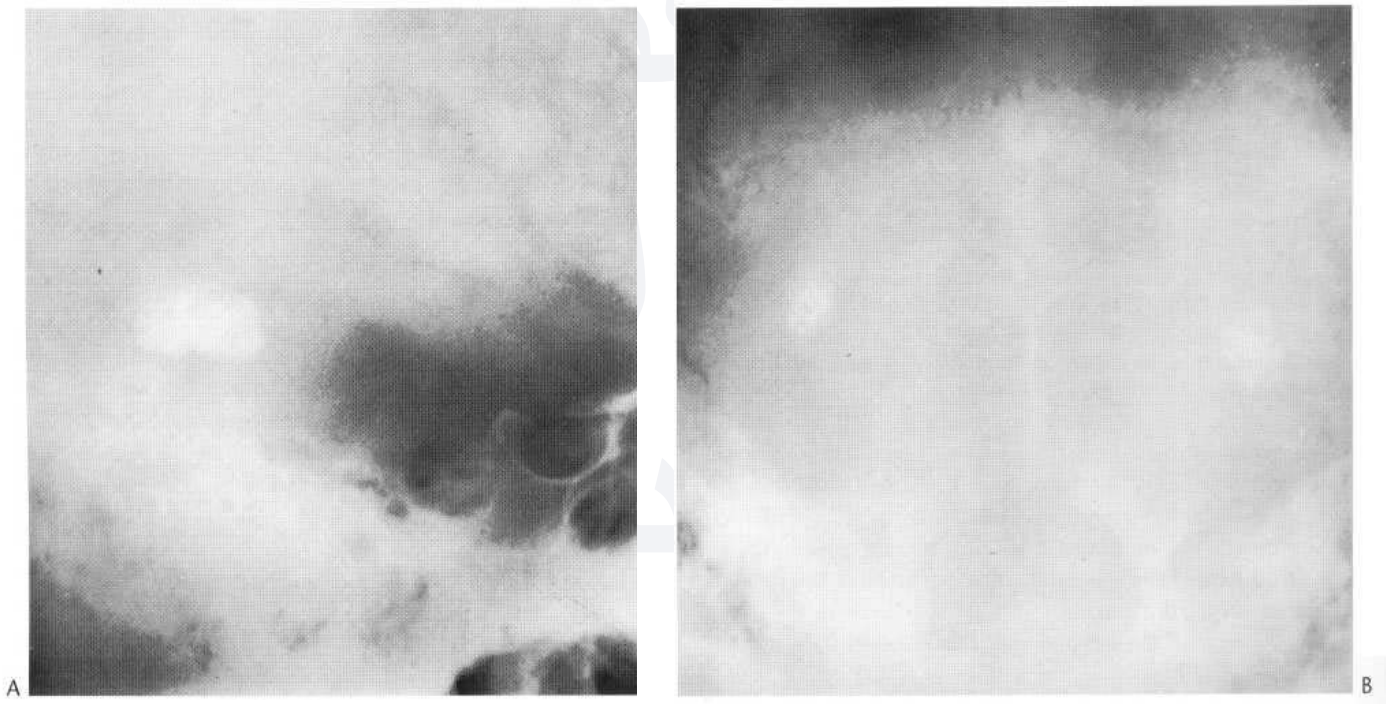


Fig. 53.14 Calcified choroid plexuses. (A) Lateral view. (B) Towne's view.

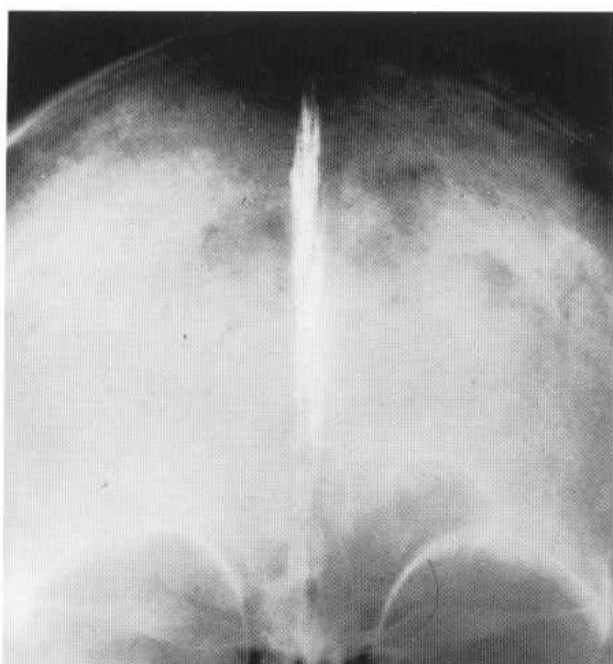


Fig. 53.15 Heavily calcified falx.

It may also occur over the vault, when it is difficult to recognise except in tangential views.

The *petroclinoid ligaments* are frequently calcified; this is identified in the lateral film as a linear calcification between the tip of the dorsum and the petrous apex. The interclinoid ligaments may also calcify, leading to so-called 'bridging' of the sella.

Pacchionian bodies can calcify, although this may be difficult to identify against the bony vault.

Pituitary calcification in normal patients has been recognised histologically but is very rarely identified by simple radiology.

Basal ganglia and *dentate nuclei* calcification are discussed below but often appear to be 'idiopathic' with no demonstrable pathological cause.

Lens calcification is recognisable in the elderly as a ring shadow in the orbit. In lateral view it appears as a linear shadow, being seen end-on.

The skull in neonates and infants

The neonate skull may appear elongated and sometimes shows overlapping of cranial bones from the moulding during birth. These appearances change to a more normal contour within a week or so.

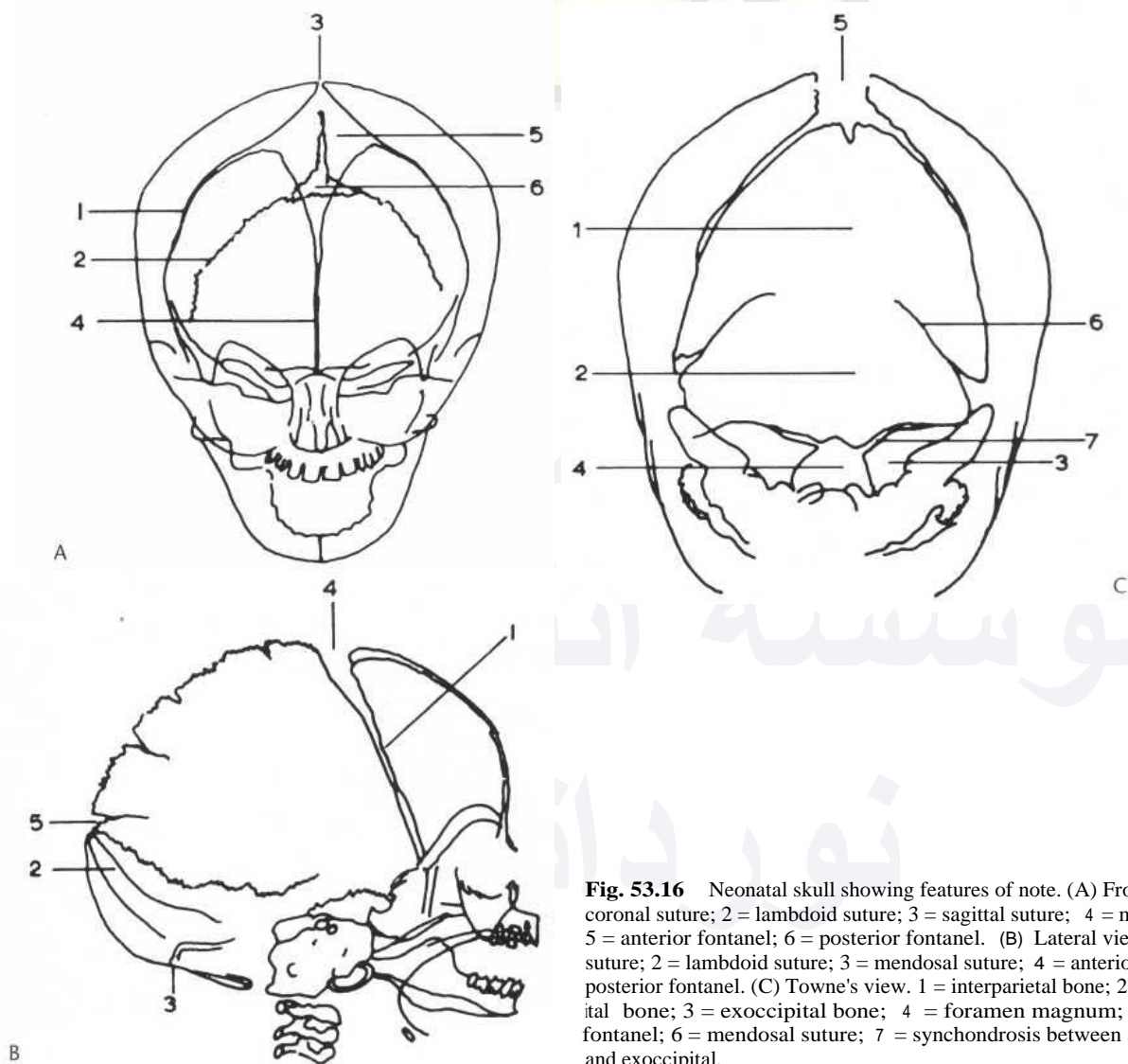


Fig. 53.16 Neonatal skull showing features of note. (A) Frontal view. 1 = coronal suture; 2 = lambdoid suture; 3 = sagittal suture; 4 = metopic suture; 5 = anterior fontanel; 6 = posterior fontanel. (B) Lateral view. 1 = coronal suture; 2 = lambdoid suture; 3 = mensoidal suture; 4 = anterior fontanel; 5 = posterior fontanel. (C) Towne's view. 1 = interparietal bone; 2 = supraoccipital bone; 3 = exoccipital bone; 4 = foramen magnum; 5 = posterior fontanel; 6 = mensoidal suture; 7 = synchondrosis between supraoccipital and exoccipital.

In the lateral view the vault is thin, with no differentiation into inner and outer tables, and no vascular markings or convolutional impressions to be seen. The sutures appear as translucent hands and the fontanelles are widely open. Within the suture lines, wormian bones are occasionally seen, although these unite with the vault as growth proceeds. The anterior and middle fossae are short and slope downward more than in the adult. These features are illustrated in Figures 53.12 and 53.16.

In premature infants the skin may be very lax and form folds which can produce linear shadows on the skull film. It is important to recognise their true nature and not mistake them for fractures.

The size of the sutures varies widely at birth and they can be from 1.5 to 10 mm wide. The wider sutures narrow rapidly and most are below 3 mm within a few months. The *spheno-occipital suture* is readily visible at birth and there is also a synchondrosis just behind the foramen magnum, dividing the occipital bone into upper and lower portions known as the supraoccipital and exoccipital regions, respectively (Fig. 53.16C). At this stage the occipital bone also shows an oblique suture (the *mendosal suture*) passing upward and medially from its lower part on each side, and this should not be confused with a fracture.

The *metopic suture* of the frontal bone is also evident at birth and begins to disappear from about the ninth month. It usually fuses by the end of the second year, although occasionally it persists into adult life.

The *posterior fontanel* closes at 3-6 months, while the larger *anterior fontanel* closes at 15-18 months. In children with hydrocephalus the fontanelles remain open longer, providing a useful window for ultrasound examinations.

THE ABNORMAL SKULL

Congenital lesions

Skulls which appear abnormal in shape are conventionally described using Greek terminology. Thus skulls that appear abnormally long in relation to their transverse diameter are referred to as *dolichocephalic*, while those that are broad in relation to their length are termed *brachycephalic*.

In some patients a step-like deformity is seen at the back of the skull where the occipital bone overlaps the parietals at the lambdoid suture. This is termed *bathrocephaly* and should not be mistaken for a traumatic lesion.

Craniosynostosis Most abnormalities of skull shape are due to premature fusion of skull sutures. While simple X-ray will usually show the sutures involved, these are more clearly and elegantly demonstrated by CT with 3D reconstruction.

Trigonocephaly (triangular head) is the term used for patients whose frontal bones appear wedge-shaped anteriorly; this is thought to be due to premature in utero fusion of the metopic suture.

Scaphocephaly (boat-shaped skull—from the resemblance to the upturned keel of a boat) refers to a narrow dolichocephalic skull resulting from premature fusion of the sagittal suture. It is the commonest form of craniosynostosis and is commoner in boys than in girls.

Plagiocephaly (oblique or slanting skull) describes a skull that is markedly asymmetric due to unilateral premature fusion of the lambdoid and coronal sutures.

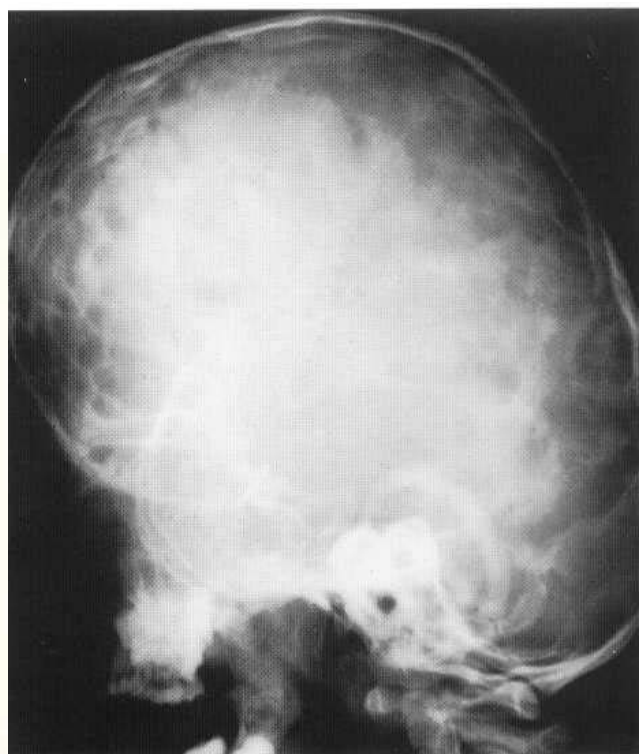


Fig. 53.17 Oxycephaly due to premature fusion of the coronal sutures. Note increased convolutional markings.

Microcephaly is associated with a generalised premature fusion of all the skull sutures and the skull vault is abnormally small. The brain is small and the subject is mentally handicapped.

Oxycephaly (pointed skull), *acrocephaly* (peak or summit skull) and *turriccephaly* (tower skull) are all terms used to describe the brachycephalic skull which results from premature fusion of the coronal and lambdoid sutures (Fig. 53.17). While many of these cases merely present a bizarre appearance, in some there is compression of the optic nerves, and others have been described with VIIIth nerve lesions, mental handicap and other neurological lesions. There is also a rare association with other anomalies, giving rise to several syndromes.

Thus, there is an association with syndactyly known as *Apert's syndrome* or acrocephalosyndactyly (Fig. 53.18), and with polydactyly, known as *Carpenter's syndrome* or acrocephalopolysyndactyly. The latter is characterised by obesity and mental handicap as well as polydactyly and mild soft-tissue syndactyly.

Crouzon's disease (hereditary craniofacial dysostosis) is a form of acrocephaly with hypoplasia of the facial bones, hypertelorism and exophthalmos. Other features are a 'parrot-beak nose', prognathism with a short upper lip, choanal atresia and a high arched palate. There is also cor pulmonale and mental handicap.

Many operations have been used for the treatment of craniosynostosis and it was hoped that preventing premature fusion of the sutures would also prevent mental handicap and neurological defects. However, it is probable that maldevelopment of the brain in microcephaly is primary rather than secondary to the skull lesions. It is therefore unlikely that operations for microcephaly can have any but cosmetic value, although they may prevent nerve compression in oxycephaly. Mere excision of the sutures is insufficient to prevent fusion, which rapidly recurs unless the bone surfaces are separated by interposing such material as tantalum foil. Operation

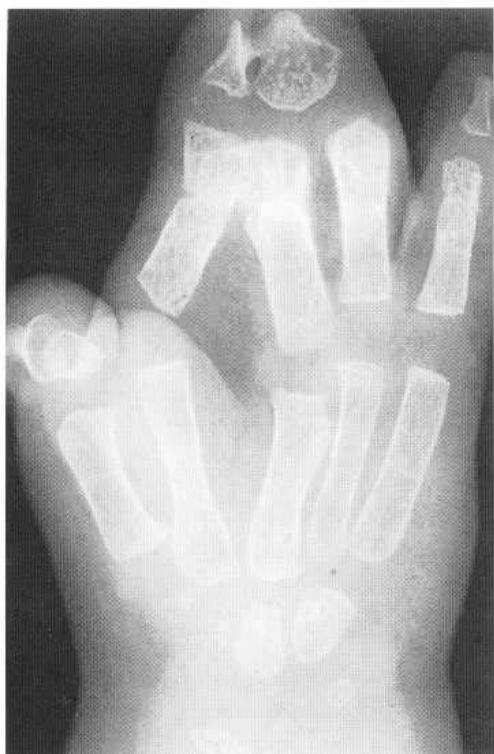


Fig. 53.18 Hand of the same patient as Fig. 53.17, showing syndactyly. The combination of oxycephaly and syndactyly comprises Apert's syndrome.

is performed as early as possible because of rapid brain growth, and before 6 weeks where two or more sutures are involved. After 9 months even cosmetic results are poor.

Lacunar skull This condition is characterised by groups of round, oval or finger-shaped pits on the inner surface of the infant skull vault. They are separated by ridges of bone and appear in fetal life on the thickest parts of the parietal, frontal and occipital bones in the skull vault (Fig. 53.19). There are usually associated anomalies of the central nervous system, the commonest being myelomeningocele and encephalocele, and there may also be

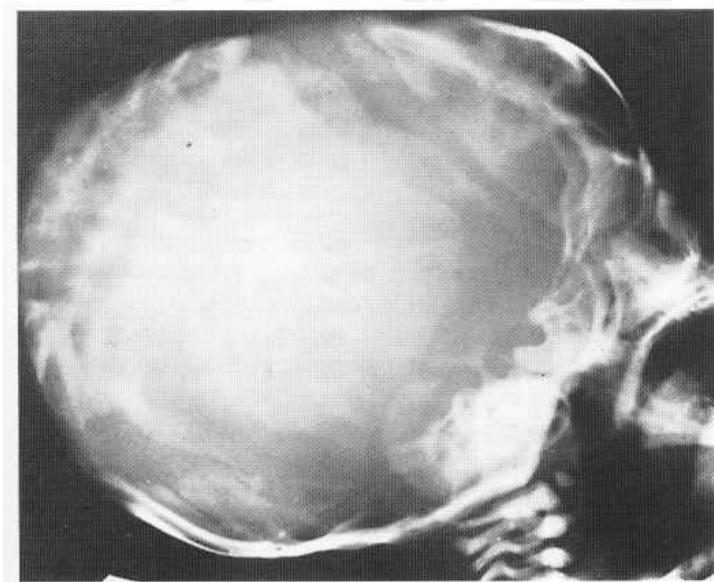


Fig. 53.19 Lacunar skull in an infant. Note the wide sutures.

hydrocephalus. These children have a high mortality, but the markings diminish rapidly after birth and if the child survives they disappear by 4-6 months.

Cranial meningocele and encephalocele These are commonest in the occipital and frontal regions, although they can occur elsewhere over the vault and also in the skull base. Diagnosis is usually clinically obvious, but can be more difficult with small lesions, particularly if lateral or basal. A hone defect beneath a scalp swelling should always raise the possibility of encephalocele.

Basal encephalocele usually presents in infants with nasal obstruction, although some cases are not diagnosed until adult life. It is vital that the nasopharyngeal mass should be correctly [diagnosed](#), as surgical intervention could prove disastrous. Clinically, hypertelorism may be noted and raise suspicion. A basal view of the skull may show a defect in the sphenoid or sphenothmoid region but CT or MRI will be necessary to define the full anatomy.

Platybasia This term is used for flattening of the base of the skull. The *basal angle* is a measurement widely used in comparative anatomy, and is defined as the angle between the plane of the clivus and the floor of the anterior fossa. In humans this is normally between 125° and 142° , while in other primates it measures over 150° . Platybasia may be symptomless and of no pathological significance. The term is sometimes used rather loosely to include basilar impression and basilar invagination, conditions with which it is usually, but not invariably, associated.

Basilar impression This indicates an elevation of the floor of the posterior fossa which occurs as a congenital anomaly, often in association with such lesions as atlanto-occipital fusion or Klippel-Feil syndrome. The foramen magnum may also be abnormal in size and shape. *Basilar invagination* is similar in appearance but is an acquired condition resulting from diseases causing bone softening. The commonest cause in the UK is Paget's disease but the condition also results from rickets, osteomalacia, scurvy and, rarely, from hyperparathyroidism. It may also be seen in such congenital bone dystrophies as fragilitas ossium and cleidocranial dysostosis.

The main significance of platybasia and basilar invagination, which are usually symptomless, is in the neurological symptoms that may sometimes result from pressure on and distortion of the brainstem and obstruction of free cerebrospinal fluid circulation. Tonsillar herniation may also be associated with atlanto-occipital fusion or Klippel-Feil syndrome.

Various lines and measurements have been used in the past for assessing platybasia and basilar impression on simple skull films. The basal angle has been described above, and can be easily measured on a lateral film. *Chamberlain's line* is drawn from the back of the hard palate to the posterior lip of the foramen magnum, and suggests platybasia when more than half the odontoid peg lies above it (Fig. 53.20A). A more reliable method is *AP tomography* in the plane of the petrous bones and occipital condyles. The atlanto-occipital joints normally lie below the level of the digastric grooves, but are elevated in basilar impression (Fig. 53.20B). Where neurological symptoms are present, further investigation will be required by CT with sagittal reformat, or by MRI, to show the bony relationships to the brainstem and tonsils (see Ch. 57).

Cleidocranial dysostosis is fully described in the skeletal section (Ch. 35) and only the skull features will be mentioned here. These include persistence of the metopic suture and anterior fontanel and

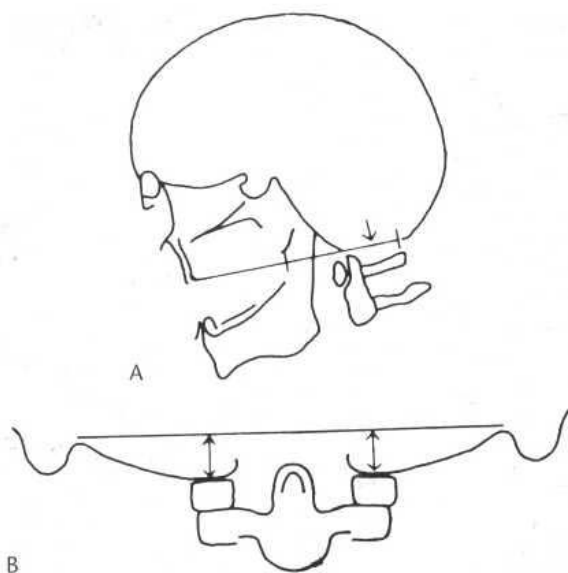


Fig. 53.20 (A) Chamberlain's line (arrow). (B) Normal relationship between digastric grooves and atlanto-occipital joint. The distance between the arrowheads normally measures 1.1 cm (± 0.4 cm).

failure of fusion of the lower lambdoid sutures. Multiple wormian bones are usually visible at the open fontanelles and sutures, and platybasia is frequently seen (see Fig. 35.32B).

Fragilitas ossium is also described above (see Fig. 35.37). In the neonate the skull is poorly mineralised, with irregular thinning and multiple wormian bones along the sutures.

Hypophosphatasia (Ch. 42) also results in defective ossification of the infant skull, leading to abnormally wide sutures with irregular margins. At a later stage premature suture fusion may occur.

Congenital parietal foramina Symmetric bilateral large parasagittal rounded or ovoid defects are present in the posterior parietal regions. These are symptomless and are seen as chance findings in a skull film taken for some other reason. The condition may be familial.

Sinus pericranii This condition, due to a small emissary vein, causes a small midline defect in the frontal bone which the vein traverses. The subcutaneous vein can be distended by raising the venous pressure or by placing the forehead in the dependent position.

Hypertelorism This is a condition in which the orbits are more widely separated than normal. It may occur as an isolated anomaly or in association with other anomalies (*Creig's syndrome*). Of radiological interest among these are syndactyly, failure of segmentation of the sternum, Sprengel's shoulder, congenital heart disease, dental abnormalities and renal hypoplasia, all of which have been recorded in varying combinations in different cases. Mental handicap is usually present and there may be soft-tissue anomalies, including muscular hypotonia, neck webbing and macroglossia.

Well-developed ethmoid cells occupy the gap between the orbits and there is usually a persistent metopic suture.

Secondary hypertelorism may result from a frontal encephalocele or mucocele of the ethmoids, while other cases may result from bone lesions such as fibrous dysplasia, or be associated with cleidocranial dysostosis and osteogenesis imperfecta; the condition can also occur with craniosynostosis.

Raised intracranial pressure

Raised intracranial pressure can produce diagnostic changes in the simple film of the skull and these are described below. However, with the advent of CT and MRI these have become of relatively little diagnostic importance, although it remains important for the radiologist to recognise the significance of such changes when they are encountered as chance findings.

The radiological signs of raised intracranial pressure are:

1. Suture diastasis
2. Sellar erosion
3. Pineal displacement
4. Increased convolutional marking.

It is important to realise that the signs seen in infants and children are quite different from those seen in adults because once the sutures are united they cannot be affected by raised pressure.

Infants and children In infants and children suture diastasis is the first and most prominent result of raised intracranial pressure, and the younger the child the more marked is the sign. The coronal and sagittal sutures are most markedly affected (Fig. 53.21). Neonates and young infants may also show unusually thin skull vaults in addition to suture diastasis and large heads. They may also show cranial lacunae (Fig. 53.19) when the raised pressure is associated with meningocele.

Older children and adolescents with chronic raised intracranial pressure have sutures which, although not obviously splayed, appear abnormal with excessive interdigitations, and the central part of the anterior fossa (cribriform plate) may be displaced downward in the lateral film.

Suture diastasis, the first and most important sign in small children, may be the only sign of raised pressure. Sellar erosion may occur but is a late sign and implies longstanding chronic pressure. In children under 10, sellar erosion without suture diastasis is likely to be due to a local erosive lesion rather than raised pressure. Above this age sellar changes are more likely to be due to raised pressure.

Increased convolutional markings, sometimes referred to as the 'copper-beaten' appearance, have often been attributed to raised intracranial pressure in the past. However, such an appearance is not necessarily pathological and is often seen in the skull films of normal children, particularly between the ages of 4 and 10 years. Conversely, severe chronic raised pressure may be present with no visible changes in the skull vault. Further, marked convolutional marking may be seen in children without raised intracranial pressure, e.g. in craniostenosis. The sign therefore has little diagnostic value.

Adults *Erosion of the dorsum sellae* is the cardinal sign of raised intracranial pressure in adults, and suture diastasis is not seen because the sutures are now united. Erosion commences as slight porosis of the anterior cortex of the dorsum and of the sellar floor cortex, best seen in a lateral film. It progresses to loss of definition of the cortex (also termed the lamina dura) and eventually to frank erosion (Figs 53.22, 53.23). The sellar porosis of raised intracranial pressure has to be distinguished from similar changes which may be seen in osteoporosis in elderly patients and in patients with chronic hypertension. Frank erosion may also result from local masses and destructive lesions; these include pituitary tumours, craniopharyngiomas, chordomas and meningiomas.

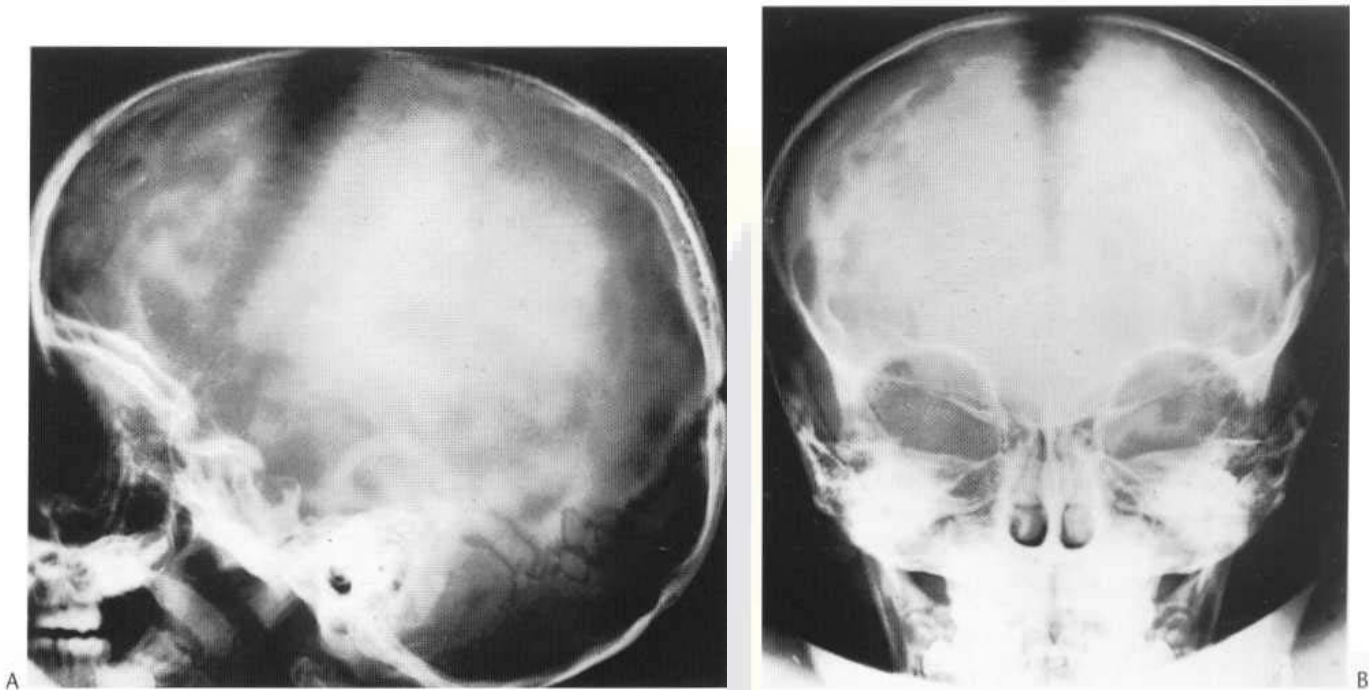


Fig. 53.21 (A) Lateral and (B) PA films of child with raised intracranial pressure and marked suture diastasis involving the coronal and sagittal sutures.

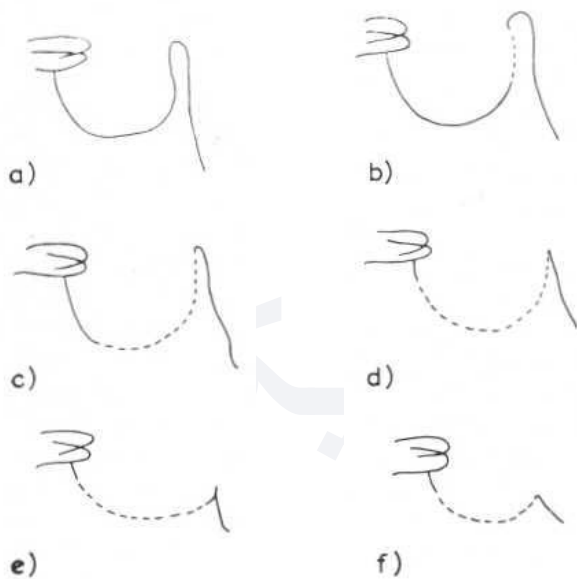


Fig. 53.22 Diagram of the sellar changes in raised intracranial pressure in the adult. (a-f) show progressive changes from slight (b) to gross (f).

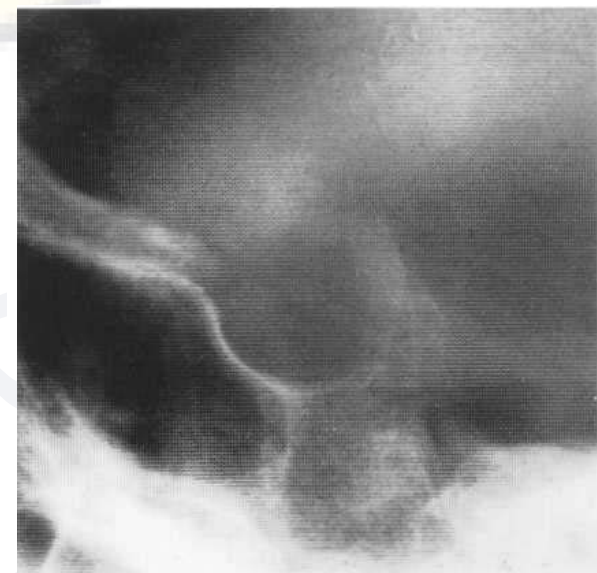


Fig. 53.23 Advanced changes due to chronic raised pressure. The dorsum sellae has become ill defined. The anterior clinoids are also affected and the floor of the sella is indistinct.

In adults, *pineal displacement* is another important sign, but it is of little use in childhood as the pineal is rarely calcified in infants and small children. The normal pineal lies within 3 mm of the midline in standard PA and Towne's views of the skull, and lateral displacement greater than this is strong presumptive evidence of a mass lesion displacing the pineal away from the affected hemisphere (Fig. 53.24). With large supratentorial masses, displacement of the pineal may also be observed in the lateral skull film, the displacement being downward and backward. Very rarely, a mass behind the pineal (usually a tentorial apex meningioma) will displace it downward and forward.

Localising evidence of cerebral tumours

The plain skull film may also show localising evidence of the presence of a cerebral tumour. In some cases this may demonstrate not only the site of the tumour, but also its pathological nature. The radiological signs may be grouped under the following headings:

1. Intracranial calcification
2. Skull erosion
3. Hyperostosis
4. Abnormal vascular markings
5. Pineal displacement.



Fig. 53.24 Displacement of the calcified pineal by a right hemisphere tumour. The displacement measures 5 mm on the original film. T = midpoint; f = pineal.

Pineal displacement has been discussed above. The other radiological signs and their differential diagnosis are described below.

Intracranial calcification

Normal or physiological intracranial calcification has already been described. Pathological intracranial calcification may be classified as in Box 53.2.

1. Tumours

Calcification occurs in many cerebral tumours. *Gliomas* are the commonest cerebral tumour, and calcification is visible on skull



Fig. 53.25 Mottled calcification in a slow-growing frontal glioma.

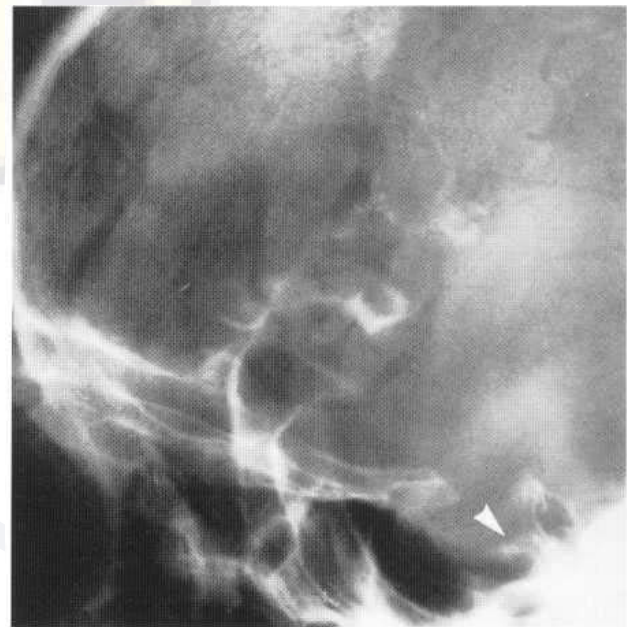


Fig. 53.26 Sinuous calcification in a frontal glioma. Note the evidence of raised pressure in the sella, which shows loss of definition of its surrounding cortex (arrowhead).

films in a little over 5%; of these. Naturally it is the slow-growing and less malignant tumours that are most likely to calcify, whereas the highly malignant tumours rarely show calcification. The rare oligodendroglioma is said to calcify in 50% of cases, and posterior fossa gliomas calcify in some 20% of cases. Oligodendrogliomas were thought at one time to show characteristic serpiginous calcification, but little reliance can be placed on the type of calcification as this is not specific, and any type of glioma can show any type of calcification. This may vary from a few punctate dots to a large calcified nodule, or linear streaks to hazy amorphous calcification (Figs 53.25-53.27).

Craniopharyngiomas, which present mainly in children, show calcification in over 75% of cases; this may vary from a few punctate dots to a densely calcified mass (Figs 53.28, 53.29). Occasionally, when the tumour is cystic, curvilinear calcification

Box 53.2 Pathological intracranial calcification**1. Neoplasms**

Craniopharyngioma
Glioma
Meningioma
Ependymoma
Papilloma of the choroid plexus
Pinealoma
Chordoma
Dermoid, epidermoid, and teratoma
Hamartoma
Lipoma
Pituitary adenoma (rarely)
Metastasis (rarely)

2. Vascular

Atheroma
Aneurysm
Angioma
Subdural haematoma
Intracranial haematoma

3. Infections and infestations

Toxoplasmosis
Cytomegalic inclusion body disease
Herpes
Rubella
Tuberculosis
Pyogenic abscess
Cysticercosis
Hydatid cyst
Paragonimus abscesses
Trichinosis
Torulosis
Coccidioides

4. Metabolic and miscellaneous

Idiopathic basal ganglia calcification
Hypoparathyroidism
Pseudohypoparathyroidism
Tuberous sclerosis
Sturge-Weber syndrome
Neurofibromatosis
Lissencephaly
Fahr syndrome
Cockayne syndrome
X-radiation and methotrexate
Haemodialysis
Lead poisoning
CO poisoning

may be seen in the cyst wall (Fig. 53.30). The characteristic feature is the position of the calcification – midline and just above the sella. Although predominantly presenting in children, the tumours are occasionally seen in adults. Diagnosis is then more difficult, as calcification is less frequent in adults. A helpful point is the shape of the sella, which is sometimes bent forward as if pressed down from above. Occasionally these turnouts with their calcification are intrasellar, or partially so (Figs 53.29, 53.30).

Meningiomas show calcification on plain film in about 10% of cases. The calcification may be characteristically ball-like and amorphous, and in a characteristic parasagittal or other typical meningioma site (Fig. 53.31). Even when calcification is less typical (and it may be speckled or nodular), other radiological signs may suggest meningioma. These include bony hyperostosis where the tumour is involving the vault or sphenoid ridge, and increased



Fig. 53.27 Hazy amorphous calcification in a glioma of the occipital lobe.

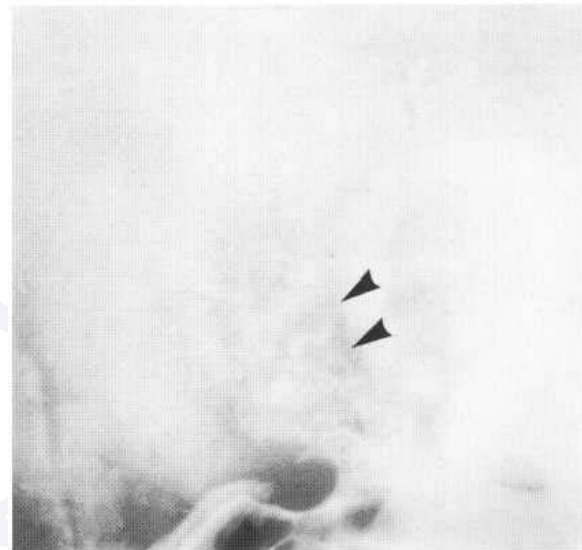


Fig. 53.28 Irregular calcification in a craniopharyngioma (arrowheads). Note the bowed shape of the dorsum sellae.

meningeal vascular markings leading up to the site of attachment (Fig. 53.32).

Dermoids are commonest in the posterior fossa or near the base of the skull. They may show arcs of calcification similar to those seen in the wall of an aneurysm (Fig. 53.33). Posterior fossa dermoids may also be associated with a characteristic small central defect in the occipital bone.

Epidermoids are much less likely to calcify but may occasionally show small arc calcifications, which can be multiple.

Teratomas are found mainly in the pineal and suprasellar regions in children. They frequently contain calcification, and, rarely, the

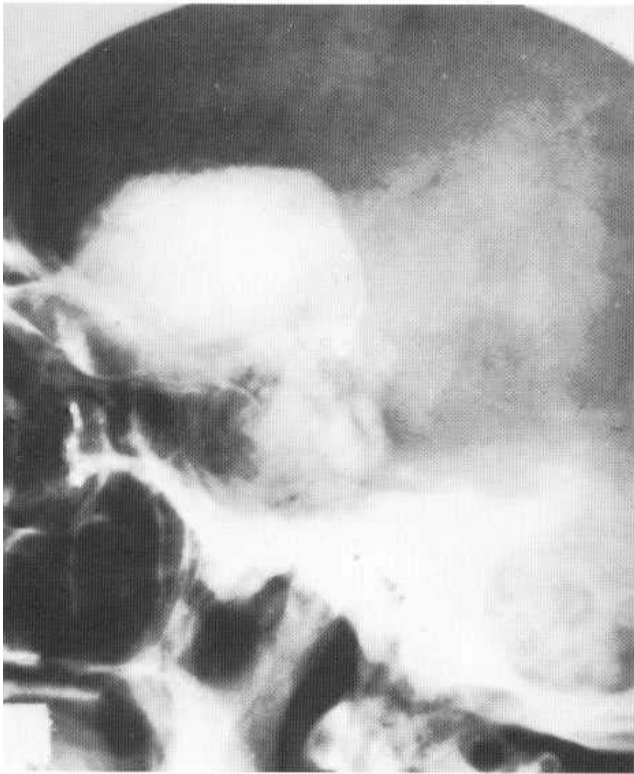
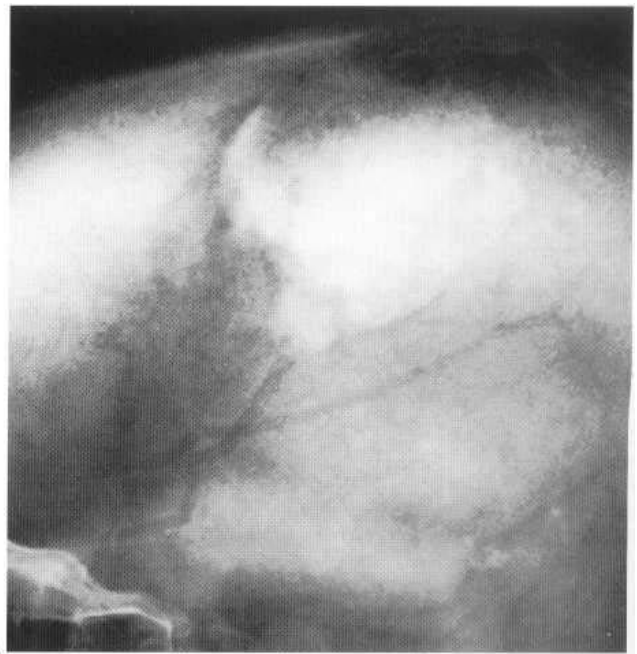
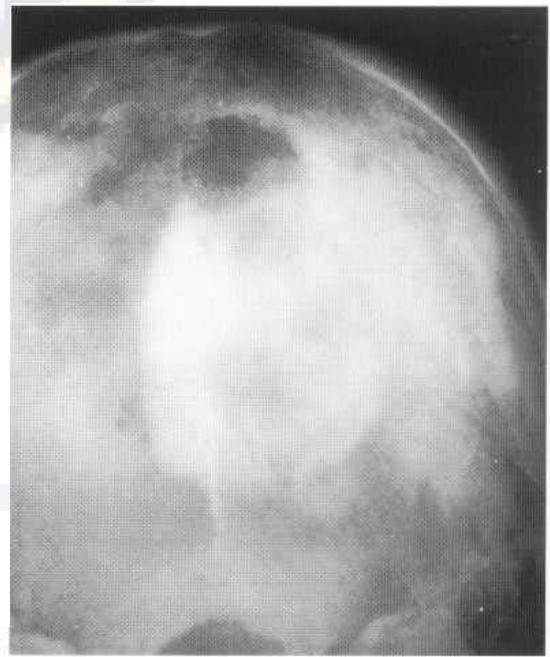


Fig. 53.29 Heavily calcified craniopharyngioma growing upward and forward from the sella.



A



B

Fig. 53.31 (A,B) Heavily calcified parasagittal meningioma. The site and type of calcification, which outlines the whole tumour, are characteristic.



Fig. 53.30 Calcified craniopharyngioma. The calcification in the upper part appears to be outlining a cyst (arrowhead) and the tumour is actually encroaching on the sella.

recognition of a dental element may establish the diagnosis on the plain film.

Pineal tumours other than teratomas can also calcify. If calcification in the pineal area is abnormal in extent, particularly in a child, it should raise suspicion of neoplasm.

Ependymomas occur mainly in the posterior fossa in children but can be seen in the supratentorial compartment, particularly in adults. Calcification is unusual but can occur and be quite dense.

Choroid plexus papillomas also occur mainly in children and show some calcification in one case in four. The characteristic site in the lateral or fourth ventricle may suggest the diagnosis, and the presence of calcification would help to differentiate from medulloblastoma, as the latter is unlikely to calcify.

Lipomas usually occur in relation to the corpus callosum, and a large lesion may show a highly characteristic marginal calcification

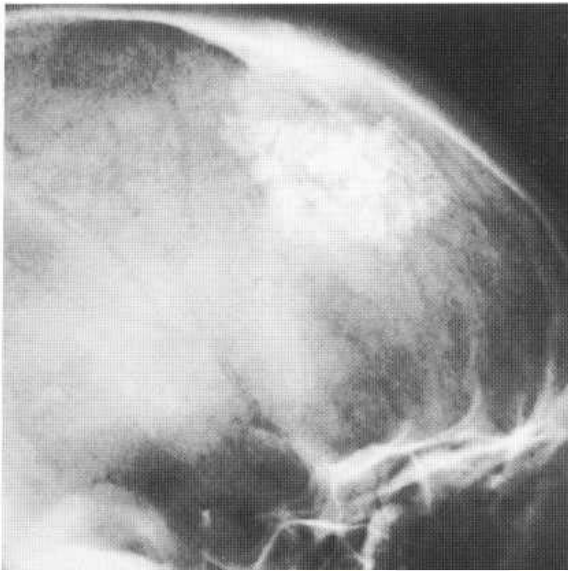


Fig. 53.32 Calcified meningioma. Calcification is less typical but again the site, with the base of the tumour against the vault in the parasagittal region, is characteristic. The presence of a local hyperostosis and prominent frontal vascular markings also help to confirm the diagnosis.

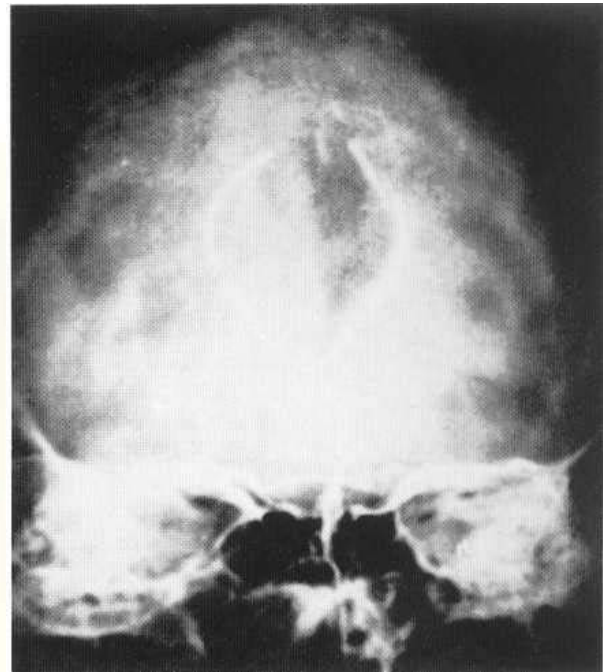


Fig. 53.34 Lipoma of corpus callosum, showing 'bracket' calcification.

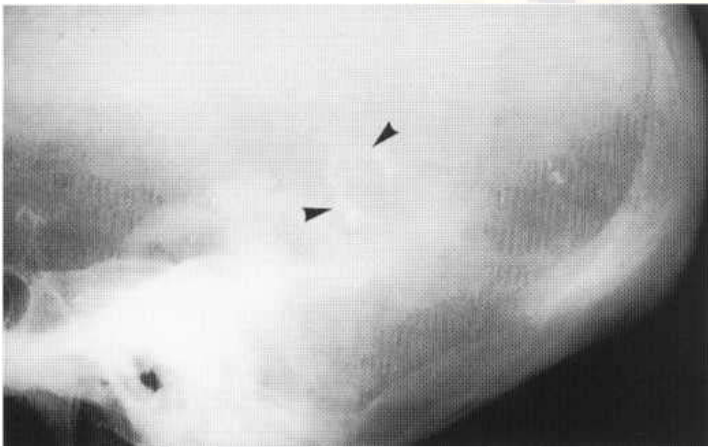


Fig. 53.33 Calcified dermoid in the posterior fossa. Note ring calcification (arrowheads).

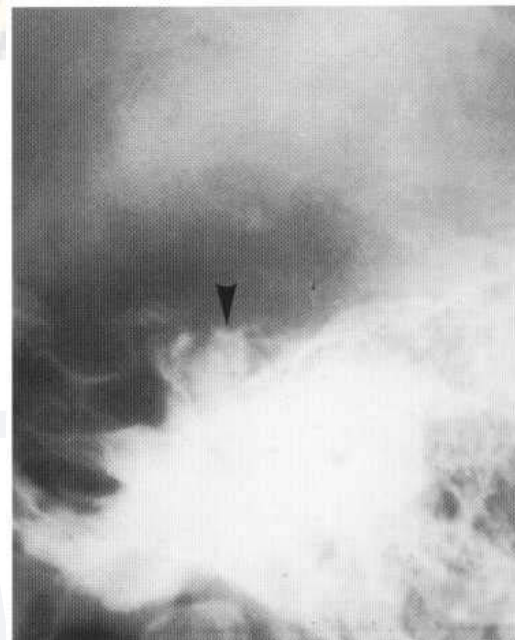


Fig. 53.35 Calcification (arrowhead) in a chordoma growing from the clivus.

('bracket sign' Fig. 53.34). Less specific calcification may also be seen.

Chordomas show irregular calcification in a minority of cases (Fig. 53.35). They usually grow from the clivus, and other radiological features such as a soft-tissue mass projecting into the nasopharynx, or basal erosion, may help to suggest the diagnosis.

Pituitary tumours sometimes contain small areas of calcification but only rarely can these be recognised radiologically.

Metastases in the brain have been recorded with radiologically demonstrable calcification, but this is so rare as to be a curiosity. It occurred in only two patients out of one series of 136 patients.

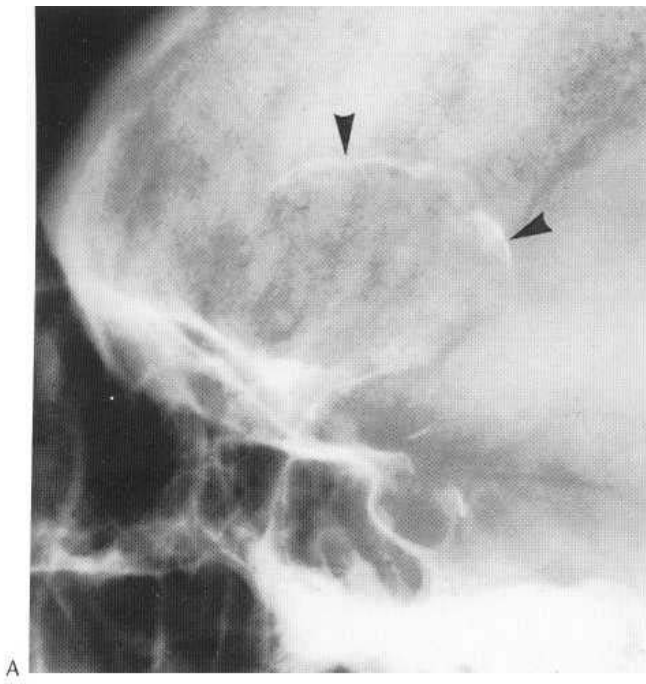
2. Vascular lesions

Aneurysms When they have been present for a long period aneurysms may show characteristic arc-like or circular marginal calcification. Most occur in the region of the circle of Willis, and a linear ring or arc of calcification in this region should always suggest an aneurysm. Although most are small (under 1 cm in

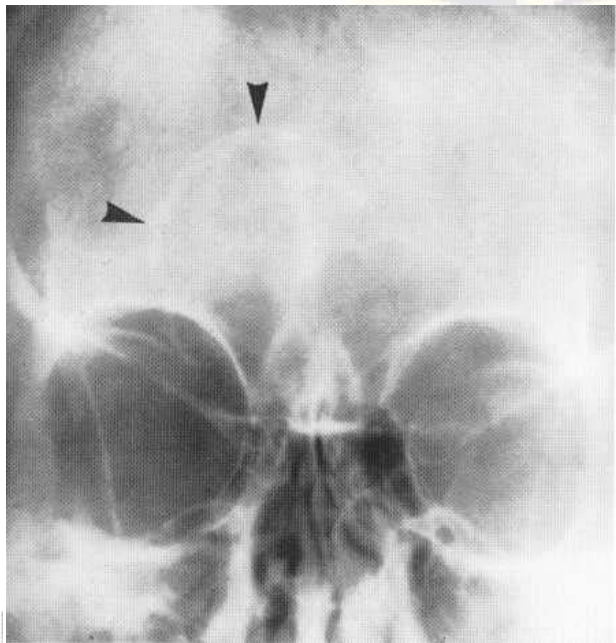
diameter), it is important to realise that some can be very large (Fig. 53.36) and mere size does not necessarily imply an alternative diagnosis of such lesions as craniopharyngioma cyst or dermoid. Occasionally calcification is seen in the margins of fusiform carotid siphon or basilar aneurysms.

Intracranial aneurysms are common lesions but calcification is rare (less than 1%), and the vast majority present with subarachnoid haemorrhage and are uncalcified.

Angioma These are also common intracranial lesions and a small proportion can show diagnostic calcification. This consists of scattered flecks of calcium associated with the presence of



A



B

Fig. 53.36 Large calcified aneurysm of the anterior communicating artery (arrowheads). The lesion is unusually large, but the marginal calcification is typical. Most calcified aneurysms are under 1 cm in diameter. (A) Lateral view. (B) PA view.

one or more ring or arc shadows. The latter are in the walls of aneurysmal dilatations of vessels on the venous side of the angioma (Figs 53.37, 53.38).

Chronic subdural haematoma This occasionally shows calcification in the membrane and is recognised by its characteristic position in relation to the skull vault (Fig. 53.39).

Intracerebral haematomas These can develop irregular calcification but this has no diagnostic features.

Atheroma Linear flecks are common in atheromatous carotid siphons and can be quite extensive (Fig. 53.40). Calcification in

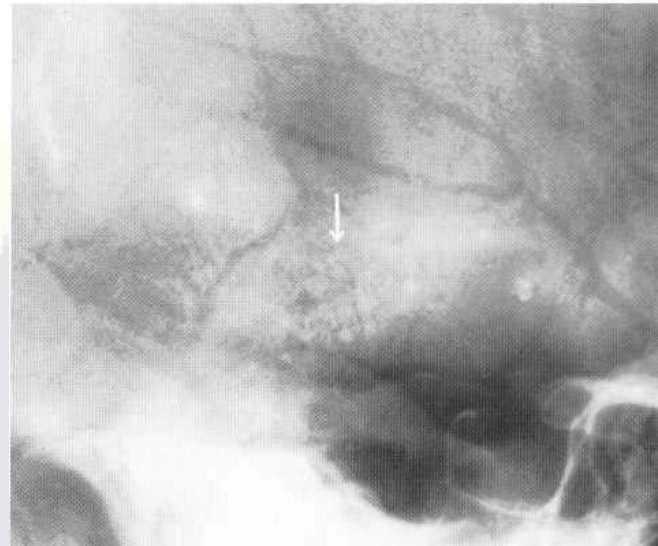


Fig. 53.37 Multiple flecks and specks of calcification in an angiomatous malformation (arrow).

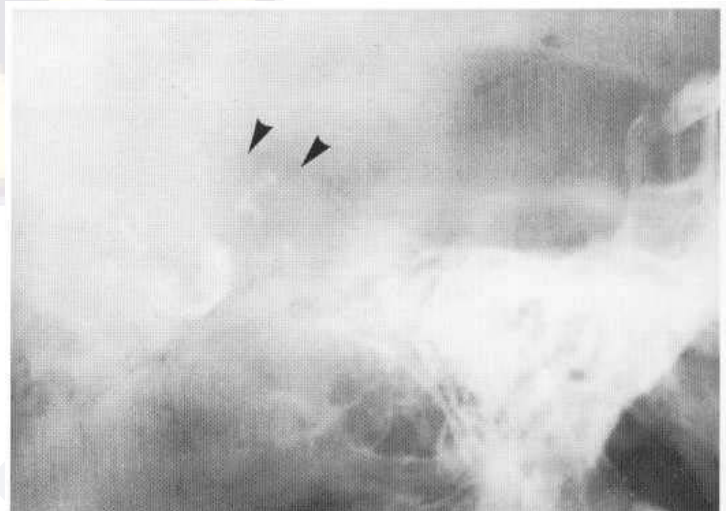


Fig. 53.38 Flecks of calcification associated with a calcified ring shadow in an angioma (arrowheads).

more distal intracranial vessels is unusual and is difficult to recognise against the bony skull. Atheromatous calcification may also be recognised at the carotid bifurcation in the neck.

3. Infections and infestations

Tuberculoma Calcification recognisable on plain films is rare and is only likely to be seen in patients successfully treated for tuberculous meningitis. Such patients may show characteristic small nodules in the healed basal exudate at the base of the brain (Fig. 53.41), and occasionally in an intracerebral lesion.

Toxoplasmosis Most human infestation with the protozoan is derived from cats. Healthy adults may be symptomless carriers but unfortunately a pregnant carrier can infect the fetus in utero. Such fetal infections involve the brain and result in widespread granulomas with calcification, severe brain atrophy with ventricular dilatation, and bilateral choroidoretinitis. The calcification in congenital toxoplasmosis is characteristic, consisting of multiple scattered flecks in the cortex and linear streaks in the basal ganglia (Fig. 53.42).

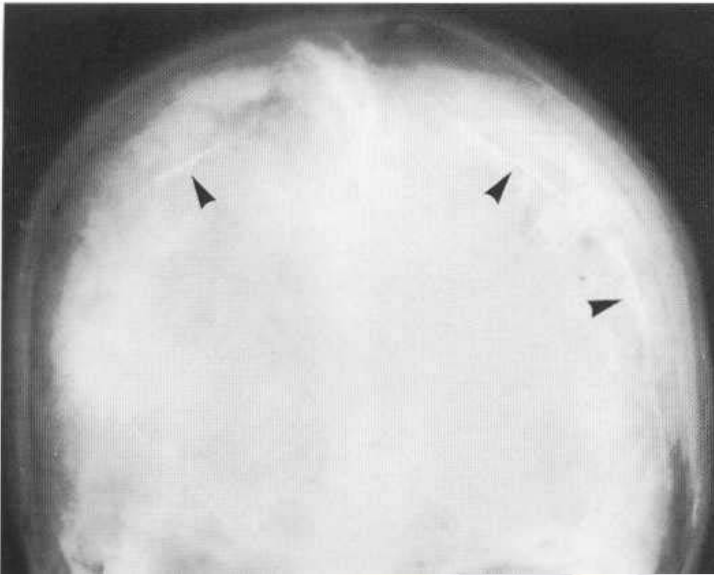


Fig. 53.39 Calcification in the margins of chronic bilateral subdural haematomas (arrowheads).

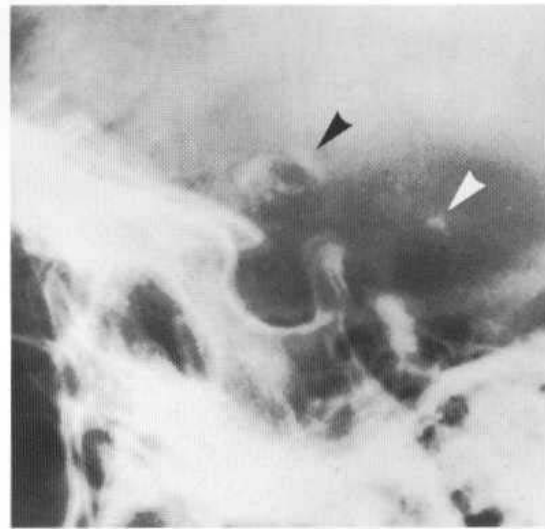


Fig. 53.41 Calcified basal exudate above the sella in a patient with healed tuberculous meningitis (arrowheads).

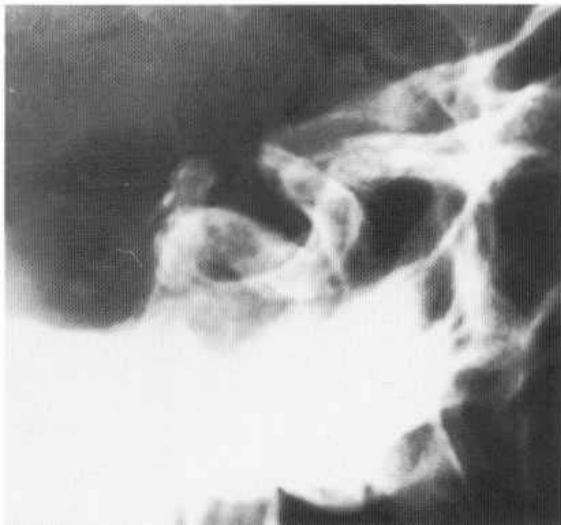


Fig. 53.40 Unusually heavy calcification outlining the whole of the carotid siphon and shown to be bilateral in the frontal projection.

Immunocompromised patients, particularly those with AIDS, may also develop cerebral toxoplasmosis, but this acute form is not associated with calcification (Ch. 58).

Cytomegalovirus (CMV) Large and characteristic intranuclear inclusions ('owl's eyes') are produced in the salivary glands and other organs by this virus, which is a member of the herpes group. It is estimated that about 1200 infants a year are born in the UK with congenital CMV infection and that about 200 a year suffer major defects, although the carrier mother is symptomless.

There may be severe intrauterine brain infection, often with microcephaly, and a characteristic widespread periventricular calcification may outline the dilated ventricles. The calcification is stippled, bilateral and symmetric, and there is usually microcephaly. Typical cells are found in the urine.

Cysticercosis This is due to human autoinfection with the tapeworm *Meniu solium* or is acquired by ingesting infected food or drink. The disease is endemic in Mexico. Central and South



Fig. 53.42 Toxoplasmosis. Note characteristic multiple flecks of calcification.

America, South Africa, India and parts of Asia. When cysts develop in human tissues, the muscle masses are mainly affected and the calcified cysts present a diagnostic picture (see Fig. 45.59). Brain infestation is less common but can also produce a characteristic picture of scattered calcified nodules (Fig. 53.43). These, however, are unlike the oat-shaped calcified muscle cysts, as only the scolex calcifies, and they appear as small (2-3 mm) calcified nodules.

Paragonimus westermani This fluke or trematode infection acquired from crabs or crayfish is endemic in the Far East, and most recorded cases are from Korea and China. Brain lesions are usually in the parietal region and can give rise to extensive 'soap-bubble' calcification in cysts measuring up to 3 or 4 cm in diameter.

4. Metabolic and miscellaneous

Basal ganglia calcification This may be observed as a chance finding on the radiograph of an adult skull. Typically this is bilateral and symmetric and commences in the region of the head of the caudate nucleus. The globus pallidus, putamen and lateral part

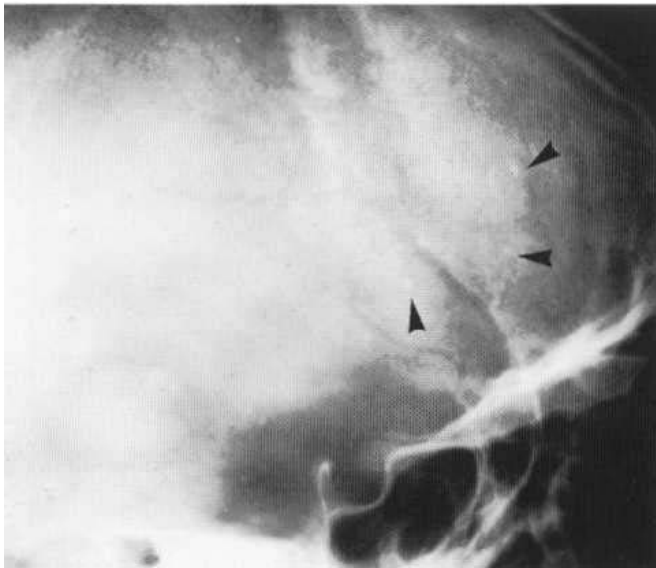


Fig. 53.43 Cysticercosis. There are multiple small calcified lesions 2-3 mm in diameter (arrowheads).

of the thalamus are also involved. The dentate nuclei in the posterior fossa can also be affected, with or without supratentorial calcification. The latter is hazy and amorphous or punctate in type (Fig. 53.44), and is due to the deposition of tiny pericapillary calcospherites plus calcification in the walls of tiny arteries and veins. For obvious reasons the calcification is more readily detected at CT (Ch. 58).

Most cases are *prima* or idiopathic and the condition is related to age.

Secondary cases are less common and most of these are due to *hypoparathyroidism*, either spontaneous or following thyroidectomy. The condition may also occur in *pseudohypoparathyroidism* (Albright's syndrome).

A *familial* type in which several members of the same family showed calcification at a relatively young age has also been described, but is much rarer.

Other rare causes include Fahr's syndrome, Cockayne's syndrome, lead and carbon monoxide poisoning, and X-radiation with methotrexate therapy. These rarer causes may also show associated subcortical calcifications.

Congenital toxoplasmosis, as noted above, may also show calcification in the basal ganglia, but this is characteristically linear and associated with flaky subcortical calcifications.

Hyperparathyroidism Scattered metastatic calcification in the brain has been recorded but is extremely rare. More common is extensive calcification in the flax and tentorium in patients with chronic renal failure and on long-term haemodialysis.

Neurofibromatosis Extensive calcification of the choroid plexuses of the third and lateral ventricles has been described as a rare accompaniment of neurofibromatosis.

Tuberous sclerosis In this condition the multiple areas of dysplasia in the brain may contain calcifications. On the plain film these appear as scattered discrete nodules of varying size (Fig. 53.45).

Sturge-Weber syndrome The characteristic radiographic finding is occipital cortical calcification described as 'tramline'. The parallel lines represent the sulci seen end-on, as the calcification lies in the atrophic cortex. Typically the calcification is unilateral

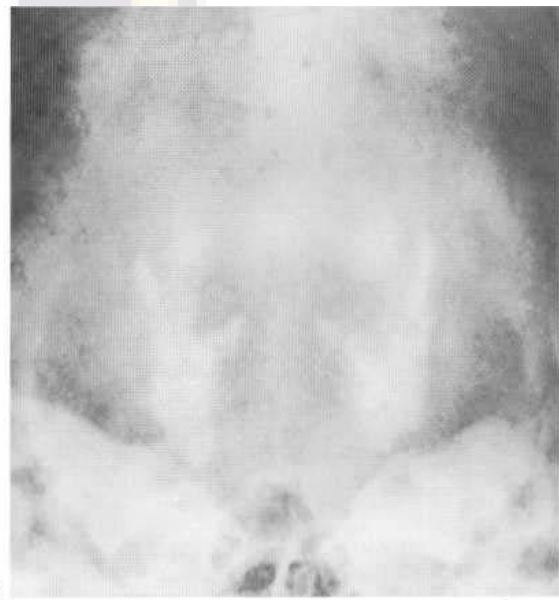


Fig. 53.44 Heavy calcification in the basal ganglia and dentate nuclei. (A) Lateral view. (B) Towne's view.

and occipital (Fig. 53.46), although in occasional severe cases it may be bilateral and more extensive.

Lissencephaly Infants born with this rare anomaly have been described as showing a characteristic small (3 mm) calcified nodule in the septum pellucidum and just behind the foramen of Monro.

Abnormal vascular markings

Meningioma This is the commonest cause of pathological vascular markings in the skull vault (Fig. 53.47). These tumours derive part of their blood supply from the middle meningeal vessels, which hypertrophy to supply them. In addition they may attract a supply from hypertrophied branches of the external carotid, particularly when they invade bone. There may also be locally enlarged diploic vascular markings and emissary venous markings in the region of the tumour. The foramen spinosum is usually

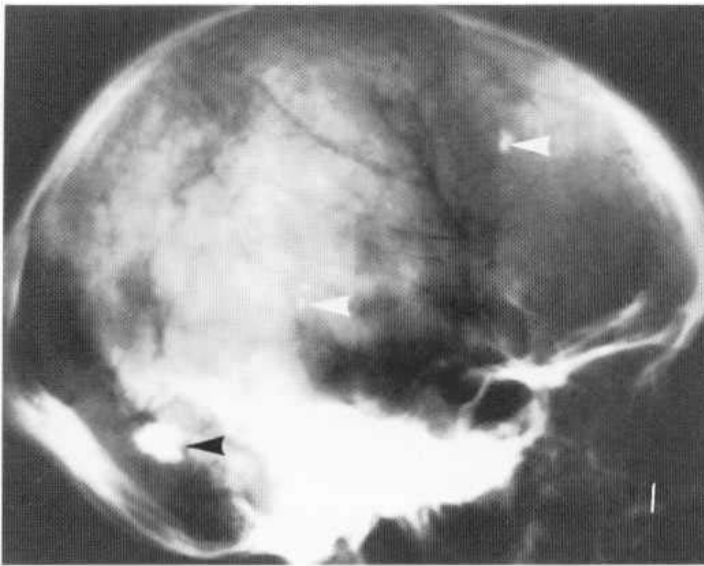


Fig. 53.45 Tuberos sclerosis. There are nodules of calcification in the posterior fossa, in the frontal region, and in the parietal region. The last is nearly superimposed on the pineal.

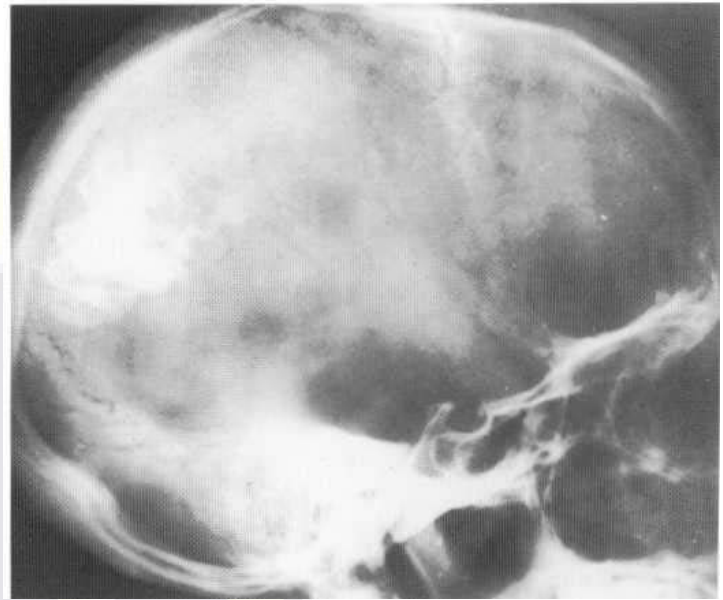


Fig. 53.46 Calcified occipital cortex in Sturge-Weber syndrome.

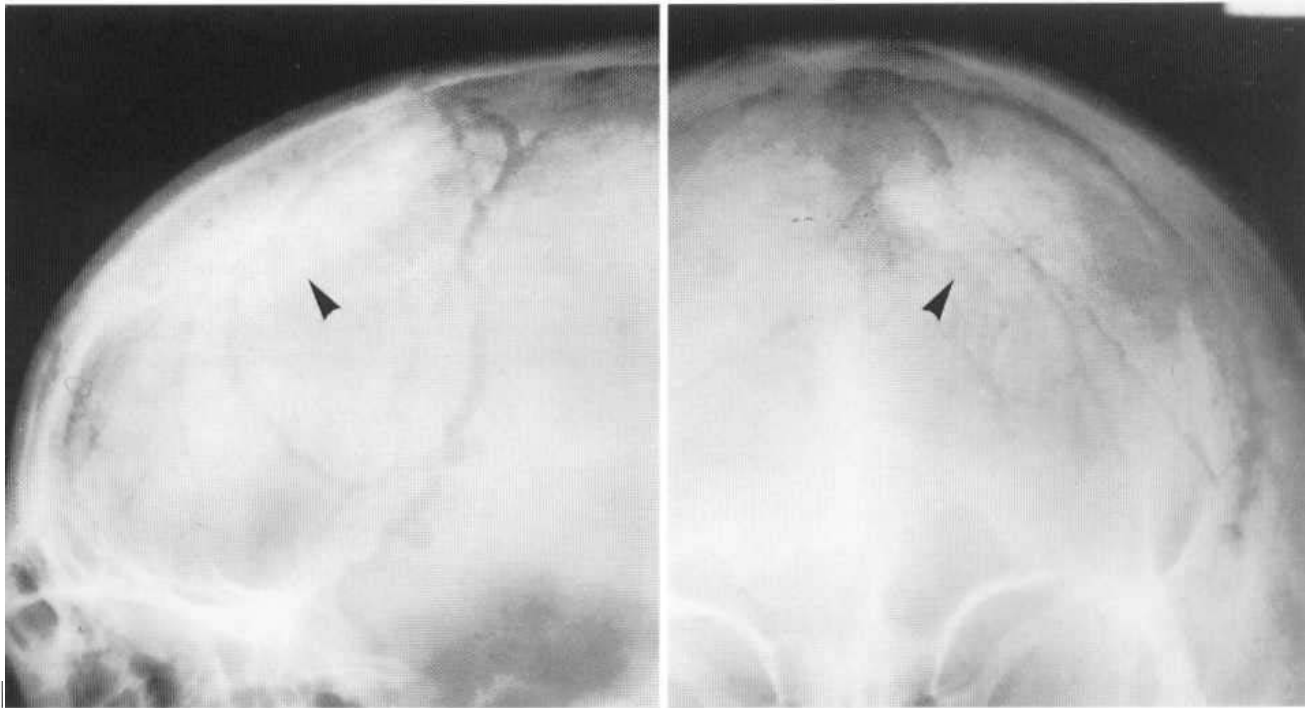


Fig. 53.47 Enlarged meningeal and diploic vascular markings associated with a parasagittal meningioma. There is also a localised hyperostosis (arrowheads). (A) Lateral view. (B) PA view.

enlarged on the side of the lesion, but, as this is commonly asymmetric, little reliance can be placed on this as an isolated sign (Figs 53.57, 53.58).

Other plain radiological signs may be present to support the diagnosis. These include local bony hyperostosis (see below), calcification in the tumour, or evidence of generally raised intracranial pressure.

Angiomatous malformations These are sometimes supplied by the meningeal arteries as well as by the internal carotid, and this results in hypertrophied meningeal vessels and markings (Fig. 53.48). Prominent emissary venous markings may also be identified, particularly with dural AV fistulas.

Erosions of the skull

Skull erosion due to tumour may arise from extracranial tumours, tumours of bone or intracranial tumours. They have to be distinguished from non-tumorous erosions, which are also discussed below.

Extracranial tumours

Erosion of the skull from extracranial tumours is rare but is occasionally seen. Thus an extracranial *dermoid cyst* can produce pressure erosion of the underlying bone, but most cases are associated with more malignant tumours.

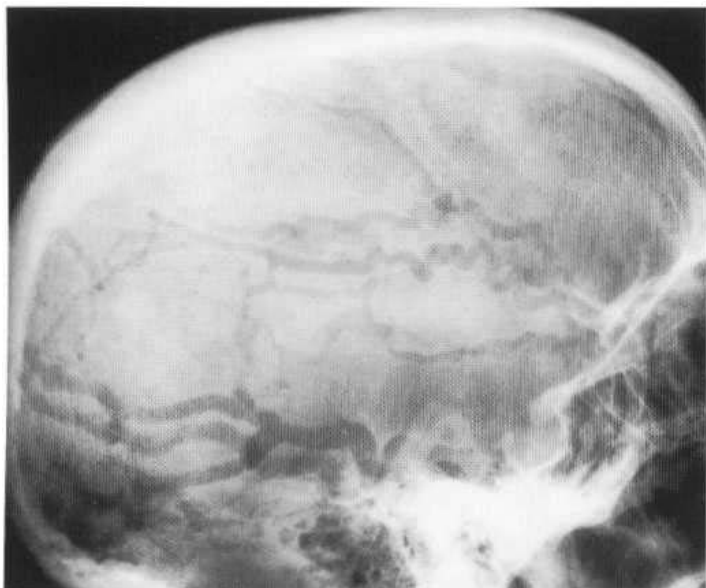


Fig. 53.48 Bilateral hypertrophy of the middle meningeal vascular markings in a patient with a large angiomatous malformation.



Fig. 53.49 Nasopharyngeal carcinoma producing erosion of the floor of the middle fossa on the left (arrows).

Rodent ulcers and *epitheliomas* can invade and erode underlying bone in face or scalp. *Carcinoma of the sphenoid* can involve and erode the skull base in the region of the pituitary fossa.

Nasopharyngeal carcinoma can also invade the skull base, usually in the middle fossa (Fig. 53.49), but more usually infiltrates through basal foramina.

Glomus jugulare tumours may invade the base of the skull in the region of the jugular foramen and undersurface of the petrous bone. This is best shown with a half axial view of the base of the skull (see Figs 52.3 and 53.50).

Bone tumours

Primary tumours with skull erosion are relatively uncommon.

Dermoids are found most commonly just above the outer angle of the orbit. They are associated with soft-tissue swelling and a rounded bone defect with a slightly sclerotic margin (see Fig. 51.34).

hemangiomas may occur in the skull vault, where they may expand the bone slightly, and in classic cases appear as an area of relative lucency with a slightly lobulated and corticated margin.

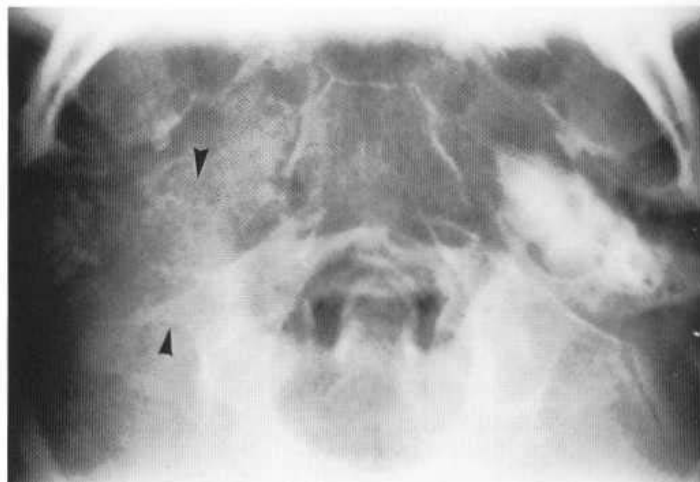


Fig. 53.50 Glomus jugulare tumour. This has completely destroyed most of the right petrous bone (arrowheads).

Hemangiomas of the skull vault also slightly expand the bone and present as a rounded lucent area with a characteristic stippled appearance (see Fig. 40.26); less frequently there is trabeculation or spiculation within the lucent lesion.

Chordomas can produce erosion of the clivus or of the petrous apex. Sometimes erosion is seen more anteriorly in the floor of the sella or at its lateral aspect. Other helpful points in diagnosis are the presence of a soft-tissue mass protruding into the nasopharynx, or calcification within the intracranial part of the tumour.

Secondary tumours producing skull erosion are encountered far more frequently than primary tumours.

Carcinoma metastases in the skull are extremely common, and are often multiple. They may have a characteristic 'moth-eaten' appearance or produce clear-cut defects (Fig. 53.51).

Myelomatosis with widespread deposits usually involves the skull vault, and the lesions are very characteristic, appearing as multiple small rounded and clear-cut defects.

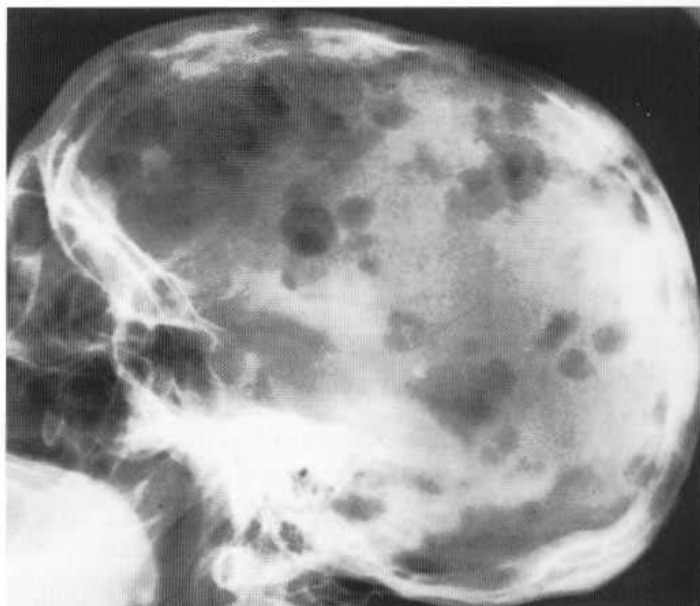


Fig. 53.51 Multiple lytic deposits in the skull vault in a patient with carcinoma of the breast.

Very rarely, a myeloma may present as a solitary myeloma or *plasmocytoma* in the skull vault. Such large solitary plasmacytomas usually present with a palpable soft-tissue swelling. Radiology shows a large irregular bone defect, most commonly in the occipital or occipitoparietal region. The lesion commences in the diploe and expands the bone. Tangential views may show spiculation extending into the soft tissues, and this, together with the intracranial extension, has led to erroneous diagnoses of sarcoma or meningioma. Eventually generalised myeloma will develop in all these cases.

Neuroblastoma in children frequently metastasises to the skull. Lesions may involve the suture margins, particularly the coronal suture, which becomes widened and irregular. The appearance may be accentuated by true suture diastasis from intracranial masses, which are usually extradural and continuous with the bony lesions. Orbital deposits with proptosis are also common in neuroblastoma. Diffuse nodular radiolucencies similar to those of metastatic carcinoma are also frequently seen in the vault. The lesions may elevate the periosteum and produce radial bone spiculation extending into the soft tissues.

Leukaemia of the meninges and central nervous system can cause raised intracranial pressure and sutural diastasis in children but bone lesions are unlikely.

Reticulosis and **lymphosarcoma** rarely affect the skull but occasionally can produce small multiple erosions which later become more confluent and widespread.

Histiocytosis commonly involves the skull, particularly in *Letterer-Siwe* and *Hanck-Schiiller-Christian* disease (Ch. 41), where the typical 'geographic' skull defects may be seen (see Fig. 41.23). *Eosinophil granuloma* may also produce similar lesions in the skull, although it may present as an isolated lesion. This can expand the bone and, unlike the more malignant lesions, may have a sclerotic margin. An isolated eosinophil granuloma may then be

difficult to differentiate from similar lesions due to epidermoids or fibrous dysplasia.

Intracranial tumours with bone erosion

Pituitary adenomas, as they increase in size, expand and erode the pituitary fossa. In the classic case this gives rise to the so-called 'ballooned' sella, with backward bowing of the dorsum, undercutting of the anterior clinoids, and downward protrusion of the floor into the sphenoid bone or sinus (Fig. 53.52).

In most cases the plain film appearances are diagnostic, but occasionally, if the dorsum is completely eroded, there may be difficulty in differentiating from the effects of chronic raised intracranial pressure. The clinical features will usually point to the correct diagnosis. In acromegaly the skull may show other diagnostic features, including thickening of the skull vault, grossly enlarged sinuses (see Fig. 42.23) and a prognathous jaw.

Microadenomas sometimes produce local bulging of the sellar floor or a 'double' floor, but this sign should be treated with great caution since similar appearances are often encountered in the normal skull.

Empty sella may be primary or secondary (Ch. 57). The sella often appears enlarged, raising suspicion of pituitary adenoma. The enlargement however is more globular and symmetric, and the cortex of the sella remains intact. The diagnosis is confirmed by CT or MRI.

Carcinoma of the pituitary is extremely rare, but when it occurs produces local erosion of the sellar floor and skull base.

Craniopharyngioma has been discussed above and is usually diagnosed from the typical calcification. However, there is often a typical deformity of the sella which can be helpful in cases without calcification. The sella appears elongated and the dorsum may be short and bowed forward as if pressed on from above (Fig. 53.53).

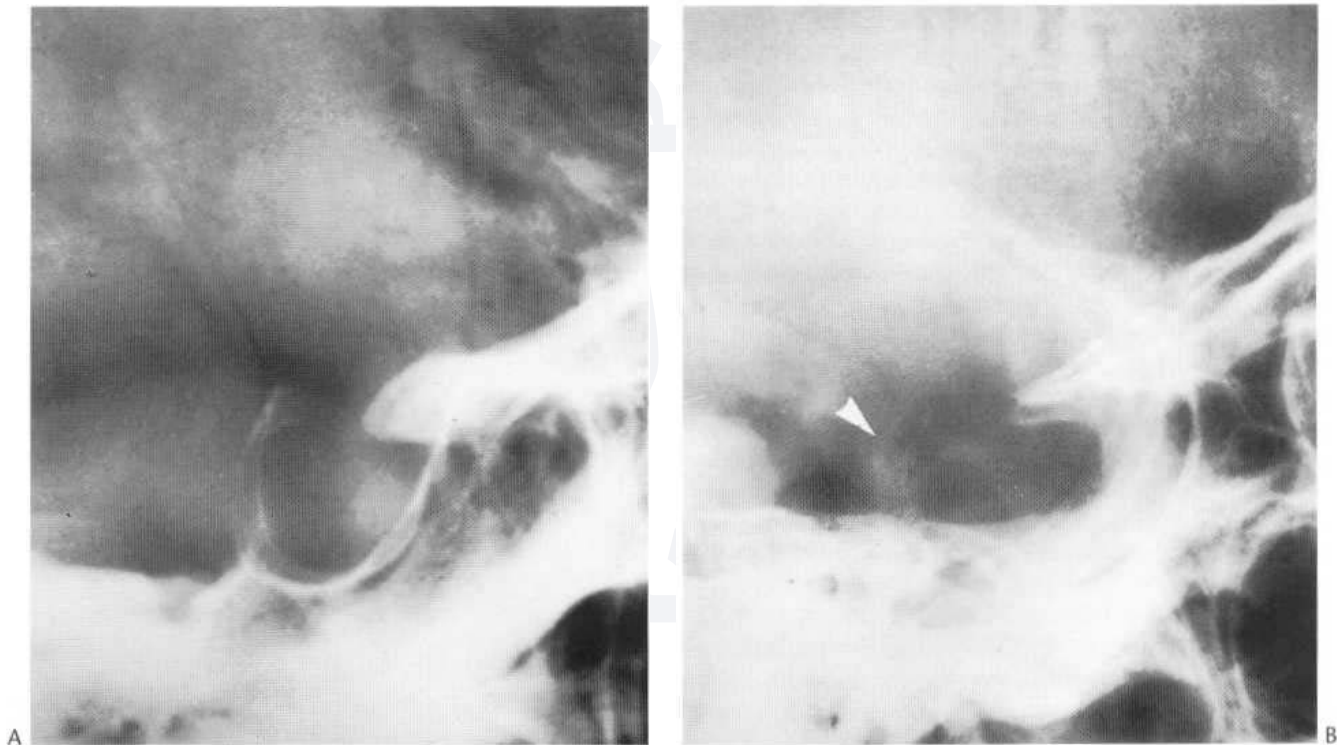


Fig. 53.52 (A) Pituitary adenoma, showing ballooning of the sella and backward bulging of the dorsum. (B) Pituitary adenoma showing ballooning of the sella with undercutting of the anterior clinoids, backward bowing and thinning of the dorsum (arrowhead).



Fig. 53.53 Craniopharyngioma without calcification. The shape of the sella, which is elongated, and the dorsum, which is slightly bowed forward, are suggestive of the cause.

Acoustic neuromas are now diagnosed at an early stage by MRI. Plain radiograph changes are only seen with the larger tumours, which are producing pressure erosion at the internal meatus, but such changes are still seen in a small proportion of cases at presentation.

Glioma of the optic nerve is a rare tumour, predominantly presenting in children. It produces a pathognomonic radiological sign consisting of localised expansion of the optic foramen (Fig. 53.54). Chiasmatic glioma may extend into both orbits and enlarge both optic canals. Other lesions that can produce unilateral enlargement of the optic canal include meningioma of the optic nerve sheath and retinoblastoma. Bilateral enlargement can also occur with meningioma and with chronic raised intracranial pressure, as the subarachnoid space extends into the canals. Very rarely, inflammatory lesions such as sarcoid or chiasmatic arachnoiditis have been responsible for, enlargement of the optic canal, either unilateral or bilateral.

Meningiomas invading bone usually produce a hyperostotic reaction (see below). Less commonly there is a mixed osteoblastic and osteolytic response, and very rarely a purely destructive reaction is seen. In these cases other radiological signs such as enlarged meningeal vascular channels may help to suggest the true diagnosis.

Gliosis growing through the dura and invading bone with visible erosion are extremely rare but have been recorded.

Non-tumorous skull erosions

Congenital and physiological skull defects have been discussed above. Erosions may also result from other non-tumorous causes, including inflammatory and traumatic lesions.

Osteomyelitis, both acute and subacute, involving the skull vault, is seen following spread of infection from the frontal sinus or following compound fracture or other trauma. It results in patchy

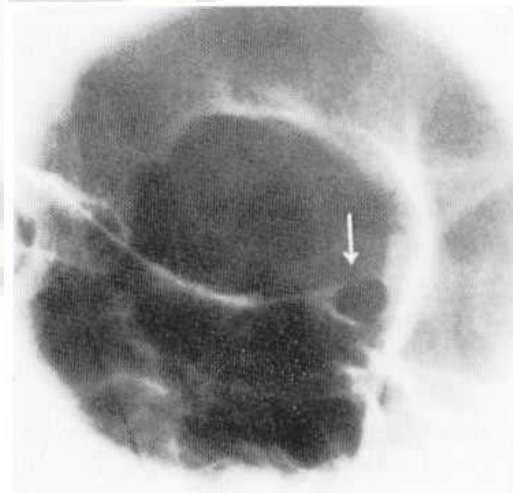
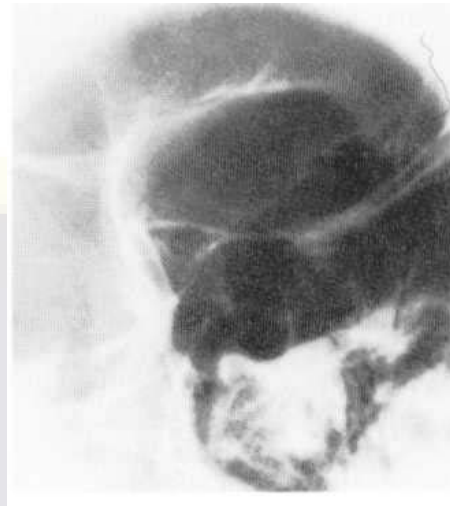


Fig. 53.54 Glioma of the left optic nerve. The left optic foramen (arrow) is markedly expanded compared with the normal right.

erosion of the affected bone. With acute osteomyelitis the diagnosis is usually obvious clinically. Occasionally, however, skull infection may follow a minor trauma which may even be forgotten by the patient (Fig. 53.55). Infection may also occur in bone flaps after a



Fig 53.55 Extensive erosion of the skull vault along the sagittal and coronal sutures. This was due to unrecognised chronic osteomyelitis following a minor scalp wound which was sutured.

craniotomy. Radiologically this is manifest by the development of radiolucent areas within the flap and erosion of the margins.

Chronic infections of the skull vault are now rarely seen except in underdeveloped countries.

Tuberculosis may produce a localised rounded destructive lesion, often associated with a soft-tissue abscess. Occasional cases with bone tuberculosis still seen in the UK are usually in Asian immigrants (see Fig. 36.xx).

Syphilis of the skull vault is now extremely rare. It produces an extensive 'moth-eaten' appearance. The clinical features permit ready differentiation from acute osteomyelitis or extensive deposits.

Hydatid cysts very rarely involve the skull vault. When they do, they give rise to a multilocular cystic mass expanding the bone and bulging it outward. Less than 2% of patients with hydatid disease have bone involvement and in only a few of these is the skull involved.

Sarcoid lesions of bone are also rare, particularly with skull involvement. However, small irregular lytic lesions involving both tables have been described in the skull.

Radiation necrosis may occur in bone flaps after radiotherapy. It results in small marginal and central bony erosions similar to those produced by infection. Very rarely such radiation changes may be encountered in the intact skull vault.

Post-traumatic skull defects are occasionally seen. There is usually a story of a skull fracture in childhood, although the original trauma may be forgotten (see Post-traumatic Cysts below).

Large retro-orbital *aneurysms* can erode the bony structures at the back of the orbit or adjacent to the sella. Erosion of the inferolateral margin of the optic foramen (the optic strut) is characteristic, and there may be slight expansion of the sphenoidal fissure at its upper end. An anterior clinoid process can also be eroded, as can the bone adjacent to it or the sella. Rarely, expansion of the sella by an intrasellar aneurysm can simulate the appearance of a pituitary tumour. Local erosion adjacent to the sella may be better shown by CT than by plain radiographs (see Fig. 55.42C).

Neurofibromatosis can be associated with congenital bone defects in the skull. The commonest site is in the occipital bone adjacent to the lower part of the lambdoid suture. Defects may also occur adjacent to the squamous temporal suture and in the greater wing of the sphenoid, where it forms the posterior wall of the orbit. Proptosis may result from the latter (Fig. 51.27).

Fibrous dysplasia of the skull vault can be cystic, sclerotic or mixed in type. The sclerotic type is discussed below under Hyperostosis. The cystic type occurs mainly in the skull vault and presents as a radiolucent area in the diploe with thinning of the adjacent tables, mainly involving the outer table. The margins are sharply defined and can be sclerotic, making differentiation from epidermoid difficult, although the latter are usually smaller and show no areas of mixed density.

Osteoporosis

Osteoporosis of the skull vault occurs in many different conditions. It may be seen as a normal physiological change in the elderly, in parallel with general osteoporosis of the skeleton. It may also be seen with the various metabolic disorders giving rise to osteomalacia and osteoporosis and discussed in detail in Chapter 42.

Hyperparathyroidism gives rise to osteoporosis of the skull with a characteristic pattern, which has been described as 'miliary' or 'pepper-pot' osteoporosis (see Fig. 42.34). Loss of the

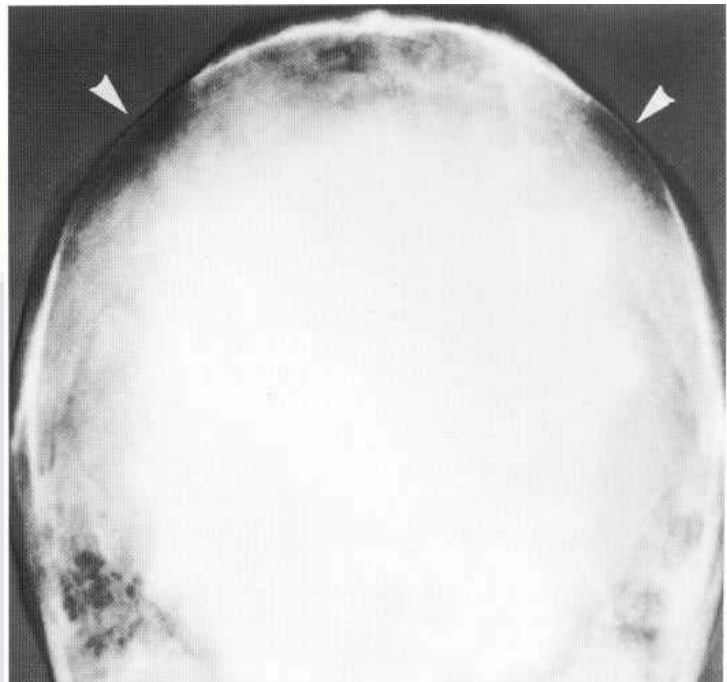


Fig. 53.56 Parietal thinning. The Towne's or PA projections show clearly that the external table and diploe are affected while the internal table remains (arrowheads).

lamina dura around the teeth is another characteristic feature in hyperparathyroidism.

Parietal thinning gives rise to a sharply demarcated localised thinning of the skull vault. This strange condition occurs mainly in elderly men and is characterised by symmetric thinning of the parietal bones, involving the outer tables. As seen in the Towne's or PA views, there is loss of the outer table and diploe of the affected areas (Fig. 53.56). The lateral view shows a sharply demarcated band of porosis in the high parietal zones.

Osteoporosis circumscripta is the name given to a type of Paget's disease affecting the skull vault. It is characterised by large areas of apparent osteoporosis with a clear-cut and well-defined margin between the normal and affected bone (see Fig. 37.37). The osteoporosis spreads upward from the base of the skull and may involve a large area without being limited by sutures. The changes are often bilateral and symmetric and there may be evidence of Paget's disease affecting other bones.

Local bulging of the skull

This is occasionally seen over intracranial mass lesions commencing in childhood where the lesion impinges on the skull. It has been described in superficial *gliomas* but is commoner with such chronic benign lesions as *arachnoid cysts*.

If they lie over the vault they can produce local bulging and thinning of the bone, while in the temporal fossa they cause it to bulge in a characteristic way.

In the basal film the middle fossa is seen to be expanded, while in the PA view close inspection of the orbit will show the sphenoidal ridge to be elevated and the innominate line (Fig. 53.3) to be absent or indistinct due to the bulging of the greater sphenoid wing.



Fig. 53.57 Small parasagittal hyperostosis in the parietal region associated with a meningeoma (arrowhead). Note the prominent vascular channels leading to the lesion.

Chronic juvenile subdural haematomas can produce similar effects both over the skull vault and in the temporal fossa.

Hyperostosis

Hyperostosis, or thickening of the skull vault, may be generalised or localised.

Generalised hyperostosis This is seen with various bone dystrophies described in Chapter 35. These include *marble bones*, *Engelntan's disease*, and *craniometaphyseal dysplasia*.

Dystrophia myotonica may also show a thickened skull vault. The small pituitary fossa in this condition has been noted above.

Acromegaly, as noted above, may also show a thickened skull vault in association with the enlarged sinuses and prognathous jaw. The vault thickening involves both tables and the diploe is encroached on and difficult to distinguish.



Fig. 53.58 Meningeoma growing through the skull vault. Note the sunray spiculation and the enlarged vascular channels of the skull vault. (A) Lateral view.

Paget's disease may lead to the grossest forms of skull thickening. At the same time as the vault becomes widened and thickened, with alterations in its bony texture, there are also osteomalacic changes and the bone becomes softer and more pliable, giving rise to platybasia with basilar invagination. The radiological appearances are quite specific (see Fig. 37.38), with a typical irregular mottled texture to the thickened bone.

Cooler's anaemia is another condition in which there may be gross generalised thickening of the skull vault, with a characteristic and diagnostic appearance (Ch. 41). The main abnormality is a widening of the diploe. Its texture also becomes abnormal with radiating linear spicules of the 'sunray' or 'hairbrush' type (see Fig. 41.6). Sometimes the bone changes in this type of anaemia may be more localised, affecting mainly the frontal region.

Localised hyperostosis of the skull This may also occur in a wide variety of conditions. These include neoplasms, dysplasia and metabolic disorders.

Meningiomas commonly invade the bony skull and produce a localised hyperostotic reaction. The diagnosis is often suggested by the classic meningeoma site, e.g. parasagittal (Fig. 53.57) or sphenoidal ridge. Originally the hyperostosis is confined to the inner table but later it may grow through the diploe and outer table and even present as a palpable lump. When protruding externally, the lesion can sometimes show sunray spicules (Fig. 53.58). Other radiological evidence of meningeoma such as enlarged vascular markings leading to the lesion, or signs of raised intracranial pressure, may also be present. If the meningeoma grows from the sphenoidal ridge into the orbit it can present with proptosis.

With meningeomas arising in the region of the jugum or anterior clinoid, a rare manifestation is local bone expansion with pneumatization, so-called 'blistering'.

Primary osteosarcoma arising in the skull is very rare but can give rise to localised hyperostosis, often with sunray spicules. It is commonest as a complication of Paget's disease.

Osteomas can occur in the skull vault, when they appear as dense flat 'ivory' nodules growing from the surface. More commonly they present as chance findings growing from the wall of a frontal sinus. They are usually small - under 1 cm in size - but occasionally larger, and cases are recorded where large osteomas have perforated through the sinus and given rise to pneumocephalus.

Ossifying fibromas involving the skull are relatively rare. They are described as most frequently commencing in the paranasal sinuses, particularly the antrum. They are particularly common in East Africa and can produce large densely calcified masses. We have personally encountered a case originating in the sphenoid sinus and growing upward into the sella.

Fibrous dysplasia is an important cause of localised hyperostosis involving the skull vault, facial bones (see Ch. 35) or skull base. It may occur as an isolated lesion, or in association with lesions in other bones (polyostotic fibrous dysplasia and Albright syndrome - see Ch. 35).

Leontiasis ossia is the descriptive term used for a form of hyperostosis affecting the frontal bones and facial bones and giving rise to severe facial deformity. Most cases are due to fibrous dysplasia, although it was once thought that a chronic periostitis was responsible.

Hyperostosis frontalis interna is a mysterious condition frequently seen in adult skulls. Its cause is unknown, although it appears to be hormone-related as it occurs almost exclusively in postmenopausal

women, male cases being relatively rare. It is characterised by irregular nodular thickening of the inner table of the skull vault, affecting mainly the frontal bones. The lesions are characteristically bilateral and symmetric and spare the midline. Occasionally they are more extensive and involve the parietal bones.

Hemiatrophy In infantile hemiplegia associated with porencephalic cyst, or other conditions in which one half of the brain is maldeveloped or atrophic, the overlying skull vault differs from that on the normal side. As well as being smaller, the affected half of the skull vault is thicker. The petrous bone and sinuses may also be larger on the affected side. These changes suggest that normal brain growth is necessary for normal growth and moulding of the overlying skull.

Skull trauma

Cephalhaematoma This is due to birth injury, and the infant presents with a soft-tissue parietal swelling which may be unilateral or bilateral. The haematoma lies under the periosteum and calcification, visible at radiography, develops at its margin. As growth proceeds, the lesion becomes less prominent and on clinical and radiological investigation is found to merge with the underlying skull.

Fractures Fractures of the skull vault have been classified as *linear*, *step* /*late* and *depressed*.

There is a tendency in many accident and emergency departments to radiograph all head injuries immediately on admission. This often results in poor-quality or non-diagnostic films, particularly if the patient is comatose or confused and non-cooperative with temporary head dressings. Since severe brain injury can occur in the absence of a fracture, and a fracture can be present without intracranial injury. Such emergency radiography is to be deprecated unless it is to show a depressed fracture or support a diagnosis of extradural haematoma by showing a fracture line involving the middle meningeal vascular markings. In most other cases, however, the procedure is of medicolegal or academic rather than of medical

importance, and it is better to radiograph the patient as an elective and non-emergency procedure when he or she is more cooperative. All cases where an intracranial haematoma or brain damage is suspected will also require CT or MRI for further assessment.

Linear fractures of the skull are readily recognised on good-quality films, where they usually appear as linear lucent lines. In some cases, however, where fracture margins overlap slightly in relation to the X-ray beam, they may appear as lines of increased density (see Fig. 53.59). Care should be taken not to confuse fractures with normal vascular markings or with the internal suture line, which is not serrated like the external suture. The internal suture line is characteristically superimposed on a serrated suture, whereas a fracture will deviate from it at some points.

Depressed fractures may require tangential views to show their exact relationships, but are often better shown by CT.

Post-traumatic cysts (leptomeningeal cysts) Where a fracture in an infant or child involves the meninges, cerebrospinal fluid may escape from the subarachnoid space and form a cyst beneath the fracture. Atrophy of the overlying bone margins may result and quite large bone defects can follow. In some of these cases the original fracture may be difficult to identify, and if the original trauma is forgotten a difficult differential diagnosis may result. Most cases present in young children either with a cystic superficial mass in the parietal or parieto-occipital region, or as a chin, c

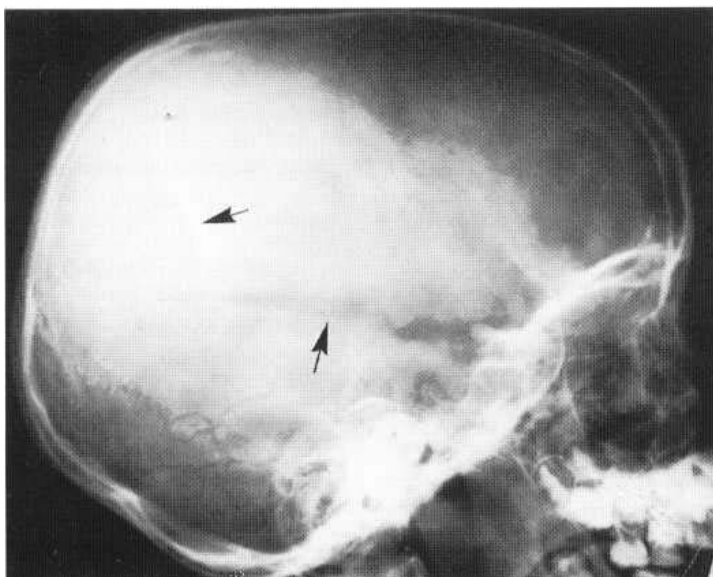


Fig. 53.59 Transverse linear fracture of the skull vault showing as a translucency (T). There is also a vertical fracture showing as an increased density (f-).

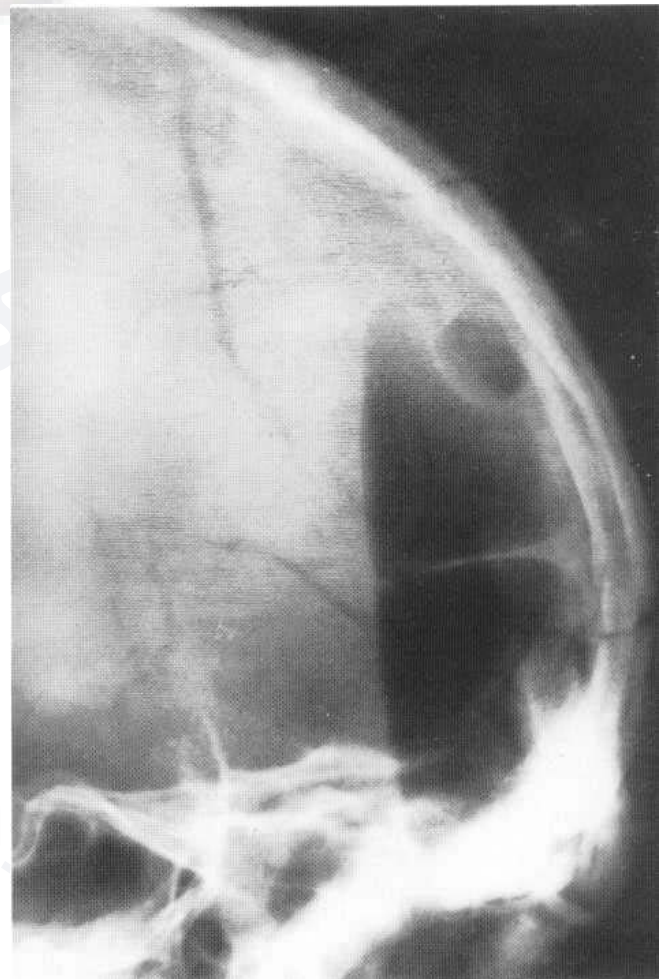


Fig. 53.60 Brow-up film showing pneumocephalus following frontal fractures. Note the air-fluid level, best seen in brow-up lateral films.

finding at X-ray. The characteristic radiographic appearance is of an elongated area of lucency with or without a fracture extending into it. Treatment is by surgical excision of the cyst and repair of the dura.

juvenile subdural haematoma These can localise around the temporal lobe and give rise to local expansion of the middle fossa as described above. Many of the cases previously diagnosed as juvenile subdural haematomas, however, would now be regarded as arachnoid cysts.

Pneumocephalus and aerocele These most commonly result from fractures involving the frontal or ethmoid sinuses. Such cases should always have follow-up films taken within a few days. These should be obtained with the head brow-up and a horizontal X-ray beam, to demonstrate possible intracranial air-fluid levels (Fig. 53.60).

Intracranial air is of course readily recognised at CT, which is more sensitive than plain radiography in identifying small quantities of air. The lateral brow-up radiograph will also demonstrate a fluid level in the *sphenoid sinus*, a finding which can indicate a fracture of the skull base.

There is usually a dural tear, and CSF rhinorrhoea may be present. The latter finding is always an indication for further investigation to localise the dural tear responsible, whether intracranial air is present or not.

CSF rhinorrhoea is characterised by a persistent drip of fluid from one or both nostrils, accentuated by stooping or straining. The fluid is usually clear, colourless and contains glucose. Surgery with closure of the dural tear is indicated, and tomographic studies or radionuclide or CT cisternography may be required for accurate localisation.

CSF otorrhoea may follow fractures involving the petrous or mastoid temporal bone. The fracture usually lies on the anterior surface of the petrous and involves the middle fossa. Localisation of the dural tear is by tomography or by radionuclide or CT cisternography.

REFERENCES AND SUGGESTIONS FOR FURTHER READING

General

- Du Boulay, G. H. (1980) *The Skull*, 2nd edn. London: Butterworth.
 Newton, T. H., Potts, D. G. (1971) *The Skull*. St Louis: Mosby.
 Taveras, J. M., Wood, E. H. (1976) *Diagnostic Neuroradiology*, 2nd edit. Baltimore: Williams & Wilkins.

Specific

- Avrahami, E., Even, I. (2000) Osteoma of the inner table of the skull: CT diagnosis. *Clinical Radiology*, 55, 435.
 Babbitt, D. P., Tang, T., Dobbs, J., Berk, R. (1969) Idiopathic familial cerebrovascular ferrocalsinosis (Fahr's disease) and review of differential diagnosis of intracranial calcification in children. *American Journal of Roentgenology*, 105, 352-358.

- Banna, M. (1976) Craniopharyngioma based on 160 cases. *British Journal of Radiology*, 49, 206-223.
 Bennett, J. C., Maffly, R. H., Steinbach, H. L. (1959) The significance of bilateral basal ganglia calcification. *Radiology*, 72, 368-378.
 Benson, M. L., Oliverio, P. J., Yuc, N. C., Zinreich, S. J. (1996) Primary craniosynostosis: imaging features. *American Journal of Roentgenology*, 166, 697-703.
 Burrows, E. H. (1963) Bone changes in orbital neurofibromatosis. *British Journal of Radiology*, 36, 549-561.
 Dorfsman, I. (1963) The radiologic aspects of cerebral cysticercosis. *Acta Radiologica (Diagnosis)*, 1, 836-842.
 Duggan, C. S., Keever, E. B., Gay, B. B. (1970) Secondary craniosynostosis. *American Journal of Roentgenology*, 109, 277-293.
 Fieldman, H. A. (1968) Toxoplasmosis. *New England Journal of Medicine*, 279, 1370-1375, 1431-1437.
 Galatius-Jensen, F., Uhm, I. K. (1965) Radiological aspects of cerebral paragonimiasis. *British Journal of Radiology*, 38, 494-502.
 Gautier-Smith, P. C. (1970) *Parasagittal and For Meningiomas*. London: Butterworths.
 Hastrup, J., Reske-Nielsen, E. (1965) Symmetrical brain calcification in infants. *Acta Neurologica Scandinavica, Suppl.* 13, 637.
 Lagos, J. C., Holman, C. B., Gomez, M. R. (1968) Tuberos sclerosi: neuroroentgenologic observations. *American Journal of Roentgenology*, 104, 171-176.
 Lorber, I. (1958) Intracranial calcifications following tuberculous meningitis in children. *Acta Radiologica*, 50, 204-210.
 McRae, D. L. (1965) Habenular calcification as an aid in the diagnosis of intracranial lesions. *American Journal of Roentgenology*, 94, 541-546.
 Musshihler, H. (1968) Radiologic study of intracranial calcifications in congenital toxoplasmosis. *Acta Radiologica (Diagnosis)*, 7, 369-379.
 Oh, S. J. (1968) Roentgen findings in cerebral paragonimiasis. *Radiology*, 90, 292-299.
 Olsen, T. G. (1963) Sarcoidosis of the skull. *Radiology*, 80, 232-235.
 Palacios, E., Schimke, N. (1969) Craniosynostosis syndactylism. *American Journal of Roentgenology*, 92, 1249-1251.
 Potts, G., Svarc, G. T. (1964) Calcification in intracranial metastases. *American Journal of Roentgenology*, 106, 144-145.
 Royal College of Radiologists (1980) Skull radiography in accident and emergency units in the UK. *Lancet*, ii, 1234-1237.
 Sage, M. R., Chan, E. S. H., Reilly, P. L. (1986) The clinical and radiological features of the empty sella syndrome. *Clinical Radiology*, 31, 513-519.
 Samiy, E., Zadeh, F. A. (1965) Cranial and intracranial hydatidosis with special reference to roentgen-ray diagnosis. *Journal of Neurosurgery*, 22, 425-433.
 Santin, G., Vargas, J. (1966) Roentgen study of cysticercosis of central nervous system. *Radiology*, 86, 520-528.
 Sutton, D. (1951) The radiological diagnosis of lipoma of the corpus callosum. *British Journal of Radiology*, 22, 534.
 Sutton, D. (1951) Intracranial calcification in toxoplasmosis. *British Journal of Radiology*, 24, 31-37.
 Tod, P. A., Yelland, J. D. N. (1971) Craniostenosis. *Clinical Radiology*, 22, 472-486.
 Tress, B. M. (1984) Skull radiography in epilepsy dementia and nonspecific neurological symptoms. *BMJ*, 289, 160.
 Vezina, J. L., Sutton, T. J. (1974) Prolactin-secreting pituitary microadenomas. *American Journal of Roentgenology*, 120, 46-54.
 Wcsenberg, R. L., Juhl, J. H., Daube, J. R. (1966) Radiological findings in lissencephaly (congenital agyria). *Radiology*, 87, 436-444.

NEURORADIOLOGY OF THE SPINE

John M. Stevens and Brian E. Kendall

Technical progress has rendered obsolete many of the radiological investigations of the spine, which were commonplace until quite recently. MRI now is widely available in developed countries and is usually the investigation of choice for the spine.

Investigations with current applications in neuroradiology

Those to be considered in this section are:

- NRI
- Plain X-rays
- CT
- Myelography and computed myelography (CTM)
- Spinal angiography
- Ultrasound
- Radioisotope studies
- Discography.

Procedures no longer used, and excluded in this edition, are endomyelography (injection of contrast medium into intradiscal cysts) and epidural venography (opacification of the anterior internal vertebral veins for the identification of epidural masses—usually disc protrusions not shown by myelography). With the exception of sonic applications more orientated to orthopaedic than neuroradiological practice, discography also falls into this obsolete category.

1. MRI

The spinal cord is a longitudinal structure, and precise localisation of the level of a lesion from clinical examination can be difficult. This factor limits the precision of siting for transverse axial imaging methods such as CT. MRI does not have this limitation because it can be easily applied in any plane, including the optimal sagittal axis.

The annulus fibrosus, spinal ligaments, and dura mater and the cortical bone of the vertebrae give low signals; the epidural and paraspinal fat provides a high-intensity signal on most commonly used sequences. The normal bone marrow contains a variable amount of fat usually sufficient to increase the signal from the vertebral regions of the vertebrae and thus display their structure and anatomy.

The gel of the nucleus pulposus of the normal intervertebral discs gives high-intensity signal on T₂-weighted sequences. In the normal

adult disc, a shelf of annulus causes a low-signal horizontal band, resulting in a characteristic hilocular appearance (Fig. 54.1), and with normal ageing the intensity of the signal from the nuclei decreases.

The T₁ and T₂ relaxation times of cerebrospinal fluid are relatively long. Using short echo-delay times the fluid appears dark, and is easily distinguished from the considerably greater signal generated from the spinal cord (Fig. 54.2). In this way the gross anatomy is well shown; distinction between the normal grey and white matter within the cord is sometimes, but not routinely, achieved. Fast spin-

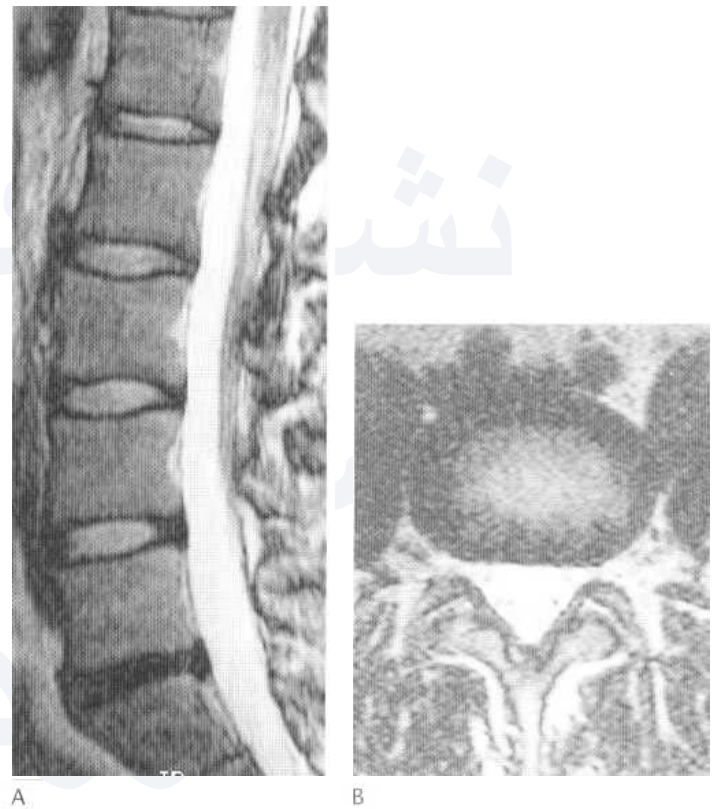


Fig. 54.1 Normal and degenerative lumbar intervertebral discs. Sagittal (A) and axial (B) MRI, T₂-weighted contrast. Normal discs are surrounded by low signal from the annulus fibrosus and partly divided horizontally by a low-signal band, not present in children's discs.



Fig. 54.2 Normal and degenerative cervical intervertebral discs and general anatomy. Sagittal MRI. (The cerebellar tonsus seem to be low lying).

echo sequences allow high-contrast, high-resolution images, especially of the intrathecal contents, which are of particular value in the examination of nerve roots and arachnoiditis (Fig. 54.1).

Most examinations consist of a multislice series acquired in the sagittal plain using conventional or preferably fast spin-echo sequences to display contrast, which is dominated by T₁ and T₂ relaxation effects. Axial multislice sequences, also with T₁ and T₂ weighting, are performed as indicated by findings on the sagittal series or by clinical considerations. If lesions of the spinal cord are suspected, axial sections 3-5 mm in thickness are preferable to improve signal from the spinal cord. If spinal root compression in the intervertebral foramina is suspected, some units perform an axial relaxation acquisition where slice thicknesses of 2 mm or less are possible with generally acceptable contrast resolution. The widespread availability of phased array coils permits the whole spinal cord to be imaged in one acquisition, and studying two regions does not require changing the coil.

The newer contrast mechanisms now finding some application in brain imaging, such as diffusion imaging and magnetisation transfer imaging, have proven insensitive to pathology readily shown by T₁- and T₂-weighted acquisitions, and similarly fluid-attenuated inversion recovery (FLAIR) acquisitions are of disappointing sensitivity in the spine. However, although rarely used in practice, diffusion-weighted imaging (DWI) could help distinguish cystic from solid or necrotic masses in the spinal cord.

It is possible to investigate aspects of cerebrospinal fluid (CSF) flow using MRI. The method most readily available uses phase-contrast imaging with cardiac gating to acquire flow-related data at points throughout the cardiac cycle and display this on a cine-loop. Spectacular moving images of CSF motion in spinal subarachnoid space, across the foramen magnum and in spinal cord cavities, can be generated but the information provided contributes little to current clinical practice.

Examination of the brachial and lumbosacral plexuses is increasingly requested in addition to the cervical and lumbar spine. If protocols suggested by many workers are followed, these are very significant additions in terms of time: they may involve acquisitions

using large fields of view in sagittal, axial and coronal plains, with both T₁- and T₂- dependent contrast (the latter with fat saturation). before and after intravenous contrast medium. A technique using carefully orientated diffusion-weighted acquisitions has been termed MR neurography. The positive yield is low and in general specificity is lacking except in clinical context. Abbreviated protocols are often used, such as only coronal acquisitions for brachial plexus and axials or coronals for lumbosacral plexus.

2. Plain spine X-rays

In most units worldwide, plain X-rays are still widely used. Anteroposterior and lateral projections of the region of interest may initiate but are now more commonly used as additional studies in the investigation of suspected spinal pathologies. Supplementary oblique views are occasionally helpful to show the intervertebral foramina in the cervical region and the pars interarticularis in the lumbar region. Stability of the cervical or lumbar spine still is best studied by lateral views in flexion and extension and plain X-rays remain the first-line investigation for spinal trauma.

3. CT (including digital imaging on the scout view facility)

Visualisation of the dura and extradural segments of nerve roots and vessels is facilitated where the epidural fat is relatively thick, as is usual in the high cervical, lumbar and sacral regions. The spinal cord and subarachnoid masses of similar density can be discriminated if they are more than 2.5 mm in diameter and separated by a 2 mm channel of CSF; thus the cervical cord is usually demonstrated, but in most patients the thoracic cord is not shown without intrathecal water-soluble contrast medium. CT remains satisfactory to diagnose disc protrusions and degenerative disease of the lumbar and occasionally cervical spine when MRI is contraindicated or impossible (see below). It also is used with high-resolution hone review algorithms to assess bone texture, structure integrity (prior to fixation for example), and to evaluate spinal fractures when necessary (Fig. 54.3). Evaluation of the spinal cord generally will require intrathecal contrast injection (see below), but every case should be viewed on its merits with an eye on the minimum that needs to be shown for management.

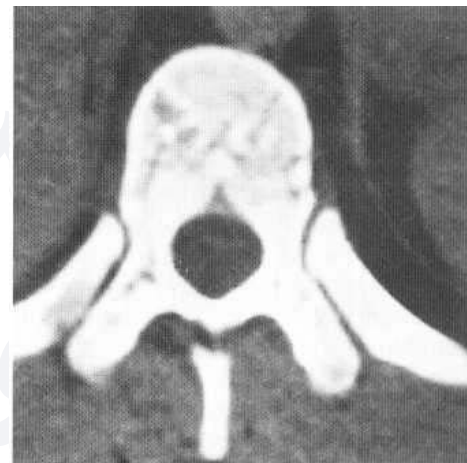


Fig. 54.3 Normal dorsal vertebral, CT axial section. Normal defects in the cortex of the vertebral body for the passage of the veins are shown; the posterior defect is for the basivertebral veins. Note the circular spinal canal with equal sagittal and coronal diameters.

To produce optimal scans, the following facilities, available on all modern machines, are required:

- Rapid scan times, as in spiral CT, to limit artefacts due to involuntary movements including swallowing and respiration.
- Digital radiograph-cursor line and tilting gantry, to allow selection of the optimal scanning plane, which for most conditions is perpendicular to the long axis of the spinal canal.
- Variable-section width. Sections as thin as 2.0 mm or less are advantageous for reducing partial volume effect in narrow structures such as cervical discs, and are necessary high-resolution reformatting of data acquired in the axial plane. Sections as thick as 8.0-10.0 mm provide the greater contrast discrimination necessary for plain scan diagnosis of lesions such as syringohydromyelia, with densities in the range between CSF and cord substance.
- Software capable of reformatting images in any desired plane.
- An extended CT number range.

4. Myelography and computed myelography (CTM)

Conventional myelography was performed using X-ray film, but most well-equipped units now go straight to CTM which requires far less radiographic and manipulative skill, a skill dissipated these days by lack of practice and obsolescence of dedicated radiographic

equipment. However, the general principles for both conventional and CT myelography are much the same, save that rarely more than 10-15 ml of contrast medium at concentrations of no more than 240 mg/ml are necessary, and manipulation generally requires only mild head-down table (or trolley) with the patient in the decubitus position, appropriate side down. CT should be performed within 30 minutes and delayed (6-12 hours) imaging may be necessary to evaluate cysts (see below) (Fig. 54.4).

A satisfactory myelogram should clearly define detail of the subarachnoid space throughout the region of interest: not only should the spinal cord, conus medullaris and nerve roots and their sheaths be clearly defined, but the spinal vessels, denticulate ligaments and arachnoid septa should also be visualised. Although many spinal pathologies cause considerable myelographic deformity, others (e.g. some angiomatous malformations) may cause only minor changes.

These water-soluble non-ionic contrast media, which are licensed for intrathecal use (e.g. Iohexol), are virtually non-neurotoxic, do not cause epileptic fits and are apparently devoid of arachnoid toxicity. They can be used without withdrawing other drugs which the patient may be taking, and anticonvulsant cover is unnecessary. The only relative contraindication is an unexpectedly severe reaction to a previous injection of the contrast medium by any route. Minor adverse reactions, which occur in about 25% of patients and are relatively more

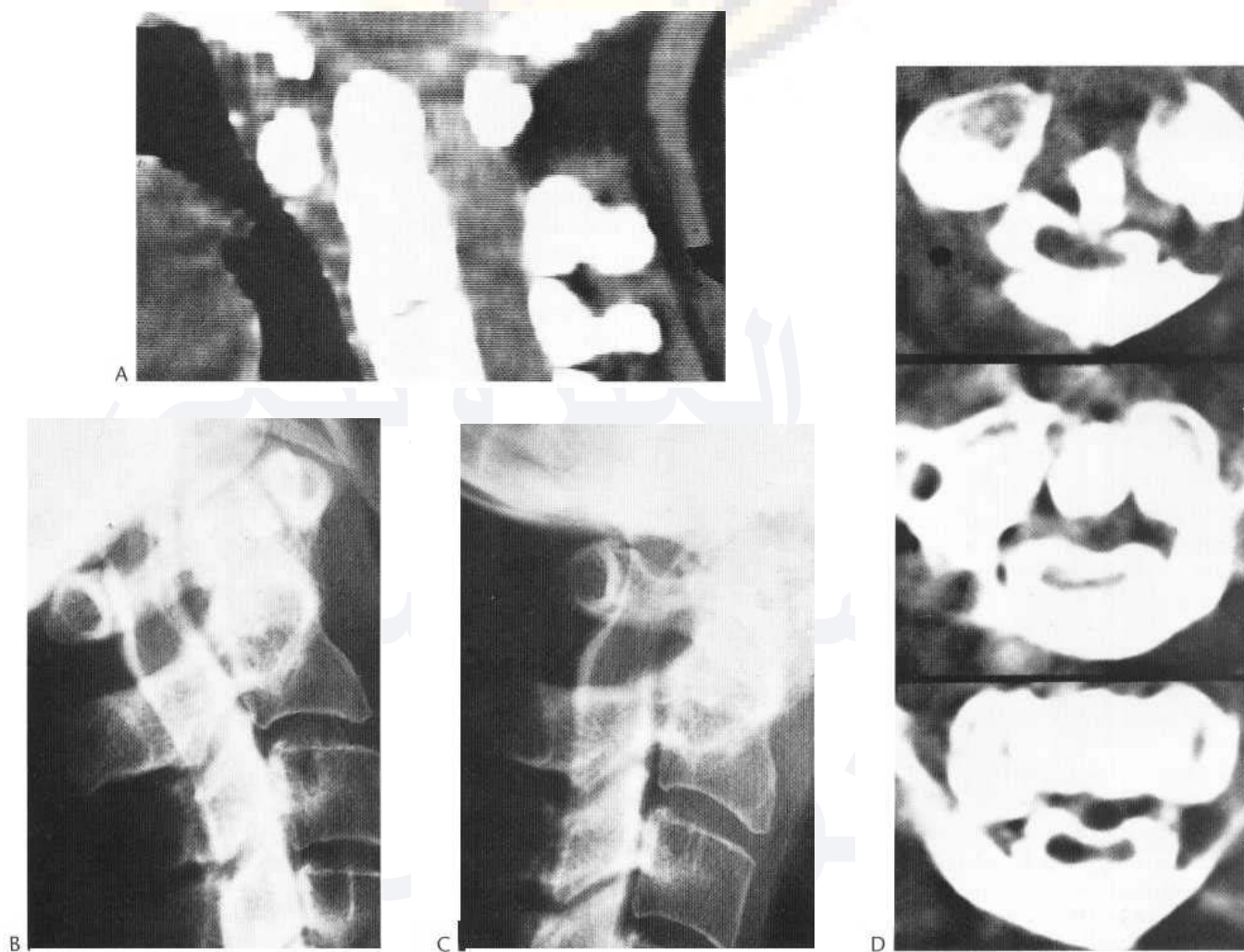


Fig. 54.4 Myelogram and CT myelography in a patient with rheumatoid arthritis and seemingly mild anterior atlanto-axial subluxation and severe spinal cord damage. (A) Sagittal image reformatted from multiple axial slices (no contrast). (B and C) Lateral views of the myelogram in flexion and extension. (D) Axial CT images of the myelogram showing the flattened damaged spinal cord.

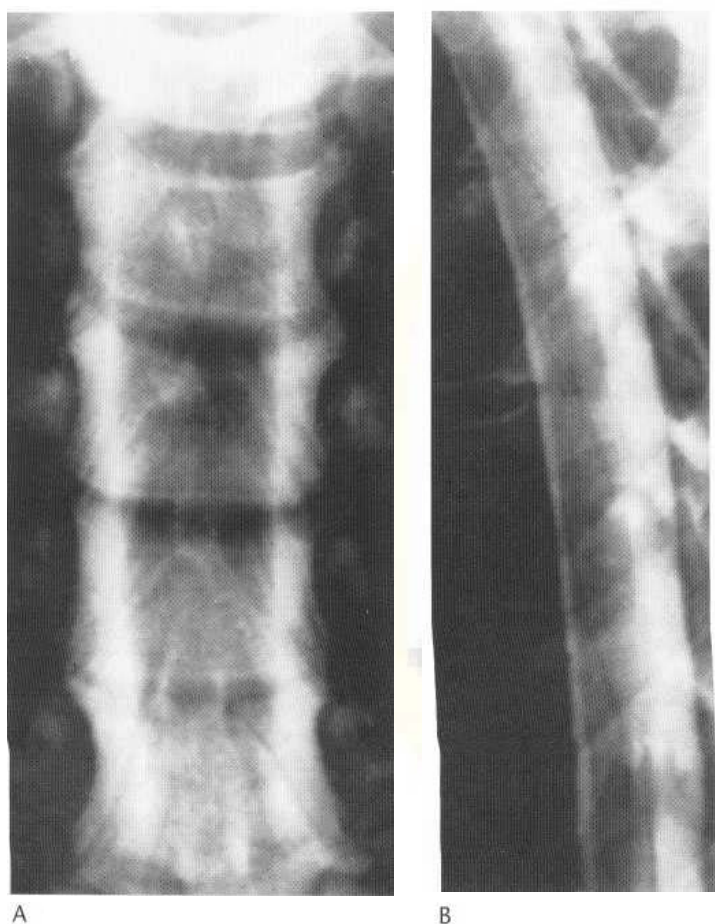


Fig. 54.5 Myelogram with non-ionic contrast medium. (A) AP projection of cervical region in prone position. The spinal cord is symmetrically situated in the opacified subarachnoid space. The nerve roots are shown descending through the root sheaths to the intervertebral foramina. An anterior radiculomedullary artery ascends to the anterior spinal artery. The periphery of the left sixth cervical nerve root sheath is obstructed by a small lateral disc protrusion. The myelogram is otherwise normal. (B) Lateral projection, supine position, dorsal region. The spinal cord tends to take the shorter route toward the convexity of the thoracic curve in the anterior part of the subarachnoid space, which is therefore wider behind the spinal cord. The descending nerve roots and denticulate ligaments are faintly visible.

frequent in women, include headache, nausea, vomiting, backache and radicular pain, but these are generally short lived. Although the empirically recommended dose is 3g I equivalent, this can be cautiously increased to 4.2g I if necessary for complete examination of large subarachnoid spaces without increasing the incidence of adverse effects. It should be noted that many of the newer water-soluble contrast media now used in angiography are not licensed for intrathecal injection: only those that are should be used (Fig. 54.5).

Myelographic technique Defects of blood clotting should be reversed if possible to reduce any tendency to sub- or extradural haemorrhage. General anaesthesia may be necessary in young children. Otherwise, unless the patient is exceptionally nervous, myelograms are performed without premeditation or special preparation, apart from an explanation of the procedure. The meal preceding the investigation is light, but a plentiful fluid intake is encouraged. A 22-gauge needle is preferred. After a CSF sample has been taken, the contrast medium is injected with fluoroscopic control, always via a connecting tube to avoid disturbing the needle or irradiating

the radiologist's hands. Lumbar puncture is used unless there is a positive contraindication. The latter include:

1. Manifest or suspected infection of the tissues overlying the lumbar theca.
2. Suspected obliteration or marked stenosis of the lumbar theca due to previous surgery, arachnoiditis, congenital abnormality or recent failure of lumbar puncture under screen control.
3. Suspected difficulty with manipulation of contrast medium to the cervical region, as in patients with a severe kyphoscoliosis or deformities of the neck, or where the head-down position induces dyspnoea, nausea, vomiting or vertigo.

Because contrast media are heavier than CSF, it can be induced to form pools under the influence of gravity by placing the patient in such a posture that the region of interest is dependent.

The *lumbar region* is most simply examined by introducing a relatively large volume of iohexol, containing 240 mg I/ml, with the feet dependent. The puncture is made away from the site of particular interest, usually high in the lumbar region with the patient prone and the back slightly flexed over a firm pad. During injection the foot of the table is at least 20° dependent, and ideally a sufficient quantity of the contrast medium (as estimated by fluoroscopy) is introduced to fill the theca to the level of the second lumbar body. Erect AP, lateral and oblique films are taken in all cases and supplemented with prone, horizontal decubitus, and supine films as necessary for diagnosis. When pathology relevant to the patient's symptoms is evident on the erect films, the examination is discontinued, but when this is not the case the study should be extended as high as the mid-dorsal level.

For examinations of the *dorsal region*, iohexol containing 240 mg I/ml is injected with the patient in the lateral decubitus position, with a firm pad beneath the head and neck to tilt the vertex toward the ceiling, and with the head of the table dependent so as to pool the contrast medium in the concavity of a dorsal curve. The injection is made under screen control, continuing until the region of interest has been adequately filled. After lateral films have been obtained, the needle is removed and the patient placed supine for AP and oblique projections.

For examination of the *cervical region* the patient is prone, with the neck extended by a soft pad under the chin and the lumbar lordosis flattened by a pillow beneath the abdomen. The contrast medium may be directly pooled in the cervical lordosis in patients with a suitably flat back, tilting the head of the table down while about 10 ml iohexol, containing up to 300 mg I/ml, is injected. Alternatively, the injection is carried out so that the contrast medium forms a pool in the lumbar region, and the head of the table is smoothly lowered to transfer the pool to the cervical theca under screen control after the injection has been completed. The latter method is usually adopted for total myelography, in which the lumbar region is examined first, then the cervical, and finally the dorsal region, by turning the patient supine, taking care to elevate the vertex in all manoeuvres to avoid intracranial spill.

Should obstruction to the upward passage of contrast medium be diagnosed while the needle is still in the lumbar theca, it can generally be overcome by further injection of iohexol or normal saline while the head of the column lies against the obstruction. The patient may be aware of some discomfort as the intrathecal pressure is increased, but this is usually tolerable, especially if it is explained that the necessity for a further puncture in the cervical region may be avoided.

For cervical studies AP and lateral films are made and supplemented with oblique projections as necessary, especially if nerve root compression is suspected. Obstruction due to cervical disc protrusion or spondylosis may be overcome by tilting the patient enough to flex the neck while obtaining sufficient lateral bowing of the head to avoid tipping the contrast medium irretrievably into the intracranial compartment. If the problem is not fully elucidated in the prone position, the patient is turned supine and the neck flexed. This is particularly necessary for examination of the cisterna magna, cerebellar tonsils, and lower posterior fossa. The neck flexion relieves the buckling of the ligamenta flava present in extension, and shows the degree of mobility of the cervical spine and the effect of these factors on canal diameter; it is thus useful in elucidating the components contributing to a canal stenosis.

Cervical puncture is best performed between the first and second vertebra in the posterior third of the canal, under fluoroscopic control. Suspicion of an upper cervical or foramen magnum mass lesion contraindicates cervical puncture; suspected mid or lower cervical obstruction is a relative contraindication to cervical puncture as the primary approach. For examination of the cervical region, the contrast medium is introduced with the patient prone and the neck extended; for the dorsal or lumbar region it is introduced with the patient supine and the neck flexed.

After myelography the patient is encouraged to resume gentle activity and to eat and drink normally. Bed rest is avoided, unless

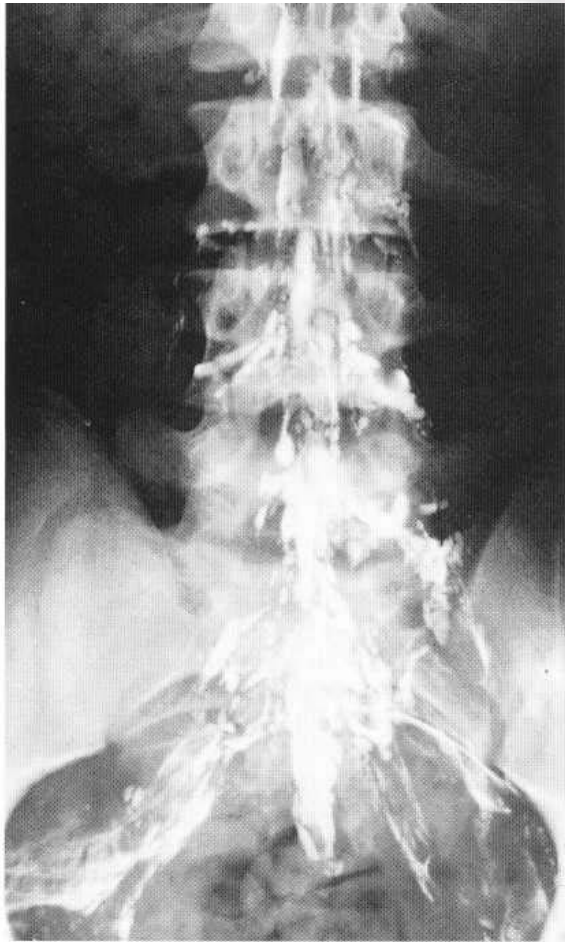


Fig. 54.6 Extradural injection of contrast medium. Myodil globules have extended throughout the lumbar and sacral epidural space, through the intervertebral foramina and along the course of the sacral plexuses.

indicated for other reasons, since it increases the incidence of minor reactions; these are treated symptomatically.

Technical errors Extra-arachnoid injection of non-ionic contrast medium is not a significant complication but it should not be mistaken for pathology. *Extradural* contrast medium extends along nerve roots and muscle planes away from the spinal theca (Fig. 54.6). *Subdural* contrast medium tends to remain localised and to flow slowly under gravity, but it may extend throughout the subdural space and simulate a swollen cord (Fig. 54.7). Since the subdural space does not normally contain fluid, the contrast medium will not layer or pool as it does in the subarachnoid space. Exceptionally, enough CSF may be present in the subdural space to allow pooling; this occurs most frequently following multiple lumbar punctures. Leakage of CSF from the punctured theca, or of blood from a blood vessel, may compress the spinal theca and simulate a mass; the site of such 'needling artefacts' at the level of the injection should suggest the correct explanation.

Computed myelography (CM). The whole spine now can be studied rapidly using modern CT with fast multislice and spiral facilities. In-plane resolution and slice thickness and spacing can be tailored to the clinical situation. Reformating in longitudinal plains is also very helpful. Once the contrast is distributed evenly the examination of all regions can be carried out with the patient supine. CTM is sometimes used to supplement MRI when it is necessary to evaluate some arachnoid cysts or diverticula, or identify the level or presence of CSF leaks, such as into the pleural cavity after spinal surgery. CTM may also be necessary in primary investigation of clinical myelopathy when MRI is unavailable,

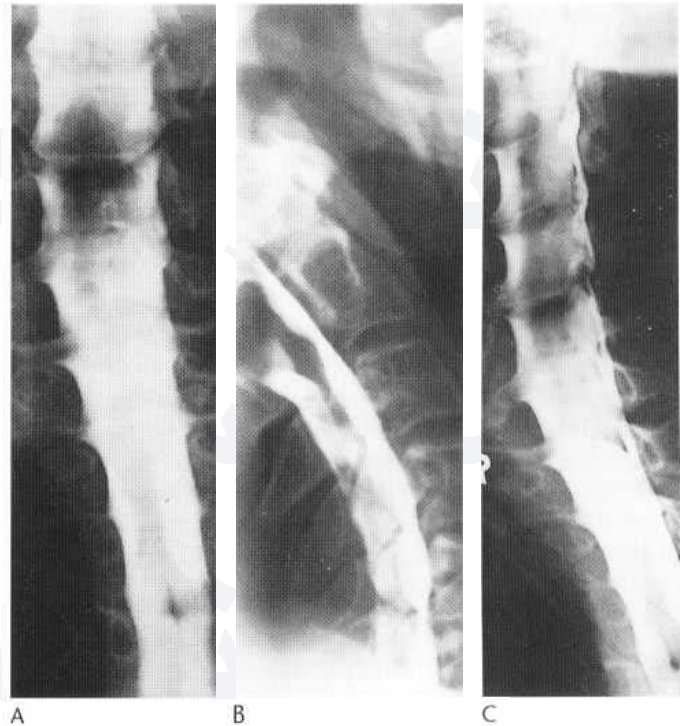


Fig. 54.7 Subdural contrast medium. (A) AP projection. (B) Lateral projection. (C) Oblique projection. The appearances superficially simulating an enlarged spinal cord are due to the contrast medium outlining the outer border of the arachnoid membrane. Note that the inner border of the contrast column appears lobulated and that its upper border does not form a fluid level with unopacified CSF.

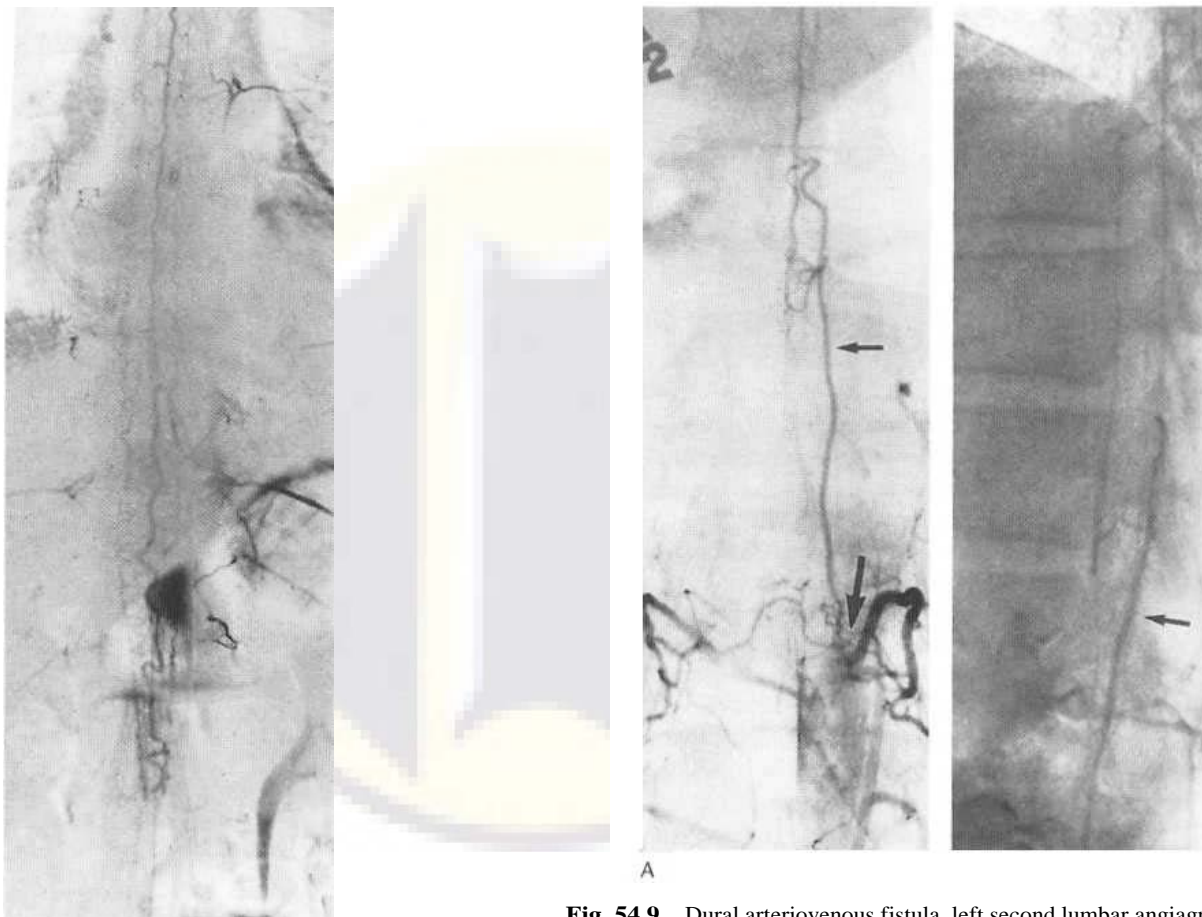


Fig. 54.8 Spinal angiogram, selective injection. Normal study. The arteria radicularis magna arises from the left tenth intercostals artery. It fills the anterior spinal artery and there is retrograde filling of other anterior radiculomedullary vessels. The posterolateral arteries of the spinal cord are also filled through the cruciate anastomosis at the conus.

Fig. 54.9 Dural arteriovenous fistula, left second lumbar angiogram. AP and lateral projections. (A and B) Large arrow, the fistula; small arrows, the draining vein.

impossible (due to skeletal deformities, excessive obesity or claustrophobia), impractical (life-support systems) or contraindicated (pacemakers or other powered implants, some intracranial aneurysm clips and mechanical heart valves).

5. Spinal angiography using digital subtraction

Spinal angiography has limited but important continuing applications (Fig. 54.8). It is essential for the preoperative or pre-embolisation elucidation of arteriovenous fistulas and angiomatous malformations involving the spinal cord, or shunting into the coronal venous plexuses which drains cord substance. Aneurysms are much less frequently associated with spinal than with intracranial angiomatous malformations, but they too can be reliably shown by angiography (Fig. 54.9).

Angiography is also used for:

a. Confirmation of haemangioblastomas suspected clinically in von Hippel-Lindau disease, or from appearances on MRI or even myelography. However, MRI before and after gadolinium enhancement has replaced angiography in most cases.

b. The preoperative investigation of hypervascular lesions of the vertebrae, including angiomas, some aneurysmal bone cysts, giant cell tumours and chordonws, which may be amenable to preoperative embolisation.

c. Showing the anatomy of the radiculomedullary arteries prior to surgical procedures in which they may be at risk, as for example in the mid and lower thoracic region in disc and scoliosis surgery.

Spinal angiography requires injection of non-ionic contrast medium into the orifices of the individual segmental vessels supplying the appropriate radiculopial and radiculomedullary arteries, and is performed using a tapered-tip 4 French catheter, generally introduced through a femoral artery. A simple cobra curve similar to that used for visceral angiography is appropriate for examination of all the vessels; in some cases catheterisation of the lumbar and sacral vessels is facilitated after the curve has been reversed by forming a loop in a renal or mesenteric artery. A complete study therefore requires a very large number of individual injections of contrast medium, and very careful technique. General anaesthesia is usually recommended because of the length of the procedure and discomfort caused by injecting small somatic arteries. A urinary catheter may be necessary to avoid a distended opacified bladder obscuring pathology. In the presence of pre-existing clinical myelography, at least some neurological deterioration should be expected in up to 15% of patients.

6. Radioisotope studies

Radionuclide bone scanning continues to be useful for:

a. Diagnosis of *spinal metastases* from a known or suspected malignancy

- h. Occasionally for the detection of *inflammatory processes* and *primary bone tumours*, especially osteoid osteoma and osteosarcoma
- c. Elucidation of *localised pain*. with normal plain X-ray.

Intrathecal injection of radionuclides may very occasionally still be useful in localising or confirming a CSF leak, especially a subarachnoid-pleural fistula, which sometimes complicates thoracic disc surgery.

7. Ultrasound

This method has limited applications for:

- a. Elucidation of the contents of meningoceles and meningomyeloceles
- b. Detection of intramedullary cysts after laminectomy
- c. Measurement of spinal diameters
- d. Detection of conus position and spinal cord tethering in infants

8. Discography

Discography has been completely replaced by CT and MRI for diagnosis of disc disease causing neurological symptoms. Lumbar discography is still applied prior to discolysis and percutaneous extraction. In orthopaedic radiology it is often used for assessing discogenic pain, for which many authorities consider the results to be of questionable significance. For details of techniques, see Ghelman 1988. Water-soluble contrast media suitable for intrathecal use should only be used.

Anatomy

The spinal canal

The spinal canal is bounded: (i) anteriorly, by the vertebral bodies and intervertebral discs, backed by the posterior longitudinal ligament; and (ii) [posterolaterally](#), by the pedicles and laminae lined by the ligamenta (lata).

Though the cross-sectional shape of the canal, which varies widely between individuals, is best shown by CT, some dimensions are visible on plain films. Of particular significance is the *minimum diameter*, which gives an indication of the amount of space for the spinal cord and/or nerve roots: it is the *sagittal diameter* in the cervical and lumbar regions, and measurements below 12 mm and 14 mm, respectively, are considered as potentially significant developmental narrowing. This may become critical if encroached on further, for example by the minor spondylosis commonly accompanying ageing. The sagittal and *interpedicular diameters* are virtually equal in the thoracic region. Interpedicular distance increases at the level of the cervical and lumbar enlargements and the increase continues down the lumbar spine in normal individuals.

Intraspinal masses growing by expansion tend to erode bone. The cortex may be thinned or destroyed if a mass is expanding quickly but tends to be reconstituted when expansion is slow. Enlargement of the spinal canal is usually associated with abnormal flattening or even medial concavity of the vertebral surfaces bordering the canal. Local expansion is generally evident from comparison with adjacent levels, a step of 3 mm or greater being abnormal. Published tables of sagittal (Ullrich et al 1980) and interpedicular diameters at every level are available. The former are made from the midpoint of the dense cortical line of the posterior border of the vertebral body to that of the conjoined laminae, which is always visible unless spina bifida is present. The latter is between the most medial points of the cortices of the



Fig. 54.10 Cystic astrocytoma, cervical spine lateral projection. The spinal canal is expanded. The posterior borders are concave. The line of the conjoined laminae bordering the posterior margin of the spinal canal is flattened and its length increased.

pedicles. These measurements are useful for reference when diffuse narrowing or widening is suspected (Fig. 54.10).

The normal intervertebral foramina are oval or boot shaped and fairly symmetrical in the absence of scoliosis. Masses extending into the foramina cause bone erosion, with thinning of the adjacent lamina and pedicles and rounding of the foramina; such masses are mainly neurogenic tumours. Other tumours, and, in the cervical region, kinked vertebral arteries, also less commonly erode foramina. All mass lesions eroding bone are large and easily shown by MRI. However failure to recognise erosion on plain X-rays may result in an important delay in diagnosis (Fig. 54.11).

The spinal cord and nerve roots

The spinal cord descends from the medulla oblongata, commencing at about the level of the foramen magnum, and terminates at the conus medullaris, which lies between the lower border of the 12th thoracic and the upper border of the third lumbar vertebra. It is approximately cylindrical, with slight enlargements in the lower cervical and thoracolumbar regions, corresponding to the cells supplying cervical and lumbosacral innervations. On anteroposterior projections it lies symmetrically in the subarachnoid space: on lateral views it tends to deviate toward the concavity of the normal curves. The nerve roots pass laterally from the anterolateral and posterolateral margins of the cord at each segment.

Normal differential growth of the axial skeleton and spinal cord causes relative cranial displacement of the segmental innervation by about one segment in the lower cervical region, two in the lower thoracic and three in the upper lumbar, so that the obliquity of descent of the nerve roots increases progressively from cervical to sacral levels. The roots generally appear straight with the spine slightly flexed and in neutral position, but they may be tortuous or redundant when the spine is extended. Especially when the canal is relatively narrow, this appearance may be exaggerated, and has occa-

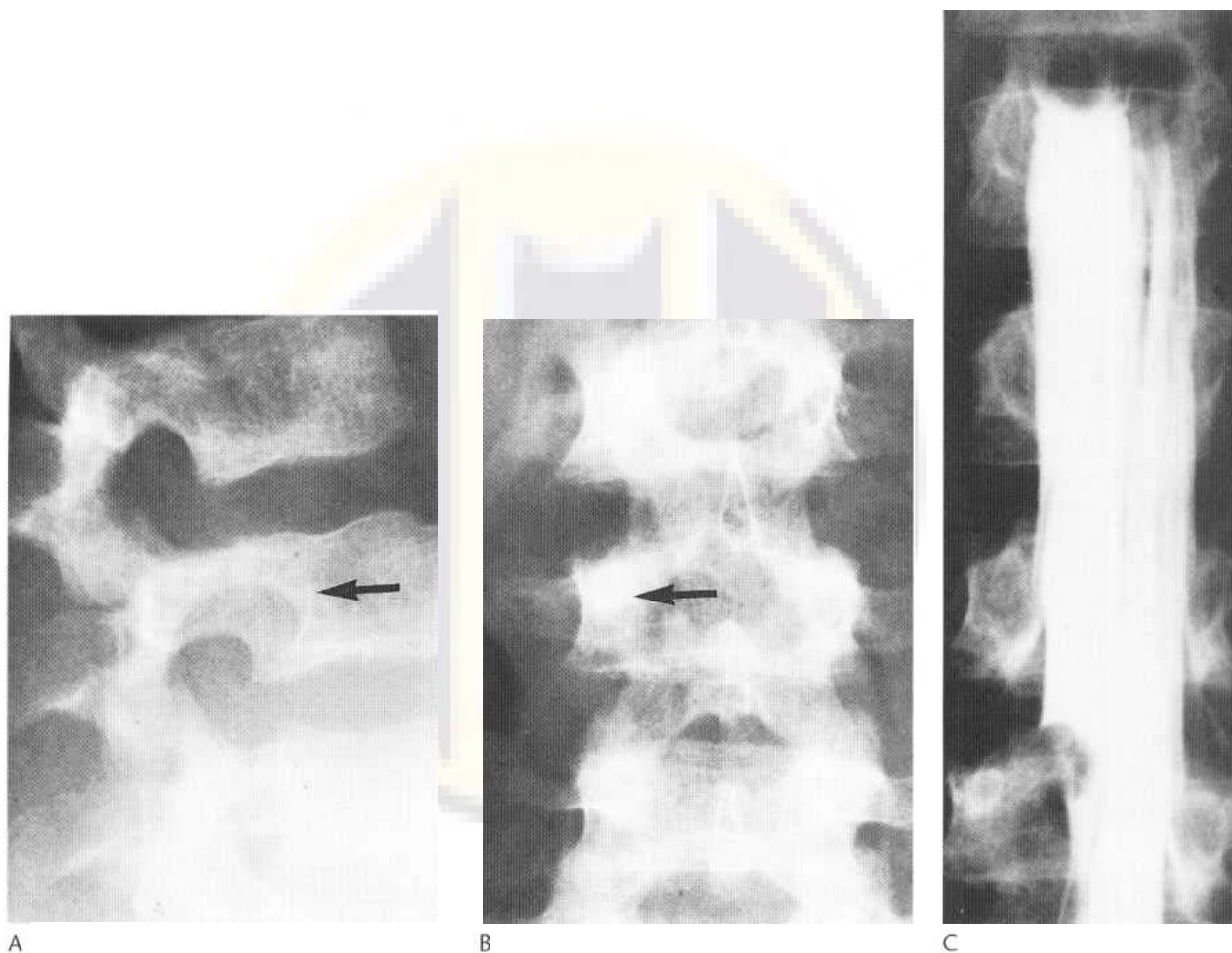


Fig. 54.11 Neurofibromatosis. (A,B) Lumbar spine X-ray. The L3/L4 intervertebral foramen is enlarged, with erosion of the inferior border of the third lumbar pedicle and the adjacent part of the posterior surface of the vertebral body. (C) Myelogram. A neurofibroma on the fourth lumbar nerve root is partly intradural, causing a well-defined filling defect within the theca at the L3 level, and partly extradural, displacing the theca medially away from the pedicle and intervertebral foramen. There is another intradural tumour at T11/T12 level which deviates the termination of the spinal cord and nerve roots toward the left and causes complete obstruction. Histology showed this tumour to be a neurofibrosarcoma.

sionally been confused with tortuous vessels. The anatomy of at least some of the roots can almost always be resolved, and distinction can be further aided by a film made in flexion to stretch the roots.

The cerebellar tonsils and biventral lobules lie posterior and lateral to the lower medulla at or just above the foramen magnum. A tonsil extending below the inferior margin of the foramen and below the biventral lobule on a coronal section is termed ectopic. Slightly more marked degrees of ectopia are evident on sagittal studies also. Minor degrees of ectopia are frequent and commonly asymptomatic, but ectopia may produce symptoms by partly obstructing the CSF pathways and/or compressing the medulla or upper cord, or be associated with syringomyelia.

The meninges

The subarachnoid space containing the CSF usually extends down to the second segment of the sacrum, but it may terminate at any level between the fifth lumbar and fourth sacral segments. Thin arachnoid suspending ligaments, the denticulate ligaments, extend from the lateral borders of the spinal cord at each level between the foramen magnum and L1, and posterior septa also divide the subarachnoid space incompletely. These structures are commonly shown on myelography and the latter may cause pocketing of CSF, which is not abnormal.

Each nerve root carries a sheath of arachnoid, extending toward the point where it penetrates the dura passing through the epidural fat to gain the appropriate intervertebral foramen. The normal sheath looks like a rose thorn, and deformity or occlusion of the sheath is an important myelographic sign of compression by an extradural mass.

The dura is closely applied to the arachnoid, but tearing of the arachnoid by any type of trauma, including surgery or puncture, will allow entry of CSF into the potential subdural space; this can compress the subarachnoid space and increase the chances of a subdural injection of myelographic contrast medium.

The epidural space contains a variable quantity of fat which outlines the nerve roots and epidural venous plexuses, facilitating visualisation by CT and MRI. When the epidural space is narrow, the contours of the spinal canal are accurately reflected by myelography and normal annuli may cause slight impressions on it. A wide epidural space may obscure disc protrusions on myelograms; although they are clearly shown on CT and/or MRI.

Blood vessels

The *anterior spinal artery* is shown by spinal angiography, but may be visible on myelograms as a linear defect approximating to the line of the anterior median sulcus of the spinal cord; the major anterior radiculomedullary arteries may also be shown, passing superi-

orly to join the anterior spinal artery at an acute angle, forming a hairpin loop.

The upper four cervical segments are supplied by the descending anterior spinal artery formed by anastomosing branches from the intracranial segments of the *vertebral* arteries.

The lower half of the cervical cord and the upper two segments of the dorsal cord are supplied by two to four anterior radicular vessels arising from the *vertebral*, *deep cervical* and/or *superior intercostal arteries* and very rarely from the *ascending cervical* artery.

The anterior spinal artery in the mid-thoracic region is usually supplied by a single anterior radicular branch from one of the adjacent *intercostal* arteries.

The lower thoracic, lumbar and sacral region is supplied mainly by the *artery of Adamkiewicz*, which may arise at any level between the eighth dorsal and the fourth lumbar artery on either side, but most commonly arises from the left tenth intercostal artery. When its origin is relatively high or low, there is usually a supplementary supplying vessel to the anterior spinal artery. Small vessels accompany the lumbar and sacral nerve roots and form an anastomosis

ing the lower cord if the artery of Adamkiewicz is occluded: it may also permit emboli introduced into lumbar vessels to cause ischaemia of the spinal cord.

The anterior spinal artery is not a continuous vessel in many patients: the most important watershed is at the periphery of the Adamkiewicz Supply (Fig. 54.9).

In addition, in all regions, a segmental radicular or radiculopial supply accompanies the posterior nerve roots; some of these give a medullary component to the peripheral part of the posterolateral aspects of the cord. From the anterior spinal artery, *sulcocommissural* arteries run through the anterior median sulcus, passing to each side to supply a hemicord. There are several arteries to each segment, with considerable overlap in their distribution, so that no nervous tissue is dependent on a single penetrating vessel. There is also a peripheral arterial anastomosis around the cord from which small arteries supply the outer parts of the white matter tracts.

Veins of the *corona/perimedullary plexus* may cause tortuous curvilinear shadows on the posterior surface of the spinal cord on supine myelography films as dark flow voids often apparently notching the dorsal surface of the spinal cord on MRI when enlarged, and as small high-signal features on the pial surface on MRI after intravenous gadolinium even when normal. They are also shown on carefully subtracted venous phase spinal angiograms.

Spinal deformity and malformation

When *kyphosis* or *scoliosis* is due to developmental vertebral anomalies such as dorsal or lateral hemivertebra, to bone destruction by inflammation or neoplasm, or to fracture or dislocation, the causative lesion is generally evident on the plain X-ray. The short kyphosis of neurofibromatosis, which generally involves about five vertebrae, and the thoracolumbar kyphosis of the mucopolysaccharidoses (particularly Morquio's disease) are recognised from the clinical and/or more diffuse radiological bony abnormalities. Also kyphosis and scoliosis may be associated with spinal tumours and syringohydromyelia; in these conditions enlargement of the spinal canal is commonly, but not necessarily, evident.

Skeletal abnormalities of the spine may be further elucidated by CT, and MRI when neural abnormalities are suspected.

Dysraphism

The most severe forms of dysraphism are due to:

1. Adhesion between the endoderm and ectoderm of the embryonic disc prior to formation of the notochord in the third week of gestation. This causes the various manifestations of the *split notochord syndrome*, which include dorsal enteric fistula, cystic remains of such a fistula (enteric duplications, foregut, gastric, enterogenous, neurenteric and spinal enteric cysts), and anterior or combined spina bifida. The intraspinal cysts are intradural and usually extratradedullary in location and typically anterior or anterolateral to the spinal cord; they are unilocular, tense, and may cause local bone erosion and enlargement of the spinal canal as well as spinal cord compression.

2. Derangements of the normal sequential closure of the neural tube and its separation from the dermis and failure of retrogressive *filum terminale*.

Disturbance of closure of the neural tube produces *myelomeningocele* or *meningocele*.

Mesoderm prematurely interposed before the neural tube is closed or the caudal cell mass fully regressed, which in normal development would have formed the primitive meninx, is induced to form lipoma between the gaping margins of the tube. The lipoma extends through the overlying local defect in the meninges (lipomyelomeningodysplasia Fig. 54.12), or simply an intramedullary lipoma. A little fat in the *filum terminale* is a frequent insignificant finding with intact overlying meninges.

Failure of separation of the neurogenic from the dermogenic ectoderm may be manifest as a dermal sinus, epidermoid or dermoid tumour.



Fig. 54.12 Lipomyelomeningodysplasia. Sagittal T-weighted image. There is high signal from the epidural fat and from the lipomatous mass. The latter is subcutaneous, within the lumbosacral spina bifida, and extends through the dura and then superiorly to blend with the posterior border of the spinal cord which extends down to the lumbosacral region. The dark band extending centrally within the intradural part of the lipoma as far as the cord is presumed to be a fibrous septum.

Plain X-rays reveal the degree of spina bifida. With overt meningocele or meningomyelocele, the pedicles and lamina are split in addition to the failure of fusion. If the vertebral bodies are split, a posterior mediastinal mass suggests an enteric cyst; gas within the mass confirms a connection to the gut.

Increased width of the spinal canal with retained medial convexity of the pedicles occurs with *diastematomyelia*. This is a dysraphic state of unknown embryogenesis, but is probably initiated by an accessory neurenteric canal or neuroentodermal adhesions. Narrowing of a disc space at the same level and interlaminar fusion are supportive evidence, and a bony spicule dividing the canal is

confirmatory; in most cases, however, the division is cartilaginous or fibrous (Fig. 54.13), and may be absent, especially when the cervical region is involved.

Bony malformations are well shown by CT, and diastematomyelia, aberrant lamina, and spina bifida are best assessed by using it. However MRI will generally allow adequate analysis of the spinal deformities (Fig. 54.14) and is the technique of choice for dysraphism requiring full elucidation. It is however true that on plain CT the low density of fat can reveal the extent of lipomas both superficial and within the spinal canal, including the infiltration of the neural placode. Meningoceles and meningomyeloceles will be shown, but details of intrathecal structures, such as position of the conus, tethering of the cord, presence of an embryonic tumour or cyst, and site of origin of nerve roots, will require elucidation by MRI. Cystic lesions without free communication with the subarachnoid space opacify only on CT sections taken late after myelography. MRI is the best technique to show the anatomy of the brainstem and cervical cord which is usually affected by a Chiari malformation (Fig. 54.15) in the presence of meningomyelocele, but usually not in other forms of dysraphism.

In caudal regression syndrome there may be absence of the caudal spine, which may involve a hemisacrum, the whole sacrum and/or a variable number of lumbar vertebrae. It is associated with neurogenic bladder and usually paralysis of some muscles innervated from sacral segments. The conus may be high, or the cord may end low in a nodular expansion. Low tethering or a lipomeningocele may be associated.

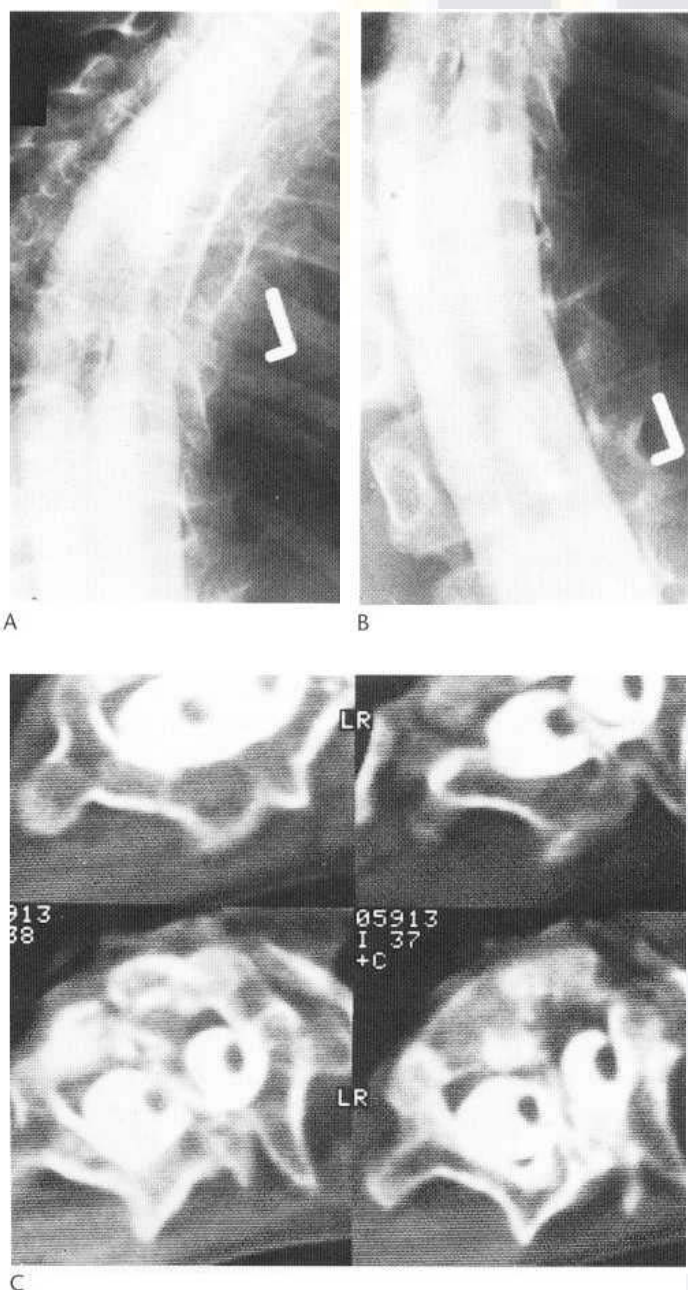


Fig. 54.13 Diastematomyelia. (A,B) Myelogram. The width of the spinal canal is increased in the lower thoracic region and it is divided by a bony spicule at T10 level. There is a long cleft of the spinal cord extending from the fourth thoracic to the second lumbar levels; the conus medullaris is at L3/4 disc level. (C) Computed myelogram. Contiguous axial sections of lower thoracic region pass through the bony spur which is dividing the spinal cord and the subarachnoid space.

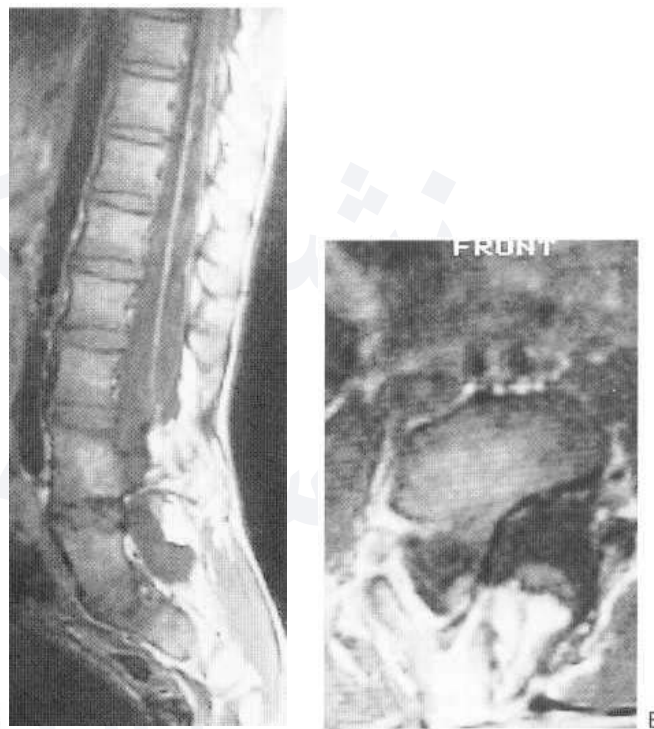


Fig. 54.14 Diastematomyelia, lipoma. (A) Sagittal T₁-weighted sequence. (B) Axial T₁ sequence. A posteriorly situated lipoma at L5 and S1 levels extends through the dura into the subcutaneous tissues. A band extends from the inferior margin of the posterior surface of the fifth lumbar vertebral body into the lipoma. The spinal cord is divided into two unequal parts, which extend one behind the other through the lumbar region and which both blend into the anterior border of the lipoma at L5 level, with the band passing between them.

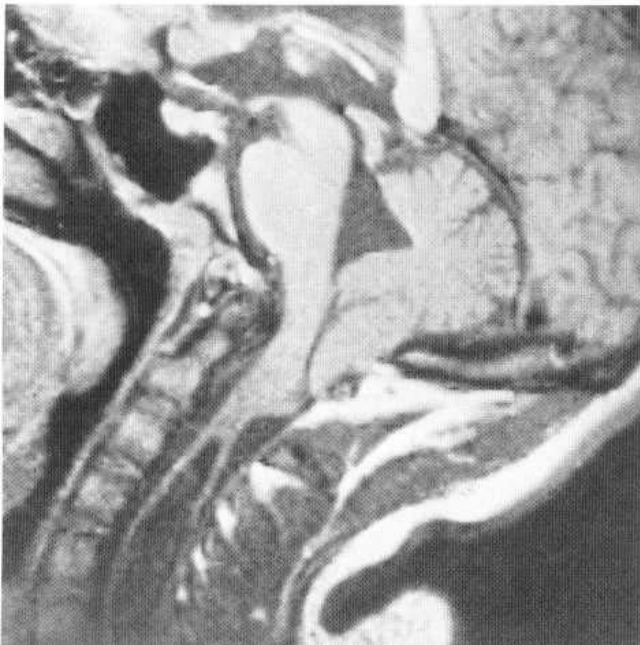


Fig. 54.15 Chiari malformation, syringomyelia. Midsagittal T₁-weighted section through brainstem and upper cervical region. The cerebellar tonsils are elongated and extend well below the level of the arch of the atlas. The medulla is elongated and the depressed dorsal column nuclei are below the tonsils. The medulla is compressed between the odontoid and the depressed cerebellar tonsils. There is a syrinx distending the spinal cord below the inferior border of C2 and there is four-ventricular hydrocephalus.

Failure of segmentation

This may affect two or more vertebral bodies and occurs in about 0.6% of the population. It is distinguished from acquired fusion by the following features:

1. The fused segments seem generally taller than adjacent unfused bodies and are reduced in AP diameter, with a tendency to 'wasp waist' at the level of the fusion (Fig. 54.16). The vertebral bodies tend to retain their fetal morphology on axial sections.
2. The arches are commonly also fused and the intervertebral foramina are round.
3. Angulation, which is common in postinflammatory fusion, is absent because there is no bone destruction.
4. Association with spina bifida is not infrequent. Though any part of the spine may be affected, the cervical region is most com-

associated with failure of segmentation. Early or accentuated spondylosis tends to affect the intervertebral discs adjoining the fused segment.

Plat ybasia, in which the angle between the central part of the anterior fossa and the clivus (basal angle) is increased to 142° or more, has little if any clinical significance.

Basilar invagination, in which the normal slope of the posterior fossa down to the foramen magnum is reversed, may cause neuraxial compression or cranial nerve dysfunction. This deformity may be congenital or acquired in conditions such as rheumatoid arthritis which destroy (basilar erosion) or soften (basilar impression) bone. The latter include Paget's disease, osteogenesis imperfecta and osteomalacia. Several measurements have been advocated to recognise

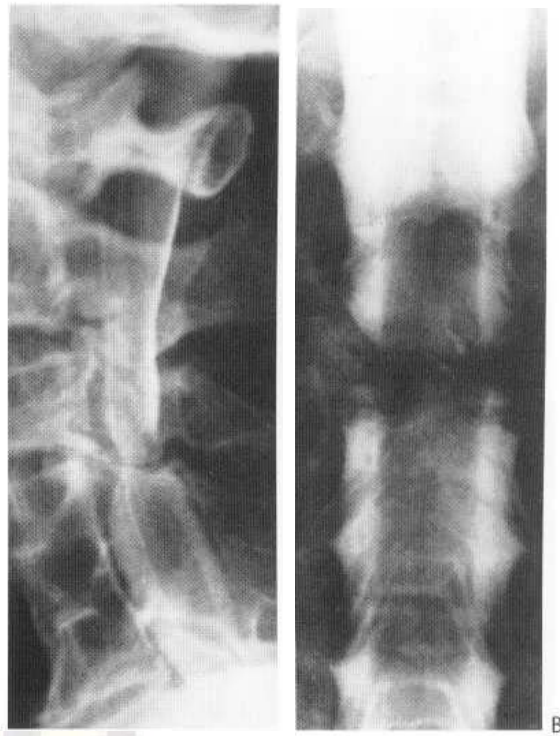


Fig. 54.16 Congenital fusion of cervical vertebrae with spondylosis: myelogram. Congenital fusion of the fourth, fifth and sixth cervical vertebrae with degenerative changes at discs above and below. Osteophytes at C3/4 level compress the spinal cord and nerve root sheaths. Osteophytes at C6/7 level compress the root sheaths only.

and quantify the deformity. These however may be abnormal in the presence of other insignificant anomalies, such as a congenitally short clivus and therefore a prominent slope of the foramen magnum.

Atlanto-occipital assimilation (Fig. 55.17) may be associated with instability at the atlanto-axial joints, with forward slip of the atlas on flexion. This may result in quadriplegia, sometimes accompanied by lower cranial nerve palsies and cerebellar dysfunction, which may be slowly progressive or related to mild trauma. Fusion of C3 and C2 vertebrae is often associated.

Spinal malformations not associated with CNS deformity

Spinal malformations are not associated with malformations of the brain. They include: failure of segmentation of basiocciput or dens, ossicles near the foramen magnum, ponticles and bipartite facets of the atlas and paracondylar and epitransverse processes), clefts of the arch of the atlas, lateral hemivertebrae, butterfly vertebrae, absent pedicle or lamina, persistent neurocentral synchondrosis, cleft and hypoplastic pedicles, and cleft lamina. Rarely, absence or hypoplasia of a pedicle is a feature of the mesodermal dysplasia of neurofibromatosis.

Absent pedicle can be mistaken for bone destruction in patients with pain or malignancy. In plain films, however, the margins of the defect are well corticated and there is generally evidence of more extensive vertebral malformation. In the cervical region this includes absence of the ipsilateral superior articular facet and retrolocation of the lateral mass of the vertebra posterior to those of the other vertebrae. The adjacent parts of the vertebral bodies and the pedi-

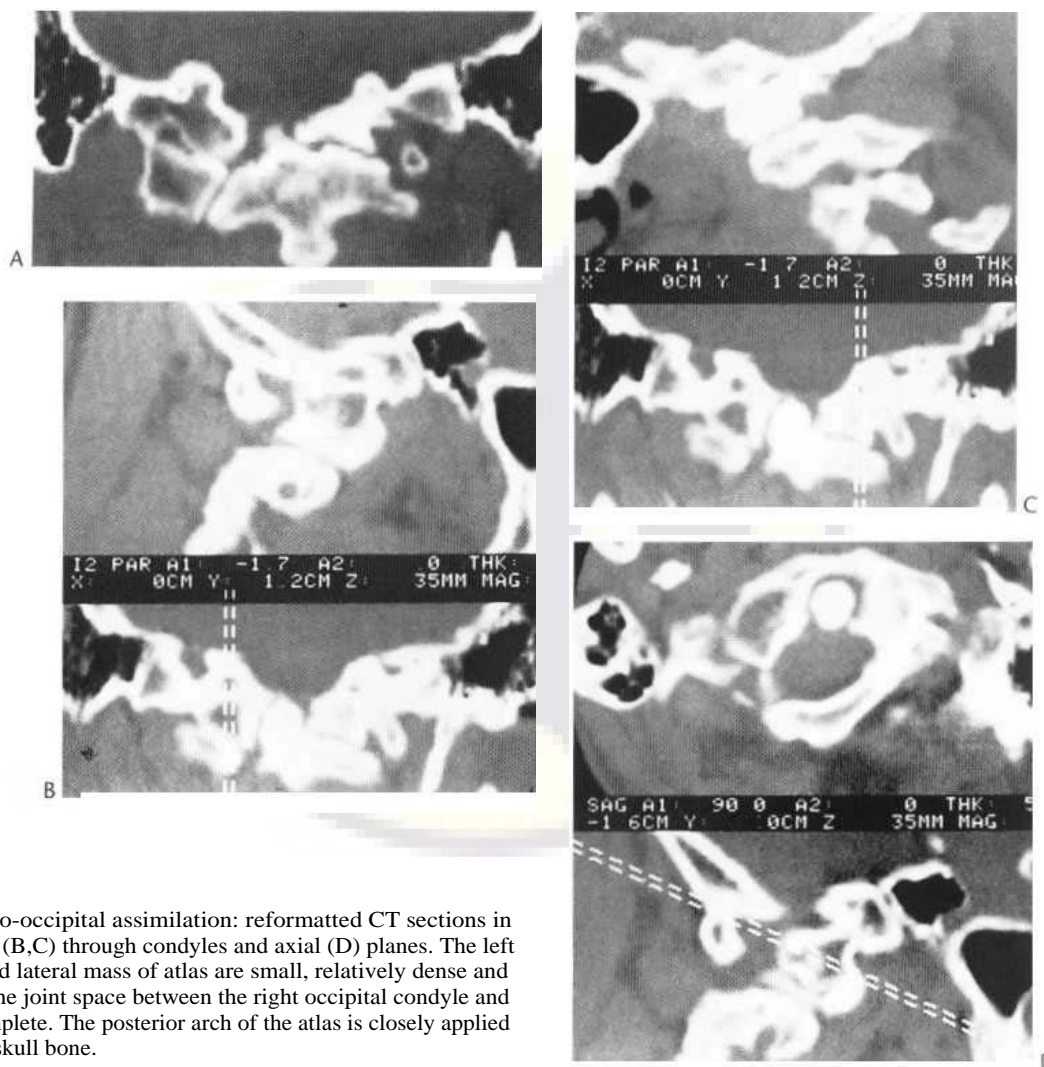


Fig 54.17 Atlanto-occipital assimilation: reformatted CT sections in coronal (A), sagittal (B,C) through condyles and axial (D) planes. The left occipital condyle and lateral mass of atlas are small, relatively dense and completely fused. The joint space between the right occipital condyle and lateral mass is incomplete. The posterior arch of the atlas is closely applied but not fused to the skull bone.

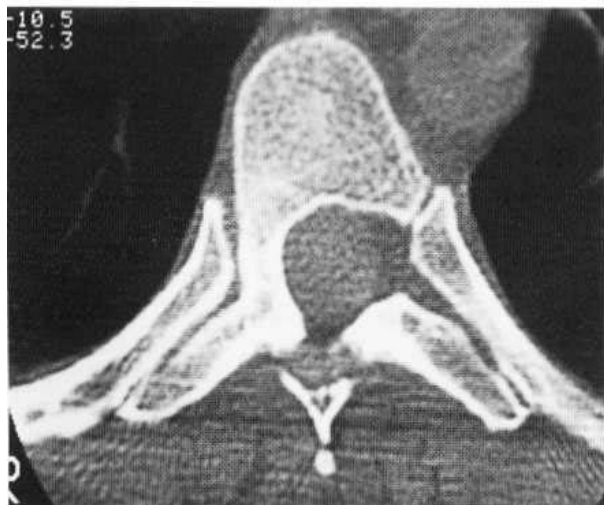


Fig. 54.18 Absent thoracic pedicle: CT. The left pedicle of the seventh thoracic vertebra is almost completely absent. The bone bordering the defect is corticated and the articulation with the corresponding rib is anomalous. The bone defect is filled by fat continuous with the epidural fat outlining the outer margin of the dura, which is in a normal position.

cles above and below the malformation are not eroded, which further excludes a neurolibroma or kinked vertebral artery. In the thoracic region the ipsilateral posterolateral border of the body of the affected vertebral is prolonged beyond the normal site of the neurocentral synchondrosis and forms an anomalous articulation with the rib. CT confirms the nature of the defect, showing the anatomical features to advantage (Fig. 54.18). The position of the pedicle is filled in by fat which overlies the normal theca; there is no soft-tissue mass, lack of definition, or irregularity of the bony margins, as would be usual with inflammatory and neoplastic processes.

With aplasia of a lumbar pedicle, there is abnormal orientation of the articular process and thickening of the contralateral neural arch. Such thickening is also present, though usually less conspicuous, in the other regions of the spine. It may be associated with sufficient increase in bone density to simulate a focal sclerosing lesion such as osteoid osteoma, but the presence of the congenital anomaly is of itself an adequate cause of the increase in bone density.

Dural ectasia (Fig. 54.19) may occur as part of the mesodermal dysplasia of neurofibromatosis; it is commonest in the thoracic region, and may be sufficiently pronounced to form a lateral meningocele. It also may complicate ankylosing spondylitis, where diffuse ectasia or pocketed localised outpouchings (sometimes containing adherent spinal roots) may be seen, and among the grossest

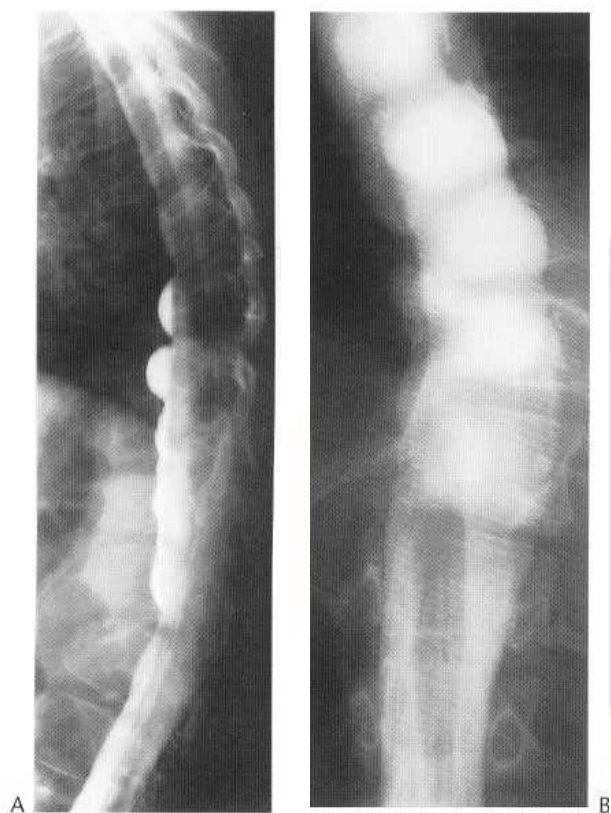


Fig. 54.19 (A,B) Dural ectasia in neurofibromatosis: myelogram. The subarachnoid space is markedly expanded in the lower half of the thoracic and upper lumbar regions. The corresponding part of the spinal canal is markedly expanded in this region and there is erosion of the posterior borders of the vertebral bodies and of the pedicles.

examples have been seen in connective tissue disorders like Ehlers-Danlos. These cause well-defined paravertebral masses associated with widened intervertebral foramina, which are usually asymptomatic incidental findings but may cause pain. They are of CSF signal intensity on MRI, and the anatomy is best shown by this technique. They are also of CSF density on CT, and though they opacify freely on myelography, the latter is rarely necessary for diagnosis.

Spinal trauma

Plain X-rays are first obtained, and in most cases provide adequate information regarding the presence of major fractures and dislocations. Careful attention to the anatomical alignment will reveal some abnormalities in all cases with displacement, though these may be subtle, as in rotatory dislocation with interlocking facets. A 'long bone' type fracture should be suspected if trauma occurs in ankylosing spondylitis.

The degree of compromise of the spinal canal is well elucidated by MRI and CT (Fig. 54.20); fractures of neural arches and vertical fractures of vertebral bodies are better shown by CT but horizontal fractures may only be adequately visualised after reformatting of axial data. Foreign bodies, herniated intervertebral discs, displaced bone and haematoma are shown and the degree of encroachment into the spinal canal is evident. Contusion and oedema may obscure soft-tissue planes and confuse the distinction between spinal cord swelling and extrinsic compression.

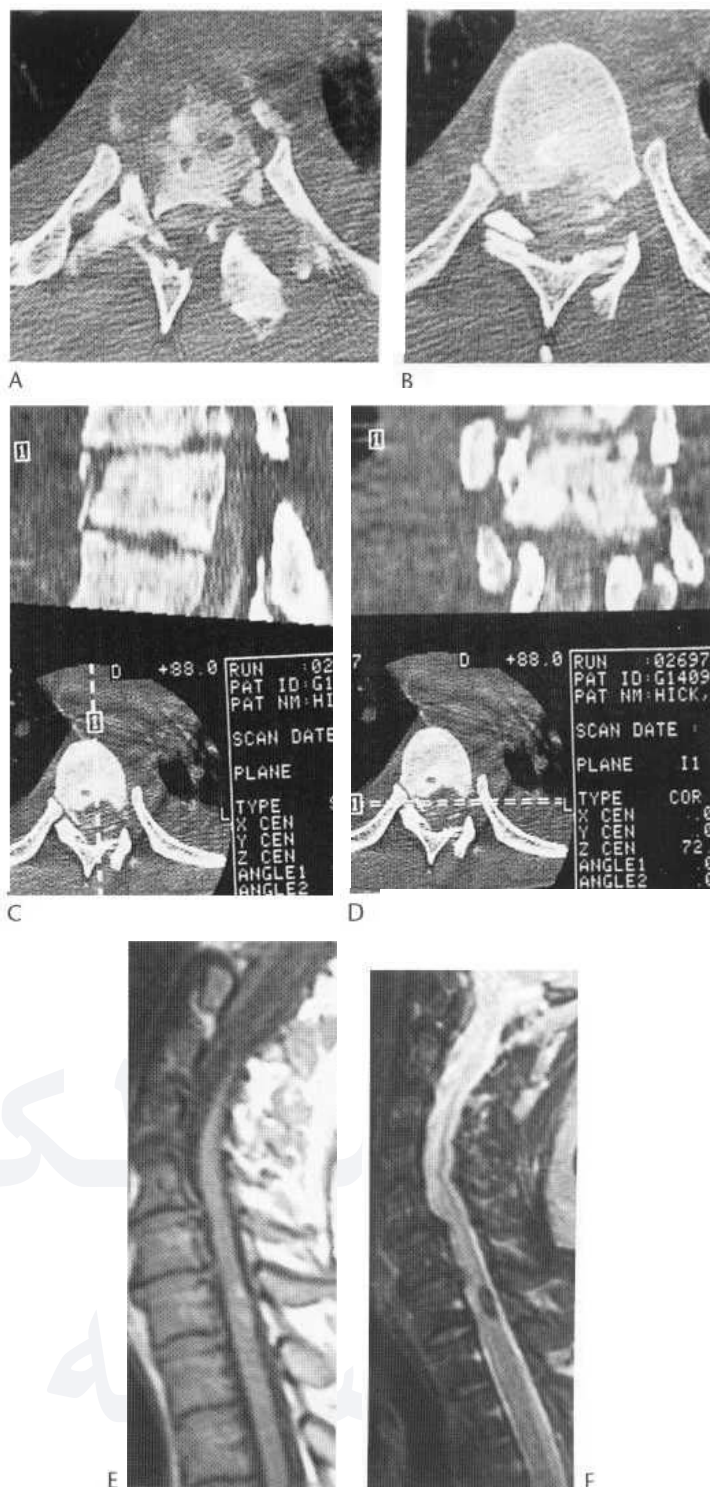


Fig. 54.20 Comminuted fracture of thoracic spine: fractures of the ninth and eighth thoracic vertebrae with anterior subluxation of the eighth. Axial sections through the ninth (A) and the eighth (B) thoracic vertebra, and reformatted sagittal (C) and coronal (D) sections. There is a comminuted fracture with disruption of the body and neural arch of the ninth thoracic vertebra. A fragment has been separated from the posterior inferior margin of the body of the eighth thoracic vertebra and there is anterior subluxation of the rest of the vertebra. The spinal canal is markedly narrowed and the spinal cord is compressed by displaced bone fragments. The subarachnoid space is opacified by a blood clot at T9 and T10 levels. (E,F) MRI of cervical spine. Whiplash injury in road traffic accident 6 months previously. Sagittal sections: T₁-weighted (E); T₂-weighted (F). The spinal canal is narrowed due to spondylosis. A small focus of aging haematoma is shown in the spinal cord at CT, possibly an unrelated cavernoma rather than an evolving haemorrhagic contusion.

MRI is particularly valuable in showing the extent of spinal cord damage by contusion, haemorrhage or disruption, and/or the degree of compression by displaced bone or haematoma. In penetrating injuries, the presence of ferromagnetic foreign bodies near the spinal cord must first be excluded by plain X-rays. In the absence of MRI, iohexol myelography and/or CT myelography is performed: (i) if there is a partial cord dysfunction which is not improving in the absence of detectable cord compression; and (ii) if there is significant persisting cord dysfunction after reduction of a dislocation to less than one-third encroachment in the spinal canal.

Traumatic meningocele

Traction on spinal nerve roots causes tearing of the arachnoid and dura of the root sheath, allowing leakage of CSF both along the course of the torn nerve root and along the epidural space. The fluid collections are surrounded by compressed areolar tissue and fibrosis, forming pseudomeningoceles. These are most common in the cervical region in association with brachial plexus avulsion, where they may encroach on the apical pleura and be visible as apical masses on the chest X-rays. Such meningoceles are well shown by MRI and CT and are outlined on myelography. In large meningoceles, dilution of contrast medium may detract from the detail of conventional myelography: the opacification is very adequate for CTM. Nerve roots may be torn without an associated meningocele, and some roots may be intact when a meningocele is present. Exact details of anatomy showing these features can be obtained from myelograms and CTM and from MRI. An extradural pseudomeningocele may displace the cord but virtually never causes signs of cord compression and is not an indication for surgery.

Traumatic subarachnoid-pleural fistula

This may follow penetrating or blunt trauma and may be suspected when persistent pleural effusion follows the injury or spinal surgery, especially costo-transversectomy in approaching a thoracic intervertebral disc; occasionally pneumocephalus occurs. The leak may be confirmed by conventional myelography or CTM.

Spinal instability

The maximum normal distance between the cortical margins of the arch of the atlas and the odontoid is 2.5 mm in adults and 5 mm in children.

Atlanto-axial subluxation and *dislocation* may cause acute or slowly progressive quadriplegia.

It may be secondary to:

1. Abnormalities of the odontoid process

These are due to: (i) fracture or (ii) congenital anomaly (os odontoideum).

Fractures of the dens are relatively common, accounting for about 1-2% of all fractures of the spine. They occur through the base of the dens, most commonly due to a hyperflexion injury, which generally also fractures the posterior arches of the atlas, allowing enlargement of the ring of the atlas to take place during anterior subluxation or dislocation without cord compression. Hyperextension fractures are much less frequent, and are also

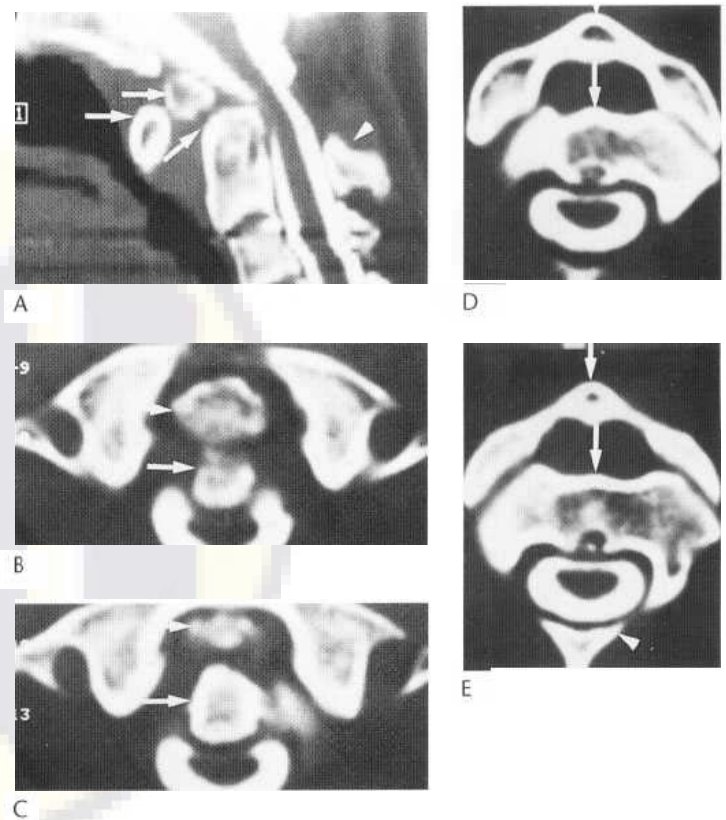


Fig. 54.21 Old fracture of odontoid peg with non-union and anterior subluxation. (A) Reformatted sagittal section. (B-E) Axial sections. B is at the level of the upper border of the anterior arch of the atlas, C at the level of the lower border of displaced odontoid, D through the upper border of the posterior arch of the second cervical vertebra, and E 3mm below D. The theca is impressed by the posterior margin of the lower fragment of the second cervical vertebra, and the spinal cord is deformed and compressed between it and the posterior arch of the first cervical vertebra. Arrows mark anterior arch of atlas, odontoid fragment, lower fragment of second cervical vertebra; arrowhead = posterior arch of second cervical vertebra.

usually associated with disruption of the posterior arch. Isolated dens fractures without subluxation may be difficult to detect in the acute stage even with tomography. Failure of union leads to pseudoarthrosis with an irregular horizontal corticated linear defect at the base of the dens; this predisposes to anterior subluxation (Fig. 54.21) with relatively minor trauma.

The *os odontoideum* is a separate ossicle which becomes significant when it carries the whole of the articular surface, with the anterior arch of the atlas being then liable to subluxation with relatively minor trauma. In such cases the odontoid itself is relatively short, and often maintains its usual superiorly convex corticated upper border. The articulation between the os odontoideum and the dens is above the usual site of the fracture through the dens. However it is recognised now that most if not all are either old fractures with remodelling, or aberrant ossification of the cartilagenous dens, as in some of the inherited connective tissue disorders, most especially Morquio's disease and spondyloepiphyseal dysplasias. This anomaly may also be isolated or associated with others, including atlanto-axial assimilation.

2. Hypoplasia of the dens

Hypoplasia of the dens occasionally complicates complex fusion anomalies of the upper cervical spine, but when isolated it usually

is a misdiagnosis because the separated dens is either small, misplaced or ankylosed to other structures, or remains unossified (Stevens et al 1994).

3. Erosions of the atlanto-axial joints by inflammatory disease

Most commonly rheumatoid arthritis but occasionally ankylosing spondylitis, tuberculous or pyogenic arthritis present with these symptoms.

Atlanto-axial subluxation occurs in over 6% of patients with rheumatoid arthritis. The atlas is usually displaced forward, with variable elements of rotatory and lateral displacement.

The dens may be subtly eroded at its base or markedly waisted, and eventually be reduced to an irregular spike of bone. Erosion of the lateral joints is accompanied by descent of the skull with pseudobasilar impression. The lower joints of the cervical spine may also be affected by the rheumatoid process, and pannus from any of the joints may encroach on the spinal canal. Limb joint affliction may cause difficulty with clinical assessment of neurological disability and of the site of neuraxial compression.

Neuroradiological assessment of rheumatoid patients using conventional myelography may be both difficult and painful. Ideally such cases are evaluated by MRI (Fig. 54.22). The site, nature, and degree of compression from bone or pannus are usually elucidated sufficiently for planning. The degree of instability is still probably best assessed by X-ray films in flexion and extension of the neck. CT myelography making reformatted thin sections from just above the foramen magnum down to the lower cervical region (Fig. 55.23) also is satisfactory. Plain CT on bone windows is useful to fully evaluate the integrity of the bones for treatment planning.

4. Presumed laxity of the joint capsules and ligaments

This may occur in association with: (i) pharyngitis or tonsillitis, particularly in children; (ii) atlanto-occipital assimilation; (iii) mucopolysaccharidoses, in which incomplete ossification of the dens and os odontoideum are a frequent feature.



Fig. 54.22 Rheumatoid arthritis. Sagittal MRI, T₂-weighted contrast. Severe erosion of the odontoid, vertical atlanto-axial subluxation and degenerate subaxial disease with spinal cord damage are shown.

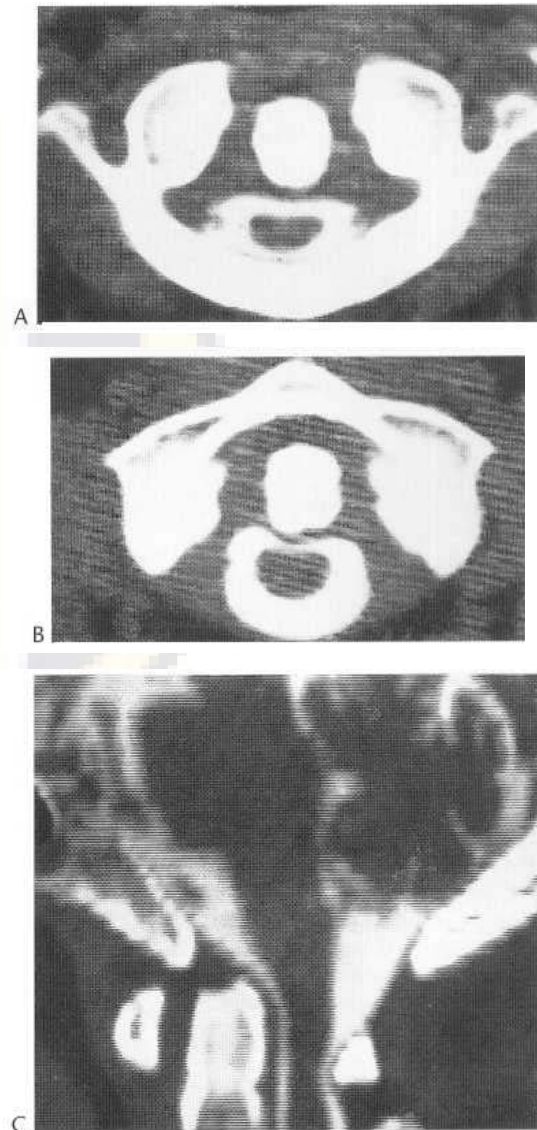


Fig. 54.23 Rheumatoid arthritis with atlanto-axial subluxation. (A,B) CT axial sections at level of the atlas. (C) Midsagittal reformatted section. There is erosion of the odontoid peg and anterior subluxation of the atlas; the spinal cord is compressed by the odontoid peg and posterior arch of the atlas.

5. Spondylolisthesis

Spondylolysis is a descriptive term referring to defects in the region of the pars intra-articularis of a vertebra, most frequently at the fifth lumbar level. Such defects, which used to be considered as congenital abnormalities, are now thought to be almost always the result of unhealed stress fractures. Spondylolisthesis indicates anterior or posterior slipping of a vertebra from any cause. It is commonly associated with separation of spondylolyses with anterior slipping of the superior vertebra, which may, but commonly does not, cause narrowing of the spinal canal.

The fractures in the pars intra-articularis are commonly visible on the routine lateral film of the lumbar spine but are better demonstrated on oblique projections or more exactly by CT. The degree of spondylolisthesis is graded by the fractional shift of vertebral body on the lateral projection but minor slips are shown on oblique projections. On the latter the axes of the apophyseal joints are normally situated progressively slightly more anteriorly as the lumbar spine is descended; this situation is reversed at the level below a forward

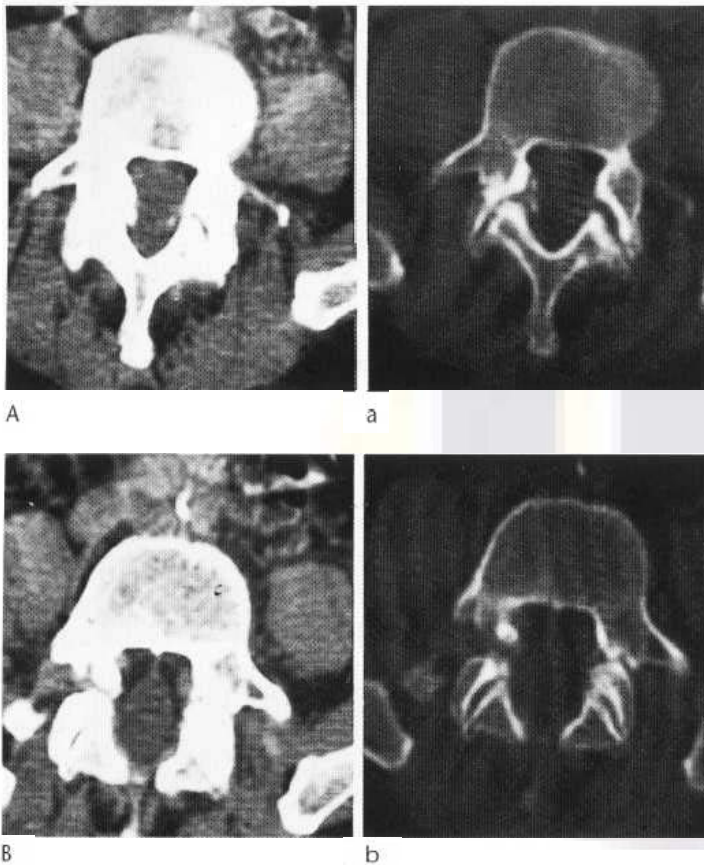


Fig. 54.24 Spondylolisthesis of the fourth lumbar vertebra at CT. (A,a) At the level of the pedicles and superior articular facets. (B,b) Through fractured pars intra-articularis. Images are made at window setting appropriate to show both soft tissue and bone. Note that the forward slip of the body of L4 has elongated the sagittal diameter of the spinal canal; there is no nerve root compression.

slip. On CT the fracture in the pars is at the level of the pedicles; it has irregular margins and adjacent sclerosis (Fig. 54.24), features which should serve to distinguish it from the apophyseal joints which cross the plane of, and are imaged at the level of, the intervertebral discs. The degree of slip and neural compromise is also shown on MRI. However, lack of signal from sclerotic but intact bone may occasionally simulate a break.

Stress fractures may heal after spondylolisthesis has occurred, and the partes interarticulares are then elongated and sometimes sclerotic.

Spondylolisthesis can also occur as a result of:

1. Trauma.
2. Pathological fractures or bone softening, as for example in Paget's disease or osteogenesis imperfecta. In such cases the abnormality causing the slip may affect partes interarticulares or pedicles.
3. Congenital dysplasia of the superior articular facets of the sacrum. In this case severe forward slipping is often associated with considerable deformity of the upper border of the sacrum and of the inferior margin of the fifth lumbar vertebra. Since the whole of the fifth lumbar vertebra is displaced anteriorly, it is easily distinguished from the common type.
4. Disc degeneration and osteoarthritis of the apophyseal joints. This is a common cause of lateral recess stenosis and clinically may stimulate disc prolapse (Fig. 54.25).



Fig. 54.25 Degenerative lumbar canal stenosis: T₂-weighted sagittal section of lumbar spine. There is low signal from all the discs, indicating ageing, but the decline in intensity is greater in the lower lumbar region due to additional disc degeneration with dehydration. The lower lumbar discs are narrowed and there is anterior subluxation of two vertebral bodies, with minor posterior protrusion of the annuli impressing the anterior surface of the theca. There is more prominent impression of the posterior surface of the theca due to infolding of the posterior ligaments associated with apophyseal osteoarthritis. The combination is causing degenerative canal stenosis.

In all types of spondylolisthesis the intervertebral disc at the level of the slip projects posterior to the plane of the displaced body; this should not be misinterpreted as significant disc prolapse or protrusion unless there is considerable encroachment on the epidural fat between the disc and the theca or root sheath.

Acute epidural haematoma

This condition may present with local and/or radicular pain, usually soon followed by signs of spinal cord or root compression. There may be a history of trauma, antecedent lumbar puncture, anticoagulation, aspirin therapy, hypertension or a blood-clotting disorder. It may also rarely be due to an angiomatic malformation. CT may be diagnostic if an extradural mass with attenuation of around 60 HU is shown. MRI is the elective study: intensity patterns will suggest the diagnosis and the degree of narrowing of the theca and neuroaxial compression will be shown. Myelography classically reveals a long extradural compression, generally from the posterior aspect of the spinal canal (Fig. 54.26).

Localised bone destruction and/or sclerosis

Such appearances on plain X-rays are generally due to neoplasm or inflammation. Inflammatory lesions tend to extend through the intervertebral discs (Fig. 54.27) and the contiguous bone, and to form paravertebral swellings which spread along soft-tissue planes. Less often, apophyseal joints are involved. On MRI the inflammatory exudate causes increase in T₁ and T₂ throughout the affected region. The disc returns high signal on T₂-weighted sequences, with diagnostic loss of the low-signal cleft, which is a feature of the normal annulus. The vertebral end-plates become indistinct and lost on T₁ weighted images early in the process. In tuberculosis, a low-

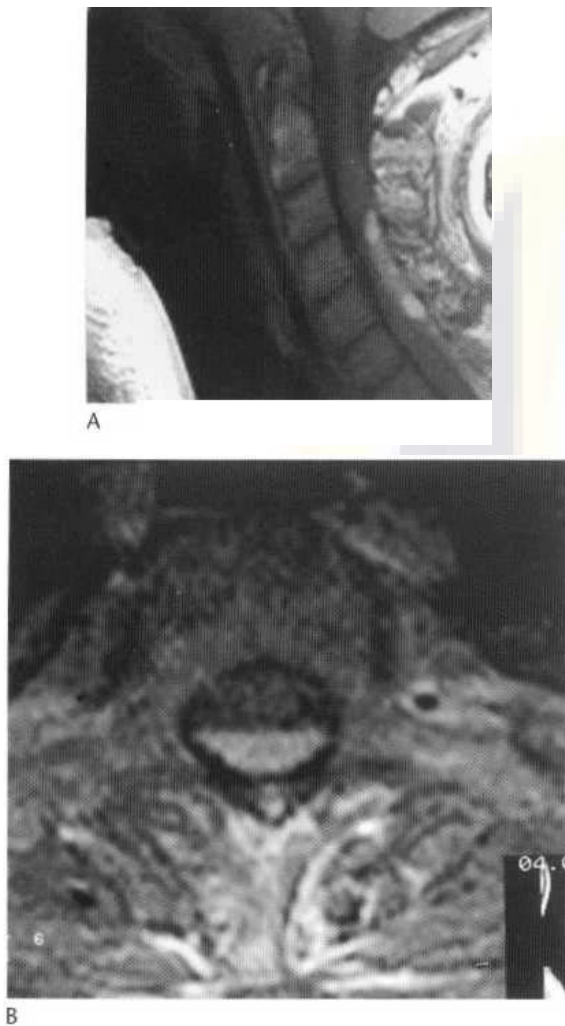


Fig. 54.26 Acute intraspinal haemorrhage. Sagittal (A) and axial (B) MRI with T₁-weighted contrast. The extensive posteriorly located haematoma is well shown. This one probably is subdural in location, and was spontaneous.

density abscess expanding psoas or other muscles may also be shown. Malignant neoplastic destruction tends to respect the intervertebral discs, and soft-tissue masses tend to be confined by the periosteum.

Paravertebral swellings may be evident on plain films. In the cervical region, widening of the retropharyngeal space (normally under 0.75 cm) or retrotracheal space (normally up to 1.5 cm in children and 2.25 cm in adults) may be caused; in the thoracic region the paramediastinal pleura is displaced laterally. They are better shown by CT or MRI (Fig. 54.28), which are valuable complementary studies, particularly in the lumbar region.

Distinction between tuberculous and pyogenic inflammation may be suggested by:

1. The presence of associated lesions in other organs, especially the lung, urinary tract and other bones in tuberculosis.
2. The tendency of untreated tuberculosis to induce less bone formation, to produce cold abscesses extending along muscle planes and beneath the anterior spinal ligament, eroding contiguous bone.
3. The tendency for pyogenic organisms to induce sclerotic bone reaction within the vertebral bodies and under the elevated periosteum. The various organisms cause generally similar reactions, which require bacteriological study for distinction. Commonly

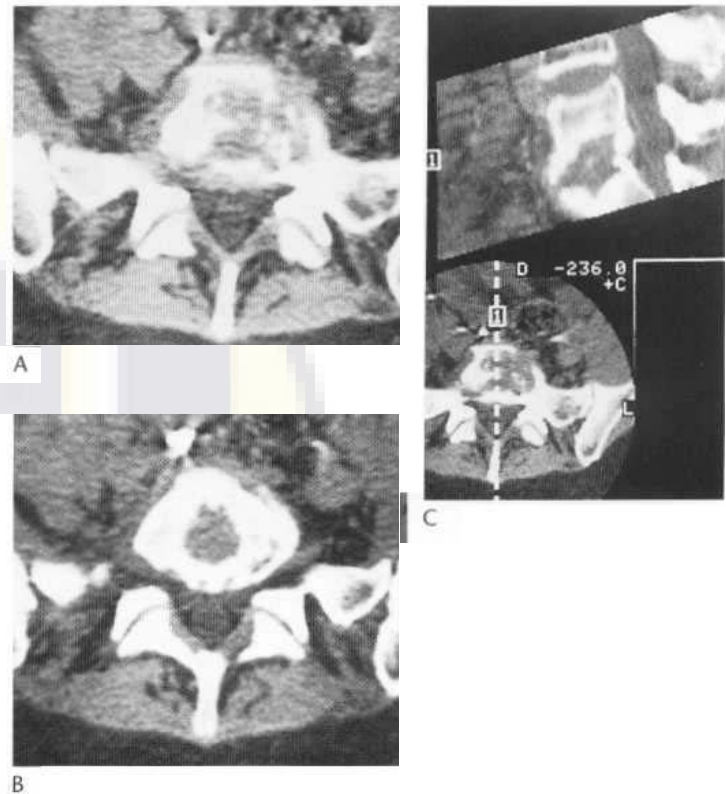


Fig. 54.27 Pyogenic infection, L5/S1 disc. (A) Axial section at level of L5; (B) at level of S1. (C) Axial reformatted section. The bone is destroyed adjacent to the disc space, leaving a large cavity with adjacent sclerosis around the disc. There is no intraspinal extension.

Staphylococcus and *Streptococcus* are implicated but many other organisms, including *Actinomyces*, *Blastomyces*, *Coccidioides*, typhus and *Brucella*, also cause spinal osteomyelitis. *Brucella* tends to cause extensive sclerosis.

4. The tendency of tuberculosis to be multifocal in the spine.
5. The tendency of tuberculosis to cause deformity, especially gibbus formation.

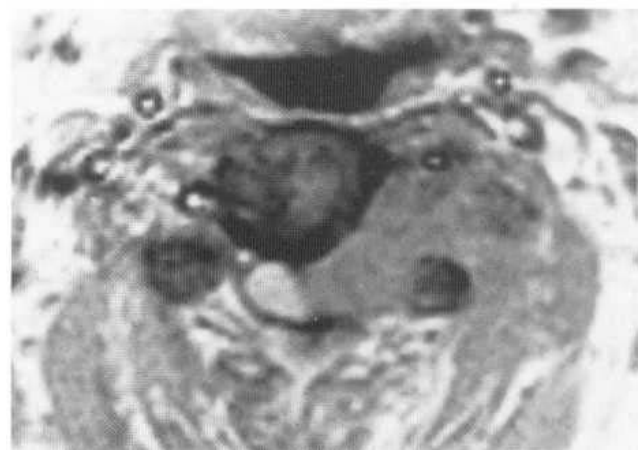


Fig. 54.28 Neurofibroma: axial section, cervical region, T₁-weighted sequence. There is a slightly lobulated mass grossly enlarging the left intervertebral foramen and eroding the adjacent bone. An intraspinal component of the mass displaces the theca and spinal cord toward the right and compresses them. A paravertebral component forms a mass displacing the deep cervical muscles. The extent of this dumb-bell neurofibroma is evident from this single study.

Hydatid cysts

These are responsible for less than 1.0% of inflammatory spinal lesions but important because their radiological appearance is suggestive. In bone, hydatids spread slowly through intertrabecular spaces by exogenous vesiculation, passing through the periosteum into the soft tissues. In the spine, the thoracic region is most commonly affected, and the disease tends to involve adjacent vertebrae and ribs and to spare the intervertebral discs. The cysts cause bubble-like round or lobulated circumscribed lytic lesions in the bones, with virtually no sclerotic reaction, and adjacent soft-tissue masses which tend to be extensive and cause extradural compression of the spinal theca.

Metastases

The commonest tumours affecting the vertebrae are metastatic. Those from the breast and prostate and neuroblastoma frequently induce sclerotic bone reactions (Fig. 54.29), also a feature of lymphoma and histiocytosis X. Sclerotic vertebra plana in children is characteristically due to the eosinophil granulomatous form of histiocytosis X.

Most metastases, including those from the commonest primary neoplasm, a bronchial carcinoma, are lytic; multiple myeloma, Burkitt's lymphosarcoma and Ewing's sarcoma cause similar destructive lesions, though the latter may cause periosteal reaction and bone expansion. In common with most tumours, metastases cause increase in T_1 (low signal) and T_2 (high signal) at M7R1. Melanoma is an exception; melanin is paramagnetic and may cause low signal on T_2 -weighted sequences. The bone lesions and soft-tissue components, including any thecal compression, are well demonstrated on MRI.

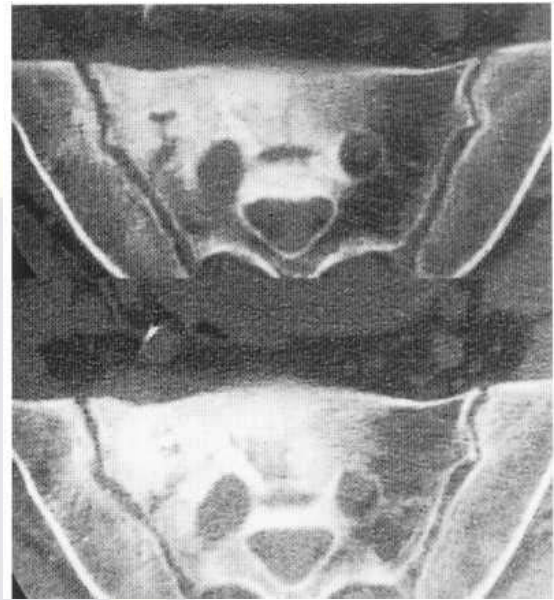


Fig. 54.29 Metastasis CT. Sclerotic metastases involving the right side of the sacrum were shown by plain films but are seen more clearly by axial CT. This also shows bone destruction around the right sacral foramen and a vertical pathological fracture through the body of the sacrum.

It should be noted that, although focal neoplastic changes are well shown, diffuse infiltration of marrow may be more difficult to recognise until T_1 and T_2 increases are pronounced. Following deep X-ray therapy, T_1 is decreased, probably due to fat replacement of haemopoietic tissue. Haemosiderin deposits after multiple transfusions of blood cause low signal on T_2 -weighted sequences due to susceptibility changes.

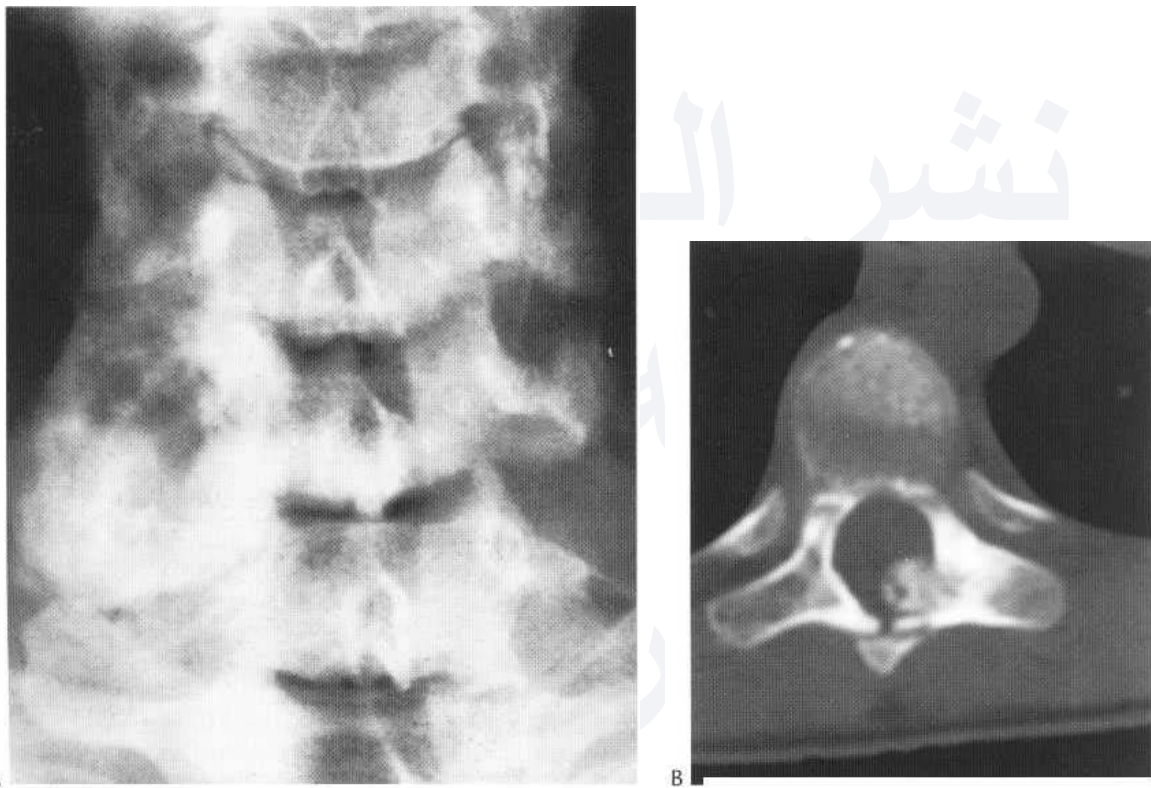


Fig. 54.30 (A) Osteoblastoma of cervical spine. The right pedicle and lateral mass of the sixth cervical vertebra are enlarged and sclerotic, with an irregular central low-density nidus. (B) Osteoid osteoma. CT scan of mid-thoracic spine. There is sclerosis with focal expansion involving the left lamina. The tumour encroaches on the epidural space and contains a small nidus which is of low density.



Fig. 54.31 Sacral chordoma. (A) A fairly well defined region of destruction involving the bodies and left lateral masses of the lowest two segments of the sacrum. (B,C) CT sections through the fourth and fifth segments of the sacrum. A mass of density slightly lower than that of muscle is expanding and destroying the bone of the bodies and left lateral masses of the fourth and fifth segments of the sacrum. (Contrast in loops of small bowel).

Osteoblastoma and osteoid osteoma

In the spine these tumours involve the neural arch; they may present with local or referred pain as well as cord compression. Sclerosis and expansion of the affected part of the neural arch may be better demonstrated with CT than plain X-rays (Fig. 54.30); a low-density nidus with or without a sclerotic centre is generally evident on CT.

Spinal chordomas (Fig. 54.31)

These primary tumours arise from notochord remnants, but usually become manifest in middle age; they are commoner in males. The majority (50%) involve the sacrococcygeal region, and only 15% arise in the remainder of the vertebral column, the rest originating in the clivus. The tumour causes bone lysis, which tends to involve several segments of the spine and to be associated with expansion. Calcification or residual bone fragments within the tumours, and some sclerotic reaction are not infrequently present. CT and MRI are particularly valuable in delineating the extent of the sacral chordomas, which may be entirely below the level of the spinal theca; higher tumours cause non-specific extradural compression.



Fig. 54.32 Haemangioma of bone, lateral lumbar spine. The secondary trabeculae of the body of the second lumbar vertebra are thickened; the vertical striate appearance is typical of a haemangioma.

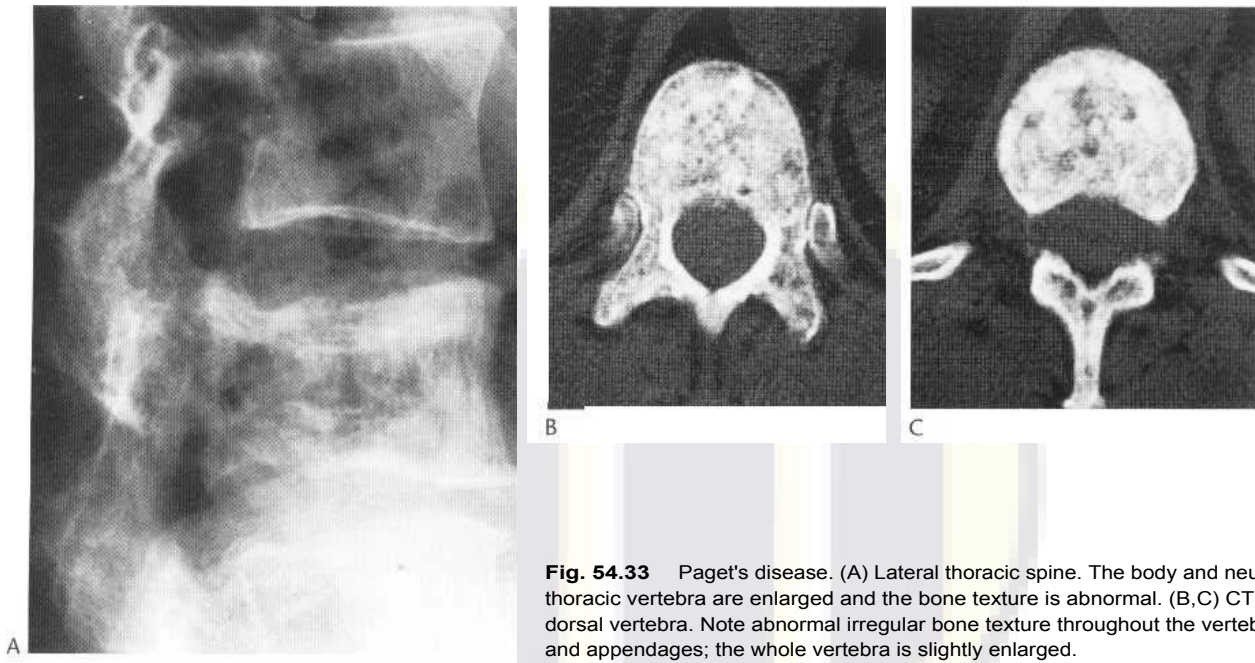


Fig. 54.33 Paget's disease. (A) Lateral thoracic spine. The body and neural arch of the twelfth thoracic vertebra are enlarged and the bone texture is abnormal. (B,C) CT axial sections, lower dorsal vertebra. Note abnormal irregular bone texture throughout the vertebral body, neural arch and appendages; the whole vertebra is slightly enlarged.

Vertebral haemangiomas

These usually asymptomatic tumours are diagnosed by observing the characteristic increase of prominence of the secondary bone trabeculae of the vertebral body causing a striate or honeycomb pattern (Fig. 54.32). Haemangiomas are commonly associated with regions of fatty change in marrow, causing lowering off, and high signal on T₂-weighted sequences. T₁ is increased, with high signal on T₁-weighted sequences: regions of signal void can occur occasionally if there is high flow. Uncommonly, expansion of the affected vertebra may cause a paravertebral swelling and symptomatic extradural compression shown on MRI or myelography. The extent of the abnormality is well shown on MRI or CT. Angiography and embolisation of the feeding arteries may reduce the morbidity of laminectomy.

Paget's disease of bone

This commonly involves vertebrae, usually affecting the neural arch and appendages in addition to the body (Fig. 54.33). The coarse trabecular structure and expansion of the whole vertebra are characteristic features, and the body often loses height due to softening. Encroachment on the spinal canal is an infrequent cause of compression of the spinal cord or cauda equina; myelography shows non-specific extradural compression, whereas MRI shows the bone thickening in addition.

Intervertebral disc prolapse and degeneration

Spondylosis is a useful general term for this process caused by wear and tear, though it is most often used when describing the cervical spine. The process involves the intervertebral discs, vertebral bodies and facet joints usually all together but to varying relative extent. The process becomes of particular relevance to neuroradiology when the spinal cord or roots become affected. It is the commonest cause of entrapment spinal neuropathy and of neurological disability due to spinal cord disease. It is extremely common, being virtually universally present in the over sixties, and it is associated with at least

some spinal root and spinal cord compression in up to 20% of asymptomatic older subjects. Therefore it is usually asymptomatic. Despite a considerable literature linking specific appearances to specific clinical features, it should be recollected that evidence for such linkages is purely circumstantial. Entrapment neuropathies due to extruded disc material and some cases of spondylotic myelopathy are clear exceptions however. Imaging is prioritised appropriately to demonstrate involvement of neural tissue.

Disc prolapse

Extrusion of the softer material from within an intervertebral disc into or through a posterior or posterolateral radial tear in the annulus fibrosus is a common cause of neural involvement. This takes the form of a focal broad-based bulge in the margin of the annulus, or a focal mass extending upwards or downwards in the anterior epidural space. Far lateral protrusions or extruded fragments involve the intervertebral foramina, not the spinal canal. They are commonest in the lumbar spine.

These lesions usually are well shown by CT and MRI. Disc material is denser than CSF in the thecal sac and is clearly visible against epidural fat on CT (Figs 54.34-54.36). There is a danger that a very large extrusion, which fills the spinal canal, will be overlooked on CT, because the disc material may closely resemble the thecal sac, and the density difference between it and CSF may not be appreciated. On MRI extruded fragments often are brighter than parent disc substance in T₂-weighted images, and may enhance after intravenous gadolinium; sometimes they are heavily calcified, which is usual in the thoracic region. MRI is more reliable than CT at demonstrating soft disc protrusions in the cervical spine, where there is less epidural fat. Myelography or CTM should be required rarely in modern departments. Only CT or MRI will demonstrate far lateral protrusions. Plain X-rays commonly are normal or show non-specific changes, such as reduction of disc space or changes in vertebral alignment due to muscle spasm.

A high proportion (70%) of extruded, soft-tissue fragments, usually yielding a higher signal than the parent disc on MRI, disappear spontaneously, usually within 3 months (Fig. 54.36).

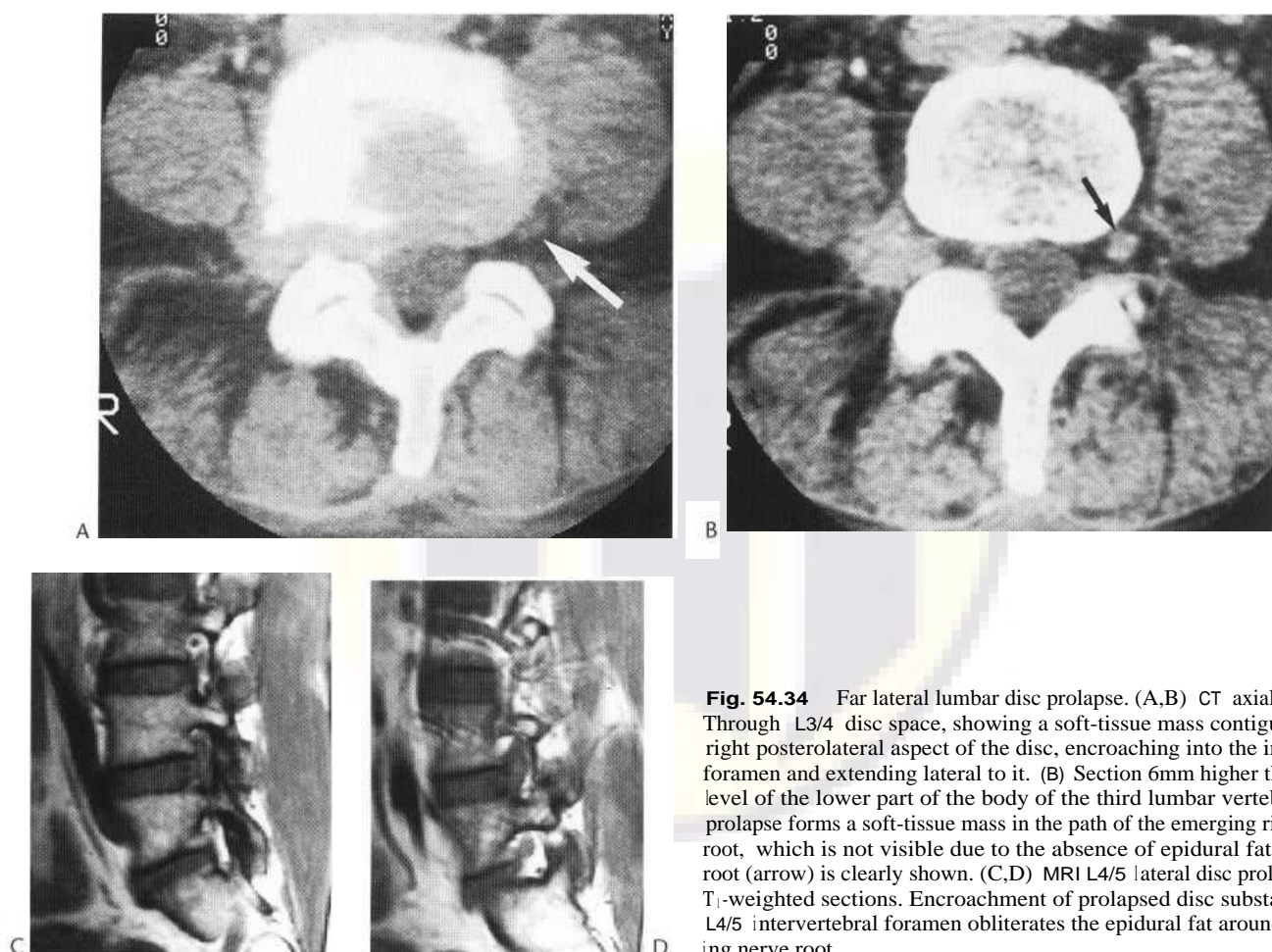


Fig. 54.34 Far lateral lumbar disc prolapse. (A,B) CT axial sections. (A) Through L3/4 disc space, showing a soft-tissue mass contiguous with the right posterolateral aspect of the disc, encroaching into the intervertebral foramen and extending lateral to it. (B) Section 6mm higher than A, and at level of the lower part of the body of the third lumbar vertebra. The disc prolapse forms a soft-tissue mass in the path of the emerging right L3 nerve root, which is not visible due to the absence of epidural fat. The left L3 root (arrow) is clearly shown. (C,D) MRI L4/5 lateral disc prolapse. Sagittal T₁-weighted sections. Encroachment of prolapsed disc substance into the L4/5 intervertebral foramen obliterates the epidural fat around the emerging nerve root.

Degenerative change

Loss of normal tension or volume in the nucleus pulposus tends to cause circumferential bulging of the annulus fibrosus and tension on the periosteum, resulting in *osteophytosis* and *marginal sclerosis*. These changes are most frequent in the lower cervical and lower lumbar regions and are accompanied by disc narrowing and altered stresses on the apophyseal joints, resulting in osteoarthritis. They are revealed by plain X-rays and CT. Reactive changes of three types occur in the adjacent vertebral bodies, and are well shown by MRI (Modic et al 1988). Degeneration in ligaments can lead to fibrocartilaginous metaplasia, calcification, ossification or myxomatous degeneration, all of which can result in diffuse thickening or a focal mass which may compress neural tissue. This process can involve the posterior longitudinal ligament, the cruciform ligament at the craniocervical junction, the ligamenta flava and the capsular ligaments of the facet joints. It includes entities such as ossification of the posterior longitudinal ligament (OPLL) (Fig. 54.37), retroodontoid pseudo-tumour, ossification of the ligamentum flavum; synovial cysts can also be accommodated in this category.

Accelerated degenerative changes are seen in such conditions as ochronosis and Charcot spine. Destructive discovertebral lesions due to non-specific degenerative processes may be seen at one or more levels in ankylosing spondylitis, rheumatoid arthritis, chronic renal failure (dialysis) or as isolated phenomenon. The process is distinguishable from infection on MRI by absent or non-uniform high signal in the involved disc, and irregularity or fragmentation of the vertebral end-plates rather than destruction.

Plain X-rays show most of the features of degeneration. If the measured sagittal diameter of the spinal canal in the cervical region is less than 10 mm, the spinal cord will be compressed. Deformation of spinal and intervertebral canals is best shown in axial sections on CT or MRI, the latter permitting direct visualisation of the effects on neural structures. As in the case of disc prolapse, myelography and CT myelography should only rarely be required in modern departments.

With the exception of focal masses directly compressing spinal roots, clinicoradiological correlation generally is poor, even with MRI. Bony stenoses of intervertebral foramina only rarely are focal enough to suggest the probability of surgical cure. Compression or moulding of the spinal cord by osteophytes in cervical spondylosis also correlates poorly with the presence and severity of clinical myelopathy. However, MRI often presents direct evidence that compression is damaging cord substance, in the form of focal signal changes in the spinal cord at or minimally below the relevant intervertebral level. The signal change is deep within the cord, often simulating accentuation of the central grey matter, unlike plaques of demyelination for example, which usually extend to the pial surface.

Postoperative changes

Recurrent myelopathy and/or radiculopathy after surgery may be discogenic or reactive. Distinction is usually evident on CT and/or MRI, with either a typical mass continuous with, and having char-

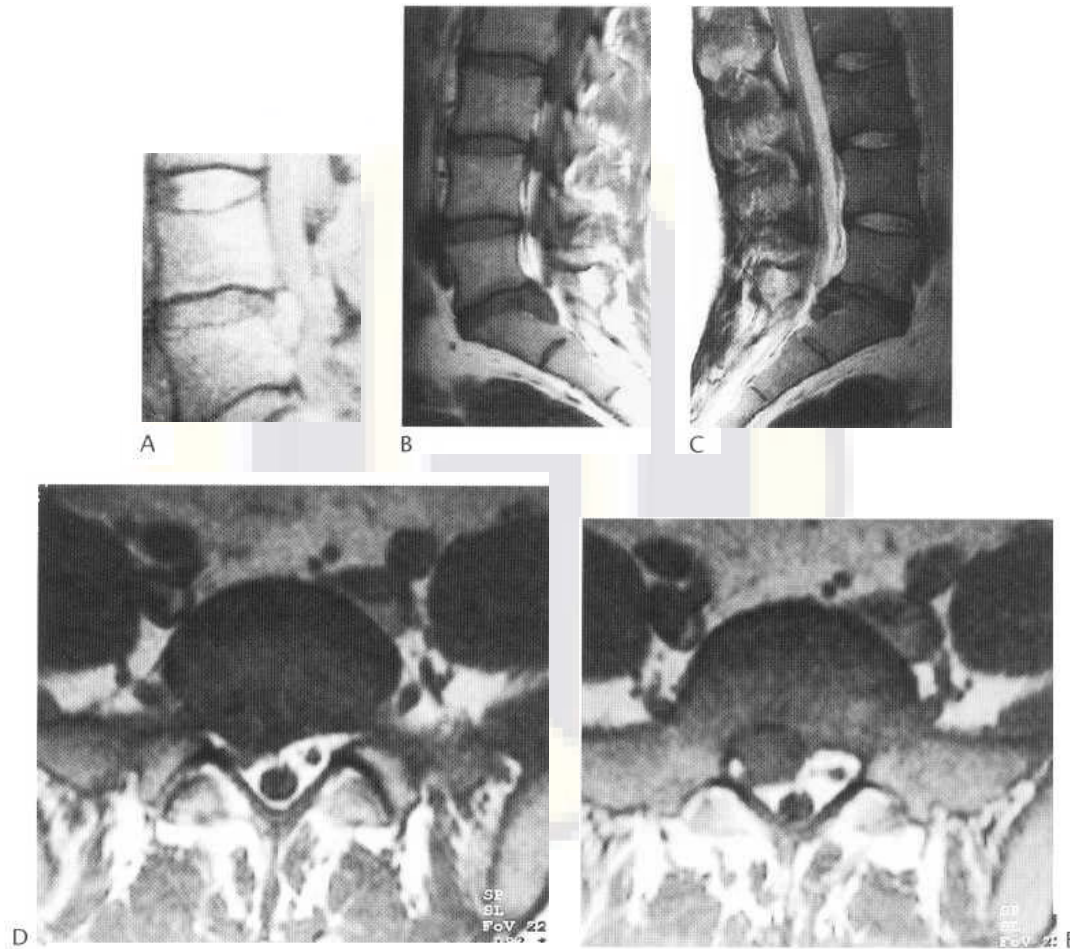


Fig. 54.35 Extruded (sequestered) disc protrusion. (A) Sagittal T₂-weighted section of lumbar spine. The L4/5 disc space is narrowed and the signal returned from the nucleus is decreased. There is a slightly lobulated extradural mass behind the L4/5 disc and upper half of the body of the fifth lumbar vertebra which is compressing the spinal theca. The signal returned from it is similar to that of the normal L3/4 nucleus. It was an extruded fragment removed at surgery. Such fragments commonly give higher signal than the damaged disc from which they originate. (B-E) Sequestered lumbosacral disc prolapse. T₁-weighted sections lumbar spine: B,C sagittal; D,E axial. The disc fragment extends behind the upper part of the right side of the body of the sacrum. It displaces the first sacral nerve root posteriorly and erodes the sacral body.

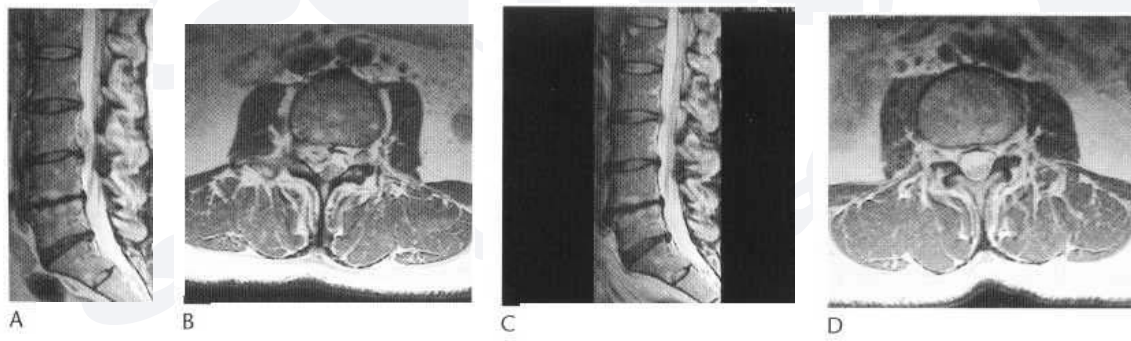


Fig. 54.36 Extruded fragment from a degenerate L3/L4 intervertebral disc. (A,B) Sagittal and axial MRI with T₂ migratory extruded disc fragment ascends on the right behind the L3 vertebral body. (C,D) Sagittal and axial MRI 8 weeks later shows spontaneous resolution of the extrusion.

acteristics of, disc substance in the former, or a contracting lesion extending around the affected part of the theca and/or nerve root and continuing into the soft tissue in the latter. On T₁-weighted MRI, disc usually returns higher signal than scar, in which signal decreases with ageing. Recent scar enhances immediately but old scar much less and more slowly. Disc fragments usually do not enhance but may do so minimally and slowly. Gadolinium-enhanced MRI appears to be more accurate than enhanced CT in this assessment.

Spinal stenosis

Although applicable in all regions, this term is most often used when describing changes in the lumbar spine. It is a feature of conditions such as achondroplasia and acromegaly, where even mild degenerative changes produce severe multilevel stenoses, especially in the lower lumbar region.

The term stenosis should be used with caution, because it has a tendency to become a diagnosis when it may be inappropriate. Clinical correlation only becomes good when the lumbar spinal

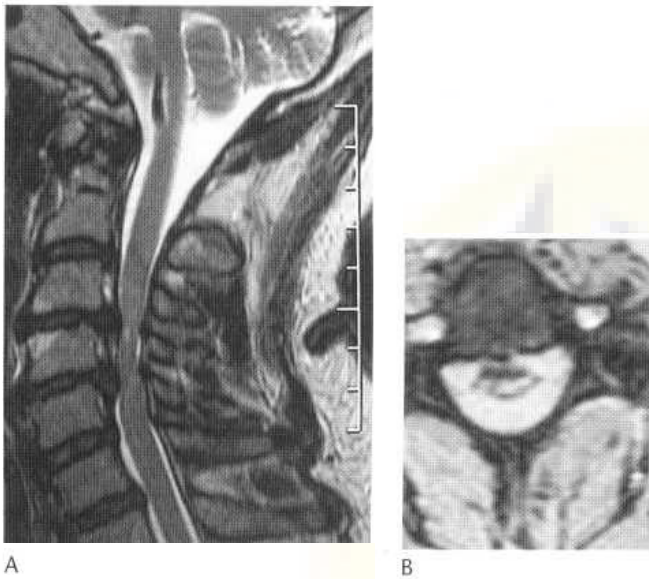


Fig. 54.37 Ossification of the posterior longitudinal ligament. Sagittal (A) and axial (B) MRI with T₂-weighted contrast. The axial image is between the intervertebral discs and shows the large low-signal thickened ligament looking somewhat like a mushroom.

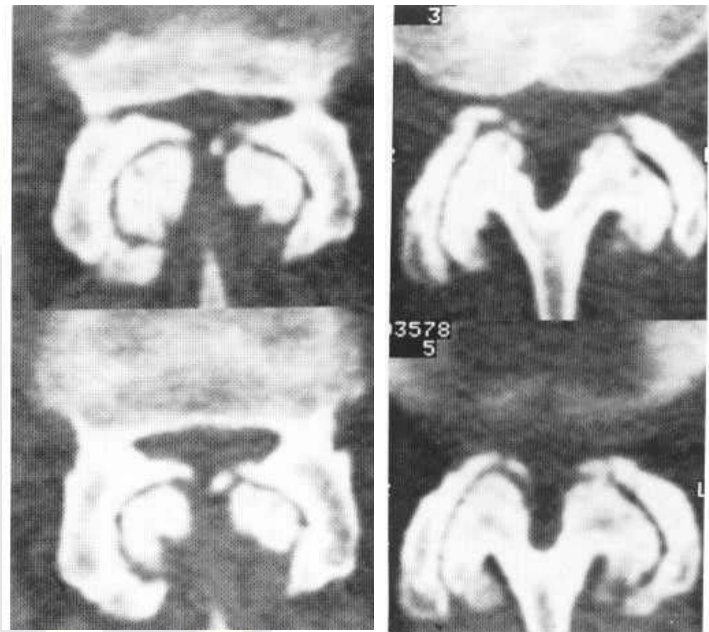


Fig. 54.39 Canal stenosis. CT sections through lumbar spinal canal. Note the short pedicles (bottom right image) and medially placed apophyseal joints. The combination causes marked reduction of the sagittal diameter of the lateral parts of the spinal canal, which is further compromised by osteoarthritic changes in the apophyseal joints.



Fig. 54.38 Lumbar spinal canal stenosis with entrapment of the cauda equina. Sagittal MRI with T₂-weighted contrast showing stenosis of the spinal canal at L4-L5; CSF signal is excluded at the level of the stenosis, and there is redundant coiling of many of the intradural spinal roots above.



Fig. 54.40 Syringomyelia. Parasagittal T₁-weighted sequence. The low-signal subarachnoid CSF outlines the expanded spinal cord and also the intramedullary cyst, which shows a typical lobulated appearance. One of the cerebellar tonsils is outlined with its lower pole extending to the level of the arch of the atlas.

canal is very narrow: cross-sectional area even less than 110 mm² on CT (Ullrich et al 1980), or narrow enough to eliminate CSF signal on T₂-weighted MRI; an additional sign of entrapment of the cauda equina is redundant coiling of intradural roots above the stenotic level on MRI, occasionally mistaken for dilated intradural

veins (Fig. 54.38). The lateral part of the spinal canal, sometimes referred to as the lateral recess, often is the most affected, usually mainly due to hypertrophy of the facet joints (Fig. 54.39). However, with the exception of S I the spinal roots are within the thecal sac as they cross the disc and simply are displaced medially rather than



Fig. 54.41 Ependymoma. Sagittal (A) and axial (B) MRI with T2-weighted contrast shows an extensive tumour filling much of the lumbosacral spinal canal and cavitated spinal cord above.

entrapped. On conventional myelograms the thecal sac assumes a waisted appearance at such levels.

Intramedullary lesions

Syringomyelia

This describes a predominantly glial lined fluid-filled cavity or cavities filled within the spinal cord usually centred on the central canal but extending into the dorsal columns through the white commissure. They may be cylindrical and extend through most of the spinal cord, or fusiform where only a localised number of segments are involved. They may enlarge the spinal cord, or be collapsed with normal or small cord size. About 80% of the extensive type are associated with a Chiari I malformation. Most of the rest are idiopathic. A small number are post-traumatic, or postarachnoiditic, and occasional reports in the past have linked them to a variety of other conditions though with less clarity. Identical cavities commonly extend through otherwise uninvolved above and below intramedullary tumours, especially haemangioblastoma (Fig. 54.40).

The cavities are well shown by MRI, together with their causative lesions; intravenous gadolinium may be necessary to exclude tumours in idiopathic cases. Plain CT may show them, but generally CTM is required, with imaging early and late (6 or 10 hours) after contrast administration.

Ependymomas

These generally very slowly growing gliomas comprise about two-thirds of all intramedullary tumours, being especially frequent in the dorsolumbar region. They may involve the filum terminale,



Fig. 54.42 Intradural lipoma. T₁-weighted MRI. Sagittal section through posterior fossa and upper cervical region. The posterior fossa and foramen magnum are normal. There is a large mass returning high signal and typical of fat. It lies within the subarachnoid space posteriorly, enlarging the spinal canal and displacing the spinal cord anteriorly. The spinal cord is markedly thinned and the cord substance appears to be almost completely replaced by fat over most of the extent of the tumour. The appearances are typical of a large intradural and partially intramedullary lipoma. These tumours typically extrude from the posterior surface of the cord between the dorsal columns.

including the extradural part within the sacrum, and cause enlargement (sometimes massive) of the spinal canal similar to that seen in giant neurofibromas. Such tumours may blend superiorly with the expanded lumbodorsal cord or simulate an intradural extramedullary mass, which may be amenable to almost complete surgical removal (Fig. 54.41).

Astrocytomas

These tumours account for about 30% of cord gliomas, but are relatively more common in children. They may cause focal or extensive expansion of the cord, sometimes continuing into the brainstem, and like ependymomas may have a considerable cystic component. Expansion of the spinal cord tends to be less marked than with ependymomas.



Fig. 54.43 Multiple sclerosis. An axial T₂-weighted MRI at C6 shows a typical plaque in the right lateral column, reaching to the pial surface of the spinal cord.

Other types of intramedullary glioma and sarcoma occur, but cannot generally be suspected prior to histological evidence. An exception is melanoma, which may give low signal due to susceptibility changes on T₂-weighted MRI sequences related to the presence of melanin.

Lipoma and dermoid

These may be associated with dysraphic features and CT may show low density within the fat; T₁-weighted MRI reflects high signal which is pathognomonic in the clinical context (Fig. 54.42). Dermoids are often extramedullary and in about 20% a dorsal dermal sinus is demonstrable by MRI.

Haemangioblastoma

This constitutes about 5% of intramedullary tumours, but it is potentially curable by surgery and can be diagnosed by spinal angiography. This tumour should be suspected in patients: (i) with previous manifestations or a family history of von Hippel-Lindau syndrome, especially cerebellar tumours or retinal angiomas; (ii) with extensive serpiginous defects in association with intramedullary swelling, especially in the absence of obstruction of the subarachnoid space. In our experience about a third of such cases will have haemangioblastomas.

The intramedullary swelling is commonly extensive, due to cyst formation. The tumour nodule reflects low signal on T₁- and high on T₂-weighted sequences and enhances markedly with gadolinium. If MRI is available angiograms usually are not necessary. The haemangioblastoma opacifies densely at angiography, usually as a homogeneous nodule, but sometimes as a ring density with central necrotic or cystic change. In contrast to angiomatous malformation, it tends to retain the contrast medium into the venous phase, but there may also be arteriovenous shunting through it (see Chapter 57).

Inflammatory lesions

The spinal cord frequently is involved in multiple sclerosis (MS) (Fig. 54.43). Plaques generally are limited in extent and involve the

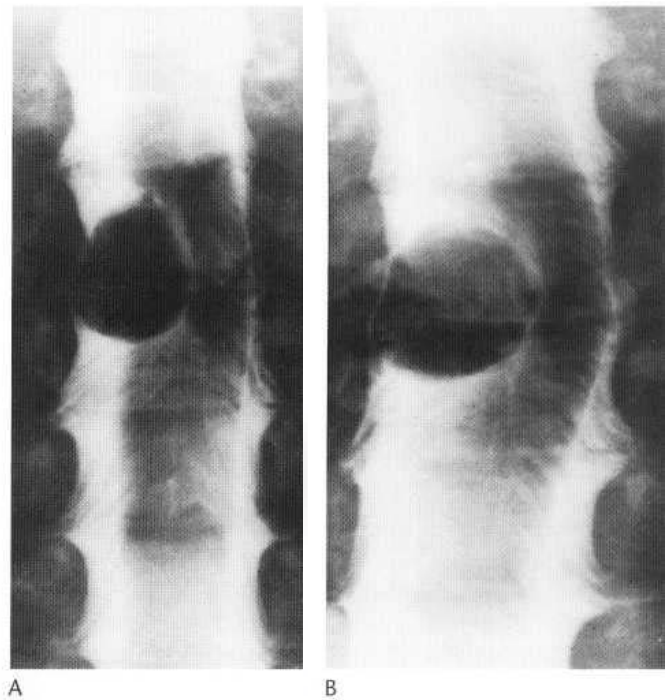


Fig. 54.44 Myelogram neurofibroma. (A) AP projection. (B) Oblique projection. The tumour is intradural on the right side at C4/5 level and its margins are clearly outlined by the contrast medium in the subarachnoid space which is widened around the tumour. The spinal cord is compressed and displaced by the mass.

dorsolateral regions most commonly, extending right to the pial surface. Mild swelling is associated with acute lesions. The lesion of acute transverse myelitis usually is far more extensive and involves most of the cord cross-section, with more swelling progressing to atrophy over time. Far more rarely intramedullary abscesses (usually associated with dermal sinuses), tuberculous or sarcoid granulomas, HTLV- I or other viral lesion, and schistosomiasis of the lumbar enlargement are encountered (Fig. 54.5).

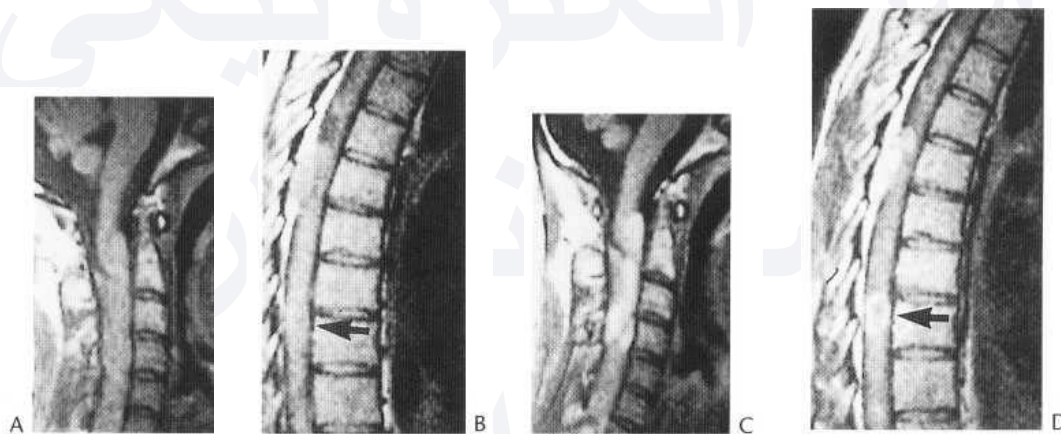


Fig. 54.45 Neurofibromatosis with multiple tumours. Sagittal T₁-weighted MRI sections. (A) Posterior fossa and cervical region. (B) Thoracic region. (C) Cervical region after gadolinium enhancement. (D) Thoracic region after gadolinium enhancement. The patient has neurofibromatosis and there are multiple tumours. Some are intradural extramedullary schwannomas. A good example is shown anteriorly at C2 level. The upper border of this tumour is outlined against the cerebrospinal fluid, but its posterior border blends with the spinal cord which gives signal of similar intensity. The extent of this tumour is evident on the enhanced scan. Some of the tumours are extradural. An example is shown posteriorly in the mid-thoracic region B; the upper and lower borders are outlined against the extradural fat behind the spinal cord. The anterior margin is only slightly denser than the cord substance. After injecting gadolinium (D), the tumour is enhanced. Its anterior border, which is compressing the dura and the cord, is more evident but the intensity of signal from the enhanced tumour is similar to that of the epidural fat, making the upper and lower limits more difficult to define. An intramedullary tumour is also present, expanding the cord in the lower dorsal region. The margins are not distinguished from cord substance on the plain scan B but are evident with ring enhancement after gadolinium (arrow in D).

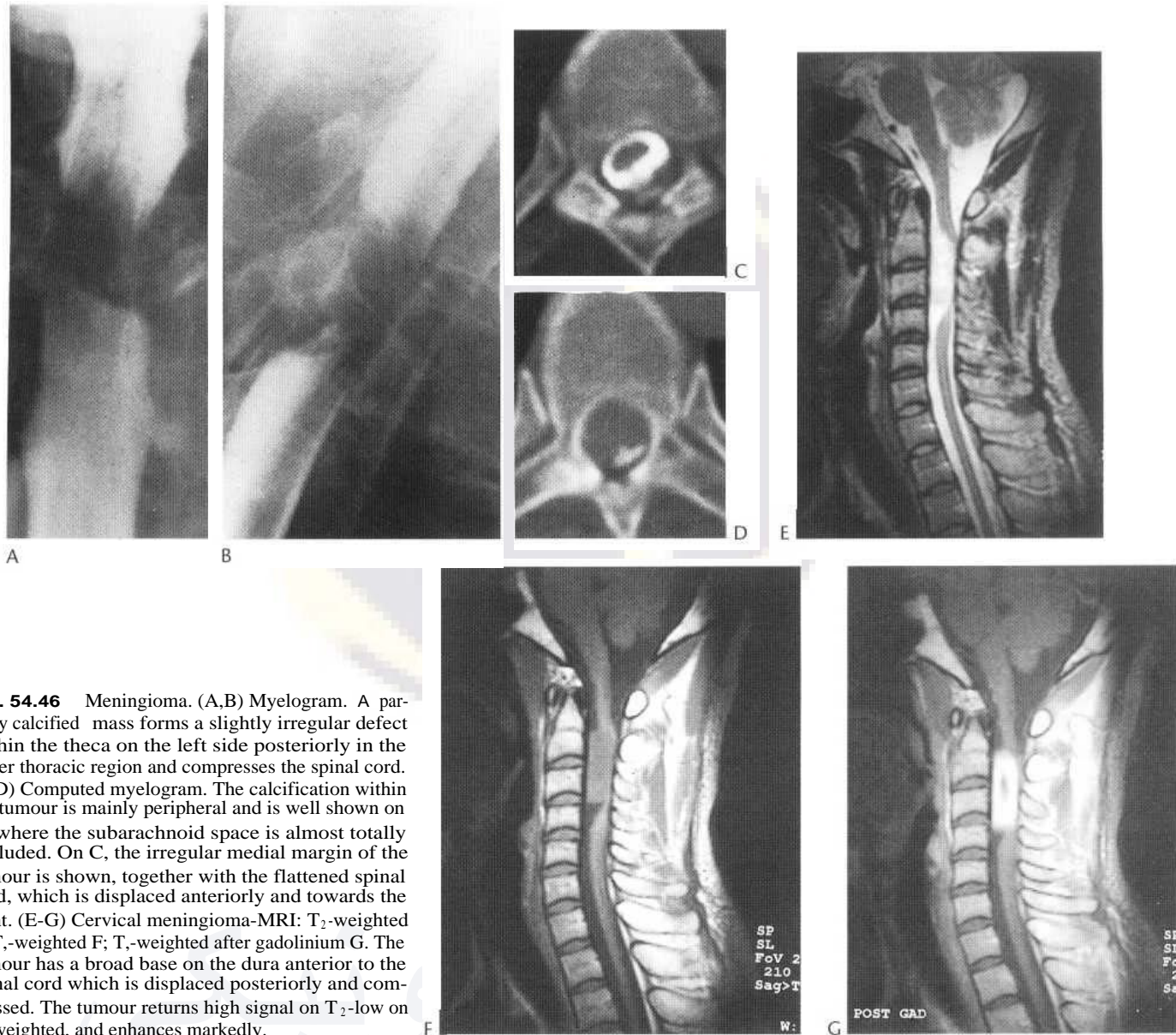


Fig. 54.46 Meningioma. (A,B) Myelogram. A partially calcified mass forms a slightly irregular defect within the theca on the left side posteriorly in the upper thoracic region and compresses the spinal cord. (C,D) Computed myelogram. The calcification within the tumour is mainly peripheral and is well shown on D, where the subarachnoid space is almost totally occluded. On C, the irregular medial margin of the tumour is shown, together with the flattened spinal cord, which is displaced anteriorly and towards the right. (E-G) Cervical meningioma-MRI: T₂-weighted E; T₁-weighted F; T₁-weighted after gadolinium G. The tumour has a broad base on the dura anterior to the spinal cord which is displaced posteriorly and compressed. The tumour returns high signal on T₂-low on T₁-weighted, and enhances markedly.

All these lesions are well shown only by MRI. Some can be difficult to distinguish from intramedullary tumours. Enhancement of the meninges after intravenous gadolinium can be helpful to indicate inflammation in some of the rarer conditions though not MS or acute transverse myelitis.

Infarction

Acute arterial and venous infarcts usually involve long segments of the spinal cord substance usually intensified centrally. Infarcts are shown only by MRI, as extensive signal change with mild swelling progressing to atrophy. Acute infarcts usually are more extensive even than acute transverse myelitis but ambiguity can exist in clinical contexts. They are seen most commonly after thoraco-abdominal aortic aneurysm repair and thrombosis of dural arteriovenous fistulas and their draining veins.

Other systemic disorders

Subacute combined degeneration of the spinal cord in congenital and acquired vitamin B₁₂ deficiency or dysmetabolic states results in extensive lesions in the dorsal and lateral columns, often but not

always visible on MRI. More acute lesions may be associated with swelling and enhancement after intravenous gadolinium administration. Striking signal change confined to the dorsal columns may be seen as a consequence of selective destruction of primary sensory neurones in the dorsal root ganglia in Sjögren's syndrome. The spinal cord may also be involved in Bichet's disease.

Intradural extramedullary lesions

These are outlined in the subarachnoid space and tend to widen the space around them by acting as wedges, displacing and flattening the spinal cord and/or nerve roots, and tending to cause local expansion of the spinal canal. Such masses are likely to be benign tumours, usually neurofibromas or meningiomas (Figs 54.44-54.46).

Meningiomas

These are especially frequent in the thoracic segment of the spinal canal (over 80%) and in the high cervical-foramen magnum region. The majority (over 80%) occur in middle-aged women. The tumours may be partly calcified and are generally entirely intradural

(over 90%); extradural involvement should suggest the possibility of malignancy. Meningioma tends to reflect MRI signal in much the same way as neural substance, but is clearly defined by marked enhancement after gadolinium injection.

Neurofibromas (schwannomas)

These usually arise from a posterior nerve root; about two-thirds are entirely intradural, the rest being either entirely extradural or having an extradural component which sometimes enlarges an intervertebral foramen.

They tend to occur in younger patients than do meningiomas, and have no predilection for either sex. They usually reflect high signal on T₂-weighted and low on T₁-weighted MRI sequences and enhance with gadolinium. Neurofibromas are often relatively larger than meningiomas by the time they present with cord or root compression, especially those in the lumbar canal or with a paraspinal extension, which may be massive tumours causing extensive bone erosion. Spinal tumours very uncommonly present with subarachnoid haemorrhage or raised intracranial pressure; neurofibroma is most frequently implicated and ependymoma less often.

Multiple intradural masses

These may be: (i) neurofibromas, or less frequently meningiomas, which may occur in combination with each other and with gliomas in patients with neurofibromatosis; (ii) metastases from a malignant neoplasm of central nervous tissue, most commonly a medulloblastoma; or (iii) metastases from a systemic primary, especially carcinoma of the breast or bronchus, which occur most frequently on the cauda equina. Suspected meningeal spread of malignancy may require intravenous contrast for visualisation even on MRI.

Extradural masses

These displace the theca away from the bony margins of the spinal canal and tend to compress the theca and nerve root sheaths. Only by considering the history and observing any local bone and/or soft-tissue changes may the traumatic, neoplastic, inflammatory or other nature of the lesion be determined.

A *disc protrusion* is generally suspected from the acute or recurrent history of pain and the position of the extradural impression, which is often, but by no means always, anteriorly placed in the spinal canal and in part opposite a disc.

A previously established or currently evident *extraspinal neoplasm*, especially in the presence of single or multiple foci of abnormal bone or radionuclide uptake, is strong evidence that an extradural mass is metastatic. However, radiological evidence of bone change is sometimes absent and the possibility of complicating haematoma or infection should be considered if the patient is receiving chemotherapy.

Direct *extension of retroperitoneal tumours*, especially lymphomas or neuroblastomas, is generally evident on CT and/or MRI. Rarely, advanced retroperitoneal fibrosis affects the extradural space and compromises neural function.

Extradural abscesses are usually localised extensions from disease of the spine; they may complicate septicaemia or be metastases from a distant known focus of infection, or apparently occur in isolation. They usually spread in the relatively unconfined segment of the extradural space in the thoracic region dorsal to the spinal cord, forming a long, smooth swelling, deviating the theca anteriorly,

and compressing the cord. The lumbar and cervical regions are less frequently affected, but any suspicion of the diagnosis is a contraindication to spinal puncture in the involved segment.

Unusual extradural masses include:

1. *Extramedullary haemopoiesis*. This occurs in severe anaemias, especially thalassaemia, and both extensive paravertebral masses and bone changes secondary to marrow hypertrophy will be evident.
2. Increase in epidural fat in patients on prolonged steroid therapy. The nature of the compression is evident on CT and/or MRI, and is rarely if ever significant.

Thickening of the dura

This may be due to:

1. *pachymeningitis*, which previously occurred as a complication of syphilis, but is usually now an exceedingly rare fibrosis of the dura of unknown aetiology.
2. *Neoplastic infiltration* by carcinoma or lymphoma.
3. *Deposition of mucopolysaccharides*, when metabolism of these substances is abnormal due to any one of a group of inherited enzyme defects. Typical clinical and biochemical abnormalities have usually been established by the time that cord compression occurs.
4. *Extension of intracranial thickening* of various causes.



Fig. 54.47 Spinal dural arteriovenous fistula with intradural drainage. Sagittal (A) and coronal (B) MRI with T₂-weighted contrast in the cervical region showing markedly enlarged intradural veins.

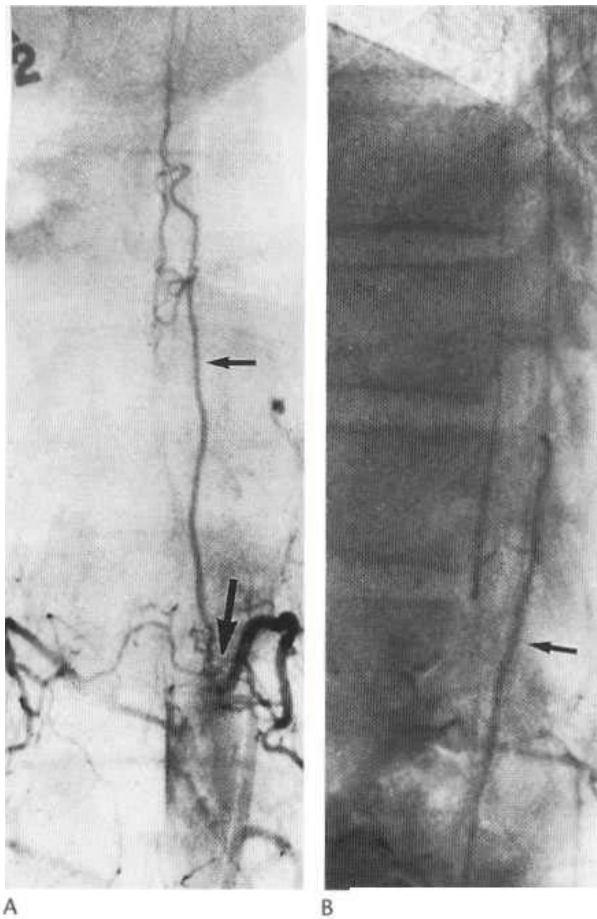


Fig. 54.48 Dural arteriovenous fistula, left second lumbar angiogram. (A) AP projection. (B) Lateral projection. The fistula is on the left side of the dura at L2 level and it drains superiorly through a vein ascending along the posterolateral aspect of the subarachnoid space to enter the posterior coronal venous system at T12 level. Veins then pass around the left side of the cord to fill the anterior coronal plexus also. Large arrow = fistula; small arrows = draining vein.

All these conditions cause concentric narrowing of the subarachnoid space which may give rise to difficulty with spinal puncture. They are well shown by MRI, but may require intravenous contrast.

Angiomatous malformation and fistula

An arteriovenous malformation or fistula draining into the spinal venous plexuses generally causes prominent dilatation of the veins, which become abnormally tortuous extending over several spinal segments and sometimes throughout the entire spinal canal. They are usually evident on T₂-weighted MRI as low-signal linear structures. High signal within the spinal cord, usually throughout its lower half or so down to the conus medullaris, usually is present also, due to oedema and/or infarction. Myelography will show the abnormal vessels; sometimes minor cord swelling is also present (Fig. 54.47).

Spinal angiography is necessary to localise the arteriovenous shunt prior to surgery or embolisation. The majority of spinal arteriovenous fistulas occur in middle-aged men and present with progressive paraparesis, usually with incontinence, often with pain; sometimes the disability increases with exercise. These fistulas are usually in the dura (Fig. 54.48), generally in the dorsal or lumbar

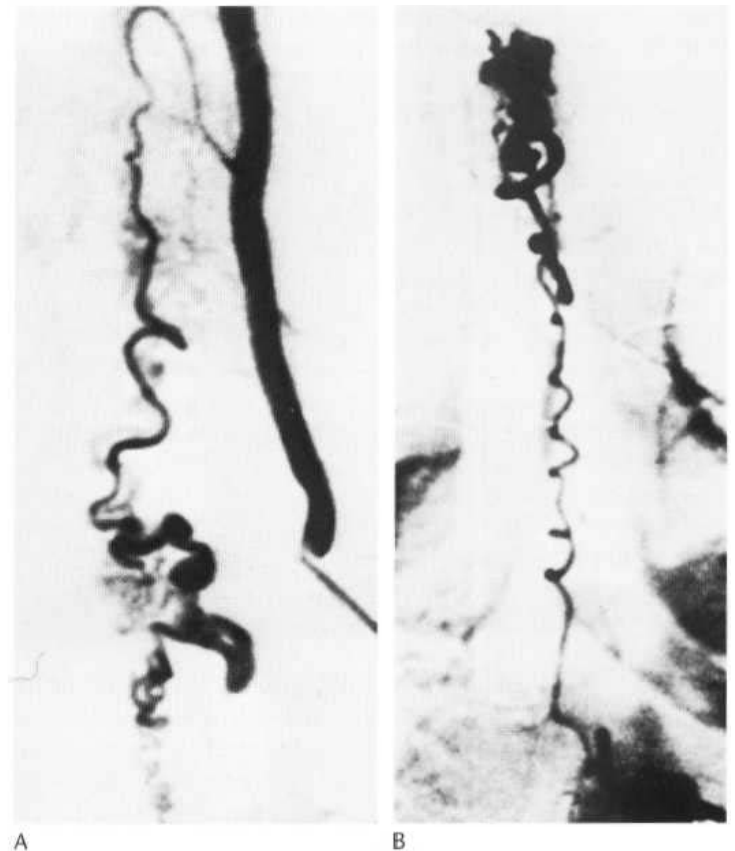


Fig. 54.49 AVM of the spinal cord. (A) Left vertebral angiogram. (B) Left sixth intercostal angiogram. The AVM is at the cervico-thoracic junction. It is supplied (A) from above by the enlarged anterior spinal artery descending from the cervical region and (B) by an enlarged tortuous vessel, presumably a posterior spinal artery, ascending along the posterolateral aspect of the cord.

regions, but they may be at any level from the sacral region to the foramen magnum. They are often related to a nerve root and are supplied by one, or occasionally two or three, radiculopial arteries, and drain through one or two veins to the coronal plexus. These fistulas are eminently suitable for embolisation procedures or surgery.

Angiomas of the spinal cord itself (Fig. 54.49) have a wider age range, not infrequently presenting in childhood, sometimes acutely with haemorrhage. They involve any region of the spinal cord, most frequently the cervical, and tend to have multiple feeding arteries, often including the anterior spinal artery.

Arachnoid cysts

Cyst-like dilatations of nerve root sheaths are a common normal variation, especially in the lumbar and sacral regions. Such root cysts and another anatomical variation, the *conjoined root sheath*, containing the nerve roots for two or more adjacent levels, have assumed significance because on plain CT they may superficially simulate an extruded disc fragment; the latter is, however, always more dense than CSF.

The term 'arachnoid cyst' refers to two separate conditions:

1. *Intratumoral arachnoid cyst*: loculated and expanding collections of CSF, usually within or adjacent to the septum posticum,

which communicate with the free subarachnoid space through narrow necks.

2. *Extradural arachnoid cysts*, which are herniations of the arachnoid through defects in the dura. They may remain within the spinal canal, expanding it, or extend through intervertebral foramina, causing erosion of the pedicles and root pain.

Cysts at the level of the spinal cord are most frequently situated posteriorly in the dorsal region, and cause backache and cord compression, sometimes varying with posture. A particular variation is the *intrasacral arachnoid cyst*, which may cause gross expansion of the sacral spinal canal with marked thinning of the bone. Such cysts may extend through into the pelvis and cause anterior displacement of the rectum. They are evident on MRI as masses spinal surgery. As well as the usual pyogenic organisms and tuberculosis, in which it generally occurs in association with extradural inflammation, sarcoidosis, schistosomiasis, cysticercosis, cryptococcal infection and coccidioidomycosis have all been implicated. The condition is associated with a variable amount of demyelination, axonal and nerve cell degeneration.

The intradural arachnoid cysts form long masses on myelography, usually posterior to the spinal cord, causing partial or complete obstruction in the dorsal region. The size of the cyst may be shown to vary with posture. Though the cyst communicates with the subarachnoid space, opacification may be slow; the cyst may be revealed only by subsequent CTM or sometimes by introducing additional contrast medium by cervical puncture.

Extradural arachnoid cysts are also generally large posteriorly situated masses, displacing the theca anteriorly or anterolaterally. The neck of the cyst is usually situated superiorly, and cyst filling, which may be free or very delayed, may be best achieved in the supine position. Where communication is free the cyst may be seen at myelography to fill and empty with posture; slow-filling cysts may be confirmed by CTM.

The cysts are usually well shown by MRI and may be suspected when different flow conditions are present in the cyst and the free subarachnoid space. Damage to the spinal cord by pulsatile expansion at the closed end of the cyst may be evident as myelopathy on T₂-weighted sequences. In both types of cyst, the diagnosis also is evident on CTM. The density of the fluid within the cyst may be similar to or less than that in the subarachnoid space, but the entire extramedullary lesion will be homogeneously opacified, and the membrane between it and the subarachnoid space may be visible. Multiple intradural arachnoid diverticula, which may erode the margins of the lumbar canal or sacrum and be associated with symptoms of radiculopathy, are an uncommon accompaniment of ankylosing spondylitis. *Herniation* of the spinal cord through a dural defect may simulate an arachnoid cyst. In this rare condition the hernia is usually anteriorly and the spinal canal may be widened locally with the spinal cord hernia extruding into the focal expansion. This is sometimes directly visualised by MRI, but more often only ventral angulation of the spinal cord is shown, sometimes wrongly diagnosed as posterior compression by an intradural arachnoid cyst. The 'empty' subarachnoid space may be mistaken for a cyst on superficial analysis.

Arachnoiditis

Infiltration of the meninges with chronic inflammatory cells and fibrosis most commonly follows chemical damage to the meninges, most often in the past by iophendylate (Myodil, Pantopaque), once widely used for myelography, or ionic myelographic contrast media, but occasionally by drugs used in therapy, including steroids and spinal anaesthetics; other causes are subarachnoid haemorrhage and infections. It used to be thought that it occurred very commonly after lumbar disc surgery, but it is now known that the cause was the contrast media used in the preoperative myelogram (Fitt & Stevens 1995). Modern myelographic media do not cause arachnoiditis, and arachnoiditis has almost disappeared as a complication of extradural

Arachnoiditis is best diagnosed by MRI, high-resolution axial T₂-weighted fast spin-echo acquisitions usually being the most helpful. Chronic adhesive arachnoiditis results in adhesions between intradural roots and with the wall of the thecal sac, producing mass-like clumps, or incorporation of roots into the thecal wall creating an empty thecal sac. The causal part of the thecal sac usually is involved. It can be very extensive, however, with distortion and cavitation of the spinal cord. The organised adhesion may calcify or even ossify, producing arachnoiditis ossificans. Clinico-radiological correlation generally is poor.

REFERENCES AND SUGGESTIONS FOR FURTHER READING

- Fitt, C. J., Stevens, J. M. (1995) Post-operative arachnoiditis diagnosed by high resolution fast spin echo MRI of the lumbar spine. *Neuroradiology*, 37, 139-145.
- Ghelman, B. (1988) Discography. In: Kricun, M. (Ed), Saunders, W. B. (eds) Imaging Modalities in Spinal Disorders, pp. 538-556. Philadelphia.
- Hueftle, M. G., Modic, M. T., Ross, J. S., et al (1988) Lumbar spine: postoperative MR imaging with Gd-DTPA. *Radiology*, 167, 817-824.
- Lacatelli, B., Laurena, R., Ballard, P., Mark, A. S. (1999) MRI in vitamin B₁₂ deficiency myelopathy. *Canadian Neurological Sciences*, 26, 60-63.
- Modic M. T., Steinberg P. M., Ross J. S., et al (1988) Degenerative disc disease: assessment of changes in vertebral bone marrow with MRI. *Radiology*, 166, 197-199.
- Ross, J. S., Masaryk, T. J., Modic, M. T., et al (1987) Magnetic resonance imaging of lumbar arachnoiditis. *American Journal of Neuroradiology*, 8, 885-892.
- Stark, D. D., Hendrick, R. E., Hahn, P. F., Ferrucci, J. T. (1987) Motion artifact reduction with fast spin-echo imaging. *Radiology*, 164, 183-191.
- Stevens, J. M. (1995) Imaging of the spinal cord. A review. *Journal of Neurology, Neurosurgery and Psychiatry*, 58, 403-408.
- Stevens, J. M., Kling Chong, W., Barber, C. et al (1994) A new appraisal of abnormalities of the odontoid process associated with atlanto-axial subluxation and neurological disability. *Brain*, 117, 133-148.
- Ullrich, C. G., Binet, E. F., Sanecki, M. G., Kieffer, S. A. (1980) Quantitative assessment of the lumbar spinal canal by computed tomography. *Radiology*, 134, 137-143.



نشر الکترونیکی
موسسه انتشاراتی
نوردانش

55

VASCULAR IMAGING IN NEURORADIOLOGY

David Sutton and John Stevens

Techniques of vascular imaging

The methods currently used include:

1. Magnetic resonance angiography (MRA)
2. CT angiography
3. Sonographic vascular imaging
4. Intravenous digital subtraction angiography (IV DSA)
5. Direct intra-arterial angiography.

Direct intra-arterial angiography using standard film has for many years provided the gold standard for angiography but is now largely replaced by minimally or non-invasive techniques in well-equipped units. Some workers, however, still prefer direct angiography for special purposes such as the investigation of subarachnoid haemorrhage. Direct angiography also remains essential for interventional work (see Ch. 56).

The different shades of meaning attached to the term 'non-invasive' have been described elsewhere in this text (see Ch. 12, p. 319, and Ch. 15, p. 416). Some procedures so referred to are better described as minimally or mildly invasive, since intravenous



Fig. 55.1 (A) MRA showing all four neck vessels in AP view. (B) Segmental MRA study of right carotid and vertebral in lateral view.



Fig. 55.2 MRAs. (A) Normal left carotid and vertebral. (B) Stenosis of right common carotid bifurcation. The stenosed channel is not outlined owing to low flow.

(I.V.) contrast and not direct intra-arterial contrast is used. These procedures include contrast enhanced magnetic resonance (CE-MR), I.V. DSA and I.V. contrast enhanced spiral CT. The procedures may also be described as without radiation hazard (MRI and ultrasound) or with radiation hazard (DSA and CT).

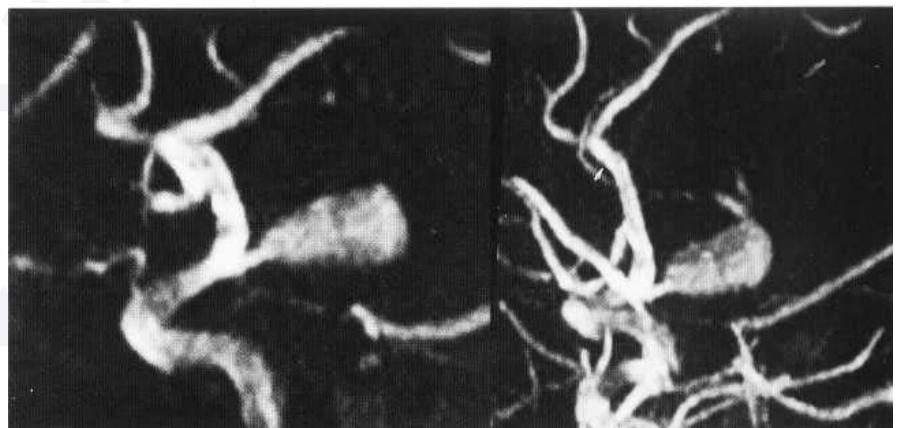
1. Magnetic resonance angiography (MRA)

(Figs 55.1–55.4 and Fig. 55.54)

This technique has expanded greatly in recent years (see Ch. 15 for more details). Two basic strategies are used for imaging, namely time of flight effects (TOF) and phase contrast (PC). These can be acquired either multislice (two-dimensional) or three-dimensionally (3D). TOE is most frequently used in imaging the cerebral circulation. Background suppression is improved by utilising magnetisation transfer (MTC), in the form of a broad-spectrum prepulse. Fixed and 'walking' presaturation slabs are also helpful to obtain selectively images of either arteries or veins. Image quality in 3D techniques can be enhanced by reducing the size of the image volume, which permits better visualisation of slower flowing protons in smaller arterial branches. Carotid and cerebral imaging is often best performed using an overlapping 3D volume technique, known as multiple overlapping thin-slice arteriography (MOTSA). Enhanced visualisation is also achieved with interactive vascular imaging (IV!), which permits segmentation of individual vessels or segments of vessels for multidirectional maximum intensity pixel (MIP) displays. Intravenous enhancement with gadolinium is now widely used in MRA. The technique most widely used is *three-dimensional contrast-enhanced MRA (3D CE MRA)*. It is necessary to acquire a time-resolved sequence so that images from the arterial phase are acquired before venous enhancement occurs. Image sets are acquired at approximately 5 s intervals. Acquisition planes generally are coronal or sagittal rather than transverse. Between 20 and 25 ml of contrast is injected into a peripheral rather than central vein. Digital subtraction of precontrast images and other post-processing may be used to improve the display and MIP projections and 3D surface renderings are produced. The technique is most commonly used to display the aortic arch and origins of the great cerebral vessels. A customised neurovascular neck coil also is a great advantage to ensure good regional coverage.



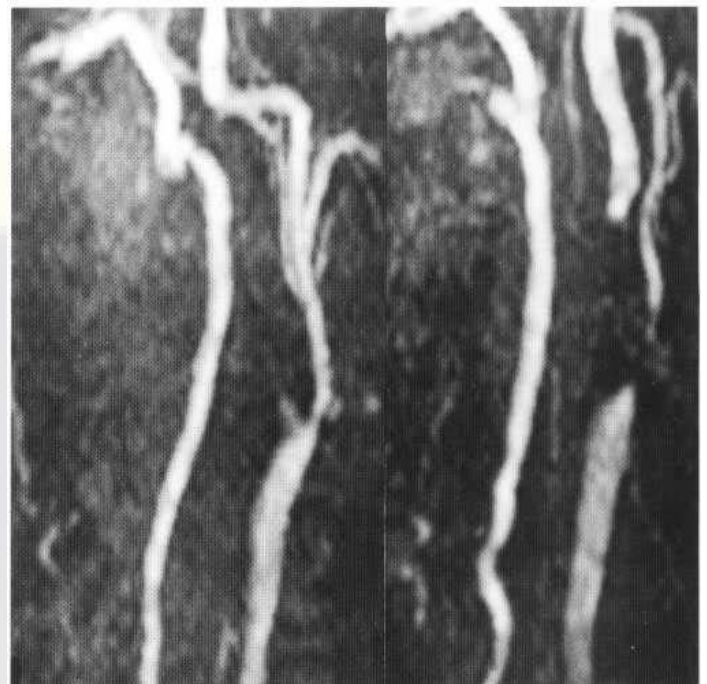
A



B

C

Fig. 55.4 MRAs. (A) Normal internal carotid bifurcation and proximal segments of the anterior and middle cerebral arteries in lateral view. Lateral (B) and rotated lateral (C) views of a posterior communicating aneurysm.



A

B

Fig. 55.3 MRAs. (A) Right internal carotid thrombosis. (B) Severe right internal carotid stenosis. Owing to low flow the proximal segment does not outline.

Perfusion imaging is also possible with both contrast-enhanced MRA and CT angiography. After an intravenous contrast bolus, a series of images are acquired over time, often of just a single slice, from which, with appropriate computer-based processing, parameters such as regional time to peak contrast, relative regional cerebral blood flow and blood volume can be calculated and presented as colour coded maps. Spatial resolution is generally better than in nuclear medicine-based techniques. These techniques are widely used, most often in research settings.

2. CT angiography (Figs 55.5,55.6; see also Ch. 15)

Spiral CT incorporates a slip ring coupling between the rotating and stationary portions of the gantry to allow for continuous tube rotation and data acquisition as the patient is transported through the

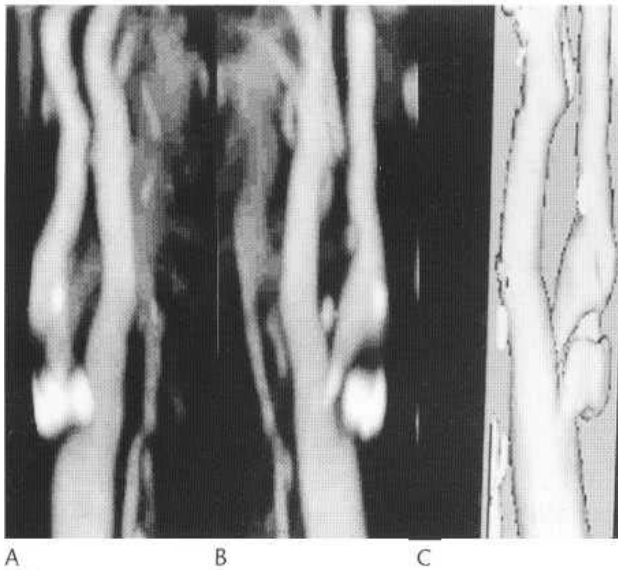


Fig. 55.5 Spiral CT of the neck vessels showing sequestered study of right carotid bifurcation. (A) In the AP view the stenosis is obscured by a calcified plaque. (B) The image is computer rotated through 180° to show the stenosed lumen. (C) 3D CT reconstruction. (Courtesy of Dr A. Al-Kutoubi.)

gantry. The dataset produced can be reconstructed at arbitrary intervals to generate overlapping sections, and the rapid acquisition time enables an entire vascular territory to be imaged within 30 s. Imaging the cerebral circulation requires the injection of approximately 90 ml of contrast medium (300 mg/ml iodine) through a cannula or catheter inserted into a peripheral arm vein, over 20–30 s. The timing of the spiral CT imaging depends on circulation time and usually requires a test dose to monitor opacification of the vessels of interest, as in CE MRA. Collimator width and table speed have important consequences on the quality of the results. As usual there is a trade-off between the volume imaged and spatial resolution, and collimator width and signal-to-noise ratio.

Images can be viewed as axial sections of any prescribed thickness. They can also be presented, like magnetic resonance angiograms, as MIP projections or as threshold shaded surface displays (SSDs). Segmentation of the arterial system from other dense structures such as bone is necessary and can be very time-consuming, but semiautomated methods are now on line; image editing is a major part of this type of angiography. 3D CT angiography in neuroradiology is used mainly to image the extracranial carotid and vertebral arteries, and to detect and display intracranial aneurysms. It generally is used when MRA is not an option.

3. Sonographic vascular imaging (see Figs 15.78, 15.82)

This is widely used for imaging the extracranial carotid vessels and can also be used to measure blood velocity in the middle cerebral and other intracranial arteries. Grey scale imaging is used to visualise the vessels and to document the state of the vessel wall. Doppler spectral analysis is used to determine blood flow velocity. Colour flow mapping is also used to enable a rapid survey of arterial segments to find sites where further spectral analysis may be beneficial. The technical details of vascular sonography are given in Chapter 15. Considerable operator skill and time are required.

4. Intravenous DSA

Digital techniques have completely replaced film-screen combinations. Computed fluoroscopy enables rapid manipulation of multiple images with subtraction of the bones and other tissues from the opacified blood vessels. Adequate arterial studies may be obtained with relatively low intra-arterial concentrations of contrast medium.

Although enjoying widespread clinical use in the early 1980s, initial enthusiasm for intravenous DSA soon became tempered with caution as limitations became apparent. The great advantage of intravenous techniques is that it is very safe to the patient. The procedure does not require hospitalisation and is performed on an outpatient basis. It is therefore cost-effective. It generally requires placement of a catheter via an arm vein, into the superior vena cava or left atrium.

Contrast resolution is not as good as with direct arteriography. For intracranial lesions all four vessels are opacified at the same time, and in lateral views there is superimposition of the vessels of the two sides. With uncooperative patients, movement can degrade the images to an unacceptable level. Large boluses of contrast agent are used for intravenous injections so that multiple projections require quite large total doses. These drawbacks led to some modification of the early enthusiasm for



Fig. 55.6 3D CT reconstruction of circle of Willis and adjacent vessels showing bilateral aneurysms. (A) AP view. (B) Computer-rotated view. (Courtesy of Dr A. Al-Kutoubi.)

the intravenous technique, and many units switched to the use of digital techniques with the more dangerous intra-arterial injections.

The main uses of *intravenous DSA* are:

1. For arch aortography for neck vessel study (Fig. 55.7).
2. For selected intracranial studies, e.g. confirmation of large aneurysms, angiomas, fistulas, or vascular tumours suggested by CT, or to show the relationships of the major arteries to a large pituitary adenoma, or to show involvement of a major venous sinus (Fig. 55.8).
3. For some postoperative and follow-up studies, particularly after aneurysm clipping and treatment of stenoses.
4. For dural sinus phlebography.

The intravenous technique ensures that all vascular territories are opacified together, allowing the generation of full-contrast venograms of good temporal resolution (Fig. 55.8).

For the reasons stated above, intravenous studies of the extra-cranial neck vessels are suboptimal in a proportion of patients. This proportion was stated to be 15-20% in the early studies, but with

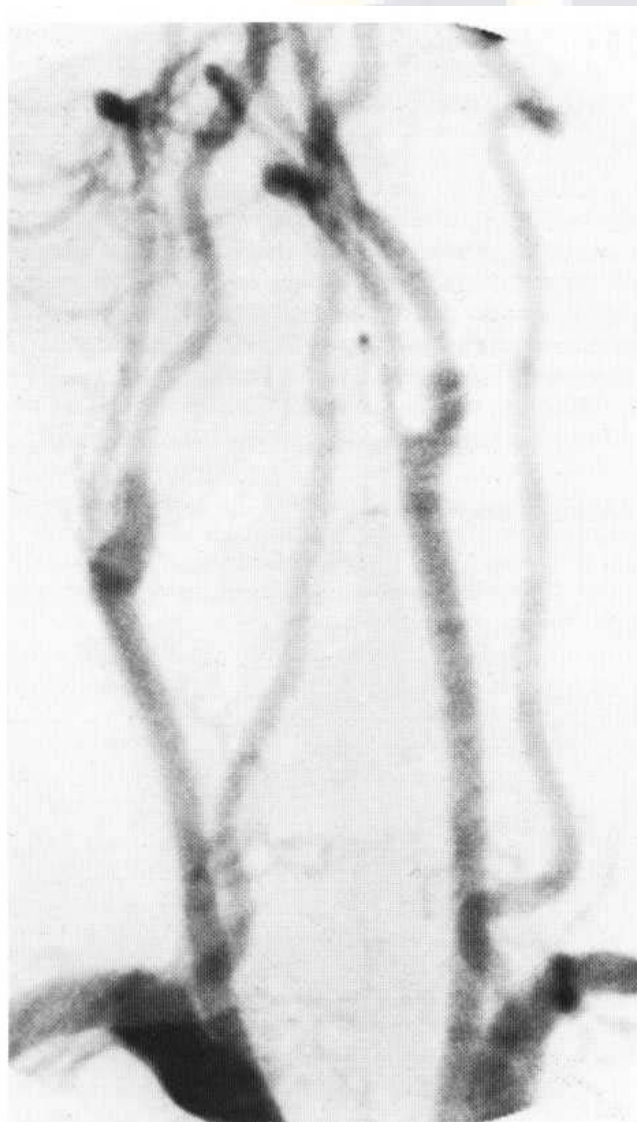


Fig. 55.7 The neck vessels shown by DSA following an intravenous injection of contrast medium. The internal carotid and vertebral origins are normal.



Fig. 55.8 DSA study showing the cortical veins, sagittal and lateral sinuses. Note large vein of Trolard and smaller vein of Labbe.

improvements of apparatus and technique should now be less than 10%; however, it may be necessary to use more than one projection to ensure this, with consequent increase in total contrast medium dose.

5. Direct intra-arterial angiography

This was originally performed by percutaneous puncture of the common carotid artery in the neck. This technique became obsolete with the increasing use of percutaneous catheterisation. Direct carotid angiography is now generally practised by the introduction of catheters into the lumen of the common carotid artery from a percutaneous transfemoral approach. This technique permits selective catheterisation of the internal and external carotid arteries; however, caution should be observed in passing catheters into the internal carotid artery in middle-aged and elderly patients, particularly if there is any suspicion of atheromatous internal carotid artery stenosis.

About 10 ml of contrast medium are usually injected within 1-2 s into the common carotid artery. A slightly smaller quantity, about 8 ml, is adequate for selective injection of the internal carotid artery. Selective injection of the external carotid artery can be accomplished with a similar amount of contrast medium (8 ml). In the case of the external carotid artery the injection can be made more slowly, taking 2-4 s.

Carotid angiography can be carried out either under local anaesthesia or under general anaesthesia. In cases where more than one artery is to be injected at one session, or if the patient is likely to be very uncooperative or nervous, general anaesthesia is more commonly used. However, the advent of DSA and low-osmolarity contrast media has further reduced the need for general anaesthesia.

As with other forms of arteriography, it is important to obtain rapid serial films as the contrast medium passes through the circulation. Many types of apparatus were available for achieving this, but today most imaging is performed by DSA. Different 'programmes' can be used and tailored to the individual case. A standard series could consist of seven images taken at 1 per second for 7 seconds and timed so that arterial, capillary and venous phases of the angiogram are all covered. With angiomas, arteriovenous fistulas and vascular tumours the early images would be taken at two or three frames per second to allow for the rapid arteriovenous shunting.

Vertebral angiography For catheter demonstration of the carotid or vertebral artery, several alternative catheters are available, and different workers have preference for different types. We prefer the Mani (5F) headhunter catheters, and even smaller catheters (4F and 3F) are now available. The smaller catheters have the added advantage of being less liable to form clot or to damage arterial walls.

Normally the left vertebral artery is easier to catheterise than the right, but if one side proves difficult the other can usually be entered. It is normally only necessary to catheterise one vertebral artery, as a forced injection will fill the contralateral vertebral artery by reflux as well as filling the basilar artery.

Sometimes the catheter can be passed into the subclavian artery but will not enter the vertebral artery. In these cases an injection can be made into the subclavian artery and an indirect vertebral arteriogram obtained. In patients whose vessels are too tortuous for the subclavian arteries to be catheterised from below, or in whom diseased iliacs prevent passage of a catheter, success can still be obtained by transaxillary catheterisation. In about 5% of cases the left vertebral artery arises direct from the aortic arch. If no vertebral artery can be found arising from the left subclavian this condition should be suspected, the catheter withdrawn into the arch, and an attempt made to manipulate it into the anomalous vertebral. If this fails, the right vertebral should be attempted.

For direct injection into the vertebral artery we use only 6-8 ml of contrast medium. Low-osmolality contrast media are now mandatory. As with carotid angiography, improved detail can be obtained by the use of magnification with a fine-focus tube and by the use of subtraction films.

Where the first part of the subclavian artery is injected, about 15 ml of contrast medium are injected in about 2 s. It may help to obtain better filling of the vertebral artery in these cases if the appropriate brachial artery is occluded at the time of injection.

Arch aortography It is still contended by some workers that cerebral symptoms may arise from stenosis or thrombosis of the origins of the internal carotid arteries or of the vertebral arteries. It has also been claimed that intrathoracic lesions of the innominate, left common carotid and left subclavian arteries can be a cause of cerebral symptoms.

Injection of contrast medium into the aortic arch enables all the Great vessels in the thorax and the vertebral arteries in the neck, together with the carotid bifurcations, to be demonstrated.

The important features of arch aortograms are illustrated in Figure 55.9. It is usual to take rapid serial films with the supine patient rotated about 45° to the right and the head turned to the right lateral position. This normally avoids superimposition of the carotid and vertebral arteries and shows the carotid bifurcations clearly.

DSA by intravenous injection has also been widely used for arch aortography.

The main indications for direct intra-arterial angiography in well-equipped departments are now limited as follows:

1. To elucidate the arterial supply and venous drainage of arteriovenous shunts for treatment planning, not simply for diagnosis.
2. Prior to endovascular therapeutic procedures such as preoperative embolisation of tumours, treatment of aneurysms or arterial stenoses, etc.
3. Investigation of definite intracranial subarachnoid haemorrhage (may not always be necessary).

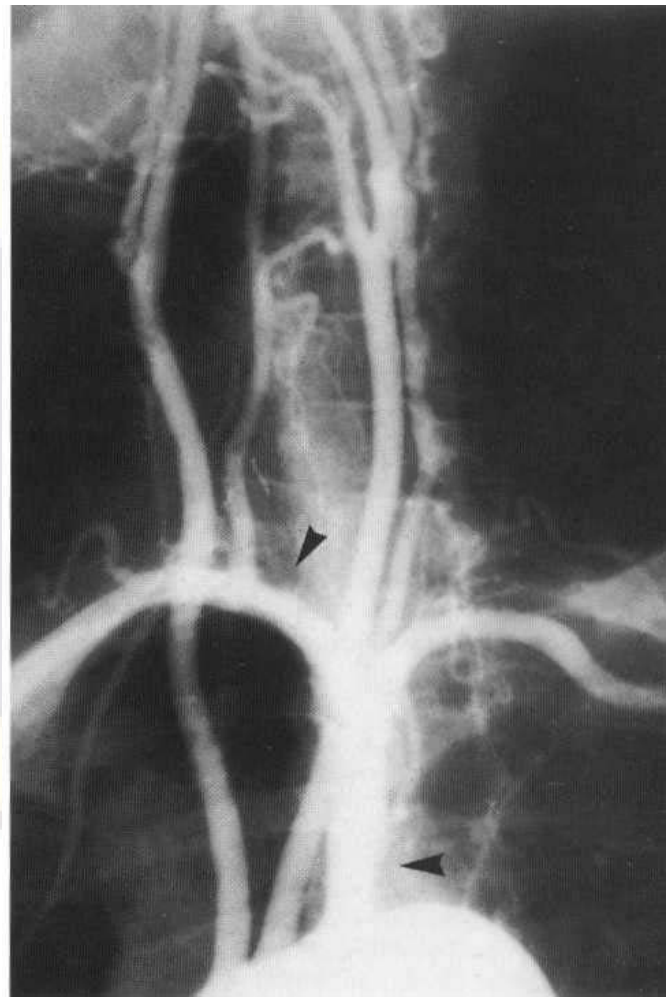


Fig. 55.9 Arch aortogram in right posterior oblique position. There is a congenital anomaly, in that the right subclavian artery arises distally from the aortic arch (arrowheads). Its origin is superimposed on the left subclavian origin. Both carotid bifurcations are well shown.

4. Very occasionally as an investigation of last resort. Most often this will be in context where less invasive imaging has been unsatisfactory.

Spinal angiography This procedure involved selective angiography and a very careful radiographic technique. The arterial supply to the spinal cord is illustrated in Figure 55.10. The main indication today is in interventional techniques (see Ch. 56).

Complications of intra-arterial cerebral angiography

The general complications of angiography have been discussed in Chapter 15. Intra-arterial techniques carry the particular risk of inducing temporary or permanent brain damage. The risks are highest in the elderly and those with pre-existing vascular disease. In the past the commonest causes of brain damage were the use of toxic contrast agents, and local damage to the carotid or vertebral arteries. Nowadays, brain damage attributable to the contrast medium is virtually non-existent, and local trauma is also relatively infrequent. The commonest cause of damage is embolism from a clot forming in or around the catheter tip. The risk of permanent

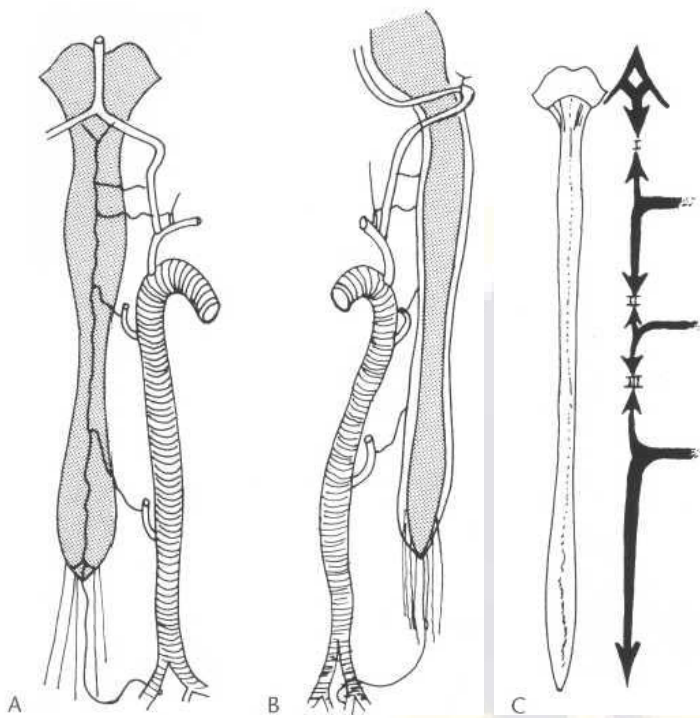
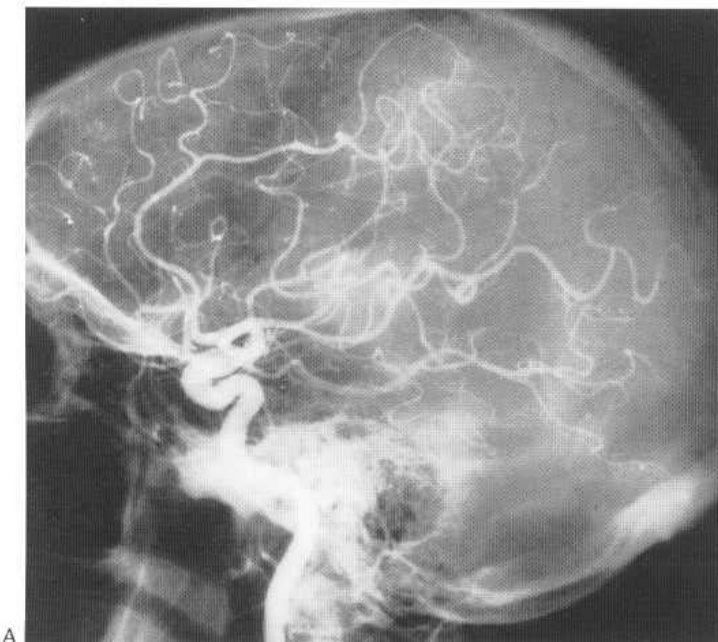


Fig. 55.10 Normal blood supply to the spinal cord as seen (A) in anterior view and (B) in lateral view. (C) Blood flow currents in the longitudinal spinal arteries. (After DiChiro & Wener 1973.)

disability or death has been variably estimated over the years, but two of the most recent assessments have put this at 1.2% and 5.2% (1995 and 1994). The best results are obtained where the procedures are carried out by experienced workers only. It must also be stressed that several recent studies from reputable centres have indicated that intra-arterial DSA is no safer than conventional film-screen techniques and, even more importantly, that arch angiography carries the same or even slightly *high* r stroke risk



than selective arteriography. These serious complication rates make it obvious that cerebral angiography should only be practised by experienced personnel who are fully aware of these hazards. Moreover, intra-arterial techniques should only be resorted to when absolutely essential on clinical grounds, and when the information required for patient management is not obtainable by less invasive techniques.

Despite a few early reports to the contrary, which were not confirmed by later studies, intravenous DSA carries no risk of stroke, but carries a small risk of usually insignificant systemic side-effects, the most frequent being angina (0.6%). Despite the earlier claims to the contrary, it is most likely that the systemic side-effects are no more frequent in intravenous DSA than in a double-dose contrast-enhanced CT or intravenous urogram. The same is probably true for 3D CT angiography. Carotid sonography and MRA carry no risk of side-effects.

Selective spinal angiography carries the risk of damage to the spinal cord and must be practised with caution. Only small doses of low-osmolar contrast medium should be injected into the posterior intercostal and lumbar arteries. In patients with arteriovenous fistulas, worsening myelopathy has been reported in up to 20% of cases. Spinal cord damage can also result from non-neuroradiological angiography, such as bronchial, thyroid and parathyroid angiography.

The normal internal carotid angiogram

The features of the normal internal carotid arteriogram are illustrated in Figures 55.11 and 55.12. The normal circulation time from injection of the contrast medium into the internal carotid artery to its disappearance from the veins of the brain varies with the individual and averages 5-7 s. In certain pathological conditions it may of course be appreciably slower. With angiomatous malformations or arteriovenous fistulas it may be extremely rapid. It is customary to divide the angiogram into four phases. The first phase lasts 1-2.5 s and is referred to as the arterial phase. Films taken during this period show the arterial tree. The second or capillary phase lasts about 1 s or less but is rarely clearly defined on the X-ray film, as

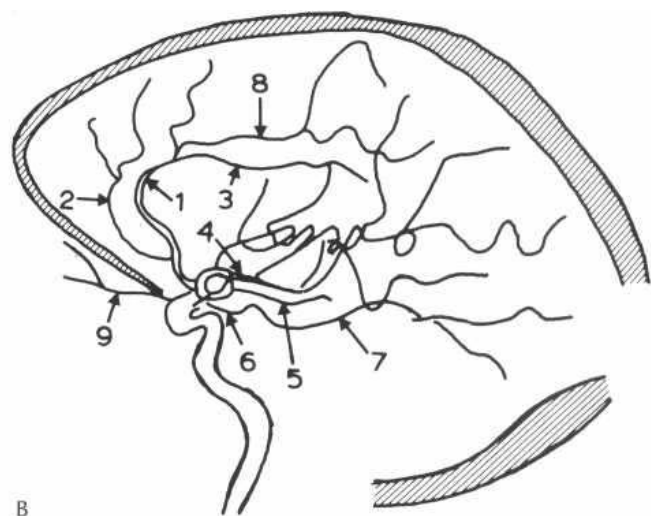


Fig. 55.11 (A) Normal internal carotid arteriogram-lateral view. (B) Diagram to illustrate (A). 1. anterior cerebral artery; 2. frontopolar artery; 3. pericallosal artery; 4. middle cerebral artery and its branches; 5. anterior choroidal artery; 6. posterior communicating artery; 7. posterior cerebral artery; 8. callosomarginal artery; 9. ophthalmic artery.

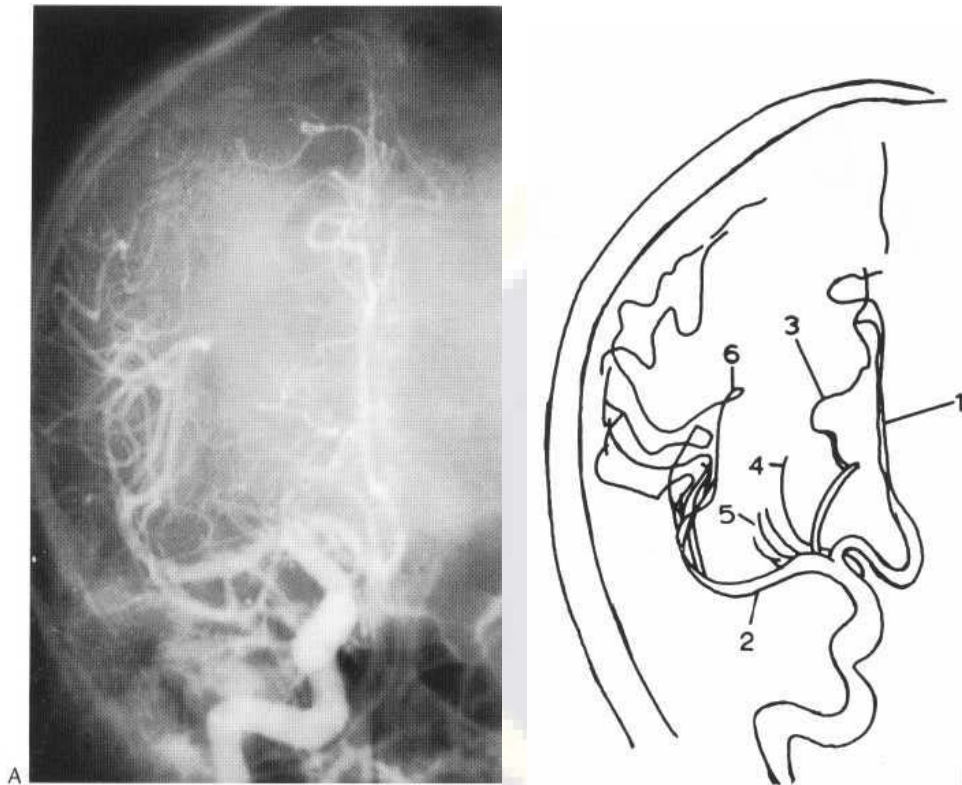


Fig. 55.12 (A) Normal internal carotid arteriogram-AP view. (B) Diagram to illustrate (A). 1. Anterior cerebral artery; 2. middle cerebral artery and its branches; 3. posterior cerebral artery; 4. anterior choroidal artery; 5. lenticulostriate arteries; 6. sylvian point.

there is usually some late arterial or early venous filling superimposed. The third and fourth phases are characterised by venous filling and last 4-5 s. They include the early and late phlebograms, respectively. The early phlebogram outlines the superficial veins of the hemisphere, and the late phlebogram shows the deep veins.

The blood flow through the internal carotid artery is considerably greater than through the external carotid artery. Thus, following injection of the common carotid artery, the intracranial vessels are usually visible in the lateral films a second or so before the branches of the external carotid become superimposed. The experienced worker has no difficulty in differentiating branches of the external from branches of the internal carotid, as the distribution of these vessels follows a standard pattern. The middle meningeal artery and its branches which stem from the internal maxillary branch of the external carotid also fill slightly later than the internal carotid branches. Early filling of the middle meningeal artery together with internal carotid branches can occur if the vessel is hypertrophied to supply a meningioma or angioma. This point is further commented on below.

The cervical internal carotid artery has no branches, but occasionally the ascending pharyngeal or other branches of the external carotid may arise from it, as may the rare proatlantal intersegmental artery and the hypoglossal artery (Figs 55.33, 55.34).

Sometimes the internal carotid artery shows a prominent loop as it lies lateral to the oropharynx, and this is known as the '*tonsillar loop*' (Fig. 55.13). It can be regarded as a normal variant. The normal internal carotid artery also forms a loop as it lies in the lateral wall of the cavernous sinus, which is usually referred to as the '*carotid siphon*'. The suprasellar portion of the internal carotid artery just before its bifurcation is normally inclined laterally (from below upward) as seen in the anteroposterior view. In this view the major branches of the anterior and middle cerebral arteries pass, respectively, medially and laterally. These two vessels, together

with the termination of the internal carotid, resemble the letter T when seen in this projection (Fig. 55.12). The major branches of the internal carotid artery all arise above the cavernous sinus, but there are some minor branches arising in its intrapetrous and pre-cavernous segments. The former include the *caroticotympanic* and

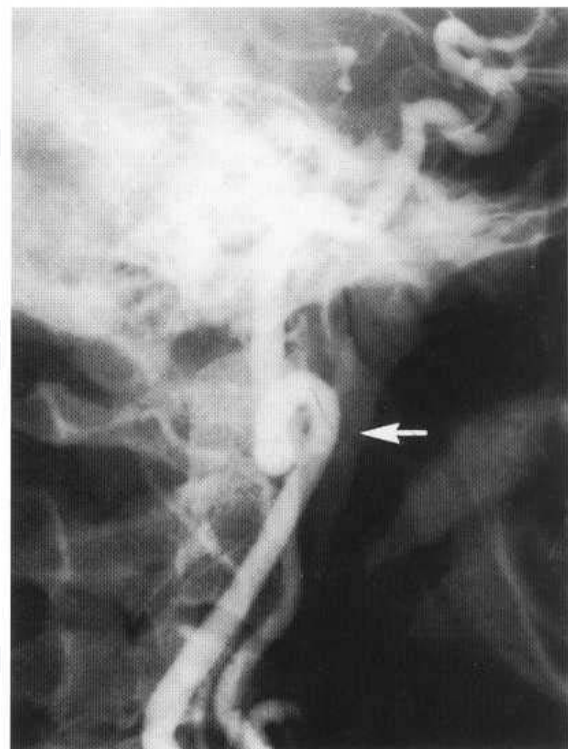


Fig. 55.13 Carotid arteriogram showing '*tonsillar loop*' (arrow) in the neck.

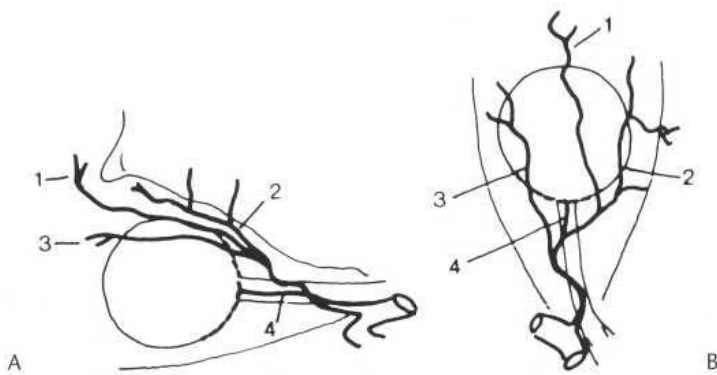


Fig. 55.14 Right ophthalmic artery. (A) In lateral view. (B) In axial view. 1. Supraorbital branch; 2. main artery with ethmoidal branches; 3. lacrimal branch; 4. central retinal branch.

pterygoid (vidian) arteries, which are rarely recognisable at angiography. The precavernous and intracavernous branches include:

1. The important *meningohypophyseal trunk* (Fig. 55.51), which gives rise to:
 - a. the *tentorial artery*
 - b. the *dorsal meningeal artery*
 - c. the *inferior hypophyseal artery*

The tentorial artery may be enlarged and easily recognisable with tentorial meningiomas.

2. The *inferior cavernous artery*, which supplies the wall of the cavernous sinus and its contents and anastomoses with the middle meningeal artery.
3. The *capsular artery*.

Under normal circumstances these arteries are only recognisable in high-quality subtraction films with magnification, as are the tiny superior hypophyseal arteries which arise above the sella. The *ophthalmic artery* arises from the internal carotid just above the sella and medial to the anterior clinoid process. It passes forward to the optic canal beneath the optic nerve and then into the orbit. A good quality film will show its terminal branches outlining the posterior aspect of the globe (Fig. 55.14). Its terminal supraorbital branch supplies a small cutaneous area above the medial aspect of the orbit.

The *artery of the falx* arises from the anterior ethmoidal branch of the ophthalmic artery and passes through the cribriform plate to supply the anterior part of the falx. It may be markedly hypertrophied to supply meningiomas or arteriovenous malformations.

The *posterior communicating* and *posterior cerebral arteries* fill in only about a third of common carotid arteriograms. However, they fill in a higher proportion of cases following selective injection of the internal carotid artery. In other cases, the dominant blood supply to the posterior cerebral artery is through the vertebrobasilar circulation. Sometimes the origin of the posterior communicating artery, as seen in lateral view, is slightly expanded. This appearance, known as the 'infundibulum' of the posterior communicating artery, has been regarded as a normal variant. On the other hand, there is some pathological evidence that it may be associated with a defect in the vessel wall and predispose to aneurysm formation.

The *anterior choroidal artery* is small but is readily identifiable. Its normal position in both lateral and anteroposterior view is illustrated in Figure 55.15. Displacements of this vessel were of considerable help in identifying and localising mass lesions.

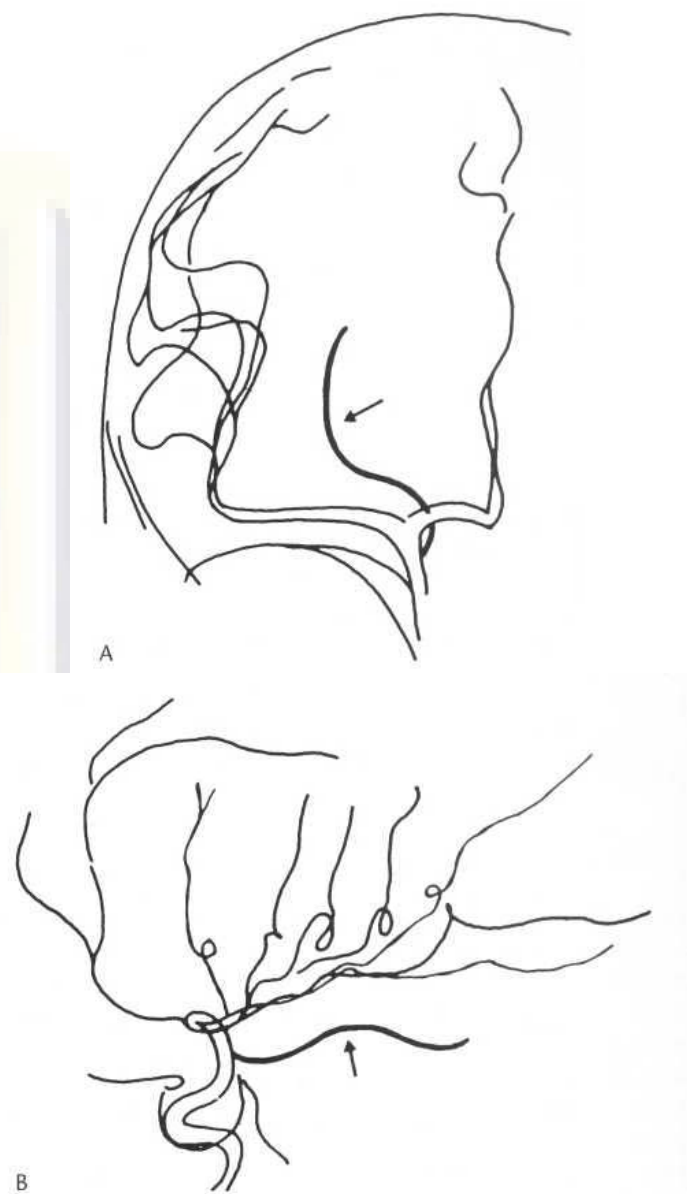


Fig. 55.15 Anterior choroidal artery (arrowed). (A) In AP projection. (B) In lateral projection.

The normal anterior choroidal artery arises from the posterior aspect of the internal carotid just distal to the origin of the posterior communicating artery, but rarely it arises from the middle cerebral or posterior cerebral artery. The artery is directed backward and medially to the medial aspect of the anterior part of the temporal lobe. It then passes round the uncus and turns laterally and backward into the choroidal fissure to enter the temporal horn. There it supplies the choroid plexus, which is sometimes seen as an ill-defined blush of contrast.

As with the posterior communicating artery, an infundibulum is occasionally seen at the origin of the artery from the internal carotid artery.

The *lenticulostriate arteries* arise in two groups of 2-4 tiny arteries, the medial and the lateral. Normally they stem from the upper surface of the middle cerebral artery trunk and pass directly up through the anterior perforated substance into the Basal ganglia and internal capsule. Some of them may also arise from the internal carotid bifurcation or the origin of the anterior cerebral. They are

readily recognised in good-quality anteroposterior films, but are usually obscured by larger overlying vessels in the lateral view. The normal disposition of these vessels is illustrated in Figure 55.16. They pass upward and medially for a short distance and then laterally in an arc that is concave inward. Masses or haematomas in the region of the external capsule displace these vessels medially, while masses in the basal ganglia or internal capsule distort or separate them.

The *anterior cerebral artery* (Figs 55.11, 55.12) passes medially from the bifurcation of the internal carotid to reach the midline. This small segment of the artery lies above the optic chiasm or optic nerve and is usually convex upward. It is best seen in the anteroposterior projection. Near the midline it is joined by the anterior communicating artery to its fellow on the opposite side. Beyond the anterior communicating artery the anterior cerebral artery turns forward and upward in the interhemispheric fissure. It passes around the anterior aspect of the corpus callosum and turns backward along its upper surface. It continues as the pericallosal artery to the back end of the corpus callosum.

In lateral view the segment between the anterior communicating artery and the genu of the corpus callosum usually has a gentle concavity downward. This is variable in degree and should not be mistaken for displacement by a mass. A few tiny perforating branches are given off from the proximal horizontal segment of the anterior cerebral artery, but these are variable and difficult to identify on angiograms.

The *frontopolar branch* is generally the first major branch of the anterior cerebral and arises proximal to the knee or bend of the vessel around the corpus callosum. This vessel passes forward and upward towards the anterior pole of the frontal lobe and is best seen in lateral view. It divides into 2-3 branches which pass to the superomedial margin of the hemisphere and over on to the convexity.

The next major branch of the anterior cerebral is the *callosomarginal*. This usually arises near the genu and passes backward and upward, giving off *anterior, middle* and *posterior internal frontal* branches. It terminates in the *paracentral branch* around the paracentral lobule. The branches just described are variable and may arise directly from the anterior cerebral. The callosomarginal artery lies in the callosomarginal sulcus for part of its course, and while in the sulcus it may be lateral to the midline. This should not be mistaken for a true displacement by a mass. The terminal branches of the artery, like those of the frontopolar artery, reach the superomedial border of the hemisphere and pass over it to the convexity. Here they anastomose with terminal ascending branches of the middle cerebral artery.

The *pericallosal artery* represents the continuation of the anterior cerebral after it has given off the major branches just described. Normally it is fairly closely applied to the upper surface of the corpus callosum and terminates in a precuneal or posterior callosal branch.

The proximal segment of the anterior cerebral artery is occasionally hypoplastic, forming one of the many variations of the circle of Willis. In these cases the major part of the vessel fills from the opposite side through the anterior communicating artery. Such congenital hypoplasia should be distinguished from spasm associated with subarachnoid haemorrhage.

The *middle cerebral artery* passes laterally and slightly forward from the bifurcation of the internal carotid artery. This segment is best seen in the AP view and is horizontal or convex upward. It gives rise to the lenticulostriate arteries, which have just been

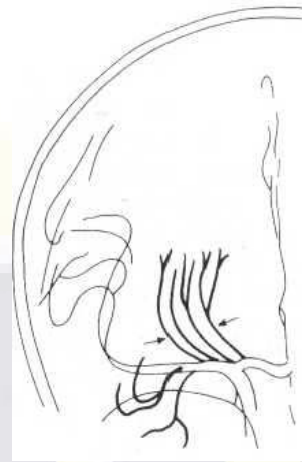


Fig. 55.16 Lenticulostriate arteries in AP projection. They are difficult to identify in lateral projection because of the superimposed middle cerebral vessels. The anterior temporal and orbitofrontal branches are also shown passing downward.

described, and also to anterior temporal and orbitofrontal branches (Fig. 55.16). These can arise from a common trunk. About 2 cm from its origin it reaches the insula (or island of *Red*), where it usually bifurcates or trifurcates. The main branches pass backward over the surface of the insula and are hidden by the opercula. These branches lie deep in the Sylvian fissure and deep to the external surface of the brain. The branches loop downward on the undersurface of the inferior parietal operculum and then pass out through the Sylvian fissure to reach the surface of the hemisphere. These

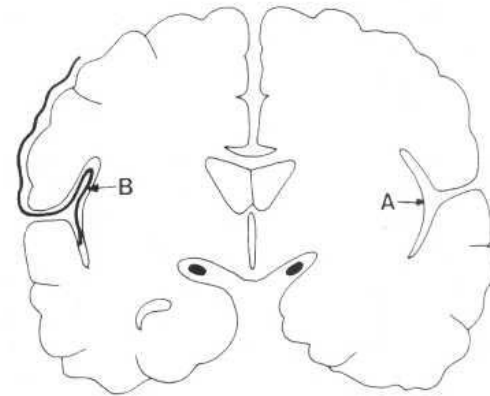


Fig. 55.17 Relationship of the middle cerebral artery and its branches to the insula in a sagittal brain section. (A) Insula. (B) Middle cerebral artery.

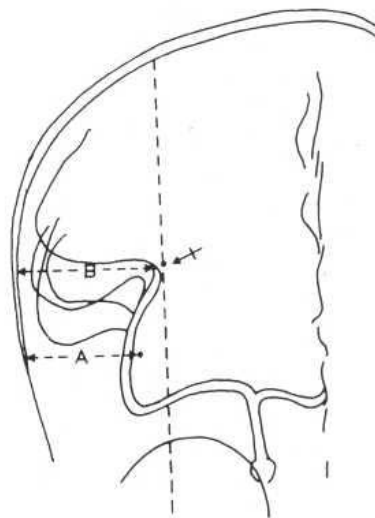


Fig. 55.18 Relationship of middle cerebral vessels to skull vault in the AP projection. Arrow points to the angiographic sylvian point which represents the posterior limit of the insula. Distance A, from the skull vault to the lateral aspect of the insula, varies from 20 to 30 mm. Distance B, from the sylvian point to the skull vault, measures 30-40 mm. (After Taveras 1969.)

downward loops can be identified in the lateral angiograms, and the margins of the triangular insula can thus be defined. The surface of the insula is also identified in the same way on the AP film (Fig. 55.17). The appearance of these vessels and their relationship to the skull vault in the frontal projection were of considerable importance in detecting displacement by tumours and other masses. Taveras refers to the posterior limit of the sylvian triangle as the 'angiographic sylvian point' and shows how this can be identified in the frontal projection. The last artery to emerge from the insula occupies at its medial bend the position of the angiographic sylvian point (Fig. 55.18). The sylvian vessels and sylvian point should appear symmetric on the two sides.

As the branches of the middle cerebral artery emerge from the sylvian fissure they turn, in the case of the anterior branches, upward, and in the case of the posterior branch, backward. The anterior or ascending branches pass upward in the prerolandic areas to supply the lateral surface of the hemisphere in the frontal and parietal regions. These arteries are rather variable and tortuous. The posterior branches are more regular and three major arteries can usually be identified. From above downward these are the *posterior parietal*, *angular* and *posterior temporal arteries*.

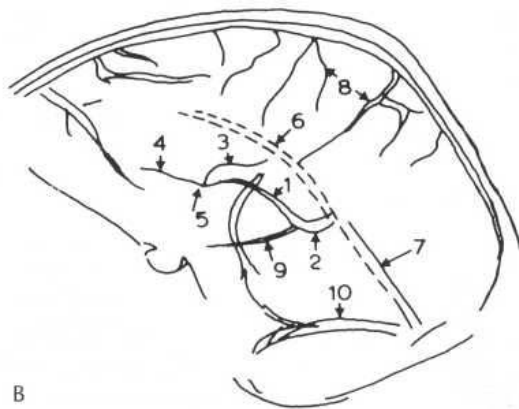
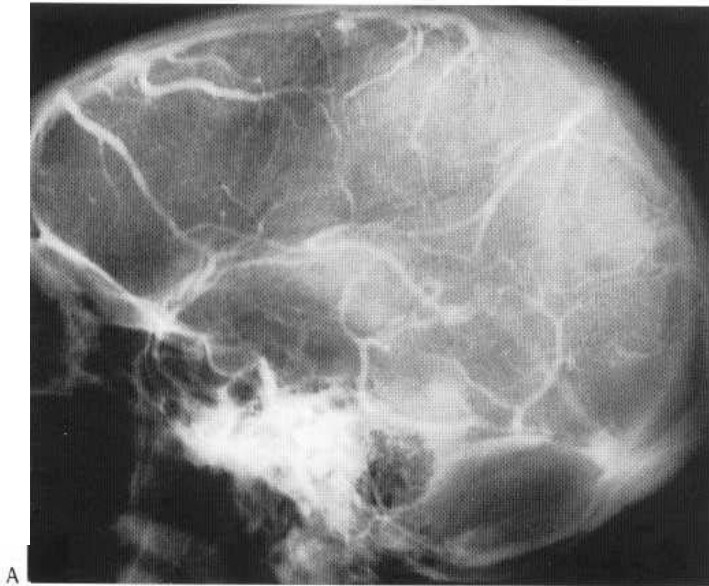


Fig. 55.19 (A) Phlebogram showing superficial and deep veins. (B) Diagram to illustrate (A) 1. Internal cerebral vein; 2. vein of Galen; 3. striothalamic vein; 4. septal vein; 5. venous angle; 6. inferior sagittal sinus; 7. straight sinus; 8. superficial cortical veins; 9. basal vein; 10. lateral sinus.

The branches of the middle cerebral artery supply the whole of the convexity of the hemisphere except a 2.5 cm band near the sagittal fissure, and the occipital lobe.

The cerebral veins

The superficial cerebral veins are very variable in position and distribution. Most of the veins of the hemisphere run upward and backward to end in the superior longitudinal sinus (Figs 55.8, 55.19). They usually enter the sinus against the direction of the blood flow, which is from before backward. Two large veins are named by the anatomists. The first, the *vein of Trolard*, is a large vein which passes upward and backward over the hemisphere to enter the superior sagittal sinus in the parietal region. The second is the *vein of Labbe*. This large vein passes horizontally across the temporal region to enter the lateral sinus. In most angiograms one or other of these veins can be recognised but it is unusual for both veins to be present in the same angiogram (Fig. 55.8). The smaller middle cerebral veins run forward in the sylvian fissure and then to the spheroidal ridge to end in the sphenoparietal sinus, which drains to the cavernous sinus.

The deep cerebral veins fill slightly later than the superficial veins just described. They are of considerable importance in angiographic diagnosis because their position is much more constant than that of the superficial veins.

The *internal cerebral veins* lie one on each side of the midline. They commence just behind the foramen of Monro and pass backward in the roof of the third ventricle, lying in the tela choroidea. Two smaller veins drain into each internal cerebral vein at its commencement. These are the *septal vein*, which runs on the medial surface of the frontal horn, and the *striothalamic vein*, which runs in the floor of the lateral ventricle to reach its lateral wall (Fig. 55.20). In the lateral view the junction of the striothalamic vein with the septal vein forms the origin of the internal cerebral vein and is known as the 'venous angle'. This provides, in most cases, a recognisable landmark, as it normally lies just behind the foramen of Monro; however, the anatomy is not constant and in some cases the striothalamic vein may enter the internal cerebral vein more posteriorly. At its posterior end the internal cerebral vein unites with its fellow on the opposite side and enters the *vein of Galen*. This is constant in position and is easily identified. Just proximal to the vein of Galen other small tributary veins may enter the internal cerebral veins. The *auricular vein* drains the area of the trigone. The *basal vein* arises anteriorly above the sella and passes round the midbrain to enter the back end of the internal cerebral vein. Less commonly, it drains directly into the vein of Galen.

Ventricular size can be assessed in the lateral view, as the septal, striothalamic and auricular veins all commence in the walls of the ventricles. Thus the shape of the ventricle can be roughly outlined by drawing in a line around the origins of these vessels. These small veins drain the subependymal veins of the cerebral white matter. Normally the latter are very tiny and are rarely recognisable in a routine angiogram. In certain pathological conditions, however, these veins may become hypertrophied. Thus, with highly malignant cerebral gliomas where there is rapid arteriovenous shunting through large tumour vessels, and with angiotomatous malformations, the subependymal veins may be quite large and readily visible.

The *vein of Galen* is a short thick vein which curves upward and backward behind the splenium of the corpus callosum. Here it joins

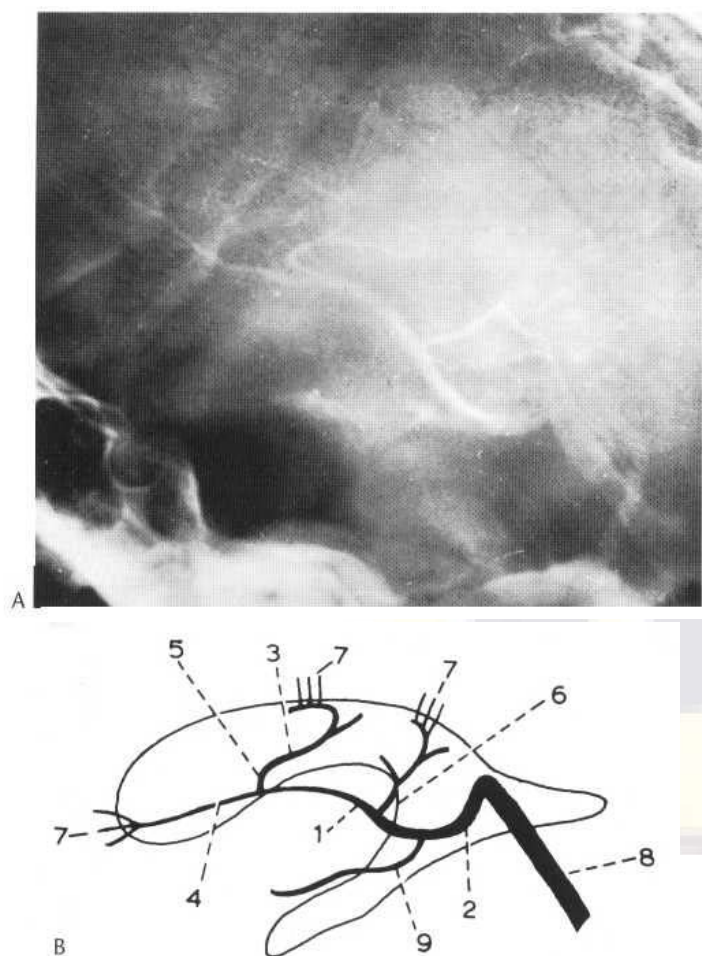


Fig. 55.20 (A) Deep veins shown at late phlebography. **(B)** Diagram of late phlebogram (lateral view) showing relationship to the ventricle. 1. Internal cerebral vein; 2. vein of Galen; 3. striothalamic vein; 4. vein of the septum pellucidum; 5. venous angle; 6. atrial vein; 7. subependymal veins; 8. straight sinus; 9. basal vein.

the inferior sagittal sinus to form the straight sinus which passes downward in the apex of the tentorium to the torcular herophili (Fig. 55.20). The straight sinus usually drains into the left lateral sinus, while the right lateral sinus usually drains the superior sagittal sinus.

The normal external carotid angiogram

The detailed angiographic anatomy of the smaller branches of the external carotid artery is described in great detail in the excellent monograph of Djindjian and Merland (1978). The named major branches of the external carotid artery may be listed as follows (Fig. 55.21):

1. Superior thyroid artery
2. Lingual artery
3. Facial artery
4. Ascending pharyngeal artery
5. Occipital artery
6. Posterior auricular artery
7. Internal maxillary artery
8. Superficial temporal artery.

The first three branches arise from the anteromedial aspect of the proximal segment of the artery. The upper or lower of these two, or

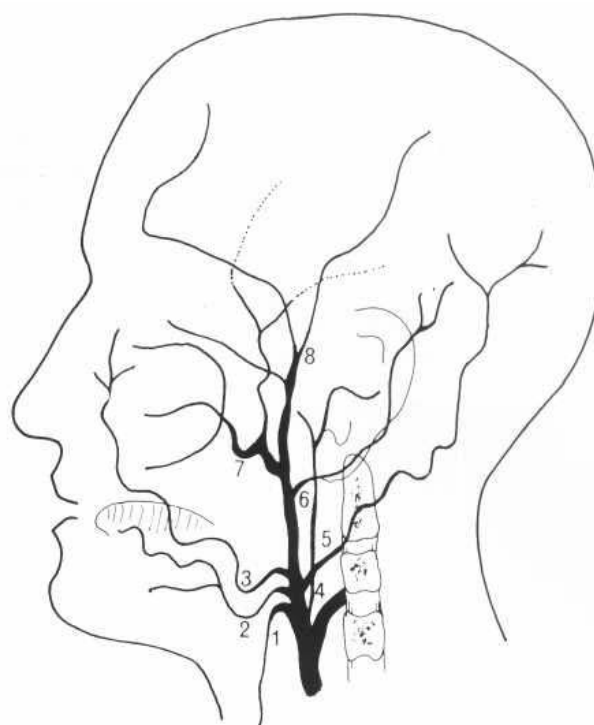


Fig. 55.21 External carotid artery branches. 1. Superior thyroid artery; 2. lingual artery; 3. facial artery; 4. ascending pharyngeal artery; 5. occipital artery; 6. posterior auricular artery; 7. internal maxillary artery; 8. superficial temporal artery.

occasionally all three arteries, may arise in common, as may the ascending pharyngeal and occipital arteries, which arise from the posterolateral aspect of the external carotid. In about 15% of cases the superior thyroid arises from the common carotid near its bifurcation, and rarely the occipital or ascending pharyngeal, or both, may arise from the internal carotid.

The posterior auricular artery is a small branch which arises just before the main terminal branches, the superficial temporal and internal maxillary. The large internal maxillary artery gives rise to the important middle meningeal artery as well as supplying the nasal fossa, palate, mandible and infraorbital region.

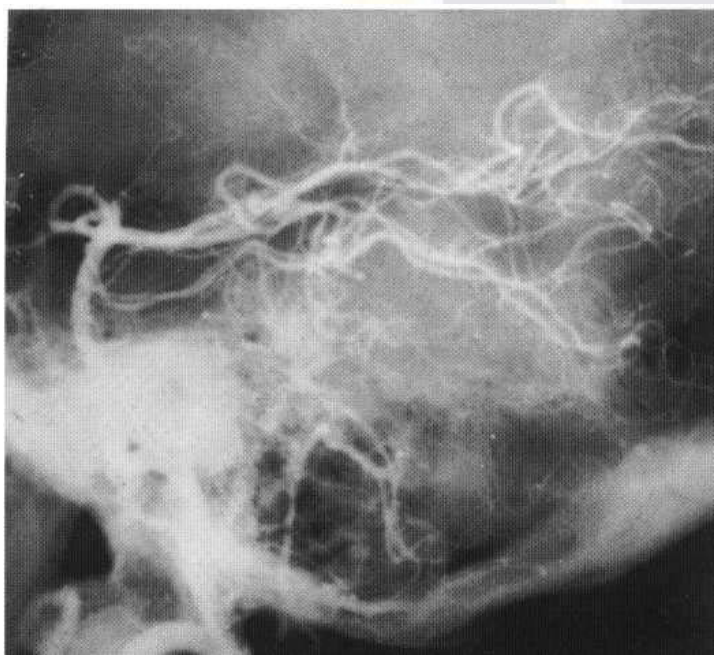
The external carotid artery normally arises at the level of the C3 vertebra from the bifurcation of the internal carotid artery. Selective injection of the external carotid has been practised in the past for the better demonstration of intracranial tumours (such as meningiomas) deriving most of their blood supply from the middle meningeal artery. It was also useful for demonstrating the contribution of the external carotid artery to the blood supply of other intracranial tumours, such as acoustic neurinomas and glomus jugulare tumours, and for the demonstration of dural arteriovenous fistulas supplied mainly or entirely by the external carotid artery.

With the greater use of embolisation techniques for the treatment of tumours and angiomatous malformations, superselective angiography of the external carotid artery is being increasingly practised. The technique has been used for the demonstration and embolisation of angiomatous malformations of the face, lips and tongue. It has also been used in the investigation and treatment of tumours. These include meningiomas, glomus jugulare tumours and nasopharyngeal angiofibromas. Another indication is the demonstration and treatment of dural arteriovenous fistula.

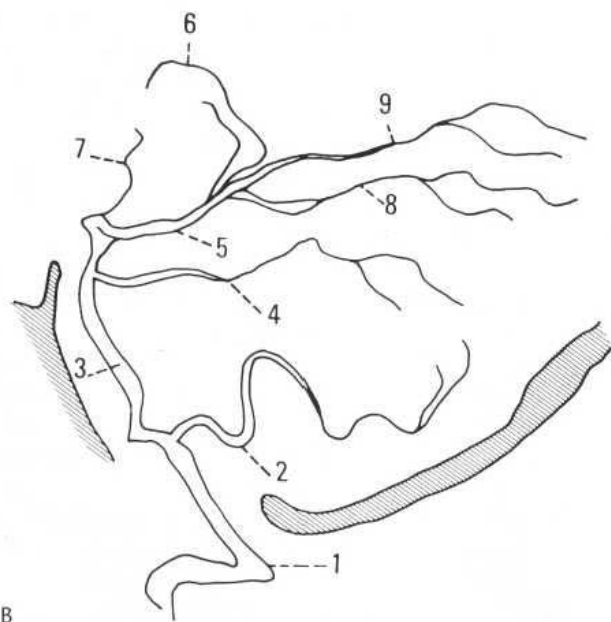
The normal vertebral angiogram

The vertebral artery arises from the subclavian artery at the root of the neck. It passes backward to enter the transverse process of C6. Occasionally it may enter a transverse process at a higher level. In its cervical course the vertebral artery gives off muscular branches that supply the paraspinous muscles. It also gives rise to tiny spinal or radicular branches.

The muscular branches anastomose with branches of the occipital artery and with the ascending pharyngeal artery. These anastomoses assume some importance in cases of carotid occlusion or stenosis of the vertebral origins and in embolisation procedures.



A



B

Fig. 55.22 (A) Normal vertebral arteriogram-lateral view. (B) Diagram to illustrate (A). 1. Vertebral artery; 2. posterior inferior cerebellar artery; 3. basilar artery; 4. superior cerebellar arteries; 5. posterior cerebellar artery; 6. posterior choroidal arteries; 7. thalamoperforate arteries; 8. posterior temporal artery; 9. internal occipital artery.

The spinal branches are tiny and are rarely recognised on routine angiograms. They supply the meninges and may anastomose with the anterior and posterior spinal arteries which supply the cord.

The normal vertebrobasilar intracranial circulation is illustrated in Figures 55.22 and 55.23. The termination of the vertebral artery in its intracranial portion gives rise to several important vessels. These are the posterior inferior cerebellar artery, the anterior and posterior spinal arteries, and small anterior and posterior meningeal arteries.

The *anterior* and *posterior spinal arteries* are tiny and difficult to identify, although the anterior spinal artery is usually visible in a good-quality vertebral arteriogram. It is seen passing downward into the spinal canal as a very fine vessel directly anterior to the cord. Like most small vessels in the posterior fossa, it is best identified in good subtraction films.

The *posterior meningeal artery*, when identified, is seen as a near midline vessel passing upward and just anterior to the occipital bone in the lateral view.

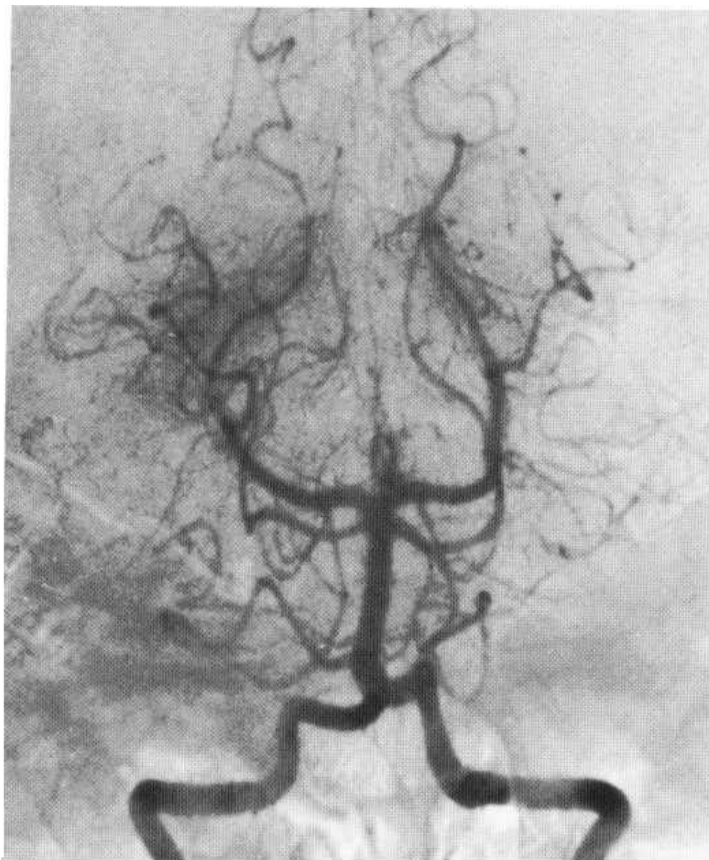
The *posterior inferior cerebellar artery* usually arises from the terminal segment of the vertebral artery. With selective catheter vertebral angiography it is usually possible to fill by reflux the termination of the contralateral vertebral artery. Thus both posterior inferior cerebellar arteries can be shown from the injection of a single vertebral artery (Fig. 55.23). The normal anatomy of the posterior inferior cerebellar artery is illustrated in Figures 55.24 and 55.25. This vessel was of considerable importance in angiographic diagnosis in the posterior fossa. There is a wide variation in its course and distribution but a fairly typical pattern is followed in most cases. The point of origin of the artery may be from the vertebral artery below the foramen magnum or as high as the junction of vertebral and basilar arteries. Sometimes it arises from the basilar or in common with the anterior inferior cerebellar artery. Normally it arises from the vertebral artery just above the foramen magnum.

The first part of the artery, as seen in lateral view, loops round the medulla and then downward to curve round the lower margin of the tonsil. It then passes up anterior and medial to the tonsil to reach the roof of the fourth ventricle in the region of the inferior medullary velum. The downward loop just described usually marks the lower limit of the tonsil and has therefore been used as an index of tonsillar herniation. However, this sign should be treated with caution since the loop may reach below the foramen magnum in normal patients as an anomaly. In these latter cases the loop tends to be narrower with a 'hairpin' appearance.

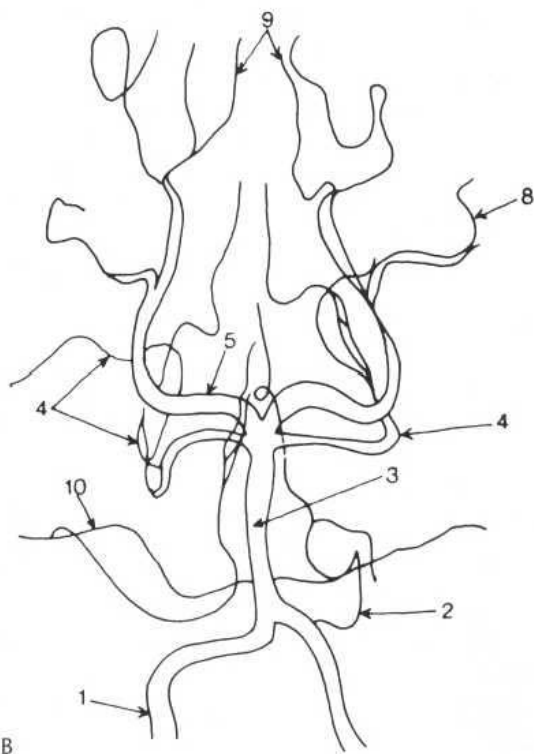
Just below the apex of the fourth ventricle the posterior inferior cerebellar artery, as seen in lateral view, loops slightly backward again before dividing into its major branches. This important landmark is known as the 'choroidal loop', as it supplies choroidal branches to the fourth ventricle and marks out the inferior roof of the fourth ventricle.

The *vermis branch*, which lies near the midline, forms a flat loop convex downward with a local exaggeration in the region of the pyramid. Its terminal portion curves round the tuber in the posterior cerebellar notch. Normally the vermis branch, as seen in the axial view, does not cross the midline; displacement across the midline can be regarded as evidence of a mass on the ipsilateral side of the posterior fossa.

The other major branch of the posterior inferior cerebellar artery is the *tonsillohemispheric*. This arises at the same point as the vermis branch but runs farther downward in lateral view along the posterior margin of the tonsil. It gives off anterior or tonsillar branches and posterior or hemispheric branches which curve down and back around the under aspect of the cerebellar hemisphere.



A



B

Fig. 55.23 (A) Vertebral arteriogram-AP view (subtraction print). (B) Diagram to illustrate (A). 1. Vertebral artery; 2. posterior inferior cerebellar artery (PICA); 3. basilar artery; 4. superior cerebellar artery; 5. posterior cerebral artery; 8. posterior temporal artery; 9. internal occipital artery; 10. anterior inferior cerebellar artery (AICA). The right PICA arises from the right AICA in this case.

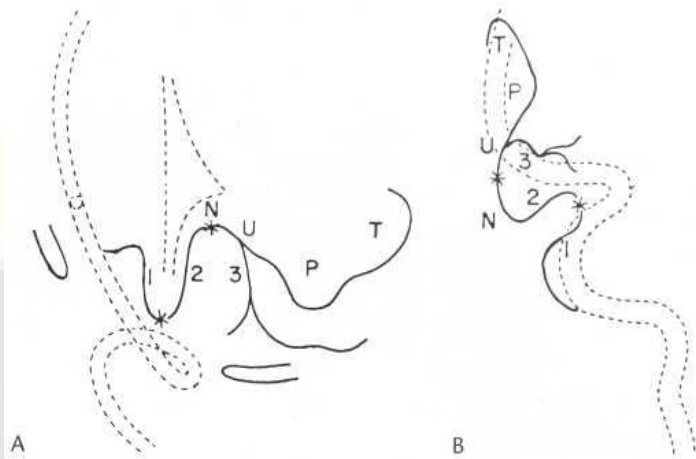


Fig. 55.24 Posterior inferior cerebellar artery. (A) Lateral view. Asterisks mark the apices of the caudal and cranial loops. The apex of the cranial loop is closely related to the nodulus (N) and roof of the fourth ventricle (dotted). The upper or vermis branch runs near the midline around the inferior vermis (including uvula-U, pyramid-P, tuber-T). The lower or tonsillohemispheric branch runs near the posterior margin of the tonsil giving off anterior or tonsillar branches and posterior or hemispheric branches. The tonsil lies between 2 and 3. (B) Anteroposterior view, in half-axial projection. The segments marked in the lateral view are identified by the same numbers and letters. Segment 3 (the tonsillohemispheric branch) may be difficult to identify in this view. The apex of the cranial loop (*N) lies usually within 2 mm of the midline and the terminal portion of the artery (T) returns to the midline. (Reproduced from Wolf, B.S., et al (1962) *American journal of Roentgenology*, 87, 322-337).

The appearance just described and illustrated can be regarded as the standard configuration of the posterior inferior cerebellar artery, but it should be appreciated that there are many variations from this standard pattern.

The basilar artery is formed by the junction of the two vertebral arteries just above the foramen magnum. It passes upward directly behind the clivus in the lateral view and it terminates behind or just above the tip of the dorsum sellae. In the anterior or Towne's projection the basilar artery lies in the midline. However, displacement from the midline, or lateral kinking, is quite common in the middle-aged and elderly, particularly in hypertensive patients, and such kinking does not necessarily imply displacement by a mass. In elderly and hypertensive patients the basilar artery may also be elongated and kinked, as seen in lateral view. Sometimes it terminates well above the dorsum sellae and these cases of a high basilar termination may cause an indent in the floor of the third ventricle. Lateral kinking of the basilar artery may also be seen in young patients. In these patients the kinking is always to the side away from a large dominant vertebral artery, and has no pathological significance.

The basilar artery has numerous small branches which supply the pons and are difficult or impossible to visualise in an angiogram. There are, however, larger branches which can be recognised in many cases. These include the paired anterior inferior cerebellar arteries. These two vessels usually arise within a centimetre of the origin of the basilar artery (Fig. 55.23). In lateral view they are obscured by the mastoids and petrous hones, and are best identified in the Towne's view or in the direct anteroposterior view. Subtraction films will usually show them well, and clear of overlying bone. They extend directly laterally to a 'floccular loop', and supply branches to the internal auditory meatus and also to the inferior surface of the cerebellum. Here they anastomose with branches of the posterior inferior cerebellar artery.

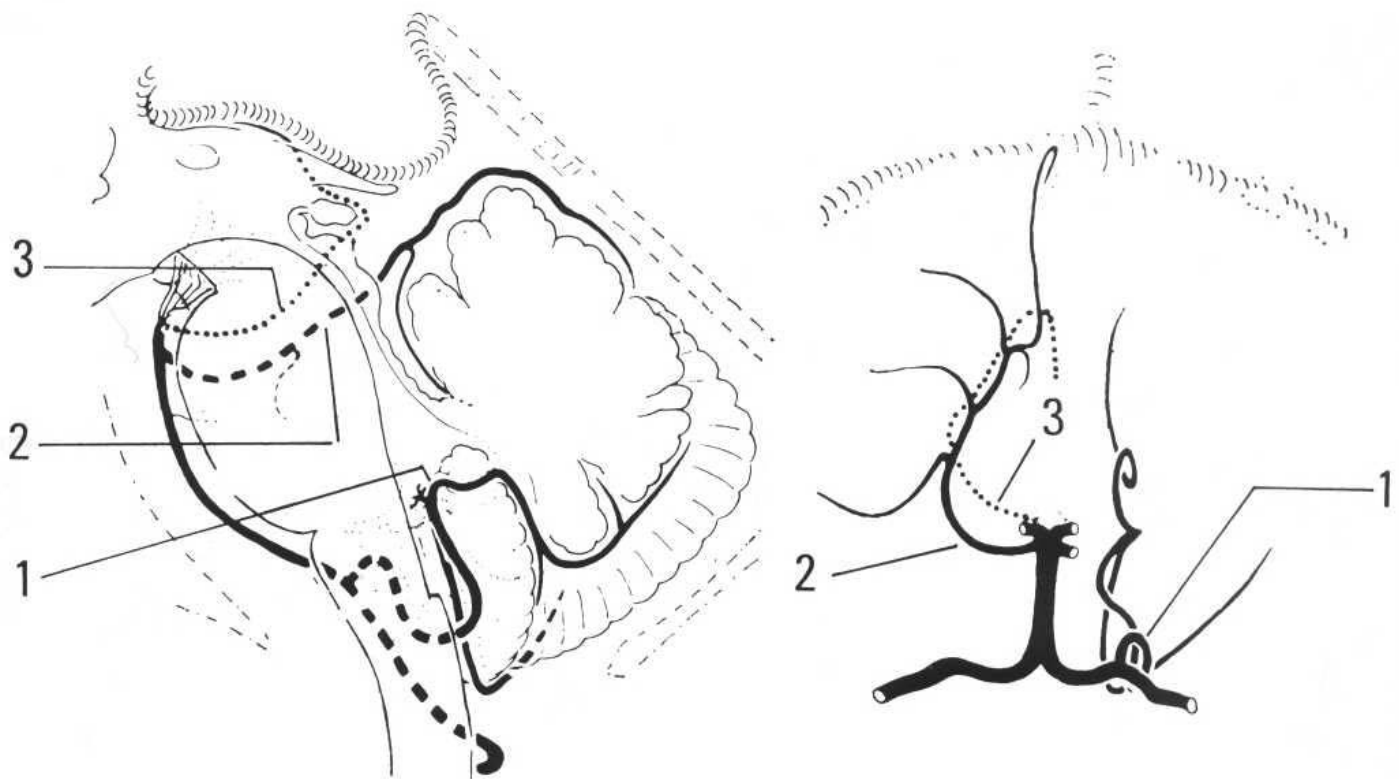


Fig. 55.25 Relationship of normal arteries in the posterior fossa to the brainstem. 1. Posterior inferior cerebellar artery; 2. superior cerebellar artery; 3. medial posterior choroidal artery. (After Huang & Wolf 1970.)

The *superior cerebellar arteries* arise just before the termination of the basilar artery. These paired arteries curve round the midbrain to reach the superior surface of the cerebellum, where they divided into several branches. In a lateral film they lie below the posterior cerebral arteries and are seen to pass over the surface of the cerebellum. In this view they are partially superimposed on the posterior temporal branch of the posterior cerebral artery, as this lies on the other side of the slanting tentorium,

The *posterior cerebral arteries* are the terminal branches of the basilar artery. Both posterior cerebral arteries fill readily through the basilar in nearly 90% of cases. In most of the remaining cases only one posterior cerebral artery fills well. Very rarely neither posterior cerebral artery is filled. In these latter cases there is a dominant supply from the carotid artery through large posterior communicating arteries. The posterior cerebral arteries curve around the cerebral peduncles to reach the dorsal aspect of midbrain. Here they pass through the tentorium to reach the undersurface of the temporal lobes. Each posterior cerebral has two main branches, a *posterior temporal*, which supplies the undersurface of the posterior part of the temporal lobe, and an *internal occipital* branch, which passes to the medial aspect of the occipital lobe. This divides into terminal branches named the *calcarine* and *parieto-occipital arteries*.

The *thalamoperforating arteries* arise from the proximal segment of the posterior cerebral artery and lie close to the midline. They are easily seen in the lateral view, where they appear to be 1-3 in number and show as fine vertical vessels passing up into the thalamus. They are difficult or impossible to define in the AP view.

Posterior choroidal arteries Each posterior cerebral artery gives off a *medial* posterior choroidal artery and also two or more *lateral* posterior choroidal arteries. The medial posterior choroidal artery arises first, just lateral to the bifurcation of the basilar

artery. It passes round the midbrain together with, and usually obscured by, the posterior cerebral artery (Fig. 55.25).

In the capillary phase the choroidal plexus is outlined as a well-defined blush of contrast. This is a normal appearance and should not be mistaken for a pathological circulation.

A small *splenium branch* of the posterior cerebral artery also supplies the pial plexus on and behind the splenium of the corpus callosum, which may thus be outlined on the vertebral angiogram.

The *posterior communicating artery* is occasionally outlined, but it is unusual to see good antegrade filling of the carotid system from the posterior communicating artery in a normal patient. However, the phenomenon can be demonstrated in certain pathological conditions. In one case we have demonstrated filling of the whole of the cerebral circulation from the vertebrobasilar system in a patient with bilateral internal carotid thromboses. Retrograde filling has also been demonstrated following compression of the carotids in the neck and simultaneous injection of the vertebral artery.

The veins of the posterior fossa

The **precentral cerebellar vein** is small but easy to recognise in the lateral phlebogram (Fig. 55.26). It passes in the midline over the superior surface of the cerebellum and lies dorsal to the midbrain. If the aqueduct and fourth ventricle are pressed backward the precentral cerebellar vein will be pressed backward with them. A mass in the upper vermin will displace the vein forward and upward. A mass in the pineal region will press the precentral cerebellar vein downward. The precentral cerebellar vein drains into the great vein of Galen at its posterior end, where it joins the straight sinus. In the frontal view the vein is difficult to recognise because of the other larger overlying midline veins. Occasionally its origin can be seen in the AP view as an inverted 'Y' draining up from the fourth ventricle.

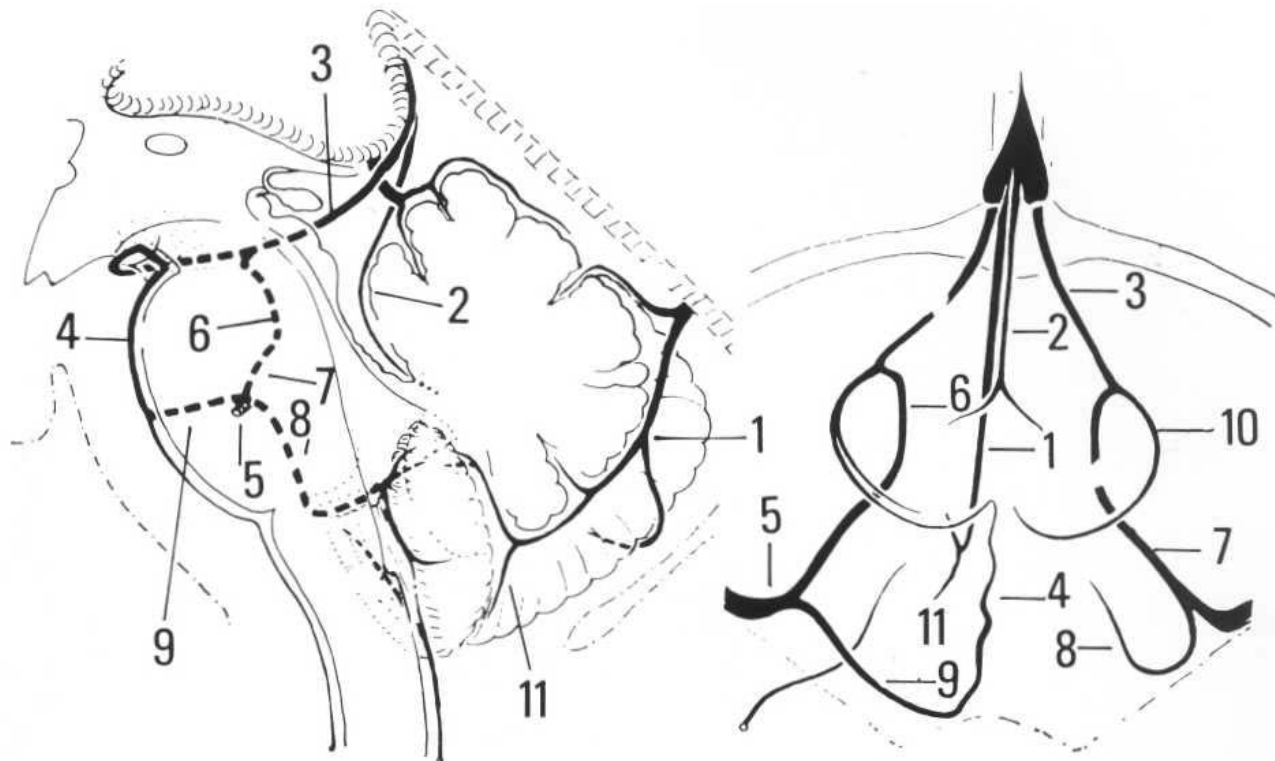


Fig. 55.26 Normal veins of the posterior fossa and their relationship to the normal structures. 1. inferior vermian vein; 2. precentral cerebellar vein; 3. posterior mesencephalic vein; 4. anterior pontomesencephalic vein; 5. petrosal vein; 6. lateral mesencephalic vein; 7. brachial vein; 8. vein of the lateral recess of fourth ventricle; 9. transverse pontine vein; 10. peduncular vein; 11. retrotonsillar veins. (After Huang & Wolf 1970.)

The *anterior pontomesencephalic vein* runs on the anterior surface of the pons, where it forms an irregular concave curve. It marks out the posterior wall of the pontine cistern and the anterior surface of the pons. Below, it communicates with the right and left petrosal vein. Above, it drains into the *posterior mesencephalic vein*. The latter is superimposed on the basal vein in lateral view and may drain into it.

The *lateral mesencephalic vein* also communicates with the posterior mesencephalic or basal vein. It passes downward and forward at an angle of about 80° in the lateral view and connects with the superior petrosal sinus, via the brachial and petrosal veins.

The *superior vermian vein* passes along the superior vermis to terminate in the great vein of Galen near the termination of the precentral cerebellar vein. It may join the precentral vein, or the basal vein, or be continuous with the inferior vermian vein. Again it is difficult to identify in the anterior view, although easily seen in the lateral view.

The paired **inferior vermian veins** lie near the midline. Both commence with a superior and inferior retrotonsillar vein outlining the back of the tonsil and drain up the inferior vermis. They usually end in the straight sinus but can join the superior vermian vein. In lateral view they are easily recognised as they lie as much as 1 cm from the occipital bone and mark the anterior margin of the cisterna magna.

The *petrosal vein* lies just above and lateral to the internal auditory meatus. It is fed by the brachial vein and drains into the superior petrosal sinus. It is best seen in the Towne's view and was of considerable importance in the assessment of angle tumours, as acoustic neurinomas or other angle tumours usually elevate or obliterate the petrosal vein.

The *brachial vein* drains into the petrosal vein and is best seen in the Towne's view where it lies at an angle of 45° to the midline. The lateral mesencephalic vein may connect it with the posterior mesencephalic vein.

The normal arch and great vessels and some anomalies

The normal aortic arch and great vessels are illustrated in Figure 55.27A. This arrangement is present in the majority of people but anomalies are seen in about a quarter of the population. In our own angiographic material the variation that was seen most often was a common origin for the innominate and the left common carotid artery (Fig. 55.27B). Obvious cases are recognised readily but it is sometimes difficult, or even impossible, to distinguish minor degrees, even in the oblique position, because of overlapping of vessels. About 20% of our white patients had this anomaly, but it appears to be even more common among blacks, being present in 36% of reported autopsies.

The remaining anomalies show a fairly constant incidence and are also of importance. Thus the left vertebral arises from the aortic arch in 5% of patients, so its origin can only be seen in these cases by arch aortography and not by subclavian catheterisation (Fig. 55.27D). An aberrant right subclavian artery is present in 1-2% of patients. This is also important because it may be a cause for right transaxillary catheterisation failing to enter the ascending aorta (Fig. 55.27E). In a few of these cases the right and left common carotid arteries arise from the aorta by a common trunk (truncus bicaroticus).

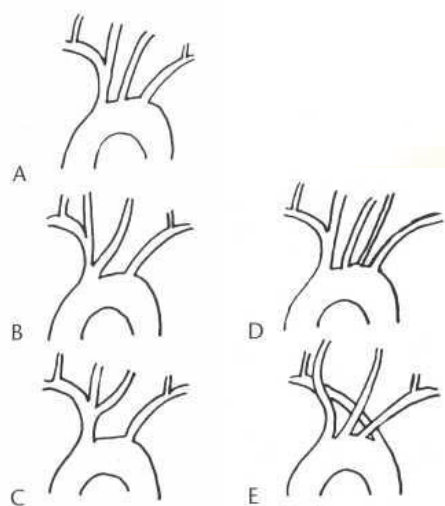


Fig. 55.27 Anomalies of the aortic arch branches. (A) Normal. (B) Joint origin of innominate and left common carotid. (C) Left common carotid arises from innominate. (D) Left vertebral arises from arch. (E) Anomalous right subclavian. (From Sutton, D., Davies, E.R. (1966) *Clinical Radiology*, 17, 330-345.)

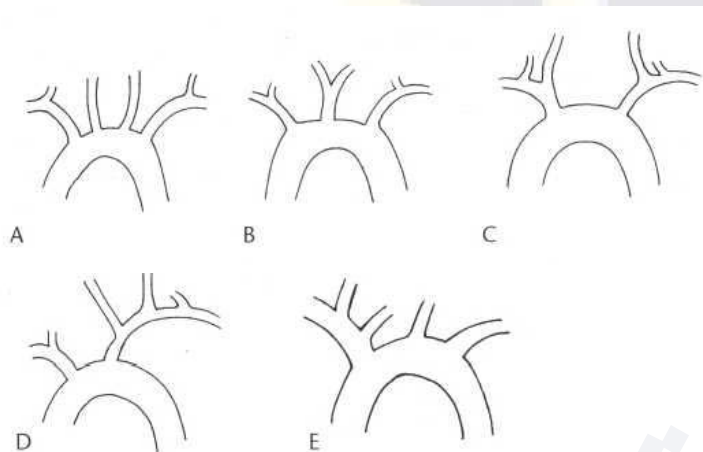


Fig. 55.28 Some rare anomalies of the great vessels (see text).

Apart from the commoner anomalies illustrated in Figure 56.27, many other rarer anomalies have been described. These include (Fig. 55.28):

1. Origin of all four great vessels independently from the arch (A)
2. Both common carotids arise together (truncus bicaroticus) between the right and left subclavians (B)
3. Origin of the left common carotid from the left subclavian (C)
4. Origin of both common carotids from the left subclavian (D)
5. The left vertebral arises from the arch, and the left common carotid from the innominate (a variant of anomalous left vertebral from the arch already described) (E).

Other congenital anomalies

Congenital anomalies of the intracranial circulation are relatively uncommon, with the exception of anomalies of the circle of Willis (Fig. 55.29). The first part of the *anterior cerebral artery* may be small or hypoplastic on one side. In these cases both anterior cerebral arteries fill from the other side with the aid of the anterior communicating artery.

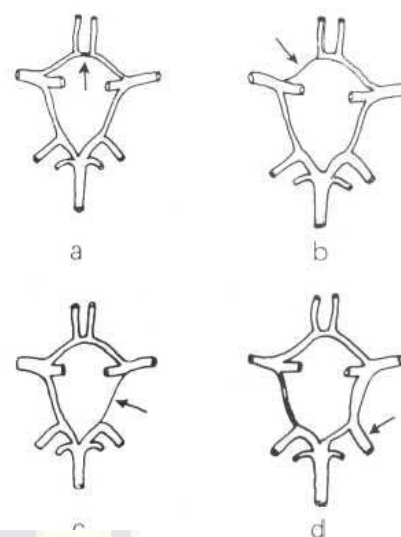


Fig. 55.29 Anomalies of the circle of Willis. The posterior communicating artery is most frequently involved and combined lesions are common. (a) Hypoplastic anterior communicating (3%); (b) hypoplastic proximal segment of anterior cerebral (2%); (c) hypoplastic posterior communicating (22%); (d) carotid origin of posterior cerebral (15%). (After Alpers et al 1959.)

The *posterior communicating artery* may also be small or hypoplastic. Such anomalies of the circle of Willis can be very important when stenosis or obstruction of a major extracranial vessel occurs, as it normally provides a collateral circulation.

Congenital hypoplasia of the *intracranial part of the internal carotid arteries* has been described and in such cases a collateral circulation may develop from the primitive vascular 'rete' or network present in the embryo at the base of the skull.

Congenital anomalies of the brain such as agenesis of the corpus callosum may also be associated with arterial anomalies. In this condition the anterior cerebral arteries may be represented by a large common trunk in the midline, or two arteries may be present. In either case the anterior cerebral artery pursues an abnormal course. It passes more vertically upward, and as there is no corpus callosum the pericallosal branch is abnormal in course and situation. The common trunk anterior cerebral artery (*azvgos anterior cerebral artery*) may also be seen as an isolated anomaly. The common carotid artery usually bifurcates at the level of C3 or C4 just below the angle of the jaw. In some 15% of cases, however, it may bifurcate at lower levels, although rarely below the C6-7 disc space. In about 2% of cases the bifurcation lies at or about the C2 level.

Anomalies of the internal and external carotid arteries are less common, but are recorded. They include:

1. External carotid artery:
 - a. Absence of the external carotid with its territory supplied by collaterals
 - b. Branches of the external carotid arising from the internal carotid
 - c. Lateral position of the external carotid instead of normal medial position relative to the internal carotid at its origin.
2. Internal carotid artery:
 - a. Aplasia of the internal carotid artery
 - b. Hypoplasia of the internal carotid artery

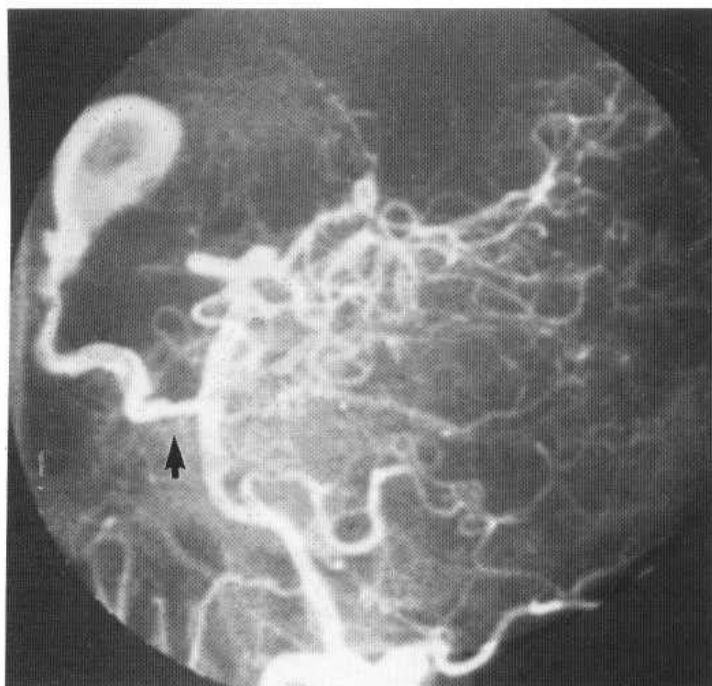


Fig. 55.32 Acoustic artery (arrow) connecting basilar artery to internal carotid. This had been ligated in the neck for an aneurysm arising from its suprasellar segment. A vertebral arteriogram shows it still filling from the basilar (intra-arterial DSA study).

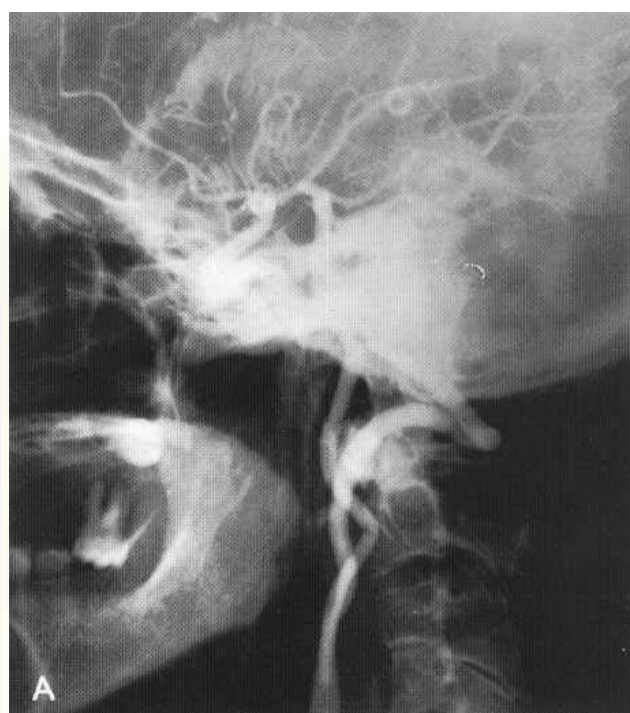


Fig. 55.34 Origin of the vertebral artery from the carotid in the neck. This is an example of the proatlantal intersegmental artery. Lateral view.

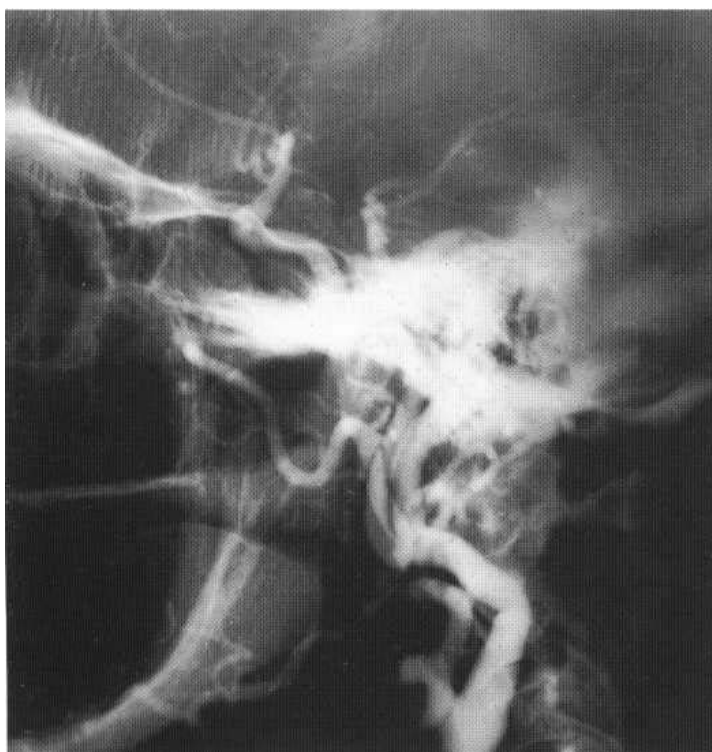


Fig. 55.33 Hypoglossal artery connecting carotid and basilar arteries. Lateral view.

Anomalous middle meningeal artery: the middle meningeal artery or its anterior branch may occasionally arise from the ophthalmic artery. The converse, an ophthalmic artery arising from the middle meningeal, may also occur. Although very rare, the anomaly is of considerable importance, as embolisation of the maxillary or

other branches of the external carotid may involve it, with resulting unilateral blindness.

Equally rare is a middle meningeal artery arising from the stapedial artery. This is an anomalous branch of the petrous segment of the internal carotid which passes through the middle ear and t(amen).

DEMONSTRATION OF PRIMARY VASCULAR LESIONS

Vascular lesions will be considered under the following headings:

1. Aneurysm
2. Angiomatous malformation
3. Arteriovenous fistula
4. Intracerebral haematoma
5. Embolus
6. Vascular stenosis and thrombosis.

In this chapter we are concerned with the findings and appearances at angiography. However, these lesions are also considered in some detail in Chapter 58, where the emphasis is mainly on the findings at scanning by CT or MR.

1. Aneurysm

Most intracranial aneurysms are berry aneurysms. Fusiform aneurysms and vascular ectasias can also occur, as can dissecting aneurysms (Fig. 55.35).

Aneurysms may present clinically in three different ways. By far the commonest mode of presentation, and that seen in over 90% of the cases encountered, is by *subarachnoid haemorrhage*. The second mode of presentation is by pressure upon cranial nerves,



Fig. 55.35 Vertebral arteriogram showing dissecting aneurysm of a posterior inferior cerebellar artery (MR study).

Box 55.1 Causes of subarachnoid haemorrhage

- A Trauma
- B Spontaneous
 1. Aneurysm
 2. Angioma
 3. Atheroma
 4. Tumour
 5. Blood dyscrasia or anticoagulants

particularly around the circle of Willis and lateral to the cavernous sinus and giving rise to *oculomotor pareses*. The third cranial nerve is the one most commonly involved. Third, in a few cases, the aneurysm may reach a very large size and *simulate an intracranial tumour*. Symptomless aneurysms are occasionally encountered as unexpected findings at cerebral CT or MRI.

Subarachnoid haemorrhage (SAH) (Box 55.1)

This is discussed in detail in Chapter 58.

In the past, suspected cases of SAH were investigated by direct angiography and often required four-vessel studies. Today, the primary investigations of choice are CT or MRI. These will often provide diagnostic evidence by showing blood in the basal cisterns or sulci or an intercerebral haematoma (see Ch. 57), but some cases may be equivocal or negative. In cases where surgery or intervention is being considered, cerebral angiography will be required. Non-invasive angiography by MRI or spiral CT is increasingly favoured but in patients considered likely to benefit from surgery or where non-invasive findings are negative or equivocal, direct angiography is still required by many neurosurgeons. It is also required where endovascular treatment by the radiologist is being considered or undertaken.

Non-invasive angiography The distinction between mildly non-invasive procedures (IV DSA and IV CE spiral CT) and non-invasive methods (MRI and ultrasound) has been explained above, as has the distinction between those with and without radiation hazards. MR angiography and 3D CT angiography have been shown to detect convincingly all aneurysms greater than 2-3 mm in size and some aneurysms smaller than this. The

advantage of being able to prescribe retrospectively an almost unlimited range of projections, free of vascular overlap, can make these forms of angiography preferable to more conventional intra-arterial studies; they may enable the neck of the aneurysm to be shown better (Fig. 55.4) and may also be better at distinguishing aneurysms from vascular loops; these can sometimes pose a diagnostic problem when only a limited number of projections are available. The non- or minimally invasive techniques are the most appropriate to use if screening for intracranial aneurysms is considered useful in high-risk populations (such as patients with polycystic disease of the kidneys) or with patients who have suffered severe sudden headache that could have been due to subarachnoid haemorrhages (thunderclap headache). These non-invasive techniques are also the most appropriate for investigating patients with cranial nerve palsies possibly due to aneurysms (Fig. 55.4). Intra-arterial angiography should no longer be used for these indications, assuming that these non-invasive techniques are available. Finally, an increasing number of patients presenting with subarachnoid haemorrhage or painful IIIrd cranial nerve palsies are now proceeding to surgery on the basis of MR or CT angiography only.

Direct angiography When the brain CT findings localise the source of bleeding, direct angiography may occasionally be limited, if clinically advisable, to a single carotid angiogram or vertebral angiogram, thus saving the patient from the more extensive four-vessel studies. The latter are, however, usually requested by the neurosurgeon, if the patient is considered fit, as aneurysms may be multiple.

Four-vessel studies These required injection of both internal carotids and either both vertebrals, or one vertebral with good reflux down the other, thus demonstrating all relevant intracranial vessels. For the carotid angiogram, lateral, AP and oblique films are usually required; it may also be necessary to take an oblique transorbital view, and occasionally an axial view. The aim is to show the aneurysm clearly and the relationship of its neck to the vessel of origin.

For the vertebral angiogram lateral and Towne's views are required with good subtraction films. A lateral oblique view, to show the origins of the posterior inferior cerebellar arteries clearly, may also be helpful.

Aneurysms are demonstrated in the majority of cases (55%) and angiomas in a significant minority (10%). Only 15-20% of cases are negative after direct angiography. Repeat angiography after 6 weeks is still advocated by some units in angiographically negative cases, and an aneurysm is then recognised a further 2% or so. Follow-up of patients with negative findings indicates that they have a much better prognosis than patients in whom an aneurysm is shown.

Cerebral aneurysms are multiple in between 5 and 15% of cases. Such multiple aneurysms can be well shown by MR (Fig. 55.36). In such cases the clinical features or CT scan may help to decide the source of the haemorrhage, or local *vascular spasm* may point to the aneurysm responsible. Following a recent bleed, the vessels in the region of the ruptured aneurysm often become spastic and narrowed. Sometimes the spasm is more widespread, involving most of the intracranial arteries. This spasm is readily identified on the arteriograms and is a factor contributing to the clinical symptoms. Other features which may help to identify the bleeding aneurysm, when multiple aneurysms are present, are the size of the

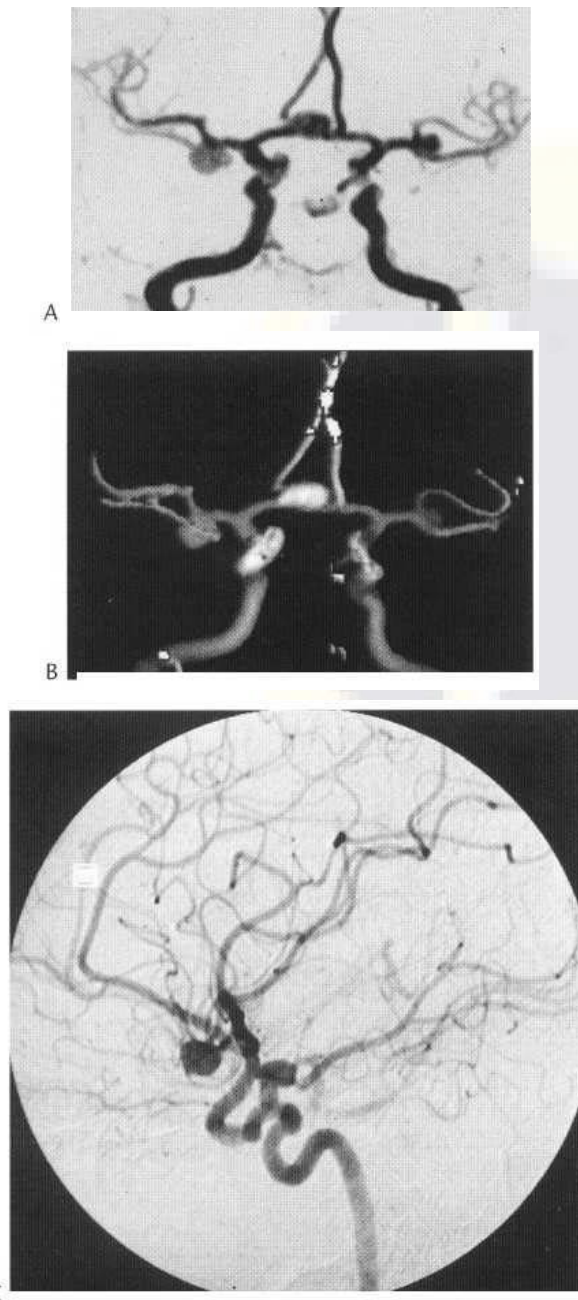


Fig. 55.36 Multiple [aneurysms](#). MR angiography without contrast injection. (A) MIP projection (contrast reversal); (B) a 3D shaded surface display; (C) direct left carotid angiogram shows anterior communicating aneurysm and posterior communicating aneurysm.

aneurysm and the presence of local haematoma. In the majority of cases it is the largest aneurysm which bleeds.

Ruptured aneurysms may haemorrhage into the brain and produce large intracerebral haematomas (Fig. 55.37). These may act as mass lesions and produce displacement of superficial vessels and even shift of the anterior cerebral artery across the midline. In these cases, and in the absence of a CT scan, the diagnosis of haematoma will be based on the history and the demonstration of a source for the haemorrhage, such as an aneurysm or angioma. CT scanning will of course show an intracerebral haematoma clearly prior to angiography. Such intracranial haematomas may themselves be the cause of symptoms and require surgical treatment by evacuation. Sometimes an anterior communicating aneurysm may

fill from one carotid yet have ruptured into the contralateral frontal lobe.

Natural history Aneurysmal subarachnoid haemorrhage is still a devastating disease: at least 50% of patients reaching hospital die or are left disabled. The cause is rebleeding in about 15% and delayed ischaemic neurological deficit in most of the rest. Exclusion of the aneurysm by operative clip or endovascular techniques reduces but does not eliminate the risk of rebleeding, and medical therapies aim to reduce the risk of ischaemia. Although the risk of rebleeding is still often stated to be 50% in the first 6 months, untreated this undoubtedly is an overestimate. Most rebleeds occur within 24 h and the risk steadily declines, perhaps to about 2% per year, or even less, by around 6 months postictus. The risk of bleeding of unruptured aneurysms, formerly given in about 2% per year, is now known to be less than 0.1%, basilar tip aneurysms having the highest risk (about 0.8% per year).

It is probable that a subarachnoid haemorrhage is a sudden incident lasting only a short time. It is followed by a drop in blood pressure, with sealing off of the point of haemorrhage by clot. It is therefore extremely unlikely that haemorrhage will be shown at angiography by contrast extravasation. However, like other investigators, we have, on isolated occasions, seen evidence that the aneurysm was actually bleeding at the time of injection. It should be emphasised that this is excessively rare and we have only seen it three times in a review of 1000 cases of subarachnoid haemorrhage examined by direct angiography.

Site of aneurysms Aneurysms giving rise to subarachnoid haemorrhage may occur anywhere in the cerebral circulation but they are most frequently around the circle of Willis and in one or two other sites. Thus, in one large series, supratentorial aneurysms occurred most frequently at:

1. The origin of the posterior communicating artery (27%)
2. The junction of anterior communicating and anterior cerebral artery (27%)
3. The bifurcation or trifurcation of the main middle cerebral trunk (20%)
4. The terminal segment of the internal carotid artery (6%).

Aneurysms of the peripheral vessels are relatively uncommon, although occasionally encountered. In the posterior fossa, aneurysms causing subarachnoid haemorrhage and shown by vertebral arteriography have been found, mainly:

1. At the basilar termination
2. At the junction of posterior communicating and posterior cerebral arteries
3. At the origin of the posterior inferior cerebellar artery from the vertebral artery (Fig. 55.35)
4. At the robasilar junction.

They have also been shown at the origin of other smaller vessels from the basilar artery and very rarely on more peripheral vessels.

Aneurysms—with the exception of the large atheromatous aneurysms, to be described later—usually arise at points of bifurcation of cerebral arteries. There is evidence of a defect in the muscle coat at this point and this has given rise to the theory of congenital origin of these lesions. However, there is no doubt that other factors, such as age, atheroma and hypertension, are most important in their aetiology.

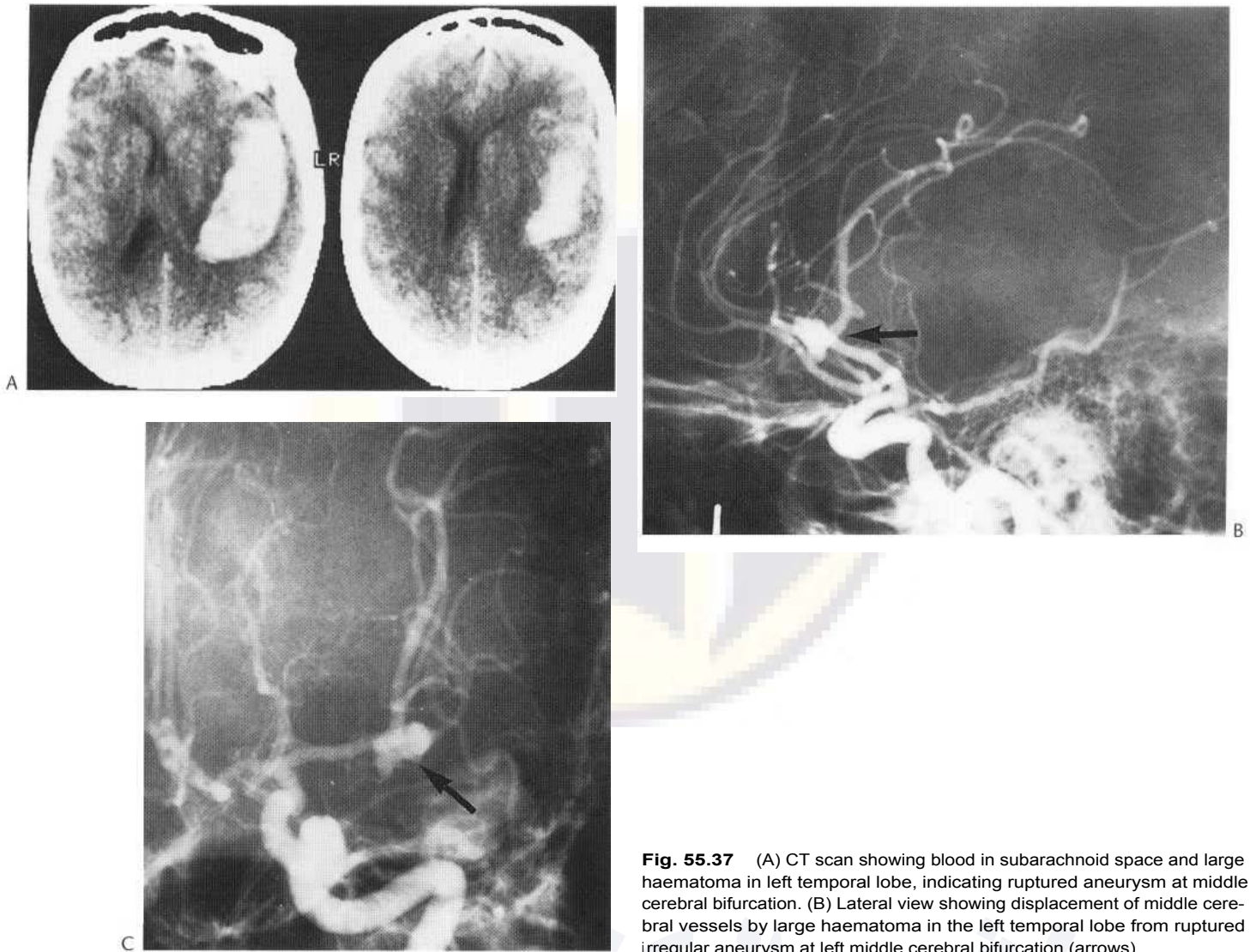


Fig. 55.37 (A) CT scan showing blood in subarachnoid space and large haematoma in left temporal lobe, indicating ruptured aneurysm at middle cerebral bifurcation. (B) Lateral view showing displacement of middle cerebral vessels by large haematoma in the left temporal lobe from ruptured irregular aneurysm at left middle cerebral bifurcation (arrows).

The vast majority of cases present in middle-aged or elderly patients and there is a higher incidence among hypertensives. This probably accounts for the recorded associations with coarctation, polycystic kidneys and fibromuscular hyperplasia.

Subdural haematomas, usually shallow, may also result from ruptured aneurysms and should be carefully looked for when inspecting the angiograms or preliminary axial scan.

Many neurosurgeons, when they consider internal carotid ligation, feel that it is important to have cross-compression angiographic studies in order to determine whether there is free flow across the anterior communicating artery. Such cross-compression studies are made by compressing the carotid on one side while injecting the other. With a freely patent anterior communicating artery, both anterior cerebrals and both middle cerebrals will fill; however, a negative result can be unreliable.

Oculomotor pareses

We have noted above that some cases of aneurysm may present by pressure upon cranial nerves leading to the orbit. The commonest nerve to be involved is the IIIrd nerve, but the IVth, Vth, and Vith nerves can also be affected. These lesions are usually produced by

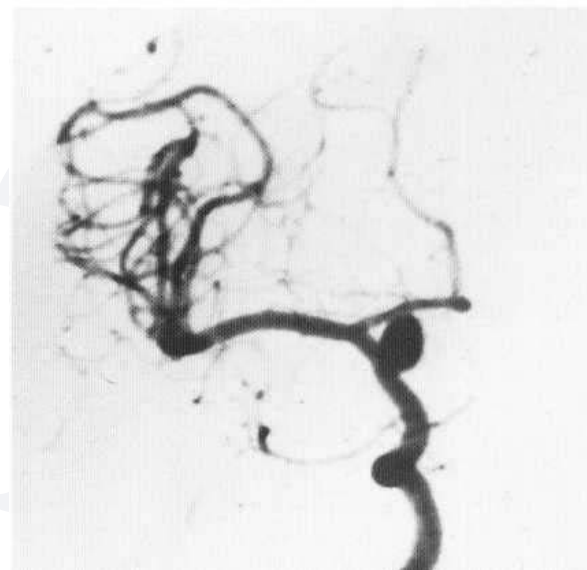


Fig. 55.38 Posterior communicating aneurysm shown in lateral view by arterial DSA study.



Fig. 55.39 Posterior communicating aneurysm shown in lateral view (MR study).

aneurysms lying in the cavernous sinus or arising from the origin of the posterior communicating artery (Figs 55.4, 55.38, 55.39). Intracavernous aneurysms are more common in women and are bilateral in 10% of cases (Figs 55.40, 55.41). Occasionally a suprasellar aneurysm may involve the optic chiasm or an optic nerve. The primary investigation for suspected pressure producing aneurysms are non-invasive (see later).

Aneurysms simulating tumours

Large supratentorial aneurysms presenting clinically as tumours are relatively rare. The true diagnosis may not be suspected before CT or angiography unless marginal calcification is present before CT or MRI, unless calcification is present on simple X-ray.

Large atheromatous aneurysms of the basilar artery are also rare, but when they do occur they may also simulate tumours. Vertebral angiography would demonstrate an aneurysm as a surprise finding in such cases unless a prior CT scan has suggested its presence. Basilar ectasia also due to atheroma can produce a dilated, elongated and kinked basilar artery with similar clinical symptoms. Again, CT or MRI will diagnose these without direct angiography. Occasionally large aneurysms of the internal carotid artery may bulge forward into the orbit. Such aneurysms will erode the sphenoidal fissure and may

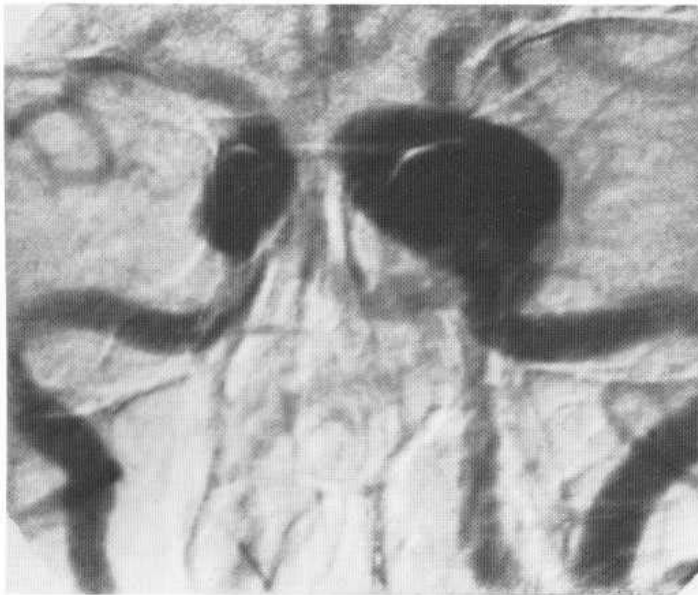


Fig. 55.40 Large left intracavernous aneurysm projecting medially and laterally. There is a smaller right intracavernous aneurysm (intravenous DSA study).

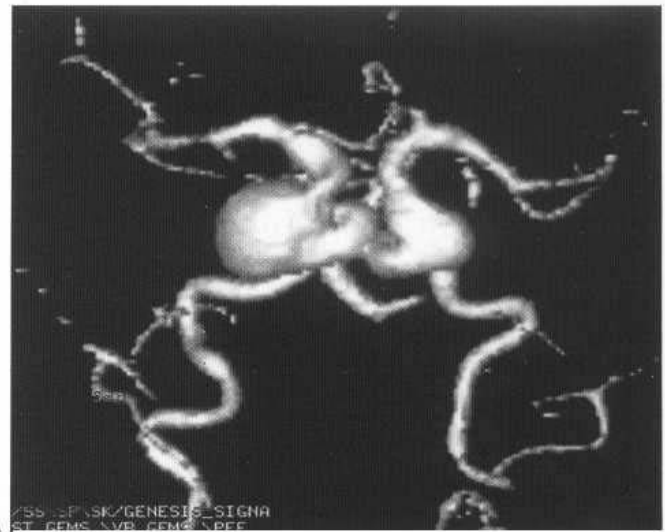


Fig. 55.41 Bilateral intracavernous aneurysms. MR angiography. (A) MIP projection. (B) 3D shaded surface display. This study was made after intravenous contrast injection: contrast-enhanced 3D MR angiography.

even produce proptosis. In these cases differential diagnosis at simple X-ray is from a secondary deposit or the rare erosive type of meningioma. However, the erosion produced by an aneurysm is fairly characteristic, and usually involves the lateral margin of the optic foramen or anterior clinoid and jugum (Figs 55.42-55.44).

2. Angiomatous malformation (synonym: *angioma or congenital arteriovenous fistula*)

These lesions are of congenital origin and are to be differentiated from the simple arteriovenous fistula which is usually due to trauma.

Although they are generally accepted as being of congenital origin, the majority of cases present in early adult life. It is probable that they increase in size with age and that this increase proceeds more rapidly once adult blood pressure has been established. The communication between the arteries and veins lies over the surface of the brain, but if large in size it extends down into the brain substance in the manner of an inverted cone. In the silent areas of the brain they may be completely symptomless. Should they lie, however, in such sensitive areas as the motor cortex or the occipital



Fig. 55.42 Huge intra- and suprasellar aneurysm of right internal carotid. (A) Lateral view. (B,C) CT cuts through anterior clinoids and suprasellar cisterns, respectively, show bony erosions (arrow) and rounded mass of aneurysm (arrow). (D) Post-enhancement CT shows the aneurysm clearly.

cortex, they will produce appropriate symptoms and physical signs. In the former case jacksonian epilepsy is likely to result; in the latter case cortical field defects may be demonstrated. Apart from the physical signs, these lesions may give rise to headaches, usually of a migrainous character. A small but significant proportion of cases present by rupture of the angioma and subarachnoid haemorrhage.

Simple X-ray of the skull in these cases has been discussed above (see Ch. 53), but CT or MRI are the usual first investigations and are often diagnostic (see Ch. 58), as is intravenous DSA (Figs 55.45, 55.46). However, arteriography will still be required for accurate delineation of the lesion for neurosurgical purposes or for intervention by the radiologist (see Ch. 56).

Angiomatous malformations vary in size from small lesions difficult to demonstrate at angiography to large and spectacular vascular masses (Fig. 56.46). It is a characteristic angiographic feature that the drainage veins fill in the normal arterial phase. This is

because the blood is passing direct from arteries to veins with no intervening capillary circulation. Depending on the size of the arteriovenous shunt, there will be compensatory hypertrophy of the afferent vessels supplying it, and also increase in size of the drainage veins. With large angiomas blood appears to be diverted away from the remaining normal cerebral vessels. Indeed, the lesion has been likened to a 'sponge' or parasite in this respect. This diversion of blood may possibly give rise to cerebral ischaemia and account for some of the symptoms.

In cases where an angioma has ruptured, an intracerebral haematoma may result, with displacement of vessels as by any other intracranial mass. Such intracranial haematomas are well shown by CT or MRI.

With small angiomas which have ruptured, the angioma may clot and it may be difficult or impossible to demonstrate the lesion at angiography. However, the clinical history of a subarachnoid haemorrhage with radiological evidence of an intracerebral

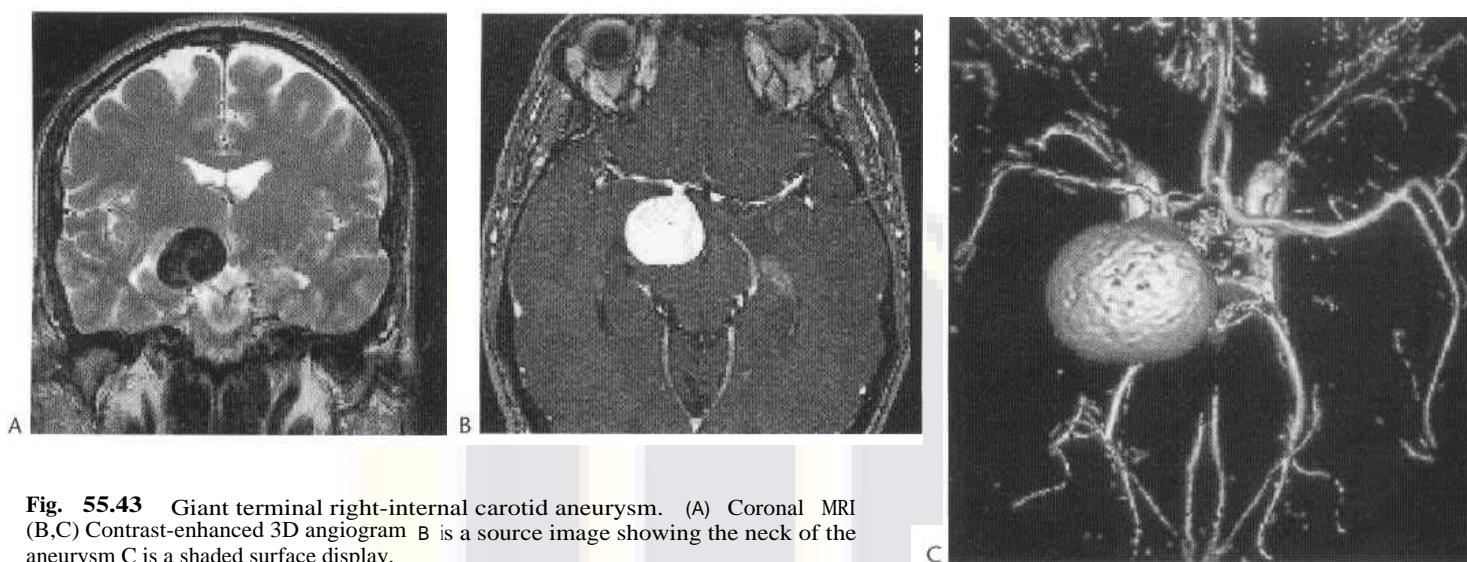


Fig. 55.43 Giant terminal right-internal carotid aneurysm. (A) Coronal MRI (B,C) Contrast-enhanced 3D angiogram B is a source image showing the neck of the aneurysm C is a shaded surface display.

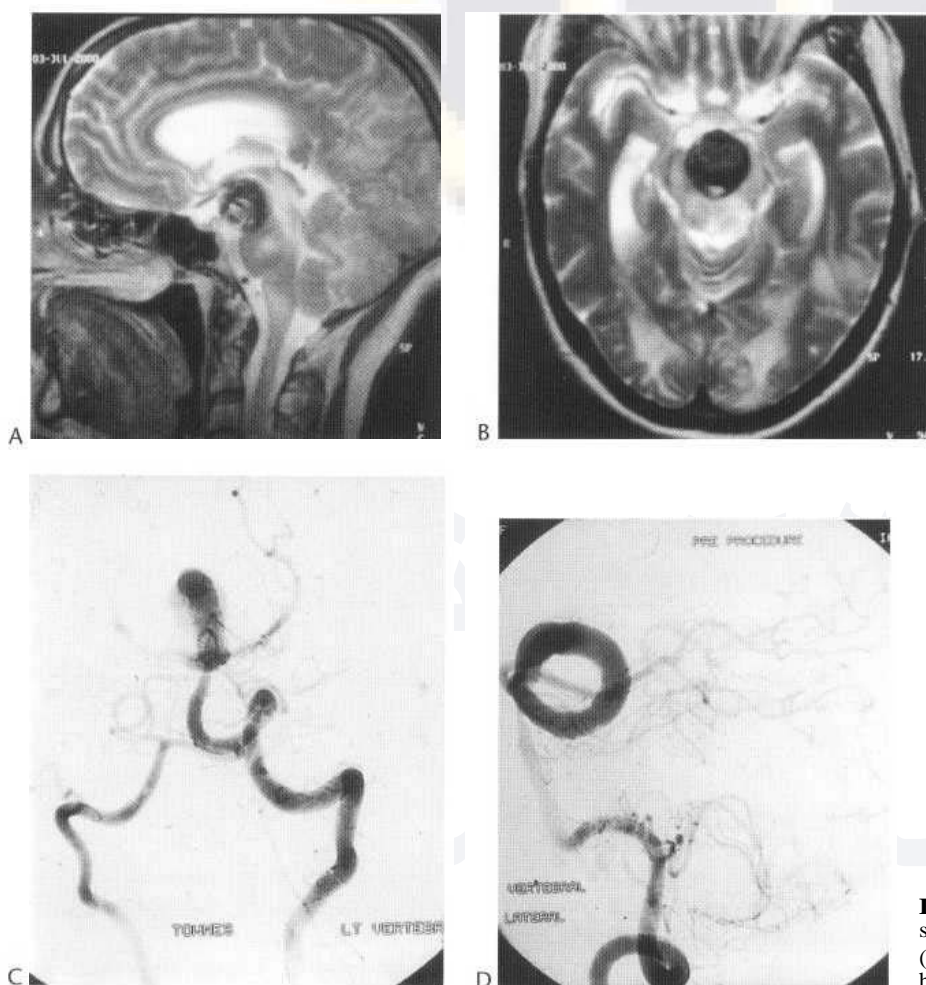


Fig. 55.44 Large basilar aneurysm presenting as a suspected pontine tumour. (A) Lateral and (B) axial MR. (C,D) Large terminal basilar aneurysm partially thrombosed; AP and lateral vertebral arteriogram.

haematoma at a peripheral site may cause suspicion. Sometimes some evidence of a lesion may remain—for example, delayed filling in a peripherally clotted vein.

Planning treatment of angiomas requires full demonstration of all feeding arteries and drainage veins. In some cases this will require bilateral carotid angiography; in others, vertebral angiography may also be required, even though the lesion is supratentorial. Some angiomas are fed by meningeal vessels as well as by branches of lesions were relatively more frequent (33%).

the internal carotid, so that the external carotid artery should be shown as well as the internal carotid. In one large series 80% of supratentorial angiomas were supplied purely by pial vessels, 15% by both pial and dural vessels, and 5% were purely dural in blood supply (see Dural AV Malformations, below). Infratentorial angiomas are not uncommon and constituted 20% of the cases in the series just quoted; among these infratentorial angiomas, dural

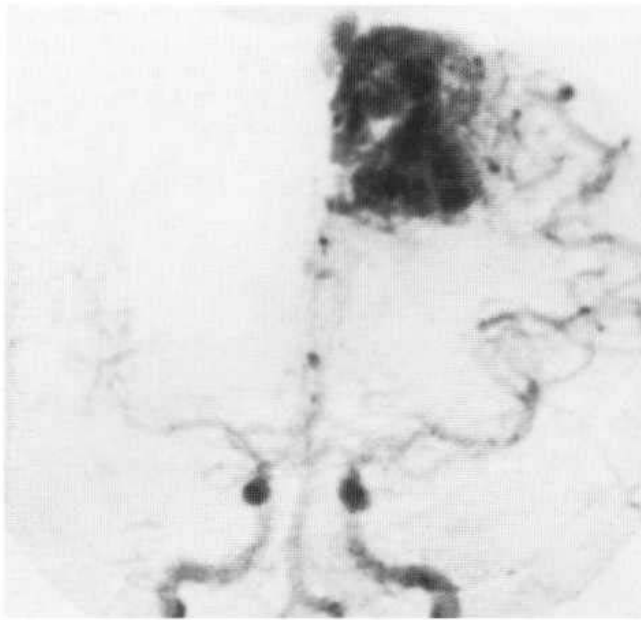


Fig. 55.45 Parasagittal angioma shown by intravenous DSA.

The above discussion concerns the common arteriovenous malformation (AVM). Other types of angioma include *cavernous angioma*, *venous angioma* and *capillary telangiectasia*. These are all less typical or negative at angiography but are shown by CT or MRI. The cavernous angioma is not shown: the venous angioma may show a small collection of venules with a single drainage vein but can easily be missed, capillary telangiectasia may show a small non-specific capillary blush.

Aneurysm of the vein of Galen (Figs 55.47, 55.48) This is in fact another manifestation of cerebral angioma, the dilated vein being secondary to AV shunting through an angioma, usually in the brainstem or medial temporal lobes. Some cases usually presenting in infancy, however, seem to be due to a congenital malformation of the venous system; the hugely dilated central venous structure is a persistent embryonic vein known as the median vein of the prosencephalon. The AV shunt is from choroid arteries

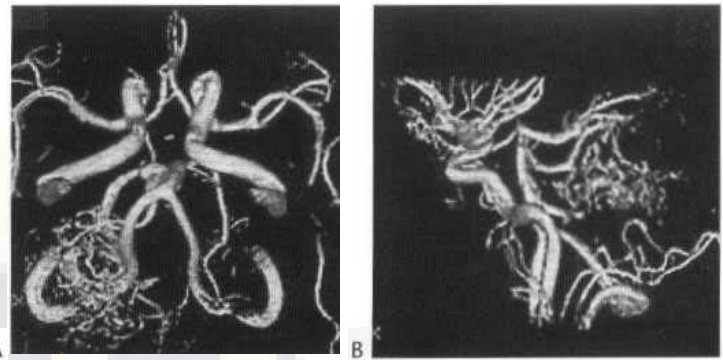


Fig. 55.46 Cerebellar arteriovenous malformation. (A,B) MR angiography without contrast injection. A 3D shaded surface display.

opening directly into the vein. Heart failure or irreversible brain damage may occur, and also a form of hydrocephalus in which ventricular shunting may be detrimental and is to be avoided.

Spinal angiomas With the increasing use of spinal angiography (see also Figs 56.10 and 56.58) spinal angiomas have been demonstrated in increasing number and treated by surgery or embolisation (see Ch. 56). Spinal angiography is of little help in the diagnosis of spinal tumours except in spinal haemangioblastoma, where a characteristic appearance similar to that seen in the posterior fossa will be shown (see Ch. 54).

3. Arteriovenous fistula

This may be due to trauma causing a direct communication between an artery and a vein. It may also be due to rupture of the wall of an aneurysm or diseased artery into an adjacent or adherent vein.

Intracranial arteriovenous fistula is rare and is most frequently seen in the cavernous sinus. Most of the cavernous sinus cases encountered are due to trauma, but a significant proportion, particularly in female patients, are due to the second of the mechanisms mentioned, i.e. spontaneous rupture of a diseased arterial wall.

The condition may be very difficult to demonstrate by angiography. If there is a large shunt through the fistula it will best be shown



Fig. 55.47 (A) Large angiomatous malformation in the region of the anterior end of the corpus callosum. (B) Drainage is mainly by a hypertrophied internal cerebral vein to the vein of Galen and straight sinus.

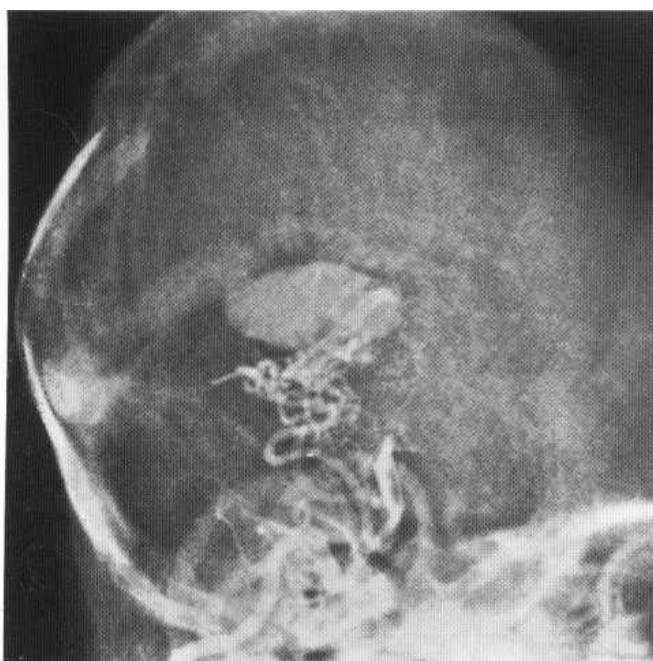


Fig. 55.48 Vertebral angiography demonstrates a vein of Galen aneurysm, secondary to an angioma.

by using larger doses of contrast medium and higher concentrations than usual. Figure 55.49 illustrates a case of spontaneous AV fistula.

In this case there is a cross-flow of contrast medium to the cavernous sinus on the opposite side. The contralateral internal carotid artery appears as a filling defect in the opacified sinus.

With cavernous sinus fistula, several different venous outflow pathways may occur. These include:

1. The superior ophthalmic vein -- the facial veins; or the inferior ophthalmic vein -- pterygoid plexus ---> the facial veins
2. The superior petrosal sinus ---> the sigmoid sinus

3. The basal vein - the straight sinus
4. The convexity veins -* various sinuses.

As already noted, the venous outflow may pass to the contralateral as well as the ipsilateral veins. Subtraction films are essential in elucidating the complex venous anatomy.

Vertebral AV fistula has been encountered in the past, mainly as a complication of vertebral angiography by needle puncture. It has also been encountered following closed trauma. So-called 'congenital' cases have also been described, although birth trauma cannot be excluded in these cases. Successful treatment of both carotico-cavernous and vertebral fistulas has been effected by detachable balloon catheters. This is described in Chapter 56.

Dural AV malformation (synonym: dural AV fistula)

It is now well known that many apparent spontaneous carotico-cavernous fistulas are dural shunts between meningeal branches of the internal or external carotid artery and dural veins near the cavernous sinus. Differentiation of these dural shunts from direct internal carotico-cavernous sinus fistula is important both for prognosis and treatment. Clinically the signs of an arteriovenous fistula are less marked with a dural shunt, but they include proptosis, chemosis and elevated intraocular pressure. The shunt is one of low pressure and low flow and needs first-class subtraction films for its demonstration. Selective angiography of both internal and external carotid arteries will be required, as the lesion may be fed by meningeal branches of the internal or external carotid artery, and can have multiple feeders. From the external carotid artery, either the middle meningeal or the distal internal maxillary branches may supply the fistula. From the internal carotid, the meningohypophysial trunk may be the source of supply (Fig. 55.50). This small vessel arises from the internal carotid just before it enters the cavernous sinus. Bilateral injections will be necessary, as once a fistula is established it can be fed from both meningohypophyseals. Similar dural arteriovenous malformations can occur at other sites,

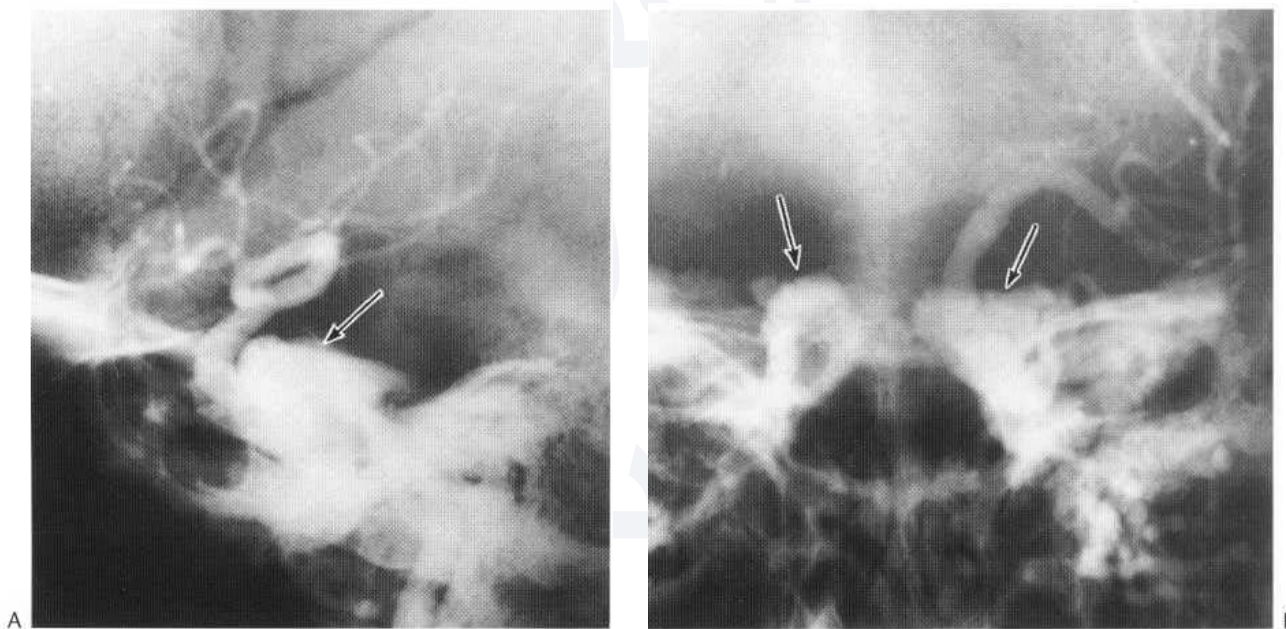


Fig. 55.49 AV fistula in the cavernous sinus (carotico-cavernous fistula). (A) Lateral view showing contrast entering cavernous and superior petrosal sinus (arrow). (B) AP view showing contrast medium entering left cavernous sinus (arrow) and crossing over to fill the right cavernous sinus (arrow). The right carotid siphon appears as a defect in the opacified sinus.

but they are commonest at the base of the skull and in the occipito-mastoid area. Figure 55.51 shows diagrammatically the meningeal vessels from which these lesions can arise.

Dural arteriovenous malformations probably arise as a fistula which progressively recruits secondary arterial feeders from the existing microcirculation or perhaps via flow-induced angioneogenesis. They drain most often via dural veins to the extracranial veins. However, some drain *intradurally* into the cerebral veins, where they may be responsible for intracranial haemorrhage or increased intracerebral venous pressure and interstitial fluid pres-

sure. These lesions may change over time due to thrombosis of draining venous pathways, and although spontaneous complete cure may occur, this is unusual. Lesions draining extracranially may suddenly begin to drain intracranially, and clinical changes such as loss of tinnitus do not necessarily mean spontaneous cure.

In a review of 28 cases it was reported that 14 lesions were basal, mostly in the middle fossa and involving the cavernous sinus, 11 were occipitomastoid, one was on the convexity, and one at the free edge of the tentorium. Lesions that are entirely fed by branches of the external carotid are eminently suitable for treatment by emboli-

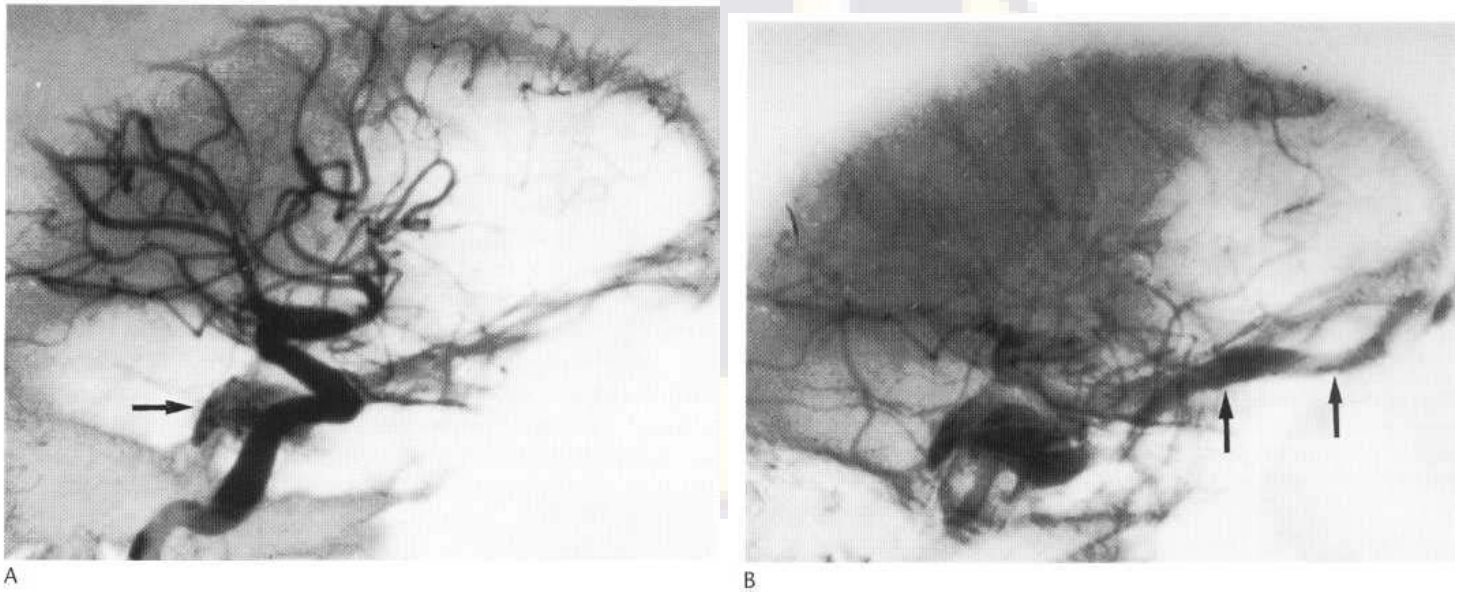


Fig. 55.50 (A) Dural AV fistula supplied by meningohypophyseal trunk (arrow). (B) The drainage is into the superior ophthalmic vein (arrows). Subtraction prints.

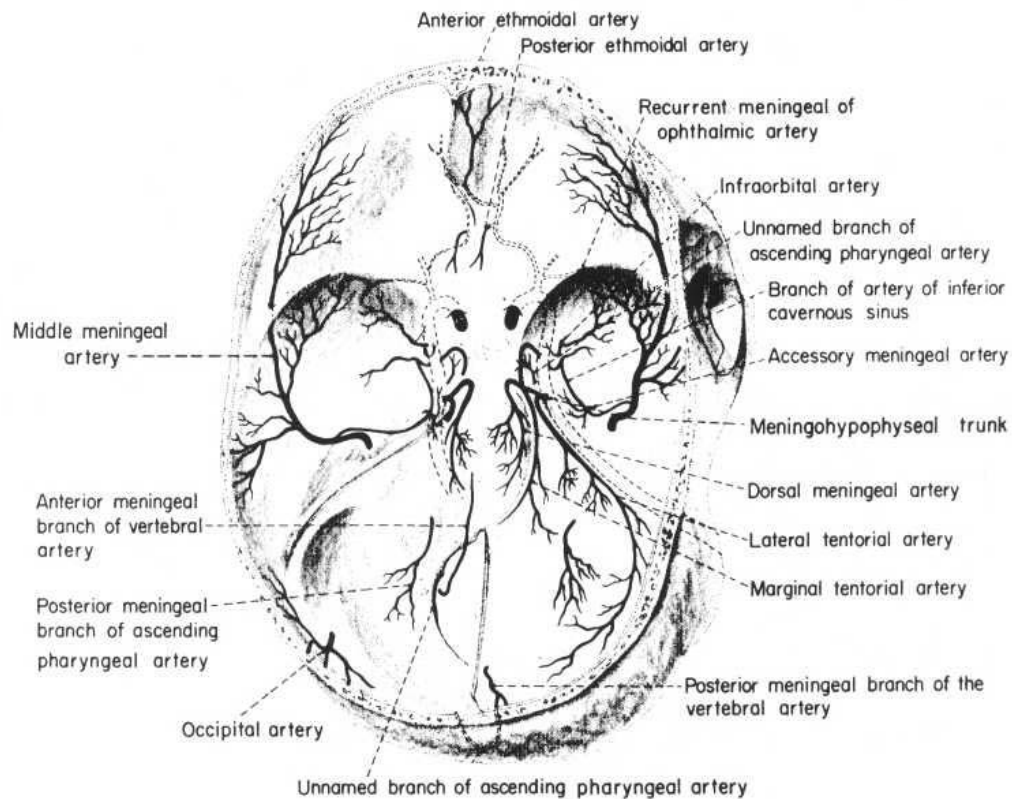


Fig. 55.51 Meningeal arterial supply to the cranial base. (From Houser, O.W., et al (1972) *Radiology*, **105**, 55-64.)

- c. Separate origins of the internal and external carotid arteries-on the right side from the innominate and subclavian, on the left side from the aortic arch.

A rare but important variant of the internal carotid is an *anomalous intrapetrous course*. Normally the vessel kinks medially and forward after entering the carotid canal and lies close to the inferior aspect of the tympanic cavity. In this anomaly it buckles laterally into the tympanic cavity. This is best seen in the AP or oblique views and the vessel is narrowed and uneven. Clinically this can give rise to pulsating tinnitus and a reddish pulsatile 'tumour' behind the tympanic membrane. The correct diagnosis can be confirmed by angiography, and a potentially fatal operation can be avoided.

Size of arteries The vertebral arteries vary markedly in size. On the one hand the vertebral artery may be almost as large as an internal carotid artery, on the other hand it may have a lumen as small as 1 or 2 mm and may appear very tiny on the arteriograms.

Such small vertebrals (usually the right) may terminate in the posterior inferior cerebellar artery, and not join the basilar artery. The average vertebral artery lies somewhere between these extremes, and on the X-ray film its lumen measures 3-4 mm in diameter. In the same individual the two vertebral arteries can be very different in size, although in approximately 30% of patients the two vertebral arteries are equal. In the remaining 70% of patients, about 40% have a left vertebral larger than the right and about 30% have a right vertebral larger than the left. The basilar artery can also vary greatly in diameter, being quite small when both posterior cerebrals are supplied from the internal carotids.

Anomalous vertebral arteries An important anomaly, the origin of the left vertebral artery direct from the aortic arch between the left common carotid and the left subclavian arteries, is described above. Left vertebral catheterisation from the femoral artery in these cases is more difficult, and from the axillary artery it is impossible. There are a number of other but much rarer anomalous origins for a vertebral artery. Thus it may arise from the innominate artery, from the inferior thyroid artery, or even from the common carotid artery in the neck. Another very rare anomaly is the origin of the right vertebral from the distal part of the aortic arch. Such a vessel must pass behind the oesophagus like an anomalous subclavian artery in order to reach the right side of the neck.

The terminal segment of one vertebral beyond the origin of the posterior inferior cerebellar artery may be hypoplastic. *Fenestration* of the terminal segment has also been described, as has fenestration of the basilar artery.

Communications between the carotid and vertebrobasilar system Normal communications exist between the muscular branches of the vertebral artery and muscular branches of the ascending pharyngeal and occipital arteries. Large abnormal communications between the internal carotid and vertebrobasilar systems may also occur. The most frequent of these (about 1 in 500 cases) is between the internal carotid artery as it enters the cavernous sinus and the termination of the basilar artery. This artery passes round the base of the sella and is termed the *trigeminal artery*, because of its close relationship to the trigeminal nerve (Fig. 55.30). Anastomosis at a more proximal level is less frequent. Named communications are the acoustic artery and the

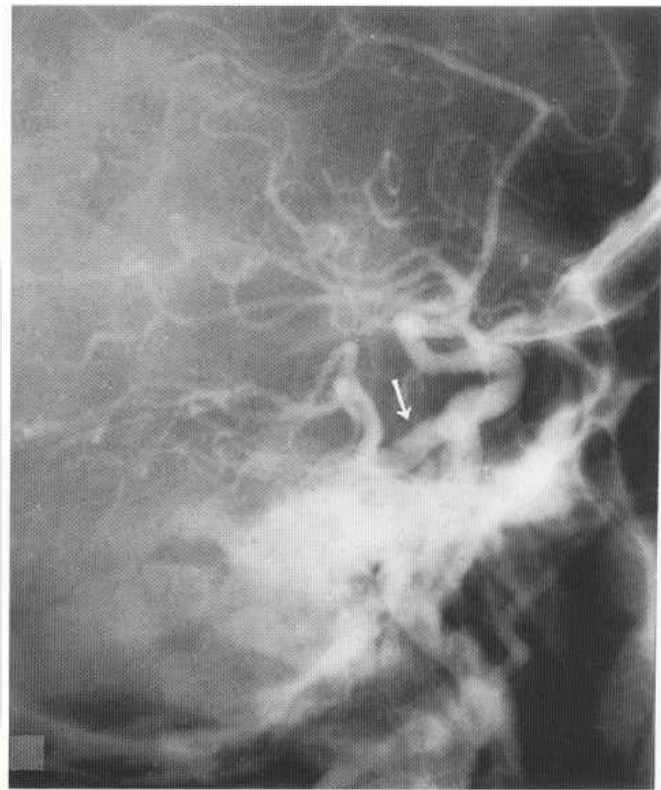


Fig. 55.30 Anomalous carotid-basilar anastomosis (arrow). This is an exam the trigeminal artery. Lateral view.

hypoglossal artery, so called because they accompany the corresponding cranial nerves (Fig. 55.31). The *acoustic artery* connects the internal carotid artery with the basilar by an artery accompanying the VIIth and VIIIth nerves through the internal auditory meatus (Fig. 55.32). It is excessively rare, and special projections, including a basal view, may be necessary before a case can be regarded as authenticated.

The *hypoglossal artery*, which passes through the anterior condyloid foramen at the base of the skull after arising from the internal carotid in the neck, is less rare, although still less common than the trigeminal artery (Fig. 55.33).

The *proatlantal intersegmental artery* is also very rare (Fig. 55.34). The essential feature is that the artery arises from the internal carotid and joins the horizontal part of the vertebral artery as it lies on the atlas.

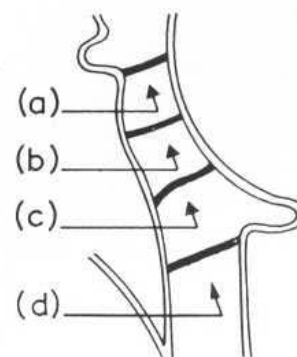


Fig. 55.31 Anomalous communications between the carotid and vertebrobasilar systems. (a) Trigeminal artery; (b) acoustic artery; (c) hypoglossal artery; (d) proatlantal intersegmental artery.



Fig. 55.52 Dural AV fistula supplied by the occipital artery and draining into the lateral sinus and internal jugular vein. Superselective occipital artery injection (subtraction print). This case was successfully treated by percutaneous embolisation.

cation (Fig. 55.52). This is a particularly valuable treatment of these lesions, as direct surgery is difficult and carries a high rate of complications and recurrence.

4. Intracranial haematoma

Intracranial haematomas may be classified as extradural, subdural and intracerebral. Arteriography can diagnose these lesions but has long been superseded by non-invasive methods, i.e. CT or MRI and, in the case of infants, ultrasound. Diagnosis is discussed in detail in Chapter 58.

5. Embolus

Cerebral embolus most commonly arises from clot in a fibrillating auricle. It is therefore most frequently seen as a complication of mitral stenosis. Like embolus elsewhere, it is sometimes seen following coronary infarction and clot formation in the left ventricle. It may also result from paradoxical embolus, or from dislodgement of clot in an aortic aneurysm. Small emboli can also result from clot forming on the surface of atheromatous plaques in the aorta and great vessels. Catheter clot embolus is a complication of arteriography and is discussed in Chapter 15. A cerebral vessel occluded by embolus is readily shown by arteriography, provided it is sufficiently large. In the writers' experience the middle cerebral artery is the commonest site for a major cerebral embolus. This is not surprising as the middle cerebral artery takes the major blood flow after bifurcation of the internal carotid artery. Embolus of smaller peripheral vessels may require careful study of rapid serial angiographic films before the lesion is recognised. A major embolus is now readily diagnosed by CT (see Ch. 58) or by MRI, but the tiny emboli which occur in transient ischaemic attacks (TIAs) cannot be so identified.

6. Vascular stenosis and thrombosis

Atheromatous stenosis and thrombosis of the internal carotid arteries before they enter the cranium can be a cause of cerebral symptoms. Thus the internal carotid artery may be stenosed or thrombosed just distal to its origin from the common carotid artery (Fig. 55.53). Less commonly, atheromatous stenosis is seen in the carotid siphon. Originally it was thought that simple stenosis produced symptoms but later it was suggested that platelet emboli from ulcerating plaques were responsible (see below). However, it is now accepted that only severe stenosis (i.e. more than 70%) is a major risk factor for stroke and an indication for surgery.

In the same way, but less frequently, the vertebral artery may be stenosed or thrombosed by atheroma near its origin from the subclavian artery (Figs 55.54, 55.55). It has also been claimed that the vertebral artery can be compressed in its cervical portion by pressure from osteophytes, and, further, that rotation of the neck may compress the vertebral artery in some elderly patients. The clinical significance of vertebral lesions is debatable, as there are still no reliable controlled studies relating them to vertebrobasilar insufficiency, and the value of surgery for vertebral stenosis remains controversial.

Finally, stenosis or thrombosis of the innominate, common carotid and subclavian arteries may occur in the thorax, and was claimed by some to affect the cerebral blood supply; however, smooth non-ulcerating lesions in these vessels are unlikely to produce cerebral symptoms. Multiple lesions are well shown by intravenous DSA (Fig. 55.56).

Collateral circulation In the case of unilateral internal carotid thrombosis, a collateral circulation may develop from several sources. Blood may reach the affected hemisphere through the circle of Willis, i.e. by flow across the anterior communicating artery from the opposite side, and by retrograde flow along the posterior communicating artery from the basilar to the internal carotid artery. In addition, anastomoses usually open up between the terminal branches of the maxillary artery and those of the ophthalmic artery. This permits blood from the external carotid artery to reach the ophthalmic artery and flow retrogradely into the cerebral circulation. Anastomoses may also develop between the muscular branches of the vertebral artery in the neck and branches of the external carotid artery, such as the occipital artery (Fig. 55.57). The usually excellent collateral circulation may explain why symptoms are often absent, or are variable and unpredictable in patients with carotid stenosis and thrombosis. Thus we have encountered symptom-free patients with bilateral carotid thrombosis at one end of the spectrum and patients with symptoms and unilateral stenosis at the other. Eventual thrombosis may result in a minor or major stroke, or paradoxically it may cure the symptoms.

Transient ischaemic attacks Symptoms in cases of internal carotid stenosis may be due to small platelet emboli detached from the surface of ulcerating atheromatous plaques. These can give rise to the so-called transient ischaemic attacks (TIAs) with focal symptoms, such as hemiparesis, hemiparaesthesia or monocular amblyopia, which recover fairly rapidly. If untreated, carotid occlusion may eventually ensue. Rather surprisingly, as already noted, this can result in clinical improvement with spontaneous cure of the TIAs. On the other hand, thrombosis may result in stroke, which may be minor, major or even fatal. Whether this is due to a major embolus or to extension of the thrombosis is

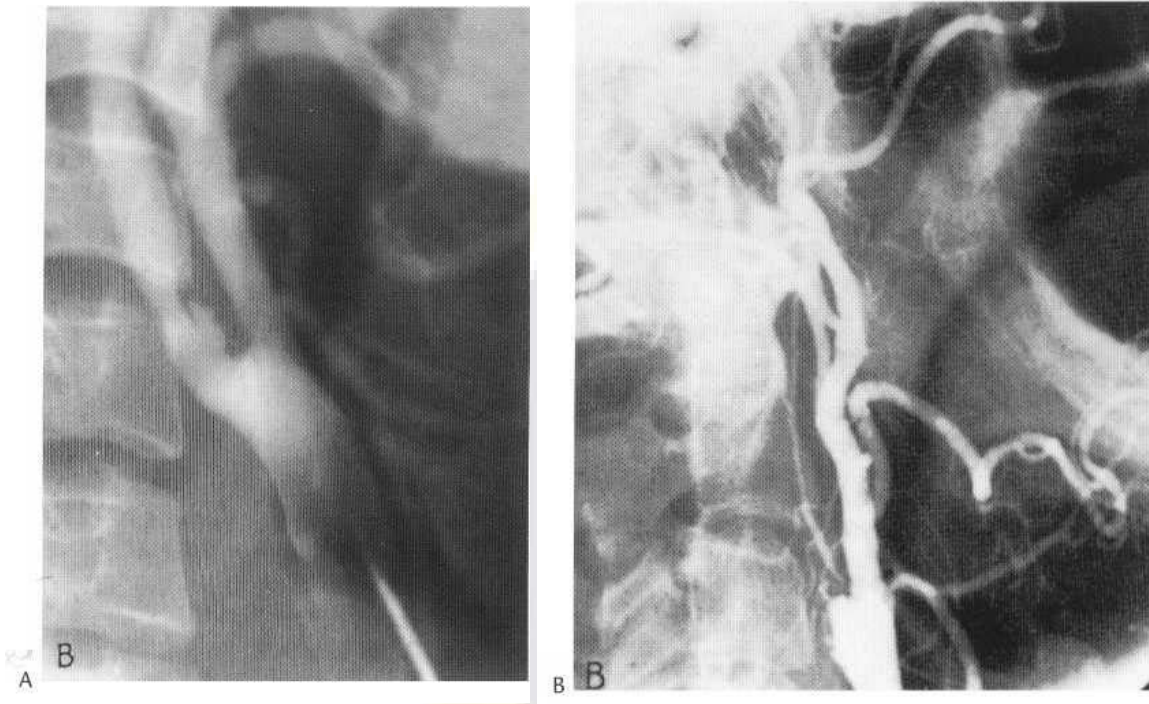


Fig. 55.53 (A) Stenosis of the internal carotid arteries. (B) Thrombosis of the internal carotid artery in the neck.

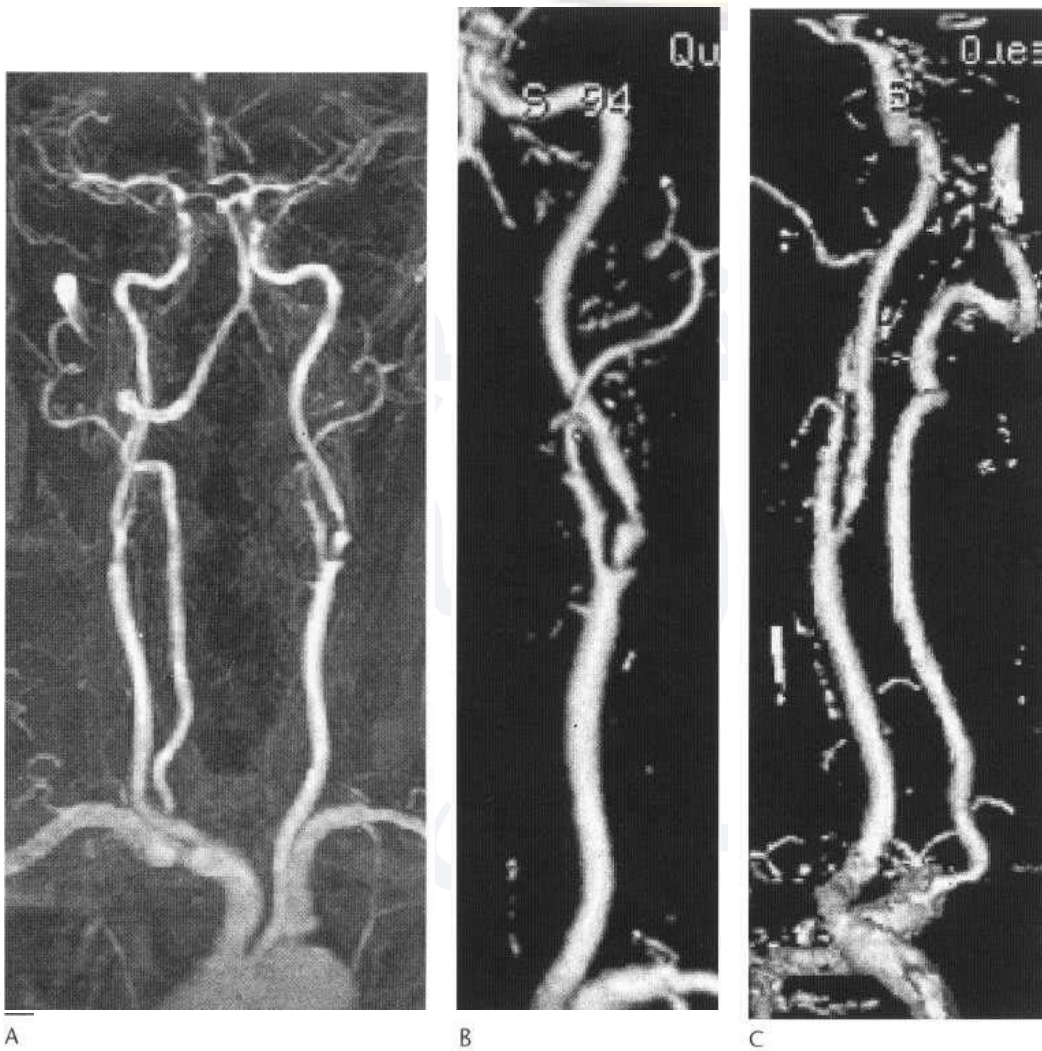


Fig. 55.54 Bilateral stenoses of the internal carotid artery sinuses. (A) MR angiography using the neurovascular coil (3D contrast-enhanced MIP projection) showing the extensive coverage achieved. (B) Higher resolution 3D contrast-enhanced image of the left carotid artery shown as a shaded surface display. The other arteries have been excluded from the image. (C) Left carotid and vertebral arteries. MR angiography contrast-enhanced 3D shaded surface display. Mild smooth narrowing of the left carotid sinus is shown. Neurovascular coil, other arteries are excluded from the display.

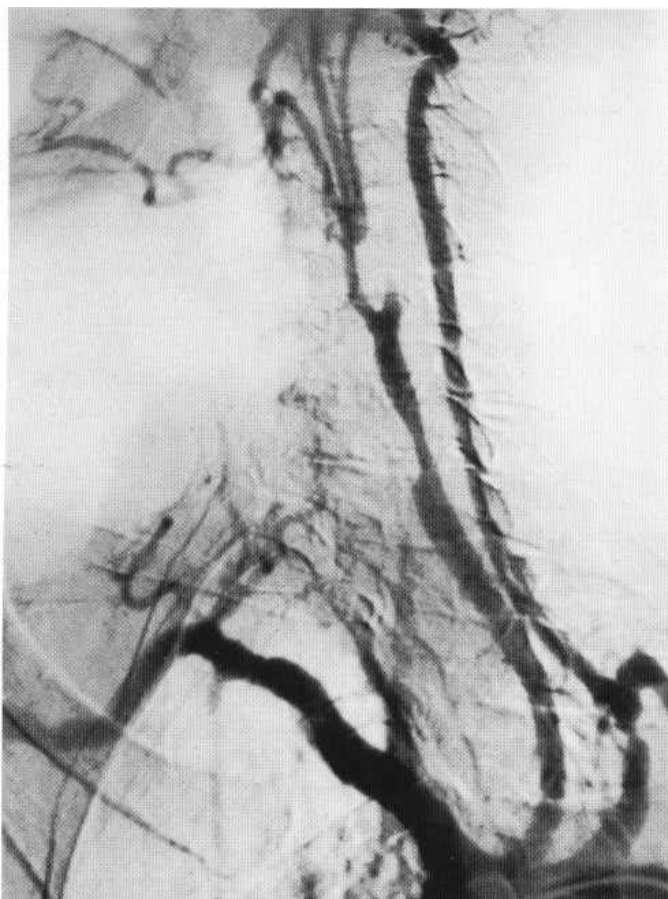


Fig. 55.55 Arch aortogram showing occlusion of right common carotid artery and left internal carotid artery and severe stenosis of the left subclavian artery. The right vertebral is also occluded. (Subtraction print.)

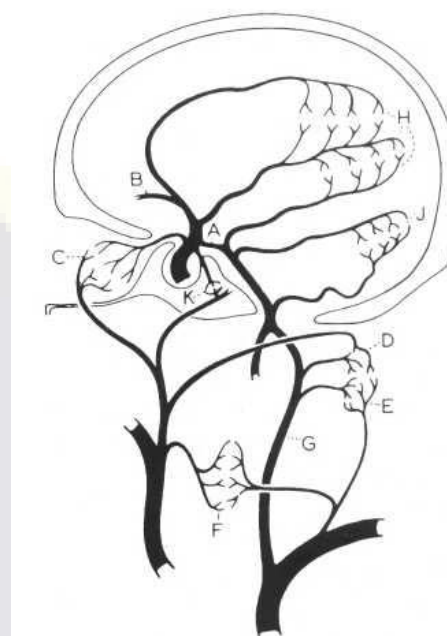


Fig. 55.57 Possible collateral pathways in cerebrovascular insufficiency. (A,B) Posterior communicating and anterior communicating arteries of the circle of Willis. (C) Communication between maxillary and ophthalmic artery. (D) Communication between muscular branches of the vertebral and the occipital artery. (E) Communication between the vertebral and ascending cervical arteries. (F) Communications between the inferior thyroid and superior thyroid arteries of the same and opposite sides. (G) The vertebral artery providing retrograde flow to the subclavian (subclavian steal). (H) Pial anastomoses between terminal branches of the anterior cerebral, middle cerebral and posterior cerebral arteries. (J) Pial anastomoses in the posterior fossa. (K) Meningeal anastomoses and rete mirabile. (From Sutton, D., Davies, E.R. (1966) *Clinical Radiology*, 17, 330-345.)

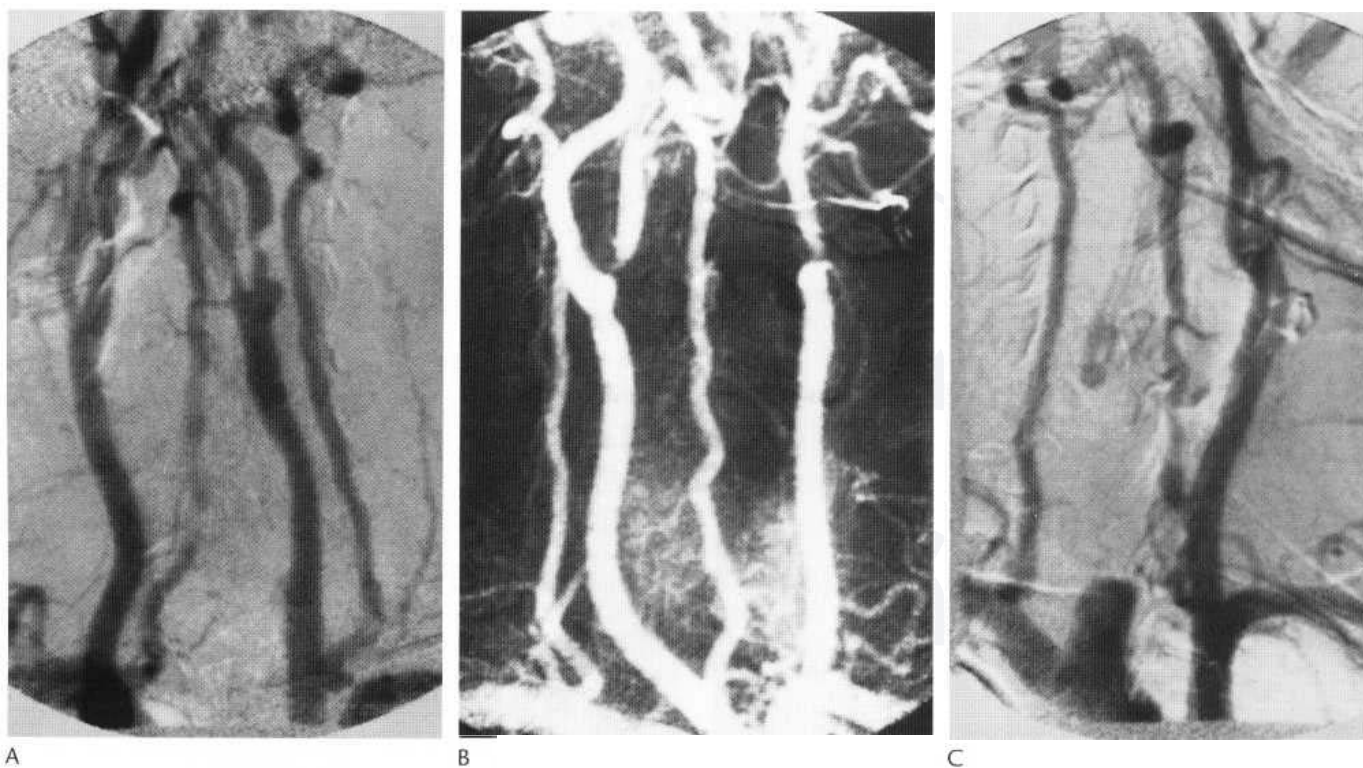


Fig. 55.56 Four-vessel neck studies by intravenous DSA in three different patients. (A) Left carotid stenosis. (B) Bilateral carotid stenosis. (C.) Right common carotid thrombosis.

difficult to determine. Other factors that may increase the risk of stroke include heart disease with poor cardiac output, hypertension or hypotension. Also relevant is the presence or absence of previous brain infarcts or other lesions.

As there was no reliable method of predicting the outcome, surgery was generally accepted as the treatment of choice and internal carotid endarterectomy, an operation pioneered at St Mary's Hospital, London, has been widely practised. The value of the operation has also given rise to much controversy and to controlled trials in Europe and North America (see below).

Subclavian steal The vertebral circulation may be seriously affected by thrombosis of the left Subclavian artery in its first part and proximal to the left vertebral origin. When this occurs, the left vertebral artery acts as a collateral to the left Subclavian artery. Blood flows up the right vertebral artery and then retrogradely down the left vertebral artery to the left subclavian artery, where blood pressure has been lowered by the proximal subclavian block. This siphonage of blood from the vertebrobasilar system to the arm has been christened the 'subclavian steal' phenomenon. It has been claimed that the diversion of blood from the brain may be considerable and result in cerebral symptoms. The lesion is well demonstrated by arch aortography. Less commonly, siphonage of blood down the right vertebral artery may occur if there is an innominate or proximal right subclavian block.

In the same way 'carotid steal' may result from occlusion of a common carotid or innominate artery.

In addition to the vertebral artery acting as a collateral to the arm, a further collateral circulation may be derived from the external carotid artery and its branches to the thyroid axis. Collaterals have also been demonstrated passing from the external carotid to the muscular branches of the vertebral and this provides a further contribution to the vertebral blood flow. Other sources of collateral supply are through the intercostals to the scapular and internal mammary arteries.

Thrombosis of the internal carotid artery This may result from several causes:

1. In the past, needle injection of the common carotid artery, particularly in the hands of an unskilled worker, was sometimes accidentally made into the arterial wall. If the injection was subintimal, an appearance resulted which superficially resembled thrombosis.

2. Thrombosis of the internal carotid artery has sometimes been wrongly diagnosed when the tip of a needle, cannula or catheter has been at the bifurcation of the common carotid artery and the main injection has entered the external carotid artery. As a result, the internal carotid artery, although patent, was not visualised. In all cases where internal carotid thrombosis is suspected, the catheter tip at test doses must be demonstrated to be below the point of bifurcation of the common carotid artery.

3. Another condition in which apparent thrombosis of the internal carotid artery may be seen is grossly raised intracranial pressure in a comatose and moribund patient. In these cases cerebral blood flow may be so reduced that, even on delayed serial films, the contrast medium passing through the internal carotid artery has still not progressed beyond the cavernous sinus. We have seen several such cases where autopsy has shown the vessels to be patent intracranially. When this phenomenon is seen it implies that cerebral perfusion is at an extremely slow rate and the prognosis is invariably bad.

An interesting feature is that the contrast medium, as it passes slowly up the cervical carotid, sinks to the posterior aspect of the vessel, producing a 'layering' effect. This is better appreciated if the radiograph is viewed in the brow-up position in which it was taken.

It has been shown experimentally in animals that spontaneous respiration invariably ceases when intracranial pressure becomes equal to the diastolic blood pressure. The parallel between this observation and the clinical fact that most of the patients with pseudo-occlusion arc in need of artificial respiration is clear.

Surgical results Multicentre trials in Europe and North America have established that severe, and only severe, atheromatous stenosis (greater than 70%) of the proximal part of the internal carotid artery is a clear and independent *risk factor* for stroke, and only infrequently is it a necessary cause. They have also demonstrated that correcting severe stenosis by carotid endarterectomy significantly reduces stroke incidence in this group, but the number of strokes thereby prevented in follow-up periods of 2-5 years is actually quite small, amounting to no more than 1 or 2% of all strokes. Little or no controlled data exist about the significance of vertebral artery stenosis or thrombosis in the presence of symptoms of vertebral vascular insufficiency, and none on the efficacy of operative treatment. Only a very small number of patients (about 2%) have more proximal stenosis, near the origins of the common carotid or subclavian arteries. These are usually smooth non-ulcerating lesions, and it is doubtful if they ever result in cerebral symptoms. It is also our experience that 'subclavian steal' is unlikely to produce cerebral symptoms and is usually a chance finding.

In assessing the stroke risk in an individual patient with a carotid stenosis, it is necessary to consider the lesion not as an isolated phenomenon, but in relation to the state of the cerebral circulation as a whole and the status of the brain itself. For example, cerebral CT or MRI may show diffuse ischaemic brain damage in white matter and basal ganglia indicative of severe intracerebral vascular disease, or cortical infarcts in multiple vascular territories. Either of these findings would suggest that an isolated carotid stenosis is of less significance as a risk factor in that particular case.

Imaging The most complete visualisation of the cerebral vasculature is routinely obtained by IV DSA (Fig. 55.56) but this now can also be achieved by MRA or invasively by arch aortography or a combination of arch and selective carotid arteriography. In general, however, the requirement of visualising all the cerebral circulation (including cervical and intracranial vessels) diminishes in importance if carotid stenosis is regarded as only a potentially remedial risk factor and not necessarily a cause of stroke. Sonography, MRA and 3D CT are usually directed only at the carotid bifurcations, but the latter two techniques now may be extended quite easily to include great vessel origins and intracranial vessels by performing further runs. For MRA this is time consuming and involves changing coils, and for 3D CT angiography it may need to be done on separate days because of concern about contrast volume and solute load. What is actually done still varies widely and continues to be driven by strongly held but often ill-founded views. This is an area where radiologists need to be more than technicians, and should be aware of the issues involved. Readers are urged to study carefully the reports of the European and North American Symptomatic Carotid Stenosis trials, and recent studies of the accuracy of intra-arterial angiogra-



Fig. 55.58 (A) Fibromuscular hyperplasia producing beaded appearance of the internal carotid. (B) Dissecting aneurysm of internal carotid artery. The channel is narrowed and irregular.

phy both in estimating stenosis and in predicting stroke risk by assessing plaque morphology, all of which are cited at the end of this chapter. Most importantly, it must be appreciated that if the stroke risk of preoperative *investigation* rises above about 2% in *appropriately operated* patients, the statistical significance of the beneficial effect of carotid endarterectomy may be wiped out. If patients eventually shown not to be in the group that benefits from carotid endarterectomy are also exposed to this level of risk, more strokes will be caused than prevented. Many centres have now opted to investigate patients with suspected carotid stenosis exclusively non-invasively, using a combination of either sonography and MRA, 3D CT or IV DSA, and they rarely if ever perform intra-arterial studies, even in operated cases. A persistent indication for intra-arterial studies, however, is when non- or less invasive techniques have suggested but not proven an occlusion, because very occasionally this turns out to be an operable very tight stenosis (Fig. 55.1).

Fibromuscular hyperplasia The internal carotid artery is occasionally involved, usually in its upper cervical segment (Fig. 55.58), although this rarely causes significant symptoms. There may be involvement of the renal arteries and associated hypertension.

Traumatic thrombosis of the internal carotid This may occur after severe direct trauma to the neck.

Dissecting aneurysm This may also follow direct trauma to the neck and usually involves the high cervical segment. Diagnosis is readily made on direct angiography if the false channel fills with contrast medium, but should also be suspected when it does not and there is merely narrowing of a segment of the artery in the same high cervical position (Fig. 55.58B). Spontaneous dissection may also occur in this area, with hypertension as a predisposing cause. Clinically there may be sudden neck or head pain and frequently a partial or complete Horner's syndrome. As noted, angiography rarely shows the false lumen, but the true lumen may be narrowed, irregular or eccentric. *MRI is not the method of choice to make a diagnosis* by using high-resolution fast spin-echo sequence to show the dissected artery in the axial plane (see Fig. 58.13A): MR angiography is not required, and may even appear normal, as it should be noted that some carotid dissections may resolve. Some dissections have an undetectable effect on the side of the true lumen. Intra-arterial angiography *should be avoided*.

Intracranial thromboses Thrombosis of intracranial vessels develops either from atheroma or, less commonly, from ruptured aneurysms. Atheromatous stenosis of the internal carotid artery occurs intracranially, either in or just above the cavernous sinus. Of the other major intracranial vessels, the middle cerebral artery is most frequently involved (Fig. 55.59).

Thrombosis of small peripheral vessels is easily missed; if it is suspected, rapid serial films may be necessary to demonstrate the lesion clearly.

With intracerebral thrombosis a collateral circulation may be demonstrated, filling the occluded vessel retrogradely.

Intracranial thrombosis of the internal carotid artery may also occur from atheroma in the cavernous sinus or just before the termination of the artery.

Basilar thrombosis is usually fatal but can occur with survival of the patient, and cases have been diagnosed by vertebral angiography.

A syndrome consisting of multiple progressive intracranial arterial occlusions in children, originally thought to occur only in

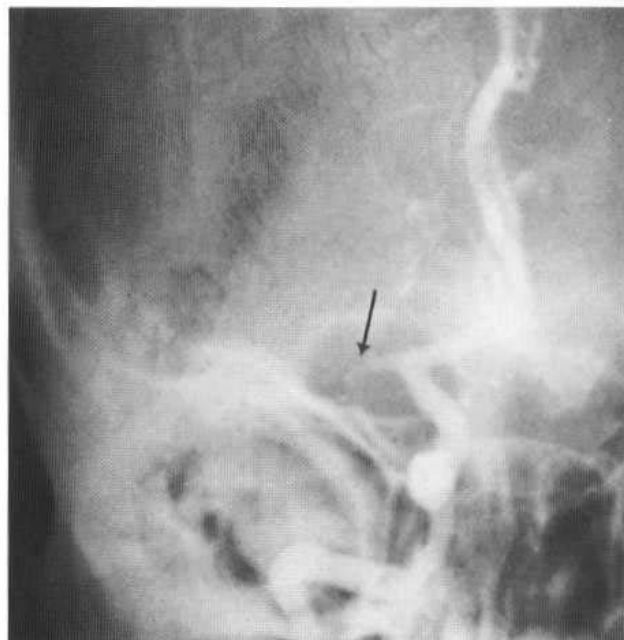


Fig. 55.59 Middle cerebral artery thrombosis (arrow).

Japanese (*moyamoya disease*), has since been reported in American and British cases. The disease results in rapidly progressive stenoses of the major vessels of the circle of Willis, leading to occlusion and multiple tiny basal collateral vessels. The process stops once occlusion occurs, so that survival is possible if collaterals are adequate. The distal arterial vessels are not involved and the aetiology is unknown.

The role of CT and MRI in the diagnosis of infarcts and TIAs is discussed in Chapter 58.

Dural sinus and cerebral vein thrombosis

Thrombosis of cerebral veins and dural sinuses is not uncommon. Clinically, the commonest cause is infection, either local or distant. Meningitis or encephalitis may be complicated by venous thrombosis, often fatal, and infection may spread from the paranasal sinuses or middle ear and mastoid. Thrombosis may also occur as a complication of pregnancy (about 1 case per 2500 births). Rare causes include skull trauma and craniotomy, cardiac disease with right heart failure, oral contraception, dehydration and blood disorders.

The symptoms and signs vary with the localisation and extent of the lesion and with associated brain oedema, infarction, haemorrhage or infection. They include hemiplegia, papilloedema and epilepsy, general or focal, and drowsiness or coma.

Superior sagittal sinus Thrombosis of the anterior part is usually asymptomatic because of excellent pial collaterals. In any case, absence of the anterior part of the sagittal sinus is a common congenital finding when the ascending frontal vein courses parallel to the midline to join the sagittal sinus more posteriorly. Thrombosis of the more posterior part of the sinus is more serious and produces symptoms of the type just described. The thrombosis may extend into the cortical veins and produce areas of infarction.

Transverse and sigmoid sinuses Thrombosis is frequently septic, arising from the middle ear or mastoid. Congenital absence of one transverse sinus may occur and should not be considered as thrombosis without supportive evidence.

Cavernous sinus Involvement of the cavernous sinus is associated with exophthalmos, chemosis, oedema of the eyelids and oculomotor palsies.

Radiological appearances Acute dural sinus thrombosis usually is obvious on unenhanced CT or MRI: the thrombosed sinuses are distended by high-density or high-signal blood clot. Once recanalisation has begun to occur, it can be difficult to diagnose, whatever modality is used. CT or MRI also demonstrate associated (parenchyma) damage. The thrombosis can be well shown by serial angiography of the internal carotid following arterial DSA (Fig. 55.8), but intravenous DSA has the advantage of displaying all the venous sinuses with uniform simultaneous opacification.

MR venography is also now widely used for this purpose, although non-visualisation of a transverse sinus is not unusual in normal individuals and turbulent flow effects can simulate intraluminal clot.

On intra-arterial angiography, thrombosis of the sagittal sinus usually slows the circulation, failure of a section of the sinus to outline, and dilated collateral venous channels bypassing the obstruction or draining to other areas. The bridging veins may be abnormal and 'corkscrew' in appearance. The lateral sinuses are best seen in the frontal projection and partial occlusions identified.

Cortical venous thrombosis, apart from local absence of venous filling and presence of surrounding collaterals, may show evidence of a local mass due to infarction and oedema.

Obstruction of venous sinuses may also occur with tumours. Thus meningiomas frequently involve the sagittal and sometimes the lateral sinus, and glomus jugulare tumours may invade the internal jugular vein and sigmoid sinus.

Arteritis

Angiography is sometimes requested to help support a clinical diagnosis of intracranial arteritis. Because some of the changes reported in these cases are subtle or involve only small branches, high-resolution infra-arterial studies are often recommended. However, even the finding of multiple small vessel occlusions or irregularities

is non-specific and can be simulated by multiple emboli or vasospasm, and the role of angiography in this context is at best controversial. In a recent review, it was concluded that CT and MRI of the brain provided better supportive evidence for arteritis than angiography, and that angiography was not indicated when these were normal.

Angiography in cerebral tumours

For many years angiography was the most important method of localising and characterising cerebral tumours. With the advent of CT in the 1970s and MRI in the 1980s its value has steadily diminished, and CT and MRI are now the primary investigations of choice. Angiography for tumour investigation is now an ancillary method for use in rare cases or for special indications. Thus, some neurosurgeons require angiography in some gliomas already diagnosed by CT or MRI, to assess the vascularity and probable degree of malignancy prior to surgery. Angiography may also be required to assess some meningiomas for similar reasons, and to assess vascular relationships or possible sinus involvement. Occasionally it is done for preoperative embolisation of large meningiomas via their external carotid feeding vessels. Vertebral angiography is still requested for *haemangioblastomas* of the posterior fossa, as it remains the most accurate method of defining small nodules, which can easily be missed by CT or MRI. Angiography is also useful for the demonstration of *glomus jugulare* and *glomus tympanicum* tumours and for the embolisation of the former. These indications are discussed in more detail in Chapters 56 and 57.

REFERENCES AND SUGGESTIONS FOR FURTHER READING

- Alpers, B. J., Berry, R. G., Paddison, R. M. (1959) Anatomical studies of the circle of Willis in normal brain. *Archives of Neurology and Psychiatry*, **81**, 409-418.
- Black, W. C. (1994) Editorial. Intracranial aneurysm in adult polycystic kidney disease: is screening with MR angiography indicated? *Radiology*, **191**, 18-20.
- Buelmke, D. A., Chambers, T. P. (1995) Editorial. Spiral CT angiography: an alternative to conventional angiography. *Radiology*, **195**, 317-319.
- Debrun, G., Legre, J., Kasbarian, M., et al (1978) Endovascular occlusion of vertebral fistulae by detachable balloons with conservation of the vertebral blood flow. *Radiology*, **130**, 141-147.
- Di Chiro, G., Wener, L. (1973) Angiography of the spinal cord. *Journal of Neurosurgery*, **39**, 1-29.
- Djindjian, R., Merland, J. J. (1978) *Superselective Angiography of the External Carotid Artery*. Berlin: Springer.

- Eastcott, H. H. G., Pickering, F. W., Rob, C. G. (1954) Reconstruction of internal carotid artery in a patient with intermittent attacks of hemiplegia. *Lancet*, *ii*, 994-995.
- European Carotid Surgery Trialist Collaboration Group (1991) MRI European Carotid Surgery Trial. Interim results (1991) of symptomatic patients with severe (70%-99%) or with mild (0%-29%) carotid stenosis. *Lancet*, *337*, 1235-1243.
- Executive Committee for the Asymptomatic Carotid Atherosclerosis Study (1995) Endarterectomy for asymptomatic stenosis. *JAMA*, *272*, 1421-1428.
- Harris, G. K., Tran, D. D., Sickels, W. J., Cornell, S. H., Yuh, W. T. L. (1994) Diagnosing intracranial vasculitis: the roles of MR and angiography. *American Journal of Neuroradiology*, *15*, 317-330.
- Huang, Y. P., Wolf, B. S. (1970) Differential diagnosis of 4th ventricle tumours from brain stem tumours in angiography. *Neuroradiology*, *1*, 4.
- Katz, D. A., Marks, M. P., Napel, S. A., Bracci, P. M., Roberts, S. L. (1995) Circle of Willis: evaluation with spiral CT angiography, MR angiography, and conventional angiography. *Radiology*, *195*, 445-449.
- Leclerc, X., Gauvrit, J. Y., Nicol, L., Provo, J. P. (1999) Contrast enhanced MR angiography of the craniocervical vessels. A review. *Neuroradiology*, *41*, 867-874.
- Lie, T. A. (1968) *Congenital Anomalies Of the Carotid Arteries*. Amsterdam: Excerpta Medica.
- National Institute of Neurological Disorders and Stroke (1995) Carotid endarterectomy in patients with asymptomatic internal carotid artery stenosis. Clinical advisory. *Journal Of the Neurological Sciences*, *129*, 76-77.
- Newton, T. H., Potts, G. G. (eds) (1974) *Radiology Of the Skull and Brain*, Vol. 2 *Angiography*. St. Louis: Mosby.
- North American Symptomatic Carotid Endarterectomy Trial Collaboration (1991) Beneficial effects of carotid endarterectomy in symptomatic patients with high grade stenosis. *New England Journal of Medicine*, *325*, 445-453.
- Osborn, A. G. (1980) *Introduction to Cerebral Angiography*. Hagerstown: Harper Row.
- Peevers, F. L. M., Kroger, R. (1979) Dural and direct cavernous sinus fistula. *American Journal Of Roentgenology*, *132*, 599-606.
- Prince, M. R., Grist, T. M., Debatin, J. F. (1998) *Contrast MR Angiography*. London: Springer.
- Rothwell, P. M., Salinas, R., Ferrando, L. A., Warlow, C. (1995) Does the angiographic appearance of a carotid stenosis predict the risk of stroke independently of the degree of stenosis. *Clinical Radiology*, *50*, 830-833.
- Stevens, J. M. (1995) Editorial. Imaging carotid stenosis. *Clinical Radiology*, *50*, 821-822.
- Stevens, J. M., Barker, C. J., Kerslake, R., Broz, M., Barter, S. (1991) Extended use of cranial CT in the evaluation of patients with stroke and transient ischaemic attacks. *Neuroradiology*, *33*, 200-206.
- Taveras, J. M. (1969) Multiple progressive intracranial arterial occlusions: a syndrome of children and young adults. *American Journal of Roentgenology*, *106*, 235-268.
- Vanninen, R., Manninen, H., Koivisto, K., Tulla, H., Partanen, K., Puvaneni, M. (1994) Carotid stenosis by digital subtraction angiography: reproducibility of the European Carotid Surgery trial and the North American Symptomatic Carotid Endarterectomy trial measurement methods and visual interpretation. *American Journal of Neuroradiology*, *15*, 1635-1641.
- Weber et al. *Asymptomatic Aneurysms*.

نشر الکترونیکی
موسسه انتشاراتی
نور دانش

INTERVENTIONAL NEURORADIOLOGY

H. R. Jäger and S. Brew

This chapter is meant to provide an overview of interventional neuroradiology. Although some general comments have been made within each section, full details of specific procedures and techniques should be obtained from dedicated texts and articles. These procedures should not be performed by occasional operators: occlusion of the main hepatic artery that interferes with the arterial supply to 750 g of liver will probably have no adverse effect and may not be noticed by the patient, while occlusion of a vessel depriving 1 g of brain of its arterial supply may leave a patient paralysed, aphasic or dead. The procedures outlined below should only be performed by experienced, well-trained operators with detailed knowledge of the relevant anatomy, anatomical variants, equipment and pathophysiology.

Even in competent hands, interventional neuroradiology is not without risks; the incidence of irreversible neurological deficit from diagnostic neuroangiography is generally accepted to be in the range of 0.3–3.0%, for interventional neuroangiography it is an *order of magnitude higher*. A neuroradiologist with ongoing hands-on experience and in-depth knowledge minimises the risks to the patient.

The decision to proceed with an interventional neuroradiological procedure necessitates a consideration of the relative risks and benefits of this modality compared to conventional surgery or other techniques such as radiosurgery. Clearly, before any procedure is undertaken, it must offer an advantage over the natural history of the condition to be treated. Careful consideration must be given to the specific risks of the procedure and these must be explicitly discussed with the patient to obtain informed consent. Interventional neuroradiology cannot exist in isolation and must be viewed as one component of a multidisciplinary team. Close interaction with anaesthetic, neurosurgical, neurological, radiotherapy and intensive care specialties is essential. High-quality biplane angiography, ideally with 3D/rotational angiography, MRI and CT are required.

ENDOVASCULAR PROCEDURES

The femoral approach is almost exclusively used. A sheath of appropriate size is always placed. Patients may have multiple diagnostic and therapeutic procedures and care should be taken to minimise trauma at puncture sites and to avoid frequent re-puncture at the same site.

Generally, a guiding catheter is used to ensure stable access and provide a route for injection of contrast for road-mapping. Microcatheters, either flow guided or over the wire, are usually used to reach the target.

The anatomy of the vessels used for access to the target and the target itself must be carefully defined by high-quality angiography. Potentially hazardous anatomical variants should be sought. The optimal endovascular route to reach the target is not necessarily the technically easiest one, minimising the chance of damage to normal tissues should always take precedence.

The possibility that flow patterns will change in the course of the procedure must always be kept in mind and close attention should be given to the appearance of previously non-visualised collateral pathways. Angiography must be repeated as often as is necessary to monitor the effects of treatment and to look for unwanted effects or alterations in flow. Angiography at the end of the procedure demonstrates the effectiveness of the technique and defines any adverse effects on normal vessels.

Heparin is often administered to decrease the risk of thrombosis during the procedure. Haemostasis at the puncture site may therefore not be easily obtained by simple manual pressure, particularly if a large calibre sheath has been used. Reversal of anticoagulation or the use of puncture site closure devices (such as Angioseal[®] or Perclose[®]) can be considered in such cases.

Endovascular procedures can be broadly divided into two categories: those that aim to restore a narrowed or obliterated endovascular lumen supplying normal tissues and those that aim to exclude abnormal blood vessels from the circulation.

Endovascular techniques for lumen restoration

Recanalisation can be achieved using mechanical devices such as dilatation balloons and stents or by using drugs with a thrombolytic or vasodilatory effect.

Intra-arterial thrombolysis

Following the result of randomised trials, intravenous thrombolysis with recombinant tissue plasminogen activator (rtPA) has now been approved for the treatment of acute ischaemic stroke, within

3 hours of onset. The potential for clot recanalisation with intra-venous thrombolysis is markedly dependent on the site of the occlusion. It is more successful in distal middle cerebral artery occlusions than in recanalisation of larger vessels such as the internal carotid artery (ICA) or proximal (M1) segment of the middle cerebral artery.

Intra-arterial thrombolysis (Fig. 56. 1) achieves a higher local concentration of the thrombolytic agent in the vicinity of the clot, which should theoretically be more efficient, but it is more complex to achieve and therefore takes longer, increasing the delay between onset and treatment. The question remains whether a more efficient lysis can prolong the therapeutic time window beyond 3 hours. A randomised trial (PROACT, Prolyse in Acute Cerebral Thrombo-embolism trial) has shown an overall benefit from intra-arterial thrombolysis in acute middle cerebral artery occlusion within 6 hours after the onset of stroke, despite a greater rate of haemorrhagic complication. In this trial 9 mg of recombinant pro-urokinase had been infused through a single end-hole microcatheter placed in the proximal third of the middle cerebral artery (MCA) thrombus over a period of 2 hours. Unfortunately urokinase has since been withdrawn from the market, however, the trial provided a proof of principle' that intra-arterial thrombolysis works and alternative pharmaceutical agents such as streptokinase and rTPA remain available for intra-arterial thrombolysis. Apart from the randomised PROACT trial there are numerous reports of successful intra-arterial throm-

bolysis, not only in the MCA but also in internal carotid artery and vertebro-basilar occlusions. Success of recanalisation is reduced in distal internal carotid artery or T-junction occlusion. A retrospective analysis of acute basilar artery occlusions showed a considerable reduction in mortality with thrombolysis within 48 hours. Young patients with short-segment basilar occlusions benefited most from thrombolytic treatment and had better chances of recovery.

It has been shown that ischaemic changes on diffusion-weighted MRI can be reversed with intra-arterial thrombolysis in certain cases. In the future it is likely that MR perfusion and diffusion imaging will play a much bigger role in selecting patients for thrombolysis, independent of rigid time-to-treatment windows. New developments in the endovascular treatment of acute stroke include the use of mechanical devices for extraction of acute thrombus. These have the advantage of reducing the treatment time (with a corresponding prolongation of the therapeutic window) and of a theoretical reduction in haemorrhagic complications associated with thrombolytic agents.

Treatment of cerebral vasospasm

Cerebral vasospasm represents a significant cause of morbidity and mortality in patients with subarachnoid haemorrhage. Early treatment of ruptured aneurysms together with refinement of endovascular (see below) and surgical techniques have led to a reduction

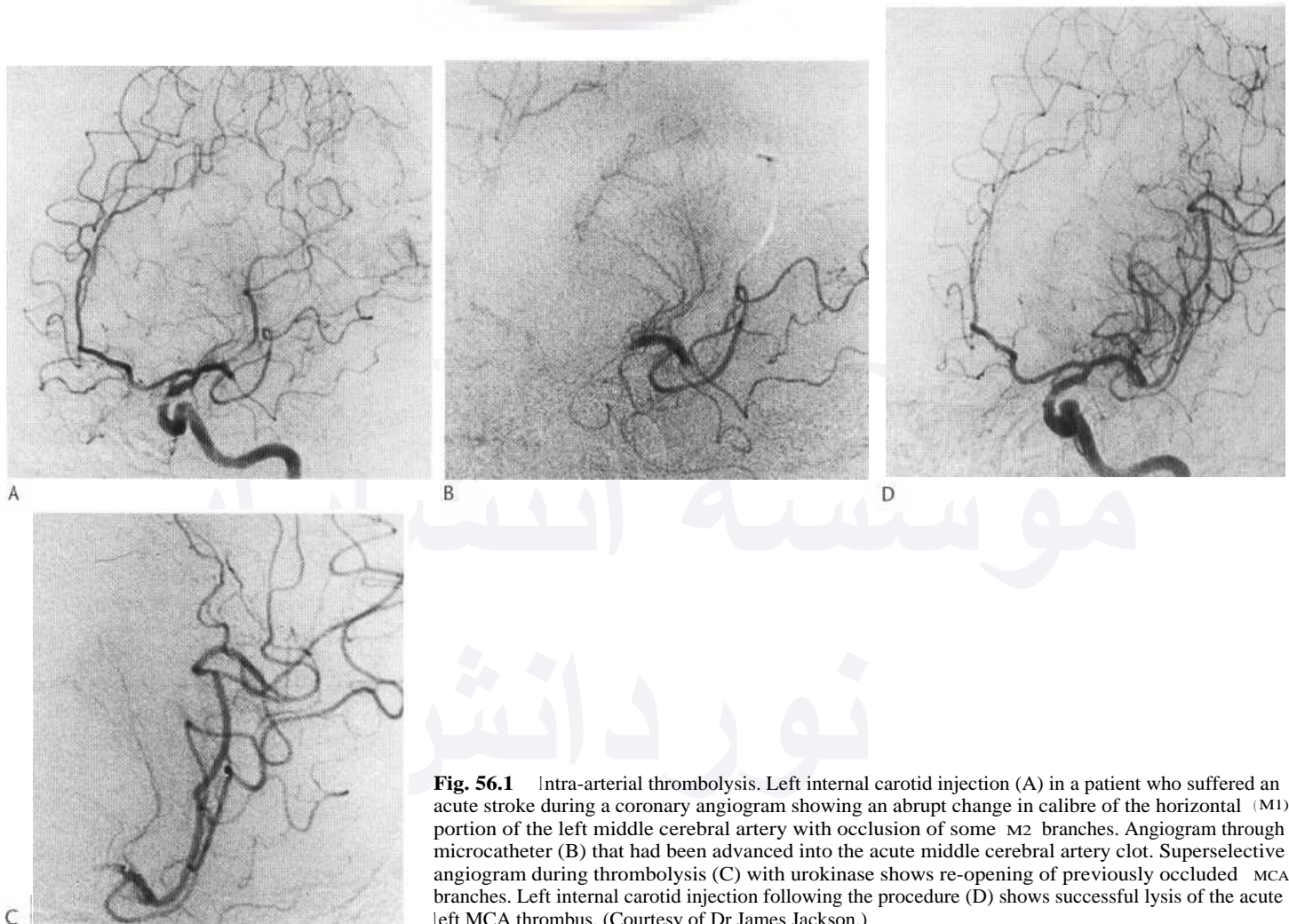


Fig. 56.1 Intra-arterial thrombolysis. Left internal carotid injection (A) in a patient who suffered an acute stroke during a coronary angiogram showing an abrupt change in calibre of the horizontal (M1) portion of the left middle cerebral artery with occlusion of some M2 branches. Angiogram through microcatheter (B) that had been advanced into the acute middle cerebral artery clot. Superselective angiogram during thrombolysis (C) with urokinase shows re-opening of previously occluded MCA branches. Left internal carotid injection following the procedure (D) shows successful lysis of the acute left MCA thrombus. (Courtesy of Dr James Jackson.)

of morbidity and mortality from aneurysm re-rupture, but management of cerebral vasospasm remains still a challenge. Approximately one-third of patients with subarachnoid haemorrhage develop symptomatic vasospasm with delayed ischaemic deficit, of which 30% will die and a further 30% will have a permanent deficit.

Medical treatment consists of hypertension, hypervolaemia and haemodilution (triple H therapy). Patients who fail to respond to medical therapy may benefit from endovascular treatment, which falls into two categories: mechanical dilatation of stenotic segments (balloon dilatation) and pharmacological relaxation of the contracted vessels with intra-arterial papaverine infusion.

Intracranial balloon angioplasty is performed with a small, compliant balloon attached to a microcatheter (Fig. 56.2). It is only suitable for treatment of the proximal segments of intracranial vessels, as dilatation of smaller branches carries a high risk of vessel rupture. Balloon dilatation has a more permanent effect than the infusion of papaverine through a microcatheter, which often leads only to a transient increase of the vessel lumen. Papaverine may, however, be useful to facilitate access for endovascular treatment of a ruptured aneurysm if this is impeded by vasospasm. It can also be used to treat vasospasm in distal branches of cerebral arteries that are not suitable for balloon dilatation. The complications of both techniques include vessel dissection and rupture, vessel thrombosis or embolus and rupture of an unsecured aneurysm. Early endovascular treatment has a higher success rate. Treatment of an obviously infarcted territory should be avoided.

Angioplasty and stenting of extracranial vessels

The European Carotid Surgery Trial (ECST) and the North American Symptomatic Carotid Endarterectomy Trial (NASCET) demonstrated that carotid endarterectomy significantly reduced the risk of recurrent stroke in patients with an over 70% carotid artery stenosis. Subsequently percutaneous transluminal angioplasty (PTA) and stenting have emerged as alternatives to surgery in these

patients. A large randomised multicentre trial, the Carotid and Vertebral Artery Transluminal Angioplasty Study (CAVATAS) showed an almost identical 30-day outcome of mortality and major stroke between surgical and endovascular treatment, however, endovascular treatment was safer in terms of minor morbidity such as cranial nerve palsies and haematoma. Three-year follow-up data suggested no difference in outcome between the two treatments, suggesting that both are equally effective in preventing stroke.

There has been a considerable evolution in endovascular techniques during and since the CAVATAS study. The majority of the patients in the endovascular arm of CAVATAS were treated with balloon angioplasty alone and only 22% were treated with stents. In the meantime primary stenting has become the endovascular technique of choice for carotid artery stenosis, replacing PTA. The majority of major strokes after carotid PTA are the result of dissection of the carotid artery at the time of balloon inflation with subsequent thrombosis. Dissection and occlusion of the carotid artery are less likely to occur with stenting because the stent maintains laminar flow across the stenosis and seals the site of dissection, preventing a free intimal flap. There is also evidence from endovascular intervention in the coronary circulation of superior outcomes with stenting compared with balloon angioplasty.

Carotid stenting (Fig. 56.3) is generally performed under local anaesthesia. The patient should receive antiplatelet therapy (ideally a combination of aspirin and clopidogrel prior to and following the procedure) to minimise the risk of thromboembolic complications. Following preliminary angiography, a guiding catheter is placed in the common carotid artery, the stenosis is crossed with a soft tip guide-wire and a self-expandable stent is placed across the stenosis, normally bridging the carotid bifurcation. The self-expandable stent allows differential expansion of its distal and proximal portions adapting to the different diameters of the common and internal carotid arteries. Additional dilatation of the stenosis with a balloon catheter placed within the stent is usually performed.

Recent developments in carotid stenting include protection devices such as filters and occlusion balloons, which can be placed

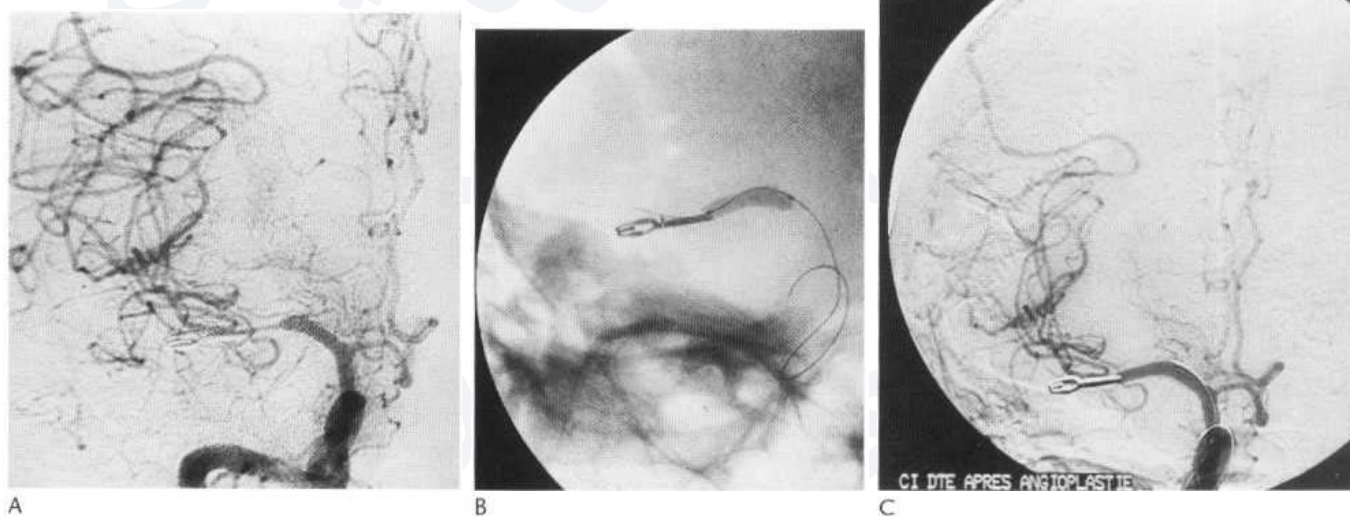


Fig. 56.2 Angioplasty of vasospasm. Right ICA angiogram following clipping of a right MCA aneurysm, which had bled, demonstrates severe vasospasm of the M1 segment of the right MCA (A). An unsubtracted image taken during balloon dilatation (B) demonstrates the inflated angioplasty balloon and aneurysms clip. Postangioplasty right ICA angiogram (C) demonstrating a normal calibre of the M1 segment.

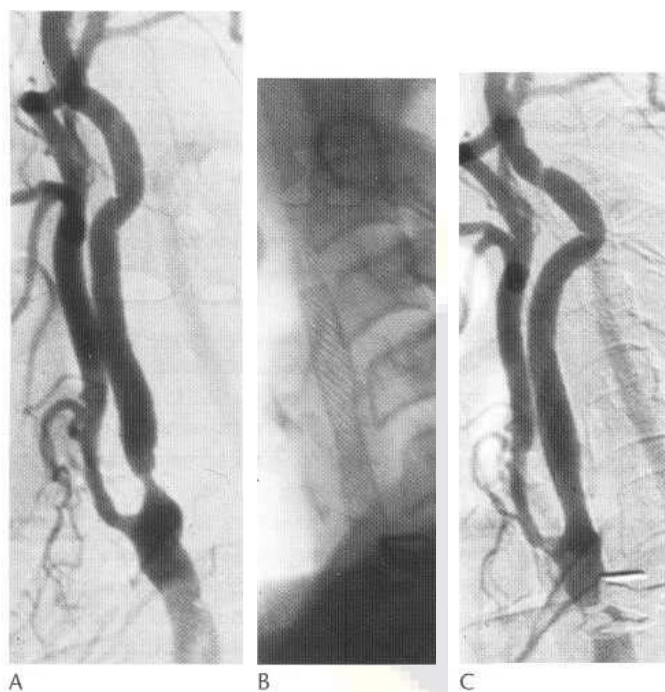


Fig. 56.3 Carotid stenting. The preceding common carotid artery angiogram (A) demonstrates a severe stenosis at the origin of the internal carotid artery. An unsubtracted image during the procedure (B) shows a self-expandable stent placed across the stenosis with a residual waist at level of stenosis. The postprocedure right CCA angiogram (C) demonstrates successful treatment of the stenosis.

distal to the carotid stenosis prior to stent deployment to catch any embolic material released during stenting. There is currently an active debate whether these protection devices should be used routinely, as they prolong and complicate the procedure and can, in rare cases, cause dissection of the distal internal carotid artery. It remains to be seen whether the benefits of these devices outweigh these drawbacks.

Larger published carotid stenting series suggest an acceptable complication rate and medium-term results comparable to endarterectomy. Prospective trials randomising surgical treatment versus carotid stenting are underway on both sides of the Atlantic.

Angioplasty and stenting for intracranial arteriosclerotic disease

Intracranial arteriosclerotic disease represents a significant cause of ischaemic strokes. It is more frequently seen in African-American or Asian ethnic groups compared to Caucasians. The Warfarin-Aspirin Symptomatic Intracranial Disease Study showed that the annual stroke risk remains as high as 10% under therapy with aspirin in patients with a greater than 50% stenosis of the MCA or distal ICA. Warfarin therapy reduced the annual stroke risk to 3.6% but was associated with a greater risk of haemorrhagic complications. The surgical treatment option consists of an extracranial-intracranial bypass operation, which has not been shown to confer any additional benefit over aspirin therapy. The possibility of treating these patients with endovascular techniques such as balloon angioplasty and stenting represents an important development. This is a technique in evolution and dedicated intracranial stents have only recently become available, after the initial use of coronary stents in the intracranial circulation. Preliminary data using recent

devices suggest that intracranial balloon dilatation and stenting have reached an acceptable safety level. Data on long-term patency, which may be compromised by a proliferative reaction of the vessel intima, are not yet available.

Endovascular techniques for lumen obliteration

A number of embolic agents are available and new agents are being developed. A broad distinction can be made between mechanical devices (such as coils and balloons), particles and liquid embolic agents.

Detachable balloons are one of the oldest mechanical devices and can be either of silicone or latex. They are used to occlude large vessels or large fistulas such as a carotico-cavernous fistula. One of the risks of this technique is the accidental detachment of a balloon in an unwanted position, which can lead to obstruction of normal cerebral vessels. Systems with non-detachable balloons are available for temporary test occlusions.

Guglielmi detachable coils (GDC) are currently the standard devices for embolisation of cerebral aneurysms. They are made of platinum and attached to a stainless steel delivery wire. The coils have a circular memory and are available in many different diameters and lengths. Detachment of the platinum coil from the delivery is achieved by electrolysis following application of an electrical current once the coil is deemed to be in a safe position. The advantage of such a system is that the coil remains firmly attached to the delivery wire until the current is applied, which allows the retrieval of a coil in an inappropriate position or of inappropriate size. Various other detachable coils have recently become available, using similar principles with various detachment systems and coil configurations.

Embolisation with particles leads to a less permanent occlusion than embolisation with liquid agents. Particles are therefore frequently used for preoperative embolisation. Polyvinyl alcohol (PVA) particles are currently the most frequently used particulate embolic agent and are supplied in sizes ranging from 50 to 1000 μm . PVA particles are diluted in radiopaque contrast medium as a suspension. Small particles (50-150 μm) are more effective in inducing tumour necrosis but carry a higher risk of cranial nerve or skin damage. Gel foam sponge is prepared from pork-skin gelatine and is a pliable material that can be cut to appropriately sized particles. It is used for occlusion of more proximal vessels, frequently following embolisation of distal vessels with PVA. It has no significant sclerosing effect and recanalises within approximately 6 weeks. Trisacryl gelatine microspheres (Embospheres) are a new non-absorbable embolic agent. They tend not to aggregate, are deformable and appear to penetrate deeper into the vascular system than PVA particles. There is also preliminary evidence that Embospheres have a longer occlusive effect.

Dehydrated (98%) alcohol is a potent liquid embolic agent. It has a sclerosing effect on cells it comes in contact with by virtue of causing dehydration and denaturation of peptides. Its main application is the percutaneous treatment of haemangiomas in the head and neck. It should be used with extreme care.

Acrylate glues such as N-butyl-cyanoacrylate (NBCA) are liquid embolic agents, mainly used for embolisation of cerebral AVMs and dural fistulas. Prior to injection, they are diluted in a lipophilic contrast agent (Lipiodol) or made radiopaque with Tantalum powder. On contact with an ionic solution, such as blood, NBCA solidifies

rapidly, causing permanent vascular occlusion. The microcatheter through which it has been delivered has to be swiftly withdrawn to avoid the risk of gluing the catheter in-situ. It is a very effective but dangerous embolic agent, which is not easy to handle, and should only be used by experienced operators.

Onyx is a new non-adhesive liquid embolic agent which consists of a mixture of ethyl-vinyl alcohol polymer (EVOH), dimethyl sulfoxide (DMSO) as a solvent and tantalum to render it radiopaque. In contrast to NBCA, it solidifies slowly, minimises the danger of in situ gluing of a microcatheter. Onyx has been used for cerebral arteriovenous malformations (AVMS) and giant cerebral aneurysms in which other forms of endovascular or surgical treatment are difficult.

Carotid and vertebral artery test occlusion

Test occlusion of the internal carotid or vertebral arteries is performed to assess the ability of the cerebral circulation to tolerate permanent sacrifice of such a vessel. Sacrifice of the internal carotid or vertebral artery may be contemplated in the context of surgery for skull base and cervical neoplasms encasing these vessels, or for the treatment of giant aneurysms, where surgical or endovascular treatment with preservation of the parent artery is not possible. Testing the clinical tolerance of an occlusion is the most important part of the procedure, which has therefore to be performed under local anaesthesia. A temporary (non-detachable) occlusion balloon, fixed at the tip of a microcatheter, is advanced to the point of the anticipated permanent occlusion and then inflated for approximately 30 minutes with careful monitoring of the patient's neurological status, which is best undertaken by a separate operator. In the event of neurological deterioration, the balloon has to be deflated immediately to prevent a permanent deficit. In addition to clinical criteria, an injection of the contralateral ICA during inflation of the test occlusion balloon is made to assess cross flow through the circle of Willis and to detect any delay in the transit of contrast medium on the side of the occlusion. This is best done by comparing the appearance of cerebral veins in the cerebral hemispheres. A delay in venous opacification of 2 seconds or more indicates that the occlusion is unlikely to be tolerated. Test occlusion

can also be combined with a number of simultaneously performed adjunctive tests, such as pharmacologically induced hypotension, transcranial Doppler, SPELT or Xenon CT. An added benefit from these procedures has, however, not been convincingly demonstrated at present. Complications of test occlusion include arterial dissection (symptomatic and asymptomatic) and transient or permanent neurological deficit. Routine use of heparin during the test occlusion limits the incidence and severity of these complications.

Traumatic carotico-cavernous fistulas

Trauma can result in a tear in the cavernous segment of the internal carotid artery, leading to a defect in the arterial wall with blood shunting directly into the cavernous sinus surrounding this arterial segment (direct carotico-cavernous fistula). From the cavernous sinus arterialised blood drains to reverse the flow in the ophthalmic veins, cerebral veins or the petrosal venous sinuses. Patients present with symptoms of venous hypertension, sometimes months after the trauma. Increased pressure in the ophthalmic veins typically causes proptosis, scleral injection and conjunctival haemorrhages. Increased cerebral venous pressure can cause headaches, seizures and venous haemorrhages.

The goal of treatment is the occlusion of the arteriovenous fistula with preservation of the lumen of the internal carotid artery. This is best achieved from an intra-arterial approach using detachable balloons (Fig. 56.4). A microcatheter with a deflated attached balloon is passed from the carotid artery through the defect in its wall into the cavernous sinus. The balloon is then gradually inflated until the fistula is occluded from the venous side, preserving patency of the ICA and flow to the ipsilateral intracranial vessels. If this is achieved the balloon is detached by a gentle pulling action. Insertion of more than one balloon may be necessary in large fistulas. In experienced hands a successful occlusion can be obtained in up to 90% with this method. This is usually followed by rapid improvement of clinical symptoms.

In the remaining cases alternative treatment options have to be considered. These include coil embolisation either transarterially, or using a transvenous approach via the inferior petrosal or ophthalmic

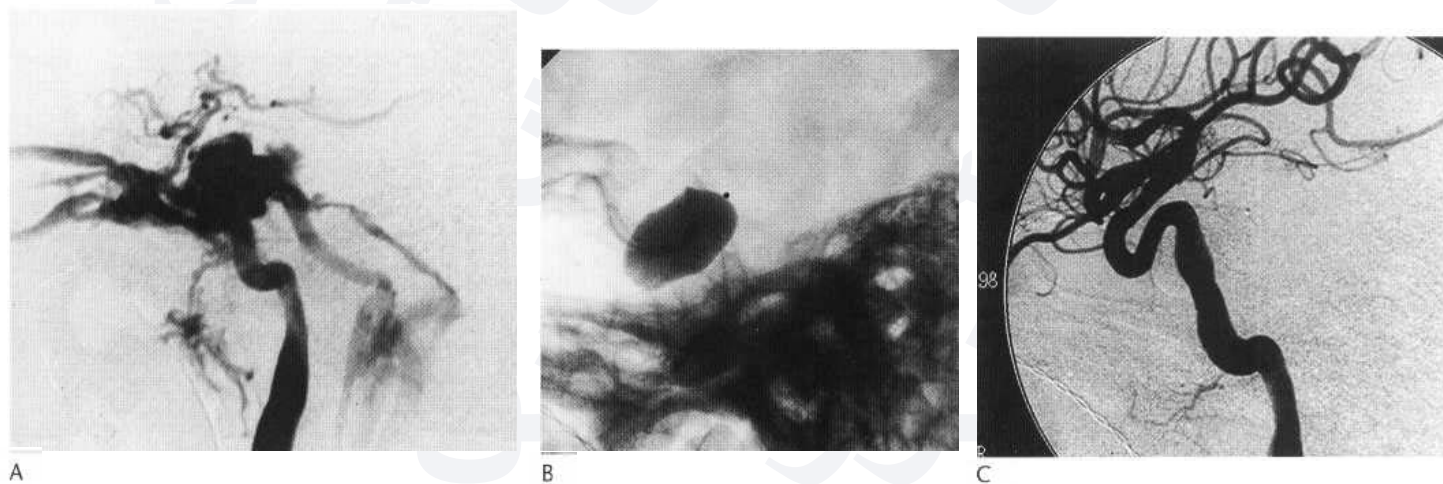


Fig. 56.4 Balloon embolisation of carotico-cavernous fistula. Internal carotid artery angiogram (A) demonstrating a traumatic carotico-cavernous fistula shunting into the ophthalmic veins and petrosal venous sinuses. Note the absence of opacification of the ipsilateral intracranial vessels due to steal through the shunt. Unsubtracted image (B) at the end of the procedure shows an inflated balloon, filled with contrast medium, within cavernous sinus. The post-procedure internal carotid angiogram (C) demonstrates complete closure of the fistula with normal anterograde opacification of the ipsilateral intracranial vessels.

veins. Sacrifice of the carotid artery, which should always be preceded by a test occlusion, represents the last treatment option.

Risks of this procedure include stroke following arterial occlusion after unintentional balloon detachment and cranial nerve palsies, usually transient, due to pressure from the balloon or coils.

Treatment of epistaxis

The most common cause of epistaxis is the spontaneous or idiopathic form, frequently related to smoking and hypertension. Other causes of epistaxis include tumours (juvenile angiofibroma in male adolescents and malignant tumours in adults), trauma (carotico-cavernous fistulas, traumatic false aneurysm or iatrogenic following endoscopic sinus surgery) and Osler-Weber-Rendu disease.

Most cases of spontaneous epistaxis occur in the anterior septal area of the nose (Kiesselbach's plexus), a location that is easily accessible for cauterity and packing. Posterior epistaxis is often more difficult to treat, requiring posterior nasal packing and endoscopic cauterisation. Endovascular embolisation is indicated if the bleeding is refractory to this initial treatment.

Blood supply to the nasal fossa derives from the internal carotid artery (ethmoidal branches of the ophthalmic artery) and external carotid artery (maxillary artery and facial artery). The main blood supply derives from the sphenopalatine artery, a branch of the maxillary artery, which can be superselectively catheterised with microcatheters.

Refractory idiopathic epistaxis is typically embolised with polyvinyl alcohol particles. This has an 87% success rate after embolisation of internal maxillary branches alone and a 97% success rate with additional facial artery embolisation. Potential complications include stroke and blindness as a result of inadvertent embolisation of ICA branches. It is therefore extremely important to check for the presence of dangerous external to internal carotid artery anastomosis before and during particle embolisation.

It should be noted that in the setting of haemorrhage in acute trauma, particle embolisation is not a suitable technique for the treatment of bleeding due to rupture of a traumatic false aneurysm or vessel transection, as the volume of fluid used to deliver the par-

articles may result in re-rupture, precipitating fresh haemorrhage. Coil or glue embolisation should be considered in this setting.

Endovascular therapy of intracranial aneurysms

Endovascular techniques are becoming more widely accepted and evolving technology is allowing endovascular treatment of arterial aneurysms that would have previously required surgery, or would have been regarded as untreatable. Published evidence suggests that endovascular techniques have comparable rates of immediate neurological complication to conventional surgery, while avoiding a craniotomy and surgical manipulation of brain.

In specific settings (aneurysms in the posterior fossa where surgical access is often difficult (Fig. 56.5), patients in poor medical condition), an endovascular approach is generally preferred. Some centres proceed directly to endovascular treatment immediately following diagnostic angiography. Endovascular treatment also has an advantage in acute subarachnoid haemorrhage (SAH) where two aneurysms are found and it remains unclear which one has ruptured; both aneurysms can be treated acutely in the same sitting from an endovascular approach (Fig. 56.6) whereas surgical treatment might require two separate craniotomies.

A large multicentre trial comparing endovascular and conventional surgical treatment of intracranial aneurysms is currently underway and it seems likely that in the future, endovascular techniques will play an increasingly important role in the management of intracranial arterial aneurysms. Because these techniques are relatively new, their long-term efficacy has not been established. Careful follow-up is therefore essential. Follow-up catheter or MR angiography has already demonstrated recurrence of aneurysms, especially at the basilar and carotid terminations.

Currently, the most widely used technique is coil embolisation. This is achieved by careful placement of a microcatheter within the aneurysm lumen, through which detachable coils are deployed, provided they could be suitably positioned. If a satisfactory position cannot be obtained, the coils are retrievable before detachment. Thermally, mechanically and electrolytically detachable coils are

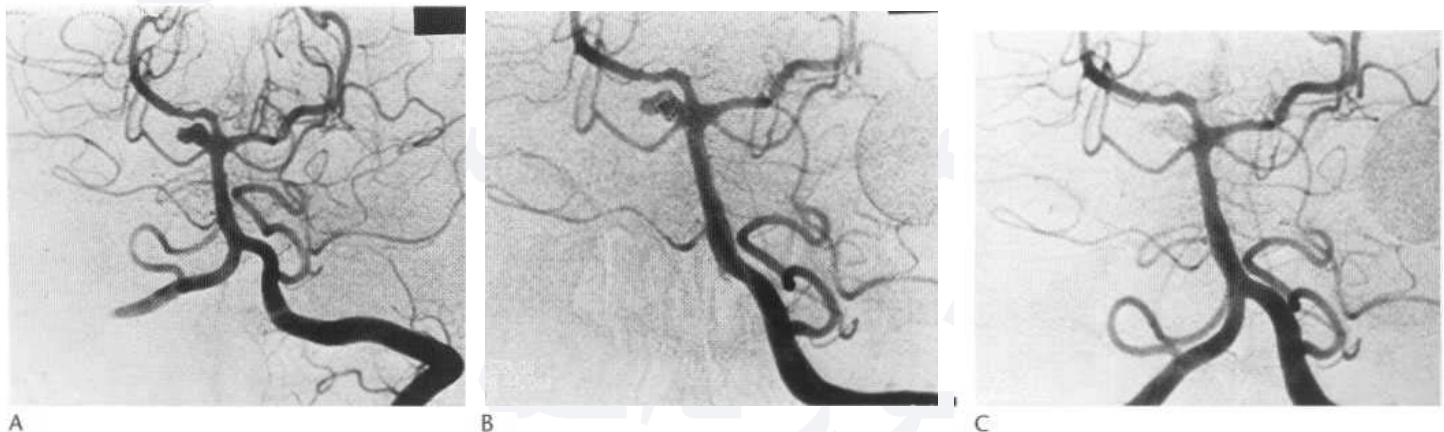


Fig. 56.5 Coil embolisation of superior cerebellar artery aneurysm. Left vertebral angiogram (A) demonstrating right superior cerebellar artery aneurysm. Note the caudal fusion and the origin of the perforating vessels off the more rostrally located P1 segment. Despite the broad neck and involvement of the superior cerebellar artery origin, it was decided to attempt endovascular treatment because of the posterior fossa location. A 3D GDC coil has been deployed (B) in good position, forming a basket across the aneurysm neck, avoiding the region of the superior cerebellar artery origin and the laterally projecting nipple, presumed to be the site of rupture. Final angiogram (C) demonstrating complete exclusion of the aneurysm without compromise of the adjacent vessels.

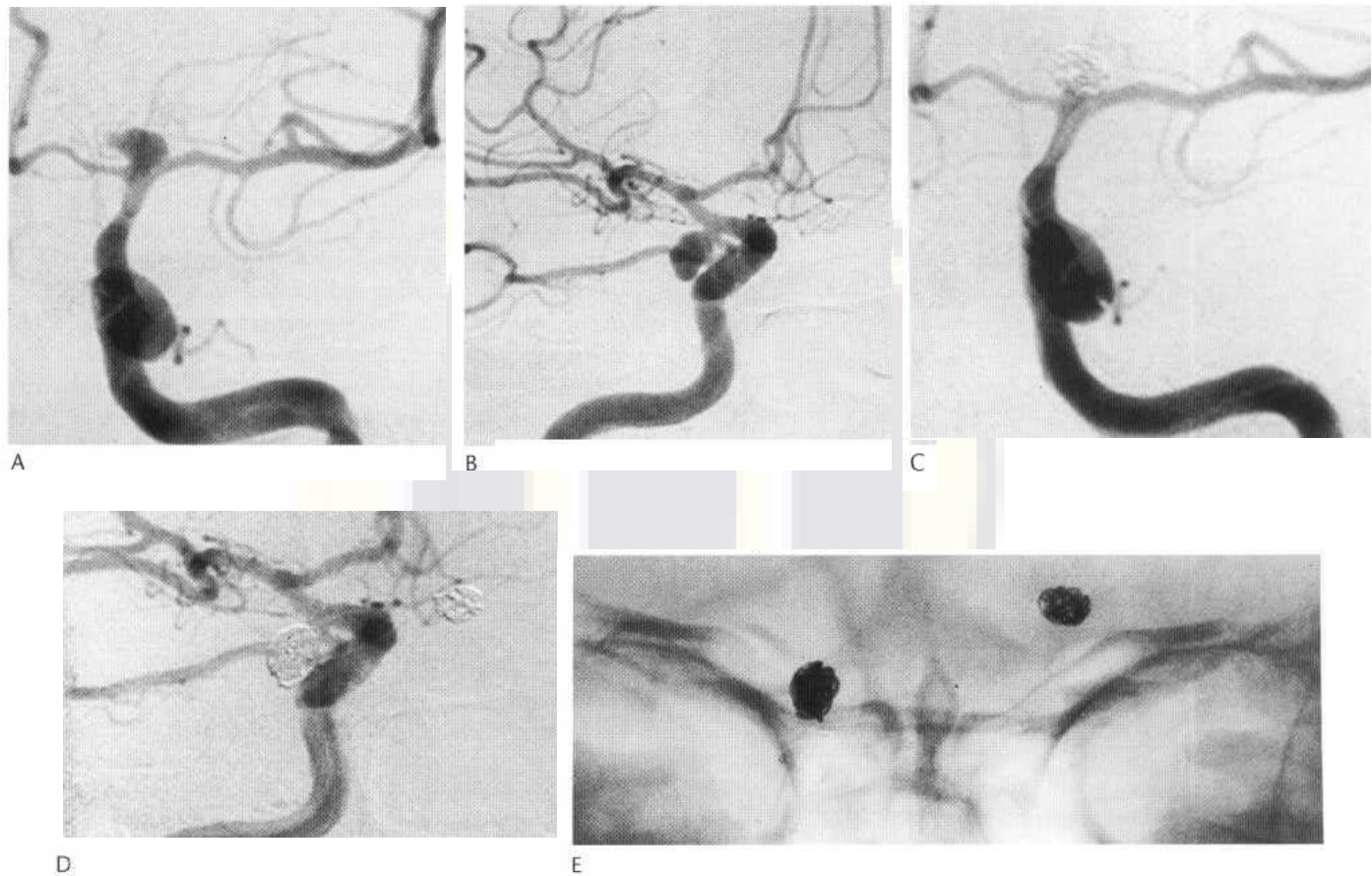


Fig. 56.6 Coil embolisation of bilateral intracranial aneurysms. Left ICA angiogram (A) demonstrating a terminal carotid aneurysm. Note the nipple pointing medially, an angiographic sign often seen in acutely ruptured aneurysms. Right ICA angiogram (B) demonstrating a posterior communicating segment aneurysm. CT (not shown) had revealed the greatest density of subarachnoid blood to lie in this region. Because of the disparity between the angiographic and CT findings, it was not certain which of the two aneurysms had bled. It was therefore decided to treat both in a single sitting, despite the risk of intervention in two different arterial territories. Bilateral surgical intervention was not considered to be a safe option. Left ICA angiogram (C) demonstrates the terminal carotid aneurysm to be excluded by coils. Right ICA angiogram (D) demonstrates the posterior communicating segment aneurysm to be excluded by coils. Unsubtracted image (E) shows the position of the coils.

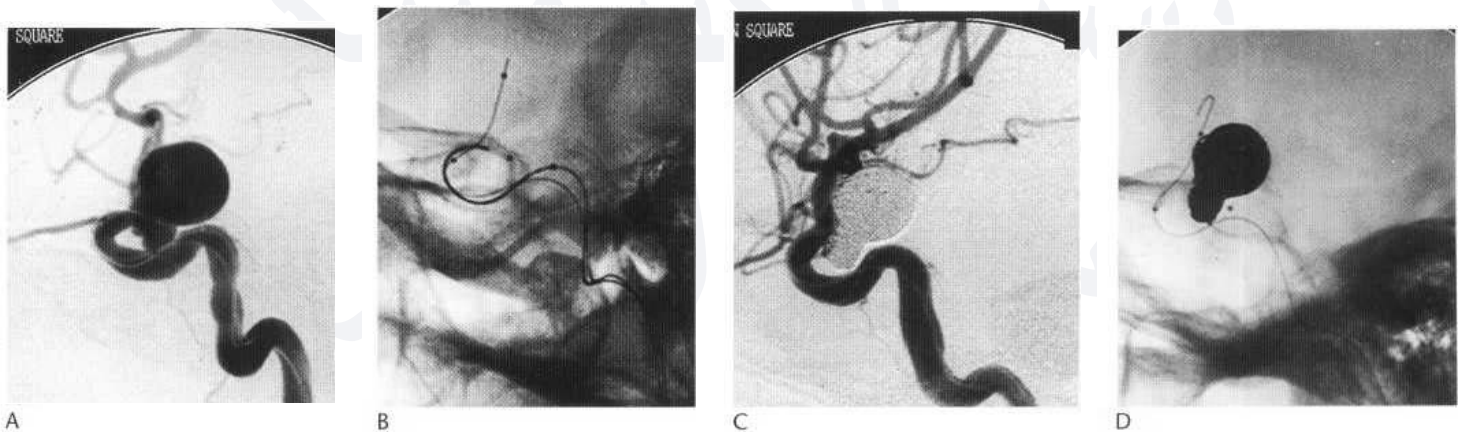


Fig. 56.7 Coil embolisation of wide-necked aneurysm with balloon remodelling. Subtracted and unsubtracted left internal carotid angiography before (A,B) and after (C,D) balloon remodelling assisted GDC coiling. The large supraclinoid aneurysm has a very wide neck (a). A remodelling balloon was placed across the neck of the aneurysm, seen on the unsubtracted image (B). Also note the microcatheter tip placed within the aneurysm lumen. The remodelling balloon was inflated for short periods during the coil deployment to prevent coil prolapse into the internal carotid artery. This enabled complete exclusion of the aneurysm, without compromise of lumen of the internal carotid artery (C). The dense coil mass is seen on the final unsubtracted image (D).

available, in a wide variety of shapes and sizes. Embolisation of aneurysms using fluid materials and exclusion of the aneurysm lumen with stents are techniques that have not yet evolved to the

point where they are suitable for widespread clinical use, though they are performed in some highly specialised centres and may be important in the future.



Fig. 56.8 Rupture during coil embolisation of intracranial aneurysms. Left vertebral angiogram (A) demonstrating extravasation of contrast from ruptured basilar tip aneurysms during coil placement. Note coils within aneurysm and extravasated contrast around the basilar artery in the interpeduncular and pre-pontine cisterns. Left vertebral angiogram (B) demonstrating cessation of extravasation after reversal of heparin with protamine and further packing of the aneurysm, to exclusion. The patient suffered no adverse consequences.

Irrespective of the technique used, the aim is total exclusion of the aneurysm lumen with preservation of the parent artery and its branches. This is most reliably achieved in narrow-necked saccular

aneurysms. Aneurysms with wide necks that would previously have been regarded as difficult to treat are increasingly amenable to endovascular treatment since the development of techniques preventing the prolapse of coils through the aneurysm neck, such as balloon remodelling (Fig. 56.7), stenting devices to bridge the aneurysm neck.

Potential complications of endovascular treatment include aneurysm perforation or rupture (Fig. 56.8) (by guide-wire, microcatheter or coil), inadvertent occlusion of the parent or branch arteries by coils (Fig. 56.9) and thromboembolic events.

Where preservation of patency of the parent vessel cannot be assured (fusiform or serpentine aneurysms, wide-necked aneurysms, false aneurysms and arterial dissection), sacrifice of the parent vessel may be considered, usually preceded by test occlusion. This can be achieved with either coils or detachable balloons, depending on the vessel configuration and indication for treatment.

Endovascular treatment of intracranial arteriovenous shunts

Endovascular treatment of cerebral arteriovenous malformations (AVMs)

Cerebral arteriovenous malformations are less common than cerebral aneurysms, with a prevalence of 0.2-0.5%. Most patients with cerebral AVMs develop symptoms before the age of 40 years, which is in contrast to cerebral aneurysms where only a quarter of patients present by the age of 40. Cerebral AVMs are an important cause of cerebral haemorrhage in young adults. Approximately 60% of patients with cerebral AVMs present with haemorrhage; epilepsy is the second commonest presentation, followed by non-haemorrhagic neurological deficit and headache.

AVMs are presumed to have usually pursued an indolent course before they present. They may occur in any location in the brain,



Fig. 56.9 Arterial occlusion due to coil embolisation of intracranial aneurysms. Left ICA angiogram (A) demonstrating coils within an aneurysm arising at the right side of the large anterior communicating artery and the origin of the right A2 segment. Note the good filling of the A2 segment. Left ICA angiogram (B) demonstrating occlusion of the A2 segment after deployment of a subsequent coil. The coil was successfully retrieved before detachment, but the vessel remained occluded. Fortunately, the patient rapidly developed collateral flow from the posterior cerebral artery and suffered no adverse consequences.

either supra- or infratentorial, from the cortical surface to the ependymal surface, or within the choroid plexus or ventricular system. Arterial supply and venous drainage may therefore be from any combination of superficial cortical vessels or deep perforating vessels. Meningeal vessels may also contribute to supply, usually after previous haemorrhage or surgery, but occasionally spontaneously.

AVMs can be treated by endovascular embolisation, microsurgery, radiosurgery or a combination of these methods. There is considerable uncertainty and lack of uniformity of opinion regarding the indications for, and strategies of, AVM treatment. The choice of treatment is often governed by local expertise and the goal of treatment may vary in individual patients depending on the clinical presentation, AVM location and size, and age of the patient. The perceived risks and benefits of treatment should be weighed up for each specific case and discussed by a multidisciplinary team. A commonly acknowledged aim is the prevention of cerebral haemorrhage or re-haemorrhage (which is associated with higher mortality and morbidity than an initial haemorrhage). The mean annual risk of haemorrhage from a cerebral AVM is probably 2-4%, but may be considerably increased in the presence of certain patient factors and angiographic features. The former include older age and initial presentation with haemorrhage and the latter include false aneurysms, venous ectasias or stenoses, a single draining vein, deep venous drainage and venous congestion.

The most commonly used endovascular approach is arterial embolisation using a permanent fluid agent such as NBCA, which is diluted and rendered radiopaque with Lipiodol or Tantalum (Fig. 56.10). The degree of dilution governs the speed of polymerisation and can be varied to suit the rapidity of arteriovenous shunting and distance to be crossed by this embolic agent. More recently Onyx has also been successfully used for embolisation of cerebral AVMs.

Small AVMs can be treated by endovascular means, radiosurgery or, if in a superficial location, by microsurgery. Radical obliteration of medium-sized or large AVMs represents a challenge for endovas-

cular treatment as well as for the other treatment modalities. It may require several staged embolisation procedures and complete AVM obliteration is often not possible. Endovascular treatment can be combined with other forms of treatment. It is sometimes performed to reduce the size of the AVM prior to radiosurgery, as the severity and incidence of side effects, such as radiation necrosis and radiation induced white matter disease, depend directly on the volume of irradiated brain tissue.

The role of partial AVM embolisation is actively debated and remains controversial. It can be effective in improving the control of epileptic seizures and in reducing the risk of haemorrhage by targeted embolisation of specific components such as false aneurysms. Partial embolisation can also bring relief of symptoms related to venous hypertension and the elimination of external carotid artery supply is often effective in alleviating headaches.

Endovascular treatment of vein of Galen aneurysmal malformations (VGAM)

VGAM is characterised by arteriovenous shunts at the choroidal level, within the subarachnoid space, in the region of the vein of Galen. They must be distinguished from cerebral arteriovenous shunts draining into the vein of Galen and producing dilatation of it as these lesions have entirely different natural histories and prognoses.

In VGAM, there is associated aneurysmal dilatation and abnormal persistence of the median vein of the prosencephalon, an embryological midline venous structure and precursor of the vein of Galen. The malformation often drains into a persistent falcine sinus and there may be agenesis of the straight sinus and anomalies of other dural venous sinuses.

VGAM and dural sinus malformations are the only intracranial AVMS, demonstrated to have been present in the fetal period. They are more common in males. Most present in either the neonatal period or in infancy. In general, the high flow arteriovenous shunt of VGAM is initially well tolerated from a neurological point of view and early presentation is with cardiac failure or altered CSF dynamics and macrocephaly.

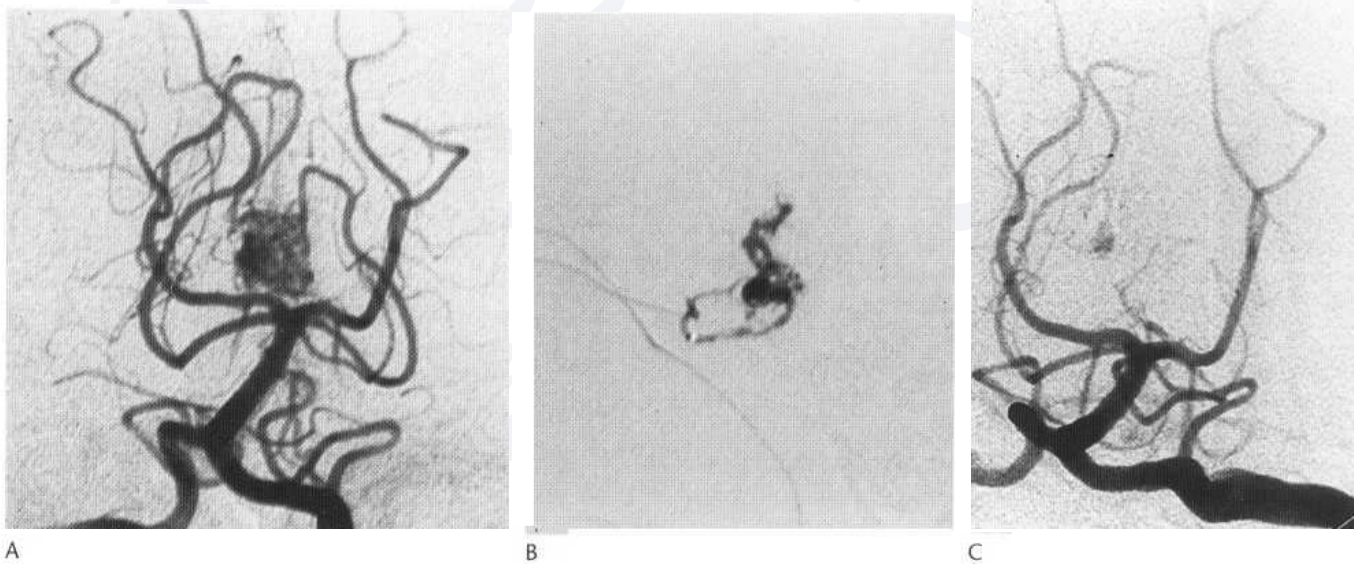


Fig. 56.10 Vermian AVM embolisation. Pre-embolisation left vertebral angiogram (A) demonstrating vermian arteriovenous malformation supplied by vermian branches of the superior cerebellar arteries. Microcatheter NBCA injection (B) into arteriovenous malformation nidus. Postembolisation of both major pedicles, left vertebral angiography (C) demonstrates almost complete obliteration of the nidus.

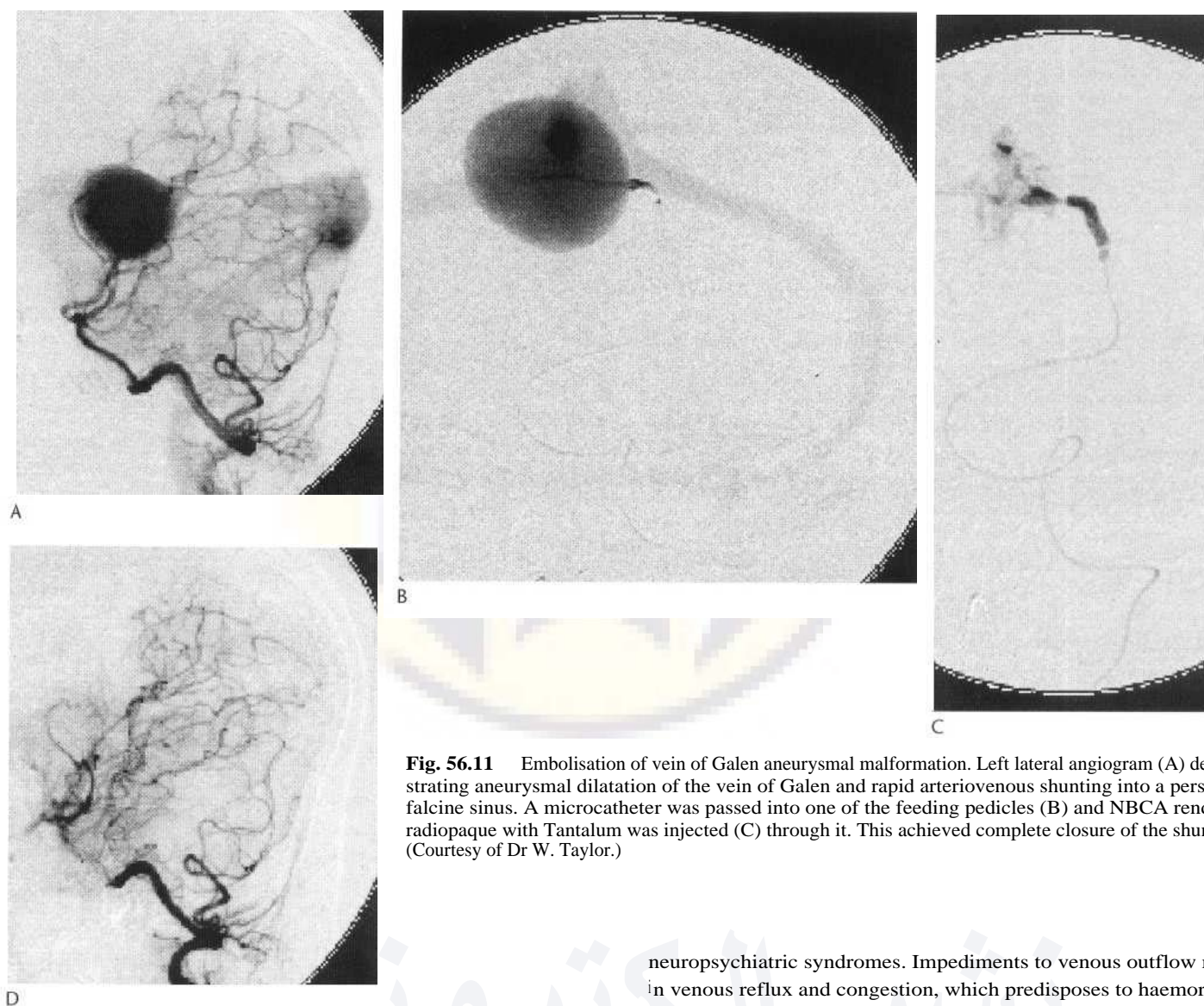


Fig. 56.11 Embolisation of vein of Galen aneurysmal malformation. Left lateral angiogram (A) demonstrating aneurysmal dilatation of the vein of Galen and rapid arteriovenous shunting into a persistent falcine sinus. A microcatheter was passed into one of the feeding pedicles (B) and NBCA rendered radiopaque with Tantalum was injected (C) through it. This achieved complete closure of the shunt (D). (Courtesy of Dr W. Taylor.)

If possible, treatment of the shunt in VGAM is deferred to allow for growth of the child, as intervention in neonates is technically difficult and hazardous. Criteria for intervention in infancy include progressive macrocephaly, developmental delay, seizures and reversible neurological deficit. Cardiac failure unresponsive to medical management is an indication for urgent embolisation in the neonatal period.

An arterial approach using a permanent embolic agent (NBCA) is most often used (Fig. 56.11). Venous approaches have also been described. The initial aim is to reduce the level of arteriovenous shunting to a degree that the cardiac failure can be managed. Further staged treatment can be performed after maturation of the child. Total cure is often possible.

Endovascular treatment of dural arteriovenous shunts

Dural arteriovenous shunts (DAVS) occur within the walls of dural venous sinuses or their tributaries. They may be related to previous episodes of sinus thrombosis. Depending on their location and severity of shunting, they may present with pulsatile tinnitus, bruit, ophthalmic symptoms (cavernous sinus DAVS), seizures, intracranial haemorrhage (Fig. 56.12) or decreased mental function and

neuropsychiatric syndromes. Impediments to venous outflow result in venous reflux and congestion, which predisposes to haemorrhage and cerebral parenchymal damage.

Cerebral venous congestion is an indication for treatment (Figs. 56.12, 56.13). Endovascular techniques are the first-line intervention in DAVS. An arterial approach utilising a permanent embolic agent is often used. The goal should be occlusion of the site of arteriovenous shunting with preservation of patency of the dural venous sinuses. Care should be taken not to redirect venous flow toward veins that drain the brain by occlusion of alternative outflow pathways. A venous approach may also be used, though this often necessitates sacrifice of a segment of dural venous sinus at the zone of arteriovenous shunting. This may be justified when there are multiple sites of shunting, multiple sources of arterial supply or inaccessible arterial sources. Venous approaches can be particularly useful in the treatment of cavernous sinus dural fistulas.

Head, neck and brain tumour embolisation, including chemotherapy

Embolisation of vascular tumour of the head, neck and CNS prior to surgery can significantly reduce intraoperative blood loss, shorten the operative procedure time and facilitate the removal of these tumours. Hypervascular tumours which may benefit from pre-operative embolisation include meningiomas, metastases, glomus

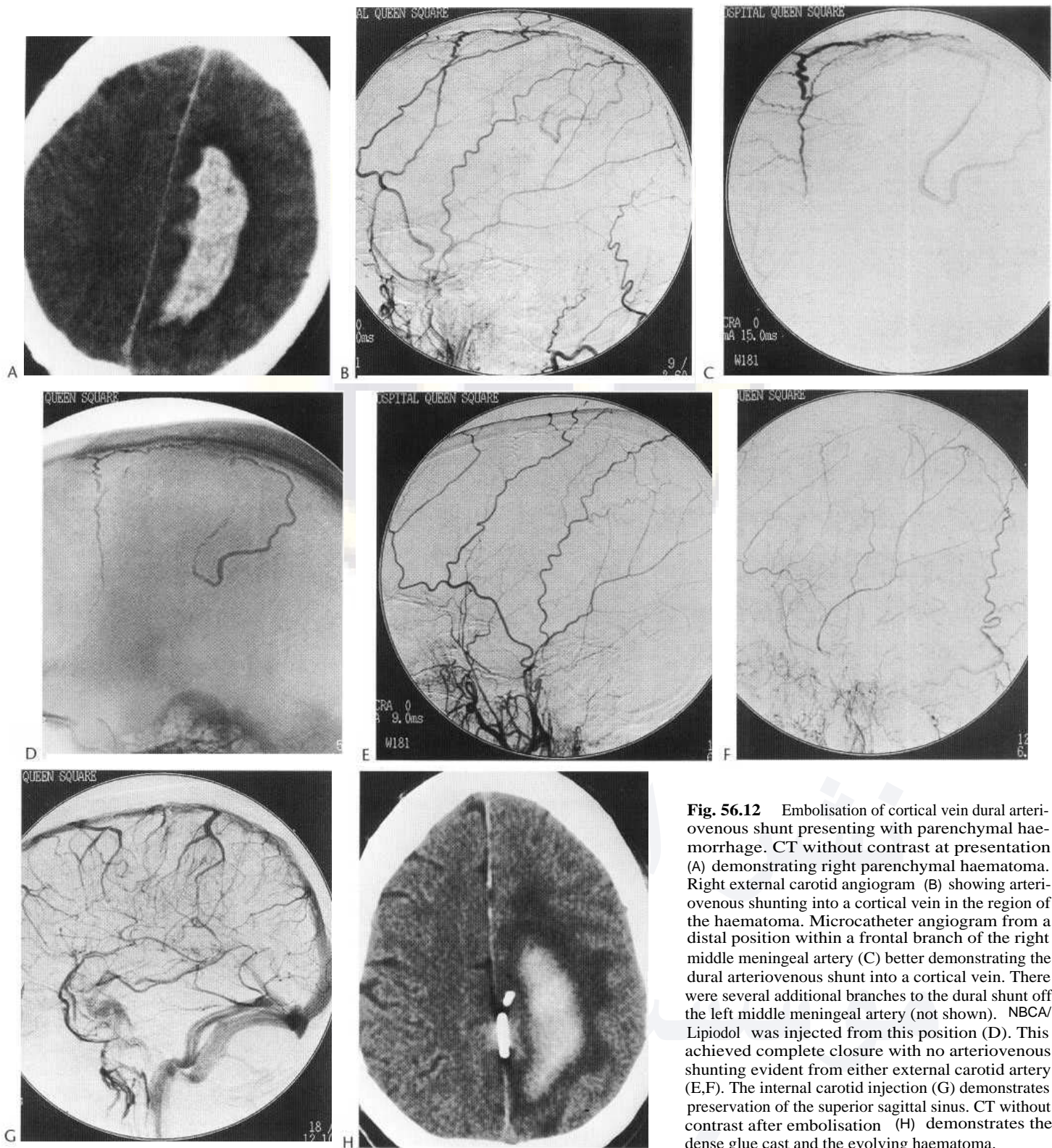


Fig. 56.12 Embolisation of cortical vein dural arteriovenous shunt presenting with parenchymal haemorrhage. CT without contrast at presentation (A) demonstrating right parenchymal haematoma. Right external carotid angiogram (B) showing arteriovenous shunting into a cortical vein in the region of the haematoma. Microcatheter angiogram from a distal position within a frontal branch of the right middle meningeal artery (C) better demonstrating the dural arteriovenous shunt into a cortical vein. There were several additional branches to the dural shunt off the left middle meningeal artery (not shown). NBCA/Lipiodol was injected from this position (D). This achieved complete closure with no arteriovenous shunting evident from either external carotid artery (E,F). The internal carotid injection (G) demonstrates preservation of the superior sagittal sinus. CT without contrast after embolisation (H) demonstrates the dense glue cast and the evolving haematoma.

jugulare tumours (Fig. 56.14), benign and malignant bone tumours and juvenile nasopharyngeal angiofibromas. Embolisation is usually performed via the endovascular route but can also be achieved by direct injection of embolic agent into the tumour (see below). The aim is a reduction of blood supply to the tumour and this is most efficient if the embolic agent can penetrate into the small vessels within the tumour, which is best achieved using parti-

cles (polyvinyl alcohol or Embosphereso) of a small size. The choice of particle size is a balance between safety and efficiency and depends on whether a highly selective catheter position could be achieved. Smaller particles penetrate deeper into the tumour but carry a higher risk of skin necrosis and cranial nerve palsies, risks they share with liquid agent such as glue or concentrate alcohol, which are occasionally used.

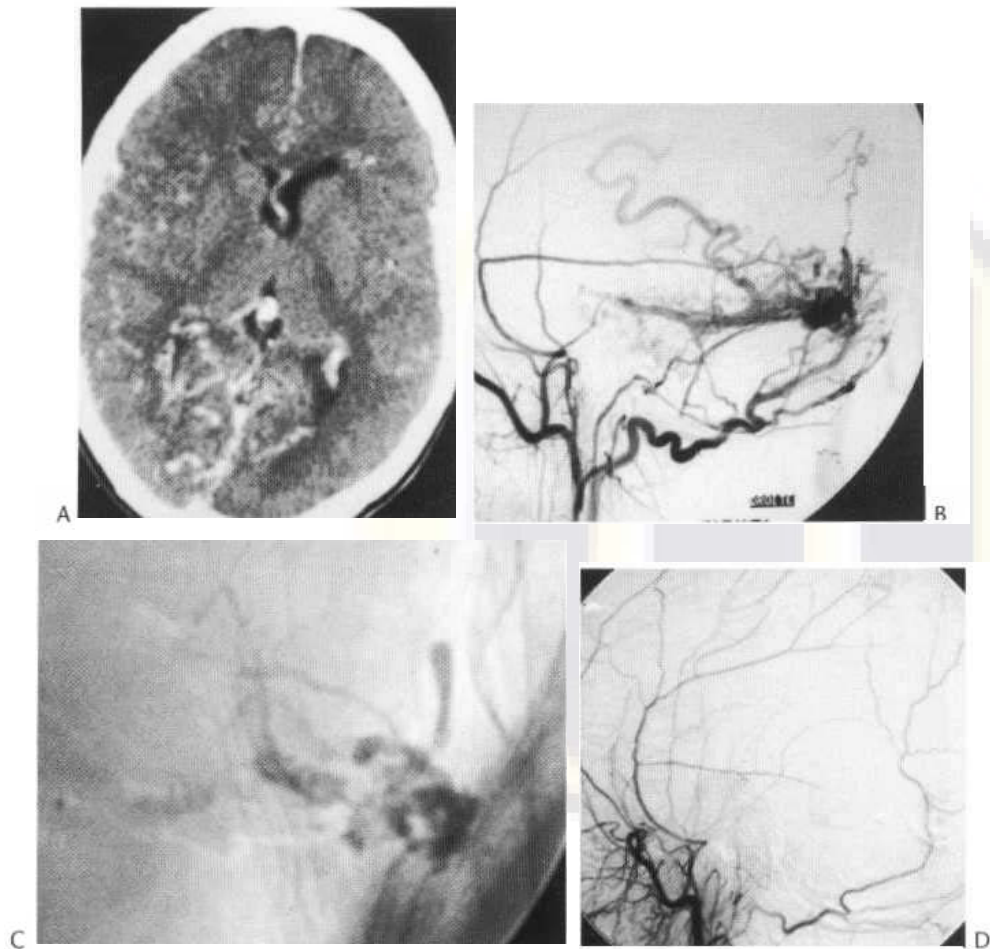


Fig. 56.13 Embolisation of dural arteriovenous shunt causing cortical venous congestion. CT with contrast (A) demonstrating dilated cortical and deep veins, including the septal vein. Right ECA angiogram (B) demonstrating a dural fistula of right transverse sinus supplied by meningeal and transosseous branches with retrograde cortical venous reflux. Unsubtracted image (C) showing NBCA glue cast at the site of the fistula. Note how the glue has penetrated the venous side of the fistula, with the cast corresponding to the zone of shunting demonstrated in (B). Right ECA angiogram (D) demonstrating complete occlusion of the fistula. Note the decrease in calibre of the occipital artery on this follow-up angiogram. (Courtesy of Prof. P. Lasjaunias.)

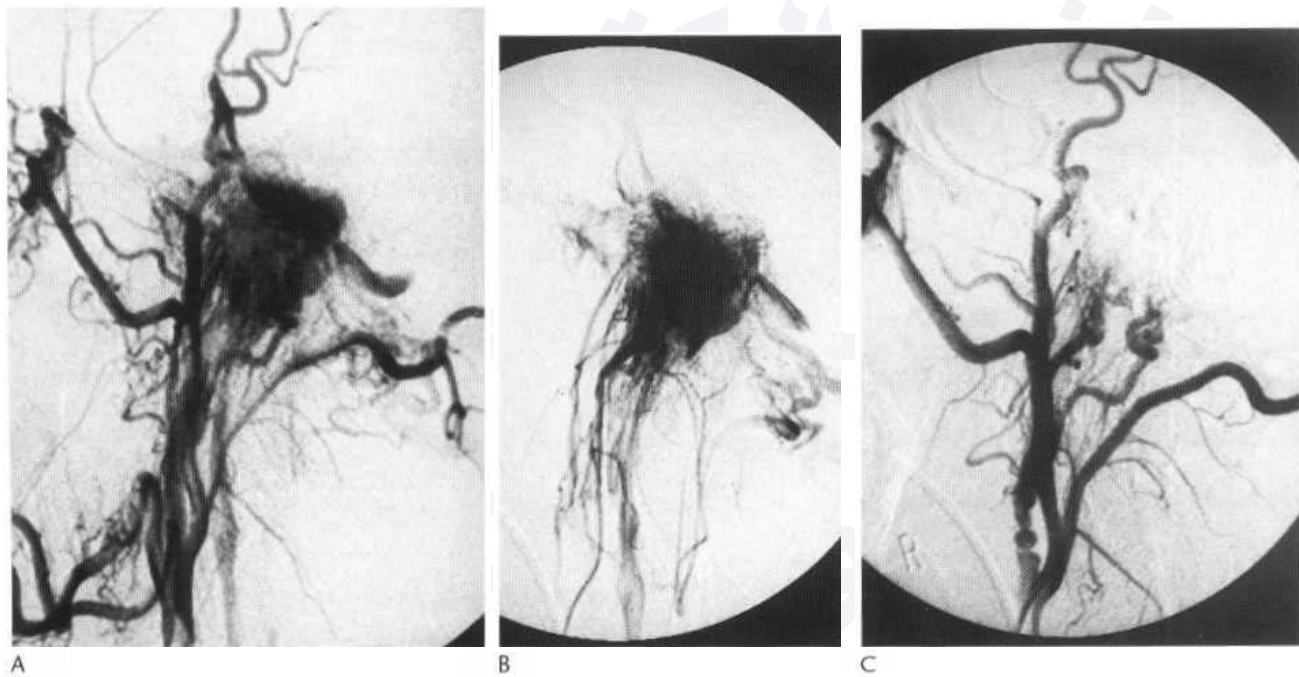


Fig. 56.14 Embolisation of glomus jugulare tumour. External carotid angiogram (A) showing a hypervascular tumour at the level of the jugular foramen. Superselective catheterisation of the ascending pharyngeal artery (B) prior to embolisation demonstrates that this vessel provides the main vascular supply to the mass, a typical finding in glomus jugulare tumours. The external carotid artery angiogram following particle embolisation (C) shows almost complete obliteration of the vascular supply. There is also some vasospasm near the catheter tip.

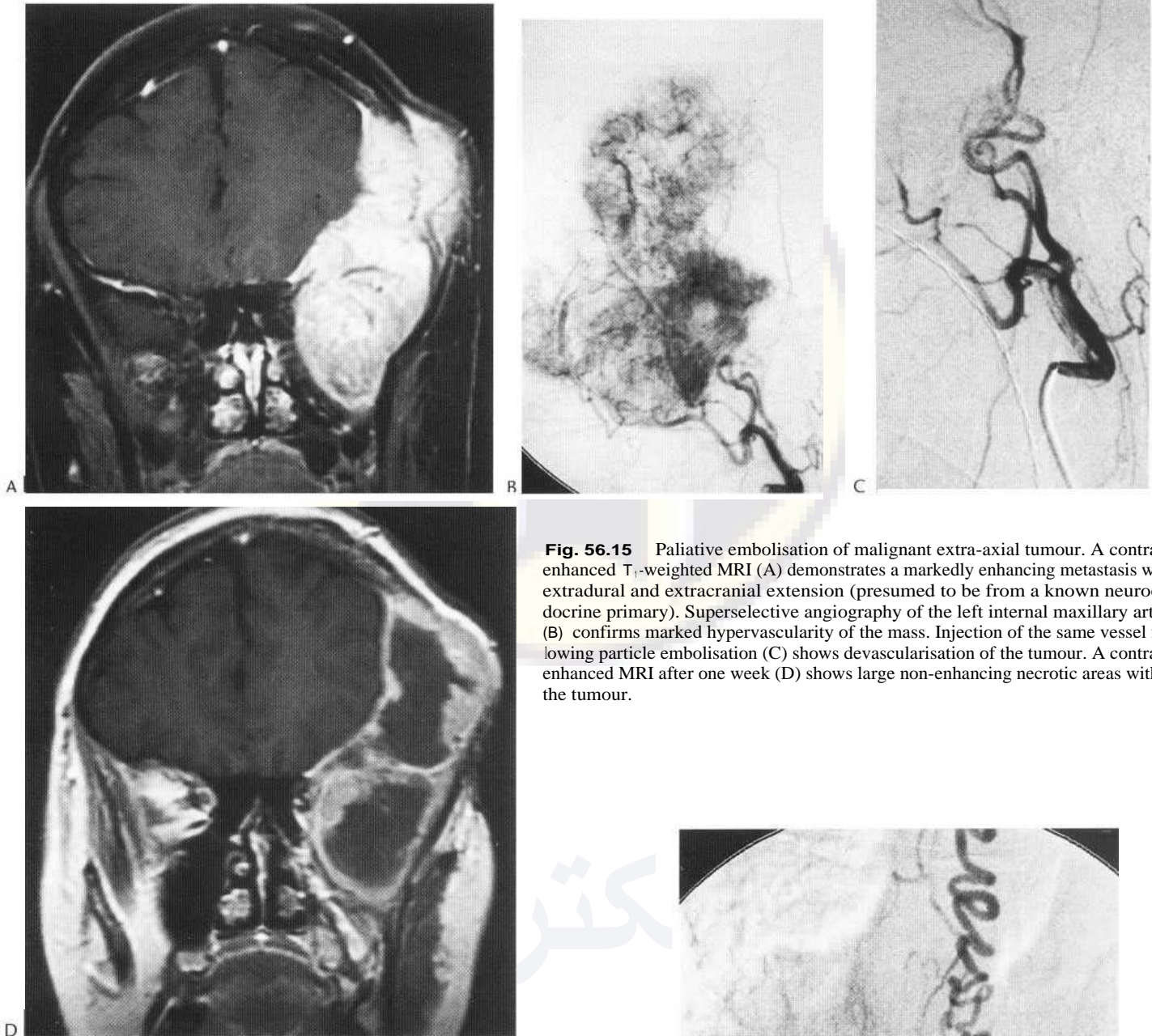


Fig. 56.15 Paliative embolisation of malignant extra-axial tumour. A contrast-enhanced T₁-weighted MRI (A) demonstrates a markedly enhancing metastasis with extradural and extracranial extension (presumed to be from a known neuroendocrine primary). Superselective angiography of the left internal maxillary artery (B) confirms marked hypervascularity of the mass. Injection of the same vessel following particle embolisation (C) shows devascularisation of the tumour. A contrast-enhanced MRI after one week (D) shows large non-enhancing necrotic areas within the tumour.

External carotid artery branches supply many of these tumours. Before and during the embolisation, a meticulous search for the presence of anastomoses from the external to the internal carotid or vertebral arteries is mandatory. It is important to realise that these collateral pathways can open during the procedure following alteration of the local haemodynamics. Anatomical variants such as ophthalmic supply from middle meningeal artery must be actively sought.

Endovascular tumour embolisation may also be indicated as a palliative procedure, to reduce tumour size or associated symptoms in patients with lesions not amenable to surgery (Fig. 56.15).

Intra-arterial chemotherapy is an established form of treatment in head and neck tumours that fail to respond to conventional therapy. Chemotherapeutic agents can be infused following catheterisation of external carotid branched via the femoral route or through an infusion pump, implanted via surgical cutdown of the



Fig. 56.16 Spinal dural arteriovenous fistula. Spinal angiogram in a patient with progressive leg weakness and sphincter disturbance. Selective injection of right thoracic intercostal vessels shows a dural arteriovenous fistula shunting into perimedullary veins, which drain superiorly and inferiorly.

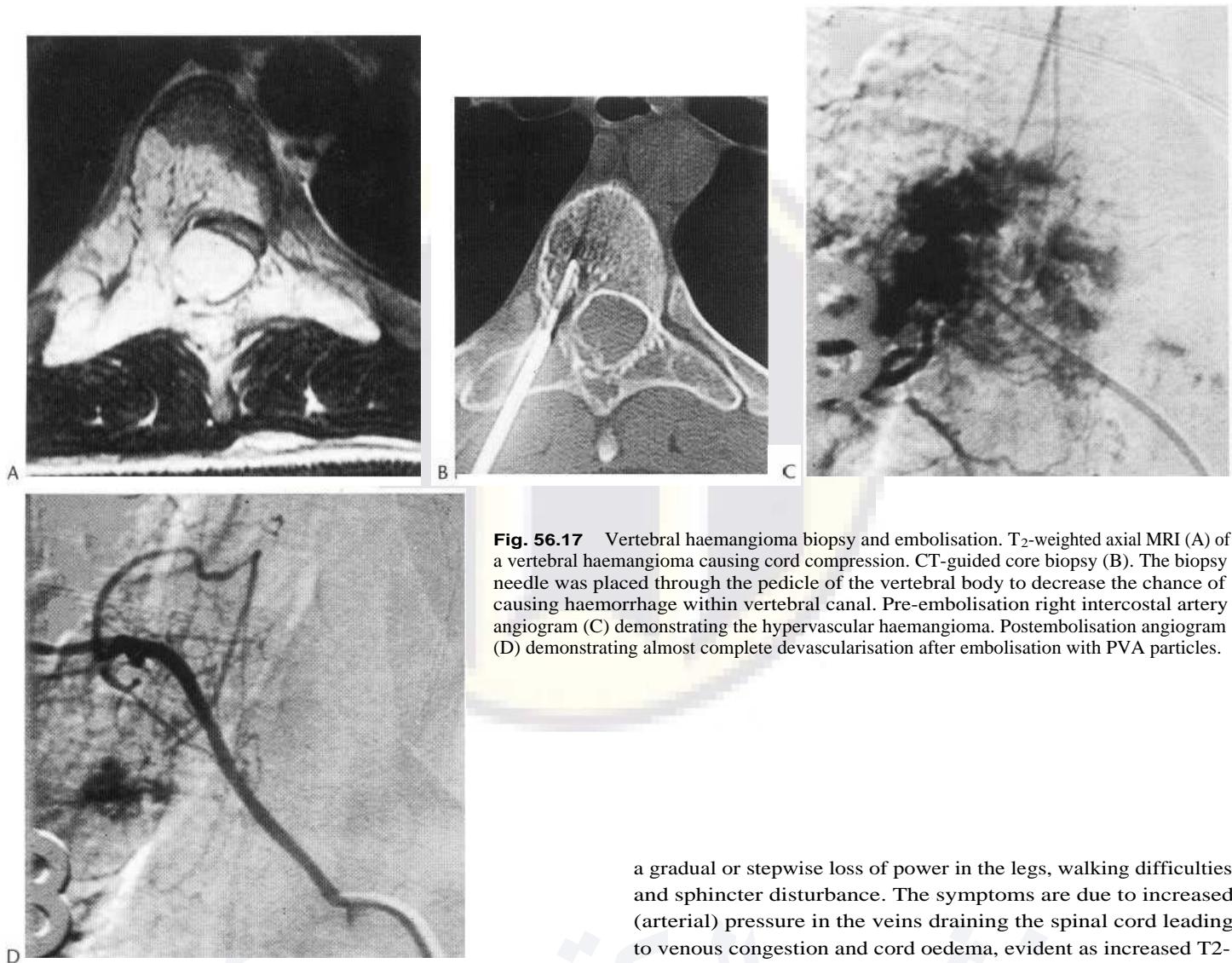


Fig. 56.17 Vertebral haemangioma biopsy and embolisation. T₂-weighted axial MRI (A) of a vertebral haemangioma causing cord compression. CT-guided core biopsy (B). The biopsy needle was placed through the pedicle of the vertebral body to decrease the chance of causing haemorrhage within vertebral canal. Pre-embolisation right intercostal artery angiogram (C) demonstrating the hypervascular haemangioma. Post-embolisation angiogram (D) demonstrating almost complete devascularisation after embolisation with PVA particles.

superficial temporal artery. Local toxicity of this treatment includes alopecia, mucositis, skin necrosis and cranial nerve palsies.

Spinal embolisation

Endovascular treatment of spinal cord arteriovenous shunts

In principal, endovascular treatment of arteriovenous malformations of the spinal cord does not differ from the brain, however, because of the small size of the vessels of the spinal cord, its dependence on one channel (the anterior spinal arterial axis) and the catastrophic consequences of occlusion of the arterial supply to even a small volume of the cord, it is an especially unforgiving territory to embolise in. Complete eradication of an arteriovenous shunt can seldom be safely achieved by embolisation. As in the brain, a permanent fluid embolic agent such as NBCA is preferred.

Whereas spinal cord AVMs are seen in young patients, spinal dural fistulas most commonly present in elderly male patients and are thought to be associated with venous thrombosis, like cranial dural fistulas. Clinical symptoms may have an insidious onset with

a gradual or stepwise loss of power in the legs, walking difficulties and sphincter disturbance. The symptoms are due to increased (arterial) pressure in the veins draining the spinal cord leading to venous congestion and cord oedema, evident as increased T₂-signal intensity within the cord on MR images. Definitive diagnosis of spinal dural fistulas requires high-quality spinal angiography, which should be performed under general anaesthesia (Fig. 56.16).

Spinal dural fistulas may be treated by embolisation or surgery. Embolisation is an option if the fistula arises from a purely radicular artery, which does not provide any arterial (either a radiculo-medullary or radiculopial artery) supply to the cord. It involves the injection of a permanent occlusive agent such as NBCA glue, which must reach and occlude the fistulous point. Surgery of these lesions is usually straightforward and consists of exposure and electrocoagulation of the fistula, which is located on the dura. The chief aim of treatment is to prevent further progression of symptoms. Recovery from existing symptoms is possible but can be slow and depends on the degree of established cord damage, which is related to the length of clinical history. Diagnosis of this relatively infrequent condition is unfortunately often delayed and patients have often had negative or inconclusive investigations for lumbar or thoracic disc disease. It is therefore important to heighten the awareness for this disease and the available treatment options. Their diagnosis is not infrequently missed, sometimes even after (usually inadequate) spinal angiography, and it must be remembered that the definitive diagnosis of spinal dural fistulas requires high-quality spinal angiography.

Endovascular treatment of vertebral tumours

Embolisation for vertebral tumours is generally performed preoperatively, aiming to reduce intraoperative bleeding (Fig. 56.17 C,D), though occasionally it may result in resolution of symptoms (either pain or cord compression). Both benign (especially haemangioma) and malignant (usually metastatic) hypervascular lesions may benefit from endovascular treatment.

High-quality diagnostic spinal angiography must be performed first. This should demonstrate the blood supply to and degree of vascularity of the lesion. The arterial supply to vertebral bodies is from the two adjacent metameric levels, and these should be examined bilaterally. The blood supply to the spinal cord must be carefully examined as inadvertent embolisation of a radiculopial or radiculomedullary artery may have terrible consequences. It will also be useful for the surgeon to know the location of any radiculomedullary artery in the region to be operated on.

If the lesion is hypervascular and there is no radiculomedullary or radiculopial artery arising from the same level, embolisation can be performed safely. It should be remembered that patterns of flow may alter in the course of embolisation, and the possibility of a previously unopacified vessel contributing to the supply of the spinal cord should be excluded. Embolisation may be performed either through a catheter positioned in the segmental artery supplying the tumour, or more selectively through a microcatheter in the feeding pedicles of the tumour itself. Occlusion of the segmental artery distal to the origin of supply to the tumour may be useful to reduce passage of embolic material to vessels supplying the skin and body wall.

DIRECT PERCUTANEOUS PROCEDURES

Imaging-guided biopsy

Fluoroscopy or cross-sectional imaging can be used to accurately place a biopsy needle and to avoid injury to adjacent vital structures, such as the spinal cord or major arteries (Fig. 56.17B). Biopsies of the spine are frequently performed under fluoroscopic or CT guidance. Imaging guided biopsies can also be performed on an interventional ('open') MR system, which allows multiplanar scanning and offers more flexibility in choosing the access route. Special MR-

compatible non-ferromagnetic instruments are required. In addition to percutaneous procedures performed in the radiology department, imaging plays an important role in neurosurgical navigation. This can be based on preoperative acquisition of volumetric CT or MR scans using a stereolactic frame or on intraoperative MR, which offers 'real-time' monitoring of neurosurgical procedures.

Imaging-guided percutaneous treatment

Percutaneous access under image guidance can also be used for minimally invasive treatment.

Direct percutaneous embolisation

Low-flow vascular malformations of the head and neck, such as haemangioma-lymphangiomas and venous malformations, can be treated with direct injections of concentrated alcohol under fluoroscopic guidance. This procedure has to be preceded by an angiographic run during the injection of a contrast medium through the percutaneously placed needle to delineate the vascular compartments and venous drainage route. Injection of concentrated alcohol should not be undertaken in the presence of intracranial venous drainage.

Spinal tumours or intracranial extradural tumours can be directly punctured using image guidance and embolised with particles or glue through a percutaneous needle, preoperatively or for palliation. Direct percutaneous tumour embolisation can be more efficient than embolisation of several feeding pedicles via the endovascular route but should only be undertaken by an experienced operator, using biplane fluoroscopy for intracranial lesions.

Percutaneous vertebroplasty

The aim of percutaneous vertebroplasty is mechanical strengthening of weakened or partially destroyed vertebral body by the percutaneous injection of acrylic cement, a substance which has been used in surgery for decades. The first image-guided percutaneous

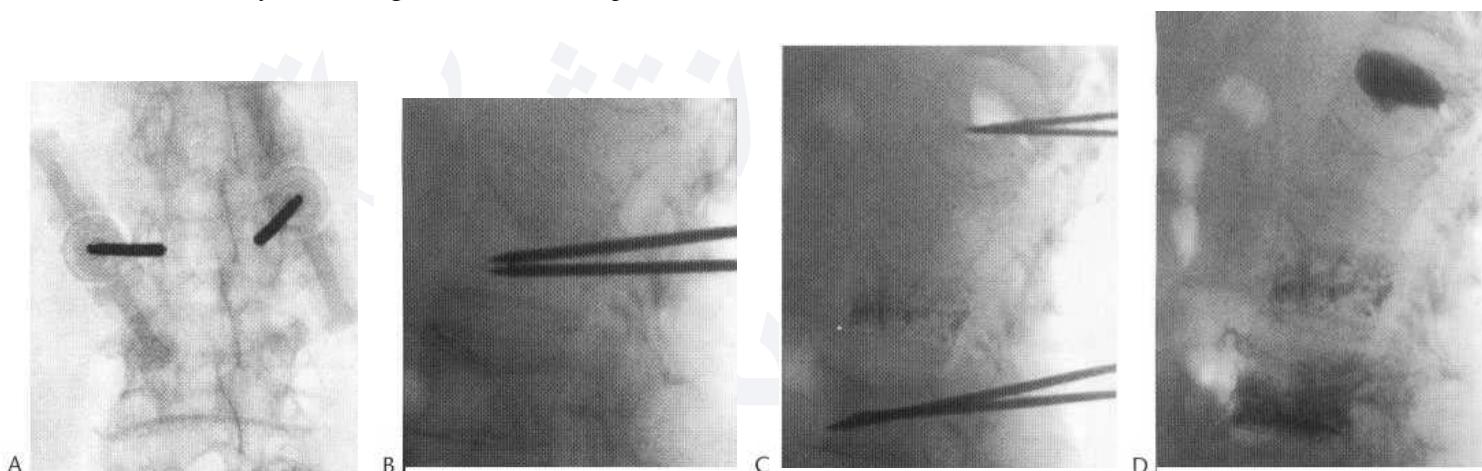


Fig. 56.18 Percutaneous vertebroplasty. Fluoroscopic images in frontal (A) and lateral (B) projections showing transpedicular course of cannulas prior to first injection of PMMA. Note marked osteopenia and loss of height of vertebral bodies in this patient with multiple myeloma. Subsequently cannulas were placed (C) in the other severely affected levels. A total of three levels were treated (D). The patient was able to cease morphine after the procedure. (Courtesy of Professor Juergen Reul.)

vertebroplasty (PVP) was performed in France in 1984, using the injection of polymethylmethacrylate (PMMA) into a C2 vertebra that had been partially destroyed by an aggressive haemangioma. Thereafter, PVP was used to treat vertebral compression fractures caused by metastatic or primary bone tumours (haemangiomas, giant cell tumours) and osteoporosis (primary or steroid induced).

PVP is able to provide rapid and lasting relief from the pain associated with vertebral compression fractures and is increasingly used for that purpose. High-quality fluoroscopic equipment is a prerequisite for PVP. It is essential for accurate placement of the cannula and real-time visualisation of the cement injection (Fig. 56.18). CT has been described as an aid to fluoroscopy, but adds considerable complexity and is most useful in the cervical spine to avoid the carotid vessels and down to approximately T4 where lateral fluoroscopy may be impossible through the shoulders.

Reported clinical complications following PVP include fever, infection, cement pulmonary embolism, radiculopathy and cord compression. Treatment of osteoporotic compression fractures has a low rate (1-2%) of mostly non-neurological complications. The complication rate increases in patients treated for malignant compression fractures, because of a higher risk of cement leakage from vertebrae destroyed by tumour. A 3-6% rate of (mostly transient) radiculopathy has been reported in this group.

Imaging-guided photodynamic therapy (PDT)

Photodynamic therapy is a minimally invasive treatment with great promise in malignant disease. It can be applied before or after chemotherapy and be repeated as necessary. It is based on the interaction of an intravenously injected photosensitising drug and locally delivered light of a specific wavelength, which activates the drug. Interaction of the activated photosensitiser with oxygen results in the production of a highly cytotoxic singlet oxygen. This technique has been used as surface illumination of superficial mucosal lesions in the past. Interstitial light delivery to solid tumours of the head and neck is greatly facilitated by imaging-guided placement of needles through which optic fibres can be inserted, providing a focused delivery of laser light (Fig. 56.19).



Fig. 56.19 Photodynamic therapy of carcinoma tongue. Sagittal (A) and axial (B) T₁-weighted scans performed on an 'open' interventional MR scanner of a patient with a carcinoma of the base of tongue causing airway obstruction. MR-compatible guiding needles, which appear as low-signal-intensity structures, were inserted into the tumour using MR guidance. Palliative treatment with PDT was carried out by inserting optic fibres through these needles.

REFERENCES AND SUGGESTIONS FOR FURTHER READING

- Bendszus, M., Klein R., Burger R., Metz M. W., Hofmann E., Solymosi L. (2000) Efficacy of trisacryl gelatin microspheres versus polyvinyl alcohol particle in the preoperative embolization of meningiomas. *American Journal of Neuroradiology*, 21, 255-261.
- Borden J. A., Wu J. K., Shucart W. A. (1995) A proposed classification for spinal and cranial dural arteriovenous fistulous malformations and implications for treatment. *Journal of Neurosurgery*, 82, 166-179.
- Brandt T., Kummer R. V., Muller-Kupfers M., Hacks W. (1996) Thrombolytic therapy of acute basilar artery occlusion: variables affecting recanalization and outcome. *Stroke*, 27, 875-881.
- Cavatas Investigators (2001) Endovascular versus surgical treatment in patients with carotid stenosis in the Carotid and Vertebral Artery Transluminal Angioplasty Study (CAVATAS): a randomised trial. *Lancet*, 357(9270), 1729-1737.
- Chimowitz M. I., Kokkinos J., Strong J., et al (1995) The warfarin-aspirin symptomatic intracranial disease study. *Neurology*, 45, 1488-1493.
- Davies M. A., Saleh J., Ter Brugge K., Willinsky R., Wallace M. C. (1997) The natural history and management of intracranial dural arteriovenous fistulae (part 1: benign lesions). *Interventional Neuroradiology*, 3(4).
- Davies M. A., Saleh J., Ter Brugge K., Willinsky R., Wallace M. C. (1997) The natural history and management of intracranial dural arteriovenous fistulae (part 2: aggressive lesions). *Interventional Neuroradiology*, 3(4).
- Dovey Z., Misra M., Thornton J., Charbel F. T., Debrun G. N., Ausman J. I. (2001) Guglielmi detachable coiling for intracranial aneurysms. The story so far. *Archives of Neurology*, 58, 559-564.
- Elliott J. P., Newell D. W., Lain D. J., et al (1998) Comparison of balloon angioplasty and papaverine infusion for the treatment of vasospasm following aneurysmal subarachnoid hemorrhage. *Journal of Neurosurgery*, 88, 277-284.
- Furlan A., Higashida R., Weschler L. (1999) Intra-arterial prothrombinase for acute ischemic stroke. The PROACT study: a randomized controlled trial. *Journal of the American Medical Association*, 282, 2003-2011.
- Gobin Y., Laurent A., Merienne L., et al (1996) Treatment of brain arteriovenous malformations by embolization and radiosurgery. *Journal of Neurosurgery*, 85, 19-28.
- Hopper C. (2000) Photodynamic therapy: a clinical reality in the treatment of cancer. *Lancet*, 1, 212-219.
- Johnson L. H., Whittle I. R., Besser M., Morgan M. K. (1987) Vein of Galen malformation: diagnosis and management. *Neurosurgery*, 20,
- Lasjaunias P. (1997) A revised concept of the congenital nature of cerebral arteriovenous malformations. *Interventional Neuroradiology*, 3(4).
- Lasjaunias P. (1997) *Vascular Diseases in Neonates, Infants and Children*. Berlin: Springer-Verlag.
- Lasjaunias P., Berenstein A. (1987) *Surgical Neuroangiography, Vol. 2; Endovascular Treatment of Craniofacial Lesions*. Berlin: Springer-Verlag.
- Lasjaunias P., Alvarez H., Rodesch G., Garcia-Monaco R., Burrows P., Taylor W. (1996) Aneurysmal malformations of the vein of Galen. Follow up of 20 children treated between 1984-1994. *Interventional Neuroradiology*, 2, 15-26.
- Lasjaunias P., Berenstein A., Terbrugge K. G. (2001) *Surgical Neuroangiography, Vol. 1; Clinical Vascular Anatomy and Variations*, 2nd edn. Berlin: Springer-Verlag.
- Massoud T. F., Hademenos G. J. (1996) Risk of intracranial arteriovenous malformation rupture due to venous drainage impairment. A theoretical analysis. *Stroke*, 27(6).
- Mathis J. M., Barr J. D., Belkoff S. M., Barr M. S., Jensen M. F., Deramond H. (2001) Percutaneous vertebroplasty: a developing standard of care for vertebral compression fractures. *American Journal of Neuroradiology*, 22, 373-381.
- Rodesch G., Hurth M., Alvarez H., Lasjaunias P. (1997) Embolisation of spinal chord arteriovenous malformations with glue through the anterior spinal axis. *Interventional Neuroradiology*, 3, 131-143.
- Roubin G. S., New G. S., Iyer S. S., et al (2001) Immediate and late clinical artery stenting in patients with symptomatic and asymptomatic carotid artery stenosis. *Circulation*, 103, 532-545.
- Terbrugge K. G. (2001) Vein of Galen management in neonatal period. *American Journal of Neuroradiology*, 22, 1236-1237.
- Tong F. C., Cloft H. J., Dion J. E. (2000) Endovascular treatment of intracranial aneurysms with Guglielmi detachable coils: emphasis on new techniques. *Journal of Clinical Neuroscience*, 7, 244-253.
- Vitek J. J. (1991) Idiopathic intractable epistaxis: endovascular therapy. *Radiology*, 181, 113-116.

INTRACRANIAL LESIONS (1)

David Sutton, John Stevens and Katherine Miszkief

Disorders of the brain will be considered in this and the following chapter under the following headings:

- Methods of investigation
- Some aspects of technique
- Congenital lesions
- Neoplasms
- Vascular lesions
- Trauma
- Inflammatory lesions
- Degenerative and metabolic lesions
- White matter disease
- Epilepsy
- Ultrasound
- Radioisotopes.

Methods of investigation

The following methods are in current use for investigation of diseases of the brain:

1. Simple radiography
2. Computed tomography (CT)
3. Magnetic resonance imaging (MRI)
4. Ultrasound
5. Angiography
6. Radionuclides.

CT and MRI are now the techniques of choice for investigating most suspected lesions of the brain, and this and the following chapter are mainly devoted to their use in defining intracranial pathology.

The use of *radioisotopes* as a method for the localisation of intracranial lesions is now obsolete, apart from a few special indications which are discussed in the section on radionuclides at the end of Chapter 58. Positron emission tomography (PET) is proving useful in certain aspects of brain disease by showing differences in local brain metabolism but is expensive and is only available at special centres. It is also discussed below.

Ultrasound is very useful in neonates and infants but not in older children and adults, since it requires the window of an open fontanelle to image the brain (see Ch. 58). However, duplex and Doppler ultrasound can be used to investigate the neck vessels and

transcranially for the circle of Willis (see Ch. 15). Ultrasound may also be used during operations to assist the neurosurgeon in defining tumour extent and cysts.

Simple radiography has been used in the past as a cheap preliminary screening technique but its accuracy and specificity are so low compared with those of CT and MRI that most workers now dispense with its use. It is, however, still valuable in the assessment of skull trauma. With suspected cerebral lesions it is helpful in lesions involving the skull vault and base and has been discussed in detail in Chapter 53.

Arteriography is no longer used for the diagnosis of tumours except in special circumstances as described below, but is still essential for the definitive diagnosis of most vascular lesions (Ch. 55). Its use has also extended into the field of interventional radiology (Ch. 56). As explained in Chapter 55, non-invasive or minimally invasive techniques for arteriography in the form of MRA and spiral CT are now preferred to direct arteriography and should be used where possible.

Some aspects of CT and MRI techniques

Data presentation CT and MRI present data as an analogue display on a console. Presentation is in the form of a 'grey scale' in which whiteness is proportional to the X-ray attenuation coefficient or nuclear magnetic resonance (NMR) signal intensity at each point in the image. The range can be varied by changing the 'window' (W) so that tissues within a wide or narrow range of CT or MRI characteristics can be evaluated. The centre point or level (L) of the window can also be varied. Standardising W and L is of more importance in CT; the range of imaging options and signal variation that occurs in MRI mitigates against rigorous standardisation. Figure 57.1 shows the relative density on the Hounsfield scale of the normal body tissues at CT. This scale is an arbitrary one with air at -1000 units and water at 0 units as fixed points. The numerical value assigned to the attenuation coefficient bears a linear relationship to the electron density of the tissue concerned. Although tissue contrast in MRI depends mainly upon proton density and T₁ and T₂ relaxation times, other contrast mechanisms come into play, and absolute values show considerable variation according to measurement method and equipment used.

Contrast enhancement Soon after the introduction of CT brain scanning, Ambrose (1973) showed that pathological lesions in the

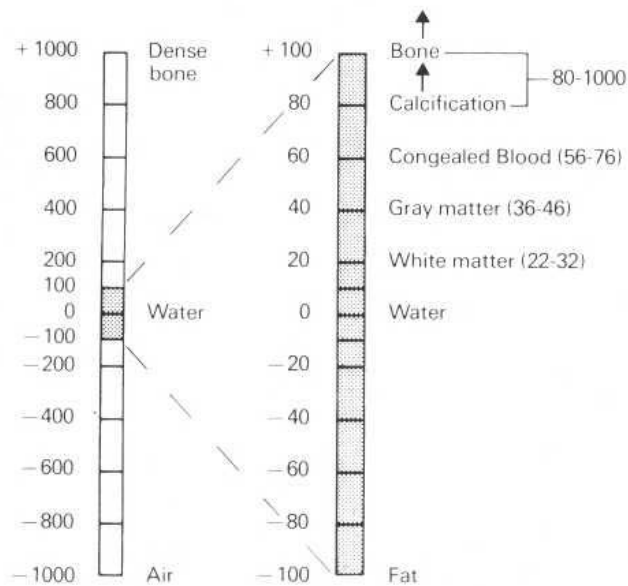


Fig. 57.1 The Hounsfield CT scale. The full scale on the left extends over 2000 units. The expanded scale on the right extends over 200 units and includes all body tissues. Head scans are usually done routinely at a window level (L) of 34-40 and a window (W) covering 0-75.

brain frequently accepted intravenous iodinated contrast media such as those used in pyelography in a manner different from normal brain. This is due partly to the breakdown of the blood-brain barrier which occurs in brain tissue damaged by disease and partly to the abnormal vascularity of some neoplasms and other pathological lesions. Aneurysms and angiomas also enhance with contrast medium, mirroring its concentration in the blood, as do vascular structures such as the choroid plexuses. Since grey matter contains considerably more blood than white matter, the difference between grey and white matter is also accentuated by contrast, and the falx and tentorium are also enhanced. Thus, some lesions not obvious on the simple scan could be revealed and many others enhanced by the contrast medium. Different workers have varied the amount of contrast medium used. A dose equivalent to 30 g of iodine for an average adult and given as a bolus is widely used, though many workers readily use up to 40 g.

Aneurysms and other vascular structures are shown best immediately following injection when blood concentrations of iodine are highest. Leakage through the blood-brain barrier shows best some 30 minutes later. In practice both types of lesion are adequately shown in sections taken 10-15 minutes following injection.

It is usual to inspect the non-enhanced scan first and then, if necessary, to proceed to injection of contrast medium followed immediately by the enhanced scan. It is not necessary to use enhancement in every case. Where the simple scan is normal and the clinical indications are vague it has been general experience that the post-enhancement scan is most unlikely to add further information.

The inert gas *xenon* has also been shown to be lipid soluble and to cross the blood-brain barrier after administration as an anaesthetic. However, its high cost and the fact that its administration often requires anaesthesia make it impractical for routine use as an enhancing agent.

MRI, despite its greater soft-tissue contrast sensitivity, also makes widespread use of contrast enhancement. T₁ and T₂ relaxation enhancement is provided by the strongly paramagnetic ion

gadolinium (Gd³⁺). This is chelated to a large carrier molecule such as DTPA and injected intravenously as a dose of 1-2 mM/litre/kg body weight.

Head positioning Most CT studies are performed with the head supine and the plane of section at 10-25° to Reid's baseline. This is comfortable for the patient and reduces radiation to the sensitive lenses of the eye. The appearances in a set of normal axial scans are illustrated in Figure 57.2.

Modern gantries are wide enough to permit coronal or near-coronal sections to be obtained directly if the patient is able to cooperate by assuming the appropriate position. Sagittal or near-sagittal sections can also be obtained (Fig. 57.3). In most cases, however, these projections are obtained by computer reconstructions of the stacked axial slices (reformat). However similar facilities are now available with the new generation of multislice spiral CT scanners.

The issue is simpler with MRI, where the scan plane is set electronically and multiplanar facilities are readily available. Figure 57.4 shows a set of normal MR scans in the usual axial plane, and Figure 57.5 a set in the coronal plane.

MRI protocols Protocol choice for MRI is much wider than for CT even in brain imaging, the longest established and in many ways simplest of all organs to image. Most modern units no longer use conventional *spin-echo* sequences, but one or more of the fast techniques are now available. In practice, this generally entails the use of *gradient-recalled echo* (GRE) imaging for three-dimensional (3D) or volumetric acquisitions, and *fast spin-echo* for multislice (2D) acquisitions. Also, fast spin-echo techniques are used mainly to demonstrate proton density and T₂-weighted contrast, T₁-weighted contrast being best displayed by gradient-recalled echo techniques, conventional spin-echo or inversion recovery. Fast spin-echo acquisitions can be used to acquire dual echoes, generating proton-density and T₁-weighted images from each excitation as in conventional spin-echo techniques. However this takes twice as long as collecting a single echo at a single effective TE, so that the advantage of collecting a single echo is that the spatial resolution can be increased for the same acquisition time. In the head GRE techniques are used mainly for volumetric acquisitions with T₁-weighted contrast, usually with some form of tissue magnetisation preparation, of which the simplest is inversion recovery (IR) prepared.

The routine MR examination of the brain performed by most units is still a sagittal scout image or multislice T₁-weighted GRE acquisition followed by an axial dual-echo fast spin-echo acquisition. Most units prefer dual to single echo for routine brain imaging because signal from CSF is lower, enabling lesions close to the ventricles or in cerebral cortex to be identified more reliably. Acquisition in the coronal plane is preferred in special situations, dictated clinically such as in patients with habitual epilepsy or dementia, or to help localise lesions shown by other sequences. When specialised post-processing is required, such as volumetry, surface rendering or registration, magnetisation-prepared GRE volumetric imaging is preferred, usually in the coronal plane using contiguous slices of 1 or 1.5 mm thickness. High-resolution techniques (single echo) are used for imaging small structures such as the pituitary gland or internal auditory meatuses (Fig. 57.5).

Newer sequences are now becoming generally available, some of them exploiting novel NMR contrast mechanisms. One, which depends on conventional T₁-weighted contrast, is fluid-attenuated

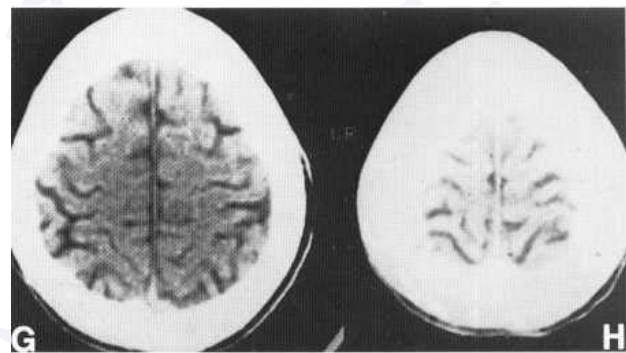
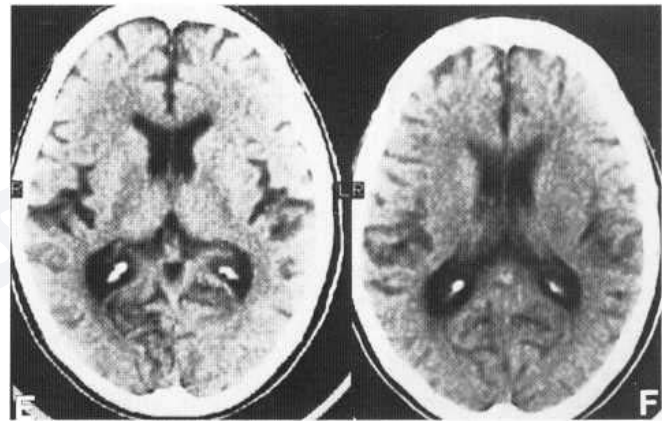
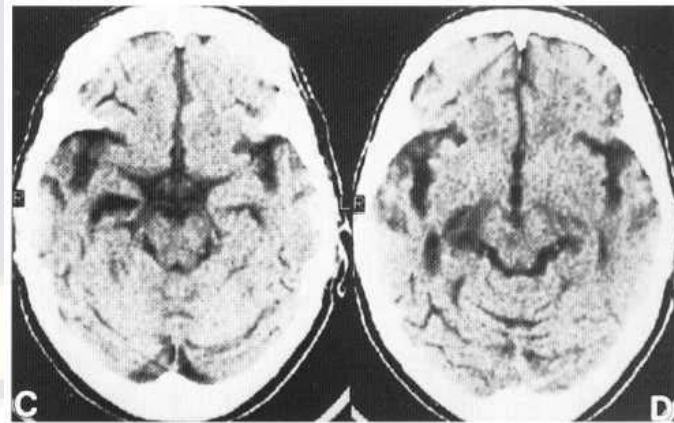
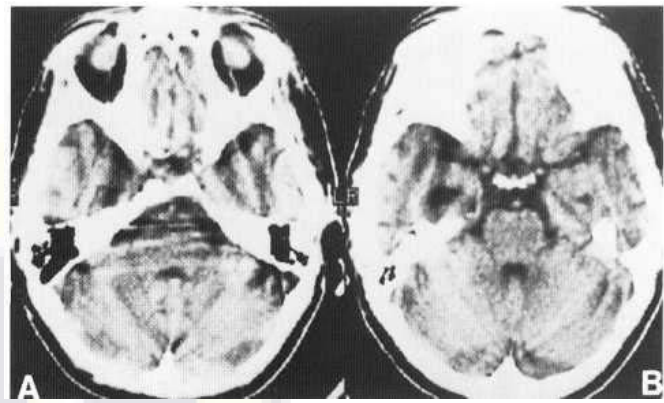
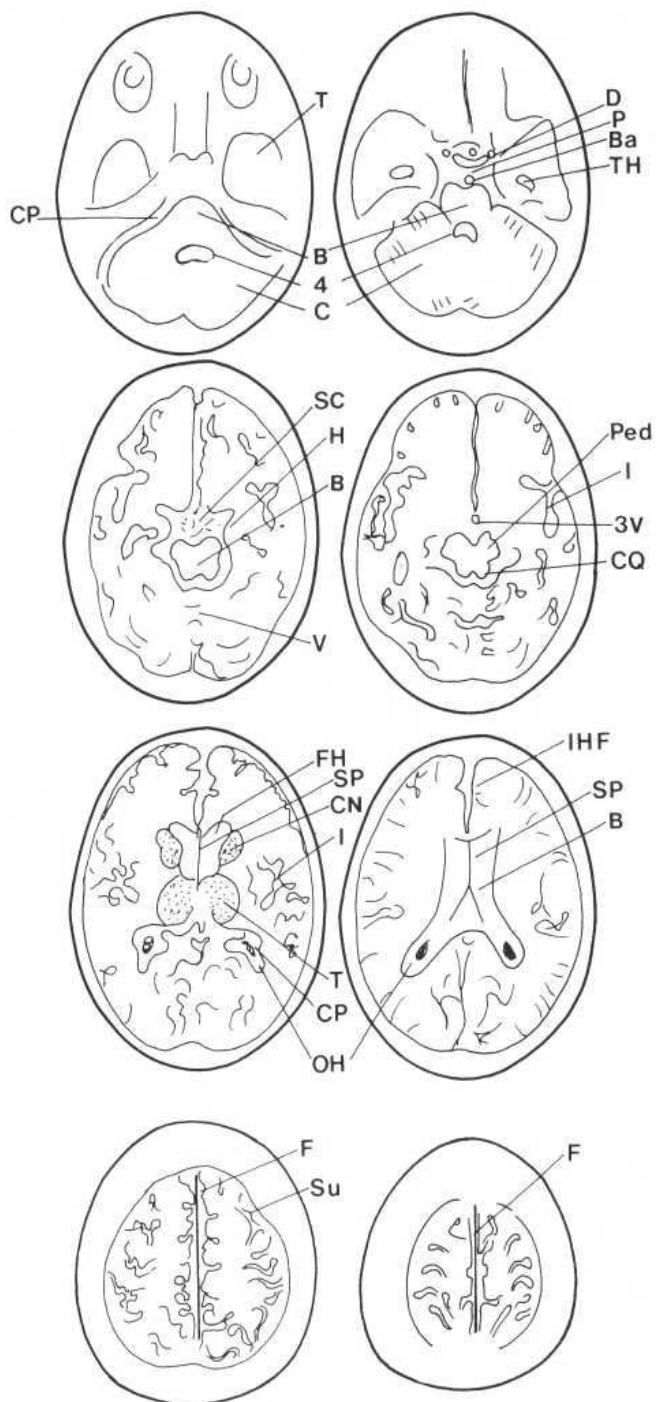


Fig. 57.2 Serial slices from below upward in an elderly patient with some degree of atrophy with diagrams to illustrate normal anatomy. (A) T = temporal lobe; CP = cerebellopontine angle; B = brainstem; 4 = fourth ventricle; C = cerebellum. (B) D = dorsum sellae; P = pontine cistern; Ba = basilar artery; TH = temporal horn. (C) SC = suprasellar cistern; H = hippocampus; B = brainstem; V = vermis. (D) Ped = peduncle; I = insula; 3V = third ventricle; CQ = corpora quadrigemina. (E) FH = frontal horn; SP = septum pellucidum; CN = caudate nucleus; T = thalamus; CP = choroid plexus; OH = occipital horn. (F) IHF = interhemispheric fissure; B = body of lateral ventricle. (G) Su = sulci; F = falx.

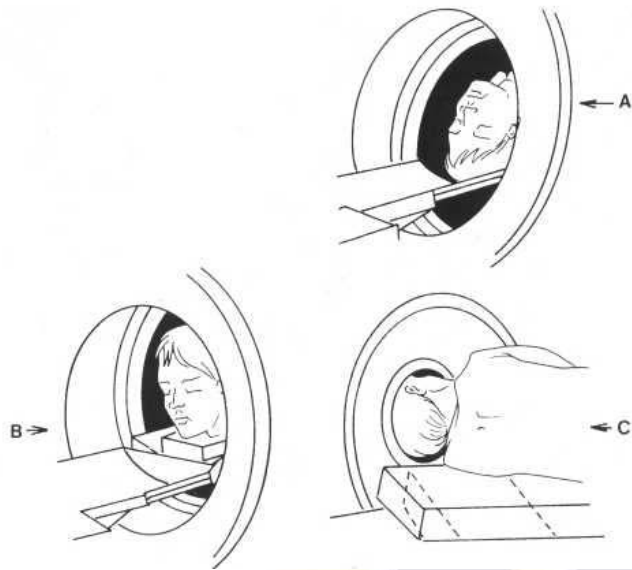


Fig. 57.3 Diagram illustrating position of patient for coronal or near-coronal sections (A, B), and sagittal or near-sagittal sections (C) at CT.

inversion recovery (FLAIR) and its variations which produce heavily T₂-weighted CSF-nulled images by coupling an inversion pulse followed by a long inversion time to a long echo time. Although FLAIR has had great success in displaying lesions not seen with conventional T₂-weighted spin-echo sequences, it has

been limited by long acquisition times. A proven but not yet widely available strategy for improving its efficiency uses sequential interleaving and rapid acquisition with relaxation enhancement (RARE). This enables very long repetition times to be used (10 seconds or more).

Magnetisation transfer contrast imaging is widely available but relatively little used in clinical practice. It emphasises contrast derived by the reduction in relaxed magnetisation induced by application of a broad-spectrum off-saturation prepulse which saturates a tightly bound water fraction not observed directly with MRL. What the water is bound to is uncertain, although in biological tissues it may be mainly macromolecules and membranes.

Diffusion weighted contrast imaging can be achieved by using strong diffusion weighting gradients, where contrast depends on the diffusion coefficient of water. Diffusion behaviour is anisotropic, especially in white matter, diffusion being greatest in the direction of the tracts and smallest transverse to them. Anisotropy can be characterised from three orthogonal directions, or better by an elliptical tensor, and directionality expressed as a trace, or one of many anisotropy indices. Diffusion weighted imaging has been used mainly in the evaluation of stroke, and now has widespread clinical application.

Perfusion imaging can be produced by analysing the signal change over time in regions of interest after the administration of a bolus of intravenous contrast medium, or by techniques such as blood oxygenation level dependent contrast imaging (BOLD) or arterial spin tagging. The latter are used in activation studies in

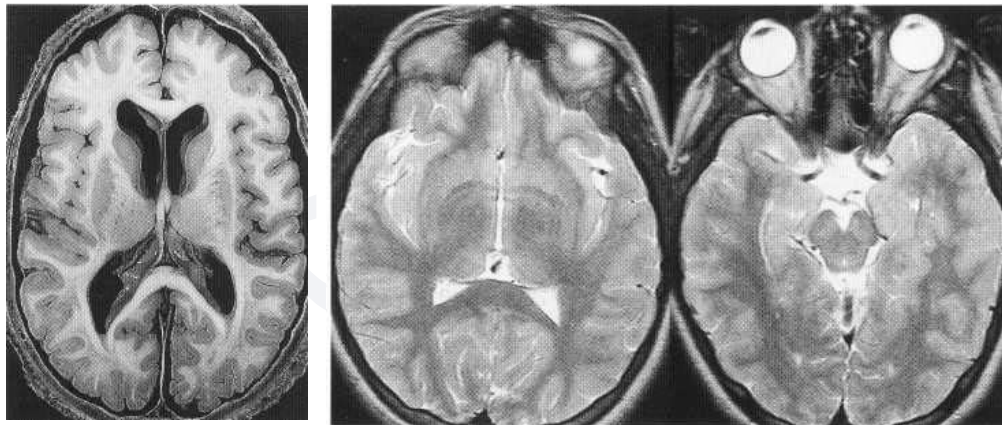
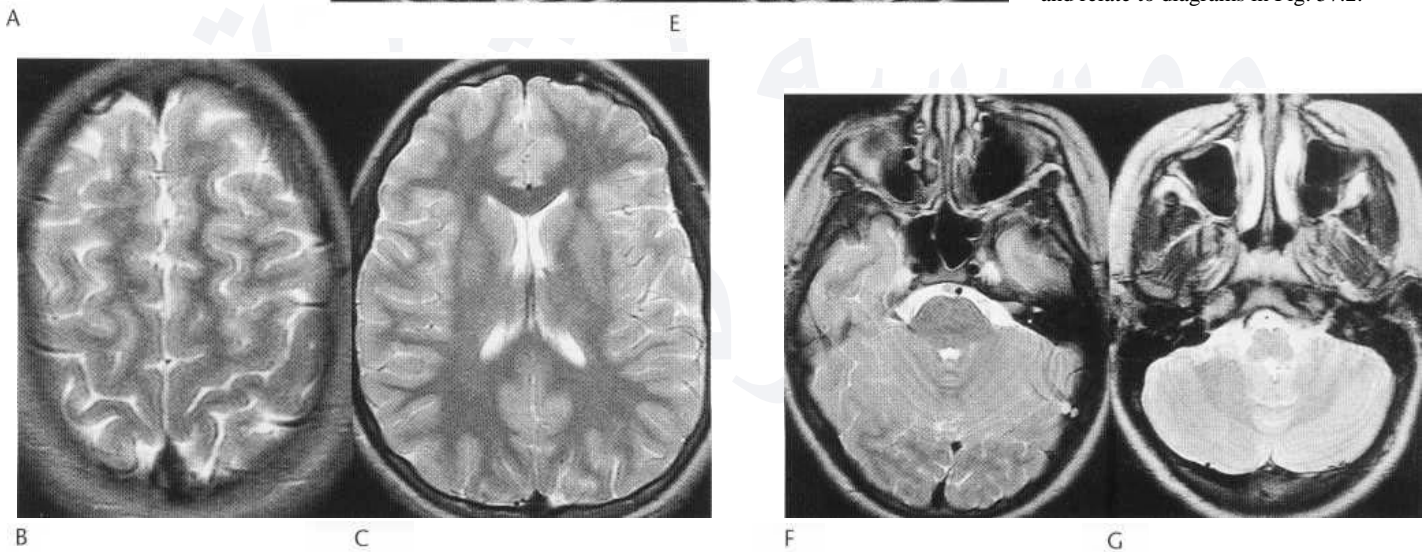


Fig. 57.4 MRI axial sections showing normal anatomy. (A) T₁-weighted section shows CSF black and clear differentiation between white and grey matter. (B-G) T₂-weighted sections in another patient show CSF white and white matter dark while grey matter remains grey. Compare with and relate to diagrams in Fig. 57.2.



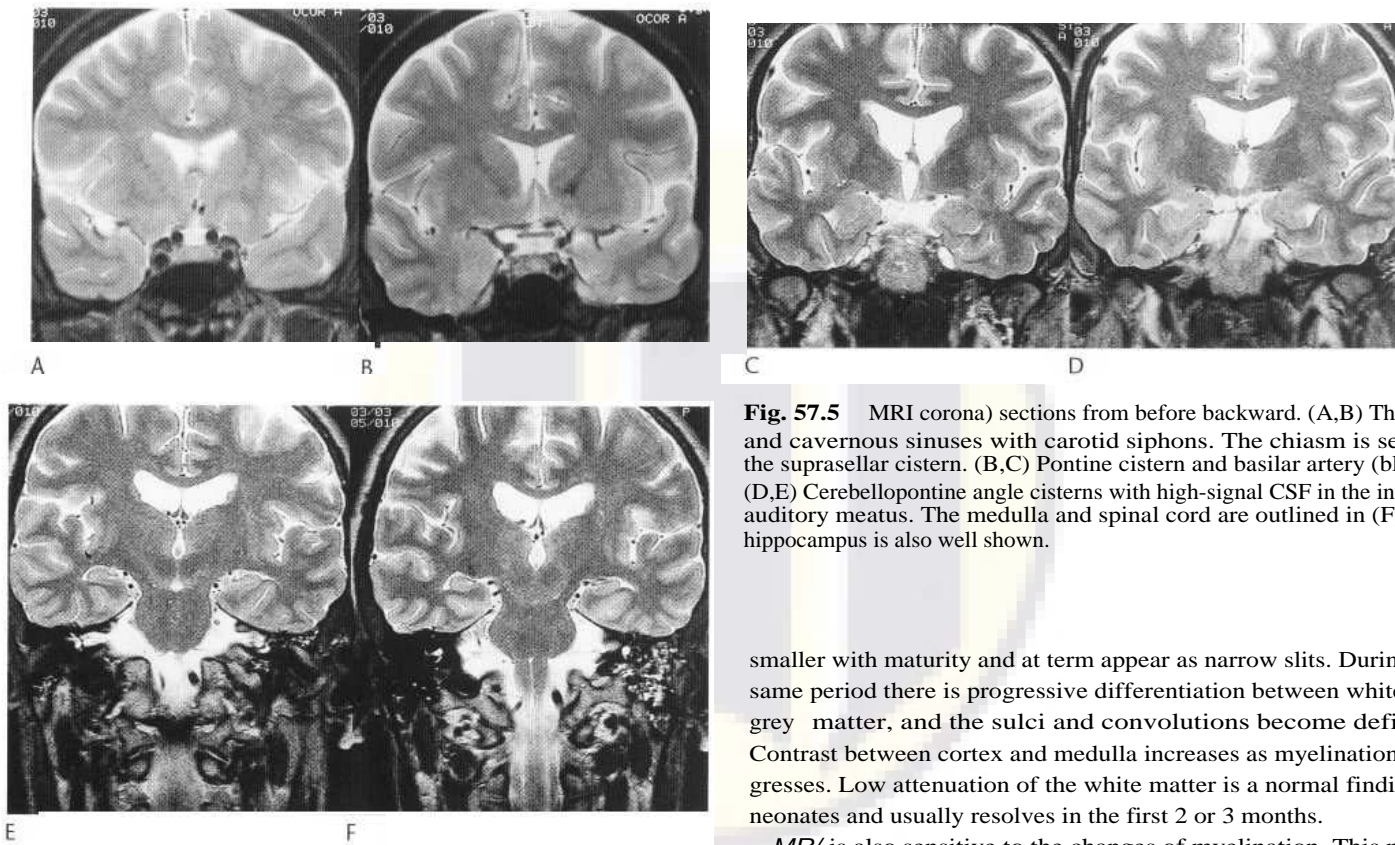


Fig. 57.5 MRI corona) sections from before backward. (A,B) The sella and cavernous sinuses with carotid siphons. The chiasm is seen in the suprasellar cistern. (B,C) Pontine cistern and basilar artery (black). (D,E) Cerebellopontine angle cisterns with high-signal CSF in the internal auditory meatus. The medulla and spinal cord are outlined in (F). The hippocampus is also well shown.

functional MRI, which is currently mainly a research rather than a clinical tool.

CT cisternography This technique greatly enhances the contrast between CSF and neural tissue enabling window and level settings to be arranged to minimise the effects of artefacts, especially in the posterior fossa and around the skull base. It requires the intrathecal injection of a water-soluble myelographic contrast medium, usually only about half or less of the amount that would be used for a myelogram. Contrast medium is run into the head by gravity, and imaging using high-resolution techniques can be performed to produce great anatomical detail of the cisternal structures. The technique is most widely used for demonstrating the site of CSF leaks in CSF rhinorrhoea but its other applications, such as demonstrating small tumours in the cerebellopontine angle, have been rendered obsolete by MRI. Air cisternography was also once used with CT but is no longer needed.

Congenital lesions and neoplasms

Congenital lesions of the brain are listed in Box 57.1. Most are well demonstrated by CT or MRI, and are discussed in this chapter. The appearance of the normal neonate brain differs from those of older children and adults and is also described here.

The neonatal brain In CT images the density of the brain is dependent on the stage of maturation/At full term the cortex shows convolutions, the cerebral sulci are well defined, and the cortex and white matter are differentiated. In premature infants before 30 weeks the brain is homogeneously low in attenuation with the cortex appearing as a thin denser rind without sulci. The sylvian fissures are shallow and wide and the ventricles appear relatively large.- They become

smaller with maturity and at term appear as narrow slits. During the same period there is progressive differentiation between white and grey matter, and the sulci and convolutions become defined. Contrast between cortex and medulla increases as myelination progresses. Low attenuation of the white matter is a normal finding in neonates and usually resolves in the first 2 or 3 months.

MR/ is also sensitive to the changes of myelination. This manifests as relative shortening of T₁ and T₂ relaxation times of white matter, thus increasing the relative contrast between white and grey matter on images as the infant brain matures.

Myelination begins in the brainstem and extends into the internal capsules and optic radiations by 6 months of life, for major and minor by 1 year, and into the gyral convolutions as in the adult by a year and a half.

Ultrasound is widely used for the examination of the neonate and infant brain. The appearances are discussed below (see Ch. 58).

Box 57.1 Congenital lesions affecting the brain

- Hydrocephalus
- Meningocele and encephalomeningocele
- Macrocephaly
- Hemimegalencephaly
- Chiari malformations
- Aqueduct stenosis
- Dandy-Walker syndrome
- Arachnoid cyst
- Ependymal cyst
- Septal agenesis
- Septo-optic dysplasia
- Cyst of the septum pellucidum
- Cyst of the cavum Vergae
- Agenesis of the corpus callosum
- Lipoma of the corpus callosum
- Hamartoma
- Coarctation of the frontal horn
- Porencephaly
- Schizencephaly
- Hydranencephaly
- Holoprosencephaly
- Disorders of neuronal migration
- Phakomatoses

Hydrocephalus Congenital hydrocephalus in infants and young children may be classified, like adult hydrocephalus, as *communicating* and *non-communicating*. In the former there is free communication between the ventricles and the basal cisterns, with obstruction to the flow of CSF in the subarachnoid space or basal cisterns. This is due to meningeal irritation by haemorrhage, infection or trauma. All the ventricles are enlarged and the basal cisterns may be prominent. In some congenital cases the cause remains obscure. In non-communicating hydrocephalus flow is obstructed within the ventricular system, usually at third ventricular, aqueductal or fourth ventricular level. The ventricles are dilated above the level of obstruction and are normal below it.

Non-communicating hydrocephalus in infants and children is commonly due to aqueduct stenosis. Other congenital causes are Dandy-Walker syndrome, arachnoid cysts and, very rarely, neoplasms.

In infants the diagnosis is confirmed by ultrasound (see Ch. 58), and a specific causative lesion such as Dandy-Walker or arachnoid cyst may be demonstrated or the level of obstruction identified. In older patients CT or MRI will usually identify the level and in most cases the cause. Rarely hydrocephalus is due to oversecretion of CSF, as in some cases of papilloma of the choroid plexus.

Low-pressure hydrocephalus This is encountered in the elderly and may be difficult to distinguish from atrophy. The distinction is discussed below (see Ch. 58).

At MRI the signal from CSF is modulated by pulsatile motion on moderately T₂-weighted images, being lowest near the choroid plexuses, in the aqueduct, along the floor of the fourth ventricle, and in the anterior cisterns of the posterior fossa where the velocity of CSF motion is greatest. In obstructive hydrocephalus this effect is diminished or absent while in communicating hydrocephalus it is often, but not always, accentuated, especially in the aqueduct. Interstitial oedema secondary to hydrocephalus is clearly shown by MRI on T₂-weighted images, appearing as well-demarcated bands of increased signal extending centrifugally from the subependymal tissues to the central white matter.

Meningocele and encephalomeningocele These lesions are usually obvious clinically though, as noted in Chapter 53, small lesions of the vault or larger lesions involving the skull base and the sphenoid can be misdiagnosed, with potentially disastrous results.

The skull defects visible at simple X-ray have already been described. The nature and extent of the cerebral deformity, particularly with basal meningocele, can be clearly defined by CT or MRI before surgical intervention. At MRI the anatomy is best shown on T₂-weighted images.

Macrocephaly (megalencephaly) Pathologically this is defined as a brain weighing more than 1800 g. Such brains may be structurally normal and occur in children from large-headed families, but more frequently there are migrational abnormalities, a diffuse glial proliferation or a pathological process. The latter include cerebral lipidoses, spongy degeneration of the white matter and Alexander's disease. Large brains may also be seen in tuberous sclerosis (Box 57.2).

In infants or children presenting with large heads the primary differentiation is from hydrocephalus, which is the commonest cause. Ultrasound in infants will readily confirm hydrocephalus or bilateral subdurals (see below).

Box 57.2 Causes of large head in infancy

Hydrocephalus
Subdural effusions
Normal (sometimes familial)
Migrational abnormalities (see below)
Lipidoses
Spongy degeneration
Alexander's disease
Tuberous sclerosis

In older children CT or MRI will be necessary to differentiate and to elucidate other pathological processes. These are discussed under their specific headings.

Hemimegalencephaly In this condition enlargement of the skull is unilateral and confined to the vault. The asymmetrical skull is secondary to, a congenital unilateral enlargement of the brain, and is associated with fits, hemiplegia and hemianopia. Pathologically there are migrational abnormalities with thickening of the grey matter and increase of the white matter and with abnormal shallow sulci on the affected side. The ventricle on this side is also enlarged. The brain lesions are identified by CT or by MRI.

Chiari malformations These were originally described by Chiari in 1891 and 1896, and were graded Types 1-4 according to degree of deformity. Types 3 and 4 have the major deformities with cerebellar hypoplasia and downward displacement of the brainstem and a high cervical or occipital encephalocele.

Type 2 This also presents in neonates or infants, virtually always with a thoracolumbar myelomeningocele. The associated brain deformities consist of caudal herniation of the medulla and vermis with a caudally displaced and elongated fourth ventricle. A backward kink may be seen at the caudally displaced junction of cervical cord and medulla. Hydrocephalus may be due to associated aqueduct stenosis or to occlusion of the ambient cisterns.

There are also various other malformations of the brain. These include hypoplasia or absence of the falx and tentorium with interdigitation of the cerebral hemispheres; absence of the corpus callosum with forward pointing of the frontal horns; deformity of the midbrain (dorsal beaking); enlargement of the cerebellar vermis and forward protrusion of the cerebellar hemispheres as pointed projections around the brainstem; gyral malformations, and other lesions. Many of these brain deformities can be identified by CT or MRI, and some by neonatal ultrasound. Simple X-ray may show a lacunar skull and forward bowing of the petrous bones and [clivus](#).

Type 1 This is the least obvious clinically and may not be diagnosed until adult life. It consists of tonsillar herniation through the foramen magnum with or without varying degrees of elongation of the medulla oblongata and fourth ventricle.

Syringohydromyelia (see Ch. 54) This is associated with the condition in up to 70% of cases. The patients do not present clinically until adult life when the symptoms and signs of syringomyelia develop; less typically, symptoms suggesting involvement of the lower cranial or cervical nerves are seen, and very rarely patients present with hydrocephalus.

Bony anomalies of the craniocervical junction are present in around 15% of cases, particularly assimilation of the atlas. Basilar invagination and dysplasias of the vault are other rare associations.

Imaging The diagnosis is best confirmed by MRI, which also shows the syrinx non-invasively (Fig. 54.4C). Caution is required when interpreting sagittal images of the craniovertebral junction as partial volume effects result in visualisation of 3-4 mm of cerebellar tissue *apparently* lying below the foramen magnum in 15-20% of normal individuals. Coronal imaging is helpful in equivocal cases.

Aqueduct stenosis In this condition there is a congenital stenosis or obstruction of the aqueduct which results in hydrocephalus involving the third and lateral ventricles. While this usually presents in infancy or childhood, the condition is occasionally diagnosed in adults. In all cases it is necessary to exclude obstructive hydrocephalus due to a local tumour or ependymitis. There are also recognised associations with neurofibromatosis and Chiari Type 2 malformation.

Imaging The diagnosis can be made by CT but is more elegantly shown by sagittal MRI sections through the aqueduct (Fig. 57.6). Hydrocephalus is present, involving the lateral and third ventricles. The latter is often markedly dilated and its suprapineal recess can be large and rounded, simulating an arachnoid cyst. Anteriorly the third ventricle may extend down into the sella, which is often flattened. The mouth of the aqueduct is dilated like a bell or trumpet, while the lower aqueduct and fourth ventricle appear normal. There is no evidence of a mass lesion in the brainstem or posterior fossa.

Dandy-Walker syndrome In this condition there is a more or less complete membranous obstruction to the foramina of Magendie and Luschka, which causes cystic dilatation of the fourth ventricle. The lesion may occur on its own or in association with other congenital anomalies such as meningocele or defects in the corpus callosum. The cerebellum is hypoplastic and in severe cases the hemispheres are vestigial and the vermis undetectable. The grossly dilated fourth ventricle extends upward to and above the tentorium and also backward to the occipital bone, which is thinned and bulging, expanding the posterior fossa. There is also marked hydrocephalus with dilatation of all the ventricles.

Imaging CT or MRI shows the anatomical features described and permits an immediate diagnosis (Figs 57.7, 57.8). In the neonate or small infant, diagnosis may be made by ultrasound (Fig. 58.86). Differential diagnosis from an arachnoid cyst, a giant

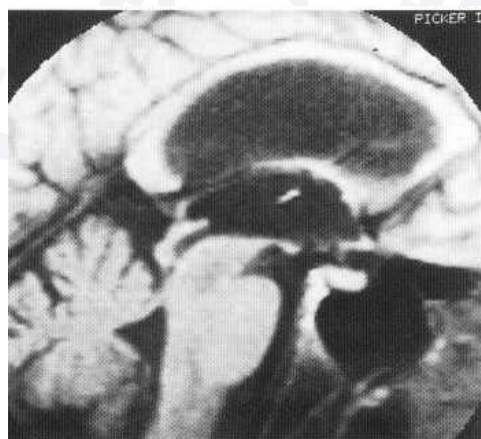


Fig. 57.6 Aqueduct stenosis shown by MRI. Sagittal midline section. (Courtesy of Dr Gordon Thomson.)

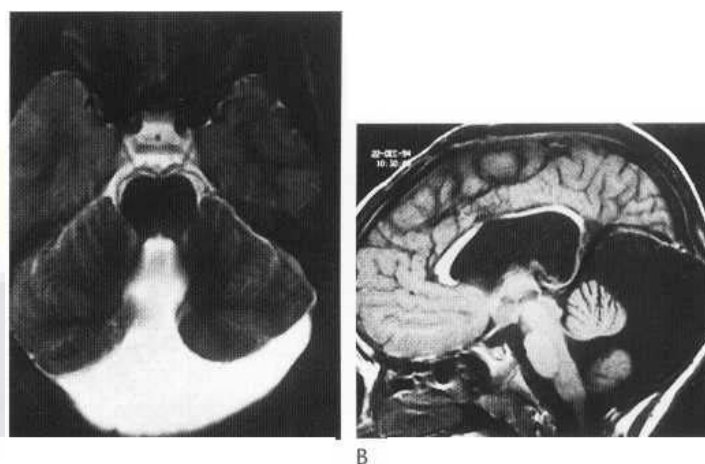


Fig. 57.7 Axial T₂- (A) and sagittal T₁- (B) weighted images in a patient with the Dandy-Walker syndrome showing an enlarged posterior fossa with a high tentorium, and a large fluid-filled fourth ventricle-cisterna magna complex in association with vermian hypoplasia.

cisterna magna, or a gliomatous cyst is normally easy, with the presence of a normal or small fourth ventricle as a key distinguishing feature. The dysplastic cerebellum in Dandy-Walker syndrome also helps to distinguish the condition.

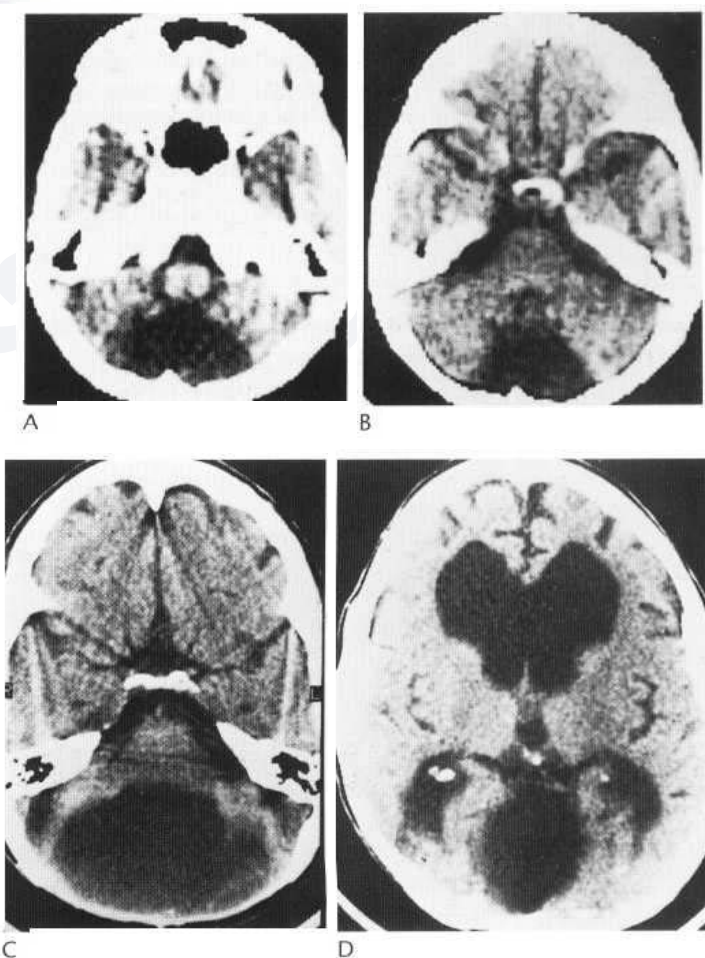
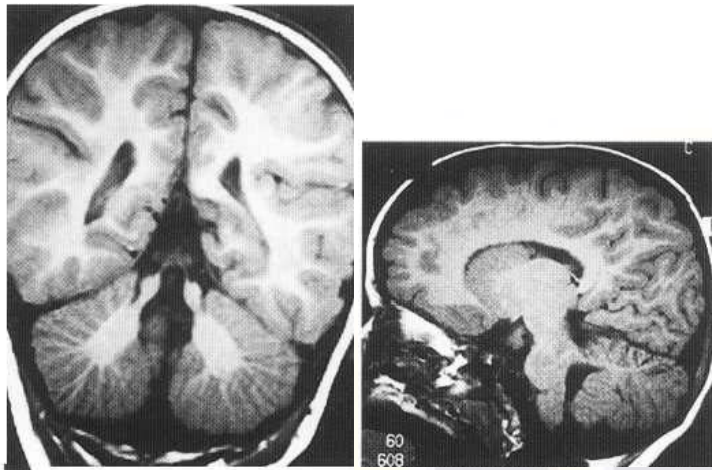


Fig. 57.8 (A-D), Dandy-Walker syndrome shown by CT.



A

B



C

Fig. 57.9 Joubert's syndrome at the level of the ponto-mesencephalic junction showing the 'molar tooth appearance' with superior cerebellar peduncles clearly seen on the coronal T₁-weighted image (A) due to absence of vermian folia. In this other patient with Joubert's syndrome the superior cerebellar peduncles are typically very horizontally orientated on the sagittal T₁-weighted image (B). (C) Axial T_{2w} view of patient with Joubert's syndrome showing molar tooth appearances.

Dandy-Walker variant This term is applied to cases where lesions are less marked and the posterior fossa is not enlarged, though the fourth ventricle is dilated and the vermis dysgenetic.

Joubert's syndrome This condition is characterised clinically by ataxia, mental retardation, episodic hyperpnoea, and abnormal eye movements, and is due to total aplasia of the cerebellar vermis. This is easily shown by CT or MRI where, in addition to absence of the vermis, the fourth ventricle appears large and triangular with the apex pointing backward at its midportion, and large and bat's wing' at a higher level (Fig. 57.9).

Giant cisterna magna In this condition the cisterna magna appears abnormally large or dilated and the posterior fossa may be enlarged. The fourth ventricle, cerebellum and vermis, however, are seen to be normal.

Arachnoid cyst Arachnoid cysts are intracranial but extra-cerebral. They may be found anywhere around the brain, but are seen particularly in the middle and posterior cranial fossae, in the suprasellar region, and behind the third ventricle. They contain clear fluid indistinguishable from CSF and are lined by arachnoid tissue. Electron microscopic studies suggest they are due to congenital splitting of the arachnoid membrane. The clear CSF content helps to distinguish them from post-traumatic lesions such as subdural hygromas and from postinflammatory loculations. Arachnoid cysts are usually unilocular, but septated cysts may occur.

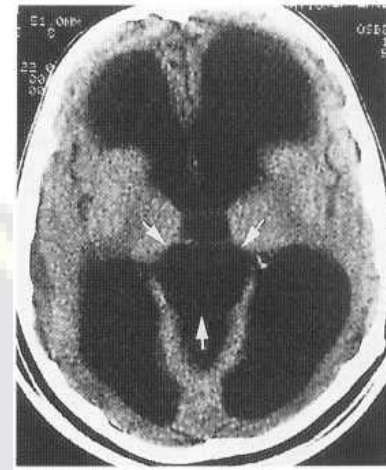
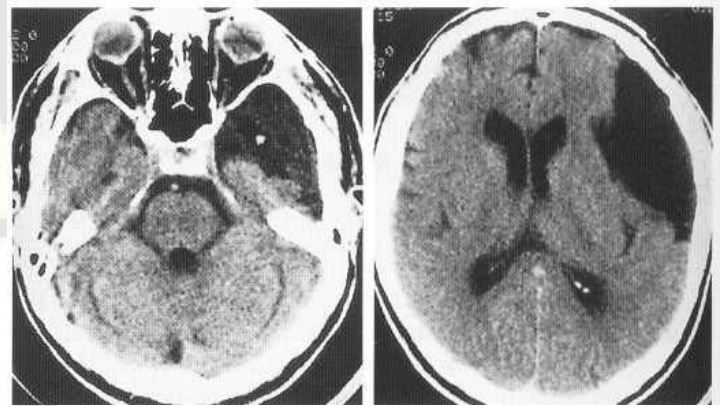


Fig. 57.10 Arachnoid cyst (arrows) involving pineal region and quadrigeminal cistern and compressing back of third ventricle, producing marked hydrocephalus.



A

B

Fig. 57.11 Arachnoid cyst in left anterior temporal (A) and Sylvian (B) region. It expands the overlying skull but produces minimal brain displacement.

They can present in adults but more usually they present in infants or children, particularly if large enough to produce a mass effect or obstructive hydrocephalus. The latter is most frequently seen with posterior fossa or quadrigeminal cistern cysts (Fig. 57.10). There may be hypoplasia of underlying cerebral tissue such as the temporal pole, considered by some to represent a coexistent congenital malformation and by others to be secondary to the mass effect (Fig. 57.11). Symptomless cases are sometimes found coincidentally at CT or MRI examination of adults for other lesions. In neonates or small infants the cysts may be diagnosed by ultrasound, but in older children or adults they are diagnosed by CT or MRI (Fig. 57.12). They usually lie in one of the classic sites mentioned above, are of CSF density, and on CT have no enhancing capsule or adjacent calcification.

With suprasellar arachnoid cysts, differential diagnosis is from a Rathke's cleft cyst or craniopharyngioma, and occasionally from a grossly dilated third ventricle. In the quadrigeminal cistern a dilated suprapineal recess or even a cystic pineal tumour may need consideration.

Ependymal cyst These very rare cysts are lined by a thin wall of ependyma and can be intra- or paraventricular. The latter can resemble a hydatid cyst at CT and show no marginal enhancement.

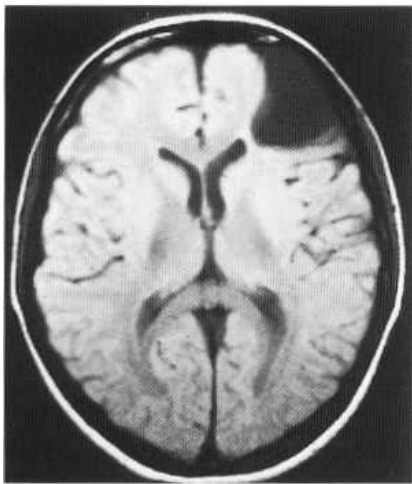


Fig. 57.12 MRI study of left anterior temporal arachnoid cyst, proton density. (Courtesy of Dr Gordon Thomson and Bristol MRI Centre.)

Large intraventricular ependymal cysts can resemble unilateral hydrocephalus since they usually occur in the lateral ventricle and the wall is difficult to define at CT. Intrathecal or intraventricular contrast agent has been used to establish a diagnosis, by outlining the cyst within the opacified ventricle.

Cyst of the septum pellucidum The double septum or fifth ventricle is due to the abnormal persistence of the fetal cavum septi pellucidi. Ultrasound will show that this is present in over one-third of neonates. The incidence falls rapidly through childhood, but nevertheless the condition persists in 1-2% of adults, when it will be seen as a chance finding at imaging by CT or MRI (Figs 57.13A, 57.14A).

Cyst of the cavum Vergae This represents the so-called 'sixth ventricle' and is a backward extension of the septal cyst, though much less commonly seen. Anatomically it lies beneath the posterior part of the corpus callosum with the velum interpositum below (Fig. 57.13B). On axial CT sections the cavum Vergae appears as a rectangular structure continuous with a septal cyst anteriorly, both being of CSF density (Fig. 57.14B). It should not be confused with the normal velum interpositum (Fig. 57.13), which is also of CSF density and lies above the third ventricle. The latter is frequently seen at axial CT, but is triangular in shape with the apex lying anteriorly, and contains the enhancing internal cerebral veins (Fig. 57.14C). Fig. 57.15 shows a cyst of the velum interpositum.

Septal agenesis Septal agenesis can occur as an isolated lesion giving rise to a single ventricle communicating across the

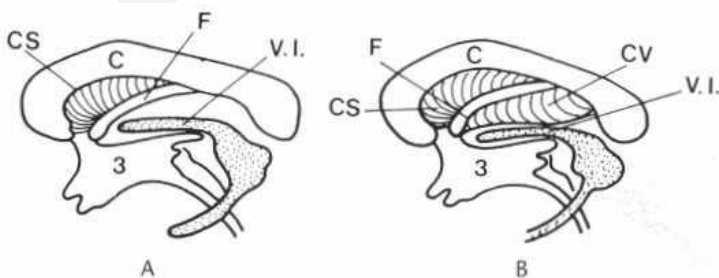


Fig. 57.13 (A) Cavum septi pellucidi: C = corpus callosum; F = fornix; CS = cavum septi pellucidi. (B) Cavum septi pellucidi and cavum Vergae: VI = velum interpositum; CV = cavum Vergae; 3 = third ventricle.

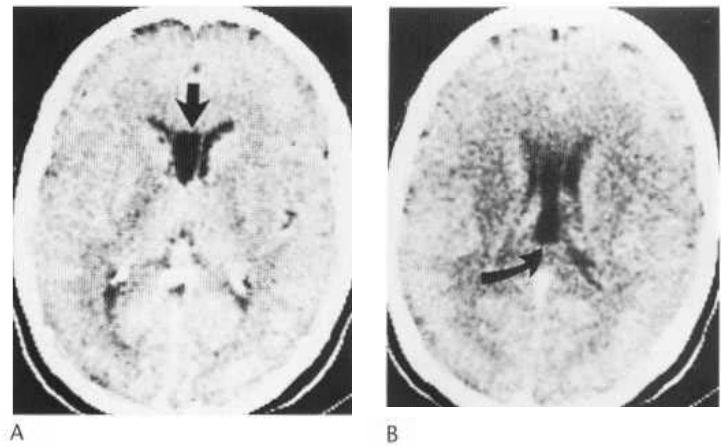


Fig. 57.14 Cyst of the septum pellucidum (arrow in A) continuous (B) with cyst of the cavum Vergae (arrow). (C) Velum interpositum (arrows) containing enhanced internal cerebral veins.

midline. A similar situation can arise in severe hydrocephalus to] rupture of the septum. Both conditions are readily identified at CT or MRI.

Septo-optic dysplasia (De Morsier's disease) This is characterized by absence of the septum pellucidum and hypoplasia of the anterior optic pathways. There is squaring of the frontal horns with a large chiasmatic cistern, and the child has retarded development and poor vision. The anatomical features may be demonstrated by CT or by MRI.

Agencies of the corpus callosum This is usually partial but sometimes complete. It may occur as an isolated finding, or in association with other malformations.

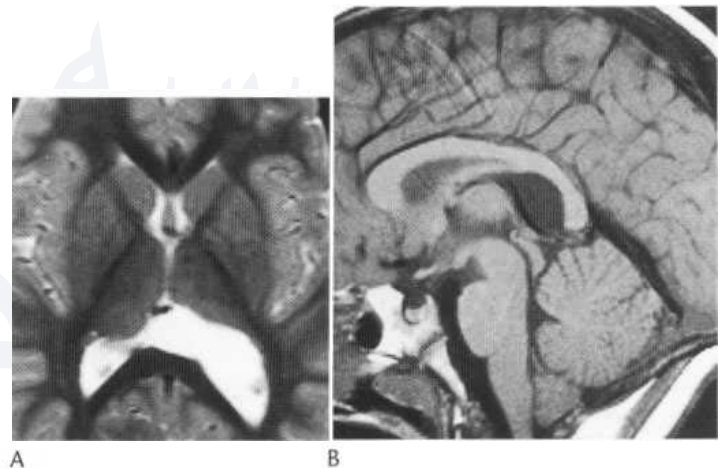


Fig. 57.15 Axial T₂- (A) and sagittal T₁- (B) weighted images showing a cyst of the velum interpositum which extends into the trigone of the left lateral ventricle.

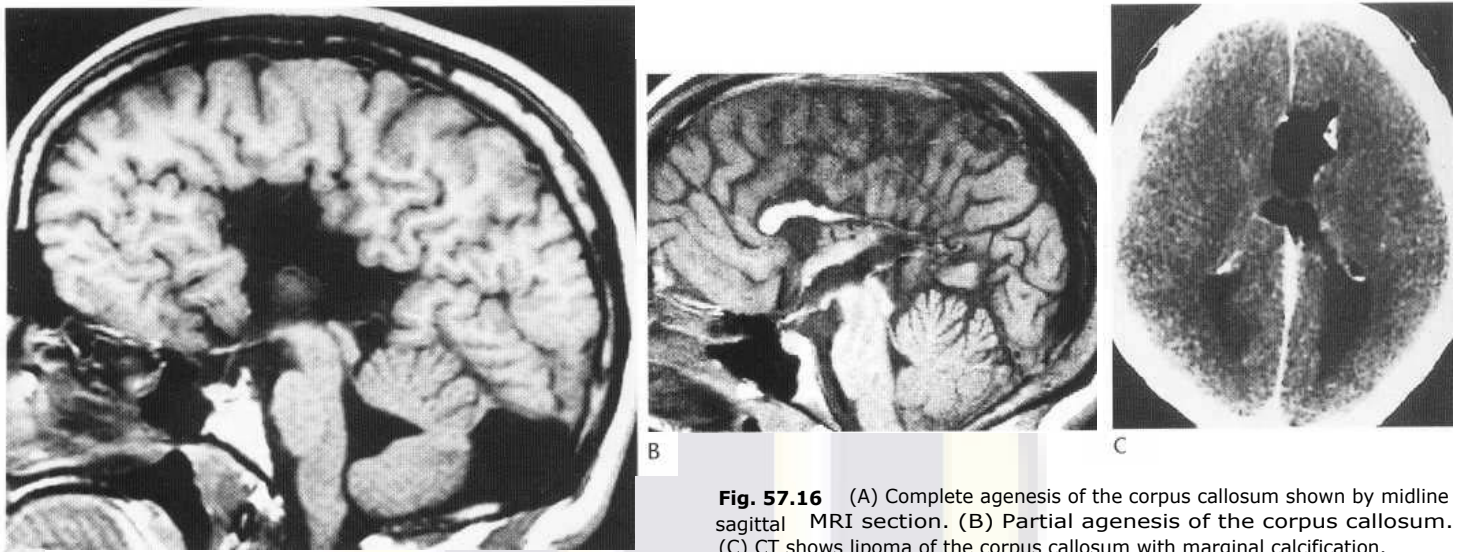


Fig. 57.16 (A) Complete agenesis of the corpus callosum shown by midline sagittal MRI section. (B) Partial agenesis of the corpus callosum. (C) CT shows lipoma of the corpus callosum with marginal calcification.

A

At CT complete agenesis is characterised by wide separation of the medial borders of the lateral ventricles, with a high third ventricle extending up between them and also enlargement of the occipital horns.

Partial agenesis usually involves the posterior part, and the anterior part may remain normal. MRI shows similar features on axial or coronal sections, but a midline sagittal section (Fig. 57.16) shows

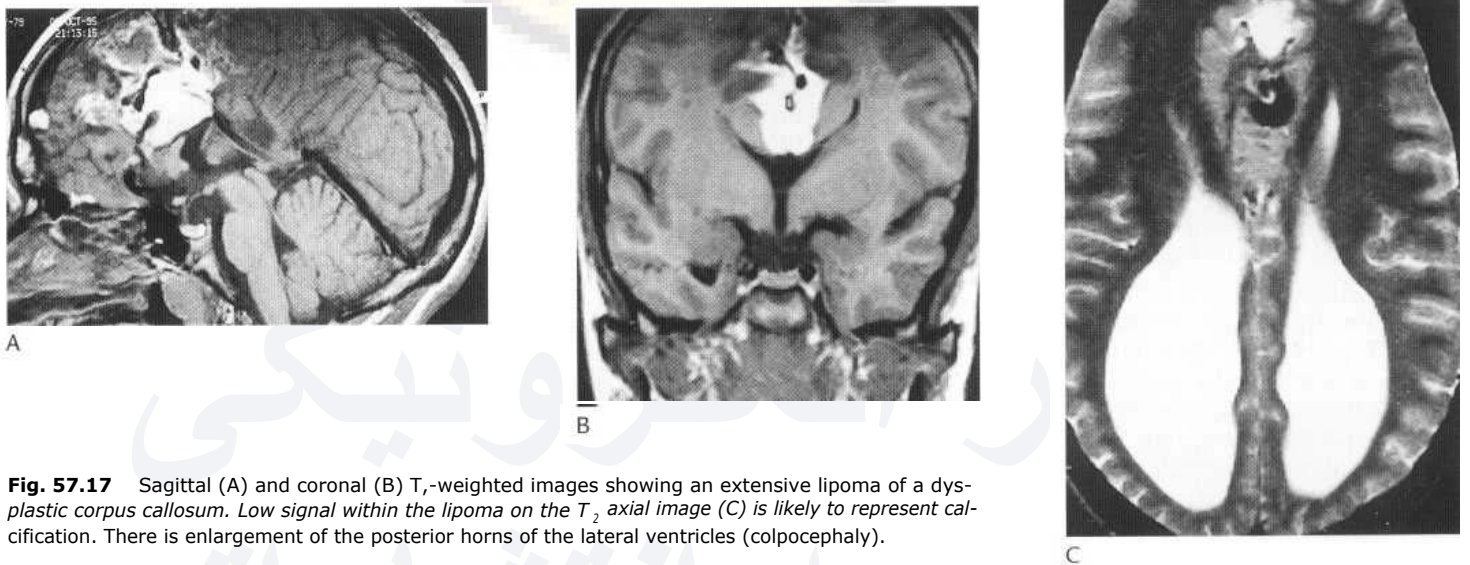


Fig. 57.17 Sagittal (A) and coronal (B) T₁-weighted images showing an extensive lipoma of a dysplastic corpus callosum. Low signal within the lipoma on the T₂ axial image (C) is likely to represent calcification. There is enlargement of the posterior horns of the lateral ventricles (colpocephaly).

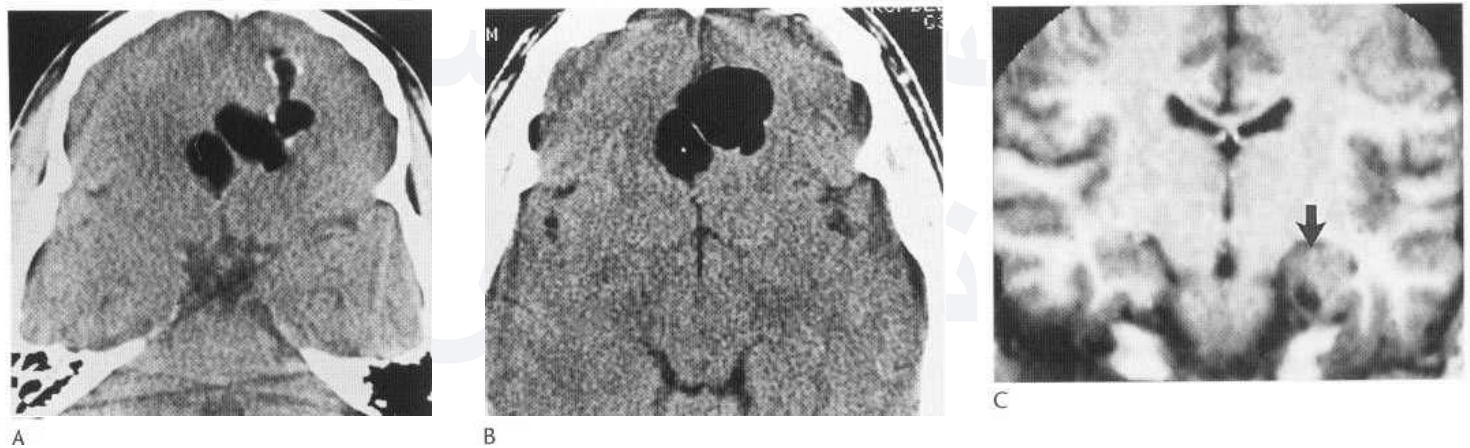


Fig. 57.18 (A,B) Midline bifrontal lobulated lipoma with marginal calcification. Shown by CT. (C) Hamartoma of the left temporal lobe. Coronal MRI study shows a small rounded lesion mainly of low signal similar to cortex.

the lesion most clearly. The third ventricle extends upward into and above the position of the absent corpus callosum. Radial configuration of the medial cerebral sulci extending through the absent callosal body region is also seen in the sagittal images. The axons which fail to cross form symmetrical longitudinal bundles along the medial surfaces of the hemispheres and impress the medial parts of the ventricles. Thus the frontal horns and bodies are laterally displaced and small. The atria and occipital horns are large and rounded due to lack of the normal forceps major impressions.

A lipoma may sometimes be found at the site of the absent corpus callosum (see below).

Lipoma of the corpus callosum Intracranial lipomas are rare tumours which occur mainly in relation to the corpus callosum, but can also occur elsewhere including the suprasellar and pineal areas. They may lie above a normal corpus callosum but are associated with partial or complete agenesis in 40% of cases. There is often marginal calcification where they merge with adjacent cortical tissue this can be of a characteristic 'brackets' type which occasionally permits diagnosis from a simple PA X-ray film (Fig. 53.34). A large lesion may also produce an area of increased radiolucency between the brackets. The pericallosal arteries are usually incorporated in the tumour and may be fused (azygos or single anterior cerebral artery).

Their typical situation together with their fatty density makes the lipomas readily identifiable at CT or MRI. Adjacent calcification is best seen at CT (Figs 57.17, 57.18A,B), but this may be minimal or absent, particularly with small lesions. The single anterior cerebral artery may be visible at MRI on T-weighted images. Sometimes streaks of fat may be evident in an otherwise normal-looking corpus callosum.

Hamartomas Hamartomas are congenital benign tumours containing an overgrowth of mature cells and tissues normally found in the affected part. Some pathologists include glial lesions of the

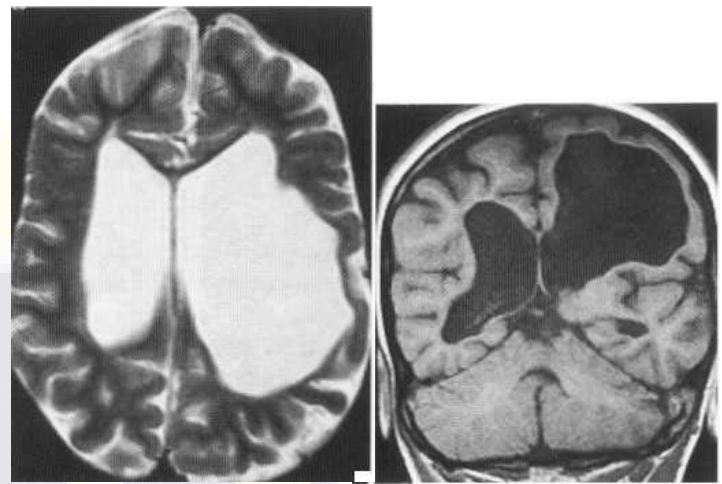


Fig. 57.19 Porencephaly (A) T₂-weighted axial study. (B) T₁-weighted coronal study. Large cavity in left hemisphere.

brain in addition to dermoids, epidermoids and nasal gliomas. These are discussed in the section on neoplasms. Hamartoma of the tuber cinereum is a specific condition associated with precocious puberty. At CT or MRI it appears as a rounded suprasellar mass of brain density and occupying the interpeduncular cistern. Hamartoma and allied lesions also occur in the temporal lobe (Fig. 57.18C) where it may present with epilepsy and contain calcification visible at simple X-ray or CT.

Ventricular coarctation In this rare condition the frontal horns fail to develop normally and the lateral and medial walls appear adherent or apposed due to ependymal fusion. The rest of the ventricular system is normal. Its importance lies in recognising its congenital nature when seen as a chance finding at imaging, and

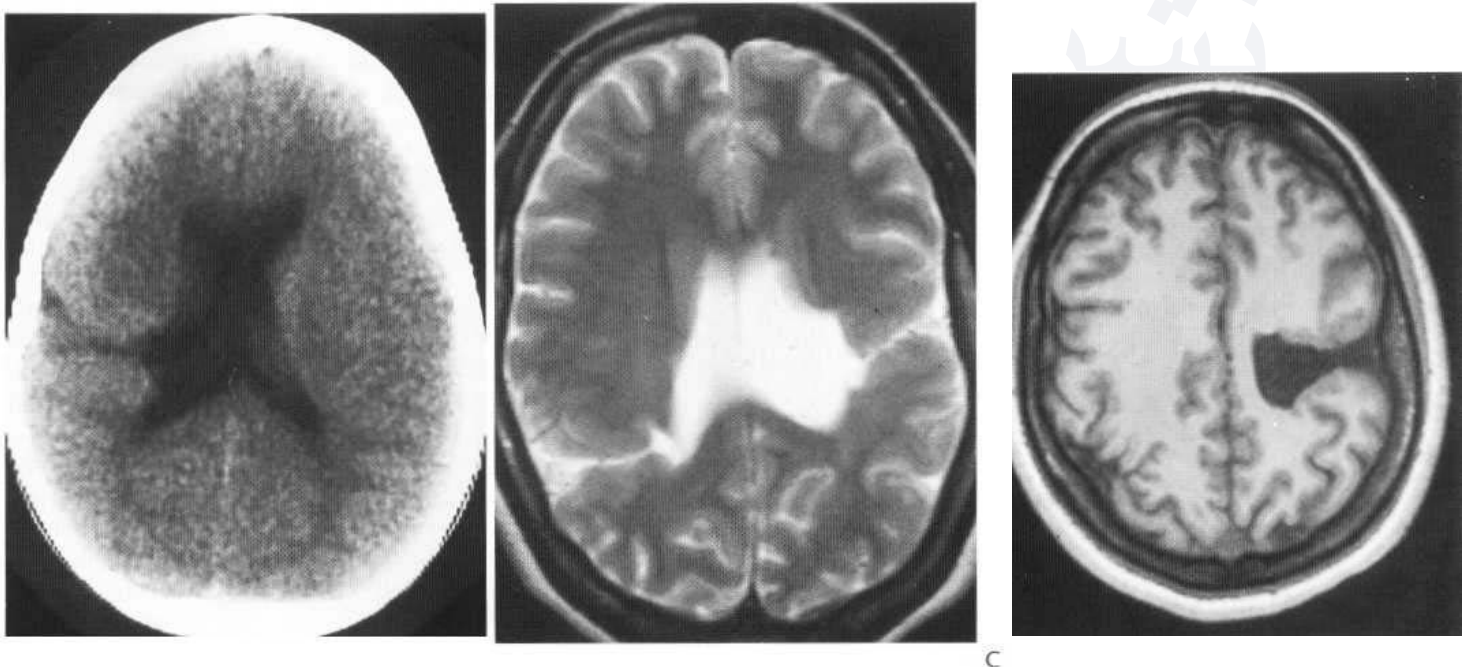


Fig. 57.20 (A) CT shows minor degree of schizencephaly presenting as lateral slit lined by cortex. Axial T₂-weighted image (B) of a patient with bilateral schizencephaly. The clefts radiate out from the lateral ventricles to the surface of the hemispheres and are lined by grey matter. The cleft on the right is closed-lipped whereas the one on the left is open-lipped and this is evident on the more superior axial T₁-weighted image (C).

in not mistaking the deformity for the effects of compression by a local tumour.

Porencephaly Porencephaly has been classified as congenital or acquired. The congenital form is due to localised agenesis of the cortical mantle resulting in the formation of a cavity or a lateral slit through which the lateral ventricle communicates with the convexity of the brain. The cavity is lined by ependyma and laterally by a thin pia-ependymal layer which may rupture into the subarachnoid space. In less severe forms the cavity may be reduced to a lateral slit lined by ependyma and partially fused.

The acquired type is secondary to any type of cerebral destructive process, ranging from trauma to infarction. Sometimes called false porencephaly, such cases are better labelled by their aetiological cause if this is known, e.g. post-traumatic or postinfarction cerebral cavities.

Porencephalic cavities or clefts can be identified or suspected by ultrasound in the neonate or infant. In children or adults they are demonstrated by CT or MRI (Fig. 57.19).

Schizencephaly This term is used for a form of porencephaly in which clefts, commonly bilateral, extend from the ventricles to the convexity in the operculoinsular regions. Injury to the germinal matrix in the early stage of gestation may result in a loss of the full thickness of cerebral substance, with a cleft extending from the ventricle to convexity subarachnoid space (Fig. 57.20). The lesion is usually symmetrical and may be associated with a single ventricle and other malformations, especially heterotopias with -topic grey matter lining the cleft margins. CT or MRI in the axial plane will demonstrate the lesions well.

Holoprosencephaly This comprises a complex craniocerebral and facial anomaly classified in grades of severity from alobar through semilobar to lobar, which is the least severe. It results from a failure of normal development of the forebrain (prosencephalon). The severe *anencephalic* form is incompatible with survival beyond infancy. The child has multiple craniofacial anomalies (cleft lip and palate, hypotelorism, anophthalmia or cyclopia). Intracranially the midline structures (falx, corpus callosum, septum pellucidum and olfactory bulbs) are absent and the two hemispheres are replaced by a single large ventricle with a thin rim of cortical mantle. The thalami are fused, unlike hydranencephaly, where they remain normal.

Semilobar holoprosencephaly, the intermediate form, shows less severe facial deformity and the brain has a thicker mantle with recognisable occipital horns (Fig. 57.21). In the mildest (*lobar*) type there are well-formed lateral ventricles and a recognisable third ventricle, though the septum and Sylvian fissures are usually absent.

The grosser forms may be suspected from the clinical appearance of the infant, but imaging will be required in all varieties to delineate the intracranial anomalies.

Hydranencephaly This condition is generally the result of a major destructive process, often in the prenatal or perinatal period, and results in massive intracerebral cavitation which can resemble gross ventricular dilatation. It tends to affect the anterior parts of the hemisphere, suggesting major involvement of the areas supplied by the internal carotids.

The falx is present (a distinguishing feature from severe holoprosencephaly), and the posterior fossa and basal ganglia appear normal. The ventricular dilatation resembles gross hydrocephalus, but the infant's head is not enlarged.

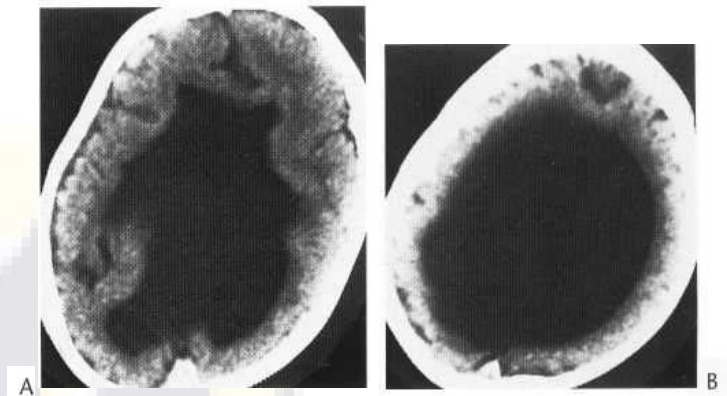


Fig. 57.21 (A,B) Semilobar holoprosencephaly.

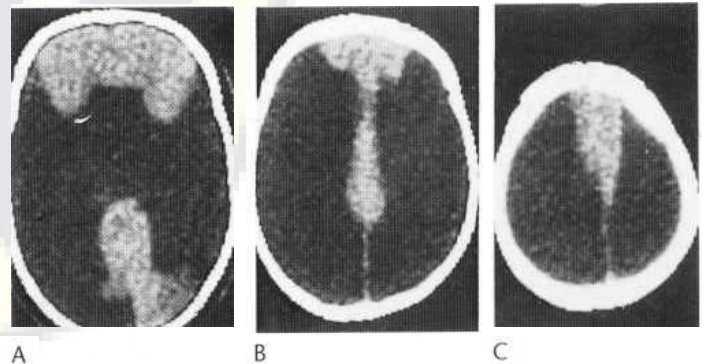


Fig. 57.22 (A-C) Hydranencephaly

The diagnosis in the neonate can be suggested by ultrasound, and the anatomical feature can be delineated by CT or MRI (Fig. 57.22).

Disorders of neuronal migration

Cortical neurones are formed in the embryonal germinal matrix which lies adjacent to the lateral ventricles. They then migrate centrifugally out to the surface of the brain where they form the cerebral cortex, the deeper layers being constituted first. Interruption of this process, which takes place at the end of the second month of fetal life, may give rise to various anomalies including lissencephaly, pachygyria, polymicrogyria and heterotopic grey matter.

Lissencephaly (agyria) This, the most severe form of migrational defect, is characterised by the absence of sulci and convolutions in the cortex, and is the normal appearance before the seventh month of fetal life. The Greek word can be translated as 'smooth brain'. It may be spontaneous or inherited as an autosomal recessive.

Its persistence to term may be total or involve only part of the hemispheres, and some degree of pachygyria may be associated. Clinically there is severe mental retardation, fits and decerebrate rigidity. There is often a characteristic nodule of calcification in the septum pellucidum near the foramen of Monro, which can be seen at simple X-ray or CT examination. The latter, like MRI (Fig. 57.23), will identify the agyria and pachygyria.

Pachygyria In this condition the convolutions and cortex are abnormally wide and thick (pachygyria = thick gyri). The condition results from disturbance of migration at a later stage than

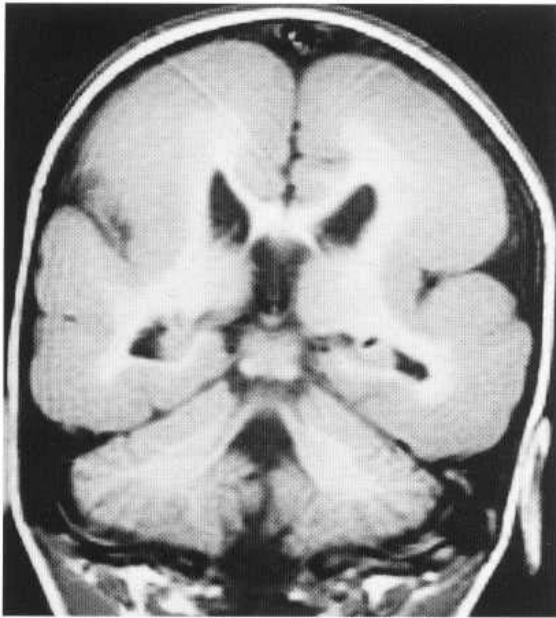


Fig. 57.23 Cerebral dysplasia with gross pachygyria and poorly formed sulci.

agyria and can occur together with it and other anomalies such as heterotopic grey matter (Figs 57.23, 57.24).

Polymicrogyria This condition is the result of a disturbance at the latest stage of neuronal migration, causing multiple small gyri to be formed. It may be focal or diffuse and accompanied by epilepsy, focal neurological deficits and mental retardation.

Heterotopias These may be observed as an isolated phenomenon due to arrest of migrating neurones in the form of small masses of grey matter. They may form subependymal nodules protruding into the lateral ventricles similar to those seen in tuberous sclerosis, or lie in the centrum ovale or subcortically, near the caudate nuclei, in the cerebellar white matter and in the brainstem. These may be nodular or band like. There are usually associated congen-

ital anomalies, but isolated nodular lesions have been mistaken for neoplastic areas at CT and they occasionally contain calcified foci. At MRI these lesions may give lower signal than does normal grey matter (Fig. 57.25).

Phakomatoses

Phakoma (from the Greek *phakos* = lentil) was the term used for a lentil-shaped object such as a spot on the body or in the retina. The term 'phakomatoses' is used to refer to a group of diseases of different aetiologies but having in common lesions of the skin, retina and nervous system and the fact that they are developmental. They are also referred to as 'neuroectodermal dysplasias', and include tuberous sclerosis, neurofibromatosis, Sturge-Weber syndrome and von Hippel-Lindau disease.

Tuberous sclerosis (synonyms: *epiloia*, *Bourneville's disease*) The lesions of this condition can affect the skin and nervous system but many other systems, including the bones (see Ch. 37), respiratory system (Ch. 4), kidneys (Ch. 32), heart and skeletal muscle.

In the brain there are multiple areas of heterotopia containing abnormal and giant glial cells and lying in the subcortical and paraventricular regions as well as the white matter and cerebellum. These often contain calcification which can be recognised on a simple X-ray film. Typically the calcifications are widely scattered small rounded discrete lesions, though they can be irregular, sinuous or densely nodular. Their multiple scattered nature should suggest the diagnosis (Fig. 53.45). Rarely a paraventricular nodule near the foramen of Monro becomes large enough to produce obstructive hydrocephalus by developing into a low-grade giant cell astrocytoma (Fig. 57.26A).

Imaging At CT the characteristic and diagnostic feature is the presence of small nodular protrusions into the ventricles, usually with calcified foci. The latter are of course much easier to see at CT (Fig. 57.26B,C) than at simple X-ray.

MRI shows the areas of dysplasia better than CT but has the disadvantage of not imaging the calcification. On T₂-weighted images

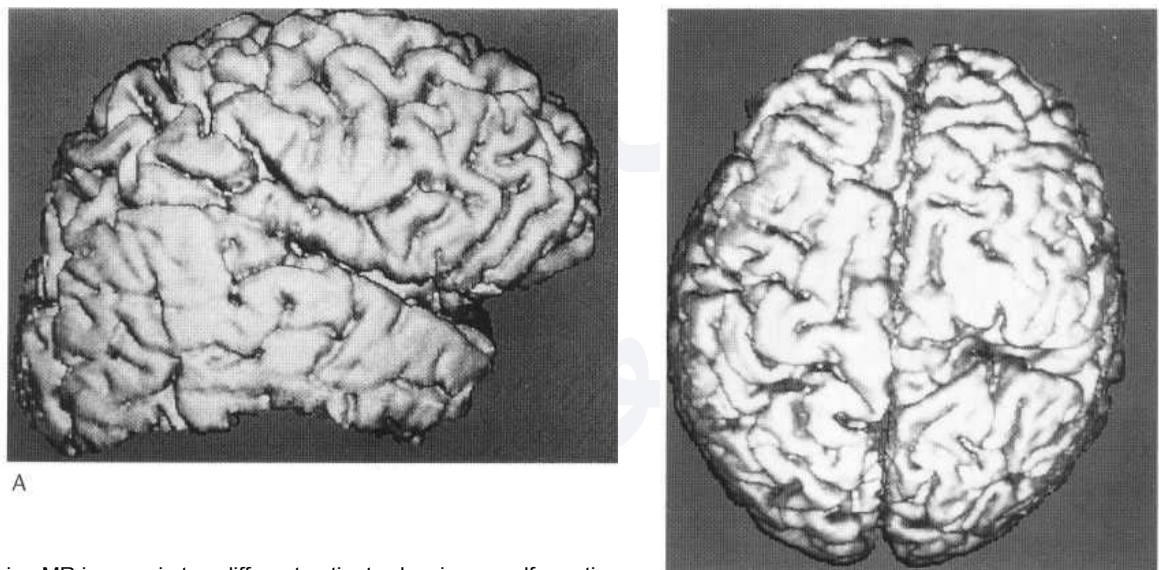


Fig. 57.24 3D surface rendering MR images in two different patients showing a malformation of cortical development in fronto-parietal region (A) and also in both parasagittal regions (B).

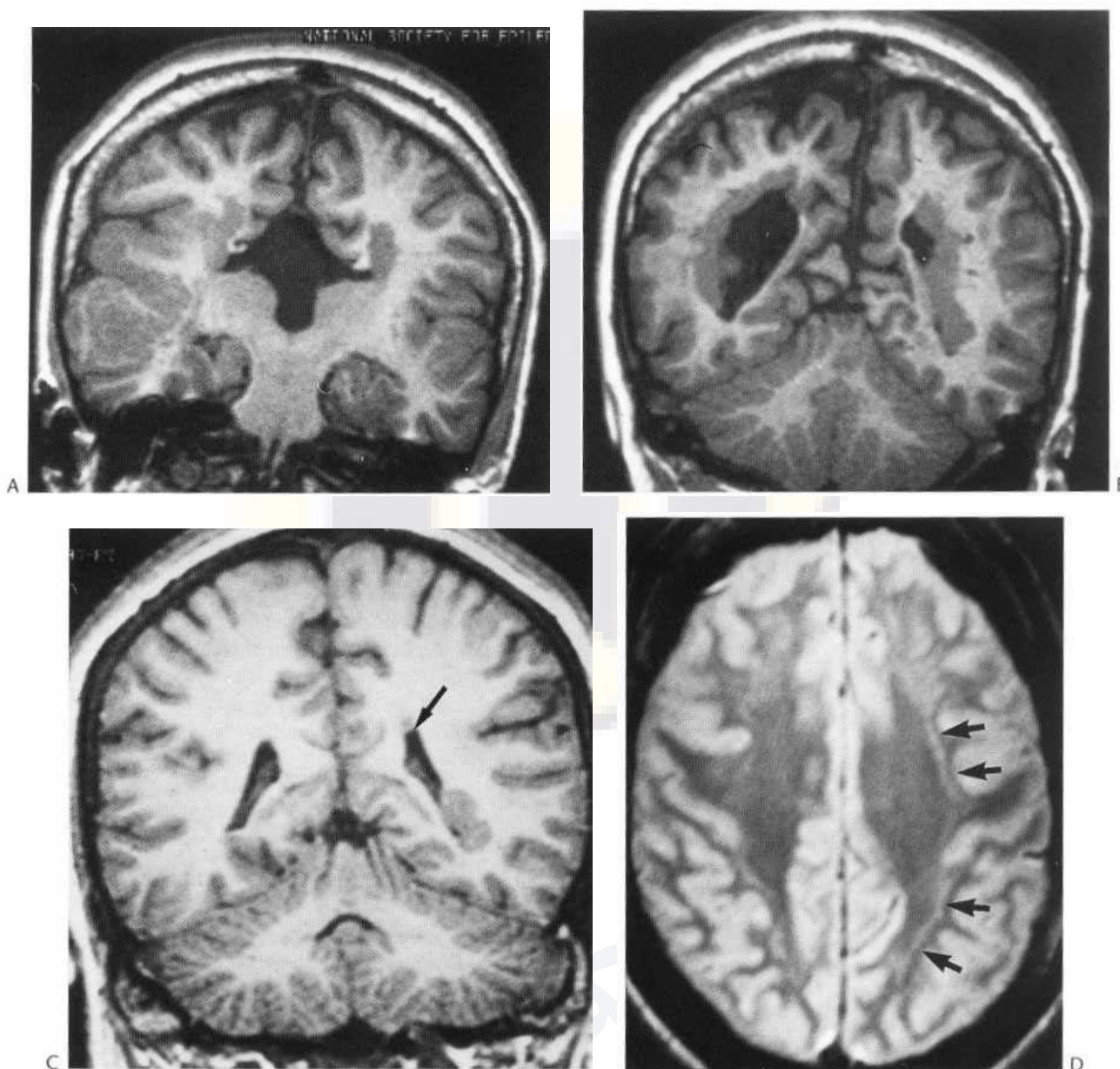


Fig. 57.25 (A) Multiple anomalies including agenesis of corpus callosum, subependymal heterotopia, subcortical heterotopia and polymicrogyria. (B) Diffuse subependymal heterotopia. (C) Unilateral nodular and subependymal heterotopia (arrow). (D) Band-like heterotopic grey matter (arrows) in a patient with epilepsy. Similar but less obvious lesions on right side. Positron density weighted MRI.

موسسه انتشاراتی
نوردانش

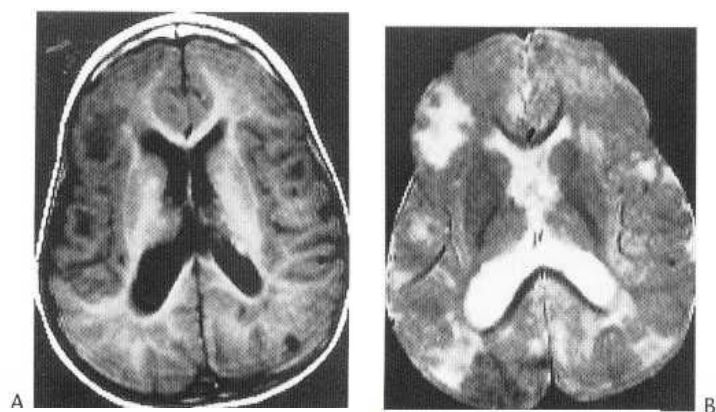


Fig. 57.27 MRI studies of a patient with tuberous sclerosis shows cortical tubers as: (A) low signal (T_1 -weighted); (B) high signal (T_2 -weighted). Calcification is not specifically identified but appears as low signal in the intraventricular tubers.

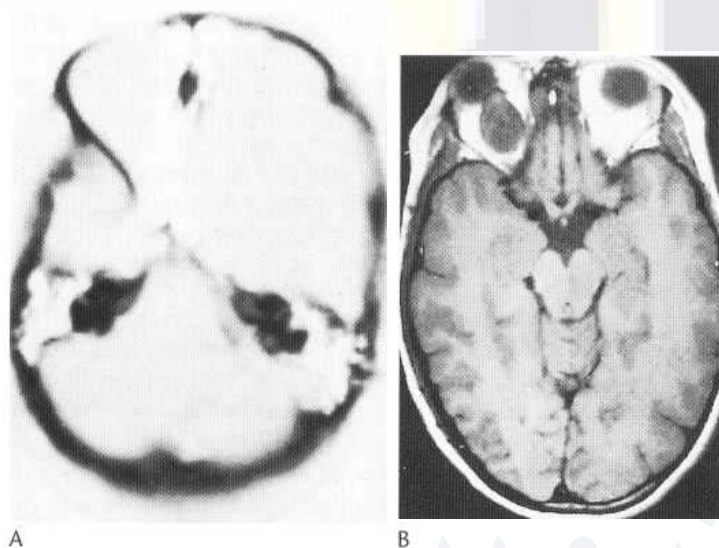


Fig. 57.28 (A) Neurofibromatosis showing absence of sphenoid wing on the right. Reversal negative at wider window for bone detail. (B) Axial MRI (T_1 -weighted) shows right optic nerve glioma as low-signal rounded mass in a patient with neurofibromatosis.

tubers appear as irregular areas of increased signal cortically, in the white matter, or paraventricular, though calcification will appear as low-signal areas (Fig. 57.27). T_2 -weighted images usually show the lesions as giving low signal and occasionally they resemble cysts.

Neurofibromatosis This manifests in several different ways, the commonest being peripheral neurofibromatosis (von Recklinghausen's disease) now classified as NF1 and affecting 1 in 4000 of the population. It is an autosomal dominant familial disorder associated with a defect in the long arm of chromosome 17, and the CNS is affected in some 15% of cases. The skull and spine are also frequently involved. The skull lesions have been described in Chapter 53; absence of the greater wing of the sphenoid is one of the causes of the 'bare orbit' causing unilateral exophthalmos (Fig. 57.28A). Spinal scoliosis or kyphoscoliosis is present in one-third of the cases, and dural ectasia and lateral thoracic meningocele are other spinal manifestations. Paraspinal neurofibromas may also occur and can occasionally become malignant (10%).

In the CNS NF1 is associated with glial tumours, including optic nerve gliomas (Fig. 57.28B) and cerebral and brainstem astrocytoma, and also with anomalies of migration resulting in various types of dysplasia and heterotopia in the white matter. Hamartomas with no mass effect are frequently present, leading to areas of high signal on T_2 MR studies. Generalised or focal cerebral atrophy may also be seen, associated with mental retardation.

Vascular dysplasias involving the terminal internal carotid or anterior or middle cerebral origins have also been described in NF1, as has the resulting moyamoya disease.

Neurofibromatosis 2 (NF2 or central neurofibromatosis), is much less commonly seen, affecting only 1 in 50 000 of the population. It is also inherited as an autosomal dominant but is due to a defect of chromosome 22. The CNS lesions are quite different from those of

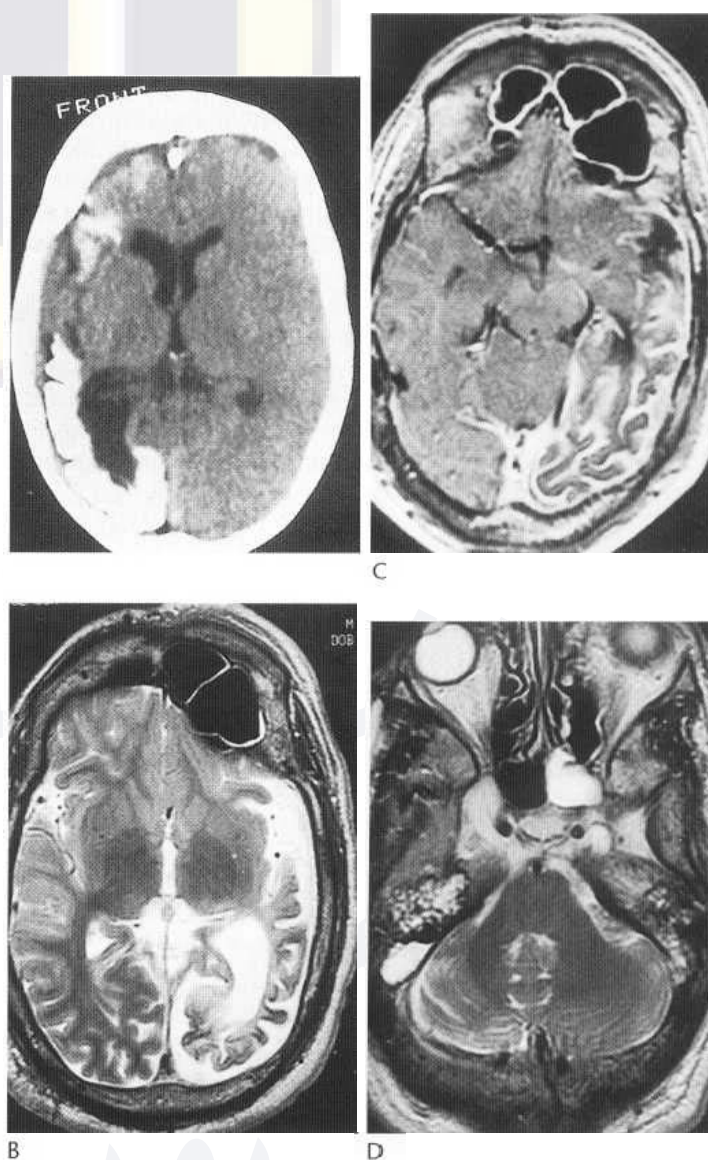


Fig. 57.29 (A) Sturge-Weber syndrome. Predominantly occipital cortical calcification with some atrophy. Axial T_2 -weighted image (B) in a patient with Sturge-Weber syndrome shows atrophy of the left cerebral hemisphere. Cortical T_2 low signal in the left occipital region is consistent with calcification. There is also some thickening of the calvarium in the left frontal region. On the postcontrast T1 axial image (C) there is marked superficial enhancement in the occipital and temporal regions due to the presence of a pial angioma. There is atrophy of the right cerebellar hemisphere (D)-crossed cerebellar diaschisis.

NF1 and consist of bilateral acoustic neuromas which may be associated with schwannomas of other cranial nerves and with meningiomas. In the spine bony abnormalities are absent but large bilateral neurofibromas may be seen, sometimes at every level (see Fig. 2.51). Spinal meningiomas also occur as does ependymoma of the cord or filum.

The intracranial lesions can be characterised by CT or MRI and are discussed below under cerebral tumours.

Other features of neurofibromatosis are described elsewhere and include skeletal deformities (Ch. 40) and a rare association with renal artery stenosis or aneurysm. There is also a very rare association with phaeochromocytoma.

Sturge-Weber disease (encephalotrigeminal angiomatosis) This condition involves a flat and often extensive unilateral angioma of the 'port wine' stain type in the facial and scalp distribution area of the trigeminal nerve. It is accompanied by a leptomeningeal angiomatosis in the parieto-occipital area on the same side, which is associated with underlying cortical gliosis and calcification. Clinically there is epilepsy and a deficit corresponding to the cortical lesion. The cortical calcification gives rise to the characteristic tramline calcification seen on simple radiographs (Fig. 3.46). This represents the margins of sulci where the calcification is seen end-on.

The occipital cortical calcification is also well shown by CT, but the classic tramline appearance is obscured at normal window since CT shows all the extensive calcification and not just that seen end-on at the sulcal margins (Fig. 57.29A). The gyriform nature of the calcification is more apparent when viewed at wide window. Occasionally CT will demonstrate bilateral changes, an important finding if hemispherectomy for intractable epilepsy is being considered.

MRI may show the calcification in the cortex but mainly by susceptibility effects, especially on gradient-recalled echo sequences. It also shows cortical atrophy, and the extent of the angiomatosis may be delineated by intravenous gadolinium (Fig. 57.29B-D). The cortex often seems to enhance as well and the choroid plexus on the side of the lesion is conspicuously larger.

Von Hippel-Lindau disease (retinocerebellar angiomatosis) This rare familial disease is characterised the occurrence of multiple haemangioblastomas in the retina and cerebellum. They may also be found in the spinal cord and rarely in the cerebrum. There is also an association with visceral tumours and cysts, particularly renal and pancreatic tumours. Patients usually present in their late teens or early twenties.

Imaging The intracranial lesions can be demonstrated by CT or MRI but angiography is more specific (Fig. 57.30). It is important to realise that haemangioblastomas occur much more commonly as isolated lesions, single or multiple in the cerebellum, and without the retinal lesions of von Hippel-Lindau disease. They can also occur as isolated lesions in the spine. Their diagnosis is discussed in the sections on cerebral tumours and spinal tumours (see also Fig. 57.27).

Ataxia telangiectasia This condition presents in infants, who show cerebellar ataxia when starting to walk followed by rapid deterioration with choreoathetosis. The mucocutaneous telangiectasias appear at 3-6 years and there is a high incidence (10-15%) of malignancy (lymphoma, and leukaemia in children and epithelial in adults). The disease is an autosomal recessive, with an incidence of 1 in 40 000 live births. Imaging by CT or MRI shows isolated gross atrophy of the cerebellum with dilated sulci and a dilated fourth ventricle. Haemorrhage as a result of cerebral telangiectasias has also been described. Such an appearance in a young child should always raise the diagnosis of ataxia-telangiectasia.

L'hermitte-Duclos disease This is a rare slow-growing cerebellar malformation which presents as a mass lesion in young adults (20-40 years). It is usually associated with Cowden's syndrome (benign skin tumours, GI polyps, goitre and breast cancer) but can occur alone. CT shows a low-density cerebellar area with thickened folia and no enhancement after contrast. Calcification may be present. MRI shows low signal on T₁ and high signal on T₂ weighting, and some enhancement after L₁-idolinium.

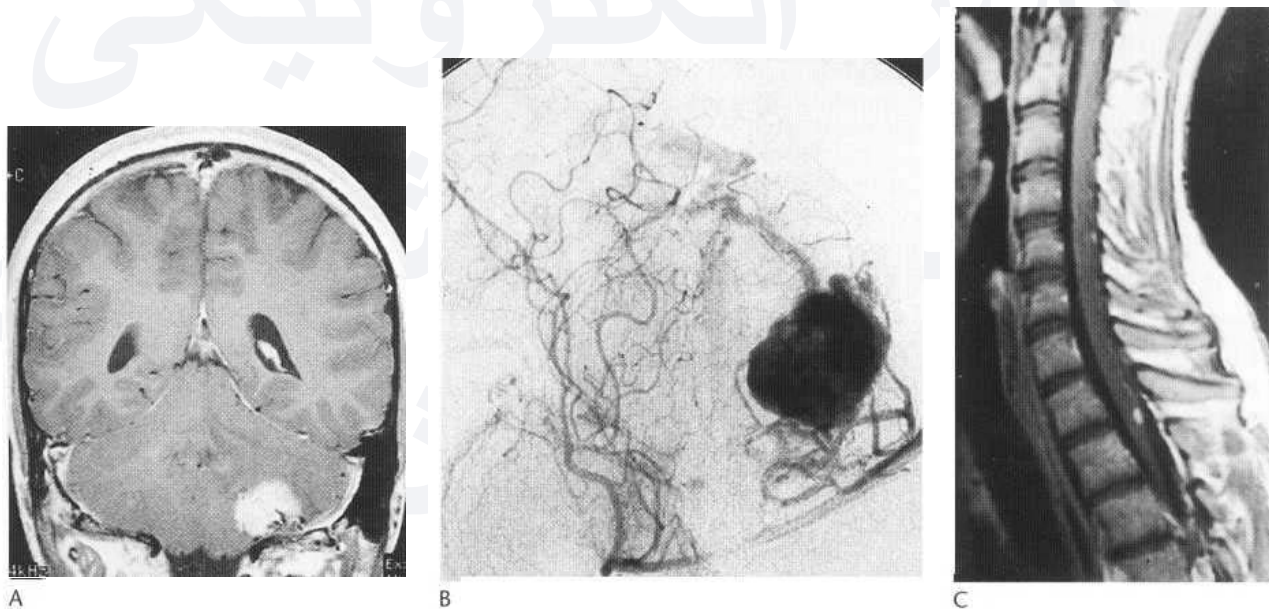


Fig. 57.30 A vascular mass is shown in the left cerebellar hemisphere in a patient with Von Hippel-Lindau syndrome. The mass shows marked enhancement on the coronal postcontrast image (A) and has a dense vascular blush on the lateral vertebral angiogram (B) with evidence of early venous shunting. Two small enhancing superficial spinal haemangioblastomas are also present in the cervical and upper thoracic region on the T₂ postcontrast sagittal image (C).

Neoplasms

Cerebral neoplasms can be classified in several ways. Topographically they may be supratentorial, posterior fossa or intermediate (straddling the tentorial notch or foramen magnum). They can also be intra-axial or extra-axial. In this section they will be discussed mainly on a histopathological basis as listed in Table 57.3.

Epidemiology

Frequency In the past many neurosurgical series have been analysed to show the relative frequency of the different cerebral tumours. However, surgical series are selected, do not reflect the natural incidence and grossly underestimate the incidence of metastases. This is because most patients with cerebral metastases are not operated on by neurosurgeons but are treated by oncologists and radiotherapists. A truer incidence is provided in the pathological series of 5199 cases analysed by Zimmerman (1971), which lists the incidence as in Table 57.1.

Age incidence Cerebral tumours are predominantly tumours of adult life with a peak incidence of 13 cases per 100 000 population at age 55-65. They are relatively uncommon in infants and children at 2 cases per 100 000.

Primary tumours While examples of most primary intracranial tumours can occur at any age, it is helpful in differential diagnosis to know that certain tumours occur mainly in certain age groups. Thus the four main tumours of childhood occur in the posterior fossa and are cerebellar glioma, pontine glioma, medulloblastoma and choroid plexus papilloma. Table 57.2 lists tumours by their usual age group.

Table 57.1 Frequency of cerebral tumours

Tumour	Frequency
Gliomas	31.4
Metastases	20.3
Meningiomas	15.4
Angiomas	5.9
Pituitary adenomas	4.4
Acoustic tumours	1.5
Congenital tumours	2.0
Granulomas	0.4
Miscellaneous	12.3

After Zimmerman 1971

Table 57.2 Primary cerebral tumours, and age groups

Tumour	Age group
Brainstem glioma, optic nerve glioma	0-5
Medulloblastoma, cerebellar astrocytoma, papilloma choroid plexus, pinealoma, craniopharyngioma	5-15
Ependymoma	15-30
Glioma, meningioma, acoustic neuroma, pituitary tumour, hemangioblastoma	30-65
Meningioma, acoustic tumour, glioblastoma	65+

Secondary tumours These affect mainly the middle-aged and elderly, with the exception of secondary neuroblastoma which occurs mainly in children.

Location In adults, supratentorial tumours outnumber posterior fossa tumours by a ratio of 7 to 3, but in children this ratio is reversed, and posterior fossa tumours are the most common.

Gliomas

These, the commonest intracranial tumours, vary greatly in malignancy. This has led to specific names being used based on the histological appearances, e.g. astrocytoma and oligodendroglioma for well-differentiated slow-growing tumours, and glioblastoma and spongioblastoma multiforme for highly malignant ones. Most workers however favour grading by degree of malignancy judged by the proportion of mitotic figures seen at microscopy. The grades range from I, which is relatively benign, through grade II to grades III and IV which are highly malignant (Kernohan). Some 50% of gliomas are of grades III and IV, and about 25% of grade I.

Gliomas can occur at any site in both children and adults, but gliomas of the optic chiasm and of the brainstem are particularly common in children, where they have a peak incidence at 1-6 years and 1-4 years respectively.

Cerebellar astrocytoma is also commoner in children, with a peak incidence at 5-10 years.

In the last decade the World Health Organisation (WHO) has introduced a more logical system based on histopathology (Table 57.3), which is now generally accepted.

Astrocytic tumours

This is the largest group of primary brain neoplasms; they vary greatly in malignancy and can exhibit either a circumscribed or diffuse growth pattern-50% of these tumours are supratentorial, 35% in the cerebellum and 15% in the brainstem. It is the most common primary brain tumour of childhood, accounting for between 30 and 40% of all CNS tumours; diffuse astrocytomas are more common in adults whereas in children the majority of astrocytomas are of the pilocytic type, only the cerebral hemispheres and brainstem being more commonly affected by the diffuse types. Tumours with a circumscribed growth pattern will initially be described followed by the more diffuse, infiltrative type.

Modern high-resolution CT will localise and characterise the vast majority of cerebral astrocytomas, and the same is true of MRI. Skull radiographs are of limited value showing calcification in only a small proportion of astrocytomas. General signs of raised intracranial pressure may be present, as described in Chapter 53, as may lateral displacement of the calcified pineal.

Pilocytic astrocytomas These low-grade (WHO grade 1) tumours account for 2-6% of all primary intracranial neoplasms and usually present in childhood between the ages of 5 and 15 years. They characteristically occur in the cerebellum, hypothalamus or optic nerves and involvement of the latter is a feature of neurofibromatosis type 1. Most series report an equal sex incidence though some series do report a slight female preponderance. Cerebellar tumours occur equally within the vermis and cerebellar hemispheres (Figs 57.31-57.33). The tumours are well circumscribed and encapsulated growing mainly by expansion. The cerebellar tumours are usually large and can be cystic, solid or both. On CT 40% of the tumours are solid, 10-20% have calcification

Table 57.3 Adapted from the World Health Organisation International Classification of tumours affecting the central nervous system

<i>Tumours of neuroepithelial tissue</i>	<i>Other CNS neoplasms</i>
1. <i>Astrocytic tumours</i>	11. <i>Tumours of the sellar region</i>
1.1 Astrocytoma-WHO grade II	11.1 Pituitary adenoma
1.2 Anaplastic (malignant) astrocytoma-WHO grade III	11.2 Pituitary carcinoma
1.3 Glioblastoma-WHO grade IV	11.3 Craniopharyngioma
1.4 Pilocytic astrocytoma-WHO grade I	12. <i>Haematopoietic tumours</i>
1.5 Subependymal giant cell astrocytoma-WHO grade I	12.1 Primary malignant lymphoma
1.6 Pleomorphic xanthoastrocytoma	13. <i>Germ cell tumours</i>
2. <i>Oligodendroglial tumours</i>	13.1 Germinoma
2.1 Oligodendroglioma-WHO grade II	13.2 Embryonal carcinoma
2.2 Anaplastic oligodendroglioma-WHO grade III	13.3 Yolk sac tumour
3. <i>Ependymal tumours</i>	13.4 Choriocarcinoma
3.1 Ependymoma-WHO grade I	13.5 Teratoma
3.2 Anaplastic (malignant) ependymoma-WHO grade III	13.6 Mixed germ cell tumours
3.3 Myxopapillary ependymoma	14. <i>Tumours of the meninges</i>
3.4 Subependymoma-WHO grade I	14.1 Meningioma
4. <i>Mixed gliomas</i>	15. <i>Non-meningothelial tumours of the meninges</i>
4.1 Mixed olig-astrocytoma-WHO grade I	15.1 Benign mesenchymal
4.2 Anaplastic (malignant) oligo-astrocytoma-WHO grade III	15.2 Malignant mesenchymal
4.3 Others (e.g. ependymal astrocytomas)	15.2.1 Chondrosarcoma
5. <i>Neuroepithelial tumours of uncertain origin</i>	15.2.2 Haemangiopericytoma
5.1 Polar spongioblastoma-WHO grade IV	15.3 Primary melanocytic lesions
5.2 Astroblastoma-WHO grade IV	15.4 Haematopoietic neoplasms
5.3 Gliomatosis cerebri-WHO grade IV	15.5 Tumours of uncertain histogenesis
6. <i>Choroid plexus tumours</i>	15.5.1 Haemangioblastoma
6.1 Choroid plexus papilloma	16. <i>Tumours of cranial and spinal nerves</i>
6.2 Choroid plexus carcinoma	16.1 Schwannoma
7. <i>Neuronal and mixed neuronal-glia tumours</i>	16.2 Neurofibroma
7.1 Gangliocytoma	16.3 Malignant Schwannoma
7.2 Dysplastic cerebellar gangliocytoma (L'hermitte-Duclos)	17. <i>Local extension from regional tumours</i>
7.3 Ganglioglioma	17.1 Paranglioma
7.4 Anaplastic (malignant) ganglioglioma	17.2 Chordoma
7.5 Desmoplastic infantile ganglioglioma	17.3 Chondroma
7.6 Central neurocytoma	17.4 Chondrosarcoma
7.7 Dysembryoplastic neuroepithelial tumour	18. <i>Metastatic tumours</i>
7.8 Olfactory neuroblastoma (esthesioneuroblastoma)	19. <i>Unclassified tumours</i>
8. <i>Pineal tumours</i>	20. <i>Cysts and tumour-like lesions</i>
8.1 Pineocytoma	20.1 Rathke cleft cyst
8.2 Pinealoblastoma	20.2 Epidermoid
8.3 Mixed pineocytoma/pinealoblastoma	20.3 Dermoid
9. <i>Embryonal tumours</i>	20.4 Colloid cyst of the third ventricle
9.1 Medulloepithelioma	20.5 Enterogenous cyst
9.2 Primitive neuroectodermal tumours	20.6 Neuroglial cyst
9.2.1 Medulloblastoma	20.7 Granular cell tumour (choristoma)
9.3 Neuroblastoma	20.8 Hypothalamic neuronal hamartoma
9.4 Retinoblastoma	
9.5 Ependymblastoma	

and up to 70% are cystic. Forty-seven per cent of the cystic tumours have an associated mural tumour nodule which is iso- or slightly hyperdense on CT. Enhancement of the cyst wall indicates it is tumour lined. On MRI the tumours are hypointense to iso- or hyperdense and enhances; the cyst wall is composed of surrounding compressed or gliotic parenchyma and thus may appear as images and enhancement patterns are similar to those seen on CT.

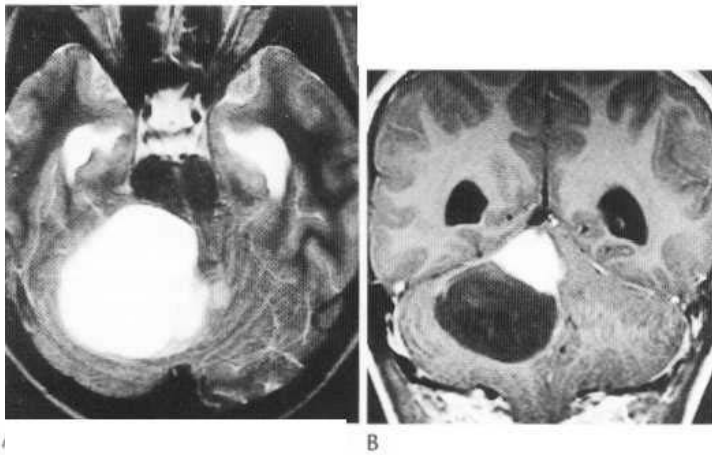


Fig. 57.31 Axial T₂-weighted image (A) in a patient with a juvenile pilocytic astrocytoma of the right cerebellar hemisphere showing a large cystic component, a little peritumoural vasogenic oedema and hydrocephalus due to obstruction of the fourth ventricle. The T₁-weighted coronal post-contrast image (B) shows a superior enhancing mural nodule and minor peripheral enhancement of the cyst wall.

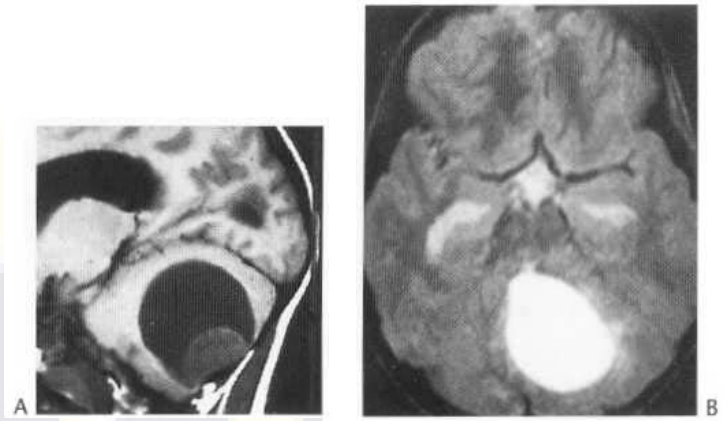


Fig. 57.33 MRI studies of cystic juvenile astrocytoma. (A) T₁-weighted: tumour and cyst are of different low signals. (B) T₂-weighted: tumour and cyst given uniform high signal.

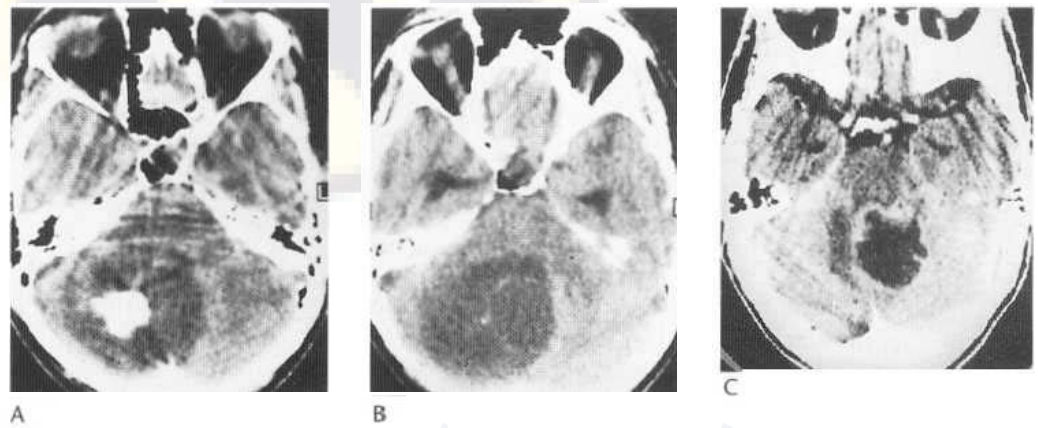


Fig. 57.32 Cerebellar astrocytomas. (A) Large nodular calcification in a right hemisphere tumour. (B) Large cystic tumour with only fair marginal enhancement. (C) Near midline tumour with irregular marginal enhancement.

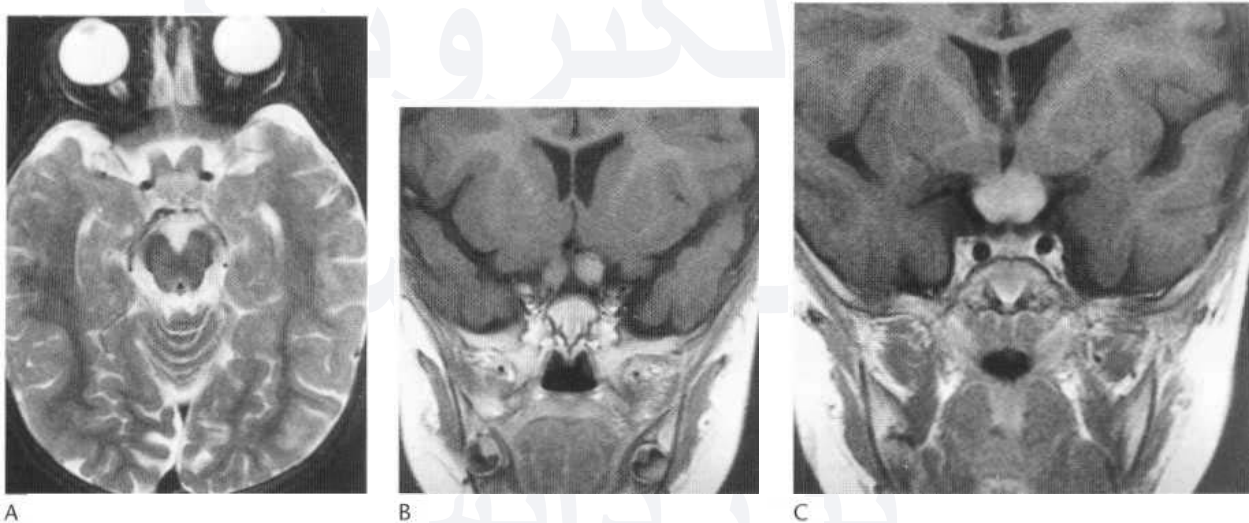


Fig. 57.34 Axial T₁-weighted MRI (A) showing enlargement of the cranial portions of both optic nerves and the chiasm in keeping with an optic glioma. On the postcontrast T₁-weighted coronal images (B,C) there is some enhancement of the tumour.

Enhancement of the solid tumours is variable ranging from complete to absent enhancement. Optic pathway gliomas can arise anywhere along the optic pathway, from orbit to the visual cortex (Figs 57.34-57.36). Between 50 and 85% involve the chiasm or

hypothalamus, and 60% of these will be pilocytic astrocytomas histologically. On imaging the optic nerve is typically enlarged and buckled and enhances: although cystic changes may be present calcification is not a feature in the absence of irradiation, which

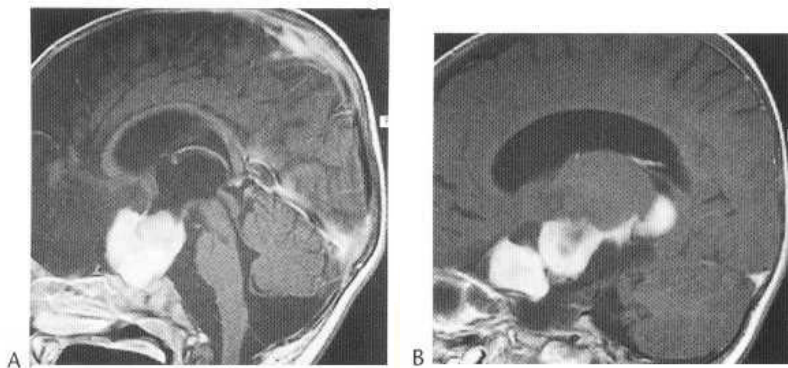


Fig. 57.35 These sagittal T₁-postcontrast images show a large enhancing sellar/suprasellar chiasmal and hypothalamic mass (A,B), which extends posteriorly along the optic tract, consistent with an optic glioma.

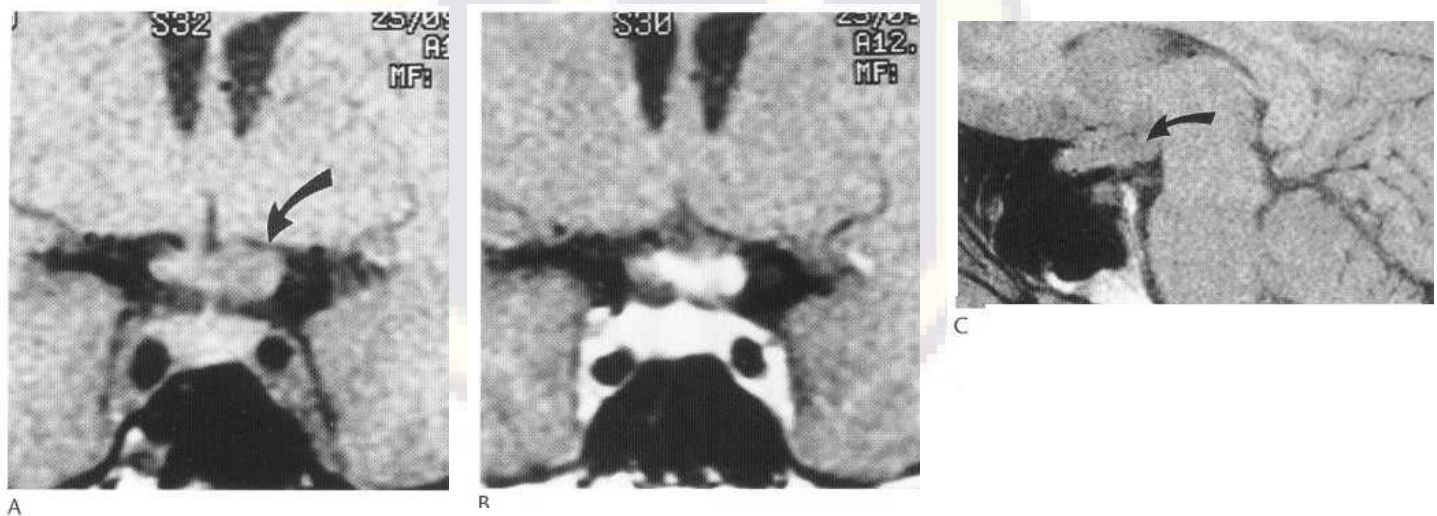


Fig. 57.36 (A) Coronal MRI section through suprasellar cistern and sella shows chiasm swollen mainly on left side (arrow). The infundibulum is also seen. (B) Postgadolinium the tumour enhances, mainly on the left. (C) Left parasagittal section through the swollen chiasm (arrow).

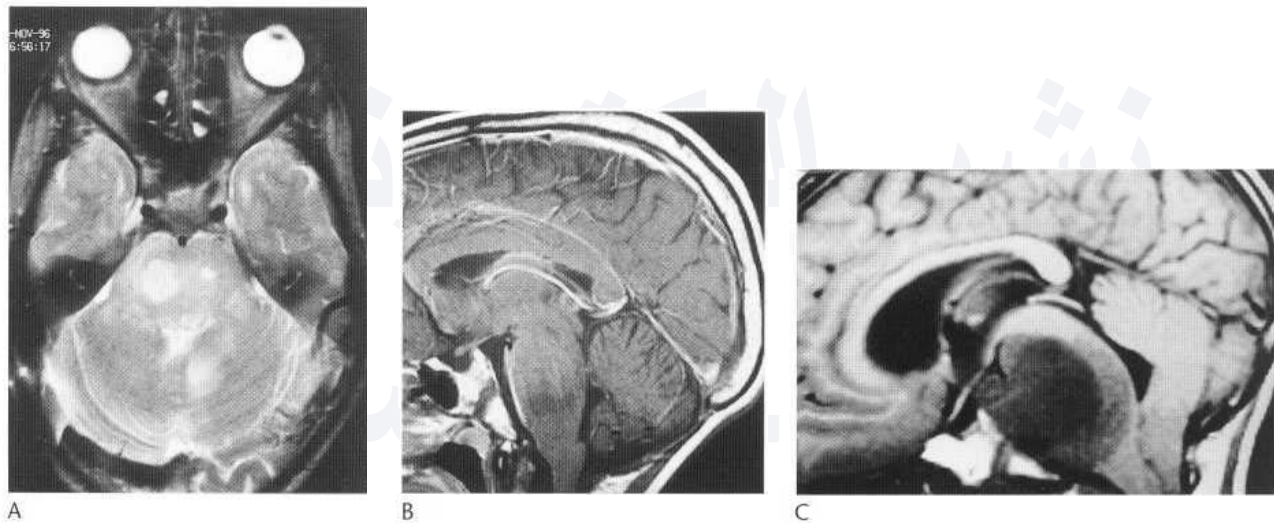


Fig. 57.37 Pontine glioma. (A) Axial T₂ image through the posterior fossa shows an expanded pons with increased signal, with flattening of the fourth ventricle and pontine cistern. (B) This case shows similar changes to A, with slight marginal enhancement after contrast medium. (C) Sagittal T₁ view shows an expanded pons and medulla compressing the pontine cistern and displacing aqueduct and fourth ventricle backwards.

may be useful in differentiating this lesion from an optic nerve sheath meningioma. The tumours involving the chiasm or hypothalamus are often large, lobulated and well circumscribed at presentation and can be partially cystic. Although haemorrhage and necrosis is uncommon, they can invade local structures and be associated with perilesional oedema. On CT they are hypodense and on MRI hypointense on T₁-weighted sequences and hyperin-

tense on T₂-weighted sequences with enhancement of the solid components (Fig. 57.37).

Subependymal giant cell astrocytomas These are also WHO grade I tumours and in 90% of cases are associated with tuberous sclerosis (TS) (Fig. 57.26); conversely 15% of patients with TS will develop this well-demarcated tumour usually in their teens

or early twenties, which is located in the vicinity of the foramen of Monro, attached to the caudate head nucleus and protrudes into the ventricle. As this tumour is covered by an intact layer of ependyma, seeding via the CSF is unlikely, but calcification is a frequent imaging feature. On CT the tumours are hypodense to isodense and on MRI they are usually hypointense to isointense on T₁- and hyperintense on T₂-weighted images, with strong enhancement. Hydrocephalus is a commonly associated feature.

Pleomorphic xanthoastrocytoma This tumour category is a new inclusion in the WHO 1993 classification with behaviour intermediate between that of a low grade II circumscribed lesion and a more infiltrative one (Fig. 57.38); it presents in children and young adults usually with seizures and has a predilection for the temporal lobe, and is rarely seen in the cerebellum or spinal cord; there is no sex predilection. It arises from subpial astrocytes which may explain its tendency to arise or involve the surface of the brain. On imaging the typical appearance is one of a superficial cortical temporal lobe mass which is partially cystic but associated with a tumoral mural nodule which is often adherent to the surface of the brain and thus there may be associated reactive meningeal thickening. On CT the solid tumour components are heterogeneous and can be either hypodense or hyperdense; calcification is variable but as the tumour is relatively slow growing and superficial there may be scalloping of the overlying calvarial inner table. On MRI the solid tumour components are hypointense or isointense on T₁- and hyperintense on T₂-weighted images. The tumoral nodule enhances, but enhancement of the cyst wall is variable.

Diffuse astrocytoma These are poorly marginated and infiltrate the surrounding brain; the histological grade varies between WHO grade II and grade IV, the latter being the most aggressive form, the glioblastoma multiforme (GBM),

The WHO grade II tumour accounts for 10% of all intracranial and one-third of all primary CNS tumours. It is uncommon in the first decade, but more common in older children and young adults up to the age of 40-45 years, being relatively uncommon after the age of 65 years. Slightly more males than females are affected and it

most frequently arises in the cerebral hemispheres though the cerebellum and brainstem may also be affected. It tends to infiltrate along white matter tracts, but the blood-brain barrier remains intact. Necrosis and haemorrhage are usually absent. On imaging there is asymmetrical enlargement within the affected brain; lesions are poorly demarcated and of low density on CT, but are well circumscribed on MRI and hypointense on T₁- and hyperintense on T₂-weighted sequences (Fig. 57.37). Contrast enhancement is notably absent in WHO grade II tumours, but they can transform into higher grade lesions.

Anaplastic astrocytoma This WHO grade III tumour is less frequent than either the aggressive glioblastoma multiforme or the lower grade II astrocytoma, and has imaging appearances intermediate between the two. It occurs in a slightly older population than the lower grade astrocytomas. The imaging appearances can be similar to those of WHO grade II tumours, but are often more heterogeneous on T₁-weighted images with more frequent enhancement. Vasogenic oedema and mass effect may be more pronounced but necrosis or heterogeneous ring enhancement should not be a feature of this tumour grade.

Glioblastoma multiforme (Figs 57.39-57.42) This WHO grade IV tumour is the most aggressive and poorly differentiated tumour accounting for 15-20% of all intracranial tumours. It usually occurs after the age of 40 and is the most common astrocytic tumour after the age of 70. The majority are of astrocytic origin, though occasionally poorly differentiated ependymomas or oligodendrogliomas are described as glioblastomas multiforme (GBM). As these tumours may arise from pre-existing lower grade lesions, appearances can be complex and approximately 5% are multicentric and 5% will seed via the CSF. On CT and MR these tumours are of complex density and T₁ and T₂ signal respectively with areas of solid and necrotic tumour, resulting in heterogeneous, solid and ring enhancement. Haemorrhage may also be a feature of these tumours and lesions are associated with a large amount of vasogenic oedema and can extend along the corpus callosum. Unfortunately no imaging technique can determine the true extent of the lesion, although will identify the main bulk of tumour.

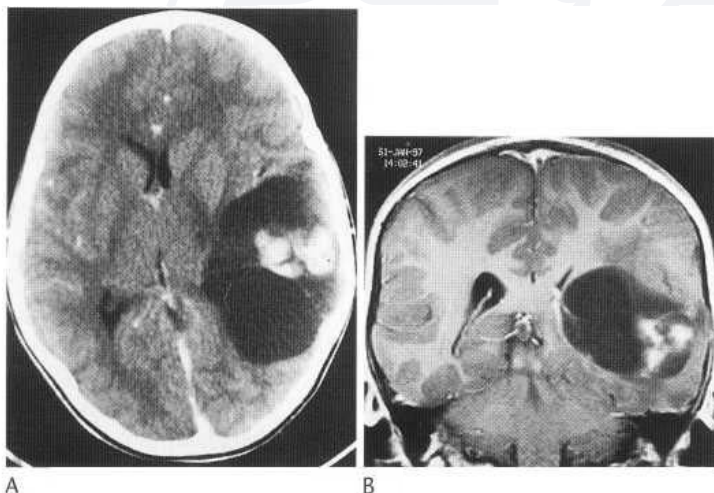


Fig. 57.38 A large complex mass in the left cerebral hemisphere shown on this postcontrast CT (A) and coronal T₁-weighted MR image (B) was proven to be a pleomorphic xanthoastrocytoma. It has a large cystic component and the peripheral lobulated solid component shows marked enhancement. Some focal resorption of the overlying skull vault is shown on the coronal MR image.

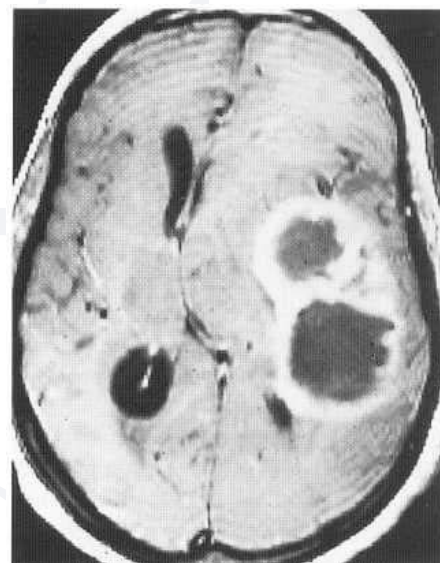


Fig. 57.39 Axial MRI study (T₁-weighted) shows tumour enhancement after IV gadolinium, resembling enhanced CT study. Mass effect and herniation under the falx are well shown. Glioblastoma multiforme.

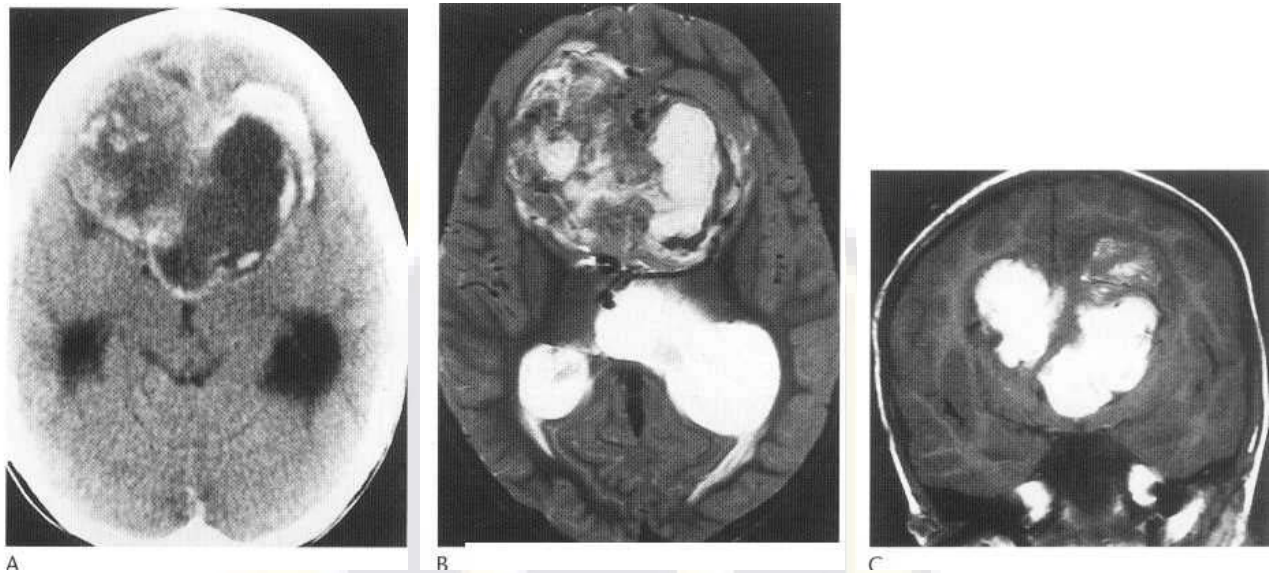


Fig. 57.40 Axial unenhanced CT (A) showing a large complex bifrontal partially cystic haemorrhagic tumour proven to be a glioblastoma. The T₂ signal characteristics are complex (B) and the coronal T₁ unenhanced image (C) shows large T₁ hyperintense components due to the presence of methaemoglobin. There is no significant vasogenic oedema despite tumour size but there is resultant obstructive hydrocephalus with early transependymal oedema around the occipital horns.

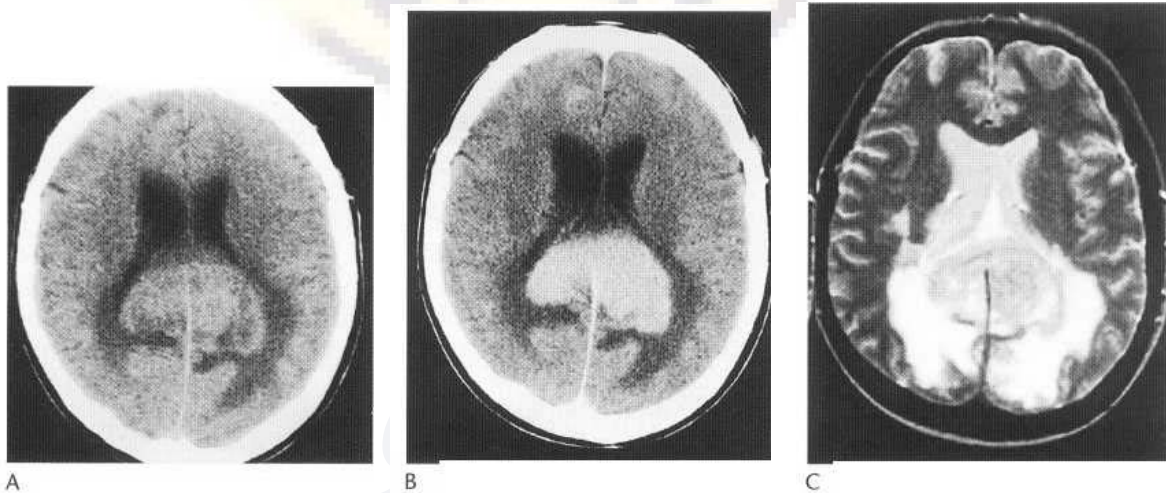


Fig. 57.41 Axial CTs pre- (A) and post- (B) contrast showing a slightly hyperdense mass precontrast involving the splenium of the corpus callosum and which shows marked enhancement. On the T₂-weighted axial image (C) the large amount of vasogenic oedema is clearly shown and there is some mass effect on the posterior aspects of the lateral ventricles. Although this mass was a glioblastoma the radiological differential would include primary central nervous system lymphoma.

Oligodendroglial tumours

Oligodendroglioma (Fig. 57.43) These glial tumours arise from oligodendrocytes which make the myelin sheaths for the central portions of the cranial and spinal nerves but often tumours comprise a mixture of oligodendrocytes and astrocytes; for a tumour thus to be classified as an oligodendroglioma, most neuropathologists require a preponderance of neoplastic oligodendrocytes in the order of 75-90%. Oligodendrogliomas account for 5-10% of all intracranial neoplasms and 18% of all gliomas. These tumours occur slightly more frequently in males, usually between the age of 35-40 years, and 85% are located in the frontal lobes, often deep within the white matter but growing towards the surface. They are slowly growing, unencapsulated and less infiltrative than diffuse astrocytomas but may infiltrate the overlying cortex. Although dystrophic tumoral calcification occurs in 90% of

tumours and cyst formation or haemorrhage in 20%, necrosis is not commonly seen. On CT the calcification may be central, peripheral or even gyriform or ribbon-like and the tumour is hypo- or isodense. Seventeen per cent of tumours scallop and become adherent to the overlying skull vault due to their superficial location and slow growth. On MRI tumours are usually hypointense on T₂- and hyperintense on T₁-weighted images to grey matter and nearly 50% show variable enhancement. Vasogenic oedema is not a striking feature.

Ependymal cell tumours

Ependymoma (Figs 57.44-57.47) These are low-grade tumours arising from the ependyma forming the epithelial lining of the ventricular system, cerebral hemispheres, brainstem and

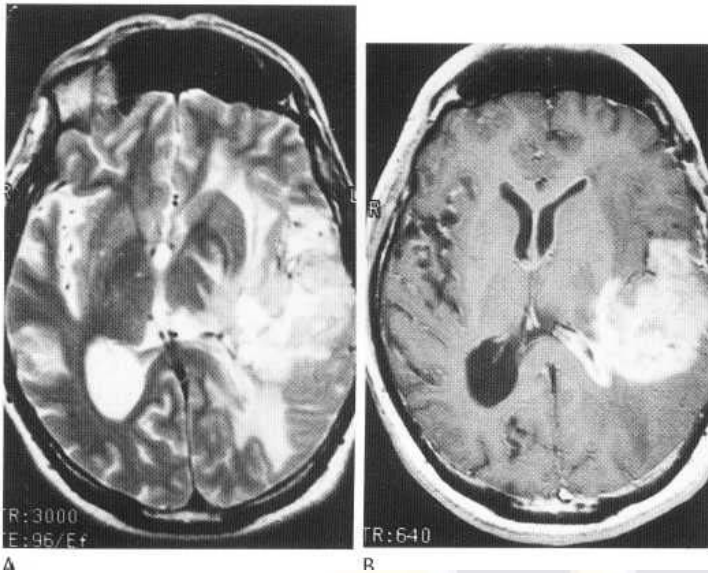


Fig. 57.42 A heterogeneous mass proven to be a glioblastoma is shown in the left cerebral hemisphere on the T_2 -weighted axial image (A) associated with mass effect and vasogenic oedema. The axial T_1 postcontrast image (B) shows marked enhancement of the tumour but also evidence of subependymal enhancement, thus spread.

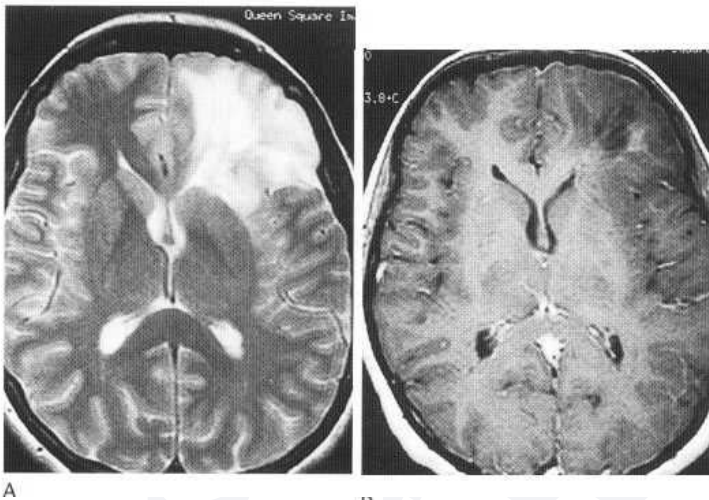


Fig. 57.43 Axial T_2 (A) and T_1 postcontrast (B) images showing a large left frontal non-enhancing tumour involving cortex and white matter which was proven to be an oligodendroglioma. There is only minimal associated mass effect.

cerebellum, central canal of the spinal cord and tip of the filum terminale, and they account for 3-5% of all intracranial tumours and 9% of all glial tumours. Their incidence is higher in the paediatric population (approximately 17%) and they are slightly more common in males. Sixty-five per cent occur infratentorially, 25% supratentorially and 10% in the spinal cord. Overall the most common location is within the fourth ventricle, arising from the ependyma lining the floor, and as they are firmly fixed tumour resection is often incomplete. On imaging they typically present as intraventricular masses which take the shape of the ventricle, and those in the fourth ventricle may extend out through the midline foramen of Magendie or laterally through the foramina of Luschka into the cerebello-pontine angles and thus seed through subarachnoid space. There may be associated obstructive hydrocephalus and they need to be differentiated from medullo-

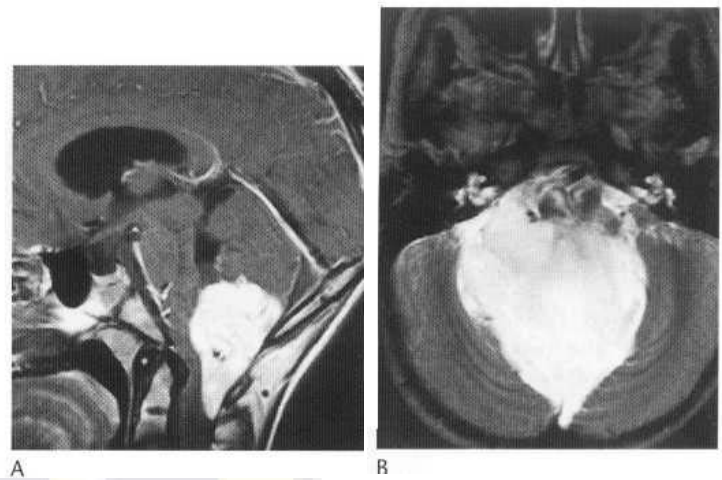


Fig. 57.44 A large avidly enhancing ependymoma is shown on the sagittal T_1 postcontrast image (A) occupying the lower part of the fourth ventricle, compressing the medulla and extending through the foramen of Magendie into the upper cervical canal. The axial T_2 image (B) shows that the mass is hyperintense and also extends out through the lateral recesses into the cerebello-pontine angles, particularly on the right.

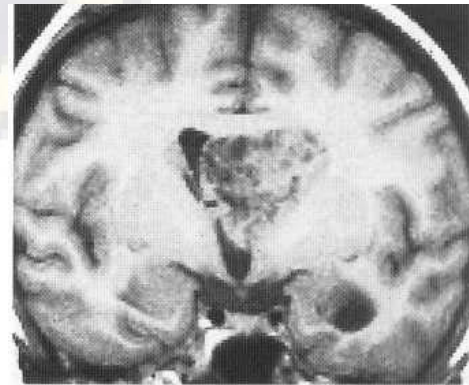


Fig. 57.45 T_2 -weighted MRI study of tumour protruding into left lateral ventricle. The tumour is of mixed but mainly low signal, suggesting multicystic ependymoma.

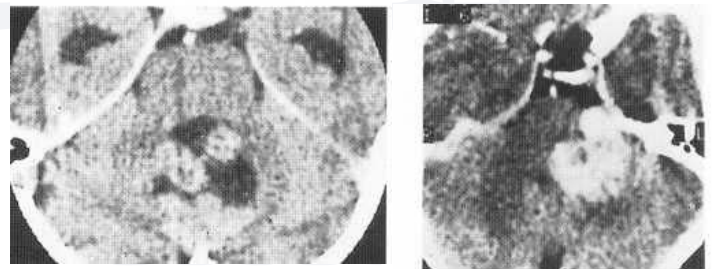


Fig. 57.46 CT demonstrates moderate contrast enhancement in tumour extending from lateral ventricle.

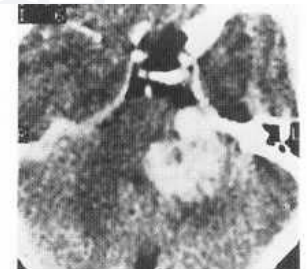


Fig. 57.47 Strongly enhancing tumour extending from lateral recess of fourth ventricle into cerebello-pontine angle. Ependymoma.

blastomas, which tend to calcify less frequently. The cerebral hemisphere ependymomas tend to arise adjacent to the ventricular system and are more frequently calcified or cystic than infratentorial tumours. *CT* shows a mass of slightly higher density than normal brain, which enhances uniformly or patchily. *MRI* shows ependymomas to have similar characteristics to gliomas, but to be more often associated with small cysts which may be multicystic. Their characteristic site projecting into and from the

fourth ventricle, or paraventricular and extending into a ventricle, should suggest the diagnosis (Fig. 57.45).

Subependymoma This variant contains both ependymal and astrocyte cells and occurs mainly in elderly males. It also presents as an intraventricular mass in the lateral or fourth ventricle but is relatively benign and does not disseminate.

Neuroepithelial tumours of uncertain origin

Gliomatosis cerebri This is relatively uncommon occurring mainly in adults in their twenties to forties, and with an equal sex incidence. Prognosis is poor as the tumour invasion is often extensive, multilobar and bihemispheric, but despite its extent patients usually present with few clinical symptoms at the time of diagnosis. On CT gliomatosis cerebri is typically hypodense and enhancement infrequent, occurring in about 12% of cases. On MRI the affected areas are fairly ill defined and are iso- or hypointense on T₁- and hyperintense on T₂-weighted sequences. Enhancement on MRI is seen in approximately 50% of tumours and is solitary or multifocal. Although the affected brain appears enlarged, surprisingly significant mass effect is uncommon.

Tumours of the choroid plexus

Choroid plexus neoplasms arise from the secretory choroid epithelium of the ventricular system and account for 1-2% of all intracranial tumours. They are most frequently seen in childhood, 85% occurring below the age 5 and 40% in the first year of life. There are two main types-the well-differentiated choroid plexus papilloma and the malignant choroid plexus carcinoma. They are invariably intraventricular tumours except those that arise in the region of the foramen of Luschka. Choroid plexus papillomas occur most commonly in the first year of life and are classified as a WHO grade I tumour. In children they occur most commonly in the lateral ventricles centred on the trigone, whereas in adults in the fourth ventricle. Approximately 30% of choroid plexus tumours are carcinomas, WHO grade III-IV, and they present at a slightly later age (2 years) than the papillomas.

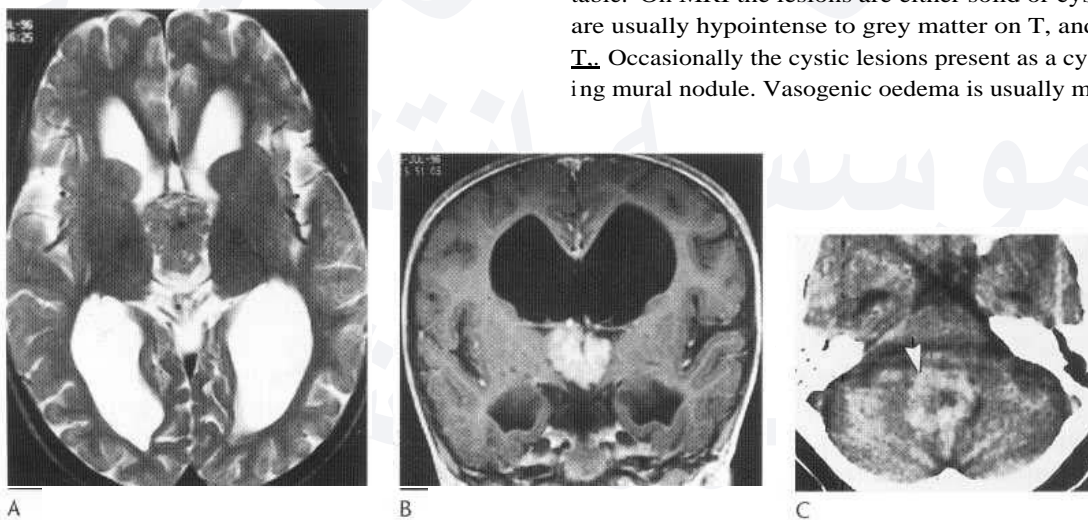


Fig. 57.48 Axial T₂-weighted image (A,B) showing a lobulated vascular mass within the third ventricle which shows avid uniform enhancement on the coronal postcontrast T₁-weighted image and is consistent with a choroid plexus papilloma. The lateral ventricles are markedly dilated due to obstructive hydrocephalus. (C) CT shows a rounded mass of increased attenuation with a low-density centre occupying the fourth ventricle. (D) After contrast medium, a slightly higher section shows strong uniform enhancement.

Overall the tumours are lobulated and friable and highly vascular and thus may present with an intraventricular haemorrhage. Approximately 65% of patients present with hydrocephalus which may be localised to the affected ventricle or more widespread due to effects on CSF production and absorption or ventricular obstruction. On CT the tumours are iso- or hyperdense intraventricular masses, with punctate calcification but avid homogeneous enhancement. If in the fourth ventricle it will be difficult to differentiate from a medulloblastoma or ependymoma (Fig. 57.48). In the lateral ventricle (more commonly the left) it lies in the region of the atrium, which is dilated. The ventricles may also be generally dilated from overproduction of CSF. On MRI the tumours are usually hypo- to isointense on T₁-weighted sequences with lower signal foci, either due to calcification or vascular signal flow voids. The resultant T₂ signal of the lesions is rather heterogeneous but on T₂-weighted images oedema is frequently visible, extending into the brain substance near the site of attachment; enhancement is avid. Parenchymal invasion or metastatic nodules within the ventricles suggests choroid plexus carcinoma.

Neuronal and mixed neuronal-glial tumours

This is a group of slow-growing benign tumours consisting of a mixture of differentiated neoplastic glial and neuronal elements or more rarely just neuronal elements (ganglioneuroma, WHO grade 1), and tumours occasionally undergo malignant transformation. They can occur anywhere in the central nervous system.

Gangliogliomas These are WHO grade I or grade II tumours, which have both neuronal and glial elements; they can occur at any site but have a predilection for the temporal lobes. A cystic form with a predilection for the cerebellum has however been described. Only 10% of these tumours behave in an aggressive fashion. They are more common in children who often present with a long history of seizures. The tumours are well circumscribed, peripheral in location but may be cystic and calcification may be prominent. On CT they are usually isodense to hypodense and up to 57% are cystic and 40% calcified. Up to 50% exhibit either homogeneous or heterogeneous enhancement and occasionally the peripheral tumours result in re-modelling of the overlying skull vault inner table. On MRI the lesions are either solid or cystic masses which are usually hypointense to grey matter on T₁, and hyperintense on T₂. Occasionally the cystic lesions present as a cyst with an enhancing mural nodule. Vasogenic oedema is usually mild.

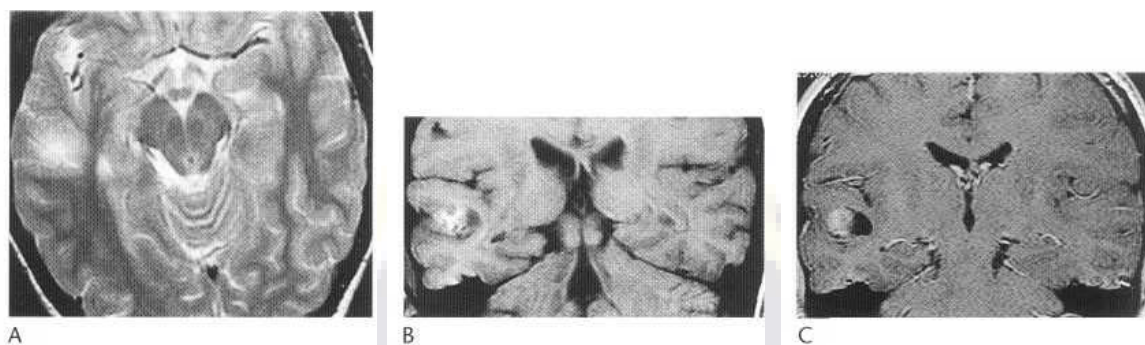


Fig. 57.49 Neuronal and mixed neuronal-glioma tumours. A poorly defined hyperintense lesion consistent with a DNT is shown in the right temporal lobe on this T₂-weighted image (A). It involves cortex and white matter and the coronal T₁ unenhanced image (B) shows it to have a medial cystic component. The lateral patchy signal hyperintensity is likely to be calcification. There is no enhancement of this lesion (C).

L'hermitte-Duclos disease This is a rare slow-growing cerebellar malformation due to the presence of a dysplastic gangliocytoma, which is of WHO grade 1. Pathologically it is thought to represent a hamartoma. A familial occurrence has been reported and associated developmental abnormalities include megalencephaly, heterotopia, microgyria, hydromelia and polydactyly. It is also associated with Cowden's syndrome (benign skin tumours, GI polyps, goitre and breast cancer) or neurofibromatosis but can occur alone. It typically presents as a mass lesion in young adults (20-40 years); CT shows a low-density cerebellar area with thickened folia and no enhancement after contrast. Calcification may be present. MRI shows low signal on T₁ and high signal on T₂ weighting with a typical striated appearance and some enhancement after gadolinium.

Central neurocytoma These are WHO grade II tumours arising from small differentiated neurones typically seen in young adult male patients and less frequently in children or older adults. It presents as an intraventricular mass near the foramen of Monro, centred on the septum pellucidum and sometimes involving the third ventricle. Calcification and cystic change are common. They are usually well-circumscribed tumours, but are often locally recurrent after surgical excision, and may also seed through the CSF.

CT shows an isodense mass which enhances strongly after contrast and which may contain calcification. MRI reveals a heterogeneous tumour, hypodense on T₁ weighting and hyperdense on T₂ weighting, which enhances with gadolinium.

Dysembryoplastic neuroepithelial tumour These mixed WHO grade I glioneuronal tumours most often presents with seizures and usually affect children, males more frequently than females, but are also encountered in the adult population. More than 80% of lesions occur in the temporal lobe (Fig. 57.49). Although they are cortically based lesions, only 38% exclusively involve the cortex and usually there is some involvement of underlying subcortical white matter. As they are slow growing and often superficial in location, scalloping of the calvarial outer table may be a feature. On CT they are often of low density; calcification is seen in 12.5% of lesions and cystic change is not uncommon. On MRI they are hypointense on T₁ and hyperintense on T₂ to grey matter with a variable enhancement pattern seen in approximately one third of tumours. There is usually very little associated perilesional vasogenic oedema or mass effect.

pineal parenchymal tumours (Figs 57.50,57.51)

There is some variation in size of the normal pineal gland. Glands which are 1 cm or larger in diameter are usually cystic, and may be

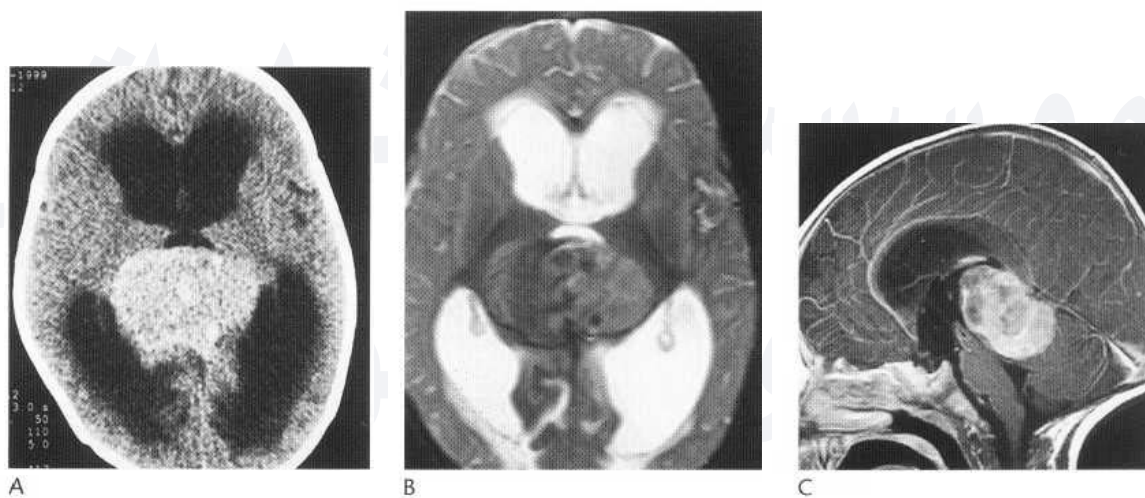


Fig. 57.50 Pineal tumours. Axial postcontrast CT (A) showing an enhancing mass centred on the pineal region invaginating into the third ventricle and resulting in obstructive hydrocephalus with transependymal oedema. This was a proven pineoblastoma. On the axial T₂-weighted MR image (B) the mass is of slightly heterogeneous T₂ signal; enhancement is also slightly heterogeneous on the sagittal T₁ postcontrast image (C).

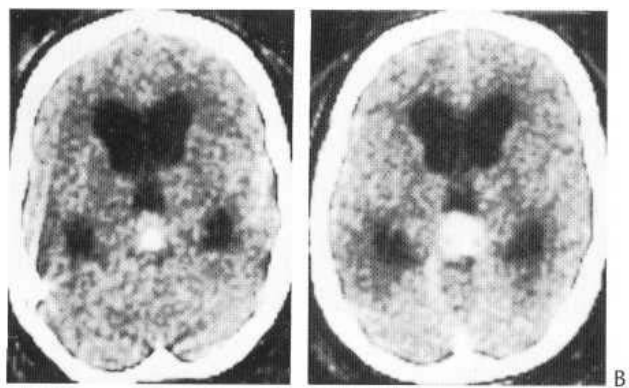


Fig. 57.51 Pineal tumour. (A) Isodense mass with calcification indenting back of third ventricle. (B) Enhancement after contrast medium (L30, W80).

a conspicuous incidental finding on T₂-weighted images as rounded lesions of high signal. However, unlike neoplasms, they do not indent the back of the third ventricle or obstruct the mouth of the aqueduct and produce hydrocephalus.

Pineal region tumours constitute approximately 1% of adult and 10% of all paediatric brain tumours. The pineal parenchymal tumours account for up to 30% of pineal region tumours and range from the moderately differentiated pineocytoma to the primitive pineoblastoma; in fact pineal germ cell tumours are much more common in this region, accounting for 50-70% of tumours.

Pineoblastomas occur in the paediatric population, with a peak incidence in the first decade and rarely over the age of 30, whereas pineocytomas in the fourth decade, but in both cases there is no sex predilection. On CT these tumours are either hypodense or isodense and 50% are calcified. On MRI they are either hypointense or isointense on T₁; pineoblastomas tend to be more isointense on T₁, and pineocytomas more hyperintense. Enhancement is prominent and hydrocephalus may be seen in up to 90% of cases due to indentation of the tectal plate and obstruction of the cerebral aqueduct. Pineocytomas are better defined than pineoblastomas; the latter tend to be rather heterogeneous in appearance, with areas of cystic change, haemorrhage and necrosis, and CSF seeding occurs in 10%. There is a rare association between bilateral retinoblastomas and pineoblastomas (trilateral retinoblastoma) which in most cases presents before the age of 2 and is hereditary.

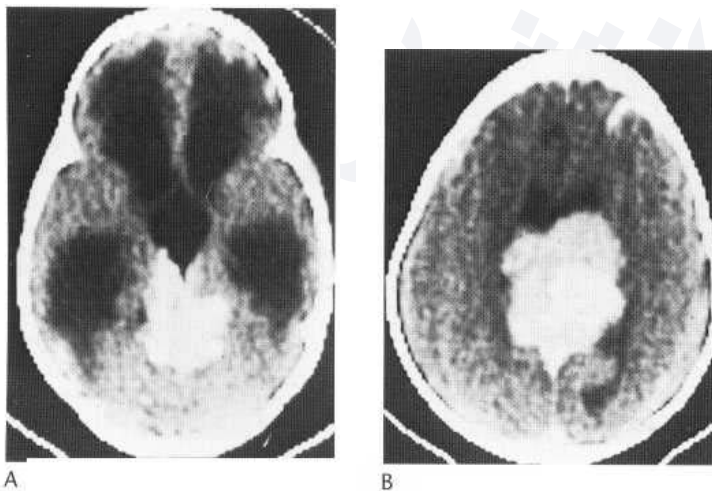


Fig. 57.52 (A,B) Pineal tumour. Large enhancing and partly calcified mass. Heavy calcification is commonest in germ cell tumours.

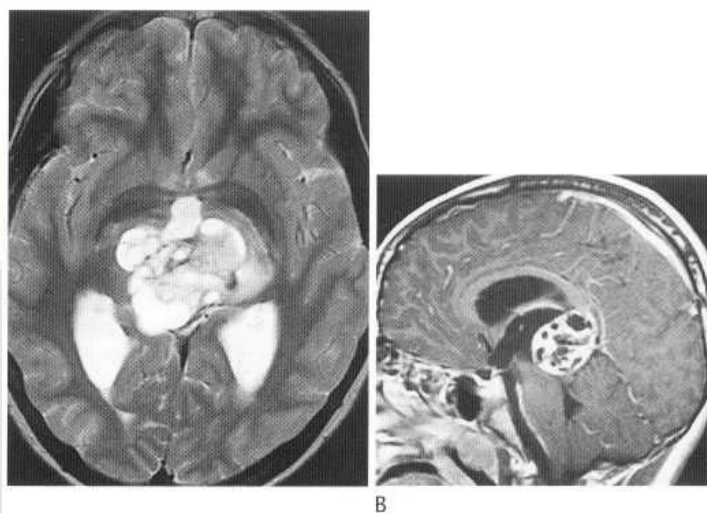


Fig. 57.53 Germ cell tumours. A large heterogeneous T₂ signal mass is shown in the pineal region on the T₂-weighted axial image (A) proven to be a pineal region teratoma. The mass comprises both solid and cystic components and there is heterogeneous enhancement after contrast on the sagittal T₁-weighted image (B) and the mass results in obstructive hydrocephalus.

Table 57.4 Pineal tumours: different types found in 54 cases

Tumour	No.
1. Pineal-cell tumours	
a. Pineoblastoma	8
b. Pineocytoma	5
2. Glial tumour	
a. Astrocytoma	
b. Glioblastoma	
3. Germ cell tumours	
a. Germinoma	18
b. Teratoma	5
c. Embryonal cell carcinoma	1
d. Choriocarcinoma	1

Other tumours which occur in this pineal situation and may sometimes enter into differential diagnosis include germ cell tumours (Figs 57.52, 57.53), arachnoid cysts in children and pineal teratoma. These are described elsewhere in the chapter. Finally glial tumours may also be found at this site (Table 57.4).

Tumours with neuroblastic or glioblastic elements (embryonal tumours)

Primitive neuroectodermal tumours (PNETs)/medulloblastomas They are predominantly tumours of childhood and comprise about 3% of large pathological series of brain tumours, but comprise 15-20% of the malignant brain tumours of childhood, and 30-40% of childhood posterior fossa tumours. The cell of origin is the external granular cell, an embryological precursor of the internal granular cell layer of the cerebellar folia. They typically occur in the posterior fossa (85%) and may present as a congenital lesion but in the majority of cases present between the ages of 5 and 15 years. Although grossly they appear quite well

circumscribed they are often invasive at their margins; 80% of midline tumours, arise in the roof of the fourth ventricle in the region of the inferior cerebellar vermis and inferior medullary velum. They usually grow to fill much of the fourth ventricle, and may extend out through the midline foramen of Magendie, but lateral extension through the foramina of Luschka is uncommon, compared with ependymomas; 90% are associated with obstructive hydrocephalus at presentation. Forty per cent of patients have metastases at presentation, either as a result of seeding via the CSF or direct CNS metastases or both. This is one of the few malignant brain tumours known to metastasise systemically, and this is usually to bone, occurring in about 5% of cases. Occasionally the tumour may primarily involve the cerebellar hemisphere, and this pattern is more frequent in adult patients. This tumour may occasionally arise within the brainstem, especially the pons, and these tumours are associated with a worse prognosis than those originating in the cerebellum. On CT the posterior fossa tumours are isodense or hypodense, with clump-like calcification present in 20%. On MRI they are isointense or hypointense on T₁- and isointense or hyperintense on T₂-weighted images. T₂ signal intensity may be heterogeneous due to calcification, cystic change, haemorrhage or necrosis. Tumour enhancement is seen in 90% of cases.

Supratentorial PNETs represent <1% of all paediatric tumours and the majority occur before the age of 10 years, with equal frequency in males and females. The most common location is the frontal lobes, the least common is the occipital lobes and occasionally the tumours can be intraventricular. Supratentorial PNETs are more frequently calcified (50-70%) than the infratentorial tumours and 40% seed via the CSR On CT the tumours are well-circumscribed large masses with relatively little vasogenic oedema compared to actual size but are often of heterogeneous density due to the presence of calcification, cystic and necrotic change or calcification. The solid components [enhance MR](#) signal characteristics are also heterogeneous.

Tumours of the sellar region

Pituitary adenomas Pituitary adenomas can be classified as *endocrine active* or *endocrine inactive*. The former can manifest clinically when still quite small but the latter are not diagnosed until large enough to produce chiasmal pressure and visual impairment or, less commonly, disturbances of eye movement. So-called microadenomas are less than 10 mm in diameter and lie within the pituitary gland. Endocrine-active tumours now form about 80% of those encountered, and non-secreting tumours about 20% (Table 57.5).

Table 57.5 Types of pituitary tumour

Tumour	%
Prolactinomas	35
Somatotrophic (acromegaly and gigantism)	25
Corticotrophic (Cushing and Nelson syndromes)	5
Miscellaneous and mixed (STH-PRL, ACTH-PRL, PRL-STH, thyrotrophic, gonadotrophic)	15
Non-secreting	20

Prolactinomas manifest with gonadal dysfunction in both sexes and with galactorrhoea in a proportion. Symptoms can be associated with large tumours, but many are microadenomas when they first present. Since hyperprolactinaemia can also be produced by a variety of different [drugs](#), it is important to exclude this cause before imaging investigation is begun.

Although MRI is the preferred imaging modality for assessing pituitary adenomas as it avoids beam hardening artefacts and can evaluate local tumour invasion and compression of critical structures such as the chiasm more accurately, CT will better demonstrate destruction of the sellar floor. For large adenomas producing chiasmal compression CT will show the extent and relationships of the suprasellar component as well as the enlarged sella, but sagittal and coronal reformats after intravenous contrast medium may be necessary to assess the full extent of a large adenoma. Macro-adenomas first extend into the normal suprasellar cistern and then into the anterior end of the third ventricle. Eventually they can extend as high as the foramen of Monro, and are often quite asymmetrical. The tumour can also extend laterally into the cavernous sinuses and temporal lobe or downward into the sphenoid sinus. Large tumours may also extend subfrontally or above and behind the sella (Figs 57.54-57.63).

On MRI the normal pituitary yields a homogeneous brain-like signal on most pulse sequences and is best shown in sagittal and coronal images. It usually envelops posteriorly a well-demarcated zone of higher signal on both T₁- and T₂-weighted images. This is



Fig. 57.54 Pituitary tumour. Contrast-enhanced CT. Direct coronal section demonstrates suprasellar extension and relationship to internal carotids and anterior cerebral arteries. The cavernous sinuses on either side are slightly denser than the tumour.

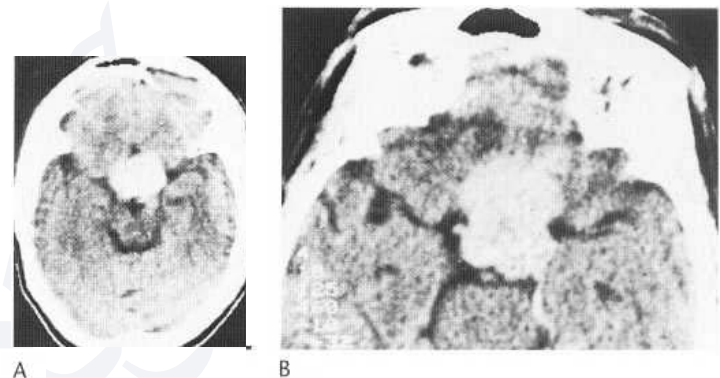


Fig. 57.55 (A) Rounded mass of slightly increased density in the suprasellar cistern. It enhances homogeneously with contrast medium. The sella was enlarged. Pituitary adenoma. (B) Irregular mass in suprasellar cistern which enhances strongly with contrast medium. As the sella was relatively normal it was thought more likely to be a craniopharyngioma than a pituitary adenoma despite absence of calcification. Histology-germinoma.

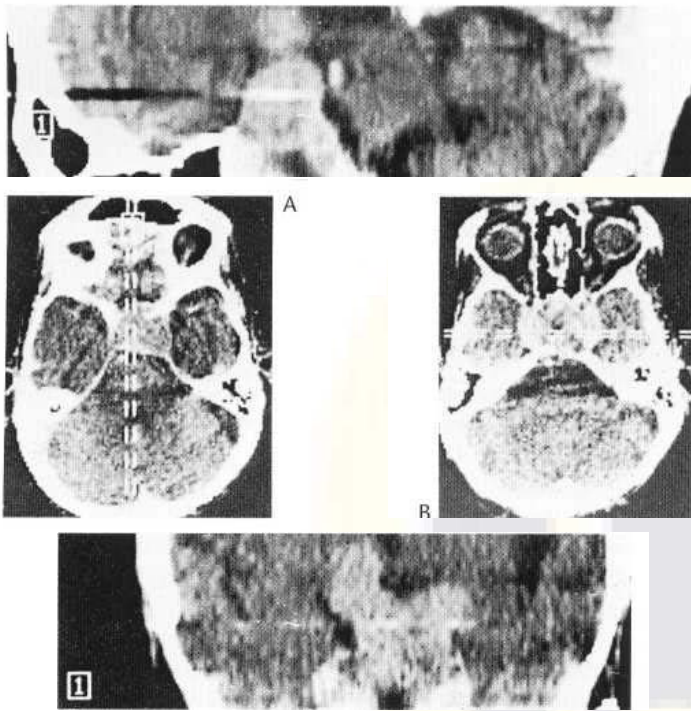


Fig. 57.56 Sagittal (A) and coronal (B) reformats of pituitary adenoma after enhancement showing asymmetrical suprasellar extension. The sella is enlarged and the cavernous sinuses bulged laterally.

now thought to represent the neurohypophysis itself, and the high signal to be related to secretory activity and possibly produced by phospholipid vehicles or neurophysin, the carrier protein for pituitary hormones.

Pituitary adenomas normally show homogeneous density similar to or slightly greater than that of normal brain tissue, and enhance uniformly after contrast medium. Five per cent however contain cystic or necrotic areas which stand out more clearly after contrast medium (Fig. 57.60).

The CT diagnosis of microadenomas requires high-resolution CT, and direct coronal sections are preferable to reformats. Contiguous 1.5 mm sections should be obtained after enhancement. The typical microadenoma can be recognised as a small low-density area within the enhancing gland (Fig. 57.61), but can be confused with artefacts or normal cysts of the pars intermedia. Other features which may be seen are deviation of the infundibulum and upward bulging of the upper surface of the gland, but these also are not diagnostic and can have other causes, as can local bulging of the sellar floor. Thus bulging of the upper gland surface occurs in menstruating, postmenopausal or oophorectomised women, and in hypothyroidism. The diagnosis of microadenoma should therefore be made with caution, especially if it is likely to affect management. Microadenomas can be imaged with up-to-date techniques and machines (Fig. 57.63). The choice of pulse sequence and mode of data collection to produce maximum differentiation between normal gland and microadenoma remains difficult but should include one heavily T₂-weighted sequence. Intravenous gadolinium-DTPA may help by showing delayed enhancement of the adenoma compared to the normal gland. Dynamic contrast-enhanced MRI using rapid field echo acquisitions may also improve sensitivity. Large adenomas and their relationships to the adjacent brain are well shown by MRI, which compares favourably with CT in this respect because of the ease with which direct sagittal and coronal

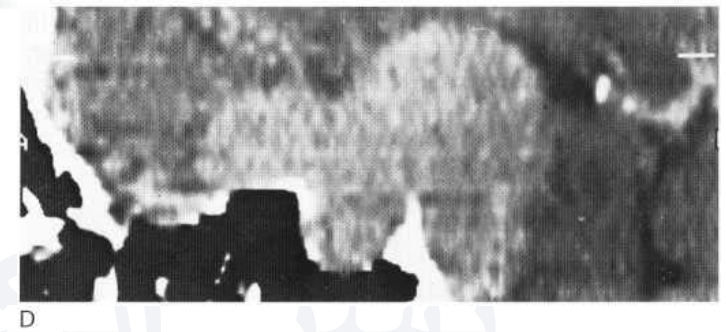
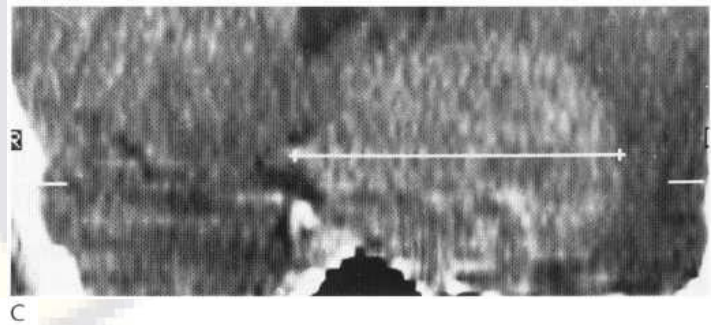
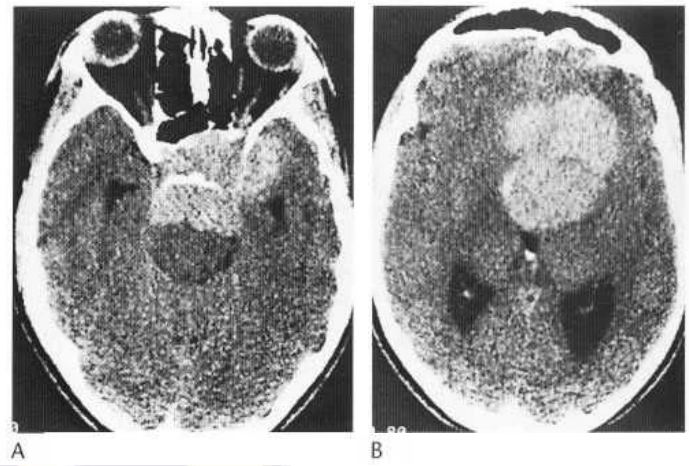


Fig. 57.57 (A,B) Large pituitary adenoma showing enlargement and erosion of sella with left lateral and retrosellar as well as suprasellar extension. (C,D) Coronal and sagittal reformat defining asymmetrical suprasellar extent.

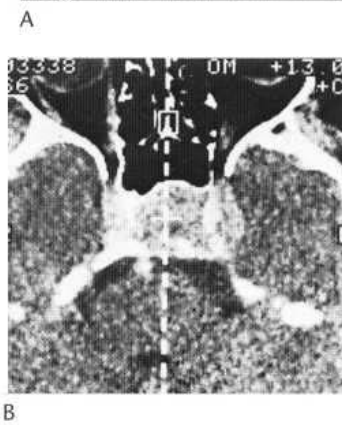


Fig. 57.58 Reformat of pituitary adenoma. Note cystic area.

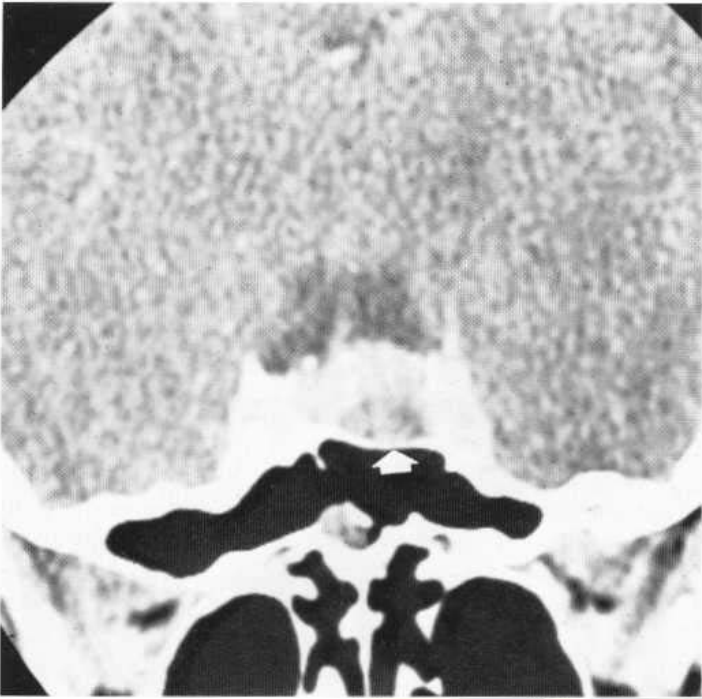


Fig. 57.59 Direct coronal scan shows a microadenoma as a hypodense lesion bulging the sellar floor (arrow). There is also upward bulging of the gland and deviation of the infundibulum.

sections can be obtained. The normal optic chiasm, carotid vessels and sphenoid sinus are also highly conspicuous at MRI (Fig. 57.62), and their relationships to the tumour well shown. The clivus, because of its fatty marrow, gives a high signal, while the sphenoid air sinus gives a low signal, anteroinferior to the sella. Macroadenomas are usually of relatively lower signal than normal brain on T_1 - and of higher signal on T_2 -weighted images. Regions of even lower signal on T_1 and higher signal on T_2 usually represent cysts when rounded and circumscribed and necrosis when more irregular. Areas of recent haemorrhage are found relatively frequently in approximately 20-30% of adenomas and are indicated by high signal on T_1 -weighted images. Tumours isointense with brain on a variety of sequences are more likely to be hard whereas



Fig. 57.61 Pituitary microadenoma shown by MRI (proton density).

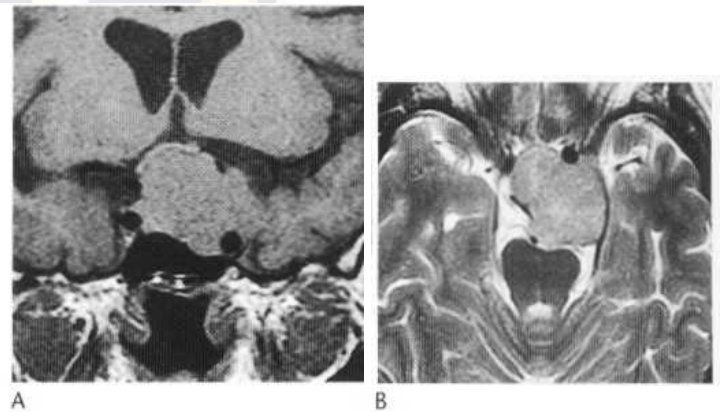


Fig. 57.62 A large isointense pituitary macroadenoma is shown on the coronal T_1 -weighted image (A) expanding the sella with suprasellar extension and compression of the optic chiasm. The left cavernous sinus is clearly involved with inferior displacement of the intracavernous internal carotid artery. On the axial T_2 -weighted image (B) the macroadenoma is hyperintense to brain and not only displaces the terminal internal carotid artery anteriorly, but posteriorly also displaces the basilar artery and indents the ventral pons.

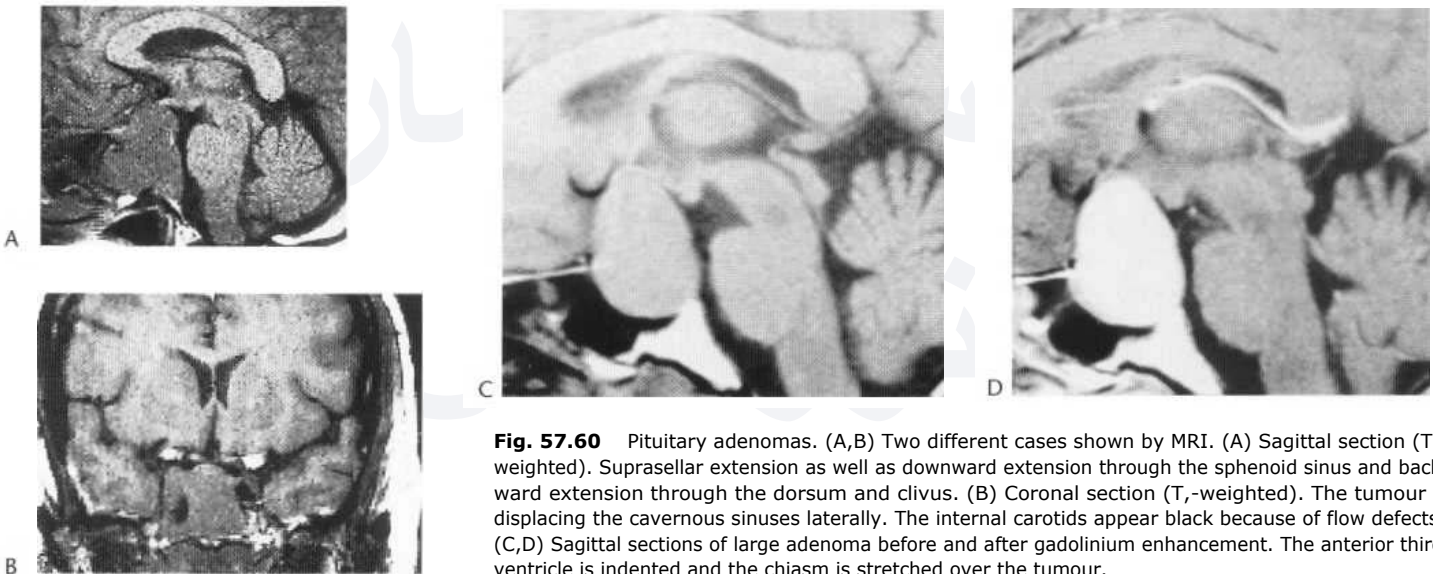


Fig. 57.60 Pituitary adenomas. (A,B) Two different cases shown by MRI. (A) Sagittal section (T_1 -weighted). Suprasellar extension as well as downward extension through the sphenoid sinus and backward extension through the dorsum and clivus. (B) Coronal section (T_1 -weighted). The tumour is displacing the cavernous sinuses laterally. The internal carotids appear black because of flow defects. (C,D) Sagittal sections of large adenoma before and after gadolinium enhancement. The anterior third ventricle is indented and the chiasm is stretched over the tumour.

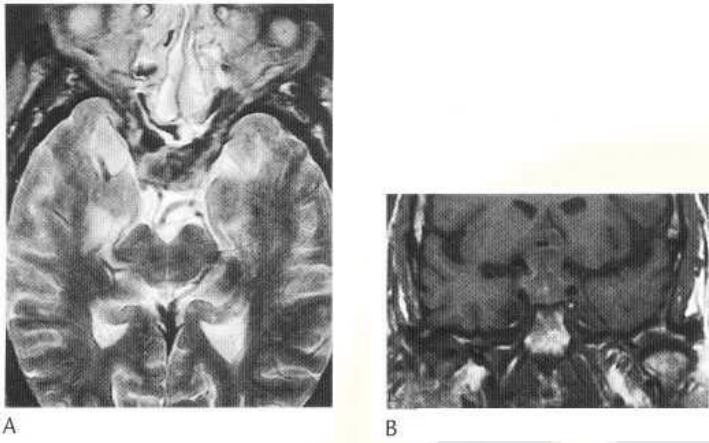


Fig. 57.63 Mixed T_2 low signal is shown in the sellar region on the T_2 -weighted axial image (A) in a patient with a known pituitary macroadenoma and who presented acutely with symptoms and signs of pituitary apoplexy. On the coronal T_1 -weighted unenhanced image (B) the sellar and suprasellar mass is largely isointense but with strands of hyperintensity. The T_2 and T_1 signal characteristics suggest the presence of deoxyhaemoglobin and methaemoglobin in a subacute haemorrhage within a pituitary macroadenoma.

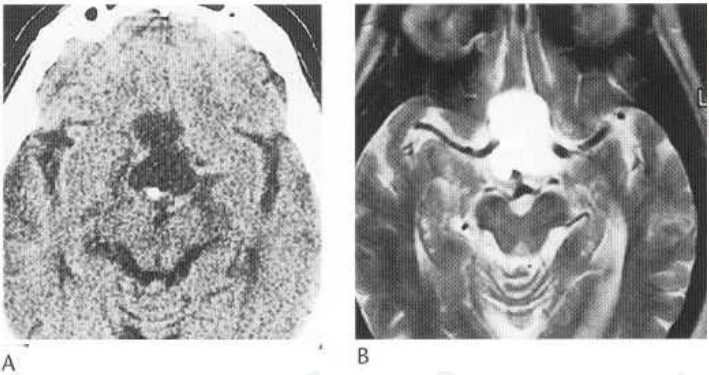


Fig. 57.64 Axial CT (A) and T_2 -weighted MRI (B) showing a largely cystic lobulated suprasellar mass. There is a small focus of calcification posteriorly within the lesion and appearances are those of a craniopharyngioma. The coronal T_1 postcontrast image (C) is of another patient with a craniopharyngioma which has both cystic and solid enhancing components.

tumours which differ from normal brain are generally softer and easier to remove.

Craniopharyngioma These tumours of epithelial origin account for up to 3% of primary intracranial tumours. They have a bimodal age distribution, with most occurring in children and adolescents usually between the ages of 6 and 10, but a second smaller peak occurs in patients in their fifties. In fact half of childhood suprasellar tumours are craniopharyngiomas (Fig. 57.64). Calcification

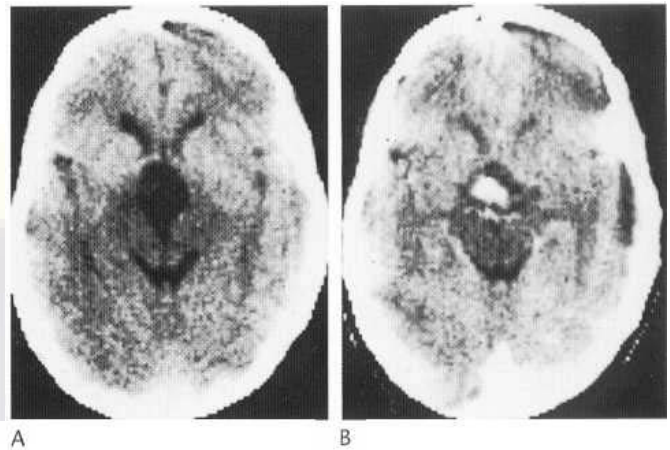


Fig. 57.65 Craniopharyngioma. Cystic tumour with solid enhancing component. Before (A) and after (B) enhancement.

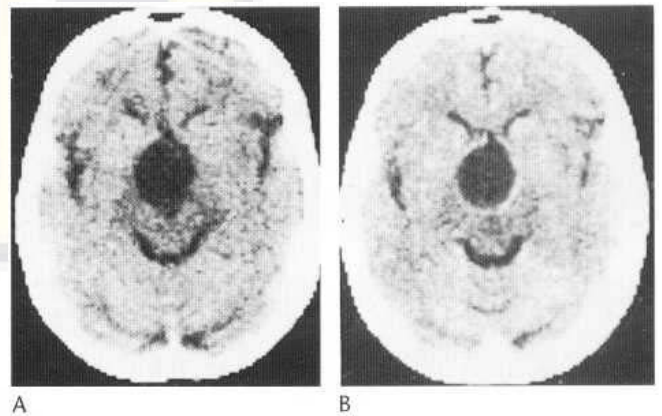


Fig. 57.66 Cystic suprasellar mass with enhancing capsule. Craniopharyngioma. Some Rathke's cleft cysts can produce a similar appearance. Before (A) and after (B) enhancement.

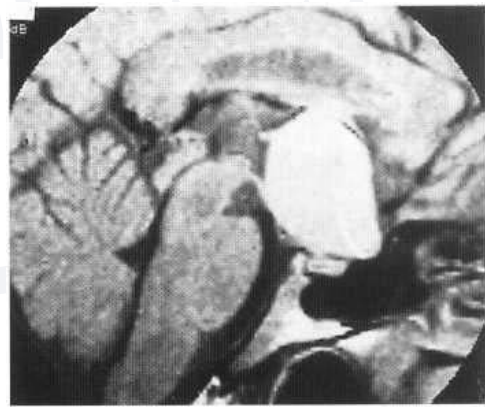
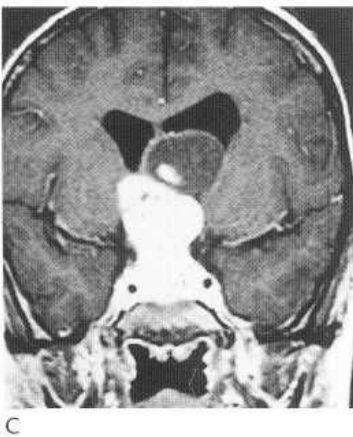


Fig. 57.67 Craniopharyngioma. Sagittal midline MRI (T_1 -weighted) shows high-signal suprasellar mass due to cystic tumour. (Courtesy of Dr Gordon Thomson and Bristol MRI Centre.)

is present in over 80% of the childhood cases, but is often absent in the less common adult cases. They usually grow above the sella and adhere tightly to the floor of the third ventricle and infundibulum, making surgical extirpation difficult or impossible. A small proportion (15%) grow into the pituitary fossa and can produce enlargement and deformity of the sella. Some of these tumours

Box 57.3 Suprasellar lesions**A. Common**

Pituitary adenoma
Craniopharyngioma
Aneurysm
Suprasellar meningioma

B. Rare

Optic chiasm glioma
Hypothalamic glioma
Germinoma
Ganglioglioma
Metastasis
Arachnoid cyst
Epidermoid
Rathke's cleft cyst
Inflammatory masses
Histiocytosis X

may appear slightly ectopic and to lie in the third ventricle or behind the sella.

Histologically they are of two main types—adamantinomatous and squamous-papillary; the former are the more common variety and are often lobulated masses with cystic components which can be hyperintense on T₁- and T₂-weighted sequences if the cyst contents are proteinaceous. The solid components enhance and calcification is a feature, but this is better demonstrated with CT. The squamous-papillary type are less often calcified or cystic and tend to have a more uniform rounded configuration. The solid components of the tumour are isointense on T₁, and hyperintense on T₂, to grey matter, and the solid components enhance. This variety of craniopharyngioma is more common in the adult population (Figs 57.65–57.67).

Differential diagnosis A wide variety of mass lesions can occur in the suprasellar region. Many of these can be indistinguishable clinically from pituitary adenomas, and some can resemble them at imaging (Box 57.3).

Many of the lesions listed have features that readily differentiate them from pituitary adenomas, and these are described under the individual lesions. Calcification, if present, suggests a craniopharyngioma; if the shape is an arc or a ring, aneurysm or craniopharyngioma is possible. Suprasellar meningiomas can also calcify but present in an older age group, and calcification, if present, is homogeneous or nodular and never in an arc. Arachnoid cysts are easily identified by their CSF density and thin capsule at CT or MRI.

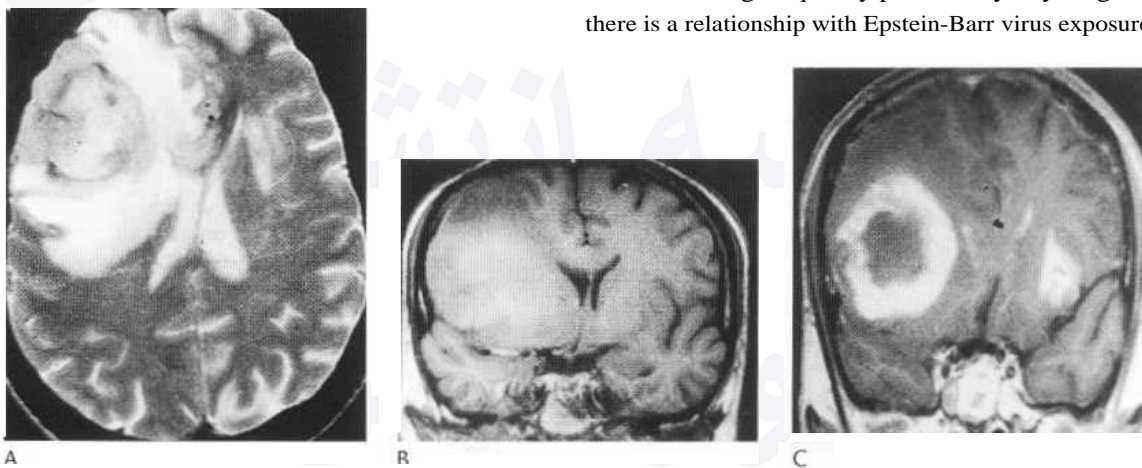


Fig. 57.68 Bilateral complex intrinsic masses are shown in the cerebral hemispheres in a patient with known AIDS. On biopsy these were proven to be primary central nervous system lymphoma. There is a large amount of vasogenic oedema on the T₂-weighted image (A) associated with the right frontal mass and there is extension across the corpus callosum. The coronal T₁, unenhanced image (B) shows faint T₁ high signal in the right frontal mass consistent with methaemoglobin. Postcontrast (C) the right frontal lesion shows thick irregular ring enhancement. Subependymal enhancement around the anterior aspects of the frontal horns is also evident, a characteristic feature of cerebral lymphoma.

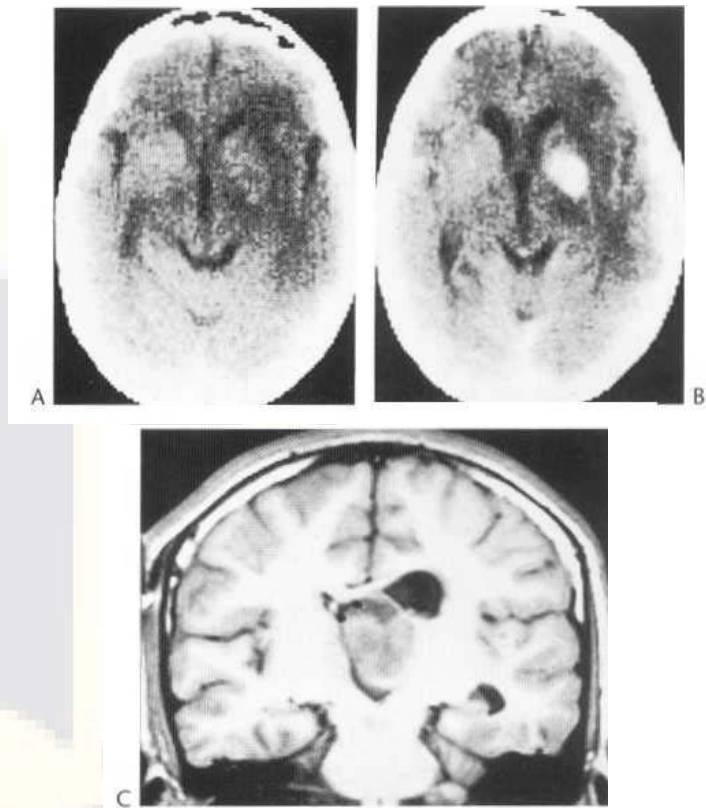


Fig. 57.69 Lymphoma of brain. (A) CT before contrast. (B) After contrast. Isodense tumour with little mass effect enhances strongly with contrast. (C) MRI, T₁-weighted, in another patient. Low-density paraventricular mass involves thalamus and extends into third and left lateral ventricles.

Haematopoietic tumours

- Primary CNS lymphoma.

Secondary lymphoma of the brain is exceedingly rare, though it can occur. More usually, however, lymphoma of the brain is found without any systemic involvement. This was previously an uncommon tumour accounting for 11% of primary brain neoplasms, but with the recent AIDS epidemic this tumour has been encountered with increasing frequency particularly in younger adults, where there is a relationship with Epstein-Barr virus exposure (Fig. 57.68);

interestingly there has also been an increase in non-HIV-related sporadic primary CNS lymphoma (PCNSL), where the peak incidence occurs in patients in their fifties (Fig. 57.69). Most of the tumours tend to be high-grade B-cell tumours and the AIDS-related tumours tend to have a poor prognosis, but that of the sporadic tumours has improved with a median survival of 5 years. In the HIV-infected population the tumour tends to be multifocal with periventricular spread, and necrosis and haemorrhage are common, whereas the sporadic form may be limited to one or two sites within the brain. Lesions are often located deep within the cerebral hemispheres, but can occur in the posterior fossa. On CT they are often hyperdense pre-contrast and show either solid or ring enhancement. On MRI signal intensity of the masses is variable and can be isointense to grey matter on T₁, or isointense or hyperintense on T₂, and signal abnormality and enhancement often extends along an ependymal surface. Vasogenic oedema and mass effect are variable and, like gliomas, PCNSL can extend along the corpus callosum. In the HIV-infected population the main radiological differential of PCNSL is toxoplasma abscesses.

Germ cell tumours

Germ cell tumours account for <1% of primary brain tumours and occur mainly in the paediatric age group. They are most commonly found in the suprasellar or pineal region, in a midline location, and between 10 and 50% are multifocal occurring at two sites—either pineal and suprasellar or pineal and third ventricle (Fig. 57.52).

Germinoma These are the most common type of intracranial germ cell tumour and 80% of these occur in the pineal region. They are usually well-circumscribed solid masses, with occasional cystic and haemorrhagic components and are slightly hypointense to grey matter on T₁ and hyperintense on T₂.

MRI.

Teratoma Pineal teratomas occur almost exclusively in males with a peak incidence around puberty, but can be seen in infants less than 1 year old. They contain all three germ layers and the mature benign teratomas contain fully differentiated tissue whereas the malignant ones contain some primitive tissue and the latter are the more common type. Calcification is present in about 50% of mature teratomas and may suggest the diagnosis, though the very rare presence of recognisable dental elements is the only true diagnostic feature. They are more heterogeneous than germinomas in appearance due to the presence of haemorrhage, cystic change, fat or calcification, thus signal characteristics on MRI are variable as is enhancement (Fig. 57.53).

The more malignant germ cell tumours such as embryonal carcinoma, endodermal sinus, tumour and choriocarcinoma have a poor prognosis, are more commonly seen in males between the ages of 10 and 20 and have a greater propensity to necrosis, haemorrhage, local invasion and CSF spread, but are otherwise radiologically indistinguishable from other pineal germ cell tumours.

Tumours of the meninges

Meningioma (Figs 57.70-57.79) These tumours of the arachnoid cells of the meninges are the most common intracranial neoplasm. They are usually well-circumscribed extra-axial lesions that cause

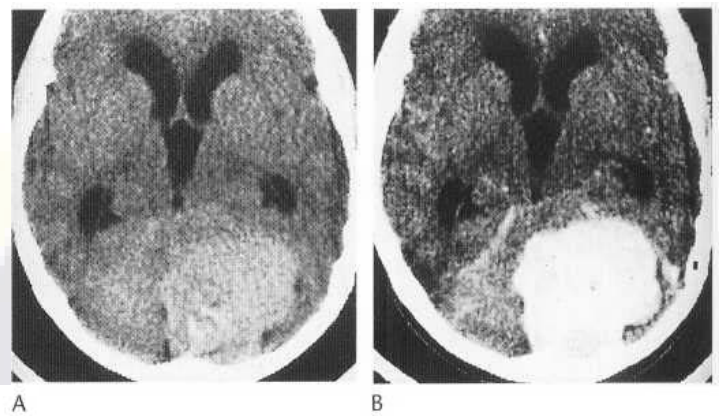


Fig. 57.70 (A) There is a high-density parasagittal mass with irregular calcification. (B) The tumour enhances strongly with contrast agent. Parasagittal meningioma.

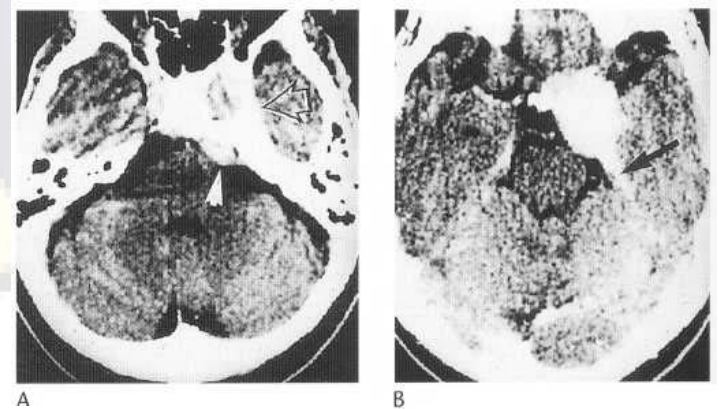


Fig. 57.71 (A,B) Cavernous sinus petrous apex meningioma. CT after IV contrast medium. The left cavernous sinus is expanded (open arrow) in continuity with a mass at the petrous apex, which extends along the tentorium (arrow) and into the posterior fossa (arrowhead).

symptoms due to mass effect on underlying structures and are thus often completely resectable unless they involve the skull base or cavernous sinuses. Although they do not tend to invade brain they can infiltrate the skull and parasagittal tumours can invade the sagittal sinus, and tumours adjacent to the lateral, sigmoid and cavernous sinuses can also invade these venous sinuses. The majority of meningiomas are benign, WHO grade I tumours but there is a histological spectrum with some sarcomatous WHO grade IV meningiomas. There is an association between meningiomas and neurofibromatosis type II and the most common associated genetic abnormality is deletion of chromosome 22 and an associated tumour suppressor gene specific to meningioma formation. Meningiomas can occur at any location where there are meningotheial cells but typical sites are the parasagittal dura, cerebral convexities, sphenoid wing and cerebello-pontine angle and up to 25% occur in the parasellar region. They typically occur in middle-aged females and up to 5% of tumours are multiple, and these tend to be parasagittal. Meningiomas can arise anywhere over or under the brain from arachnoid cell rests, but have several sites of predilection, as shown by Table 57.6.

Although skull radiographs are no longer routinely performed as part of the imaging work-up of intracranial tumours, radiographs may show the presence of a meningioma (either from bone changes or from calcification) in about one-third. The specific bone changes

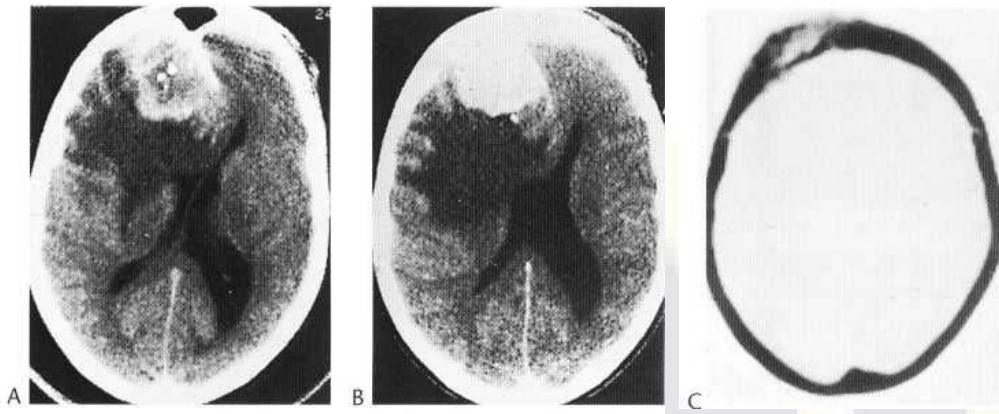


Fig. 57.72 (A) Frontal meningioma. High-density lesion with some calcification. Unusual degree of oedema. (B) Strong enhancement with contrast medium. (C) Reversal print at wide window to show bone involvement ([80 W400]) (D) Parietal meningioma. Superficial isodense mass effacing sulci. (E) Strong enhancement after contrast medium outlines the tumour.

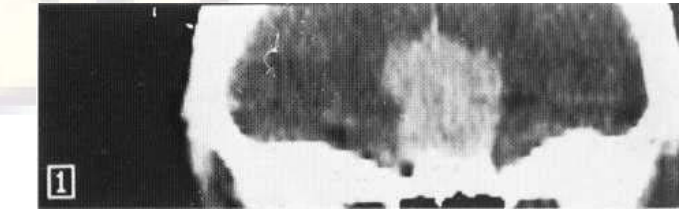
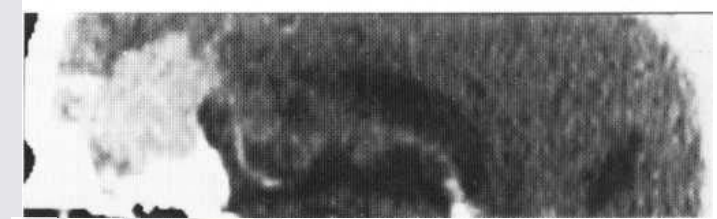
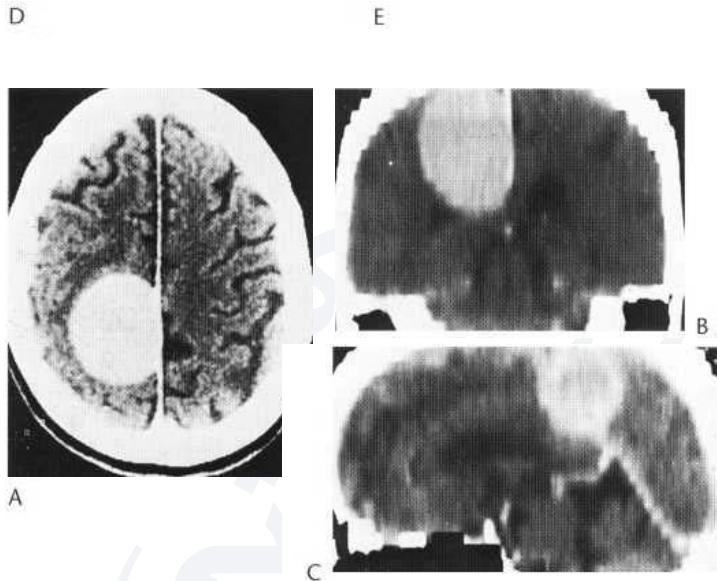
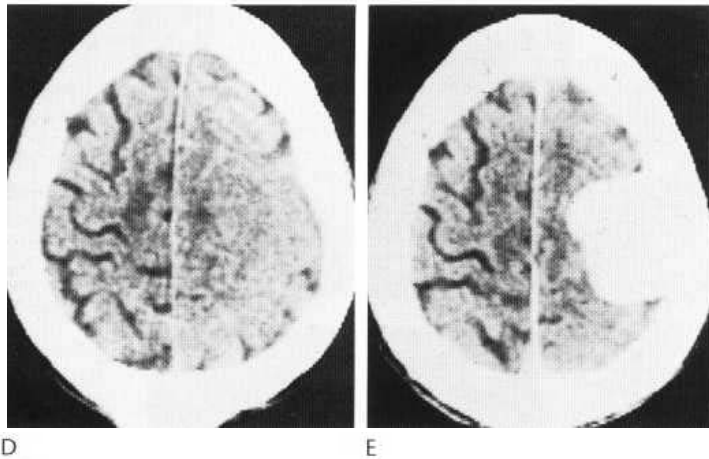


Fig. 57.74 Olfactory groove meningioma. Midline sagittal (A) and coronal (B) reformats after contrast medium showing extent of tumour and bony hyperostosis.

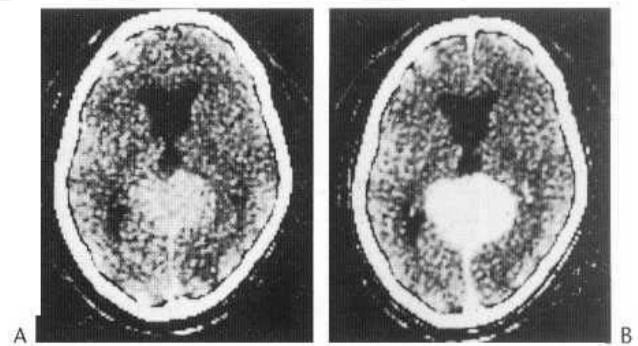


Fig. 57.75 Meningioma of territorial apex before (A) and after (B) enhancement.

Fig. 57.73 (A) Strongly enhancing parasagittal falx meningioma. No adjacent oedema but brain compressed and sulci effaced. Coronal (B) and midline (C) sagittal reformats show attachment to falx but no growth across the midline.

have been described above (see Ch. 53). Calcification in these tumours is sufficient to make them radiopaque in around 15% and is often specific. Thus homogeneous ball-like calcification at a typical site is virtually diagnostic, as is less regular or dense calcification adjacent to typical bony changes (Figs 53.70 and 53.71).

On CT 60% are usually homogeneous well-defined hyperdense solid masses pre-contrast and calcification of a variable pattern is seen in up to 20% of them; there is usually intense enhancement

and there may be hyperostosis of the adjacent calvarium or skull base, either a reactive process or a consequence of direct tumour infiltration. The 'en plaque' type of tumour may be more difficult to identify, particularly adjacent to the cavernous sinus (Fig. 57.71) or sphenoid ridge. However the bony involvement often seen in these tumours may be more obvious on bone windows. Oedema surrounding the tumour tends to be absent or minimal and circumscribed; only occasionally is it extensive and with the characteristic digital elongation of more malignant tumours (Fig. 57.72). Low-

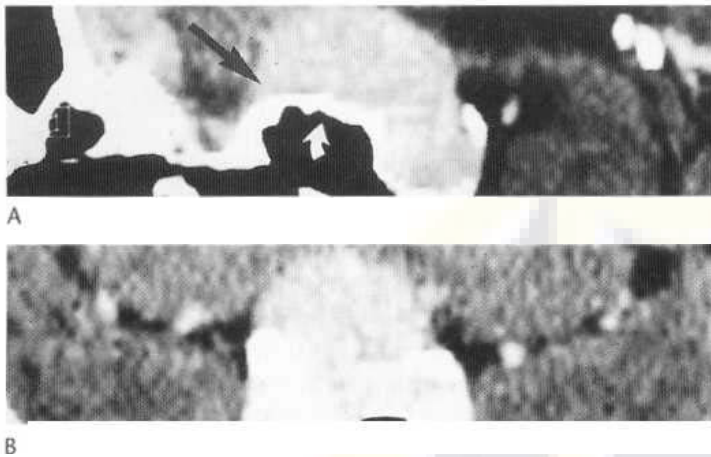


Fig. 57.76 Meningioma of the planum sphenoidale. Sagittal (A) and coronal (B) reformats of contrast-enhanced CT. The tumour is contiguous with the enhancing pituitary gland and extends forward along the planum (black arrow). There is blistering of the sphenoidal sinus.

density or cystic components to meningiomas are very uncommon, but in a few cases they can be a major feature. Mass effect is moderate in most cases, though it can be marked in around 10%. The appearances just described, together with the characteristic sites, are sufficient to permit a specific diagnosis in over 95% of cases. The occasional false-negative diagnoses reported in past series should not occur with modern high-resolution apparatus, provided the appropriate area is adequately covered. An occasional false-positive diagnosis may still occur in the differential diagnosis from a superficial intracerebral tumour, which is usually a metastasis. The rare intraventricular meningioma has to be differentiated from an intraventricular papilloma or ependymoma.

MRI can better demonstrate dural sinus invasion or patency than CT. On MRI the tumours are isointense to hypointense on T₁- and hypo- to hyperintense on T₂-weighted sequences with avid enhancement but associated variable vasogenic oedema. The sign of an enhancing dural tail, which can be either a reactive phenomenon or

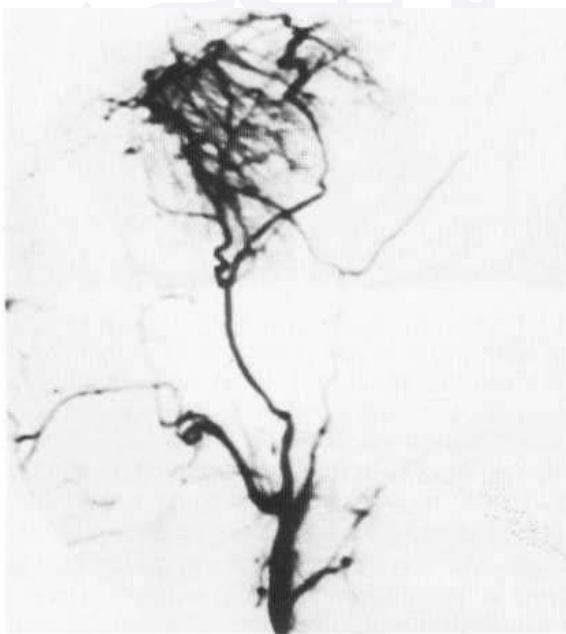


Fig. 57.78 Selective external carotid angiogram showing meningeal vessels supplying a frontal meningioma (arterial DSA study).

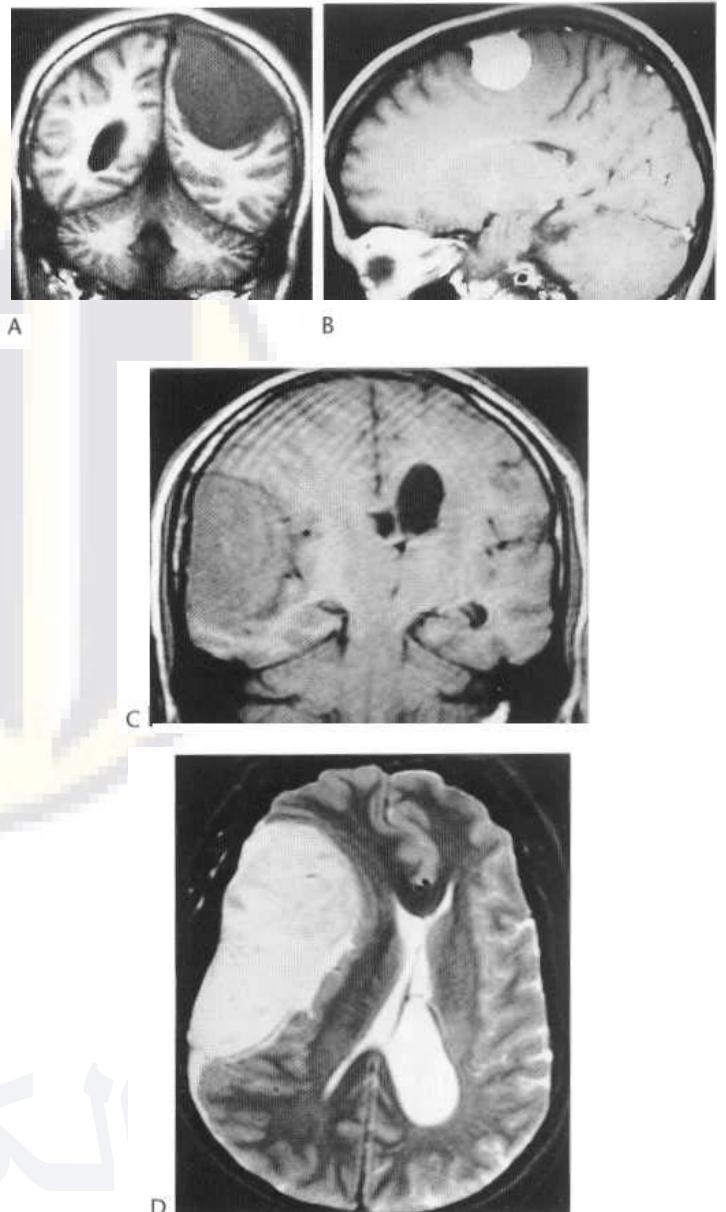


Fig. 57.77 (A) Coronal MRI section (T₁-weighted) shows uniformly low signal of a large parasagittal meningioma. (Courtesy of Dr Gordon Thomson and Bristol MRI Centre.) (B) Sagittal MRI study (T₁-weighted). A small parasagittal meningioma shows strong uniform enhancement with gadolinium. (C) Coronal MRI, T₁-weighted, shows low signal from large meningioma, broadly based on dura and with lower signal rim at brain-meningioma interface. (D) Axial view of same large tumour, T₂-weighted, shows inhomogeneous high signal.

represent direct tumour extension, is seen in approximately 70% of cases, but is not specific for meningiomas.

Although angiography is now little used in tumour diagnosis, it still has a place in the assessment of some meningiomas. This is particularly so where the tumour is adjacent to the sagittal or other major sinus and may be involving or occluding the sinus and there remains some uncertainty on MRI and MRV sequences. The major sinuses are well shown by intravenous digital subtraction angiography, which can be performed on an outpatient basis without the risks of arterial puncture. Some neurosurgeons still require arterial studies of the blood supply and vascular relationships before surgery in highly vascular or potentially more malignant menin-

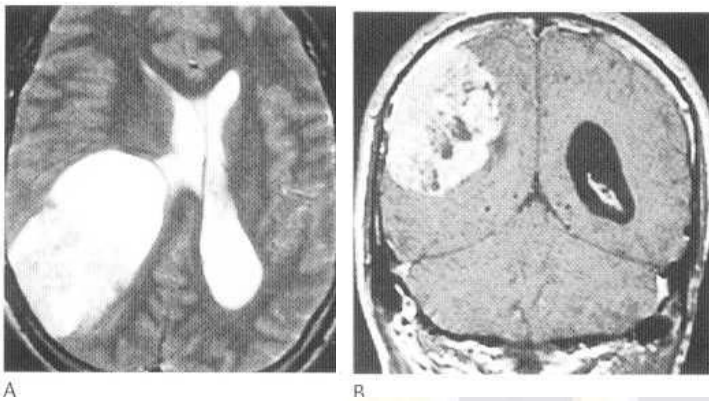


Fig. 57.79 A large mixed cystic and solid extra-axial mass is shown in the right parietal region on the T₂-weighted axial image (A) with marked mass effect on the ipsilateral lateral ventricle. The postcontrast T₁ coronal (B) image shows the lesion is durally based and shows some heterogeneous enhancement; this was proven to be a haemangiopericytoma.

Table 57.6 Sites of meningiomas (from a consecutive series of 100 cases)

Site of meningioma	No.
Parasagittal	26
Convexity	32
Tuberculum sellae (suprasellar)	13
Sphenoidal ridge and pterion	12
Cerebellopontine angle	8
Subfrontal	3
Cerebellar convexity	3
Tentorium	2
Intraventricular	1

From Sutton & Claveria 1977

giomas. Prior to surgery some tumours of this type have been treated by embolisation from the external carotid artery of meningeal feeding vessels not supplying cerebral tissue.

The blood supply of most meningiomas is mainly from the meningeal branches of the external carotid (Fig. 57.78) but there is often a major supply from the internal carotid.

Malignant mesenchymal-haemangiopericytoma Haemangiopericytoma, a tumour arising from perivascular pericytes of Zahn, was a new tumour category incorporated into the WHO 1993 classification. It is usually fairly well differentiated and generally of low WHO grade II, but anaplastic forms occur with a high proliferative rate and a tendency to invade brain. Overall it tends to be more aggressive than the ordinary meningiomas, may invade brain and local recurrence after surgical excision is common. On imaging it is a well-defined durally based mass but often more lobulated and heterogeneous than meningiomas and tends to be highly vascular. On CT like meningiomas it is hyperdense to brain precontrast, but calcification and hyperostosis of the adjacent calvarium are not frequent features. On MRI the tumours tend to be isointense, enhance signal flow void structures indicative of its hypervascularity are frequently detectable (Fig. 57.79).

Tumours of uncertain histogenesis—haemangioblastoma

Haemangioblastoma, is a benign WHO grade I tumour and accounts for 1% of all intracranial tumours. It occurs in isolation in 80% of cases but is linked with Von Hippel-Lindau (VHL) syndrome. Although it is the most common primary intra-axial tumour of the posterior fossa predominantly in the cerebellum, even so it only accounts for 10% of posterior fossa tumours; it can also occur in the brainstem and spinal cord. Supratentorial tumours are very rare and appear to occur only with VHL. It occurs in adults between the ages of 30 and 65, but is seen in younger patients in association with VHL where lesions tend to be multiple. The classical imaging appearances are seen in 60% of cases and on CT this comprises a smooth walled-cystic mass with an enhancing mural nodule that abuts the pial surface of the brain. As they are vascular tumours the large cysts can mask the underlying vascular nodule. The cyst wall

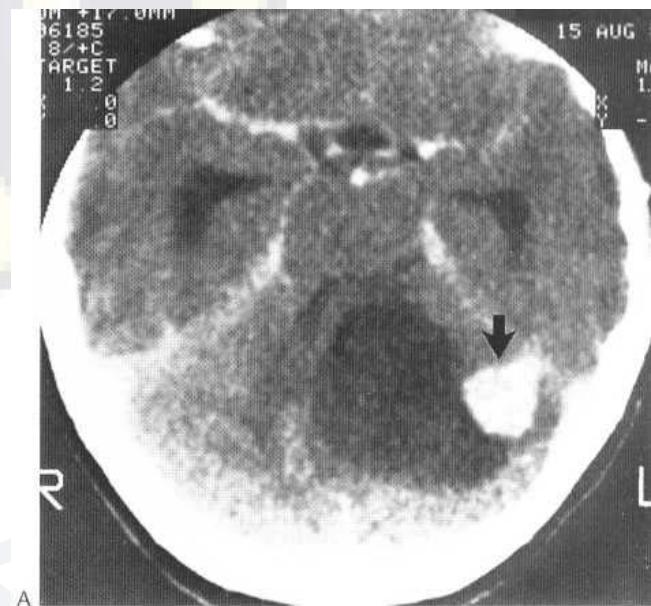


Fig. 57.80 (A) Haemangioblastoma cyst with enhancing mural nodule (arrow) in left cerebellar hemisphere. (B) Vertebral angiogram also shows the nodule (thick arrow) and a vessel stretched around the cyst.

is non-enhancing, and although oedema is typically relatively mild, mass effect will depend on overall cyst size. A solitary nodule with a large cyst can easily be mistaken for a low-density glioma or gliomatous cyst, unless the mural nodule is identified in the post-enhancement scan. The tumour nodule is isodense or slightly hyperdense, and enhances strongly after contrast medium (Fig. 57.80A). Multiple tumours are often small and may measure a few millimetres only in diameter. Thus they are easily missed, even on high-quality scans, if not included in the section. On MRI the signal return from the cyst is that of CSF and the mural nodule is normally isointense on T₁, and hyperintense on T₂ with intense enhancement. In the 40% of solid tumours, on imaging they are of less homogeneous signal, particularly on T₁-weighted images though largely isointense on T₁, and hyperintense on T₂. Radiologically the differential diagnosis of a typical cystic cerebellar haemangioblastoma would include a pilocytic astrocytoma in a younger patient or cystic metastases, although in the latter the cyst wall may be enhancing.

As already mentioned haemangioblastomas are highly vascular tumours and show a characteristic appearance at angiography. There is a dense blush of contrast, commencing in the arterial phase and continuing through into the venous phase. The larger nodules can be 1-2 cm in diameter and can resemble angiomas or even aneurysms. They may show arteriovenous shunting with one or more large drainage veins visible in the arterial phase. Smaller nodules appear as smears of contrast in the arterial phase (Figs 57.80B, 57.81).

Vertebral angiography may be indicated in some cases of suspected haemangioblastoma, even after CT or MRI, since it is the most accurate method of identifying multiple small lesions which may be missed on CT or MRI (Fig. 57.82; see also Fig. 57.30).

Tumours of cranial and spinal nerves

Schwannoma These tumours of the Schwann cells which form the nerve sheath can arise from any of the cranial nerves in the posterior fossa, although the most commonly affected nerves are the superior and inferior vestibular divisions of the eighth cranial nerve, the facial and trigeminal nerves. Vestibular schwannomas in fact account for 80-90% of cerebello-pontine angle (CPA) masses and occur mainly in the middle-aged and elderly. They are

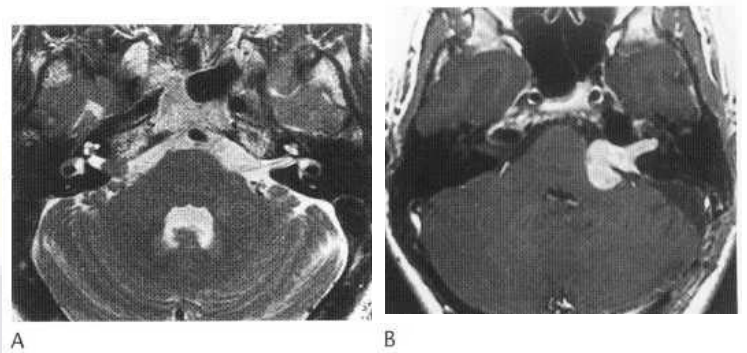


Fig. 57.83 Axial T₂-weighted high-resolution image (A) showing a rounded right acoustic neuroma isointense with brain straddling the porous acousticus. The internal auditory canal is consequently slightly enlarged. The axial T₁-weighted postcontrast image in another patient (B) shows an enhancing left acoustic neuroma with mild mass effect on the pons and extending into and filling the left internal auditory canal.

firm encapsulated tumours, which vary greatly in size at presentation. The larger tumours may become irregular and lobulated and can become cystic and 10% of vestibular schwannomas are associated with arachnoid cysts presumably due to the formation of adhesions. As a rule they are single solitary tumours, but in central neurofibromatosis (NF2) bilateral acoustic tumours may be seen. They can either be confined to the internal auditory canal or CPA cistern, but more commonly straddle both. Although the major radiological differential of a vestibular schwannoma is a meningioma, the former are more often centred on the porous acousticus of the internal auditory canal resulting in some widening of the canal and form a relatively acute angle with the petrous ridge. Meningiomas tend to be more eccentric to the internal auditory canal, extending into it less frequently and form an obtuse angle with the petrous ridge. On CT large and medium acoustic tumours are generally isodense and difficult to visualise on the un-enhanced scan. Rotational deformity of the fourth ventricle however may suggest their presence, as may symmetrical hydrocephalus. On giving contrast medium, most of these tumours will enhance strongly (Figs 57.83, 57.84). The rare cystic tumours are of low density and may simulate an arachnoid cyst or epidermoid in the cerebellopontine angle. Only the solid part of the tumour will enhance. Small acoustic tumours (less than 10 mm in diameter), or tumours lying in or just protruding from the internal auditory meatus, are more difficult or impossible to demonstrate on conventional CT. They can however be readily shown by the special techniques of CT with air meatography or CT cisternography with water-soluble contrast medium. These are no longer justified if MRI is available.

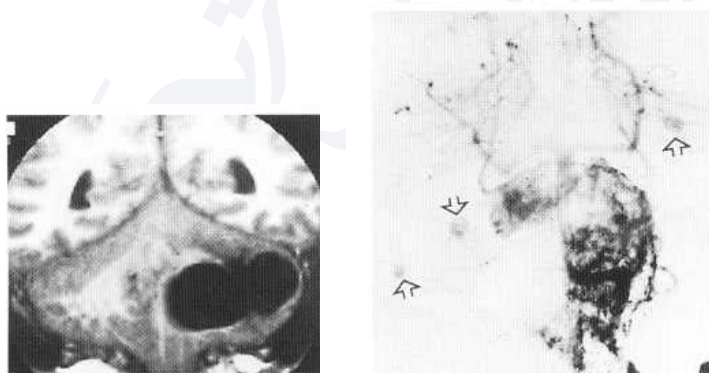


Fig. 57.81 Coronal MRI (T₁-weighted). A large haemangioblastoma cyst is well shown. (Courtesy of Dr Gordon Thomson and Bristol MRI Centre.)

Fig. 57.82 Vertebral angiography demonstrates two large vascular haemangioblastomas and several smaller nodules (arrows).

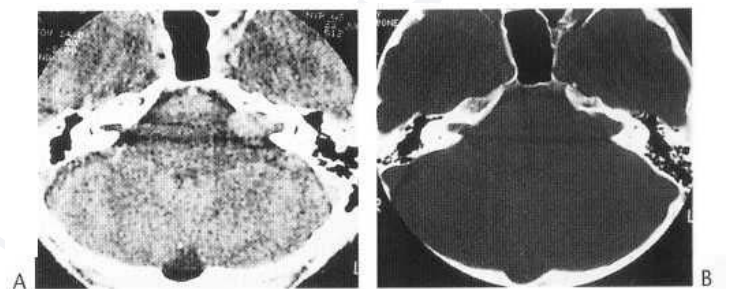


Fig. 57.84 (A) A small acoustic tumour in the left cerebellopontine angle is demonstrated after contrast enhancement. The dark bands across the pons are artefacts from the dense petrous bones. (B) Imaging at bone window shows bony erosion around the IAM.

On CT meningiomas are more likely to be hyperdense to brain pre-contrast and may contain calcification (Fig. 57.84). The dural tail is a non-specific radiological sign and can be seen with both tumours.

The MRI appearances of schwannomas will vary according to their histological make-up; those of the Antoni-A subtype contain densely packed neural and fibrous tissue with little extracellular fluid, thus will be hypointense to brain on T_2 -weighted sequences; the reverse is true of the Antoni-B subtype where the cells are more loosely arranged with more extracellular fluid thus the tumour will be hyperintense on T_2 ; both types of tumour are iso-hypointense on T_1 -weighted sequences.

Other neuromas

Though much less common than acoustic neuromas, lesions of the other lower cranial nerves and of the fifth nerve are occasionally seen. Tumours of the lower cranial nerves occur more inferiorly and may involve the skull base (petrous bone, jugular foramen or hypoglossal canal). Fifth nerve tumours may involve the petrous apex and floor of the middle fossa as well as the pons. Large tumours may become cystic.

There may be evidence of bony erosion in the sites mentioned above. CT is at a disadvantage at the skull base and foramen magnum region, and small tumours can be easily missed without high-quality films of the appropriate areas; larger tumours are more



Fig. 57.85 Fifth nerve tumour with marked enhancement after contrast medium. The tumour at the petrous apex extends into both the middle and posterior fossae (L36, W80).

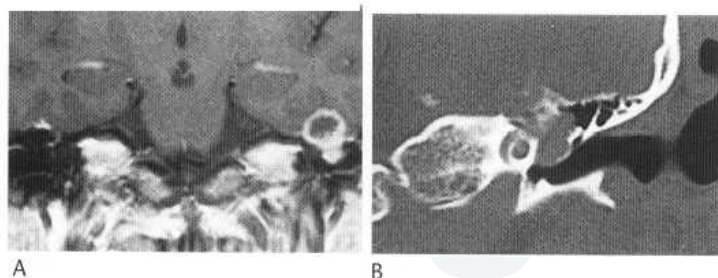


Fig. 57.86 Coronal T_1 -weighted postcontrast image (A) showing a lobulated ring-enhancing mass in the region of the geniculate ganglion of the left facial nerve. The dedicated coronal CT (B) acquired on a bone algorithm shows associated bone destruction by the soft-tissue tumour with some involvement of the cochlea.

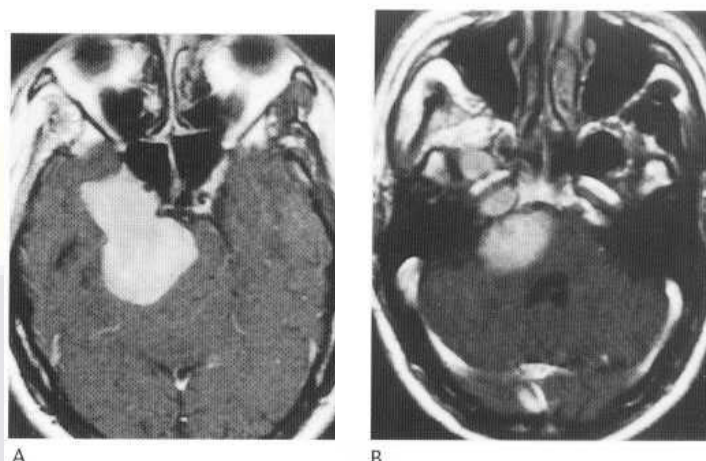


Fig. 57.87 A lobulated enhancing mass is shown on these T_1 axial images. It involves the right cavernous sinus and extends posteriorly with marked mass effect on the pons (A). More inferiorly it extends towards the skull base and the region of the foramen ovate (B). This was a neuroma of the trigeminal nerve.

readily identified, particularly after contrast enhancement (Fig. 57.85). High-quality reformats or even CT cisternography may be required in equivocal cases, though bone erosion is well shown by CT on bone windows.

MRI, with its capacity for easy sagittal and coronal imaging and freedom from bone interference, is the ideal method for demonstrating these tumours. The anatomical features and relationships are well shown on T_2 -weighted images, while the neuromas invariably yield a higher signal on T_1 -weighted images. Like acoustic neuromas they enhance well with intravenous gadolinium-DTPA (Figs 57.86, 57.87).

Local extensions from regional tumours

Paraganglioma These tumours are also termed chemodectomas or non-chromaffin paragangliomas. They occur within the tympanic cavity (glomus tympanicum) or in the jugular body situated in the wall of the jugular bulb (glomus jugulare). They can proliferate into the middle ear and can present at the drum as a 'cherry-red' polyp.

Glomus jugulare tumours can also extend into the posterior fossa and down into the neck. They are commoner in females.

CT will show the bone destruction well, and, after enhancement, any associated intracranial extension (Fig. 57.88A,B) and downward extension into the neck (see Figs 52.29 and 52.30).

On MRI the tumour gives a higher signal than brain on T_2 - and is isointense on T_1 -weighted images. It commonly appears stippled, due to signal void from the large vascular channels. Enlarged veins are often apparent in the region and the jugular bulb may be obstructed and show unexpectedly high signal due to absence of flow. If direct coronal sections can be obtained, they will be helpful in assessing the full extent of the tumour, and particularly useful in showing involvement of the internal jugular vein (see Figs 52.29, 52.30).

These tumours, are highly vascular and are well demonstrated by angiography. Selective external carotid angiography with subselective catheterisation of the occipital and ascending pharyngeal arteries has been used both for diagnosis and for therapeutic embolisation (Fig. 57.88C).

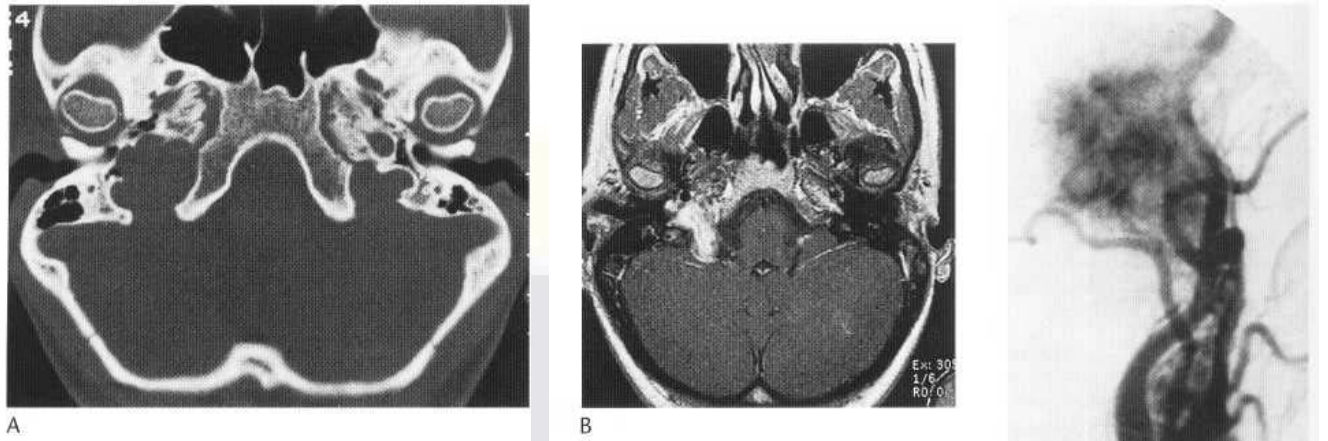


Fig. 57.88 (A) CT at bone window demonstrates erosion of skull base around right jugular foramen. (B) Enhanced MRI shows strongly enhancing tumour extending into posterior fossa. (C) Large glomus jugulare tumour at the skull base and a concomitant carotid body tumour at the carotid bifurcation are both shown by carotid angiography.

Chordoma This low-grade malignant lesion probably arises from primitive notochord remnants. 35% of tumours arise in the intracranial extension impinges on the brainstem and may present with symptoms and signs suggesting a brainstem or cerebellopontine angle tumour, and cranial nerves and vessels may be encased by tumour (Fig. 57.89). Occasionally a tumour involving the skull base arises from an upper cervical vertebra. The larger and more aggressive basisphenoid tumours can also involve the sella or even the back of the orbit. Though usually central, the tumour is often asymmetrical and can grow mainly on one side. They are

extend intracranially as well as forward into the nasopharynx. The larger and more aggressive basisphenoid tumours can also involve the sella or even the back of the orbit. Though usually central, the tumour is often asymmetrical and can grow mainly on one side. They are

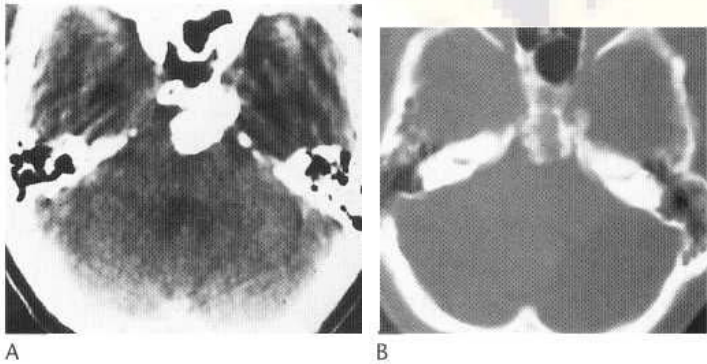


Fig. 57.89 Chordoma of skull base. (A) CT at brain window. Bony density mass protrudes back from the clivus. (B) CT at bone window (slightly lower section) confirms osteochondromatous nature.



Fig. 57.90 Chordoma. Calcified mass growing backward and upward from the clivus. It is displacing the brainstem and extending up above the sella.

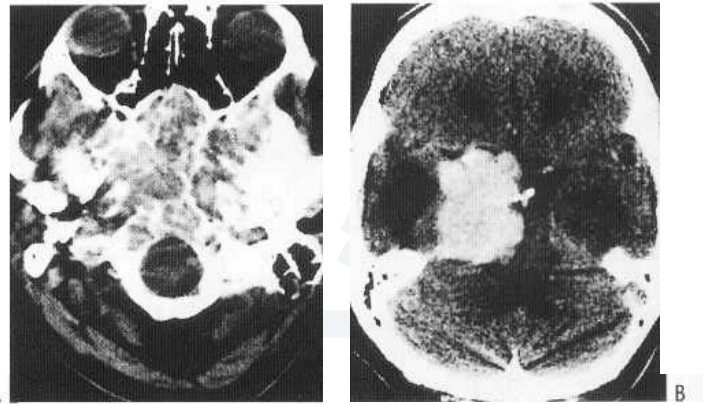


Fig. 57.91 Chordoma. (A) Extensive infiltrative destruction of the skull base. (B) Enhancing tumour mass extends up into the posterior and middle fossa on the right side involving the right clivus and sella.

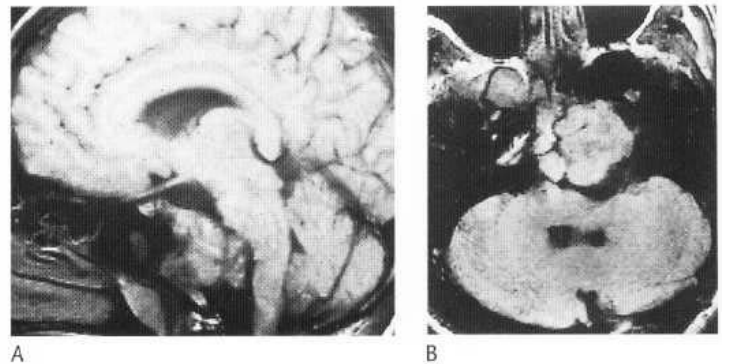


Fig. 57.92 Chordoma. MRI (T₁-weighted). (A) Sagittal midline section. (B) Axial section. The tumour arising from the clivus is isointense with brain and protrudes backward, deforming the brainstem. It also protrudes forward into the nasopharynx.

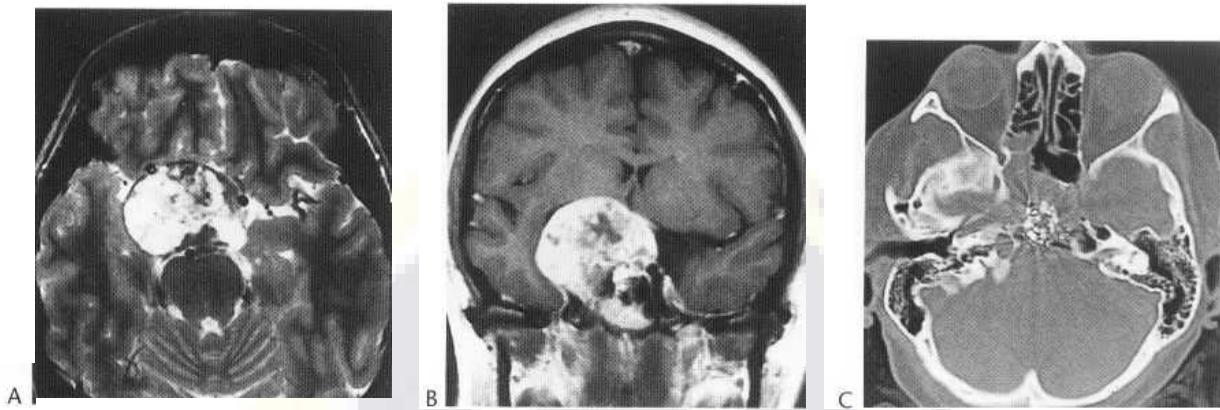


Fig. 57.93 A large heterogeneous T_2 signal eccentric suprasellar chondrosarcoma (A) displaces the terminal internal carotid arteries. (B) On the postcontrast coronal T_1 -weighted image the mass involves the clivus and shows heterogeneous enhancement. The axial CT (C) shows that the mass is partially calcified.

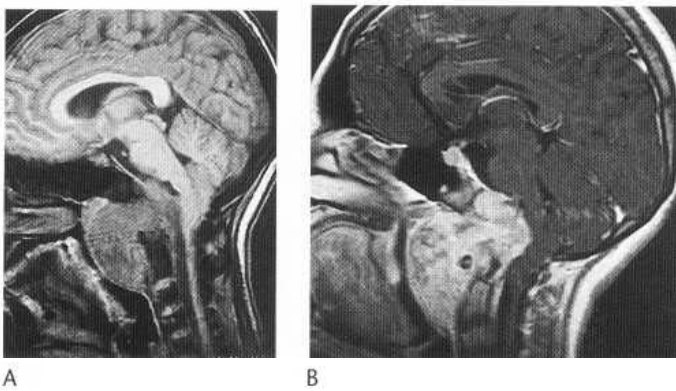


Fig. 57.94 Sagittal T_1 unenhanced (A) and postcontrast (B) images showing an expansile enhancing chordoma involving the clivus and dens with compression of the craniocervical junction and a large extrasosseous soft-tissue component extending into the nasopharynx, ethmoids and prevertebral space.

almost exclusive to the adult population occurring in those in their twenties to sixties, and are rare in children. They are slow-growing lesions spreading by local infiltration, destroying adjacent bone, thus surgical resection is usually incomplete and the ultimate course is one of disease progression. CT is optimal for demonstrating the full extent of the bone involvement and shows the calcification better which is usually a prominent though not a constant feature (Figs 57.90, 57.91). MRI has the great advantage of permitting sagittal sections, which often show the lesion best and, together with coronal and axial sections, permit full demonstration of the extent and relations of the tumour (Fig. 57.92). The tumour appears as a lobulated inhomogeneous mass; 75% of the tumours are isointense with brain on T_1 and 25% hypointense; T_2 signal is heterogeneous although overall mildly hyperintense and enhancement is also heterogeneous.

Chondroma and chondrosarcomas These tumours arise from cartilage or embryonal cell rests at the skull base and can sometimes be difficult to distinguish from chordomas; chondrosarcomas arise most commonly in the petrous region and extend to the sella but may also arise in the midline; chondroid tumours often have a scooped margin. Bone destruction and calcification is better seen on CT though the full extent of the lesion is better appreciated on MRI. Chondromas and chondrosarcomas are hyperintense on T_2 and of variable signal on T_1 ; the soft-tissue

component enhances on both CT and MRI and curvilinear and ring-like enhancement has been described (Figs 57.93, 57.94).

Metastatic tumours (Figs 57.95-57.101) Metastasis to the brain, skull or meninges can occur in most forms of systemic cancer. Skull metastases have been described in Chapter 53. Rather surprisingly, most have little effect on the brain, but occasionally a large deposit will grow inward and involve the meninges and underlying brain. Cerebral metastases occur in up to 20% of all cancer patients and account for nearly 40% of intracranial tumours in adults. The most

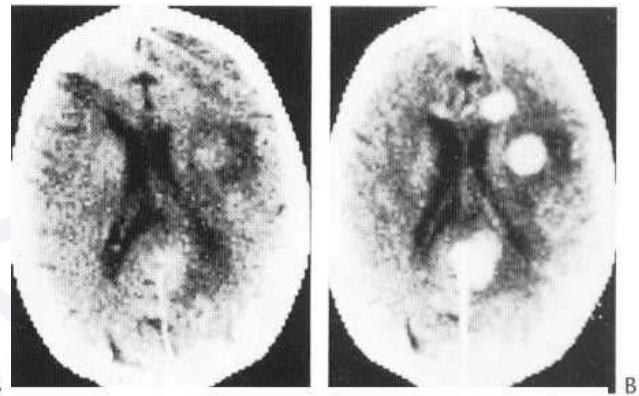


Fig. 57.95 Metastases. Three separate lesions, all isodense and enhancing strongly with contrast medium. Oedema around the larger secondaries (L40, W60). Before (A) and after (B) enhancement.

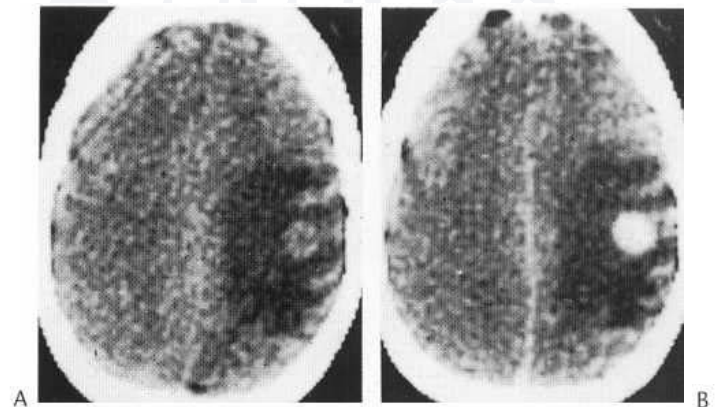
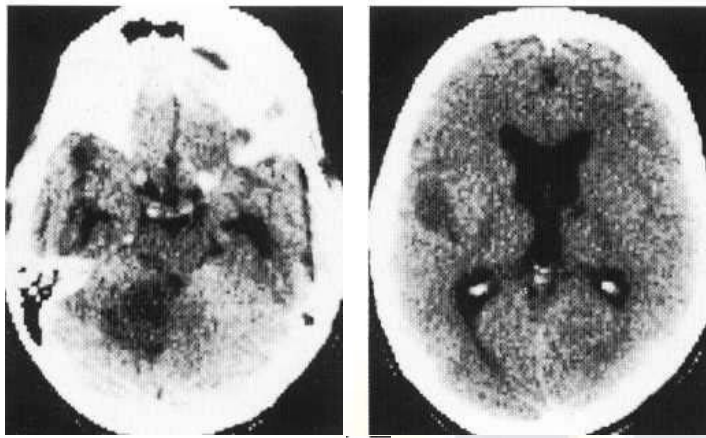
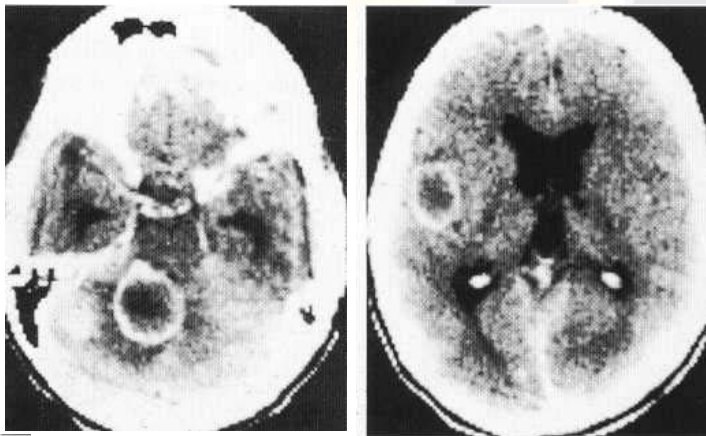


Fig. 57.96 (A,B) Metastasis. Small isodense enhancing tumour with marked oedema (L36, W80).



A

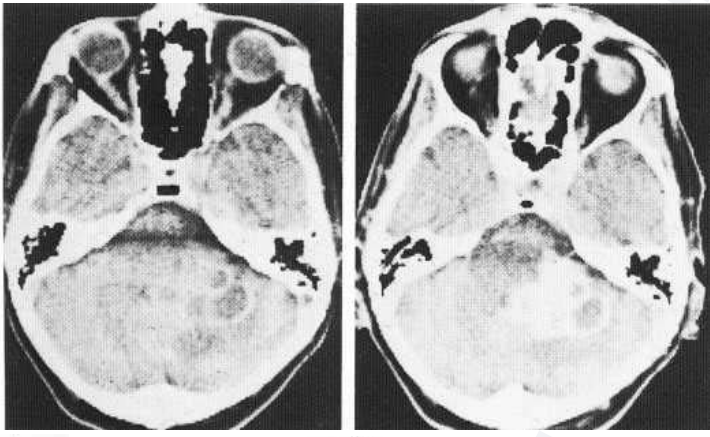
B



C

D

Fig. 57.97 (A,B) Metastases. Two low-density lesions, one in left cerebellum and one in left temporal lobe. (C,D) After contrast there is ring enhancement of both tumours ([40, W80]).

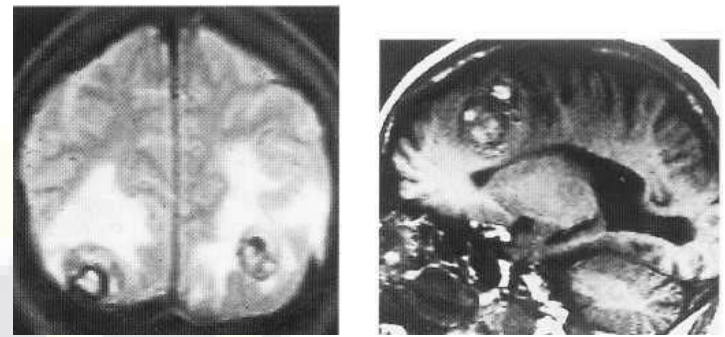


A

B

Fig. 57.98 Metastases. (A) Multiple adjacent ring shadows with low-density centres. (B) Mainly ring enhancement after contrast.

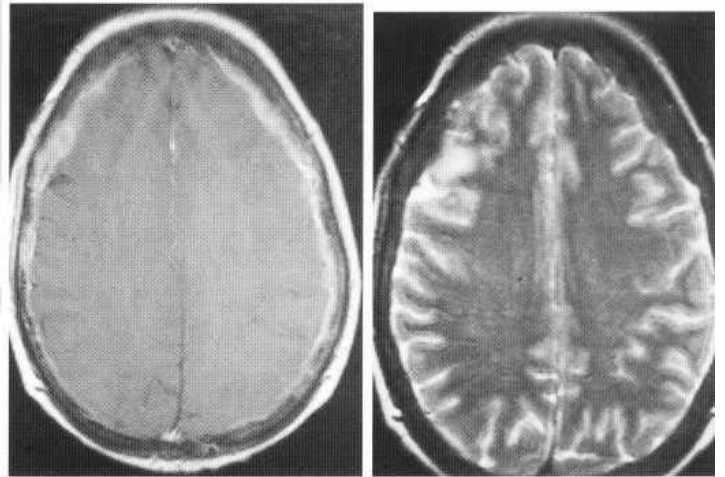
common primary tumours to metastasise intracranially include lung (30%), breast (20%), melanoma (10%), kidney (10%) and gastrointestinal tract (5%). Eighty per cent of metastases are supratentorial in distribution, but infratentorial metastases still account for the most common intra-axial posterior fossa neoplasm. Haemorrhage can be seen in association with metastases from melanoma, renal, chorio-



A

B

Fig. 57.99 Metastases. (A) Coronal MRI (T₁-weighted). Symmetrical deposits in the occipital lobes. High signal within the deposits probably due to haemorrhage. Surrounding oedema also shown as high signal. (B) Sagittal MRI (T₁-weighted). Frontal lobe adjacent deposits.



A

B

Fig. 57.100 Axial T₁-weighted postcontrast image (A) showing bilateral diffuse nodular dural thickening and enhancement in a patient with metastatic breast carcinoma. A small area of underlying cortical signal abnormality is present in the right frontal lobe on the T₂-weighted axial image (B).

carcinoma, thyroid, lung or breast primary tumours. Lymphoma can metastasise to brain but this is very uncommon. In one large series it occurred in only 1 % of cases, all of these being non-Hodgkin's lymphoma.

Metastatic disease of the brain in children is less common than in adults and arises from different tumours. The most common are: neuroblastoma, Wilms' tumour, rhabdomyosarcoma and osteogenic sarcoma.

MRI is not surprisingly more sensitive than CT in detecting small metastatic deposits, even if double-dose intravenous contrast and delayed imaging is performed with CT. On imaging cerebral metastases are usually well-defined lesions on both CT and MRI, typically located at the grey-white matter interface and they are associated with a disproportionately large amount of vasogenic oedema considering their size, even with a very small superficial lesion. Deposits can occur anywhere including brainstem, cerebellum, basal ganglia and white or grey matter. Interestingly, cortical metastases are associated with very little vasogenic oedema. On CT metastases are usually isodense or hyperdense, hyperdensity being a frequently encountered feature of melanoma secondaries. Calcification is very rare and is a point against the diagnosis of metastasis. However, it

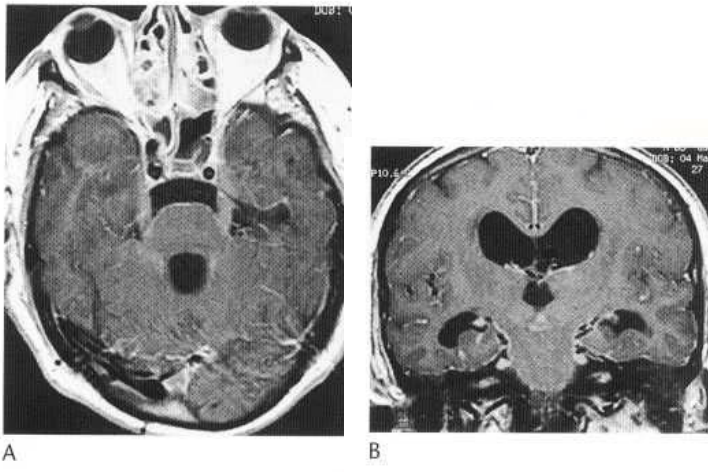


Fig. 57.101 Axial (A) and coronal (B) T₁-weighted postcontrast images in a patient with meningeal leukaemic infiltration. There is meningeal enhancement and thickening around the brainstem and temporal lobes with thickened enhancing 5th nerves and 7th/8th nerve complexes bilaterally.

can occur and has been described from bone sarcoma and colonic carcinoma. It may also be seen after radiation treatment. Larger metastases tend to become necrotic centrally and may appear cystic. Contrast medium enhancement, often very marked, is an almost universal feature of metastases. This may be seen as a well-defined nodule within an area of surrounding oedema, or, if the centre is necrotic or cystic, as marginal or ring enhancement (Figs 57.95–57.98). Superficial nodules easily missed on the pre-enhancement scan may be more easily recognised after contrast enhancement. On MRI metastases are hypointense on T₁ and hyperintense on T₂ and enhancement patterns are similar to those described for CT.

The presence of multiple discrete lesions within the brain should always suggest the diagnosis of metastases. Similar appearances may be seen with multiple small abscesses or granulomas, though the clinical features will often help to differentiate. In the posterior fossa multiple haemangioblastomas may have to be considered.

Unfortunately a high proportion of patients (50% or more in some series) present with a solitary metastasis, and unless there is a known primary this can raise a difficult problem of differentiation from a primary brain tumour or cerebral abscess. In some cases this can only be resolved by biopsy.

Cysts and tumour-like lesions

Rathke cleft cyst These rare lesions are important to differentiate from craniopharyngiomas since they are much easier to treat surgically. The cell type lining the cyst wall distinguishes craniopharyngiomas from Rathke's cleft cysts; the latter are benign thin-walled unilocular cysts, which do not recur even after simple evacuation. They have no solid components and do not calcify. They are lined with cuboidal or columnar epithelium and contain mucinous cyst fluid, often brownish in colour. Craniopharyngiomas are lined by squamous or basal cell line epithelium. Purely suprasellar Rathke's cleft cysts are rare and the density and signal characteristics of the cyst on imaging will depend on its content.

CT shows a round mass in the sellar and suprasellar cistern with no calcification. The value of the density varies from that of CSF

when the contents are serous fluid (in which case the mass cannot be differentiated from an arachnoid cyst before histological examination of the cyst wall) to more solid looking when the contents are viscid, proteinaceous and pus like. The capsule may then enhance slightly, resembling a cystic craniopharyngioma.

On MRI cysts with serous fluid are of similar signal characteristics to CSF, but those with proteinaceous fluid are of high T₁ signal. Peripheral cyst wall enhancement may be seen due to their origin in the pars intermedia, but there is a nodular enhancing component. Displacement of the infundibulum anteriorly is easily detectable on MRI.

Epidermoid

Histologically epidermoids are tumours with a thin capsule of epidermis (squamous keratinised epithelium); they contain desquamated epithelial debris and cholesterol, which gives rise to their characteristic metallic or 'pearly' sheen.

They usually present in adults and are commonest in the cerebellopontine angle or suprasellar region in the subarachnoid space. Other sites are in the sylvian fissure and in the ventricles. The exact site of origin is often difficult to determine, since the tumours can infiltrate widely around vessels and nerves as they extend in the subarachnoid space (Fig. 57.102).

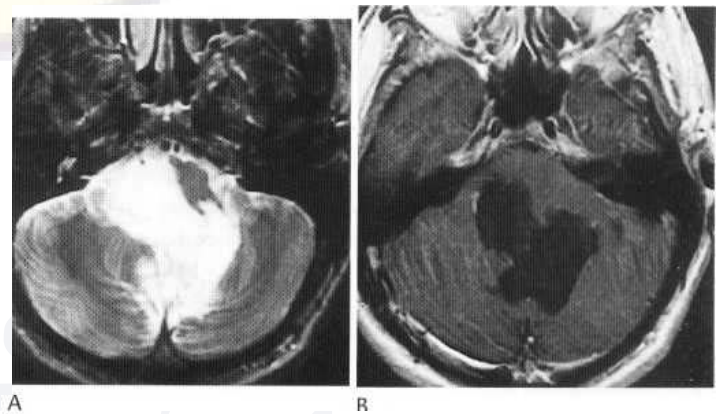


Fig. 57.102 Axial T₂- (A) and T₁-weighted postcontrast images (B) show a large lobulated epidermoid in the posterior fossa filling and expanding the fourth ventricle and causing marked displacement of the brainstem. The signal characteristics of the mass are similar to CSF and there is no enhancement.

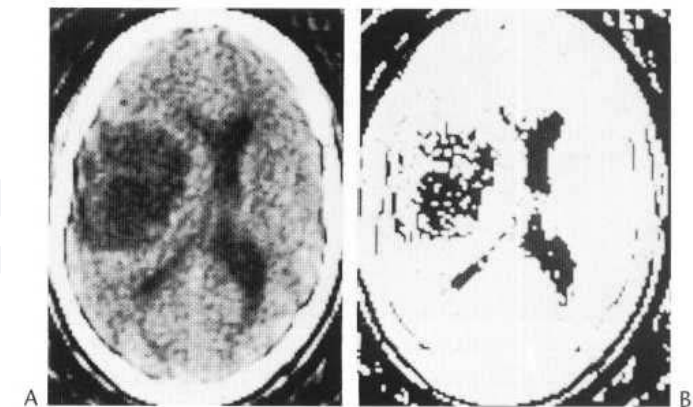


Fig. 57.103 Epidermoid (pearly tumour) in the left temporal region. (A) At L36, W80. (B) Same case at L8, W1.

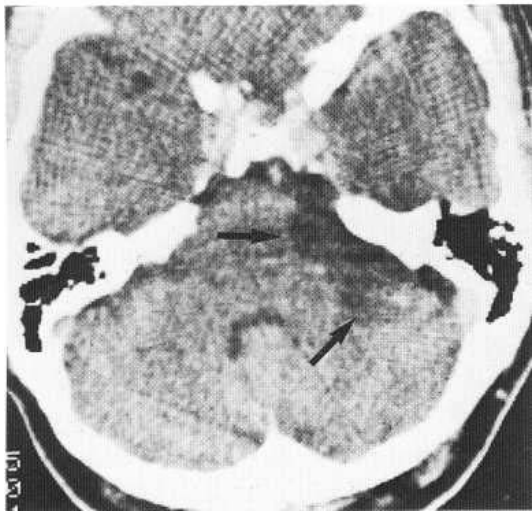


Fig. 57.104 Epidermoid (arrow) of left cerebellopontine angle.

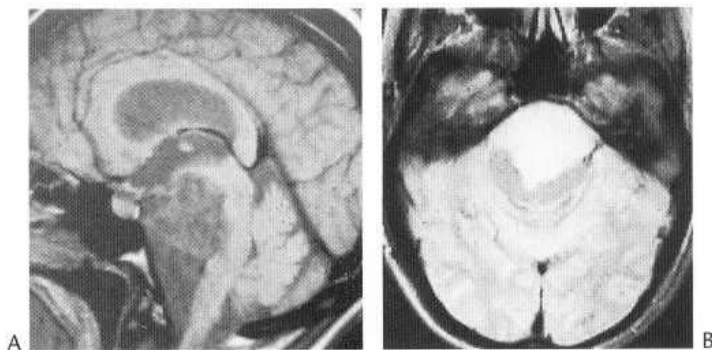


Fig. 57.105 Epidermoid. (A) Sagittal MRI (T₁-weighted). An irregular tumour in the pontine cistern is displacing the pons and appears to be invading it. (B) Axial MRI (T₂-weighted). The tumour is shown as high signal displacing and compressing the central pons.

On CT the tumours are usually of low (fatty) density, but the density can be as high as that of CSF or higher, depending on the content. The margins may be ill defined and they do not enhance with contrast medium (Figs 57.103, 57.104). Calcification is unusual but flecks of calcification have occasionally been noted at the capsule. They may be difficult to differentiate from arachnoid cysts.

On MRI signal characteristics and appearances depend on the relative proportions of cholesterol (short T₁) and keratin (long T₁) within the tumour. They are usually isointense with CSF on T₁- and isointense or slightly brighter on T₂-weighted images. On FLAIR sequences they are of slightly higher signal to CSF whereas arachnoid cysts are usually isointense with CSF. Diffusion-weighted sequences may also be helpful in differentiating epidermoid tumours from arachnoid cysts if difficulty arises, since there is free diffusion of water within arachnoid cysts, hence they are of low signal; there is some restriction of diffusion in epidermoids due to the presence of protein macromolecules, hence they are of increased signal, although there is also a contribution from T₂ shine-through. Epidermoids often expand the prepontine or cerebellopontine cisterns in which they usually arise, and distort the adjacent neural structures such as pons, medulla or cerebellar peduncle, often with a lobulated or scalloped margin. Larger lesions may invaginate deeply into the brain and appear continuous with it (Fig. 57.105), though the extra-axial origin remains apparent. Surgical resection is often incomplete.

Dermoids

These are more complex cystic slow-growing tumours accounting for 0.04-0.6% of intracranial tumours. Their wall contains a full width of dermis, which may contain hair and sebaceous glands, and an outer layer of connective tissue, as well as a connective-tissue capsule. The cyst may contain matted hair and glandular secretions as well as desquamated keratinised epithelium. They normally present in children, and may lie in the midline at the base of the brain or near the fourth ventricle. The latter may show an occipital skin dimple with a stalk leading through the bone to the lesion. Such dermoids can become infected.

As noted above (see Ch. 53), posterior fossa dermoids in children may be suggested by an occipital hone defect, which may be detected on a plain skull radiograph. Wherever sited, calcification of an arc-like type resembling that seen in aneurysms may occur in the capsule and is seen in 20% of cases (see Fig. 53.33).

On CT the cysts are usually of fatty or low density and more rounded than epidermoids. They are seen in the posterior fossa near the midline, or above the floor of the anterior fossa, but they can occur over the convexity or elsewhere. Capsular calcification occurs more commonly than with epidermoids (Fig. 57.106). Rupture of a cyst may occur, with escape of the fatty contents into the CSF resulting in a chemical meningitis followed by arachnoid scarring

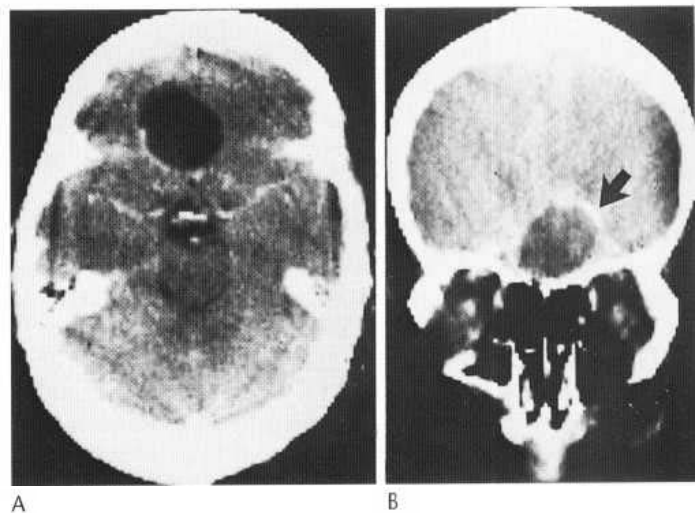


Fig. 57.106 (A,B) Basal dermoid arising from ethmoids. Note marginal calcification (arrow).

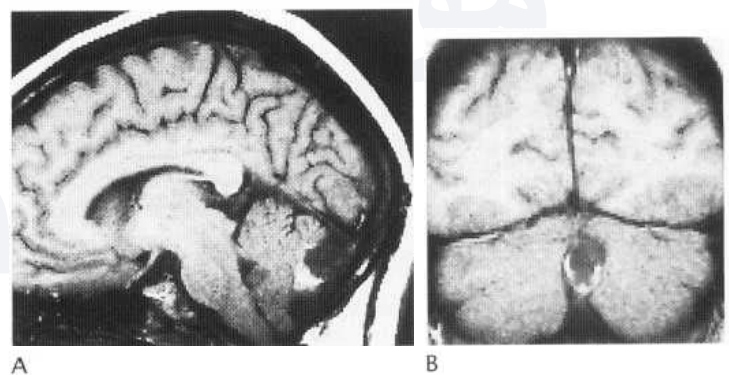


Fig. 57.107 Dermoid. Sagittal (A) and coronal (B) MRI sections (T₁-weighted) demonstrate small ovoid mass in lower vermis with high signal in lower part and low signal in upper part.

and hydrocephalus; rupture into a ventricle has also been reported, and this has been recognized at CT by a fat-fluid level.

On MRI signal characteristics are heterogeneous but will fail to show calcification (Fig. 57.107). Dermoids without fat or calcification within them may be indistinguishable from epidermoids or arachnoid cysts; the presence of material other than fat within a lesion is also useful in distinguishing a dermoid from a suprasellar lipoma.

Colloid cysts

According to one theory these tumours are derived from the paraphysis and have been termed paraphyseal cysts. The paraphysis is a gland normally found in the human fetus at one stage of development but later disappears; it is present in some lower vertebrates but its function is unknown. Other workers are sceptical of this theory and prefer to use the non-committal term 'neuroepithelial cyst'. The cyst lies in the roof of the third ventricle behind the foramen of Monro and contains amorphous gelatinous material (colloid). Because of its position it can give rise to intermittent obstruction of the foramen of Monro even when quite small. These tumours usually present in adults at any age, but have been described in children. They are usually 1-2 cm in diameter at presentation, but can be larger.

The CT appearances are usually diagnostic on the unenhanced scan. Symmetrical hydrocephalus of the lateral ventricles is present

with a high-density spherical cyst at the base of the septum pellucidum in the region of the foramen of Monro (Fig. 57.108A). The appearances are normally unchanged after intravenous contrast. Marginal enhancement may be seen in these cases either from opacified capsule or from stretched veins around it (Fig. 57.108B). MRI will also characterise the cyst and shows it well in the coronal plane (Fig. 57.108C). These tumours are also described as of low signal or similar to surrounding brain on T₁-weighted images, but of high signal on T₂-weighted images sometimes with a low signal centre.

Granular cell tumour (choristoma, pituicytoma)

This rare tumour originates in the neurohypophysis and the pituitary infundibulum and its location in the posterior pituitary gland is useful in making the diagnosis. On CT appearances are those of a hyperdense mass on unenhanced images with intense enhancement post contrast. On MRI the mass is isointense to brain on all sequences with moderate enhancement after gadolinium contrast agent.

Hypothalamic neuronal hamartoma

This is a congenital lesion of non-neoplastic heterotopic grey and white matter with a varying degree of differentiation. It is usually situated around the tuber cinereum, between the infundibular stalk and the mamillary bodies, inferior to the hypothalamus and can be either sessile or pedunculated and although is not strictly a neoplasm can grow slowly. Patients often present with precocious puberty and/or gelastic seizures, but it may also be associated with mental impairment, other structural abnormalities such as microgyria, heterotopias, callosal agenesis/dysgenesis, polydactyly, facial and cardiac anomalies, and the Lawrence-Moon-Biedl syndrome. There are also metabolic associations such as diabetes insipidus and growth hormone secreting pituitary adenomas. The CT appearances are those of an isodense well-circumscribed, non-enhancing mass and on MRI the mass is isointense to grey matter on T₁ and isointense or slightly hyperintense on T₂-weighted images; occasionally signal characteristics can be heterogeneous, with a peripheral rim of T₁/T₂ isointensity, and a central focus of T₁ and T₂ hypointensity.

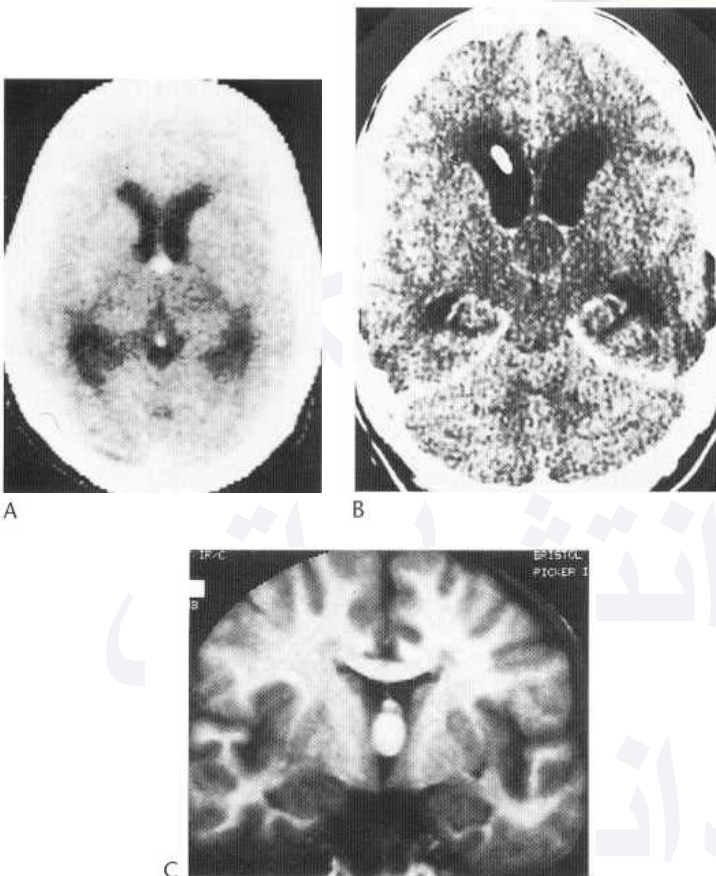


Fig. 57.108 Colloid cysts. (A) Small high-density cyst at base of septum pellucidum. This is the classic appearance seen in most cases. (B) Isodense cyst with marginal enhancement after contrast medium—a rare variant. (C) Coronal MRI study (T₂-weighted) shows the cyst as a high-signal lesion in the third ventricle. (Courtesy of Dr Gordon Thomson and Bristol MRI Centre.)

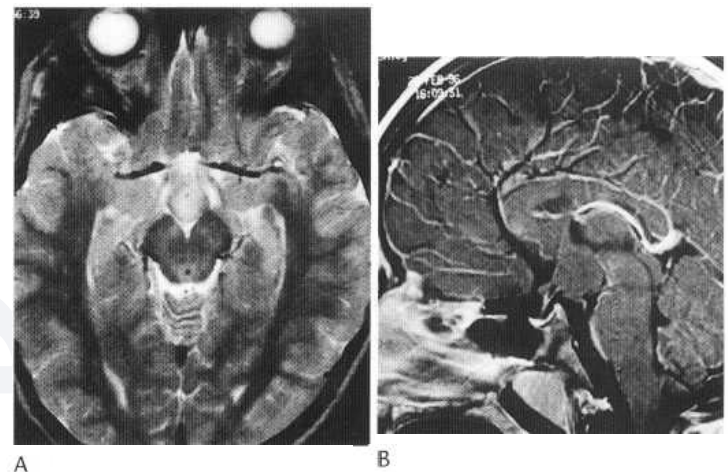


Fig. 57.109 Axial T₂-weighted image (A) showing a rounded mass, slightly hyperintense to brain in the hypothalamic region consistent with a hamartoma. The mass is isointense to brain on the T₁-weighted post-contrast image (B) and does not enhance.

Cystic components within these lesions have been described extending into the temporal fossa, and the lesions can thus appear very similar to arachnoid cysts (Fig. 57.109).

The main radiological differential of a hypothalamic hamartoma lies between a hypothalamic glioma.

Esthesioneuroblastoma (nasal glioma)

This rare tumour arises from neuroepithelial cells of the olfactory mucosa. It spreads downward into the nares and, in 20% of cases, upward through the cribriform plate into the subfrontal region. CT or MRI will define its full extent.

Miscellaneous

Radionecrosis Interpretation of follow-up examinations after surgery and radiotherapy of gliomas is complicated in the early stages by normal postoperative changes and later by the occurrence of radionecrosis. This can give rise to features similar to those of gliomas—mixed density, mass effect, contrast enhancement and even calcification. Radionecrosis changes may occur months or even years after radiotherapy and may only be distinguished from recurrence by biopsy.

Empty sella (Fig. 57.110)

The 'empty sella syndrome' is discussed here because it sometimes enters into the differential diagnosis (both clinically and radiologically) of pituitary tumours. An empty sella may be classified as primary or secondary:

1. Primary (idiopathic) empty sella
2. Secondary empty sella:
 - (i) after hypophysectomy or after tumour removal
 - (ii) after radiation therapy of sellar contents
 - (iii) after infarction of pituitary (normal or tumour).

Primary empty sella is due to a congenital defect in the diaphragma sellae, permitting suprasellar arachnoid and CSF to herniate into the sella. The pituitary gland is compressed against the back and floor of the sella and much or most of the sella is occupied by CSF. The condition is usually entirely symptom free and only discovered as a chance finding at imaging or autopsy for other causes. Symptomatic cases are commoner in females and there is usually

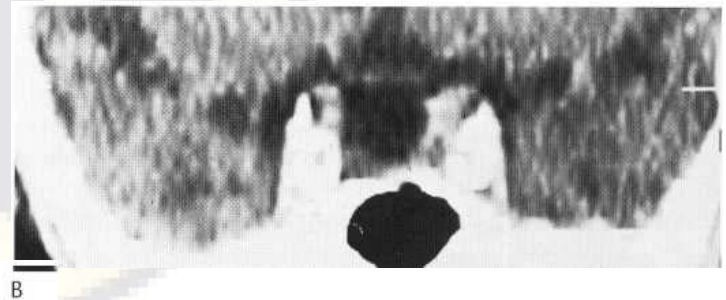


Fig. 57.110 (A,B) Empty sella confirmed by reformat.

an association with raised intracranial pressure, since the patients are often obese, multiparous and hypertensive. Visual field defects can occur due to prolapse of optic nerve or chiasmal tissue into the empty sella. The sella itself is often enlarged, presumably from pulsating CSF, and this, together with the clinical findings, can lead to an erroneous diagnosis of pituitary tumour.

Secondary empty sella may be due to any of the causes listed above and can also give rise to symptoms suggesting tumour recurrence.

REFERENCES AND SUGGESTIONS FOR FURTHER READING

See end of Chapter 58.

58

INTRACRANIAL LESIONS (2)

David Sutton, John Stevens and Katherine Miszkiel

with contributions from Keith Dewbury and Phillip J. A. Robinson

VASCULAR LESIONS

Intracerebral haematoma

In adults intracerebral haemorrhages can be classified as traumatic or 'spontaneous' (Box 58.1). The vast majority of spontaneous haemorrhages occur in the elderly and middle-aged and are due to rupture of a microaneurysm on a small intracerebral artery, with hypertension and atheroma as predisposing factors. Intracerebral haemorrhage may also occur in patients on anticoagulants or with haemorrhagic blood disorders (although subdural haematomas are commoner in the latter). Neoplasms are a rare cause (1%) and malignant melanoma deposits are particularly liable to haemorrhage.

Ruptured aneurysms or angiomas can also give rise to intracerebral haemorrhage, usually in association with subarachnoid haemorrhage, although sometimes without the latter, which is normally the outstanding clinical feature. Amyloid angiopathy of the cortical arterioles is a rare cause of superficial haematomas in the elderly and may also be associated with subarachnoid haemorrhage.

CT Because of the clear distinction between the high attenuation of extravasated blood and that of the surrounding brain, CT scanning is by far the most accurate radiological method for demonstrating these lesions. Of intracerebral haemorrhages that are hypertensive in origin, around 60% occur in the basal ganglia or centre sylvian areas; the remaining 40% involve the pons (20%), cerebellum (10%), and less commonly the cerebral white matter (Figs 58.1-58.3).

On CT the haemorrhage shows as an area of increased attenuation ranging from 50 to 90 Hounsfield units and is surrounded by a thin low-attenuation ring which probably results from clot retraction.

Box 58.1 Causes of intracerebral haematoma

Traumatic	Aneurysm
Spontaneous	Angioma
Hypertension and atheroma	Blood disorder and anticoagulants
Amyloid angiopathy	Tumour

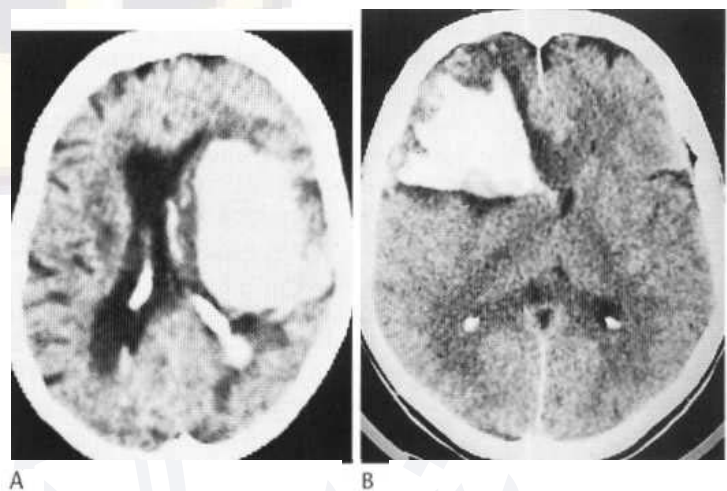


Fig. 58.1 (A) Massive capsular haematoma with blood in the ventricles. (B) Spontaneous haemorrhage into right frontal lobe, minor extension into right lateral ventricle. Low density around haematoma due to clot retraction.

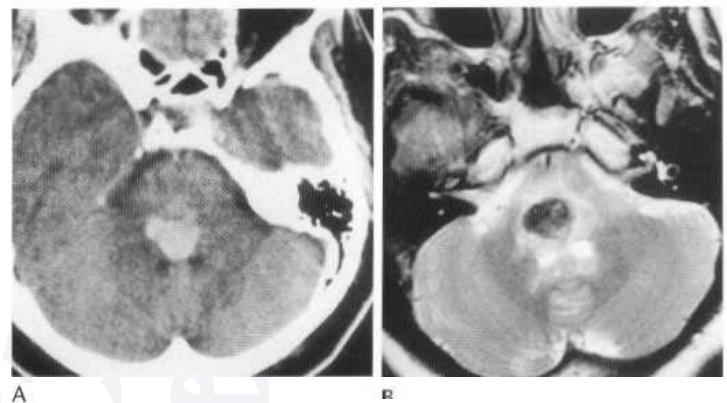


Fig. 58.2 (A) Axial unenhanced CT and (B) T₂-weighted MR image demonstrating an acute intrinsic pontine haemorrhage.

tion and damage to the blood-brain barrier. Haemorrhage can rupture into the subarachnoid space or ventricles (Fig. 58.1A). In subarachnoid extension the normal low-attenuation CSF appears isodense with brain or has areas of increased attenuation. The mass

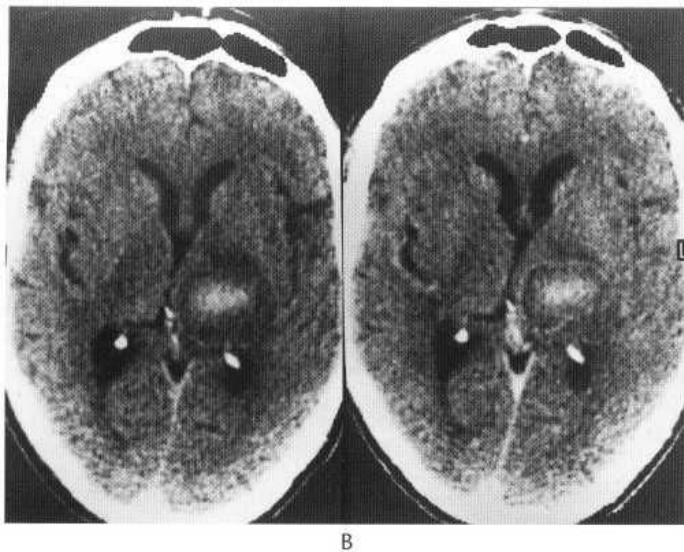


Fig. 58.3 CT of resolving left thalamic haemorrhage 10 days after onset. (A) Before contrast there is some residual high density centrally. (B) After contrast there is marginal enhancement.

effect depends on the size of the bleed but is frequently less than with tumours of comparable size. Congealed blood appears as an area of high attenuation. The absorption values increase with progressing haemoconcentration. A haematoma which is 48 hours old may develop slightly higher values than were present initially because of fluid loss during clot retraction. It is the tightly packed haemoglobin molecules which are responsible for the high attenuation values.

A blood specimen with 15 g haemoglobin has a Hounsfield number of approximately 50 units, i.e. only slightly greater than grey matter. The 50 mg of iron present contribute only 7% of the total value. A contracted clot, however, has a haemoglobin value of 30 g with an absorption value of approximately 80. The iron percentage here contributes about 4 units and the tightly packed haemoglobin molecules the rest of the increase. The baseline for plasma is 24 and each gram per cent of haemoglobin adds 2 HU.

The high attenuation of intracerebral haematomas is seen immediately from the time of haemorrhage. It decreases slowly over the subsequent weeks, until eventually a low-density cystic area remains.

Resolution of the haematoma density takes place from the periphery (Fig. 58.3). Resolution at CT does not necessarily mean that the haematoma is absorbed but merely that it has become isodense with surrounding brain. Enhancement may occur round a clot due to damage to the blood-brain barrier and neovascularity. This is unusual in the first week, but with a large haemorrhage it can persist up to 3 months. At the stage where the clot is isodense or of low density there is a clear danger of confusing the CT appearances with those of an abscess or tumour postenhancement. Differentiation will then depend on the history.

MRI Acute haematomas may be isointense with normal brain in both T₁- and T₂-weighted images and therefore may escape detection. Often, however, by the time of examination, they are hypointense on T₂-weighted images, because the paramagnetic effect of deoxyhaemoglobin causes predominantly T₂ proton-relaxation enhancement. After 3-4 days haemoglobin begins to break down at the periphery of the haematoma, accompanied by oxidation of deoxyhaemoglobin to methaemoglobin, which causes predomi-

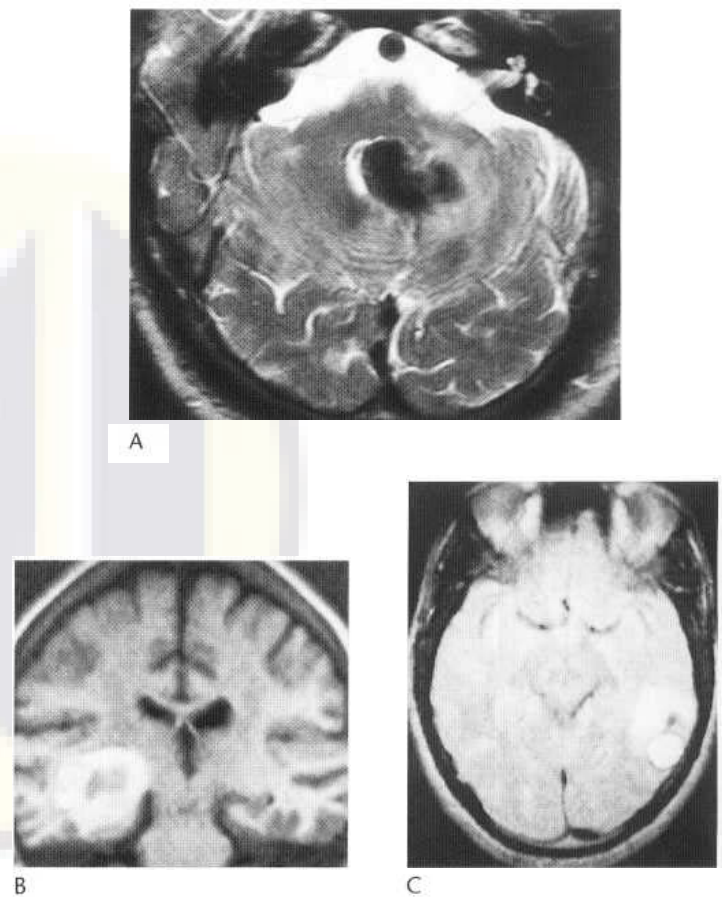


Fig. 58.4 (A) MR of subacute posterior fossa haemorrhage. T₂-weighted, and 3-4 days after onset. Low signal lesion with some marginal high signal. (B) MR T₂-weighted, and 3-4 days after onset. Low-signal lesion with some marginal high signal. (C) MR (T₂-weighted). Large haematoma in right temporal lobe 10 days after ictus. Peripheral high signal. (C) MR (T₂-weighted). Cortical haematoma at 4 weeks. Note rim of low density.

nantly T₁ proton-relaxation enhancement. The result is high signal at the periphery on both T₁- and T₂-weighted images which spreads inward over the next few days (Fig. 58.4A) until the entire haematoma becomes markedly hyperintense, which may persist for many months (Fig. 58.4B). Haematomas are commonly surrounded by a thin rim of hypointensity, best shown on T₂-weighted images, presumed to represent the predominantly T₂ proton-relaxation enhancing effect of tissue haemosiderin (Fig. 58.4C). Oedema is variable, but usually does not persist beyond 2-3 weeks. Administration of intravenous gadolinium-DTPA usually results after about 1 week in a thin rim of peripheral enhancement which persists for several weeks, similar to the enhancement rim seen on CT after administration of iodinated contrast agent. Old intracerebral haemorrhages are usually represented by a cyst or cleft-like cavity in the brain commonly associated with surrounding atrophy. The cavity contains hypointense material on T₂-weighted images, but the T₁ shortening caused by haemosiderin in the wall probably persists indefinitely.

Subarachnoid haemorrhage (SAH)

Subarachnoid haemorrhage from any cause (see Ch. 55) may be associated with a number of abnormalities on the CT scan. These include:

1. Subarachnoid blood
2. Intracerebral and/or intraventricular blood

3. Areas of infarction or ischaemia
4. Hydrocephalus
5. Demonstration of the causative lesion (aneurysm, angioma, or tumour).

1. **Extravasated blood** may be identified anywhere in the subarachnoid space from its high attenuation. It is usually confined to the basal cisterns (Fig. 58.5A). If the subarachnoid blood is localised, e.g. in the insula, this can be very helpful in identifying which of multiple aneurysms is responsible for the haemorrhage. Such extravasated blood can be demonstrated in about 90% of cases during the first 2 days after the haemorrhage, but during the second week this proportion falls to less than 40%.

2. The characteristics of **intracerebral haematomas** have been described above. The main indication that a haematoma may have arisen from a ruptured aneurysm is its situation near a typical aneurysm site. One-third of intracranial bleeds are secondary to ruptured aneurysms, and a high proportion of ruptured aneurysms (30-60% in different series) bleed into adjacent brain. CT is therefore helpful in identifying the site of the bleed if there is associated intracerebral clot.

Haematoma in the medial frontal lobes, septum pellucidum or corpus callosum can indicate an anterior cerebral artery aneurysm bleed (Fig. 58.5B,D). A middle cerebral artery aneurysm can be recognised by fresh clot in the sylvian cistern (Fig. 58.5C). Haematoma in the region of the external capsule may be hypertensive or may be from an internal carotid or middle cerebral artery aneurysm.

Thus CT can be helpful in selecting the first vessel to be examined by direct angiography. If two or more aneurysms are shown, the presence of intracerebral clot or of a low-density area representing ischaemia secondary to spasm may identify the aneurysm which has bled. Occasionally the CT scan may be positive, although the aneurysm is not shown by angiography. Conversely, if the CT study is negative soon after a presumed haemorrhage, the likelihood of showing a vascular lesion by angiography is reduced.

The presence of blood in both the cisterns and ventricles has a graver prognosis and is associated with a higher mortality. Small

amounts of intraventricular blood usually gravitate to the occipital horns, where they are readily identified.

3. **Low-density areas** representing infarcted or ischaemic brain are frequently shown. It is thought that they are related to the arterial spasm which often accompanies subarachnoid haemorrhage.

4. **Dilated ventricles** are shown in 50% of patients scanned within 48 hours of a subarachnoid haemorrhage, as communicating hydrocephalus may develop quite rapidly, due to blood clot obstructing the CSF flow. Later posthaemorrhagic hydrocephalus also occurs in up to 20% of cases: the initial examination is then of use as a baseline.

5. If the haemorrhage arises from an **aneurysm**, it is rare for the aneurysm to be visible, even after intravenous contrast medium. **Angiomas**, however, are shown before injection in more than 50% of cases, and after contrast medium in more than 90%. In the rare cases in which subarachnoid haemorrhage is a manifestation of a **tumour**, the main findings are those of the tumour itself, with an associated haematoma.

MRI MRI is less sensitive than CT in detecting subarachnoid haemorrhage within the first few days. Detection of subarachnoid blood clot depends on it yielding a relatively higher signal than the low signal of CSF: blood dispersed throughout the mobile cisternal CSF is unlikely to be detected. MRI becomes increasingly reliable at detecting subarachnoid or intraventricular clot over several days, but after the clot has liquefied and been dispersed throughout the CSF as xanthochromia there is little chance of detection, and this has usually occurred by 10-14 days. FLAIR is more sensitive than other sequences as the CSF signal may not be suppressed due to increased protein content: pathological appearances still need to be distinguished from signal variation due to CSI motion effects. Intracerebral clot adjacent to an aneurysm behaves like intracerebral haemorrhage in general.

Complications of subarachnoid haemorrhage are shown well. Hydrocephalus is best shown on T₁-weighted images, interstitial oedema of hydrocephalus and areas of cerebral ischaemia on T₂-weighted images. Delayed pial hemosiderosis after SAH can also be demonstrated as low signal on T₂-weighted images.

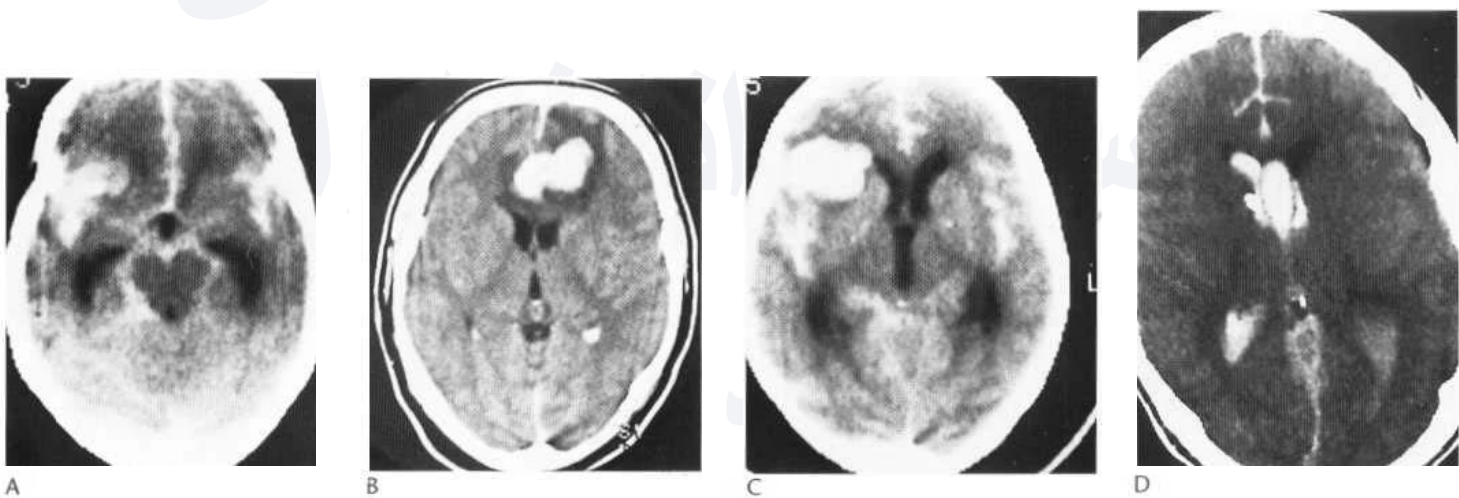


Fig. 58.5 (A) Subarachnoid haemorrhage. Congealed blood in the basal cisterns, insulae and interhemispheric cleft. (B) Clot in both frontal lobes from anterior communicating ruptured aneurysm. (C) Subarachnoid haemorrhage from right middle cerebral aneurysm. In addition to blood in the subarachnoid space, there is a local clot in the anterior part of the right insula indicating the site of the ruptured aneurysm. (D) Ruptured anterior communicating aneurysm with blood between frontal lobes, in septal cyst and in ventricles.

Superficial siderosis

This is a condition thought to be caused by continuous or intermittent, usually subclinical, subarachnoid haemorrhage. It results in haemosiderin being deposited in the pia mater and superficial cortical layers. Brainstem, cerebellum (especially the superior vermis), cranial nerves and upper spinal cord usually are mainly affected. The clinical picture generally is of a progressive neurological disorder in which ataxia and deafness are prominent features. A source of bleeding is rarely found despite extensive investigation, which can include spinal angiography. It is a chronic condition but outcomes can become fatal if a source of bleeding cannot be found and dealt with. CT may show hyperdense leptomeninges, but MRI shows the siderotic changes very clearly indeed. Atrophy supervenes in involved regions.

Aneurysms

The vast majority of cerebral aneurysms present clinically as subarachnoid haemorrhage. A smaller proportion present with oculomotor palsies or, if large and in an appropriate area, as suspected cerebral tumours. Thus a large basilar aneurysm can give rise to a brainstem syndrome and a large anterior communicating aneurysm can arouse suspicion of a suprasellar tumour.

The investigation of *subarachnoid haemorrhage* is discussed also in Chapter 55, and CT scanning is the most important primary investigation in this condition. However, if surgery is to be undertaken, some form of angiography will also be required, which is still usually intra-arterial. The **CT scan**, by demonstrating the site of the bleed, can sometimes be followed by simple unilateral carotid angiography and obviate the necessity for four-vessel angiography in a seriously ill patient. Non-invasive angiography (CT or MRI) is generally regarded as adequate in cases of only possible or doubtful SAH.

In patients with an *oculomotor palsy* the aneurysm, if large enough, will be demonstrated as a high-density suprasellar or parasellar lesion on the simple scan, and this may enhance strongly and be clearly related to the circle of Willis on the postenhancement scan (Fig. 58.6A). If the aneurysm lies within the cavernous sinus, it will only be shown if large enough to bulge the sinus. Thin

-section contrast-enhanced CT or high-resolution continuous slice MRI, MR or CT angiography, either alone or in combination, should exclude the presence of aneurysmal compression without the need for direct intra-arterial angiography.

Large aneurysms, i.e. those more than 1 cm in diameter, show well at CT scanning as high-density rounded lesions at the base of the brain. These enhance strongly and immediately after contrast medium injections (Fig. 58.6B-D). Since large aneurysms frequently contain thrombus, the enhancement may involve only part of the lesion: paradoxically, a lesion showing marked enhancement in only one portion is more likely to be an aneurysm. Occasionally they show characteristic marginal calcification.

In an appropriate situation there may be a difficult differential diagnosis to be made, e.g. a large suprasellar aneurysm (Fig. 58.6C,D) may simulate a suprasellar meningioma, craniopharyngioma, or pituitary tumour, and a large basilar aneurysm can simulate a clivus chordoma or meningioma (Fig. 58.8).

Basilar aneurysms can be fusiform or serpentine and they sometimes show peripheral increased density representing calcification or mural thrombosis.

Dynamic CT after a bolus injection has been used in some cases where there is difficulty in differentiating between basal meningiomas and a large aneurysm. The density of an aneurysm increases, then falls, with the circulating contrast medium, while that of a meningioma rises more gradually as the contrast medium leaks from the capillaries and the meningioma remains dense longer. Differentiation between meningioma and a large basal aneurysm is more simply made by MRI.

MRI Large aneurysms are shown by standard MR techniques (Fig. 58.7), commonly appearing as areas of signal void along the course of named arteries close to the circle of Willis. Giant aneurysms may be variable in appearance. They present as rounded or slightly lobular clearly extra-axial masses, although they may burrow into brain substance. They usually enclose an eccentric, circumscribed area of signal void representing the residual lumen, surrounded by regions of variable signal representing clot in different stages of organisation. The configuration of clot and residual lumen may change on serial examinations.

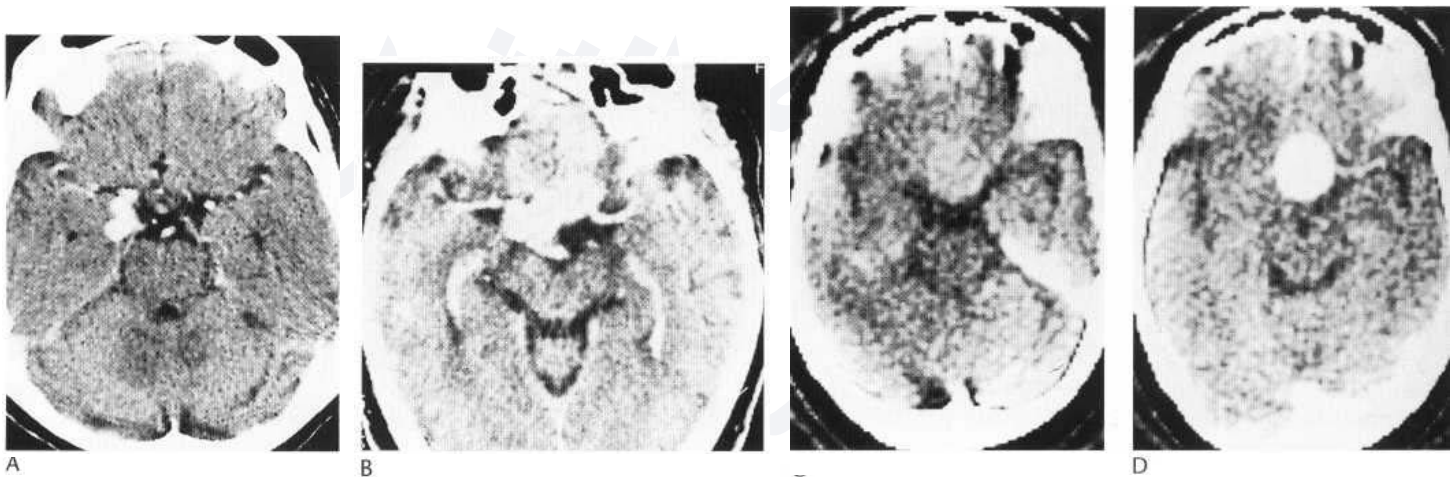


Fig. 58.6 (A) Enhanced CT shows a right posterior communicating aneurysm. (B) Large irregular suprasellar aneurysm after enhancement. (C) High-density rounded mass in suprasellar region. (D) The mass enhances strongly with contrast medium. Large aneurysm confirmed at angiography (L36, W80).

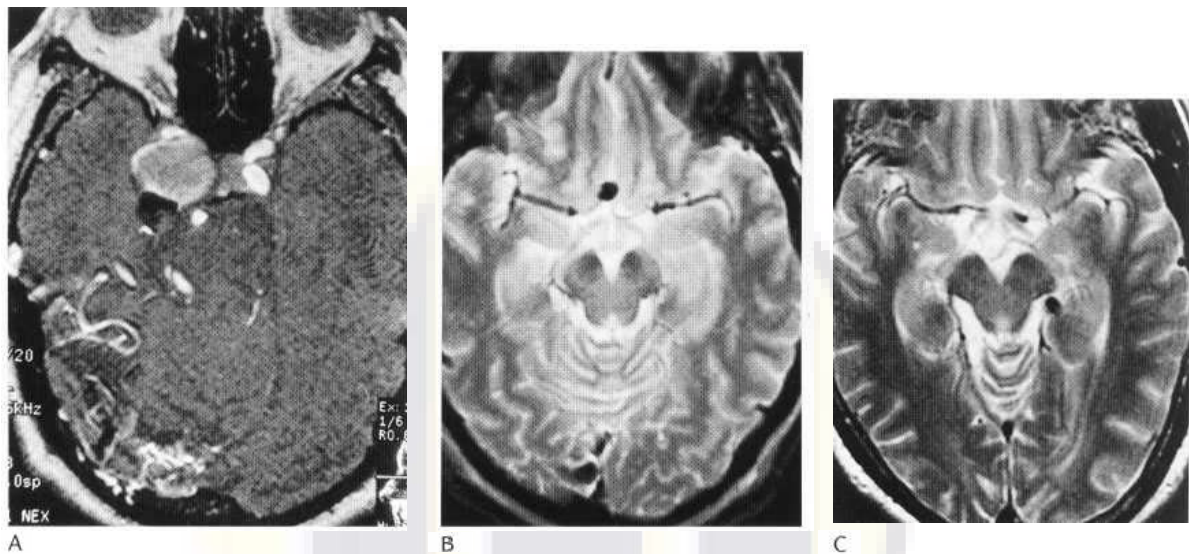


Fig. 58.7 (A) MRA axial study. Large aneurysm of the right carotid artery bifurcation is shown protruding up from the right cavernous sinus. There is also a small occipital angioma supplied by the right posterior cerebral artery. (B) Axial T₂-weighted MR image showing a small anterior communicating artery aneurysm. (C) Axial T₂-weighted MR showing a small aneurysm of the distal left posterior cerebral artery.

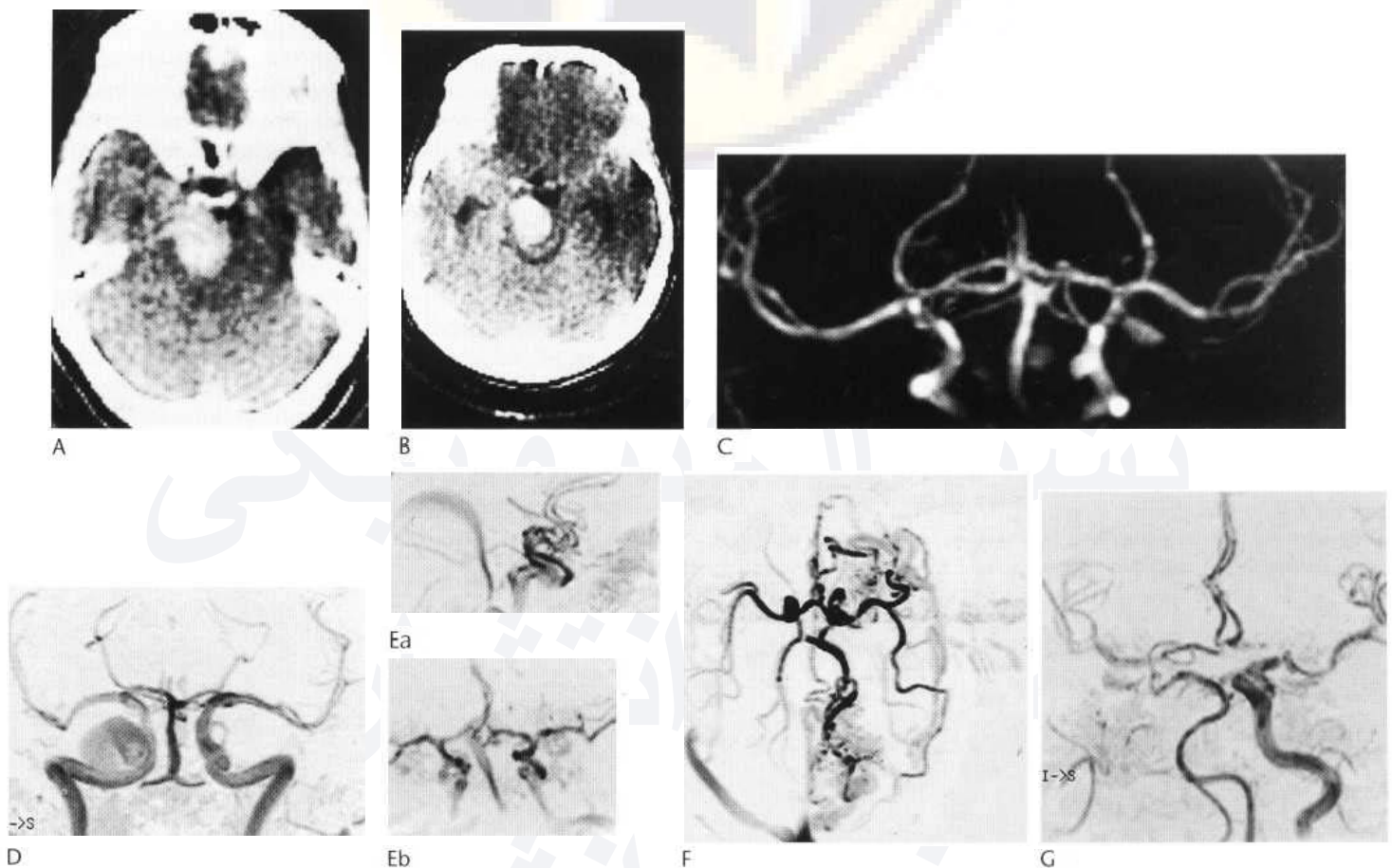


Fig. 58.8 (A,B) Basilar aneurysms confirmed at angiography. Two different patients with high-density enhancing rounded masses behind the sella and extending into brainstem. (C) MRA shows left posterior communicating aneurysm. (D) Giant right intracavernous carotid aneurysm (3D MRA, TOF). (E) Lateral (a) and (b) views of giant basilar tip aneurysm. Flow arches up and over the invisible main cavity. (F) MRA (compressed axial 3D TOF). Two angiomas, one temporo-occipital, one anterior temporal. (G) MRA (3D TOF). Occluded right internal carotid artery cross-filling from left to right.

The lumens of arteries and aneurysms do not enhance after the administration of intravenous gadolinium-DTPA, because the velocity of blood flow in arteries prevents detection of the effect of contrast medium. Occasionally, however, blood flow in an

aneurysm sac can be slow enough for some enhancement to be apparent. Nevertheless the wall of the aneurysm, and sometimes parts of organising blood clot, may enhance after intravenous gadolinium. Calcification in the wall may be apparent as a thin,

usually discontinuous, rim of signal void, but is not as reliably shown as on CT.

MR angiography (MRA) (Fig. 58.8C-G) and CT angiography (see Figs 55.55.5 and 55.6) are being used increasingly to demonstrate intracranial aneurysms, and because segmentation enables single vessels to be viewed at multiple different projections, a better demonstration of the aneurysm neck can often be obtained by these non-invasive methods than by conventional angiography. Similarly, it can be easier to distinguish possible aneurysms from loops. With non-invasive techniques being increasingly used in practice, patients are being operated on on the basis of these techniques alone without formal angiography. However, doubt about the sensitivity remains, and aneurysms below 3 or 4 mm in size may not be detected. High-quality MRA is probably good enough to exclude aneurysms which warrant consideration for prophylactic treatment, but its role as a replacement technique in subarachnoid haemorrhage is currently being established (Fig. 58.8C).

Dissecting aneurysm

This can occur in the internal carotid artery, usually in its high cervical portion, and has been discussed elsewhere (see Fig. 55.58B). The lesion may be suggested or even caused by intra-arterial angiography but is best demonstrated non-invasively by axial MR sections (Fig. 58.9A) and direct angiography should be avoided for diagnosis.

Vascular compression of cranial nerves by kinked arteries

The theory that vascular compression at the Vth nerve root exit zones can be a cause of trigeminal neuralgia was suggested by direct observations at surgery. The compression is usually due to a kinked branch of the superior cerebellar artery, and recent advances in MRA have made non-invasive confirmation possible in these cases.

It is also now well recognised that the distressing condition of hemifacial spasm can be due to kinked vessels arching into the cerebellopontine angle and impinging on the facial nerve. In the past we have demonstrated this with conventional CT (Fig. 58.9B), and the lesion can now be shown by 3D helical CT, or even more elegantly and non-invasively by 3D MRI. The arteries implicated

are either the vertebral artery, the anterior inferior cerebellar artery, or the posterior inferior cerebellar artery. Other cranial nerves which may be affected by vascular compression include the VIIIth nerve, giving rise to tinnitus and vertigo, and the IXth nerve, leading to glossopharyngeal neuralgia. Central hypertension and even non-insulin-dependent diabetes has been attributed to neurovascular compression of the medulla or vagus nerve.

Angiomas and AV fistulas

CT Angiomas or arteriovenous malformations involving the brain parenchyma or its overlying meninges may be demonstrated well by CT. A distinction must be made between those presenting with subarachnoid haemorrhage and those presenting with other symptoms.

Patients with subarachnoid haemorrhage will usually show an intracerebral haematoma recognisable by its characteristic density, and blood may also be shown in the basal cisterns, ventricles or sulci, as with a ruptured aneurysm. Direct evidence of the angioma may be seen near the site of the haemorrhage and will consist of features similar to those seen in patients without subarachnoid haemorrhage.

This latter group of patients will show no obvious lesion in 10-20% of cases; this happens where the lesion is relatively small and superficial. However, with the larger lesions the simple scan may show characteristic appearances. The most typical of these are serpiginous high-density shadows suggesting thrombosed enlarged vessels or hypertrophied veins. Calcification, characteristically ring-like or curvilinear and serpiginous, may also be shown in some cases. The exact appearance of the vessels in a large angioma will vary depending on the angle relative to the tomographic cuts. Usually tubular or vermiform shadows may be recognised when cut longitudinally, and rounded or ovoid shadows when transected.

The multiple vessels in a large lesion may give rise to a mottled appearance (Fig. 58.10). There may be low-density areas adjacent to or around the malformation, representing posthaemorrhagic cysts or ischaemic brain.

After the injection of contrast medium the appearances become more characteristic and the tortuous vascular shadows may be easily recognised. Large lesions may penetrate deeply into the brain

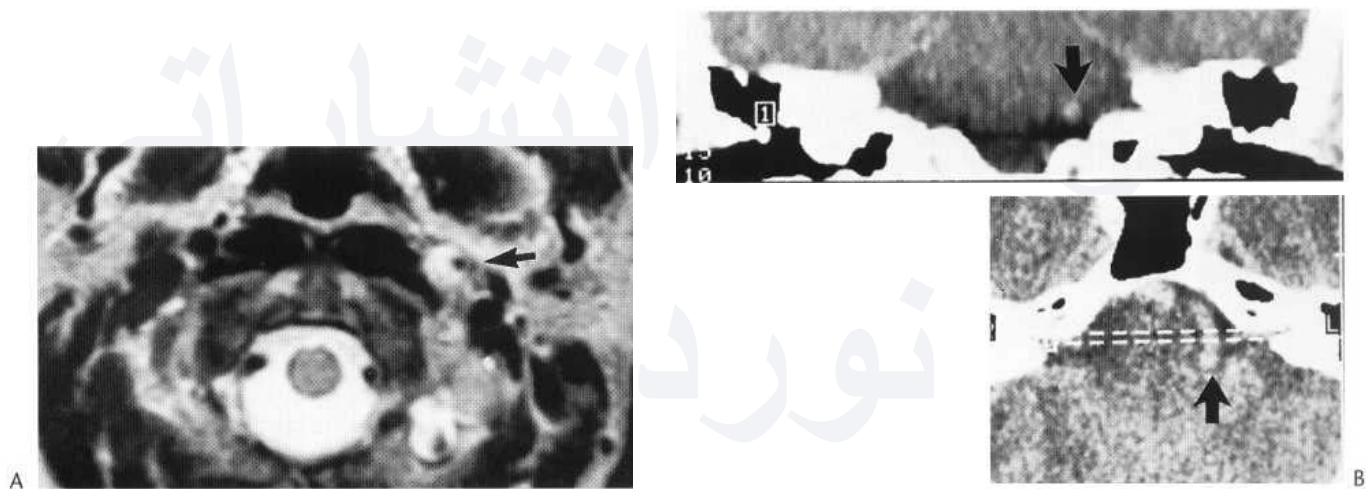


Fig. 58.9 (A) Axial MR section (T_2 -weighted) at base of skull. The right carotid and both vertebrals (lateral to the cord) show no signal due to normal flow. The dilated left internal carotid shows dissection with high signal in the false channel due to low or no flow (arrow). (B) CT with coronal reformat shows kinked vertebral artery arching high into left cerebellopontine angle (arrows) and compressing 7th nerve in a patient with facial tic.

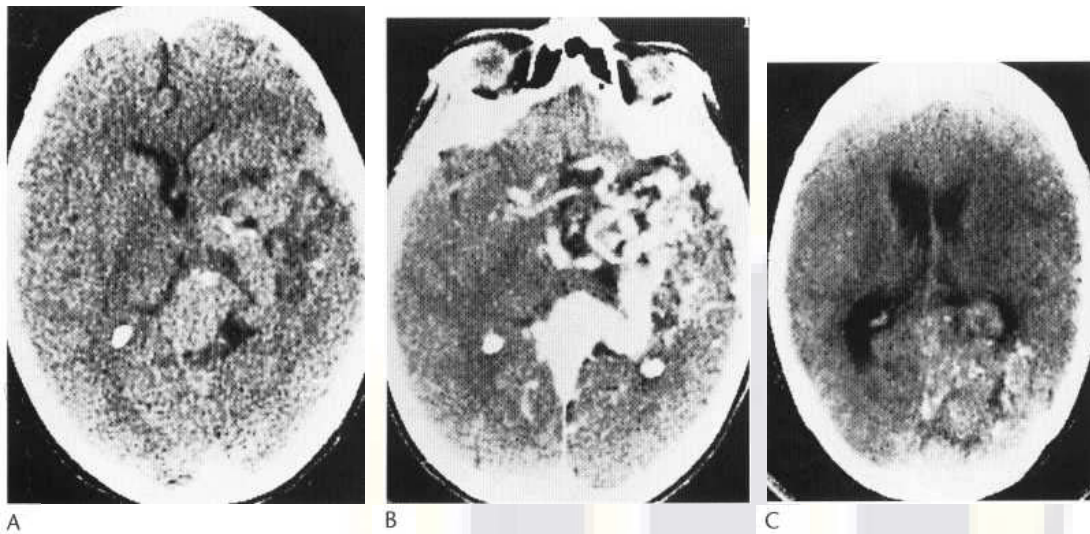


Fig. 58.10 (A) Large temporal angiomatous malformation. Note mottled appearance. The dilated vessels are of slight increased density and there are small 'cystic' and low-density areas. (B) After contrast medium, the dilated serpiginous vessels are well shown. Major drainage is to an aneurismal vein of Galen. (C) Large occipital angioma. CT shows mottled area of mixed high and low densities with flecks of calcification. (D) After enhancement multiple dilated vascular shadows are shown.

like wedges, although the majority will be superficial. Most angiomas produce little mass effect unless there has also been a large haemorrhage. Nevertheless, it is possible to mistake the appearances for gliomas or infarcts and the differential diagnosis should be borne in mind when the appearances are not characteristic.

Although the diagnosis of angioma may be certain on a CT scan, most of these cases will require angiography before surgery in order to define the exact anatomy of the feeding vessels and draining veins.

Purely dural lesions, or dural AV fistulas, are difficult to detect because of their proximity to the bony vault or base, although in a few cases enlarged drainage veins may be demonstrated (Fig. 58.11).

The rare *cavernous* type of intracerebral angioma, like a thrombosed angioma, may show clearly at CT but be invisible at angiography.

The unenhanced scan shows a hyperdense lesion 2 or 3 cm in diameter and with calcification in about 30% of cases. Unless thrombosed, or after haemorrhage, the lesions show homogeneous enhancement. When superficial they can resemble meningiomas but there is no oedema or mass effect.

MRI MR signal from *arteriovenous malformations* is variable, but it may have a punctate appearance, especially on T₁-weighted images, due to signal void in relatively large abnormal vessels.

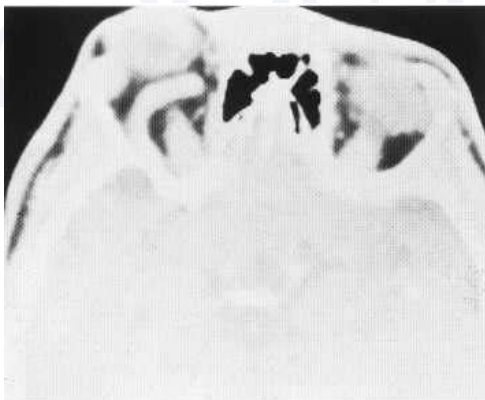


Fig. 58.11 Patient with proptosis and orbital bruit due to dural AV fistula. CT shows grossly dilated superior ophthalmic vein.

Calcification is rarely appreciable and cannot be distinguished from flow void in small vessels. Large arteries and draining veins are a particularly characteristic feature (Figs 58.12-58.14), usually shown as signal void rather than flow-related enhancement. There may be regional brain atrophy, or occasionally some local mass effect. Intracerebral haematoma may be shown in or adjacent to the malformation, usually clearly evident on MR as high signal on T₁-weighted images. Frequently there are areas of hypointensity on T₂-weighted images, indicating tissue haemosiderin. Sometimes high signal is shown extending into the adjacent brain on T₂-weighted images, probably representing ischaemic changes. Intravenous gadolinium-DTPA does not facilitate the detectability of these lesions on MR as does intravenous iodinated contrast medium on CT.

Telangiectatic and *cavernous haemangiomas* are usually shown clearly on MRI. They commonly appear as small circumscribed lesions, hypointense on T₁- and hyperintense on T₂-weighted images; the lesions generally look larger on T₂- than on T₁-weighted images or on CT. A characteristic feature is the presence of a hypointense rim of variable thickness on T₁-weighted images indicating tissue haemosiderin, which suggests that the lesion is vascular (Fig. 58.15). Calcification may not be appreciated. Sometimes areas of recent haemorrhage may be shown, or the

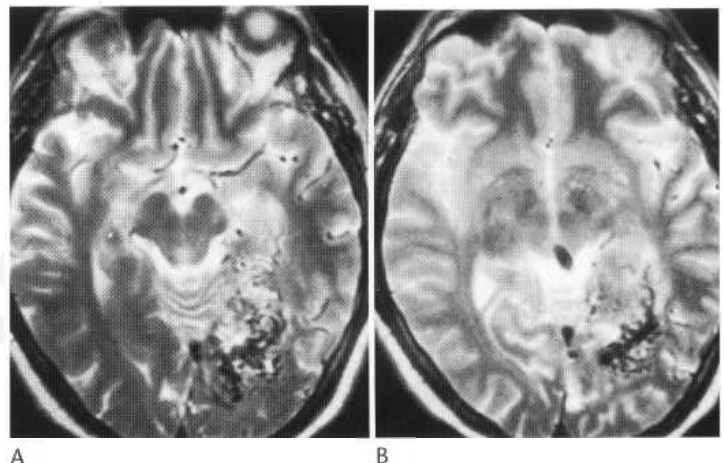


Fig. 58.12 (A,B) MR T₂-weighted image shows an angioma lying with tortuous vessels mainly in the left temporal lobe.

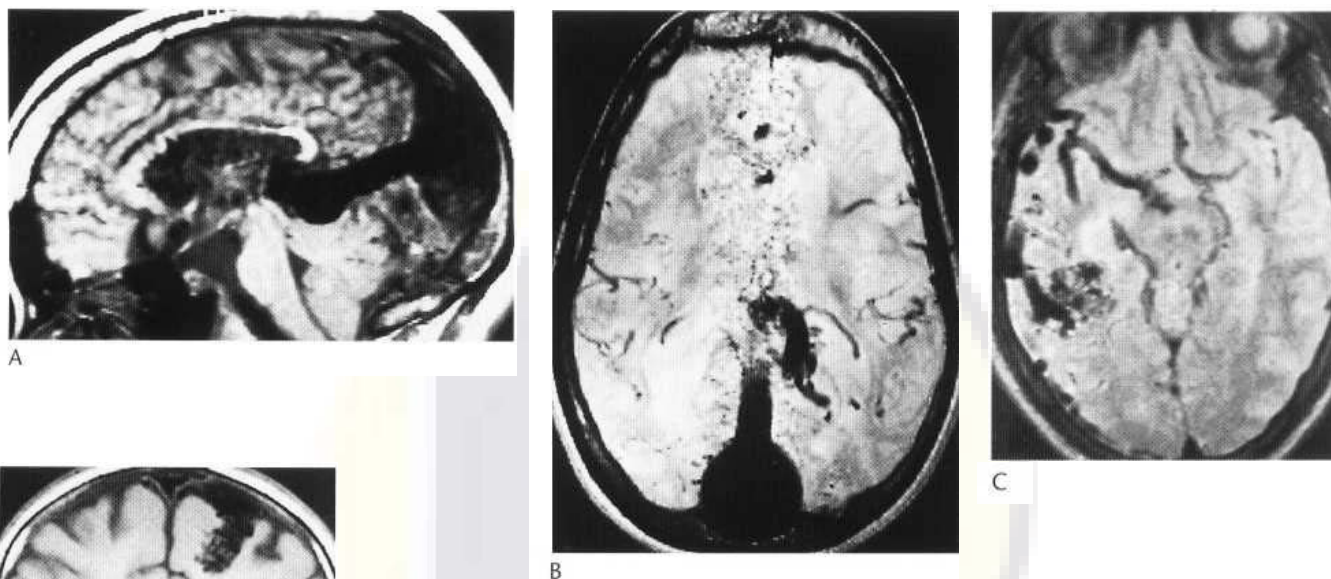


Fig. 58.13 MR study (T₁-weighted). (A) Midline sagittal section. (B) Axial section. A large complex midline angioma drains into an aneurismal vein of Galen, and there is a dilated straight sinus and aneurysmal torcular. (C) MR study (T₁-weighted). Right temporoparietal angioma supplied by hypertrophied middle cerebral artery. (D) Coronal MR study (T₁-weighted) of small left parasagittal angioma showing cone-like extension into brain.

lesion presents as an intracerebral, cerebellar or brainstem haematoma. Intracerebral cavernomas usually do not enhance after intravenous gadolinium, telangiectatic haemangiomas usually do.

Venous angiomas are simply aberrant venous drainage of one or both cerebral hemispheres. They are shown on MRI as a slightly curved linear structure traversing cerebral substance, representing a single draining vein into which numerous cerebral veins converge. They are often incidental findings, but may be associated with (parenchyma) haemorrhage or focal brain damage (Fig. 58.14C,D).

Arteriovenous fistulas occur most commonly in the dura mater, and drain extradurally via superficial veins which may be visible in the dura, orbit or scalp, usually as areas of signal void, but sluggish (low flow may result in flow-related enhancement). Occasionally, dural arteriovenous fistulas drain intradurally, and enlarged tortuous cerebral veins may then be visible. Dural sinus thrombosis may complicate these lesions and the thrombus may then be visible as high signal on T₁- and T₂-weighted images.

Occasionally, arteriovenous fistulas may occur deep within the brain and shunt into the great cerebral vein of Galen, or in infants into an embryonic vein which becomes grossly enlarged and appears as a pear-shaped area of signal void on axial T₁- and T₂-weighted images (aneurysm of the vein of Galen). Hydrocephalus and extensive ischaemic changes throughout the cerebral white matter of the brain are frequent accompanying findings (Fig. 58.13A,B).

Infarcts

Ischaemic infarction is due to interruption of the blood supply to a portion of the brain. It may be thrombotic, embolic or hypoxic but the distinction cannot be made by imaging.

CT The cardinal sign of infarction is an area of decreased attenuation within the cerebral substance. Typical locations are within

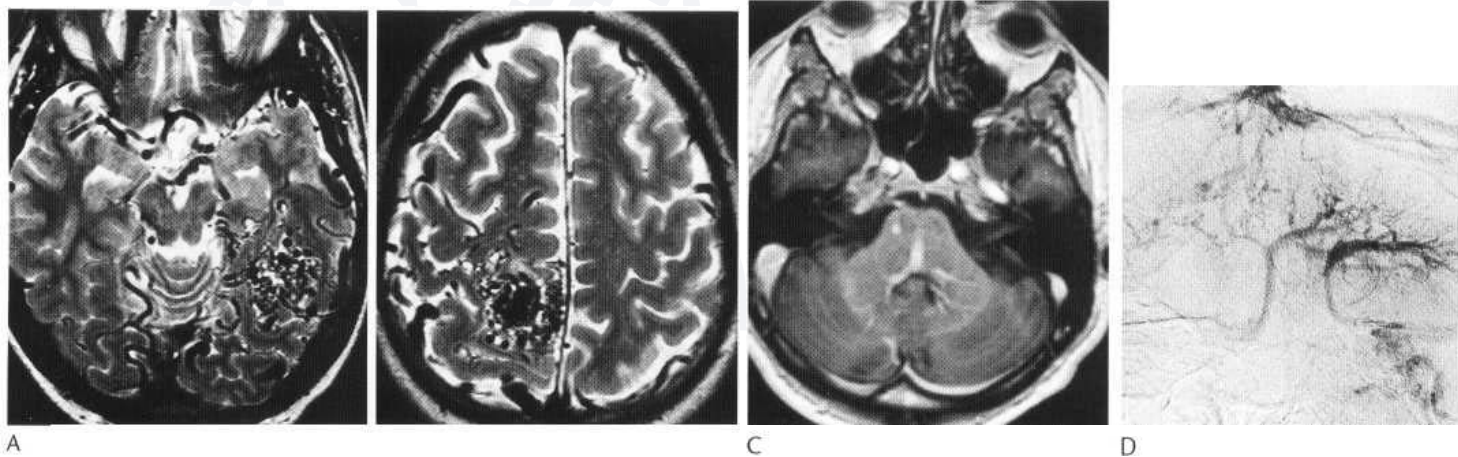


Fig. 58.14 (A,B) Extensive bilateral AVMs are demonstrated on these two axial T₂-weighted MR images. There are multiple enlarged superficial drainage veins. (C) Axial MR shows transpontine venous angioma. (D) Angiogram shows abnormal drainage veins.

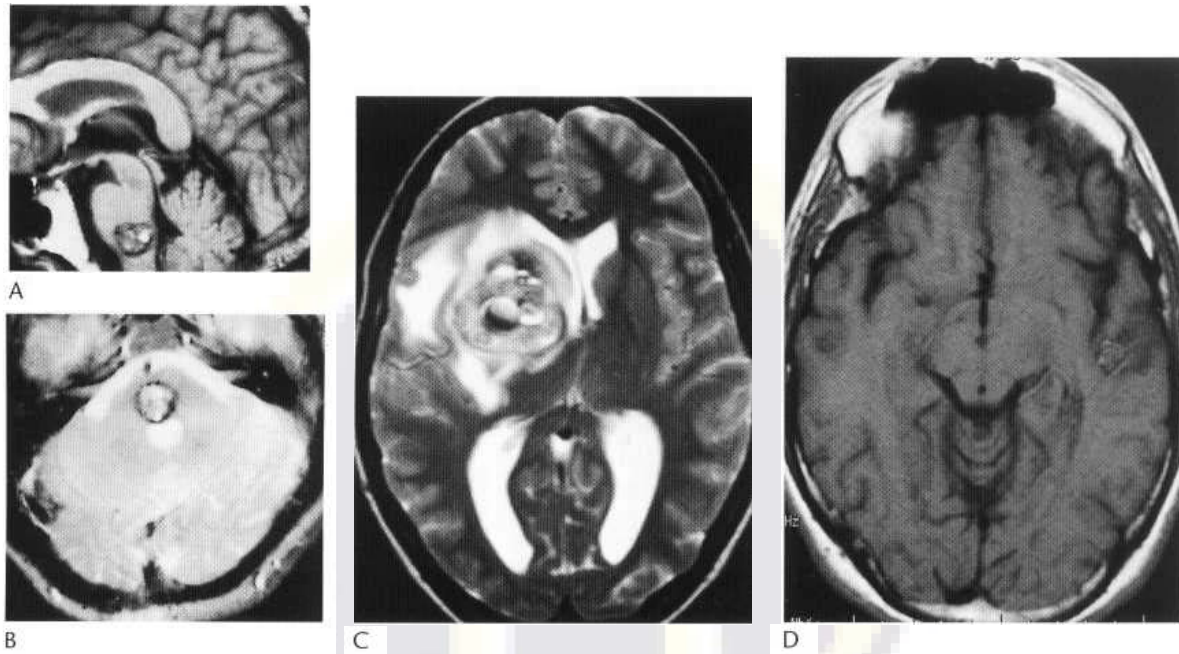


Fig. 58.15 (A) Sagittal midline MR (T1-weighted). Cavernous angioma of pons appears as in homogeneous mixed-signal lesion with peripheral low-signal halo. (B) Axial section (T1-weighted) shows the lesion equally well. (C,D) Axial MR scans T_2 -weighted show large haematoma, which showed cavernomatous features on histology, on the right frontal lobe.

the known territory of a major vessel (e.g. the middle or posterior cerebral arteries), or in the region of the basal ganglia and internal capsule. So-called watershed infarcts may be seen at the margins of a major vascular territory, e.g. the posterior frontal and parieto-occipital zones (Fig. 58.16). Infarcts are often triangular in shape, although they can appear rounded in axial cross-section. They involve both the white and superficial grey matter, whereas vasogenic oedema (around a tumour, for example) usually affects mainly the white matter.

This area of diminished density, accompanied by mild mass effect, may be seen as early as 6 hours after the onset of symptoms, but in many cases is not clearly visible during the first 24 hours,

depending on the quality of the CT images. At first the margins of the infarcted area are poorly defined, although a few infarcts are clearly margined from the outset. The density of the lesion becomes progressively lower over the succeeding weeks, until it approaches that of cerebrospinal fluid in a mature infarct (Figs 58.17-58.21). However, about 2 weeks after the onset, and

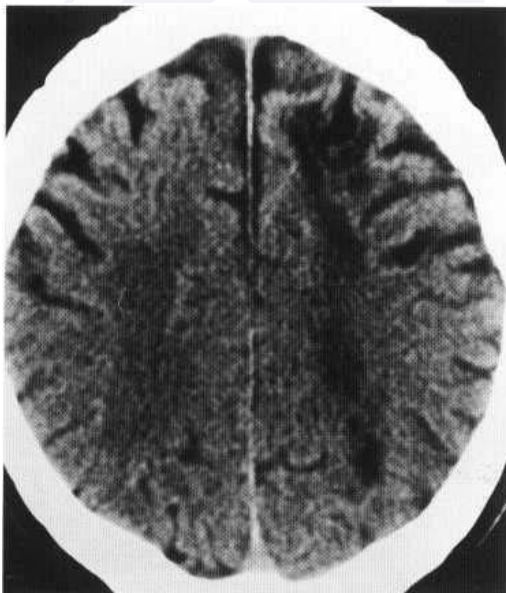


Fig. 58.16 CT shows watershed infarct at junction of LMCA and ACA territory.



Fig. 58.17 CT shows basal ganglia calcification in a child with HIV/AIDS. There are also small established vascular infarcts, the largest in the right frontal region.

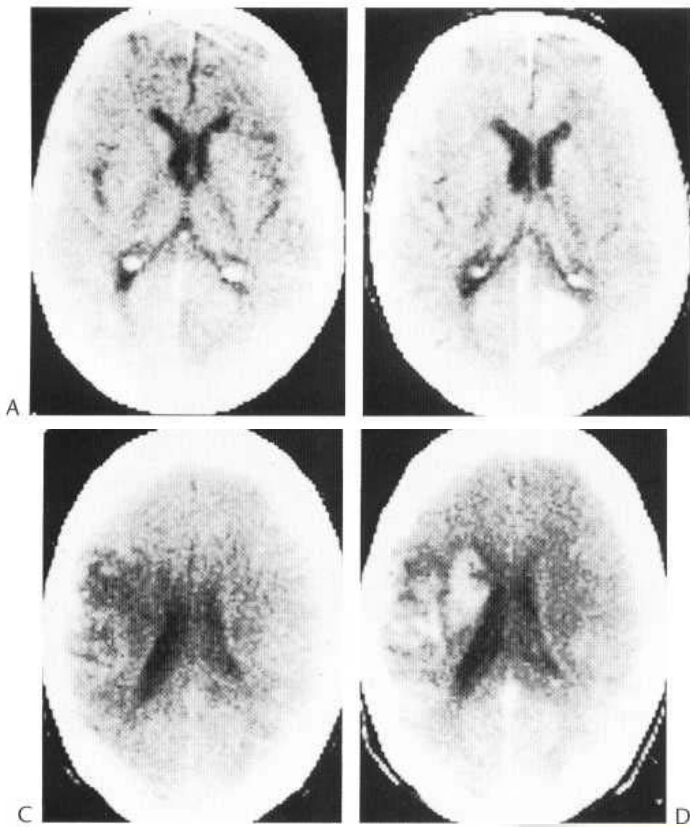


Fig. 58.18 Acute infarct. (A) Doubtful low-density in the left occipital region. No mass effect. (B) Strong enhancement with contrast medium. (C) Middle cerebral infarct. Mixed low-density and isodense lesion in right parietal region. No mass effect. (D) Patchy enhancement after contrast medium.

corresponding to a phase of resolution of oedema and of macrocytic and vascular infiltration, infarcts may be less evident than at other times. Thus some infarcts may appear isodense at about the third week. In the last week there is often some swelling of the affected part of the brain, but persistent mass effect is rare, and eventually there is loss of volume, with enlargement of the adjacent cerebrospinal fluid spaces in most cases. Complete healing is very rare.

Enhancement of an infarct may be seen after a few hours from the onset of symptoms, but is often not seen until some days have passed. Such enhancement may be around the lesion, suggesting hypervascularity of the adjacent brain, or within it, indicating a breakdown of the blood-brain barrier (Figs 58.17, 58.18). Patterns

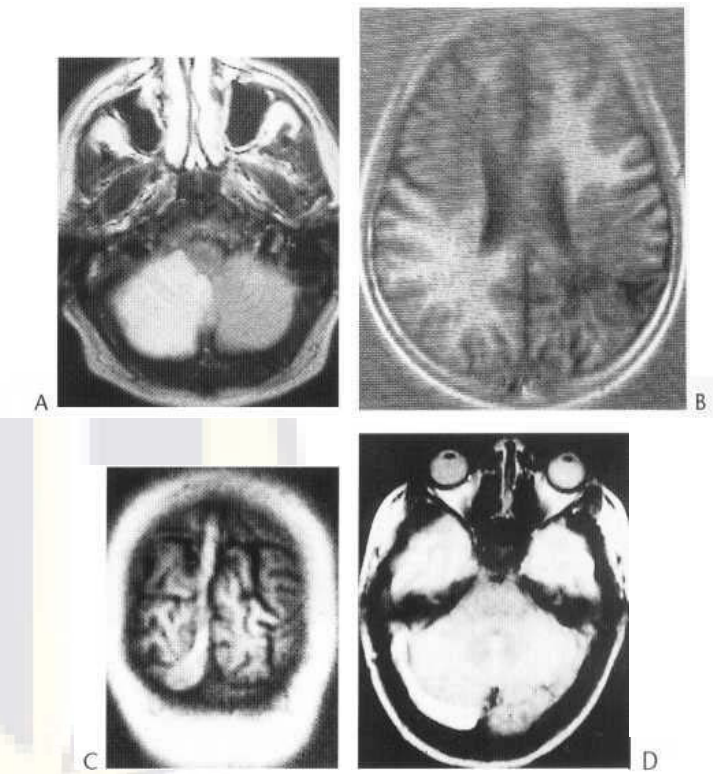


Fig. 58.19 (A,B) MR axial sections showing infarcts in two different patients (A) T₂-weighted. Right cerebellar infarct appears as high signal. (B) T₁-weighted. Large areas of low signal in both hemispheres from embolic infarcts in a patient with hypertrophic cardiomyopathy. (C,D) MR axial sections (T₁-weighted) showing high signal from sagittal and transverse sinuses which are thrombosed.

of enhancement vary widely. They include total enhancement of the infarcted area, central enhancement and ring enhancement, and such appearances can simulate a tumour or abscess. In some cases purely cortical enhancement is seen and this is more specific. There is no clear relationship between the type of enhancement and the prognosis.

It has been suggested that infarcts which flood with contrast medium will go on to marked necrosis. Since it is possible that the contrast medium may have a deleterious effect, administration in cases of obvious infarction is contraindicated. Occasionally, as noted above, enhancement may be the only definite indication of ischaemia, the infarct itself being isodense with the surrounding

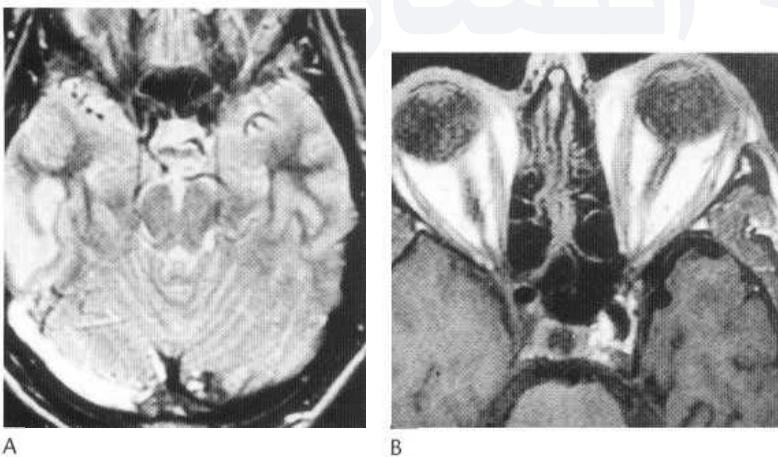


Fig. 58.20 (A) Axial section shows thrombosed right transverse sinus with evidence of venous infarcts in temporal lobe. (B) Left cavernous sinus occluded shows high signal around patent internal carotid; axial MR section shows left proptosis.



Fig. 58.21 MRA shows occlusion of left internal carotid at its origin.

brain (Fig. 58.17). Such infarction is one of the very few situations in which contrast medium injection may show previously undetected lesions. The majority of infarcts will show enhancement at some stage during the first 2 weeks though some do not (Fig. 58.19A). The proportion showing enhancement is related to the dose of contrast medium, being low with a small bolus (50 ml) but high with the large-dose technique (300 ml by drip infusion). After 6 weeks, however, persisting enhancement should suggest an alternative diagnosis, even though occasional cases are encountered with enhancement persisting at 12 weeks.

A type of infarct whose appearances differ markedly from those described above is the uncommon haemorrhagic infarct. This is commonest with a major embolus but may also be seen with patients on anticoagulants. There is patchy increased density throughout the affected region, often with some mass effect, or there may be haemorrhage at the cortical margins of the infarct (Fig. 58.19B). The ability to differentiate this type of infarct is important in its contraindication to the use of anticoagulant drugs. The CT appearances may resemble those of a haemorrhage or haemorrhagic contusion rather than a simple infarct.

Venous and sinus thrombosis, either spontaneous, or more commonly in association with an inflammatory process, may lead to infarction. In severe cases the white matter is predominantly affected and the changes are often bilateral, showing as areas of



Fig. 58.22 MRA shows atheromatous irregularity of proximal segments of carotid arteries.

diminished density. The affected cerebral hemispheres are frequently swollen and may show haemorrhages and marked contrast enhancement. Increased density of the dural sinuses or cortical veins with lack of the normal intraluminal enhancement may be detected at CT (Fig. 58.22).

Transient ischaemic attacks (TIAs)

These have been generally regarded as being due to small emboli arising from atheromatous plaques, which are most commonly situated at the origin of the internal carotid artery. The causative lesions are very well shown by angiography (see Ch. 56) and are amenable in some cases to surgical treatment. It is characteristic that the symptoms are transient unless a major stroke supervenes, and CT studies during the prodromal and TIA phase have proved focally negative in most cases. It appears that the cerebral lesion, although producing transient clinical symptoms, is not severe enough to produce detectable focal CT changes.

However, it is increasingly being realised that mechanisms in TIAs are multifactorial, and it can easily be argued that artery-to-artery embolism is an infrequent cause. Modest benefit from surgical correction of a carotid stenosis has been shown in symptomatic patients with a stenosis measuring greater than 70%. Both CT and MRI in patients with TIAs show diffuse, rather non-specific, ischaemic abnormalities in up to 40% of cases, often in basal ganglia and white matter, and their relevance to the clinical symptoms is speculative.

MRI T₁ and T₂ are prolonged in infarcted and severely ischaemic tissue. This may be detectable a few hours after onset but is usually not shown until after 1-2 days. Infarcts commonly seem more extensive than on CT (Fig. 58.23A,B), although changes with time are less conspicuous so their age can be more difficult to estimate. Moreover MRI may be less sensitive than CT at detecting areas of haemorrhage within the first few days. Most cerebral infarcts show enhancement with gadolinium-DTPA towards the end of the first week, although earlier enhancement has been observed.

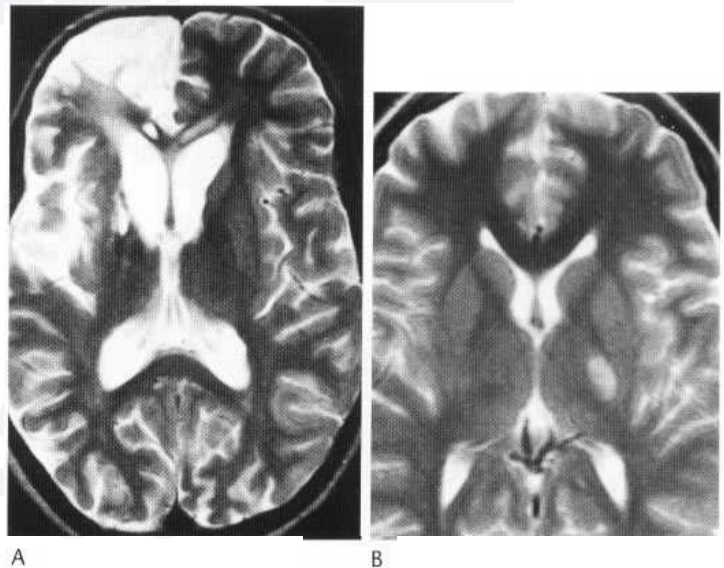


Fig 58.23 (A) Axial MR T₁ weighted child with AIDS mature right ACA and right MCA territory infarcts show as high-signal. (B) Axial MR T₂

increased signal.

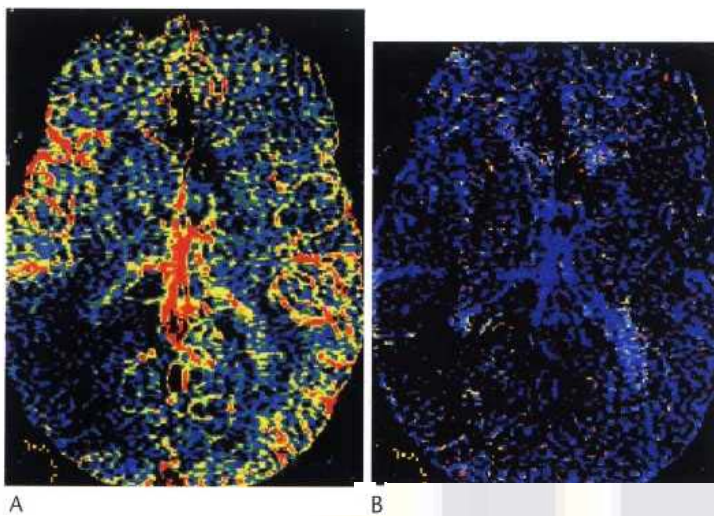


Fig. 58.24 (A,B) Perfusion MR. Occlusion of right internal carotid artery.

Sometimes an occluded artery is visible on MRt. Arteries normally show signal void, and the presence of signal from within the lumen of an artery suggests that it is thrombosed or has pathologically slow flow, due either to proximal severe stenosis or occlusion more distally.

Chronic ischaemic change in the white matter is seen in over 50% of patients over the age of 60 years. This is usually shown as areas of multifocal or confluent signal change in the cerebral white matter. CT is much less sensitive than MRI at detecting these changes. Only large areas of signal change have corresponded to areas of macroscopic cerebral softening. The smaller areas, and especially those close to the lateral ventricles, have been associated with textural changes in the tissue accompanied by a reactive astrogliosis presumed to be of ischaemic origin. The clinical significance of these lesions with regard to both pathogenesis and their relation to transient ischaemic attacks, stroke and dementia has yet to be adequately elucidated.

Diffusion MRI now enjoys considerable clinical use, especially in recognising infarction, the first 3 days or so. In this period diffusion is restricted, so that the area yields high signal on diffusion weighted images and low signal on apparent diffusion coefficient maps (ADC maps) (Fig. 58.24). This reverts to increased diffusion over time to variable degrees. Perfusion imaging often shows a larger area of reduced regional blood flow than indicated by spin-echo and diffusion weighted MRI; the area of perfusion-diffusion,

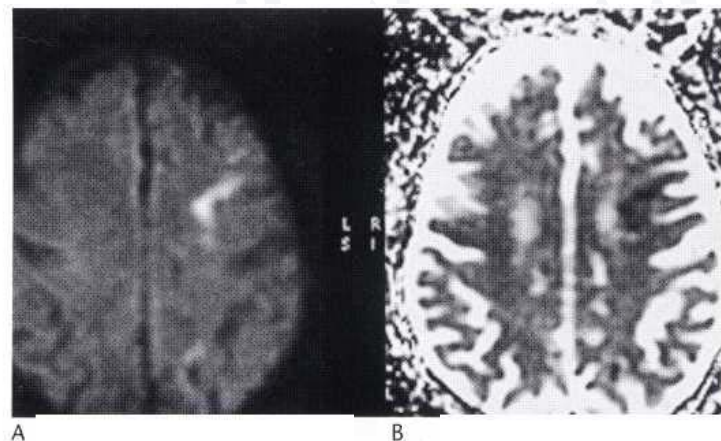


Fig. 58.25 Diffusion MR shows recent small left frontal cortical infarct.

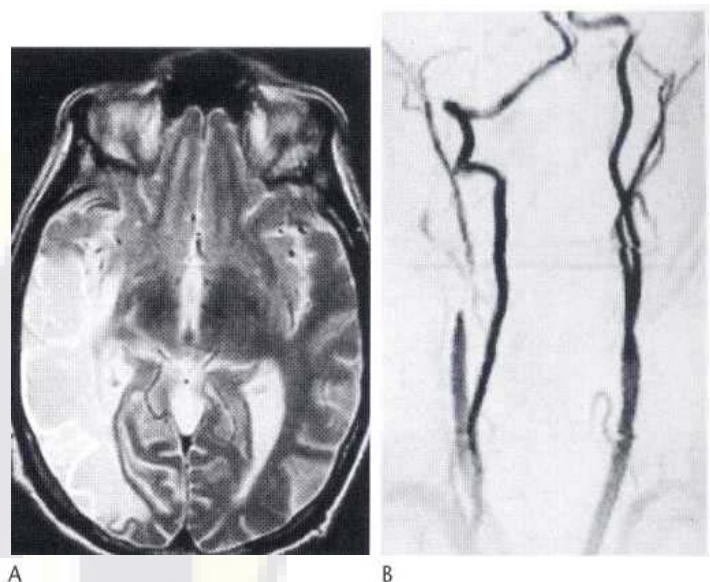


Fig. 58.26 (A) MRI shows large area of right hemisphere with high signal. (B) MRA shows occlusion of right internal carotid artery.

mismatch, as it is often called, is believed to be the ischaemic penumbra of potentially salvageable but at risk tissue (Figs 58.25, 58.26).

Venous infarction in brain substance appears similar to arterial infarction although it is not confined to arterial supply territories. It is commonly haemorrhagic but this may not be apparent on MR images within the first few days. Bilateral involvement is also relatively characteristic when present. It may be possible to diagnose the condition directly by recognizing signal changes in the dural sinuses and larger cerebral veins. In general, signal from within the lumen of the thrombosed vein is higher than expected, and higher than normal veins in the vicinity.

Hypoxic ischaemic brain damage

Global hypoxia, hypotension or hypoglycaemia can damage the whole brain, usually but not always symmetrically. It is seen most often in the newborn. Two patterns are recognisable in the newborn on CT and MRI: *acute asphyxia* for more than 6 minutes results in signal changes in the thalami (not basal ganglia) and sometimes also the peri-Rolandic regions of the cerebral hemispheres; *partial asphyxia* (hypoxic ischaemic brain damage) results in periventricular leucomalacia in premature infants and more peripheral cortical watershed infarcts in full-term infants. In adults, patterns vary from total cerebral infarction to predominantly white matter infarction, cortical watershed or white matter terminal zone infarction, basal ganglia infarcts (especially globus pallidus), and pure cortical damage in cerebral hemisphere or cerebellum such as in severe hypoglycaemia. Severe clinical disability can occur with little or no changes on CT or MR.

TRAUMA

Cranial trauma is a major problem in accident and emergency departments and in one series provided 10% of the patients seen. It is also responsible for 150 000 hospital admissions per year in the UK.

It is not necessary for every patient who suffers a head injury to undergo a CT scan. In the acute phase, the indications are deteriora-

tion of the patient's conscious level, with or without focal neurological signs. Sedation and/or general anaesthesia should be employed without hesitation when indicated, since the recently traumatised patient may be very restless.

CT in acute trauma

Extradural haematomas These are seen as biconvex high-density areas immediately subjacent to the vault (Fig. 58.27A). They are most frequent in the frontoparietal regions, but may occur in the posterior fossa, when they are particularly likely to be missed if the CT scan is of poor quality. Occasionally less dense areas appear within them, perhaps due to unclotted blood, and if they should recur after surgery the classic shape may be lost. The lateral ventricles are characteristically displaced to the contralateral side, and there is usually some swelling of the affected cerebral hemisphere, although obvious oedema may not be apparent.

Subdural haematomas The appearances vary considerably depending mainly on age. The acute subdural haematoma, i.e. within 48 hours of the injury, can sometimes closely resemble the acute extradural lesion, but is more frequently concavoconvex, spreading over the surface of the cerebral hemisphere (Fig. 58.27B). In the acute stage, the haematoma is usually of high density, often situated in the frontoparietal regions or middle cranial fossa, and associated with ipsilateral brain swelling.

Subdural collections are generally of higher attenuation than brain for about 2 weeks, and after 3-4 weeks are of lower attenuation, eventually approaching that of CSF (Figs 58.28, 58.29).

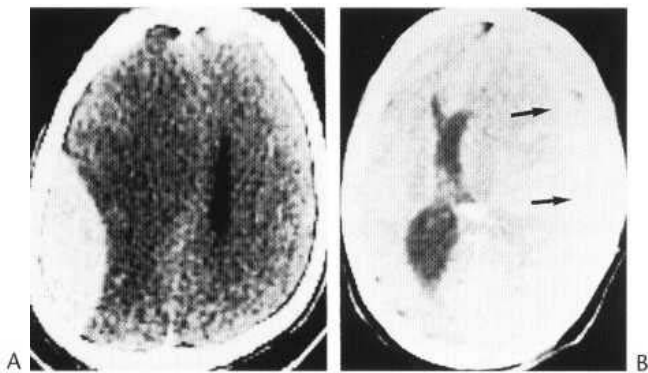


Fig. 58.27 (A) Acute extradural haematoma. High-density biconvex mass in right occipitoparietal region with mass effect following trauma (L34, W75). (B) Acute subdural haematoma. Superficial high-density concavoconvex lesion (arrows) with marked mass effect.



Fig. 58.28 Subdural haematoma 3 weeks after onset. The clot is largely absorbed and the subdural fluid is now of low density.



Fig. 58.29 Bilateral subdural as a complication of shunt operation.

Between 2 and 4 weeks after injury, however, they pass through a stage when they are isodense with the underlying brain. **Isodense haematomas** (Fig. 58.30) can present major problems in diagnosis, as the lesion is not directly visible, and it may be necessary to rely on indirect signs. The problem was most marked with older scanners but is still occasionally seen with modern scanners, particularly with uncooperative patients. The indirect signs include ventricular or pineal displacement, and absence of visible sulci on the affected side; the former sign will, however, be absent in the not uncommon case of bilateral lesions. Squeezing together of the frontal horns, to give a 'rabbit's ears' appearance, and effacement of the basal cisterns may suggest the diagnosis when bilateral isodense lesions are present. Intravenous iodinated contrast medium may help by causing enhancement of the capsule of such haematomas but this is not invariable. With high doses of contrast medium, however, isodense subdurals can be identified because the surface of the brain is usually clearly outlined (Fig. 58.30B). Subdural haematomas of mixed density, probably indicating fresh bleeding into a chronic lesion, may be seen. With the patient in the supine position, the denser blood tends to sink to the posterior, dependent portion of the lesion, giving rise to a fluid level.

Very longstanding chronic subdural haematomas are invariably of low attenuation. They may be associated with atrophy of the underlying brain and occasionally with expansion and thinning of the skull vault. They should not be confused with cases of post-

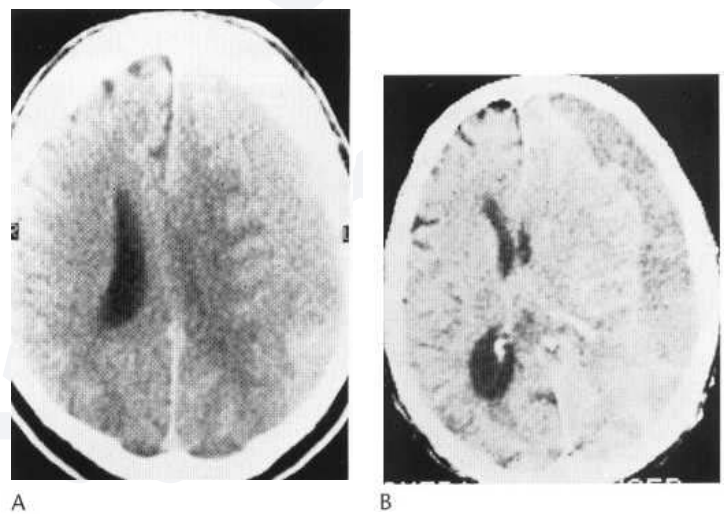


Fig. 58.30 (A) Isodense subdural. Note mass effect and effacement of sulci which suggest diagnosis prior to contrast medium. (B) Post-enhancement scan of another isodense subdural. The lesion stands out against the enhanced surface of the brain.

traumatic hemiatrophy, in which the affected hemicranium is the smaller.

CT scanning is invaluable in the management and follow-up of both extra- and subdural haematomas, since it permits the detection of residual or recurrent lesions, of undiagnosed contralateral haematomas, or the presence of infection. Infection may be suggested by loculation of air within the haematoma cavity, by increase in density of the fluid contents, and by marked enhancement of the capsule.

Calcification of the capsule may occur in chronic lesions, without or without complications such as infection.

Subdural collections also are well shown by MRI, and FLAIR may occasionally be helpful in distinguishing chronic subdural collections from wide subarachnoid spaces. On coronal images, subdural collections exhibit a biconvex shape, like extradural collections.

CT is also invaluable in the diagnosis and management of extracerebral fluid collections which may occur as a complication of neurosurgery (Fig. 58.29).

Traumatic intracerebral haematomas It may be impossible to distinguish these from spontaneous intracerebral haemorrhage, and in this context even the history may be unhelpful. The frontal and temporal lobes are classic sites, which are less commonly affected by spontaneous episodes (Fig. 58.31 A). Both types are of high density, but traumatic bleeding is more frequently multifocal and in cases with a poor prognosis may be seen to involve the

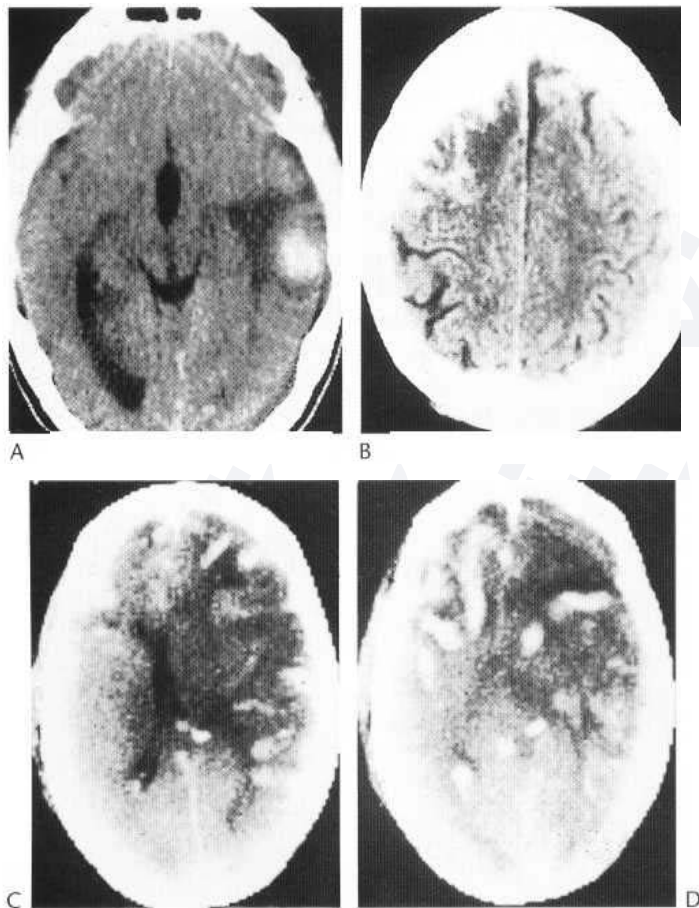


Fig. 58.31 (A) Subcortical traumatic haematoma. (B) Haemorrhagic contusions in right frontal region. (C-D) Multifocal haemorrhages and contusions in both hemispheres.

brainstem. It is also more commonly associated with low-density areas and brain swelling, even in the acute stages. The blood may extend to the ventricles or the subarachnoid space. Purely intraventricular haemorrhage is uncommon as a result of trauma. Subarachnoid haemorrhage is, however, relatively frequent, although often overlooked. It is commonly manifest as a line of high attenuation alongside the falx, especially posteriorly.

Retrobulbar or subperiosteal orbital haematomas are readily diagnosed in the context of head trauma as high-density lesions within the orbits or applied to the bone. Without a history of head injury, the differential diagnosis is that of a retrobulbar mass.

It is also possible to demonstrate soft-tissue extracranial haemorrhage in the acute stage.

Cerebral contusion and oedema Two types of cerebral contusion may be detected by CT scanning: haemorrhagic and non-haemorrhagic. The latter may be impossible to distinguish from focal cerebral oedema due to other causes.

Haemorrhagic contusion (Fig. 58.31 B-D) is commonly seen in the frontal and temporal lobes, although any part of the cerebrum, cerebellum or brainstem may be affected. It appears as a mass lesion of mixed high and low density not dissimilar to multifocal traumatic haemorrhage, but generally more diffuse—the area of swelling may be very extensive. The haemorrhagic areas may not be evident in the very acute stage, occurring only 24 hours or more later.

Non-haemorrhagic contusion (Fig. 58.32A,B) cannot reliably be distinguished from cerebral oedema, but tends to be more focal and space-occupying. Considerable enhancement may be seen with intravenous contrast medium; this does not occur with oedema.

Diffuse brain damage About 50% of patients who suffer immediate prolonged unconsciousness following a head injury have no obvious mass or focal lesions of the types just described; this is true of about one-third of fatal cases. In these patients the lesions present have been classified into four types:

1. Multiple petechial haemorrhages
2. Diffuse axonal injury
3. Brain swelling
4. Hypoxic brain damage.

Multiple petechial haemorrhages This type of injury is seen throughout the white matter and brainstem and is rapidly fatal. It is therefore more likely to be seen at postmortem than in an imaging department.

Diffuse axonal injury (white matter shearing) This severe injury may show virtually no macroscopic change in the affected brain. There is disruption of axons in the subcortical parasagittal white matter and in various other sites, including the internal and external capsules, fornix and cerebellum. It is claimed to result from acute lateral acceleration or deceleration of the brain within the rigid cranium and can occur without anything actually striking the head. It occurs most commonly in automobile accidents.

The patient is unconscious from the moment of impact and remains unconscious, vegetative or severely disabled until death. Despite the severe brain damage and the very grave state of the patient there may be little or nothing shown at imaging.

Small focal haemorrhages have been described in the corpus callosum and in the posterolateral quadrant of the rostral brainstem and such lesions could theoretically be demonstrated, as can small

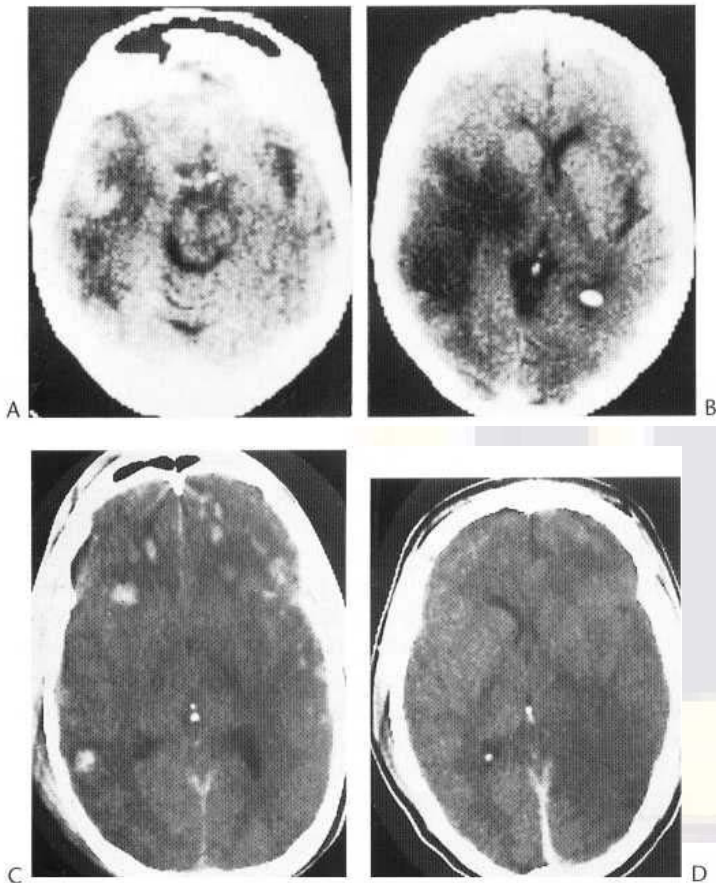


Fig. 58.32 (A,B) Cerebral trauma. Contusions in left temporal lobe. (C) Subcortical small haemorrhages associated with shearing injury, and a few large haemorrhages. (D) Head injury in a child. There is cerebral oedema mainly on the right, associated with compression of the ventricles and some shift to the right.

subcortical haemorrhages (Fig. 58.32C). Susceptibility weighted (T2*) MRI is most sensitive at detecting haemorrhage, including old haemorrhage.

Brain swelling Diffuse swelling of the entire brain occurs mainly in children and adolescents. The pathogenesis is debated and it is thought to be due to vasodilatation and increased cerebral blood volume in the first place. This is recoverable, but if it persists for any length of time true oedema may follow.

Diffuse swelling of the ipsilateral hemisphere can also occur with local and mass lesions described above, including acute subdural haematoma and extensive unilateral contusions. Focal oedema may also occur with haemorrhages and contusions.

With diffuse bilateral swelling the ventricles are compressed and appear small, like slits, at imaging; the basal cisterns may be occluded and the sulci effaced. The white matter shows no reduction in density and appears normal at CT, although evidence of oedema may be seen in cases with prolonged coma (Fig. 58.32D).

Hypoxic damage This is due either to a prolonged drop in systolic blood pressure, or to arterial spasm, or to both. Evidence of hypoxic damage is seen in the first place at major arterial boundary zones, and frank infarction may later ensue.

Hypoxia and subsequent infarction may also result from brain swelling and tentorial herniation compromising the posterior cerebral circulation, or from trauma to major vessels. Imaging may

show little in the early stages but later will demonstrate evidence of infarction.

Skull fractures Fractures are, in most instances, best diagnosed by a combination of clinical features and plain radiography. However, basal fractures, which are often difficult to demonstrate or to assess fully by these means, may be shown very clearly by CT scanning.

Depressed fractures can be clearly demonstrated and their relationship to the underlying brain better shown than by plain X-ray films (Fig. 58.33A,B). However, the chief value of the CT scan is in the assessment of underlying brain damage and haematoma formation.

Intracranial air Whether subdural or subarachnoid, air is well shown by CT and implies a dural tear communicating with a sinus or other air-containing cavity. Intracerebral air (aerococle) is also well shown and its site of origin can be identified prior to surgery (Fig. 58.33C,D).

Foreign bodies Intracranial foreign bodies may be accurately localised by CT scanning. The value of the technique is in the demonstration of the position of the foreign body relative to, and

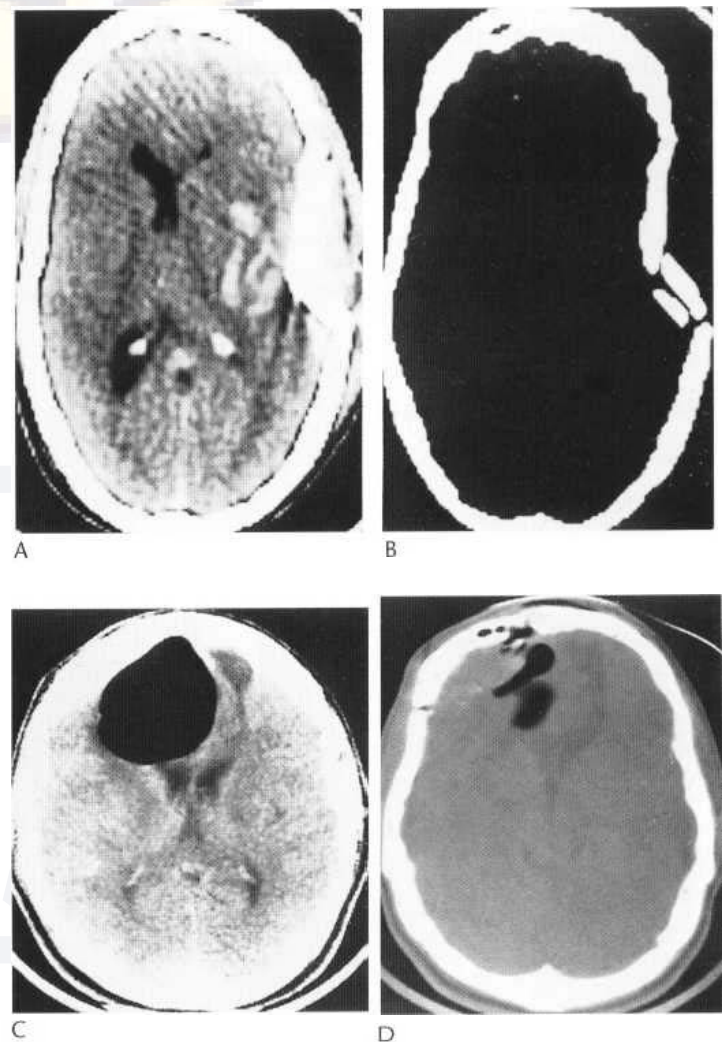


Fig. 58.33 (A) Depressed fracture in the left temporal region with underlying haemorrhagic contusions (134, W75). (B) Same case at higher level (L) to show bone detail (L128, W75). (C) Frontal aerococle. (D) Bone window film showing frontal fracture and connection with top of frontal sinus.

its effects on, the intracranial structures, features which cannot be seen on plain radiographs. Good demonstration of the relationships of metallic objects may, however, be prevented by the resulting artefacts. Wooden fragments may appear less dense than brain.

MRI in acute trauma

Cerebral contusions These appear on MRI as regions of poor grey/white matter discrimination on T₁-weighted images and as ill-defined areas of hyperintensity on T₂-weighted images, changes which become apparent within a few hours of injury. Haemorrhagic contusion may not be recognised as such within the first few days of injury, and traumatic intracerebral haematomas, which can appear a few days after the traumatic event, may also not be easily detected initially. The amount of mass from the cerebral contusion, and the size of any associated haemorrhages, tend to increase in the first few days and subsequently diminish. CT may be better at recognising haemorrhages in the first few days.

Generalised brain swelling and hemispheric swelling, which occurs particularly in children, are not necessarily associated with any signal changes in the brain, and diagnosis can be difficult. The ventricles are small but this does not necessarily mean brain swelling. The cisterns around the brainstem may also be obliterated; this is perhaps a better guide. Such changes are best detected on T₂-weighted spin-echo images.

Extracerebral haematomas MRI is superior to CT at demonstrating extracerebral fluid collections. Although initially the extracerebral collection may be isointense with adjacent brain, the displaced cortex is usually clearly evident, especially on axial or coronal images (Fig. 58.34). The extracerebral collection becomes progressively more hyperintense on T₁-weighted images, which increases its conspicuity.

Post-traumatic sequelae

These may include:

1. Cerebral infarction
2. Cerebral atrophy
3. Hydrocephalus

4. Infection
5. Aerocele
6. CSF fistula.

1. **Cerebral infarction.** Vascular occlusion or spasm caused by trauma to the head or neck may cause cerebral infarction, the appearances of which are indistinguishable from those of cerebral infarction arising from thromboembolic lesions. Infarction can on rare occasions follow some weeks or months after trauma to the great vessels of the neck.

2. **post-traumatic atroph.** This can be focal or generalised. It may clearly reflect cerebral infarction, affecting a known vascular territory, or affect one cerebral hemisphere. If the latter occurs in infancy or childhood or from perinatal trauma, the whole hemisphere may be underdeveloped. The appearances are those of cerebral atrophy. There is enlargement of the fissures and sulci and ventricular dilatation. Porencephalic cyst cavities may be present, whose communication with the ventricular system may or may not be obvious (Fig. 58.35).

3. **Hydrocephalus.** Ventricular enlargement commonly occurs in the subacute phase after head trauma. It may then resolve or become progressive and symptomatic. In the early stages, development of hydrocephalus may be difficult to distinguish from resolution of generalised cerebral swelling. Enlargement of the temporal horns strongly suggests the former, but further follow-up is indicated.



Fig. 58.35 Post-traumatic porencephalic cyst or encephalomalacia. Large cortical and subcortical defect in the left frontal region several years after a severe head injury.

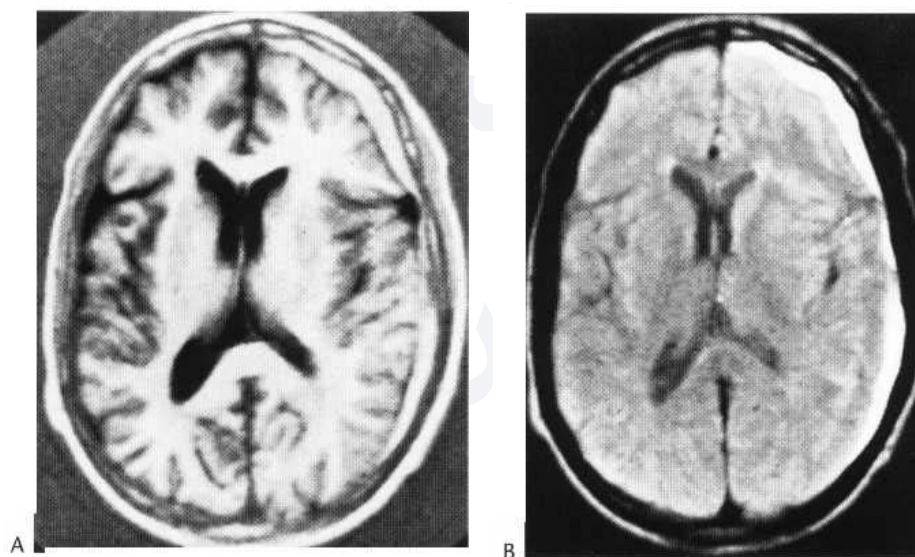


Fig. 58.34 Subdural haematoma shown by MR (T₁-weighted) as high signal overlying left hemisphere. (A) IR 1400/400 (B) SE 1400/40 (Courtesy of Dr Graeme Bydder).

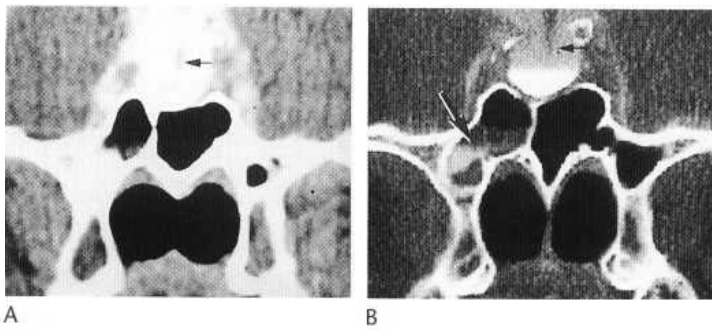


Fig. 58.36 CSF fistula. CT cisternography. Direct corona) sections with patient prone. Soft tissue (A) and bone (B) window. Contrast medium has entered an empty sella. Pituitary stalk is arrowed. Bone window shows level of contrast fluid in the sphenoid sinus on the left.

4. *Infection* may follow penetrating injury or fractures involving air cavities.

5. *Aerocele* has been mentioned above and may require urgent treatment, as there may be progressive enlargement causing further damage to the compromised brain (Fig. 58.33C,D).

6. *CSF fistulas* resulting from basal fracture are notoriously difficult to localise and may require CT cisternography (Fig. 58.36) or radionuclide cisternography (see below).

INFECTIONS

Cerebritis and abscess

Abscesses may be pyogenic, tuberculous, fungal, or parasitic. *Pyogenic abscesses* are the most frequently encountered in clinical practice, and due to improvements in diagnosis and treatment of bacterial abscesses the mortality rate has fallen to approximately 14%. Although cerebral abscesses may occur at any age, they are most common in the first four decades of life and males are more commonly affected than females. They are either secondary to local or haematogenous spread, resulting from cardiac, paranasal sinus or aural disease, but may occur as a result of suppurative chest diseases such as bronchiectasis, lung abscesses or operations. Intravenous drug users also have an increased incidence of cerebral abscesses, as do immunocompromised patients.

Cerebritis and abscesses may occur anywhere in the brain and the subdural space may also become involved. The temporal lobe and cerebellum are commonly affected as a result of suppurative otitis media or mastoiditis and implicated organisms include *Bacteroides* and *Streptococcus*. Septic thrombophlebitis of the draining emissary veins may also result in abscess formation. Bilateral frontal abscesses clearly implicate the frontal sinuses or face and scalp as a source of infection. Untreated dural tears involving the anterior cranial fossa may also result in frontal abscesses and here the implicated organisms are most commonly *Strepto-*

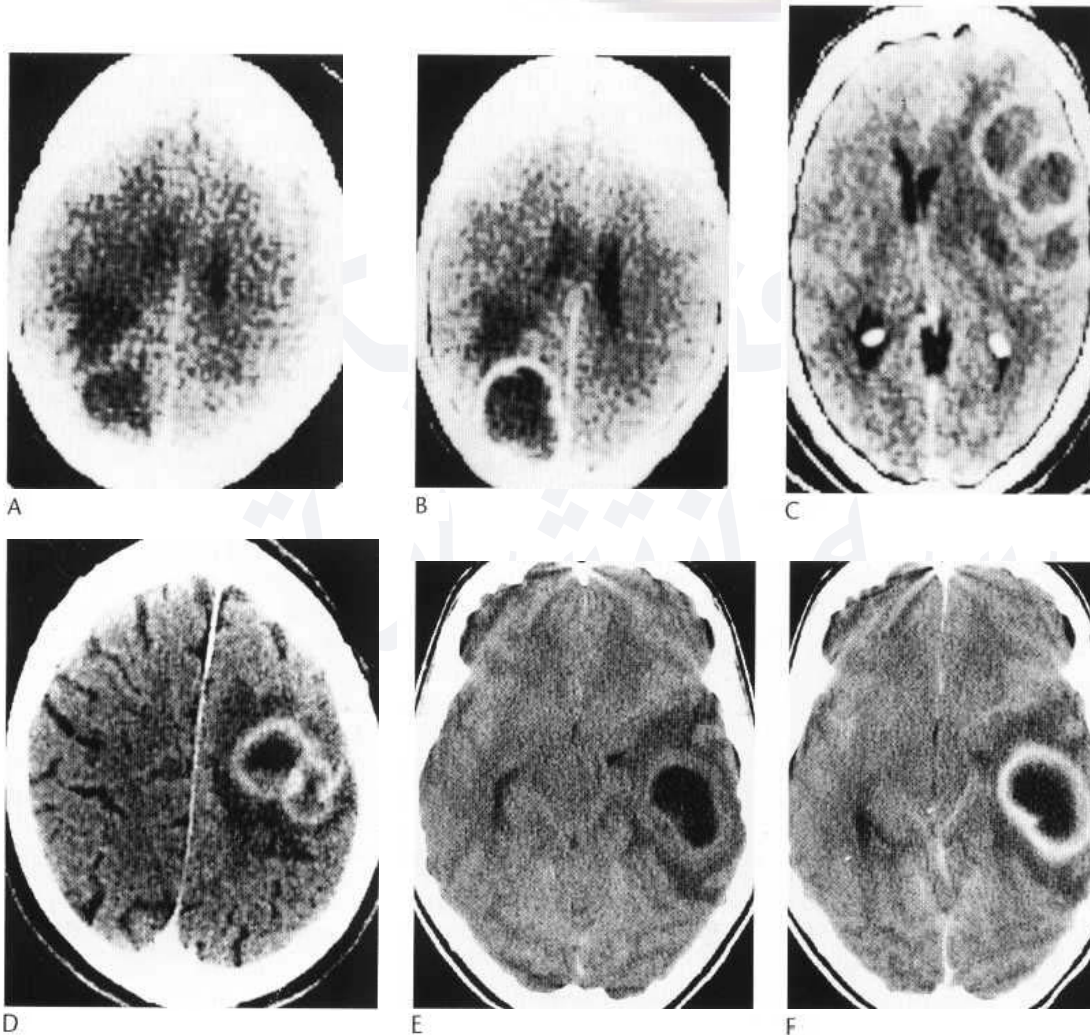


Fig. 58.37 (A,B) Cerebral abscess. (A) Low-density lesion in occipital region with some mass effect. (B) After contrast medium, note thin ring of enhancement round the abscess with oedema anteriorly. (C) Multiple abscesses in frontoparietal area showing capsular enhancement after contrast medium (L34, W75). (D) Capsular enhancement in bilocular abscess. (E,F) Otogenic abscess in left posterior temporal region with thick enhancing capsule and oedema posteriorly.

coccus, *Bacteroides* and *Staphylococcus aureus*. CT may provide more direct evidence by showing opaque sinuses or air cells, or bone defects. In children, congenital malformations such as meningomyeloceles, encephaloceles, ectodermal defects and cyanotic heart disease frequently predispose to abscess formation.

Cerebritis precedes abscess formation whereby the organism involved results in an area of parenchymal softening with necrosis, oedema, vascular congestion, petechial haemorrhage and an inflammatory exudate. On imaging, early cerebritis is better demonstrated with MRI than CT, whereby the affected area is hyperintense on T₂, proton density of FLAIR sequences, and hypointense on T₁. There is often associated mass effect and heterogeneous contrast enhancement. As the cerebritis progresses an abscess develops once there is a central, liquefied necrotic zone, which is surrounded by a collagen capsule and zone of gliosis. The capsule is often less well formed on the side closest to the ventricle, probably an effect of differential blood supply, and tends to be thinner and more uniform than that of a cystic or necrotic tumour. Abscesses can be unilocular or multilocular and those that result from haematogenous dissemination of an organism tend to be located at the grey-white matter interface, usually in the frontal or parietal lobes.

CT The CT scan will show an area of low density in the large majority of cases, and injection of intravenous contrast medium will demonstrate the abscess capsule as a thin-walled regular ring of enhancement (Fig. 58.37A,B). Occasionally it may be clear that the lesion is multilocular (Fig. 58.37C,D). The capsule may sometimes be seen as a ring of increased density before enhancement, but this is not a general feature of abscesses.

Gas may be present adjacent to or within an abscess; it usually indicates that the cavity has been tapped, but in rare cases is present preoperatively, when it may indicate either infection with gas-forming organisms or, more commonly, a fistulous connection with the exterior.

There is usually some mass effect but this may not be marked in relation to the extent of the oedema. Extension of the inflammatory process to the ventricular system is a bad prognostic sign. After successful tapping of the abscess, enhancement of the capsule may persist for some months.

MR1 The appearances of an abscess on MRI will vary according to the stage of the lesion. The central zone of liquefying necrosis in a mature abscess is similar to that of CSF and the surrounding brain oedema on T₂-weighted images (Fig. 58.38A), slightly

hyperintense to CSF on T₂-weighted images. On unenhanced images the collagenous capsule is commonly isointense to slightly hyperintense on T₂- and hypointense to brain on T₁-weighted images, and these signal characteristics are probably attributed to the presence of paramagnetic free radicals. As with CT, the abscess capsule usually enhances strongly on MRI and administration of intravenous gadolinium is also important in recognising whether the abscess cavity is unilocular or multilocular. Associated disease in the paranasal sinuses may also be visible on images.

Although the sensitivity of MRI is greater than CT in detecting an abscess, the radiological differential of a ring-enhancing lesion includes primary and secondary brain neoplasms, lymphoma, septic and aseptic infarcts, resolving haematoma, thrombosed aneurysm and tumefactive multiple sclerosis plaques. Recent studies with diffusion-weighted imaging seem promising in differentiating an abscess from a liquefied/cystic tumour, as the former is of hyperintense signal with a reduced apparent diffusion coefficient (ADC) due to viscosity of the cavity contents, and tumours have increased free diffusion of water, hence an increased ADC.

Ventriculitis/ependymitis Ventriculitis is an uncommon but potentially serious infective process of the cerebral ependyma. It may follow spontaneous or iatrogenic rupture of an abscess into the ventricles, and may sometimes result from leptomeningitis or from shunt infection. It is characterised at CT or MRI by linear contrast enhancement outlining the ventricular wall. Ventriculomegaly, septation and compartmentalisation of the ventricles may also be seen and there may be associated reactive transependymal oedema. Abnormally swollen choroid plexi, indicative of a choroid plebitis, may also be a feature. In chronic ventriculitis parenchymal periventricular calcification may be present and this is particularly seen in neonatal ventriculitis, classically in association with the TORCH infections.

Meningitis This is an infective/inflammatory process of the dura mater, leptomeninges (pia and arachnoid maters) and the cerebrospinal fluid within the subarachnoid space. It may be associated with underlying cerebral parenchymal inflammation meningoencephalitis. The overall mortality for meningitis in adults is 19%. As with cerebral abscesses, meningitis can be classified as aseptic (usually viral), acute pyogenic (usually bacterial) and chronic (any infectious agent including fungi and parasites).

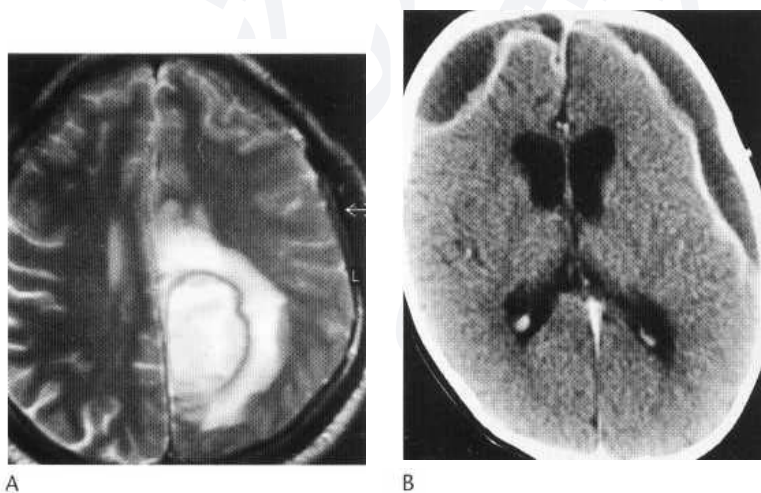


Fig. 58.38 (A) Axial T₂-weighted image of a left parietal abscess and associated vasogenic oedema. The central contents are hyperintense but the low-signal rim is thought to be secondary to the paramagnetic effects of the free radicals present. **(B)** Axial post-contrast CT in a child demonstrating bilateral low-density subdural empyemas with enhancement of the inner membranes.

The role of imaging in meningitis is largely to detect complications such as hydrocephalus, venous thrombosis and infarction, as often in early uncomplicated meningitis imaging may be normal.

Viral meningitis This is usually a self-limiting infection and the most common pathogen is an enterovirus, commonly echovirus, coxsackievirus and non-paralytic poliovirus. In most cases CT and MRI are normal, unless associated with a viral encephalitis. Brain swelling and meningeal enhancement may be seen in some cases.

Pyogenic meningitis The causative organisms will vary according to the age of the patient; in neonates these will often be *Escherichia coli* and the group B streptococci, whereas in older children *Haemophilus influenzae* is more common; in young adults *Neisseria meningitidis* is most frequently encountered, whereas in elderly patients it is *Strep. pneumoniae*. In early cases of pyogenic meningitis there may be obliteration of the basal cisterns and cerebral and cerebellar sulci due to the presence of an inflammatory exudate and brain swelling. After contrast administration there may be either dural or leptomeningeal enhancement, and both of these are easier to appreciate on MRI than CT.

Communicating hydrocephalus is the most common complication associated with meningitis, resulting from blockage of the CSF flow and resorption pathways by debris, mainly at the level of the arachnoid villi. Leptomeningeal-ependymal fibrosis may be a later complication resulting in irreversible communicating-obstructive hydrocephalus. Subdural effusions are also sometimes demonstrated in patients with acute meningitis and these may be infected or sterile. Most commonly they are sterile hygromas, and presumably these are either secondary to irritation of the dura or subdural veins by the infectious agent.

Subdural abscesses (empyemas)

These are usually secondary to bacterial or fungal disease of the calvaria and subdural space, and frontal sinusitis is in fact the most common cause of a subdural empyema. Although small collections may be largely obscured by the overlying bone, the cerebral convexities and interhemispheric fissure are the most common locations; on CT these are seen as crescentic or lentiform collections of variable attenuation (usually reduced), whose margins, and occasionally contents, enhance markedly (Fig. 58.38B). The inner enhancing membrane represents an inflammatory membrane of granulation tissue on the leptomeningeal surface. Hypodensity of the adjacent brain may result from secondary thrombophlebitis of the subdural bridging veins, resulting in venous infarction. MRI may be useful in differentiating a sterile from an infected subdural collection, as the former is likely to be isointense to CSF on T₂, whereas the latter is more hyperintense due to proteinaceous contents. The enhancing internal and external inflammatory membranes are easily appreciated with MRI. When subdural empyemas are adjacent to the tentorium, coronal sections may be indicated to show whether the lesion is supra- or infratentorial. They are readily detected by coronal MRI, especially on T₂-weighted images, where the collection is variably hyperintense with respect to normal brain.

Epidural abscess (empyema)

When associated with meningitis, these are usually the result of direct extension from an external source such as the frontal sinuses, petromastoid air cells and middle ear cavity, but they may also

occur secondary to surgery or penetrating trauma. On CT and MRI the fluid collection is usually of slightly higher density and signal intensity than CSF and the involved dura is markedly thickened and enhances. The underlying brain is usually normal, as the dura prevents intracranial dissemination of the infection, but with advanced cases retrograde thrombophlebitis may occur.

Tuberculosis

Central nervous system infection with the bacillus *Mycobacterium tuberculosis hominis* occurs with increased frequency in the immunocompromised population, including those with HIV infection, alcoholics, drug abusers, the poor and the aged. Spread to the CNS is most frequently haematogenous and intracranial manifestations include leptomeningitis, pachymeningitis, cerebritis, abscesses and tuberculomas.

Tuberculous meningitis (TBM) primarily affects the basal meninges, resulting in a thick proliferative arachnoiditis and meningeal exudate, which may result in varying degrees of communicating or even obstructive hydrocephalus. Traversing arteries and veins may become involved, resulting in a vasculitis. On CT the basal cisterns are obliterated by an isodense or hyperdense exudate, and postcontrast there is avid enhancement of the basal meninges extending into the ambient, sylvian, pontine and chiasmatic cisterns. The meningeal enhancement may extend over the cerebral and cerebellar hemispheres. Hydrocephalus is present in 45-87% of patients at the time of diagnosis, although usually no detectable signal abnormality of the meninges on unenhanced MR sequences is present.

MRI is more sensitive for the detection of the meningeal enhancement and any additional parenchymal changes that may be present. Infarcts due to vasculitis are most frequently seen in the basal ganglia due to involvement of the perforating arteries but also occur in the cerebral cortex, pons and cerebellum, and up to 50% of patients with TBM may have infarcts on MRI. The radiological differential of TBM includes pyogenic, carcinomatous and fungal meningitis as well as neurosarcomatous.

Granulomatous basal meningitis is a relatively uncommon presentation of TBM. The diffuse granulomatous involvement of the basal meninges commonly results in visual disturbances and compression of the optic nerve and chiasm. On CT there is dense basal meningeal enhancement in association with irregular enhancing nodular masses. On MRI this granulomatous process exhibits low signal on T₁, and is isointense to brain on T₂-weighted sequences and enhances postcontrast.

Chronic tuberculous leptomeningitis can rarely result in a pachymeningitis, with the dura of the cavernous sinuses, floor of middle cranial fossa, cerebral convexities and tentorium involved. The affected thickened dura may be calcified, on non-contrast CT it is hyperdense and on MRI it is isointense to hypointense on T₁, and T₂-weighted sequences and enhances avidly.

Intracranial tuberculomas may be single or multiple, of variable size and situated above or below the tentorium (Fig. 58.39A,B). Brainstem involvement is infrequent, accounting for 2.5-8% of intracranial tuberculomas, and other uncommon sites include the cavernous sinus, sella turcica, suprasellar cistern and hypothalamus. There may or may not be an associated tuberculous meningitis. The tuberculous focus starts off as an area of cerebritis and at this stage it is of low density on CT and hyperintense on T₂-weighted MR

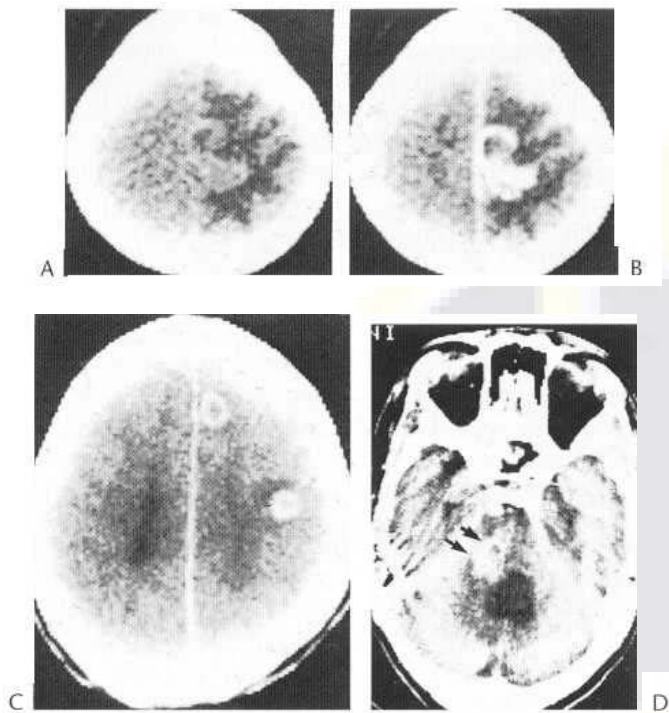


Fig. 58.39 Tuberculoma. (A) Isodense lesion with surrounding oedema. (B) Mixed enhancement after contrast. (C) Tuberculomas. Two small lesions with thick ring enhancement ([40, W80]). (D) Small brainstem tuberculomas with ring enhancement anterior to dilated fourth ventricle.

images. although there may not be any T₂ signal change or homotomous enhancement. The cerebritis then progresses to a focal non-caseating granuloma, which is isodense or mildly hyperdense on CT, surrounded by perilesional low-density oedema. Postcontrast there is dense nodular enhancement. On MRI these solid granulomas are isointense to hypointense on T₁, and hyperintense on T₂, with homo-

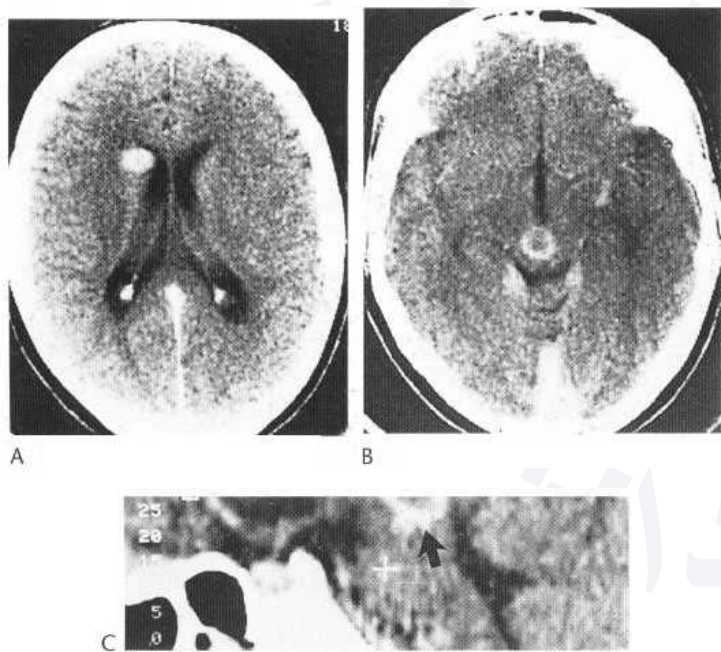


Fig. 58.40 Tuberculomas in right frontal region with nodular enhancement (A) and upper midbrain with ring enhancement (B). (C) Sagittal reformat of midbrain lesion. Note infundibulum and pituitary gland well shown.

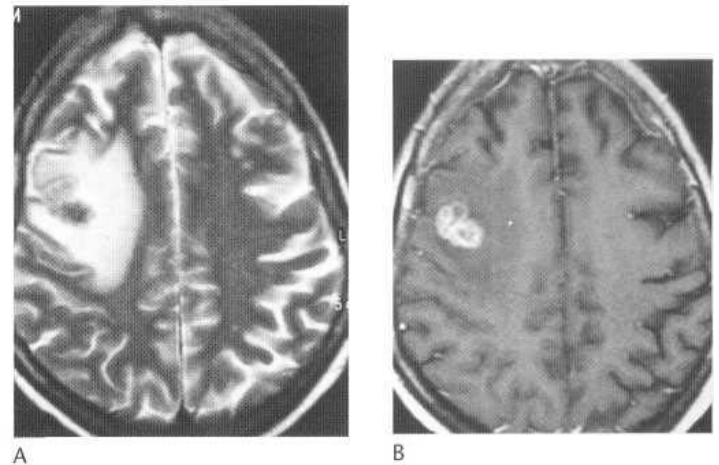


Fig. 58.41 Axial T₂-weighted image (A) showing a hypointense caseating tuberculous granuloma in the right frontal lobe in association with vasogenic oedema. The lesion is situated at the grey-white matter junction and on the postcontrast T₁ axial image (B) has a multiloculated ring enhancing appearance.

geneous enhancement. As caseation occurs, the granuloma becomes isodense or slightly hypodense on CT. On MRI the caseating granuloma is isointense to hypointense on T₁, but also now hypointense on T₂-weighted images. The lesion now shows ring-enhancement on both CT and MRI and perilesional oedema remains. The radiological differential of such ring-enhancing lesions includes abscess, neurocysticercosis, glioma, metastases, lymphoma and other granulomatous processes such as sarcoid (Figs 58.39-58.41, 58.42A,B).

With disseminated miliary tuberculosis, multiple enhancing small (<5 mm) granulomas are seen scattered throughout the brain and sometimes these lesions may become calcified in the long term. Tuberculous abscesses are rare, and usually on imaging a single supratentorial abscess is seen at the grey-white matter interface, which has a hyperdense rim and low-density centre on CT. On MRI the abscess wall is slightly hyperintense on T₁- and hypointense on T₂-weighted images, with the central contents being hypointense and hyperintense, respectively. There is irregular dense enhancement of the wall and a large amount of associated perilesional oedema (Fig. 58.42C,D).

Fungal infections

Fungal infection of the CNS is only rarely seen in healthy people. In these cases it is usually spread by the bloodstream from a primary focus in the lungs or elsewhere in the body and a chest radiograph may show evidence of a primary fungal infection or of an opportunist infection.

Most cases occur in patients whose resistance to infection is lowered by conditions such as leukaemias, lymphomas, malignant disease, or AIDS, or by prolonged use of antibiotics, steroids, cytotoxic drugs or immunosuppressive agents.

The commonest fungal infections are candidiasis and cryptococcosis. They can give rise to granulomatous meningitis as well as parenchymatous abscesses or granulomas. Mucormycosis may complicate uncontrolled diabetes or acute leukaemia.

The infecting fungus can also be one of the usual human pathogens, such as the fungi of aspergillosis, actinomyces or histoplasmosis. Blastomycosis, coccidiomycosis, cladosporiosis, nocardiosis and rarer fungal infections have also been recorded.

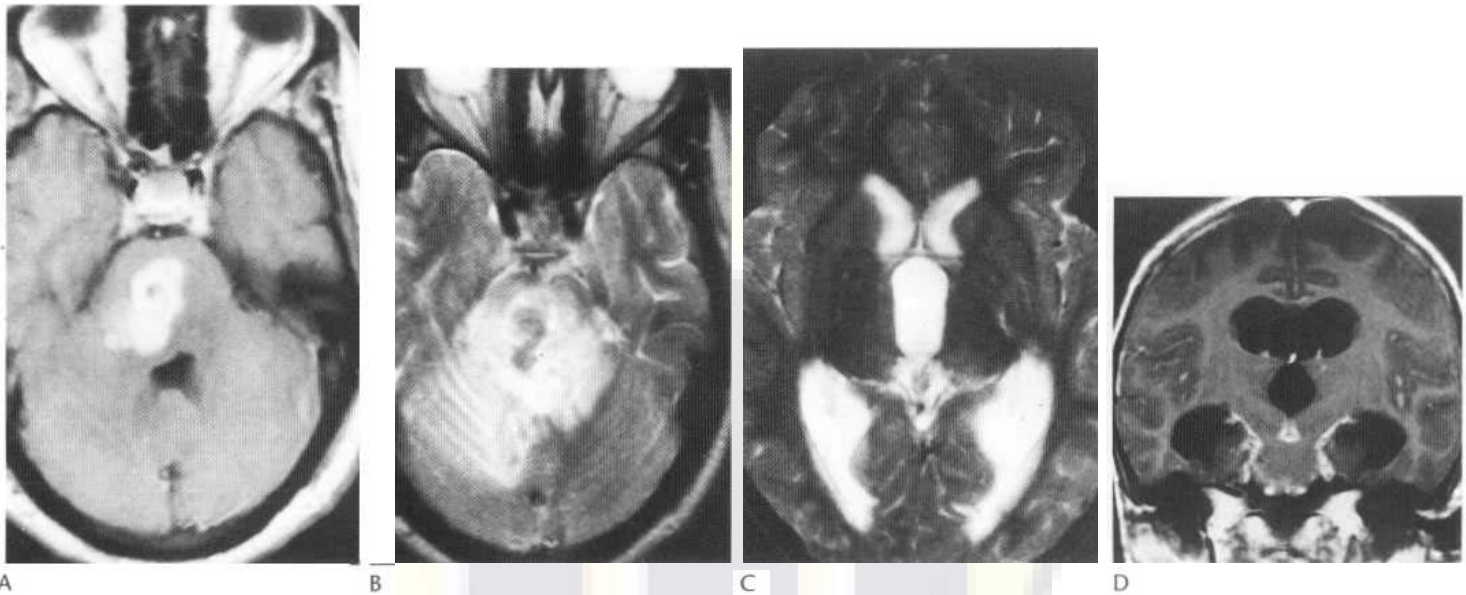


Fig. 58.42 An irregular enhancing tuberculoma is shown within the pons on the postcontrast axial T₁-weighted MR image. (A) The lesion is of relatively low signal on the T₂ axial image (B) and there is extensive vasogenic oedema and some modest mass effect with distortion of the 4th ventricle. Axial T₂-weighted MR (C) demonstrating third and lateral ventricular hydrocephalus with transependymal oedema around the occipital horns. This was secondary to tuberculous meningitis. On the coronal T₁ postcontrast image (D) there is nodular meningeal thickening and enhancement around the brainstem and cerebellum.

Cryptococcal infection This is the most common fungal infection of the CNS, particularly affecting patients with AIDS. The fungus is ubiquitous encapsulated yeast, most commonly found in the soil, thus entry into the body is via inhalation. Imaging findings in patients with CNS cryptococcosis are variable, and in patients who have meningitis are often negative. The most common imaging finding is a communicating or obstructive hydrocephalus, which occurs more commonly in immunocompetent patients (25%) compared with immunocompromised patients (9%), probably due to an inability to mount an adequate immune response in the latter: thus leptomeningeal enhancement is only rarely seen (Fig. 58.43A,B).

Low-density non-enhancing lesions in the basal ganglia are seen on CT: on MRI these are seen as hyperintense on T₂ and hypointense on T₁, often with a punctate appearance in the early stages, with a tendency to coalescence with progression. Pathologically, these lesions represent dilated perivascular spaces, which become

distended with mucoid material from the yeast. Although these cryptococcomas can be associated with slight mass effect, they are not usually associated with any vasogenic oedema or enhancement. Miliary/cryptococcal granulomas may also occur in the immunocompromised population, but less commonly than the pattern of basal ganglia cryptococcomas.

In immunocompetent patients, however, more commonly present with cryptococcomas that enhance after contrast medium.

Candidiasis This yeast is normally present as part of the gastrointestinal flora: with disseminated haematogenous spread, the most commonly involved organs are the kidney and the brain, and the frequency of CNS involvement in the setting of disseminated disease is up to 50%. CNS candidiasis can give rise to a spectrum of radiological appearances including meningitis, meningococcalitis, microabscess, abscess and granuloma formation as well as ependymitis: mycotic aneurysms as well as vascular inva-

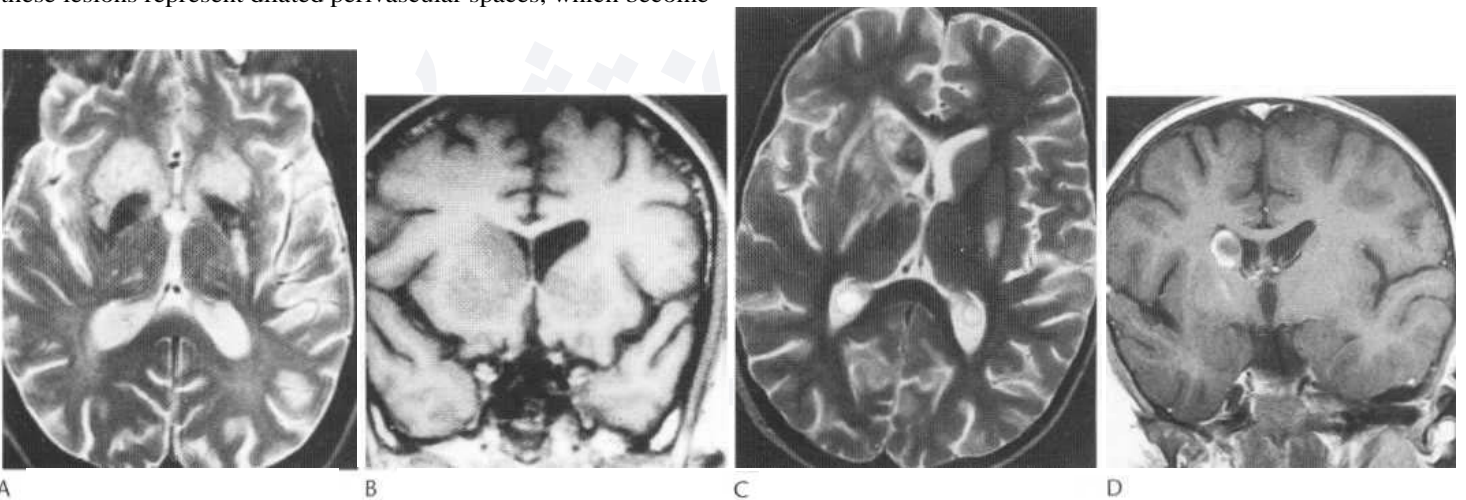


Fig. 58.43 (A,B) Bilateral basal ganglia cryptococcomas, which have a slightly punctate appearance on the T₂-weighted images. On the T₁ coronal images, the lesions are slightly hypointense and those on the right exert some mass effect on the right frontal horn. (C,D) Axial and coronal sections T₂-weighted and T₁-weighted show small enhancing abscess impinging on the right ventricle.

sion with endarteritis have also been described. On CT the microabscesses and granulomas typically show enhancement, and on MRI a target appearance has been described on T₂-weighted images with a well-delineated hyperintense area surrounded by a hyperintense rim (Fig. 58.43C,D).

Aspergillosis This is a ubiquitous mould and primary intracerebral infection may present as a granuloma, encephalitis, abscess or a vasculitis with resultant infarction, which may be haemorrhagic. Imaging findings in this infection that have been described include cortical and subcortical low-density lesions on CT, which on MRI are hyperintense on T₂-weighted sequences; basal ganglia and thalamic lesions have also been described and a significant proportion of patients with such parenchymal lesions have evidence of haemorrhagic change. Mycotic aneurysms may also occur and patients may present with subarachnoid haemorrhage. Brain abscesses have non-specific imaging appearances on both CT and MRI. Involvement of the paranasal sinuses by aspergillus infection is fairly common; on CT the sinuses are filled with hyperdense material but on MRI these secretions, unlike other inflammatory secretions, are hypointense on both T₁- and T₂-weighted sequences. The reduction in T₁ signal is thought to be secondary to the high concentration of paramagnetic calcium, magnesium, manganese and iron in the secretions and postcontrast rim enhancement may also be seen. Dural enhancement may be associated with sinonasal, calvarial or orbital involvement.

Mucormycosis This group of fungi are ubiquitous in bread and fruit mould and patients with diabetes are at an increased risk of the rhinocerebral form of this infection, and account for approximately 70% of cases. The moulds have a propensity for vascular structures; hence, radiological findings include arteritis, ischaemic lesions, haemorrhagic infarction and aneurysms. Intracranial granulomas are rare. Meningitis is uncommon in the haematogenous form of this infection, and more common with rhinocerebral or skull base involvement resulting from direct spread.

Imaging findings include low-density lesions on unenhanced CT, some with associated oedema and haemorrhage, which may show ring enhancement after contrast. On MRI such lesions may be hyperintense on both T₁- and T₂-weighted sequences secondary to haemorrhage. The signal changes associated with sinus infection are as described above for those seen with aspergillosis.

Spirochaete infections

Lyme disease This rare condition, due to spirochaetal infection with *Borrelia burgdorferi* has been increasingly diagnosed in both America and Europe in the last decade. Central nervous system involvement occurs in 15-20% of cases but the clinical presentation is variable, meningovascular features being common and some patients presenting with cranial nerve palsies, mild encephalopathy or polyneuropathy, but the clinical picture may be confusing. Definitive diagnosis is by serology or culture of the organism. CT scanning is relatively insensitive in this disease, although vague low density in involved white matter may sometimes be seen. On MRI T₂ hyperintense lesions in the periventricular and subcortical cerebral white matter, basal ganglia and brainstem have been described and these may be either granulomas or areas of vasculitis. There may also be contrast enhancement of the meninges in the acute phase on MRI and delayed imaging may show contrast leakage into the CSF, enhancing the

basal cisterns (Fig. 58.41 B). The parenchymal lesions may or may not enhance.

Syphilis This sexually transmitted disease is caused by the spirochete *Treponema pallidum*, which penetrates intact mucous membranes. CNS involvement usually occurs as a late manifestation of the disease, usually in the tertiary stage, but patients with secondary syphilis can also develop meningeal signs. There has recently been a resurgence of syphilis with the AIDS epidemic and these patients usually develop neurological symptoms earlier, within 3-18 months. Aseptic syphilitic meningitis is the most common manifestation occurring within 2 years of infection, and chronic encephalitis and tabes dorsales do not seem to be a feature in patients with AIDS.

Normally signs of tertiary syphilis develop after a long, latent phase of 6-40 years; neurosyphilis occurs in approximately 8% of untreated patients; in meningovascular syphilis, there is invasion of the intracranial vessels and meninges, resulting in meningeal thickening and arteritis with consequent infarction, often in the middle cerebral artery territory or affecting small vessels, with a predilection for the basal ganglia. These areas of infarction are shown on CT and MRI and as there is an underlying vasculitis the abnormalities affect multiple vascular territories. Gummas can occur in the brain, but are rare and arise secondary to a leptomeningeal inflammatory reaction with involvement of local blood vessels, and thus are usually found near the cerebral convexities adherent to the dura and brain parenchyma. On CT, gummas are well-circumscribed homogeneously or ring-enhancing soft-tissue masses, and on MRI have been reported to be hyperintense on T₁ and hypointense on T₂.

Parasitic infections

Box 58.2 lists the different parasitic infections that can involve the brain.

The incidence of parasitic infections of the nervous system varies greatly in different geographic regions. They may involve the brain, producing cysts, granulomas or abscesses, and they can also involve the meninges.

Toxoplasmosis The causative organism (*Toxoplasma gondii*) is an obligatory intracellular parasite. The definitive hosts are the cat family, in whom the entire life cycle can be completed. Other mammals and birds can become infected, as can humans, either from cats or from eating meat from chronically infected animals.

Two types of brain infection are seen in humans: the congenital and the adult. This is because the CNS is only involved in humans with an immature immune system (as in the fetus) or with compromised immunity (as in AIDS or immunosuppression). Most toxoplasmosis infection in immunocompetent individuals is subclinical.

The congenital type results in a child with more or less extensive brain damage at birth, which may include encephalomyelitis,

Box 58.2 Parasitic infection of the brain

A. Protozoal	B. Metazoal
Toxoplasmosis	Tapeworm (cestodiasis)
Amoebiasis	Fluke (trematode)
Malaria	
Trypanosomiasis	
Chagas' disease	

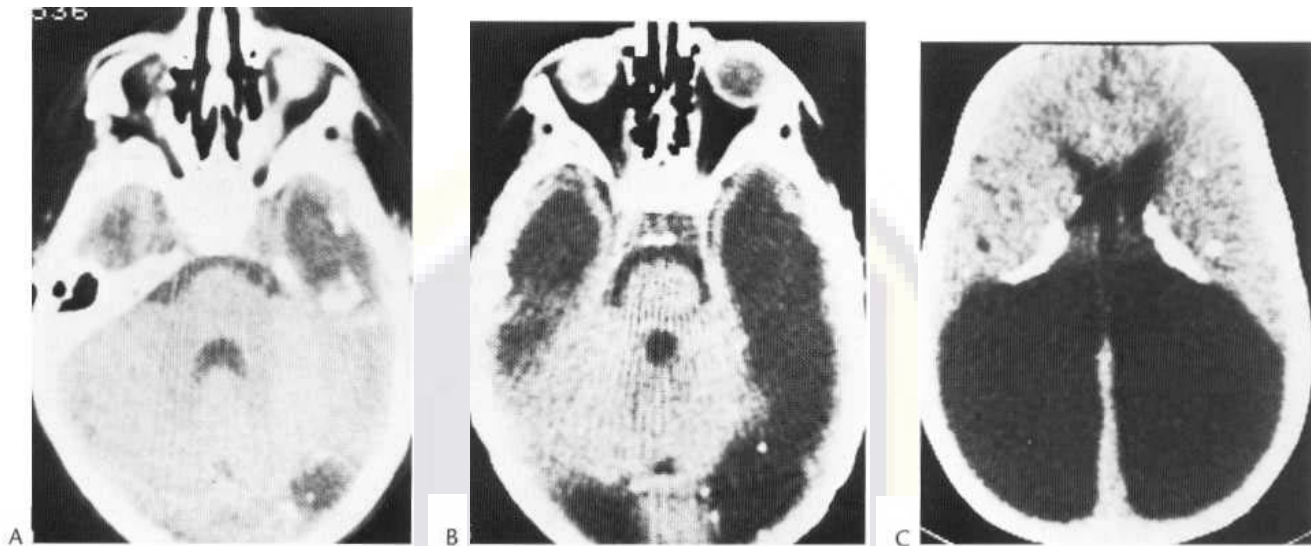


Fig. 58.44 (A,C) Congenital toxoplasmosis. Grossly dilated ventricles and calcified granulomas in atrophic cortex and basal ganglia.

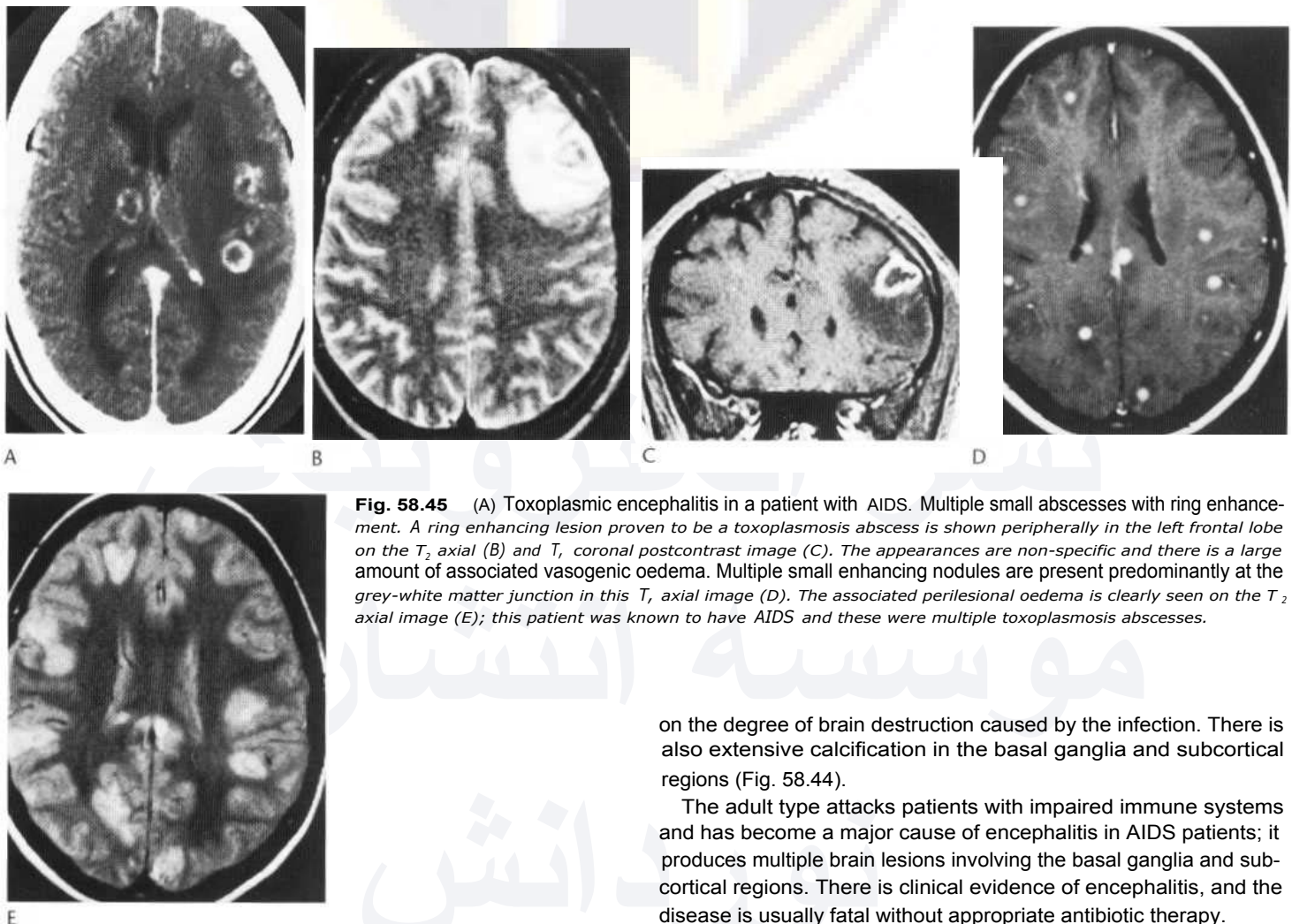


Fig. 58.45 (A) Toxoplasmic encephalitis in a patient with AIDS. Multiple small abscesses with ring enhancement. A ring enhancing lesion proven to be a toxoplasmosis abscess is shown peripherally in the left frontal lobe on the T_2 axial (B) and T_1 coronal postcontrast image (C). The appearances are non-specific and there is a large amount of associated vasogenic oedema. Multiple small enhancing nodules are present predominantly at the grey-white matter junction in this T_1 axial image (D). The associated perilesional oedema is clearly seen on the T_2 axial image (E); this patient was known to have AIDS and these were multiple toxoplasmosis abscesses.

hydrocephalus or microcephaly as well as bilateral choroidoretinitis. The lesions remain apparently healed and the condition does not progress. Plain radiographs may be helpful in the congenital type and may show characteristic intracranial calcification. On CT there is a more or less gross degree of ventricular dilatation, depending

on the degree of brain destruction caused by the infection. There is also extensive calcification in the basal ganglia and subcortical regions (Fig. 58.44).

The adult type attacks patients with impaired immune systems and has become a major cause of encephalitis in AIDS patients; it produces multiple brain lesions involving the basal ganglia and subcortical regions. There is clinical evidence of encephalitis, and the disease is usually fatal without appropriate antibiotic therapy.

The adult type shows focal, usually multiple (Fig. 58.45D,E) lesions of slightly reduced density in the thalamus and basal ganglia or subcortically. They are best identified after high-dose contrast enhancement when most will show ring or nodular enhancement, although some will not (Fig. 58.45A-C). There is usually mass effect and some local oedema. In the appropriate context the

appearances are suggestive but not specific, as other inflammatory lesions can produce similar appearances, as can neoplastic lesions.

MRI appears to be more sensitive than CT in detecting the intracerebral lesions and is thus claimed to permit earlier biopsy and appropriate treatment.

Amoebiasis Amoebic abscess of the brain is rare and is usually a late and fatal haematogenous complication of intestinal, hepatic or pulmonary infection with *Entamoeba histolytica*. There is usually a single abscess in the subcortical or basal ganglia region.

Infections of the CNS with other types of amoeba (*Naegleria fowleri*; *Hartmannella acanthamoeba* group) have also been described. *N. fowleri* produces a primary amoebic meningoencephalitis. It is acquired by previously healthy children and young adults swimming in contaminated water and is usually fatal within a few days. *H. acanthamoeba*, on the other hand, affects debilitated or immunocompromised individuals and produces a granulomatous amoebic encephalitis that is also fatal although the course is more prolonged.

Malaria Cerebral malaria occurs only in malignant tertian malaria due to *Plasmodium falciparum*. There is a high mortality and the main macroscopic abnormalities in the brain are oedema, vascular congestion and petechial haemorrhages.

Tapeworms (cestodes)

The tapeworm infestations which can involve the brain include cysticercosis, hydatid disease and coenurosis.

Cysticercosis *Cysticercus cellulosae* is the larval stage of *Taenia solium*, a tapeworm whose permanent host is humans. Animals, including the pig, are intermediate hosts and harbour the cysts after ingesting eggs excreted in human faeces. The eggs release the embryos in the intestine of the animal; they penetrate the intestinal wall and are carried to all organs, including brain and muscles. Here the larvae develop a cystic wall (Fig. 58.46).

Humans can become intermediate hosts from self-infection with eggs. The disease is widespread in India and Latin America, where it accounts for a high proportion of brain tumours.

Simple X-ray Calcification is commonest in the muscle cysts and shows a pathognomonic appearance already described (see Fig. 48.24). Calcification can also occur in the cerebral cysts. It is

also characteristic but is far less common and looks different (see Fig. 53.43).

CT The appearances depend on the number, size and distribution of the cysts as well as on their stage of evolution. Their number can vary from just one to over a hundred. They are commonest in the brain but can involve the meninges and the ventricles.

In the acute stage parenchymatous cysts appear as small, rounded low-density lesions that enhance strongly with contrast medium (Fig. 58.45) in a ring or nodular manner. In the chronic stage they do not enhance but may develop punctuate calcification. Obstructive hydrocephalus may develop from cysts obstructing the ventricles or basal cisterns, where they may form racemose groups.

MRI This will demonstrate the lesions well, particularly in the acute stages or subacute stages, when small rounded cyst-like structures due to the individual bladders may be visualised. Complex arachnoid cysts may burrow into the brain and the walls of partly degenerate bladders may be recognised within them. Intraventricular bladders may be difficult to recognise because their signal may be similar to that from CSF, although slight differences usually permit detection. As cysts degenerate, oedema often appears in adjacent brain and is readily shown by MRI. However, small calcified foci representing the residual scolex are not identified.

Hydatid disease (echinococcosis) This is produced by the larval stage of the dog tapeworm. The eggs are ingested by sheep, who form the usual intermediate host. Humans can become the intermediate host through contact with infected dogs or by ingesting contaminated food. The embryos pass via the portal system to the liver and thence to the lungs and general circulation. Hydatid cysts of the brain are usually solitary and unilocular. They commonly lie in middle cerebral territory in the parietal region and can reach a large size, often over 6 cm in diameter (Fig. 58.47).

CT Typical cases show a large cystic lesion lying subcortically in the parietal lesion. There is some mass effect but there is no enhancement after contrast medium and no surrounding oedema or adjacent calcification. In rare cases there may be more than one cyst, or the cyst may be deeply sited adjacent to the ventricle.

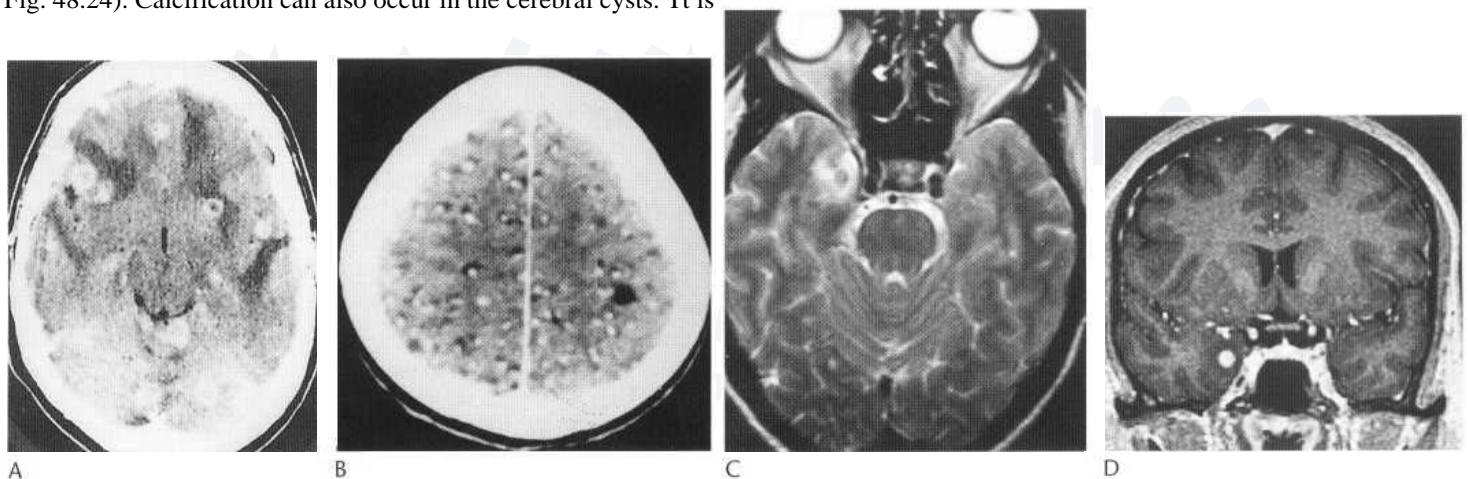


Fig. 58.46 Enhanced CT in acute cysticercosis. (A) Multiple ring and nodular lesions inconstantly accompanied by oedema. (B) Another patient with chronic quiescent cysticercosis. The brain was riddled with cysts and calcified nodules. (C) The axial T₂-weighted MR in this patient who presented acutely with epileptic seizures showed a small hypointense lesion in the medial right temporal lobe associated with a small amount of vasogenic oedema. (D) On the postcontrast T₁ coronal image, this lesion showed almost uniform enhancement and resolved on treatment for cysticercosis.

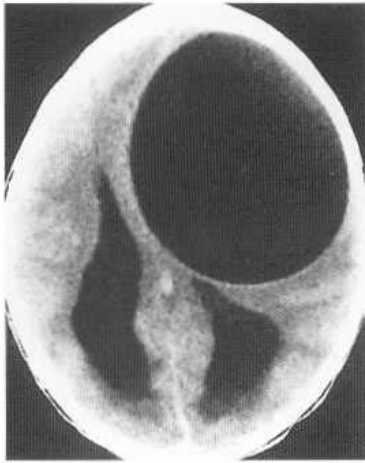


Fig. 58.47 Huge hydatid cyst in the left frontal lobe. It is of CSF density and shows no capsular enhancement of adjacent oedema. It expands the overlying skull vault.

MRI This also shows the lesions well but has no particular advantage over CT.

Coenurosis This is infection by another dog tapeworm, *Taenia nut/beeps*, which has occasionally infected humans. The cysts are similar to hydatid cysts but not as large. In the brain they are usually single, but multiple racemose groups have been described in the ventricles or basal cisterns.

Trematodes (flukes)

Paragonimiasis This infection is caused by the lung fluke, *Paragonimus trwesteroicmii*, and may affect other organs, notably the brain. Human infection is caused by eating poorly cooked crustacea infected by the larval stage of the parasite. The disease was endemic in the Far East, from which most recorded cases have been reported, and in South Korea it was one of the commonest causes of brain tumour, although now less frequent. The organism gives rise to a large granuloma, usually in the temporal or parieto-occipital regions, which may later heal with marginal calcification.

Simple X-ray In the chronic healed stage radiographs may demonstrate characteristic 'soap bubble' calcification outlining the margins of the large granuloma.

CT In the acute stage there is a large irregular low-density area within the affected lobe, and some mass effect. Marginal ring enhancements occur after intravenous contrast medium, suggesting a multiloculated abscess or tumour. Later, in the chronic stage, the characteristic marginal calcification may be demonstrated.

Schistosomiasis (bilharzia) Although human infection is common, involvement of the brain is very rarely seen, and is always secondary to infection elsewhere in the body. When it occurs it gives rise to multiple small granulomas, which can involve the brain, spinal cord or meninges.

Nematodes (roundworms)

Loa/oa, a filarial worm, is prevalent in West Africa and can cause multiple small cerebral granulomas. Similar lesions may occur in trichinosis, due to *Trichinella spiralis*, which has a worldwide distribution.

Viral infections

Acute lymphocytic meningitis

This is a common response to many different viral infections. The diagnosis is made clinically and imaging has no contribution.

Parenchymatous viral disease may be classified as:

1. Non-specific
2. Specific.

Non-specific virus infection of the CNS

This is variously described as *postinfectious encephalitis*, *post-infectious perivenous encephalitis*, *acute disseminated encephalomyelitis* and *acute disseminated leucoencephalitis*. The condition may complicate many viral diseases 7-14 days after onset, but in particular the exanthemas such as measles, chickenpox, rubella and smallpox, or it may follow smallpox vaccination. The basic mechanism is thought to be immunoallergic and the histological features are characteristic, consisting of lymphocytic and plasma-cell infiltrates around the venules of the neural parenchyma, with perivenous foci of demyelination. Clinically, most cases present with seizures or focal neurological signs and recover within 2-3 weeks, although 10-20% may suffer permanent damage.

CT CT may show no changes, but in the more severe cases there may be areas of patchily reduced density reflecting vasogenic oedema in the white matter.

MRI This is more sensitive than CT in demonstrating areas of oedema and demyelination in the white matter and may show changes more extensive than suggested by CT, or even when CT is negative (Fig. 58.48). As in other forms of encephalitis, the main change is increased signal on T₂-weighted images with multifocal lesions. The brainstem is often involved, sometimes selectively, and the spinal cord may also be affected.

Reye's syndrome This condition, as originally described, predominantly affected children below the age of 16 years, but is now known to affect adults as well. The patients are recovering from an illness of viral or presumed viral aetiology when they develop both hepatitis and encephalitis. About one-third of the patients die within a few days from raised intracranial pressure.

Liver function is severely affected and half the patients have enlarged livers. Toxic agents, particularly salicylates, have been associated with the syndrome, and the interaction of toxin and virus has been postulated as the cause.



Fig. 58.48 Multiple T₂ hyperintense lesions in the basal ganglia, thalami, internal capsules and periventricular white matter are present in this patient with acute disseminated encephalomyelitis (ADEM).

CT or *MRI* in the acute phase shows widespread cerebral oedema with compression of the ventricles. Patients who recover may show enlargement of the ventricles and sulci and diminished attenuation of the cerebral white matter.

Specific infection

This is usually referred to as viral encephalitis or acute infective encephalitis and may be due to many different viruses. These can be classified as follows:

- a. RNA viruses
 - (i) Enteroviruses
 - (ii) Arboviruses (arthropod-borne)
 - (iii) Rabies virus
 - (iv) Paramyxoviruses
- b. DNA viruses
 - (i) Herpes simplex viruses
 - (ii) Cytomegalovirus
 - (iii) Herpes zoster
 - (iv) Papovaviruses
 - (v) Unidentified viruses (encephalitis lethargica; subarachnoid meningitis; Behcet's disease).

The best known of the enteroviruses is the poliovirus, responsible for acute anterior poliomyelitis. The arboviruses spread by mosquitoes are responsible for the St Louis, Eastern and Western equine, Japanese B and Murray Valley encephalitides; those spread by ticks result in Russian spring-summer and Central European encephalitis.

Imaging Changes at both *CT* and *MRI* can be focal or multifocal or involve the greater part of one or both cerebral hemispheres, depending on the severity and type of infection. *MRI* is generally more sensitive than *CT* but the latter is occasionally positive when *MRI* is negative, usually because a time interval has allowed changes to resolve. *CT* shows areas of reduced density in the white matter, while *MRI* shows areas of higher signal on T-weighted images. The abnormalities may be evanescent and fluctuate over periods of a few days.

Among the paramyxoviruses, measles can cause subacute sclerosing panencephalitis as well as the quite different postinfectious encephalitis already described.

Subacute sclerosing panencephalitis (SSPE) This occurs in children or young adults several years after a known episode of measles. The precise mechanism of this delayed or prolonged viral infection is still poorly understood but is presumably related

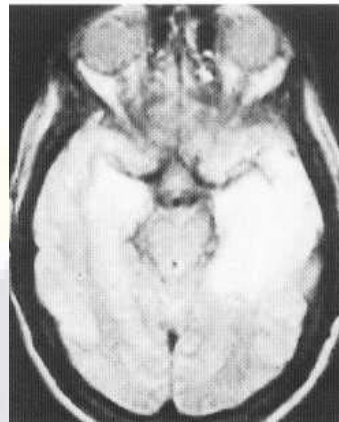


Fig. 58.50 MR (T₁-weighted) shows high signal in both temporal lobes. Herpes encephalitis.

to immunological factors. The disease runs a protracted course ending in death or severe disablement.

Imaging *CT* and *MRI* may show low attenuation in the white matter, similar to that already described for non-specific encephalitis, with *MRI* being the more sensitive.

Herpes simplex type I encephalitis This involves predominantly the temporal lobes and is a grave illness with a mortality of 55%. The severity of the infection can lead to haemorrhagic necrosis and considerable mass effect. The changes are bilateral but may appear predominantly unilateral in the acute phase, and this may lead to a false diagnosis of tumour at imaging.

CT This shows reduced density in the affected temporal lobe(s) and the adjacent posterior frontal region, usually with mass effect (Figs 58.49, 58.50). The changes may be minimal in the first 2–3 days despite severe neurological impairment and should be carefully sought. Haemorrhage rarely shows a clear haematoma but may give rise to patchy areas of slightly increased density.

After contrast medium, enhancement is seen in most cases and may be patchy, peripheral or gyral. As already noted, mainly unilateral cases can give rise to diagnostic error. In the chronic stage there may be large low-density areas with associated local atrophy in the affected regions.

MRI *MRI*, which is more sensitive to white-matter changes, may show the lesions to be more extensive than they appear at *CT*, and will identify them at an earlier stage as high signal on T₁-weighted images. Haemorrhage may occur as increased signal on T₁-weighted images and usually implies extensive necrosis. *MRI* also shows extensive periventricular signal change not apparent at *CT*.

Herpes simplex virus type 2 This may affect neonates and infants, being acquired either transplacentally or at birth.

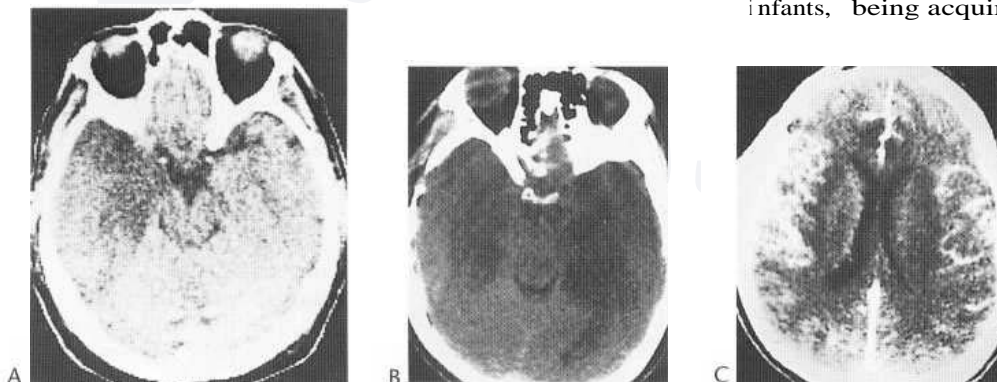


Fig. 58.49 Herpes encephalitis. (A) Low-density area in right temporal region with slight mass effect. (B) Bilateral low-density areas in both temporal lobes. Burr hole for brain biopsy on right. (C) After contrast medium there is marked irregular enhancement, mainly gyral.

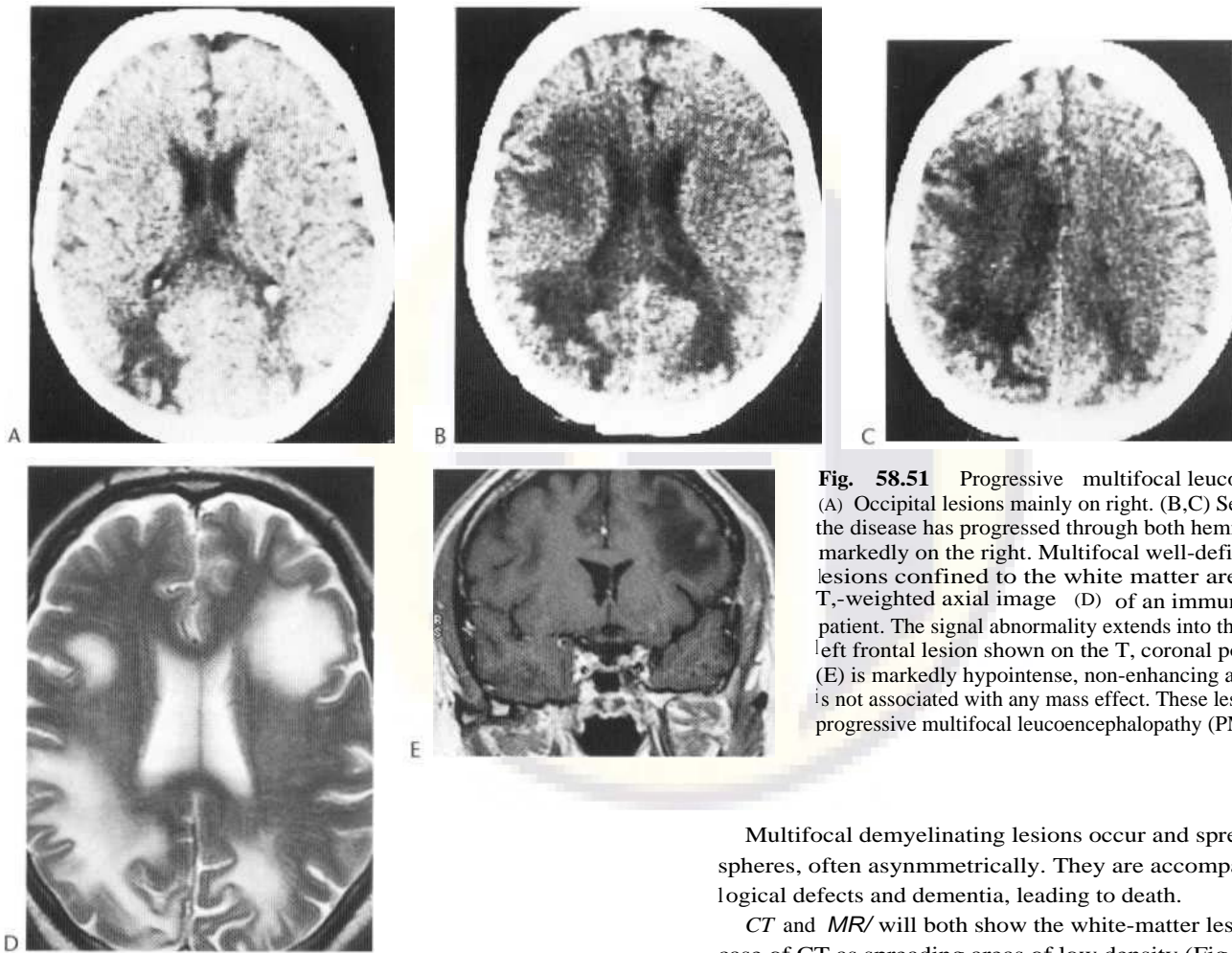


Fig. 58.51 Progressive multifocal leucoencephalopathy. (A) Occipital lesions mainly on right. (B,C) Several weeks later, the disease has progressed through both hemispheres but most markedly on the right. Multifocal well-defined hyperintense lesions confined to the white matter are shown on this T₂-weighted axial image (D) of an immuno-compromised patient. The signal abnormality extends into the gyral cores. The left frontal lesion shown on the T₁ coronal postcontrast image (E) is markedly hypointense, non-enhancing and despite its size is not associated with any mass effect. These lesions are typical of progressive multifocal leucoencephalopathy (PML).

Intrauterine infection of the fetal brain may give rise to microcephaly and intracranial calcification, both periventricular and in white and grey matter. This may be recognised both at simple X-ray and at CT.

Cytomegalovirus (CMV) CMV infection is widespread but does not normally involve the CNS except in patients with compromised immunity, as in AIDS, or where immunity is undeveloped, as in the fetus, which is infected from a carrier mother across the placental barrier. It is estimated that each year around 1200 infants are born in the UK with congenital CMV infection and 200 suffer major defects.

Simple X-ray The skull radiograph of an affected infant may show microcephaly and in some cases calcification which is characteristic, being stippled, bilateral and symmetric and mainly subependymal and periventricular. Other causes of calcification are toxoplasmosis.

CT or MRI These will show dilated ventricles due to atrophy with paraventricular and cortical calcifications.

Progressive multifocal leucoencephalopathy (PML) PML is due to a papovavirus and occurs only in special pathological circumstances. It particularly affects patients with compromised immunity, e.g. Sufferers from chronic lymphatic leukaemia or Hodgkin's disease, or those receiving immunosuppressive therapy.

Multifocal demyelinating lesions occur and spread in the hemispheres, often asymmetrically. They are accompanied by neurological defects and dementia, leading to death.

CT and MR will both show the white-matter lesions well: in the case of CT as spreading areas of low density (Fig. 58.51). MRI is more sensitive than CT and shows more widespread brain involvement. It may be positive when CT is still normal. There is increased signal on T₂ weighted images, and less conspicuous reduced signal on T₁-weighted images. Rarely, necrosis and mass effect may occur.

AIDS

CNS infections are a common complication of AIDS, and manifest clinically as meningitis, focal lesion or generalised abnormalities.

Meningitis This is most commonly due to *Cryptococcus neoformans*, but can arise from mycobacteria or herpes simplex.

Focal lesions These are mainly due to infections giving rise to abscesses and granulomas. The commonest organism responsible is *Toxoplasma gondii*. Other organisms seen are mycobacteria and the fungi *Cryptococcus*, *Aspergillus fumigatus* and *Candida albicans*.

Focal brain lesions in patients with intracranial calcification in neonates are rubella and in patients with AIDS can be neoplastic as well as inflammatory. In particular, lymphoma and rarely Kaposi's sarcoma are found in the brain.

More generalised changes are seen with viruses, in particular cytomegalovirus, herpes simplex and the JC papovavirus responsible for PML. The HIV virus itself has been found in the brain of AIDS patients at autopsy, and is considered to be responsible for a direct cytopathic effect leading to the encephalopathy, dementia and atrophy frequently encountered.

Imaging CT and MR will identify focal lesions such as abscesses due to toxoplasmosis (Fig. 58.44) or cryptococcus

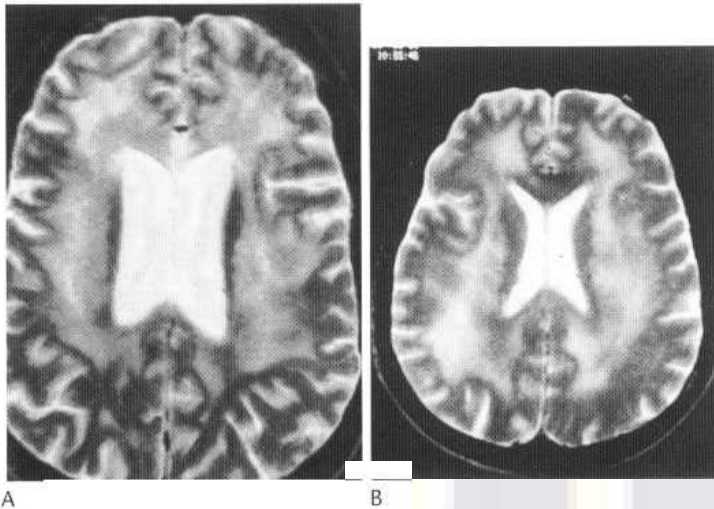


Fig. 58.52 (A) Axial T₂-weighted image in a patient with AIDS showing widespread signal abnormality in the white matter of HIV encephalitis. There is also background atrophy with ventricular enlargement and mild sulcal widening. (B) AIDS encephalitis.

(Fig. 58.43). The appearances seen in PML and involvement by lymphoma have been described above. In some cases brain biopsy may be necessary to distinguish between abscess and neoplasm. However, toxoplasmosis is the commonest cause of focal lesions in AIDS patients, and anti-infective treatment with pyrimethamine and sulfadiazine may be given a trial before resorting to brain biopsy.

Non-specific changes such as brain atrophy with cortical shrinkage and ventricular dilatation are readily identified by CT or MRI. The latter can also demonstrate non-specific white-matter signal changes on T₁-weighted images in 50% of patients who are HIV positive and in 70% of cases with established AIDS (Fig. 58.52). They are thought in most cases to be due to a direct HIV infection.

Other techniques that have been used to investigate HIV encephalopathy include MR spectroscopy and radioisotopes (PET and SPECT). In both cases sensitivity is higher than MRI but specificity is low and neither method is as yet widely accepted.

Other lesions

Sarcoidosis Involvement of the CNS is not uncommon, occurring in around 15% of affected patients. It manifests either as a basal

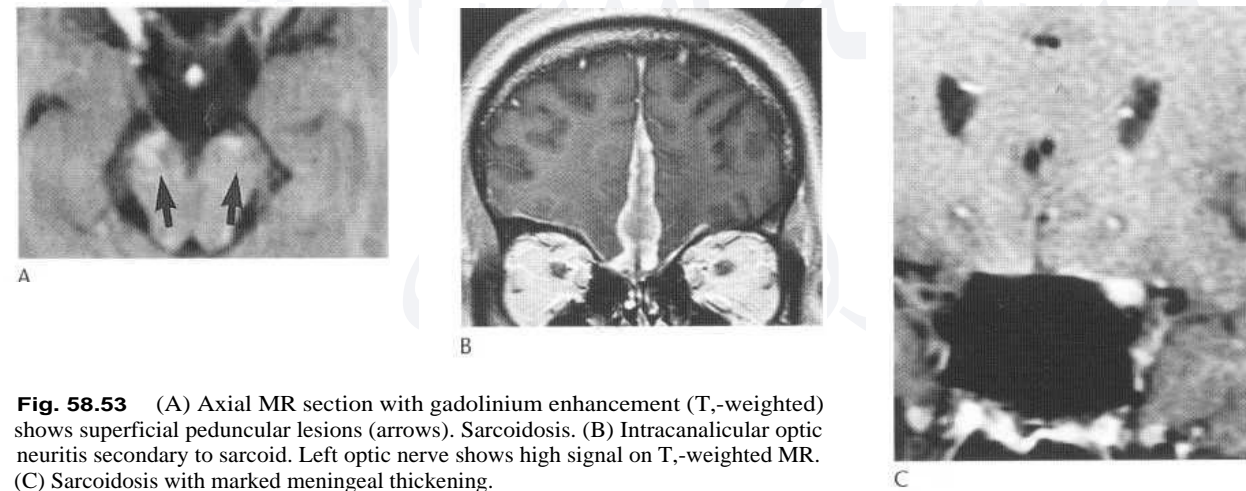


Fig. 58.53 (A) Axial MR section with gadolinium enhancement (T₁-weighted) shows superficial peduncular lesions (arrows). Sarcoidosis. (B) Intracanalicular optic neuritis secondary to sarcoid. Left optic nerve shows high signal on T₁-weighted MR. (C) Sarcoidosis with marked meningeal thickening.

leptomeningitis or as intracerebral granulomas, although both may be present. Clinically patients with chronic leptomeningitis present with hydrocephalus and those with granulomas with focal signs, depending on the site of the lesion (Fig. 58.53).

CT In the meningitic form CT will demonstrate communicating hydrocephalus associated with enhancing hyperdensities in the basal cisterns, an appearance which is non-specific. Granulomas are also hyperdense and enhance with contrast medium. They may be multiple and small, resembling metastases, although there is no surrounding oedema. A single large lesion is occasionally seen and simulates a neoplasm.

MRI A variety of changes have been described. Many of these have not been detected by CT, but they are non-specific. The commonest abnormalities are areas of hyperintensity on T₂-weighted images in the cerebral white matter, usually located more superficially than the lesions of multiple sclerosis, although periventricular lesions do occur. Surface granulomas may be shown, especially adjacent to the major cisterns (Fig. 58.50), and also deeper lesions involving the basal ganglia typically with marginal enhancement after contrast.

Behcet's syndrome MRI commonly reveals non-specific changes, characterised by hyperintensity on T₂-weighted images. The optic chiasm, hypothalamus and brainstem are frequently involved.

DEGENERATIVE AND METABOLIC DISORDERS

Cerebral atrophy and low-pressure hydrocephalus

Cerebral atrophy may be focal or generalised.

Focal atrophy may be vascular, infective or traumatic in origin and the causes have been discussed above. It may also be degenerative, as in olivopontocerebellar atrophy, which is discussed below.

Generalised atrophy is more commonly degenerative or idiopathic, although vascular, inflammatory, toxic and traumatic types also occur or may be associated. Toxic atrophy may follow alcohol or drug abuse.

Generalised atrophy of the brain is a routine concomitant of the ageing process and is a normal finding in the elderly, increasing with age. The loss of neural tissue in the senile brain occurs in a cranium of unchanged size and is therefore compensated by an

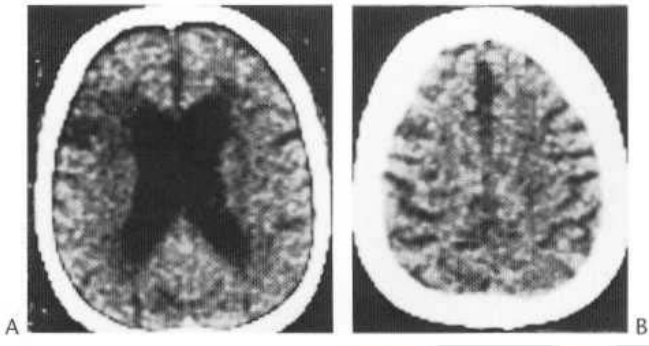


Fig. 58.54 Generalised atrophy. (A) Dilated lateral ventricle. (B) Enlarged sulci and interhemispheric fissure (L36, W80).

increased volume of CSF, which occupies the resulting enlarged ventricles, sulci and subarachnoid space.

Imaging CT or MR/ of patients with cerebral atrophy shows in varying degrees:

1. Ventricular dilatation with rounding of the ventricular angles
2. Enlargement of the cerebral and cerebellar sulci
3. Increased width of the subarachnoid space and basal cisterns, with increased prominence of the interhemispheric and sylvian fissures.

Diagnosis is usually obvious (Fig. 58.54) but can occasionally be more difficult in patients with communicating hydrocephalus, particularly in the elderly patient with 'normal-pressure' or 'low-pressure' hydrocephalus.

Communicating hydrocephalus (Fig. 58.55) The ventricular bodies and frontal horns are often more rounded: the temporal horns are also characteristically more dilated and prominent. They are usually normal or relatively small with atrophy. In addition the sulci are less prominent with hydrocephalus, rather than dilated as in atrophy. Periventricular lucencies at CT, usually most marked around the frontal horns, are also a feature of hydrocephalus, and are due to seepage of CSF through the ependyma. Nevertheless, cases do arise where imaging remains equivocal and in these cases further investigation may be required.

The problem is usually to decide whether patients with dementia are suffering from normal pressure hydrocephalus (NPH) or merely atrophy, as the former have been said to benefit from a shunting operation. Many investigations have been advocated to distinguish central atrophy (mainly ventricular enlargement) from NPH, and

none are reliable and hence are rarely used in most centres. *Radionuclide cisternography* or *CT cisternography* have been advocated. With both methods the ventricles of hydrocephalus patients may be outlined at 12-24 hours and remain so for 48-72 hours: normal patients or those with atrophy show little radionuclide or contrast within the ventricles but much over the cortex. However these methods are rarely used.

Pseudoatrophy Fluid shift from the brain may result from high doses of steroids and from anti diuretics. It is also described in anorexia, protein starvation, and severe dehydration. The resulting pseudoatrophy may simulate the CT appearances of true atrophy, but is reversible with appropriate treatment.

Primary neurodegenerative conditions

In this section, the following will be considered:

1. The dementias
 - Alzheimer's disease (AD)
 - Frontotemporal dementia (FTD)
 - Lewy body dementia
 - Vascular dementia (including CADASIL)
2. Extraparainidal and other movement disorders with or without dementia
 - Parkinson's disease
 - Multiple system atrophy (MSA)
 - Progressive supranuclear palsy (PSP)
 - Motor neurone disease (MND)
 - Corticobasal degeneration (CBD)
 - Huntingdon's disease
3. Prion diseases
 - Sporadic and iatrogenic Creutzfeldt-Jacob disease (CJD)
 - Familial CJD
 - New variant CJD (nvCJD)
 - Gerstmann-Strussler-Scheinker disease (GSSD)
 - Fatal familial insomnia (FFI)
4. Cerebellar atrophy.

These are usually diseases of the ageing population. Most patients progress to death within 5-10 years. In the early stages, the diseases can be difficult to differentiate from normal ageing, or between one another at a clinical level. Interest has been greatly enhanced in recent years by advances in molecular pathology and

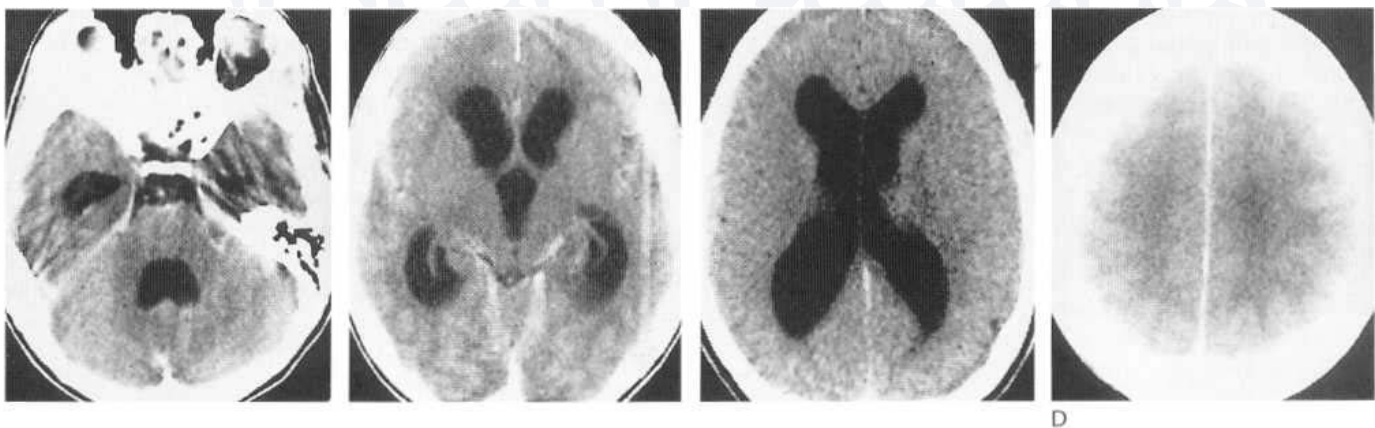


Fig. 58.55 (A-D) Communicating hydrocephalus complicating meningitis. All four ventricles are dilated and the sulci are effaced.

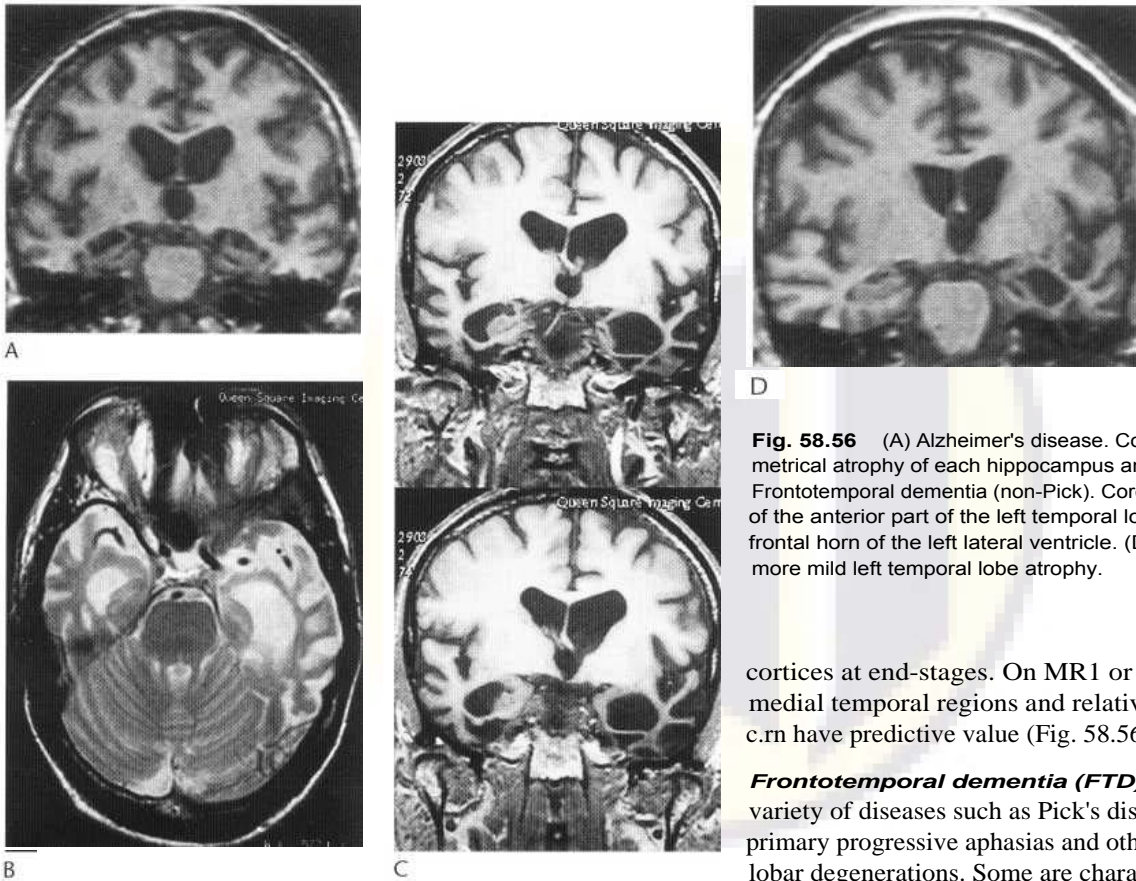


Fig. 58.56 (A) Alzheimer's disease. Coronal MRI showing bilateral symmetrical atrophy of each hippocampus and parahippocampal gyrus. (B,C) Frontotemporal dementia (non-Pick). Coronal MRI showing severe atrophy of the anterior part of the left temporal lobe and mild enlargement of the frontal horn of the left lateral ventricle. (D) True Pick's disease, showing more mild left temporal lobe atrophy.

genetics. As well as neurone loss and gliosis, most of these conditions are characterised pathologically by intracytoplasmic inclusions in neurones or glia, or mainly extracellular amyloid deposits. Many of the proteins in these materials have been characterised and the genes which encode them identified. Familial trends are recognisable in an increasing proportion. At this moment, however, these diseases are still classified syndromically, but the molecular pathologies suggest that there is enough phenotypic variation for syndromes to overlap, adding to diagnostic difficulties. This is a rapidly evolving area. The role of imaging traditionally has been to exclude symptomatic causes such as neoplasms, chronic infections, arteritis, diffuse vascular malformations, or to diagnose intercurrent disease. The development of newer forms of treatment, both symptomatic and directed at molecular mechanisms, has increased the need for precise early diagnosis, and the importance of the positive predictive value of imaging has become considerably enhanced. Because structural imaging has been perceived as wanting in this area, clinical roles for functional imaging using radionuclides (PET and SPECT) or functional or perfusion MRI have been advocated. Despite a large and encouraging literature developed over many decades, functional imaging has proved disappointing as a discriminator, especially in difficult cases, or in early stages of disease, and is little used by many centres except in ongoing research.

Alzheimer's disease This is characterised pathologically by neurofibrillary tangles within neurones, and neuritic plaques. Progressive neurone loss, manifesting on CT and MRI mainly as volume loss (atrophy), occurs in the hippocampus in the preclinical and early stages and progresses to involve temporal and medial parietal lobes, only affecting primary motor and sensory

cortices at end-stages. On MRI or CT, accentuated atrophy in medial temporal regions and relative sparing of the cerebellum c.rn have predictive value (Fig. 58.56A).

Frontotemporal dementia (FTD) This category includes a variety of diseases such as Pick's disease, semantic dementia, the primary progressive aphasia and other mainly frontal or temporal lobar degenerations. Some are characterised by very specific isoforms of tau protein, such as Pick, and others are non-tau, such as MND-like inclusion body frontal lobe degeneration. Clinically early stages are characterised by behavioural or speech disturbances. On MRI and CT, striking accentuated atrophy in temporal and/or frontal lobes (usually mainly temporal), with an equally striking anteroposterior gradient of decreasing severity, can be seen, which will then have considerable positive predictive value (Fig. 58.56B).

Lewy body dementia The molecular structure and genes for Lewy bodies have not been fully characterised as yet. Difficult to distinguish from AD clinically, fluctuation in cognition and visual hallucinations are suggestive, together with overlaps with Parkinson's disease. There are no suggestive MRI or CT features.

Vascular dementia The almost iniquitous finding of some ischaemic damage in cerebral white matter and basal ganglia in MRI in the ageing population, its poor correlation with cognitive impairment, and the relative rarity of extensive cortical infarction manifesting mainly as dementia, have cast serious doubt on the existence of this as an independent entity. A familial form affecting younger patients is currently very topical: CADASIL (cerebral autosomal dominant arteriopathy, subcortical infarcts and leucoencephalopathy); stroke and migraine as well as dementia are common clinical features. The gene is known, but sporadic mutations occur. On MRI there is usually striking confluent ischaemic damage throughout the cerebral white matter (including temporal lobes, often spared in arteriosclerotic disease) and basal ganglia (Fig. 58.57).

Parkinson's disease Lewy body intracellular inclusions and neurone loss, maximal in the pars compacta of the substantia nigra, are the pathological hallmarks. Loss or reduction of the

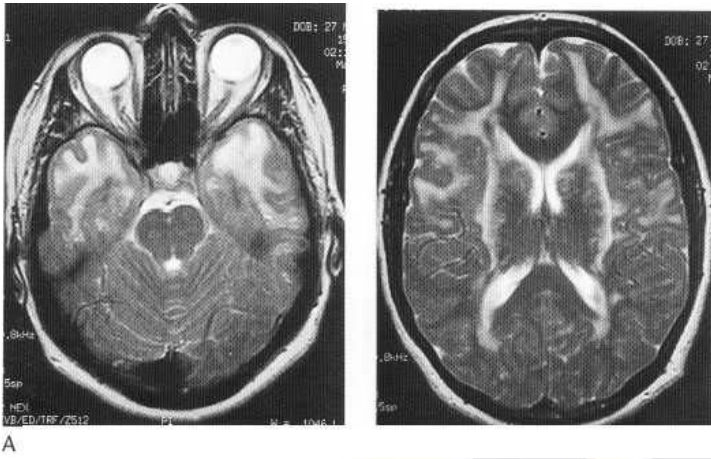


Fig. 58.57 T₂-weighted axial images in a patient with CADASIL (cerebral autosomal dominant arteriopathy, subcortical infarcts and leucoencephalopathy) showing predominantly confluent signal hyperintensity in the cerebral white matter, fairly symmetrical in distribution. The changes are particularly marked in the temporal lobes (A). The basal ganglia also exhibit a lacunar state (B).

normally higher signal of the substantia nigra between the cerebral peduncle and red nucleus in the midbrain on T₂-weighted MRI has been emphasised by some but is highly unreliable.

Multiple system atrophy This is characterised by mainly glial inclusions consisting of alpha-synuclein. There are two main forms. (1) The pontocerebellar type: cerebellum and pons show atrophy on MRI, pontine involvement being characterised by loss of pontine nuclei and shrinkage of the middle cerebellar peduncles (Fig. 58.58). (2) Striatonigral type: the putamen may show reduced signal on MRI due to increased iron deposition and a thin longitudinal cleft may appear in its lateral portion; neither are specific.

Progressive supranuclear palsy Deposition of tau protein and neurone loss accentuated in the midbrain tegmentum may be indicated on MRI by shrinkage and slight signal changes in the midbrain, sparing the cerebral peduncles.

Motor neurone disease Non-(au inclusions and degeneration in spinal motor neurones and pyramidal tracts usually leave no indications on MRI. Occasionally signal change in the tracts can be seen in the brain.

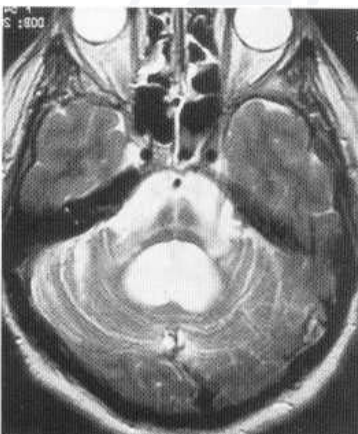


Fig. 58.58 Axial T₂-weighted image in a patient with multisystem atrophy showing marked atrophy of the pons and middle cerebellar peduncles. Abnormal T₂ high signal is present in the pons in the form of a cross (hot cross bun sign) with more confluent signal hyperintensity in the middle cerebellar peduncles. The cerebellum is also atrophic and the 4th ventricle is consequently enlarged.

Corticobasal degeneration This is another tau-opathy. MRI is usually unhelpful, but some cases show selective asymmetric, mainly parietal lobe atrophy, not seen in other conditions.

Huntington's disease A direct gene test is now available for a gene which encodes for the protein Huntingtin. On CT and MRI the caudate nuclei are selectively atrophic in established cases, giving rise to a characteristic appearance of the frontal horns of the lateral ventricles.

Prion diseases These are the spongiform encephalopathies affecting mainly grey matter. Some are hereditary, others are sporadic and transmissible. MRI and CT usually show only progressive cerebral cortical atrophy in CJD, but diffusion-weighted images often show altered diffusion in large areas of cerebral cortex. In a minority of cases (10%), diffuse, symmetrical mildly increased signal in the caudate nucleus and putamen may be seen. In new variant CJD, symmetrically increased signal in the pulvina of each thalamus is a consistent and specific diagnostic feature on MRI, sometimes also involving the medial thalamus and upper midbrain. Progressive mainly cerebellar atrophy may be seen on MRI in GSSD.

cerebellar atrophy Apart from those already mentioned, the main causes are paraneoplastic, toxic (e.g. phenytoin, alcohol), genetic (spinocerebellar atrophies, Friedreich's ataxia, hereditary telangiectasia), and of course, unknown. Involvement of the pons on MRI usually indicates multiple system atrophy; atrophy of the lower brainstem and upper spinal cord is suggestive of Friedreich's ataxia (Fig. 58.59).

Wilson's disease (hepatolenticular degeneration) Hepatolenticular degeneration is a familial metabolic disease due to an abnormality of copper metabolism in which cirrhosis of the liver is associated with degeneration of the corpus striatum. It usually commences in the second decade. Clinically there is progressive rigidity and tremor, dysarthria and dysphagia, and in the terminal stages some degree of dementia. A characteristic feature is a ring of brown pig-

CT The brain may show no significant changes, but low-density lesions may be seen in the basal ganglia of more advanced cases.

MRI MRI may show increased signal in the basal ganglia on T₂-weighted images and low signal on T₁-weighted images. The



Fig. 58.59 Cerebellar atrophy showing widened sulci and fissures. The brainstem is also atrophic.

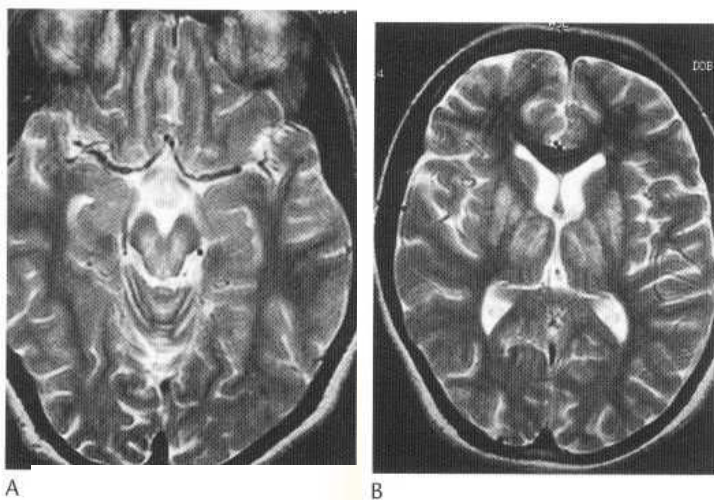


Fig. 58.60 T₂-weighted axial images demonstrating basal ganglia, thalamic and midbrain lesions in Wilson's disease.

lentiform nucleus is most commonly affected. In a few cases low signal has been observed in T₂-weighted sequences, associated with either copper or iron deposited in the basal ganglia.

Calcification of the basal ganglia

Bilateral symmetric calcification of the basal ganglia is not uncommon. Pathologically, the heaviest calcifications are found in the globus pallidus, caudate nucleus and putamen. The dentate nuclei of the cerebellum and the internal capsule may also be involved. Smaller collections, which are only rarely visible at imaging, occur at the junction of cortex and white matter and in the cerebellar cortex. Histopathologically the calcifications are deposits of tiny pericapillary calcospherites plus calcification in the medial walls of tiny arteries and veins (Fig. 58.61).

The major causes, and some other conditions in which calcification of a less typical type may be found in the basal ganglia, are listed in Box 58.3.

Idiopathic calcification is by far the commonest type and is seen mainly in the elderly, where it may be regarded as a normal variant of little pathological significance. The condition is usually encountered as a chance finding either at simple X-ray of the skull (see Ch. 53) or more frequently at CT. The latter is far more sensitive than simple X-ray and has shown the condition to be more common than previously realised (Fig. 58.54), being present in 0.6% of one large series of 7000 consecutive CT examinations.

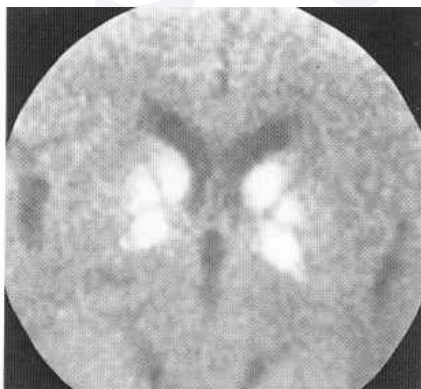


Fig. 58.61 Calcification of the basal ganglia.

Box 58.3 Causes of calcification in the basal ganglia

Major	Cockayne's syndrome
Idiopathic	Carbon monoxide poisoning
Familial	Lead poisoning
Hypoparathyroidism	Toxoplasmosis
Pseudohypoparathyroidism	Mineralising microangiopathy
Minor or atypical	Secondary hyperparathyroidism
Fahr's syndrome	Mitochondrial cytopathy

Familial calcification is very rare but when it occurs affects young as well as elderly members of the same family.

Hypoparathyroidism, either idiopathic or following thyroidectomy, is the most important aetiological cause because it is potentially treatable.

Pseudohypoparathyroidism (Albright's syndrome) may also be associated with similar calcification. This rare condition is described in the bone section (see Ch. 42).

Fahr's syndrome (idiopathic familial cerebrovascular ferrocaldinosis) is a rare familial condition commencing in childhood and characterised by the deposition of iron and calcium in the basal ganglia, dentate nuclei and subcortical regions. It presents with spasticity and choreoathetoid movements, proceeding to progressive mental deterioration (Fig. 58.62).

Cockayne's syndrome, which is inherited as an autosomal recessive, is characterized by dwarfism and progeria. There is microcephaly and a thick cranial vault as well as the intracranial calcification (Fig. 58.63).

The calcification in *toxoplasmosis* is linear or nodular rather than amorphous (Fig. 58.43) and in the other conditions the diagnosis is usually clear from the history and clinical findings.

Carbon monoxide poisoning is usually due to attempted suicide. Classic cases show necrosis of the globus pallidus, giving rise to bilaterally symmetric small lucent areas in this characteristic site. Calcification is unusual but has been described.

Mineralising microangiopathy is also referred to as disseminated necrotising leucoencephalopathy. It is a rare condition seen mainly in patients with leukaemia treated with cerebral radiotherapy followed by intrathecal methotrexate. In the acute phase there is bilat-

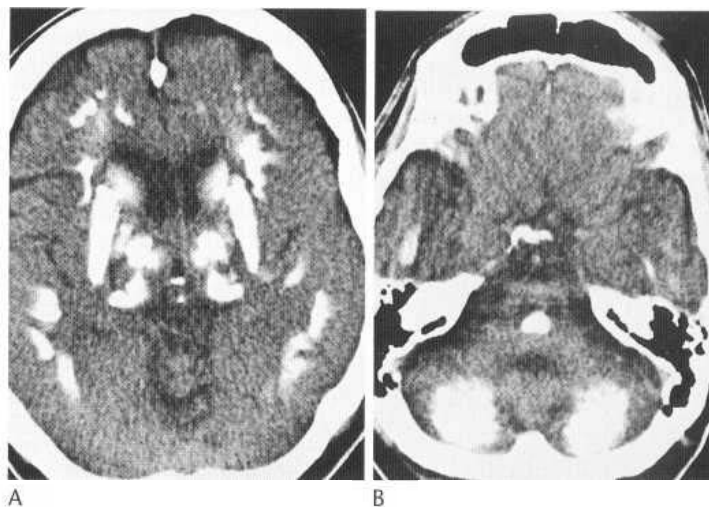


Fig. 58.62 Axial CT scans demonstrating extensive calcification in the basal ganglia, thalami, subcortical white matter, brainstem and dentate nuclei of the cerebellum in Fahr's syndrome.

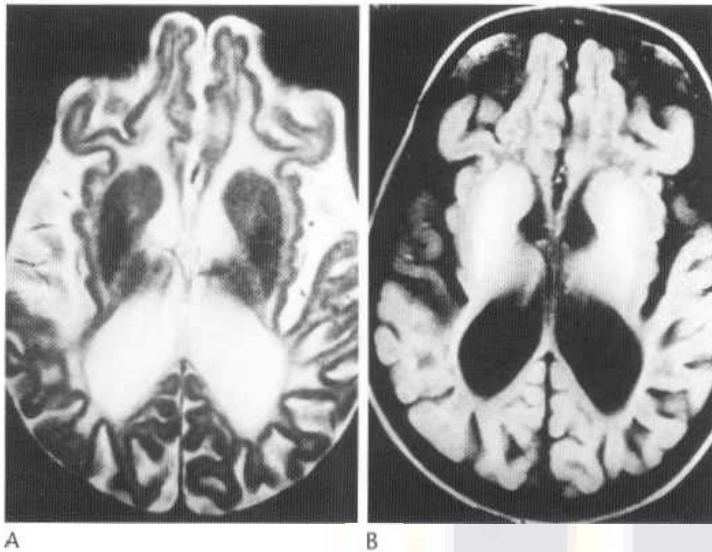


Fig. 58.63 Axial T₂- and T₁-weighted images in Cockayne's syndrome demonstrating gross supratentorial atrophy and diffuse signal abnormality and reduction in bulk of the white matter. T₁ high and T₂ low signal in the basal ganglia is indicative of calcification.

oral leucoencephalopathy, and CT may show bifrontal low density in the white matter, but atrophy follows later.

Mineralising microangiopathy shows low attenuation in the white matter, mainly near the corticomedullary junction and with relative sparing of the deeper white matter. Thin reticular or serrated linear calcification is also present at the corticomedullary junction as well as in the basal ganglia and posterior fossa, giving rise to a very characteristic appearance.

Secondary hyperparathyroidism is often associated with extensive calcification in the falx and tentorium, and this is evident at simple X-ray of the skull. Rarely, intracerebral calcification is identified at CT and occurs in the basal ganglia and also in the white matter.

White-matter disorders

Under this heading we shall discuss conditions of differing aetiologies which have in common predominant involvement of the white matter. White-matter diseases have been classified as *dysmyelinating*, where there is abnormal formation or maintenance of myelin, and *demyelinating*, where there is destruction of normally formed myelin (Box 58.4). To these may be added miscellaneous causes of what may be termed 'secondary' demyelination inflammatory and postinflammatory lesions and neoplastic, vascular, toxic and other disorders.

Some of these have already been discussed, e.g. disseminated encephalomyelitis, progressive multifocal encephalopathy (PML) and Reye's syndrome. Other conditions which fall into this category are described below.

Box 58.4 Disorders of white matter

Dysmyelinating	Schilder's disease
Leucodystrophies	Central pontine myelinolysis
Metabolic disorders	Marchiafava-Bignami disease
Demyelinating (myelinoclastic)	Secondary to other disorders
Multiple sclerosis	

Changes in the white matter are well shown by CT, but there is no doubt that MRI is even more sensitive in demonstrating white-matter lesions. The changes in specific pathological conditions are described below, but it should be realised that there are also many physiological causes of changes in white-matter density at CT or in its signal at MRI.

Neonates, particularly premature infants, normally show low-attenuation white matter at CT and poorer differentiation between white and grey matter at MRI. This is due to incomplete myelination and improves as myelination progresses. Low-attenuation white matter at CT and abnormal contrast at MRI is also seen in the elderly, usually in association with generalised senile atrophic changes.

Other causes of generalised low attenuation of the white matter at CT and altered signal at MRI include *uraemic* and *hepatic coma* and *hypertensive crises: malignant disease* and *muscular dystrophy* are other rare causes. *Vasogenic oedema* associated with tumour or trauma can also produce focal or more generalised low density, as can radiation damage.

Multiple sclerosis (MS) This is one of the commonest neurological disorders and is characterised by disseminated plaques of demyelination and gliosis throughout the neuraxis. The sites of election are:

1. Periventricular
2. Optic pathways
3. Brainstem
4. Cerebellar white matter and peduncles
5. Spinal cord.

Most authorities consider the aetiology to be immunopathological, and there is an increased incidence of certain tissue type antigens in the affected patients. There is also raised gamma globulin in the CSF. Young adults are primarily affected, with an increased incidence in the colder wet temperate zones of the northern hemisphere.

CT CT may show no abnormality even in the acute stages. In about one-third of patients, small low-density areas are seen in the white matter, particularly adjacent to the atria or in other periventricular sites (Fig. 58.64). In the acute stage these may show marked enhancement (Fig. 58.64B.C), but chronic lesions fail to enhance. Occasionally enhancing small lesions are seen which were isodense before adding contrast medium. Classic cases show no mass effect or surrounding oedema, but very rarely mass effect and oedema are encountered which can simulate tumour, particularly with a single large lesion.

MRI This is far more sensitive than CT in the demonstration of MS plaques, and it has been claimed that an accuracy of nearly 100% can be obtained with modern machines. The most characteristic appearance is that of periventricular nodular hyperintense lesions on T₂-weighted images, most numerous posteriorly (Fig. 58.65), and plaques are also well shown at the grey-white matter interfaces. MRI can even image lesions in the spinal cord, as well as the brainstem and cerebellum. Multiple cerebral lesions are demonstrated in over half the patients presenting with a single episode of optic neuritis, or with clinically isolated brainstem or cord lesions.

As already noted, some lesions may have enough mass effect to simulate a tumour, although this is rare. Others may show a central area of greater signal intensity, resembling a target.

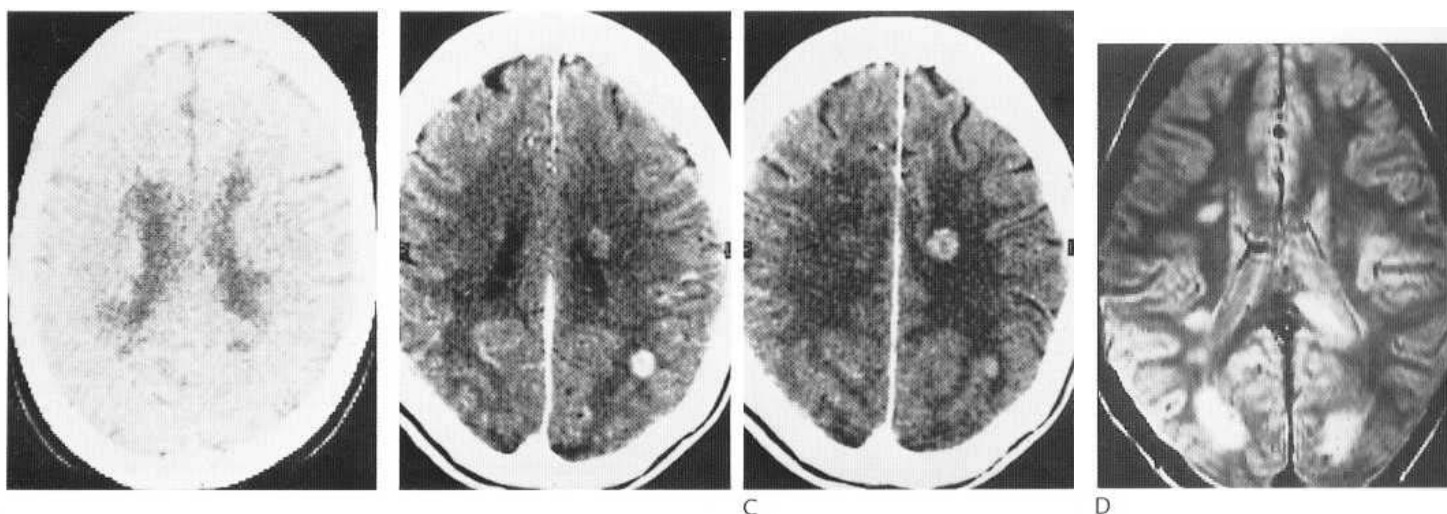


Fig. 58.64 Multiple sclerosis. (A) Paraventricular and white-matter low-density areas. (B,C) Enhancing paraventricular and white-matter low-density areas. (D) Axial MRI section J, -weighted). Multiple sclerosis plaques are seen as areas of high signal.

Contrast enhancement after giving gadolinium occurs in the acute phase, presumably indicating activity, as it later subsides.

It should be remembered that the MRI lesions are non-specific and must be considered in the clinical context. MRI is so sensitive that it shows similar periventricular lesions in around 25% of elderly patients. These may represent ischaemic lesions, as they are particularly noted in patients with multi-infarct dementia. Similar lesions have also been noted following radiotherapy and in encephalomyelitis.

Schilder's disease (diffuse sclerosis) This condition affects children as well as young adults. Histopathologically, the lesions are similar to those of MS, but are more extensive, and clinically the course is continuous and progressive, even fulminant, rather than intermittent and relapsing. The main lesions extend through the corpus callosum into both parieto-occipital regions.

CT Bilateral low-attenuation areas are shown in both parieto-occipital regions which enlarge progressively but not symmetrically. Contrast enhancement is uncommon.

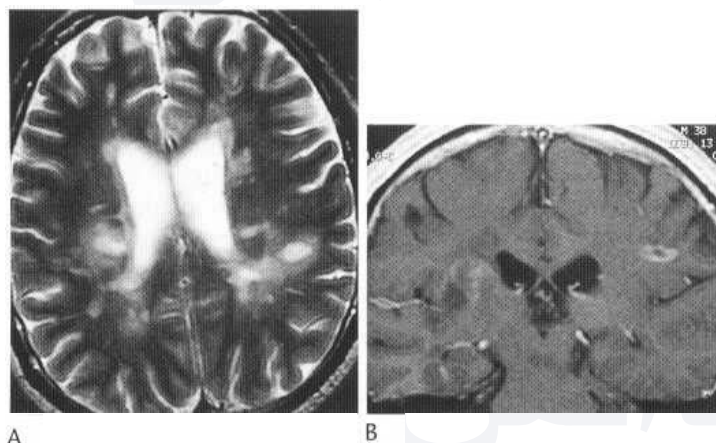


Fig. 58.65 The T₂ axial image (A) demonstrates multiple hyperintense lesions in the cerebral white matter, many of which are periventricular in distribution and typical of multiple sclerosis. A couple of the lesions are associated with perilesional oedema, giving a target appearance, and on the postcontrast T₁ coronal image (B) show patchy and ring enhancement; these lesions are plaques of active demyelination.

MRI This shows the white-matter lesions better than CT, and their true extent is more clearly reflected.

Central pontine myelinolysis This rare condition, primarily affecting the pontine white matter, was originally thought to be due to chronic alcoholism and malnutrition, but was later shown to be, associated with many other chronic illnesses, including neoplasia and liver and kidney diseases. The underlying cause may be an abnormality of plasma sodium, and in most cases hyponatremia has been observed, although the relationship is not a simple one. It is often fatal, but recovery can occur, with varying degrees of neurological deficit.

Imaging CT may demonstrate low density in the affected pons, usually only when the disease is well advanced. MRI is more sensitive and reveals more extensive change. There is increase in T₁ and T₂ within the pons, and changes can be more widespread, extending into the midbrain and thalami and even into the subcortical white matter.

Marchiafava-Bignami disease This is another rare condition, with a peculiar white-matter localisation. The corpus callosum is mainly affected, although other central pathways may also be involved. There is an association with chronic alcoholism, but this is not invariable, and chronic cyanide intoxication can produce similar lesions.

Radiation leucoencephalopathy Radiation used in the treatment of malignant tumours can itself produce harmful effects. This is mainly due to occlusion of small vessels and resulting infarction. In the acute stage there are changes in the white matter indistinguishable from tumour at both CT and MRI. Since the radiation damage is sometimes delayed, and can occur months later this can give rise to a difficult differential diagnosis from tumour recurrence or extension both clinically and on imaging. In this situation PET may help by showing hypermetabolism in tumour recurrence and hypometabolism in radiation necrosis (see below). Radiation changes will eventually progress to local atrophy, although white-matter low density on CT and signal change on MRI will persist (Fig. 58.66).

The association between radiotherapy, methotrexate and PML has been discussed above.

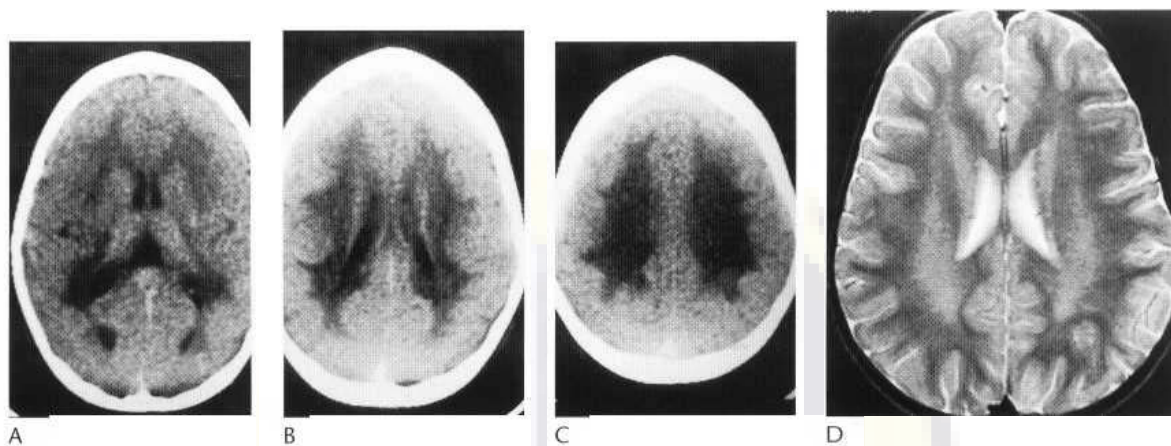


Fig. 58.66 (A-C) Axial CT scans demonstrating confluent and symmetrical low-density change in the deep and peripheral supratentorial white matter in metachromatic leucodystrophy. (D) Axial MR T_2 W shows widespread low density in white matter.

Leucodystrophies

Leucodystrophy is a term commonly used to refer to dysmyelination disorders. They are mainly due to genetic defects in the formation and maintenance of myelin, usually present in infants and children, with increasing developmental delay, progressive dementia and neurological deficits. They include the following conditions, which, like most disorders of lipid metabolism, are inherited as autosomal recessives and are associated with lysosomal enzyme deficiencies:

- Metachromatic leucodystrophy
- Globoid leucodystrophy (Krabbe's disease)
- Spongiform degeneration (Canavan's disease).

Metachromatic leucodystrophy This is one of the commoner hereditary leucodystrophies; clinical symptoms usually commence in infancy, although they can be delayed into adolescence or later. It is due to a deficiency of the enzyme arylsulphatase A.

There is mental retardation or regression and other neurological which are progressively fatal.

Globoid leucodystrophy (Krabbe's disease) This is characterised by a lack of the enzyme P-galactocerebrosidase. It presents in infancy with retardation and spasticity, and is usually fatal by the second year. Rarely, it presents in later childhood with a more chronic course and early visual failure (Fig. 58.67).

Spongiform degeneration The condition is so-called because of the characteristic spongy degeneration produced in the white matter of the affected infant. It is one of the few leucodystrophies that produces enlargement of the head, others being Alexander's disease and GM, gangliosidosis (Tay-Sachs disease).

X-linked leucodystrophies These are less frequent, but two important ones are adrenoleucodystrophy and Pelizaeus-Merzbacher disease.

Adrenoleucodystrophy This is an X-linked genetic disease that was at one time confused with Schilder's disease. It affects

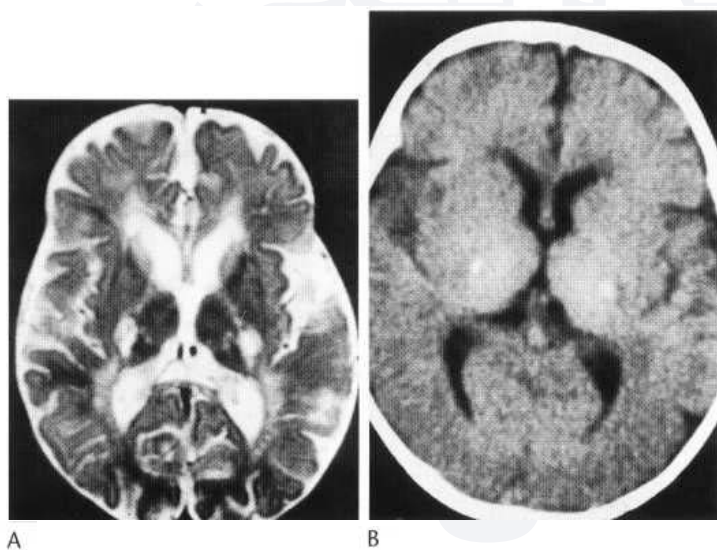


Fig. 58.67 (A,B) Axial CT and T_2 -weighted MRI in Krabbe's disease showing focal bilateral thalamic and posterior internal capsular lesions which are calcified on CT. T_2 signal abnormality is also present in the deep periventricular white matter with some cavitary change adjacent to the frontal horns.

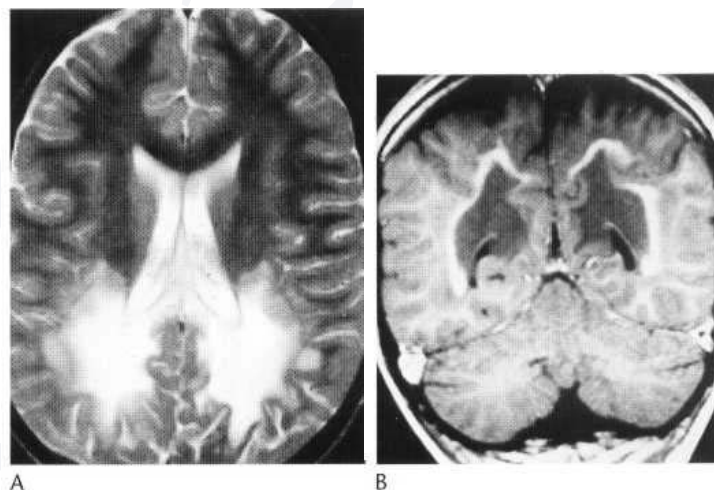


Fig. 58.68 (A,B) Axial T_2 signal abnormality in the periventricular occipitoparietal white matter is fairly symmetrical and extends across the corpus callosum; there are zones of differential T_2 signal hyperintensity representing the different phases of demyelination and appearances are typical of X-linked adrenoleucodystrophy. On the T_1 coronal image a band of enhancement is present at the active edge of the demyelination.

boys aged 4-6 years and occasionally a little older. The victims develop adrenal insufficiency, resembling that in Addison's disease, together with dementia, cortical blindness, ataxia and spasticity (Fig. 58.68).

Pelizaeus-Merzbacher disease This is also X-linked. It presents mainly in infancy, but can begin later. There is progressive dementia, ataxia and nystagmus, often with extrapyramidal features such as dystonic postures and torsion spasms. The metabolic basis remains obscure.

Alexander's disease is one of the few leucodystrophies that occurs sporadically and is characterised histopathologically by the abundant presence of Rosenthal fibres in the affected brain. Definitive diagnosis thus depends on brain biopsy (Fig. 58.69).

Batten's disease (neuronal ceroid lipofuscinosis) This was also referred to as *cerebrum macrum degeneration*, and in contrast to the above the brain is atrophic, often markedly so.

CT CT in the leucodystrophies shows low-density areas in the white matter which are bilateral but not necessarily symmetric and become more extensive as the disease process progresses (Fig. 58.56).

In *adrenoleucodystrophy* the parieto-occipital regions are involved and in thin curvilinear or serrated rim of contrast enhancement may be seen, representing perivascular inflammation at the margins of the extending process. Such enhancement is not seen in the other leucodystrophies described above. Another unusual finding described in adrenoleucodystrophy is dystrophic calcification in the affected white matter.

Krabbe's disease has been described as showing increased density in the basal ganglia as well as hypodensity of the white matter, while *Alexander's disease* has been reported as showing unusual enhancement of the caudate nuclei and periventricular areas in one reported case. Considerable atrophy has been reported to accompany the white-matter changes in *Pelizaeus-Merzbacher disease*.

MRI MRI is more sensitive than CT in the demonstration of white-matter disease. Changes can be diagnosed earlier, are shown more clearly, and appear more extensive. T₂-weighted sequences produce a high signal from affected white matter

(Figs 58.68, 58.69). In *adrenoleucodystrophy* maternal carriers have in some cases shown white-matter changes with mild neurological symptoms. Similar findings have been reported in carriers of *Pelizaeus-Merzbacher disease*.

Amino and organic acidopathies

This is a wide group of metabolic disorders caused by enzyme defects resulting in accumulation of toxic metabolites in the body and in the brain, where they interfere with normal myelin synthesis or cause destruction of myelin sheaths. They present in infants and with improved methods of biochemical assay many different types have now been defined, some of which are listed in Box 58.5. Diagnosis is usually made biochemically but imaging may help by showing the degree of myelin damage or the effect of treatment on progression.

Imaging CT may show small low-density foci in the white matter but MRI shows the white-matter lesions best as small areas of high signal on T₂-weighted studies, and lying subcortically or in the centrum ovate. Sagittal T₂ sections may demonstrate small low-density lesions in the corpus callosum. The findings are non-specific.

Phenylketonuria This is a congenital disorder of amino acid metabolism due to absence of phenylalanine hydroxylase which hydrolyses phenylalanine to tyrosine. Severe mental impairment may ensue if the condition is unrecognised and untreated, and

Box 58.5 Amino and organic acidopathies

- | | |
|---------------------------------------|------------------------------|
| Phenylketonuria | Homocystinuria |
| Hyperphenylalaninaemia | Cystathioninuria |
| Tyrosinaemia | Hypermethioninaemia |
| Maple syrup urine disease | Propionic acidaemia |
| Argininosuccinicaciduria | Methylmalonic acidaemia |
| Citrullinaemia | Non-ketotic hyperglycinaemia |
| Ornithine transcarbamylase deficiency | Lactic acidaemia |
| Hyperargininaemia | |

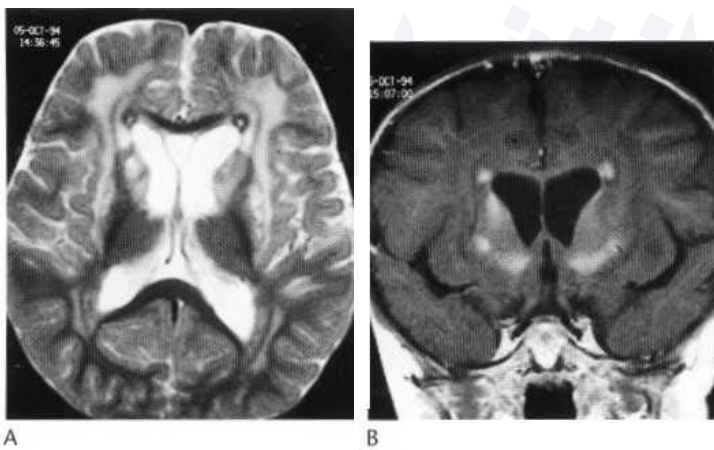


Fig. 58.69 (A) Axial T₂ and (B) T₁ coronal postcontrast images in a patient with Alexander's disease showing signal abnormality in the white matter, which has a predilection for the frontal lobes. There is some basal ganglia involvement and enhancement postcontrast.

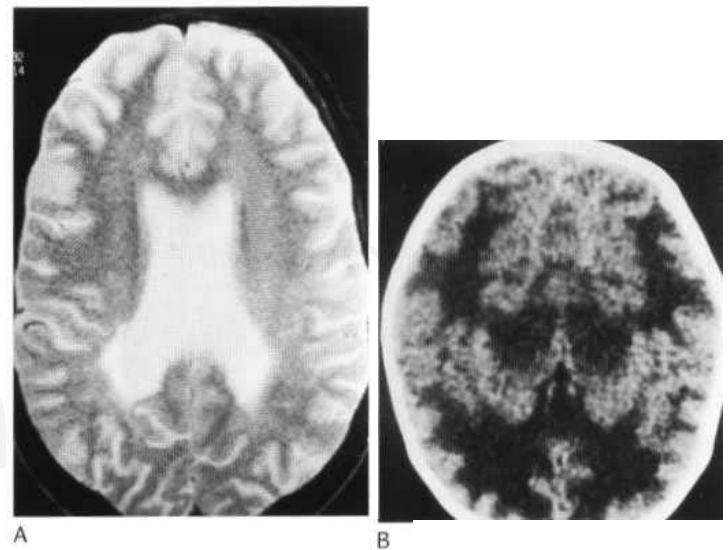


Fig. 58.70 (A) Axial T₂-weighted MRI showing bilateral parietal periventricular signal abnormality in a patient with classical phenylketonuria. (B) Axial CT showing extensive very low density change in the cerebral white matter and thalami in maple syrup urine disease.

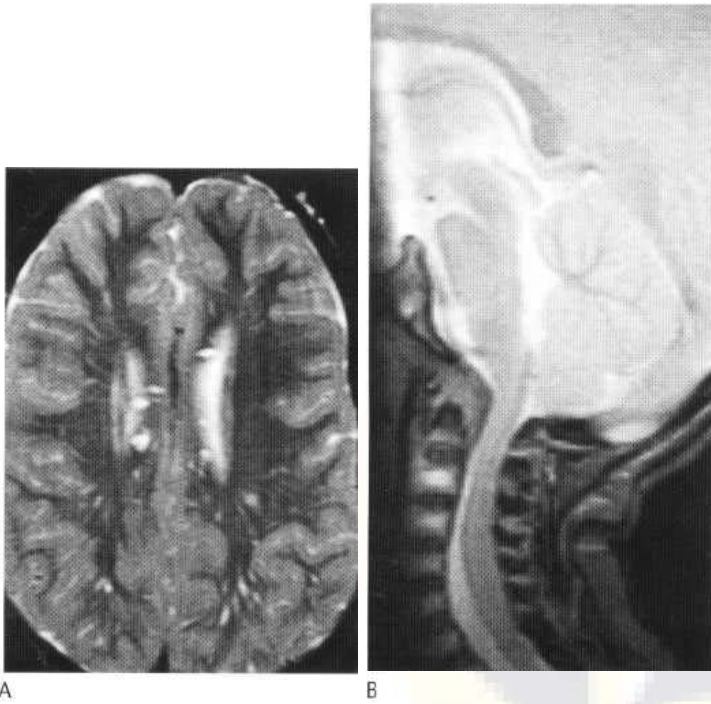


Fig. 58.71 (A) Multiple dilated perivascular spaces are present on the T₂-weighted axial image in this patient with mucopolysaccharidoses. (B) T₂ sagittal image through the craniocervical junction in Morquio's syndrome showing a small foramen magnum and some cervical cord impingement. There is odontoid hypoplasia and ligamentous and dural thickening contributing to the small foramen magnum.

there are alterations in the hemisphere myelin resembling leukodystrophy. The white-matter changes have been characterised by MRI (Fig. 58.70).

Mucopolysaccharidoses The skeletal abnormalities seen in these lysosomal storage disorders have been described in Chapter 35. Diagnosis is made by the characteristic urinary mucopolysaccharides combined with the clinical picture (Fig. 58.71).

Imaging The brain shows atrophy and hydrocephalus and in some cases megalencephaly. White-matter changes appear as diffuse low attenuation at CT or as high signal on T₂-weighted MRI images.

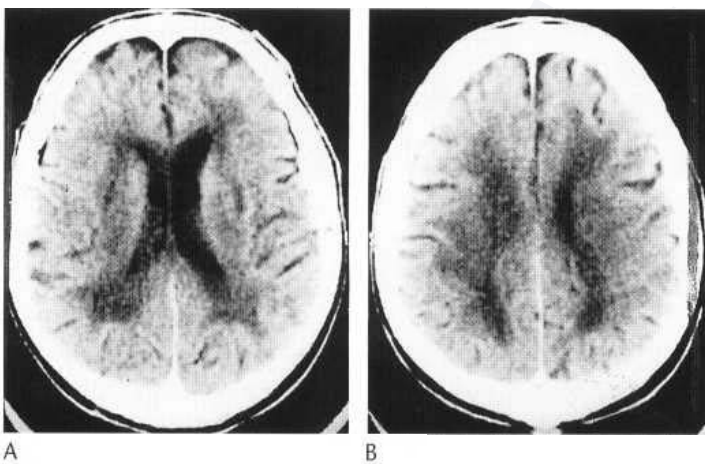


Fig. 58.72 (A,B) CT of elderly demented patient. Cortical atrophy is mild but there are extensive areas of patchy low density in the deep cerebral white matter. Binswanger's disease.

Binswanger's disease (subcortical arteriosclerotic encephalopathy) There is a frequent association between hypertension, arteriosclerosis and dementia or other neuropsychiatric manifestations. The deep penetrating arteries of the brain are affected, leading to ischaemic changes in the deep white matter, associated with generalised atrophy. Some authorities consider this to be a form of multi-infarct dementia, but others regard the changes as non-specific senile changes.

CT There is generalised atrophy with multifocal or generalised low attenuation of the white matter, particularly around the ventricles (Fig. 58.72). There is no enhancement after contrast medium. Other findings reported in some cases include lacunar infarcts in the basal ganglia. However, similar low-attenuation changes may be seen in the brains of many elderly people who are normotensive and without dementia or other neurological signs. Lacunar infarcts and atrophy are also non-specific.

MRI MRI will demonstrate the white-matter changes more sensitively than CT and will also show the generalised atrophy. Periventricular lesions are well shown but it should be realised that these are not specific and similar lesions may be seen in some symptomless elderly patients.

Mitochondrial cytopathy

This is a group of diseases that have in common a defect in mitochondria, with consequent deficiency of enzymes controlling oxidative phosphorylation and/or the respiratory chain. They frequently involve muscle and may cause a proximal myopathy. Involvement of the CNS can result in very varied clinical presentations associated with elevation of the serum and CSF lactate (Figs 58.73, 58.74). The typical presentations include:

1. Myoclonic epilepsy with ataxia
2. Ophthalmoplegia with retinal degeneration, which is often associated with heart block and elevated CSF protein
3. Stroke-like episodes, often associated with episodic vomiting and cortical blindness.

The disease is transmitted through the maternal cytoplasm and is non-mendelian. The affected persons are often short in stature.

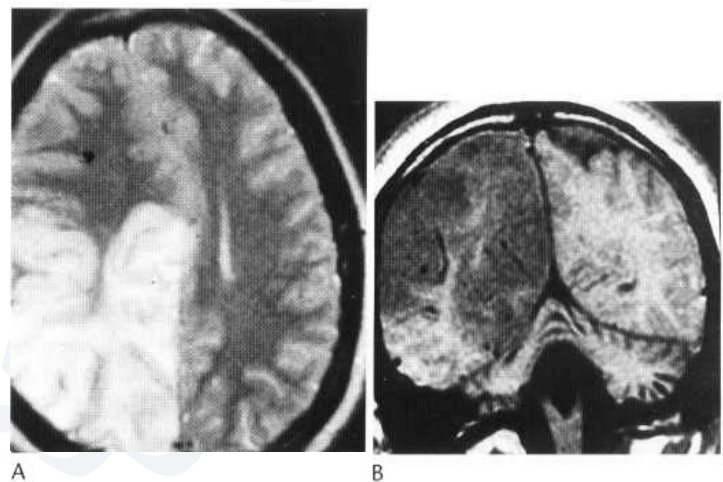


Fig. 58.73 (A) Axial T₂- and (B) coronal T₁-weighted images showing extensive signal abnormality in the cortex and white matter of the right cerebral hemisphere in MELAS. There is some mass effect and note that the signal change involves all three vascular territories, although is largely posterior in distribution. There is also cerebellar atrophy.

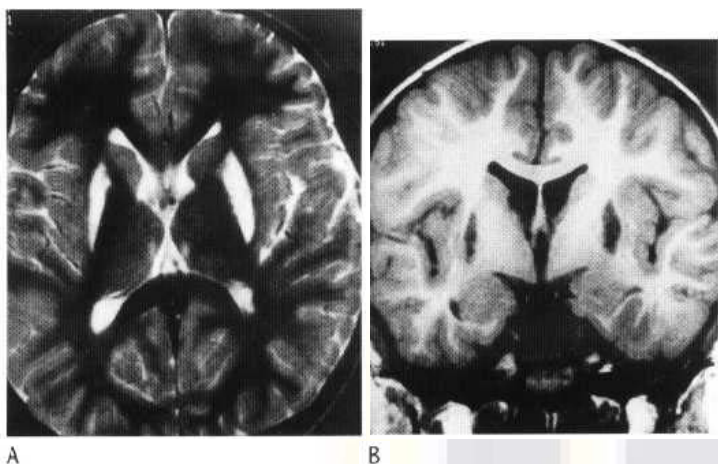


Fig. 58.74 Bilateral mature cystic cleft-like lesions have occurred in the lentiform nuclei in this patient with a mitochondrial cytopathy. (A) Axial MR T₂ W. (B) Coronal MR T₂ W.

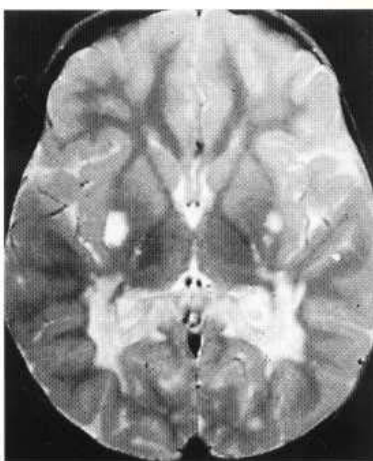


Fig. 58.75 Mitochondrial cytopathy. Four-year-old boy with ataxia, myoclonus and drowsiness. MRI (T₁-weighted) reveals loci of high signal in the lentiform nuclei and parietal white matter extending into posterior limbs of internal capsule.

The histopathology includes subacute necrotising encephalomyelopathy associated with proliferation of capillaries and glia and with spongiform degeneration. The distribution, reflected in the MRI appearances, includes symmetric necrosis in the basal ganglia, spongiform change with increase in T₁ and T₂ in the thalamus, brainstem and/or hemispheric white matter (Fig. 58.75). In the more chronic presentations such as *Kearn-Sayer syndrome* there may be basal ganglia calcification associated with atrophy, which may be marked in the cerebellum and brainstem. The stroke-like episodes are reflected in focal abnormalities closely resembling [infarcts](#).

EPILEPSY

Box 58.6 gives the classification of seizures by the Commission of Classification of the International League Against Epilepsy; Box 58.7 gives the classification of myoclonus and epilepsy syndromes.

Partial seizures are further subdivided into the suspected lobe or region of origin based on seizure semiology. Thus we have temporal lobe seizures (mesial or lateral temporal neocortex), frontal (jacksonian, supplementary motor, premotor, cingulate, orbito-frontal) and parieto-occipital. There is also an important distinction between *habitual* and *recent onset* seizures, and *symptomatic* epilepsy where seizures occur as part of other diseases.

Box 58.6 Classification of seizures

Partial seizures (localisation related, focal)

Simple (consciousness unimpaired)

- Motor
- Somatosensory
- Autonomic
- Psychic

Complex (impaired consciousness)

- Beginning as simple
- Complex at onset
- Secondary generalised

Generalised seizures

- Absence seizures
- Myoclonic seizures
- Clonic seizures
- Tonic seizures
- Tonic-clonic seizures
- Atonic seizures

Box 58.7 Classification of myoclonus and epileptic syndromes

Infantile and childhood epilepsies

- Infantile spasm
- Lennox-Gastaut syndrome
- Cryptogenic myoclonic epilepsy

Adolescent epilepsies

- Early morning myoclonus with tonic-clonic seizures
- Myoclonus simple absence

Progressive myoclonic epilepsies

- Lipidoses
- Ceroid lipofuscinosis (Kufs' disease)
- Lafora body disease
- Sialidosis
- Mitochondrial cytopathy
- Baltic myoclonus

In the generalised epilepsies imaging is usually negative or shows only evidence of trauma due to the seizures; but if a causative focal lesion is found, the diagnosis will change from generalised to secondary generalised epilepsy.

In patients with seizures of recent onset, imaging (either CT or MRI) is recommended in most cases: in developed countries, causative lesions will be found in only 5-10% (usually neoplasms); in some less developed countries it can be as high as 50% due to tuberculosis or cysticercosis. Malformations of cortical development, whether focal, lobar or generalised, are much more common in focal childhood epilepsies, and are rarely found with late-onset seizures.

In patients with partial epilepsy of habitual type, the causative lesions are shown by MRI in about 20% of cases overall, and in up to 60% in some types. The lesions found, in approximate order of prevalence, are:

- Hippocampal sclerosis (over 50% of the total) (Figs 58.76, 58.77)
- Benign neoplasms
- Cortical scars
- Vascular lesions (Fig. 58.78)
- Malformation of cortical development.

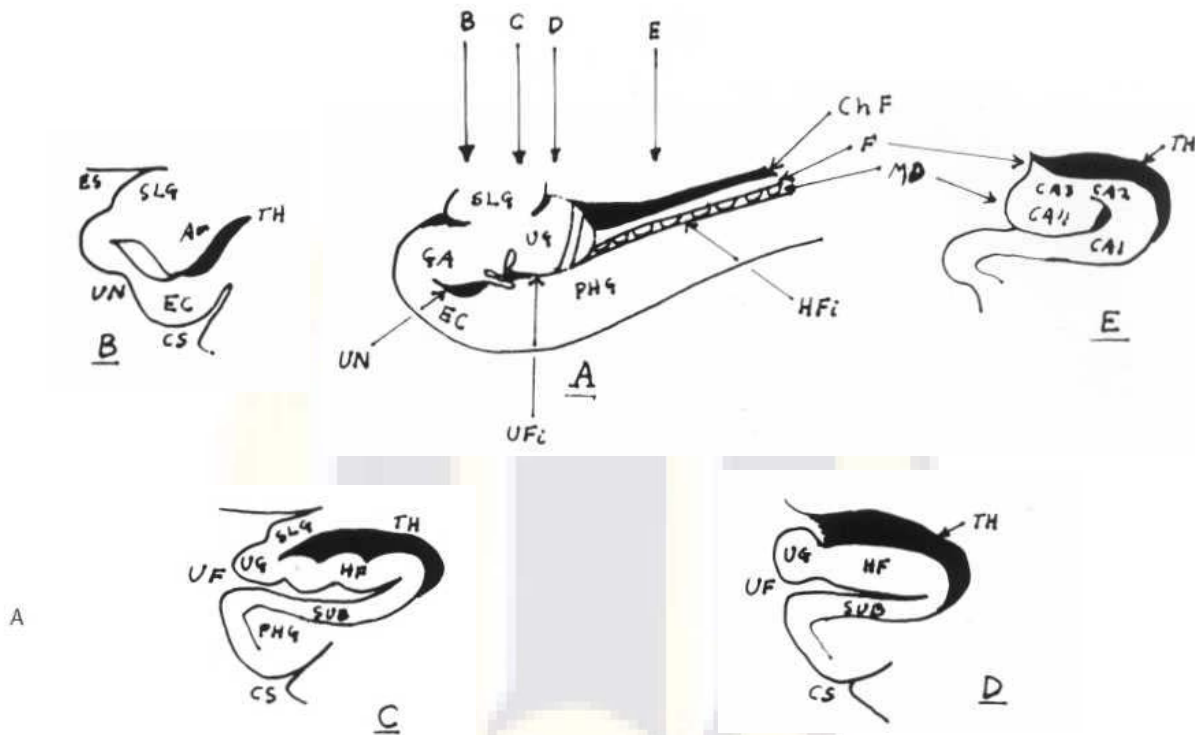
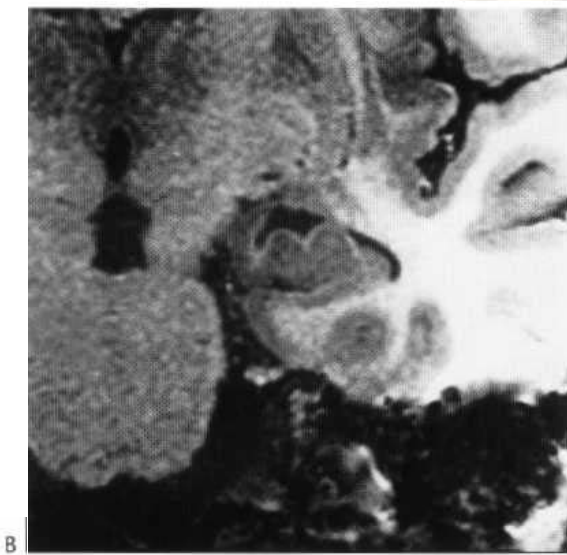


Fig. 58.76 (A) Diagram of hippocampus and its relationships. A. Lateral aspect of left temporal lobe. B-E Coronal sections from before backward at levels shown in A. Ch F = choroidal fissure; F = fimbria; MD = margo denticulatus (dentate gyrus); HF = hippocampal fissure; TH = temporal horn; CA1 = four regions within hippocampus itself; PHG = parahippocampal gyrus; UN = uncus; EC = entorhinal cortex; UG = uncinatus gyrus; SLG = semilunar gyrus (part of amygdala); GA = gyrus ambiens; HF = hippocampal formation; OF = uncus fissure; CS = collateral sulcus; UN = uncus notch; SUB = subiculum. (B) Coronal MRI section through left medial temporal lobe at level of C above. T₂-weighted.



Hippocampal sclerosis (HS) Neurone loss and gliosis maximal in hippocampal subfields CA1 and CA4 manifests on MRI as (I) reduction in volume, and (O) increased signal on T₂-weighted images. These features are confined to the hippocampus. Although many extrahippocampal abnormalities have been described on MRI, none are reliable in isolation and the significance and even the existence of some are doubtful. The optimal MRI protocol for detection of HS is as follows.

Dual-echo fast spin-echo acquisition in the coronal plane, slice thickness 5 mm, and a T₂-weighted volumetric acquisition also in the coronal plane, with slice thickness 1.5 mm or less. The dual echo acquisition is designed to maximise contrast resolution for detection of T₂-dependent signal change, and the volumetric acquisition for volume loss. We usually also add a coronal FLAIR acquisition: it sometimes aids recognition of small cortical abnormalities that might otherwise be overlooked. This protocol is therefore

appropriate for investigating habitual epilepsy in general. HS usually seems unilateral on imaging, so diagnosis is affected by comparing the two sides. Measurements of volume and relaxometry are not usually necessary but may aid detection of bilateral abnormalities. CT does not detect HS at all.

Neoplasms These are benign and are usually centred on cerebral cortex of usually temporal or frontal lobes. They are often circumscribed. The commonest in this context is dysplastic neuroepithelial tumour (DNT), described elsewhere.

Cortical scars These may be small or extensive. They usually involve frontal lobes. They result from trauma, infarction or infections, in descending order of frequency.

Vascular lesions These are usually cavernous and sometimes arteriovenous malformations involving cortex of usually frontal or temporal lobes. Their appearances on MRI and CT are described elsewhere.

Malformations of cortical development (MCD) These can take many forms, and appearances on MRI and CT are described elsewhere. An important one in the context of partial epilepsy is *focal cortical dysplasia*, which manifests on MRI as focal cortical thickening, blurring of the underlying grey-white matter interface and variable signal change in the underlying white matter. Most involve frontal or temporal lobes; they usually are 1-2 cm in size, but can be more extensive. They are indistinguishable from cortical

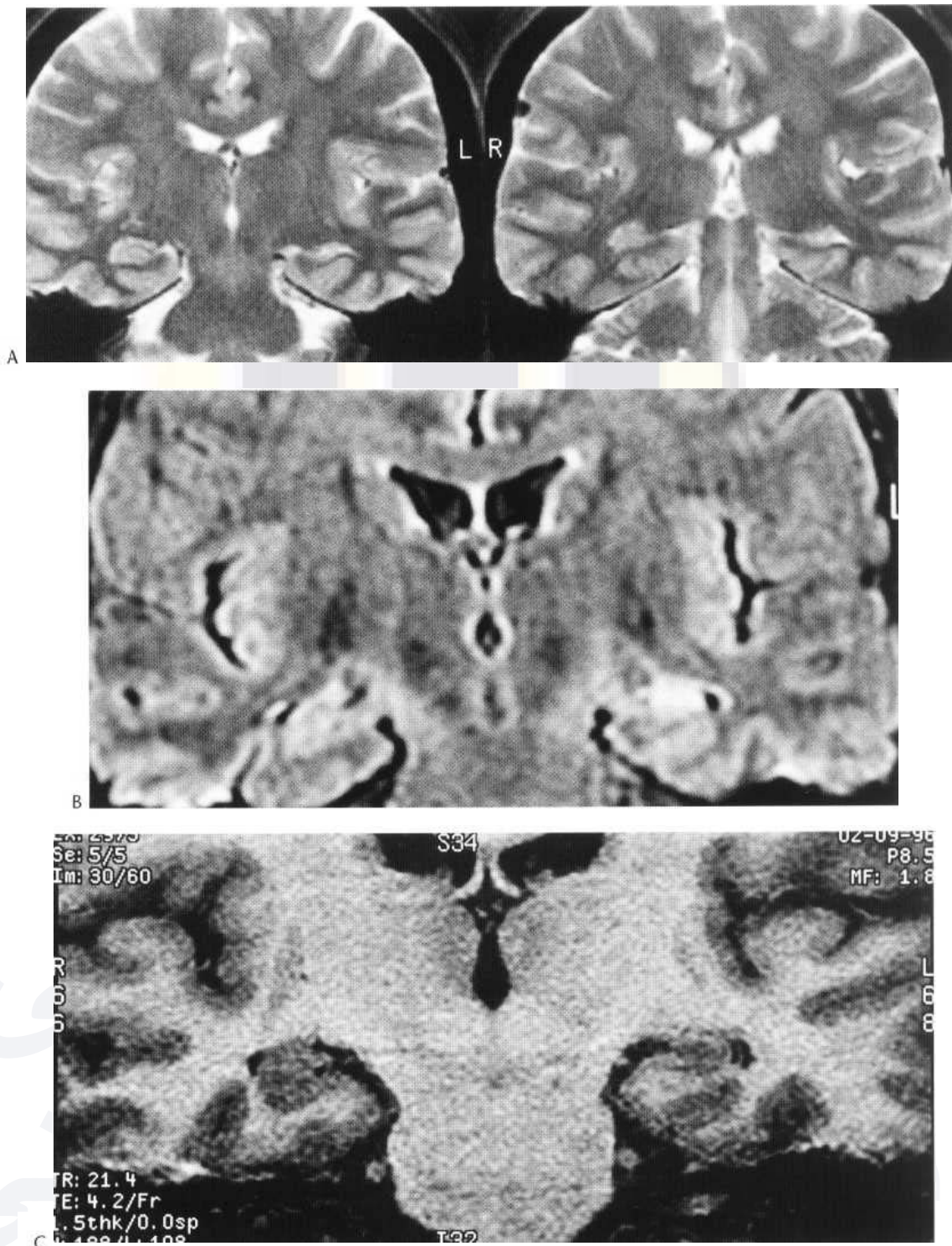


Fig. 58.77 (A) Coronal MRI sections, T₂-weighted, through hippocampal bodies, corresponding to level E of Fig. 58.76A. The left hippocampus is smaller than the right and shows higher signal. Hippocampal sclerosis. (B) Coronal MRI (FLAIR) image at level of hippocampal body accentuating high signal in left hippocampus. (C) T₁-weighted image at similar level from a 3D accumulation, showing the left hippocampus to be much smaller than the right.

cal tubers in tuberous sclerosis. A special case is the hypothalamic hamartoma, found very frequently in patients with gelastic seizures.

Neurosurgery and epilepsy

Symptomatic epilepsy may require neurosurgery to treat progressive pathology for its own sake. Patients with habitual epilepsy

refractory to drug treatment may benefit from surgery designed to cure or ameliorate the epilepsy itself. Seizure outcomes are best after resection of hippocampal sclerosis, about 80% of carefully selected patients can expect to become seizure-free and off drugs. Focal resections of neocortical lesions usually result in only 50% or less being seizure-free, and resection of histologically normal tissue, less than 20%. Non-resective surgery is used sometimes to

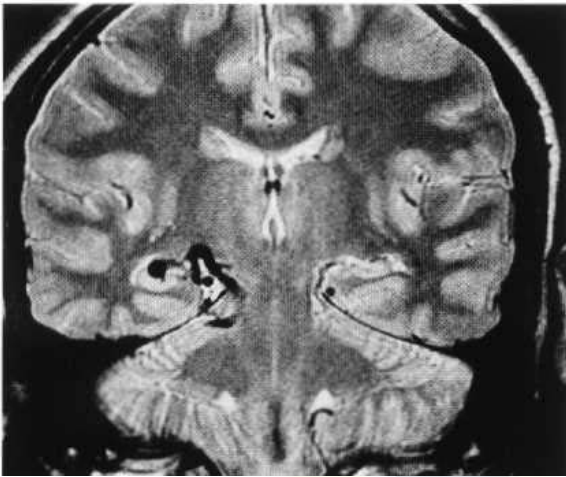


Fig. 58.78 Coronal MRI (T₂-weighted). Abnormal vessels are shown in the right medial temporal lobe involving the hippocampus. Angioma.

ameliorate devastating epilepsy: corpus callosotomy, functional hemispherectomy and multiple subpial cortical transection. Diagnostic neurosurgical procedures include depth electrode and surface grids placement, usually designed to test a hypothesis concerning site of seizure onset.

Functional imaging in epilepsy

PET and especially SPECT have a long history of clinical application in epilepsy. However, in recent years their role has diminished because of the much greater specificity of MRI. The reliability of localisations achieved by PET and SPECT in *MRI-negative cases* is questionable; depth electrodes or surface grids are necessary and they often fail to confirm localisations in such cases. Some units still practise what has been termed multimodality convergence in presurgical work-up: the results from MRI, SPECT (and PET), neuropsychology and videotelemetry are compared to clinical features, and surgery is considered in the context of how well they converge. In most units, however, less than 10% of MRI-negative cases come to surgery. MRI therefore is paramount.

ULTRASOUND OF THE INFANT BRAIN

Keith Dewbury

Technique The ideal equipment for the examination of the infant brain is a high-resolution sector real-time scanner, fitted with a 5 MHz (or higher frequency) transducer. The scan head should ideally be as small and manoeuvrable as possible. The sector field of view is particularly well suited for showing the maximum area of information through a small acoustic window. This type of equipment is usually mobile. It is taken to the infant and the transducer applied to the head via a port-hole in the incubator. In this way the baby is almost undisturbed by the examination.

If this type of equipment is not available it is possible and reasonable to examine the brain with either conventional static or linear-array real-time equipment, provided that a suitable high-frequency transducer is available (5 MHz). The linear-array transducer has a long rectangular scan head and field of view. Provided the acoustic window is suitable, it is increasingly used to optimise detail.

In each examination a series of closely spaced scans is made in both the coronal and sagittal planes by altering the angulation of the transducer to the fontanelle. The aim is to include as much as possible of the brain on each scan. A more limited access may also be possible through the posterior fontanelle and through the sutures. Occasionally it may be of value to image directly through the skull vault. The larger the fontanelle and therefore the freer the access, the better will be the images. As the fontanelle begins to decrease in size the access becomes more limited and the visualisation of the brain less complete. Ultrasound studies of the brain are most valuable in the first 6 months of life.

Indications The two most common abnormalities of the neonatal brain requiring confirmation or exclusion by imaging techniques are *hydrocephalus* and *intracranial haemorrhage*. These are the major indications for an ultrasound scan in the neonatal period. It is now widely accepted that ultrasound reliably and accurately demonstrates the size of the lateral ventricles and also sensitively detects the presence of intracerebral haemorrhage. Hydrocephalus may result from congenital malformation. Haemorrhage into the ventricles or subarachnoid space may also cause hydrocephalus. It may also develop following intrauterine infection such as toxoplasmosis. The definitive surgical management of hydrocephalus is to perform a shunt procedure of some type. The success of the procedure and the early complications such as shunt failure may also be followed by ultrasound.

The incidence of intracerebral haemorrhage is considerably increased in premature infants. With the growth of high-risk nurseries, allowing the survival of very premature infants, this complication is increasingly frequently seen and needs evaluation. The diagnosis of intracerebral and intraventricular haemorrhage may be made with ultrasound.

Meningitis is a comparatively common infection in some parts of the world. In young infants the progress of the disease and the results of medical and surgical treatment may be monitored effectively and simply with ultrasound. The common complications are *ventricular enlargement, subdural cysts and cerebral oedema*, all of which may be well shown with trans fontanelar scanning.

Normal appearances

Ultrasound is able to demonstrate the normal brain structure in considerable detail. The coronal sections are particularly valuable for showing focal abnormalities as advantage may be taken of the brain's symmetry. A series of landmarks in both coronal and sagittal planes has been described which allows recognition of the position at which the scan has been taken, and subsequently the acquisition of standard reproducible sections. The position of these sections is illustrated diagrammatically in Figure 58.79.

Within the brain, structures containing CSF, such as the ventricles and cisterns, appear anechoic; normal brain tissue generates low to mid-level echoes; higher-level echoes are generated from the cerebellum, the sulci and vascular structures. It is likely that a great deal of the internal echo reflection in the brain is due to the collagen content of the pia, ependyma and the vascular sheaths. One of the most echogenic intracerebral structures seen with ultrasound is choroid plexus. This stretches around the floor of the lateral ventricles from the foramen of Monro into the temporal horns, enlarging at the level of the glomus in the trigone before sweeping down into the temporal horns. The bones of the vault also produce highly echogenic reflections and so may be useful as landmarks.

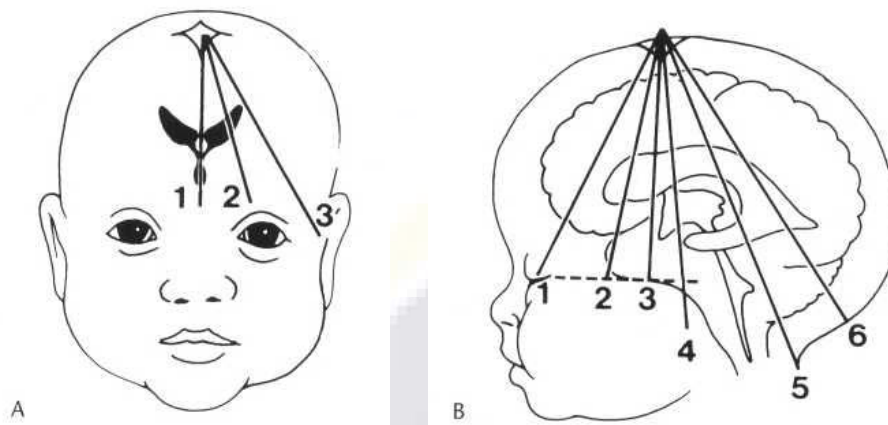


Fig. 58.79 Diagram showing three standard sagittal sections (A) and six coronal sections (B).

In the *first coronal* plane the transducer is angled anteriorly in the fontanelle, producing a section through the frontal lobes, seen separated centrally by the interhemispheric fissures and the falx. The lateral ventricles will not be seen in this section. The far field landmark is the high-amplitude echoes from the orbital roofs and the central echoes from the ethmoid complex extending downward to a lower level.

As the transducer is angled slightly back to the *second* position the far field landmark changes so that the lesser wings of the sphenoid, with the greater wings of the sphenoid behind, are seen forming the anterior floor of the temporal fossa. The anterior horns of the lateral ventricles may be seen in this section as small slit-like spaces either side of the central midline echo.

Angling the transducer slightly further back so that it is almost vertical produces the *third* coronal section where the most prominent landmarks are the sylvian fissures. These are seen just behind the lesser wings of the sphenoid and run laterally and outward, becoming Y-shaped between the temporal and frontal lobes. Within this echo complex, pulsation from branches of the middle cerebral artery will be readily seen. This section lies just anterior to the foramen of Monro, and between the lateral ventricles the echo-free box-like structure of the *cavum septi pellucidi* may be seen (Fig. 58.80). This is present during fetal life where it is used as a landmark to optimise a measurement of biparietal diameter in the

fetus. It is also present in about half of all full-term infants. It is seen more commonly in premature infants. Its incidence decreases sharply with age, and by 6 months compares with the low percentage reported in adults. The roof of the lateral ventricle is formed by the corpus callosum, which is echogenic, and the floor by the head of the caudate nucleus, with lower-level echoes.

With the transducer angled vertically the *fourth* coronal plane passes through the third ventricle which is not usually resolved in this plane when of normal size. A very prominent far field landmark is formed by the paired C-shaped echoes from the parahippocampal gyri and medial surface of the temporal lobes (Fig. 58.81). Part of the sylvian fissure will again be seen in this section. The bodies of the lateral ventricles now lie more horizontally and reflections from the choroid plexus may be seen in the floor of the ventricles.

Angling the transducer posteriorly on the fontanelle leads to the *fifth* coronal section where the prominent landmark is the highly echogenic tentorium and cerebellum shaped like an inverted V. Slight further angulation will bring into view the echogenic divergent bands characteristic of the glomus of the choroid plexus. These are the landmarks for the *sixth* section (Fig. 58.82). In the normal infant the choroid plexus will always be seen in this section, although the fluid-filled ventricles will not always be separately distinguished around the choroid.

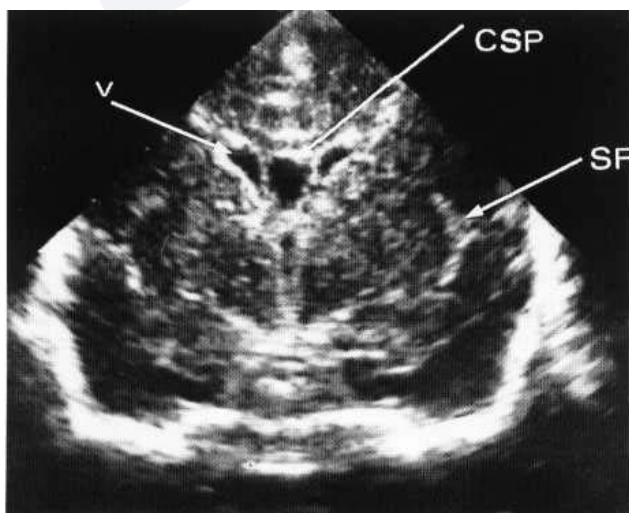


Fig. 58.80 A coronal section in the third position showing the bodies of the lateral ventricles (V) and the sylvian fissures (SF). Lying between the lateral ventricles is the cavum septi pellucidi (CSP).

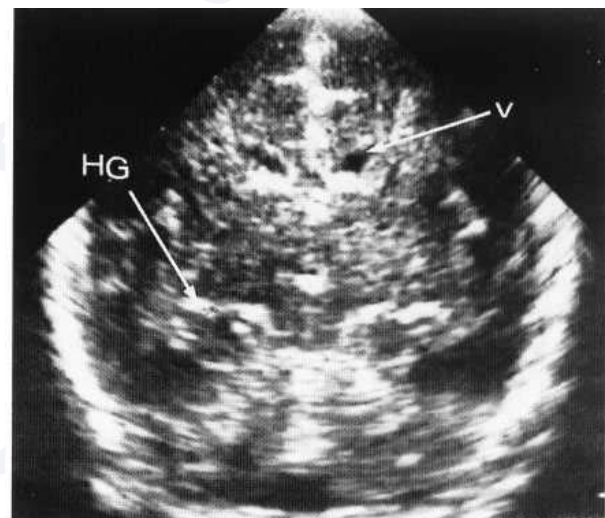


Fig. 58.81 A coronal section in the fourth position showing the prominent landmark of the parahippocampal gyri (HG). V = lateral ventricles.

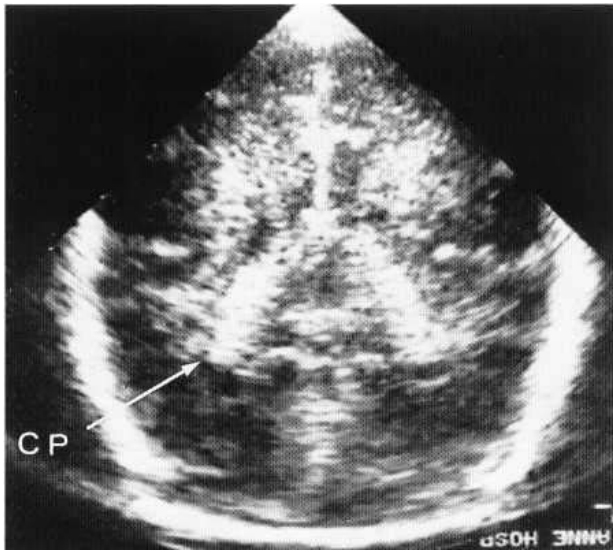


Fig. 58.82 A coronal section in the sixth position showing the characteristic echogenic choroid plexus (CP).



Fig. 58.83 A sagittal section in the midline showing the echogenic cerebellum and the fourth ventricle (arrow) posteriorly.

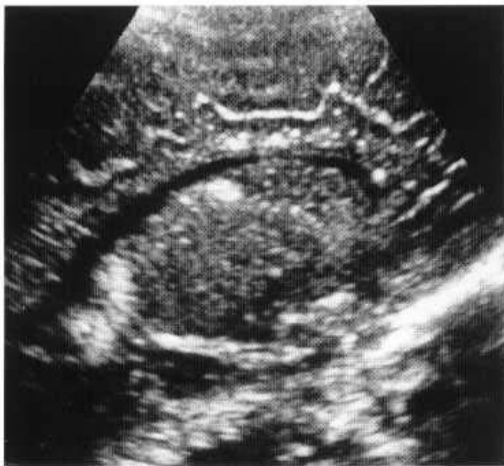


Fig. 58.84 An angled sagittal section showing the full sweep of one lateral ventricle around the caudate nucleus and thalamus.

Rotating the transducer through 90° into the sagittal plane, the *first sagittal section* is taken in the midline. The sulcal detail is usually prominent and the cingulate sulcus containing the branches of the anterior cerebral artery can be identified. The echogenic cerebellum is seen posteriorly, and anterior to this the fourth ventricle can be recognised. Above this the third ventricle and the massa intermedia are demonstrated, and often the aqueduct of Sylvius is outlined. The clivus forms the far field landmark (Fig. 58.83).

The *second parasagittal section* is angled about 15° away from the midline and shows almost the full sweep of the lateral ventricle containing the echogenic choroid plexus. Within the sweep of the ventricles the rounded mass is formed by the thalamus and caudate nucleus (Fig. 58.84). The far field landmark is the floor of the middle fossa. The *third parasagittal* section is angled outward about 30° , lateral to the ventricle and through the sylvian fissure.

Hydrocephalus and cystic lesions

The lateral ventricles in the normal neonate may be small and difficult to define accurately. The mean width of the lateral ventricle in the full-term infant is 12 mm and in the 30-week premature infant 9 mm, measured at the level of the body of the lateral ventricle (*coronal section 3*). In the past the measurement of the width of the lateral ventricle has usually been expressed as a ratio of the distance to the skull vault. In axial CT scanning, deviation of the medial walls of the lateral ventricle is an early sign of dilatation but the normal ratio of up to 30% appears too large when measured by ultrasound in the coronal plane and the ratio may not be valid in this circumstance.

The trigone and occipital poles of the ventricles are generally the largest part of the entire ventricular system, but no convenient landmark exists to monitor changes in size accurately and in any event there may be considerable variation in the shape of these structures. However, early dilatation is often most prominently featured in the trigone, occipital and temporal horns, possibly reflecting the lesser compliance of the supporting structures in this region.

Ultrasound has proved to be accurate and reliable in detecting and grading the severity of hydrocephalus and is ideally suited to following progress. Figure 58.85 is a coronal section at the level of the bodies of the lateral ventricles showing the appearances of established hydrocephalus. Further evaluation of hydrocephalus to establish a precise aetiology may require diagnostic procedures in addition to ultrasound. However, in certain instances, ultrasound may provide most or all of the answers. In addition to the diagnosis and follow-up of hydrocephalus, ultrasound may also be helpful in following shunt procedures, particularly in the evaluation of complications.

Besides hydrocephalus other cystic lesions within the brain may show well. In *hydranencephaly* no brain parenchyma is present above the level of the midbrain and no cortical mantle is seen. The *Dandy-Walker syndrome* has a characteristic appearance where cystic dilatation of the fourth ventricle can be recognised (Fig. 58.86). This condition must, however, be distinguished from a retrocerebellar *arachnoid cyst* which may produce a similar appearance. In the latter instance, however, a normal fourth ventricle is identified compressed anteriorly by the cyst (Fig. 58.87). A wide variety of other cystic lesions has been described, such as holoprosencephaly (Fig. 58.88).

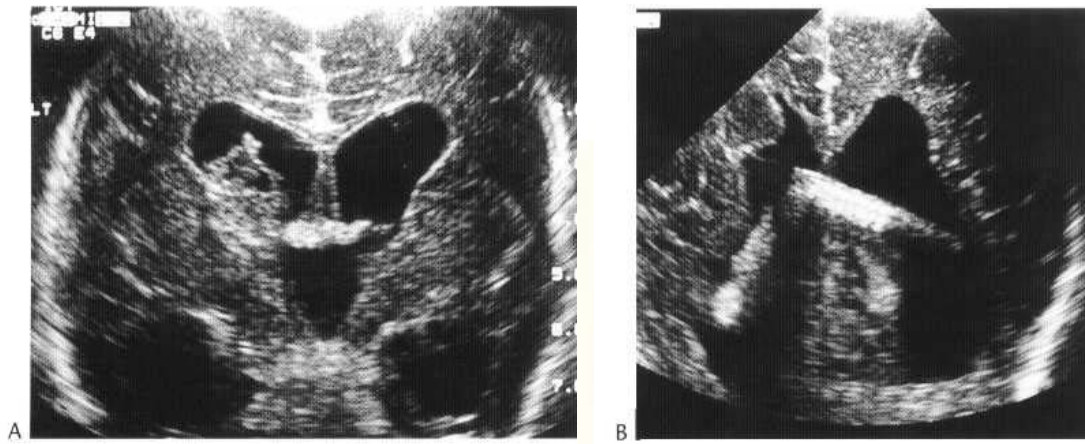


Fig. 58.85 (A) A coronal section showing the typical appearance of hydrocephalus involving the lateral and third ventricles. The section is through the foramen of Monro. Echogenic haemorrhage is within the ventricle. (B) A ventricular shunt in position more posteriorly.

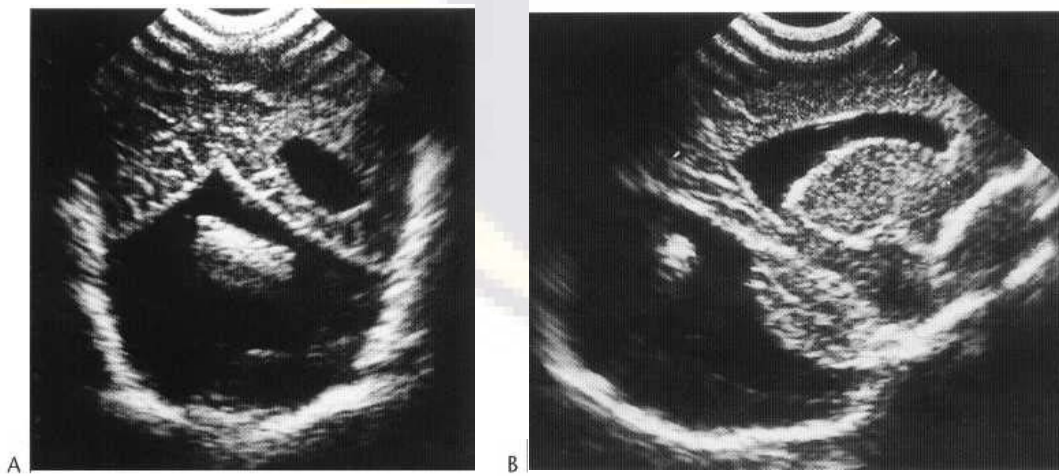


Fig. 58.86 (A) A coronal section. (B) A sagittal section showing the characteristic findings of the Dandy-Walker syndrome. There is cystic dilatation of the fourth ventricle filling the posterior fossa. A shunt is in place.

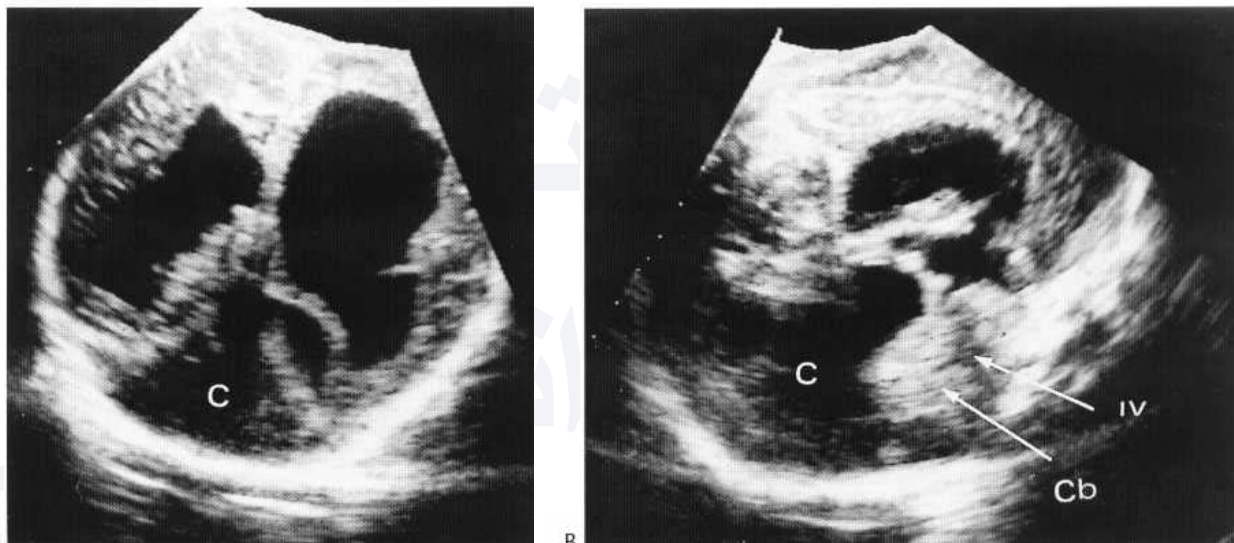


Fig. 58.87 (A) A coronal section. (B) A sagittal section showing the findings of a retrocerebellar arachnoid cyst for comparison. Note that in the sagittal section the cerebellum (Cb) and the fourth ventricle (iv) can be seen compressed forward by the cyst.

Haemorrhage

The *germinal matrix* is a neural vascular tissue in the fetus which is normally involuted by term. It is situated subependymally in the ventricles and is prominent in the groove between caudate nucleus and thalamus. This is a frequent site for haemorrhage in premature infants (Fig. 58.89).

The vascular choroid is also an important site for cranial haemorrhage in infants. The shape of the choroid plexus as it surrounds the caudate nucleus and thalamus is fairly constant so that any irregular increase in size is suspicious of haemorrhage (Fig. 58.90). The symmetry of the two sides may also be of value in detecting abnormality.

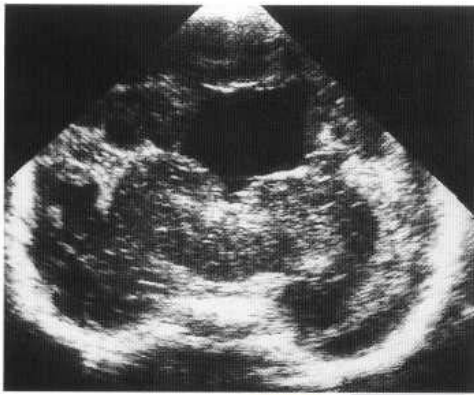


Fig. 58.88 Coronal section showing the single fused ventricle typical of holoprosencephaly.



Fig. 58.91 A sagittal section showing the characteristic appearances of advanced periventricular leucomalacia (PML) as periventricular cystic spaces.

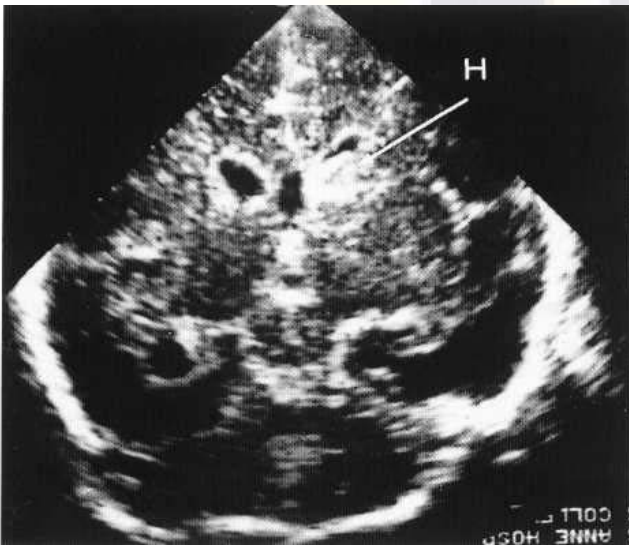


Fig. 58.89 A coronal section in a premature infant showing a typical reflective haemorrhage (H) from the germinal matrix. A mass effect from the haemorrhage is distorting and elevating the lateral ventricle on this side.



Fig. 58.92 Coronal section showing extensive reflective intraparenchymal haemorrhage.

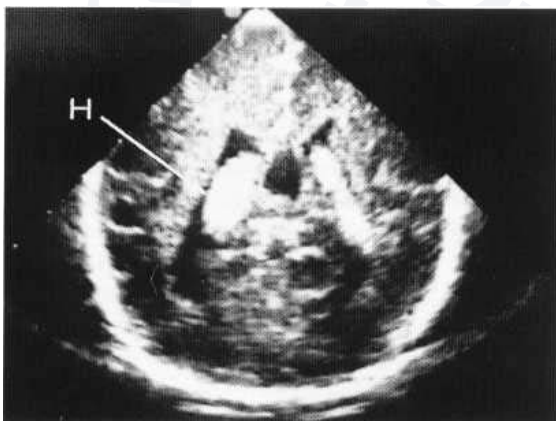


Fig. 58.90 A posterior coronal section showing asymmetric enlargement of one choroid plexus (H) typical of haemorrhage.

White-matter haemorrhage occurs in both preterm and full-term infants. In the former it is associated with *periventricular leucomalacia* (Fig. 58.91). This lesion is attributed to underperfusion of the boundary zones between different arterial territories within the

periventricular white matter, which may develop during episodes of hypotension. Ultrasound may show a periventricular increase in echo amplitudes, with follow-up studies showing formation of cystic spaces. In term neonates, intraparenchymal haemorrhage may be diffuse and petechial in the cortical areas.

The diagnosis of intracerebral, periventricular and intraventricular haemorrhages may be made reliably using ultrasound where the haemorrhage shows as a brightly reflective area (Fig. 58.92). This is mainly due to the fibrin mesh formed, which produces multiple reflecting interfaces for the ultrasound beam. *Subarachnoid haemorrhage* is not reliably demonstrated using ultrasound, but *subdural haemorrhage* is usually shown as a crescentic echo-poor region separating brain from the skull vault (Fig. 58.93). Haemorrhage, particularly in premature infants, may rupture into the lateral ventricles. This may enlarge the ventricles, either due to brain tissue loss and atrophy or to hydrocephalus due to CSF flow obstruction. The combination of both may occur, and monitoring to show progress or stabilisation is important in these circumstances.

Trauma to the infant brain due to birth or accidental injury produces a combination of the types of haemorrhagic or ischaemic change already described. Non-accidental injury to the brain may produce pathognomonic shearing injuries at the grey-white matter interface. This appears typically as small linear slit-like cavities, optimally demonstrated with the linear-array transducers.



Fig. 58.93 A transcranial section showing a large crescentic subdural haematoma.

RADIONUCLIDE IMAGING OF THE BRAIN

Phillip J. A. Robinson

Numerous different approaches have been employed for brain imaging using radionuclides. Anatomical studies using pertechnetate and other extracellular fluid tracers have been superseded by CT and MRI. Techniques for mapping regional cerebral blood flow have important clinical applications, which are described below. Specific agents targeted at neurotransmitter sites and other receptors are used extensively in research and are beginning to enter the clinical arena, particularly in relation to Parkinson's disease. Tracer studies of CSF flow are now rarely required, but may occasionally be helpful.

Instrumentation and radiopharmaceuticals

Dedicated PET imagers provide the best spatial resolution for scintigraphic studies of the brain. Proximity to a cyclotron is essential for receptor studies using short-lived tracers labelled with carbon-11, or flow studies using oxygen-15 labelled water as a marker. Although much of the research and development work in brain metabolism has involved the use of PET tracers for blood flow, glucose metabolism using ^{18}F FDG, neurotransmitter and other receptor activity, these have not yet been widely translated into routine clinical applications. A brief review of the current and potential clinical applications of PET is given in Chapter 59.

SPECT using a conventional single or multiheaded gamma camera mounted on a rotating gantry offers tomographic imaging of useful diagnostic quality. Improved resolution is obtained by using a dedicated single-photon brain imaging array, with the disadvantage that the device is unsuitable for other scintigraphic applications.

Tracers for regional cerebral blood flow (rCBF) imaging

Because brain tissue has no mechanism for storage of oxygen or glucose, local blood flow in the normal brain correlates well with

neuronal activity. Inert gases are effective markers of regional blood flow, but have technical drawbacks. Krypton-81m with its low solubility in blood and its short half-life of 14 s, allows continuous measurement of regional blood flow, but the same properties require its delivery by intracarotid infusion. A rebreathing method using xenon-133 (half-life 5.3 days) offers a non-invasive method for assessment of regional blood flow, but the greater solubility and long half-life of xenon allow recirculated activity in the scalp, which causes image noise. A more practical approach emerged with the development of tracers based on small lipophilic molecules which readily cross the blood-brain barrier and are retained within brain cells. The first of these to be widely used was iodoamphetamine labelled with iodine-123 (^{123}I -IMP), but for most clinical applications agents labelled with $^{99\text{m}}\text{Tc}$ and commercially available in kit form have major practical advantages. Two of these agents are currently widely available—exametazime ($^{99\text{m}}\text{Tc}$ -HMPAO) and ethylcysteine dimer ($^{99\text{m}}\text{Tc}$ -ECD). HMPAO has a high extraction efficiency by brain tissue. About 5% of the injected dose is taken up by brain tissue and only a small proportion of this is washed out in the first few hours after injection, giving an ample time window for imaging. ECD has some practical advantages in that it is more stable in vitro and its extraction efficiency is slightly better than HMPAO, but the kinetics of ECD in abnormal brain are as yet less well established than those of HMPAO.

rCBF imaging: HMPAO technique

$^{99\text{m}}\text{Tc}$ -HMPAO (exametazime) requires no patient preparation. The typical activity of 500 MBq is injected intravenously with the patient in a quiet stable environment. Images may be obtained from 20 min to several hours after injection because the tracer distribution in the brain is stable during this time. Dedicated multidetector imaging devices will produce the best resolution, but diagnostic results may also be obtained using a rotating gamma camera, taking care to position the camera head as close as possible to the patient during rotation. Volumetric data are displayed in standardised axial, coronal and sagittal planes, and colour displays may be used to increase the conspicuity of low contrast features in the reconstructed images.

rCBF imaging: interpretation

Absolute uptake of exametazime is affected by numerous factors which vary between individual subjects, so interpretation generally relies upon the use of specific reference areas in the image to give an indication of normal flow. For most purposes, the cerebellar hemispheres may be taken as normal flow indicators. Cortical uptake is normally fairly homogeneous and white-matter structures are identified as areas of low uptake in the subcortical, periventricular and capsular areas. Increased separation between the heads of the caudate nuclei indicate dilatation of the lateral ventricles. Sagittal slices are helpful in comparing regional uptake in frontal, parietal and occipital lobes with the cerebellum, although cortical atrophy may lead to partial volume effects causing spurious hypoperfusion on sagittal images, particularly in the frontal region. Coronal images overcome this problem and should also demonstrate the mesial and lateral components of the temporal cortex.

rCBF imaging: applications

Cerebrovascular disease

In acute stroke, symptoms and signs of brain injury are associated with changes in regional cerebral blood flow; however, the consequent structural abnormalities may take hours or even days to become visible on CT or MRI. For example, 8 h after the clinical onset of acute stroke, only about 20% of patients will show CT abnormalities in the affected area, whereas 90% will show local blood flow abnormalities on SPECT imaging. Although the diagnosis of stroke is essentially clinical, early SPECT imaging may be used to establish the presence and extent of the blood flow deficit. The magnitude of the deficit, when SPECT is performed in the first few hours after onset of a stroke, is a fairly good indicator of the eventual outcome—the more extensive the initial deficit, the worse the prognosis for recovery. A further guide to prognosis may be obtained by repeating the SPECT study about 24 h after onset, an early recovery in the perfusion deficit being a good prognostic indicator.

After the initial ischaemic insult, cell death in the infarcted area effectively reduces the oxygen and glucose requirement so that a continuing deficit in blood flow may not result in further neuronal damage. However, a common finding in the subacute phase of stroke is that the blood flow deficit shown on SPECT is more extensive than the structural changes of infarction which appear on CT. This discrepant area, described as the SPECT 'penumbra', may indicate an area of ischaemic but viable tissue which is potentially recoverable.

The appearance of 'luxury perfusion' commonly occurs 2-28 days after the onset of a stroke. This is a variety of reactive hyperaemia with increased flow through the infarcted area. Experimental work suggests that much of this flow is non-nutritive, so that the normal consistent relationship between flow and the uptake of oxygen and glucose in the local tissues is lost. However, the uptake of HMPAO is unchanged or in some cases more avid than normal, so SPECT studies carried out during this period are likely to underestimate the true ischaemic deficit. The correlation of long-term abnormalities on SPECT with chronic infarcts shown on CT is fairly good, except that the resolution of SPECT is inadequate for small cortical and lacunar infarcts.

Crossed cerebellar diaschisis describes the phenomenon in which cerebral infarction leads to diminished perfusion in the contralateral cerebellar hemisphere, due to loss of linkages which normally stimulate neuronal activity in the cerebellum. This deficit is often seen when there is extensive cortical infarction, and it persists throughout the period of luxury perfusion in the subacute phase. A similar reactive fall in perfusion may occur in the cortical areas which overlie deep-seated infarcts. Since cerebellar blood flow is usually used as a reference point for assessing regional cortical flow, it is important to bear in mind the possibility of unilateral perfusion loss when cerebellar activity is asymmetric.

As a prelude to surgery or angiographic intervention, SPECT imaging may be used to assess the degree and extent of functional deficit which is associated with arterial stenosis or occlusion. An alternative approach uses acetazolamide stress testing to measure perfusion reserve. Acetazolamide (Diamox) is a carbonic anhydrase inhibitor which mimics the effect on the cerebral circulation of increasing the concentration of circulating carbon dioxide. An intravenous injection of 1 g of acetazolamide normally causes an increase in cerebral blood flow that reaches a peak about 20-30 min

later and then declines gradually over the next 1-2 h. The degree of augmentation of flow after Diamox, described as 'cerebral perfusion reserve', may be as much as 40% increase over resting flow in normal subjects. The degree of reserve in patients is often unrelated to the severity of vascular stenoses, particularly in the extracranial arteries. Loss of perfusion reserve carries a poor prognosis, with a high risk of subsequent stroke, and this assessment may be used as a selection criterion for patients who are candidates for carotid artery surgery or stenting. Pre- and post-Diamox studies can be carried out either on the same day or on consecutive days, and subtraction images can be used to highlight the areas of abnormal reserve. Diamox should not be given to patients who suffer from migraine, since it may induce severe headache.

In summary, the value of rCBF SPECT imaging in suspected stroke is:

1. For triage—to distinguish stroke from TIA in the acute stage.
2. To show the extent and distribution of abnormality, which will help to identify the likely site of arterial occlusion (Fig. 58.94).
3. To demonstrate areas at risk of further damage, and those areas with possibility of recovery (Fig. 58.95).
4. To monitor thrombolytic therapy.

Dementia

A gradual and global reduction in cortical blood flow is a feature of normal ageing in asymptomatic subjects. Specific variations in rCBF are associated with different types of dementia.

Alzheimer's disease accounts for about 50% of patients with progressive dementia. Pathology shows loss of neurones, fibrillary tangles, amyloid deposition, granulovacuolar degeneration and neuritic plaques. Clinical criteria for Alzheimer's disease (AD) are helpful, but are relatively non-specific, so that autopsy studies show the typical pathological changes of AD in only 50% of patients with

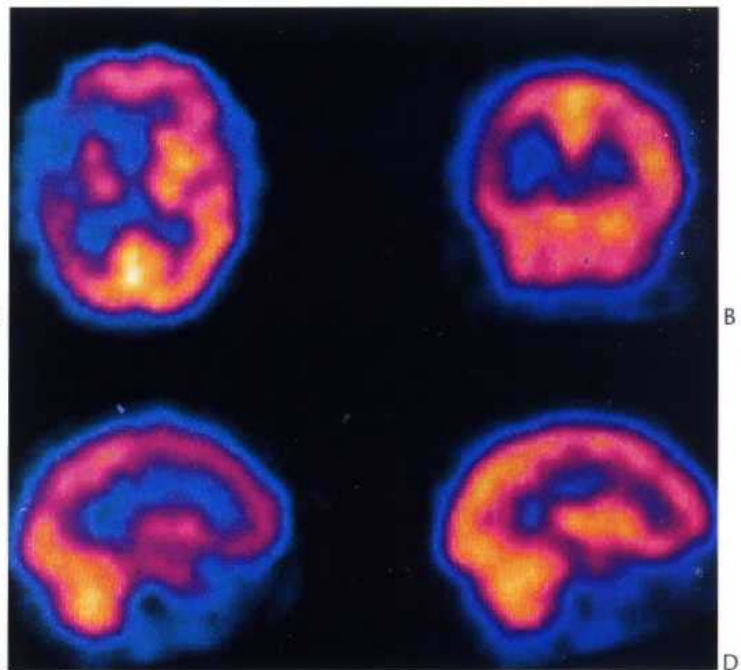


Fig. 58.94 ^{99m}Tc-exametazime brain SPECT: axial (A), Coronal (B), right parasagittal (C) and left parasagittal (D) sections in a patient with massive infarction of the right middle cerebral artery territory. Note severe ischaemia of the frontal, temporal and parietal cortex and also of the basal ganglia on the right.

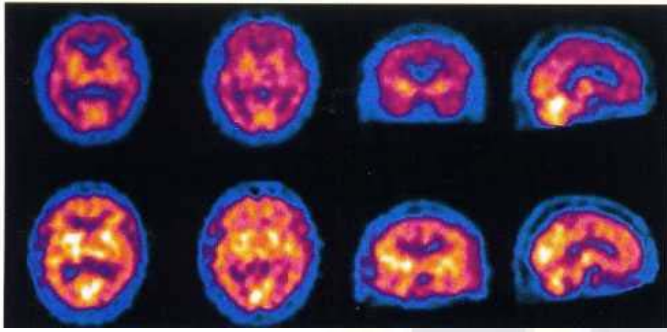


Fig. 58.95 ^{99m}Tc-exametazime brain SPECT: axial, coronal and right parasagittal images showing *very* extensive perfusion deficits during the acute ischaemic phase (top row) and substantial improvement several months later after clinical recovery (bottom row).

clinically 'probable' AD. The addition of SPECT rCBF studies improves the accuracy of diagnosis to the extent that 80% of patients with clinically probable AD and positive brain SPECT are found to have typical pathological changes at autopsy. The typical defect of AD is a reduction of flow in the posterior parietal and temporal areas (Figs 58.96, 58.97). This pattern of abnormality is highly specific in discriminating between AD and normals, and a little less specific in distinguishing between AD and other demential, but still highly characteristic. The blood flow changes may precede the onset of clinical symptoms. Brain atrophy is also a feature of AD, but is non-specific. The blood flow response to Diamox is relatively normal in AD. Flow to the basal ganglia is normal in most patients with AD, while in Parkinson's disease cortical flow is well maintained. However, there is a recognised subgroup of patients who present with a combination of Parkinson's disease and AD, and these show the typical cortical abnormalities of AD. An important differential diagnosis to be made by SPECT is in distinguishing AD from similar clinical presentations in occa-

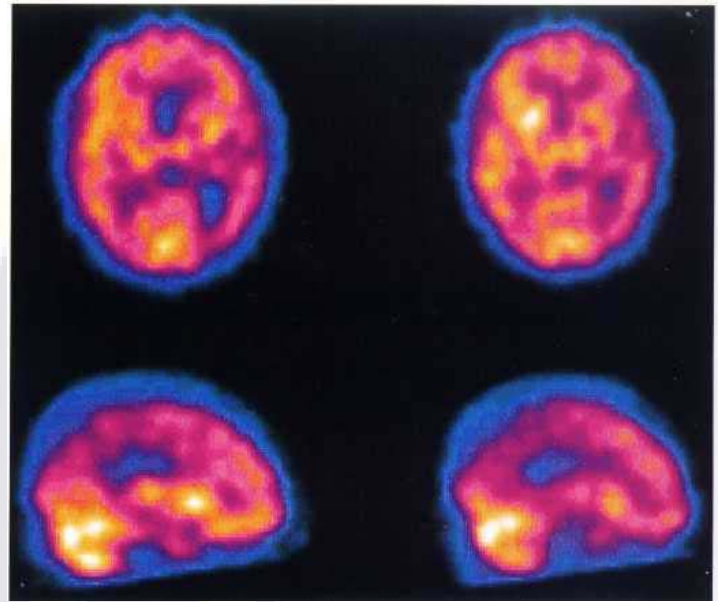


Fig. 58.97 ^{99m}Tc-exametazime brain SPECT: axial (top row) and left and right parasagittal (bottom row) sections in a patient with suspected Alzheimer's disease. The distribution is primarily posterior but quite asymmetric, unlike Fig. 58.96.

sional patients with multiple sclerosis, and in those with multiple drug and alcohol abuse.

Lewy body disease (LBD) is the cause of about 20% of dementias in patients over 70. Lewy bodies are intracellular inclusions found in the basal ganglia and substantia nigra in Parkinson's disease, but when they are also found in the cerebral cortex they are associated with progressive dementia. The perfusion abnormality is less specific than that of AD, but broadly similar in distribution, although the calcarine and occipital cortices are often also affected.

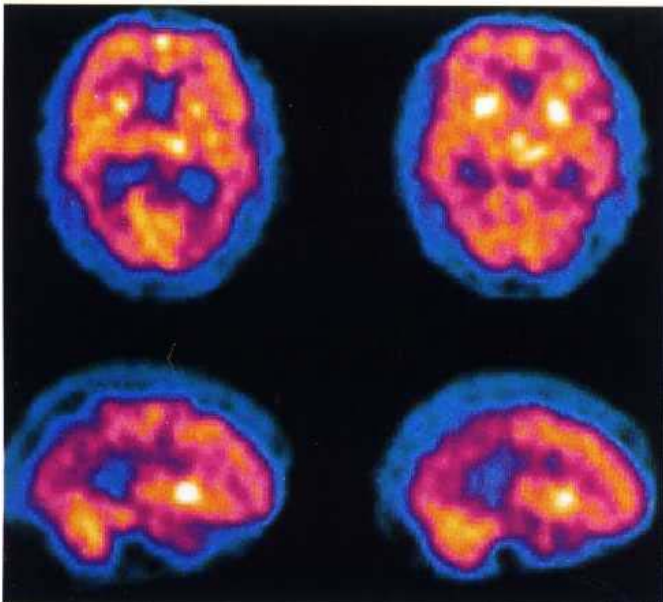


Fig. 58.96 ^{99m}Tc-exametazime brain SPECT: axial (top row) and left and right parasagittal (bottom row) sections in a patient with suspected Alzheimer's disease. Note the posterior distribution of the major ischaemic areas.

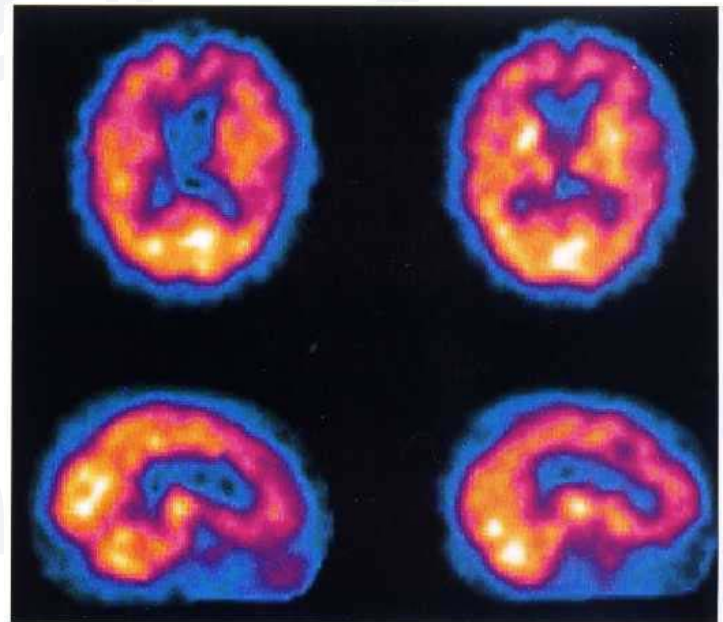


Fig. 58.98 ^{91m}Tc-exametazime brain SPECT: axial (top row) and left and right parasagittal (bottom row) sections in a patient with dementia of frontal lobe type. Note the ischaemic lesions are predominantly in the frontal lobes on both sides.

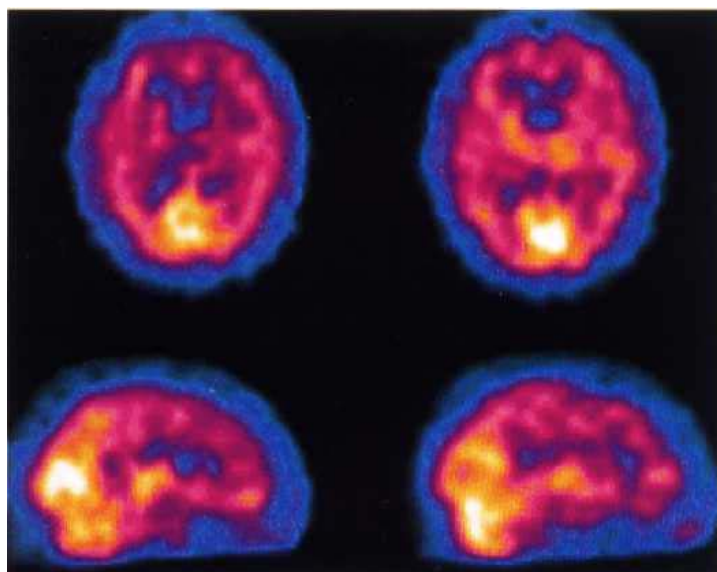


Fig. 58.99 ^{99m}Tc-exametazime brain SPECT: axial (top row) and left and right parasagittal (bottom row) sections in a patient with dementia of frontal lobe type. Note the marked frontal and temporal ischaemia with central atrophy as well.

Progression is typically faster than with AD. In addition, the basal ganglia are typically abnormal in LBD, but normal in AD. Patients with LBD, who show the typical pattern of bilateral frontal, temporal, parietal and occipital abnormalities of flow, may also have a parkinsonian presentation, and in other cases LBD and AD may coexist in the same patient.

Frontal lobe and frontotemporal dementias, including **Pick's disease**, account for about 15% of demented patients. SPECT studies show symmetrical reduction in rCBF in both frontal lobes initially, and in later stages both temporal lobes are affected as well (Figs 58.98, 58.99). In **multiinfarct dementia** (MID) flow abnormalities are related to multiple episodes of cortical infarction. The distribution of abnormalities is sporadic but tends to be related to the major arterial territories, rather than the lobar distributions seen in AD and the other primary neuronal dementias. Abnormalities are often asymmetrical, and may involve frontal, temporal and parietal lobes, usually with multiple areas of diminished flow. The uptake of CBF agents into white matter is normally about one-third of that in grey matter. Focal white-matter infarcts (Binswanger's disease) may show no abnormality on SPECT studies in the early stages, but more advanced disease can be detected as diffuse or focal loss of white-matter uptake, often associated with cortical infarcts and atrophy.

In summary, the aims of rCBF imaging in dementia are:

1. To distinguish the different aetiologies of dementia, as treatment and prognosis are both influenced by the cause of the disease.
2. To detect disease as early as [possible](#), as treatment is more likely to be effective than in the later stages of progression.
3. To show the extent and severity of the lesion and to indicate prognosis.
4. In follow-up, to monitor the progress of disease and the effect of treatment.

Epilepsy

Surgery for intractable focal epilepsy—usually excision of the anterior two-thirds of the temporal lobe and in some cases the whole of

the mesial cortex—is successful in eliminating seizures in over 90% of cases where the abnormal focus can be identified preoperatively. Results are much worse if the focus is not identified. The accuracy of external EEG alone is about 25% and, although intracranial EEG gives a much better accuracy of 85-90%, it is an invasive and costly procedure. Mesial temporal sclerosis shown on MRI is often associated with the abnormal focus, but the sensitivity of about 60%—is still less than desirable for selecting patients for surgery.

In focal epilepsy, the affected area of the brain shows abnormal blood flow. During focal fits, the flow to the abnormal cortex is sharply increased, and it then falls in the immediate postictal period. In about half of patients, blood flow to the abnormal focus is lower than normal in the resting (interictal) phase. A recent meta-analysis of SPECT imaging in focal epilepsy suggested that the sensitivity for detecting the abnormal focus was 97% when the SPECT was obtained during seizure, 75% for examinations done in the postictal stage, and 44%—for interictal studies. Those patients in whom flow is normal during the ictal or immediate postictal phases will show a marked hypoperfusion in the interictal phase, so although ictal studies are the most sensitive, interictal studies are also worthwhile. Ictal studies require patients to be under continuous observation, with a tracer dose ready prepared and available for immediate injection when a seizure occurs. Since the tracer is fixed within the first few minutes after injection, imaging can be delayed until the patient has been stabilised.

The pattern of abnormality seen in CBF during seizures may vary from day to day even in the same patient, so multiple studies are worthwhile. Patients with bilateral foci are less likely to benefit from surgery. Chronic motor seizures are usually associated with a frontal cortex focus, again best identified in ictal studies. About one-third of patients with refractory temporal lobe seizures over a long period will develop diminished flow in the cerebellum.

Although the main value of radionuclide studies is to identify a temporal lobe focus as a prelude to surgery, SPECT may also be used to exclude from surgery those psychiatric patients with non-epileptic seizures in whom perfusion remains normal throughout.

Trauma

Delayed neurological sequelae of trauma after head injury are characteristically associated with blood flow abnormalities in the acute stage. SPECT studies in the early period after head injury may give a useful prognostic indicator, as those with normal SPECT are unlikely to develop late sequelae.

Tracers for imaging the dopamine transporter system

Several tracers have been developed for investigating the pathophysiology of movement disorders and their response to drug therapy. The preferred agent for demonstrating the presynaptic dopamine transporter is ¹²³I-FP-CIT (ioflupane). ¹²³I-beta-CIT has similar properties but its uptake into the target sites is slower, so imaging has to be done 18-24 h after injection, while with ¹²³I-FP-CIT images can be obtained on the same day as injection. For investigation of the postsynaptic dopamine receptors, the favoured agent is ¹²³I-iodobenzamide (IBZM).

Dopamine transport imaging: technique Uptake of these agents is related to the presynaptic dopamine transporter activity. Patient preparation includes 5 days of thyroid blockade with potassium iodide. Dopaminergic drugs *need* not be stopped but tricyclic antidepressants may interfere with the technique and should be withheld—prior to the test. High-resolution SPELT images are obtained 3–6 h after intravenous injection of 150–185 mBq of ^{123}I -FP-CIT, or 18–24 h after a similar activity of ^{123}I -beta-LIT.

Dopamine transport imaging: interpretation Normal subjects show a crescent-shaped area of specific uptake in the corpus striatum, a lesser degree of uptake in the substantia nigra and little or none in white matter. The specific uptake in the striatum is normally about four times that of the rest of the brain.

Application: the investigation of movement disorders The diagnosis of idiopathic Parkinson's disease is confirmed in only about one-half of patients with the initial clinical diagnosis of Parkinson's. About one-quarter of presenting patients have parkinsonian syndromes, which may be drug-induced or associated with other degenerative disorders including Huntington's chorea, Wilson's disease, progressive supranuclear palsy and multiple system atrophy. In the remainder of patients presenting with Parkinson-like symptoms, the true diagnosis may be essential tremor, early dementia or 'gait apraxia', all conditions that do not benefit from anti-Parkinson medication. SPELT imaging of the dopamine transporter system helps to distinguish between the various neuropathologies that may be associated with parkinsonian clinical presentation (Fig. 58.100).

Idiopathic Parkinson's disease (IPD) is characterised by loss of dopamine-containing cells in the substantia nigra. SPELT imaging shows reduced uptake in the corpus striatum, the degree of which is proportional to the severity of clinical manifestations. A qualitative grading system may be used to indicate the degree of abnormality:

- Grade 1—reduced uptake in putamen, caudate normal.
- Grade 2—reduced uptake in both putamen and caudate.
- Grade 3—reduced uptake in caudate, zero uptake in putamen.

Studies on a mixed group of patients with Parkinson's disease showed uptake in the striatum to be approximately half that of

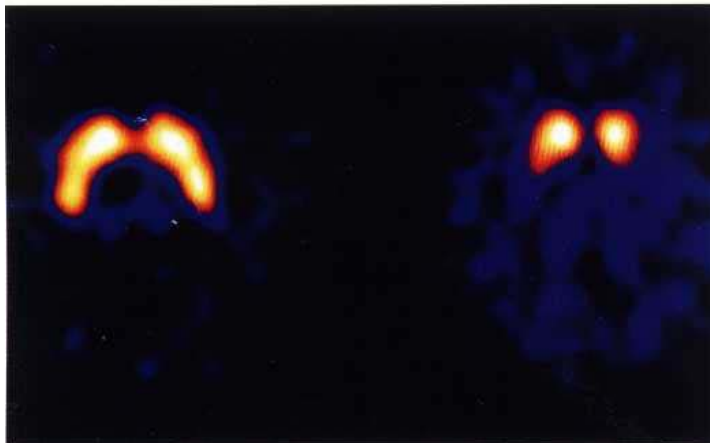


Fig. 58.100 ^{123}I -beta CIT SPECT imaging showing normal distribution of activity in a patient with essential tremor (A) and diminished putamen and caudate uptake in a patient with Parkinson's disease (B). (Courtesy of Dr M. Buxton-Thomas.)

normal controls, i.e. 1.5–2 times the uptake in the rest of the brain. Initial changes in IPD occur in the putamen and later progress to the caudate. The abnormality is often bilateral but also typically asymmetrical, being worse on the clinically more affected side.

Similar findings to those in IPD are seen in patients with progressive supranuclear palsy and multiple system atrophy. Asymmetry is more likely in IPD but there is too much overlap to make a distinction in individual cases. Uptake of dopamine transporter tracers in the striatum is normal in patients with drug-induced parkinsonism and in those with essential tremor. Patients with 'vascular Parkinson's disease' show an overlap between normal and IPD appearances, but in these cases deep infarcts may be visible on CT.

Dopamine receptor levels normally decline with age, so in population controls the reduction in uptake of tracers in the corpus striatum declines by about 2–3% per year. Consecutive studies in IPD show a much more rapid decline of 6–10% per year. Consecutive studies in patients with essential tremor and in parkinsonian syndromes associated with cerebrovascular disease, drug therapy, previous trauma and psychogenic origins typically show a normal rate of decline of dopamine receptors.

In summary, the objectives of clinical SPELT imaging for movement disorders are:

1. To differentiate IPD from essential tremor and other mimics of IPD.
2. To establish the diagnosis of IPD as early as possible (images may be abnormal 3 years or more before the onset of clinical symptoms).
3. To monitor disease evolution, particularly the effect of 'neurorescue' drugs in slowing or arresting the progression of the disease.

The postsynaptic D2-receptor ligand iodobenzamide (^{123}I BZM) may be useful in some clinical situations but its role has not yet been firmly established. Initial studies suggest that uptake of this agent is normal or increased in IPD, particularly in the early stages of the disease, while uptake is reduced in progressive supranuclear palsy, multiple system atrophy, Huntington's chorea and Wilson's disease.

A further application of $^{231}\text{FP-CIT}$ may be in the differentiation of Alzheimer's disease (normal striatal uptake) from Lewy body dementia (similar pattern to IPD).

Radionuclide cisternography

CSF dynamics can be investigated by injecting a suitable tracer into the subarachnoid space, either by lumbar puncture or preferably by lateral cervical or direct cisternal puncture. One such agent is indium-111-DTPA, which is not absorbed by the meninges, and has a sufficiently long half-life (68 h) to allow useful images to be obtained at 24 or 48 h after injection. The normal pattern of flow of CSF is from the lateral ventricles, where it is formed, out through third and fourth ventricles to the basal cisterns, where it mixes with spinal CSF, and then over the surface of the cerebral hemispheres, where absorption takes place. Obstruction to flow may prevent the appearance of the tracer over the cerebral hemispheres on delayed images and in severe cases CSF may apparently reflux into the lateral ventricles. The main application for this technique has been in patients with normal pressure hydrocephalus, in whom the demonstration of obstruction to flow of CSF was used to assist in the selection of patients for bypass surgery. The same technique has also been used to search for CSF leaks following trauma, or in patients with sponta-

neous intracranial hypotension in whom leaks of CSF are often found in the cervical or dorsal spine. However, in both of these applications, cisternography is now considered to add little to assessment based on high-resolution CT and clinical criteria.

REFERENCES AND SUGGESTIONS FOR FURTHER READING

Textbooks

- Atlas, S. W. (1991) *MR of the Brain and Spine*. New York: Raven Press.
- Barkovich, A. J. (1990) *Pediatric Neuroimaging*. New York: Raven Press.
- Brain Tumours (1999) *Neuroimaging Clinics of North America*, 9(4).
- Graham, I., and P. L. (eds) (1997) *Greenfield's Neuropathology*, 6th edn. London: Arnold.
- Intracranial Infectious Diseases (2000) *Neuroimaging Clinics of North America*, 10(2).
- Kleihues, P., Cavenee, W. K. (2000) *World Health Organization Classification of Tumours. Pathology and Genetics of Tumours of the Nervous System*. Lyon: IARC Press.
- Orison, W. W., Lewine, J. D., Sandes, J. A., Hartshorne, M. A. (1995) *Functional Brain Imaging*. St Louis: Mosby.
- Osborn, A. G. (1994) *Diagnostic Neuroradiology*. St Louis: Mosby.
- Russell, L. T. (1988) *Pathology of Tumours of the Nervous System* 5th edn. London: Arnold.
- Scott, W. (1995) *MR of the Brain and Spine*, 2nd edn. New York: Raven Press.

CT

- Altman, N. R., Alhnan, D. H., Sheldon H., et al (1984) Holoprosencephaly classified by CT. *American Journal of Neuroradiology*, 5, 433-437.
- Ambrose, J. (1973) Computerised transverse axial scanning (tomography). 2. Clinical applications. *British Journal of Radiology*, 46, 1023-1047.
- Barber, C. I., Rowlands, P. C., McCarty, M., et al (1990) Clinical utility of cranial CT in HIV positive and AIDS patients with neurological disease. *Clinical Radiology*, 42, 164-165.
- Bentsen, J. R., Wilson, G. H., Iletmer, E., Winter, J. (1977) CT in intracranial cysticercosis. *Journal of Computer Assisted Tomography*, 1, 464-471.
- Brismar, J., Ageel, A., Gascon, G., et al (1990) Malignant hyperphenylalaninemia: CT and MRI of the brain. *American Journal of Neuroradiology*, 11, 135-138.
- Brismar, J., Brismar G., Coates, R., et al (1990) Increased density of the thalamus in CT of patients with GM2 gangliosidosis. *American Journal of Neuroradiology*, 11, 125-130.
- Cone, L., Spinavasan, H., Romanui, F. C. A. (1990) Granular cell tumour (choristoma) of the neurohypophysis. *American Journal of Neuroradiology*, 11, 403-406.
- Davis, P. C., Hoffman, J. C. Jr., Tindall, G. T., Braun, L. F. (1985) Prolactin secreting pituitary microadenomas-inaccuracy of high resolution CT imaging. *American Journal of Roentgenology*, 144, 151-156.
- Deibler, C., Dussler, A., Dulac, O. (1985) Congenital toxoplasmosis. Clinical and radiological evaluation of the cerebral lesions. *Neuroradiology*, 27, 125-130.
- Dome, H. L., O'Gorman, A. M., Melanson, D. (1986) CT of intracranial aneurysms. *American Journal of Neuroradiology*, 7, 281-285.
- Fitz, C. R. (1983) Holoprosencephaly and related entities. *Neuroradiology*, 25, 225-285.
- Ganti, S. R., Hilal, S. K., Stein, B. M., Silver, A. J., Mawad, M., Sane, P. (1986) CT of pineal region tumours. *American Journal of Neuroradiology*, 7, 97-104.
- Holtas, S., Nyman, U., Cronquist, S. (1984) CT of malignant lymphoma of the brain. *Neuroradiology*, 26, 33-38.
- Hounsfield, G. N. (1973) Computerised transverse axial scanning (tomography). I. Description of system. *British Journal of Radiology*, 46, 1016-1022.
- Illurn, F., Dupont, E. (1985) Prevalences of CT detected calcification in the basal ganglia. *Neuroradiology*, 27, 32-37.
- Jack, C. R., Reese, D. F., Scheithauer, B. W. (1985) Radiographic findings in 32 cases of primary CNS lymphoma. *American Journal of Neuroradiology*, 6, 899-904.

- Klein, H. M., Bertalanffy, I., Mayfrank, A., et al (1994) 3D spinal CT for neurosurgical planning. *Neuroradiology*, 36, 435-439.
- Levy, M., Rosenbloom, S., Perrett, R. V. (1986) Neuroradiological findings in AIDS: review of 200 cases. *American Journal of Neuroradiology*, 7, 833-839.
- Liang, E. Y., Shan, M., Hsiang, J. H. K. (1995) Detection and assessment of intracranial aneurysms; value of CT angiography with shadow surface display. *American Journal of Roentgenology*, 165, 1497-1502.
- Lott, P. R., Bellinger, W. E., Quisling, R. C. (1986) Subcortical arteriosclerotic encephalopathy: the CT spectrum. *American Journal of Neuroradiology*, 7, 817-822.
- Naidich, T. P., Fulling, K. H. (1983) Congenital malformations of the brain. *Neuroradiology*, 5, 177-304.
- Post, M. J. D., Kursonoglu, S. J., Hensky, G. T., Chan, J. C., Moskowitz, L. B., Hoffman, T. A. (1985) Cranial CT in AIDS. *American Journal of Neuroradiology*, 6, 743-754.
- Ronald, A. A., Patel, M., Casey, S., et al (1995) Evaluation of circle of Willis with 3D CT angiography in patients with suspected intracranial aneurysms. *American Journal of Neuroradiology*, 15, 1571-1579.
- Savoiardi, M., Strada, L., Paserini, N. (1983) Intracranial cavernous haemangiomas review of 36 operated cases. *American Journal of Neuroradiology*, 4, 945-950.
- Suss, P. A., Maravilla, K. R., Tompson, J. (1986) MR of intracranial cysticercosis: comparison with CT and anatomopathological features. *American Journal of Neuroradiology*, 7, 235-242.
- Sutton, D., Claveria, L. E. (1977) Meningiomas diagnosed by scanning. A review of 100 intracranial cases. In: Du Boulay, G. H., Moseley, T. F. (eds) *Computerised Axial Tomography in Clinical Practice*, pp. 102-110. Berlin: Springer.
- Welchman, J. M. (1979) CT of intracranial tuberculomata. *Clinical Radiology*, 30, 567-573.
- Zeumler, H., Schonsky, B., Sturm, K. W. (1980) Predominant white matter involvement in subcortical arteriosclerotic encephalopathy (Binswanger's disease). *Journal of Computer Assisted Tomography*, 4, 14-19.
- Zimmerman, H. M. (1971) The ten most common types of brain tumour. *Seminars in Roentgenology*, 6, 48-54.

MRI

- Boltshauser, E., Schinzel, A., Wichmann, W., Haller, D., Valavanis, A. (1988) Pelizaeus Merzhafer disease: identification of heterozygotes with magnetic resonance imaging. *Human Genetics*, 80, 363-394.
- Braffman, B. H., Bilanick, L. T., Zimmerman, R. A. (1988) Central nervous system manifestation of the phakomatoses on MR. *Radiologic Clinics of North America*, 26, 773-782.
- Bryant, R. N., Wells, S. W., Hiller, T. L., et al (1997) Infarct like lesions in the brain at MR imaging of the elderly. *Radiology*, 202, 47-54.
- Coates, T. L., Hinshaw, D. B., Peckman, N., et al (1989) Paediatric choroid plexus neoplasms: MR, CT and pathologic correlation. *Radiology*, 173, 81-90.
- Earnest, F. I. V., Kelly, P. J., Scheithauer, B. W., et al (1988) Cerebral astrocytomas: histopathologic correlation of MR and CT contrast enhancement with stereotactic biopsy. *Radiology*, 166, 823-830.
- Ellis, P. K. (1996) Case report; I, hermitte-Duclos disease; enhancement following gadolinium DTPA. *Clinical Radiology*, 51, 222-224.
- Elster, A. D., Challa, V. R., Gilbert, T. H., et al (1989) Haemangiomas: MR and histopathologic features. *Radiology*, 170, 857-863.
- Feinberg, D. A., Mark, A. S. (1987) Human brain motion and cerebrospinal fluid circulation demonstrated with MR velocity imaging. *Radiology*, 163, 793-798.
- Freeborough, P. A., Woods, R. P., Fox, N. C. (1996) Accurate registration of serial 3D MR brain imaging in neurodegenerative disorders. *Journal of Computer Assisted Tomography*, 20, 1012-1022.
- Freeman, M. P., Kessler, R. M., Allen, J. H., et al (1987) Craniopharyngioma: CT and MR imaging in nine cases. *Journal of Computer Assisted Tomography*, 11, 810-818.
- Hayman, L. A., Taber, K. H., Ford, T. J., Bryan, R. N. (1991) Mechanisms of MR signal alteration by acute intracranial blood clot: old concepts and new theories. *American Journal of Neuroradiology*, 12, 897-907.
- Hesselink, J. R., Dowd, C. F., Healy, M. L., et al (1988) MR imaging of brain contusions: a comparative study with CT. *American Journal of Neuroradiology*, 9, 269-275.

- Imakita, S., Nishimura, T., Yamada, N., et al (1988) Magnetic resonance imaging of cerebral infarction: time course of Gd-DTPA enhancement and CT comparison. *Neuroradiology*, **30**, 372-381.
- Jack, Jr, C. K. (1993) Epilepsy; surgery and imaging. *Radiology*, **89**, 635-646.
- Joubert, M., Eisenring, J. J., Robb, J. P., Andermann, F. (1969) Familial agenesis of the cerebellar vermis. *Neurology*, **19**, 813-825.
- Kucharczyk, J., Kucharczyk, W., Bern, I., et al (1988) Histochemical characterisation and functional significance of the hyperintense signal on MR images of the posterior pituitary. *American Journal of Neuroradiology*, **9**, 1079-1083.
- Kulkarni, M. V., Lee, K. F., McArdle, C. B., et al (1988) 1.5 T MR Imaging of pituitary microadenomas: technical considerations and CT correlation. *American Journal of Neuroradiology*, **9**, 5-15.
- Lee, S. R., Sanches, J., Mark, A. S., et al (1989) Posterior fossa haemangioblastomas MR Imaging. *Radiology*, **171**, 463-470.
- Li, L. M., Fish, D. R., Sisodia, S. M., et al (1995) High resolution MRI in adults with partial or secondary generalised epilepsy attending a tertiary referral unit. *Journal of Neurology, Neurosurgery and Psychiatry*, **59**, 384-387.
- McAndrew, P. T., Land, N., Sellar, R. J. (1995) A case of intracranial septated arachnoid cyst. *Clinical Radiology*, **50**, 502-504.
- McArdle, C. B., Richardson, C. J., Nicholas, D. A., et al (1987) Developmental features of the neonatal brain: MR Imaging. I. Grey-white matter differentiation and myelination. II. Ventricular size and extracerebral space. *Radiology*, **162**, 223-245.
- McMurdo, S. K., Brand-Zawadzki, M., Bradley, W. G., et al (1986) Dural sinus thrombosis: a study using intermediate field strength MR Imaging. *Radiology*, **161**, 83-86.
- Marshall, V. G., Bradley, W. G., Marshall, C. E., et al (1988) Deep white matter infarction: correlation of MR imaging and histopathological findings. *Radiology*, **167**, 517-522.
- Miller, D. A., Albert, P. I., Berkhof, F., et al (1996) Guide lines for the use of MR techniques in monitoring the treatment of MS. *Annals of Neurology*, **39**, 6-16.
- Moseley, I. (1995) Imaging the adult brain. *Journal of Neurology, Neurosurgery and Psychiatry*, **58**, 7-21.
- Muller-Forell, W., Schroth, G., Egan, P. J. (1988) MR Imaging in tumours of the pineal region. *Neuroradiology*, **30**, 224-229.
- Pickworth, S., Leutloth, U. (1996) CT and MRI findings in primitive neuroectodermal tumours in adults. *British Journal of Radiology*, **69**, 1-5.
- Pirker, W., Asenbaum, S., Bencsits, G., et al (2000) SPECT in multiple system atrophy, supranuclear palsy, and cortico basal degeneration. *Movement Disorders*, **15**, 1158-1167.
- Post, M. J. D., Tate, L. G., Quencer, R. M., et al (1988) CT, MR and pathology in HIV encephalitis and meningitis. *American Journal of Neuroradiology*, **9**, 469-473.
- Roosen, N., Sahlen, D., Stork, W., et al (1987) Magnetic resonance imaging of colloid cysts of the third ventricle. *Neuroradiology*, **29**, 10-21.
- Savader, S. J., Murtagh, F. R., Savader, B. L., et al (1989) Magnetic resonance imaging of intracranial epidermoid tumours. *Clinical Radiology*, **40**, 282-290.
- Schwaighofer, B. W., Hesselink, J. R., Press, G. A., et al (1989) Primary intracranial CNS lymphoma: MR manifestations. *American Journal of Neuroradiology*, **10**, 725-732.
- Sherman, J. L., Citrin, C. M., Sangarossa, R. E., et al (1986) The MR appearances of CSF How in patients with ventriculomegaly. *American Journal of Neuroradiology*, **7**, 1025-1031.
- Smirniotopoulos, J. G., Murphy, F. N. (1992) The phacomatoses. *American Journal of Neuroradiology*, **13**, 725-746.
- Stack, J. P., Ramsden, R. T., Antowa, N. M., et al (1988) Magnetic resonance imaging of acoustic neuromas: the role of gadolinium-DTPA. *British Journal of Radiology*, **61**, 800-806.
- Stevens, J. M. (1998) Neuroradiology in epilepsy. In: Scaravilli, F. (ed.) *Neuropathology of Epilepsy*, pp. 77-139. London, *World Scientific*.
- Stevens, J. M., Fox, N. (2001) Structural imaging. In: Hodges, J. R. (ed.) *Early Onset Dementia. A Multidisciplinary Approach*, pp. 124-142. Oxford: Oxford University Press.
- Tolly, T. L., Wells, R. G., Sty, J. R. (1989) MR features of the fleeting lesions associated with Epstein-Barr virus infection. *Journal of Computer Assisted Tomography*, **13**, 665-669.
- Van Paerschen, W., Sisodiya, S., Connelly, A., et al (1995) Quantitative hippocampal MRI and intractable temporal lobe epilepsy. *Neurology*, **45**, 2233-2240.
- Weishman, U. C., Free, S. L., Everitt, A. D., et al (1996) MRI in epilepsy with a fast FLAIR sequence. *Journal of Neurology, Neurosurgery and Psychiatry*, **61**, 357-361.
- Yeakley, J. W., Kulkarni, M. V., McArdle, C. B., et al (1988) High resolution MR imaging of juxtacellar meningiomas with CT and angiographic correlation. *American Journal of Neuroradiology*, **9**, 279-283.
- Yoshiura, T., Wu, O., Sorensen, A. (1994) Diffusion MRI, perfusion MRI and spectroscopy. *New Imaging Clinics of North America*, **9**, 439-453.
- Zee, C. S., Segall, H. D., Boswell, W., et al (1988) MR Imaging of neurocysticercosis. *Journal of Computer Assisted Tomography*, **12**, 927-936.
- Ultrasound**
- Babcock, D. S., Hann, B. K., Lequesne, G. W. (1980) B mode grey scale ultrasound in the head of the newborn and young infant. *American Journal of Roentgenology*, **134**, 457-468.
- Brown, J. K., Minns, R. A. (1993) Non accidental head injury with particular reference to whiplash shaking injury. *Developmental Medicine and Child Neurology*, **35**, 849-869.
- Cremin, B. N., Chilton, S. J., Peacock, W. J. (1983) Anatomical landmarks in anterior fontanelle ultrasonography. *British Journal of Radiology*, **56**, 511-526.
- Dewbury, K. C., Bates, R. I. (1983) Neonatal intracranial haemorrhage: the cause of the ultrasound appearances. *British Journal of Radiology*, **56**, 783-789.
- Fisher, R. M., Lipinski, J. K., Cremin, B. J. (1984) Ultrasonic assessment of infectious meningitis. *Clinical Radiology*, **35**, 267-273.
- Gaissie, G., Roberts, M., Bouldin, T. W., Scatlifi, J. H. (1990) The echogenic wall in intracranial haemorrhage; sonographic pathological correlation. *Paediatric Radiology*, **20**, 297-300.
- Jaspan, T. (1994) Assessment of infant intracranial trauma by high resolution ultrasound. *BMUS Bulletin*, **2**, 14-22.
- Jaspan, T., Narborough, G., Punt, J. A. G., Lowe, I. (1992) Cerebral contusion tears as markers of child abuse - detection by cranial sonography. *Pediatric Radiology*, **22**, 237-245.
- Khaw, K-T. (1997) Does carotid duplex imaging render angiography redundant before carotid endarterectomy? *British Journal of Radiology*, **70**, 235-238.
- Levene, M. I. (1981) Measurement of the growth of the lateral ventricles in preterm infants with real time ultrasound. *Archives of Disease in Childhood*, **56**, 900-904.
- Radionuclide Imaging**
- Asenbaum, S., Baumgartner, C. (2001) Nuclear medicine in the preoperative evaluation of epilepsy. *Nuclear Medicine Communications*, **22**, 835-840.
- Benamer, T. S., Patterson, J., Grosset, D. G., et al (2000) Accurate differentiation of parkinsonism and essential tremor using visual assessment of [¹²³I]-FP-CIT SPECT imaging: the [¹²³I]-FP-CIT study group. *Movement Disorders*, **15**, 503-510.
- Iacoboni, M., Baron, J. C., Frackowiak, R. S., et al (1999) Emission tomography contribution to clinical neurology. *Clinical Neurophysiology*,

59

RECENT TECHNICAL ADVANCES

Andrew P. Jones and Jeremy P. R. Jenkins (MR), Philip J. A. Robinson (Nuclear Medicine), Paul L. Allan (Ultrasound), Richard W. Whitehouse, Andrew R. Wright (CT), Nicola H. Strickland and Philip Gishen (Computing (digital workflow)).

MAGNETIC RESONANCE IMAGING

The application of MR techniques to medicine appears to advance each year with a relentless pace and it would almost seem foolish for someone to suggest what its limitations will be and when these will be reached. We constantly see refinements and improvements in existing techniques, providing enhanced diagnostic information. This is hand

in hand with the emergence of new applications, which have been enabled by hardware advances linked to new sequence and acquisition protocols, which in turn reflect the development of new contrast agents. Increasingly, MR is providing new, non invasive alternatives to existing imaging techniques, often with improved diagnostic information. There is also a move towards more quantitative imaging techniques, providing data quicker than using other modalities and without the requirement for multiple imaging investigations. There is always the temptation to suggest that, as MR becomes more advanced and faster, the possibility of reduced examination times may result in higher patient throughputs. However, it is often more realistic to accept that these advances, while giving some benefits in shorter examination times, will in the main result in the ability to make additional measurements, producing more extensive and improved quality of diagnostic information.

In this section, covering the recent advances of MRI, we hope to provide an insight into a few examples of where MR may be positioned relative to the 'routine' in 2-3 years time. Hopefully, if the development of MR continues unabated at its current pace, further new and exciting advances will rapidly supersede the information presented here.

Hardware advances

Magnets

Standard clinical imaging systems have generally embraced patient comfort aspects in terms of their design. Superconducting magnets have become shorter in bore length and the internal patient apertures are enhanced by use of strongly flared entrances (Fig. 59.1). These changes in bore size have been accomplished without compromising the maximum image field of view or main magnetic field homogeneity.

The development of MR systems designed for specialist niche applications has continued. Smaller, low-field, open resistive systems still find widespread applications in, for example, extremity

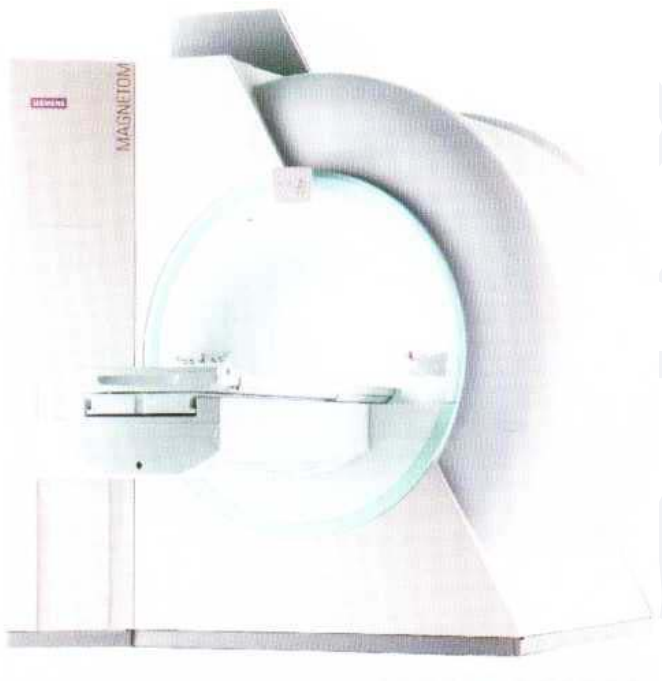


Fig. 59.1 Siemens Symphony 1.5 tesla MR system typical of the patient friendly features, incorporating short magnet bore length and flared patient aperture. (Courtesy of Siemens Medical Solutions.)

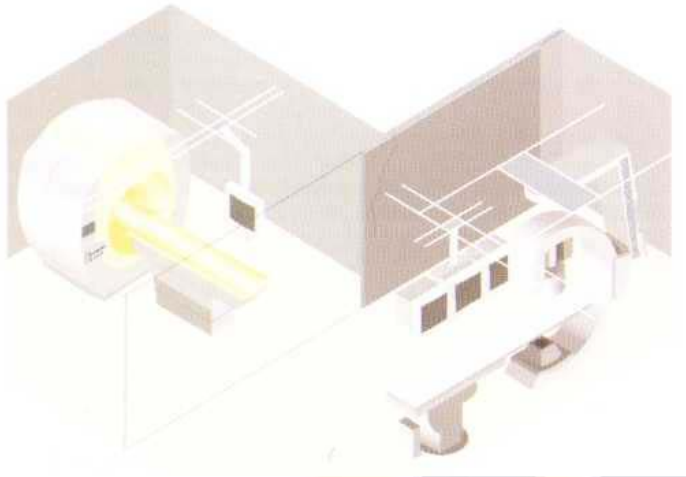


Fig. 59.2 An interventional MR suite incorporating a high-field superconducting magnet and a digital X-ray fluoroscopy facility. Patient transfer between the MR system and the X-ray fluoroscopy unit is possible while still within the general environment of an operating theatre. Patient coordinates relative to the two imaging modalities can be maintained via a patient couch transport system. (Courtesy of Philips Medical Systems.)

musculoskeletal imaging. In addition, higher field (0.5-1.0 T) open architecture systems are emerging, essentially aimed at interventional MR installations. These new interventional systems, although significantly heavier than standard superconducting magnets (typically around 10 tons and above), provide the ability to perform surgical intervention during imaging, along with therapeutic applications such as focused radiofrequency and ultrasound. Uniquely, MR techniques can provide measurements of tissue temperature during therapy, or in the future, monitor drug delivery using new MR-visible agents. Furthermore, recent trends in the development of interventional installations have seen the linking of MR systems with digital X-ray fluoroscopic units in a single examination/operating room or in contiguous rooms, thus allowing patient movement between modalities (Fig. 59.2).

For general clinical imaging, most users now choose 1.5 T superconducting systems, with field strengths of 1 T and below primarily being applied in niche situations. There is an increasing emergence of very high field (VHF) systems, with a growing number of 3 T systems being used for routine and research applications and a small number of 7-9 T whole-body magnets installed worldwide. For an optimised 3 T magnet, there are significant advantages for many neurological applications, in particular spectroscopy, tMRI and spin-tagging perfusion imaging. In terms of general imaging, there are significant hurdles to overcome at 3 T. The main issues relate to increased T₂ relaxation times, RF power problems in relation to specific absorption rate (SAR) and receiver coil design issues for efficient transfer of a uniform B₁ (radiofrequency excitation) field. However, for neurological applications the improved signal-to-noise can give significant benefits (Fig. 59.3).

Gradient coils

Magnetic field gradient coils continue to develop, with increasingly greater maximum amplitudes and faster rise times. Maximum amplitudes are now typically 30-40 mT/m or even 50-60 mT/m on some of the dedicated cardiac and neurological systems operating at reduced field of view with shorter gradient coils. At optimum performance, many systems now accomplish these maximum amplitudes with rise times of 200 μ s or below, at a 100% duty cycle. As a result of reduced duration of the RF pulse, improvements in gradient performance result in reduced minimum echo and repetition times (TE and TR), and improved spatial resolution via increased matrices and reduced image fields of view (Fig. 59.4). In addition, high-performance gradients provide the ability to perform echo-planar imaging (EPI), and enhancements in many other sequence applications. Improvements in diffusion-weighted sequences are enabled by higher b-values (sensitivity to diffusion) and increased speed of acquisition. Contrast-enhanced angiography (CE-MRA) benefits from shorter TEs. Bolus injection-based dynamic perfusion imaging achieves greater temporal resolution via shorter TRs, and



Fig. 59.3 (A) T₂-weighted FSE and (B) time-of-flight angiography of a cerebral arteriovenous malformation acquired at 3 Tesla. (Courtesy of Malcolm Randall, VA Medical Center, University of Florida.)

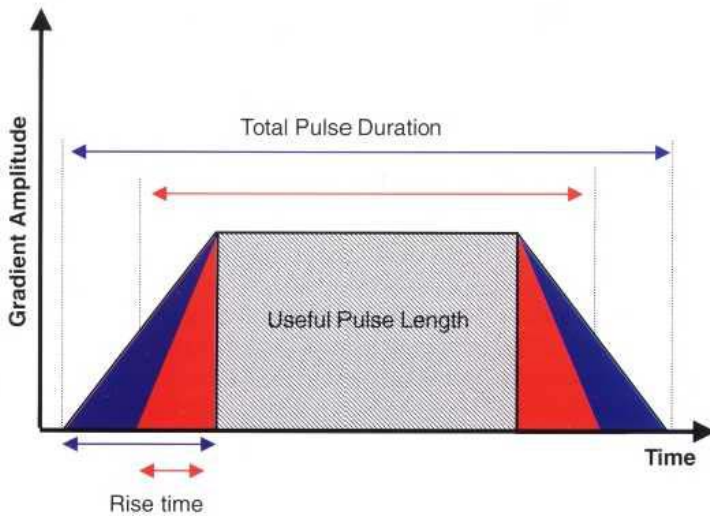


Fig. 59.4 The effects of improved gradient performance on duration of gradient pulses. Increased gradient rise times result in a reduction in the total pulse length within a sequence for the same useful pulse length.

cardiac imaging has improved significantly, with faster acquisitions now permitting real-time imaging and navigator-echo corrections.

Ultimately, the limit to gradient performance development is constrained by considerations for patient safety. Peripheral nerve stimulation is now a real safety issue when running many routine rapid sequences. Unfortunately, the geometry of the patient within the magnet and individual patient sensitivity to the phenomena are factors dictating the probability of induced nerve stimulation. Therefore, it is for this reason that current estimations on the likelihood of any possible effects are empirical. Some manufacturers are now producing double gradient systems and gradient coil inserts which reduce the high dB/dt (rate of change of magnetic field) values produced at the ends of standard gradient designs, while facilitating the possibility of even greater maximum amplitudes and rise times.

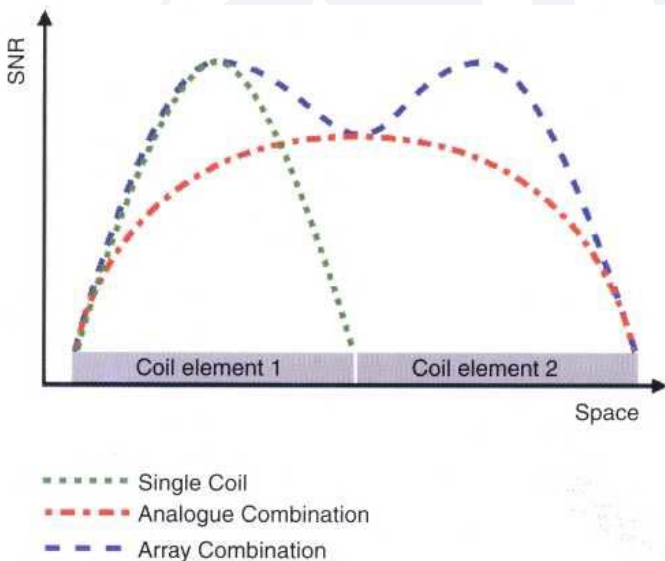


Fig. 59.5 Principle of phased array coil technology. Multiple coil arrays provide the benefits of large fields of view along with the signal-to-noise properties of small single-coil elements when signals are combined in an array combination.

Receiver coils

Manufacturers continue to produce an ever-expanding series of receiver coils, many of which are aimed at specific applications and parts of the body. The majority are now quadrature/circularly polarised in operation, with resulting improved signal-to-noise ratio. Increasingly, new coil designs are enhancements on previous coils, based on developments in techniques, for example combined neck and head coils for neurological applications and peripheral leg coils for contrast-enhanced angiography. Phased array coils are now considered standard for spine, body and pelvic examinations. The principle of phased array coils is to combine the signal-to-noise properties of small surface coils with large image fields of view (Fig. 59.5). Wherever possible, phase array technology is being applied to other body areas such as the shoulder, to give the benefits of greater signal-to-noise.

The increasing use of several coils at the same time, and multiple-element phased array coils, has led to the provision of multiple data receive channels and the option of duplexing coils into a single channel. Some systems have eight independent data channels, allowing the possibility of up to 16 separate coils or coil elements to be used simultaneously. Alongside these developments have been significant enhancements in data handling and processing power.

Image processing and computers

Significant developments in computing power have had to be made in order to benefit from the many hardware innovations already discussed. Rapid imaging strategies can easily produce hundreds of images per examination. Dedicated array processors can now perform thousands of Fourier transforms per second, providing the ability to achieve real-time imaging. The use of multiple-element phased array coils and multiple data acquisition channels also require enhanced computing power, if data reconstruction times are not to be detrimental to new imaging strategies.

Innovative techniques, for manipulating k-space data, have produced significant image quality benefits and new methods for reducing image acquisition times. Partial k-space acquisition strategies, such as half-Fourier and partial echo acquisitions, are now widely used techniques. Developments in the flexibility of k-space filling routines have enabled improvements for triggered acquisition routines in cardiac imaging and non-triggered methods in free-breathing sequences for abdominal imaging. Reordering of k-space filling can now produce optimum contrast rendition in contrast-enhanced angiography. New partial/parallel acquisition techniques, such as SENSE and SMASH, have provided the ability to produce

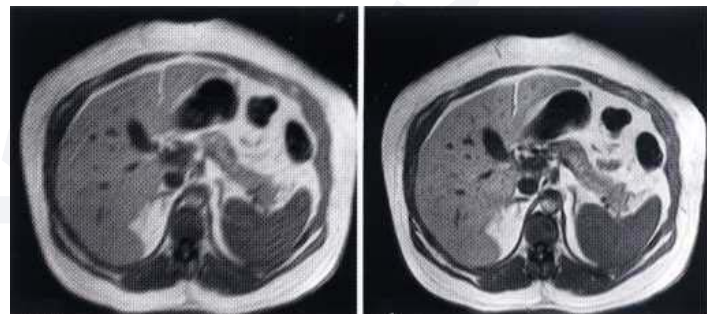


Fig. 59.6 Example of the application of SENSE to abdominal breath-hold imaging for an elderly patient unable to sustain a long breath-hold. (A) 23 s without SENSE; (B) 12 s with SENSE. (Courtesy of Philips Medical Systems.)

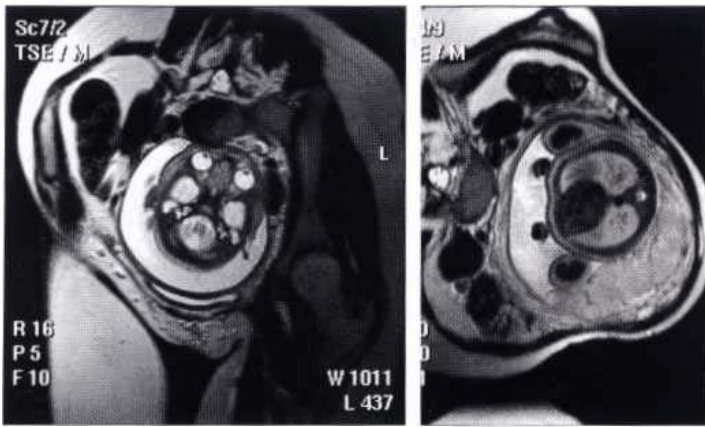


Fig. 59.7 (A,B) Rapid T_2 -TSE imaging using SENSE illustrating the imaging of a fetus in utero. The fast imaging in less than 20 s minimises any possible artefacts from fetal movement with high signal-to-noise and high spatial resolution. (Courtesy of Philips Medical Systems.)

significant reductions in acquisition times for sequences setup with a single signal excitation/average. These new techniques require multiple coil elements in specific directions within the desired imaging volume. Existing coils permit the use of these new techniques; however, new designs consisting of coil arrays along multiple axes will extend their application. The resulting shorter acquisition times will benefit CE-MRA, for example in breath-hold abdominal imaging and cardiac studies, where temporal resolution is paramount. Figures 59.6 and 59.7 show examples of the benefits of the shorter acquisition times in minimising the deleterious effects of patient movement.

Sequence advances

The hardware developments already described have enabled a series of new sequences to be applied to routine clinical practice. These sequences, in conjunction with phase array technology, have permitted refinements to existing examination types as well as the opportunity for MR to be used in innovative and exciting areas of diagnostic imaging and spectroscopy. The following examples of clinical applications serve to reflect the breadth of the advances that MR has achieved.

MR cholangiopancreatography (MRCP)

The refinement of fast/turbo spin-echo (FSE/TSE) sequences to permit single shot acquisitions has made breath-hold T_2 -weighted sequences a practical technique. Long echo train lengths of 128 spin echos, often linked with a half Fourier k-space filling (HASTE), produce heavily T_2 -weighted images from a single excitation pulse, as shown schematically in Figure 59.8.

The visualisation of the static, long T_2 , pancreaticobiliary fluids resulting from long effective echo times gives perfect contrast for MRCP techniques (Fig. 59.9). Single thick-slab acquisitions, which mimic maximum intensity projection (MIP) images, can be made in 2-3 s. Multiple 2D slices can be acquired in 10-15 s or even 3D variations in a single breath-hold. Data can then be viewed as an MIP, with the ability to remove overlying high signal from stomach or small bowel.

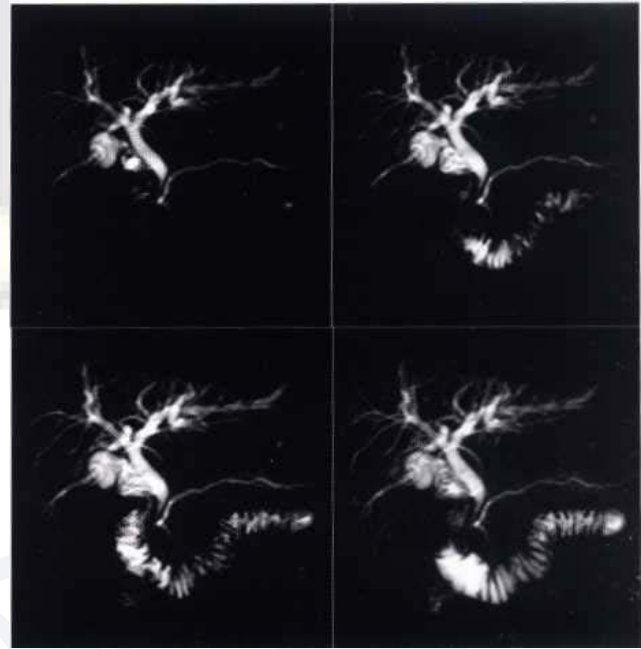


Fig. 59.9 Single-shot breath-hold MRCP examination. Heavily T_2 -weighted FSE/TSE images demonstrate high contrast fluid signal from pancreatic and biliary systems.

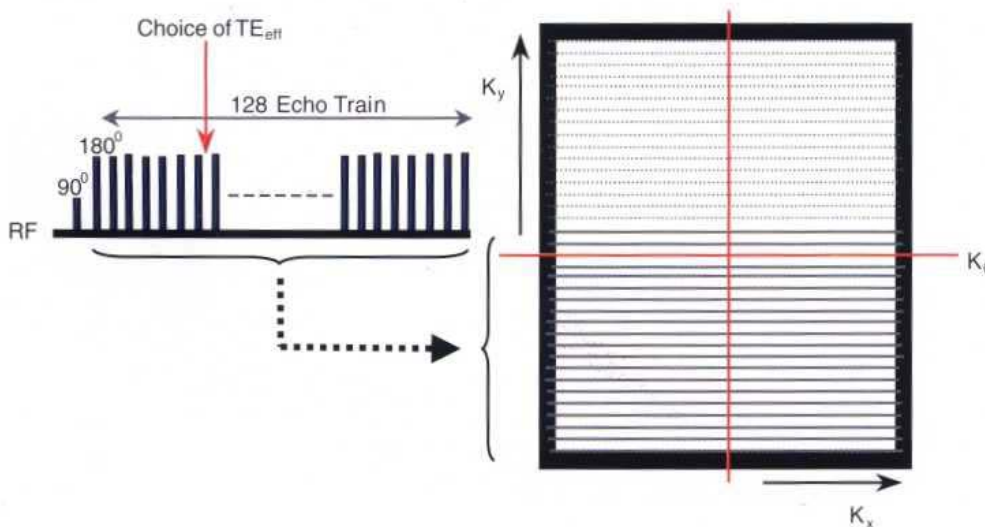


Fig. 59.8 Schematic diagram for a single shot FSE/TSE sequence. An echo train length of 128 180 pulses, following a single 90 excitation pulse, fills half of k-space. The effective echo time TE_{eff} corresponds to those data lines written to the centre of k-space. The significant number of very long TE echos give a heavily T_2 -weighted contrast.

Whole-body screening

High-performance gradients linked to automated table movements enables rapid imaging, covering the whole of the body. Fast T₁- and T₂-weighted FSE/TSE sequences can be planned with automatic, sequential movements of the patient through the MR scanner. The whole body can then be scanned in coronal or sagittal planes, giving full body views (Fig. 59.10). Additional transverse imaging can be carried out as required at each relevant table position incrementation, while still maintaining short, practical examination times. The technique offers exciting alternative imaging methods for some aspects of oncological screening. Whole-body STIR imaging can provide a sensitive and fast screening process for bone tumours and lymph nodes.

Comprehensive stroke examination

Rapid diffusion-weighted imaging and T₂-weighted, gadolinium-based perfusion imaging require high specification gradients. Fast acquisitions minimise problems with patient motion for diffusion images and provide good temporal resolution for dynamic, first-pass perfusion studies. Diffusion- and perfusion-weighted protocols can provide key, unique diagnosis for the assessment of acute stroke patients. Early diagnostic imaging can give essential information,

which can dictate strategies for patient management using new antithrombotic drugs. New high-specification systems can now perform a comprehensive brain study in a practical examination time. Diffusion and perfusion sequences can be added to routine neurological sequences such as FSE/TSE or GRASE T₂, FLAIR and time of flight angiography. Subsequent analysis of the diffusion data can give an apparent diffusion coefficient map (ADC) to complement the diffusion weighted images. Similarly, analysis of the dynamic perfusion images produces time to peak (TTP) and mean transit time (MTT) maps, along with integral data implying relative cerebral blood volume (rCBV).

An example of a typical stroke examination protocol, which includes routine imaging along with diffusion and perfusion sequences, is shown in Figure 59.11. The value of imaging acute patients in the first few hours following a stroke is illustrated by the diffusion and perfusion data, as conventional imaging shows no change until approximately 24 h after the stroke.

Contrast-enhanced angiography and vascular imaging

CE-MRA has recently developed into a standard vascular imaging routine for systems with high-performance gradient systems. The

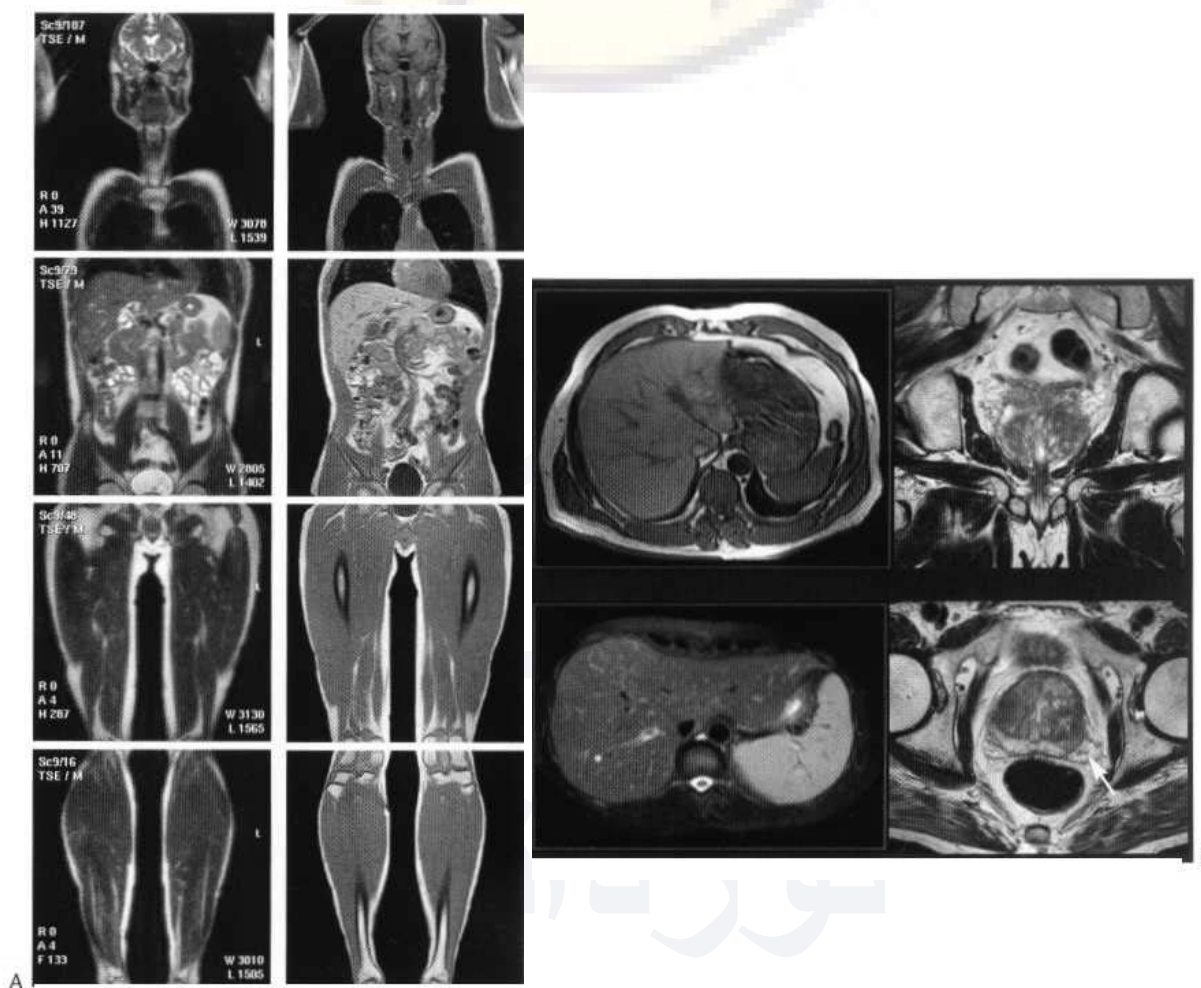


Fig. 59.10 (A) Rapid whole-body screening using a moving table facility. Four sets of coronal images with both T₁ and T₂ weighting are acquired to cover the entire length of the body. (B) Additional transverse images are also acquired at chosen anatomical positions. In total, 750 images are produced in 5 min. Note the high resolution with demonstration of a contained prostatic carcinoma (low signal, arrow) in the left peripheral zone. (Courtesy of Philips Medical Systems.)

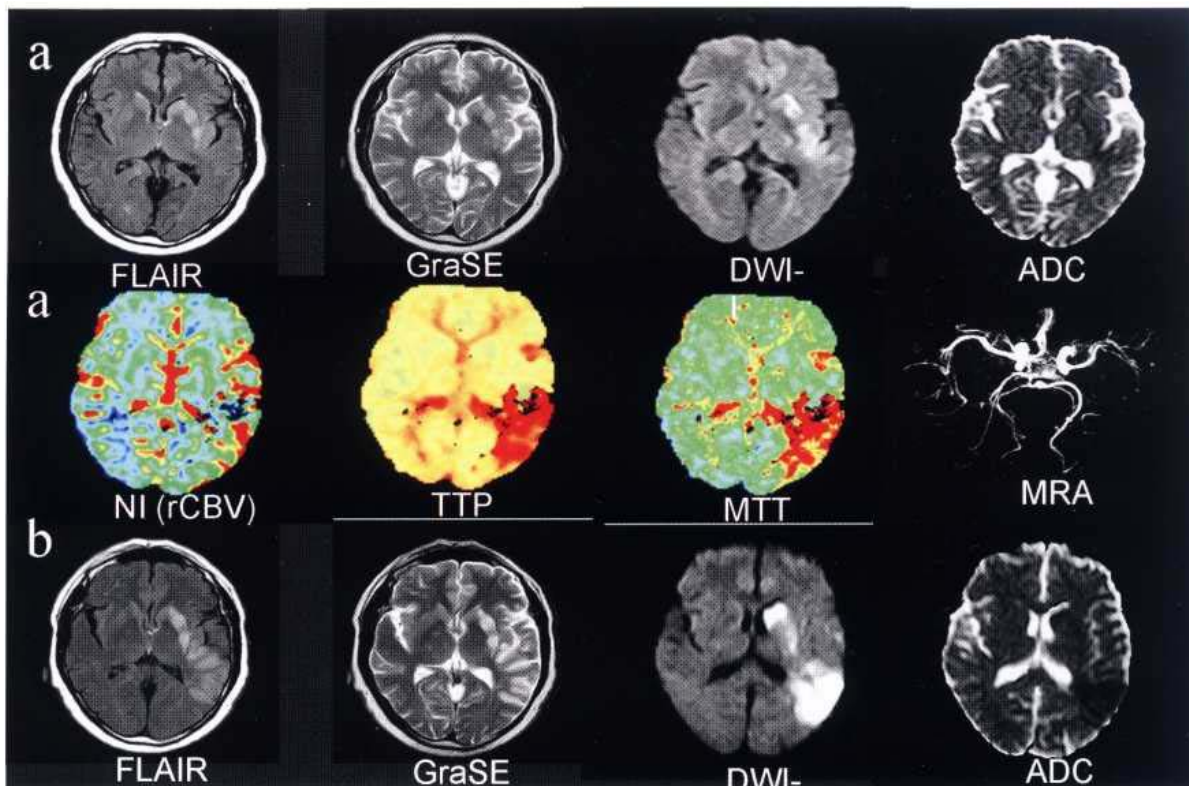


Fig. 59.11 Comprehensive stroke examination performed after (a) 6 h and (b) 24 h from an acute stroke. The protocol includes routine brain sequences in addition to diffusion weighted and dynamic perfusion protocols. The whole examination can be carried out in less than 10 min. The early perfusion and diffusion imaging clearly shows areas of infarct not visible in the standard T_2 and FLAIR images until after 24 hours. (Courtesy of Philips Medical Systems.)

technique does not rely on either the inflow signal enhancement associated with time-of-flight, or the signal phase shift for moving spins utilised in phase-contrast techniques. Essentially, it is based on the simple, longstanding principle of T_1 -weighted signal

enhancement following the administration of a gadolinium-based contrast agent.

The high equipment performance requirements for CE-MRA relate to the ability to perform a 3D T_1 -weighted acquisition while a

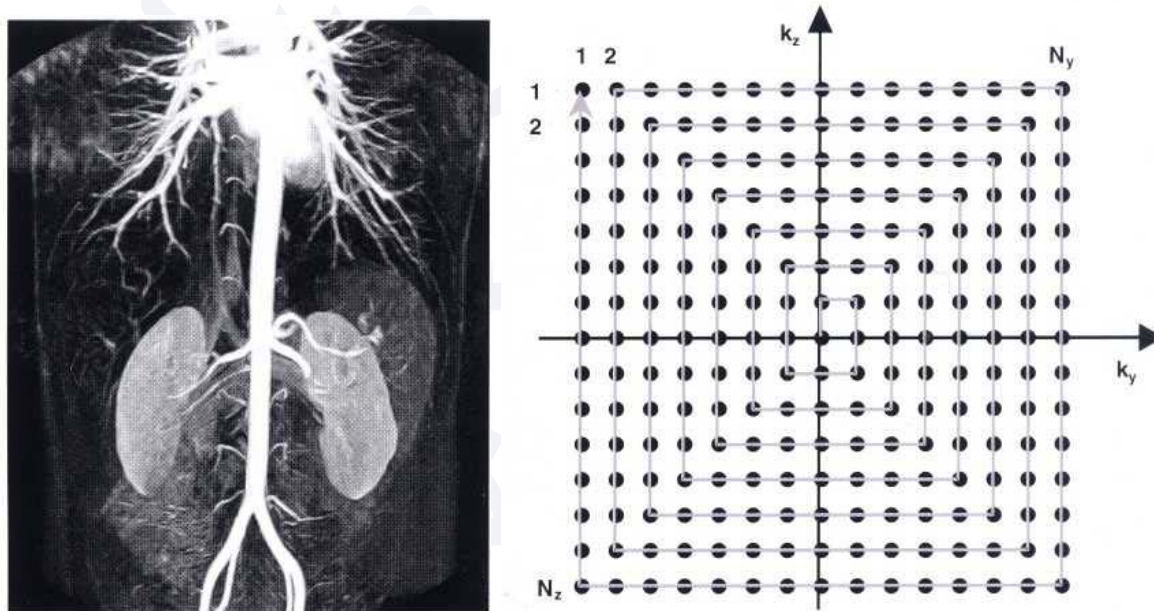


Fig. 59.12 (A,B) Contrast-enhanced abdominal angiography. A maximum intensity projection image from the CE-MRA 3D acquisition performed during a 15 s breath-hold and triggered using real-time image monitoring of the contrast bolus arrival. The centre of k-space is acquired at the start of the sequence, using an elliptical filling strategy to provide optimal signal as the bolus of contrast passes through the vasculature. (Courtesy of Siemens Medical Solutions.)

bolus of contrast passes through the particular vasculature of interest. Therefore, short repetition times, using a flip angle optimised for the shortened T₁ of contrast-enhanced blood, are needed to ensure the 3D acquisition takes place while the bolus is within the area of interest. For abdominal and thoracic applications, the acquisition additionally needs to be made within a breath-hold period (Fig. 59.12). Furthermore, exceptionally short echo times (typically less than 1.5 ms) are also required to minimise intravoxel signal phase losses due to flow. Real-time imaging routines are used to monitor the arrival of the bolus of contrast in order to ensure correct timing of the acquisition. The CE-MRA sequences are also linked to dedicated k-space filling strategies as alternatives to the standard linear filling routines. These specialised strategies enable the centre of k-space (which controls low spatial frequency, contrast information), to be captured at the peak of the signal enhancement from the bolus of contrast agent (Fig. 59.12). Filling strategies include elliptical or centric k-space trajectories, with the central portion of the k-space volume being filled at the start of the 3D sequence (see Fig. 15.134).

The use of short echo times in CE-MRA minimises the possibility of dephasing signal losses arising from complex or turbulent flow. The well-recognised signal voids associated with complex and turbulent flow in time-of-flight angiography and exaggeration of vessel stenosis do not normally occur in CE-MRA. Therefore CE-MRA offers significant improvements over standard MR angiographic techniques, providing diagnostic information to rival conventional angiography in a non-invasive way. Adaptation of bolus contrast injection strategies is used to perform multiple acquisitions over different areas of the body for peripheral angiography. Typically, a steady-state injection of contrast is linked with automatic incrementation of the patient couch position. Acquisitions are performed over three to four positions. The series of images can then be linked together for display purposes and maximum intensity projection images generated (see Fig. 15.149). Furthermore, multi-

planar reconstructions and surface rendering routines can be used to produce virtual endoscopy images.

Further important contributions to vascular imaging have been made by the use of high-resolution imaging in conjunction with dedicated small field-of-view, vascular coils. The main application has been in the visualisation of thrombus and plaque formation for carotid artery imaging (Fig. 59.13). The dedicated coils can be used to obtain high signal-to-noise, high-resolution, black-blood images demonstrating areas of thrombus.

Cardiac imaging

The ability to perform rapid sequences using cardiac triggering with the latest highest performing gradient systems has catapulted MR as an important tool for cardiac imaging. One of the main strengths of MR is the versatility it brings to cardiac imaging, permitting investigations previously performed using several different imaging modalities to be carried out in a single, one-stop cardiac examination. Established techniques of black-blood prepared FSE/TSE and bright-blood, cine gradient-echo acquisitions (TrueFISP/BalancedFFE/FIESTA) can provide several slices in a single breath-hold. Higher performing gradients, linked with improved cardiac triggering regimens, permit multiple cardiac phases to be measured with excellent R-to-R wave coverage. Figure 59.14 demonstrates examples of the different types of image data that can contribute to a generalised cardiac examination.

Motion of the myocardium can be imaged and assessed quantitatively using tagging routines, which use a narrow grid of saturation lines applied repeatedly across the image field of view during the cardiac cycle. Perfusion can be assessed using a rapid series of gated acquisitions following a bolus of contrast. Measurements can be made in terms of signal changes in the myocardium. The technique can be used in conjunction with stress induction, using, for example, dobutamine administration, to give diagnostic information that matches both ultrasound- and radioisotope-based techniques. Reductions in image acquisition times and the use of the latest navigator-echo correction methods have enabled coronary artery imaging to be a realistic technique for MR. Issues do remain, however, for patients who are unable to hold their breath for even short periods. Interestingly, it has been found that a very useful byproduct of contrast administration during the cardiac examination has been the development of myocardial viability measurements. Images acquired approximately 10 min postcontrast, using an inversion recovery sequence to null-out normal myocardium, demonstrate residual signal from trapped contrast within any infarcted myocardial tissue.

¹H-MR spectroscopy and chemical shift imaging

Clinical spectroscopy continues to develop and remains a key research tool for the investigation of many neurological diseases, including stroke, psychiatric disorders, multiple sclerosis, HIV and oncology. The use of shorter echo times to provide data on important, short T₂ metabolites and multiple voxel acquisitions (chemical shift imaging, CSI) has extended the clinical application of spectroscopy. A huge reduction in examination times for spectroscopy measurements and automated setup and adjustment routines for shimming and water suppression have helped ease ¹H-spectroscopy

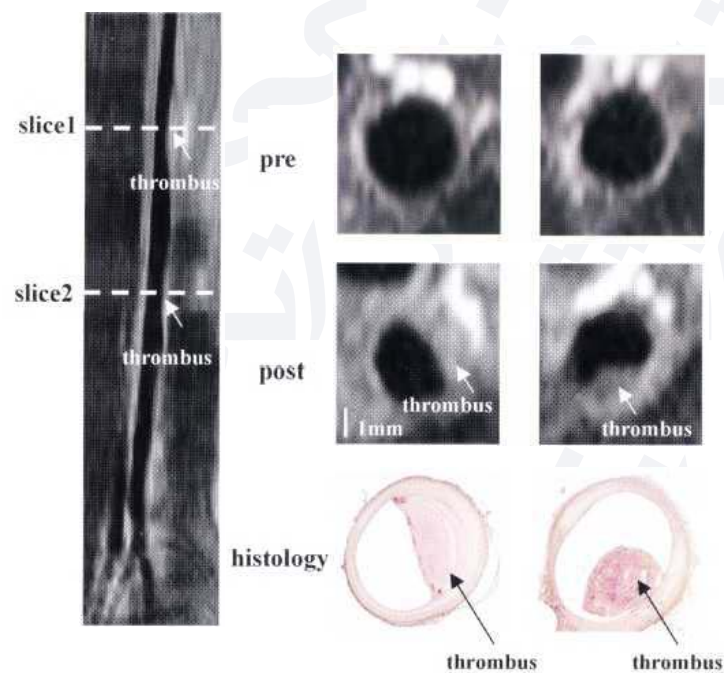


Fig. 59.13 High-resolution carotid imaging for the visualisation of thrombus. Transverse images through the area of thrombus show excellent correlation with histology.

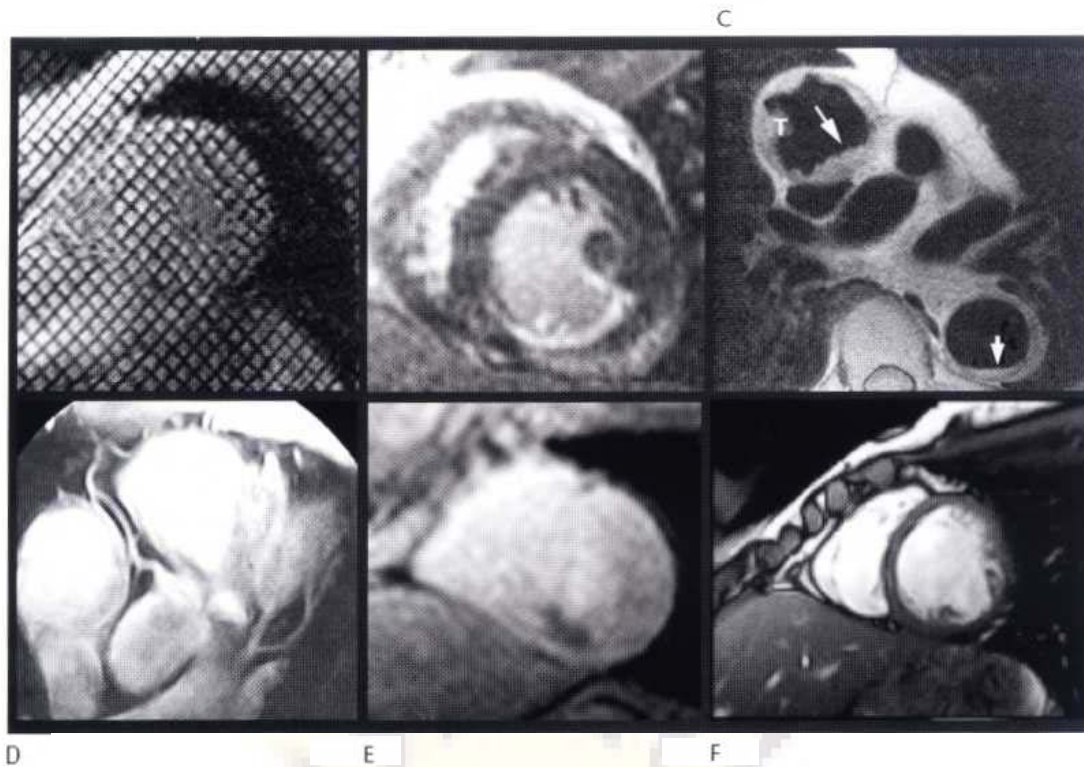


Fig. 59.14 A comprehensive MR cardiac examination. The *one-stop* investigation provides diagnostic information on: (A) myocardial motion using saturation tagging techniques to visualise wall movement through the cardiac cycle; (B) myocardium viability using an inversion recovery technique, 10 min postcontrast administration; (C) black blood-prepared FSE anatomical images showing atherosclerotic plaques (arrows); (D) coronary artery angiography; (E) myocardial perfusion-weighted images acquired immediately after a bolus injection of contrast; (F) cine gradient echo, bright-blood images, for ventricular volume analysis. (Courtesy of GE Medical Systems.)

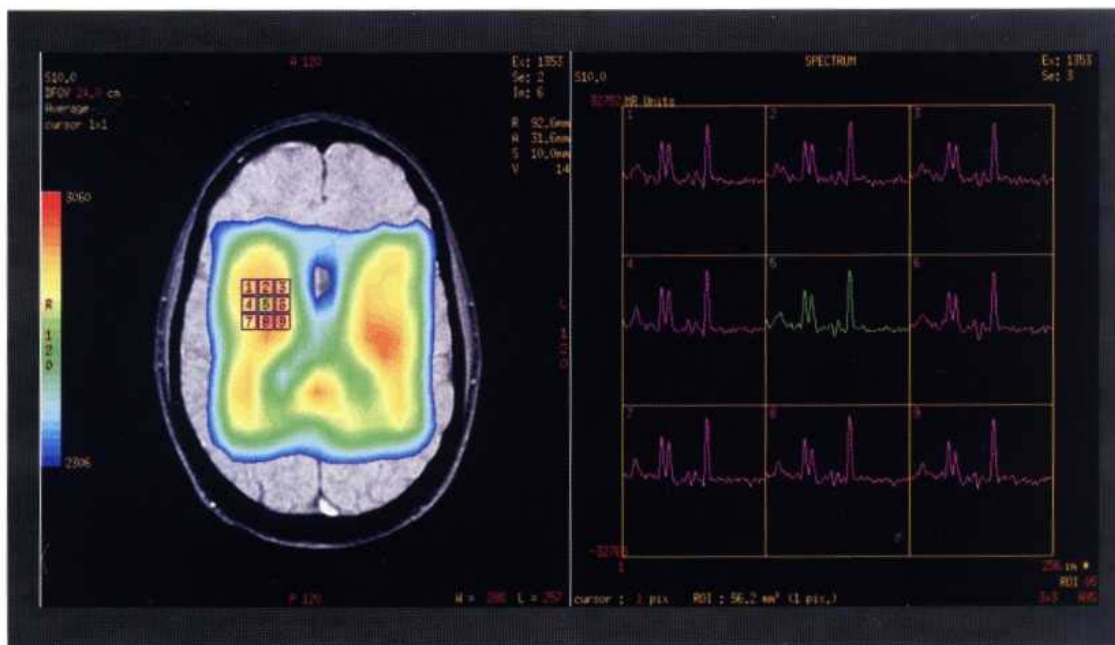


Fig. 59.15 Chemical shift imaging in the brain. Multiple voxels are acquired over slices through the brain. Analysis of the spectra provides quantification of the measured metabolites using an overlaid map on a reference anatomical image. Individual spectra can be viewed and interrogated from within the metabolite maps. The spatial distributions of the various metabolites seen can give important clinical information. (Courtesy of GE Medical Systems.)

into the clinical routine. Single voxel acquisitions, including system setup, can now be made in about 10 min, with only a further 10 min being required for multiple slice CSI.

This reduction in examination time and the increased numbers of clinical MR systems with the capability to perform MR spec-

troscopy have resulted for the first time in spectroscopy being used as a routine clinical tool. It has been in the investigation of brain tumours that the most significant diagnostic benefits have been seen. MR spectroscopy can provide important information to aid the identification and grading of brain tumours, discriminating

lesions from other pathologies and differentiating tumour from postradiotherapy signal changes. FSE/TSE approaches have permitted the extension of the single voxel techniques to CSI methods where several slices are acquired, each consisting of a 32 x 32 voxel array. Importantly, the CSI data allow metabolite maps to be created and overlaid upon conventional MR images as an alternative to standard MR spectra (Fig. 59.15). Individual spectra from each voxel can be viewed as required. The metabolite maps provide the clinician with spectroscopic data in an image-like format, which lends itself more readily to a routine clinical interpretation.

An important, new application of ¹H-MR spectroscopy has been in the study of prostate cancer. Single voxel or CSI can be used to identify tumour and monitor disease spread. Within the prostate, MR signals from citrate only occur within malignant tissue, therefore the visualisation of citrate is indicative of tumour. Using CSI techniques, the individual voxel resolution is sufficient to monitor disease spread from within the gland into, for example, the seminal vesicles, and also to monitor response to treatment therapies (Fig. 59.16). The analysis of citrate signal in each spectrum provides information on disease spread. In a similar manner to the brain metabolite maps, citrate maps can be overlaid on to reference T₂ anatomical images of the prostate. Evidence appears to suggest that the best quality data are currently obtained using endorectal coils.

Contrast agents

Over a decade, extracellular space (ECS) gadolinium chelate contrast agents (the first being gadolinium DTPA (Magnovist, Schering, AG)) have been the only agents available for MRI. Newer contrast agents have been, and are currently being, developed, with some of these agents due for general release shortly, further extending the role of MRI into new areas, as well as consolidating existing practices.

MR contrast agents can be classified as T₁ or T₂ agents, but are better subdivided into four groups by their distribution in the body: (i) ECS; (ii) hepatobiliary; (iii) reticuloendothelial system (RES);

(iv) blood-pool agents. New developments in each of these areas are becoming available, extending the clinical utility of MRI.

Extracellular space agents are routinely used in MR in CNS and body imaging, and have a high safety profile. Recent developments in the assessment of brain function described above, CE-MRA and the improved detection of intracranial disease with double or triple dosing (0.2-0.3 mmol/kg body weight) require the use of a rapid bolus of increased volumes of contrast. Newer agents with lower viscosity and increased concentration of gadolinium (e.g. 1 molar formulation gadobutrol (Gadovist, Schering, AG), as opposed to the original 0.5 molar agents, can reduce the volume load injected by a half.

Extracellular space agents, using a dynamic acquisition, can be used for improved detection of liver lesions. There are, however, several other agents (e.g. Mn DPDP (Teslascan, Nycomed); Gd EOB-DTPA (Eovist, Schering); Gd BOPTA/dimeglumine (MultiHance, Bracco)) that are actively taken up by hepatocytes and lead to prolonged T₁, shortening of the liver. These hepatobiliary agents remain in the liver for a long period of time, allowing a wide imaging window for delayed scanning, providing increased flexibility in sequence selection and imaging planes compared with the ECS agents. The hepatobiliary agents provide an increased liver-to-lesion contrast and improved lesion conspicuity.

Reticuloendothelial system agents are iron oxide-based particles with a covering of polysaccharides that specifically target the RES or blood pool. They can be formulated in different sizes: those of >50 nm are termed superparamagnetic iron oxides (SPIO), and those of <50 nm ultrasmall superparamagnetic iron oxides (USPIO). The main difference between the two groups is that the SPIO particles (e.g. Endorem, Guerbet; SH U 555 (Resovist, Schering, AG)) are phagocytosed by the RES of the liver in the majority, with only a small percentage of the particles ending up in the spleen and bone marrow. One advantage with Resovist is that it can be injected as a bolus, whereas Endorem has to be administered as an infusion. The SPIO agents are mainly designed for liver applications, with resultant signal void from T₁, shortening of normal liver due to its uptake of the superparamagnetic particles. Metastases do not show any signal change as they do not take up the contrast agent, and therefore

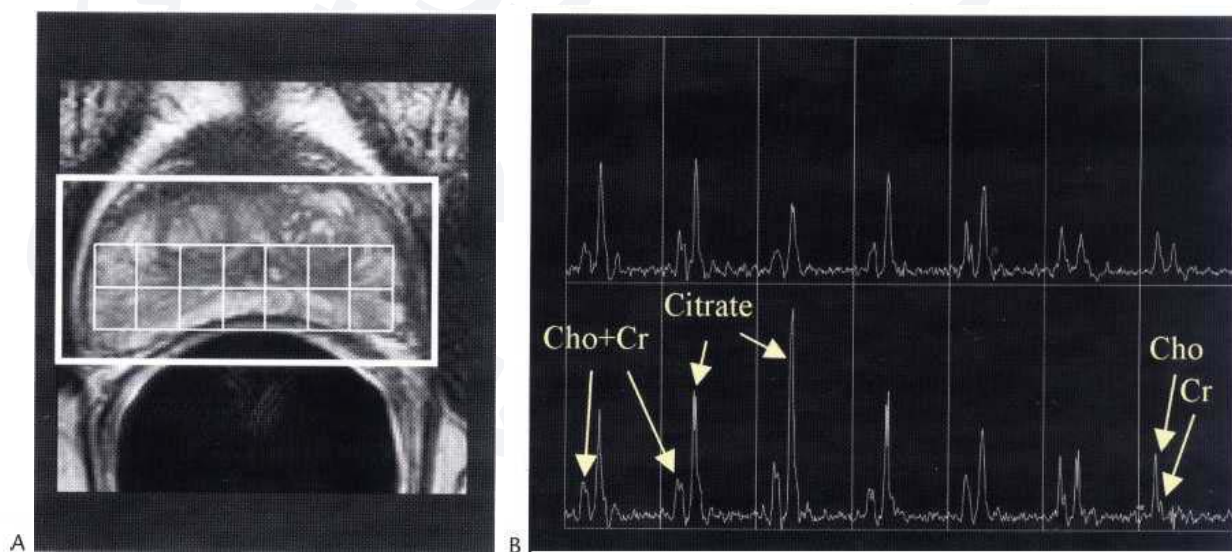


Fig. 59.16 Chemical shift imaging of the prostate. Multiple voxels are acquired over the area of the prostate gland and seminal vesicles. The position of the voxels is shown along with the measured spectra for each voxel. Citrate occurs only within tumour, indicating the extent and spread of the malignancy both within and outside the gland.



Fig. 59.17 Coronal T_1 -weighted image (A) pre-USIOP showing nodes (arrows) and inguinal veins (v) with intermediate signal intensity. In (B) following USIOP administration the lymph nodes demonstrate signal void due to iron oxide uptake. Veins (v) have high-signal intensity. Histology showed normal lymph nodes. (Courtesy of Guerbet.)

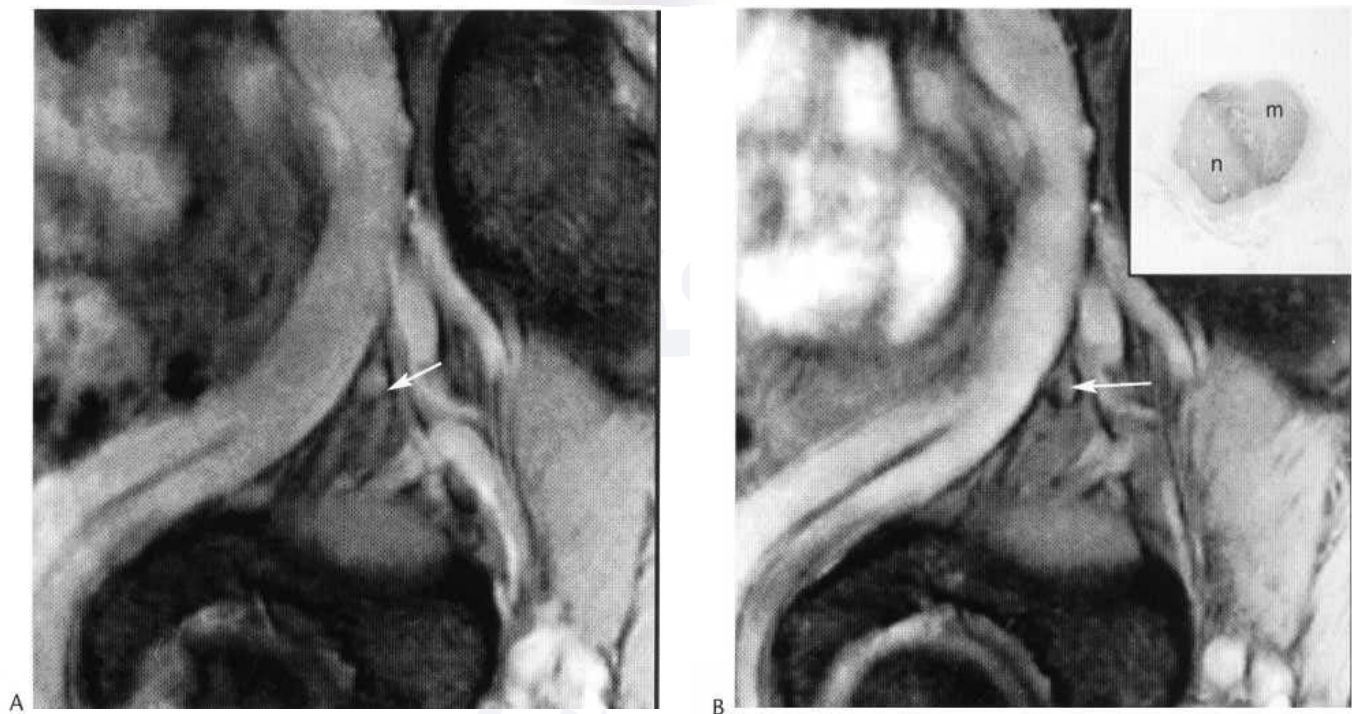


Fig. 59.18 Sagittal T_2 GRE (A) pre-USIOP image with a small (6 x 5 mm) inguinal node (arrow) showing a high signal intensity appearance. (B) Post-USIOP image with the node demonstrating in its ventral part a normal low signal, whereas the dorsal part (4 x 3 mm) remains high signal, in keeping with metastasis. Histology confirmed partially normal (n) and partially metastatic (m) node.

are more conspicuous following SPIO administration. The USPIO particles (e.g. ferumoxitan (Sinerem, Guerbet)) are designed for lymph node imaging (Figs 59.17, 59.18), and have the potential to be used for CE-MRA (Fig. 59.17), lymphocytic marking and receptor imaging targeted to other specific organs.

CE-MRA is now in widespread clinical practice using ECS gadolinium chelate agents. These agents produce T_1 shortening, leading to an increase in signal intensity within the blood but only providing a narrow window for scanning (blood-pool phase) because of rapid ECS redistribution. Blood-pool agents are

designed to remain within the blood pool and can provide improved assessment of blood flow. These agents give a wide imaging window, during which an MR angiogram can be obtained, although clinically useful delayed blood-pool images using standard MIP algorithms may be difficult to achieve due to enhancing veins and overlying structures. Many of the agents are paramagnetic compounds complexed with other substances designed to prevent redistribution outside the blood pool. These agents shorten the T₁ of blood, producing selective enhancement of vascular structures. Some iron oxide agents have MR angiographic capability, having a prolonged blood-pool phase producing T₁ shortening of the blood (Fig. 59.17).

Virtual intraluminal endoscopy

New paradigms are opening up with the manipulation of 3D datasets, particularly in conjunction with contrast enhancement, producing virtual imaging endoscopy (VIE) (e.g. virtual colonoscopy and virtual gastroscopy). These techniques emulate standard endoscopic procedures without being invasive, producing iatrogenic injury or patient discomfort. They can also be used in areas inaccessible to standard endoscopy (e.g. virtual angiography) (see Fig. 25.149). Computer-simulated endoscopy allows for a fly-through facility and interactive viewing. This is a powerful tool requiring more work and development to determine its true clinical efficacy.

RADIONUCLIDE IMAGING

Positron emission tomography (PET)

Positron-emitting radionuclides were discovered in the 1940s and PET imaging devices were first developed in the 1970s but the early instruments were costly and cumbersome. For the last quarter of the century, PET imaging has been extensively used in research, but only in the last few years has the technology become more widely available for clinical application.

PET tracers

The only isotopes of carbon, nitrogen and oxygen that are suitable for imaging *in vivo* are the positron emitters ¹¹C, ¹³N and ¹⁵O. Unfortunately, all these nuclides are short-lived, so they can only be used in close proximity to the cyclotron in which they are produced. Even so, they have been used to label a wide range of naturally occurring small organic molecules for physiological research and larger molecules for pharmacological investigation, but none are yet in routine clinical use.

Currently the mainstay of clinical PET is deoxyglucose labelled with fluorine-18 (¹⁸F-FDG). Malignant tumours show an increased rate of glucose metabolism, probably due to the presence on cell surfaces of an abnormally large number of glucose transporters, together with increased hexokinase-mediated glycolysis and a reduced level of dephosphorylation by glucose 6-phosphate. In general, the rate of glycolysis increases in proportion to the rate of cell growth. FDG undergoes glycolysis in tumours but the dephosphorylation of FDG-6-phosphate is relatively slow, so FDG gradu-

ally accumulates within the cells. The concentration of FDG reaches a plateau when the rate of dephosphorylation equals the rate of uptake into the cell. In experimental studies, this occurs about 45-60 min after injection, so clinical imaging is normally carried out after this interval. The kidney does not recognise FDG as glucose, so it is largely excreted by glomerular filtration, although there is some reabsorption in the proximal tubule. In a normal subject about half of the injected dose is excreted in the urine in 2-2.5 h after injection. The half-life of fluorine-18 is 110 min, so a daily production run is required, and the location of imaging needs to be within 1-2 h of the cyclotron production site.

Absolute measurement of glucose uptake into lesions or specific organs is difficult because of differences in the size and body composition of patients, and individual variations in glucose metabolism. Approximate quantitation is achieved by using the standardised uptake value (SUV), which is an estimate of the uptake of FDG into the lesion or organ of interest compared with the mean uptake in the rest of the body.

Instrumentation for PET

Each positron gives rise to two 511 keV photons travelling in diametrically opposed directions. The recognition of such coincident pairs of photons by detectors placed on opposite sides of the body allows the position of the source of the radiation to be determined. Since collimators are not needed, the efficiency of detection is considerably improved compared with the conventional gamma camera approach. Either a multihead gamma camera or a dedicated PET ring or partial ring detector system can be used, but the dedicated PET systems have several advantages. Using thicker crystals, more crystal elements and more photon multipliers, PET systems are superior in terms both of resolution and sensitivity. The high-energy photons require detector crystals with increased 'stopping power' and bismuth germanate (BGO) has been the standard for the last few years. The recent introduction of lutetium-based detectors, together with faster electronics, offers a further increase in sensitivity so that examination times for whole-body examinations can be considerably reduced.

Using a dual- or multiheaded gamma camera for PET has the obvious advantage that the same instrument can also be used for single-photon imaging as well, but the performance of these systems is inferior to dedicated PET instruments. Initial comparisons have shown that both types of system perform equally well in detecting lesions larger than about 2 cm, but for the detection of small lesions dedicated PET systems have a significant advantage.

One of the major limitations of PET is the lack of anatomical landmarks, particularly in the thorax, abdomen and pelvis, so, for applications in oncology, PET images need to be interpreted in conjunction with CT or MR anatomy. Although coregistration of images obtained from separate examinations can be carried out on an image processing workstation, the advantages of simultaneous acquisition of anatomical and functional data are self-evident. Mounting both a spiral CT and a partial ring PET device on a single imaging gantry offers the possibility of combining functional and anatomical data in the same examination. Typically, the CT acquisition is performed first, followed by PET acquisition. The anatomical CT data can then be used to apply attenuation correction for the PET data and the resulting images can be displayed separately or fused together.

PET applications

Much of the early work with PET focused on brain metabolism, partly because of the smaller size of detector needed to study the head. With the introduction of improved instruments allowing acquisition of whole-body images in under an hour, applications in oncology have developed into the major clinical use of PET.

Lung tumours Small cell lung cancer is usually multifocal at the time of presentation, so surgery is rarely indicated. Since systemic chemotherapy is the mainstay of treatment, precise staging is less important than in surgical cases, and the use of FDG-PET is of limited value. Non-small cell lung cancer is much more likely to be amenable to surgery, so careful staging is needed. FDG-PET is highly accurate in staging mediastinal nodes in this condition, and is at least as accurate as the combination of CT and bone scintigraphy for detecting metastases in the abdomen, pelvis or skeleton, although not in the brain, where MRI is superior. Residual soft-tissue abnormality after treatment may be non-specific on CT, and in these conditions a negative FDG-PET study may eliminate the need for biopsy. Consecutive studies that show a fall in FDG uptake in the lesion during treatment may be used as a predictor of anatomical response.

About one-half of non-calcified, solitary pulmonary nodules which present for investigation turn out to be benign. FDG-PET offers a non-invasive method for discriminating between benign and malignant pathologies with sensitivity about 95% and specificity greater than 80%, so a negative PET result is more reassuring than a negative biopsy. However, the accuracy of PET falls off with decreasing lesion size, so its value is less clear for lesions of under 1 cm.

Colorectal cancer The major value of FDG-PET is in detecting local recurrence after treatment, and finding metastatic disease. For preoperative staging of the primary tumour and local nodes, PET has not so far proved superior to colonoscopy, CT/MRI and surgery. In the more problematic patients with suspected local recurrence, PET appears to be the most accurate non-invasive procedure for distinguishing fibrosis from tumour, with reported accuracy of about 90% (Fig. 59.19). PET is also superior to CT for detecting extrahepatic metastatic disease, and about equal to CT for liver secondaries (Fig. 59.20). It is proposed that PET should be used as the first imaging test in working up patients

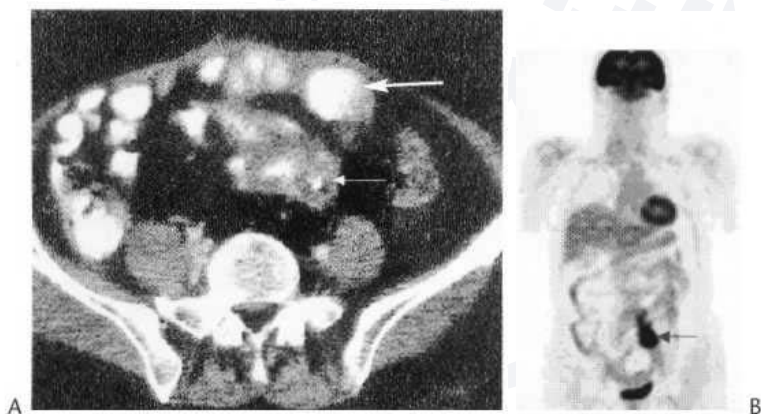


Fig. 59.19 Following surgery for colorectal cancer CT (A) shows indeterminate soft-tissue thickening (arrow), FDG-PET image (B) shows an intensely active focus at the site of recurrent tumour (arrow). (Courtesy of Professor P. J. Ell, Institute of Nuclear Medicine, Middlesex Hospital, London.)

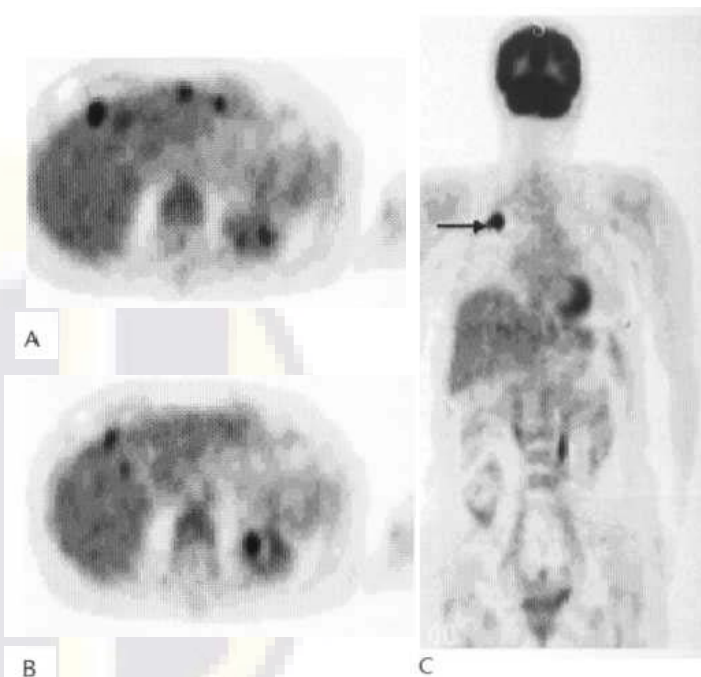


Fig. 59.20 FDG-PET images in two patients with small-volume colorectal metastases, in the liver (A,B) and in the lung (C). (Courtesy of Professor P. J. Ell, Institute of Nuclear Medicine, Middlesex Hospital, London.)

with suspected recurrence, and may also be used in patients with rising carcinoembryonic antigen (CEA) and negative CT. Response to treatment may also be monitored by PET—baseline levels of uptake should be reached by 6 months after local radiotherapy.

Lymphoma Most types of lymphoma show avid uptake of FDG, and it is suggested that those patients with the most intense uptake at presentation have the worst prognosis. When PET has been used as a staging procedure for lymphoma, it has proved to be more accurate than CT. PET is more likely to determine the presence or absence of disease in nodes that are close to the normal size limits, it will show additional sites of disease in 10–20% of patients, and it may lead to a change of stage in about 10% of cases. A fall in FDG uptake which may be seen after 1–2 cycles of chemotherapy is a useful predictor of later clinical response. In patients with a residual mass after radiotherapy or chemotherapy, PET is a fairly good predictor of future recurrence, although relapse still occurs in a small minority of patients with negative PET studies.

Head and neck cancer The majority of primary head and neck tumours show avid uptake of FDG, and PET is particularly advantageous over CT/MRI for detecting occult primary tumours in patients who first present with metastatic nodes in the neck (Fig. 59.21). PET is equivalent to CT/MR for staging in patients with overt primaries and metastatic disease (Fig. 59.22), but its most valuable application is probably in differentiating recurrence from fibrosis after treatment. PET may also be used as a prognostic indicator: persistent FDG uptake during treatment indicates lack of response and/or likely recurrence.

Breast cancer In the early detection of breast tumours, PET may be a useful addition to mammography, particularly in patients with dense breasts, fibrocystic disease, previous surgery or radiotherapy, and in those with breast implants. Increased uptake of FDG is also

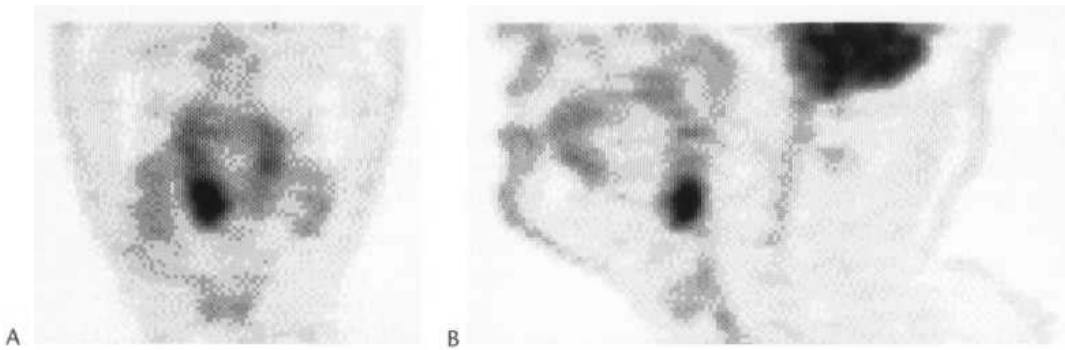


Fig. 59.21 FDG-PET axial (A) and sagittal (B) images in a patient with a small primary carcinoma arising in the vallecula. (Courtesy of Dr P. Julyan, Christie Hospital, Manchester.)

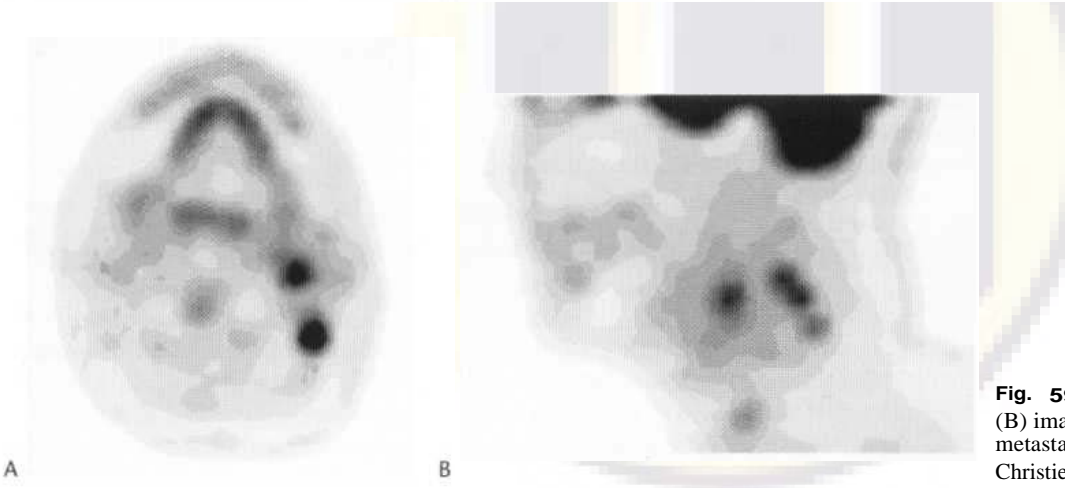


Fig. 59.22 FDG-PET axial (A) and sagittal (B) images in a patient with small volume nodal metastases in the neck. (Courtesy of Dr P. Julyan, Christie Hospital, Manchester.)

seen after surgery, with inflammatory breast conditions, and in some fibroadenomas. With tumours smaller than 1 cm, some false-negative PET results may be expected. For local node staging, sentinel node biopsy is probably the procedure of choice, but PET is effective for detecting distant metastases at initial presentation. For detecting bone metastases, PET is more sensitive than bone scintigraphy for lytic lesions, but less sensitive for detecting sclerotic deposits. As with other tumours, a sharp fall in FDG uptake during treatment is a good prognostic indicator.

Other tumours In malignant melanoma, PET is highly effective in detecting distant metastases, although for staging of local lymph nodes CT or sentinel node biopsy may still be preferred. Primary oesophageal tumours are FDG-avid and PET appears superior to CT in detecting distant metastases. For local nodal staging of oesophageal tumours, PET is probably better than CT but still has limitations due to the small size of involved nodes, and their proximity to the primary lesion.

Specific applications in relation to other tumours are still being explored. Initial experience points to a broad role for FDG-PET as a procedure that is complementary to CT and MRI in the initial staging of many types of malignancy, is particularly useful in the assessment of recurrent or residual disease after treatment, and may be a very useful early indicator of prognosis and response to treatment.

Other clinical applications of PET In patients with refractory epilepsy, where surgical excision of a temporal lobe lesion may be indicated, preoperative localisation of the abnormal focus is critically important. Although this can be achieved fairly accurately with regional cerebral blood flow studies using SPECT if the radiopharmaceutical can be injected during a seizure (ictal SPECT), interictal studies are less reliable. Metabolic brain

imaging using PET appears to be more sensitive, and will localise a high proportion of abnormal foci during the interictal phase. Similarly, myocardial viability is usually assessed using perfusion studies with SPECT, but in the case of inconclusive results, metabolic assessment with short-lived PET tracers may be more decisive.

Sentinel node imaging

The conventional surgical approach to the excision of lymph node metastases as an adjunct to the removal of primary malignancies has been to remove as many nodes as possible in the expected area of drainage from the tumour. The concept of the sentinel node, i.e. the first node which receives lymphatic drainage from the primary tumour, is no longer new, but has only recently been adopted as a possible basis for modifying surgical practice. Both experimental data and empiric clinical observation supports the view that lymphatic spread of malignancy is a sequential process. Nodes in a direct chain are not bypassed, so if the more proximal nodes are uninvolved, then the likelihood of nodal deposits existing further from the tumour is remote. Usually one or two nodes are recognised as the 'sentinels', although occasionally there may be several.

Techniques

The aim of sentinel node imaging is to localise the sentinel nodes, which can then be excised for histological examination. In patients in whom the sentinel nodes show no evidence of tumour involvement, further surgical dissection can be avoided, reducing both the morbidity of the surgery itself, and eliminating the secondary effects of lymphoedema, etc., which commonly result. Techniques are still being refined, but so far a combination of radionuclide

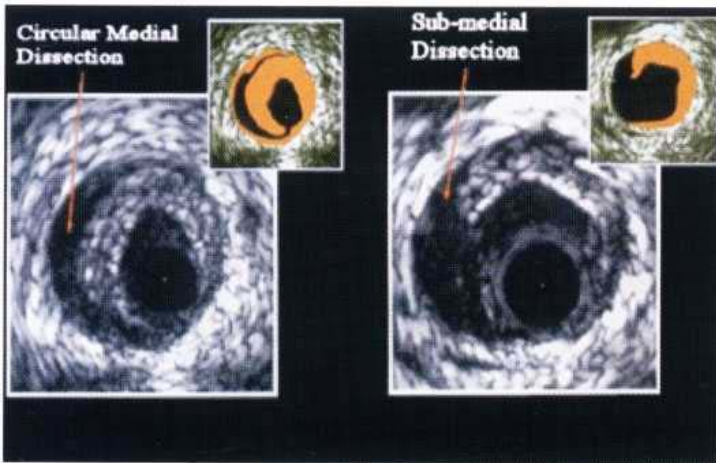


Fig. 59.29 Intravascular ultrasound images of coronary artery dissections: *Left panel:* An extensive medial dissection is shown extending from 6 o'clock to 1 o'clock associated with balloon angioplasty. *Right panel:* A deep submedial dissection is shown between 7 o'clock and 11 o'clock after balloon angioplasty subsequently associated with acute coronary occlusion successfully treated by intracoronary stenting. (Courtesy of Dr N. Uren, Royal Infirmary, Edinburgh.)

The addition of further rows of elements transversely across the transducer face also allows beam manipulation in the transverse, or elevation (across the slice thickness), plane (Fig. 59.28). Among other things, this allows the beam to be focused in two dimensions, thus improving resolution.

The increase in the number of elements means that new methods of transducer construction are required to accommodate, insulate, connect and control individually all the elements. Much progress has been made in this area and, although true 2D arrays are not yet commercially available, several manufacturers now offer 1.5 D transducers with between 3 and 7 rows of elements across the transducer face.

As well as increasing the complexity of transducers, modern technology has made it possible to reduce the size, so that quite complex transducers can now be mounted on catheters small enough to pass into coronary arteries. Specialised transducers are now available for a variety of applications and can be used for transrectal, transvaginal, transurethral or transoesophageal scans, laparoscopic surgery, endoscopic ultrasound and intravascular ultrasound, among others (Fig. 59.29).

Echo-enhancing agents

These were originally developed to improve the signal-to-noise ratio in Doppler examinations but, by the time the first ones became

available, the improvements in system design and performance resulted in their use for this purpose being less important, although they may still be useful in confirming patency or otherwise of a vessel. However, during their development it became apparent that they had other interesting properties that may be useful in clinical ultrasound. Several materials have been developed as echo-enhancing agents by different manufacturers but they all result in microbubbles in the body; typically these are now less than 10 µm in diameter, so they can pass through the pulmonary capillary bed after injection and reach the systemic circulation.

It has become apparent that the response of microbubbles to ultrasound is more complex than originally expected and depends on the acoustic power. At low powers, represented by a low mechanical index (MI) of 0.1-0.3, they reflect and scatter ultrasound. At moderate power levels (MI of 0.5 approximately) they resonate; the frequency of this resonance happens to lie in the diagnostic range of 1-20 MHz and the strength of the reflected signal is maximal at this level. A further increase in acoustic power (MI of 0.7-0.8) results in the microbubbles oscillating in a non-linear fashion and the production of harmonic signals, which are specific to the agent. At high acoustic powers (MI of >>1.0), the microbubbles are disrupted and burst.

This behaviour of echo-enhancing agents results in new varieties of imaging techniques for these agents. At the most basic level they can be used to improve the signal-to-noise ratio in spectral, colour and power Doppler examinations to rescue inadequate examinations. Transit times can also be measured and arteriovenous shunts can be identified. Using low-MI imaging allows detection of the agent in the blood vessels and tissues with minimal destruction of the microbubbles; this allows imaging of the agent in blood vessels on real-time imaging. Pulse inversion imaging detects the non-linear echoes from microbubbles and enables areas containing agent to be distinguished from areas without agent (Fig. 59.30B). High-MI imaging destroys the agent but this produces high-amplitude signals from areas where the agent is present (stimulated acoustic emission (Fig. 59.30C)), which contrast with the absent signals from areas without the agent. This is particularly useful in the liver, where it has been discovered that several agents have a delayed hepatosplenic-specific phase (Fig. 59.31). Sequential high-MI scans at intervals can be used to provide an estimate of blood flow into the area of interest, calculated from the rate of reaccumulation between scan sweeps.

Research is now developing in the area of tissue-specific agents containing a variety of therapeutic substances. These could be targeted at specific areas of disease, such as tumours or blood clots; when the agent has accumulated in the target area, the microbubbles are then destroyed using ultrasound at the appropriate fre-



Fig. 59.30 (A) shows a liver tumour on real-time imaging; (B) shows low MI imaging of the vascular phase; (C) shows the same lesion with high MI imaging producing bubble destruction and stimulated acoustic emission. (Courtesy of Dr P. Sidhu, Kings College Hospital.)

imaging and visual inspection with injection of patent blue dye has produced the best results. The radiotracer technique gives better detection of nodes in unexpected sites, and with dynamic imaging is more likely to indicate the sequence of drainage when several nodes are shown. The ideal tracer would be easy to prepare, stable and securely labelled, and would migrate rapidly from the injection site to the sentinel nodes. Early studies have used various technetium-labelled colloids, but more recently technetium-dextran compounds have shown promise.

The technique requires injection of the tracer directly into or closely adjacent to the primary tumour, or into the overlying skin if the tumour is superficial. Imaging over the next 1-4 h typically identifies one or more sentinel nodes, the position of which can then be marked on the patient's skin.

Surgical excision, which may follow immediately after the imaging or the next day, is assisted by using a handheld scintillation detector (gamma probe) to find the sites of tracer concentration. Injection of patent blue dye immediately prior to surgery improves the detection rate of sentinel nodes, and offers the additional advantage of identifying the lymphatic vessels that lead from the tumour towards the sentinel nodes.

The successful application of a sentinel node technique requires effective expertise not only in imaging but particularly also in surgical and pathological techniques. The routine use of immunohistochemistry has improved the sensitivity of conventional H & E staining for nodal staging, and the introduction of reverse transcriptase-polymerase chain reaction (RT-PCR) offers a further improvement in accuracy. However, the sensitivity of pathological examination for detecting microscopic tumour deposits in otherwise normal lymph nodes remains uncertain, as does the ultimate significance of such micrometastases.

Applications

Most of the early experience with sentinel node techniques is in breast cancer and melanoma.

Breast cancer About one-third of patients with breast cancer have axillary nodal disease at the time of presentation. Routine dissection of the axilla creates morbidity and is of no benefit to that large group of patients whose nodes are negative.

Identification of sentinel nodes in breast cancer is achievable in about 95% of cases, with greater than 95% success in correctly identifying whether the axilla is involved. Follow-up studies have shown that nodal recurrence in patients whose axilla is negative at the time of sentinel node biopsy is very rare.

Sentinel node biopsy is inappropriate for patients with clinically involved axillary nodes, and is also unreliable in patients who have had just radiotherapy. The application of sentinel node biopsy in patients with multifocal tumours and in those with previous local excision of the primary breast lesion is still not clear. Sentinel node techniques can be carried out on patients with impalpable tumours by using ultrasound-guided injection.

Melanoma The patterns of lymphatic drainage from melanoma are less consistent than with breast cancer, and simultaneous drainage to multiple sites is not uncommon. For this reason, imaging after local radiotracer injection is of critical importance and the distinction of primary from second tier nodes may be helpful in planning subsequent surgery. The status of sentinel

lymph nodes is a powerful indicator of prognosis from the time of presentation. As with breast cancer, the majority of new patients show negative sentinel nodes. Patients spared extensive nodal dissection on the basis of an initial negative sentinel node biopsy have shown on follow-up a small but worrying incidence of subsequent relapse, so the adoption of this technique as best surgical practice is still in doubt.

Other tumours Promising results for sentinel node imaging and biopsy have been obtained in various gastrointestinal tumours, particularly colorectal and oesophageal cancer. The original description of the techniques arose from observations in patients with penile cancer; more recent applications include patients with cancer of the cervix, vulva, squamous tumours of the head and neck, and papillary carcinoma of the thyroid.

ULTRASOUND

In common with other clinical imaging techniques, ultrasound has benefited significantly from the massive improvements in computing power and data storage that have taken place over the last few years. These have allowed major advances in signal generation and processing techniques to be achieved. In parallel with these developments in data processing, the advent of echo-enhancing agents has opened up many new opportunities for developing the role of ultrasound as a diagnostic and therapeutic technique.

The rapid advance of computing power, together with the trend to miniaturisation, has enabled manufacturers to provide either more processing power in the same size of system, or the same functionality in a smaller system. Several handheld systems are available with excellent frame rates and resolution comparable to high-end systems of 4-5 years ago, and which increase the availability of ultrasound in many areas of medical practice (Fig. 59.23).



Fig. 59.23 Two modern ultrasound systems, the larger one on the left is a fully configured system; the smaller one on the right on the couch is nevertheless capable of abdominal and small parts examinations, including Doppler studies.

Signal generation and processing techniques

All aspects of Doppler signal generation, reception and subsequent processing are undergoing intense development. *Harmonic imaging*, using harmonic frequencies that are generated at two, three or four times the fundamental frequency, reduces the amount of noise in the image and enhances the relative signal-to-noise ratio. Initially used with echo-enhancing agents, it is now also used for improved real-time imaging, especially in technically 'difficult' patients. Harmonics are produced only by pulses with high amplitude (a violin string stroked gently produces a single, pure tone; stroked more forcefully, it produces a much coarser sound due to the harmonics that are generated), so pulses in the focused beam tend to produce harmonics, whereas those in side lobes and reverberations are too weak, thus reducing noise and speckle in the image (Fig. 59.24A,B). *Pulse inversion* harmonic techniques produce pulses of alternating phase, with the returning echoes being summated; these might be expected to cancel themselves but, because of the non-linear effects relating to the propagation of ultrasound waves through tissues, summation of pulse pairs produces a detectable signal containing diminished amounts of noise and clutter. As with 'ordinary' harmonic imaging, pulse inversion techniques can be used with both echo-enhancing agents and imaging techniques. Further variations in pulse generation can be used, including pulse coding techniques, initially developed for radar transmissions, and tailoring of the pulses to the characteristics of specific echo-enhancing agents. *Compound imaging* can be achieved by interrogating a volume of tissue with scan lines steered electronically at different angles; this results in noise and speckle reduction, together with improved visualisation of margins and small structures, such as microcalcifications. Initially used for

superficial scans, it has now been further developed for abdominal use (Fig. 59.24).

Echoes from flowing blood can sometimes be seen on real-time imaging, typically in the common femoral veins. With modern systems and appropriate processing techniques, these can be displayed in real time to show flowing blood without the use of Doppler techniques (Fig. 59.25).

The stiffness or compliance of different tissues can be assessed using ultrasound, the technique is known as *elastography*. A set of digital radiofrequency (RF) echo data from the region of interest is obtained. The tissue is then compressed, usually by the transducer, and a further set of RF echo data is obtained. This is then cross-correlated with the initial data and any changes in arrival time of pulses from equivalent volumes of tissue can be identified. An estimate of the local tissue strain can be made and from this the degree of tissue stiffness can be assessed. This technique is still being developed but shows some promise for identifying abnormal areas



Fig. 59.25 A 'B flow' image of an internal carotid artery stenosis with the echoes from the moving blood clearly shown in the lumen of the vessel. (Courtesy of GE Ultrasound.)

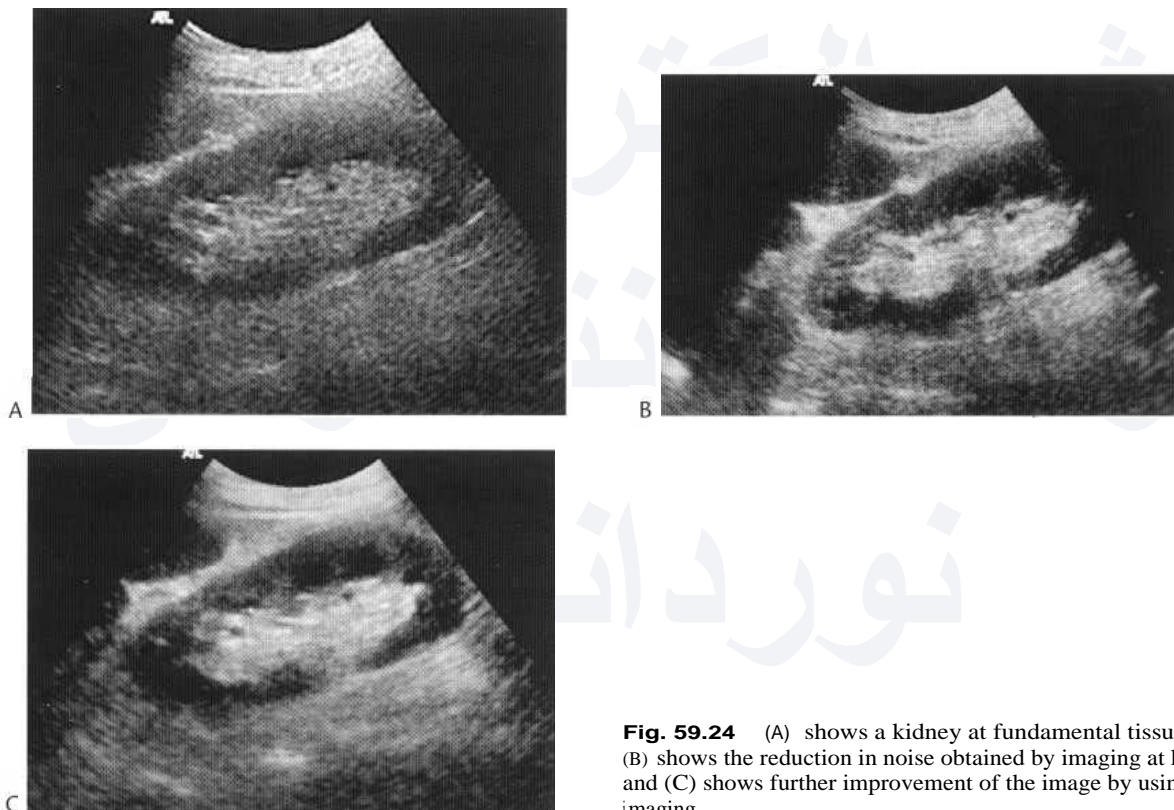


Fig. 59.24 (A) shows a kidney at fundamental tissue imaging frequency; (B) shows the reduction in noise obtained by imaging at harmonic frequencies; and (C) shows further improvement of the image by using dynamic compound imaging.



Fig. 59.26 3D ultrasound. (A) shows a reconstruction of a fetal face and arm; (B) shows planar reconstructions from the data volume shown at the bottom right. (Courtesy of Acuson.)

in tissues, which may not have sufficiently different echo properties to register on an amplitude image, such as a scirrhus breast carcinoma compared with a fibroadenoma.

The increased computing power now available allows the storage and manipulation of the large amounts of data required for 3D imaging. The two-dimensional ultrasound beam is swept through the region of interest and the data processed to produce a three-dimensional representation of the volume scanned, which can then be viewed and manipulated in a variety of ways (Fig. 59.26). Increased capabilities for data storage also allow extended field of view imaging, which allows the display of larger regions of interest, such as muscles and tendons, or large masses (Fig. 59.27).

Transducer developments

Developments in transducer design and construction have been responsible for many of the advances in ultrasound techniques and applications over the years. New materials are being developed to improve transducer performance. Multiple elements, broadband transmission and reception, and improved beam forming techniques have all contributed to improved performance in terms of both spatial and contrast resolution. In the 1980s abdominal scans were typically performed at 3.5 MHz, and 'small parts' scanning at

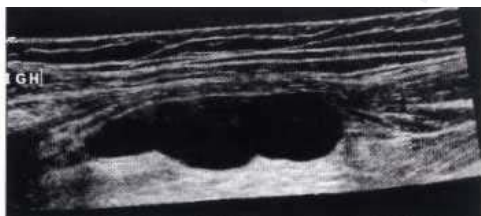


Fig. 59.27 Extended field of view image of an iliopsoas bursa.

5 MHz; today the equivalent frequencies are 5-7 MHz and 12-15 MHz. Some specialist applications, such as dermatology and intravascular ultrasound, use transducers with frequencies up to 30-40 MHz. Broadband technology allows the transducer's operating frequency to be adjusted to the scanning conditions and harmonic and non-linear imaging techniques to be undertaken.

Multielement array transducers have made it possible to focus and steer the ultrasound beam electronically; different groups of elements can be used for different tasks, such as pulsed Doppler and imaging. The elements in these transducers have been arranged in a single row along the length of the transducer, allowing beam manipulation in the lateral (across the slice length) direction only.

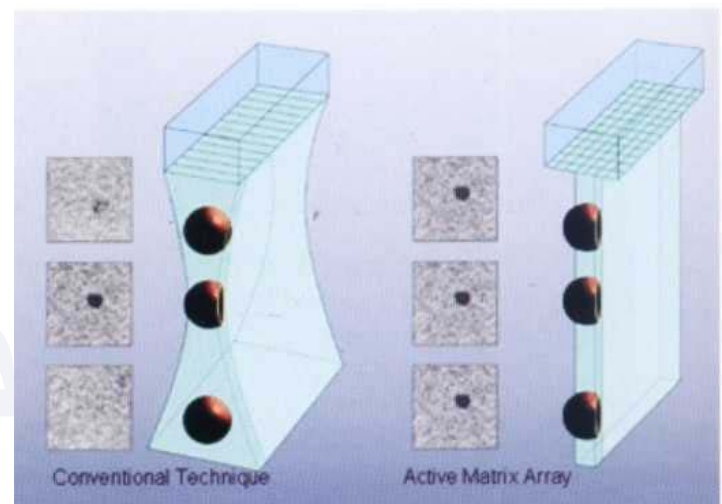


Fig. 59.28 Diagram of a 2D transducer showing the improvement in beam formation and the associated improvement in spatial and contrast resolution. (Courtesy of GE Ultrasound.)

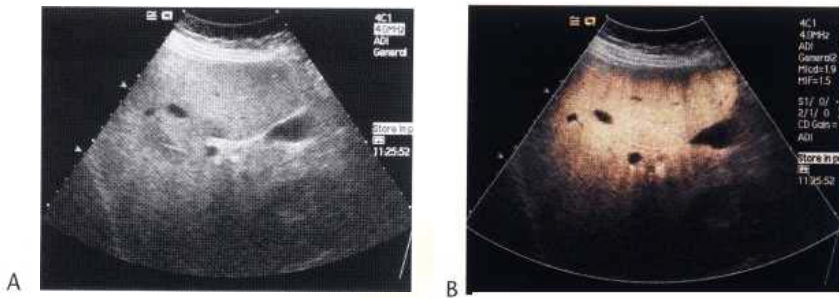


Fig. 59.31 (A) shows two focal areas of relatively reduced echogenicity in a fatty liver; (B) shows filling in of these areas after the administration of an echo-enhancing agent with a liver-specific phase, confirming the presence of normal liver tissue in these areas consistent with focal fatty sparing in a fatty liver. (Courtesy of Professor D. O. Cosgrove, Hammersmith Hospital.)

quency and thereby release chemotherapeutic or thrombolytic agents within the tumour or blood clot.

Despite developments in other imaging techniques, such as CT, MRI and computed radiography, the role of ultrasound continues to expand. Its unrivalled ability to show events within the body in real time, the continuing improvements in contrast sensitivity and resolution, technological advances in equipment, together with the emergence of new techniques such as elastography, will mean that the prominent role of ultrasound in clinical imaging will continue to expand over the years to come.

COMPUTED TOMOGRAPHY

Over the last decade, computed tomography has developed rapidly, from conventional, single-slice machines through helical (spiral) CT to the current multidetector (multislice) scanners. A number of advances in hardware and software have enabled this: in particular, the use of slip rings to allow the scanner gantry to rotate continuously in one direction; the development of X-ray tubes with great heat capacity for long continuous X-ray exposure (up to 60 s); cheaper, more stable solid-state detectors and multidetector arrays; improved computer power and hardware to handle and store the large amounts of data produced; and improvements in software to allow effective image postprocessing.

Slip rings

Prior to the development of slip ring technology, the high tension supply to the gantry-mounted X-ray tube was made via cables. The gantry therefore had to return to the starting position after each rotation to unwind the cables. During this period the table would increment to the next slice position, and the patient would begin another cycle of suspended respiration. Slip rings (large circumference electrically conducting rings) allow power to be conducted to the tube on the CT gantry via electrical brushes instead of cables. The gantry is therefore able to rotate continuously in one direction. The data from the detectors may also be transferred back to the reconstruction computer by slip rings. This has several advantages: with single-slice CT, the cycle time per slice was reduced, allowing a number of slices to be acquired within a single breath-hold; a faster rotation speed can be achieved giving shorter scan acquisition times; continuous exposure is possible at a single table position, allowing functional studies, better temporal resolution, and 'CT fluoroscopy' for interventional procedures. The combination of continuous exposure with continuous table movement through the gantry is the basis of helical CT. A helical volume dataset is acquired,

which is reconstructed into axial slices by interpolating between adjacent points in the helix.

X-ray tubes

Helical CT calls for continuous X-ray exposure over the entire period of the scan (up to 60 s) with reasonable levels of tube current. The tube heating associated with this requires a tube with a very high heat capacity, and these have been developed especially for helical CT. Delays due to overheating of the tube can cause problems in high throughput departments, and where high tube load examinations are carried out (for example, back-to-back helical scans for triphasic liver CT). This is not such a problem with multislice CT because the scan times are so much quicker, reducing tube loading compared with single-detector helical CT.

X-ray detectors

For many years CT scanners have used xenon gas detectors which have a conversion efficiency (X-rays to signal strength) of around 60%. This diminishes further if the detectors are not maintained, but xenon detectors are relatively stable. Solid-state crystal detectors may have conversion efficiencies of nearly 100%, with a consequent potential for a 40% reduction in patient radiation dose for the equivalent scan appearances. Technical difficulties of stability of output, continuing emission of light after the X-rays have terminated (afterglow), and other problems with respect to the size of the front face of the individual detectors and the interspace material between adjacent detectors, have been largely overcome or compensated for in the data processing.

Developments in solid-state detectors and the ease with which they can be stacked in parallel adjacent channels have facilitated the development of multislice scanners. Although different approaches to the multidetector array have been adopted by the various manufacturers, all current multislice machines are able to acquire four slices per rotation. With rotation times as low as 0.5 s, the slice acquisition rate of a multislice scanner is thus eight times that of a typical single-slice helical unit. Scanners capable of acquiring 16 slices per rotation (32 slices/s) are presently under evaluation.

The width of the detector array produces problems of image quality due to the cone shape of the X-ray beam. Special reconstruction algorithms are needed to compensate for the divergence of the beam along the long axis of the patient.

Computing power and hardware

With helical and particularly multislice CT, a vast amount of data per unit time is produced from the gantry detectors. The rapid trans-

fer of the data to the reconstructing computer is crucial and may be carried out via specialised cables or radiofrequency/infrared links. With multislice CT datasets typically containing 250-300 images, rapid reconstruction is vital. Powerful computers are needed to apply the interpolation and reconstruction algorithms to give adequate reconstruction speed. Current scanners reconstruct each slice in less than 1 s, but further improvements are likely to be needed as multislice scanners evolve and produce even larger numbers of thinner slices. Rapid links between the scanner console and other elements in the scanner network, such as workstations, PACS systems and teleradiology units, are important, and each of these elements must have sufficient computing power to handle the large datasets ergonomically. Archiving of data should be efficient and economical.

CT 'fluoroscopy'

Continuous scanning in the same table location results in a repeatedly updated image at the same slice location. Using rapid reconstruction algorithms (often omitting some of the usual data filtration steps), images can be updated several times a second with an effective delay between acquisition and display of less than half a second. This gives a 'near real-time' image, which can be used to guide interventional procedures. Radiation dose to the patient is significantly higher than from conventional fluoroscopy, so minimum tube current settings and minimum exposure times should be used. The potential for increased dose to the operator is also high with this technique. Interventional devices designed to keep the operator's hands out of the primary beam, audible timers, fluoroscopy exposure time limits and routine logging and review of fluoroscopy times are advocated.

Multidetector CT

Although similar in many respects to helical CT, multidetector CT represents a considerable advance. The essential difference lies in the detector array, which contains multiple detector elements. Most current (circa 2002) machines allow four slices to be acquired simultaneously, scanners acquiring 16 simultaneous slices are on the market and detector arrays in some machines already contain 32 rows of detectors. Large volumes can be scanned rapidly with relatively narrow slice width (typically 0.5-3.0 mm). The advantages of multidetector CT can be summarised as improvement in speed, quality and scope. The manufacturer's eventual aim must be to acquire all the sections required in a single rotation of the gantry, although currently the corrections to the acquired data for the cone-beam geometry of the volume swept by the X-ray beam are still under development. Consequently the increasing number of detector rows in current machines are being used to reduce the individual slice thicknesses more than increasing the total beam width. As multislice CT is up to eight times as fast as single-detector helical CT, there is even less likelihood of movement or respiration artefacts in routine scanning. Examination of the chest, for example, is feasible in less than 10 s. It is particularly suited to imaging of children, trauma patients and the seriously ill, monitored patient where speed is important (Fig. 59.32). Further refinements are possible in contrast examinations, such as precise arterial and portal phase liver scans, and reduction in contrast medium dose is seen in vascular studies because of the shorter acquisition times.

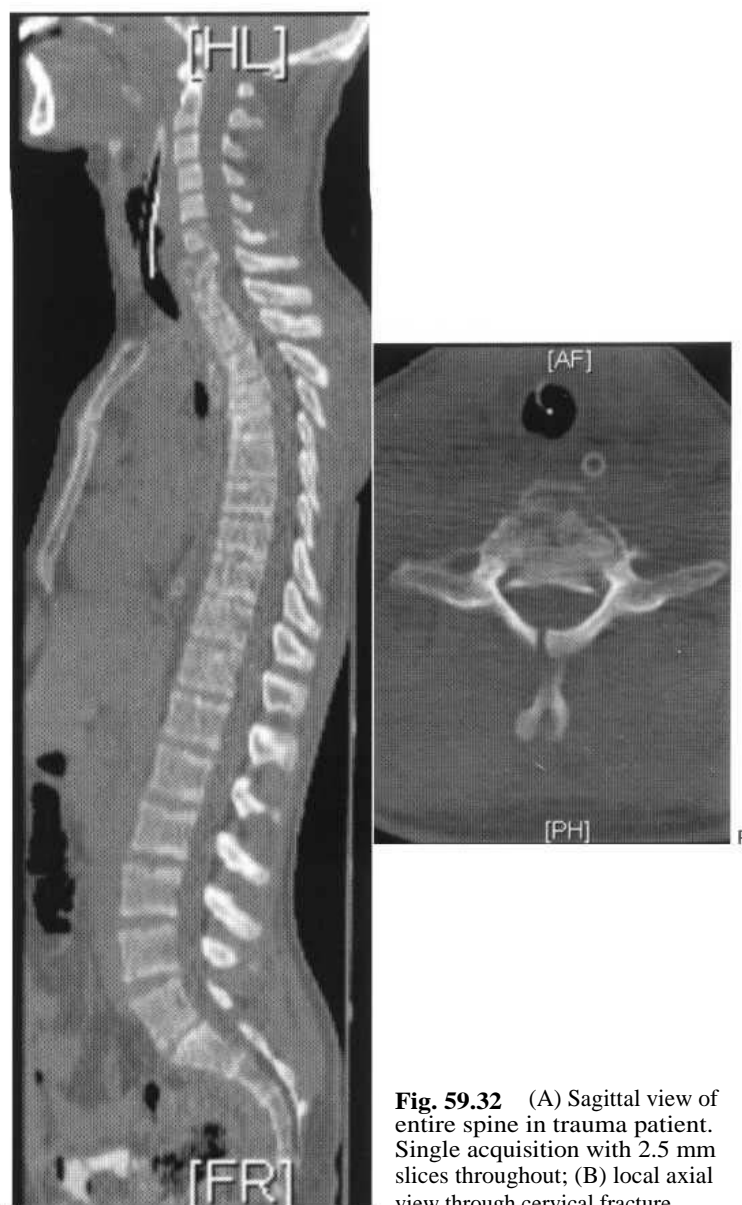


Fig. 59.32 (A) Sagittal view of entire spine in trauma patient. Single acquisition with 2.5 mm slices throughout; (B) local axial view through cervical fracture.

As there is no longer any compromise between volume coverage and slice width, thin slices can be used in all cases. This leads to better spatial resolution inplane and along the z-axis. Multiplanar reconstruction (MPR) and other image processing can be carried out routinely, thus improving diagnostic precision (Fig. 59.33). For high-definition imaging of small volumes, very thin slices can give virtually isotropic imaging (where spatial resolution in any reconstructed plane approaches that of the inplane resolution) (Fig. 59.34). The thinnest slice collimation is currently achieved by collimating the X-ray beam to half the width of the two central detector rows, to give two slices each half the width of the individual detector row. Thus, however many simultaneous sections the scanner is capable of as a maximum, only two are available at the thinnest slice width. Such accurate beam collimation is technically difficult, and may be aided by postpatient collimation, with consequent potential for significantly increased patient radiation dose.

Helical CT led to many new CT applications but many of these have only become clinical reality with the advent of multislice CT. The large-volume, thin-slice datasets obtained are well suited to all forms of image processing. Possibilities include CT angiography,

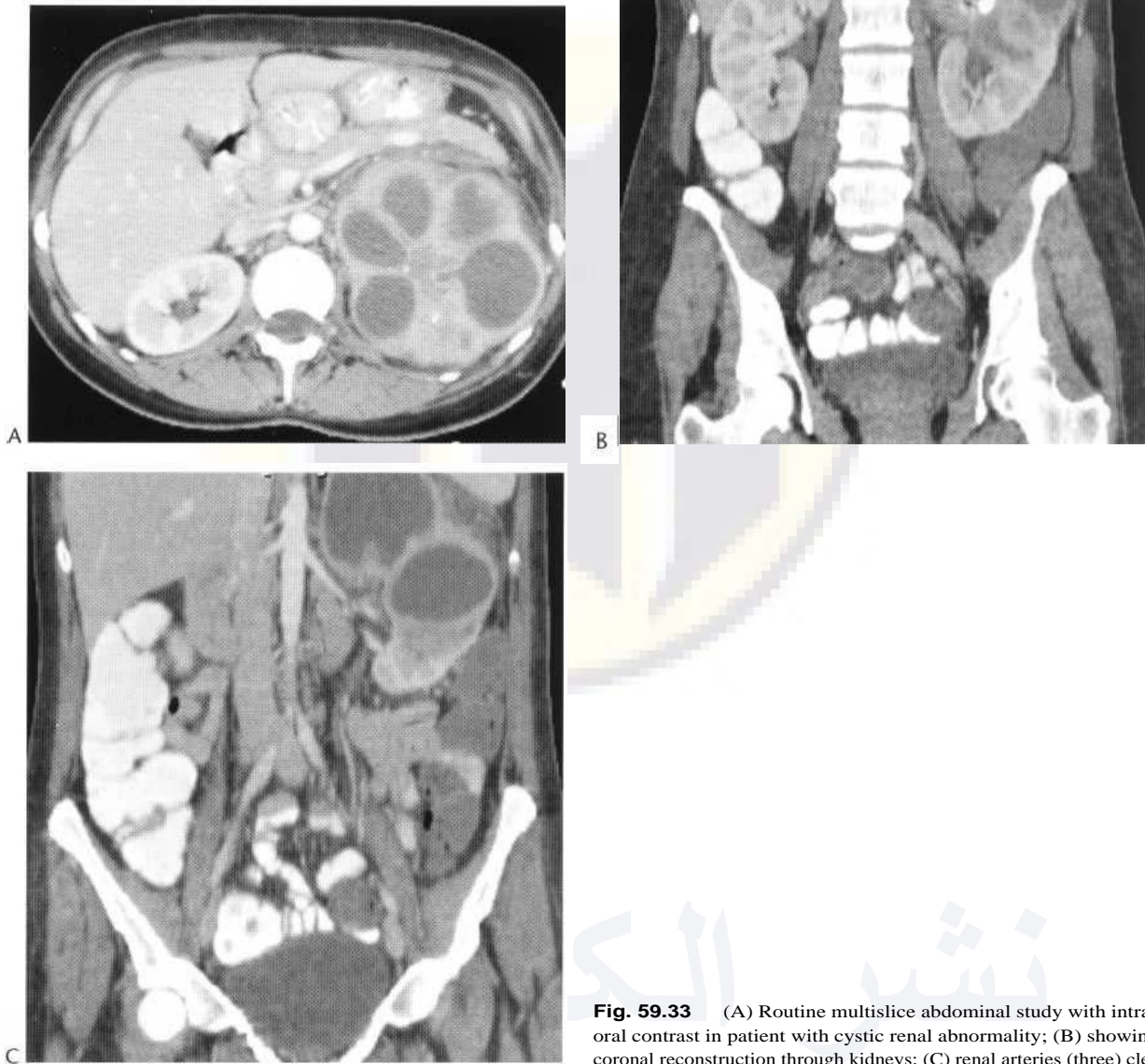


Fig. 59.33 (A) Routine multislice abdominal study with intravenous and oral contrast in patient with cystic renal abnormality; (B) showing quality of coronal reconstruction through kidneys; (C) renal arteries (three) clearly visible.

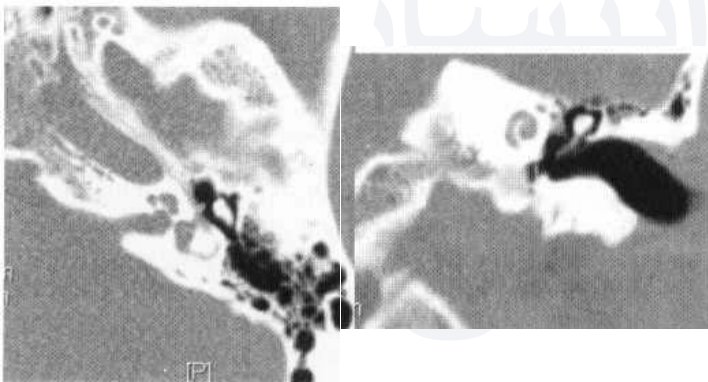


Fig. 59.34 (A) Axial 0.5 mm acquisition through petrous temporal bone with overlapping reconstructions; (B) coronal reconstructions from axial dataset have similar resolution to source images (isotropic resolution).

CT of the colon with 'virtual' endoluminal views (Fig. 59.35), virtual bronchoscopy, routine MPR from axial acquisition in sinus/ENT and orthopaedic imaging, cardiac CT with prospective and retrospective ECG-triggered gating and functional and perfusion imaging.

As with helical CT, pitch can be increased to increase coverage or reduce dose or acquisition time. However, the relationship between pitch and image degradation is complex and non-linear with multislice CT. Optimal pitch values are given by the scanner manufacturer.

Radiation dose

In 1989 the National Radiological Protection Board estimated that CT scanning accounted for 2% of radiological investigations but 20% of the population collective radiation dose. By 2000, further

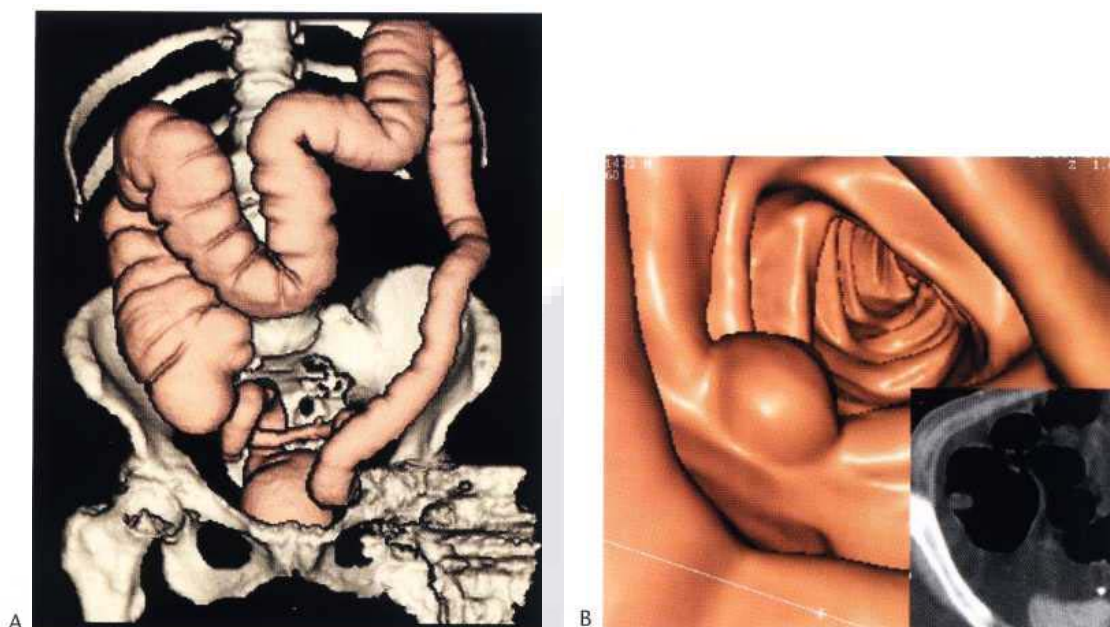


Fig. 59.35 (A) 3D image of air-insufflated colon; (B) endoluminal view of colon ('virtual colonoscopy') demonstrates a rounded submucosal lesion seen at conventional colonoscopy; inset image, oblique axial reformatted profiles the lesion and demonstrates fat density within it, confirming a colonic lipoma.

studies suggested the latter figure had risen to 40% in the UK and 67% in one USA department.

The routine use of thin slices does confer a slight increase in radiation dose, partly because increasing rows of thinner detectors in multislice machines will require more rows of interspace material, resulting in 'dead space'-irradiated but not contributing to image data. This had been partly offset by solid-state detectors, used in all multislice machines, which have X-ray conversion efficiencies approaching 100%. However, this leaves negligible scope for further improvements in detector efficiency. Multidetector scanners may use slightly overlapping pitch values in routine practice, as accurate prepatient collimation of the X-ray beam to the exact limits of the detector rows requires very high engineering precision. This may also increase radiation dose if scanning parameters are not adjusted. It has been estimated that absorbed dose may be up to 40% higher for a multislice helical CT examination than for the equivalent conventional CT scan.

Otherwise, dosimetry is similar to single-slice helical scanners, with the caveat that the speed and versatility of these scanners may encourage scanning of larger volumes or multiphasic examinations, with an associated increase in radiation exposure. Protocols for scanning the liver, for example, may now include arterial, early venous and late venous scans (triphasic). Such extended scanning protocols will inevitably suffer from a 'law of diminishing returns'. For every individual patient, a clear indication for each phase of the scan is required, performing only those phases relevant to the investigation. This clearly necessitates the direct supervision of every examination by an experienced radiologist. The development of new indications for multislice CT and the increasing demand for established CT indications will also result in increased population radiation exposure from CT. The role of the experienced radiologist in vetting requests for CT to minimise unnecessary examinations remains of paramount importance. Reduction in scanner mAs to the lowest values consistent with acceptable noise in the resultant image is a further responsibility of the supervising radiologist. This is of the greatest importance in the scanning of children, where the consequences of radiation exposure are potentially greater and yet the small size of the patient makes reduction in mAs easier to

achieve. Modulation of the X-ray beam mAs during the scan can be used to reduce patient radiation dose with negligible effect on image quality. The chest, abdomen and pelvis are usually thinner from front to back than side to side, consequently a lower mAs suffices in those portions of the gantry rotation where the beam traverses the patient in these directions. Dose reductions of 25-40% can be achieved by this method. Reconstruction algorithms designed to reduce streak artefact (particularly useful for scans in the pelvis or across the shoulders) can also be used to reduce radiation dose by reducing the selected mAs, and can be combined with the modulated mAs described above.

Image processing

The CT computer workstation is now, more than ever, a pivotal part of the scanning unit. Radiologist interaction with the workstation is now routine, and many radiologists will report entirely from the workstation. A fast and ergonomic system is therefore essential. The computer must be powerful enough to handle and store the large datasets with ease. A typical workstation will contain software to allow viewing in the axial and reconstructed planes (including curved planes), surface shading, maximum and minimum intensity projection, endoluminal imaging (virtual endoscopy) and volume rendering.

Volume rendering has become available on CT scanners relatively recently. The software assigns variable degrees of opacity and brightness to all voxels within the dataset within a certain HU range. Parameters can be changed interactively to give varying degrees of translucency and conspicuity to different structures. The result is a more comprehensive image which can show soft tissue, bone and vascular features (Figs 59.36, 59.37). As the algorithm uses the whole dataset, it requires great computing power to work effectively. An advantage of volume rendering is that very little editing or segmentation of the dataset is needed compared with maximum intensity projection.

Cardiac imaging using CT is becoming increasingly important. Gating techniques can be used to freeze cardiac motion. Coronary artery calcification assessment is now well established with CT

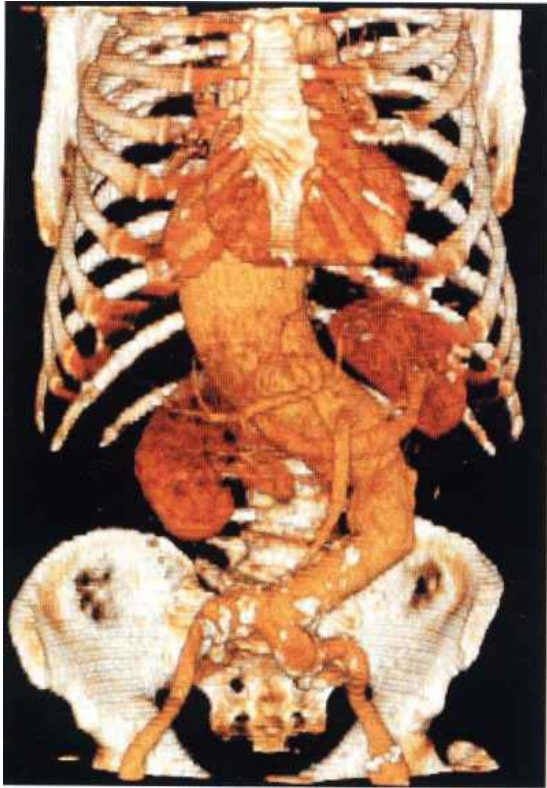


Fig. 59.36 Volume-rendered image of thoracoabdominal aortic aneurysm.



Fig. 59.37 Volume-rendered image of abdomen combined with cut-surface reformations to demonstrate viscera.

(Fig. 59.38), and angiographic techniques to visualise the coronary arteries directly are being evaluated. Tumour permeability imaging and functional and perfusion studies in various sites are possible. Modality matching software allows, for example, CT and PET images to be superimposed, giving anatomical and functional information in one image.

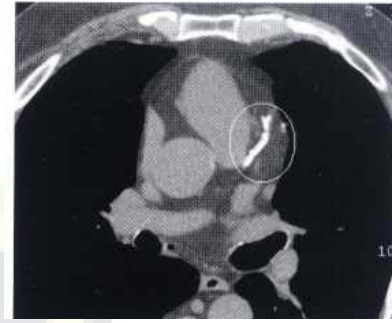


Fig. 59.38 Coronary calcification scoring. Calcification is highlighted in each vessel (here in left anterior descending) and a cumulative score obtained.

Because of the large number of images produced in a typical multislice dataset, printing of all images to hard copy is no longer feasible. Thin slice images can be fused together into a thicker image for presentation to the hard-copy printer. As much CT reporting is currently performed from the workstation, images from abnormal studies only may be selected from the workstation for printing by the radiologist. As PACS systems become more prevalent, the need for hard-copy imaging will decline further.

Advantages of multislice helical CT

The ability to acquire CT data continuously while moving the patient through the scanner aperture confers a number of significant advantages. The speed of acquisition allows large volumes, for example the entire chest, to be scanned within a single breath-hold. This guarantees contiguity of the reconstructed slices, avoiding the misregistration often seen with conventional single-slice CT, caused by variable depth of respiration. Rapid scanning also minimises the risk of movement artefact.

The helical dataset can be thought of as a volume of data within which scans can be reconstructed at any level. This means that overlapping slices can be reconstructed without the need for further scanning or X-ray exposure. The above features give a marked

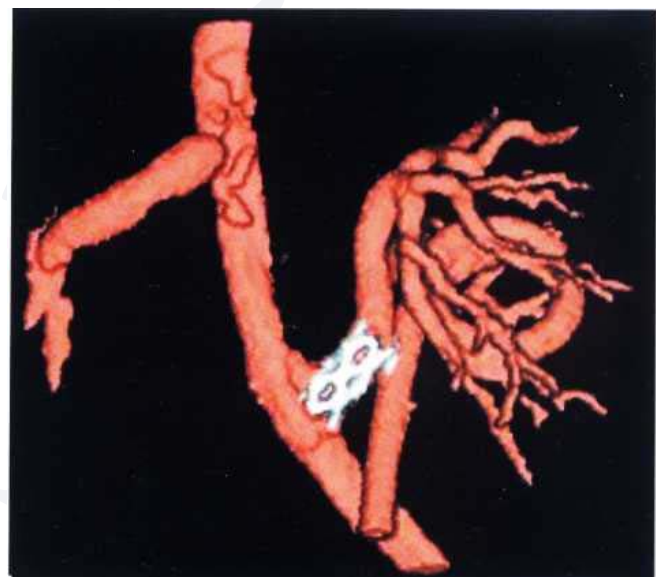


Fig. 59.39 3D segmented CT angiogram image of renal transplant artery with arterial stent.

improvement in spatial resolution in the z-axis (long axis of the patient), allowing good quality MPR and 3D reconstruction from the dataset.

A further advantage of rapid scanning is that contrast medium can be deployed with greater precision, whether used for imaging of solid organs or vascular structures. Data can be acquired entirely within the arterial phase of a peripheral intravenous injection, giving the possibility of performing angiographic studies (Fig. 59.39).

By increasing the speed of table movement during data acquisition, coverage in a given time can be increased and radiation dose reduced. The relationship between slice width and table travel per gantry rotation is known as pitch. The disadvantage of increasing pitch is that the image quality decreases as pitch increases, primarily due to an increase in the effective slice width. Pitches greater than 1.5-2.0 are not recommended. By using multiple banks of detectors, multislice scanners acquire several interlaced datasets simultaneously. This can be used to both decrease the individual slice collimation (slice thickness) and increase the table increment per tube rotation, giving rise to faster scans with even better z-axis resolution. The relationship between slice collimation and table increment per rotation is then modified by the number of simultaneous slices in order to retain an effective pitch ratio of less than 2.

Image quality and radiation dose do not inherently differ in any significant way from conventional single-slice CT. However, the rapidity and ease of scanning may mean that larger volumes than before are routinely imaged. Moreover the versatility of helical CT is such that more CT is being used in clinical practice. The radiation dose to the population from CT is therefore likely to be increasing. The massive increases in computer power, coupled with the more rapidly acquired, thinner slice data from multislice helical CT, has resulted in a plethora of image display techniques such as surface-shaded 3D, maximum and minimum intensity projections, and endoluminal surface reconstructions such as virtual colonoscopy. The clinical value of these techniques is currently being actively investigated.

COMPUTERS IN RADIOLOGY: DIGITAL WORKFLOW

A number of hospitals throughout the world have recently become filmless using a picture archiving and communication system (PACS), but the major challenge now is to re-engineer the whole clinical workflow process to become digital, so that hospitals may become paperless as well as filmless, not just with respect to radiological examinations but for the whole of clinical workflow. Seamless integration of all the various electronic systems throughout the hospital (and beyond, if telemedicine is being considered) is the critical issue that now needs to be solved.

Steps in digital workflow

1. The examination is electronically requested, with the relevant clinical history (Weccails) provided.
2. The request is justified electronically or manually, as appropriate to the investigation, and accepted, modified or rejected, with

an explanation of the action taken being provided in the latter two cases.

3. The examination appointment is made, with a date, time and room booking.
4. Any patient instructions or pharmacological preparation are dispensed to the patient.
5. On the day of the examination a DICOM (digital imaging and communication in medicine) modality worklist is generated, including that patient's examination scheduled to be acquired on a specific piece of imaging apparatus.
6. The completed examination is verified as being technically adequate by the person acquiring the examination (usually a radiographer/technologist).
7. The examination is sent to the PACS and PACS confirms receiving the images it contains using DICOM storage commitment.
8. Postprocessed images or later image acquisitions relating to the same examination (imaging study) may be added to the examination on PACS using DICOM performed procedure step (PPS).
9. The examination is viewed on a diagnostic PACS workstation, in conjunction with the clinical details relating to the examination (as stated when the examination was requested) and any pertinent past imaging examinations.
10. The examination is reported (dictated) using a digital speech recognition system and the resultant text report generated is visible on PACS and the radiological information system (RIS), as well as being accessible on the hospital information system (HIS) and via the electronic patient record (EPR).

1. The report is verified (electronically signed) by one of the reporting radiologists.

2. Possible addenda are added to the report when the examination is later reviewed or audited, and these addenda are electronically signed by the radiologists responsible for them.

Integration It is clear that a number of information technology systems are involved in the digital workflow scenario outlined above, and all these must be integrated seamlessly with one another for the digital workflow to function smoothly. In most health care environments there will be a number of legacy computerised systems already in place, which function well in isolation but are not integrated with one another. It is essential that demographic (textural) data, such as the patient's name and personal details, be entered only once on the hospital network of computer systems, to avoid typographical errors generating spurious patients with different hospital numbers for the same individual. It should also be possible for the person accessing the system to navigate from one dataset to another on the same patient, without having to log-in again, or to re-enter the patient's demographic details. Thus one virtual database must exist linking all these disparate computer systems. Even if a completely new health care institution is being created, different medical specialists may wish to install electronic systems from different manufacturers, choosing the 'best of breed' information technology (IT) solution best suited to fulfilling their specialised requirements, rather than making do with the solution that happens to be provided by a single vendor chosen to equip the entire institution.

This important issue of streamlining workflow and integrating the various hospital IT systems is being addressed by the ME (Integrating the Healthcare Enterprise) initiative launched at the Radiological Society of North America (RSNA) international

meeting 1999. This initiative is bringing together for the first time vendors of clinical information systems with manufacturers of PACS and imaging equipment, and there is thus broad industry support for the work of IHE. IHE is not introducing new standards, but merely facilitating those which already exist by defining profiles that specify an unambiguous way to communicate integration requirements.

Web-based integration One of the simplest solutions to this integration dilemma is to use a web-based protocol so that all the different computer systems, such as the RIS and the HIS, are merely web-based clients, allowing the user to browse different datasets on the same patient in much the same way as the worldwide web allows users to access different computer servers around the world over the internet, and to pass easily (by pointing and clicking) from one internet site to another. PACS manufacturers are using web browsers to allow review of PACS images and reports from ordinary desktop PCs. Indeed, a growing number of PACS vendors are using web technology for their entire PACS, not just for review workstations. Web technology used in this manner has much to commend it: upgrades can be carried out on central servers without the need for software packages to be upgraded on many specialised workstations; training requirements are minimal, as the majority of modern health care professionals are familiar with the use of web browsers; and navigation between different modules is facilitated by pointing and clicking on hyperlinks.

DICOM Digital imaging and communication in medicine is a standard, now accepted worldwide by vendors and users of imaging equipment, which precisely describes the various attributes of pieces of apparatus one might wish to connect together on a network, and thereby specifies whether they will be able to integrate with one another and to what extent they will interact.

HL7 Health level 7 is a standard which is less well defined than DICOM and is used by vendors of patient information systems such as HIS and RIS. Originally a standard used predominantly by North American manufacturers, it has now superseding other, less well accepted European standards. HL7 and DICOM equipment can be relatively easily integrated together using standard brokers (protocol converters).

The electronic patient record (EPR) The EPR (or electronic medical record, EMR) can be thought of as an almost virtual entity linking the other health care computer systems together (Fig. 50.40); however, it must also ultimately accommodate the electronic patient case notes, discharge summaries, clinic letters and prescribing data.

The databases of all the various computer systems in the hospital need to be linked (or be the same database) so that, when any relevant items of that patient's demographic details are entered on any part of the system (patient name, hospital number, NHS number, date of birth, etc.), that patient will be accessed. Input of demographic data only once minimises error. Any update to a patient's demographic data on any part of an integrated EPR system (e.g. the HIS, RIS or PACS) means that that updated information is propagated to all systems automatically, ensuring that all systems contain accurate information.

Hospital information system (HIS) Other names for the HIS include the CIS (clinical information system) and PAS (patient administration system). The HIS is a computer system that holds

data such as patient demographics (name, address, hospital number, family doctor name, and other personal information on the patient), the numerical results from laboratory tests (biochemistry, haematology, bacteriology, virology, immunology), and reports from clinical investigations (such as endoscopic and bronchoscopic studies, pathological examinations of tissue): as well as scheduling information such as outpatient clinic appointments, hospital admissions, the bed state and occupancy, and patient discharge information. The HIS is currently the most important computer system in the majority of extant hospitals. It forms a major part of the EPR, but also needs to integrate with the RIS and other specialised reporting systems (such as in histopathology) so that all the radiological and other reports are visible from within the HIS. HIS needs to integrate with PACS for prefetching old examinations on patients attending outpatient clinics but not necessarily having a new radiological examination. (These patients will not be scheduled on RIS if they are not undergoing a new radiological procedure and therefore their old images will not be prefetched by the RIS.)

Electronic remote requesting system (RRS) Such systems are also referred to as remote order entry and order communications (order comms). They provide an electronic means of requesting and booking investigative examinations from a remote location (wards, outpatient clinics and general practitioner surgeries). It is suggested that the entire health care facility be served by a common electronic remote requesting system (RRS), but that the requests to different departments will have customised front-end software. Thus there will be menus tailored to suit an imaging request, a haematology request, a biochemistry request, a histopathology request, and so forth. In this way the remote requesting system can be kept as generic as possible.

The RRS is frequently regarded as being a module of the HIS, but must be integrated with the RIS and with the PACS. There needs to be a very close integration of the RRS with the RIS because a list of the previous imaging examinations that a patient has had, with their reports (known to the RIS), must automatically be presented to, or easily accessed by, the requesting doctor. Also, procedures booked on the RRS will need to be closely linked with the RIS procedure code, and the RRS needs access, via the RIS, to the room availability for booking the various imaging procedures within the imaging department.

The clinical details pertaining to the requested imaging examination are entered onto the system (typed or entered by a speech recognition system) and are thus legible, and already in digital form, thereby rendering the examination-requesting process paperless. An RRS is very advantageous in the presence of a PACS since it ensures the typed clinical details relating to the examination will appear on the diagnostic PACS workstations in conjunction with the associated images at the time of reporting. There is thus no need for these details to be typed from a paper request form, nor for paper request forms to be digitised.

Radiological information system (RIS) The RIS is the computer system responsible for the scheduling of the various rooms within the imaging department and booking of examinations into those rooms, and it serves as the repository of the radiological reports once they have been typed. The workflow of the imaging department and its radiologists, radiographers and typists can be audited from the RIS data. Every imaging procedure is allocated a

specific RIS code. Many patients are known to the RIS but not to the HIS, as they have only attended the hospital for an imaging procedure (referred directly from their family doctors) but have not been seen as an inpatient or outpatient at the hospital and therefore will not have been given an HIS-based hospital number. This illustrates one reason why the various IT computer systems in the hospital must share a common database, or have their databases seamlessly integrated. When a patient is scheduled for an imaging procedure, the RIS must first check to see whether a patient with the same (or very similar) name already exists in the HIS/EPR database, and only if no match is found will a new id (identification) number be allocated to the patient.

Modern RIS and imaging acquisition modalities support the DICOM service of 'modality worklists', whereby a list of patients whose examinations are to be acquired on a particular modality is passed automatically to that piece of image acquisition apparatus (e.g. a CT scanner, a computed radiography phosphor plate imaging device), thus generating a worklist. This is an extremely important aspect of departmental workflow facilitated by DICOM, as it obviates the need for the operator to retype the patient name and other identification details onto the acquisition apparatus and thus avoids the generation of typographical errors and the mismatch of data that would otherwise result. This is particularly important when working in a PACS environment because images on the acquisition modalities will only be accurately sent to their destination on PACS if the demographic details match exactly; if they do not, and the images are still sent, they end up as 'orphan' examinations, usually labelled 'unspecified', and require manual reallocation or merger with the correct PACS entry by a PACS systems administrator. Such housekeeping database 'clean-up' operations are time consuming, inefficient, wasteful of resources and interfere with departmental workflow.

Acquisition devices When purchasing new apparatus (or PACS components), it is crucial for radiologists to specify the role that they expect that apparatus to play in the setting of departmental workflow so that it can be established which DICOM attributes that piece of apparatus will need to support. The DICOM attributes of any piece of modern imaging equipment are listed in its DICOM conformance statement, and a technical expert will thus be able to determine whether or not two pieces of DICOM conformant apparatus will be able to interface with each other and carry out the desired functions, as this will depend upon comparing their respective DICOM conformance statements and determining which common DICOM attributes they possess. DICOM is an international standard composed of numerous subparts. It is continually being expanded and improved in such a way that none of the additions negates pre-existing parts of the standard, but builds upon them.

In a digital workflow environment, images clearly need to be acquired digitally rather than in analogue format. This is already the case for most of the specialised examinations: computed tomography, magnetic resonance, digital fluoroscopy and angiography, radioisotope scanning, the newer ultrasound scanners and positron emission tomography. The bulk (>70%) of the imaging workload of any imaging department, however specialised, is composed of plain radiographic image acquisition. The newer direct digital acquisition systems for plain radiography capture remain very expensive, but produce a signal in direct digital format. Some are more directly digitally acquired than others: those using a scintillator (generally

caesium iodide) produce light photons locally, which are then converted into electrical signals. The earlier photostimulable phosphor plate technology, generally known as computed radiography (CR), is the most widespread means of acquiring plain digital radiographic images, although in fact this technology produces an analogue signal in photons, which is converted to a digital signal as a final step by cathode ray tube.

PACS Regardless of the size of the PACS project, it should always be founded on a formal contract between the institution and the PACS vendor, and it should define in detail the responsibilities of each. Different vendors are contributing to the [project](#), it is highly desirable to have one who contractually assumes ultimate responsibility for the integration of each part of the network so there can be no argument when an interface problem arises.

Clearly a PACS must replace the traditional roles of conventional film, namely: the acquisition, display, transport, storage and retrieval of images. The major added value provided by a PACS is the institution-wide efficiency with which those roles are achieved. This operational efficiency is only truly realised when film has been withdrawn and the entire institution has an electronic digital workflow. The two critical characteristics of a PACS are its performance and the access it provides to radiological examinations.

The physical architectures of most PACS installations today are similar, consisting of fast networks connecting multiple servers, modalities and workstations. The physically distributed, but logically centralised, architecture provides the most powerful capabilities to PACS users, especially in large PACS installations.

The network is the critical link for all the individual components in a PACS. Its performance is a major factor in determining the ability of a PACS to support the examination volume of the hospital.

Most PACS products now use industry-standard networks, usually consisting of a high-speed network (backbone) that spans the entire institution, with branches that connect individual components or groups of components to the backbone. Networks can be differentiated in several ways, including cable type, speed, communication protocol and topology.

Ethernet is the most common network in use today: 100 megabit per second (100 Mbps) is the minimum Ethernet speed required for efficiently transmitting the large amount of data contained in radiological imaging examinations (8-10 megabytes of data in a chest radiograph) in a PACS network.

For a PACS used for high-volume primary diagnosis (at least 50 000 procedures per year), the network traffic is very large. Such a system should not share a network with other functions in the enterprise if it is to guarantee consistently high performance. This usually means that a network will have to be installed specifically for the PACS.

All PACS products have a database to store information identifying patients and cataloguing their imaging studies. Most PACS installations use a single relational database (like Sybase, Oracle or Microsoft Access) to store identifying information for patients and studies. The user interacts directly with the database to find the imaging study of current interest, and thus the database performance is critical to the performance of the whole PACS.

The radiologists' participation in the digital workflow process is highly dependent upon having a user-friendly seamless reporting process in place. The PACS software plays a crucial role in facilitating rapid reporting from PACS, which must be at least as rapid as reporting from hard-copy film in a conventional film-based radio-

ogy department. It is also essential, as discussed above, to have satisfactory integration of other computerised health care systems closely related to reporting from PACS: in particular, the electronic RRS (which supplies the typed clinical details associated with each imaging study); the speech recognition system (which immediately converts the radiologists' dictated reports into text on the system); and the RIS (which stores these typed reports).

The PACS software concepts required for efficient soft copy reporting are: availability of relevant historical images for comparison (often known as prefetching), compilation of reporting worklists, ordered arrangements of the current and previous images on the PACS workstation monitors by default (often called default display protocols (DDPs), or hanging protocols), and reporting or 'dictation macro' software to facilitate the mechanics of the soft-copy reporting process. The compilation of worklists of unreported imaging studies (particularly for plain radiography reporting) should be automatic but flexible and institution configurable. The triggers for building such worklists are generally within the RIS.

E-mail Easy intranet e-mail access from all modules forming part of the EPR, but especially the electronic RRS and the PACS, is desirable in allowing rapid correspondence with requesters of imaging procedures. This can be useful, for example, in alerting a requesting clinician to a rejected or modified request for an imaging procedure on the RRS, or drawing his or her urgent attention to an abnormal imaging result. Restricting the e-mail access to the intranet rather than the internet reduces the stringency of requirements for protective firewalls and the need for data encryption.

On-line journals The reporting radiologist can benefit from accessing on-line journals and textbooks as sources of reference during reporting. Ideally, these should be accessible from the same workstation the radiologist is using for viewing PACS images and dictating reports on the speech recognition systems, as it is cumbersome and time consuming to have to log into, and activate, a separate computer system for every task and this interferes with streamlined workflow.

Image library/museum and teaching modules The transfer of digital images to an on-line image library and/or personal teaching or academic folders should be considered part of the digital workflow. This area has been rather neglected until recently, being seen as a non-essential part of digital workflow of interest only to academic centres (even though it is actually of concern to the majority of radiologists and other clinicians) and possibly also because it was not considered by PACS vendors to be a financially rewarding area for investment.

Speech recognition dictation system Speech recognition (voice activation) systems are now beginning to achieve sufficient accuracy (>95%) to be acceptable for clinical use and use in radiological reporting (dictation). The accuracy and speed of learning of such systems is an important issue affecting departmental workflow: radiologists require an extensive customised word database for their work (which is specific to imaging and to the appropriate form of English used to generate reports), and time spent correcting the text must be low enough not to impact significantly on the time spent generating the report. It is crucial that a speech recognition system be integrated into the departmental RIS and into the hospital PACS, rather than acting as a stand alone system, which is still often the case.

Conclusion

It is clear that digital workflow (filmless and paperless) throughout a hospital, or other health care enterprise, is utterly dependent upon seamless integration of the various computer systems contributing to that workflow. It requires efficient appropriate networks and conscientious round-the-clock maintenance and management.

REFERENCES AND SUGGESTIONS FOR FURTHER READING

MRI

- Castillo, M. (ed.) (1998) Proton spectroscopy of the brain. *Neuroimaging Clinics of North America*, 8(4).
- Drayer, B. P. (ed.) (2001) *Selected topics in neuroradiology. Neuroimaging Clinics, of North America*. 11(3).
- Elster, A. D., de Roos, A. (1999) Multiple perspectives in MR contrast. *Journal of Computer Assisted Tomography*. 23 (suppl. 1), S1-S217.
- Heiserman, J. E. (ed.) (1999) Fast scan and echoplanar MR imaging. *Neuroimaging Clinics of North America*, 9(2).
- Melhem, E. R. (ed.) (2002) Diffusion imaging. *Neuroimaging Clinics of North America*, 12(1).
- Naidich, T. P., et al (eds) (2001) Anatomic basis of functional imaging. *Neuroimaging Clinics of North America*. 11(2).
- Nesbit, G. M. (ed.) (1999) Acute ischemic stroke. *Neuroimaging Clinics of North America*, 9(3).
- Padhani, A. R., Nccma n. M. (2001) Challenges for imaging angiogenesis. *British Journal of Radiology*, 74. 886-890.
- Semelka, R. C. (ed.) (2001) MR imaging of the liver 1: techniques and contrast agents. *Magnetic Resonance Imaging Clinics of North America*, 9(4).
- Truwit, C. L. (ed.) (2001) MR-guided therapy in neurosurgery. *Neuroimaging Clinics of North America*, 11(4).
- Yucel, E. K. (ed.) (1999) New techniques in body MR imaging. *Magnetic Resonance Imaging Clinics of North America*, 7(2).
- Magnetic Resonance in Medicine* and *Journal of Magnetic Resonance Imaging* (published by John Wiley & Sons, Chichester) are both official journals of the International Society for Magnetic Resonance in Medicine: good sources of original articles and works in progress.

Radionuclide imaging

- Barrington, S. F. (2000) Clinical uses of PET in neurology. *Nuclear Medicine Communications*, 21, 237-240.
- Bar-Shalom, R., Valdivia, A. Y., Blafox, M. D. (2000) PET imaging in oncology. *Seminars in Nuclear Medicine*. 30. 150-185.
- Beyer, T., Townsend, D., Brun, T., et al (2000) A combined PET/CT scanner for clinical oncology. *Journal of Nuclear Medicine*. 41. 1369-1379.
- Haigh, P. J., Hansen, N. M., Giuliano, A. E., et al (2000) Factors affecting sentinel node localisation during pre-operative breast lymphoscintigraphy. *Journal of Nuclear Medicine*, 41, 1682-1688.
- Kcshtgar, M. R. S., Waddington, W. A., Lakhani, S. R., Ell, P. J. (1999) *The Sentinel Node in Surgical Oncology*. Berlin: Springer.
- Maisey, M. N. (2000) Clinical PET in cardiology and cardiac surgery. *Nuclear Medicine Communications*, 21, 234-236.
- Nunan, T. O., Hait, S. F. (2000) PET in oncology II-other tumours. *Nuclear Medicine Communications*, 21. 229-233.
- O'Doherty, M. J. (2000) PET in oncology I-lung, breast, soft tissue sarcoma. *Nuclear Medicine Communications*. 21. 224-229.

Ultrasound

- Harvey, C. J., Blomley, M. J. K., Eckersley, R. J., Cosgrove, D. O. (2001) *Review: Developments in ultrasound contrast media. European Journal of Radiology*, 11. 675-689.
- Laing, F. C. (2001) Update on ultrasonography. *Radiologic Clinics of North America*, 39, 385-590.
- (1999) Ultrasound today and tomorrow: new developments and contrast media. *European Radiology*. 9(suppl. 3), S298-S414.
- WFUM13 Symposium on the Future of Biomedical Ultrasound (2000) A celebration of medical and biological ultrasound at the dawn of the third millennium. *Ultrasound in Medicine and Biology*, 26. S1-S172.

CT

- Broderick, L. S., Shemesh, J., Wilensky, R. L. (1996) Measurement of coronary artery calcium with dual-slice helical CT compared with coronary angiography: evaluation of CT scoring methods, interobserver variations, and reproducibility. *American Journal of Roentgenology*, 167, 439-444.
- Calhoun, P. S., Kuszyk, B. S., Heath, D. G., Carley, J. C., Fishman, E. K. (1999) Three-dimensional volume rendering of spiral CT data: theory and method. *Radiographics*, 19, 745-764.
- Daly, B., Templeton, P. A., Krebs, T. L., Carroll, K., Wong You Cheong, J. J. (1998) Evaluation of biopsy needles and prototypic needle guide devices for percutaneous biopsy with CT fluoroscopic guidance in simulated organ tissue. *Radiology*, 209, 850-855.
- Dawson, P., Lees, W. R. (2001) Multi-slice technology in computed tomography. *Clinical Radiology*, 56, 302-309.
- De Mey, J., Op de Beeck, B., Meysman, M., et al (2000) Real time CT-fluoroscopy: diagnostic and therapeutic applications. *European Journal of Radiology*, 34, 32-40.
- Golding, S. J., Shrimpton, P. C. (2002) Radiation dose in CT: are we meeting the challenge? *British Journal of Radiology*, 75, 1-4.
- Johnson, C. D., Dachman, A. H. (2000) CT colonography: the next colon screening examination? *Radiology*, 216, 331-341.
- Johnson, P. T., Halpern, E. J., Kuszyk, B. S., et al (1999) Renal artery stenosis: CT angiography-comparison of real-time volume-rendering and maximum intensity projection algorithms. *Radiology*, 211, 337-343.
- Kalender, W. A. (1995) Thin-section three-dimensional spiral CT: is isotropic imaging possible? *Radiology*, 197, 578-580.
- Remy-Jardin, M., Remy, J. (1999) Spiral CT angiography of the pulmonary circulation. *Radiology*, 212, 615-636.

نشر الکترونیکی
موسسه انتشاراتی
نور دانش



نشر الکترونیکی
موسسه انتشاراتی
نوردانش

APPENDIX A

CENTRES OF OSSIFICATION

The following illustrations show diagrammatically the dates of appearance of the primary and secondary ossification centres in the various regions of the body. Primary ossification centres are identified by capital letters; secondary ossification centres are identified by small letters.

These three epiphyses fuse with one another in the 6th year and with the shaft in the 20th year.

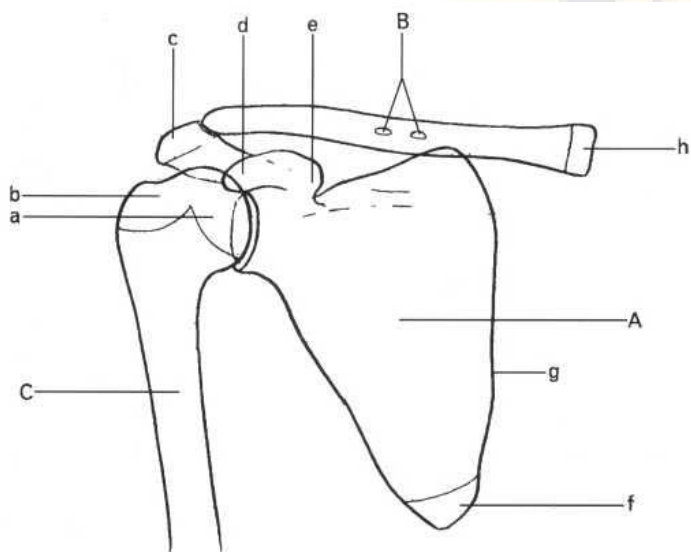


Fig. A1 Ossification of bones of the shoulder. A, 8th week of fetal life. B, 5th and 6th weeks of fetal life, fuse about the 45th day of life. C, 8th week of fetal life.

- a. Head of humerus 1 year
- b. Greater tuberosity 3 years
Lesser tuberosity 5 years
- c. Two epiphyses for acromion 15-18 years, fuse by 25th year
- d. Middle of coracoid process 1 year, fuses 15th year
- e. Root of coracoid process 17 years, fuses 25th year
- f. Inferior angle of scapula 14-20 years, fuses 22-25 years
- g. Medial border of scapula 14-20 years, fuses 22-25 years
- h. Sternal end of clavicle 18-20 years, fuses 25th year.

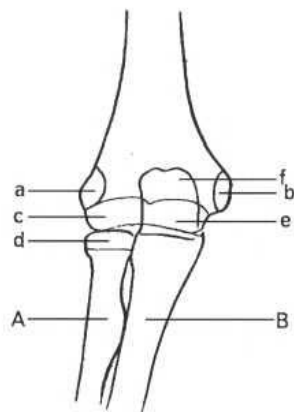


Fig. A2 Ossification of bones of the elbow. A, 8th week of fetal life. B, 8th week of fetal life.

- a. External epicondyle 10-12 years, fuses 17-18 years
- b. Internal epicondyle 5-8 years, fuses 17-18 years
- c. Capitellum 1-3 years, fuses 17-18 years
- d. Head of radius 5-6 years, fuses 16-19 years
- e. Trochlea 1 1 th year, fuses 18th year
- f. Olecranon 10 13 years, fuses 16-20 years.

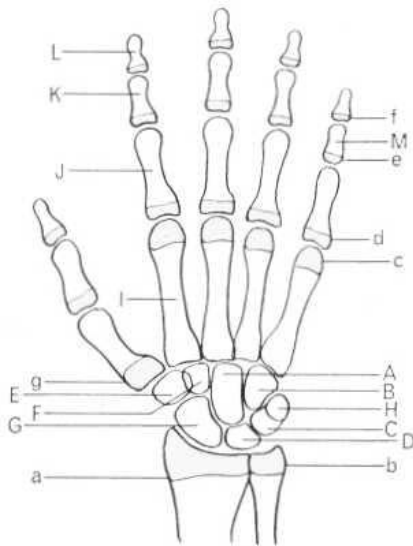


Fig. A3 Ossification of the wrist, carpus, and hand. A, Capitate 4 months. B, Hamate 4 months. C, Triquetral 3 years. D, Lunate 4-5 years. E, Trapezium 6 years. F, Trapezoid 6 years. G, Scaphoid 6 years. H, Pisiform 11 years. I, Metacarpals 10th fetal week. J, Proximal phalanges 11th fetal week. K, Middle phalanges 12th fetal week. L, Distal phalanges 9th fetal week. M, Middle phalanx of 5th digit 14th fetal week.

- a. Lower end of radius 1-2 years, fuses 20th year
- b. Lower end of ulna 5-8 years, fuses 20th year
- c. Metacarpal heads 2; years, fuse 20th year
- d. Base of proximal phalanges 2; years, fuse 20th year
- e. Base of middle phalanges 3 years, fuse 18-20 years
- f. Base of distal phalanges 3 years, fuse 18-20 years
- g. Base of I st metacarpal 2z years, fuses 20th year.

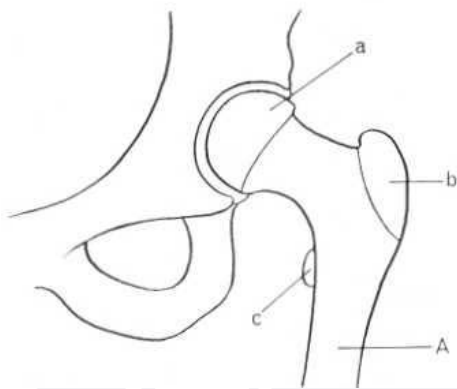


Fig. A4 Ossification of bones of the hip. A, 7th fetal week.

- a. 1st year, fuses 18-20 years
- b. 3-5 years, fuses 18-20 years
- c. 8-14 years, fuses 18-20 years.

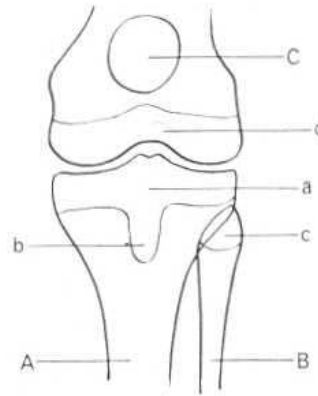


Fig. A5 Ossification of bones of the knee. A, 7th fetal week. B, 8th fetal week. C, 5 years.

- a. At birth, fuses 20th year
- b. Tibia) tubercle 5-10 years, fuses 20th year
- c. 4th year. fuses 25th year
- d. At birth, fuses 20th year.

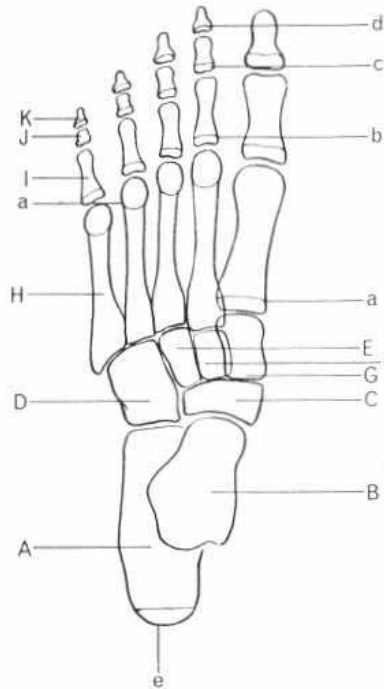


Fig. A6 Ossification of bones of the foot. A, Calcaneus 6th fetal month. B, Talus 6th fetal month. C, Navicular 3-4 years. D, Cuboid at birth. E, Lateral cuneiform 1 year. F, Middle cuneiform 3 years. G, Medial cuneiform 3 years. H, Metatarsal shafts 8-9th fetal week. I, J, K, Phalangeal shafts 10th week.

- a. Metatarsal epiphyses 3 years, fuse 17-20 years
- b. Proximal phalangeal base 3 years, fuse 17-20 years
- c. Middle phalangeal base 3 years, fuse 17-20 years
- d. Distal phalangeal base 5 years, fuse 17-20 years
- e. Posterior epiphysis of calcaneus 5th year, fuses at puberty.

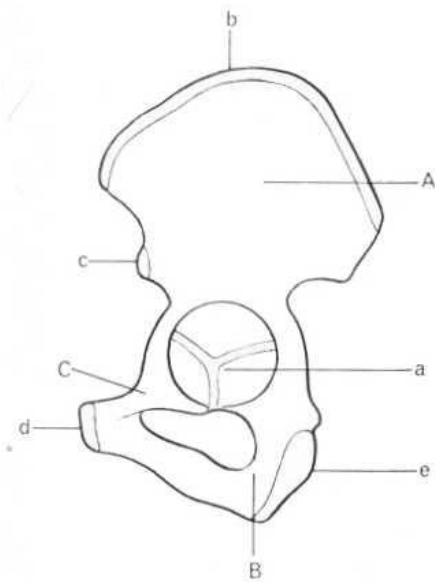


Fig. A7 Ossification of bones of the pelvis. A, Ilium 3rd fetal month. B, Ischium 4th fetal month. C, Pubis 5th fetal month. *Note:* ischiopubic ramus fuses at 7th year.

- a. Y-shaped cartilage-2 or more centres
 b. Iliac crest
 c. Anterior inferior iliac spine
 d. Pubic symphysis
 e. Ischial tuberosity.

Appear about puberty-fuse 20-25 years.

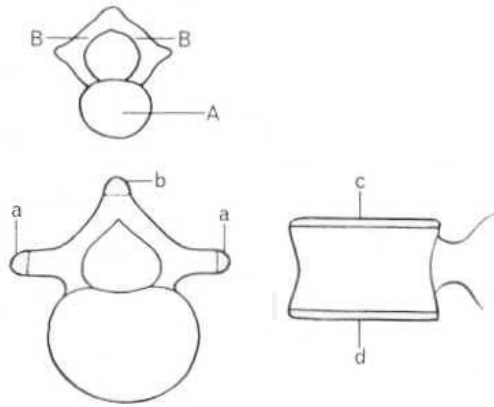


Fig. A8 Ossification of vertebrae. A, Body 8th fetal week. B, Neural arch-one for each side-8th fetal week.

- a. Transverse process
 h. Spinous process
 c. Upper surface of the body
 d. Lower surface of the body

All appear at about 16 years and fuse by the 25th year.

Note:

Atlas: 3 centres; one for each lateral mass and one for the anterior arch-unite 6-8 years

Axis: 5 primary centres; one for the body, two for the arch, two for the odontoid process

2 secondary centres; one for the tip of the odontoid, one for the inferior rim of the body

7th Cervical vertebra: extra primary centre for each costal process

Lumbar vertebrae: have two extra secondary centres for the mammillary processes.

Detailed assessment of bone age is discussed in Greulich, W. W., Pyle, S. I. (1959) *Radiographic Atlas of Skeletal Development of the Hand and Wrist*. Stanford University Press.

APPENDIX B

GLOSSARY OF CT TERMS

Richard W. Whitehouse

The terms included in this glossary are some of those commonly used for CT scanning and subsequent image manipulation. Some of the terms are common to the manipulation of other digital images, being generic to image manipulation rather than to CT. Other terms have accepted clinical, radiological or anatomical meanings but are included here as they carry specific connotations when applied to CT scanning. Some terms vary between manufacturers.

Algorithm Computer program which modifies the raw data to alter the characteristics of the final image; e.g. bone or high spatial frequency algorithm gives high spatial resolution to the image but increases image noise, soft-tissue or low spatial frequency algorithm reduces image resolution but reduces image noise.

Artefact A fault in the image not representing an object in the scanned volume. Artefacts may be generated by the imaging equipment, by patient motion during scanning, or by many other confounding factors.

Back projection The computer technique used to convert the raw CT data into all image. Filtered back projection is performed, the digital filtration alters the data prior to back projection in order to optimise the image spatial resolution and noise (see Algorithm) and to reduce artefacts.

Collimation The use of lead shutters to control the effective thickness of the X-ray beam and thus the slice thickness. Prepatient collimation is next to the X-ray tube. Positioning of the shutters requires high precision and accuracy as the beam will diverge, thus the shutter collimation has to be less than the nominal slice thickness. Prepatient collimation markedly affects patient radiation dose. Postpatient collimation is next to the detectors. This will reduce scatter and also controls the nominal slice thickness. Thin-section CT can be more easily acquired with postpatient collimation, but accurate alignment between pre- and postpatient collimation is required to optimise radiation (dose).

Cone beam Descriptive term for the shape of the 'swept volume' passed through by the CT beam for a detector row away from the centre of the fan-beam on multislice CT. Because this beam is not perpendicular to the detectors, it generates image artefacts. Corrections for the 'cone beam geometry' of the data acquisition from multislice scanners are under development to enable wider banks of detectors to further increase the volume scanned per rotation.

Contiguous Sections which are nominally immediately adjacent to each other.

Contrast resolution Ability to resolve structures according to density difference. Influenced on CT by the noise in the image, improved by higher mAs (radiation dose).

Convolution Computer manipulation of raw data to generate an image (usually by back projection).

CTDI CT dose index. A measurement of radiation dose per 100 mAs on tile surface of. 1 cm into or at the centre of a plexiglass cylinder 16 or 32 cm in diameter. Used to make comparisons of dose between scanners as simple mAs exposure levels do not give comparable doses between different scanners.

CT fluoroscopy Rapid serial display of images from a single-slice location to provide an image updated between one and several times a second, used to guide interventional procedures by CT. Fast image reconstruction algorithms, often without the usual correction steps and utilising some of the

already back-projected data from the previous image, can result in a moving image in 'near real-time', less than 250 ms later.

Detector Hardware used to convert incident X-rays into electrical impulses. Xenon gas detectors are stable and relatively inexpensive but only approximately 60% efficient. Solid-state crystal detectors are expensive and some are less stable but are over 99% efficient in converting X-rays to electrical impulses. Higher conversion efficiency can allow radiation dose reduction.

Direct coronal Patient positioning to allow scans to occur in the coronal plane.

Direct sagittal Patient positioning to allow scans to occur in the sagittal plane.

Dose-radiation dose Measurement of radiation dose on CT is more complicated than for other radiological techniques as the patient is irradiated from all directions around the circumference of the scan (unless a partial scan is performed). Calculation of the effective dose can be performed from a combination of measurements and computer simulations. Radiation doses for CT tend to be higher than for most other diagnostic imaging techniques. While only 2% of radiological examinations are by CT, they account for 20% of the population diagnostic radiology dose in the UK.

Dynamic scan Rapid scan acquisitions, which may all be at the same site over a period of time (dynamic sequential scan) or with table increments between each scan (dynamic incremental scan). Dynamic scanning on conventional equipment is being superseded by spiral scanning.

Flying focal spot Electromagnetic oscillation of the X-ray tube focal-spot position during scanning, performed at every data acquisition point during gantry rotation, give two sets of data from slightly different positions for each gantry position, consequently improving spatial resolution to a level that would otherwise require twice as many detectors, each of half the front face area.

Gantry The scanner gantry contains the X-ray tube and detectors mounted around a central tunnel through which the patient and table pass. The gantry can be angled away from the vertical over a limited range. Some spiral scanners also have the generator mounted on the gantry.

Helical scanning Correct terminology for what is usually referred to as spiral scanning, where the use of slip rings allows the X-ray tube and detector assembly to rotate continuously in one direction at 0.5-1 revolution per second. Continuous smooth table motion results in a helical path of the X-ray beam through the patient with no pauses between adjacent loops of the helix. Images can be reconstructed centred on any point in the helix, allowing overlapping sections to be generated.

Hounsfield unit (HU) This is the corrected or accurate value of the CT number, measured from the scanner image, although CT number and Hounsfield unit are often used interchangeably. The Hounsfield unit is defined by the relationship between the linear attenuation value of the material being scanned and that of water. A vacuum has a Hounsfield unit value of -1000, while water has a value of zero. The upper end of the scale is open ended but image data storage limitations usually result in a scale from -1024 to +3096 (12 bit).

HRCT High-resolution computed tomography usually applied to pulmonary imaging. See CT Scanning of the Lungs, Chapter I.

Interpolation A mathematical process used to estimate the value to ascribe to a point lying between known measurements. Interpolation is used in spiral

scanning using data from the adjacent loops of a helix to produce a correction for the helical scan path.

Matrix A grid of picture elements (pixels) from which the CT image is composed. Most scanners use 512 x 512 pixel matrices: 256 x 256 and 320 x 320 are becoming less commonly used as scanner resolutions improve and data storage media get cheaper. Many scanners now have display consoles with 1024 x 1024 matrices.

Maximum intensity projection Computed image derived from a stack of CT images which displays the slack from any direction, with the image density related to the peak pixel value seen from that direction throughout the stack volume. This technique is used to demonstrate vascular enhancement in an 'angiogram-like' way.

Minimum intensity projection As for maximum intensity projection but with image density related to the minimum pixel value.

Multislice CT scanner in which the detector bank is split into several adjacent rows so that the data acquisition from a single gantry rotation can be used to produce multiple adjacent thin slices from a beam collimated to one thicker section.

Pitch (Pitch prime) The usual definition of pitch (see above) can cause confusion when applied to multislice CT. A scanner with a 2 cm wide beam hitting four 5 mm detector rows to give four simultaneous sections with a table increment of 2 cm per rotation has a pitch of 4 (table increment over individual detector width) but a pitch prime of 1 (table increment over nominal beam width).

Pitch factor In spiral scanning, this is the ratio of the distance travelled by the table per rotation of the gantry to the X-ray beam collimation. A pitch factor of 1 is standard: increasing the pitch factor to 1.25 or 1.5 results in thicker effective slices, more image noise, greater image artefacts, and lower patient radiation dose. It requires greater interpolation of data but allows a shorter scan time or an extended scan volume.

Pixel Picture element in the image display (cf. Voxel).

Postprocessing Manipulation of the image data.

Preprocessing Manipulation of the 'raw data' to enhance certain features in subsequent image reconstructions.

QCT Quantitative computed tomography—the use of a calibration procedure to identify the values of the CT numbers in an image in terms of a reference material. QCT is most commonly used to measure the mineral density of trabecular bone in the spine. Techniques have been described using two different scan energies (kVp) to allow for correction of the error introduced by the presence of marrow fat in trabecular bone (dual energy QCT-DEQCT). QCT can also be calibrated to measure the iron content of the liver.

Real-time CT Rapid image reconstruction such that the image is available almost as soon as the data acquisition for that slice is finished. See CT fluoroscopy.

Reconstruction The production of an image from the 'raw data'.

Reformation (reformatted image) The generation of images in an alternative plane from the original CT images. Reformats can now be in any plane or even curved, as computer speeds have improved. Multiple overlapping sections such as those obtained from spiral acquisitions produce markedly improved reformat image quality.

Region of interest (ROI) Any Part of a CT image on which measurements are being made—particularly measurements of the mean CT number.

Scout view CT scanner digital radiograph acquired by keeping the X-ray tube and detectors stationary while moving the table through the gantry. The resultant image can be used to identify the start and stop points for the subsequent CT sections.

Segmentation Removal of part of each image in a stack in order to allow subsequent manipulations to be applied to the area of interest, e.g. removing the spine from an angiographic CT to allow MIP projections without the bone densities obscuring the vascular contrast densities.

Slice thickness The nominal thickness of the slice which the image represents. As the X-ray beam is divergent, the sampled volume in the patient is thicker around the edges than centrally. The alignment of pre- and post-patient collimation may also affect the true slice thickness. Image noise is reduced with thicker slices but partial volume averaging effects become apparent in larger structures.

Slip ring A component of the gantry transferring data or electrical energy to or from the stationary (fixed) part of the scanner to the rotating part of the gantry, allowing continuous rotation of the gantry. Low-voltage slip rings can supply current to an onboard generator. High-voltage slip rings allow the generator to be separate from the gantry and supply high kV to the tube.

Spatial resolution Ability to resolve structures according to size. Formally assessed by calculation of the modulation transfer function. Influenced on CT by choice of field of view (targeting), mAs (radiation dose) and reconstruction algorithm (bone or high spatial frequency algorithm).

Spiral See Helical.

Surface rendered A computer-generated image of the surface defined by a specified minimum pixel intensity in a stack of images. Used to generate a 'three-dimensional' image.

Surface shaded Computer enhancement of a three-dimensional CT image to give a 'realistic' shaded effect to the surface of the object.

Voxel The volume within the scan plane that is represented by a pixel in the image.

Window The window width is the range of CT numbers that will occupy the entire greyscale of the display monitor: the window level is the CT number at the midpoint of that range. Altering the width and level therefore alters the contrast and brightness of the image, allowing the entire image density range to be interrogated on the monitor.

APPENDIX C

GLOSSARY OF MR TERMS

Jeremy P. R. Jenkins, Andrew. P. Jones

Aliasing An artefact that occurs, as a result of the nature of the image encoding process, when the field of view (FOV) is smaller than the area being imaged. There is folding-over of the anatomy outside the FOV back into the image. Also called 'fold-over' or 'wrap-around' artefact.

Angular frequency Frequency of oscillation or rotation (measured in radians/second) represented by the Greek symbol omega (ω). $\omega = 2\pi\nu$, where ν is the frequency in Hertz.

Artefact An error that occurs in the reconstructed image which does not correspond to any anatomical region or pathological lesion within the patient. There are many sources of artefact in MRI.

Averaging A method for improving the signal-to-noise ratio (SNR). The data lines in k-space are acquired multiple times by repeat acquisitions of the same phase encoding steps. The same MR signal is added up and the sum divided by the number of signals (i.e. number of signal excitations (NEW)/signal averages (NSA)).

B_0 , The symbol used for the static main magnetic field in the MR system measured in Tesla. The orientation of this field is along the z axis.

B_1 The symbol used to denote the radiofrequency (RF) magnetic field in an MR system measured in Tesla

Bandwidth A measure of the range of frequencies within which the MR system is tuned to receive the signal (receiver bandwidth) or the range of frequencies within an RF pulse delivered by the transmitter (transmitter bandwidth). Alteration in the receiver bandwidth affects the SNR, with narrowing of the bandwidth increasing SNR and vice versa. RF pulses of different bandwidths are used for various applications within pulse sequences.

Coil Single or multiple loops of wire (or other electrical conductor such as tubing) designed to either produce (transmit) a magnetic field from current flowing through the wire or measure (receive) an induced voltage in the loop arising from a changing magnetic field.

Diamagnetic A substance that will slightly reduce the strength of a magnetic field in which it is placed. The polarity of the magnetisation induced in a diamagnetic substance (most organic material) is opposite to that of the surrounding magnetic fields, and has negative *magnetic susceptibility*. These substances have no unpaired orbital electrons.

Diffusion A process whereby water and other small molecules in a tissue undergo random microscopic translational movement from Brownian motion (thermal processes). MR is a sensitive technique for measuring diffusion effects, e.g. in strokes, differentiating cysts from solid tumour and in CSF dynamic studies.

Echo rephasing The re-establishment of MR signal coherence which is achieved with either a 180° RF pulse or by gradient switching.

Echo train length (ETL) This is the number of echoes individually phase encoded for a fast (turbo) spin-echo sequence. The ETL corresponds to the number of lines of k-space measured per *repetition time* (TR) interval. ETLs can range typically from 3 to 128 depending on the pulse sequence type.

Eddy currents Small electrical currents induced by the changing magnetic fields within the gradient coils or the structure of the magnet. These induced electrical currents degrade image quality unless either properly compensated for or eliminated.

Even echo rephasing Re-establishment of spin-echo coherence of moving spins on symmetric even echoes (e.g. 2, 4, 6, etc.) in multiecho sequences as a result of sequential integration of signal phase shifts summing to zero.

Fat/water suppression A method that suppresses the signal within the imaging volume from either fat or water protons by application of a frequency-selective saturation RF pulse.

Ferromagnetic A substance, such as iron, cobalt or nickel, that is attracted by a magnetic field and retains its magnetism once removed from the effects of the magnetic field.

Flip angle The angle through which the magnetisation vector moves, relative to the longitudinal axis of the static magnetic field, as a result of the application of an RF pulse. This variation in flip angle is used in *gradient-echo* imaging to obtain the various tissue-weighted images (a low flip angle (typically $10\text{--}30^\circ$) produces a T_1 -weighted image and a 90° flip angle pulse provides T_2 -weighting).

Flow-related enhancement A process by which the signal intensity of moving fluids can be increased as compared with signal from stationary tissue; it occurs when in-flowing, unsaturated fully magnetised spins replace saturated spins within the imaging slice between successive RF pulses.

Fourier transform A mathematical process by which the frequency components of a signal are separated from its amplitudes as a function of time, and vice versa.

Free induction decay (FID) A transient signal that occurs as the transverse magnetisation decays towards zero following application of an RF pulse.

Gauss (G) An old unit used for measuring magnetic field strength. The internationally accepted unit is the Tesla ($1 \text{ Tesla} = 10\,000 \text{ Gauss}$). The earth's magnetic field is approximately 0.5 Gauss.

Gradient coils These are magnetic coils designed to alter the main magnetic field (in order that the magnetic field is stronger in some areas compared with other parts) by a few per cent. The magnetic field gradient generated by a coil is controlled by the electrical current passed through the coil. They are used to localise a slice and spatially encode slice information.

Gradient echo (GE/GRE) A basic pulse sequence which only uses magnetic field gradient reversal to rephase the transverse magnetisation and produce echoes of the MR signal. This allows shorter repetition times thus faster scanning, and flip angles less than 90° (see *flip angle*).

Image acquisition time This is the scanning time to produce a set of images from a measurement sequence. For a 2D sequence it is the product of the repetition time (TR), number of signal excitations/averages (NEX/NSA), and the number of *phase encoding* steps (N_y). For a 3D volume sequence the acquisition time is as for the 2D sequence together with the product of the number of partitions (z phase encoding steps, N_z). For *fast (turbo) 2D* sequences the acquisition time is the product of the 2D sequence divided by the *echo train length* (ETL).

Inhomogeneity The slight variation in uniformity of the static magnetic field expressed in parts per million (ppm) as a fractional deviation from the average value of the field.

Inversion recovery (IR) A basic pulse sequence which inverts the magnetisation and measures the recovery rate as the nuclei return to equilibrium. This rate of recovery is dependent on the T_1 relaxation rate.

Inversion time (TI) The time from the centre of the first inversion pulse (180°) to the beginning of the second (90°) excitation pulse in an IR sequence.

K-space The space which is filled with information (let's call it *rate duty matrix*) and undergoes a Fourier transform to form the MR image. The points at the centre of this data matrix represent low spatial frequencies (which give gross signal levels, i.e. contrast in the MR image). Increasing the offset from the centre corresponds to higher spatial frequencies (edge detection, i.e. image sharpness). By manipulating K-space faster sequences can be implemented as *in/fast* (or *1111-ho*) imaging.

Larmor equation $w = \gamma B_0$, [The expression of the proportional relationship between the precessional angular frequency of a nuclear magnetic moment (w , expressed in Hertz) and the main magnetic field (B_0 , in Tesla). The gyromagnetic ratio (γ) is a proportionality constant fixed for the nucleus. being 42.6 MHz/Tesla for hydrogen. For B_0 of 1.5 T $w = 42.6 \times 1.5 = 64$ MHz.]

Longitudinal magnetisation (M_z) The part of the macroscopic magnetisation vector parallel to the main static magnetic field (B_0). Following RF excitation the M_z returns to its equilibrium value (M_{z0}) as a function of the characteristic time constant T_1 of the tissues excited.

Longitudinal relaxation time See T_1 .

Magic angle artefact In joint imaging if a tendon is orientated at a certain angle (55°) to the static main magnetic field, the tendon appears brighter on T_2^* and proton density (intermediate)-weighted images but normal low signal on T_1 -weighted images. This artefactual increase in signal within the tendon is termed the *magic angle effect* and can be potentially confused with pathology. This effect is due to the highly ordered structure of tendons, which are composed of type I Collagen. This ordered structure restricts the motion and orientation of water protons, with consequent reduction in the dipolar interaction and thus an increase in signal.

Magnetic moment A measure of the magnitude and direction (vector quantity) of the magnetic properties of an object or particle that cause it to align with the static main field and create its own local magnetic field.

Magnetic resonance (MR) The absorption or emission of electromagnetic energy by nuclei (hydrogen protons in imaging) in a static magnetic field following excitation by a RF pulse. The resonant frequency of the RF pulse and emitted signal is proportional to the magnetic field (the relationship given by the Larmor equation).

Magnetic resonance signal The electromagnetic signal produced by the precession of the transverse magnetisation of the spins. The rotation of the transverse magnetisation induces a voltage in the receiver coil. It is this voltage that is amplified by the receiver and forms the signal.

Magnetic susceptibility The ability of a substance to become magnetised or to distort a magnetic field, denoted as the Greek symbol χ . This is described in terms of *diarrotgaene*, *paramagnetic*, *superparamagnetic* and *ferromagnetic* materials and refers to their respective electronic magnetic moments.

Magnetisation transfer contrast (MTC) This is a relatively new technique in which the image contrast is manipulated by selectively saturating a pool of protein-bound water. It should be noted that protons in the protein-bound water have a resonant frequency, approximately 500-2500 Hz away from the bulk water protons. By applying an off-resonance pulse (i.e. the centre frequency of the pulse being 1000-2000 Hz removed from the Larmor frequency for protons together with a wide bandwidth) these protons are suppressed. Because the protein-bound water and the bulk water protons are in rapid exchange, the saturation is transferred to the bulk phase of the water protons. This leads to a reduction in the signal from bulk water. MTC is used in the following situations: (i) in MRA of the brain as a means of enhancing visualisation of small peripheral vessels and aneurysms by suppressing the background brain tissue; (ii) in conjunction with gadolinium chelate enhancement, making the enhanced areas more conspicuous; (iii) combined with T_2 -weighted images in the detection of early demyelination or protein destruction.

Maximum intensity projection (MIP) An algorithm for producing multiple projections from a 2D or 3D volume data set. This volume data set is processed along selected angles in which the highest signal intensity pixel is projected as a 2D image. This technique is used in *MRA*, whereby flowing blood has a high signal intensity, and in MR cholangiopancreatography (MRCP) in which bile is of high signal.

MRA Magnetic resonance angiography.

NEX Number of signal excitations repeated in a given acquisition. This is a way of increasing SNR at the expense of time.

Nuclear spin An intrinsic property of certain nuclei (i.e. those with an odd number of neutrons and/or protons, e.g. ^1H , ^{23}Na , ^{13}C , ^{15}O) that gives them an angular momentum and magnetic moment. The spins of nuclei have

characteristic fixed values. Nuclei of paired neutrons and protons align to cancel out their spins and thus do not resonate.

Off-centre field of view A field of view (FOV) that is not centred at the isocentre of the magnet.

Paramagnetic This describes a substance (e.g. gadolinium, methaemoglobin) with positive magnetic susceptibility (opposite of diamagnetic). The substances align themselves with the static magnetic field and affect the relaxation times of tissues containing them. Gadolinium-chelate contrast agents are used for this effect, reducing the T_1 relaxation times (with subsequent increase in signal) of tissues containing them.

Phase-contrast (PC) angiography A 2D or 3D imaging technique relying on velocity induced phase shifts to distinguish flowing blood from stationary tissues. This technique relies on the fact that the phase gain of flowing blood is proportional to its velocity, assuming constant velocity. The *magnitude* image shows the vasculature with the direction of flow given by the *phase* image (also called *phase map*).

Phase encoding This allows the localisation of an MR signal by applying a series of varying phase encode gradient pulses in order to alter the phase of spins prior to signal readout. The spins themselves retain memory of the effect of the separate phase encode pulses.

Pixel An acronym for picture element describing the smallest component of a digital image display.

Proton density (ρ) weighted image These images show contrast related to the number of mobile protons in the structure and require scanning parameters that minimise the effects of T_1 (long TR) and T_2 (short TE) to obtain the appropriate weighting. Images usually have T_1 , T_2 and bulk flow contributions, however, and are thus better termed *'mixed'* (between T_1 and T_2) weighted.

Repetition time (TR) The time between successful excitations of a slice (i.e. the time from the beginning of one RF pulse sequence to the start of the next). In cardiac gated studies this can vary depending on the heart rate of the patient and as such an *effective* repetition time is obtained.

Saturation A non-equilibrium state in which equal numbers of spins are aligned with and against the magnetic field. This occurs immediately following a 90° RF pulse with the longitudinal magnetisation aligned in the x-y (transverse) plane and thus the system is said to be saturated. A few moments later, with some T_1 recovery, the system is partially saturated. Saturation effects are used in the slice direction to minimise signal from flowing blood.

Signal-to-noise ratio (SNR) The ratio of signal amplitude to the noise. Methods of improving the SNR are: increasing the number of signal excitations (NEX) with subsequent time penalty; increasing the field of view (FOV) with corresponding reduction in spatial resolution of the resultant image, and increasing the strength of the main magnetic field used.

Spin echo (SE) The reappearance of an MR signal, after the initial signal (FID) has disappeared following a 90° RF pulse, by the application of a refocusing 180° RF pulse. This refocusing pulse results in an effective reversal of the dephasing of the spins by eliminating the effects of inhomogeneity in the main magnetic field.

Superparamagnetic This describes a substance (e.g. haemosiderin, superparamagnetic iron oxide liver, lymph node, and oral bowel contrast agents) with magnetic susceptibilities 100-1000 times stronger than paramagnetic substances. These substances produce marked shortening of the T_2^* relaxation time, producing areas of signal void.

T_1 relaxation time Also called the *'spin-lattice'* or *'spin-office'* relaxation time, referring to the time taken for the spins to give up the energy obtained from the initial RF pulse back to the surrounding lattice (environment) and return to equilibrium. T_1 relaxation time represents the time required for the longitudinal magnetisation (M_z) to increment from 0 to 63% of its final maximum value.

T_2 relaxation time This is termed *transverse* or *spin-spin* relaxation time, and is the characteristic time constant for loss of phase coherence among spins orientated at an angle to the static main magnetic field. This time constant arises from interaction between the spins (hence the term 'spin-spin'). This can be mathematically represented by the time required for the transverse magnetisation (M_x or M_y) to decay to about 37% of its maximum value.

TE This refers to the *echo time*, i.e. the time between the centre of the excitation pulse and the peak of the echo.

TI This refers to the *inversion time* and represents the time after the middle of the 180° RF inverting pulse in the IR sequence to the middle of the 90° read pulse. This time monitors the amount of longitudinal magnetisation (M_z) and can be varied in the IR [sequence, e.g. as](#) in STIR (short TI (or tau)

Inversion Recovery) where the TI interval is short, being at the null point (zero signal) for fat; and FLAIR (Fluid Attenuation Inversion Recovery) where the TI interval is very long, being at the null point for fluids (e.g. CSF).

Time-of-flight (TOF) angiography Also referred to as *in-flow* angiography. It is used in 2D or 3D mode based on the principle of flow-related enhancement, i.e. blood flowing into a slice appearing brighter than surrounding tissue because it has not become saturated by previous RF pulses.

Voxel An acronym for volume element, being a 3D region of an imaged object represented in 2D by a pixel.

FURTHER READING

- Adamis, M. K. (1996) Glossary of MR terms. In Edelman, R. E., Hesselink, J. R., Zlatkin, M. B. (eds) *Clinical Magnetic Resonance Imaging*, 2nd edn, pp. 2177-2196. Philadelphia: WB Saunders.
- Elster, A. D., Burdette J. H. (2001) *Questions and Answers in Magnetic Resonance Imaging*. St Louis: Mosby.
- Floyd, L. J., Williams, R. F., Stark, D. D. (1999) Glossary. In *Magnetic Resonance Imaging*, 3rd edn. St Louis: Mosby.
- Hashemi, R. H., Bradley, G. W. (1997) *MRI: The Basics*. Baltimore Williams & Wilkins.

نشر الکترونیکی
موسسه انتشاراتی
نوردانش

APPENDIX D

RADIOPHARMACEUTICALS FOR IMAGING

Philip J. A. Robinson

Radiopharmaceutical

Nuclide	Chemical form	Investigation	Route of administration	Typical maximum activity given (MBq)	Effective dose (mSv)	Dose to the uterus (mGy)	Interrupt breast feeding?
⁵¹ Cr	EDTA	GFR measurement	IV	3	0.006	0.008	No
⁶⁷ Ga	Gallium citrate	Infection /Inflammation and tumour imaging	IV	150	1.7	12	Stop
⁷⁵ Se	23-Seleno-25-homo-taurocholate (SeHCAT)	Bile salt absorption	Oral	0.4	0.3	0.3	No
^{81m} Kr	Krypton gas	Lung ventilation	Inhalation	6000	0.2	<0.001	No
^{99m} Tc	Pertechnetate	Thyroid imaging	IV	80	1	0.6	24 hours
^{99m} Tc	Pertechnetate	Salivary gland imaging	IV	40	0.5	0.3	24 hours
^{99m} Tc	Pertechnetate	Meckel's diverticulum imaging	IV	400	5	3	48 hours
^{99m} Tc	Pertechnetate	First pass cardiovascular imaging	IV	800	10	6	48 hours
^{99m} Tc	Human albumin macro-aggregates	Lung perfusion imaging	IV	100 200 SPECT	1 2	0.3 0.6	12 hours
^{99m} Tc	Phosphonates	Bone imaging	IV	600 800 SPECT	3 5	4 5	No
^{99m} Tc	DTPA	Renal imaging	IV	300 excretion 800 perfusion	2 5	2 6	No
^{99m} Tc	DMSA	Renal imaging	IV	80	0.7	0.4	No
^{99m} Tc	Colloid	Liver imaging	IV	80	0.8	0.2	No
^{99m} Tc	Colloid	Lymph node imaging	Interstitial	40	0.4	<0.5	No
^{99m} Tc	Colloid	GI bleeding	IV	400	4	0.8	No
^{99m} Tc	Iminodiacetates	Biliary system imaging	IV	150	2	2	No
^{99m} Tc	Erythrocytes	GI bleeding	IV	400	4	2	12 hours
^{99m} Tc	Erythrocytes	Cardiac imaging	IV	800	8	4	18 hours
^{99m} Tc	Non-absorbable compounds	Gastric emptying	Oral	12	0.3	0.2	No
^{99m} Tc	Non-absorbable compounds	Oesophageal transit & reflux	Oral	40	0.9	0.6	No
^{99m} Tc	DTPA	Lung ventilation	Aerosol	80	0.4	0.5	No
^{99m} Tc	MAG3	Renal imaging	IV	100 excretion 200 perfusion	0.7 1	0.7 1.4	No

Radiopharmaceutical (cont'd)

Nuclide	Chemical form	Investigation	Route of administration	Typical maximum activity given (MBq)	Effective dose (mSv)	Dose to the uterus (mGy)	Interrupt breast feeding?
^{99m} Tc	Exametazime-labelled leucocytes	Infection/inflammation imaging	IV	200	3	0.8	No
^{99m} Tc	Sestamibi	Parathyroid & breast imaging	IV	900	11	11	No
^{99m} Tc	Sestamibi	Myocardial imaging	IV	300* 400*SPECT	4 5	4 5	No
^{99m} Tc	Exametazime	Cerebral blood flow imaging	IV	500	5	4	No
^{99m} Tc	Sulesomab	Infection/inflammation imaging	IV	750	6	4	No
^{99m} Tc	Technegas	Lung ventilation	Inhalation	40	0.6	0.07	No
^{99m} Tc	Arcitumomab	Tumour imaging	IV	750	7	4	No
^{99m} Tc	Tetrofosmin	Parathyroid imaging	IV	900	9	9	No
^{99m} Tc	Tetrofosmin	Myocardial imaging	IV	300 400 SPECT	3 4	3 4	No
^{99m} Tc	ECD	Brain imaging	IV	500	5	4	No
¹¹¹ In	DTPA	Cisternography	Intra-cisternal	30	2	0.9	No
¹¹¹ In	Leucocytes	Infection/inflammation imaging	IV	20	9	3	No
¹¹¹ In	Pentetreotide	Somatostatin receptor imaging	IV	110 220 SPECT	9 1.7	8 15	No
¹²³ I	Iodide	Thyroid imaging	Oral or IV	20	4	0.3	27 hours
¹²³ I	Iodide	Imaging metastases after thyroid ablation	Oral or IV	400	5	6	N/A
¹²³ I	meta-iodo benzyl-guanidine (mIBG)	Neuro-ectodermal tumour imaging	IV	400	6	4	N/A
³³ Xe	Xenon gas	Lung ventilation studies	Inhalation	400	0.4	0.3	No
²⁰¹ Tl	Thallous chloride	Myocardial & Parathyroid imaging	IV	80	18	4	No
¹¹ C	L-methyl-Methionine	Brain tumour & parathyroid imaging	IV	400	2	1	No
¹³ N	Ammonia	Myocardial blood flow imaging	IV	550	2	1	No
¹⁵ O	Water (bolus)	Cerebral & myocardial blood flow imaging	IV	2000	2	1	No
¹⁸ F	FDG	Tumour & myocardial imaging	IV	400	10	7	No

نشر الکترونیکی
موسسه انتشاراتی
نور دانش

INDEX

A

- Abdomen, acute, 663-89
aortic aneurysm leakage, 688
appendicitis, 683-5
 children, 867, 869
 calcified lesions, 689
cholecystitis
 acute, 685-6
 emphysematous, 686
 colitis, 679-80
 contrast studies, 668
 gynaecological disorders, 688
 intestinal obstruction, 668
 large bowel, 675, 676-8
 small bowel, 670-5
intra-abdominal abscess, 681-3
intramural gas, 687-8
intrapertoneal fluid, 680-1
pancreatitis, 686-7
plain films, 663
 abdomen, 664-8
 chest, 663-4
 pneumoperitoneum, 663, 664, 665-8
 renal colic, 688
- Abdominal circumference, 1042, 1046
Abdominal cysts, paediatric, 867, 868
Abdominal disorders in childhood *see*
 Paediatric abdomen
Abdominal lymph nodes, 512-13
Abdominal trauma, 691-708
 imaging, 691-2
Abdominal vessels
 Doppler ultrasound, 468-9
 magnetic resonance angiography,
 479-80
 phlebography, 489-97
Abdominal wall defects, 864, 1058-9
 associated abnormalities, 857-8,
 1059
Aberrant carotid artery, 1599, 1605,
 1606
Abetalipoproteinaemia, 629
Abscess
 adrenal, neonate, 877
 appendix, 673, 683
 breast, 1475, 1479
 Brodie's, 1159-60
 cerebral, 1520, 1783-4, 1790
 dental, 1532
 epidural, 1785
 intra-abdominal, 681-3
 liver, 715, 740, 742, 758, 771, 785,
 880
 lung, 19, 20, 22, 23, 72, 95, 138,
 139
 orbit, 1578
 paracolic, 645, 682
 parotid gland, 538
 pelvic, 991
 perinephric, 943-4
 renal, 876, 942-3
 retropharyngeal, 1497
 soft tissues, 1418, 1432, 1444
 spleen, 748-9, 758, 775-6, 882
 subdural, 1785
 subhepatic, 681-2
 subphrenic, 46, 53, 231, 681-2,
 738-40
 tubo-ovarian, 1079, 1093
Acalculous cholecystitis, 715, 723, 881
Acceleration index (AI), 463
Acceleration time (AT), 463
Accessory breast tissue, 1454
Accessory diaphragm, 52
Accessory foot bones, 1114
Accessory nipples, 1454
Accessory renal vessels, 933
Accessory soleus muscle, 1417
Accessory spleen, 747, 775
Acetabular fracture, 1402-3
Achalasia, 76, 552-3, 866
 secondary (pseudoachalasia), 553-4
Achilles tendon
 calcification, 1437
 injury, 1413
Achochondrognathia, 1062, 1149
Achochondroplasia, 1062, 1138-40, 1141,
 1664
Acoustic artery, 1689, 1690
Acoustic neuroma, 1597, 1611, 1612,
 1613, 1638, 1758, 1759
Acquired immune deficiency syndrome
 see AIDS/HIV infection
Acro-osteolysis (Hajdu-Cheney
 syndrome), 1124
Acrocephaly, 1624
Acromegaly, 976, 977, 1360, 1361,
 1362, 1538, 1640, 1664
Acromioclavicular joint dislocation,
 1406
Acrylate glue embolic agents, 456,
 1710
Ae inonuces, 145, 627, 1659
Actinomycosis, 49, 72, 145, 146, 558,
 652, 1174, 1523, 1786
Adactyly, 1107
Adamantinoma of long bone, 1291-2
Addison's disease, 826, 828, 1438,
 1439
Adenoid cystic carcinoma
 intra-thoracic, 122, 124
 lacrimal gland, 1592-3
 nasopharynx/paranasal sinuses,
 1494, 1527, 1528
Adenoid hyperplasia, 1492
Adenolipoma, breast, 1462, 1463
Adenolymphoma (Warthin's tumour),
 540, 1515
Adenoma
 adrenal cortex, 458, 830, 835, 839,
 840, 841, 842, 878
 islet cells *see* Islet cell tumours
 kidney, 442, 950, 995
 liver, 443-4, 757-8, 761, 770, 782,
 879
 oesophagus, 563
 paranasal sinuses, 1524
 parathyroid, 68, 69, 458, 1507,
 1508, 1509, 1510, 1515
 pituitary, 495, 660, 839-40, 1637,
 1749-52
 small bowel, 625
 thyroid, 62, 64, 1510, 1512-13
Adenomatous polyps
 adenoma-carcinoma sequence,
 640-1
 duodenum, 588, 589
 large bowel, 637, 638, 1540
 small bowel, 625, 626
 stomach, 587-8, 589, 591
Adenomyosis (endometriosis interna),
 1075-6, 1077, 1089, 1096-7
Adenovirus, 72, 172
 pneumonia, 135, 137, 259
Adhesions
 intrauterine, 1087, 1088
 small bowel obstruction, 618, 670,
 671
Adnexal cyst, 1078-9, 1084, 1091
Adnexal mass, 1078-81, 1091-2,
 1102-3
 benign/malignant features, 1083-4
Adnexal torsion, 884
Adolescent kyphosis (Scheuermann's
 disease), 1188
Adrenal abscess, neonate, 877
Adrenal arteriography, 825
Adrenal calcifying fibrous
 pseudotumour, 828-9, 838
Adrenal cortex, 825
 hormones, 825
 radionuclide imaging, 831
Adrenal cortical adenoma, 830, 835,
 878
 Conn's syndrome, 835, 840, 841,
 842
 Cushing's syndrome, 835, 839
 hormone secretion, 835, 839
 therapeutic embolisation, 458
Adrenal cortical carcinoma, 829, 835,
 836, 837, 878
 Conn's syndrome, 835, 840
 Cushing's syndrome, 835, 839
 staging, 836
Adrenal cyst, 829, 838-9, 878
Adrenal gland, 825-48, 886
 anatomy, 825, 826, 827
 blood supply, 825-6
 calcification, 828-9
 childhood masses, 876-8
 enlargement in infants, 826
 imaging investigations, 827-33
 radionuclide imaging, 830-3
 infections, 826
 needle biopsy, 830, 831
 pathology, 826-7
Adrenal haemorrhage, 826, 838-9
 neonate, 876-7
Adrenal hyperplasia, 826
 congenital, 939, 878
 Conn's syndrome, 840
 Cushing's syndrome, 839
Adrenal lipoma, 829-30, 836, 838
Adrenal medulla, 825
 hormones, 825
 radionuclide imaging, 832
Adrenal myelolipoma, 836, 838
Adrenal phlebography, 825
Adrenal pseudocyst, 838
Adrenal rests, scrotal extratesticular,
 1026
Adrenal tumours, 826, 827, 828-9
 calcification, 829
 embolisation, 458
 metastatic, 835-6, 837, 838
 venous sampling, 495
Adrenal vein phlebography, 495, 829
Adrenocorticotrophic hormone,
 Cushing's syndrome, 839-40
Adrenogenital syndrome, 826, 839
Adrenoleucodystrophy, 1801-2
Adriamycin-induced cardiomyopathy,
 90
Adult respiratory distress syndrome, 43,
 139, 175, 210, 220, 230, 242-4
Aerocele, 1642
 post-traumatic, 1783
Aesthesioneuroblastoma (nasal
 glioma), 1766
Afferent loop syndrome, post-gastric
 surgery, 607-8
Agammaglobulinaemia, 163
Age-related macular degeneration,
 1556
Agyria (lissencephaly), 1634, 1734
AIDS/HIV infection, 153-60

- AIDS/HIV infection -contcl
 biliary strictures, 729
 central nervous system infections,
 †786, 1787, 1788, 1793-4
 children
 diffuse infiltrative lymphocytosis
 syndrome (DILS), 882
 intrahepatic cholangiopathy, 722
 pneumonia, 260
 colorectal disease, 652-3
 duodenitis, 586
 fungal infections, 157, 772, 948,
 †786, 1787, 1793
 Kaposi's sarcoma, 121-2, 158, 599,
 626, 644, 652, 821
 lung cancer, 159-60
 lymphocytic interstitial pneumonia
 (LIP), 121, 158-9
 lymphomas, 159, 160, 625, 652, 821
 CNS, 1753-4
 mediastinal lymphadenopathy, 70,
 72
 mycobacterial infection, 156-7
 tuberculosis, 140, 141
 non-specific pneumonitis, 159
 oesophagitis, 558, 559
 pancreatic changes, 820-1
 parotid enlargement, 539
 protease inhibitor crystals, urinary
 tract obstruction, 967
 pulmonary infections, 153-7
 small bowel infections, 628
 splenic lesions, 776
 toxoplasmosis, 157, 1788, 1789
 Ainhum (dactylitis spontanea), 1 177
 Air block phenomena/pulmonary
 interstitial emphysema, 257
 Air bronchogram, 14-16, 17, 35
 causes, 16
 lung collapse, 175, 176
 lung consolidation, 182, 183
 Air embolus, angiography
 complication, 422
 Air enema, 647, 850, 873
 Air swallowing, 664, 665, 668, 669,
 688
 Airway disease, 161-86
 Alagille's syndrome (arteriohepatic
 dysplasia), 720
 Albers-Schonberg disease *see*
 Osteopetrosis
 Albright's syndrome *see*
 Pseudohypoparathyroidism
 Alcohol intake, 564, 790, 791, 816,
 840
 chronic pancreatitis, 817, 819
 osteoporosis, 1366
 Alcoholic hepatitis, 766
 Alexander's disease, 1728, 1802
 Algodystrophy *see* Regional pain
 syndrome
 Alkaptonuria (ochronosis), 50, 1366,
 †367, 1438
 Allen test, 357
 Allergic angiitis and granulomatosis
 (ChumStrauss syndrome),
 200.202
 Allergic bronchopulmonary
 aspergillosis, 148-9, 150, 174
 Allergic contrast media reactions *see*
 Anaphylactoid contrast media
 reactions
 AlphaU luanitrypsin deficiency, 168,
 240, 720, 722
 Alport's syndrome, 554, 977
 Aluminium toxicity, 1353, 1365
 Alveolar cell carcinoma
 (bronchiolar/bronchioloalveolar
 carcinoma), 107, 117, 119
 Alveolar disease, acute, 35, 36
 Alveolar microlithiasis, 24-5, 213, 214
 Alveolar process of jaw, 1531
 Alveolar protcinosis (pulmonary
 alveolar protcinosis), 35, 180,
 212, 213, 262, 263
 Angina, 295
 Alveoli, 9
 Alzheimer's disease, 999, 1796
 regional cerebral blood flow
 imaging, 1813-14
 Ambiguous genitalia, 1021, 1022
 Amelia, 1 107
 Ameloblastoma, 1545-6
 Amino acidurias, 1354, 1802-3
 Amiodaronchepatotoxicity, 756
 Ammonia inhalation, 195
 Amniocentesis, 1048, 1050
 Amniotic fluid volume, 1059
 Amoebiasis, 150
 biliary tract, 731
 brain, 1790
 colitis, 652
 liver abscess, 740, 742, 758, 771
 lung abscess, 23
 Amplatz catheter, 280, 350, 456
 Amplatzer device, 376, 378
 Ampulla of Vater, 711
 Ampullary carcinoma, 732, 733, 794,
 803
 Amyloidosis, 976, 1161, 1339, 1767
 dialysis-related, joint lesions, 1311,
 †312, 1313
 diffuse lung disease, 210-12
 gastrointestinal involvement, 580-1,
 629
 inediastinal lymph node calcification,
 70, 72
 primary/secondary, 210-11
 restrictive card iomyopathy, 299, 325
 tracheal involvement, 162, 211-12
 Anal canal, 635
 tumours, 655
 Anal endosonography, 637, 655
 Anal incontinence, 654-5
 Anal sphincter, 635
 lesions, 654-5
 Analgesic nephropathy, 977, 978
 Anaphylactoid contrast media
 reactions, 429, 927, 1086
 emergency treatment, 421, 927
 gadolinium-based MR contrast
 agents, 481
Ancylostoma eluodenale, 627
 Androgen-secreting tumours, 835
 Anencephaly, 1050-1
 Aneurysm, 412, 423-9
 aortic *see* Aortic aneurysm
 carotid space, 1501, 1502
 congenital, 423-4
 degenerative, 424-5
 dissection
 internal carotid artery, 1704
see also Aortic dissection
 embolisation, 458, 459
 endovascular repair, 452
 imaging techniques, 425
 infective, 424
 intracranial
 angiography, 1690-4
 calcification, 1631, 1632
 left ventricular, 321, 322
 mycotic, 1787, 1788
 necrotising vasculitis, 428
 poststenotic, 429
 subclavian stenosis, 433
 retro-orbital, skull erosion, 1639
 traumatic, 425-6, 427
 Aneurysmal bone cyst, 49, 1293,
 †295-6, 1297
 jaws, 1544, 1545
 Angelchik prosthesis, 562
 Angina, 295
 stable, 295-6
 Angiodysplasia, 441
 Angiography, 41 1-46
 adrenal mass imaging, 829
 aneurysms, 423-9
 angiomatous malformations, 437,
 438, 439
 aortic dissection, 428
 arteriovenous fistula, 439-40
 arteritis, 435-6
 bladder, 906
 bone tumours, 1250
 cardiac imaging, 279-81, 282, 320
 aortic coarctation, 380-1, 382
 atrioventricular septal defect,
 390-1
 congenital cardiac disease, 363,
 364
 interventional procedures, 281
 paediatric, 280
 patent ductus arteriosus, 377
 pulmonary stenosis, 379
 tetralogy of Fallot, 384
 total anomalous pulmonary
 venous connection, 397
 transposition of great arteries,
 387-8
 congenital lesions, 423
 contrast media, 927
 direct intra-arterial carotid/cerebral
 vessel imaging, 1676-7
 complications, 1677-8
 embolus, 436-7, 439
 erectile dysfunction, 906, 1035, 1036
 haemorrhage, 441
 historical aspects, 411
 indications, 422-3
 indirect phlegraphy, 483
 interventional *see* Endovascular
 neuroradiological procedures;
 Interventional angiographic
 techniques
 islet cell tumours, 787, 795
 liver disease, 742-6
 masses/tumours, 442-6
 neuroradiological techniques,
 †673-7
 paediatric chest, 248
 petrous temporal bone, 1599
 prostate, 906
 pulmonary, 46-7
 pulmonary embolism, 343
 renal, 906
 renal artery stenosis, 965
 spinal, 1648
 stenoses/thromboses, 429-33
 subclavian stenosis, 433
 trauma, 435, 436
 abdomen, 692
 liver, 697-8
 major blood vessels, 708
 spleen, 694
 urogenitaltract, 703
 uterine arteries, 1092
see also Arterial imaging
 Angioma *see* Angiomatous
 malformation
- Angiomatous (arteriovenous)
 malformation, 412, 437, 438,
 439
 capillary telangiectasia, 1697, 1773
 carotid angiography, 1678, 1679,
 †680
 cavernous, 1697, 1773, 1775, 1805
 embolisation, 458, 1683, 1710,
 †711, 1714-15, 1719, 1720
 heart, 337
 high-output cardiac failure, 401
 intracerebral, 1694-7, 1710, 1711,
 †714-15, 1772-4, 1820
 angiography, 1677, 1695-6
 calcification, 1631-2
 clinical presentation, 1694-5
 computed tomography (CT),
 †772-3
 epilepsy, 1805, 1807
 intracranial haematoma, 1695,
 †767
 subarachnoid haemorrhage, 1769
 vein of Gal en aneurysm, 1697
 kidney, 949
 liver, children, 880
 magnetic resonance angiography,
 479
 magnetic resonance imaging (MRI),
 †773-4
 pulmonary, 22, 46, 47, 401-2
 selective external carotid
 angiography, 1683
 skull vault vascular marking
 abnormalities, 1635, 1636
 small bowel, 630
 spine, 1669, 1670, 1697, 1719, 1720
 upper gastrointestinal haemorrhage,
 440
 uterus, 1092
 venous angioma, 1697, 1774
 Angiomatous polyp, paranasal sinuses,
 †525-6
 Angiomyolipoma, 876
 kidney, 949, 952-3, 963
 angiography, 442
 haemorrhage, 953
 Angiomyoliposis, liver, 771
 Angiosarcoma
 bone, 1300
 heart, 337, 338
 liver, 772
 Angioscopy
 angioplasty success assessment, 449
 arterial imaging, 412
 Aniridia, 874
 Anisakiasis, 627, 652
 Ankle joint
 congenital anomalies, 1114-17
 hall and socket joint, 1116
 imaging, 1240-3
 injuries, 1413-14
 classification, 1413
 Ankylosing spondylitis, 50, 1216,
 †218-21
 genetic aspects, 1218-19
 juvenile, 1215
 peripheral joint changes, 1220-1
 pulmonary involvement, 199, 201
 sacroiliac joint changes, 1219
 senile (diffuse idiopathic skeletal
 hyperostosis; Forestier's
 disease), 1221-2
 spinal changes, 1220, 1221, 1654,
 †655, 1671
 Ankylostomui, †50
 Annular pancreas, 604, 605, 790

- Anomalous first rib, 432
- Anomalous left subclavian artery, 269
- Anomalous origin of left pulmonary artery (pulmonary artery sling), 400-1
- Anomalous pulmonary venous connection, 395-7
 partial, 395
 total, 395-7
- Anomalous right subclavian artery, 269, 272, 290, 399, 573, 1687
- Anorectal atresia, 861, 862
- Anorectal malformations, 859, 861-2, 863
- Anorexia nervosa, ovulation disorders, 1073
- Antegrade pyelography, 900, 901
- Antegrade ureteric stenting, 900, 902, 903
- Anterior cerebral artery, 1681, 1688
- Anterior choroidal artery, 1680
- Anterior fontanel, 1624
- Anterior inferior cerebellar arteries, 1685
- Anterior spinal artery, 1650, 1651
- Antheor filter, 453
- Anthracycline cardiotoxicity, 403
- Anticoagulant excess, 88
- Antiplatelet drug therapy, 447-8
- Antithrombin III deficiency, 436
- Antral diaphragm, 603-4
- Antral web, 853
- Antrochoanal polyp, 1492
- Anus, 654-5
- Aorta, 265, 266, 267, 268, 272, 309, 365
 abdominal, magnetic resonance angiography, 479
 impressions on thoracic oesophagus, 572
 lesion terminology, 310
 selective catheterisation, 418
 thoracic, 57, 60, 61, 83, 309
 contrast-enhanced magnetic resonance angiography (CE-MRA), 476-7
 pathology, 312, 338-42
 wall structure, 309
- Aortic aneurysm, 50, 58, 83, 664, 1840
 abdominal, 412, 414, 415, 416, 424, 472
 ureteric displacement, 980
 definition, 310
 endovascular repair, 452, 453
 imaging, 425
 CT angiography, 412, 413, 414
 magnetic resonance angiography, 415, 416, 475, 476, 477
 plain chest film, lateral view, 13
 leakage, acute abdomen, 688
 oesophageal displacement, 573
 thoracic, 72-4, 338, 341, 412, 414, 415, 416, 424, 425, 475, 476, 477
 atheromatous disease, 312
 Marfan's syndrome, 312, 313
 mycotic, 314
 syphilitic aortitis, 313
- Aortic annular ectasia, 327
- Aortic arch, 268, 309, 1687
 traumatic aneurysm, 425, 427
 imaging, 425-6
- Aortic arch anomalies, 367, 380, 399, 400, 407-10, 1687-8
- Aortic atresia (hypoplastic left heart syndrome), 368, 394-5
- Aortic bifurcation, percutaneous transluminal angioplasty, 448
- Aortic body tumour, 446
- Aortic coarctation, 73, 74, 83, 368, 370, 380-I, 423, 424, 426
 imaging, 380-I, 382
 magnetic resonance angiography, 477, 478
 impressions on thoracic oesophagus, 573
- interventional cardiac catheterisation, 364
 poststenotic aneurysms, 429
 rib notching, 48, 290
 treatment, 381, 382
 balloon valvuloplasty, 382
 surgical repair, 228, 364
 ventricular septal defect association, 371-81
- Aortic dissection, 58, 62, 63, 73-4, 83, 309-10, 327, 426
 chest trauma, 22, 23, 224
 De Blakely classification, 309-10, 426, 427
 definition, 310
 imaging, 427-8
 CT angiography, 412, 414
 Doppler ultrasound, 472
 magnetic resonance angiography, 415, 475, 476, 477
 Stanford classification, 310
 thoracic aorta, 338, 339-41, 475, 476, 477
 chronic, 340-1
 type A/type B, 73, 74, 339
- Aortic false aneurysm, 63
- Aortic hypoplasia, 423
- Aortic penetrating ulcer, 74
- Aortic pseudocoarctation, 74, 423
- Aortic regurgitation, 300, 301, 327
 ventricular septal defect, 374
- Aortic root, 309
- Aortic rupture
 definition, 310
 thoracic aorta, 338, 341, 342
 traumatic (traumatic transection), 222, 224, 310-11
- Aortic sarcoma, radiation-induced, 236
- Aortic stenosis, 300, 326-7, 370, 381-2, 426
 balloon dilatation, 360-I
 quantitation by continuous wave Doppler, 326-7
 aortic insertion, 451
 subaortic, 381
 supraaortic, 381
- Aortic thrombosis (Leriche's syndrome), 417, 429-30, 431
- Aortic trauma, 31, 1, 707
 traumatic transection, 222, 224, 310-11
- Aortic valve, 265, 266, 268, 270, 271, 309
 acquired disease, 300, 301
 left ventricular angiography, 348
- Aortitis
 syphilitic, 313
 Takayasu's, 314
- Aortocaval fistula, 440, 441
- Aortoduodenal fistula, 602
- Aortography, 280, 354, 355, 356, 411
 adrenal mass imaging, 829
 aortic rupture, 224
 chest trauma, 217
 complications, 422
 contrast media dosage, 420
 see also Arch aortography
- Aortopulmonary window, 61, 81, 511
- Apert's syndrome, 1060, 1109, 1624, 1625
- Aphthous ulceration. Crohn's disease, 648, 649
- Apical cyst, 1542, 1543
- Appendicitis, 652, 683-5
 children, 867, 868, 869
 computed tomography (CT), 684-5
 localised ileus (sentinel loop), 621
 peritoneal abscess, 633
 signs, 683
 ultrasound, 683-4
- Appendix abscess, 673, 683
- APUD (amine precursor uptake and decarboxylation) system, 794
- Apudomas, somatostatin receptor scintigraphy, 660
- Aqueductal stenosis, 1054, 1728, 1729
- Aqueous humour, 1552
- Arachnodactyly see Marfan's syndrome
- Arachnoid cyst, 1639, 1728, 1730, 1731
 infant/neonate, 1809, 1810
 spine, 1670-1
- Arachnoiditis, 1671
- Arboriform pulmonary ossification (idiopathic pulmonary ossification), 214
- Arch aortography, 1677
 aortic arch traumatic aneurysm, 425-6
 complications, 1678
- Armilli-Jeromillors, 151, 1438
- Arnold-Chiari malformation, 1053
- Arrhenoblastoma (ovarian Sertoli cell tumour), 1082
- Arrhythmic right ventricular dysplasia, 323, 324, 403
- Arterial calcification, 412, 1435, 1473
- Arterial congenital anomalies, 423
- Arterial embolism, 436-7, 439
 transluminal angioplasty
 complication, 449
- Arterial extrinsic obstruction, 429
- Arterial graft surveillance, 412
- Arterial imaging, 41, 122
 angiography, 412
 computed tomography (CT), 412-13, 417
 contrast arteriography, 418
 complications, 421-2
 percutaneous catheterisation see Percutaneous arterial catheterisation
 pharmacovascular angiography, 421
 digital subtraction angiography (DSA), 415-16
 indications, 422-3
 magnetic resonance angiography, 472-81
 magnetic resonance imaging (MRI), 413, 415, 416, 417, 418
 plain films, 411-12
 radionuclide imaging, 412
 selective/superselective catheterisation, 418
 ultrasound, 411, 417, 418
 Doppler, 460-72
 venous angiography, 412
- Arterial spasm, peripheral, 435
 transluminal angioplasty
 complication, 449, 454
- Arterial stenosis, 412, 429-33
 congenital, 429
- Arterial stents, 451
- Arterial thrombosis, 429, 436
 angiography complication, 421
 aorta (Leriche's syndrome), 417, 429-30, 431
- Arterial trauma, 435, 436
 fracture-related, 1381-2
- Arterial wall damage
 angiography, 421, 428
 transluminal angioplasty
 complication (subintimal dissection), 449
- Arteriohepatic dysplasia (Alagille's syndrome), 720
- Arteriography, 483, 501, 502
- Arteriovenous fistula, 439-40
 congenital, 440
 dural (dural arteriovenous malformation), 1698-9, 1774
 high-output cardiac failure, 440
 iatrogenic, 440, 449
 intracranial, 1772-4
 angiography, 1678, 1697-700
 orbit, 1568-9
 peripheral artery bypass grafts, 467
 renal trauma, Doppler examination, 471
 spine, 1669, 1671
 steal insertion, 451
 therapeutic embolisation, 458, 459
 see also Angiomatous malformation
- Arteritis, 435-6
 arterial stenoses, 429
- Artery of Adamkiewicz, 1651
- Arthritis, childhood disorders, 1213-15
- Arthrography, 1235
 ankle joint, 1240-I
 congenital hip dysplasia (congenital dislocation), 1111-13
 elbow joint, 1243-4
 intercarpal ligament disruption, 1410
 knee, 1235, 1236
 Perthes' disease (osteochondritis of femoral capital epiphysis), 1183-4, 1185, 1186
 rheumatoid arthritis, 1207-8
 shoulder joint, 1237-8
 wrist joint, 1244
- Arthrogryposis multiplex congenita, 1434
- Arthroscopy, 1235
- Asbestos exposure, 17, 107, 633
 associated malignant disease, 192
 lung cancer, 192
 malignant mesothelioma, 102-3, 192
 pleural of fusions, 194
 pleural plaques/calcification/fibrosis, 98, 100, 101, 102, 193-4, 196
 pulmonary fibrosis, 194
- Asbestos fibre subtypes, 192
- Asbestos-related pleural disease, 35
- Asbestosis, 34, 35, 187, 192-4
 asbestos fibre subtype relationship, 192
 Caplan's syndrome, 198
- A. ecaris* (roundworm), 627, 715
 biliary tract infection, 730
 brain infection, 1791
 Loeffler's syndrome, 150
- Ascinic sinonasal carcinoma, 1527
- Ascites, 633, 680
 acute pancreatitis, 817
 obstetric ultrasound, 1058
 pancreatic malignancy, 788
 transjugular intrahepatic portosystemic shunt (TIPS), 453

- Aseptic necrosis *see* Osteonecrosis
- Asherman's syndrome, 1088, 1089
- Aspergilloma (*Aspergillus* mycetoma), 23, 24, 147-8
- Aspergillosis, 25, 147-9, 157, 158, 166
allergic bronchopulmonary, 148-9, 150
central nervous system, 1786, 1788, 1793
invasive, 148, 149, 150, 153
paranasal sinuses, 1522-3
ureteric inflammation, 979
- Aspergillus*, 142, 199, 294, 880, 882
- Aspergillus flavus*, 1522
- Aspergillus fumigates*, 147, 148, 157, 204, 1522
- Asphyxiating thoracic dystrophy (Jeune's disease), 1109, 1142, 1144
- Aspiration, 138-9, 153, 195, 544
barium swallow examination, 544-5, 547
lung consolidation, 180
paediatric contrast use, 849, 850
swallowing modification, 547-8
- Aspiration pneumonia/pneumonitis, 77, 227, 230
- achalasia-related risk, 552
- Aspiration thrombectomy, 456
- Asplenia (Ivermark's syndrome), 749, 882
bronchial tree abnormalities, 250
- Assisted conception, 1084
- Asteroid hyalosis, 1558
- Asthma, 19, 28, 79, 165-6
children, 260
definition, 165
extrinsic (atopic), 166
intrinsic, 166
mucoid impaction, 174
pulmonary eosinophilia, 204
- Astrocytic tumours, 1739
- Astrocytoma, 1739
anaplastic, 1743
diffuse, 1743
pilocytic, 1739-42
cerebellar, 1739, 1740
pontine, 1742
spine, 1649, 1666-7
subependymal giant cell, 1742-3
- Ataxia telangiectasia, 1738
- Atelectasis, 220, 227, 228, 230
- Atheroma removing devices, 450
- Atheromatous disease, 422
aortic displacement of oesophagus, 573
arterial calcification, 412, 1435
carotid arteries, 1632, 1633
coronary arteries, 320
arterial embolism, 437
arterial stenoses, 429-30
Doppler ultrasound measurement, 463
coeliac/superior mesenteric stenosis, 431
coronary heart disease, 295, 320, 354
degenerative aneurysms, 424-5
internal carotid artery
stenosis/thrombosis, 1700-5
intracranial vessel
angioplasty/stenting, 1710
mesenteric ischaemia, 630
Raynaud's phenomenon, 433
renal artery stenosis, 480, 964
Athletes, ovulation disorders, 1073
- Atlanto-axial subluxation/dislocation, 1432, 1656-8
- Atlanto-occipital assimilation, 1653, 1654
- Atlas, Jefferson burst fracture, 1397-8
- Atrial baffle operation, 388
- Atrial myxoma, 308-9, 336, 337, 338
peripheral microaneurysms, 428
- Atrial septal defect, 47, 368, 374-6
cardiac catheterisation/angiography, 375
clinical presentation, 374-5
left-to-right shunt, 369
non-invasive diagnosis, 375
ostium primum *see* Atrioventricular septal defect
ostium secundum, 374
treatment, 375
transcatheter occlusion, 375-6
- Atrial switch operation, 389
- Atrioventricular septal defect, 368, 390
imaging, 390-1
non-invasive diagnosis, 375
treatment, 390
- Atypical mycobacterial infection, 157
- Atypical pneumonias, 135-8
- Augmentation/substitution cystoplasty, 1000, 1001
- Auricular vein, 1682
- Autoimmune adrenal gland atrophy, 828
- Automatic implantable cardiac defibrillators, 294
- Autonomic neuropathy, oesophageal motility disorders, 552
- Avascular necrosis *see* Osteonecrosis
- Avulsion fractures, 1377, 1378
sites, 1379
- Axial osteomalacia, 1356
- Axillary artery catheterisation, 418
brachial plexus damage, 422
- Axillary artery stenosis, 449
- Axillary lymph nodes, 513, 1463
metastases, 1475
- Axillary lymphadenopathy, 1467-8
- Azygo-oesophageal recess, 61
- Azygos fissure, 7, 32
- Azygos vein, 5, 60, 61
dilated, 74
- Azzopardi tumour, 1033
- B-cell lymphomas, 523
- Bacterial pneumonia, 17, 131-5
opportunistic infections, 153, 156
pleural effusion, 87
- Bacteroides*, 1783, 1784
- Bagassosis, 195
- Baker's cyst, 1208, 1211, 1225, 1235, 1236, 1383
rupture, 1239
- Ball and socket ankle joint, 1116
- Balloon angioplasty
cerebral vasospasm, 1709
intracranial arteriosclerotic disease, 1710
- Balloon dilatation of pelviureteric junction obstruction, 904
- Balloon embolic devices, 1710
- Balloon valvuloplasty, 281
- Balloon-expandable stents
arterial, 451
biliary drainage/stenting, 734
- Bands, congenital (Streeter's bands), 1107, 1177
- Bankart lesion, 1405
- Banti syndrome, 747
- Barium aspiration, paediatric patient, 849, 850
- Barium enema, 636
colorectal cancer, 641-2
screening, 644
colorectal polyps, 639-40
colostomy enema, 637
Crohn's disease, 648-9, 650
diverticular disease, 645
instant enema, 636, 648
intussusception reduction, 873
ovarian carcinoma, 1085, 1086
paediatric examination, 850
procedure, 636
ulcerative colitis, 647-8, 650
- Barium follow-through, 615-16
compression paddle, 616
enterocolysis comparison, 617
procedure, 616
- Barium laryngogram, 1489
- Barium meal
duodenitis, 586
duodenum anatomy, 577-8
gastric surgery complications, 607
paediatric abdomen, 850
pancreas examination, 788-9
peptic ulceration, 581-2
benign gastric ulcers, 581-2
biphasic examination, 581-2
duodenal ulcers, 583-4
procedure/filming sequence, 575-6
stomach anatomy, 576-7
- Barium peritonitis, 636
- Barium studies
Bochdalek's hernia, 78
oesophageal duplication cyst, 78
paediatric abdomen, 849
- Barium swallow
congenital cardiac disease, 405
oesophageal lesions, 77
tears, 571
varices, 571
webs, 548-9
oesophageal motility assessment, 549
paediatric imaging, 247
pancreatic tumours, 788
pharyngeal motility/swallowing disorders, 544
aspiration risk, 544-5, 547
examination technique, 544-5
interpretation, 545-8
pharynx/larynx examination, 1489, 1490
respiratory disease, 2
- Barrel chest, 169
- Barrett's oesophagus, 554, 557, 558
adenomas, 563
oesophageal adenocarcinoma risk, 565
- Barton's fracture, 1408
- Barytosis, 195
- Basal ganglia calcification, 1361, 1623, 1633-4, 1798-9
- Basilar artery, 1685
size variation, 1689
- Basilar impression, 1625-6
- Basilar invagination, 1625, 1653
- Bathrocephalic skull, 1624
- Batten's disease (neuronal ceroid lipofuscinosis), 1802
- Battered child, 1126, 1384-5, 1811
- Beaded peripheral arterial spasm, 435
- Bechterew's disease *see* Ankylosing spondylitis
- Beckwith-Wiedemann syndrome, 792, 874, 878, 881, 930, 1059
- Behcet's disease, 325, 630, 1216, 1668, 1794
- Benign lymphoepithelial lesion (myoepithelial sialadenitis; Mikulicz's disease), 539
- Benign papillary stenosis, 733
- Benign peritoneal mesothelioma, 1081
- Benign prostatic hyperplasia, 993, 1004-5
- Bennet fracture, 1410
- Berry aneurysm, congenital, 423, 424
- Berylliosis, 194, 196
- Beuford complex, 1407
- Bezoars, 607, 608-9
gastric in children, 866
small bowel obstruction, 674
- Biceps long head damage, 1237, 1240
- Bicornuate uterus, 1075, 1087, 1094
- Bicuspid aortic valve, 300, 326, 327, 363, 380, 382, 426
- Bilateral superior vena cava, 402
- Bile duct disorders, 725-35
biliary drainage/stenting indications, 733-4
spontaneous perforation, 722
- Bile duct stones, 725-7, 816
endoscopic interventions, 733
- Bile duct stricture
benign
balloon dilatation, 733
biliary drainage/stenting, 734
malignant, endoscopic interventions, 733
- Bile duct tumours, 722, 731-2
endoscopic interventions, 733
- Bile ducts
angiographic interventions, 735
biliary tree gas, 714
endoscopic interventions, 733-5
extrahepatic, 711
intrahepatic, 711
- Bile leak
post-liver transplantation, 774
post-liver trauma, 728, 729
scintigraphy, 718
- Bile, limy, 713
- Biliary atresia, 720, 760, 879
- Biliary colic, 686
- Biliary cystadenocarcinoma, 732
- Biliary cystadenoma, 732, 769
- Biliary dilatation, 733
- Biliary drainage/stenting, 733-4
stent types, 734
metallic, 734, 735
- Biliary hypoplasia, 720
- Biliary obstruction
cholangiocarcinoma, 732
computed tomography (CT), 717
hepatic metastases, 734
liver transplantation complication, 774-5
pancreatic tumours, 813
scintigraphy, 718
ultrasound, 716-17, 813
- Biliary strictures
AIDS-related cholangiopathy, 729
benign postsurgical, 727-8
children, 722
chronic pancreatitis, 729-30
liver trauma, 728, 729
malignant, 732
post-liver trauma, 728
primary sclerosing cholangitis, 728-9

- Biliary tract, 711-35
 abdominal plain film, 712-14
 anatomy, 711-12
 blood supply, 711
 childhood disorders, 720-2
 computed tomography (CT), 717
 developmental anomalies, 711-12, 720
 embryonal cell sarcoma, 879
 embryonal rhabdomyosarcoma, 879
 endoscopic retrograde
 cholangiopancreatography (ERCP), 719
 gas, 673, 674
 intravenous cholangiography, 719
 magnetic resonance cholangiography (MRC), 717
 operative cholangiography, 719-20
 oral cholecystography, 718-19
 parasitic infection, 730-1
 percutaneous cholangiography (PTC), 719
 radionuclide imaging, 717-18, 760
 trauma, 698-9
 complications, 699
 ultrasound, 714-17
- Binswanger's disease (subcortical arteriosclerotic encephalopathy), 1803, 1815
- Biophysical profile, 1047
- Biparietal diameter, 1041-2
- Bipartite patella, 1114, 1411
- Birth asphyxia, cardiac manifestations, 370
- Bismuth poisoning, 1368
- Bite wounds, osteomyelitis complicating, 1161
- Bladder, 989-1004
 anatomy, 888-9
 benign tumours, 995
 blood supply, 889
 calculi, 997, 998
 computed tomography (CT), 910
 congenital lesions, 989-90
 extrinsic compression/displacement, 1003-4
 fistulas into gastrointestinal tract, 994-5
 herniation, 994
 inflammatory lesions, 991-3
 magnetic resonance imaging (MRI), 911, 912, 1007-8
 major surgical procedures, 999-1002
 postintervention imaging appearances, 1002-3
 malignant tumours, 995-7
 mechanical problems of wall, 993-5
 micturition physiology, 921
 neck, 888
 neuromuscular disorders, 999
 obstetric ultrasound, 1059-61
 percutaneous procedures, 905
 schistosomiasis, 992-3
 trauma, 703-4, 997, 998
 rupture, 997-9
 trigone, 889
 tuberculosis, 991-2
 ultrasound, 894-5
 urodynamics, 921
 wall thickness, 993
 wall trabeculation, 993
- Bladder agenesis, 989
- Bladder cancer
 fistulas into gastrointestinal tract, 994
 local bone destruction, 1253
 lymphoma, 997
 magnetic resonance imaging (MRI), 1008-11
 rhabdomyosarcoma, 997
 TNM staging, 1008
 total cystectomy with urinary diversion/neobladder construction, 999-1000, 1001
 postintervention imaging appearances, 1002-3
 urachal carcinoma, 997
 urothelial carcinoma, 995-6
- Bladder diverticulum, 921, 993-4
 congenital, 990
- Bladder duplication, 989
- Bladder extrophy, 989
- Bladder outflow obstruction, 921, 993, 1004
- Blalock shunt, 384, 385, 386
- Blalock-Taussig shunt placement, 228, 229
- Blastomyces*, 146, 1659
- Blastomycosis, 25, 72, 146, 627, 1786
- Blighted ovum, 1045
- Blount's disease (tibia vara), 1189, 1358
- 'Blue bloaters', 171
- Blue rubber bleb naevus syndrome, 630
- Boari bladder flap, 1000, 1001, 1003
- Bochdalek's hernia, 53, 77, 78, 560, 562
 neonate, 254
- Boerhaave's syndrome, 79, 224, 571
- Bone
 biopsy, 1159
 blood supply, 1155
 bruise injury, 1374, 1419
 density measurement, 1351-2
 invasion/destruction by extrasosseous primary malignant tumours, 1253-4
- Bone cyst
 aneurysmal, 1293, 1295-6, 1297
 jaws, 1544, 1545
 solitary (unicameral), 1312-14, 1315, 1316
- Bone dysplasias, 1122-49
 jaw/teeth involvement, 1539-40
 obstetric ultrasound, 1061-2
 focal abnormalities, 1062
 petrous temporal bone involvement, 1612-14
 skull hyperostosis, 1640
 temporomandibular joint involvement, 1546
- Bone haemangioma, 1296-8, 1299, 1300, 1301, 1302
- Bone infarction
 Gaucher's disease, 1344, 1346
 sickle cell disease, 1324, 1325, 1326
 see also Osteonecrosis
- Bone infection, 1155-72, 1173-7
 sickle cell disease, 1324-5, 1327
- Bone island (enostosis), 1254, 1256
- Bone marrow hyperplasia
 chronic haemolytic anaemias, 1321
 iron deficiency anaemia in children, 1326
 jaw/facial skeleton changes, 1541
 sickle cell disease, 1324
 thalassaemia, 1322, 1323
- Bone tumours, 1247-85, 1287-320
 angiography, 445
 blood vessels, 1296-300
 bone-forming, 1254-69
 cartilage-forming, 1269, 1272-85
 classification, 1247, 1248
 diagnostic principles, 1248-9
 epithelial, 1306
 fatty tissue, 1303-4
 fibrous, 1287-92
 giant cell-containing, 1292-6
 imaging investigations, 1248-9
 angiography, 1250
 computed tomography (CT), 1249-50
 magnetic resonance imaging (MRI), 1250-1
 plain films, 1249
 radionuclide imaging, 1248, 1249
 tomography, 1249
- lymphoma, 526
 metastatic, 50, 113, 125, 1248, 1251-3
 nerve tissue, 1300-3
 notochord, 1305-6
 primary tumour preoperative embolisation, 458
 sites, 1249
 skull erosion, 1636-7
- Bony metaplasia of lung (idiopathic pulmonary ossification), 214
- Borrelia burgdorferi*, 1788
- Bourneville's disease see Tubercous sclerosis
- Boutonniere deformity, 1203, 1204
- Bowel trauma, 705-7
- Boxer's fracture, 1411
- Brachial artery
 catheterisation, 357, 418
 congenital anomalies, 423
 stenosis, transluminal angioplasty, 449
- Brachial plexus, 1418, 1512
 angiography-related injury, 422
 imaging, 1644
- Brachicephalic skull, 1624
- Brachydactyly, 1107
- Brachymesophalangy, 1107
- Brain damage
 arteriography-related, 422
 diffuse, 1780
 brain swelling, 1781
 diffuse axonal injury (white matter shearing), 1780-1
 hypoxic, 1781
 multiple petechial haemorrhages, 1780
- Brain, ultrasound examination
 infant, 1723, 1807-12
 indications, 1807
 normal appearances, 1807-9
 technique, 1807
 obstetric ultrasound, 1049
- Branchial cleft cysts, 540, 1500-1, 1502, 1510, 1512
- BRCA1*, 1081
- BRCA2*, 1081
- Breast, 50, 1451-86
 anatomy, 1454-5, 1456, 1476-7
 architectural distortion (stellate lesion), 1460, 1461-2
 asymmetrical soft-tissue density, 1462
 axillary node abnormalities, 1467-8
 circumscribed mass, 1462-8
 mixed density, 1462-3
 radiolucent lesions, 1462
 radiopaque (soft-tissue density) lesions, 1464-6
 women under 35 years, 1467
 complex sclerosing lesion (radial scar), 1461
 fat necrosis, 1457, 1473, 1474
 image-guided practical procedures, 1478-82
 preoperative localisation of non-palpable lesions, 1482
 magnetic resonance imaging (MRI), 1476-8
 mammography, 1451-5, 1475
 microcalcifications, 1458, 1461, 1468-74
 differential diagnosis, 1472-3
 ductal, 1469-70
 lobular, 1470-2
 management, 1473
 outside glandular tissue, 1473-4
 normal variants, 1454
 oedematous, 1474-5
 plain chest film appearances, 11
 skin lesions, 1468
 spiculate mass, 1458-60, 1476
 surgical scar, 1460, 1461
 trauma, 1462, 1463
 ultrasound, 1455-8, 1475
 indications, 1455-6
- Breast abscess, 1475
 ultrasound-guided aspiration, 1479
- Breast adenosis, 1471
 sclerosing, 1471, 1472
- Breast cancer screening, 1483-6
 effectiveness, 1483
 interval cancers, 1484
 organisational aspects, 1483-4
 quality assurance, 1484, 1485
 recent UK results, 1486
 research studies
 age trials, 1484
 one-view vs. two-view
 mammography, 1485
 screening frequency, 1485
- Breast carcinoma
 architectural distortion (stellate lesion), 1461-2
 asymmetrical soft-tissue density, 1462, 1463
 circumscribed mass, 1464, 1465-6
 management, 1466-7
 ductal carcinoma in situ, 1469-70, 1471, 1477
 follow-up, 1478
 interval cancers, 1484
 intracystic, 1464, 1465, 1467
 invasive ductal, 1465, 1467
 mammography see Mammography
 medullary, 1457, 1465-6
 metastases, 117, 597, 792, 835, 1251, 1252, 1548, 1636, 1660, 1762
 microcalcifications, 1468, 1472, 1473
 mucinous, 1457, 1466
 oedematous breast, 1474-5
 papillary, 1466
 positron emission tomography (PET), 1830-I
 screen-detected, 1484
 sentinel node imaging, 1832
 somatostatin receptor scintigraphy, 661
 spiculate mass, 1458-60, 1476
- Breast cyst, 1456, 1464, 1473, 1474, 1477
 ultrasound-guided aspiration, 1479
- Breast fibroadenoma, 1456-7, 1464-5, 1466, 1467, 1468, 1473, 1474, 1477

- Breast fibromatosis, 1460
- Breast implants, 1474, 1476-7, 1478
rupture, 1477, 1478
siliconorna formation, 1478, 1479
- Breast lipoma, 1462
- Breast masses
benign, 1456-7, 1464
lymphoma, 1466
malignant, 1456, 1457, 1464
see also Breast carcinoma
matatastic tumours, 1466
- Breast microcystic change, 1471, 1472
- Breast papilloma, 1465, 1473
- Breast sarcoma, 1465, 1467
- Brenner's tumour, 1082
- Bridge stent, 451
- Broad thumb, congenital, 1 107
- Brodie's abscess, 1159-60
- Bronchi, 9, 10, 60
impressions on thoracic oesophagus, 572
- Bronchial arteries, 9
congenital anomalies, 423
emholisation, 248, 457
enlarged, 9
- Bronchial arteriography, 47, 164
- Bronchial atresia, 174, 175,250
- Bronchial benign clear cell tumour, 124
- Bronchial carcinoid, 122-3, 125
- Bronchial carcinoma, 9, 17, 35, 107-18
aetiology, 107
AIDS patients, 159-60
airway obstruction, 108
asbestos exposure-rela(ed, 192
biopsy, 113-14, 116
bronchopleural fistula, 95
chylothorax, 88
clinical presentation, 108
diagnosis, 113-15
ectopic ACTH production, 840
epidemiology, 107
hypertrophic osteoarthopathy, 1231
lung consolidation, 180
mediastinal involvement, 34,
111-12, 118, 127
lymphadenopathy, 71, 82, 108,
111-12, 116
metastases, 117-18, 119, 120, 126,
626, 777, 835, 838, 1660, 1762
hone, 1248, 1250, 1251, 1253
scintigraphic detection, 42
pathology, 107-8, 113-14
adenocarcinoma, 107, 108, 112
adcnosquamous carcinoma, 107
alveolar cell carcinoma, 107, 1 17,
119
basal cell carcinoma, 107
carcinosarcoma, 107
clear cell carcinoma, 107
large cell undifferentiated, 107
small (oat) cell carcinoma, 107,
108,113,115
squamous cell, 107, 108, 109,
111,113
pericardial invasion, 126, 335, 336
peripheral pulmonary mass, 108-11
pleural involvement, 87, 89, 95,
109,112,126
positron emission tomography
(PET), 43, 1830
rib involvement (Pancoast tumour),
113, 125, 1254
screening investigations, 113
staging, 115-16, 117
treatment assessment, 117
- Bronchial chondroma, 124
- Bronchial cystadenoma, 122
- Bronchial disease, 163-5
- Bronchial lipoma, 124
- Bronchial mucoid impaction, 173-4
- Bronchial myoblastoma (granular-cell
tumour), 124
- Bronchial obstruction, 26, 163, 175
- Bronchial papilloma, 124
- Bronchial sites, 365-6
- Bronchial trauma, 221
- Bronchial tree congenital
abnormalities, 250
- Bronchial wall thickening, 19
- Bronchiectasis, 9, 19, 21, 23, 29, 33,
34, 43, 152, 163-4, 165, 1231
allergic bronchopulmonary
aspergillosis, 148
bronchial arteriography with
embolisation, 47
bronchography, 45
children, 261
cylindrical (tubular), 163, 164
cystic fibrosis, 261
saccular (cystic), 163, 164
varicose, 163
- Bronchiolar|bronchioloalveolar
carcinoma (alveolar cell
carcinoma), 107, 117, 119
- Bronchioles, 9
- Bronchiolitis, 172-3
acute, 172
obliterative, 139, 172-3
drug-induced, 210
lung transplantation complication,
242
panhronchiolitis (Japanese
panhronchiolitis), 173
respiratory with interstitial lung
disease, 173
- Bronchiolitis obliterans organizing
pneumonia (BOOP), 173, 174
- Bronchitis, chronic, 43, 152, 105,
166-8
emphysema, 167, 170-1
- Bronchocele, 19, 108, 112, 173-4
- Bronchocentric granulomatosis, 200,
202,203
- Bronchogenic cyst, 22, 38, 74-5, 252
- Bronchography, 45
Bronchiectasis, 163
paediatric chest, 248
bronchopleural fistula, 51, 95, 226-7
- Bronchopneumonia, 131, 132, 133
aspergillosis, 148
tuberculosis, 142, 143,144
- Bronchopulmonary aspergillosis, 16,
19, 21, 163
allergic, 148-9, 150, 174
- Bronchopulmonary dysplasia|chronic
lung disease of prematurity,
257-8
- Bronchopulmonary foregut
malformations, 252
- Bronchopulmonary lymph nodes, 10
- Bronchoscopy
bronchial carcinoma, 113
lung biopsy, 44
Brown tumours, 49, 1293, 1295, 1363,
1364, 1539
- Brucellosis, 1659
bone infection, 1173-4
- Brunner's gland
hamartoma, 590
hyperplasia, 586-7, 590
- Budd-Chiari syndrome *see* Hepatic
vein thrombosis
- Buerger's disease (thromboangitis
obliterans), 433-5
- Bullous emphysema, 23
- Bullous lung disease, 169-70
- Buphthalmos, 1588
- Burkiit's lymphoma, 871, 881, 882-3,
1528-9
skeletal features, 1336, 1337, 1546,
1660
- Bursae, 1426
enlargement, 1426
- Buscopan, 636
- Butterfly vertebra, 1117, 1119, 1653
- Butylcyanoacryl|Lite embolisation, 456,
458, 1710-11, 1715, 1720
- Bypass graft stcnosis, Doppler
ultrasound examination, 466-7
- C-reactive protein assay, 483, 485
- CA-125, ovarian cancer screening,
1084
- CADASIL, 1796, 1797
- Cadmium toxicity, 1353
- Caecal adenocarcinoma, 619
- Caecal (right colon) volvulus, 669,
676-7,679
- Caecum, 635
- Cafley's disease (infantile cortical
hyperostosis), 1 192
- Caisson disease (dysbaric
osteonecrosis), 1191-2, 1385
- Calcaneal fracture, 1373, 1414
- Calcaneonavicular fusion, 1117
- Calcitic tendinopathy, 1421, 1422,
1437
- Calcifying fibrous pseudotumour,
adrenal gland involvement,
828-9, 838
- Calcinosis circmnscripta, 1439
- Calcinosis interstitialis universalis,
1439
- Calve's disease, 1 187, 1341
- Campylohaeter*, 627, 651, 870
- Candida*, 146, 153, 880, 882
- Candidiasis
acute parotitis, 537
central nervous system, 1786,
1787-8, 1793
chronic mucocutaneous, 558
emphysematous cystitis, 991
liver infection, 772
ocspthagitis, 557-8, 866
oral, 1539
pulmonary infection, 146-7, 153,
154
pyelonephritis, 948
ureteric inflammation, 979
- Caplan's syndrome, 191, 192, 193, 198
- Capsular artery, 1680
- Captopril scintigraphy, 917, 919
- Carbon monoxide poisoning, 1634,
1798
- Carcinoid syndrome, 123, 626
tricuspid/pulmonary valve
regurgitation, 303
- Carcinoid tumours, 42
hone metastases, 1251, 1253
bronchi, 122-3, 125
hepatic metastases, 626, 785
embolisation, 458, 460, 746
hormone production, 123, 840
large bowel, 644, 660, 661
small bowel, 626, 633
- somatostatin receptor scintigraphy,
6W661,761,702
- stomach|duodenum, 599, 600
thymus, 65
- Carcinosarcoma
lung, 122
oesophagus, 569, 570
- Cardiac anatomy, 265-71
morphological approach to congenital
cardiac disease, 364-5
ventricular wall
terminology, 271
thickness, 265
- Cardiac catheterisation
aortic coarctation, 380-1, 382
atrial septa] defect, 375
atrioventricular septal defect, 390-1
complications, 417
congenital cardiac disease, 348, 363,
364,406-7
contrast media, 407
coronary angiography *see* Coronary
angiography
historical aspects, 411
indications, 347-8
interventional procedures, 358-62,
364
infra-aortic balloon pump support,
361
left ventricular angiography, 348,
349,350
patent ductus arteriosus, 377
pulmonary stenosis, 379
right heart, 356
screening of prostheses, 362
tetralogy of Pal lot, 384
total anomalous pulmonary venous
connection, 397
transposition of great arteries, 387-8
vascular access, 357
ventricular septa] defect, 373-4
- Cardiac contour, 271, 272, 283, 284-6,
317
- Cardiac disease, acquired, 317-45
childhood disorders, 402-4
plain chest film, 283-316
postcardiac surgery, 291, 292-3
- Cardiac disease, congenital, 363-410
adult patients (grown-up congenital
cardiac disease), 363
associated congenital
emphysemal|loharoverinflation,
251
associated oesophageal atresia, 852
birth asphyxia, 370
cardiac catheterisation, 348, 363,
364,406-7
cardiac connections, 367
chest X-ray appearances, 9, 405,
406
circulation
common mixing, 370
left-|right-sided obstruction, 370
left-to-right shunt, 369
classification, 365-70
developmental aspects, 368-9
imaging techniques, 318, 319, 320,
405-7
incidence, 363, 371
interventional catheter techniques,
363,364
looping (topology), 367
malformations, 367-8
morphological approach, 364-5
obstetric ultrasound examination,
1055-6

- physiological changes at birth, 369
position, 367
situs variations, 365-7
surgery, 363-4
- Cardiac enlargement, 283, 284-6
oesophageal extrinsic impressions, 573
- Cardiac failure, 74, 87, 318
high-output, 440
- Cardiac fat pad, 307
- Cardiac fibroma, 308
- Cardiac foreign body retrieval, 361
- Cardiac imaging
angiography, 279-81, 282, 320
chest X-ray, 5-6, 271-3, 275, 317-18
computed tomography (CT), 278-9, 280, 319, 1839-40
echocardiography, 273-7
transoesophageal, 318-19
transthoracic, 318
fetal heart, 1055
invasive/interventional techniques, 347-62
magnetic resonance imaging (MRI), 279, 280, 281, 319-20, 1825, 1826
radionuclide imaging, 277-8, 319
- Cardiac implants, 294-5
- Cardiac lipoma, 337, 338
- Cardiac masses/tumours, 307-9
primary, 308-9
secondary, 309
- Cardiac rhabdomyoma, 308, 1055, 1056
- Cardiac size, 271, 283-4, 317
intensive care postoperative X-ray, 290
transverse diameter, 5
- Cardiac surgery
incisions, 228, 292
postoperative chest, 227, 228-9, 292-3
devices seen on plain film, 293
postoperative haemorrhage, 227, 228, 292
see also intensive care patient
- Cardiac transplantation, 239, 293-4
- Cardiac trauma, 224
- Cardiac tumours, 336-8
benign, 336-7
children/neonates, 402-3
fetal sonographic detection, 1055, 1056
incidence, 336
lymphoma, 337
magnetic resonance imaging (MRI), 338
malignant, 337-8
metastases, 337
- Cardiac steel filter, 452
- Cardiogenic pulmonary oedema, 180
- Cardiomyopathy, 322-6
dilated, 299, 322-3
hypertrophic, 299, 323-5, 329, 403
infants/children, 403
restrictive, 299, 325-6
- Cardiopulmonary transplantation, 239-42
heart, 239, 293-4
lung, 239-42
lymphoproliferative disease following, 242, 293
- Cardiothoracic ratio, 5, 272-3, 283-4, 290
children/neonate, 249, 273, 284
Caroli's disease, 721, 725, 937
- Caroticotympanic artery, 1679
- Carotid angiography, 411, 1676, 1678-82
carotid siphon, 1679
cerebral veins, 1682-3
complications, 1677-8
congenital anomalies of intracranial circulation, 1688-90
external carotid, 1679, 1683
internal carotid, 1679
tonsillar loop, 1679
- Carotid arteries
aberrant, 1599, 1605, 1606
aneurysm, 464
dissection, 465
Doppler ultrasound examination, 461, 462, 463-5, 466
indications, 462-4
magnetic resonance angiography, 474, 475, 478-9
high-resolution imaging, 1825
stent placement, 451, 1709-10
- Carotid artery stenosis, 1509
carotid bifurcation, 1675
Doppler ultrasound examination, 463-5
accuracy, 465
diagnostic criteria, 464
internal carotid artery occlusion, 464
intima-medial thickness (IMT) measurement, 465
plaque morphology, 464
percutaneous transluminal angioplasty, 450, 1709-10
stent insertion, 451, 1709-10
- Carotid body tumour, 1501, 1502, 1510, 1511
angiography, 445
Doppler ultrasound, 464, 465
- Carotid endarterectomy, 1703, 1709, 1710
- Carotid space
anatomy, 1509
aneurysm, 1501, 1502
lesions, 1501-3
masses, 1510-11
- Carotid-cavernous fistula, 1568-9, 1580, 1581, 1584, 1585, 1710, 1712
traumatic, endovascular occlusion, 1711-12
- Carpal bone fusions, 1108-9
- Carpal tunnel syndrome, 1244
- Carpenter's syndrome, 1624
- Carpus
dislocation, 1409-10
fractures, 1378, 1408-9
- Cartilage-hair hypoplasia, 1137
- Castleman's disease, 70, 72
- Cat scratch fever, 537
- Cataract, 1554
- Catheter clot embolus, 422, 437
- Caudal regression syndrome, 1652
- Caustic oesophagitis, 559
- CAVATAS (Carotid and Vertebral Artery Transluminal Angioplasty Study), 1708
- Cavernosography, 906, 1035, 1036
- Cavernous sinus fistula, 1697, 1698
- Cavernous sinus thrombosis, 1705
- Cavitating pulmonary lesions, 22-3, 37
bacterial pneumonia, 132
lung cancer, 109, 113
metastatic tumours, 117
tuberculosis, 141
- Cavum Vergae cyst, 1731
- Cellulitis, 483, 1426, 1432, 1435
orbit, 1520, 1521, 1578
- Cementoma, 1535, 1544
- Cementum, 1531
- Central European encephalitis, 1792
- Central nervous system
interventional neuroradiology, 1707-22
lymphomas, 525-6, 529
- Central neurocytoma, 1747
- Central pontine myelinosis, 1800
- Central retinal artery occlusion, 1554
- Central retinal vein occlusion, 1554
- Central venous catheters, 232, 233, 293, 454
- Cephalhaematoma, 1641
- Cerebellar atrophy, 1795, 1797
- Cerebellar tonsils, 1650
ectopic, 1650
- Cerebral abscess, 1520, 1783-4, 1790
- Cerebral atrophy, 1794-5
focal, 1794
generalised, 1794
post-traumatic, 1782
pseudotrophy, 1795
- Cerebral contusion, 1780, 1781, 1782
- Cerebral cystic lesions, 1763-6
infant/neonate, 1809, 1810
- Cerebral embolus, 1700
- Cerebral hypoxic ischaemic brain damage, 1778
- Cerebral infarcts, 1774-8
computed tomography (CT), 1774-7
haemorrhagic, 1777
head injury, 1782
diffuse traumatic brain damage, 1781
magnetic resonance imaging (MRI), 1777-8
venous and sinus thrombosis, 1777
watershed, 1775
- Cerebral infection, 1783-94
post-traumatic, 1783
- Cerebral oedema, 1780
cerebral abscess, 1784
diffuse traumatic brain damage, 1781
pyogenic meningitis, 1785
- Cerebral tumours, 1739-66
age incidence, 1739
angiography, 1705
classification, 1740
embolisation, 1716
epidemiology, 1739
epilepsy, 1804, 1805
lymphoma, 525, 1753-4
magnetic resonance spectroscopy, 1826-7
metastatic, 1631, 1761-3
plain skull film, 1627-8
intracranial calcification, 1628-31
skull erosions, 1637-8
- Cerebral vasospasm, 1708-9
intracranial balloon angioplasty, 1709
- Cerebral veins, 483
carotid angiography, 1682-3
thrombosis, 1705
- Cerebritis, 1783-4
- Cerebrospinal fluid fistula, 1783
- Cerebrospinal fluid
otorrhoeal/rhinorrhoea, 1389, 1642
- Cerebrovascular disease, regional
cerebral blood flow imaging, 1813
- Cervical carcinoma, 1091, 1097-100
- destructive bone lesions, 1253
- FIGO/TNM staging, 1097
- lymphadenopathy, 1099
metastases, 1248
recurrent disease, 1100, 1101
- Cervical cerclage, 1065
- Cervical lymph nodes, 510-I 1
anterior superficial (external jugular), 511
deep (internal jugular) chain, 511
groups/levels, 511
inflammatory adenopathy, 1510, 1511
metastases, 1510, 1511
ultrasound, 1515-16
- Cervical rib, 432, 1109, 1120
- Cervical spine
C2/C3 pseudoluxation in children, 1393
degenerative disease, 1227, 1229, 1230
imaging, 1644
myelography, 1646-7
normal radiographic anatomy, 1392, 1394
trauma, 1392-9
associated aortic transection, 311
axial loading, 1397-8
burst fracture, 1398
classification, 1395
flexion teardrop fracture, 1395, 1396
hangman's fracture, 1396-7
hyperextension injuries, 1396-7
hyperflexion sprain, 1395, 1396
Jefferson fracture (C1 burst fracture), 1397-8
odontoid fracture, 1398
rotational injuries, 1398, 1399
spinous process fracture, 1398
unilateral facet dislocation, 1396
wedge fracture, 1395
- Cervicothoracic sign, 14
- Cervix, 1070, 1078, 1090, 1093, 1094
obstetric ultrasound evaluation, 1065
- Cestode infection *see* Cysticercosis:
Tapeworm
- Chagas' disease, 76, 553
- Chamberlain's line, 1625, 1626
- Chance fracture, 1400
- Charcot joints, 1386
- Chemodectoma (chromaffinoma), 75, 833
angiography, 445-6
preoperative embolisation, 458
- Chemotherapy, intra-arterial, 455
head and neck tumours, 1719-20
hepatocellular carcinoma, 455, 458
- Cherubism, 1539, 1544
- Chest imaging, 1-54
barium swallow, 2
bronchial arteriography, 47
bronchography, 45
computed tomography (CT), I, 30-7, 45
diagnostic pneumothorax, 2
fluoroscopy, 29
magnetic resonance imaging (MRI), 2-38
paediatric chest, 247-62
plain film, I, 2-29
positron emission tomography (PET), 43-4
pulmonary angiography, I, 46-7
radionuclide imaging, I, 38-43
toniography, I, 29
ultrasound, I, 45-6

- Chest pain, non-cardiac, 550
- Chest trauma, 217-24
- Chest wall, II
- cardiac disease-related changes, 290
 - imaging, 47-54
 - artefacts, 50
 - bones, 47-50
 - diaphragm, 51-4
 - soft tissues, 50-I
 - trauma, 217-18
- Chiari malformation, 267, 270, 1652, 1653, 1728-9
- Chickenpox, 1791
- pneumonia, 24, 25, 136, 137, 138
- Chilaiditi's syndrome, 1f, 12, 667, 742
- Children
- biliary tract disorders, 720-2
 - fractures, 1383-5
 - patient support, 849
 - urogenital tract investigation, 923-6
 - see also* Paediatric abdomen; Paediatric chest
- Chlamydia psittaci* pneumonia (psittacosis; ornithosis), 131, 135, 137
- Chlamydia trachomatis*, 1017, 1024
- Chlonorchis sinensis*, 730
- Chlorine inhalation, 195
- Cholangiocarcinoma, 729, 731-2, 757, 772, 783, 1248
- biliary drainage/stenting, 733
- Cholangiography
- intravenous, 719
 - operative, 719-20
 - percutaneous (PTC), 719
- Cholangiopathies of childhood, 722
- Cholangioscopy, 733
- Cholecystectomy, 725, 727
- Cholecystitis
- acalculous, 715, 723, 881
 - acute, 685-6, 715
 - biliary scintigraphy, 686, 718
 - childhood, 722, 881
 - chronic, 715, 716
 - emphysematous, 686, 687, 713, 714, 723
 - gallstones (calculous cholecystitis), 723, 881
 - localised ileus (sentinel loop), 621
 - ultrasound, 685-6, 715, 716
 - xanthogranulomatous, 724
- Cholecystitis glandularis proliferans (gallbladder adenomyomatosis), 724, 725
- Cholecystoduodenal fistula, 602
- Cholecystography, 718-19
- Choledochal cyst, 717, 720-1, 725, 733, 760, 880
- classification, 721, 880-1
- Choledochal fistula, 733
- Choledochal varices, 731
- Choledocholithiasis *see* Bile duct stones
- Cholchiliasis *see* Gallstones
- Cholesteatoma, 1607-9
- acquired, 1608-9
 - congenital, 1607
- Cholesterol deposits, 715
- Cholesterol embolus, 422, 437, 449
- Cholesterol granuloma, 1607, 1608
- Cholesterosis of gallbladder, 723-4
- Chondroblastoma, 1249, 1269, 1276-7
- Chondrocytoma, 69
- Chondrodystrophia calcificans
- congenita (chondrodysplasia punctata: dysplasia epiphysealis punctata), 1134-5
- Chondroectodermal dysplasia *see* Ellis-van Crevald syndrome
- Chondroma, 49, 1269, 1272-6
- intracranial, 1761
 - juxtacortical, 1275, 1276
 - laryngeal, 1498, 1499
 - tracheo bronchial, 124, 161
- Chondromyxoid fibroma, 1269, 1277-8
- Chondrosarcoma, 1250, 1272, 1281-5, 1761
- central, 1269, 1281, 1282
 - clear cell, 1285
 - mesenchymal, 1284, 1285
- Chordoma, 1305-6, 1307
- intracranial calcification, 1631
 - mediastinal mass, 69
 - nasopharynx, 1494
 - presacral space widening, 654
 - skull base/intracranial extension, 1760-I
 - skull erosion, 1636
 - spine, 1661
- Choriocarcinoma, mediastinum, 66
- Chorionic villus sampling, 1048
- Choristoma (granular cell tumour; pituicytoma), 1765
- Choroid plexus calcification, 1622, 1630
- Choroid plexus cyst, 1053
- Choroid plexus papilloma, 1630
- Choroid plexus tumours, 1746
- Choroidal detachment, 1557, 1576
- Choroidal haemangioma, 1563
- Choroidal melanoma, 1560-2
- Choroidal osteoma (osseous choristoma), 1562-3
- Christmas disease, 1346
- Chromaffinoma *see* Chemodectoma
- Churg-Strauss syndrome (allergic angiitis and granulomatosis), 200, 202
- Chyloma, 228
- Chylothorax, 2, 88, 224, 228
- Ciclosporin nephrotoxicity, 984
- Ciliary body, 1552
- melanoma, 1560-2
- Cineradiography
- pharynx/larynx examination, 1489, 1491
 - swallowing disorders, 1489, 1495
- Circle of Willis
- aneurysm, 1675
 - subarachnoid haemorrhage, 1692
 - congenital anomalies, 1688
 - magnetic resonance angiography, 479
 - transcranial Doppler ultrasound, 462, 466
- Cirrhosis, 737, 743, 749, 755-6, 766-7, 779, 783
- portal hypertension, 767, 779
 - portal vein thrombosis, 768
- Cisterna chyli, 509
- Cladosporiosis, 1786
- Clavicle, 12, 47
- fracture, 218, 1404
- Clay shoveller's fracture, 1398
- Clear cell carcinoma
- bronchus, 124
 - ovary, 1082
 - renal cell, 480
- Clear cell chondrosarcoma, 1285
- Clear cell renal sarcoma, 874-5
- Cleft palate, 1538
- Cleidocranial dysplasia (cleidocranial dysostosis), 47, 1114, 1122-3, 1539, 1540, 1625-6
- Clinodactyly, 1107
- Clostridium difficile*, 651, 680
- Clostridium perfringens*, 1433
- Clostridium welchii*, 686, 687, 723
- Club foot (talipes equinovarus), 1115-16
- Coagulation disorders, skeletal abnormalities, 1346-9
- Coal worker's pneumoconiosis, 191-2
- progressive massive fibrosis, 191, 193
- Coats' disease, 1563, 1591
- Cobblestone duodenal cap, 586
- Cocaine abuse, nasal granuloma, 1523
- Coccidioidomycosis, 25, 72, 80, 145, 149, 157, 1659
- honeycomb lesions, 1176
 - central nervous system, 1786
- Cochlea, 1598, 1599
- congenital bony abnormalities, 1601, 1602, 1603
- Cochlear implants, 1607, 1608, 1614
- Cockayne's syndrome, 1634, 1798
- Codman's triangle, 1154
- Coeliac artery stenosis, 450
- Coeliac axis, 810, 812
- congenital anomalies/anatomical variations, 423, 812
 - Doppler ultrasound examination, 472
 - stenosis, 431, 472
- Coeliac compression syndrome, 429, 431
- Coeliac disease (gluten-sensitive enteropathy), 598, 625, 629
- Coenurosis, 1791
- Coil embolisation, 456, 457, 458, 459
- intracranial aneurysms, 1712-14
- Cold virus pneumonias, 131
- Colectomy and ileorectal anastomosis, 650
- Colitis, 646
- acute, 679-80
 - children, 871-2
 - eosinophilic, 652
 - infective/non-infective, 651-2
 - ischaemic, 651, 652, 680
 - microscopic, 652
 - neutropenic (typhlitis), 632, 652, 872
 - pseudomembranous, 651, 680
 - radiation, 652
- Collagen vascular diseases *see* Connective tissue disorders
- Collateral ligament damage, 1235, 1238
- Colles' fracture, 1408
- Colloid cyst, 1765
- Coloboma, 1587, 1588
- Colon, 635, 665
- Colon cancer
- gastrointestinal invasion, 597-8
 - metastasis tumours, 644
 - pulmonary metastases, 117
 - see also* Colorectal cancer
- Colonic angiodysplasia, 653
- Colonic atresia, 859, 861, 862
- Colonic functional immaturity (small left colon syndrome), 859, 861
- Colonic lymphoma, 644
- Colonic malrotation, 635
- Colonic motility, 635-6
- Colonic transit studies, 637
- Colonoscopic colorectal cancer screening, 644
- Colorectal cancer, 640-2, 646
- adenoma-carcinoma sequence, 640-I
 - bladder fistulas, 994
 - colorectal stenting, 642, 643
 - Crohn's disease-related risk, 649
 - Dukes's staging, 641
 - familial adenomatous polyposis-related risk, 639, 641
 - familial risk, 641
 - large bowel obstruction, 676
 - metastases, 642, 757, 1251, 1253
 - positron emission tomography (PET), 1830
 - recurrent disease, 643
 - screening, 644
 - small bowel obstruction, 673
 - TNM classification, 641
 - ulcerative colitis-related risk, 648
- Colorectal polyps, 637-40
- polyposis syndromes, 637, 638-9, 1540
- Colorectal stenting, 642, 643
- Colorectal tumours, 637-44
- Colour flow ultrasound
- acute pancreatitis, 817
 - aortic coarctation, 382
 - arterial imaging, 412
 - atrial septal defect, 375
 - atrioventricular septa) defect, 390
 - carotid artery stenosis, 464
 - carotid/cerebral vessel imaging, 1675
 - cavernous liver haemangioma, 770
 - dialysis graft examination, 467, 468
 - Doppler echocardiography, 274, 276
 - epididymo-orchitis, 471
 - equipment, 461
 - eye, 1553-4
 - hepatic vein thrombosis (Budd-Chiari syndrome), 469, 768
 - orbital carotid-cavernous fistuladural cavernous arteriovenous malformation, 1569
 - paediatric abdomen, 851
 - patent ductus arteriosus, 377
 - peripheral artery bypass graft occlusion, 466
 - portosystemic shunt patency assessment, 769
 - pulsatile necklumps, 464
 - total anomalous pulmonary venous connection, 397
 - transcranial Doppler ultrasound, 465
 - ureteric obstruction, 471
 - uterine arteriovenous malformation, 1092
 - ventricular septal defect, 373
 - vertebral artery stenosis, 415
- Colovesical fistula, 645, 994
- Common atrium, 370
- Common bile duct, 711, 796
- obstruction, 686, 716, 813
 - stones, 725-7
- Common carotid artery, 268, 269
- catheterisation, 418
- Common femoral artery
- Doppler ultrasound, 461, 466
 - false aneurysm, 467
- Common iliac artery aneurysm, ureteric displacement, 980
- Common truncus arteriosus, 370
- Communicating veins, 485, 486

- Compartment syndrome, 1381, 1425
 Complete spontaneous abortion, 1045
 Computed tomography (CT)
 adrenal glands, 826, 827
 adrenal masses, 829-30, 833
 aneurysms, 425, 1770
 aortic dissection, 339-40, 414, 428
 aortic rupture, 224
 appendicitis, 684-5
 arterial imaging, 412-13
 aspergilloma, 147
 biliary tract, 717
 bone density measurement, 1352
 bone tumours, 1249-50
 bronchial carcinoma, 108, 109, 110, 111, 113, 115, 116, 124-5
 cardiac disease, congenital, 405-6
 cardiac imaging, 278-9, 280, 319, 331, 1839-40
 colorectal cancer, 642
 contrast media, 515, 795, 927, 1724
 Crohn's disease, 623-4
 duodenum, 576
 emphysema, 169, 170
 gastric carcinoma staging, 594
 glossary of terms, 1850-1
 gynaecological imaging, 1090-2
 head injury
 acute trauma, 1779-82
 extradural haematomas, 1779
 indications, 1778-9
 subdural haematomas, 1779-80
 high resolution (HRCT), 33-4
 adult respiratory distress syndrome, 244
 asbestosis, 194, 195
 asthma, 166
 bronchiectasis, 163, 164, 165
 bronchiolitis, 173
 cryptogenic organizing pneumonitis (COP), 173
 diffuse lung disease, 187
 idiopathic pulmonary fibrosis, 205
 opportunistic pulmonary infections, 153
 paediatric chest, 247-8
 pleural plaques, 193
 Pneumocystis carinii pneumonia, 154
 sarcoidosis, 188, 189
 silicosis, 191
 inflammatory bowel disease, 650
 intra-abdominal sepsis, 682
 intracranial lesions, 1723-4, 1725
 aneurysms, 1770
 intracerebral haematoma, 1767-8
 large bowel, 637
 liver, 753-8
 lungs, 30-7
 collapse, 176, 177, 180, 182
 lymph nodes, 515
 micrometastases, 516
 lymphoma
 abdomen, 528
 head and neck, 528-9
 stomach, 599
 thorax, 526-8
 malignant disease
 staging, 519, 567-9, 599
 treatment response evaluation, 520
 mediastinum, 58, 59, 60-1, 81, 111
 neck, 1509-12
 obstetric imaging, 1065
 oesophageal cancer staging, 567-9
 oesophagus, 543-4
 orbit, 1574
 osteomyelitis, 1 158
 paediatric abdomen, 851
 paediatric chest, 247-8
 Paget's disease, 1194-5
 pancreas, 787, 795-6
 pericarditis/pericardial effusion, 333-4
 pericolic abscess/peritonitis, 645
 petrous temporal bone, 1597-8, 1599, 1600, 1601, 1602
 pheochromocytoma, 843-4
 pharynx/larynx, 1489-90, 1492
 pleural disease, 37
 pleural effusion, 88, 91, 92-3, 97
 pneumoperitoneum, 666-7
 pulmonary embolism, 342
 recent technical advances, 1836-41
 advantages of rapid scanning, 1840-1
 computing requirements, 1836-7
 CT 'fluoroscopy', 31, 1837
 image processing, 1839-40
 multidetector CT, 1837-8
 multislice helical CT, 1840-1
 radiation dose, 1838-9
 slip rings, 1836
 X-ray tubes/detectors, 1836
 rheumatoid arthritis, 1209
 salivary glands, 533-4, 535-6
 sinuses, 1519
 small bowel, 618
 small bowel obstruction, 619-20, 671, 672
 soft tissues, 1442-5
 spine, 1644-5
 spleen, 753, 758-9
 stomach, 576, 577
 subarachnoid haemorrhage, 1768-9, 1770
 thoracic biopsy guidance, 31
 trauma, 1415-16
 abdomen, 691
 aortic arch aneurysm, 425
 bladder, 704
 bowel, 705
 chest, 217
 facial bones, 1390-1
 head, 1778-82
 kidney, 700-1, 702, 973-4
 liver, 695-6
 major vessels (IVC/aorta), 707
 pancreas, 704, 705
 pelvis, 1404
 skull fracture, 1389
 spine, 1391-2, 1393
 spleen, 692-3, 694, 695
 urogenital tract, 906, 910
 children, 925-6
 veins (phlebography), 483
 Computed tomography (CT)
 angiography, 412-13, 417, 1837
 carotid/cerebral imaging, 1674-5
 complications, 1678
 pulmonary angiography, pulmonary embolism imaging, 238, 239
 Computed tomography (CT)
 cisternography, 1727, 1783, 1795
 Computed tomography (CT)
 fluoroscopy, 31, 1837
 Computed tomography myelography (CTM), 1645, 1647-8
 Condylomata acuminata (venereal warts), 1020
 Conjoined twins, 1063
 Connective tissue disorders
 bronchiectasis, 163
 diffuse lung disease, 197-202
 pleural effusion, 87
 pulmonary eosinophilia, 204
 tracheal widening, 163
 valvular heart disease, 327
 Conn's syndrome (primary hyperaldosteronism), 495, 826, 840-1
 adrenal cortical adenoma, 835, 840, 841, 842
 adrenal cortical carcinoma, 835, 840
 adrenal scintigraphy, 831-2, 833
 blood sampling/hormone assay, 829
 Conradi-Hunermann syndrome, 1 135
 Conray *see* lothalamate meglumine
 Constipation, 653
 Constriction rings (Streeter's hands), 1 107, 1177
 Constrictive pericarditis, 74, 87, 306, 307
 Continuous diaphragm sign, 221
 Continuous-wave Doppler
 echocardiography, 274, 275
 equipment, 460
 Contrast echocardiography, 276-7
 Contrast media
 brain damage following cerebral angiography, 1677
 computed tomography (CT), 515, 795, 927, 1724
 congenital cardiac disease, 407
 coronary angiography, 350, 351, 420
 intravenous cholangiography, 719
 lymph node imaging, 515
 magnetic resonance imaging (MRI), 1827-9
 extracellular space agents, 1827
 liver-specific, 778
 ultra-small superparamagnetic iron oxides, 1827, 1828
 myelography, 1645, 1646
 injection errors, 1647
 nephrotoxicity, 927
 non-ionic, 926-7
 percutaneous arterial catheterisation, 419
 dosage, 419-20
 phlebography, 486
 reactions, 420, 486, 891, 893, 926, 1645-6
 drug interactions, 927
 iodism, 420-1
 management, 927
 mild/intermediate/severe, 420
 nephrotoxicity, 421
 organ damage, 422
 risk factors, 420
 treatment, 420, 421-2
 sialography, 535
 small bowel examination, 617-18
 ultrasound, 763
 urogenital tract investigations, 926-7
 see also Barium studies
 Contrast phlebography, 483
 Contrast studies
 acute abdomen, 668, 671
 gynaecological imaging, 1085-90
 paediatric abdominal imaging, 849-50
 Cooley's anaemia *see* Thalassaemia
 Copper deficiency, 1367
 Cor triahiatum, 394
 Core biopsy, breast lesions, 1458, 1462, 1464, 1467, 1473, 1475
 stereotactic-guided, 1481
 ultrasound-guided, 1480
 vacuum-assisted, 1481-2
 Cornea, 1551-2
 Cornual polyps, 1089
 Coronal cleft vertebra, 1117
 Coronary angiography, 279-80, 347, 350-4
 complications, 350, 353, 422
 contrast media, 420
 injection dose, 350, 351
 coronary artery pathological appearances, 354-5
 examination procedure/projections, 351-2
 mortality risk, 353
 percutaneous Seldinger approach, 280
 safety requirements, 350-1
 vascular access, 357
 Coronary angioplasty, 358-9
 see also Percutaneous transluminal angioplasty, coronary arteries (PTCA)
 Coronary arteries, 269-71, 273, 274, 309
 calcification, 295, 296, 320, 1839, 1840
 congenital abnormalities/anatomical variations, 355, 356, 357, 401
 intravascular ultrasound, 1835
 left ventricular angiography, 348
 Coronary artery aneurysm, 354, 355
 Kawasaki's disease, 428-9
 Coronary artery bypass graft, 228
 devices seen on postoperative plain film, 293
 graft angiography, 355, 356
 Coronary artery dissection, 354, 355
 Coronary artery stenting, 293, 358, 359, 360, 451
 Coronary fistula, 354, 355
 Coronary heart disease, 295-9, 320-2, 347, 354, 429, 451
 screening, 320
 stable angina, 321
 see also Myocardial infarction
 Coronary sinuses, 269-70, 273
 Corpus callosum agenesis, 1055, 1066, 1688, 1731-3
 Corpus callosum lipoma, 1732, 1733
 Corpus luteum, 1072
 Corpus luteum cyst, 1102
 Corrosive oesophageal stricture, 558, 559
 Corticobasal degeneration, 1797
 Costophrenic angles, 7
 Cough fracture of ribs, 49, 217-18
 Covered arterial stents, 451
 Cowden's disease, 564, 589, 627, 639
 Cowper's duct syringocoele, 1017
 Cowper's glands, 1017
 Coxa vara
 acquired, 1114
 idiopathic of childhood, 1 113, 1114
Coxiella burnetii infection (Q fever), 131, 135, 137-8
 Cranial meningocele, 1625
 Cranial nerves, 1574
 orbital anatomy, 1574
 tumours, 1758-9
 vascular compression, 1772
 Craniofacial microsomia, 1605
 Craniometaphyscal dysplasia, 1640

- Craniopharyngioma, 1752-3
 intracranial calcification, 1628-9,
 † 630
 skull erosion, 1637, 1638
- Craniosynostosis, 1624-5
- CREST syndrome, 197
- Cretinism see Hypothyroidism*
- Creutzfeldt-Jakob disease, 456, 1797
- Crohn's disease, 621-4, 991, 994, 995,
 † 353
 aphthous ulceration, 648, 649
 children, 870, 872, 883
 colonic disease, 621, 648-9
 duodenitis, 586
 gastric involvement, 580
 gastrointestinal malignancy
 associations, 625, 649
 inflammatory polyps, 637, 638
 joint disease, 1216, 1221
 non-caseating granuloma, 648
 peritoneal abscess, 633
 postinflammatory polyposis, 649
 postoperative appearances, 622-3
 radionuclide imaging, 659, 660
 small bowel disease, 617, 621-2
 obstruction, 618, 673
 surgery, 651
 toxic megacolon, 648
 ulcerative colitis differentiation, 650
- Cronkhite-Canada syndrome, 627,
 638-9
- Croup (laryngotracheobronchitis), 161,
 † 497
- Croton's disease (hereditary
 craniofacial dysostosis), 1624
- Crown-rump length, 1041, 1044
- Cruciate ligament damage, 1235, 1238
- Cryptococcosis (torulosis), 146, 149,
 † 54, 157, 1786, 1787, 1793
- Cr. vptococcus aeu%onrums*, † 46, 157,
 880, 882
- Cryptogenic fibrosing alveolitis
 (unusual interstitial
 pneumonitis), 204-6
- Cryptogenic organizing pneumonitis
 (COP), 173, 174
- Cryptorchidism (undescended testes),
 † 022, 1028, 1033
- Crvlnsporidiron*, 586, 628, 729, 821,
 870
- Curtis-Fitz-Hugh syndrome, 1081
- Cushing's disease, 49
 adrenal tumour embolisation, 458
 osteoporosis, 1358, 1359
- Cushing's syndrome, 66, 495, 826,
 839-40, 1539
 adrenal cortical adenoma, 835, 839
 adrenal cortical carcinoma, 835, 839
 adrenal scintigraphy, 831, 833
 adrenal tumour embolisation, 458
 micronodular adrenal dysplasia, 840
 osteoporosis, 839
- Cutis laxa, 162
- Cystadenocarcinoma, hilar tract, 732
- Cystadenoma
 biliary tract, 732, 769
 liver, 780
- Cystic adenomatoid malformation of
 lung, 252-3, 254
 fetal sonographic detection, 1057
- Cystic angiomatosis of bone, 1300,
 † 303
- Cystic duct, 711
 developmental anomalies, 712
- Cystic fibrosis, 34, 72, 165, 166, 1058
 bronchial artery embolisation, 248
 bronchiectasis, 163, 166, 167, 261
 colitis/fibrosing colonopathy, 652
 duodenal changes, 581
 intrahepatic cholangiopathy, 722
 lung disease, 42, 43, 152, 260-1, 262
 mconium dens, 859-60
mconium ilcus equivalent, 629
 mucoid impaction, 174
 pancreatic disease, 789, 791, 820
 pneumothorax, 165, 167
 small bowel
 involvement/intimal absorption, 629
- Cystic hygroma, 68, 81, 262, 1056,
 † 057
 neck, 1501
 soft tissues, 1426, 1427
- Cystic pneumatosis (pneumatosis
 cystoides intestinalis), 687
- Cysticercosis, 51, 1437
 brain infection, 1790, 1804
 intracranial calcification, 1633,
 † 634
- Cystinuria, 967
- Cystitis
 acute bacterial, 991
 chronic, 991
 emphysematous, 687-8, 991
 encrustation, 993
 focal, 991
 haemorrhagic, 993
 interstitial, 993
 viral, 991
- Cystocele, 994
- Cystography, 898-9, 927
 radionuclide, 917-18, 920-1
- Cylomegalovirus, 586, 729, 790
- acute pancreatitis, 820-1
 colitis, 652
 encephalitis, 1793
 intracranial calcification, 1633
 ocular infection, 1592
 oesophagitis, 558, 559, 866
 pneumonia, 88, 137, 157, 260
 small bowel infection, 628
- Cytotoxic drugs, pulmonary toxicity,
 210
- Dacryoadenitis, 1594
- Dacryocystography, 1573, 1594
- Dactylosis spontanea (ainhum), 1177
- Dandy-Walker syndrome, 1053, 1054,
 † 060, 1728, 1729, 1809, 1810
- Dandy-Walker variant, 1730
- De Morsier's disease (septo-optic
 dysplasia), 1731
- de Quervain's (subacute) thyroiditis,
 † 507, 1514
- Deep central vein lipoma, 490
- Deep vein thrombosis, 483, 486-7,
 503-4, 505, 506
 C-reactive protein assay, 483, 485
 inferior vena cava filters, 453
 thrombolysis, 456
- Dcfecography (evacuation
 proctography), 637, 654
- Degenerative aneurysms, 424-5
- Degenerative arthritis *see Osteoarthritis*
- Degenerative disc disease, 1376, 1643,
 † 644, 1662
 degenerative changes, 1663
 disc prolapse, 1662-3
 postoperative changes, 1663-4
 spondylolisthesis, 1658
- Delphinian node, 511
- Dementias, 1795-6
 regional cerebral blood flow
 imaging, 1813-14
- Demyelinating disorders, 1799
- Dens in dente, 1538, 1544
- Dens fracture*, 1656
- Dens hypoplasia, 1656-7
- Dental abscess, 1532
- Dental caries, 1531-2, 1535
- Dental charting, 1531
- Dental cysts
 apical/radicular, 1542, 1543
 dentigerous/follicular, 1542, 1543
 primordial/dontogenic keratocyst,
 † 542, 1543
- Dental eruption, 1532
- Dental radiographic techniques, 1531
- Dentate nuclei calcification, 1623
- Dentigerous (follicular) cyst, 1542,
 † 543
- Dentine, 1531
- Dermal sinus, 1651
- Dermatomyositis/polymyositis, 197
 diffuse lung disease, 199, 200
 soft tissue calcification, 1439, 1440
- Dermoid cyst (benign cystic teratoma),
 † 079, 1085, 1091, 1103-4
 bone lesions, 1306, 1308
 intracranial, 1764-5
 calcification, 1629, 1631
 lacrimal gland, 1592
 mediastinum, 66
 orbit, 1582-3
 ovary, 1082-3
 presacral space, 654
 skull erosion, 1635, 1636
 spinal dysraphism, 1651
 spine, 1667
- Desmoid tumour
 chest wall, 69
 familial polyposis coli, 626, 627, 639
 ovary, 688
 peritoneal cavity, 633
 soft tissues, 1443-4
- Desmoplastic fibroma, 1287-8, 1289
- Desquamative interstitial pneumonitis,
 204
- Detrusor function, 921
- Detrusor instability/overactivity, 921
- Diabetes mellitus, 403, 976
 contrast media risks, 420, 421, 927
 infections, 979, 1163, 1432
 pancreatic ultrasound, 820
 vessel calcification, 412, 1435
- Diagnostic peritoneal lavage (DPL),
 691-2
- Diagnostic pneumothorax, 2
- Dialysis
 acquired arthropathy, 1311, 1312,
 † 313, 1365
 acquired renal cysts, 952
- Dialysis access grafts (fistulas), 467-8
 thrombolysis, 456
 venous stents, 452
- Diaphragm, 6-7, 8, 13
 congenital abnormalities, 254-6
 elevation, 52-3, 227
 movement, 52
 normal variants, 51-2
 thickness, 53
 traumatic laceration/rupture, 54,
 218, 560, 563
 tumours, 53
- Diaphragmatic eventration, 52, 255-6,
 863, 865
- Diaphragmatic hernia *see* Hiatus hernia
- Diaphragmatic hiatus, 554
- Diaphragmatic lymph nodes, 51, 1
- Diaphyseal aclasis (hereditary multiple
 exostosis), 1137-8, 1139, 1249,
 † 272, 1278, 1280, 1281
- Diastematomyelia*, 1652
- DICOM (digital imaging and
 communication in medicine),
 † 842, 1843
- Diethylstilboestrol (DES) exposure,
 uterine abnormalities, 1087,
 † 088
- Diffuse idiopathic skeletal hyperostosis
 (Forstner's disease, senile
 ankylosing spondylitis), 1221
- Diffuse infiltrating lymphocytosis
 syndrome (DIES), 882
- Diffuse liver disease, 755-6, 764-9,
 779
- Diffuse lung disease, I, 17-18, 19,
 † 87-214
- Diffuse oesophageal spasm, 550, 552
- Diffuse sclerosis (Schilder's disease),
 † 800
- DiGeorge syndrome, 65
- Digital cardiac angiography imaging,
 407
- Digital ischaemia, 433
- Digital mammography systems,
 † 452-3
- Digital obstetric ultrasound systems,
 † 041
- Digital subtraction angiography,
 415-16
 arch aortography, 1677
 carbon dioxide, 416, 417
 carotid/cerebral vessel imaging,
 † 675-6
 intravenous, 416, 417
 complications, 1678
 phlebography, 483
 spine, 1648
- Digital workflow, 1841-4
 acquisition devices, 1843-4
 E-mail, 1844
 electronic patient record (EPR),
 † 842
 electronic remote requesting system
 (RRS), 1842-3, 1844
 hospital information system (HIS),
 † 842
 image library/museum, 1844
 imaging equipment standards, 1842,
 † 843
 integration, 1841-2
 web-based, 1842
 on-line journals, 1844
 radiological information system
 (RIS), 1843
 speech recognition dictation system,
 † 844
 steps, 1841
 teaching modules, 1844
- Dilated cardiomyopathy, 299, 322-3,
 403
- Diploic vascular markings, 1619
- Direct arteriography, 418
 carotid/cerebral vessels, 1676-8
- Disciform lesions, 1556
- Discitis, infective, 1162, 1163
- Discography, 1228, 1649
- Discoid meniscus, 1235, 1236
- Dissecting aneurysm
 internal carotid artery, 1704
see also Aortic dissection

- Disseminated encephalomyelitis/
leucoencephalitis, acute, 1791
- Disseminated infiltrative lymphocytic
syndrome. 26(1)
- Diverticula, gastrointestinal
haemorrhage, 454
- Diverticular disease. 644-6
- Diverticulitis. 633, 645, 646, 991
- Diverticulosis, 441, 645
- Dolicephalic skull. 1624
- Dopamine transport system imaging,
1815-16
- Doppler equation. 460
- Doppler ultrasound, 460-72
abdominal vessels, 468-9
aorta. 472
carotid artery stenosis. 46, 3-5
echo-enhancing agents, 462
equipment, 460-2
colour Doppler. 461
continuous-wave Doppler, 460
Duplex Doppler, 460-I
power Doppler. 461-2
eye. 1553-4
fetoplacental/uteroplacental
circulation, 1046-7
gastric motility, 609
inferior vena cava. 472
intracranial vessels, 463-5, 1723
obstetric examinations, 1039
ovarian blood flow, 1(171), 1072
paediatric abdomen, 851
pancreatic adenocarcinoma, 814
pelvis
female, 471
male. 471-2
peripheral arteries, 466-8
portal hypertension. 767
principle, 460
recent technical advances, 1833-4
renal vein thrombosis, 965
stenosis measurement. 463
transcranial, 462, 465-6
uterine arteries. 1071
venous, 503-5
vertebral artery stenosis, 415
see also Colour flow ultrasound:
Duplex ultrasound:
Echocardiography
- Doppler-based indices, 463
- Dorsal meningeal artery, 1680
- Double aortic arch, 4(10), 853
- Double bubble sign, 855
- Double decidual sac sign. 1044, 1047
- Double inferior vena cava, 489, 491
- Double superior vena cava, 498
- Double-inlet ventricle, 367, 392, 393
- Double-outlet ventricle, 367, 399
- Down's syndrome see Trisomy 21
- Dracwtcuhts aiecliuen.sis* (guinea
worst), 1437
- Drash syndrome, 874
- Dressler's (post-myocardial infarction)
syndrome, 87, 298, 299, 321
- Driller's disease (vibration syndrome),
13811
- Dromedary diaphragm, 52
- Drug-induced oesophagitis, 559
- Drug-induced osteomalacia, 1353
- Drug-induced osteonccrosis, 1 181
- Drug-induced osteoporosis, 1366
- Drug-induced pancreatitis, 790
- Drug-induced pulmonary disease,
209-10, 211
- Drusen, 1556
- Dual photon absorption, 1351
- Dual X-ray absorption, 1351
- Duchenne muscular dystrophy, 1434
- Duct ectasia, 1470
- Ductal carcinoma in situ. 1469-70,
1471, 1477
- Ductography, 1482, 1483
- Dumping syndrome, 608, 610-I 1
gastric motility investigation, 61 I,
612
- Duodenal atresia, 855, 1057-8
- Duodenal disorders in children, 866
- Duodenal displacement, 599
- Duodenal diverticuluni, 604
- Duodenal duplication cyst, 590
- Duodenal extrinsic involvement, 601-2
- Duodenal haemangioma, 590
- Duodenal haematoma*, 630, 866
- Duodenal lipoma, 589-90
- Duodenal liposarcoma, 590
- Duodenal obstruction, neonate. 855-8
- Duodenal polyps, 588, 589
- Duodenal stenosis, congenital, 855
- Duodenal stromal tumours, 588
- Duodenal ulcer, 579, 581, 583-4
Helicobacter pylori, infection. 578
upper gastrointestinal haemorrhage,
440
see also Peptic ulcer disease
- Duodenal villous tumour, 588-9
- Duodenal web, 604, 855, 856
- Duodenitis, 585-7, 866
- Duodenum. 575-612
anatomy, 577-8, 615
examination methods, 575-6
- Duplex kidney. 933, 934-5
- Duplex ultrasound
angioplasty assessment, 449
arterial imaging. 412
equipment. 460-I
erectile dysfunction, 906, 1035-6
hepatic vein thrombosis
(Budd-Chiari syndrome), 768
intracranial vessels. 1723
portosystemic shunt patency
assessment, 769
- Duplex ureter, 933-4
- Duplication cyst, 859
- oesophagus, 564
small bowel, 866-7
stomach/duodenum, 590
- Dural arteriovenous fistula (dural
arteriovenous malformation),
1648, 1698-700
cavernous malformation, 1568-9
endovascular treatment. 1716, 1717,
1718
spine, 1719, 1720
percutaneous embolisation,
1699-700
selective external carotid
angiography, 1683
- Dural calcification, 1622-3
- Dural ectasia. 1654-5
- Dural sinus thrombosis, 1705
- Dynamic cystography, 898
- Dyschondroplasia (Caisson
disease), 1191, 1385
- Dyschondroplasia, 1249, 1275-6, 1281
- Dyschondrosteosis (Leri-Weil
syndrome). 1108, 1109, 1144,
1145
- Dysembryoplastic neuroepithelial
tumour. 1747
- Dysgerminoma, 1083
- Dyskinetic ciliary syndromes,
congenital. 152
- Dysmyelinating disorders. 1799
- Dysplasia epiphysealis
hemimelica (tarsoepiphyseal aplasia:
Trevor's disease). 1136-7
multiplex (multiple epiphyseal
dysplasia), 1135-6
punctata (chondrodystrophia
calcificans congenita:
chondrodysplasia punctata),
1134-5
- Dysplastic neuroepithelial tumour,
1805
- Dysraphism. 1651-2
- Dystrophia myotonica, 1640
- ## E
- E-mail for digital workflow, 1844
- Ear
carcinoma. 1611-12, 1614
congenital deformities. 1600-5
petrous temporal bone imaging
techniques. 1597-600
- Eastern equine encephalitis, 1792
- Ebslein's anomaly, 398
- Echinococcosis see Hydatid disease
- Echinococcus multilocularis*, 771
- Echo-enhancing agents, 462, 1835-6
- Echocardiography. 273-7
aortic coarctation, 380, 382
aortic valve regurgitation, 327
aortic valve stenosis, 326-7
atrial septal defect. 375
atrioventricular septa) defect, 375,
390
cardiac tumours, 336, 337
cardiomyopathy
dilated, 322
hypertrophic, 324-5
congenital cardiac disease, 363, 364,
405
left-to-right shunts, 369
continuous-wave imaging, 274, 275
contrast technique. 276-7
examination procedure. 274, 275-6
fetal, 403-4, 1055
M-mode imaging, 274, 275
mural valve regurgitation. 329, 330
mitral valve stenosis, 328
myocardial infarction, 321
patent ductus arteriosus, 377
pericarditis/pericardial effusion.
332-3
pulmonary stenosis, 379
pulsed-wave imaging, 274, 275-6
sinus of Valsalva fistula, 399
stress see Stress echocardiography
tetralogy of Fallot, 383
thoracic aorta pathology. 339
total anomalous pulmonary venous
connection, 397
transoesophageal, 276, 318-19
transposition of great arteries, 387
transthoracic. 318
truncus arteriosus, 398
two-dimensional imaging. 273
anatomical planes. 274, 275
ventricular septa) defect, 372-3
- Ectodermal dysplasia, 1108, 1539-40
- Ectopia lentis, 1554, 1555
- Ectopic kidney. 423
- Ectopic pancreatic tissue. 590-1, 790
- Ectopic pregnancy, 1045, 1047-8,
1179
- Doppler ultrasound. 471
pseudogestational sac, 1044
rupture, 688
- Ectopic lesion, 493
- Ectopic thyroid tissue. 1504, 1506
- Ehlers-Danlos syndrome. 73, 75, 162,
163, 309, 488, 937, 1439-40,
1655
- Eisenmenger's syndrome. 287-8, 369,
370
- Elastography, 1833
- Elbow joint imaging, 1243-4
- Elbow trauma. 1407
- Elderly people
gastric ulcer. 581
plain chest film. 28-9
- Electrocardiographically (ECG) gated*
blood pool scan, 3 19
- Electrocardiography, 609
- Electronic patient record (EPR), 1842
- Electronic remote requesting system
(RRS). 1842-3, 1844
- Ellis-van Creveld syndrome
(chondroectodermal dysplasia),
931, 1 109, 1 142, 1 144, 1145,
1537, 1540
- Embolic agents. 456, 171(1-1 1
- Embolisation, 447, 456-60
acute haemorrhage, 456-7
arteriovenous communication
(haemohilia). 735
carotid/vertebral artery test
occlusion. 1711
cerebral arteriovenous malformation,
1710, 171 1, 1714-15
cerebral tumours, 1716
complications, 459-60, 1714
direct percutaneous procedures in
head and neck. 1721
dural arteriovenous malformation
(dural arteriovenous fistula),
1699-700
epistaxis. 1712
glomusjugulare tumour, 1705
head and neck tumours, 1716
indications. 456
intracranial aneurysms. 1712-14
liver trauma, 697, 698
liver tumours, 443, 742, 744, 745-6
liver vascular lesions. 744
organ function ablation. 458-9
pelvic arterial injuries, 708
post-prostatectomy haemorrhage,
906, 908
renal arteriovenous abnormalities,
907
renal cell carcinoma, 906, 907
renal tract trauma, 703
spinal cord arteriovenous shunts,
1719, 1720
splenic artery. 752
splenic trauma. 694
testicular vein. 9(16), 909
transvenous, 497
traumatic carotid-cavernous fistula,
1711-12
tumour management. 458
uterine arteries, 1092
varicocele. 1024, 1025
vascular abnormalities, 458
vertebral tumours, 1720, 1721
- Embolus
cerebral. 1700
thrombolysis indications, 455
- Emboluses, 1710, 1717
- Embryonal cell carcinoma. 66

- Embryonal cell sarcoma, 879
- Embryonal rhabdomyosarcoma, 879
- Emphysema, 33, 168-72
- bullous, 42, 168, 169-70
 - centriacinar/centrilobular, 168, 171
 - chronic bronchitis, 167, 170-1
 - compensatory, 168, 172
 - congenital (congenital lobar overinflation), 251-2
 - definition, 165
 - intestinal, 687
 - lung scintigraphy, 41-2
 - ventilation/perfusion (VQ) imaging, 39, 40
 - mediastinal, 221
- obstructive, 28, 168, 171-2
- children, 260, 261
- panacinar, 168-9, 171
- paracatricial, 168
 - paraseptal, 168
 - pulmonary interstitial, 221, 243
 - premature infant, 257
 - subcutaneous, 217, 218, 221, 243, 244
 - surgical, 50-1, 79, 1433-4
- Emphysematous cholecystitis, 686, 687, 713, 714, 723
- Emphysematous cystitis, 687-8, 991
- Emphysematous enterocolitis, 687
- Emphysematous gastritis, 687
- Emphysematous pyelonephritis, 688, 942, 943
- Empty sella, 1637, 1766
- Empyema
- chest, 45, 87, 91-2, 94, 95, 98, 225-6
 - percutaneous drainage, 45-6
 - tuberculosis, 141
 - urokinase instillation, 92, 96
- epidural, 1785
- gallbladder, 686, 722, 723
 - subdural, 1785
- Enamel, 1531
- Encephalitis, vital, 1792
- Encephalocle, 1051, 1625
- Encephalomeningocele, 1728
- Encephalotrigeminal angiomatosis *see* Sturge-Weber syndrome
- Encrustation cystitis, 993
- Endocrine disorders
- fibrous dysplasia, 1 134
 - osteoporosis, 1358-66
- Endodermal sinus (yolk sac) tumour, 66
- Endometrial abnormalities, 1077-8
- Endometrial carcinoma, 1078, 1101-2
- Endometrial hyperplasia, 1077-8, 1087, 1088
- Endometrial polyp, 1077, 1087, 1088
- Endometrioid carcinoma, 1082, 1090-1
- Endometrioma, 1095
- Endometriosis, 1079-80, 1084, 1085, 1095-6
- interna (adenomyosis), 1075-6, 1077, 1089, 1096-7
 - large bowel involvement, 653
 - ureter involvement, 980
- Endometrium, 1070
- hormonal responses, 1073
 - thickness measurement, 1070
- Endomyocardial fibrosis, 325, 403
- Endoscopic bile duct interventions, 733-5
- Endoscopic monitoring, magnetic resonance imaging (MRI), 1446-7
- Endoscopic pycolysis (endopyelotomy), 903
- Endoscopic retrograde cholangiopancreatography (ERCP), 719, 787, 806-9
- chronic pancreatitis, 791, 792
 - pancreatic adenocarcinoma, 792
 - pancreatic pseudocyst, 792
- Endoscopic sphincterotomy, 733
- Endoscopic ultrasound, 1835
- biliary tract, 717
 - equipment, 544
 - gastric carcinoma staging, 594-5
 - gastric varices, 572
 - oesophageal cancer staging, 567
 - oesophagus, 544
 - pancreas, 787, 821
 - stomach/duodenum, 576, 577
- Endosteal apposition of bone ('bone within a bone'), 1324
- Endosteal cortical erosions, 1344
- Endotracheal intubation, 234, 292
- Endovascular aneurysm repair, 452, 453, 1712-14, 1715-16
- Endovascular neuroradiological procedures, 1707-21
- angioplasty/stenting
 - extracranial vessels, 1709-10
 - intracranial arteriosclerotic disease, 1710
 - carotid/vertebral artery test occlusion, 1711
 - cerebral arteriovenous malformations, 1714-15
 - cerebral vasospasm, 1708-9
 - dural arteriovenous shunts, 1716, 1717, 1718
 - intra-arterial chemotherapy, 1719-20
 - intra-arterial thrombolysis, 1707-8
 - intracranial aneurysms, 1712-14
 - spinal embolisation, 1720-1
 - spinal cord arteriovenous shunts, 1719, 1720
 - vertebral tumours, 1720, 1721
- technical aspects, 1707
- traumatic carotid-cavernous fistula, 1711-12
- tumour embolisation, 1716-19
- vein of Galen aneurysm, 1715-16
- Endovascular ultrasound *see* Intravascular Ultrasound
- Engelman's disease, 1640
- Enostosis (bone island), 1254, 1256
- Enlamoeha histolytica*, 771, 880, 1790
- biliary tract infection, 731
 - lung infection, 150
- Enteric cysts, 252
- Enteroclysis (small bowel enema), 616-17
- Enteropathic spondyloarthropathies, 1221
- Eosinophilic colitis, 652
- Eosinophilic gastritis/gastroenteritis, 580, 628
- Eosinophilic granuloma, 49, 1637
- skeletal abnormalities, 1340-2
 - see also* Langerhans' cell histiocytosis
- Eosinophilic pneumonia, 16, 17
- Epanutin teratogenesis, 1 107
- Ependymal cell tumours, 1744-6
- Ependymal cyst, 1730-1
- Ependymitis, 1784
- Ependymoma, 1630, 1666, 1744-6
- Epidermoid cyst
- intracranial, 1763-4
 - calcification, 1629
 - skull erosion, 1636
- lacrimal gland, 1592
- orbit, 1582-3
- presacral space, 654
- spinal dysraphism, 1651
- testes, 1028
- Epidermolysis bullousa, 549, 559
- Epididymal adenomatoid tumour, 1026
- Epididymal appendix torsion, 1027
- Epididymal cyst, 1023-4
- Epididymis, 890
- post-vasectomy appearances, 1024, 1025
- Epididymitis, 1023, 1024-6
- Epididymo-orchitis, 471, 1034
- Epidural abscess, 1785
- Epidural haematoma, acute, 1658, 1659
- Epidural space, 1650
- Epidiottis, 543
- Epilepsy, 1804-7
- classification, 1804
 - cortical developmental malformations, 1804, 1805-6
 - cortical scars, 1804, 1805
 - functional imaging, 1807
 - hippocampal sclerosis, 1804, 1805, 1806
 - neoplasms, 1804, 1805
 - neurosurgery, 1806-7
 - positron emission tomography (PET), 1831
 - regional cerebral blood flow imaging, 1815
 - vascular lesions, 1804, 1805, 1807
- Epiloia *see* Tuberous sclerosis
- Epiphyseal injury, 1383, 1384
- Epistaxis, 1712
- Epithelial bladder tumours, 995
- Epithelioma, skull erosion, 1636
- Epstein-Barr virus, 242, 260, 1336, 1528, 1753
- Erectile dysfunction, 906, 1035-6
- Ergot poisoning, 435
- Erosions
- ankylosing spondylitis, 1219, 1220
 - gout, 1229-30
 - osteoarthritis, 1226
 - psoriatic arthritis, 1216
 - Reiter's syndrome, 1217
- Erythroblastosis fetalis (haemolytic disease of newborn), 1325-6
- Escherichia coli*, 651, 687, 870, 1024, 1785
- pneumonia, 133, 259
 - urinary tract infection, 941, 942, 944, 979, 991
- Escherichia coli* 1057, 872
- Ethanol embolisation, 456, 458, 1710
- Ethmoid mucocele, 1522
- Ethmoid sinus, 1520
- Evacuation proctography (defecography), 637, 654
- Eventration of diaphragm, 52, 255-6, 863, 865
- Ewing's sarcoma, 1315, 1317-20
- jaws, 1546, 1547
 - orbit, 1569
 - paravertebral mass, 77
 - periosteal new bone, 1154
 - spine, 1660
- Exercise-induced compartment syndrome, 1425
- Exomphalos (omphalocele), 864, 1058, 1059
- External carotid artery
- anomalous communications with vertebralbasilar system, 1689
 - branches, 1683
 - congenital anomalies, 1688
 - normal angiographic findings, 1683
- External ear, congenital abnormalities, 1601, 1604-5
- External iliac lymph nodes, 512
- Extracorporeal membrane oxygenation (ECMO), 258-9
- Extracorporeal shock-wave lithotripsy (ESWL), 725, 905-6, 969
- Extradural empyema, 1520
- Extradural haematoma, 1389, 1390, 1779
- Extrahepatic bile duct, 711
- developmental anomalies, 712
 - ultrasound, 716-17
- Extramedullary haemopoiesis, 78-9, 85, 1321
- sickle cell disease, 1323
 - thalassaemia, 1322
- Extraocular muscles, 1574
- lymphoma infiltration, 1579-80
 - rhabdomyosarcoma, 1579
- Extrapyramidal movement disorders, 1795, 1796-7
- Extrinsic allergic alveolitis, 36, 195-7, 198
- Eye, 1551-66, 1587-92
- anatomy, 1551-3, 1574-5
 - foreign bodies, 1566
 - infection, 1591-2
 - ocular masses, 1560-4, 1589-91
 - metastatic tumours, 1560, 1590
 - shape/size disorders, 1587-9
 - 'tenting' of globe, 1587
 - trauma, 1564-6, 1575-6
 - globe rupture, 1565
 - ultrasound imaging, 1551, 1553-4
 - B-scan, 1553
 - clinical applications, 1554-66
 - Doppler techniques, 1553-4
 - indications, 1554
- Facial bone fracture, 1389-91, 1575
- Facial lymph nodes, 510
- Faecal occult blood testing, 644
- Fahr's syndrome, 1634, 1798
- Fallopian tubes, 1070, 1104
- Fallot's tetralogy, 9
- False aneurysm
- Doppler ultrasound, 467
 - iatrogenic, 422, 431, 449
 - stent insertion, 451
 - ultrasound-guided compression, 467
- Falx, arterial supply, 1680
- Familial basal ganglion calcification, 1798
- Familial hypophosphataemia, 1356
- Familial hypophosphatasia (vitamin D-resistant rickets), 1353-4
- Familial polyposis coli, 633, 639, 871
- colon cancer risk, 639
 - colorectal polyps, 639
 - desmoid disease, 626, 627, 639
 - gastroduodenal polyps, 589
 - small bowel adenomas, 626
- Fanconi's anaemia, 879, 1108, 1109, 1327
- Farmer's lung, 195, 197
- Fascia of Zuckerkandl, 886
- Fat embolism, 220, 243
- Fat necrosis, breast, 1457, 1473, 1474

- Fatty liver, 742, 754, 755, 756, 765, 779, 785, 839
- FDG-PET *see* Positron emission tomography (PET)
- Feline oesophagus, 556
- Female infertility, 1084, 1085
- Female pelvic anatomy, 1069-71
- Feminising syndrome, 835
- Femoral artery
 - atheromatous disease, 429
 - catheterisation, 357, 418
 - congenital anomalies, 423
- Femoral artery aneurysm, 426
- Femoral artery angioplasty, 447, 448, 449
- Femoral nerve palsy, 422
- Femoral phlebography, 489
- Femoral vein, 485, 486
- Femur fracture, 1379
 - distal, 1411
 - neck/intertrochanteric, 1378, 1411, 1416
 - shaft, 1411
- Femur length, 1042-3
- Femur, proximal focal deficiency (congenitally short femur), 1113
- Fetal blood sampling, 1048
- Fetal echocardiography, 403-4, 1055
 - heart rate/rhythm, 404
- Fetal gender determination, 1049
- Fetal growth, 1046-7
- Fetal heart rate, 404, 1055
- Fetal malformation
 - cardiorespiratory system, 1055-7
 - central nervous system, 1049-55
 - cystic hygroma, 1056, 1057
 - gastrointestinal system, 1057-9
 - genitourinary system, 1059-61
 - magnetic resonance imaging (MRI), 1066
 - musculoskeletal system, 1061-3
- Fetal malpresentation, 1040
- Fibroadenoma, breast, 1456-7, 1464-5, 1466, 1467, 1468, 1473, 1474, 1477
- Fibrodysplasia ossificans progressiva *see* Myositis ossificans
- Fibrogenesis imperfecta ossium, 1126, 1127, 1356
- Fibrolamellar carcinoma, 772
- Fibrolamellar hepatoma, 757
- Fibroma
 - bone
 - desmoplastic, 1287-8, 1289
 - non-ossifying, 1287, 1289
 - heart, 308, 337, 1056
 - lung, 124
 - mediastinum, 69
 - oesophagus, 564
 - ovary, 1082
 - pleura (benign mesothelioma), 100, 104
 - scrotum (extratesticular), 1026
 - trachea, 161
- Fibromuscular hyperplasia, 414, 432, 435
 - renal artery stenosis, 432, 480, 481
- Fibrosarcoma, 445
 - bone, 1288-90
 - heart, 337
 - lung, 122, 129
 - mediastinum, 69
 - peritoneal cavity, 633
 - soft tissues, 1428
- Fibrosing atherosclerosis, 18, 34, 187, 204
 - cryptogenic (unusual interstitial pneumonitis), 204-6
 - lung transplantation, 240, 242
 - rheumatoid disease, 198-9
- Fibrosing mediastinitis, 80, 85, 145, 148, 161, 499, 500
- Fibrothorax, 97
- Fibrous cortical defect, 1249, 1287, 1288
- Fibrous dysplasia, 49, 1114, 1130-4, 1249
 - complications/endocrine disorders, 1134
 - jaw lesions, 1534, 1535-6, 1544
 - petrous temporal bone involvement, 1614
 - skull erosion, 1639
 - skull local hyperostosis, 1640
- Fibrovascular oesophageal polyp, 564
- Fibula, congenital pseudarthrosis, 1114
- Fifth metatarsal base avulsion injury, 1414
- Filariasis, 88, 204, 516, 1474, 1475
- Fine needle aspiration cytology
 - adrenal gland, 830, 831
 - breast, 1458, 1462, 1464, 1467, 1468, 1473, 1475
 - stereotactic-guided, 1480-1
 - ultrasound-guided, 1479-80
- cervical lymph nodes, 1516
 - lung, 44
- malignant mesothelioma, 103
- mediastinal mass, 59
- pancreas, 820
 - adenocarcinoma, 814, 820
 - cystic tumours, 815
- paravertebral mass, 78
- salivary gland mass, 543, 1515
- thyroid nodule, 1505
- First branchial cleft cyst, 540
- Fistula-in-ano, 649, 655
- Fistulation
 - Crohn's disease, 649
 - diverticular disease, 645
- Flail segment, 217
- Flat foot, congenital, 1116, 1117, 1118
- Fleischner lines (plate atelectasis), 19
- Fluke infection, brain, 1791
- Fluoroscopy
 - chest, 29, 247
 - computed tomography, 31, 1837
 - congenital cardiac disease, 405
 - paediatric imaging, 247, 924-5
 - urogenital tract, 896-900, 924-5
- Fluorosis, 49, 1368, 1369
- Focal bacterial nephritis, 876
- Focal cortical dysplasia, 1805-6
- Focal nodular hyperplasia, 757-8, 761, 770, 782, 785, 879
- Follicular aspiration, 1092
- Follicular (dentigerous) cyst, 1542, 1543
- Fontan procedure, 393
- Foot
 - accessory bones, 1114
 - congenital anomalies, 1114-17
 - fusions, 1117
 - osteomyelitis, 1161
 - trauma, 1413-14
- Forearm abnormalities, 1062
- Forearm fractures, 1407, 1408
 - around wrist, 1408
- Foregut duplication cyst, 252
 - oesophageal extrinsic compression, 866
 - obstruction in neonate, 853
- Foreign bodies
 - inhaled, 5, 260, 261
 - intracranial, 1781-2
 - intraocular, 1566
 - intravascular, retrieval, 447
 - orbit, 1577, 1578
 - small bowel obstruction, 618
 - soft tissues, 1432-3
 - upper aerodigestive tract, 570, 865-6, 1495, 1496
- Forestier's disease (diffuse idiopathic skeletal hyperostosis: senile ankylosing spondylitis), 1221-2
- Fractures, 1371-87, 1389-416
 - arterial injury, 1381-2
 - avulsion, 1377, 1378, 1379
 - 'butterfly' fragment, 1371, 1372
 - childhood, 1383-5
 - battered child, 1384-5
 - growth arrest classification, 1384
 - closed, 1371
 - comminuted, 1371, 1372, 1373
 - complications, 1375, 1376
 - delayed union, 1375, 1376
 - evaluation, 1374-5
 - greenstick, 1372, 1383
 - healing, 1374
 - imaging problems, 1414-16
 - incomplete/complete, 1371
 - malunion, 1374, 1377
 - non-union, 1374, 1375, 1377
 - oblique, 1371
 - open, 1371
 - pathological, 49, 1196, 1197, 1340, 1344-5, 1377
 - soft-tissue associated abnormalities, 1372-4
 - spiral, 1371
 - stress, 49, 217, 1371, 1374, 1375, 1376-7, 1413, 1416, 1419
 - terminology, 1371-2
 - 'torus/huckle', 1371, 1372, 1383
 - transverse, 1371
- Fragilitas ossium, 1625, 1626
- Francisella tularensis*, 134-5, 136
- Freiherg's infarction (osteochondritis of metatarsal head), 1187
- Frieberg's disease, 1378
- Friclandr's bacillus, 17, 132
- Frontal lobe/frontotemporal dementia, 1796
 - regional cerebral blood flow imaging, 1815
- Frontal sinus, 1520
 - mucocele, 1522
- Frostberg's sign, 597, 601, 789
- Frostbite, 436, 455, 1385, 1438, 1439
- Functional endoscopic sinus surgery, 1519, 1521
- Fungal infection
 - central nervous system, 1786-8
 - lungs, 145-9, 157
 - mediastinal lymphadenopathy, 72
 - paranasal sinuses, 1522-3
 - pneumonia, 153, 260
 - pyelonephritis, 948
 - ureteric inflammation, 978-9
- use in pregnancy/lactating women, 482
- Gadolinium-DTPA contrast
 - digital subtraction angiography (DSA), 416
 - paediatric imaging, 851
- Gadoxetic acid contrast agent, 778
- Galactocoele, 1462, 1463
- Galactosaemia, 879
- Galeazzi fracture, 1407, 1408
- Gallbladder
 - anatomy, 711
 - cholesterol deposits, 715
 - developmental anomalies, 712
 - mural calcification (porcelain gallbladder), 713, 724
 - mural gas, 713, 714
 - polyps, 715, 716
 - spontaneous perforation, childhood, 722
 - trauma, 698-9
 - ultrasound, 715
- Gallbladder adenomyomatosis (cholecystitis glandularis proliferans), 724, 725
- Gallbladder carcinoma, 598, 724-5, 783-4
- Gallbladder cholesterosis, 723-4
- Gallbladder disorders, 722-5
 - interventions, 725
- Gallbladder empyema, 686, 723
- Gallbladder hydrops, 881
- Gallium-67 imaging, 42
 - lymph nodes, 515
 - osteomyelitis, 1157-8
 - sarcoidosis, 189
- Gallstone empyema, 722
- Gallstone ileus, 602, 673-4, 714
- Gallstones, 722-3
 - acute cholecystitis, 685, 723
 - acute pancreatitis, 790, 816
 - calcified, 712-13
 - children, 722, 881
 - computed tomography (CT), 717
 - gallbladder carcinoma association, 724
 - interventions, 725
 - operative cholangiography, 719
 - oral cholecystography, 718, 719
 - small bowel obstruction, 618
 - types, 723
 - ultrasound, 715
- Gamma-Gandy bodies, 786
- Ganglioglioma, 1746-7
- Ganglion, 1426
 - intraosseous, 1311-12, 1314
- Ganglion cell tumours, 75
- Ganglioneuroma, 75
- Ganglioneuroma, 834-5
 - calcification, 829, 834
 - carotid sheath, 1502
 - ectopic ACTH production, 840
 - posterior mediastinum, 261
- Gangosa, 1175
- Gardner's syndrome (ostomatosis-intestinal polyposis syndrome), 639, 871
 - colorectal adenomatous polyps, 1540
 - facial osteomas, 1254
 - gastrointestinal polyps, 589
 - jaw/teeth involvement, 1540
- Garre's osteomyelitis, 1159
- Gas gangrene, 1433, 1434, 1444
- Gas, soft tissues, 1433-4, 1444
- Gas-forming infections, 687-8

G

- Gastric atresia, 853
- Gastric cancer, 591-8, 739
 advanced carcinoma, 592-3, 595, 596, 597
 staging, 593, 594-5
 early carcinoma, 591-2
 gastric outlet obstruction, 669
 linitis plastica ('leather bottle' stomach), 592, 593, 595
 metastases, 757, 777, 1251, 1253
 risk factors, 591
 screening, 591
- Gastric cardia, 577
- Gastric dilatation, 668-9
- Gastric disorders in children, 866
- Gastric displacement, 599
- Gastric diverticulum, 603
- Gastric duplication cyst, 590, 853
- Gastric extrinsic compression, 599, 600
- Gastric haemangioma, 590
- Gastric lipoma, 589-90
- Gastric liposarcoma, 590
- Gastric lymphoma, 524, 598-9
- Gastric motility, 609-12
 factors affecting, 610
 gastric emptying curve, 610
 indications for investigation, 609
 investigation methods, 609
 liquid phase, 610
 normal ranges, 610
 postoperative, 610-11
 radionuclide imaging, 609
 interpretation, 611-12
 technique, 611
 solid phase, 610
- Gastric obstruction
 gastric dilatation, 668, 669
 neonate, 853-5
 post-gastric surgery, 607
- Gastric polyps
 adenomatous, 587-8, 591
 hamartomatous, 589
 hyperplastic, 587
- Gastric stasis, 61 L 612
- Gastric stromal tumours
 benign, 588, 589
 malignant, 599
- Gastric surgery, 604, 605, 606-9
 complications
 early, 606-7
 late, 607-8
 gastric motility following, 610-11
- Gastric tumours
 benign mucosal, 587-9
 benign submucosal, 58) 91
 malignant, 591-9
 metastatic, 597-8
- Gastric ulcer, 578, 579, 581, 582-3
 geriatric, 581
 giant, 581
 non-steroidal anti-inflammatory drug-related, 578
 upper gastrointestinal haemorrhage, 440
 see also Peptic ulcer disease
- Gastric varices, 572, 602-3, 779
- Gastric volvulus, 599, 600, 668, 669, 866
- Gastrinoma, 587, 794, 800, 815, 822, 881
 see also Zollinger-Ellison syndrome
- Gastritis, 577, 578-80
 acute erosive, 579
 atrophic, 591, 599
 children, 866
 chronic, 579-80
 emphysematous, 687
 eosinophilic, 580
 gastrointestinal haemorrhage, 440
 intra-arterial vasoconstrictor infusion, 454
 lymphocytic, 580
 reactive, 579-80
- Gastro-oesophageal junction, 543, 544, 554
 gastro-oesophageal ring (B-ring), 554, 555
 interior oesophageal sphincter (A-ring), 554, 555
 Z-line, 543, 554
- Gastro-oesophageal reflux
 children, 864-5
 see also Reflux oesophagitis
- Gastroenterostomy, 604, 605, 607
- Gastrografin, 585
 caustic oesophagitis, 559
 large bowel examination, 636-7
 oesophageal perforation, 571
 paediatric abdominal imaging, 850
 small bowel examination, 618
 small bowel obstruction, 620
- Gastrointestinal haemorrhage
 intraarterial vasoconstrictor infusion, 454
 radionuclide imaging, 412
 see also Lower gastrointestinal haemorrhage; Upper gastrointestinal haemorrhage
- Gastrointestinal masses
 lymphoma, 524-5
 paediatric abdomen, 882-3
- Gastrointestinal tract
 lymphatic tissue, 509
 neonate, 851-64
 obstetric ultrasound, 1057-9
 older child, 864-74
 trauma, 705-7
- Gastroschisis, 864, 865, 1059
- Gaucher's disease, 49, 1180, 1181, 1344-5, 1346, 1347, 1366, 459, 1710
- Gel foam embolisation, 456, 457, 458, 459, 1710
- Generalised fibromatosis, congenital (infantile myofibromatosis), 1288
- Genitography, 925
- Geodes
 osteoarthritis, 1223
 rheumatoid arthritis, 1205, 1206, 1207
- Germ cell tumours
 brain, 1754
 mediastinum, 58, 66
 ovary, 883, 1081, 1082
 malignant, 1083, 1084
 retroperitoneum, 845
 testis, 1028
 classification, 1028
- Germinoma, intracranial, 1754
- Gerota's fascia, 886
- Gestational age assessment, 1040, 1041-3
 anatomical parameters, 1041
 multiple fetal growth parameters, 1043
- Gestational sac, 1040, 1041, 1043
 discriminatory size, 1043-4
 double decidual sac sign, 1044
 growth rates, 1046
 non-viable pregnancy, 1045, 1046
- Giant cell arteritis, 436
- Giant cell reparative granuloma, 1544, 1545
- Giant cell tumour
 hone, 1249, 1292-3, 1294
 tendon sheath, 1428
- Giant cell-rich osteosarcoma, 1293, 1294
- Giant cisterna magna, 1730
- Gianturco Z stent, 451, 452
- Gianturco-Roehm bird's nest filter, 453
- Gianturco-Rosch Z stent, 734
Giardia, 587, 627, 870
- Gigantism, jaw enlargement, 1538-9
- Glandular fever see Infectious mononucleosis
- Glaucoma, 1554
- Glioblastoma multiforme, 1743, 1744, 1745
- Gliomas, 1739
 grading, 1739
 intracranial calcification, 1628, 1629
 local skull bulging, 1639
 optic nerve, 1569-70, 1585, 1638
 skull erosion, 1638
- Gliomatosis cerebri, 1746
- Globoid leucodystrophy (Krahe's disease), 1801, 1802
- Globulomaxillary cyst, 1544
- Glomerular filtration rate, 912-13
- Glomerulonephritis, chronic, 976, 977
- Glomus jugular tumour, 446, 1501, 1599, 1759, 1760
 angiography, 1705
 selective external carotid artery, 1683
 embolisation, 1716-17, 1718
 petrous temporal bone, 1609, 1610
 skull erosion, 1636
- Glomus tumours, 1599
 bone, 1300, 1303
 petrous temporal bone, 1609-10
 soft tissues, 1428
- Glomus tympanicum tumour, 1759
 angiography, 446, 1705
 petrous temporal bone, 1609, 1611
- Glomus vagale tumour, 1501
 angiography, 446
- Glossopharyngeal neuralgia, 1772
- Glottic turnouts, 1498
- Glucagonoma, 822
 embolisation, 458, 460
- Gluten-sensitive enteropathy see Coeliac disease
- Glycogen acanthosis, 563
- Glycogen storage disease, 720, 756, 879, 1366
 type 1, 879
- Goitre, 1510
 multinodular, 1513
 'simple' colloid, 1507
 thyroid scintigraphy, 1504, 1507
 see also Graves' disease (diffuse toxic goitre)
- 'Golden S sign', 27
- Gonadal veins, 493
- Gonococcal urethritis, 1017
- Goodpasture's syndrome, 208, 209
- Gorham's disease (vanishing bone disease), 1299-300, 1302
- Gorlin-Goltz syndrome, 1541
- Goundou, 1175
- Gout, 1229-31, 1233
 calcific tophi, 1230, 1231, 1233, 1234
 soft tissue deposits, 1438
 urate calculi association, 966
- Graft-versus-host disease
 colitis, 652
 gastrointestinal tract involvement, 632
 children, 870
- Granular cell tumour
 bronchial myohlastoma, 124
 choristoma (pituicytoma), 1765
 oesophagus, 564
- Granulocytic sarcoma, 1529
- Granulomas
 dental pulp, 1532, 1536
 paranasal sinuses, 1523
 solitary pulmonary nodule, 22, 36
- Granulomatous disease, chronic (Landing-Shirky disease), 152
 skeletal lesions, 1163, 1164, 1342
 ureteric malacoplakia, 979-80
- Granulosa cell tumour of ovary, 1082
- Graves' disease (diffuse toxic goitre), 1504, 1505, 1513
 ophthalmopathy, 1567, 1579
- Great vessel anomalies, 399-401, 1687, 1688
- Great vessel trauma, 707-8
- Greater trochanter bursitis, 1426
 tuberculosis, 1167
- Greenfield titanium filter, 452
- Greig's syndrome, 1626
- Groshong catheters, 454
- Guglicmi detachable coils, 1710
- Guinea worm (*Dracmefulus meelinensis*), 1437
- Gunther tulip filter, 453
- Gynaecological disorders, acute abdomen, 688
- Gynaecological imaging, 1069-104
 computed tomography (CT), 1090-2
 contrast studies, 1085-90
 interventional radiology, 1092-3
 magnetic resonance imaging (MRI), 1093-104
 plain film, 1085
 ultrasound, 1069-84
 endovaginal, 1069
 transabdominal, 1069
- Habenular commissure calcification, 1622
- Haemangioblastoma
 angiography, 1705
 intracranial, 1757-8
 spine, 1667
- Haemangiocndothelial sarcoma see Angiosarcoma
- Haemangiocndothelioma
 infantile, 771, 879
 mediastinum, 69
- Haemangioma, 49, 1473
 bone, 1296-8, 1299, 1300, 1301, 1302
 choroid, 1563
 heart, 1056
 large bowel, 644
 liver, 739, 743, 757, 769-70, 781-2, 879
 angiography, 443, 444
 mediastinum, 69
 neck, 1501
 oesophagus, 564
 orbit, 1568, 1580-1
 globe, 1590

- pancreas, 788
salivary gland, 540
skull erosion, 1636
small bowel, 625, 630
soft tissues, 1428, 1429, 1430, 1431.
 | 443
 calcification, 1436, 1437, 1443
stomach/duodenum, 590
trachea, 161
vertebrae, 1661, 1662
 embolisation, 172(1), 1721
- Haemangiopericytoma
angiography, 446
bone, 1300
intracranial, 1757
lung, 122
mediastinum, 69
orbit, 1581-2
- Haemarthrosis, 1347, 1348, 1373
- Haematocele, 1027
- Haematoma
breast, 1462
duodenum, 630, 866
iatrogenic, 422, 449
oesophagus, 571
pancreas, 788
soft tissues, 1422-4, 1444
 calcification, 1439
 stages of evolution, 1423
- Haematopoietic disorders, skeletal abnormalities, 1321-7
- Haemobilia, angiographic embolisation, 735
- Haemochromatosis, 756, 779, 1366
cardiomyopathy, 299
 magnetic resonance imaging (MRI), 323
 liver radiodensity enhancement, 741
- Haemoglobinopathics, 962, 1541
- Haemolytic anaemias, chronic, 78, 79, | 321
- Haemolytic disease of newborn (crythroblastosis fetalis), 1325-6
- Haemolytic uraemic syndrome, 872
- Haemoperitonum, 691, 693
- Haemophilia, 88, 1346-9
 intra-articular haemorrhage, 1347, | 348, 1349
 intraosseous haemorrhage, 1347
 subperiosteal haemorrhage, 1347-9
haemophilus influenzae, | 52, 1785
 pneumonia, 131, 133, 135, 136, 259
- Haemopneumothorax, 95, 217, 218
- Haemoptysis
 bronchial arteriography with embolisation, 47
 pulmonary siderosis, 208
- Haemorrhage
 arteriographic diagnosis, 440
 embolisation, 456-7
- Haemorrhagic cystitis, 993
- Haemorrhoids, 653
- Haemosiderosis, 289, 302, 303
- Haemospuria, 1005-6
- Haemothorax, 88, 98, 217, 218, 219, | 404, 1415
- Hajdu-Cheney syndrome (acro-osteolysis), 1124
- Hamartoma
 Brunner's gland, 590
 fetal renal (mesoblastic nephroma), 962
 hypothalamic, 1765-6, 1806
 intracranial, 1732, | 733
 lung, 22, 37, 123-4, 125, 126
- in mesenchymal, 879
 oesophagus, 564
- Hamartomatous polyps
 gastrointestinal, 589, 626-7
 | large bowel, 638
- Hamman-Rich disease, 204
- Hampton's hump, 315
- Hand
 congenital defects, 1108-9
 osteoarthritis, 1225
 osteomyelitis, 1161
 trauma, 1410-11
 | tuberculous dactylitis, 1168, | 169
- Hand-Schieller-Christian disease.
 | 582, 1637
- Pulmonary involvement, 1343, 1344
 skeletal abnormalities, 1342-3
 .see also Langerhans' cell histiocytosis
- Hangman's fracture, 1396-7
- Hartmannella acanthisamoeba*, | 790
- Hashimoto's thyroiditis, 62, 828, 1507, | 514
- Head circumference, 1042
- Head injury, 999, 1389, 1778-83
 computed tomography (CT)
 acute trauma, 1779-82
 indications, 1778-9
 hearing loss, 1605-6
 infant, accidental/non-accidental trauma, 1811
 magnetic resonance imaging (MRI), | 782
 post-traumatic segnae, 1782-3
 regional cerebral blood flow
 | imaging, 1815
 skull fracture, 1389
- Head, large in infancy, 1728
- Head and neck, lymphatic drainage.
 510-11
- Head and neck tumours
 embolisation, 1716-19
 intra-arterial chemotherapy, 1719-20
 lymphoma, 526
 positron emission tomography (PET), 1830, 1831
- Helicobacter pylori*, 525, 578-9
 children, 866
 duodenitis, 586
 gastric carcinoma, 591
 gastric lymphoma, 598, 599
 gastritis, 579
 lymphocytic, 580
- Heiniatropathy, 1641
- Hemifacial spasm, 1772
- Hemihypertrophy, 874, 937, 976
- Hemimegalencephaly, 1728
- Hemivertebrae, 1108, 1119, 1653
- Henoch-Schönlein purpura, 202, 630, 866, 870, 874
- Heparin-related osteoporosis, 1366
- Heparinisation, 421, 448
- Hepatic adenoma, 757-8, 761, 770, 782, 879
 angiography, 443-4
- Hepatic arteriovenous malformation, 880
- Hepatic artery, 753, 764
 aneurysm, 468, 469
 congenital anomalies, 423
 Doppler ultrasound examination, 468
 embolisation, 455, 456, 458
 trauma management, 697, 698
 liver transplantation-related thrombosis, 774
- Hepatic cyst, 758, 769, 780, 781
 congenital, 879
- Hepatic fibrosis, congenital, 769
- Hepatic focal nodular hyperplasia, 879
- Hepatic haemangioma, 879
 angiography, 443, 444
- Hepatic portal vein, 753, 754, 755, 763-4
 imaging, 501-3
 Doppler ultrasound, 468
 magnetic resonance angiography, 507
 thrombosis, 731, 768, 774, 779
- Hepatic vein, 753, 754, 763, 764
 catheterisation, 751
 Doppler ultrasound examination, 469
 magnetic resonance angiography, 507
 phlebography, 493
- Hepatic vein stenosis, stent placement, 452
- Hepatic vein thrombosis (Budd-Chiari syndrome), 469, 493-4, 496, 507, 737, 751, 756, 767, 768-9, 780
 causes, 497, 507
 liver transplantation complication, 774
 thrombolysis, 456
 transjugular intrahepatic portosystemic shunt (TIPS), 453
- Hepatitis, 765
 alcoholic, 766
 viral, 765-6
- Hepatitis A, 766
- Hepatitis B, 766
- Hepatitis C (non-A, non-B), 766
- Hepatobiliary masses, children, 878-81
- Hepatoblastoma, 762, 878
- Hepatocellular carcinoma (hepcoma), 740, 741, 743, 754, 756-7, 760, 761, 766, 772, 782-3, 785
 angiography, 444
 biliary drainage/stenting, 734
 children, 879
 Doppler ultrasound, 468
 embolisation, 458, 745
 intra-arterial chemotherapy, 455, 458
- Hepatolenticular degeneration (Wilson's disease), 1366, | 797-8
- Hepatomegaly, 737, 738, 764-5
- Hereditary craniofacial dysostosis (Crouzon's disease), 1624
- Hereditary haemorrhagic telangiectasia (Osler-Weber-Rendu syndrome), 316, 564, 743, | 712
- Hereditary multiple exostosis .see Diaphyseal aclasis
- Hereditary non-polyposis colorectal cancer (Lynch syndrome), 641
- Hereditary tyrosinaemia, 879
- Hernia
 congenital
 lesser sac, 631
 paracacal, 631
 paradaodenal (mesocolic), 631
 small bowel obstruction, 618, 67(1), 671, 672-3
 .see also Hiatus hernia
- Herpes simplex oesophagitis, 558, 866
- Herpes simplex type 1 encephalitis, | 792
- Herpes simplex type 2 encephalitis, | 792-3
- Heterotopia, 1735, 1736
- Hexabrix, 420
- Hiatus hernia, 53-4, 58, 75-6, 85, 554, 555, 556, 560-3
 congenital, 254-5, 561, 863, 864, | 057
 fetal sonographic detection, 1056, | 057
 gastric ulcer, 581
 mixed, 561
 peptic stricture, 556, 557
 rolling (paraesophageal), 561
 sliding, 554, 556, 560-1
 surgery, 561-2
- Hickman catheters, 454
- High-output cardiac failure, arteriovenous fistula, 440
- Highly-selective vagotomy, 608
- Hilar enlargement, 27
- Hilar lymphadenopathy, 513
 bronchial carcinoma, 108, 111, 115
 cystic fibrosis, 165
 fibrosing alveolitis, 205
 Hodgkin's disease, 118, 122, 123
 lymphoma, 527
 sarcoidosis, 188
 silicosis, 191
 tuberculosis, 141, 142-3, 144, 146
- Hilar tumours, ventilation/perfusion (VQ) imaging, 38, 39
- Hill-Sachs (hatchet) defect of humeral head, 1238, 1240, 14(15)
- Hilum
 computed tomography (CT), 31, 32
 plain chest film, 8
 small, 27, 28
 tomography, 29
- Hilum overlay sign, 14
- Hip dysplasia, congenital (congenital dislocation), 1109-13
 arthrography, | 111-13
 Graf classification, | 110
 imaging indications, | 109
 imaging, 1244
 ultrasound, 1109-10
- Hip fracture
 acetabulum, 1402-4
 femoral neck, 1411
- Hip joint
 arthritis in infants (Tom Smith arthritis), 1164-6
 idiopathic chondrolysis, 1367
 imaging, 1244
 irritable hip syndrome, | 182
 osteoarthritis, 1223-4
 tuberculosis, | 170
- Hip prosthesis loosening/infection, | 242, 1243, 1244
- Hippocampal sclerosis, 1804, 1805, | 806
- Hirschsprung's disease, 654, 850, 859, 860-1
- Histiocytic lymphomas, 523
- Histiocytosis X, 17, 1340-4
 jaw lesions, 1542
 orbital involvement, 1580, 1582, | 584
 skull involvement, 1637
 spinal involvement, 1660
 .see also Langerhans' cell histiocytosis
- Histoplasma capsulatum*, | 45, 157

- Histoplasmosis, 29, 145, 148, 157, 16L499, 826
 bowel infection, 627, 652
 central nervous system, 1786
 mediastinal fibrosis, 80, 145, 148
 mediastinal lymphadenopathy, 70, 72
 pulmonary infection, 24, 25, 147
 HL7 (health level 7), 1842
 Hodgkin's disease, 511, 512, 513, 521-3, 1330
 Ann Arbor staging system (Cotswold modification), 519, 522, 527
 cross-sectional imaging, 527, 528
 intrathoracic, 118, 122, 123, 526
 lymph node involvement, 70, 71-2, 82, 118, 122, 123, 522
 lymphocyte-depleted, 522, 1330
 lymphocyte-predominant, 522, 1330
 mixed cellularity, 522, 1330
 nodular sclerosing, 522, 1330
 skeletal lesions, 1330-1, 1332, 1333, 1334
 somatostatin receptor scintigraphy, 661
 treatment, 522-3
 Hoffman-Rigler sign, 285
 Holoprosencephaly, 1054, 1809, 1811
 Holt-Oram syndrome, 47, 1107, 1108, 1109
 Homocystinuria, 1366, 1367
 lens pathology, 1554, 1555
 skeletal features, 1148-9
 Hookworm, 627
 Hormone assay
 Conn's syndrome (primary hyperaldosteronism), 829
 phaeochromocytoma, 829, 844
 Horseshoe kidney, 861, 874; 913, 931
 accessory arteries, 423
 Hospital information system (HIS), 1842
 Haglund's disease, 1210
 Human chorionic gonadotrophin.
 ectopic pregnancy, 1047
 Human herpes virus 8 (Kaposi's sarcoma associated herpes virus; KSHV), 158
 Human immunodeficiency virus (HIV)
 see AIDS/HIV infection
 Human papilloma virus, 1526
 Humerus fracture, 1406
 medial epicondyle avulsion, 1407
 supracondylar, 1407
 Humerus hatchet deformity (Hill-Sachs defect), 1238, 1240, 1405
 Huntington's disease, 1797
 Hurler's syndrome, 49, 1145-6
 Hurtle cell tumour, 1514
 Hyaline membrane disease (respiratory distress syndrome), 17, 256-7
 Hydatid disease (cchinococcosis), 730-1
 biliary tract, 730-1
 bone lesions, 1174, 1175
 brain, 1790-1
 liver, 758, 771-2, 780, 781, 879
 calcification, 740, 741
 lung, 23, 24, 151-2
 pericardium, 308, 335, 336
 skull erosion, 1639
 urinary tract, 946
 Hydatid of Morgagni (testicular appendix) torsion, 1027
 Hydatidiform mole, 1045
 Hydranencephaly, 1054-5, 1734, 1809
 Hydrocele, 1023, 1029
 Hydrocephalus, 999
 communicating, 1728, 1785, 1795
 congenital, 1728, 1807, 1809, 1810
 low-pressure/normal pressure, 1728, 1795, 1816
 non-communicating, 1728
 obstetric ultrasound, 1053
 persistently open fontanels, 1624
 post-traumatic, 1782
 Hydrolyser catheter, 456
 Hydronephrosis, 861, 970-1, 972, 976, 981
 obstructive causes, 970
 post-obstructive, 970
 pregnancy, 971
 Hydropneumothorax, 95, 100
 Hydrops fetalis, 1056, 1058
 immune, 1063
 non-immune, 1062
 obstetric ultrasound, 1057, 1063
 Hydrosalpinx, 1104
 see also Pelvic inflammatory disease
 Hydrothorax, 87
 Hydrometer, 970-1, 976, 981
 pregnancy, 971, 973
 Hypaque, 419, 420
 Hyperaldosteronism, primary *See* Conn's syndrome
 Hypercalcaemia, 790, 791, 1354
 chronic pancreatitis, 818
 hyperparathyroidism, 1507
 medullary nephrocalcinosis, 977
 multiple myeloma, 1339
 renal calculi, 965
 Hypercalcuria
 multiple myeloma, 1339
 renal calculi, 965
 Hypercementosis, 1534-5
 Hyperinflation, chest trauma, 220
 Hyperlipidaemia, 295
 Hypernephroma *see* Renal cell carcinoma
 Hyperostosis frontalis interna, 1640-1
 Hyperoxaluria, 1366
 nephrocalcinosis, 977
 osteoporosis, 1366
 Hyperparathyroidism, 47, 48, 790, 842, 1362-6, 1514-15
 arterial calcification, 412
 brown tumours, 49, 1293, 1295, 1363, 1364, 1539
 intracranial calcification, 1634
 jaw/teeth involvement, 1539
 nephrocalcinosis, 977
 osteoporosis of skull vault, 1639
 primary, 1362, 1507, 1514-15
 skeletal features, 1363-4
 secondary, 1364, 1507
 basal ganglion calcification, 1799
 renal osteodystrophy, 1364, 1365
 temporomandibular joint involvement, 1546, 1548
 soft tissue/blood vessel calcification, 1435, 1438
 tertiary, 1366, 1507
 Hyperphalangism, 1107
 Hyperplastic polyposis, 638
 Hyperplastic polyps
 large bowel, 637, 638
 stomach, 587, 589
 Hypersensitivity pneumonitis *see* Extrinsic allergic alveolitis
 Hypersplenism, 459
 Hypertelorism, 1626
 Hypertension
 renal artery stenosis, 964
 renal trauma sequelae, 975
 Hypertthyroidism *see* Thyrotoxicosis
 Hypertrophic arthritis *see* Osteoarthritis
 Hypertrophic cardiomyopathy, 299, 323-5, 329
 infants/children, 403
 Hypertrophic (pulmonary)
 osteoarthritis, 102, 113, 1231, 1359, 1360
 periosteal new bone, 1154
 skeletal features, 1231, 1234
 Hypertrophic pyloric stenosis,
 adult/infantile form, 604
 Hyperuricuria, urate calculi association, 966
 Hypervitaminosis A, 1367-8
 Hypochondroplasia, 1141-2
 Hypogammaglobulinaemia, 65, 152, 587
 Hypoglossal artery, 1679, 1689, 1690
 Hypogonadism, osteoporosis, 1358-9
 Hypoparathyroidism, 1360-1
 basal ganglion calcification, 1361, 1634, 1798
 jaw/teeth involvement, 1539
 osteoporosis, 1360
 soft tissue calcification, 1438
 Hypophalangism, 1107
 Hypopharyngeal carcinoma, 1497, 1498
 Hypopharynx, 543
 Hypophosphataemia
 acquired, 1354
 familial, 1356
 Hypophosphatasia, 1353-5, 1626
 skeletal features, 1147, 1148
 Hypopituitarism, 1539
 Hypoplastic left heart syndrome (aortic atresia), 368, 394-5
 Hypoproteinaemia, 87
 Hypospadias, 1017
 Hypothalamic neuronal hamartoma, 1765-6
 Hypothyroidism, 47
 jaw/teeth involvement, 1539
 neonate, thyroid scintigraphy, 1506
 skeletal features, 1359, 1360, 1361
 Hypotonic duodenography, 789, 790
 Hypoxic brain damage, 1781
 Hysterosalpingo-contrast sonography, 462
 tubal patency assessment, 1084, 1085
 Hysterosalpingography, 1085-90
 complications, 1086
 technique, 1085-6
 Idiopathic basal ganglion calcification, 1798
 Idiopathic coxa vara of childhood, 1113, 1114
 Idiopathic juvenile osteoporosis, 1126, 1127, 1356-7
 Idiopathic male osteoporosis, 1357
 Idiopathic Parkinson's disease, 1816
 Idiopathic pulmonary haemosiderosis, 262
 Idiopathic pulmonary ossification, 214
 Idiopathic scoliosis, 1121, 1122
 Ileal atresia/stenosis, 858-9, 860
 Ileal conduit, 1000, 1001, 1002
 loopography, 898
 reflux nephropathy, 947, 948
 heal faccolith (enterolith), 674
 Ileoanal pouch, 650
 Crohn's disease, 622, 623
 water-soluble pouchography, 650, 651
 Ileocaecal valve, 636
 hyperplasia, 653
 Ileosigmoid knot, 678
 Ileostomy enema, 617
 Ilcum, 615
 Ileus, 620-1
 gallstone, 673-4, 714
 paralytic, 620, 678-9, 688
 children, 871
 gastric dilatation, 668
 Iliac artery
 angioplasty, 446, 448
 Doppler ultrasound examination, 466
 stenosis/thrombosis, 425, 426, 429, 430
 Dacron grafts, 430, 431
 stent insertion, 451
 Iliac horns, 1117
 Iliac vein, 486, 489
 extrinsic displacement/obstruction, 491
 spontaneous rupture, 491-2
 stenosis, stent insertion, 452
 thrombosis, 489-90, 491, 492, 493
 Image library for digital workflow, 1844
 Immature lung disease, 256
 Immotile cilia syndrome, 152
 Immunocompromised patient, 210
 childhood chest disease, 260
 fungal pyelonephritis, 948
 non-specific pneumonitis, 159
 ocular infections, 1592
 oesophagitis, 557, 558
 toxoplasmosis, 1788, 1789
 see also AIDS/HIV infection
 Imperforate anus, 790
 Implantation dermoid cyst, 1306, 1308
 Impotence, 472
 Incomplete abortion, 1045
 Indium-111 I-DTPA-labelled octreotide
 see Somatostatin receptor scintigraphy
 Indium-111 I-labelled leucocyte scan
 arterial graft infection, 412
 inflammatory bowel disease, 659
 infra-abdominal sepsis, 682-3
 osteomyelitis, 1158
 Indwelling catheter balloon deflation, 905
 Inevitable abortion, 1045
 Infantile cortical hyperostosis (Caffey's disease), 1192
 Infantile haemangioid endothelioma, 879
 liver, 771
 Infantile myofibromatosis (congenital generalised fibromatosis), 1288
 Infectious enteritis, 627-8
 Infectious mononucleosis, 72, 136, 790
 Infective aneurysm, 424
 Infective colitis, 651-2
 Infective discitis, 1162, 1163
 Infective endocarditis, 300, 303, 327, 329, 330-1, 424
 Inferior cavernous artery, 1680
 Inferior hypophyseal artery, 1680
 Inferior mesenteric artery
 Doppler ultrasound, 472
 ilcoecolic branches, 635

- Inferior vena cava, 265, 266, 267
 congenital anomalies. 402, 489
 Doppler ultrasound, 472
 extrinsic displacement, 491
 obstruction, venous stent placement, 452
 phlebography, 486, 489
 therapeutic interruption, 492
 thrombosis, 489-90, 491, 492, 493, 506
 trauma, 707
- Inferior vena cava filters. 452-3, 492, 497
 Doppler ultrasound assessment, 472
- Interior vena cavography, 906
 phaeochromocytoma imaging, 829
- Infertility
 female. 1084, 1085
 male, 1036
 treatment, Doppler ultrasound monitoring, 471
- Inflammatory bowel disease, 646, 729
 acute colitis, 679-80
 computed tomography (CT), 650
 magnetic resonance imaging (MRI), 650
 radionuclide imaging, 659-60
 ultrasound, 650
see also Crohns' disease; Ulcerative colitis
- Inflammatory bowel mass, children, 882-3
- Inflammatory myopathy, 1425-6
- Inflammatory polyp
 large bowel, 637, 638
 oesophagogastric, 563
- Influenza pneumonia. 131, 135, 136, 137, 259
- Informed consent
 interventional vascular radiology, 447
 intussusception reduction, 850
- Infrapatellar bursitis, 1426
- Infratemporal fossa lesions, 1498-503
 congenital/developmental anomalies, 1500-1
- Inguinal hernia, 859
- Inguinal lymph nodes, 512
- Inhalation damage, 163, 195
see also Pneumoconioses
- Inhaled foreign body, 5, 260, 261
- Inhaled irritant gases, 195
- Inner ear, 1597, 1598, 1599
 congenital abnormalities, 1601, 1602-4
- Innominate artery stenosis, 450
- Inoue mitral valve balloon
 commissurotomy, 360, 361
- Inspissated bile plug syndrome, 721-2
- Insulinoma, 794, 795, 800, 804, 815, 822, 881
 embolisation, 458, 460
- Intensive care patients, 217, 231-5
 central venous catheters, 232, 233, 293
 endotracheal intubation, 234, 292
 intra-aortic balloon pump, 23.5
 mediastinal drains, 234, 292
 nasogastric intubation, 233, 234
 pacemakers, 235
 plain chest film, 290
 pleural tubes, 234
 positive pressure ventilation, 234
 Swan-Ganz (pulmonary artery flotation) catheters, 232, 233
 tracheostomy tubes, 234
- Intermittent claudication, 429, 447
 limb artery Doppler ultrasound, 466
- Internal auditory meatus, 1597, 1598, 1599
- Internal carotid artery
 anomalous communications with vertebrobasilar system, 1689-90
 atheromatous stenosis, 429, 450, 1700-5, 1833
 collateral circulation, 1700, 1702
 imaging, 1703-4
 stroke risk, 1703
 subcalvian steal, 1703
 thrombosis, 1703, 1704-5
 transient ischaemic attacks, 1700, 1703
 congenital anomalies, 1688-9
 anomalous intrapetrous course, 1689
 dissecting aneurysm, 1704
 Doppler ultrasound, 461
 fibromuscular hyperplasia, 1704
 occlusion
 infra-arterial thrombolysis, 1708
 lesl, 1711
 transluminal angioplasty, 450
 traumatic thrombosis, 1704
 vascular stenosis, 450
- Internal carotid/common carotid (IC/CC) ratio, 463
- Internal iliac lymph nodes, 512
- Internal mammary lymph nodes, 511
- Intersex disorders, 1021, 1022
- Interstitial cystitis, 993
- Interstitial lung disease, 34-5
- Interventional neuroradiology, 1707-22
 direct percutaneous procedures, 1721-2
 endovascular procedures *see* Endovascular/neuroradiological procedures
 risks, 1707
- Interventional vascular techniques, 446-60
 bile ducts, 735
 central venous catheter insertion, 454
 informed consent, 447
 intravascular stenosis, 451-4
 scope of procedures, 447
 therapeutic embolisation, 456-60
 transluminal angioplasty, 447-51
 vascular foreign bodies retrieval, 454
 vascular infusion therapy, 454-5
see also Endovascular neuroradiological procedures
- Interventricular septum, 60, 265, 266, 270
 rupture, 297
- Intervertebral discs
 calcification, 50
 imaging, 1643, 1644
- Intestinal emphysema, 687
- Intestinal ischaemia, 472
- Intestinal lymphangiectasia, 629
- Intestinal membranes, 618
- Intestinal obstruction
 acute abdomen, 668
 gastric dilatation, 668-9
 neonate, 85 1-62
 causes, 862
 small/large bowel dilatation, 669
see also Large bowel obstruction; Small bowel obstruction
- Intra-abdominal abscess, 681-3
- Intra-aortic balloon pump, 235, 361-2
- Intra-arterial chemotherapy, 455
 head and neck tumours, 1719-20
 hepatic tumours, 443, 455
- Intracranial air, 1781
- Intracranial aneurysm, 1724, 1770-2
 angiography, 1690-4
 calcification, 1631
 clinical presentation as tumour, 1694, 1695, 1696
 congenital berry aneurysm, 423
 dissection, 1772
 embolisation, 1712-14
 complications, 1714
 intracranial haematoma, 1767
 oculomotor pareses, 1691, 1693-4
 subarachnoid haemorrhage, 1690, 1769
 cerebral vasospasm, 1709
- Intracranial arteritis, 1705
- Intracranial balloon angioplasty, 1709
- Intracranial calcification, 1621-3
 basal ganglia, 1633-4
 cerebral tumours, 1628-31
 infections/infestations, 1632-3
 metabolic disorders, 1633-4
 pathological, 1629
 vascular lesions, 1631-2
- Intracranial circulation
 carotid angiography, 1678-82
 cerebral veins, 1682-3
 congenital anomalies, 1688-90
- Intracranial foreign body, 1781-2
- Intracranial haematoma, 1700, 1767-8, 1769
 acute trauma, 1779-80
 angiomatous malformation rupture, 1695
 calcification, 1632
 causes, 1767
 extracerebral, 1782
 intracranial aneurysm rupture, 1692, 1693
- Intracranial haemorrhage, 1389
 neonate, 1807, 1810
 periventricular leucomalacia, 1811
 pre-term infants, 1810, 1811
- Intracranial lesions, 1723-66, 1767-816
 congenital, 1727-34
 neuronal migration disorders, 1734-8
 degenerative/metabolic disorders, 1794-804
- Infant brain ultrasound examination, 1807-12
- Infections, 1783-94
 investigation methods, 1723-7
 patient positioning, 1724, 1726
 neoplasms, 1739-66
 radionuclide imaging, 1812-16
 trauma, 1778-83
 vascular, 1767-78
- Intracranial pressure elevation, 1626-7
- Intracranial thrombosis, 1703, 1704-5
- Intraductal mucin hypersecreting tumours, pancreas, 794
- Intrahepatic bile duct, 71 1
 developmental anomalies, 71 1-12
 stones, 725-7
 ultrasound, 716-17
- Intramural gas, 687-8
- Intramural pseudodiverticulosis, 559-60
- Intramural small bowel haemorrhage, 630
- Intramuscular myxoma, 1426-7
- Intraocular foreign bodies, 1566
- Intraocular lens implant, 1554, 1555
- Intraoperative ultrasound
 islet cell tumours, 795
 pancreas examination, 787
- Intraosseous ganglion, 131 1-12, 1314
- Intraosseous geodes
 osteoarthritis, 1223
 rheumatoid arthritis, 1205, 1206, 1207
- Intrapulmonary lymph nodes, 10
- Intraspinal masses, 1649
- Intratubular germ cell neoplasia, 1033
- Intrauterine adhesions, 1087, 1088
- Intrauterine contraceptive devices (IUCDs), 1073, 1074, 1075
 magnetic resonance imaging (MRI), 1093, 1094
- Intrauterine growth retardation, 471, 1046-7, 1065
 asymmetric, 1046
 diagnosis, 1046
 Doppler ultrasound of fetoplacental/uteroplacental circulation, 1046-7
 symmetric, 1046
- Intravascular foreign body retrieval, 447
- Intravascular stents, 451-4
 arterial, 451
 endovascular aneurysm repair, 452
 venous, 452
- Intravascular ultrasound, 1835
 angioplasty success assessment, 449
 arterial imaging, 412
- Intravenous cholangiography, 719
- Intravenous urodynamicogram, 922
- Intravenous urography, 891-4
 adrenal mass, 829
 benign prostatic hyperplasia, 1005
 bladder cancer, 995, 996
 children, 925
 contrast media, 927
 contrast reactions, 891, 893
 modifications, 893
 renal colic, 688
 renal trauma, 972
 shock nephrogram, 965
 ureteric calculi, 967, 968, 969
- Intussusception, 1058
 air enema reduction, 850
 children, 872-4
 radiological reduction, 873
 small bowel obstruction, 674-5
- Iobitridol, 927
- Iodamide, 926
- Iodinated contrast agents, 926-7
 vascular agents, 419
- Iodine-123 scintigraphy
 adrenal medulla, 832
 renal imaging, 912
 retrosternal goitre, 64
 thyroid imaging, 1504, 1505
 whole body imaging for metastases detection, 42
- Iodine-131-labelled agents
 adrenal cortex imaging, 831
 renal scintigraphy, 912
 therapeutic applications, 1504, 1507
- Iodixanol (Visipaque), 419
- Ioglycamide (Biligram), 719
- Iohexol, 421, 618, 849, 927, 1645
- Iomeprol (Iomeron), 419, 927

- loperamide, 420, 849, 927
 loperol, 927
 loperamide (Ultravist), 419, 927
 lophthalmate meglumine, 419, 420, 850, 926
 lotrolan (Isovist), 419
 lotroximale (Biliscopin), 719
 loxerol, 927
 loxithalamate, 926
 Iris, 1552
 Iron deficiency anaemia, 549, 1326
 Irritable bowel syndrome, 653
 Irritable hip syndrome, 1181, 1379
 Irritant gas inhalation, 139-40
 Ischaemic colitis, 651, 652, 680
 Ischaemic optic neuropathy, 1586
 Islet cell tumours, 42, 787, 788, 794-5, 800, 803, 804, 805, 815, 881
 angiography, 444, 445
 hepatic metastases, 785
 intraoperative ultrasound, 795
 radionuclide imaging, 821-2
 somatostatin receptor scintigraphy, 66 M61
 venous blood sampling, 445, 495
 Isolated dextrocardia, 6, 366
/Sporobolus, 870
 Ivalon embolisation, 456, 457, 458, 459
 Ivermark's syndrome (asplenia), 250, 749, 882
 Ivory osteoma, 1255, 1256

 Jacoud's arthropathy, 1234
 Jansen's metaphyseal chondrodysplasia, 1137.1 138
 Japanese B encephalitis, 1792
 Japanese panbronchiolitis, 173
 Jaundice
 childhood, 720, 721, 722
 biliary scintigraphy, 718
 ultrasound investigation, 813
 Jaws, 1531-49
 benign neoplasms, 1544
 bone dysplasias, 1539-40
 cysts, 1542-4
 dental origin, 1542, 1543
 developmental (fissural), 1544
 non-epithelialised bone cysts, 1544, 1545
 developmental abnormalities, 1537-8
 endocrine disorder involvement, 1538-9
 haemoglobinopathy-related changes, 1541
 histiocytosis X, 1542
 malignant tumours, 1544-6
 metastatic, 1546, 1548
 radiation changes, 1533-4
 sclerosing lesions, 1534-6
 trauma, 1536-7
 mandibular fracture, 1549
 Jefferson fracture (C1 burst fracture), 1397-8
 Jejunal atresia/stenosis, 858-9
 Jejunal diverticulum, 440
 Jejunum, 615
 Jeune's disease (asphyxiating thoracic dystrophy), 1109, 1142, 1144
 Joint disorders, 1201-44
 childhood, 1213-15
 effusions, 1372, 1373, 1432
 imaging, 1235-44
 tumour involvement, 1308-12
 Joint trauma, 1382-3
 chronic (neuroma-in-arthropathy), 1386
 dislocation/subluxation, 1382
 Jones fracture (fifth metatarsal proximal diaphysis), 1414
 Jostent, 451
 Joubert's syndrome, 1730
 Judkins catheter, 280, 350
 Jugular bulb, large, 1605, 1606
 Jugulodigastric lymph node, 510
 Juvenile angiofibroma *see* Nasopharyngeal angiofibroma
 Juvenile ankylosing spondylitis, 1215
 Juvenile idiopathic arthritis, 1213-15
 classification, 1214
 Juvenile polyp, 871
 Juvenile polyposis, 638, 871
 Juvenile subdural haematoma, 1640, 1642

 Kaposi's sarcoma, 72, 158, 626, 652
 gastrointestinal tract, 599, 626, 644
 lung, 121-2, 158
 pancreas, 821
 Kaposi's sarcoma associated herpes virus (KSHV, human herpes virus 8), 158
 Kartagener's syndrome, 152, 163
 Kasai operation, 720, 727
 Kawasaki's disease, 355, 402, 428-9
 Kearn-Sayer syndrome, 1804
 Keloid scar, breast, 1468, 1469
 Kensey catheter, 450
 Kerley lines, 12
 A lines, 12
 B lines, 9, 11, 12, 19, 131, 145, 289
 Kidney
 anatomy, 885-8
 computed tomography (CT), 906
 congenital lesions/variants, 913-14, 929-41
 associated anorectal malformations, 861
 persistent fetal lobulation, 929
 development, 885, 886
 diffuse/multifocal abnormalities, 975-8
 inflammatory disease, 941-8
 magnetic resonance imaging (MRI), 910-11
 scarring, 914
 small scarred, 976
 small smooth, 976
 smooth enlargement, 976
 supernumerary, 930
 ultrasound, 894-5
 children, 923-4
 Doppler examination of vasculature, 469-71
 obstetric, 1059-61
 vascular supply, 887
 Kienbock's disease (osteochondritis of scaphoid), 1189, 1378, 1380
 Killian-Jamieson diverticulum (lateral cervical oesophageal diverticulum), 547
 Klatskin's tumour, 756, 757, 772, 783
Klebsiella, 119, 131, 132, 134, 135, 138, 152, 687, 979, 991
 Klinefelter's syndrome, 1033
 Klippel-Feil syndrome, 50, 1108, 1119, 1120, 1625, 1653
 Klippel-Trenaunay syndrome, 488, 497, 500
 Knee joint
 fractures, 1411-12
 imaging, 1235-7
 osteoarthritis, 1225, 1227
 tuberculosis, 1170
 Kock ileostomy/Kock pouch, 623, 65(1), 1000
 Kohler's disease (osteochondritis of patella), 1188, 1189
 Kohler's disease I (osteochondritis of tarsal navicular), 1187
 Kohler's disease II (osteochondritis of metatarsal head), 1187
 Krabbe's disease (globoid leucodystrophy), 1801, 1802
 Krukenberg tumour, 595, 596, 1083, 1104
 Krypton-SI in ventilation scintigraphy, 39
 KUB (kidney, ureters and bladder) film, 890-1
 Kveim test, 187
 Kyphosis, 1651
 adolescent (Scheuermann's disease), 1188
 cervical spinal trauma, 1393
 elderly person, 28

L
 Labral injuries, 1407
 congenital deformities, 1602-4
 Labyrinthitis, 1598, 1599
 Labyrinthitis ossificans, 1607, 1608
 Lacrimal gland, 1575
 drainage apparatus
 disorders/tumours, 1594
 masses, 1592-4
 benign, 1592
 inflammatory, 1593-4
 malignant, 1592-3
 Lacrimal gland cyst, 1592, 1593
 Lacteas, 509
 Lactobezoar, 866
 Lacunar skull, 1625
 Ladd's hands, 618, 631, 856
 Ladd's procedure, 857
 Landing-Shirkey disease *see* Granulomatous disease, chronic
 Langerhans' cell histiocytosis, 1637
 diffuse lung disease, 187, 206, 207, 261, 262
 intrahepatic cholangiopathy, 722
 Large bowel, 635-61
 anatomy, 635
 childhood disorders, 871-4
 function, 635-6
 radiological investigation, 636-7
 rotational anomalies, 635
 tumours, 637-44
 Large bowel dilatation, acute abdomen, 669
 Large bowel haemangioma, 644
 Large bowel obstruction, 665, 675, 676-8
 colorectal cancer, 676
 colorectal stenting, 642, 643
 diverticular disease, 645
 ileocaecal valve competence, 675, 676
 neonate, 859-62
 obstetric ultrasound, 1058
 pseudo-obstruction, 676, 677
 types, 675
 Large bowel volvulus, 676
 Laryngeal carcinoma, 1510
 Laryngocoele, 1497
 Laryngotracheobronchitis (croup), 161, 1497
 Larynx, 543, 1489
 benign tumours, 1498
 cysts, 1497
 functional disorders, 1495
 imaging techniques, 1489-91, 1492, 1493
 infections, 1497
 malignant tumours, 1498-9
 trauma, 1495-7
 Laser-assisted angioplasty, 45(1-1)
 Lateral cervical oesophageal diverticulum (Killian-Jamieson diverticulum), 547
 Lateral epicondylar fracture, 141(1)
 Lateral pharyngeal pouch, 547
 Laurence-Moon-Biedl syndrome, 930, 936, 11(19)
 Le Fort fractures, 1389-9(1), 1575
 Lead poisoning, 1368, 1634
 Left atrial appendage, 267-8, 270, 272
 enlargement, 284
 Left atrium, 267-8
 enlargement, 284
 Left paracolic abscess, 682
 Left ventricle, 265
 aneurysm, 297-8, 321, 322
 enlargement, 285
 rupture, 297
 heft ventricular angiography, 280, 281, 348, 349, 350
 left ventricular volume/ejection fraction, 348
 Left-sided inferior vena cava, 489
 Left-sided superior vena cava, 498
 Legg-Calve-Perthes' disease *see* Perthes' disease
Legionella pneumophila pneumonia (Legionnaire's disease), 131, 132-3, 135, 153
 Leiomyoma
 bladder, 995
 oesophagus, 76, 563, 564
 scrotal extratesticular, 1026
 small bowel, 624-5
 uterus (fibroids), 1075, 1(176), 1077, 1087, 1085, 1090, 1091, 1094-5
 Leiomyomatosis, oesophagus, 554
 Leiomyosarcoma
 lung, 122
 oesophagus, 76, 569-70
 retroperitoneum, 845
 soft tissues, 1428
 Lens, 1552, 1553
 calcification, 1623
 dislocation/traumatic displacement, 1564, 1576
 pathology, 1554, 1555
 Lenticulostriate arteries, 1680-1
 Leontiasis ossia, 1198, 1640
 Leprosy, 1175-6, 1436, 1437, 1523
 Leptomeningeal cyst, 1641-2
 LeWeb syndrome (dyschondroplasia), 1108, 1109, 1144, 1145
 Leriche's syndrome (aortic thrombosis), 417, 429-A431
 Leri's disease (melorheostosis), 1129

- Lesser sac hernia, 631
 Letterer-Siwe disease, 1582, 1637
 pulmonary involvement, 1343
 skeletal abnormalities, 1343-4, 1345
 see also Langerhans' cell
 histiocytosis
 Leucocyte scan
 intra-abdominal sepsis, 682-3
 see also Indium-111-labelled
 leucocyte scan
 Leucodystrophies, 1801-2
 Leukaemia
 axillary lymphadenopathy, 1468
 CNS involvement, 1637
 intrathoracic disease, 27, 121
 mediastinal lymphadenopathy,
 70, 71, 121
 lymphocytic, 1335
 orbital deposits, 1569
 paranasal sinuses involvement, 1529
 renal infiltration, 958
 children, 876
 skeletal abnormalities, 1328, 1329
 children, 1327, 1328, 1329
 Leukoplakia, urinary tract, 947-8, 979
 Lewy body dementia, 1796
 regional cerebral blood flow
 imaging, 1814-15
 Leydig cell turnouts, 1028
 LGM Venatech filter, 453
 L'hermitte-Duclos disease, 1738, 1747
 Ligament injury, 1419
 Limb salvage
 angioplasty, 447
 thrombolysis, 455
 'Limy bile', 713
 Linitis plastica ('leather bottle'
 stomach), 592, 593, 595
 Lipiodol, 419
 Lipohaemarthrosis, 1372, 1373, 1434,
 1435
 Lipoid pneumonia, 138-9, 140, 195
 Lipoma
 adrenal gland, 829-30, 836, 838
 arborescens, 131(1-11), 1312
 bone, 1303-4, 1306
 parosteal, 1303, 1307
 breast, 1462
 chest, 49, 50, 53
 bronchial, 124
 corpus callosum, 1732, 1733
 deep central veins, 490
 heart, 337, 338
 intracranial calcification, 1630-1
 kidney, 950
 large bowel polyps, 638
 liver, 771
 mediastinum, 58, 68-9, 7(1
 oesophagus, 564
 pleura, 100, 102, 105
 retroperitoneum, 848
 salivary glands, 1515
 scrotal extratesticular, 1026
 small bowel, 625
 soft tissues, 1418, 1428, 1429, 1434,
 1441, 1443
 neck, 1502, 1511
 spine, 1666, 1667
 stomachoduodenum, 589-90
 Lipomatosis
 renal sinus, 949, 950
 synovium, 1311
 Lipomyelomeningodysplasia, 1651
 Liposarcoma
 bone, 1303-4
 parosteal, 1304
 hepatic metastases, 784
 mediastinum, 58, 68-9
 retroperitoneum, 845
 soft tissues, 1428, 1430, 1441, 1444
 stomachoduodenum, 590
 Lisfranc fracture-dislocation, 1414, 1415
 Lissencephaly (agyria), 1634, 1734
 Liver, 737-46, 749
 anatomy, 711, 753, 754, 763
 computed tomography (CT), 753-8
 imaging techniques, 737
 magnetic resonance imaging (MRI),
 777-85
 contrast agents, 778
 radionuclide imaging, 759-62
 ultrasound, 763-75
 Doppler examination of
 vasculature, 468-9
 Liver abscess, 758, 771, 785
 amoebic, 740, 742, 758, 771
 Ascaris, 715
 children, 880
 pyogenic, 771
 Liver biopsy, 751
 transjugular, 453, 751
 Liver disease
 angiography, 742-6
 interventional, 744-6
 osteomalacia, 1353
 plain abdominal film, 737-42
 calcification, 740
 portal hypertension, 749-53
 Liver enlargement, 738, 764-5
 Liver transplantation, 760, 773-5
 hiliary anastomosis, 774
 strictures, 728
 complications, 774-5
 Doppler ultrasound examination of
 liver vasculature, 468
 hepatic artery aneurysm, 469
 preoperative assessment, 773-4
 vascular anastomosis, 774
 Liver trauma, 695-8, 759, 760
 hiliary leak/stricture formation, 728,
 729
 complications, 699
 CT grading, 697
 management, 697
 vascular involvement, 697-8
 Liver tumours, 738, 739, 754, 755
 angiography, 443-4, 445
 benign, 757-8
 lymphoma, 772
 malignant, 756-7, 772
 metastases, 577, 643, 740, 741,
 745-6, 757, 772-3, 784-5, 803,
 814
 hiliary obstruction, 734
 children, 879
 embolisation, 456, 458, 459, 460,
 742, 745-6
 intra-arterial chemotherapy, 455
 Loa lot, 1438
 Lobar overinflation,
 congenital/congenital
 emphysema, 251-2
 Lobectomy, 225
 Loeffler's endomyocarditis, 325-6
 Loeffler's syndrome (simple pulmonary
 eosinophilia), 150-1, 203
 Loopography, 898, 925
 Looser's zones, 49, 1354, 1355
 Low-osmolality contrast media, 419,
 927
 paediatric abdominal imaging,
 849-50
 Lower gastrointestinal haemorrhage,
 645
 arteriographic diagnosis, 440
 embolisation, 456
 radionuclide imaging, 655-7
 Lower limb
 congenital disorders, 1109-17
 fracture, 1372
 stress, 1413
 ischaemia
 thrombolysis, 455
 see also Peripheral vascular
 disease
 trauma, 141 1-14
 veins, 484, 485
 duplication anomalies, 488
 Lower limb phlebography, 483-8
 complications, 486
 congenital anomalies, 488
 normal appearances, 485, 486
 technique
 ascending, 485-6
 descending, 486
 Lower oesophageal sphincter, 554
 hypertrophy, 550
 Lumbar spine
 degenerative disease, 1228, 1231,
 1232
 imaging, 1644
 myelography, 1646
 Lumbosacral plexus imaging, 1644
 Lunate
 dislocation, 1409, 1410
 osteochondritis (Kienbock's
 disease), 1189, 1378, 1380
 Lung abscess, 19, 20, 22, 23, 72, 95,
 138, 139
 Lung biopsy, 1, 44-5
 CT guidance, 31
 Lung cancer *see* Bronchial carcinoma
 Lung collapse, 4, 26, 108, 175-9, 290,
 667
 complete, 176
 definition, 175
 lobar, 15, 17, 26, 176-9
 left upper lobe, 179, 181, 182
 lingula, 178-9, 181
 lower lobe, 177-8, 179, 180
 right middle lobe, 177, 178
 right upper lobe, 176-7
 mechanisms, 175
 radiological signs, 175-9
 rounded atelectasis, 179, 183
 Lung consolidation, 179-80
 bacterial pneumonia, 131, 132
 lobar, 14, 15, 17, 183-4
 left upper lobe, 184, 186
 lingula, 184, 186
 lower lobe, 183, 184, 186
 right middle lobe, 183, 185
 right upper lobe, 183, 185
 radiation injury, 236
 tuberculosis, 141-2
 Lung cyst, 22-3
 Lung scintigraphy, 41-3, 171
 gallium imaging, 42
 lung capillary permeability, 43
 mucociliary escalator function,
 43
 regional lung function, 41-2
 turnouts, 42
 see also Ventilation/perfusion (VQ)
 imaging
 Lung transplantation, 239-42
 complications, 240-2
 single/double lung, 240
 Lung trauma, 219-20, 221
 radiation injury, 235-6, 237
 Lung tumours, 19, 23, 29, 107-29
 computed tomography (CT), 35-7
 lymphoma, 526, 527
 magnetic resonance imaging (MRI),
 124-6, 127, 128
 scintigraphic detection, 42
 Lungs
 calcified lesions, 24, 25, 109, 117,
 142, 147, 189
 computed tomography (CT), 31-2
 respiratory phase, 32-3
 drug toxicity, 209-10, 211
 fissures, 7, 13, 32
 thickening, 19
 lateral view, 13
 lymphatic drainage, 9, 51 1-12
 obstetric ultrasound, 1056-7
 postero-anterior film, 7
 acini, 9, 11
 apices, 8
 hidden areas, 8
 lymphatic system, 9
 pulmonary segments, 9, 11
 subdiaphragmatic features, 10-11
 scarring, 19
 underdevelopment, 250-1
 Lyme disease, 1788
 Lymph circulation, 509-10
 Lymph nodes, 509, 510
 acute inflammation, 517
 calcification, 25, 1437
 chest film, 10, 25, 27
 disorders, 516-18
 benign, 517
 malignant, 518
 fibrofatty deposits, 517
 imaging techniques, 514-15
 metastases, 516, 518
 TNM staging system (N-staging),
 519
 treatment planning, 519-20
 reactive hyperplasia, 510, 517
 Lymphadenopathy, 513
 acute lymph node inflammation,
 517
 benign lymph node disorders, 517
 fibrofatty deposits, 517
 granulomatous disease, 517
 malignant disease, 516
 reactive hyperplasia, 510, 517
 Lymphangiography, 2, 512
 Lymphangioliomyomatosis, 35, 187,
 207, 208
 Lymphangioma, 68, 81
 cavernous pancreatic, 788
 children, 867
 neck, 1501, 1511, 1512
 orbit, 1581
 retroperitoneum, 848
 see also Cystic hygroma
 Lymphangiomyomatosis, 88
 Lymphangitis carcinomatosa, 19, 35,
 108, 118, 121, 126, 187
 Lymphatic aplasia/hypoplasia, 516
 Lymphatic capillaries, 509
 Lymphatic ducts
 disorders, 516
 lymphography, 513-14
 lymphoscintigraphy, 514
 Lymphatic system
 anatomical aspects, 509-10
 function, 509-10
 imaging, 513-15
 malignant disease, 519-21

- Lymphatic system *-contd*
topography, 510-13
abdomen, 512-13
head and neck, 510-11
pelvis, 512-13
thorax, 511-12
- Lymphocytic gastritis, 580
- Lymphocytic interstitial pneumonitis (LIP), 120-1, 158-9, 260
- Lymphocytic meningitis, acute, 1791
- Lymphoedema, 483
praecox, 493, 494
primary/secondary, 516
- Lymphography, 513-14
lymph node micrometastases, 516
lymphatic ducts, 513-14
disorders, 516
- Lymphoid granulomatosis, 200
diffuse lung disease, 202
- Lymphoid hyperplasia
duodenal involvement, 587
large bowel, 636
- Lymphoma, 42, 509, 517, 521-30, 1330
AIDS-related, 159, 160, 821
bladder, 997
brain, 1753-4
breast, 1466
cervical lymph node involvement, 1516
chylothorax, 88
colon, 644
cross-sectional imaging
abdomen, 528
head and neck, 528-9
spine, 529
thorax, 526-8
extranodal invasion, 529, 530
gallium-67 scintigraphy, 515
heart, 337, 338
intrathoracic, 118-19, 123, 124
ivory vertebra, 50
kidney, 957-8
children, 875, 876
liver, 772
lung, 23
mediastinum, 59, 70, 71, 72, 82
nasolacrimal, 1594
oesophagus, 570
orbital involvement, 1568, 1569,
1579-80, 1582, 1583, 1593
pancreas, 792, 800
paranasal sinuses, 1528-9
pleural effusions, 89, 91
positron emission tomography (PET), 1830
pulmonary hilar enlargement, 27
retroperitoneal tumours, 845
salivary glands, 539, 540
small bowel, 625-6
somatostatin receptor scintigraphy, 661
spine, 1660
spleen, 759, 776
staging, 519
stomach, 598-9
testis, 1028, 1032-3
thyroid, 62, 1514
treatment complications, 521,
529-30
- Lymphomatoid granulomatosis, 121,
124
- Lymphoproliferative disease, post-transplantation, 242, 293
- Lymphoreticular system disorders
skeletal abnormalities, 1330-46
storage disorders, 1345-6
- Lymphosarcoma, 1637
- Lymphoscintigraphy, 514
- Lynch syndrome (hereditary non-polyposis colorectal cancer), 641
- Macleod's (Swyer-James) syndrome, 28, 171, 172
- Macrocephaly (megalencephaly), 1728
- Macroactyly, 1107
- Macrodyostrophia lipomatosa, 1304
- Madlung's deformity, 1108, 1138,
1139
- Madura foot, 1161, 1176, 1177
- Maffucci's syndrome, 1276, 1281
- Magnetic field gradient coils, 1820-1
- Magnetic resonance angiography (MRA), 271, 472-81
abdominal vessels, 479-80
arterial imaging, 413, 415, 416, 417,
418, 474, 475-6
carotid arteries, 474, 475, 478-9,
1673, 1674
cerebral imaging, 1673, 1674
contrast agent safety, 481-2
contrast-enhanced (CE-MRA), 472,
473, 475, 476, 477, 478, 479,
481, 1823-5
contrast agents, 1828-9
three-dimensional, 1674
iatrogenic hilar tree trauma, 698
imaging principles, 473-5
maximum intensity projection (MIP), 474, 475
phase contrast (gradient refocused) method, 473, 474,
480, 1674
subtraction techniques, 474
time-of-flight (saturation) method,
473-4, 481, 1674
intracranial aneurysm, 1770-2
liver, 778
paediatric abdomen, 851
paediatric chest, 248
perfusion imaging, 1674
peripheral vessels, 474, 475-6, 481,
482
petrous temporal bone, 1600
portal vein imaging, 507
pulmonary arteries, 475, 477-8
renal arteries, 480-1
thoracic aorta, 476-7
- Magnetic resonance cholangiography (MRC), 716, 717, 1822
- Magnetic resonance cholangiopancreatography (MRCP), 787, 801, 803, 804,
805
iatrogenic biliary tree trauma, 698
paediatric imaging, 851
technical aspects, 802
- Magnetic resonance imaging (MRI)
abdominal trauma, 692
adrenal gland, 826, 830, 833
aortic dissection, 427, 428
benign prostatic hyperplasia, 1005
hiliary tract *see* Magnetic resonance cholangiography (MRC);
Magnetic resonance cholangiopancreatography (MRCP)
bladder, 1007-8
cancer, 1008-11
bone density measurement, 1352
breast, 1476-8
cardiac imaging, 265, 266, 267, 271,
279, 280, 281, 319-20, 1825,
1826
cardiac tumours, 338
congenital cardiac disease, 363,
373, 406-7
hypertrophic cardiomyopathy,
325
valvular heart disease, 331-2
ventricular function assessment,
323
chest, 2, 38
complex biopsies, 1446
contraindication with cardiac
implanted devices, 295
contrast agents, 82, 515, 778,
1827-9
Crohn's disease, 623-4
fat suppression/saturation
techniques, 1417-19
gastric motility, 609
glossary of terms, 1852-4
gynaecological imaging, 1093-104
head injury, acute, 1782
inflammatory bowel disease, 650
interventional, 1445-8
biomechanical investigations,
1448
endoscopic monitoring, 1446-7
open surgery guidance, 1447-8
intracranial lesions, 1723, 1724,
1726-7
haematoma, 1768
subarachnoid haemorrhage, 1769
joint imaging, 1235
ankle, 1241, 1243
degenerative disc disease, 1228-9,
1233
knee, 1235, 1236, 1237, 1412
rheumatoid arthritis, 1211-13
shoulder, 1239-40
wrist, 1244
large bowel, 637
liver, 777-85
lung tumours, 124-6, 127, 128
bronchial carcinoma, 108, 110-11
lymph nodes, 515
microretastases, 516, 517
lymphoma, 529
malignant disease
residual mass, 520-I
staging, 519
malignant mesothelioma, 103
mediastinum, 58, 80, 111
neck soft tissues, 1500
obstetric imaging, 1065-6
orbit, 1574
osteomyelitis, 1158-9
osteonecrosis, 1181
paediatric abdomen, 851
paediatric chest, 248
Paget's disease, 1195-6
pancreas, 787, 801-2, 805
pericarditis/pericardial effusion, 334
Perthes' disease (osteochondritis of femoral capital epiphysis),
1185, 1186
petrous temporal bone, 1598-9,
1602
pharynx/larynx examination, 1491,
1493
prostate, 1011-12
cancer, 1112-15
recent technical advances, 1819-29
clinical applications, 1822-7
computing power requirements,
1821
gradient coils, 1820-1
image processing, 1821-2
magnets, 1819-20
receiver coils, 1821
sequence advances, 1822
rectal cancer, 643
salivary glands, 533-5, 536
sinuses, 1519-20
small bowel examination, 618
soft tissues, 1417-32, 1445-8
tumours, 1427-8, 1429-31
spinal injury, 1392, 1393
spine, 1643-4
spleen, 785-6
thermal ablation procedures, 1446
urogenital tract, 910-12, 926
veins, 505-7
- SI-Magnetic resonance spectroscopy, 1825-7
- Major blood vessel trauma, 707-8
- Malabsorption, 628-9
osteomalacia, 1353
- Malacoplakia, urinary tract, 947-8,
979-80, 991
- Malaria, cerebral, 1790
- Male genitalia, 889-90, 895-6
- Male infertility, 1036
- Male pseudohermaphroditism, 1033
- Malignant disease
diagnosis, 519
lymphatic system imaging, 519-21
residual masses, 520-I
TNM staging, 518, 519
treatment planning, 519-20
treatment response, 520
- Malignant fibrous histiocytoma, 83,
1428, 1444
bone, 1290-I
retroperitoneal tumours, 845
- Malignant otitis externa, 1612, 1614
- Malignant peripheral nerve sheath tumour, 1428, 1431
- Malignant round cell tumours, 1315
- Mallory-Weiss tear, 440, 571
- Malrotation, 630-I, 672, 856-7
- Malta fever *see* Brucellosis
- Mammography, 1451-5
abnormal findings *see* Breast digital imaging, 1452-3
full field, 1452-3
image display modes, 1453
small field, 1452
normal appearances, 1454, 1455
diffuse increase in density,
1454-5
projections, 1453-4
screening *see* Breast cancer screening
technical aspects, 1451-2
viewing procedure, 1458
- Mandibular cyst, 1544
- Mandibular fracture, 1389, 1391,
1392, 1549
- Mandibular osteomyelitis, 1161
subacute, 1533, 1534
- Mandibulofacial dysostosis (Treacher Collins syndrome), 1604
- Mangafodipir, 778
- Marble bones *see* Osteopetrosis
- Marchiafava-Bignami disease, 1800
- Marfan's syndrome, 47, 48, 62, 73,
163, 290, 309, 314, 327, 423
aortic aneurysm, 312, 313, 341

- aortic dissection, 426, 427
 intraocular pathology, 1554
 skeletal features, 1147-8
 thoracic aorta dilatation, 476, 477
 valvular heart disease, 300, 303
- Marie Strumpell arthritis see Ankylosing spondylitis
- Mastectomy, 28, 50, 51
 Mastitis, 1470
 Mastocytosis, 629, 1336-7
 Mastoid lymph nodes, 510
 Mastoiditis, acute, 1606-7
 Mastoids, 1597, 1598, 1619
 Maternal serum alpha-fetoprotein screening, 1048-9, 1050
- Maxillary cyst, 1544
 Maxillary sinus, 1520, 1542
 fracture, 1391, 1392
 Mazahraud's syndrome, 1427
 Measles, 72, 163, 1791
 giant cell pneumonia, 136, 138
 subacute sclerosing panencephalitis, 1792
- Mechanical hull thumb, 1411
 Mechanical embolisation devices, 456
 Mechanical rotating devices, 450
 Mechanical thrombectomy devices, 456
- Meckel-iruber syndrome, 1060
 Meckel's diverticulum, 440, 631, 867
 radionuclide imaging, 657-8, 659
- Meconium, 1057
 aspiration syndrome, 258-9
 ileus, 859-60, 1158
 peritonitis, 1058
- Medial epicondylar fracture, 1407
 Mediastinal cyst, 58, 59, 81
 Mediastinal drains, 234, 292
 Mediastinal emphysema, 221
 Mediastinal fat deposition/ lipomatosis, 66, 68
 Mediastinal fibrosis, 80, 236, 729
 Mediastinal haemorrhage, 80, 222, 223
 Mediastinal hernia, 58
 Mediastinal lipoma, 58, 68-9, 70
 Mediastinal lymph nodes, 11, 57, 511-12
 anterior, 10, 511
 calcification, 70, 81, 155
 CT guided biopsy, 61, 62, 63
 middle, III, 12
 posterior, 10, 511
 Mediastinal lymphadenopathy, 58, 69-72, 81-2, 142, 146, 155, 188, 205, 513
 bronchial carcinoma, 108, 111-12, 115, 116, 118, 127
 drug-induced, 210
 Hodgkin's disease, 118, 122, 123
 lymphoma, 527
 oesophageal displacement, 573
- Mediastinal mass, 57, 58, 61, 65, 66, 67, 573
 calcification, 58, 60
 children, 248, 252, 261
- Mediastinal neurogenic tumours, 75, 84
 Mediastinal radiotherapy, 72
 Mediastinal trauma, 221-4
 Mediastinal vascular pathology, 61-2
 venous abnormalities, 74, 83
- Mediastinal widening, 58, 66, 68, 76-7, 224
 Mediastinitis, acute, 79, 229
 Mediastinoscopy, 115
- Mediastinum
 anatomy, 57-8, 59, 60-1
 anterior division, 57
 middle division, 57
 posterior division, 57
 radiological investigation, 58-60
 computed tomography (CT), 60-1
 magnetic resonance imaging (MRI), 58, 80, 111
 plain chest film, 5-6, 8
- Medullary cystic disease, 937, 976
 Medullary sponge kidney, 937-8, 976, 977
- Medullary thyroid carcinoma, 840, 842-3, 1514
 radionuclide imaging, 1507
 somatostatin receptor scintigraphy, 660
- Medulloblastoma (primitive neuroectodermal Wntour; PNET), 1748-9
- Meigal colon, 665
 congenital, 654
- Megaesophagus, 76-7
 Megarectum, congenital, 654
 Meigal rectr. primary, 940, 941
 Megluntine/sodium see Gastrogralin
 Meigs' syndrome, 87, 1082
- Melanoma
 anal canal, 655
 choroid/ciliary, 1560-2, 1589
 metastases, 117, 596, 597, 626, 777, 784, 785, 792, 1762
 oesophageal involvement, 570
 paranasal sinuses, 1528
 positron emission tomography (PET), 1831
 sentinel node imaging, 1832
- MELAS, 1803
 Melioidosis, 134
 Melorheostosis (Levi's disease), 1129
 Memotherm, 451
 Mendelson's syndrome, 139, 141, 195
 Menetrier's disease, 580
 Meningeal tumours, 1754-7
 Meningeal vascular markings, 1619, 1621
- Meninges of spinal cord, 165(1)
 Meningioma, 1754-7
 carotid angiography, 1679, 168(1)
 selective external carotid artery, 1683
 carotid space, 1502
 cerebropontine angle, 1611, 1613
 intracranial
 calcification, 1629, 1630, 1631
 preoperative embolisation, 458
 optic nerve, 1585-6
 optic nerve sheath, 1570
 sites, 1757
 skull erosion, 1638
 skull local hyperostosis, 1640
 skull vault vascular marking abnormalities, 1634-5
 spine, 1668-9
- Meningitis, 1784-5
 acute lymphocytic, 1791
 fungal infections, 1786
 infants, 1807
 pyogenic, 1785
 tubercular, 1785-6
 viral, 1785
- Meningocele, 78, 1050, 1051, 1052, congenital abnormalities, 1601, 1492, 1651, 1652, 1728
 cranial, 1625
 presacral, 654
- traumatic, 1656
- Meningohypophysial trunk, carotid angiography, 1680, 1699
- Meniscal cyst, 1235, 1237
 Meniscal tears, 1235, 1236, 1237, 1383, 1412
 MRI grading, 1235, 1237
- Menopause, 1072
 premature (primary ovarian failure), 1073
- Menstrual cycle, 1071-2, 1084
 follicular phase, 1071
 luteal phase, 1071-2
- Mesenchymal chondrosarcoma, 1284, 1285
- Mesenchymal hamartoma, 879
 Mesenteric cyst, 633, 867
 Mesenteric disease, 633-4
 Mesenteric ischaemia, 455, 630, 651
 Mesenteric lymph nodes, 512
 Mesenteric panniculitis, 633, 634
 Mesenteric trauma, 7117
 Mesiodens, 1537, 1538
- Mesohlastic nephroma (fetal renal hamartoma), 876, 962
- Mesothelioma
 benign (scrotal extratesticular), 1026
 malignant, 37, 38, 49, 102-3, 105, 106, 192
 biopsy tract seeding, 103, 106
 peritoneal cavity, 633
- Metabolic bone disease, 1351-69
 laboratory findings, 1352
 vitamin D abnormalities, 1352-6
- Metachromatic leucodystrophy, ISO 1
 Metallic coils see Coil embolisation
 Metallic dust disease, 17
 Metallic sterns, hiliary
 drainagelstenting, 734, 735
- Metanfetamine abuse, 428
 Metaphyscal chondrodysplasia/dysplasia/dysostosis, 1137
 Metaplastic polyps see Hyperplastic polyps
- Metastatic malignancy, 518
 Metazoan pulmonary infections, 150-2
 Metcorism, 665
 Me(hyrcrgidc, 80
- MIBG (metaio(lobenzylguanidine) scintigraphy, 42, 832, 844
- Michel deformity, 1602
 Microaneurysms, 428
 Microcephaly, 1624
 Microdontia, 1537
 Microgastria, 853
 Micronodular adrenal dysplasia, 840
 Microphthalmia, 1588-9
 Mii ropohvsporit /iieni, 195
- Microscopic colitis, 652
 Micturating cystourethrography, 898, 899
 children, 924-5
 vesicoureteric reflux grading, 946
- Micturition, 921
- Middle cerebral artery
 carotid angiography, 1681-2
 embolus, 1700
 occlusion, infra-arterial thrombolysis, 1708
- Middle ear, 1597, 1598
 carcinoma, 1611, 1612, 1614
 congenital abnormalities, 1601, 1604-5
- Middle meningeal artery, 1679
 anomalies, 1690
- Midgut volvulus, 856-7
 chronic, 857, 858
- Midline granuloma, paranasal sinuses, 1523, 1528
- Mikity-Wilson syndrome, 257
 Mikulicz's disease (mucopolysaccharidosis: benign lymphopitthelial lesion), 539
- Milroy's disease, 516
 Mineralising microangiopathy, basal ganglion calcification, 1798-9
- Miner's pneumoconiosis, 171
 Mirena coil, 1075
- Mirrizzi syndrome, 712, 722, 723, 734
 Missed abortion, 1044-5
- Mitochondrial cytopathy, cerebral manifestations, 1803-4
- Mitral prolapse, 290
 Mitral regurgitation, 302, 304, 329, 331
 acute, 296-7
 continuous wave Doppler quantitation, 329
 left ventricular angiography, 348
- Mitral stenosis, 284, 301-2, 303, 328-9
 cerebral embolus, 1700
 congenital, 394
 continuous wave Doppler quantitation, 328
- Mitral valve, 265, 266, 270
 congenital abnormalities, 394
 replacement, 291
- Mitral valve disease, 301-3
 percutaneous balloon commissurotomy, 359, 361, 361
- Mitrofanoff procedure, 1000, 1003
- Mixed connective tissue disease, 197, 1234-5
- Mixed neuronal-filial honours, 1746-7
 Monckberg's medial atherosclerosis, 1435
- Mondini deformity, 1602
 Monteggia fracture, 1407, 1408
 Morbid obesity, 606
- Morgagni's hernia, 54, 67-8, 69, 560, 562
- Morquio-Braileford syndrome
 mucopolysaccharidosis IV, 145, 1146, 1651, 1656
- Morton's neuroma, 1430
 Motor neurone disease, 1797
 Mounier-Kahn syndrome, 75, 162, 163
- Movement disorders, dopamine transport system imaging, 1816
- Moyamoya disease, 1704-5
- Mucinous cystadenocarcinoma, ovary, 1081-2, 1104
- Mucinous cystadenoma
 ovary, 883
 pancreas, 793-4, 799, 815
- Mucocele, 108, 1522
 Mucociliary escalator function, lunc scintigraphy, 43
- Mucoepidermoid tumours
 intrathoracic, 122
 sinonasal, 1527, 1528
- Mucopolysaccharidosis, skeletal abnormalities, 1144
- Mucopolysaccharidosis
 atlanto-axial subluxation/dislocation, 1656, 1657
 cerebral manifestations, 1803
 classification, 1145
 skeletal abnormalities, 1144-6, 1651

- Mucopolysaccharidosis I-H (Hurler's syndrome), | 145-6
- Mucopolysaccharidosis IV (Morquio-Brailsford syndrome), | 145, 1146, 1651, 1656
- Mucormycosis, | 47, 154, 1786, 1788
- Mucosa-associated lymphoid tissue (MALT) lymphoma, 524-5 stomach, 579, 598
- Mullerian duct remnants, | 107
- Multicystic/multicystic dysplastic kidneys, 913-14, 935, 1060
- Multielement array transducers, | 834
- Mullininfarct dementia, regional cerebral blood flow imaging, | 815
- Multilocal cystic nephroma, 876, 962
- Multilocular cystic renal lesions, 963
- Multipartite patella, 11 | 4
- Multiple enchondromas, | 275-6
- Multiple endocrine neoplasia type I, 587, 794
- Multiple endocrine neoplasia type 11 (Sipple's syndrome), 842, 1507
- Multiple endocrine neoplasia type IIa, 878
- Multiple endocrine neoplasia type IIb, 878
- Multiple endocrine neoplasia type 111, 843
- Multiple epiphyseal dysplasia (dysplasia epiphysealis multiplex), | 135-6
- Multiple fetal growth parameters, | 1043
- Multiple fibromatosis, congenital, | 288
- Multiple myeloma, 49, 1366 contrast media risks, 421 skeletal features, | 1338-40, 1529, | 1546, 1636, 1660 pathological fractures, | 1340
- Multiple pregnancy, | 1040 chorionicity establishment, | 1003, | 1064 obstetric ultrasound, | 1063-4
- Multiple sclerosis, 999, 1586, 1666, | 1667, 1799-800
- Multiple system atrophy, | 1797
- Mumps, 537, 790, 1026
- Munchmeyer's disease *see* Myositis ossificans
- Murray Valley encephalitis, | 792
- Muscle denervation, | 426 inflammatory myopathy, | 425-6 injury, | 422, 1423, 1444-5
- Muscular dystrophy, | 434
- Musculotendinous junction injury, | 420
- Mushroom growers, extrinsic allergic alveolitis, | 195
- Mustard procedure, 388, 389
- Myasthenia gravis, 58, 65
- Mycetoma, | 42, 143, 147-8, 199, 201, | 176-7 bronchial arteriography with embolisation, 47
- Mycobacterial pulmonary infection, | 44-5 *see also* Tuberculosis
- Mycobacterium avium intracellulare*, 70, 72, 156-7, 559, 586, 628, 653
- Mycobacterium batteri*, 144
- Mycobacterium kansasii*, 144
- Mycobacterium leprae*, 1175
- Mycobacterium tuberculosis*, 140, 156, 559, 870, 1785
- Mycobacterium xenopi*, 144
- Mycoplasma infection, 72 pneumonia, | 131, 135-6, 259, 517
- Mycoplasma pneumoniae*, 131, 135-6, 259
- Mycotic aneurysm, 314, 424, 1787, | 788
- Myclofibrosis, 49, 78, 1328, 1329, 1330
- Myelography, | 1645-8 complications, | 1647 contrast media, | 1645, 1646 injection errors, | 1647 technique, | 1646-7
- Myeloid metaplasia *see* Myclofibrosis
- Myelolipoma, adrenal gland, 836, 838
- Myelomeningocele, | 1050, 1051, 1052, | 1651, 1652
- Myoblastoma of bronchus (granular cell tumour), | 124
- Myocardial infarction, 295 acute, 296, 321 interventricular septum rupture, 297 late complications, 321-2 left ventricular aneurysm, 297-8 left ventricular rupture, 297 mitral regurgitation, 296 papillary muscle rupture, 296-7 pericardial effusion, 298-9 plain chest film, 296 thrombolysis, 455 transluminal angioplasty complications, 449
- Myocardial perfusion scanning, 277, 319
- Myocardial pharmacological stress studies magnetic resonance imaging (MRI), 279 radionuclide imaging, 278 stress echocardiography, 277
- Myodil, 51
- Myoepithelial sialadenitis (benign lymphoepithelial lesion; Mikulic's disease), 539
- Myopia, | 1587-8
- Myositis ossificans, | 149, 1150, | 1424-5, 1440, 1445 post-traumatic, | 1376, 1380-I
- Myotonia congenita, | 619
- Myxoedema pleural effusion, 87 *see also* Hypothyroidism
- Myxoma cardiac, 308-9, 336, 337, 338, 403, | 1056 intramuscular, | 426-7 pulmonary, | 124
- Naegleria fowleri*, 1790
- Naevi, chest wall, 50
- Nail-patella syndrome, | 1114, 1117, | 1118
- Nasal bone fracture, | 1389, 1391
- Nasal glioma (aesthesioneoblastoma), | 766
- Nasogastric intubation, 233, 234
- Nasogastric tube oesophagitis, 559
- Nasopharyngeal angiofibroma (juvenile angiofibroma), | 492-3, 1494, | 1524-5, 1712
- angiography, 446 selective external carotid artery, | 1683 preoperative embolisation, 457, 458
- Nasopharyngeal carcinoma, 518, 1636
- Nasopharynx, 543 developmental lesions, | 492 imaging techniques, | 489-91
- turnours, | 502-3 benign, | 492-4 lymphoid, | 494, 1495 malignant, | 494, 1495
- Nasopalatine cyst, | 1544
- Near drowning, | 139
- Necator americanus*, 627
- Neck, | 489-516 anatomy, | 509 imaging techniques, 11, | 489-91, | 492, 1493 computed tomography (CT), | 509-12 ultrasound, | 512-16 infratemporal fossalparapharyngeal lesions, | 498-503 lymphatic drainage, 510-11 soft tissue inflammatory disease, | 503 soft tissue neoplasms, | 501-3 lipoma, | 502, 1511 staging, | 503
- Necrotising enteritis, 628
- Necrotising enterocolitis, 687, 859, 862-3, 864
- Necrotising fasciitis, | 425-6
- Necrotising sarcoid granulomatosis, 200, 202
- Necrotising vasculitis, 428-9
- Needle biopsy bronchial carcinoma, | 114, 116 *see also* Fine needle aspiration cytology
- Neisseria meningitidis*, 1785
- Nelson's syndrome, 840
- Neonate abdominal contrast studies, 849, 850 adrenal haemorrhage, 838-9, 876-7
- brain congenital lesions, | 727, 1728-38 cystic lesions, | 809 hypoxic ischaemic damage, | 778 imaging, | 727 low-attenuation white matter at CT, 1799 ultrasound examination, | 807-12 chest radiology, 256-9 fontanels, | 624 gastrointestinal obstruction, 851-62 duodenum, 855-8 high intestinal, 858-9 low intestinal, 859-62 oesophagus, 852-3 stomach, 853-5 gastrointestinal tract, 851 hepatitis syndrome, 720 hydrocephalus, | 807, 1809, 1810 intracranial haemorrhage, | 807, | 1810 jaundice, 720 biliary scintigraphy, 718 pneumonia, 259 renal ultrasound, 923-4 skull radiography, | 623-4 skull sutures, | 1621, 1624 intracranial pressure elevation, | 626
- Nephroblastoma *see* Wilms' tumour
- Nephroblastomatosis, 962
- Nephrocalcinosis, 976, 977
- Nephrogenic adenoma, 995
- Nephroma mesohlastic, 876, 962 multilocular cystic, 876, 962
- Nephronia, acute, 914
- Nephrostogram, 902
- Nerve damage, iatrogenic, 422, 449
- Nerve sheath tumours malignant, | 428, 1431 mediaslinum, 75
- Neural tube defects, obstetric ultrasound examination, | 1050-3
- Neurenteric cyst, 78, 252
- Neurilemmoma (schwannoma) bone, | 1311-2 intracranial, | 1758-9 Antoni-A/Antoni-B subtypes, | 1759 large bowel, 644 mediaslinum, 75 optic nerve, | 1569 retroperitoneum, 848 small bowel, 625 soft tissues, | 428
- Neurinoma, orbit, | 582
- Neuroblastoma, 42, 261, 262, 826, 830, 834, 9W877, 881, 1660 adrenal medulla, 832, 833 calcification, 829, 834 imaging, 877 mediastinum, 75, 84 MIBG scintigraphy, 832-3 olfactory, | 528 orbit, | 569 skeletal features, 832-3, 1327 skull erosion, | 637 somatostatin receptor scintigraphy, 660 staging, 877
- Neurocytoma, central, | 747
- Neurodegenerative disorders, | 1795-8 white matter, | 1799-800
- Neuroendocrine tumours, somatostatin receptor scintigraphy, 660
- Neuroepithelial cerebral tumours of uncertain origin, | 746
- Neurofibroma bone, | 1301-2, 1304, 1305 dumb-bell tumour, | 1301, 1304 chest, 49, 53 large bowel, 644 mediastinum, 75, 76, 84 oesophagus, 564 orbit, | 582, 1583 retroperitoneum, 848 small bowel, 625 soft tissues, | 428, 1430, 1443 spine, | 669
- Neurofibromatosis, 48, 50, 432, 842, | 1437, 1441, 1468, 1738 bone turnours, | 1302-3, 1305, 1306 clinical presentation, | 1302 congenital pseudarthroses, | 1114 extraskeletal manifestations, | 1303, | 1306 gastrointestinal polyps, 039 intracranial calcification, | 634 orbital involvement, | 582 skull erosion, | 639 spinal involvement, | 1650, 1651, | 1654, 1655, 1659, 1667, 1669 scoliosis, | 1121, 1122

- Neurofibromatosis I (NFI; von Recklinghausen's disease)
diffuse lung disease, 207-8
intracranial lesions, 1737, 1739
jawltooth involvement, 1541
- Neurofibromatosis 2 (NF2)
acoustic neuromas, 1611, 1612
intracranial lesions, 1737-8, 1758
- Neurofibrosarcoma, mediastinum, 75
- Neurogenic tumours
carotid sheath, 1502
mediastinum, 75
- Ncuroma
carotid sheath, 1502
intracranial, 1758, 1759
petrous temporal bone, 1610-11
- Neuromuscular disorders, bladder control abnormalities, 999
- Neuronal cerebral tumours, 1746-7
- Neuronal ceroid lipofuscinosis (Batten's disease), 1802
- Neuropathic arthropathy, 1386
- Neuropathic bladder, 999
- Neurosurgery, epilepsy, 1806-7
- Neurosurgical navigation, 1721
- Neutropenic colitis (typhlitis), 632, 652, 872
- Niemann-Pick disease, 1346
- Nissen fundoplication, 561-2
- Nitrates, dietary, 591
- Nitrofurantoin, pulmonary hypersensitivity reaction, 195
- Nitrogen oxides inhalation, 195
- Nocardia asteroides*, 145, 146, 153
- Nocardiosis, 145, 146, 147, 153, 260, 294, 1786
- Nodular lymphoid hyperplasia, 631
- Nodular regenerative hyperplasia, 770
- Non-accidental injury *see* Battered child
- Non-cardiac chest pain, 550
- Non-cardiogenic pulmonary oedema, 180
- Non-Hodgkin's lymphoma, 512, 513, 523-6, 1331
cardiopulmonary transplantation complication, 242
cellular subtypes, 523
cross-sectional imaging, 528
diffuse, 523
extranodal presentations, 524-6
central nervous system, 525-6
gastrointestinal tract, 524-5
head and neck, 526
skeletal lesions, 526, 1331-6
testes, 526
thorax, 526
follicular (nodular), 523, 524
high-grade, 1335-6
intrathoracic, 118-19
low-grade, 1332-3
mesenteric involvement, 633
nodal presentations, 523-4
REAL classification, 523
staging, 524
treatment, 524, 1333
- Non-ionic contrast agents, 419, 618, 926-7
- Non-ossifying fibroma, 1249, 1287, 1289
- Non-rotation anomaly, 858
- Non-seminomatous germ cell tumours, 1028, 1029, 1031, 1032
- Non-specific urethritis, 1017
- Non-steroidal anti-inflammatory drug (NSAID) enteritis, 632
- Noonan's syndrome, 403, 936
- Nose, sinonasal physiology/anatomy, 1520
- Nuchal translucency, 1040, 1041, 1049, 1055
- Nutcracker oesophagus, 550
- Oat cell bronchial carcinoma *see* Small cell bronchial carcinoma
- Ohlterative bronchiolitis, 172-3, 199
- Obscure gastrointestinal bleeding syndrome, 630
- Obstetric ultrasound, 1039-66
biophysical profile, 1047
cardiorespiratory system, 1055-7
central nervous system, 1049-55
cervix evaluation, 1065
computerised reporting systems, 1041
cystic hygroma, 1056, 1057
Doppler ultrasound, 1039
ectopic pregnancy, 1047-8
equipment, 1039
fetal anomaly scanning, 1041
fetal gender, 1049
fetal growth, 1046-7
fetal malpresentation, 1040
fetal structures detection, 1043
first trimester (early pregnancy), 1040, 1041, 1043-4
complications, 1044-6
human chorionic gonadotrophin levels, 1045-6
gastrointestinal system, 1057-9
genetic screening, 1048-9
genitourinary system, 1059-61
gestational age assessment, 1040, 1041-3
hydrops fetalis, 1057, 1063
indications, 1040
multiple pregnancy, 1040, 1063-4
musculoskeletal system, 1061-3
normal examination, 1040-1
nuchal translucency measurement, 1040, 1041, 1049, 1055
placenta, 1064-5
second and third trimester, 1040, 1041, 1042
three-dimensional imaging, 1039-40, 1834
tissue harmonic imaging, 1039
transabdominal, 1039, 1043
transvaginal, 1039, 1043, 1044
- Obstructive pulmonary disease, chronic, 75, 161, 165-72, 240, 290
- Obturator lymph nodes, 512
- Occipital lymph nodes, 510
- Occipito-mental (Waters) view, 1390, 1391, 1519
- Ochronosis (alkaptonuria), 50, 1366, 1367, 1438
- Ocular masses, 1589-91
- Ocular prostheses, 1592
- Oculomotor pareses, 1691, 1693-4, 1770
- Odontogenic keratocyst (primordial cyst), 1542, 1543
- Odontoid fracture/relapsed fracture (Mach effect), 1398
- Odontomes, jaw, 1535
complex, 1535
compound, 1535, 1536
- Oesophageal adenoma, 563
- Oesophageal atresia, 161, 790, 1057
associated tracheal abnormalities, 249, 250
tracheo-oesophageal fistula, 852-3
without tracheo-oesophageal fistula, 852
- Oesophageal cancer, 76, 564-9, 1510
adenocarcinoma, 565
advanced, 565-6
early, 565
leiomyosarcoma, 569-70
lymphoma, 570
malignant melanoma, 570
management, 569
metastatic tumours, 569
spindle cell carcinoma (carcinosarcoma: pseudosarcoma), 569, 570
squamous cell carcinoma, 564
staging, 566-9
lymphadenopathy, 568-9
- Oesophageal disorders, 76-7, 84
children, 864-6
- Oesophageal diverticulum, 553, 554, 853
- Oesophageal duplication cyst, 78, 564, 868
- Oesophageal extrinsic compression, 866
- Oesophageal foreign body, 570, 865-6
- Oesophageal haematoma, 571
- Oesophageal intramural pseudodiverticulosis, 559-60
- Oesophageal leiomyoma, 563, 564, 866
- Oesophageal leiomyomatosis, 554
- Oesophageal lipoma, 564
- Oesophageal manometry, 549, 550
- Oesophageal motility, 549-54
abnormalities, 549-50
peristalsis, 549
transit test, 549, 550-2
- Oesophageal obstruction, neonate, 852-3
- Oesophageal papillomatosis, 563
- Oesophageal perforation, 571
- Oesophageal reflux, 555
- Oesophageal retention cyst, 564
- Oesophageal rupture, 79, 224, 225
- Oesophageal scintigraphy (transit test), 549, 550-2
- Oesophageal stenosis, congenital, 853
- Oesophageal stricture, 76
children, 866
corrosive, 558, 559
reflux oesophagitis, 556, 557
- Oesophageal tears, infra-arterial vasoconstrictor infusion, 454
- Oesophageal tumours
benign, 563-4
malignant, 564-70
- Oesophageal varices, 571-2
bleeding, 750
children, 866
haemorrhage, 440
- Oesophageal web, 548-9, 853, 1497, 1498
- Oesophagitis
caustic, 559
children, 866
drug-induced, 559
nasogastric tube, 559
opportunistic infections, 557-8
radiation, 559
reflux, 550, 552, 556-7
- Oesophagus
anatomy, 543
segments, 543-4
extrinsic impressions, 572-3
imaging, 543-4
- Oil cyst, breast, 1462, 1463
- Olecranon fracture, 1407
- Olciothorax, 231
- Olfactory neuroblastoma, 1528
- Oligodendroglial tumours, 1744
- Oligodendroglioma, 1744, 1745
- Oligohydramnios, 1057
- Omental cyst, 867
- Omphalocele (exomphalos), 864, 1058, 1059
- On-line journals for digital workflow, 1844
- Onyx embolic agent, 1711, 1715
- Operative cholangiography, 719-20
- Ophthalmic artery, 1574, 1575
carotid angiography, 1680
- Ophthalmic vein, 1574
thrombosis, 1584
- Optic canal/foramen, skull radiography, 1573, 1618-19, 1620
- Optic nerve, 1574, 1575
trauma, 1577
- Optic nerve drusen, 1592
- Optic nerve glioma, 1569-70, 1585
skull erosion, 1638
- Optic nerve meningioma, 1585-6
- Optic nerve sheath meningioma, 1570
- Optic nerve tumours, 1569-70
- Optic nerve-sheath complex abnormalities, 1584-7
- Optic neuritis, 1586, 1587
- Oral cancer, 1497, 1544-6
- Oral cholecystography, 718-19
- Oral contraceptive pill, 1073
- Orbit, 1566-70, 1573-94
anatomy, 1574-5
arteriovenous fistula, 1568-9
examination techniques, 1566, 1573-5
ultrasound, 1566-70
haemangioma, 1568
infection, 1577-8
inflammatory disease (orbital pseudotumour), 729, 1567-8, 1578-9
masses, 1569, 1579-84
lymphoma, 525, 1568, 1569, 1593
metastatic tumours, 1569, 1582, 1583, 1587
trauma, 1575-7
varices, 1568
vascular lesions, 1568-9
- Orbital cellulitis, 1520, 1521, 1578
- Orbital emphysema, 1374, 1391
- Orbital foreign body, 1577, 1578
- Orbital fracture, 1389, 1391
blow-out, 1374, 1391, 1575, 1577
- Orbital implants, 1592
- Orchitis, 1026
- Organic acidopathies, 1802-3
- Ornithosis, 137
- Oroantral fistula, 1537
- Oropharyngeal carcinoma, 1497, 1498
- Oropharynx, 543
- Orthoptic nystagmus, 1000, 1001, 1003
- Os odontoideum, 120, 1398, 1656
- Os peroneum, 1114
- Os tibiae externum, 1114
- Os trigonum, 1114, 1115

- Osgood-Schlatter disease (tibial tubercle osteochondritis), 1186-7, 1377, 1378
- Osler-Weber-Rendu syndrome (hereditary haemorrhagic telangiectasia), 316, 564, 743, 1712
- Osseous choristoma (choroidal osteoma), 1562-3
- Ossicular dislocation, 1605-6, 1607
- Ossification centres, 1847-9
- Ossifying fibroma, 1640
- Ossifying pneumonitis (idiopathic pulmonary ossification), 214
- Osteitis deformans *see* Paget's disease
- Osteitis pubis, 1161
- Osteoarthritis, 1222-9
 - cysts and geodes, 1223, 1224, 1312
 - erosive, 1226
 - hands, 1225
 - hip joint, 1223-4
 - joint space narrowing, 1222
 - joint space remodelling, 1222-3
 - knee joint, 1225, 1227
 - loose bodies, 1223, 1224, 1225
 - secondary to rheumatoid arthritis, 1207
 - houlderjoint, 1224-5, 1227
 - spine *see* Spinal degenerative disease
- Ostoclastoma, 1258-61, 1661
- Osteochondritis dissecans (osteochondral fracture), 1190-1, 1374, 1375, 1386, 1387
- Osteochondritis (osteochondrosis), 1181-91, 1377
 - adults, 1189-90
 - capitellum, 1188
 - femoral capital epiphysis, 1182-6
 - innate, 1189, 1378, 1380
 - medial tibia condyle (tibia vara), 1189
 - metatarsal head, 1187
 - patella, 1188-90, 1377
 - tarsal navicular, 1187
 - tibial tubercle, 1186-7, 1377, 1378
 - types, 1182
 - vertebral body (vertebra plana), 1187, 1341
 - vertebral epiphyseal plates (adolescent kyphosis), 1188
- Osteochondroma, 1272, 1278-9
 - diaphyseal aclasis, 1278, 1280, 1281
- Osteoclastoma (giant cell tumour), 1292-3, 1294
 - jaws, 1539, 1544
- Osteogenesis imperfecta, 1062, 1114, 1124-6, 1366
 - petrous temporal bone, 1612-14
 - spinal involvement, 1653, 1658
 - type I, 1124
 - type 2, 1125
 - type 3, 1125
 - type 4, 1125-6
- Osteogenic sarcoma
 - Paget's disease malignant
 - degeneration, 1196, 1197
 - soft tissues, 1441
 - solitary pulmonary metastases, 117
- Osteoid osteoma, 1249, 1255-8, 1259, 1260, 1661
- Osteolytic lesions
 - Burkitt's lymphoma, 1336, 1337
 - eosinophilic granuloma, 1341
 - Hand-Schuller-Christian disease, 1343
 - Hodgkin's disease, 1331
 - leukaemia in children, 1327, 1329
 - multiple myeloma, 1339, 1340
 - non-Hodgkin's lymphoma, 1336
 - plasmacytoma, 1337, 1338, 1339
- Osteoma, 1254-5
 - jaws, 1544
 - paranasal sinuses, 1523-4
 - petrous temporal bone, 1609, 1610
 - skull local hypostosis, 1640
- Osteomalacia, 49, 1353, 1354, 1355, 1377
 - axial, 1356
 - spinal involvement, 1653
- Osteomyelitis, 1155-63, 1520
 - adults, 1155
 - bone biopsy, 1159
 - Brodie's abscess, 1159-60
 - children, 1155
 - cloacae, 1156, 1158
 - complications, 1161
 - computed tomography (CT), 1158
 - feet, 1161
 - hands, 1161
 - infants, 1155
 - involucrum formation, 1156
 - magnetic resonance imaging (MRI), 1158-9
 - mandible, 1160
 - osteonecrosis, 1180
 - pelvis, 1161
 - plain film, 1156-7
 - radionuclide imaging, 1157-8
 - sclerosing of Garre, 1159
 - sequestra, 1156, 1158
 - skull, 1160, 1161, 1638-9
 - spine, 1161-2, 1659
 - subacute of mandible, 1533, 1534
 - Osteonecrosis, 1179-81, 1385
 - causes, 1181, 1182
 - drug-related, 1181
 - dysbaric (Caisson disease), 1191-2
 - epiphyseal abnormalities, 1180
 - magnetic resonance imaging (MRI), 1181
 - pathology, 1179
 - radiation-induced, 236, 238
 - radionuclide imaging, 1180, 1181
 - stages, 1179-80
 - Osteopathia condensans dissimminata (osteopoikylolysis), 1130
 - Osteopathia racemosa, 24
 - Osteopathia striata (Voorhoeve's disease), 1130
 - Osteonetrosis (marble bones; Albers-Schonberg disease), 49, 1126, 1127, 1128
 - hyperostosis of skull, 1640
 - jawteeth involvement, 1128, 1541
 - Osteopoikylolysis (osteopathia condensans dissimminata), 1130
 - Osteoporosis, 49, 1234, 1356-8, 1377
 - ankylosing spondylitis, 1220
 - causes, 1356
 - Cushing's syndrome, 839, 1358, 1359
 - dissuse, 1363
 - drug-toxin-induced, 1366
 - endocrine disorders, 1358-66
 - hyperthyroidism, 1359
 - hypogonadims, 1358-9
 - hypoparathyroidism, 1360-1
 - idiopathic juvenile, 1126, 1127, 1356-7
 - idiopathic male, 1357
 - localised, 1367
 - osteomyelitis, 1156
 - postmenopausal, 1356
 - regional migratory, 1367
 - rheumatoid arthritis, 1202
 - senile (involutional), 1356
 - skull vault, 1639
 - transient (regional), 1367, 1380
- Osteosarcoma, 1250, 1261-9, 1270
 - anaplastic, 1262
 - central, 1266-7, 1272
 - chondroblastic, 1262
 - diaphyseal, 1263, 1266, 1271
 - fibroblastic, 1262
 - giant cell-rich, 1293, 1294
 - imaging features, 1263
 - jaws, 1546, 1547
 - metastatic spread, 1262, 1264, 1265
 - multifocal, 1267
 - osteoblastic, 1262, 1265, 1267
 - Paget's disease, 1262, 1268-9, 1274
 - parosteal, 1268, 1273
 - radiation-induced, 1267, 1272
 - skull local hyperostosis, 1640
 - soft tissue, 1267, 1272
 - mediastinum, 69
 - telangiectatic, 1262, 1263
 - Osteosclerosis
 - benign in jaw, 1535, 1536
 - metaphyseal, leukaemia in children, 1327
 - Ostiomeatal complex, 1520
 - Otitis externa, malignant, 1612, 1614
 - Otosclerosis (otospongiosis), 1612-13
 - central, 1613-14
 - Ovarian carcinoma, 1081, 1085, 1086, 1092, 1104
 - metastases, 632, 633, 757, 777
 - risk factors, 1081
 - screening, 1084
 - Ovarian cyst, 1078-9, 1084, 1091, 1102, 1103
 - aspiration/drainage, 1092-3
 - children, 883, 884
 - torsion, 688, 1091
 - Ovarian cystadenocarcinoma, 1104
 - Ovarian cystadenoma, 1104
 - Ovarian failure, primary (premature menopause), 1073
 - Ovarian follicles, 1102
 - Ovarian hyperstimulation syndrome, 1084
 - Ovarian torsion, 884, 1079
 - Doppler ultrasound, 471
 - Ovarian turnouts, 1004, 1081-4
 - children, 883
 - diagnostic features, 1083-4
 - Doppler ultrasound, 471
 - epithelial, 1081-2
 - malignant, 1081
 - metastatic (Krukenberg's tumours), 1083
 - Ovarian vein syndrome, 493
 - Ovaries, 1070-1, 1090, 1102-3
 - blood supply, 1071, 1072
 - Doppler ultrasound, 471
 - multifollicular, 1072-3
 - ovulation disorders, 1072-3
 - size/volume estimation, 1070, 1102
 - Ovulation disorders, 1072-3
 - Ovulation induction, 1084
 - Oxalosis (primary hyperoxaluria), 1366
 - Oxycephaly, 1624
 - Oxygen toxicity, pulmonary damage, 195
- Pacchionian body calcification, 1623
- Pacemakers, 235, 294, 295
- Pachydermoperiostosis, 1232
- Pachygyria, 1734-5
- Paediatric abdomen, 849-84
 - adrenal masses, 876-8
 - cysts, 867, 868
 - gastrointestinal masses, 882-3
 - hepatohiliary masses, 878-81
 - imaging techniques, 849-51
 - pelvic masses, 883-4
 - renal masses, 874-6
 - splenic masses, 882
- Paediatric chest, 247-62
 - cardiothoracic ratio, 249
 - congenital abnormalities, 249-50, 251-4
 - diaphragm, 254-6
 - pulmonary underdevelopment, 250-1
 - imaging techniques, 247-8
 - immunocompromised child, 260
 - inhaled foreign body, 260, 261
 - newborn infant, 256-9
 - older child, 259-63
 - pleural effusions, 249
 - soft tissue artefacts, 249
 - thymus *see* Thymus
 - trachea, 249
- Paget's disease (osteitis deformans), 49, 50, 1192-8
 - complications, 1196, 1197
 - differential diagnosis, 1196, 1198
 - imaging, 1193-6
 - jaw lesions, 1534, 1536
 - long bones, 1193
 - malignant degeneration, 1196, 1197
 - osteoporosis circumscripta, 1193, 1639
 - pathological phases, 1193
 - pelvis, 1193-4, 1195
 - petrous temporal bone, 1614
 - sarcomas, 1262, 1268-9, 1274
 - skull, 1193, 1194, 1640
 - spinal involvement, 1194, 1195, 1653, 1658, 1662
- Palmz stem, 451, 734
- Panbronchiolitis (Japanese panbronchiolitis), 173
- Pancoast (superior sulcus) tumours, 25, 97, 109-10, 113, 114, 125, 126, 128, 1254
- Pancreas, 787-822
 - anatomy, 796, 811
 - ductal, 806, 807, 812
 - relations, 810, 812
 - variations, 812
 - blood supply, 812
 - calcification, 787, 788, 791, 792, 796, 798, 819, 821
 - congenital disorders, 789-90
 - development, 808-9, 810
 - investigation methods, 787-9
 - computed tomography (CT), 795-6
 - endoscopic retrograde pancreatography (ERP/ERCP), 806-9
 - endoscopic ultrasound, 821
 - magnetic resonance imaging (MRI), 801-2
 - ultrasound, 810-12
 - trauma, 704-5
 - ultrasound-guided interventions, 820

- Pancreas divisum. 790, 791, 806.
808-9, 810, 818
- Pancreatic adenocarcinoma. 441, 788,
792-3, 798, 799, 802, 803, 804,
805, 807-8, 913, 840
angiography, 444
hiliary drainage/scintigraphy, 733
differential diagnosis, 815
fine needle aspiration biopsy, 814
gastroduodenal
infiltration/displacement, 597,
601
pancreatic duct abnormalities. 732.
807, 813
staging, 814
uncinate process, 814
- Pancreatic agenesis. 790
- Pancreatic aplasia. 790
- Pancreatic cavernous lymphangioma.
788
- Pancreatic cyst. 792, 796, 800, 819
congenital, 792, 881
- Pancreatic cystadenocarcinoma, 799
- Pancreatic cystadenoma. 444, 445
- Pancreatic cystic tumours, 793-4, 799,
815
- Pancreatic duct
calculi, 806, 808, 809, 819
obstruction, 807, 808, 818
tumours, 794
- Pancreatic false aneurysm
embolisation, 456
- Pancreatic haemangioma. 788
- Pancreatic haematoma, 788
- Pancreatic mass in children, 881
- Pancreatic microcystic adenoma, 800
- Pancreatic pseudocyst, 78, 686-7, 788,
791, 792, 819, 820, 881
percutaneous drainage, 821
- Pancreatic transplantation, 800, 801
- Pancreatic trauma, 800, 820
- Pancreatic tumours, 788, 789, 792-4,
799-800, 813-15
angiography, 444
calcification, 788
see also Islet cell tumours
- Pancreaticoblastoma. 792, 881
- Pancreatitis
acute. 87, 686-7, 788, 789, 790-1,
792, 796-7, 805, 806, 815-16
aneurysms, 428, 429
complications, 806, 816, 817
localised ileus (Sertini loop), 621
recurrent, 817
severity indicators, 817
chronic. 789, 791, 792, 798, 804,
805, 816, 808, 817-18, 881
hiliary strictures. 729-30
pancreatic duct calculi, 808, 809,
819
local, 816
hereditary, 789, 791
- Papilla of Santorini. 578
- Papilla of Vater, 578
- Papillary epithelial pancreatic tumours,
794, 799
- Papillary fibroblastoma, 337
- Papillary necrosis, 977-8
- Papilloma
breast, 1465, 1473
bronchus, 124
larynx, 1498
paranasal sinuses, 1524
trachea, 161
- Paracaecal hernia. 631
- Peracolic abscess. 645, 682
- Paraduodenal hernia, 599-600, 631
- Paraffin aspiration, 195
- Paraganglioma. 833, 845, 1759
somatostatin receptor scintigraphy.
660, 661
- Paragonitiasis
brain infection. 1633, 1791
lung manifestations, 151
- Paragonimus westermani*. 1633, 1791
- Parainfluenza pneumonia, 259
- Paralytic ileus, 620, 668, 678-9, 688,
871
- Paramesenteric cyst. 1426
- Parapharyngeal lesions, 1498-503
masses, 1501-3
- Parapharyngeal space. 534
- Parasitic disease
biliary system, 730-1
brain, 1788-91
colitis. 652
small bowel, 627
soft tissue calcifications. 1437-8
- Paraspinal lines, 6, 58
- Paraspinal mass, 61, 62
- Parathyroid adenoma, 68, 69, 1510,
1515
radionuclide imaging. 1507, 1508,
1509
therapeutic embolisation, 458
- Parathyroid carcinoma. 1515
- Parathyroid gland
positron emission tomography
(PET). 1508-9
radionuclide imaging, 1507-9
ultrasound, 1514-15
- Parathyroid hyperplasia, 1515
radionuclide imaging. 1507, 1508
- Parathyroid tumours, 495
- Paratracheal stripelline. 5, 58, 61
- Paratracheal/paratracheobronchial
lymph nodes, 5, 61
- Paravertebral lesions, 77-8
- Parietal foramina, congenital. 1626
- Parietal lymph nodes, 10
- Parkinson's disease, 999, 1796-7
dopamine transport system imaging,
1816
- Parosteal osteosarcoma. 1268, 1273
- Parotid abscess, 538
- Parotid gland, 1515
anatomy. 533, 534
parapharyngeal masses. 1501, 1502
- Parotid haemangioma, 540
- Parotid lymph nodes. 510
- Parotid sialosis, 538
- Parotid tumours, 535, 540, 541, 542,
543
- Parotitis. acute. 537-8
- Partial anomalous pulmonary venous
connection, 74, 395
- Partial gastrectomy
Billroth I. 605, 606
Billroth II (Polya operation), 606,
607, 608
early/late complications, 591, 607,
608, 610-11
- Patella
congenital anomalies, 1114
fracture, 1411
osteochondritis. 1188-9, 1377
- Patent ductus arteriosus, 363, 374,
376-8
imaging, 377
physiological changes at birth, 369
treatment. 228, 377-8
transcatheter occlusion, 364, 378
- Patent foramen ovale. 267, 374
paradoxical embolus, 437
- Patent processus vaginalis, 1022-3
- Patent urachus, 989
- Paterson-Brown Kelly syndrome,
1497, 1498
- Pathological fractures. 1377
Gaulche's disease, 1344-5
multiple myeloma, 1340
Paget's disease, 1196, 1197
ribs, 49
- Pectoralis muscle, congenital
absence/hypoplasia. 1454,
1455
- Pectus excavatum, 47-8, 290, 291
- Pellicular-Merzbacher disease. 1802
- Pelligrini-Stieda lesion, 1381, 1437
- Pelvic abscess. 991
- Pelvic congestion syndrome. 1170
- Pelvic extraperitoneal spaces, 888
- Pelvic floor. 888
- Pelvic fracture. 1400-4
acetabulum, 1402-4
anteroposterior compression, 1401,
1402
avulsion injuries, 1402
classification, 1400-1
isolated, 1402
lateral compression. 1401
major blood vessel damage, 707
mixed patterns, 1402, 1403
straddle, 1402, 1403
vertical shear, 1402
- Pelvic inflammatory disease. 884,
1080-1, 1089, 1104
- Pelvic kidney. 913, 930-1
- Pelvic lipomatosis, 654, 991, 1004
- Pelvic lymph nodes, 512-13
- Pelvic masses in children. 883-4
- Pelvic phlebography, 489-97
- Pelvic varicosities. 493
- Pelviometry. 1065
- Pelviureteric junction obstruction, 970
congenital, 938-40
dynamic radionuclide studies. 918
endoscopic pyelosis
(endopyelotomy), 903
percutaneous balloon dilatation, 904
prenatal diagnosis, 1060-1
- Pelviureteric junction trauma. 702,
703, 975
- Pemphigoid, oesophageal involvement.
549, 559
- Pendred's syndrome, 1506, 1603
- Penile carcinoma, 1033-4
- penis, 889, 896, 1033-4
haemodynamics assessment. 1035
trauma, 1034
- Pentology of Cantrell, 1059
- Peptic ulcer disease
anastomosis site. 608
hiphasic barium meal examination,
581-2
children, 866
gastric outlet obstruction, 669
oesophageal reflux. 555, 557
perforation, 585, 668
- Percutaneous arterial catheterisation,
418
anaesthesia, 418-19
complications, 421-2, 436
contrast media. 419
dosage. 419-20
reactions, 420-1
historical aspects. 411
pharmacology, 421
- Seldinger technique. 418
selective/superselective
catheterisation. 418
systemic heparinisation, 421
technique, 418-20
- Percutaneous hiliary tract stone
procedures. 725, 733
- Percutaneous biopsy
hepatobiliary. 733
kidney. 905
magnetic resonance imaging (MRI),
1446
pancreas, 787
- Percutaneous cholangiography (PTC),
719
- Percutaneous gastrostomy. 609
- Percutaneous mitral balloon
commissurotomy, 359, 360,
361
- Percutaneous nephrolithotomy, 900,
901, 902-3, 904
- Percutaneous nephrostomy, 900,
901-2, 969
- Percutaneous ovarian
aspiration/drainage, 1092-3
- Percutaneous pancreatography, 787
- Percutaneous renal cyst aspiration.
904-5
- Percutaneous transluminal angioplasty.
446, 447-51
adjuvant techniques. 450-1
atheronur removing devices, 450
laser-assisted angioplasty, 450-1
mechanical rotating devices. 450
antiplatelet drug therapy, 447-8
carotid artery, 450, 1709-11
coeliac artery. 450
coronary arteries (PTCA). 281,
358-9
restenosis. 358
innominate artery. 450
peripheral vascular disease. 447-9
renal artery. 450, 965
superior mesenteric artery. 450
vertebral artery. 450
- Percutaneous vertebroplasty, 1721-2
- Pericardial calcification, 333, 334
- Pericardial cyst. 61, 307, 308, 335, 336
- Pericardial defect, congenital, 308
- Pericardial disease, 305-7, 332-5
- Pericardial effusion. 112, 305, 306,
307, 309
computed tomography (CT), 333-4
echocardiography, 332-3
fetal sonographic detection, 1056
magnetic resonance imaging (MRI),
334
post-myocardial infarction, 298-9
- Pericardial hydatid disease, 308
- Pericardial masses. 335
- Pericardial space. 265, 268
- Pericarditis, 306, 307
computed tomography (CT), 333-4
echocardiography. 332-3
magnetic resonance imaging (MRI),
334
- Pericardium, 265
congenital absence, 334-5
Pericolic abscess. 645, 649
- Perilunate dislocation, 1409-10
- Perinephric abscess, 943-4
- Perinephric space. 886-7
- Periodontal disease. 1532-3
- Periodontal ligament, 1531
- Perioptic subarchnoid space dilatation.
1596

- Periosteal reaction, 1153-5
causes, 1153
Gaucher's disease, 1345
leukaemia in children, 1327
non-Hodgkin's lymphoma, 1335
rheumatoid arthritis, 1204, 1209
stress fractures, 1413
thyroid acropachy, 1 155
tumours, 1153-4, 1249
vascular insufficiency, 1154
- Peripancreatic varices, 779
- Peripheral arterial spasm, 435
- Peripheral arteries
Doppler ultrasound examination, 466-8
bypass graft stenosis, 466-7
dialysis grafts, 467-8
false aneurysm, 467
magnetic resonance angiography, 474, 481, 482
contrast-enhanced (CE-MRA), 474, 475-6
- Peripheral vascular disease, 417
percutaneous transluminal angioplasty, 447-9
adjuvant techniques, 450-1
balloon size, 448
haemodynamic pressure measurements, 448-9
subintimal procedure, 448
- Perisplenic varices, 779
- Peritoneal cavity, 632-4
abnormal fluid collections, 633, 680-1
anatomy, 632-3
infectious disease, 618, 633, 643
primary disease, 633-4
spread of infection, 681
- Peritoneal fluid, 680-1, 817
- Periventricular leucomalacia, 1811
- Pernicious anaemia, 591, 828
- Persistent fetal circulation, 258
- Persistent hyperplastic primary vitreous, 1557, 1564, 1591
- Persistent primitive sciatic artery, 423
- Perthes' disease (osteochondritis of femoral capital epiphysis), 1114, 1182-6, 1378-9
Catterall classification, 1 183
imaging, 1183-6
stages of disease, 1183
- Pes anserinus bursitis, 1426
- Petroclinoid ligament calcification, 623
- Petrol aspiration, 195
- Petrous temporal bone, 1597-614, 838
benign neoplasms, 1609-11
bone dysplasias, 1612-14
cholesteatoma, 1607-9
congenital ear deformities, 1600-5
congenital vascular anomalies, 1605
imaging techniques, 1597-600
skull radiography, 1597, 1619, 621
inflammatory disease, 1606-7
malignant neoplasms, 1611-12
trauma
Fracture, 1605
ossicular dislocation, 1605-6, 607
- Peutz-Jeghers syndrome, 638, 792, 871
gastrointestinal hamartomatous polyps, 589, 626-7, 638
- Peyronie's disease, 896, 1034
- pH probe 24h monitoring, gastro-oesophageal reflux, 865
- Phaeochromocytoma, 42, 75, 495, 785, 826, 829, 841-5, 846, 847, 848, 878
blood sampling/hormone assay, 829, 844
ectopic tumours, 841, 844, 846
hormone secretion, 840, 841
imaging investigations, 832, 833, 843-5
somatostatin receptor scintigraphy, 660, 661
- Phakomatoses, 1735-8
- Phalangeal distal atrophic changes, 124
- Pharyngeal pouch, 1495, 1496
lateral, 547
posterior (Zenker's diverticulum), 547
- Pharyngo-oesophageal pouch, 76
- Pharynx, 1489-504
anatomy, 543
cysts, 1497
functional disorders, 1495, 1496
imaging techniques, 1489-91, 1492, 493
infections, 1497
motility assessment, 544-8
trauma, 1495-7
tumours, 1497-8
- Phased array coils, 1417, 1821
- Phenylketonuria, 1802-3
- Phlebography, 483-507
contrast media, 486
hepatic veins, 493
lower limb, 483-8
pelvis/abdomen, 489-97
portal system, 501-3
renal veins, 494, 497
superior vena cava, 497-8
upper limb, 497-8
- Phlebolith, 1435, 1436, 1441, 1443
- Photodensitometry (radiographic absorptiometry), 1351
- Photodynamic therapy, image-guided, 1722
- Phrenic nerve, iatrogenic damage, 227, 228
- Phthisis bulbi, 1566, 1589
- Phyllodes tumour, 1465, 1466
- Phytobezoar, 607, 608, 866
- Pick's disease, 1796, 1815
- Picture archiving and communication system (PACS), 1841, 1842, 843
networks, 1843-4
- Pigeon breeders, extrinsic allergic alveolitis, 195-6
- Pigmented villonodular synovitis, 1308, 1309, 1310, 1311, 1422, 1428
- Pineal calcification, 1621-2, 1630
- Pineal displacement, 1627
- Pineal tumours, 1630, 1747-8
- Pineoblastoma, 1748
- Pineocytoma, 1748
- 'Pink puffers', 171
- MOPED (Prospective Investigation of Pulmonary Embolism), 343, 344, 345
- Pituicytoma (granular cell tumour; choristoma), 1765
- Pituitary adenoma, 495, 1749-52
classification, 1749
Cushing's syndrome, 839-40
macroadenomas, 1751, 1752
microadenomas, 1637, 1749, 1750, 751
skull erosion, 1637
somatostatin receptor scintigraphy, 660
- Pituitary carcinoma, 1637
- Pituitary fossa, 1619, 1621
- Pituitary gland calcification, 1623
- Pituitary tumour calcification, 1631
- Placenta, 1066
ultrasound examination, 1064-5
- Placenta praevia, 1064, 1066
- Placental abruption, 1064
- Placental infarcts, 1064-5
- Plagiocephaly, 1624
- Plain abdominal film
acute abdomen, 663, 664-8
adrenal glands, 827-8, 833
biliary tract, 712-14
gynaecological imaging, 1085
intra-abdominal sepsis, 682
large bowel examination, 636
liver disorders, 737-42
normal appearances, 664-5
paediatric abdomen, 849
pancreas, 787-8
pancreatitis, acute, 791
postoperative abdomen, 679
small bowel examination, 615
small bowel obstruction, 618-19, 670, 671
spleen, 747
ulcerative colitis, 646-7
- Plain chest film, 1, 2-29
acute abdomen, 663-4
air bronchogram, 14-16
air-space filling, 16-17
aortic aneurysm, 425
aortic arch traumatic aneurysm, 425
aortic dissection, 427
apical shadowing, 25
apical view, 4
asbestosis, 194, 195
asthma, 166, 167
bacterial pneumonia, 131-3, 134, 135
band shadows, 18-19
bronchial carcinoma, 115
bronchiectasis, 163, 164
calcification, 24-5
cardiac disease, acquired, 283-90
cardiac enlargement, 283-4
left atrial enlargement, 284
pulmonary vascular patterns, 286, 287-90
right atrial enlargement, 284-5
right ventricular enlargement, 285-6
thoracic cage changes, 290
cardiac disease, congenital, 363, 364, 405
left-to-right shunt, 369
cardiac imaging, 271-3, 275, 317-18
cardiac size, 271, 283-4
cardiac implants, 294-5
cardiac transplantation, 293-4
cavitating lesions/cysts, 22-3
chest trauma, 217
chronic bronchitis, 167, 168
coal worker's pneumoconiosis, 191
cystic fibrosis, 165
decubitus view, 4, 5
diffuse lung disease, 17-18
elderly person, 28-9
emphysema, 168, 169
fluid levels, 23-4
fungal chest infection, 145-9
hilar enlargement, 27
inspiratory/expiratory paired films, 5
intensive care patient, 290
interpretation of abnormalities, 14-29
Kerley B lines, 9, 11, 12, 19, 131, 145, 289
lateral view, 2, 13
limitations, 29
linear shadows, 18-19
lordotic view, 4, 177
lung cancer, 108-11
lung consolidation, 183, 185, 186
lung/lobar collapse, 26-7, 176, 177, 178, 179, 180, 181, 182
lymphadenopathy, 513
mediastinal disease, 57, 58
mediastinum, 57
oblique view, 3-4
opaque hemithorax, 28
paediatric chest, 247
pericardial disease, 305-7
pleural effusion, 88
pneumothorax, 94
postcardiac surgery, 227, 228-9, 292-3
postero-anterior (PA) view, 1, 2
bones, 12-13
hidden areas, 8
soft tissues, 11-12
viewing procedure, 5-13
pulmonary arterial hypertension, 287-8
pulmonary embolism, 237
pulmonary nodule, 19-22
pulmonary oligoemia, 290
pulmonary plethora, 289, 290, 372, 376, 378, 386
pulmonary vascular pattern, 271, 273, 286-90
abnormal patterns, 287-90
regional abnormalities, 290
pulmonary venous hypertension, 288-90
silhouette sign, 14
silicosis, 189, 191
subphrenic abscess, 53
supine view, 4-5
technical aspects, 5
tuberculosis, 140-2
unilateral hypertranslucency, 27-8
viral pneumonia, 136, 137
- Plain film radiology
arterial imaging, 41 1-12
hip dysplasia, congenital (congenital dislocation), 11 10-1 1
lymphatic system, 513
neck lateral view, 1489, 1490
salivary glands, 535
skull see Skull radiography
soft tissue artefacts, 1432
soft tissues, 1432-42
spine, 1644
- Plasma cell granuloma, pulmonary, 124
- Plasmacytoma, 69, 1337-8, 1339, 1498, 1529, 1637
- Plastic stents, 734
- Plate atelectasis (Fleischner lines), 19
- Platybasia, 1625, 1653
- Pleomorphic adenocarcinoma, 793
- Pleomorphic adenoma
lacrimal gland, 1592
paranasal sinuses, 1528
salivary glands, 534, 536, 540, 502, 1515

- Pleomorphic xanthoastrocytoma, 1743
- Pleura
 anatomy, 87
 calcification, 98-100, 101, 102
 asbestos exposure-related
 plaquescalcification, 193, 196
 physiology, 87
 scarring, 19
 thickening, 95-8, 100, 101, 108,
 : 43, 145, 194, 229
 apical (pleural cap), 25
 trauma, 218-19
- Pleural adenocarcinoma, 91
- Pleural disease, 37, 87-106
- Pleural effusion, 3, 4, 14, 29, 37, 87-93
 acute pancreatitis, 817
 asbestos exposure, 194
 bronchial carcinoma, 1 12.126
 chemical pleurodesis, 46
 chest wall trauma, 219
 exudates, 87-8
 Hodgkin's disease, 118, 527
 intensive care patient, 290
 lamellar, 89
 Legionnaire's disease, 132
 malignant mesothelioma, 102
 massive, 88-9
 myocardial infarction, 296, 298
 paediatric imaging, 249
 percutaneous drainage, 45-6
 postoperative, 227, 228, 230
 radiation injury, 236
 radiological appearances, 88-93
 free fluid, 88-91
 loculated fluid, 91
 rheumatoid disease, 198
 small, 88
 subphrenic abscess, 681
 subpulmonary, 89
 systemic lupus erythematosus, 198
 transudates, 87
 tuberculosis, 141, 143
 ultrasound, 45
 fetal sonographic detection, 1056
- Pleural fibrosis, 97
- Pleural lipoma, 100, 102, 105
- Pleural mesothelioma, 35, 37, 38
- Pleural tubes, 218, 219, 234
- Pleural tumours, 87, 100-5
 metastatic disease, 37, 100, 103
- Pleurisy, 98
- Pleuropericardial cyst, 66-7, 68
- Plombage, 229, 231
- Plummer-Vinson syndrome, 549, 564
- Plummet's disease (autonomous toxic
 nodule), 1504, 1505
- Pneumatocele, 19, 20, 23
- Pneumatosis coli, 653
- Pneumatosis cystoides intestinalis
 (cystic pneumatosis), 687
- Pneumatosis intestinalis, 631-2
- Pneumocephalus, 1642
- Pneumococcus (Streptococcus
 pneumoniae)*, : 7, 19, 131, 132,
 : 136, 156, 1 163, 1 165
- Pneumococci, 189, 191-5
- Pneumococcus (Streptococcus
 pneumoniae)*, : 6, 23, 29, 70,
 72, 97, 154-6, 260, 729, 821
- Pneumocystography, 1464
- Pneumomediastinum, 79, 221-2, 223,
 243, 244, 257
- Pneumectomy, postoperative chest,
 225,226
- Pneumonia, 131, 180
 acute, 131-5
 atypical, 135-8
 bacterial, 131-5, 156
 bronchitis obliterans organizing
 pneumonia (BOOP), 173, 174
 bronchopneumonia, 131
 fungal, 145, 146, 147, 148
 lipoid, 138-9, 140
 lobar, 131
 neonate, 259
 older child, 259, 260
 opportunistic infections, 153, 156,
 260
 pleural effusion, 87
 postoperative, 231
 viral, 136, 137
- Pneumonitis, 131
- Pneumopericardium, 221-2, 228, 257,
 292
- Pneumoperitoneum, 6, 7, 10, 50, 228,
 665-7, 668, 679
 plain abdominal film, 664, 666
 plain chest film, 663, 665
 without peritonitis, 667, 668
- Pneumothorax, 5, 50, 87, 93-5, 97,
 : 41, 143, 155, 165, 167, 243,
 244, 257, 290
 aetiology, 94
 complications, 95
 post-lung biopsy, 44
 postoperative, 228, 230, 292
 post-pacemaker implantation, 294,
 295
 radiological appearances, 94-5
 tension, 94, 98, 99
 traumatic, 217, 218-19, 1404, 1415
- POEMS syndrome, 1340
- Poland's syndrome, 50, 1454
- Poliomyelitis, 48, 1426, 1792
- Polyarteritis nodosa, 197, 201-2, 428,
 630,1154
- Polycystic kidney disease, 792, 879,
 881,936
 autosomal dominant (adult type), 936
 autosomal recessive (infantile type),
 936, 976, 1059, 1060
 hepatic cysts, 758, 769
 syndromic associations, 936
- Polycystic liver disease, 769, 781
- Polycystic ovaries, 1072, 1073, 1088,
 : 102
- Polycythaemia, 1327, 1328
- Polydactyly, 1107, 1 109
- Polyhydramnios, 1051, 1058, 1063
- Polymicrogyria, 1735
- Polyp
 adenomatous, 637, 638, 1540
 adenoma-carcinoma sequence,
 640-I
 age-related incidence, 640-I
 colorectal distribution, 641
 antrochoanal, 1492
 cervix, 1078
 endometrial, 1077, 1087, 1088
 gallbladder, 715, 716
 juvenile, 871
 large bowel, 637-40, 1540
 oesophagus, 563, 564
 paediatric gastrointestinal tract, 871
 postinflammatory, 648, 649
 sinonasal, 1521-2, 1525-6
- Polyposis syndromes, 624, 626-7, 637,
 638-9, 871
- Polysplenia, 250, 749, 775, 790, 882
- Polyvinyl alcohol embolisation, 456,
 : 092, 1710, 1712, 1717
- Popliteal artery aneurysm, 413, 425
- Popliteal artery angioplasty, 448, 449
- Popliteal cyst, 429, 430, 431
- Popliteal entrapment, 429, 431
- Popliteal primary thrombosis, 431
- Porcelain (calcified) gallbladder, 713.
- Porencephalic cyst, post-traumatic,
 : 782
- Porencephaly, 1733, 1734
- Portal hypertension, 602, 749-53, 755,
 767-8,779
 causes, 501
 Doppler ultrasound examination,
 468
 interventional procedures, 751-3
- Positive pressure ventilation
 complications, 223, 230, 234
- Positron emission tomography (PET)
 brain imaging, 1812
 epilepsy, 1807, 1831
 breast cancer, 1830-I
 bronchial carcinoma, 1 15,1830
 colorectal cancer, 1830
 head and neck cancer, 1830, 1831
 lymph nodes, 515
 lymphoma, 1830
 melanoma, 1831
 myocardial imaging, 278
 oesophageal cancer staging, 569
 parathyroids imaging, 1508-9
 recent technical advances, 1829-31
 applications, 1830-1
 instrumentation, 1829
 tracers, 1829
 respiratory disease, 38, 43-4
 sinonasal malignancy, 1526
- Postembolisation syndrome, 460
- Posterior cerebral arteries, 1686
 carotid angiography, 1680
- Posterior cervical space, 1509
- Posterior choroidal arteries, 1686
- Posterior communicating artery
 aneurysm, 1674
 carotid angiography, 1680, 1688
- Posterior fontanel, 1624
- Posterior fossa veins, 1686-7
- Posterior inferior cerebellar artery,
 : 684-5
- Posterior longitudinal ligament
 ossification, 1222
- Posterior meningeal artery, 1684
- Posterior pararenal spaces, 886-7
- Posterior pharyngeal
 diverticulum/pouch (Zenker's
 diverticulum), 76, 547
- Posterior urethral valves, 1017, 1061
- Posterior vitreous detachment, 1559,
 : 565
 incomplete, 1559-60
- Postinfectious encephalitis/perivenous
 encephalitis, 1791
- Postmenopausal osteoporosis, 1356
- Post-myocardial infarction (Dressler's)
 syndrome, 87, 298, 299, 321
- Postoperative abdomen, 679
- Postoperative chest, 217, 224-31, 290,
 291
 cardiac surgery, 227, 228-9, 292-3
 general surgery, 230-1
 thoracotomy, 225-7
 late appearances, 229, 230
 see also Intensive care patient
- Postoperative pneumoperitoneum, 668
- Postpericardotomy syndrome, 229
- Post-prostatectomy haemorrhage, 906,
 908
- Poststenotic aneurysm, 429, 433
- Post-styloid space lesions, 1501
- Post-thrombotic syndrome, 483, 487
- Post-traumatic avascular necrosis,
 : 374, 1377-80
- Post-traumatic myositis/myositis
 ossificans, 1376, 1380-I, 1441,
 : 445
- Post-traumatic skull defects, 1639
- Potter's syndrome (renofacial
 dysplasia), 930, 1017, 1059
- Power Doppler
 carotid artery stenosis, 464
 equipment, 461-2
 transcranial, 466
- Preaortic lymph nodes, 512
- Precentral cerebellar vein, 1686
- Pregnancy
 computed tomography (CT), 1065
 double decidual sac sign, 1044, 1047
 ectopic see Ectopic pregnancy
 first trimester (early pregnancy),
 : 040, 1041, 1043-4
 complications, 1044-6
 gestational age assessment, 1040,
 : 041-3
 human chorionic gonadotrophin,
 : 045-6
 hydronephrosis/hydroureter, 971,
 973
 magnetic resonance imaging (MRI),
 : 065-6
 multiple see Multiple pregnancy
 obstetric ultrasound examination see
 Obstetric ultrasound
 osteoporosis, 1366
 second and third trimester, 1040,
 : 041, 1042
- Pre-laryngeal lymph nodes, 511
- Premature infant, 256-8
 bronchopulmonary dysplasia/chronic
 lung disease of prematurity
 257-8
- Prenatal diagnosis, 1048-9
 see also Obstetric ultrasound
- Prepatellar bursitis, 1426
- Presacral space, 654
- Preshyoesophagus, 550, 552
- Pretracheal lymph nodes, 511
- Prevertebral space, 1509, 1511
- Priapism, internal pudenda) artery
 embolisation, 459
- Primary sclerosing cholangitis, 728-9
- Primitive neuroectodermal tumour
 (PNET/medulloblastoma),
 : 748-9
- Primordial cyst (odontogenic
 keratocyst), 1542, 1543
- Priori disease, 1795, 1797
- PROACT, 1708
- Proatlantal intersegmental artery,
 : 679, 1689, 1690
- Processus vaginalis, 890
- Proctitis, 654
- Progesterone-only pill, 1073
- Progressive massive fibrosis, 191, 193
- Progressive multifocal
 leucoencephalopathy, 1793,
 : 794
- Progressive supranuclear palsy, 1797
- Prolactinoma, 1749
- Prostate, 1004-7
 anatomy, 888, 889
 magnetic resonance imaging (MRI),
 911, 912, 1011-12
 ultrasound, 896, 897

- Prostate cancer, 472, 1006-7, 1012-15
 Gleason grading, 1006
 magnetic resonance spectroscopy, 1827
 metastases, 777, 1251, 1252, 1253, 1660
 prostate specific antigen (PSA) levels, 1006
 radical prostatectomy, 1000, 1002, 1003
 urinary tract reconstruction, 1002
 TNM staging, 1012
 Prostate specific antigen (PSA), 1006
 Prostatic cyst, congenital, 990-1
 Prostatitis, 472, 1005
 Prosthetic heart valves, 228, 294, 330
 angiographic screening, 362
 Protease inhibitor crystals, urinary tract obstruction, 967, 968
 Protein C deficiency, 436
 Protein S deficiency, 436
Proteus, 944, 965, 966, 979, 993
 Protozoal pulmonary infections, 149-50
 Proximal femoral focal deficiency (congenitally short femur), 1113
 Prune-belly syndrome, 864, 940-1, 942, 990, 1061
 Pseudo-obstruction
 idiopathic intestinal, 676, 677
 large bowel, 653
 small bowel, 620-1
 Pseudoachalasia (secondary achalasia), 553-4
 Pseudoachondroplasia, 1142, 1143
 Pseudogestational sac, 1044
 Pseudohypoparathyroidism (Albright's syndrome), 1134, 1361, 1362
 basal ganglion calcification, 1634, 1798
 soft tissue calcification, 1438
 Pseudolymphoma, intrathoracic, 120, 124
 Pseudomembranous colitis, 651, 680
Pseudomonas, 133, 152, 156, 165, 991
Pseudomonas pseudomallei infection (melioidosis), 134
 Pseudomyxoma peritonei, 633
 Pseudoperitoneum, 667
 Pseudopseudohypoparathyroidism, 1361
 Pseudosarcoma, oesophagus, 569, 570
 Pseudotumour cerebri, 1586
 Pseudoxanthoma elasticum, 1440, 1473
 Psittacosis (*Chlamydia psittaci* pneumonia), 131, 137
 Psoas muscle hypertrophy, ureteric displacement, 981
 Psoriatic arthritis, 1216-17
 Pterygoid (vidian) artery, 1680
 Pulmonary agenesis, 26, 28, 250
 Pulmonary angiography, 1, 46-7, 280, 281
 Pulmonary aplasia, 250
 Pulmonary arterial hypertension, 287-8, 290, 301, 477
 Pulmonary arteriovenous malformation, 254, 315, 316, 401-2
 cunbolisation, 46, 47, 458, 460
 Pulmonary artery, 8, 60, 62, 265, 266, 267, 269, 272, 273, 286, 365
 contrast-enhanced magnetic resonance angiography (CE-MRA), 475, 477-8
 Pulmonary artery aneurysm, 46, 315
 Pulmonary artery angiosarcoma, 122
 Pulmonary artery atresia, 477
 Pulmonary artery banding, 228, 364, 374
 Pulmonary artery flotation (Swan-Ganz) catheter, 232, 233, 454
 Pulmonary artery sling (anomalous origin of left pulmonary artery), 400-1
 Pulmonary artery stenosis, 477-8, 479
 Pulmonary artery thrombosis, 315
 Pulmonary atresia, 9, 368, 369, 391
 circulation, 370
 ductus dependence, 369, 377
 with intact ventricular septum, 392
 with ventricular septal defect, 391-2
 Pulmonary confluence, 9
 Pulmonary contusion, 219, 220, 221
 Pulmonary embolism, 1, 29, 30, 58, 81237-9, 290, 342-5, 436, 487, 492
 acute massive, 314-15
 chronic, 315
 computed tomography (CT), 342
 computed tomography angiography, 62, 412-13
 diagnostic investigations, 40-1, 237-9, 342-3
 inferior vena cava filters, 453
 magnetic resonance angiography, 478
 non-acute, 315
 plain chest film, 314-15
 post-therapeutic embolisation, 460
 postoperative, 227, 231
 pulmonary angiography, 46, 280, 343
 recurrent, 453
 subsegmental emboli, 238
 thrombolysis, 455
 ventilation perfusion scan, 38, 39, 40-1, 343, 344-5
 Pulmonary eosinophilia, 150, 151, 202-4, 210
 Pulmonary fibroma, 124
 Pulmonary fibrosis, 163, 175, 188, 197, 290
 asbestos exposure, 194
 diffuse, 204-8
 drug-induced, 210
 radiation injury (radiation fibrosis), 235, 236, 238
 Pulmonary haematoma, 219, 220, 222
 Pulmonary haemorrhage, 208, 209, 217
 Pulmonary haemosiderosis, 194, 208-9, 262
 Pulmonary hamartoma, 22, 37, 123-4, 125, 126
 Pulmonary hypertension, 46
 congenital cardiac disease, 258, 369, 374, 375
 see also Pulmonary arterial hypertension; Pulmonary venous hypertension
 Pulmonary hypoplasia, 46
 lobar underdevelopment, 250-1
 Pulmonary infarction, 19, 87
 Pulmonary infections, 19, 131-60, 290
 predisposing conditions, congenitally acquired, 152-3
 see also Pneumonia
 Pulmonary interstitial emphysema, 221, 243
 premature infant, 257
 Pulmonary laceration, 219, 221
 Pulmonary myxoma, 124
 Pulmonary nodule
 computed tomography (CT), 35-7
 multiple, 22, 124
 ossific, 290, 302
 rheumatoid disease, 198
 solitary, 19-22, 33, 35, 42, 113-14, 117, 124
 positron emission tomography (PET), 43-4
 Pulmonary oedema, 16, 17, 19, 288, 289
 adult respiratory distress syndrome, 243
 chest trauma, 220
 drug-induced, 210
 inhalation injury, 195
 lung consolidation, 180
 myocardial infarction, 296, 297
 postoperative, 227, 230
 re-expansion, 95
 Pulmonary oligaemia, 290
 Pulmonary ossification, idiopathic, 214
 Pulmonary plethora, 289, 290
 congenital cardiac disease, 369, 372, 376, 378, 386
 Pulmonary sarcoma, 121-2
 Pulmonary segments, 9, 11
 Pulmonary sequestration, 253-4
 congenital, 152, 153
 fetal sonographic detection, 1056-7
 Pulmonary stenosis, 370, 378-80
 tetralogy of Fallot, 383
 treatment, 364, 379-80
 Pulmonary talcosis, 210, 211, 212
 Pulmonary torsion, 220
 Pulmonary valve, 265-6
 Pulmonary varix, 316
 Pulmonary veins, 9, 265, 266, 267, 268, 271, 273, 286
 magnetic resonance angiography, 477
 Pulmonary venolobular syndrome, congenital (scimitar syndrome), 251, 315, 395
 Pulmonary venous hypertension, 288-9, 302
 Pulsatility index (PI), 463
 Pyelography, 927
 Pyelonephritis
 acute, 914, 941-2
 emphysematous, 688, 941, 943
 fungal, 948
 xanthogranulomatous, 944
 Pyeloureteritis cystica, 947, 979
 Pyknodysostosis, 1123, 1124
 Pyloric stenosis, hypertrophic in neonate, 853-5
 Pyloroplasty, 604, 605
 Pyonephrosis, 944
 Pyopneumothorax, 95, 100
 arterial damage/thrombosis, 436
 colitis, 652
 enteritis, 618, 628
 lucoencephalopathy, 1800
 lung, 235-6, 237
 pneumonitis, 236, 237
 radiation fibrosis, 235, 236, 238
 mediastinitis, 72
 oesophagitis, 559
 optic neuropathy, 1586
 see also Radionecrosis
 Radiation-induced sarcomas, 236, 239, 1267, 1272
 Radical prostatectomy, 1000, 1001, 1003
 Radicular cyst, 1542, 1543
 Radiographic absorptiometry (photodensitometry), 1351
 Radiological information system (RIS), 1843
 Radionecrosis, 1385
 chest wall, 236, 238
 intracranial, 1766
 jaws, 1534
 ribs, 49
 skull erosion, 1639
 Radionuclide cysternography, 1816
 Radionuclide imaging
 acute cholecystitis, 686
 adrenal gland, 830-3
 angiography, 412
 hiliary tract, 717-18
 bone tumours, 1248, 1249
 brain
 dopamine transport system imaging, 1815-16
 radionuclide cysternography, 1816
 regional cerebral blood flow imaging, 1812-15
 bronchial carcinoma staging, 115
 cardiac disease, congenital, 405
 left-to-right shunt, 369
 cardiac imaging, 277-8, 319
 chest disease, 1, 38-44
 coronary artery stress perfusion studies, 320, 321
 gastric motility, 609-12
 gastrointestinal bleeding, 440, 655-7
 hip prosthesis loosening/infection, 1244
 hypertrophic osteoarthropathy, 1231, 1234
 inflammatory bowel disease, 659-60
 islet cell tumours, 787, 821-2
 liver, 759-62
 lymph nodes, 515
 Meckel's diverticulum, 657-8, 659
 osteomyelitis, 1157-8
 osteonecrosis, 1180, 1181
 paediatric abdomen, 851
 paediatric chest, 248
 Paget's disease, 1194, 1196
 parathyroids, 1507-9
 Perthes' disease, 1184-5, 1186
 phaeochromocytoma, 844, 846
 pulmonary embolism see Ventilation perfusion scan
 recent technical advances, 1829-32
 rheumatoid arthritis, 1208, 1209
 somatostatin receptor scintigraphy, 660-1
 spine, 1648-9
 spleen, 762-3
 testes, 1034-5
 thyroid, 1504-7
 urinary tract, 912-21

- Radiotherapy planning, 520
Radium ingestion, 1267
Radius
 congenital defects, 1 108
 distal fracture, 1372, 1407, 1408
 head fracture, 1407, 1416
Radius-ulna synostosis, 1 108
Ramstedt's pyloromyotomy, 855
Rapunzel's syndrome, 609
Rashkind device, 378
Rashkind septostomy, 364, 386, 388
Rastelli procedure, 390, 392
Rathke cleft cyst, 1763
Raynaud's disease, 455, 1439
Raynaud's phenomenon, 433
Reactive gastritis, 579-80
Rectal carcinoma, 643, 655
Rectal disorders, 653-4
Rectal prolapse syndromes, 654
Rectum, 635
Red blood cell disorders, skeletal abnormalities, 1321-7
Red cell aplasia, 65
Reed-Sternberg cells, 118, 521
Reflex sympathetic dystrophy .see Regional pain syndrome
Reflex nephropathy, 946-7, 976
 ileal conduit-related, 947, 948
Relux oesophagitis, 550, 552, 556-7
Regional cerebral blood flow imaging, 1812-16
 applications, 1813-15
 HMPAO technique, 1812
 interpretation, 1812
 tracers, 1812
Regional pain syndrome (reflex sympathetic dystrophy; Sudeck's atrophy; algodystrophy), 1367, 1380, 1426
Reiter's syndrome, 1216, 1217-18
Relapsing polychondritis, 62, 75, 161, 162, 201
Renal abscess, 876, 942-3
Renal adenoma, 442, 950, 995
Renal agenesis, 861, 929-30, 1065
 bilateral, 930, 1059-60
 unilateral, 1060
Renal angiography, 906, 907
Renal angiomyolipoma, 442
Renal arteriovenous malformation, 949
 embolisation, 456
Renal artery, 887
 accessory, 423
 contrast-enhanced magnetic resonance angiography (CE-MRA), 475
 magnetic resonance angiography, 480-1
Renal artery aneurysm, 414, 965
Renal artery embolisation, 456, 957
Renal artery occlusion, thrombolysis, 456
Renal artery stenosis, 429, 431-2, 919, 964-5, 976, 980
 computed tomography (CT) angiography, 964
 Doppler ultrasound, 469, 470, 964
 magnetic resonance angiography, 480, 481, 964-5
 percutaneous transluminal angioplasty, 450
 stem insertion, 450, 451
Renal artery trauma, 974
Renal biopsy, percutaneous, 905
Renal calculi, 965-70
 treatment options, 969
 urinary tract obstruction, 967-8
Renal calyceal diverticulum, 938
Renal cell carcinoma, 953-7, 963
 angiography, 442
 children, 876
 duodenal invasion, 598
 embolisation, 456, 457, 458, 906, 907, 957
 metastases, 1 17, 956, 957, 1251, 1252-3, 1254
 Robson classification, 954
 TNM staging, 954-5
 vascular involvement, 956
Renal colic, 688
Renal cyst, 950-2, 1838
 angiography, 442
 dialysis-related, 952
 percutaneous aspiration, 904-5
 simple, 950, 963
 classification of malignant potential, 951-2
 parapelvic/peripelvic, 951
Renal duplication abnormalities, 933-5
Renal dysplasia, 930, 931
Renal ectopia, 913-14, 930-1, 932
Renal failure, acute, 919
Renal failure, chronic, 976-7, 1474, 1475
 arterial calcification, 412
 contrast media risks, 421
 skeletal manifestations, 1364, 1365-6
Renal function, scintigraphic assessment, 912-21
 captopril scintigraphy, 917
 children, 925
 DMSA scintigraphy, 913
 dynamic studies, 914-17
 radiopharmaceuticals, 914-15
 renogram, 916
 response to diuresis, 916-17
 glomerular filtration rate, 912-13
 pharmacological stress tests, 912
 renal transplant, 917
 tracers, 912
Renal hypoplasia, 930
Renal infarct, 963-4
Renal lipoma, 950
Renal lymphoma, 957-8
Renal masses, 442-3, 914, 949-63
 benign, 949-53
 Doppler ultrasound, 471
 indeterminate, 963
 malignant, 953-63
 metastatic tumours, 958
 paediatric abdomen, 874-6
Renal medullary carcinoma, 962-3
Renal mcgcalycosis/polycalycosis, 940, 941
Renal mesenchymal tumours, 949-50
Renal oncocytoma, 958-9
 angiography, 442
Renal osteodystrophy, 1364, 1365
 temporomandibular joint involvement, 1546, 1548
Renal pelvis carcinoma, 442
Renal pelvis obstruction
 dynamic radionuclide studies, 918
 urodynamic studies, 922-3
Renal pseudotumour, 443, 929
Renal rotational abnormalities, 930, 931
Renal sarcoma, 963
Renal sinus lipomatosis, 949, 950
Renal squamous cell carcinoma, 960, 961
Renal transitional cell carcinoma, 959-60, 961, 963
Renal transplantation, 982-6
 acute rejection, 984
 angiography, 443
 ciclosporin nephrotoxicity, 984
 computed tomography (CT) angiography, 1840
 Doppler ultrasound, 471
 early graft failure, 983-4
 fluid collections, 986
 scintigraphic function assessment, 917, 919-20
 surgery, 982-3
 transplant artery transluminal angioplasty, 450
 transplant trauma, 699, 703
 ureteric obstruction, 985-6
 vascular complications, 984-5
Renal trauma, 699-703, 971-5
 classification, 974
 imaging, 700-2, 972-4
 Doppler ultrasound, 470, 471
 indications, 702, 971
 management, 703
 staging systems, 702, 703
Renal tubular acidosis, 1128, 1129
 type I (distal), 977
 vitamin D-resistant rickets, 1354
Renal tubular necrosis, acute post renal transplantation, 983-4
Renal vascular abnormalities, 932-3
Renal vascular disease, 963-5
 hypertension, 480, 919
Renal vein, 483, 887
 phlebography, 494, 497
 renin assay, 495
Renal vein thrombosis, 494-5, 965
 Doppler ultrasound, 469-70
Renin-secreting juxtaglomerular cell tumour, 442-3
Reninoma, 949
Renofacial dysplasia (Potter's syndrome), 930, 1017, 1059
Renogram, 916
Residual tumour mass, 520-1
Resistance index (RI), 463
Respiratory acinus, 9, 11
Respiratory distress syndrome (hyaline membrane disease), 256-7
Respiratory syncytial virus, 135, 172, 259
Respiratory tract infection in children, 259
Restrictive cardiomyopathy, 299, 325-6
Retention cyst
 oesophagus, 564
 paranasal sinuses, 1523, 1524
Retina, 1552
 pathology, 1555-6
 post-traumatic holes, 1565
Retinal detachment, 1554, 1555, 1557, 1576
Retinoblastoma, 1563, 1590-1
 differential diagnosis, 1563-4
Retinocerebellar angiomatosis see Von Hippel-Lindau disease
Retinopathy, 1564, 1589
Retinoschisis, acquired, 1556
Retrocaval ureter, 940
Retrograde pyelography, 897-8
Retrolental fibroplasia, 1564, 1589
Retroperitoneal air insufflation, adrenal mass imaging, 829
Retroperitoneal fibrosis, 80, 729, 981-2
Retroperitoneal haemorrhage, 449
Retroperitoneal lipoma, 848
Retroperitoneal para-aortic lymph nodes, 512
Retroperitoneal tumours, 845, 848
Retroperitoneum, 885-8
Retropharyngeal abscess, 1497
Retropharyngeal lymph nodes, 510
Retropharyngeal space, 1509, 1511
Retrosternal goitre, 62, 64
Reversible ischaemic neurological deficits (RINDS), 463
Reye's syndrome, 1791
Rhabdoid tumour, 874-5
Rhabdomyoma, 308, 337, 402, 1055, 1056
Rhabdomyosarcoma, 883
 bile duct, 722
 bladder, 997
 orbit, 1569, 1579
 paranasal sinuses, 1529
 soft tissues, 1428
Rhabdosarcoma, 337
Rhesus incompatibility, haemolytic disease of newborn, 1063, 1326
Rheumatic heart disease, 403
 aortic valve, 326, 327
 regurgitation, 300
 stenosis, 300
 mitral valve, 328, 329
 regurgitation, 303
 stenosis, 301, 302
 pulmonary artery thrombosis, 315
 tricuspid valve disease, 303
Rheumatoid arthritis, 47, 48, 197, 538, 539, 630, 661, 1201-13, 1421, 1468
 arthrography, 1207-8
 atlanto-axial subluxation, 1657
 childhood form, 1214
 computed tomography (CT), 1209
 intraosseous cysts/geodes, 1205, 1206
 magnetic resonance imaging (MRI), 1211-13
 periosteal reaction, 1204, 1209
 plain film joint changes, 1201
 alignment deformities, 1202-4
 Boutonniere deformity, 1203, 1204
 erosions, 1204-7, 1211
 joint space widening/narrowing, 1202-3
 osteoporosis, 1202
 periostitis, 1204
 sacroiliac joints, 1216
 secondary osteoarthritis, 1207
 soft-tissue, 1201, 1202
 terminal phalangeal sclerosis, 1202, 1203
 radionuclide imaging, 1208, 1209
 spine, 1206-7, 1653
 CII2 lesions, 1212-13, 1214
 temporomandibular joint, 1546, 1548
 ultrasound, 1209-11
Rheumatoid disease, 163, 1312
 Caplan's syndrome, 191, 192, 198
 chest disorders, 198-9
Rheumatoid nodule, 23, 37
Rhinoscleroma, 161, 1523
Rhinosinusitis, chronic, 1521
Rib fracture, 49, 217-18, 1404, 1415
 aortic transection, 311
 lung tissue herniation, 218
 stress fracture, 217

- Rib notching, 48, 229, 230, 290, 380.
| 301
- Ribs, 48-9
cervical, 1 120
congenital anomalies, 48
destruction, 49, 113, 125
intrathoracic, 48
localized expansion, 49
plain chest film, 12
post-thoracotomy defect, 225, 229,
230
sclerosis, 49
- Rickets, 49, 50, 1114, 1353, 1354
acquired hypophosphataemic, 1354
vitamin D-resistant
familial hypophosphatasia,
| 353-4
renal tubular disorders, 1354
- Riedl's thyroiditis, 80, 729, 1514
- Right atrium, 267
enlargement, 284-5
- Right colon (caecal) volvulus, 669,
676-7, 678
- Right heart catheterisation, 356
- Right lymphatic duct, 509
- Right paracolic abscess, 682
- Right ventricle, 265
enlargement, 285-6
- Right-sided aortic arch, 63, 269, 367,
368, 399, 410
impressions on thoracic oesophagus,
573
tetralogy of Fallot, 383
- Rigler's sign, 863, 864
- Rocky Mountain spotted fever, 138
- Rodent ulcer, skull erosion, 1636
- Rokitansky-Aschoff sinuses, 724, 725
- Rotablator, 450
- Rotational Transluminal Angioplasty
Catheter System (ROTACS),
450
- Rotator cuff
calcific deposits, 1421, 1422, 1436
injuries, 1237, 1238, 1239, 1240,
| 382, 1383, 1406-7
- Round ligament, 1070
- Rounded atelactasis, 35, 179, 183
- Roundworm *see Anaris*
- Rubella, 1791
- Russian spring summer encephalitis,
| 792
- Ruvalcaba-Myhre-Smith syndrome,
639
- Saber-sheath trachea, 161
- Sacral region imaging, 1644
- Sacrocoxygeal teratoma, 883, 1063
- Sacroiliac joint
fracture *see* Pelvic fracture
osteomyelitis, 1 161
tuberculosis, 1 171
- Sacrum
isolated fracture, 1402
stress fracture, 1375
- St Louis encephalitis, 1792
- Salazopyrine, pulmonary
hypersensitivity reaction, 195
- Salivary gland calculi (sialolithiasis),
535, 536, 537
- Salivary gland lesions, 537-43
- Salivary gland lipoma, 1515
- Salivary gland mass, 1515
- Salivary gland strictures, 538
- Salivary gland tumours, 540-3
benign, 540-1
fine needle aspiration cytology, 543
lymphoma, 539, 540
malignant, 541-3
pathology, 541
- Salivary gland-type lung tumours, 122
- Salivary glands, 1501
anatomy, 533-5
imaging, 535-6
ultrasound, 1515
- Salivary inclusion defect (Stafne's
defect), 1538
- Salmonella*, 627, 651, 870
- Salpingitis isthmica nodosa, 1089
- Salter-Harris epiphyseal injury
classification, 1383, 1384
- Saphenous veins, 485
Doppler ultrasound mapping, 505
- Sarcoidosis, 161, 1468
arthritis, 1 173
bone lesions, 1172-3, 1639
CNS involvement, 1794
gastric involvement, 580-1
mediastinal disease, 70, 71, 72, 75
nephrocalcinosis, 977
orbital involvement, 1568, 1580,
| 586, 1588, 1593, 1594
paranasal sinuses, 1523
respiratory disease, 20, 25, 27, 35,
36, 42, 187-9, 190, 240
restrictive cardiomyopathy, 299,
325-6
- Scaphocephaly, 1624
- Scaphoid fracture, 1408, 1409, 1416
- Scapholunate dissociation, 1409, 1410
- Scapula, 12
- Scapular fracture, 1404-5, 1415
- Sehatzki's ring, 554-5
- Schuermann's disease (vertebral
epiphysitis; adolescent
kyphosis), 1 188
- Schilder's disease (diffuse sclerosis),
| 800
- Scistosoma*, 992
- Schistosomiasis, 627, 651, 992-3
brain infection, 1791
lung infection, 151
urinary tract disease, 946, 980, 992,
993
- Schizencephaly, 1733, 1734
- Schwannoma *see* Neurilemmoma
- Scimitar syndrome (congenital
pulmonary venolohular
syndrome), 251, 315, 395
- Sclera, 1551-2
- Scleroderma (systemic sclerosis), 197,
538, 565, 1353
acro-osteolysis, 1439
calcinosis circumscripta, 1439
intestinal pseudo-obstruction, 620-1
lung disease, 34, 199, 200
oesophageal involvement, 76, 552,
553, 554, 555
phalangeal involvement, 1233-4, 1235
- Sclerosing cholangitis, 722, 724
- Sclerosing encapsulating peritonitis,
633
- Sclerosing osteitis, postinflammatory in
jaw, 1535
- Sclerosing sialolithiasis, chronic, 537
- Scoliosis, 13, 49, 50, 1108, 1121-2,
| 256, 1259, 1651
classification, 1121-2
Cobb curve measurement method,
| 122
hemivertchrac, 1119, 1121
- Screening investigations
breast cancer *see* Breast cancer
screening
colorectal cancer, 644
lung cancer, 113
ovarian cancer, 1084
- Scrotal extratesticular tumours, 1026
- Scrotal trauma, 1027
- Scrotoliths/scrotal pearls, 1027
- Scrotum, 889-90
congenital disorders, 1022-3
extratesticular disorders, 1023-7
scintigraphy, 1034-5
ultrasound, 895-6
- Scrub typhus, 138
- Scurvy, 49.
- Scwachman-Diamond syndrome, 789
- Seat-belt injuries, 1462
bowel, 705
Ihoracolumbar spine, 1400
- Sebaceous gland calcification, 1473
- Segmental lung resection, 225
- Segmental oriental infarction, 633-4
- Seizures
classification, 1804
see also Epilepsy
- Selective arterial catheterisation, 418
- Selective fallopian tube
catheterisation/lrccanalisation,
| 090
- Selenium-75-labelled seleno-nor-
cholesterol, 831
- Self-expanding stents
arterial, 451
biliary, 734
- Sellar region
raised intracranial pressure-related
changes, 1626, 1627
tumours, 1749-53
differential diagnosis, 1753
- Semicircular canals, 1597, 1598
congenital abnormalities, 1603
- Seminal vesicle cyst, 990, 991
- Seminal vesicles, 889, 896
- Seminoma, 66, 1028, 1029, 1032
- Senile (involutional) osteoporosis,
| 356
- Senile macular degeneration, 1556
- Senning procedure, 388
- SENSE acquisition technique, 1821,
| 822
- Sentinel lines, 19
- Sentinel node imaging, 1831
clinical applications, 1832
radionuclide techniques, 515,
| 831-2
- Septa] agenesis, 1731
- Septate uterus, 1075, 1087, 1094
- Septic arthritis, 1163-4, 1432
infants, 1155
hip (Tom Smith arthritis), 1164-6
- Septo-optic dysplasia (De Morsier's
disease), 1731
- Septum pellucidum cyst, 1731
- Scronegative spondyloarthropathies,
| 215-22, 1432
diagnostic criteria, 1215
juvenile chronic arthritis, 1214
- Serous cystadenocarcinoma, ovary,
| 081
- Serous cystadenoma
ovary, 883
pancreas, 793, 815
- Serrated adenomatous polyposis, 638
- Sertoli cell tumours, 1028, 1082
- Sesamoids at metatarsal heads, 1114,
| 115
- Sex cord stromal tumours, 1081, 1082
- Shigella*, 651, 870
- Shock bowel, 706, 707
- Shoulder joint
dislocation, 1405-6
anterior, 1404, 1405
inferior, 1406
posterior, 1405
imaging, I I, 1237-40
osteoarthritis, 1224-5, 1227
trauma, 1404-7
tuberculosis, 1 170
- Sialadenitis
acute, 535
chronic, 535
myoepithelial (benign
lymphoepithelial lesion), 539
- Sialectasis, 538, 539
- Sialography, 535
- Sialolithiasis (salivary gland calculi),
535, 536, 537
- Sialosis, 538
- Sicca syndrome, 199, 200
- Sickle cell disease, 315, 962, 1323
skeletal features, 1180, 1323-5,
| 326, 1327, 1541
extramedullary haemopoiesis, 78
soft tissue involvement, 1325
splenic infarcts, 749
- Siderosis, 18, 194
- Sigmoid volvulus, 677-8
- Silhouette sign, 14
- Silicosiderosis, 194
- Silicosis, 27, 187, 189, 191, 192, 240
Caplan's syndrome, 198
lymph node calcification, 25, 70, 72
progressive massive fibrosis, 191
- Simon nitinol filter, 453
- Simpson atherectomy catheter, 450
- Sinding-Larsen disease
(ostochondritis of patella),
| 188-9, 1377
- Single photon absorptiomctry, 1351
- Single photon emission tomography
(SPECT)
epilepsy, 1807
knee joint imaging, 1236-7, 1239
liver, 759
myocardial imaging, 277, 278, 279
regional cerebral blood low
imaging, 1812
Alzheimer's disease, 1814
cerebrovascular disease, 1813
epilepsy, 1815
trauma, 1815
regional lung function, 41
rheumatoid arthritis, 1209
- Single ventricle, 370, 392-3
- Single X-ray absorptiomctry, 1351
- Sinonasal cancer, 1526-9
- Sinonasal polyposis, 1521-2
- Sinus pericranii, 1626
- Sinus of Valsalva, 268, 269-70, 309
aneurysm, 73, 314
fistula, 399
- Sinus venosus defect, 374, 375
- Sinuses, 1519-29
anatomy, 1520
fungal infection, 1522-3
imaging, 1519-20, 1619
for functional endoscopic surgery,
| 521
inflammatory conditions, 1520-3
physiology, 1520

- skull fracture, 1642
tumours
benign, 1523-6
lymphoma, 1528-9
malignant, 1526-9
orbital invasion, 1569, 1570
- Sinusitis
acute, 1520
chronic, 163, 1521
- Sipple's syndrome (multiple endocrine neoplasia type II), 842, 878, 1507
- Sites ambiguous, 366
inverses, 366, 635, 712
solitus, 366
variations, 365-7
- Sjögren's syndrome, 121, 1594
lung involvement, 163, 199
primary (sicca syndrome), 199, 200
salivary gland disease, 538, 539
lymphoma, 539
spinal involvement, 1668
- Skeletal congenital disorders, 1107-22
lower limb, 1109-17
pelvis, 1117
spine, 1117, 1119-22
upper limb, 1107-9
- Skeletal trauma, 1371-87
regional, 1389-416
Fractures
- Skin lesions, chest wall, 5(1)
- Skull, 1617-42
congenital lesions, 1624-6
erosions, 1635-9
hypostosis, 1640-I
local bulging, 1639-40
osteomyelitis, 116(1), 1161, 1638-9
osteoporosis, 1639
post-traumatic cysts, 1641-2
premature fusion of sutures, 1624
trauma, 1641-2
tuberculosis, 1169
- Skull fracture, 1389, 1390, 1641, 1781
base of skull, 1389, 1575, 1642
paranasal sinuses, 1642
- Skull radiography
cerebral tumours, localising
evidence, 1627-31
erosions, 1635-9
intracranial calcification, 1621-3.
| 628-31
intracranial pressure elevation
diagnosis, 1626-7
mastoids, 1597, 1619
neonate/infant, 1621, 1623-4
optic foramen view, 1573, 1618-19,
| 620
paranasal sinuses, 1519, 1619
petrous bones, 1597, 1619, 1620
internal auditory meatus, 1619.
| 620, 1621
pituitary fossa, 1619, 1621
skull trauma assessment, 1723
skull vault, 1621
special views, 1617-18
standard AP projection, 1617, 1618
standard basal view, 1617, 1621
standard lateral projection, 1617,
| 618
sutures, 1621, 1624
Towne's view, 1617, 1619, 1620,
| 622
vascular markings, 1619, 1621
abnormalities, 1634-5
- Sleep apnoea syndrome, 62
- Slipped femoral capital epiphysis, 1384
- Small bowel, 615-32
anatomy, 615
radiological investigation, 615-18
barium follow-through, 615-16
computed tomography (CT), 618
enteroclysis (small bowel enema),
616-17
ileostomy enema, 617
magnetic resonance imaging
(MRI), 618
ultrasound, 618
water-soluble contrast studies,
617-18
- Small bowel adenocarcinoma, 625
- Small bowel adenoma, 625
- Small bowel atresia, 1057-8
- Small bowel carcinoids, 626, 633
- Small bowel dilatation, 670
acute abdomen, 669
- Small bowel disorders in children,
866-71
- Small bowel duplication cyst, 866-7
- Small bowel duplications, 631
- Small bowel enema (enteroclysis),
616-17
- Small bowel enteritis, 627-8
- Small bowel fluid levels, 664
- Small bowel haemangioma, 625, 630
- Small bowel infarction, 675
- Small bowel lipoma, 625
- Small bowel lymphoma, 524, 625-6
- Small bowel malrotation, 630-I
- Small bowel obstruction, 618-20, 670-5
closed-loop, 618
fluid-filled loops, 670-I
gallstone ileus, 673-4
infants/older children, 871
intestinal volvulus, 672
intrinsic/extrinsic causes, 618
intussusception, 674-5
management, 671-2
neonate, 858-9
obstetric ultrasound, 1057-8
strangulated external hernia, 670,
671, 672
strangulation, 618, 672
'string of heads' sign, 670, 671
- Small bowel thickening, children,
869-70
- Small bowel tumours, 624-7
benign, 624-5
children, 871
malignant, 625-6
metastases, 626
neurogenic, 625
polyposis syndromes, 624, 626-7
small bowel obstruction, 618
stromal, 624, 626
- Small bowel vascular disease, 630
- Small bowel volvulus, 672
- Small cell (oat cell) bronchial
carcinoma, 30, 107, 108, 110,
| 5, 660-1
somatostatin receptor scintigraphy,
660-I
- Smallpox, 1791
- SMASH acquisition technique, 1821
- Smith fracture (scat-hell spinal injury),
1400
- Smith's fracture of forearm, 1408
- Sodium tetradecyl sulphate (SDS)
cmholisation, 456, 458
- Soft tissue abscess, 1418, 1432, 1444
- Stilt tissue lipoma, 1418, 1428, 1429,
| 434, 1441, 1443
- neck, 1502, 1503
- Soft tissue osteosarcoma, 1267, 1272
- Soft tissue sarcoma, 445, 1428-9,
| 431, 1444
- Soft tissue tumours, 1427-32, 1441-2.
| 443-4
angiography, 445
multiple, 1431
recurrence, 1431-2
- Soft tissues, 1417-48
calcification, 1249, 1421, 1422,
| 435-40, 1445
compartment syndrome, 1425
computed tomography (CT), 1442-5
cystic lesions, 1426-7
foreign bodies, 1432-3
gas, 1433-4
haematomas, 1422-4
infection/inflammation, 1432, 1435,
| 444
magnetic resonance imaging (MRI),
| 417-32
interventional procedures, 1445-8
necrosis, 1439
oedema, 1435
ossification, 1249, 1440-I
plain films, 1432-42
chest, 11-12
trauma, 1419-25
fracture associations, 1372-4
- Solitary bone cyst, 1312-14, 1315,
| 316
- Solitary rectal ulcer syndrome, 654
- Somatostatin receptor scintigraphy, 42,
660-1, 759, 761-2
adrenal medulla tumours, 833
islet cell tumours, 821-2
- Sonohysterography, 1077, 1078
- South American trypanosomiasis, 76
- Speech recognition dictation system for
digital workflow, 1844
- Spermatic cord, 890
- Spermatic cord sarcoma, 1026
- Sphenoid carcinoma, 1636
- Sphenoid osteocoele, 1522, 1523
- Sphenoid sinus, 1520
- Spheroctyosis, 1326
- Spina hilda, 1050, 1051-3, 1121,
| 651, 1652, 1653
occulta, 1121
- Spinal accessory lymph node chain,
1121
- Spinal angiography, 1677, 1678
- Spinal angioma (arteriovenous
malformation), 1669, 1670, 1697
- Spinal arteries, 1684
- Spinal canal, 1649
- Spinal cord, 1649-50
biopsy, 1721
compression, 999, 1432
- Spinal degenerative disease, 1226-9
cervical spine, 1227, 1229, 1230
discography, 1228, 1232, 1233
lumbar spine, 1228, 1231, 1232
- Spinal degenerative disease, 1226-9
cervical spine, 1227, 1229, 1230
discography, 1228, 1232, 1233
lumbar spine, 1228, 1231, 1232
- magnetic resonance imaging (MRI),
| 228-9
disc high-intensity zones (HIZ),
| 228, 1233
vertebral body Modic changes,
| 228
thoracic spine, 1228
- Spinal dysraphism, 1651-2
- Spinal infection, 1658-9
osteomyelitis, 1161-2
infective discitis, 1162, 1163
tuberculosis, 1166, 1167-8
- Spinal lipoma, 1666, 1667
- Spinal nerve roots, 1649-50
root sheaths, 1650
- Spinal nerve tumours, 1758-9
- Spinal stenosis, 1664-6
- Spinal trauma, 1391-400, 1655-6, 1837
associated aortic transection, 311
cervical spine, 311, 1392-9
cervicothoracic junction imaging
problems, 1415
thoracolumbar spine, 218, 1399-400
- Spinal ununions, 1666-7, 1668-9
metastases, 1660, 1669
- Spindle cell carcinoma, oesophagus,
569, 570
- Spine, 1643-71
anatomy, 1649-51
arachnoid cysts, 1670-I
blood vessels, 1650-I
congenital abnormalities, 1117,
| 119-22
bony without CNS involvement,
| 653-4
deformity, 1651
extradural masses, 1669-70
instability, 1656-8
intradural extramedullary lesions,
| 668-9
intradural lesions, 1666-8
infarction, 1668
inflammatory, 1667-8
investigations, 1643-9
localised bone destruction/sclerosis,
| 658-62
obstetric ultrasound examination,
| 049-50
plain chest film, 13, 49-51
segmentation failure, 1653
spondylolisthesis/Degenerative disc
disease
- Spleen, 509, 746-9
calcification, 748
computed tomography (CT), 753,
758-9
magnetic resonance imaging (MRI),
785-6
radionuclide imaging, 762-3
Thorotrast deposition, 748
trauma, 692-5, 759, 762, 763
grading, 693, 694
imaging pitfalls, 693
management, 693-4
recovery monitoring, 694-5
ultrasound, 775-7
- Splenic abscess, 748-9, 758, 775-6,
882
- Splenic accessory tissue, 882
- Splenic angiosarcoma, 759
- Splenic cyst, 748, 749, 776, 882
- Splenic cmholisation, 459, 694, 752
- Splenic focal lesions, 882
- Splenic infarcts, 749, 775
- Splenic masses in children, 882
- Splenic rupture, 749
- Splenic turnouts, 749, 759, 776
lymphoma, 759, 776
metastases, 759, 776, 777
- Splenic vein, 755
- Splenomegaly, 746, 747-8, 776
causes, 747, 882
children, 882
- Splenorenal shunt, 779, 780
- Splenosis, 775
- Splenunculus, 747
- Split notochord syndrome, 1651
- Spondylocyphoseal dysplasia, 1146-7

- Spondylolisthesis, 1376, 1378, 1657-8
 Spondylometaphyseal dysostosis, 1 137
 Spondylosis see Degenerative disc disease
 Spongiform degeneration, 1801
 Sprengle's shoulder, 1 108
 Springwater (benign pericardial) cyst, 307, 308, 335, 336
 Squamous cell carcinoma
 bladder, 995
 kidney, 960, 961
 nasopharynx, 1494, 1495
 oesophagus, 564
 oral cavity, 1544
 paranasal sinuses, 1525, 1526
 ureter, 979
 Squamous papilloma, oesophagus, 563
 Stable angina, 321
 Stafne's defect (salivary inclusion defect), 1538
 Stannosis, 194-5
Staphylococcus, 537, 627, 1659
 lung abscess, 22, 23, 138, 139
 osteomyelitis, 1 155
 pneumonia, 19, 23, 259
 septic arthritis, 1 163, 1 165
Staphylococcus aureus, 1 52, 165, 942, 1 784
 pneumonia, 131-2, 133, 136, 156
 toxic shock, 243
 Stein-Leventhal syndrome, 1072
 Stent placement
 hiliary tract, 734
 carotid artery stenosis, 1709-10
 intracranial arteriosclerotic disease, 1 710
 veins, 497
 Stentography, urinary tract, 898
 Stenver's (oblique posteroanterior) view, 1597
 Sternal dehiscence, post-cardiac surgery, 229
 Sternotomy, 228, 292
 Sternum, 12, 13, 47-8
 depressed (pectus excavatum), 47-8
 developmental abnormalities, 47
 fracture, 48, 218
 Still's disease (acute systemic onset juvenile arthritis), 1214
 Stomach, 575-612
 anatomy, 576-7
 examination methods, 575-6
 gastric motility, 609-12
 Stomatitis, 549
 Storage disorders, skeletal abnormalities, 1344-6
 Straddle fracture, 1402, 1403
 Straight back syndrome, 50
 Strecker stent, 451
 Streeter's bands (constriction rings), 1 107, 1177
Streptococcus, 259, 537, 1659, 1783-4, 1 785
 osteomyelitis, 1 155
 septic arthritis, 1163, 1164, 1 165
Streptococcus pneumoniae see *Pneumococcus*
 Stress echocardiography, 277
 coronary heart disease screening, 320
 stable angina, 321
 Stress fracture, 49, 217, 1371, 1374, 1 375, 1376-7, 1413, 1416, 1419
 Stroke
 carotid artery stenosis, 1709
 cholesterol emboli, 437
 Doppler ultrasound examination, 464, 466
 infra-arterial thrombolysis, 1707-8
 intracranial arteriosclerotic disease, 1 710
 magnetic resonance imaging (MRI), 1 823, 1824
 transluminal angioplasty complication, 449
 Stromal tumours
 benign gastric, 588, 589
 large bowel, 644
 peritoneal cavity, 633
 sex cord, 883
 small bowel, 624, 626
 Strongyloidiasis, 627, 652
 Loeffler's syndrome, 150-1
 Sturge-Weber syndrome (encephalotrigeminal angiomatosis), 1563, 1590, 1 634, 1635, 1737, 1738
 Subacute combined degeneration of spinal cord, 1668
 Subacute (de Quervain's) thyroiditis, 1 507, 1514
 Subacute sclerosing panencephalitis, 1 792
 Subarachnoid haemorrhage, 1673, 1 768-9
 aneurysmal, 1690, 1691
 embolisation, 1712
 natural history, 1692
 site of aneurysms, 1692-3
 angiography, 1691-2
 angiomas/arteriovenous fistulas, 1 772
 causes, 1691
 cerebral vasospasm, 1708-9
 intracerebral haematoma, 1692, 1 693, 1767, 1769
 neonate, 1811, 1812
 superficial siderosis, 1770
 transcranial Doppler ultrasound, 466
 Subarachnoid-pleural fistula, traumatic, 1 656
 Subarticular geode, 1293, 1295, 1312, 1 314
 Subclavian arteries, 268, 269
 compression syndromes, Doppler ultrasound, 467
 Subclavian artery stenosis, 432-3, 465, 473
 arteriography, 433
 transluminal angioplasty, 449
 Subclavian sarcoma, radiation-induced, 236
 Subclavian steal syndrome, 433, 434, 449, 465, 1703
 Subclavian vein stenosis, venous stents, 452
 Subcortical arteriosclerotic encephalopathy (Binswanger's disease), 1803, 1815
 Subcutaneous emphysema, 217, 218, 221, 243, 244
 Subdeltoid/subacromial bursitis, 1426
 Subdural abscess, 1785
 Subdural empyema, 1520
 Subdural haematoma, 1693, 1779, 1 782
 chronic, 1632, 1633
 Subdural haemorrhage, neonate, 181 1
 Subependymoma, 1746
 Subglottic tumours, 1498, 1500
 Subhepatic abscess, 681-2
 Sublingual gland, 533, 534, 1509, 1515
 Sublingual lymph nodes, 510
 Sublingual space, 535
 Submandibular gland, 533, 534, 1509, 1515
 Submandibular gland tumours, 535
 Submandibular lymph nodes, 510
 Submandibular space, 535
 Submental lymph nodes, 510
 Subphrenic abscess, 46, 53, 231, 681-2, 738-40
 Subsegmental lung resection, 225
 Sudeck's atrophy see Regional pain syndrome
 Superconducting magnets, 1819-20
 Superficial siderosis, intracranial, 1770
 Superior accessory fissure, 7
 Superior cerebellar arteries, 1686
 Superior labrum anterior posterior (SLAP) injury, 1407, 1419
 Superior mesenteric artery, 615
 anatomical variations, 812
 ileocolic branches, 635
 position with malrotation, 857, 858
 ultrasound examination, 472, 810
 Superior mesenteric artery acute occlusion, 630
 Superior mesenteric artery stenosis, 431, 472
 percutaneous transluminal angioplasty, 450
 vascular stents, 450
 Superior mesenteric artery syndrome, 601, 602
 Superior mesenteric artery thrombosis/embolism, 439, 675
 Superior mesenteric vein, 615, 635
 position with malrotation, 857, 858
 thrombosis, 630
 Superior rectal artery, 635
 Superior sulcus tumours see Pancoast tumours
 Superior vena cava, 60, 265, 266, 267, 272
 congenital anomalies, 498
 dilated, 74
 left-sided, 63, 74
 phlelography, 497-8
 Superior vena caval obstruction, 74, 83, 111 -12, 497, 499-500
 thrombolysis, 456
 venous stents, 452
 Supernumerary kidneys, 930
 Supernumerary teeth, 1537
 Superparamagnetic iron oxides, 778, 783, 786
 see also Ultrasmall superparamagnetic iron oxides
 Superselective arterial catheterisation, 418
 Supraclavicular (transverse) lymph nodes, 511
 Supracondylar fracture, 1407
 Supraglottic tumours, 1498, 1500, 1 503
 Supramitral ring, 394
 Surgical emphysema, 50-I, 1433-4
 pneumothorax/pneumomediastinum, 50.79
 Sutures, skull radiography, 1621, 1624
 Swan-Ganz (pulmonary artery flotation) catheter, 232, 233, 454
 Swyer-James (Macleod's) syndrome, 28, 171, 172
 Symphalangism, 1 107
 Synchysis scintillans, 1559
 Syndactyly, 1107, 1 109
 Synovial chondromatosis, 1308, 1309
 Synovial osteochondromatosis, 1426
 Synovial sarcoma, 1428, 1441-2
 Synovioma, 1311, 1313
 Syphilis, 73, 341, 424, 1788
 bone/joint lesions, 117 1, 1523, 1639
 congenital, 1171-2
 Syringohydrumyelia, 1728-9
 Syringomyelia, 1665, 1666
 Systemic lupus erythematosus, 48, 197, 198, 210, 538, 630, 976
 diffuse lung disease, 198
 microaneurysms, 428
 peripheral arthropathy, 1233
 pleural effusion, 87, 198
 Systemic sclerosis see Scleroderma
 Systemic vasculitides, 200-2
 Systemic-to-pulmonary shunt insertion, 364
 Systolic/diastolic ratio, 463
- ## T
- T-cell lymphoma, 523, 524, 598, 629
Taenia multiceps, 1 791
Taenia saginata, 627
Taenia solium, 627, 1437, 1790
 Tailgut cysts, 654
 Takayasu's disease, 73, 314, 431, 435-6
 aortic arch syndrome, 436
 arterial stenoses, 429
 Talar fracture, 1378, 1413-14
 Talipes deformity, 11 14-15
 Talipes equinovarus (club foot), 1 115-16
 Talocalcaneal fusion, 1 117
 Tamoxifen, 1073, 1 101
 Tapeworm (cestode), 627, 1437
 brain infection, 1790-1
 Loeffler's syndrome, 150
 Tarsoepiphyseal aclerosis, 1136-7
 Tattoos, 1433
 Taurodontia, 1538
 Taussig-Bing anomaly, 399
 Technetium-labelled colloid
 gastric motility investigation, 611
 gastrointestinal haemorrhage, 440, 456, 655-6
 Technetium-labelled depreotide, 42
 Technetium-labelled red blood cells, gastrointestinal bleeding, 412, 440, 456
 Technetium-labelled tracers
 acute cholecystitis, 686
 biliary tract examination, 717-18
 bone scan
 bone tumours, 1248
 rheumatoid arthritis, 1209
 cardiac blood pool imaging, 277-8
 inflammatory bowel disease, 659
 liver imaging, 759
 lung capillary permeability, 43
 lymphoscintigraphy, 514
 myocardial imaging, 277, 278, 279
 osteomyelitis, 1 157
 parathyroid imaging, 1508
 adenoma, 68
 regional cerebral blood flow imaging, 1812
 renal scintigraphy, 912
 DMSA, 913-14
 MAG3, 914-15
 retrosternal goitre, 64

- thyroid imaging, 1504, 1505
 perchlorate discharge test, 1506-7
 transit test (oesophageal scintigraphy), 550
 ventilation/perfusion (VQ) imaging, 38, 39
- Teeth, 1531-49
 absent, 1537
 anatomy, 1531
 bone dysplasias, 1539-40
 charting, 1531
 chronology of development, 1532
 cysts, 1542, 1543
 developmental abnormalities, 1537-8
 endocrine disorder involvement, 1538-9
 fusion, 1537
 hypoplasia (microdontia), 1537
 infection, 1531-3
 postinflammatory sclerosing osteitis, 1535
 radiographic techniques, 1531
 supernumerary, 1537
 trauma, 1536-7
- Temporal arteritis, 436
- Temporomandibular joint disorders, 1546-7, 1548, 1549
- Tendon calcification, 1421, 1422, 1437
- Tendon injury, 1419-20
 musculotendinous junction, 1420
 subluxation/dislocation, 1421
 tears, 1420-1
- Tendon myxoid degeneration (tendinopathy: tendinosis), 1420, 1421
- Tenosynovitis, 1421, 1432
- Tension pneumothorax, 94, 98, 99
- Tentorial artery, 1680
- Teratoma
 carotid space, 1502
 intracranial, 1754
 calcification, 1629-30
 mediastinum, 66, 67, 81
 ovary, 883, 884, 1083
 presacral space, 654
 retroperitoneum, 848
- Terson's syndrome, 1558
- Testes
 anatomy, 8911
 blood supply, 890
 calcification, 1033
 magnetic resonance imaging (MRI), 911
 trauma, 1027
 ultrasound, 895-6
- Testicular appendix (hydatid of Morgagni) torsion, 1027
- Testicular cancer, 117, 472, 1028-33
 germ cell tumours, 1028
 non-seminomatous, 1028, 1029, 1031, 1032
 seminomas, 1028, 1029, 1032
- imaging, 1028-9
 staging, 1030-2
- Leydig cell tumours, 1028
- lymph node involvement, 512, 514, 518, 519, 520, 1029, 1031
- lymphoma, 526, 1028, 1032-3
 metastatic tumours, 1028, 1032
- Royal Marsden staging system, 1029-30
- Sertoli cell tumours, 1028
 treatment planning, 519-20
- Testicular cysts, 1027, 1028
- Testicular masses, 1027-33
- Testicular microlithiasis, 1033
- Testicular torsion, 1026-7, 1035
 Doppler ultrasound, 472
- Testicular vein embolisation, 906, 909
- Tetralogy of Fallot, 367, 368, 369, 370, 382-5
 balloon dilatation of pulmonary outflow tract, 384
 cardiac catheterisation, 384
 non-invasive imaging, 383
 pulmonary stenosis, 383
 right-sided aortic arch, 383
 treatment, 384-5
 ventricular septa defect, 382, 383, 384
- Thalassaemia (Cooley's anaemia), 49, 1321-3
 extramedullary haemopoiesis, 78
 skeletal features, 1322, 1323
 jawfacial skeleton, 1541
 skull vault, 1640
- Thalidomide embryopathy, 1107, 1108
- Thallium-201 imaging
 myocardium, 278
 parathyroid adenoma, 68
 tetralogy of Fallot, 383
- Thanatophoric dysplasia, 1061-2, 1142, 1144
- Thecoma, 1082
- Thermal ablation, magnetic resonance imaging (MRI), 1446
- Thoracic biopsy, computed tomography (CT) guidance, 31
- Thoracic duct, 509, 510
- Thoracic inlet syndrome, 429, 432, 434
- Thoracic lymphoma, 526
 cross-sectional imaging, 526-8
- Thoracic soft tissues/artefacts, paediatric chest, 249
- Thoracic spine, 49-50
 degenerative disease, 1228
 fracture, 218
 associated aortic transection, 311
- Thoracolumbar spinal trauma, 1399-400
- Thoracoplasty, 49, 229, 230
- Thoracotomy, 225, 228
 bronchopleural fistula, 226-7
 complications, 225-7
 late appearances, 229, 230
 diaphragmatic elevation, 227
 empyema, 225-6
 pleural fluid, 227
 postoperative spaces, 225
- Thorium dioxide (Thorotrast) contrast medium, 419, 1267
 Thorotrast spleen, 748
- Threatened abortion, 1044-5
- Thrombocytopenia-absent radius syndrome, 1108
- Thromboangitis obliterans (Buerger's disease), 433-5
- Thrombolysis, 455-6, 497
 acute ischaemic stroke, 1707-8
 complications, 455
 hepatic vein thrombosis, 751
 indications, 455, 456
 procedure, 455
- Thrombosis
 angiography complication, 420, 422
 intracranial vessels, 1703, 1704-5
 thrombolysis indications, 455
 transluminal angioplasty complication, 449
- Thumb injuries, 1382, 1383, 1410-11, 1414, 1415
- Thymic hyperplasia, 65
- Thymic tumours, 64-5
- Thymolipoma, 58, 65
- Thymoma, 58, 59, 61
 computed tomography (CT), 65, 66
 ectopic ACTH production, 840
 magnetic resonance imaging (MRI), 81
 plain chest film, 13
- Thymus, 248-9, 509
 computed tomography (CT), 60, 64-5
 magnetic resonance imaging (MRI), 81
 plain chest film, 6
- Thyroid acropachy, 1155
- Thyroid adenoma, 62, 64, 1510, 1512-13
- Thyroid carcinoma, 62, 64, 1510, 1513-14
 anaplastic, 1513
 bone metastases, 1251, 1253, 1255
 follicular, 1513
 medullary *see* Medullary thyroid carcinoma
 papillary cell, 1513
 radionuclide imaging, 1507
- Thyroid cyst, 1512
- Thyroid gland, 1510
 enlargement
 multinodular, 62
 oesophageal displacement, 573
see also Goitre
 radionuclide imaging, 1504-7
 applications, 1504, 1505-7
 normal appearances, 1505
 perchlorate discharge test, 1506-7
 preparation, 1504-5
 ultrasound, 1512-14
- Thyroid mass
 computed tomography (CT), 62, 64
 magnetic resonance imaging (MRI), 81
- Thyroid nodules, scintigraphy, 1504, 1505, 1506
- Thyroid ophthalmopathy, 1567, 1579
- Thyroid tumours, 1512-14
 Hurthle cell, 1514
 lymphoma, 1514
 malignant, 1513-14
 metastatic, 1251, 1253, 1255, 1514
 functional, 1504, 1507
 scintigraphic detection, 42
- Thyroiditis, scintigraphy, 1504, 1507
- Thyrotoxicosis, 62, 1513
 osteoporosis, 1359
 thyroid scintigraphy, 1504, 1505-6
- Tibia
 congenital pseudarthrosis, 1114
 osteochondritis of tubercle, 1186-7, 1377, 1378
- Tibia vary (Blount's disease), 1189, 1358
- Tibia artery angioplasty, 448, 449
- Tibia plateau fracture, 1411, 1412
 avulsion injury, 1383
- Tibial shaft fracture, 1372, 1412
- Tietze's syndrome, 49
- Tissue adhesive embolisation materials, 456
- TNM staging system, 518, 519
 bladder cancer, 1008
 bronchial carcinoma, 115, 117
 gastric carcinoma, 593
 lymph node imaging, 519
 oesophageal cancer, 567
 prostate cancer, 1012
 renal cell carcinoma, 954-5
- Tom Smith arthritis, 1164-6
- Tomography, 30
 aspergilloma, 147
 chest imaging, 1, 29
- Tongue carcinoma, 1722
- Tophi, 1230, 1231, 1233, 1234
- Torulosis *see* Cryptococcosis
- Torus mandibularis, 1544
- Torus palatines, 1544
- Total anomalous pulmonary venous connection, 370, 395-7
 diagnostic imaging, 397
- Total cystectomy, 999
- Total gastrectomy, 606
- Total proctocolectomy and ileostomy, 650
- Towne's view, 1391, 1573, 1617, 1619, 1620, 1622, 1685, 1687, 1691
- Toxic megacolon, 636, 647, 680
 Crohn's disease, 648
 differential diagnosis, 647
 intestinal emphysema, 687
 ulcerative colitis, 647
- Toxins, effects on skeleton, 1367-9
 osteomalacia, 1353
 osteoporosis, 1366
- Tosocara cams*, ocular infection, 1591-2
- Toxoplasmosis
 cerebral infection, 1788-90, 1793, 1798
 congenital intracranial lesion
 calcification, 1632, 1633, 1634
 lung infection, 150, 157
 ocular infection, 1592
- Trachea
 computed tomography (CT), 60, 62
 congenital abnormalities, 161
 narrowing, 75, 161-2
 paediatric imaging, 249
 plain chest film, 5, 13
 widening, 75, 162-3
- Tracheal agenesis, 249
- Tracheal bronchus (PIG bronchus), 250
- Tracheal carcinoma, 161, 162
- Tracheal intubation-related stricture, 161-2
- Tracheal lesions, 75
- Tracheal stenosis, 161-2, 249
 congenital abnormalities, 249
- Tracheal trauma, 221, 222
- Tracheal tumours, 75, 84, 161
- Trachcobronchomegaly, 75, 162, 163
- Trachcomalacia
 tracheobronchomalacia, 62, 63, 75, 162
 congenital abnormalities, 249
- Trachco-oesophageal fistula, 161
 congenital abnormalities, 249-50
 H-type, 852
 with oesophageal atresia, 852-3
- Tracheopathia osteoplastica, 161, 162
- Tracheopathia/tracheobronchopathia osteochondroplastica, 75, 212
- Tracheostomy tubes, 218, 234
 complications, 234
 tracheal strictures, 161, 162
- Transcranial Doppler ultrasound, 462, 465-6
- Transducers, 1039, 1834-5
- Transhepatic portal phlebography, 502-3

- Transhepatic venous sampling, 795
- Transient ischaemic attacks, 463, 1700, 1703, 1777
- carotid angioplasty, 450
- cholesterol emboli, 437
- Transient (regional) osteoporosis, 1367, 1380
- Transient tachypnoea of newborn (wet lung disease), 258
- Transit test (oesophageal scintigraphy), 549, 550-2
- Transitional cell carcinoma
- bladder, 995, 996
- synchronous/metachronous tumours, 996
- kidney, 959-60, 961, 963
- risk factors, 959
- ureter, 979
- Transitional papilloma, 995
- Transjugular intrahepatic portosystemic shunt (TIPS), 453, 454, 752-3, 775, 780
- stenosis, Doppler ultrasound examination, 468
- Transjugular liver biopsy, 453, 751
- Transluminal Endarterectomy Catheter (TEC), 450
- Transoesophageal echocardiography, 269, 270, 271, 276
- congenital cardiac disease, 363
- sinus venosus defect, 375
- Transoesophageal ultrasound, chest trauma, 217
- Transposition of great arteries, 74, 367, 385-90
- cardiac catheterisation, 387-8
- circulation, 369-70
- D-loop, 385-6
- associated abnormalities, 386
- L-loop (corrected transposition), 367, 386-7
- non-invasive imaging, 387
- treatment, 388-90
- Rashkind balloon septostomy, 364, 370
- Transrectal ultrasound, 637
- benign prostatic hyperplasia, 1005
- male infertility investigation, 1036
- prostate, 896, 897
- cancer, 1006, 1007, 1014-15
- rectal cancer, 643
- Transvaginal ultrasound, 471, 1069
- Transvenous interventional procedures, 497
- Transverse limb defects, 1107
- Transverse (supraclavicular) lymph nodes, 511
- Trauma
- abdomen, 691-708
- imaging, 691-2
- aneurysms, 425-6, 427
- arterial, fracture-related, 1381-2
- hilar tree, 698-9
- bladder, 703-4, 997-9
- bowel, 705-7
- breast, 1462, 1463
- causes of death, 691
- chest, 217-24
- cranial/skull, 1641-2, 1778-83
- see also Head injury
- epidemiology, 691
- gallbladder, 698-9
- jaws, 1536-7
- joints, 1382-3
- kidney, 470, 471, 699-703, 971-5
- liver, 695-8, 759, 760
- lung, 219-20, 221
- major blood vessels, 707-8
- male urethra, 1018-19
- mesentery, 707
- orbit, 1575-7
- pancreas, 704-5, 800, 820
- penis, 1034
- petrous temporal bone, 1605-6
- pharynx/larynx, 1495-7
- scrotum, 1027
- skeletal, 1371-87
- imaging difficulties ('problem' fractures), 1414-16
- regional, 1389-416
- soft tissues, 1372-4, 1419-26
- spine, 1655-6, 1837
- spleen, 692-5, 759, 761, 763
- rupture, 749
- teeth, 1536-7
- Treacher Collins syndrome (mandibulofacial dysostosis), 1604
- Trematode (fluke) infection, brain, 1791
- Treponema pallidum*, 1788
- Treponematoses (yaws), 1174-5
- Trevor's disease (dysplasia epiphysealis hemimelica; tarsometatarsal aetiology), 1136-7
- Trichinella spiralis*, 1791
- Trichinosis, brain infection, 1791
- Ti ichobezoar, 608, 609, 866
- Tricuspid atresia, 370, 393-4
- Tricuspid regurgitation, 373
- Tricuspid stenosis, 304
- Tricuspid valve, 265, 266
- Tricuspid valve disease, 74, 303, 329, 330
- Trigeminal artery, 1689
- Trigeminal nerve neuroma, 1759
- Trigeminal neuralgia, 1772
- Trigonocephaly, 1624
- Triosil, 419, 420
- Triquetrolunate dissociation, 1409
- Triquetrum dorsal avulsion fracture, 1408
- Trisomy 13, 1059, 1109
- Trisomy 18, 1053, 1059, 1063, 1108, 1109
- Trisomy 21 (Down's syndrome), 47, 48, 790
- associated abnormalities, 860, 1033, 1058, 1063, 1107, 1537
- duodenal atresia, 855
- oesophageal atresia, 852
- skeletal features, 1149-51
- Trochlear apparatus calcification, 1583-4
- Tropheryma whippelii*, 628
- Trophoblastic disease, 471
- Tropical sprue, 629
- Tropical ulcer, 1176
- Trosier's lymph nodes, 511
- Truncus arteriosus, 397-8
- Truncus bicaroticus, 1687, 1688
- Tubal disease, 1089
- selective fallopian tube catheterisation and recanalisation, 1090
- see also Pelvic inflammatory disease
- Tubal filling pressure measurement, 1090
- Tubal patency, 1084
- assessment
- hysterocontrastsonography, 1084, 1085
- hysterosalpingography, 1085, 1086
- Tuberculoma, 142, 144
- calcification, 1632, 1633
- Tuberculosis, 29, 140-4, 1468
- acute parotitis, 537
- adrenal gland, 826, 828
- AIDS/immunocompromised patients, 153, 156, 157
- airway involvement, 144
- arthritis, 1169-71
- hip, 1170
- knee, 1170
- sacroiliac joint, 1171
- shoulder, 1170
- wrist, 1170-1
- bladder, 991-2
- bone, 1166-9
- bronchiectasis, 163
- bronchopneumonia, 142, 143, 144
- cerebral disease, 1632, 1633, 1785-6, 1787
- epilepsy, 1804
- children, 259
- primary pulmonary disease, 259-60
- secondary disease, 260
- colitis, 652, 653
- dactylitis, 1168, 1169
- empyema, 141
- epidemiology, 140
- greater trochanter, 1167
- hilar enlargement, 27
- hydrocele, 1023
- hypertrophic osteoarthropathy, 1231
- intestinal disease, 627, 628
- lymphadenopathy, 70, 71, 72, 141, 142-3, 144, 146
- mediastinal disease, 61, 62, 70, 71, 72, 75
- fibrosis, 80
- miliary, 17, 18, 36, 141, 142, 144, 260
- neck soft tissue spaces, 1504, 1510
- oesophagitis, 558, 559
- otitis media, 1607
- paranasal sinuses, 1523
- pericardial cyst, 308, 335
- peritoneal infection, 633
- pleural disease, 87, 95, 97, 141, 143-4, 145
- plombage, 229, 231
- pneumothorax, 141, 143
- pulmonary lesions, 25, 168
- calcification, 24, 25
- cavitation, 22-3
- Ghon focus, 141
- healed, 142
- lung consolidation, 141-2
- post-primary, 140, 141, 142
- pulmonary, 140-1
- renal involvement, 944, 945, 946
- skull, 1169
- erosion, 1639
- somatostatin receptor scintigraphy, 661
- spine, 1166, 1167-8, 1658-9, 1667
- splenic abscess, 776
- superior vena caval obstruction, 499
- synovium, 1242
- thoracoplasty, 229
- tracheitis/tracheal stenosis, 161
- ureter involvement, 980
- uterus/tubular disease, 1087, 1088, 1089
- Tuberous sclerosis, 207, 403, 442, 771, 1056, 1198, 1728
- intracranial lesions, 1735-7
- calcification, 1634, 1635
- renal angiomyolipoma, 876, 949
- renal manifestations, 936-7
- skeletal features, 1198
- Tubo-ovarian abscess, 1079, 1093
- Tularaemia, 134-5, 136
- Tumoral calcinosis, 1440, 1445
- Tumour blood supply, angiographic investigations, 442
- Tumour doubling time, 518
- Tumour spread, 518
- Tumour staging systems, 518
- Turcot's syndrome, 639, 871
- Turner's syndrome, 314, 931, 936, 1108, 1109, 1151, 1358
- Turricephaly, 1624
- Tylosis palmaris et plantaris, 564
- Typhlitis (necrotic colitis), 632, 652, 872
- Typhoid enteritis, 440
- Ulcerative colitis, 646-8
- hack-wash ileitis, 648
- children, 872
- colorectal carcinoma risk, 648
- contrast studies, 647-8
- Crohn's disease differentiation, 650
- joint disease, 1216, 1221
- plain films, 646-7
- postinflammatory polyps, 638, 648
- radionuclide imaging, 660
- surgery, 650-1
- Ulnar congenital defects, 1108
- Ulnar fracture, 1407, 1408
- Ultrasound
- supramagnetic iron oxides (USPIOs), 515, 1827, 1828
- bladder cancer imaging, 1011
- pelvic lymphadenopathy imaging, 1099
- Ultrasound
- abdominal trauma, 691
- acute cholecystitis, 685-6
- adrenal mass, 829
- amoebiasis, 150
- anal endosonography, 637, 655
- aneurysms, 425
- appendicitis, 683-4
- children, 867, 869
- arterial imaging, 412, 417, 418
- biliary tract examination, 714-17
- bladder, 894-5
- bone density measurement, 1352
- breast, 1455-8
- abnormal findings see Breast image-guided procedures, 1479-80
- carotid/cerebral vessels, 1675
- cervical lymph nodes, 1515-16
- chest imaging, 1, 45, 248
- chest trauma, 217
- fluid collections percutaneous drainage, 45-6
- children
- abdomen, 851
- chest, 248
- infant brain see Brain, ultrasound examination
- urogenital tract, 923-4
- contrast media, 763
- Crohn's disease, 623-4
- cystodynamogram, 921-2
- eye examination, 1551
- pathology, 1554-64
- trauma, 1564-6

- female infertility, 1084, 1085
gastric motility, 609
gynaecological imaging, 1069-84
 endovaginal/transabdominal, 1069
hip dysplasia, congenital (congenital dislocation), 1109-10
inflammatory bowel disease, 650
intravascular, 412, 449, 1835
joint imaging
 ankle, 1243
 knee, 1235-6
 shoulder, 1240, 1241
 wrist, 1244
kidneys, 894-5
 trauma, 972-3
liver, 763-75
lung consolidation, 183, 184
lymph nodes, 514-15
mediastinal disease
 lymphangioma, 68
 pleuropericardial cyst, 67
neck, 1512-16
orbit, 1566-70
pancreas, 787, 810-21
 guidance for interventions, 820
parathyroid glands, 1514-15
Perthes' disease, 1184, 1185
phaeochromocytoma, 843, 844
pleural effusions, 88, 91, 92
recent technical advances, 1832-6
 3D imaging, 1039-40, 1834
 compound imaging, 1833
 echo-enhancing agents, 1835-6
 elastography, 1833
 harmonic imaging, 763, 1039, 1833
 signal generation/processing, 1833-4
 transducers, 1834-5
rectal examination, 637
 see also Transrectal ultrasound
rheumatoid arthritis, 1209-11
salivary glands, 535, 1515
scrotum/male genitalia, 895-6
small bowel, 618
spine, 1649
spleen, 775-7
transoesophageal, 217
transvaginal, 471, 1069
venous, 503-5
 see also Doppler ultrasound;
 Endoscopic ultrasound;
 Obstetric ultrasound
Umbilical-urachal sinus, 989
Undescended testes (cryptorchidism), 1022, 1028, 1033
Undulant fever *see* Brucellosis
Unicameral (solitary) bone cyst, 1312-14, 1315, 1316
Unicornuate uterus, 1075, 1087, 1094
Unusual interstitial pneumonitis (cryptogenic fibrosing alveolitis), 204-6
Upper gastrointestinal endoscopy, 575
Upper gastrointestinal haemorrhage
 arteriographic diagnosis, 440
 radionuclide imaging, 655-7
 therapeutic embolisation, 456
Upper limb
 arteries, Doppler ultrasound, 467
 congenital disorders, 1107-9
 classification, 1107
 critical ischaemia, thrombolysis, 456
 phlebography, 497-8
 trauma, 1372, 1404-11
 venous drainage, 497, 498
Urachal anomalies, 989-90
Urachal carcinoma, 997
Urachal cyst, 989, 990
Urachus, 888
Urate calculi, 966-7
Ureter, 885, 888, 910
 duplication abnormalities, 933-4, 935
Ureteric calculi, 965-70, 978
 hydronephrosis, 970
 imaging, 967-8, 969
 obstruction, 967-8, 971, 972
 percutaneous nephrostomy, 969
Ureteric colic, 967, 969
Ureteric deviation, 982
Ureteric dilatation, 900
Ureteric diverticulum, 935
Ureteric intramural haemorrhage, 979
Ureteric lesions, 978-82
 extrinsic, 980-2
 intraluminal, 978-9
 mural, 979-80
Ureteric mucosal oedema, 979
Ureteric obstruction
 Doppler ultrasound, 470-1
 dynamic radionuclide studies, 918
 renal colic, 688
 renal transplant graft failure, 985-6
Ureteric strictures, 980
 congenital, 940
Ureteric trauma, 975
Ureteric tumours, 979
Ureterocele, 935
Uretroperitoneal junction *see* Pelviureteric junction
Ureterosigmoidostomy, 1001, 1002-3
Ureterovesical junction obstruction, prenatal diagnosis, 1061
Urethra, 888, 889-90
 male, congenital lesions, 1017
Urethral calculi, 1020
Urethral carcinoma, 1019
Urethral diverticulum, 1020-1
Urethral duplication, 1017
Urethral fibroepithelial polyp, 1019
Urethral fistula, 1021-2
Urethral papilloma, 1019
Urethral sinus, 1020, 1021-2
Urethral stricture, 993, 1017-18
 inflammatory, 1017-18
 traumatic, 1018
Urethral trauma, 1018-19
 anterior, 1019
 posterior, 1018-19
Urethral tumours, 1019-20
 benign, 1019
 malignant, 1019
 metastatic, 1019-20
Uretrography, 899-900, 927
 ascending, 900, 901
Urinary diversion/obliterated bladder construction, 999-1000, 1001
Urinary incontinence, 921
Urodynamics studies, 921-3
 intravenous urodynamicogram, 922
 ultrasound cystodynamogram, 921-2
 upper urinary tract, 922-3
 videocystometry, 922
Urogenital tract, 885-928
 anatomy, 885-90
 computed tomography (CT), 906, 910, 925-6
 contrast media, 891, 893, 926-7
 direct contrast studies, 896-900, 924-5
 dynamic radionuclide studies, 918-19
 intravenous urography, 891-4, 925
 investigations, 890-900
 children, 923-6
 KUB (kidney ureters and bladder) film, 890-1
 lithotripsy, 725, 905-6, 969
 magnetic resonance imaging (MRI), 910-12, 926
 percutaneous interventional procedures, 900-5, 925
 radionuclide imaging, 912-21, 925
 ultrasound, 894-6, 923-4
 urodynamic studies, 921-3
 vascular procedures, 906
Urografin, 420
Uroselectan (lopax), 419
Urothelial chronic irritation, 948
Urothelial mass, 903
Uterine adenomyosis (endometriosis interna), 1075-6, 1077, 1089
Uterine fibroids (leiomyomas), 1004, 1075, 1076, 1087, 1088, 1090, 1091, 1094-5
 cervix, 1078
 differential diagnosis, 1077
 embolisation, 458, 1092
 uterine, 1070, 1090, 1093, 1094
 blood flow, Doppler ultrasound, 471
 congenital abnormalities, 1075, 1086-7, 1094
 size measurement, 1069
 tumours, 1094-7
 uterus didelphys, 1074, 1075, 1094
 Vaandrager's metaphysal chondrodysplasia, 1137
 VACTERL association, 852
 Vagina, 1069-70, 1090, 1093
 Vaginal fistula, 1085
 Vaginal tampon, 1069
 Vagotomy, 608
 gastric motility following, 611, 612
 Valgus angulation, 1372
 Valves of Houston, 635
 Valvular heart disease, 318, 326-32
 interventional valve dilatation, 359
 plain chest film, 299-304
 sectional imaging, 331-2
 Vanishing bone disease (Gorham's disease), 1299-300, 1302
 Varicella zoster pneumonia, 24, 25, 136, 137, 138
 Varices
 choledochal, 731
 embolisation, 457
 gastric, 572
 oesophageal, 571-2
 children, 866
 orbit, 1568
 transjugular intrahepatic portosystemic shunt (TIPS), 453, 454
 Varicocele, 493, 1024
 Doppler ultrasound, 472
 embolisation, 458, 906, 909, 1024, 1025
 Varicose ulcers, 483
 Varicose veins, 483, 487-8, 504-5
 Varix, 488
 orbit, 1584
 Varus angulation, 1372
 Vas deferens, 890
 Vascular contrast media, 419
 Vascular dementia, 1796
 Vascular foreign bodies retrieval, 454
 Vascular infusion therapy, 447, 454-5
 see also Chemotherapy, intra-arterial
 Vascular ring, 407-10, 866
 neonatal oesophageal obstruction, 853
 Vascular stent insertion, 447
 congenital cardiac disease, 364
 Vasculitides, small bowel disease, 630
 Vasectomy, epididymis appearances following, 1024, 1025
 Vasoconstrictors, intra-arterial infusion, 454
 Vasodilators, intra-arterial infusion, 454-5
 peripheral angioplasty arterial spasm prophylaxis, 449, 454
 Vasography, 906, 1036
 Vasopressive, intra-arterial infusion, 454
 Vasovagal reaction, 422, 429, 449, 1086
 VATER syndrome, 161, 250, 851, 929
 anorectal malformations, 861
 duodenal atresia, 855
 Vein of Galen
 aneurysm, 1697, 1698
 endovascular treatment, 1715-16
 carotid angiography, 1682-3
 Veins
 magnetic resonance imaging (MRI), 505-7
 phlebography *see* Phlebography
 ultrasound, 503-5
 Venous access, 497
 Venous angiography, 412
 Venous angioma, 488
 Venous blood sampling, 445, 495
 Venous calcification, 1435, 1436
 Venous congenital abnormalities, 402
 Venous incompetence, 483, 485
 Venous insufficiency, chronic, 505
 Venous stasis, periosteal reaction, 1154
 Venous stents, 452
 Venous thrombosis, 503, 505-6
 acute, 487
 cerebral infarcts, 1777
 iliac veins, 489-90, 491, 492, 493
 inferior vena cava, 489-90, 491, 492, 493, 506
 upper limb, 497, 498
 see also Deep vein thrombosis
 Venous valves, 485, 486
 congenital absence, 488
 Ventilation/perfusion (VQ) imaging, 38-9
 interpretation, 39-40
 perfusion scintigraphy, 39
 pulmonary embolism, 237, 238, 239, 343, 344-5
 ventilation scintigraphy, 39
 Ventricular coarctation, 1733-4
 Ventricular function assessment, 318, 320
 Ventricular septal defect, 47, 368, 371-4
 aneurysmal perimembranous, 373
 aortic coarctation association, 371-81
 aortic regurgitation, 374
 cardiac catheterisation, 373-4
 clinical presentation, 372
 common mixing circulation, 370

- Ventricular septal *defect-could*
 Gerbode defect, 371
 left-to-right shunt, 369
 malalignment, 371
 muscular, 371
 non-invasive imaging, 372-3
 patent ductus arteriosus association, 374
 per-fine membranous, 371
 with pulmonary atresia, 391-2
 surgical treatment, 374
 tetralogy of Fallot, 382, 383, 384
 tricuspid regurgitation, 373
- Ventricular wall
 terminology, 271
 thickness, 265
- Ventriculitis, 1784
- Ventriculoatrial septum, 266
- Ventriculomegaly, 1053
- Vermian veins, 1687
- Vertebra plana (osteochondritis of vertebral body; Calve's disease), 1187
 eosinophilic granuloma, 1341
- Vertebral anomalies, 1653-4
 absent pedicle, 1653, 1654
 butterfly, 1117
 coronal cleft, 1117
 fusion, 1119-20
 hemivertebrae, 1119
 lumbosacral facet anomalies (trochism), 1121
 malfusion of appendages, 1119
 sacralisation/lumbarisation, 1120-1
- Vertebral arteriovenous fistula, 1698
- Vertebral artery, 268
 angiography, 1677
 complications, 422
 normal findings, 1684-6
 anomalous communications with carotid arteries, 1689-90
 atheromatous disease, 429, 1700, 1702
 congenital anomalies, 1689
 Doppler ultrasound examination, 415, 466
 size variation, 1689
 test occlusion, 1711
- Vertebral artery stenosis, 415, 429, 1700, 1702
 percutaneous transluminal angioplasty, 450
- Vertebral body compression fracture, 1373
- Vertebral burst fracture, cervical spine, 1398
 Jefferson fracture (C I), 1397-8
- Vertebral epiphysitis (adolescent kyphosis; Scheuermann's disease), 1188
- Vertebral haemangioma, 1661, 1662
- Vertebral tumour embolisation, 1720, 1721
- Vertebrobasilar insufficiency/occlusion
 carotid angioplasty, 450
 infra-arterial thrombolysis, 1708
- Vertebrobasilar intracranial circulation, 1684, 1685
- Vertebroplasty, percutaneous, 1721-2
- Vertical handed gastroplasty, 606, 607
- Vertical talus, congenital, 1116, 1117
- Vesicoenteric fistula, 995
- Vesicourachal diverticulum, 989, 990
- Vesicoureteric reflux, 861, 898, 924, 925, 946
 grading, 946
 radionuclide imaging, 917, 918, 920-1
 urodynamic studies, 922-3
- Vesicovaginal fistula, 995
- Vestibular apparatus, 1598, 1599
- Vestibular aqueduct, 1602
- Vibration syndrome (driller's disease), 1380
- Videocystometry, 922
- Videofluoroscopy
 paediatric abdomen, 850
 pharynx/larynx examination, 1489, 1495
- Vidian (pterygoid) artery, 1680
- Villous tumour, duodenum, 588-9
- Vinyl chloride poisoning, 1368-9
- Vipoma
 embolisation, 458
 somatostatin receptor scintigraphy, 660
- Viral central nervous system infections, 1791-4
- Viral cystitis, 991
- Viral encephalitis, 1792
- Viral hepatitis, 765-6
- Viral meningitis/encephalitis, 1785
- Viral pneumonia, 136, 137
- Virchow's lymph nodes, 511
- Virilising syndrome, 835
- Virtual bronchoscopy, 1838
- Virtual colonoscopy, 1829, 1839
 colorectal cancer screening, 644
- Virtual endoscopy, 1838, 1839
 intraluminal, 1829
- Virtual gastroscopy, 1829
- Visceral space of neck, 1509
- Visceroatrial situs, 365, 366
- Vitamin A overdose, 1367-8
- Vitamin C deficiency, 1356
- Vitamin D deficiency, 1353
- Vitamin D metabolism, 1352-3
 abnormalities, 1352-6
- Vitamin D-resistant rickets (familial hypophosphatasia), 1353-4
- Vitreous body, 1552, 1553
- Vitreous detachment, posterior, 1559, 1565
 incomplete, 1559-60
- Vitreous haemorrhage, 1558, 1576
 traumatic, 1565
- Vitreous pathology, 1557-60
- Volkman's ischaemia of forearm, 1381, 1407
- Volumetric computed tomography (CT)
 paediatric chest, 248
 quantitative computed tomography (QCT), bone density measurement, 1352
- Volvulus, 1058
 caecal (right colon), 669, 676-7, 678
 gastric, 599, 866
 gastric dilatation, 668, 669
 large bowel, 653, 676
 midgut, 856-7
 chronic, 857, 858
 sigmoid, 677-8
 small bowel, 672
- Von Hippel-Lindau disease, 769, 792, 800, 842, 879, 881, 1590, 1667
 clinical presentation, 936, 937
 intracranial lesions, 1738, 1757
 renal cell carcinoma, 949, 953
- Von Recklinghausen's disease *see* Neurofibromatosis I (NFL)
- Von Willebrand's disease, 1346
- Voorhoeve's disease (osteopathia striata), 1130
- Vulval varices, 492-3
- Waldenström's disease, 1384
- Waldenström's macroglobulinaemia, 629
- Wallstent, 451, 452, 734
- Wandering spleen, 882
- Warfarin, 448
- Warthin's tumour (adenolymphoma), 540, 1515
- Water-soluble contrast studies
 paediatric abdomen, 850
 pouchography, 641, 650
 small bowel obstruction, 620
- Watermelon stomach, 580
- Waters (occipito-mental) view, 1390, 1391, 1519
- Wegener's granulomatosis, 75, 200, 202
 diffuse lung disease, 23, 201
 extraocular muscle involvement, 1580
 microaneurysms, 428
 orbit involvement, 1568
 paranasal sinuses, 1523
 renal appearances, 976
 tracheal narrowing, 161
- Werner's syndrome, 412
- Westermark sign, 315
- Western equine encephalitis, 1792
- Wet lung disease (transient tachypnoea of newborn), 258
- Wharton's duct, 533
- Whipple's disease, 628
 joint involvement, 1216, 1221
- Whitaker test, 923
- White blood cell disorders, skeletal abnormalities, 1327-30
- White matter disorders, 1799-800
- Whole body magnetic resonance screening, 1823
- Whooping cough, 72, 79
- William's syndrome, 381
- Wilms' tumour (nephroblastoma), 874, 875, 961, 962
 angiography, 442
 associated disorders, 874, 961
 metastases, 961, 1569
 nephroblastomatosis transformation, 962
 staging, 874
- Wilson's disease (hepatolenticular degeneration), 1366, 1797-8
- Wolman's disease (Abramov-Wolman disease), 826, 828, 878
- Wrist
 congenital defects, 1108-9
 imaging, 1242, 1244
 tuberculosis, 1170-1
- Wrist trauma
 carpus dislocation, 1409-10
 carpus fractures, 1408-9
 forearm fractures, 1408
 triangular fibrocartilage complex disruption, 1408
- X
- X-linked leucodystrophies, 1801-2
- Xanthine calculi, 967
- Xanthogranulomatous cholecystitis, 724
- Xanthogranulomatous pyelonephritis, 944
 angiography, 442
- Xenon contrast agent, 1724
- Xenon-133 ventilation scintigraphy, 39
- Yaws (treponematosis), bone involvement, 1174-5
Yersinia, 627, 651, 870
 Young's syndrome, 152
- Z-line, 543, 554
- Zenker's diverticulum (posterior pharyngeal diverticulum/pouch), 76, 547
- Zollinger-Ellison syndrome, 555, 557, 579, 583, 587, 866
 gastric carcinoids, 599
 small bowel involvement, 629
- Zygomatic arch fracture, 1389, 1391, 1575

- Goodman, L. R. (1980) Postoperative chest radiograph: II. Alterations after major intrathoracic surgery. *American Journal of Roentgenology*, 134, 803-813.
- Goodman, L. R., Kuzo, M. D. (eds) (1996) Intensive care radiology. *Radiologic Clinics of North America*, 34, 1.
- Spirn, P. W., Gross, G. W., Wechsler, R. J., Steiner, R. M. (1988) Radiology of the chest after thoracic surgery. *Seminars in Roentgenology*, 23, 9-31.
- Thorsen, M. K., Goodman, L. R. (1988) Extracardiac complications of cardiac surgery. *Seminars in Roentgenology*, 23, 32-48.

Radiation injury of the lung

- Boushy, S. F., Belgason, A. II., Borth, L. B. (1970) The effect of radiation on the lung and bronchial tree. *American Journal of Roentgenology*, 108, 284-292.
- Davis, S. D., Yankelevitz, D. F., Henschke, C. I. (1992) Radiation effects on the lung: clinical features, pathology and imaging findings. *American Journal of Roentgenology*, 159, 1157-1164.
- Huvos, A. G., Woodward, H. Q., Cahan, W. B., et al (1985) Post irradiation osteogenic sarcoma of bone and soft tissue: a clinico-pathologic study in 66 patients. *Cancer*, 55, 1244-1255.
- Ikezoe, J., Takashima, S., Morimoto, S., et al (1988) CT appearance of acute radiation-induced injury in the lung. *American Journal of Roentgenology*, 150, 765-770.
- Libshitz, H. I., Shuman, L. S. (1984) Radiation-induced pulmonary change: CT findings. *Journal of Computer Assisted Tomography*, 8, 15-19.
- Polansky, S. M., Ravin, C. E., Prosnitz, I. R. (1980) Lung changes after breast irradiation. *American Journal of Roentgenology*, 139, 101-105.
- Rowinsky, E. K., Abeloff, M. D., Wharam, M. D. (1985) Spontaneous pneumothorax following thoracic irradiation. *Chest*, 88, 703-708.
- Wencel, M. L., Sitrin, R. G. (1988) Unilateral lung hyperlucency after mediastinal irradiation. *American Research into Respiratory Disease*, 137, 955-957.

Pulmonary embolism

- Baile, E. M., King, G. G., Muller, N. L., et al (2000) Spiral computed tomography is comparable to angiography for the diagnosis of pulmonary embolism. *American Journal of Respiratory and Critical Care Medicine*, 161, 1010-1015.
- Burkill, G. J., Bell, J. R., Padley, S. P. (1999) Survey on the use of pulmonary scintigraphy, spiral CT and conventional pulmonary angiography for suspected pulmonary embolism in the British Isles. *Clinical Radiology*, 54, 807-810.
- Garg, K., Welsh, C. II., Feyerabend, A. J., et al (1998) Pulmonary embolism: diagnosis with spiral CT and ventilation-perfusion scanning-correlation with pulmonary angiographic results or clinical outcome. *Radiology*, 208, 201-208.
- Goodman, L. R., Lipchik, R. J. (1996) Diagnosis of acute pulmonary embolism: time for a new approach. *Radiology*, 199, 25-27.
- Huisman, M. V., Bulle, H. R., ten Cate, J. W., et al (1989) Unexpected high prevalence of silent pulmonary embolism in patients with deep venous thrombosis. *Chest*, 95, 498-502.
- Invasive and noninvasive diagnosis of pulmonary embolism. Preliminary results of the Prospective Investigative Study of Acute Pulmonary Embolism Diagnosis (PISA-PED). (1995) *Chest*, 107 (1 Suppl), 33S-38S.
- Remy-Jardin, M., Remy, J., Deschildre, F., et al (1996) Diagnosis of pulmonary embolism with spiral CT: comparison with pulmonary angiography and scintigraphy. *Radiology*, 200, 699-706.
- Robinson, P. J. (1996) Ventilation-perfusion lung scanning and spiral computed tomography of the lungs: competing or complementary modalities? *European Journal of Nuclear Medicine*, 23, 1547-1553.
- Task force report (2000) Guidelines on the diagnosis and management of acute pulmonary embolism. *European Heart Journal*, 21, 1301-1336.
- Value of the ventilation/perfusion scan in acute pulmonary embolism. Results of the prospective investigation of pulmonary embolism diagnosis (PIOPED). The PIOPED Investigators. (1999) *JAMA*, 263, 2753-2759.

- van Erkel, A. R., van Rossum, A. B., Bloem, J. L., Kievit, J., Pattynama, P. M. (1996) Spiral CT angiography for suspected pulmonary embolism: a cost-effectiveness analysis. *Radiology*, 201, 29-36.
- Wells, P. S., Anderson, D. R., Ginsberg, J. (2000) Assessment of deep vein thrombosis or pulmonary embolism by the combined use of clinical model and noninvasive diagnostic tests. *Seminars in Thrombosis and Hemostasis*, 26, 643-656.

Transplantation

- Anderson, D. C., Glazer, H. S., Semenkovich, J. W., et al (1995) Lung transplant edema: chest radiography after lung transplantation-the first 10 days. *Radiology*, 195, 275-281.
- Collins, J., Kuhlman, J. F., Love, R. 13. (1998) Acute, life-threatening complications of lung transplantation. *Radiographics*, 18, 21-43.
- Collins, J., Muller, N. L., Leung, A. N., et al (1998) Epstein-Barr virus-associated lymphoproliferative disease of the lung: CT and histologic findings. *Radiology*, 208, 749-759.
- Dauber, J. H., Paradis, L. L., Dummer, J. S. (1990) Infectious complications in pulmonary allograft recipients. *Clinics in Chest Medicine*, 11, 291-308.
- Herman, S. J. (1994) Radiologic assessment after lung transplantation. *Radiologic Clinics of North America*, 31, 663-678.
- Kesten, S., Chaparro, C. (1999) Mycobacterial infections in lung transplant recipients. *Chest*, 115, 741-745.
- Levine, S. M., Angel, L., Anzueto, A., et al (1999) A low incidence of posttransplant lymphoproliferative disorder in 109 lung transplant recipients. *Chest*, 116, 1273-1277.
- Leung, A. N., Fisher, K., Valentine, V., et al (1998) Bronchiolitis obliterans after lung transplantation: detection using expiratory HRCT. *Chest*, 113, 365-370.
- Loubeyre, P., Revel, D., Delignette, A., Loire, R., Mornex, J. F. (1995) High-resolution computed tomographic findings associated with histologically diagnosed acute lung rejection in heart-lung transplant recipients. *Chest*, 107, 132-138.
- Mihalov, M. L., Gattuso, P., Abraham, K., Holmes, E. W., Reddy, V. (1996) Incidence of post-transplant malignancy among 674 solid-organ-transplant recipients at a single center. *Clinical Transplantation*, 10, 248-255.
- Murray, J., McAdams, H., Erasmus, J., Pat/ Jr, E., Tapson, V. (1996) Complications of lung transplantation: radiologic findings. *American Journal of Roentgenology*, 166, 1405-1411.
- Schulman, L. L., Scully, B., McGregor, C. C., Austin, J. H. (1997) Pulmonary tuberculosis after lung transplantation. *Chest*, 111, 1459-1462.
- Shepard, J. A. (1999) Imaging of lung transplantation. *Clinics in Chest Medicine*, 20, 827-844.
- Shreenivas, R., Schulman, L. L., Berkmen, Y. M., McGregor, C. C., Austin, J. H. (1996) Opportunistic bronchopulmonary infections after lung transplantation: clinical and radiographic findings. *Radiology*, 200, 349-356.
- Spickerkoetter, E., Krug, N., Hoepfer, M., et al (1998) Prevalence of malignancies after lung transplantation. *Transplantation Proceedings*, 30, 1523-1524.
- Rappaport, D. C., Chamberlain, D. W., Shepherd, F. A., Hutcheon, M. A. (1998) Lymphoproliferative disorders after lung transplantation: imaging features. *Radiology*, 206, 519-524.
- Venuta, F., Boehler, A., Rendina, E. A., et al (1999) Complications in the native lung after single lung transplantation. *European Journal of Cardiothoracic Surgery*, 16, 54-58.

ARDS

- Andrews, C. P., Coalson, J. J., Smith, J. D., Johanson Jr., W. G. (1981) Diagnosis of nosocomial bacterial pneumonia in acute, diffuse lung injury. *Chest*, 80, 254-258.
- Bernard, G. R., Artigas, A., Brigham, K. L., et al (1994) The American-European Consensus Conference on ARDS: definitions, mechanisms, relevant outcomes, and clinical trial coordination. *American Journal of Respiratory and Critical Care Medicine*, 149, 818-824.

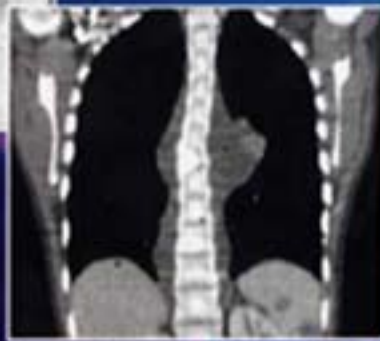
- Chastre, J., Trouillet, J. L., Vuagnat, A., et al (1998) Nosocomial pneumonia in patients with acute respiratory distress syndrome. *American Journal of Respiratory and Critical Care Medicine*, 157, 1165-1172.
- Desai, S. R., Wells, A. U., Rubens, M. B., Evans, T. W., Hansell, D. M. (1999) Acute respiratory distress syndrome: computed tomographic abnormalities at long-term follow-up. *Radiology*, 210, 29-35.
- Gattinoni, L., Pelosi, P., Vitale, G., Pesenti, A., D'Andrea, L., Mascheroni, D. (1991) Body position changes redistribute lung computed-tomographic density in patients with acute respiratory failure. *Anesthesiology*, 74, 15-23.
- Gattinoni, L., Bombino, M., Pelosi, P., et al (1994) Lung structure and function in different stages of severe adult respiratory distress syndrome. *Journal of the American Medical Association*, 271, 1772-1779.
- Gattinoni, L., Pelosi, P., Suter, P. M., Pedoto, A., Vercesi, P., Lissoni, A. (1998) Acute respiratory distress syndrome caused by pulmonary and extrapulmonary disease: different syndromes? *American Journal of Respiratory and Critical Care Medicine*, 158, 3-11.
- Goodman, L. R., Fumagalli, R., Tagliabue, P., et al (1999) Adult respiratory distress syndrome due to pulmonary and extrapulmonary causes: CT, clinical, and functional correlations. *Radiology*, 213, 545-552.
- Hansell, D. M. (1996) Imaging the injured lung. In: Evans, T.W., Haslett, C. (eds) *ARDS: Acute Respiratory Distress in Adults*, pp. 361-379. London: Chapman & Hall.
- Snow, N., Bergin, K. T., Horrigan, T. P. (1990) Thoracic CT scanning in critically ill patients: information obtained frequently alters management. *Chest*, 97, 1467-1470.
- Winer-Muram, H. T., Rubin, S. A., Ellis, J. V., et al (1993) Pneumonia and ARDS in patients receiving mechanical ventilation: diagnostic accuracy of chest radiography. *Radiology*, 188, 479-485.
- Wright, J. L. (1995) Adult respiratory distress syndrome. In: Thurlbeck, W. M., Churg, A. M. (eds) *Pathology of the Lung*, 2nd edn, pp. 385-399. New York: Thieme.

نشر الکترونیکی
موسسه انتشاراتی
نور دانش

SEVENTH EDITION

Textbook of RADIOLOGY AND IMAGING

VOLUME 1



CHURCHILL
LIVINGSTONE

An imprint of Elsevier Science



Visit our website for
additional outstanding
products

www.elsevierhealth.com



ISBN 0-443-07108-X



9 780443 071089

INTERNATIONAL EDITION